

Proceedings of the 12<sup>th</sup> International Conference on  
Computational Fluid Dynamics in the Oil & Gas,  
Metallurgical and Process Industries

# Progress in Applied CFD – CFD2017



SINTEF Proceedings

Editors:

Jan Erik Olsen and Stein Tore Johansen

## **Progress in Applied CFD – CFD2017**

Proceedings of the 12<sup>th</sup> International Conference on Computational Fluid Dynamics  
in the Oil & Gas, Metallurgical and Process Industries

SINTEF Academic Press

SINTEF Proceedings no 2

Editors: Jan Erik Olsen and Stein Tore Johansen

**Progress in Applied CFD – CFD2017**

Selected papers from 10<sup>th</sup> International Conference on Computational Fluid Dynamics in the Oil & Gas, Metallurgical and Process Industries

Key words:

CFD, Flow, Modelling

Cover, illustration: Arun Kamath

ISSN 2387-4295 (online)

ISBN 978-82-536-1544-8 (pdf)

© Copyright SINTEF Academic Press 2017

The material in this publication is covered by the provisions of the Norwegian Copyright Act. Without any special agreement with SINTEF Academic Press, any copying and making available of the material is only allowed to the extent that this is permitted by law or allowed through an agreement with Kopinor, the Reproduction Rights Organisation for Norway. Any use contrary to legislation or an agreement may lead to a liability for damages and confiscation, and may be punished by fines or imprisonment

SINTEF Academic Press

Address:       Forskningsveien 3 B  
                  PO Box 124 Blindern  
                  N-0314 OSLO

Tel:             +47 73 59 30 00

Fax:            +47 22 96 55 08

[www.sintef.no/byggforsk](http://www.sintef.no/byggforsk)

[www.sintefbok.no](http://www.sintefbok.no)

**SINTEF Proceedings**

SINTEF Proceedings is a serial publication for peer-reviewed conference proceedings on a variety of scientific topics.

The processes of peer-reviewing of papers published in SINTEF Proceedings are administered by the conference organizers and proceedings editors. Detailed procedures will vary according to custom and practice in each scientific community.

## PREFACE

This book contains all manuscripts approved by the reviewers and the organizing committee of the 12th International Conference on Computational Fluid Dynamics in the Oil & Gas, Metallurgical and Process Industries. The conference was hosted by SINTEF in Trondheim in May/June 2017 and is also known as CFD2017 for short. The conference series was initiated by CSIRO and Phil Schwarz in 1997. So far the conference has been alternating between CSIRO in Melbourne and SINTEF in Trondheim. The conferences focuses on the application of CFD in the oil and gas industries, metal production, mineral processing, power generation, chemicals and other process industries. In addition pragmatic modelling concepts and bio-mechanical applications have become an important part of the conference. The papers in this book demonstrate the current progress in applied CFD.

The conference papers undergo a review process involving two experts. Only papers accepted by the reviewers are included in the proceedings. 108 contributions were presented at the conference together with six keynote presentations. A majority of these contributions are presented by their manuscript in this collection (a few were granted to present without an accompanying manuscript).

The organizing committee would like to thank everyone who has helped with review of manuscripts, all those who helped to promote the conference and all authors who have submitted scientific contributions. We are also grateful for the support from the conference sponsors: ANSYS, SFI Metal Production and NanoSim.

Stein Tore Johansen & Jan Erik Olsen



Organizing committee:

Conference chairman: Prof. Stein Tore Johansen

Conference coordinator: Dr. Jan Erik Olsen

Dr. Bernhard Müller

Dr. Sigrid Karstad Dahl

Dr. Shahriar Amini

Dr. Ernst Meese

Dr. Josip Zoric

Dr. Jannike Solsvik

Dr. Peter Witt

Scientific committee:

Stein Tore Johansen, SINTEF/NTNU

Bernhard Müller, NTNU

Phil Schwarz, CSIRO

Akio Tomiyama, Kobe University

Hans Kuipers, Eindhoven University of Technology

Jinghai Li, Chinese Academy of Science

Markus Braun, Ansys

Simon Lo, CD-adapco

Patrick Segers, Universiteit Gent

Jiyuan Tu, RMIT

Jos Derksen, University of Aberdeen

Dmitry Eskin, Schlumberger-Doll Research

Pär Jönsson, KTH

Stefan Pirker, Johannes Kepler University

Josip Zoric, SINTEF

## CONTENTS

<b>PRAGMATIC MODELLING .....</b>	<b>9</b>
On pragmatism in industrial modeling. Part III: Application to operational drilling .....	11
CFD modeling of dynamic emulsion stability .....	23
Modelling of interaction between turbines and terrain wakes using pragmatic approach .....	29
<b>FLUIDIZED BED .....</b>	<b>37</b>
Simulation of chemical looping combustion process in a double looping fluidized bed reactor with cu-based oxygen carriers.....	39
Extremely fast simulations of heat transfer in fluidized beds.....	47
Mass transfer phenomena in fluidized beds with horizontally immersed membranes .....	53
A Two-Fluid model study of hydrogen production via water gas shift in fluidized bed membrane reactors .....	63
Effect of lift force on dense gas-fluidized beds of non-spherical particles .....	71
Experimental and numerical investigation of a bubbling dense gas-solid fluidized bed .....	81
Direct numerical simulation of the effective drag in gas-liquid-solid systems .....	89
A Lagrangian-Eulerian hybrid model for the simulation of direct reduction of iron ore in fluidized beds.....	97
High temperature fluidization - influence of inter-particle forces on fluidization behavior .....	107
Verification of filtered two fluid models for reactive gas-solid flows .....	115
<b>BIOMECHANICS.....</b>	<b>123</b>
A computational framework involving CFD and data mining tools for analyzing disease in carotid artery .....	125
Investigating the numerical parameter space for a stenosed patient-specific internal carotid artery model.....	133
Velocity profiles in a 2D model of the left ventricular outflow tract, pathological case study using PIV and CFD modeling.....	139
Oscillatory flow and mass transport in a coronary artery.....	147
Patient specific numerical simulation of flow in the human upper airways for assessing the effect of nasal surgery.....	153
CFD simulations of turbulent flow in the human upper airways .....	163
<b>OIL &amp; GAS APPLICATIONS .....</b>	<b>169</b>
Estimation of flow rates and parameters in two-phase stratified and slug flow by an ensemble Kalman filter .....	171
Direct numerical simulation of proppant transport in a narrow channel for hydraulic fracturing application .....	179
Multiphase direct numerical simulations (DNS) of oil-water flows through homogeneous porous rocks .....	185
CFD erosion modelling of blind tees .....	191
Shape factors inclusion in a one-dimensional, transient two-fluid model for stratified and slug flow simulations in pipes .....	201
Gas-liquid two-phase flow behavior in terrain-inclined pipelines for wet natural gas transportation .....	207

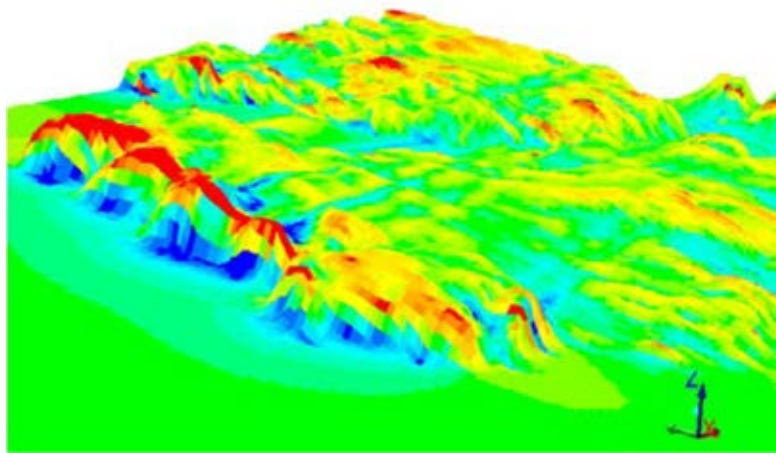
<b>NUMERICS, METHODS &amp; CODE DEVELOPMENT .....</b>	<b>213</b>
Innovative computing for industrially-relevant multiphase flows .....	215
Development of GPU parallel multiphase flow solver for turbulent slurry flows in cyclone.....	223
Immersed boundary method for the compressible Navier–Stokes equations using high order summation-by-parts difference operators .....	233
Direct numerical simulation of coupled heat and mass transfer in fluid-solid systems .....	243
A simulation concept for generic simulation of multi-material flow, using staggered Cartesian grids.....	253
A cartesian cut-cell method, based on formal volume averaging of mass, momentum equations.....	265
SOFT: a framework for semantic interoperability of scientific software .....	273
 <b>POPULATION BALANCE .....</b>	 <b>279</b>
Combined multifluid-population balance method for polydisperse multiphase flows .....	281
A multifluid-PBE model for a slurry bubble column with bubble size dependent velocity, weight fractions and temperature.....	285
CFD simulation of the droplet size distribution of liquid-liquid emulsions in stirred tank reactors .....	295
Towards a CFD model for boiling flows: validation of QMOM predictions with TOPFLOW experiments .....	301
Numerical simulations of turbulent liquid-liquid dispersions with quadrature-based moment methods.....	309
Simulation of dispersion of immiscible fluids in a turbulent couette flow .....	317
Simulation of gas-liquid flows in separators - a Lagrangian approach.....	325
CFD modelling to predict mass transfer in pulsed sieve plate extraction columns .....	335
 <b>BREAKUP &amp; COALESCENCE .....</b>	 <b>343</b>
Experimental and numerical study on single droplet breakage in turbulent flow .....	345
Improved collision modelling for liquid metal droplets in a copper slag cleaning process .....	355
Modelling of bubble dynamics in slag during its hot stage engineering.....	365
Controlled coalescence with local front reconstruction method .....	373
 <b>BUBBLY FLOWS .....</b>	 <b>381</b>
Modelling of fluid dynamics, mass transfer and chemical reaction in bubbly flows .....	383
Stochastic DSMC model for large scale dense bubbly flows.....	391
On the surfacing mechanism of bubble plumes from subsea gas release.....	399
Bubble generated turbulence in two fluid simulation of bubbly flow .....	405
 <b>HEAT TRANSFER .....</b>	 <b>413</b>
CFD-simulation of boiling in a heated pipe including flow pattern transitions using a multi-field concept .....	415
The pear-shaped fate of an ice melting front .....	423
Flow dynamics studies for flexible operation of continuous casters (flow flex cc).....	431
An Euler-Euler model for gas-liquid flows in a coil wound heat exchanger.....	441
 <b>NON-NEWTONIAN FLOWS.....</b>	 <b>449</b>
Viscoelastic flow simulations in disordered porous media .....	451
Tire rubber extrudate swell simulation and verification with experiments .....	459
Front-tracking simulations of bubbles rising in non-Newtonian fluids.....	469
A 2D sediment bed morphodynamics model for turbulent, non-Newtonian, particle-loaded flows.....	479

<b>METALLURGICAL APPLICATIONS.....</b>	<b>491</b>
Experimental modelling of metallurgical processes .....	493
State of the art: macroscopic modelling approaches for the description of multiphysics phenomena within the electroslag remelting process .....	499
LES-VOF simulation of turbulent interfacial flow in the continuous casting mold .....	507
CFD-DEM modelling of blast furnace tapping .....	515
Multiphase flow modelling of furnace tapholes .....	521
Numerical predictions of the shape and size of the raceway zone in a blast furnace.....	531
Modelling and measurements in the aluminium industry - Where are the obstacles? .....	541
Modelling of chemical reactions in metallurgical processes.....	549
Using CFD analysis to optimise top submerged lance furnace geometries .....	555
Numerical analysis of the temperature distribution in a martensic stainless steel strip during hardening.....	565
Validation of a rapid slag viscosity measurement by CFD.....	575
Solidification modeling with user defined function in ANSYS Fluent.....	583
Cleaning of polycyclic aromatic hydrocarbons (PAH) obtained from ferroalloys plant.....	587
Granular flow described by fictitious fluids: a suitable methodology for process simulations .....	593
A multiscale numerical approach of the dripping slag in the coke bed zone of a pilot scale Si-Mn furnace.....	599
<b>INDUSTRIAL APPLICATIONS .....</b>	<b>605</b>
Use of CFD as a design tool for a phosphoric acid plant cooling pond .....	607
Numerical evaluation of co-firing solid recovered fuel with petroleum coke in a cement rotary kiln: Influence of fuel moisture .....	613
Experimental and CFD investigation of fractal distributor on a novel plate and frame ion-exchanger .....	621
<b>COMBUSTION .....</b>	<b>631</b>
CFD modeling of a commercial-size circle-draft biomass gasifier.....	633
Numerical study of coal particle gasification up to Reynolds numbers of 1000.....	641
Modelling combustion of pulverized coal and alternative carbon materials in the blast furnace raceway .....	647
Combustion chamber scaling for energy recovery from furnace process gas: waste to value .....	657
<b>PACKED BED.....</b>	<b>665</b>
Comparison of particle-resolved direct numerical simulation and 1D modelling of catalytic reactions in a packed bed .....	667
Numerical investigation of particle types influence on packed bed adsorber behaviour .....	675
CFD based study of dense medium drum separation processes .....	683
A multi-domain 1D particle-reactor model for packed bed reactor applications.....	689
<b>SPECIES TRANSPORT &amp; INTERFACES .....</b>	<b>699</b>
Modelling and numerical simulation of surface active species transport - reaction in welding processes .....	701
Multiscale approach to fully resolved boundary layers using adaptive grids.....	709
Implementation, demonstration and validation of a user-defined wall function for direct precipitation fouling in Ansys Fluent.....	717



<b>FREE SURFACE FLOW &amp; WAVES .....</b>	<b>727</b>
Unresolved CFD-DEM in environmental engineering: submarine slope stability and other applications.....	729
Influence of the upstream cylinder and wave breaking point on the breaking wave forces on the downstream cylinder .....	735
Recent developments for the computation of the necessary submergence of pump intakes with free surfaces .....	743
Parallel multiphase flow software for solving the Navier-Stokes equations .....	752
 <b>PARTICLE METHODS .....</b>	 <b>759</b>
A numerical approach to model aggregate restructuring in shear flow using DEM in Lattice-Boltzmann simulations .....	761
Adaptive coarse-graining for large-scale DEM simulations.....	773
Novel efficient hybrid-DEM collision integration scheme.....	779
Implementing the kinetic theory of granular flows into the Lagrangian dense discrete phase model.....	785
Importance of the different fluid forces on particle dispersion in fluid phase resonance mixers .....	791
Large scale modelling of bubble formation and growth in a supersaturated liquid.....	798
 <b>FUNDAMENTAL FLUID DYNAMICS .....</b>	 <b>807</b>
Flow past a yawed cylinder of finite length using a fictitious domain method .....	809
A numerical evaluation of the effect of the electro-magnetic force on bubble flow in aluminium smelting process.....	819
A DNS study of droplet spreading and penetration on a porous medium.....	825
From linear to nonlinear: Transient growth in confined magnetohydrodynamic flows.....	831

# PRAGMATIC MODELLING





# ON PRAGMATISM IN INDUSTRIAL MODELING PART III: APPLICATION TO OPERATIONAL DRILLING

Stein T. JOHANSEN<sup>1,2</sup>, Ernst A. MEESE<sup>1</sup>, Josip ZORIC<sup>1</sup>, Aminul ISLAM<sup>3</sup>, Dwayne W. MARTINS<sup>4</sup>

<sup>1</sup> SINTEF Materials and Chemistry, Trondheim, NORWAY

<sup>2</sup> Norwegian University of Science and Technology (NTNU), Trondheim, NORWAY

<sup>3</sup> Statoil, Trondheim, Norway

<sup>4</sup> Engie E&P, Stavanger, Norway

\* Corresponding author, E-mail address: [Stein.T.Johansen@sintef.no](mailto:Stein.T.Johansen@sintef.no)

## ABSTRACT

In this paper, we will apply the concepts of pragmatic industrial modelling to the development of a real time drilling support tool. We develop requirements to such a modelling tool, regarding both input and output, model response times, and accuracy requirement.

The selected application will next be the subject to more theoretical discussions on analyses, standards, technologies, design of the database, and the interface for the modelling framework

On the selected pragmatic modelling case, we evaluate the proposed solutions and outline requirements for the realization of the described tool. We give a proposal of the architecture for such a system, and examples of analysis / modelling workflows, presented in pseudo-code.

We summarize the findings and discuss how this specific "pragmatism in industrial modelling" case should be concluded and prepared for further software/hardware implementation, reuse, sharing, and collaboration. Partial standardization of work processes (illustrated as workflows in pseudo-code), data, and metadata is a necessity for building more consistent and informative industrial models. It will answer to customer needs for relevant results, actual accuracy, and delivery speed, and will definitely pave a way towards a tool, which can enable an automated drilling process.

**Keywords:** Industrial modelling, pragmatism, drilling, real-time simulation, multiphase flow, hydraulics, robotized drilling operation

## INTRODUCTION

Building industrially relevant models is handled in many text books, such as (Cameron, I. and Gani, R., 2011). From the software perspective, fields like software engineering and systems engineering has become highly developed over the last decades. However, how these areas can be exploited to build useful industrial applications does not have sufficient focus. A particular

need is to arrive at standards for development and workflows that can help to improve the final quality. In the area of CFD we have seen attempts to develop standards, such as (Casey et al., 2000) and (Mendenhall et al., 2003). However, in many applications CFD will only be part of a larger picture.

At CFD2014 in Trondheim, Norway, a framework (FW) for pragmatic industrial modelling was suggested and demonstrated on industrial use cases with a process centric approach (Zoric et al., 2014). The framework was further elaborated (Zoric et al., 2015) at CFD2015 in Melbourne, Australia, with focus on metadata describing modelling and experimental data. Their organization, syntax, and semantics were exemplified on a use case related to drilling of oil & gas wells. In this paper, the objective is to apply previous principles of pragmatic industrial modelling to develop a drilling application for the oil & gas industry. The elements of such a development process are established knowledge, but how these elements are assembled into an application driven workflow is new.

In order to develop a successful application the pragmatic workflow can be seen as a procedure that can support quality of both the development work and the final application. The second element and success factor is the Solution Architect Team (SAT), as discussed in (Zoric et al., 2014). SAT will make numerous decisions on software engineering, model concepts, numerical methods and control strategies. In this way, the final solutions will reflect the level of knowledge in the SAT. This will become evident in the present paper, where we will decide on which concepts to work with, and at that point disregarded all other possible methods.

Well operations vary from operation to operation, and are tailored for each field. In this paper, we will focus specifically on the drilling processes. To date, several components for drilling operations pose phase specific challenges during each of the stages beginning from the initial planning phase to drill-stem testing. As services are provided by various vendors and, integrating multiple service interfaces into a single platform is often challenging. On several occasions, operators often

receive un-scalable raw data with noise, replication, and missing values, instead of a comprehensive standardized format. Similarly, data storage poses a challenge due to heterogeneous database systems and analogue data. Hence, organizing inputs for modelling simulation studies has been inadequate, not precise, and time consuming. Data authenticity is often questionable as it is stored in several non-standardized formats, thereby escalating the uncertainty in the simulated results. The streaming of real-time data needs to be easily accessible and scaled in reliable and standard formats.

The literature reviewed is an integral and introductory part of the pragmatic analysis. As this paper merely demonstrates the pragmatic approach, we restrict the literature review accordingly. Over the last 60 years, a substantial amount of work on models and simulations of drilling operations has been published.

Examples of leading software for drilling are Drillbench® from Schlumberger and the software from eDrilling. Examples of publications on hydrodynamic models are (Bourgoyne Jr. et al., 1986) and (Hansen et al., 1999). Real time simulations are discussed in (Mathis and Thonhauser, 2007), (Cayeux et al., 2011a), (Cayeux et al., 2013b), (Cayeux et al., 2016) and (Rommetveit et al., 2017). Examples of mechanical models for the drill string are found in (Cayeux et al., 2011b) and (Cayeux and Skadsem, 2014). Tools for automated drilling and discussed in (Lohne et al., 2008), (Florence and Iversen, 2010), and (Cayeux et al., 2013a). The general impression is that the papers on real-time simulations are quite general and industrial, with limited scientific information. Information on modelling software design methods and design principles seems to be scarce. A major reason for limited information is that most of the work is confidential and thus not available to the public. Based on the authors' knowledge existing application programs within drilling operations have several hardware and software limitations. The accuracy of physical models may in some cases be critical, and contribute to software limitations. In this paper, we primarily focus on the conceptual workflow: How do we (with above-mentioned challenges) develop a software, capable of delivering the required information and knowledge support?

In order to develop applications for drilling, we need to understand the physical and operational challenges. The root causes of downhole problems are generally not well understood (Nazari et al., 2010). Typically, some downhole problems occur due to lack of implementation of lessons learned and best practices, but sometimes are also due to unforeseeable downhole mechanical failures. By developing a better understanding of root causes and using best practices, we could improve efficiency by 50 to 75%. Evaluation of daily drilling data should not only be accessed at the end of the well drilling operation, but should be reviewed regularly by competent personnel within drilling along with subsurface team members. Additionally, as drilling engineers during training and operations may need to better understand the effects of fluid properties, rotation and flow rate, an interpolation calculator tool may be used to interpolate between the set-up parameters. These parameters could be used to address pressure losses, thresholds for transferring

cuttings from beds to suspension phase based on shear rate at surface, in a more complete simulation.

The autonomous solutions are not available for different activities in drilling. For example, the industry needs real-time characterization of the drilling fluids because as of today, insufficient sampling rate and volume correlations have incorrectly represented the true downhole mud properties. Similarly, standardized verification tools both in the laboratory and operations are not available to QC a cement's density and rheology prior to pumping downhole. We need instantaneous assessment of the mineralogy and morphology of drilling cuttings, cuttings cleaning and transport treatment and mechanistic hole cleaning models that could be applied to real-time advisory and decision-making systems.

Industrial solutions within enhanced kick and losses detection methods, particularly when using oil-based muds and in complex geological areas compromising of formations that are naturally faulted, have heterogeneous stress regimes and negative drilling window challenges yet to be determined. A real-time advisory system offers consistent results and this has been discussed in (Islam et al., 2016) and (Moi et al., 2017). The industry is also currently investigating more enhanced techniques towards monitoring and mitigating bottom hole drilling dysfunctions including buckling, vibrations, stuck pipe etc. An autonomous historical case-based digitalized database system should be applied from the laboratory testing phase up to field deployment, as this will help mitigate inconsistencies due to lack of competency.

Hence, a pragmatic approach to address the above-mentioned limitations can be roughly described by the following steps:

1. Accurately define *what each model should predict*. In addition, specify requirements addressing the computational speed (delivery time) and accuracy of the derived results, along with the key data input parameters. This includes the system configuration and field input data. This data can be accessed from various sources, e.g. adaptive real-time computations, stored experimental data, correlations, stored simulated data etc.

2. Provide integrated *conceptual design* approaches, which incorporate perceptive techniques for estimating model input parameters from different sources (and meet the case-specific requirements).

3. Decide and identify which *model framework* (e.g. 1D transient multiphase 3-phase model) and its sub models or elements should be included. Their orchestration during the drilling operation should be well defined, e.g. formalized by workflows and described in pseudo-code. This step must also resolve issues regarding standardization of data formats (obtained from multiple resources including experimental, field and simulated data).

4. The analysis workflow provides various parametric inputs at different *decision gate stages*. This process should be continuously evaluated, and verified to check if the current requirements meet the original data input criterion or the requirements need to be relaxed. If the bottlenecks in the modelling framework show up, the workflow should be corrected and new model elements (sometimes also including sub-models) developed.

5. The qualification of the *uncertainties* within the model framework is critical and hence needs a robust workflow wherein it is easy to adapt, implement, and increase accuracy.

This paper will investigate a case specific scenario wherein the drilling operation is carried out from a platform. During the drilling process, a drill bit is rotated at the end of a drill pipe. Non-Newtonian drilling fluid is pumped through the drill pipe and the bit, and is circulated back to the platform through the annular space to the surface. Should these cuttings accumulate in the annular space, this may lead to several problems eventually causing the drill pipe to be stuck if the necessary preventative actions are not taken. This could also be a result from caving collapsing within the newly drilled hole. When the mud flows through the annulus, some mud may be lost to the formation for various reasons. Sometimes this may lead to a kick wherein formation fluids enter the borehole and displace the mud, thereby reducing the bottom hole pressure. Should the losses be severe, this may lead to the hole collapse. In some cases drilling with a mud weight much lower than the formation pressure, also leads to the hole collapsing or induces a kick that could unfold into a blowout.

An application that addresses such challenges should handle all these possibilities.

Human intervention and responsiveness influences heavily drilling processes; hence, human errors tend to reduce the efficiency. Drilling operations are very expensive and the multi-dimensional challenges do occur, hence a more automated drilling approach should be advantageous.

By using the appropriate models, correctly interpreting the data, and providing appropriate remedial actions during operations, faster and more cost effective drilling operations will be possible.

### PRAGMATISM - STEP 1: REQUIREMENTS FOR AUTOMATED DRILLING TOOL

The tool will be limited, but still designed to handle all drilling hydraulics, including gas kicks. Issues related to interaction between drill-bits, drilling fluids, and formation is included. The same goes for the tools and materials involved into the drilling operation (mud pump, motors, Bottom Hole Assembly, mechanics, and integrity of drill-string and drill-bits). Any failure of tools, risk for stuck pipe, and remediation of stuck pipe is part of what we will address. Prediction of the true drilling window is of major importance. The drilling window is the range of mud pressures, exposed to the formation, within which the operation is safe. If the mud pressure is too low, oils and gas may be produced into the drilling fluid (risk of blow out) and we have the possibility for rock collapse (have to give up well). At the other end (too high mud pressure), the drilling fluid may be lost to the formation. That will delay operation, block pores for future production, and trigger additional costs. On top of that, formation may be fractured and the well has to be abandoned.

A simplified example of a typical drilling scenario is illustrated in Figure 1. In Figure 2 we see the mud pump, supplying the drill pipe with high pressure drilling fluid.

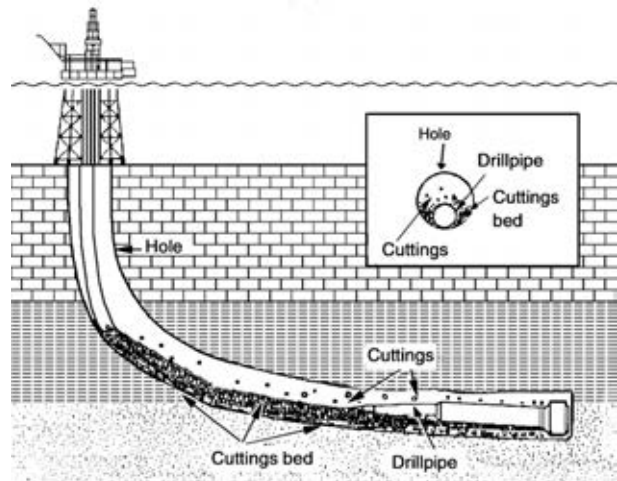


Figure 1 Typical scenario during drilling. Three types of rock is seen (from [http://petrowiki.org/Hole\\_cleaning](http://petrowiki.org/Hole_cleaning)).

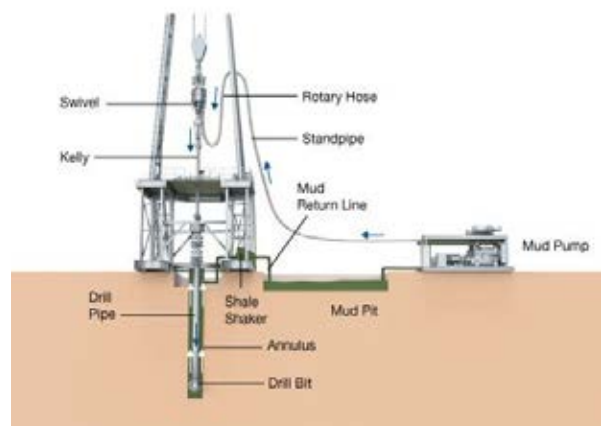


Figure 2 Drill platform with mud pump and shale shaker (from <http://www.petroleonline.com/>)

The return flow of drilling fluid and cuttings is passed through the shale shaker where cuttings are separated from the drilling fluid. The drilling fluid is then circulated back to well bore through the mud pit.

The following considerations were shortlisted based on the current industrial requirements:

1. An automated tool capable of handling hydraulics during drilling operations from a platform or vessel.
2. Real-time assessment for drilling fluid characterization and rheological effects
3. A tool that mitigates uncertainty towards organising input parameters for the real-time drilling models during the drilling process, such as stuck-pipe events and wellbore breakout.

The tool will perform drilling process optimization – mostly monitoring critical parameters and their influences while drilling. The tool may comprise both software and hardware, and should integrate well into already existing database frameworks. As illustrated in Figure 5, the tool should support at least three distinctive modes of interaction: monitoring, predictions and recommendations.

The system must be a *real-time advisory system*. This includes full and transient predictions of hydraulics, adjustment of density and rheological mud properties, information on the interaction between drilling fluid and formation, torque and drag (T&D) on drill string. The drilling parameters, annular velocity, drill string rotation speed (RPM), Rate of Penetration (ROP), weight-on-bit (WOB), cuttings mineralogical and morphological info, particle transportation, well geometry, and drilling practices must be highlighted and made available to the user. In addition, online measurements must be made available and used by the system to improve predictions and analysis of the ongoing drilling operation.

Specific features that the model system should handle are:

- Enable ROP optimization. This includes prediction of T&D, effects of flow rate, WOB, effects of selection of bit type and size, and RPM.
- Interaction with the rock formation:
  - Predict rate of mudflow into the formation.
  - Predict rate of inflow of hydrocarbons from the formation.
  - Provide risk assessment for formation damage, and effects of the applied bits.
- Drilling window management: At any time, the model shall know the drilling window and be able to advice the best way to operate within the limits of formation pore and fracture pressure.
- Hole cleaning:
  - The tool should predict the amount of solids being laid up into sediments at any time and at any position in the annulus. In addition, the mass flux of cuttings being transported should be known at any time and location.
  - The tool should predict the cuttings size produced at the bit, including the particle shape factor and the mineral composition of the cuttings.
  - Included into the tool should be a device to perform on-the-fly fluid characterization of the drilling fluid. Both fluid density and viscosity shall be measured. The measured properties should be available at the latest 30 seconds after the fluid has been sampled.
  - The tool must make faster than real-time predictions, in order to assess the required mud-properties in advance. Based on the most favourable scenario for next near future drilling operations, the tool will instruct the mixing of the mud on the fly.
- Predict filter cake creation and properties of the filter cake (thickness, permeability).
- The tool shall assess enhanced Kick & Loss detection.
- The tool shall include an auto drill pipe handling system – accounting for fatigue and buckling. Based on the mechanical and thermal history of each drill pipe element, risk of failure shall be assessed and drill pipe elements with high failure risk will automatically be replaced by new elements.
- The model system should be integrated into a live data streaming system.

*Prediction speed requirement:*

The tool should be able to predict key parameters at least 20 times faster than real-time. This will allow look-ahead simulations that can be used to optimize the drilling strategy in the nearest future.

*Requirement of spatial resolution of model:*

The largest grid cells allowed is 100 m.

*Model / operation input parameters:*

- Borehole trajectory is available on digital format,
- Rock information (as this is not available in real time, we will use Mechanical Specific Energy (MSE) equations),
- Fluid rheology and fluid properties,
- Mud temperature out from mud pump,
- Formation temperature along borehole trajectory,
- Critical mud pressure for fracking of formation,
- Formation fluid pressure and permeability along borehole trajectory,
- Formation fluid properties along borehole trajectory,
- Dimensions and properties of tools, pipe, casings, cement, rock (mass of system elements, sound speed, thermal properties),
- Actual ROP (measured),
- Average cuttings size (measured),
- Pump pressure,
- Both applied torque and drill string rotation data is available,
- Hook load data is available in real time (hook load represents the force acting on the drill string at the platform),
- Block position is available in real time (block position versus time represents the axial velocity of the drill string at the platform end).

We note that uncertainty measures for all input parameters must be given. If uncertainty is unknown, the quantity must be labelled with "*Uncertainty unknown*".

## **Output parameters from prediction model**

*Primary prediction parameters:*

- Transient flowrate at surface versus actual pump pressure
- Mass flow of cuttings to the surface versus time
- Mud temperature at shale shaker
- Hook load as function of measured or suggested block position.

The model should allow on-the-fly tuning of the model. However, tuning methods and selection of tuning parameters are not part of the present tool, but will be a future extension possibility.

The required prediction accuracy of the primary output parameters is assumed given. For the accuracy of the pressure, and mudflow rate predictions, a minimum accuracy of  $\pm 10$  bar is assumed required. The temperature of the mud should be critically assessed based on the climatic and field specific conditions.

*Secondary prediction parameters:*

- Dynamic updates of the drilling window,
- Optimal method selection to drill safely within drilling window,
- Based on primary output parameters, issue immediate warning if a kick is appearing,
- Information of where the cuttings are located in the system,
- Highlight differences between model and monitored data. Give interpretation of deviations and suggested actions.

At this point, proven accuracy in primary parameters prediction are sufficient for early kick detection. For example, this can be performed using existing multiphase flow codes such as LedaFlow® or OLGAR®.

*Monitor parameters, used to check the model, or to support, or to tune the model*

- Hook load,
- Block position (hook load taken as input),
- ROP (input),
- Torque and RPM,
- Motor power,
- Mud temperature (both out from pump and for return flow into shale shaker),
- Cuttings mass flow into the shakers,
- Cuttings size (separated at the shakers),
- Mudflow rate out from pump (pump pressure as input),
- Mud pump pressure (mud flowrate as input),
- Return fluid flow rate,
- Density of fluid after the shaker.

Specification of requirements and the necessary information concludes Step 1. This pragmatic model approach closely resembles the use case specifications and scenarios, often adapted during software development. We recognize that some elements may be too generic and in a real project development, it would demand reiterating the above-mentioned specifications into further sub-classes .

## **STEP 2 CONCEPTUAL MODEL DESIGN**

In Step 1 the process is led by Solution Architects Team (SAT), but is under strict control of the end user of the application. In this second step, the SAT will take a stronger lead. The team will now look at the specifications above and work out possible conceptual design possibilities. At this stage, it may be necessary to develop mock-ups, i.e. rudimentary and simple demonstration of sub-models, for assessing possible solutions. We will point to this possibility when necessary.

Based on the need to have a fast and accurate transient hydraulic calculation as part of the tool we realize that multidimensional Computational Fluid Dynamics (CFD) is out of the question for the system model. Presently, we realize two possible approaches for the system model:

### **A. A transient 1D multiphase flow model, solving masse, momentum and energy conservation equations for the flow of liquid, gas (from kick), and solids.**

The model is formulated by individual transient transport equations for the mass of mud, cuttings, and fluids entering from the formation (oil, gas). Similarly, we formulate individual transport equations for momentum of liquid, gas and cuttings, as well as mixture energy (temperature) of the fluids/solids and near well-bore region.

### **B. A simplified transient 1D multiphase flow model, based on a mixture approach: The approach is computationally similar to a single-phase description. The phases are handled through a drift flux concept where phase slip velocity relations relative to mixture is known.**

The model has mass conservation equations for mud, cuttings, reservoir fluids, and free gas. The velocity of free gas and cuttings is related to a mixture velocity by a slip relation. The slip relation may be obtained from existing data (lab, field, simulation). The prediction of temperature is the same as in A.

I.e., both flow simulation strategies are based on a 1D Eulerian-based flow code, and the system model should be able to represent pressure waves in the mud. This can be done by solving for the pressure waves directly in the model, or by using a characteristics methods (Skalle et al., 2014). This may be critical for prediction of pressure waves and enable early kick detection.

### **Use of pre-calculated data, field data or laboratory data**

As we have decided that applying a 1D model is the only possibility to reach time requirements, we realize that such simplified models may need heavy support in order to give realistic predictions. Based on the current knowledge of non-Newtonian flows with particles, we see that it is possible to arrive at CFD models with acceptable accuracy in relatively short time. During drilling the drill-pipe is rotating, but also whirling. As a result, the transport rate of cuttings will depend on a balance between sedimentation, convection and dispersion effects (granular and turbulent dispersion), and where drill string position, RPM and whirling frequency are critical elements. Another important factor is inclination of the well trajectory.

Another option for simulating the transient drilling process is to use steady state data, coming from lab experiments or some steady state simulation tool. In this case the transient phenomena can be approximated by applying Succession-of-steady-states (SSS) solutions (Modisette et al., 2001). Such an approach is useful if the phenomena we want to model have a time scale that is significantly longer than the time scale of the transport processes in the system. E.g., formation and movement of cuttings bed is often orders of magnitude slower than the mudflow. Laboratory data are typically obtained at a much a smaller spatial scale than the field operation. I.e., such data need to be supported by either CFD of field data to ensure proper scaling of the model from laboratory to field conditions.



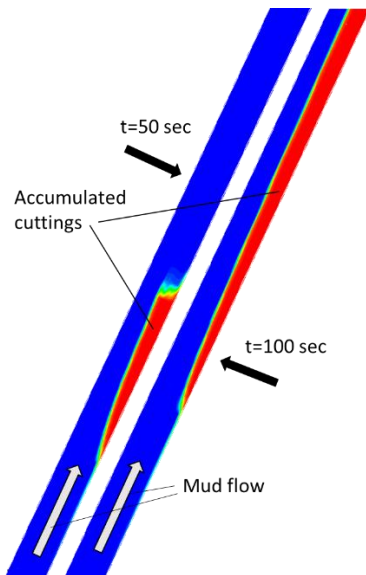


**Figure 3** Flow of liquid and cuttings particles of 1.0 mm diameter. The red colour shows a compacted bed of cuttings.

A fast method to produce rheology online is critical. It is suggested to apply a number of pipe rheometers operating in parallel on the field, to obtain robust data with a good measure of uncertainty.

A task will be defined to clarify how lab data, possibly field data, and simulated data from 3D CFD can be saved, processed, and retrieved (to provide the input for the system model). The processed data may supply both pressure drop data (wall stresses) and slip data. The data is supposed to be steady state, and it is required that an uncertainty measure of the data is provided with the data.

#### **Application of CFD to build database or to improve closures**

It is fully possible to use CFD (Computational Fluid Dynamics) to provide useful data. CFD is slow, compared to online applications, but can be used, over time, to build a substantial database. It is therefore preferred that a case database be established initially, and is dynamically extended over the time to improve the prediction power of the system model. As an example we have used a previously developed granular flow model (Laux, 1998) to predict the flow of liquid (superficial velocity of 1.5 m/s, and solids fraction in the lower boundary inflow is 2%) and solids in a 65 degree inclined, 40 mm diameter, channel. The fluid is here water and the solids density is 2600 kg/m<sup>3</sup>. As seen from Figure 3, the 2.0 mm solids separate in the lower wall and form rather quickly a thick deposit layer. The compacted bed is assumed to have an internal angle of friction (repose) of 30°. The cuttings accumulate fast and may build a large bed along the annulus (here a channel). If the mud pump is switched off, the shear stress from the fluid supporting the bed will disappear, and the cuttings will avalanche to the lowest possible point. In Figure 4, we see that a few seconds after the pump is shut off, an avalanche is taking place. Such avalanches may lead to pressure build-up of roughly 15 bar for each 100 m of open hole. This effect alone can lead to substantial pressure variations, and it must be considered in order to understand the drilling window.

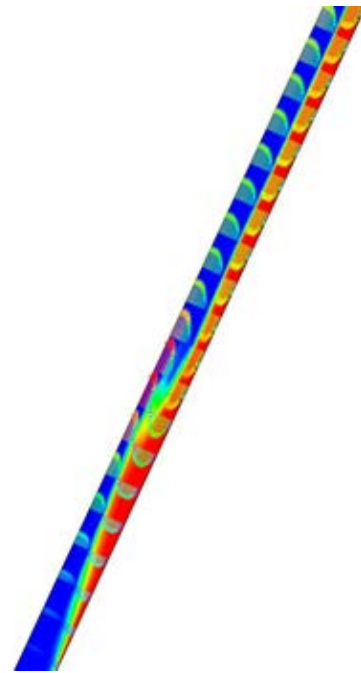


**Figure 4** The blue colour shows liquid, red is the cuttings concentration and the vectors show the liquid flow. The maximum velocity is 5.8 m/s.

The mechanical model will apply a Lagrangian framework to handle drag and torque related phenomena. For the mechanical model, we have two overall approaches:

- C. The mechanical model integrated into the flow model.**
- D. The mechanical model computed independently, and the data exchanged between the flow model and the mechanical model.**

For the Pipe Auto handling system, this system will be designed based on that the mechanical model is keeping track of the temperature and stress history. I.e., the work to make such a system is separated from the overall model and can be handed over to a team with the necessary knowledge. As all teams delivering into the project, they will have a deadline for when their work is to be finished and well as necessary documentation of uncertainty in the actual sub-models input and prediction parameters.

All fluid and material properties is to be made available to the models through a database. These data will at the time of execution of the tool, be made available in a fast and efficient manner. Data from online monitoring may also be provided through the same database, or if very high transmission speed is needed, through an industrial API for data communication. However, a filter for validation of these data is needed in case the measuring equipment is failing. A strategy for handling this may be to continue with the latest data available. Depending on the variation in the recorded data, it can be decided if the drilling operation should be aborted or not.

#### **STEP 3 SELECTION OF APPROACH**

We are now at a point where we should choose between the sketched approaches. What we can say is that system model A: "A transient 1D multiphase flow model,

solving mass, momentum and energy conservation equations for the flow of liquid, gas (from kick), solids and energy" and mechanical model C: "The mechanical model is integrated into the flow model", is the set which is expected to give the most robust simulations. In addition, this set of coupled models will allow simulation of the most important physics involved.

On the other hand, the system model B: "A simplified transient 1D multiphase flow model, based on a mixture approach", together with mechanical model D: "The mechanical model is computed independently, and where data is exchanged between the flow and the mechanical model", may offer the fastest simulation strategy.

We will briefly give some design considerations and implementation techniques that will be part of the development. These methods and techniques are mostly well established, but have to be walked through in order to get an understanding of the pragmatic workflow.

#### *Mock-up solutions*

To select between the above-mentioned modelling options, it may be necessary to develop mock-up solutions to demonstrate and compare capabilities of the different modelling approaches. The mock-ups are good starting approach for concretization of such systems, and they should be constructed as sets of simplified collaborative functional modules and processes.

#### *Workflows*

To create realistic mock-ups one should specify well the overall operational drilling process. Good starting point can be describing them as workflows, modelled in pseudo-code (example given in Table 1). An information system usually supports many different workflows, representing various work and process situations and necessary actions. The system should support monitoring activities, give various predictions and operational information, and finally give recommendations for operational situations and actions (particularly in urgency situations). Formalization and modelling of the important (if possible) complete set of workflows is necessary if we want automatization of the operations and well-functioning reasoning engines (see Figure 5).

Based on the mock-up evaluation results and the overall judgement of the System Architects Team (see also (Zoric et al., 2014)), the application system design can be started. Of course, if new and critical information arrives, the selection of the basic methods and models may have to be changed.

Maybe not necessary to mention, but it is critical that the users and application owners are continuously involved into the development. Workflows, exemplified by pseudo-code in Table 1, with well-defined (inputs, outputs, transformation functions and activities), are a good tool for specifying both the user interactions and other design and implementation details.

#### *System design considerations*

Software design and implementation technology, programming languages, database technology, and data communication technology require also careful

evaluation (Zoric et al., 2015). However, for all of these choices it is likely that some legacy issues must be addressed. For the software design, it means that probably the existing codes might be modified and used. However, if the existing code does not satisfy critical requirements some parts may have to be redesigned or replaced. The choice of programming language to some extent will rely on developer's competence and preferences, as well as on the implementation of the existent systems that have to be interfaced with.

#### *Information and data handling*

Heterogeneous field data is collected in all major drilling operations today, and the most cost-effective solution will be to rely on the database and communication technology already in use, which requires respecting the existing and hopefully standardized interfaces, APIs and data handling protocols and formats. Some additional data/information processing might be involved to solve the aspects as, data formatting, data curation, enrichment with metadata and contextualization of data, as well as filtering of the data/information that is worth preserving.

One possible solution could be SOFT (SINTEF Open Framework and Tools (Hagelien et al, 2017)). This is a framework for semantic interoperability of scientific and industrial software, making it possible to make software data-exchange seamlessly, according to given semantic rules. Parts of the SOFT system is in industrial use in the commercial LedaFlow™ software and is applied in the Porto software (Hagelien et al., 2015). Porto is designed to effectively exchange data between a number of different software, ranging from atomistic scale models, meso-scale models, CFD and system models. SOFT is based on a data-centric design, and can tap into numerous data-streams and collect the external data needed for given tasks. The application data could at the same time be available for external applications, with the granted access. For maintenance and further development of an application, established industrial standards should be preferred.

Detailed discussions and analyses of software frameworks are outside the scope of this paper, but we can conclude that a well-designed pragmatic modelling system should follow good SW engineering practices.

## **STEP 4 SUMMARY AND CONCLUSIONS**

In this paper, we have investigated how a more automated drilling approach can be obtained. We have used principles of a workflow and a set of methods we have named "Pragmatic industrial modelling".

In Step 1, we discussed "Requirements for an automated drilling tool". Here we found it rather challenging to give the necessary acceptance level on input and prediction results. The numbers in the paper must be considered as suggestions. Within a technological development project, detailed work must be performed to quantify which uncertainties are acceptable. It is important that during this process we identify and explore critical components within automated drilling systems.

Furthermore, we have identified various possibilities to build simulation tools to cater to new requirements. As a

basis, we could build on existing models, current streams of monitored wellbore data, as well as historical data from laboratory and field applications.

As CFD is too slow to meet the requirements for system analyses, CFD will not fulfil the requirements. On the other hand, drilling operations include numerous complex flow situations, not represented or reproduced by current 1D-flow models. In this perspective, CFD would be capable to represent the flow physics, provided that: we understand the phenomena, have these cast into mathematical models, and correctly implemented and validated. The CFD results should be handled similar to the experimental data and field data. CFD results have their strength in that input is well defined, and models may scale well with geometries and fluid properties.

On the other hand, lab data and operational data is reflecting the reality, even if the conditions for the data may be poorly defined. It is clear that we have only succeeded when models supported by CFD and lab/operational data agree, and show similar qualitative and quantitative results.

CFD models, if validated in conjunction with lab/operational data, can be used to build lookup tables for the simulation tool, or it may serve as a sub-element applied to improve the closure laws for the system hydraulics code. As demonstrated above, CFD modelling has the capability to reveal poorly understood issues (e.g. cutting avalanches) that may be critical for successful operation of an automated drilling system. Other examples may be cuttings, which during tripping out of the hole, may result in cuttings pile-up in front of the Bottom Hole Assembly. Such a phenomenon may lead to unexpected and high-pressure losses, and possibly stuck pipe.

Based on the requirements and above indicated approaches it seems quite likely that it would be possible to produce an automated drilling system. Verification that a complete tool can be developed to meet the requirements ("Step 1: Requirements for automated drilling tool") is a staged process. As part of this process the different modelling solutions must be properly assessed, based on developed mock-ups when necessary. The described system was planned be able to operate without relying on advanced downhole monitoring systems. If this is actually possible, it can only be substantiated by suggested mock-ups or by making tests using available 1D-flow simulators.

Based on our preliminary assessments, the tool that would answer to the requirements could be a transient multiphase flow model, directly linked to a mechanical model. However, the necessary assessments described above (part of the pragmatic modelling workflow) could show that this combination of models may be too slow to meet the requirements. In that case a different overall solution may have to be selected.

A critical element in an automated system is that existing operational data streams are seamlessly interpreted and integrated into computations, with no additional costs.

At the current stage, the degree of user-interaction and control over the drilling process cannot be established. However, it seems clear that a much higher degree of automation than what is the case today will be possible.

In order to get closer to a real recommendation for the actual components in an automated drilling system, a development project has to be initiated.

## ACKNOWLEDGEMENTS

The project Advanced Wellbore transport Modelling (AdWell) with its sponsor, the Research Council of Norway and its partners Statoil, ENGIE E&P Norge AS, IRIS, UiS, NTNU and SINTEF are gratefully acknowledged for funding and supporting this work.

## REFERENCES

- Cameron, I., Gani, R., 2011. Product and Process Modelling 1st Edition A Case Study Approach. Elsevier.
- Casey, M., Wintergerste, T., European Research Community on Flow, T., Combustion, 2000. ERCOFTAC Best Practice Guidelines: ERCOFTAC Special Interest Group on "quality and Trust in Industrial CFD." ERCOFTAC.
- Cayeux, E., Amare, L., Roald, K., Jarle, H., 2016. Use of a Transient Cuttings Transport Model in the Planning, Monitoring and Post Analysis of Complex Drilling Operations in the North Sea. Presented at the IADC/SPE Drilling Conference and Exhibition, Fort Worth.
- Cayeux, E., Daireaux, B., Dvergsnes, E., 2011a. Automation of mud-pump management application to drilling operations in the north-sea. SPE Drill. Complet. 26, 41–51.
- Cayeux, E., Daireaux, B., Dvergsnes, E.W., 2011b. Automation of drawworks and topdrive management to minimize swab/surge and poor-downhole-condition effect. SPE Drill. Complet. 26.
- Cayeux, E., Daireaux, B., Dvergsnes, E.W., Florence, F., 2013a. Toward drilling automation: On the necessity of using sensors that relate to physical models. Presented at the SPE/IADC Drilling Conference and Exhibition, Amsterdam, the Netherlands.
- Cayeux, E., Mesagan, T., Tanripada, S., Zidan, M., Fjelde, K.K., 2013b. Real-time evaluation of hole cleaning conditions using a transient cuttings transport model. Presented at the SPE/IADC Drilling Conference and Exhibition, Amsterdam, the Netherlands.
- Cayeux, E., Skadsem, H.J., 2014. Estimation of weight and torque on bit: Assessment of uncertainties, correction and calibration methods. Presented at the ASME 2014 33rd International Conference on Ocean, Offshore and Arctic Engineering, San Francisco, California, USA.
- Florence, F., Iversen, F.P., 2010. Real-Time Models for Drilling Process Automation: Equations and Applications, in: SPE-128958-MS. Society of Petroleum Engineers, SPE. doi:10.2118/128958-MS
- Islam, M.A., Helstrup, O.A., Moi, S., Carlsen, L.A., 2016. Automated Pressure Integrity Testing APIT-A Step Change Approach, in: SPE-183273-MS. Society of Petroleum Engineers, SPE. doi:10.2118/183273-MS
- Laux, H., 1998. Modeling of dilute and dense dispersed fluid-particle two-phase flow (PhD thesis). NTNU, Trondheim.
- Lohne, H.P., Gravdal, J.E., Dvergsnes, E.W., Nygaard, G.H., Vefring, E.H., 2008. Automatic calibration of real-time computer models in intelligent drilling control systems - results from a north sea field trial. Presented at the International Petroleum Technology Conference, Kuala Lumpur, Malaysia.

- Mathis, W., Thonhauser, G., 2007. Mastering real-time data quality control - how to measure and manage the quality of (rig) sensor data. Presented at the SPE Middle East Intelligent Energy Conference and Exhibition, Cairo, Egypt.
- Mendenhall, M.R., Childs, R.E., Morrison, J.H., 2003. Best practices for reduction of uncertainty in CFD results, in: 41st AIAA Aerospace Sciences Meeting.
- Modisette, J.L., Modisette, J.P., others, 2001. Transient and Succession-of-Steady-States Pipeline Flow Models, in: PSIG Annual Meeting. Pipeline Simulation Interest Group.
- Moi, S., Carlsen, L.A., Skadsem, H.J., Islam, A., Helstrup, O.A., 2017. Nonlinear Regression Analysis and System Stiffness Approach for Formation Integrity Test Interpretation, in: SPE-184602-MS. Society of Petroleum Engineers, SPE. doi:10.2118/184602-MS
- Nazari, T., Hareland, G., Azar, J.J., 2010. Review of Cuttings Transport in Directional Well Drilling: Systematic Approach, in: SPE Western Regional Meeting. Society of Petroleum Engineers, Anaheim. doi:10.2118/132372-MS
- Rommetveit, R., Davidson, I., Svendsen, M., 2017. Real Time Engineering-Based Simulation Training Addresses Risk in Managed Pressure Drilling, in: SPE-184700-MS. Society of Petroleum Engineers, SPE. doi:10.2118/184700-MS
- Skalle, P., Toverud, T., Johansen, S.T., 2014. Attenuation of pump pressure in long wellbores (v02). J. Pet. Sci. Eng. 122, 159–165. doi:10.1016/j.petrol.2014.07.005
- Zoric, J., Busch, A., Meese, E.A., Khatibi, M., Time, R.W., Johansen, S.T., Rabenjafimanantsoa, H.A., 2015. On Pragmatism in industrial modeling - Part II: Workflows and associated data and metadata, in: The 11th International Conference on CFD in the Minerals and Process Industries. Presented at the Eleventh International Conference on CFD in the Minerals and Process Industries CSIRO, CSIRO Publishing, Melbourne.
- Zoric, J., Johansen, S.T., Einarsrud, K.T., Solheim, A., 2014. On pragmatism in industrial modeling, in: Johansen, S.T., Olsen, J.E. (Eds.), CFD 2014 - 10th International Conference on Computational Fluid Dynamics in the Oil & Gas, Metallurgical and Process Industries. SINTEF, Trondheim, pp. 1–16.
- Hagelien, T.F., S. Radl, C. Kloss, C. Goniva, P.I. Dahl, S. M. Nazir, P. Fede, S. Amini, "Porto: A framework for information interchange and multi-scale fluid mechanics simulations", 3rd EUMMC Workshop, Jyväskylä, Finland, 2015
- Hagelien, T.F., Chesnokov, A., Johansen, S.T., Meese, E. A., Løvfall, B.T., "SOFT: A framework for semantic interoperability of scientific software", To appear in Proceedings of CFD 2017 - 12th International Conference on Computational Fluid Dynamics in the Oil & Gas, Metallurgical and Process Industries, SINTEF, Trondheim, May 30th – June 1st, 2017

LedaFlow®, [www.ledaflow.com](http://www.ledaflow.com)

OLGA®, <https://www.software.slb.com/products/olga>

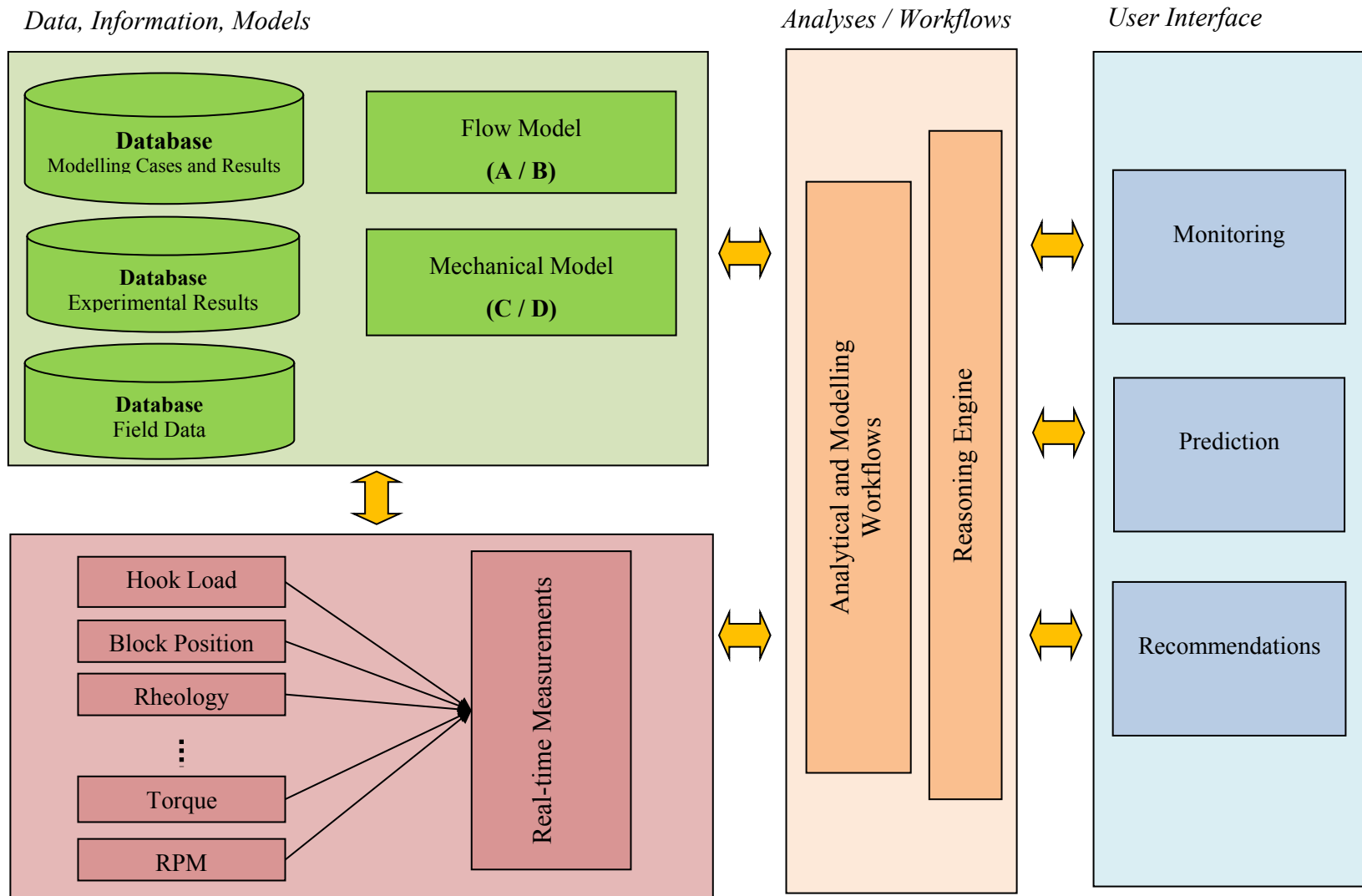


**Figure 5** Architecture of the Conceptual Model - Operational Drilling Decision Support System. Four possible combinations of modelling approaches for flow and mechanical models (AC, AD, BC and BD) are discussed in the section "STEP 2 CONCEPTUAL MODEL DESIGN".

**Table 1.** Workflow / Pseudo-code for one of the analyses (modelling combination A-D), which supports drilling operations discussed above. Mechanical and flow model may be run in parallel.

<b>OPERATION</b>	<b>COMMENT</b>
<b>INITIALIZE</b>	
Prepare for drilling operation	
Check that input data for simulation is available	
Initialize simulation software: i) Flow model ii) Mechanical model iii) All other models	Ensure that monitoring systems are OK Read initial and boundary conditions for all models
<b>BEGIN</b>	
Start drilling operation	
Simulation software starts	
<b>WHILE drilling in operation DO</b>	
Continuous update on drilling operational parameters from monitoring system	Pump pressure, Hook load, Block position, Torque, RPM etc.
Continuous update of boundary conditions for mechanical model	Based on current position of the drill string, and monitored flow conditions.
Continuous update of boundary conditions, geometry and fluid properties for the flow model	Based on previous model runs and on monitor data.
Communicate coupling set-up between mechanical and flow model.	Ensure that the models are consistent with each other at all stages of operation
Run mechanical and flow models in parallel	Many look-ahead simulations may be run simultaneously, each with variations of initial and boundary conditions, and variation of other parameters. Communication between the models will happen also on a per time step basis, e.g., exchanging gradients for numerical stability.
Monitoring activity	Data is continuously retrieved from the monitoring system.
Collect simulation results into database	Database will contain all data needed to identify a drilling operation, and will be an asset for historical learning (some information may be added post-operation)
Analyse accuracy of simulation results	Compare with monitor data and estimate uncertainties.
<b>IF mismatch between model and monitor data THEN</b>	
Identify most likely sources of errors	Mismatch is defined as deviations larger than what is acceptable, based on uncertainty in input and simulation results.
Determine if deviation must lead to operational action or/and correction of model parameters	
Tuning of model input parameters and/or adjusting the model set-up parameters	Conditional; depending on the previous step
<b>ENDIF</b>	
Update borehole model geometry.	The modelling geometry essentially is the borehole angle and hole size as a function of length along the borehole. This information must be updated as the drilling progresses. Setting of casings: Update on thermal data
Analyse simulation results and monitor data	Find recommendation for settings of operation parameters. Identify eventual issues, e.g., risk for gas kick, etc.
Update status and result in operator view	Includes updating history server.
Provide adjusted settings to the drilling robot	Settings may be adjusted automatically, or overridden by a human operator.
<b>END WHILE</b>	
Stop drilling operation	
<b>END</b>	



# CFD MODELING OF DYNAMIC EMULSION STABILITY

**A.V. Patil<sup>1</sup>, S. T. Johansen<sup>1</sup>**

<sup>1</sup> SINTEF Materials and Chemistry, 7465 Trondheim, NORWAY

\* E-mail: amit.patil@sintef.no

## ABSTRACT

Assuring transport and separation of oil and water crude emulsions is of significant importance to the oil and gas industries. The crude oil, due to its profuse chemical composition, has complex dispersion and emulsion flow behavior with water. As a result, of the interface chemistry, the bubbles and droplets may separate easily, or not separate at all, impacting flow regime, water holdup, pressure drop and separation efficiency during pipe transport. Using a recently developed new stirred tank characterization technique for emulsion stability droplet relaxation parameters can be studied. Multiple model oils and crude oils were characterized by this technique. This work discusses development of a pragmatic modeling method that can validate the experimental measurements. A time averaged velocity profile in a stirred tank is used to obtain a 1-D flux flow profile in the vertical direction. This 1-D flux profile is used as a simplified flow equation and scalar equations for droplet size and dispersed phase fraction is used for modeling the emulsion stability and relaxation. This method can help in fast simulation of emulsion stability that involves long time scales of coalescence and breakage evolution for crude oil and water.

**Keywords:** Multiphase flow, oil-water emulsion, flow assurance.

## NOMENCLATURE

A complete list of symbols used, with dimensions, is required.

### *Greek Symbols*

- $\rho$  Mass density, [kg/m<sup>3</sup>].
- $\mu$  Dynamic viscosity, [kg/m.s].
- $\Gamma$  Dispersed phase viscosity, [m<sup>2</sup>/s].
- $\Omega$  relaxation coefficient, [1/s].

### *Latin Symbols*

- $a$  Characteristic area, [m<sup>2</sup>].
- $p$  Pressure, [Pa].
- $\mathbf{u}$  Velocity, [m/s].

$\bar{U}$  Averaged velocity, [m/s].

$\bar{d}$  mean droplet size, [m].

$\alpha$  dispersed phase fraction, [-].

$\bar{V}$  Dispersed phase velocity, [m/s].

$\tau$  Relaxation time scale for droplets, [s].

### *Sub/superscripts*

- c Continuous phase.
- A upward flow direction.
- B downward flow direction.
- E Exchange flow between A and B.
- z z- direction representing height direction of tank
- eq Equilibrium

## INTRODUCTION

The pipeline transport of crude oil-water dispersions or emulsions is typical for many oil fields and flow assurance studies has been hampered by limited understanding of how to handle the possible behavior of the flow when stabilizing surfactants are present. The cost of crude oil production is strongly related to pressure drop produced in transport pipes. It is well known that pressure drop is strongly dependent on the rheological behavior, which is strongly influenced by emulsion stability. Therefore oil-water emulsion stability has been a subject to several studies in the past.

Emulsion stability or droplet size evolution is strongly influenced by interfacial tension (IFT) and surface chemistry (Aichele 2009; Mullins et. al. 2007; Sjoblom 2005). So there has been a need to quantify the droplet size evolution behaviour for given characteristics of oil-water emulsions. This has been achieved by an advanced imaging technique developed recently and presented in Patil et. al. (2017). In this method, the measurement of droplet size alongside torque provides the necessary understanding of dissipation on emulsion stability.

Experiments with model oils-water emulsion has shown that the droplet size in turbulent regimes is governed by Kolmogorov scale criteria (Kolmogorov, 1949). Depending on the regime defined by the inertial and viscous subrange; the equilibrium droplet size agree well with the theoretical correlations (Boxall et. al.



2010; Boxall et. al. 2012; Patil et. al. 2017). Further the dynamic droplet size relaxation of emulsions have also been studied by measuring the time dependent droplet relaxation and hence its coefficient (Calderbank, 1958; Patil et. al., 2017).

Dispersion of two phases by emulsification in a stirred tank has long been modeled using various multiphase modelling methods. Most common models for such fluid-fluid systems is the Euler-Euler method (Murthy et. al. 2007). Besides CFD methods using Population Balance models (PBM) to represent the dynamic dispersed phase have also been developed (Trætlie-Einarsrud et. al. 2014, Raikar et. al. 2009).

Generally for model oil-water emulsions the time scales for relaxations is several seconds (Patil et. al. 2017). For crude oil-water emulsions which have stabilizing components these time scales are higher (few minutes) (Patil et. al. 2017b). The challenges with using Euler-Euler methods (in 3D) is that they are slow and time consuming due to the small time steps needed ( $<10^{-4}$ s). The CFD-PBM approach is still a useful modelling method. But a number of challenges were encountered in using such a method for emulsions where surface active components influence the droplet behavior.

For a normal stirred tank cell with a single impeller the radial and angular variation in dissipation is very small relative to the height. Therefore, a pragmatic 1-D model in height direction can make the model simplistic and fast. This will essentially also make emulsion stabilization modelling easy. Initially only the Sauter mean diameter (SMD) of the droplet will be modelled and later a size distribution model can be developed with a PBM kind of technique, like in Einarsrud et. al. (2014). In this work we describe the development of such a pragmatic 1-D model.

## MODEL DESCRIPTION

The oil and water phase in the emulsion stability study are of nearly the same density and hence the 3-D flow patterns in the tank will not be much different from a single phase flow. So the flow pattern for the 3 speed levels of impeller can be evaluated using a single phase flow simulations. The properties of the continuous phase can be used for such a simulation.

The continuity and momentum equation for the 3D system is represented by;

$$\frac{\partial \rho_c}{\partial t} + \nabla \cdot (\rho_c \tilde{\mathbf{u}}_c) = 0 \quad (1)$$

$$\frac{\partial \rho_c \tilde{\mathbf{u}}_c}{\partial t} + \nabla \cdot \{ \rho_c \tilde{\mathbf{u}}_c \tilde{\mathbf{u}}_c \} + \{ \overline{\rho_c \mathbf{u}_c'' \mathbf{u}_c''} \} - \tau_c \} = -\nabla p + \rho_c g \quad (2)$$

Where,  $\rho_c$  is the density of continuous phase. Turbulent fluctuations are modelled with the k- $\epsilon$  model.

In these single phase simulations the impeller blade moments is integrated to obtain the torque. The torque is

monitored till equilibration is achieved. The simulation is continued further by time averaging the velocity field to obtain the averaged flux.

It is well known that the averaged velocity field for a baffled and flat blade impeller based stirred tank has a profile that looks like in Fig. 1. There are 2 circulation currents in the vertical z-direction. Both currents start at the impeller in radially outward direction. This results in a two large scale counter-rotating vortices. The upper vortex is moving up along the wall, above the impeller, while the lower vortex moving down along the wall, below the impeller. The flow recirculates back along the shaft as shown in Fig. 1. The upwards and downwards flow field sections is shown in Fig. 1 where the areas are marked. Within this flow pattern note that the upward and downward flow mass rate is always the same. The difference in the area is balanced by difference in mean velocities (z-directional).

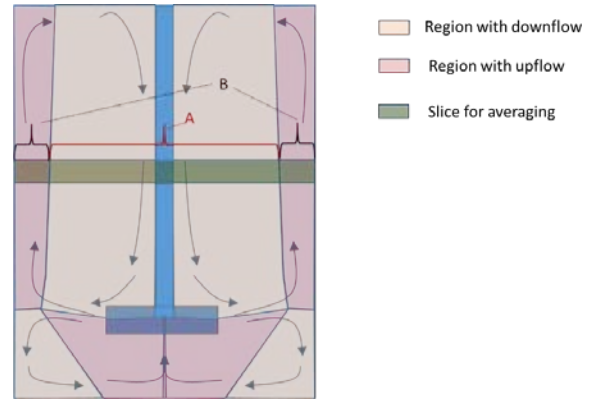


**Figure 1:** Regions with upward and downward flows are marked

This 3-D time averaged velocity field data is utilized to obtain a pseudo 1-D flow field in the vertical direction (z-direction) and horizontal directions. For this purpose, the flow fields in the cross section is averaged for upward and downward flow defined by region A and B at discrete cross sections along the z direction. Thus the upward and downward mean velocity and the upward and downward, and the corresponding cross sectional areas are evaluated. The averaged upward and downward velocity is given by;

$$\overline{U}_A = \frac{\int_A u_{c,z} da}{\int_A da} \quad \text{and} \quad \overline{U}_B = \frac{\int_B u_{c,z} da}{\int_B da} \quad (3)$$

Where,  $u_{c,z}$  is the z-direction component velocity of the fluid velocity field  $\tilde{\mathbf{u}}_c$ . The flow area for the streams A and B are given by;

$$a_A = \int_A da \quad \text{and} \quad a_B = \int_B da \quad (4)$$

For evaluation of the average turbulent dissipation  $\epsilon$  in horizontal slices, denoted A and B we define:

$$\overline{\varepsilon_A} = \frac{\int_A \varepsilon dV}{\int_A dV} \quad \text{and} \quad \overline{\varepsilon_B} = \frac{\int_B \varepsilon dV}{\int_B dV} \quad (5)$$

These dissipation rates, averaged over horizontal slices with finite thickness  $\Delta z$ , are critical input for evaluation of the equilibrium droplet sizes used by the model.

The mass conservation on a slice, for the zones A and B, is then given by:

$$\begin{aligned} [a_A \overline{U_A}]_z^+ - U_E a_I &= 0 \\ [a_B \overline{U_B}]_z^+ + U_E a_I &= 0 \end{aligned} \quad (6)$$

Here  $U_E$  is the average radially directed velocity (horizontal exchange velocity), communicating through area  $A_I$ , which is easily determined based on the interface location between zones A and B. The radial velocity  $U_E$  can be computed from any of the two relations in Eq.(6).

The above description for total flow balance is summarized in Fig. 2. It is to be noted that for each tank cross sectional area, the upward and downward volumetric flow is the same. This means that;

$$\overline{U_{A,k+\frac{1}{2}} a_{A,k+\frac{1}{2}}} = \overline{U_{B,k+\frac{1}{2}} a_{B,k+\frac{1}{2}}} \quad (7)$$

This is consistent with the global mass conservation equations, Eq. (6)

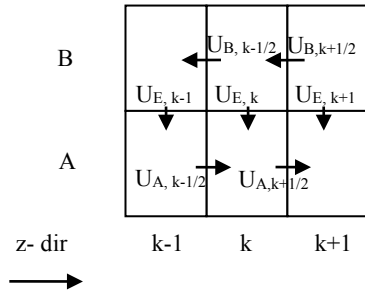


Figure 2: Grid description for the 1-D model

This 1-D averaged data is utilized in the dynamic droplet size model equation provided by;

$$\begin{aligned} \frac{\partial}{\partial t} a_A \overline{d_{A,z}} + \frac{\partial}{\partial z} (a_A V_z \overline{d_{A,z}}) &= \frac{\partial}{\partial z} \Gamma a_A \frac{\partial \overline{d_{A,z}}}{\partial z} \\ + a_A \frac{\overline{d_{eq,A,z}} - \overline{d_{A,z}}}{\tau} + \Omega a_I (\overline{d_{B,z}} - \overline{d_{A,z}}) & \quad (8) \\ + \frac{a_I}{\Delta z} (\max(U_E, 0) \overline{d_{B,z}} - \max(-U_E, 0) \overline{d_{A,z}}) & \end{aligned}$$

The above equation formulation is a passive scalar transport equation with source terms. The 3-D version of this can be found in Laux and Johansen (1999). Similarly for the droplet size in zone B:

$$\begin{aligned} \frac{\partial}{\partial t} a_B \overline{d_{B,z}} + \frac{\partial}{\partial z} (a_B V_z \overline{d_{B,z}}) &= \frac{\partial}{\partial z} \Gamma a_B \frac{\partial \overline{d_{B,z}}}{\partial z} \\ + a_B \frac{\overline{d_{eq,B,z}} - \overline{d_{B,z}}}{\tau} - \Omega a_I (\overline{d_{B,z}} - \overline{d_{A,z}}) & \quad (9) \\ - \frac{a_I}{\Delta z} (\max(U_E, 0) \overline{d_{B,z}} - \max(-U_E, 0) \overline{d_{A,z}}) & \end{aligned}$$

Where;  $\overline{d_{A,z}}$  is the averaged droplet size in the zone of upward flow at position z. The above 1-D model is further simplified by neglecting the shear term defined by the viscosity of the continuous phase. Since this model is not taking the detailed flow into consideration the shear effect can be essentially lumped into Equilibrium droplet size  $\overline{d_{eq,A,z}}$ . The  $\overline{d_{eq,A,z}}$  is a function of multiple factors defined by fluid properties and the presence of surface-active components. If the surface-active components are not present then depending on the flow regime the droplet size is governed by inertial or viscous sub-range correlations in (Patil et. al. 2017).

In these two equations ((8),(9))  $\Omega$  is a dispersion transfer coefficient, expressing the turbulence induced exchange rate of particle size between the two zones. The last term in Eqs. (8) and (9) express the convective transport between zones A and B.

The droplet fraction in zone A is conserved by:

$$\begin{aligned} \frac{\partial}{\partial t} a_A \overline{\alpha_{A,z}} + \frac{\partial}{\partial z} (a_A V_z \overline{\alpha_{A,z}}) &= \frac{\partial}{\partial z} \Gamma a_A \frac{\partial \overline{\alpha_{A,z}}}{\partial z} \\ + \Omega a_I (\overline{\alpha_{B,z}} - \overline{\alpha_{A,z}}) & \quad (10) \\ + \frac{a_I}{\Delta z} (\max(U_E, 0) \overline{\alpha_{B,z}} - \max(U_E, 0) \overline{\alpha_{A,z}}) & \end{aligned}$$

The above equation is a general mass conservation equation for dispersed phase assuming phase densities are constant. It is averaged over all the control volumes in the system. Similarly for zone B, we have

$$\begin{aligned} \frac{\partial}{\partial t} a_B \overline{\alpha_{B,z}} + \frac{\partial}{\partial z} (a_B V_z \overline{\alpha_{B,z}}) &= \frac{\partial}{\partial z} \Gamma a_B \frac{\partial \overline{\alpha_{B,z}}}{\partial z} \\ + \Omega a_I (\overline{\alpha_{B,z}} - \overline{\alpha_{A,z}}) & \quad (11) \\ - \frac{a_I}{\Delta z} (\max(U_E, 0) \overline{\alpha_{B,z}} - \max(U_E, 0) \overline{\alpha_{A,z}}) & \end{aligned}$$

The dispersed phase velocity in z-direction  $V_z$  has essentially two components, which are convective velocity  $U_z$  and terminal velocity.

$$V_z = U_z + V_t \quad (12)$$

Here  $V_t$  is the dispersed phase velocity component from Stokes law given by;

$$V_t = \frac{(\rho_c - \rho_d) d^2 g}{18\mu} \quad (13)$$

Further discretization and rearranging Eq. (8) gives the following equation to solve the (Sauter mean) droplet size equations in height direction.

$$\begin{aligned}
& \frac{a_{A,k}}{\Delta t} (\overline{d_{A,k,n+1}} - \overline{d_{A,k,n}}) + \frac{1}{\Delta z} \left[ a_{A,k} (\overline{U_A} + \overline{V_t}) \overline{d_{A,k,z}} \right]_{z^-}^+ = \\
& \frac{1}{\Delta z} \left[ \Gamma a_{A,k} \frac{\partial \overline{d_{A,k,z}}}{\partial z} \right]_{z^-}^+ \\
& + a_{A,k} \frac{\overline{d_{eq,A,k,z}} - \overline{d_{A,k,z}}}{\tau} + \Omega a_{I,k} (\overline{d_{B,k,z}} - \overline{d_{A,k,z}}) \\
& + \frac{a_{I,k}}{\Delta z} (\max(U_{E,k}, 0) \overline{d_{B,k,z}} - \max(-U_{E,k}, 0) \overline{d_{A,k,z}})
\end{aligned} \quad (14)$$

In equations (15) and (16) the notation  $z^+$  and  $z^-$  denotes the cell boundary positions for the slice where the droplet size is computer. The averaged velocities  $U_A$  and  $U_B$  are always computed at these cell boundaries (staggered grid arrangement).

Before proceeding, we subtract the product of droplet size and fluid mass conservation eq. (6), and rearrange.

$$\begin{aligned}
& \frac{a_{A,k}}{\Delta t} (\overline{d_{A,k,n+1}} - \overline{d_{A,k,n}}) + \frac{1}{\Delta z} (a_{A,k} \overline{U_{A,k}})^+ (\overline{d_{A,k,n}} - \overline{d_{A,k,n}}) \\
& - \frac{1}{\Delta z} (a_{A,k} \overline{U_{A,k}})^- (\overline{d_{A,k,n}} - \overline{d_{A,k,n}}) \\
& + \frac{1}{\Delta z} \left[ (a_{A,k} \overline{V_t})^+ \overline{d_{A,k,n}} - (a_{A,k} \overline{V_t})^- \overline{d_{A,k,n}} \right] = \\
& \frac{1}{\Delta z} \left[ \Gamma_k a_{A,k} \frac{\partial \overline{d_{A,k,n}}}{\partial z} \right]_{z^-}^+ + a_{A,k} \frac{\overline{d_{eq,A,k,n}} - \overline{d_{A,k,n}}}{\tau} \\
& + \Omega_k a_{I,k} (\overline{d_{B,k,n}} - \overline{d_{A,k,n}}) \\
& + \frac{a_{I,k}}{\Delta z} (\max(U_{E,k}, 0) (\overline{d_{B,k,n}} - \overline{d_{A,k,n}}))
\end{aligned} \quad (15)$$

The values at the cell faces ( $\overline{d_{A,k,z}^+}$  and  $\overline{d_{A,k,z}^-}$ ) are now approximated by the upwind value, controlled by  $U_A$  or the terminal velocity  $V_t$ .

Note that here by convention,  $\overline{U_{A,k}}$  and  $\overline{U_{B,k}}$  are always positive representing the upward and downward velocity direction respectively. However,  $\overline{V_t}$  and  $\overline{U_E}$  can be positive or negative depending on density difference and direction of the flow respectively. If continuous phase density is larger than dispersed phase  $\overline{V_t}$  is positive (in z direction). Else it is negative when dispersed has higher density.

At any given cross sectional grid say 'k' in z direction, if the exchange of mass is from B zone (downward flow) to A zone (upward flow) then the  $\overline{U_{E,k}}$  is positive.

Similarly, vis-versa it is negative.

$$\begin{aligned}
& \frac{a_{A,k}}{\Delta t} (\overline{d_{A,k,n+1}} - \overline{d_{A,k,n}}) - \frac{1}{\Delta z} (a_{A,k} \overline{U_{A,k}})^- (\overline{d_{A,k,n}} - \overline{d_{A,k,n}}) \\
& + \frac{1}{\Delta z} \left[ (a_{A,k} \overline{V_t})^+ \overline{d_{A,k,n}} - (a_{A,k} \overline{V_t})^- \overline{d_{A,k,n}} \right] = \\
& \frac{1}{\Delta z} \left[ \Gamma_k a_{A,k} \frac{\partial \overline{d_{A,k,n}}}{\partial z} \right]_{z^-}^+ + a_{A,k} \frac{\overline{d_{eq,A,k,n}} - \overline{d_{A,k,n}}}{\tau} \\
& + \Omega_k a_{I,k} (\overline{d_{B,k,n}} - \overline{d_{A,k,n}}) \\
& + \frac{a_{I,k}}{\Delta z} (\max(U_{E,k}, 0) (\overline{d_{B,k,n}} - \overline{d_{A,k,n}}))
\end{aligned} \quad (16)$$

Similarly, a formulation for the downward flow droplet size equation exists given by;

$$\begin{aligned}
& \frac{a_{B,k}}{\Delta t} (\overline{d_{B,k,n+1}} - \overline{d_{B,k,n}}) + \frac{1}{\Delta z} (a_{B,k} \overline{U_{B,k}})^+ (\overline{d_{B,k,n}} - \overline{d_{B,k,n}}) \\
& + \frac{1}{\Delta z} \left[ (a_{B,k} \overline{V_t})^+ \overline{d_{A,k,n}} - (a_{B,k} \overline{V_t})^- \overline{d_{A,k,n}} \right] = \\
& \frac{1}{\Delta z} \left[ \Gamma_k a_{B,k} \frac{\partial \overline{d_{B,k,n}}}{\partial z} \right]_{z^-}^+ + a_{B,k} \frac{\overline{d_{eq,A,k,n}} - \overline{d_{A,k,n}}}{\tau} \\
& - \Omega_k a_{I,k} (\overline{d_{B,k,n}} - \overline{d_{A,k,n}}) \\
& - \frac{a_{I,k}}{\Delta z} (\max(U_{E,k}, 0) (\overline{d_{B,k,n}} - \overline{d_{A,k,n}}))
\end{aligned} \quad (17)$$

The conservation equations for the dispersed phase is given by eqs. (10) and (11). These equations as well, may be discretised, using explicit time integration and first order unwinding for convection.

It should be noted that the vertical dispersion coefficient  $\Gamma$  as well as the horizontal exchange coefficient  $\Omega$  has not been determined yet. These may be estimated based on the mixing length hypothesis, or may be extracted from the CFD simulations. As a first approach we may neglect the effects of turbulent dispersion and convective dispersion will dominate in most cases.

Both the terminal velocity and the equilibrium size may be made explicitly depending on the droplet fractions. Accordingly, the terminal velocity  $V_t$  in equations (16) and (17), will depend on the solution of the droplet fraction equations (10) and (11).

For the top and bottom slices the boundary condition is that there is no flux of droplet size or droplet mass (volume fraction) across these external boundaries. The droplet fraction may build to large values in the end-of-domain cells. In this case over compaction may, as an example, be avoided by enforcing the droplet velocities to become stagnant at a maximum packing.

The 3-D single phase flow simulations of stirred tank was performed using ANSYS Fluent 17.1. The 3-D time averaged velocity field data was imported in MATLAB to obtain time averaged 1-D volumetric flow rate in height direction.

## RESULTS

The averaged velocity vector plot for the 3-D flow field is shown hereby in Fig. 3 for a 3500 RPM impeller speed. This plot illustrates the flow field description provided earlier in the previous section Fig. 1.

The z-direction velocity field is shown in Fig. 4. Note that close to the impeller tip the fluid velocities are very high. Therefore, the scale in this fig has been limited to +1.5 and -1.5 m/s velocity range so that remaining flow features are better visible.

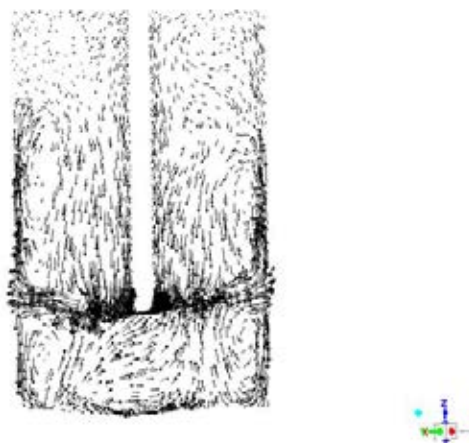


**Figure 3:** Cross sectional cut view of velocity vector field

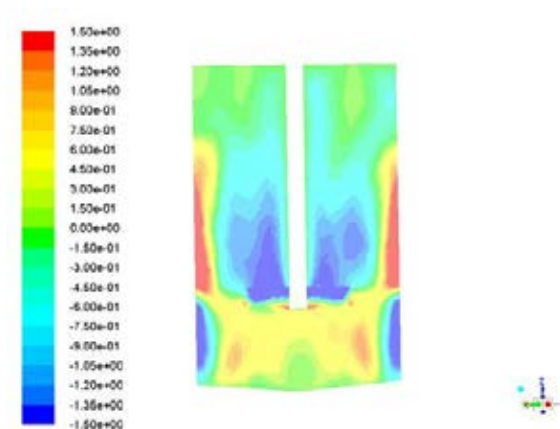


**Figure 4:** Cross sectional cut view of z-directional velocity colour profile

The data from the time averaging done over a 3-D simulation data for 25 s gave a profile that equilibrated and changed negligibly with time. Using this profile data the positive and negative averaged velocity fields were averaged at discrete cell faces in z direction. These cell face velocities are weighted with respect to cell face area as per Eq. (3) to give averaged upward and downward velocities.

Besides, integrating the upward and downward flow area provides averaged area of A and B. The volumetric flow rate in upward and downward direction can thus be obtained which both should be equal from Eq. (7).

Further using Eq. (6) the exchange velocity and volumetric flow rate between the two zones (A and B) can be obtained. The dimensions of the tank is summarized in Table 1.

**Table 1:** Model dimension.

Dimensions	
Tank diameter	0.095 m
Tank height	0.148 m
Impeller diameter	0.05 m
Number of cells in z direction	10
Grid size (z-direction)	0.0148 m

It is to be noted that though the averaging takes place for a long enough time there is always some small difference between the upward and downward flow

rates. Though this numerical difference is negligibly small they need to be removed for the 1-D simulation as this may cause numerical leakages for the dispersed phase equation.

Therefore, the upward and downward volumetric flow rate are averaged out as a reasonable approximation. Fig. 5 shows a plot of the averaged upward and downward volumetric flow rate for the 3-D simulation at 3500 RPM impeller speed. These are at cell face positions. Besides, it also shows a plot of cell exchange flow rate between A and B zone at cell centre position.

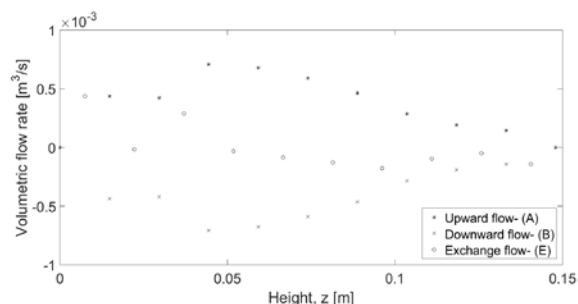


**Figure 5:** Upward and downward volumetric flow rate and exchange flow rate

This has provided a complete internally balanced velocity field that can be used for dispersed phase simulations. Using such a 1-D method, fast simulation of dispersed phase evolution is possible. With this method, the long time scales of emulsion droplet size relaxation can be modelled.

## CONCLUSION

A simplified 1-D modelling method has been proposed to mimic emulsion stability in stirred tank. This method uses time averaged velocity fields from 3-D single phase simulations to obtain 1-D flow rate in z direction (upward and downward direction). This balanced flow rate field can be further used for modelling the size evolution of a dispersed phase in the height or z direction. Using such a method long time scales of emulsion evolution can be modelled fast. These models can be fitted with emulsion evolution parameters obtained experimentally using a stirred tank. Such models can in future be used in 1-D pipe simulation software.

## REFERENCES

- AICHELE, C., (2009), "Characterizing Water-in-oil Emulsions with Application to Gas Hydrate Formation", *PhD thesis, Rice University*, 2009.
- MULLINS O., SHEU E., HAMMAMI A., MARSHALL A., (2007), "Asphaltenes, Heavy Oils, and Petroleomics", *Springer New York*.
- J. SJOBLM, (2005), "Emulsions and Emulsion Stability: Surfactant Science Series/61", *Surfactant Science, CRC Press*.
- PATIL A.V., MARTI X.S., TETLIE P., JOHANSEN S.T., "Development of an advanced imaging technique

for dynamic emulsion stability”, accepted by *Chem. Engg. J.*

KOLMOGOROV, A., (1949), “On the disintegration of drops in a turbulent flow”, *Dok. Akad. Nauk.*, **66**, 825-828.

BOXALL J. A., KOH C. A., SLOAN E. D., SUM A. K., and WU D. T., (2010), “Measurement and calibration of droplet size distributions in water-in-Oil emulsions by particle video microscope and a focused beam reflectance method”, *Ind. and Engg. Chem. Res.*, **49**, 1412-1418.

BOXALL, J. A., KOH, C. A., SLOAN, E. D., SUM, A. K., and WU, D. T., (2012), “Droplet size scaling of water-in-oil emulsions under turbulent flow”, *Langmuir: The ACS Journal of Surfaces and Colloids*, **28**, 104-110.

CALDERBANK P., (1958), “Physical rate processes in industrial fermentation. Part i; the interfacial area in gas-liquid contacting with mechanical agitation”, *Trans. Instn. Chem. Eng.* 36 443-463.

MURTHY B.N., GHADGE R.S., JOSHI J.B., (2007), “CFD simulations of gas-liquid-solid stirred reactor: Prediction of critical impeller speed for solid suspension”, *Chem. Engg. Sci.*, **62**, 7148-7195.

TRÆTTLI-EINARSRUD K. E., PANJWANI B., PAUCHARD V., (2014), “A pragmatic approach to CFD modelling of separation processes”, *Proceedings of 10th International Conference on CFD in Oil & Gas, Metallurgical and Process Industries, Trondheim, Norway, June 2014.*

RAIKAR N. B., BHATIA S. R., MALONE M. F., HENSON M. A., (2009), “Experimental studies and population balance equation models for breakage prediction of emulsion drop size distributions”, *Chem. Engg. Sci.*, **64(10)**, 2433-2447.

LAUX H., and JOHANSEN S.T., (1999), “A CFD analysis of the air entrainment rate due to a plunging steel jet combining mathematical models for dispersed and separated multiphase flows”, *Fluid Flow Phenomena in Metal Processing, Edited by N. El-Kaddah et al., The Minerals, Metals and Materials Society*, 21-30.

# MODELLING OF INTERACTION BETWEEN TURBINES AND TERRAIN WAKES USING PRAGMATIC APPROACH

Kjersti Røkenes<sup>1</sup>, Balram Panjwani<sup>2</sup>, Berit Floor Lund<sup>1</sup>, Jon Samseth<sup>2</sup>

<sup>1</sup>Kongsberg Digital, Trondheim, Norway

<sup>2</sup>SINTEF Materials and Chemistry, 7465 Trondheim, NORWAY

\* E-mail: balram.panjwani@sintef.no

## ABSTRACT

Kongsberg Digital (KDI) is currently developing a decision support system for wind farms (Kongsberg EmPower). The objectives of Kongsberg EmPower are to optimize the total power production from a wind farm, forecast the power production and monitor the performance and condition of the wind turbines. Power production from a wind farm depends on the flow field around the wind turbine, which is highly influenced by the interaction between turbine and terrain wakes. Furthermore, increased turbulence due to wake-wake interaction increases structural and fatigue loads on the wind turbine blades, leading to higher operational and maintenance (O&M) cost. An improved understanding on the wake-wake interaction is extremely important for optimizing the power production and for reducing the O&M cost. Performing extensive velocity measurements for an entire wind farm is time consuming and expensive. The traditional approach within wind research and industry has been to use full CFD models when complex flow phenomena have to be taken into consideration, but this is computationally demanding. On the other hand, simple engineering models are unable to capture the interaction of flow over complex terrain and wind turbine wakes. KDI and SINTEF are running a project to develop a fast response simulator with simplified representations of terrain effects and turbine wakes. In the proposed approach a pragmatic model for turbines and terrain wakes interaction is presented. Complex flow over a terrain is estimated with mass consistent model and wake from wind turbine is computed using well established wake models i.e. Jensen and Ainslie model. The pragmatic model for coupling the interaction between turbine wakes and terrain approach is presented. The results obtained from the mass consistent approach are verified with CFD using OpenFoam.

**Keywords:** CFD, OpenFoam, Wakes, Turbines, Terrains

## INTRODUCTION

Wind energy is one of the oldest sources of renewable energy that has been harvested to a large

extent. The current state of turbine technology is mature and available from several manufacturers. The size of the wind turbines is increasing steadily and current size of the wind turbine in terms of power is around 6 MW in operational and up to 10 MW is being developed. Irrespective of the size of the wind turbine, the energy extracted by a wind turbine depends on the local wind conditions. The wind conditions varies significantly from one region to another. Furthermore, local terrain effects can also change the wind conditions and these are significantly different from one site to another. Some countries have relatively flat terrain whereas other countries, i.e. Norway, have very complex terrain. Most of the onshore wind farms in Norway are located in complex terrain and just to name a few: Hundhammerfjellet, Havøygavlen and Hitra Wind Farms. The wind conditions in a complex terrain are relatively harsh and transient in nature. Furthermore, an interaction of wakes generated from a complex terrain with a wind turbine results in increased turbulence and velocity deficit. This leads to reduced power production and higher loads on turbines compared with those located in a flat terrain. The knowledge of the local wind conditions is extremely important for a successful operation of wind farms. The most accurate way to estimate behaviour of such flow is to perform experiments in a full scale wind farm or in reduced scale wind tunnel testing. However, performing experiments on full scale is very challenging and not economically feasible. Wind tunnel testing on a scaled size wind farm is also prohibitive. The other approach is to use numerical simulation of the wind parks.

There are numerous models available for estimating the wind turbine wakes and interaction of wakes generated from neighbouring wind turbines. A review of these models can be found in the review paper by Göçmen (Gocmen et al. 2016) . Similarly there had been some research for estimating the flow over complex terrain (Barthelmie R.J. 2008; Bitsuamlak, Stathopoulos, and Bédard 2004; Cabezón D 2010). Most of the studies performed so far the interaction between turbine and terrain wakes have not caught much attention. One common approach for estimating the wake interaction is to superimpose wake due to

wind turbines and wake due to the complex terrain. This approach is adequate for moderately complex terrain, but not for complex terrain (Cabezón D 2010). The models, except computational fluid dynamics (CFD), developed up to present day for wind farm modelling do not explicitly take into account the complex interaction of flow due to wind turbines and the complex terrain.

The models for flow analysis over a complex terrain can be divided into two categories: "prognostic" and "diagnostic" models (Ratto 1996). Prognostic models solve time dependent mass, momentum and energy conservation equations. Since these models are based on the fundamental of mass, momentum (Navier-Stokes) and energy conservation, they are accurate and descriptive. In the past 50 years, these model has increasingly been developed and applied to wind flow over complex topography. However, the solution of the full set of equations is a computationally demanding task and the cost increases with domain size. Due to their complexity and computational cost, these models are normally run for only a few scenarios to understand the detailed description of the flow i.e. turbulence characteristics and local speed. Brief reviews on assessment of the wind farm performance over complex terrains have been provided by Politis (Politis et al. 2012). According to the authors, one of the major problems with Reynolds-Averaged Navier–Stokes (RANS) approach is turbulence models. These turbulence models have been validated in freestream flow conditions, rather than for atmospheric boundary layer conditions. Nevertheless, Reynolds averaged models predict reasonably accurate overall flow field around the complex terrain. The prognostic models have also been used for verification of simple models. The diagnostic models on the other hand, are based on a simplified approach and do not satisfy all the constraint such as mass, momentum and energy conservation. One of the objectives of the present work is to use these models to verify simple engineering models.

One of the major objectives of the ongoing KonWake project (NFR) is to develop a quasi-real time, user friendly and computationally light simulator for the flow field throughout a wind farm and the near surroundings. The model will be integrated with Kongsberg EmPower, which among other things, will optimize the total power from the wind farm and forecast the power production. SINTEF in collaboration with Kongsberg is developing the wind simulator in EmPower. The wind simulator mainly consists of a simplified model for flow over a complex terrain and turbine wake models. The simulator is designed to simulate wind conditions for a complex terrain in quasi-real time, and therefore it has to be computationally fast and also accurate enough to capture the essential global physics. Wind models for simulating flow over complex terrain based on diagnostic models are chosen due to the relative simplicity. Diagnostic models, either based on linearized Jackson and Hunt (JH) (Jackson and Hunt 1975) theory or mass consistent approaches (Sasaki 1970), are much faster than prognostic models, but the

accuracy is also affected due to unresolved physics. Software such as WAsP (WASP), based on linearized JH theory, predicts the wind accurately when the terrain is sufficiently smooth for the flow to be attached. However, these linear models are not accurate for complex terrain where flow separation dominates. Although some modifications, such as site ruggedness index (RIX) (Troen 1990), has been proposed in order to account for complex geometries, these modifications are still not able to capture the flow field for complex terrain. A wind model based on the mass-consistent approach (Sasaki 1970), satisfying the physical constraints of mass conservation has been chosen in the current research work. Verification of mass consistent model for complex terrain have been performed by Panjwani et al. (Panjwani B. 2015)

## MODEL DESCRIPTION

The mass consistent models are based on the numerical solution of the steady state three-dimensional continuity equation for the mean wind components. The momentum and energy equations are not solved explicitly, but introduced through observed wind data and by adding wake effects in the initial flow field. The mass consistent wind models are attractive for a computationally light simulator for several reasons: 1) they do not require much input data, 2) many simulations for different wind conditions can be performed efficiently 3) Accuracy can be improved via improved initial condition. However, according to Troen (Troen 1990), the JH approach should be preferred compared to the mass-consistent method, due to the fact that it uses more physical constraints than just the continuity equation. An advantage with the mass-consistent models is possibility to add more physical constraints in the initial field. Furthermore, steep slopes affect the JH approach more critically than mass-consistent models (Ratto 1996). The theoretical basis for mass consistent models was developed by Sasaki (Sasaki 1970). Mass consistent models have been applied to many other applications but mostly related to the wind, such as pollutant dispersion in the rural and urban areas where the geometry is complex, fire spreading in forest. Sherman (Sherman 1978) and Ross (Ross et al. 1988) applied mass conservation for understanding the atmospheric flows over complex terrain. Ratto (Ratto 1996) has provided a review on mass-consistent models over complex terrain. In the present work a mass consistent model "Wind 3D" developed by G. Montero et al. (Montero, Montenegro, and Escobar 1998; Wind3D) has been used. A brief theoretical development of a mass consistent model is provided here.

Since the wind model conserves mass, we start with the continuity equation

$$\nabla \cdot \vec{u} = 0 \quad (1)$$

Assuming a field is initialized with an initial condition  $u_0$ , but this initial field does not follow any physical constraint i.e. mass or momentum. Assuming  $\vec{u}$  is the intermediate field, then the least square

problem is formulated in the computational domain

$$E(\vec{u}) = \int \left[ \alpha_1^2 (\vec{u} - u_0)^2 + (\vec{v} - v_0)^2 + \alpha_2^2 (\vec{w} - w_0)^2 \right] d\Omega \quad (2)$$

The initial conditions,  $u_0$ , can be obtained either from the experimental measurements or from other theoretical methods such as CFD. The constants  $\alpha_1$  and  $\alpha_2$  are the Gauss precision moduli, which are also wind vector-partitioning factors in the horizontal and vertical directions respectively. These parameters are used for velocity adjustment in horizontal and vertical direction. The essential requirement in the mass consistent model is the minimization of the objective function:

$$E(u, v, w) = \min \left[ E(\vec{u}) + \int (\Phi \vec{\nabla} \cdot \vec{u}) d\Omega \right] \quad (3)$$

$$\begin{aligned} u &= u_0 + \lambda_1 \frac{\partial \Phi}{\partial x}; \\ v &= v_0 + \lambda_2 \frac{\partial \Phi}{\partial y} \\ w &= w_0 + \lambda_3 \frac{\partial \Phi}{\partial z} \end{aligned} \quad (4)$$

$$\lambda = [\lambda_1, \lambda_2, \lambda_3] \quad (5)$$

The continuity equation (Eq. 1) and the least square function are inserted in the objective function Eq. 3, which leads to the following equation

$$E(u, v, w) = \int \left[ \alpha_1^2 (\vec{u} - u_0)^2 + (\vec{v} - v_0)^2 + \alpha_2^2 (\vec{w} - w_0)^2 + \lambda \left( \frac{\partial u}{\partial x} + \frac{\partial v}{\partial y} + \frac{\partial w}{\partial z} \right) \right] d\Omega \quad (6)$$

The Lagrange multipliers method (Eq. 4) is employed to minimize Eq. 6, which minimum leads to form the Euler-Lagrange equation.

$$\frac{\partial^2 \Phi}{\partial x^2} + \frac{\partial^2 \Phi}{\partial y^2} + \frac{\partial^2 \Phi}{\partial z^2} = -\frac{1}{\lambda} \left( \frac{\partial u_0}{\partial x} + \frac{\partial v_0}{\partial y} + \frac{\partial w_0}{\partial z} \right) \quad (7)$$

A Dirichlet boundary condition ( $\lambda = 0$ ) at the lateral and top boundaries and the Neumann boundary condition ( $\frac{\partial \lambda}{\partial x} = 0$ ) for the terrain was employed.

The mathematical formulation in the mass-consistent model is a Poisson equation for the Lagrange multiplier (Eq.7) and it is discretised using the finite element method. The accuracy and speed of the model relies on the solution algorithm employed for solving the discretised Poisson equation and on the initial condition. Some common algorithms for solving the Poisson equation are Gauss-Seidel (GS), strongly implicit procedure (SIP), the alternating direction implicit (ADI), the conjugate gradient (CG) and the multigrid approach (Weng, Taylor, and Walmsley 2000). Wind3D

employs, a non-symmetric variant of the classical Conjugate Gradient method, "BICGSTAB", for solving the Poisson equation.

## GENERATION OF INITIAL FIELD

The accuracy of the results obtained from a mass consistent model depends on the initial condition. A most common way to obtain the initial field is to interpolate the 3D field from station data available on the site. The accuracy of the initial field will then be affected by both the accuracy of the station data and the interpolation algorithm. A general procedure for interpolation includes both horizontal and vertical interpolation. A horizontal interpolated velocity field is generated from the few station points, as a function of distance from the stations.

$$u(z) = \varepsilon \frac{\sum_{n=1}^N V_n / d_n^2}{\sum_{n=1}^N 1 / d_n^2} + (1 - \varepsilon) \frac{\sum_{n=1}^N V_n / |\Delta h_n|}{\sum_{n=1}^N 1 / |\Delta h_n|} \quad (8)$$

Where,  $V_n$  is the velocity observed at the  $n^{\text{th}}$  station.  $N$  is the number of stations considered in the interpolation,  $d_n$  is the horizontal distance from station  $n$  to the point in the domain where we are computing the wind velocity,  $|\Delta h_n|$  is the height difference between station  $n$  and the studied point, and  $\varepsilon$  is a weighting parameter which allows the assignment of weights to these interpolation criteria.

A logarithmic velocity profile (Eq.9) is used in vertical interpolation.

$$u(z) = \frac{v^*}{k} \left( \log \frac{z}{z_0} - \Theta \right) \quad (9)$$

The velocity profile (Eq.9) takes into account the friction velocity ( $v^*$ ), the effect of roughness ( $z_0$ ) and the atmospheric stability ( $\Theta$ ). The friction velocity is calculated using the velocities obtained from horizontal interpolation. For further details see the Wind3D manual (Wind3D)

The friction velocities were calculated from the reference plane and reference velocity. The reference plane and reference velocity were estimated from the station data.

## ACCOUNTING OF WAKE EFFECTS IN THE MASS CONSISTENT MODEL

The initial field described in the section above does not account for the local windward and leeward effects explicitly. Measurements data might be consisting implicitly some of effects but not the local effects. For explicitly accounting windward and leeward effects in the initial field, a method proposed by Röckle (Röckle 1990) has been utilized. According to Röckle (Röckle 1990) the flow field around an isolated object generates mainly three regions; displacement zone, cavity zone and wake zone. The displacement zone is established on the windward side of obstacles. The flow in this region might be separated, depending on the slope and aspect ratio of the obstacle on the windward side. The distance



of the displacement zone is determined by the obstacle's dimensions including slope. The cavity zone is the region on the leeward side of the obstacle where the flow separates. The detailed description of the model is provided here [17].

## TURBINE WAKE MODEL

The wake models have been developed for estimating the wake behind the wind turbines. An extensive review of the wake models have been carried out by DTU (Gocmen et al. 2016). Most commonly wake models used for the wake calculation are Jensen, Larsen, Fuga and Ainslie. For the current pragmatic modelling two wake models Jensen and Ainslie are used. Jensen model is one of the most popular models among engineering application due to simplicity. In Jensen model, it is assumed that the wake expanded linearly with a prescribed expansion factor. Modelling of the multiple wind turbine wake interaction is rather straightforward with Jensen model. In the Ainslie mode, the flow behind the turbine is treated in two separate regime, near wake and far wake regime. The near wake regime dominates around 2 to 3 time of rotor diameter from the wind turbine. In the near wake regime, flow expansion mainly take place due to the pressure recovery, and effect of turbulence mixing is not that significant. Ainslie proposed expansion of the wake in the near wake regime based on the experimental data. The wake expansion in the near wake depends on the motor thrust coefficient, ambient turbulence intensity, and wake width. In the far wake regime, pressure effects are not dominating and most of the wake expansion take place due to turbulence mixing. In this region, thin shear Navier stokes equations are solved to obtain both axial and radial velocities.

## WAKE SUPERPOSITION

In the offshore park, power production at any turbine mainly depends on the number of upstream turbines, wind speed and turbulence intensity. Wake produced from the upstream turbine strongly influences the approaching wind speed at the downstream wind turbines. The wake at the downstream turbine is estimating by superimposing the wake from the upstream wind turbines. For wake superposition mainly 2 approaches are used.

Linear Sum

$$\left(1 - \frac{u_{n+1}}{U_\infty}\right) = \sum_{j=1}^n \left(1 - \frac{u_{j+1}}{U_j}\right) \quad 10$$

Quadratic sum

$$\left(1 - \frac{u_{n+1}}{U_\infty}\right)^2 = \sum_{j=1}^n \left(1 - \frac{u_{j+1}}{U_j}\right)^2 \quad 11$$

Where n is the total number of upstream wind turbines and  $u_{n+1}$  is velocity at the downstream wind turbine.  $U_\infty$  is free stream wind speed.  $j$  is an index for  $j^{\text{th}}$  wind turbine.

In onshore wind park the effect of terrain wake is very important. In the present study, the wake superposition approach is extended to account for the terrain wake. In

this model we assumed that wake from the terrain behave similar to the wind turbine wake. The terrain and wind turbine wake interaction is estimated using following approaches.

Linear Sum

$$\left(1 - \frac{u}{U_\infty}\right) = \left(1 - \frac{u_{ter}}{U_\infty}\right) + \left(1 - \frac{u_{tur}}{U_\infty}\right) \quad 12$$

Quadratic sum

$$\left(1 - \frac{u}{U_\infty}\right)^2 = \left(1 - \frac{u_{ter}}{U_\infty}\right)^2 + \left(1 - \frac{u_{tur}}{U_\infty}\right)^2 \quad 13$$

Where subscript ter is used for the terrain and tur is used for the wind turbines.

## VALIDATION OF THE MASS CONSISTENT APPROACH

The validation of the mass consistent approach has been done in an earlier work with Bolund measurement hill data (Panjwani B. 2015). In the current publication, flow over the complex terrain (shown in Figure 1) is performed using CFD and also using mass consistent model. It should be mentioned that the flow over a complex terrain is mainly governed by conservation of mass and momentum for an isothermal system. The mass consistent approach only accounts for the mass conservation, and momentum conservation is not accounted in the mass consistent model. A major difference in the flow fields calculated by CFD and mass consistent models are normally obtained on the leeward and windward side of the hill.

## FLOW SIMULATIONS OF THE TERRAIN

Accurate and reliable flow simulations of wind flow over a complex terrain are important for a wide range of applications, and especially for wind resource assessment and condition monitoring of an operational wind farm. In the present study OpenFoam (OpenFoam 2009) and mass consistent simulation of the entire wind farm located on a complex terrain is carried out. The computational geometry of the complex terrain is based on GIS data with a horizontal resolution of 2 m. The maximum height of the terrain surface is about 300 m above sea level and the extent of the domain is 18 km in the longitudinal direction and 15 km in the lateral direction. The terrain geometry was generated from orography data using MATLAB. The surfaces are discretised with triangular cells that provided the basis for the generation of 3D hexahedral cells for application of the control volume method. The surface geometry of terrain was imported into the OpenFoam pre-processor. The size of the computational box in longitudinal, lateral and normal directions was (18 km x 15 km x 2 km). The mesh was refined close to the terrain surface and the initial mesh includes 2e06 hexahedrons. The accuracy in the results improves with finer mesh. The computational grid (Figure 2) is generated using the TerrainBlockMesher mesh generator (TerrainBlockMesher). A problem with the OpenFoam build-in mesh generator, "snappy hex approach", is generation of unstructured mesh near to the terrain

surface. The mesh on the terrain surface is highly irregular, and this is a major source of numerical error near to the boundary surface. On the other hand TerrainBlockMesher generates high quality of the meshes for the complex geometries. The TerrainBlockMesher first generates a basic mesh, which is mainly an extensive blockMeshDict file consisting of many multi blocks. The number of mesh points for each box is given in the control parameter available with TerrainBlockMesher. This technique allows a large degree of control over the size and shape of the computational cells. This grid technique only uses hexahedral and prismatic cells, and no tetrahedral and pyramid cells. In this case, all cell faces are either vertical or parallel to the underlying terrain surface. This reduces the numerical discretisation errors and allows the use of a second-order discretisation scheme without compromising convergence. This technique has been successfully applied in other CFD studies to model complex urban areas (Peralta et al. 2014).

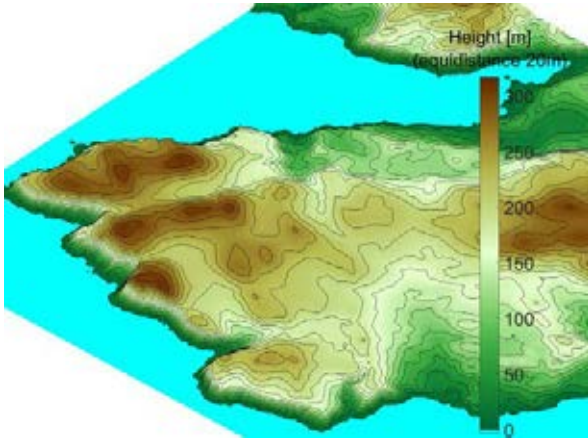


Figure 1: Complex terrain located in Norway

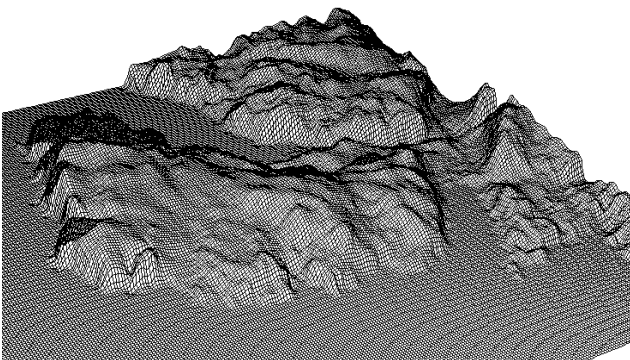


Figure 2: Grid on the terrain using TerrainBlockMesher

### Simulation of the complex terrain

The 3D steady Reynolds-Averaged Navier–Stokes (RANS) equations are solved with the open source CFD code "OpenFoam". The realizable  $k-\epsilon$  model is used for estimating the turbulent kinetic energy and turbulent dissipation. Second-order discretization schemes are used for both the convective and viscous terms of the

governing equations. The SIMPLE algorithm is used for pressure-velocity coupling.

In reality, turbulent kinetic energy and dissipation varies with height above the terrain. The variation in turbulent kinetic energy and dissipation depend on the atmospheric condition. However, in the present study a constant fixed value of turbulent kinetic energy and dissipation rate were used at the inlet of the domain. The inlet turbulent intensity was 0.15 and the turbulent viscosity ratio was 0.2. Furthermore, the default wall functions available in OpenFoam were employed.

### Inlet Boundary condition

A logarithmic boundary condition have been used at the inlet to the boundary of the domain. A logarithm velocity profile, as shown in Figure-3 and described in Eq. (14), is used to approximate the atmospheric boundary layer (ABL).

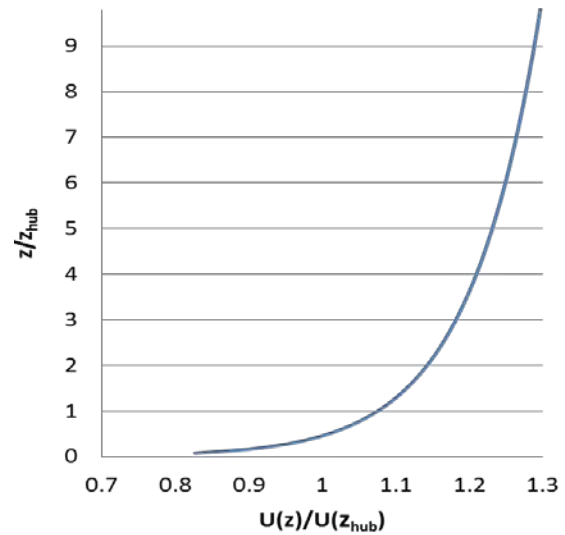


Figure 3 : Vertical profiles of the atmospheric boundary layer (ABL)

$$U = \frac{u_*}{\kappa} \ln \left( \frac{z}{z_o} \right) \quad 14$$

Where  $\kappa$  is the von Kármán constant,  $z$  is height,  $z_o$  is the aerodynamic roughness length and  $u_*$  is the friction wind speed defined by  $\sqrt{\tau/\rho}$ , is the wind stress, and  $\rho$  is air density and  $\tau$  is shear stress at the ground surface.

There are mainly two types of roughness (Blocken 2015); (1) the roughness of the terrain that is included in the computational domain, which is part of the terrain geometry and (2) the roughness of the terrain that is not included in the computational domain i.e.  $z_o$ . This roughness is accounted through boundary layer profile (Eq.14). The knowledge of the roughness  $z_o$  is important because it determines the shape of the inlet profiles of mean wind speed and turbulence properties.

The roughness,  $z_o$  of the surface was around 0.03 m in the current simulations. We have assumed that the selected terrain is relatively smooth and it does not have any dense trees and therefore the chosen roughness should be enough.

A no-slip boundary condition is used on the bottom terrain surface. On the sides and top surface of computational domain a free slip boundary condition is applied. At the exit of the computational domain an outlet boundary condition is used.

## Results and Discussion

CFD studies of flow over complex terrain that consists of an irregular succession of hills and valleys are presented in this section. The CFD data files obtained from the OpenFoam was converted into FLUENT format for visualization purpose. The velocity near to the terrain surface is shown in Figure 4. Dominating flow changes near the terrain surface due to the terrain topography is clearly visible.

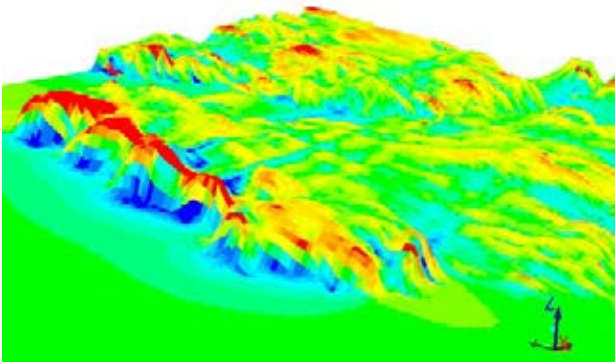


Figure 4: Contour plot of velocity near the terrain surface using OpenFoam

Flow accelerates at the upper edge of the mountain and deaccelerates on the leeward side. A mass consistent simulation of the same terrain was carried out, and a contour plot of the velocity near the terrain surface is shown in Figure 5.

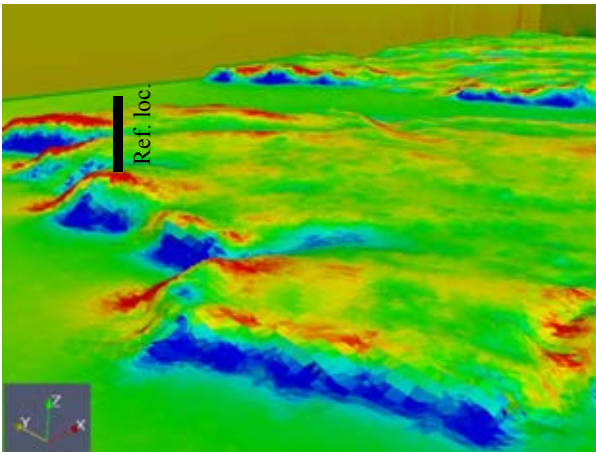


Figure 5: Contour plot of velocity near the terrain surface using mass consistent model

The estimated flow field using both approaches show roughly similar behavior (see Figure 4 and 5). The velocity profile at different downstream positions (along x direction) from reference location is shown in Figure 6, 7 and 8 for mass consistent and CFD results. The reference location is marked in Figure 5. The mass

consistent model under-predicts the velocity at most locations. The reason for this discrepancy is unresolved momentum term in the mass consistent model.

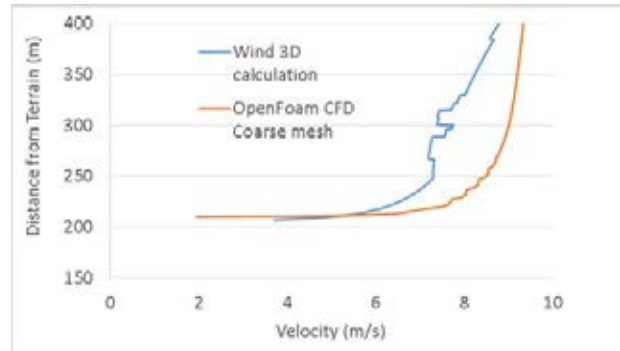


Figure 6: Velocity profile along vertical direction from the terrain surface at reference location (reference location is shown in Figure 5)

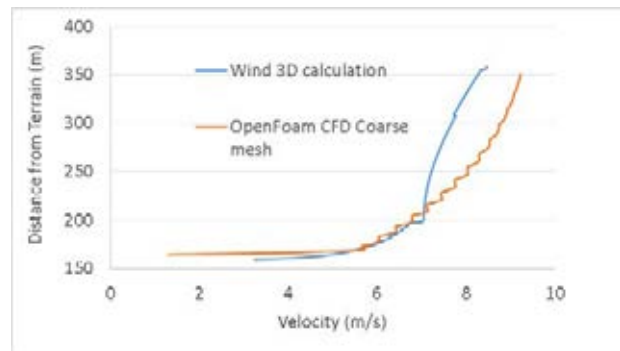


Figure 7: Velocity profile along vertical direction from the terrain surface at 2 km along x direction from reference location (reference location is shown in Figure 5)

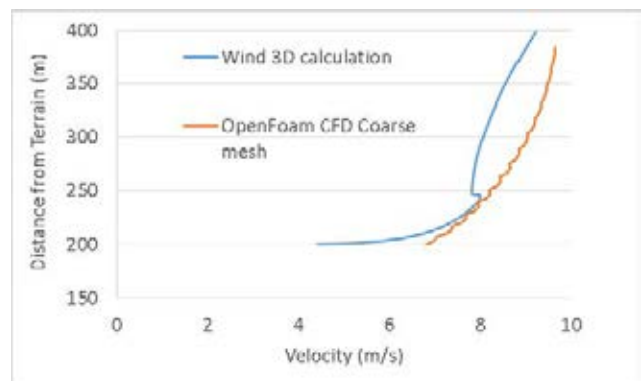


Figure 8: Velocity profile along vertical direction from the terrain surface at 3 km along x direction from reference location (reference location is shown in Figure 5)

Method for coupling the terrain and turbine wake has been described in theory section. In order to verify the approach, a simplified geometrical model setup was generated. In this simplified setup, one small turbine

was mounted on the Bolund hill geometry as shown in Figure 9.

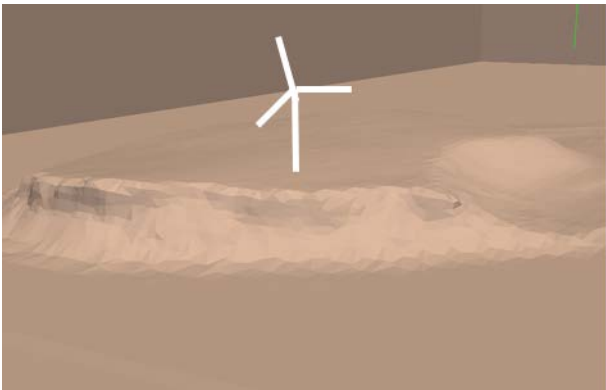


Figure 9: Turbine location on the Bolund terrain

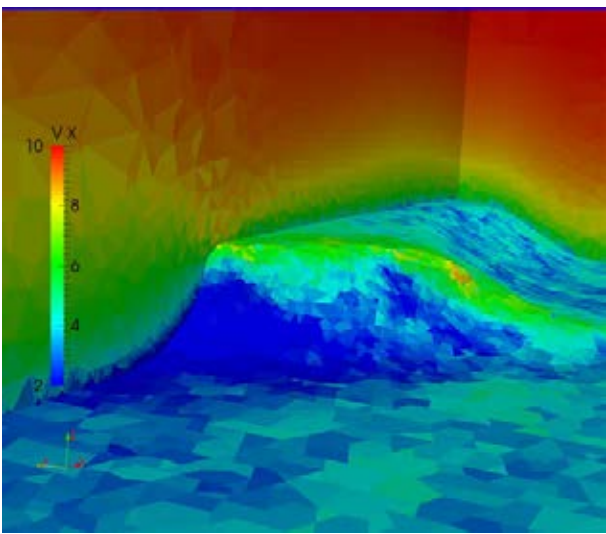


Figure 10: Contour plot of the velocity near the Bolund terrain without wind turbine

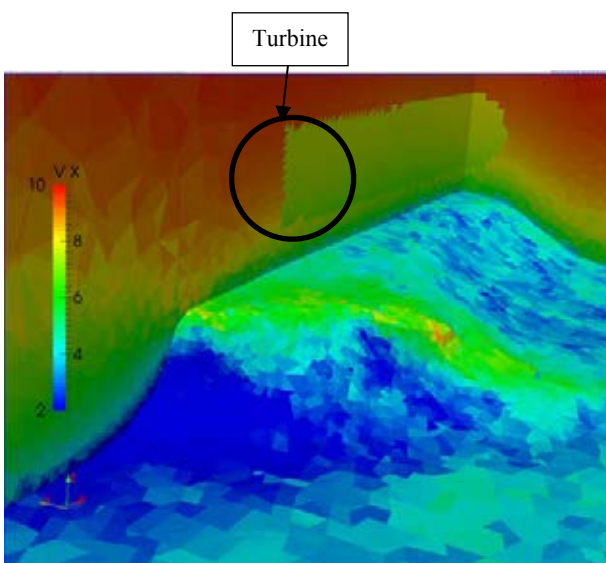


Figure 11: Contour plot of the velocity on the terrain and in turbine cross section

Mass consistent simulation of the Bolund hill without wind turbine was performed and velocity distribution

for this configuration is shown in Figure 10. Wake behind the wind turbine was calculated using Jensen approach. Wake from the wind turbine and wake from the terrain were superimposed using approach described in earlier section. The resulting flow field without wind turbine is shown in Figure 10. The resulting wind flow field due to the turbine and terrain wake interaction is shown in Figure 11. It can be seen that the flow over the terrain interacts with wake generated from the wind turbine. In the present study superposition of terrain and turbine wakes is presented. Verification of the approach is under progress and hopefully, the verification results will be presented in the conference.

## Conclusions

CFD and mass consistent simulations of flow over complex terrain have been carried out. The mass consistent model is able to capture local acceleration and deceleration of flows due to terrain geometry. However, predicted wind velocities using the mass consistent are under-predicted compared with CFD data. The under-prediction of the velocity is mainly due to un-accounting of the momentum equation in the mass consistent model. In the mass consistent model the displacement zone, windward and leeward effects are not considered in the initial field. Accounting for these effects might improve the results. Integration approach of the wind turbine wakes and terrain wake is presented.

## References

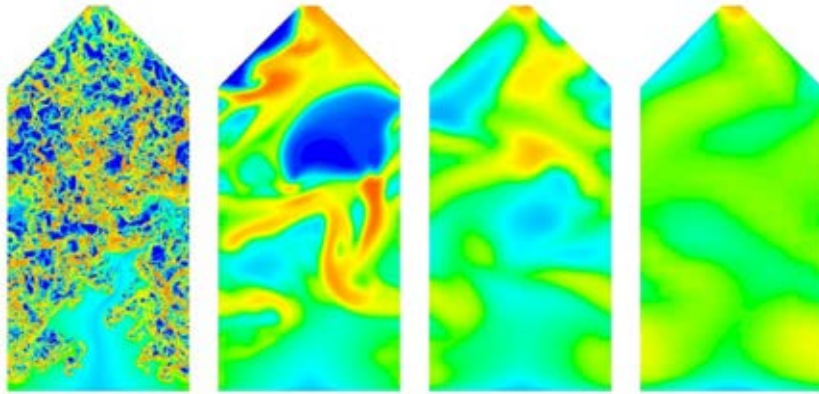
- Barthelmie R.J., Frandsen S.T., Rathmann O. , Hansen K. . 2008. "Flow and wakes in large wind farms in complex terrain and offshore." In *EWEA 2008*. Brussels.
- Bitsuamlak, G. T., T. Stathopoulos, and C. Bédard. 2004. 'Numerical Evaluation of Wind Flow over Complex Terrain: Review', *Journal of Aerospace Engineering*, 17: 135-45.
- Blocken, Bert. 2015. 'Computational Fluid Dynamics for urban physics: Importance, scales, possibilities, limitations and ten tips and tricks towards accurate and reliable simulations', *Building and Environment*, 91: 219-45.
- Cabezón D, Hansen KS, . Barthelmie RJ. 2010. "Analysis and validation of CFD wind farm models in complex terrain Effects induced by topography and wind turbines." In *EWEC2010*. Warsaw, Poland.
- Gocmen, T., P. Van der Laan, P. E. Rethore, A. P. Diaz, G. C. Larsen, and S. Ott. 2016. 'Wind turbine wake models developed at the technical university of Denmark: A review', *Renewable & Sustainable Energy Reviews*, 60: 752-69.
- Jackson, P. S., and J. C. R. Hunt. 1975. 'Turbulent wind flow over a low hill', *Quarterly Journal of the Royal Meteorological Society*, 101: 929-55.
- Montero, G., R. Montenegro, and J. M. Escobar. 1998. 'A 3-D diagnostic model for wind field adjustment', *Journal of Wind Engineering and Industrial Aerodynamics*, 74-76: 249-61.

NFR.

<https://www.forskningsradet.no/prosjektbanke/n/#!/project/235754/en>, Accessed 28/04/2017.

- OpenFoam. 2009. *OpenFOAM. The Open Source CFD Toolbox. User Guide* (Free Software Foundation, Inc.).
- Panjwani B. , Lund B.F. Røkenes R., Popescu M. and Samseth J. 2015. "Fast response simulator for flow over a complex terrain: A case study." In *EWEA 2015*. Paris.
- Peralta, C., H. Nugusse, S. P. Kokilavani, J. Schmidt, and B. Stoevesandt. 2014. 'Validation of the simpleFoam (RANS) solver for the atmospheric boundary layer in complex terrain', *ITM Web of Conferences*, 2.
- Politis, E. S., J. Prospathopoulos, D. Cabezón, K. S. Hansen, P. K. Chaviaropoulos, and R. J. Barthelmie. 2012. 'Modeling wake effects in large wind farms in complex terrain: the problem, the methods and the issues', *Wind Energy*, 15: 161-82.
- Ratto, C.F. 1996. "An overview of mass-consistent models. Modeling of Atmosphere Flow Fields." In *D. P. Lalas and C. F. Ratto, Eds, World Scientific Publications*, 379–400.
- Ross, D. G., I. N. Smith, P. C. Manins, and D. G. Fox. 1988. 'Diagnostic Wind Field Modeling for Complex Terrain: Model Development and Testing', *Journal of Applied Meteorology*, 27: 785-96.
- Röckle, R. 1990. 'Determination of flow relationships in the field of complex building structures (in German)', der Technischen Hochschule.
- Sasaki, Yoshikazu. 1970. 'SOME BASIC FORMALISMS IN NUMERICAL VARIATIONAL ANALYSIS', *Monthly Weather Review*, 98: 875-83.
- Sherman, Christine A. 1978. 'A Mass-Consistent Model for Wind Fields over Complex Terrain', *Journal of Applied Meteorology*, 17: 312-19.
- TerrainBlockMesher.  
<https://github.com/jonasIWES/terrainBlockMesher>, Accessed 28/04/2017.
- Troen, I.B. 1990. "A high resolution spectral model for flow in complex terrain." In *Ninth Symposium on Turbulence and Diffusion*. Roskilde.
- WASP. <http://www.wasp.dk/>, Accessed 28/04/2017.
- Weng, W., P. A. Taylor, and J. L. Walmsley. 2000. *J. Wind. Eng. Ind. Aerodyn.*, 86: 169.
- Wind3D. <http://www.dca.iusiani.ulpgc.es/Wind3D/en/>  
Accessed 28/04/2017.

# FLUIDIZED BED





## SIMULATION OF CHEMICAL LOOPING COMBUSTION IN A DOUBLE LOOPING FLUIDIZED BED REACTOR WITH CU-BASED OXYGEN CARRIERS

Yuanwei ZHANG<sup>1\*</sup>, Øyvind LANGØRGEN<sup>2†</sup>, Inge SAANUM<sup>2‡</sup>, Zhongxi CHAO<sup>3§</sup>, Hugo A.

JAKOBSEN<sup>1¶</sup>

<sup>1</sup>NTNU Department of Chemical Engineering, 7034 Trondheim, NORWAY

<sup>2</sup>SINTEF Energy Research, Sem Sælands vei 11, 7034 Trondheim, Norway

<sup>3</sup>Safetec Nordic AS, 7037 Trondheim, Norway

\* E-mail: yuanwei.zhang@ntnu.no

† E-mail: oyvind.langorgen@sintef.no

‡ E-mail: inge.saanum@sintef.no

§ E-mail: zhongxi.chao@safetec.no

¶ E-mail: hugo.a.jakobsen@ntnu.no

### ABSTRACT

Chemical looping combustion (CLC) is an attractive technology that produces a pure CO<sub>2</sub> stream and therefore the CO<sub>2</sub> can be readily recovered by condensing water vapour. In order to understand the physical phenomena and to explore the chemical process performance of the CLC process, a CFD model has been developed. The model is implemented numerically in an in-house code including the kinetic theory of granular flow and reaction models. Methane is used as fuel and CuO is chosen as oxygen carrier. This process is configured with an air reactor and a fuel reactor. The two reactors are simulated by a sequential approach. The connection between the two reactors is realized through time-dependent inlet and outlet boundary conditions. The widely used drag models were selected to examine their effects on the flow behaviour. The results indicating that the cluster effect in the FR is higher than in the AR. The frequency factor in the reaction model was varied to fit with the experimental measurements. The predicted result with the frequency factor of  $1.35 \times 10^{-3}$  gives a reasonable prediction in comparison to the experimental data.

**Keywords:** CFD, Double loop circulating fluidized bed, Drag model, Reactive flow .

### NOMENCLATURE

#### Greek Symbols

$\alpha_k$	Volume fraction of phase $k$ , [-]
$\beta$	Inter-phase momentum transfer coefficient, [kg/m <sup>3</sup> s]
$\gamma_s$	Collisional energy dissipation, [J/m <sup>3</sup> s]
$\Gamma$	Interfacial mass transfer rate, [kg/m <sup>3</sup> s]
$\epsilon_g$	Turbulent energy dissipation rate, [m <sup>2</sup> /s <sup>3</sup> ]
$\Theta$	Granular temperature, [m <sup>2</sup> /s <sup>2</sup> ]
$\kappa_s$	Conductivity of granular temperature, [kg/ms]
$\lambda_k$	Thermal conductivity of phase $k$ , [m <sup>2</sup> /s]
$\mu_k$	Viscosity of phase $k$ , [kg/ms]
$\nu_j$	Stoichiometric coefficient, [-]
$\rho_k$	Density of phase $k$ , [kg/m <sup>3</sup> ]
$\rho_M$	Molar density, [mol/m <sup>3</sup> ]
$\tau$	Time for complete solid conversion, [s]
$\bar{\tau}_k$	Stress tensor of phase $k$ , [N/m <sup>2</sup> ]
$\bar{\tau}_t$	Turbulent stress tensor, [N/m <sup>2</sup> ]
$\omega$	Mass fraction, [-]

#### Latin Symbols

A Frequency factor, [mol<sup>1-n</sup>m<sup>3n-2</sup>/s].

$C$	Gas concentration, [mol/m <sup>3</sup> ].
$C_1, C_2, C_b, C_\mu$	Turbulence model parameter, [-].
$C_d$	Drag coefficient, [-].
$d_s$	Particle diameter, [m].
$D_{ji}$	Binary diffusion coefficient, [m <sup>2</sup> /s].
$D_{k,j}$	Diffusion coefficient for component $j$ in phase $k$ , [m <sup>2</sup> /s].
$e_{ss}$	Particle restitution coefficient, [-].
$E$	Activation energy, [kJ/mol].
$\vec{g}$	Gravity acceleration, [m/s <sup>2</sup> ].
$g_0$	Radial distribution function, [-].
$\bar{I}$	Unit tensor, [-].
$k$	Reaction rate coefficient, [mol <sup>1-n</sup> m <sup>3n-2</sup> /s].
$k_g$	Gas turbulent kinetic energy, [m <sup>2</sup> /s <sup>2</sup> ].
$K$	Scale factor, [-].
$\vec{M}_k$	Interfacial momentum transfer, [kg/m <sup>2</sup> s <sup>2</sup> ].
$M$	Mole mass, [kg/kmol].
$n$	Reaction order, [-].
$p_k$	Pressure of phase $k$ , [Pa].
$Pr$	Prandtl number, [-].
$r$	Reaction rate, [mol/m <sup>3</sup> s].
$r_g$	Radius of a grain, [m].
$R$	Gas constant, [J/mol <sup>-1</sup> K <sup>-1</sup> ].
$Re_p$	Particle Reynolds number, [-].
$S_t$	Turbulent kinetic energy production, [kg/ms <sup>3</sup> ].
$t$	Time, [s].
$T$	Temperature, [K].
$\vec{v}_k$	Velocity of phase $k$ , [m/s].
$V_M$	Molar volume, [m <sup>3</sup> /mol].
$X$	Gas conversion, [-].
$z$	Axial coordinate, [m].

#### Sub/superscripts

0	Initial.
B	Bulk.
dilute	Dilute.
e	Effective.
g	Gas.
i	Reaction number.
k	Gas ( $k = g$ ) or solid ( $k = s$ ) phase.
m	Molecular.
max	Maximum.
mf	Minimum fluidization.
s	Solid.
t	Turbulent.



## INTRODUCTION

Chemical-looping combustion (CLC) is an efficient and low cost combustion process that can be explored to limit CO<sub>2</sub> emissions. This new type of combustion is a two-step combustion process. Typically, it consists of two interconnected fluidized bed reactors, the fuel reactor and the air reactor. A solid oxygen carrier (OC) gets oxidized and reduced in a cyclic manner, carrying the oxygen from one reactor to the other. First, the fuel is introduced to the FR and reacts with the oxidized OC, to give CO<sub>2</sub> and steam. The oxidized OC being reduced from MeO<sub>α</sub> to MeO<sub>α-1</sub>. In a subsequent step, this oxygen carrier is reoxidized to its initial state with air in the AR, from MeO<sub>α-1</sub> to MeO<sub>α</sub>. The overall reaction obtained summing the oxidation and reduction of the OC is equivalent to the conventional combustion of the fuel and releases exactly the same amount of energy. Since the mixing of fuel and air is avoided, CO<sub>2</sub> will inherently not be diluted with nitrogen (Ishida and Jin, 1996).

In order to get sufficiently high fuel conversion, enhance gas-solid contact and realize flexible operation, SINTEF Energy Research and the Norwegian University of Science and Technology have designed a double loop circulating fluidized bed (DLCFB) reactor for the CLC process, as shown in Figure 1. The design is sized to be used with gaseous fuel. It consists of two circulating fluidized beds interconnected by means of divided loop seals and a bottom extraction. The fluidizing gas (methane in the FR and air in the AR) is fed from bottom of the reactors. The solid outflow from one reactor will inject into the bottom of the other reactor through the cyclones and divided loop seals. The propose of the divided loop seal is both to avoid the gas mixing between the two reactors and to lead flow of solids entrained by one reactor into the other one or recirculate it back to the reactor of origin. The air reactor as well as the fuel reactor are operated in the turbulent or fast fluidization regime for a better gas-solid contact. This special design is meant to be flexible with respect to OCs and to be extrapolated to other chemical looping applications. In addition, the arrangement is compact in order to ease the up-scaling as well as for the prospective of pressurizing the reactor as a further step.

Computational fluid dynamics (CFD) is expected to play an important role in studying the hydrodynamic and chemical process performance of gas-solid system. In order to understand the physical phenomena, explore the reactive performance of the CLC process in the DLCFB system, it is beneficial to develop a simulation model, which further can be used to optimize the operating conditions, and for scale-up and design of industrial scale reactors.

In this work, a reactive multiphase CFD model for an interconnected DLCFB reactor has been developed and implemented using an in-house Fortran code. Euler-Euler approach with the kinetic theory of granular flow (KTGF) has been selected. Methane is used as the gaseous fuel and CuO is chosen as OC. The main objective of this investigation is to validate the model based on the real experimental data and make preparation for the further research.

## MODEL DESCRIPTION

A two-fluid reactive flow model based on the KTGF implemented in an in-house code is used to describe the hydrodynamics and the reacting system in the fluidized reactors. In the two-fluid model, each phase is described by a set of governing equations and closures. For the gas phase, the transport equations can be derived by adopting suitable averaging process for local instantaneous equations, while the transport

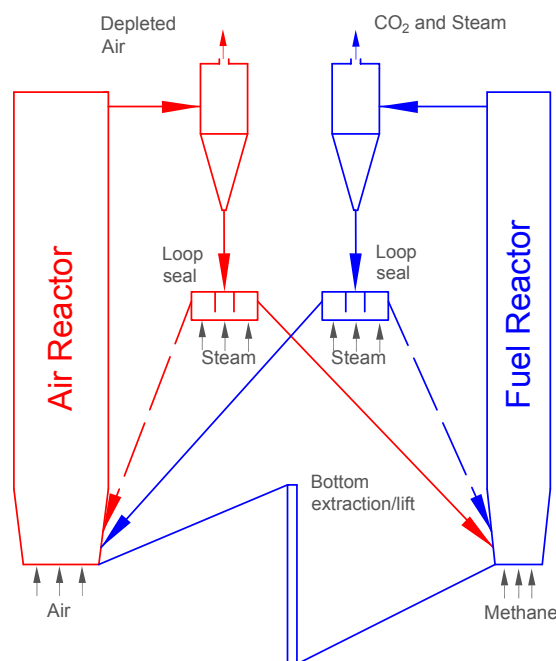


Figure 1: Sketch of the DLCFB reactor.

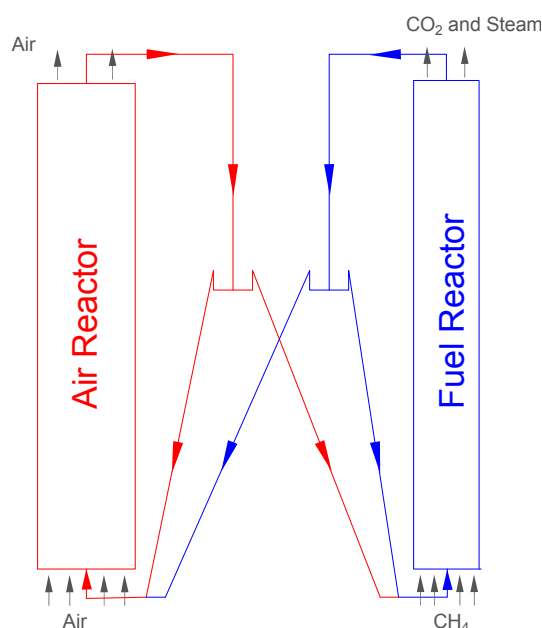
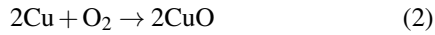
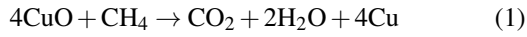


Figure 2: Sketch of the DLCFB reactor.

equations for solid phase originate from the ensemble average of a single-particle quantity over the Boltzmann integral-differential equation. Detailed descriptions of the model can be found in (Jakobsen, 2014). The governing equations are summarised in Table 1. The standard  $\kappa - \epsilon$  turbulence model is chosen for characterizing the gas phase turbulence phenomena, the corresponding closure models are shown in Tables 2 and 3. The KTGF is adopted to derive the physical properties of solid phase by introducing the granular temperature,  $\Theta$ . The two phases are coupled through the interfacial momentum transfer, which is dominated by the drag force. In this study, the most commonly used drag coefficient models proposed by Gidaspow (Gidaspow, 1994), Syamlal and O'Brien (Syamlal and O'Brien, 1988) and Gibilaro (Gibilaro *et al.*, 1985) are selected to examine their influence on the simulated results. In addition, McKeen and Pugsley (McKeen and Pugsley, 2003) model was used for accounting the cluster effect. The description of the drag models are given in the Appendix A. The internal phases constitutive equations are listed in Tables 4 and 5.

The oxygen carrier material used in the simulation is a copper oxide based material with a CuO content of 14.7%. The particle density and diameter are 1700 Kg/m<sup>3</sup> and 149  $\mu\text{m}$  respectively. One step reactions are assumed both for the fuel and air reactors and given as follows:



The particle was assumed to be composed by spherical grains of CuO. The shrinking core model (SCM) with the reaction controlled by the chemical reaction in the grain was applied. The equations that describe the reaction model are follows (Abad *et al.*, 2007):

$$X = \frac{t}{\tau} \quad (3)$$

where  $X$  is the degree of conversion,  $\tau$  is the time for complete conversion of the carrier and is calculated from:

$$\tau = \frac{r_{g,\text{CuO}}}{vV_{M,\text{CuO}}kC^n} \quad (4)$$

$C, n, v, r_g$  and  $V_M$  represent the concentration of the gas reactant, reaction order, stoichiometric factor, mean radius of the grains, and molar volume, respectively. The reaction constant  $k$  follows:

$$k = A \exp(-E/RT) \quad (5)$$

where  $A$  is the pre-exponential factor of the rate constant, also known as the frequency factor.  $E$  is the activation energy, and  $R$  is the constant of the ideal gas ( $R = 8.314\text{J/mol}^{-1}\text{K}^{-1}$ ).

The reaction rate of equation 1 and 2 is expressed as follows:

$$(-r)_i = \left( \frac{\rho_{M,\text{CuO}} \alpha_s \omega_{\text{CuO}}}{v} \frac{dX}{dt} \right)_i \quad (6)$$

where  $i$  and  $\rho_M$  represent the  $i$ th reaction and molar density. The detailed kinetic parameters are listed in table 6 (Abad *et al.*, 2007).

The source term in the species mass balance equation for the  $j$  th species in the gas can be modelled by:

$$\Gamma_{g,j}^\omega = v_j M_j r \quad (7)$$

The mass transfer between the gas phase and the solid phase is calculated as following the relation proposed by Jung and Gamwo (Jung and Gamwo, 2008):

$$\Gamma_g = v_{\text{O}_2} M_{\text{O}_2} r = -\Gamma_s \quad (8)$$

### Numerical implementation of the coupling between reactors

The chemical looping combustion process is simulated by utilizing the DLCFB system as described above. A 2D plane geometry is chosen for the simulation of the fuel and air reactors, which is shown in Figure 2, having the same dimensions as the experimental setup. The computational domain is meshed by using uniform grids in each direction.

Two different sets of coordinates and parameters are adopted to solve the governing equations for the AR and the FR respectively. The solid flowing out of the AR is fed into the bottom of the FR, and in a similar way all the solids that exited at the outlet of FR will be injected into the bottom of the AR. The exchange of the solid flow between the reactor units is realized through the time-dependent inlet and outlet boundary conditions. At each simulation time step, the processes in the two risers are simulated by a sequential approach, the solid flux of the inlet of one riser is calculated from the solid flowing out of the outlet of the other riser with the same OC condition. In the experiment, this kind of continuous solid exchange is achieved by means of cyclones, divided loop-seals and the bottom lift. The cyclones are neglected in the simulation by assuming the efficiency of the cyclones are equal to one. The bottom extraction/lift is replaced by an internal recirculation mechanism in order to keep the mass balance inside each reactor. In this way, a full loop is fulfilled for one time step. Then, another computation loop for next time step will run repeatedly.

### Initial and boundary condition

Initially, there is no gas flow in the reactor and the bed is at rest with a particle volume fraction of 0.4. A uniform plug gas flow is applied at the inlets of the reactors, the inlet solid flux of one of the reactors is kept consistent with the outlet solid flux of the other one with a prescribed solid volume fraction at the inlet. The normal velocities at all boundaries are set to zero. No-slip wall boundary condition is set for the gas phase while the solids are allowed to slip along the wall, following the equation (9) from (Jakobsen, 2014).

$$\vec{v}_{s,z}|_{\text{wall}} = \frac{d_s}{\alpha_s^{1/3}} \frac{\partial \vec{v}_{s,z}}{\partial r} \quad (9)$$

where  $\vec{v}_{s,z}$  is the axial velocity of the particles.  $r$  denotes the direction normal to the wall.

For all the scalar variables but pressure, Dirichlet boundary conditions are used at the inlets, while Neumann conditions are used at the other boundaries. For the pressure correction equations, all the boundaries except outlet, Neumann conditions are adopted. At the outlet a fixed pressure (101325 Pa) is specified.

### Numerical Procedure

The two-fluid model equations are discretized by finite volume method and implemented in a Fortran program. The algorithm is based on the work by Lindborg (Lindborg, 2008) and Jakobsen (Jakobsen, 2014). The second order central differential scheme is used to discretize the diffusion terms. In order to reduce the oscillation and keep higher-order accuracy of the numerical solution, a total variation diminishing

(TVD) scheme is employed for discretizing the convection term (van Leer, 1974). In this scheme, cell face values are calculated from the combination of upwind scheme part and a suitable anti-diffusive part, which controlled by a smoothness function. In this way, a higher-order discretization scheme is used in smooth regions and reduce to the first order at local extrema of the solution. The upwind part is treated fully implicitly while the anti-diffusive part is treated explicitly. The SIMPLE algorithm for multiphase flow is selected for the pressure-velocity coupling (Jakobsen, 2014). Due to the strong coupling of the two phases, the coupling terms are handled specially in the discretized transport equations, and then the coupled equations are solved simultaneously by using a coupled solver. The species mass balance equations are solved by applying a fractional step scheme which decouples the chemistry (i.e., kinetics) and the transport (i.e., convection and diffusion) terms. All the linear equation systems are solved by the preconditioned Bi-conjugate gradient (BCG) algorithm (Lindborg, 2008).

## RESULTS

The chemical looping combustion experiments have been conducted in the DLCFB system at SINTEF Energy Research in Trondheim. Pressure transducers were placed along the reactor bodies to measure the local pressure distribution.  $\text{CH}_4$ ,  $\text{CO}_2$  and  $\text{O}_2$  concentration were measured in the exhaust from the FR and the AR. The operating and initial conditions of the simulation are adopted the same as the actual experiment, summarized in Table 8. The first part of this section presents the validation of the hydrodynamics and reactive model by using different drag models. Then the chemical process performances were analysed. The simulations were conducted for 20 seconds of real time. To ensure the initial transient effects are not included in the analysis, the last 10 seconds of the simulations are used for extracting the mean results.

### Verification of the hydrodynamic model

For the simulation procedure, grid sensitivity study was carried out in advance in previous work by Zhang et al (Zhang *et al.*, 2017). The drag model plays a critical role for the successful simulation of the hydrodynamics in a gas-solid system. Three widely used drag models were selected to examine their effects on the flow behaviour.

Figure 3 shows the predicted axial profiles of the pressure in the FR. The corresponding axial solid concentration distribution can be found in Figure 5. It can be seen that the Gidaspow (Gidaspow, 1994), Syamlal and O'Brien (Syamlal and O'Brien, 1988) models give nearly identical results, which are overestimate the inter-phase momentum transfer in the FR, and hence predict a more uniform distribution of solids across the riser. That is why the predicted pressure was far away from the experimental data, especially in the upper part of the reactor. The discrepancy was ameliorated a little by using the Gibilaro (Gibilaro *et al.*, 1985) model, but still overestimate the interphase drag force. This could be explained by the cluster effect inside the FR. The existence of cohesive interparticle forces would lead to grouping of particles, resulting in larger effective particle sizes, and hence reduced fluid-particle drag forces.

In order to account for the aggregation of particles, some modifications have been proposed. McKeen and Pugsley et al. (McKeen and Pugsley, 2003) proposed an empirical method to reduce the Gibilaro (Gibilaro *et al.*, 1985) drag correction using a constant scale factor,  $K$ . This scale factor

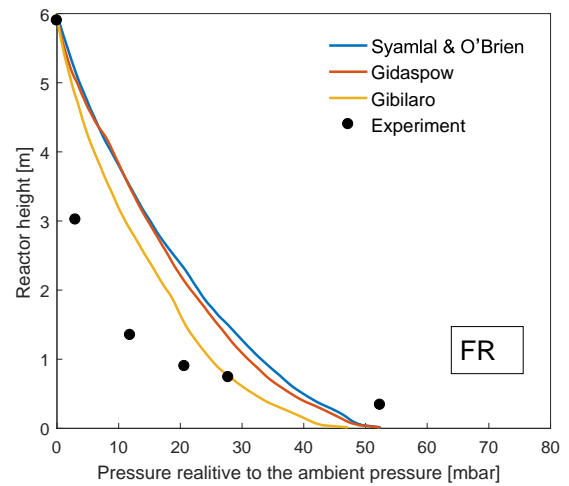


Figure 3: Axial pressure distribution.

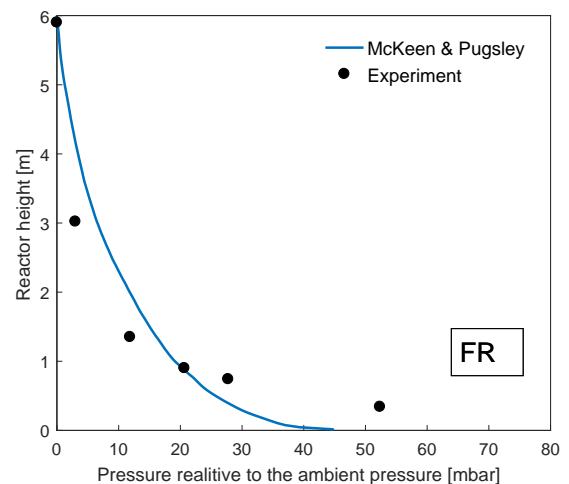


Figure 4: Axial pressure distribution.

could be adjusted to take in to account the effect of interparticle cohesive forces on particle agglomeration. In this study, the scale factor is set to 0.6.

The predicted axial pressure and solid distribution with McKeen and Pugsley model (McKeen and Pugsley, 2003) shown in the Figure 4 and Figure 5 respectively. It can be seen that the predicted results calculated by McKeen and Pugsley model (McKeen and Pugsley, 2003) are in good agreement with the experimental data, except for the reasonable deviation occurring in the dense bottom zone, which can be mostly attributed to the incomplete 2-D description of a real 3-D geometry according to our numerical experiences. From Figure 5, the basic feature of the turbulent fluidization regime was achieved with coexisting the dilute and dense phase.

Figure 6 displays the predicted axial profiles of the pressure in the AR with aforementioned drag models. For the AR, the predicted result calculated by the Gibilaro (Gibilaro *et al.*, 1985) model shows the best agreement with the experimental data. However, the McKeen and Pugsley model (McKeen and Pugsley, 2003) underestimated the drag force. It should be pointed out that the inlet gas velocity in the AR is higher compared with FR due to the air to fuel ratio, which could result in the different fluidization regimes of the two reactors and hence lead to the different degrees of cluster effect. Besides, as the reactions go on, the particle density increases in the AR and decreases in the FR, which could be another factor to the difference of fluidization regimes of the FR and the

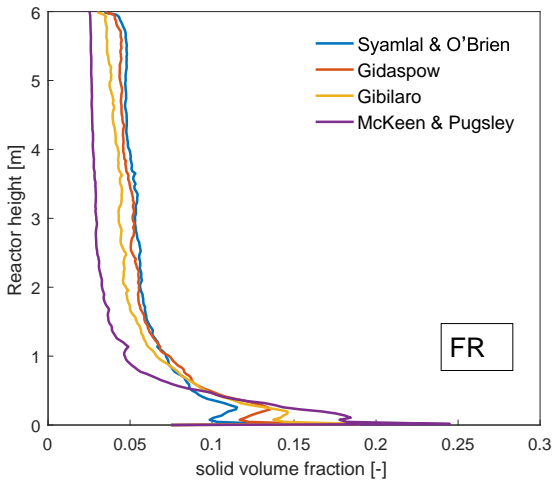


Figure 5: Axial solid volume fraction.

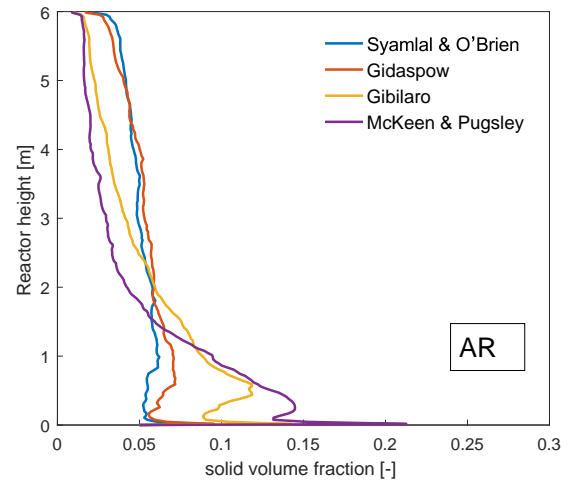


Figure 7: Axial solid volume fraction.

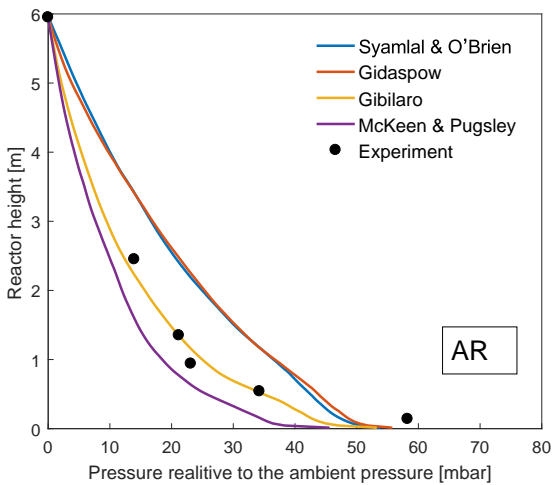


Figure 6: Axial pressure distribution.

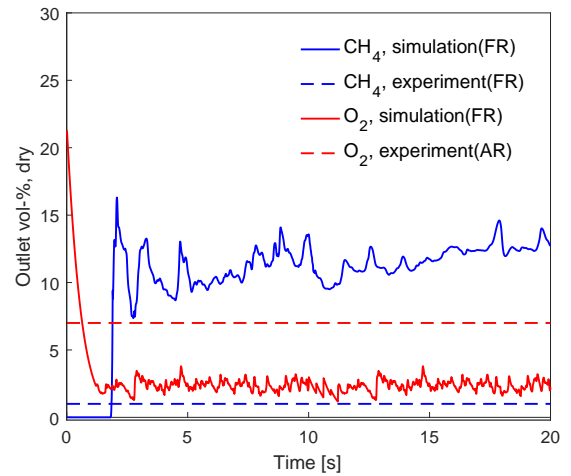


Figure 8: Concentration of CH<sub>4</sub> in the FR exhaust and O<sub>2</sub> concentration out from the AR.

AR. Since the Gibilaro (Gibilaro *et al.*, 1985) model gives reasonable prediction in the AR whereas overpredicts the drag force in the FR, it could be concluded that the degree of clustering in the FR is higher than in the AR. The corresponding solid distribution is shown in 7.

### Verification of the chemical reaction model

In this section, the chemical reaction model was validated based on the experimental results of the CH<sub>4</sub> concentration in the fuel reactor exhaust as well as the O<sub>2</sub> concentration out from the air reactor.

Figure 8 displays the CH<sub>4</sub> and O<sub>2</sub> concentration calculated from the simulation and the measurements from the experiments. For both reactors, relatively stable outlet concentrations of the gas species are achieved in just a few seconds of simulation time, hence the reactive flow can be said to be at a quasi-steady-state. It can be observed that the predicted O<sub>2</sub> concentration agrees reasonably with the experiment data although the result is slight under-predicted. However, the predicted CH<sub>4</sub> concentration is far away from the experimental data. This can be explained as the CuO used in the current study is slight different from the literature (Abad *et al.*, 2007), which would lead to a certain amount of error of the kinetic parameters. So in order to match the experimental result, three more frequency factors (A, in equation 5) for reduction reaction were evaluated, as shown in Figure 9. The best agreement between the simulation result and the experi-

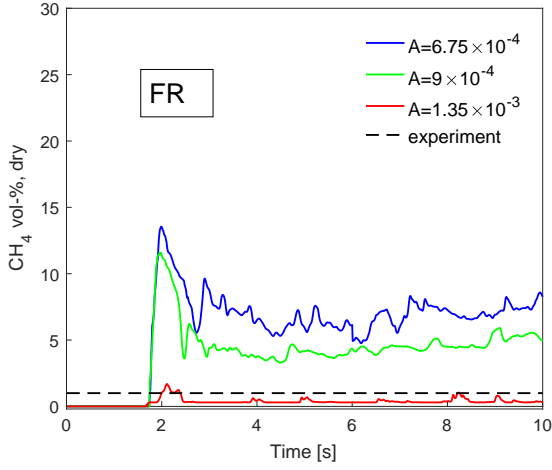
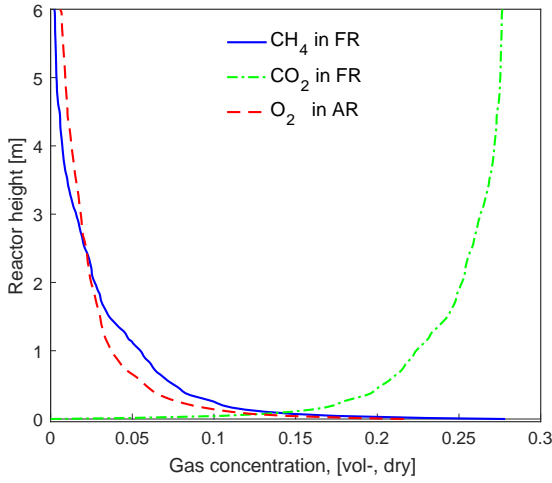
mental data was found when the frequency factor was equal to  $1.35 \times 10^{-3}$ .

With a frequency factor of  $1.35 \times 10^{-3}$ , McKeen and Pugsley (McKeen and Pugsley, 2003) model in the FR and Gibilaro (Gibilaro *et al.*, 1985) model in the AR, the vertical profiles of gas concentration in both reactors are examined. As illustrated in Figure 10, the reactants, CH<sub>4</sub> and O<sub>2</sub>, are rapidly consumed at a very short entrance length, where there is a larger concentration gradient. At the upper part of the reactors, the concentration gradient is much smaller. The reverse trend is observed for gas products CO<sub>2</sub>.

### CONCLUSION

The conclusions are:

1. The degree of clustering is higher in the FR than in the AR, which needs different drag models for each reactor. The predicted results given by McKeen and Pugsley (McKeen and Pugsley, 2003) model in the FR and Gibilaro (Gibilaro *et al.*, 1985) model in the AR show good agreement with the experimental data.
2. Due to the difference between the OC used in this study and the one for deriving the kinetic parameters, the frequency factor need to be modified according to the experimental measurements, and The best agreement between the simulation result. The frequency factor of


**Figure 9:** Concentration of CH<sub>4</sub> in the FR exhaust.

**Figure 10:** Axial distribution of CH<sub>4</sub>, CO<sub>2</sub> and O<sub>2</sub> along the reactors.

**Table 1:** Governing equations.

(Jakobsen, 2014; Lindborg, 2008)

Continuity equation for phase $k$ ( $k = g, s$ )
$\frac{\partial}{\partial t} (\alpha_k \rho_k) + \nabla \cdot (\alpha_k \rho_k \vec{v}_k) = \Gamma_k$
Momentum equation for phase $k$ ( $k = g, s$ )
$\frac{\partial}{\partial t} (\alpha_k \rho_k \vec{v}_k) + \nabla \cdot (\alpha_k \rho_k \vec{v}_k \vec{v}_k) = -\alpha_k \nabla p - \nabla \cdot \alpha_k \bar{\tau}_k + \vec{M}_k + \alpha_k \rho_k \vec{g} + \Gamma_k \vec{v}$
Species mass balance for phase $k$ ( $k = g, s$ )
$\frac{\partial}{\partial t} (\alpha_k \rho_k \omega_{k,j}) + \nabla \cdot (\alpha_k \rho_k \vec{v}_k \omega_{k,j}) = \nabla \cdot (\alpha_k \rho_k D_{k,j}^e \nabla \omega_{k,j}) + \Gamma_{k,j}^{\omega}$
Gas turbulent kinetic energy equation
$\frac{\partial}{\partial t} (\alpha_g \rho_g k_g) + \nabla \cdot (\alpha_g \rho_g k_g \vec{v}_g) = \alpha_g (-\bar{\tau}_t : \nabla \vec{v}_g + S_t) + \nabla \cdot (\alpha_g \frac{\mu_g^t}{\sigma_g} \nabla k_g) - \alpha_g \rho_g \varepsilon_g$
Gas turbulent energy dissipation rate equation
$\frac{\partial}{\partial t} (\alpha_g \rho_g \varepsilon_g) + \nabla \cdot (\alpha_g \rho_g \varepsilon_g \vec{v}_g) = \alpha_g C_1 \frac{\varepsilon_g}{k_g} (-\bar{\tau}_t : \nabla \vec{v}_g + S_t) + \nabla \cdot (\alpha_g \frac{\mu_g^t}{\sigma_\varepsilon} \nabla \varepsilon_g) - \alpha_g \rho_g C_2 \frac{\varepsilon_g^2}{k_g}$
Granular temperature equation
$\frac{3}{2} \left[ \frac{\partial}{\partial t} (\alpha_s \rho_s \Theta_s) + \nabla \cdot (\alpha_s \rho_s \Theta_s \vec{v}_s) \right] = -\bar{\tau}_s : \nabla \vec{v}_s + \nabla \cdot (\kappa_s \nabla \Theta_s) - 3\beta \Theta_s - \gamma_s$

**Table 2:** Closure for turbulent model

Turbulent viscosity
$\mu_g^t = \rho_g C_\mu \frac{k_g^2}{\varepsilon_g}$
Turbulent kinetic energy production (Jakobsen, 1993)
$S_t = C_b \beta (\vec{v}_s - \vec{v}_g)^2$
Turbulent stress tensor (Jakobsen, 2014)
$\bar{\tau}_t = -\frac{2}{3} \rho_g k_g \bar{\mathbb{I}} + 2 \mu_g^t \bar{S}_g$

**Table 3:** Empirical parameters for the  $\kappa - \varepsilon$  model

(Jakobsen, 2014)					
$C_\mu$	$\sigma_0$	$\sigma_\varepsilon$	$C_1$	$C_2$	$C_b$
0.09	1.00	1.30	1.44	1.92	0.25

**Table 4:** Closure for internal momentum transfer

 (Lun *et al.*, 1984; Gidaspow, 1994)

Gas phase stress
$\bar{\tau}_g = 2 \alpha_g \mu_g \bar{S}_g$
Solid phase stress
$\bar{\tau}_s = -(-p_s + \alpha_s \mu_{B,s} \nabla \cdot \vec{v}_s) - 2 \alpha_s \mu_s \bar{S}_s$
Deformation rate for phase $k$ ( $k = g, s$ )
$\bar{S}_k = \frac{1}{2} (\nabla \vec{v}_k + (\nabla \vec{v}_k)^T) - \frac{1}{3} (\nabla \cdot \vec{v}_k) \bar{\mathbb{I}}$
Solid phase pressure
$p_s = \alpha_s \rho_s \Theta_s [1 + 2(1 - e) \alpha_s g_0]$
solid bulk viscosity
$\mu_{B,s} = \frac{4}{3} \alpha_s \rho_s d_p g_0 (1 + e) \sqrt{\frac{\Theta_s}{\pi}} + \frac{4}{5} \alpha_s \rho_s d_p g_0 (1 + e)$
Solid phase shear viscosity
$\mu_s = \frac{2 \mu_s^{dilute}}{\alpha_s g_0 (1 + e)} \left[ 1 + \frac{4}{5} \alpha_s g_0 (1 + e) \right]^2 + \frac{4}{5} \alpha_s \rho_s g_0 (1 + e) \sqrt{\frac{\Theta_s}{\pi}}$
Conductivity of the granular temperature
$\kappa_s = \frac{15}{2} \frac{\mu_s^{dilute}}{(1 + e) g_0} \left[ 1 + \frac{6}{5} \alpha_s g_0 (1 + e) \right]^2 + 2 \alpha_s^2 \rho_s d_p (1 + e) g_0 \sqrt{\frac{\Theta_s}{\pi}}$
Collisional energy dissipation
$\gamma_s = 3(1 - e^2) \alpha_s^2 \rho_s g_0 \Theta_s \left[ \frac{4}{d_p} \sqrt{\frac{\Theta_s}{\pi}} - \nabla \cdot \vec{v}_s \right]$
Radial distribution function
$g_0 = \frac{1 + 2.5 \alpha_s + 4.5904 \alpha_s^2 + 4.515439 \alpha_s^3}{\left[ 1 - \left( \frac{\alpha_s}{\alpha_s^{max}} \right)^3 \right]^{0.67802}}$
Dilute viscosity
$\mu_s^{dilute} = \frac{5}{96} \rho_s d_p \sqrt{\pi \Theta_s}$

**Table 5:** Constitutive equations for internal mass transfer

(Jakobsen, 2014; Lindborg, 2008)

Effective diffusivity
$D_{k,j}^e = D_{k,j}^m + D_k^t$
Molecular diffusion coefficient
$D_{g,j}^m = \frac{1 - \omega_j}{M_m \sum_{j \neq i} \frac{\omega_j}{M_j D_{ji}}}$
Binary diffusion coefficient
$D_{ji} = \frac{T_0^{1.75} \sqrt{1/M_j + 1/M_i}}{101.325 P \left( (\Sigma V)_j^{1/3} + (\Sigma V)_i^{1/3} \right)^2}$
Turbulent diffusion coefficient
$D_g^t = \frac{\mu_g^t}{\rho_g S_c^t}$
$D_s^t = \frac{d_p}{16 \alpha_s} \sqrt{\pi \Theta}$

$1.35 \times 10^{-3}$  gives a reasonable prediction in comparison to the experimental data.

**Table 6:** Main geometric and operating parameters

(Abad *et al.*, 2007)

	CH <sub>4</sub>	O <sub>2</sub>
Physical parameters		
$\rho_{M,CuO}$ (mol/m <sup>3</sup> )	80402	80402
$r_{g,CuO}$ (m)	$1.4 \times 10^{-6}$	$1.4 \times 10^{-6}$
$v$	4	2
Kinetic parameters		
$A$ (mol <sup>1-n</sup> m <sup>3n-2</sup> s <sup>-1</sup> )	$4.5 \times 10^{-4}$	$4.7 \times 10^{-6}$
$E$ (kJ/mol)	60	15
$n$	0.4	1

**Table 7:** Main geometric and operating parameters

Description	Unit	Value
Reactor geometry		
AR height	<i>m</i>	6
AR diameter	<i>m</i>	0.23
FR height	<i>m</i>	6
FR diameter	<i>m</i>	0.154
Particle properties		
Mean particle size	$\mu\text{m}$	149
Particle density	$\text{kg/m}^3$	1700
Active NiO content	%	14.7
Operational condition		
Operating pressure	<i>atm</i>	1.0
Fuel power	<i>kW</i>	100
Lower heating value of fuel	<i>MJ/kg</i>	50
Inlet composition of FR	–	27 % CH <sub>4</sub>
Temperature in FR	<i>K</i>	1100
Temperature in AR	<i>K</i>	1100
Global air-fuel ratio	–	1.1

**Table 8:** Main geometric and operating parameters

Description	Unit	Value
No. of control volume	–	22800
Gas viscosity	<i>kg/ms</i>	$1.82 \times 10^{-5}$
Sphericity of particle	–	1
Restitution coefficient of particles	–	0.99
Initial bed height of FR	<i>m</i>	0.9
Initial bed height of AR	<i>m</i>	1.2
Time step	<i>s</i>	$1.0 \times 10^{-4}$

## REFERENCES

- ABAD, A., ADÁNEZ, J., GARCÍA-LABIANO, F., LUIS, F., GAYÁN, P. and CELAYA, J. (2007). “Mapping of the range of operational conditions for cu-, fe-, and ni-based oxygen carriers in chemical-looping combustion”. *Chemical Engineering Science*, **62**(1), 533–549.
- ERGUN, S. (1952). “Fluid flow through packed columns”. *Chem. Eng. Prog.*, **48**, 89–94.
- GIBILARO, L., DI FELICE, R., WALDRAM, S. and FOSCOLO, P. (1985). “Generalized friction factor and drag coefficient correlations for fluid-particle interactions”. *Chemical engineering science*, **40**(10), 1817–1823.
- GIDASPOW, D. (1994). *Multiphase flow and fluidization: continuum and kinetic theory descriptions*. Academic press, San Diego, US.
- ISHIDA, M. and JIN, H. (1996). “A novel chemical-looping combustor without nox formation”. *Ind. Eng. Chem. Res.*, **35**, 2469–2472.
- JAKOBSEN, H.A. (1993). *On the modelling and simulation of bubble column reactors using a two-fluid model*. Ph.D. thesis, Norwegian Institute of Technology, Trondheim, Norway.
- JAKOBSEN, H.A. (2014). *Chemical Reactor Modeling*. 2nd ed. Springer-Verlag, Multiphase Reactive Flows, Berlin, Germany: Springer-Verlag.
- JUNG, J. and GAMWO, I.K. (2008). “Multiphase cfd-based models for chemical looping combustion process: fuel reactor modeling”. *Powder Technol.*, **183**(3), 401–409.
- LINDBORG, H. (2008). *Modeling and Simulation of Reactive Two-Phase Flows in Fluidized Bed Reactors*. Ph.D. thesis, Norwegian Institute of Technology, Trondheim, Norway.
- LUN, C., SAVAGE, S.B., JEFFREY, D. and CHEPURNIY, N. (1984). “Kinetic theories for granular flow: inelastic particles in couette flow and slightly inelastic particles in a general flowfield”. *J. Fluid Mech.*, **140**, 223–256.
- MCKEEN, T. and PUGSLEY, T. (2003). “Simulation and experimental validation of a freely bubbling bed of fcc catalyst”. *Powder Technol.*, **129**(1), 139–152.
- SYAMLAL, M. and O’BRIEN, T. (1988). “Simulation of granular layer inversion in liquid fluidized beds”. *International Journal of Multiphase Flow*, **14**(4), 473–481.
- VAN LEER, B. (1974). “Towards the ultimate conservation difference scheme. ii. monotonicity and conservation combined in a second-order scheme”. *J. Comput. Phys.*, **14**, 361–370.
- WEN, C. and YU, Y. (1966). “A generalized method for predicting the minimum fluidization velocity”. *AIChE Journal*, **12**(3), 610–612.
- ZHANG, Y., CHAO, Z. and JAKOBSEN, H.A. (2017). “Modelling and simulation of hydrodynamics in double loop circulating fluidizedbed reactor for chemical looping combustion process”. *Powder Technology*, **310**, 35–45.

## APPENDIX A

The drag force acting on a particle in gas-solid system can be presented by the product of a momentum transfer coefficient ( $\beta$ ) and slip velocity between the two phases

$$\vec{M} = \frac{3}{4} C_d \frac{\alpha_s \rho_g}{d_s} f(\alpha_g) |\vec{u}_g - \vec{u}_s| = \beta (\vec{u}_s - \vec{u}_g) \quad (\text{A.1})$$

The correlations of  $\beta$  are usually obtained from pressure drop measurements.

Gidaspow et al.(Gidaspow, 1994) employed the Ergun (Ergun, 1952) equation for the dense phase and the Wen-Yu (Wen and Yu, 1966) equation for the dilute phase.

$$\beta = \begin{cases} 150 \frac{\mu_g (1 - \alpha_g)^2}{\alpha_g d_s^2} + 1.75 (1 - \alpha_g) \frac{\rho_g}{d_s} |\vec{u}_g - \vec{u}_s| & \alpha_g < 0.8 \\ 0.75 C_d \frac{(1 - \alpha_g) \alpha_g}{d_s} \rho_g |\vec{u}_g - \vec{u}_s| \alpha_g^{-2.65} & \alpha_g > 0.8 \end{cases} \quad (\text{A.2})$$

where the drag coefficient  $C_D$  was expressed by

$$C_d = \begin{cases} \frac{24}{Re_p} [1 + 0.15 Re_p^{0.687}] & Re_p \leq 1000 \\ 0.44 & Re_p > 1000 \end{cases} \quad (\text{A.3})$$

The particle Reynolds number is:

$$Re_p = \frac{\alpha_g d_s \rho_g |\vec{v}_s - \vec{v}_g|}{\mu_g} \quad (\text{A.4})$$

Syamlal and O'Brien(Syamlal and O'Brien, 1988) proposed a new drag coefficient based on the measurements of the terminal velocities of particles in the form

$$\beta = \frac{3}{4} C_d \frac{\alpha_s \rho_g}{d_s} \frac{\alpha_g}{f^2} |\vec{u}_g - \vec{u}_s| \quad (\text{A.5})$$

$$C_D = (0.63 + 4.8/\sqrt{f/Re_p})^2 \quad (\text{A.6})$$

where  $f$  is the ratio of the failing velocity of a suspension to the terminal velocity of a single particle.

$$f = \frac{1}{2} (A - 0.06 Re_p + \sqrt{((0.06 Re_p)^2 + 0.12 Re_p (2B - A) + A^2)}) \quad (\text{A.7})$$

with

$$A = \alpha_g^{4.14} \quad (\text{A.8})$$

$$B = \begin{cases} \alpha_g^{2.65} & \alpha_s < 0.15 \\ 0.8 \alpha_g^{1.28} & \alpha_s \geq 0.15 \end{cases} \quad (\text{A.9})$$

Gibilaro et al.(Gibilaro *et al.*, 1985) considered an effective buoyancy force to produce drag coefficient correlation for individual particles in a fluidized suspension as follows:

$$\beta = [\frac{17.3}{Re_p} + 0.336] \frac{\rho_g}{d_s} |\vec{v}_s - \vec{v}_g| \alpha_s \alpha_g^{-1.8} \quad (\text{A.10})$$

McKeen and Pugsley et al.(McKeen and Pugsley, 2003) proposed an empirical method to reduce the Gibilaro(Gibilaro et al., 1985) drag correction using a constant scale factor  $K$ . This scale factor could be adjusted to take in to account the effect of interparticle cohesive forces on particle agglomeration.

$$\beta = K [\frac{17.3}{Re_p} + 0.336] \frac{\rho_g}{d_s} |\vec{v}_s - \vec{v}_g| \alpha_s \alpha_g^{-1.8} \quad (\text{A.11})$$

# EXTREMELY FAST SIMULATIONS OF HEAT TRANSFER IN FLUIDIZED BEDS

Thomas LICHTENEGGER<sup>1,2\*</sup>, Stefan PIRKER<sup>1†</sup>

<sup>1</sup>Department of Particulate Flow Modelling, Johannes Kepler University, 4040 Linz, AUSTRIA

<sup>2</sup>Linz Institute of Technology (LIT), Johannes Kepler University, 4040 Linz, AUSTRIA

\* E-mail: thomas.lichtenegger@jku.at

† E-mail: stefan.pirker@jku.at

## ABSTRACT

Besides their huge technological importance, fluidized beds have attracted a large amount of research because they are perfect playgrounds to investigate highly dynamic particulate flows. Their overall behavior is determined by short-lasting particle collisions and the interaction between solid and gas phase. Modern simulation techniques that combine computational fluid dynamics (CFD) and discrete element methods (DEM) are capable of describing their evolution and provide detailed information on what is happening on the particle scale. However, these approaches are limited by small time steps and large numerical costs, which inhibits the investigation of slower long-term processes like heat transfer or chemical conversion.

In a recent study (Lichtenegger and Pirker, 2016), we have introduced recurrence CFD (rCFD) as a way to decouple fast from slow degrees of freedom in systems with recurring patterns: A conventional simulation is carried out to capture such coherent structures. Their re-appearance is characterized with recurrence plots that allow us to extrapolate their evolution far beyond the simulated time. On top of these predicted flow fields, any passive or weakly coupled process can then be investigated at fractions of the original computational costs.

Here, we present the application of rCFD to heat transfer in a lab-scale fluidized bed. Initially hot particles are fluidized with cool air and their temperature evolution is recorded. In comparison to conventional CFD-DEM, we observe speed-up factors of about two orders of magnitude at very good accuracy with regard to recent measurements.

**Keywords:** recurrent patterns, fluidized beds, multiphase heat and mass transfer, multiscale simulations .

## NOMENCLATURE

### Greek Symbols

$\alpha$  volume fraction,  $[\ ]$   
 $\Delta t$  time step,  $[s]$   
 $\rho$  density,  $[kg/m^3]$   
 $\boldsymbol{\tau}$  deviatoric stress tensor,  $[kg/s^2m]$

### Latin Symbols

$C$  specific heat capacity,  $[m^2/s^2K]$ .  
 $D$  diameter,  $[m]$ .  
 $D$  random fluctuations parameter,  $[m^2/s]$ .  
 $D$  dissimilarity norm,  $[\ ]$ .  
 $d\mathbf{w}$  random step,  $[m]$ .  
 $\mathbf{f}$  force density,  $[kg/s^2m^2]$ .  
 $\mathbf{F}$  force,  $[kgm/s^2]$ .

$k$  thermal conductivity,  $[kgm/s^3K]$ .  
 $m$  mass,  $[kg]$ .  
 $\dot{Q}$  heat transfer,  $[kg/s^3m]$ .  
 $R$  recurrence norm,  $[\ ]$ .  
 $t$  time,  $[s]$ .  
 $T$  temperature,  $[K]$ .  
 $\mathbf{u}$  field velocity,  $[m/s]$ .  
 $\mathbf{v}$  point velocity,  $[m/s]$ .

### Sub/superscripts

$f$  fluid.  
 $n$  normal.  
 $p$  particle.  
 $p$  pressure.  
 $rec$  recurrence.  
 $t$  tangential.  
 $v$  volume.

## INTRODUCTION

Modeling and simulation of fluidized beds is extremely demanding due to the various scales present. In the spatial domain, submillimeter particles are to be contrasted with the geometric dimensions of industrial-size plants. In the temporal domain, collisions set the lower limit of time scales at small fractions of a second while heat transfer or chemical conversion happens much more slowly.

Substantial progress has been made in up-scaling well-established mesoscopic methods like CFD-DEM (Cundall and Strack, 1979; Tsuji *et al.*, 1993) or the two-fluid model (TFM) (Anderson and Jackson, 1967; Gidaspow, 1994) to macroscopic sizes. To allow for coarser meshes so that larger systems can be described, sub-grid heterogeneities need to be modeled appropriately (Heynderickx *et al.*, 2004; Igci *et al.*, 2008; Igci and Sundaresan, 2011a,b; Milioli *et al.*, 2013; Ozel *et al.*, 2013; Parmentier *et al.*, 2012; Radl and Sundaresan, 2014; Schneiderbauer *et al.*, 2013; Schneiderbauer and Pirker, 2014; Wang *et al.*, 2008, 2010; Yang *et al.*, 2003; Zhang and VanderHeyden, 2002).

Although industrial-size reactors may be simulated with these methods, they are still bound to short-term investigations. Here, we show a systematic way to circumvent this problem and apply it to heat transfer in a lab-scale fluidized bed. In a recent paper, we introduced the idea of rCFD (Lichtenegger and Pirker, 2016) to time-extrapolate the behavior of systems dominated by reappearing structures. We use fields from short-term simulations with conventional



CFD-DEM or TFM to create long sequences of flow patterns with the aid of recurrence plots (Eckmann *et al.*, 1987).

On these sequences, we simulate heat transfer between gas and solid particles as measured by Patil *et al.* (Patil *et al.*, 2015) and obtain speed-up factors of about two orders of magnitude.

## MODEL DESCRIPTION

In the following, we briefly summarize the CFD-DEM method and refer the interested reader to extensive reviews (Deen *et al.*, 2007; Zhou *et al.*, 2010). Afterwards, the rCFD strategy is explained.

### Fluid equations

If a secondary, particulate phase is present, the Navier Stokes equations for a fluid with density  $\rho_f$  and velocity field  $\mathbf{u}_f$  become (Anderson and Jackson, 1967)

$$\frac{\partial}{\partial t} \alpha_f \rho_f + \nabla \cdot \alpha_f \rho_f \mathbf{u}_f = 0 \quad (1)$$

$$\frac{\partial}{\partial t} \alpha_f \rho_f \mathbf{u}_f + \nabla \cdot \alpha_f \rho_f \mathbf{u}_f \mathbf{u}_f = -\alpha_f \nabla p_f + \alpha_f \nabla \cdot \boldsymbol{\tau}_f + \mathbf{f}_{\text{drag}} + \mathbf{f}_{\text{ext}}. \quad (2)$$

Various correlations for particle-fluid drag  $\mathbf{f}_{\text{drag}}$  can be found in literature, we use one obtained from lattice-Boltzmann simulations (Beetstra *et al.*, 2007).

To picture heat transfer, we assume incompressible conditions and neglect contributions due to pressure variations to the enthalpy transport equation from which we derive

$$C_f^{(p)} \frac{\partial}{\partial t} \alpha_f \rho_f T_f + C_f^{(p)} \nabla \cdot \alpha_f \rho_f \mathbf{u}_f T_f = \nabla \cdot \alpha_f k_f^{(\text{eff})} \nabla T_f + \dot{Q}_{p-f}. \quad (3)$$

Both heat conduction  $\nabla \cdot \alpha_f k_f^{(\text{eff})} \nabla T_f$  and particle-fluid heat transfer  $\dot{Q}_{p-f}$  have to be modeled with empirical correlations (Syamlal and Gidaspow, 1985; Gunn, 1978). Note that for incompressible flows, Eq. (3) is decoupled from Eqs. (1) and (2) if density and viscosity are assumed to be temperature-independent.

### Particle equations

Solid particles are often modeled as perfect spheres which interact with each other via contact forces  $\mathbf{F}_i^{(p-p)}$ , with a surrounding fluid  $\mathbf{F}_i^{(p-f)}$  and possibly other sources  $\mathbf{F}_i^{(\text{ext})}$ . For each particle  $i$  with mass  $m_i$ , Newton's second law

$$m_i \dot{\mathbf{v}}_i = \mathbf{F}_i^{(p-p)} + \mathbf{F}_i^{(p-f)} + \mathbf{F}_i^{(\text{ext})} \quad (4)$$

determines its trajectory. The particle-particle force

$$\mathbf{F}_i^{(p-p)} = \sum_{j \neq i} (\mathbf{F}_{i,j}^{(n)} + \mathbf{F}_{i,j}^{(t)}) \quad (5)$$

on particle  $i$  due to all surrounding particles  $j$  consists of normal and tangential components which depend on the relative positions and velocities of  $i$  and  $j$  and are often described via spring-dashpot models (Cundall and Strack, 1979). The interaction of particles with a fluid  $\mathbf{F}_i^{(p-f)}$  is related to the drag force and the pressure gradient in Eq. (2).

Each particle is assumed to have a homogeneously distributed temperature  $T_i$ . We neglect particle-particle heat exchange because of the extremely short collision times so that only heat transfer from/to the fluid can change a particle's temperature via

$$m_i C_p^{(p)} \dot{T}_i = -\pi k_f D_i \text{Nu}_p (T_i - T_f(\mathbf{r}_i)) \quad (6)$$

in terms of the Nusselt number  $\text{Nu}_p$  (Gunn, 1978).

## Recurrence CFD

In a first step, we define norms for recurrence and dissimilarity of states, respectively, e.g.

$$R(t, t') \equiv 1 - \frac{1}{\mathcal{N}} \int d^3 r (\alpha_f(\mathbf{r}, t) - \alpha_f(\mathbf{r}, t'))^2 \quad (7)$$

$$D(t, t') \equiv 1 - R(t, t'), \quad (8)$$

to assess the similarity of flow fields obtained from the solution of Eqs. (1) – (4) at two times  $t, t' \leq t_{\text{max}}$ .

$$\mathcal{N} \equiv \max_{t, t'} \int d^3 r (\alpha_f(\mathbf{r}, t) - \alpha_f(\mathbf{r}, t'))^2 \quad (9)$$

ensures normalization in Eq. (7). We stress that it is an assumption that similarity according to Eq. (7) carries over to other fields like the particle velocity  $\mathbf{u}_p$ . As a matter of fact, it has to be checked *a posteriori* if they are sufficiently correlated to justify it.

Compared to binary recurrence statistics (Eckmann *et al.*, 1987), definition (7) allows for continuous degrees of similarity, which is referred to as unthresholded recurrence statistics (Marwan *et al.*, 2007).

Given a large enough recurrence statistics  $R(t, t')$ , it is possible to extrapolate the underlying system's behavior. Starting at some given begin time  $t_i^{(b)}$ , one randomly picks an interval of length  $\Delta t_i$ . In this study, we used uniformly distributed  $\Delta t_i$  in the range of  $t_{\text{max}}/20$  and  $t_{\text{max}}/5$ . Within  $\Delta t_i$ , the corresponding fields are taken as first elements of the desired sequence. Then, the most similar state to that at the end of the interval  $t_i^{(e)} = t_i^{(b)} + \Delta t_i$  is identified with the aid of  $R(t, t')$  and reconstruction is continued from there on. Again, an interval length is chosen and its fields are appended to the sequence. Obviously, this procedure can be repeated arbitrarily often. Figure 2 shows an example of two states that could be identified with each other because of a sufficiently high degree of similarity.

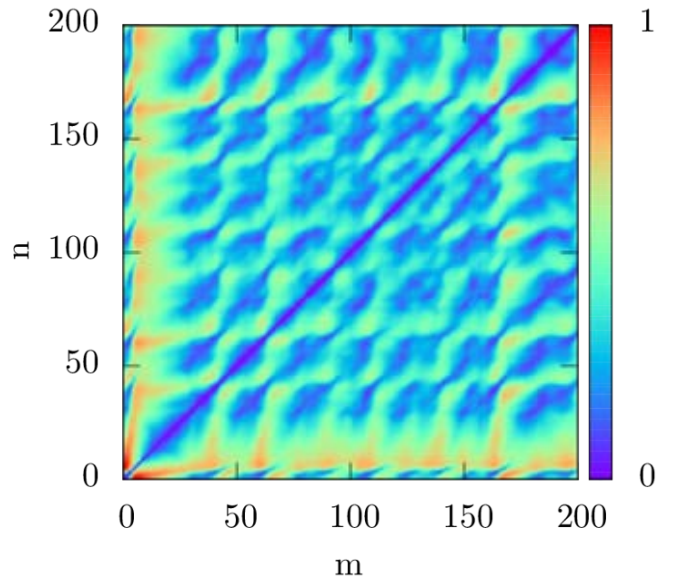


**Figure 1:** Degree of dissimilarity  $D(t, t')$  for the first 5 s of simulation of a fluidized bed corresponding to 200 snapshots. Besides the main diagonal with dissimilarity 0, a pattern of local minima and maxima is clearly visible, corresponding to more or less similar states. Their alignment approximately parallel to the main diagonal indicates pseudo-periodic behavior.

Finally, any passive processes can now be simulated on these fields in an extremely efficient way. The CFD-side problem of Eqs. (1), (2) and (3) is replaced with the temperature equation (3) alone. Other information like volume fraction, density and velocity are obtained from the recurrence process, only the temperature distribution is really calculated. The motion of the particles is simplified with tracers that follow the solid phase's velocity field  $\mathbf{u}_p^{(\text{rec})}$  and undergo random fluctuations  $d\mathbf{w}_i$ , viz.

$$d\mathbf{r}_i = \mathbf{u}_p^{(\text{rec})}(\mathbf{r}_i, t)dt + \sqrt{2D^{(\text{rec})}(\mathbf{r}_i, t)}d\mathbf{w}_i. \quad (10)$$

The latter act to avoid too high tracer concentrations in comparison to actual solid particles. A phenomenological, possibly position-dependent parameter  $D^{(\text{rec})}$  controls the strength of the fluctuations, e.g. via

$$D^{(\text{rec})}(\mathbf{r}, t) = D_0 \frac{\max[\alpha_p(\mathbf{r}, t) - \alpha_p^{(\text{rec})}(\mathbf{r}, t), 0]}{\alpha_p(\mathbf{r}, t)}. \quad (11)$$

The constant  $D_0$  has to be chosen empirically such that neither excessive clustering occurs nor that particle diffusion is enhanced dramatically. In neither case, the passive process under consideration could be pictured accurately.

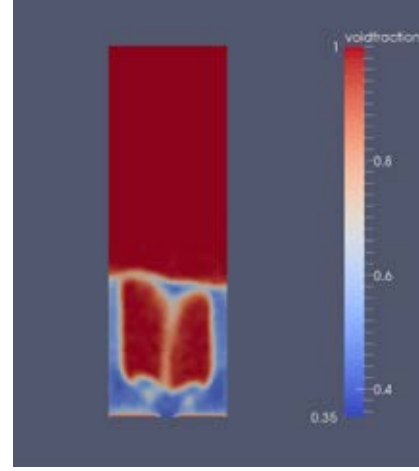
## SIMULATION SETUP

We set up simulations in close resemblance to recent experiments and simulations of heat transfer in a fluidized bed (Patil *et al.*, 2015) which we took as reference data. A  $8\text{ cm} \times 1.5\text{ cm} \times 25\text{ cm}$  cuboid was discretized into  $35 \times 110 \times 6$  equal cells and approximately 57000 1-mm spheres with material values of glass and initial temperature  $T_p^{(0)} = 90^\circ\text{C}$  were inserted. Air with ambient temperature  $T_f^{(0)} = 20^\circ\text{C}$  fluidized them with a superficial inlet velocity of  $u_{\text{inlet}} = 1.2\text{ m/s}$  and slowly cooled them.

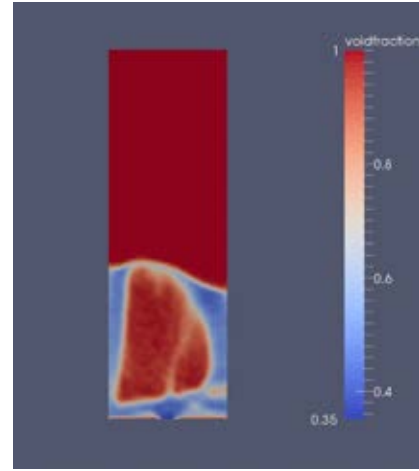
Since unresolved CFD-DEM requires larger cells than particles, the above grid could not be used to resolve the flux of heat through the domain walls happening over a very thin layer. Instead, its thickness was introduced as modeling parameter within reasonable bounds to control heat loss through the walls (Patil *et al.*, 2015). Since the focus of this work was rather the comparison of full CFD-DEM with rCFD than with experiments, we chose its value (in roughly the same range, but somewhat larger) such that our CFD-DEM results were in agreement with the reference simulation. We opted for this procedure because in contrast to the reference simulation which was carried out for an ideal, compressible gas, we approximated the system as incompressible to enable a recurrence-based treatment. Future work will address this shortcoming (Lichtenegger *et al.*, 2017) and allow for a meaningful comparison with measurements.

For the full CFD-DEM simulations, Eqs. (1) – (3) were solved under incompressible conditions employing the PISO algorithm (Issa, 1986). On the DEM side, we used velocity-Verlet integration (Verlet, 1967) for Eq. (4). The full CFD-DEM simulations were carried out for 10 s process time, the first 5 s were then used as basis for rCFD. We stress that this duration was chosen quite generously and smaller recurrence statistics would probably work equally well.

In this study, each particle was represented by exactly one tracer. Of course, one could also employ a parcel approach to combine clusters of particles into fewer tracers or conversely try to resolve coarse-grained CFD-DEM data with higher numbers of tracers.



(a)



(b)

**Figure 2:** Example of two equivalent states in the sense of dissimilarity norm Fig. 1. Although the volume fraction fields are not identical, they are close enough so that substituting one with the other does not lead to any significant inaccuracies.

Special care had to be taken with the choice of the fluctuation control parameter  $D_0$ . We found empirically that with  $d\mathbf{w}$  distributed uniformly on the unit sphere,  $D_0 = 10^{-4} \text{ m}^2/\text{s}$  was large enough to avoid too high particle concentrations and sufficiently small not to increase particle diffusion and consequently heat transfer and the mean cooling rate.

## RESULTS

According to the rCFD strategy outlined above, the first quantity to look at is the dissimilarity norm (or equally useful the recurrence norm) displayed in Fig. 1. 200 snapshots corresponding to 5 s real time are compared with each other, leading to a structure of local minima and maxima approximately parallel to the main diagonal. These minima are caused by very similar states that evolve in an analogous fashion, which demonstrates local pseudo-periodicity.

The degree of similarity is indicated in Fig. 2. Two volume fraction fields which give rise to a local minimum in the dissimilarity norm are shown. While small quantitative differences can be found, their qualitative features clearly agree: a large bubble was formed in the center of the bed with a few particles moving downwards in the middle of the bubble.

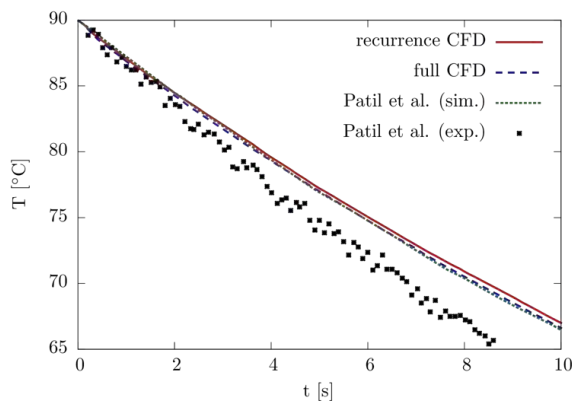


**Figure 3:** Particle mean temperature over time. Per construction, the full CFD simulations closely resembled the reference data (Patil *et al.*, 2015). As a consequence, the cooling rate was somewhat too low in comparison with measurements. Most importantly, recurrence CFD led to almost identical results as the full model.

If such semiquantitative agreement was sufficient to obtain a meaningful extrapolation of the fluidized bed's evolution is finally answered by looking at the particle mean temperatures from full and recurrence-based simulations in Fig. 3. As discussed above, the thickness of the boundary layer over which temperature drops to its wall value allowed for some "tuning" of the cooling rate. With a value to match the reference data (Patil *et al.*, 2015), the agreement of the present CFD-DEM results with them was of course to be expected. More importantly, however, the curves from rCFD and CFD-DEM agree very well. After 10 s their deviation is much less than  $1^\circ\text{C}$  at a speed-up of approximately two orders of magnitude.

Furthermore, Fig. 3 demonstrates that particle cooling happened over much longer times than the bed's fast dynamics. Such a clear separation of scales is clearly vital for the rCFD procedure because it minimizes the impact of switching between most similar but nevertheless different flow states on the passive process under consideration.

## CONCLUSION AND OUTLOOK

In this paper, we have demonstrated how to decouple the fast dynamics of a fluidized bed from the much slower heat transfer between solid particles and surrounding gas to accelerate the calculations. To facilitate the procedure, we assumed incompressible conditions in contrast to the treatment in the reference simulation (Patil *et al.*, 2015) and used a tuning parameter for wall heat loss to match our full CFD-DEM simulations to them. Upon these results, we built the recurrence statistics used for rCFD.

Future work (Lichtenegger *et al.*, 2017) will deal with rCFD for the compressible case, where we expect a superposed transient behavior due to a slow decrease of the mean gas temperature in the center of the bed. Besides more realistic results from the CFD-DEM calculation for a meaningful comparison with measurements, this will allow to study the bed over much longer times. Furthermore, a detailed performance analysis of the method's implementation might reveal optimization potential for even faster simulations.

## ACKNOWLEDGEMENT

This work was partly funded by the Linz Institute of Technology (LIT), Johannes Kepler University, Linz. We furthermore acknowledge support from K1-MET GmbH metallurgical competence center.

## REFERENCES

- ANDERSON, T.B. and JACKSON, R. (1967). "A fluid mechanical description of fluidized beds. Equations of motion". *Ind. Eng. Chem. Fundam.*, **6(4)**, 527–539.
- BEETSTRA, R., VAN DER HOEF, M.A. and KUIPERS, J.A.M. (2007). "Drag force of intermediate Reynolds number flow past mono- and bidisperse arrays of spheres". *AIChE J.*, **53(2)**, 489–501.
- CUNDALL, P.A. and STRACK, O.D.L. (1979). "A discrete numerical model for granular assemblies". *Géotechnique*, **29(1)**, 47–65.
- DEEN, N.G., VAN SINT ANNALAND, M., VAN DER HOEF, M.A. and KUIPERS, J.A.M. (2007). "Review of discrete particle modeling of fluidized beds". *Chem. Eng. Sci.*, **62(1-2)**, 28–44.
- ECKMANN, J.P., KAMPHORST, S.O. and RUELLE, D. (1987). "Recurrence plots of dynamical systems". *Europhys. Lett.*, **4(9)**, 973–977.
- GIDASPOW, D. (1994). *Multiphase flow and fluidization: continuum and kinetic theory descriptions*. Academic press.
- GUNN, D. (1978). "Transfer of heat or mass to particles in fixed and fluidised beds". *Int. J. Heat Mass Transfer*, **21(4)**, 467–476.
- HEYNDERICKX, G.J., DAS, A.K., DE WILDE, J. and MARIN, G.B. (2004). "Effect of clustering on gas-solid drag in dilute two-phase flow". *Ind. Eng. Chem. Res.*, **43(16)**, 4635–4646.
- IGCI, Y. and SUNDARESAN, S. (2011a). "Constitutive models for filtered two-fluid models of fluidized gas-particle flows". *Ind. Eng. Chem. Res.*, **50(23)**, 13190–13201.
- IGCI, Y. and SUNDARESAN, S. (2011b). "Verification of filtered two-fluid models for gas-particle flows in risers". *AIChE J.*, **57(10)**, 2691–2707.
- IGCI, Y., ANDREWS, A.T., SUNDARESAN, S., PANNALA, S. and O'BRIEN, T. (2008). "Filtered two-fluid models for fluidized gas-particle suspensions". *AIChE J.*, **54(6)**, 1431–1448.
- ISSA, R.I. (1986). "Solution of the implicitly discretised

- fluid flow equations by operator-splitting". *J. Comput. Phys.*, **62(1)**, 40–65.
- LICHTENEGGER, T., PETERS, E.A.J.F., KUIPERS, J.A.M. and PIRKER, S. (2017). "A recurrence CFD study of heat transfer in a fluidized bed". in preparation.
- LICHTENEGGER, T. and PIRKER, S. (2016). "Recurrence CFD - a novel approach to simulate multiphase flows with strongly separated time scales". *Chem. Eng. Sci.*, **153**, 394–410.
- MARWAN, N., ROMANO, M.C., THIEL, M. and KURTHS, J. (2007). "Recurrence plots for the analysis of complex systems". *Phys. Rep.*, **438(5-6)**, 237–329.
- MILIOLI, C.C., MILIOLI, F.E., HOLLOWAY, W., AGRAWAL, K. and SUNDARESAN, S. (2013). "Filtered two-fluid models of fluidized gas-particle flows: New constitutive relations". *AIChE J.*, **59(9)**, 3265–3275.
- OZEL, A., FEDE, P. and SIMONIN, O. (2013). "Development of filtered Euler–Euler two-phase model for circulating fluidised bed: high resolution simulation, formulation and a priori analyses". *Int. J. Multiph. Flow*, **55**, 43–63.
- PARMENTIER, J.F., SIMONIN, O. and DELSART, O. (2012). "A functional subgrid drift velocity model for filtered drag prediction in dense fluidized bed". *AIChE J.*, **58(4)**, 1084–1098.
- PATIL, A.V., PETERS, E.A.J.F. and KUIPERS, J.A.M. (2015). "Comparison of CFD-DEM heat transfer simulations with infrared/visual measurements". *Chem. Eng. J.*, **277**, 388–401.
- RADL, S. and SUNDARESAN, S. (2014). "A drag model for filtered Euler–Lagrange simulations of clustered gas–particle suspensions". *Chem. Eng. Sci.*, **117**, 416–425.
- SCHNEIDERBAUER, S. and PIRKER, S. (2014). "Filtered and heterogeneity-based subgrid modifications for gas–solid drag and solid stresses in bubbling fluidized beds". *AIChE J.*, **60(3)**, 839–854.
- SCHNEIDERBAUER, S., PUTTINGER, S. and PIRKER, S. (2013). "Comparative analysis of subgrid drag modifications for dense gas–particle flows in bubbling fluidized beds". *AIChE J.*, **59(11)**, 4077–4099.
- SYAMLAL, M. and GIDASPOW, D. (1985). "Hydrodynamics of fluidization: prediction of wall to bed heat transfer coefficients". *AIChE J.*, **31(1)**, 127–135.
- TSUJI, Y., KAWAGUCHI, T. and TANAKA, T. (1993). "Discrete particle simulation of a two-dimensional fluidized bed". *Powder Technol.*, **77**, 79.
- VERLET, L. (1967). "Computer" experiments" on classical fluids. I. Thermodynamical properties of Lennard-Jones molecules". *Phys. Rev.*, **159(1)**, 98.
- WANG, J., GE, W. and LI, J. (2008). "Eulerian simulation of heterogeneous gas–solid flows in CFB risers: EMMS-based sub-grid scale model with a revised cluster description". *Chem. Eng. Sci.*, **63(6)**, 1553–1571.
- WANG, J., VAN DER HOEF, M.A. and KUIPERS, J.A.M. (2010). "Coarse grid simulation of bed expansion characteristics of industrial-scale gas–solid bubbling fluidized beds". *Chem. Eng. Sci.*, **65(6)**, 2125–2131.
- YANG, N., WANG, W., GE, W. and LI, J. (2003). "CFD simulation of concurrent-up gas–solid flow in circulating fluidized beds with structure-dependent drag coefficient". *Chem. Eng. J.*, **96(1)**, 71–80.
- ZHANG, D.Z. and VANDERHEYDEN, W.B. (2002). "The effects of mesoscale structures on the macroscopic momentum equations for two-phase flows". *Int. J. Multiph. Flow*, **28(5)**, 805–822.
- ZHOU, Z.Y., KUANG, S.B., CHU, K.W. and YU, A.B. (2010). "Discrete particle simulation of particle-fluid flow: model formulations and their applicability". *J. Fluid Mech.*, **661**, 482–510.



## MASS TRANSFER PHENOMENA IN FLUIDIZED BEDS WITH HORIZONTALLY IMMERSSED MEMBRANES

**Ramon J.W. VONCKEN<sup>1</sup>, Ivo ROGHAIR<sup>1\*</sup>, Martin VAN SINT ANNALAND<sup>1</sup>**

<sup>1</sup>Chemical Process Intensification, Department of Chemical Engineering and Chemistry, Eindhoven University of Technology, THE NETHERLANDS

\* Corresponding author e-mail: i.roghair@tue.nl

### ABSTRACT

Mass transfer phenomena in fluidized bed reactors with horizontally immersed membranes have been investigated using a verified and validated Two-Fluid Model. A binary hydrogen-nitrogen mixture was injected into the fluidized bed which was operated in the bubbling fluidization regime, and hydrogen was extracted via horizontally immersed membranes. The hydrogen flux is lowest on top of the membranes and highest at the bottom of the membranes. The main causes for the low flux on top of the membranes are densified zones and insufficient hydrogen replenishment due to the flow pattern of the gas. Gas pockets do not have a negative effect on the mass transfer towards the membranes. In systems with membrane tube banks, the membranes located at the walls perform worst, because solids mostly flow downwards near the walls of a fluidized bed, which causes gas back-mixing, which hinders hydrogen replenishment and thereby decreases the driving force for hydrogen transport. Removing the membranes closest to the wall increases the overall efficiency of the system. Replacing wall membranes with inactive tubes has no significant effect on the system. The membrane tube banks also have a significant effect on the hydrodynamics.

**Keywords:** Two-Fluid Model, mass transfer, hydrodynamics, fluidized bed, membrane.

### NOMENCLATURE

#### Latin Symbols

$A$	area	[m <sup>2</sup> ]
$C_d$	drag coefficient	[-]
$D$	diffusion coefficient	[m <sup>2</sup> /s]
$e$	restitution coefficient	[-]
$g$	gravitational acceleration	[m/s <sup>2</sup> ]
$M$	molar weight	[kg/mol]
$n$	power in Sieverts' law	[-]
$p$	pressure	[Pa]
$Q$	membrane permeance	[mol/(m <sup>2</sup> .s.Pa <sup>n</sup> )]
$R$	universal gas constant	[J/(mol.K)]
$Re$	Reynolds number	[-]
$S$	membrane mass source term	[kg/(m <sup>3</sup> .s)]
$t$	time	[s]
$T$	temperature	[K]
$u$	velocity	[m/s]
$V$	volume	[m <sup>3</sup> ]

$X$	molar fraction	[-]
$Y$	mass fraction	[-]

#### Greek Symbols

$\alpha$	hold-up fraction	[-]
$\beta$	interphase drag coefficient	[kg/(m <sup>3</sup> .s)]
$\gamma$	dissipation of fluctuation energy	[kg/(m.s <sup>3</sup> )]
$\theta$	granular temperature	[m <sup>2</sup> /s <sup>2</sup> ]
$\kappa$	conductivity of fluctuation energy	[kg/(m.s)]
$\mu$	shear/dynamic viscosity	[Pa.s]
$\rho$	density	[kg/m <sup>3</sup> ]
$\tau$	shear stress tensor	[N/m <sup>2</sup> ]

#### Sub/superscripts

$c$	cell
$H_2$	hydrogen
$g$	gas
$i$	phase
$m$	membrane
$mf$	minimum fluidization
$p$	particle
$ret$	retentate
$s$	solid
$sim$	simulation
$tot$	total
$w$	wall

### INTRODUCTION

Hydrogen is commonly produced by Steam Methane Reforming (SMR), which can be performed in (multi-tubular) packed bed reactors. In the packed beds, methane reacts with steam to form carbon monoxide and hydrogen at temperatures around 1000 °C. Consecutively, the Water Gas Shift (WGS) reaction occurs; the carbon monoxide reacts with steam to form carbon dioxide and hydrogen. To ensure a high methane conversion, high temperatures and low hydrogen concentrations are required. Separating the unwanted byproduct CO<sub>2</sub> from the outlet gas mixture requires complex and energy intensive separation units such as pressure swing adsorption columns, and will result in an increase in cost and energy usage, and a decrease in system performance (Medrano et al. (2014)). A promising new approach to circumvent the drawbacks of the current hydrogen production methods is

integrating the reaction and separation steps in one unit. Extracting hydrogen from the gas mixture with modern, high-flux hydrogen perm-selective palladium membranes purifies the hydrogen whilst simultaneously driving the chemical reaction equilibria towards the product side. The reactor can therefore operate at a lower temperature (600-700 °C) than the industrial process. The integration of hydrogen perm-selective membranes in packed bed reactors has already been investigated by Tsotsis et al. (1992), Tiemersma et al. (2006) and many others.

In packed bed membrane reactor systems, catalyzed reactions and separation of product and waste are performed in the same unit. However, a major drawback of packed bed membrane reactors is the low mixing efficiency, causing temperature and concentration gradients in the reactor. When using state-of-the-art membranes, the system is not limited by the permeation rate, but limited by the mass transfer rate of hydrogen towards the membranes, which is called concentration polarization (Caravella et al. (2009)). To circumvent these drawbacks, fluidized bed membrane reactors have been proposed to extract hydrogen from the reaction mixture, see Adris et al. (1994), Gallucci (2008), Mleczko et al. (1996) and Hommel et al. (2012).

Compared to packed bed membrane reactors, fluidized bed membrane reactors have better mixing properties, resulting in reduced mass transfer limitations towards the membranes. The hydrodynamics and mass transfer phenomena of the fluidized suspension can be strongly affected by the membrane configuration. Possible hydrodynamic consequences of installing membranes in fluidized beds have been demonstrated by e.g. De Jong et al. (2011), Dang et al. (2014), Tan et al. (2014), Wassie et al. (2015) and Medrano et al. (2015). Industrially, membranes immersed in the particle emulsion of a fluidized bed may be damaged due to attrition, so for large scale applications a protective nano-layer coating or a porous filter could be applied to prevent this. Having said this, Helmi et al. (2016) have successfully demonstrated the long term (over 900 hours) performance of a fluidized bed membrane reactor utilizing very high flux membranes for ultra-pure hydrogen production via WGS.

Membranes are mostly inserted vertically in reactors. Helmi et al. (2017) have demonstrated that when using state-of-the-art high-flux palladium membranes to extract hydrogen from a hydrogen/nitrogen gas mixture, mass transfer limitations from the bed to the membrane (concentration polarization) can severely limit the extracted flux. Furthermore, recent experimental findings suggest that vertically immersed membranes hardly affect the gas bubbles that are passing by. By inserting the membranes perpendicular to the flow direction (i.e. horizontally), the membranes can cut large gas bubbles into smaller ones, hereby improving the mixing efficiency of the bed. Previous studies by Medrano et al. (2015), De Jong et al. (2012), Asegehegn et al. (2011), Rong et al. (1999), Solnordal et al. (2015), Wang et al. (2015), Yang et al. (2014) and Sarkar et al. (2013) on horizontal tubes immersed in fluidized beds have already proven that tubes have a significant effect on the bed hydrodynamics. However, very little work

has been done on mass transfer phenomena in fluidized bed reactors with horizontally immersed membranes.

This work is a numerical study on the mass transfer phenomena in fluidized bed reactors with horizontally immersed membranes. The goal of this work is to describe, identify and explain the most important mass transfer phenomena occurring in fluidized beds with horizontally immersed membranes. Explaining the mass transfer phenomena will also require relating the observed mass transfer phenomena to the hydrodynamics. For example, Medrano et al. (2015) found that gas pockets (solids free, non-rising gas bubbles) occur underneath and densified particle zones occur on top of horizontally submerged membranes. The gas pockets and densified zones may affect the mass transfer towards the membranes and could therefore have a noticeable effect on the system performance.

Because palladium-based membranes are quite expensive, placing them at locations where they perform sub-optimally should be avoided. Exploratory simulations have already indicated that reduced hydrogen concentrations are mostly found at membranes near the bed walls (see Voncken et al. (2015)), so the performance of these membranes are especially worth investigating. Therefore, we have simulated fluidized beds with various membrane tube bank configurations with and without membranes near the bed walls. However, simply removing membranes near the wall could also affect the solids circulation patterns, the bubble cutting behavior of the tube banks and could induce gas bypassing via the walls, so fluidized beds with inactive tubes instead of membranes near the walls were also simulated.

A Two-Fluid Model (TFM) was used to perform the simulations and to obtain detailed information on the mass transfer phenomena occurring near the membranes. The OpenFOAM v.2.3.0 TFM (*twoPhaseEulerFoam*) was used as hydrodynamic framework, and was extended with a species balance equation and realistic membrane models to simulate selective extraction of hydrogen from the system.

First, the model equations, verification and validation will be discussed. Special attention will be given to the implementation of the species balance, the implementation of the membrane source term and the membrane boundary condition. Next, the simulation settings and the tube bank geometries will be presented. In the results section, the most important mass transfer phenomena and hydrodynamics will be presented and explained.

## MODEL DESCRIPTION

A TFM considers the gas and solids phase as interpenetrating continua. The most important governing and constitutive equations are presented in equations 1 through 6. The continuity equations (1) of both gas and solids phase are very similar. The source term  $S$  is added to the gas continuity equation to take into account the extraction of gas via membranes. The membrane source term will be presented in the mass transfer and membranes section. Compared to the Navier-Stokes equations of the gas phase (2), the Navier-Stokes equations for the solids phase (3) contain

an additional solids pressure term  $p_s$ . For both phases a Newtonian stress tensor  $\boldsymbol{\tau}$  is employed. The gas phase density is described with the ideal gas law. Furthermore, the granular temperature equation (4) is solved. The granular temperature equation incorporates the mean particle velocity and a superimposed fluctuating component, taking into account the vibrations of particles due to collisions.

$$\frac{\partial(\alpha_i \rho_i)}{\partial t} + \nabla \times (\alpha_i \rho_i \mathbf{u}_i) = S_m, \quad i = s, g \quad (1)$$

$$\begin{aligned} & \frac{\partial(\alpha_g \rho_g \mathbf{u}_g)}{\partial t} + \nabla \times (\alpha_g \rho_g \mathbf{u}_g \mathbf{u}_g) \\ &= -\nabla \times (\alpha_g \boldsymbol{\tau}_g) - \alpha_g \nabla p - \beta \times (\mathbf{u}_g - \mathbf{u}_s) + \alpha_g \rho_g \mathbf{g} \end{aligned} \quad (2)$$

$$\begin{aligned} & \frac{\partial(\alpha_s \rho_s \mathbf{u}_s)}{\partial t} + \nabla \times (\alpha_s \rho_s \mathbf{u}_s \mathbf{u}_s) = -\nabla \times (\alpha_s \boldsymbol{\tau}_s) \\ & - \alpha_s \nabla p - \nabla p_s + \beta \times (\mathbf{u}_g - \mathbf{u}_s) + \alpha_s \rho_s \mathbf{g} \end{aligned} \quad (3)$$

$$\begin{aligned} & \frac{3}{2} \left( \frac{\partial(\alpha_s \rho_s \theta)}{\partial t} + \nabla \times (\alpha_s \rho_s \mathbf{u}_s \theta) \right) = -\gamma_s - 3\beta\theta \\ & - (p_s \mathbf{I} + \alpha_s \boldsymbol{\tau}_s) : \nabla \mathbf{u}_s + \nabla \times (\alpha_s \boldsymbol{\kappa}_s \nabla \theta) \end{aligned} \quad (4)$$

The drag between the solids and the gas phase is modelled according to Gidaspow (1994), which combines the drag model of Ergun et al. (1949) and Wen et al. (1966). Ergun's model is valid for high solids hold-ups (20% and higher) and Wen's model is valid at lower solids hold-ups (below 20%). The drag coefficient  $C_d$  is determined based on the Reynolds particle number. The drag models are described in equations 5 until 9.

$$\beta = 150 \frac{\alpha_s^2 \mu_g}{\alpha_g d_p^2} + 1.75 \frac{\alpha_s \rho_g |\mathbf{u}_g - \mathbf{u}_s|}{d_p} \quad (\alpha_s \geq 0.20) \quad (5)$$

$$\beta = \frac{3}{4} C_d \frac{\alpha_s \alpha_g \rho_g}{d_p} |\mathbf{u}_g - \mathbf{u}_s| \alpha_g^{-2.65} \quad (\alpha_s < 0.20) \quad (6)$$

$$C_d = \frac{24}{\text{Re}_p} (1 + 0.15 \text{Re}_p^{0.687}) \quad \text{for } \text{Re}_p \leq 1000 \quad (7)$$

$$C_d = 0.44 \quad \text{for } \text{Re}_p > 1000 \quad (8)$$

$$\text{Re}_p = \alpha_g \frac{\rho_g d_p |\mathbf{u}_g - \mathbf{u}_s|}{\mu_g} \quad (9)$$

### Kinetic Theory of Granular Flow

To simulate the rheological and collisional properties of the solids phase's continuum approximation more realistically, various KTGF closure equations are required. The closure equations used in this work are

presented in **Table 1**. Further details on the TFM-KTGF can be found a.o. in Lun et al. (1984), Kuipers et al. (1992), Gidaspow (1994), Van Wachem (2000), Rusche (2003) and Van Der Hoef et al. (2006). Details on the OpenFOAM TFM can be found in Passalacqua et al. (2011) and Liu et al. (2014).

**Table 1:** KTGF closures used for TFM simulations.

Quantity	Closure
Solids shear viscosity	Nieuwland et al. (1996)
Solids bulk viscosity	Lun et al. (1984)
Solids pressure	Lun et al. (1984)
Frictional stress	Srivastava & Sundaresan (2003)
Conductivity of fluct. energy	Nieuwland et al. (1996)
Radial distribution function	Ma & Ahmadi (1984)
Dissipation of gran. energy	Nieuwland et al. (1996)

### Mass transfer and membranes

Mass transfer phenomena and hydrogen extraction via membranes was modeled similar to the approach of Coroneo et al. (2009). A hydrogen mass balance with Fickian diffusion was added to the model. The mass balance is a transient convection-diffusion equation as shown in equation 10. The diffusion coefficient can have a significant effect on the hydrogen flux. The selective extraction of hydrogen via the membranes was taken into account via the source term,  $S_m$ , which is applied to the computational cells adjacent to a membrane boundary (the red cells in **Figure 1**). The source term in equation 10 is the membrane flux calculated with Sieverts' law, multiplied by the boundary cell's area  $A_c$ , divided by the cell volume  $V_c$ , see equation 11.

$$\begin{aligned} & \frac{\partial \alpha_g \rho_g Y_{H_2}}{\partial t} + \nabla \times (\alpha_g \rho_g \mathbf{u}_g Y_{H_2}) \\ &= \nabla \times (\alpha_g \rho_g D_{H_2} \nabla Y_{H_2}) + S_m \end{aligned} \quad (10)$$

$$S_m = \frac{A_c}{V_c} Q_m M_{H_2} \times \left[ (X_{H_2}^{ret} P_{tot})^n - (X_{H_2}^{perm} P_{tot})^n \right] \quad (11)$$

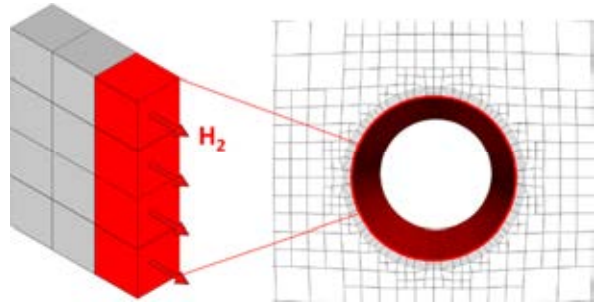


**Figure 1:** Schematic representation of how and where the membrane source term has been implemented in the grid.

The extraction of mass via a membrane will also result in momentum extraction from the system. Therefore, a boundary condition was added for the membranes to ensure momentum leaves the system. The momentum flux is based on the magnitude of the extractive flux. The boundary condition ultimately imposes a velocity normal to the membrane boundary (see equation 12). For fluidized beds momentum extraction could be an



important topic, because the it can cause densified zones to form near the membranes. Extracting a large amount of the momentum from a fluidized bed can even alter the flow pattern of the solids, as shown by De Jong et al. (2012) and Dang et al. (2014). The work of Helmi et al. (2017) has shown that selective extraction of hydrogen has an effect on the bed hydrodynamics, but that this effect is relatively small.

$$u_m = \frac{S_m RT}{pM_{H_2}} \frac{V_c}{A_c} \quad (12)$$

### Boundary conditions

All simulations have been performed with a 2D computational domain. For the gas mixture, a no-slip boundary condition was applied to the left and right walls, a constant gas velocity was imposed at the inlet, an imposed pressure condition was set at the outlet and the boundary condition of equation 12 was applied at the membranes. For the solids velocity and granular temperature, a Johnson & Jackson partial slip boundary condition with a specularity coefficient of 0.50 was applied on the walls and membranes (see Johnson et al. (1987)).

### Numerical schemes and accuracy

The temporal discretization was done with the second order Crank-Nicolson scheme. All simulations were run with an adjustable time-step, with a maximum time-step of  $1 \cdot 10^{-5}$  s. The selected time-step value each iteration was selected based on a maximum Courant number of 0.1. A combination the second order Gauss linear and Van Leer scheme were used for spatial discretization. The numerical tolerances for the residuals were set to  $1 \cdot 10^{-11}$  for each quantity.

## VERIFICATION, VALIDATION, GEOMETRIES AND SETTINGS

### Verification and validation

The fluid, solid and mass transfer part of the TFM have all been verified and validated. The fluid part of the model has been verified by comparing gas flow profiles, convection and diffusion of a chemical specie to their respective analytical solutions. Gas flow profiles and the pressure drop in a flat rectangular column (pseudo 2D) match very well with the analytical solution of White et al. (1991), even for very coarse grids. Furthermore, combined convection-diffusion of a specie were compared to the analytical solution found in Mohsen et al. (1983). Especially at finer grids and time-steps of 0.001 s and below, the TFM results match well with the analytical solution and the numerical diffusion decreases significantly.

Helmi et al. (2017) have used this TFM to simulate an experimental reactor with one vertically immersed membrane in the center. The TFM was able to predict the experimental fluxes very well and proved to be a useful tool to determine concentration profiles in fluidized bed membrane reactors.

The model was also validated by comparing experimental bubble properties to the simulated ones. The bubble properties match well with experimental

bubble diameter and velocity data obtained via Digital Image Analysis of thousands of gas bubbles.

The accuracy of the model for densely packed systems is important because densified zones are expected to occur frequently in fluidized bed membrane reactors, especially on top of the membranes and near the walls. Therefore, the predicted TFM pressure drop over a pseudo 2D packed bed injected with air ( $\rho_g=1.2 \text{ kg/m}^3$ ,  $\mu_g=1.84 \cdot 10^{-5} \text{ Pa}\cdot\text{s}$ ) was compared to the Ergun equation and experimental pressure drop data for 500  $\mu\text{m}$  particles with a density of 2500  $\text{kg/m}^3$  (see **Figure 2**). The TFM results match well with the experimental data and with the Ergun equation. The minimum fluidization velocities determined by experiments and TFM are 0.218 and 0.212 respectively, and match very well. The small difference between the slopes of the experimental and TFM/Ergun equation is caused by the difference between the TFM and experimental porosity at minimum fluidization velocity.

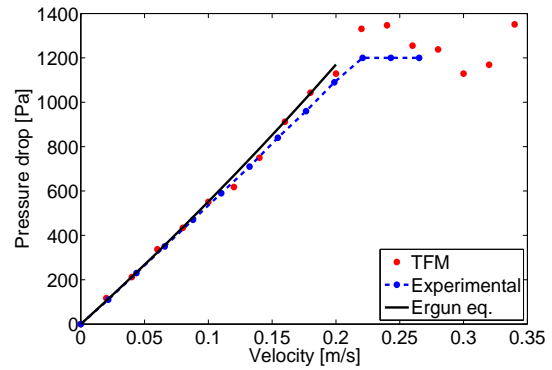


**Figure 2:** Pressure drop versus gas velocity for experiments, TFM simulations and Ergun equation calculations based on the TFM porosity.

### Geometries and model settings

A grid sensitivity study was performed for fluidized bed membrane reactors with one membrane in the center of the bed. The flux around the membrane is not uniform and is lowest on top of the membrane. Furthermore, the time-averaged solids hold-up on top of the membranes is higher than elsewhere around the membrane, which could suggest there is a relation between the reduced flux and increased solids hold-up. Further details will be discussed in the results section.

The tested grids are displayed in **Figure 3** and are labeled coarse (28 cells counted around the circumference of the membrane), middle (64 cells) and fine (128 cells). The computed fluxes of the different grids were time-averaged over 25 seconds of simulation time and compared to each other to verify whether grid independent results were obtained. The coarse grid was not yet grid independent, whereas the middle and fine grid are relatively close to each other. The large number of grid cells in the fine grid would however require the simulations to be run at unfeasibly small time-steps, which would result in very long simulation times, especially when extending this to systems with membrane tube banks. Therefore, the middle grid was used for all further cases studied in this work.

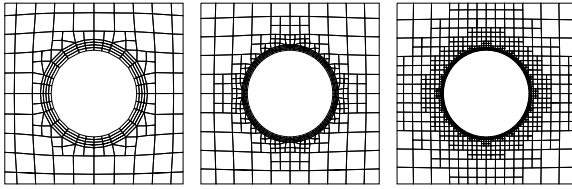


**Figure 3:** Grids around membranes for a coarse grid with 28 cells (left), middle grid with 64 cells (middle) and fine grid with 128 cells (right) adjacent to the membrane boundary.

Various horizontal membrane configurations were simulated. To keep practical simulation times, full 2D simulations were performed. As Asegehehn et al. (2011) reported, bubble behavior is quite similar for 2D and 3D systems with immersed tubes. The simulation settings are given in **Table 1**. The configurations and dimensions of the tube banks are presented in **Figure 4**. Configurations (a)–(d) are the base cases called Wall Membranes (WM), because membranes are present close to the bed walls. In configurations (e)–(h) the membranes closest to the walls have been removed, so they are called No Wall Membranes (NWM). In configurations (i)–(l) the membranes near the walls have been replaced with inactive tubes (portrayed as open black circles), so they are referred to as Tubes (T). The Tubes cases have the same membrane area as the No Wall Membranes cases, but the same membrane/tube locations as the Wall Membranes cases. The hydrodynamic effect that objects near the bed walls have on the system performance can hereby be quantified. The membrane tube banks have either been placed in a staggered or in an in-line configuration. The Full Staggered (FS) cases are configured in the same way as the Half Staggered (HS) cases, except they have double the number of membranes. This is also the case with the Full In-line (FI) and Half In-line (HI) configurations. Industrially, the half tube bank cases could be useful for auto-thermal reactions; the empty bottom section can be used to generate heat for the reaction by combustion. Furthermore, overloading the system with too many modern high flux membranes will result in a low performance per membrane, which would make the system less feasible.

**Table 1:** Summary of TFM simulation settings for all horizontal membrane cases.

Par.	Value	Par.	Value
<i>Width</i>	0.30 m	$\rho_p$	2500 kg/m <sup>3</sup>
<i>Height</i>	0.90 m	$D_{H_2}$	1.0 · 10 <sup>-4</sup> m <sup>2</sup> /s
$N_{c,width}$	150	$Q_{pd}$	4.3 · 10 <sup>-3</sup> mol/(m <sup>2</sup> s Pa <sup>n</sup> )
$N_{c,height}$	450	$n$	0.50
$d_m$	9.6 mm	$T$	405 °C
$d_p$	500 μm	$X_{H_2,in}$	0.25
$e_{pp}$	0.97	$p_{outlet}$	1.6 · 10 <sup>5</sup> Pa
$e_{pw}$	0.97	$p_{perm}$	0.01 · 10 <sup>5</sup> Pa
$u/u_{mf}$	3.0	$t_{sim}$	30 s
$u_{mf}$	0.21 m/s	$\Delta t_{max}$	1 · 10 <sup>-5</sup> s

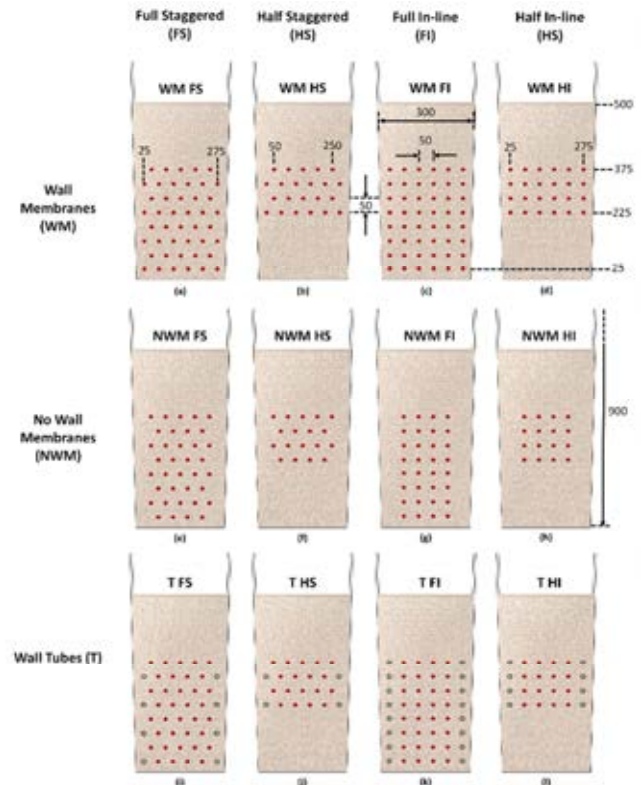


**Figure 4:** Membrane tube bank configurations:

- Wall Membranes**  
 (a) Full Staggered (WM FS); (b) Half Staggered (WM HS);  
 (c) Full In-line (WM FI); (d) Half In-line (WM HI).  
**No Wall Membranes**  
 (e) Full Staggered (NWM FS); (f) Half Staggered (NWM HS);  
 (g) Full In-line (NWM FI); (h) Half In-line (NWM HI).  
**Wall Tubes (black open circles)**  
 (i) Full Staggered (T FS); (j) Half Staggered (T HS); (k) Full In-line (T FI); (l) Half In-line (T HI). All given measurements are in mm.

## RESULTS

### Mass transfer limitations

The main mass transfer limitations in fluidized beds with horizontally immersed membranes are at the membranes located near the bed walls (**Figure 5**). The time-averaged hydrogen mole fractions are lowest on top of the membranes near the walls. For the full in-line configuration (**Figure 4 c**) the time averaged hydrogen flux of the membranes at the walls is in some cases half of the flux of the all membranes in the middle. The flux of the membranes in the middle does show a similar trend as the flux of the membranes near the walls. Mass transfer is mostly limited on top of the membranes, whereas the best performance is found at the bottom of the membranes. This flux profile can be related to hydrodynamic effects that have already been observed by Medrano et al. (2015). In their work, densified zones and gas pockets were found to be potential mass transfer limitations for horizontally immersed membranes. In the next section, the effect of these densified zones and gas pockets on mass transfer of hydrogen towards horizontally immersed membranes will be discussed in more detail.

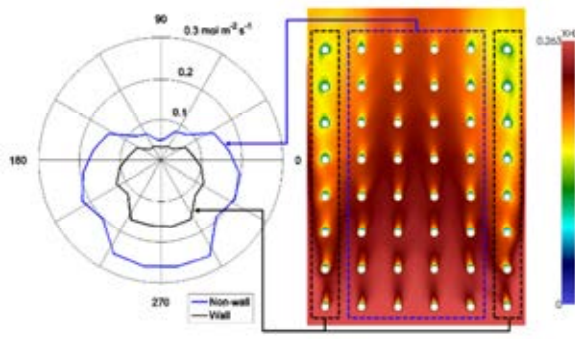


**Figure 5:** Time-averaged hydrogen flux at various angles around the membranes, and a snapshot of time-averaged hydrogen mole fractions, both for the full inline membrane tube bank configuration.

### Densified zones, gas pockets and gas flow patterns

Gas pockets and densified zones are observed both in TFM simulations and during experiments. Gas pockets are formed because the downward movement of solids shields the underside, which can cause areas with very little solids content to form underneath the membranes. Gas pockets mostly appear near the walls, but they can be found underneath any horizontally immersed membrane.

No significant effect of gas pockets on the mass transfer towards the membranes was found. **Figure 6** shows two snapshots, one taken right before the gas pocket occurs, and one while the gas pocket is at its largest. Similar to regular bubbles in fluidized beds, the gas mixture follows the path of least resistance and therefore flows through areas with the lowest particle content, such as gas pockets. The streamlines show that the gas flowing around the membrane has a significant effect on where reduced hydrogen concentrations are observed. The gas cannot easily flow to the top of the membranes, which enables solids to accumulate here (densified zones), making it more difficult to quickly replenish hydrogen here.

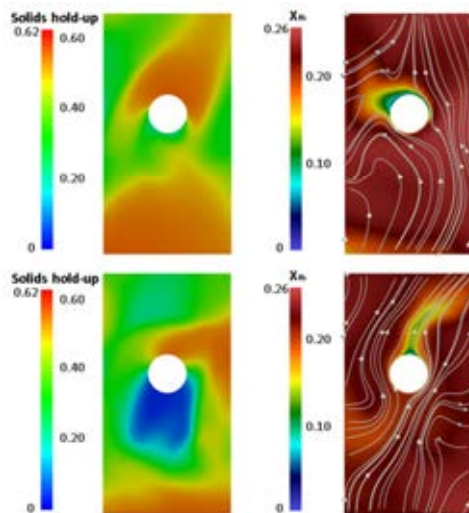


**Figure 6:** Snapshot of the solids hold-up, hydrogen mole fraction and gas velocity streamlines around a horizontally immersed membrane with and without a gas pocket.

Densified zones can be present on top of membranes anywhere in the reactor. Similar to gas pockets, they mostly occur at the membranes that are located near the bed walls, because the solids flow downwards onto the top of the membranes there. Next to solids down flow, **Figure 7** shows that an important reason for densified zones to form is that gas cannot easily reach the top of the membranes. The gas velocities are especially low near the membranes close to the walls. Because of the no-slip behavior of the gas near the walls, the gas has insufficient momentum to move the downward flowing solids away from the membranes near the walls. In the middle of the reactor, less densified zones are present, but they still occur because the gas cannot always reach the top of the membrane easily.

The time-averaged hydrogen mole fractions in **Figure 7** show that densified zones have a detrimental effect on mass transfer towards the membrane. On top of the membrane, the hydrogen mole fractions (thus also the hydrogen fluxes) are significantly lower compared to elsewhere around the membrane. The effect is mostly noticeable near the walls, where clearly some gas back-mixing is visible, but also in the middle of the reactor a reduced hydrogen flux was observed on top of the membrane. This is intrinsic to the way the membranes are placed compared to the flow direction. The gas cannot always reach the top of the membrane easily, because the membrane itself shields the top-side of the membrane. In **Figure 5** this is visible, because the time-averaged hydrogen flux is also lower on top of the membranes in the middle.

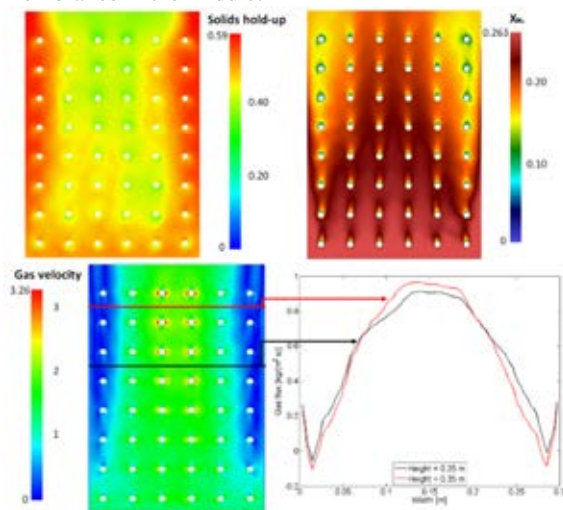


**Figure 7:** Snapshot of the time-averaged solids hold-up, hydrogen mole fractions and gas velocities (in m/s) in a fluidized bed with a full in-line membrane tube bank.

### Effect of tube bank configuration on hydrogen flux

The main mass transfer limitations towards the membranes have already been identified near the bed walls. This section will quantify how much the mass transfer limitations affect the flux for various membrane tube bank configurations. **Figure 8** and **Figure 9** present the time-averaged hydrogen flux profiles at various width positions and various angles around the membranes for all the full in-line and half in-line configurations from **Figure 4**. The membranes near the

walls perform approximately three to five times worse than the membranes in the middle of the reactor for the full and half in-line configurations. Adding inert tubes near the walls does not have a significant effect on the system performance. The polar plots in **Figure 8** and **Figure 9** show that when active membranes are placed close to the walls, the averaged flux of all membranes is reduced. The in-line configurations with half tube banks show similar behavior to the full tube bank configurations.

In general, the flux over the reactor width in the full staggered configurations is more equal over the width than in the full in-line one (see **Figure 10**). However, some of the membranes that have not been removed in the full staggered configuration still have reduced flux, even though the difference between the highest and the lowest flux is about a factor two. In general the results show that membranes that are approximately within 8 cm distance of the walls (about 20% of the total bed width) suffer from reduced flux. Because bubbles cannot channel through the staggered membrane tube banks, the membranes near the walls perform better in a staggered configuration than in an in-line one. The flux is slightly higher for the membranes in the middle of the half tube bank configurations, because in the full tube bank configurations a lot of the hydrogen has already been extracted before it reaches the membranes in the top of the tube bank, which results in lower fluxes for the top membranes.

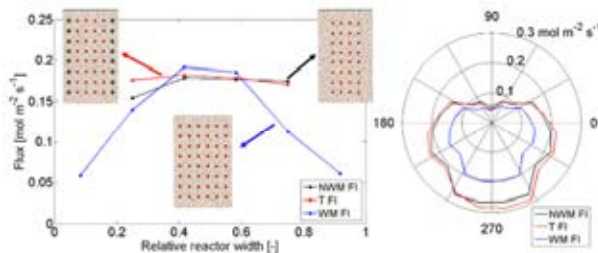


**Figure 8:** Time-averaged flux for the full in-line tube bank configurations without wall membranes, with inert tubes at the walls and with wall membranes; (left) flux versus relative reactor width (right) flux averaged over all membranes at various angles around the membranes.

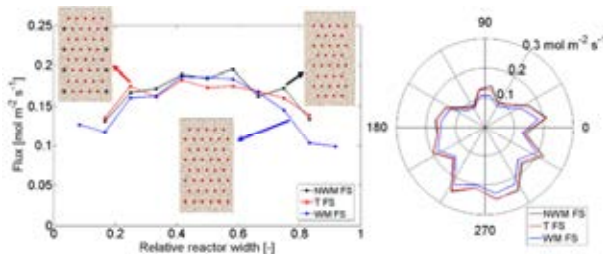


**Figure 9:** Time-averaged flux for the full staggered tube bank configurations without wall membranes, with inert tubes at the walls and with wall membranes; (left) flux versus relative reactor width (right) flux averaged over all membranes at various angles around the membranes.

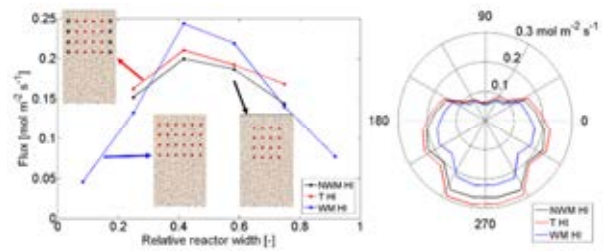


**Figure 10:** Time-averaged flux for the half in-line tube bank configurations without wall membranes, with inert tubes at the walls and with wall membranes; (left) flux versus relative reactor width (right) flux averaged over all membranes at various angles around the membranes.

## CONCLUSION

The performance of fluidized bed membrane reactors with various horizontally immersed membrane tube bank configurations was investigated. The flux is lowest at the top of the membranes and highest below the membranes. The densified zones and the gas flow patterns have a significant negative effect on the hydrogen permeation flux. Gas pockets have no negative effect on the mass transfer from the emulsion phase to the membrane. However, gas pockets could reduce the reaction rate of systems in which the extracted product is produced via a catalytic reaction.

In systems with tube banks, membranes that are placed close to the fluidized bed walls show significantly lower performance than the membranes in the center of the bed. The down flowing solids and reduced gas flow near the walls keeps the flux low here. Replacing the wall membranes with inactive tubes does not have a significant positive effect on the system, so removal of the wall membranes is therefore advised. In case of exothermal or endothermal reactions, wall tubes can perhaps be used for internal cooling or heating.

Future work on fluidized beds with horizontally immersed membranes should focus on methods to reduce the mass transfer limitations towards the membranes. Potential methods include having a non-uniform gas feed, pulsating gas inlet flow rate, changing the membrane pitch and using as large as possible particles to increase the dispersion effects.

## ACKNOWLEDGEMENTS

The authors are grateful to TTW and NWO for their financial support through the VIDI project ClingCO<sub>2</sub>, project number 12365.

## REFERENCES

- ADRIS, A.M., LIM, C.J. and GRACE, J.R., (1994), "The fluidized bed membrane reactor system: a pilot scale experimental study", *Chem. Eng. Sc.*, **49**, 5833-5843.
- ASEGEHEGN, T.W., SCHREIBER, M. and KRAUTZ, H.J., (2011), "Numerical simulation and experimental validation of bubble behavior in 2D gas-solid fluidized beds with immersed horizontal tubes", *Chem. Eng. Sc.*, **66**, 5410-5427.
- CARAVELLA, A., BARBIERI, G. and DRIOLI, E., (2009), "Concentration polarization analysis in self-

supported Pd-based membranes”, *Purif. Technol.*, **66**, 613-624.

CORONEO, M., MONTANTE, G., CATALANO, J. and PAGLIANTI, A., (2009), “Modelling the effect of operating conditions on hydrodynamics and mass transfer in a Pd-Ag membrane module for H<sub>2</sub> purification”, *J. Memb. Sc.*, **343**, 34-41.

DANG, T.Y.N., GALLUCCI, F. and VAN SINT ANNALAND, M., (2014), “Micro-structured fluidized bed membrane reactors: solids circulation and densified zones distribution”, *Chem. Eng. J.*, **239**, 42-52.

DE JONG, J.F., VAN SINT ANNALAND, M. and KUIPERS, J.A.M., (2011), “Experimental study on the effects of gas permeation through flat membranes on the hydrodynamics in membrane-assisted fluidized beds”, *Chem. Eng. Sc.*, **66**, 2398-2408.

DE JONG, J.F., VAN SINT ANNALAND, M. and KUIPERS, J.A.M., (2012), “Membrane-assisted fluidized beds - part 2: numerical study on the hydrodynamics around immersed gas-permeating membrane”, *Chem. Eng. Sc.*, **84**, 822-833.

ERGUN, S. and ORNING, A., (1949), “Fluid flow through randomly packed columns and fluidized beds”, *Ind. Eng. Chem.*, **41**, 1179-1184.

GALLUCCI, F., VAN SINT ANNALAND, M. and KUIPERS, J.A.M., (2008), “Autothermal reforming of methane with integrated CO<sub>2</sub> capture in a novel fluidized bed membrane reactor. Part 1: experimental demonstration”, *Top. Catal.*, **51**, 133-145.

GIDASPOW, D., (1994), “Multiphase flow and fluidization: continuum and kinetic theory descriptions”, *Academic Press Inc.*

HOMMEL, R., Cloete, S. and AMINI, S., (2012), “Numerical investigations to quantify the effect of horizontal membranes on the performance of a fluidized bed reactor”, *Int. J. Chem. React. Eng.*, **10**.

HELMI, A., FERNANDEZ, E., MELENDEZ, J., PACHECO TANAKA, D.A., GALLUCCI, F. and VAN SINT ANNALAND, M., (2016), “Fluidized Bed Membrane Reactors for Ultra Pure H<sub>2</sub> Production - A Step forward towards Commercialization”, *Molecules*, **21**, 376.

HELMI, A., VONCKEN, R.J.W., RAIJMAKERS, T., ROGHAIR, I., GALLUCCI, F., and VAN SINT ANNALAND, M., (2017), “On concentration polarization in fluidized bed membrane reactors”, *Submitted to Chem. Eng. J.*

JOHNSON, P.C. and JACKSON, R., (1987), “Frictional-collisional constitutive relations for granular materials, with application to plane shearing”, *J. Fluid Mech.*, **176**, 67-93.

KUIPERS, J.A.M., VAN DUIN, K.J., VAN BECKUM, F.P.H., and VAN SWAAIJ, W.P.M., (1992), “A numerical model of gas-fluidized beds”, *Chem. Eng. Sci.*, **47**, 1913-1924.

LIU, Y. and HINRICHSEN, O., (2014), “CFD modeling of bubbling fluidized beds using OpenFOAM®: Model validation and comparison of TVD differencing schemes”, *Comp. & Chem. Eng.*, **69**, 75-88.

LUN, C.K.K., SAVAGE, S.B., JEFFREY, D.J., and CHEPURNIY, N., (1984), “Kinetic theories for granular flow: inelastic particles in Couette flow and slightly

inelastic particles in a general flowfield”, *J. Fluid Mech.*, **140**, 223-256.

MA, D. and AHMADI, G., (1988), “A kinetic model for rapid granular flows of nearly elastic particles including interstitial fluid effects”, *Powder Technol.*, **56**, 191-207.

MEDRANO, J.A., SPALLINA, V., VAN SINT ANNALAND, M. and GALLUCCI, F., (2014), “Thermodynamic analysis of a membrane-assisted chemical looping reforming reactor concept for combined H<sub>2</sub> production and CO<sub>2</sub> capture”, *Int. J. Hydrogen Energy*, **39**, 4725-4738.

MEDRANO, J.A., VONCKEN, R.J.W., ROGHAIR, I., GALLUCCI, F. and VAN SINT ANNALAND, M., (2015), “On the effect of gas pockets surrounding membranes in fluidized bed membrane reactors: An experimental and numerical study”, *Chem. Eng. J.*, **282**, 45-57.

MLECZKO, L., OSTROWSKI, T. and WURZEL, T., (1996), “A fluidised-bed membrane reactor for the catalytic partial oxidation of methane to synthesis gas”, *Chem. Eng. Sc.*, **51**, 3187-3192.

MOHSEN, M.F.N. and BALUCH, M.H., (1983), “An analytical solution of the diffusion-convection equation over a finite domain”, *Appl. Math. Model.*, **7**, 285-287.

NIEUWLAND, J.J., VAN SINT ANNALAND, M., KUIPERS, J.A.M. and VAN SWAAIJ, W.P.M., (1996), “Hydrodynamic modeling of gas/particle flows in riser reactors”, *AIChE J.*, **42**, 1569-1582.

PASSALACQUA, A. and FOX, R.O., (2011), “Implementation of an iterative solution procedure for multi-fluid gas-particle flow models on unstructured grids”, *Powder Technol.*, **213**, 174-187.

RONG, D., MIKAMI, T. and HORIO, M., (1999), “Particle and bubble movements around tubes immersed in fluidized beds – a numerical study”, *Chem. Eng. Sc.*, **54**, 5737-5754.

RUSCHE, H., (2002), “Computational fluid dynamics of dispersed two-phase flows at high phase fractions”, PhD thesis, *University of London*.

SRIVASTAVA, A. and SUNDARESAN, S., (2003), “Analysis of a frictional-kinetic model for gas-particle flow”, *Powder Technol.*, **129**, 72-85.

SARKAR, A., SUN, X. and SUNDARESAN, S., (2013), “Sub-grid drag models for horizontal cylinder arrays immersed in gas-particle multiphase flows”, *Chem. Eng. Sc.*, **104**, 399-412.

SOLNORDAL, C.B., KENCHE, V., HADLEY, T.D., FENG, Y., WITT, P.J. and LIM, K.-S., (2015), “Simulation of an internally circulating fluidized bed using a multiphase particle-in-cell method”, *Powder Technol.*, **274**, 123-134.

WANG, Q., YANG, H., FENG, Y., WITT, P.J., LU, J. and YIN, W., (2015), “Numerical study of the effect of operation parameters on particle segregation in a coal beneficiation fluidized bed by a TFM-DEM hybrid model”, *Chem. Eng. Sc.*, **131**, 256-270.

YANG, S., LUO, K., FANG, M., FAN, J. and CEN, K., (2014), “Discrete element study of solid circulating and resident behaviors in an internally circulating fluidized bed”, *Chem. Eng. J.*, **248**, 145-157.

TAN, L., ROGHAIR, I. and VAN SINT ANNALAND, M., (2014), “Simulation study on the effect of gas permeation on the hydrodynamic

characteristics of membrane-assisted micro fluidized beds”, *Appl. Math. Model.*, **38**, 4291-4307.

TIEMERSMA, T.P., PATIL, C.S., VAN SINT ANNALAND, M. and KUIPERS, J.A.M., (2006), “Modelling of packed bed membrane reactors for autothermal production of ultrapure hydrogen”, *Chem. Eng. Sc.*, **61**, 1602-1616.

TSOTSIS, T.T., CHAMPAGNIE, A.M., VASILEIADIS, S.P., ZIACA, Z.D. and MINET, R.G., (1992), “Packed bed catalytic membrane reactors”, *Chem. Eng. Sc.*, **47**, 2903-2908.

VAN DER HOEF, M.A., YE, M., VAN SINT ANNALAND, M., ANDREWS IV, A.T., SUNDARESAN, S. and KUIPERS, J.A.M., (2006) “Multi-scale modeling of gas-fluidized beds”, *Adv. Chem. Eng.* **31**, 65–149.

VAN WACHEM, B.G.M., (2000), “Derivation, implementation, and validation of computer simulation models for gas-solid fluidized beds”, PhD thesis, Delft University of Technology.

VONCKEN, R., ROGHAI, I., GALLUCCI, F. and VAN SINT ANNALAND, M., (2015), “Mass transfer phenomena in fluidized beds with vertically and horizontally immersed membranes”, *Proc. 11th Int. Conf. Comput. Fluid Dyn. Miner. Process Ind. (CFD 2015)*, 031VON 1-6.

WASSIE, S.A., GALLUCCI, F., CLOETE, S., ZAABOUT, A., VAN SINT ANNALAND, M., and AMINI, S., (2015), “The effect of gas permeation through vertical membranes on chemical switching reforming (CSR) reactor performance”, *Int. J. Hydrogen Energy*, **41**, 8640-8655.

WEN, C. and YU, Y., (1966) “A generalized method for predicting the minimum fluidization velocity” *AICHEJ.* **12**, 610-612.

WHITE, F.M., (1991), “Viscous fluid flow”, *McGraw-Hill Inc.*



## A TWO-FLUID MODEL STUDY OF HYDROGEN PRODUCTION VIA WATER GAS SHIFT IN FLUIDIZED BED MEMBRANE REACTORS

Ramon J.W. VONCKEN<sup>1</sup>, Ivo ROGHAI<sup>1\*</sup>, Martin VAN SINT ANNALAND<sup>1</sup>

<sup>1</sup> Chemical Process Intensification, Department of Chemical Engineering and Chemistry, Eindhoven University of Technology, THE NETHERLANDS

\* Corresponding author e-mail: i.roghair@tue.nl

### ABSTRACT

Fluidized bed membrane reactors have been proposed as a promising reactor concept for the production of ultra-pure hydrogen via Water Gas Shift (WGS). High-flux thin-film dense palladium-based membranes are used to selectively extract hydrogen from the reaction medium, which shifts the thermodynamic equilibrium towards the products' side, increasing the conversion. A Two-Fluid Model (TFM) has been used to investigate the effect of hydrogen extraction via perm-selective membranes on the WGS reaction rates in the fluidized bed. A thorough TFM verification study was performed, which showed that the model is able to accurately predict the concentration profiles for various types of  $n^{\text{th}}$  order and equilibrium chemical reactions. Also, the implementation of the WGS reaction rate in the TFM was checked. The results have shown a clear positive effect of the hydrogen permeation on the WGS reaction rates, both for vertically and horizontally immersed membranes. In systems with horizontally immersed membranes, gas pockets that contain a very small amount of catalyst develop underneath the membrane tube, resulting in reduced local reaction rates. Densified zones on top of the membrane tube show increased local reaction rates. Mass transfer limitations from the emulsion phase to the membrane surface is the most pronounced effect that reduces the overall reactor performance. The developed model allows further investigating different configurations and operation modes to further optimize the reactor's performance.

**Keywords:** Two-Fluid Model, Water Gas Shift, hydrogen, fluidized bed, membrane.

### NOMENCLATURE

#### Latin Symbols

$A$	area	[m <sup>2</sup> ]
$A_{WGS}$	pre-factor WGS reaction rate	[mol/(bar kg <sub>cat</sub> s)]
$B_{WGS}$	Relative equilibrium ratio eq.	[-]
$C_d$	drag coefficient	[-]
$C_1$	constant for Gibbs calc.	[J/(mol K <sup>3</sup> )]
$C_2$	constant for Gibbs calc.	[J/(mol K <sup>2</sup> )]
$C_3$	constant for Gibbs calc.	[J/(mol K)]
$C_4$	constant for Gibbs calc.	[J/mol]
$D$	diffusion coefficient	[m <sup>2</sup> /s]
$E_{act}$	Activation energy	[J/mol]
$e$	restitution coefficient	[-]

$G$	Gibbs free energy	[J/mol]
$H$	enthalpy	[J/mol]
$g$	gravitational acceleration	[m/s <sup>2</sup> ]
$k_{WGS}$	WGS reaction rate constant	[mol/(bar kg <sub>cat</sub> s)]
$K_{eq,WGS}$	WGS equilibrium constant	[-]
$M$	molar weight	[kg/mol]
$n$	power in Sieverts' law	[-]
$p$	pressure	[Pa]
$P$	partial pressure	[Pa]
$Q$	membrane permeance	[mol/(m <sup>2</sup> s Pa <sup>n</sup> )]
$R$	universal gas constant	[J/(mol.K)]
$R_{WGS}$	chemical reaction rate	[mol/(kg <sub>cat</sub> s)]
$Re$	Reynolds number	[-]
$S$	membrane mass source term	[kg/(m <sup>3</sup> .s)]
$t$	time	[s]
$T$	temperature	[K]
$u$	velocity	[m/s]
$V$	volume	[m <sup>3</sup> ]
$X$	molar fraction	[-]
$Y$	mass fraction	[-]

#### Greek Symbols

$\alpha$	hold-up fraction	[-]
$\beta$	interphase drag coefficient	[kg/(m <sup>3</sup> s)]
$\gamma$	dissipation of fluct. energy	[kg/(m s <sup>3</sup> )]
$\theta$	granular temperature	[m <sup>2</sup> /s <sup>2</sup> ]
$\kappa$	conductivity of fluct. energy	[kg/(m s)]
$\mu$	shear/dynamic viscosity	[Pa.s]
$\rho$	density	[kg/m <sup>3</sup> ]
$\tau$	shear stress tensor	[N/m <sup>2</sup> ]
$\omega_{cat}$	catalyst mass fraction	[-]

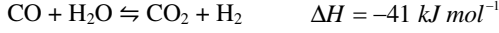
#### Sub/superscripts

$c$	cell
$g$	gas
$i$	phase
$m$	membrane
$mf$	minimum fluidization
$p$	particle
$ret$	retentate
$s$	solid
$sim$	simulation
$tot$	total
$w$	wall



## INTRODUCTION

Hydrogen is industrially mostly produced via Steam Methane Reforming (SMR) carried out in multi-tubular packed bed reactors. First, methane reacts with steam to form carbon monoxide and hydrogen at temperatures around 1000 °C. Consecutively, the formed carbon monoxide reacts with steam to form carbon dioxide and hydrogen via the Water Gas Shift (WGS) reaction, given by



WGS is thermodynamically favoured at low temperatures and kinetically favoured at higher temperatures. Traditionally, WGS reactors consist of two stages; in the first reactor most of the CO is converted at 300-450 °C and in the second reactor the remaining CO is converted at 200-300 °C. However, to produce hydrogen efficiently, low hydrogen concentrations are required to achieve high CO conversions. Costly and energy intensive separation units, such as pressure swing adsorption units, are required to separate the hydrogen from the outlet gas mixture. The process will have an additional cost and energy penalty, if the unwanted byproduct CO<sub>2</sub> should be separated from the gas mixture and stored underground (Medrano et al. (2014)).

Both packed bed membrane reactors (Tiemersma et al. (2006)) and fluidized bed membrane reactors (Fernandez et al. (2015)) have been proposed as alternative reactor systems for hydrogen production via WGS. This work will focus on the development of fluidized bed membrane reactors (FBMRs) for hydrogen production via WGS. In FBMRs, the reaction and separation steps have been integrated in one single unit; ultra-pure hydrogen is obtained from the reactor by extracting it from the gas mixture with modern high-flux hydrogen perm-selective supported palladium-based membranes. The hydrogen extraction drives the reaction equilibrium towards the products' side, which will increase the reaction rate and reactant conversion. The WGS reaction is highly suitable for hydrogen production in an FBMR, because hydrogen can be produced at 400 °C, high enough to avoid problems associated with membrane embrittlement and low enough to circumvent problems related to the membrane chemical/mechanical stability and membrane sealing.

Fluidized bed membrane reactors have already been investigated by a.o. Adris et al. (1994), Gallucci (2008) and Mleczko et al. (1996), and many others. Most of the previous fluidized bed membrane reactor studies were either focused on experimental demonstration or using phenomenological models. More recently, various CFD studies on fluidized bed membrane reactors have been performed, which have mostly investigated the bed hydrodynamics (De Jong et al. (2012), Tan et al. (2014) and Medrano et al. (2015)). Only a few studies have investigated FBMRs with CFD models focused on mass transfer phenomena and chemical reactions (e.g. Hommel et al. (2012), Voncken et al. (2015) and Helmi et al. (2017)).

The present work uses CFD simulations to visualize and quantify the mass transfer phenomena and reaction rates throughout FBMR systems in which hydrogen is produced via WGS. The OpenFOAM v.2.3.0 solver *twoPhaseEulerFoam*, a Two-Fluid Model (TFM), was used to model hydrodynamics, mass transfer and chemical reactions occurring in various fluidized bed membrane reactor configurations. The chemical species balances, selective membrane extraction and chemical reactions are our own implementations that were coupled to the TFM hydrodynamics. A thorough verification was carried out for all these aspects. To ensure the reaction terms have been implemented properly, numerous simple chemical reactions in a batch reactor have been simulated and compared to analytical and numerical solutions. The more complex kinetics of the WGS reaction have also been implemented in the TFM and compared to a batch reactor model.

The objective of this research is to understand and quantify the effect of selective hydrogen permeation on the performance of fluidized bed reactors for hydrogen production via WGS. The Numaguchi and Kikuchi (1988) reaction kinetics for WGS were implemented in the TFM. Both horizontally and vertically immersed membrane configurations were studied. These results were compared to the performance of a fluidized bed reactor without membranes.

First, the model equations and the verification of their implementation will be discussed. Special attention will be given to the species balance and the reaction kinetics. Next, the used simulation settings and geometries will be presented. In the results section, the effect of the extraction via the membranes on the reaction rates and reactor performance will be discussed.

## MODEL DESCRIPTION

The TFM considers the gas and solids phases as interpenetrating continua. The most important governing and constitutive equations are presented in equations 1 through 4, showing the continuity and Navier-Stokes equations of both the gas and solids phases. The source term  $S$  is added to the gas continuity equation to account for the extraction of gas via the membranes, which will be detailed later. The gas phase is considered as an ideal, Newtonian fluid. The solids phase rheology (solids pressure  $p_s$  and stress tensor  $\boldsymbol{\tau}_s$  is described with closures from the Kinetic Theory of Granular Flow, for which the granular temperature equation (4) is solved.

$$\frac{\partial(\alpha_i \rho_i)}{\partial t} + \nabla \cdot (\alpha_i \rho_i \mathbf{u}_i) = S_m, \quad i = s, g \quad (1)$$

$$\begin{aligned} & \frac{\partial(\alpha_g \rho_g \mathbf{u}_g)}{\partial t} + \nabla \cdot (\alpha_g \rho_g \mathbf{u}_g \mathbf{u}_g) \\ & = -\nabla \cdot (\alpha_g \boldsymbol{\tau}_g) - \alpha_g \nabla p - \beta (\mathbf{u}_g - \mathbf{u}_s) + \alpha_g \rho_g \mathbf{g} \end{aligned} \quad (2)$$

$$\begin{aligned} & \frac{\partial(\alpha_s \rho_s \mathbf{u}_s)}{\partial t} + \nabla \cdot (\alpha_s \rho_s \mathbf{u}_s \mathbf{u}_s) = -\nabla \cdot (\alpha_s \boldsymbol{\tau}_s) \\ & - \alpha_s \nabla p - \nabla p_s + \beta (\mathbf{u}_g - \mathbf{u}_s) + \alpha_s \rho_s \mathbf{g} \end{aligned} \quad (3)$$

$$\frac{3}{2} \left( \frac{\partial(\alpha_s \rho_s \theta)}{\partial t} + \nabla \times (\alpha_s \rho_s \mathbf{u}_s \theta) \right) = -\gamma_s - 3\beta\theta \quad (4)$$

$$-(p_s \mathbf{I} + \alpha_s \boldsymbol{\tau}_s) : \nabla \mathbf{u}_s + \nabla \times (\alpha_s \kappa_s \nabla \theta)$$

The fluid-particle drag is modelled according to Gidaspow (1994), which combines the drag models by Ergun et al. (1949) and Wen et al. (1966), where Ergun's model is valid for high solids hold-ups (above 20%) and Wen's model is applied at lower solids hold-ups (below 20%). The drag coefficient  $C_d$  is determined based on the Reynolds particle number. The drag models are described in equations 5 until 9.

$$\beta = 150 \frac{\alpha_s^2 \mu_g}{\alpha_g d_p^2} + 1.75 \frac{\alpha_s \rho_g |\mathbf{u}_g - \mathbf{u}_s|}{d_p} \quad (\alpha_s \geq 0.20) \quad (5)$$

$$\beta = \frac{3}{4} C_d \frac{\alpha_g \alpha_s \rho_g}{d_p} |\mathbf{u}_g - \mathbf{u}_s| \alpha_g^{-2.65} \quad (\alpha_s < 0.20) \quad (6)$$

$$C_d = \frac{24}{\text{Re}_p} (1 + 0.15 \text{Re}_p^{0.687}) \quad \text{for } \text{Re}_p \leq 1000 \quad (7)$$

$$C_d = 0.44 \quad \text{for } \text{Re}_p > 1000 \quad (8)$$

$$\text{Re}_p = \alpha_g \frac{\rho_g d_p |\mathbf{u}_g - \mathbf{u}_s|}{\mu_g} \quad (9)$$

### Kinetic Theory of Granular Flow

To simulate the rheological properties of the solids phase's continuum approximation, various KTGF closure equations are required. The closure equations used in this work are summarized in **Table 1**.

**Table 1:** KTGF closures used for TFM simulations.

Quantity	Closure
Solids shear viscosity	Nieuwland et al. (1996)
Solids bulk viscosity	Lun et al. (1984)
Solids pressure	Lun et al. (1984)
Frictional stress	Srivastava & Sundaresan (2003)
Conductivity of fluct. energy	Nieuwland et al. (1996)
Radial distribution function	Ma & Ahmadi (1984)
Dissipation of gran. energy	Nieuwland et al. (1996)

Further details on the TFM-KTGF can be found a.o. in Lun et al. (1984), Kuipers et al. (1992), Gidaspow (1994), Van Wachem (2000), Rusche (2003) and Van Der Hoef et al. (2006). Details on the OpenFOAM TFM can be found in Passalacqua et al. (2011) and Liu et al. (2014).

### Mass transfer, membranes and reactions

Mass transfer phenomena and extraction of hydrogen via membranes were modeled with an approach similar to that described by Coroneo et al. (2009), see equation 10. Extraction of hydrogen via the membranes was modeled via source term,  $S_m$ , to the species equation of hydrogen. This membrane source term is applied to the

computational cells adjacent to a membrane. The membrane source term is calculated with Sieverts' law, which is commonly used to describe the hydrogen flux through dense palladium membranes (see equation 11). The parameters in Sieverts' law are obtained from experiments. The extraction of mass via a membrane will also result in momentum extraction from the system. Therefore, a boundary condition was added for the membranes to ensure momentum leaves the system via the membranes, see equation 12.

$$\frac{\partial \alpha_g \rho_g Y_i}{\partial t} + \nabla \times (\alpha_g \rho_g \mathbf{u}_g Y_i) \quad (10)$$

$$= \nabla \times (\alpha_g \rho_g D_i \nabla Y_i) + S_m + R_i$$

$$S_m = \frac{A_c}{V_c} Q_m M_{H_2} \times \left[ (X_{H_2}^{ret} p_{tot})^n - (X_{H_2}^{perm} p_{tot})^n \right] \quad (11)$$

$$u_m = \frac{S_m RT}{p M_{H_2} A_c} \quad (12)$$

The Numaguchi and Kikuchi (1988) kinetics for the WGS reaction were implemented in the TFM model. The reaction rate equation and their corresponding parameters (reaction rate constants, pre-factors, equilibrium constants) are presented in **Table 2** and **Table 3**.

**Table 2:** Chemical reaction rates for WGS.

$$R_{WGS} = k_{WGS} \frac{P_{CO} P_{H_2O} - \frac{P_{CO_2} P_{H_2}}{K_{eq,WGS}}}{P_{H_2O}}$$

$$k_{WGS} = A_{WGS} \exp\left(-\frac{E_{act}}{RT}\right)$$

$$K_{eq,WGS} = \exp\left(\frac{-\Delta G_{WGS}}{RT}\right)$$

$$\Delta G_{WGS} = C_1 T^3 + C_2 T^2 + C_3 T + C_4$$

**Table 3:** Parameters for reaction rate expressions.

Parameter	Value
$A_{WGS}$	$2.45 \times 10^2 \text{ mol}/(\text{bar kg}_{cat} \text{ s})$
$E_{act}$	$54.5 \times 10^3 \text{ J}/(\text{mol K})$
$C_1$	$1.760 \times 10^{-6} \text{ J}/(\text{mol K}^3)$
$C_2$	$-1.065 \times 10^{-2} \text{ J}/(\text{mol K}^2)$
$C_3$	$48.04 \text{ J}/(\text{mol K})$
$C_4$	$2.075 \times 10^2 \text{ J}/\text{mol}$

Extraction of hydrogen via the membrane should move the reaction away from equilibrium, towards the product side. The relative equilibrium ratio will be used to quantify the deviation from equilibrium (see equation 13). The addition of membranes to a fluidized bed is expected to significantly lower the local equilibrium ratio compared to a fluidized bed without membranes.

$$B_{WGS} = \frac{\left( \frac{P_{CO_2} P_{H_2}}{P_{CO} P_{H_2O}} \right)}{K_{eq,WGS}} \quad (13)$$

### Boundary conditions

All simulations have been performed with a 2D computational domain. For the gas mixture, a no-slip boundary condition was applied to the left and right walls, a constant gas velocity was imposed at the inlet, an imposed pressure condition was set at the outlet and the boundary condition of equation 12 was applied at the surface of the membranes. For the solids velocity and granular temperature, a Johnson & Jackson partial slip boundary condition with a specular coefficient of 0.50 was applied on the walls and the membranes (see Johnson et al. (1987)).

### Numerical schemes and accuracy

The temporal discretization was done with the second order Crank-Nicolson scheme. All simulations were run with an adjustable time-step, with a maximum time-step of  $1 \cdot 10^{-5}$  s. The time-step was selected each iteration based on a maximum Courant number of 0.1. A combination the second order Gauss linear and Van Leer scheme was used for the spatial discretization. The model's absolute tolerances for all quantities were within  $1 \cdot 10^{-11}$  each iteration.

## VERIFICATION, GEOMETRIES AND SETTINGS

### Reaction verification

The hydrodynamics and mass transfer parts of the model have been carefully verified and validated in our earlier works, see Medrano et al. (2015), Voncken et al. (2015) and Helmi et al. (2017). Gas flow profiles, packed bed pressure drop, convection-diffusion and diffusion only systems have all been verified with their respective analytical solutions. The fluidized bed's bubble properties and the membrane's hydrogen flux have been validated with experimental data. To verify whether the WGS reaction terms were implemented correctly, different types of basic reactions were compared to their analytical solutions. Furthermore, the WGS reaction has been simulated with the TFM and compared to a simple MATLAB numerical batch reactor model.

A first and second order reaction have been performed in a gas only batch reactor. The TFM mass fraction profiles in **Figure 1** match very well with the analytical solution. The mass fraction profiles for an equilibrium reaction with two species reacting to a product was also predicted correctly by the TFM (**Figure 2**).

The implementation of the WGS reaction rate equation was then checked by simulating a simple gas batch reactor system with the TFM, and comparing it with a gas batch reactor system in MATLAB. For this gas only verification study the catalyst efficiency for the WGS reaction was removed from the reaction rate equation.

**Figure 3** shows that the TFM results for WGS compares well with the gas batch reactor results obtained from the MATLAB code. These results verify that the TFM can be used to simulate various types of chemical reactions

and can predict the resulting concentration profiles accurately. To ensure equilibrium concentrations are correctly predicted by the TFM, the WGS verification simulation will be run for a longer period of time in future studies.

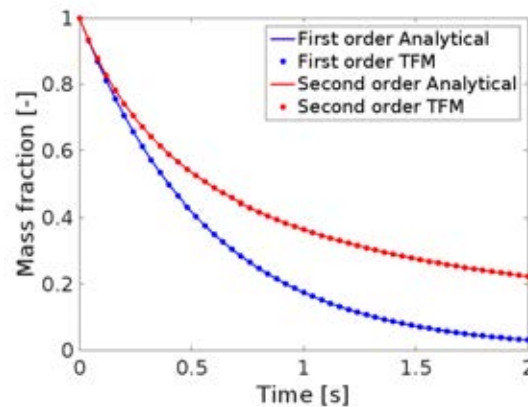


**Figure 1:** Analytical solution and TFM simulation result for a first and second order reaction.

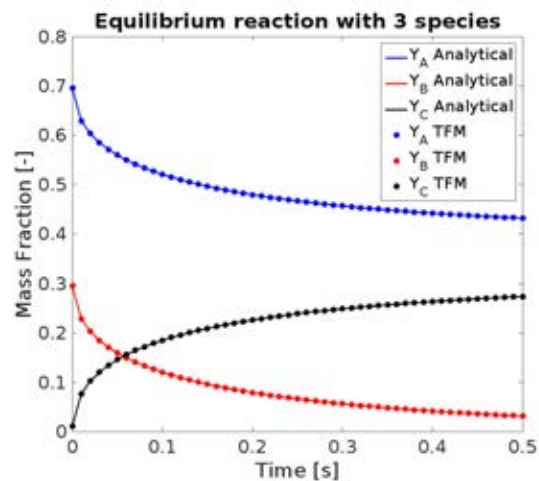


**Figure 2:** Analytical solution and TFM simulation result for a three species equilibrium reaction  $A + B \rightleftharpoons C$ .

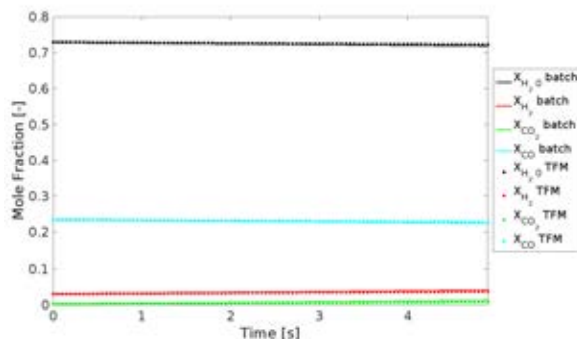


**Figure 3:** TFM simulation and batch reactor model comparison for the WGS reaction.

### Geometries and model settings

To quantify the effect of hydrogen extraction via a membrane on the reaction rate, systems with and without membranes were simulated. Both vertically and horizontally positioned membranes were looked into.

Fully 2D simulations have been performed. The geometries of all simulations are presented in **Table 4** and **Figure 4**. The horizontal membrane's diameter was set to 3.5 mm. Only one horizontal membrane has been simulated to show the effects that can occur in the system, in general, tube banks are best to be used to avoid hydrogen bypassing. The bed depths are only important for the calculation of the membrane area and do not hold any physical meaning in these 2D cases. The simulation settings can be found in **Table 5**. The vertical membrane was always placed at the left boundary. The horizontal membrane was placed at half of the reactor width.

**Table 4:** Geometries of all TFM WGS simulations.

Case	Width	Height	Depth
Vertical/no membrane	0.0356 m	0.0712 m	0.016 m
N <sub>cells</sub> vert./no memb.	40	80	-
Horizontal membrane	0.0356 m	0.0712 m	0.032 m
N <sub>cells</sub> horizontal memb.	40	80	-

**Table 5:** Summary of simulation settings for the WGS cases.

Quantity	Value	Unit
$d_p$	250	$\mu\text{m}$
$\rho_p$	1700	$\text{kg}/\text{m}^3$
$e_{pp}, e_{pw}$	0.97	-
$w/u_{mf}$	3	-
$D$	$1.0 \cdot 10^{-4}$	$\text{m}^2/\text{s}$
$Q_{pd}$	$4.3 \cdot 10^{-3}$	$\text{mol}/(\text{m}^2\text{sPa}^n)$
$n$	0.50	-
$T$	678	K
$X_{H_2}$	0.1	-
$X_{CH_4}$	0.1	-
$X_{H_2O}$	0.35	-
$X_{CO}$	0.35	-
$X_{CO_2}$	0.1	-
$\omega_{cat}$	0.10	-
$p_{outlet}$	3	bar
$p_{perm}$	$0.01 \cdot 10^5$	Pa
$t_{sim}$	10	s
$\Delta t$	$5 \cdot 10^{-6}$	s

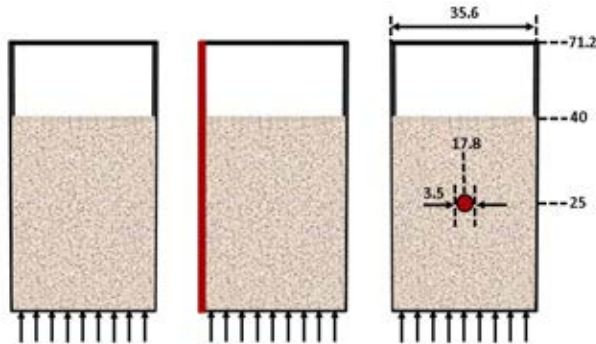


**Figure 4:** A fluidized bed: (left) without membranes; (middle) with a membrane at the left boundary; (right) with a horizontally immersed membrane. Dimensions are in mm.

## RESULTS

### Water Gas Shift

This section presents the results obtained by simulating fluidized beds with and without membranes in which the WGS reaction takes place. The reaction rate and equilibrium ratio will be used to assess the effect of the membrane on the system. The different types of membranes are not directly comparable, because they have different amount of hydrogen bypass and because the horizontal membrane affects the hydrodynamics. However, the effects that occur in these reactors can be described.

#### Reaction rate and equilibrium

The instantaneous and time-averaged reaction rates, and the time-averaged relative equilibrium ratio for a regular fluidized bed, fluidized bed with a vertical membrane and fluidized bed with a horizontal membrane are displayed in **Figure 5**. From the plot showing spatial distribution of the instantaneous reaction rates the position of the gas bubbles can be easily discerned as areas with reduced reaction rates related to the lower catalyst concentration inside the bubbles. The time-averaged reaction rates near the vertical membrane (the red line in the second row of **Figure 5**) are a factor 2 to 2.5 higher than the ones in a regular fluidized bed without membranes. The reaction is also further from its equilibrium state near the membrane than elsewhere in the reactor, which shows that the membrane flux is so high that kinetic and mass transfer limitations start to play a role.

Temporary gas pockets with low catalyst content occur underneath horizontally immersed membranes (Medrano et al. (2015)). Similar to bubbles, lower reaction rates are expected inside gas pockets compared to elsewhere in the reactor. This reduction in reaction rate is slightly visible in the time-averaged reaction rate plots for the horizontal membrane case. When the membrane tube is placed lower in the bed and closer to the wall the effect of gas pockets on a catalytic reaction rates is more pronounced (not shown). Contrary to the gas pockets, densified zones on top of the horizontal membrane increase the reaction rate locally with about a factor 4 to 5 compared to regular fluidized beds. However, despite the increased driving force, the hydrogen flux is still lowest on top of the horizontal membrane. Further investigation is required to quantify the mass transfer limitations in these densified zones and the effect of the position of the membranes in the bed.

#### Hydrogen concentrations and membrane geometry

**Figure 6** shows the hydrogen mole fraction profiles for a fluidized bed with a vertically and a horizontally immersed membrane. In both systems the membranes suffer from mass transfer limitations from the emulsion phase towards the membrane surface. Insufficient hydrogen is supplied to the membrane, so its flux is significantly lower than its maximum theoretical flux, which is referred to as concentration polarization. Caravella et al. (2009) and Helmi et al. (2017) have shown that concentration polarization are to be expected for systems with high flux membranes to extract one

chemical component from a gas mixture. Extraction of hydrogen increases the reaction rate and thus the hydrogen production. Clearly, the mass transfer rates of reactants and hydrogen towards the membrane is insufficient to maintain high hydrogen concentrations near the membrane, which are required to keep the driving force for permeation and the fluxes high. The differences in hydrogen mole fraction profiles clearly shows how differently vertically and horizontally

immersed membranes behave. The vertically immersed membrane is able to extract a large amount of hydrogen, hereby causing severe concentration polarization via a vertical concentration boundary layer. The underside of the horizontally immersed membranes is hardly limited by concentration polarization due to the direction of the gas flow, whereas the top has a high degree of concentration polarization, partially due to densified (defluidized) zones (see Voncken et al. (2015)).

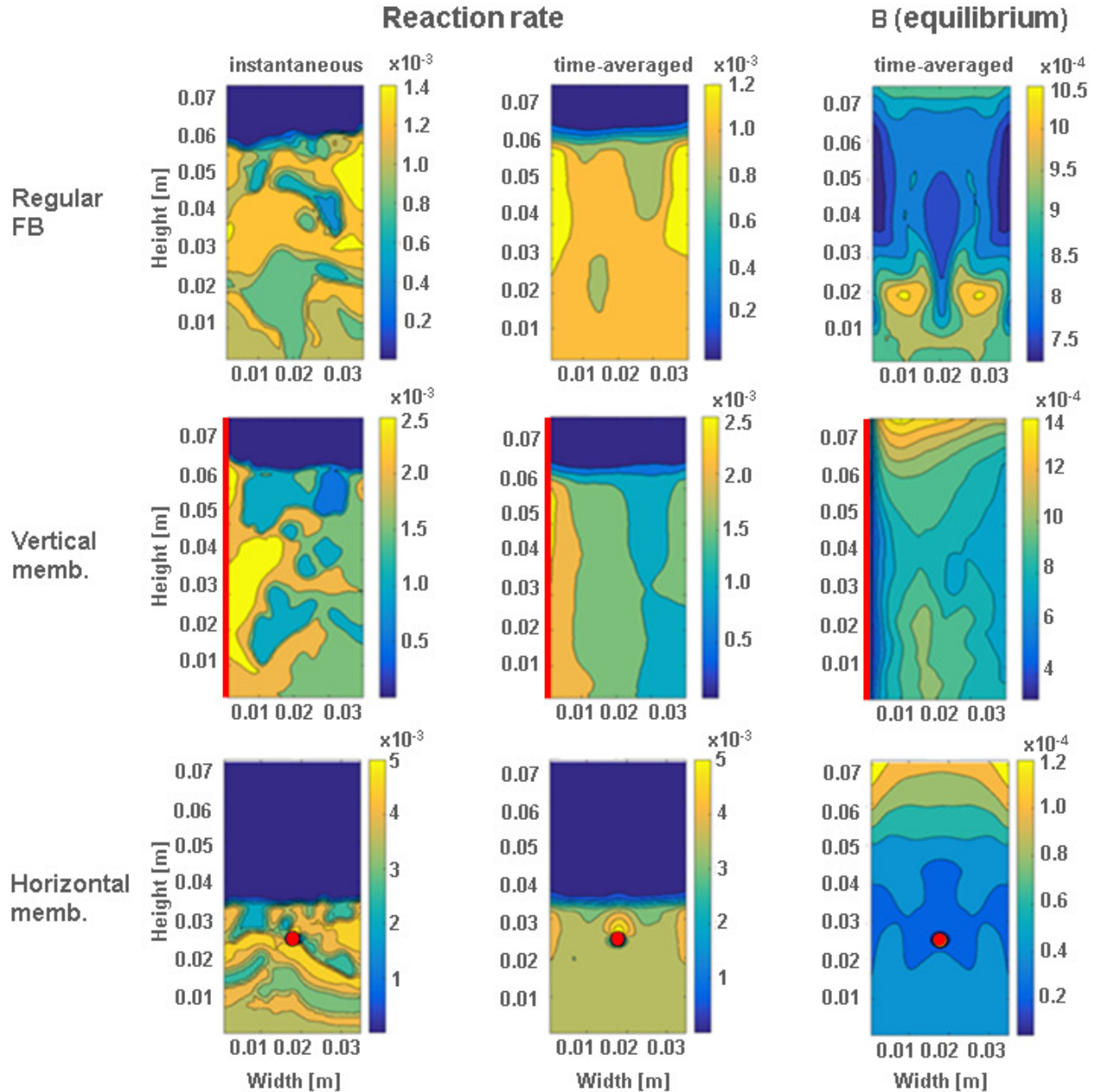


**Figure 5:** Instantaneous and time-averaged WGS reaction rates and time-averaged relative equilibrium ratio. Membranes are portrayed in red.

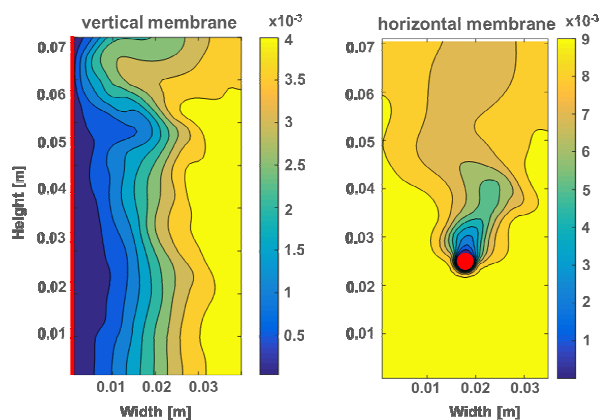


**Figure 6:** Hydrogen mole fraction profiles for fluidized bed reactors with a horizontally and vertically immersed membrane. The membranes are portrayed in red.

## CONCLUSION

A TFM with mass transfer, membranes and reactions was verified with various simple reactions such as  $n^{\text{th}}$  order, multi-species equilibrium reactions and Water Gas Shift. The verified TFM was then used to simulate WGS in fluidized beds without and with membranes. The membranes increase the reaction rate by a factor 2 to 5, depending on the geometry and orientation of the membrane. The extraction of hydrogen shifts the equilibrium of the reaction, especially in the vicinity of the membrane. For systems with vertically immersed membranes vertical mass transfer boundary layers develop, whereas for systems with horizontally immersed membranes, gas pockets with reduced reaction rates and densified zones with increased reaction rates prevail. Future studies will focus on the quantification of the concentration polarization effects and extend the investigations to Steam Methane Reforming.

## ACKNOWLEDGEMENTS

The authors are grateful to TTW and NWO for their financial support through the VIDI project ClingCO<sub>2</sub>, project number 12365. The authors thank Evert van Noort for his contribution to the simulation results.

## REFERENCES

- ADRI, A.M., LIM, C.J. and GRACE, J.R., (1994), "The fluidized bed membrane reactor system: a pilot scale experimental study", *Chem. Eng. Sc.*, **49**, 5833-5843.
- CARAVELLA, A., BARBIERI, G. and DRIOLI, E., (2009), "Concentration polarization analysis in self-supported Pd-based membranes", *Purif. Technol.*, **66**, 613-624.
- CORONEO, M., MONTANTE, G., CATALANO, J. and PAGLIANTI, A., (2009), "Modelling the effect of operating conditions on hydrodynamics and mass transfer in a Pd-Ag membrane module for H<sub>2</sub> purification", *J. Memb. Sc.*, **343**, 34-41.
- DANG, T.Y.N., KOLKMAN, T., GALLUCCI, F. and VAN SINT ANNALAND, M., (2013), "Development of a novel infrared technique for instantaneous, whole-

field, non invasive gas concentration measurements in gas-solid fluidized beds", *Chem. Eng. J.*, **219**, 545-557.

DE JONG, J.F., VAN SINT ANNALAND, M. and KUIPERS, J.A.M., (2012), "Membrane-assisted fluidized beds - part 2: numerical study on the hydrodynamics around immersed gas-permeating membrane", *Chem. Eng. Sc.*, **84**, 822-833.

ERGUN, S. and ORNING, A., (1949), "Fluid flow through randomly packed columns and fluidized beds", *Ind. Eng. Chem.*, **41**, 1179-1184.

FERNANDEZ, E., HELMI, A., COENEN, K., MELENDEZ, J., VIVIENTE, J.L., PACHECO TANAKA D.A., VAN SINT ANNALAND, M. and GALLUCCI, F., (2015), "Development of thin Pd-Ag supported membranes for fluidized bed membrane reactors including WGS related gases", *Int. J. Hydrogen Energy*, **40**, 3506-3519.

GALLUCCI, F., VAN SINT ANNALAND, M. and KUIPERS, J.A.M., (2008), "Autothermal reforming of methane with integrated CO<sub>2</sub> capture in a novel fluidized bed membrane reactor. Part 1: experimental demonstration", *Top. Catal.*, **51**, 133-145.

GIDASPOW, D., (1994), "Multiphase flow and fluidization: continuum and kinetic theory descriptions", *Academic Press Inc.*

HELMI, A., VONCKEN, R.J.W., RAIJMAKERS, T., ROGHAI, I., GALLUCCI, F., and VAN SINT ANNALAND, M., (2017), "On concentration polarization in fluidized bed membrane reactors", *Submitted to Chem. Eng. J.*

HOMMEL, R., Cloete, S. and AMINI, S., (2012), "Numerical investigations to quantify the effect of horizontal membranes on the performance of a fluidized bed reactor", *Int. J. Chem. React. Eng.*, **10**.

JOHNSON, P.C. and JACKSON, R., (1987), "Frictional-collisional constitutive relations for granular materials, with application to plane shearing", *J. Fluid Mech.*, **176**, 67-93.

KUIPERS, J.A.M., VAN DUIN, K.J., VAN BECKUM, F.P.H., and VAN SWAAIJ, W.P.M., (1992), "A numerical model of gas-fluidized beds", *Chem. Eng. Sc.*, **47**, 1913-1924.

LIU, Y. and HINRICHSEN, O., (2014), "CFD modeling of bubbling fluidized beds using OpenFOAM®: Model validation and comparison of TVD differencing schemes", *Comp. & Chem. Eng.*, **69**, 75-88.

LUN, C.K.K., SAVAGE, S.B., JEFFREY, D.J., and CHEPURNIY, N., (1984), "Kinetic theories for granular flow: inelastic particles in Couette flow and slightly inelastic particles in a general flowfield", *J. Fluid Mech.*, **140**, 223-256.

MA, D. and AHMADI, G., (1988), "A kinetic model for rapid granular flows of nearly elastic particles including interstitial fluid effects", *Powder Technol.*, **56**, 191-207.

MEDRANO, J.A., SPALLINA, V., VAN SINT ANNALAND, M. and GALLUCCI, F., (2014), "Thermodynamic analysis of a membrane-assisted chemical looping reforming reactor concept for combined H<sub>2</sub> production and CO<sub>2</sub> capture", *Int. J. Hydrogen Energy*, **39**, 4725-4738.

MEDRANO, J.A., VONCKEN, R.J.W., ROGHAI, I., GALLUCCI, F. and VAN SINT ANNALAND, M., (2015), "On the effect of gas pockets surrounding membranes in fluidized bed membrane reactors: An experimental and numerical study", *Chem. Eng. J.*, **282**, 45-57.

MLECZKO, L., OSTROWSKI, T. and WURZEL, T., (1996), "A fluidised-bed membrane reactor for the catalytic partial oxidation of methane to synthesis gas", *Chem. Eng. Sc.*, **51**, 3187-3192.

NIEUWLAND, J.J., VAN SINT ANNALAND, M., KUIPERS, J.A.M. and VAN SWAAIJ, W.P.M., (1996), "Hydrodynamic modeling of gas/particle flows in riser reactors", *AIChE J.*, **42**, 1569-1582.

NUMAGUCHI, T. and KUKUCHI, K., (1988), "Intrinsic kinetics and design simulation in a complex reaction network: Steam-Methane Reforming", *Chem. Eng. Sc.*, **43**, 2295-2301.

PASSALACQUA, A. and FOX, R.O., (2011), "Implementation of an iterative solution procedure for multi-fluid gas-particle flow models on unstructured grids", *Powder Technol.*, **213**, 174-187.

PATIL, C.S., VAN SINT ANNALAND, M. and KUIPERS, J.A.M., (2007), "Fluidised bed membrane reactor for ultrapure hydrogen production via methane steam reforming: Experimental demonstration and model validation", *Chem. Eng. Sci.*, **62**, 2989-3007.

RUSCHE, H., (2002), "Computational fluid dynamics of dispersed two-phase flows at high phase fractions", PhD thesis, *University of London*.

SRIVASTAVA, A. and SUNDARESAN, S., (2003), "Analysis of a frictional-kinetic model for gas-particle flow", *Powder Technol.*, **129**, 72-85.

TAN, L., ROGHAI, I. and VAN SINT ANNALAND, M., (2014), "Simulation study on the effect of gas permeation on the hydrodynamic characteristics of membrane-assisted micro fluidized beds", *Appl. Math. Model.*, **38**, 4291-4307.

TIEMERSMA, T.P., PATIL, C.S., VAN SINT ANNALAND, M. and KUIPERS, J.A.M., (2006), "Modelling of packed bed membrane reactors for autothermal production of ultrapure hydrogen", *Chem. Eng. Sc.*, **61**, 1602-1616.

VAN DER HOEF, M.A., YE, M., VAN SINT ANNALAND, M., ANDREWS IV, A.T., SUNDARESAN, S. and KUIPERS, J.A.M., (2006) "Multi-scale modeling of gas-fluidized beds", *Adv. Chem. Eng.* **31**, 65-149.

VAN WACHEM, B.G.M., (2000), "Derivation, implementation, and validation of computer simulation models for gas-solid fluidized beds", PhD thesis, Delft University of Technology.

VONCKEN, R., ROGHAI, I., GALLUCCI, F. and VAN SINT ANNALAND, M., (2015), "Mass transfer phenomena in fluidized beds with vertically and horizontally immersed membranes", *Proc. 11th Int. Conf. Comput. Fluid Dyn. Miner. Process Ind. (CFD 2015)*, 031VON 1-6.

WEN, C. and YU, Y., (1966) "A generalized method for predicting the minimum fluidization velocity" *AIChE J.* **12**, 610-612.

## EFFECT OF LIFT FORCE ON DENSE GAS-FLUIDIZED BEDS OF NON-SPHERICAL PARTICLES

Ivan MEMA<sup>1\*</sup>, Vinay V. MAHAJAN<sup>1</sup>, Barry W. FITZGERALD<sup>1</sup>, Hans KUIPERS<sup>2</sup>, Johan T. PADDING<sup>1</sup>

<sup>1</sup>Delft University of Technology, Process & Energy Department, Intensified Reaction & Separation Systems, Leeghwaterstraat 39, 2628 CB Delft, The Netherlands

<sup>2</sup>Department of Chemical Engineering and Chemistry, Multiphase Reactors Group, Eindhoven University of Technology, 5600 MB Eindhoven, The Netherlands

\* E-mail: i.mema@tudelft.nl

### ABSTRACT

In industry we encounter many processes that rely on equipment in which particles are suspended by a gas flow, such as pneumatic conveyors, CFB gasifiers, combustors and fluidized bed reactors. In numerical models of these processes, particles have traditionally been represented as spheres, thus limiting complexities associated with drag or lift forces. However, spherical particles are not representative of the entities encountered in real systems. For example, non-spherical biomass particles of varying aspect ratios are used in the production of biomass fuels.

Thus far literature is quite limited when it comes to hydrodynamic forces experienced by non-spherical particles under fluidized conditions. In fluidized beds, particles will experience varying lift force conditions dependent on the orientation of the particle relative to the direction of the flow. In this study, we investigate numerically the effect of different lift force coefficient correlations on fluidization of spherocylindrical particles. We employ correlations derived from previous simulations on non-spherical particles and aerofoil dynamics in simulations. We also look into the effect of the Di Felice approximation, in this case applied to take into account the effect of surrounding particles on the lift force. Particle interactions are modelled using the Open Source engine CFDEM, which uses the OpenFOAM computational fluid dynamics (CFD) solver to describe the fluid component and LIGGGHTS to implement discrete element method (DEM) calculations. We investigate the importance of lift forces on non-spherical particles under dense fluidised conditions and compare results to the case of spherical particles where lift forces are often neglected.

**Keywords:** Fluidized bed, granular flow, CFD-DEM, non-spherical particle, lift force.

### NOMENCLATURE

*DEM - Spherocylinder particles*

$\mathbf{v}_i$  Particle velocity, [m/s].  
 $m_i$  Mass, [kg].  
 $\rho_p$  Density, [kg/m<sup>3</sup>].  
 $\boldsymbol{\omega}_i$  Angular velocity, [rad/s].  
 $\mathbf{I}_i$  Moment of inertia, [kg/m<sup>2</sup>].  
 $P_i$  Identification for the  $i^{\text{th}}$  particle, [-].  
 $\mathbf{r}_i$  Position of centre of mass, [m].  
 $L$  Shaft length, [m].  
 $R$  Characteristic radius, [m].

$\mathbf{u}_i$  Orientation unit vector, [-].  
 $k_n$  Normal spring constant, [N/m].  
 $\eta_n$  Normal damping coefficient, [kg/s].  
 $\mathbf{n}_{12}$  Normal unit vector, [-].  
 $\mathbf{t}_{12}$  Tangential unit vector, [-].  
 $k_t$  Tangential spring constant, [N/m].  
 $\eta_t$  Tangential damping coefficient, [kg/s].

*CFD - Fluid*

$\varepsilon_f$  volume fraction, [-].  
 $\rho_f$  Density, [kg/m<sup>3</sup>].  
 $\mathbf{v}_f$  Fluid velocity, [m/s].  
 $C_D$  Drag coefficient [-].  
 $\mathbf{F}_D$  Drag force [N].  
 $Re_p$  Reynolds number of particle in fluid [-].  
 $C_L$  Lift coefficient [-].  
 $\mathbf{F}_L$  Lift force [N].  
 $U_{mf}$  Minimum fluidization velocity [m/s].

### INTRODUCTION

Many industrial processes such as fluidized bed reactors, cyclone separators, dust collectors and pulverized-coal combustors involve particle-laden in gas flows. These devices are categorized as gas-solid contactors, of which the fluidized bed reactor is a proto-typical example (Werther, 2000; Warnecke, 2000; Grace *et al.*, 1997). Due to their favourable mass and heat transfer characteristics, gas-fluidized beds are employed in many branches of industry such as the chemical (Son and Kim, 2006), petrochemical (Williams and Williams, 1999) and energy industries (Nikoo and Mahinpey, 2008). In addition, fluidized bed reactors are used in large-scale operations involving the granulation, drying and synthesis of fuels, base chemicals and polymers (Grace *et al.*, 1997). In recent years there has been increased application of fluidized beds in biomass energy production (McKendry, 2002; Bridgwater, 2003, 2006; Alauddin *et al.*, 2010). Therefore predicting the response of dense gas-solid flows in fluidized reactors via computational investigation is crucial for both reactor design and determination of optimal operating conditions. However simulations of dense gas-solid flows generally represent the solid phase as perfect spherical entities whereas, in reality, the solid phase is composed of particles of varying geometry. For example, in biomass energy production, biomass particles are usually non-spherical (Kruggel-Emden and Vollmari, 2016; Gil *et al.*, 2014).



With regards to implementation, describing non-spherical particles in simulations gives rise to a number of issues. While spheres can be described by a single parameter, i.e. diameter, non-spherical particles require more parameters. Even regular non-spherical shapes, such as ellipsoids and spherocylinders, require at least two parameters. When the particles become significantly irregular, it becomes computationally more demanding to detect particle-particle interactions and subsequently calculate the resulting contact force. An additional concern is the determination of the hydrodynamic forces and torques on particles due to interaction with the fluid flow. For non-spherical particles, both the hydrodynamic forces, such as drag and transverse lift, and pitching and rotational torque can vary appreciably with particle orientation and thus crucially dictate the translational motion of the particles. Drag force, lift force and torques are characterised by dimensionless coefficients that depend on particle velocity and orientation relative to the flow and Reynolds number ( $Re$ ). A number of drag force coefficients for a variety of non-spherical particles have been formulated (Tran-Cong *et al.*, 2004; Loth, 2008; Hölzer and Sommerfeld, 2008, 2009) while, recently, lift coefficient correlations have also been derived for non-spherical particles (Zastawny *et al.*, 2012; Richter and Nikrityuk, 2013; Ouchene *et al.*, 2015, 2016).

In the case of a dilute suspension, depending on the Reynolds number, the lift force can be more than half the drag force for non-spherical particles in a gas flow and, as a result, significantly influence the trajectory of non-spherical particles (Richter and Nikrityuk, 2013). However, it is not clear what effect lift force will have on non-spherical particles in dense systems such as those encountered in dense gas-fluidized systems. In this study we will investigate numerically the effect of differing lift force expressions and coefficients on non-spherical particles, specifically spherocylindrical particles, in a laboratory scale gas-fluidized bed reactor. We will employ lift force correlations derived from previous studies on non-spherical particles (Zastawny *et al.*, 2012) and from aerofoil dynamics (Hoerner, 1965). Particle interactions are numerically described using the Open Source engine CFDEM, which combines the OpenFOAM computational fluid dynamics (CFD) solver to describe the fluid component with the LIGGGHTS software package to implement discrete element method (DEM) calculations (Mahajan *et al.*, 2017). We present results on the importance of lift forces on non-spherical particles by studying the evolution of void fraction, particle velocity and particle alignment in the reactor.

This paper is arranged as follows. We will first outline the CFD-DEM numerical model used in this study focusing on the implementation of contact detection, drag forces and lift forces for spherocylindrical particles. In the results section we will explore the effect of differing lift force expressions on particle dynamics in dense fluidized beds. Specifically we will focus on the variation of particle velocity along the direction of fluid flow, the evolution of voidage conditions in the reactor and particle alignment. Finally we will draw conclusions from this study and provide an outlook for future studies.

## NUMERICAL MODEL

For this study we implement the CFD-DEM algorithm to simulate a coupled particle-fluid system, which has been extensively employed to simulate systems where particle-fluid interactions are relevant (Tsuji *et al.*, 1993; Zhu *et al.*, 2007; Deen *et al.*, 2007; Zhu *et al.*, 2008; Zhao and Shan,

2013; Salikov *et al.*, 2015). The CFD component of the algorithm is solved using the Open Source package OpenFOAM while the DEM component is implemented using LIGGGHTS, which stands for LAMMPS Improved for General Granular and Granular Heat Transfer Simulations, and is an Open Source package for modelling granular material via the discrete element method (DEM). Coupling of the CFD and DEM components is facilitated by the Open Source coupling engine CFDEM which executes both the DEM solver and CFD solver consecutively. The CFDEM engine allows for execution of the program for a predefined number of time steps after which data is exchanged between the OpenFOAM solver and LIGGGHTS solver (Kloss *et al.*, 2012).

## Discrete Element Method (DEM)

The discrete element method (DEM) is a soft contact model first introduced by Cundall and Strack (1979) to describe interactions between granular particles (Cundall and Strack, 1979). The simplest DEM contact model approximates grains as either disks in 2D or spheres in 3D, an approach that is sufficient to replicate laboratory-scale force chains (Aharonov and Sparks, 1999) and depict percolation-like contact networks (Fitzgerald *et al.*, 2014). Individual particles are tracked and their trajectories are numerically integrated over time and subject to local contact forces and torques, which develop when adjacent particles spatially overlap.

In this study we have adapted the DEM model to describe the interaction of spherocylinders with rotational and translational degrees of freedom. Consider spherocylinder  $i$  in a dense gas-fluidized reactor. The translational motion for spherocylinder  $i$  can be calculated by integrating

$$m_i \frac{d\mathbf{v}_i}{dt} = \mathbf{F}_{i,n} + \mathbf{F}_{i,t} + \mathbf{F}_{i,f} + \mathbf{F}_{i,p} + \mathbf{F}_{i,b} \quad (1)$$

where  $\mathbf{F}_{i,n}$  is the total normal contact force acting on the particle,  $\mathbf{F}_{i,t}$  is the total tangential contact force acting on the particle,  $\mathbf{F}_{i,f}$  is the total hydrodynamic force acting on the particle (further details on these forces in the next section),  $\mathbf{F}_{i,p}$  represents the pressure gradient acting on the particle and  $\mathbf{F}_{i,b}$  is the total body force acting on the particle including gravity. The rotational motion of the particles can be solved using the expression

$$\mathbf{I}_i \frac{d\boldsymbol{\omega}_i}{dt} = \mathbf{T}_i \quad (2)$$

where  $\mathbf{I}_i$  is the particle moment of inertia,  $\boldsymbol{\omega}_i$  is the angular velocity of the particle and  $\mathbf{T}_i$  is the net torque acting on the particle. Spherocylinder orientations are described by quaternions in the algorithm. For this study the equations of motion are integrated using the Velocity Verlet method.

In the case of spherical particles, particles overlap when the distance between the particle centres is less than the sum of the particle radii. For spherocylinder particles, the identification of contacts between particles, and the subsequent calculation of the overlap region, is more complicated than for spheres. Two adjacent spherocylinder particles are deemed to be overlapping once the distance between their shafts is smaller than the sum of their radii. Figure 1 shows an example of an overlapping contact between two spherocylinder particles  $P_1$  and  $P_2$ . For particle  $P_i$ ,  $R$  is the characteristic radius or radius of the spherical part of the spherocylinder,  $\mathbf{r}_i$  is the centre of mass,  $L$  is the shaft length,  $\mathbf{u}_i$  is the orientation unit vector originating at  $\mathbf{r}_i$  and  $\mathbf{v}_i$  is the translational

velocity. A spherocylinder contact detection algorithm originally developed for granular flows has been used in this study (Vega and Lago, 1994; Pournin *et al.*, 2005). For the sample contact illustrated in Figure 1 the shortest distance between the particles is given by  $|s_2 - s_1|$ , where  $s_1$  and  $s_2$  are points on the central axes of  $P_1$  and  $P_2$  respectively. The mid-point between the points  $s_1$  and  $s_2$  is  $r_c$  and the degree of overlap between the particles is expressed as  $\delta_n$ .  $\mathbf{n}_{12}$  and  $\mathbf{t}_{12}$  are the normal and tangential unit vectors for the contact respectively.

To calculate the normal contact force exerted on particle  $P_1$  by particle  $P_2$  we use a linear spring-dashpot model such that the normal contact force is given by

$$\mathbf{F}_{12,n} = -k_n \delta_n \mathbf{n}_{12} - \eta_n \mathbf{v}_{12,n} \quad (3)$$

where  $k_n$  is the normal spring constant,  $\eta_n$  is the normal damping coefficient and  $\mathbf{v}_{12,n}$  is the normal relative velocity between the particles. The tangential contact force is calculated from the Coulomb-type friction expression

$$\mathbf{F}_{12,t} = \min(-k_t |\delta_t| \mathbf{t}_{12} - \eta_t \mathbf{v}_{12,t}, -\mu |\mathbf{F}_{12,n}| \mathbf{t}_{12}). \quad (4)$$

In this expression  $k_t$ ,  $\delta_t$ ,  $\eta_t$ ,  $\mu$  and  $\mathbf{v}_{12,t}$  are the tangential spring constant, tangential overlap, tangential damping coefficient, friction coefficient and tangential relative velocity respectively.  $\delta_t$  is calculated from the time integral of the tangential relative velocity since the development of the initial particle contact and given by

$$\delta_t = \int_{t_{c,0}}^t \mathbf{v}_{12,t} \Delta t \quad (5)$$

where  $t_{c,0}$  is the time of initial contact between the particles. This expression represents the elastic tangential deformation of the particles since the onset of particle contact.

## CFD

The fluid phase is described on basics of the volume-averaged Navier-Stokes equations which are discretized on a uniform grid. The equation of continuity is given by

$$\frac{\partial(\epsilon_f \rho_f)}{\partial t} + \nabla \cdot (\epsilon_f \rho_f \mathbf{v}_f) = 0 \quad (6)$$

where  $\epsilon_f$  is fluid volume fraction,  $\rho_f$  is fluid density and  $\mathbf{v}_f$  is the fluid velocity. The expression for momentum conservation is given by

$$\begin{aligned} \frac{\partial(\epsilon_f \rho_f \mathbf{v}_f)}{\partial t} + \nabla \cdot (\epsilon_f \rho_f \mathbf{v}_f \mathbf{v}_f) = \\ -\epsilon_f \nabla p + \nabla \cdot (\epsilon_f \boldsymbol{\tau}_f) + \mathbf{R}_{f,p} + \epsilon_f \rho_f \mathbf{g} \end{aligned} \quad (7)$$

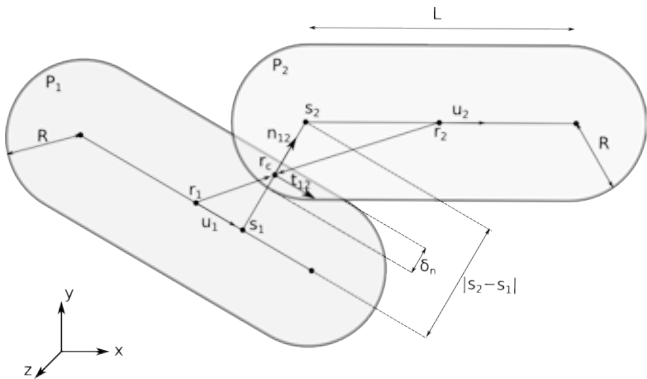


**Figure 1:** A schematic of a sample contact between two spherocylinders with each having a shaft length  $L$  and characteristic radius  $R$ .

where  $\boldsymbol{\tau}_f$  is the stress tensor,  $\mathbf{R}_{f,p}$  represents the momentum exchange between the fluid and particle phases and  $\mathbf{g}$  is gravity.

## Drag Force

The drag force on a single particle  $\mathbf{F}_{D0}$  in a suspended flow in the absence of other particles acts in the direction of flow and is given by

$$\mathbf{F}_{D0} = \frac{1}{2} C_D \rho_f \epsilon_f^2 \frac{\pi}{4} d_p^2 |\mathbf{v}_f - \mathbf{v}_i| (\mathbf{v}_f - \mathbf{v}_i) \quad (8)$$

where  $C_D$  is the drag coefficient,  $d_p$  is the particle volume equivalent diameter or the diameter of a sphere with the same volume as the spherocylinder,  $\mathbf{v}_f$  is the gas velocity interpolated to the location of particle  $i$ , and  $\mathbf{v}_i$  is the velocity of particle  $i$ . A precise expression for the drag force coefficient for spherocylinders is currently unavailable. However, a number of drag coefficients have been developed in the past that account for particle shape (Rosendahl, 2000; Loth, 2008; Hölzer and Sommerfeld, 2008; Zastawny *et al.*, 2012; Richter and Nikrityuk, 2013; Ouchene *et al.*, 2016). In this study, as an approximation, we employ the drag force correlation for arbitrary shaped particles established by Hölzer and Sommerfeld (Hölzer and Sommerfeld, 2008), which is given as

$$\begin{aligned} C_D = \frac{8}{\text{Re}_p} \frac{1}{\sqrt{\Phi_\perp}} + \frac{16}{\text{Re}_p} \frac{1}{\sqrt{\Phi}} + \frac{3}{\sqrt{\text{Re}_p}} \frac{1}{\Phi^{3/4}} \\ + 0.42 \times 10^{0.4(-\log \Phi)^{0.2}} \frac{1}{\Phi_\perp} \end{aligned} \quad (9)$$

where  $\text{Re}_p$  is the particle Reynolds number and for particle  $i$  is given as  $\text{Re}_p = \epsilon_f \rho_f d_p |\mathbf{v}_f - \mathbf{v}_i| / \eta_f$  with  $\eta_f$  being the fluid viscosity,  $\Phi$  is the particle sphericity and  $\Phi_\perp$  is the crosswise sphericity. Besides being universally applicable to different shapes and easy to implement, this expression is accurate in that it has a mean relative deviation from experimental data of only 14.1%, significantly lower than previous expressions (Haider and Levenspiel, 1989; Ganser, 1993).

In a dense gas-fluidized system the drag force acting on a given particle will be affected by neighbouring particles. To account for this effect we implement a modified drag force expression (Felice, 1994)

$$\mathbf{F}_D = \frac{1}{2} C_D \rho_f \epsilon_f^{1-\chi} \frac{\pi}{4} d_p^2 |\mathbf{v}_f - \mathbf{v}_i| (\mathbf{v}_f - \mathbf{v}_i) \quad (10)$$

where  $\chi$  is a correction factor given by

$$\chi = 3.7 - 0.65 \exp \left[ -(1.5 - \log(\text{Re}_p))^2 / 2 \right]. \quad (11)$$

## Lift Force

For non-spherical particles suspended in fluid flows a shape induced lift force on particles, similar to the concept of an aerofoil in aerodynamics, can significantly affect the trajectory of the particle. When the axis of elongated, rod-like or spherocylinder particle is inclined to the direction of fluid flow the flow fields on the upper and lower sides of the particle differ. The pressure drops in regions of rapid flow while the pressure increases in regions where the fluid velocity decreases (Richter and Nikrityuk, 2013), thus leading to an asymmetric pressure distribution and inducing a lift force perpendicular to the direction of fluid flow. An example of the lift force  $\mathbf{F}_L$  due to a fluid flow for a spherocylinder that is not aligned with the direction of fluid flow is shown in

Figure 2. The lift force  $\mathbf{F}_L$  does not align with the flow velocity, is orthogonal to  $\mathbf{v}_{rel}$  and lies in the plane defined by the particle orientation vector  $\mathbf{u}_i$  and  $\mathbf{v}_{rel}$ . For spherocylinder particles, there is no lift force when the central particle axis is aligned or perpendicular to the direction of fluid flow since there will be no resulting pressure difference. However arbitrary shaped particles can still be subject to a lift force even when they are aligned with the flow direction, similar to effects observed for a cambered airfoil.

The magnitude of the lift force  $F_L$  on a spherocylindrical particle is calculated from

$$F_L = \frac{1}{2} C_L \rho_f \epsilon_f^2 \frac{\pi}{4} d_p^2 |\mathbf{v}_f - \mathbf{v}_i|^2 \quad (12)$$

where  $C_L$  is the lift force coefficient. To ensure that the lift force for a particle is orientated correctly,  $F_L$  is multiplied by the lift force orientation vector  $\mathbf{F}_{Lo}$  which is given by

$$\mathbf{F}_{Lo} = \frac{\mathbf{u}_i \cdot \mathbf{v}_{rel}}{|\mathbf{u}_i \cdot \mathbf{v}_{rel}|} \frac{(\mathbf{u}_i \times \mathbf{v}_{rel}) \times \mathbf{v}_{rel}}{\|(\mathbf{u}_i \times \mathbf{v}_{rel}) \times \mathbf{v}_{rel}\|} \quad (13)$$

Thus the resultant lift force experienced by a particle is  $\mathbf{F}_L = F_L \mathbf{F}_{Lo}$ . Similar to drag force, the lift force exerted on a given particle can be influenced by other particles in proximity. In the absence of a proper correlation to account for the effect of surrounding particles on lift force, we have adapted the Di Felice correction originally intended for drag forces (Felice, 1994) and applied it to lift force such that the lift force  $F_L$  is given by

$$F_L = \frac{1}{2} C_L \rho_f \epsilon_f^{1-\chi} \frac{\pi}{4} d_p^2 |\mathbf{v}_f - \mathbf{v}_i|^2. \quad (14)$$

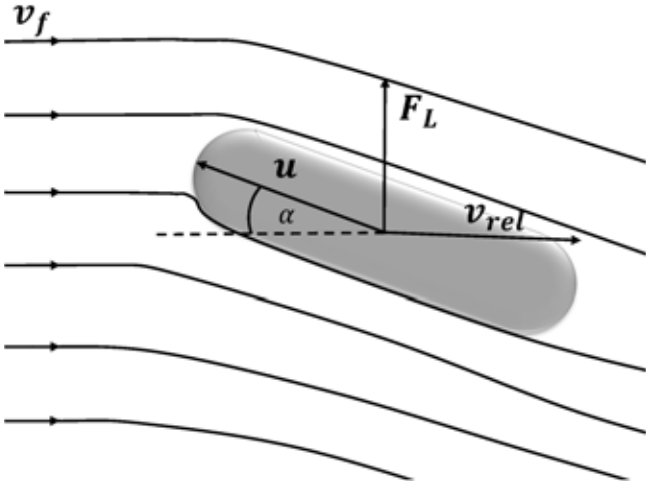


**Figure 2:** Lift vector orientation based on relative velocity  $\mathbf{v}_{rel} = \mathbf{v}_f - \mathbf{v}_i$  and particle orientation vector  $\mathbf{u}_i$ . The angle of incidence of the fluid flow  $\alpha$  is also indicated on the figure.

The lift force correlations considered in this study are presented in Table 1. In the expression from Hoerner,  $C_L$  is a function of the angle of incidence  $\alpha$  and the drag coefficient  $C_D$  while particle shape and the flow characteristics are incorporated in the calculation of the drag coefficient (Hoerner, 1965). On the other hand, in the expression from Zastawny *et. al*,  $C_L$  is independent of  $C_D$ , and is dependent on Reynolds number and the angle of incidence while the shape of the particle is taken in to account with a number of fitting parameters  $b_1$  to  $b_{10}$  (Zastawny *et. al.*, 2012). These parameters can be estimated by fitting data from DNS simulations and have already been calculated for ellipsoids, disc-shaped particles

**Table 1:** Expressions for the lift correlations used in this study.

Authors	Correlation
Hoerner (1965)	$\frac{C_L}{C_D} = \sin^2 \alpha \cos \alpha$
Zastawny <i>et. al</i> (2012)	$C_L = \left( \frac{b_1}{Re^{b_2}} + \frac{b_3}{Re^{b_4}} \right) \times \sin(\alpha)^{b_5 + b_6 Re^{b_7}} \times \cos(\alpha)^{b_8 + b_9 Re^{b_{10}}}$

and fibres with an aspect ratio of 5 (Zastawny *et. al.*, 2012). Since these parameters are not applicable for the spherocylinders in this study, we use parameters for spherocylinders that have been fitted using in-house DNS simulations (Sanjeevi *et. al.*, 2017). These parameters are presented in Table 2.

**Table 2:** Values for the fit parameters for the Zastawny *et. al* (2012) lift coefficient expression specific for spherocylinder particles with an aspect ratio of 4.

Coefficient	Value	Coefficient	Value
$b_1$	1.884	$b_6$	0.003624
$b_2$	0.1324	$b_7$	0.6598
$b_3$	0.001668	$b_8$	-0.2621
$b_4$	-0.8159	$b_9$	0.8021
$b_5$	0.8562	$b_{10}$	0.04384

## Simulation Parameters and Void Fraction

**Table 3:** Parameters for the CFD-DEM algorithm

CFD parameters	
Parameter	Value
Reactor dimensions	0.1 m $\times$ 0.1 m $\times$ 1.0 m
Number of cells	10 $\times$ 10 $\times$ 100
Minimum fluidisation velocity	$U_{mf} = 1.3$ m/s
Fluid velocity	$1.5U_{mf} = 1.95$ m/s
Time step ( $t_{CFD}$ )	$1 \times 10^{-4}$ s
Fluid density ( $\rho_f$ )	1.2 kg/m <sup>3</sup>
Spherocylinder & DEM parameters	
Parameter	Value
Number of particles	8000
Particle length	12 mm
Particle width	3 mm
Particle aspect ratio	4
Time step ( $t_{DEM}$ )	$1 \times 10^{-5}$ s
Particle density ( $\rho_p$ )	1297 kg/m <sup>3</sup>
Coefficient of friction ( $\mu$ )	0.3
Initial bed height	0.1 m

Simulation parameters for the CFD-DEM algorithm are given in Table 3. The particle material properties represent those of the alumide particles used in previous experiments (Mahajan *et. al.*, 2017). In addition, the dimensions of the fluidized bed reactor are equivalent to a laboratory scale apparatus. The fluid velocity is set such that we are operating in the bubbly regime, which was previously determined with experiments (Mahajan *et. al.*, 2017). Simulation results correspond to a fluidization process over a laboratory timescale of 18 seconds, which is sufficiently long to ensure that the system has reached steady-state fluidization.

For this study we have defined a grid such that the length of each grid side is equal to approximately two diameters of the volume equivalent sphere, which in turn is equivalent to length of one spherocylindrical particle. For this preliminary investigation we have not explored the effect of grid size on the results presented. We anticipate that an increase in grid size will lead to changes in the drag and lift forces given the dependency of these forces on the void fraction (Equation 10 and Equation 12). Thus variation of the grid size will be examined in a future study.

Finally we present the approach used to calculate the fluid void fraction  $\epsilon_f$ , which is required to solve the continuity equation (Equation 6) and the momentum conservation equation (Equation 7), in addition to calculating both the drag force (Equation 8) and lift force (Equation 12). To allow for the calculation of the solid fraction  $(1 - \epsilon_f)$  contribution of any spherocylinder to the grid cells, the spherocylinder is assigned  $n_{sp}$  evenly spaced satellite points throughout its volume such that each satellite point carries an equal volume weight. First the parent cell for a particle is identified based upon the position vector  $\mathbf{r}_i$  after which the particle volume is assigned to the parent cell and the neighbouring cells subject to the position of the satellite points. If the entire particle volume is contained within the parent cell then no distribution of particle volume is required. This approach for the calculation of  $\epsilon_f$  in all cells can be optimised by varying  $n_{sp}$ .

## RESULTS

We now present results from simulations subject to four different lift force conditions. In the first case we exclude lift forces such that particles are subject only to the drag force described by the Hölzer and Sommerfeld correlation with the Di Felice approximation that accounts for the effect of surrounding particles (Equation 10). In the second case, in addition to drag force, we include the lift force as described by the Hoerner correlation given in Table 1. In the third case, the lift force is described by the expression from Zastawny (Table 1) with the Di Felice approximation originally derived for drag force but adapted here for lift force (Equation 14). In the final case, we use the lift force expression from Zastawny without the Di Felice approximation (Equation 12).

A snapshot of a fluidized bed reactor subject to a fluid velocity of  $1.5U_{mf}$  is shown in Figure 3(a). Boundaries are included along both the  $x$ -axis and  $y$ -axis. For all lift force cases, we present results pertaining to particle dynamics at three positions,  $z = 0.075$  m,  $z = 0.155$  m and  $z = 0.245$  m, along the  $z$ -axis in the fluidized bed reactor as shown in Figure 3(b). The lowest  $z$ -position corresponds to a location close to the bottom of the reactor while the higher  $z$ -positions represent locations with more dilute particle conditions. All positions are midway along the  $y$ -axis as indicated in Figure 3(b). At each position we present analysis of the temporally averaged particle velocity in the direction of fluid flow ( $v_z$ ), temporally-averaged void fraction measurements and temporally-averaged particle alignment with the  $z$ -direction along the  $x$ -axis. Thus we construct temporally averaged profiles along on the  $x$ -direction ( $0.0 \text{ m} \geq y \geq 0.1 \text{ m}$ ) for a fixed  $z$ -position and fixed  $y$ -position, which is in the range  $0.05 \text{ m} \geq y \geq 0.06 \text{ m}$ . Typically a steady-state recirculation state is reached after approximately 5 s. Thus all temporal averages are calculated over the remaining simulation time, which is a period of approximately 13 s.

## Particle Velocity

Figure 4 shows profiles of the temporally-averaged particle velocity parallel to the direction of the fluid flow along the  $x$ -axis  $v_z(x)$  for the three analysis positions illustrated in Figure 3(b) and four lift force conditions. The value of  $v_z$  represents the temporal average of particles moving upwards and downwards in the reactor and can be used to study the resultant circulation pattern. The temporally-averaged particle velocity along the  $z$ -direction  $v_z$  at a given grid cell in the fluidized bed reactor over a specific time interval is calculated using the expression

$$v_z = \frac{\sum_{t=t_0}^{t_{\text{end}}} \sum_{p=1}^{N_{\text{cell}}(t)} v_z(p, t)}{\sum_{t=t_0}^{t_{\text{end}}} N_{\text{cell}}(t)} \quad (15)$$

where  $t_0$  is the start time,  $t_{\text{end}}$  is the end time,  $N_{\text{cell}}(t)$  is the number of particles in the grid cell at time  $t$ ,  $p$  is the particle label and  $v_z(p, t)$  is the velocity of particle  $p$  in the grid cell at time  $t$ .

Overall it can be seen that the inclusion of lift forces in the particle dynamics affects the form of  $v_z(x)$ . In general we find that the inclusion of any type of lift force leads to an overall increase in  $v_z$ . There are exceptions to this statement however. For example, at  $x \approx 1$ , without lift force,  $v_z$  is larger than all cases with lift force while at  $z = 0.245$  m we find that a overall change in the form of  $v_z$  is only discernible for the case where the Zastawny lift force with the Di Felice approximation is used. The inability to resolve circulation patterns at the highest position is due to the fact that particle flow is quite dilute in this sector of the reactor. The larger value of  $v_z$  next to the wall in case without lift force is more likely due to the grid size rather than channeling effects. Given that we are operating above  $U_{mf}$ , a bubbling response will dominate over channeling, which is prominent just below  $U_{mf}$  (Mahajan *et al.*, 2017). We plan to explore the effect of grid size on the  $v_z$  profiles in a future study.

We also find that employing the Zastawny drag force expression with the Di Felice correction (Equation 14) leads to

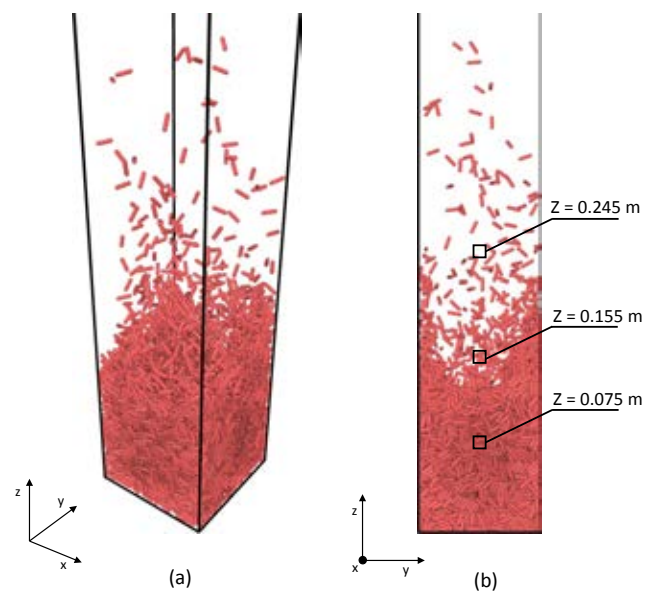


**Figure 3:** (a) Snapshot of the fluidized bed reactor with fluid velocity  $1.5U_{mf}$ . (b) Analysis positions in the bed reactor along the  $z$ -direction. These system snapshots were visualized using OVITO (Stukowski, 2010).

a much larger estimation of the lift force midway along the  $x$ -axis. In the case of results where the lift force is described by the Zastawny drag force without Di Felice (Equation 12), we resolve the average circulation pattern at  $z = 0.075$  m where particles tend to rise on the left side of the reactor and fall on the right side of the reactor. Finally the velocity profiles for simulations using the Hoerner correlation are quite close to the case with no lift force, indicating that the Hoerner correlation has little or no effect on the velocity profiles.

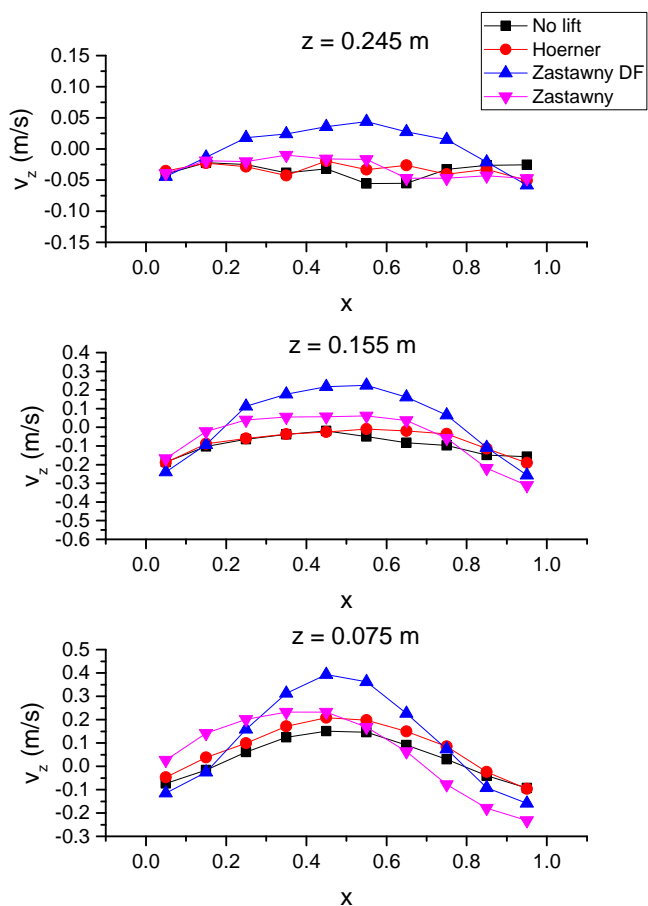
### Void Fraction

Figure 5 shows temporally-averaged void fraction profiles at the positions defined in Figure 3(b) for four lift force conditions. Variations in the void fraction reflect the trends observed in the  $v_z$  profiles presented in the previous section. The void fraction measure is linked to particle velocity as an increase in particle velocity can lead to increased dispersion of the particles in the reactor and hence an increase in void fraction at specific locations. For the case with the Zastawny lift force correlation with the Di Felice correction (Zastawny DF), we find an increase in the void fraction midway along the  $x$ -axis at  $z = 0.075$  m and  $z = 0.155$  m. This is similar to the increase observed in the  $v_z$  profiles. For the Zastawny lift force without the Di Felice correction (Zastawny), there

is an obvious change in the recirculation pattern. Similar to the  $v_z$  profiles, void fraction profiles for the Hoerner correlation are analogous to the profiles for the case with no lift force. Finally at  $z = 0.245$  m, the void fraction profiles for all lift forces cases are effectively indistinguishable with only minute variations in the profiles observed. In this domain of the reactor the particle flow is quite dilute and as a result, it is difficult to observe fluctuations in particle density.

### Particle Orientation

The lift force crucially depends on particle orientation relative to the fluid and is a measure that certainly merits examination. Figure 6 shows temporally-averaged particle orientation profiles for the three analysis positions illustrated in Figure 3(b) and four lift force conditions. For this analysis we are only concerned with fluctuations in the  $z$ -component of the particle orientation and for each particle we calculate  $u_z^2$  in order to scale the component between 0 and 1, thus avoiding negative orientation contributions. When a particle is perfectly aligned with the  $z$ -axis  $u_z^2 = 1$ . On the other hand,  $u_z^2 = 0$  indicates that a particle is perpendicular to the  $z$ -axis or parallel to the  $xy$ -plane. A particle with  $u_z^2 = 1/3$  is randomly orientated and does not preferentially align parallel or perpendicular to the  $z$ -axis. To emphasise the transi-



**Figure 4:** Comparison of the temporally-averaged  $v_z$  along the  $x$ -axis for the positions defined in Figure 3(b) in a fluidized bed reactor for the lift force cases: without lift force (No lift), lift force described by Hoerner correlation (Hoerner), lift force described by Zastawny correlation and Di Felice approximation (Zastawny DF) and lift force described by the Zastawny correlation (Zastawny). In these plots  $x$  is the position normalised by the length of reactor along the  $x$ -axis (0.1 m).

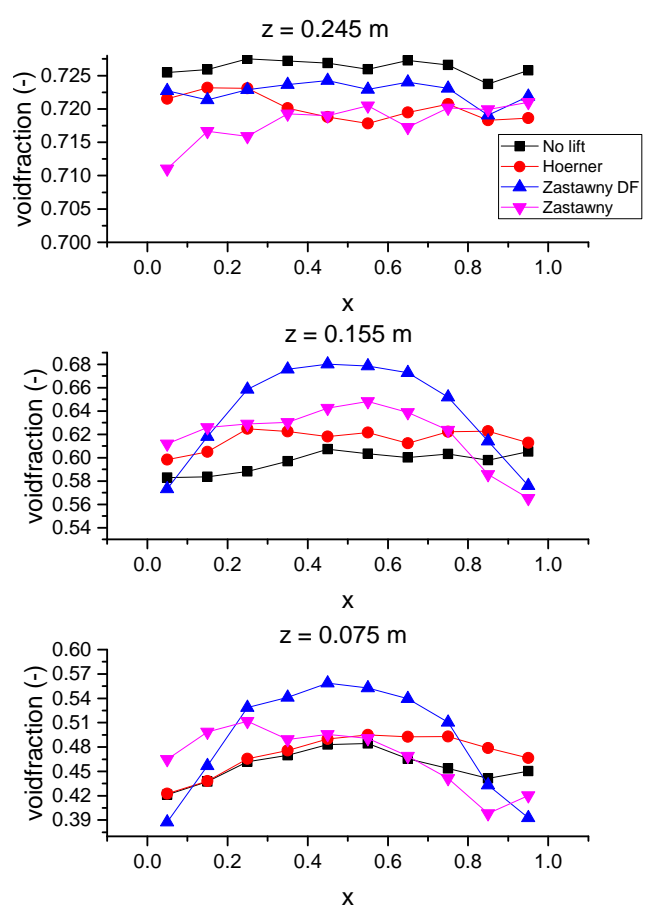


**Figure 5:** Comparison of the temporally-averaged void fraction along the  $x$ -axis for the positions defined in Figure 3(b) in a fluidized bed reactor for the lift force cases: without lift force (No lift), lift force described by Hoerner correlation (Hoerner), lift force described by Zastawny correlation and Di Felice approximation (Zastawny DF) and lift force described by the Zastawny correlation (Zastawny). In these plots  $x$  is the position normalised by the length of reactor along the  $x$ -axis (0.1 m).

tion in particle orientation that occurs at  $u_z^2 = 1/3$ , we study the variation of  $u_z^2 - 1/3$  with  $x$  position such that a positive value is more aligned with the direction of flow or  $z$ -axis and a negative value indicates that particles are more aligned perpendicular to the flow.

From the profiles shown in Figure 6, boundary effects due to the walls are clearly visible in the profiles at  $z = 0.075$  m and  $z = 0.155$  m. At these positions particles tend to be more aligned with the  $z$ -axis close to the boundaries however contrasting behaviours are evident near the centre of the reactor. At  $z = 0.075$  m, particles have a stronger tendency to align with the  $z$ -axis independent of the type of lift force. In contrast, at  $z = 0.155$  m, particles have a much weaker tendency to align with the  $z$ -axis. In addition, at  $z = 0.155$  m, for simulations with the Zastwany correlation (Zastwany), particles have a stronger inclination to align perpendicular with the  $z$ -axis while with the Zastwany correlation and Di Felice approximation (Zastwany DF) the orientation expression fluctuates around 0 at the centre of the reactor. At  $z = 0.245$  m where the solid fraction is lowest, particles are randomly orientated with no discernible dependence on position relative

to the rigid boundaries. Overall the results indicate that differing lift force cases do not affect particle orientation at bed positions studied here.

## CONCLUSION AND OUTLOOK

We have investigated through simulation the relevance of lift forces on spherocylinder particles in dense gas-fluidized beds. To account for the coupling between the solid particle phase and fluid phase, we have implemented the CFD-DEM algorithm where the CFD component solves the fluid motion and the DEM component evaluates spherocylinder particle-particle interactions. The CFDEM engine, an Open Source software, has been used for program execution and coupling of the fluid and solid phases (Kloss *et al.*, 2012). Central to this study has been the implementation of a series of lift force closures in an attempt to establish the importance of lift forces on spherocylinder particle dynamics in a fluidized bed reactor. We have considered a lift force expression from aerofoil dynamics (Hoerner, 1965) and a lift force correlation derived for non-spherical particles of varying geometry (Zastwany *et al.*, 2012). In addition, we have accounted for the effect of neighbouring particles on the lift force experienced by a particle by combining the Di Felice condition (Felice, 1994) originally derived for drag forces with the Zastwany lift force correlation.

To quantify the effect of differing lift force expressions we have studied temporally-averaged particle velocity, void fraction and particle orientation at specific positions in a fluidized bed. Overall the results show that shape-induced lift force can have a considerable effect on the fluidization of spherocylinder or elongated particles with different lift force expressions predicting distinct responses. Using a lift force consisting of the Zastwany lift force correlation and the Di Felice neighbourhood approximation leads to a significantly higher values of the velocity along the  $z$ -axis ( $v_z$ ) in comparison to the other lift force expressions (Figure 4). Trends in void fraction profiles have been shown to be comparable to those observed in the  $v_z$  profiles (Figure 5). For a given position in the reactor, an increase in particle velocity is suggestive of an increase in the local void fraction. Regions with low void fractions can also be indicative of increased particle interactions, leading to increased particle dissipation and therefore slower moving particles. However, during fluidization, clusters of co-aligned particles may develop in specific regions of the bed where the particles do not undergo appreciable dissipative interactions yet move faster than other similarly dense regions in the reactor. We plan on testing this proposal in a future study. Finally we examined particle orientation at different positions in the bed (Figure 6) where particles were found to align with the direction of flow near boundaries and in the middle of the bed near the fluid inflow region. However some distance above the base of the bed at  $z = 0.245$  m where fewer particles are recorded as shown in Figure 3(b), particle orientation is effectively random with no preferred alignment of particles measured.

In this study we have demonstrated the relevance of lift force for the fluidization of spherocylinder particles in that the incorporation of a description of lift force clearly affects particle dynamics. As a result, we must identify conclusively the appropriate lift force expressions for spherocylinder particles that account for different particle aspect ratios and can be applied to flow conditions at high Reynolds numbers ( $Re < 2000$ ). This may involve further investigation with current expressions such as those developed specifically for ellipsoidal particles (Ouchene *et al.*, 2016) or the formula-

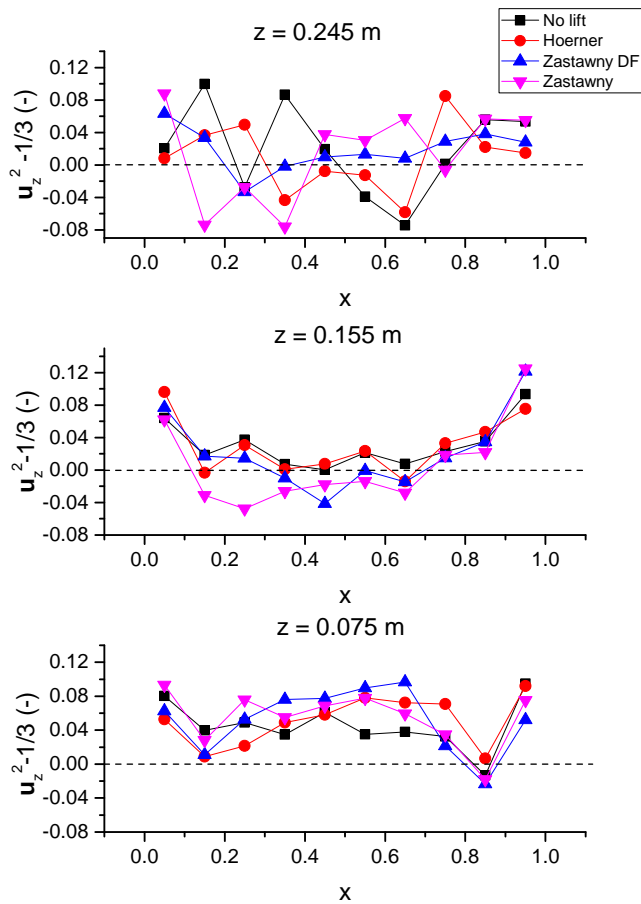


**Figure 6:** Comparison of the temporally-averaged  $z$ -component of particle orientation for the positions defined in Figure 3(b) in a fluidized bed reactor for the lift force cases: without lift force (No lift), lift force described by Hoerner correlation (Hoerner), lift force described by Zastwany correlation and Di Felice approximation (Zastwany DF) and lift force described by the Zastwany correlation (Zastwany). Each figure plots  $u_z^2 - 1/3$  with  $x$ , where  $u_z^2$  scales the component between 0 and 1 and  $1/3$  is subtracted to allow for more intuitive comparison of the profiles. In these plots  $x$  is the position normalised by the length of reactor along the  $x$ -axis (0.1 m).

tion of expressions using DNS simulations. We will also explore the influence of grid size on the results presented in this study. In addition it may be necessary to develop more accurate drag force closures specific to spherocylinder particles. To gain a better insight into the fluidization response in real systems we will perform Magnetic Particle Tracking (MPT) experiments (Buist *et al.*, 2014) to compare results obtained experimentally with simulations subject to different lift force conditions. We also plan on implementing relevant torque expressions for the particles, studying larger systems, different particle aspect ratios and higher fluidization velocities.

## ACKNOWLEDGEMENTS

The authors thank the European Research Council for its financial support under its consolidator grant scheme, contract no. 615906 (NonSphereFlow).

## REFERENCES

- AHARONOV, E. and SPARKS, D. (1999). “Rigidity phase transition in granular packings”. *Phys. Rev. E*, **60**, 6890–6896.
- ALAUDDIN, Z.A.B.Z., LAHIJANI, P., MOHAMMADI, M. and MOHAMED, A.R. (2010). “Gasification of lignocellulosic biomass in fluidized beds for renewable energy development: A review”. *Renewable and Sustainable Energy Reviews*, **14**(9), 2852 – 2862.
- BRIDGWATER, A. (2003). “Renewable fuels and chemicals by thermal processing of biomass”. *Chemical Engineering Journal*, **91**(2-3), 87 – 102.
- BRIDGWATER, T. (2006). “Biomass for energy”. *Journal of the Science of Food and Agriculture*, **86**(12), 1755–1768.
- BUIST, K.A., VAN DER GAAG, A.C., DEEN, N.G. and KUIPERS, J.A.M. (2014). “Improved magnetic particle tracking technique in dense gas fluidized beds”. *AIChE J.*, **60**, 3133–3142.
- CUNDALL, P. and STRACK, O. (1979). “A discrete numerical model for granular assemblies”. *Geotechnique*, **21**, 47 – 65.
- DEEN, N., ANNALAND, M.V.S., DER HOEF, M.V. and KUIPERS, J. (2007). “Review of discrete particle modeling of fluidized beds”. *Chem. Eng. Sci.*, **62**(1-2), 28 – 44.
- FELICE, R.D. (1994). “The voidage function for fluid-particle interaction systems”. *International Journal of Multiphase Flow*, **20**(1), 153 – 159.
- FITZGERALD, B.W., CLANCY, I. and CORCORAN, D. (2014). “Bridging percolation and particle dynamics models of the granular rigidity transition”. *Physica A: Statistical Mechanics and its Applications*, **410**, 582 – 594.
- GANSER, G.H. (1993). “A rational approach to drag prediction of spherical and nonspherical particles”. *Powder Technology*, **77**(2), 143 – 152.
- GIL, M., TERUEL, E. and ARAUZO, I. (2014). “Analysis of standard sieving method for milled biomass through image processing. effects of particle shape and size for poplar and corn stover”. *Fuel*, **116**, 328 – 340.
- GRACE, J.R., AVIDAN, A. and KNOWLTON, T. (1997). *Circulating Fluidized Beds*. Hoerner Fluid Dynamics.
- HAIDER, A. and LEVENSPIEL, O. (1989). “Drag coefficient and terminal velocity of spherical and nonspherical particles”. *Powder Technology*, **58**(1), 63 – 70.
- HOERNER, S.F. (1965). *Fluid-Dynamic Drag*. Hoerner Fluid Dynamics.
- HÖLZER, A. and SOMMERFELD, M. (2008). “New simple correlation formula for the drag coefficient of non-spherical particles”. *Powder Technology*, **184**(3), 361 – 365.
- HÖLZER, A. and SOMMERFELD, M. (2009). “Lattice boltzmann simulations to determine drag, lift and torque acting on non-spherical particles”. *Computers and Fluids*, **38**(3), 572 – 589.
- KLOSS, C., GONIVA, C., HAGER, A., AMBERGER, S. and PIRKER, S. (2012). “Models, algorithms and validation for Open Source DEM and CFD-DEM”. *Progress in Computational Fluid Dynamics*, **12**(2/3), 140 – 152.
- KRUGGEL-EMDEN, H. and VOLLMARI, K. (2016). “Flow-regime transitions in fluidized beds of non-spherical particles”. *Particuology*, **29**, 1 – 15.
- LOTH, E. (2008). “Drag of non-spherical solid particles of regular and irregular shape”. *Powder Technology*, **182**(3), 342 – 353.
- MAHAJAN, V.V., NIJSSEN, T.M.J., FITZGERALD, B.W., HOFMAN, J., KUIPERS, H. and PADDING, J.T. (2017). “Fluidization of spherocylindrical particles”. *Powders and Grains*.
- MCKENDRY, P. (2002). “Energy production from biomass (part 3): gasification technologies”. *Bioresource Technology*, **83**(1), 55 – 63.
- NIKOO, M.B. and MAHINPEY, N. (2008). “Simulation of biomass gasification in fluidized bed reactor using ASPEN PLUS”. *Biomass and Bioenergy*, **32**(12), 1245 – 1254.
- OUCHENE, R., KHALIJ, M., TANIÈRE, A. and ARCEN, B. (2015). “Drag, lift and torque coefficients for ellipsoidal particles: From low to moderate particle reynolds numbers”. *Computers and Fluids*, **113**, 53 – 64.
- OUCHENE, R., KHALIJ, M., ARCEN, B. and TANIÈRE, A. (2016). “A new set of correlations of drag, lift and torque coefficients for non-spherical particles and large reynolds numbers”. *Powder Technology*, **303**, 33 – 43.
- POURNIN, L., WEBER, M., TSUKAHARA, M., FERREZ, J.A., RAMAIOLI, M. and LIEBLING, T.M. (2005). “Three-dimensional distinct element simulation of spherocylinder crystallization”. *Granular Matter*, **7**(2), 119–126.
- RICHTER, A. and NIKRITYUK, P.A. (2013). “New correlations for heat and fluid flow past ellipsoidal and cubic particles at different angles of attack”. *Powder Technology*, **249**, 463 – 474.
- ROSENDAHL, L. (2000). “Using a multi-parameter particle shape description to predict the motion of non-spherical particle shapes in swirling flow”. *Appl. Math. Modelling*, **24**(1), 11 – 25.
- SALIKOV, V., ANTONYUK, S., HEINRICH, S., SUTKAR, V.S., DEEN, N.G. and KUIPERS, J. (2015). “Characterization and CFD-DEM modelling of a prismatic spouted bed”. *Powder Technology*, **270**, Part B, 622 – 636.
- SANJEEVI, S., ZARGHAMI, A. and PADDING, J. (2017). “in preparation”.
- SON, S.R. and KIM, S.D. (2006). “Chemical-looping combustion with NiO and Fe<sub>2</sub>O<sub>3</sub> in a thermobalance and circulating fluidized bed reactor with double loops”. *Industrial & Engineering Chemistry Research*, **45**(8), 2689–2696.
- STUKOWSKI, A. (2010). “Visualization and analysis of atomistic simulation data with OVITO, the Open Visualization Tool”. *Modelling and Simulation in Materials Science and Engineering*, **18**(1), 015012.
- TRAN-CONG, S., GAY, M. and MICHAELIDES, E.E. (2004). “Drag coefficients of irregularly shaped particles”. *Powder Technology*, **139**(1), 21 – 32.
- TSUJI, Y., KAWAGUCHI, T. and TANAKA, T. (1993). “Discrete particle simulation of two-dimensional fluidized bed”. *Powder Technology*, **77**(1), 79 – 87.
- VEGA, C. and LAGO, S. (1994). “A fast algorithm to

evaluate the shortest distance between rods”. *Computers and Chemistry*, **18(1)**, 55 – 59.

WARNECKE, R. (2000). “Gasification of biomass: comparison of fixed bed and fluidized bed gasifier”. *Biomass and Bioenergy*, **18(6)**, 489 – 497.

WERTHER, J. (2000). *Fluidized-Bed Reactors*, 320–366. Wiley-VCH Verlag.

WILLIAMS, P.T. and WILLIAMS, E.A. (1999). “Fluidised bed pyrolysis of low density polyethylene to produce petrochemical feedstock”. *Journal of Analytical and Applied Pyrolysis*, **51(1-2)**, 107 – 126.

ZASTAWNY, M., MALLOUPPAS, G., ZHAO, F. and VAN WACHEM, B. (2012). “Derivation of drag and lift force and torque coefficients for non-spherical particles in flows”. *International Journal of Multiphase Flow*, **39**, 227 – 239.

ZHAO, J. and SHAN, T. (2013). “Coupled CFD-DEM simulation of fluid-particle interaction in geomechanics”. *Powder Technology*, **239**, 248 – 258.

ZHU, H., ZHOU, Z., YANG, R. and YU, A. (2007). “Discrete particle simulation of particulate systems: Theoretical developments”. *Chemical Engineering Science*, **62(13)**, 3378 – 3396.

ZHU, H., ZHOU, Z., YANG, R. and YU, A. (2008). “Discrete particle simulation of particulate systems: A review of major applications and findings”. *Chemical Engineering Science*, **63(23)**, 5728 – 5770.





# EXPERIMENTAL AND NUMERICAL INVESTIGATION OF A BUBBLING DENSE GAS-SOLID FLUIDIZED BED

Lei YANG<sup>1</sup>, J.T. PADDING<sup>2\*</sup>, J.A.M. KUIPERS<sup>1</sup>

<sup>1</sup> TUE Department of Chemical Engineering and Chemistry, 5600MB Eindhoven, the Netherlands

<sup>2</sup> TUD Department of Process and Energy, 2826BL Delft, the Netherlands

Corresponding author's e-mail: J.T.Padding@tudelft.nl

## ABSTRACT

Eulerian models incorporating kinetic theory of granular flow (KTGF) are widely used to simulate gas-solids flow. The most widely used KTGF models have been derived for dilute flows of slightly inelastic, frictionless spheres. In reality, however, granular materials are mostly frictional. Attempts to quantify the friction effect have been somewhat limited. In this work, we focus on the validation of the KTGF model for rough spheres derived by Yang et al. (2016a, b) and the corresponding BCs from Yang et al. (2016c) for frictional walls. The present TFM simulations are validated by comparing with magnetic particle tracking (MPT) experimental data and results obtained from discrete particle model (DPM) simulations of a pseudo-2D bubbling fluidized bed. Numerical results are compared with respect to particle distribution, solids velocities, and energy balance in the bed. On comparison with a simple kinetic theory derived by Jenkins and Zhang (2002), we find that present model improves the predictions for particle axial velocity and flux upon simulation of inelastic rough particles. In conclusion, the current KTGF model obtains excellent agreement with experiment and discrete particle simulation for the time-averaged bed hydrodynamics.

## NOMENCLATURE

$e$	normal restitution coefficient
$p$	pressure, Pa
$\mathbf{v}$	velocity, m/s
$\mathbf{F}$	force, N
$m$	mass, kg
$\mathbf{T}$	torque, Nm
$\rho$	density, kg/m <sup>3</sup>
$\Theta$	granular temperature, m <sup>2</sup> /s <sup>2</sup>
$\beta_0$	tangential restitution coefficient
$\sigma$	particle diameter, m
$\gamma$	energy dissipation rate, kg/(m <sup>3</sup> ·s)
$\beta_A$	inter-phase momentum transfer coefficient
$\boldsymbol{\tau}$	stress tensor, Pa
$\varepsilon$	volume fraction
$\boldsymbol{\omega}$	rotational velocity, rad/s
$\kappa$	thermal conductivity, kg/(m·s)
$\mathbf{g}$	gravitational acceleration, m/s <sup>2</sup>

## INTRODUCTION

Gas-solid fluidized beds are widely encountered in the chemical, petrochemical, metallurgical industries due to high heat and mass transfer rates resulting from large gas-solids contact. In order to improve existing processes and scale up new processes, the hydrodynamics of gas-solids fluidized beds need to be better understood. However, obtaining sufficient experimental data can be difficult, costly and becomes more complicated for large scale systems. Thus, with increasing computational power and more efficient numerical solver, numerical modelling becomes critical in complementing experimental investigation to provide valuable insights into gas-solids flow.

The continuum two fluid model (TFM) incorporated with kinetic theory of granular flow (KTGF) is commonly used for simulation of industrial scale gas-fluidized beds. In this approach, constitutive equations are solved using additional closure equations for particle phase (Kuipers et al., 1992). The most widely used KTGF models (Ding and Gidaspow, 1990; Nieuwland, 1996) have been derived for dilute flows of slightly inelastic, frictionless spheres. However, granular materials are mostly frictional in reality. Attempts to quantify the friction effect have been somewhat limited. Yang et al. (2016a) derived a kinetic theory of granular flow (KTGF) for frictional spheres in dense systems which includes the effects of particle rotation and friction explicitly. Moreover, this theory has been validated by Yang et al. (2016b) for the simulation of a dense solid-gas bubbling fluidized bed.

Both experiments by Sommerfeld and Huber (1999) and numerical simulations, e.g. Lan et al. (2012) and Loha et al. (2013), have reported the importance of wall boundary conditions in determining the characteristics of granular flow. However, there is no consensus on the value of this coefficient. Moreover, the physical meaning is not clear. In rapid granular flows, a rapid succession of almost instantaneous collisions between particles and wall cause random fluctuations of the particle velocities, which determine the amount of momentum and fluctuation energy transferred through the walls (Louge, 1994). Yang et al. (2016c) derived new boundary conditions (BCs) for collisional granular flows of spheres at flat frictional walls. They characterized the influence of frictional wall by the normal and tangential restitution coefficients and friction coefficient. Their theory described the collisions between frictional particles and flat walls physically, and adopted both rotational and translational granular temperature. They performed simulations of a bubbling pseudo-2D

fluidized bed using new BCs. The results showed that the new BCs were better capable of predicting solids axial velocity profiles, solids distribution near the walls. However, the most noticeable effect was the better agreement of rotational granular temperature with that from DPM simulations.

Even though numerical simulations are widely used to predict detailed understanding of flow structures in fluidized beds. However, validation of those numerical models using advanced and detailed experiments are still crucial. Due to the opaqueness of fluidized beds, non-invasive techniques are preferred like electrical resistance tomography, electrical capacitance tomography, positron emission particle tracking and magnetic resonance imaging. MPT has been emerged as a promising tool to investigate hydrodynamics in the process of fluidization due to its long-term stability and low computational effort. This method uses a magnetic tracer particle, which follows the bulk particle flow and is continuously detected by multiple magnetic field sensors located outside the bed. In MPT, a series of anisotropy magnetoresistive sensors detect the instantaneous position and orientation of the magnetic tracer. Based on statistical analysis of the tracer trajectory, characteristic measures of the bulk particle flow, such as the average particle velocity and particle circulation pattern, can be determined as a function of operating conditions. The application of magnetic particle tracking (MPT) in fluidization has been first initiated by Mohs et al. (2009) for the study of a spouted bed. Recently, MPT improved by Buist et al. (2015) has been employed in dense granular flow of bubbling fluidized beds.

The present study focuses on the validation of the present KTGF model and the corresponding BCs from Yang et al. (2016c) for rough walls. Experimental work of Lorenz et al. (1997) reported several impact properties for collisions of small, nearly spherical particles. Due to limited choice of magnetic tracker, we adopted the stainless steel 316 which is non-magnetisable and has a quite rough surface. A systematic quantitative comparison among Eulerian-Eulerian two fluid simulation, DPM and one-to-one MPT experiment is carried out in a pseudo 2D bubbling fluidized bed. In particular, we investigate the effect of different inlet gas velocities on the hydrodynamics in the bed. We compare the time- and space- averaged quantities, i.e. particle velocity, particle flux, particle circulation pattern and distribution. The aim of this comparison is to show the level of agreement between simulations and experiments encountered in particle phase. Further, a careful comparison is made between the present model and the effective model by Jenkins and Zhang (2002) (represented as old TFM).

## NUMERICAL MODELS

### Two fluid model

The two fluid model describes both gas phase and solid phase as fully interpenetrating continua. The continuity equations for gas and solid phases are given in equation 2.1 with the subscript  $k$  denoting the gas ( $k = g$ ) or solid ( $k = s$ ). The momentum equations are given by 2.2 and 2.3.

$$\frac{\partial(\varepsilon_k \rho_k)}{\partial t} + \nabla \cdot (\varepsilon_k \rho_k \mathbf{v}_k) = 0 \quad (1)$$

$$\begin{aligned} \frac{\partial(\varepsilon_g \rho_g \mathbf{v}_g)}{\partial t} + \nabla \cdot (\varepsilon_g \rho_g \mathbf{v}_g \mathbf{v}_g) = \\ -\nabla \cdot (P_g \mathbf{I} + \varepsilon_g \boldsymbol{\tau}_g) + \varepsilon_g \rho_g \mathbf{g} - \beta_A (\mathbf{v}_g - \mathbf{v}_s) \end{aligned} \quad (2)$$

$$\begin{aligned} \frac{\partial(\varepsilon_s \rho_s \mathbf{v}_s)}{\partial t} + \nabla \cdot (\varepsilon_s \rho_s \mathbf{v}_s \mathbf{v}_s) = \varepsilon_s \rho_s \mathbf{g} \\ -\nabla \cdot (P_s \mathbf{I} + \varepsilon_s \boldsymbol{\tau}_s) + \beta_A (\mathbf{v}_g - \mathbf{v}_s) - \varepsilon_s \nabla P_g \end{aligned} \quad (3)$$

The gas and solid phases are coupled through the interphase momentum transfer coefficient  $\beta_A$ . To describe the solid phase, KTGF with friction is used. In this work, particle surface friction and rotation are considered explicitly. In order to describe the solid phase rheology thoroughly, an extra energy balance equation for the rotational granular temperature was derived.

$$\begin{aligned} \frac{3}{2} \left[ \frac{\partial(\varepsilon_s \rho_s \Theta_t)}{\partial t} + \nabla \cdot (\varepsilon_s \rho_s \mathbf{v}_s \Theta_t) \right] = -3\beta_A \Theta_t \\ -\nabla_{\mathbf{v}_s} : (P_s \mathbf{I} + \varepsilon_s \boldsymbol{\tau}_s) + \varepsilon_s \nabla \cdot (\kappa_t \nabla \Theta_t) - \gamma_t \end{aligned} \quad (4)$$

$$\begin{aligned} \frac{3}{2} \left[ \frac{\partial(\varepsilon_s \rho_s \Theta_r)}{\partial t} + \nabla \cdot (\varepsilon_s \rho_s \mathbf{v}_s \Theta_r) \right] = \\ \varepsilon_s \nabla \cdot (\kappa_r \nabla \Theta_r) - \gamma_r \end{aligned} \quad (5)$$

The definitions of the translational and rotational granular temperatures are respectively  $\Theta_t \equiv \langle C^2 \rangle / 3$ ,  $\Theta_r \equiv I \langle \Omega^2 \rangle / 3m$ , where  $I$  is particle's moment of inertia,  $C$  is the fluctuating translational velocity and  $\Omega$  is the fluctuating angular velocity. All the closures can be referred to Yang et al. (2016a).

Additionally, it is known that BCs on the gas and solid phases velocities and solid granular temperature, need to be specified at the wall. In the simulations, a no-slip wall boundary condition for side walls (left, right, front and back side of the rectangular domain) is used for the gas phase. At the bottom inlet, a uniform gas velocity is specified, whereas at the top outlet, atmospheric pressure (101 325 Pa) is prescribed. For the solid phase, a partial slip boundary condition is used for the side walls. We applied the relations for solids velocity gradient, translational and rotational energy dissipation rate per unit area derived by Yang et al. (2016c). The boundary conditions for solid velocity and granular temperatures at a flat frictional wall have the form

$$-(\mu_t + \mu_r) \frac{\partial v_i}{\partial n} = \quad (5)$$

$$\begin{aligned} \mu m n (1 + e) g_0 \cot \theta_c \frac{\Theta_t V_i}{\sqrt{2\pi\Theta_t}} \max(A1, A2) \\ -\kappa_t \frac{\partial \Theta_t}{\partial n} = Q_t \end{aligned} \quad (7)$$

$$-\kappa_r \frac{\partial \Theta_r}{\partial n} = Q_r \quad (8)$$

where  $n$  is direction perpendicular to the wall and  $i$  is the velocity component.  $V_i$  is the local mean contact velocity.

$\mu_{i_s}$  and  $\mu_{i_r}$  are the shear viscosities based on the KTGF of Yang et al. (2016a). A1 and A2 are functions regarding three measurable collisional parameters, rotational and translational granular temperatures and slip velocity. The details expressions can be referred to the Appendix and Yang et al (2016c).

### Discrete particle model

In DPM, the gas phase is described in the same way as in TFM (equations 2.1 and 2.2). However the solid phase is treated more detailed. The motion of every particle in the DPM is computed with Newton's second law of motion,

$$m_p \frac{d\mathbf{v}_p}{dt} = \sum \mathbf{F} = \mathbf{F}_{external} + \mathbf{F}_{contact} \quad (9-10)$$

$$I \frac{d\boldsymbol{\omega}}{dt} = \mathbf{T}$$

where  $m_p$ ,  $\mathbf{v}_p$ ,  $\mathbf{T}$  are particle mass, velocity, and torque acting on the particle. The sum of all external forces acting on a particle  $\mathbf{F}_{external}$  is calculated using:

$$\mathbf{F}_{external} = m_p \mathbf{g} - V_p \nabla p_g + \frac{V_p \beta_A}{1 - \varepsilon_g} (\mathbf{v}_g - \mathbf{v}_p) \quad (11)$$

where  $V_p$  is the volume of particle. We use a linear spring-dashpot contact force, where the friction coefficient  $\mu$  is limiting the tangential contact force:

$$\mathbf{F}_{contact,n} = -k_n \delta_n \mathbf{n}_{ab} - \eta_n \mathbf{v}_{ab}$$

$$\mathbf{F}_{contact,t} = \begin{cases} -k_t \delta_t - \eta_t \mathbf{v}_{ab,t}, & \text{(sticking)} \\ -\mu |\mathbf{F}_{contact,n}| \mathbf{t}_{ab}, & \text{(sliding)} \end{cases} \quad (12-13)$$

where  $k_n$ ,  $\mathbf{n}_{ab}$ ,  $\delta_n$ ,  $\eta_n$ ,  $\mathbf{v}_{ab}$ ,  $\delta_t$ ,  $\eta_t$  are respectively the spring stiffness in the normal direction, the normal unit vector, the overlap and damping coefficient in the normal direction, relative velocity at the contact point, and the overlap and damping coefficient in the tangential direction. We do not include a rolling friction. We refer to Hoomans et al. (1996) for details on the DPM model.

Parameters	Values
Particle type	Stainless steel 316
Particle density, kg/m <sup>3</sup>	8000
Particle diameter (mm),	3.0
Initial bed height (m),	0.15
Domain size (m),	0.15 × 0.015 × 1.0
Grid number (x × y × z)	15 × 2 × 60
p-p collisional parameters,	$e_n=0.91, \beta_0=0.33, \mu=0.15$
p-w collisional parameters,	$e_w=0.93, \beta_w=0.40, \mu_w=0.13$
Superficial gas velocity,	3.75 m/s
Simulation time	35 s
Flow solver time-step	10 <sup>-4</sup> s

**Table 1:** Properties of particles and simulation settings.

## MODEL VALIDATION

### Simulation settings

In the old TFM, we employ the same BCs for the gas phase. However, partial slip BCs from Sinclair and Jackson (1987) are used for four side walls with a specular coefficient of 0.2. The simulation settings are specified in Table 1. In the experiment, the pseudo 2D bed

has the same height, width and depth as is in the simulation. The four side walls are made of plastic glass. The porous distributor plate made of bronze has an average pore size of 10  $\mu\text{m}$  and a thickness of 3 mm. The distance between the measuring domain and the sensors is maintained less than 2 cm during experiment. To ensure statistical data, experiments are carried out for 2.5-3.0 h. The averaged bed dynamics are inferred from the motion of the tracker. The principle of the MPT measurement technique has been given by Buist et al. (2015). We followed the same method to filter data and deal with the corresponding post-process. Finally, an overview of all settings and properties is listed in Table 1.

### Results and discussion

In the experiment, we found that the minimum fluidization velocity is 3.91 m/s. Meanwhile the minimum fluidization velocity is 3.75 m/s in the simulation with the Ergun/Wen and Yu drag law. In the present pseudo 2D bed, the depth is only 5 times larger than the particle diameter, which reveals that particle bridge can occur. Consequently, this bridging leads to difficulties in determining local drag. This explains the mismatch of the minimum fluidization velocity between the experiment and the simulation. To make comparison with MPT experiment, we adopted the same excess background velocity. In this part, we focus on the validation of our current KTGF model and BCs for rough spheres impacting on a flat frictional wall.

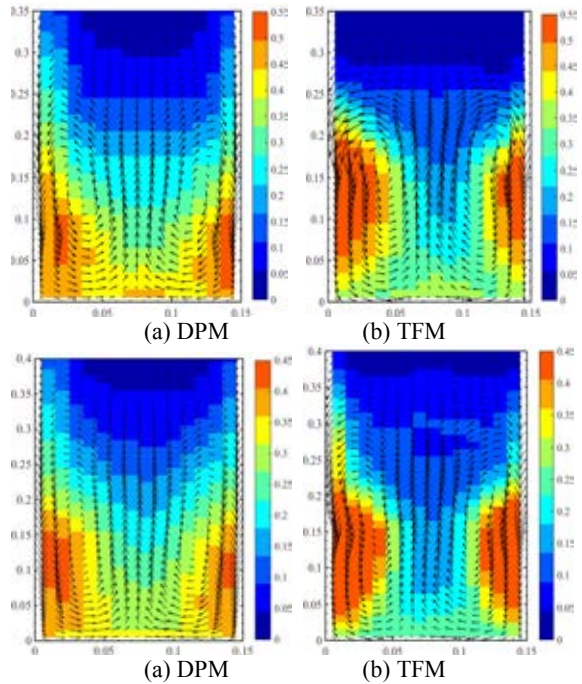
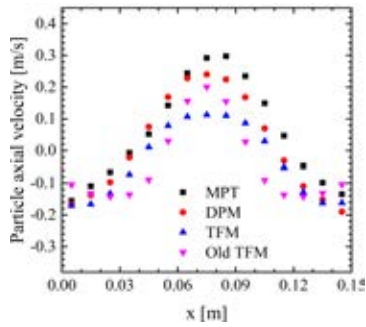


**Figure 1:** Time-averaged (10-35s) solids flux pattern and solids volume distribution at various superficial gas velocity, top row:  $U_g = 1.5U_{mf}$ , bottom row:  $U_g = 2.0 U_{mf}$ .

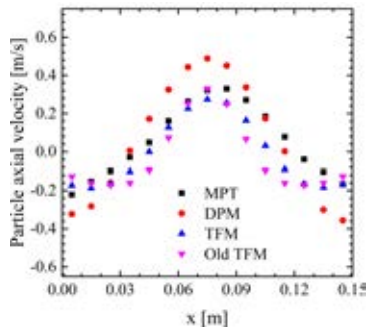
In order to study the overall behaviour of the bubbling bed, the time-averaged volume distribution and solids flux pattern are plotted in Figure 1. The DPM simulations show dense zones of solids close to the side walls and at the bottom of the bed. This type of solids volume fraction distribution reveals that bubbles are mostly formed at the bottom and move towards the center. On the other hand,

animations of the porosity patterns indicate that in TFM simulations more bubbles than in DPM are generated at the bottom of the bed and larger bubbles are formed (due to coalescence) in the center of the bed. Therefore, the DPM simulations, produces slightly more dilute zones in the lower part of the bed and more dilute zones in the center, and consequently larger dense zones near the side walls in comparison with the TFM simulations. Besides, the very low solids concentration at the top of the bed from both DPM and TFM simulations indicates the bursting of bubbles. With increasing superficial gas velocity, in both DPM and TFM simulations bubble coalescence is enhanced and more pronounced lateral motion of bubbles occurs, leading to a more dilute zone in the center of the bed.

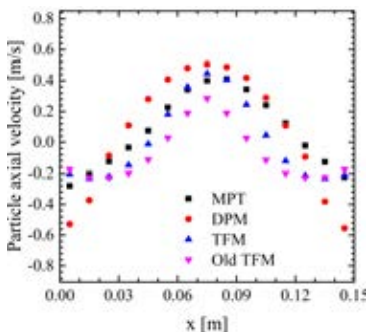
TFM and DPM simulations show very similar solids flux pattern. Particles move laterally close to the distributor, flow upwards in regions of more intense bubble activity and downwards in regions of lesser bubble activity. Consequently, a pronounced global solids circulation pattern with two symmetric vortices in the middle of the bed is formed. Since the height of the dense zone grows due to the increasing superficial gas velocity. It can be noticed that the size of the vortices has enlarged, which was also observed by Lindborg et al. (2007).



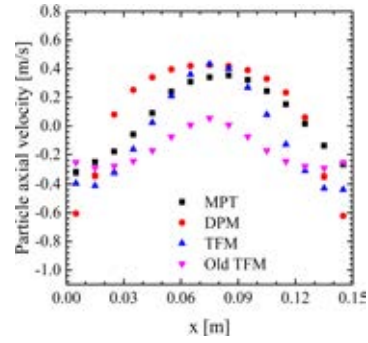
(a) height=0.05 m



(b) height=0.1 m



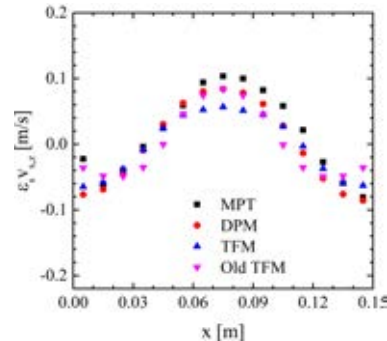
(c) height=0.15 m



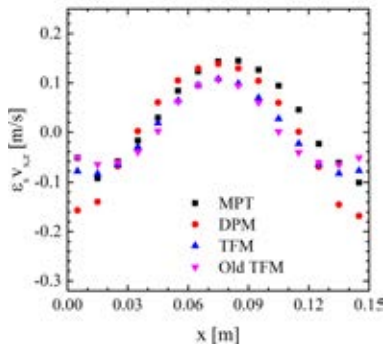
(d) height=0.2 m

**Figure 2:** Comparison of the time-averaged (10-35s) particle axial velocity between MPT experiment, DPM and TFM simulations at various heights,  $U_g = 1.5U_{mf}$ .

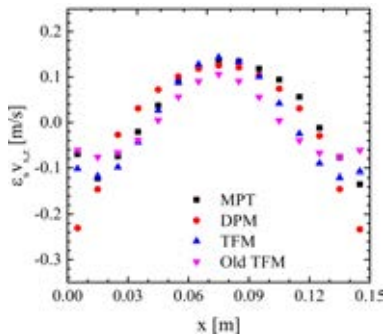
**Figure 2** overlays the profiles of time-averaged particle axial velocity at different heights measured in the experiment and the numerical simulations at  $U_g = 1.5U_{mf}$ . Overall, the particles ascend in the center and descend near the side walls due to the preferred path of the rising bubbles. Note that rough wall BCs are employed also at the bottom wall in our TFM simulations, which probably hinders particle upwards motion close to the distributor. Additionally, in the dense bottom region, long-term and multi-particle collisions are dominant, which are not accounted for in the TFM simulations. As a consequence, the new TFM simulations underpredict the particle velocity in the center at the lower height of 0.05 m (**Figure 6.2(a)**), but produce good agreement near the wall and in the annulus. At all other heights, a good match is obtained among the new TFM, DPM simulations and MPT experiments in the bulk. In contrast, the old TFM obtains good agreement with the MPT experiments and DPM simulations in the lower part of the bed, but underpredicts the particle axial velocity in the upper parts of the bed. In the dense wall region, DPM overestimates the downward solid velocity. This deviation between MPT experiments and DPM simulation was also reported by Buist et al. (2015) for a bubbling bed. They pointed out that it was necessary to add particle rolling friction to make corrections. However, the present TFM simulations are in excellent agreement with the experiments.



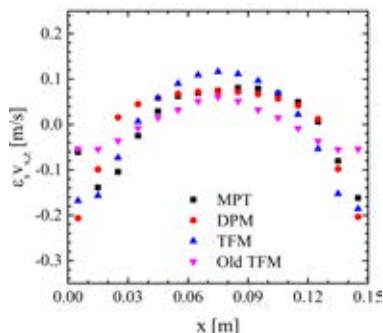
(a) height=0.05 m



(b) height=0.1 m



(c) height=0.15 m



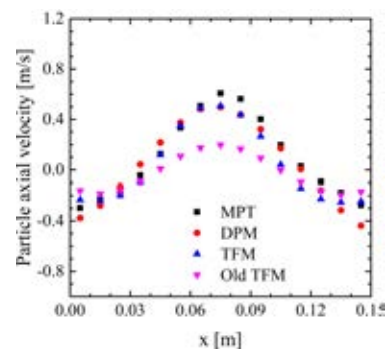
(d) height=0.2 m

**Figure 3:** Comparison of the time-averaged (10-35s) particle axial flux between MPT experiment, DPM and TFM simulations at various heights,  $U_g = 1.5 U_{mf}$ .

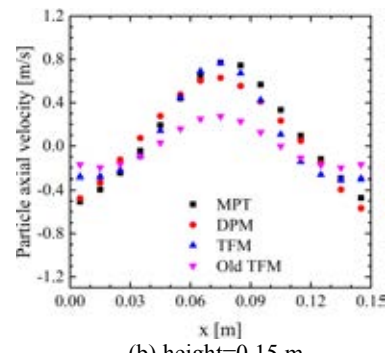
**Figure 3** shows the downward and upward particle axial flux for different heights from experiment and simulations at a background velocity of  $U_g = 1.5 U_{mf}$ . The upward solid flux is located in the center and the downward solid flux is observed in the near wall region. As can be seen from **Figure 1(a)** and **2(a)**, the upward solid flux close to the distributor is underestimated in present TFM simulations as a consequence of rough wall BCs at the bottom. Small bubbles are generated close to the distributor and side walls, carry particles in their wakes, which produces voids filled by downward owing particles. Due to the coalescence of these bubbles, the amount of downward solids flux increases with increasing bed height, particularly in the near wall region. As bubbles move up in the bed center, particles ow vertically upward at higher axial area (0.05-0.15 m), which indicates an increase in upward solids flux. The number of particles close to the freeboard is so limited that lower amount of upwards solids flux is observed at the height of 0.2 m. All of these corresponds well to the results in **Figure 1**. In

total, current TFM, old TFM and DPM simulations are in good agreement with the experiment.

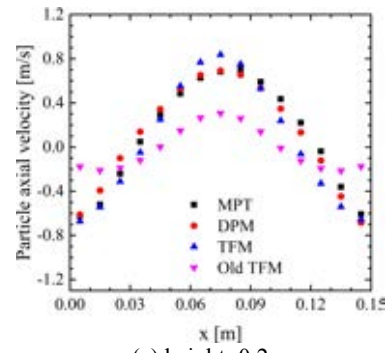
**Figure 4** shows profiles of the particle axial velocities at various heights from experiment and simulations at  $U_g = 2.0 U_{mf}$ . In general, the current TFM simulations agree well with the results from DPM and the experiment. Due to the roughness of the distributor, both TFM simulations underestimate the particle axial velocity. Unfortunately, the old TFM from Jenkins and Zhang (2002) underpredicts particle axial velocity in the center and captures lower amount of particle velocity value close to the wall. Similar underestimation of particle axial velocity is reported in the work of Lu and Gidaspow (2003). The particle surface friction leads to the formation of bed heterogeneous structures. For rough particles, more energy is dissipated during particle-particle and particle-wall collisions.



(a) height=0.1 m



(b) height=0.15 m



(c) height=0.2 m

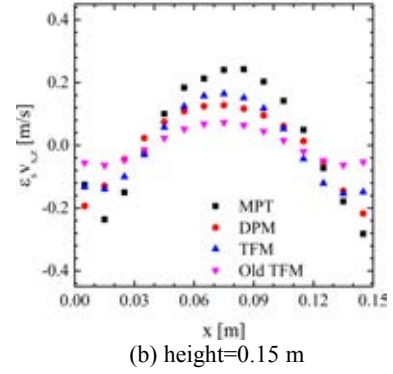
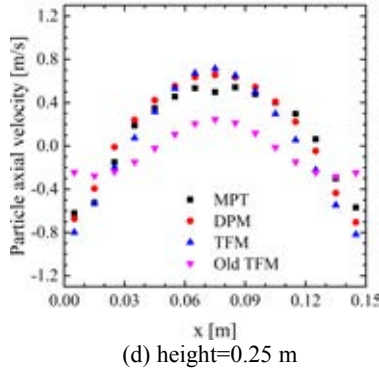
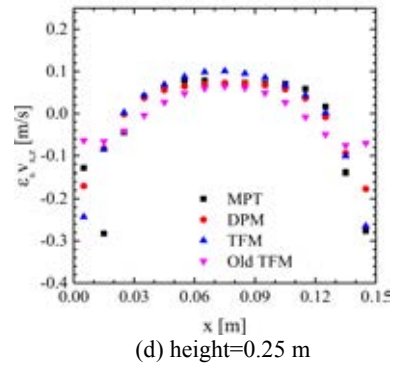
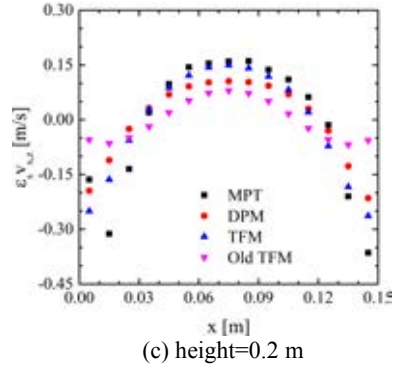


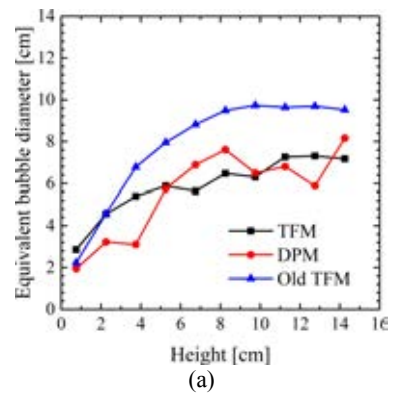
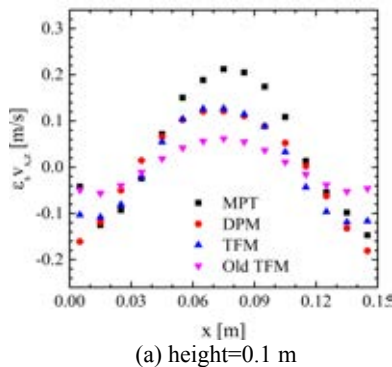
**Figure 4:** Comparison of the time-averaged (10-35s) particle axial velocity between MPT experiment, DPM and TFM simulations at various heights,  $U_g = 2.0 \text{ Umf}$ .

Comparisons of the time-averaged solid flux are depicted in **Figure 5**. In all cases, the current TFM simulations obtain best match with the DPM simulations among the results from MPT experiment and the old TFM. Note that characteristic measurements of the bulk particle flow is based on statistical analysis of the tracer trajectory in MPT experiment. Consequently, the MPT experiment just provides the information of  $\langle \epsilon_s \rangle \langle v_s \rangle$ . In contrast,  $\langle \epsilon_s v_s \rangle$  is applied in simulations. It is clear that  $\langle \epsilon_s v_s \rangle$  is not equal to  $\langle \epsilon_s \rangle \langle v_s \rangle$ . Thus, for this part we focus on the comparisons among simulations. With increasing height, both TFM simulations are in better accordance with the DPM simulation. Finally, the current TFM achieves significant improvement of the modelling results.



Time-averaged bubble size and count are presented in **Figure 6** to investigate the bubble motion. Note that the equivalent bubble diameter is evaluated using the bubble area  $A$ , i.e.  $De = \sqrt{4A/\pi}$  particle value of gas fraction equal to 0.8 is applied as the bubble boundary. Moreover, we exclude bubbles in contact with the free-board to avoid ambiguity. **Figure 6(a)** shows that the bubble size increases with increasing bed height. As is shown in **Figure 6(b)**, large number of bubbles near the bottom indicates that small bubbles emerge, and less bubbles with increasing bed height reveals the bubble coalescence. The old TFM predicts larger bubble size and less bubbles than the DPM and present TFM models. This is due to the fact that bubbles from the DPM and present TFM simulations burst into the free-board and form an obvious slugging fluidization.

**Figure 5:** Comparison of the time-averaged (10-35s) particle axial flux between MPT experiment, DPM and TFM simulations at various heights,  $U_g = 2.0 \text{ Umf}$ .



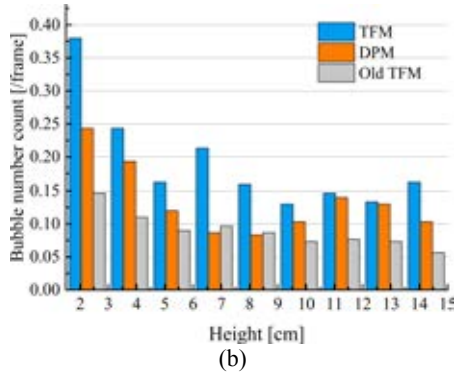


**Figure 6:** Comparison of time-averaged (10-25s) equivalent bubble diameter at different height,  $U_g = 1.5U_{mf}$ .

## CONCLUSION & OUTLOOK

This work focus on the validation of the present KTGF model for rough spheres and the corresponding BCs for rough wall. Current KTGF model are validated by comparing with one-to-one MPT experiment and DPM simulations of the same dense solid-gas fluidized bed both in a pseudo-2D. We have performed comparisons between the present KTGF model and the results of a simple kinetic theory derived by Jenkins and Zhang (2002). On comparison with DPM simulation and MPT experiment, it can be concluded that our present model improves the predictions obtained from the Jenkins and Zhang's model for the simulation of inelastic rough particles. The energy distributions from the current TFM is almost the same as that from DPM simulation. Consequently, Jenkins and Zhang's model under predicts particle axial velocity in the bed center and captures lower amount of particle velocity close to the wall, especially at high superficial fluidization velocity. Then, because of including of particle surface friction and rotation, larger densely packed zones are formed both in DPM and present TFM simulations, which is not clear in the old TFM simulation. In conclusion, further validation of current TFM for type Geldart A and B should be carried out. Additionally, since industrial fluidized beds are generally large and cylindrical in shape, therefore validation of current TFM model in cylindrical bed is also necessary.

## REFERENCES

- HOOMANS, B.P.B., et al., (1996), "Discrete particle simulation of bubble and slug formation in a two-dimensional gas-fluidised bed: a hard-sphere approach". *Chemical Engineering Science* **51(1)**, 99-118.
- JENKINS, J.T. and ZHANG, C., (2002), "Kinetic theory for identical, frictional, nearly elastic spheres". *Physics of Fluids*, **14**, 1228-1235.
- LOUGE, M.Y. (1994), "Computer-simulations of rapid granular flows of spheres interacting with a flat, frictional boundary". *Physics of Fluids* **6**, 2253-2269.
- LAN, X., et al., (2012), "Influence of solid-phase wall boundary condition on CFD simulation of spouted beds". *Chemical Engineering Science* **69(1)**, 419-430.
- LOHA, C. et al., (2013), "Euler-Euler CFD modelling of fluidized bed: Influence of specular coefficient on hydrodynamic behaviour". *Particuology* **11** 673-680.
- KUIPERS, J. A. M., et al., (1992), "A numerical model of gas-fluidized beds". *Chemical Engineering Science* **47**, 1913-1924.

DING, J. M., and GIDASPOW, D., (1990), "A bubbling fluidization model using kinetic theory of granular flow". *AIChE Journal* **36**, 523-538.

NIEUWLAND, J. J., et al., (1996), "Hydrodynamic modelling of gas/particle flows in riser reactors". *AIChE Journal* **42(6)**, 1569-1582.

SOMMERFELD, M. and HUBER N. (1999), "Experimental analysis and modelling of particle-wall collisions". *Int. J. Multiphase Flow* **25**, 1457-1489.

LINDBORG, H., et al., (2007), "Practical validation of the two-fluid model applied to dense gas-solid flows in fluidized beds". *Chemical Engineering Science* **62(21)**, 5854-5869.

LORENZ, et al., (1997). "Measurements of impact properties of small, nearly spherical particles". *Experimental Mechanics* **37(3)**, 292-298.

SINCLAIR, J., JACKSON R., (1987), "Gas-Particle Flow in a Vertical Pipe with Particle-Particle Interactions". *AIChE Journal* **35** 1473-1486.

Yang, L., et al., (2016a), "Modification of Kinetic Theory for Frictional Spheres, Part I: Two-fluid model derivation and numerical implementation". *Chemical Engineering Science* **152**, 767-782.

Yang, L., et al., (2016b), "Modification of kinetic theory of granular flow for frictional spheres, part II: Model validation". *Chemical Engineering Science* **152**, 783-794.

Yang, L., et al., (2016c), "Partial slip boundary conditions for collisional granular flows at flat frictional walls". *AIChE Journal*, 10.1002/aic.15534

LU, H.L., GIDASPOW, D., (2003). "Hydrodynamics of binary fluidization in a riser: CFD simulation using two granular temperatures". *Chemical Engineering Science* **58(16)**, 3777-3792.

MOHS, G., et al., (2009). "Magnetic monitoring of a single particle in a prismatic spouted bed". *Chemical engineering science* **64(23)**, 4811-4825.

BUIST, K. A., et al., (2015). "Determination and comparison of rotational velocity in a pseudo 2D fluidized bed using magnetic particle tracking and discrete particle modelling". *AIChE Journal* **61(10)**, 3198-3207.

## ACKNOWLEDGEMENT

The authors thank the European Research Council for its financial support, under its Advanced Investigator Grant scheme, Contract no. 247298 (Multi-scale Flows).

## APPENDIX

The expressions in the BCs for particle slip velocity are as follows,

$$A1 = \frac{1}{2(1+X^2)} + \frac{Y^2(1-X^2)}{8X^2(1+X^2)^2} + \frac{(4X^2-Y^2)\arctan[X]}{8X^3}$$

$$A2 = \frac{\sqrt{\pi}}{2Y} \operatorname{erf}(Y) - \frac{X^2 e^{-Y^2}(2Y^2-1)}{4Y^2} - \frac{\sqrt{\pi}X^2}{8Y^3} \operatorname{erf}(Y)$$

$$\text{Where } X = \sqrt{1+\lambda} \cot \theta_c, \quad Y = \sqrt{\frac{V_t^2}{2\Theta_c}} \cot \theta_c$$

The corresponding boundary conditions for granular temperatures are



$$\begin{aligned}
-\kappa_t \frac{\partial \Theta_t}{\partial n} &= g_0 \rho_s \varepsilon_s \left\{ \mu^2 (1+e)^2 \left( 1 - \frac{e^{-\frac{Y^2}{1+X^2}}}{1+X^2} \right) - (1-e^2) \right\} \sqrt{\frac{\Theta_t}{2\pi}} \Theta_t \\
&+ g_0 \rho_s \varepsilon_s \frac{2(1+\beta)}{7} (1+\lambda) \frac{2-ee_p}{2+ee_p} \min \left[ \frac{(2\Theta_t(1+\lambda)B1 - V_t^2 A1)}{V_t^2 (B2 - A2)}, \right] \sqrt{\frac{\Theta_t}{2\pi}} \\
-\kappa_r \frac{\partial \Theta_t}{\partial n} &= \frac{5}{4} (1+e)^2 \mu^2 m n g_0 \Theta_t \frac{2-ee_p}{2+ee_p} \sqrt{\frac{2\Theta_t}{\pi}} \left( 1 - \frac{e^{-\frac{Y^2}{1+X^2}}}{1+X^2} \right)
\end{aligned}$$

Where

$$\begin{aligned}
B2 &= \frac{\sqrt{\pi}}{2Y} \operatorname{erf}(Y) + \frac{X^2 \sqrt{\pi}}{8Y^3} \operatorname{erf}(Y) + \frac{3-2Y^2}{4Y^2} X^2 e^{-Y^2} + \frac{\sqrt{\pi} X^4}{64Y^5} \operatorname{erf}(Y) \\
B1 &= \frac{2X^2(X^2+1) + Y^2(X^2 - Y^2 + 3)}{4X^2(1+X^2)^2} + \frac{3Y^4(1+7X^4)}{96X^4(1+X^2)^3} \\
&+ \frac{8X^2(2X^2+Y^2) - Y^4}{32X^5} \arctan X
\end{aligned}$$

# DIRECT NUMERICAL SIMULATION OF THE EFFECTIVE DRAG IN GAS-LIQUID-SOLID SYSTEMS

**Maïke W. BALTUSSEN<sup>1\*</sup>, J. A. M. KUIPERS<sup>1†</sup>, Niels G. DEEN<sup>2‡</sup>**

<sup>1</sup>Multiphase Reactors Group, Eindhoven University of Technology, Postbus 513, 5600 MB Eindhoven, THE NETHERLANDS

<sup>2</sup>Multiphase and Reactive Flows Group, Eindhoven University of Technology, Postbus 513, 5600 MB Eindhoven, THE NETHERLANDS

\* E-mail: m.w.baltussen@tue.nl

† E-mail: j.a.m.kuipers@tue.nl

‡ E-mail: n.g.deen@tue.nl

## ABSTRACT

Due to the increase in the oil prices and the depletion of the oil reserves, Fischer-Tropsch processes for the production of synthetic fuels, methanol synthesis and other gas-to-liquid processes are rapidly gaining interest. These reactions are commonly performed in slurry bubble columns, i.e. three-phase gas-liquid-solid reactors. Although slurry bubble columns are already widely used, challenging scale-up and operational issues are encountered when these reactors are used for the Fisher-Tropsch process. To improve the fundamental understanding of these complex reactors, this work focuses on the effective drag acting on particles and bubbles in dense flows, using Direct Numerical Simulations. We combined the Front Tracking method of Roghair *et al.* (2013b) and the second order implicit Immersed Boundary method of Deen *et al.* (2012), resulting in a resulting hybrid Front Tracking Immersed Boundary method that is able to simulate dense three phase flows and quantify the effects. For a system consisting of 2 mm bubbles and 1 mm particles, effective drag closures are developed for both the bubbles and the particles at several phase volume fractions. In future research, the developed methodology will be applied to study the effect of the bubble and particle size and their ratio as well as heat and mass transfer.

**Keywords:** Multiphase flow, Slurry bubble column, multiscale modeling, gas-liquid-solid flows, fluid structure interaction, Front Tracking, Immersed Boundary method .

## NOMENCLATURE

### Greek Symbols

$\alpha$  Void fraction.  
 $\mu$  Viscosity, [Pa · s].  
 $\rho$  Density, [kg/m<sup>3</sup>].  
 $\sigma$  Surface tension coefficient, [N/m].  
 $\tau$  Stress tensor, [Pa].  
 $\phi$  Solid volume fraction.  
 $\psi$  Velocity component, [m/s].  
 $\omega$  Rotational velocity, [1/s].

### Latin Symbols

$a, b, C$  Coefficient.  
 $d$  Diameter, [m].  
 DNS Direct Numerical Simulation.  
 $Eo$  Eötvös number,  $g_z d_b^2 \Delta\rho / \sigma$ .  
**F** Force density or Force, [N/m<sup>3</sup>] or [N].

FT Front Tracking.  
**g** Gravity acceleration, [m/s<sup>2</sup>].  
 IB Immersed Boundary.  
 $I$  Moment of inertia, [kg · m<sup>2</sup>].  
 MCFD Multiphase Computational Fluid Dynamics.  
 Mo Morton number,  $g_z \mu_l^4 \Delta\rho / (\rho_l^2 \sigma^3)$ .  
**n** Normal.  
 $p$  Pressure, [Pa].  
 $t$  Time, [s].  
**r** Distance, [m].  
 Re Reynolds number,  $\rho |\mathbf{v}| d_b / \mu_l$ .  
**u** Liquid, fluid velocity, [m/s].  
**v** Bubble velocity, [m/s].  
 $V$  Volume, [m<sup>3</sup>].  
**w** Particle velocity, [m/s].

### Sub/superscripts

$b$  Bubble.  
 $B$  Buoyancy.  
 $c$  Central.  
 $col$  Due to particle-particle collisions.  
 $D$  Drag.  
 $g$  Gas phase.  
 $l$  Liquid phase.  
 $nb$  Neighboring.  
 $P$  Pressure.  
 $rel$  Relative.  
 $s$  Solid phase.  
 $z$  Direction of the gravitation.  
 $\sigma$  Surface tension.  
 $\infty$  Single bubble or particle infinite liquid.

## INTRODUCTION

The interest in Fischer-Tropsch processes for the production of synthetic fuels, methanol synthesis and other prominent gas-to-liquid processes has rapidly expanded in recent years, due to depletion of oil reserves and increasing oil prices. In these gas-to-liquid processes, a reactant gas is converted into liquid products over a solid catalyst. These type of three-phase gas-liquid-solid processes are often performed in slurry bubble columns. To accurately scale-up and design these columns, the fundamental understanding of the complex three phase interactions needs to be improved (Kantarci *et al.*, 2005; Wang *et al.*, 2007; Yang *et al.*, 2007; Pan *et al.*, 2016).

The introduction of particles in a bubble column causes a decrease in the bubble size and an increase in the void fraction. Besides, the bubble rise velocity decreases with increasing solids volume fraction even when neutrally buoyant particles are used (Kantarci *et al.*, 2005; Wang *et al.*, 2007; Hooshyar *et al.*, 2013; Baltussen *et al.*, 2013; Pan *et al.*, 2016). By using neutrally buoyant particles, Hooshyar *et al.* (2013) reported that the interaction mechanism depends on the Stokes relaxation time of the particles. When the Stokes relaxation time is relatively small, the bubble rise velocity is only affected via an increase in the apparent viscosity. For larger particles, which also have a larger Stokes relaxation time, the bubble rise velocity is only slightly influenced by the change in the apparent viscosity, while the main effect is caused by the encounters between the particles and the bubbles.

Because slurry bubble columns are often several meters in diameter and tens of meters in height, it is not possible to resolve all the details of the bubble-particle interactions for a full slurry bubble column. Therefore, a multiscale modeling approach is used to simulate industrial size columns. In this approach, coarse grained models, which do not capture the particle/bubble scale transport phenomena (like the Euler-Lagrange or Euler-Euler models), need closures for the bubble-bubble, bubble-particle and particle-particle interactions. This effective drag acting on the particles and the bubbles in dense can will be determined using smaller scale models, like the novel hybrid Direct Numerical Simulation (DNS) approach in this work (van Sint Annaland *et al.*, 2003; Deen *et al.*, 2004; Yang *et al.*, 2007; Raessi *et al.*, 2010; Roghair *et al.*, 2011; Baltussen *et al.*, 2013; Pan *et al.*, 2016). Several hybrid three-phase DNS methods have already been developed. Li *et al.* (2001) combined a Euler-Lagrange model for the particles with a DNS method for the bubbles. Although the particles are in reality much smaller than the bubbles, the method still requires closures for the solid-liquid interactions. Ge and Fan (2006), Jain *et al.* (2012) and Baltussen *et al.* (2016) combined a front capturing technique (Level-Set, Volume of Fluid and Volume of Fluid methods, respectively) for the gas-liquid interfaces with an Immersed Boundary (IB) method, to enforce the no-slip boundary condition at the surface of rigid immersed bodies. The disadvantage of these front capturing methods is the numerical coalescence which occurs when bubbles are close to each other. To overcome the numerical coalescence, Deen *et al.* (2009) and Baltussen *et al.* (2013) combined the Front Tracking (FT) method with a IB method. In FT, the bubbles are tracked directly using a triangular mesh. However, the separate mesh for each of the bubbles, the used FT currently prevents all coalescence between bubbles.

In this work, the swarm effects on the apparent drag of the bubbles and the particles is studied, requiring a constant bubble size during the simulation to facilitate the ease of interpretation. Therefore, we combined the FT method of Roghair *et al.* (2013a) with the second order implicit IB method of Deen *et al.* (2012). This specific IB method is chosen, because the method does not require a calibration of the effective particle size.

This paper starts with a short discussion of the applied numerical method and a short overview of the chosen numerical parameters. Subsequently, the effect of the void fraction and the solids volume fraction on the effective drag of the bubbles and the particles is discussed.

## NUMERICAL METHOD

Our novel hybrid three phase DNS method is a combination of the FT method of Roghair *et al.* (2013a) and the second order IB method of Deen *et al.* (2012). Here, we present only a brief discussion of both methods, particularly focusing on the combination of both methods and the modification required to enable the calculation of three-phase systems.

The hybrid FT-IB model solves the continuity equation, equation 1, and the Navier-Stokes equations, equation 2, assuming incompressible flow:

$$\nabla \cdot \mathbf{u} = 0 \quad (1)$$

$$\rho \frac{\partial \mathbf{u}}{\partial t} = -\nabla p - \rho \nabla \cdot (\mathbf{u}\mathbf{u}) - \nabla \cdot \boldsymbol{\tau} + \rho \mathbf{g} + \mathbf{F}_\sigma \quad (2)$$

Because the velocity field is continuous across the gas-liquid interface, the Navier-Stokes equations can be solved using an one-field approximation. The surface tension at the gas-liquid interface is taken into account by an extra force density,  $\mathbf{F}_\sigma$ , which is introduced near the interface. This force is directly calculated from the triangular mesh by summing the tensile forces exerted by the three neighboring markers, triangular element, on a reference marker and subsequent force mapping to the Eulerian grid using mass-weighting (Dijkhuizen *et al.*, 2010b; Roghair, 2012). To alleviate the parasitic currents that arise due to the mismatch between the discretisation of the surface tension and the pressure field, the surface tension calculations is augmented with the so-called "pressure-jump correction" (Renardy and Renardy, 2002; Francois *et al.*, 2006; Dijkhuizen *et al.*, 2010b). The local density and viscosity are obtained by normal and harmonic averaging, respectively.

The no-slip boundary condition at the particle surface is taken into account implicitly. At the level of the discretised Navier-Stokes equations, each velocity component at a certain node in the fluid,  $\psi_c$ , can be described as a function of the velocity components of the neighboring nodes,  $\psi_{nb}$ , with equation 3.

$$a_c \psi_c + \sum_{nb} a_{nb} \psi_{nb} = b_c \quad (3)$$

where the coefficients  $a_{nb}$  indicate the coupling of the velocity at node  $c$  with the velocities of the neighboring nodes,  $nb$ .

Using a second order (1D) polynomial fit, each neighboring fluid node inside a particle can be eliminated from equation 3. Together with the local velocity field and the velocity at the particle surface, the coefficients of the two velocity nodes involved in the polynomial fit are adjusted. A similar function is obtained for fluid nodes that are in close proximity of two particles, when there is only 1 grid point in between the particles, by using the velocity of the central node and the velocity of both particles. Because both equations are singular when the particle surface is close to the central cell, a linear fit is used when the distance between the surface and the central point is less than  $10^{-4}$  times the grid size.

The velocity field given by equation 2 is obtained on a staggered grid using a projection-correction method. In the projection step, all terms in this equation are treated explicitly except for the diffusion term, which is treated semi-implicitly. The implicit part of the diffusion term is chosen such that it only depends on the velocity component that is solved for, whereas the remaining (small) terms are treated explicitly. The diffusion terms are discretised using

a second order central difference scheme, while a second order flux-delimited Barton scheme is used for the convective terms. The projected velocity field is corrected to satisfy the continuity equation (equation 1). The equations in both the projection step and the correction step are solved using a OpenMP parallelised block ICCG matrix solver.

### Particles

When the velocity field is calculated, the positions of the particles,  $m$ , are updated by solving the Newtonian equations of motion:

$$V_m \rho_m \frac{d\mathbf{w}_m}{dt} = m\mathbf{g} + \oint_{\Gamma_m} -(\boldsymbol{\tau} \cdot \mathbf{n}) dS + \iiint_{\Omega_m} -\nabla p dV + F_{d,col} \quad (4)$$

$$I_m \frac{d\boldsymbol{\omega}_m}{dt} = \oint_{\Gamma_m} (\mathbf{r}_{i,j,k} - \mathbf{r}_m) \times -(\boldsymbol{\tau} \cdot \mathbf{n}) dS \quad (5)$$

where the moment of inertia is given by:

$$I_m = \frac{1}{10} V_m \rho_m d_m^2 \quad (6)$$

In the three-phase system, the transpose part of the Stokes stress tensor in equation 4 and 5 should be included, because the viscosity is not constant. Both the pressure gradient and the velocity gradients, which are needed in the stress tensor, can be obtained directly from the second order fit, which was used to apply the no-slip boundary condition.

In the continuous limit, the calculation of the pressure force can be performed with either a surface integral or a volume integral using Gauss's theorem. Although the pressure inside the particle is unknown, the volume integral of the pressure gradient over the total particles will effectively result in a calculation depending on the pressures outside the particle due to the employed discretisation. When the calculation via the surface integral and the volume integral are compared with the results of Zick and Homsy (1982), the calculation of the force via the surface integral is not able to accurately capture the drag of a particle in a dense array. Therefore, the drag force will be calculated via the volume integral in this paper.

The interactions between the particles are included using a hard sphere model (Hoomans *et al.*, 1996). Therefore the drag force as discussed before does not include the collisions with other particles. However, the collisions with the bubbles are not separately treated and therefore their effects will be lumped in the drag force.

### Bubbles

Following the update of the particle positions and velocities, the position of the bubbles is updated. Every marker point at the surface is displaced separately with the local velocity, which is interpolated from the Eulerian grid using cubic spline interpolation, by fourth order Runge-Kutta time stepping. Because each marker point is advected separately, the bubbles will change both its position and its shape. Nevertheless, this also changes the distance between the marker points leading to a decreased surface mesh quality. To restore the mesh quality, the surface is remeshed, using four elementary operations: edge splitting, edge collapsing, edge swapping and smoothing (Roghair, 2012).

Due to the separate advection of the marker points and the remeshing, small volume changes in the bubble volume arise, which accumulate over the total simulation time. To locally restore the volume losses during the remeshing a smoothing

**Table 1:** Simulation settings for the base case of the slurry bubble swarms.

Property	Value	Unit
Void fraction, $\alpha$	0.30	
Solid volume fraction, $\phi$	0.05	
Computational grid	171	
Grid size	$1.0 \cdot 10^{-4}$	m
Time step	$1.0 \cdot 10^{-5}$	s
Bubble diameter	$2.0 \cdot 10^{-3}$	m
Particle diameter	$1.0 \cdot 10^{-3}$	m
Liquid density	$1.0 \cdot 10^3$	kg/m <sup>3</sup>
Liquid viscosity	$1.0 \cdot 10^{-3}$	Pas
Gas density	100.0	kg/m <sup>3</sup>
Gas viscosity	$1.8 \cdot 10^{-5}$	Pas
Solids density	$2.0 \cdot 10^3$	kg/m <sup>3</sup>
Surface tension	0.073	N/m
Normal restitution coefficient	1.00	
Tangential restitution coefficient	1.00	
Friction coefficient coefficient	0.00	
$-\log(\text{Mo})$	10.6	
Eo	0.48	

procedure described by Kuprat *et al.* (2001) is implemented. Moreover, the volume changes due to the separate advection of each marker are compensated by distributing the lost volume over all the interface cells. This procedure might cause unphysical overlap with other bubbles and particles. Marker points that are close to another bubble or particle, within the maximal edge length of a marker, are therefore excluded from this operation.

### Simulation set-up

The simulations are started with a random initial configuration of bubbles and particles, generated using a Monte-Carlo method. In this method, the dispersed elements (bubbles/particles) are first placed in a lattice structure in the domain. Subsequently, each element is displaced slightly 200 times. The procedure is repeated until no overlap between the elements is found.

In the simulations, periodic boundaries are used to mimic an infinite bubble/particle swarm. To ensure that the finite box size does not influence the results, a minimum number of bubbles and particles is required. Roghair *et al.* (2011) and Bunner and Tryggvason (2002) established that the minimum number of bubbles needed is 12. By changing the number of particles for simulations with the settings of table 1, there is no effect when the number of particles exceeds 40. Therefore, the minimum number of bubbles and particles used in the simulations is conservatively set to respectively 16 and 60.

Besides the number of bubbles and particles, the resolution of both the particles and the bubbles should be sufficient to obtain grid independent results. Dijkhuizen *et al.* (2010a) showed that at least 20 grid cells across a bubble diameter are needed in the used FT method. Furthermore, simulations using again the settings of table 1 with a different resolution for the particles showed negligible effect of the grid resolution. Therefore, the number of grid cells inside a particle and a bubble diameter is set to 10 and 20, respectively.

To study the effect of the void fraction and the solids volume fraction, 27 different simulations have been performed, which are grouped in four different cases listed in table 2. All

**Table 2:** Gas fraction, solids volume fraction and averaging time for the four different cases studied to determine the effect of solids volume fraction and the void fraction. All cases have the same settings as listed in table 1, except for the parameters listed here.

Case	$\alpha$	$\phi$	$t_{avg}$
1	0.20	0.02...0.14	0.8
2	0.40	0.02...0.14	0.25...0.8
3	0.15...0.45	0.05	0.55...0.8
4	0.15...0.45	0.10	0.8

simulations are initiated with a time step of  $1.0 \cdot 10^{-5}$  s and continued for 1 s. To remove any start-up effects, the first 0.2 s is discarded from the analysis, which was sufficient to yield the time-averaged slip velocity within 2% from the final results for two phase flows (Roghair *et al.*, 2011).

## RESULTS

First, the effect of the particles on the bubble drag force is quantified by varying the solids volume fraction and the void fraction. The drag coefficient of the bubbles is determined using a macroscopic force balance for the bubbles similar to the work of Roghair *et al.* (2011). At a pseudo steady state, the time-averaged drag will exactly balance the gravitational force and the hydrostatic pressure force in the flow direction.

$$\begin{aligned} \langle \mathbf{F}_D \rangle &= \langle \mathbf{F}_G \rangle + \langle \mathbf{F}_P \rangle \\ &= V_b \rho_g \mathbf{g} - \nabla p V_b \\ \frac{1}{2} \rho_l v_{rel,b}^2 C_D \frac{\pi d_b^2}{4} &= \left( 1 - \alpha - \phi \frac{\rho_l - \rho_s}{\rho_l - \rho_g} \right) (\rho_l - \rho_g) g_z V_b \quad (7) \end{aligned}$$

The relative drag coefficient can be obtained by normalizing the drag coefficient of equation 7 with the drag coefficient of a single bubble rising in an infinite pool of liquid obtained by Tomiyama (1998). This definition results in a direct correspondence between the relative drag coefficient and the terminal rise velocity of a single bubble with the same size and the average velocity of the bubbles in the simulation. Because the addition of particles and the other bubbles results in a difference in hydrostatic pressure in comparison with a single rising bubble, the bubble rise velocity has to be corrected with the void fraction and the solids volume fraction, equation 8. It should be noted that this equation reduces to the form of Roghair *et al.* (2011) in the absence of particles or when the particles are neutrally buoyant.

$$C_{D,rel} = \frac{C_D}{C_{D,\infty} \left( 1 - \alpha - \phi \frac{\rho_l - \rho_s}{\rho_l - \rho_g} \right)} = \frac{\langle \mathbf{v}_{b,\infty} \rangle^2}{(\langle \mathbf{v}_b \rangle - \langle \mathbf{u} \rangle)^2} \quad (8)$$

Figure 1 shows the relative drag coefficients resulting from the three-phase simulations including the standard deviations. For case 2, two different simulations with a solids volume fraction of 8% but different initial positions are shown. The figure shows that the relative drag coefficients differ only 12%, which is within the large and overlapping standard deviation. In addition, the standard deviations obtained in this work are larger than those obtained for gas-liquid bubble swarms, which is probably due to the interactions with the (heavier) particles.

According to figure 1, the drag coefficient of the bubbles increases with increasing void fraction and solids volume fraction. The increase of the relative drag force with increasing void fraction was also determined in two-phase flows (Roghair *et al.*, 2011; Martínez-Mercado *et al.*, 2007). However, the effects in the three-phase flow are larger due to the addition of particles, which is in good agreement with the experimentally observed decrease in the bubble rise velocity upon the introduction of particles (Kantarci *et al.*, 2005; Wang *et al.*, 2007; Hooshyar *et al.*, 2013; Pan *et al.*, 2016). The data of figure 1 was used to derive a correlation for the relative bubble drag coefficient. With respect to the form of the correlation, we constrained the form such that the correlation will lead to the correlation of Roghair *et al.* (2011) in the limit that there are no particles ( $\phi = 0$ ) and that the drag coefficient of a single bubble ( $\alpha = 0$ ) is higher in a liquid containing particles. This resulted in the fit in equation 9.

$$C_{D,rel} = 1 + \frac{18}{\text{Eo}} \alpha + 1.8 \cdot 10^5 \alpha^5 \phi^{1.1} + 2.7 \cdot 10^3 \phi^2 \quad (9)$$

In addition to the close match of the symbols and the lines in figure 1, the parity plot of figure 2 shows that most of the results are within 10% of the fit. On average, the differences between the correlation and the simulation results amounts 7.6%, which is less than the spread in results obtained by using different initial conditions. The maximum difference, which is obtained for low solids volume fractions and low void fractions, is 20%.

Secondly the effect of the bubbles on the drag coefficient of the particles can be determined in a similar manner as the drag coefficient of the bubbles. In the case of the particles, the drag coefficient is now normalized with the drag coefficient of a single particle in an infinite fluid, given by Schiller and Nauman (Clift *et al.*, 1978):

$$C_{D,\infty,p} = \frac{4d_p(\rho_l - \rho_p)g_z}{3\rho_l w_z^2} = \frac{24}{\text{Re}_p} \left( 1 + 0.15 \text{Re}_p^{0.687} \right) \quad (10)$$

The resulting relative drag coefficient is given by:

$$C_{D,rel,p} = \frac{C_D}{C_{D,\infty,p} \left( 1 - \phi - \alpha \frac{\rho_g - \rho_l}{\rho_s - \rho_l} \right)} = \frac{\langle \mathbf{w}_\infty \rangle^2}{(\langle \mathbf{w}_p \rangle - \langle \mathbf{u} \rangle)^2} \quad (11)$$

Figure 3 clearly shows that the drag force on the particles occasionally changes direction. In these circumstances, a bubble and particle will mutually rise, because the combination of one bubble and one particle is buoyant with respect to the liquid. The large standard deviations indicate that particles have two different modes: almost free movement and movement that is obstructed by bubbles. Because particles appear to alternate between these modes, the standard deviations are much larger than the averaged drag coefficient. The calculation of the drag coefficient will be improved when the drag coefficient is calculated for each of these two modes separately. However, this is beyond the scope of this work. In addition, the simulations of case 2 with a solids fraction of 8% only show a difference of 8% for the drag coefficient of the particles.

The obtained drag coefficients are also fitted to quantify the effect of the void fraction and the solids volume fraction on the drag coefficient. The correlation should meet two criteria: the relative drag coefficient of the particles should be equal to 1 when the solids volume fraction and the void fraction are zero. Secondly, it is expected that the drag coefficient of a

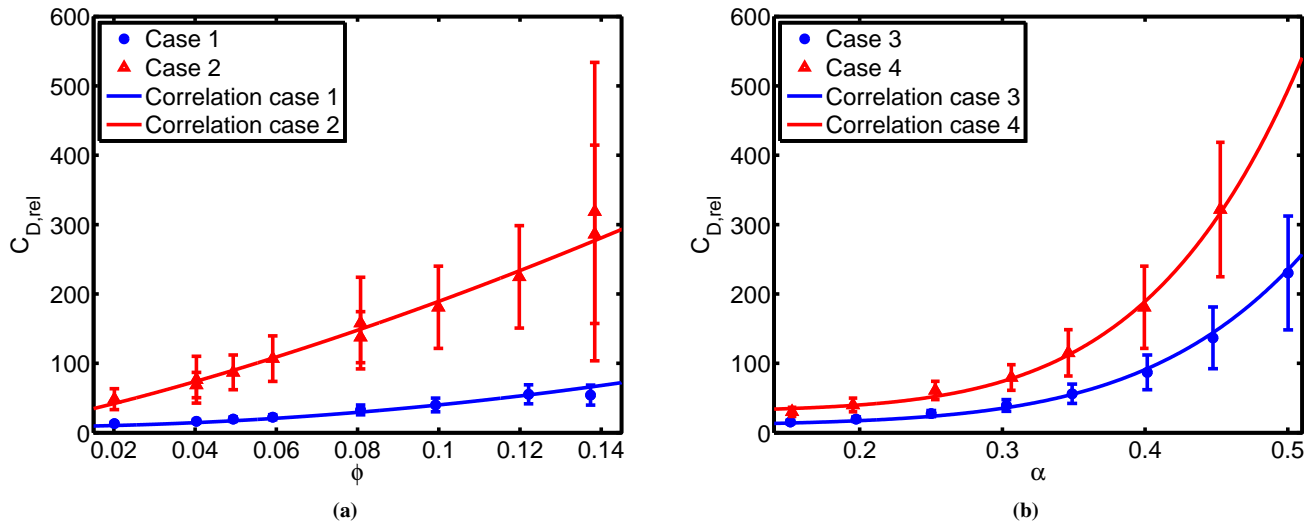


**Figure 1:** Effect of the solids volume fraction, figure a, and the effect of the void fraction, figure b, on the normalized drag coefficient of the bubbles. The drag is normalized using equation 8. The lines in the figures represent the fit of equation 9. The bars indicate the standard deviation.

single particle in a bubble swarm or in a particle swarm have a relatively higher drag than a single particle in an infinite liquid. The obtained fit is shown in equation 12.

$$C_{D,rel,p} = 1 + 10\alpha^{2.5} + 200\phi^2 + 1.41 \cdot 10^7 \phi^{4.5} \alpha^5 \quad (12)$$

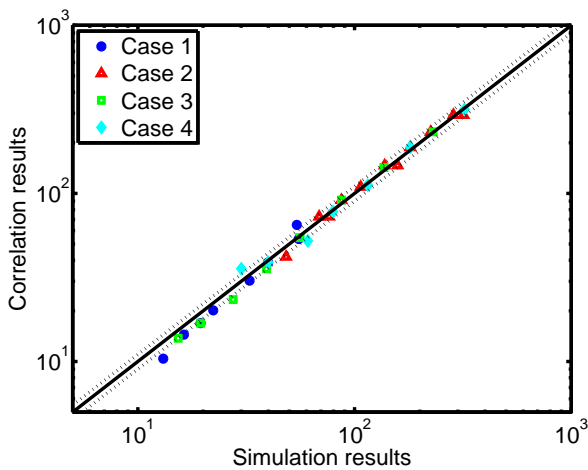


**Figure 2:** Parity plot containing the relative drag coefficient of the particles obtained from the simulations and the correlation given by equation 9. The dashed lines indicate an error of 10%.

In addition to a proper capture of the trends in the drag coefficient, the parity plot in figure 4 shows an average absolute difference between the simulation and the correlation results of only 7.1% with a maximum of 22.5%.

The increase of the drag coefficients of both the bubbles and the particles can partly be explained by the micro structuring of the bubbles. The bubbles cluster in a dynamic system of horizontal layers, as shown in figure 5. The horizontal clustering was already observed by Roghair *et al.* (2013b) for bubble swarms and by Baltussen *et al.* (2013) for slurries, and is probably caused by the lack of large scale circulations. The clustering of the particles prevails due to hindrance by the bubbles. The particles partly cluster on top of the bubbles, effectively hindering the rise of the bubbles, which decreases the particle velocity or even reverses its direction. The particles will eventually roll down the side of the bubble, due to a combination of buoyancy forces and surface tension.

## CONCLUSION

In this paper, a combined FT second order implicit IB method was used to simulate dense bubble/particle swarms. By using this method, the effect of the void fraction and the solids volume fraction on the drag coefficient of 1 mm particles and 2 mm bubbles was determined. For both the particles and bubbles, a combined effect of the void fraction and the solids volume fraction was found on the drag coefficient. Using the simulation results, drag correlations for both the bubbles and the particles were developed, which provides an accurate description for  $15\% \leq \alpha \leq 50\%$  and  $2\% \leq \phi \leq 14\%$ .

Because of the limited range in physical properties, particle and bubble diameter used in this paper, the applicability of the obtained correlations is limited to the range of conditions investigated. To obtain a broader applicability, the simulation

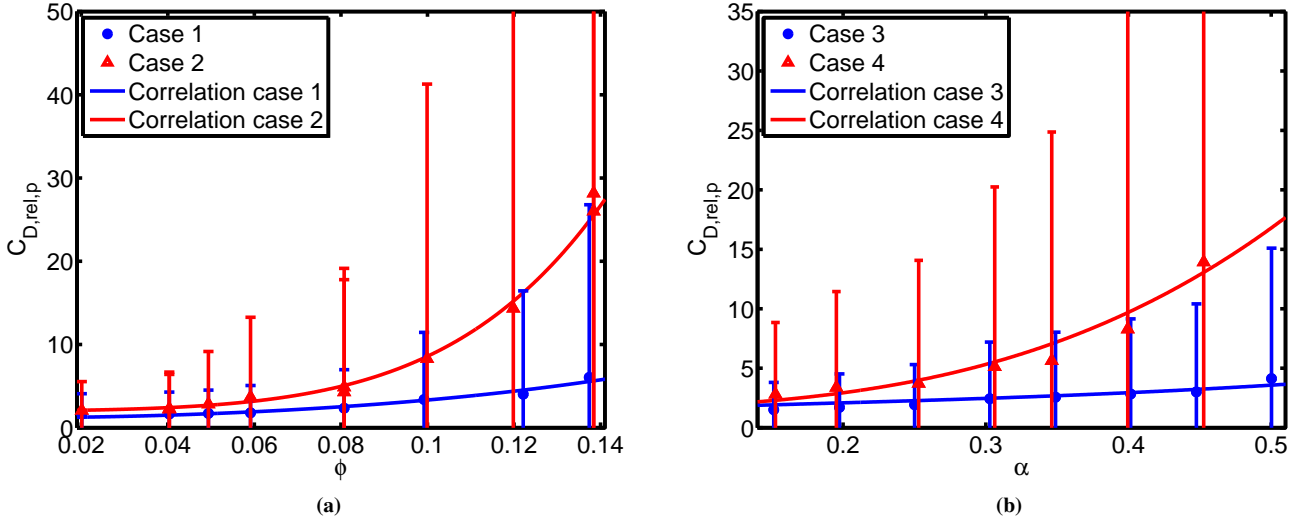


**Figure 3:** Effect of the solids volume fraction (a), and the effect of the void fraction (b) on the normalized drag coefficient of the particles. The drag is normalized using equation 11. The lines in the figures represent the fit of equation 12. The bars indicate the standard deviation.

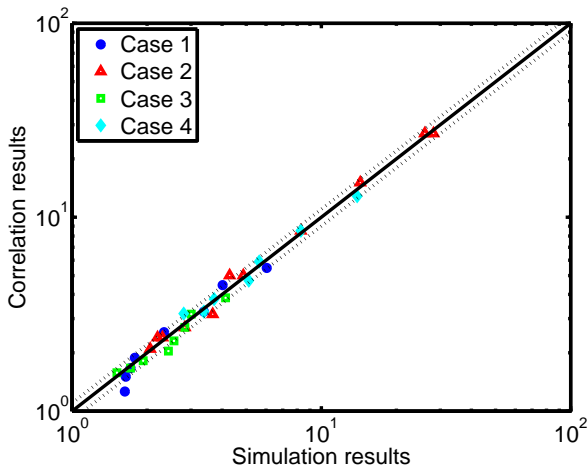


**Figure 4:** Parity plot containing the relative drag coefficient of the particles obtained from the simulations and the correlation given by equation 12. The dashed lines indicate an error of 10%.

range should be extended. Preliminary results to assess the effect of the bubble diameter show similar trends in void fraction and solids volume fraction. An increasing bubble diameter will lead to a decrease in the drag coefficient for both the bubbles and the particles. It is expected that the size of the particles will influence the drag coefficient. However, because the increase of inertia of the particles might lead to larger deformation and even to break-up of the bubbles, it is hard to predict the effect of the particle size on the drag of both particles and bubbles.

Simulating particles with a high inertia in combination with bubbles with a relatively low surface tension is still difficult for the FT-IB model. In such cases, particles can fall through bubbles, leading to the formation of a doughnut shaped bubble or even the break-up of the bubble. To enable capturing these events, a break-up model needs to be included in the method. Another option is to combine the currently used FT model with the Volume of Fluid model, which prevents unphysical merging of the bubbles while break-up is incorporated in the model (Torres and Brackbill, 2000; Walker *et al.*, 2013). Another option is to implement FT without connectivity, like the Local Front Reconstruction Method (Shin and Juric, 2002).

Although the second order IB method is tested thoroughly, the rotation of freely moving particles at high Reynolds numbers is not accurately calculated. However, the disturbance of the bubbles and the frequent collisions with both particles and bubbles are expected to diminish any effect of unphysical rotation. To prevent any unphysical rotation of the particles, the calculation of the rotational velocity should be improved.

Finally, the currently used size ratio between the bubbles and the particles ( $d_b/d_p = 2$ ) is much larger than the ratio which is common in slurry bubble columns ( $d_b/d_p \approx 10 - 100$ ). To obtain a realistic effect of the particles on the drag of the bubbles and vice versa, this diameter ratio should be decreased drastically. Clearly this will put challenges on the allowable number of grid cells, which can probably only be solved by applying adaptive grid refinement.

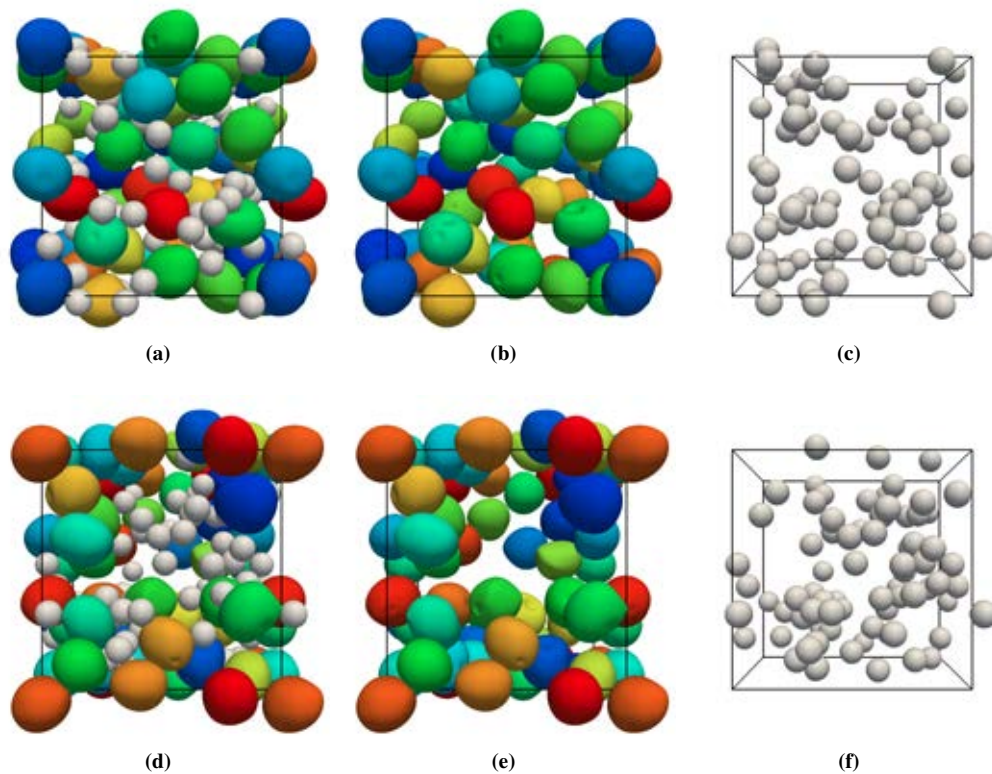


**Figure 5:** Two snapshots of a simulation with a void fraction of 25% and a solids volume fraction of 5%. Figure (a) and (d) show both the particles and the bubbles, while the middle and the right figures only show the bubble configuration and the particle configuration.

## ACKNOWLEDGMENT

The authors would like to thank the European Research Council for its financial support, under its Starting Investigator Grant scheme, contract number 259521 (CuttingBubbles).

## REFERENCES

- BALTUSSEN, M.W., SEELLEN, L.J.H., KUIPERS, J.A.M. and DEEN, N.G. (2013). "Direct numerical simulations of gas-liquid-solid three phase flows". *Chemical Engineering Science*, **100**, 293–299.
- BALTUSSEN, M.W., SEGERS, Q.I.E., KUIPERS, J.A.M. and DEEN, N.G. (2016). "Cutting bubbles with a single wire". *Chemical Engineering Science (accepted)*.
- BUNNER, B. and TRYGGVASON, G. (2002). "Dynamics of homogeneous bubbly flows part 1. rise velocity and microstructure of the bubbles". *Journal of Fluid Mechanics*, **466**, 17–52.
- CLIFT, R., GRACE, J.R. and WEBER, M.E. (1978). *Bubbles, drops and particles*. Academic Press, New York.
- DEEN, N.G., van Sint Annaland, M. and KUIPERS, J.A.M. (2004). "Multi-scale modeling of dispersed gas-liquid two-phase flow". *Chemical Engineering Science*, **59(8-9)**, 1853–1861.
- DEEN, N.G., van Sint Annaland, M. and KUIPERS, J.A.M. (2009). "Direct Numerical Simulation of complex multi-fluid flows using a combined Front Tracking and Immersed Boundary method". *Chemical Engineering Science*, **64(9)**, 2186–2201.
- DEEN, N.G., KRIEBITZSCH, S.H.L., van der Hoef, M.A. and KUIPERS, J.A.M. (2012). "Direct Numerical Simulation of flow and heat transfer in dense fluid-particle systems". *Chemical Engineering Science*, **81**, 329–344.
- DIJKHUIZEN, W., ROGHAIR, I., van Sint Annaland, M. and KUIPERS, J.A.M. (2010a). "DNS of gas bubbles behaviour using an improved 3D Front Tracking model—drag force on isolated bubbles and comparison with experiments". *Chemical Engineering Science*, **65(4)**, 1415–1426.
- DIJKHUIZEN, W., ROGHAIR, I., van Sint Annaland, M. and KUIPERS, J.A.M. (2010b). "DNS of gas bubbles behaviour using an improved 3D Front Tracking model—model development". *Chemical Engineering Science*, **65(4)**, 1427–1437.
- FRANCOIS, M.M., CUMMINS, S.J., DENDY, E.D., KOTHE, D.B., SICILIAN, J.M. and WILLIAMS, M.W. (2006). "A balanced-force algorithm for continuous and sharp interfacial surface tension models within a volume tracking framework". *Journal of Computational Physics*, **213(1)**, 141–173.
- GE, Y. and FAN, L.S. (2006). "3-D Direct Numerical Simulation of gas-liquid and gas-liquid-solid flow systems using the Level-Set and Immersed-Boundary methods". *Advances in Chemical Engineering*, **31**, 1–63.
- HOOMANS, B.P.B., KUIPERS, J.A.M., BRIELS, W.J. and van Swaaij, W.P.M. (1996). "Discrete Particle simulation of bubble and slug formation in a two-dimensional gas-fluidised bed: A hard-sphere approach". *Chemical Engineering Science*, **51(1)**, 99–118.
- HOOSHYAR, N., VAN OMMEN, J.R., HAMERSMA, P.J., SUNDARESAN, S. and MUDDE, R.F. (2013). "Dynamics of single rising bubbles in neutrally buoyant liquid-solid suspensions". *Physical Review Letters*, **110(24)**, 244501.
- JAIN, D., DEEN, N.G., KUIPERS, J.A.M., ANTONYUK,



- S. and HEINRICH, S. (2012). "Direct Numerical Simulation of particle impact on thin liquid films using a combined Volume of Fluid and Immersed Boundary method". *Chemical Engineering Science*, **69**(1), 530–540.
- KANTARCI, N., BORAK, F. and ULGEN, K.O. (2005). "Bubble column reactors". *Process Biochemistry*, **40**(7), 2263–2283.
- KUPRAT, A., KHAMAYSEH, A., GEORGE, D. and LARKEY, L. (2001). "Volume conserving smoothing for piecewise linear curves, surfaces, and triple lines". *Journal of Computational Physics*, **172**, 99–118.
- LI, Y., YANG, G.Q., ZHANG, J.P. and FAN, L.S. (2001). "Numerical studies of bubble formation dynamics in gas-liquid-solid fluidization at high pressures". *Powder Technology*, **116**(2-3), 246–260.
- MARTÍNEZ-MERCADO, J., PALACIOS-MORALES, C. and ZENIT, R. (2007). "Measurement of pseudo-turbulence intensity in monodispersed bubbly liquids for  $10 < \text{Re} \leq 500$ ". *Physics of Fluids*, **19**(10).
- PAN, H., CHEN, X.Z., LIANG, X.F., ZHU, L.T. and LUO, Z.H. (2016). "Cfd simulations of gas-liquid-solid flow in fluidized bed reactors - a review". *Powder Technology*, **299**, 235–258.
- RAESSI, M., MOSTAGHIMI, J. and BUSSMANN, M. (2010). "A Volume-of-Fluid interfacial flow solver with advected normals". *Computers & Fluids*, **39**(8), 1401–1410.
- RENARDY, Y. and RENARDY, M. (2002). "PROST: A parabolic reconstruction of surface tension for the Volume-of-Fluid method". *Journal of Computational Physics*, **183**(2), 400–421.
- ROGHAIR, I. (2012). *Direct Numerical Simulations of Hydrodynamics and Mass Transfer in Dense Bubbly Flows*. Ph.D. thesis, Eindhoven, University of Technology.
- ROGHAIR, I., LAU, Y.M., DEEN, N.G., SLAGTER, H.M., BALTUSSEN, M.W., van Sint Annaland, M. and KUIPERS, J.A.M. (2011). "On the drag force of bubbles in bubble swarms at intermediate and high reynolds numbers". *Chemical Engineering Science*, **66**, 3204–3211.
- ROGHAIR, I., BALTUSSEN, M.W., van Sint Annaland, M. and KUIPERS, J.A.M. (2013a). "Direct Numerical Simulations of the drag force of bi-disperse bubble swarms". *Chemical Engineering Science*, **95**, 48–53.
- ROGHAIR, I., VAN SINT ANNALAND, M. and KUIPERS, J.A.M. (2013b). "Drag force and clustering in bubble swarms". *AIChE Journal*, **59**(5), 1791–1800.
- SHIN, S. and JURIC, D. (2002). "Modeling three-dimensional multiphase flow using a level contour reconstruction method for Front Tracking without connectivity". *Journal of Computational Physics*, **180**, 427–470.
- TOMIYAMA, A. (1998). "Struggle with computational bubble dynamics". *Third International Conference on Multiphase Flow*, 369–405.
- TORRES, D.J. and BRACKBILL, J.U. (2000). "The Point-Set method: Front-Tracking without connectivity". *Journal of Computational Physics*, **165**(2), 620–644.
- van Sint Annaland, M., DEEN, N.G. and KUIPERS, J.A.M. (2003). *Multi-level modeling of dispersed gas-liquid two-phase flows*. Heat and mass transfer. Springer, Berlin (edited by M. Sommerfeld and D. Mewes).
- WALKER, E., NIKITOPOULOS, D. and TROMEUR-DERVOU, D. (2013). "Parallel solution methods for poisson-like equations in two-phase flows". *Computers & Fluid*, **80**, 152–157.
- WANG, T., WANG, J. and JIN, Y. (2007). "Slurry reactors for gas-to-liquid processes: A review". *Industrial and Engineering Chemistry Research*, **46**(18), 5824–5847.
- YANG, G.Q., DU, B. and FAN, L.S. (2007). "Bubble formation and dynamics in gas-liquid-solid fluidization. a review". *Chemical Engineering Science*, **62**(1-2), 2–27.
- ZICK, A.A. and HOMSY, G.M. (1982). "Stokes flow through periodic arrays of spheres." *Journal of Fluid Mechanics*, **115**, 13–26.

## A LAGRANGIAN-EULERIAN HYBRID MODEL FOR THE SIMULATION OF DIRECT REDUCTION OF IRON ORE IN FLUIDIZED BEDS

Simon SCHNEIDERBAUER<sup>1\*</sup>, Mustafa E. KINACI<sup>1†</sup>, Franz HAUZENBERGER<sup>2‡</sup>, Stefan PIRKER<sup>3§</sup>

<sup>1</sup>Christian-Doppler Laboratory for Multi-Scale Modelling of Multiphase Processes, Johannes Kepler University, 4040 Linz, AUSTRIA

<sup>2</sup>Primetals Technologies Austria GmbH, 4031 Linz, AUSTRIA

<sup>3</sup>Department of Particulate Flow Modelling, Johannes Kepler University, 4040 Linz, AUSTRIA

\* E-mail: simon.schneiderbauer@jku.at

† E-mail: mustafa\_efe.kinaci@jku.at

‡ E-mail: franz.hauzenberger@primetals.com

§ E-mail: stefan.pirker@jku.at

### ABSTRACT

Fluidized bed and moving bed reactors are one of the most important technologies in several branches of process industry. Especially, it is known since decades that iron can be reduced rapidly and efficiently from iron carrier materials using such. The primary energy sources and reducing agents are natural gas, coal, coke, pulverized coal, which are finally released as CO<sub>2</sub> and in a lesser extent as H<sub>2</sub>O to the environment. Iron reduction consumes about 70% of the energy during steelmaking therefore offering potential in energy and CO<sub>2</sub> savings. Due to the limited accessibility for measurements, simulation methods have become one of the most important tools for optimizing the iron making processes. While the two-fluid model (Schneiderbauer *et al.*, 2012) would be a good candidate to attack the simulation of large-scale multi-phase processes it lacks from a proper representation of the particle size distribution and the related physical phenomena. This, in turn, gives rise to particle-based approaches, such as the coupling between CFD and DEM methods, which can easily handle particle segregation, particle growth and particle mixing. Furthermore, chemical reactions can be evaluated per particle and it is not required to transfer these reactions to a continuum representation. However, CFD-DEM approaches require an appropriate coarse-graining to considerably reduce their computational demands. We, therefore, present a generalization of the Lagrangian-Eulerian hybrid model for the numerical assessment of reacting poly-disperse gas-solid flows (Schneiderbauer *et al.*, 2016b) to fluidized beds used for iron ore reduction. The main idea of such a modeling strategy is to use a combination of a Lagrangian discrete phase model (DPM) and a coarse-grained two-fluid model (TFM) to take advantage of the benefits of those two different formulations. On the one hand, the DPM model unveils additional information such as the local particle size distribution, which is not covered by TFM. On the other hand, the TFM solution deflects the DPM trajectories due to the inter-particle stresses. This hybrid approach further enables the efficient evaluation of the gas-solid phase reduction of iron ore at a particle level using DPM. The predictive capability and numerical efficiency of this reactive hybrid modeling approach is demonstrated in the case of a lab-scale fluidized bed. The results show that the model is able to correctly predict fractional reduction of the iron ore. The results further give a closer insight about the temperatures and reaction gas consumption due to the reduction process.

**Keywords:** fluidized bed, iron ore reduction, two-fluid model.

A complete list of symbols used, with dimensions, is re-

quired.

### NOMENCLATURE

#### Greek Symbols

$\beta$	drag coefficient, [ $kg/m^3s$ ]
$\rho$	Mass density, [ $kg/m^3$ ]
$\epsilon$	volume fraction, (-)
$\mu_g$	viscosity of gas phase, [ $Pa s$ ]
$\tau$	Tortuosity, (-)

#### Latin Symbols

$a, b, c$  Stoichiometric coefficients of relative species

$A, B, C$  Species

$A_p$	Particle surface area, [ $m^2$ ]
$C_i$	Molar Concentration of species $i$ , [ $mol/m^3$ ]
$D_{j,i}$	Binary gas diffusion, [ $m^2/s$ ]
$d$	Particle diameter, [ $m$ ]
$E_a$	Activation energy, [ $kJ/mol$ ]
$f_j$	Local fractional reduction of the $j^{th}$ layer, [ $kJ/mol$ ]
$G_\Delta$	Box filter defined by numerical grid, (-)
$k_0$	Pre-exponential factor, [ $m/s$ ]
$Ke_j$	Equilibrium constant of layer $j$ , (-)
$k_f$	Mass transfer coefficient, [ $m/s$ ]
$k_j$	Reaction rate constant, [ $m/s$ ]
$m_i$	Mass of species $i$ , [ $kg$ ]
$M_i$	Molecular mass of species $i$ , [ $kg/mol$ ]
$N_i$	Number of moles of species $i$ , [ $mol$ ]
$n$	Number density, [ $1/m^3$ ]
$Nu$	Nusselt number, (-)
$Pr$	Prandtl number, (-)
$P_t$	Total pressure, [ $bar$ ]
$R$	Universal gas constant, [ $kJ/molK$ ]
$Re$	Reynolds number, (-)
$r_p$	Particle radius, [ $m$ ]
$r_j$	Layer radius, [ $m$ ]
$Sc$	Schmidt number, (-)
$Sh$	Sherwood number, (-)
$T$	Temperature, [ $K$ ]
$u$	velocity, [ $m/s$ ]
$\dot{Y}_{i,j}$	Mass fraction of species $i$ layer $j$ , (-)
$X_i$	Molar fraction of species $i$ , (-)

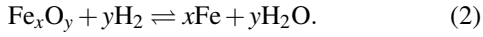
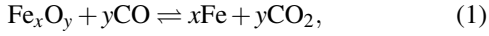
#### Sub/superscripts

$g$	Gas phase
$i$	species $i$
$j$	layer $j$

s solid phase

## INTRODUCTION

The main conversion process to gain metallic iron from oxidic iron compounds is the reduction of iron ores by suitable reducing agents, where iron oxides are reduced to metallic iron by gaseous reducing agents (CO and H<sub>2</sub>). During the reduction of iron ores, oxygen is removed according to the thermodynamic equilibrium conditions, until the next oxidation level is reached. The gaseous reduction of iron oxides as well as the oxidation of the reducing agents can be described by the following reaction mechanism (Valipour, 2009)



These equations reveal that the reduction reactions of iron ores can be considered as elementary reactions, which means that the number of moles of the gaseous components does not change during the reactions. Thus, the equilibrium of reactions is independent of the total pressure of the reaction system and the chemical equilibrium conditions only depend on temperature.

The leading process used in iron-making is the blast furnace, which consists of a moving bed reactor with countercurrent flow of the solid reactants against a reducing gas. In the lower part the iron is molten and carburized. However, in the blast furnace process iron ore fines, which build up around 80% of the total iron ore, needs to go through a preparation step (i.e. pelletizing or sintering process; Schenk (2011)). In contrast, by using fluidized bed technology fine ores can directly be charged into the reduction process. Such fluidized bed reactors are used, for example, in the FINEX<sup>®</sup> process (Habermann *et al.*, 2000; Primetals Technologies Austria GmbH and POSCO E&C, 2015). The FINEX<sup>®</sup> process, which was jointly developed by POSCO (Korea) and Primetals Technologies (Austria), produces hot metal in the same quality as traditional blast furnaces, however the coke making and sintering of the fine ores are avoided. The iron-ores that are charged into the process go through fluidized bed reactors where they are heated and reduced to DRI (Direct Reduced Iron), charged into the melter gasifier, where final reduction and melting as well as the production of reducing gas by gasification of coal with oxygen takes place (Plaul *et al.*, 2009).

Due to the limited accessibility for measurements, simulation methods have become one of the most important tools for optimizing the iron making processes (Valipour, 2009; Natsui *et al.*, 2014; Valipour *et al.*, 2006; Fu *et al.*, 2014). However, either these numerical models neglect the impact of the reduction of iron ore (Fu *et al.*, 2014) or these are restricted to very small scale processes such as, individual pellets (Valipour, 2009; Valipour *et al.*, 2006) or lab-scale fluidized beds (Natsui *et al.*, 2014). It has to be noted that the latter utilized the CFD-DEM approach to model the gas-solid flow, where the continuous phase is governed by computational fluid dynamics (CFD) and the particle trajectories are computed by using the discrete element method (DEM), which is rather computationally demanding (Goniva *et al.*, 2012).

Since the total number of particles in fluidized bed reactors is extremely large, it may be impractical to solve the equations of motion for each particle. It is, therefore, common to investigate particulate flows in large process units using averaged equations of motion, i.e. two-fluid models (TFM),

which include the inter-particle collisions statistically by kinetic theory based closures of the particle stresses (Lun *et al.*, 1984; Schneiderbauer *et al.*, 2012; Agrawal *et al.*, 2001). However, each representative particle diameter requires an additional momentum and continuity equation, which considerably raises the computational demand with increasing number of particle diameters (Iddir and Arastoopour, 2005; Schellander *et al.*, 2013). One may restrict the calculations to spatially constant particle size distributions to evaluate the gas-solid drag force (Schneiderbauer *et al.*, 2015a). To overcome this deficiency of TFM, we follow our previous work (Schneiderbauer *et al.*, 2016a; Schellander *et al.*, 2013; Pirker *et al.*, 2010; Schneiderbauer *et al.*, 2015b; Pirker and Kahrmanovic, 2009) and employ a hybrid model for the numerical assessment of poly-disperse gas-solid fluidized beds. The main idea of such a modeling strategy is to use a combination of a Lagrangian discrete phase model (DPM) and a TFM to take advantage of the benefits of those two different formulations. On the one hand, the local degree of poly-dispersity (i.e. the local particle size distribution), which is essential for the evaluation of the gas-solid drag force, can be obtained by tracking statistically representative particle trajectories for each particle diameter class. On the other hand, the computationally demanding tracking of the inter-particle collisions can be obtained from the inter-particle stresses, which are deduced from the TFM solution. These then appear in addition to the gas-particle drag as a body force in the equation of motion of each DPM-trajectory. Thus, the hybrid model represents a TFM simulation with additional DPM particles, which are used, for example, to provide a closure for the poly-disperse drag law. Finally, by employing the above Lagrangian-Eulerian hybrid model, the reduction of the iron ore as well as the corresponding reaction heat can be computed based on the representative Lagrangian particles. This, in turn, includes the conversion of iron oxides to iron.

In this paper, we employ a Eulerian-Lagrangian hybrid model (Schneiderbauer *et al.*, 2016a,b) to the direct reduction of iron ore in fluidized beds. Here, the reduction is computed based on representative Lagrangian trajectories, where the reduction model is based on literature (Hanel *et al.*, 2015; Valipour, 2009; Valipour *et al.*, 2006; Natsui *et al.*, 2014).

## POLY-DISPERSE GAS-SOLID FLOWS

### Two-fluid model (TFM)

In this work, we used a kinetic-theory based two-fluid model (TFM) to study fluidized beds. Since these equations have been extensively discussed in our previous work (Schneiderbauer *et al.*, 2013, 2012; Schneiderbauer and Pirker, 2014), we do not repeat all the details here and solely present the continuity and momentum equations for the solid phase below:

$$\frac{\partial}{\partial t} \varepsilon_s \rho_s + \nabla \cdot (\varepsilon_s \rho_s \mathbf{u}_s) = \mathcal{R}_s, \quad (3)$$

$$\frac{\partial}{\partial t} (\varepsilon_s \rho_s \mathbf{u}_s) + \nabla \cdot (\varepsilon_s \rho_s \mathbf{u}_s \mathbf{u}_s) = -\varepsilon_s \nabla p - \nabla \cdot (\boldsymbol{\Sigma}_s^{\text{kc}} + \boldsymbol{\Sigma}_s^{\text{fir}}) + \beta (\mathbf{u}_g - \mathbf{u}_s) + \varepsilon_s \rho_s \mathbf{g}. \quad (4)$$

Here,  $\rho_s$ ,  $\varepsilon_s$  and  $\mathbf{u}_s$  denote density, volume fraction and local-average velocity of the solid phase, respectively;  $\mathcal{R}_s$  denotes the rate of oxygen removal due to chemical reactions;  $p$  is the gas phase pressure;  $\mathbf{u}_g$  is the local-average velocity of the gas phase;  $\beta$  is the microscopic drag coefficient, which is closed by the poly-disperse drag law of Beetstra *et al.* (2007) (see

table 1);  $\mathbf{g}$  is the gravitational acceleration; finally,  $\Sigma_s^{\text{kc}}$  and  $\Sigma_s^{\text{fr}}$  are the stress tensors associated with the solids phase, where the frictional contribution,  $\Sigma_s^{\text{fr}}$ , arises from enduring or multi-particle collision events in dense areas. The kinetic-collisional part,  $\Sigma_s^{\text{kc}}$ , is closed using kinetic theory (Hrenya and Sinclair, 1997; Lun *et al.*, 1984), which requires an additional equation for the granular temperature. It has to be further noted that in our previous study (Schellander *et al.*, 2013) we considered an additional term on the right hand side of the solids momentum equation, which accounted for the impact of particle rotation (Magnus force). Particle rotation is assumed to be non-significant in fluidized beds and is therefore included in this work.

### Lagrangian discrete phase model (DPM)

We follow our previous work (Schneiderbauer *et al.*, 2016a,b) and obtain the local volume fraction of the different particle size classes  $\varepsilon_{s,i} = x_i \varepsilon_s$ , which is required for the evaluation of the gas-solid drag force (compare with table 1), by tracking statistically representative particle trajectories for each particle diameter class along the solids flow obtained from TFM. In particular, such a trajectory  $k$  represents  $a_k$  real particles, which are referred to parcels (Radl and Sundaresan, 2014). Thus, we obtain for the number density of size class  $i$

$$n_i(\mathbf{x}) = \sum_{k \in \mathcal{P}_i} a_k G_{\Delta_g}(\mathbf{x} - \mathbf{x}_{p,k}), \quad (5)$$

which is connected to the volume fraction  $\varepsilon_{s,i}$  by

$$\varepsilon_{s,i} = n_i \pi \frac{d_{s,i}^3}{6} \quad (6)$$

yielding

$$x_i = \pi \frac{d_{s,i}^3}{6} \frac{n_i}{\varepsilon_s} \quad (7)$$

In equation (5),  $\Delta_g$  denotes the grid spacing of the Eulerian grid and the set  $\mathcal{P}_i$  contains all parcels of particle size class  $i$ . We further obtain the local Sauter diameter, which is required for the evaluation of the drag force and the kinetic theory stresses, from

$$\langle d_s \rangle = \left[ \sum_{i=1}^{N_{sp}} \frac{x_i}{d_{s,i}} \right]^{-1}, \quad (8)$$

where  $N_{sp}$  the number of particle size classes.

It remains to discuss the equation of motion of such a tracer parcel  $k$ , which reads (Schneiderbauer *et al.*, 2016a, 2015b)

$$\frac{d\mathbf{u}_{p,k}}{dt} = \frac{1}{\tau_{c,k}} (\mathbf{u}_s - \mathbf{u}_{p,k}) + \mathbf{F}_k^{\text{poly}} + \mathbf{g}, \quad (9)$$

where  $\mathbf{u}_{p,k}$  denotes the velocity of the Lagrangian tracer parcel  $k$ ,  $\mathbf{u}_s$  the solids velocity,  $\mathbf{g}$  the gravitational acceleration and  $\tau_{c,k}$  is a collisional time scale required to accelerate a single particle to the average solids velocity (Syamlal *et al.*, 1993; Schneiderbauer *et al.*, 2016a, 2015b)

$$\frac{1}{\tau_{c,k}} = \frac{3(1+e)}{4} \varepsilon_s \|\mathbf{u}_{p,k} - \mathbf{u}_s\| \sum_j^{N_{sp}} \frac{x_j (d_{s,k} + d_{s,j})^2 g_{0,kj}}{d_{s,k}^3 + d_{s,j}^3}. \quad (10)$$

Here,  $e \approx 0.9$  is the coefficient of restitution,  $N_{sp}$  is defined in equation (8),  $d_{s,j}$  the particle diameter of class  $j$  and  $x_j$  is

defined in table 1.  $g_{0,jk}$  denotes the radial distribution function, which accounts for the poly-disperse mixture of hard spheres (Iddir and Arastoopour, 2005). Note that equation (10) accounts for the contribution coming from the inter-particle stresses, i.e. inter-particle collisions. These are determined by the coarse-grained TFM solution and affect the trajectories of the tracer parcels by the collisional time scale  $\tau_{c,k}$ .

Since the tracers show different particle diameters  $\mathbf{F}_k^{\text{poly}}$  is the acceleration of a single particle of diameter  $d_{s,k}$  within the local poly-disperse mixture of particles (units force per unit parcel mass, i.e.  $\text{m s}^{-2}$ ) due to the gas-solid drag force. Thus, the acceleration of parcel  $k$  due to the drag force can be written as (Schneiderbauer *et al.*, 2016a)

$$\mathbf{F}_k^{\text{poly}} = \frac{1}{x_k \varepsilon_s \rho_s} \beta_k (\mathbf{u}_g - \mathbf{u}_{p,k}), \quad (11)$$

where  $\tilde{\beta}_k$  is presented in table 1. Note that here  $\beta_k$  is computed based on the Reynolds number computed from the local velocity of the tracer instead of the local velocity of the solid phase.

### DIRECT REDUCTION OF IRON ORE

In the following, we briefly present the reduction model. For more details the reader is referred to Kinaci *et al.* (2017).

### Species Transport and Heat Transfer

The local concentration of the reactant  $i$  is described by a transport equation for a corresponding species  $Y_i$  of the gas phase, which reads

$$\frac{\partial \varepsilon_g \rho_g Y_i}{\partial t} + \nabla \cdot (\varepsilon_g \rho_g \mathbf{u}_g Y_i) = -\nabla \varepsilon_g \mathbf{J}_i + \varepsilon_g \mathcal{R}_i, \quad (12)$$

where  $\rho_g$  is the density of the gas phase given by the equation of state for ideal gases and  $\mathcal{R}_i$  accounts for net rate of generation/destruction of species  $i$  by chemical reactions. Finally, the diffusion flux  $\mathbf{J}_i$  is written as

$$\mathbf{J}_i = -\rho_g D_{m,i} \nabla Y_i - D_{T,i} \frac{\nabla T_g}{T_g}, \quad (13)$$

where  $D_{m,i}$  is the mass diffusion coefficient for species  $i$  and  $D_{T,i}$  is the thermal (Soret) diffusion coefficient (ANSYS, 2011).

To describe the conservation of energy in fluidized bed reactors, a separate transport equation is solved for the specific enthalpy,  $h_q$ , of each phase:

$$\frac{\partial \varepsilon_q \rho_q h_q}{\partial t} + \nabla \cdot (\varepsilon_q \rho_q \mathbf{u}_q h_q) = \Sigma_q : \nabla \mathbf{u}_q - \nabla \cdot \mathbf{q}_q + S_q + Q_{gs}, \quad (14)$$

where the heat flux  $\mathbf{q}_q$  is modeled by using Fourier's law  $\mathbf{q}_q = k_q \nabla T_q$  and  $S_q$  accounts for the reaction heat. In case of the gas phase the heat conductivity  $k_g$  is computed employing a weighted average of the individual heat conductivities of the monomers. For the heat exchange between the gas and the solid phase,  $Q_{gs}$ , we employ the correlation proposed by Gunn (1978). Assuming constant specific heats  $c_{p,q}$  the phase temperature and phase enthalpy are correlated as follows

$$h_q = c_{p,q} T_q. \quad (15)$$

**Table 1:** Summary of microscopic poly-disperse drag coefficient of Beetstra *et al.* (2007), which has been adapted in our previous work (Schneiderbauer *et al.*, 2015a). Here,  $\bar{\epsilon}_g$  denotes the filtered gas volume fraction,  $\langle d_s \rangle$  the Sauter diameter,  $\epsilon_{s,i}$  the volume fraction of particle size class  $i$  and  $N_{sp}$  the number of particle size classes.

$$\tilde{\beta} = 18\mu_g \bar{\epsilon}_s \bar{\epsilon}_g^2 F(\bar{\epsilon}_s, \bar{\epsilon}_g, \widetilde{\text{Re}}_{\langle d_s \rangle}) \left( \sum_{i=1}^{N_{sp}} \bar{x}_i F_{\text{poly}}(y_i) \right),$$

with

$$\begin{aligned} \widetilde{\text{Re}}_{\langle d_s \rangle} &= \frac{\bar{\epsilon}_g \rho_g \langle d_s \rangle \|\tilde{\mathbf{u}}_g - \tilde{\mathbf{u}}_s\|}{\mu_g}, \\ F_{\text{poly}}(y_i) &= \bar{\epsilon}_g y_i + \bar{\epsilon}_s y_i^2 + 0.064 \bar{\epsilon}_g y_i^3, \\ F(\bar{\epsilon}_s, \bar{\epsilon}_g, \widetilde{\text{Re}}_{\langle d_s \rangle}) &= \frac{10\bar{\epsilon}_s}{\bar{\epsilon}_g^3} + \bar{\epsilon}_g (1 + 1.5\bar{\epsilon}_s^{1/2}) + \frac{0.413 \widetilde{\text{Re}}_{\langle d_s \rangle}}{24\bar{\epsilon}_g^3} \left( \frac{\bar{\epsilon}_g^{-1} + 3\bar{\epsilon}_g \bar{\epsilon}_s + 8.4 \widetilde{\text{Re}}_{\langle d_s \rangle}^{-0.343}}{1 + 10^{3\bar{\epsilon}_s} \widetilde{\text{Re}}_{\langle d_s \rangle}^{-(1+4\bar{\epsilon}_s)/2}} \right) \end{aligned}$$

and the dimensionless parameters

$$\bar{x}_i = \frac{\bar{\epsilon}_{s,i}}{\bar{\epsilon}_s}, \quad y_i = \frac{d_i}{\langle d_s \rangle}$$

## Thermochemical Aspects

Modelling direct reduction of iron ore can be related to equilibrium phase diagrams. One such diagram demonstrates the reduction processes of the iron-oxygen-carbon system, which is also called the *Baur-Glaessner Diagram*. In this diagram, the stabilities for the iron-oxides and iron phases are depicted as a function of temperature and CO/CO<sub>2</sub> (H<sub>2</sub>/H<sub>2</sub>O) mixture with the available correlations for the equilibrium constant from literature and the ones calculated.

The concentration molar fraction of the relative gas species can be determined with the use of the equilibrium constant as

$$\frac{x_{\text{CO}_2}}{x_{\text{CO}}} = K e_{\text{Fe}_x\text{O}_y, \text{CO}}, \quad (16)$$

thus the molar fraction of the mixture can be defined with,

$$x_{\text{CO}_2} = k_c \frac{K e_{\text{Fe}_x\text{O}_y, \text{CO}}}{1 + K e_{\text{Fe}_x\text{O}_y, \text{CO}}} \quad (17)$$

or

$$x_{\text{CO}} = k_c \frac{1}{1 + K e_{\text{Fe}_x\text{O}_y, \text{CO}}}, \quad (18)$$

in which  $k_c$  represents the total content of carbon in the system that can be expressed with

$$x_{\text{CO}} + x_{\text{CO}_2} = k_c. \quad (19)$$

As a more advanced method one might consider a four-component gas mixture of CO, H<sub>2</sub>, CO<sub>2</sub> and H<sub>2</sub>O to be represented in a single Baur-Glaessner Diagram with an abscissa of CO + H<sub>2</sub> or H<sub>2</sub>O + CO<sub>2</sub> content.

## Reaction Kinetics

The most common types of representation models for the non-catalytic reactions of solids submerged in fluids is the shrinking particle model (SPM) and the unreacted shrinking core model (USCM) (Levenspiel, 1999), where the unreacted shrinking core model is accepted as the most precise model to represent direct reduction of iron ore (Valipour *et al.*, 2006; Valipour, 2009; Natsui *et al.*, 2014). In particular, the three layer unreacted shrinking core model developed by Philbrook, Spitzer and Manning (Tsay *et al.*, 1976) is able

to represent the three interfaces of hematite/magnetite, magnetite/wustite and wustite/iron. For further details about the current implementation of the USCM the reader is referred to Kinaci *et al.* (2017).

According to Tsay *et al.* (1976) the removal rate of oxygen is determined through the following mechanisms: (i) The reducing gas is transported through the gas film onto the particle surface ( $F$ ); (ii) diffusion through the porous iron layer ( $B_3$ ); (iii) reactants react with wustite at the wustite/iron interface and form iron ( $A_3$ ); (iv) remaining reactants diffuse through the wustite layer to the wustite/magnetite interface ( $B_2$ ); (v) reaction with magnetite at layer surface forming wustite and gaseous products ( $A_2$ ); (vi) remaining reactants diffuse through the magnetite layer to the magnetite/hematite interface ( $B_1$ ); (vii) reaction with hematite core forming magnetite and a gaseous products ( $A_1$ ); (viii) The gaseous products diffuses outwards through the pores of the pellet. Since each step is a resistance to the total reduction of the pellet, the reduction pattern of a single pellet can be considered to follow a resistance network such as an electrical resistance circuit network. The solution of this resistance network yields the reaction flow rate of  $\dot{Y}_{j,i}$  of the gas species for the relative layers yields:

### From hematite to magnetite:

$$\begin{aligned} \dot{Y}_{h,i} &= ([A_3(A_2 + B_2 + B_3 + F) + (A_2 + B_2)(B_3 + F)](Y - Y_1^{eq}) \\ &\quad - [A_3(B_2 + B_3 + F) + B_2(B_3 + F)](Y - Y_2^{eq}) \\ &\quad - [A_2(B_3 + F)](Y - Y_3^{eq})) \frac{1}{W_{3,i}}, \end{aligned} \quad (20)$$

### From magnetite to wustite:

$$\begin{aligned} \dot{Y}_{m,i} &= ([A_1(A_2 + B_2 + B_3 + F) + A_3(B_3 + F)](Y - Y_2^{eq}) \\ &\quad - [B_2(A_3 + B_3 + F) + A_3(B_3 + F)](Y - Y_1^{eq}) \\ &\quad - [(A_1 + B_1)(B_3 + F)](Y - Y_3^{eq})) \frac{1}{W_{3,i}}, \end{aligned} \quad (21)$$

### From wustite to iron:

$$\begin{aligned} \dot{Y}_{w,i} &= ([A_1(A_2 + B_2 + B_3 + F) + A_2(B_2 + B_3 + F)] \\ &\quad (Y - Y_3^{eq}) - [A_2(B_3 + F)](Y - Y_1^{eq}) \\ &\quad - [(A_1 + B_1)(B_3 + F)](Y - Y_2^{eq})) \frac{1}{W_{3,i}} \end{aligned} \quad (22)$$

where the index  $i$  denotes the gas-species  $i$  (i.e. either CO or H<sub>2</sub>). Furthermore,  $A_j$  represents the relative chemical reaction resistance term,  $B_j$  the relative diffusivity resistance

term,  $j$  represents the layers hematite, magnetite and wustite and  $i$  the reducing gas species.  $F$  is the mass transfer resistance term, which is defined with  $1/k_f$ .  $Y$  is the bulk gas mole fraction and  $Y_j^{eq}$  the relative layer equilibrium mole fractions. The denominator  $W_{3,i}$  is expressed as

$$W_{3,i} = [(A_1 + B_1)(A_3(A_2 + B_2 + B_3 + F) + (A_2 + B_2)(B_3 + F)) + A_2(A_3(B_2 + B_3 + F) + B_2(B_3 + F))] \quad (23)$$

The chemical reaction resistance term  $A_{j,i}$  can be expressed as

$$A_{j,i} = \left[ \frac{1}{(1-f_j)^{\frac{2}{3}}} \frac{1}{k_j \left(1 - \frac{1}{Ke_j}\right)} \right]_i \quad (24)$$

in which  $j$  represents the reduction layer,  $i$  the reducing gas,  $k$  the reaction rate constant and  $f_j$  is the local fractional reduction of the relative layer that is calculated as

$$f_j = 1 - \left( \frac{r_j}{r_g} \right)^3. \quad (25)$$

The diffusivity resistance term  $B_{j,i}$  can be calculated for the relative iron oxide component as (Valipour *et al.*, 2006; Valipour, 2009)

$$B_{h,i} = \left[ \frac{(1-f_m)^{\frac{1}{3}} - (1-f_h)^{\frac{1}{3}}}{(1-f_m)^{\frac{1}{3}}(1-f_h)^{\frac{1}{3}}} \frac{r_g}{De_h} \right]_i, \quad (26)$$

$$B_{m,i} = \left[ \frac{(1-f_w)^{\frac{1}{3}} - (1-f_m)^{\frac{1}{3}}}{(1-f_w)^{\frac{1}{3}}(1-f_m)^{\frac{1}{3}}} \frac{r_g}{De_m} \right]_i, \quad (27)$$

$$B_{w,i} = \left[ \frac{1 - (1-f_w)^{\frac{1}{3}}}{(1-f_w)^{\frac{1}{3}}} \frac{r_g}{De_w} \right]_i, \quad (28)$$

in which  $De_j$  represents the diffusion coefficient of the relative layer.

With the use of the reaction flow rate  $\dot{Y}_{j,i}$  the relative mass flow rates between layers can be defined as

$$\frac{dm_i}{dt} = C_i M_i A_p \dot{Y}_{j,i}. \quad (29)$$

#### Mass and Heat Transfer Coefficient

The mass transfer coefficient  $k_f$  which is used in the determination of the mass transfer term can be calculated through the Sherwood number or the Nusselt number as

$$\begin{aligned} Sh &= \frac{k_f d}{D_e}, \\ Nu &= \frac{k_f}{k}, \end{aligned} \quad (30)$$

where  $d$  is the diameter of pellet,  $D_e$  the diffusion coefficient and  $k$  the thermal conductivity. A number of correlations for determining the Sherwood number exist in literature. Lee and Barrow (Lee and Barrow, 1968) proposed a model through investigating the boundary layer and wake regions around the sphere leading to a Sherwood number of

$$Sh_t = (0.51Re^{0.5} + 0.02235Re^{0.78})Sc^{0.33}, \quad (31)$$

where  $Sc$  stands for the Schmidt number and defined as  $\frac{\nu}{\rho D}$ . In more recent works from Valipour (Valipour, 2009) and

Nouri *et al.* (Nouri *et al.*, 2011) the Sherwood and Nusselt numbers are expressed as

$$\begin{aligned} Sh &= 2 + 0.6Re^{0.5}Sc^{0.33}, \\ Nu &= 2 + 0.6Re^{0.5}Pr^{0.33}. \end{aligned} \quad (32)$$

$Pr$  represents the Prandtl number and is expressed as the specific heat times the viscosity over thermal conductivity  $c\mu/k$ . However, since fluidized beds usually show very dense regions we use the correlation proposed by Gunn (1978) to compute the Nusselt number and consequently the heat transfer coefficient.

#### Diffusivity Coefficient

Diffusivity of a gaseous species depends on properties such as the pore size distribution, void fraction and tortuosity. For example, according to Tsay *et al.* (1976) a pore size of  $2\mu$  to  $5\mu$  the Knudsen diffusion has been found to be 10 times faster than molecular diffusion, therefore in their work the Knudsen diffusion has been neglected, since slowest process mostly determines the final reaction rate. Thus, the effective binary gas diffusion was calculated with

$$D_{eff} = D_{12} \frac{\epsilon}{\tau} \quad (33)$$

where  $\epsilon$  represents the dimensionless void fraction,  $\tau$  the tortuosity. (Valipour, 2009; Valipour *et al.*, 2006) has used the Fuller-Schettler-Giddings equation to determine the effective diffusivity as

$$D_{j,i} = \frac{10^{-7} T^{1.75}}{(P_t(\dot{v}_j^{1/3} + \dot{v}_i^{1/3}))^2} \left( \frac{1}{M_j} + \frac{1}{M_i} \right)^{0.5} \quad (34)$$

in which the  $\dot{v}$  is the diffusion volume of the relative species,  $M$  is the molecular weight,  $P_t$  the total flow pressure and  $T$  the temperature in Kelvin.

#### Reaction Rate Coefficient

For many reactions the rate expression can be expressed as a temperature-dependent term. It has been established that in these kinds of reactions, the reaction rate constant can be expressed with the Arrhenius' law (Levenspiel, 1999) as follows

$$k = k_0 \exp\left(\frac{-E_a}{RT}\right), \quad (35)$$

in which  $k_0$  represents the frequency factor or the pre-exponential factor,  $E_a$  the activation energy,  $R$  the universal gas constant and  $T$  the temperature. The values for the pre-exponential factor and the activation energy can be found through various works (Tsay *et al.*, 1976; Valipour, 2009).

## IMPLEMENTATION

Since the motion equation of the Lagrangian particles (equation (9)) does only account for collision implicitly by using equation (10) the total volume fraction of the tracer particles,  $\epsilon_{s,p} = \sum_{i=1}^{N_{sp}} n_i \pi d_{s,i}^3 / 6$  (compare with equation (5)) may exceed the maximum packing locally. This, in turn, may yield an unphysical accumulation of tracer particles in dense regions. Thus, we introduce an additional repulsive mechanism  $\mathbf{F}_k^{\text{pack}}$  (units  $\text{m s}^{-2}$ ), which prevents the Lagrangian tracer particles from forming dense aggregates exceeding the maximum packing fraction. Finally, the reduction model is evaluated at each parcel at each parcel time step. The resulting mass transfer and reaction heats have to be mapped to

the Eulerian grid to compute  $\mathcal{R}_i$  (equations (3) and (12)) and  $\mathcal{S}_q$  (equation (14)). For more details the reader is referred to equations (26) and (28) in our previous study (Schneiderbauer *et al.*, 2016b). Finally, it has to be noted that in the case where no tracer particle is in a specific numerical cell we apply a diffusive smoothing approach to the exchange fields locally (i.e. to the Sauter mean diameter; Pirker *et al.* (2011)).

For the numerical simulation we use the commercial finite volume CFD-solver FLUENT (version 16). For the discretization of all convective terms the QUICK (Quadratic Upwind Interpolation for Convection Kinematics) scheme is used. The derivatives appearing in the diffusion terms are computed by a least squares method and the pressure-velocity coupling is achieved by the phase coupled SIMPLE algorithm (Cokljat *et al.*, 2006). The trajectories of the Lagrangian tracer particles (equation (9)) is integrated after each fluid flow time step using a third-order Runge-Kutta method. Further it has to be noted that the gas velocity and the solid phase velocity in equation (9) are linearly interpolated to the particle positions by using a first order Taylor approximation. For fluidized bed simulations we employ a time step size of 0.001. More details on the implementation can be found in our previous studies (Schneiderbauer *et al.*, 2016a,b).

## RESULTS

To validate the presented reduction model, we investigate the direct reduction of hematite ore within a lab-scale fluidized bed with 68 mm diameter (Spreitzer, 2016). The small dimensions of the vessel allow to use very fine grid spacings (i.e.  $\approx 2$  mm), which resolve all relevant heterogeneous structures, and therefore no sub-grid corrections are required (Schneiderbauer *et al.*, 2013; Schneiderbauer and Pirker, 2014). The pressure in the fluidized bed was 140000 Pa and the superficial gas velocity  $0.25 \text{ m s}^{-1}$ . The detailed process conditions are given in tables 2, 3 and 4. According to table 3 we use four different types of tracer parcel representing the different size fractions. In total we found that 120000 tracer parcels are appropriate to gather sufficient statistics (Schneiderbauer *et al.*, 2016a,b).

**Table 2:** Experimental conditions for the different reduction steps. The concentrations of the reactants are given in volume percent.

	R1 (W→Fe)	R2 (M→W)	R3 (H→M)
H <sub>2</sub>	13.4%	15.9%	13.0%
H <sub>2</sub> O	3.4%	6.8%	6.8%
CO	37.0%	37.4%	30.3%
CO <sub>2</sub>	14.0%	27.4%	26.4%
N <sub>2</sub>	32.2%	12.4%	23.5%
T [°C]	720	750	480

**Table 3:** Particle size distribution of the iron ore.

$d_p$	fraction [vol. %]
0 – 0.063	0
0.063 – 0.125	15.4
0.125 – 0.25	33.2
0.25 – 0.5	28.6
0.5 – 1	22.8

Figure 1 shows snapshots of the solid volume fraction, the mass fraction of CO, the mass fraction of CO<sub>2</sub> and the frac-

**Table 4:** Parameters for DRI-model (Hanel *et al.*, 2015).

		H→M	M→W	W→Fe
H <sub>2</sub>	$k_0$ [m/s]	160	29	6
	$E_a$ [J]	68600	75000	65000
	$Ke$ [-]	$e^{\frac{-362.6}{T_s} + 10.334}$	$10^{\frac{-3577}{T_s} + 3.74}$	$10^{\frac{-827}{T_s} - 0.468}$
CO	$k_0$ [m/s]	437	45	17
	$E_a$ [J]	102000	86000	68000
	$Ke$ [-]	$e^{\frac{3968.37}{T_s} + 3.94}$	$10^{\frac{-1834}{T_s} + 2.17}$	$10^{\frac{914}{T_s} - 1.097}$

tional reduction of individual parcels during the conversion of hematite to magnetite. On the one hand, figure 1a unveils that the bed is operated in the bubbling regime to optimize the solid mixing, the gas-solid contact as well as the reaction heat removal. On the other hand, figures 1b – 1d clearly reveal the removal of oxygen from the hematite ore due to the conversion of CO to CO<sub>2</sub>, which increases the fraction reduction of the individual iron ore particles. In particular, the content of CO considerably decreases as the gas passes the particle bed while the content of CO<sub>2</sub> increases.

Figure 2 shows the cumulative distribution function of the fractional reduction. The figure indicates that after about 150 s approximately 50% of the hematite ore was converted to magnetite. In particular, the smallest particles are already converted after 150 s while the larger particles still contain hematite (figure 3). This is clear, since the larger particles contain much more hematite ore than compared to their surface area than the smaller particles.

Finally, figure 4 shows the fractional reduction as a function of time for the different reduction steps. Both, experiment and simulation unveil that the conversion of hematite to magnetite (R3) is the fastest reduction step (Hanel *et al.*, 2015). After approximately 500 s the fractional reduction approaches a plateau, where the fractional reduction is about 11.1%. Here, the total amount of hematite was already converted to magnetite. The subsequent conversion from magnetite to wustite is known to be the second fastest reduction step, which is also correctly predicted by the presented conversion model. Again, the fractional reduction approaches a plateau region, where the fraction reduction is about 33.3%, which is in fairly good agreement with the experiment. It has to be noted that we stopped the simulations after reaching the plateau regions of fractional correction during R3 and R2 and extrapolated the fractional correction in time in figure 4 till the next reduction step to reduce the computational demands. The final reduction step, where wustite is converted to metallic iron, unveils the slowest conversion rate. This is also indicated by the kinetic parameters given in table 4. Similar to the previous reduction steps, the present model is able to correctly predict the conversion of wustite to iron.

## CONCLUSION

We have presented the application of our previously published hybrid-TFM (Schneiderbauer *et al.*, 2015b; Schellander *et al.*, 2013; Pirker and Kahrmanovic, 2009; Schneiderbauer *et al.*, 2016a,b) to the conversion of iron ore to iron using fluidized bed technology. Such a modelling strategy enables the efficient numerical analysis of reactive poly-disperse gas-phase reactors without requiring computationally demanding multi-fluid models, which are coupled to population balance approaches.

To conclude, the results clearly show that the reactive hybrid-TFM is able to picture the correct conversion rates within the fluidized bed. Nevertheless, the conversion model has to

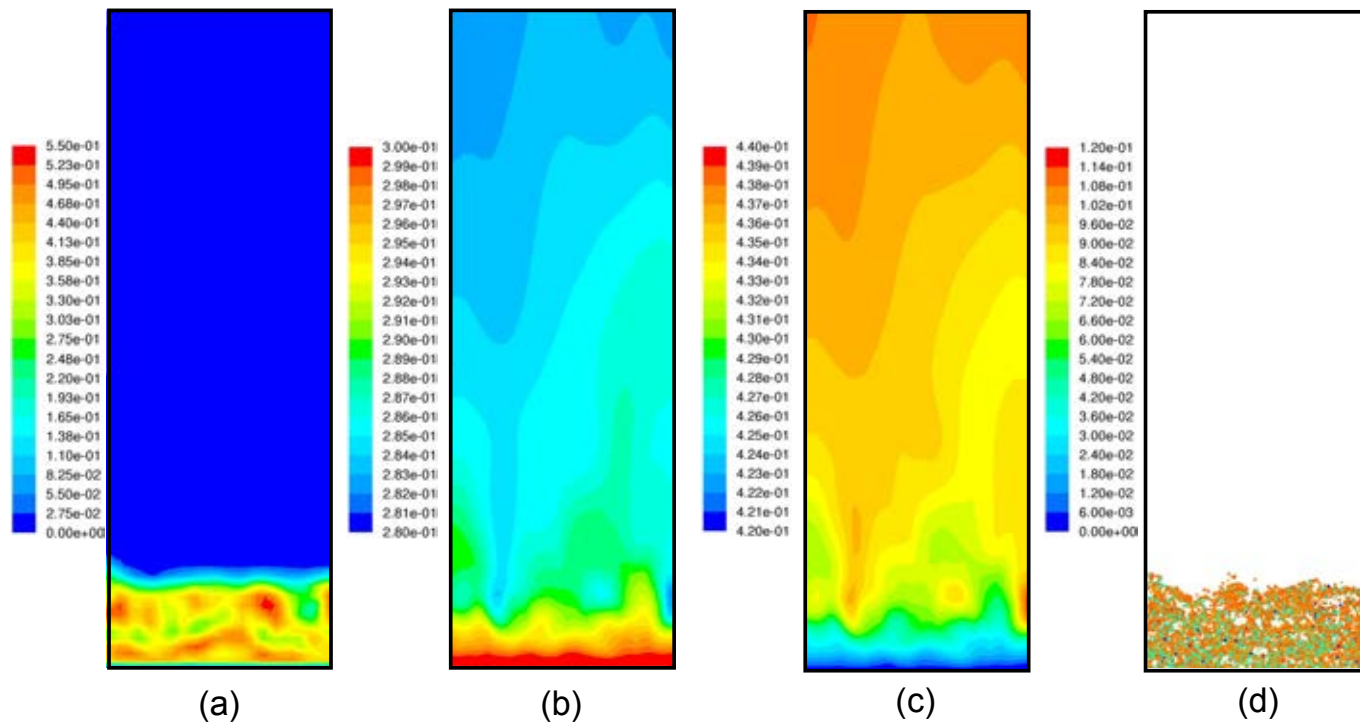


**Figure 1:** Snapshots at  $t = 228$  s (i.e. within  $R_3$ ) of a) the solid volume fraction, b) the mass fraction of CO, c) the mass fraction of CO<sub>2</sub> and d) the fractional reduction of individual parcels.

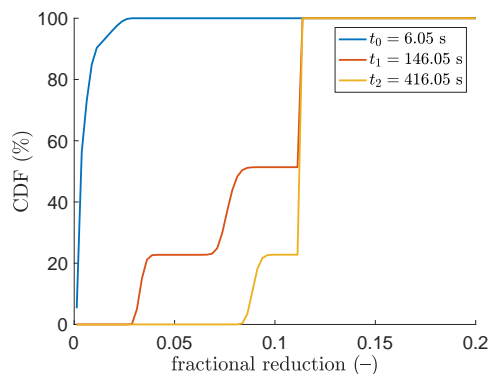


**Figure 2:** Snapshots of cumulative distribution of the fractional reduction during the conversion of hematite to magnetite.

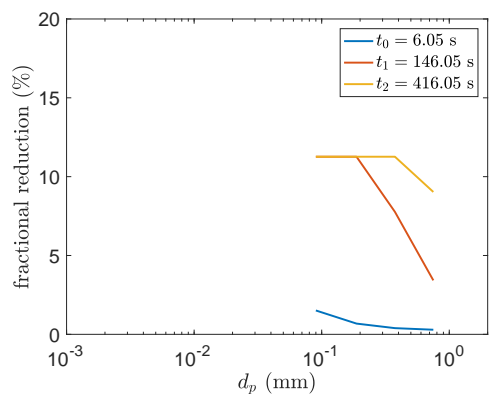


**Figure 3:** Snapshots of the fractional reduction as a function of the particle diameter during the conversion of hematite to magnetite.

be verified further against more different gas compositions. I.e. future efforts will concentrate on the numerical analysis

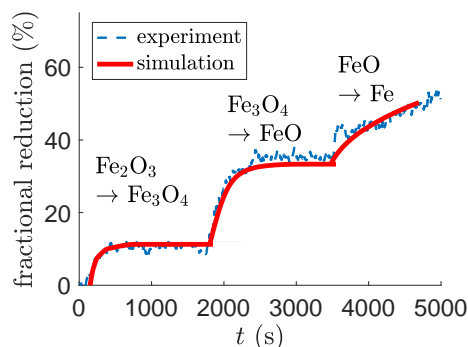


**Figure 4:** ractional reduction as a function of time for the different reduction steps.

of different process conditions and their detailed evaluation against experimental data. Finally, large-scale applications should be investigated, where sub-grid corrections will be required to account for the unresolved small scales on the behaviour of the fluidized bed and the conversion rates (Schneiderbauer, 2017).

### ACKNOWLEDGEMENTS

The authors want to acknowledge the support of Dr. Christoph Klaus-Nietrost, who provided the c-code for the reduction model developed during his PhD work "Development of Conversion Models for Iron-Carriers and Additives within a Melter-Gasifier or Blast Furnace" (Institute for Energy Systems and Thermodynamics, TU Vienna, 2016). This work was funded by the Christian-Doppler Research Association, the Austrian Federal Ministry of Economy, Family and Youth, and the Austrian National Foundation for Research, Technology and Development. The author also wants to acknowledge the financial support from the K1MET center for metallurgical research in Austria ([www.k1-met.com](http://www.k1-met.com)).



## REFERENCES

- AGRAWAL, K., LOEZOS, P.N., SYAMLAL, M. and SUNDARESAN, S. (2001). "The role of meso-scale structures in rapid gas-solid flows". *Journal of Fluid Mechanics*, **445**, 151–185.
- ANSYS (2011). *ANSYS FLUENT Theory Guide*, vol. 15317. ANSYS, Inc., Canonsburg, PA.
- BEETSTRA, R., Van der Hoef, M.A. and KUIPERS, J.A.M. (2007). "Drag Force of Intermediate Reynolds Number Flow Past Mono- and Bidisperse Arrays of Spheres". *AIChE Journal*, **53**(2), 489–501.
- COKLIJAT, D., SLACK, M., VASQUEZ, S.A., BAKKER, A. and MONTANTE, G. (2006). "Reynolds-Stress Model for Eulerian multiphase". *Progress in Computational Fluid Dynamics, An International Journal*, **6**(1/2/3), 168.
- FU, D., ZHOU, C.Q. and CHEN, Y. (2014). "Numerical Methods for Simulating the Reduction of Iron Ore in Blast Furnace Shaft". *Journal of Thermal Science and Engineering Applications*, **6**(2), 021014.
- GONIVA, C., KLOSS, C., DEEN, N.G., KUIPERS, J.A.M. and PIRKER, S. (2012). "Influence of rolling friction on single spout fluidized bed simulation". *Particuology*, **10**(5), 582–591.
- GUNN, D.J. (1978). "Transfer of Heat or Mass to Particles in Fixed and Fluidized Bed". *International Journal of Heat Mass Transfer*, **21**, 467–476.
- HABERMANN, A., WINTER, F., HOFBAUER, H., ZIRNGAST, J. and SCHENK, J.L. (2000). "An Experimental Study on the Kinetics of Fluidized Bed Iron Ore Reduction". *ISIJ International*, **40**(10), 935–942.
- HANEL, M.B., SCHENK, J.F., MALI, H., HAUZENBERGER, F., THALER, C. and STOCKER, H. (2015). "Characterization of Ferrous Burden Material for Use in Ironmaking Technologies". *BHM Berg- und Hüttenmännische Monatshefte*, **160**(7), 316–319.
- HRENYA, C.M. and SINCLAIR, J.L. (1997). "Effects of particle-phase turbulence in gas-solid flows". *AIChE Journal*, **43**(4), 853–869.
- IDDIR, H. and ARASTOPOUR, H. (2005). "Modeling of multitype particle flow using the kinetic theory approach". *AIChE Journal*, **51**(6), 1620–1632.
- KINACI, M.E., LICHTENEGGER, T. and SCHNEIDERBAUER, S. (2017). "Modelling of Chemical Reactions in Metallurgical Processes". J.E. Olsen (ed.), *Proceedings of the 12th International Conference on Computational Fluid Dynamics in the Oil & Gas, Metallurgical and Process Industries (CFD 2017)*. SINTEF, Trondheim, Norway, Trondheim, Norway.
- LEE, K. and BARROW, H. (1968). "Transport processes in flow around a sphere with particular reference to the transfer of mass". *International Journal of Heat and Mass Transfer*, **11**(6), 1013–1026.
- LEVENSPIEL, O. (1999). *Chemical Reaction Engineering*.
- LUN, C.K.K., SAVAGE, S.B., JEFFREY, D.J. and CHEPURNIY, N. (1984). "Kinetic theories for granular flow: inelastic particles in Couette flow and slightly inelastic particles in a general flowfield". *Journal of Fluid Mechanics*, **140**, 223–256.
- NATSUI, S., KIKUCHI, T. and SUZUKI, R.O. (2014). "Numerical Analysis of Carbon Monoxide-Hydrogen Gas Reduction of Iron Ore in a Packed Bed by an Euler-Lagrange Approach". *Metallurgical and Materials Transactions B*, **45**(6), 2395–2413.
- NOURI, S.M.M., Ale Ebrahim, H. and JAMSHIDI, E. (2011). "Simulation of direct reduction reactor by the grain model". *Chemical Engineering Journal*, **166**(2), 704–709.
- PIRKER, S. and KAHRIMANOVIC, D. (2009). "Modelling Mass Loading Effects in Industrial Cyclones by a Combined Eulerian-Lagrangian Approach". *Acta Mechanica*, **204**(2), 203–216.
- PIRKER, S., KAHRIMANOVIC, D., KLOSS, C., POPOFF, B. and BRAUN, M. (2010). "Simulating coarse particle conveying by a set of Eulerian, Lagrangian and hybrid particle models". *Powder Technology*, **204**(2-3), 203–213.
- PIRKER, S., KAHRIMANOVIC, D. and GONIVA, C. (2011). "Improving the applicability of discrete phase simulations by smoothing their exchange fields". *Applied Mathematical Modelling*, **35**(5), 2479–2488.
- PLAUL, F.J., BÖHM, C. and SCHENK, J.L. (2009). "Fluidized-bed technology for the production of iron products for steelmaking". *Journal of the Southern African Institute of Mining and Metallurgy*, **109**(2), 121–128.
- Primetals Technologies Austria GmbH and POSCO E&C (2015). "The finex® process – economical and environmentally safe ironmaking". <http://www.primetals.com/en/technologies/ironmaking/finex%C2%AE/Lists/FurtherInformation/The%20Finex%20process.pdf>. Accessed: 2017-02-28.
- RADL, S. and SUNDARESAN, S. (2014). "A drag model for filtered Euler-Lagrange simulations of clustered gas-particle suspensions". *Chemical Engineering Science*, **117**, 416–425.
- SHELLANDER, D., SCHNEIDERBAUER, S. and PIRKER, S. (2013). "Numerical study of dilute and dense poly-dispersed gas-solid two-phase flows using an Eulerian and Lagrangian hybrid model". *Chemical Engineering Science*, **95**, 107–118.
- SCHENK, J.L. (2011). "Recent status of fluidized bed technologies for producing iron input materials for steelmaking". *Particuology*, **9**(1), 14–23.
- SCHNEIDERBAUER, S. (2017). "A spatially-averaged two-fluid model for dense large-scale gas-solid flows". *AIChE Journal*.
- SCHNEIDERBAUER, S. and PIRKER, S. (2014). "Filtered and heterogeneity based sub-grid modifications for gas-solid drag and solids stresses in bubbling fluidized beds". *AIChE Journal*, **60**(3), 839–854.
- SCHNEIDERBAUER, S., AIGNER, A. and PIRKER, S. (2012). "A comprehensive frictional-kinetic model for gas-particle flows: analysis of fluidized and moving bed regimes". *Chemical Engineering Science*, **80**, 279–292.
- SCHNEIDERBAUER, S., PUTTINGER, S. and PIRKER, S. (2013). "Comparative Analysis of Subgrid Drag Modifications for Dense Gas-Particle Flows in Bubbling Fluidized Beds". *AIChE Journal*, **59**(11), 4077–4099.
- SCHNEIDERBAUER, S., PUTTINGER, S., PIRKER, S., AGUAYO, P. and KANELLOPOULOS, V. (2015a). "CFD Modeling and Simulation of Industrial Scale Olefin Polymerization Fluidized Bed Reactors". *Chemical Engineering Journal*, **264**, 99–112.
- SCHNEIDERBAUER, S., PUTTINGER, S. and PIRKER, S. (2015b). "Numerical study of a bi-disperse gas-solid fluidized bed using an Eulerian and Lagrangian hybrid model". *Procedia Engineering*, **102**, 1539–1545.
- SCHNEIDERBAUER, S., HAIDER, M.F., HAUZENBERGER, F. and PIRKER, S. (2016a). "A Lagrangian-Eulerian Hybrid Model for the Simulation of Industrial-scale

Gas-solid Cyclones”. *Powder Technology*, **304**, 229—240.

SCHNEIDERBAUER, S., PIRKER, S., PUTTINGER, S., AGUAYO, P., TOULOUPIDIS, V. and Martínez Joaristi, A. (2016b). “A Lagrangian-Eulerian Hybrid Model for the Simulation of Poly-disperse Fluidized Beds: Application to Industrial-scale Olefin Polymerization”. *Powder Technology* (*in press*).

SPREITZER, D. (2016). *Optimierung der Prozessparameter für die Reduktion von Feineisenerzen mittels Wirbelschichtverfahren*. Master thesis, Montanuniversität Leoben.

SYAMLAL, M., ROGERS, W. and O’BRIEN, T.J. (1993). “MFX documentation theory guide, Technical note”. Tech. Rep. December, U.S. Department of Energy, Office of Fossil Energy, Morgantown, West Virginia.

TSAY, Q.T., RAY, W.H. and SZEKLEY, J. (1976). “The modeling of hematite reduction with hydrogen plus carbon monoxide mixture”. *AIChE J*, **22(6)**, 1064–1076.

VALIPOUR, M.S. (2009). “Mathematical Modeling of a Non-Catalytic Gas-Solid Reaction : Hematite Pellet Reduction with Syngas”. *Transactions C: Chemistry and Chemical Engineering*, **16(2)**, 108–124.

VALIPOUR, M.S., Motamed Hashemi, M.Y. and SA-BOOHI, Y. (2006). “Mathematical modeling of the reaction in an iron ore pellet using a mixture of hydrogen, water vapor, carbon monoxide and carbon dioxide: an isothermal study”. *Advanced Powder Technology*, **17(3)**, 277–295.



# HIGH TEMPERATURE FLUIDIZATION – INFLUENCE OF INTER-PARTICLE FORCES ON FLUIDIZATION BEHAVIOR

Milan MIHAJLOVIC<sup>1</sup>, Ivo ROGHAIR<sup>1\*</sup>, Martin van Sint ANNALAND<sup>1</sup>

<sup>1</sup> Eindhoven University of Technology, 5600 MB Eindhoven, NETHERLANDS

\* E-mail: I.Roghair@tue.nl

## ABSTRACT

Recent experiments have shown an influence of temperature on the minimum fluidization conditions in gas-solid fluidized beds, even when the gas phase density and viscosity were kept constant (Campos Velarde et al., 2016). Correlations that are available in the open literature, for predicting the minimum fluidization velocity and the bed voidage at minimum fluidization conditions at elevated temperatures, fail to describe their experimental data, in particular how the bed porosity at incipient fluidization conditions is changing with temperature.

It is hypothesized that at higher temperatures inter-particle forces play an important role in this phenomenon. Inter-particle forces, specifically van der Waals forces, are known to be important in the fluidization of very fine powders, and may incur detrimental effects on the process such as the formation of particle agglomerates or reduced particle mixing. However, the experimental results by Campos Velarde et al. (2016) have indicated that such forces may also become important during the fluidization of larger particles at increased temperatures. In this work, we characterize the effects of inter-particle forces using simulations with a Discrete Particle Model (DPM).

DPM is an Euler-Lagrange type model with a discrete description of the solids phase and a continuous description of the gas phase. The motion of each individual particle is tracked and described with Newton's second law, with van der Waals forces used to describe the inter-particle forces. Van der Waals forces are described with a Hamaker constant, which depends on the particle material and fluidization gas properties and may depend on temperature (Castellanos et al., 2003). Particle-particle interactions are dealt with using a soft-sphere collision model, which allows multiple simultaneous contacts between several pairs of particles. The gas phase is described with a set of volume-averaged Navier-Stokes equations, and full two-way coupling between the phases is implemented.

In this work we investigate the influence of the inter-particle forces (by variation of the Hamaker constant) on the minimum fluidization velocity ( $U_{mf}$ ) and the bed porosity at minimum fluidization ( $\varepsilon_{mf}$ ), and relate the effects to the dominating phenomena prevailing at high-temperature fluidization.

**Keywords:** Discrete Particle Model, fluidized beds, minimum fluidization, interparticle forces.

## NOMENCLATURE

### Greek Symbols

- $\rho$  density, [kg/m<sup>3</sup>].
- $\varepsilon$  porosity, [-].
- $\mu$  dynamic viscosity, [kg/m.s].
- $\tau$  viscous stress tensor, [kg/m s<sup>2</sup>].
- $\beta$  inter-phase momentum exchange coefficient, [-].
- $\omega$  rotational velocity, [rad/s].
- $\phi$  sphericity, [-].

### Latin Symbols

- $Ar$  Archimedes number, [-].
- $d$  particle diameter, [m].
- $\mathbf{F}$  force, [N].
- $g$  gravitational acceleration, [m/s<sup>2</sup>].
- $H$  Hamaker constant, [J].
- $I$  moment of inertia, [kg m<sup>2</sup>].
- $K$  slope, [m/s<sup>2</sup>].
- $m$  mass, [kg].
- $N_{part}$  number of particles, [-].
- $p$  pressure, [Pa].
- $Re$  Reynolds number, [-].
- $\mathbf{r}$  particle position, [m].
- $r$  particle radius, [m].
- $S$  inter-surface distance between two spheres, [m]
- $\mathbf{T}$  torque, [N m].
- $t$  time, [s].
- $\mathbf{u}$  velocity, [m/s].
- $U_0$  superficial gas velocity, [m/s].
- $v$  particle velocity, [m/s].
- $V$  volume, [m<sup>3</sup>].

### Sub/superscripts

- 0 initial state
- $a$  particle index
- $g$  gas phase.
- $p$  particle phase.
- $cont$  contact forces.
- $vdW$  van der Waals forces.
- $mf$  minimum fluidization point
- $mb$  minimum bubbling point

## INTRODUCTION

Fluidized bed reactors are often used in the chemical process industry. Due to their sheer size, many studies have been and are being performed to optimize the operation of these reactors. Most industrial processes using fluidized beds are operated at reactive conditions, i.e. at elevated temperatures (Kunii and Levenspiel, 1991). Research has shown that operation at elevated temperature has an effect on the bed voidage and minimum fluidization velocity (Lettieri et al., 2001). However, there is an ongoing debate on the mechanism by which the temperature influences the fluidization process.

Since the early work by Geldart (1972), we know that different particle classes show very different fluidization behaviour even at ambient conditions. The boundaries between the different classes change at higher temperatures (Botterill et al., 1982). For instance, Botterill et al. (1982) and Lettieri et al. (2001) showed that particles that are originally classified as one Geldart type can change their fluidization characteristics to those belonging to another Geldart type with increasing temperature. One possible explanation for these changes in fluidization behaviour, according to Lattieri and Botterill, is that at high temperatures the gas phase properties (i.e. density and viscosity) change. However, other research suggests that also inter-particle forces (IPF) can have an important additional influence (Baerns (1966), Formisani et al. (1998)). Although the influence of the gas properties and IPFs occurs simultaneously during fluidization at elevated temperatures, researchers have debated about the relative contributions of these phenomena at different conditions. For example, Shabaniyan (2013) and Baerns (1966) have found that IPFs have a significant role using Geldart C type particles, whereas for Geldart B and D not much influence of IPFs were found. For Geldart A type particles, the debate is still ongoing.

Numerical analysis was performed in different studies in order to investigate the influence of the van der Waals (denoted as vdW) forces on the fluidization behaviour. Ye et al. (2004) and Kobayashi et al. (2006) performed an analysis on the fluidization of Geldart A type particles including vdW forces between adjacent particles. Ye et al. (2004) specifically examined the influence of the Hamaker constant on the fluidization behaviour. Results showed, for example, that for higher values of the Hamaker constant, Geldart A particles can exhibit the fluidization behaviour of Geldart C type particles. In their study, the value of the Hamaker constant was chosen with the objective to demonstrate the influence, but the value was not directly related to actual particle properties. In this work, we adopt a similar approach, where we extend the study to Geldart B type particles.

In a recent study done by Campos Velarde et al. (2016), a novel experimental approach was used for high temperature fluidization. The authors have carried out experiments where fluidization was performed with two different gas mixtures that possessed the same properties (density and viscosity) at different temperatures. It was shown that these two cases show different fluidization behaviour. This has lead the authors to suggest that IPFs could be the reason behind the observed phenomena.

In the work of Castellanos (2003) it is shown that the Hamaker constant is dependent on temperature which indicate that the magnitude of the IPFs will also change with temperature. This work gives a first look on how the change of IPFs could influence the fluidization.

Specifically, this work uses DEM simulations to show the influence of the vdW forces via the Hamaker constant on the minimum fluidization conditions ( $U_{mf}$  and  $\varepsilon_{mf}$ ) and average particle circulation patterns of Geldart A and Geldart B particles.

## MODEL DESCRIPTION

The model used in this work originates from the work of Hoomans et al. (1996), Ye et al. (2004), and Tan et al. (2014). The gas flow is modelled by the volume-averaged Navier–Stokes equations

$$\frac{\partial(\varepsilon\rho_g)}{\partial t} + \nabla \cdot (\varepsilon\rho_g \mathbf{u}) = 0 \quad (1)$$

$$\frac{\partial(\varepsilon\rho_g \mathbf{u})}{\partial t} + \nabla \cdot (\varepsilon\rho_g \mathbf{u}\mathbf{u}) = -\varepsilon\nabla p - \mathbf{S}_p - \nabla \cdot (\varepsilon\boldsymbol{\tau}) + \varepsilon\rho_g \mathbf{g} \quad (2)$$

where  $\varepsilon$  is the porosity, and  $\rho_g$ ,  $\mathbf{u}$ ,  $\boldsymbol{\tau}$  and  $p$  are the density, velocity, viscous stress tensor, and pressure of the gas phase, respectively. The source term  $\mathbf{S}_p$  is defined as:

$$\mathbf{S}_p = \frac{1}{V} \int \sum_{a=0}^{N_{part}} \frac{\beta V_a}{1 - \varepsilon} (\mathbf{u} - \mathbf{v}_a) \delta(\mathbf{r} - \mathbf{r}_a) dV \quad (3)$$

Note that  $V$  is the volume of the fluid cell,  $V_a$  the volume of particle,  $\mathbf{v}_a$  the particle velocity,  $\mathbf{r}_a$  is the position of a particle,  $N_{part}$  the number of particles and  $\beta$  is the inter-phase momentum exchange coefficient. The  $\delta$ -function ensures that the drag force acts as a point force at the (central) position of a particle. The distribution function for mapping the properties from the Lagrangian particle positions to the Eulerian computational grid and vice versa is implemented in a straightforward manner through volume-weighting techniques (Hoomans et al., 1996), which is often used when the volume of the smallest computational cell for the fluid is (much) larger than the volume of a particle. The integration calculates the total drag force between the gas phase and the particles in a computational cell.

For the solids phase, the motion of each particle is described with Newton's second law of motion. The translational motion of a single particle with mass  $m_a$  and volume  $V_a$  is computed with the following equation:

$$m_a \frac{d^2 \mathbf{r}_a}{dt^2} = \mathbf{F}_{cont,a} + F_{vdw,a} + \frac{V_a \beta}{1 - \varepsilon} (\mathbf{u} - \mathbf{v}_a) - V_a \nabla p + m_a \mathbf{g} \quad (4)$$

The forces on the right hand side of Equation (4) represent the contact force, vdW force, drag force, pressure gradient and gravity respectively. The rotational force balance is given by

$$I_a \frac{\partial \boldsymbol{\omega}_a}{\partial t} = \mathbf{T}_a \quad (5)$$

where  $T_a$  is the torque,  $I_a$  the moment of inertia, and  $\omega_a$  the rotational velocity.

The contact force between two particles (or a particle and a sidewall) is calculated by use of the soft-sphere model developed by Cundall and Strack (1979). In this model, a linear-spring and a dashpot are used to formulate the normal contact force, while a linear-spring, a dashpot and a slider are used to compute the tangential contact force, where the tangential spring stiffness is  $\frac{2}{7}$ th of the normal spring stiffness.

In order to resolve the time-dependent motion of particles and the dynamics of the gas phase, two different time steps are used to solve the particle collisions and the Navier–Stokes equations. The time step in the soft-sphere model depends on the duration of a contact and should be sufficiently small to make sure that the contact lasts for a certain number of time steps. Doing so helps to avoid problems concerning energy conservation due to the numerical integration, which is inevitable in the soft-sphere model. The time step for the particle phase can be calculated from:

$$\Delta t = \frac{1}{K_N} t_{contact,n} = \frac{1}{K_N} \sqrt{\frac{\pi^2 + (\ln e_n)^2}{k_n/m_{ab}}} \quad (6)$$

where  $K_N$  is the minimum number of steps during one contact and normally in the range of 15–50. Using the normal stiffness  $k_n$  determined from the Youngs modulus will result a very small time step which will require a large computation time. It has been found (Tsuji, 1993), however, that one can set  $k_n$  to a lower value than the one derived from material properties without loss of accuracy for gas–solid fluidized beds. At the same time,  $k_n$  should be a value sufficiently large so that the maximum overlap between particles is below 1% of the particle diameter to ensure that the computed hydrodynamics are not affected. As shown in Table 1,  $k_n$  is set to a value such that at the very least 15 particle time steps are taken to evaluate a single contact, which gives  $1 \times 10^{-6}$  s as the time step for the selected particle phase in this work.

To calculate the inter-particle vdW forces, we adopt the Hamaker scheme (Israelachvili, 1991):

$$F_{vdw,ab} = \frac{H}{3} \frac{2r_1 r_2 (S + r_1 + r_2)}{[S(S + 2r_1 + 2r_2)]^2} \times \left[ \frac{(S + 2r_1 + 2r_2)}{(S + r_1 + r_2)^2 - (r_1 - r_2)^2} - 1 \right]^2 \quad (7)$$

where,  $S$  is the inter-surface distance between two spheres,  $H$  the Hamaker constant, and  $r_1$  and  $r_2$  the radii of the two spheres, respectively. However, Eq. (7) exhibits an apparent numerical singularity that the vdW interaction diverges if the distance between two particles approaches zero. In reality, such a situation will never occur, because of the short-range repulsion between particles. In the present model, we have not included this repulsion, however, we can avoid the numerical singularity by defining a cut-off (maximal) value of the vdW force between two spheres. In the simulations only particle-particle vdW forces have been used, no particle-

wall interactions other than collisions have been considered.

## Numerical simulations

### Input parameters

In order to investigate the influence of vdW forces we consider two systems: one with Geldart A type particles with diameter of 100  $\mu\text{m}$  and a density of 900  $\text{kg/m}^3$ , and a second one with Geldart B type particles with diameter of 500  $\mu\text{m}$  and a density of 2525  $\text{kg/m}^3$ . Input parameters used for both systems are shown in Table 1.

**Table 1:** Parameters used in simulation for vdW forces.

Particle type	Geldart A	Geldart B	
Number of particles	7000	12000	
Particle diameter, $d_p$	100	500	$\mu\text{m}$
Particle density, $\rho$	900	2525	$\text{kg/m}^3$
Normal restitution coefficient, $e_n$	0.9	0.97	-
Tangential restitution coefficient, $e_t$	0.9	0.33	-
Friction coefficient, $\mu_t$	0.3	0.1	-
Normal spring stiffness, $k_n$	420	7000	$\text{N}\cdot\text{m}$
Tangential spring stiffness, $k_t$	120	2000	$\text{N}\cdot\text{m}$
CFD time step	$1 \times 10^{-5}$		s
Particle time step, $\Delta t$	$1 \times 10^{-6}$		s
Minimum interparticle distance, $S_0$	0.4		nm
System height, $Z_{max}$	15	45	mm
System width, $X_{max}$	2	10	mm
System depth, $Y_{max}$	1	10	mm
CFD grid height, $\Delta x$	250	1250	$\mu\text{m}$
CFD grid width, $\Delta y$	250	1250	$\mu\text{m}$
CFD grid depth, $\Delta z$	250	1250	$\mu\text{m}$
Shear viscosity of gas, $\mu$	$1.8 \times 10^{-5}$		$\text{Pa}\cdot\text{s}$
Gas temperature, $T$	293		K
Hamaker constant, $H$	$10^{-19}/10^{-20}/10^{-21}/10^{-22}$		J

### Procedure and initial condition

The Hamaker constant is known to be dependent on particle properties and the gas properties between the particles (Lefèvre (2009), Hamaker (1937)). In this research the primary goal is to investigate how the vdW forces affect the minimum fluidization conditions, so a value range of the Hamaker constant will be taken from  $10^{-19}$  down to  $10^{-22}$  J. All simulations start by fluidizing the particles by a relatively large gas velocity for 2 s (Geldart A at 0.04 m/s; Geldart B at 0.45 m/s), and after the initial fluidization the gas supply is switched off causing the particles to drop down to form a packed bed. After a short settling period, the superficial gas velocity  $U_0$  is set to increase slowly and linearly in time:

$$U_0 = Kt \quad (8)$$

Here the rate constant  $K$  is 0.03  $\text{m/s}^2$ , which is by Ye et al. (2005) optimal in the sense that this yields a reasonable speed-up compared to the step-wise method, where the deviation in the predicted pressure drop and bed height is minimal (again compared to the results from the step-wise method).

## Simulation results

### Geldart A type particles

The main focus of this part of the study is to investigate the influence of vdW forces on the minimum fluidization velocity. A number of snapshots of the simulations from a central slice of the bed (using no vdW forces, and Hamaker constants in the range of  $10^{-21}$  to  $10^{-19}$  J) are shown in Figure 1. We observe that bubble formation is suppressed for higher Hamaker constants.

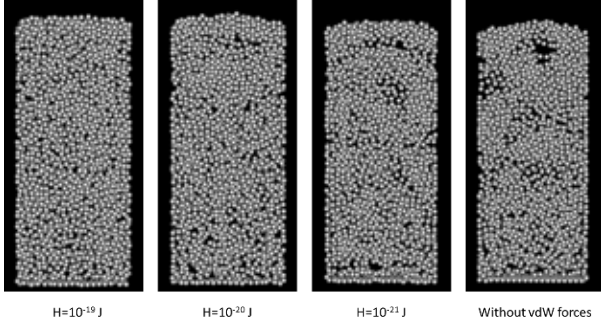


**Figure 1:** Snapshots from simulations showing the influence of the Hamaker constant on fluidization. Simulations were performed for Geldart A particles with the same superficial gas velocity.

From Figure 2, showing the pressure drop over the bed as a function of the superficial gas velocity, we can draw the quantitative conclusion that vdW forces have a negligible influence on  $U_{mf}$ . The biggest influence is observed during the transition from a fixed bed to the fluidized bed. Simulations that include vdW forces in the  $\Delta p-U_{mf}$  graph show a more smooth transition from packed bed state towards the fluidized state as the Hamaker constant increases. One explanation for this behaviour would be that with a higher Hamaker constant particles form channels and clusters and by doing so allow gas to pass through the bed (Ye et al., 2004). We can take a look at snapshots from simulations presented in the Appendix (Figure 7), showing the gas density on a slice in the middle of the bed at the specific times. These snapshots show that for  $H = 10^{-19}$  and  $10^{-20}$  J there is a longer homogeneous fluidization, which may be due to formed small clusters or channels. A further investigation on the emergence, whereabouts and possibly disintegration of these structures (channels and clustered particles) will be reported in a future work. An algorithm that can accurately locate such structures is under development.

Values of  $U_{mf}$  determined from the simulations for different Hamaker constants are given in Table 2:

**Table 2:** Determined  $U_{mf}$  for various Hamaker constants

Hamaker constant $H$ [J]	Determined $U_{mf}$ [m/s]
0	$3.94 \times 10^{-3}$
$10^{-22}$	$3.94 \times 10^{-3}$
$10^{-21}$	$4.01 \times 10^{-3}$
$10^{-20}$	$4.07 \times 10^{-3}$
$10^{-19}$	$3.8 \times 10^{-3}$

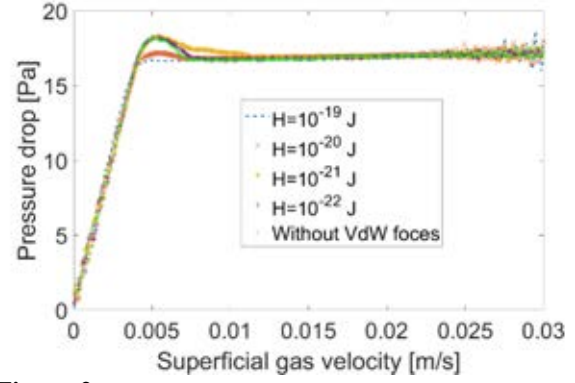


**Figure 2:** Influence of the Hamaker constant on the pressure drop as a function of the gas velocity for Geldart A particles.

We conclude that these changes are unimportant and that the biggest influence of the Hamaker constant is the reduction of the hysteresis and a slight decrease in the  $\Delta p-U_{mf}$  slope of the homogeneous part of the fluidization. This effect could be explained in two ways; firstly, a reason could be a numerical artefact due to the soft sphere method that was employed in the DPM code for the particle collisions. As indicated in the model description, we assume a certain value of the spring stiffness that will avoid particle overlap exceeding 1% of their particle diameter during the simulation. Although for all the other types of simulation with fluidized beds this maximum overlap yielded satisfactory results, for simulations with higher Hamaker constants this maximally allowed overlap of 1% could still be too large. We can take a look at snapshots from simulations presented in the Appendix (Figure 9), showing the particle overlap for different Hamaker constants at the same gas velocity. Further investigation is ongoing on this topic to investigate whether it is necessary reduce the maximally allowed overlap. The second explanation lies in a possible existence of clusters and channels that would allow gas bypass which would reduce the pressure drop. Compared with work of Ye et al. (2004), our conclusions are matching well, the biggest difference is that their approach for determining  $U_{mf}$  was a step-wise method of increasing the gas velocity instead of a continuous incrementing gas flow rate. The values determined from the simulations are slightly higher in comparison to the values calculated using the basic Ergun equation (Eq 9) with the bed porosity taken from our simulations.

$$\frac{1.75}{\varepsilon_{mf}^3 \phi} (\text{Re}_{mf})^2 + \frac{150(1 - \varepsilon_{mf})}{\varepsilon_{mf}^3 \phi^2} (\text{Re}_{mf}) = Ar \quad (9)$$

where the Reynolds number at minimum fluidization and the Archimedes number are defined as

$$\text{Re}_{mf} = \frac{\rho_g d_p U_{mf}}{\mu_g} \quad (10)$$

$$Ar = \frac{(\rho_p - \rho_g) g \rho_g (d_p)^3}{(\mu_g)^2} \quad (11)$$

Substituting the simulation data into these equations we obtain a value for the minimum fluidization velocity of 0.0034 m/s for  $\epsilon_{mf}=0.4$ . This value is not significantly different from the values obtained from Figure 2.

Simulations including Van der Waals forces show a clear influence on the average bed porosity (Figure 3). The bed porosity for increasing Hamaker constant is increasing, however, we observe for the largest Hamaker constant that the bed height and porosity are lower than the case without vdW forces. As noted before, this effect could be due to the soft sphere method.

The minimum bubbling velocity  $U_{mb}$  can be determined by using a combination of the snapshots of the bed porosity and from  $\Delta p-U_0$  graph. For all cases, bubbles start to appear at around 0.023 m/s, which is lower than the value reported in Ye et al.'s (2004) work. It is important to mention that our simulations were performed in 3D, whereas Ye et al. (2004) used 2D simulations.

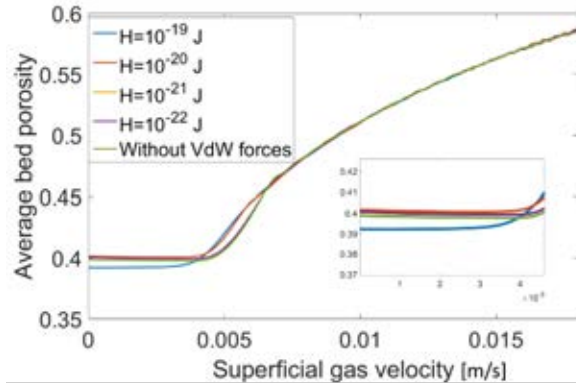


**Figure 3:** Average bed porosity as a function of the superficial gas velocity.

The influence of van der Waals forces on the time-averaged solids velocity is shown in Figure 8 in the Appendix.

The time averaged solids velocities were plotted for  $H=10^{-19/20/21}$  J at gas velocities 0.004 m/s and 0.014 m/s. For all the cases the circulation patterns follow the anticipated profile with solids flowing upwards in the centre of the bed and downwards near the walls of the column. For cases with the superficial gas velocity close to the minimum velocity, the solids circulation rate is somewhat reduced for cases with higher Hamaker constants, as expected. At higher superficial gas velocities this effect is similar, but somewhat less pronounced.

#### Geldart B type particles

As a first step in the investigation of high-temperature fluidization of Geldart B type particles, we have examined the minimum fluidization conditions. Compared to Geldart A particles, a similar effect on  $U_{mf}$  was observed also for Geldart B particles. For higher Hamaker constants, the superficial gas velocity at incipient fluidization conditions is slightly higher (see Figure 4). However, we do not observe a decrease in the minimum fluidization gas velocity for  $H=10^{-19}$  J, but found a significant increase in the minimum fluidization velocity. The values for the minimum fluidization

velocity determined from the simulation results are given in Table 3:

**Table 3:** Determined  $U_{mf}$  for various Hamaker constants

Hamaker constant $H$ [J]	Determined $U_{mf}$ [m/s]
0	0.2224
$10^{-22}$	0.2274
$10^{-21}$	0.2277
$10^{-20}$	0.2321
$10^{-19}$	0.2885

When calculating  $U_{mf}$  using Ergun's equation with characteristics for Geldart B particles and with the porosity from simulations ( $\epsilon_{mf}=0.4$ ), we find 0.226 m/s, which is very close to the simulated values.

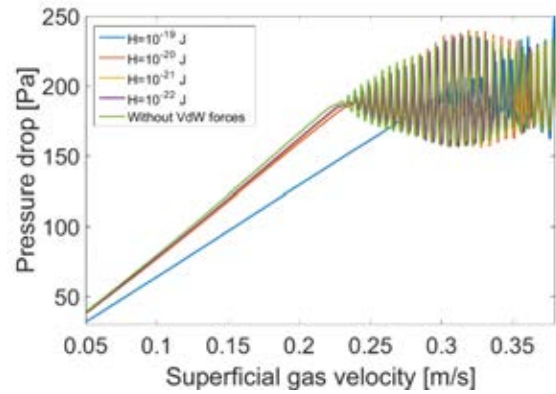


**Figure 4:** Influence of the Hamaker constant on the pressure drop vs. the superficial gas velocity for Geldart B particles.

For the time-averaged bed porosity a slightly different behaviour was observed compared to our findings for Geldart A particles. It was also found that by increasing the gas velocity the bed porosity tends to increase (Figure 5). However, for a very high Hamaker constant, the bed porosity was larger than for the case without vdW forces, which is clearly different from the Geldart A simulations.

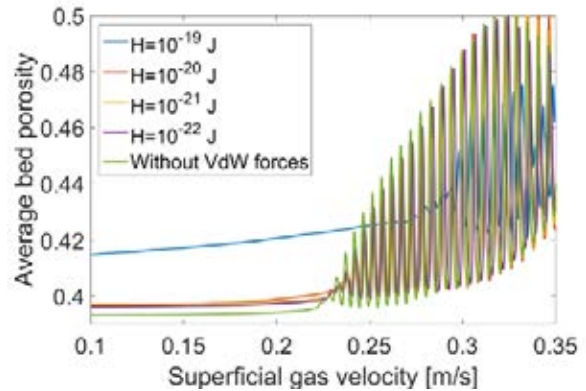


**Figure 5:** Bed porosity as a function of the gas velocity, influence of the Hamaker constant on the bed compaction.

A possible reason for this behaviour we can find in the fact that simulations start by fluidizing the particles with a relatively large gas velocity for 2 s, after which the gas flow is switched off and the particles drop down to form the initial situation before the velocity starts to increase linearly in time. By doing so, the particles in the simulations with a larger Hamaker constant tend to form clusters that affect the overall bed porosity with the formation of larger voids. In comparison, the case without vdW forces shows that particles have been



distributed more uniformly over the bottom of the reactor (Appendix, Figure 10) resulting in a higher overall bed porosity.

Similar to the results for Geldart A particles, the average overlap is higher for the case with a stronger Hamaker constant (Figure 6) and this needs to be further investigated.

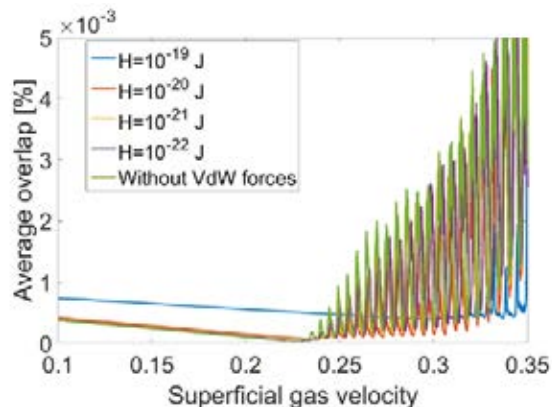


**Figure 6:** Average overlap between particles during the simulations, the effect of the Hamaker constant on the bed porosity may be related to the increased particle overlap.

In a future work a more detailed comparison will be carried out between the experiments at high temperatures and DPM simulations including vdW forces.

## CONCLUSIONS

The main conclusions are:

1. For both Geldart A and Geldart B particles vdW forces increase the minimum fluidization bed porosity (increased bed height).
2. For higher Hamaker constants Geldart B particles tend to form unstable channels and clusters.
3. The effect of the maximum particle overlap has to be further investigated. The current maximum allowed overlap may not be suitable for the cases of the strongest considered Hamaker constants, where the average particle overlap is higher.

## ACKNOWLEDGMENTS

The authors wish to thank the European Commission for supporting this work as part of the research project "Intensified by Design platform for the intensification of processes involving solids handling", IbD®, under the H2020 SPIRE programme (SPIRE-08-2015-680565).

## REFERENCES

BAERNS, M., (1966), "Effect of Interparticle Adhesive Forces on Fluidization of Fine Particles", *Ind. Eng. Chem. Fundamen.*, **5** (4), 508–516

BOTTERILL, J.S.M., TEOMAN, Y., YÜREGIR, K.R., (1982), "The Effect of Operating Temperature on the Velocity of Minimum Fluidization, Bed Voidage and General Behavior", *Powder Technology*, **31**, 101 – 110

CAMPOS VELARDE, I., GRIM, R., GALLUCCI, F., VAN SINT ANNALAND, M., (2016), "Influence of Temperature on

Minimum Fluidization Properties of Gas-Solid Fluidized Beds", *Powder Technology*, Submitted.

CASTELLANOS, A. J., GARCIA-SUCRE, M., URBINA-VILLALBA G., (2003), "Temperature dependence of Hamaker constants for fluorocarbon compounds" *The Journal of Physical Chemistry B*, **107**, 8532-8537

CUNDALL, P.A., STRACK, O.D., (1979), "A discrete numerical model for granular assemblies", *Geotechnique*, **29**, 47.

FORMISANI, B., GIRIMONTE, R., MANCUSO, L., (1998) "Analysis of the fluidization process of particle beds at high temperature", *Chemical Engineering Science*, **53**(5), 951–961

GELDART, D. (1972), "The Effect of Particle Size and Size Distribution on the Behaviour of Gas-Fluidised Beds", *Powder Technology*, **6**, 201-215

GELDART, D. (1973), "Types of gas fluidization", *Powder Technology*, **7**, 285-292

HAMAKER, H.C., (1937) "The London – van der Waals attraction between spherical particles", *Physica*, **4**(10), 1058–1072.

HOOMANS, B.P.B., KUIPERS, J.A.M., BRIELS, W.J., VAN SWAAIJ, W.P.M., (1996) "Discrete particle simulation of bubble and slug formation in a two-dimensional gas-fluidised bed: a hard-sphere approach" *Chemical Engineering Science*, **51**, 99–118.

ISRAELACHVILI, J., (1991) "Intermolecular and Surface Forces", *Academic Press, London*

KOBAYASHI, T., MUKAI, T., KAWAGUCHI, T., TANAKA T., TSUJI Y., (2006), "DEM Analysis on Flow Patterns of Geldart's Group A Particles in Fluidized Bed-Effect of Adhesion and Lubrication Forces", *Journal of the Society of Powder Technology, Japan*, **43**, 737-745

KUNII, D., LEVENSPIEL, O., (1991.) "Fluidization engineering", Butterworth-Heinemann, London

LEFÈVRE, G., JOLIVET, A., (2009), "Calculation of Hamaker constants applied to the deposition of Metallic oxide particles at high temperature", *Proceedings of International Conference on Heat Exchanger Fouling and Cleaning VIII*

LETTIERI, P., NEWTON, D., YATES, J.G., (2001), "High temperature effects on the dense phase properties of gas fluidized beds", *Powder Technology*, **120**, 34–40

SHABANIAN, J., FOTOVAT, F., CHAOUKI, J., BOUFFARD, J., (2013) "Fluidization Behavior in a Gas- Solid Fluidized Bed with Thermally Induced Inter-Particle Forces" *10th International Conference on Circulating Fluidized Beds and Fluidization Technology - CFB-10*, Eds, *ECI Symposium Series, Volume RP7*

SEVILLE, J.P.K., WILLET, C.D., KNIGHT P.C., (2000), "Interparticle forces in fluidisation: a review", *Powder Technology*. **113**, 261–268

SUBRAMANI, H.J., BALAIYYA, M.B.M., MIRANDA, L.R., (2007), "Minimum fluidization velocity at elevated temperatures for Geldart's group-B powders", *Experimental Thermal and Fluid Science*, **32**, 166–173

TAN, L., ROGHAI, I., VAN SINT ANNALAND, M., (2014) "Simulation study on the effect of gas permeation on the hydrodynamic characteristics of membrane-assisted micro fluidized beds", *Applied Mathematical Modeling*, **38**, 4291-4307

TSUJI, Y., KAWAGUCHI, T., TANAKA, T., (1993) "Discrete particle simulation of two-dimensional fluidized bed", *Powder Technology*, **77**, 79–87.

YE, M., VAN DER HOEF, M.A., KUIPERS, J.A.M., (2004) "A numerical study of fluidization behavior of Geldart A particles using a discrete particle model", *Powder Technology*, **139**, 129-139

YE, M., VAN DER HOEF, M.A., KUIPERS, J.A.M., (2005) "The effects of particle and gas properties on the fluidization of Geldart A particles", *Chemical Engineering Science* **60**, 4567 – 4580

APPENDIX

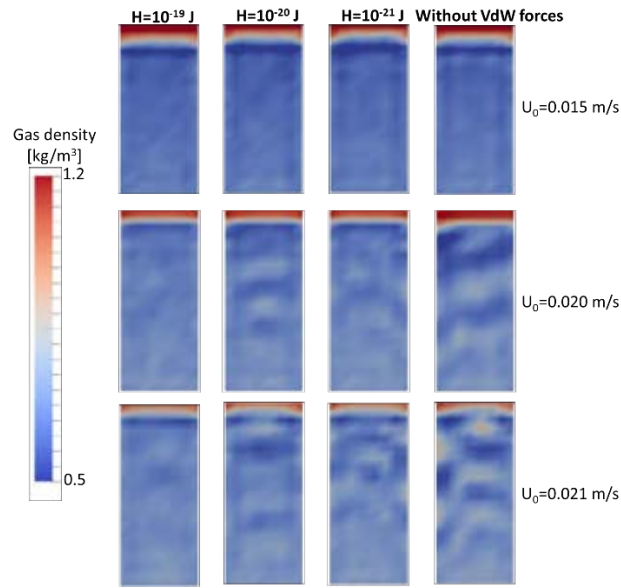


Figure 7: Gas density distribution in the bed of Geldart A particles.

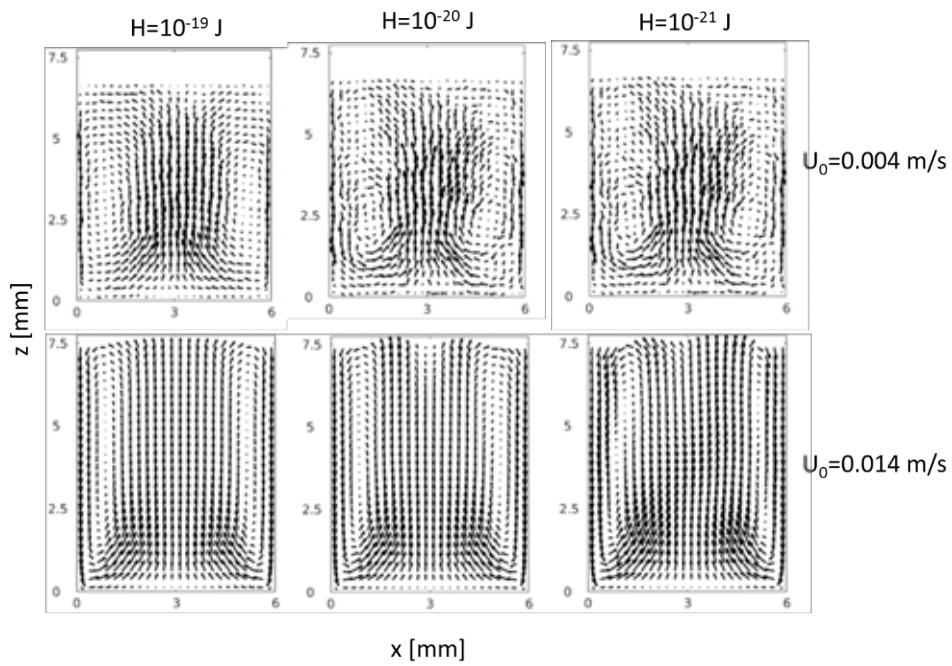
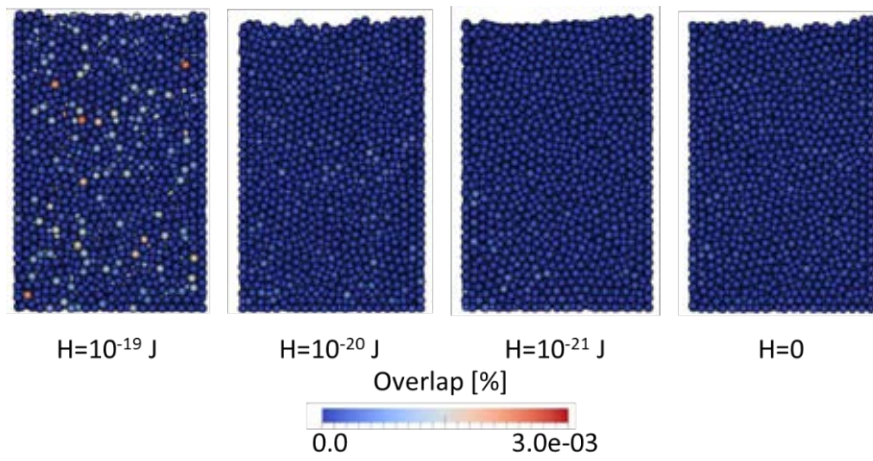
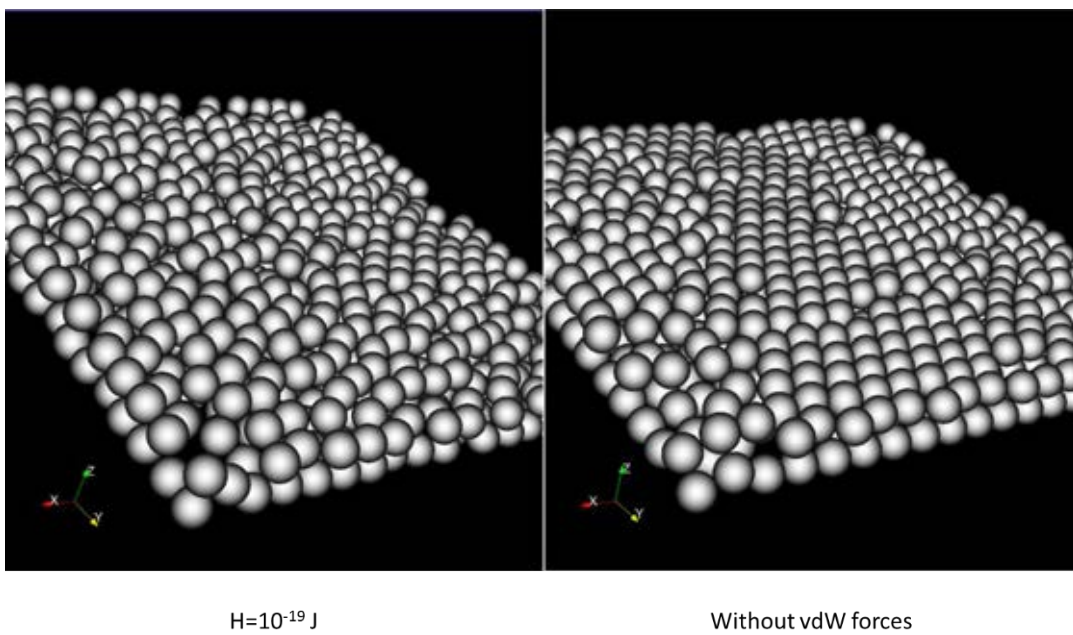


Figure 8: Average particle velocity for different Hamaker constants. Geldart A particles.



**Figure 9:** Overlap between the particles for different Hamaker constants at  $U_0=0.0035$  m/s



**Figure 10:** Slice of the bottom of the bed after the particle drop. Influence of vdW forces on fixed bed.

# VERIFICATION OF FILTERED TWO FLUID MODELS FOR REACTIVE GAS-SOLID FLOWS

Jan Hendrik CLOETE<sup>1</sup>, Schalk CLOETE<sup>2</sup>, Stefan RADL<sup>3</sup>, Shahriar AMINI<sup>1,2\*</sup>

<sup>1</sup> Department of Energy and Process Engineering, Norwegian University of Science and Technology (NTNU), 7491 Trondheim, NORWAY

<sup>2</sup> Flow Technology Department, SINTEF Materials and Chemistry, NO-7465 Trondheim, NORWAY

<sup>3</sup> Institute of Process and Particle Engineering, Graz University of Technology, Graz, AUSTRIA

\*Corresponding author's e-mail: [shahriar.amini@sintef.no](mailto:shahriar.amini@sintef.no)

## ABSTRACT

CFD simulations of fluidized bed reactors are generally limited to the laboratory scale because of the fine grid sizes that are required to resolve complex particle clustering phenomena. The filtered Two Fluid Model (fTFM) approach has recently emerged as a promising method for allowing reasonable predictions of large-scale fluidized beds. This paper presents a verification study of new two-marker fTFM closures. In general, the fTFMs matched well to the resolved simulations. It was shown that the two-marker models significantly increased the predicted degree of phase segregation (resolved in coarse grid simulations), and hence have superior capabilities compared to simpler one-marker models. Also, the two-marker model predicted a more dynamic transient flow behaviour. However, further work is recommended to extend the present study over a wider range of flow conditions.

Keywords: CFD, Fluidized beds, verification, filtered two-fluid model.

## NOMENCLATURE

### Greek Symbols

- $\alpha$  Volume fraction, [].  
 $\mu$  Dynamic viscosity, [kg/m.s].  
 $\rho$  Density, [kg/m<sup>3</sup>].  
 $\overline{\overline{\tau}}_s$  Stress tensor, [Pa].  
 $\mathcal{V}$  Velocity, [m/s].  
 $\Delta_f$  Filter size, [m].

### Latin Symbols

- $d$  Particle diameter, [m].  
 $D$  Mass diffusivity, [m<sup>2</sup>/s].  
 $g$  Gravitational acceleration, [m/s<sup>2</sup>].

$K_{sg}$  Momentum exchange coefficient, [kg/m<sup>3</sup>s].

$p$  Pressure, [Pa].

$S$  Shear rate magnitude, [1/s].

$t$  Time, [s].

$v_t$  Terminal settling velocity, [m/s].

$X_A$  Mass fraction of species A, [].

### Subscripts, superscripts and accents

$f$  Filtered.

$g$  Gas.

$s$  Solids.

– Algebraic volume average.

~ Phase-weighted volume average.

$\langle \rangle$  Time average.

$\vec{\phantom{x}}$  Vector quantity.

\* Scaled or non-dimensionalized quantity.

' Fluctuating quantity.

## INTRODUCTION

Fluidized beds are widely used in industry due to their excellent mass and heat transfer properties. In the last three of decades, CFD has emerged as a useful tool with which to investigate the reactive flow in these reactors, although significant challenges remain (Cloete et al., 2012). The most important limitation of this approach remains the excessive computational times involved in simulating industrial scale reactors, due to the large number of particles (in the order of  $10^{12}$ ).

The filtered Two-Fluid Model (fTFM) (Igci et al., 2008) offers a solution to this problem. The TFM closed by the Kinetic Theory of Granular Flow (KTGF) (Lun et al., 1984, Gidaspow et al., 1992), where the fluctuations in the particle velocities are treated analogous to that of gas molecules in the kinetic theory of gases, are often employed in fluidized bed simulations. However,

KTGF-based TFMs suffer from the limitation that they require a high enough grid resolution to resolve the small scale structures (particle clusters and gas bubbles) for accurate model predictions, leading to computationally expensive simulations. The fTFM aims to reduce the required computational time substantially by relying on spatially-averaged (i.e., “filtered”) governing equations. However, this leads to additional terms in these equations (that account for small-scale fluctuations) which must be closed. These closures are generally formulated as a function of the size of the averaging region, and additional marker quantities. Closures may be obtained by fitting a proposed functional form to data obtained from fine grid TFM simulations.

Most of the research in this field has been limited to developing models for the filtered hydrodynamics (Ozel et al., 2013, Schneiderbauer and Pirker, 2014, Sarkar et al., 2016), where sub-grid corrections to the interphase drag and solids stresses are essential. However, in reactive flows further closures are required to correct the reaction rate and species dispersion for sub-grid effects. Models have been proposed for these effects (Holloway and Sundaresan, 2012, Agrawal et al., 2013), but have not been verified so far.

This paper will therefore evaluate the reactive fTFM closures developed by the Princeton group (Igci and Sundaresan, 2011, Holloway and Sundaresan, 2012, Agrawal et al., 2013). Additionally, a new set of closures for the filtered drag, solids pressure and reaction rate will be tested. These comparisons will give an indication of the ability of the fTFM approach to predict reactive flow on coarse grids and will help identify areas of improvement for the existing models.

## MODEL DESCRIPTION

### Governing equations

Two types of simulations are performed in this study: coarse grid simulations using fTFM closures and resolved TFM simulations against which to verify the coarse grid results. The resolved TFM simulations follow a standard KTGF approach as commonly employed in the literature, e.g. (Cloete et al., 2017), and the equations and closures used will therefore not be described here in detail.

However, the equations and fTFM closures employed in the coarse grid simulations warrant further discussion. Two sets of fTFM closures are evaluated in this verification study: a model from the Princeton group and a new model proposed in this study. To derive filtered equations, a spatial average is performed on all equations and averages of products are rearranged by defining the instantaneous value of a quantity as the sum of its averaged value and a fluctuating component. Employing this procedure to the solids momentum equation, the following equation is obtained.

$$\begin{aligned} \frac{\partial}{\partial t}(\rho_s \bar{\alpha}_s \bar{v}_s) + \nabla \cdot (\rho_s \bar{\alpha}_s \bar{v}_s \bar{v}_s) = -\bar{\alpha}_s \nabla p - \nabla \bar{p}_s \\ - \nabla \cdot (\overline{\rho_s \alpha_s v_s' v_s'}) + \nabla \cdot \bar{\bar{v}}_s + \bar{\alpha}_s \rho_s \bar{g} + K_{gs} (\bar{v}_g - \bar{v}_s) - \alpha_s' \nabla p' \end{aligned} \quad (1)$$

For the hydrodynamics, closures are required for the filtered kinetic theory stresses (second term and fourth term on the right), the meso-scale solids stresses (third term on the right), the filtered drag force (sixth term on the right) and an added mass-like force due to the subgrid pressure gradient fluctuations (last term on the right). Additionally, similar meso-scale stresses in the gas momentum equation will require closure. However, in this study these stresses are neglected, since they are generally considered to be much smaller than the particle phase meso-scale stresses (Milioli et al., 2013).

For the fTFM hydrodynamics from the Princeton group, the model by Igci and Sundaresan (2011) is used, which closes the filtered solids stresses and the filtered drag as a function of the filter size and the filtered solids volume fraction. Although more advanced models using an additional marker have been published, a recent hydrodynamic verification study (Cloete et al., 2017) showed that these advanced models perform poorly in predicting the hydrodynamics in 2D flows, whereas the simpler Igci model performed very well.

For the fTFM proposed in this study, the following closures are suggested. The filtered drag force and the pressure gradient fluctuation term are modelled together as a correction to the microscopic drag law, as follows.

$$C = \frac{K_{gs} (\bar{v}_{g,i} - \bar{v}_{s,i}) - \alpha_s' \frac{dp'}{dx_i}}{K_{gs, microscopic} (\bar{v}_{g,i} - \bar{v}_{s,i})} \quad (2)$$

The drag correction factor,  $C$ , is calculated as a function of the dimensionless filter size (Igci et al., 2008), the filtered solids volume fraction and the filtered slip velocity magnitude scaled by the steady state slip velocity (Cloete et al.). This scaling of the slip velocity was shown to lead to a better distribution of data in the parameter space and to a simple dependency of the drag correction factor on the filtered slip velocity, resulting in a better fit of the correlation to the resolved simulation data. The following correlation is used:

$$\begin{aligned} -\log(C) = \frac{\left( \begin{aligned} & \text{atan} \left( x_1 \left( \Delta_f^* - \Delta_{fine}^* \right)^{x_2} \bar{\alpha}_s \right) \times \\ & \text{atan} \left( \frac{x_2 \left( \Delta_f^* - \Delta_{fine}^* \right)^{x_3} \times}{\left( \bar{\alpha}_{max} - \bar{\alpha}_s \right)} \right) \times \\ & \text{atan} \left( x_3 \left( \Delta_f^* - \Delta_{fine}^* \right) \right) \times \\ & \left( x_4 \log \bar{v}_{slip} + x_5 \left( \Delta_f^* - \Delta_{fine}^* \right)^{x_6} + \right. \\ & \left. x_7 \left( \log \bar{v}_{slip} \right)^2 \left( 1 - \right. \right. \\ & \left. \left. \text{atan} \left( x_8 \left( \Delta_f^* - \Delta_{fine}^* \right) \right) / \left( \frac{\pi}{2} \right) \right) \right) \right) \left/ \left( \frac{\pi}{2} \right)^3 \right. \end{aligned} \right) \quad (3) \end{aligned}$$

Where  $x_1 = 46.75$ ,  $x_2 = 51.51$ ,  $x_3 = 1.370$ ,  $x_4 = 0.8632$ ,  $x_5 = 0.05360$ ,  $x_6 = 0.4776$ ,  $x_7 = 364.1$ ,  $x_8 = 260.7$ ,  $x_9 = 0.889$ ,  $x_{10} = 0.494$ , and  $\bar{\alpha}_{max} = 0.55$ . The fine grid scaled filter size is set to  $\Delta_{fine}^* = 0.1286$ .

It is assumed that the filtered kinetic theory stresses are much smaller than the meso-scale stresses for filter sizes large enough for practical use (Igci et al., 2008). Therefore closures for the former stresses are neglected. However, the following closure is proposed for the

dimensionless filtered frictional pressure, which was found to be significant:

$$\frac{P_{s,fric}}{\rho_s v_t^2} = \bar{\alpha}_s^{x_1} (\Delta_f^* - \Delta_{fine}^*)^{x_2} \times \left( x_3 \bar{S}_s^{x_4} (\Delta_f^* - \Delta_{fine}^*)^{x_5} + x_6 \frac{\bar{\alpha}_s^{x_7}}{(\bar{\alpha}_{s,max} - \bar{\alpha}_s)^{x_8}} \right) \quad (4)$$

Where  $x_1 = 4.016$ ,  $x_2 = -0.005543$ ,  $x_3 = 0.1905$ ,  $x_4 = 1.939$ ,  $x_5 = 1.658$ ,  $x_6 = 0.03935$ ,  $x_7 = 12.78$ ,  $x_8 = 5.084$  and  $\bar{\alpha}_{s,max} = 0.63$ . The dimensionless filtered solids shear rate magnitude,  $\bar{S}_s^*$ , is calculated as done by Milioli et al. (2013).

It was found that the effect of modelling the off-diagonal component of the solids meso-scale stress on the coarse grid simulations were small, therefore a new model was not derived as part of this study and the model of (Sarkar et al., 2016) is used. For the diagonal components of the solids meso-scale stresses the following correlation is proposed:

$$\frac{\rho_s \overline{\alpha'_s v'_{s,x} v'_{s,x}}}{\rho_s v_t^2} = \frac{\rho_s \overline{\alpha'_s v'_{s,y} v'_{s,y}}}{\rho_s v_t^2} = \bar{\alpha}_s^{x_1} \operatorname{atan}(x_2 (\bar{\alpha}_{max} - \bar{\alpha}_s)) \times \left( \Delta_f^* - \Delta_{fine}^* \right)^{x_3} \left( x_4 \bar{S}_s^{x_5} + x_6 \bar{\alpha}_s^{x_7} \right) / \left( \frac{\pi}{2} \right) \quad (5)$$

Where  $x_1 = 1.522$ ,  $x_2 = 15.49$ ,  $x_3 = 1.162$ ,  $x_4 = 0.5660$ ,  $x_5 = 1.385$ ,  $x_6 = 0.07166$ ,  $x_7 = -0.9543$ , and  $\bar{\alpha}_{max} = 0.6043$ . The correlation shape is based on a Smagorinsky-type model as used by Sarkar et al. (2016), with modifications to have zero meso-scale stresses at the filter size where the resolved simulations were performed, and non-zero meso-scale stresses at zero filtered shear rates. The latter is motivated by an observation of Schneiderbauer (2016).

A simple irreversible, first-order, solids-catalysed reaction of species A to species B is considered in this study. The filtered gas species transport equation, formulated for the mass fraction of species A, is:

$$\frac{\partial}{\partial t} (\rho_g \overline{\alpha_g \widetilde{X}_A}) + \nabla \cdot (\rho_g \overline{\alpha_g \widetilde{X}_A \widetilde{v}_g}) = \nabla \cdot (D \overline{\alpha_g \rho_g \nabla X_A}) - \nabla \cdot (\rho_g \overline{\alpha_g X'_A \widetilde{v}'_g}) - k_A \rho_g \overline{\alpha_g X_A} \quad (6)$$

The first term on the right is neglected, considering that the molecular diffusion is small relative to species dispersion due to the meso-scale velocity fluctuations (i.e., the second term on the right). The species dispersion due to the meso-scale velocity fluctuations is modelled as an added diffusivity as proposed by Agrawal et al. (2013).

The last term on the right hand side of the species transport equation is modelled as follows:

$$\overline{\alpha_g X_A} = R \overline{\alpha_g \widetilde{X}_A} \quad (7)$$

The reaction rate correction factor  $R$  accounts for the effect of unresolved concentration and voidage fluctuations on the filtered reaction source term. It can

be calculated from finely-resolved reaction rate data, and can be defined such that it also accounts for non-local effects (i.e., gradient terms) as suggested by Holloway and Sundaresan (2012). This was also done in our present contribution. For the Princeton fTFM setup the model by Holloway and Sundaresan (2012) is used. A new model for  $R$ , adding an additional marker for the scaled slip velocity, is proposed as part of this study. The proposed model is limited to the specific case of a reaction rate constant giving a Thiele modulus of 0.16.

$$-\log(R) = \operatorname{atan} \left( x_1 (\Delta_f^* - \Delta_{fine}^*)^{x_2} \bar{\alpha}_s \right) \times \operatorname{atan} \left( x_2 (\Delta_f^* - \Delta_{fine}^*)^{x_3} \times \left( \bar{\alpha}_{max} - \bar{\alpha}_s \right) \right) \times \operatorname{atan} \left( x_3 (\Delta_f^* - \Delta_{fine}^*) \right) \times \left( \frac{\pi}{2} \right)^3 \left( \frac{\operatorname{atan}(x_4 \widetilde{v}_{slip}^*)}{\operatorname{atan} \left( x_3 (\Delta_f^* - \Delta_{fine}^*) \right)} \right) \times \left( x_5 \log \widetilde{v}_{slip}^* + x_6 \right) \quad (8)$$

Where  $x_1 = 7.925$ ,  $x_2 = 17.31$ ,  $x_3 = 0.3511$ ,  $x_4 = 0.7772$ ,  $x_5 = 0.1366$ ,  $x_6 = 1.007$ ,  $x_7 = -0.09253$ ,  $x_8 = -0.003722$  and  $\bar{\alpha}_{max} = 0.5627$ .

### Verification cases

The average superficial inlet gas velocity for this study is chosen to be at the geometric center of the bubbling fluidization regime, according to Bi and Grace (1995), giving an average superficial velocity of  $0.468 \frac{m}{s}$  at the inlet. A solids flux of  $150 \frac{kg}{m^2 s}$  is specified.

Furthermore, the profile of the velocity, solids volume fraction and reactant mass fraction at the inlet is specified to be non-uniform. This allows more rigorous testing of the filtered models by creating mean gradients in the flow. The gas phase superficial velocity is chosen to be half the average superficial velocity at the sides of the domain and increases linearly towards the center. Zero slip between the phases is specified at the inlet. The solid volume fraction is set to a minimum at the centre and increases linearly to the sides. The value of the minimum solids volume fraction is set equal to half the solids volume fraction required to deliver the specified solids flux at the mean gas superficial velocity. Finally, the reactant species mass fraction is set to 1 at the center and 0 at the sides.

The simulation domain consists of a rectangular reactor region, 0.96 m by 1.6 m, and a small outlet region with walls sloping at  $45^\circ$  towards the outlet. The wall boundary condition is set as free slip for the solids to minimize the effect of the outlet region on the flow in the rest of the domain. The outlet has a small width of 10 cm to prevent backflow, which could potentially cause numerical instabilities. The sides of the fluidization region are specified as periodic boundaries, since the models evaluated in this study was derived for periodic flows far away from wall-effects.

Due to the large computational expense of performing resolved simulations (performed at a grid size equal to

11.8 times the particle diameter) in such a large domain, all simulations were performed in 2D. Testing filtered models in 2D remains a valid approach, since filtered models derived from 2D and 3D simulations have been shown to be qualitatively similar (Igeci et al., 2008).

The particle and fluid properties used in the simulations are summarized in Table 1.

**Table 1:** Summary of particle and fluid properties

$d$	Particle diameter	$75 \times 10^{-6}$ m
$\rho_s$	Particle density	1500 kg/m <sup>3</sup>
$\rho_g$	Gas density	1.3 kg/m <sup>3</sup>
$\mu_g$	Gas viscosity	$1.8 \times 10^{-5}$ kg/m s
$v_t$	Terminal settling velocity	0.2184 m/s
$D$	Mass diffusivity	$1.385 \times 10^{-5}$ m <sup>2</sup> /s

The coarse grid simulations are allowed to run for 10 s of simulation time to reach a statistical steady state, after which the results are time averaged for 50 s. The resolved simulation has been time-averaged for 9 s. Two values are used to quantify the overall reactor behaviour: the average solids holdup and the average scaled conversion. The average solids holdup is calculated as the time-averaged solids volume fraction averaged over the rectangular region of the geometry. The scaled conversion of the reactant is calculated as  $-\log_{10}(\overline{X_A})$ . To calculate  $\overline{X_A}$  the time-average reactant mass fraction is averaged over a horizontal line at a height of 1.5 m (0.1 m below the start of the outlet region). The averaging regions for both quantities are chosen in such a way as to minimize the effect of the outlet region on the results.

## RESULTS

Results will be presented and discussed in two main sections. Firstly, the overall model performance will be compared using the holdup and conversion performance parameters discussed in the previous paragraph. Then, a more detailed comparison between the different model predictions for the spatial distribution of key quantities will be presented and discussed.

### Overall comparison

Model performance is summarized in Figure 1. Firstly, the need for filtered modelling on coarse grids is readily visible from the cases without any filtered models. Predictions of the holdup without any filtered modelling are lower by about 20% because clusters are not resolved and drag is over-predicted. A much larger error is observed for the reaction rate because mass transfer limitations caused by clustering are strongly under-predicted when not resolving the clusters. It is notable that the overall conversion is over-predicted by up to 100% even though a substantially lower solids holdup is predicted.

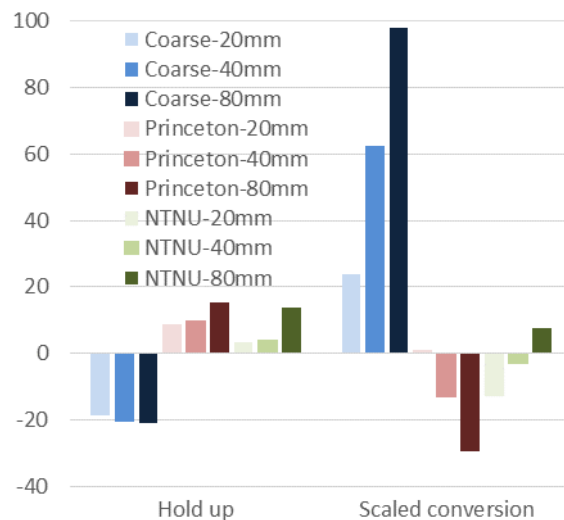


**Figure 1:** Deviation of model predictions from the resolved simulations for the solids holdup and reactant conversion.

Both filtered models investigated in this work resulted in substantial improvements relative to the cases without any filtered modelling. However, it is also clear that both models show significant grid dependencies, implying that work is still needed to improve the filter size dependency on the models. The primary difference between the performance of the Princeton and NTNU model setups is the trend of reactant conversion with an increase in grid size. The Princeton model increasingly under-predicts the reactant conversion at larger grid sizes, whereas the NTNU model over-predicts it. For the NTNU model, this trend is aligned with the increase in solids holdup at larger filter sizes, so the trend can be partly explained by the imperfect hydrodynamic models. For the Princeton models, on the other hand, the trend is in opposition to the holdup trend, implying that significant improvements to the reaction rate model are required.

### Detailed comparison

A good idea about model behaviour can be formed by inspecting the contours of instantaneous solids volume fraction and conversion presented in Figure 2 and Figure 3.

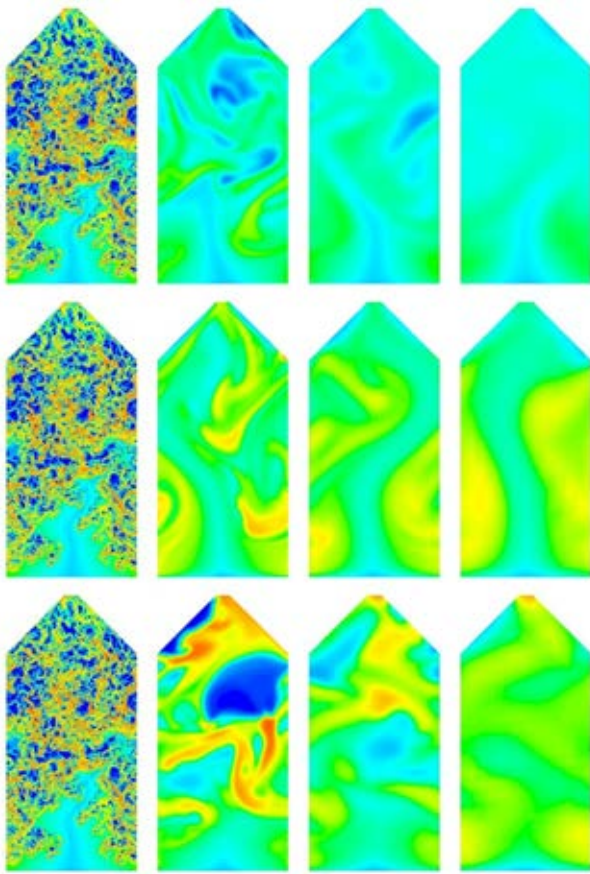


**Figure 2:** Instantaneous contours of solids volume fraction. Top row: no filtered modelling. Middle row: Princeton model. Bottom row: NTNU model. Each row shows the resolved simulation on the left and then the coarse grid simulations on grids of 20, 40 and 80 mm. The blue-red colour map spans a range of 0-0.6.

Figure 2 clearly shows the increased holdup simulated by the filtered models relative to the coarse grid simulations with no filtered modelling. In addition, the NTNU models (two-marker models) generally predict more phase segregation than the Princeton models (i.e., primarily one-marker models). This is the result of a wider range of variation for each filtered quantity ensured by a two-marker model relative to a one-marker model. The variation of filtered quantities (e.g. drag, pressure, etc.) will therefore be more pronounced in adjacent cells and the resulting force gradients will lead to greater phase segregation. As expected, it is also clearly visible that the amount of phase segregation reduces as the grid size (and filter size) is increased.

When inspecting the resolved simulation profiles, it appears as if the prediction of denser “clusters of clusters” by the filtered model is correct. Denser regions with many clusters and more dilute regions with fewer clusters are clearly visible in the resolved simulation. The resolution of these denser regions is gradually lost as the grid size is increased in the filtered simulations, especially for the one-marker Princeton models.

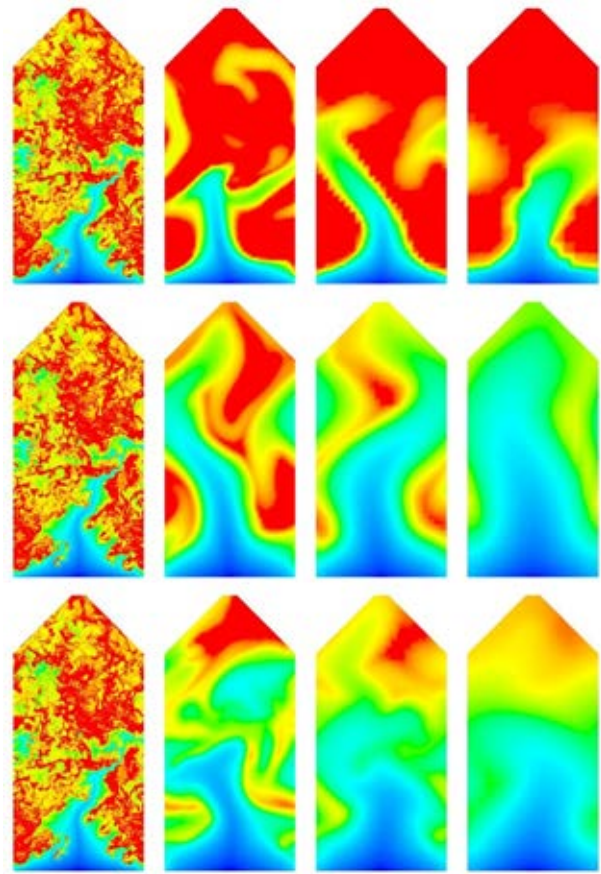


**Figure 3:** Instantaneous contours of reactant conversion ( $-\log_{10}(\overline{X_A})$ ). Top row: no filtered modelling. Middle row: Princeton model. Bottom row: NTNU model. Each row shows the resolved simulation on the left and then the coarse grid simulations on grids of 20, 40 and 80 mm. The blue-red colour map spans a range of 0-7.

The reactant conversion profiles in Figure 3 show that the filtered models generally capture the reactant transport correctly: low conversion in the central part of the inlet (high velocities and reactant mole fractions, and low volume fractions) with higher conversions at the sides of the domain. In addition, regions of low and high conversion in the developed flow regions seem to be qualitatively captured by the filtered models. As may be expected, these regions are aligned with the regions of low and high solids volume fraction in Figure 2.

It should be noted that the conversion looks misleadingly low in the filtered simulations because of the log scaling used to visualize the conversion. Spatial averages over a range of conversions ( $-\log_{10}(\overline{X_A})$ ) would be heavily weighted towards lower sample values.

Another perspective is given by the time-averaged solids volume fraction and conversion plots given in Figure 4 and Figure 5. The solids volume fraction contours show that the Princeton models generally predict higher solids volume fraction regions on the sides of the domain than the NTNU models. This is accentuated as the grid size is increased until a central spout between two dense regions is predicted on the 80 mm grid. In this measure, the NTNU models appear to match more closely with the resolved simulations,



although the triangular shape of the central inlet spout is gradually lost as the grid size is increased.

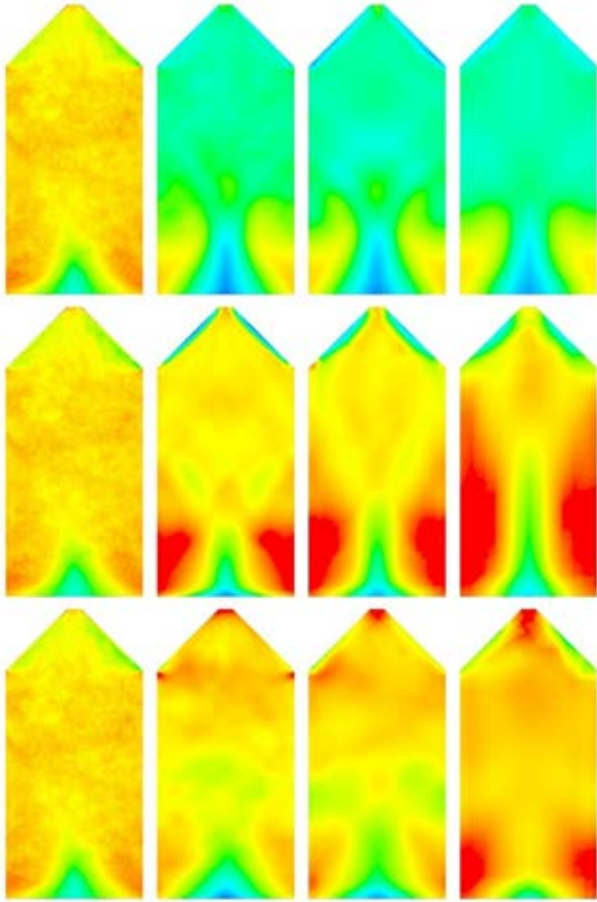


**Figure 4:** Time-averaged contours of solids volume fraction. Top row: no filtered modelling. Middle row: Princeton model. Bottom row: NTNU model. Each row shows the resolved simulation on the left and then the coarse grid simulations on grids of 20, 40 and 80 mm. The blue-red colour map spans a range of 0.1-0.36.

In general, it appears as if dense regions over the sides of the inlet tend to form more easily when less flow dynamics (driven primarily by phase segregation) are resolved. This may be expected since dynamically moving dense regions will have a lower tendency to stagnate in regions with low fluidization velocity, but rather move through that region to again be swept up by the stronger central gas stream. The greater phase segregation resolved by the two-marker NTNU models therefore appears to improve the prediction in this case.

When inspecting the reactant conversion contours in Figure 5, it is seen that the profiles qualitatively align with the volume fraction profiles in Figure 4: denser regions align with higher conversion and vice versa. However, significant improvement still seems to be possible. Both models appear to under-predict the conversion in the bottom-side regions of the domain. The Princeton models over-predicted solids holdup in these regions, so it would be expected that a similar over-prediction in conversion will result. This becomes particularly evident at larger filter sizes where large regions of high volume fraction were predicted, but conversion is increasingly under-predicted. Similarly, the NTNU models predict the solids holdup with

reasonable accuracy in the bottom-side regions of the domain, but the conversion in these regions is significantly under-predicted. This may be related to a over-prediction of the scalar dispersion rate.

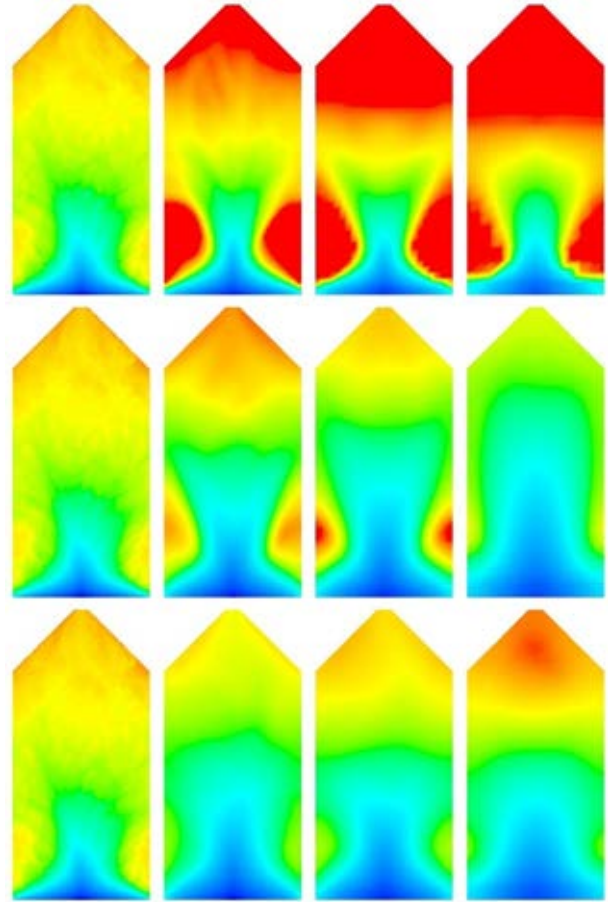


**Figure 5:** Time-averaged contours of reactant conversion ( $-\log_{10}(\overline{X_A})$ ). Top row: no filtered modelling. Middle row: Princeton model. Bottom row: NTNU model. Each row shows the resolved simulation on the left and then the coarse grid simulations on grids of 20, 40 and 80 mm. The blue-red colour map spans a range of 0-6.

As shown in Figure 6, exclusion of the scalar dispersion model led to a reactant conversion profile that is better aligned with the solids volume fraction profiles shown in Figure 4. The dense regions at the sides of the domain above the inlet now show greater conversion. However, the effect of the scalar dispersion model is small and it did not significantly affect the overall conversion in the domain.

Aside from this moderate discrepancy in the lateral direction at the bottom of the domain, conversion also appears to proceed too slowly along the height of the domain despite reasonably accurate predictions of the solids volume fraction in Figure 4. For the NTNU model, one possible explanation for this trend is that the phase segregation is too strong, leading to excessive mass transfer limitations. Further investigation is required to determine whether these moderate discrepancies are caused by inaccuracies from the hydrodynamic models or the reaction rate model. Given the relative simplicity of deriving a reaction rate model, the hydrodynamic models appear to be the more likely source of error. For the Princeton models, the filter size

dependency of the reaction rate model appears to be too weak, leading to progressively larger under-predictions of conversion with an increase in the grid size.

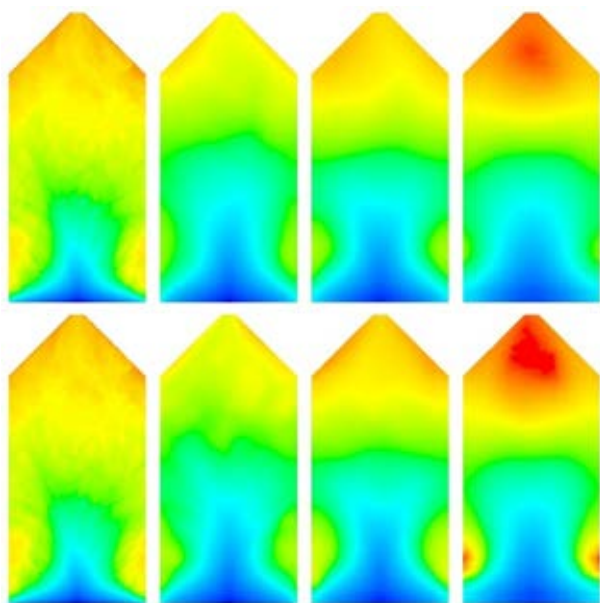


**Figure 6:** Time-averaged contours of reactant conversion ( $-\log(X_A)$ ) with the NTNU model. Top row: with scalar dispersion model. Bottom row: without scalar dispersion model. Each row shows the resolved simulation on the left and then the coarse grid simulations on grids of 20, 40 and 80 mm. The blue-red colour map spans a range of 0-6.

## CONCLUSION

A new two-marker filtered Two Fluid Model formulation is presented for solving reactive flows in fluidized beds. The model is verified against a computationally expensive resolved simulation to show good agreement. However, significant grid dependency is still present, which must be addressed in future model development work.

The two-marker model is compared to earlier one-marker models from the literature. Greater phase segregation is resolved by the two-marker model relative to the one-marker model, thereby capturing more flow dynamics even on a coarse mesh. In this case, the increased resolution of flow prevented excessive stagnation in low velocity regions of the domain.

The proposed two-marker reaction rate model performed significantly better than the existing one-marker model where the filter size dependency was found to be too weak. It is likely that the required improvements to conversion predictions can be more readily achieved by improving the more complex hydrodynamic models than the relatively simple reaction rate model. Finally, it was found that the inclusion of a model for dispersion of the reactant due to meso-scale velocity fluctuations appeared to have a slightly negative effect on model accuracy.

In general, this successful verification study shows the promise of the two-marker model approach. Further verification work over a wider range of flow conditions is recommended for future study.

## ACKNOWLEDGEMENTS

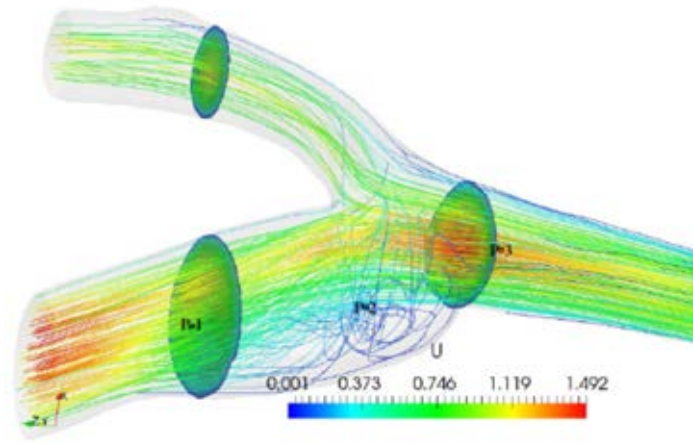
The authors would like to express their gratitude for the financial support from the European Commission under the NanoSim grant (project number: 604656), as well as for the computational resources provided at NTNU by UNINETT Sigma2 AS, <https://www.sigma2.no>.

## REFERENCES

- AGRAWAL, K., HOLLOWAY, W., MILIOLI, C. C., MILIOLI, F. E. and SUNDARESAN, S., (2013), "Filtered models for scalar transport in gas-particle flows", *Chem. Eng. Sci.*, **95** (0), 291-300.
- BI, H. T. and GRACE, J. R., (1995), "Flow regime diagrams for gas-solid fluidization and upward transport", *Int. J. Multiphase Flow*, **21** (6), 1229-1236.
- CLOETE, J. H., CLOETE, S., MUNICCHI, F., RADL, S. and AMINI, S., (2017), "The sensitivity of filtered Two Fluid Model to the underlying resolved simulation setup", *Powder Technol.*
- CLOETE, J. H., CLOETE, S., RADL, S. and AMINI, S., (2017), "Verification of filtered Two-Fluid Models in different flow regimes", *CFB-12.Krakow*.
- CLOETE, J. H., CLOETE, S., RADL, S., MUNICCHI, F. and AMINI, S., "A new anisotropic drag closure for filtered Two Fluid Models", *AIChE J.*, **Submitted**.
- CLOETE, S., JOHANSEN, S. T. and AMINI, S., (2012), "An assessment of the ability of computational fluid dynamic models to predict reactive gas-solid flows in a fluidized bed", *Powder Technol.*, **215-216** (0), 15-25.
- GIDASPOW, D., BEZBURUAH, R. and DING, J., (1992), "Hydrodynamics of Circulating Fluidized Beds, Kinetic Theory Approach", *7th Engineering Foundation Conference on Fluidization* 75-82.
- HOLLOWAY, W. and SUNDARESAN, S., (2012), "Filtered models for reacting gas-particle flows", *Chem. Eng. Sci.*, **82** (0), 132-143.
- IGCI, Y., ANDREWS, A. T., SUNDARESAN, S., PANNALA, S. and O'BRIEN, T., (2008), "Filtered two-fluid models for fluidized gas-particle suspensions", *AIChE J.*, **54** (6), 1431-1448.
- IGCI, Y. and SUNDARESAN, S., (2011), "Constitutive Models for Filtered Two-Fluid Models of Fluidized Gas-Particle Flows", *Ind. Eng. Chem. Res.*, **50** (23), 13190-13201.
- LUN, C. K. K., SAVAGE, S. B., JEFFREY, D. J. and CHEPURNIY, N., (1984), "Kinetic Theories for Granular Flow: Inelastic Particles in Couette Flow and Slightly Inelastic Particles in a General Flow Field", *J. Fluid Mech.*, **140**, 223-256.
- MILIOLI, C. C., MILIOLI, F. E., HOLLOWAY, W., AGRAWAL, K. and SUNDARESAN, S., (2013), "Filtered two-fluid models of fluidized gas-particle flows: New constitutive relations", *AIChE J.*, **59** (9), 3265-3275.
- OZEL, A., FEDE, P. and SIMONIN, O., (2013), "Development of filtered Euler-Euler two-phase model for circulating fluidised bed: High resolution simulation, formulation and a priori analyses", *Int. J. Multiphase Flow*, **55** (0), 43-63.
- SARKAR, A., MILIOLI, F. E., OZARKAR, S., LI, T., SUN, X. and SUNDARESAN, S., (2016), "Filtered sub-grid constitutive models for fluidized gas-particle flows constructed from 3-D simulations", *Chem. Eng. Sci.*, **152**, 443-456.
- SCHNEIDERBAUER, S., (2016), "Cluster induced turbulence (CIT) - A spatially averaged two-fluid model (SA-TFM) for dense gas-solid flows", *24th ERCOFTAC ADA Pilot Center Meeting*.
- SCHNEIDERBAUER, S. and PIRKER, S., (2014), "Filtered and heterogeneity-based subgrid modifications for gas-solid

drag and solid stresses in bubbling fluidized beds", *AIChE J.*,  
**60** (3), 839-854.

# BIOMECHANICS





## A COMPUTATIONAL FRAMEWORK INVOLVING CFD AND DATA MINING TOOLS FOR ANALYZING DISEASE IN CAROTID ARTERY BIFURCATION

Mandar TABIB<sup>1\*</sup>, Adil RASHEED<sup>1†</sup>, Eivind FONN<sup>1‡</sup>

<sup>1</sup>SINTEF Digital, Trondheim, NORWAY

\* E-mail: mandar.tabib@sintef.no

† E-mail: adil.rasheed@sintef.no

‡ E-mail: eivind.fonn@sintef.no

### ABSTRACT

Cardiovascular diseases, like Carotid Artery Disease and Coronary Artery Disease (CAD) are associated with the narrowing of artery due to build-up of fatty substances and cholesterol deposits (called plaque). Carotid Artery Disease increases the chances of brain stroke. Hence, the main objective of this work is to apply computational tools to help differentiate between the healthy and unhealthy artery (with 25% stenosis) using a combination of Computational Fluid Dynamics (CFD) and data mining tools. In this work, first, the CFD has been qualitatively shown to provide similar results as the experimental Phase-Contrast Magnetic Resonance Imaging (PCMRI) technique. The CFD simulation shows that wall shear stress is an ideal parameter to identify the location of plaque formation and the existence of plaque conditions in the body (due to overall higher spatially averaged wall shear stress in the clogged case at all times in the cycle). Then data mining tools like Fast Fourier Transform (FFT) and Proper Orthogonal Decomposition (POD) have been used to unearth a pattern that can be useful for diagnosis. FFT shows that the flow constriction induced by plaque leads to lesser variation in magnitudes of energy of dominant frequencies at different locations like, wake region, mid-Internal Carotid Artery (mid-ICA) and mid-Common Carotid Artery (mid-CCA) regions, while for cleaner artery, there is more variation in the magnitude of energy of these dominant frequencies when measured at wake, mid ICA and mid CCA region. POD helps by confirming the location of regions with high energy in decomposed velocity modes for both the cases. More studies are required to develop a data mining based modern 21st century cardio-vascular patient care.

**Keywords:** Carotid Artery Bifurcation, CFD, Cardiovascular, data mining.

### NOMENCLATURE

#### Greek Symbols

$\rho$  Mass density, [ $kg/m^3$ ]  
 $\phi$  Orthogonal modes, []  
 $\lambda$  Eigen values, []

#### Latin Symbols

$a$  POD Coefficients, [].  
 $p$  Pressure, [ $Pa$ ].  
 $\mathbf{u}$  Velocity, [ $m/s$ ].  
 $\mathbf{A}$  Eigen vectors, [ $m/s$ ].

#### Sub/superscripts

$i$  Index  $i$ .

$j$  Index  $j$ .

### INTRODUCTION AND OBJECTIVE

Cardiovascular diseases, like Carotid Artery Disease and Coronary Artery Disease (CAD), both have some similarities. The similarities in disease progression pertains to the narrowing or hardening of the artery due to build-up of fatty substances and cholesterol deposits (called plaque). Carotid Artery Disease refers to this disease in the artery located in the neck region, and it increases the chances of ischemic strokes and transient ischemic attacks (brain stroke for example). For treatment of such diseases, an in-vivo assessment of physiologic hemodynamics can prove to be beneficial as it might help in understanding the physics behind the development of the vascular diseases. Such investigations may play an important role in designing novel and efficient treatment plans, like Magnetic Drug Targeting (MDT), wherein the magnetized drug particles are added to the blood in the artery and they are made to concentrate around the diseased region by applying a magnetic field at that location. This minimizes the side effects in the rest of the body. However, for such drug delivery methods, it is necessary to accurately determine the flow profiles in the Carotid Artery and to understand the progression of disease. Current methods of evaluating progression of vascular diseases (stenosis, atherosclerosis and aneurysms) involve: a) Experimental techniques (like Phase-Contrast Magnetic Resonance Imaging (PCMRI) (Barker *et al.*, 2010; Markl *et al.*, 2003; Cebal *et al.*, 2009), doppler ultrasound (US), etc) that provide information on the temporal evolution of the velocity profiles, and b) Computational Fluid Dynamic (CFD) techniques (Cebal *et al.*, 2009; Rispoli *et al.*, 2012) where patient-specific angiogram acquired by either Magnetic Resonance Angiography (MRA), or Computed Tomography Angiography (CTA) or 3D Rotational Angiography (3DRA) provide required geometry and flow or pressure waveforms obtained from phase-contrast MRI (PCMRI) as boundary conditions to numerically solve blood flow motion equations in the region of interest and predict hemodynamic parameters over the whole 3D computational domain. Both CFD and experimental techniques have proven to be immensely useful despite the known limitations with both of them (like in experimental techniques, there is low spatial and temporal resolution of PCMRI which limits detection of high velocity gra-

dients, secondary flows and complex flows in recirculation zones, while in CFD - there is the issue of realistic velocity profiles and rigid wall boundary). This success, despite the limitations, can be further enhanced by introducing the ability to unearth more information (and patterns) in order to enable diagnosis from the CFD and experimental dataset. This can be done through application of data mining tools. Researchers involved in evidence-based cardiological practice have suggested that data mining can be the 21st century approach towards patient care (Hu *et al.*, 2009). Data mining (DM) techniques can make cumbersome CFD / Experimental analyses more productive for future everyday clinical practice. Hence, this work focusses on developing a computational framework involving a combination of CFD and data mining techniques like Proper Orthogonal Decomposition (POD) and Fast Fourier Transform (FFT) with the aim of making data mining the workhorse in carotid artery examination and stenosis classification. POD has been widely used to extract dominant modes and structures from massive dynamic computational data to improve the understanding and discovery of the phenomena. The objective of the current work is then to:

### Objectives

Develop and demonstrate a computational framework involving CFD and data mining tools (involving feature extraction through POD and FFT) for efficient diagnosis of carotid artery disease progression.

### APPROACH AND METHODS

The approach involves investigating two cases: one with carotid artery bifurcation for a healthy person and another for a patient with about 25 % stenosis (meaning that about 25% of the area has been blocked by the plaque formation). First, results from simulations are validated using existing experimental PCMRI data for a similar geometry for a healthy person. In the following step deviations in the flow patterns and wall shear stress for healthy and patient case is demonstrated. Then, the simulated result data is subjected to FFT and POD analysis to obtain more information, and extract the differences. The next section describes the numerical methods (CFD and POD) that are used in the analysis.

### CFD

A transient 3D Navier Stokes equation have been solved to simulate the laminar flow in the artery. The model computes the flow fields (velocity, pressure). The Navier–Stokes equations are represented by the mass continuity equation (equation 1) and the momentum transport equation (Equation 2).

$$\nabla \cdot (\rho \mathbf{u}) = 0 \quad (1)$$

$$\frac{D\mathbf{u}}{Dt} = -\nabla \left( \frac{p}{\rho} \right) + \frac{1}{\rho} \nabla \cdot \mathbf{R} \quad (2)$$

where, where  $\rho$  is the density,  $u$  refers to flow velocity, operator  $\frac{D}{Dt}$  refers to total derivative,  $\nabla$  refers to gradient-vector operator,  $\nabla \cdot$  refers to a partial derivative operator that computes dot product,  $p$  is pressure,  $t$  is time.  $\mathbf{R}$  is referred to stresses arising due to viscosity. Components of  $\mathbf{R}$  can be computed as  $R_{ij} = \nu \left( \frac{\partial u_i}{\partial x_j} + \frac{\partial u_j}{\partial x_i} \right) - \frac{2}{3} k \delta_{ij}$ , where subscripts  $i$ ,  $j$  refers to components of vector,  $k$  is turbulent kinetic energy and  $\nu$  is molecular diffusivity.

### Proper Orthogonal Decomposition (POD)

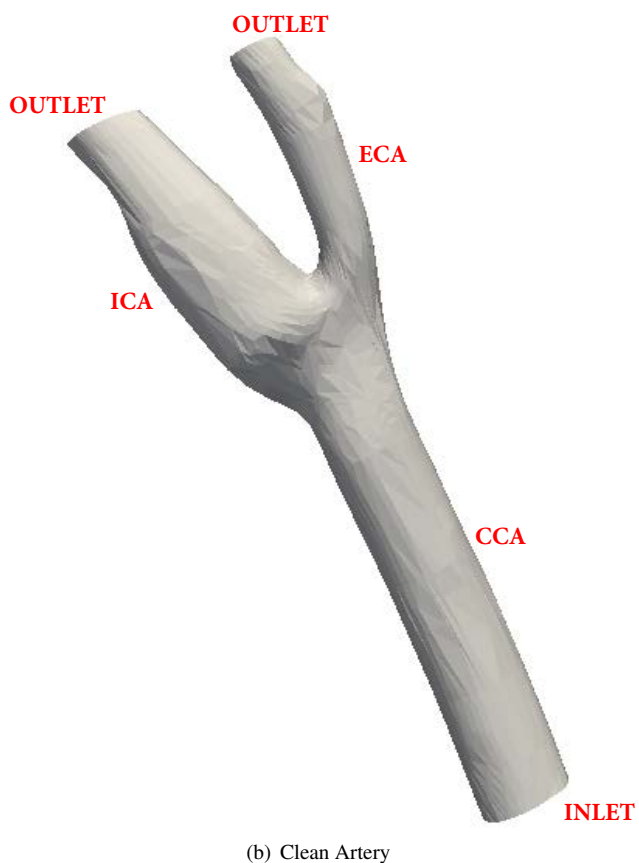
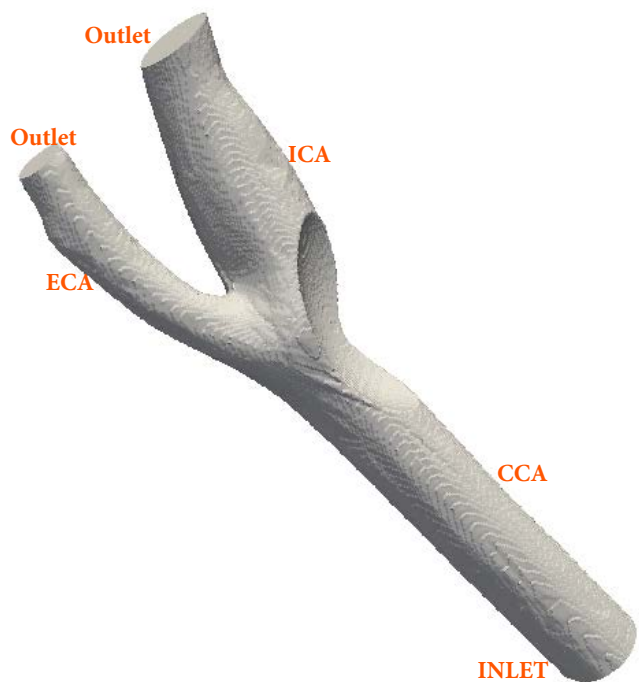
For the computation of the POD modes two dimensional snapshots of any variable (velocity components here) is required. The  $N$  snapshots are represented by  $\mathbf{U} = [\mathbf{u}^1, \mathbf{u}^2 \dots \mathbf{u}^N]$  which is used to compute the covariance matrix given by  $\mathbf{C} = \mathbf{U}^T \mathbf{U}$ . After this an eigenvalue problem  $\mathbf{C} \mathbf{A}^i = \lambda_i \mathbf{A}^i$  is solved to obtain the eigenvalues  $\lambda^i$  and eigen vectors  $\mathbf{A}^i$  which are sorted in a decreasing order as  $\lambda_1 > \lambda_2 > \dots > \lambda_N$ . POD modes are then computed as

$$\phi^i = \frac{\sum_{n=1}^N A_n^i \mathbf{u}^n}{\left\| \sum_{n=1}^N A_n^i \mathbf{u}^n \right\|}, i = 1, \dots, N \quad (3)$$

With POD modes arranged as  $\Psi = [\phi^1 \phi^2 \dots \phi^N]$ . POD coefficients  $a_i$  can be found from the snapshot  $n$  as  $\mathbf{a}^n = \Psi^T \mathbf{u}^n$ . From this a snapshot can be reconstructed as  $\mathbf{u}^n = \Psi \mathbf{a}^n$ . Relative energy given by any  $i^{th}$  mode is given by  $\lambda_i / \sum_{j=1}^N \lambda_j$

### MODEL DESCRIPTION

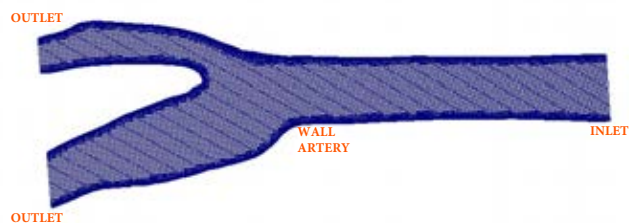
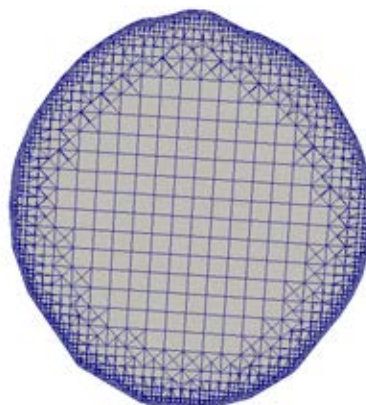
Figure 1 shows the geometry of the clean healthy artery and an unhealthy clogged artery. In both the cases, the structure involves the main artery (CCA) which bifurcates into the Internal Carotid Artery (ICA) and the External Carotid Artery (ECA). In case of clogged artery, 25% of the flow area in Carotid sinus region has been blocked by plaque deposits. Figure 2 shows the hexahedral mesh that is used to spatially discretize the geometry and the boundary conditions are also labeled. The mesh size is about 3 million element mesh. The mesh resolution is such that across the inlet diameter there are 20 mesh points, resulting in a grid size of  $2.5 \times 10^{-4} m$  with the grid becoming much finer near the artery surface (about  $3 \times 10^{-5} m$ ) to capture the high velocity gradients here. The inlet profile used for the study is shown in Figure 3. This inlet velocity profile is based on a heart rate of 72 beats per minute (resulting in 0.8 s time period for one cycle or one beat) which involves the diastolic period for first 0.36 s of cycle (where sinusoidal pulsatile inflow varies with 1.25 Hz frequency ( $f$ )) and a systolic period for rest of cycle where inlet velocity is held constant at 0.15 m/s. As a result of this, the normal Peak systolic Velocity (PSV) in the CCA reaches about 0.8 m/s, however in general, the PSV is patient or person specific and depends upon cardiac output or stroke volume, heart rate, systolic blood pressure, and age. The PSV in the normal CCA ranges from 0.70 to 1 m/s while the diastolic velocity is around 0.1-0.2 m/s. Thus, the current inlet profile used is justifiable. The equation used for inlet profile is as proposed by Sinnott (Sinnott *et al.*, 2006). The simulations have been conducted over a time period of 12 cycles and the averaging of results has been done over last 2 cycles. An adaptive time-step has been used to maintain a courant number of 1 for accurate and stable simulation, as a result the simulation time step varied between  $2.5 \times 10^{-5} s$  to  $1 \times 10^{-4} s$  during the course of simulation. The CFD takes about 1.5 hrs of computational time to simulate one cardiac cycle (time period of one cardiac cycle is 0.8 s) on 8 processors run (with each processor having 1.2GHz CPU speed). For 12 cardiac cycles, about 18 hrs of computational time is required. In the model (Figure 2), the blood flows through the bifurcating artery from the inlet and exits from the two outlets. The density of blood is  $1060 \text{ kg/m}^3$ . The diameter of the artery at the inlet is around 6 mm. The diameter of ICA outlet is around 4.5mm and the diameter of ECA outlet is around 3.0mm. The Reynolds number based on input diameter varies from around 50 to 300 during the cycle and the flow is considered laminar. The systolic pressure of a healthy



(b) Clean Artery



(a) Clogged Artery



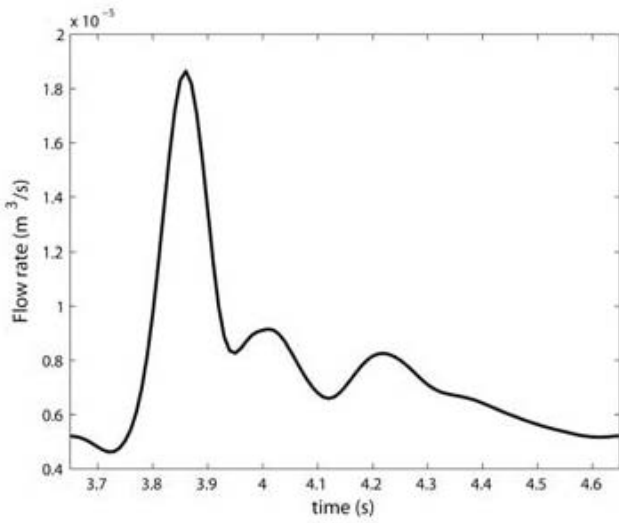
(c) Clean Artery

Figure 2: Mesh and boundary details for clogged and clean case.

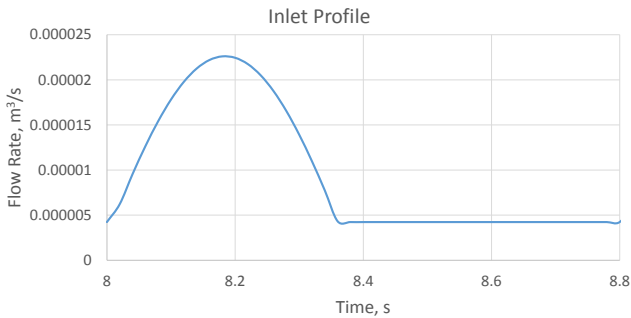
Figure 1: 3D Geometry of Carotid Artery for clogged and clean case.



human is around 120 mmHg and the diastolic pressure of a healthy human is around 80 mmHg. Thus taking the average pressure of the two phases, we use 100 mmHg (around 13332 Pascal) as the static gauge pressure at the outlets. In the next section, the results obtained from the CFD and data mining tools are discussed.



(a) Experimental Inlet Profile is taken from (Gharahi *et al.*, 2016)



(b) Idealized CFD Inlet

**Figure 3:** Inlet profiles of experimental and CFD study used in validation.

## RESULTS

### Validation

Figure 4 involves a quantitative and qualitative comparison study with experimental data obtained from (Gharahi *et al.*, 2016). An attempt is made to check whether CFD is able to predict similar flow patterns in the post bifurcation regions: Internal Carotid Artery (ICA) and External Carotid Artery (ECA) as the experimental data if they begin with similar velocity magnitude in the main artery region. The maximum value of velocity in the contour plot in Figure 4 measured by PCMRI for CCA section is 0.7 m/s, and for the ECA/ICA section is 0.5 m/s. The comparison is done at a time instant corresponding to peak systolic inlet velocity. The velocity from CFD simulations is normalized to match those of the inlet conditions of the experimental data, though some variations in the inflow profile exist as inflow profile in the CFD simulation is an idealized form of the experimental conditions (see figure 3). Qualitatively, CFD is able to predict similar flow patterns as captured by MRI, but quantitatively CFD is over-predicting the magnitude. The deviation ( $U_{experimental}$

$- U_{simulation})/U_{experimental}$  in predicting the maximum velocity is around 15%. The difference can be attributed to either low resolution of the MRI data (as seen in figure 4) or variations in the inflow conditions at CCA (again see figure 3). The inflow conditions are shown over one cardiac cycle and it is periodic over this time period. However, the qualitative similarities between the experimental and CFD approach establishes credibility of the CFD study to a certain degree. The major drawback of experimental technique like PCMRI is that owing to its low resolution, it is difficult to compute the wall shear stress, which is known to play a big role in facilitating plaque deposition. Hence, CFD is used to compare the flow field and wall shear stress profiles.

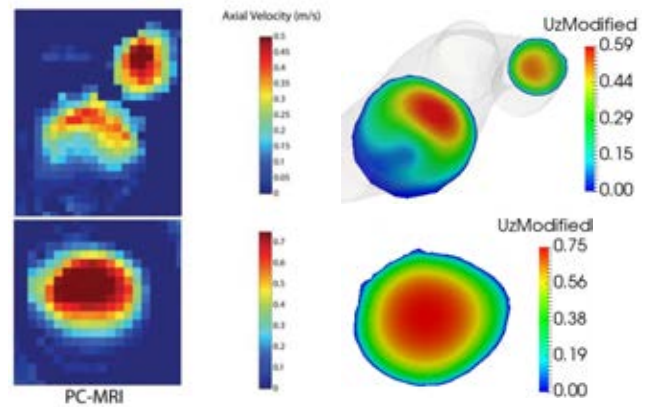


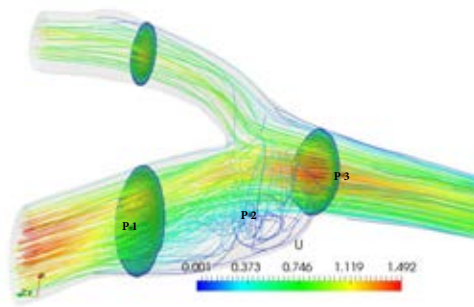
**Figure 4:** Comparison CFD with PC-MRI Flow pattern. Experimental results in figure on left from (Gharahi *et al.*, 2016)

### Comparison of flow patterns

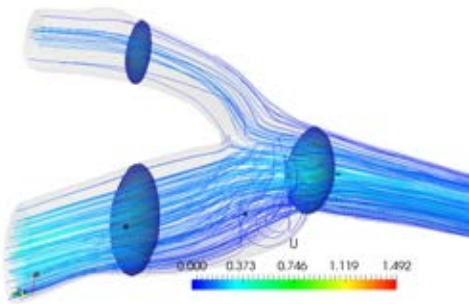
Figure 5 compares the flow patterns for a healthy clean artery and an unhealthy clogged artery for similar inflow conditions. The flow patterns are compared at two instances in each case: at the maximum inlet velocity condition (Figure 5(a) and 5(c)) and at the minimum inlet velocity condition (figure 5(b) and 5(d)). In the clogged case (figure 5(c)-5(d)), the streamlines show higher flow separations and flow recirculations than the clear artery case (figure 5(a)-5(b)) near the carotid bulb both at the minimum velocity and maximum velocity inlet conditions. The resulting helical and secondary flows (due to flow separations around complex artery geometry) are higher at maximum inlet velocity conditions than the minimum velocity conditions. The impact of these flow patterns is felt on the wall shear stress as well as the associated frequencies (the FFT's are conducted at the probe locations denoted by black dots between the text P1, P2 and P3 in figure 5 and discussed in the section on FFT comparison).

### Comparison of wall shear stress

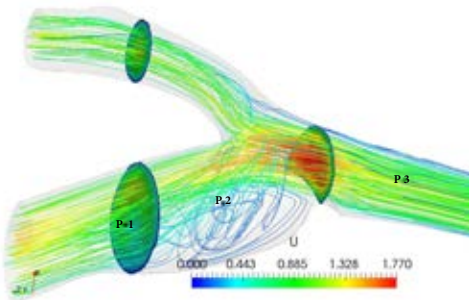
Figure 6 and 7 compare the wall shear stresses for the two conditions. Figure 6 presents the wall stress at two instances for both healthy and unhealthy case one at the maximum inlet velocity condition and another at the minimum inlet velocity condition. In the clogged case (Figure 7(c)-7(d)), a higher wall shear stress compared to the clear artery case (figure 7(a)-7(b)) is seen. This can be attributed to the higher velocity gradients owing to the blockage of the flow area and higher flow recirculations behind the plaque deposits. The location of the plaque is at the ICA region, where sudden divergence cause recirculation with low velocity gradient region causing regions of lower shear stress. In both the cases,



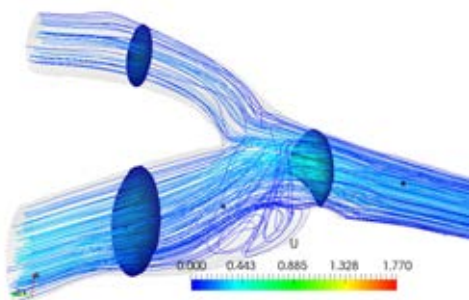
(a) Clean Artery at Max  $U_{inlet}$



(b) Clean Artery at Minimum  $U_{inlet}$



(c) Blocked Artery at Max  $U_{inlet}$

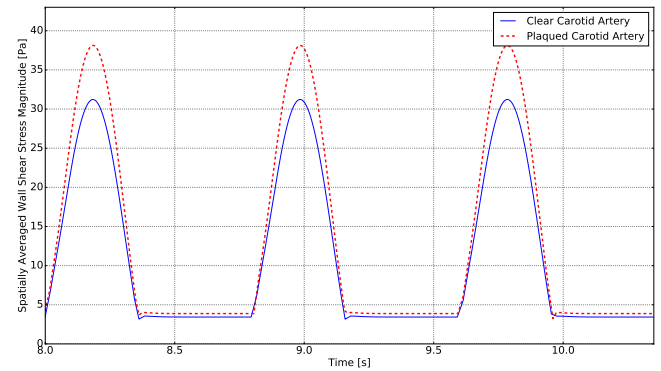


(d) Blocked Artery at Minimum  $U_{inlet}$

**Figure 5:** Flow pattern and streamlines comparison for clogged and clean artery.

the wall shear stress has the highest magnitude near the inner wall of the carotid bifurcation and conversely, the ICA displays lower wall shear stress.

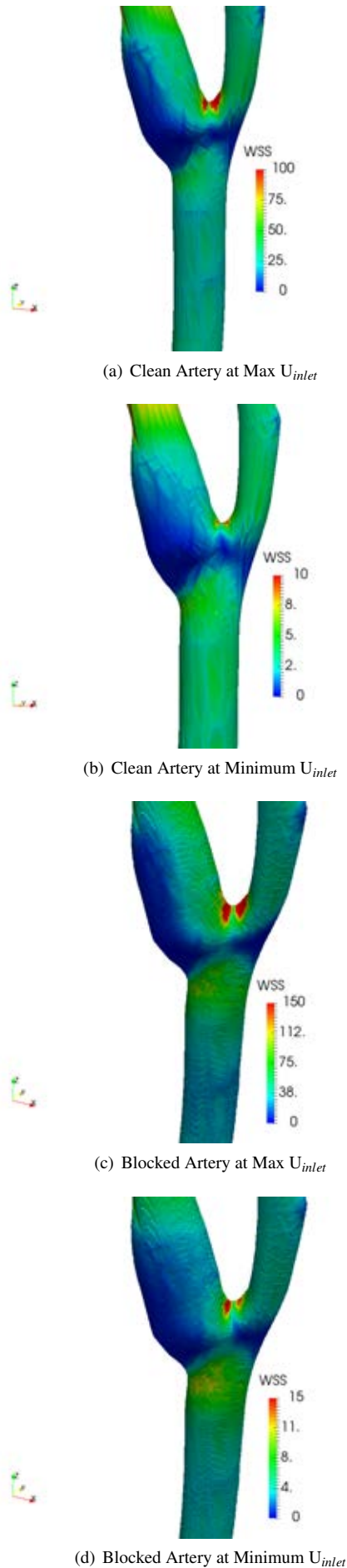
Figure 7 compares the spatially averaged wall shear stress over the whole artery over two period of cycles. Here too, it can be seen that wall shear stress values are consistently higher for the clogged case over the whole cycle. Thus, the simulation shows that wall shear stress is an ideal parameter to confirm both the location of plaque formation (low wall shear stress region) and the existence of plaque conditions in the body (overall higher spatially averaged wall shear stress in clogged case at all times in the cycle). Next we look at feature extraction from the accumulated dataset to help in the diagnosis of Carotid Artery Disease. FFT and POD have been used in this work.



**Figure 6:** Comparison of wall shear stress at different times in a cycle for clogged and clean artery case.

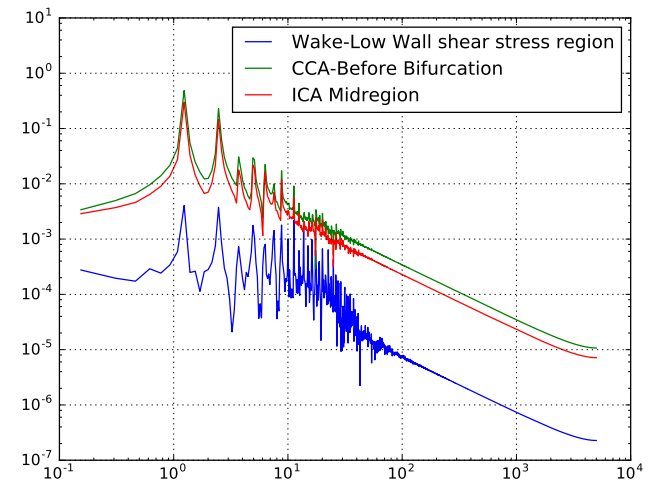
### FFT Comparison

Figure compares the energy spectrum obtained from the application of FFT on the velocity signal at the probe locations for both the clean and clogged artery cases. FFT provides the energies associated with various frequencies and helps to identify the dominant frequencies. The location of probes is shown as black dot in Figure 5. FFT is compared at probes located in the CCA, ECA and wake regions. The data is sampled at a frequency of 10000 Hz over a period of 2 cycles. All the probe locations in both the cases are able to detect the dominant frequency of 1.25 Hz present in the inlet pulsatile flow at varying magnitudes. The bifurcation region which creates a diverging section at the ICA leads to the presence of eddies in flow separation, with these eddy having its own length and time-scale. For the clean artery case, figure 8(a) shows that the energy of dominant frequency (1.25 Hz) in the wake region is less than that at the CCA and ICA case but a high amount of fluctuations in frequency range 10-20 Hz range is seen. These fluctuations could be representative of eddies arising out of flow separation and some of them possess similar energy content as the dominant frequency in the wake region (energy range above  $1 \times 10^{-3} m^2/s^2$ ). While in the wake region of clogged artery case, figure 8(b) shows the energy in dominant frequency (1.25Hz) and energy in fluctuations in 10-20 Hz in to be more nearer to the energy in corresponding frequencies in the ICA and CCA region (as compared to the clean artery case). The blockage induced by plaque leads to higher velocity magnitudes and higher flow recirculation leading to higher energy frequencies (at both 1.25Hz and 10-20 Hz range) and leading them to be closer to energies associated with these frequencies in ICA and CCA

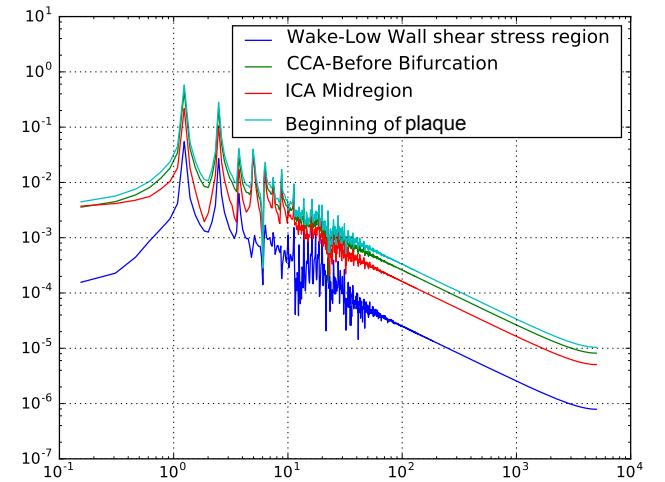


**Figure 7:** Wall Shear Stress contour comparison for clogged and clean artery case.

(as compared to clear artery case). Such patterns as this, which has been identified by FFT can be an useful detection and diagnosis tool. Though more studies are required to ascertain presence of such patterns. The location of regions of higher energies can be obtained from the POD analysis as shown below.



(a) Clean Artery, X axis is Frequency in Hz, and Y axis is Energy in  $m^2/s^2$



(b) Clogged Artery, X axis Frequency in Hz, and Y axis is Energy in  $m^2/s^2$

**Figure 8:** FFT results for clogged and clean artery case.

### POD comparison

For Artery, the 2D planar data for each simulation is sampled at 5 Hz and then interpolated on a uniform rectilinear grid measuring  $510 \times 159$  elements (corresponding to a grid-size of  $0.0509mm \times 0.0158mm$ ). The original snapshots (defined on the original mesh) have been interpolated on a uniform mesh (defined on a rectangle), so the modes are also defined on the whole rectangle, even though they are zero outside of the artery region. The results regarding the energy spectra can be observed in Figure 9, which reveals that there is not much difference in energy captured by different modes. In both the cases, almost more than 99% of energy is captured within the first two modes itself, the first mode being the large scale flow and second mode being mostly the separated flow in the wake region (as seen in figure 10- 11 which shows the decomposed velocity modes for the two cases). Despite similar energy content of the modes in the two cases, the location of concentration of energy is different. Figures (10-

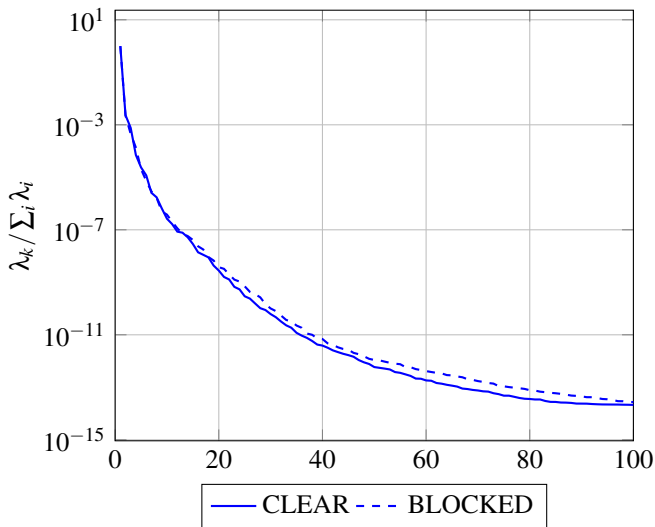


**Figure 9:** ENERGY SPECTRA OF CLEAR AND BLOCKED ARTERY.

11) show the decomposed velocity modes, where the Red color regions represent regions with highest decomposed velocity values and blue color regions represents regions with lowest decomposed velocity values. The values of these decomposed modes are not relevant. These figures (figure 10-11) reveal that mode 1 has similar energy of around 99.7% for both case, but in case of clogged artery, most of this energy is concentrated in the region above the plaque where the flow constriction leads to higher by the plaque. Similarly, de-

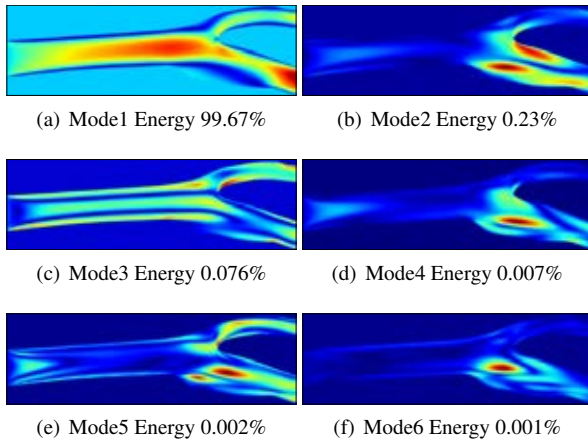


**Figure 10:** First six modes of a healthy artery showing decomposed velocity. Red color regions represent regions with highest decomposed velocity values and blue color regions represents regions with lowest decomposed velocity values.

spite mode 2 capturing the energy content of around 0.22%, the clogged one has energy concentrated around wake region while the clean artery case has this energy distributed in both wake at outer wall of ICA and energy at the inner wall of the ICA. This energy distribution also shows the reasoning behind the pattern observed through FFT analysis. Thus, the POD and FFT together as data mining tools helped to unearth the differences between healthy and unhealthy patients artery. These tools can be applied on experimental dataset as well if there is a possibility to obtain suitable vari-

able dataset at the required locations at high sampling rate. CFD provides a cost effective way of obtaining data at high sampling rates and at all locations in the geometry (which is sometimes difficult to do using experiments).

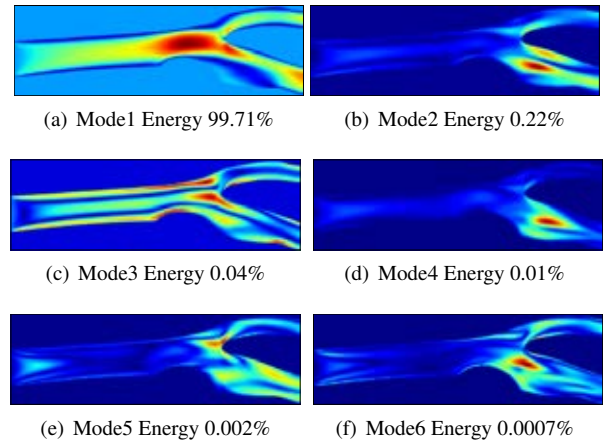


**Figure 11:** First six modes of an unhealthy clogged artery showing decomposed velocity. Red color regions represent regions with highest decomposed velocity values and blue color regions represents regions with lowest decomposed velocity values.

## CONCLUSION

The work demonstrates an application of combination of CFD along with data mining techniques in unearthing differences between a healthy and an unhealthy patient with carotid artery disease. The conclusions are enumerated below :

1. First, the CFD has been qualitatively shown to provide similar results as the experimental PCMRI technique. Owing to lower resolution of the experimental technique, CFD has been used to analyze further differences in the flow pattern.
2. CFD simulation shows that wall shear stress is an ideal parameter to show existence of plaque conditions in case of unhealthy artery (overall higher spatially averaged wall shear stress in clogged case at all times in the cycle). Further CFD shows the observation of lower wall shear stress in regions of carotid sinus where build up of plaque occurs.
3. Use of data mining tools (FFT and POD) along with CFD has helped to unearth patterns to distinguish between healthy and unhealthy case. FFT shows that the flow constriction induced by plaque leads to lesser variation in magnitudes of energy of dominant frequencies at different locations (like, wake region, mid-ICA and mid-CCA region), while for cleaner artery, there is more variation in magnitude of energy of these dominant frequencies when measured at wake, mid ICA and mid CCA region. POD helps by confirming the location of regions with high energy in decomposed velocity modes for both cases. Such patterns as this, which has been identified by FFT can be an useful detection and diagnosis tool.

This work is one of the steps towards using data mining for modern 21st century cardiovascular patient care. Future

work involves using this methodology for more studies involving different patients and healthy persons to confirm the observed patterns and develop a diagnosis toolkit.

## REFERENCES

- BARKER, A., BOCK, J., LORENZ, R. and MARKL, M. (2010). "4d flow mr imaging". *Am J Neuroradiol.*, **18**, 46.
- CEBRAL, J., PUTMAN, M., ALLEY, M., HOPE, T., BAMMER, R. and CALAMANTE, F. (2009). "Hemodynamics in normal cerebral arteries: Qualitative comparison of 4d phase-contrast magnetic resonance and image-based computational fluid dynamics." *J Eng Math.*, **64**, 367.
- GHARAH, H., ZAMBRANO, B., ZHU, D., DEMARCO, J. and BAEK, S. (2016). "Computational fluid dynamic simulation of human carotid artery bifurcation based on anatomy and volumetric blood flow rate measured with magnetic resonance imaging". *Int J Adv Eng Sci Appl Math.*, **8**, 40.
- HU, D., NGUYEN, T., KIM, M., KWAN, T. and SAITO, S. (2009). "Evidence-based cardiology practice: A 21st century approach". *PMPH*, **1**, ISBN: 978-1-60795-095-0.
- MARKL, M., CHAN, F., ALLEY, M., WEDDING, K., DRANEY, M. and ELKINS, C. (2003). "Time-resolved three-dimensional phase-contrast mri". *J Magn Reson Imaging*, **17**, 499.
- RISPOLI, V., CARVALHO, L., NIELSEN, J. and NAYAK, K. (2012). "Assessment of carotid flow using magnetic resonance imaging and computational fluid dynamics". *Fluid dynamics, computational modeling and applications*. Editor Juarez LH. *InTech*, **64**, 513.
- SINNOTT, M., CLEARY, P. and PRAKASH, M. (2006). "An investigation of pulsatile blood flow in a bifurcating artery using a grid-free method". *Fifth International Conference on CFD in the Process Industries CSIRO, Melbourne, Australia*.

## INVESTIGATING THE NUMERICAL PARAMETER SPACE FOR A STENOSED PATIENT-SPECIFIC INTERNAL CAROTID ARTERY MODEL

Viviana MANCINI<sup>1</sup> & Aslak BERGERSEN<sup>2</sup>, Patrick SEGERS<sup>1</sup>, Kristian VALEN-SENDSTAD<sup>2\*</sup>

<sup>1</sup> Ghent University, IBItech-bioMMeda, 9000 Ghent, BELGIUM

<sup>2</sup> Simula Research Laboratory, Computational Cardiac Modelling, 1325 Lysaker, NORWAY

\* E-mail: kvs@simula.com

### ABSTRACT

Systemic risk factors are known to correlate with cardiovascular diseases, but e.g., atherosclerotic plaques are focally distributed and highlight the role of hemodynamically induced forces on vascular remodeling. Computational fluid dynamics (CFD) shows great promise for revealing mechanisms of atherosclerotic plaque progression, but the utility of CFD depends on the robustness of the numerical methods. The aim of the study was to investigate the parameter space of the numerical solutions to understand the resulting flow effects in a stenosed patient-specific internal carotid artery model. Simulations were performed on meshes consisting of 2 to 50M-elements meshes with a kinetic energy-preserving and minimally-dissipative solver, and time step size ranging from  $1 \cdot 10^{-4}$  to  $5 \cdot 10^{-6}$  seconds. The spatial refinement study revealed large differences in the instantaneous velocity fields, and the coarsest simulation did not provide any meaningful insight into the flow. That being said, the time-averaged results were in acceptable agreement for all spatial and temporal refinement levels. The variations in temporal resolution had minor effects, and the coarsest resolution was found to suffice. In conclusion, even for a highly accurate solver, a relatively high spatial resolution was needed to sufficiently resolve the flow, and we found the 22M-element mesh to offer an optimal balance between computational cost and time-averaged quantities.

**Keywords:** Stenosis, Computational Fluid Dynamics, Turbulence, Atherosclerotic plaque, Direct Numerical Simulation.

### NOMENCLATURE

#### Latin Symbols

M Million, [-]  
 PSD Power spectral density, [ $\text{m}^2/\text{s}$ ].

TKE Turbulent kinetic energy, [ $\text{m}^2/\text{s}^2$ ]  
 $\mathbf{u}(\mathbf{x}, t)$  Instantaneous velocity, [ $\text{m}/\text{s}$ ].

#### Greek Symbols

$\nu$  Kinematic viscosity, [ $\text{m}^2/\text{s}$ ].  
 $\Delta t$  Time steps size, [s].  
 $\tau$  Kolmogorov time scale, [s].  
 $\Delta x$  Mesh node spacing, [m].  
 $\eta$  Kolmogorov length scale, [m].  
 $\varepsilon$  Dissipation rate of TKE, [ $\text{m}^2/\text{s}^3$ ].

#### Sub/superscripts

$\bar{\mathbf{u}}$  Mean velocity component, [ $\text{m}/\text{s}$ ].  
 $\mathbf{u}'$  Fluctuating velocity component, [ $\text{m}/\text{s}$ ].  
 $|\mathbf{u}'|$  Magnitude of  $\mathbf{u}'$ , [ $\text{m}/\text{s}$ ].

### INTRODUCTION

Atherosclerotic plaque is a leading cause of death in the western world, and causes a local narrowing of the arterial lumen also known as stenosis. The stenosis severity may increase over time to the point where it completely obstructs the blood flow. It is also known that blood clots can form downstream of the stenoses or that unstable plaques can loosen; both of which can result in ischemic stroke or heart attacks.

Computational fluid dynamics (CFD) shows great potential for revealing mechanisms of atherosclerotic plaque progression, e.g., in the carotid bifurcation by modeling patient-specific local hemodynamic forces (Steinman, 2002). However, the efficacy of CFD depends on the robustness of the methods and ability of reproduce results. This has shown to be challenging, especially for transitional biomedical flows, as demonstrated by Steinmann *et al.* (2012) who reported a large variability of jet penetration and complexity of patient-specific internal carotid artery aneurysm. In particular, it is not uncommon in the biomechanics literature to see the use of first order accurate and stabilized numerical schemes, which are well known to

be far too dissipative (Roache *et al.*, 1986). Such schemes have been argued applicable because of the relatively low Reynolds numbers of cardiovascular flows (Stewart *et al.*, 2012), relative to the transition point for steady flow in an infinitely long pipe (Reynolds, 1883). However, we have previously argued that Reynolds experiments might not be the best point of reference and showed that the use of “black-box” CFD solvers using default settings may be misleading us about the nature of the flow in the cardiovascular system (Valen-Sendstad and Steinman, 2014).

The aim of the current study was to use a verified and validated solver for laminar, transitional, and turbulent flows to find an adequate (under-resolved) direct numerical simulation reference solution from a spatial and temporal refinement study, with respect to point of transition and resolution of the flow instabilities through rigorous analysis, but also to determine the required resolution from a pragmatic biomedical point of view.

## MODEL DESCRIPTION

Medical images of a common carotid bifurcation with severe stenosis (82% by area) located in the ICA of a 75 years old man were obtained from computed tomography angiography. The medical image was segmented using 3D Slicer (Iannaccone *et al.*, 2014), to obtain a plausible model of the vasculature. The Vascular Modelling Toolkit (Piccinelli *et al.*, 2009) was used to create meshes with a local refinement in the stenotic- and downstream region, but a constant global refinement between each mesh, resulting in four meshes with mean cell length ( $\Delta x$ ) of  $3.19 \cdot 10^{-4}$ ,  $2.14 \cdot 10^{-4}$ ,  $1.38 \cdot 10^{-4}$ , and  $1.05 \cdot 10^{-4}$  m. The meshes consists of 2, 6, 22, and 50 million (M) linear tetrahedral cells, and is referred to as the 2, 6, 22, and 50M-element mesh, respectively.

Simulations were performed using the open-source finite element CFD solver *Oasis* (Mortensen and Valen-Sendstad, 2015), where special care was taken to ensure a kinetic energy-preserving and minimally-dissipative numerical solution. We used continuous Lagrange elements with polynomial degree one for both the velocity, and pressure. The fluid properties were set to mimic water, with kinematic viscosity of  $\nu = 1 \cdot 10^{-6}$  m<sup>2</sup>/s to allow for direct comparison with *in-vitro* experiments. The inlet flow rate was set to be peak systolic, 585.52 ml/min, which corresponds to a Reynolds number of 1550 at the inlet. This deliberate choice was made to enable rigorous assessment of the temporal and spatial resolution with respect to the smallest scales present in the flow, however at the cost of a physiological artificial flow condition. A parabolic velocity profile was prescribed as inlet condition and no-slip condition was set along the walls. Figure 1 shows a curve fit based on work from Groen *et al.* (2010) that measured the flow split between the common and internal carotid artery as a function of degree of stenosis using MRI in 33 patients. The shape of the curve shows that most of the flow resistance occurs in the micro-vasculature for stenosis severity less than 65%, whereas the pressure drop across the stenosis dominates the resistance above this threshold. Using this

model, the flow split between the internal and external carotid artery was set as to 31.8% and 68.2%, respectively.

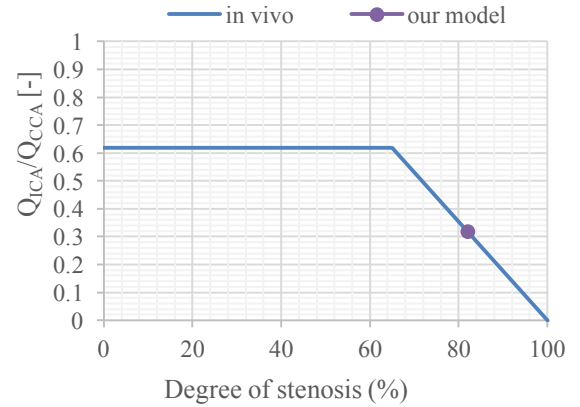


**Figure 1:** Outflow boundary conditions were set in order to match *in-vivo* values. The model is taken from the work of Groen *et al.* (2010) [10], who measured flow split as a function of degree of stenosis using MRI.

The flow was computed for 2 physical seconds on the coarsest mesh in order to cheaply washout initial transients associated with the artificial initial conditions. This simulation time was then the equivalent of 2 flow-throughs as the length of the model was 0.2 m, and the mean flow at the inlet was 0.1954 m/s. This flow field was then projected onto the 6, 22, and 50M-element meshes as initial conditions. To obtain a velocity field that was statistically converged, the mean velocities were based on simulations from 0.1 to 2.0 seconds. However, due to limitations on CPU hours, the 50M-element simulation was only simulated for 0.7 seconds, and the 22M-element simulation for 1.4 s.

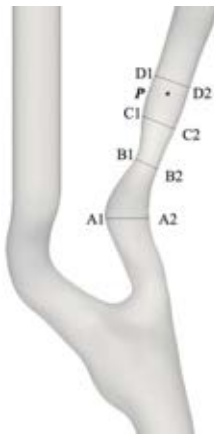
We first performed a spatial refinement study at a fixed time step ( $\Delta t$ ) of  $2 \cdot 10^{-5}$  seconds. Using the least computationally expensive mesh that gave adequate results, a temporal refinement study was performed, with  $\Delta t$  ranging from  $1 \cdot 10^{-4}$  to  $5 \cdot 10^{-6}$  seconds.

Figure 2 shows the region of interest with four lines (A to D) and a point  $P$ , located 1.7 cm (2.2 diameters) downstream of the center of the stenosis, where instantaneous velocity  $\mathbf{u}(\mathbf{x}, t)$ , was sampled. Reynolds decomposition was used to separate the instantaneous velocity from the time averaged,  $\bar{\mathbf{u}}(\mathbf{x})$ , and fluctuating,  $\mathbf{u}'(\mathbf{x}, t)$ , components, i.e.,  $\mathbf{u} = \bar{\mathbf{u}} + \mathbf{u}'$ . Taking the fluctuating velocity magnitude signal,  $|\mathbf{u}'|$ , as input we computed the power spectral density (PSD) using Welch’s method (Welch, 1967) with 32 segments, and a Hanning windowing function with 50 % overlap.

The coherent vortical structures were identified by the Q-criterion, which is a spatial region where the Euclidean norm of the vorticity tensor  $\vec{\omega}$  dominates the strain rate tensor  $\vec{S}$  (Equation 1) (Hunt *et al.*, 1988).

$$Q = \frac{1}{2} \left[ |\vec{\omega}|^2 - |\vec{S}|^2 \right] > 0$$

**Equation 1:** The comparison between the vorticity and strain rate tensors obtained through decomposition of the velocity gradient can be used as three-dimensional vortex identification criterion.



**Figure 2:** Region of interest of the model with lines A to D and point *P*. Flow is going from bottom and up, or alternatively, the common carotid artery is branching into the external carotid (left), and internal carotid artery (right), respectively. The center of stenosis is defined as the midpoint of line B, and is based on the minimum area.

## RESULTS

We first focus on basic flow features obtained on the 22M-element mesh shown in Figure 3, which depicts the volumetric velocity magnitude within the common carotid artery and ICA. The top of Figure 3 shows that the flow in the common artery is stable up until the carotid bifurcation, as the flow is uniform and there are no visible minor flow structures. At the bifurcation, the flow develops into a skewed profile towards the external wall of the ICA. Moreover, because of the pronounced curvature of the ICA the flow becomes unstable upstream of the stenosis, as observed in the left most bottom part of Figure 3. The stenosis causes the disturbed flow to accelerate into the stenosis, before the jet breaks down into an unstable flow downstream of the stenosis. However, the flow instabilities quickly dissipate further downstream, and the flow relaminarizes.

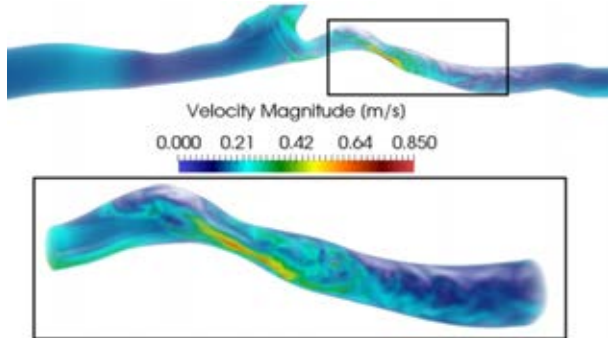


**Figure 3:** The top shows the volumetric rendering of the instantaneous velocity magnitude in the common and internal carotid arteries, and the bottom part is an enlargement of the box in the top part, showing the stenosis and downstream region.

Firstly, the Q-criterion was used to perform a quantitative comparison of the instantaneous velocity fields as shown in Figure 4. Moving from 2M through 50M there was a consistent increase in the number of vortices. In particular, upstream of the stenosis, the 22 and 50M-element simulations were phenotypically different from the 2 and 6M-element simulations, as there were smaller and more complex structures. In the

downstream region in the 50M-element simulation the vortices were visually easier to see than in the 22M, however we can observe the same type and number of vortices. Visually there are large differences between mesh resolutions based on instantaneous flow fields. Moreover, the 2 and 6M-element simulations does not provide any physical insight into the flow.

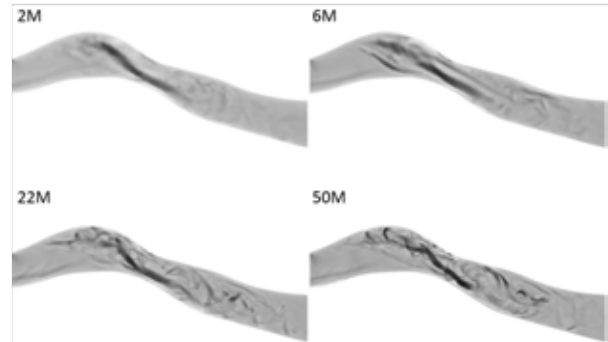


**Figure 4:** Volumetric rendering of coherent vortical structures at identical times within ICA identified by the Q-criterion.

To further assess the results from the spatial refinement study, we first consider the time-averaged velocities across the lines A to D, shown in Figure 5. In line A, upstream of the stenosis, we observe that the 2 and 6M-element simulations were similar, however relatively different from the 20 and 50M-element simulations which were phenotypically similar.

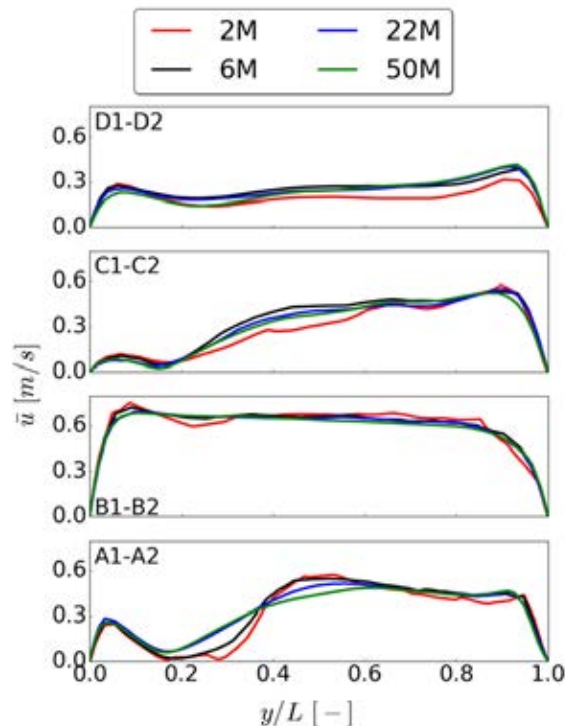


**Figure 5:** Time-averaged velocity along the four lines of interest for the spatial refinement study.

The time-averaged results were for all practical purposes equal at the stenosis (line B). In line C, when the jet from the stenosis breaks down the 22 and 50M-element simulations were similar, while the 2 and 6M-element simulations were under resolved, and under- and overestimated the centerline velocities, respectively. Finally, in line D at the end of the disturbed flow region, the 2M-element simulation under-estimates the time-



averaged velocity, while the other simulations were similar.

The PSD analysis of the fluctuating velocity signal at point *P* from Figure 2 is illustrated in Figure 6. The 2, 6, and 22M-element simulation seems to converge towards the 50M-element simulation. The 22 and 50M-element simulations were practically identical up until ~2000 Hz, however the spectra differs slightly at the higher frequencies. That being said, the analysis was admittedly based on different time-periods, and we would expect even better agreement if simulated for an equal period of time.

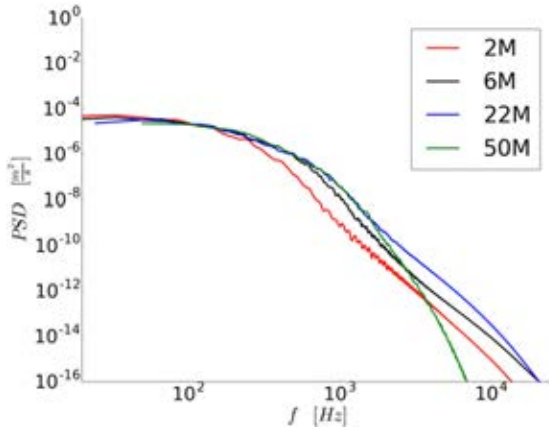


**Figure 6:** Power spectral density of the velocity field at point *P* from Figure 2, for the spatial refinement study.

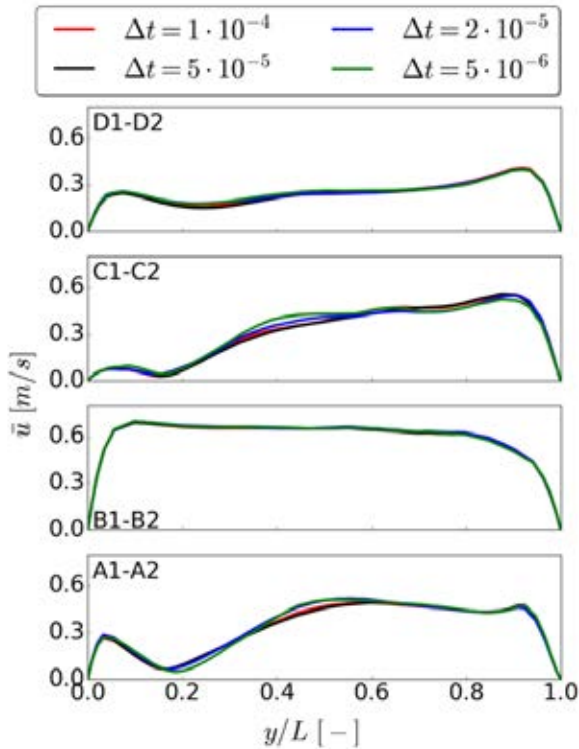


**Figure 7:** Time-averaged velocity along the four lines of interest for the spatial refinement study.

The temporal refinement study was evaluated similarly to the spatial refinement study. First, we considered the time-averaged velocity in the lines A to D, as shown in Figure 7. In all lines  $1 \cdot 10^{-4}$ ,  $5 \cdot 10^{-5}$ ,

and  $2 \cdot 10^{-5}$  were close to indistinguishable. In contrast, the  $5 \cdot 10^{-6}$  simulation differed both in line A and C.

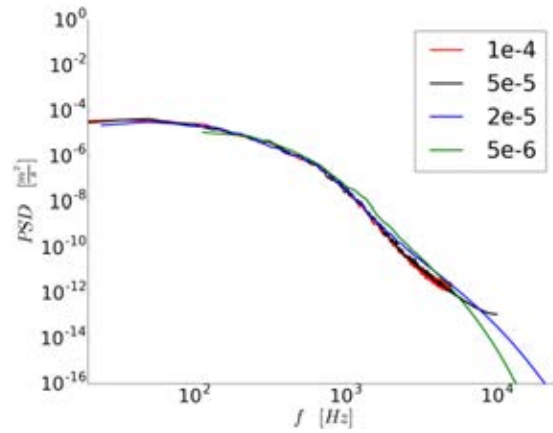


**Figure 8:** Power spectral density of the velocity field at point *P* from Figure 2, for the temporal refinement study.

The PSD analyses of the velocity traces recorded in point *P* are shown in Figure 8. We can observe that all of the different temporal simulations were from a pragmatic point of view equal. However, the temporally coarsest simulations naturally cannot capture the highest frequencies.

## DISCUSSION

The aim of this study was to find an adequate (under-) resolved solution relative to the reference solution. From the spatial and temporal refinement study performed, a 22M-element mesh with a time step of  $1 \cdot 10^{-4}$  seconds was found to be an optimal choice between computational cost and accuracy. This reference solution will be used in future studies on stenotic carotid bifurcations for comparison with turbulence modeling techniques. That being said, there is admittedly a minor difference between 22 and 50M-element meshes in Figure 5, in addition the simulations were not computed over the same number of physical seconds. To assess if the 50M-element simulation was close enough to a proper direct numerical simulation we compared the spatial ( $\Delta x$ ) and temporal ( $\Delta t$ ) scales in the numerical simulation to the Kolmogorov length scale ( $\eta$ ) and time scale ( $\tau$ ) (Kolmogorov, 1941), respectively, which can be calculated from the dissipation as shown in equation 2.

$$\eta = (v^3/\varepsilon)^{1/4}$$

$$\tau = (v/\varepsilon)^{1/2}$$

**Equation 2:** Kolmogorov scales depend on the kinematic viscosity ( $\nu$ ) and the rate of dissipation per unit mass of the turbulent kinetic energy ( $\varepsilon$ ).

One of the assumptions behind the Kolmogorov hypothesis is that the turbulence is homogenous isotropic. It is obvious from Figure 3 that the (turbulent) kinetic energy is not homogenous. To assess whether the post-stenotic flow instabilities were isotropic, we computed the time-averaged mean squared fluctuating

velocities along the centerline between lines A and D in Figure 2. Figure 9 shows that the mean squared fluctuating velocities are at the same order of magnitude, however there are large variations, and thus cannot be called isotropic. Therefore, computing the Kolmogorov scales is a very conservative estimate of the smallest length scales in this mildly unstable flow.

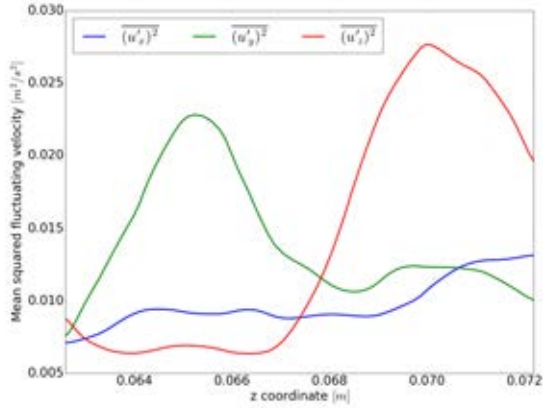


**Figure 9:** Mean squared fluctuating component of the velocity recorded along the centreline of the internal carotid artery.

The results of spatial assessment can be found in Table 1, displaying the characteristic node spacing  $\Delta x_{mean}$ , the smallest Kolmogorov length scale  $\eta_{min}$ , and the maximum ratio between  $\Delta x$  and  $\eta$ . There are two things to notice, first the Kolmogorov length scale converges, as the mesh is refined. Second, the maximum ratio between  $\Delta x$  and  $\eta$  on the two finest meshes are below 10, which is typically sufficient to capture  $> 95\%$  of the dissipation (Pope, 2001). If the simulations, from a numerical point of view, were truly converged, the ratio should be unity. However, the Kolmogorov scales only can be considered a conservative estimate as none of the rigid assumptions behind the hypothesis are met in this weakly unstable flow. Moreover, the differences between the 22M, and 50M-element simulations were negligible, and a finer simulation will most likely not provide additional insight. We therefore consider the 50M-element simulation sufficiently refined from a pragmatic point of view, and by extension the 22M-element mesh for biomedical applications, where one is typically interested in a rapid classification once the tools are validated.

Furthermore, the difference in CPU hours is substantial, the 22M simulation with  $\Delta t = 1 \cdot 10^{-4}$  seconds used 1420 CPU hours on 96 cores, while the 50M simulation  $\Delta t = 2 \cdot 10^{-5}$  seconds would have spent 16 496 CPU hours on 128 cores to simulate 2 physical seconds, thus an order of magnitude difference.

**Table 1:** Comparison between Kolmogorov length scale  $\eta$  and the spatial scale of the numerical grid  $\Delta x$ .

Number of cells	2M	6M	22M	50M
$\Delta x_{mean}$ [m]	3.19E-4	2.14E-4	1.38E-4	1.05E-4
$\eta_{min}$ [m]	9.81E-6	9.30E-6	8.91E-6	8.58E-6
$(\Delta x/\eta)_{max}$ [-]	21.93	14.04	9.31	7.49

The temporal assessment of the flow simulation can be found in Table 2, showing the minimum Kolmogorov time scale  $\tau_{min}$  and the ratio between the numerical time scale  $\Delta t$  and  $\tau_{min}$ . The two best resolved simulations were below the Kolmogorov time scale. However, we can observe from the PSD in Figure 8, that there was energy at higher fluctuations than the Nyquist frequency for the suggested  $\Delta t$ . If we are interested in the mean flow features, this cutoff is not important as there are for all practical purposes, no energy in the fluctuating component above 5000 Hz. However, since we are studying the fluctuations in the post-stenotic region, these high frequency fluctuations might be important. If such high frequency fluctuations were of interest, then the mesh itself might be the limiting factor, as the eddies associated with the high frequencies cannot be represented in mesh.

All quantitative analyses shown here were based on time-averaged results. However, there are evidences from the biomedical literature that temporal changes might play an important role in remodeling of the arteries (Valen-Sendstad *et al.*, 2011, 2013, 2014).

From a numerical point of view, an even larger time step might have been acceptable, but  $\Delta t = 1 \cdot 10^{-4}$  seconds is very close to the stability criteria of the numerical scheme used in the solver. The Courant–Friedrichs–Lewy (CFL) number for the 22M-element mesh simulation was 1.3, and the typical limit for this solver is 3-4 CFL.

**Table 2:** Comparison between Kolmogorov time scale  $\tau$  and the temporal scale of the simulations  $\Delta t$ .

$\Delta t$ [s]	1.00E-4	5.00E-5	2.00E-5	5.00E-6
$\tau_{min}$ [s]	7.96E-5	7.96E-5	7.93E-5	7.92E-5
$\Delta t/\tau_{min}$ [-]	1.2563	0.6281	0.2522	0.0631

We have admittedly not tested all parameters of the complete solution strategy space, exemplified by numerical schemes, viscosity models, compliant walls, etc.

A limitation of the current study is first of all that the simulations were not run for the same period of time. Secondly, the simulations were performed assuming rigid walls. However, compliant effects are normally considered negligible, and is nevertheless not of any importance in arterial growth and remodeling (Malek *et al.*, 1999). That being said, the effect of a compliant model in combination with turbulent-like flows remains to be assessed. Furthermore, the fluid used for these simulations was water instead of blood to allow for direct comparison against *in-vitro* experiments, which will be the focus of future work. However, non-Newtonian effects have shown to have negligible effects on the hemodynamics of carotid bifurcations and intracranial aneurysms (Lee and Steinman, 2007; Khan *et al.*, 2016).

As part of a larger consortium, the final aim of this line of investigation is to build a non-contact device to diagnose severe stenosis in the carotid arteries through the analysis of neck's skin displacement. We will therefore compute the sensitivity of the flow split and of noise in the inflow pulse through *in-silico* experiments,

since both factors can be challenging to control in the in-vitro experiments.

## CONCLUSION

We analyzed the flow field of a patient-specific carotid artery bifurcation with severe stenosis. The flow was found to become unstable already upstream of the stenosis because of flow separation at the bifurcation. The acceleration and deceleration of the flow caused by the stenosis itself led to the occurrence of vortices which propagated downstream of the stenosis until relaminarization started around 4 cm downstream.

We found an adequate under-resolved solution relative to the reference solution. From the spatial and temporal refinement study performed, a 22M mesh with a time step of  $\Delta t = 1 \cdot 10^{-4}$  seconds was found to be an optimal choice between computational cost and accuracy.

## REFERENCES

- GROEN, H.C., SIMONS, L., VAN DEN BOUWHUIJSEN, Q.J., BOSBOOM, E.M.H., GIJSEN, F.J., VAN DER GIESSEN, A.G., VAN DE VOSSE, F.N., HOFMAN, A., VAN DER STEEN, A.F., WITTEMAN, J.C. *et al.* (2010). “MRI-based quantification of outflow boundary conditions for computational fluid dynamics of stenosed human carotid arteries”. *Journal of Biomechanics*, **43**(12), 2332–2338.
- HUNT, J.C., WRAY, A.A. and MOIN, P. (1988). “Eddies, streams, and convergence zones in turbulent flows”. *Center for Turbulence Research, Report CTR-888*.
- IANNACCONE, F., DE BOCK, S., DE BEULE, M., VERMASSEN, F., VAN HERZEELE, I., VERDONCK, P., SEGERS, P. and VERHEGGHE, B. (2014). “Feasibility of a priori numerical assessment of plaque scaffolding after carotid artery stenting in clinical routine: proof of concept.” *The International Journal of Artificial Organs*, **37**(12), 928–939.
- KHAN, M., STEINMAN, D. and VALEN-SENDSTAD, K. (2016). “Non-Newtonian versus numerical rheology: Practical impact of shear-thinning on the prediction of stable and unstable flows in intracranial aneurysms”. *International Journal for Numerical Methods in Biomedical Engineering*.
- KOLMOGOROV, A.N. (1941). “The local structure of turbulence in incompressible viscous fluid for very large Reynolds numbers”. *Dokl. Akad. Nauk SSSR*, **30**, 301–305.
- LEE, S.W. and STEINMAN, D.A. (2007). “On the relative importance of rheology for image-based CFD models of the carotid bifurcation”. *Journal of Biomechanical Engineering*, **129**(2), 273–278.
- MALEK, A.M., ALPER, S.L. and IZUMO, S. (1999). “Hemodynamic shear stress and its role in atherosclerosis”. *JAMA*, **282**(21), 2035–2042.
- MORTENSEN, M. and VALEN-SENDSTAD, K. (2015). “Oasis: A high-level/high-performance open source Navier–Stokes solver”. *Computer Physics Communications*, **188**, 177–188.
- PICCINELLI, M., VENEZIANI, A., STEINMAN, D.A., REMUZZI, A. and ANTIGA, L. (2009). “A framework for geometric analysis of vascular structures: application to cerebral aneurysms”. *IEEE Transactions on Medical Imaging*, **28**(8), 1141–1155.
- POPE, S.B. (2001). *Turbulent flows*. IOP Publishing.
- REYNOLDS, O. (1883). “An experimental investigation of the circumstances which determine whether the motion of water shall be direct or sinuous, and of the law of resistance in parallel channels.” *Proceedings of the Royal Society of London*, **35**(224–226), 84–99.
- ROACHE, P.J., GHIA, K.N. and WHITE, F.M. (1986). “Editorial policy statement on the control of numerical accuracy”. *Journal of Fluids Engineering*, **108**(1), 2–2.
- STEINMAN, D.A. (2002). “Image-based computational fluid dynamics modeling in realistic arterial geometries”. *Annals of Biomedical Engineering*, **30**(4), 483–497.
- STEINMAN, D.A., HOI, Y., FAHY, P., MORRIS, L., WALSH, M.T., ARISTOKLEOUS, N., ANAYIOTOS, A.S., PAPA HARILAOU, Y., ARZANI, A., SHADDEN, S.C. *et al.* (2013). “Variability of computational fluid dynamics solutions for pressure and flow in a giant aneurysm: the ASME 2012 summer bioengineering conference CFD challenge”. *Journal of Biomechanical Engineering*, **135**(2), 021016.
- STEWART, S.F., PATERSON, E.G., BURGREN, G.W., HARIHARAN, P., GIARRA, M., REDDY, V., DAY, S.W., MANNING, K.B., DEUTSCH, S., BERMAN, M.R. *et al.* (2012). “Assessment of CFD performance in simulations of an idealized medical device: results of FDAs first computational interlaboratory study”. *Cardiovascular Engineering and Technology*, **3**(2), 139–160.
- VALEN-SENDSTAD, K. and STEINMAN, D. (2014). “Mind the gap: impact of computational fluid dynamics solution strategy on prediction of intracranial aneurysm hemodynamics and rupture status indicators”. *American Journal of Neuroradiology*, **35**(3), 536–543.
- VALEN-SENDSTAD, K., MARDAL, K.A., MORTENSEN, M., REIF, B.A.P. and LANGTANGEN, H.P. (2011). “Direct numerical simulation of transitional flow in a patient-specific intracranial aneurysm”. *Journal of Biomechanics*, **44**(16), 2826–2832.
- VALEN-SENDSTAD, K., MARDAL, K.A. and STEINMAN, D.A. (2013). “High-resolution CFD detects high-frequency velocity fluctuations in bifurcation, but not sidewall, aneurysms”. *Journal of Biomechanics*, **46**(2), 402–407.
- VALEN-SENDSTAD, K., PICCINELLI, M. and STEINMAN, D.A. (2014). “High-resolution computational fluid dynamics detects flow instabilities in the carotid siphon: Implications for aneurysm initiation and rupture?” *Journal of Biomechanics*, **47**(12), 3210–3216.
- WELCH, P. (1967). “The use of fast Fourier transform for the estimation of power spectra: a method based on time averaging over short, modified periodograms”. *IEEE Transactions on Audio and Electroacoustics*, **15**(2), 70–73.

## VELOCITY PROFILES IN A 2D MODEL OF THE LEFT VENTRICULAR OUTFLOW TRACT, PATHOLOGICAL CASE STUDY USING PIV AND CFD MODELING

Paul R. LEINAN<sup>1\*</sup>, Paal SKJETNE<sup>2†</sup>, John MORUD<sup>2‡</sup>, Stig URHEIM<sup>3§</sup>, Sigrid K. DAHL<sup>2¶</sup>

<sup>1</sup>SINTEF Petroleum AS, 7465 Trondheim, NORWAY

<sup>2</sup>SINTEF Materials and Chemistry, 7465 Trondheim, NORWAY

<sup>3</sup>Department of Heart Disease, Haukeland University Hospital, Bergen, Norway

\* E-mail: paul.roger.leinan@sintef.no

† E-mail: paal.skjetne@sintef.no

‡ E-mail: john.c.morud@sintef.no

§ E-mail: stig.urheim@gmail.com

¶ E-mail: sigrid.dahl@sintef.no

### ABSTRACT

In the current study, we present an experimental (in vitro) 2D flow model for studying blood flow in the human left ventricular outflow tract (LVOT) and the first part of the aorta using particle image velocimetry (PIV) and computational fluid dynamics (CFD). Two cardiac pathologies were investigated in this study; 1) anterior mitral leaflet (AML) billowing, and 2) asymmetric septal hypertrophy (ASH). Each of these conditions has the potential to alter the normal direction of the flow entering the aortic valve apparatus from the LVOT and therefore place an abnormal stress distribution on the aortic valve leaflets. We found good agreement between the PIV results and the CFD calculations. The largest discrepancy between the experimental data and the numerical results was found in the recirculation zone adjacent to the left coronary leaflet. The main limitations in the current study when evaluating the clinical significance of the results are the choice of a 2D geometry with stiff and stationary walls. Keeping this in mind, our results show that AML billowing and ASH bulging alone does not alter the flow field in the LVOT dramatically. However, when the two conditions combine, we see a significant flow separation and re-circulation zone forming at the left coronary leaflet, covering half of the aortic outflow tract at peak systole.

**Keywords:** In-vitro, PIV, CFD, Left ventricle.

### NOMENCLATURE

#### Greek Symbols

$\rho$  Mass density, [kg/m<sup>3</sup>]  
 $\mu$  Dynamic viscosity, [cP]  
 $\psi$  Drag correction factor, [-]

#### Latin Symbols

$p$  Pressure, [Pa].  
 $u$  Fluid velocity, [m/s].  
 $d$  Diameter, [m].  
 $Re$  Reynolds number, [-].  
 $St$  Stokes number, [-].

#### Sub/superscripts

$x$  Cartesian  $x$  component..  
 $y$  Cartesian  $y$  component.  
 $p$  Particle

### INTRODUCTION

In the current study, we present an experimental (in vitro) 2D flow model for studying blood flow in the human left ventricular outflow tract (LVOT) and the first part of the aorta using particle image velocimetry (PIV), under both physiological and pathological conditions. The same setup was analyzed using computational fluid dynamics (CFD) and the results compared. Two cardiac pathologies were investigated in this study; 1) anterior mitral leaflet (AML) billowing, and 2) asymmetric septal hypertrophy (ASH). Each of these conditions has the potential to alter the direction of the flow entering the aortic valve apparatus from the LVOT and therefore alter the stress distribution on the aortic valve leaflets. In order to investigate the hemodynamic effects of AML billowing and ASH bulging on the aortic valve apparatus, the degree of AML billowing and ASH bulging was parametrized through parameters L1 and L2 in Figure 1.

There is a general agreement that the velocity profile in the LVOT and aortic annulus is flat but skewed, in previous Doppler ultrasound studies (at rest) (Sjöberg *et al.*, 1994; Kupari and Koskinen, 1993; Zhou *et al.*, 1993). Abnormal conditions such as AML and ASH which alters the geometry of the LVOT may have significant influence on the flow profiles in the same area (Matre *et al.*, 2003; Zhou *et al.*, 1993). However, previous studies on the hemodynamical influence of AML on LVOT are more scarce in the literature, while some geometrical studies exist (Kvitting *et al.*, 2010). Some authors have used CFD models to study the hemodynamical effects of AML (Dahl *et al.*, 2011; Dimasi *et al.*, 2012; Xiong *et al.*, 2008), and reports that there is a non-negligible effect on the flow conditions in the aortic annulus due to AML billowing. In this work, we have build a simplified parametrized 2D model (both in an experimental lab setup and CFD) of the LVOT and aortic annulus where we can test hypotheses regarding the hemodynamical effects of AML billowing and ASH on the velocity profile in the aortic annulus and the load on the aortic valve leaflets. With this model setup, we also believe that we will be better equipped to point out directions where more detailed studies are needed, e.g. with 3D CFD and fluid-structure simulation models as well as 3D Doppler and 4D MRI studies of blood flow in the LVOT.

The two main limitations in our choice of model setup are; 1) the flow field is 2D, which may introduce unnatural flow conditions compared to the real 3D case, such as increased vortex formation, and 2) the walls are non-deformable and stationary. However, our model offers very good visual and

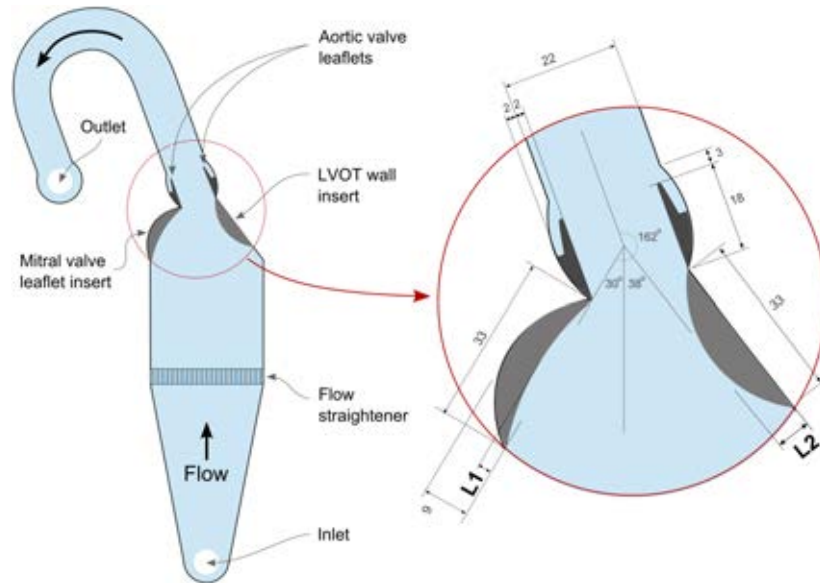


**Figure 1:** The flow domain geometry (blue area) which is cut into a 10mm thick Plexiglass plate by a water jet. A 40/60% glycerol-water mixture enters the model through the "inlet" port, then flows through the "flow straightener" before entering the LVOT and the aortic valve apparatus, finally the flow follows the aortic arc and exits through the "outlet". The degree of AML billowing and ASH are parametrized with Plexiglass inserts with different widths defined by the lengths L1 and L2.

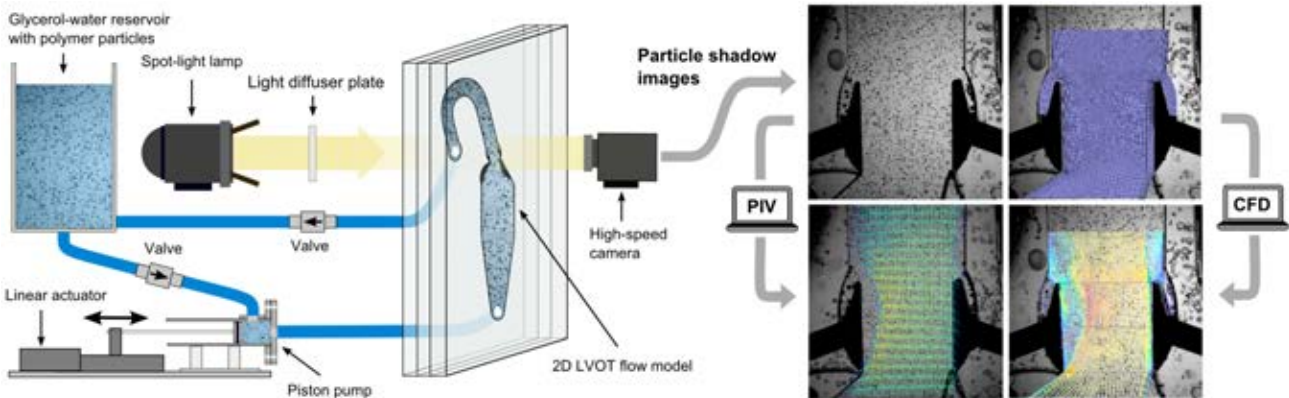


**Figure 2:** Illustration of the experimental setup, which consists of a fluid reservoir, the 2D LVOT flow model, a piston pump, a linear actuator (Zaber, X-LRQ-E) and connecting fiber reinforced 1" tubes and one-way polymer ball valves (SXE PVC-U, 1"). Fluid can be pumped through the loop and the LVOT model a pulsatile manner, determined by the waveform given to the linear actuator. The flow field in the 2D LVOT model was visualized by tracking the movement of polymer particles by recoding their shadows projection with a high-speed camera (Photron, FASTCAM 1024 PCI). The particle shadows were projected into the camera from a spot-light lamp (dedolight DLH400DT) and a light diffuser plate inline with the camera.

quantifiable access to the LVOT flow field. Our geometry was based on conditions at peak systole when aortic leaflets are fully open, we will therefore focus our measurements on this period of the cardiac cycle. At the onset of the systole the aortic valve opens fully in typically less than 30 ms.

## METHODS

### Experimental setup

The LVOT flow model consists of three Plexiglass plates. The geometry of the flow domain, seen in Figure 1, was cut out of the middle plate by a water jet. This plate was then sandwiched between the two uncut Plexiglass plates, as illustrated in Figure 2. In this way, the 2D flow domain was sealed inside the plates providing excellent visual access to the flow field. The middle plate was 10mm thick. Flow inlet and outlet ports were mounted on the uncut plates. The LVOT geometry is extracted from ultrasound recording provided by Dahl (2012) at peak systole, and is given by the

so-called long axis view from such recordings defined as the 2D plane through the center of the aortic valve annulus, the mitral valve annulus and the apex of the left ventricle.

A flow loop was built so that fluid could be circulated through the LVOT model in a pulsatile manner. The flow loop is illustrated in Figure 2, and is made up of; the 2D LVOT flow model, a fluid reservoir, a piston pump and connecting tubes and one-way valves. The piston pump was connected to a programmable linear actuator (Zaber, X-LRQ-E) so that an arbitrary flow pulse could be injected into the model in displacement control. Two ball valves (SXE PVC-U, 1") and fiber reinforced 1" transparent PVC tubing connected the loop components and ensured that unidirectional pulsatile flow could be circulated through the flow loop setup.

The blood analog fluid consisted of 60% deionized water and 40% Glycerol, which at room temperature gives a Newtonian fluid with a dynamic viscosity of  $\mu = 3.6\text{mPa}\cdot\text{s}$  (Yousif *et al.*, 2011).

The velocity field in the 2D plane of the LVOT model (i.e. the flow domain described by Figure 1) was quantified by particle image velocimetry (PIV). In our case we added polymer particles to the reservoir tank, which were circulated in the loop, hence there was a uniform concentration of particles in the system. The particles were visualized by spot-light lamp (dedolight DLH400DT) inline with a light diffuser plate, the 2D LVOT flow domain and a high-speed camera (Photron, FASTCAM 1024 PCI), as seen in Figure 2. In this setup the shadows of the particles could clearly be seen in the flow domain on a white background because of the light diffuser plate. However, the quality of the visualization depended on several factors such as the distance between the spot-light lamp, the diffuser and the flow domain, the polymer particle size and the high-speed camera resolution (other important factors where also particle concentration, light intensity, camera shutter speed and aperture). The particle size compared to the camera resolution was particularly important, i.e. the size of the shadow needed to be larger than the size of the image pixels. In our current setup with the necessary zoom and a camera resolution of 512x512 (needed in order to have a frame rate of 3000 frames/sec), we achieved a pixel resolution of 0.013 pixels/ $\mu\text{m}$ . Hence, we used 80  $\mu\text{m}$  polymer particles (Dynoseeds®TS 80), having a density of 1050 kg/m<sup>3</sup>. According to Tropea *et al.* (2007) tracing accuracy errors for spherical traces are below 1% if the Stokes number is significantly smaller than 0.1. Stokes number with Reynolds number drag correction (Israel and Rosner, 1982) may be given by

$$St = \frac{\rho_p d_p u}{18\mu} \psi(Re_d) \quad (1)$$

where  $\rho_p$  and  $d_p$  are the particle density and diameter, respectively, and  $\psi(Re_d)$  is the drag correction factor. In the current setup flow velocities around 1.0 m/s are expected in the LVOT, which by Eq. 1 gives a Stokes number of  $St \approx 0.75$ .

The recorded shadow particle images were post processed using the open source software OpenPIV (python version, 0.20.5) (Taylor *et al.*, 2010). Default settings in the software was used during PIV calculations with a window size of 24 and overlap of 20 pixels.

#### Experimental protocol

The two pathologies investigated in this study can be seen in Figure 1, defined by the parameters L1 and L2. L1 defines the degree of AML billowing and L2 defines the degree of ASH. Four cases were studied in the current work, as given in Table 1 the normal physiological geometry, case 1; AML billowing, case 2; ASH, case 3; and a combination of AML billowing and ASH, case 4.

**Table 1:** Model parameter matrix with; the normal physiological geometry, case 1; AML billowing, case 2; ASH, case 3; and a combination of AML billowing and ASH, case 4, as depicted in Figure 1

Case	AML		ASH	
	L1 (mm)	L2 (mm)	L1 (mm)	L2 (mm)
1	0	0	0	0
2	0	0	9	9
3	9	9	0	0
4	9	9	9	9

The experiments started with preparing the 40/60% glycerol-water mixture which was added to the reservoir

tank, as seen in Figure 2. Polymer trace particles were then added (Dynoseeds®TS 80) until the particle density was sufficient to achieve good PIV quality. Care was taken to evacuate all air pockets and bubbles from the connecting tubes and vales, and the fluid mixture was circulated in the loop until a uniform distribution was obtained. The software controlling the inflow waveform (given by the linear actuator and the piston pump) was able to trigger the high-speed camera at a predetermined point in the cardiac cycle. Six full cardiac cycles were recorded with a frame rate of 3000 frames per second, for each of the four geometry cases in Table 1. The LVOT inflow waveform was obtained from ultrasound recording provided by Dahl (2012), defined by the volumetric change of the left ventricle during systole.

#### CFD model

The LVOT flow model described in the previous subsection was simulated using ANSYS Fluent 16.2. The computational domain was limited to the section after the flow straightener and the outlet was simplified to a simple in-plane rectangular outlet. The actual dimensions of the CFD domain and the flow loop were the same since the same underlying CAD was used to generate both the machined loop geometry and the CFD domain.

A hexahedral mesh was used, with a nominal grid resolution of 500  $\mu\text{m}$  in the region of interest, i.e. the aortic root and lower part of the ascending aorta. A boundary layer was attached to the mitral and septal sides of the flow conduit with a starting size of 100  $\mu\text{m}$  expanding with a factor of 1.2 in 9 layers. In the out of plane direction the resolution was 1 mm, and in the distal parts relative to the aortic root (inlet and outlet regions) the lateral resolution was decreased to 2 mm.

The flow is highly transient, the whole outflow lasting 360 ms. Thus, there is not enough time for steady state boundary layers to develop, and not time enough time for turbulence to develop. For these reasons we opt to use a laminar flow model, although at the aortic root the Reynolds number briefly rises to a value of approximately 6000 at peak systole (peak flow). The SIMPLE method was used for the pressure-velocity coupling, a second order upwind scheme for the momentum equation, a second order scheme for pressure, and gradient reconstruction was done using cell based least squares. A first order implicit formulation was used for the transient formulation. Estimated peak flow velocities are 1.5 m/s, and with a 100 $\mu\text{m}$  resolution this results in a time step requirement of 30  $\mu\text{s}$ , we have employed a time step of 20  $\mu\text{s}$ . Furthermore, constant density, 1050 kg/m<sup>3</sup>, and Newtonian viscosity, 3.5 mPa.s, were employed.

At the outlet a pressure boundary condition was implemented, with zero gauge pressure, as the reference point for the pressure was also located at the center of the outlet. The inlet was modeled as a velocity inlet. The inlet velocity was determined in the following way: The volume curve obtained from a subject using ultrasound (Dahl, 2012) was used to give a physiological realistic time varying profile. This volume curve was converted into a time varying piston position, and the velocity was simply the derivative of this curve and is depicted in Figure 3. The inlet velocity was implemented using ANSYS Fluents user defined functions (UDF).

## RESULTS

PIV and CFD results from the four LVOT geometry cases is presented in Figure 4. Additionally, the maximum axial velocities for the velocity profiles (blue solid lines) are given in

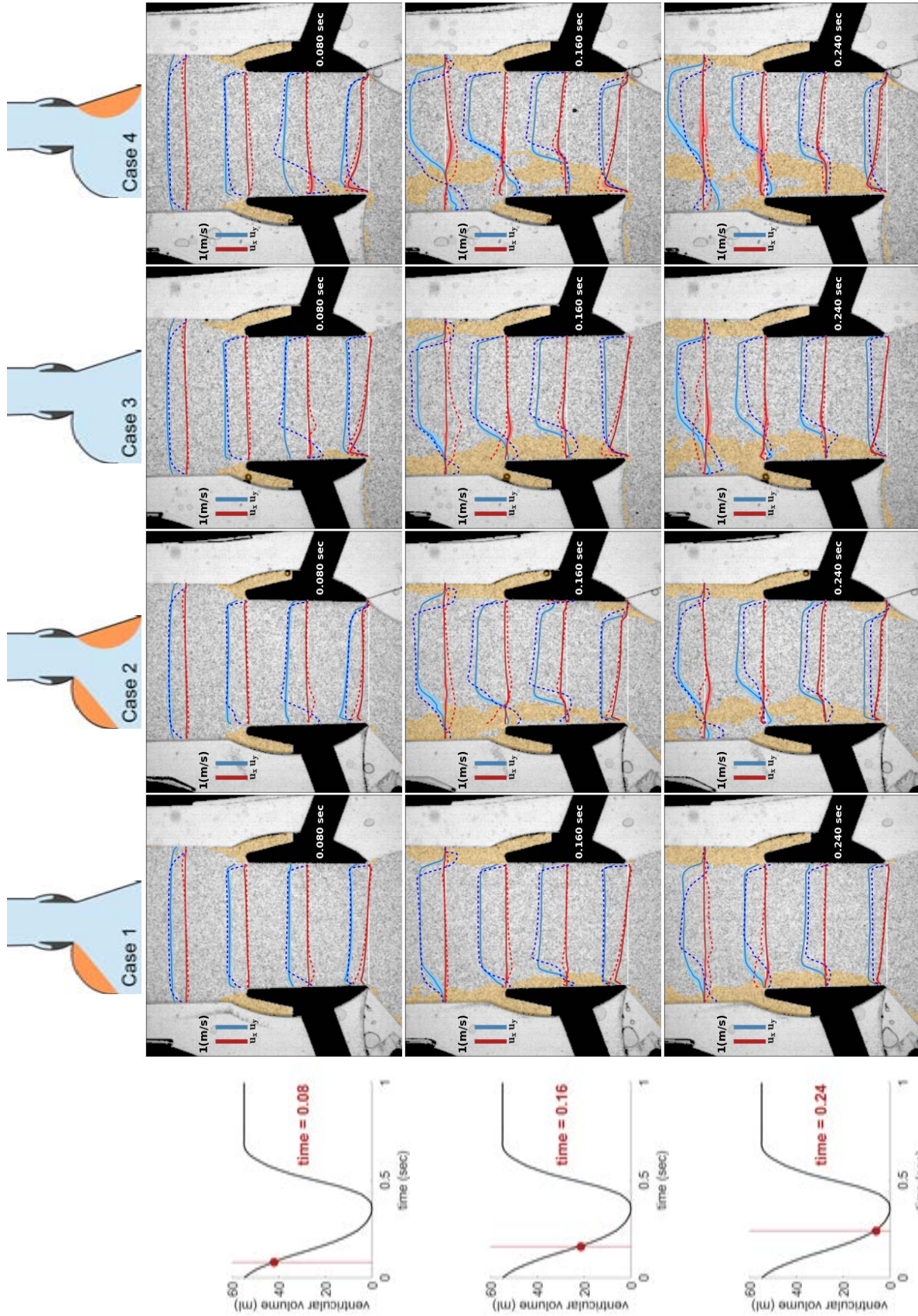


**Figure 4:** PIV and CFD results from the four LVOT geometry cases. The top row shows illustrations of the geometry of the LVOT for the four cases, where the inserts are colored orange. The inflow waveform used in the experiments is given in the left column from the top. The curves shows remaining ventricular ejection volume as a function of time which determines the volume flow in the loop. Systole begins at time zero and ends at 0.360 sec. Velocity profiles at three times during systole are given in the figure, at 0.08, 0.16 and 0.24 sec, respectively. The blue velocity profiles gives the velocity components in the axial direction (y-direction) and the red velocity profiles gives the velocity components in the transverse direction (x-direction). The PIV results from the in-vitro flow loop is given by solid lines, and is averaged from six cardiac cycles. Additionally, at the three selected times, velocities are averaged over a time span of 3 milliseconds. The plotted blue and red shaded areas give the standard deviation in the PIV data. The velocity profiles components from the CFD calculations are given by blue and read dashed lines, for the y and x direction respectively. The red and blue vertical bars in each figure gives the velocity profile scale of 1 m/s. Areas where the velocity magnitude is smaller than 0.1 m/s are marked in yellow.

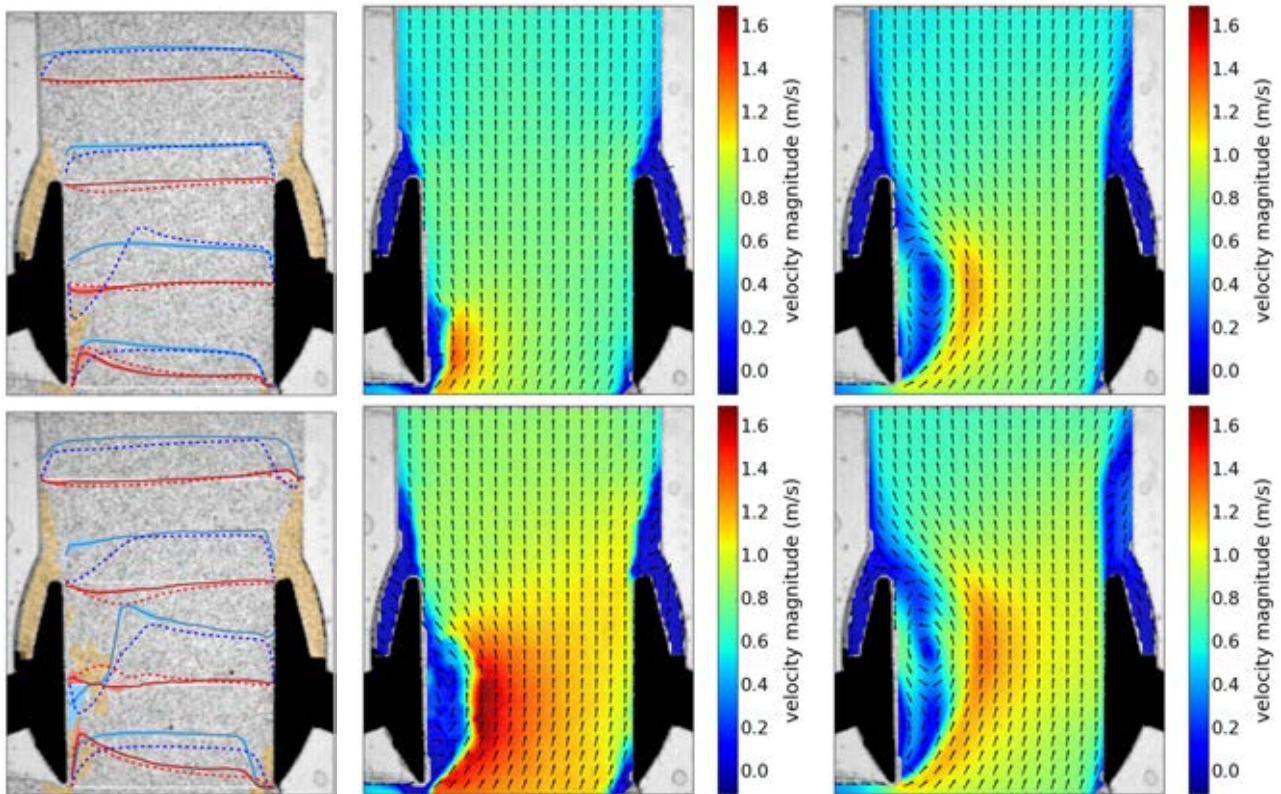


**Figure 5:** **Left column:** PIV and CFD velocity profiles for Case 4 at 0.08 and 0.1 sec, respectively. **Middle column:** PIV velocity vectors for Case 4 at 0.08 and 0.1 sec, respectively. **Right column:** CFD velocity vectors for Case 4 at 0.08 and 0.1 sec, respectively. The PIV velocity vector plot at 0.08sec (1st row and 2nd column) shows that a wake is forming at the left coronary leaflet. The CFD velocity profile at 0.08sec (1st row and 3rd column) shows that a large wake is already present in the CFD simulation. Additionally, the PIV velocity vector plot at 0.1sec shows (2st row and 2nd column) show that the PIV analysis is not able to pick up the detailed flow field in the wake at the left coronary leaflet where the velocities are small

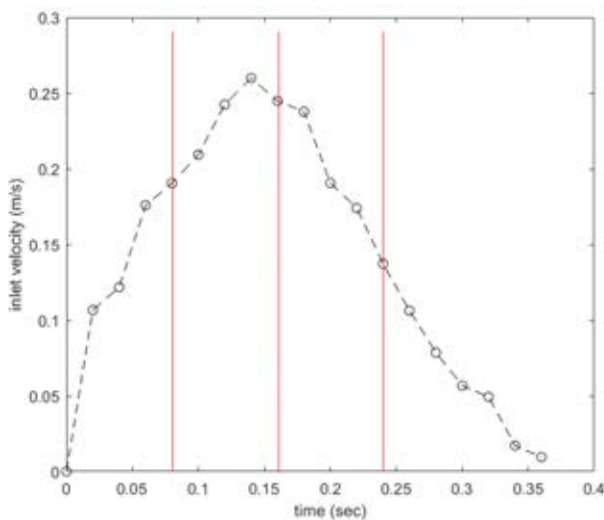


**Figure 3:** The inlet flow velocity derived from the volume change between successive frames in a patient specific ultrasound recording. The volume curve at the top of Figure 4 represents the accumulated ejection volume and is thus smoother than the velocity curve. The vertical red lines indicate the times visualized in Figure 4.

Table 2. In Figure 4, the top row shows illustrations of the geometry of the LVOT for the four cases, where the removable inserts are colored orange. The inflow waveform used in the experimenters is given in the left column of Figure 4 and

3. The curves in Figure 4 shows remaining ejection volume of the ventricle as a function of time and defines the volume flow in the loop, Figure 3 shows the corresponding development in inlet velocity. The systole begins at time zero and ends at 0.360 sec. Velocity profiles at three times and four different positions in the aortic valve apparatus during systole is given in the figure, at 0.08, 0.16 and 0.24 sec. The blue velocity profiles give the velocity components in the axial direction (y-direction) and the red velocity profiles give the velocity components in the transverse direction (x-direction). The PIV results from the in-vitro flow loop is given by solid lines, and is averaged over six cardiac cycles. Additionally, at the three selected times, velocities are averaged in a time span of 3 milliseconds (i.e. 3 PIV frames). The plotted blue and red areas give the standard deviation in the PIV data. The velocity profiles components from the CFD calculations are given by blue and red dashed lines, for the axial and transverse direction respectively.

Velocity profiles for Case 1, where there is no AML billowing nor ASH bulging, remains relatively flat throughout systole, as can be seen in Figure 4. There is however a recirculation zone adjacent to the left coronary leaflet. The recirculation zone develops during systole due to the angle between the anterior mitral leaflet and the left coronary leaflet. For Case 2, with an ASH bulging of 9mm, a small re-circulation zone can be seen at the root of the right coronary leaflet. The re-circulation zone does not extend into the aorta and is caused by the angle between the ASH bulging right coronary leaflet. A 9 mm AML billowing, as defined in Case 3, causes a larger recirculation zone adjacent to the left coronary leaflet



**Table 2:** Maximum axial velocities for the velocity profiles (blue solid lines) given in Figure 4, at flow times 0.08, 0.16 and 0.24 seconds, for Case 1, 2, 3 and 4. At each flow time, four velocity profiles are plotted at regular increments in the vertical direction starting at the root of the aortic vales, as seen in Figure 4. The maximum velocities given in the table are arranged in the same vertical order as the velocity profiles in Figure 4.

Time [s]	Case 1 [m/s]	Case 2 [m/s]	Case 3 [m/s]	Case 4 [m/s]
0.08	0.57	0.61	0.69	0.68
	0.70	0.71	0.85	0.82
	0.67	0.79	0.84	0.88
	0.85	1.03	0.90	0.99
0.16	0.92	0.99	1.00	1.27
	0.92	1.10	1.09	1.34
	1.03	1.17	1.11	1.24
	0.87	0.94	0.86	0.92
0.24	0.78	0.94	0.99	1.31
	0.74	1.03	1.04	1.19
	0.87	0.95	0.91	0.97
	0.66	0.81	0.74	0.80

compared to the physiological case (Case 1). However, the axial velocity profiles remains relatively flat throughout the systole, and there are little cross flow in the transverse direction. Large re-circulations zones adjacent to the left coronary leaflet were found for Case 3 and Case 4. They are indicated as areas shadowed by yellow color in Figure 4. These areas were discriminated by having a velocity magnitude smaller than 0.1 m/s. There is also significant back flow downstream of the left coronary leaflet in the ascending aorta. Case 4 has the highest presence of transverse flow through the aortic vales and also exhibits a re-circulation zone similar to that of Case 2 at the root of the right coronary leaflet.

The PIV velocity vector plot at 0.08 sec (Figure 5, top left panel) shows that a wake is forming at the left coronary leaflet. The CFD velocity profile shows that a large wake is already present in the CFD simulation at 0.08 sec. Additionally, the PIV velocity vector plot at 0.1 sec shows (Figure 5, top left panel) show that the PIV analysis is not able to pick up the detailed flow field in the wake at the left coronary leaflet where the velocities are small.

## DISCUSSION

In this work, we performed both in-vitro experiments and CFD calculations on the 2D LVOT model. The 2D models were parametrized according to Table 1, where Case 1 represents the normal physiological geometry. AML billowing was simulated by removing a 9mm wide insert (Case 2, Table 1) in the mitral valve position, as seen in Figure 1. ASH was simulated by inserting a 9mm wide insert (Case 3, Table 1) on the right LVOT wall, as seen in Figure 1. Finally, both AML billowing and ASH was simulated in Case 4.

The agreement between the PIV results and the CFD calculations can be seen in Figure 4 and 5. The largest discrepancy between the experimental data and the numerical results can be seen in the re-circulation zone adjacent to the left coronary leaflet. The timing of the development of the circulations zone is not exactly the same for the CFD and the experimental results. From the axial velocities one can observe that there is some time shift between the experimental and the CFD results. The most likely cause of this time lag

originate from some compliance present in the experimental setup which delays the flow wave form into the LVOT compared to the CFD results, as seen in Figure 5. Moreover, the current PIV setup was not able to map the small velocities in the re-circulation zone at the left coronary leaflet as seen in Figure 4 and 5, this was also confirmed by testing an alternative PIV software (PIVlab). The velocity field in the recirculation zone can be determined by analyzing this region with higher spatial resolution, i.e. smaller polymer particles and increased camera resolution/zoom.

Flow velocity measurements based on particle shadows allows for low-power illumination compared to a conventional laser PIV setup. Additionally, since the light source in shadow PIV can illuminate continuously, the temporal resolution is only restricted by the frame rate of the high-speed camera and not on a laser system. A drawback with the shadow PIV technique is that it is not possible to isolate particles in a specific plane in the depth direction of the flow domain (i.e. in the line defined by the camera and the light source), which is the strong point of laser PIV where typically a laser sheet is used to illuminate particles in a specific 2D plane (Estevadeordal and Goss, 2005). However, by adjusting the focus point of the camera in the center of the flow domain (in the depth direction) we were to some extent able to favorize particles in the center plane of the flow model. A second issue with shadow PIV technique in the current setup is the particle size. As shown in Sec. *Experimental setup*, the particles in our setup have a Stokes number in the order of 0.75, which is somewhat high for following the flow as true tracers. A smaller Stokes number could be achieved in our setup with a high speed camera with higher resolution, which will be considered for future studies.

The main limitations in the current study when evaluating the clinical significance of the results are the choice of a 2D geometry with stiff and stationary walls. The 2D geometry will introduce unnatural flow conditions compared to the real 3D case, such as increased vortex formation. Moreover, the aortic valves are not allowed to move in our current flow model. In the real physiologic case, the aortic valve leaflets are highly deformable structures and the final fully open position during systole is believed to be significantly influenced by the local flow conditions in the LVOT. A more realistic in-vitro setup for future studies might involve a full 3D geometry with a biological prosthetic aortic valve.

## CONCLUSION

In conclusion, while keeping in mind the limitations of the current study from a clinical perspective as discussed above, our results show that ASH bulging alone does not alter the flow field in the LVOT dramatically. However, for AML billowing and for the combination of AML billowing and ASH, we see a significant re-circulation zone covering half of the aortic outflow tract at peak systole (i.e. 160ms into the cardiac cycle), as seen in e.g. Case 4 in Figure 4. This result is not surprising since these two cases produce large expansion angles between the LVOT and the aortic outflow tract. Which in turn, might cause asymmetrical hemodynamical loads on the aortic valve leaflets and downstream compactions.

## REFERENCES

- DAHL, S.K. (2012). *Numerical simulations of blood flow in the left side of the heart*. Ph.D. thesis.
- DAHL, S.K., FAGERHOLT, E., KISS, G., PROT, V.E., AMUNDSEN, B.H., HELLEVIK, L.R. and SKALLERUD, B.H. (2011). "3d moving boundary conditions for heart

CFD simulations - from echocardiographic recordings to discretized surfaces". *MekIT'11: Sixth National Conference on Computational Mechanics*, 33–46. Tapir Akademisk Forlag.

DIMASI, A., CATTARINUZZI, E., STEVANELLA, M., CONTI, C.A., VOTTA, E., MAFFESSANTI, F., INGELS JR, N.B. and REDAELLI, A. (2012). "Influence of mitral valve anterior leaflet in vivo shape on left ventricular ejection". *Cardiovascular Engineering and Technology*, **3(4)**, 388–401.

ESTEVADEORDAL, J. and GOSS, L. (2005). "An investigation of particle-shadow velocimetry (psv) for transonic-flow applications". *35th AIAA Fluid Dynamics Conference and Exhibit*, 5009.

ISRAEL, R. and ROSNER, D.E. (1982). "Use of a generalized stokes number to determine the aerodynamic capture efficiency of non-stokesian particles from a compressible gas flow". *Aerosol Science and Technology*, **2(1)**, 45–51.

KUPARI, M. and KOSKINEN, P. (1993). "Systolic flow velocity profile in the left ventricular outflow tract in persons free of heart disease". *The American journal of cardiology*, **72(15)**, 1172–1178.

KVITTING, J.P.E., BOTHE, W., GÖKTEPE, S., RAUSCH, M.K., SWANSON, J.C., KUHL, E., INGELS, N.B. and MILLER, D.C. (2010). "Anterior mitral leaflet curvature during the cardiac cycle in the normal ovine heart: clinical perspective". *Circulation*, **122(17)**, 1683–1689.

MATRE, K., KVITTING, P., ZHOU, Y. and FAERESTRAND, S. (2003). "The effect of body weight on the degree of blood velocity profile skewness in the aortic annulus in domestic pigs". *Laboratory animals*, **37(1)**, 72–80.

SJÖBERG, B.J., ASK, P., LOYD, D. and WRANNE, B. (1994). "Subaortic flow profiles in aortic valve disease: a two-dimensional color doppler study". *Journal of the American Society of Echocardiography*, **7(3)**, 276–285.

TAYLOR, Z.J., GURKA, R., KOPP, G.A. and LIBERZON, A. (2010). "Long-duration time-resolved piv to study unsteady aerodynamics". *IEEE Transactions on Instrumentation and Measurement*, **59(12)**, 3262–3269.

TROPEA, C., YARIN, A.L. and FOSS, J.F. (2007). *Springer handbook of experimental fluid mechanics*, vol. 1. Springer Science & Business Media.

XIONG, F., YEO, J.H., CHONG, C.K., CHUA, Y.L., LIM, K.H., OOI, E.T. and GOETZ, W.A. (2008). "Transection of anterior mitral basal stay chords alters left ventricular outflow dynamics and wall shear stress". *Journal of Heart Valve Disease*, **17(1)**, 54.

YOUSIF, M.Y., HOLDSWORTH, D.W. and POEPPING, T.L. (2011). "A blood-mimicking fluid for particle image velocimetry with silicone vascular models". *Experiments in fluids*, **50(3)**, 769–774.

ZHOU, Y., FAERESTRAND, S., MATRE, K. and BIRKELAND, S. (1993). "Velocity distributions in the left ventricular outflow tract and the aortic annulus measured with doppler colour flow mapping in normal subjects". *European heart journal*, **14(9)**, 1179–1188.



## OSCILLATORY FLOW AND MASS TRANSPORT IN A CORONARY ARTERY

Sargon A. GABRIEL<sup>1\*</sup>, Yan DING<sup>1</sup>, John A. GEAR<sup>1</sup>, Yuqing FENG<sup>2†</sup>

<sup>1</sup>Mathematics, School of Science, RMIT University, Melbourne, Victoria 3001, AUSTRALIA

<sup>2</sup>Mineral Resources, CSIRO, Clayton South, Victoria 3169, AUSTRALIA

\* E-mail: sargon.gabriel@rmit.edu.au

† E-mail: yuqing.feng@csiro.au

### ABSTRACT

Pulsatile flow is intrinsic to the cardiovascular system and is driven by the rhythmic beating of the heart. As a system for mass transport, the cardiovascular system hosts a variety of biochemical and cellular species whose transport is subjected to the corresponding flow oscillations. The influence is most prevalent near the heart and particularly within arteries, where pressure fluctuations are most significant. This makes modelling of long-term mass transport difficult to evaluate, since intermediate oscillations need to be explicitly resolved. By applying Reynolds averaging to the governing flow and mass transport equations on a representative period of oscillation, this problem may be alleviated. However, doing so introduces extra terms akin to the Reynolds stresses in the flow equations as well as perturbed-flux terms in the mass transport equations. These terms are investigated in the present study and their distributions assessed. A human right coronary artery is used as the subject geometry, wherein the oscillatory transport behaviour of blood flow and low density lipoprotein is studied.

**Keywords:** coronary artery, oscillation, period-average, pulsatile flow, species transport.

### NOMENCLATURE

#### Greek Symbols

$\partial$	partial derivative
$\delta_{ij}$	Kronecker delta tensor
$\mu$	dynamic viscosity, [kg/m/s]
$\rho$	density, [kg/m <sup>3</sup> ]
$\tau_{ij}$	viscous stress tensor, [kg/m/s <sup>2</sup> ]
$\boldsymbol{\tau}_w$	wall shear stress vector, [kg/m/s <sup>2</sup> ]
$\phi$	arbitrary scalar field variable
$\Delta_{ij}$	strain-rate tensor, [1/s]
$\Gamma$	domain boundary
$\Omega$	domain

#### Latin Symbols

$c$	normalised species concentration
$d$	diameter, [m]
$\mathbf{n}$	surface normal vector
$p$	pressure, [kg/m/s <sup>2</sup> ]
ps	pulsatile-state (period-averaged)
ss	steady-state
$t$	time, [s]
$\mathbf{u}$	velocity vector, [m/s]
$\mathbf{x}$	spatial position vector, [m]

$C$	species concentration
$D$	species diffusivity, [m <sup>2</sup> /s]
$J$	flux into a boundary
Pe	Péclet
Re	Reynolds

#### Sub/superscripts

0	reference condition (at the inflow)
$i, j$	Cartesian tensor indices <sup>1</sup>
F	fluid
I	inflow
O	outflow
W	wall

### INTRODUCTION

The cardiovascular system is a circulatory transport system for blood that carries erythrocytes, thrombocytes, lipoproteins and other species throughout the body. The flow of blood within the cardiovascular system is driven by pressure differentials generated at the heart. As the heart periodically contracts and relaxes, the pressure differentials fluctuate, causing blood flow to oscillate about a non-zero net-period flow-rate. Correspondingly, the transport of blood-borne species is inherently oscillatory<sup>2</sup>, with oscillations imparted by the advecting blood medium. Advective transport by blood flow is one of two dominant transport processes governing species within the cardiovascular system, with the other being diffusive transport. The net transport of a species may be therefore regarded as a competing balance between the two transport processes, with advection generally dominating within the bulk blood flow and diffusion near the vascular walls. This collective behaviour is quantified by the dimensionless Péclet number (Pe), which measures the respective rates of advective and diffusive transport.

At any point in the flow, advective transport is perceived almost equally amongst relatively passive blood-borne species (i. e. that do not significantly influence the flow field). However, diffusive transport can vary since diffusivity varies amongst species and hence, their corresponding Péclet numbers. A low Péclet number species (i.e. of high diffusivity

<sup>1</sup>The subscripts  $i, j$  are reserved for index notation of Cartesian tensors; all other subscripts are for designating variables and should not be interpreted as tensor indices. Repeated indices in a term imply Einstein summation notation. For the generic vector variable  $\boldsymbol{\phi}$ , the element-wise absolute is designated by  $|\phi_i|$  and the Euclidean magnitude (2-norm) by  $\|\boldsymbol{\phi}\| = \sqrt{\phi_i \phi_i}$ .

<sup>2</sup>The terms *oscillatory* and *pulsatile* are herein used interchangeably to describe the flow and are not differentiated with any distinct meaning.

within blood plasma), would be little influenced by the oscillatory flow and would conform to a near-regular transport. However, most blood-borne species are generally of high Péclet numbers in the bulk flow, such as low density lipoproteins ( $Pe \sim 2 \times 10^8$ ) and oxygen ( $Pe \sim 1 \times 10^6$ ) (Stangeby and Ethier, 2002). In such species, the dominance of advective transport implies a strong influence from the flow, and hence its oscillatory behaviour on their transport. From a modelling perspective, this presents a potential constraint for high Péclet number species transport, since the strong coupling to the flow in the bulk flow and increasing influence of diffusivity in the near-wall flow implies an interplay of varying length and time scales. That is, the corresponding response of the species to perturbations from the oscillating flow would spatially vary between the bulk and near-wall flow, requiring a large number of periods (i. e. computational time) to achieve a steady-periodic equilibrium state.

This is demonstrated in the transport of high Péclet number blood-borne species, in that whilst the flow may resolve to a steady-periodic regime within a reasonable  $\sim 5$  periods of oscillation from resting-state initial conditions (Liu *et al.*, 2011), the same is not necessarily true for the species, which may take considerably longer (Sun *et al.*, 2007). This is especially problematic near vascular walls where other types of interactions may occur, such as transport into the walls and reactions with other species (Tarbell, 2003). For computational models of such species, this presents an inconvenience that may be infeasible to resolve within reasonable time and computational resources. Indeed, oscillatory flow and mass transport has been extensively investigated in past studies, such as those of Hong *et al.* (2012), Liu *et al.* (2011), Sakellarios *et al.* (2013) and Sun *et al.* (2007). However, the difficulty of attaining a steady-periodic regime still remains to be realised within feasible computational resources. In the objective of resolving this difficulty, the mechanics that influence the steady-periodic regime for flow and species transport are therefore investigated in the present study. Period-averaging techniques akin to those of turbulence modelling are applied to the governing flow and species transport equations, so that they may be compared to their equivalent steady-state conditions.

## METHODOLOGY

A human right coronary artery (RCA) segment is selected as the subject geometry of study for this investigation. This is because coronary arteries are inherent with relatively small diameters and longitudinal variations in their geometry; the former is useful for reducing computational requirements as multiple periods of oscillation are to be computed, and the latter is useful for inducing variations in the distribution of near-wall species concentration. For this study, the species to be investigated is low density lipoprotein (LDL).

### Geometry

The RCA geometry<sup>3</sup> to be investigated comprises of a single stem with no bifurcations or branches. The geometry comprises of the volumetric flow space (lumen)  $\Omega_F$ , which is bounded by the wall  $\Gamma_W$ , inflow  $\Gamma_I$  and outflow  $\Gamma_O$  boundaries; see figure 1 (a). To ensure that the flow and species entering  $\Omega_F$  are sufficiently developed from their boundary condition states, the inflow and outflow boundaries are extended by flow extensions of 5 [mm] and 10 [mm] respectively.

The geometry is discretised using a longitudinally swept O-grid mesh that comprises of 2385 hexahedral elements per cross-section, which amounts to about  $7.75 \times 10^5$  elements for the collective geometry; see figure 1 (b). For most of the volumetric flow space, the concentration of LDL is expected to be uniform, except near the wall where a thin mass transport boundary layer develops. The near-wall mesh is thus refined to sufficiently resolve the mass transport boundary layer, such that the first element layer height is about 2200 times smaller than the average inflow diameter  $d_I$ .

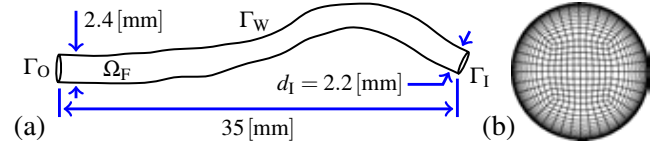


**Figure 1:** Detail of the RCA segment used for this study, with (a) geometry schematic (not including flow-extensions) and (b) cross-section O-grid mesh (coarsened for display).

### Governing equations

To investigate the oscillatory behaviour of flow and mass transport of blood and blood-borne species, a continuum description is considered. That is, though it is recognised that blood comprises a heterogeneous suspension of particulates, the collective fluid is approximated as continuous on a sufficiently large macroscale level. For blood vessels with diameters significantly larger than that of an erythrocyte (i. e. red blood cell), the continuum fluid assumption is found to satisfactorily hold. However, special care needs to be made in resolving macroscale level properties such as rheology, which need to be described via constitutive models (Thiriet, 2008). For the present study, the arterial wall is assumed to be rigid and hence non-compliant. This assumption is made so that data processing of oscillatory blood flow and blood-borne species transport can be made within a fixed (i. e. Eulerian) reference frame. For example, the Eulerian reference frame allows for a spatially-invariant definition of period-averaging to be naturally realised. Otherwise, if the arterial wall is allowed to deform, then so would the volumetric flow space  $\Omega_F$ . In such a case, special treatment would be required to define a spatially-invariant period-average within  $\Omega_F$ .

#### Blood flow transport

To describe blood flow, the incompressible mass and momentum conservation (Navier–Stokes) equations are used. In conservative-form, these are respectively expressed by

$$\partial_i u_i = 0 \quad (1)$$

$$\rho \partial_t u_i + \partial_j (\rho u_i u_j - \tau_{ij} + p \delta_{ij}) = 0, \quad (2)$$

where  $u_i$  is a component of the blood's velocity field vector  $\mathbf{u}$  and  $p$  is its scalar pressure field;  $\delta_{ij}$  is the Kronecker delta. The viscous stress tensor is defined  $\tau_{ij} = 2\mu \Delta_{ij}$  and the strain-rate tensor  $\Delta_{ij} = \frac{1}{2} (\partial_i u_j + \partial_j u_i)$ . Material properties are provided by the blood's density  $\rho$  and viscosity  $\mu$ , which are assumed constant for the present formulation, such that  $\rho = 1050$  [kg/m<sup>3</sup>] and  $\mu = 3.45 \times 10^{-3}$  [kg/m/s].

Whilst it is recognised that blood viscosity is non-Newtonian (i. e. having a strain-rate dependence), its equivalent Newtonian approximation may be acceptable for arteries with diameters significantly larger than that of an erythrocyte  $\sim 8 \times 10^{-6}$  [m] (Ambrosi *et al.*, 2012). The RCA geometry of figure 1 is sufficiently large to satisfy this condition and since

<sup>3</sup>Geometry provided by the Biofluid Mechanics Lab, Charité Universitätsmedizin Berlin.

multiple periods of oscillation are to be computed in this study, the Newtonian approximation is used so that computational needs are reduced. However, it is recommended that in general, a high fidelity model of blood flow within coronary arteries should use a non-Newtonian viscosity formulation; see for example the models presented in Cho and Kensey (1991). It is also noted that the near-wall computational elements (required to resolve the mass transport boundary layer) are smaller than the diameter of an erythrocyte and hence, should resolve greater detail than the continuum description of blood would allow. Such flow detail is beyond the scope of the present study and may necessitate local corrections to the material properties of the blood fluid if required. This has been addressed in studies such as Huang *et al.* (2009), which have resolved such detail as the Fahraeus–Lindqvist effect (migration of erythrocytes away from the wall) and resulting variations in blood rheology.

### Species transport

As with the flow, the distribution of blood-borne species is modelled as a continuum. That is, rather than tracking individual particles, their concentration is resolved on an Eulerian framework. For this study, the species of interest is low density lipoprotein (LDL); a single particle has a diameter of approximately  $2.0 \times 10^{-8}$  [m] (Teerlink *et al.*, 2004), which is about  $10^5$  times smaller than the internal diameter of a coronary artery. Thus, with such large difference between their respective diameters, the continuum description is expected to satisfactorily hold for the transport of LDL.

The presence of LDL is assumed to have no influence on the flow field. Therefore, LDL concentration transport is modelled as a passive scalar  $c$  that is advected with the flow (one-way coupling). The governing transport equation can be expressed in conservative form as

$$\partial_t c + \partial_i (u_i c - D \partial_i c) = 0, \quad (3)$$

where  $D$  is the isotropic diffusion coefficient, which for LDL is about  $5.0 \times 10^{-12}$  [m<sup>2</sup>/s] (Stangeby and Ethier, 2002). For the present case,  $c$  is a normalised concentration which has been scaled by its inflow value, such that  $c = C/C_0$ , where  $C$  is the concentration and  $C_0$  is its inflow boundary value.

### Boundary conditions

For a boundary  $\Gamma$  enclosing the volumetric flow space  $\Omega_F$ , its inward-pointing surface normal is designated by  $\mathbf{n}^+$  and outward-pointing surface normal by  $\mathbf{n}^-$ . The boundary conditions described here are for pulsatile flow conditions. Under steady-state conditions (i. e. when  $\partial_t u_i = 0$  and  $\partial_t c = 0$  in equations 2 and 3 respectively), the boundary conditions take their period-average values. At the inflow boundary  $\Gamma_I$ , a pulsatile Poiseuille flow profile of the form

$$u_i(\mathbf{x}, t) = 2u_0(t) \left( 1 - \left( \frac{\|\mathbf{x} - \mathbf{x}_c\|}{\frac{1}{2}d_I} \right)^2 \right) n_i^+ \quad (4)$$

is assigned, where  $u_0$  is the boundary-average velocity, which follows the time-periodic waveform defined in figure 2 and has period-average  $\bar{u}_0$ . The characteristic parabolic profile of the Poiseuille flow has its maximum at the boundary centroid  $\mathbf{x}_c$ , where  $\mathbf{x}$  is a spatial coordinate on the boundary. To gauge-fix the pressure field, an arbitrarily selected Dirichlet condition  $p = 0$  is assigned to the outflow boundary  $\Gamma_O$ ; the precise value is not important under the present conditions. For the wall boundary  $\Gamma_W$ , a no-slip wall condition is assigned, such that  $u_i = 0$ .

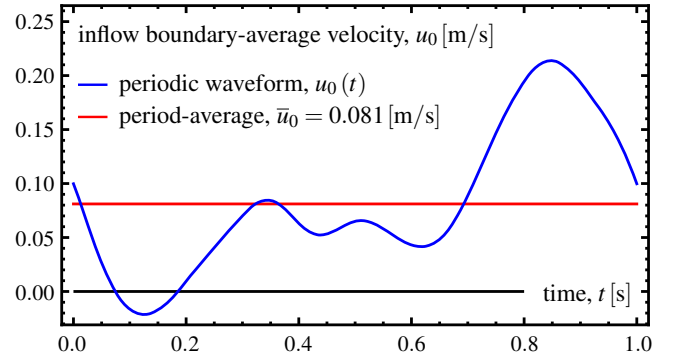


**Figure 2:** Plot of the RCA inflow waveform and its period-average; using an 8-term truncated Fourier series representation of the waveform provided in (Johnston *et al.*, 2006).

Since the LDL concentration field has been normalised by its inflow value, the inflow boundary  $\Gamma_I$  is therefore ascribed with the uniform condition  $c = 1$ . At the outflow boundary  $\Gamma_O$ , a zero flux condition  $(\partial_i c) n_i^- = 0$  is assigned. Both these conditions are whole-boundary approximations and locally misrepresent the near wall LDL concentration due to the presence of a spatially growing boundary layer. However, due to the high Péclet number of LDL, its species transport equation is weakly elliptic, and so with the added flow-extensions, the effect of the misrepresented boundary conditions is not significant within the domain of interest. On the wall boundary  $\Gamma_W$ , the flux equilibrium condition

$$(u_i c - D \partial_i c) n_i^- = J_c \quad (5)$$

is ascribed, which describes the balance between advective flux into the wall and diffusive flux away from it. The net influx  $J_c$  of LDL into the arterial wall is set to be zero for the present conditions. The advecting velocity into the wall is set to be constant and equivalent to the water filtration velocity  $J_u = 4.0 \times 10^{-8}$  [m/s] (Stangeby and Ethier, 2002), such that  $u_i n_i^- = J_u$ . Note that this boundary condition has only been enforced in the species transport and has been omitted from the flow equations for this study. A more appropriate boundary condition for the flow equations should therefore correct the no-slip wall condition, such that

$$u_i n_i^- = J_u \quad (6)$$

$$u_i - (u_j n_j^-) n_i^- = 0. \quad (7)$$

The effect of the misrepresented boundary condition is not expected to influence the flow field significantly, because  $J_u$  is much smaller than  $\bar{u}_0$  and the domain  $\Omega_F$  is small; see the analytical solution for a straight artery with a semi-permeable wall in Wada and Karino (2000) for the influence of  $J_u$ .

### Oscillatory flow data processing

An arbitrary scalar field variable  $\phi$  that is transported within an oscillating flow of period-length  $T_p$  is considered. To compare the oscillating field variable with its steady-state, it is first necessary to decompose it into a time-invariant state. This is achieved with Reynolds periodic-decomposition, which decomposes the field variable into its period-average  $\bar{\phi}$  and time-dependent perturbation  $\phi'$  components. Reynolds periodic-decomposition is defined

$$\phi(t) = \left\{ \bar{\phi} + \phi'(t) \mid \bar{\phi} = \frac{1}{T} \int_T \phi(t) dt, t \in T \right\}, \quad (8)$$

where  $T = kT_p$  is the integration time and  $k \geq 1$  is an integer multiplier. Under laminar flow conditions, the flow field is periodic at all relevant length scales; therefore, the decomposition may be made over a single period of oscillation ( $k = 1$ ). However, under turbulent flow conditions, a sufficiently large number of periods ( $k \gg 1$ ) would be required for  $\bar{\varphi}$  to become temporally invariant.

Applying the Reynolds periodic-decomposition to the flow (equations 1 and 2) and species transport (equation 3), and period-averaging, respectively yields

$$\partial_i \bar{u}_i = 0 \quad (9)$$

$$\rho \partial_i \bar{u}_i + \partial_j \left( \rho \left( \bar{u}_i \bar{u}_j + \overline{u'_i u'_j} \right) - \bar{\tau}_{ij} + \bar{p} \delta_{ij} \right) = 0 \quad (10)$$

$$\partial_i \bar{c} + \partial_i \left( \bar{u}_i \bar{c} + \overline{u'_i c'} - D \partial_i \bar{c} \right) = 0. \quad (11)$$

It is noted that the period-averaged flow and mass equations are similar to their original form, except for the presence of added terms, which have emerged from the non-linear advective components of the equations. These added terms describe the period-aggregate influence of fluctuations about the period-average of their respective field variable. For the flow (equation 10) and species (equation 11), these added terms are respectively referred as the oscillatory advective-stress and oscillatory advective-flux.

Due to the presence of the oscillatory advective-stress and oscillatory advective-flux in the flow and species transport equations respectively, variations may emerge between the period-average and equivalent steady-state of their respective field variables. These variations may be subtle and difficult to qualitatively differentiate. A quantitative measure is therefore required, and is provided with the Steady Representation Index (SRI), which is defined

$$\text{SRI}\{\varphi\} = \frac{\varphi|_{\text{ss}} - \bar{\varphi}|_{\text{ps}}}{\varphi|_{\text{ss}} + \bar{\varphi}|_{\text{ps}}}. \quad (12)$$

This index quantifies variations in a generic field variable  $\varphi$  that arise due to flow pulsatility, relative to its equivalent steady-state. The SRI is signed and bounded by the range  $-1 \leq \text{SRI} \leq 1$ , such that a positive value  $\text{SRI}\{\varphi\}$  denotes that the steady-state value locally overestimates the field variable  $\varphi$ , and a negative value if it underestimates; at  $\text{SRI}\{\varphi\} = 0$ , both steady and pulsatile conditions are locally equivalent.

For the flow field, oscillatory fluctuations have generally been measured via the Oscillatory Shear Index (OSI), which was designed to measure fluctuations in the wall shear stress  $\boldsymbol{\tau}_w$  (He and Ku, 1996). In a previous study by the authors (Gabriel *et al.*, 2016), the Oscillatory Shear Index was generalised to the Oscillatory Flow Index (OFI), which extended the domain space of the index onto the flow-field, where

$$\text{OFI} = \begin{cases} 1 - \frac{\|\bar{\mathbf{u}}\|}{\|\mathbf{u}\|} & \text{on } \Omega_F \cup \partial\Omega_F \setminus \Gamma_W \\ 1 - \frac{\|\bar{\boldsymbol{\tau}}_w\|}{\|\boldsymbol{\tau}_w\|} & \text{on } \Gamma_W. \end{cases} \quad (13)$$

Note that the OSI is generally scaled to have a maximum value of 0.5; the scaling multiplier is removed in the above definition as it presents no added value. In the same study (Gabriel *et al.*, 2016), the Oscillatory Kinetic Energy Index (OKEI) was also introduced to measure the significance of the oscillatory fluctuations; by measures the trace (i. e. energy) of the oscillatory advective-stress tensor relative to that

of the period-average flow. The OKEI was also extended to flow and wall spaces, and is defined

$$\text{OKEI} = \begin{cases} \frac{\overline{\mathbf{u}' \cdot \mathbf{u}'}}{\bar{\mathbf{u}} \cdot \bar{\mathbf{u}} + \overline{\mathbf{u}' \cdot \mathbf{u}'}} & \text{on } \Omega_F \cup \partial\Omega_F \setminus \Gamma_W \\ \frac{\overline{\boldsymbol{\tau}'_w \cdot \boldsymbol{\tau}'_w}}{\bar{\boldsymbol{\tau}}_w \cdot \bar{\boldsymbol{\tau}}_w + \overline{\boldsymbol{\tau}'_w \cdot \boldsymbol{\tau}'_w}} & \text{on } \Gamma_W. \end{cases} \quad (14)$$

By applying the OFI to the OKEI, direction-reversing (DR) and non direction-reversing (NDR) oscillations can be segregated and their significance measured, such that

$$\text{OKEI}_{\text{DR}} = \text{OKEI} \times \text{OFI} \quad (15)$$

$$\text{OKEI}_{\text{NDR}} = \text{OKEI} \times (1 - \text{OFI}). \quad (16)$$

It is noted that a similar period-averaging technique was applied by Hong *et al.* (2012) to derive the period-average species concentration equations for LDL transport within the arterial wall. In that study, the authors argued that within the arterial wall, the period-averaged LDL concentration is significantly larger than its oscillatory perturbations and can thus be represented satisfactorily by the steady-state equivalent. In the present analysis, the period-averaged species equations within the lumen are demonstrated to inherit the period-aggregated influence of oscillatory perturbations via the oscillatory advective-flux term, which depending on its magnitude, can spatially modify the period-average species concentration from its steady-state equivalent. Therefore, in the same manner as the OKEI for the flow, the Oscillatory Species Advective-Flux Index (OSAFI) is proposed to measure the significance of the oscillatory advective-stress term in equation 11; the OSAFI is defined

$$\text{OSAFI} = \frac{\|\overline{\mathbf{u}' c'}\|}{\|\bar{\mathbf{u}} \bar{c}\| + \|\overline{\mathbf{u}' c'}\|} \quad \text{on } \Omega_F \cup \partial\Omega_F \setminus \Gamma_W. \quad (17)$$

## Computational implementation

The system of flow and species transport equations was implemented into the cell-centred finite-volume solver ANSYS Fluent v17.2, with in-house user-defined functions for customisation of the solver and data-processing. Computations were made with double-precision on a 64-bit serial machine. For the flow equations, pressure-velocity coupling was attained via the SIMPLE algorithm. Flow variable discretisation was made using a second-order upwind scheme and pressure discretisation using the *standard* ANSYS Fluent scheme (a neighbour-cell interpolation method using momentum equation coefficient weighting). For species (LDL concentration) discretisation, a first-order upwind scheme was used; this scheme was implemented to avoid numerical instabilities arising due to the high Péclet number associated with the species transport. Temporal discretisation of all equations was made with an implicit first-order forward-differencing scheme. Field variable gradients were derived using least-squares cell-based interpolation.

## RESULTS AND DISCUSSION

For the pulsatile flow (i. e. temporal) case, computations were terminated at the end of the 20th period of oscillation. It was found that from zero initial conditions, the flow field had converged to a steady-periodic state by the fourth period (i. e. the period-average remained unchanged with successive periods). However, as expected of the high Péclet number associated with LDL transport, the LDL concentration field

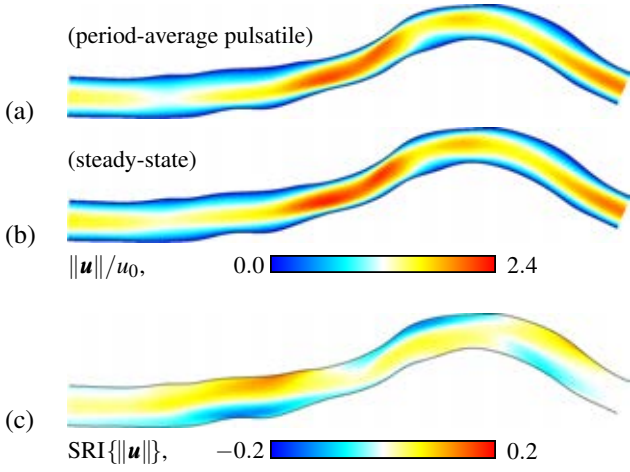


**Figure 3:** Plot of normalised velocity magnitude on a longitudinal mid-cut of the artery; for (a) period-average of pulsatile flow, (b) steady-state flow and (c) Steady Representation Index of both conditions.

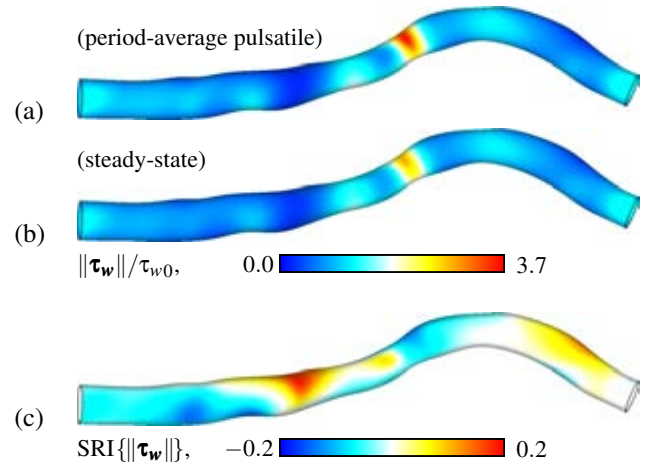


**Figure 4:** Plot of normalised wall shear stress magnitude on the wall; for (a) period-average of pulsatile flow, (b) steady-state flow and (c) Steady Representation Index of both conditions, where  $\tau_{w0} = 8\mu u_0/d_1$  is the inflow's equivalent Poiseuille wall shear stress.

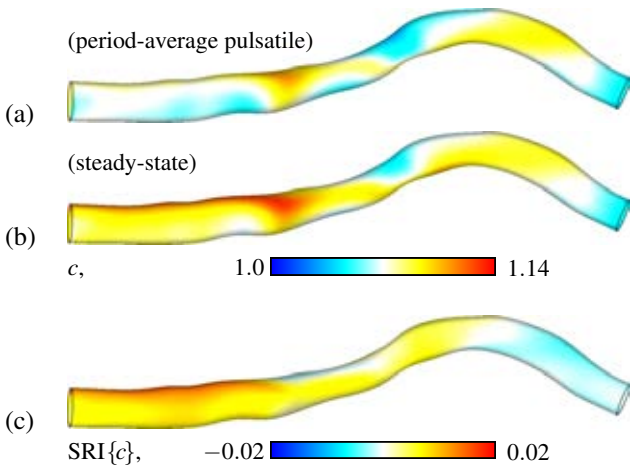


**Figure 5:** Plot of normalised LDL concentration on the wall; for (a) period-average of pulsatile flow, (b) steady-state flow and (c) Steady Representation Index of both conditions.

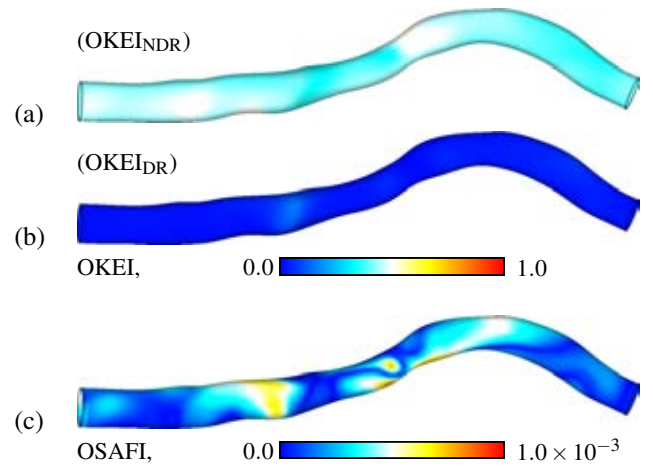


**Figure 6:** Plot of OKEI on the wall; for (a) NDR and (b) DR oscillations. Also, a plot of (c) OSAFI on a near-wall surface within  $\Omega_F$  (i. e. taking measurements at the first element layer from the wall).

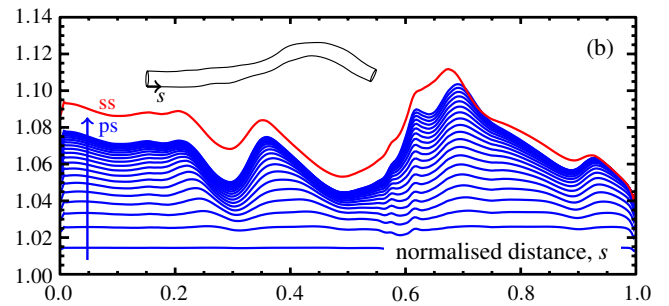
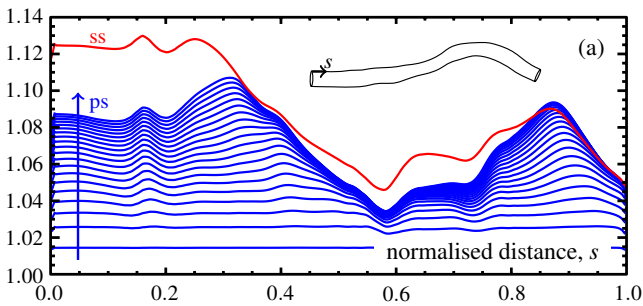


**Figure 7:** Plot of normalised LDL concentration along the normalised distance of the (a) upper and (b) lower span of the RCA; comparing period-averaged pulsatile-state (ps) and equivalent steady-state (ss) conditions. The direction of the arrow is from period 1–20.

was yet to converge onto a steady-periodic state from initial conditions  $c = 1$  (see figure 7). Nevertheless, to give preliminary insight into what is expected of a converged periodic state for the LDL concentration field, the 20th period results are investigated for the present study.

Observation of the flow and wall shear stress distributions in

figures 3 and 4 respectively, reveals that the period-average of the pulsatile flow displays similar characteristic to that of its equivalent steady-state condition. However, subtle variations can be observed, particularly in the magnitude of the velocity and wall shear stress at the narrowing of the artery (near its longitudinal centre) and at the expansion thereafter



(just before the outflow). This is confirmed by the SRI for these respective indices, which also reveals that its sign is not homogeneous but a seemingly even distribution of positive and negative; indicating that the period-average of the pulsatile flow is both overestimated and underestimated relatively evenly by its steady-state equivalent.

For the LDL concentration (figure 5), it is noted that the period-average distribution for the 20th period is significantly far from converged, and many more periods are required before a steady-periodic state is achieved. When compared to the steady-state case, it appears that both distributions resemble each other (since regions of high and low concentrations seem to spatially coincide), though their respective magnitudes substantially differ. Correspondingly, it is expected that the steady-periodic state may also behave similarly to the 20th period. From the corresponding signed SRI distribution, it is noted that the period-average of the oscillatory concentration field is mostly less than that of its steady-state equivalent. Observation of successive period-averaged concentration profiles along the span of the artery (figure 7) reveals that the concentration field is currently incrementally increasing in magnitude away from its initial condition  $c = 1$ . This behaviour appears to be monotonic and slowing down with each successive period, indicating that the steady-periodic state is a converging limit.

It is difficult to ascertain the influence of flow oscillations on the flow and species field variables, from their respective distributions alone. However, this information can be determined from their corresponding oscillatory indices. From figure 6, it can be observed that the OKEI is significant throughout the artery, with NDR oscillations dominating. A small distribution of  $OKEI_{DR}$  is also observed, though this is insignificant relative to that of the  $OKEI_{NDR}$ . The magnitude of these distributions is generally equal to or less than 0.5, indicating that the oscillatory advective-stress is not dominant though moderately influential in modifying the period-average flow field from its equivalent steady-state.

For the OSAFI, a more diverse distribution is observed, where there seems to be little correlation with that of the OKEI. However, a similar distribution is observed with the  $SRI\{\|\tau_w\|\}$  (figure 4), indicating a possible relation with the gradient of the flow velocity. Though, further analysis is required before this can be ascertained.

## CONCLUSION

The oscillatory transport of pulsatile blood flow and blood-borne species (low density lipoprotein) has been investigated in the present study. It was determined from their respective period-averaged transport equations that oscillatory influence is inherent to the period-average transport. This influence is prominent in the advective terms of the equations and manifests as the period-aggregate of oscillatory advective-stresses and advective-fluxes within the flow and species transport respectively. These terms are identified to be the cause for parting the period-average transport from its equivalent steady-state condition. To investigate these terms, pulsatile blood flow within a human right coronary artery is investigated and oscillatory indices developed to measure their significance. It was observed that though a direct correlation could not be ascertained between the oscillatory indices for flow and species transport respectively, there was sufficient similarity to imply a potential relationship. It is the objective of this study that such a relationship can be determined and modelled, so as to better resolve pulsatile species transport without explicitly resolving all periods of oscillation.

## ACKNOWLEDGEMENTS

This work was supported by an Australian Government Research Training Program Scholarship and a grant from the CSIRO through the ATN Industry Doctoral Training Centre. The Biofluid Mechanics Lab, Charité Universitätsmedizin Berlin is acknowledged for providing the RCA geometry.

## REFERENCES

- AMBROSI, D., QUARTERONI, A. and ROZZA, G. (eds.) (2012). *Modeling of Physiological Flows*, vol. 5 of *Modeling, Simulation & Applications*. Springer Milan, Milano.
- CHO, Y.I. and KENSEY, K.R. (1991). "Effects of the non-Newtonian viscosity of blood on flows in a diseased arterial vessel. Part 1: Steady flows." *Biorheology*, **28(3-4)**, 241–62.
- GABRIEL, S.A., DING, Y. and FENG, Y. (2016). "Extending the Oscillatory Index to discern oscillatory flow modes". *20th Australasian Fluid Mechanics Conference*, 1–4. Australasian Fluid Mechanics Society, Perth, Australia.
- HE, X. and KU, D.N. (1996). "Pulsatile flow in the human left coronary artery bifurcation: average conditions." *Journal of Biomechanical Engineering*, **118(1)**, 74–82.
- HONG, J., FU, C., LIN, H. and TAN, W. (2012). "Non-Newtonian effects on low-density lipoprotein transport in the arterial wall". *Journal of Non-Newtonian Fluid Mechanics*, **189-190**, 1–7.
- HUANG, J., LYCZKOWSKI, R.W. and GIDASPOW, D. (2009). "Pulsatile flow in a coronary artery using multiphase kinetic theory". *Journal of biomechanics*, **42(6)**, 743–54.
- JOHNSTON, B.M., JOHNSTON, P.R., CORNEY, S. and KILPATRICK, D. (2006). "Non-Newtonian blood flow in human right coronary arteries: transient simulations." *Journal of biomechanics*, **39(6)**, 1116–28.
- LIU, X., FAN, Y., DENG, X. and ZHAN, F. (2011). "Effect of non-Newtonian and pulsatile blood flow on mass transport in the human aorta". *Journal of Biomechanics*, **44(6)**, 1123–1131.
- SAKELLARIOS, A.I. *et al.* (2013). "Patient-specific computational modeling of subendothelial LDL accumulation in a stenosed right coronary artery: effect of hemodynamic and biological factors." *American journal of physiology. Heart and circulatory physiology*, **304(11)**, H1455–70.
- STANGEBY, D.K. and ETHIER, C.R. (2002). "Computational analysis of coupled blood-wall arterial LDL transport". *Journal of biomechanical engineering*, **124(1)**, 1–8.
- SUN, N. *et al.* (2007). "Influence of pulsatile flow on LDL transport in the arterial wall". *Annals of biomedical engineering*, **35(10)**, 1782–90.
- TARBELL, J.M. (2003). "Mass transport in arteries and the localization of atherosclerosis". *Annual review of biomedical engineering*, **5(1)**, 79–118.
- TEERLINK, T., SCHEFFER, P.G., BAKKER, S.J.L. and HEINE, R.J. (2004). "Combined data from LDL composition and size measurement are compatible with a discoid particle shape". *Journal of lipid research*, **45(5)**, 954–66.
- THIRIET, M. (2008). *Biology and Mechanics of Blood Flows. Part II: Mechanics and Medical Aspects*. Springer, New York, NY.
- WADA, S. and KARINO, T. (2000). "Computational Study on LDL Transfer from Flowing Blood to Arterial Walls". T. Yamaguchi (ed.), *Clinical Application of Computational Mechanics to the Cardiovascular System*, 157–173. Springer Japan, Tokyo.

## PATIENT SPECIFIC NUMERICAL SIMULATION OF FLOW IN THE HUMAN UPPER AIRWAYS FOR ASSESSING THE EFFECT OF NASAL SURGERY

**Maria R. JORDAL<sup>1\*</sup>, Sverre G. JOHNSEN<sup>2</sup>, Sigrid K. DAHL<sup>2</sup>, Bernhard MÜLLER<sup>1</sup>**

<sup>1</sup> NTNU Department of Energy and Process Engineering, 7491 Trondheim, NORWAY

<sup>2</sup> SINTEF Materials and Chemistry, 7465 Trondheim, NORWAY

\* E-mail: mariarjordan@gmail.com

### ABSTRACT

The study is looking into the potential of using computational fluid dynamics (CFD) as a tool for predicting the outcome of surgery for alleviation of obstructive sleep apnea syndrome (OSAS). From pre- and post-operative computed tomography (CT) of an OSAS patient, the pre- and post-operative geometries of the patient's upper airways were generated. CFD simulations of laminar flow in the patient's upper airway show that after nasal surgery the mass flow is more evenly distributed between the two nasal cavities and the pressure drop over the nasal cavity has increased. The pressure change is contrary to clinical measurements that the CFD results have been compared with, and this is most likely related to the earlier steps of modelling – CT acquisition and geometry retrieval.

**Keywords:** CFD, upper airways, OSAS, biomechanics

### NOMENCLATURE

#### Greek Symbols

$\rho$  Mass density, [kg/m<sup>3</sup>].

$\mu$  Dynamic viscosity, [Pa s].

#### Latin Symbols

A Cross sectional area [m<sup>2</sup>].

D<sub>H</sub> Hydraulic diameter [m].

p Pressure, [Pa].

P Perimeter [m].

Q Volumetric flow rate, [ml/s].

R Resistance, [Pa s/ml].

U<sub>avg</sub> Average velocity [m/s]

V Velocity vector, [m/s].

#### Abbreviations

AHI	Apnea-hypopnea index
CFD	Computational fluid dynamics
CT	Computed tomography
HU	Hounsfield units
OSAS	Obstructive sleep apnea syndrome
PNIF	Peak nasal inspirational flow
RANS	Reynold averaged Navier Stokes
RMM	Rhinomanometry
RRM	Rhinoresistometry

### INTRODUCTION

Obstructive sleep apnea syndrome (OSAS) is a disorder characterized by repeated collapses of the upper airways, preventing air from flowing freely during sleep, causing apneas (pauses in breath) and hypopneas (shallow breathing). The severity of sleep apnea is indicated by the number of apnea/hypopnea events per hour during sleep, which defines the apnea-hypopnea index (AHI), where <5 is considered normal and >30 severe. The most prevalent symptoms are daytime sleepiness, unrefreshing sleep and snoring, but OSAS has also been shown to increase the chance of cardiovascular diseases (AASM, 1999).

Several surgical and non-surgical treatment options exist for alleviation of OSAS, but it is difficult to predict the outcomes of the treatments. As the success rates of the treatments are highly varying from patient to patient, a tool for predicting their outcome is needed. CFD may aid as such a tool, and may provide a non-invasive and cost-efficient guidance to medical personnel on what surgery procedure to choose.

### Outline

In the current paper we have simulated the flow in the upper airways of one OSAS patient before and after intranasal surgery. The work is based on the treatments for OSAS at St. Olav University Hospital in Trondheim, Norway. Here, intranasal surgery is being performed on patients with OSAS. Only one third of the patients experience improvement in OSAS after surgery. It is not known why there is such a low success rate after surgery, and why some patients improve and others do not (Moxness and Nordgård, 2014). By studying the geometry and flow patterns of the upper airways before and after surgery, the impact of intranasal surgery on the airflow in the upper airway might become clearer. The method for creating computational models from CT images follows in the next section. Selected results (pressure, velocity and nasal resistance) will be discussed and compared with measured results. This article is based on the M.Sc. thesis by Jordal (2016).

A schematic of the upper airways and definitions of the anatomical planes and directions can be seen in Fig. 1.

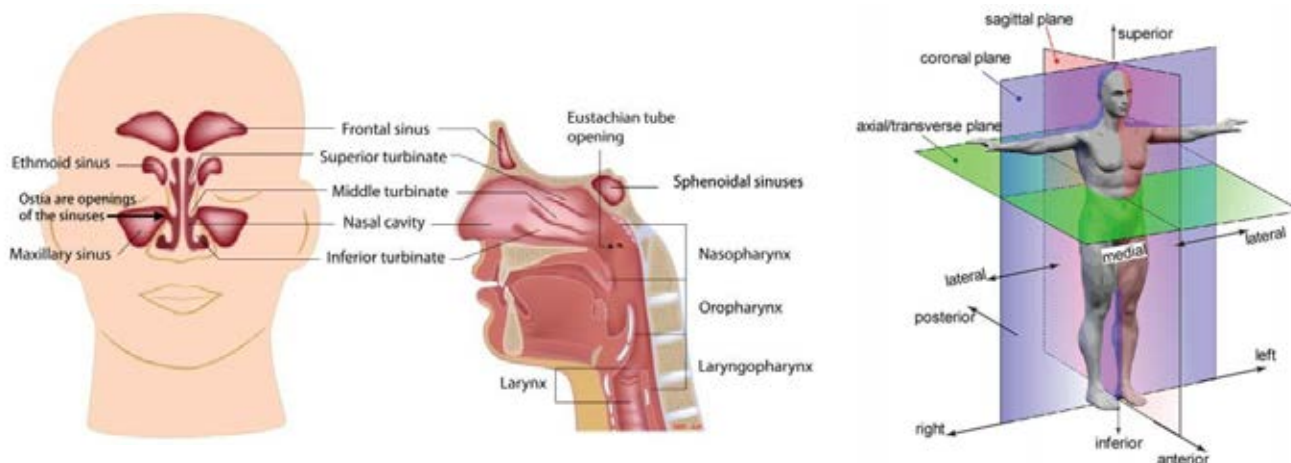


**Figure 1:** Schematic of the upper airways (Southlake sinus and snoring center, 2017) and of the anatomical planes and directions (Tu et al., 2013).

## METHOD

### Geometry Retrieval

#### Data Acquisition

The pre- and post-operative geometries were reconstructed from CT images provided by the Department of Radiology and Nuclear Medicine at St. Olav University Hospital, Trondheim. The CT was done with a Siemens Sensation 64 in the transverse plane. The pre-operative scan provided 342 slices with a slice thickness of 1.0 mm, and the post-operative scan provided a total of 423 slices with a slice thickness of 1.5 mm. All of the 2D CT images consisted of 512x512 pixels.

#### Patient Data

The patient chosen for this particular study is a man born in 1948 with a body mass index of 28. He underwent intranasal surgery at St. Olav Hospital in the fall of 2015 for alleviation of OSAS. The patient had a narrow nasal passage in his left nostril obstructing the airflow, and had surgery to increase the volume of this passage. A result of this intranasal surgery was a reduction in AHI from 23 to 5.7. As  $AHI < 5$  is considered normal, this indicates that the patient is almost alleviated of OSAS.

#### Segmentation Procedure and Editing of Geometry

The segmentation of the upper airways was done using ITK-SNAP 3.4.0 (Yushkevich, 2006). The automatic segmentation was performed using the Active Contour Method with thresholding. Air defines the lower limit of the Hounsfield Unit (HU)-scale at -1024HU, but there is no standard as to what the upper limit should be. Upper HU-values such as -300 (Ito et al., 2011), -400 (De Backer et al., 2007), -460 to -470 (Nakano et al., 2013) and -587 (Weissheimer et al., 2012) have been used for automatic segmentation in previous works. Although there is a big range of the upper limit, all of the above mentioned reported good results with these settings. For this segmentation, -300 as the upper HU-value has been chosen based upon trial and error (Jordal, 2015).

In addition, manual segmentation was necessary in order to capture the geometry. For this, the paint brush mode was used on the slices in all planes (coronal, axial and sagittal). For simplicity of the model, the paranasal sinuses were excluded from the model. The entire segmentation process was done in cooperation with an ear-nose-throat surgeon and a radiologist to make sure the model was anatomically correct.

The segmented volume was extracted from ITK-SNAP as a triangulated surface mesh. Netfabb basic (Netfabb basic v.7.3) was used to analyze and check the quality of the mesh, and MeshLab (Cignoni et al., 2008) for further post-processing. In MeshLab, the mesh was reduced using the built-in function Quadratic Edge Collapse Decimation with topology preservation and a target number of faces of 100 000. This reduces the size of the mesh and the size of the file, which all reduces the time on editing the geometry in the steps that follows. Finally, the mesh was smoothed using the Laplacian Smooth Filter with default settings to avoid any artefacts from digitalization.

Since the patient had been positioned differently on the pre- and post-operative CT the pharynx appeared rather different for the two models (Fig. 2). The bend in the neck post-operatively is a result of a head-rest that was used during CT. The result of this is that the angle between the nasal cavity and the pharynx is larger post-operatively, in addition to some changes in the pharynx and larynx as the walls are elastic.

However, the only difference between the two models should be between geometry of the nasal cavities. To make sure the only difference between the two models was the surgery, and avoid any effects that may be caused from the different positioning during CT, the post-operative nasal cavity was combined with the pre-operative pharynx and larynx. In order to do this, the models were first aligned in MeshLab, converted from surface mesh (stl file) to a solid body (stp file) in ANSYS Spaceclaim, and then combined in ANSYS DesignModeler. The two models had different circumferences, and in order to join the two parts together without creating a stair-step, a small volume (length of 3 mm.) between the two parts was created. In

addition, the outlet was extended by cutting the model at the larynx and extending it in the flow direction using ANSYS DesignModeler in order to avoid reverse flow and to smooth the air flow at the outlet (Fig. 3).

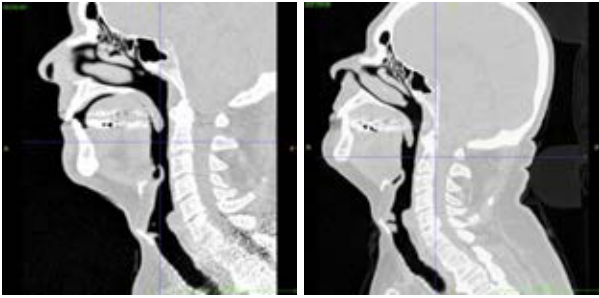


**Figure 2:** Pre- and post-operative CT images of the patient showing the difference in head positioning, respectively. Sagittal view from the left side.

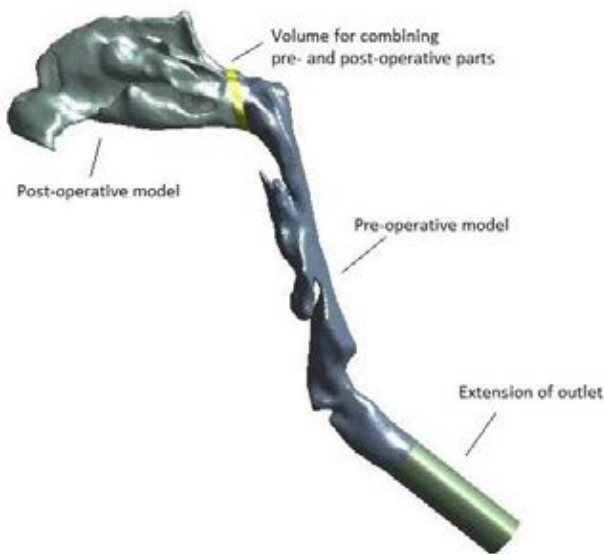


**Figure 3:** The final post-operative geometry showing the different parts that were combined into one single geometry. Viewed from the left side.

### Grid Generation

A grid convergence test was carried out on tetrahedral and polyhedral grids made in Ansys Meshing (ANSYS inc, v.16.2). Coarse, medium and fine (mostly) tetrahedral grids were made in Ansys Meshing by choosing “no set cell type” as the cell type in Ansys Meshing. The same grids were then converted to polyhedral cells in Ansys Fluent. In addition to these six grids, a coarse grid with inflation layers was included in the test. The computational time was about 30% lower on the polyhedral grids, and a medium type grid showed grid independence. Based on the grid convergence test, grids were made for both pre- and post-operative models. The post-operative grid was made with the medium settings which resulted in a grid with 19 783 513 nodes and 3 489 365 polyhedral cells. The pre-operative grid was then made to approximately match the number of cells, and consists of 17 023 087 nodes and 2 993 762 polyhedral cells.

### Numerical Simulation

The incompressible Navier-Stokes equations were solved for the entire domain. They read:

$$\operatorname{div} \mathbf{V} = 0 \quad (1)$$

$$\rho \frac{D\mathbf{V}}{Dt} = -\nabla p + \mu \nabla^2 \mathbf{V} \quad (2)$$

where  $\mathbf{V}$ ,  $p$ ,  $\rho$ ,  $\mu$  are the velocity vector, pressure, mass density and dynamic viscosity, respectively. The software ANSYS Fluent was used for numerical simulations. The flow simulated is modelled as incompressible, hence the pressure-based solver was chosen. This solver is also default in Fluent. The pressure based solver couples the velocity and pressure and for this SIMPLE (semi-implicit method for pressure-linked equations) was chosen. SIMPLE is default in ANSYS Fluent. For the spatial discretization, the following default settings were used; Gradient: Least square cell based, pressure: second order, momentum: second order upwind. For the transient formulation (when applied), the second order implicit was used. Inspirational flow was simulated by defining the nostrils as inlets with atmospheric pressure (0 Pa total pressure), and the end of larynx as the outlet with a uniform outflow velocity corresponding to 250ml/s. The no-slip condition was applied at the walls. The flow was simulated as laminar with  $\rho = 1.225 \text{ kg/m}^3$  and  $\mu = 1.7894 \cdot 10^{-5} \text{ Pas}$ .

Because of the large amount of grid cells, the simulations were done on a high performance computer available at NTNU. With 12 CPUs, this took about two days, but the solution was not fully stable. The flow was modelled as steady-state, but to reach a solution, the flow was solved as transient with a time step of 10e-6 seconds with a maximum of 20 iterations per time step. This went on until the solution converged with the scaled residuals in the order of e-09 to e-13.

### Clinical Measurements

From St. Olav Hospital, data from rhinometric measurements, such as rhinoresistometry (RRM) and rhinomanometry (RMM) were available. RRM and RMM measure the resistance in the nose at different flow rates. The resistance,  $R$ , is defined as  $R = \Delta P/Q$  where  $\Delta P$  is the pressure difference from the nostrils to the posterior nose/beginning of nasopharynx, and  $Q$  is the volumetric flow rate. The resistances of the left and right nasal cavities are measured individually. The test procedure is to close one of the nostrils, placing a mask over the nose and mouth, and letting the patient breathe in and out at normal pace. All tests have been done both pre- and post-operatively, before and after decongestion of the nose. The tests were first taken when the nose was at its normal state. After this, the patient was given nasal spray, and waited 15 minutes before the tests were retaken. This was done to decongest the nose and eliminate the effect of mucosa

To compare the measured values, the resistance was calculated from the CFD-results. The volumetric flow rate was calculated from the mass flow rates of

each of the nostrils, and the pressure drop was defined from the inlets (nostrils) to the posterior nose. The results were compared with the results from RMM and RRM at the same flow rates.

## RESULTS

### Geometry

The difference between the two final geometries is the nasal cavity, and a more detailed view of this can be seen in Fig. 4-6.



**Figure 4:** The nasal cavity pre(left)- and post(right)-operative viewed from the left side. Planes used for cross sections in Fig. 5-6 are marked.

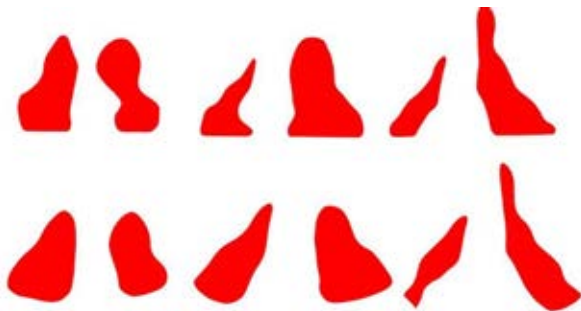


**Figure 5:** Cross sections at planes 1-3. Pre-operative model on top, and post-operative below.

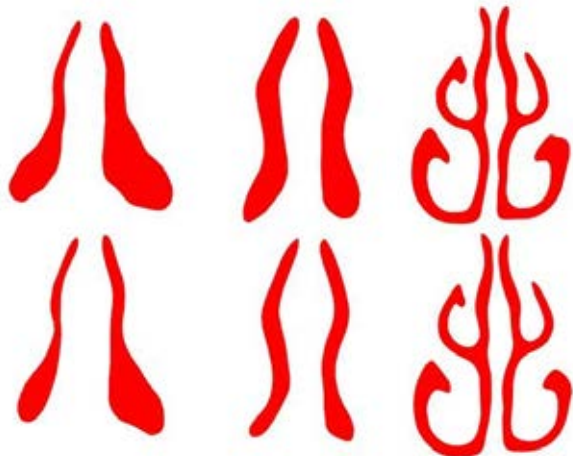


**Figure 6:** Cross sections at planes 4-6. Pre-operative model on top and post-operative model below.

The surgery was performed in order to open up the narrow airway on the anterior left nasal cavity, and straighten out the septum. As seen in Fig. 5-6, this volume has increased on both left and right side in the anterior nose. However, the volume appears to have decreased after surgery posterior in the nose. This will be discussed further. The inlets of the pre- and post-operative models are angled slightly different, but this is not affecting the air flow remarkably (Taylor et.al. 2010).

### Velocity

The velocity distribution in the upper airways both pre- and post-operatively showed lower velocities in the nasal cavity, and an increase in velocity as the cross sectional area becomes narrower in the pharynx. The velocity magnitudes across a sagittal cut plane can be seen in Fig.10. The plane is positioned in the middle of the pharynx and the larynx, and close to the septum on the left nasal cavity.

The highest velocities are found in the smallest cross sectional area, which is behind the epiglottis. This narrowing creates a pharyngeal jet. A large change in the angle between the pharynx and larynx creates swirling and recirculation in the larynx. The maximum velocities are almost identical pre- and post-operative at 7.783 and 7.827 m/s, respectively. As the mass flow is constant and identical in both cases, and the pre- and post-operative geometry is the same from the nasopharynx and below, the velocity is expected to be similar in these areas. Differences in the pre- and post-operative nasal cavities can be observed as the geometry has changed (Fig. 9).

It can be seen that the velocity magnitude has increased on the left side after surgery. The highest velocities are found in the inferior nasal cavity around the inferior turbinate and close to the septum. The lowest velocities are observed in the olfactory zone and at the edges. The findings correspond with the description of flow patterns in the literature (Schreck et al., 1993, Hahn et al., 1993, Keyhani et al., 1995). The flow is more evenly spread out in the right nasal cavity. The differences between the left and right nasal cavity and the pre- and post-operative nasal cavities are well illustrated by the velocity streamlines (Fig. 11).

In Fig. 11 it can be seen that the majority of the flow is in the inferior nasal cavity. After surgery, the velocities are higher in the left nasal cavity. This is a result of an increased volume in the left anterior nasal cavity allowing more air in. Before surgery 15% more of the flow went through the right nasal cavity than the left. After surgery, this difference is reduced to 8%. Even though the mass flow rate in the right nasal cavity is lower after surgery, the velocity has not decreased. However, the cross sectional area appear to have decreased. This will be discussed further below.

From the velocity, the Reynolds Number was calculated at the cross sections marked in Fig. 8 as follows:

$$Re = \frac{\rho U_{avg} D_H}{\mu} \quad (3)$$

where  $D_H$  is the hydraulic diameter,  $D_H = 4A/P$ , where  $A$  is the cross-sectional area and  $P$  the perimeter. For the nasal cavity, both  $P$  and  $A$  are summations of both the left and the right side of the cavity.  $U_{avg}$  is the area averaged velocity at the cross section. The result is plotted in Fig 7.

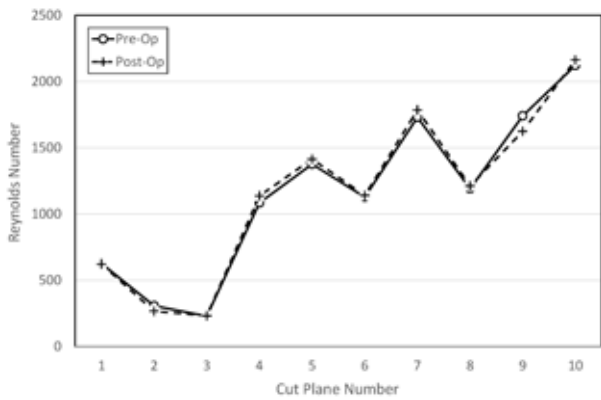


**Figure 7:** Calculated Reynolds numbers at selected cut planes (see Fig. 8) based on area averaged velocity and hydraulic diameter of the cut plane

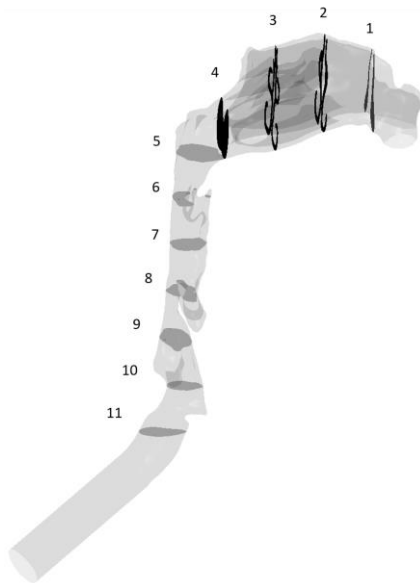


**Figure 8:** Location and numbering of cut planes used for calculation of Reynolds number.

The Reynolds number ranges from 621 to 2160, which is within the laminar regime. Based on this, the laminar approach is suitable.

### Pressure

At a flow rate of 250 ml/s, the calculated pressure drop from inlet to the larynx is 34.46 Pa pre-operatively, and 44.56 Pa post-operatively. This means that a greater pressure difference and more effort are needed to inhale the same amount of air after surgery. The major change in pressure drop is found over the nasal cavity. This has increased with 5.41 Pa after surgery. The pressure on the wall in the nasal cavities can be seen in Fig. 12.

The major change in the pressure distribution after surgery is the high pressure gradient at the smallest cross section in the anterior nose. This change can be seen on both sides post-operatively, and is the main reason for the total change in pressure drop over the nasal cavities after surgery. Besides from this pressure change in the anterior nose, the pressure development follows the same trend pre- and post-operatively, but the pressure is overall lower post-operatively. Another change between the two models can be observed at the posterior laryngopharynx. The pressure drop at this region was lower before surgery.

### Nasal Resistance

The nasal resistance was measured with RRM and RMM both pre- and post-operatively. Pre-operative, measured results are only available for the right nasal cavity. This is because the nasal passage was too narrow for the tests to work. Post-operative measurements are available for both sides. However, even post-operatively the results are limited and only available for measurements after decongestion. Both measured and CFD results are presented in Table 1.

**Table 1:** Nasal resistance, measured and calculated results.

	Flow rate [ml/s]	R, RRM [Pa s/ml]	R, CFD [Pa s/ml]
Pre, right	143.8	0.1732	0.0429
Pre, left	106.2	Not Measured	0.0581
Post, right	135.1	0.1145	0.0888
Post, left	114.9	0.6167	0.1044

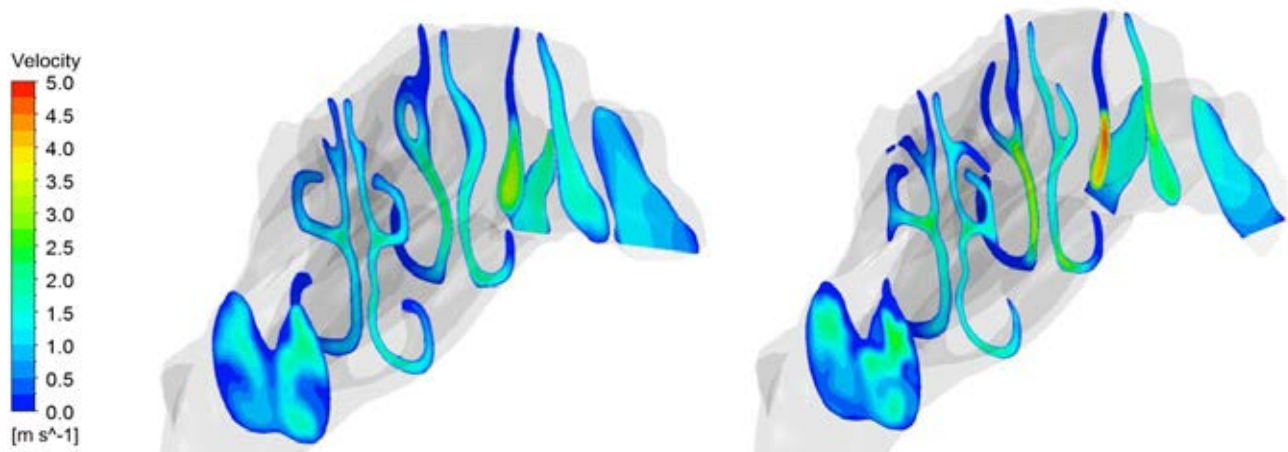


**Figure 9:** Contour plot of the velocity across coronal cross sections in the nasal cavity pre-operative (left) and post-operative (right). The models are viewed from the right side.

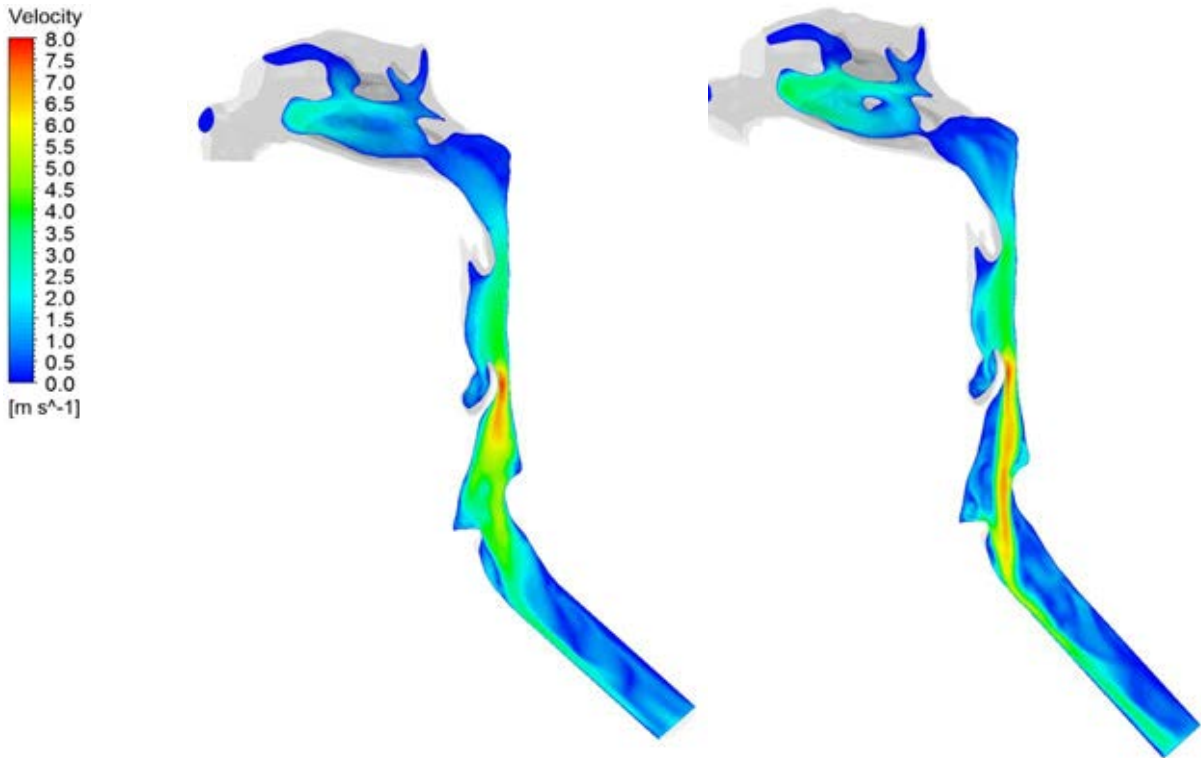


**Figure 10:** Contour plot of the velocity of the velocity across a sagittal cut plane at the middle of pharynx and larynx, and the left nasal cavity. The pre-operative results to the left, and the post-operative results to the right.

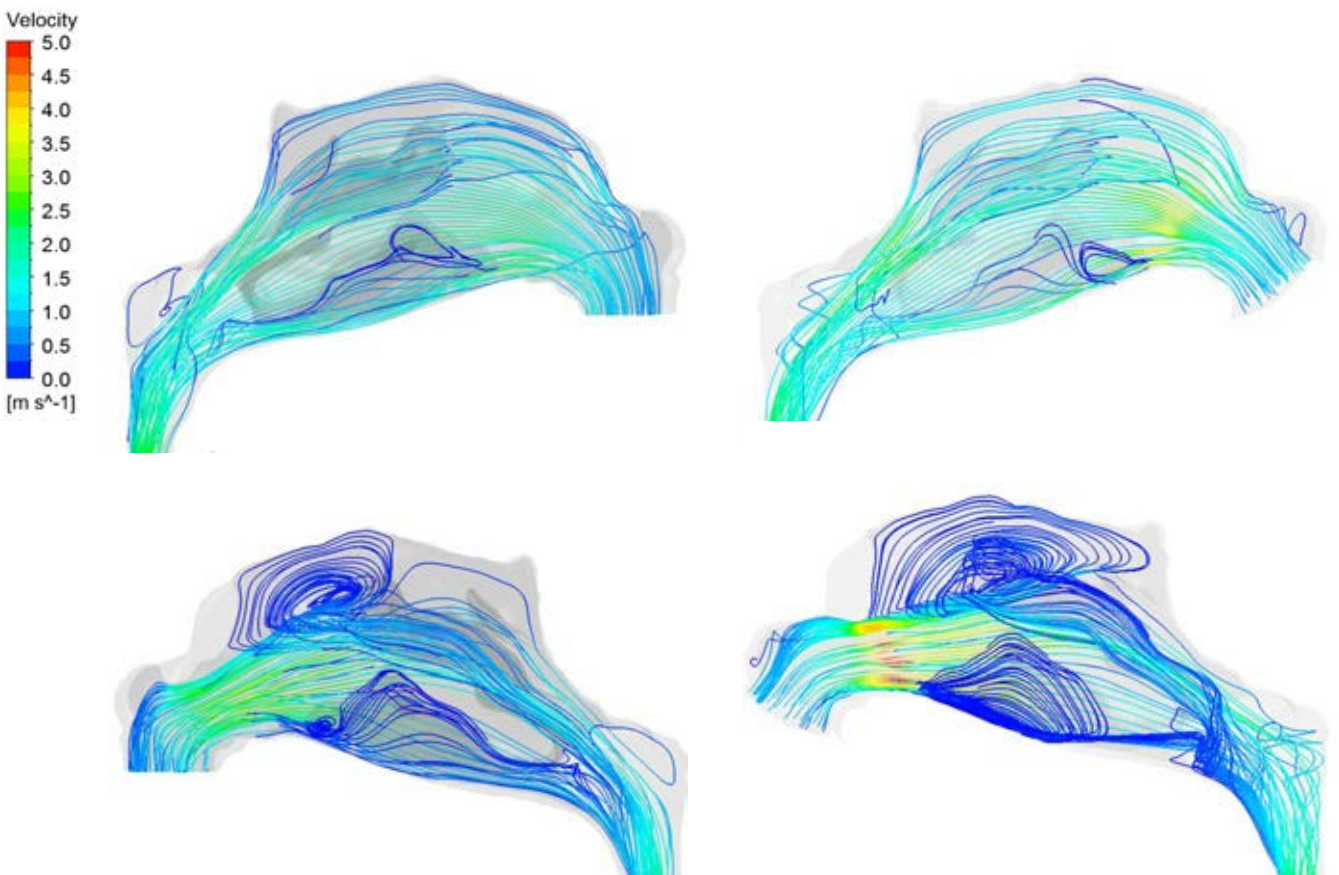


**Figure 11:** Velocity streamlines in the right (upper) and left (lower) nasal cavity pre (left)- and post (right)-operative.

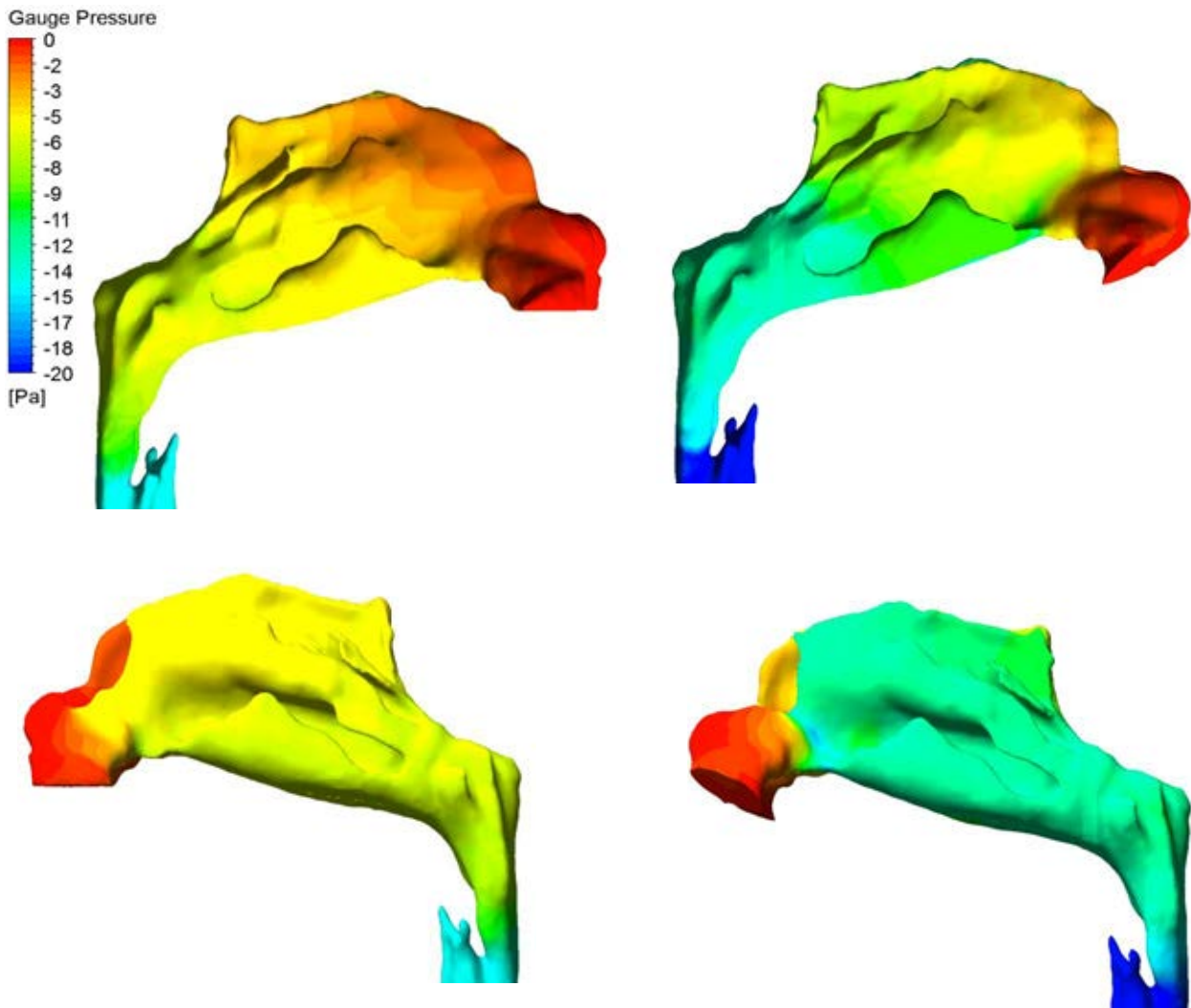


**Figure 12:** Contour plots of the pressure distribution at the wall in the nasal cavity pre (left) – and post (right)-operative. The nasal cavity is viewed from the right (upper) and left (lower).

## DISCUSSION

### CFD and geometry approach

The CFD results show airflow-patterns similar to previous modelling work and experiments reported in the literature. However, the calculated nasal resistance values from the CFD results differ remarkably from the rhinometric measurements. A possible source of error is the CFD approach. This study established a laminar base-case, and based on the Reynolds number, the flow is within the laminar flow regime. However, the geometry of the upper airways varies greatly and turbulent effects may be present at certain regions. The turbulent approach has been studied by Aasgrav (2016) and Aasgrav et.al (2017). The CFD-simulations with laminar and turbulent models gave similar results for both pressure and velocities and indicate that the errors must be related to earlier steps in the modelling procedure such as geometry retrieval and/or CT acquisition.

As pointed out (Shreck et al., 1993) the nasal resistance is highly dependent on the cross sectional area. A comparison of the measured and calculated hydraulic diameter on the pre-operative model shows that the hydraulic diameter is significantly larger (about 60%) in the CFD model (decongested RMM). This may account for the large deviation between the measured and calculated nasal resistance. A decrease in hydraulic diameter by 60% is approximately a layer of one voxel off the model (0.3mm on the left side, and 0.5mm on the right side). When reducing the geometry, by a trial and error approach, the reduction of a voxel layer corresponds to an upper HU-value of approximately -600 HU. It should be noted that this value is higher than those reported in the literature, but nevertheless, this strongly indicates that the geometry is too large, and that the HU-values for segmentation should be reevaluated. Finding a suitable HU-range by calculating the hydraulic diameter after simulating the air flow is easy, but not ideal. Predicting the right HU-range and segmentation procedure earlier on in the process is



challenging, and a standard approach for setting the upper HU-value is needed. However, more work is needed in order to study the effect of a reduction of the hydraulic diameter, and the sensitivity to HU values. Overall, it should be noted that the segmentation procedure is both time consuming and prone to human errors as a large amount of manual segmentation is needed.

As mentioned, the model was smoothed in order to reduce digitalization artefacts. This creates a smooth surface, with less friction on the walls. By doing so, an idealized, and perhaps unrealistic, nasal cavity may be created. In reality, the walls of the nasal cavity are covered by mucosa and nasal hair in the anterior nose, which will make a more irregular surface. While eliminating the unrealistic stair-steps of the model created by digitalization, the smoothing may have resulted in much less friction than in the real case. This may have contributed to the overall low nasal resistance, but does not explain the increase in pressure drop over the nasal cavity after surgery.

Another simplification of the model is that all the walls are assumed to be rigid. For most of the nasal cavity this is a good approximation, but the pharyngeal walls are known to be less rigid. By modelling these walls with fluid-structure-interaction (FSI), effects not captured by the CFD approach so far may be evident. In particular, a collapse of the airways during inspirational flow may occur. However, the hysteresis effects in RMM data are expected to be negligible as the calculated flow resistance behaves similar during inhalation and expiration.

### Physiological effects

Whether or not the difference in measured and calculated hydraulic diameter is solely based on the segmentation procedure, or if there actually is a physical difference between the patient at the time of CT scans and at the time when the rhinometric tests were taken is not yet clear. In addition to the segmentation procedure, the geometry difference may also be caused by physical effects captured on CT. One concern is the nasal cycle – of which the effect it has on the model is not yet determined. CT gives an instantaneous representation of the upper airway, but the geometry of the upper airway is in fact constantly changing because of the nasal cycle. The cyclic movement works in a way so that the volume of the left and the right side most of the time is asymmetric. This means that CT from the same day can give different geometries. When comparing pre- and post-operative CT data, the differences in the geometry can be greater or smaller depending on which nasal cavity is dominant at the time. A comparison of the CT images shows indications of the patient being in different cycles pre- and post-operatively. A comparison of a coronal slice in the anterior nasal cavity can be seen in Fig. 13.

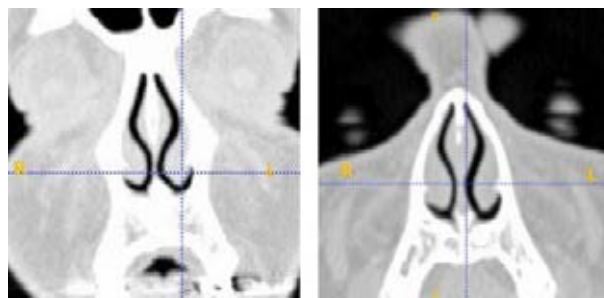


**Figure 13:** Coronal CT view of the nasal cavity pre (left) - and post (right) -operative showing indications of a change in the nasal cycle in pre- and post-operative CT.

The right side appears to be larger in the pre-operative CT than in the post-operative one, and hence there is a more distinct difference between in the left and right nasal cavities after surgery. This also corresponds with the hydraulic diameter that is especially large on the right side. The need for taking the nasal cycle into account when modelling the nose has been pointed out in previous studies. Patel et al. (2015) compared pre- and post-operative models to study nasal airway obstruction and had to limit their study subjects to those that seemed to be in the mid cycle (symmetric) of the nasal cycle both pre- and post-operatively. In order to include more subjects into the study, they came up with a method for modelling the nasal cycle. By changing the thickness of the inferior and middle turbinate in addition to the septal swell body, the nasal cycle is taken into account. Patel found that the surgical effect was more correctly simulated when the geometry has been adjusted to eliminate the influence of the nasal cycle. Another option is to simply try to avoid the nasal cycle as a source of error. This could be done by obtaining the CT after the patients nose have been decongested by nasal spray. It is, however, important to keep in mind that the decongested state is unnatural. When measuring the AHI during a sleep study, the nasal cycle is present, and including the nasal cycle in the model instead of eliminating it may give a more realistic result. As long as the nasal cycle is ignored, the CT scan image data can make show different geometries of the same nasal cavity, and make it more difficult to reproduce data.

The high reduction in AHI measured clinically is not as clearly observed in the CFD results. The simulation results show a significant change in the flow patterns in the nasal cavities, but only a small change in the flow patterns in the pharynx and larynx between the pre- and post-operative models. The major differences after surgery are a more evenly distributed flow between the two nasal cavities, and an increase in the pressure drop over the nasal cavity. The change from mouth breathing to nasal breathing can be the cause of the major improvement in AHI. It can be hypothesized that the obstructions in the nose of the patient made it too difficult to breathe through the nose, and that he instead was breathing through his mouth during sleep. When breathing through the mouth (and opening the mouth), the volume in the pharynx decreases as the tongue and soft palate moves posterior towards the pharyngeal walls. This might even close the pharynx, and can result in both apneas and hypopneas which can explain the high AHI reported before surgery. After surgery, the

simulation results show a more symmetrical flow in the nose which might make it easier to breathe through the nose - perhaps enough for the patient to breathe only, or mostly, through his nose. If this is the case, the pharyngeal volume will be significantly larger than it is when the mouth is open, and the risk for collapse will be reduced. It is, however, not known if the patient changed from mouth- to nasal breathing after surgery as there are no available data for this, and more information about the patients sleeping habits is needed to verify this. If the patient did sleep with an open mouth, the geometry should also include the oral cavity (a third inlet), and a CFD study on that geometry should be included as well to relate the CFD-results with the AHI. Modelling of open mouth breathing calls for a more complex model as this requires the soft palate to be movable, and FSI is needed in order to do so.

It should be noted that all the mechanisms of OSAS are not known and understood, and there can be other mechanisms causing apneas and hypopneas that are not visible by studying the flow. It has been suggested that neurological mechanisms also may influence the breathing pattern. It is currently unknown how this can be affected by nasal surgery (Moxness and Nordgård, 2016). A last remark is that the CT data, which is the basis for the numerical simulations, is obtained when the patient is awake, while the AHI is measured during a sleep study. During sleep, the muscles relax and the pharyngeal wall can become narrower as the muscles that are supporting it are relaxed. In addition, the muscle-relaxation may also make the tongue relax and fall posterior, when sleeping in the supine position, due to gravity.

## CONCLUSIONS AND FURTHER WORK

In the current paper, the airflow in the human upper airways has been simulated for an OSAS patient to study the effect of intranasal surgery for alleviation of OSAS. A base-case with laminar flow was made and the results from CFD were compared with clinical measurements, in particular measurements of the nasal resistance. The CFD results and the measured results did not correspond, and the main errors are expected to be caused by differences between the geometry of the upper airway and the airway being modelled. Further work will be focused on making an anatomical correct geometry before proceeding further with numerical simulations.

## ACKNOWLEDGEMENTS

This project work is part of a collaborative research project, "Modeling of Obstructive Sleep Apnea by Fluid-Structure Interaction in the Upper Airways", between NTNU, SINTEF Materials and Chemistry, and St. Olavs Hospital, Trondheim University Hospital, Norway. The project is funded by the Research Council of Norway, under the FRINATEK program (OSAS, 2017).

## REFERENCES

- AASGRAV, E., (2016), "CFD simulations of turbulent flow in the upper airways", *The Norwegian University of Science and Technology*, Project work.
- AASGRAV, E., JOHNSEN, S.G., SIMONSEN, A.J., and MÜLLER, B., (2017), "CFD simulations of turbulent flow in the human upper airways", *CFD 2017 (12th International Conference on CFD in Oil & Gas, Metallurgical and Process Industries)*, Trondheim, Norway, May 30th - June 1st.
- AASM - American Academy of Sleep Medicine, (1999), "Sleep-related breathing disorders in adults: Recommendations for syndrome definition and measurement techniques in clinical research", *SLEEP*, **22**, 667-689.
- ANSYS Inc., ANSYS v.16.2, <http://www.ansys.com>.
- CIGNONI, P., CALLIERI, M., CORSINI, M., DELLEPIANE, M., GANOVELLI, F., and RANZUGLIA G., (2008), "MeshLab: an Open-Source Mesh Processing Tool", *Sixth Eurographics Italian Chapter Conference*, 129-136.
- DE BACKER, J. W., VANDERVEKEN, O., VOS, W., DEVOLDER, A., VERHULST, S., VERBRAECKEN, J., PARIZEL, P., BRAEM, M., DE HEYNING, P. V., BACKER, W. D., (2007), "Functional imaging using computational fluid dynamics to predict treatment success of mandibular advancement devices in sleep-disordered breathing", *Journal of Biomechanics*, **40**, 3708-3714.
- HAHN, I., SCHERER, P. W., and MOZELL, M. M., (1993), "Velocity profiles measured for airflow through a large-scale model of the human nasal cavity", *Journal of Applied Physiology*, **75**, 2273-2287.
- ITO, Y., CHENG, G. C., SHIH, A. M., KOOMULLIL, R. P., SONI, B. K., SITTIAVORNWONG, S. and WAITE, P. D., (2011), "Patient-specific geometry modeling and mesh generation for simulating obstructive sleep apnea syndrome cases by maxillomandibular advancement", *Mathematics and Computers in Simulation*, **81**, 1876-1891.
- KEYHANI, K., SCHERER, P. W., and MOZELL, M.M., (1995), "Numerical simulation of airflow in the human nasal cavity", *Journal of Biomechanical Engineering*, **117**, 429-441.
- JORDAL, M.R., (2015), "Geometry retrieval from CT and MRI of the human upper airways", *The Norwegian University of Science and Technology*, Project work.
- JORDAL, M.R., (2016), "Patient Specific Numerical Simulation of Flow in the Human Upper Airways", *The Norwegian University of Science and Technology*, M.Sc thesis.
- MATERIALISE, "3D Medical Image Processing Software", <http://biomedical.materialise.com/mimics>.
- MOXNESS, M.H. and NORDGÅRD, S., (2014), "An observational cohort study of the effects of septoplasty with or without inferior turbinate reduction in patients with obstructive sleep apnea," *BMC Ear, Nose and Throat Disorders*, **14**.
- MOXNESS, M. H., and NORDGÅRD, S., (2016), *Personal communication*.
- NAKANO, H., MISHIMA, K., UEDA, Y., MATSUSHITA, A., SUGA, H., MIYAWAKI, Y., MANO, T., MORI, Y. and UHEYAMA, Y., (2013), "A

new method for determining the optimal CT threshold for extracting the upper airway”, *Dentomaxillofacial Radiology*, **42**.

NETFABB basic v7.3 – Software for 3D printing - <http://www.netfabb.com/products/netfabbbasic>.

OSAS (2017), “Modeling of Obstructive Sleep Apnea by Fluid-Structure Interaction in the Upper Airways”, <http://osas.no/description>.

PATEL, R. G., GARCIA, G. J. M., FRANK-ITO, D. O., KIMBELL, J. S. and RHEE, J. S., (2015), “Simulating the nasal cycle with computational fluid dynamics”, *Otolaryngology - Head and Neck Surgery*, **152**, 353-360.

SCHRECK, S., SULLIVAN, K.J, HO, C.M. and CHANG, H.K., (1993), “Correlations between flow resistance and geometry in a model of the human nose”, *Journal of Applied Physiology*, **75**, 1767-1775.

SOUTHLAKE SINUS AND SNORING CENTER, (2017), “Nasal Airway Anatomy ”, <http://dfwsinus.com/nasal-airway-obstruction/nasal-airway-anatomy/>.

TAYLOR, D. J., DOORLY, D.J. and SCHROTER, R. C., (2010), Inflow boundary profile prescription for numerical simulation of nasal airflow”, *J R Soc Interface*, **7**, 515-527.

TU, J., INTHAVONG, K., and AHMADI, G., (2013), “Computational Fluid and Particle Dynamics in the Human Respiratory System”, *Springer*.

WEISSHEIMER, A., DE MENEZES, L. M., SAMESHIMA, G. T., ENCISCO, R., PHAM, J. and GRAUER, D., (2012), “Imaging software accuracy for 3-dimensional analysis of the upper airway”, *American Journal of Orthodontics and Dentofacial Orthopedics*, **142**, 801-813.

YUSHKEVICH, P.A., PIVEN, J., HAZLETT, H. C., SMITH, R. G., HO, S., GEE, J. C., and GERIG G., (2006), “User-guided 3D active contour segmentation of anatomical structures: Significantly improved efficiency and reliability”, *Neuroimage*, **31**, 1116-1128.

# CFD SIMULATIONS OF TURBULENT FLOW IN THE HUMAN UPPER AIRWAYS

**Elin AASGRAV<sup>1\*</sup>, Sverre G. JOHNSEN<sup>2</sup>, Are J. SIMONSEN<sup>2</sup>, Bernhard MÜLLER<sup>1</sup>**

<sup>1</sup> NTNU, dept. Energy and Process Technology, 7491 Trondheim, NORWAY

<sup>2</sup> SINTEF Materials and Chemistry, 7465 Trondheim, NORWAY

\* E-mail: eaasgrav@gmail.com

## ABSTRACT

In this paper, investigations are conducted using Reynolds-averaged Navier-Stokes (RANS) turbulence models to investigate the importance of turbulence modelling for nasal inspiration at a constant flow rate of 250 ml/s. Four different, standard turbulence models are tested in a model geometry based on pre-operative CT images of a selected obstructive sleep-apnea syndrome (OSAS) patient. The results show only minor differences between them. Furthermore, the turbulence models do not give significantly different results than a laminar flow model. Thus, the main conclusion is that effects of turbulence are insignificant in CFD modelling of the airflow in the pre-operative model of the upper airways of the chosen patient.

**Keywords:** CFD, Biomechanics, Obstructive Sleep Apnea, Turbulence, Upper airways.

## NOMENCLATURE

### *Greek Symbols*

- $\delta_{ij}$  Kronecker delta, [-].  
 $\rho$  Mass density, [kg/m<sup>3</sup>].  
 $\nu$  Kinematic viscosity, [m<sup>2</sup>/s].  
 $\nu_T$  Turbulence eddy viscosity, [m<sup>2</sup>/s].

### *Latin Symbols*

- $k$  Turbulence kinetic energy, [m<sup>2</sup>/s<sup>2</sup>].  
 $p$  Pressure, [Pa].  
 $\mathbf{U}$  Velocity vector, [m/s].  
 $U_i$  Mean velocity component in the  $i$  direction, [m/s].  
 $x, y, z$  Cartesian coordinates, [m].

### *Sub/superscripts*

- $i, j, k$  Spatial coordinate indexes.  
 $w$  Wall.

## INTRODUCTION

Snoring is caused by the soft parts of the upper airways collapsing and preventing the air from flowing freely. In some cases, snoring is so severe that medical attention is required. The most severe form, called obstructive sleep apnea syndrome (OSAS) involves complete blocking of the airway during sleep because of the collapse of e.g. relaxed muscles and soft tissue due to e.g. Venturi effect and gravity, in particular when the patient is lying in the supine position. It affects 2-4 % of the population. A variety of treatment options exists, but currently there are no available methods for predicting the outcome of the treatment. In order to gain insight into the biomechanical mechanisms of OSAS, computational fluid dynamics (CFD) simulations of flow in the human upper airways have been performed.

In short, the conclusions from previous studies indicate that the turbulence model that compares best with experimental data varies from case to case. Mihaescua et al. (2008) conclude that the Large Eddy Simulation (LES) modelling approach is a better option compared to the standard Reynolds-Averaged Navier-Stokes (RANS) models  $k-\epsilon$  and  $k-\omega$ , with  $k-\omega$  being slightly better than  $k-\epsilon$ . The RANS modelling approach is not able to capture flow separation effects, which are important for the understanding of the flow, as well as the LES approach. Riazuddin et al. (2011) conducted a study of inspiratory and expiratory flow in the nasal cavity using a  $k-\omega$  SST turbulence model. The results were validated with experimental and numerical data from other studies, and they showed good correlation. The conclusion of the study was that the  $k-\omega$  SST model gave accurate and reliable results for the flow involving adverse pressure gradients. Ma et al. (2009) used a realizable  $k-\epsilon$  model when simulating flow and aerosol delivery in the human airways, and obtained good agreement with experimental data. Stapleton et al. (2000) used a standard  $k-\epsilon$  model and concluded that CFD simulation do not compare very well with experimental data. They argued that the reason for this could be that particle deposition is very sensitive to pressure drop and recirculation, highlighting the need for accuracy in the reproduction of these flow characteristics to obtain good results. Longest et al. (2007) considered variations of the

k- $\omega$  turbulence model. The standard k- $\omega$  model gave good agreement with experimental results, but a low-Reynolds number (LRN) k- $\omega$  model improved the results. They also emphasized the importance of accurate inlet conditions to obtain good results.

The studies all agree that CFD analysis of the human upper airways is a great tool for giving a realistic representation of flow related problems. Choosing a specific turbulence model can be challenging, because it depends, among other things, on the geometry and Reynolds number. The literature suggests that standard turbulence models are not always accurate enough, but improved models that take into consideration effects such as recirculation and separation, can provide results that agree well with empirical data. However, to our knowledge, no systematic studies have been published to compare and assess various turbulence models in the human upper airways (Quadrio et al., 2014).

The human upper airways consist of complex meatuses of highly varying cross-sections with hydraulic diameters ranging from milli- to centimeter-scale. Additionally, the sinusoidal nature of the intrathoracic pressure, due to the inhalation/expiration cycle, results in a wide range of flow velocities, hence Reynolds numbers. Most likely, the airflow is transitional, due to the relatively low maximum Reynolds number and the limited time to develop the turbulent boundary layers.

The current paper focuses on investigating the qualitative and quantitative differences between standard turbulence models applied to a patient-specific, rigid-wall geometry of the upper airways, investigated by Aasgrav (2016) based on CT images (Jordal, 2016). The study includes a sensitivity study with respect to grid size as well as turbulence boundary conditions. The present work is a part of the collaboration project “Modelling of obstructive sleep apnea by fluid-structure interaction in the upper airways” aiming to demonstrate the applicability of CFD as a clinical tool in OSAS diagnostics and treatment (OSAS, 2016). The project is a collaboration between NTNU, SINTEF and St. Olavs Hospital, the university hospital in Trondheim, and is funded by the Research Council of Norway.

## MODEL DESCRIPTION

### Computational Geometry and Mesh of the Human Upper Airways

The geometry retrieval is based on pre-operative CT scans of "Patient 12" (Moxness, 2014), provided by the Department of Radiology and Nuclear Medicine at St. Olavs Hospital, the university hospital in Trondheim. A detailed description of the process of retrieving the geometry can be found in the M.Sc. thesis by Jordal (2016). The resulting 3D geometry was modified to get an even distribution of outflow. The final pre-operational geometry used for further investigations is shown in Figure 1. The geometry has two inlets (left and right nostrils) and one outlet (trachea). The oral cavity was not considered in the model, and neither were the paranasal sinuses.



**Figure 1:** Final pre-operative model used in simulations, seen from the left (Jordal, 2016)

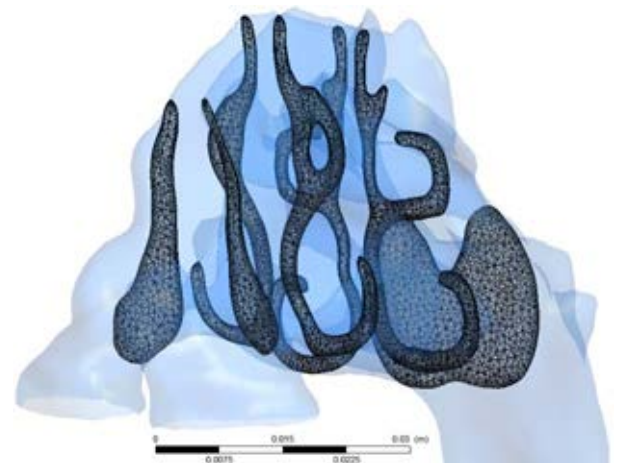


**Figure 2:** Base-case computational mesh in the nasal cavity, displayed on the cut-planes 1-4 (see Figure 4)

The meshing was done in ANSYS Meshing (Ansys, 2017), version 16.2. In order to get good results for the near-wall effects, an inflation layer consisting of five layers was utilized at the wall. The option “Size Function” in ANSYS Meshing was set to “Proximity and Curvature”, where proximity captures the effects of tight gaps and thin sections, like for instance in the nasal cavity, and curvature captures sharp changes in flow direction, like we have in the nasopharynx. For the base-case, the size limitation was set to 1 mm. This resulted in a mesh with ca. 1.4 million grid cells. Details of the grid can be seen in figures 2 and 3. The grid sensitivity was investigated by comparing the base-case mesh to a refined mesh consisting of 6.8 million grid cells (size limitation of 0.8mm) and a coarser mesh consisting of 0.81 million grid cells (size limitation of 2.0mm), using the realizable k- $\epsilon$  turbulence model (see next section).

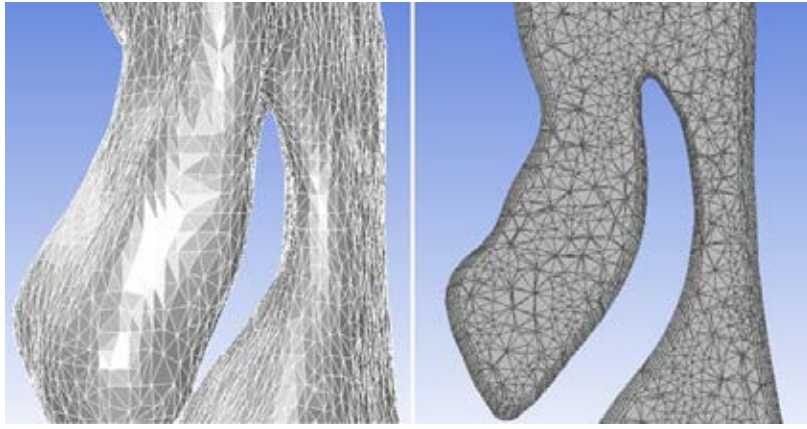


**Figure 3:** Details of the base-case mesh at the epiglottis; on the wall and in an arbitrary cut-plane

### Mathematical Models for Turbulent Flow in the Human Upper Airways

The Navier-Stokes equations describe fluid flow and thus are the foundation for the mathematical modelling of the airflow in the human upper airways. Due to the low Mach number ( $Ma \ll 0.3$ ), the flow is considered incompressible, and the governing equations take the following form (Pope, 2000):

*Continuity equation*

$$\nabla \cdot \mathbf{U} = 0 \quad (1)$$

*Momentum equation*

$$\frac{D\mathbf{U}}{Dt} = -\frac{1}{\rho}\nabla p + \nu\nabla^2\mathbf{U} \quad (2)$$

Here,  $\mathbf{U}$  is the velocity vector,  $p$  is the pressure,  $\rho$  is the mass density and  $\nu$  is the kinematic viscosity.

Even though we have a relatively low maximum Reynolds number of about 2000, we include effects of turbulence. Several solution approaches exist, with Reynolds-averaged Navier-Stokes (RANS) modelling being the most utilized one. Other popular methods are Large Eddy Simulation (LES) and Direct Numerical Simulation (DNS). DNS is solving the Navier-Stokes equations numerically for all significant spatial and temporal scales and does not involve any additional modelling of turbulence. LES involves explicit representation of the large-scale turbulent eddies containing anisotropic energy, while the smaller-scale, more isotropic turbulent motions are modelled. Although LES has a significantly lower computational cost than DNS, the RANS approach is far less computationally demanding. This makes RANS the desired approach in most practical cases. Here, we consider the RANS equations, where the Reynolds stress tensor is determined by the Boussinesq approximation.

*RANS equations*

$$\frac{\partial U_i}{\partial x_i} = 0 \quad (3)$$

$$\frac{\partial U_i}{\partial t} + U_j \frac{\partial U_i}{\partial x_j} = -\frac{\partial p}{\rho \partial x_i} + \nu \frac{\partial^2 U_i}{\partial x_j \partial x_j} - \frac{\partial \overline{u'_i u'_j}}{\partial x_j} \quad (4)$$

*Boussinesq approximation*

$$-\overline{u'_i u'_j} = 2\nu_T S_{ij} - \frac{2}{3}k\delta_{ij} \quad (5)$$

*Mean strain-rate tensor*

$$S_{ij} = \frac{1}{2} \left( \frac{\partial U_i}{\partial x_j} + \frac{\partial U_j}{\partial x_i} \right) \quad (6)$$

Here,  $U_i$  and  $U_j$  are the mean velocity components in the  $i$  and  $j$  directions, respectively ( $i, j \in \{x, y, z\}$ ),  $p$  is the mean pressure,  $k$  is the turbulence kinetic energy,  $\nu_T$  is the eddy viscosity to be defined by the RANS model,  $\delta_{ij}$  is the Kronecker delta, and the Einstein summation convention is employed. The Reynolds stress models are generally divided into categories based on how many equations need to be solved, with the two-equation models being the most used and the most verified RANS types.

### Numerical Approximation

The governing equations were solved using the commercial CFD software ANSYS Fluent 16.2 (Ansys, 2017). In the following, simulation results from the upper airways geometry shown in the previous section are shown, for various standard RANS turbulence models as well as laminar flow. Coupled solver was employed for the pressure-velocity coupling. For pressure and momentum, second order upwind solvers were chosen, while for the turbulent kinetic energy and turbulent dissipation rate, a first order upwind solver was determined to be accurate enough. Standard material properties for air was employed (mass density of  $1.225 \text{ kg/m}^3$  and viscosity of  $1.7894 \cdot 10^{-5} \text{ Pa s}$ ).

Boundary conditions were:

- Atmospheric total pressure at the inlets (nostrils)
- Velocity outlet corresponding to an inspiratory volumetric flow rate of 250 ml/s
- No-slip condition at the walls
- Turbulence intensity of 5%
- Turbulent viscosity ratio of 10

The sensitivity to turbulence boundary conditions at the inlets were investigated by testing the sensitivity to reducing the turbulence intensity at the inlets to 1% and increasing it to 10%.

## RESULTS

The described setup was simulated with four different turbulence models, namely the standard  $k-\epsilon$  and  $k-\omega$  models, as well as realizable  $k-\epsilon$  and  $k-\omega$  SST. The four models were checked against laminar flow by comparing the area-averaged pressure at selected cross-sections throughout the geometry (see Figure 4). The results are shown in Figure 5. The models showed only minor differences in results upstream of the epiglottis. Some differences are observed downstream of the epiglottis, but it is believed that the effects so far down do not affect the flow further up where the airway collapses in OSAS.

It is to be expected that the difference between a laminar model and various turbulence models is minor, because the maximum Reynolds number in the flow is about 2000, indicating that the flow is mainly laminar. Because of the complex geometry inducing separated flow, the flow most likely has some turbulence features as well. The total pressure,  $p_{tot} = p_{stat} + 0.5\rho U^2$ , decreases throughout the geometry as it should, while the static pressure depicted in Figure 5 does not show this behavior for all the models because of the highly varying velocity.

Both of the  $k-\epsilon$  models' residuals converged to an acceptable value, where the residuals for continuity,  $k$ ,  $\epsilon$ , and  $x$ -,  $y$ - and  $z$ -velocities started at about 1, and converged to values between  $10^{-4}$  and  $10^{-8}$ , with a steady state solver. None of the  $k-\omega$  models' residuals converged as desired with steady state. Thus, a transient simulation was needed to achieve residuals in the range of  $10^{-4}$ - $10^{-8}$ . Despite the steady-state boundary conditions, the solution might be transient due to unsteady vortices in regions with separated flow. In this case, a converged steady-state solution would be unfeasible.

The realizable  $k-\epsilon$  model was chosen for the grid and turbulence boundary condition sensitivity studies. First, a sensitivity study was conducted to investigate the sensitivity to turbulent intensity at the inlets, as described in the Model Description chapter. In Figure 6, it is seen that the turbulent kinetic energy differences that exist close to the inlets, due to the different turbulence intensity boundary conditions, decay as the air progresses through the nasal cavity, such that the effect of changing the inlet boundary condition is negligible when considering the flow entering the nasopharynx. Furthermore, we found that the velocity streamlines and velocity magnitude are largely unaffected by the turbulence intensity. Second, a grid sensitivity study as described in the previous chapter was performed utilizing a base-case grid (1.4M grid cells), a refined grid (6.8M grid cells) and a coarser grid (0.81M grid cells). Figure 7 shows a comparison of the area-averaged pressure at the selected cross-sections for the different grids. It is evident that the coarsest mesh differs from the base case and the finer mesh, leading to the conclusion that grid independency is achieved for the base case sizing and finer resolutions. The velocity streamlines in Figure 8 show that the three different meshes give some differences in the flow patterns. This is especially prominent right after the epiglottis and in the oropharynx behind the oral cavity. Here, the refined mesh portrays more swirl in the flow, indicating higher vorticity in these regions, a characteristic of the flow pattern that could be an important factor in the understanding of OSAS. The

coarser mesh has less swirl than the two other meshes, indicating that the mesh is too coarse to capture the complexity and turbulence effects of the flow. The wall pressure was found not to show any difference between the three meshes. The turbulence kinetic energy plot was similar for the two finer meshes, while it differed greatly for the coarser mesh, giving the same conclusion that the coarser mesh does not have a large enough resolution to capture the turbulence effects.

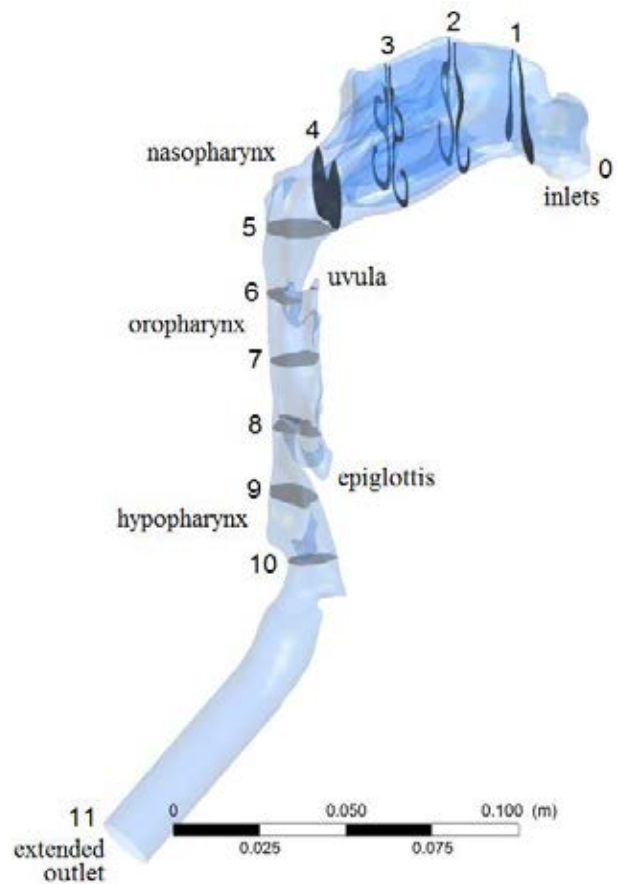


**Figure 4:** Location and numbering of cross-sections in the final pre-op geometry

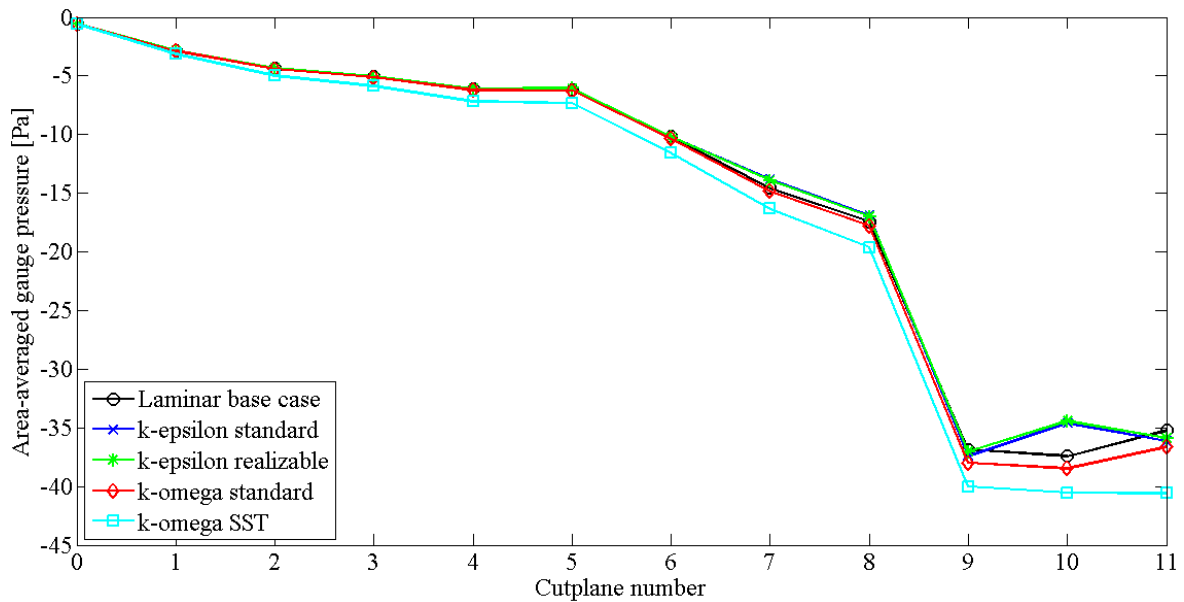


Figure 5: Comparison of area-averaged pressure for the laminar base-case and four different turbulence models

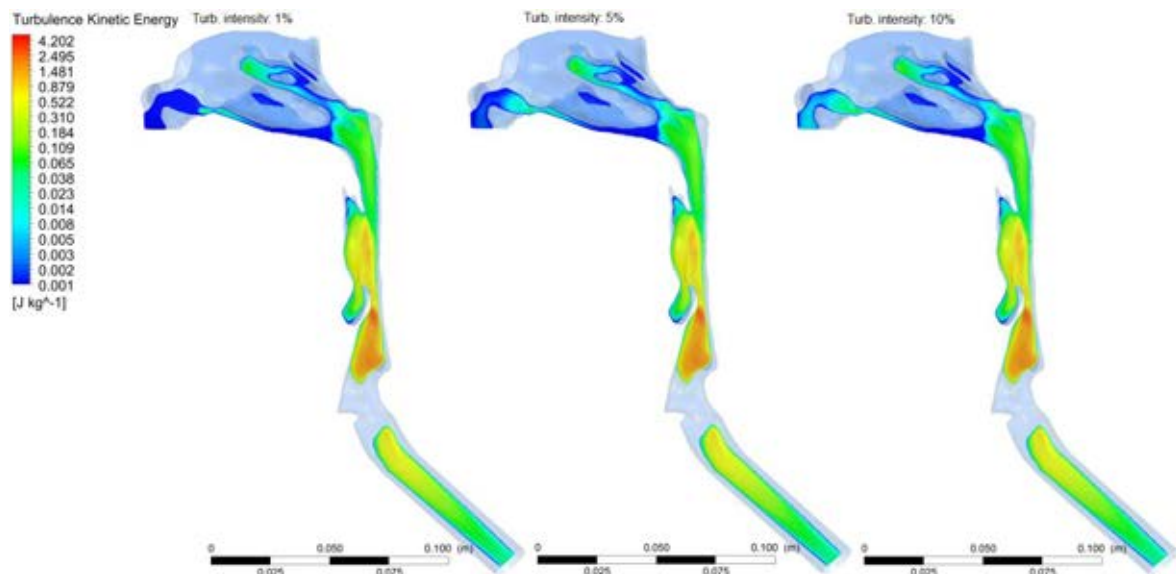


Figure 6: Turbulence kinetic energy for different turbulent intensities using the base case mesh, logarithmic scale

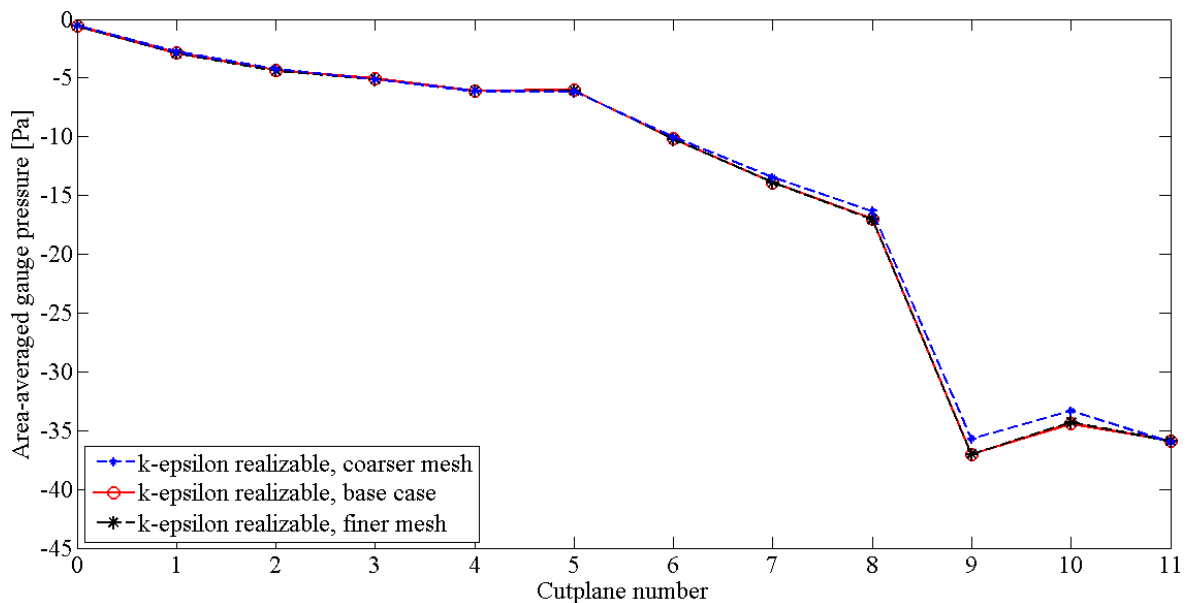
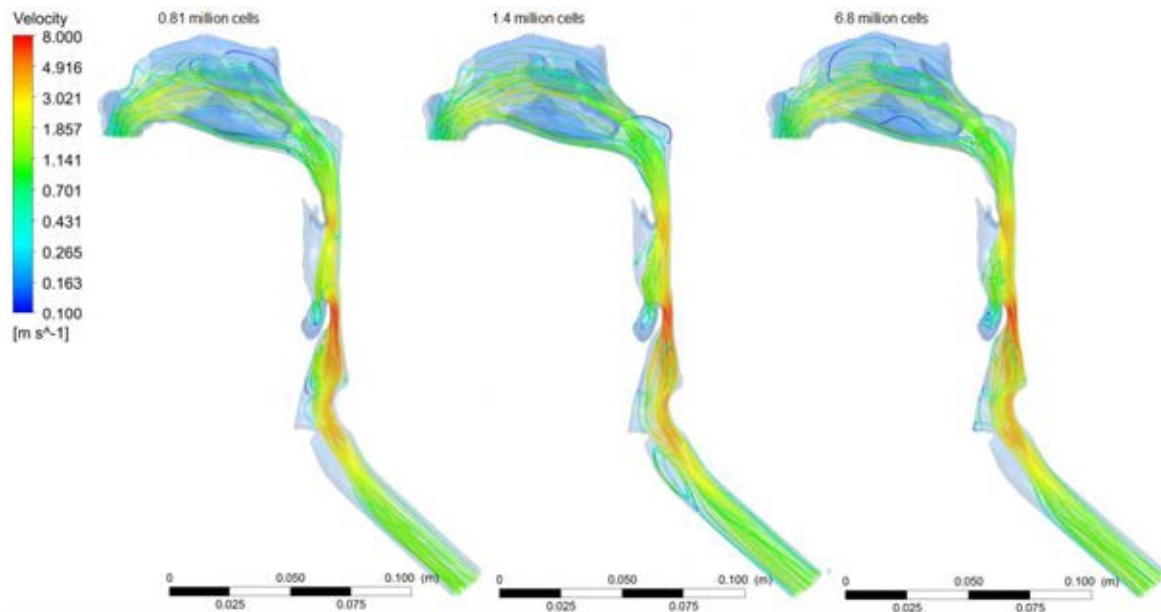


Figure 7: Comparison of area-averaged pressure for the turbulent base-case, and a finer and coarser mesh





**Figure 8:** Velocity streamlines for different meshes, logarithmic scale

## CONCLUSIONS

CFD simulations of airflow in the human upper airways were performed to investigate and assess the importance of turbulence modelling. Four different standard RANS turbulence models were compared to a laminar flow model at a constant inspiratory volumetric flow rate of 250 ml/s in a model geometry based on pre-operative CT images of an OSAS patient. The area-averaged pressure at selected cross-sections upstream of the epiglottis were largely unaffected by the choice of laminar or turbulent flow models. Thus, the main conclusion of the study is that effects of turbulence are insignificant in CFD modelling of the airflow in the pre-operative model of the upper airways of the chosen patient. It remains to investigate other volumetric flow rates.

Employing the realizable  $k-\epsilon$  model, the effect of varying turbulence inlet boundary conditions was investigated by varying the turbulent intensity at the inlets from 1% to 10%. No significant effect was observed downstream of the nasal cavities.

Finally, a grid sensitivity study was conducted to assess the grid independency of the computed results. The base-case mesh, based on a cell size limitation of 1 mm and consisting of 1.4 million cells, showed some discrepancy in the flow pattern in some regions, but produced almost exactly the same pressure loss results as a refined mesh consisting of 6.8 million cells (size limitation of 0.8 mm). A coarser mesh consisting of 0.81 million cells was not able to reproduce the results and thus did not have the required resolution to capture the turbulence effects.

## REFERENCES

AASGRAV, E., (2016), "CFD simulations of turbulent flow in the upper airways", NTNU, M.Sc. specialization project.  
 ANSYS (2017), <http://www.ansys.com>.  
 JOHNSEN, S.G., (2016), Private communication.  
 JORDAL, M. R., (2016), "Patient Specific Numerical Simulation of Flow in the Human Upper Airways", NTNU, M.Sc. thesis.

LONGEST, P.W., and VINCHURKAR, S., (2007), "Validating CFD predictions of respiratory aerosol deposition: Effects of upstream transition and turbulence", *Journal of Biomechanics*, **40**, 305-316.

MA, B., and LUTCHEN, K.R., (2009) "CFD simulation of aerosol deposition in an anatomically based human large-medium airway model", *Annals of Biomedical Engineering*, **37**, 271-285.

MIHAESCUA, M., MURUGAPPAN, S., KALRAC, M., S. KHOSLAB, S., and GUTMARK, E., (2008), "Large Eddy Simulation and Reynolds-Averaged Navier–Stokes modeling of flow in a realistic pharyngeal airway model: An investigation of obstructive sleep apnea", *Journal of Biomechanics*, **41**, 2279–2288.

MOXNESS, M.H. and NORDGÅRD, S., (2014), "An observational cohort study of the effects of septoplasty with or without inferior turbinate reduction in patients with obstructive sleep apnea," *BMC Ear, Nose and Throat Disorders*, **14**.

OSAS, (2016), "Modeling of Obstructive Sleep Apnea by Fluid-Structure Interaction in the Upper Airways", <http://www.osas.no>.

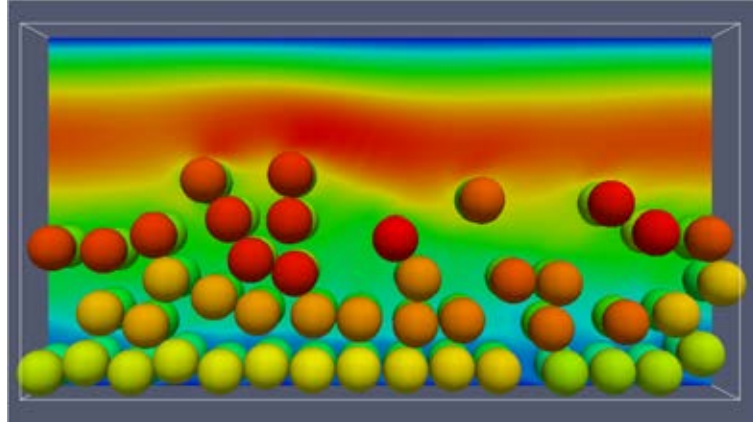
POPE, S.B., (2000). *Turbulent Flows*. Cambridge University Press.

QUADRIO, M., PIPOLO, C., CORTI, S., LENZI, R., MESSINA, F., PESCI, C., and FELISATI, G., (2014), "Review of computational fluid dynamics in the assessment of nasal air flow and analysis of its limitations", *Eur Arch Otorhinolaryngol*, **271**, 2349-2354.

RIAZUDDIN, V.N., ZUBAIR, M., ABDULLAH, M.Z., RUSHDAN, I., SHUAIB, I.L., HAMID, S.A., and AHMAD, K.A., (2011), "Numerical study of inspiratory and expiratory flow in a human nasal cavity", *Journal of Medical and Biological Engineering*, **31**, 201-206.

STAPLETON, K.W., GUENTSCH, E., HOSKINSON, M.K., and FINLAY, W.H., (2000), "On the suitability of  $k-\epsilon$  modeling for aerosol deposition in the mouth and throat: A comparison with experiment", *Journal of Aerosol Science*, **31**, 739-749.

# OIL & GAS APPLICATIONS





## ESTIMATION OF FLOW RATES AND PARAMETERS IN TWO-PHASE STRATIFIED AND SLUG FLOW BY AN ENSEMBLE KALMAN FILTER

Marco FERRARI<sup>1\*</sup>, Arianna BONZANINI<sup>2†</sup>, Gianni ARIOLI<sup>1‡</sup>, Pietro POESIO<sup>2§</sup>

<sup>1</sup>Politecnico di Milano, Department of Mathematics, 20133 Milan, ITALY

<sup>2</sup>Università degli Studi di Brescia, Department of Mechanical and Industrial Engineering, 25123 Brescia, ITALY

\* E-mail: marco2.ferrari@polimi.it

† E-mail: a.bonzanini001@unibs.it

‡ E-mail: gianni.arioli@polimi.it

§ E-mail: pietro.poesio@unibs.it

### ABSTRACT

Data assimilation methods were introduced to reduce production costs and to optimize processes in different industrial fields, such as oil & gas reservoir industry or transport of multiphase flows in pipelines. In flow assurance, these methods, called also soft-sensing techniques, allow to avoid the use of expensive and complex multiphase meters to measure some flow characteristics. Moreover, they allow the estimation of some flow parameters, whose actual values are unknown. Using these techniques, flow meters may be substituted by numerical simulations that solve a real-time dynamic model.

Among data assimilation methods, sequential filtering techniques allow flow estimation using a mathematical recursive filter where the estimated state of the physical model is updated in real-time through a comparison with few available and easy to obtain measurements of the actual system. If an explicit matrix structure of the model is available, the Extended Kalman filter (EKF) can be used as a recursive filter; otherwise, in the case of a more complex physical model, the Ensemble Kalman filter (EnKF), that is a stochastic extension of the original Kalman filter, can be used in combination with a numerical code to estimate various pieces of information of a multiphase flow in pipe.

Previous Authors (see Gryzlov et al. (2010)) used the Extended or the Ensemble Kalman filter in combination with the simplified one-dimensional no-pressure wave and drift-flux models to estimate the inlet flow rate or some correlation parameters in liquid/gas two-phase flow.

In this work, the application of the Ensemble Kalman filter to the more complex Two-Fluid model for two-phase flow is investigated. The possibility to extend flow rate estimations to simulations where a flow regime transition from stratified to slug flow occurs, simulated with a one-dimensional slug capturing numerical code previously developed, is shown. The estimation of the pipe diameter by the real-time soft-sensing technique is performed in order to show the possibility of evaluating the presence of possible pipe restrictions or obstructions along the pipe due to wax deposition, solid phase scaling or other similar processes, without the use of ad-hoc physical model or invasive examination of the pipe. All the measurements used in this work for the soft-sensing process are obtained from previous numerical simulations of artificial actual systems kept as reference.

**Keywords:** Multiphase pipeline transport, Oil & Gas .

### NOMENCLATURE

#### Greek Symbols

$\alpha$	Volume fraction.
$\rho$	Density, [ $kg/m^3$ ].
$\mu$	Dynamic viscosity, [ $Pa \cdot s$ ].
$\theta$	Inclination angle, [ $rad$ ].
$\tau$	Shear stress, [ $N/m^2$ ].
$\Delta$	Interval.
$v$	Measurements Gaussian error.

#### Latin Symbols

$x$	Axial length coordinate, [ $m$ ].
$t$	Time coordinate, [ $s$ ].
$p$	Pressure, [ $Pa$ ].
$u$	Phase velocity, [ $m/s$ ].
$g$	Gravity acceleration, [ $m/s^2$ ].
$F$	Frictional force, [ $N/m^3$ ].
$r_p$	Pressure relaxation parameter, [ $(Pa \cdot s)^{-1}$ ].
$c$	Speed of sound, [ $m/s$ ].
$f$	Friction factor.
$Re$	Reynolds number, [ $m/s$ ].
$D$	Pipe diameter, [ $m$ ].
$L$	Pipe length, [ $m$ ].
$S$	Wetted perimeter, [ $m$ ].
$A$	Cross-sectional area, [ $m^2$ ].
$\mathbf{Q}$	Numerical vector of variables.
$\mathbf{L}$	Numerical operator.
$\mathbf{s}$	State vector.
$v$	General parameter.
$\mathbf{w}$	Gaussian noise.
$\mathbf{W}$	Covariance matrix.
$M$	Ensemble number.
$\mathbf{T}$	Covariance factor.
$\mathbf{P}$	Approximated covariance matrix.
$\mathbf{z}$	Measurements vector.
$\mathbf{R}$	Measurements covariance matrix.
$\mathbf{H}$	Selector matrix.
$\mathbf{K}$	Kalman gain.

#### Sub/superscripts

$k$	General phase.
$g$	Gas phase.
$l$	Liquid phase.
$i$	Interface.
$s$	Superficial.
$0$	Reference or initial.

$h$	Hyperbolic.
$i$	Cells index $i$ .
$n$	Time index $n$ .
$j$	Ensemble index $j$ .

## INTRODUCTION

Multiphase flows have a relevant role in many engineering applications such as in oil and gas industries. The possibility to control and measure flow parameters in wellbore and pipelines can strongly reduce costs and make growing production rate. However, real-time measurements along a wellbore or a pipe are often expensive and complex to realize. Therefore, in the last years, substitute methods to optimize and manage wellbore mining or pipeline transport process have reached a great importance and development.

Among these replacement methods, multiphase soft-sensors allow to estimate flow rates and flow parameters from cheap probes easy to place along a pipe, such as pressure gauges, combined with dynamic mathematical and numerical model. A great variety of soft-sensing techniques is available (often called data assimilation methods), as briefly explained by (Gryzlov *et al.*, 2010). According to them, two approaches are possible to soft-sensing: variational data assimilation methods, that use a minimization of a cost function, and sequential methods which, by a filtering technique, update the state of a system every time measurements are available. A widely used filtering technique is Kalman filtering, see (Kalman, 1960), initially developed for linear models and then derived into some extensions, such as the extended Kalman filter and the ensemble Kalman filter, suitable also for more complex and non-linear problems.

In the last decade, although soft-sensing techniques have not been widely employed in multiphase flow applications in pipes, some few important works have been presented on this topic. (Lorentzen *et al.*, 2003) applied the ensemble Kalman filter to the estimation of flow and closure parameters by a drift-flux model in a two-phase flow; then, the possibility to estimate both flow rate and parameters through the extended Kalman filter, applied to a drift-flux model, was discussed in (Leskens *et al.*, 2008). (Gryzlov *et al.*, 2010) presented an application of the ensemble Kalman filter, in combination, once again, with a drift-flux model, to estimate inflow along an horizontal wellbore under stratified conditions by measuring only pressure along the pipe and the other characteristics at the outlet section. Recently, a further application of the extended Kalman filter has been presented in (Gryzlov *et al.*, 2013), this time combined to the simplified no-pressure wave model, in order to estimate inflow along a horizontal pipe.

In this work, we try to extend the soft-sensing scheme presented by (Gryzlov *et al.*, 2010) to a more complex two-fluid model. (Ferrari *et al.*, 2017) developed a numerical scheme for a five equation, one-dimensional, hyperbolic two-fluid model able to capture transitions from stratified to slug flow. Here, this scheme is adopted in combination with an ensemble Kalman filter in order to create a soft-sensor model for flow estimations in horizontal pipe. First of all, the final objective is the estimation of inlet flow rates, knowing only pressure measurements along the pipe and outlet quantities. Then, the same technique is applied to a first attempt of estimation of a variable pipe diameter along the pipe, which can represents obstructions or constrictions in the pipe due, for example, to wax deposition. This phenomenon, in actual pipelines, can create issues and reduce the efficiency of hydrocarbon transportation and it is often difficult to predict,

except through invasive and expensive inspections. So, the possibility to estimate this type of phenomenon using real-time dynamical numerical model, through only few easy and cheap measurements, can achieve a relevant importance in the optimization of multiphase flow industrial process.

For the applications presented here, the same five equation model by (Ferrari *et al.*, 2017) is kept also as reference system for actual values to be estimated and from which take pressure and outlet measurements.

The paper is organized as follows: first, the five equation model and its numerical solution are briefly recalled; then, the ensemble Kalman filter adopted is presented. Finally, before conclusion, results are shown, both for the inlet flow rate and for the diameter estimation.

## MODEL AND NUMERICAL SCHEME

### Model

In this paper, to describe a two-phase flow, we adopt the five equation, hyperbolic, one-dimensional, two-fluid model widely investigated by (Ferrari *et al.*, 2017). The flow is assumed to be isothermal; hence, the energy equations are not accounted for. The model consists in five time-dependent partial differential equations, four obtained from the conservation of mass and momentum for each phase. A fifth equation is added to the system: it expresses the evolution of the gas volume fraction. The system reads

$$\frac{\partial \alpha_g}{\partial t} + u_i \frac{\partial \alpha_g}{\partial x} = r_p (p_{ig} - p_{il}) \quad (1)$$

$$\frac{\partial (\alpha_g \rho_g)}{\partial t} + \frac{\partial (\alpha_g \rho_g u_g)}{\partial x} = 0 \quad (2)$$

$$\frac{\partial (\alpha_l \rho_l)}{\partial t} + \frac{\partial (\alpha_l \rho_l u_l)}{\partial x} = 0 \quad (3)$$

$$\begin{aligned} \frac{\partial (\alpha_g \rho_g u_g)}{\partial t} + \frac{\partial (\alpha_g \rho_g u_g^2)}{\partial x} + \alpha_g \frac{\partial p_{ig}}{\partial x} + \rho_g \alpha_g g \frac{\partial h}{\partial x} \cos(\theta) = \\ - \rho_g \alpha_g g \sin(\theta) - F_{gw} - F_i \end{aligned} \quad (4)$$

$$\begin{aligned} \frac{\partial (\alpha_l \rho_l u_l)}{\partial t} + \frac{\partial (\alpha_l \rho_l u_l^2)}{\partial x} + \alpha_l \frac{\partial p_{il}}{\partial x} + \rho_l \alpha_l g \frac{\partial h}{\partial x} \cos(\theta) = \\ - \rho_l \alpha_l g \sin(\theta) - F_{lw} + F_i. \end{aligned} \quad (5)$$

where the subscripts  $l$  and  $g$  stand for liquid and gas phase, respectively, interfacial variables have the subscript  $i$  and the subscript  $w$  indicates the wall.  $\alpha$  is the volume fraction,  $\rho$  is density,  $u$  stands for phase velocity and  $p$  for pressure;  $p_{ig}$  and  $p_{il}$  indicate gas and liquid interfacial pressures;  $\theta$  is the inclination angle, see Fig. 1, and  $g$  is the gravity acceleration. The  $F$  terms are the frictional forces per unit volume: they need closure relations, which are introduced at the end of this Section. Finally,  $h$  is the height of the liquid surface, as shown in Fig. 1. Pressure formulation derives from the average pressure value at each phase in stratified conditions, as shown by (Brauner and Maron, 1992). Finally, the equations are complemented by  $\alpha_g + \alpha_l = 1$ .

Thanks to the addition of the further Eq. (1), the five equation system becomes hyperbolic. Eq. (1) needs a closure relation for the interfacial velocity: (Saurel and Abgrall, 1999) proposed to estimate it as the velocity of the centre of mass

$$u_i = \frac{\sum \alpha_k \rho_k u_k}{\sum \alpha_k \rho_k}. \quad (6)$$

The right-hand side of Eq. (1), in which the pressure relaxation parameter  $r_p$  appears, takes into account the instantaneous pressure relaxation process. More details about instantaneous pressure relaxation process are discussed in (Ferrari

*et al.*, 2017), (Saurel and Abgrall, 1999), and (Munkejord and Gran, 2009).

The five-equation system (1) - (5), with instantaneous pressure relaxation, provides a strictly hyperbolic alternative to the traditional four-equation two-fluid model and it is suitable for slug capturing, as shown and discussed in (Ferrari *et al.*, 2017).

### Equations of State (EOS)

In the model adopted here, liquid and gas phases are both assumed to be compressible, hence the balance Eqs. (1) - (5) must be complemented with the equation of state (EOS) of each phase

$$p_{ik} = c_k^2(\rho_k - \rho_{k,0}) - p_0, \quad (7)$$

which relates pressures to densities;  $c_k$  is the speed of sound in phase  $k$ ,  $\rho_{k,0}$  is the reference density and  $p_0$  is the reference pressure.

### Closure models

The closure relations for the liquid-wall  $F_{lw}$ , gas-wall  $F_{gw}$  and interfacial  $F_i$  shear forces are defined as

$$F_{lw} = \frac{\tau_{lw}S_l}{A}, \quad F_{gw} = \frac{\tau_{gw}S_g}{A}, \quad F_i = \frac{\tau_i S_i}{A}, \quad (8)$$

where, see Fig. 1,  $A$  is the cross-section area,  $S_l$ ,  $S_g$  stand for the perimeters wetted by the liquid and gas phases, respectively, and  $S_i$  is the cross section of the interfacial surface between the two phases.

Shear stresses  $\tau$  are expressed as

$$\begin{aligned} \tau_{lw} &= \frac{1}{2}f_{lw}\rho_l|u_l|u_l, & \tau_{gw} &= \frac{1}{2}f_{gw}\rho_g|u_g|u_g, \\ \tau_i &= \frac{1}{2}f_i\rho_g|u_g - u_l|(u_g - u_l). \end{aligned} \quad (9)$$

In this work, we adopt the same friction factors formulation adopted by (Issa and Kempf, 2003) and (Ferrari *et al.*, 2017). For the gas-wall friction factors and for interfacial friction factors the correlations used for turbulent flow are

$$f_g = \begin{cases} \frac{16}{Re_g} & \text{if } Re_g < 2100, \\ 0.046(Re_g)^{-0.2} & \text{if } Re_g \geq 2100; \end{cases} \quad (10a)$$

$$f_i = \begin{cases} \frac{16}{Re_i} & \text{if } Re_i < 2100, \\ 0.046(Re_i)^{-0.2} & \text{if } Re_i \geq 2100. \end{cases} \quad (11a)$$

$$f_i = \begin{cases} \frac{16}{Re_i} & \text{if } Re_i < 2100, \\ 0.046(Re_i)^{-0.2} & \text{if } Re_i \geq 2100. \end{cases} \quad (11b)$$

For liquid wall friction force we use

$$f_l = \begin{cases} \frac{24}{Re_l} & \text{if } Re_l < 2100, \\ 0.0262(\alpha_l Re_{sl})^{-0.139} & \text{if } Re_l \geq 2100. \end{cases} \quad (12a)$$

$$f_l = \begin{cases} \frac{24}{Re_l} & \text{if } Re_l < 2100, \\ 0.0262(\alpha_l Re_{sl})^{-0.139} & \text{if } Re_l \geq 2100. \end{cases} \quad (12b)$$

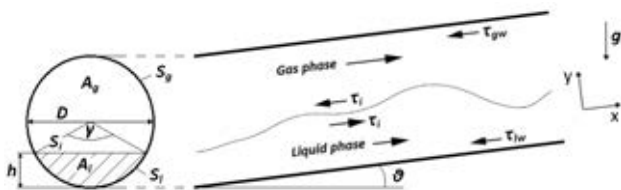


Figure 1: Geometry.

The Reynolds numbers are defined as

$$\begin{aligned} Re_g &= \frac{4A_g u_g \rho_g}{(S_g + S_i)\mu_g}, & Re_i &= \frac{4A_g |u_g - u_l| \rho_g}{(S_g + S_i)\mu_g}, \\ Re_l &= \frac{4A_l u_l \rho_l}{S_l \mu_l}, & Re_{sl} &= \frac{D u_{sl} \rho_l}{\mu_l}, \end{aligned} \quad (13)$$

where, as indicated in Fig. 1,  $D$  is the pipe diameter,  $A_g$  and  $A_l$  are the pipe cross section occupied by the gas and liquid phase, respectively;  $\mu$  is the dynamic viscosity and  $u_{sl}$  stands for the superficial liquid velocity.

### Numerical method

Following previous works by (Ferrari *et al.*, 2017) and (Munkejord and Gran, 2009), Eqs. (1) - (5) are discretised on a uniform one-dimensional grid, by a finite volume method and a first order explicit time discretisation. The numerical solution is obtained through a succession of operators in a fractional-step process

$$\mathbf{Q}_i^{n+1} = \mathbf{L}_s^{\Delta t} \mathbf{L}_h^{\Delta t} \mathbf{Q}_i^n \quad (14)$$

where  $\mathbf{Q}_i^n$  stands for the numerical approximation of the vector of variables in the cell  $i$  at time  $n$  and  $\mathbf{Q}_i^{n+1}$  is the same vector at time  $n+1$ . Therefore, the solution is updated, at each numerical iteration, in two sequential sub-steps.

In the first sub-step, the hyperbolic operator  $\mathbf{L}_h^{\Delta t}$  is applied, in each control volume  $i$ , to solve the hyperbolic system containing non-conservative terms

$$\frac{\partial \mathbf{q}}{\partial t} + \mathbf{A}(\mathbf{q}) \frac{\partial \mathbf{q}}{\partial x} = 0. \quad (15)$$

This requires the solution of the linear Riemann problem at interface of each cell, by a Roe method, and leads to an upwind resolution of the wave phenomena appearing in the problem. The solution of the Riemann problem is obtained basing on the high-resolution *Roe5* solver by (Munkejord and Gran, 2009). To solve the hyperbolic system (15), at each iteration, the value of the unknown vector  $\mathbf{Q}_i^{h,n+1}$  is computed using a high resolution extension of Godunov's method. The use of a high resolution correction guarantees a second order accuracy in space.

In (Ferrari *et al.*, 2017) the *Roe5* scheme is modified to take into account the pressure terms for stratified flow, shear forces, and transition from two (i.e. stratified flow) to one phase (i.e. slug flow).

Finally, in a second sub-step, the operator  $\mathbf{L}_s^{\Delta t}$  is applied to add source terms, appearing in momentum Eqs. (4) - (5), and to take into account the pressure relaxation process.

As pointed out by (Munkejord and Gran, 2009) and (Ferrari *et al.*, 2017), the five equation system with instantaneous pressure relaxation can be adopted as an alternative numerical method to solve the four-equation two-fluid model, gaining the hyperbolicity.

Since in a slug capturing process, during the slug onset process, the transition from two-phase flow to single phase flow occurs, the liquid volume fraction grows and tends to unity; conversely, gas volume fraction tends to zero and this generates numerical problems as discussed by (Munkejord and Gran, 2009). Ferrari *et al.* (Ferrari *et al.*, 2017) introduce a slug criterion to handle these numerical issues.

This numerical method is implemented in a code called **5ES-CARGOTS**. Details are discussed in (Ferrari *et al.*, 2017).

## ENSEMBLE KALMAN FILTER

To solve the inverse problem, since the system of Eqs. (1) - (5) adopted in this work is non-linear, we need to use the *ensemble Kalman filter* (EnKF), an extension of the Kalman filter. This filter has been used by (Gryzlov *et al.*, 2010) and (Lorentzen *et al.*, 2003) in their works.

The main difference between EnKF and traditional Kalman filter is how the error covariance matrix is calculated. The ensemble Kalman filter calculates the approximation of the covariance matrix using an ensemble of model forecasts. The members of the ensemble can be generated randomly from a Gaussian distribution, as done in (Gryzlov *et al.*, 2010).

First, a state vector is introduced

$$\mathbf{s} = [\alpha_{l,i} \ u_{g,i} \ u_{l,i} \ p_i \ v_i]^T \quad (16)$$

where the primitive variable  $\alpha_l$ ,  $u_g$ ,  $u_l$  and  $p$  are extrapolated, each time the filter is used, from the numerical solution of the five equation system (1) - (5), in which the values of the two densities are rounded up in the common value of pressure  $p$ . The subscript  $i$  is the cell index of the numerical discretization. If the final purpose is also the estimate of model parameters, these are accounted for in the generic variable  $v$ .

In order to initialize the filter, the initial ensemble of the state vector is generated (for semplicity, the cell index  $i$  is omitted)

$$\mathbf{s}_{0,j} = \bar{\mathbf{s}}_0 + \mathbf{w}_{0,j} \quad (17)$$

where  $j$  indicates the  $j$ 'th member of the ensemble,  $\bar{\mathbf{s}}_0$  is the initial mean state vector and  $\mathbf{w}_{0,j}$  is a Gaussian noise with zero mean.

So, the state vector is estimated through a recursive scheme, composed by the following two steps:

1. **forecast step** - the direct model is run one time step forward for each member of the ensemble obtaining the updated forecast state vector

$$\bar{\mathbf{s}}_{n,j}^- = \chi(\bar{\mathbf{s}}_{n-1,j}) + \mathbf{w}_{n,j} \quad (18)$$

where  $\mathbf{w}_{n,j}$  corresponds to the model error covariance matrix  $\mathbf{W}_n$ ,  $n$  denotes the time step and  $\chi$  is the model's numerical solution function.

The model error is usually added only to the components of the state vector  $\mathbf{s}$  that have more uncertainty on their values, as in the case of parameters or input quantities.

Then, through the mean value of the state vector

$$\bar{\mathbf{s}}_n^- = \frac{1}{M} \sum_{j=1}^M \bar{\mathbf{s}}_{n,j}^- \quad (19)$$

and the factor

$$\mathbf{T}_n^- = \frac{1}{\sqrt{M-1}} [(\bar{\mathbf{s}}_{n,1}^- - \bar{\mathbf{s}}_n^-), (\bar{\mathbf{s}}_{n,2}^- - \bar{\mathbf{s}}_n^-), \dots, (\bar{\mathbf{s}}_{n,M}^- - \bar{\mathbf{s}}_n^-)] \quad (20)$$

we obtain the error covariance matrix

$$\mathbf{P}_n^- = \mathbf{T}_n^- (\mathbf{T}_n^-)^T \quad (21)$$

where  $M$  is the number of the members of the ensemble;

2. **analysis step** - measurements  $\mathbf{z}_{n,j}$ , distributed with known variances, are take into account. As pointed out by (Gryzlov *et al.*, 2010), assuming that measurement errors are statistically independent, the measurements

covariance matrix  $\mathbf{R}$  is diagonal and constant. The matrix  $\mathbf{H}$  is used to select data or physical characteristics from the actual system to obtain the measurements that will be compared to the corresponding values of the forecast state vector, as follows

$$\mathbf{z}_n = \mathbf{H}_n \mathbf{s}_n + \mathbf{v}_n \quad (22)$$

where  $\mathbf{v}_n$  is the measurement Gaussian error identified by the covariance matrix  $\mathbf{R}$ .

Therefore the Kalman gain is calculated as follows

$$\mathbf{K}_n = \mathbf{P}_n^- \mathbf{H}^T (\mathbf{H} \mathbf{P}_n^- \mathbf{H}^T + \mathbf{R})^{-1} \quad (23)$$

and the analyzed state for each member of the ensemble is given by

$$\mathbf{s}_{n,j} = \bar{\mathbf{s}}_{n,j}^- + \mathbf{K}_n (\mathbf{z}_{n,j} - \mathbf{H} \bar{\mathbf{s}}_{n,j}^-). \quad (24)$$

Finally, the mean value of the analyzed ensemble is

$$\bar{\mathbf{s}}_n = \frac{1}{M} \sum_{j=1}^M \mathbf{s}_{n,j}. \quad (25)$$

and it represents the best estimate of the actual system.

Now, the cycle can restart from the step 1.

To avoid poor quality performances of the filter due to truncation errors, since variables involves in the Kalman filtering process can have different orders of magnitude, the variables in the state vector  $\mathbf{s}$  have to be adimensionalized on some reference values  $\mathbf{s}_{ref}$ , as suggested by (Gryzlov *et al.*, 2010)

$$\mathbf{s}_{ad} = \mathbf{s} / \mathbf{s}_{ref}, \quad (26)$$

obtaining the adimensionalized state vector  $\mathbf{s}_{ad}$  in which quantities have the same order of magnitude. In this work, the reference values are ones assumed by the variables of the problem in the last cell of the discretized geometries, corresponding to the outlet section. Therefore

$$\mathbf{s}_{ref} = [\alpha_{l,o} \ u_{g,o} \ u_{l,o} \ p_o \ v_o]^T, \quad (27)$$

where the subscript  $o$  stands for outlet. The same procedure is applied to the measurement vector  $\mathbf{z}$ .

## RESULTS

### Flow rate estimate

In a first test case we try to estimate inlet flow rates in slug flow conditions. First, using the 5ESCARGOTS code by (Ferrari *et al.*, 2017), we simulate an air/water two-phase flow reference problem in a horizontal pipe to keep as actual system to be estimated. The pipe is 36 m long with a diameter equal to 0.078 m. The simulation starts with stratified conditions; inlet superficial velocities are chosen to guarantee that slug flow conditions will develop during the simulation. Therefore, gas and liquid superficial velocities are fixed to 2.0 m/s and 1.5 m/s, respectively. Cells number is set to 900, corresponding to a CFL condition of 0.25. Outlet is open to ambient pressure. The liquid phase is water ( $\mu_l = 1.14 \cdot 10^{-3} \text{ Pa} \cdot \text{s}$ ,  $\rho_{0,l} = 1000.0 \text{ kg/m}^3$ ) and the gas phase is air ( $\mu_g = 1.79 \cdot 10^{-5} \text{ Pa} \cdot \text{s}$ ,  $\rho_{0,g} = 1.0 \text{ kg/m}^3$ ). In Fig. 2 the liquid volume fraction profile along the pipe after 8 s of simulation is reported: it is clearly visible a slug in the second half of the pipe.

Then, by the combination of the same 5ESCARGOTS code

with an ensemble Kalman filter, a soft-sensing scheme is implemented in order to estimate actual inlet flow rate (i.e. inlet superficial velocities of the first simulation) starting from a initial guess, for example  $1.0 \text{ m/s}$  for both gas and liquid superficial velocities. The state vector, in this case, is defined as

$$\mathbf{s} = [\alpha_{l,i} \ u_{g,i} \ u_{l,i} \ p_i]^T \quad (28)$$

where inlet superficial velocities are extrapolated directly from the left boundary condition. The ensemble Kalman filter is initialized by gaussian errors based on standard deviations about 1% of the value of the characteristics of the state vector  $\mathbf{s}$ .

In a first test, we run a soft-sensor with the so-called twin simulation, see (Gryzlov *et al.*, 2010), i.e. a simulation with

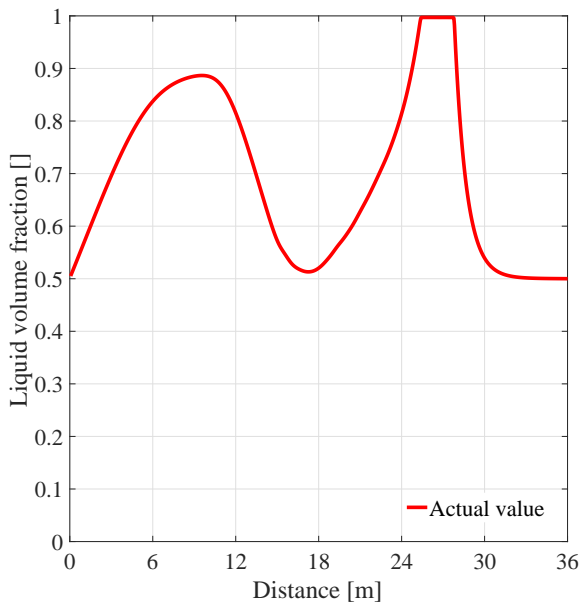


**Figure 2:** Slug flow after 8 s of simulation. Liquid volume fraction profile.

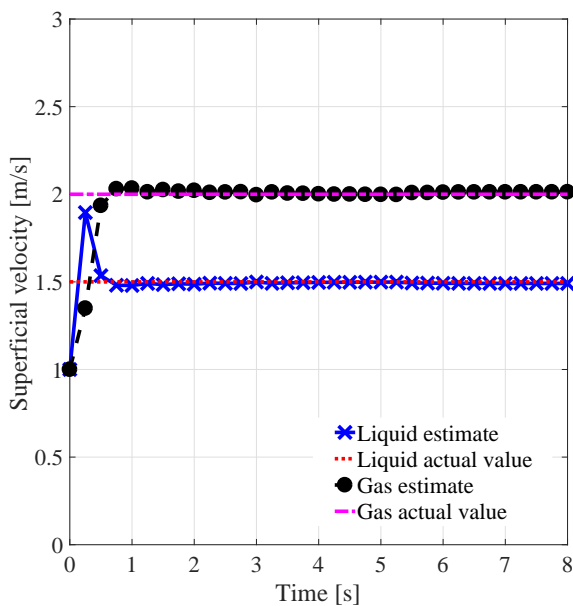


**Figure 3:** Inlet flow rate estimation by pressure measurements in every cell along the pipe.

the same conditions of the actual one, except for inlet superficial velocities. Inlet conditions are estimated through measurements of pressure in each cell along the pipe and by the measure of the other characteristics at the outlet section every 0.25 s.

Figure 3 shows the estimated inlet superficial velocities compared to the actual values of the first simulation: the soft-sensor, with the ensemble number set to 100, estimates very well actual values for both phases, also when slug flow arises and develops, i.e. after about 5 seconds of simulation. On the other hand, the great number of pressure measurements used in this case is unrealistic for an application.

If we try to reduce the number of numerical pressure gauges

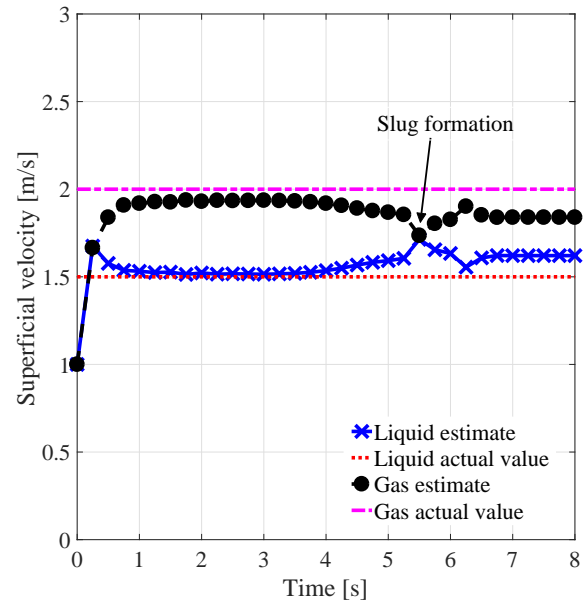


**Figure 4:** Inlet flow rate estimation by 36 pressure measurements along the pipe.

along the pipe, the soft-sensor system becomes quickly unstable, due probably to the great number of unknown that characterized the five equation model adopted, if compared to the number of measurements chosen to use here.

Therefore, in a second test case, we decide to run the soft-sensor reducing the number of cell to 36, measuring pressure from the actual simulation only in the 36 positions along the pipe, corresponding to the centre of each of the 36 cells used in the soft-sensor. If that, on one hand, leads to a more poor physical description of the slug phenomenon, it allows, on the other hand, to reduce computational costs and the number of pressure measurements along the pipe, making the soft-sensor more suitable for real application.

Figure 4 shows results in the case of 36 pressure measurements. It is clearly visible that the estimate is very good only for the first five seconds of simulation, i.e. when the flow is stratified. Then, when slug conditions arise (after about 5 seconds of simulation, as indicated in Fig. 4), estimates leave the actual values and the estimate error becomes a little higher, in the order of 5-10%. This fact is due to the inadequate description of the slug flow since the number of cells is insufficient. Therefore, in future applications, a better compromised between the accuracy in the simulation of the physical phenomena and the efficiency of the soft-sensing technique would be investigated.



## Diameter estimate

In actual pipelines, wax deposition can create obstructions or constrictions reducing the efficiency of hydrocarbon transportation. This phenomenon is often difficult to predict, except through invasive and expensive inspections. Therefore, the possibility to estimate the entity and the position of a potential obstructions along a pipe, using real-time dynamical numerical model, through only few easy and cheap measurements, can be very important in the optimization of multi-phase flow industrial process.

This can be obtained, through a soft-sensing technique, considering the diameter not as a constant parameter but as a variable, that can assume, at the same instant,  $N$  possible different values, where  $N$  is the number of cells, taking into account the presence of potential reduction of the local cross-section.

Therefore, the same technique presented in the previous Section is here applied to a first attempt of estimate of a variable pipe diameter along the pipe. Geometrical and flow conditions are the same of the previous test case, but now the unknowns to be estimated are not inlet flow conditions but the values of a variable diameter along the pipe. So the state vector, in this case, becomes

$$\mathbf{s} = [\alpha_{l,i} u_{g,i} u_{l,i} p_i d_i]^T, \quad (29)$$

where  $d_i$  are the different diameters in the cells.

First of all, a simulation with a constant diameter, set to the value of  $0.078\text{ m}$ , is run and it is kept as actual reference for the following estimate process. Then, by the use of an ensemble Kalman filter, a soft-sensor simulates the same test case but with a diameter value expressed for each cell. As initial guess, the soft-sensor starts with a distributed diameter with same value in each cells, fixed to  $0.13\text{ m}$ , to which is added a Gaussian noise.

Preliminary tests have showed that the estimate of non con-

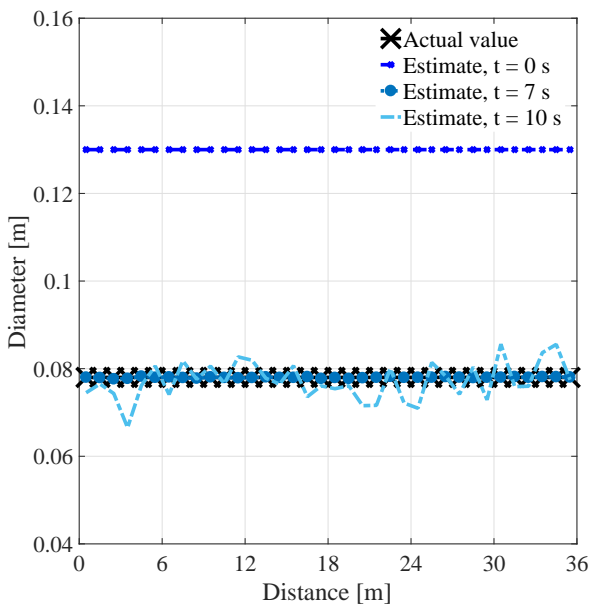


**Figure 5:** Diameter estimate along the pipe at three different time instants.

stant diameter makes the soft-sensor unstable and not efficient. In fact, as pointed out by (Gryzlov *et al.*, 2010), the attempt to estimate parameters, in particular if their number

is large, as in this case, increases the size of the state vector  $\mathbf{s}$ , in which the variable diameter must be included. This leads to a dramatical decreasing of the robustness of the method. Therefore, as first attempt, we decide to include among measurements to be used for the estimate process, beside pressure values, also liquid volume fraction values along the pipe, in order to decrease the great disparity between the size of the state vector and the number of the available measurements. Obviously, this compromise is quite unrealistic for actual applications, but it allows us to obtain and discuss some first results. As for the inlet flow rate estimate, soft-sensor is set to a cell number equal to 36.

Figure 5 shows the estimated diameter along the pipe at dif-

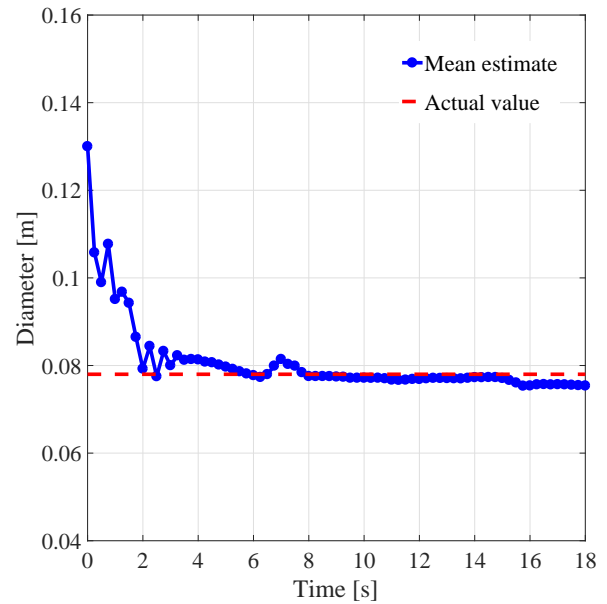


**Figure 6:** Mean diameter estimate during simulation.

ferent times in comparison with the actual diameter value. The estimate quickly reaches the actual value along all the pipe in the first seconds of simulation, i.e. when the flow is stratified; then, after the development of the first slug, the estimate becomes less accurate, with significant oscillations. In Fig. 6 the profile of the estimate of the mean diameter during the simulation, calculated along cells, is compared to the actual value. In this last case, the less accuracy of the soft-sensor when the flow is under slug regime is less visible. This results lead to the conclusion that the estimate of a variable diameter along the pipe is feasible also under slug flow conditions; however, the five equation model adopted here seems to be too complex for a soft-sensing application, since the great size of the state vector badly affects the filter accuracy.

## CONCLUSION

In this paper, a soft-sensing technique, composed by a five equation two-fluid model and an ensemble Kalman filter, is presented. The 5ESCARGOTS code, numerically developed for slug capturing purposes by (Ferrari *et al.*, 2017), guarantees to capture the transition from stratified to slug flow; here it is combined with an ensemble Kalman filter, in order to estimate real-time inlet flow rate and variable diameter along the pipe, using the less possible number of measurements from the actual system.

Results shows estimate in quite good agreement with actual

values, but they demonstrate also some limits of the soft-sensor presented in this paper. In fact, this work leads to the conclusion that the estimate of inlet flow rate and variable diameters along the pipe seems to be feasible also under slug flow conditions; however, in some cases, the five equation model appears too complex for a soft-sensing application since the great size of the state vector badly affects the filter accuracy. In future applications, a better compromised between the accuracy of the slug phenomenon simulation and the efficiency of the soft-sensing technique would be investigated.

## REFERENCES

- BRAUNER, N. and MARON, D.M. (1992). "Stability analysis of stratified liquid-liquid flow". *Int. J. Multiph. Flow*, **18**, 103–121.
- FERRARI, M., BONZANINI, A. and POESIO, P. (2017). "A five-equation, transient, hyperbolic, one-dimensional model for slug capturing in pipes". Accepted for publication in *Int. J. Numer. Meth. Fluids*.
- GRYZLOV, A., SCHIFERLI, W. and MUDDE, R.F. (2010). "Estimation of multiphase flow rates in a horizontal wellbore using an ensemble kalman filter". *Proc. 7th Int. Conf. on Multiph. Fl.* ICMF2010, Tampa, FL USA.
- GRYZLOV, A., SCHIFERLI, W. and MUDDE, R.F. (2013). "Soft-sensors: model-based estimation of inflow in horizontal wells using the extended kalman filter". *Flow Meas. Instrum.*, **34**, 91–104.
- ISSA, R.I. and KEMPF, M.H.W. (2003). "Simulation of slug flow in horizontal and nearly horizontal pipes with the two-fluid model". *Int. J. Multiph. Flow*, **29**, 69–95.
- KALMAN, R.E. (1960). "A new approach to linear filtering and prediction problems". *J. Basic Eng.*, **82**, 35–45.
- LESKENS, M., DE KRUIF, B., BELFROID, S., SMEULERS, J. and GRYZLOV, A. (2008). "Downhole multiphase metering in wells by means of soft-sensing". *Proc. SPE Intel. Energy Conf. and Exhib.* Amsterdam, The Netherlands.
- LORENTZEN, R.J., NAEVDAL, G. and LAGE, A.C.V.M. (2003). "Tuning of parameters in a two-phase flow model using an ensemble kalman filter". *Int. J. Multiph. Flow*, **29**, 1283–1309.
- MUNKEJORD, S.T. and GRAN, I.R. (2009). *Modelling and numerical methods for two-phase flow*, vol. Phd Thesis 2005, NTNU, Trondheim, Norway. VDM Verlag Dr. Müller Aktiengesell & Co. KG, Saarbrücken, Germany.
- SAUREL, R. and ABGRALL, R. (1999). "A multiphase godunov method for compressible multifluid and multiphase flow". *J. Comput. Phys.*, **150**, 425–467.



## DIRECT NUMERICAL SIMULATION OF PROPPANT TRANSPORT IN A NARROW CHANNEL FOR HYDRAULIC FRACTURING APPLICATION

R. V. MAITRI<sup>1\*</sup>, I. KOIMTZOGLOU<sup>1</sup>, S. DAS<sup>1</sup>, J.A.M. KUIPERS<sup>1</sup>, J.T. PADDING<sup>2</sup>, E.A.J.F. PETERS<sup>1</sup>

<sup>1</sup>Multiphase Reactors Group, Department of Chemical Engineering and Chemistry,  
 Eindhoven University of Technology, THE NETHERLANDS

<sup>2</sup>Intensified Reaction & Separation Systems, Process and Energy Department,  
 Delft University of Technology, THE NETHERLANDS

\* E-mail: r.maitri@tue.nl

### ABSTRACT

An efficient and accurate model for the direct numerical simulations (DNS) of liquid-solid flows is presented in this work. In this numerical model, fluid-solid coupling is achieved by implementing the no-slip boundary condition at the particles' surfaces by using a second order ghost-cell immersed boundary method, allowing for a fixed Cartesian grid to be used for solving the fluid equations. The particle-particle and particle-wall interactions are implemented using the soft sphere collision model. Lubrication forces are included through a sub-grid scale model because of its range of influence on a scale smaller than the grid size.

After the validation of the model, the transport of solid particles in a narrow channel is simulated to mimic the proppant transport in rock fractures in fracking process. The simulations are performed for solids volume fractions ranging from 1.7 to 20 % with the range of Reynolds and Archimedes number: 100-400 and 0-7848, respectively.

**Keywords:** Direct Numerical Simulation (DNS), Immersed Boundary Method (IBM), Multiphase flow, fracking

$p$	Pressure, [ $N/m^2$ ]
$\bar{r}$	Position vector, [ $m$ ]
$Re$	Reynolds number
$St$	Stokes number
$t$	Time, [ $s$ ]
$\bar{T}_{f \rightarrow s}$	Torque exerted by fluid on solid, [ $N.m$ ]
$\bar{u}$	Fluid velocity, [ $m/s$ ]
$\bar{w}$	Translational velocity, [ $m/s$ ]
$\bar{y}$	Vertical height [ $m$ ]

### Sub/superscripts

$f$	Fluid phase
$p$	Particle
$s$	Solid phase

### Operators

$\nabla$	Gradient [ $1/m$ ]
$\nabla \cdot$	Divergence [ $1/m$ ]
$\nabla^2$	Laplace [ $1/m^2$ ]

### NOMENCLATURE

#### Greek Symbols

$\varepsilon_s$	Solids volume fraction
$\mu$	Dynamic viscosity, [ $kg/m.s$ ]
$\xi_s$	Dimensionless distance
$\rho$	Density, [ $kg/m^3$ ]
$\tau$	Viscous stress, [ $N/m^2$ ]
$\phi$	Variable in the equation to be solved
$\bar{\omega}, \bar{\Omega}$	Rotational velocity, [ $1/s$ ]

#### Latin Symbols

$a$	Coefficients in discretized equation
$Ar$	Archimedes number
$b_c$	Explicit part in the discretized equation
$D$	Diameter, [ $m$ ]
$\bar{F}_{f \rightarrow s}$	Force exerted by fluid on solid, [ $N$ ]
$\bar{F}_{s \rightarrow s}$	Force in solid-solid interaction, [ $N$ ]
$\bar{g}$	Gravitational acceleration, [ $m/s^2$ ]
$H$	Height of the channel, [ $m$ ]
$I$	Moment of inertia, [ $kg.m^2$ ]
$m$	Mass, [ $kg$ ]
$\bar{n}$	Unit normal vector,
$N$	Total number of particles

### INTRODUCTION

Particle laden flows are encountered in many industrial as well as natural processes. These include proppant transport in fracking, biological flows, sediment transport in river and environmental flows. The fundamental understanding of fluid-solid multiphase flows is important for the optimization of these processes and computational fluid dynamics (CFD) is an effective numerical tool to obtain an insight in such complex processes.

For fluid-solid interaction, the immersed boundary method (Peskin, 1972) was introduced to couple the movement of the flexible membrane and the fluid around it. This method used the feedback forcing method to enforce the no-slip boundary condition on the particle surface. A different approach was proposed by (Fadlun *et al.*, 2000) to have a direct forcing to impose the no-slip boundary condition. (Uhlmann, 2005) combined the direct forcing method with the regularized delta function to remove oscillations in moving particles' simulation. This method was improved later (Breugem, 2012; Kempe and Fröhlich, 2012) to account for the lower solid to fluid density ratios and to improve the order of accuracy of the original method. Another efficient variant of the IBM named ghost cell method (Tseng and Ferziger, 2003) is also often used. Here the ghost node inside the solid is given a velocity to impose the no-slip boundary condition

on the particle surface. This method was later modified and extended for moving particles in fluidized beds (Deen *et al.*, 2012) and is used with further modification in this paper for the simulations.

Particle laden flows can be categorized in two classes: free-surface flow like sediment transport in a river and narrow channel flow like proppant transport in a rock fracture. The relevant length scales and the flow structures in both the phenomena are quite different to each other. This work focuses on the narrow channel flow to obtain an insight into the proppant transport phenomenon. Previous numerical studies of particle transport in a narrow channel were performed for 2D circular particles using Arbitrary-Lagrangian-Eulerian (ALE) method (Choi and Joseph, 2001; Patankar *et al.*, 2001). In this paper, fully resolved 3D simulations are performed to capture the effect of flow structures in the transverse direction as well.

## MODEL DESCRIPTION

Our DNS model solves the coupled fluid-solid flow where the fluid phase is governed by continuity and Navier-Stokes equation and the solid motion is governed by Newton-Euler equations. The mathematical formulation of these equations is as follows (Eq. 1 - 4):

### Fluid phase:

The governing equations for incompressible Newtonian fluid flow are:

$$(\nabla \cdot \bar{u}) = 0 \quad (1)$$

$$\frac{\partial \rho_f \bar{u}}{\partial t} + (\nabla \cdot \rho_f \bar{u} \bar{u}) = -\nabla p + \mu_f \nabla^2 \bar{u} + \rho_f \bar{g} \quad (2)$$

The viscous term in the Navier-Stokes equation is discretized with the standard second-order central difference scheme. For the convective terms, the total variation diminishing minmod scheme is used, with a deferred correction. In the deferred correction, first order upwind (FOU) is implemented implicitly and the corrector step is carried out explicitly. The velocity and pressure variable are solved on a staggered grid with the standard fractional step method.

### Solid phase:

The translational and rotational motion of particles is governed by the following equations:

$$m_p \frac{d\bar{w}_p}{dt} = m_p \bar{g} + \bar{F}_{f \rightarrow s} + \bar{F}_{s \rightarrow s} \quad (3)$$

$$I_p \frac{d\bar{\omega}_p}{dt} = \bar{T}_{f \rightarrow s} \quad (4)$$

The force and torque exerted by the fluid on a spherical particle is:

$$\bar{F}_{f \rightarrow s} = - \iint_{S_p} (\tau_f \cdot \bar{n} + p \bar{n}) dS \quad (5)$$

$$\bar{T}_{f \rightarrow s} = - \iint_{S_p} (\bar{r} - \bar{r}_p) \times (\tau_f \cdot \bar{n}) dS \quad (6)$$

The particle-particle interaction ( $\bar{F}_{s \rightarrow s}$ ) is accounted for by the standard soft-sphere collision (Cundall and Strack, 1979) for the normal forces whereas a sub-grid scale lubrication model (Brenner, 1961) is used for the correction of the unresolved hydrodynamic interaction between particles.

## Fluid-solid interaction

The fluid-solid interaction takes place through momentum exchange at the particle surface and is incorporated in this study using the second order ghost-cell immersed boundary method (Deen *et al.*, 2012; Das *et al.*, 2016). In this method, the no-slip boundary condition on the particle surface is enforced implicitly by modifying the coefficient matrix of the fluid velocities at the level of the discrete equivalent of Eq. 2. In Fig. 1,  $\phi_i$  denotes a flow variable in cell at position  $i$ , such as a velocity component. The velocity at ghost cell 0 in Fig. 1 is extrapolated based on the particle velocity and the neighbouring fluid velocities and is represented as:

$$\phi_0 = -\frac{2\xi_s}{1-\xi_s} \phi_1 + \frac{\xi_s}{2-\xi_s} \phi_2 + \frac{2}{(1-\xi_s)(2-\xi_s)} \phi_p \quad (7)$$

It can be noted that the velocity at point  $\phi_1$  and  $\phi_2$  are to be solved for the new time step as well and hence, the extrapolation modifies the coefficients for the equation of velocity at  $\phi_1$ . The generic form of the discretized momentum equation and the updated coefficients are given in Eq. 8 - 11, where  $a_i$  and  $b_i$  indicate the coefficients and the explicit terms, respectively, before incorporating boundary conditions at the fluid-solid interface and  $\hat{a}_i$  and  $\hat{b}_i$  are the modified values after IBM implementation.

$$a_1 \phi_1 + \sum_{nb} a_{nb} \phi_{nb} = b_c \quad (8)$$

$$\hat{a}_1 = a_1 - a_0 \frac{2\xi_s}{1-\xi_s} \quad (9)$$

$$\hat{a}_2 = a_2 + a_0 \frac{\xi_s}{2-\xi_s} \quad (10)$$

$$\hat{b}_c = b_c - a_0 \frac{2}{(1-\xi_s)(2-\xi_s)} \phi_p \quad (11)$$

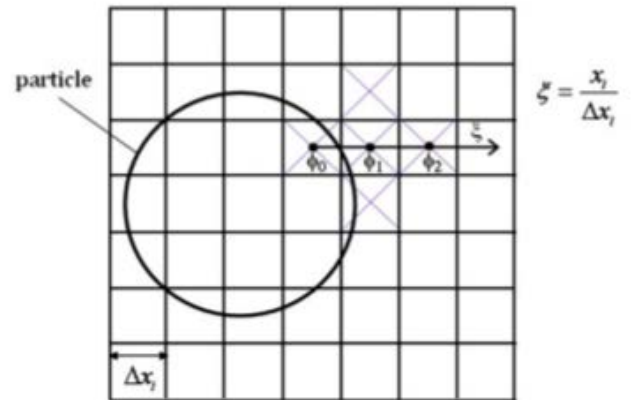


**Figure 1:** Representation of the fluid-solid interface on the Cartesian grid (Deen *et al.*, 2012)

## VERIFICATION AND VALIDATION

The original IBM (Deen *et al.*, 2012) is modified to compute the torque on spherical particles accurately. The performance of the new algorithm is quantified by comparing the torque computations with the analytical solution of the slowly rotating sphere in a large body of quiescent fluid in a creeping flow regime (Fig. 2) and the sedimentation of a single particle in a box filled with the liquid.

## Torque on a sphere

The torque on a sphere in a creeping flow (Bird *et al.*, 2007):

$$T = \pi\mu_f\omega_p D_p^3 \quad (12)$$

The results of the improved IBM method are presented in the Table 1. It is found that the error associated with the torque computation is reduced by 3-13 times (depending on the resolution) after the implementation of an improved algorithm. The accurate torque computation is very important in the particle laden flows as the particle rotation affects the fluid flow which in turn affects the particles again and hence, the small error can amplify over the time.

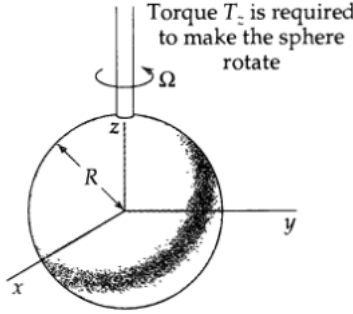


**Figure 2:** Freely rotating sphere in the quiescent fluid (Bird *et al.*, 2007)

**Table 1:** Error estimation of the numerical values of torque with the original and improved IBM ( $\mu_f = 2 \text{ kg/m.s}$ ,  $\omega = 10^{-5} \text{ s}^{-1}$ ,  $D_p = 0.2 \text{ m}$ ),  $\text{Torque}_{analytical} = 5.03 \times 10^{-7} \text{ N.m}$

$D_p/\Delta x$	Torque (N.m)		% Error	
	Original	Improved	Original	Improved
10	$4.52 \times 10^{-7}$	$4.86 \times 10^{-7}$	10.14 %	3.31 %
20	$4.60 \times 10^{-7}$	$4.96 \times 10^{-7}$	8.55 %	1.29 %
40	$4.88 \times 10^{-7}$	$5.00 \times 10^{-7}$	2.98 %	0.47 %
80	$4.92 \times 10^{-7}$	$5.02 \times 10^{-7}$	2.2 %	0.17 %

## Sedimentation of a single particle

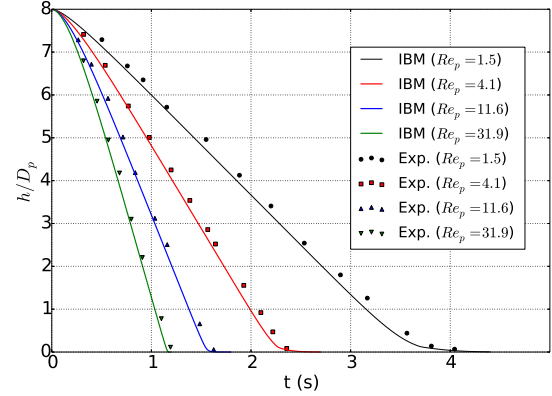
As a next validation case, numerical simulation of a single particle sedimentation in a large box is performed and the results are compared with the experimental measurements (Ten Cate *et al.*, 2002). The simulation is carried out in the domain of the size  $6.67D_p \times 10.67D_p \times 6.67D_p$  with initial particle centre position at  $8.5D_p$  from the bottom wall. The diameter of the particle is 0.015 m and the density is 1120  $\text{kg/m}^3$ . Free-slip boundary condition is applied on the walls for velocity. The comparison results for the position of the bottom surface of the particle from bottom wall and its vertical velocity are presented in Fig. 3. An excellent agreement between the simulation and experimental results is obtained.

## RESULTS

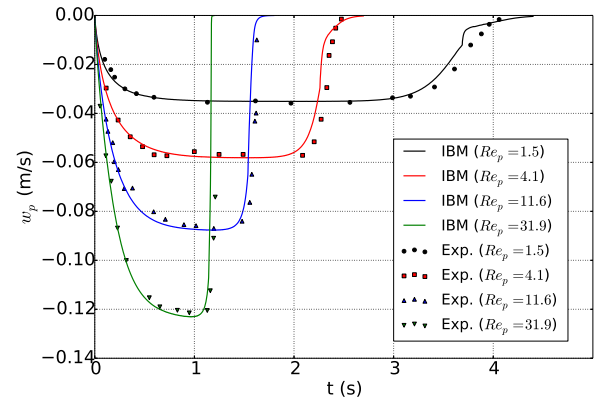
To mimic the proppant transport phenomenon in rock fractures, multi-particle simulations in the narrow channel are performed in this paper. Especially, the influence of the initial particle configuration and the solids volume fraction is studied. The transport of particles is governed by the two important non-dimensional numbers:

**Table 2:** The details of the simulation for single particle sedimentation case

Case	$Re_p$	St	$\rho_f$	$\mu_f$
1	1.4	0.19	970	0.373
2	4.1	0.53	965	0.212
3	11.6	1.50	962	0.113
4	31.9	4.13	960	0.058



a) Particle location



b) Particle velocity

**Figure 3:** Comparison of numerical simulation with the experimental results for the case of single particle sedimentation

$$Re = \frac{2\rho_f u_f H}{\mu_f}$$

$$Ar = \frac{\rho_f^2 (\rho_p / \rho_f - 1) g D_p^3}{\mu_f^2}$$

The boundary conditions in the x & z directions are periodic and in y-direction, no-slip condition with zero velocity is applied on the upper and lower wall. The pressure gradient is applied in the x-direction to drive the flow.

## Effect of initial particle configuration

In this section, the results for the effect of the particle configuration is presented. The simulations are carried out for 2 different cases - **Case 1:** The particles are stacked in three layers with each subsequent layer touching the layer below, **Case 2:** The particles are placed with a gap of  $D_p/2$  between each layer. Other relevant simulation parameters are summarized in Table 3.

**Table 3:** Simulation parameters used to study the effect of initial particle configuration

Simulation parameter	Value
# CV	300 x 160 x 60
# particles	135
$\Delta x$	0.01 m
$D_p/\Delta x$	20
Re	100
Ar	39.24
$\epsilon_s$	19.6 %

The simulation for both these cases is performed to study the behaviour of particles according to their initial configuration. It is found that for the given cases, the dynamics is substantially different although the non-dimensional parameters are kept constant (Figs. 4 & 5). It can be commented that for Case 2, the spacing between particles allows the particles to move freely due to gravity and lift forces affecting the flow field around it. With the evolution of time, the disturbance in the flow field leads to more pronounced asymmetric forces on the particles and consequently they remain in fluidized state (Fig. 5). On the contrary, no such fluidization is observed for Case 1 and particles remain sedimented during the entire simulation. This might be caused due to the restricted motion of particles in a closed packing. Hence, it is important to have a thin gap of fluid between particles to produce realistic simulations mimicking the proppant transport.

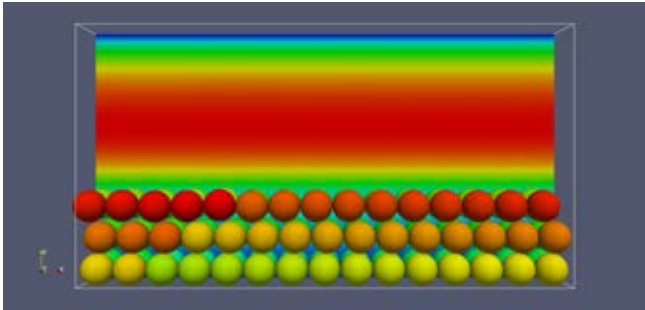


**Figure 4:** Particle configuration and the velocity distribution (on centre  $x$ - $y$  plane) at  $t^*(tu_f/D_p) = 17$  (Case 1)

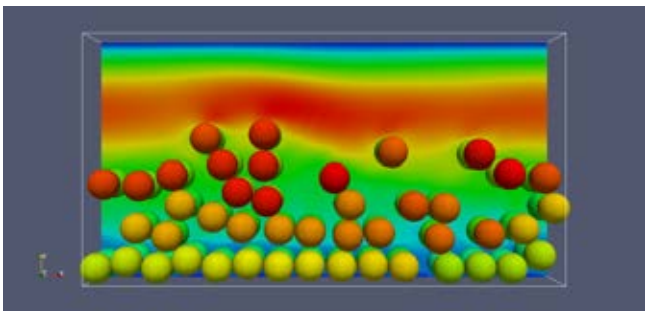
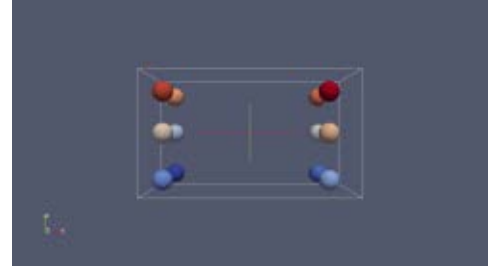


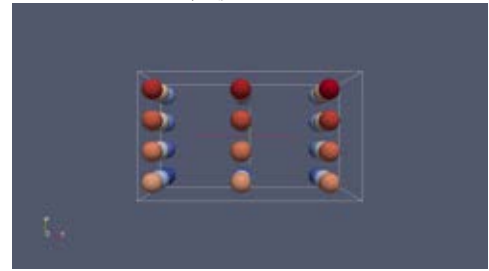
**Figure 5:** Particle configuration and the velocity distribution (on centre  $x$ - $y$  plane) at  $t^*(tu_f/D_p) = 17$  (Case 2)

### Effect of solids volume fraction

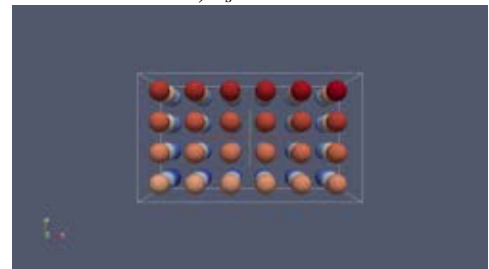
In this section, the effect of solids volume fraction on the particle transport and specifically, on the sedimentation times is studied. The initial particle configuration is shown in Fig. 6 whereas Table 4 lists the detailed simulation parameters.



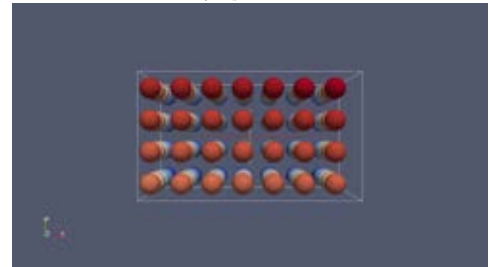
a)  $\epsilon_s = 0.017$



c)  $\epsilon_s = 0.05$



e)  $\epsilon_s = 0.1$



g)  $\epsilon_s = 0.2$

**Figure 6:** Initial configuration of particles for different solids volume fraction.

In these simulations, the average vertical location (Eq. 13) of all particles is monitored to obtain the sedimentation time. The time at which  $y_{avg}$  reaches a steady state value, is used as the sedimentation time and is listed in Table 5 for the chosen parameter space.

$$y_{avg} = \frac{1}{N} \sum_{n=i}^{n=N} y_i \quad (13)$$

The aim of the fracking process is to attain operating conditions with a longer sedimentation time such that particles are carried deeper into a fracture. It can be observed from the results that the sedimentation time increases by decreasing  $Ar$  owing to the reduced effect of the gravitation force. However,

**Table 4:** Simulation parameters used to study the effect of solids volume fraction

Simulation parameter	Value
# CV	200 x 120 x 120
$\Delta x$	0.01 m
$D_p/\Delta x$	20
Re	100 - 400
Ar	0-7848
$\epsilon_s$	1.7 - 20%

with the higher sedimentation times, it is also important for the particles not to fluidize in the flowback stage of the fracking process. The lighter particles will tend to fluidize quickly in the flowback and the efficiency of the process would be reduced. Hence, it would be important to use the heavier particles and still have a longer sedimentation time. From Table 5, it can be observed that the sedimentation time for  $Re = 400$  is comparable for the cases  $\{\epsilon_s = 0.017, Ar = 1569.6\}$  and  $\{\epsilon_s = 0.2, Ar = 7848\}$  which signifies that the heavier particles can also be transported at a longer distances if the higher solids volume fraction is used. The pattern for the influence of the Reynolds number on the sedimentation time is not consistent for all the volume fractions, however, the Reynolds number tends to increase the sedimentation time at higher value of  $\epsilon_s$ .

Ar \ Re	100	200	300	400
0	-	-	-	-
1569.6	13.4	11.2	10.5	9.3
3924	6.7	6.9	6.4	6.1
7848	3.9	4.2	4.7	4.8

a) Sedimentation time (s)  $\epsilon_s=0.017$

Ar \ Re	100	200	300	400
0	-	-	-	-
1569.6	20.2	24.7	23.4	35.2
3924	9.8	10.3	10	12.8
7848	4.7	5.3	6.1	7.4

b) Sedimentation time (s)  $\epsilon_s=0.05$

Ar \ Re	100	200	300	400
0	-	-	-	-
1569.6	21.1	25.6	23.2	18.3
3924	18.4	18.6	18.9	13.2
7848	8.7	9.1	10.2	7.6

c) Sedimentation time (s)  $\epsilon_s=0.1$

Ar \ Re	100	200	300	400
0	-	-	-	-
1569.6	17.2	15.2	22.4	23.2
3924	10.3	13.7	12.8	15.6
7848	8.6	12.6	9.9	11.3

d) Sedimentation time (s)  $\epsilon_s=0.2$

**Table 5:** Sedimentation time for all cases simulated, various  $\epsilon_s$

## CONCLUSION

In this work, an efficient and accurate model for the direct numerical simulation (DNS) of liquid-solid flows is presented. The torque computation results with the improved immersed boundary method (IBM) are presented for the single rotating sphere in a quiescent fluid in comparison with the original IBM. It is found that the improved IBM reduces the error around 3-13 times. The verified and validated IBM is then used to simulate the transport of solid particles in a narrow channel to mimic the proppant transport in rock fractures in a fracking process. Initially, the simulation of transport of 135 particles with two different particle arrangements is performed and it was found that the spacing between the particles leads to a fluidization, contrary to the packed particle system with the same non-dimensional flow parameters. Hence, it is important to have a gap between particles while performing simulations to attain closer similarity with the real process.

As a next step, 48 simulation cases are performed to study the influence of the solids volume fraction, Archimedes number and Reynolds number on the proppant transport phenomenon. It was found that the sedimentation time of the heavier particles can be increased by increasing the solids volume fraction and it is even comparable to the sedimentation time of the lighter particles in the dilute system. Moreover, the influence of increasing Reynolds number is more pronounced and consistent in the higher volume fraction cases and contributes positively to keep the particles fluidized for a longer period.

In reality, the process of proppant transport is quite complex due the rough walls in the rock fractures with the varying widths, visco-elastic fracking fluids, randomly oriented cracks, high aspect ratio in dimensions of a crack and polydispersity in the proppant sizes. Moreover, large number of particles are used in this process. Hence, the numerical model has to be extended with the complex boundary conditions for rough walls, visco-elastic flow modeling and polydispersity of particles. To simulate the larger system, full parallelization of the fluid solver as well as particle part is also very important.

## ACKNOWLEDGEMENTS

This work is supported by the programme ‘Computational Sciences for Energy Research (CSER)’ of the Foundation for Fundamental Research on Matter (FOM) which is now part of the Netherlands Organisation for Scientific Research Institutes (NWO-I). This research is also co-financed by Shell Global Solutions International B.V. We thank NWO and Dutch Supercomputing Consortium SURFsara ([www.surfsara.nl](http://www.surfsara.nl)) for granting us the computational time on Cartesius cluster.



## REFERENCES

- BIRD, R.B., STEWART, W.E. and LIGHTFOOT, E.N. (2007). *Transport phenomena*. John Wiley & Sons.
- BRENNER, H. (1961). “The slow motion of a sphere through a viscous fluid towards a plane surface”. *Chemical Engineering Science*, **16(3-4)**, 242–251.
- BREUGEM, W.P. (2012). “A second-order accurate immersed boundary method for fully resolved simulations of particle-laden flows”. *Journal of Computational Physics*, **231(13)**, 4469–4498.
- CHOI, H.G. and JOSEPH, D.D. (2001). “Fluidization by lift of 300 circular particles in plane poiseuille flow by direct numerical simulation”. *Journal of Fluid Mechanics*, **438**, 101–128.
- CUNDALL, P.A. and STRACK, O.D. (1979). “A discrete numerical model for granular assemblies”. *Geotechnique*, **29(1)**, 47–65.
- DAS, S., DEEN, N.G. and KUIPERS, J. (2016). “Immersed boundary method (ibm) based direct numerical simulation of open-cell solid foams: Hydrodynamics”. *AIChE Journal*.
- DEEN, N.G., KRIEBITZSCH, S.H.L., VAN DER HOEF, M.A. and KUIPERS, J.A.M. (2012). “Direct numerical simulation of flow and heat transfer in dense fluid-particle systems”. *Chemical Engineering Science*, **81**, 329–344.
- FADLUN, E., VERZICCO, R., ORLANDI, P. and MOHD-YUSOF, J. (2000). “Combined immersed-boundary finite-difference methods for three-dimensional complex flow simulations”. *Journal of Computational Physics*, **161(1)**, 35–60.
- KEMPE, T. and FRÖHLICH, J. (2012). “An improved immersed boundary method with direct forcing for the simulation of particle laden flows”. *Journal of Computational Physics*, **231(9)**, 3663–3684.
- PATANKAR, N., KO, T., CHOI, H. and JOSEPH, D. (2001). “A correlation for the lift-off of many particles in plane poiseuille flows of newtonian fluids”. *Journal of Fluid Mechanics*, **445**, 55–76.
- PESKIN, C.S. (1972). “Flow patterns around heart valves: a numerical method”. *Journal of Computational Physics*, **10(2)**, 252–271.
- TEN CATE, A., NIEUWSTAD, C., DERKSEN, J. and VAN DEN AKKER, H. (2002). “Particle imaging velocimetry experiments and lattice-boltzmann simulations on a single sphere settling under gravity”. *Physics of Fluids*, **14(11)**, 4012–4025.
- TSENG, Y.H. and FERZIGER, J.H. (2003). “A ghost-cell immersed boundary method for flow in complex geometry”. *Journal of Computational Physics*, **192(2)**, 593–623.
- UHLMANN, M. (2005). “An immersed boundary method with direct forcing for the simulation of particulate flows”. *Journal of Computational Physics*, **209(2)**, 448–476.

## MULTIPHASE DIRECT NUMERICAL SIMULATIONS (DNS) OF OIL-WATER FLOWS THROUGH HOMOGENEOUS POROUS ROCKS

H.V. PATEL<sup>1\*</sup>, J.A.M. KUIPERS<sup>1</sup>, E.A.J.F. PETERS<sup>1</sup>

<sup>1</sup>Multiphase Reactors Group, Dept. of Chemical Engineering and Chemistry, Eindhoven University of Technology, P.O. Box 513, 5600 MB Eindhoven, THE NETHERLANDS

\* E-mail: h.v.patel@tue.nl

### ABSTRACT

Water flooding is commonly used to recover oil from porous rocks using pressurized water. Present study focuses on fully resolved pore-scale level multiphase Direct Numerical Simulations (DNS) of oil-water flows through homogeneous porous rocks. A second order accurate implicit Immersed Boundary Method (IBM) is used to resolve fluid-solid interactions on a non-body fitted Cartesian computational grid. Dynamic evolution of the fluid-fluid interface is tracked by a mass conservative sharp interface Volume of Fluid (VOF) method. The IBM and VOF method are coupled by a prescribed contact angle boundary condition at the fluid-fluid-solid contact line. Our method has been extensively validated especially for the test cases involving oil-water flows. Simulations of water flooding process through periodic homogeneous configurations of spheres are performed based on typical pore-scale capillary and Reynolds numbers. Effect of wettability on the mobility of oil through oil-wet and neutrally-wet rocks has been quantified as well.

**Keywords:** water flooding, porous rocks, Immersed Boundary Method (IBM), Volume of Fluid (VOF), contact angle .

### NOMENCLATURE

#### Notations

$p$	Pressure, [Pa]
$F$	Fluid phase fraction, [-]
$M$	Dynamic viscosity ratio, [-]
$Re$	Reynolds number, [-]
$Ca$	Capillary number, [-]
$S$	Fluid phase saturation, [-]
$k$	Permeability, [ $m^2$ ]
$x$	x co-ordinate, [ $m$ ]
$y$	y co-ordinate, [ $m$ ]
$z$	z co-ordinate, [ $m$ ]

#### Greek Symbols

$\rho$	Mass density, [ $kg/m^3$ ]
$\mu$	Dynamic viscosity, [ $Pa \cdot s$ ]
$\sigma$	Surface tension, [ $N/m$ ]
$\Delta$	Grid size, [ $m$ ]
$\theta$	(Static) contact angle, [ $degree$ ]
$\phi$	Porosity, [-]

#### Vectors

$\mathbf{u}$	Velocity, [ $m/s$ ]
$\mathbf{F}_\sigma$	Surface tension force, [ $N$ ]
$\mathbf{g}$	Gravitational acceleration, [ $m/s^2$ ]

#### Sub/superscripts

1,2	Fluid phase number
$w$	Wetting fluid
$nw$	Non-wetting fluid

### INTRODUCTION

Multiphase flows in complex structures are encountered widely in nature and technology. One such example is water flooding (Sheng, 2014) used for oil recovery. After the primary (natural) recovery of the oil from reservoir, large amount of oil remains trapped in the porous rocks. Secondary and ternary recovery processes (e.g. water flooding, gas injection, thermal processes, chemical flooding etc.) are then used for further recovery of such residual oil. In water flooding high pressure and/or high temperature water is pushed through porous rocks which carries oil out of the porous bed. Focus of the current work is to perform pore-scale simulations of oil-water multiphase flows through complex rock structures during such a water flooding process. To serve this purpose, three different problems need to be tackled: i) oil-water multi-fluid interface tracking, ii) interactions between fluids (oil or water) and complex solid geometries, and iii) three-phase contact line dynamics.

A wide range of numerical methods (e.g. Front Tracking, Volume of Fluid, Level Set etc.) has been developed and tested successfully to track multi-fluid interfaces (Wörner, 2003). They all differ with respect to tackling the following complexity: i) interface advection based on local velocity field and ii) surface tension force based on local interface curvature. The volume of fluid (VOF) method (Hirt and Nichols, 1981; Youngs, 1982) uses a color function  $F$  which denotes the local fluid phase fraction in the immiscible mixture of fluids. Advection of  $F$  is governed by pseudo-Lagrangian geometrical advection schemes to minimize numerical diffusion. This particular feature makes VOF the most mass conservative among all multi-fluid interface tracking methods. The density-scaled continuum surface force (CSF) model proposed by Brackbill *et al.* (1992) is used to evaluate the surface tension force for its simplicity and robustness especially in the presence of complex solid boundaries.

The immersed boundary method (IBM) (Mittal and Iaccarino, 2005) is a set of computational techniques which

uses non-body fitted (mainly Cartesian) grids for simulating fluid-solid interactions through complex geometries. It eliminates the need of traditional unstructured body fitted grids and hence provides simplicity in grid generation and discretization, ease of code development, less memory requirement and higher computational efficiency. A direct forcing approach used in IBM produces a sharp fluid-solid interface without spatial spreading. So, in the present work a direct forcing, implicit, second order IBM (Deen *et al.*, 2012; Das *et al.*, 2016) is used which does not require any calibration for the different complex geometries.

Fluid-fluid interfaces in contact with solid boundaries produce a three-phase contact line. The contact line behavior is determined by microscopic physicochemical interactions between molecules of two different immiscible fluids and the solid substrate, and it can drastically affect the statics and dynamics of the bulk flow (Snoeijer and Andreotti, 2013). An apparent contact angle at the macroscopic length scales is a result of these microscopic interactions at the contact line. In the present work, a coupled IBM-VOF method has been used to simulate contact line dynamics.

This paper deals with validation/verification and application of the developed IBM-VOF solver specifically for multiphase flows involving oil and water. It is organized as follows: We first describe the governing Navier-Stokes equations for multiphase flows along with the  $F$ -advection equation. Next, we discuss numerical and implementation details in brief. Further, the coupled IBM-VOF solver is extensively validated/verified for the test cases involving oil-water flows. Last, a water flooding process is simulated on the pore-scale and the effect of wettability on the mobility of oil has been quantified for oil-wet and neutrally-wet homogeneous rocks.

## MODEL DESCRIPTION

### Governing equations

For incompressible multiphase flows the Navier-Stokes equations can be combined into a single equation for  $\mathbf{u}$  in the entire domain. Surface tension due to the presence of a curved deformable fluid-fluid interface is taken into account by a local volumetric  $\mathbf{F}_\sigma$ . The governing mass and momentum conservation equations for unsteady, incompressible, Newtonian, multiphase flows are expressed as follows:

$$\nabla \cdot \mathbf{u} = 0 \quad (1)$$

$$\rho \frac{\partial \mathbf{u}}{\partial t} + \rho \nabla \cdot (\mathbf{u}\mathbf{u}) = -\nabla p + \nabla \cdot \boldsymbol{\tau} + \rho \mathbf{g} + \mathbf{F}_\sigma \quad (2)$$

where  $\boldsymbol{\tau} = \mu[\nabla \mathbf{u} + (\nabla \mathbf{u})^T]$  is the fluid stress tensor. Advection of  $F$  is governed by the following equation:

$$\frac{DF}{Dt} = \frac{\partial F}{\partial t} + \mathbf{u} \cdot \nabla F = 0 \quad (3)$$

This equation expresses that the interface is advected with the local fluid velocity. To evaluate the local averaged density, linear averaging of the densities of the fluid 1 ( $F = 1$ ) and fluid 2 ( $F = 0$ ) is used:

$$\rho = F\rho_1 + (1-F)\rho_2 \quad (4)$$

Similarly, the local average  $\mu$  could also be evaluated by linear averaging of the dynamic viscosities of individual fluid phase. Alternatively, following a fundamental approach proposed by Prosperetti (2002), the local average kinematic viscosity is evaluated by harmonic averaging of the kinematic viscosities of the individual fluid phases:

$$\frac{\rho}{\mu} = F \frac{\rho_1}{\mu_1} + (1-F) \frac{\rho_2}{\mu_2} \quad (5)$$

In all the computations reported in this paper, Eq. (4) and Eq. (5) are used to evaluate the local average density and dynamic viscosity, respectively.

### Numerical and Implementation Details

In the current implementation, the finite volume method is used to solve the mass and momentum conservation equations in each control volume of a staggered computational grid. To simulate multiphase flows involving multi fluid-solid interactions three things need to be dealt with: i) dynamic interactions between fluids and non-deformable solids, ii) dynamics of deformable fluid-fluid interfaces, and iii) contact line dynamics at the three phase contact lines.

An implicit (direct) second-order accurate IBM proposed by Deen *et al.* (2012) and described in detail by Das *et al.* (2016) has been used to apply no-slip boundary conditions for fluids-solid interactions at immersed boundaries. VOF (Van Sint Annaland *et al.*, 2005) to track fluid-fluid interface consists of three main parts: i) solution of  $F$ -advection equation, ii) computation of the volumetric  $\mathbf{F}_\sigma$ , and iii) smoothing of  $F$ . In presence of fluid-fluid interfaces with immersed solids, contact line dynamics plays a major role in wetting-dewetting phenomena. It is incorporated in our coupled IBM-VOF framework (Patel *et al.*, 2017) by applying the apparent contact angle as a boundary condition at contact lines. The contact angle may have a single value (static) or different values (dynamic) depending upon the local contact parameters and fluid properties. The effect of the contact angle is taken into account by modifying the interface normals at the solid boundaries. Readers may refer to the mentioned literature for intrinsic numerical and implementation details.

### VERIFICATION AND VALIDATION

The IBM and VOF implementations have been tested individually by Das *et al.* (2016) and Van Sint Annaland *et al.* (2005) respectively for various cases and they obtained excellent agreement with numerical and experimental results published in literature. The 3D coupled IBM-VOF implementation with contact line dynamics has been validated by Patel *et al.* (2017) with static and/or dynamic contact angles for i) the equilibrium shape of a droplet on a flat surface, ii) the equilibrium shape of a droplet on a spherical surface, and iii) temporal evolution of droplet contact radius on flat surface (generated with and without IBM).

In this section, we investigate additional validation/verification test cases specifically addressing the oil-water multiphase flows. First, a test case of 2D multiphase Poiseuille flow is considered to compare the velocity profiles and relative permeabilities with analytical expressions. Further, a viscous fingering phenomenon is simulated in a 2D channel and finger characteristics parameters i.e. dimensionless finger width and tip radius have been compared with results published in literature. Last, a grid independence study for the contact force is presented for 3D coupled IBM-VOF implementation.

### 2D Multiphase Poiseuille Flow

In this section, we investigate the co-current multiphase Poiseuille flow of two immiscible fluids namely wetting and non-wetting fluid. The wetting fluid is in contact with the channel walls ( $a < |y| < L$ ) whereas the non-wetting fluid resides between the layers of wetting fluid ( $0 < |y| < a$ ) as shown in Figure 1. No-slip boundary conditions are applied at the

channel walls ( $|y| = L$ ) and the flow in  $x$ -direction is periodic. Both fluids have the same density ( $\rho_w = \rho_{nw}$ ) and different dynamic viscosities giving the definition of  $M = \mu_{nw}/\mu_w$ . A constant body force  $G$  is applied to both fluids in the  $x$ -direction such as the flow remains in the Stokes regime ( $Re \ll 1$ ). Due to the existence of a flat fluid-fluid interface, the surface tension force doesn't play any role in this problem.

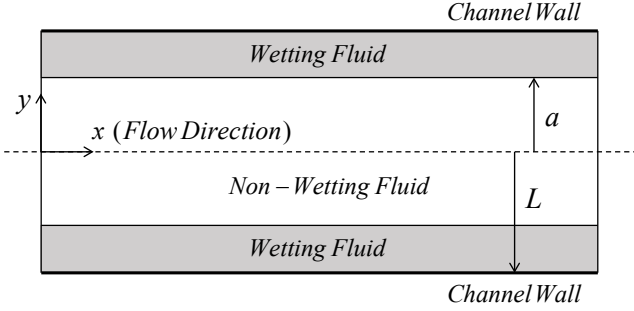


**Figure 1:** Schematic diagram of 2D multiphase Poiseuille flow.

For the given value of wetting and non-wetting saturation ( $S_w = (1 - a)/L$  and  $S_{nw} = a/L$ ), the analytical expressions for the velocity of the wetting and non-wetting fluids ( $u_w$  and  $u_{nw}$ ) are given by:

$$\begin{aligned} u_w(y) &= \frac{G}{2\mu_w}(L^2 - y^2) \\ u_{nw}(y) &= \frac{G}{2\mu_w}(L^2 - a^2) + \frac{G}{2\mu_{nw}}(a^2 - y^2) \end{aligned} \quad (6)$$

Similarly, the analytical expressions for the relative permeability of each fluid ( $k_{r,w}$  and  $k_{r,nw}$ ) can be given as,

$$\begin{aligned} k_{r,w} &= \frac{1}{2}S_w^2(3 - S_w) \\ k_{r,nw} &= S_{nw} \left[ \frac{3}{2}M + S_{nw}^2 \left( 1 - \frac{3}{2}M \right) \right] \end{aligned} \quad (7)$$

Readers are referred to Yiotis *et al.* (2007) for the detailed derivation of Equation (6) and (7). Equation (7) suggests that  $k_{r,w}$  is always bounded between 0 to 1 as it is only function of  $S_w$ . However,  $k_{r,nw}$  may become greater than 1 in case  $M > 1$  due to the 'lubricating' effect of the wetting fluid.

Simulations have been performed for  $M = 0.01, 1$  and 100 with  $S_w$  ranging from 0 to 1 with increment of 0.1. Total 100 grid cells have been taken across  $L$ . Figure 2 shows analytical and numerical velocity profiles for the case of  $M = 100$  and  $S_w = 0.5$ . Figure 3 compares analytical and numerical relative permeabilities for wetting and non-wetting fluids for  $M = 100$ . Our simulations show an excellent agreement with analytical results having maximum error in relative permeability to be less than 0.2%. Huang and Lu (2009) reports this error to be nearly 7% using multiphase Lattice-Boltzmann method. Also, in their results, continuity of the shear stress is not maintained at the interface and hence a velocity jump is observed.

### Viscous Finger in a 2D Channel

A viscous finger is an instability that may occur when a low viscosity fluid displaces high viscosity fluid. In this section, we simulate the single viscous finger formation phenomenon in a 2D channel. Initially, a channel with finite width  $H$  is fully saturated with high viscosity fluid 2. Fluid 1 with low

viscosity is introduced in  $x$ -direction with fully developed velocity profile and displaces Fluid 2 from channel. During this displacement process the viscous finger gets developed and produces a steady state shape (constant finger tip velocity) as shown in Figure 4.

Average velocity of the inlet fluid 1 is  $U_1$ . Viscosity ratio  $M = \mu_2/\mu_1$  is 20 which is generally experienced during water flooding process where water displaces oil. No-slip boundary conditions are applied at the channel walls in  $y$ -direction whereas velocity inlet and pressure outlet boundary conditions are applied in  $x$ -direction. Densities of fluid 1 and 2 have been chosen equal ( $\rho_1 = \rho_2 = \rho$ ) for the simplicity as the density ratio does not affect the finger formation and

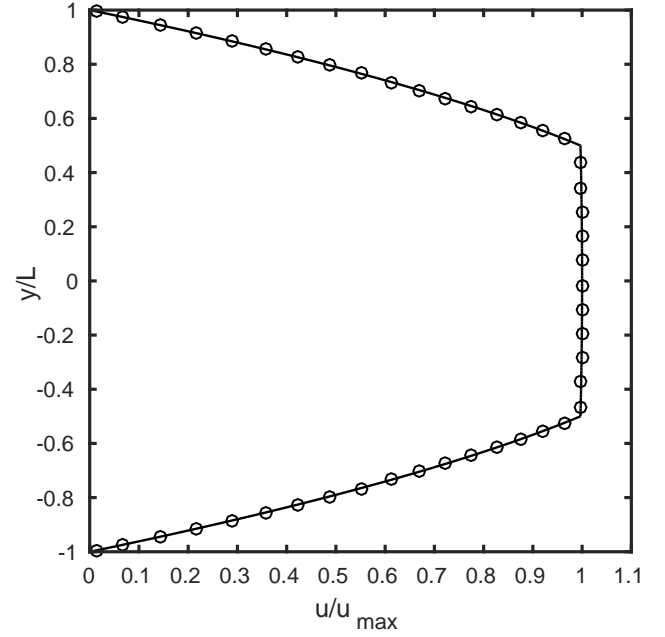


**Figure 2:** Analytical (—) and numerical (○) velocity profiles for  $M = 100$  and  $S_w = 0.5$ .

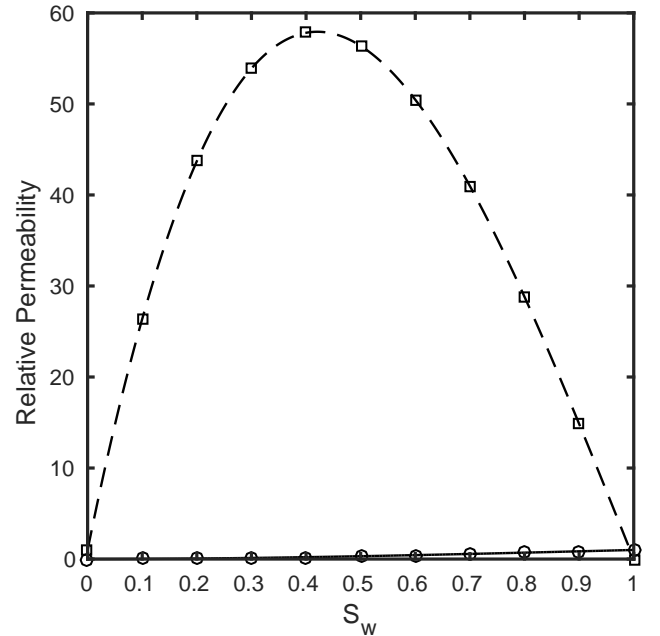


**Figure 3:** Relative permeability with  $S_w$  for  $M = 100$ : analytical  $k_{r,w}$  (—), numerical  $k_{r,w}$  (○), analytical  $k_{r,nw}$  (---) and numerical  $k_{r,nw}$  (□).

its properties. Capillary and Reynolds number defined using the steady state finger tip velocity  $U_t$  are  $Ca = \mu_2 U_t / \sigma$  and  $Re = \rho U_t H / \mu_2$ . From the mass balance, one can find  $U_t = U_1 H / W$ . To maintain the flow in Stokes regime, value of  $Ca$  and  $Re$  have been chosen such that  $ReCa = 10^{-3}$ .

Simulations have been performed with different  $Ca$  ranging from 0.025 to 3 with 64 grid cells across the height  $H$ . The steady state finger width  $W$  and finger tip radius  $R$  have been obtained. Figure 5 compares the same finger characteristics parameters in dimensionless form with the results obtained using boundary element method by Halpern and Gaver (1994). Our results of  $W/H$  show an excellent match with maximum deviation to be less than 2%. Also,  $R/H$  shows an excellent match at low  $Ca$ . However at higher  $Ca$ , deviation is higher due to higher tip curvatures.

### Contact Force Calculation

In this section, we present the grid independence study for contact force at three phase contact line in 3D. Initially, an oil droplet of equivalent radius  $R_{eq} = 1$  mm (Volume  $V = \frac{4}{3}\pi R_{eq}^3$ ) is placed on the solid sphere of radius  $R_s = 1$  mm such that it inscribes  $\theta = 60^\circ$  as shown in Figure 6. In this position,

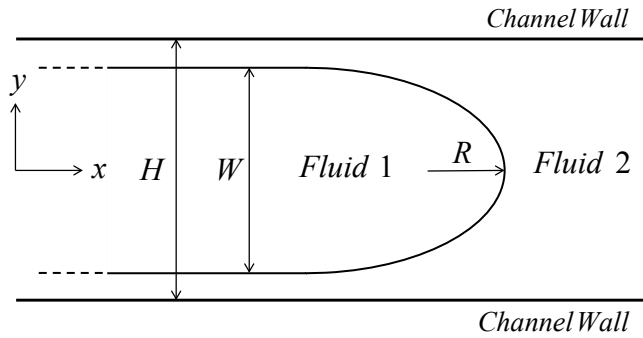


**Figure 4:** Schematic diagram of steady state viscous finger in 2D channel.

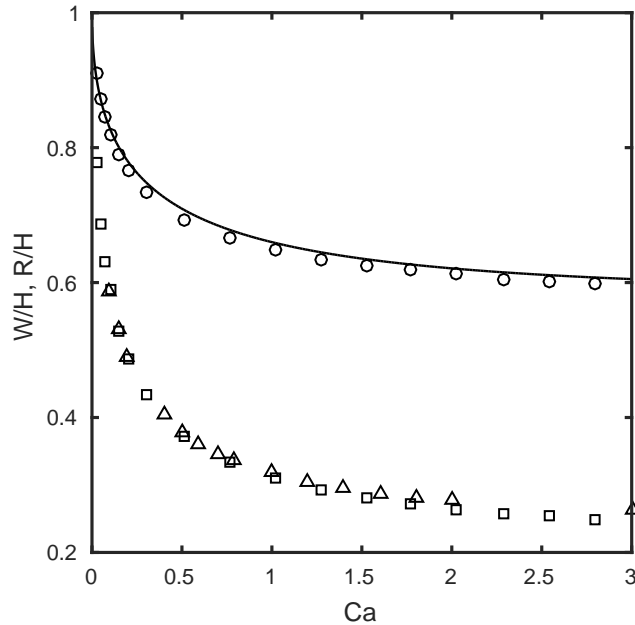


**Figure 5:** Dimensionless characteristics parameters of steady state viscous finger in 2D channel with  $Ca$  a) finger width  $W/H$ : present (○), Halpern and Gaver (1994) (—) b) finger tip radius  $R/H$ : present (□), Halpern and Gaver (1994) (△).

droplet radius  $R_d = 1.1082R_{eq}$ , contact radius  $R_c = 0.9069R_{eq}$  and  $\psi = 35.08^\circ$  (Patel *et al.*, 2017). The oil droplet is surrounded by water with  $\sigma = 0.03$  N/m. Using a force balance, contact force can be given by following expression,

$$\begin{aligned} F_{y,analytical} &= 2\pi\sigma R_c \sin\psi \\ F_{x,analytical} &= F_{z,analytical} = 0 \end{aligned} \quad (8)$$

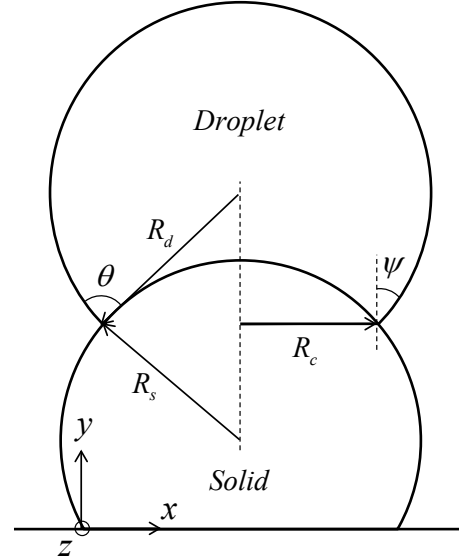


**Figure 6:** Schematic diagram of droplet on solid sphere for contact force calculation ( $xy$  cross section).

Numerical values of the contact force in all three directions have been calculated using the method proposed by Washino *et al.* (2013). The relative error in the contact force in the  $y$ -direction is given by following expression,

$$Error(\%) = \frac{|F_{y,analytical} - F_{y,numerical}|}{F_{y,analytical}} \times 100\% \quad (9)$$

Figure 7 shows the relative error in the contact force in  $y$ -direction with different grid resolutions. It follows a 1<sup>st</sup> order trend. However, even at lower grid resolution ( $R_c/\Delta \approx 5$ ) the relative error is lower than 4%. Moreover, the maximum value of the numerical contact forces in  $x$ - and  $z$ -directions ( $F_x/F_y$  and  $F_z/F_y$ ) is less than  $10^{-6}$  which affirms the accuracy of present coupled IBM-VOF implementation.

### RESULTS

In this section, we present pore-scale simulations of a water flooding process such as encountered in enhanced oil recovery. Our aim is to investigate the wettability effects on the mobility of oil through oil-wet and neutrally-wet rocks.

The physical properties of an oil-water system are:  $\mu_{oil} = 0.02$  Pa·s,  $\mu_{water} = 0.001$  Pa·s,  $\rho_{water} = \rho_{oil} = 1000$  kg/m<sup>3</sup> and  $\sigma = 0.03$  N/m. Initial distribution of oil and water phases in homogeneous configuration of spheres (rock structure) is shown in Figure 8a. Saturation of oil  $S_{oil} = 0.5$  and structure porosity  $\phi = 0.5$ . Wettability is altered by varying  $\theta$  for oil-wet ( $\theta < 90^\circ$ ) and neutrally-wet ( $\theta = 90^\circ$ ) rocks.

Simulations are performed on a 3D periodic domain with  $100 \times 100 \times 100$  grid cells of size  $\Delta = 1.5 \times 10^{-5}$  m. In this case, the number of grid cells across the radius of the sphere is around 39 which is quite sufficient to resolve accurate contact force. A constant body force of  $10^5$  N/m<sup>3</sup> is applied in

$x$ -direction to both oil and water phases. Superficial velocities of both phases are monitored to decide if the flow has reached steady state. Figure 9 shows the plot of superficial velocity of oil  $U_{oil}$  with time for oil-wet rocks with  $\theta = 45^\circ$ . One can observe that  $U_{oil}$  repeats itself after a fixed time interval and hence the flow has reached (pseudo) steady state. A snapshot of this (pseudo) steady state is presented in Figure 8b. Using the time averaged superficial velocity of oil  $\bar{U}_{oil}$ , one can calculate  $Re$ ,  $Ca$  and  $k_{r,oil}$  by means of the following expressions,

$$\begin{aligned} Re &= \frac{\rho_{oil} \bar{U}_{oil} D}{\mu_{oil}} \\ Ca &= \frac{\mu_{oil} \bar{U}_{oil}}{\sigma} \\ k_{r,oil} &= \frac{\bar{U}_{oil}(S_{oil})}{\bar{U}_{oil}(S_{oil} = 1)} \end{aligned} \quad (10)$$

where  $D$  is the diameter of sphere and  $\bar{U}_{oil}(S_{oil})$  is  $\bar{U}_{oil}$  at given  $S_{oil}$ . Maximum value of  $Re$  and  $Ca$  numbers among all simulations are 0.5 and 0.006 respectively ensuring the flow in the Stokes regime.

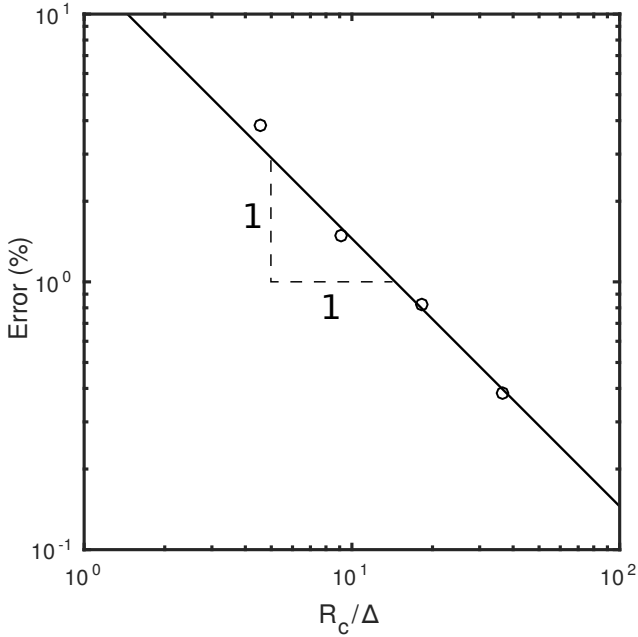


**Figure 7:** Grid independence study for contact force in  $y$ -direction: present (○) and 1<sup>st</sup> order line (–) for reference

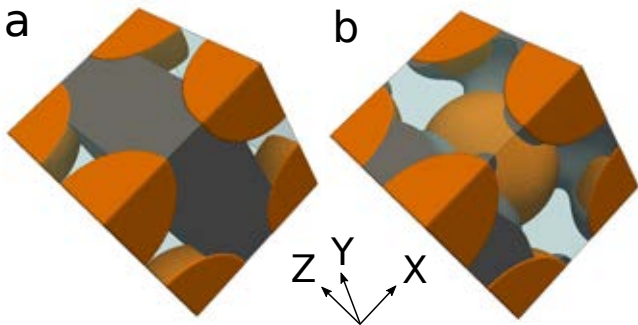


**Figure 8:** (a) Initial and (b) (pseudo) steady state fluid phase distribution for oil-wet rocks with  $\theta = 45^\circ$ ,  $\phi = 0.5$  and  $S_{oil} = 0.5$ . Oil, water and rocks are represented by grey, transparent blue and brown color respectively.

Figure 10 shows the  $k_{r,oil}$  with  $\theta$  for oil-wet ( $\theta < 90^\circ$ ) and neutrally-wet ( $\theta = 90^\circ$ ) rocks. Oil is more mobile in the neutrally-wet rocks as oil and water both have equal wettability towards rocks. As the rocks become more and more oil-wet ( $\theta \rightarrow 0^\circ$ ), the tendency of oil to adhere with rocks increases and hence its mobility decreases. Interestingly, this decrement is non-linear and it may fully choke the flow at a lower body force. The maximum difference in  $k_{r,oil}$  compared to its mean value is around 50% which suggests that the wettability has a strong effect on the oil recovery during water flooding process.

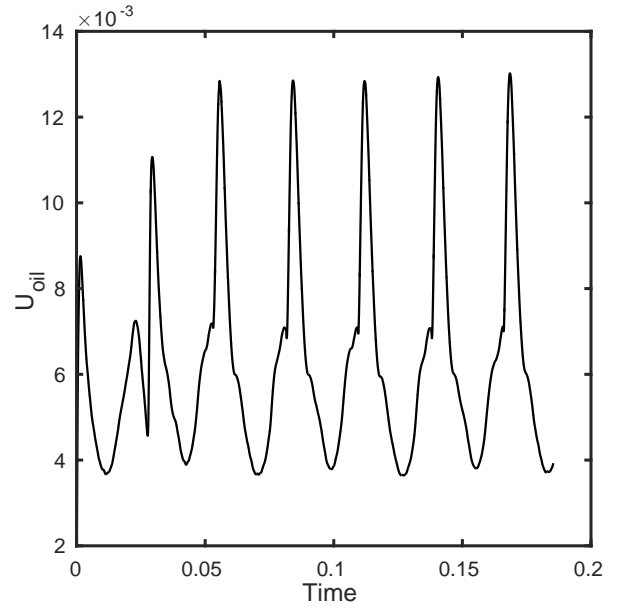


**Figure 9:**  $U_{oil}$  with time for oil-wet rocks with  $\theta = 45^\circ$ ,  $\phi = 0.5$  and  $S_{oil} = 0.5$ .

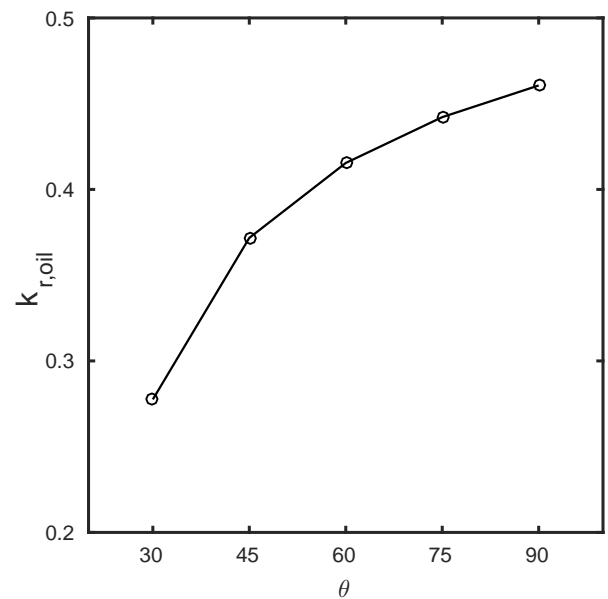


**Figure 10:**  $k_{r,oil}$  with  $\theta$  for oil-wet ( $\theta < 90^\circ$ ) and neutrally-wet ( $\theta = 90^\circ$ ) rocks with  $\phi = 0.5$  and  $S_{oil} = 0.5$

## CONCLUSION

In this paper a methodology is presented to simulate the multiphase flows involving oil and water from complex geometries. IBM is used to simulate the dynamic interactions between fluids and complex geometries on a Cartesian computational grid. Present IBM is second order, direct forcing, implicit and doesn't require any calibration for different geometries. Sharp interface VOF method is used to track multi-fluid interfaces. IBM and VOF are coupled at the three phase contact line via the apparent contact angle. Present methodology works perfectly well for the validation/verification test cases involving oil-water flows and yields more accurate results compared to simulations performed using the Lattice-Boltzmann method. Pore-scale water flooding simulations are presented to quantify the effect of wettability on the mobility of oil through oil-wet and neutrally-wet homogeneous rocks. Obtained results show that the oil-wet rocks can drastically reduce the mobility of oil.

In future, this work will be continued on large randomized structures with number of spheres in order of 100 to quantify the effect of wettability, porosity, capillary number, saturation, viscosity ratio etc. on the mobility of oil-water flows.

## ACKNOWLEDGMENTS

This work is part of the Industrial Partnership Program (IPP) 'Computational sciences for energy research' of the Foundation for Fundamental Research on Matter (FOM), which is part of the Netherlands Organization for Scientific Research (NWO). This research program is co-financed by Shell Global Solutions International B.V.

## REFERENCES

- BRACKBILL, J.U., KOTHE, D.B. and ZEMACH, C. (1992). "A continuum method for modeling surface tension". *Journal of computational physics*, **100**(2), 335–354.
- DAS, S., DEEN, N.G. and KUIPERS, J.A.M. (2016). "Immersed boundary method (ibm) based direct numerical simulation of open-cell solid foams: Hydrodynamics". *AIChE Journal*.
- DEEN, N.G., KRIEBITZSCH, S.H.L., VAN DER HOEF, M.A. and KUIPERS, J.A.M. (2012). "Direct numerical simulation of flow and heat transfer in dense fluid-particle systems". *Chemical engineering science*, **81**, 329–344.
- HALPERN, D. and GAVER, D.P. (1994). "Boundary element analysis of the time-dependent motion of a semi-infinite bubble in a channel". *Journal of Computational Physics*, **115**(2), 366–375.
- HIRT, C.W. and NICHOLS, B.D. (1981). "Volume of fluid (vof) method for the dynamics of free boundaries". *Journal of computational physics*, **39**(1), 201–225.
- HUANG, H. and LU, X.Y. (2009). "Relative permeabilities and coupling effects in steady-state gas-liquid flow in porous media: A lattice boltzmann study". *Physics of Fluids*, **21**(9), 092104.
- MITTAL, R. and IACCARINO, G. (2005). "Immersed boundary methods". *Annu. Rev. Fluid Mech.*, **37**, 239–261.
- PATEL, H.V., DAS, S., KUIPERS, J.A.M., PADDING, J.T. and PETERS, E.A.J.F. (2017). "A coupled volume of fluid and immersed boundary method for simulating 3d multiphase flows with contact line dynamics in complex geometries". *Chemical Engineering Science*, **166**, 28–41.
- PROSPERETTI, A. (2002). "Navier-stokes numerical algorithms for free-surface flow computations: An overview". *Drop-Surface Interactions*, 237–257. Springer.

SHENG, J.J. (2014). "Critical review of low-salinity waterflooding". *Journal of Petroleum Science and Engineering*, **120**, 216–224.

SNOEIJER, J.H. and ANDREOTTI, B. (2013). "Moving contact lines: scales, regimes, and dynamical transitions". *Annual review of fluid mechanics*, **45**, 269–292.

VAN SINT ANNALAND, M., DEEN, N.G. and KUIPERS, J.A.M. (2005). "Numerical simulation of gas bubbles behaviour using a three-dimensional volume of fluid method". *Chemical Engineering Science*, **60**(11), 2999–3011.

WASHINO, K., TAN, H.S., HOUNSLOW, M.J. and SALMAN, A.D. (2013). "A new capillary force model implemented in micro-scale cfd-dem coupling for wet granulation". *Chemical Engineering Science*, **93**, 197–205.

WÖRNER, M. (2003). *A compact introduction to the numerical modeling of multiphase flows*. Forschungszentrum Karlsruhe.

YIOTIS, A.G., PSIHOGIOS, J., KAINOURGIAKIS, M.E., PAPAIOANNOU, A. and STUBOS, A.K. (2007). "A lattice boltzmann study of viscous coupling effects in immiscible two-phase flow in porous media". *Colloids and Surfaces A: Physicochemical and Engineering Aspects*, **300**(1), 35–49.

YOUNGS, D.L. (1982). "Time-dependent multi-material flow with large fluid distortion". *Numerical methods for fluid dynamics*, **24**(2), 273–285.

## CFD EROSION MODELING OF BLIND TEES

Arnaud SANCHIS\*, Alexander SKORGEN

TechnipFMC, Philip Pedersens vei 7, 1366 Lysaker, NORWAY

\* E-mail: arnaud.sanchis@technipfmc.com

### ABSTRACT

In subsea components such as Production Trees (XT) where the production flow path is machined out of steel blocks, the flow changes direction abruptly at blind tees or sharp elbows, causing increased erosion risks compared to a piping design. The risk of erosion is largely controlled by the depth of the cavity inside a flow-turning element, which may vary between zero for a sharp elbow and more than one time the Inner Diameter (ID) for a full blind tee. In this paper, a comparison between the erosion response of three different flow-turning elements is performed by using Computational Fluid Dynamics (CFD) with transient particle tracking: a blind tee with a deep cavity, a blind tee with a shallow cavity (depth < 1 ID) and a sharp elbow. The DNVGL-RP-O501 (2015) erosion response model is implemented in the simulations with a modification to the angle function which aims at filtering out erosion results due to impacts at low angle. The transient formulation causes the sand particles to be dispersed naturally by the flow field, yielding time-averaged realistic erosion results without any need for area-averaging or numerical dispersion schemes. The CFD model is successfully benchmarked against the DNVGL-RP-O501 (2015) guidelines for standard piping components such as bends.

The simulation results reveal that the shallow cavity blind tee creates a very high risk of erosion inside the cavity which is not predicted by the guidelines, with peak erosion rates one order of magnitude higher than for a sharp elbow. This is observed both for a gas and liquid production case, and a physical explanation for this behaviour is provided based on an analysis of the transient flow and sand particle dynamics. Although further numerical sensitivities and experimental evidence are required to confirm this result, it is advised to avoid blind tees with a shallow cavity (less than one time the inner diameter of the flow path) for designing subsea production systems where sand production can be expected.

**Keywords:** Erosion, CFD, SPS design

### NOMENCLATURE

#### Greek Symbols

$\alpha$  Impact angle, [rad]  
 $\rho_{MAT}$  Wall material density [kg/m<sup>3</sup>]

#### Latin Symbols

$A_{IMPACT}$  Area of impact [m<sup>2</sup>]  
 CFD Computational Fluid Dynamics  
 DPM Discrete Phase Modeling  
 $E_{MF}$  Erosion mass flux, [kg/m<sup>2</sup>]  
 $E_{RATE}$  Erosion rate, [mm/year]

$E_{RATIO}$  Erosion ratio, [kg/kg]  
 $f$  Impact angle function  
 GF Geometry Factor  
 ID Inner Diameter, [mm]  
 $k$  Material coefficient, [-]  
 $\dot{m}$  Sand mass rate, [kg/s]  
 SPS Subsea Production System  
 $V_p$  Particle velocity, [m/s]  
 XT Production tree

### INTRODUCTION

Solid particles consisting of sand, gravel or proppants may be produced from subsea wells for certain conditions related to rock formation stability, well completion design and production parameters such as flow rate or bottom hole pressure. As they pass through the Subsea Production System (SPS), solid particles impact on the inner walls of equipment conveying the flow of hydrocarbons to topside, causing over time loss of material. This phenomenon is generally described as "erosion" and, if not managed properly, may have serious consequences for the integrity and functionality of the SPS.

The prediction of material loss caused by erosion over life of the field is one of the key competence area within the Flow Assurance discipline at TechnipFMC. Erosion analysis relies on two different tools: screening calculations, which are based on empirical models applicable to standard types of components, and detailed calculations based on Computational Fluid Dynamics (CFD) which solve the equation of motion for the flow and solid particles within a 3D geometry of the SPS.

### Erosion response model

Both screening and detailed erosion calculation use a wall response model, which determines the amount of material removed from the wall at particle impact as a function of the mass, impact angle and impact velocity of the particle. The erosion ratio  $E_R$  is expressed in kg of material removed per kg of incoming particle and takes the form

$$E_{RATIO} = k \mathcal{N}_p^n \times f(\alpha) \quad (1)$$

In Equation (1), the velocity exponent  $n$ , material constant  $k$  and the angle function  $f(\alpha)$  vary depending on the model employed. This study is based on the erosion



response model from DNVGL-RP-O501 (2015). Multiplying  $E_R$  by the mass flow rate of incoming sand and dividing by the density of inner wall material and area of impact, the thickness of material lost per unit of time (erosion rate) is obtained:

$$E_{RATE} = \frac{E_{RATIO} \dot{m}}{\rho_{MAT} \times A_{IMPACT}} \quad (2)$$

Erosion rates are usually expressed in mm/year, and cumulated over several years of production to calculate the total erosion wear over life of the field. The erosion wear is finally compared to the allowance, i.e. the thickness of material which may be eroded without compromising the integrity or functionality of the equipment.

### Erosion screening calculations

DNVGL-RP-O501 (2015) contains empirical models applicable to standard components such as reducers, bends or blind tees which are typical "hot-spots" for erosion in a SPS. Based on the component's dimensions, solid and fluid (carrier) phase properties and production parameters, an erosion rate is provided from a simple model validated by experimental data.

These empirical models may easily be implemented in a spreadsheet or script and applied to large datasets of production cases for early risk screening and sensitivity purposes. However, they rely on important assumptions which may limit their applicability for certain geometries and / or flow conditions:

1. The sand particles are considered uniformly distributed across the flow area upstream of the component
2. A single fluid phase (with mixed properties based on volume fraction average for multiphase flows) is considered with a uniform velocity profile upstream of the component
3. The erosion rate is predicted for a single hot-spot per component corresponding to the main impact area of sand particles
4. The geometry of the component evaluated should be similar to the samples tested experimentally to validate the empirical models.

An example is provided in Figure 1 for a component referred to as "blind tee" in DNVGL-RP-O501 (2015). The geometry shown represents one of the samples tested at DNVGL. The cavity depth is 50 mm, more than the Inner Diameter (ID) of the inlet flow cross-section. The hot-spot considered in the empirical model corresponds to an impact area situated at the extrados outlet wall. Uniform flow conditions and sand particle concentration are assumed in the vertical inlet upstream of the tee.

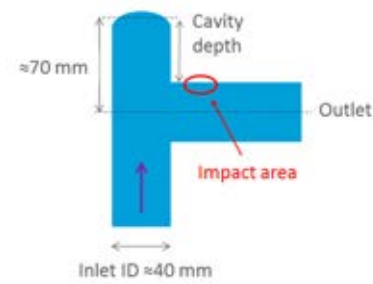


**Figure 1:** Example of blind tee experimental geometry tested at DNVGL (courtesy of DNVGL).

### Erosion detailed calculations based on CFD

Erosion CFD computations combine two simulation processes, performed either sequentially (steady-state models) or simultaneously (transient models):

- The simulation of the carrier flow in the system consisting of one or several fluid phases, using an Eulerian approach
- The simulation of the sand particles (solid phase) using a Lagrangian approach whereby individual particles are tracked in space (steady-state models) or time and space (transient models).

The number of individual sand particles tracked in one simulation is in the range of 50 000 to several millions in order to yield statistically representative results. Each time a sand particle impacts a wall boundary and rebounds into the domain, the erosion model from Equation (1) is used to compute the mass of material removed from the wall. The greatest potential added value of the CFD approach compared to screening calculations is that no assumption on the sand distribution and flow profile upstream of a component is needed as long as the upstream extent of the computational domain is sufficient. Also, CFD simulations consider the actual geometry of the SPS and should be used when assessing erosion on components for which no empirical screening model is available.

### Geometry Factors (GF)

Geometry Factors (GF) have been introduced in DNVGL-RP-O501 (2015) to account for the effect of the upstream flow path layout on erosion results. These factors are directly applied to the empirical models used for screening calculations and may vary between 1 and 4:

$$E_{RATE-CORR} = GF \times E_{RATE} \quad (3)$$

A value of 1 is used if the component of interest is placed downstream a long straight section of piping so that the flow and sand concentration profile can be considered as uniform. A value of 4 corresponds to a case where multiple flow-turning elements are present upstream of the component with the flow path in several planes. This induces a swirl component in the flow that contributes to focusing the sand particles and creating enhanced erosion locally.

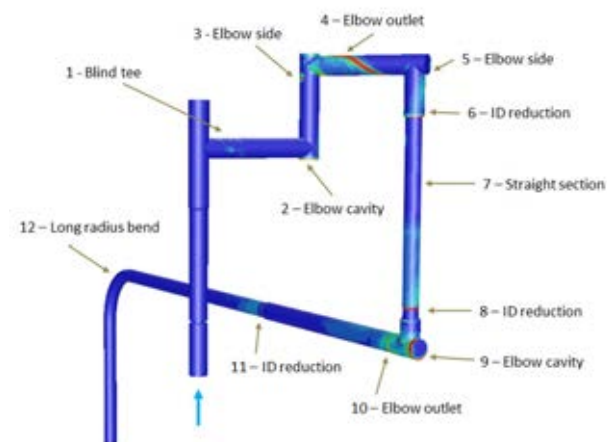
Geometry Factors may also be directly obtained from CFD simulations by dividing the simulated erosion rate by the result from an empirical model, provided that the

extent of the computational model is sufficient to capture all relevant upstream effects.

Based on TechnipFMC's experience, the GF values specified in DNVGL-RP-O501 (2015) are retrieved when comparing CFD and screening results for most of the hot-spots encountered in an SPS erosion analysis, i.e. values in the range of 1 to 4 are usually obtained. However, in subsea components such as Production Trees (XT) where the production flow path is machined out of steel blocks, the Geometry Factors are sometimes found to be much larger, as illustrated in the following.

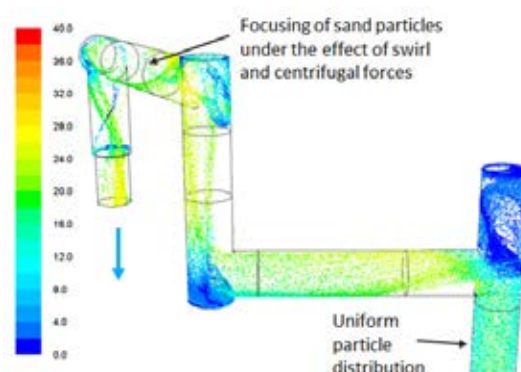
### Application of screening and CFD erosion calculations for SPS design

The flowpath in a SPS from the well tubing to the flowline consists of a succession of flow-turning elements (bends, elbows, blind tees) and ID variations separated by straight sections. In Figure 2, erosion contours from a detailed CFD erosion analysis on part of a SPS are displayed. A single phase, transient simulation with particle tracking has been run with a total of 15 million particles injected into the domain. Twelve erosion hot-spots have been identified at locations which could not always be predicted by the screening empirical models (for example, hot-spot 3 in Figure 2 upstream of the second elbow). The elbow geometry itself is not described in DNVGL-RP-O501 (2015), where the only flow-turning elements considered consist of bends or blind tees.



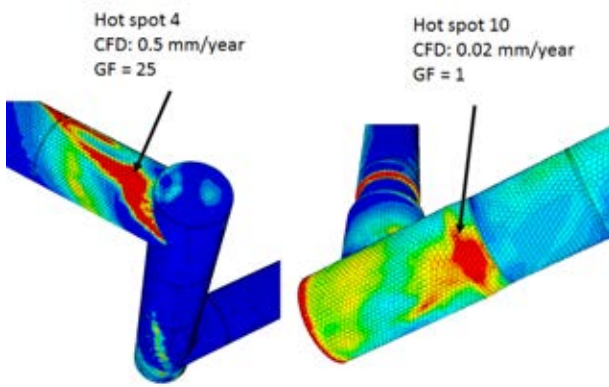
**Figure 2:** Example of SPS flowpath and erosion results.

Figure 3 shows the instantaneous location of the sand particles in the domain and their velocity. Upstream of the first blind tee, which is preceded by a long vertical section corresponding to the well tubing, the sand particles are homogeneously distributed across the inner bore cross-section. However, the close succession of flow-turning elements in multiple planes distorts the velocity profile and introduces a swirl component which tends to focus the sand particles. It is obvious that downstream of the second elbow, the assumption of homogeneous sand concentration is no longer valid.



**Figure 3:** Instantaneous sand particle tracks coloured by velocity magnitude (m/s).

A comparison of CFD erosion results to screening calculations indicates that Geometry Factors are in the range of 0.3 to 3.4 for most of the hot-spots shown in Figure 2. However, much higher values are obtained for some components. In Figure 4, CFD erosion results at the outlet of two elbows corresponding to hot-spots 4 and 10 in Figure 2 are shown. Both flow-turning elements have similar inlet ID and geometry. The application of DNVGL-RP-O501 (2015) to these elbows, represented as a bend with a radius of 0.5 ID and a Geometry Factor of 1, yields an erosion rate of 0.02 mm/year. Hot-spot 10 is situated downstream a long vertical section of piping which allows the flow profile and sand concentration to recover before entering the elbow. The CFD results obtained at the outlet confirm the erosion rate from the screening methodology with GF of 1. On the contrary, hot-spot 4 is situated downstream three flow-turning elements (one blind tee and two elbows), in different planes and separated by 4 to 6 IDs only. The erosion rate is 0.5 mm/year, corresponding to a Geometry Factor of 25 ( $0.5 / 0.02$ ). The configuration upstream of hot-spot 4 is representative of designs where the flow path is machined out of steel blocks. This reduces the streamwise separation between flow-turning elements and replaces pipe bends or blind tees with sharp elbows, creating added distortion of the flow velocity profile and focusing of sand particles compared to a piping design. Some care and engineering judgement should be used when applying Geometry Factors from CFD results to the screening of SPS designs. However, such information may be used to provide useful feedback to designers: adding an inline cavity with a depth  $> 1$  ID to the elbow situated upstream of hot-spot 4 may reduce the Geometry Factor for hot-spot 4, for example.



**Figure 4:** Comparison of CFD to screening results at the outlet of two elbows with different upstream flow configuration.

### CASE EXAMPLE: EROSION IN BLIND TEES

In the following, the effect of the cavity depth on the erosion performance of a blind tee is investigated using the same approach as described previously. The purpose of this work is to compare erosion results for actual flow-turning element geometries to the results provided by the DNVGL-RP-O501 (2015) empirical models.

#### Blind tee cavity depth

There is ample experimental and numerical evidence that blind tees have a dampening effect on erosion compared to sharp bends. Due to the local increase of the inner cross-section as the flow changes direction, the fluid and sand particle velocity at the outlet of a blind tee are lower than for a 90 degrees, short radius bend. In addition, at least part of the sand particles penetrate the low-velocity, high pressure zone inside the cavity where they lose momentum and recirculate instead of impacting the wall at the extrados outlet. Both of those effects are illustrated in Figure 13 by comparing particle trajectories and velocity for the “full” blind tee (top) and the sharp elbow (bottom). For more insight on particle dynamics inside bends and blind tees, reference is made to Chen (2004). This behaviour is captured in the empirical models of DNVGL-RP-O501 (2015): for gas flow conditions and small particle diameters, the erosion rate for a blind tee is about 5 times lower than for a short radius bend of similar ID. DNVGL-RP-O501 (2015) does not contain any definition of the geometrical characteristics of a blind tee. Presumably, it is assumed that the term “blind tee” refers to a standard piece of equipment which corresponds to the sketch provided in Figure 1, where the cavity depth is large enough to provide the benefits described above in terms of erosion performance. However, tees machined out of steel blocks may have cavities deeper or shallower than presented in Figure 1, depending on the drilling length for each perpendicular section of the flow path. Therefore, there is an uncertainty regarding the minimum cavity depth that such a component should have to qualify as a “blind tee” according to DNVGL-RP-O501 (2015).

#### Model set-up

##### Softwares and hardware used

The work reported here has been performed using the following softwares:

- BETA ANSA version 16 for pre-processing (geometry and mesh generation)
- ANSYS Fluent version 17.1 for solving and post-processing.

All simulations have been run on a 128 cores cluster and have required approximately one day of computational time for each case. The cluster consists of 4<sup>th</sup> generation Xeon E5 CPUs with 32 GB RAM, interconnected with Infiniband at 56 Gb/s.

#### Geometry

The geometries investigated are shown in Figure 5. The flow-turning element is preceded by a 13 ID section of straight piping. A square-step contraction equal to 50% of the cross-sectional area is placed 10 ID upstream of the tee to trigger transient effects in the flow and enhance the dispersion of sand particles upstream of the tee. The particle injection plane is placed 6 ID upstream of the tee. Three different flow-turning elements have been investigated:

1. A “full” blind tee with a cavity depth equal to the inlet ID
2. A “shallow” blind tee with a cavity depth equal to 38% of the inlet ID
3. A sharp elbow (i.e. a blind tee with cavity depth reduced to zero).

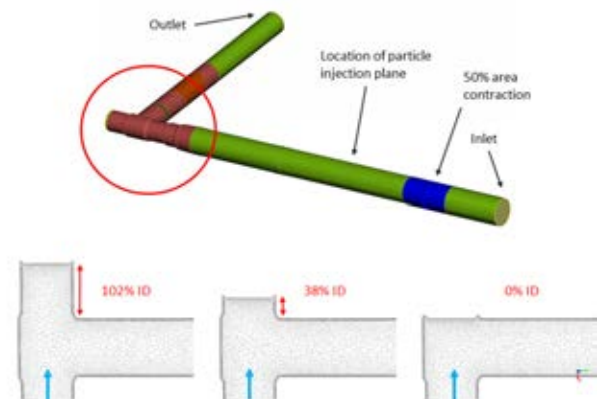


**Figure 5:** Geometries investigated in blind tee erosion CFD study

#### Production cases

Two production cases have been simulated which aim to represent typical gas and liquid production from a subsea well through a 5-inch ( $\approx 130$  mm ID) XT. Production parameters are listed in Table 1. The fluid is considered as single phase. In this work, the solid particles in the flow are assumed to be sand grains with a density of 2650 kg/m<sup>3</sup> and uniform size. All surfaces of impact consist of Inconel with a density of 8440 kg/m<sup>3</sup>.

**Table 1:** Production cases simulated

	Gas case	Liquid case
Fluid mass flow rate	40.0 kg/s	85.8 kg/s
Fluid bulk velocity upstream of tee	32.9 m/s	8.1 m/s
Fluid density	110 kg/m <sup>3</sup>	961 kg/m <sup>3</sup>
Fluid viscosity	0.017 cP	0.696 cP
Sand mass flow rate	0.074 g/s	0.858 g/s
Sand particle size	50 μm	250 μm

### Transient methodology

The computational model used in this study relies on the simultaneous solution of the fluid and sand particle equations of motion with a time-dependent (i.e. transient) approach. At each time step in the simulation, the flow field and position of the particles are computed. Erosion wear accumulates over time and is monitored at the different hot-spots in the model. The simulation is run until sufficient statistics are accumulated to calculate a rate of erosion in mm/year.

The transient approach yields results which are much more realistic than the “steady-state” approach, whereby the motion of the sand particles is solved onto a frozen flow field. It is especially recommended for designs such as presented in Figure 2 and Figure 5 where the flow-turning elements consist of sharp elbows rather than smooth pipe bends. Downstream of each elbow, the flow separates from the wall and forms large-scale turbulent vortices which are conveyed downstream to the next flow-turning element. Sand particles will tend to coalesce into “packets” or narrow bands under the effect of swirl, recirculation and vortex shedding. This is illustrated in Figure 6, where snapshots of the sand particle concentration in the domain at two different instants are shown.

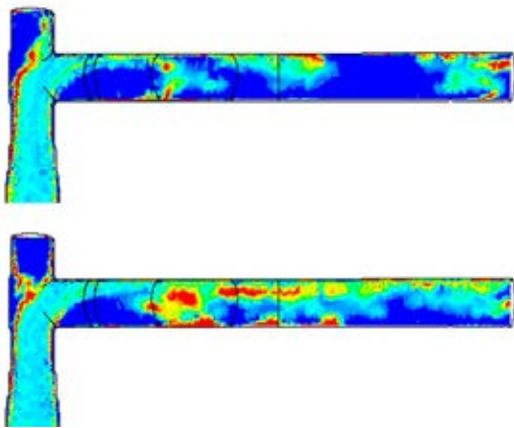


**Figure 6:** Contours of sand particle concentration at two different instants in the simulation (full blind tee, gas production case).

The instantaneous rate of erosion at any location may vary considerably with time, as illustrated in Figure 7 for the case of an intrusive erosion probe. The total simulation time should therefore be much larger than the time scale of the flow and particle dynamics, so that a linear rate of erosion can be calculated. Reference is made to Equation (4) for the relation between the erosion rate and erosion mass flux.

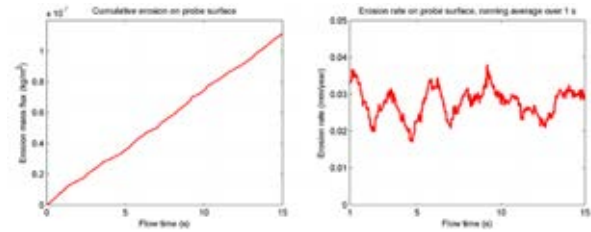


**Figure 7:** Transient CFD erosion results: increase of erosion mass flux (kg/m<sup>2</sup>) with simulation time on an erosion probe placed in the flow path (left), and instantaneous erosion rate (mm/year) calculated based on 1 s running average (right)

### Fluid and discrete phase modelling

The continuous fluid phase is modelled as incompressible. Turbulence effects are resolved using a  $k-\omega$  SST model with automatic wall treatment, because the constraints placed on the mesh aspect ratio do not allow to use a low  $y^+$  approach, especially for the gas phase. The time step in the simulation is set to obtain a Courant number below 5.

Fluent’s Discrete Phase Modeling (DPM) approach is used to model the sand particles and their interaction with the fluid. In DPM, particles are modeled as point masses with no physical volume, an assumption which is valid as long as the effect of collisions between particles is negligible. Sommerfeld (2016) indicates that particle-particle interactions become important for sand volume fractions above 0.001, which is several orders of magnitude above the value for this case.

Numerical “parcels” representing sand particles are injected at each time step from a plane situated 6 ID upstream of the tee, and consisting of 648 points distributed as a grid across the flow cross-section (Figure 8). The parcels are subject to inertial, gravity and drag forces only. Given the high Reynolds number and low Stokes relaxation times, turbulent dispersion may play an important role. For steady-state erosion CFD analyses, turbulent dispersion must be accounted for because it is the only term which causes dispersion of sand particles in the domain. However, in the present case, it is assumed that the effects of turbulent dispersion are inherently captured by the transient simulation procedure, whereby parcels are tracked in the domain with the same time step as the flow solution. A two-way fluid coupling approach is used.

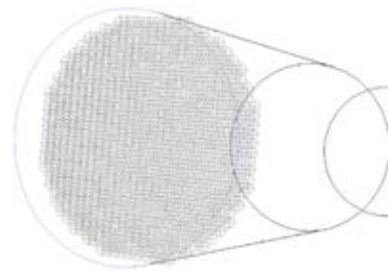


**Figure 8:** Sand particle injection locations

### Erosion wall response model

The erosion response model from DNVGL-RP-O501 (2015) has been implemented as a boundary condition at all walls in the domain by entering the parameters

introduced in Equation (1). For every impact of a sand particle with the walls, the following computational steps are performed:

- The particle rebounds into the domain (energy restitution coefficients of 0.8 and 1.0 are used in the normal and tangential directions, respectively)
- The mass of metal lost at the cell where the impact occurs is calculated according to Equation (1).

The mass of metal lost is normalized by the cell surface to compute an erosion mass flux expressed in kg of metal removed per unit area of wall. This value increases monotonically with simulation time in each cell as more sand particles collide with the wall.

The model from DNVGL-RP-O501 (2015) is modified by setting the angle function to zero for all impact angles less than 5° (see Figure 9). This correction has been implemented based on numerous observations of high erosion predicted by CFD in areas of flow recirculation with low particle density and / or low velocities such as cavities, dead legs or separation bubbles. For numerical reasons which have not yet been clarified, the presence of sand particles at those locations (not directly impacting but rather “brushing” along the wall) produces significant, unphysical erosion results. The DNVGL-RP-O501 (2015) erosion response model only applies to particle impacts with high enough angle, at which the sand grains “cut” through the metal. Therefore, it is considered that applying a cut-off angle to the function  $f$  in Equation (1) is a valid approach to filter out unphysical erosion results from the simulations.

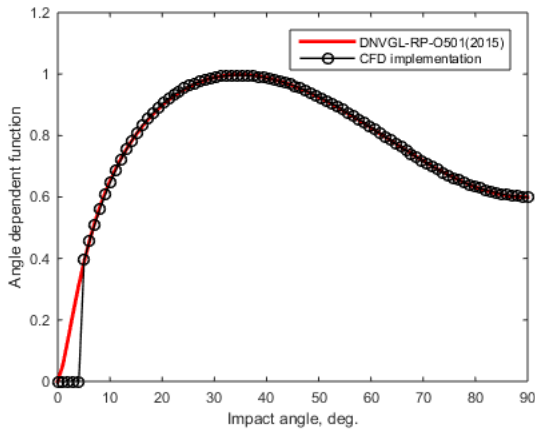


Figure 9: Angle function implemented in CFD simulations

Sensitivities have been performed to ensure that the erosion rate in areas of direct particle impact is not affected by this modification. An example is provided in Figure 10: the erosion rate at the intrados of the blind tee has been reduced by a factor of 3 with the application of the cut-off angle, whereas the erosion rate at the extrados is unchanged.

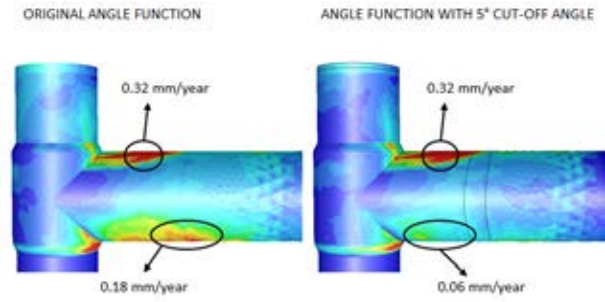


Figure 10: Effect of cut-off angle on erosion results for a blind tee. Gas production case with 250 μm particles.

Mesh design

The same mesh is used to resolve the Eulerian fluid motion and the Lagrangian particle trajectories, and is applied to both production cases listed in Table 1. The mesh was first designed as an unstructured grid with tetrahedral elements and prisms in the inflation layers, then converted to polyhedral elements. The thickness of the first inflation layer is 150 μm and the quality metrics are listed in Table 2.

Table 2: Mesh parameters and quality metrics

Element type	Polyhedrals (prisms in inflation layers)
Number of cells	1.1 million
First layer thickness	150 μm
Element base size	7 mm (5% of ID)
Minimum orthogonal quality	0.11
Maximum equiangle skewness	0.87
Maximum aspect ratio	154

In DNVGL-RP-O501 (2015), it is recommended that the first layer thickness of the mesh on which the particle trajectories are solved should be 3 to 5 times larger than the sand particle diameter. In the present study, this criterion is met for the gas production case, but not for the liquid production case with 250 μm particles. However, sensitivities have been performed on the first layer thickness and showed that with the numerical setup used, no variations in the erosion results were observed with first layer thickness varying between 5 and 0.4 times the particle size. Unphysical erosion results have been observed in cells with a high aspect ratio, though. Therefore, attention has been given in the mesh design to the orthogonal quality and aspect ratio, rather than the ratio between the first layer thickness and the sand particle size.

Results

The simulations for the gas and liquid production cases have been conducted in three steps:

1. The transient flow solution is computed without sand particles, until stationary velocity fluctuations are obtained downstream of the tee
2. Particles are injected at each time step and progressively fill the domain. The total mass of sand in the domain is monitored: when steady state conditions are reached, the erosion mass flux at the walls is monitored

3. The simulation is stopped when a constant erosion rate has been calculated at each hot-spot from the erosion mass flux values monitored:

$$E_{RATE} = \frac{\partial}{\partial t} E_{MF} \times \frac{1}{\rho_{MAT}} \quad (4)$$

It is important to note that all erosion mass fluxes used to compute erosion rates are maximum values over all vertices forming the “hot-spot”, i.e. no area-averaging of results is performed (Figure 11). Such post-processing techniques are often necessary in steady-state simulations to account for the lack of dispersion in the sand particle impacts. TechnipFMC’s practice is to area-average all steady-state erosion results over a circular surface equal to 10% of the pipe ID as suggested in DNVGL-RP-O501 (2015) and described in Leong (2016). In the present case, impact points vary in time due to the dynamics of the flow and sand particles, so that no post-treatment of the erosion results is required.

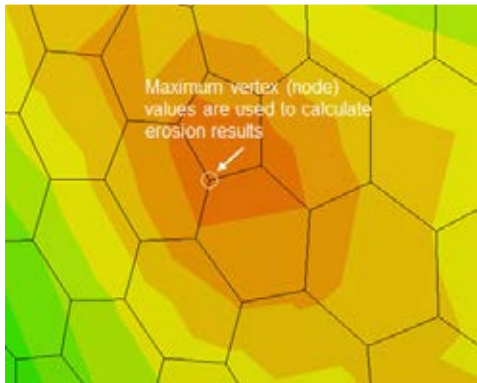


**Figure 11:** Example of erosion mass flux contours at one hot-spot

Approximately 10 seconds of flow time have been simulated for each production case, with a time step of 0.1 milliseconds for the gas production case and 0.5 milliseconds for the liquid case. The corresponding total number of parcels tracked in the simulation is around 60 million and 12 million, respectively.

#### *Sand mass in the domain*

The evolution of the sand mass present in the computational domain with simulation time is presented in Figure 12. Particle are injected at  $t = 1$  s and progressively fill up the domain until a steady-state regime is established for the sand load. This indicates that the time-averaged mass of sand in the domain is constant, i.e. there is no accumulation of sand. A lower value is obtained for the sharp elbow than for the full blind tee since the volume of fluid in the domain is smaller. Important fluctuations of the sand load are obtained for the shallow tee geometry, especially for the liquid case. This is due to the periodic accumulation and release of sand particles in the shallow cavity.

There were no incomplete particle path in the simulation, meaning that all particles injected exited the domain at the outlet.

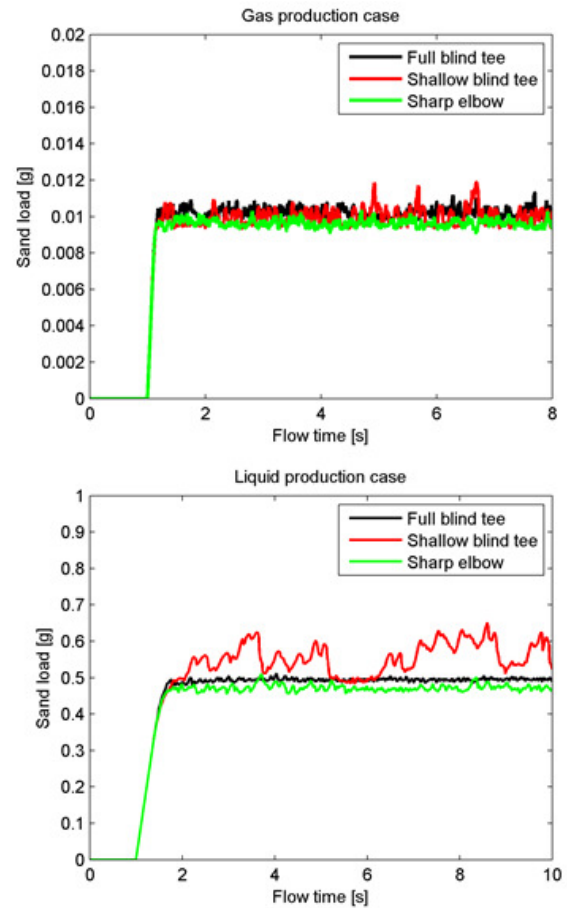


**Figure 12:** Time evolution of sand mass in the domain. Top: gas production case, bottom: liquid production case

#### *Particle tracks*

In Figure 13, tracks of the sand particles at one instant in the simulation are shown, coloured by velocity magnitude and residence time, for the liquid production case. Similar results are obtained for the gas production case.

As the cavity depth is reduced, the maximum velocity of the particles downstream of the flow-turning element increases because the flow cross-sectional area is smaller. The particle tracks for the shallow blind tee indicate the presence of a strong vortex cell inside the cavity which entrains particles with quite high velocity. This is confirmed by the flow velocity and vorticity results plotted in Figure 14: the vortex is much weaker for the full blind tee, and almost disappears for the sharp elbow. An analysis of the animations of the particle tracks over the full simulation time allows to link observations made from Figure 12, Figure 13 and Figure 14. The vortex cell inside the shallow blind tee cavity is unstable: as it grows in strength, a large number of sand particles are entrained inside the cavity and recirculate with high velocity. They are projected against the back wall of the cavity, creating important erosion at this location. Then, with a periodicity which is visible in the sand loading plot in Figure 12, the vortex collapses and all sand particles are released in the flow. This behaviour is unique to the shallow blind tee: inside the full blind tee, the flow of sand particles into and out of the cavity is almost steady and velocities are low. For the sharp elbow, the cavity is reduced to the upper back corner of the elbow, and this volume does not appear to be large enough to sustain the

same flow mechanism as observed for the shallow blind tee.

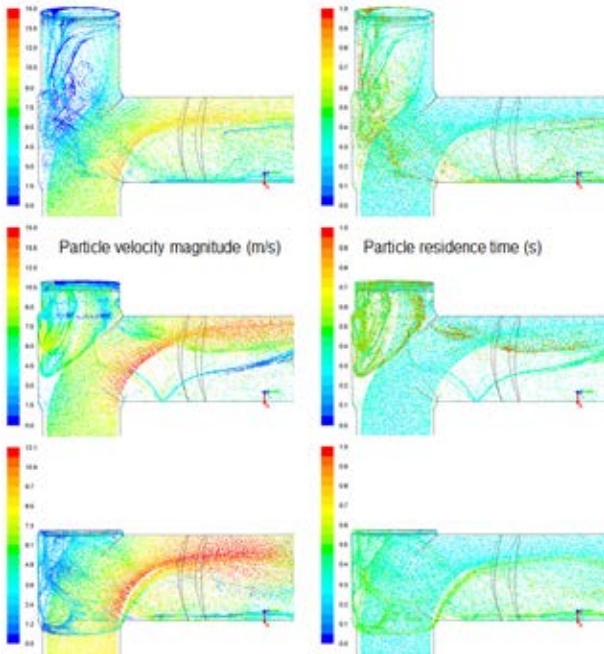


**Figure 13:** Particle tracks coloured by velocity magnitude (left) and residence time (right), liquid production case, for the three geometries investigated

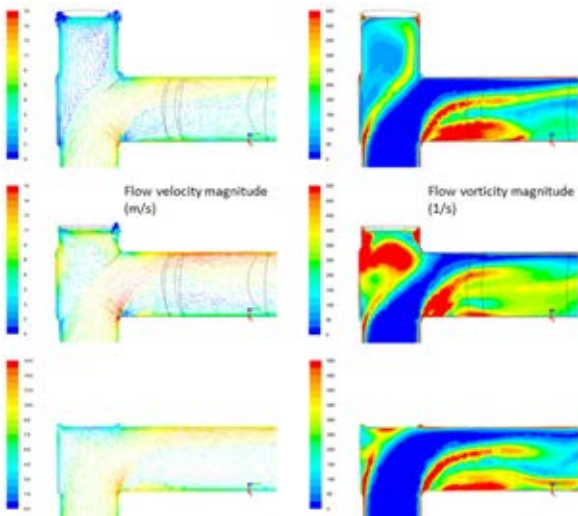


**Figure 14:** Flow velocity vectors coloured by velocity magnitude (left) and vorticity contours (right), liquid production case, for the three geometries investigated.

*Erosion results*

Contours of the erosion mass flux at simulation end are displayed in Figure 15. For each geometry and each production case, the maximum erosion rate obtained over the whole geometry is listed in Table 3 and compared to the screening result from the application of DNVGL-RP-O501 (2015). The “blind tee” empirical model has been used for the full blind tee geometry, and the “bend” model with a radius of 0.5 ID has been used for the shallow blind tee and sharp elbow geometries. A Geometry Factor of 1 has been considered for the

screening calculations, since the upstream flow path only consists of a straight, vertical section.

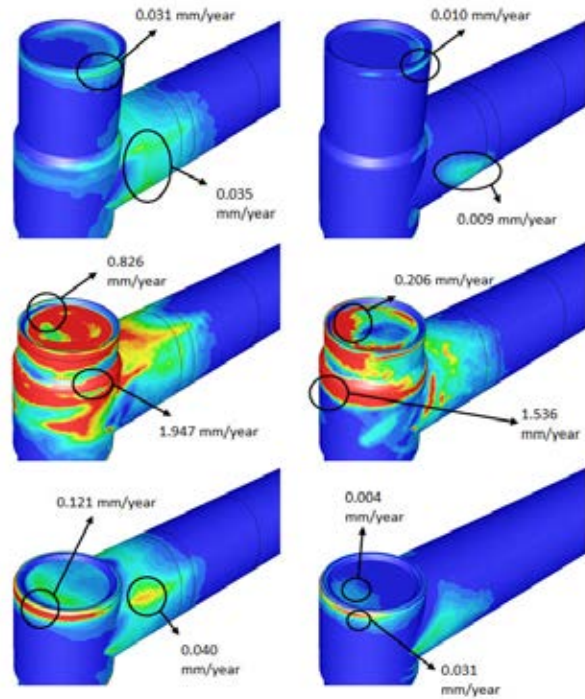


**Figure 15:** Contours of erosion mass flux at simulation end and erosion rates at hot-spots for the three geometries investigated. Left: gas production case, right: liquid production case. Different scaling is used for the two production cases.

**Table 3:** Comparison of CFD results to screening results

Geometry	DNVGL-RP-O501 model (GF = 1)	Prod. case	Screening result (mm/year)	CFD result (mm/year)	Geometry Factor (CFD / screening)
Full blind tee	Blind tee	Gas	0.028	0.035	1.2
		Liquid	0.004	0.010	2.5
Shallow blind tee	0.5 ID radius bend	Gas	0.154	1.947	12.6
		Liquid	0.024	1.536	64.0
Sharp elbow	0.5 ID radius bend	Gas	0.154	0.121	0.8
		Liquid	0.024	0.031	1.3

A massive increase in the erosion rate is observed for the shallow blind tee, both for the gas and liquid production cases. The maximum erosion rate is increased by one order of magnitude when comparing results between the full and shallow blind tees. The most severe erosion is reported at the cavity back wall, and is caused by the presence of the unstable vortex cell described earlier. When reducing the cavity depth down to zero (sharp elbow), erosion rates drop back to expected values for a sharp flow-turning element.

The comparison of the CFD and screening results shows that the full blind tee and sharp elbow may be described using the “blind tee” and “0.5 ID bend radius” models. Proportionality factors between the CFD and screening results are comprised between 0.8 and 2.5. However, factors of 12.6 and 64.0 are obtained from the CFD results for the shallow blind tee, indicating that the erosion performance of such geometries may be much worse than either a “blind tee” or a “sharp elbow”.

*Limitations and uncertainty*

The erosion results obtained inside the blind tee with shallow cavity are caused by a large-scale instability in the flow. The representation of this flow structure in CFD is subject to large uncertainties due to limitations of the turbulence modeling, insufficient discretization of near-wall regions and other numerical effects. It is therefore recommended to perform further sensitivities to confirm this result, particularly related to the mesh density and turbulence model employed.

Another important source of uncertainty is the assumption of single phase flow which has been taken to represent the flow. Virtually all production streams contain both a liquid and gas phase at subsea conditions. Multiphase flow effects on erosion CFD simulations have been briefly discussed in Leong (2016) and may be significant in the present case: in a gas production case, liquid will most likely accumulate inside the tee cavity and may have a “cushioning” effect on erosion. The presence of a second fluid phase may also affect the unstable vortex structure which creates the present results for the shallow blind tee.

**CONCLUSIONS**

The geometry of blind tees inside SPS parts which are machined out of steel blocks may deviate from standardized flow-turning elements found in piping designs. In particular, the depth of the blind tee cavity may vary between zero (sharp elbow) and more than one time the ID. In this paper, the impact of the cavity depth on the erosion performance of such blind tees has been assessed by considering three geometries with cavity depth of 1 ID (“full” blind tee), 0.38 ID (“shallow” blind tee) and 0 ID (no cavity, i.e. sharp elbow).

Results are compared to the DNVGL-RP-O501 (2015) empirical models for a standard blind tee component and a sharp bend with a radius of 0.5 ID. The cavity depth of the blind tee empirical model is not defined explicitly in DNVGL-RP-O501 (2015) but is assumed to be greater than the flowpath ID. Two cases which are representative of single phase gas and liquid flow conditions with produced sand have been assessed.

CFD results for both production cases indicate that erosion results inside the “full” blind tee and sharp elbow (cavity depth of 0 ID) are in line with predictions from the empirical models. However, erosion rates inside the shallow blind tee with cavity depth of 0.38 ID are found to be one to two orders of magnitude greater than empirical model predictions using a short radius bend. An explanation for this behaviour is proposed based on the transient flow dynamics observed inside the cavity, both for the gas and liquid production cases.

These results should be confirmed by further numerical sensitivities and experimental evidence.

**ACKNOWLEDGEMENTS**

An important part of this work has been inspired by discussions with the DNVGL erosion modelling experts from Høvik, Norway. Their contribution is gratefully acknowledged.

**REFERENCES**

- CHEN, X. *et al.*, (2004), “Application and experimental validation of a computational fluid dynamics (CFD)-based erosion prediction model in elbows and plugged tees”, *Computers & Fluids*, **33**, 1251-1272.
- DNVGL-RP-O501, (2015), “Managing sand production and erosion”.
- LEONG M. and SANCHIS, A., (2016), “Intrusive erosion probes on subsea equipment – Design and placement considerations”, *Offshore Technology Conference*, Kuala Lumpur, Malaysia, March 22-25.
- SOMMERFELD M. *et al.*, (2016), “Best practice guidelines for computational fluid dynamics of dispersed multiphase flows”, *ERCOFTAC*.





## SHAPE FACTORS INCLUSION IN A ONE-DIMENSIONAL, TRANSIENT TWO-FLUID MODEL FOR STRATIFIED AND SLUG FLOW SIMULATIONS IN PIPES

Arianna BONZANINI<sup>1\*</sup>, Davide PICCHI<sup>2†</sup>, Marco FERRARI<sup>3‡</sup>, Pietro POESIO<sup>1§</sup>

<sup>1</sup>Università degli Studi di Brescia, Dipartimento di Ingegneria Meccanica ed Industriale, Via Branze, 38, 25123 Brescia, ITALY

<sup>2</sup>Tel-Aviv University, Faculty of Engineering, School of Mechanical Engineering Ramat Aviv, 69978 Tel-Aviv, ISRAEL

<sup>3</sup>Politecnico di Milano, PoliMi Department of Mathematics, 20133 Milan, ITALY

\* E-mail: a.bonzanini001@unibs.it

† E-mail: davide.picchi@gmail.com

‡ E-mail: marco2.ferrari@polimi.it

§ E-mail: pietro.poesio@unibs.it

### ABSTRACT

In previous works, (Ferrari *et al.*, 2017) have shown that a one-dimensional, hyperbolic, transient five equations two-fluid model is able to numerically describe stratified, wavy, and slug flow in horizontal and near-horizontal pipes. Slug statistical characteristics, such as slug velocity, frequency, and length can be numerically predicted with results in good agreement with experimental data and well-known empirical relations. In this model some approximated and simplified assumptions are adopted to describe shear stresses at wall and at phase interface.

In this paper, we focus on the possibility to account for the cross sectional flow by including the shape of the velocity profiles, inserting shape factors into the momentum balance equations. Velocity profiles are obtained by the pre-integrated model proposed by (Biberg, 2007) and they are computed at each time step and at each computational cell. Once that the velocity profiles are known, the obtained shape factors are inserted in the numerical resolution. In this way it is possible to recover part of the information lost due to the one-dimensional flow description.

Velocity profiles computed in stratified conditions are compared against experimental profiles measured with PIV technique - see (Ayati *et al.*, 2015), showing good agreement. Finally, first results in slug flow configuration are shown.

**Keywords:** Multiphase pipeline transport, Oil & Gas .

### NOMENCLATURE

#### Greek Symbols

$\alpha$	Phase volume fraction, $[-]$
$\beta$	Wetted angle, $[rad]$
$\gamma$	Shape factor, $[-]$
$\delta$	Boundary layer thickness, $[m]$
$\theta$	Pipe inclination angle, $[rad]$
$\lambda$	Eigenvalues vector, $[m/s]$
$\mu$	Dynamic viscosity, $[kg/ms]$
$\rho$	Mass density, $[kg/m^3]$
$\tau$	Shear stress, $[Pa]$

#### Latin Symbols

$A$	Pipe section, $[m^2]$ .
$A_j$	Pipe section occupied by phase $j$ , $[m^2]$ .
$c$	Sound speed, $[m/s]$ .
$D$	Pipe diameter, $[m]$ .
$f$	Friction factor, $[-]$ .
$F_i$	Interfacial friction term, $[N/m^3]$ .
$F_w$	Wall friction term, $[N/m^3]$ .

$g$	Gravity acceleration, $[m/s^2]$ .
$h$	Liquid height, $[m]$ .
$k_s$	Sand roughness, $[m]$ .
$p_i$	Interfacial pressure, $[Pa]$ .
$r_p$	Pressure relaxation parameter, $[1/Pas]$ .
$\mathbf{R}$	Eigenvector matrix, $[m/s]$ .
$Re$	Reynolds number, $[-]$ .
$S_j$	Pipe perimeter wetted by phase $j$ , $[m]$ .
$S_i$	Interfacial perimeter, $[m]$ .
$t$	Time coordinate, $[s]$ .
$u$	Phase velocity, $[m/s]$ .
$u_i$	Interfacial velocity, $[m/s]$ .
$u_s$	Superficial velocity, $[m/s]$ .
$v$	Cross-sectional velocity, $[m/s]$ .
$x$	Space coordinate in the axial direction, $[m]$ .
$y$	Space coordinate in the cross-sectional direction, $[m]$ .

#### Sub/superscripts

$g$	Gas phase.
$l$	Liquid phase.
$j$	Generic phase, gas or liquid.

### INTRODUCTION

Stratified and slug flow are two-phase flow regimes frequently encountered in multiphase pipeline transport of oil and gas. In the past decades, the interest in the numerical description of these flow regimes has significantly increased, aiming at obtaining predictions about the behaviour of the fluids employed in petroleum transport pipelines, chemical and nuclear industries, and buoyancy driven fermentation devices. The one-dimensional averaged two-fluid model is often employed (see (Issa and Kempf, 2003), (Renault, 2007)) and pipelines are usually simulated adopting mono-dimensional models to keep reasonable simulation times. Closure relations to describe shear stresses at interface and at wall are required, and friction factors are often described adopting models or correlations (see (Bonizzi *et al.*, 2009)); however, wall and interfacial shear stresses are related via the velocity distribution and, therefore, the cross-sectional flow description is required to obtain consistent modelling. Two-dimensional and three-dimensional models are computationally expensive and require too long computational times; to solve the issue of speed versus consistency, the cross-sectional velocity profiles can be described by a pre-integrated model, which leads to a consistent set of near-

algebraic friction models suitable for one-dimensional two-phase flow simulations.

In the present work, we aim at introducing the velocity profiles shape description in the mono-dimensional, transient, five-equation two-fluid model by (Ferrari *et al.*, 2017): they assumed that the profiles coefficients were unitary ( $\gamma_l = \gamma_g = 1$ ), representing a completely flat profile. The profiles coefficients are correction factors adopted to describe the curvature of the velocity profile, since the latter is not constant over the entire cross section and, for turbulent flows, the profile coefficient is slightly above one. To account for the cross-sectional velocity, we need to modify the five-equation system eigenstructure, inserting the  $\gamma$  factors in the modelisation; then, we adopted the pre-integrated model developed by (Biberg, 2007), to describe the shear stresses at interface and at wall consistently with the modelling of the velocity profiles.

In this paper, the comparison of the computed velocity profiles against the experimental ones measured by (Ayati *et al.*, 2015) will be reported, showing a fairly good agreement; then, first results in slug flow will be presented, showing how to describe numerically the velocity profiles during the transition from two-phase to single phase flow.

## MODEL DESCRIPTION

In this work, we adopted the mono-dimensional, hyperbolic, transient, five-equation, two-fluid model proposed by (Ferrari *et al.*, 2017), which is able to compute well flow regimes transitions and slug flow characteristics. The first modification performed on the model consists in adding the shape factors  $\gamma_g$  and  $\gamma_l$ , both for gas and liquid phase, in the momentum balance equations, Eqs. (4) - (5)

$$\frac{\partial \alpha_g}{\partial t} + u_i \frac{\partial \alpha_g}{\partial x} = r_p(p_{ig} - p_{il}) \quad (1)$$

$$\frac{\partial(\alpha_g \rho_g)}{\partial t} + \frac{\partial(\alpha_g \rho_g u_g)}{\partial x} = 0 \quad (2)$$

$$\frac{\partial(\alpha_l \rho_l)}{\partial t} + \frac{\partial(\alpha_l \rho_l u_l)}{\partial x} = 0 \quad (3)$$

$$\frac{\partial(\alpha_g \rho_g u_g)}{\partial t} + \frac{\partial(\gamma_g \alpha_g \rho_g u_g^2)}{\partial x} + \alpha_g \frac{\partial p_{ig}}{\partial x} + \rho_g \alpha_g g \frac{\partial h}{\partial x} \cos(\theta) = -\rho_g \alpha_g g \sin(\theta) - F_{wg} - F_i \quad (4)$$

$$\frac{\partial(\alpha_l \rho_l u_l)}{\partial t} + \frac{\partial(\gamma_l \alpha_l \rho_l u_l^2)}{\partial x} + \alpha_l \frac{\partial p_{il}}{\partial x} + \rho_l \alpha_l g \frac{\partial h}{\partial x} \cos(\theta) = -\rho_l \alpha_l g \sin(\theta) - F_{wl} + F_i \quad (5)$$

The introduction of the shape factors in the model equations modifies the eigenstructure of the system; since the numerical resolution of the model is based on the Roe linearisation, the knowledge of the system eigenstructure is required. Thus, as first step of this work, the modified eigenvalue and eigenvectors were computed; we remark that, if the shape factors in the modified eigenstructure are set to one (as supposed in the previous work by (Ferrari *et al.*, 2017)), the original version of the eigenstructure is recovered (the comparison of the old eigenvalues against the new ones including shape factors is reported in Appendix A). The numerical resolution is largely based on the one proposed by (Ferrari *et al.*, 2017), which adopts the finite volume method and an explicit first order time discretisation. The source term on the right-hand side of the advection equation –Eq. (1)– is taken into account by a pressure relaxation process, described by (Munkejord, 2005), which requires the solution of a second degree polynomial equation: in the hyperbolic step, the gas volume fraction  $\alpha_g$  is modified to restore pressure equality at the interface. Some modifications were applied in the computation of the shear stresses at wall and at

interface and the pre-integrated model proposed by (Biberg, 2007) was adopted to compute the cross-sectional velocity profiles, which are required to obtain the shape factors (see (Picchi *et al.*, 2014))

$$\gamma_j = \frac{1}{A_j v_j^2} \int v_j^2(y) dA. \quad (6)$$

The velocity distribution  $v_j$  in the  $y$  direction is computed as proposed by (Biberg, 2007)

$$v_j = \text{sgn}(\tau_{wj}) \frac{u^*}{\kappa} \Delta_j + C_j, \quad (7)$$

where  $\Delta_j$  and  $C_j$ , reported in Appendix B, are function of  $Y$ , the adimensional position along the pipe cross section, of  $R_j$ , the ratio between the shear stress at interface and at wall,

$$Y = \frac{y}{h}, \quad R_j = \frac{\tau_i}{\tau_{wj}} \quad (8)$$

and of  $K_j$ , a parameter accounting for the interface shape, which reads, respectively for gas and liquid phase,

$$K_g = \frac{8v_g}{|u_g - u_l|}, \quad K_l = 1 \quad (9)$$

in case of smooth interface, and

$$K_g = \frac{0.065 \rho_g}{\rho_l - \rho_g} \frac{u_g - u_l}{g h_g \cos \theta}, \quad K_l = 10 \sqrt{\frac{\rho_g}{\rho_l}} \left| \frac{u_g - u_l}{u_l} \right| \quad (10)$$

in case of wavy interface.

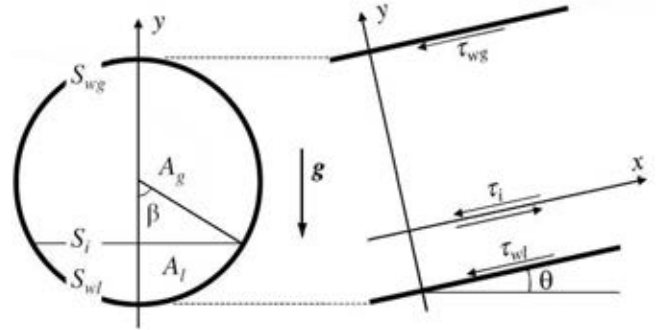


**Figure 1:** Schematic diagram of geometry.

The parameters  $R_j$  and  $K_j$  are introduced also in the computation of the shear stresses at wall and at interface through the corrected hydraulic diameter proposed by (Biberg, 2007)

$$D_{ej} = \frac{4A_j}{S_{wj}} \left( \frac{S_{wj}}{S_{wj} + S_i} \right)^{F(R_j, K_j)}, \quad (11)$$

where the wetted perimeter  $S_{wl}$  and  $S_{wg}$  and the interface perimeter  $S_i$  are shown in Figure 1. The corrected hydraulic diameter is employed to compute the Reynolds number

$$Re_j = |u_j| \frac{\rho_j}{\mu_j} D_{ej}, \quad (12)$$

which is then used to obtain the friction factor  $f_j$  by the Colebrook-White interpolation

$$\frac{1}{\sqrt{f_j}} = -2 \log_{10} \left( \frac{2.51}{Re_j \sqrt{f_j}} + \frac{k_s}{3.7D} \right) \quad (13)$$

in the case of turbulent flow and

$$f_j = \frac{64}{Re_j} \quad (14)$$

in the case of laminar flow. In this work, both smooth and rough flow can be described thanks to the sand roughness  $k_s$ . The gas shear stress at wall is computed as

$$\tau_{wg} = \frac{f_g \rho_g |u_g| u_g}{4} \quad (15)$$

the value of  $\tau_i$  and  $\tau_{wl}$  are computed by knowing  $\tau_{wg}$ ,  $R_g$  and  $R_l$ .

The value of  $R_g$  is computed in every computational cell and at every time step by a root search algorithm, imposing the equality of gas and liquid velocity at the interface, while computing the shear stresses. Once that  $R_g$  is known, it is possible to obtain the velocity profile in the cross-sectional direction and, by integration, the shape factors value, which will be inserted in the Roe matrix in the subsequent time step.

## RESULTS

### Stratified flow

In this Section, the computed cross-sectional velocity profiles in stratified flow conditions will be validated against the experimental measurements performed by (Ayati *et al.*, 2015): the geometry adopted in the experiments consists in a horizontal 31 m long PVC pipe, with an internal diameter  $D = 0.1$  m; the fluids used in the test cases are water and air at 22 °C, whose density are, respectively, 997 kg/m<sup>3</sup> and 1.2 kg/m<sup>3</sup>.

Concerning the numerical simulations, the space discretisation consists in 620 cells, leading to a  $\Delta x = D/2$ ; the time step is  $\Delta t = 10^{-5}$  s, with a corresponding CFL

$$CFL = \frac{\Delta t}{\Delta x} |\lambda_{max}| \approx 0.2, \quad (16)$$

since the maximum eigenvalue is approximately 10<sup>3</sup> m/s (for further information on the eigenvalues, see Appendix A).

We perform four comparisons, with four different couples of superficial velocities, which are reported in Table 1: two of the chosen configurations are characterized by a smooth sub-regime and two by a 2D waves sub-regime, as stated by (Ayati *et al.*, 2015). In the case of smooth sub-regime (and therefore smooth interface), in our numerical simulations we adopted the relation for  $K_f$  in Equation (9), while in case of 2D waves, we employed Equation (10). The PVC pipe roughness, required in Equation (13), was set to the representative value  $5 \cdot 10^{-3}$  mm, since the actual value is not reported by (Ayati *et al.*, 2015).

(Ayati *et al.*, 2015) perform the PIV measurements in a vertical plane located at 260D downstream from inlet and, thus, our numerical results are extracted at the same position along the pipe.

Figures 2 and 3 compare the experimental results with the numerical ones: we can observe that the shapes of the computed velocity profiles are in good agreement with the experimental one (the experimental profiles present some discontinuities because of strong background reflections or restricted optical access in proximity of the interface, as explained by (Ayati *et al.*, 2015)). In the case of smooth regime, there is a small discrepancy in the velocity magnitude: this can be due to the fact that the numerical code forecasts an equilibrium liquid volume fraction slightly higher than the one observed

in the experiments: therefore, the flow section for the gas phase is smaller and the velocity at the nose of the profile is higher, while the opposite happens for the liquid phase, whose velocity magnitude of the flat profile is slightly lower than the observed one.

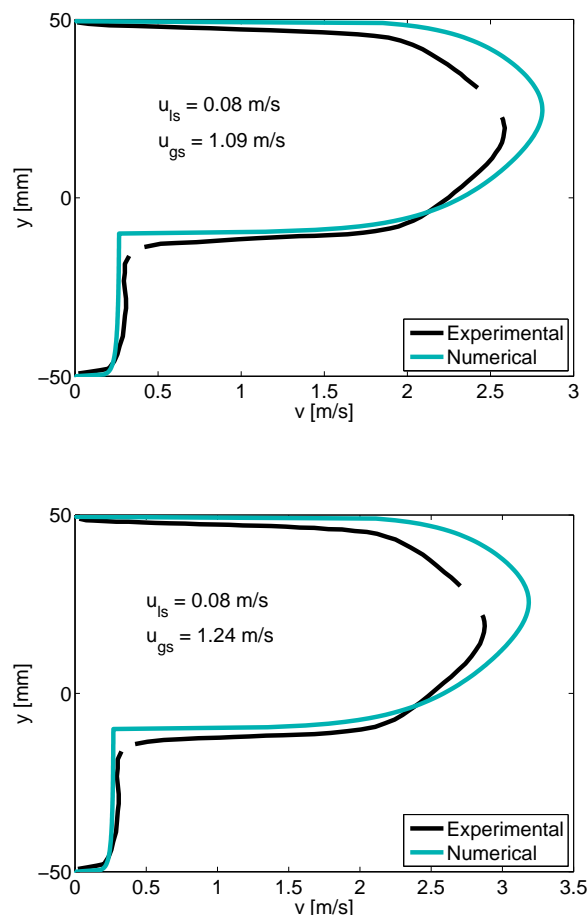


**Figure 2:** Comparison of the experimental and the numerical profiles. Smooth sub-regime.

In Table 1 the computed shape factor for gas and liquid phase are reported.

**Table 1:** Superficial liquid and gas velocities adopted in the numerical simulations.

$u_{ls}$ [m/s]	$u_{gs}$ [m/s]	Sub-regime	$\gamma_l$	$\gamma_g$
0.08	1.09	Smooth	1.10	1.03
0.08	1.27	Smooth	1.09	1.04
0.10	2.03	2D waves	1.09	1.04
0.10	2.29	2D waves	1.10	1.04

### Slug flow

First results in slug flow configuration will be now discussed. For the numerical simulations in slug conditions, the adopted geometry consists in a 36 m long pipe, with an internal diameter  $D = 0.078$  m (see (Issa and Kempf, 2003)); in this case we adopt  $\Delta x = 0.577D$  and  $\Delta t = 10^{-5}$  s. The liquid and gas superficial velocities are, respectively,  $u_{ls} = 1.5$  m/s and  $u_{gs} = 2.0$  m/s; the simulated fluids are again water and air.

(Ferrari *et al.*, 2017) developed a criterion to simulate the transition from two-phase to single phase flow, which takes place as a slug emerges and grows: this method consists in setting to zero the gas velocity when the gas volume fraction drops under a certain threshold; the threshold value is in the range  $3 \div 8 \cdot 10^{-3}$ . A special treatment for the shape factors and velocity profile inside the slug body was added to the existing transition criterion: this method prescribes that, when a slug forms, the shape factor of the gas phase is no longer computed, since it is no more required in the calculation concerning the gas momentum balance equation. Regarding the liquid phase, we prescribe that the velocity profile inside the slug body follow the relation proposed by (Biberg, 2007) in the case of Poiseuille-type flow: although this kind of flow is normally laminar, thanks to the turbulent viscosity employed in the computations, we obtain a turbulent shaped profile. (Dukler *et al.*, 1985) adopted the one-seventh power law to describe the velocity profile in the slug body

$$v_l = v_0 \left( \frac{y}{\delta} \right)^{1/7} \quad (17)$$

and, later, (Gopal and Jepson, 1997) supported their assumptions by experimental observations. In Figure 4 the computed profile in a slug body is compared against the one-seventh power law profile, which was calculated with  $\delta = D/2$  and

$v_0 = u_{ls} + u_{gs} = 3.5 \text{ m/s}$ : this choice is justified by the fact that the centerline velocity  $v_0$  is very close to the slug velocity, which is obtained by summing the gas and liquid superficial velocities, as reported by (Jepson, 1989). The shape factor in the slug body is in the range  $1.02 \div 1.04$ .

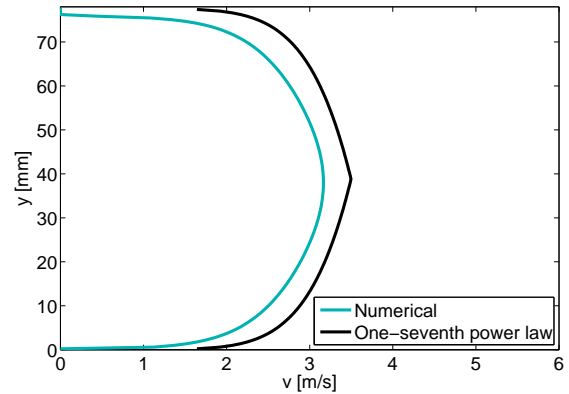


Figure 4: Comparison of the one-seventh power law profile against the computed one.

Finally, Figure 5 reports the qualitative behaviour of the velocity profiles before (top) and after (bottom) slug formation.

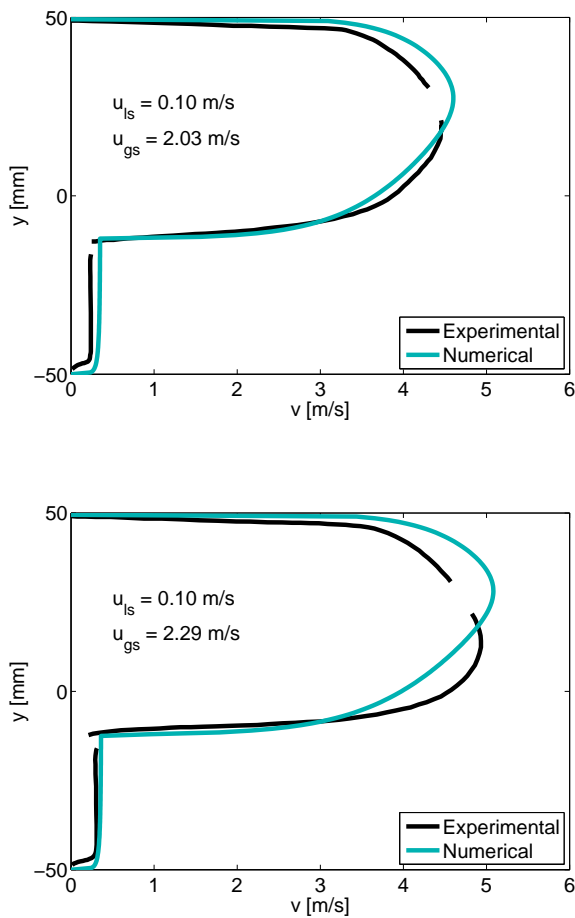


Figure 3: Comparison of the experimental and the numerical profiles. 2D waves sub-regime.

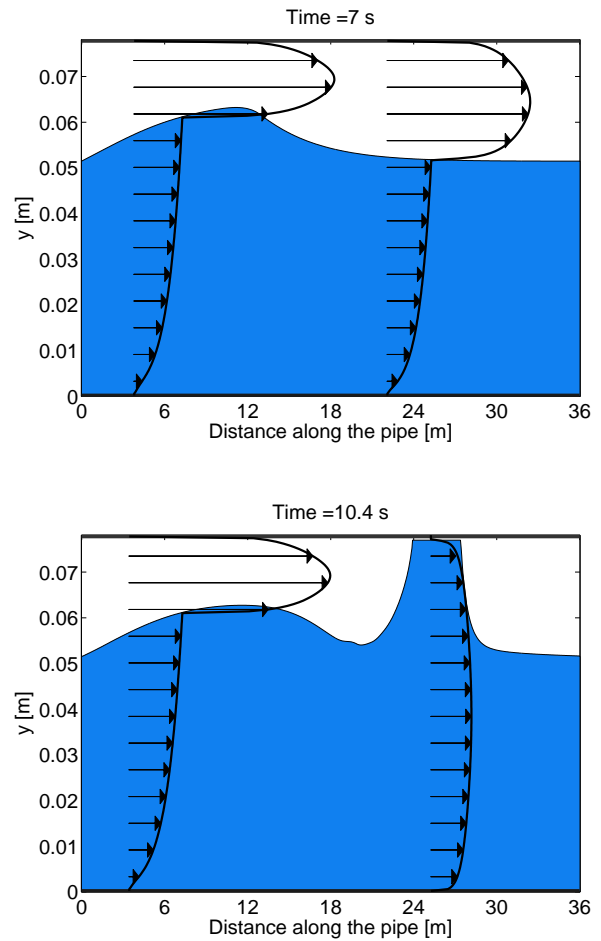


Figure 5: Example of computed velocity profiles before (top) and after (bottom) slug formation.

## CONCLUSION

In this work, a transient, five-equation two-fluid model accounting for cross-sectional velocity distribution has been presented. Starting from the existing numerical code by (Ferrari *et al.*, 2017), the model has been modified to account for the velocity profiles shape by the  $\gamma$  factor in the momentum balance equations; the inclusion of these correction coefficients modifies the five-equation system eigenstructure, which explicit form has been computed including  $\gamma$  factors. The pre-integrated model proposed by (Biberg, 2007) has been embodied in the numerical code, to compute shear stresses at wall and at interface and to obtain a consistent description of the cross-sectional velocity distribution. Numerical results both in stratified and in slug flow regime have been presented. The computed velocity profiles in smooth and wavy stratified regime were compared against experimental measurements, showing good agreement. Moreover, a method to compute the velocity profile during the transition from two-phase to single phase flow (which occurs during slug formation) has been developed; the computed velocity distribution in the liquid phase follows quite accurately the one-seventh power law profile, which has been experimentally observed to occur in the slug body.

## REFERENCES

- AYATI, A., KOLAAS, J. and JOHNSON, G. (2015). "Combined simultaneous two-phase piv and interface elevation measurements in stratified gas/liquid pipe flow". *International Journal of Multiphase Flow*, **74**, 45 – 58.
- BIBERG, D. (2007). "A mathematical model for two-phase stratified turbulent duct flow". *Multiphase Science and Technology*, **19**, 1 – 48.
- BONIZZI, M., ANDREUSSI, P. and BANERJEE, S. (2009). "Flow regime independent, high resolution multi-field modelling of near-horizontal gas-liquid flows in pipelines". *International Journal of Multiphase Flow*, **35**, 34 – 46.
- DUKLER, A.E., MOALEM MARON, D. and BRAUNER, N. (1985). "A physical model for predicting the minimum stable slug length". *Chemical Engineering Science*, **40**, 1379 – 1385.
- FERRARI, M., BONZANINI, A. and POESIO, P. (2017). "A five-equation, transient, hyperbolic, one-dimensional model for slug capturing in pipes". *International Journal for Numerical Method in Fluids*. Accepted for publication.
- GOPAL, M. and JEPSON, W.P. (1997). "Development of digital image analysis techniques for the study of velocity and void profiles in slug flow." *International Journal of Multiphase Flow*, **23**, 945 – 965.
- ISSA, R.I. and KEMPF, M.H.W. (2003). "Simulation of slug flow in horizontal and nearly horizontal pipes with the two-fluid model". *International Journal of Multiphase Flow*, **29**, 69 – 95.
- JEPSON, W.P. (1989). "Modelling the transition to slug flow in horizontal conduit". *Canadian Journal of Chemical Engineering*, **67**, 731 – 740.
- MUNKEJORD, S.T. (2005). *Analysis of the two-fluid model and the drift-flux model for numerical calculation of two-phase flow*, vol. Phd Thesis 2005, NTNU, Trondheim, Norway.
- PICCHI, D., CORRERA, S. and POESIO, P. (2014). "Flow pattern transition, pressure gradient, hold-up predictions in gas/non-newtonian power-law fluid stratified flow". *International Journal of Multiphase Flow*, **63**, 105 – 115.
- RENAULT, F. (2007). *A lagrangian slug capturing scheme for gas-liquid flows in pipes*, vol. Phd Thesis 2005, NTNU, Trondheim, Norway.

## APPENDIX A: COMPARISON OF THE EIGENSTRUCTURE WITH AND WITHOUT THE INCLUSION OF THE SHAPE FACTORS IN THE MODEL

We report here the eigenvalues and the eigenvectors of the five-equation system with and without the shape factor inclusion in the model, to show how deeply the description of the velocity profiles affects the eigenstructure of the five-equation system.

First, the eigenvalues employed by (Ferrari *et al.*, 2017) are

$$\lambda = \begin{bmatrix} u_i \\ u_g - c_g \\ u_g + c_g \\ u_l - c_l \\ u_l + c_l \end{bmatrix}, \quad (18)$$

while the ones adopted in the present work are

$$\lambda = \begin{bmatrix} u_i \\ \frac{u_g}{2}(1 + \gamma_g) - \frac{\sqrt{4c_g^2 + [u_g(\gamma_g - 1)]^2}}{2} \\ \frac{u_g}{2}(1 + \gamma_g) + \frac{\sqrt{4c_g^2 + [u_g(\gamma_g - 1)]^2}}{2} \\ \frac{u_l}{2}(1 + \gamma_l) - \frac{\sqrt{4c_l^2 + [u_l(\gamma_l - 1)]^2}}{2} \\ \frac{u_l}{2}(1 + \gamma_l) + \frac{\sqrt{4c_l^2 + [u_l(\gamma_l - 1)]^2}}{2} \end{bmatrix}, \quad (19)$$

where  $c_g = 316.22$  m/s and  $c_l = 1000$  m/s are the speed of sound respectively for gas and liquid phase.

The eigenvectors without the shape factors are

$$\mathbf{R} = \begin{bmatrix} 1 & 0 & 0 & 0 & 0 \\ -\frac{c_g^2 \rho_g + \alpha_g \rho_g \zeta}{[(u_g - u_i)^2 - c_g^2]} & 1 & 1 & 0 & 0 \\ -\frac{c_g^2 \rho_g + \alpha_g \rho_g \zeta}{[(u_g - u_i)^2 - c_g^2]} u_i & u_g - c_g & u_g + c_g & 0 & 0 \\ \frac{c_l^2 \rho_l - \alpha_l \rho_l \zeta}{[(u_l - u_i)^2 - c_l^2]} & 0 & 0 & 1 & 1 \\ \frac{c_l^2 \rho_l - \alpha_l \rho_l \zeta}{[(u_l - u_i)^2 - c_l^2]} u_i & 0 & 0 & u_l - c_l & u_l + c_l \end{bmatrix}, \quad (20)$$

where  $\zeta = -\frac{\pi D g \cos \theta}{4 \sin(\beta)}$ ; the eigenvectors including  $\gamma$  factors are

$$\mathbf{R} = \begin{bmatrix} 1 & 0 & 0 & 0 & 0 \\ r_{21} & 1 & 1 & 0 & 0 \\ r_{31} & \frac{\gamma_g u_g^2 - c_g^2}{\lambda_3} & \frac{\gamma_g u_g^2 - c_g^2}{\lambda_2} & 0 & 0 \\ r_{41} & 0 & 0 & 1 & 1 \\ r_{51} & 0 & 0 & \frac{\gamma_l u_l^2 - c_l^2}{\lambda_5} & \frac{\gamma_l u_l^2 - c_l^2}{\lambda_4} \end{bmatrix}, \quad (21)$$

with

$$\begin{aligned} r_{21} &= -\frac{c_g^2 \rho_g + \alpha_g \rho_g \zeta}{[\gamma_g u_g^2 - u_g u_i (1 + \gamma_g) + u_i^2 - c_g^2]}, \\ r_{31} &= -\frac{c_g^2 \rho_g + \alpha_g \rho_g \zeta}{[\gamma_g u_g^2 - u_g u_i (1 + \gamma_g) + u_i^2 - c_g^2]} u_i, \\ r_{41} &= \frac{c_l^2 \rho_l - \alpha_l \rho_l \zeta}{[\gamma_l u_l^2 - u_l u_i (1 + \gamma_l) + u_i^2 - c_l^2]}, \\ r_{51} &= \frac{c_l^2 \rho_l - \alpha_l \rho_l \zeta}{[\gamma_l u_l^2 - u_l u_i (1 + \gamma_l) + u_i^2 - c_l^2]} u_i. \end{aligned} \quad (22)$$

It is possible to observe that, when in Equations (19) and (21)  $\gamma_g$  and  $\gamma_l$  are unitary, the expressions without the shape factor of Equations (18) and (20) are recovered. Therefore, the eigenstructure of the model including shape factors can be seen as an extension of the one by (Ferrari *et al.*, 2017).

## APPENDIX B: FURTHER EQUATIONS ADOPTED IN THE MODEL

In this Appendix, we report the equations developed by (Biberg, 2007) and adopted in the presented model.

$\Delta_j$  and  $C_j$ , adopted in Eq. (7), are (the subscript  $j$  has been removed for clarity)

$$\begin{aligned} \Delta = & \ln(1-Y) + \frac{(K^3 + R^3)\ln(Y + K(1-Y))}{|R|^{5/2} - K^3} \\ & + \frac{(R + \sqrt{|R|})\sqrt[3]{|R|}\ln(Y + |R|^{5/6}(1-Y))}{3(K - |R|^{5/6})} \\ & - \frac{(R + \sqrt{|R|})(K + 2|R|^{5/6})|R|^{5/6}\sqrt[3]{|R|}}{\ln Y^2 - (1-Y)(Y - (1-Y)|R|^{5/6})} \\ & \cdot \frac{6(K^2 + |R|^{5/6}K + |R|^{5/3})}{K(R + \sqrt{|R|})\sqrt[3]{|R|}} \\ & + \frac{K(R + \sqrt{|R|})\sqrt[3]{|R|}}{\sqrt{3}(K^2 + |R|^{5/6}K + |R|^{5/3})} \\ & \cdot \tan^{-1}\left(\frac{2(Y-1)|R|^{5/3} + (2Y-1)|R|^{5/6} + 2Y}{\sqrt{3}|R|^{5/6}}\right) \end{aligned} \quad (23)$$

and

$$C = C^1 + \text{sgn}(\tau_w) \frac{u^*}{\kappa} \Psi, \quad (24)$$

where

$$C^1 = \text{sgn}(\tau_w) \frac{u^*}{\kappa} \left( \ln\left(\frac{h}{k_s}\right) + A\kappa \right), \quad (25)$$

and

$$\Psi = -\frac{K(R + \sqrt{|R|})\sqrt[3]{|R|}}{\sqrt{3}(K^2 + |R|^{5/6}K + |R|^{5/3})} \tan^{-1}\left(\frac{1 + 2/|R|^{5/6}}{\sqrt{3}}\right). \quad (26)$$

The exponent  $F(R_j, K_j)$  reported in Eq. (11) is (the subscript  $j$  has been removed for clarity)

$$F(R, K) = \frac{\Lambda + \Psi}{\Lambda^P}, \quad (27)$$

where

$$\begin{aligned} \Lambda = & \frac{5(R + \sqrt{|R|})(|R|^{5/2} + K^2 + K)R^2 \ln(|R|)}{6(K^3 - |R|^{5/2})(|R|^{5/2} - 1)} \\ & - \frac{K(K^3 + R^3)\ln(K)}{(K-1)(K^3 - |R|^{5/2})} \\ & + \frac{(R + \sqrt{|R|})\sqrt[3]{|R|}}{\sqrt{3}(|R|^{5/3} + |R|^{5/6} + 1)(K^2 + K|R|^{5/6} + |R|^{5/3})} \\ & \cdot \left( (K - |R|^{5/3}) \tan^{-1}\left(\frac{1 + 2/|R|^{5/6}}{\sqrt{3}}\right) \right. \\ & \left. - (K + (K+1)|R|^{5/6})|R|^{5/6} \tan^{-1}\left(\frac{2|R|^{5/6} + 1}{\sqrt{3}}\right) \right), \end{aligned} \quad (28)$$

and

$$\Lambda^P = -\frac{2}{27}(2\sqrt{3} + 9). \quad (29)$$

## GAS-LIQUID TWO-PHASE FLOW BEHAVIOR IN TERRAIN-INCLINED PIPELINES FOR WET NATURAL GAS TRANSPORTATION

Yan Yang<sup>1</sup>, Jingbo Li<sup>1</sup>, Shuli Wang<sup>1</sup>, Chuang Wen<sup>2\*</sup>

<sup>1</sup> School of Petroleum Engineering, Changzhou University 213016 Changzhou, CHINA

<sup>2</sup> Department of Mechanical Engineering, Technical University of Denmark, 2800 Kgs. Lyngby, DENMARK

\* E-mail: cwen@mek.dtu.dk

### ABSTRACT

The liquid slug formation in a hilly-terrain pipeline is simulated using the Volume of Fluid model and RNG k- $\epsilon$  turbulence model. The numerical model is validated by the experimental data of the horizontal slug flow. The influence of pipe diameter on liquid slug formation is discussed in detail. The results show that the pipe is blocked by the liquid slug at the moment of slug formed. The pipe pressure suddenly increases, and then decreases gradually in the process of liquid slug formation and motion. The pipe diameter has little effect on liquid slug formation, while the pipe pressure drop and liquid holdup change small.

**Keywords:** gas-liquid two-phase flow, CFD, natural gas, pipe flow.

### NOMENCLATURE

A complete list of symbols used, with dimensions, is required.

#### Greek Symbols

$\alpha$	Volume fraction, [-].
$\alpha_k$	Constant, [-].
$\alpha_\epsilon$	Constant, [-].
$\beta$	Constant, [-].
$\epsilon$	Turbulent dissipation rate, [-].
$\delta_{ij}$	Kronecker delta, [-].
$\mu$	Dynamic viscosity, [ $\text{m}^2\text{s}^{-1}$ ].
$\mu_t$	Turbulent viscosity, [ $\text{m}^2\text{s}^{-1}$ ].
$\eta_0$	Constant, [-].
$\rho$	Density, [ $\text{kgm}^{-3}$ ].
$\theta$	Inclination angle of pipe, [ $^\circ$ ].
$\theta_1$	Inclination angle of descending pipe, [ $^\circ$ ].
$\theta_2$	Inclination angle of ascending pipe, [ $^\circ$ ].

#### Latin Symbols

$C_{1\epsilon}$	Constant, [-].
$C_{1\epsilon}^*$	Constant, [-].
$C_{2\epsilon}$	Constant, [-].
$C_\mu$	Constant, [-].
$D$	Pipe diameter, [mm].
$E_{ij}$	Mean strain rate, [-].

$\vec{F}$	External body force, [N].
$F_{vol}$	Surface force, [N].
$G_k$	Generation of turbulence kinetic energy, [-].
$g$	Acceleration of gravity, [ $\text{m/s}^2$ ].
$h$	Level of stagnant liquid, [mm].
$k$	Turbulent kinetic energy, [ $\text{m}^2\text{s}^{-2}$ ].
$L$	Pipeline length [m].
$\dot{m}_{pq}$	Mass transfer from phase $p$ to phase $q$ , [ $\text{kgs}^{-1}$ ].
$\dot{m}_{qp}$	Mass transfer from phase $q$ to phase $p$ , [ $\text{kgs}^{-1}$ ].
$p$	Pressure, [Pa].
$Q$	Volume of pipe, [ $\text{m}^3\text{s}^{-1}$ ].
$Q_L$	Volume of stagnant liquid, [ $\text{m}^3\text{s}^{-1}$ ].
$S_{aq}$	Source term, [-].
$t$	Time, [s].
$u$	Velocity, [ $\text{ms}^{-1}$ ].
$V_G$	Inlet gas velocity [ $\text{ms}^{-1}$ ].
$V_{SL}$	Superficial liquid velocity [ $\text{ms}^{-1}$ ].
$V_{SG}$	Superficial gas velocity [ $\text{ms}^{-1}$ ].

#### Sub/superscripts

$G$	Gas.
$L$	Liquid.
$i$	Index $i$ .
$j$	Index $j$ .

### INTRODUCTION

Natural gas field usually locates in hilly or basin region, and then the hilly-terrain pipelines are used inevitably. The water in wet gas can assemble in the low-lying pipes, and becomes stagnant liquid in the process of transporting wet gas. It leads to the formation of the liquid slug or the slug flow which can cause the shapely pressure and liquid holdup fluctuation in the pipeline. Therefore, it is important to study and predict the slug flow in the hilly-terrain pipelines.

For the slug flow, the study mainly focuses on the horizontal pipe, vertical pipe and hilly-terrain pipes. For the horizontal pipelines, a prediction method based on one-dimensional two-fluid model was presented for



predicting hydrodynamic slug initiation and growth by Issa and Kempf (2003). Al-Safran et al. (2015) proposed a new empirical relationship for predicting slug liquid holdup in high viscosity liquids. For the studies of a slug in the vertical pipelines, Taha and Cui (2006) used the Volume of Fluid (VOF) model to simulate the motion of a single Taylor bubble in the vertical tubes and obtained the shape and flow parameters of the slug. Abdulkadir et al. (2015) conducted the experimental and numerical studies in the vertical pipes with 6 m long and 0.067 m internal diameter. Henau and Raithby (1995) investigated the slug behavior in two-phase pipes which contained several uphill and downhill sections. Ersoy et al. (2011) investigated gas-oil-water three-phase slug flow in hilly-terrain pipelines.

The gas-liquid slug flow attracts attention all the time. However, the formation and motion of a single liquid slug still needs to be further studied in hilly-terrain pipelines, in particular the existence of the stagnant liquids. In this paper, the numerical study is carried out to understand the formation process of a single liquid slug in hilly-terrain pipelines. The influence of pipe diameter on liquid slug formation is analysed in detail.

## MODEL DESCRIPTION

The slug flow is a sort of complex gas-liquid flow which has a distinct phase interface. The interface catching is a key step for the simulation of the liquid slug. The Volume of Fluid (VOF) model is a kind of surface-tracking technology based on fixed Eulerian mesh and it can be used for modelling two or more immiscible fluids. Therefore, the VOF model is employed here to track the gas-liquid phase interface in hilly-terrain pipelines. In addition, the turbulence model is necessary due to the flow is turbulent in our simulation.

### Governing Equation

Continuity equation

$$\frac{\partial \rho}{\partial t} + \frac{\partial}{\partial x_i} (\rho u_i) = 0 \quad (1)$$

Momentum equation

$$\begin{aligned} \frac{\partial}{\partial t} (\rho \vec{u}) + \nabla \cdot (\rho \vec{u} \vec{u}) \\ = -\nabla p + \nabla \cdot \left[ \mu (\nabla \vec{u} + \nabla \vec{u}^T) \right] + \rho \vec{g} + \vec{F} \end{aligned} \quad (2)$$

where  $\rho$  is the density,  $\vec{u}$  is the velocity,  $p$  is the static pressure,  $\mu$  is the dynamic viscosity,  $\vec{g}$  is the gravitational acceleration and  $\vec{F}$  is external body force.

Volume fraction equation

$$\frac{1}{\rho_q} \left[ \frac{\partial}{\partial t} (a_q \rho_q) + \nabla \cdot (a_q \rho_q \vec{v}_q) \right] = S_{a_q} + \sum_{p=1}^n (\dot{m}_{pq} - \dot{m}_{qp}) \quad (3)$$

where  $\dot{m}_{pq}$  is the mass transfer from phase  $q$  to phase  $p$  and  $\dot{m}_{qp}$  is the mass transfer from phase  $p$  to phase  $q$ ,

$\alpha_q$  is the volume fraction of phase  $q$ ,  $S_{\alpha_q}$  is the source term.

### Continuum Surface Force Model

The effect of surface force along the interface is included in the VOF model. The continuum surface force (CSF) model proposed by Brackbill et al (1992) is used in this paper. It is implemented as a source term in the momentum equation. The surface force  $F_{vol}$  is expressed as follows:

$$F_{vol} = \sigma_{ij} \frac{\rho \kappa_i \nabla \alpha_i}{\frac{1}{2} (\rho_i + \rho_j)} \quad (4)$$

where

$$\rho = \alpha_2 \rho_2 + (1 - \alpha_2) \rho_1 \quad (5)$$

$$\kappa = \nabla \cdot \hat{n} \quad (6)$$

$$\hat{n} = \frac{n}{|n|} \quad (7)$$

$$n = \nabla \alpha_q \quad (8)$$

### Turbulence Model

The RNG  $k$ - $\varepsilon$  turbulence model has an additional term in its  $\varepsilon$  equation that significantly improves the accuracy for rapidly strained flows. It also provides an option to account for the effects of swirl or rotation by modifying the turbulent viscosity appropriately. Therefore, the RNG  $k$ - $\varepsilon$  turbulence model is employed here because the flow turns at the elbow of the pipe which connects the uphill section and downhill section in hilly-terrain pipelines. The turbulence kinetic energy,  $k$ , and its rate of dissipation,  $\varepsilon$ , are as follows:

$$\begin{aligned} \frac{\partial (\rho k)}{\partial t} + \frac{\partial (\rho k u_i)}{\partial x_i} \\ = \frac{\partial}{\partial x_j} \left[ \alpha_k \mu_{eff} \frac{\partial k}{\partial x_j} \right] + G_k + \rho \varepsilon \end{aligned} \quad (9)$$

$$\begin{aligned} \frac{\partial (\rho \varepsilon)}{\partial t} + \frac{\partial (\rho \varepsilon u_i)}{\partial x_i} \\ = \frac{\partial}{\partial x_j} \left[ \alpha_\varepsilon \mu_{eff} \frac{\partial \varepsilon}{\partial x_j} \right] + \frac{C_{1\varepsilon}^* \varepsilon}{k} G_k - C_{2\varepsilon} \rho \frac{\varepsilon^2}{k} \end{aligned} \quad (10)$$

where

$$\mu_{eff} = \mu + \mu_t \quad (11)$$

$$\mu_t = \rho C_\mu \frac{k^2}{\varepsilon} \quad (12)$$

$$C_{1\varepsilon}^* = C_{1\varepsilon} - \frac{\eta(1 - \eta / \eta_0)}{1 + \beta \eta^3} \quad (13)$$

$$\eta = (2E_{ij} \cdot E_{ij})^{1/2} \frac{k}{\varepsilon} \quad (14)$$

$$E_{ij} = \frac{1}{2} \left( \frac{\partial u_i}{\partial x_j} + \frac{\partial u_j}{\partial x_i} \right) \quad (15)$$

where  $C_\mu=0.0845$ ,  $\alpha_k=\alpha_\varepsilon=1.39$ ,  $C_{1\varepsilon}=1.42$ ,  $C_{2\varepsilon}=1.68$ ,  $\eta_0=4.377$ ,  $\beta=0.012$ .

**GEOMETRY AND MESH**

The sketch of hilly-terrain pipeline is shown in Figure 1. This pipeline contains a descending pipe and an ascending pipe, respectively. The inclination angles of two pipes are  $\theta_1$  and  $\theta_2$ . The stagnant liquid is water and the gas phase is methane. Two pressure monitoring points (P1 and P2) are set at the center of the pipe cross section which locates in  $x = -15 D$  and  $x = 15 D$ . The pipe pressure drop is the value of  $|P1 - P2|$  in this paper.

The computational domain should be meshed after the geometric model is established. The commercial software ANSYS ICEM CFD is selected as the meshing tool. The hexahedral mesh and O-block technology are selected as the grid partition strategy for improving the quality of grid. The grid system is shown in Figure 2. Around 300 000 cells are performed for our simulations after the grid independence test.

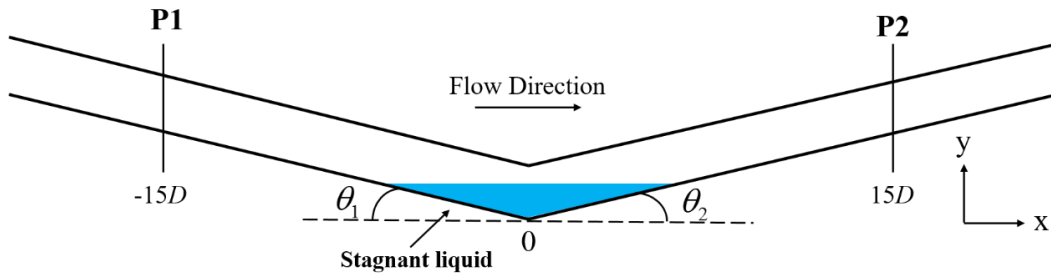


Figure 1 Sketch of the hilly-terrain pipeline

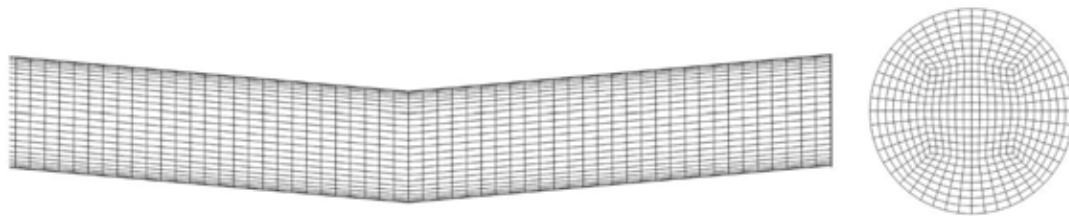


Figure 2 Mesh generation

**RESULTS AND DISCUSSION**

**Model Validation**

In this paper the experimental data obtained by Heywood and Richardson (1979) are employed to validate our numerical method. The experiments were carried out in an air-water flow loop system, which included a horizontal pipeline of 42 mm inner diameter. The  $\gamma$ -ray absorption method was used to measure the slug liquid holdup (liquid volume fraction). Six experimental data in the same superficial liquid velocity (0.978 m/s) were selected for the model validation in different superficial gas velocities. The results of the comparison between the experimental and numerical data are shown in Figure 3. It presents that the maximum relative error is 5.9% in superficial gas velocity of 4.145 m/s. Therefore, the numerical results are in good agreement with the experimental data.

$x$  is the position coordinates of pipe along the flow direction.

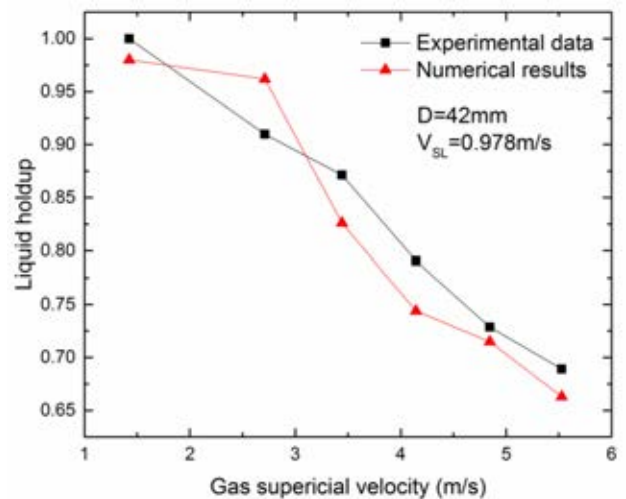


Figure 3 Comparison between experimental and numerical results in a horizontal pipe

**Liquid Slug Formation Process**

Figure 4 shows the formation process of a liquid slug in the 150 mm diameter pipe with the inclination angle of  $\theta_2 = \theta_2 = 5^\circ$ . The inlet gas velocity is 6.5 m/s, and the ratio of the stagnant liquid height,  $h$ , to the pipe diameter is 0.75 ( $h/D=0.75$ ). The phase fraction distribution with different moment ( $t$ ) is described in the contours. The blue region represents the gas phase, while the red one represents the liquid phase. The axis,

The flow area decreases due to the stagnant liquid accumulated at the bottom of hilly-terrain pipes, which cause the increase of the gas velocity. This flow structure further induces the decline of the pressure above the liquid level. Then suction force generates in the vertical upward, which destroys the stability of gas-liquid interface. For this reason, a wave crest forms. When the liquid level uplifts to the top of the pipe and

blocks the entire pipe cross section, the liquid slug flow finally appears ( $t=0.005$  s - $0.100$  s in Figure 4). The liquid slug then goes into the next process of moving

forward under the pressure difference between the upstream and downstream of the slug flow ( $t=0.105$ - $0.120$  s in Figure 4).

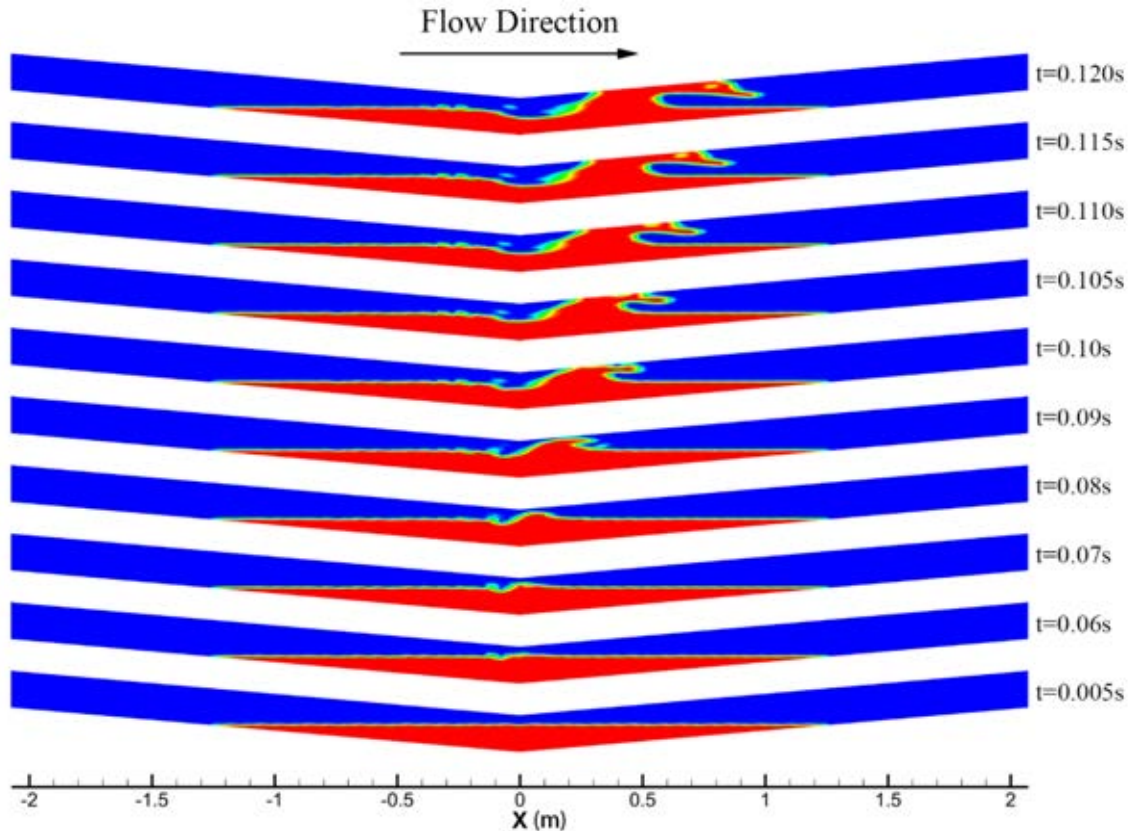


Figure 4 Formation process of a liquid slug

### Pipe Diameter Effect

In this section, the influence of the pipe diameter on the formation of a liquid slug is discussed in detail. The pipe diameters are 90 mm, 120 mm, 150 mm, 180 mm and 210 mm, respectively. The length of the ascending and descending pipes is  $50 D$ , while the inclination angle is set to be  $5^\circ$ . The numerical simulation is implemented in the identical condition which the inlet gas velocity is  $6.5$  m/s with  $h/D=0.75$ .

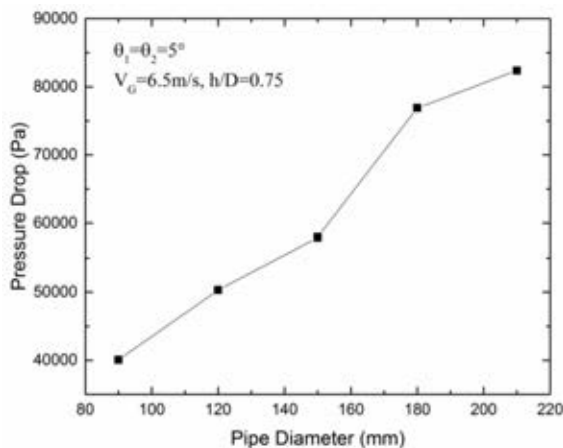


Figure 5 Influence of pipe diameter on pressure drop at the moment of slug formed

The pressure drops in different pipe diameter at the moment of slug formed are shown in Figure 5. The pressure drop increases along with the pipe diameter.

The pressure drop ranges from  $40,000$  Pa to  $82,000$  Pa. The rate of increasing pressure drop is about 30% with the pipe diameter from  $90$  mm to  $210$  mm. Figure 6 describes the slug liquid holdup in different pipe diameters. We can see that the liquid holdup increases slowly in the pipe diameters from  $90$  mm to  $180$  mm, while it declines slightly in the  $210$  mm diameter pipe. However, the value of slug liquid holdup distributes approximately  $0.5$  in the entire pipe diameters.

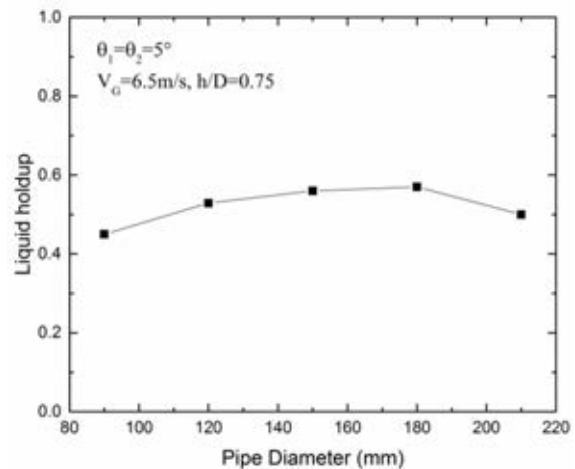


Figure 6 Influence of pipe diameter on liquid holdup at the moment of slug formed

### CONCLUSIONS

The VOF and RNG  $k-\epsilon$  turbulence models show the reasonable results in simulating the formation process

of a liquid slug. The distinct gas-liquid two-phase distribution and the formation process of a liquid slug are obtained by numerical simulation. The pipe cross-section is blocked by the liquid phase at the moment of a liquid slug formed. The pressure suddenly increases, and then declines gradually in process of liquid slug formation and motion. The pipe diameter has tiny effect on the slug formation, since the pressure drop and the liquid holdup change little.

#### ACKNOWLEDGEMENTS

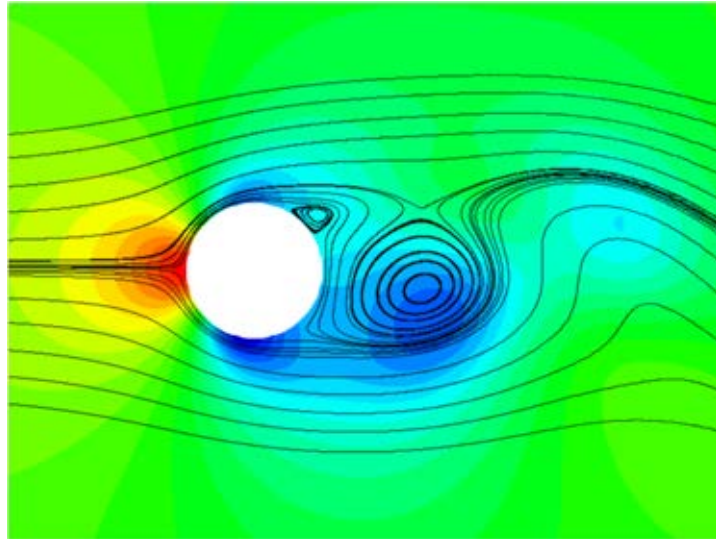
This work was supported by the National Natural Science Foundation of China (51444005, 51574045).

#### REFERENCES

- ABDULKADIR, M., HERNANDEZ-PEREZ, V., LO, S., LOWNDES, I.S. and AZZOPARDI, B.J., (2015), "Comparison of experimental and Computational Fluid Dynamics (CFD) studies of slug flow in a vertical riser", *Exp. Therm Fluid Sci.*, **68**, 468-483.
- AL-SAFRAN, E., KORA, C. and SARICA, C., (2015), "Prediction of slug liquid holdup in high viscosity liquid and gas two-phase flow in horizontal pipes", *J. Pet. Sci. Technol.*, **133**, 566-575.
- BRACKBILL, J.U., KOTHE, D.B. and ZEMACH, C., (1992), "A continuum method for modeling surface tension", *J. Comput. Phys.*, **100**, pp.335-354.
- CLARKE, A. and ISSA, R.I., (1997), "A numerical model of slug flow in vertical tubes", *Comput. Fluids*, **26**, 395-415.
- ERSOY, G., SARICA, C., AL-SAFRAN, E. and ZHANG, H.Q., (2011), "Experimental Investigation of Three-Phase Gas-Oil-Water Slug Flow Evolution in Hilly-Terrain Pipelines", *SPE Annual Technical Conference and Exhibition*, Denver, Colorado, USA, 30 October - 2 November.
- DE HENAU, V. and RAITHBY, G.D., (1995), "A study of terrain-induced slugging in two-phase flow pipelines", *Int. J. Multiphase Flow*, **21**, 365-379.
- HEYWOOD, N.I. and RICHARDSON, J.F., (1979), "Slug flow of air—water mixtures in a horizontal pipe: Determination of liquid holdup by  $\gamma$ -ray absorption", *Chem. Eng. Sci.*, **34**, 17-30.
- ISSA, R.I. and KEMPF, M.H.W., (2003), "Simulation of slug flow in horizontal and nearly horizontal pipes with the two-fluid model", *Int. J. Multiphase Flow*, **29**, 69-95.
- TAHA, T. and CUI, Z.F., (2006), "CFD modelling of slug flow in vertical tubes", *Chem. Eng. Sci.*, **61**, 676-687.



# NUMERICS, METHODS & CODE DEVELOPMENT





## INNOVATIVE COMPUTING FOR INDUSTRIALLY-RELEVANT MULTIPHASE FLOWS

**Damir JURIC<sup>1\*</sup>, Jalel CHERGUI<sup>1</sup>, Seungwon SHIN<sup>2</sup>,  
Lyes KAHOUADJI<sup>3</sup>, Richard V. CRASTER<sup>4</sup>, Omar K. MATAR<sup>3</sup>**

<sup>1</sup>Laboratoire d'Informatique pour la Mécanique et les Sciences de l'Ingénieur (LIMSI),

Centre National de la Recherche Scientifique (CNRS), Rue John von Neumann, 91405 Orsay, FRANCE

<sup>2</sup>Department of Mechanical and System Design Engineering, Hongik University, Seoul, 121-791 SOUTH KOREA

<sup>3</sup>Department of Chemical Engineering, Imperial College London,  
South Kensington Campus, London SW7 2AZ, UK

<sup>4</sup>Department of Mathematics, Imperial College London,  
South Kensington Campus, London SW7 2AZ, UK

\* E-mail: damir.juric@limsi.fr

### ABSTRACT

The ability to predict the behaviour of multiphase flows accurately, reliably, and efficiently addresses a major challenge of global economic, scientific, and societal importance. These flows are central to virtually every processing and manufacturing technology. Significant advances have been made in the numerical methods to simulate these flows; examples of these include the use of Large Eddy Simulations to simulate turbulence, and interface-capturing or tracking techniques to deal with the free surface. These codes have made progress in simulating the interaction of a turbulent flow field with an interface, however, there remains a large gap between what is achievable computationally and 'real-life' systems. We will present the latest on the modelling framework that we are currently developing within the Multi-scale Examination of MultiPhase physics in flowS (MEMPHIS) programme that will enable the use of numerical simulations as a reliable design tool. The framework features Front-Tracking/Level-Set hybrids, an Immersed Boundary approach to Fluid-Structure Interaction and sophisticated multi-scale, multi-physics models. The code we call BLUE is fully parallelised and can run on various platforms: from laptops to supercomputers (on over 250,000 cores). This allows the user the flexibility to choose between a quick 'answer' with a degree of uncertainty common to engineering applications or a high-fidelity solution, for targeted cases, that requires more time. BLUE also has built-in, user-friendly meshing capabilities that allow rapid construction of complex geometries. We present a number of simulations of problems of interest to process industries and biomedical applications, which include the design of container-filling processes, two-fluid mixing with a rotating impeller, high-speed atomization, microfluidic droplet encapsulation, falling film reactors featuring non-Newtonian fluids, and surfactant-driven non-isothermal flows.

**Keywords:** CFD, Multiphase flow, Surfactants, Chemical reactors, Atomization, Filling, Mixing, Microfluidics, Non-Newtonian fluids, Fluid Structure Interaction.

### NOMENCLATURE

#### *Greek Symbols*

- $\rho$  Mass density, [kg/m<sup>3</sup>].
- $\mu$  Dynamic viscosity, [kg/m.s].
- $\kappa$  Curvature, [m<sup>-1</sup>].
- $\sigma$  Surface tension, [kg/s<sup>2</sup>].
- $\delta$  Dirac delta function, [m<sup>-3</sup>].
- $\alpha$  Arrhenius exponent
- $\dot{\gamma}$  Shear rate, [s<sup>-1</sup>].

#### *Latin Symbols*

- $t$  Time, [s].
- $P$  Pressure, [Pa].
- $T$  Temperature, [K].
- $\mathbf{u}$  Fluid velocity, [m/s].
- $\mathbf{V}$  Interface velocity, [m/s].
- $\mathbf{g}$  Gravitational acceleration, [m/s<sup>2</sup>].
- $\mathbf{n}$  Normal vector.
- $n$  Power-law index.
- $I$  Indicator function.
- $\mathbf{F}$  Force per unit volume, [N/m<sup>3</sup>].
- $N_c$  Number of computation cores.
- $T_c$  Elapsed computation time.

#### *Sub/superscripts*

- 1 Fluid phase 1.
- 2 Fluid phase 2.
- ref Reference value for parallel performance.
- $\alpha$  Reference value for Arrhenius temperature.
- 0 Zero value for non-Newtonian viscosity.
- $\infty$  Infinite value for non-Newtonian viscosity.



## INTRODUCTION

It is very common in nature as in industrial processes that two or more phases are present simultaneously. One of the most striking examples is probably the aerodynamic breakup atomization caused by shear stresses at the liquid-gas interface. This process consists of a liquid jet projected at high speed in a gas that destabilizes gradually until breaking up into a myriad of droplets. This mechanism, which is widely used in fuel injection or perfumery, for example, is only one aspect of a broad class of phenomena that can be gathered under the name of multiphase flows. General fluid-fluid interfaces are found in an extraordinary variety of situations and scales such as free-surface waves, jets, bubbles and drops just to name a few examples.

From a numerical perspective, the typical issues faced in multiphase flows lead immediately to questions such as: What is the actual shape of the interface or what are the interactions between the phases? In the wide field of multiphase flow, analytical approaches are useful but extremely limited to the most trivial cases. The natural extension is direct numerical simulation, helped by the continuing growth of information technology resources. Such flows are generally three-dimensional and require advanced numerical methods for many reasons. First, physical parameter discontinuities at the interface require particular techniques and several popular methods could be chosen such as Volume of Fluid (VOF) (Hirt and Nichols, 1981), Level Set (Osher and Sethian, 1988), Front Tracking (Unverdi and Tryggvason, 1992) or their recently developed hybrid combinations. The history of the development and descriptions of such methods for multiphase flows is thoroughly covered in Tryggvason et al. (2011). The discretized systems involve different and widely ranging spatio-temporal scales and therefore a large number of degrees of freedom. It is often necessary to scan the parameter space to study robustness of a system. Our approach in the code BLUE is based on an innovative hybridization of the Front-Tracking and Level Set methods which is fully parallelized and able to run on a variety of computer architectures (Shin et al. 2017a). Below we briefly describe the techniques implemented in BLUE, discuss the code's parallel performance and present a variety of simulation results in various challenging multiphase flow regimes.

## DESCRIPTION OF THE CODE BLUE

In this section, we will describe the basic solution procedure for the Navier-Stokes equations with a brief explanation of the hybrid interface method implemented in BLUE. Details of the numerical implementation can be found in several articles by Shin and Juric (2002, 2007, 2009a, 2009b), Shin (2007) and Shin et al. (2011, 2017a).

The governing equations for transport of an incompressible two-phase flow can be expressed by a single field formulation:

$$\text{Continuity equation} \\ \nabla \cdot \mathbf{u} = 0$$

(1)

*Momentum equation*

$$\rho \left( \frac{\partial \mathbf{u}}{\partial t} + \mathbf{u} \cdot \nabla \mathbf{u} \right) = -\nabla P + \nabla \cdot \mu (\nabla \mathbf{u} + \nabla \mathbf{u}^T) + \rho \mathbf{g} + \mathbf{F}$$

(2)

where  $\mathbf{u}$  is the velocity,  $P$  the pressure,  $\mathbf{g}$  the gravitational acceleration and  $\mathbf{F}$  the local surface tension force at the interface and is described by the formulation:

$$\mathbf{F} = \sigma \kappa_H \nabla I$$

(2)

where  $I$  is the indicator function which is zero in one phase and one in the other phase, resolved with a sharp but smooth transition across 3 to 4 grid cells and is essentially a numerical Heaviside function generated using a vector distance function computed directly from the tracked interface (Shin and Juric, 2009a). This formulation was shown to essentially eliminate the spurious currents which had plagued most numerical techniques for surface-tension driven flows.  $\kappa_H$  is twice the mean interface curvature field calculated on the Eulerian grid using:

$$\kappa_H = \frac{\mathbf{F}_L \cdot \mathbf{G}}{\sigma \mathbf{G} \cdot \mathbf{G}}$$

(4)

where

$$\mathbf{F}_L = \int_{\Gamma(t)} \sigma \kappa_f \mathbf{n}_f \delta_f(\mathbf{x} - \mathbf{x}_f) ds$$

(5)

and

$$\mathbf{G} = \int_{\Gamma(t)} \mathbf{n}_f \delta_f(\mathbf{x} - \mathbf{x}_f) ds$$

(6)

Here  $\mathbf{x}_f$  is a parameterization of the interface,  $\Gamma(t)$ , and  $\delta(\mathbf{x} - \mathbf{x}_f)$  is a Dirac distribution that is non-zero only when  $\mathbf{x} = \mathbf{x}_f$ .  $\mathbf{n}_f$  is the unit normal vector to the interface and  $ds$  is the length of the interface element.  $\kappa_f$  is again twice the mean interface curvature but obtained from the Lagrangian interface structure. The geometric information, unit normal,  $\mathbf{n}_f$  and length of the interface element,  $ds$ , in  $\mathbf{G}$  are computed directly from the Lagrangian interface and then distributed onto an Eulerian grid using the discrete delta function. The details follow Peskin's (1977) pioneering immersed boundary approach.

The Lagrangian interface is advected by integrating

$$\frac{d\mathbf{x}_f}{dt} = \mathbf{V}$$

(7)

with a second order Runge-Kutta method where the interface velocity,  $\mathbf{V}$ , is interpolated from the Eulerian velocity. Material properties such as density or viscosity are defined in the entire domain with the aid of the indicator function,  $I(\mathbf{x}, t)$ :

$$\rho(\mathbf{x}, t) = \rho_1 + (\rho_2 - \rho_1)I(\mathbf{x}, t)$$

(8)

$$\mu(\mathbf{x}, t) = \mu_1 + (\mu_2 - \mu_1)I(\mathbf{x}, t) \quad (9)$$

where the subscripts 1 and 2 stand for the respective phases.

The code's solution structure consists of essentially two main modules:

- A module for solution of the incompressible Navier-Stokes equations as well as transport of energy, species or surfactant when applicable.
- A module for the interface solution including tracking the Lagrangian mesh of triangular interface elements, initialization and reconstruction of the interface when necessary.

The parallelization of the code is based on an algebraic domain decomposition technique. The code is written in the computing language Fortran 2008 and communications are managed by data exchange across adjacent subdomains via the Message Passing Interface (MPI) protocol. The Navier-Stokes solver computes the primary variables of velocity,  $\mathbf{u}$ , and pressure,  $P$ , on a fixed and uniform Eulerian mesh by means of the well-known projection method (Chorin, 1968, Temam, 1968, Goda, 1979). Depending on the physical problem, numerical stability requirements and user preferences, the user has a choice of explicit or implicit time integration to either first or second-order. For the Eulerian 3D spatial discretisation we use the staggered mesh, MAC method pioneered by Harlow and Welch (1965). All spatial derivative operators are evaluated using standard centered differences, except in the nonlinear term where we use a second-order Essentially-Non-Oscillatory (ENO) scheme (Shu and Osher, 1989 and Sussman et al., 1998).

We use a multigrid iterative method for solving the elliptic pressure Poisson equation

$$\nabla \cdot \left( \frac{1}{\rho} \nabla P \right) = S \quad (10)$$

where  $S$  denotes the source term and is a function of the non-projected velocities, interfacial tension and any body or external forces. In the case of two-phase flow with large density ratio the now non-separable Poisson equation is solved for the pressure by a modified multigrid procedure implemented for distributed processors. We have developed a modified parallel 3D V-cycle multigrid solver based on the work of Kwak and Lee (2004). The solver incorporates a parallel multigrid procedure whose restriction and prolongation operators are not associated with each other, contrary to what is commonly used. This method has been successfully implemented to solve 3D elliptic equations where coefficients can be highly discontinuous (see Wesseling, 1988). The procedure can handle large density discontinuities. The key features of the modified multigrid implementation can be summarized as: (i) cell centered second order finite difference approximation of Eq. (10), (ii) Harmonic approximation of the discontinuous coefficient  $1/\rho$  (iii) linear interpolation of the residual during the restriction process, (iv) cell flux

conservation of the error on coarse grids during the prolongation process, (v) a parallel Red-Black SOR technique to relax the linear systems on fine grids and (vi) solution of the error using a parallel GMRES algorithm on the coarsest grid. Further detail is described in Shin et al. (2017a).

### Code BLUE Performance

There are two ways to evaluate the performance of parallel codes. The first method is called ‘‘heavy scaling’’ parallel performance which is based on program execution timings with varying number of cores (processors) while keeping the global mesh resolution fixed. The second method is called ‘‘weak scaling’’ based on program execution timings with varying number of cores while keeping the local (subdomain) resolution fixed. In BLUE, we are more concerned with the latter for two main reasons: (i) on large supercomputers such as the IBM BlueGene each core has a small memory of 512MB, and (ii) we are more concerned with using the finest global mesh resolution while increasing the number of cores (subdomains) instead of increasing the local mesh resolution. BLUE has been successfully run on over 250k cores on the IBM BlueGene/Q machine at IDRIS in Orsay, France with excellent linear scalability performance as shown in Fig. 2 for the case of drop splash on a thin film in Fig. 1 (Shin et al., 2017a). Fixing  $32 \times 32 \times 32$  as the resolution per core and using up to  $8192 = 16 \times 16 \times 32$  cores gives a global resolution of  $512 \times 512 \times 1024$ . The speedup and efficiency of BLUE for weak scaling is defined as:

$$\text{Speedup} = \frac{N_c}{N_{c_{ref}}} \text{Efficiency} \quad (11)$$

where  $N_c$  is the number of cores,  $N_{c_{ref}}$  is the reference number of cores (here 128) and Efficiency is defined as

$$\text{Efficiency} = \frac{T_{c_{ref}}}{T_c} \quad (12)$$

where  $T_{c_{ref}}$  is the elapsed time measured from  $N_{c_{ref}} = 128$  cores.  $T_c$  is the elapsed time measured for  $N_c = 512, 1024, 2048, 4096, \text{ or } 8192$  cores, respectively. We show the speedup with number of cores in Fig. 2 (top). The scalability of the code is sufficient to overcome communication overhead as the number of cores increases. Up to 8192 cores, speedup is linear. With 8192 cores, the code runs 42 times faster than with 128 reference cores if the global mesh resolution would have been fixed to  $512 \times 512 \times 1024$ . The efficiency, shown in Fig. 2 (bottom), demonstrates that the average core utilization is about 68% and is maintained constant up to 8192 cores. For less physically demanding cases, the efficiency of BLUE reaches over 90%. In all cases, the performance timings we gather are for code run times over many thousands of time steps. We note that parallel performance is highly dependent on, among many other things, the physical case simulated as well as the machine, thus comparisons between different codes, cases or machines must be conducted and interpreted with a great deal of caution.

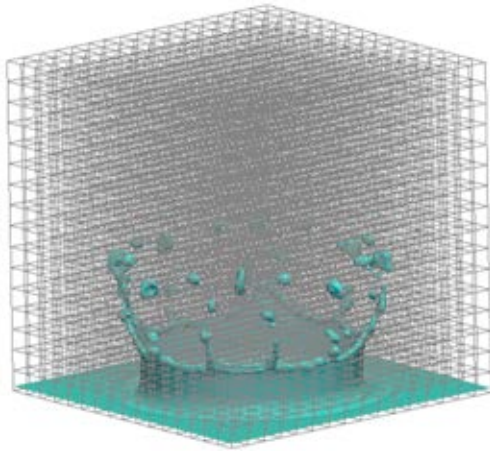


**Figure 1:** Water drop impact onto a thin film of water. 4096 core parallel computation.

we intend to perform complete rigorous investigations and mesh refinement studies in the future. Nevertheless, in the past several years we have gained considerable confidence in the fidelity of the code when comparing simulation results to experimental studies and analytical benchmarks. During the code development, validation and verification process, we maintain a growing test suite of more than two dozen single- and multiphase flow benchmark solutions with which simulations using BLUE are compared.

Fig. 1 shows a snapshot of the canonical droplet splash phenomenon. Here a 9mm diameter drop of water falling through air impacts a 1mm thick water film at 2.2 m/s creating an annular crown which ruptures and ejects small droplets at its rim. The simulation is performed on  $16 \times 16 \times 16 = 4096$  subdomains (processor cores). Each subdomain is resolved by a  $32 \times 32 \times 32$  grid. The global resolution is thus  $512^3$ .

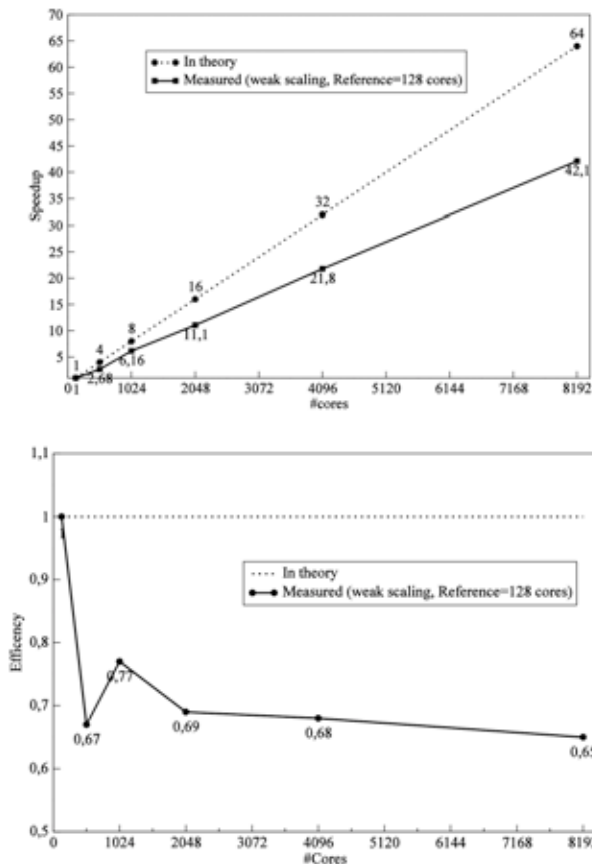


**Figure 2:** (Top): BLUE speedup on IBM BlueGene/Q for drop splash on a free surface. Performance increase with number of cores. (Bottom): BLUE efficiency on IBM BlueGene/Q for drop splash on a free surface. Efficiency vs. number of cores.

## RESULTS

In order to demonstrate the range of applicability of BLUE to many different industrially-relevant multiphase flow scenarios, we present a variety of examples of both small-scale laptop (typically 8 core) calculations as well as massively parallel computations on thousands of cores. The very recent simulations presented here are presented as demonstrator, proof-of-concept simulations which explore flexible use of the code toward engineering design scenarios and for which

In Fig. 3 we demonstrate the simulation of flow in a complex solid geometry where a fluid 500 times more viscous than water exits a nozzle at 30 mL/s and fills a 6mm inner diameter mug and its hollow handle. The annular nozzle and mug were quickly constructed in BLUE by combining simple geometric forms without using a body-fitted mesh but rather using Immersed Boundary techniques. The simulation was conducted to demonstrate the capability of BLUE to deliver quick laptop simulations (~2 hour simulation time) of complex flows on a rather coarse  $64 \times 64 \times 128$  mesh, while still capturing the essential features of the filling process.



**Figure 3:** Container filling with complex geometry. Simulation on 8 cores.

In the simulation shown in Fig. 4 we construct a complex microfluidic cross-junction to the exact dimensions of the experimental cell geometry, again using the Immersed Boundary technique. The main

channel branches have a width of 390 microns and a depth of 190 microns. In this three-phase flow, oil flows into the horizontal side branches which focus the aqueous stream entering from the top branch. Within this aqueous stream, a third oil phase is simultaneously introduced. This combined stream descends into the focusing junction whereupon the stream pinches further in the downstream branch to produce a drop of oil encapsulated within a drop of water.

In Fig. 5, a 12.5 cm deep layer of water is agitated by the action of an impeller spinning at 100 rotations per second. The resulting vortex causes the air/water surface to descend toward the impeller blades. Here we compute on a 64x64x128 mesh using 16 cores. Higher resolution would be necessary to capture the details of further entrainment of the free surface and formation of small bubbles.

The simulation in Fig. 6 is inspired by the experimental studies of jet atomization by Marmottant and Villermaux (2004) using an annular injector of 7.8 mm inner diameter and an annular gap of 1.7 mm. Our simulation results were generated on a 256x256x1024 mesh using 2048 cores. For this case, a liquid jet flows out of the centre of the nozzle at 0.5 m/s while the gas flows from the annulus at a much higher speed of 15 m/s inducing wave formation on the liquid jet surface with subsequent ligament formation and breakup into droplets. The results are qualitatively very similar to the experiment and a further quantitative comparison of the spray characteristics is being undertaken.

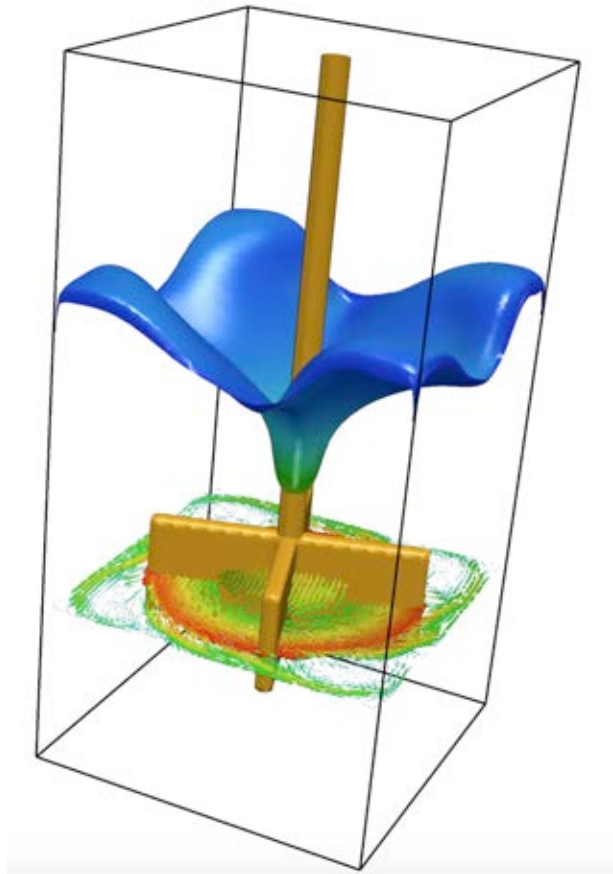


Figure 5: Rotating impeller with free surface deformation.

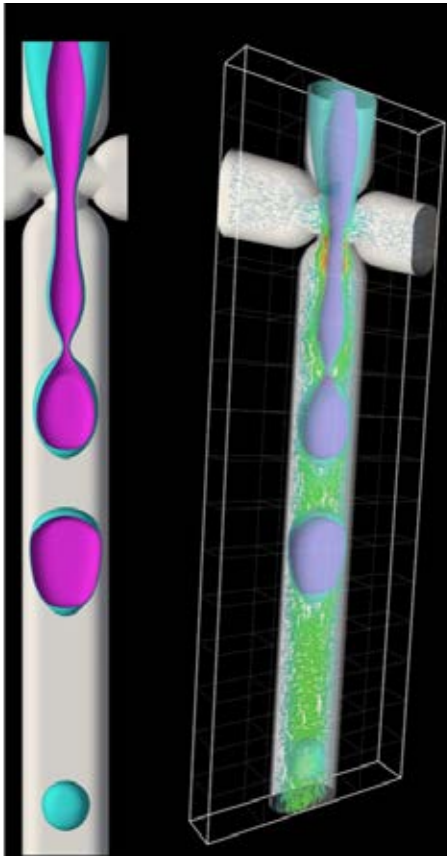


Figure 4: Microfluidic encapsulation. An example of a three-phase simulation.

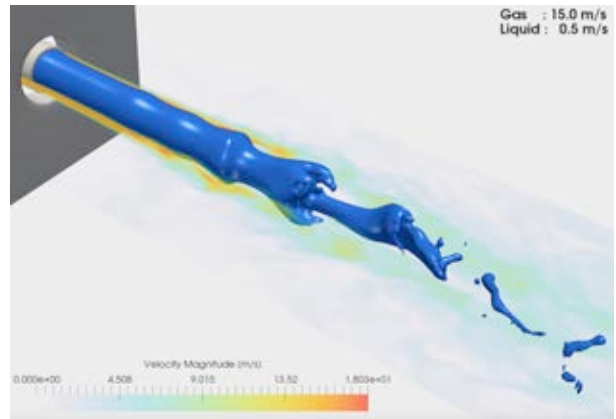


Figure 6: Jet atomization simulation on 2048 cores.

An annular falling film is studied in Fig. 7. Here an initially 4 mm thick liquid film falls downward inside of a 32.4 mm diameter solid tube together with a co-current flow of air in the core of the tube. The liquid is a non-Newtonian, shear-thinning fluid obeying a non-isothermal Carreau law with viscosity defined as:

$$\mu = H(T) \left( \mu_{\infty} + \frac{\mu_0 - \mu_{\infty}}{\left[1 + (\dot{\gamma}\lambda)^2\right]^{\frac{1-n}{2}}} \right) \quad (13)$$

where  $\dot{\gamma}$  is the shear rate,  $n$  is the power-law index,  $\lambda$  is the time constant and  $\mu_0$  and  $\mu_\infty$  are, respectively, the zero- and infinite-shear viscosities.  $H(T)$  is the Arrhenius law temperature dependence:

$$H(T) = \exp \left[ \alpha \left( \frac{1}{T - T_0} - \frac{1}{T_\alpha - T_0} \right) \right] \quad (14)$$

where  $T$  is the temperature of the liquid,  $\alpha$  is the ratio of the activation energy to the thermodynamic constant.  $T_\alpha$  is a reference temperature for which  $H(T) = 1$ .  $T_0$  is the temperature shift and corresponds to the lowest temperature that is thermodynamically acceptable. In this simulation we use  $n=0.1$  corresponding to a shear thinning fluid,  $\lambda=0.1$  s,  $\mu_0=0.009$  kg/m.s and  $\mu_\infty=10^{-7}$  kg/m.s. In the Arrhenius relation, we use  $\alpha=0.5$ ,  $T_0=0$  K and  $T_\alpha=300$  K. The simulation was performed on 8 cores with a  $64 \times 64 \times 256$  grid. For this relatively thick initial liquid layer, we observe quite strong interface deformation leading to ligament formation and bubble entrainment. In further annular falling film simulations, not shown here, we have studied the effect of soluble surfactant transport on flooding in counter-current flows (Shin et al., 2017b).

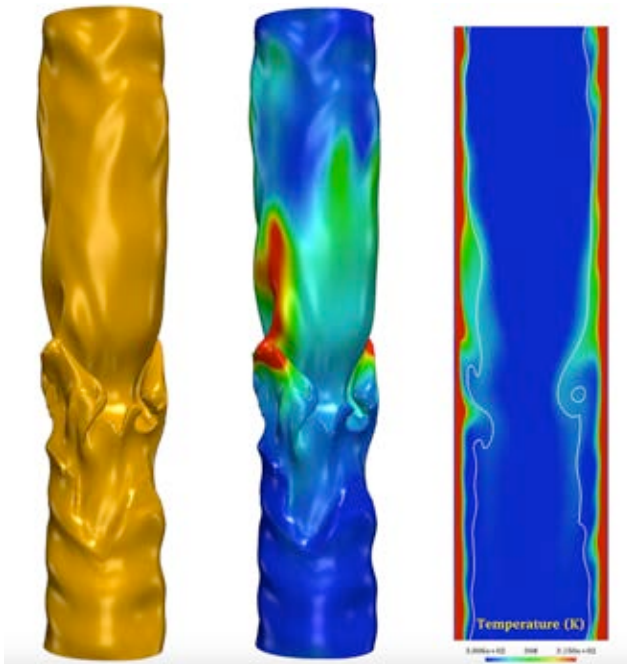


**Figure 7:** Annular falling film. Non-Newtonian fluid inside of a heated solid cylinder with co-current gas core flow. Simulation using the code BLUE on an 8 processor laptop.

## CONCLUSION

We present BLUE a simulation and design tool for multiphase flows in industrial processes. We combine in BLUE recently developed innovative algorithms for high precision interface-tracking, novel multigrid and GMRES linear solvers and the immersed boundary

approach for meshless construction of solid objects and fluid-structure interaction. The code is fully parallelised and has been tested on a number of different architectures from laptops and small clusters to massively parallel HPC machines. BLUE has been written entirely from scratch to take advantage of modern object-oriented programming features, compiles and runs using MPI and is otherwise independent of any external software libraries. These advances have allowed simulations of industrially-relevant multiphase and multi-physics problems where complex interface dynamics, extreme density and viscosity differences, fluid rheology and chemistry pose great challenges. In this article, we have only presented a brief outline of the numerical techniques in BLUE, discussed the code's parallel performance and shown a small sample of simulation examples. The large range of spatial scales present in the drop splash or jet atomization cases necessitate very fine grids and benefit from large scale parallelism. However, many cases have been run on relatively coarse grids on a handful of cores in order to demonstrate that quick design type simulations on a laptop or desktop machine could be accessible while still retaining an excellent approximation of the main features in the flow process. Other capabilities of BLUE which we have not demonstrated here include surfactant-laden flows, flows with phase change in boiling or solidification, rotating flows subject to Coriolis and centrifugal forces, thermal and solutal Marangoni convection and input of CAD generated solid geometries. Continuing developments of BLUE will allow the ability to handle compressible flows and also incorporate adaptive mesh refinement.

## ACKNOWLEDGEMENTS

This work is supported by (1) the Engineering & Physical Sciences Research Council, United Kingdom, through the MEMPHIS program grant (EP/K003976/1), (2) the Basic Science Research Program through the National Research Foundation of Korea (NRF) funded by the Ministry of Science, ICT and future planning (NRF-2014R1A2A1A11051346) and (3) by computing time at the Institut du Developpement et des Ressources en Informatique Scientifique (IDRIS) of the Centre National de la Recherche Scientifique (CNRS), coordinated by GENCI (Grand Equipement National de Calcul Intensif). Graphical visualizations are produced via ParaView.

## REFERENCES

- CHORIN, J., (1968), "Numerical solution of the Navier-Stokes equations", *Mathematics of Computation*, **22**, 745-762.
- GODA, K., (1979), "A multistep technique with implicit difference schemes for calculating two- or three-dimensional cavity flows", *J. Comput. Phys.* **30**, 76-95.
- HARLOW, F.H. and WELCH, J.E., (1965), "Numerical calculation of time dependent viscous incompressible flow of fluid with free surface", *Physics of Fluids*, **8**, 2182-2189.
- HIRT, C. W. and NICHOLS, B. D., (1981), "Volume

of Fluid (VOF) method for the dynamics of free boundaries”, *J. Comput. Phys.*, **39**, 201-226.

KWAK, D. Y. and LEE, J. S., (2004), “Multigrid algorithm for the cell-centered finite-difference method ii: Discontinuous coefficient case”, *Numer. Meth. Part. Differ. Equ.* **20**, 723-741.

MARMOTTANT, P. and VILLERMAUX, E., (2004), “On spray formation”, *J. Fluid Mech.*, **498**, 73-111.

OSHER, S. and SETHIAN, J., (1988), “Fronts propagating with curvature-dependent speed: algorithms based on Hamilton-Jacobi formulations”, *J. Comput. Phys.*, **79**, 12-49.

PESKIN, C. S., (1977), “Numerical analysis of blood flow in the heart”, *J. Comput. Phys.* **25**, 220-252.

SHIN, S. and JURIC, D., (2002), “Modeling three-dimensional multiphase flow using a level contour reconstruction method for front tracking without connectivity”, *J. Comput. Phys.*, **180**, 427-470.

SHIN, S. and JURIC, D., (2007), “High order level contour reconstruction method”, *Journal of Mechanical Science and Technology*, **21**(2), 311-326.

SHIN, S., (2007), “Computation of the curvature field in numerical simulation of multiphase flow”, *J. Comput. Phys.* **222**, 872-878.

SHIN, S. and JURIC, D., (2009a), “A hybrid interface method for three-dimensional multiphase flows based on front-tracking and level set techniques”, *Int. J. Num. Meth. Fluids*, **60**, 753-778.

SHIN, S. and JURIC, D., (2009b), “Simulation of droplet impact on a solid surface using the level contour reconstruction method”, *Journal of Mechanical Science and Technology*, **23**, 2434-2443.

SHIN, S., YOON, I. and JURIC, D., (2011), “The Local Front Reconstruction Method for direct

simulation of two-and three-dimensional multiphase flows”, *J. Comput. Phys.*, **230**, 6605-6646.

SHIN, S., CHERGUI, J. and JURIC, D., (2017a), “A solver for massively parallel direct numerical simulation of three-dimensional multiphase flows”, *Journal of Mechanical Science and Technology*, to appear, arXiv 1410.8568.

SHIN, S., CHERGUI, J., JURIC, D., KAHOUADJI, L., MATAR, O. K. and CRASTER, R. V., (2017b), “An interface-tracking technique for multiphase flow with soluble surfactant”, *J. Comput. Phys.*, submitted. ArXiv 1702-02478.

SHU, C.-W. and OSHER, S., (1989), “Efficient implementation of essentially non-oscillatory shock capturing schemes II”, *J. Comput. Phys.*, **83**, 32-78.

SUSSMAN, M., FATEMI, E., SMEREKA and OSHER, S., (1998), “An improved level set method for incompressible two-phase flows”, *Computers and Fluids*, **27**, 663-680.

TEMAM, R., (1968), “Une méthode d'approximation de la solution des équations de Navier-Stokes”, *Bull. Soc. Math. France*, **96**, 115-152.

TRYGGVASON, G., SCARDOVELLI, R. and ZALESKI, S., (2011), “Direct Numerical Simulations of Gas-Liquid Multiphase Flows,” *Cambridge University Press*.

UNVERDI, S. O. and TRYGGVASON, G., (1992), “A front-tracking method for viscous, incompressible, multi-fluid flows”, *J. Comput. Phys.*, **100**, 25-37.

WESSELING, P., (1988), “Cell-centred multigrid for interface problems”, *J. Comput. Phys.*, **79**, 85-91.



## DEVELOPMENT OF GPU PARALLEL MULTIPHASE FLOW SOLVER FOR TURBULENT SLURRY FLOWS IN CYCLONE

Kumar MAYANK<sup>1\*</sup>, Raja BANERJEE<sup>2†</sup>, Narasimha MANGADODDY<sup>1‡</sup>

<sup>1</sup>IIT Hyderabad Department of Chemical Engineering, 502285 Medak, India

<sup>2</sup>IIT Hyderabad Department of Mechanical Engineering, 502285 Medak, India

\* E-mail: ch15resch02001@iith.ac.in

† E-mail: rajabanerjee@iith.ac.in

‡ E-mail: narasimha@iith.ac.in

### ABSTRACT

The development of GPU parallelized unstructured multiphase solver and its application in predicting turbulent swirling flow of slurries inside cyclones is presented. Algebraic slip mixture model (ASM) is modified with additional shear lift forces and slurry rheology is corrected with fines fraction. The modified ASM model coupled with LES is used to predict particle classification inside hydrocyclone. During hydrocyclone operation the residence time of the fluid is very small and hence there is insufficient time for the larger eddies to cascade into smaller eddies. LES can accurately resolve flow structures that are few times the Kolmogorov scale at an increased computational cost due to finer mesh requirement. Therefore, the solver has been parallelized using general purpose graphics processing units (GPGPUs). In the current solver, the Pressure Poisson equation has been parallelized with an algebraic multigrid solver on GPU architecture using CUDA programming language for unstructured grids. The single phase flow field predicted by LES shows good agreement with experimental results obtained from open literature. The turbulent flow fields, the size segregation and the particle efficiency curve obtained from multiphase simulations are presented. Additionally, computational speedup due to GPU parallelization is reported over its serial version of the solver.

**Keywords:** CFD, hydrodynamics, LES, GPU, ASM .

### NOMENCLATURE

A complete list of symbols used, with dimensions, is required.

### NOMENCLATURE

#### Greek Symbols

- $\rho_m$  Mixture density, [ $kg/m^3$ ]  
 $\mu_c$  viscosity of the continuous phase, [ $kg/ms$ ].  
 $\mu_m$  viscosity of the mixture, [ $kg/ms$ ].  
 $\alpha_k$  Volume fraction of phase.  
 $\alpha_p$  Total particle volume fraction.  
 $\alpha_{pm}$  Maximum packing fraction.  
 $\omega_{mj}$  Vorticity vectors.  
 $\varepsilon_{ijk}$  Kronecker delta.

#### Other Symbols

- $p$  Pressure, [ $Pa$ ].  
 $\mathbf{u}_m$  Mixture velocity, [ $m/s$ ].

- $\mathbf{u}_{cp}$  Slip velocity for phase p, [ $m/s$ ].  
 $d_p$  diameter of the particle, [ $m$ ].  
 $Re_p$  Reynolds number of the particle.  
 $C_{lp}$  lift coefficient.  
 $S_f$  Face area vector.  
 $F_f$  mass flux through face f.

#### Sub/superscripts

- $i, j$  Spatial coordinate index .  
 $k$  Phase Index.  
 $f$  Face Index .

### INTRODUCTION

The use of computational fluid dynamics(CFD) for design exploration has been prevalent for the past couple of decades. Most of these studies have relied on RANS based approach to model the entire range of turbulence length scales in the flow. Though computationally efficient RANS based approach fail to account for the dynamic interactions between the large and small scales of motion, and has been observed to have limited predictive capabilities for decay of isotropic turbulence even in simpler configurations(Pope, 2004). With the availability of increased computational power recently, LES and DNS have been used extensively to model turbulence in complex flow configuration. While, DNS typically resolves all turbulence length scales down to the smallest Kolmogorov scale. LES uses a spatial filter to separate the larger scale motions from the smaller scales. The larger scales of motion are anisotropic and LES resolves all the scales above the specified cutoff length. While using a sub-grid scale model (Germano *et al.*, 1991; Lilly, 1992) to incorporate the effects of the small scale motions on the resolved scales. This feature makes LES much less computationally extensive as compared to DNS where even the universally isotropic smaller scales(Leonard, 1975) are resolved, requiring mesh resolution in the order of  $Re^{9/4}$  for DNS computations. LES has been reported to have good turbulence predictive capabilities for channel flow (Deardorff, 1970; Moin and Kim, 1982), recirculating flows (Kobayashi, 1992) as well as in complex flow configuration such as in gas turbine combustion (Moin and Apte, 2006). LES has been used to simulate highly strained flows in complex geometries was first performed by (Slack *et al.*, 2000) and since has been used to predict flow dynamics inside hydrocyclones(Brennan, 2006) as well as predicting the cut size(Narasimha *et al.*, 2006).



The comparatively high mesh requirement for LES as compared to RANS based models is the major drawback that limits the scope of LES simulations for design exploration at realistic industrial configurations. Using general purpose GPU for parallelizing linear equation solvers was explored by (Sanders and Kandrot, 2010) and further development for method of parallelisation for unstructured and hybrid mesh solvers was presented in (Xu *et al.*, 2014) and for two phase flow problems in (Reddy and Banerjee, 2015). The massive parallel compute capability of the GPU allows conducting high fidelity LES simulations for industrial configurations computationally feasible.

The work presented in this study explains the development of a high fidelity LES multiphase solver using the algebraic slip model to study flow of poly dispersed slurry system. The solver was parallelized by porting the pressure poisson equation solver on the GPU. The single phase LES solver is validated against LDA measurements for cyclone flows reported in open literature. The multiphase code is tested for particle segregation inside a hydrocyclone. The cut point predicted by the multiphase code was found to be agreeable with the simulation results presented in literature. Finally the speed up obtained for parallel implementation over serial version is reported in the final section.

## MODEL DESCRIPTION

The slurries consists of mixture of poly dispersed solid particles within a continuous phase mostly water. The governing equation for multiphase fluid flow following (Ishii 1975) notations is given by

*Continuity equation*

$$\frac{\partial \rho_m}{\partial t} + \frac{\partial \rho_m u_{mi}}{\partial x_i} = 0 \quad (1)$$

*Momentum Equation*

$$\frac{\partial \rho_m u_{mi}}{\partial t} + \frac{\partial \rho_m u_{mi} u_{mj}}{\partial x_j} = \frac{\partial p}{\partial x_i} + \frac{\partial}{\partial x_j} (\tau_{\mu,ij} + \tau_{D,ij}) + \rho_m g_i \quad (2)$$

where the density and the velocity of the mixture is given by farve-averaged quantities explained in (Soo 1990).

$$\rho_m = \sum_{k=1}^n \alpha_k \rho_k \quad (3)$$

$$u_m = \frac{1}{\rho_m} \sum_{k=1}^n \alpha_k \rho_k u_k \quad (4)$$

Each dispersed phase is tracked using a scalar transport equation of the form

$$\frac{\partial}{\partial t} \alpha_k + \nabla \cdot (\alpha_k u_m) = -\nabla \cdot (\alpha_k u_{Mk}) \quad (5)$$

The viscous diffusive flux for the mixture ( $\tau_{\mu,ij}$ ) is calculated using model by (Ishii-Mishima 1980) as

$$\mu_m = \mu_c \left(1 - \frac{\alpha_p}{\alpha_{pm}}\right)^{-2.5 \alpha_{pm}} \quad (6)$$

The extra term in the Eq. 2, ( $\tau_{D,ij}$ ) is the diffusion flux arising due to phase slip and is given by

$$\tau_{D,ij} = - \sum_{k=1}^n \alpha_k \rho_k u_{mk} u_{mk} \quad (7)$$

The phase diffusion velocity  $u_{Mk}$ , is represented in terms of individual phase slip velocity as

$$u_{mp} = u_{cp} - \sum_{k=1}^n \alpha_k u_{ck} \quad (8)$$

The individual phase slip velocity using force balance on the particles experiencing drag was derived by (Manninen and Taivassalo, 1996) and extended to include the effects of lift forces by (Narasimha *et al.*, 2007) and is given by

$$u_{cpi} = \frac{d_p^2 (\rho_k - \rho_m)}{18 f_{Rep} \mu_c} \left( g_i - \frac{\partial}{\partial t} u_{mi} - u_{mj} \frac{\partial}{\partial x_j} u_{mi} + 0.75 \frac{\rho_c}{\rho_k - \rho_m} C_{lp} \epsilon_{ijk} \omega_{mj} u_{pck} \right) \quad (9)$$

Where the term  $f_{Rep}$  is given by

$$f_{Rep} = (1 + 0.15 Re_p^{0.687}) \alpha_p^{-4.65}$$

$$Re_p = \frac{d_p \rho_c |u_{cp}|}{\mu_m}$$

## Numerical Implementation

The solver presented is capable of handling unstructured grid in CGNS format. Unstructured grids are preferred for industrial applications as the complex equipment geometry can be represented much easier as compared to structured grid arrangement. The implementation of numerical schemes for unstructured grids are complicated though, with increased and random inter-dependence of grid point variables. The geometric and neighbor data information of each cell is stored before the start of the solution. A collocated grid arrangement (Date, 2005) is used wherein all the solution variables are stored at the cell centers. Finite volume method is used to discretize the governing equation on the grid. A first order explicit scheme was used for the temporal term. A combination of first order and central difference scheme with the deferred correlation approach (Khosla and Rubin, 1974) was used to approximate the convective fluxes. Volumetric interpolation was used to calculate the face center values from the stored cell center variables. The diffusive fluxes and other terms are approximated in a similar method as followed by (Dalal *et al.*, 2008). The pressure correction method (Davidson, 1996) was used for the pressure velocity decoupling. The diffusive flux due to phase slip is implemented as a volumetric source term. The starting point of the solver is to initialize the grid points, initial and boundary conditions. In case of a velocity inlet both the primary phase and the secondary phase velocity as well as volume fraction for each secondary phases are specified. The solver then proceeds to calculate the density and mixture velocities at each boundary using eq. 3 and 4. These calculated mixture properties act as the actual boundary values for the solution. The mass flux for the mixture is calculated with the divergent field velocity obtained by solving the discrete form of eq. 2 without the pressure term. Then we solve the pressure poisson equation using the calculated mass flux value which is of the form.

$$\sum_f (\nabla p_f^{n+1}) \cdot S_f = \frac{\rho}{\Delta t} \sum_f F_f^* \quad (10)$$

Finally the mass flux is corrected by subtracting the pressure gradient term from the initially calculated mass flux and the divergent free velocity is obtained for the new time step. The discrete form of the phase tracking eq. 5 is then solved and

density and viscosity values are updated using eq. 6. Slip velocity is calculated with the difference between the primary and secondary phase velocities as initial guess. We calculate the term  $f_{Rep}$  which is used to calculate the individual slip velocity using eq. 9 iteratively as long as the final value reaches the desired convergence criterion. The slip velocities are used to calculate the phase diffusion velocity using eq. 8. Finally the diffusion flux due to phase slip is calculated using eq. 7, gradient of which is stored as the source term for the next time step. The gradient of the volume flux of the scalar is stored to be as the source term for the scalar transport equation for the next time step. The algorithm of the solver is explained below

#### Initialization:

Initialize grid points, initial and boundary condition;

Calculate mixture velocity and density boundary values;

#### Solution:

**while**  $T < Final\ Time$  **do**

Calculate mass velocity ( $u^*$ ) and the mass flux for each face( $F^*$ );  
Solve pressure poisson equation using the mass flux( $F^*$ );  
Correct velocities ( $u^{n+1}$ ) and flux( $F^{n+1}$ ) value using pressure correction;  
Solve the phase tracking equations;  
Update density and viscosity Calculate the slip velocities for each phase;  
Calculate the source terms for the momentum and phase tracking equation for the next time step;

**end**

**Algorithm 1:** Algorithm of the solver

## GPU PARALLELIZATION

A standard V-cycle algebraic multigrid (AMG) implementation was used for solving the pressure poisson equation. The equation is of the form  $Au = f$  with the coefficient matrix(A) being a symmetric matrix with six dominant diagonals. Instead of working on one mesh AMG uses a hierarchy of mesh, which starts from the finest mesh and uses the coarsening algorithm suggested by (Haase *et al.*, 2010) to construct levels of coarser mesh. For each level the coefficient matrix( $A_c$ ), the prolongation matrix(P) and the restriction matrix( $P^T$ ) are populated. For a two level multigrid system which can be extended to multilevel system the algorithm can be summarized as

- Compute estimate  $u^*$  for  $u$  in  $Au = f$ ;
- Compute the residual  $r = f - Au^* = Ae$ ;
- Solve for  $e_c$  in the coarser system  $A_c e_c = P^T r$ ;
- Correct  $u^* \leftarrow u^* + P e_c$ .

CUDA programming module was used to implement the AMG solver on the GPU. The implementation is rather difficult for unstructured meshes as the interdependencies between the nodes are not in an ordered arrangement. The interdependencies of the nodes though irregular, remains constant for non deforming grids. Therefore, the neighbor element data is stored at the start of the solution. Greedy coloring scheme (Hege and Stuben, 1991) was used to identify set of independent nodes. Each independent set of nodes are

assigned a color class. The total number of color class was referred to as maximum degree. Which for tetrahedral element meshes comes out to be six independent sets. The nodes are updated in order of color class. Updating all the independent set of nodes simultaneously helps preventing any unrealistic solutions due to data race condition. The nodes are ordered in such a way that inter dependent nodes can be co located resulting in a coalesced memory access pattern thereby reducing the time required for the data transfer operations. Gauss Seidel method is used for the smoothening operation. In CUDA terminology, the CPU is referred to as the host and the GPU is referred to as the device. The device function is called a kernel and is identified by `__global__` identifier. The kernel is called, and the number of threads to be launched is specified from the host code. The number of threads to be launched is specified in terms of grids and blocks. For the current implementation we use grid size equal to the maximum degree and the block size is equal to the maximum number of cells within a color class. We use V-cycle multigrid, which is made up of a down cycle and up cycle. Down cycle is a sequence of smoothing and restriction operations performed alternately starting from finest grid till we reach coarsest grid. Up cycle is a combination of prolongation and smoothing operations performed alternately starting with the coarsest grid till we reach finest grid. The multigrid V-cycle is repeated till the desired convergence is reached. The algorithm for the parallelization code for the solution of the equation of the form  $Ax = B$  is given in algorithm 2.

## RESULTS

The parallel solver was tested for two cases. First is the single phase LES prediction for flow in industrial flow configuration within a gas cyclone. Second being the multiphase flow prediction of phase segregation under turbulent slurry flow conditions. The simulation setup and results are presented in the subsections below

### Validation of LES solver

The single phase LES solver is tested for the flow configuration similar to the one presented in (Slack *et al.*, 2000). The dimensions of the geometry and the mesh used is given in the figure 1. Air with density  $1.225\text{ kg/m}^3$  and viscosity  $1.78943 \times 10^{-5}\text{ kg.m}^{-1}\text{s}^{-1}$  was used to define the fluid properties. For the cyclone volume of  $0.0203\text{ m}^3$  around  $6.5 \times 10^5$  hexahedral cells were used to discretize the flow domain. The inlet, overflow and the underflow are the boundary patches composed of quadrilateral cells. The inlet air flow rate was maintained at  $0.08\text{ kg/m}^3$ , the residence time at this flow rate was 0.25 s. The pressure at the overflow was specified as gauge pressure and the velocity was specified homogeneous neumann boundary condition, whereas the underflow was specified wall boundary condition. The time step size was  $1 \times 10^{-5}$  s. The mean velocity magnitude, axial velocity and tangential velocity profile along the central plane is given in figure 2. Velocity magnitude profile shows an increase in the magnitude as we proceed from the walls to the central axis, while the central core is the region of lowest magnitude. Typically fluid stream upon entering the cyclone moves along the outer wall while descending down, then accelerating due to the constriction of the area and reaches the bottom wall where the flow reversal happens and the stream moves towards the exit overflow. Vortex formation can be observed due to low dynamic pressure in the

**Host Code:**

Populate Coefficient matrix(A), Initial Guess pressure matrix(x) and RHS matrix(b) ;

Create levels of multigrid ;

**for**  $i = 0; i < \text{number of levels} : i++$  **do**

    Calculate  $A_p[i], P[i]$  and  $P^T[i]$ ;

    Color the nodes using procedure explained by (Hege and Stuben, 1991);

    Rearrange the node for interdependent nodes to be collocated;

    Transfer data from the host to the device;

**end**

**Device Code:**

**while**  $\text{residual} \geq \text{convergence criterion}$  **do**

**for**  $\text{Numlevel} = 1; \text{Numlevel} < \text{MaxNumlevel};$

**Numlevel++ do**

            Calculate the residual for the finer mesh

            ( $\text{NumLevel} - 1$ ) level using kernel `calculateResiduals()` ;

            Update the residual at the coarse level( $\text{NumLevel}$ ) using kernel `updateResiduals()`;

**for**  $\text{ClrId} = 0; \text{ClrId} < \text{MaxDegree} - 1; \text{ClrId}++$  **do**

                Smooth the error on the coarse mesh level( $\text{NumLevel}$ ) for color class  $\text{ClrId}$  using `gaussSiedeliteration()` kernel;

**end**

**end**

**for**  $\text{Numlevel} = \text{MaxNumlevel} - 2; \text{Numlevel} > 0;$

**Numlevel - do**

            Update the pressure of the coarse mesh level( $\text{Numlevel} + 1$ ) `updatepressure()` kernel;

**for**  $\text{ClrId} = 0; \text{ClrId} < \text{MaxDegree} - 1; \text{ClrId}++$  **do**

                Smooth the error on the coarse mesh level( $\text{Numlevel}$ ) for the color class  $\text{ClrId}$  using `gaussSiedeliteration()` kernel;

**end**

**end**

**for**  $\text{ClrId} = 0; \text{ClrId} < \text{MaxDegree} - 1; \text{ClrId}++$  **do**

        Smooth the error on the finest mesh level(0) using `gaussSiedeliteration()` kernel;

**end**

    Calculate the residuals for the finest mesh level(0);

**end**

**Algorithm 2:** Parallelization of standard V cycle algebraic multigrid solver

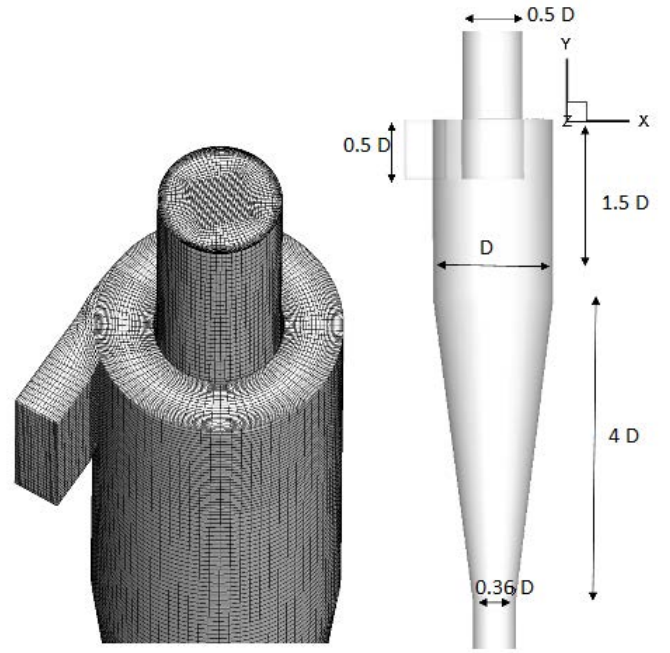


**Figure 1:** Geometry specifications and unstructured mesh of the stairmand cyclone(Slack *et al.*, 2000)

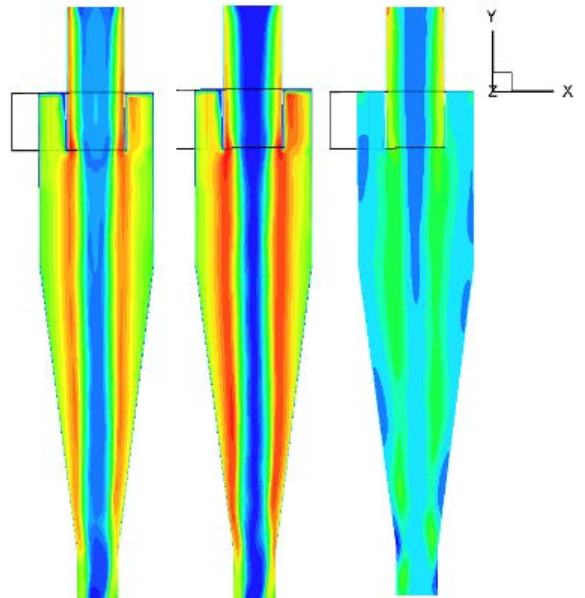


**Figure 2:** Contours of Left:Mean velocity magnitude(red is 40 m/s or higher and blue is 1 m/s or lower), Center: Mean tangential velocity (red is 36 m/s or higher and blue is 1m/s or lower) Right: Mean axial velocity (red is 20m/s or higher and blue is -10 m/s or lower)

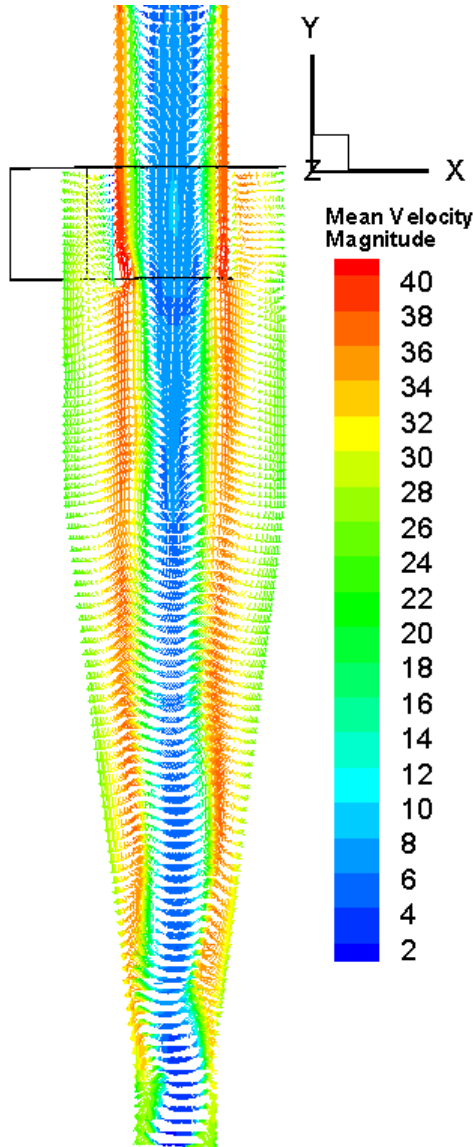


**Figure 3:** Velocity vectors for cyclone flow at feed air flow rate of  $0.0203\text{m}^3$  colored by velocity magnitude

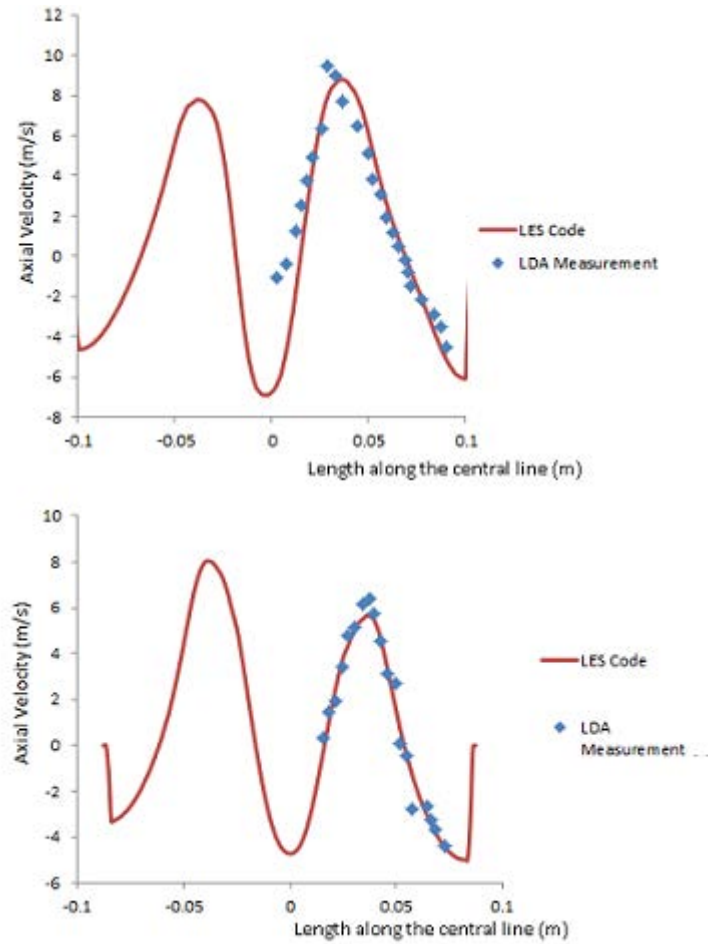


**Figure 4:** Comparison of axial velocity with LDA measurements from (Slack *et al.*, 2000) at left:0.38 m from top of the overflow and right: 0.59m from the top of the overflow

central core regions for such highly strained flows. The axial velocity profile show flow reversals near the central core region. Where the central core has downward flow towards the underflow while the region outside the central core has predominantly upward flow except near the walls where the flow is downwards towards the underflow. Similarly the tangential velocity also shows an increase in magnitude as we proceed from the walls towards the center reaching a maximum at a region where flow reversal start to take place and the tangential component reduces to a minimum value close to zero near the center. The comparison of the mean axial velocity and tangential velocity along the center line with the LDA measurements reported in (Slack *et al.*, 2000) for two different axial location are given in figure 4 and 5 respectively. Good quantitative comparison for the two velocity components at stations located at 0.38 m from the top and at 0.59 m from the top can be observed between the LES simulated value and the experimental results.

### Phase segregation in a hydrocyclone

The multiphase code is tested for a poly dispersed slurry flow problem and study the phase segregation within the cyclone. As the algebraic slip mixture multiphase solver has not been successfully tested for higher density ratio, air core free design from (Vakamalla *et al.*, 2017) having a rod along the central core is chosen for the study. The geometry and the unstructured grid containing around  $5 \times 10^5$  hexahedral cells is shown in figure 6.

Water with density  $998.1\text{ kg/m}^3$  and viscosity  $0.00103\text{ kg}$ .

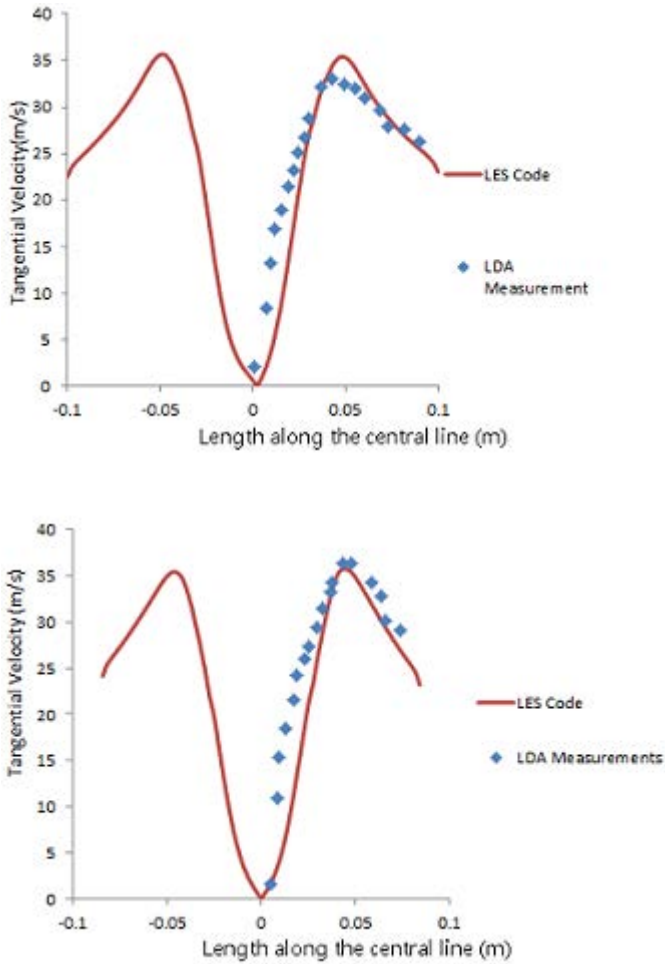


**Figure 5:** Comparison of tangential velocity with LDA measurements from (Slack *et al.*, 2000) at left: 0.38 m from top of the overflow and right: 0.59m from the top of the overflow

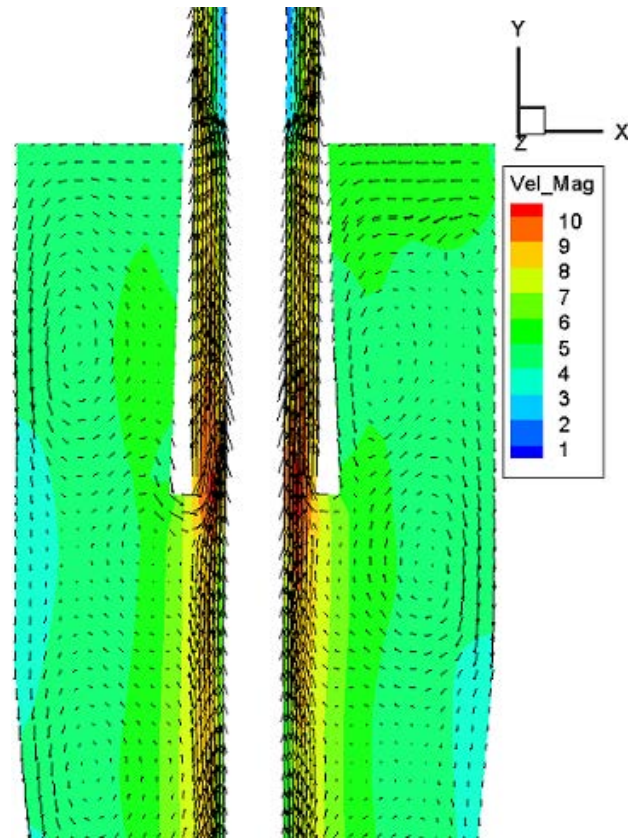


**Figure 7:** Vector plot for the slurry flow

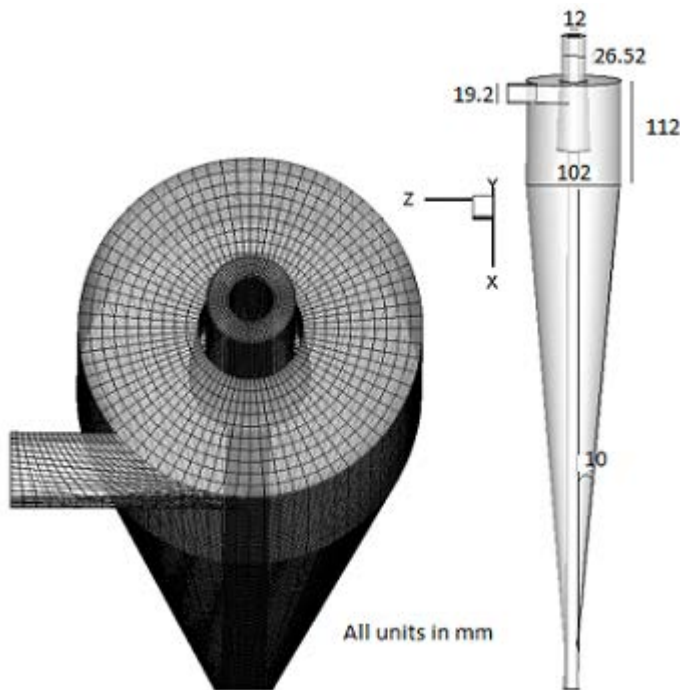


**Figure 6:** Geometry specifications and unstructured mesh prepared for the cyclone similar to (Vakamalla *et al.*, 2017)



**Figure 8:** Iso surface for contour level 0.005 volume fraction for phases left to right: phase 6 to phase 1



**Figure 9:** Iso surface for contour level 0.01 volume fraction for phases left to right: phase 6 to phase 1

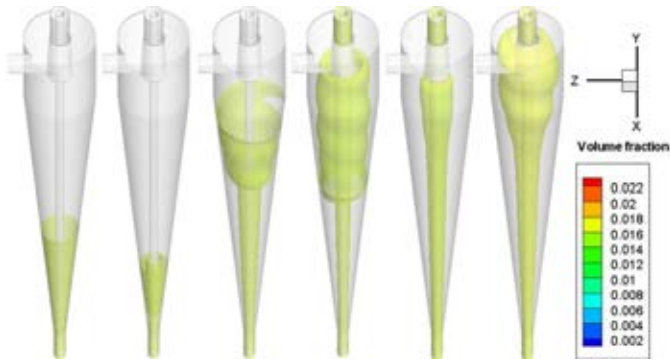


**Figure 10:** Iso surface for contour level 0.015 volume fraction for phases left to right: phase 6 to phase 1

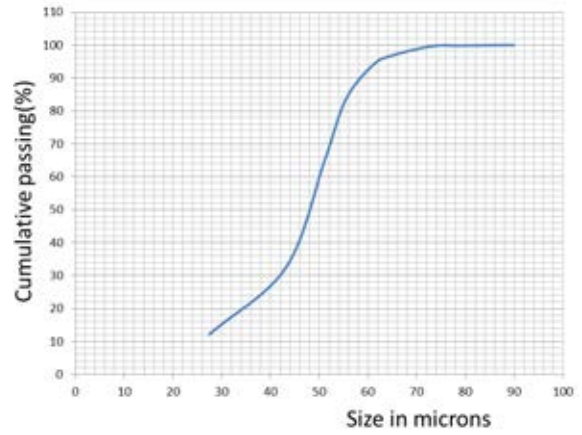


**Figure 12:** Particle classification curve for the air core free hydro-cyclone design for water flow rate of  $1.665 \text{ kg/m}^3$

$\text{m}^{-1} \text{s}^{-1}$  is used as the continuous phase fluid. Varying sizes of silica powder with density  $2650 \text{ kg/m}^3$  was used to specify the different secondary phases properties. The different phase size and volume fraction at the inlet is given in the table 1. Inlet flow rate of water was maintained at 1.664

**Table 1:** Phase size and distribution.

Phase	Diameter ( $\mu \text{m}$ )	Feed Volume fraction
Phase 1	3.35	0.0174
Phase 2	10.25	0.0124
Phase 3	19.37	0.01158
Phase 4	28.27	0.00509
Phase 5	38	0.01329
Phase 6	68	0.00252

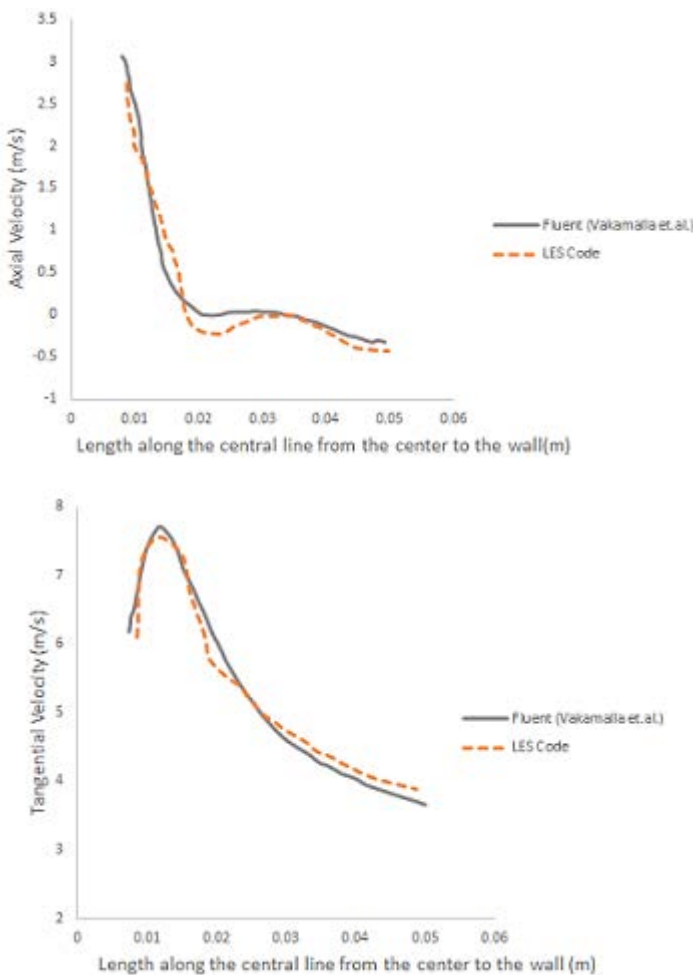


**Figure 11:** Comparison of left: Axial velocity and right: Tangential velocity at the mid plane along the line at the intersection of the conical and cylindrical sections

$\text{kg/s}$ . Both the overflow and the underflow are specified gauge pressure values and the velocities and phase fractions were specified homogeneous neumann boundary conditions. The central rod was specified with no slip wall boundary condition. The secondary phase was introduced after the steady state velocity profile for the single phase water flow is obtained. The velocity magnitude profile at the mid plane for the single phase flow and the comparison of results with the fluent simulation performed in the study(Vakamalla *et al.*, 2017) is presented in the figure 11. The slurry flow patterns can be visualized using the vector plots given in figure 7 along the mid plane parallel to the inlet flow direction. Plots show the central region of positive axial velocity towards the overflow while minor circulations near in the central region. The phase segregation is studied using the iso contour for three different concentration. The low concentration contour at volume fraction value 0.005 is given in figure 8. The contour show that the smallest size fraction is more evenly distributed with very small regions near the overflow having smaller concentration. The regions of low concentration for the larger phases changes from the central rod region to regions near the wall as the size increases. The medium and high concentration iso contour at level 0.01 and 0.015 are given in figure 9,10 respectively. The smallest phase medium concentration regions are still the central core region while similar trend of segregation towards the walls for larger sizes can be observed. The largest phase fraction is located mainly near the walls and the underflow. The high concentration iso contour plots show the evenly distributed

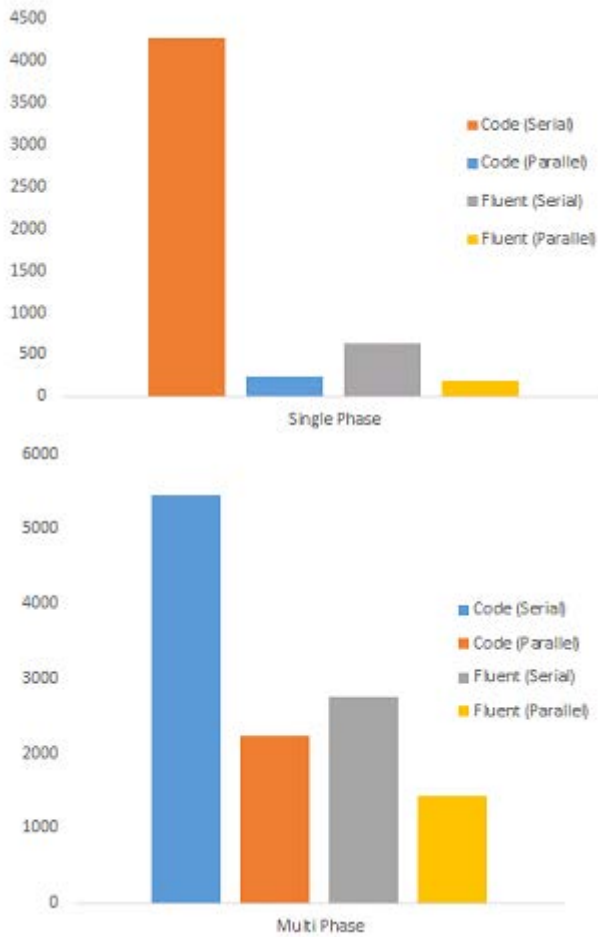


**Figure 13:** Comparison of time required in seconds for 100 timesteps of simulation

smallest size fraction. The cut-point for the said design was calculated using the particle efficiency curve given in figure 12, which comes out to be  $48.1 \mu\text{m}$

### Speed up obtained

The comparison of time required for the completion of 100 time steps of transient simulations due to the parallel GPU implementation with the serial implementation of the code along with the serial and parallel versions of commercial code Fluent is given in figure 13. The single phase parallel implementation reported speed up of around 11.3X over the serial code implementation. Compared to the serial version of fluent the speed up obtained is around 2.75 X. The code performs slower as compared to the parallel version of fluent using 4 cores where a speed up of 1.6X is recorded for fluent parallel implementation over the parallel code. While for the multiphase implementation a speed up of 2.3X is obtained for the parallel implementation of the code over the serial one. Whereas, the speed up obtained over fluent serial implementation is 1.25X. The multiphase parallel implementation also performs slower as compared to the parallel implementation of fluent. Where the parallel fluent solver is reported to be 1.9 X faster than the parallel code implementation. This slower operation of the multiphase code as compared to the single phase solver is due to the amount of time expended on solving the phase tracking equations which is done on the CPU. The parallelisation of the solver for the phase tracking equation and the validation of the multiphase solver is the scope of the future work.

### CONCLUSION

The development of an unstructured LES multiphase solver was presented for simulating highly strained slurry flows. Algebraic slip model was used to model the poly-dispersed slurry system. Where local velocity fields cause phase segregation due to varying inter phase momentum exchange due to drag and lift based on size of the particle. The solver is tested for single phase cyclone flows and validated against LDA measurements provided in (Slack *et al.*, 2000). The multiphase implementation was tested for particle classification with hydrocyclone geometry suggested in (Vakamalla *et al.*, 2017). The velocity profiles and the cut point obtained from the predicted particle separation curve was similar to the one obtained using the same design in the reference. Implementation of GPU parallelization for the compute intensive LES methodology is presented and the speed up obtained for the parallel implementation is reported. The parallel solver makes it computationally feasible to conduct design explorations even at industrial configuration.

## REFERENCES

- BRENNAN, M.S. (2006). "CFD Simulations of Hydrocyclones with an Air Core: Comparison Between Large Eddy Simulations and a Second Moment Closure". *Chemical Engineering Research and Design*, **84**(6), 495–505.
- DALAL, A., ESWARAN, V. and BISWAS, G. (2008). "A Finite-Volume Method for Navier-Stokes Equations on Unstructured Meshes". *Numerical Heat Transfer, Part B: Fundamentals*, **54**(3), 238–259.
- DATE, A.W. (2005). "Solution of transport equations on unstructured meshes with cell-centered colocated variables. Part I: Discretization". *International Journal of Heat and Mass Transfer*, **48**, 1117–1127.
- DAVIDSON, L. (1996). "A Pressure Correction Method for Unstructured Meshes with Arbitrary Control Volumes". *International Journal for Numerical Methods in Fluids*, **22**, 265–281. URL [http://doi.wiley.com/10.1002/\(SICI\)1097-0363\(19960229\)22:4{ }3C265::AID-FLD359{ }3E3.0.CO;2-J](http://doi.wiley.com/10.1002/(SICI)1097-0363(19960229)22:4{ }3C265::AID-FLD359{ }3E3.0.CO;2-J).
- DEARDORFF, J.W. (1970). "A numerical study of three-dimensional turbulent channel flow at large Reynolds numbers". *Journal of Fluid Mechanics*, **41**(1970), 453. URL <http://www.journals.cambridge.org/abstract{ }S0022112070000691>.
- GERMANO, M., PIOMELLI, U., MOIN, P. and CABOT, W.H. (1991). "A dynamic subgrid-scale eddy viscosity model". *Phys. Fluids A Fluid Dyn.*, **3**(7), 1760. URL <http://scitation.aip.org/content/aip/journal/pofa/3/7/10.1063/1.857955>.
- HAASE, G., LIEBMANN, M., DOUGLAS, C.C. and PLANK, G. (2010). "A parallel algebraic multigrid solver on graphics processing units". *Lecture Notes in Computer Science (including subseries Lecture Notes in Artificial Intelligence and Lecture Notes in Bioinformatics)*, **5938 LNCS**, 38–47.
- HEGE, H.C. and STUBEN, H. (1991). "Vectorization and parallelization of irregular problems via graph colouring". *Proceedings of the 5th International Conference on Supercomputing*, 47–56.
- KHOSLA, P.K. and RUBIN, S.G. (1974). "A diagonally dominant second-order accurate implicit scheme". *Computers and Fluids*, **2**(2), 207–209.
- KOBAYASHI, T. (1992). "Large eddy simulation of backward-facing step flow". *Communications in applied numerical methods*, **8**(October 1991), 431–441.
- LEONARD, A. (1975). "Energy Cascade in Large-Eddy Simulations of Turbulent Fluid Flows". *Turbulent Diffusion in Environmental Pollution Proceedings of a Symposium held at Charlottesville, Volume 18*, 237–248. URL <http://www.sciencedirect.com/science/article/pii/S0065268708604641>.
- LILLY, D.K. (1992). "A proposed modification of the Germano subgrid-scale closure method". *Physics of Fluids A: Fluid Dynamics*, **4**(3), 633.
- MANNINEN, M. and TAIVASSALO, V. (1996). "On the mixture model for multiphase flow".
- MOIN, P. and APTE, V. (2006). "Large-Eddy Simulation of Realistic Gas Turbine Combustors". *AIAA Journal*, **44**(4), 698–708.
- MOIN, P. and KIM, J. (1982). "Numerical investigation of turbulent channel flow". *Journal of Fluid Mechanics*, **118**, 341–377.
- NARASIMHA, M., BRENNAN, M. and HOLTHAM, P. (2006). "Large eddy simulation of hydrocyclone prediction of air-core diameter and shape". *International Journal of Mineral Processing*, **80**(1), 1–14. URL <http://linkinghub.elsevier.com/retrieve/pii/S0301751606000032>.
- NARASIMHA, M., BRENNAN, M., HOLTHAM, P. and NAPIER-MUNN, T. (2007). "A comprehensive CFD model of dense medium cyclone performance". *Minerals Engineering*, **20**(4), 414–426. URL <http://www.sciencedirect.com/science/article/pii/S0892687506002494>.
- POPE, S.B. (2004). "Ten questions concerning the large-eddy simulation". *New Journal of Physics*, **6**(1), 35.
- REDDY, R. and BANERJEE, R. (2015). "Computers & Fluids GPU accelerated VOF based multiphase flow solver and its application to sprays". *COMPUTERS AND FLUIDS*, **117**, 287–303. URL <http://dx.doi.org/10.1016/j.compfluid.2015.05.013>.
- SANDERS, J. and KANDROT, E. (2010). *CUDA by Example*, vol. 54. arXiv:1011.1669v3, URL <http://wwwzb.fz-juelich.de/contentenrichment/inhaltsverzeichnisse/2010/9780131387683.pdf>.
- SLACK, M., PRASAD, R., BAKKER, A. and BOSYAN, F. (2000). "Advances in cyclone modelling using unstructured grids". *Chemical Engineering Research and Design*, **78**(November), 1098–1104.
- VAKAMALLA, T.R., KORUPROLU, V.B.R., ARUGONDA, R. and MANGADODDY, N. (2017). "Development of novel hydrocyclone designs for improved fines classification using multiphase CFD model". *Separation and Purification Technology*, **175**, 481–497.
- XU, C., DENG, X., ZHANG, L., FANG, J., WANG, G., JIANG, Y., CAO, W., CHE, Y., WANG, Y., WANG, Z., LIU, W. and CHENG, X. (2014). "Collaborating CPU and GPU for large-scale high-order CFD simulations with complex grids on the TianHe-1A supercomputer". *Journal of Computational Physics*, **278**, 275–297. URL <http://www.sciencedirect.com/science/article/pii/S0021999114005786>.





# IMMERSED BOUNDARY METHOD FOR THE COMPRESSIBLE NAVIER–STOKES EQUATIONS USING HIGH ORDER SUMMATION-BY-PARTS DIFFERENCE OPERATORS

M. EHSAN KHALILI<sup>1\*</sup>, MARTIN LARSSON<sup>2†</sup>, BERNHARD MÜLLER<sup>1‡</sup>

<sup>1</sup>Department of Energy and Process Engineering, Norwegian University of Science and Technology (NTNU), Kolbjørn Hejes vei 2, NO-7491 Trondheim, Norway

<sup>2</sup>Sportradar AS, Ferjemannsveien 10, NO-7014 Trondheim, Norway

\* E-mail: mohammadtaghi.khalili@ntnu.no

† E-mail: m.larsson@sportradar.com

‡ E-mail: bernhard.muller@ntnu.no

## ABSTRACT

A ghost-point immersed boundary method is devised for the compressible Navier–Stokes equations by employing high order summation-by-parts (SBP) difference operators. The immersed boundaries are treated as sharp interfaces by enforcing the solid wall boundary conditions via flow variables at ghost points using bilinearly interpolated flow variables at mirror points. The approach is verified and validated for compressible flow past a circular cylinder at moderate Reynolds numbers.

**Keywords:** High order finite difference method, Immersed boundary method, Compressible viscous flow .

## NOMENCLATURE

### Greek Symbols

$\rho$	Mass density
$\mu$	Dynamic viscosity
$\tau$	Viscous stress tensor
$\gamma$	Ratio of specific heats
$\kappa$	Heat conduction coefficient
$\phi$	Generic variable
$\mathcal{G}$	Set of body intercept points that are part of the interpolation stencil
$\Lambda$	Parameter
$\sigma$	Source term in steady state heat equation
$\xi, \eta$	Transformed coordinates in computational domain

### Latin Symbols

$t$	Physical time
$E$	Specific total energy
$H$	Total enthalpy
$p$	Pressure
$S_c$	Sutherland constant
$T$	Temperature
$\mathbf{U}$	Vector of conservative variables
$\mathbf{V}$	Vandermonde matrix
$x, y$	Cartesian coordinates in physical domain
$J^{-1}$	Jacobian determinant

### Sub/superscripts

$GP$	Ghost point
$IP$	Image point
$BI$	Body intercept
$c'$	Conservative perturbation
$v'$	Viscous perturbation

## INTRODUCTION

Many applications in engineering, biology and medicine involve low and moderate Reynolds number flow problems with complex boundaries between fluid and structure. Simulating these problems with conventional methods requires the process of generating high quality and body-conforming grids which is challenging and time-consuming. Recently, there has been a growing interest in the development of non-boundary conforming methodologies for the solution of the Navier–Stokes equations (Mittal and Iaccarino, 2005). In such methods, the requirement that the grid should conform to a solid boundary is dropped, and the effect of the immersed boundary of the solid body on the flow is introduced through the proper treatment of the solution variables near the boundary. The basic advantage of these formulations is the simplicity compared with conventional body-conforming grid generation, especially in cases of complex stationary or moving boundaries where the demand for regeneration or deformation of the grid is eliminated. Therefore, efficient non boundary conforming strategies with robust Cartesian coordinate solvers can directly be applied to a wide range of flow problems.

Over the past decades a variety of non-body conforming approaches with various degrees of accuracy and complexity have been proposed. The so-called immersed-boundary method (IBM) was introduced by (Peskin, 1972). IB methods are categorized into continuous forcing and discrete (direct) forcing approaches. In the first category, a continuous forcing term is added to the governing equations to represent the interaction between the immersed boundary and the fluid, and a discrete Dirac–delta function is used to smooth this singular force on the Euler grid (Peskin, 1972; Goldstein *et al.*, 1993; Saiki and Biringen, 1996). Numerous modifications and improvements have been implemented in this category (Haeri and Shrimpton, 2012; Sotiropoulos and Yang, 2014). The second category, including the sharp interface method, mimics the presence of a surface force exerted by the boundary on the fluid by adjusting the discretization in the vicinity of the immersed boundary in order to directly take into account the boundary conditions at the IB (Ye *et al.*, 1999; Fadlun *et al.*, 2000; Mohd-Yusof, 1997; Balaras, 2004). The ghost cell immersed boundary (GCIB) method as sharp interface method is proposed in the studies by (Tseng and Ferziger, 2003; Ghias *et al.*, 2007; Mittal *et al.*, 2008). Ghost cells are defined as a layer of cells within the solid body having at least one nearby point in the fluid domain

i.e., adjoining to the immersed boundary. The flow variables at the ghost points are calculated with the boundary conditions at the immersed boundary and the flow variables at grid points near the IB in the fluid domain. The presence of the immersed boundary is introduced by the flow variables at the ghost points. The idea of image points inside the fluid domain is adopted to ensure suitable weighting coefficients in the reconstruction formula in order to avoid numerical instability caused by the large, negative weighting coefficients in the extrapolation formulation (Tseng and Ferziger, 2003). The ghost point method has shown large potential to deal with different fluid-solid interaction problems, including those involving highly complex geometries and moving or deforming bodies (Mittal *et al.*, 2008).

In the IBM, all the equations can be solved on a body non-conformal, Cartesian grid which does not require to be updated for moving or deforming bodies. Due to the flexibility of the method, many different types of IBM have been developed in incompressible and compressible flow solvers. However, most of the attention on IBM is devoted to incompressible flows (Mittal and Iaccarino, 2005). Works on viscous compressible flows are still scarce and a few IBM for viscous compressible flows has been developed (De Palma *et al.*, 2006; Ghias *et al.*, 2007; de Tullio *et al.*, 2007; Brehm *et al.*, 2015). Due to the different nature of the Navier–Stokes equations for compressible and incompressible flows, i.e. the requirement of equation of state for compressible flows, there are differences in implementation of the boundary conditions between these two types of equations as well as in the spatial discretisation schemes employed.

In this study, the ghost point IB approach has been adopted for a high order finite difference method based on summation-by-parts operators (SBP) to provide an accurate and efficient approach for studying low Mach number compressible viscous flows. The major ambition of the present work is to extend this approach for fluid structure interaction (FSI) in the upper airways to study the obstructive sleep apnea syndrome. The main focus in our study is subsonic flow which permits us to characterize the acoustic wave propagation induced by the structure oscillation in FSI to obtain a better understanding of snoring. The proposed approach is verified and validated for two dimensional flows over a circular cylinder. In the following sections, a brief review of the governing equations and their numerical solution is given. Then, the IB approach is described in detail. Finally, results are provided and compared with numerical and experimental ones available in the literature.

## MODEL DESCRIPTION

### Governing equations

The 2D compressible Navier–Stokes equations in perturbation form are solved. To minimize cancellation errors when discretizing the Navier–Stokes equations for compressible low Mach number flow, the perturbation formulation is employed (Sesterhenn *et al.*, 1999; Müller, 2008). The conservative form of the 2D compressible Navier–Stokes equations in perturbation formulation can be written as

$$\mathbf{U}'_t + \mathbf{F}'_x + \mathbf{G}'_y = \mathbf{F}''_x + \mathbf{G}''_y \quad (1)$$

where  $\mathbf{U}' = \mathbf{U} - \mathbf{U}_0$  is the vector of conservative perturbation variables with  $\mathbf{U} = (\rho, \rho u, \rho v, \rho E)^T$  the vector of the conservative variables and  $\mathbf{U}_0 = (\rho_0, 0, 0, (\rho E)_0)^T$  the stagnation values.

The conservative perturbation variables  $\mathbf{U}'$  and the inviscid ( $\mathbf{F}^{c'}$ ,  $\mathbf{G}^{c'}$ ) and viscous perturbation flux vectors ( $\mathbf{F}^{v'}$ ,  $\mathbf{G}^{v'}$ ) are defined by  $\mathbf{F}^{c'} = \mathbf{F}^c(\mathbf{U}) - \mathbf{F}^c(\mathbf{U}_0)$ , etc.

$$\mathbf{U}' = \begin{pmatrix} \rho' \\ (\rho u)' \\ (\rho v)' \\ (\rho E)' \end{pmatrix},$$

$$\mathbf{F}^{c'} = \begin{pmatrix} (\rho u)' \\ (\rho u)'u' + p' \\ (\rho v)'u' \\ ((\rho H)_0 + (\rho H)')u' \end{pmatrix}, \mathbf{G}^{c'} = \begin{pmatrix} (\rho v)' \\ (\rho u)'v' \\ (\rho v)'v' + p' \\ ((\rho H)_0 + (\rho H)')v' \end{pmatrix},$$

$$\mathbf{F}^{v'} = \begin{pmatrix} 0 \\ \tau'_{xx} \\ \tau'_{xy} \\ u'\tau'_{xx} + v'\tau'_{xy} + \kappa T'_x \end{pmatrix}, \mathbf{G}^{v'} = \begin{pmatrix} 0 \\ \tau'_{yx} \\ \tau'_{yy} \\ u'\tau'_{yx} + v'\tau'_{yy} + \kappa T'_y \end{pmatrix},$$

where  $t$  is physical time and  $x$  and  $y$  are the Cartesian coordinates.  $\rho$  denotes density,  $u$  and  $v$  the  $x$ - and  $y$ -direction velocity components,  $E$  the specific total energy,  $T$  the temperature and  $\kappa$  the heat conduction coefficient calculated from the constant Prandtl number  $\text{Pr} = 0.72$ .  $\rho_0$ ,  $(\rho E)_0$  and  $(\rho H)_0$  denote the stagnation values of density, total energy density and total enthalpy density. The perturbation variables are defined as:

$$\rho' = \rho - \rho_0, \quad (\rho \mathbf{u})' = (\rho \mathbf{u}),$$

$$(\rho E)' = \rho E - (\rho E)_0, \quad (\rho H)' = (\rho E)' + p', \quad \mathbf{u}' = \frac{(\rho \mathbf{u})'}{\rho_0 + \rho'},$$

$$\tau' = \mu(\nabla \mathbf{u}' + (\nabla \mathbf{u}')^T) - \frac{2}{3}\mu(\nabla \cdot \mathbf{u}')\mathbf{I}, \quad T' = \frac{p'/R - \rho'T_0}{\rho_0 + \rho'}$$

Here,  $R$  is the specific gas constant and  $\mu$  is the viscosity which is determined from the Sutherland law  $\frac{\mu}{\mu_0} = \left(\frac{T}{T_0}\right)^{1.5} \left[ \frac{1 + S_c}{1 + S_c} \right]$  with the non-dimensional Sutherland constant  $S_c = \frac{110}{301.75}$ .

Since perfect gas is considered, the pressure perturbation can be related to the conservative perturbation variables by  $p' = (\gamma - 1)[(\rho E)' - \frac{1}{2}((\rho \mathbf{u}') \cdot \mathbf{u}')]'$ , where the ratio of specific heats  $\gamma = c_p/c_v = 1.4$  for air.

The viscous flux vectors  $\mathbf{F}^{v'}$  and  $\mathbf{G}^{v'}$  are the same as for the standard conservative form, except for using the temperature perturbation  $T'$  instead of temperature  $T$  for the heat flux terms. The momentum density and velocity perturbations are taken as the same as their unperturbed counterparts, i.e.  $(\rho \mathbf{u})' = \rho \mathbf{u}$  (Larsson and Müller, 2009). For convenience the variables are non-dimensionalized with  $\rho_0$ , stagnation speed of sound  $c_0$  and  $\rho_0 c_0^2$  as reference values. In order to generalize the geometry for non-uniform Cartesian grids, the equations of motions are transformed from the physical domain  $(x, y)$  to the computational domain  $(\xi, \eta)$  by the following relations,

$$\begin{aligned} x &= x(\xi, \eta) \\ y &= y(\xi, \eta) \end{aligned} \quad (2)$$

Thus, the transformed 2D compressible Navier–Stokes equations in perturbation form are expressed as:

$$\hat{\mathbf{U}}'_t + \hat{\mathbf{F}}'_\xi + \hat{\mathbf{G}}'_\eta = 0 \quad (3)$$

where  $\hat{\mathbf{U}}' = J^{-1}\mathbf{U}'$ ,  $\hat{\mathbf{F}}' = J^{-1}(\xi_x(\mathbf{F}^{c'} - \mathbf{F}^{v'}) + \xi_y(\mathbf{G}^{c'} - \mathbf{G}^{v'}))$  and  $\hat{\mathbf{G}}' = J^{-1}(\eta_x(\mathbf{F}^{c'} - \mathbf{F}^{v'}) + \eta_y(\mathbf{G}^{c'} - \mathbf{G}^{v'}))$ . The chain rule for partial differentiation provides the expressions for Cartesian derivatives in the viscous flux vectors  $\mathbf{F}^{v'}$  and  $\mathbf{G}^{v'}$ , e.g.

$u'_x = u'_\xi \xi_x + u'_\eta \eta_x$  and  $u'_y = u'_\xi \xi_y + u'_\eta \eta_y$ . The Jacobian determinant of the transformation is  $J^{-1} = x_\xi y_\eta - x_\eta y_\xi$  and metric terms are

$$\begin{aligned} J^{-1} \xi_x &= y_\eta, & J^{-1} \xi_y &= -x_\eta, \\ J^{-1} \eta_x &= -y_\xi, & J^{-1} \eta_y &= x_\xi. \end{aligned} \quad (4)$$

### Numerical methodology

The summation-by-parts (SBP) operator  $Q$  is an approximation to the first  $\xi$ - and  $\eta$ - derivatives in (4) and (3). In the interior, it corresponds to the standard sixth order central operator, while being third order accurate near the boundaries. Through a special boundary treatment, SBP operators permit energy estimates for discrete problems similar to those for the continuous ones that are approximated. Therefore, SBP operators can yield strictly stable schemes for general boundary conditions (Strand, 1994; Gustafsson *et al.*, 1995; Gustafsson, 2008). The global order of accuracy of the present SBP operator  $Q$  is fourth order (Müller, 2008). The energy method and the summation-by-parts operators are discussed in the Appendix A and B, respectively.

Second derivatives of viscous parts of  $\hat{\mathbf{F}}'_\xi$  and  $\hat{\mathbf{G}}'_\eta$  are approximated by applying the SBP operator for first derivatives twice. However, successively applying the first derivative operator makes the scheme wider, which requires special treatment for the immersed boundary method, and will be discussed in section boundary conditions below. Spurious high wave number oscillations are suppressed by a sixth order explicit filter (Visbal and Gaitonde, 2002; Müller, 2008). The classical fourth order explicit Runge–Kutta method is employed for time integration.

### Immersed boundary formulation

The sharp interface method is well suited for compressible viscous flow, due to imposing the boundary conditions at immersed boundaries, without computing any forcing term and introducing any force distribution function. The ghost point immersed boundary method employed in this study is based on the ghost cell immersed boundary approach for second order methods (Ghias *et al.*, 2007; Mittal *et al.*, 2008).

The basic idea in this method is to compute the value of the flow variables at each of the ghost points (referring to the layer of points inside the solid body adjoining the immersed boundary) such that the boundary conditions at the immersed boundary are satisfied. As illustrated in Fig. 1, the procedure begins by determining the immersed boundary and then distinguishing the solid points, i.e. the nodes lying inside the solid body, and the fluid points, i.e. the nodes lying outside the body in the fluid domain. The ghost points (denoted by GP) are identified by those nodes that lie inside the body and adjacent to the immersed boundary which have at least one neighbour node in the fluid domain with the difference stencil centered at the ghost point. The image point (denoted by IP) can be found by extending a normal probe, i.e. a line normal to the immersed boundary, from the ghost point to intersect with the immersed boundary at the body intercept point (denoted by BI) such that the body intercept point lies at the midpoint of the line connecting the ghost point and the image point. Once the flow variables at the image point are computed, the ghost point variables can be determined by imposing the boundary conditions. In other words, the general strategy is to compute the flow variables at the image point by taking into account the nodal values at the surrounding fluid points and then use the boundary conditions to obtain the values at the ghost point.

Among the available options for determining the flow variables at the image points, the computationally most efficient scheme will be the bilinear interpolation scheme in 2D (Ghias *et al.*, 2007; Mittal *et al.*, 2008) where the flow variables are linearly interpolated from four nodal points surrounding the image points. This interpolation scheme leads to a nominally second order accuracy of the immersed boundary condition. The high order SBP operator used in this study for spatial discretization, corresponding to the sixth order central finite difference method at interior grids, requires three layers of ghost points inside the immersed boundary in order to maintain the overall high order of accuracy, as shown in Fig. 2.

In the case of bilinear interpolation, the interpolating polynomial involves four nodes and hence four nodal values need to be specified. The bilinear interpolation for a generic variable  $\phi$  can be expressed as

$$\phi(x, y) = C_1 + C_2x + C_3y + C_4xy. \quad (5)$$

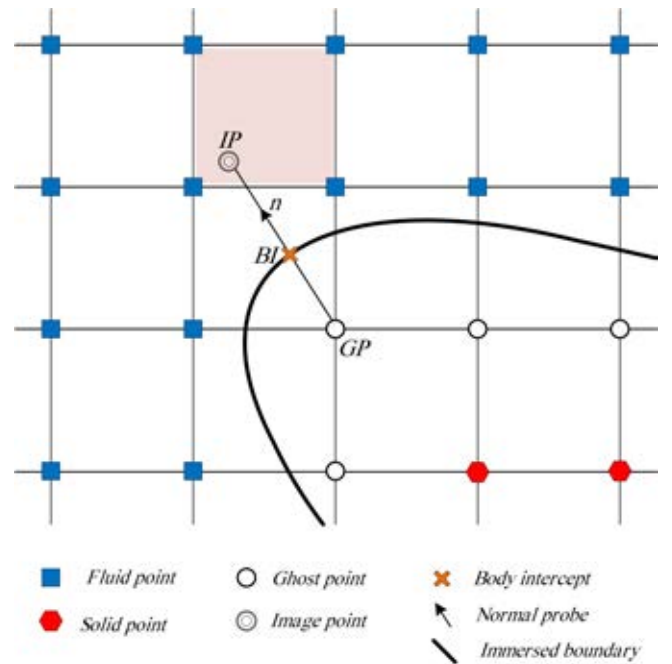


**Figure 1:** Schematic of points used to interpolate the variable located at a ghost point.

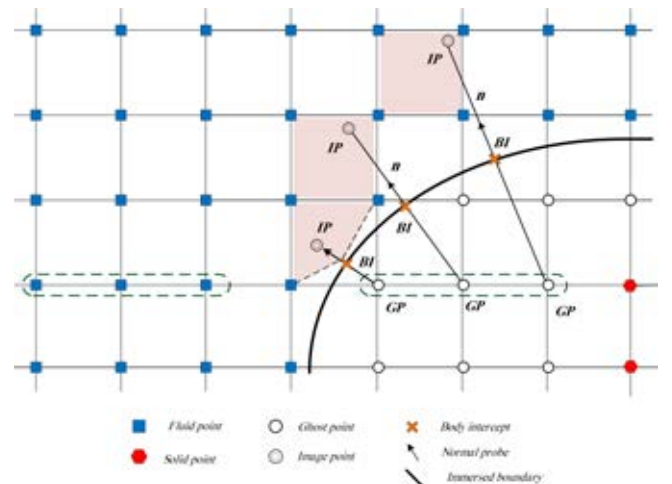


**Figure 2:** Schematic of 3 layers of ghost points inside immersed body on a Cartesian mesh.

The four unknown coefficients  $C_i, i = 1, \dots, 4$ , can be determined using values at the four nodes surrounding the image point. Thus, the variable at the image point is reconstructed through bilinear interpolation using unknown coefficients and known flow variables at surrounding fluid nodes. The four weighting coefficients are evaluated as the solution of the linear system

$$\mathbf{VC} = \phi, \quad (6)$$

where

$$\mathbf{C} = \{C_1, C_2, C_3, C_4\}^T \quad (7)$$

is the vector of the unknown coefficients and

$$\phi = \{\phi_1, \phi_2, \phi_3, \phi_4\}^T \quad (8)$$

is the vector of the four surrounding node values. The matrix  $\mathbf{V}$  is the Vandermonde matrix which is expressed as

$$\mathbf{V} = \begin{bmatrix} 1 & x_1 & y_1 & x_1 y_1 \\ 1 & x_2 & y_2 & x_2 y_2 \\ 1 & x_3 & y_3 & x_3 y_3 \\ 1 & x_4 & y_4 & x_4 y_4 \end{bmatrix} \quad (9)$$

In this classical formulation, the unknown coefficient values  $C_i, i = 1, \dots, 4$ , would depend on the solution at each time step. However, the approach can be reformulated such that new coefficients are only dependent on the coordinates of the image point and the geometry of the grids. The reformulation is discussed in detail in Appendix C. Thus, the image point value can be expressed as

$$\phi_{IP} = \sum_{i=1}^4 \alpha_i \phi_i \quad (10)$$

where  $\alpha_i, i = 1, \dots, 4$ , are coefficients depending on the coordinates only. They can be established once the grid, immersed boundary and image point coordinates are specified. When a ghost point is close to the immersed boundary, its corresponding image point might not have four surrounding fluid points. One case would be that the ghost point itself is part of the interpolation scheme. Since the ghost point value in an interpolation scheme would be unknown, the ghost point is then replaced by the body intercept point where the values are determined by the boundary conditions, cf. Fig. 3.

For Dirichlet boundary condition in this case, the corresponding row in Eq. (9) is replaced by

$$\phi_{BI}(x, y) = C_1 + C_2 x_{BI} + C_3 y_{BI} + C_4 x_{BI} y_{BI} \quad (11)$$

where  $x_{BI}$  and  $y_{BI}$  are the coordinates of the body intercept point. Thereby, for a Dirichlet boundary condition the linear system corresponding to Eq.(6) for this case becomes

$$\begin{bmatrix} 1 & x_1 & y_1 & x_1 y_1 \\ 1 & x_2 & y_2 & x_2 y_2 \\ 1 & x_3 & y_3 & x_3 y_3 \\ 1 & x_B & y_B & x_B y_B \end{bmatrix} \begin{bmatrix} C_1 \\ C_2 \\ C_3 \\ C_4 \end{bmatrix} = \begin{bmatrix} \phi_1 \\ \phi_2 \\ \phi_3 \\ \phi_{BI} \end{bmatrix} \quad (12)$$

For a Neumann boundary condition, the variable gradient at the body intercept is known instead of the actual value. The most obvious choice in such a case is to use the specified gradient value  $\frac{\partial \phi_{BI}}{\partial n}$  to compute the value at the image point. The gradient of  $\phi_{BI}$  at the boundary can be determined by taking the normal derivative of Eq.(11),

$$\frac{\partial \phi_{BI}}{\partial n} = C_2 n_x + C_3 n_y + C_4 (y_{BI} n_x + x_{BI} n_y) = \zeta \quad (13)$$

where  $n_x$  and  $n_y$  are the components of the unit vector normal to the boundary.

Thus, the linear system corresponding to Eq.(6) for this case becomes

$$\begin{bmatrix} 1 & x_1 & y_1 & x_1 y_1 \\ 1 & x_2 & y_2 & x_2 y_2 \\ 1 & x_3 & y_3 & x_3 y_3 \\ 0 & n_x & n_y & y_{BI} n_x + x_{BI} n_y \end{bmatrix} \begin{bmatrix} C_1 \\ C_2 \\ C_3 \\ C_4 \end{bmatrix} = \begin{bmatrix} \phi_1 \\ \phi_2 \\ \phi_3 \\ \zeta \end{bmatrix} \quad (14)$$

As shown in Fig. 4, it might also be the case that two interpolation points would lie inside the immersed body, one at the corresponding ghost point itself and one at another ghost point. The procedure we used to handle this case is to repeat the above steps for the other ghost point as well, resulting in a Vandermonde matrix where another row is also replaced by Eqs. (11) or (13) in the same way as the fourth row, in contrast to (Ghias *et al.*, 2007; Mittal *et al.*, 2008). Applying our procedure for this case, it is no longer necessary to solve a coupled linear system by using iterative processes like (Ghias *et al.*, 2007; Mittal *et al.*, 2008). This situation does not pose any consistency issues and ensures that the interpolation procedure for the image point is well-posed without affecting the accuracy of the interpolation.

The value of the variable at the ghost point is computed by employing a linear approximation along the normal probe which takes into account the boundary condition at the boundary intercept. For a Dirichlet boundary condition this can generally be expressed as

$$\phi_{GP} = \frac{1}{2}(\phi_{IP} + \phi_{GP}) + O(\Delta l^2) \quad (15)$$

where  $\Delta l$  is the length of the normal probe from GP to IP. Solving for  $\phi_{GP}$  using Eq. (15) and neglecting the truncation gives

$$\phi_{GP} = \left(2 - \sum_{j \in \mathcal{G}} \alpha_j\right) \phi_{BI} - \sum_{i \notin \mathcal{G}} \alpha_i \phi_i \quad (16)$$

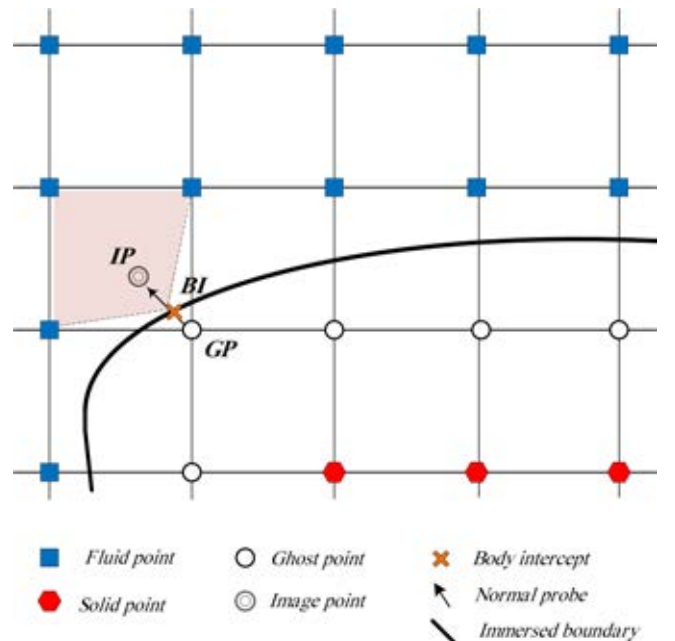


**Figure 3:** Schematic of the situation when one surrounding interpolation point is the boundary intercept.

where  $\mathcal{G}$  is the set of body intercepts that are part of the interpolation stencil. For a Neumann boundary condition on the immersed boundary, the following second-order central-difference is written along the normal probe

$$\left(\frac{\partial\phi}{\partial n}\right)_{BI} = \frac{\phi_{IP} - \phi_{GP}}{\Delta l} + O(\Delta l^2) \quad (17)$$

Thereby, the general formulation for a non-homogeneous Neumann boundary condition is expressed as

$$\phi_{GP} = \left(\sum_{j \in \mathcal{G}} \alpha_j - \Delta l\right) \left(\frac{\partial\phi}{\partial n}\right)_{BI} + \sum_{i \notin \mathcal{G}} \alpha_i \phi_i \quad (18)$$

## Boundary conditions

The no-slip boundary condition at the immersed boundary for a stationary body is considered. Thereby, Dirichlet boundary conditions are employed for the velocity components at the IB. For each velocity components, the corresponding value at the body intercept  $\phi_{BI} = 0$  is set in Eq. (11). Applying the no-slip condition at the body surface, the convective flux contribution should be zero. The pressure gradient normal to the immersed interface is set zero as a boundary layer approximation,  $\frac{\partial p}{\partial n} = \frac{\partial \phi_{BI}}{\partial n} = 0$  in Eq. (13). The boundary condition for the temperature depends on whether the immersed surface of the body is adiabatic or isothermal. Assuming an adiabatic boundary condition at the immersed body, the temperature gradient normal to the surface  $\frac{\partial T}{\partial n} = 0$  is set to zero by enforcing a zero density gradient  $\frac{\partial \rho}{\partial n} = 0$ . Thus, for the variables  $\rho$  and  $p$  Neumann boundary conditions are employed. According to the boundary conditions considered for the immersed body, the values of the conservative perturbation variables at the ghost points are determined once the flow variables at the image points

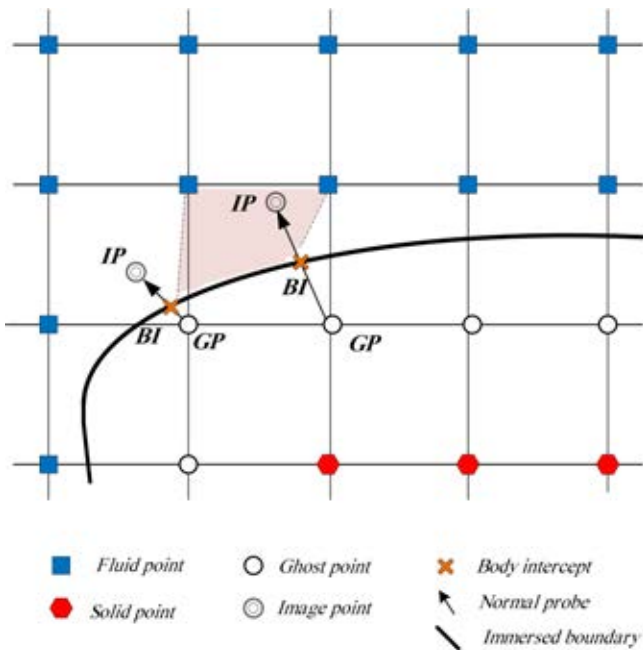


**Figure 4:** Schematic of the situation when two of the surrounding interpolation points lie inside the immersed body.

are interpolated using:

$$\begin{aligned} \rho'_{GP} &= \rho'_{IP} \\ (\rho u)'_{GP} &= -(\rho u)'_{IP} \\ (\rho v)'_{GP} &= -(\rho v)'_{IP} \\ (\rho E)'_{GP} &= (\rho E)'_{IP} \end{aligned} \quad (19)$$

As mentioned above, applying the first derivative approximation twice for computing the second derivative will make the stencil wider. For the proper treatment of wide stencils in computing the second derivative, the first derivatives of the viscous terms are computed up to and including the ghost points, treating the solid points inside the ghost point layers as domain boundaries when employing the differencing stencil. Using this procedure, we ensure that the derivatives of the viscous fluxes at the fluid points closest to the immersed boundary are computed with high order.

Non-reflecting characteristic boundary conditions are employed at the inflow and outflow boundaries to minimize wave reflections. The Navier–Stokes characteristic boundary conditions (NSCBC) developed by (Poinsot and Lele, 1992) are employed to approximate incoming waves based on local one-dimensional inviscid (LODI) relations. The primitive variables can be related to the wave amplitude ( $\mathcal{L}_i$ ) by LODI relations. The amplitudes of the characteristic waves are  $\mathcal{L}_1 = \lambda_1(\frac{\partial p}{\partial x} - \rho c \frac{\partial u}{\partial x})$ ,  $\mathcal{L}_2 = \lambda_2(c^2 \frac{\partial p}{\partial x} - \frac{\partial p}{\partial x})$ ,  $\mathcal{L}_3 = \lambda_3(\frac{\partial v}{\partial x})$  and  $\mathcal{L}_4 = \lambda_4(\frac{\partial p}{\partial x} + \rho c \frac{\partial u}{\partial x})$ . Since fully non-reflecting conditions may lead to an ill-posed problem (Poinsot and Lele, 1992), this approach is partially reflecting. Imposing a constant pressure at the outlet requires  $\mathcal{L}_1 = -\mathcal{L}_4$ . To keep the reflections low and the pressure close to atmospheric pressure, the incoming wave amplitude is set to

$$\mathcal{L}_1 = K(p - p_{\text{atm}}) \quad (20)$$

where  $K$  is a relaxation coefficient. Rudy and Strikwerda proposed the relaxation coefficient as  $K = \Lambda(1 - \text{Ma}^2)(c/L_t)$  where  $\text{Ma}$  is the Mach number,  $c$  the speed of sound,  $L_t$  the total length of the domain and  $\Lambda$  a parameter (Rudy and Strikwerda, 1980). The optimum value  $\Lambda = 0.25$  derived by (Rudy and Strikwerda, 1980) is employed. For reverse flow (negative velocity in  $x$ -direction) at the outlet,  $\mathcal{L}_1$ ,  $\mathcal{L}_2$  and  $\mathcal{L}_3$  are set to zero. A similar boundary treatment at inflow and outflow was used by (Khalili *et al.*, 2016).

## RESULTS

In order to assess the accuracy of the immersed boundary methodology, a two-dimensional steady state heat problem is first solved. Then, the IBM is applied to a two-dimensional flow past a circular cylinder at a range Reynolds numbers to demonstrate the ability and performance of the method for simulating compressible viscous flow.

### Steady state heat equation

To verify the order of spatial accuracy of the current immersed boundary scheme, a steady state heat transfer problem has been considered. Since the ghost point immersed boundary method is second-order accurate (Ghias *et al.*, 2007; Mittal *et al.*, 2008), care has been taken to maintain a second-order spatial accuracy in the imposition of boundary conditions on the immersed boundary. The steady state heat equation reads

$$\nabla^2 T = \sigma \quad (21)$$

where  $\sigma$  is a source term, i.e.  $-\kappa\sigma$  is the rate of heat generation per unit volume. The exact solution for this case in polar coordinates can be expressed as

$$T(r) = \sigma \frac{r^2}{4} + A \ln(r) + B \quad (22)$$

where  $A$  and  $B$  depend on the boundary conditions type and their values.

The numerical solution by means of IBM is implemented to solve Eq.(21) in Cartesian coordinates. The second and fourth order central finite difference methods for second derivatives are employed for spatial discretization of the regular fluid points.

$$T_{xx}^{(2)} = (T_{i+1} - 2T_i + T_{i-1})/\Delta x^2 \quad (23)$$

$$T_{xx}^{(4)} = (-T_{i+2} + 16T_{i+1} - 30T_i + 16T_{i-1} - T_{i-2})/(12\Delta x^2) \quad (24)$$

The temperature distribution is solved between two concentric cylinders with inner and outer diameters  $D_{\text{inner}} = 3.5$  and  $D_{\text{outer}} = 8.5$ , respectively, embedded in a square domain of edge length  $L = 10$ . The  $\sigma = -0.45$  is chosen and the temperatures of the inner and outer cylinders are  $T_{\text{inner}} = 5$  and  $T_{\text{outer}} = 10$ , respectively. The immersed boundary approach is implemented at the cylinder interfaces. The results from different grids on a uniform Cartesian grid ( $N \times N$ ) from  $N = 100$  to  $1000$  are compared with the exact solution to compute the  $L_2$  and  $L_\infty$  norms. Fig. 5 shows the errors for different grids.

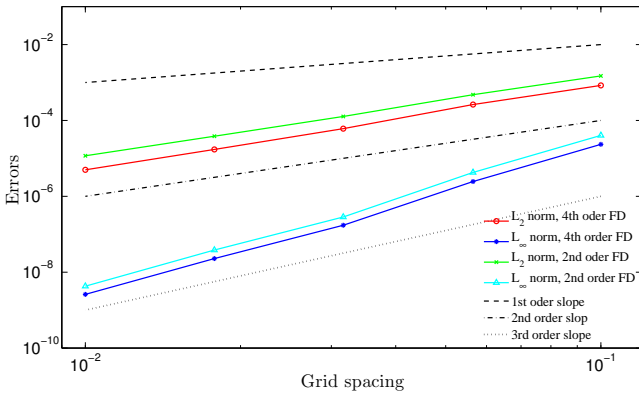


**Figure 5:**  $L_2$  and  $L_\infty$  norms computed at various grid levels with IBM for 2D steady heat Eq. (21).

The first, second and third-order convergence rates are also included in Fig. 5 for reference. This figure indicates that a second-order rate of convergence has been achieved by the Poisson solver for Dirichlet boundary conditions at immersed boundaries. The error are slightly lower for the fourth order difference method than for the second order one.

### Flow past circular cylinder

To verify and validate the present immersed boundary treatment for a compressible flow solver, the benchmark flow over a circular cylinder is firstly simulated at the Reynolds numbers of 20 and 40 based on the free-stream velocity and diameter of the cylinder. It is known that steady flow over a circular cylinder can persist up to Reynolds numbers of about 40. The free-stream Mach number for the simulation is set as a small number  $Ma = 0.03$  in order to be comparable to the simulations performed using incompressible solvers. Then, the unsteady flow over a circular cylinder has been chosen

to verify the proposed IB method at the Reynolds number of 100 and Mach number 0.25.

The computational domain size is  $90D \times 40D$  where  $D$  is the diameter of the cylinder. The center of the cylinder is located at the point  $(20D, 20D)$  of the coordinate system. The computational domain is sizeable to reduce the effects of domain boundaries and wave reflections form the inlet and outlet boundaries. It has been observed that those could lead to a momentous error when computing the lift and drag coefficients. In the present work, the block structured computational domain has been discretized with non-uniform Cartesian grids, where the block corresponding to the cylinder has a much finer grid spacing of  $(\Delta x = \Delta y = D/25)$  at  $Re = 20$  and 40, and grid spacing of  $(\Delta x = \Delta y = D/50)$  at  $Re = 100$ . At these grid resolutions, the lift and drag coefficients are sufficiently converged. Sufficient grid resolution around the cylinder is crucial to obtain the drag and lift coefficients accurately. Additionally, to capture the von Kármán vortex shedding, the wake region needs to be resolved properly. The grid spacing  $\Delta x$  and  $\Delta y$  was smoothly stretched from  $(\Delta x = \Delta y = D/25)$  at  $Re = 20$  and 40, and  $\Delta x = \Delta y = D/50$  for  $Re=100$  to  $\Delta x = \Delta y = D/2$  near the inflow, outflow, top and bottom boundaries. Symmetry boundary conditions are applied on the top and bottom of the computational domain. At the inflow, the velocities in the  $x$ - and  $y$ -directions are imposed using a uniform inlet profile normal to the boundary,  $u(x = 0, t) = U_\infty$  and  $v = 0$ . In addition, the inlet temperature is set to  $T = T_0 = 310$  K. The outlet pressure is set to atmospheric pressure, i.e.,  $p' = p - p_0 = p - p_{\text{atm}} = 0$  Pa.

The drag and lift coefficients are defined as  $C_D = \frac{F_D}{\frac{1}{2}\rho_\infty U_\infty^2 D}$  and  $C_L = \frac{F_L}{\frac{1}{2}\rho_\infty U_\infty^2 D}$ , respectively, where  $F_D$  and  $F_L$  are the drag and lift forces. The total force on the cylinder is given by the sum of the pressure and viscous force integrated over the cylinder surface  $F = -\oint p_B \cdot \mathbf{n} ds + \oint \tau_B \cdot \mathbf{n} ds$  where  $\mathbf{n}$  is the outer unit vector normal to the cylinder, and  $p_B$  and  $\tau_B$  are pressure and the viscous stress tensor on the body surface, respectively. These quantities are based on the evaluation of surface pressure and viscous stress. The procedure used to compute these surface quantities needs some explanation. In the current solver, four nodes surrounding a body-intercept point corresponding to the first layer of ghost points are identified and then a bilinear interpolation is used to estimate the pressure and viscous stress tensor at the body intercept. The viscous stress at the involved ghost points and fluid points are computed in a straightforward manner by using our high order method.

Figs. 6 - 9 show streamlines and vorticity contours for  $Re = 20$  and  $Re = 40$ , respectively. The geometrical properties of the vortices behind the cylinder are schematically illustrated in Fig. 10 (Canuto and Taira, 2015). The quantitative comparison of these parameters as well as the drag coefficient with available numerical and experimental results are given in Table 1.

Fig. 11 presents the instantaneous spanwise vorticity  $\omega_z$  contours for  $Re = 100$  indicating the presence of the von Kármán vortex street. The vortex shedding leads to time-varying lift and drag forces until they reach to a periodic oscillatory form. The Strouhal number  $St = \frac{fD}{U_\infty}$ , where  $f$  is the vortex shedding frequency, is computed from the temporal variation of the lift coefficient. Due to the unsteadiness of the flow, the comparison of the average values of the lift and drag coefficients as well as the amplitude of the sinusoidal variation in time of the lift and drag coefficients is central. The results for the time-averaged lift and drag coefficients, the amplitude of

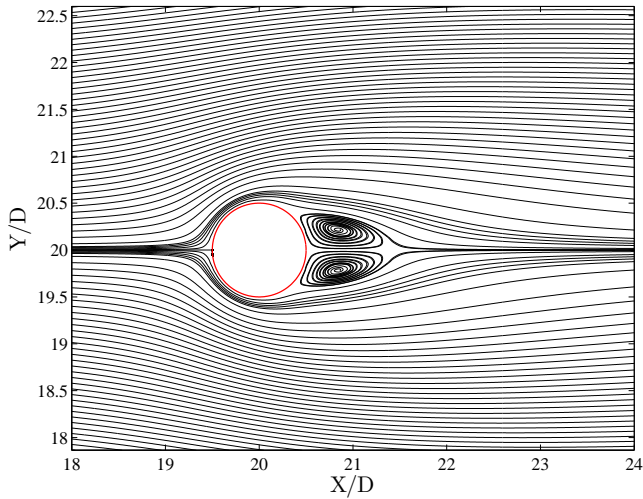


**Figure 6:** Streamlines for computed flow past a circular cylinder at  $Re = 20$  and  $Ma = 0.03$ .

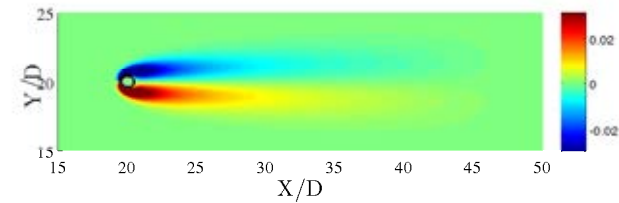


**Figure 7:** Vorticity contours for computed flow past a circular cylinder at  $Re = 20$  and  $Ma = 0.03$ .

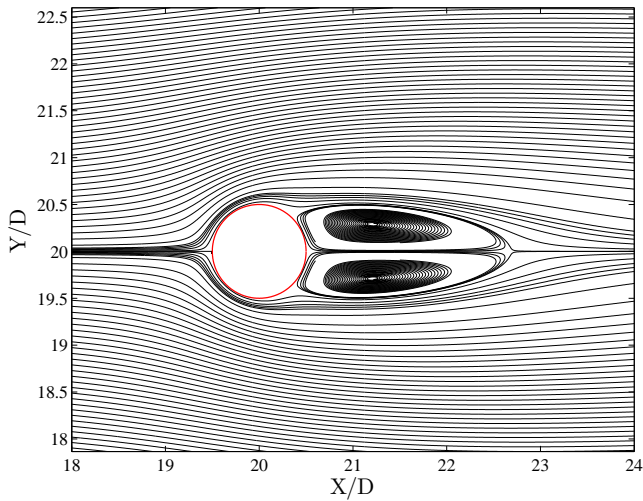


**Figure 8:** Streamlines for computed flow past a circular cylinder at  $Re = 40$  and  $Ma = 0.03$ .

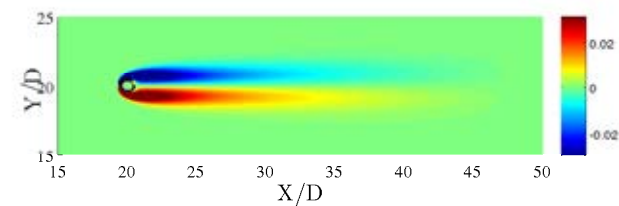


**Figure 9:** Vorticity contours for computed flow past a circular cylinder at  $Re = 40$  and  $Ma = 0.03$ .

**Table 1:** Comparison of computed data with available numerical and experimental data at  $Re = 20$  and  $Re = 40$ . (Exp.) indicates the experimental results.

	Re = 20					
	Ma	L	a	b	$\theta(deg)$	$C_D$
(Tritton, 1959)(Exp.)	-	-	-	-	-	2.09
(Dennis and Chang, 1970)	0	0.94	-	-	43.7	2.05
(Coutanceau and Bouard, 1977)(Exp.)	-	0.93	0.33	0.46	45.0	-
(Fornberg, 1980)	0	0.91	-	-	45.7	2.0
(Linnick and Fasel, 2003)	0	0.93	0.36	0.43	43.5	2.06
(De Palma <i>et al.</i> , 2006)	0.03	0.93	0.36	0.43	44.6	2.05
(Canuto and Taira, 2015)	0	0.92	0.36	0.42	43.7	2.07
<b>Present study</b>	<b>0.03</b>	<b>0.93</b>	<b>0.36</b>	<b>0.43</b>	<b>43.9</b>	<b>2.05</b>
	Re = 40					
	Ma	L	a	b	$\theta(deg)$	$C_D$
(Tritton, 1959)(Exp.)	-	-	-	-	-	1.59
(Dennis and Chang, 1970)	0	2.35	-	-	53.8	1.52
(Coutanceau and Bouard, 1977)(Exp.)	-	2.13	0.76	0.59	53.8	-
(Fornberg, 1980)	0	2.24	-	-	55.6	1.50
(Linnick and Fasel, 2003)	0	2.28	0.72	0.60	53.6	1.52
(De Palma <i>et al.</i> , 2006)	0.03	2.28	0.72	0.60	53.8	1.55
(Canuto and Taira, 2015)	0	2.24	0.72	0.59	53.7	1.54
<b>Present study</b>	<b>0.03</b>	<b>2.22</b>	<b>0.72</b>	<b>0.59</b>	<b>53.1</b>	<b>1.52</b>

their changes as well as the Strouhal number of the present study are compared to published results in Table 2. Table 1 and 2 confirm that for the present study all results compare very well with results reported in the literature.

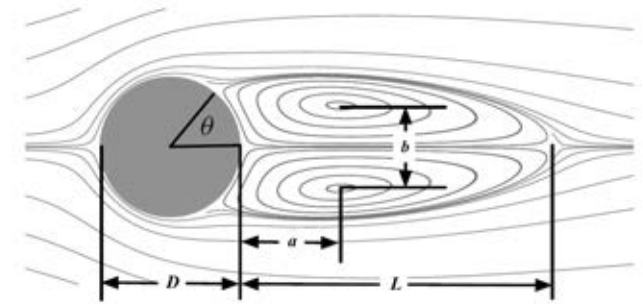


**Figure 10:** Definitions of the relevant geometrical parameters of the symmetric deperation region behind the cylinder (Canuto and Taira, 2015).

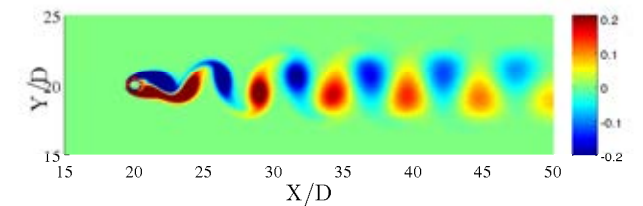


**Figure 11:** Vorticity contours for computed flow past a circular cylinder at  $Re = 100$  and  $Ma = 0.25$



**Table 2:** Comparison of computed data with available numerical and experimental data at  $Re = 100$ .

	Re = 100			
	Ma	St	$C_D$	$C_L$
(Berger and Wille, 1972)	0	0.16-0.17	-	-
(Liu <i>et al.</i> , 1998)	0	0.165	$1.35 \pm 0.012$	$\pm 0.339$
(Linnick and Fasel, 2003)	0	0.166	$1.34 \pm 0.009$	$\pm 0.333$
(Mittal <i>et al.</i> , 2008)	0	-	1.35	-
(Karagiozis <i>et al.</i> , 2010)	0.25	0.168	1.336	$\pm 0.319$
(Canuto and Taira, 2015)	0.25	0.163	1.378	$\pm 0.325$
<b>Present study</b>	<b>0.25</b>	<b>0.1667</b>	<b><math>1.33 \pm 0.013</math></b>	<b><math>\pm 0.323</math></b>

## CONCLUSION

In this paper, we have combined highly stable high-order SBP operators with an immersed boundary method which permits us to use Cartesian grids for arbitrary geometries for solving the compressible Navier–Stokes equations accurately and efficiently. SBP operators which are 6<sup>th</sup> order accurate in the interior and 3<sup>rd</sup> order accurate near the boundaries is employed. To achieve high accuracy and easy parallelization, the 4<sup>th</sup> order explicit Runge–Kutta method is applied. The methodology is applied to compute steady and unsteady flow problems to demonstrate its versatility as well as its accuracy. The flow past a circular cylinder for moderate values of Reynolds number and Mach number is assessed. A good agreement with available experimental and numerical results is achieved.

## ACKNOWLEDGMENTS

The present research is a part of a research project entitled "Modeling of obstructive sleep apnea by fluid-structure interaction in the upper airways" funded by the Research Council of Norway. The simulations in our work are done on the Vilje cluster at NTNU which is gratefully acknowledged.

## REFERENCES

BALARAS, E. (2004). "Modeling complex boundaries using an external force field on fixed Cartesian grids in large-eddy simulations". *Computers & Fluids*, **33**(3), 375–404.

BERGER, E. and WILLE, R. (1972). "Periodic flow phenomena". *Annual Review of Fluid Mechanics*, **4**(1), 313–340.

BREHM, C., HADER, C. and FASEL, H.F. (2015). "A locally stabilized immersed boundary method for the compressible navier–stokes equations". *Journal of Computational Physics*, **295**, 475–504.

CANUTO, D. and TAIRA, K. (2015). "Two-dimensional compressible viscous flow around a circular cylinder". *Journal of Fluid Mechanics*, **785**, 349–371.

COUTANCEAU, M. and BOUARD, R. (1977). "Experimental determination of the main features of the viscous flow in the wake of a circular cylinder in uniform translation. Part 1. Steady flow". *Journal of Fluid Mechanics*, **79**(02), 231–256.

DE PALMA, P., DE TULLIO, M., PASCAZIO, G. and NAPOLITANO, M. (2006). "An immersed-boundary method for compressible viscous flows". *Computers & Fluids*, **35**(7), 693–702.

DE TULLIO, M.D., DE PALMA, P., IACCARINO, G., PASCAZIO, G. and NAPOLITANO, M. (2007). "An immersed boundary method for compressible flows using local grid refinement". *Journal of Computational Physics*, **225**(2), 2098–2117.

DENNIS, S. and CHANG, G.Z. (1970). "Numerical solutions for steady flow past a circular cylinder at Reynolds

numbers up to 100". *Journal of Fluid Mechanics*, **42**(03), 471–489.

FADLUN, E., VERZICCO, R., ORLANDI, P. and MOHD-YUSOF, J. (2000). "Combined immersed-boundary finite-difference methods for three-dimensional complex flow simulations". *Journal of Computational Physics*, **161**(1), 35–60.

FORNBERG, B. (1980). "A numerical study of steady viscous flow past a circular cylinder". *Journal of Fluid Mechanics*, **98**(04), 819–855.

GHIAS, R., MITTAL, R. and DONG, H. (2007). "A sharp interface immersed boundary method for compressible viscous flows". *Journal of Computational Physics*, **225**(1), 528–553.

GOLDSTEIN, D., HANDLER, R. and SIROVICH, L. (1993). "Modeling a no-slip flow boundary with an external force field". *Journal of Computational Physics*, **105**(2), 354–366.

GUSTAFSSON, B. (2008). *High order difference methods for time dependent PDE*. Springer, Berlin.

GUSTAFSSON, B., KREISS, H.O. and OLIGER, J. (1995). *Time dependent problems and difference methods*. John Wiley & Sons, New York.

HAERI, S. and SHRIMPTON, J. (2012). "On the application of immersed boundary, fictitious domain and body-conformal mesh methods to many particle multiphase flows". *International Journal of Multiphase Flow*, **40**, 38 – 55.

KARAGIOZIS, K., KAMAKOTI, R. and PANTANO, C. (2010). "A low numerical dissipation immersed interface method for the compressible navier–stokes equations". *Journal of Computational physics*, **229**(3), 701–727.

KHALILI, M., LARSSON, M. and MÜLLER, B. (2016). "Interaction between a simplified soft palate and compressible viscous flow". *Journal of Fluids and Structures*, **67**, 85–105.

LARSSON, M. and MÜLLER, B. (2009). "Numerical simulation of confined pulsating jets in human phonation". *Computers & Fluids*, **38**(7), 1375–1383.

LINNICK, M. and FASEL, H. (2003). "A high-order immersed boundary method for unsteady incompressible flow calculations". *41st Aerospace Sciences Meeting and Exhibit*, 1124.

LIU, C., ZHENG, X. and SUNG, C. (1998). "Pre-conditioned multigrid methods for unsteady incompressible flows". *Journal of Computational Physics*, **139**(1), 35–57.

MITTAL, R. and IACCARINO, G. (2005). "Immersed boundary methods". *Annual Review of Fluid Mechanics*, **37**, 239–261.

MITTAL, R., DONG, H., BOZKURTTAS, M., NAJJAR, F., VARGAS, A. and VON LOEBBECKE, A. (2008). "A versatile sharp interface immersed boundary method for incompressible flows with complex boundaries". *Journal of Computational Physics*, **227**(10), 4825–4852.

MOHD-YUSOF, J. (1997). "Combined immersed-boundary/B-spline methods for simulations of flow in complex geometries". *Center for Turbulence Research Annual Research Briefs*, 317–325.

MÜLLER, B. (2008). "High order numerical simulation of aeolian tones". *Computers & Fluids*, **37**(4), 450–462.

PESKIN, C.S. (1972). "Flow patterns around heart valves: A numerical method". *Journal of Computational Physics*, **10**(2), 252–271.

POINSOT, T.J. and LELE, S. (1992). "Boundary conditions for direct simulations of compressible viscous flows". *Journal of Computational Physics*, **101**(1), 104–129.

RUDY, D.H. and STRIKWERDA, J.C. (1980). “A non-reflecting outflow boundary condition for subsonic Navier-Stokes calculations”. *Journal of Computational Physics*, **36**(1), 55–70.

SAIKI, E. and BIRINGEN, S. (1996). “Numerical simulation of a cylinder in uniform flow: Application of a virtual boundary method”. *Journal of Computational Physics*, **123**(2), 450–465.

SESTERHENN, J., MÜLLER, B. and THOMANN, H. (1999). “On the cancellation problem in calculating compressible low Mach number flows”. *Journal of Computational Physics*, **151**(2), 597–615.

SOTIROPOULOS, F. and YANG, X. (2014). “Immersed boundary methods for simulating fluid-structure interaction”. *Progress in Aerospace Sciences*, **65**, 1–21.

STRAND, B. (1994). “Summation by parts for finite difference approximations for  $d/dx$ ”. *Journal of Computational Physics*, **110**(1), 47–67.

SVÄRD, M. and NORDSTRÖM, J. (2014). “Review of summation-by-parts schemes for initial-boundary-value problems”. *Journal of Computational Physics*, **268**, 17–38.

TRITTON, D. (1959). “Experiments on the flow past a circular cylinder at low Reynolds numbers”. *Journal of Fluid Mechanics*, **6**(04), 547–567.

TSENG, Y.H. and FERZIGER, J.H. (2003). “A ghost-cell immersed boundary method for flow in complex geometry”. *Journal of Computational Physics*, **192**(2), 593–623.

VISBAL, M.R. and GAITONDE, D.V. (2002). “On the use of higher-order finite-difference schemes on curvilinear and deforming meshes”. *Journal of Computational Physics*, **181**(1), 155–185.

YE, T., MITTAL, R., UDAYKUMAR, H. and SHYY, W. (1999). “An accurate Cartesian grid method for viscous incompressible flows with complex immersed boundaries”. *Journal of Computational Physics*, **156**(2), 209–240.

## APPENDIX A. ENERGY METHOD

To demonstrate the energy method, we apply the procedure to a simplified PDE, that is, rather than analysing the full Navier–Stokes equations in this section, we only focus on the 1D convection–diffusion equation as a model equation.

$$\begin{aligned} u_t + au_x &= bu_{xx}, & 0 \leq x \leq 1 & \quad t \geq 0 \\ u(x, 0) &= f(x) \\ u(0, t) &= u(1, t) = g(t) = 0 \end{aligned} \quad (25)$$

where  $a$  and  $b$  are assumed to be constant and positive, and  $u$  is the dependent variable. The  $L_2$  scalar product for two real functions  $v$  and  $w$  is defined by

$$(v, w) = \int_0^1 v(x)w(x)dx \quad (26)$$

which then defines the  $L_2$  norm of the continuous solution at time  $t$  and energy  $E(t) = \|u(\cdot, t)\|^2 = (u, u)$ . Using integration by parts  $(v, w_x) = v(1, t)w(1, t) - v(0, t)w(0, t) - (v_x, w)$ , the energy method leads to

$$\begin{aligned} \frac{dE}{dt} &= \frac{d}{dt} \|u(\cdot, t)\|^2 = (u_t, u) + (u, u_t) \\ &= (-au_x + bu_{xx}, u) + (u, -au_x + bu_{xx}) \\ &= -a[u^2(1, t) - u^2(0, t)] + 2b[u(1, t)u_x(1, t) - u(0, t)u_x(0, t)] \\ &\quad - 2b(u_x, u_x) \leq au^2(0, t) + 2b[u(1, t)u_x(1, t) - u(0, t)u_x(0, t)] \\ &= 0 \end{aligned} \quad (27)$$

which yields a non growing solution, i.e.  $E(t) \leq E(0) = \|f(x)\|^2$ . Thus, the energy is bounded by the initial condition.

## APPENDIX B. SUMMATION BY PARTS OPERATORS

(Khalili *et al.*, 2016)

The SBP operators are constructed to guarantee a discrete energy estimate similar to the continuous energy estimate above.

$$\begin{aligned} u_t + au_x &= bu_{xx}, & 0 \leq x \leq 1 & \quad t \geq 0 \\ u(x, 0) &= f(x) \\ u(0, t) &= u(1, t) = g(t) = 0 \end{aligned} \quad (28)$$

where  $a$  and  $b$  are assumed to be constant and positive, and  $u$  is the dependent variable.

The basis of getting such an energy estimate is to satisfy integration by parts in the discrete sense called Summation–By–Parts (SBP) property (Gustafsson, 2008; Svärd and Nordström, 2014). To outline this technique for model problem (28), we consider  $u_j = u_j(t)$  the numerical solution of the convection–diffusion equation at grid point  $x_j = jh$ ,  $j = 0, \dots, N$ , with grid spacing  $h = \frac{1}{N}$ . The solution vector containing the solution at the discrete grid points is  $\mathbf{u} = [u_0(t), u_1(t), \dots, u_N(t)]^T$ . Using a difference operator  $Q$  approximating the first derivative in space, the semi-discrete form of the model equation can be expressed as

$$\frac{d\mathbf{u}}{dt} = -aQ\mathbf{u} + bQQ\mathbf{u}, \quad u_j(0) = f(x_j) \quad (29)$$

The discrete scalar product and corresponding norm and energy can be defined by

$$\begin{aligned} (\mathbf{u}, \mathbf{v})_h &= h\mathbf{u}^T H\mathbf{v}, \\ E_h(t) &= \|\mathbf{u}\|_h^2 = (\mathbf{u}, \mathbf{u})_h \end{aligned} \quad (30)$$

where  $H$  is a diagonal and positive definite matrix defined by  $H = \text{diag}(H_L, I, H_R)$ . The SBP property is satisfied by the difference operator  $Q$ , if

$$(\mathbf{u}, Q\mathbf{v})_h = u_N v_N - u_0 v_0 - (Q\mathbf{u}, \mathbf{v})_h \quad (31)$$

or if  $Q$  can be written on the form  $hQ = H^{-1}P$  for  $P$  satisfying

$$P + P^T = E_N - E_0 = \text{diag}(-1, 0, \dots, 0, 1) \quad (32)$$

where  $E_0 = \text{diag}(1, 0, \dots, 0)$  and  $E_N = \text{diag}(0, 0, \dots, 1)$ . Using the semi-discrete equation 29, the energy estimate for the semi-discrete problem can be obtained as

$$\begin{aligned} \frac{dE}{dt} &= \frac{d}{dt} \|u(\cdot, t)\|^2 = (u_t, u)_h + (u, u_t)_h \\ &= (-aQu + bQQ\mathbf{u}, \mathbf{u})_h + (u, -aQu + bQQ\mathbf{u})_h \\ &= -a[u_N^2 - u_0^2] + 2b[u_N(Q\mathbf{u})_N - u_0(Q\mathbf{u})_0] \\ &\quad - 2b(Q\mathbf{u}, \mathbf{u})_h \leq au_N^2 + 2b[u_N(Q\mathbf{u})_N - u_0(Q\mathbf{u})_0]. \end{aligned} \quad (33)$$

We would get non-growing energy in time if the homogeneous boundary conditions could directly be imposed in (33). However, this will change the difference operator  $Q$  such that its SBP property might be lost. To avoid this problem, boundary conditions are weakly imposed by the simultaneous approximation term (SAT) technique (Gustafsson, 2008). A first derivative SBP operator with diagonal quadrature matrix  $H$  in 30 is a  $O(h^{2s})$  accurate central difference operator which is  $O(h^s)$  accurate at and near boundaries  $s = 1, 2, 3$ . Such an SBP operator is globally  $O(h^{s+1})$  accurate.

## APPENDIX C. REFORMULATION OF COEFFICIENTS

The four unknown coefficients  $C_i, i = 1, \dots, 4$  can be determined using values of the four variables surrounding the image point. It can be expressed as

$$\mathbf{C} = \mathbf{V}^{-1}\{\phi\} \quad (34)$$

where  $\mathbf{V}$  is the Vandermonde matrix corresponding to the bi-linear interpolation scheme for four surrounding nodes. The value at the image point can be expressed as

$$\phi_{IP} = \begin{bmatrix} 1 & x_{IP} & y_{IP} & x_{IP}y_{IP} \end{bmatrix} \begin{bmatrix} C_1 \\ C_2 \\ C_3 \\ C_4 \end{bmatrix} \quad (35)$$

The vector in bracket can be expressed as

$$\mathbf{V}_{IP} = \begin{bmatrix} 1 & x_{IP} & y_{IP} & x_{IP}y_{IP} \end{bmatrix} = \sum_{i=1}^4 \alpha_i V_i \quad (36)$$

where  $V_i$  is the  $i$ th row of  $\mathbf{V}$  and  $\alpha_i$  depends on the coordinates of the image point and the four surrounding nodes.

Thereby, the matrix equation for  $\alpha$  can be written as

$$\begin{bmatrix} 1 \\ x_{IP} \\ y_{IP} \\ x_{IP}y_{IP} \end{bmatrix} = \begin{bmatrix} 1 & 1 & 1 & 1 \\ x_1 & x_2 & x_3 & x_4 \\ y_1 & y_2 & y_3 & y_4 \\ x_1y_1 & x_2y_2 & x_3y_3 & x_4y_4 \end{bmatrix} \begin{bmatrix} \alpha_1 \\ \alpha_2 \\ \alpha_3 \\ \alpha_4 \end{bmatrix} \quad (37)$$

By rearranging,  $\alpha$  can be obtained as

$$\alpha = \mathbf{V}^{-T} \mathbf{V}_{IP}^T. \quad (38)$$

Thus, the value at the image point can be expressed as

$$\phi_{IP} = \phi^T \mathbf{V}^{-T} \mathbf{V}_{IP}^T \quad (39)$$

Inserting the result obtained in Eq. (38), the value at the image point can be obtained as

$$\phi_{IP} = \sum_{i=1}^4 \alpha_i \phi_i \quad (40)$$

## DIRECT NUMERICAL SIMULATION OF COUPLED HEAT AND MASS TRANSFER IN FLUID-SOLID SYSTEMS

Jiangtao Lu\*, E.A.J.F. Peters, J.A.M. Kuipers

Multiphase Reactors Group, Department of Chemical Engineering and Chemistry, Eindhoven University of Technology, P.O. Box 513, 5600 MB Eindhoven, The Netherlands

\* E-mail: J.Lu1@tue.nl

### ABSTRACT

In this paper, an efficient ghost-cell based immersed boundary method is introduced to perform direct numerical simulation (DNS) of particulate flows. The fluid-solid coupling is achieved by implicit incorporation of the boundary conditions into the discretized momentum, thermal and species conservation equations of the fluid phase. Taking the advantage of a second order quadratic interpolation scheme, different boundary conditions could be realized consistently in our ghost-cell based immersed boundary method. The heat and mass transport in a fluid-particle system is coupled through the solid temperature, which offers a dynamic boundary condition for the fluid thermal equation.

The present simulations are performed for three different fluid-solid systems. The first one is the unsteady mass and heat diffusion in a large pool of quiescent fluid. The solution of the solid temperature development obtained from DNS is compared with the “exact” solution obtained from a standard second-order finite difference technique. Following that, we consider a stationary sphere under forced convection. The steady state temperature of the particle can be calculated from the fluid-solid mass and heat transfer rates, which are obtained from the well-known empirical Ranz-Marshall and Frössling correlations. The last simulation case is an in-line array of three spheres, the so-called three-bead reactor. The computed adiabatic temperature rise obtained from DNS shows good agreement with the value calculated from the overall species conversion ratio of the reactor.

**Keywords:** Direct numerical simulation, ghost-cell based immersed boundary method, particulate flows, multiphase heat and mass transfer.

### NOMENCLATURE

#### Greek Symbols

$\alpha, \beta$  Coefficients of Robin boundary condition.  
 $\alpha_h$  Heat transfer coefficient, [W/m<sup>2</sup>/K].  
 $\lambda_f$  Fluid thermal conductivity, [W/m/K].  
 $\mu_f$  Fluid dynamic viscosity, [kg/m/s].  
 $\xi_f$  Species conversion ratio, [1].  
 $\rho_f$  Fluid density, [kg/m<sup>3</sup>].  
 $\phi$  General fluid variable.  
 $\Delta H_r$  Reaction enthalpy, [J/mol].

$\Delta t$  Time step, [s].  
 $\Delta T_a$  Adiabatic temperature rise, [K].  
 $\Phi_{h,f \rightarrow s}$  Heat transfer rate from fluid to solid, [J/s].  
 $\Phi_{m,f \rightarrow s}$  Molar transfer rate from fluid to solid, [mol/s].

#### Latin Symbols

$a, b$  Coefficients in generic discretised equations.  
 $c_f$  Molar concentration, [mol/m<sup>3</sup>].  
 $c_{f,0}$  Initial molar concentration, [mol/m<sup>3</sup>].  
 $c_{f,in}$  Inlet molar concentration, [mol/m<sup>3</sup>].  
 $c_{ijk}$  Coefficients in second-order polynomial.  
 $C_{p,f}$  Fluid heat capacity, [J/kg/K].  
 $C_{p,s}$  Solid volumetric heat capacity, [J/m<sup>3</sup>/K].  
 $C_h$  Convective heat transport per unit of volume, [W/m<sup>3</sup>].  
 $C_m$  Convective species transport per unit of volume, [mol/m<sup>3</sup>/s].  
 $C_m$  Convective momentum flux, [N/m<sup>3</sup>].  
 $d_s$  Sphere diameter, [m].  
 $D_f$  Mass diffusivity, [m<sup>2</sup>/s].  
 $D_h$  Diffusive heat transport per unit of volume, [W/m<sup>3</sup>].  
 $D_m$  Diffusive species transport per unit of volume, [mol/m<sup>3</sup>/s].  
 $D_m$  Diffusive momentum flux, [N/m<sup>3</sup>].  
 $f$  Coefficient of Robin boundary condition.  
 $g$  Gravitational acceleration, [m/s<sup>2</sup>].  
 $k_m$  Mass transfer coefficient, [m/s].  
 $n$  Unit normal vector, [1].  
 $p$  Pressure, [Pa].  
 $r$  Spherical coordinate, [m].  
 $R_s$  Sphere radius, [m].  
 $S$  Area, [m<sup>2</sup>].  
 $S_S$  Particle surface area, [m<sup>2</sup>].  
 $t$  Time, [s].  
 $T_f$  Fluid temperature, [K].  
 $T_{f,0}$  Initial fluid temperature, [K].  
 $T_{f,in}$  Inlet fluid temperature, [K].  
 $T_{f,out}$  Outlet fluid temperature, [K].  
 $T_s$  Solid temperature, [K].  
 $u$  Velocity, [m/s].  
 $V_s$  Particle volume, [m<sup>3</sup>].  
 $x, y, z$  Relative Cartesian coordinate, [m].

$X, Y, Z$  Cartesian coordinate, [m].

*Sub/superscripts*

$f$  Fluid phase.  
 $s$  Solid phase.

## INTRODUCTION

Fluid-particle flows are frequently encountered in a wide range of industrial processes, such as chemical, petrochemical and energy industries. Often these processes are accompanied with significant heat effects. Understanding the mass and heat transport processes in such complex heterogeneous systems is of great importance to improve performance and facilitate optimal design of process equipment.

For prediction of particulate flows in engineering scale equipment, accurate closures for fluid-solid interaction are of utmost importance. This requirement has led to the adoption of a multiscale modelling approach (van der Hoef *et al.*, 2008), which offers the possibility to compute and parameterize closures for application in more coarse-grained models. With the development of computational technology, DNS has become a powerful tool to resolve all the details at the smallest relevant length scales and quantitatively derive microscale transport coefficients to gain fundamental insight in fluid-solid interactions. In recent years the immersed boundary method (IBM), as a branch of DNS, has received a lot of attention. Taking the advantages of efficient CPU/memory utilization and easy grid generation, IBM is applied in various studies including complex situations of moving particles, complex geometries and deformable immersed objects (Fadlun *et al.*, 2000; Udaykumar *et al.*, 2001; Tseng and Ferziger, 2003). Following the fluid flow equations, additional equations for species and thermal energy transport can be added using the same methodology.

The IBM was first introduced by Peskin for simulation of blood around the flexible leaflet of a human heart (Peskin, 1977). The main idea of this method is to use a Cartesian grid for fluid flow simulation whereas the immersed boundary is represented by Lagrangian marker points. A forcing term is introduced to represent the interaction between the immersed boundary and the fluid, whose magnitude is taken such that the boundary conditions are fulfilled in an interpolated manner. A regularized Dirac delta function is used to distribute this singular force over a belt of cells surrounding each Lagrangian point. This method is categorized as continuous forcing method (CFM), and many researchers have contributed to the further development of this method (Goldstein *et al.*, 1993; Saiki and Biringen, 1996; Uhlmann, 2005). The second category of IBM is referred to as discrete forcing method (DFM), which was first proposed by Mohd-Yusof (1997), and later extended by Fadlun *et al.* (2000), Tseng and Ferziger (2003), Marella *et al.* (2005), Ghias *et al.* (2007), Haugen and Kragset (2010), Seo and Mittal (2011) and Lee and You (2013). In this method the ghost point approach is applied, where the virtual (i.e. inside the immersed body) variable value is calculated through the boundary

condition and the fluid variables near the boundary. DFM treats the immersed boundary as a sharp interface, and does not require the explicit addition of a force in the governing equations, thus the stability limit is the same as that without the immersed boundaries.

Although IBM has been widely used for studies of momentum transfer in fluid-solid system, very few computational results are available in the field of mass and heat transfer (Bagchi *et al.*, 2000; Zhang *et al.*, 2008; Wang *et al.*, 2009; Shu *et al.*, 2013; Tavassoli *et al.*, 2013; Tenneti *et al.*, 2013; Xia *et al.*, 2014). Coupled mass and heat transfer has been reported by Dierich *et al.* (2011) using 2D DNS, Li *et al.* (2013) using Lattice Boltzmann method and Deen and Kuipers (2014) using 3D DNS with directional quadratic interpolation scheme.

In this paper, an efficient ghost-cell based immersed boundary method is proposed for the simulation of coupled heat and mass transfer problems in fluid-solid system. The reconstruction procedures involve a second order quadratic interpolation scheme. As the unique feature, different boundary conditions are realized consistently and enforced exactly at the particle surface. The organisation of this paper is as follows. First, the description of the model is given. Subsequently, the results are presented, through which the strength of our DNS model is demonstrated. Single sphere unsteady diffusion, forced convection to a single stationary sphere and a three-bead reactor are considered and analysed. Finally, the conclusions are presented.

## MODEL DESCRIPTION

In this part, we describe the governing equations that need to be solved in DNS, the numerical details involved in the finite difference scheme, as well as the fluid-solid coupling. For the model presented in this paper, the following main assumptions are applied:

- The fluid phase is incompressible and Newtonian.
- The solid phase consists of spherical particles, and intra-particle temperature gradients are negligible.
- Both fluid and solid phase have constant physical properties.

### Governing equations of fluid phase

The transport phenomena in the fluid phase are governed by the conservation equations for mass, momentum, species and thermal energy, respectively defined as:

$$\nabla \cdot \mathbf{u} = 0 \quad (1)$$

$$\frac{\partial \rho_f \mathbf{u}}{\partial t} + \nabla \cdot (\rho_f \mathbf{u} \mathbf{u}) = -\nabla p + \mu_f \nabla^2 \mathbf{u} + \rho_f \mathbf{g} \quad (2)$$

$$\frac{\partial c_f}{\partial t} + \nabla \cdot (c_f \mathbf{u}) = D_f \nabla^2 c_f \quad (3)$$

$$\rho_f C_{p,f} \left[ \frac{\partial T_f}{\partial t} + \nabla \cdot (T_f \mathbf{u}) \right] = \lambda_f \nabla^2 T_f \quad (4)$$

In above equations,  $\rho_f$  is the fluid density,  $\mu_f$  is the fluid viscosity,  $D_f$  is the species mass diffusivity in the fluid

whereas  $C_{p,f}$  and  $\lambda_f$  are the heat capacity and thermal conductivity of the fluid phase respectively.

### Governing equation of solid phase

The particle temperature is governed by the following equation with the assumption of a uniform particle temperature:

$$V_s C_{p,s} \frac{dT_s}{dt} = \Phi_{h,f \rightarrow s} + \Phi_{m,f \rightarrow s} (-\Delta H_r) \quad (5)$$

In this equation, the first term on the right hand side is the fluid-solid heat transfer rate while the second term represents the rate of reaction heat liberated from a chemical reaction. The heat transfer rate and mass transfer rate, with the normal pointing outward of the solid, are calculated by the following two equations respectively:

$$\Phi_{h,f \rightarrow s} = -\iint_{S_s} (-\lambda_f \nabla T_f \cdot \mathbf{n}) dS \quad (6)$$

$$\Phi_{m,f \rightarrow s} = -\iint_{S_s} (-D_f \nabla c_f \cdot \mathbf{n}) dS \quad (7)$$

Considering an exothermal chemical reaction proceeding at the exterior surface of the particles, the heat liberation is assumed to be rapidly transported to the interior of the particle with a negligible intra-particle temperature gradient. The coupling between the fluid thermal energy equation and the fluid species conservation equation is fulfilled through the particle thermal energy equation. In other words, the particle temperature of individual particle offers a dynamic boundary condition for the thermal energy equation of the fluid phase.

For longer times, the particle temperature will become constant, which implies the liberated reaction heat is fully carried away by the fluid. In this case, Equation (5) reduces to the following one which is often encountered in descriptions of coupled heat and mass transport phenomena.

$$\Phi_{m,f \rightarrow s} (-\Delta H_r) = -\Phi_{h,f \rightarrow s} \quad (8)$$

### Numerical solution method

The governing equations are solved by a finite difference scheme implemented for a staggered Cartesian grid. The grid is defined in three dimensions (3D) with a uniform grid spacing in all three directions. Building on the work of Deen *et al.* (2012), the numerical solution of the equations described in previous section is acquired by using both high order discretization schemes and small computational stencils. The momentum equation is discretised in time by a first order Euler scheme:

$$\rho_f \mathbf{u}^{n+1} = \rho_f \mathbf{u}^n + \Delta t \left[ -\nabla p^{n+1} - \left( \frac{3}{2} \mathbf{C}_m^n - \frac{1}{2} \mathbf{C}_m^{n-1} \right) + \mathbf{D}_m^{n+1} + \rho_f \mathbf{g} \right] \quad (9)$$

In this equation,  $n$  is the time step index. The convective and diffusive momentum fluxes  $\mathbf{C}_m$  and  $\mathbf{D}_m$  are calculated by the spatial discretization of:

$$\mathbf{C}_m = \rho_f (\nabla \cdot \mathbf{u}\mathbf{u}) \quad (10)$$

$$\mathbf{D}_m = \mu_f \nabla^2 \mathbf{u} \quad (11)$$

The solution of Equation (9) is achieved by using a two-step projection method where a tentative velocity field  $\bar{\mathbf{u}}^{**}$  is first computed by neglecting the pressure gradient contribution. As the second step, the velocity field at the new time step  $n+1$  is obtained based on the new pressure gradient calculated from Poisson equation at time step  $n+1$ . For the interested reader, we refer for a more detailed description of this method to the work of Deen and Kuipers (2013).

The species and thermal energy convection-diffusion equations are temporally discretised in the same way as for the momentum equation, namely the Adams-Bashforth scheme is applied for the convective transport while the fully implicit Euler backward scheme is used for the diffusion term.

$$c_f^{n+1} = c_f^n + \Delta t \left[ -\left( \frac{3}{2} C_m^n - \frac{1}{2} C_m^{n-1} \right) + D_m^{n+1} \right] \quad (12)$$

$$T_f^{n+1} = T_f^n + \frac{\Delta t}{\rho_f C_{p,f}} \left[ -\left( \frac{3}{2} C_h^n - \frac{1}{2} C_h^{n-1} \right) + D_h^{n+1} \right] \quad (13)$$

with the convective species molar flux  $C_m$  and convective heat flux  $C_h$  given by:

$$C_m = \nabla \cdot (c_f \mathbf{u}) \quad (14)$$

$$C_h = \rho_f C_{p,f} \nabla \cdot (T_f \mathbf{u}) \quad (15)$$

and the diffusive molar flux  $D_m$  and diffusive heat flux  $D_h$  computed as:

$$D_m = D_f \nabla^2 c_f \quad (16)$$

$$D_h = \lambda_f \nabla^2 T_f \quad (17)$$

For momentum, species and thermal energy equations, the convection term is spatially discretized by a second-order total variation diminishing scheme, whereas the diffusion term is computed with a standard second-order central differencing scheme. The boundary condition is enforced at exactly the immersed boundary surface, which is handled at the level of the discretized equations and will be introduced in detail in next section.

The solid phase equation is solved after the fluid phase equations. The trapezoidal rule is used for the time integration, which maintains second order accuracy.

$$T_s^{n+1} = T_s^n + \frac{\Delta t}{V_s C_{p,s}} \left[ \Phi_{h,f \rightarrow s}^{n+\frac{1}{2}} + (-\Delta H_r) \Phi_{m,f \rightarrow s}^{n+\frac{1}{2}} \right] \quad (18)$$

### Fluid-solid coupling

The fluid-solid coupling constitutes the key element of our model. In order to impose variable boundary conditions in a sharp interface way, a ghost-cell based immersed boundary method is developed. The discretization of momentum, species and thermal energy equation leads to algebraic equations of the following generic form:

$$a_c \phi_c + \sum_1^6 a_{nb} \phi_{nb} = b_c \quad (19)$$

where  $\phi$  is the fluid variable for which we want to find a solution, namely velocity, concentration and temperature

fields for momentum, species and thermal energy equation, respectively. This equation provides the relationship between any fluid quantity  $\phi_c$  and its six neighbouring points indicated as  $\phi_{nb}$ .

Since the surfaces of the immersed objects do not coincide with the mesh boundaries, we need a special treatment for the nodes near the fluid-solid interface. In our method, the first step is to identify all ghost points, which are defined as points inside the solid phase but having at least one neighbour in fluid phase. These points are used to obtain a solution of the governing equations for the exterior of the solid phase. The second step is to check every fluid node whether any of its six surrounding neighbours represents a ghost point. If this is the case, a boundary condition has to be applied.

Figure 1 demonstrates the quadratic interpolation scheme used in our model. It is given in a 2D domain for illustration purpose, in which the shadow in cross shape represents the initial computational stencil containing four neighbours. In the end, i.e. after imposing the boundary condition, G is removed from the stencil, while  $F_1$  and  $F_2$  are added to it. It should be noted that this reconstruction procedure is of best suitability in case the description of the gradient in the normal direction is required, specifically the non-homogeneous Neumann boundary condition encountered in species transport calculation.

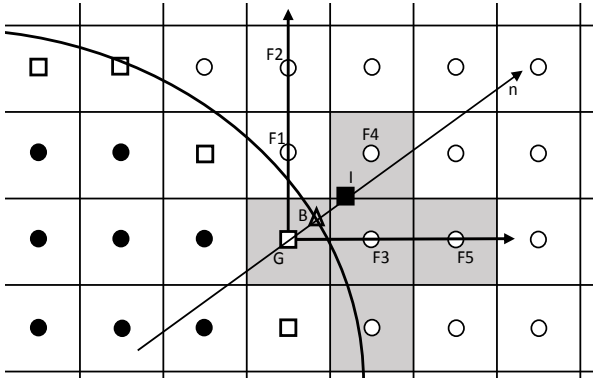


**Figure 1:** Schematic representation of the interpolation procedures for quadratic interpolation. Filled circles indicate the solid phase points, while open circles indicate the fluid phase points and open squares indicate the ghost points. The triangle and solid square are the boundary point and image point, respectively.

A generic variable  $\phi$  in the vicinity of the immersed object surface could be approximated in terms of a second-order polynomial as follows:

$$\phi = \sum_{i=0}^2 \sum_{j=0}^2 \sum_{k=0}^2 c_{ijk} x^i y^j z^k, i + j + k \leq 2 \quad (20)$$

where relative coordinates are applied based on the location of boundary point  $(X_B, Y_B, Z_B)$ , which is the interception of normal direction and immersed boundary surface.

$$x = X - X_B \quad (21)$$

$$y = Y - Y_B \quad (22)$$

$$z = Z - Z_B \quad (23)$$

Equation (20) is in fact the approximation of  $\phi$  using the Taylor expansion near the boundary point:

$$\begin{aligned} \phi(x, y, z) = & \phi_B + \frac{\partial \phi_B}{\partial x} x + \frac{\partial \phi_B}{\partial y} y + \frac{\partial \phi_B}{\partial z} z \\ & + \frac{1}{2} \frac{\partial^2 \phi_B}{\partial x^2} x^2 + \frac{1}{2} \frac{\partial^2 \phi_B}{\partial y^2} y^2 + \frac{1}{2} \frac{\partial^2 \phi_B}{\partial z^2} z^2 + \dots \end{aligned} \quad (24)$$

In the 3D case, the number of coefficients for a second-order polynomial is ten. In order to determine these coefficients  $c_{ijk}$ , we need  $\phi$  values from nine neighbouring fluid points and one image point. The image point is defined as the mirror point of the ghost point through the boundary in normal direction, which has the same distance to the boundary point as the ghost point. For the 2D case, only five fluid points plus one image point are required for computation of  $c_{ij}$  coefficients, as indicated in Figure 1.

With adequate data points (ten values at fluid/image point for ten coefficients in a second-order polynomial), the resulting equation for solving coefficients  $c_{ijk}$  can be written as a matrix vector multiplication:

$$\boldsymbol{\phi} = \mathbf{X}\mathbf{c} \quad (25)$$

where  $\boldsymbol{\phi}$  and  $\mathbf{c}$  are the vectors for species concentrations and coefficients respectively, and  $\mathbf{X}$  is the Vandermonde matrix given by:

$$\mathbf{X} = \begin{bmatrix} 1 & x_1 & y_1 & z_1 & x_1^2 & y_1^2 & z_1^2 & x_1 y_1 & x_1 z_1 & y_1 z_1 \\ 1 & x_2 & y_2 & z_2 & x_2^2 & y_2^2 & z_2^2 & x_2 y_2 & x_2 z_2 & y_2 z_2 \\ \vdots & \vdots & \vdots & \vdots & \vdots & \vdots & \vdots & \vdots & \vdots & \vdots \\ 1 & x_{10} & y_{10} & z_{10} & x_{10}^2 & y_{10}^2 & z_{10}^2 & x_{10} y_{10} & x_{10} z_{10} & y_{10} z_{10} \end{bmatrix} \quad (26)$$

To solve Equation (25), the Vandermonde matrix is inverted by applying LU decomposition with Crout algorithm. The coefficients  $c_{ijk}$  are obtained by multiplication of the inversed matrix  $\mathbf{X}^{-1}$  and the concentration vector  $\boldsymbol{\phi}$ , which can be written as a linear combination of  $\phi$  values.

$$c_{000} = \phi_B = \sum_{m=1}^{10} \mathbf{X}_{1m}^{-1} \phi_m \quad (27)$$

$$c_{100} = \frac{\partial \phi_B}{\partial x} = \sum_{m=1}^{10} \mathbf{X}_{2m}^{-1} \phi_m \quad (28)$$

$$c_{010} = \frac{\partial \phi_B}{\partial y} = \sum_{m=1}^{10} \mathbf{X}_{3m}^{-1} \phi_m \quad (29)$$

$$c_{001} = \frac{\partial \phi_B}{\partial z} = \sum_{m=1}^{10} \mathbf{X}_{4m}^{-1} \phi_m \quad (30)$$

Therefore, for a general Robin boundary condition at the immersed object surface:

$$\alpha \phi_B + \beta \frac{\partial \phi_B}{\partial n} = f \quad (31)$$

the image point value can be evaluated by satisfying the boundary condition at the boundary point:

$$\phi_I = \frac{f - \sum_{m=2}^{10} M_m \phi_m}{M_0} \quad (32)$$

where  $M_m$  is defined according to the following equation, with the components of the normal unit vector indicated as  $n_x$ ,  $n_y$  and  $n_z$  respectively:

$$M_m = \alpha X_{1m}^{-1} + \beta (n_x X_{2m}^{-1} + n_y X_{3m}^{-1} + n_z X_{4m}^{-1}) \quad (33)$$

Considering the correlation between image point and ghost point ( $\Delta l$  is the mutual distance):

$$\phi_B = \frac{\phi_G + \phi_I}{2} \quad (34)$$

$$\frac{\partial \phi_B}{\partial n} = \frac{\phi_G - \phi_I}{\Delta l} \quad (35)$$

the value at the ghost point can be computed as:

$$\phi_G = \frac{(2\Delta l M_1 - \alpha \Delta l + 2\beta) f + (\alpha \Delta l - 2\beta) \sum_{m=2}^{10} M_m \phi_m}{(\alpha \Delta l + 2\beta) M_1} \quad (36)$$

With Equation (36), the matrix coefficients in Equation (19) can be updated. Altered coefficients within the original stencil are incorporated in the implicit scheme, while neighbours outside the original stencil are accounted for in an explicit way. The procedure described above needs to be carried out for all ghost points to ensure that the desired local boundary condition applies everywhere at the immersed boundary surface. Note that the pressure, velocity, concentration and temperature field are obtained for the entire computation domain, i.e. also for the cells inside the particles, with our DNS model proposed above.

## RESULTS

In this section, three fluid-solid systems will be presented for coupled heat and mass transfer. The results obtained from our DNS model demonstrate its strong power in engineering applications. In the next sub-sections, comparisons are made between DNS and the “exact” solution for the limiting case of unsteady molecular diffusion and empirical values for forced convection, whereas a three-bead reactor will be considered lastly.

### Unsteady mass and heat transport

Here we consider the unsteady diffusion of a certain species to a sphere, where species vanishes and reaction heat is liberated. The sphere is positioned in the centre of a large pool of quiescent fluid. The governing equations for unsteady mass and heat diffusion in the fluid phase are described by Equation (3) and (4) respectively, with  $\mathbf{u}$  set as zero. The initial conditions are defined by the following two equations, for species and thermal energy conservation equation respectively:

$$c_f = c_{f,0} \quad (37)$$

$$T_f = T_{f,0} \quad (38)$$

The boundary conditions are:

$$c_f|_{wall,t} = c_{f,0} \quad (39)$$

$$T_f|_{wall,t} = T_{f,0} \quad (40)$$

at the boundaries of the simulation domain, and

$$c_f|_{R_s,t} = 0 \quad (41)$$

$$T_f|_{R_s,t} = T_s \quad (42)$$

at the sphere surface. Equation (39) and (40) are valid as long as the diffusion fronts have not reached the confining walls. The particle temperature  $T_s$  in Equation (42) serves as a dynamic boundary condition for the fluid phase thermal energy equation, and governed by the particle thermal energy equation (Equation (5)).

For the DNS the particle is located in the centre of a cubic box with a length of 0.12m. The data used for the numerical simulation are given in Table 1. The simulation is computed in a  $120 \times 120 \times 120$  grid with uniform grid spacing in all directions.

**Table 1:** Data used for the simulation of unsteady mass and heat transport.

Parameter	Value
Time step [s]	$5 \times 10^{-5}$
Sphere diameter [m]	0.015
Fluid density [ $\text{kg}/\text{m}^3$ ]	1.0
Fluid diffusivity [ $\text{m}^2/\text{s}$ ]	$2 \times 10^{-5}$
Fluid thermal conductivity [W/m/K]	0.025
Fluid heat capacity [J/kg/K]	1000
Particle volumetric heat capacity [J/m <sup>3</sup> /K]	1000
Reaction enthalpy [J/mol]	$-10^{-5}$
Fluid initial concentration [mol/m <sup>3</sup> ]	1.0
Fluid initial temperature [K]	293
Particle initial temperature [K]	293

To offer an “exact” solution for the particle temperature as well as concentration and temperature profiles in the fluid phase, the model composed the spherical symmetric problem (so only  $r$  dependence) is solved by a standard second order finite difference technique. In this case, the governing equations for unsteady mass and heat diffusion in the fluid phase are respectively described as:

$$\frac{\partial c_f}{\partial t} = \frac{D_f}{r^2} \frac{\partial}{\partial r} \left( r^2 \frac{\partial c_f}{\partial r} \right) \quad (43)$$

$$\rho_f C_{p,f} \frac{\partial T_f}{\partial t} = \frac{\lambda_f}{r^2} \frac{\partial}{\partial r} \left( r^2 \frac{\partial T_f}{\partial r} \right) \quad (44)$$

The heat and mass transfer rates required in particle thermal energy equation are redefined as:

$$\Phi_{h,f \rightarrow s} = \lambda_f \frac{\partial T_f}{\partial r} \Big|_{r=R_s} \quad 4\pi R_s^2 \quad (45)$$

$$\Phi_{m,f \rightarrow s} = D_f \frac{\partial c_f}{\partial r} \Big|_{r=R_s} \quad 4\pi R_s^2 \quad (46)$$

It should be noted here that a very large number of grid points in the radial direction was used to obtain this highly accurate numerical solution. In theory, the particle temperature at final steady state can be computed by Equation (8), which gives:

$$T_s = T_{f,0} + \frac{\Delta T_a}{Le} \quad (47)$$

In this equation,  $\Delta T_a$  is the adiabatic temperature rise calculated as:

$$\Delta T_a = \frac{(-\Delta H_r) c_{f,0}}{\rho_f C_{p,f}} \quad (48)$$



and  $Le$  is the Lewis number defined as the ratio of the thermal diffusivity and the mass diffusivity:

$$Le = \frac{\lambda_f}{D_f} = \frac{\rho_f C_{p,f}}{Pr} = \frac{Sc}{Pr} \quad (49)$$

The simulation results obtained from DNS are compared with the “exact” solution obtained from the standard second order finite difference technique. Using the data listed in Table 1 the analytical temperature difference between the particle and the infinite far fluid is 80K at final steady state. From our DNS, a value of 81.6K is obtained, which matches well with the analytical one. In Figure 2, the particle temperature evolution profiles are plotted along the time scale, to give a comparison between the solutions. As clearly demonstrated in Figure 2, these two solutions reach a good agreement. The behaviour of the evolution curve can be explained as follows. At initial few time steps, the species flux is relatively high so that the heat liberated from the exothermal reaction rapidly heats the particle up from initial temperature. After that, a temperature difference between the particle and the surrounding fluid is established, so that the heat is transferred from the particle to the fluid through unsteady heat conduction. Finally, the heat removal rate goes to the same value as the heat liberation rate, which leads to the final steady state of a constant particle temperature.

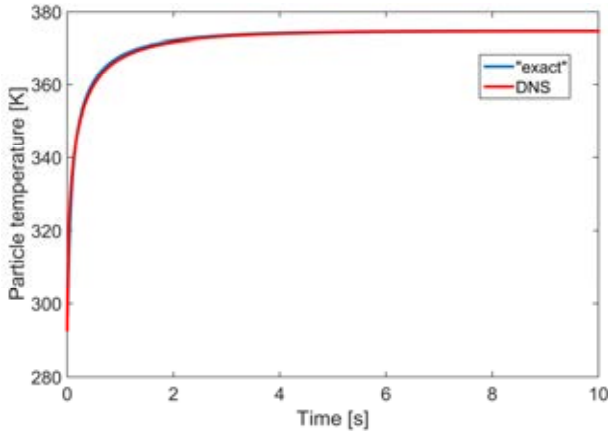


**Figure 2:** Comparison of particle temperature evolution profiles between simulation and the “exact” solution.

### Convective heat and mass transfer to a stationary sphere

In this system, we consider an exothermic chemical reaction under forced convection, which is external mass transfer limited and proceeds at the surface of a single stationary sphere in an enclosure. The sphere is located at the centre of the domain laterally while it is positioned at a distance of two times of the sphere size from the inlet in the flow direction. The data used for the numerical simulation are summarized in Table 2. The simulations are computed in a  $240 \times 240 \times 240$  grid with uniform grid spacing in all directions. The ratio of domain size to the particle size is eight whereas the mesh resolution applied to the particle is thirty.

The particle Sherwood number  $Sh_s$  and Nusselt number  $Nu_s$  are predicted by the well-known empirical Frössling and Ranz-Marshall correlations for a single sphere subject to a Dirichlet boundary condition:

$$Sh_s = \frac{k_m d_s}{D_f} = 2.0 + 0.6 (Re_s)^{\frac{1}{2}} (Sc)^{\frac{1}{3}} \quad (50)$$

$$Nu_s = \frac{\alpha_h d_s}{\lambda_f} = 2.0 + 0.6 (Re_s)^{\frac{1}{2}} (Pr)^{\frac{1}{3}} \quad (51)$$

where  $Re_s$  is the particle Reynolds number,  $Sc$  and  $Pr$  are the Schmidt number and Prandtl number, respectively. These three dimensionless numbers are defined as follows:

$$Re_s = \frac{\rho_f u_0 d_s}{\mu_f} \quad (52)$$

$$Sc = \frac{\mu_f}{\rho_f D_f} \quad (53)$$

$$Pr = \frac{\mu_f C_{p,f}}{\lambda_f} \quad (54)$$

**Table 2:** Data used for the simulations of coupled heat and mass transfer to a single stationary sphere under forced convection.

Parameter	Value
Time step [s]	$1 \times 10^{-4}$
Grid size [m]	$5 \times 10^{-4}$
Sphere diameter [m]	0.015
Fluid density [ $\text{kg}/\text{m}^3$ ]	1.0
Fluid viscosity [ $\text{kg}/\text{m}\cdot\text{s}$ ]	$2 \times 10^{-5}$
Fluid diffusivity [ $\text{m}^2/\text{s}$ ]	$2 \times 10^{-5}$
Fluid thermal conductivity [ $\text{W}/\text{m}\cdot\text{K}$ ]	0.025
Fluid heat capacity [ $\text{J}/\text{kg}\cdot\text{K}$ ]	1000
Particle volumetric heat capacity [ $\text{J}/\text{m}^3\cdot\text{K}$ ]	1000
Reaction enthalpy [ $\text{J}/\text{mol}$ ]	$-10^5$
Fluid initial concentration [ $\text{mol}/\text{m}^3$ ]	1.0
Fluid initial temperature [K]	293
Particle initial temperature [K]	293

As explained in the second section, the particle temperature at final steady state is described by:

$$\Phi_{m,f \rightarrow s} (-\Delta H_r) = -\Phi_{h,f \rightarrow s} \quad (55)$$

The empirical value can be calculated from the mass transfer coefficient  $k_m$  and heat transfer coefficient  $\alpha_h$ .

$$S_s k_m (c_f - c_{f,s}) (-\Delta H_r) = -S_s \alpha_h (T_s - T_f) \quad (56)$$

where  $S_s$  is the particle surface area and  $c_{f,s}$  is zero considering the precondition of a completely mass transfer limited chemical reaction proceeding at the sphere surface. Equation (56) can be rearranged to the following expression:

$$T_s = T_f + \frac{k_m c_f (-\Delta H_r)}{\alpha_h} \quad (57)$$

Substitute Equation (50) and (51) into above equation, the steady state particle temperature can be calculated empirically:

$$T_s = T_f + \frac{Sh_s}{Nu_s} \frac{c_f (-\Delta H_r)}{\rho_f C_{p,f} Le} \quad (58)$$

In Table 3, the comparison between the simulation results obtained from our DNS model and the empirical values

(indicated as EMP) calculated from Equation (58) is demonstrated. In this table, we also list the particle Sherwood number and Nusselt number calculated from simulation work and the values given by the empirical correlations (Equation (50) and (51)). All results reach a good agreement.

**Table 3:** Comparison of steady state particle temperature, particle Sherwood number and Nusselt number between DNS and empirical values.

$Re_s$	$T_s$		$Sh_s$		$Nu_s$	
	DNS	EMP	DNS	EMP	DNS	EMP
30	377.7	376.7	5.13	5.29	4.83	5.05
60	378.4	377.2	6.52	6.65	6.11	6.31
120	379.1	377.7	8.51	8.57	7.91	8.10
240	379.8	378.0	11.53	11.30	10.63	10.63
480	379.9	378.3	15.60	15.15	14.28	14.20

It should be noted here, the particle temperature at final steady state is found to be insensitive to the change of particle Reynolds number. This can be explained by Equation (58). In case of high fluid velocity, the convection term dominates so that the equation can be simplified to the following one, which is independent of particle Reynolds number.

$$T_s = T_f + \frac{(Sc)^{\frac{1}{3}} c_f (-\Delta H_r)}{(Pr)^{\frac{1}{3}} \rho_f C_{p,f} Le} = T_f + \frac{c_f (-\Delta H_r)}{\rho_f C_{p,f} Le^{\frac{2}{3}}} \quad (59)$$

### An in-line array of three stationary spheres

In this sub-section, we consider an in-line array of three spheres, the so-called three-bead reactor. The spheres are positioned in a cuboid domain with 0.21m in length and 0.02m in cross-sectional diameter. Free slip boundary condition is applied at the domain boundary for velocity calculation, while Neumann boundary condition (non-penetrating walls) is used for concentration and thermal energy equations. The first sphere is located at a distance of two times of the sphere size from the inlet in the flow direction, and the other two spheres are located in such a way that the mutual distance between all sphere centres is one and half times of the sphere diameter. Table 4 lists the simulation data.

**Table 4:** Data used for the simulations of coupled heat and mass transfer in a three-bead reactor.

Parameter	Value
Domain size in grid points	420×40×40
Time step [s]	1×10 <sup>-4</sup>
Grid size [m]	5×10 <sup>-4</sup>
Sphere diameter [m]	0.015
Fluid density [kg/m <sup>3</sup> ]	1.0
Fluid viscosity [kg/m/s]	2×10 <sup>-5</sup>
Fluid diffusivity [m <sup>2</sup> /s]	2×10 <sup>-5</sup>
Fluid thermal conductivity [W/m/K]	0.025
Fluid heat capacity [J/kg/K]	1000
Particle volumetric heat capacity [J/m <sup>3</sup> /K]	1000
Reaction enthalpy [J/mol]	-10 <sup>-5</sup>
Fluid initial concentration [mol/m <sup>3</sup> ]	0.0
Fluid initial temperature [K]	293
Particle initial temperature [K]	293
Fluid inlet velocity [m/s]	0.32
Fluid inlet concentration [mol/m <sup>3</sup> ]	1.0
Fluid inlet temperature [K]	293

For this three-bead reactor system, we consider two cases. One is of a fast exothermal chemical reaction proceeding at the surface of all three spheres (Case 1), whereas the other one contains an inert (non-reactive) sphere which is located at the second position (Case 2).

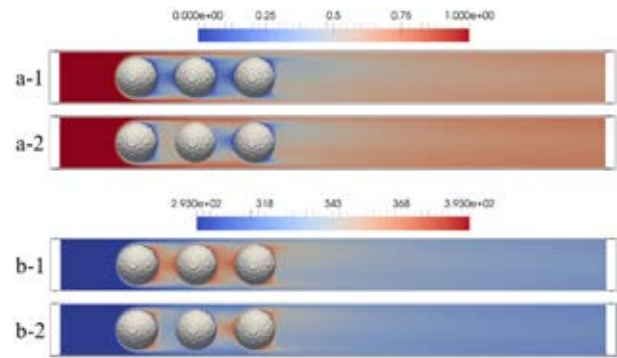


**Figure 3:** Fluid phase species concentration (a) and thermal temperature (b) distribution inside the reactor, in the central plane. Index 1 and 2 refer to Case 1 and 2 respectively.

Figure 3 illustrates the simulation results of concentration and temperature distribution at steady state for both cases. The corresponding particle temperature evolution profiles are presented in Figure 4. A thermal energy wave is moving through the in-line array of three spheres. The first sphere rapidly heats up due to the exothermal chemical reaction proceeding at its surface. Due to a temperature difference between the particle and the surrounding fluid, the thermal energy is transferred from the solid phase to the fluid phase. The sphere temperature finally reaches a constant value when the removed heat equals to the generated reaction heat. For the first particle, the thermal behavior is almost identical for Case 1 and Case 2. For the second sphere, it has completely different behaviors as it is reactive in Case 1 while an inert surface is assumed in Case 2. For Case 1, there are two contributors to the rise of sphere temperature: liberated reaction heat and convective heat transfer. The unconverted reactant which has passed the first sphere is partly converted at the surface of the second sphere. The thermal energy transferred from the first sphere to the fluid is further transferred to the second sphere. For Case 2, the only heat source is the convective heat transfer as there is no reaction proceeding at the sphere surface. Due to the initial large temperature difference between the fluid and the sphere, it heats up quickly and as a consequence the temperature difference decreases and finally the second sphere reaches the same temperature as the surrounding fluid. For the third sphere, it has the same boundary condition in Case 1 and Case 2. The remaining reactant is partly converted at the surface of the particle and the thermal energy in solid phase is subsequently transferred to the fluid. However, slight differences are noticed in the temperature evolution curves of the third sphere. The particle temperature develops faster in Case 2. This can be explained by the larger driving force of the chemical reaction as the second sphere does not consume any reactant in Case 2. It should be noted that the thermal energy in fluid phase is only generated by the first sphere and partly used for heating up the second sphere in Case 2, which means the convective heat transfer from fluid to the third sphere is

lower comparing with the case of both first and second sphere contributing to the fluid thermal energy in Case 1. This demonstrates the dominant role of reaction heat in the development of particle temperature.

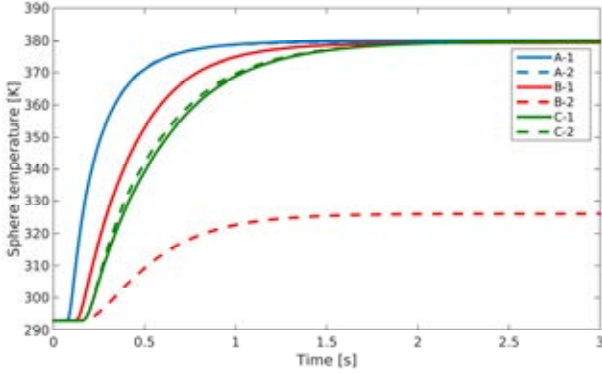


**Figure 4:** Evolution of particle temperatures for the three-bead reactor. A, B and C are the first, second and third sphere respectively, and index 1 and 2 correspond to Case 1 and 2 respectively.

The axial profiles of cup-average concentration and temperature are shown in Figure 5, which demonstrates the relative contribution of individual sphere to the overall reactant conversion and temperature rise. In both cases, the first sphere has the highest contribution. In Case 1, the second sphere has a lower contribution compared to the first sphere, while the third sphere contributes even less. In Case 2, as expected, the second sphere has no contribution to the reactant conversion and temperature rise. It can be seen from the figure that, both profiles maintain nearly constant between the first sphere and the third sphere. However, the third sphere in Case 2 is noticed to have a higher contribution compared to the second sphere in Case 1. Excluding the influence of concentration driving force, this can be explained by the increased mass transfer rate as no sphere is behind the third sphere, which allows the full development of the fluid flow.

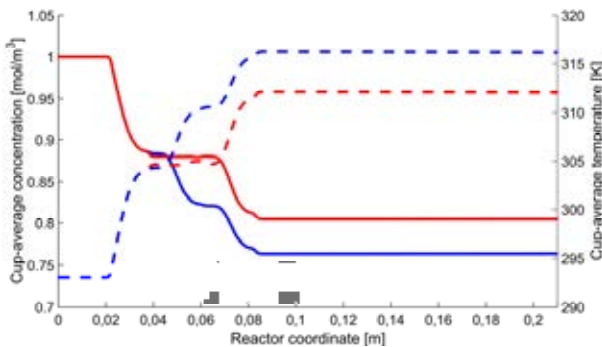


**Figure 5:** Fluid phase cup-average concentration and temperature profiles along the flow direction. The blue curves are of Case 1 while the red curves are of Case 2. The solid line and the dashed line stand for concentration and temperature respectively.

From the simulation, the overall conversion of the reactant in this three-bead reactor is obtained, which is 0.236 and 0.195 for Case 1 and Case 2 respectively. The theoretical fluid outlet temperature can be computed from the adiabatic temperature rise (Equation (60)). The fluid outlet temperatures given by the simulations are

316.2 and 312.1 for Case 1 and Case 2 respectively, which have a good agreement with the theoretically calculated values - 316.6 and 312.5.

$$T_{f,out} = T_{f,in} + \frac{(-\Delta H_r)c_{f,in}\xi_f}{\rho_f C_{p,f}} \quad (60)$$

In this equation,  $\xi_f$  is the ratio of converted species which is obtained from the simulation. The Nusselt numbers and Sherwood numbers of individual sphere at the time moment of 3 second obtained from our simulations are listed in Table 5, which correspond well with the behaviors of individual sphere contribution in Figure 4. The Nusselt number and Sherwood number are computed by the following expressions:

$$Sh = \frac{\Phi_{m,f \rightarrow s}}{4\pi R_s^2 c_{f,in} D_f} \frac{d_s}{\lambda_f} \quad (61)$$

$$Nu = \frac{\Phi_{h,f \rightarrow s}}{4\pi R_s^2 (T_{f,in} - T_s) \lambda_f} \frac{d_s}{\lambda_f} \quad (62)$$

It should be noted that the negative Nusselt number in the following table indicates the heat flux is still flowing from the fluid phase to the solid phase.

**Table 5:** Nusselt numbers and Sherwood numbers of individual sphere at the time moment of 3s.

		Sphere 1	Sphere 2	Sphere 3
Nu	Case 1	12.90	7.67	6.99
	Case 2	13.34	-0.0013	9.21
Sh	Case 1	14.02	8.29	7.59
	Case 2	14.46	0.00	10.01

## CONCLUSION AND FUTURE WORK

In this paper a ghost-cell based immersed boundary method is presented for direct numerical simulation of coupled heat and mass transfer process in fluid-solid systems. In this method, a quadratic interpolation scheme is applied and the boundary condition is incorporated into the governing equations at the discrete level implicitly. Considering an external mass transfer limited exothermal reaction proceeding at the sphere surface, the heat and mass transport is coupled through the particle temperature.

For the case of single sphere unsteady diffusion, the temperature rise of the sphere obtained from DNS has a good agreement with the value calculated theoretically, and the simulation result of particle temperature evolution agrees well with the “exact” solution obtained from a numerical solution using a standard second-order finite difference technique. After that, forced convection to a stationary sphere is considered, the steady state particle temperature matches the empirical value well which is calculated from the mass transfer coefficient and heat transfer coefficient. Besides that, the particle Sherwood number and Nusselt number obtained from DNS are compared with those values given by the well-known empirical Frössling and Ranz-Marshall correlations. In the last simulation, a three-bead reactor is studied which is composed of an in-line array of three spheres. One case consists only of active spheres while the other case assumes the middle sphere is inert. The

temperature evolution of individual particle together with the cup-average concentration and temperature profiles along the flow direction give a detailed description of the behavior of the reactor system. The adiabatic temperature rise obtained from DNS is in good agreement with the value computed from the overall species conversion.

Based on the examples discussed in this work, it is evident that DNS models are a powerful tool to obtain improved correlations for interfacial transfer which could be applied in coarser scale models. The three fluid-solid systems presented in this paper serve as good verifications for our proposed model of coupled heat and mass transfer. Further work related to the extension of the current model to random arrays of particles is ongoing, where more parameters, such as Reynolds number, Damköhler number and solid phase packing density, are of high interest.

## ACKNOWLEDGEMENTS

This work was supported by the Netherlands Center for Multiscale Catalytic Energy Conversion (MCEC), an NWO Gravitation programme funded by the Ministry of Education, Culture and Science of the government of the Netherlands.

## REFERENCE

- BAGCHI, P., HA, M.Y. and BALACHANDAR, S., (2000), "Direct Numerical Simulation of Flow and Heat Transfer From a Sphere in a Uniform Cross-Flow", *J. Fluids Eng.*, **123**(2), 347-358.
- DEEN, N.G., KRIEBITZSCH, S.H.L., VAN DER HOEF, M.A. and KUIPERS, J.A.M., (2012), "Direct numerical simulation of flow and heat transfer in dense fluid-particle systems", *Chem. Eng. Sci.*, **81**(0), 329-344.
- DEEN, N.G. and KUIPERS, J.A.M., (2013), "Direct Numerical Simulation of Fluid Flow and Mass Transfer in Dense Fluid-Particle Systems", *Ind. Eng. Chem. Res.*, **52**(33), 11266-11274.
- DEEN, N.G. and KUIPERS, J.A.M., (2014), "Direct numerical simulation of fluid flow accompanied by coupled mass and heat transfer in dense fluid-particle systems", *Chem. Eng. Sci.*, **116**(0), 645-656.
- DIERICH, F., NIKRITYUK, P.A. and ANANIEV, S., (2011), "2D modeling of moving particles with phase-change effect", *Chem. Eng. Sci.*, **66**(22), 5459-5473.
- FADLUN, E.A., VERZICCO, R., ORLANDI, P. and MOHD-YUSOF, J., (2000), "Combined Immersed-Boundary Finite-Difference Methods for Three-Dimensional Complex Flow Simulations", *J. Comput. Phys.*, **161**(1), 35-60.
- GHIAS, R., MITTAL, R. and DONG, H., (2007), "A sharp interface immersed boundary method for compressible viscous flows", *J. Comput. Phys.*, **225**(1), 528-553.
- GOLDSTEIN, D., HANDLER, R. and SIROVICH, L., (1993), "Modeling a No-Slip Flow Boundary with an External Force Field", *J. Comput. Phys.*, **105**(2), 354-366.
- HAUGEN, N.E.L. and KRAGSET, S., (2010), "Particle impaction on a cylinder in a crossflow as function of Stokes and Reynolds numbers", *J. Fluid Mech.*, **661**, 239-261.
- LEE, J. and YOU, D., (2013), "An implicit ghost-cell immersed boundary method for simulations of moving body problems with control of spurious force oscillations", *J. Comput. Phys.*, **233**, 295-314.
- LI, X., CAI, J., XIN, F., HUAI, X. and GUO, J., (2013), "Lattice Boltzmann simulation of endothermal catalytic reaction in catalyst porous media", *Appl. Therm. Eng.*, **50**(1), 1194-1200.
- MARELLA, S., KRISHNAN, S., LIU, H. and UDAYKUMAR, H.S., (2005), "Sharp interface Cartesian grid method I: An easily implemented technique for 3D moving boundary computations", *J. Comput. Phys.*, **210**(1), 1-31.
- MOHD-YUSOF, J., (1997), "Combined Immersed-Boundary and B-spline methods for simulations of flow in complex geometries", *Cen. Turb. Res., Annual Research Brief*, 317-327.
- PESKIN, C.S., (1977), "Numerical analysis of blood flow in the heart", *J. Comput. Phys.*, **25**(3), 220-252.
- SAIKI, E.M. and BIRINGEN, S., (1996), "Numerical Simulation of a Cylinder in Uniform Flow: Application of a Virtual Boundary Method", *J. Comput. Phys.*, **123**(2), 450-465.
- SEO, J.H. and MITTAL, R., (2011), "A high-order immersed boundary method for acoustic wave scattering and low-Mach number flow-induced sound in complex geometries", *J. Comput. Phys.*, **230**(4), 1000-1019.
- SHU, C., LI, X., REN, W.W. and YANG, W.M., (2013), "Novel immersed boundary methods for thermal flow problems", *Int. J. Numer. Method H*, **23**(1), 124-142.
- TAVASSOLI, H., KRIEBITZSCH, S.H.L., VAN DER HOEF, M.A., PETERS, E.A.J.F. and KUIPERS, J.A.M., (2013), "Direct numerical simulation of particulate flow with heat transfer", *Int. J. Multiphase Flow*, **57**(0), 29-37.
- TENNETI, S., SUN, B., GARG, R. and SUBRAMANIAM, S., (2013), "Role of fluid heating in dense gas-solid flow as revealed by particle-resolved direct numerical simulation", *Int. J. Heat Mass Transfer*, **58**(1-2), 471-479.
- TSENG, Y.-H. and FERZIGER, J.H., (2003), "A ghost-cell immersed boundary method for flow in complex geometry", *J. Comput. Phys.*, **192**(2), 593-623.
- UDAYKUMAR, H.S., MITTAL, R., RAMPUNGGON, P. and KHANNA, A., (2001), "A Sharp Interface Cartesian Grid Method for Simulating Flows with Complex Moving Boundaries", *J. Comput. Phys.*, **174**(1), 345-380.
- UHLMANN, M., (2005), "An immersed boundary method with direct forcing for the simulation of particulate flows", *J. Comput. Phys.*, **209**(2), 448-476.
- VAN DER HOEF, M.A., VAN SINT ANNALAND, M., DEEN, N.G. and KUIPERS, J.A.M., (2008), "Numerical Simulation of Dense Gas-Solid Fluidized Beds: A Multiscale Modeling Strategy", *Annu. Rev. Fluid Mech.*, **40**(1), 47-70.
- WANG, Z., FAN, J., LUO, K. and CEN, K., (2009), "Immersed boundary method for the simulation of flows with heat transfer", *Int. J. Heat Mass Transfer*, **52**(19-20), 4510-4518.
- XIA, J., LUO, K. and FAN, J., (2014), "A ghost-cell based high-order immersed boundary method for inter-phase heat transfer simulation", *Int. J. Heat Mass Transfer*, **75**, 302-312.
- ZHANG, N., ZHENG, Z.C. and ECKELS, S., (2008), "Study of heat-transfer on the surface of a circular cylinder in flow using an immersed-boundary method", *Int. J. Heat Fluid Flow*, **29**(6), 1558-1566.



# A SIMULATION CONCEPT FOR GENERIC SIMULATION OF MULTI-MATERIAL FLOW USING STAGGERED CARTESIAN GRIDS

**Ernst A. MEESE<sup>1</sup>, Stein T. JOHANSEN<sup>1,2\*</sup>**

<sup>1</sup> SINTEF Materials and Chemistry, Trondheim, NORWAY

<sup>2</sup> Norwegian University of Science and Technology (NTNU), Trondheim, NORWAY

\* Corresponding author, E-mail address: Stein.T.Johansen@sintef.no

## ABSTRACT

Simulation of multiphase flows is generally treated by various classes of Eulerian methods, Lagrangian methods, and various combinations of these. In the SIMCOFLOW initiative, we have set out to develop a framework for simulation of multi-material flows, using a Eulerian description. A fundamental part is the application of Cartesian grids with cut cells, and with a staggered representation of the grid for velocities and scalars. The model equations are derived based on formal volume and ensemble averaging (Quintard and Whitaker, 1995), (Gray and Lee, 1977) and (Cushman, 1982). Solid walls or moving solid materials are treated in the same manner as any flowing material (fluid, deforming material). The interface is characterized by a level set or by a 3D surface. In grid cells that are cut by a large-scale interface, the stress acting at the cut surface can be computed based on the level set or volume fractions. The exchange of mass, energy, and momentum between continuous fluids (note: walls are also considered a continuous fluid) can be estimated using wall functions in the case of coarse grids. The methods applied to the flow in a general geometry are closely related to the FAVOR method (Hirt and Sicilian, 1985) and the LS-STAG method (Chen and Botella, 2010).

In this paper, we discuss the derivation of the equations and the numerical solution strategy needed to handle such complex physics within the framework of finite volume methods.

We further discuss briefly the ongoing developments such as adaptive gridding and the computational framework.

The results of this work will end up as open source software.

**Keywords:** Multi-material flows, Cartesian cut-cells, staggered grid, volume averaging, dispersed fields, large scale interface

## NOMENCLATURE

Greek Symbols

$\alpha$  volume fraction

$\beta$  interface specific volume fraction (m)  
 $\rho$  density (kg/m<sup>3</sup>)  
 $\rho_l$  intrinsic density of phase  $l$  (kg/m<sup>3</sup>)  
 $\hat{\rho}^{k;l}$  extensive phase density (kg/m<sup>3</sup>),  $\hat{\rho}^{k;l} = \alpha^{k;l} \rho_l$   
 $\chi_p$  multiphase compressibility factor  
 $\tau$  viscous stress tensor (Pa)

Latin Symbols

**A** interfacial area vector (m<sup>2</sup>)  
**A** matrix, defined by Eqs. (55) and (56)  
*DU* defined by equation (64)  
 $\mathcal{A}$  index set for cell faces of grid cell **i**  
**g** gravity vector (m/s<sup>2</sup>)  
 $K_{m;n}^{k;l}$  interface friction coefficient between velocity fields  $m;n$  and  $k;l$   
LSI Large Scale Interface  
**n** normal vector to interface  
*p* pressure at end of time step (Pa)  
*S* generic source term  
 $\Delta t$  time step (s)  
*p'* pressure correction,  $p' = p - p^0$  (Pa)  
*T* temperature (K)  
*T'* temperature correction,  $T' = T - T^0$  (K)  
 $u^{k;l}$  field velocity of phase  $k$ , dispersed into phase  $l$  (m/s)  
 $u^*$  defined by equation (53)

Superscripts

0 previous time step  
*k;l* field  $k$ , submerged into phase  $l$

Subscripts

**i** multi-index for grid cells, e.g.,  $\mathbf{i} = (i,j,k)$   
**k** generic index for grid cell faces  
**w** wall index

Other symbols

$\langle \rangle$  volume averaged

## INTRODUCTION

In Computational Fluid Dynamics (CFD), a number of different technical and scientific elements must play



**Figure 1: Oil boom operated in calm sea.**

together to create powerful methods that reliably can simulate real world behaviour. Multiphase and multi-material flows are of the most complex flows, and here the development of models with predictive power is generally lagging behind single phase flow models. An exception in the multiphase domain is free surface flows, which has shown some impressive developments over the last decade.

In an attempt to answer to challenges in multiphase pipe flow, we developed the LedaFlow Q3D model (Laux et al., 2007). In this model, multiple coexisting continuous and disperse phases can be represented. However, the code was tailored for pipe flows and could not readily be extended to complex geometries. The Research Council of Norway has now supported further development of these concepts through the SIMCOFLOW project. The target for this development is to simulate the flow of air, oil, and water in an operated oil boom (see Figure 1), interacting dynamically with wind, waves and sea current. Here we have set out to develop an open source CFD code that can handle any moving interface problem, using Cartesian grids with local grid refinement. The discretization of the governing equations is made on staggered grids, where the velocity component cells are centred at the faces of the scalar (primary) cell faces. A Cartesian Cut-Cell approach is applied to represent the immersed boundaries (Cheny and Botella, 2010; Hirt and Sicilian, 1985). The justification for working with this particular concept is a) relative ease of implementing new physical models using finite volumes on a regular mesh, b) exploit more accurate interpolation of fluxes, also due to grid regularity, c) easy automation of grid generation for any geometries using the cut-cell concept, and d) staggered mesh provides a tighter pressure-velocity coupling than what can be obtained using co-located grids. Previously it was unsuccessfully attempted to implement the CDP (Compressible Disperse Phase) method (Johansen and Laux, 1995) using a co-located mesh. Based on that experience, dealing with granular flows, it turned out that a staggered arrangement ensured positive pressures for all solid fractions, while the co-located approach generated from time to time negative pressures that killed the simulations.

In this paper, we present a theoretical and numerical framework for this development. To limit the scope of this paper, we only discuss discretization on regular Cartesian meshes. However, work is in progress for establishing a dynamic mesh structure, based on a graded

octree representation (i.e., a 2:1 balance so that neighbouring cells are at most one level apart in the tree). The aim is to apply dynamic grid refinement in regions of interest, such as close to walls and to fluid-fluid interfaces. Using local grid refinement in Cartesian meshes introduces the additional complexity of hanging nodes, i.e., a grid cell may have two (2D) or four (3D) neighbouring cells in either coordinate direction, or it may be a connected to a neighbour through only half (2D) or a quarter (3D) of the neighbour's cell face. Due to space limitations, these additional discretization complexities and the actual procedure for dynamic refinement are not discussed here. We will focus on the model formulations that can allow such complex simulations.

## MODEL DESCRIPTION

### Cut-cell approach based on formal volume averaging

In order to handle the complex multiphase flows referred to above, we need a mathematical and numerical framework that can handle both complex wall geometries and fluid-fluid interfaces. An attempt to do so is represented by the FAVOR method (Hirt and Sicilian, 1985). However, in our case we want to extend the method to handle multiphase flows with any number of dispersed fields and continuous phases, as well as moving or stationary solids.

For the sake of simplicity, in the first part of this paper we go through some fundamental concepts looking only at single phase flow, extending the method to multiphase flow in the latter part. The extension to generic multiphase flows is quite straightforward. The only new issue that will enter is that the moving fluids and fields are coupled through mass, momentum, and energy transfer. Stiffness due to these interactions can be handled locally in each cell using a fractional step approach, which is a very desirable feature for enabling good parallel performance of the simulation code.

### Scalar transport

In order to familiarize ourselves with cut-cell related issues we start by investigating the evolution of enthalpy in a cut-cell domain. We investigate the conservation of enthalpy  $h$  where only conduction, convection, and simple energy sources  $S_h$  are allowed to change the enthalpy field.

It is assumed that the relation between enthalpy and temperature is known. Currently we assume that  $h = C_p T$ . Using the generic formalism ((Quintard and Whitaker, 1995), (Gray and Lee, 1977) and (Cushman, 1982)), a very simplified conservation of enthalpy that is sufficient to demonstrate the concepts can be expressed as,

$$\begin{aligned} \frac{\partial}{\partial t} \int_{V_f} \rho_f h dV &= - \int_{S_f} \rho_f h \mathbf{u}_f \cdot \mathbf{n}_f dS \\ &\quad - \int_{A_w} \rho_k h (\mathbf{u}_f - \mathbf{u}_l) \cdot \mathbf{n}_{f,w} dS \\ &\quad - \int_{S_f} \mathbf{q} \cdot \mathbf{n}_f dS - \int_{A_w} \mathbf{q} \cdot \mathbf{n}_f dS + \int_{V_f} \rho_f S_h dV \end{aligned} \quad (1)$$

where  $V_f$  is a fluid volume,  $S_f$  is the part of the volume surface interfacing a neighbouring fluid volume, and  $A_w$

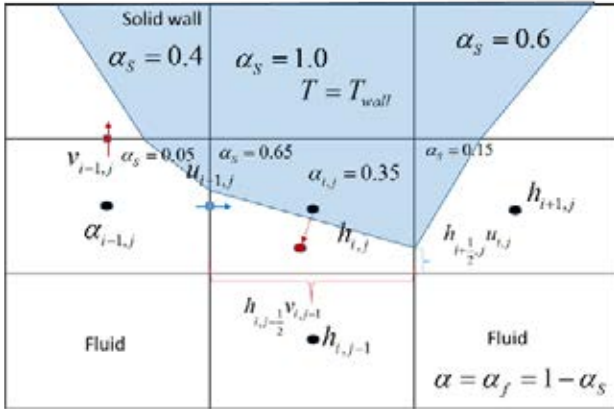


**Figure 2** Cartesian cut cell domain with solid walls (blue) and enthalpy in cell  $(i,j)$  is  $h_{i,j}$ .

is the part of the volume surface interfacing a neighbouring solids region, see Figure 3.

The first term on the right hand side of Eq. (1) express the convection of enthalpy across cell faces, and the second term is the mass transfer between wall and fluid. RHS terms three and four express thermal conduction across the fluid cell boundary and into the solid wall, respectively. The last term is a general volumetric heat source.

The discrete enthalpy equations on a Cartesian grid cell  $\mathbf{i}$  with fluid volume  $V_f = \alpha_{f,i} \Delta V_i$  becomes,

$$\begin{aligned} \frac{\Delta(\alpha_f \rho_f h)_i \Delta V_i}{\Delta t} &= - \sum_{\mathbf{k} \in \mathcal{F}_i} (\rho_f \mathbf{h} \mathbf{u}_f \cdot \mathbf{n}_f \alpha_f \Delta A)_k \\ &- \sum_{\mathbf{k} \in \mathcal{F}_i} (\mathbf{q} \cdot \mathbf{n}_f \alpha_f \Delta A)_k \\ &- \sum_{\mathbf{w} \in \mathcal{W}_i} (\mathbf{q} \cdot \mathbf{n}_f \Delta A)_w + \int_{V_f} \rho_f S_h dV \end{aligned} \quad (2)$$

where  $\Delta(\alpha_f \rho_f h)_i$  is the update of enthalpy over a time step,  $\mathcal{F}_i$  is the index set for the faces of cell  $\mathbf{i}$ , and  $\mathcal{W}_i$  is the set of walls embedded in cell  $\mathbf{i}$ . Note that we use a short-hand notation where the index of all variables inside parentheses is indicated on the parentheses itself.

In Eq. (2), the wall mass transfer term is absorbed into the generic source term. It is assumed that the velocity field is mass conserving. We will now discuss the implications of Eq. (2) when it comes to handling of the cut-cells.

Firstly, the transient term in Eq. (2) allows for a change in geometry, i.e., the solid fraction  $\alpha_s = 1 - \alpha_f$  is changing between time steps.

For the convective term, i.e., the first term on the right hand side of Eq. (2), it becomes important that we have good estimates of the fluid fraction  $(\alpha_f)_k$  at cell boundaries. At the cell-face between cells  $\mathbf{i} = (i,j)$  and  $(i,j+1)$ , the cell-face solid fraction in Figure 2 is clearly equal to one. If we compute the cell-face fraction by simple averaging, we have a situation where energy will flow between the two cells by conduction through the fluid phase. This is not acceptable. To avoid this problem, we have to introduce the following rules for cell interface fractions:

#### Rule I

*A cell which is fully loaded by one phase will have that all the cell-face fractions of that phase is 1.*

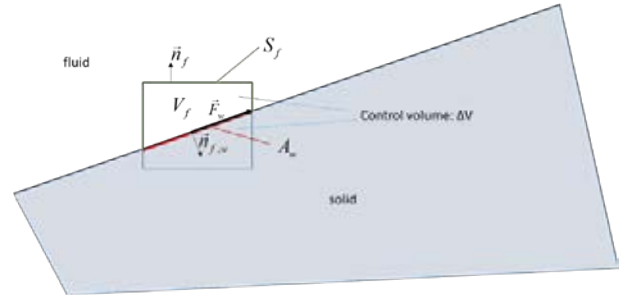


**Figure 3** Control volume cut by solid. Force  $\vec{F}_w$ , acting on the fluid from the wall.

#### Rule II

*A cell which have one, or more, but not all of the cell-faces dictated by Rule I will have a special method available to compute cell fractions for the remaining cell faces.*

The values of the density  $\rho_f$  and enthalpy  $h_f$  at the cell-face that are needed to calculate the convective flux,

$$F_{k,\text{conv}} = (\rho_f h_f \mathbf{u}_f \cdot \mathbf{n}_f \alpha_f \Delta A)_k, \quad (3)$$

are interpolated from neighbouring values using any preferred interpolation method. We note that the flux  $F_{k,\text{conv}}$  is to be understood as the time averaged flux over the time step.

#### Wall treatment:

The wall flux is the generic transfer of heat between the fluid in the cell and the wall. The flux is generally treated as,

$$F_{w,\text{wall}} = (\mathbf{q} \cdot \mathbf{n}_f \Delta A)_w = -\lambda \nabla T \cdot \mathbf{n}_w \Delta A_w = -\lambda \frac{T_{w,i,j} - T_{i,j}}{\delta_{w,n}} \Delta A_w \quad (4)$$

Equation (4) can be replaced by wall functions in the case of turbulent flows.

Here  $\lambda$  is the thermal conductivity,  $\Delta A_w$  is the actual area (Rule III) of the wall cutting through the cell, and  $\delta_{w,n}$  is the distance between the wall and the mass centre of the cell (Rule IV).

#### Rule III

*The heat transfer area  $\Delta A_w$  of a cell cut by a wall is computed by a specific method (not detailed here).*

#### Rule IV

*The distance between a wall and the cell centre inside the fluid part of the cell is computed by a specific method. The first version of the method is based on computation of the mass centre in the fluid part of the cell and computation of the normal distance  $\delta_{w,n}$  between this point and the cell-face.*

The fluid conduction flux can be treated in a similar manner as for the convective fluxes. An example for the  $x$ -direction flux at the positive  $x$ -cell-face is,

$$F_{k,\text{cond}}^{x^*} = (q_x \cdot n_{f,x} \alpha_f \Delta A)_k^{x^*} = -(\alpha_f \Delta A \lambda)_k^{x^*} \frac{T_{i+i,j} - T_{i,j}}{\Delta x} \quad (5)$$

The computations and application of the cell interface fractions  $\alpha_f$  are identical for conduction and convection. However, we note that due to Rule IV, the location point



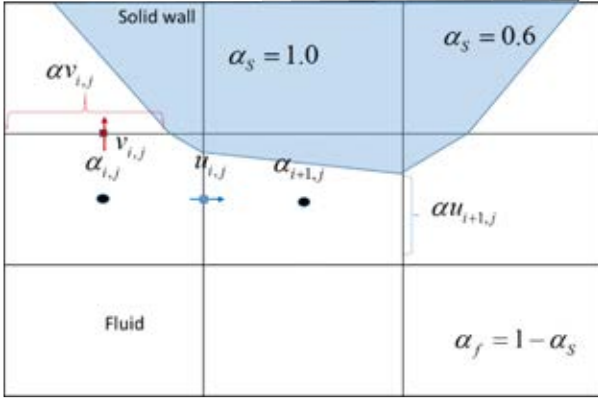


**Figure 4 Staggered grid layout in 2D**

for the temperature and enthalpy is moved from the cell centre to a new position (red circle in Figure 2). The movement of the point will impact the conductive fluxes across the neighbouring cell faces. It is therefore suggested that the offset of points in the cut cells are accounted for in the conductive flux calculations.

#### Rule V

*The offset of cell centre points for a fluid in a cut cell is used to correct the diffusive exchange fluxes with neighbouring fluid cells.*

#### Mass equations

According to the formalism (Cushman, 1982; Gray and Lee, 1977; Quintard and Whitaker, 1995) the transport equation for fluid mass is

$$\frac{\partial}{\partial t} \int_{V_f} \rho_f dV = - \int_{S_f} \rho_f \mathbf{u}_f \cdot \mathbf{n}_f dS - \int_{A_w} \rho_f (\mathbf{u}_f - \mathbf{u}_l) \cdot \mathbf{n}_{f,w} dS, \quad (6)$$

Referring again to Figure 3 for definition of  $V_f$ ,  $S_f$  and  $A_w$ . Integrating  $\rho_f(\mathbf{x})$  over the fluid volume  $V_f$  we find the intrinsic average of the density. The fluid mass per volume in a grid cell may then be defined as

$$\hat{\rho} = \alpha_f \rho_f = (1 - \alpha_s) \rho_f, \quad (7)$$

where  $\alpha_f$  and  $\alpha_s$  are the fluid and solids fraction (solid wall fraction) respectively, and  $\rho_f = \rho(p, T)$  is the intrinsic density of the fluid phase.

For a grid cell with volume  $\Delta V_i$ , we may write the discrete mass equation as

$$\frac{\partial \hat{\rho}_i}{\partial t} \Delta V_i + \sum_{\mathbf{k} \in \mathcal{F}_i} (\hat{\rho} \mathbf{u}_f \cdot \mathbf{n} \Delta A)_k = - \rho_f (\mathbf{u}_f - \mathbf{u}_l) \cdot \mathbf{n}_{f,w} \Delta A_w \quad (8)$$

Note that the term on the right hand side of Eq. (8) may represent both a flow (mass source) coming through the wall, or any combination with an interface moving with velocity  $\mathbf{u}_l$ .

If the solid (walls, external domain) is stationary the mass equation will simplify to,

$$\frac{\partial \hat{\rho}_i}{\partial t} \Delta V_i + \sum_{\mathbf{k} \in \mathcal{F}_i} (\hat{\rho} \mathbf{u}_f \cdot \mathbf{n} \Delta A)_k = S_i \quad (9)$$

where  $S_i$  is a generic source term in cell  $\mathbf{i}$ . In Figure 4, we see a typical staggered grid layout in 2D that is used to construct the discretization.

#### Momentum equations

The momentum equation over a fluid volume  $V_f$  may be formulated as,

$$\begin{aligned} \frac{\partial}{\partial t} \int_{V_f} \rho \mathbf{u} dV &= \int_{V_f} \rho \mathbf{g} dV \\ &+ \int_{S_f} (-p \mathbf{I} + \boldsymbol{\tau}) \cdot \mathbf{n}_f dS + \int_{A_w} (-p \mathbf{I} + \boldsymbol{\tau}) \cdot \mathbf{n}_{f,w} dS \\ &- \int_{S_f} \rho \mathbf{u} \mathbf{u} \cdot \mathbf{n}_f dS - \int_{A_w} \rho \mathbf{u} (\mathbf{u} - \mathbf{u}_l) \cdot \mathbf{n}_{f,w} dS \end{aligned} \quad (10)$$

For the volume integrals at the top line of Eq. (10), we have for grid cell  $\mathbf{i}$ , where  $V_f = \alpha_{f,i} \Delta V_i$ , that

$$\frac{\partial}{\partial t} \int_{V_f} \rho \mathbf{u} dV = \frac{\partial \hat{\rho}_i \mathbf{u}_i}{\partial t} \Delta V_i \text{ and } \int_{V_f} \rho \mathbf{g} dV = \hat{\rho}_i \mathbf{g} \Delta V_i, \quad (11)$$

where the values  $\hat{\rho}_i$  and  $\mathbf{u}_i$  on the right hand sides are volume averaged magnitudes over  $V_f$ , and  $\hat{\rho}_i$  is defined as in Eq. (7).

For the stress terms, we have that

$$\int_{S_f} (-p \mathbf{I} + \boldsymbol{\tau}) \cdot \mathbf{n}_f dS = \sum_{\mathbf{k} \in \mathcal{F}_i} [(-p \mathbf{I} + \boldsymbol{\tau}) \cdot \mathbf{n} \alpha_f \Delta A]_k \quad (12)$$

and for wall stresses,

$$\int_{A_w} (-p \mathbf{I} + \boldsymbol{\tau}) \cdot \mathbf{n}_{f,w} dS = (-p \mathbf{I} + \boldsymbol{\tau})_w \cdot \mathbf{n}_{f,w} \Delta A_w \quad (13)$$

The advection term becomes

$$\int_{S_f} \rho \mathbf{u} \mathbf{u} \cdot \mathbf{n}_f dS = \sum_{\mathbf{k} \in \mathcal{F}_i} (\rho \mathbf{u} \mathbf{u} \cdot \mathbf{n} \alpha_f \Delta A)_k \quad (14)$$

Note that all variables on the right-hand sides of Eqs. (12) – (14) are face-averaged values, so that no approximations have been made yet.

To arrive at a discretization of Eq. (10), several interesting observations can be made.

- i) The surface averages of pressure in the stress terms (12) and (13) can be approximated closely by the volume averages.
- ii) For the stress term in Eq. (12), some cell faces may have zero fluid fraction ( $\alpha_{f,k} = 0$ ). The contribution from these cell faces will disappear for the pressure and the shear stress.
- iii) The wall effect is reintroduced by the stress term in Eq. (13). The stress contribution will have to be computed based on the surrounding discrete velocity values and volume fractions. In addition, the pressure contribution here involves only the pressure internally in the fluid in the cell, not a pressure behind the interface. As a consequence of ii) and iii) there will be no fluid pressure (and no need for it) in a cell which is fully solid.
- iv) The transfer term

$$\int_{A_w} \rho \mathbf{u} (\mathbf{u} - \mathbf{u}_l) \cdot \mathbf{n}_{f,w} dS$$

will only have values for the case where mass is entering or leaving through the wall face. In the case of an inert wall surface, moving through space, we will have zero contribution from this term. This applies to typical fluid-structure interaction cases.

#### Treatment of wall boundary conditions

In Figure 3 we see the wall shear force  $\vec{F}_w$  acting on the fluid in the volume  $V_f$ . The shear force acts in the direction of the fluid velocity, tangential to the wall. The wall may have any velocity  $\mathbf{u}_w$ . First we need the relative velocity between the fluid and the wall, tangential to the

wall. The relative velocity vector  $\Delta \mathbf{u}$  between the fluid and the wall is,

$$\Delta \mathbf{u} = \mathbf{u} - \mathbf{u}_w \quad (15)$$

so that the relative velocity normal to the wall is,

$$\Delta \mathbf{u}_n = [(\mathbf{u} - \mathbf{u}_w) \cdot \mathbf{n}] \mathbf{n} \quad (16)$$

where  $\mathbf{n}$  is the unit vector normal to the wall. The relative velocity tangential to the wall is then,

$$\Delta \mathbf{u}_t = \Delta \mathbf{u} - \Delta \mathbf{u}_n = \Delta \mathbf{u} - [\Delta \mathbf{u} \cdot \mathbf{n}] \mathbf{n} \quad (17)$$

The unit normal vector for the relative flow, parallel to the wall is now,

$$\mathbf{n}_t = \frac{\Delta \mathbf{u}_t}{|\Delta \mathbf{u}_t|} = \frac{\Delta \mathbf{u} - [\Delta \mathbf{u} \cdot \mathbf{n}] \mathbf{n}}{|\Delta \mathbf{u} - [\Delta \mathbf{u} \cdot \mathbf{n}] \mathbf{n}|} \quad (18)$$

The force acting on the fluid at a wall will be in the direction of  $\mathbf{n}_t$  and can be given as,

$$\vec{F}_w = -|\tau_w| A_w \mathbf{n}_t \quad (19)$$

The wall force decomposed into each Cartesian coordinate direction can now be written as,

$$\begin{aligned} F_{w,x} &= -|\tau_w| A_w \mathbf{n}_t \cdot \mathbf{e}_x \\ F_{w,y} &= -|\tau_w| A_w \mathbf{n}_t \cdot \mathbf{e}_y \\ F_{w,z} &= -|\tau_w| A_w \mathbf{n}_t \cdot \mathbf{e}_z \end{aligned} \quad (20)$$

In the case of no flow, a tangential vector is easily computed from the cross product of any of base vectors which are not parallel with the normal vector.

For the stability of a numerical implementation without having to excessively limit the time step size, it is critical to linearize the wall stress in velocity for use in an implicit scheme for the viscous terms. This is done in the following (example for Cartesian  $x$ -direction). The wall stress is Taylor-expanded in the required direction, here  $x$ -direction,

$$|\tau_w| \approx |\tau_w|^0 + \left( \frac{\partial |\tau_w|}{\partial |\Delta \mathbf{u}_t|} \frac{\partial |\Delta \mathbf{u}_t|}{\partial \Delta u_{t,x}} \right)^0 (\Delta u_{t,x} - \Delta u_{t,x}^0) \quad (21)$$

We use the wall function concept, stating that,

$$|\Delta \mathbf{u}_t(y)| = u_\tau u^+(y^+), \quad (22)$$

where  $u_\tau$  is the friction velocity,  $u^+$  the velocity normalized by the friction velocity, and  $y^+$  the normalized wall distance. Eq. (22) is equivalent to,

$$|\tau_w| = \rho u_\tau^2 = \rho \left( \frac{|\Delta \mathbf{u}_t(y)|}{u^+(y^+)} \right)^2 \quad (23)$$

Using (23) in (21) we have that,

$$|\tau_w| \approx |\tau_w|^0 + \left\{ \frac{2|\tau_w|}{|\Delta \mathbf{u}_t|} \frac{\Delta u_{t,x}}{|\Delta \mathbf{u}_t|} \right\}^0 (\Delta u_{t,x} - \Delta u_{t,x}^0) \quad (24)$$

We may now write the viscous stress, linearized in the fluid and wall velocities in the  $x$ -direction, as

$$\begin{aligned} |\tau_w| &\approx |\tau_w|^0 - \underbrace{\left\{ \frac{2|\tau_w|}{|\Delta \mathbf{u}_t|} \frac{\Delta u_{t,x}}{|\Delta \mathbf{u}_t|} \right\}^0}_{\tau_A} \Delta u_{t,x}^0 \\ &\quad + \underbrace{\left\{ \frac{2|\tau_w|}{|\Delta \mathbf{u}_t|} \frac{\Delta u_{t,x}}{|\Delta \mathbf{u}_t|} \right\}^0}_{\chi} (u_x - u_{w,x}) \end{aligned} \quad (25)$$

$$= \tau_A + \chi (u_x - u_{w,x})$$

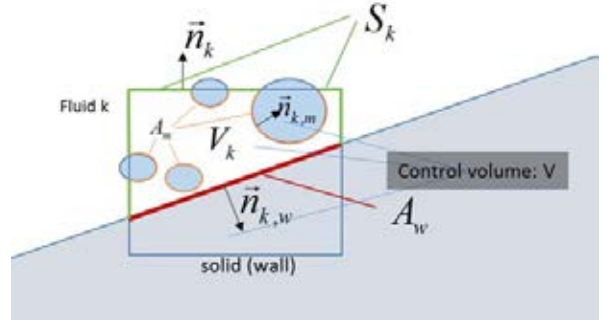


**Figure 5** Control volume  $V$ , containing field  $k$ , cut by solid (or fluid-fluid interface), and by dispersed fields  $m$ .

The  $x$ -direction force can in turn be written as

$$F_{w,x} = -\tau_A n_{t,x} \Delta A_w - \chi n_{t,x} (u_x - u_{w,x}) \Delta A_w \quad (26)$$

Test: Flow parallel to wall.  $n_y = 1$ ,  $n_{t,x} = 1$ ,  $u_w = 0.0$  m/s:

$$|\tau_w| \approx -\underbrace{|\tau_w|^0}_{\tau_A} + \underbrace{\left\{ \frac{2|\tau_w|}{|\Delta \mathbf{u}_t|} \right\}^0}_{\chi} u_x \quad (27)$$

The resulting force is:

$$F_{w,x} = \left( |\tau_w|^0 - \frac{2|\tau_w|^0}{|\Delta \mathbf{u}_t|^0} u_x \right) \Delta A_w \quad (28)$$

This result is as expected. Note that due to the properties of Eq. (23), the linearization factor becomes  $\frac{2|\tau_w|^0}{|\Delta \mathbf{u}_t|^0}$  and

not  $\frac{|\tau_w|^0}{|\Delta \mathbf{u}_t|^0}$  !

## MULTIPHASE FLOW EQUATIONS

We now introduce multiple phases and the fields used to represent them (Laux et al., 2007). We use notation  $\alpha^{k;l}$  to tell that this is the volume fraction of a field with index  $k$  that is submerged in a phase  $l$ . The continuous field for phase  $l$  is denoted as  $\alpha^{l;l}$ . The field velocity is  $u^{k;l}$ , and accordingly the continuous phase velocity is  $u^{l;l}$ .

In order to support the functionality that only some fields are active in various parts of the solution domain, we may apply a field indicator  $\Upsilon^{k;l}$ , where

$$\Upsilon^{k;l} = \begin{cases} 1 & \text{if field } k \text{ in phase } l \text{ exists} \\ 0 & \text{if field } k \text{ in phase } l \text{ is non-existing} \end{cases} \quad (29)$$

For convenience, in the computer code we may attach string tables to the indices, where the entries in the table could be, e.g., ["gas", "oil", "water", "sand", "wall\_1"]. The pair  $(k;l) = (1;2)$  would then refer to dispersed gas in the oil phase. In this notation,  $k = l$  represents the case where the field is the continuous phase. I.e., in our example, all fields carried by the continuous water phase are represented by  $\alpha^{k;3}$ , continuous water is  $\alpha^{3;3}$ , gas bubbles in water is  $\alpha^{1;3}$ , and sand particles in water is  $\alpha^{4;3}$ . Since sand cannot be a continuous phase, we will have that  $\Upsilon^{4;4} = 0$ , and accordingly  $\alpha^{4;4}$  do not exist. In this example, we have only one wall type, represented by wall fraction  $\alpha^{5;5}$ , and where  $\Upsilon^{5;5} = 1$  and  $\Upsilon^{i<5;5} = 0$ .

Note also that the total number of fields in our system is given by

$$N_{\text{fields}} = \sum_{l=1}^{N_{\text{phases}}} \sum_{k=1}^{N_{\text{phases}}} \Upsilon^{k;l} \quad (30)$$

### Special interface notation

For interfaces, we will use a special notation which handle the precise situation. We use the following notation, exemplified by the interfacial area:

$$A_{k;m\uparrow m;m}$$

Here the area is represented at the interface between field  $k$  submerged into phase  $m$  ( $k;m$ ) and the continuous field ( $m;m$ ). For dispersed fields, we may use the shortcut  $A_{k;m\uparrow m;m} \equiv A_{k;m}$  without loss of generality. However, for continuous fields, having an interface between ( $k;k$ ) and ( $m;m$ ) we have to apply  $A_{k;k\uparrow m;m}$  since  $A_{k;k\uparrow m;m} \neq A_{k;m}$ .

### Multiphase mass equations

To arrive at the formal transport equation for mass we, as for single phase above, use the formalism provided in ((Quintard and Whitaker, 1995), (Gray and Lee, 1977) and (Cushman, 1982)). The transport equation for the mass of a field  $k$ , submerged in continuous phase  $m$ , can then be formulated as,

$$\begin{aligned} \frac{\partial}{\partial t} \int_{V^{k;m}} \rho^{k;m} dV = & - \int_{S_k} \rho^{k;m} \mathbf{u}^{k;m} \cdot \mathbf{n}^{k;m} dS \\ & - \underbrace{(1 - \delta_{km}) \int_{A_{k;m\uparrow m;m}} \rho^{k;m} (\mathbf{u}^{k;m} - \mathbf{u}_{I,k;m\uparrow m;m}) \cdot \mathbf{n}_{k;m\uparrow m;m} dS}_{\text{k is dispersed in m}} \quad (31) \\ & - \underbrace{\delta_{km} \sum_{j=1}^L \int_{A_{m;m\uparrow j;m}} \rho^{m;m} (\mathbf{u}^{m;m} - \mathbf{u}_{I,m;m\uparrow j;m}) \cdot \mathbf{n}_{m;m\uparrow j;m} dS}_{\text{j is dispersed in m}} \end{aligned}$$

Here the summation over  $j$  includes all dispersed fields present in the control volume. The Kronecker delta

$$\delta_{km} = \begin{cases} 0 & \text{if } k \neq m \\ 1 & \text{if } k = m \end{cases} \quad (32)$$

is introduced to select the correct form of the equations for continuous phases and non-continuous phases. The first term on the right-hand side of Eq. (31) accounts for mass leaving or entering the control volume. The two other terms correspond to mass transfer terms and will be non-zero only if the fluid velocity is different from the interface velocity.

In general, all walls are treated as a phase or field which is stationary or moving. In this way, there is no difference in the treatment of fluid-fluid, fluid-solid, or solid-solid interfaces. This will allow for any dynamics of the "solids".

Areas, volumes, and vectors are handled as discussed in the single-phase section and as explained in Figure 5, which sketches a typical multiphase situation. In Figure 5, the field marked as "wall" could be any continuous field, represented by a volume fraction  $\alpha^{k;k}$  and a velocity  $\mathbf{u}^{k;k}$ . The dispersed field denoted  $m$  could be a collection of different fields.

The mass transfer terms in Eq. (31) involves sub-grid velocities, and will typically be modelled by source terms that will be specific to different mechanisms for mass transfer. For the discussion in this paper, we introduce a

generic volumetric source term  $S^{k;m}$  to represent these models for net mass transfer into field ( $k;m$ ).

When we now integrate over the fluid volume  $V^{k;m}$  we find the intrinsic average of the density. Using  $\alpha^{k;m}$  as field fraction of the control volume, the field mass per volume in the complete control volume is

$$\hat{\rho}^{k;m} = \alpha^{k;m} \rho^{k;m}$$

Here,  $\rho^{k;m}(p,T)$  is the intrinsic density of the field phase, or rather of the phase labelled  $k$  since the fields represent subsets of all mass there is of a phase, where the thermodynamic properties, such as density, belongs to the phase.

The mass equation for the field ( $k;m$ ) on a Cartesian grid cell with index  $\mathbf{i}$  can now be written as,

$$\frac{\partial \hat{\rho}_{\mathbf{i}}^{k;m}}{\partial t} \Delta V_{\mathbf{i}} + \sum_{\mathbf{k} \in \mathcal{F}_{\mathbf{i}}} (\hat{\rho}^{k;m} \mathbf{u}^{k,m} \cdot \mathbf{n} \Delta A)_{\mathbf{k}} = S_{\mathbf{i}}^{k;m} \Delta V_{\mathbf{i}} \quad (33)$$

where  $\hat{\rho}_{\mathbf{i}}^{k;m}$  is mass per volume in the cell, the values of  $\hat{\rho}$  and  $\mathbf{u} \cdot \mathbf{n}$  in the parenthesis under the sum are average values over the cell faces, and  $\mathbf{n}$  is the outward unit normal at the cell face.

### Volume constraint

For multiphase flows, we get an algebraic constraint for volume that has to be fulfilled. It is stating that the sum of the volume occupied by all fields must equal the total available volume. I.e., the volume fractions have to fulfil the condition,

$$\sum_{m=1}^{N_{\text{phases}}} \sum_{k=1}^{N_{\text{phases}}} \Upsilon^{k;m} \alpha^{k;m} = 1 \quad (34)$$

Note that we have used the field indicator (29) to exclude fields that are not present in the model. At this stage we note that we in Eq. (34) have a total of  $N_{\text{phases}}$  different phases and types of walls, where these may have different appearances, but they are each represented by a field.

### Multiphase momentum equations

#### Dispersed fields and single continuous fields in a grid cell

By following the suggestions above we arrive at the following momentum equation for a field  $k;l$ . The field  $k;l$  may be a continuous field containing other dispersed fields or a dispersed field submerged into a continuous field. At this point we do not consider multiple continuous fields with-in a single grid cell. In addition, the considered flow is laminar. Turbulence may later be introduced by one more layer of ensemble averaging of the model equations.

$$\begin{aligned}
& \frac{\partial}{\partial t} (\alpha^{k,l} \rho^{k,l} \mathbf{u}^{k,l}) + \nabla \cdot (\alpha^{k,l} \rho^{k,l} (\overline{\delta \mathbf{u}^{k,l}} \delta \mathbf{u}^{k,l} + \mathbf{u}^{k,l} \mathbf{u}^{k,l})) \\
&= \alpha^{k,l} \rho^{k,l} \mathbf{g} + \alpha^{k,l} \nabla \cdot (-\langle p^{l,l} \rangle \mathbf{I} + \langle \boldsymbol{\tau}^{l,l} \rangle) \\
&+ \underbrace{(1 - \delta_{kl}) K^{k,l} \left\{ (\mathbf{u}^{j,l} - \mathbf{u}^{k,l}) + \frac{\alpha^{j,l} \mathbf{u}^{j,l}}{\alpha^{k,l}} \right\}}_{k \text{ is dispersed in } l} \\
&+ \underbrace{\delta_{kl} \sum_{j=1}^L K^{j,l} \left\{ (\mathbf{u}^{j,l} - \mathbf{u}^{l,l}) - \frac{\alpha^{j,l} \mathbf{u}^{j,l}}{\alpha^{l,l}} \right\}}_{j \text{ is dispersed in } l} \quad (35) \\
&- (1 - \delta_{kl}) \frac{1}{\Delta V} \int_{A_{k,j \uparrow l,j}} \rho^{k,l} \mathbf{u}^{k,l} (\mathbf{u}^{k,l} - \mathbf{u}_{l,k,j \uparrow l,j}) \cdot \mathbf{n}_{k,j \uparrow l,j} dS \\
&\quad \underbrace{\hspace{10em}}_{k \text{ is dispersed in } l} \\
&- \delta_{kl} \frac{1}{\Delta V} \sum_{j=1}^L \int_{A_{l,j \uparrow j,l}} \rho^{l,l} \mathbf{u}^{l,l} (\mathbf{u}^{l,l} - \mathbf{u}_{l,l,j \uparrow j,l}) \cdot \mathbf{n}_{l,j \uparrow j,l} dS \\
&\quad \underbrace{\hspace{10em}}_{j \text{ is dispersed in } l}
\end{aligned}$$

Here we again have used the Kronecker delta  $\delta_{kl}$  to distinguish between dispersed and continuous fields.  $\Delta V$  is the size of the control volume in which the areas  $A_{k,j \uparrow l,j}$  and  $A_{l,j \uparrow j,l}$  are defined. The LHS terms represent transient variation, stresses due to sub-cell mixing and convection. The RHS terms are external forces (gravity), fluid pressure and viscous stress, the two next groups of terms contain hydrodynamic drag and dispersion due to sub-volume mixing, and the last two groups of terms are momentum exchange due to mass transfer.

#### Extension to multiple continuous fields within a grid cell

Based on the generic averaging theorems ((Quintard and Whitaker, 1995), (Gray and Lee, 1977) and (Cushman, 1982)), the momentum equation for a continuous field is written as

$$\begin{aligned}
& \frac{\partial}{\partial t} \int_{V^{l,l}} \rho^{l,l} \mathbf{u}^{l,l} dV = \int_{V^{l,l}} \rho^{l,l} \mathbf{g} dV + \int_{S^{l,l}} (-p^{l,l} \mathbf{I} + \boldsymbol{\tau}^{l,l}) \cdot \mathbf{n}^{l,l} dS \\
&- \sum_{\substack{\text{All dispersed} \\ \text{fields } k,l \text{ in } l}} \int_{A_{k,j \uparrow l,j}} (-p^{l,l} \mathbf{I} + \boldsymbol{\tau}^{l,l}) \cdot \mathbf{n}_{k,j \uparrow l,j} dS \\
&- \underbrace{\sum_{\substack{\text{All continuous fields } m,m, \\ \text{interacting with } l,l}} \int_{A_{m,m \uparrow l,l}} (-p^{l,l} \mathbf{I} + \boldsymbol{\tau}^{l,l}) \cdot \mathbf{n}_{m,m \uparrow l,l} dS}_{LSI\_wall} \quad (36) \\
&- \int_{S^{l,l}} \rho^{l,l} \mathbf{u}^{l,l} \mathbf{u}^{l,l} \cdot \mathbf{n}^{l,l} dS \\
&- \sum_{\substack{\text{All other fields} \\ \text{inside volume}}} \int_{A_{k,j \uparrow l,j}} \rho^{k,l} \mathbf{u}^{k,l} (\mathbf{u}^{k,l} - \mathbf{u}_{l,k,j \uparrow l,j}) \cdot \mathbf{n}_{l,j \uparrow k,j} dS
\end{aligned}$$

All terms in Eq. (36) except one has been introduced through Eq. (35). The new term is marked with *LSI\_wall* and represents the force acting at the large scale interface between two continuous fields. Shear and normal stresses at solid walls or LSIs are handled by this term, as these are stresses and pressures resolved on the scale of the control volume  $\Delta V$ .

For now disregarding the interfacial pressure difference due to curvature, we may drop the pressure contributions acting inside the grid cell and assume that all phases share the same pressure. This simplification may lead to problems in certain cases and will be analysed at a later stage. At the LSI, as well as at solid walls, the jump condition for mass flow normal to the interface must always be fulfilled.

By application of the method discussed under the section "Treatment of wall boundary conditions" we may write the tangential LSI exchange force as

$$\int_{A_{m,m \uparrow l,l}} \boldsymbol{\tau}^{l,l} \cdot \mathbf{n}_{m,m \uparrow l,l} dS_{m,m \uparrow l,l} = (\boldsymbol{\tau}^{l,l})_{m,m \uparrow l,l} \cdot \mathbf{n}_{m,m \uparrow l,l} \Delta S_{m,m \uparrow l,l} \quad (37)$$

This may further be linearized in the velocities; take for example the  $x$ -velocity component (ref. Eq. (26)), being expressed as

$$F_{w,x} = -\tau_A n_{t,x} \Delta S_{m,m \uparrow l,l} - \chi n_{t,x} (u_x - u_{LSI,x}) \Delta S_{m,m \uparrow l,l}, \quad (38)$$

which we generalize to

$$\begin{aligned}
& (\boldsymbol{\tau}^{l,l})_{m,m \uparrow l,l} \cdot \mathbf{n}_{m,m \uparrow l,l} \Delta S_{m,m \uparrow l,l} = \\
& \Theta_{m,m \uparrow l,l} + \Phi_{m,m \uparrow l,l} (\mathbf{u}_{m,m \uparrow l,l} - \mathbf{u}^{l,l}) \quad (39)
\end{aligned}$$

The coefficients  $\Theta_{m,m \uparrow l,l}$  and  $\Phi_{m,m \uparrow l,l}$  are defined by Eqs. (20) - (26). We may further note that for a solid wall, in Eq. (39) we will use  $\mathbf{u}^{m,m}$  as the wall velocity. If the interface is moving, we must consider Newton's 3<sup>rd</sup> law. For each interface, we have the relation,

$$\begin{aligned}
& (\boldsymbol{\tau}^{l,l})_{m,m \uparrow l,l} \cdot \mathbf{n}_{m,m \uparrow l,l} \Delta S_{m,m \uparrow l,l} = (\boldsymbol{\tau}^{m,m})_{l,l \uparrow m,m} \cdot \mathbf{n}_{l,l \uparrow m,m} \Delta S_{l,l \uparrow m,m} \\
& \quad \Downarrow \\
& \Theta_{m,m \uparrow l,l} + \Phi_{m,m \uparrow l,l} (\mathbf{u}_{m,m \uparrow l,l} - \mathbf{u}^{l,l}) = \\
& \quad \Theta_{l,l \uparrow m,m} + \Phi_{l,l \uparrow m,m} (\mathbf{u}_{l,l \uparrow m,m} - \mathbf{u}^{m,m}) \quad (40)
\end{aligned}$$

which couples the two continuous fields over the interface.

As a result of Eq. (40), we obtain the interface velocity:

$$\mathbf{u}_{m,m \uparrow l,l} = \frac{\Theta_{m,m \uparrow l,l} - \Theta_{l,l \uparrow m,m} + (\mathbf{u}^{m,m} \Phi_{l,l \uparrow m,m} - \mathbf{u}^{l,l} \Phi_{m,m \uparrow l,l})}{(\Phi_{l,l \uparrow m,m} - \Phi_{m,m \uparrow l,l})} \quad (41)$$

And, finally, for the exchange force, we get,

$$\begin{aligned}
& (\boldsymbol{\tau}^{l,l})_{m,m \uparrow l,l} \cdot \mathbf{n}_{m,m \uparrow l,l} \Delta S_{m,m \uparrow l,l} = \\
& \left( \frac{\Phi_{l,l \uparrow m,m} \Theta_{m,m \uparrow l,l} - \Phi_{m,m \uparrow l,l} \Theta_{l,l \uparrow m,m}}{\Phi_{l,l \uparrow m,m} - \Phi_{m,m \uparrow l,l}} \right) \\
& + \left( \frac{\Phi_{m,m \uparrow l,l} \Phi_{l,l \uparrow m,m}}{\Phi_{l,l \uparrow m,m} - \Phi_{m,m \uparrow l,l}} \right) (\mathbf{u}^{m,m} - \mathbf{u}^{l,l}) \quad (42)
\end{aligned}$$

The suggested method is ready for application of wall functions since the quantities entering into Eq. (38), like  $n_{t,x}$ ,  $\tau_A$ , and  $\chi$  are readily computed from wall functions. As a result, the LSI forces acting on the field  $k,l$  is given by,

$$\delta_{kl} \sum_{\substack{\text{All continuous fields } m,m, \\ \text{interacting with } l,l}} (\psi_{l,j \uparrow m,m} + \vartheta_{l,j \uparrow m,m} (\mathbf{u}^{m,m} - \mathbf{u}^{l,l})), \quad (43)$$

where the coefficients are given by,

$$\begin{aligned}
\psi_{l,j \uparrow m,m} &= \psi_{m,m \uparrow l,l} = \left( \frac{\Phi_{l,l \uparrow m,m} \Theta_{m,m \uparrow l,l} - \Phi_{m,m \uparrow l,l} \Theta_{l,l \uparrow m,m}}{\Phi_{l,l \uparrow m,m} - \Phi_{m,m \uparrow l,l}} \right) \\
\vartheta_{l,j \uparrow m,m} &= \vartheta_{m,m \uparrow l,l} = \left( \frac{\Phi_{m,m \uparrow l,l} \Phi_{l,l \uparrow m,m}}{\Phi_{l,l \uparrow m,m} - \Phi_{m,m \uparrow l,l}} \right) \quad (44)
\end{aligned}$$

#### Simplified model equations

Here we neglect molecular and mechanical mass transfer. Then the mass conservation equation (33) becomes:

$$\frac{\partial \hat{\rho}_i^{k,m}}{\partial t} \Delta V_i + \sum_{\mathbf{k} \in \mathcal{S}_i} (\hat{\rho} \mathbf{u} \cdot \mathbf{n} \Delta A)_k = 0 \quad (45)$$

Similarly, the momentum equation in (35) is written

$$\begin{aligned}
& \frac{\partial}{\partial t} (\alpha^{k,l} \rho^{k,l} \mathbf{u}^{k,l}) + \nabla \cdot (\alpha^{k,l} \rho^{k,l} \mathbf{u}^{k,l} \mathbf{u}^{k,l}) = \alpha^{k,l} \rho^{k,l} \mathbf{g} + \\
& \alpha^{k,l} \nabla \cdot \left( -\langle p^{l,j} \rangle^i \mathbf{I} + \langle \boldsymbol{\tau}^{l,j} \rangle^i \right) + \nabla \cdot (\alpha^{k,l} \rho^{k,l} \Gamma_{sub}^{k,l} \nabla \mathbf{u}^{k,l}) \\
& + (1 - \delta_{kl}) K^{k,l} \left\{ (\mathbf{u}^{l,j} - \mathbf{u}^{k,l}) + \left( \frac{v_t^{l,j}}{Sc_t^{l,j}} \frac{\nabla \alpha^{l,j}}{\alpha^{l,j}} - \frac{v_t^{l,j}}{Sc_t^{k,l}} \frac{\nabla \alpha^{k,l}}{\alpha^{k,l}} \right) \right\} \quad (46) \\
& \underbrace{\hspace{10em}}_{k \text{ is dispersed in } l} \\
& + \delta_{kl} \sum_{j=1}^L K^{j,l} \left\{ (\mathbf{u}^{j,l} - \mathbf{u}^{l,j}) - \left( \frac{v_t^{j,l}}{Sc_t^{j,l}} \frac{\nabla \alpha^{j,l}}{\alpha^{j,l}} - \frac{v_t^{j,l}}{Sc_t^{l,j}} \frac{\nabla \alpha^{l,j}}{\alpha^{l,j}} \right) \right\} \\
& \underbrace{\hspace{10em}}_{j \text{ is dispersed in } l} \\
& + \delta_{kl} \sum_{\substack{\text{All continuous fields } m,m, \\ \text{interacting with } l}} (\psi_{l,j \uparrow m,m} + \mathcal{G}_{l,j \uparrow m,m} (\mathbf{u}^{m,m} - \mathbf{u}^{l,j}))
\end{aligned}$$

Here, the last term contains all the large-scale interfaces (LSI) and fluid-solid wall stresses. This will work fine as long as the interface are located away from cell boundaries. For LSIs adjacent of coinciding with a cell boundary (will not be very frequent), the LSI exchange force will have to be modified. In the normal case, the exchange force in the Cartesian  $x$ -direction may look like:

$$(\psi_{l,j \uparrow m,m} + \mathcal{G}_{l,j \uparrow m,m} (\mathbf{u}^{m,m} - \mathbf{u}^{l,j})) \bar{\mathbf{e}}_x = A_L + B_L (u_L^{m,m} - u_L^{l,j}) \quad (47)$$

The index  $L$  is here the cell index. However, if the LSI is very close to the cell face  $L$ - $LYM$  ( $LYM$  is neighbour on  $y^-$  side of the cell face) we will have to replace (47) with:

$$(\psi_{l,j \uparrow m,m} + \mathcal{G}_{l,j \uparrow m,m} (\mathbf{u}^{m,m} - \mathbf{u}^{l,j})) \bar{\mathbf{e}}_x = A_L + B_L (u_{LYM}^{m,m} - u_L^{l,j}) \quad (48)$$

In this case the computational stencil is slightly changed, as we have momentum exchange between two different fluids in two neighbouring computational cells.

We note that here the mixing stress term  $\nabla \cdot (\alpha^{k,l} \rho^{k,l} \Gamma_{sub}^{k,l} \nabla \mathbf{u}^{k,l})$  is simplified for the discussion purpose.

## NUMERICAL DISCRETIZATION

### Momentum equations

The momentum equation, disregarding mass transfer (Eq.(46)), may be reformulated into

$$\begin{aligned}
& \frac{\partial}{\partial t} (\hat{\rho}^{k,l} \mathbf{u}^{k,l}) + \nabla \cdot (\hat{\rho}^{k,l} \mathbf{u}^{k,l} \mathbf{u}^{k,l}) = \hat{\rho}^{k,l} \mathbf{g} \\
& + \alpha^{k,l} \nabla \cdot \left( -\langle p^{l,j} \rangle^i \mathbf{I} + \langle \boldsymbol{\tau}^{l,j} \rangle^i \right) + \nabla \cdot (\hat{\rho}^{k,l} \Gamma_{sub}^{k,l} \nabla \mathbf{u}^{k,l}) \\
& + (1 - \delta_{kl}) K^{k,l} (\mathbf{u}^{l,j} - \mathbf{u}^{k,l}) + \delta_{kl} \sum_{j=1}^L K^{j,l} (\mathbf{u}^{j,l} - \mathbf{u}^{l,j}) \quad (49) \\
& + \delta_{kl} \sum_{\substack{\text{All continuous fields } m,m, \\ \text{interacting with } l}} (\psi_{l,j \uparrow m,m} + \mathcal{G}_{l,j \uparrow m,m} (\mathbf{u}^{m,m} - \mathbf{u}^{l,j})) + \mathbf{S}^{k,l}
\end{aligned}$$

where the source term, assumed to be treated fully explicit, is given by:

$$\begin{aligned}
\mathbf{S}^{k,l} = & \underbrace{(1 - \delta_{kl}) K^{k,l} \left( \frac{v_t^{l,j}}{Sc_t^{l,j}} \frac{\nabla \alpha^{l,j}}{\alpha^{l,j}} - \frac{v_t^{l,j}}{Sc_t^{k,l}} \frac{\nabla \alpha^{k,l}}{\alpha^{k,l}} \right)}_{k \text{ is dispersed in } l} \\
& - \delta_{kl} \underbrace{\sum_{j=1}^L K^{j,l} \left( \frac{v_t^{j,l}}{Sc_t^{j,l}} \frac{\nabla \alpha^{j,l}}{\alpha^{j,l}} - \frac{v_t^{j,l}}{Sc_t^{l,j}} \frac{\nabla \alpha^{l,j}}{\alpha^{l,j}} \right)}_{j \text{ is dispersed in } l} \quad (50)
\end{aligned}$$

The terms of type  $K^{k,l} (\mathbf{u}^{l,j} - \mathbf{u}^{k,l})$  and  $K^{j,l} (\mathbf{u}^{j,l} - \mathbf{u}^{l,j})$  denotes friction between fields, and where we in the latter case sum over all fields  $j$ , dispersed in  $k = l$ .

As long as we can provide sub-models for the large-scale interface friction we may simulate any fluid-fluid, or fluid-solid system, allowing both direct simulations and more coarse-grained simulation possibilities.

The semi-discretized momentum equation for  $k$  in  $l$  now reads:

$$\begin{aligned}
& \hat{\rho}^{0,k,l} \frac{u_i^{k,l} - u_i^{0,k,l}}{\Delta t} \\
& + \frac{\partial}{\partial x_j} (\hat{\rho}^{0,k,l} u_j^{0,k,l} u_i^{0,k,l}) - u_i^{0,k,l} \frac{\partial}{\partial x_j} (\hat{\rho}^{0,k,l} u_j^{0,k,l}) \\
& = -\alpha^{0,k,l} \frac{\partial}{\partial x_i} p + \alpha^{0,k,l} \frac{\partial}{\partial x_j} \tau_{ji}^{k,l} + \frac{\partial}{\partial x_j} \left( \hat{\rho}^{k,l} \Gamma_{sub}^{k,l} \frac{\partial}{\partial x_j} u_i^{k,l} \right) \\
& + \sum_{m;n} \widehat{K}_{m;n}^{k,l} (u_i^{m;n} - u_i^{k,l}) + S_i^{0,k,l} \quad (51)
\end{aligned}$$

The drag force in (51) has been generalized by:

$$\begin{aligned}
& \sum_{m;n} \widehat{K}_{m;n}^{k,l} (\mathbf{u}^{m;n} - \mathbf{u}^{k,l}) \equiv (1 - \delta_{kl}) K^{k,l} (\mathbf{u}^{l,j} - \mathbf{u}^{k,l}) \\
& + \delta_{kl} \sum_{j=1}^L K^{j,l} (\mathbf{u}^{j,l} - \mathbf{u}^{l,j}) \quad (52) \\
& + \delta_{kl} \sum_{\substack{\text{All continuous fields } m,m, \\ \text{interacting with } l}} (\psi_{l,j \uparrow m,m} + \mathcal{G}_{l,j \uparrow m,m} (\mathbf{u}^{m,m} - \mathbf{u}^{l,j}))
\end{aligned}$$

We may note that  $\widehat{K}_{m;n}^{k,l}$  is defined by equations (47) and (52). For now we have not included the special cases for the LSI or wall perfectly aligned with the computational cell face, here represented by Eq. (48).

Similar to how we proceed for single phase flow, we first do a predictor step where we use explicit operators for all terms except for diffusion terms, which are solved implicitly. I.e., we use the momentum equation on the form,

$$\begin{aligned}
& \hat{\rho}^{0,k,l} \frac{u_i^{*,k,l} - u_i^{0,k,l}}{\Delta t} \\
& + \frac{\partial}{\partial x_j} (\hat{\rho}^{0,k,l} u_j^{0,k,l} u_i^{0,k,l}) - u_i^{0,k,l} \frac{\partial}{\partial x_j} (\hat{\rho}^{0,k,l} u_j^{0,k,l}) \\
& = -\alpha^{0,k,l} \frac{\partial}{\partial x_i} p^0 + \alpha^{0,k,l} \frac{\partial}{\partial x_j} \tau_{ji}^{k,l} (\mathbf{u}^*) \\
& + \frac{\partial}{\partial x_j} \left( \hat{\rho}^{k,l} \Gamma_{sub}^{k,l} \frac{\partial}{\partial x_j} u_i^{*,k,l} \right) \\
& + \sum_{m;n} \widehat{K}_{m;n}^{k,l} (u_i^{0,m;n} - u_i^{0,k,l}) + S_i^{0,k,l} \quad (53)
\end{aligned}$$

As external forces, friction, stress and pressure gradient balance out by large, the explicit friction term is included.

By subtracting (53) from (51) we obtain:

$$\begin{aligned}
& \hat{\rho}^{0,k;l} \frac{u_i^{k;l} - u_i^{*,k;l}}{\Delta t} \\
&= -\alpha^{0,k;l} \frac{\partial}{\partial x_j} (p - p^0) + \alpha^{0,k;l} \frac{\partial}{\partial x_j} \left( \frac{\tau_{j,i}^{k;l}}{\tau_{j,i}^{k;l}} (\mathbf{U}^*) \right) \\
&+ \frac{\partial}{\partial x_j} \left( \hat{\rho}^{k;l} \Gamma_{sub}^{k;l} \frac{\partial}{\partial x_j} (u_i^{k;l} - u_i^{*,k;l}) \right) \\
&+ \sum_{m,n} \widehat{K}_{m;n}^{k;l} (u_i^{m;n} - u_i^{k;l} - u_i^{0,m;n} + u_i^{0,k;l})
\end{aligned} \quad (54)$$

The crossed-out terms are neglected at this stage of the algorithm following the reasoning behind the fractional step approach, i.e., the diffusion terms are completed in the predictor step, and do not carry over to the corrector step. This essentially introduces a first order error in time, however, for most practical purposes it performs almost as well a second order methods (LeVeque, 2007). When neglecting the crossed-out term in equation (54) we find that:

$$\begin{aligned}
& u_i^{k;l} - K_{m;n}^{k;l} \frac{\Delta t}{\hat{\rho}^{0,k;l}} (u^{m;n} - u^{k;l}) \\
&= u_i^{*,k;l} - K_{m;n}^{k;l} \frac{\Delta t}{\hat{\rho}^{0,k;l}} (u^{0,m;n} - u^{0,k;l}) - \alpha^{0,k;l} \frac{\Delta t}{\hat{\rho}^{0,k;l}} \frac{\partial}{\partial x_i} p'
\end{aligned} \quad (55)$$

Here we assume the summing convention for the terms involving  $K_{m;n}^{k;l}$ . We recognize that Eq. (55) may be written on matrix form as

$$\mathbf{A}\mathbf{u} = \mathbf{b} - \Delta t \mathbf{a} \frac{\partial p'}{\partial x_i} \quad (56)$$

where

$$\mathbf{a} = \begin{bmatrix} \vdots \\ \alpha^{0,k;l} / \hat{\rho}^{0,k;l} \\ \vdots \end{bmatrix} \quad (57)$$

and

$$\mathbf{b} = \begin{bmatrix} \vdots \\ u_i^{*,k;l} - K_{m;n}^{k;l} \frac{\Delta t}{\hat{\rho}^{0,k;l}} (u^{0,m;n} - u^{0,k;l}) \\ \vdots \end{bmatrix} \quad (58)$$

So the solution for the velocities may be written as,

$$\mathbf{u} = \mathbf{A}^{-1} \mathbf{b} - \Delta t \mathbf{A}^{-1} \mathbf{a} \frac{\partial p'}{\partial x_i} \quad (59)$$

Note that since we have used an explicit operator for the convective terms, and used the fractional step approach for diffusion terms, the matrix  $\mathbf{A}$  only couples terms within a single grid cell. In a two-phase flow with 4 fields  $\mathbf{A}$  is a 4×4 matrix, in three-phase flows we have a 9×9 matrix. If we had carried over the implicit diffusion operator from the predictor step, or used an implicit scheme for convection, the matrix  $\mathbf{A}$  would also need to couple to the neighbouring cells, which we want to avoid. I.e., in the present approach, except for the diffusion operators of the predictor, there is no need for solving global matrices, which is a large benefit in terms of potential for achieving good parallel performance of the simulation code.

The main reason why we do not treat all terms explicitly, and dispose of the coupling matrix  $\mathbf{A}$  altogether is that the terms coupling the field velocities within a cell can be

quite stiff. Linearizing and coupling through the matrix  $\mathbf{A}$  has been seen to be sufficient for stability.

### Obtaining a pressure equation

To derive an equation for pressure, we use the volume constraint given in Eq. (34), which we may restate in terms of field masses  $\hat{\rho}^{k;m}$  and densities  $\rho_i^{k;m}$  as

$$\sum_{m=1}^{N_{\text{phases}}} \sum_{k=1}^{N_{\text{phases}}} \Upsilon^{k;m} \frac{\hat{\rho}_i^{k;m}}{\rho_i^{k;m}} = 1 \quad (60)$$

Note that Eq. (60) is also valid for single phase  $N_{\text{phases}}=1$ , where it will express that the density transported by the mass equation must equal the density determined by the equation of state.

The same is true for multiphase. Eq. (60) states that the cell masses must satisfy the thermodynamic relations so that the cell volume is exactly filled. Conceptually, in the corrector step of the algorithm we want to find a pressure that projects the solution onto the volume conserving manifold.

We start out by substituting for the masses from the solution of the mass equation (33). The mass equation can be reformulated as,

$$\hat{\rho}_i^{k;m} = (\hat{\rho}_i^{k;m})^0 - \frac{\Delta t}{\Delta V_i} \sum_{\mathbf{k} \in \mathcal{J}_i^-} \left( (\hat{\rho}^{k,m})^0 \mathbf{u}^{k;m} \cdot \mathbf{n} \Delta A \right) + \Delta t S_i^{k;m} \quad (61)$$

where masses are explicit and velocities implicit in the convection term. We want to use an explicit scheme for masses to keep numerical diffusion low, but we need the implicit velocities since they will be adjusted by the pressure, allowing for a volume consistent solution.

Now defining,

$$\mathbf{u}^{**} = \mathbf{A}^{-1} \mathbf{b} \quad \text{and} \quad \mathbf{u}' = \mathbf{u} - \mathbf{u}^{**} \quad (62)$$

we may rewrite Eq. (59) as,

$$\mathbf{u}' = -\Delta t \mathbf{A}^{-1} \mathbf{a} \frac{\partial p'}{\partial x_i} \quad (63)$$

which we on component form write as,

$$(u_i^{k;m})' = -DU_i^{k;m} \frac{\partial p'}{\partial x_i} \quad (64)$$

where  $DU_i^{k;m}$  is the element in the vector preceding the pressure gradient in Eq. (63) that correspond to the velocity  $u_i^{k;m}$ . For the velocities normal to the cell faces in Eq. (61), we may then write

$$\mathbf{u}^{k;m} \cdot \mathbf{n} = (\mathbf{u}^{k;m})^{**} \cdot \mathbf{n} - DU^{k;m} \nabla p' \cdot \mathbf{n} \quad (65)$$

Further, defining a predicted field mass as,

$$\begin{aligned}
& (\hat{\rho}_i^{k;m})^{**} = (\hat{\rho}_i^{k;m})^0 \\
& - \frac{\Delta t}{\Delta V_i} \sum_{\mathbf{k} \in \mathcal{J}_i^-} \left( (\hat{\rho}^{k,m})^0 \left( (\mathbf{u}^{k;m})^{**} \cdot \mathbf{n} \right) \Delta A \right) + \Delta t S_i^{k;m}
\end{aligned} \quad (66)$$

we may write the mass equation (61) as

$$\hat{\rho}_i^{k;m} = (\hat{\rho}_i^{k;m})^{**} + \frac{\Delta t}{\Delta V_i} \sum_{\mathbf{k} \in \mathcal{J}_i^-} \left( (\hat{\rho}^{k,m})^0 (DU^{k;m} \nabla p' \cdot \mathbf{n}) \Delta A \right) \quad (67)$$

Substituting Eq. (67) into the volume constraint, we get the pressure equation

$$\begin{aligned}
& \sum_{m=1}^{N_{\text{phases}}} \sum_{k=1}^{N_{\text{phases}}} \Upsilon^{k;m} \frac{\Delta t}{\Delta V_i} \sum_{\mathbf{k} \in \mathcal{J}_i^-} \left( (\hat{\rho}^{k,m})^0 (DU^{k;m} \nabla p' \cdot \mathbf{n}) \Delta A \right) \frac{1}{\rho_i^{k;m}} \\
& 1 - \sum_{m=1}^{N_{\text{phases}}} \sum_{k=1}^{N_{\text{phases}}} \Upsilon^{k;m} \frac{(\hat{\rho}_i^{k;m})^{**}}{\rho_i^{k;m}}
\end{aligned} \quad (68)$$

where we recognize the right-hand side of the equation as the volume error in the predicted masses. We have not discussed the details of the discretization of the gradient of the pressure correction, but essentially, the left hand side of Eq. (68) will be a weighed discrete Laplace operator for the pressure correction.

Note that for constant densities, Eq. (68) is a linear equation for pressure, i.e., after solving the equation we will get a velocity field and masses that exactly satisfies the volume constraint.

However, generally the density will be a function of pressure. I.e., taking the thermodynamics into account makes Eq. (68) non-linear, and we may need to iterate on the pressure equation to satisfy the volume constraint to some specified tolerance. To improve convergence, we linearize the equation in pressure, essentially getting a Newton iteration for pressure. Experience shows that this iteration indeed exhibit quadratic convergence. Note also that we iterate only on the pressure equation, only updating density, velocities, and masses ( $\hat{\rho}_i^{k:m}$ )<sup>\*\*</sup> between each iteration.

Linearizing the pressure equation in pressure, we get,

$$-\chi_p p'_i + \sum_{m=1}^{N_{\text{phases}}} \sum_{k=1}^{N_{\text{phases}}} \Upsilon^{k:m} \frac{\frac{\Delta t}{\Delta V_i} \sum_{\mathbf{k} \in \mathcal{S}_i} \left( (\hat{\rho}^{k,m})^0 (DU^{k:m} \nabla p' \cdot \mathbf{n}) \Delta A \right)_{\mathbf{k}}}{\rho_i^{k:m}} = 1 - \sum_{m=1}^{N_{\text{phases}}} \sum_{k=1}^{N_{\text{phases}}} \Upsilon^{k:m} \frac{(\hat{\rho}_i^{k:m})^{**}}{\rho_i^{k:m}} \quad (69)$$

where  $\chi_p$  is the multiphase compressibility factor,

$$\chi_p = \sum_{m=1}^{N_{\text{phases}}} \sum_{k=1}^{N_{\text{phases}}} \Upsilon^{k:m} \frac{\alpha_i^{k:m}}{\rho_i^{k:m}} \frac{\partial \rho^{k:m}}{\partial p} \quad (70)$$

Finally, we may note that since the updated velocities are always inserted into Eq. (61), mass will always be conserved. The error we may have is a deviation from the volume constraint. However, since the volume error is the driving term at right hand side of Eq. (69), and it is at all time based on the latest estimate of cell masses, the solution will always relax towards the solution manifold where the volume constraint is satisfied.

### The solution procedure

- 1) Prediction of extensive densities, by Eq. (66).
- 2) A first prediction of the phase velocities, Eq. (53). Here the stress terms are treated implicitly.
- 3) Establishing the momentum exchange matrix coefficients, equation (55) and (56), for the final momentum equation.
- 4) Computing inverse of the **A** matrix for each grid cell, Eq. (56).
- 5) Establish the coefficients in the relation between final velocity and pressure update gradient, Eq. (64)
- 6) By using the pressure correction (update) equation (69), compute the pressure correction  $p' = p - p^0$ .
- 7) Update pressures.
- 8) Update all field velocities, Eq. (65).
- 9) Update extensive phase densities, Eq. (67).
- 10) Update thermodynamic properties, in particular densities, based on new pressures (and temperatures if the energy equation is solved for).

- 11) Recalculate the right-hand side of the pressure equation (69) using new extensive densities and field densities, i.e., calculate the volume error for the solution.
- 12) If the volume error is greater than some tolerance, go to 6).
- 13) Advance to next time step

Note that no iterations are needed, except possibly for the pressure equation to reduce volume error. Our preliminary testing indicates, however, that most of the time no iterations are needed. Further, the iterations exhibit quadratic convergence, so only one or maybe two iterations are always sufficient.

### DISCUSSION

The method described above has this far only been implemented and validated for single phase, including moving walls. In these laminar flow test cases good results have been obtained, and will be presented in a separate publication (Dang, S. T. et al., 2017). In the general case of multiple moving materials we need a reliable method to compute interface propagation and at the same time provide the geometric information needed to handle the flow in the cut cells. The most promising strategy here seems to be the level-Set-VOF method (Chakraborty et al., 2013). As probably noted by the reader, the discretization schemes for convection has not been discussed in detail. SIMCOFLOW will however be open to plugging in any scheme which is supported by the code infrastructure. In the case of an octree grid we may not allow the use of large grid stencils for interpolation.

The method proposed herein will not need gridding in the way we normally do. The entire geometry is placed inside a cube and a regular Cartesian grid is established based on a surface geometry file (STL format). Based on this a level set function is established, describing the initial geometry.

Adaptive grid refinement is being allowed, using an octree grid arrangement. However, the code may run with or without adaptive grids. An important design element here is that all the moving interfaces will be on the same grid level during one time step to facilitate high accuracy and ease of implementation of boundary and interface phenomena.

The SIMCOFLOW code is being designed for parallel execution.

The results of this work will be published under a GNU Open Source licence.

### CONCLUSIONS

A method to simulate generic multi material flows in a Cartesian framework, using a staggered grid arrangement, is proposed.

The method is using Cartesian cut-cells, where the volume fractions in grid cells, or the value of the level set function, describe the positions of the materials inside the system.

The method is capable of simulating any number of flowing fluids, containing dispersed fields. Here the dispersed fields may be entrained from or deposit on the large scale interfaces.

The proposed method allows to use detailed boundary conditions, for all fields represented, at the large scale interfaces.

Introduction of floating objects such as boats and vessels will be easy to integrate if these are described by a level set function.

## ACKNOWLEDGEMENTS

The Norwegian Research Council, through the researcher program SIMCOFLOW (proj. 234126), is acknowledged for supporting this work.

## REFERENCES

- Chakraborty, I., Biswas, G., Ghoshdastidar, P.S., 2013. A coupled level-set and volume-of-fluid method for the buoyant rise of gas bubbles in liquids. *Int. J. Heat Mass Transf.* 58, 240–259.
- Chen, Y., Botella, O., 2010. The LS-STAG method: A new immersed boundary/level-set method for the computation of incompressible viscous flows in complex moving geometries with good conservation properties. *J. Comput. Phys.* 229, 1043–1076.
- Cushman, J.H., 1982. Proofs of the volume averaging theorems for multiphase flow. *Adv. Water Resour.* 5, 248–253.
- Dang, S. T., Johansen, S.T., Meese, E. A., 2017. A Cartesian cut-cell method based on formal volume averaging of mass momentum and energy equations. Presented at the CFD2017, SINTEF Proceedings, Trondheim.
- Gray, W.G., Lee, P.C.Y., 1977. On the theorems for local volume averaging of multiphase systems. *Int. J. Multiph. Flow* 3, 333–340.
- Hirt, C.W., Sicilian, J.M., 1985. A porosity technique for the definition of obstacles in rectangular cell meshes (Flow Science Inc.). New Mexico.
- Johansen, S.T., Laux, H., 1995. An alternative method for numerical solution of dispersed multiphase flow equations. Presented at the The 2nd International Conference on Multiphase Flow '95 Kyoto, April 3 -7, p. NU 8.
- Laux, H., Meese, E., Johansen, S.T., Ladam, Y., Bansal, K.A., Danielson, T.J., Goldszal, A., Monsen, J.I., 2007. Simulation of multiphase flows composed of large scale interfaces and dispersed fields. *Proc. ICMF 2007 Leipz.*
- LeVeque, R.J., 2007. *Finite volume methods for hyperbolic problems*, 6th ed. Cambridge University Press.
- Quintard, M., Whitaker, S., 1995. Aerosol filtration: An analysis using the method of volume averaging. *J Aerosol Sci* 26, 1227–1255.





# A CARTESIAN CUT-CELL METHOD, BASED ON FORMAL VOLUME AVERAGING OF MASS, MOMENTUM EQUATIONS

Son Tung DANG<sup>2,\*</sup>, Stein T. JOHANSEN<sup>1,2</sup>, Ernst Arne MEESE<sup>1</sup>

<sup>1</sup> SINTEF Materials and Chemistry, Trondheim, NORWAY

<sup>2</sup> Norwegian University of Science and Technology (NTNU), Trondheim, NORWAY

\* Corresponding author, E-mail address: [son.tung.dang@ntnu.no](mailto:son.tung.dang@ntnu.no)

## ABSTRACT

Simulation of multiphase flows are generally treated by various classes of Eulerian methods, Lagrangian methods and various combinations of these. In the SIMCOFLOW initiative we have set out to develop a framework for simulation of multi-material flows, using an Eulerian description. A fundamental part is the application of Cartesian grids with cut cells, and with a staggered representation of the grid for velocities and scalars. The model equations are derived based on formal volume and ensemble averaging (Gray and Lee, 1977; Quintard and Whitaker, 1995; Cushman, 1982). Solid walls or moving solid materials are treated in the same manner as any flowing material (fluid, deforming material). The interface is characterized by a level set or by a 3D surface. In grid cells which are cut with a large scale interface the stress acting at the cut surface can be computed based on the level set or volume fractions. The exchange of mass, energy and momentum between continuous fluids (note: walls are also considered a continuous fluid) can be estimated by wall functions in the case of coarse grids. The methods applied to the flow in a general geometry is closely related to the FAVOR method (Hirt and Sicilian, 1985), the LSSTAG method (Chen and Botella, 2010) and the cut-cell method of (Kirkpatrick et al., 2003). In this paper we present the derived equations and applications of the method to a single phase two-dimensional flow, and where solid walls are treated as a non-moving secondary phase. Simulations are performed for flow over a cylinder in crossflow. Simulation results are compared with experiments from literature. The results are discussed and critical issues are pointed out.

**Keywords:** CFD, Cartesian grid, Cut-Cell, immersed boundary method, Level-set.

## NOMENCLATURE

### Greek Symbols

$\alpha^c$  cell fraction

$\alpha^f$  face fraction

$\rho$  density (kg/m<sup>3</sup>)

$\rho$  intrinsic density (kg/m<sup>3</sup>)

$\hat{\rho}$  extensive phase density (kg/m<sup>3</sup>),  $\hat{\rho} = \alpha^c \rho$

$\tau$  viscous stress term (Pa)

### Latin Symbols

G total external force (N/m<sup>3</sup>)

p pressure at end of time step (Pa)

Se source term

$\Delta t$  time step (s)

p'  $p' = p - p^0$

$n, N$  normal vector

$V$  cell volume

$A$  cell face area

$\Delta h$  distance from velocity location to the wall

$U$  velocity component

$\mathbf{u}$  the volume averaged velocity vector

$\Delta_i$  grid spacing

### Superscripts

0 previous time step

c cell

f face

S solid

F fluid

w wall

b boundary

e eastern face

w western face

n northern face

P present cell

E eastern cell

N northern cell

## INTRODUCTION

Simulating multiphase and multi-material flows are among the most challenging topics of computational fluid dynamic. It is not only because of the presence of numerous phases or materials but also due to the difficulty of interface treatment. Therefore, in order to model accurately the physical interactions between phases or materials, it is crucial to predict accurately the flow fields in the regions which are close to interfaces. In recent years, among many approaches, the immersed boundary method (IBM) is increasingly used in many applications to handle the coupling between materials such as in fluid-structure interactions (Ng et al., 2009; Schneiders et al., 2016) or two-phase flow (Lauer et al., 2012; Schwarz et al., 2016). In this method, the Cartesian grid is used for the whole domain, and where conventional numerical method can be applied for almost the entire flow field except for those cells which are near the boundary. Based on how the boundary condition on the immersed surface is imposed, the IBM may be classified into the continuous forcing method, the discrete forcing method and sharp interface method (Mittal and Iaccarino, 2005). Belonging to sharp interface method, the cut-cell finite volume approach is widely used due to the strict conservation of mass and

momentum which is crucial in prediction of multiphase flows. Moreover, in this approach, the accurate local boundary condition is used to calculate fluxes across the cell face. Therefore, the cut-cell method is preferred and applied by several research groups (Bouchon et al., 2012; Cheny and Botella, 2010; Hirt and Sicilian, 1985; Kirkpatrick et al., 2003). Following the same approach, our code is designed to use a staggered grid representation and Cartesian Cut-Cell method (Kirkpatrick et al., 2003) to represent the immersed boundaries. In this paper, the continuity and momentum equations are derived by using a formal volume averaging method. In addition, the level-set function is applied to calculate the face and volume fractions.

It should be noted that we are now developing a dynamic grid structure, based on an octree representation. Hence, we will apply dynamic grid refinement in regions of interest, such as close to walls and fluid-fluid interfaces. This part will not be discussed herein as we will concentrate of the model formulations which can allow such complex simulations.

## MODEL DESCRIPTION

The model equations are derived based on formal volume and ensemble averaging (Gray and Lee, 1977; Quintard and Whitaker, 1995; Cushman, 1982). The application of the formal volume averaging is not critical for this paper. An importance element is however that based on volume fractions, accurate boundary positions can be located and correct boundary conditions can be applied at internal as well as external boundaries. However, when we later extend our cut cell method to complex multiphase flows, the usefulness of formal volume averaging will become clearer. This will be presented in a companion paper at CFD2017.

### Mass equations

According to the formalism (Cushman, 1982; Gray and Lee, 1977; Quintard and Whitaker, 1995) the transport equation for the mass is:

$$\frac{\partial}{\partial t} \int_{V_F} \rho dV = - \int_{S_F} \rho \mathbf{u} \cdot \mathbf{n}_F dS - \int_{A_w} \rho (\mathbf{u} - \mathbf{u}_I) \cdot \mathbf{n}_{F,w} dS \quad (1)$$

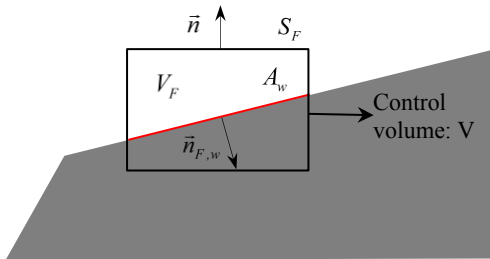


**Figure 1. Control volume cut by solid**

Here wall areas  $A_{F,w}$ , fluid volumes  $V_F$  and normal vectors  $\bar{n}_F$  are explained in Figure 1. When we integrate over the fluid volume  $V_F$  we find the intrinsic average of the density. Using  $\alpha_F^c$  as fluid fraction of the control volume the fluid mass per volume in the complete control volume is  $\hat{\rho} = \alpha_F^c \rho_F = (1 - \alpha_S^c) \rho_F$ . Here  $\alpha_S^c$  is the solids

fraction (solid wall fraction) and  $\alpha_F^c = 1 - \alpha_S^c$ , and where  $\rho_F(p, T)$  is the intrinsic density of the fluid phase.

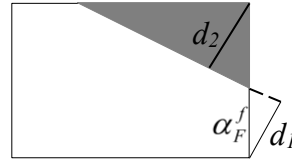
In Figure 2 we see a typical staggered grid layout in 2D. While the location of pressure is unchanged for both standard cell and boundary cell, the location of velocity is located at the face centre of pressure cell.

The discrete mass equation can now be represented by:

$$\begin{aligned} & \alpha_{i,j} \Delta V_{i,j} \frac{\rho_{i,j} - \rho_{i,j}^0}{\Delta t} \\ & + A_x (\alpha_{F,u}^f)_{i,j} \rho_{i+\frac{1}{2},j} u_{i,j} - A_x (\alpha_{F,u}^f)_{i-1,j} \rho_{i-\frac{1}{2},j} u_{i-1,j} \\ & + A_y (\alpha_{F,v}^f)_{i,j} \rho_{i,j+\frac{1}{2}} v_{i,j} - A_y (\alpha_{F,v}^f)_{i-1,j} \rho_{i,j-\frac{1}{2}} v_{i-1,j} = Se \end{aligned} \quad (2)$$

Where,  $Se = \rho (\mathbf{u} - \mathbf{u}_I) \cdot \mathbf{n}_{F,w} A_w$

The quantities  $\alpha_{F,u,i,j}^f$  and  $\alpha_{F,v,i,j}^f$  are computed from the level-set function. The simplest and first approach is:



$$\alpha_F^f = \frac{d_1}{(d_1 + d_2)} \quad (3)$$

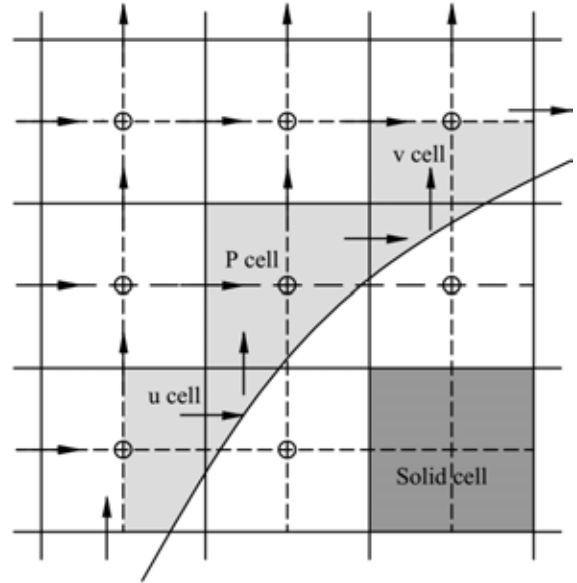


**Figure 2. Staggered grid layout in 2D**

### Momentum equations

Similarly, the momentum equation reads:

$$\begin{aligned} \frac{\partial}{\partial t} \int_{V_F} \rho \mathbf{u} dV = & \int_{V_F} \rho \mathbf{g} dV + \int_{V_F} \nabla p I dV + \int_{S_F \cap A_w} \boldsymbol{\tau} \cdot \mathbf{n}_F dS - \\ & \int_{S_F} \rho \mathbf{u} \mathbf{u} \cdot \mathbf{n}_F dS - \int_{A_w} \rho \mathbf{u} (\mathbf{u} - \mathbf{u}_I) \cdot \mathbf{n}_{F,w} dS \end{aligned} \quad (4)$$

The volume integrals are first evaluated,  $\frac{\partial}{\partial t} \int_{V_F} \rho \mathbf{u} dV = \Delta V \frac{\partial}{\partial t} \hat{\rho} \mathbf{u}$  and  $\int_{V_F} \rho \mathbf{g} dV = \Delta V \hat{\rho} \mathbf{g}$ . Here the velocity and density are the volume averages, where  $\hat{\rho} = \alpha_F^c \rho$ . Next we do the surface integrals:

$$\Delta V \frac{\partial}{\partial t} \hat{\rho} \mathbf{u} = \Delta V \hat{\rho} \mathbf{g} - \alpha_F^c \Delta V \nabla p \mathbf{I} + \sum_{S_F} \boldsymbol{\tau} \cdot \mathbf{n}_F \alpha_F^f A + \boldsymbol{\tau} \cdot \mathbf{n}_{F,w} A_{F,w} - \sum_{S_F} \rho \mathbf{u} \cdot \mathbf{n}_F \alpha_F^f A - \int_{A_{F,w}} \rho \mathbf{u} (\mathbf{u} - \mathbf{u}_l) \cdot \mathbf{n}_{F,w} dS \quad (5)$$

From equation (5) we see several interesting consequences:

i) The pressures gradient in term  $\alpha_F^c \Delta V \nabla p \mathbf{I}$  is represented by the volume averages, which can be approximated by the difference of two adjacent pressure cell (which cell centre remains unchanged).

ii) In term  $\sum_{S_F} \boldsymbol{\tau} \cdot \mathbf{n}_F \alpha_F^f A$ , some cell faces have a zero fluid fraction ( $\alpha_F^f = 0$ ). The contribution from these cell faces will disappear for the shear stress.

iii) The wall effect is reintroduced by the term  $\boldsymbol{\tau} \cdot \mathbf{n}_{F,w} A_w$ . The stress contribution will have to be computed based on the surrounding velocities.

iv) The transfer term  $\int_{A_w} \rho \mathbf{u} (\mathbf{u} - \mathbf{u}_l) \cdot \mathbf{n}_{f,w} dS$  will only have

values for the case where mass is entering/leaving through the wall face. In the case of an inert wall surface, moving through space, we will have zero contribution from this term. This applies to typical fluid-structure interaction cases.

### Treatment of wall boundary conditions

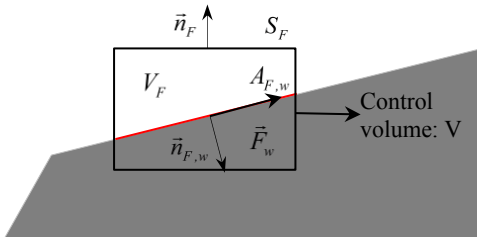


**Figure 3. The force  $\vec{F}_w$ , acting on the fluid from the wall**

In Figure 3 we see the wall shear force  $\vec{F}_w$  acting on the fluid in the volume  $V_F$ . The shear force acts in the direction of the fluid velocity, tangential to the wall. The wall may have any velocity  $\mathbf{u}_w$ . First we need the relative velocity between the fluid and the wall, tangential to the wall. The relative velocity between fluid and wall is represented by:

$$\Delta \mathbf{U} = \mathbf{u} - \mathbf{u}_w \quad (6)$$

The force acting on the fluid in a wall cell is now given by:

$$\vec{F}_w = -\tau_w A_w \mathbf{n}_t \quad (7)$$

The wall force decomposed into each direction follows:

$$F_{w,x} = -\tau_w A_w \mathbf{n}_t \cdot \mathbf{e}_x \quad (8)$$

$$F_{w,y} = -\tau_w A_w \mathbf{n}_t \cdot \mathbf{e}_y$$

With

$$\tau_w \cdot \mathbf{n}_t \cdot \mathbf{e}_x \approx \mu \frac{u - u_w}{\Delta h} \quad (9)$$

$$\tau_w \cdot \mathbf{n}_t \cdot \mathbf{e}_y \approx \mu \frac{v - v_w}{\Delta h}$$

### Numerical implementation

The implementation can follow the general method for doing multiphase flows. However, for simplicity we start with single phase compressible flows.

The semi discretized momentum equation for momentum in Cartesian direction i reads:

$$\Delta V \alpha_F^c \rho \frac{U_i - U_i^0}{\Delta t} + \sum_j (\alpha_F^f \rho U^0 A)_j U_i^0 = -\alpha_F^c \Delta V \frac{(p_{i+1} - p_i)}{\Delta_i} + \sum_j (\tau_{ij}(U_i) \alpha_F^f A)_j - \tau_w(U_i) A_{F,w} n_{t,i} + \Delta V G_i^0 - (\rho U^0 n_{F,w})_j (U_i - U_{w,i})^0 A_{F,w} \quad (10)$$

We next do the first fractional step for the momentum equation, solving for the temporary velocity  $U_i^*$ :

$$\Delta V \alpha_F^c \rho \frac{U_i^* - U_i^0}{\Delta t} + \sum_j (\alpha_F^f \rho U^0 A)_j U_i^0 = -\alpha_F^c \Delta V \frac{(p_{i+1}^0 - p_i^0)}{\Delta_i} + \sum_j (\tau_{ij}(U_i^*) \alpha_F^f A)_j - \tau_w(U_i^*) A_{F,w} n_{t,i} + \Delta V G_i^0 - (\rho U^0 n_{F,w})_j (U_i - U_{w,i})^0 A_{F,w} \quad (11)$$

In this first step we solved implicitly for the viscous stresses (turbulent stresses are straight forward, can easily be included later). In next step, by subtracting equation (11) from equation (10), we obtain:

$$\Delta V \alpha_F^c \rho \frac{U_i' - U_i^*}{\Delta t} = -\Delta V \alpha_F^c \frac{p_{i+1}' - p_i'}{\Delta_i} - (\tau_w(U_i^* + U_i') - \tau_w(U_i^*)) A_{F,w} + \sum_j \left\{ (\tau_{ij}(U^* + U') - \tau_{ij}(U^*)) \alpha_F^f A \right\}_j \approx -\Delta V \alpha_F^c \frac{(p_{j+1}' - p_j')}{\Delta_j} - \mu \frac{A_w}{\Delta h} U_i' \quad (12)$$

We should note that  $\alpha_F^f$  is the cell-face value, telling exactly the fraction of a cell face area being available for flow.

In equation (12) we have an equation for the implicit correction of the velocity. Similar to SIMPLEC method, we assume the error of neighbour cells are equal to the centre cell. However, in this case the convective momentum terms are discretized fully explicit, and formally we do not have any influence of neighbour cells as in the case of the SIMPLEC method.

### Obtaining a pressure equation

The pressure equation will be based on the mass equation.

$$\Delta V \alpha_F^c \frac{\rho - \rho^0}{\Delta t} + \sum_j \left\{ \rho^0 (U^* + U') \alpha_F^f A \right\}_j = S e^* \quad (13)$$

For incompressible flow  $\rho = \rho^0$ , and inserting the velocity correction from equation (12), we have:

$$-\sum_j \{\rho^0 U' \alpha_f^i A\}_j = Se^* - \sum_j \{\rho^0 U^* \alpha_f^i A\}_j \quad (14)$$

And where

$$U'_j = -\frac{\alpha_f^c \Delta V}{\frac{\alpha_f^c \Delta V \rho^0}{\Delta t} + \mu \frac{A_w}{\Delta h}} (p'_{j+1} - p'_j) \quad (15)$$

We take a two dimensional example, using equations (14) and (15), and having a wall at the right boundary, as illustrated in pressure cell (i+1,j) in Figure 2. The pressure equation in a cell (i,j) with this wall configuration is represented by:

$$\begin{aligned} & -\{\rho^0 u' \alpha_f^i \Delta A_x\}^+ + \{\rho^0 u' \alpha_f^i \Delta A_x\}^- - \\ & \{\rho^0 v' \alpha_f^i \Delta A_y\}^+ - \{\rho^0 v' \alpha_f^i \Delta A_y\}^- \\ & = Se^* - \{\rho^0 u^* \alpha_f^i \Delta A_x\}^+ + \{\rho^0 u^* \alpha_f^i \Delta A_x\}^- - \\ & \{\rho^0 v^* \alpha_f^i \Delta A_y\}^+ - \{\rho^0 v^* \alpha_f^i \Delta A_y\}^- \end{aligned} \quad (16)$$

Here we have that:

$$\begin{aligned} u^{*+} &= -\frac{\alpha_f^c \Delta V}{\frac{\alpha_f^c \Delta V \rho^0}{\Delta t} + \mu \frac{A_w}{\Delta h}} (p'_{i+1,j} - p'_{i,j}) \\ u^{*-} &= -\frac{\alpha_f^c \Delta V}{\frac{\alpha_f^c \Delta V \rho^0}{\Delta t} + \mu \frac{A_w}{\Delta h}} (p'_{i,j} - p'_{i-1,j}) \\ v^{*+} &= -\frac{\alpha_f^c \Delta V}{\frac{\alpha_f^c \Delta V \rho^0}{\Delta t} + \mu \frac{A_w}{\Delta h}} (p'_{i,j+1} - p'_{i,j}) \\ v^{*-} &= -\frac{\alpha_f^c \Delta V}{\frac{\alpha_f^c \Delta V \rho^0}{\Delta t} + \mu \frac{A_w}{\Delta h}} (p'_{i,j} - p'_{i,j-1}) \end{aligned} \quad (17)$$

These two equations (16) and (17) define our Poisson equation for the pressure. Once pressure is solved for we can compute the final velocities, using equation (17).

The handling of in/out-flow boundary conditions should be quite standard, and is not discussed here.

In the paper, we use a finite volume method where all fluxed across cell faces are balanced. Therefore, the cut-cell method will conserve mass, momentum and energy. In addition, the advective and diffusive fluxes across the cell face will be evaluated in the following sections.

### Calculating advective flux

Based on the cut-cell method in (Kirkpatrick et al., 2003) the advective flux in the cut cell is calculated for U-momentum equation as follows:

$$\begin{aligned} F_{adv} &= (\alpha_f^i \rho A U^2)_f \quad \text{for } x \text{ direction} \\ F_{adv} &= (\alpha_f^i \rho A U V)_f \quad \text{for } y \text{ direction} \end{aligned} \quad (18)$$

Here  $\alpha_f^i$  is the fluid fraction at the cell face and A is the area of the face. In the x direction, for the standard cell, a typical central interpolation is used to compute the velocity at the centre of cell face

$$u_e = [(1-\theta)u_p + \theta u_N] \quad (19)$$

Where,  $\theta = \frac{\Delta x_e}{\Delta x_E}$

For boundary cell the interpolated velocity is slight off the centre of cell face as shown in Figures 4 and 5. Therefore, a modification is needed to correct the velocity at this position.

$$u_{ec} = \alpha_c (u_e - u_b) + u_b \quad (20)$$

With,  $\alpha_c = \frac{h_{ec}}{h_e}$

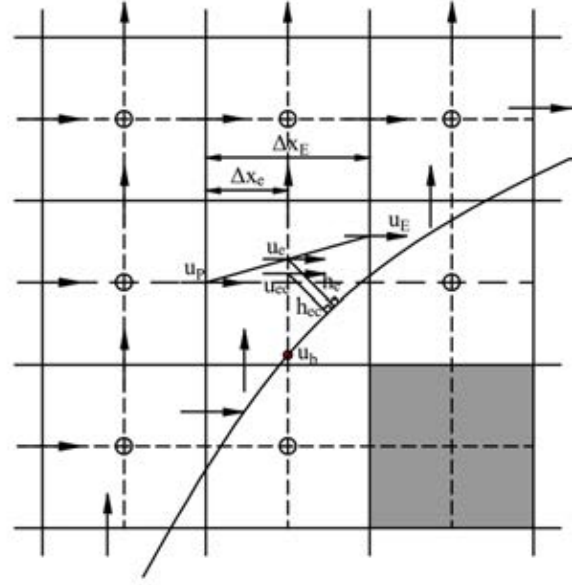


Figure 4. The schematic of interpolation and correction method for u at cell face

In y direction,

$$v_n = [(1-\theta_e)v_{ne} + \theta_w v_{mw}] \quad (21)$$

Where,  $\theta_e = \frac{\Delta x_w}{\Delta x_{we}}$  and  $\theta_w = \frac{\Delta x_e}{\Delta x_{we}}$

$$u_n = [(1-\theta)u_p + \theta u_N] \quad (22)$$

The correct velocity at cell centre:

$$u_{nc} = \alpha_c (u_n - u_b) + u_b \quad (23)$$

With  $\alpha_c = \frac{h_{nc}}{h_n}$

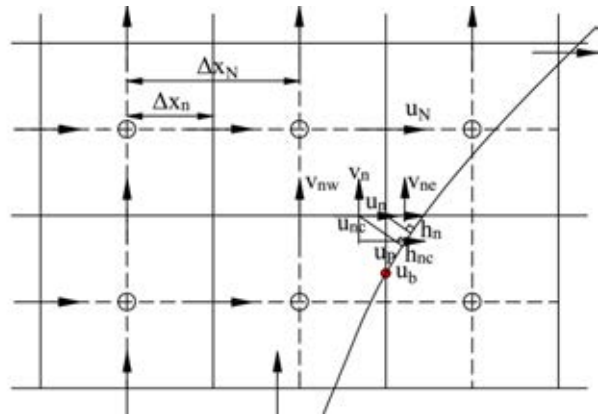


Figure 5. The location of interpolation and correction velocity at north face

### Calculating diffusive flux

The diffusive flux for U-momentum equation is given as flow

$$\begin{aligned} F_{diff} &= \left( \mu \alpha_f^i \Delta A \frac{\partial u}{\partial x} \right) \quad \text{for } x \text{ direction} \\ F_{diff} &= \left( \mu \alpha_f^i \Delta A \frac{\partial u}{\partial y} \right) \quad \text{for } y \text{ direction} \end{aligned} \quad (24)$$

As seen from Figure 6, the new velocity locations, making the vector connect points E and P, may not be perpendicular to the cell face. Therefore, a modification from conventional central difference is needed in order to compute the derivative  $\frac{\partial u}{\partial x}$  and  $\frac{\partial u}{\partial y}$  at the cell face. Taking

derivative of  $u$  along the vector  $\vec{s}$  gives,

$$\frac{\partial u}{\partial s} = s_x \frac{\partial u}{\partial x} + s_y \frac{\partial u}{\partial y} \quad (25)$$

Using central difference to approximate  $\partial u / \partial s$  yields,

$$\frac{u_E - u_P}{S} \approx s_x \frac{\partial u}{\partial x} + s_y \frac{\partial u}{\partial y} \quad (26)$$

Therefore,

$$\frac{\partial u}{\partial x} \approx \frac{1}{s_x} \left( \frac{u_E - u_P}{S} - s_y \frac{\partial u}{\partial y} \right) \quad (27)$$

With

$$\frac{\partial u}{\partial y} \approx N_y \frac{(u_e - u_b)}{h_e} \quad (28)$$

Where,  $N_y$  is  $y$  component of normal vector  $\vec{N}$  at the surface which passes through  $e$ . The velocity  $u_e$  is evaluated by the similar interpolation as was used for advective flux.

$$\frac{\partial u}{\partial x} \approx \frac{u_E - u_P}{S_x} - \left[ \frac{(1-\theta)u_P + \theta u_e - u_b}{S_x h_e} S_y N_y \right] \quad (29)$$

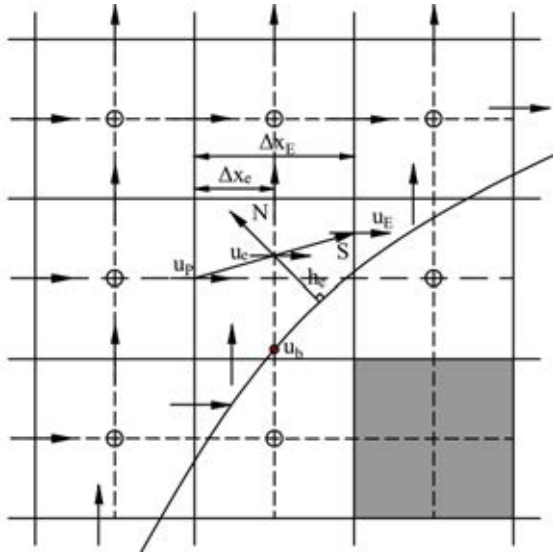


Figure 6. The vector  $S$  connects two cells and the normal vector  $N$  from the surface through the point  $e$

### Small cell problem

The presence of interface creates several velocity cells which connect to only one pressure cell. Those cells are defined as small cell (slave cell) and linked to master cell as shown in Figure 7. The detail of this method was presented in (Kirkpatrick et al., 2003).

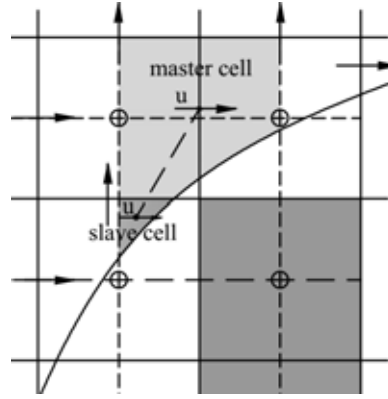


Figure 7. Linking between slave cell and master cell

## RESULTS AND EXTENSION TO TRUE MULTIMATERIAL FLOWS

### Taylor-Couette flow

This test is performed to check the order of accuracy of the scheme. The schematic of Taylor-Couette is shown in the Figure 8. While the outer cylinder is stationary, the inner cylinder rotates with the angular velocity  $\omega$ . The inside and outside radius is  $R_1 = 1$  and  $R_2 = 2$ , respectively. The Taylor number  $Ta$  which presents characterization of the Taylor-Couette flow is defined by:

$$Ta = \frac{\omega^2 (R_1 + R_2)(R_2 - R_1)^3}{2\nu^2} \quad (30)$$

As reported by (Dou et al., 2008), the flow fields are stable with  $Ta$  smaller than 1708. According to (Cheny and Botella, 2010), the velocity fields in steady state is given as follows:

$$\begin{aligned} u(x, y) &= -K \left( \frac{R_2^2}{r^2} - 1 \right) (y - y_c) \\ v(x, y) &= K \left( \frac{R_2^2}{r^2} - 1 \right) (x - x_c) \end{aligned} \quad (31)$$

$$\text{Where, } K = \frac{\omega R_1^2}{R_2^2 - R_1^2} .$$

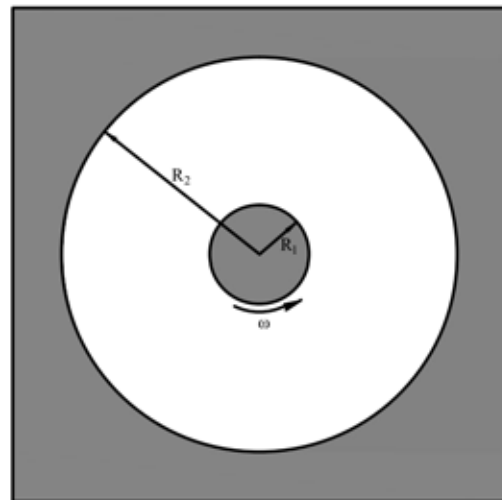


Figure 8. The geometry of Taylor-Couette flow

In this paper, the  $Ta$  is equal to 1000 and the centre of cylinder  $(x_c, y_c)$  is  $(0.023, 0.013)$ . The computational domain is from -5 to 5 in each direction. The grid spacing  $h$  is approximated by  $1/N$ , which  $N$  is grid size. The Figures 9 and 10 show the order of accuracy of the scheme for 2-norm and infinity norm. Whereas, the current method shows second order of accuracy for the 2-norm of  $u$  and  $v$  velocity, the infinity norm is slightly off from 2<sup>nd</sup> order slope.

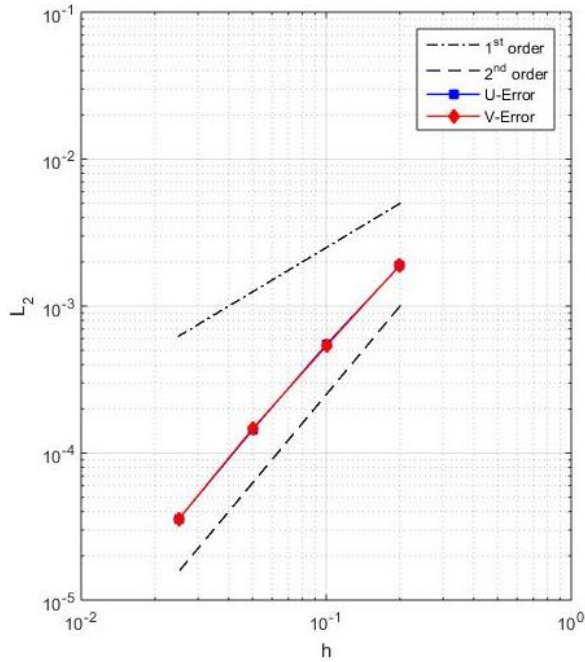


Figure 9.  $L_2$  norm of the error for velocity  $u$  and  $v$

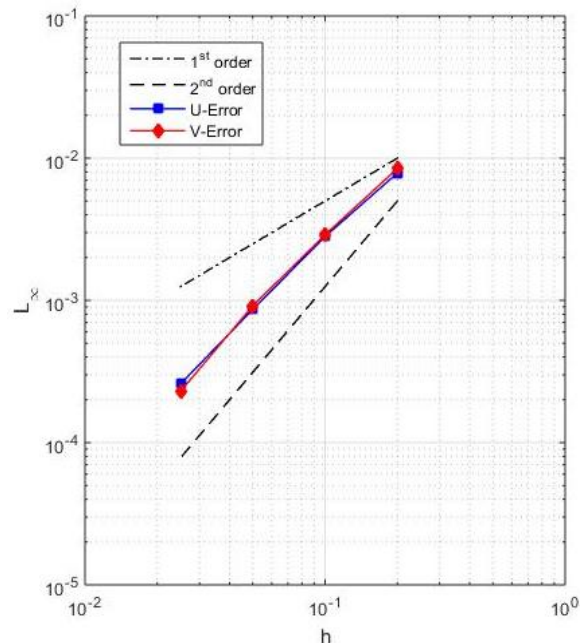


Figure 10.  $L_\infty$  norm of the error for velocity  $u$  and  $v$

*Flow past a circular cylinder*

Due to a significant amount of well documented test cases published in literature, the second test is the flow past a circular cylinder. The Reynolds number in this case is calculated based on the inlet velocity  $U_{inlet}$  and the

diameter of cylinder  $D$ . The computational domain is illustrated in Figure 11.

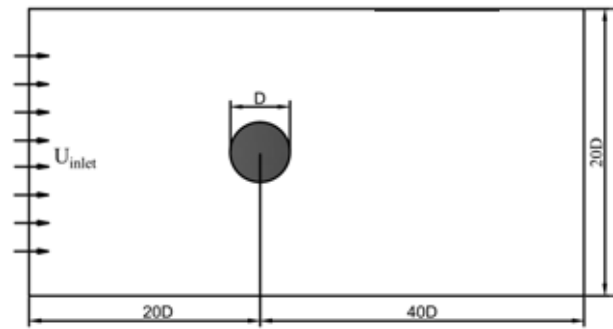


Figure 11. The computational domain

Figure 12 shows the comparison of pressure coefficient over cylinder, as obtained by present study, experiment data (Grove et al., 1964) and numerical result (Jeff Dietiker, 2009). As seen from the figure, good agreement with these reference results is observed. In addition, it can be seen that the current method can predict the pressure distribution quite accurately for coarse grids. Additional predicted properties of the flow, such as the drag coefficient, the separation angle and the size of flow separation bubble is in Table 1 seen to compare well with previous studies.

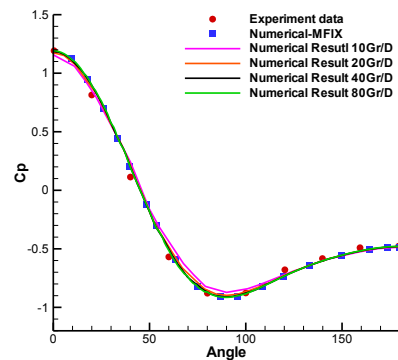
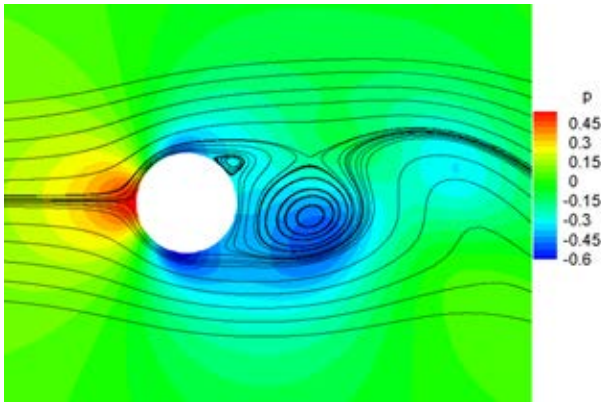


Figure 12. The pressure coefficient over cylinder at  $Re = 40$

$Re = 40$	$C_D$	$\theta$	$L/D$
Linnick and Fasel, 2005	1.54	53.6	2.28
Taira and Colonius, 2007	1.54	53.7	2.30
Kirkpatrick et al., 2003	1.535	53.5	2.26
MFIX(Jeff Dietiker, 2009)	1.542	53.7	2.27
Present Study	1.55	53.5	2.26

Table 1. The drag coefficient  $C_D$ , the separation angle  $\theta$  and the length of recirculation bubble  $L/D$  behind the cylinder

Figure 13 shows the pressure contour and streamline at  $Re = 100$ . As shown in this figure, the flow became unsteady as vortex shedding formed behind cylinder. Tables 2 and 3 show that for the drag coefficient, the maximum lift coefficient and Strouhal number, our simulation results compared well with other results published in literature.



**Figure 13. The pressure contour and streamline at  $Re = 100$ .**

$Re = 100$	$C_D$	$C_{L,max}$	$St$
Linnick and Fasel, 2005	$1.34 \pm 0.009$	0.333	0.166
King, 2007	1.41	-	-
He et al., 2000	1.353	-	0.167
Present Study	$1.374 \pm 0.01$	0.337	0.169

**Table 2. The Drag Coefficient  $C_D$ , the maximum Lift Coefficient  $C_{L,max}$  and Strouhal number  $St$  at  $Re = 100$**

$Re = 200$	$C_D$	$C_{L,max}$	$St$
Linnick and Fasel, 2005	$1.34 \pm 0.044$	0.69	0.197
Taira and Colonius, 2007	$1.35 \pm 0.048$	0.68	0.196
He et al., 2000	1.356	-	0.198
Present Study	$1.346 \pm 0.046$	0.7	0.196

**Table 3. The Drag Coefficient  $C_D$ , the maximum Lift Coefficient  $C_{L,max}$  and Strouhal number  $St$  at  $Re = 200$**

## CONCLUSION

A method to establish discrete transport equations for mass and momentum is presented. A semi-implicit predictor-corrector method for solving for velocities and pressure. The near interface advective flux and diffusive flux are calculated based on the interpolation technique presented by (Kirkpatrick et al., 2003). The numerical results show that our method can achieve global second order of accuracy and well predict the physical phenomena.

## REFERENCES

Bouchon, F., Dubois, T., James, N., 2012. A second-order cut-cell method for the numerical simulation of 2D flows past obstacles. *Comput. Fluids* 65, 80–91. doi:10.1016/j.compfluid.2012.02.011

Chen, Y., Botella, O., 2010. The LS-STAG method: A new immersed boundary/level-set method for the computation of incompressible viscous flows in complex moving geometries with good conservation properties. *J. Comput. Phys.* 229, 1043–1076. doi:10.1016/j.jcp.2009.10.007

Cushman, J.H., 1982. Proofs of the volume averaging theorems for multiphase flow. *Adv. Water Resour.* 5, 248–253.

Dou, H.-S., Khoo, B.C., Yeo, K.S., 2008. Instability of Taylor–Couette flow between concentric rotating cylinders. *Int. J. Therm. Sci.* 47, 1422–1435. doi:10.1016/j.ijthermalsci.2007.12.012

Gray, W.G., Lee, P.C.Y., 1977. On the theorems for local volume averaging of multiphase systems. *Int. J. Multiph. Flow* 3, 333–340.

Grove, A.S., Shair, F.H., Petersen, E.E., 1964. An experimental investigation of the steady separated flow past a circular cylinder. *J. Fluid Mech.* 19, 60–80. doi:10.1017/S0022112064000544

He, J.-W., Glowinski, R., Metcalfe, R., Nordlander, A., Periaux, J., 2000. Active Control and Drag Optimization for Flow Past a Circular Cylinder. *J. Comput. Phys.* 163, 83–117. doi:10.1006/jcph.2000.6556

Hirt, C.W., Sicilian, J.M., 1985. A porosity technique for the definition of obstacles in rectangular cell meshes (Flow Science Inc.). New Mexico.

Jeff Dietiker, 2009. Implementation of Cartesian Cut-Cell Technique into the Multiphase Flow Solver MFIX.

King, R. (Ed.), 2007. *Active Flow Control, Notes on Numerical Fluid Mechanics and Multidisciplinary Design (NNFM)*. Springer Berlin Heidelberg, Berlin, Heidelberg. doi:10.1007/978-3-540-71439-2

Kirkpatrick, M.P., Armfield, S.W., Kent, J.H., 2003. A representation of curved boundaries for the solution of the Navier–Stokes equations on a staggered three-dimensional Cartesian grid. *J. Comput. Phys.* 184, 1–36.

Lauer, E., Hu, X.Y., Hickel, S., Adams, N.A., 2012. Numerical modelling and investigation of symmetric and asymmetric cavitation bubble dynamics. *Comput. Fluids* 69, 1–19. doi:10.1016/j.compfluid.2012.07.020

Linnick, M.N., Fasel, H.F., 2005. A high-order immersed interface method for simulating unsteady incompressible flows on irregular domains. *J. Comput. Phys.* 204, 157–192. doi:10.1016/j.jcp.2004.09.017

Ng, Y.T., Min, C., Gibou, F., 2009. An efficient fluid–solid coupling algorithm for single-phase flows. *J. Comput. Phys.* 228, 8807–8829. doi:10.1016/j.jcp.2009.08.032

Quintard, M., Whitaker, S., 1995. AEROSOL FILTRATION: AN ANALYSIS USING THE METHOD OF VOLUME AVERAGING. *J. Aerosol Sci* 26, 1227–1255.

Schneiders, L., Günther, C., Meinke, M., Schröder, W., 2016. An efficient conservative cut-cell method for rigid bodies interacting with viscous compressible flows. *J. Comput. Phys.* 311, 62–86. doi:10.1016/j.jcp.2016.01.026

Schwarz, S., Kempe, T., Fröhlich, J., 2016. An immersed boundary method for the simulation of bubbles with varying shape. *J. Comput. Phys.* 315, 124–149. doi:10.1016/j.jcp.2016.01.033

Taira, K., Colonius, T., 2007. The immersed boundary method: A projection approach. *J. Comput. Phys.* 225, 2118–2137. doi:10.1016/j.jcp.2007.03.005





## SOFT: A FRAMEWORK FOR SEMANTIC INTEROPERABILITY OF SCIENTIFIC SOFTWARE

Thomas F. HAGELIEN<sup>1\*</sup>, Andrey CHESNOKOV<sup>2†</sup>, Stein Tore JOHANSEN<sup>2,3‡</sup>, Ernst A. MEESE<sup>3§</sup>,  
Bjørn Tore LØVFALL<sup>3¶</sup>

<sup>1</sup>SINTEF Ocean, 7465 Trondheim, NORWAY

<sup>2</sup>NTNU, Department of Energy and Process Engineering, 7491 Trondheim, NORWAY

<sup>3</sup>SINTEF Materials and Chemistry, 7465 Trondheim, NORWAY

\* E-mail: thomas.hagelien@sintef.no

† E-mail: andrey.chesnokov@ntnu.no

‡ E-mail: stein.t.johansen@sintef.no

§ E-mail: ernst.a.meese@sintef.no

¶ E-mail: bjortore.lovfall@sintef.no

### ABSTRACT

In this paper we present our strategy and implementation of a datacentric modelling framework (SOFT, SINTEF Open Framework and Tools) with focus on information interchange in through-process and multiscale applications. SOFT needs to accommodate for a inhomogeneous set of in-house open source and proprietary simulators, often written in different programming languages, and storing data in different formats. The complexity and diversity of such a system requires that we have formal schemas and structures of metadata that allow for information interpretation regardless of the original storage formats, which application produced the data, and which application processes the data. We propose a standard for data exchange, separately describing metadata specific to different knowledge domains.

SOFT, via a mechanism of plugins, offers the possibility to utilize different tools for storage of such data and metadata. Further, SOFT facilitates scientific software development by clear separation of numerical routines and platform-dependent input, output, and analysis routines. Automated testing and simulation data analysis are also achieved in SOFT via external plugins and interfaces to scripted languages such as Python and Javascript.

The framework has been developed and tested within such flow modelling projects as LedaFlow, NanoSim and SimcoFlow.

**Keywords:** Metadata, information interchange, semantic interoperability, software framework, JSON .

### INTRODUCTION

Modern scientific modelling software often has to operate with large amounts of data coming from different sources. A typical example is flow or process simulators where phenomena on different time and spatial scales has to be connected and data exchanged. If sub-models or relevant experimental information are available, it would be very efficient if we could “plug in” such models or data and have them available inside of a simulator with a minimum of work. In our development of the open source software SimcoFlow, the target is to develop a multi-material simulator which can handle complex multiphase flows with coexisting dynamic materials, free surfaces, and dispersed phases. In such a framework, it would be of great advantage if we could, with a minimum of work, use available sub-models for physics, available Cartesian cut-cell grid generation methods, visualization methods, as well as models/data for thermodynamic and material properties.

Most often such simulation software has to function as part of a pipeline, producing data for post processing, analysis and input for a higher level simulator. The data is often stored in a variety of formats, ranging from proprietary and closed formats, to well-documented open standards. In addition to this, the data often lacks information, such as which unit is used for a data point, how the data was produced, what are the uncertainties of the data etc. — as this is either implicit or simply just “understood” by the systems interpreting the data.

In this paper we describe a framework that is operating on a high level of abstraction, allowing for loose coupling between syntactic data representation (data structures and file formats) and internal representation in a software system. The framework operates within concepts of metadata and metamodels, representing different entities and their domain specific relationship, and how this can be used to connect different scientific modelling tools in a workflow. The framework also eases identification, traceability and reproducibility of simulations, and allows for easier separation of different knowledge domains, while also reducing development time.

### HISTORICAL APPROACHES

The information technology has evolved into a world of largely loosely coupled systems and as such, needs increasingly more explicit, machine-interpretable semantics. There have been several approaches to formalizing interoperability, arising from different areas of knowledge.

A good example of an important problem is an effective data sharing across government agencies and other organizations. Such sharing relies upon agreed meanings and representations. A key technological challenge in electronic governance is to ensure that the meaning of data items is accurately recorded, and accessible in an economical, preferably, fully automatic fashion. In response, a variety of data and metadata standards have been put forward: from government departments (DHS, 2012), from industry groups (Chieu *et al.*, 2003), and from organizations such as the ISO (ISO, 2013) and W3C (Lassila and Swick, 1997). A short review of several challenges and initiatives in the area is presented in the works (Obrst, 2003) and (Davies *et al.*, 2008).

Standardization activity in software engineering was originally focused upon language and protocol design: upon the intended interpretation of programming statements, and upon

the concrete representation of data and commands. Since then, there has been a significant shift in focus towards metadata standards, such as descriptions of intended functionality and meaning that can be associated with particular items of data, in order to ensure consistent treatment and interpretation.

There could be mentioned several serious failures in industry due to misinterpreting of metadata. Probably the most well known example is the NASA Mars Climate Orbiter (NASA, 1999), that was lost after two different subsystems did not agree on communication. The first was sending values in US Customary units, the second assumed that the values arriving were measured in SI units. In this example the data itself, i.e. number, was passed correctly, but the metadata, i.e. unit, was lost during communication. This kind of mistake is hard to avoid when data is processed and integrated automatically, while its semantic consistency, such as the compatibility of units and intended interpretation, is checked only manually.

Importance of specification and recycling of standard metadata elements has led to development of the ISO 11179 standard (ISO, 2013), an international standard for metadata registration. The standard addresses “the semantics of data, the representation of data, and the registration of the descriptions of that data”.

An important initiative in the domain of material modelling is the SimPhoNy project (Hashibon, 2014). The main concept of the SimPhoNy framework is to augment existing open-source and commercial simulation tools and supplement them with sophisticated interface software libraries that allow for flow of information from one component to the other and from one scale to another. The integrated tools range from those describing the electronic structure and atomistic scales up to those modelling mesoscopic and macroscopic device level scales.

On the low level, the metadata model in SimPhoNy specifies a basic knowledge-based set of keywords that cover all aspects of the models and associated numerical computational methods. For example, temperature is a fundamental concept that is used in numerous models in different contexts. In continuum models it is the macroscopic thermodynamic temperature of a whole domain or on specific mesh elements. While for atomistic systems it may be the local kinetic temperature or a global parameter defining the interaction with a thermal bath. It can be associated therefore with either a parameter of the system or a variable. In either case, one keyword is associated with temperature in SimPhoNy with appropriate basic metadata. This metadata is then augmented with the associations and relations between different model components to obtain readily the exact nature of the particular temperature and its context in the model.

## GENERAL IDEAS

In this section we define basic concepts of metadata, semantic modelling and data interchange.

### Metadata

To achieve interoperability, the data that is communicated needs to be labeled, categorized and described. This description is generic, and is called metadata. Usually this is a means to define the data syntactically. It is also possible to think about metadata as extra information that can be attached to data. A good example of this is EXIF-info, which

is attached to images and stores metadata such as date and time information, camera settings, etc. These two definitions of metadata are one and the same, with just a different set of attributes.

## Ways of data interoperability

Interoperability between two or more scientific simulators is the process of taking some input into one simulation tool, producing the output and transforming the data into a suitable form that can be read and interpreted by the second simulator. Often the data is stored to disk, but can also be exchanged directly between two simultaneously running simulations via RPC, MPI etc. Here we focus on file based information exchange.

The data that is written to disk needs to be structured such that data can be retrieved. The format (syntax) of the data files can be either proprietary (closed) or open. To generalize information exchange from proprietary formats is difficult. Using open file formats is better, but it requires that wrappers are written and placed in the pipeline between the simulators in a defined workflow. The wrappers allow for the conversion of an application specific representation to a generic representation understood by a framework. If the formal specification of the generic representation contains enough information to be self-contained and allow for data sharing between different simulators and domains, we call this a schema for semantic interoperability.

A framework for semantic interoperability should allow for the exchange of information with any other "context compatible" system that shares the same attributes, purely based on a formal description of the semantics, without regards to the underlying syntax or file formats. This, however, requires that there exists wrappers that handles application specific file formats. The semantic framework builds on top of a set of syntactic layers, without exposing the details to the scientific simulator.

## Defining semantic interoperability

Semantic interoperability can be achieved by formally describing all properties of the data that is to be exchanged, along with domain specific relationships between categories of data (entities). Necessary information includes attributes such as property names, types, units, rank (dimensionality), etc. This allows for reading and writing the data at the syntactic level. The schema for describing the semantics needs to be formal such that information can be shared between platforms and domains. Relationships between different entities need to be described explicitly as to define how they are connected. Any given relationship between two or more entities is bound to a certain domain, and might not be true for another, as such it is important to separate the relationship descriptions from the data descriptions. With this, it is possible to have interoperability across domains, where the semantically equivalent data points are used in two different contexts.

There are certain desired requirements to a formal schema-describing language that would be used as a building block for domain-specific schemas. It should be well-defined, minimalistic, be able to describe itself and provide versioning for handling of changes during the development process. There already exist several industry-wide languages that supersede these requirements, such as XML, YAML, JSON and others.

## Concepts in semantic modelling

An entity is a fundamental concept in semantic interoperability approach. The entity is a generic concept that can represent anything, and according to Merriam-Webster is defined as “Something that exists by itself, something that is separate from other things”. This means that entities have unique identities and sets of attributes. Such identities and attributes are described using formal schemas in a selected language. The schemas represent self-contained information about some object or concept.

While during well-known entity-relationship modelling (Chen, 1976) a model is composed of entity types, which classify the things of interest, and specifies relationships that can exist between instances of those entity types, we allow an entity to also include information about the state data, accompanying metadata, entity relations, workflow semantics and more.

Similarly to the Resource Description Framework data model (Lassila and Swick, 1997), we define facts as binary relations between entities. Then a system that is being modelled can be represented as a set of entities combined into collections by a fact-based semantic data model. Since a collection is an entity, collections can define relationships between collections as well as data-entities and model-entities.

While entity definitions are shared between knowledge domains, relationships between entities change between the domains. It is therefore important to separate these two concepts. Relationships in SOFT are expressed using triples. Each triple has a subject-predicate-object structure. To illustrate this, let us define a person as an entity, and give it properties such as name, date of birth, social security number etc. Instances of the entity person will represent an actual human being. To add relationships we can consider an example of a family business named FamCo, where the oldest son, Peter, is running the firm, while his sister Susan and father John are employees. In this domain the relationships can be defined like this:

"Peter"	"works at"	"FamCo"
"Susan"	"works at "	"FamCo"
"John"	"works at"	"FamCo"
"Peter"	"title"	"CEO"
"Peter"	"is-the-boss-of"	"Susan"
"Peter"	"is-the-boss-of"	"John"

In a different domain — say genealogy, we can consider the same entities, but the relations are completely different:

"John"	"is father of"	"Peter"
"John"	"is father of"	"Susan"

## Instantiation of semantic models

To reduce dependencies to a specific piece of computational software, it is useful to classify the mathematical models that is realized in the software, and create a generic description that allows for the computational software to be interchangeable.

A mathematical model defines a transformation of a set of values (Input  $\rightarrow$  Transformation  $\rightarrow$  Output). Let these inputs, outputs and state data be described by a semantic data model. Then such a mathematical model can be considered as yet another abstraction level, namely, as a metamodel. By

using this concept, we can describe a complete solution of a given business case, where the actual realization will not depend on any one given piece of computational software or file format. A suitable set of software simulators and data sources will be chosen then at runtime, which is called as an instantiation of a business case.

An important application of these ideas in the SOFT framework is an ability to build data agnostic simulators, that is, simulators working with different formats and storage technologies. With standardized formal metadata-schemas, we can allow reusable backend storage systems to handle I/O, thus letting computational models know only about the semantic data model and not the implementation details.

The current representation of the semantics in SOFT is targeted towards scientists and programmers with domain knowledge. The choice of representation syntax is intentionally kept minimalistic and pragmatic, without loosing the mapping to other representations, such as OSF.

## EMMC initiative

The work presented here lies in heart of the EU cluster EMMC CSA (European Materials Modelling Council, <https://emmc.info/>), where framework development, semantic interoperability and metadata are key enablers for the coupling of new and existing materials modelling tools.

## SOFT FRAMEWORK: PRACTICAL IMPLEMENTATION OF GENERAL CONCEPTS

### Scientific software development — a datacentric approach

It is a common practice to start out the development of scientific software with implementing core functionality around numerical methods or other algorithms. We propose an alternative, namely, to start with data modelling of the system in the context of a framework such as SOFT (Domain Driven Design). We have experienced that this way the development will greatly benefit from the architectural quality attributes maintainability, interchangeability/interoperability and modifiability.

The modelling process starts with building a taxonomy of the domain for which the software system should be built. This will require expertise from both domain experts and data modelling experts. The taxonomy will be a blueprint of what will later be defined as entities and relationships. The taxonomy should include all relevant actors and properties the scientific software will address, without regards for what will be the workflow, transformations, inputs and output of the system. The next step in the process is formalizing the model into a recognized/standardized format suitable for metadata interchange.

The associations and dependencies defined in the taxonomy are candidates for the decoupled structuring of the information in data collections. The first step here is to formally define the entities. Then code generators can be employed to generate classes, templates, wrappers, serialization code, documentation, etc. In addition, the developed schemata can be published such that others working in a similar knowledge domain can benefit from the classification work, without having to redo all the work.

SOFT includes an autogenerator which can take any JSON data as input, and transform it into a custom text output, by

defining a template that mixes pure text and Javascript code identified by a special markup. One of the greatest benefits of this is that an entity can be changed anytime by changing only its corresponding JSON description. The changes are then applied to the rest of project automatically, without having to worry about updating all dependent code and documentation. Code autogeneration happens at compile time.

While developing formal schemata for the entities it seems to be beneficial to employ namespaces in the descriptions of the entities for avoiding name-clashes between domains, as well as version numbers for supporting a semi-automatic versioning system. This is the way the entities are named in the SOFT system.

SOFT supports I/O through a storage plug-in mechanism, which hides the I/O machinery from the modelling code. In cases where data needs to be communicated between multiple simultaneously running processes, the entities can be used to generate code used to serialize the data between the processes. Examples of this can be MPI (<http://pages.tacc.utexas.edu/~eijkhout/pcse/html/mpi-data.html>) and protobuf (<https://developers.google.com/protocol-buffers/>) messages. In these cases, the interfacing of the simulation software components is written or autogenerated based on entities, as part of the modelling code.

Exchanging data only requires that data is described in the formal semantic description and there exists support for the given syntax (data format) in the SOFT framework as a plugin. The APIs for entities and collections are used in the modelling code (and are usually embedded in the autogenerated code) to get access to the data. Except from this, no other APIs are necessary.

### Example 1: Describing an entity

In SOFT, we have selected to use JSON as this is widely supported, human readable/writable and integrates nicely with the scripting engine of SOFT which is based in JavaScript. The proposed JSON schema for defining entities is currently being reviewed in the EMMC-CSA project and is subject for future standardization. The standard will be open and publicly available. An example of the JSON definition of an entity is shown in Figure 1. The entity is uniquely defined with a name, namespace and a version. Attributes are listed under the *properties* keyword. In this case there is only one property *foo*.

```
{
  "name": "example",
  "namespace": "com.example",
  "version": "0.1-SNAPSHOT-1",
  "properties": [
    {
      "name": "foo",
      "type": "string",
      "description": "A metasynth. variable"
    }
  ]
}
```

Figure 1: An example of a formal schema for defining an entity

### Example 2: Taxonomy of a simplified simulation case

An example of an instantiation of a semantic model is a simulation case. Let us consider some imaginary case that has an inlet condition and an outlet condition. The case also has a set of predefined user inputs, such as physical constants, and computational results, such as velocity fields. The case also has a numerical solver that requires a matrix structure and some settings, such as tolerances, that can be changed by the user. In Figure 2 we have defined the relations between six different *Entities* (grey ovals) and two *Collections* (blue ovals).

All *Entities* are described by their formal JSON-metadata. These JSON-files are registered in the SOFT system and their counterpart in the desired programming language is autogenerated. Before running the simulation a Case Creator instantiates these *Entities* with input data and other parameters and stores them in a Domain *Collection* with a certain ID.

When the simulation is run, one gives this unique ID of the instance of the Domain *Collection* and the URI of a place where the raw data is stored, to SOFT. This is all that is needed; SOFT takes care of the rest. Thus, the simulation core does not have to take into account how the data is stored, provided that it complies to a given semantic, i.e. JSON, description. A *Collection* can be dynamic, such that, for example, the solver tolerance or inlet type can be changed at a runtime.

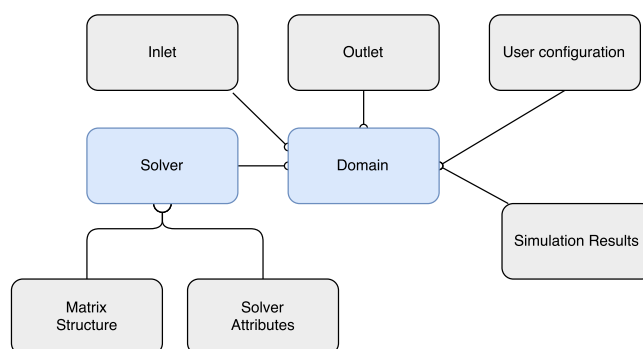


Figure 2: Taxonomy of a simulation case

### Example 3: Entities and couplings in the NanoSim project

The NanoSim project (Singhal *et al.*, 2016) employs SOFT in a multiscale coupling workflow. In this example we demonstrate data transformations and exchange of information from an atomic scale simulation to a resolved CFD simulation. Figure 3 illustrates a workflow, which starts with available intermolecular scale data (DFT), that was generated using VASP software (<https://www.vasp.at>). Raw data files are represented by using SOFT entities named *Reference*. These are instantiated and registered in a *Collection*. The next step of the workflow is to feed this to the REMARC software to generate information for chemical kinetics models. The REMARC (owned by SINTEF) package already reads the VASP data formats, so there is no need to transform the data further. In addition, the DFT files can be very large, so it makes no sense to store duplicates or transfer these files.

Additional input files to REMARC are handled via the entity named *File*, which stores information about an arbitrary block of data, a name, size and a cryptographic hash

string for consistency checking. REMARC is embedded in SOFT by using a wrapper that converts information from the *Collection* into the native file format and back again. In this case the CHEMKIN-II data files are read and written using a SOFT storage plugin. This enables the REMARC wrapper to work purely on semantic information along with a URI to the location of the actual data. One of the output entities from the REMARC wrapper is called *chemkinReaction*, whose corresponding JSON-description could be accessed online at <https://github.com/NanoSim/Porto/blob/master/porto/src/entities/chemkinreaction.json>. A part of it is shown on Figure 4. The data generated from REMARC is stored in a MongoDB database.

The URI to the MongoDB location, along with the unique case ID is then passed to a SOFT code generator, which generates a plugin for ANSYS Fluent. The code generator uses a general template for generating FLUENT UDFs as well as data that came from VASP through REMARK. The entire workflow is put together as a single SOFT script. The simulation is then run simply by passing the input files (VASP DFT data and REMARC configuration files) to the script, which, in its turn, generates the *Collection*, and attaches all entities automatically.

On Figure 3 we show the complete workflow. The DFT-prepare step creates a *Collection*, a *File* and a *Reference* entity, and instantiates these with data given from input. The output from the preparation step is the ID of the *Collection*, which is passed to the REMARC wrapper. The wrapper makes call to the REMARC simulator and appends REMARC data to the *Collection* using relevant entities, such as *chemkinReaction*. The output from the wrapper has the same ID as was given as input. The code generator receives the ID and builds a model based on the relevant entities found in the *Collection*. It then uses the SOFT code generator utility to produce a User Defined Function (UDF) that can be compiled and read by ANSYS Fluent.

#### Example 4: Workflow in the SimcoFlow project

A typical run of a SimcoFlow simulation could be divided into three parts: Case Creator, Simulator and Postprocessor. Simulator operates on initial data provided by Case Creator and, in its turn, generates the data for the Postprocessor. All data exchange happens via the SOFT framework, that takes care of several low-level details. Figure 5 shows data flow chart of the project. The datacentric architecture is noticeable by the data storage that is initially declared, and later used during the simulation run.

The Case Creator generates a *Collection* with all information describing a full simulation case. This will be typically written in a high level (scripting) language, or produced with

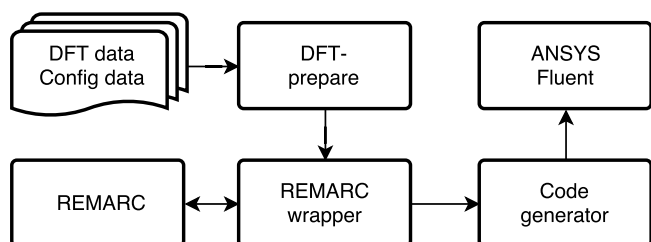


**Figure 3:** A workflow going from an atomic scale simulation to a CFD simulation using SOFT

a graphical user interface. The SOFT system provides the autogenerated code in this selected language for the Entities described with JSON-schemas. The process of working with metadata is shown on Figure 6. The language can be potentially different from what is used for the core numerical method. The *Entities* are then instantiated with the user provided input data and united in a *Collection*. This instance of a *Collection* is stored in a storage solution provided by SOFT, resulting in a unique UUID referring to the simulation case.

We assume that the main Simulator module has the following structure:

1. Fetch data from storage
2. Initialize simulation
3. Time stepper
  - (a) Initialize time step
  - (b) Do time step
  - (c) Finalize time step
4. Finalize the simulation

```

{"name": "chemkinReaction",
 "version": "0.1",
 "namespace": "eu.nanosim.vasp",
 "description": "Description of a
  thermodynamical reaction with rate
  constant: k(T) = A * T**b * exp(-Ea
  /(R*T)) where A, b and Ea are
  parameters, T the temperature and R
  the molar gas constant (8.31451 J
  /(mol K)).",
 "dimensions": [
  {
    "name": "nreactants",
    "description": "Number of reactants"
  },
  {
    "name": "nplog",
    "description": "Number of intervals
    the pressure dependency of the
    rate coefficients is described."
  } ],
 "properties": [
  {
    "name": "reactants",
    "type": "string",
    "dims": ["nreactants"],
    "description": "Name of each reactant
    species."
  },
  {
    "name": "P_plog",
    "type": "double",
    "dims": ["nplog+1"],
    "unit": "Pa",
    "description": "Pressures defining
    the borders of the nplog pressure
    intervals for defining pressure
    dependency of the rate constant."
  } ]
}
  
```

**Figure 4:** An extract of *chemkinReaction* entity.

This workflow is represented on Figure 5.

Each of the steps corresponds to a specific function, that can be written in any supported programming language. The only requirement is that its function pointer has to be registered in the system by Case Creator.

During step 1 the Simulator reads in input data using SOFT drivers, given the UUID from Case Creator, and initializes the native programming language structures, using metadata description autogenerated from JSON. During step 2 some physical parameters could be set. During step 3 the main computation is done. In principle, different programming languages can be used for different functions in step 3, if their argument structures follow the documented C API.

Each of the functions on steps 1-4 can in principle dump some data to the storage, using SOFT drivers and metadata description. However, we feel that it is natural to restrict dumping to steps 3c (store some information available at a working time step) and 4 (store the final result or the whole simulation with all intermediate steps). A generated UUID

will refer to the stored simulation results.

Given this UUID and metadata descriptions, different applications can access the data storage independent from the simulation module, either in the process of the simulation or when it is finished. A natural use case here is postprocessing of data for visualization.

## CONCLUSION

In this paper we presented a datacentric approach for designing and developing scientific software that enables interoperability, and illustrate this approach with examples based on the SOFT framework and several projects that are employing it. By starting with the classification of the domain and transferring this into formal definitions of entities and associations/relations, a researcher creates a solution model that is both maintainable and flexible.

Employing a framework like SOFT makes it uncomplicated to share data between different areas of knowledge, by bridging the different domains with a semantic layer. This is done by the exchange of formal definitions of entities. The framework itself takes care of low-level data input and outputs in reusable modules, letting the physicians focus on the physics and software scientists focus on the data modelling within the same project.

## ACKNOWLEDGEMENTS

The Norwegian Research Council, through the research program SimcoFlow (project 234126), is acknowledged for supporting this work.

## REFERENCES

- CHEN, P.P.S. (1976). "The entity-relationship model&mdash;toward a unified view of data". *ACM Trans. Database Syst.*, **1**(1), 9–36.
- CHIEU, T.C., FU, S.S., PINEL, F. and YIH, J.S. (2003). "Unified solution for procurement integration and b2b stores". *Proceedings of the 5th International Conference on Electronic Commerce, ICEC '03*, 61–67. ACM, Pittsburgh, Pennsylvania, USA.
- DAVIES, J., HARRIS, S., CRICHTON, C., SHUKLA, A. and GIBBONS, J. (2008). "Metadata standards for semantic interoperability in electronic government". *Proceedings of the 2nd International Conference on Theory and Practice of Electronic Governance*, 67–75. ACM.
- DHS (2012). *National Information Exchange Model, 3.0*. Dept. of Justice and Dept. of Homeland Security.
- HASHIBON, A. (2014). "SimPhoNy: Simulation framework for multiscale phenomena in micro and nano systems".
- ISO (2013). *ISO 11179. Information Technology Specification and Standardization of Data Elements*. International Organization for Standardization (ISO).
- LASSILA, O. and SWICK, R. (1997). "Resource Description Framework (RDF) Model and Syntax". Tech. rep., W3C.
- NASA (1999). "Mars Climate Orbiter Mishap Investigation Board Phase I Report". Tech. rep., NASA.
- OBRST, L. (2003). "Ontologies for semantically interoperable systems". *Proceedings of the Twelfth International Conference on Information and Knowledge Management, CIKM '03*, 366–369. ACM, New Orleans, LA, USA.
- SINGHAL, A., CLOETE, S., RADL, S., FERREIRA, R. and AMINI, S. (2016). "Cfd-dem predictions of heat transfer in packed beds using commercial and open source codes". *MAYFEB Journal of Chemical Engineering*, **1**(1), 1–17.

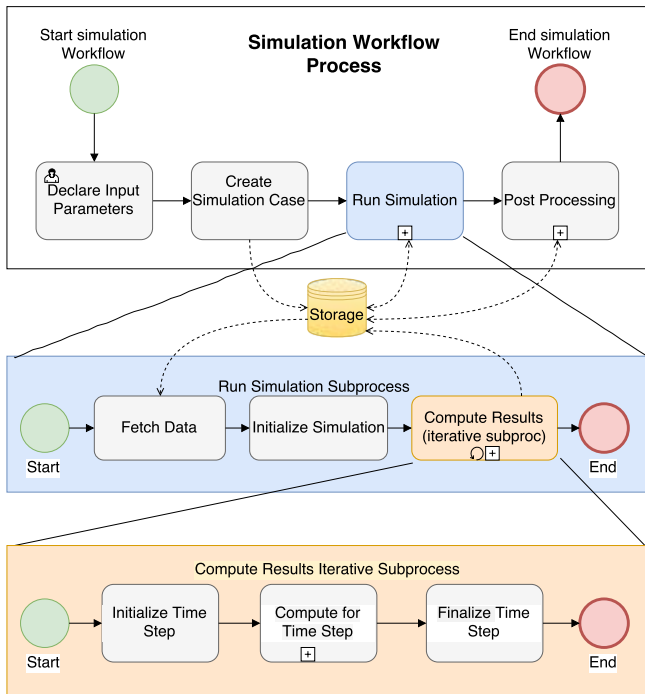


Figure 5: BPMN diagram illustrating the process of running a simulation with SimCoFlow

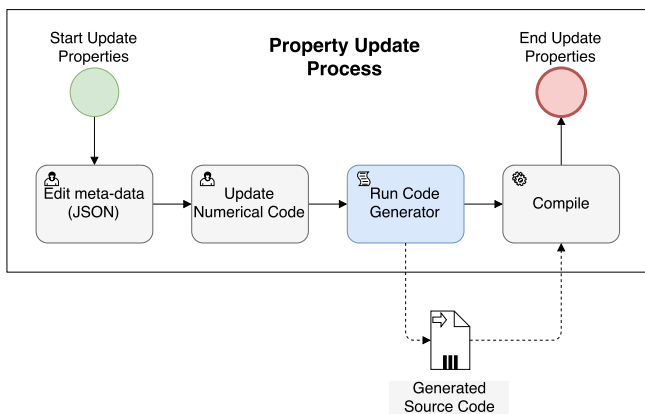
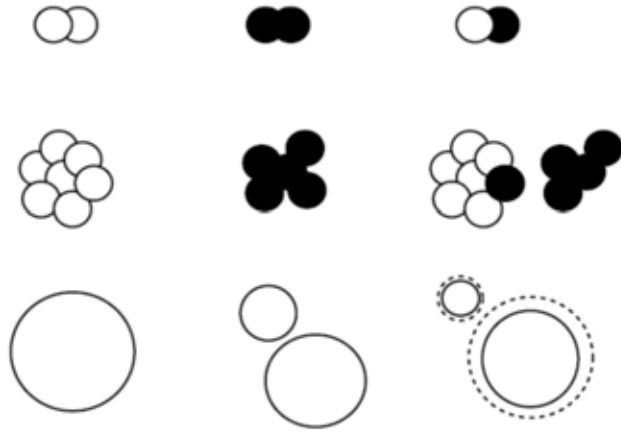


Figure 6: BPMN diagram illustrating the process of updating properties/state data

# POPULATION BALANCE







## COMBINED MULTIFLUID-POPULATION BALANCE METHOD FOR POLYDISPERSE MULTIPHASE FLOWS

**Alexander VIKHANSKY**

Siemens PLM Software, Trident House, Basil Hill Road, Didcot OX11 7HJ, UK

E-mail: alexander.vichansky@cd-adapco.com

### ABSTRACT

In the present work we analyse applicability of the adaptive multiple size-group (A-MuSiG) population balance method to modelling of multiphase flows. The dispersed phase is split into  $M$  size-groups, each one having its own mass- and momentum balance. An additional equation for the number density makes the method adaptive, that is, the groups sizes are not prescribed a priori, but calculated. A special attention is paid to the effect of the turbulent diffusion on size distribution. The method is implemented in the multiphase CFD code STAR-CCM+ of Siemens PLM Software.

**Keywords:** CFD, population balance, two-phase flows .

### NOMENCLATURE

<i>Greek Symbols</i>		$m_{ij}$	Group-to-group mass flux, $[kg/m^3s]$ .
$\alpha$	Volume fraction.	$n$	Number density, $[m^{-3}]$ .
$\rho$	Mass density, $[kg/m^3]$ .	$\mathbf{u}$	Velocity, $[m/s]$ .
$\tau$	Reynolds stress, $[Pa]$ .	$P$	Pressure, $[kg/ms^2]$ .
<i>Latin Symbols</i>		$S$	Number density source, $[m^{-3}s^{-1}]$ .
$D_T$	Coefficient of turbulent diffusion, $[m^2/s]$ .	$v$	Volume of a particle, $[m^3]$ .
$L$	Particle size, $[m]$ .	<i>Sub/superscripts</i>	
$M$	Number of size groups.	$p$	Particle.

### INTRODUCTION

Population balance equations (PBE) are the general mathematical framework describing different physical, chemical, biological, and technological processes (Ramkrishna, 2000). They deal with bubbles, droplets, bacteria, molecules, etc. Hereafter we call them “particles”. Main object of a population balance equation is number density  $n$ , e.g., the number of particles having size, density, velocity and temperature in the intervals  $[L, L + dL]$ ,  $[\rho, \rho + d\rho]$ ,  $[\mathbf{u}, \mathbf{u} + d\mathbf{u}]$ ,  $[T, T + dT]$ , respectively, is

$$n(L, \rho, \mathbf{u}, T) \times dL \times d\rho \times du_x \times du_y \times du_z \times dT. \quad (1)$$

In the most general form the PBE reads:

$$\frac{\partial n}{\partial t} = B(n) - D(n), \quad (2)$$

where  $B$  and  $D$  are “birth” and “death” rates due to transport, coalescence, breakup, mass transfer, etc. If a particle is characterised by a single parameter, e.g., size, Eq. (2) for  $n(L)$  is called *univariate* PBE, otherwise it is *multivariate* PBE.

Eq. (1) provides a very detailed description of the system, e.g., momentum is given by the integral

$$\int (\rho \mathbf{u} n) dL d\rho d\mathbf{u} dT. \quad (3)$$

Therefore, by solving the PBE one gains more information than from solution of a Navier-Stokes (NS) equation. It is clear, that being a “theory of everything”, the PBE in form of Eq. (2) is prohibitively time-consuming and has very little practical value; it is why more restricted, more tractable formulations are sought.

As an example imagine an isothermal bubbly flow. Inertia of the bubbles is low and one can assume with high confidence that the gas-liquid slip velocity depends on the local flow conditions and the bubble size only; the multivariate number density (1) can be represented as

$$n(L, \mathbf{u}) \approx n(L) \delta(\mathbf{u} - \mathbf{U}(L)), \quad (4)$$

where  $\mathbf{U}(L) = \langle \mathbf{u} | L \rangle$  is the conditional mean velocity. Method of classes (Kumar and Ramkrishna, 1996; Bhole *et al.*, 2008), also known as multisize-group (MuSiG) method (Lo, 1996) splits the dispersed (gas) phase into  $M$  size-groups, that is

$$n(L, \mathbf{u}) \approx \sum_{i=1}^M n(L_i) \delta(\mathbf{u} - \mathbf{U}(L_i)). \quad (5)$$

From the modelling point of view each group is a separate phase in every aspect but the name; the groups move with their own velocities and exchange mass, momentum and energy with other groups and with the continuous phase (Lo, 1996). Note that the method of classes in form (5) occupies an intermediate position between the univariate and full multivariate PBEs, to be precise, it is a *multivariate method with a first-order univariate conditional moment closure* (Klimenko and Bilger, 1999).

Recently, an adaptive discretisation has been proposed for the method of classes (Vikhansky, 2013; Vikhansky and Splawski, 2015), that is, the size-groups are not prescribed a priori, but follow the evolution of the size distribution. The first (simplified) version of the new adaptive multiple size-group method (A-MuSiG) has been implemented in a development version of the STAR-CCM+ simulation software of

Siemens PLM Software. The final version, described in the present paper, deals with the full set of the transport equations including turbulent dispersion and correct treatment of spurious dissipation.

## MULTIFLUID MODEL

Reynolds-averaged (RA) mass conservation equation for the  $i^{\text{th}}$  group reads:

$$\frac{\partial \rho_p \bar{\alpha}_i}{\partial t} + \nabla \cdot (\rho_p \bar{\alpha}_i \langle \mathbf{u}_i \rangle_i) = m_{ij} - m_{ji}, \quad (6)$$

where  $\rho_p$  is density of the dispersed phase,  $\bar{\alpha}_i$  is RA volume fraction of the  $i^{\text{th}}$  group and  $m_{ij}$ ,  $m_{ji}$  are (averaged) mass fluxes from the  $j^{\text{th}}$  group to the  $i^{\text{th}}$  group and from the  $i^{\text{th}}$  group to the  $j^{\text{th}}$  group, respectively;  $\langle \mathbf{u}_i \rangle_i$  is phase-averaged velocity of the group (Fox, 2014):

$$\langle \mathbf{u}_k \rangle_l = \frac{\langle \alpha_l \mathbf{u}_k \rangle}{\bar{\alpha}_l}, \quad (7)$$

where  $\alpha_l$ ,  $\mathbf{u}_k$  are instantaneous values of volume fraction and velocity; angular brackets mean Reynolds averaging.

Reynolds-averaged momentum conservation equation for the  $i^{\text{th}}$  group reads:

$$\frac{\partial \rho_p \bar{\alpha}_i \langle \mathbf{u}_i \rangle_i}{\partial t} + \nabla \cdot (\rho_p \bar{\alpha}_i \langle \mathbf{u}_i \rangle_i \langle \mathbf{u}_i \rangle_i) = -\bar{\alpha}_i \nabla P - \nabla \cdot \boldsymbol{\tau}_i + \langle \mathbf{F}_i \rangle + m_{ij} \langle \mathbf{u}_j \rangle_j - m_{ji} \langle \mathbf{u}_i \rangle_i, \quad (8)$$

where  $\boldsymbol{\tau}_i$  is Reynolds stress and  $\mathbf{F}_i$  is interaction force between the continuous phase and the  $i^{\text{th}}$  group. The Reynolds stress  $\boldsymbol{\tau}_i$  is modelled by a RANS model, which can be found elsewhere (Pope, 2000).

In order to calculate the phase interaction forces the size of the particles in the  $i^{\text{th}}$  group has to be specified. Prescribing a constant size for the group one obtains the MuSiG method (Lo, 1996). If the particles size distribution varies significantly across the system, the fixed discretisation in the size space is not efficient from the numerical point of view. In order to track the size distribution adaptively, Eqs. (6), (8) have to be augmented by an equation for the number density of the  $i^{\text{th}}$  group:

$$\frac{\partial \bar{n}_i}{\partial t} + \nabla \cdot \langle n_i \mathbf{u}_i \rangle = \langle S_i \rangle, \quad (9)$$

where  $S_i$  is the source term due to the breakage and coalescence of the particles, the RA number density flux is given below by Eq. (14). Knowing the number density one calculates the equivalent diameter of a particle as

$$d_i = \sqrt[3]{\frac{6\bar{\alpha}_i}{\pi\bar{n}_i}}. \quad (10)$$

In order to close the model described by Eqs. (6), (8), (9) one has to specify  $m_{ij}$  and  $\langle S_i \rangle$ ; it is done by a population balance algorithm. Note that the population balance algorithm is local, that is, below we ignore the spatial variations of the parameters of interest and concentrate on a single cell of a finite volume method. Details of the A-MuSiG method are given in (Vikhansky, 2013; Vikhansky and Splawski, 2015). In a nutshell the method works as shown in Fig. 1; size of the circle on the diagram corresponds to the volume fraction of the size-group.

I Initially, all size-groups have the same volume fraction.

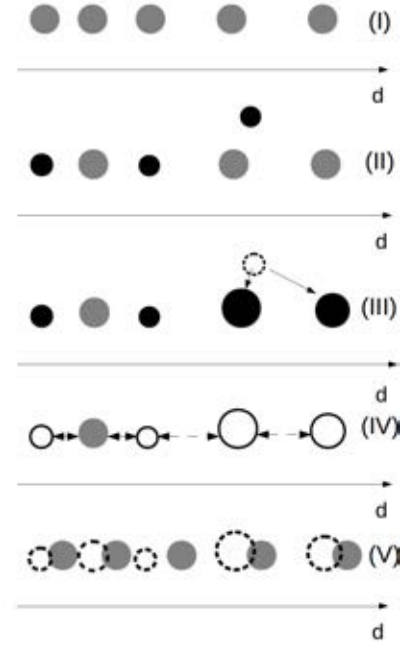


Figure 1: Schematic representation of the A-MuSiG method.

- II When two size-groups undergo coalescence, a new particle is created, while the volume fraction and number densities of the parent size-groups reduces.
- III Volume fraction and number density of the newly created particle is redistributed among two nearest size-groups using a version of the DQMoM method (Marchisio and Fox, 2005). At that step we locally conserve the first three moments of the distribution, namely, number density, mean volume (i.e., volume fraction), and mean square of the particles volume.
- IV One can see that coalescence leads to depletion of the size-groups with small diameters and accumulation of the mass of the entire ensemble in the size-groups with higher diameters. In order to restore the equal distribution of the volume fractions, we redistribute the number density and volume fraction between each pair of neighbour groups. In each pair-wise redistribution event the first three moments of size distribution are conserved locally.
- V By the end, each size-group has the same volume fraction, the size-groups have new diameters.

## NUMBER DENSITY TRANSPORT

Note that it follows from Eq. (7)  $\langle n_i \mathbf{u}_i \rangle \neq \bar{n}_i \langle \mathbf{u}_i \rangle_i$ ; in order to model the RA number density flux one can represent  $n_i$  as

$$n_i = \frac{\alpha_i}{v_i}. \quad (11)$$

Then

$$\langle n_i \mathbf{u}_i \rangle = \left\langle \alpha_i \mathbf{u}_i \frac{1}{v_i} \right\rangle = \bar{\alpha}_i \langle \mathbf{u}_i \rangle_i \frac{1}{\bar{v}_i} + \left\langle \alpha_i \mathbf{u}_i \left( \frac{1}{v_i} - \frac{1}{\bar{v}_i} \right) \right\rangle, \quad (12)$$

where the phase-averaged volume of a single particle is

$$\bar{v}_i = \frac{\bar{\alpha}_i}{\bar{n}_i}. \quad (13)$$

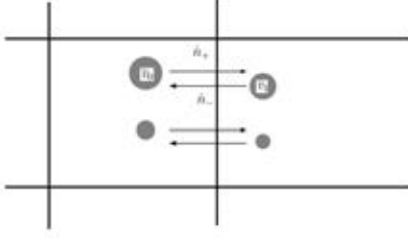


**Figure 2:** Schematic view of the diffusive flux.

Eq. (12) can be modelled using the gradient hypothesis:

$$\langle n_i \mathbf{u}_i \rangle = \bar{n}_i \langle \mathbf{u}_i \rangle_i - \bar{\alpha}_i D_T \nabla \frac{1}{\bar{v}_i} = \bar{n}_i (\langle \mathbf{u}_i \rangle_i + D_T \nabla \ln \bar{v}_i), \quad (14)$$

where  $D_T$  is coefficient of turbulent diffusion. There is no particular physical justification for (14) except that we use the same hypothesis for other scalars transported by turbulent flow field, e.g., kinetic energy of turbulence, temperature, etc. Note that if the group's volume  $\bar{v}_i$  is constant, the diffusive flux in Eq. (14) vanishes.

The turbulence disperse the particles not just in the physical space, but also in the phase space. In order to illustrate this effect let us consider transport of the particles without breakup and coagulation. Since  $\alpha_i = v_i n_i$  multiplication of the number density transport equation by  $v_i$  and subtraction from mass conservation after some algebra yields the equation for transport of the group's volume:

$$\frac{\partial v_i}{\partial t} + \mathbf{u}_i \cdot \nabla v_i = 0. \quad (15)$$

It can be multiplied by  $v_i$  to result in

$$\frac{\partial v_i^2}{\partial t} + \mathbf{u}_i \cdot \nabla v_i^2 = 0. \quad (16)$$

Eqs. (15)-(16) are averaged using the gradient closure:

$$\begin{aligned} & \frac{\partial \langle v_i \rangle}{\partial t} + \langle \mathbf{u}_i \rangle \cdot \nabla \langle v_i \rangle + \langle \mathbf{u}_i \cdot \nabla v_i' \rangle \\ &= \frac{\partial \langle v_i \rangle}{\partial t} + \langle \mathbf{u}_i \rangle \cdot \nabla \langle v_i \rangle - \nabla \cdot (D_T \nabla \langle v_i \rangle) = 0, \end{aligned} \quad (17)$$

$$\begin{aligned} & \frac{\partial \langle v_i^2 \rangle}{\partial t} + \langle \mathbf{u}_i \rangle \cdot \nabla \langle v_i^2 \rangle + \langle \mathbf{u}_i \cdot \nabla (v_i^2)' \rangle \\ &= \frac{\partial \langle v_i^2 \rangle}{\partial t} + \langle \mathbf{u}_i \rangle \cdot \nabla \langle v_i^2 \rangle - \nabla \cdot (D_T \nabla \langle v_i^2 \rangle) = 0. \end{aligned} \quad (18)$$

In order to obtain equation for the second central moment of the group's volume  $\sigma_{v_i}^2 = \langle v_i^2 - \langle v_i \rangle^2 \rangle$  Eq. (17) is multiplied by  $\langle v_i \rangle$  and subtracted from Eq. (18); after some algebra one obtains:

$$\frac{\partial \sigma_{v_i}^2}{\partial t} + \langle \mathbf{u}_i \rangle \cdot \nabla \sigma_{v_i}^2 - \nabla \cdot (D_T \nabla \sigma_{v_i}^2) = 2D_T |\nabla \langle v_i \rangle|^2. \quad (19)$$

Ignoring of the RHS in Eq. (19) leads to the spurious dissipation (underestimation of the standard deviation of the size distribution) obtained in (Marchisio and Fox, 2005; Fox, 2003).

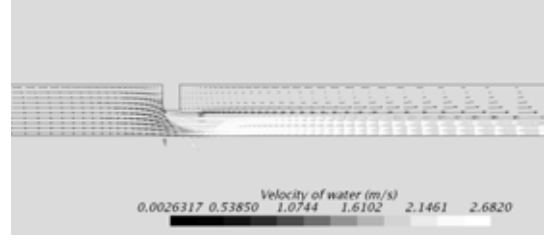


**Figure 3:** Water flow field.

Since the spurious dissipation is a result of the turbulent diffusion, proper discretisation of the diffusive flux might solve the problem (Vikas *et al.*, 2013). The root cause of the spurious dissipation can be illustrated by Fig. 2; the particles belonging to the same size-group at different neighbour cells have different diameters. It is not enough to calculate the total number density flux; one has to know the number  $\dot{n}_+$  of the particles of size  $\bar{v}_0$  moving from left to right, and number  $\dot{n}_-$  of the particles of size  $\bar{v}_1$  moving from right to left. Hereafter we use two conditions. Firstly, the difference between  $\dot{n}_+$  and  $\dot{n}_-$  is equal to the diffusive flux across the cell face:

$$\dot{n}_+ - \dot{n}_- = \bar{n}_f D_T \mathbf{v} \cdot \nabla \ln \bar{v}, \quad (20)$$

where  $\mathbf{v}$  is normal to the cell face and  $\bar{n}_f$  is number density at the face. Secondly, the total mass flux by diffusion is zero, that is

$$\bar{v}_0 \dot{n}_+ = \bar{v}_1 \dot{n}_-. \quad (21)$$

Solution of Eqs. (20)-(21) yields:

$$\begin{aligned} \dot{n}_+ &= \bar{n}_f \frac{\bar{v}_1}{\bar{v}_1 - \bar{v}_0} D_T \mathbf{v} \cdot \nabla \ln \bar{v}, \\ \dot{n}_- &= \bar{n}_f \frac{\bar{v}_0}{\bar{v}_1 - \bar{v}_0} D_T \mathbf{v} \cdot \nabla \ln \bar{v}. \end{aligned} \quad (22)$$

Once the fluxes  $\dot{n}_+$ ,  $\dot{n}_-$  are calculated, corresponding numbers of particles with size  $\bar{v}_0$ ,  $\bar{v}_1$  are added to the right (left) cell according to the algorithm described in Fig. 1, (Vikhan-sky, 2013).

## RESULTS AND DISCUSSION

Performance of the A-MuSiG method can be illustrated on a liquid-liquid pipe flow downstream of a restriction (Percy and Sleicher, 1983; Galinat *et al.*, 2005). The continuum phase is water, the dispersed phase is *n*-heptane. There is a recirculation zone behind the obstacle as shown in Fig. 3; the shear at the edge of the jet produces high dissipation rate, which causes intensive breakup of the droplets.

The adaptive nature of the method is demonstrated in Fig. 4; we perform the calculations with 5 size-groups and plot group diameters at the axis of the pipe. Initially, size of the biggest group increases because of coalescence, as the flow passes the orifice (at  $x = 0$ ) a strong breakup happens. Fig. 4 can be interpreted in the following way: since there are 5 groups, one can say that approximately 10% of the droplets volume is below the first group diameter, 30% is below the second group diameter, etc., 90% is below the fifth group diameter. Since the A-MuSiG method is adaptive, only 5 size-groups suffice for quite detailed description of the size distribution.

For an  $M$ -independent characterisation of the droplets size distribution we use different definitions of mean diameters:

$$d_{pq} = \sqrt[p-q]{\frac{\sum n_i d_i^p}{\sum n_i d_i^q}}, \quad (23)$$

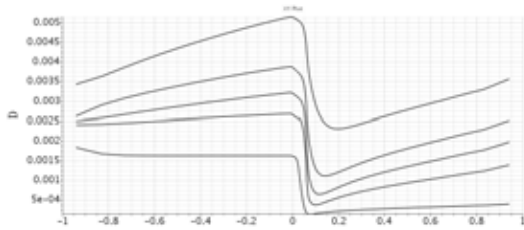


Figure 4: Group diameters at the pipe axis.

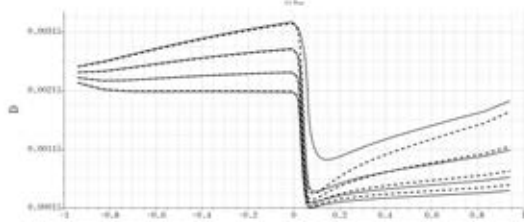


Figure 5: Mean diameters at the pipe axis with (dashed lines) and without (solid lines) spurious dissipation.

where the most important for applications are  $d_{43}$  (volume-mean diameter),  $d_{32}$  (Sauter mean diameter),  $d_{30}$  (volume-based diameter), and  $d_{10}$  (arithmetic mean diameter);  $d_{43} \geq d_{32} \geq d_{30} \geq d_{10}$ . For a mono-disperse system all diameters are equal; a high difference between, e.g.,  $d_{43}$  and  $d_{10}$  implies a high standard deviation of the size distribution.

In order to examine the effect of the often-neglected spurious dissipation we plot all four mean diameters mentioned above in Fig. 5. As one could expect, the biggest error is just behind the obstacle where the size distribution undergoes the fastest change, and therefore the RHS in Eq. (19) is biggest. Calculations without a proper treatment of the spurious dissipation term significantly narrower size distribution than that using Eq. (22).

The  $M$ -dependence of the results is illustrated in Fig. 6. Apart from the fact that smaller  $M$  implies a narrower predicted distribution, one can see that  $M = 3, 5, 9$  give quite close prediction of  $d_{43}, d_{32}, d_{30}$ , while calculation of  $d_{10}$  is less precise. It follows from the current formulation of the A-MuSiG method; since each size-group represents the same portion of volume fraction, more small particles are lumped together in the same (smallest) size-group. Even  $M = 3$  resolves the distribution quite well up to  $x \leq 0.2$ , that is, breakup is less sensitive to the number of size-groups. For many applications the Sauter mean diameter  $d_{32}$  is the single most important particles size characteristics; our numerical experiments suggest that reliable engineering estimates can

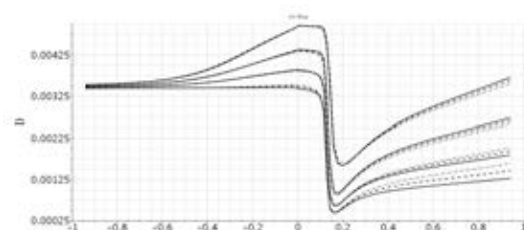


Figure 6: Mean diameters at the axis of the pipe calculated with 3 groups (dash-dotted), 5 groups (dotted), 9 groups (solid).

be done with a small ( $M = 3 - 5$ ) number of the size-groups.

## CONCLUSIONS

The paper presents an adaptive method for combined modelling of multiphase flows and breakup/coalescence processes; few size groups suffice for reliable prediction of mean characteristics of the polydisperse ensemble. The method solves for mass, momentum balance of each size-group, what extends it beyond a simple univariate population balance method. The effect of turbulent diffusion on size distribution is analysed and a special treatment is proposed to neutralize the spurious dissipation.

## REFERENCES

- BHOLE, M., JOSHI, J. and RAMKRISHNA, D. (2008). "CFD simulation of bubble columns incorporating population balance modeling". *Chemical Engineering Science*, **63**, 2267 – 2282.
- FOX, R.O. (2003). *Computational models for turbulent reacting flows*. Cambridge University Press.
- FOX, R.O. (2014). "On multiphase turbulence models for collisional fluid – particle flows". *JFM.*, **742**, 368 – 424.
- GALINAT, S., MASBERNAT, O., GUIRAUD, P., DALMAZZONE, C. and NOÏK, C. (2005). "Drop break-up in turbulent pipe flow downstream of a restriction". *Chemical Engineering Science*, **60**, 6511 – 6528.
- KLIMENKO, A. and BILGER, R. (1999). "Conditional moment closure for turbulent combustion". *Progress in Energy and Combustion Science*, **25**, 595 – 687.
- KUMAR, S. and RAMKRISHNA, D. (1996). "On the solution of population balance equations by discretization - I. A fixed pivot technique". *Chem. Eng. Sci.*, **51**, 1311–1332.
- LO, S. (1996). "Application of the MUSIG model to bubbly flows". *AEAT-1096, AEA Technology*, **230**, 8216–8246.
- MARCHISIO, D.L. and FOX, R.O. (2005). "Solution of population balance equations using the direct quadrature method of moments". *J. Aerosol Sci.*, **36**, 43–73.
- PERCY, J.S. and SLEICHER, C.A. (1983). "Drop breakup in the flow of immiscible liquids through an orifice in a pipe". *AIChE Journal*, **29**, 161–164.
- POPE, S.B. (2000). *Turbulent Flows*. Cambridge University Press.
- RAMKRISHNA, D. (2000). *Population balances*. Academic press.
- VIKAS, V., WANG, Z. and FOX, R. (2013). "Realizable high-order finite-volume schemes for quadrature-based moment methods applied to diffusion population balance equations". *Journal of Computational Physics*, **249**, 162 – 179.
- VIKHANSKY, A. (2013). "Direct quadrature spanning tree method for solution of the population balance equations". *Journal of Aerosol Science*, **55**, 78 – 88.
- VIKHANSKY, A. and SPLAWSKI, A. (2015). "Adaptive multiple size group method for CFD-population balance modelling of polydisperse flows". *Canadian J. Chem. Eng.*

## A MULTIFLUID-PBE MODEL FOR A SLURRY BUBBLE COLUMN WITH BUBBLE SIZE DEPENDENT VELOCITY, WEIGHT FRACTIONS AND TEMPERATURE

Camilla Berge VIK<sup>1\*</sup>, Jannike SOLSVIK<sup>1†</sup>, Mathias ENGH<sup>1‡</sup>, Magne HILLESTAD<sup>1§</sup>, Hugo Atle JAKOBSEN<sup>1¶</sup>

<sup>1</sup>NTNU Department of Chemical Engineering, 7491 Trondheim, NORWAY

\* E-mail: camilla.berge.vik@ntnu.no

† E-mail: jannike.solsvik@ntnu.no

‡ E-mail: mathias.engh@ntnu.no

§ E-mail: magne.hillestad@ntnu.no

¶ E-mail: hugo.a.jakobsen@ntnu.no

### ABSTRACT

With kinetic gas theory as a starting point, equations of change for total mass, species mass, momentum and inner energy are developed for the dispersed gaseous phase and implemented to describe the Fischer-Tropsch synthesis carried out at industrial scale. The resultant model describes bubble velocity, composition and temperature in the gaseous phase as function of axial position and bubble size. The bubble size is found from the population balance equation (PBE) using a continuous mass density function which is calculated explicitly and used as basis for the gas-liquid transfer fluxes of species mass, momentum and heat. In the Fischer-Tropsch synthesis reactants are transported from inside gas bubbles through the gas-liquid interface into the liquid phase and subsequently into the catalyst pores to form hydrocarbon products at the active sites on the catalyst surface. Higher catalyst loading requires a higher mass transfer from the gas bubbles to the liquid phase and may cause the overall reaction to become mass transfer limited. In order to optimize reactor design, knowledge of the bubble size may thus be of importance. The liquid and solid phases are modelled using conventional continuum mechanics equations of change. The results of the simulations show that the weight percent of reactant varies by 20 percentage points from the smallest to the largest bubble size and thus a significant level of detail is added to the model when including bubble size in the mass fraction variable. For temperature the particle size dependency is negligible at the same conditions. It is noted that firm conclusions on the mass and heat transfer limitations can only be drawn when reliable estimates of the transfer coefficients are available.

**Keywords:** population balance methods, chemical reactors, slurry bubble column, multiphase mass transfer, Fischer-Tropsch synthesis, bubble size .

### NOMENCLATURE

#### Greek Symbols

$\alpha$  Volume fraction,  $[-]$ .  
 $\gamma$  Size dependent mass transfer term,  $[1/s]$ .  
 $\gamma_s$  Size dependent mass transfer term for species  $s$ ,  $[1/s]$ .  
 $\Gamma$  Mass transfer term,  $[kg/m^3 s]$ .  
 $\zeta$  Bubble diameter,  $[m]$ .  
 $\lambda$  Effective turbulent conductivity in spatial space,  $[W/m K]$ .  
 $\mu$  Dynamic viscosity,  $[kg/ms]$ .  
 $\xi$  Bubble diameter,  $[m]$ .

$\Xi$  Microscopical velocity in property space,  $[m/s]$ .  
 $\rho$  Mass density,  $[kg/m^3]$ .  
 $\rho_{cat}$  Catalyst density in reactor,  $[kg/m^3]$ .  
 $\Psi$  Generic quantity.  
 $\omega$  Weight fraction,  $[-]$ .

#### Latin Symbols

$A$  Bubble surface area,  $[m^2]$ .  
 $a_L$  Gas-liquid interfacial area per unit dispersion mixture,  $[m^2/m^3]$ .  
 $b$  Breakage frequency,  $[1/s]$ .  
 $c$  Coalescence frequency,  $[1/s]$ .  
 $c$  Microscopical velocity in physical space,  $[m/s]$ .  
 $C_D$  Drag coefficient,  $[-]$ .  
 $c_p$  Specific heat capacity,  $[J/kg K]$ .  
 $d_s$  Sauter mean diameter,  $[m]$ .  
 $D$  Diameter of column,  $[m]$ .  
 $D_{eff}$  Eff. axial dispersion coefficient,  $[m^2/s]$ .  
 $f$  Number density function,  $[\#/m^3 m]$ .  
 $f_d$  Mass density function,  $[kg/m^3 m]$ .  
 $f_{drag}$  Size dependent drag force per mass,  $[N/kg]$ .  
 $\mathbf{F}$  Force,  $[N]$ .  
 $g$  Standard acceleration of gravity,  $[m/s^2]$ .  
 $h$  Heat transfer coefficient,  $[W/m^2 K]$ .  
 $h$  Specific enthalpy,  $[J/kg]$ .  
 $h_b$  Daughter size redistribution function,  $[1/m]$ .  
 $J$  Source term,  $[kg/m^3 s]$ .  
 $k_L$  Liquid side mass transfer coefficient,  $[m/s]$ .  
 $K$  Equilibrium constant describing the relationship  $y_i^*/x_i^*$  at given conditions,  $[-]$ .  
 $m$  Mass,  $[kg]$ .  
 $p$  Microscopical density function,  $[\#/(m^3 m m/s K kg)]$ .  
 $P$  Microscopical normalized density function,  $[\#/(m/s K)]$ .  
 $p$  Pressure,  $[Pa]$ .  
 $\mathbf{P}$  Pressure tensor,  $[kg/m s^2]$ .  
 $\mathbf{p}_\xi$  Space-property pressure vector,  $[kg/m s^2]$ .  
 $\mathbf{q}$  Kinetic energy flux vector,  $[W/m^2]$ .  
 $\mathbf{q}_\xi$  Space-property kinetic energy flux vector,  $[W/m^2]$ .  
 $\mathbf{r}$  Physical coordinates,  $[m]$ .  
 $r_{CO}$  Reaction rate in terms of CO conversion,  $[kmol s/kgcat]$ .  
 $R$  Reaction term,  $[kg/m^3 s]$ .  
 $S$  Source term not due to collisions,  
 $t$  Time,  $[s]$ .  
 $T$  Temperature,  $[K]$ .  
 $v$  Velocity,  $[m/s]$ .  
 $V$  Bubble volume,  $[m^3]$ .

$v_{\xi}$  Growth velocity, [m/s].  
 $z$  Dispersion height, [m].

#### Sub/superscripts

$B - D$  Birth and death terms.  
*coll* Collisions.  
*d* (mass) density function.  
*eff* Effective.  
*G* Gas.  
*G - L* Gas-liquid.  
*in* (Reactor) inlet.  
*L* Liquid.  
*m* Mass.  
*max* Maximum.  
*min* Minimum.  
*p* Particle.  
*r* Physical space.  
*s* Superficial (superscript).  
*s* Chemical species (subscript).  
*S* Solid.  
*S - L* Solid-liquid.  
*SL* Slurry.  
*z*  $z$  (axial) direction.  
 $\xi$  Property space.

## INTRODUCTION

### Background

In the modelling of multiphase chemical reactors the interfacial transfer fluxes play an important role. Chemical species are transported between the phases to form products, interfacial forces influence the relative velocities of the phases and heat is transferred from one phase to another. Mathematical models for reactive *dispersed* flows (as opposed to *stratified*) are developed on basis of continuum mechanics and kinetic theory of gases (Jakobsen, 2008). With emphasis on modelling the interfacial transfer fluxes, the latter framework is of interest as it provides a density function describing the number of entities at a location in physical space and property space. Solving for the density function explicitly, the transfer of chemical species, momentum and heat can thus be calculated as the product of the transfer coefficient, the density function and a property dependent driving force. In particular, choosing size (diameter) as the property space / inner coordinate the influence of the bubble size distribution on mass, momentum and heat transfer can be studied.

### Development of a reactive multifluid-PBE model

A multifluid-PBE model, where PBE denotes the population balance equation, was developed by Dorao (2006), Zhu (2009), Patruno *et al.* (2009), Sporleder (2011), Nayak *et al.* (2011) and Solsvik and Jakobsen (2014) to describe isothermal non-reactive flow with size dependent velocity. Based on the works by Andresen (1990) and Simonin (1996) a model for reactive, non-isothermal solid particles in gas was developed by Lathouwers and Bellan (2000) to describe the gasification of biomass. Chao (2012) extended their model to allow for two types of particles in a gas and applied it to sorption enhanced steam methane reforming. With the kinetic theory of gases in common, this work extends the above models to describe reactive, non-isothermal gas bubbles in a liquid phase with size dependent velocity, weight fractions and temperature. An explicit and continuous mass density function describes the mass of bubbles at a point in physical space  $z$  (axial direction) and property space  $\xi$  (diameter).

## Application of the multifluid-PBE to the Fischer-Tropsch synthesis

The multifluid-PBE model is applied to the Fischer-Tropsch synthesis of liquid hydrocarbons from biomass carbon sources, termed Biomass-to-Liquid (BtL). Torrefication and gasification of wood residue such as branches and tops gives synthesis gas which is fed to a reactor where it is converted to hydrocarbons over a catalyst.

A potential reactor for this process is the slurry bubble column (Figure 1) where the reactants are fed as gas through a slurry composed of solid catalyst submerged in a liquid phase. In order to form products, carbon monoxide and hydrogen are transported from the gas bubbles to the liquid phase and into the catalyst pores where they form hydrocarbons of various lengths in a very exothermal reaction. With high gas flow rates and the requirement of efficient mass transfer and heat removal the Fischer-Tropsch process requires accurate description of size dependent interfacial transfer fluxes and field variables such as weight fraction, velocity and temperature.

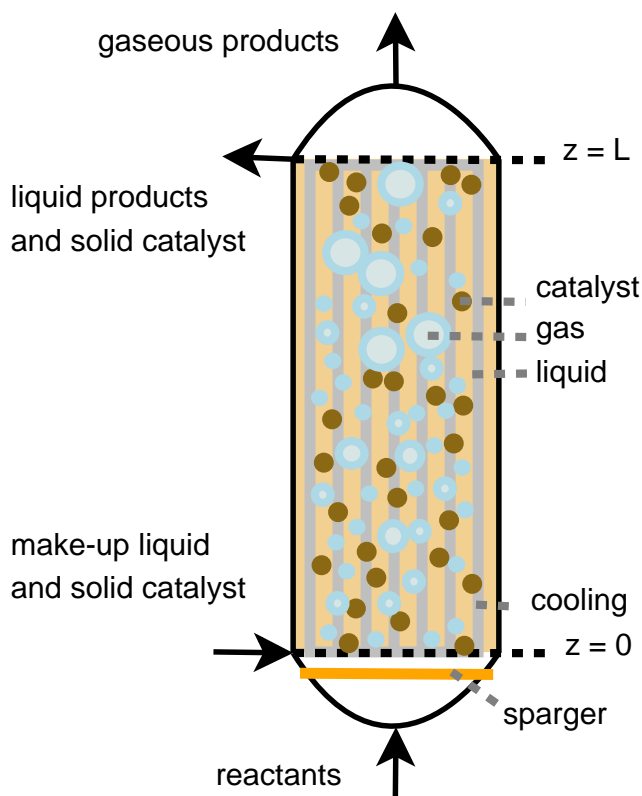


**Figure 1:** Slurry bubble column reactor for the Fischer-Tropsch synthesis. Solid catalyst is submerged in the liquid phase. Gas bubbles with reactant are injected through a sparger. Cooling rods along the axial direction facilitate removal of reaction heat from the liquid phase.

### Mass transfer

Efficient mass transfer of reactants from gas phase to liquid phase along with fast reaction kinetics are important for the overall reactor efficiency for the Fischer-Tropsch synthesis in a slurry bubble column. In this work, the kinetic model by Yates and Satterfield (1991) is applied to study the conversion of reactants and a standard Anderson-Schultz-Flory distribution is applied to estimate the chain length of the hydrocarbon products.

A schematic view of the mass transfer resistances in the Fischer-Tropsch synthesis in a slurry bubble column is shown in Figure 2. It is known that among all the mass transfer resistances from gas bubble to inside the catalyst pellet the liquid side mass transfer is the limiting (Kohler, 1986). Values for the liquid side mass transfer coefficient for Fischer-Tropsch fluids vary by an order of magnitude (Vandu *et al.*, 2004). In this work the model by Calderbank and Moo-Young (1961) for small bubbles is applied. While the authors denoted small bubbles as those with diameter less than 2.5 mm, they remarked that most industrial reactors exhibit conditions where the small bubble correlation was better than their large bubble correlation.

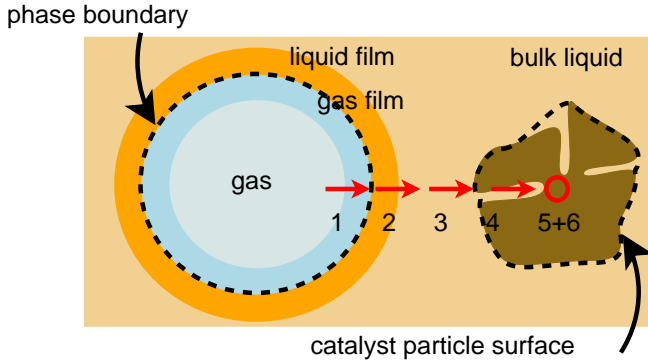


**Figure 2:** Possible mass transfer limitations (Kohler, 1986), whereas step (2) is the most important.

### Momentum transfer

The main momentum transfer is the drag force between the gas bubbles and the liquid phase. The gas bubbles are fed at a velocity of 0.5 m/s while the liquid phase initial velocity is 0.02 m/s, thus the drag force is significant. Bubble size dependent velocity is known from the literature to give a valuable additional information compared to all bubbles having the same average velocity (e.g. Frank *et al.* (2005)). As shown before for the Fischer-Tropsch synthesis in a slurry bubble column (Vik *et al.*, 2015) the velocity varies significantly with bubble size - mainly as a result of the drag force dependency on bubble size.

### Heat transfer

The interfacial gas-liquid heat flux is modelled using the heat transfer coefficient by Calderbank and Moo-Young (1961). The reaction heat is removed from the liquid using axial cooling rods. In this work we have assumed only the liquid phase to be in contact with the axial cooling rods (See Figure 1) and thus only the gas-liquid interfacial heat transfer is relevant for the bubble size dependent gas temperature.

## THEORY

### The Boltzmann equation

An analogy to the kinetic theory of granular flow is applied to describe reactive bubbles in an interstitial liquid. The starting point is a microscopical density function  $p = p(\mathbf{r}, \xi, \mathbf{c}, \Xi, \omega_{s,p}, T_p, m_p, t)$  which describes the number of bubbles located at point  $\mathbf{r}$  with size  $\xi$ , physical velocity  $\mathbf{c}$ , property velocity (growth)  $\Xi$ , weight fraction of species  $s$   $\omega_{s,p}$ , temperature  $T_p$ , mass  $m_p$  at time  $t$ . Compared to the model of Lathouwers and Bellan (2000)/ Chao (2012) the coordinate set is extended to include the size in form of the

diameter  $\xi$  and velocity in diameter; growth  $\Xi$ . A Boltzmann-like equation for  $p$  is formulated as

$$\frac{\partial p}{\partial t} + \mathbf{c} \cdot \frac{\partial p}{\partial \mathbf{r}} + \mathbf{F} \cdot \frac{\partial p}{\partial \mathbf{c}} + \Xi \frac{\partial p}{\partial \xi} + F_\xi \frac{\partial p}{\partial \Xi} + \dot{T}_p \frac{\partial p}{\partial T_p} + \sum_s \omega_{s,p} \frac{\partial p}{\partial \omega_{s,p}} + m_p \frac{\partial p}{\partial m_p} = \left( \frac{\partial p}{\partial t} \right)_{\text{collision}} + S \quad (1)$$

The two terms on the right hand side denote the changes in  $p$  due to collision events and other (not collision) events. Equation 1 is multiplied with a microscopical quantity  $\psi_p$  and the mass  $m_p$  and then integrated. Lathouwers and Bellan (2000) multiplied with the particle mass and integrated over the entire space except physical location and time. Nayak *et al.* (2011) assumed constant particle mass and integrated over the entire space except physical location, size and time. We here multiply with particle mass and integrate over the entire space except physical location, size and time. This gives a mass averaged momentum equation:

$$\begin{aligned} & \frac{\partial}{\partial t} (f_d \langle \psi_p \rangle) + \frac{\partial}{\partial \mathbf{r}} \cdot (f_d \langle \psi_p \mathbf{c} \rangle) + \frac{\partial}{\partial \xi} (f_d \langle \Xi \psi_p \rangle) = \\ & f_d \left[ \left\langle \frac{\partial \psi_p}{\partial t} \right\rangle + \left\langle \mathbf{c} \cdot \frac{\partial \psi_p}{\partial \mathbf{r}} \right\rangle + \left\langle \mathbf{F}_r \cdot \frac{\partial \psi_p}{\partial \mathbf{c}} \right\rangle + \left\langle \Xi \frac{\partial \psi_p}{\partial \xi} \right\rangle \right] \\ & + f_d \left[ \left\langle F_\xi \frac{\partial \psi_p}{\partial \Xi} \right\rangle + \left\langle \dot{T}_p \frac{\partial \psi_p}{\partial T_p} \right\rangle + \sum_s \left\langle \omega_{s,p} \frac{\partial \psi_p}{\partial \omega_{s,p}} \right\rangle \right] \\ & + f_d \left[ \left\langle m_p \left( \frac{\partial \psi_p}{\partial m_p} + \frac{1}{m_p} \right) \right\rangle + \left\langle J_{\psi_p} \right\rangle \right] \end{aligned} \quad (2)$$

Equations of change for the dispersed fluid are found by introducing appropriate quantities for  $\psi_p$ . We shall introduce coordinates for  $\psi_p$  thus using an Eulerian framework.

### Definitions

We define an average of the macroscopical number density:

$$f(\mathbf{r}, \xi, t) = \int_{-\infty}^{+\infty} p(\mathbf{r}, \xi, \mathbf{c}, \Xi, \omega_{s,p}, T_p, m_p, t) d\mathbf{c} d\Xi d\omega_{s,p} dT_p dm_p \quad (3)$$

and mass density:

$$f_d(\mathbf{r}, \xi, t) = \int_{-\infty}^{+\infty} m_p p(\mathbf{r}, \xi, \mathbf{c}, \Xi, \omega_{s,p}, T_p, m_p, t) d\Omega \quad (4)$$

where  $d\Omega = d\mathbf{c} d\Xi d\omega_{s,p} dT_p dm_p$  for brevity. Fluid properties are found from moments of  $\psi_p$ , defined as:

$$\langle \psi_p \rangle = \int_{-\infty}^{+\infty} \psi_p m_p P(\mathbf{r}, \xi, \mathbf{c}, \Xi, \omega_{s,p}, T_p, m_p, t) d\Omega \quad (5)$$

where  $P(\mathbf{r}, \xi, \mathbf{c}, \Xi, \omega_{s,p}, T_p, m_p, t)$  is a normalized microscopical density function, defined as:

$$P(\mathbf{r}, \xi, \mathbf{c}, \Xi, \omega_{s,p}, T_p, m_p, t) = \frac{p(\mathbf{r}, \xi, \mathbf{c}, \Xi, \omega_{s,p}, T_p, m_p, t)}{f_d(\mathbf{r}, \xi, t)} \quad (6)$$

This yields and alternative formulation of the moment:

$$\begin{aligned} \langle \psi_p \rangle &= \int_{-\infty}^{+\infty} \psi_p m_p \frac{p(\mathbf{r}, \xi, \mathbf{c}, \Xi, \omega_{s,p}, T_p, m_p, t)}{f_d(\mathbf{r}, \xi, t)} d\Omega \\ &= \frac{1}{f_d(\mathbf{r}, \xi, t)} \int_{-\infty}^{+\infty} \psi_p m_p p d\Omega \end{aligned} \quad (7)$$

Average, or macroscopical bubble mass is found by:

$$m(\mathbf{r}, \xi, t) = \langle m_p \rangle = \frac{1}{f_d(\mathbf{r}, \xi, t)} \int_{-\infty}^{+\infty} m_p m_p p d\Omega \quad (8)$$



and we adopt the relation:

$$f_d(\mathbf{r}, \xi, t) = f(\mathbf{r}, \xi, t)m(\mathbf{r}, \xi, t) \quad (9)$$

from Lathouwers and Bellan (2000). Macroscopical or average dispersed fluid properties such as velocity, growth velocity, weight fraction of species  $s$ , temperature and enthalpy are then given as:

$$\mathbf{v}_r(\mathbf{r}, \xi, t) = \frac{1}{f_d(\mathbf{r}, \xi, t)} \int_{-\infty}^{+\infty} \mathbf{c} m_p p d\Omega \quad (10)$$

$$v_\xi(\mathbf{r}, \xi, t) = \frac{1}{f_d(\mathbf{r}, \xi, t)} \int_{-\infty}^{+\infty} \Xi m_p p d\Omega \quad (11)$$

$$\omega_s(\mathbf{r}, \xi, t) = \frac{1}{f_d(\mathbf{r}, \xi, t)} \int_{-\infty}^{+\infty} \omega_{s,p} m_p p d\Omega \quad (12)$$

$$T(\mathbf{r}, \xi, t) = \frac{1}{f_d(\mathbf{r}, \xi, t)} \int_{-\infty}^{+\infty} T_p m_p p d\Omega \quad (13)$$

$$h(\mathbf{r}, \xi, t) = \frac{1}{f_d(\mathbf{r}, \xi, t)} \int_{-\infty}^{+\infty} h_p m_p p d\Omega \quad (14)$$

Peculiar velocity, growth velocity, weight fraction, temperature and enthalpy are defined as the difference between the microscopical and macroscopical velocity and the average of the fluctuation is zero. The pressure tensor and heat flux are defined by:

$$\mathbf{P}(\mathbf{r}, \xi, t) = \int_{-\infty}^{+\infty} m_p \mathbf{C} \mathbf{C} p d\Omega = f_d \langle \mathbf{C} \mathbf{C} \rangle \quad (15)$$

$$\mathbf{q}(\mathbf{r}, \xi, t) = \int_{-\infty}^{+\infty} m_p \mathbf{C} h' p d\Omega = f_d \langle \mathbf{C} h' \rangle \quad (16)$$

We define a space-property pressure vector and a space-property kinetic energy flux as:

$$\mathbf{p}_\xi = \int_{-\infty}^{+\infty} m_p v'_\xi \mathbf{C} p d\Omega = f_d \langle v'_\xi \mathbf{C} \rangle \quad (17)$$

$$q_\xi = \int_{-\infty}^{+\infty} m_p v'_\xi h' p d\Omega = f_d \langle v'_\xi h' \rangle \quad (18)$$

From Equation 2 the equations of change for total mass, species mass, momentum and enthalpy (temperature) are found by inserting for 1,  $\omega_{s,p}$ ,  $\mathbf{c}$  and  $h_p$  for  $\psi_p$ , respectively, and applying definitions 10-18.

## MODEL DESCRIPTION

### Assumptions

With the kinetic theory of gases originally developed for dilute monoatomic gases in vacuum, the application has moved far from the original intentions of the theory, as shown in Figure 3.

The *particles* in this work are bubbles with a significant mass and occupying a significant volume that may vary. The interstitial fluid is a liquid exerting a drag force on the particles and the bubbles are injected into the reactor with an initial velocity, thus not moving freely. The equations are cross-sectionally averaged to reduce the number of spatial dimensions to one. Furthermore, the implemented model is steady-state.

## Equations of change

The article presents a novel model particularly designed to describe interfacial mass transfer limited chemical processes in a slurry bubble column. The developed equations of change are 3D and transient, but in order to simulate a practical process such as the Fischer-Tropsch synthesis, a reduced 1D steady state model is applied. The developed equations of change are shown below. The population balance equation formulated in terms of a mass density function  $f_d(z, \xi)$  is given as:

$$\frac{\partial(f_d(z, \xi)v_z(z, \xi))}{\partial z} + \frac{\partial(f_d(z, \xi)v_\xi(z, \xi))}{\partial \xi} = f_d(z, \xi)\gamma(z, \xi) + J_m(z, \xi) \quad (19)$$

with initial conditions:

$$\begin{aligned} f_d|_{z=z_{\min}} &= f_{d,\text{in}} \\ f_d|_{\xi=\xi_{\min}} &= 0 \end{aligned} \quad (20)$$

In addition, the growth flux  $v_\xi f_d$  is set to zero at the  $\xi$  boundaries so that no bubbles enter or leave the domain through growth. The growth velocity is defined as Morel (2015), extending it to a density as a function of  $z$  and  $\xi$ :

$$v_\xi(z, \xi) = -\frac{\xi}{3\rho(z, \xi)} \left[ \frac{\partial \rho(z, \xi)}{\partial t} + \mathbf{v}_r(z, \xi) \cdot \nabla_r \rho(z, \xi) \right] \quad (21)$$

The continuity equation is subtracted from the equations of change for species mass, momentum and enthalpy (temperature). For the gas phase the dispersion, turbulent dissipation and conduction terms are omitted because the gas phase experiences negligible backmixing. For species mass this gives:

$$\begin{aligned} v_G(z, \xi) f_d(z, \xi) \frac{\partial \omega_{G,s}(z, \xi)}{\partial z} + v_\xi(z, \xi) f_d(z, \xi) \frac{\partial \omega_{G,s}(z, \xi)}{\partial \xi} \\ = f_d(z, \xi) \gamma_s(z, \xi) - \omega_s(z, \xi) f_d(z, \xi) \gamma(z, \xi) \\ + \langle J_{\omega_{s,p}} \rangle - \omega_s(z, \xi) J_m(z, \xi) \end{aligned} \quad (22)$$

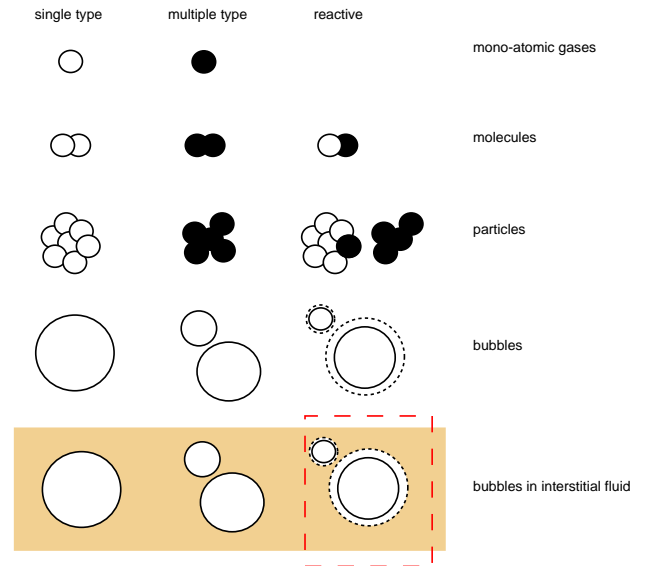


**Figure 3:** Extension of the subjects to the kinetic theory of gases. The upper left corner represents the origin of kinetic gas theory - a monoatomic gas in a vacuum. Gas atoms of different type, denser gases, particles, bubbles and finally bubbles subject to chemical reactions and in an interstitial fluid, which is considered in this work (inside red dashed line).

The initial conditions are given as:

$$\begin{aligned}\omega_{G,s}|_{z=z_{\min}} &= \omega_{G,s,\text{in}} \\ \omega_{G,s}|_{\xi=\xi_{\min}} &= K_s \omega_{L,s}(z)\end{aligned}\quad (23)$$

The initial condition at  $\xi_{\min}$  implies that the smallest bubbles with diameter  $\xi_{\min}$  are assumed to be in equilibrium with the liquid phase at all times. For momentum:

$$\begin{aligned}v_G(z, \xi) f_d(z, \xi) \frac{\partial v_G(z, \xi)}{\partial z} + v_\xi(z, \xi) f_d(z, \xi) \frac{\partial v_G(z, \xi)}{\partial \xi} \\ = f_d(z, \xi) F_z(z, \xi) + \langle J_e \rangle - v_G(z, \xi) J_m(z, \xi)\end{aligned}\quad (24)$$

with the initial conditions:

$$\begin{aligned}v_G|_{z=z_{\min}} &= v_{G,\text{in}} \\ v_G|_{\xi=\xi_{\min}} &= v_L(z)\end{aligned}\quad (25)$$

where the smallest bubbles are assumed to have the same velocity as the liquid. For temperature:

$$\begin{aligned}c_p v_G(z, \xi) f_d(z, \xi) \frac{\partial T_G(z, \xi)}{\partial z} + c_p v_\xi(z, \xi) f_d(z, \xi) \frac{\partial T_G(z, \xi)}{\partial \xi} \\ = f_d(z, \xi) q_z(z, \xi) + \langle J_T \rangle - T_G(z, \xi) J_m(z, \xi)\end{aligned}\quad (26)$$

with initial conditions:

$$\begin{aligned}T_G|_{z=z_{\min}} &= T_{G,\text{in}} \\ T_G|_{\xi=\xi_{\min}} &= T_{SL}(z)\end{aligned}\quad (27)$$

as the smallest bubbles are assumed to have the same temperature as the slurry.

### Interfacial transfer terms

Interfacial mass, momentum and heat transfer terms are defined in terms of the size dependent variables weight fraction, velocity and temperature.

#### Mass transfer

$$f_d(z, \xi) \gamma_s \approx \frac{f_d(z, \xi) A(\xi) k_{L,s}(z) \rho_L}{\rho_G(z, \xi) V(\xi)} \left( \frac{1}{K_s} \omega_{G,s}(z, \xi) - \omega_{L,s}(z) \right)\quad (28)$$

where  $A(\xi)$  is the surface area of a bubble,  $k_{L,s}(z, \xi)$  is the liquid side mass transfer coefficient,  $\rho_L$  is the liquid density (constant in this work),  $\omega_{L,s}(z)$  the weight fraction of component  $s$  in the liquid phase and  $K_s$  an equilibrium constant for component  $s$ . The mass transfer term  $\gamma$  is obtained by summing over all  $s$ :

$$f_d(z, \xi) \gamma = \sum_s f_d(z, \xi) \gamma_s\quad (29)$$

It is noted that integration of Equation 28 and 29 yield the  $\xi$ -averaged mass transfer terms for the liquid phase.

#### Momentum transfer

The force terms are given by Nayak *et al.* (2011):

$$F_z(z, \xi) = - \frac{f_d(z, \xi)}{\rho_G(z, \xi)} \frac{\partial p(z)}{\partial z} + f_d(z, \xi) g_z + f_{\text{drag}}^{G-L}(z, \xi)\quad (30)$$

where

$$f_{\text{drag}}^{G-L} = - \frac{3}{4} \rho_L \frac{C_D}{\xi} \frac{f_d(z, \xi)}{\rho_G(z, \xi)} |v_G(z, \xi) - v_L(z)| (v_G(z, \xi) - v_L(z))\quad (31)$$

Integrating Equation 31 over  $\xi$  gives the momentum exchange term for use in the liquid phase momentum equation.

#### Heat transfer

The heat transfer term for heat transfer by convection is similar to the species mass transfer term in mathematical structure:

$$f_d(z, \xi) q_c(z, \xi) = \frac{f_d(z, \xi) A(\xi) h_{G-L}(z, \xi)}{\rho_G(z, \xi) V(\xi)} (T_G(z, \xi) - T_{SL}(z))\quad (32)$$

Integrating Equation 32 over  $\xi$  gives the heat exchange term for use in the slurry temperature equation.

#### Source terms

The source terms due to coalescence and breakage in the population balance equation (Equation 19) are modelled as:

$$\begin{aligned}J_m(z, \xi) &= -b(\xi) f_d(z, \xi) \\ &+ \rho_G(z, \xi) V(\xi) \int_{\xi}^{\xi_{\max}} h_b(\xi, \zeta) b(\zeta) \frac{f_d(\mathbf{r}, \zeta, t)}{\rho_G(z, \zeta) V(\zeta)} d\zeta \\ &- f_d(z, \xi) \int_{\xi_{\min}}^{(\xi_{\max} - \xi^3)^{1/3}} c(\xi, \zeta) \frac{f_d(\mathbf{r}, \zeta, t)}{\rho_G(z, \zeta) V(\zeta)} d\zeta \\ &+ \frac{\xi^2}{2} \rho_G(z, \xi) V(\xi) \int_{\xi_{\min}}^{(\xi^3 - \xi_{\min}^3)^{1/3}} \dots \\ &\frac{c([\xi^3 - \zeta^3]^{1/3}, \zeta) f_d(\mathbf{r}, [\xi^3 - \zeta^3]^{1/3}, t) f_d(\mathbf{r}, \zeta, t)}{[\xi^3 - \zeta^3]^{2/3} \rho_G(z, \zeta) V(\zeta) \rho_G(z, [\xi^3 - \zeta^3]^{1/3}) V([\xi^3 - \zeta^3]^{1/3})} d\zeta\end{aligned}\quad (33)$$

where the closure models by Coulaloglou and Tavlarides (1977) for breakage frequency and daughter size redistribution are applied. A pre-factor of  $K_B = 2 \times 10^{-3}$  was multiplied to the breakage terms to adjust the resultant breakage frequency to reasonable numbers within the bubble size domain along the axial direction of the reactor. Coalescence was not included in the simulations as bubble column flows generally are breakage dominated Sporleder *et al.* (2011). Breakage and coalescence terms for the species mass, momentum and energy equations are in general not known. As continuity is subtracted from the species mass, momentum and energy equations, two source terms appear in each equation. These are assumed to be equal (but with opposite sign) through the assumption that the product of averages equal to average of products and thus cancel. The result is that only the continuity equation has source terms due to coalescence and breakage.

#### Liquid and solid phase equations

The liquid and solid phase equations are the standard axial dispersion model equations coupled with a momentum equation for each phase. The solid phase is assumed to have the same temperature as the liquid phase. The liquid and solid phases is collectively referred to as the slurry temperature. No species mass equation is applied for the solid phase. The liquid and solid equations along with Fischer-Tropsch specific reactor parameters are given in Vik *et al.* (2015).

#### SOLUTION METHOD AND IMPLEMENTATION

The equations of change for species mass, total mass, momentum and enthalpy (temperature) for the dispersed, liquid and solid phases were implemented in MATLAB® and solved using the orthogonal collocation method. 22 points were used in the axial direction and 35 points in the property (diameter) direction. Convergence was taken as when the global iteration error was less than  $10^{-5}$ . The mass loss/gain in the model was calculated for each phase as the difference

between phase specific mass flux entering and leaving the model, divided by the phase specific mass flux entering the reactor.

## Operating conditions

The operating conditions are given in Table 1.

**Table 1:** Operating conditions.

Reactor inlet temperature	$T$	220 °C
Reactor outlet pressure	$p_0$	3 MPa
Inlet superficial gas velocity	$v_G^{s,0}$	0.26 m/s
Inlet superficial liquid velocity	$v_L^{s,0}$	0.01 m/s
Dispersion (reactor) height	$H$	50 m
Reactor diameter	$D$	9 m
Mass of catalyst per mass of dispersion	$\alpha_s$	0.05
Product distribution parameter	$\alpha_{ASF}$	0.9
H <sub>2</sub> /CO feed (mole based) ratio	-	2
Liquid density (constant)	$\rho_L$	687 kg/m <sup>3</sup>
Bubble size range	$\xi$	0.1 - 15 mm

## RESULTS

### Interfacial transfer fluxes

The interfacial fluxes for mass, momentum and energy for a single bubble as defined in Equations 28/29, 31 and 32 are shown in Figures 4, 5 and 6 for bubbles of size 0.1 to 15 mm. Available surface area for a single bubble as function of diameter is shown in Figure 7. Mass and heat flux are directly proportional to the available surface area and this is seen in the left plot of Figures 4 and 6. All three fluxes are inversely proportional to  $\xi$ . But as the driving force is squared in the drag force (as opposed to linear in mass and heat flux) the drag force has a different slope than do the mass and heat flux.

The interfacial gas-liquid mass transfer flux occurs as the reaction alters the liquid concentrations and thus gives a driving force between them. The interfacial mass transfer flux reaches a peak as the reaction rate is at its maximum level in the liquid phase.

The interfacial momentum flux is more of a constant magnitude over the axial direction of the reactor. As the bubbles are injected with a high velocity of 0.5 m/s and the liquid phase moves slowly with 0.02 m/s, the gas bubbles are slowed down by the liquid phase along the reactor height.

The interfacial heat transfer flux occurs first with a positive sign (observed from the gas side) as the bubbles are heated by the heat of the reaction in the liquid phase. Then with a negative sign as the liquid is cooled by the installed cooling rods (Figure 1) and successively cools the gas bubbles. The gas-liquid heat flux shows a peak slightly higher in the dispersion than does the mass flux, reflecting the peak of the heat of the reaction. The smaller bubbles have their maximum heating rate slightly lower in the reactor than do the larger bubbles, showing quicker heat transfer due to their higher available surface area for heat transfer.

### Size dependent weight fractions

Figure 8 shows the weight fraction of CO as function of bubble size and axial direction. The field value is lower than the average for the smallest bubble sizes and higher for the largest bubble sizes. The largest difference seen between the field value and the average value at the smallest bubble size is 12 wt% units higher for the average than the field. For the

largest bubble the field value is up to 8 wt% units lower than the average. The difference is at its largest at the middle of the reactor height (around 25 m). The maximum difference in concentration between the smallest and largest bubble size is 20 wt% units at the middle of the reactor height. CO is the reactant and is thus transported out of the bubble. Smaller bubbles have higher surface area per mass of gas and thus allow for more mass transport. A lower concentration of reactant for the smaller bubbles and vice versa for the large bubbles is thus an expected result.

The main difference between the size dependent model in this work and the average model is the use of a size dependent mass transfer term. A size dependent mass transfer term takes the difference in surface area per bubble gas mass into account and can predict the effect of bubble size on mass transfer. As mentioned above, mass transfer coefficients for the Fischer-Tropsch synthesis are claimed to vary by one order of magnitude. Figure 9 shows the effect of increasing and decreasing the value of the liquid side mass transfer coefficient

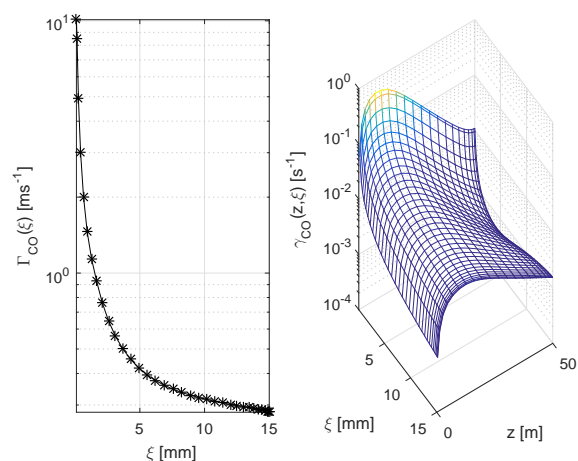


**Figure 4:** Mass flux of CO for a single bubble as function of bubble size for bubble sizes 0.1 mm to 15 mm. Left: Mass transfer flux for a single bubble integrated over the entire height of the reactor. Right: Mass transfer flux as function of bubble size and axial direction for a single bubble.

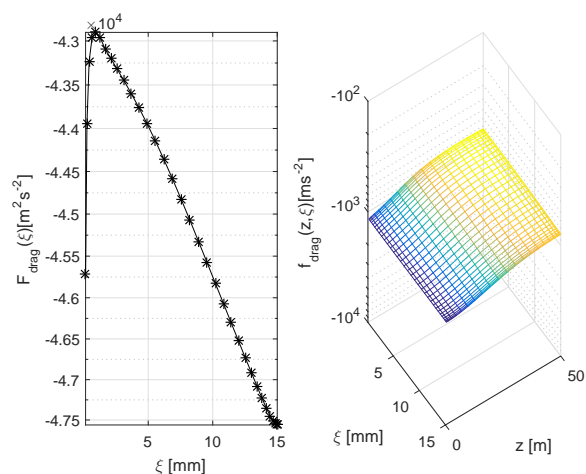


**Figure 5:** Drag force for a single bubble as function of bubble size for bubble sizes 0.1 mm to 15 mm. Left: Drag force for a single bubble integrated over the entire height of the reactor. Right: Drag force as function of bubble size and axial direction for a single bubble.

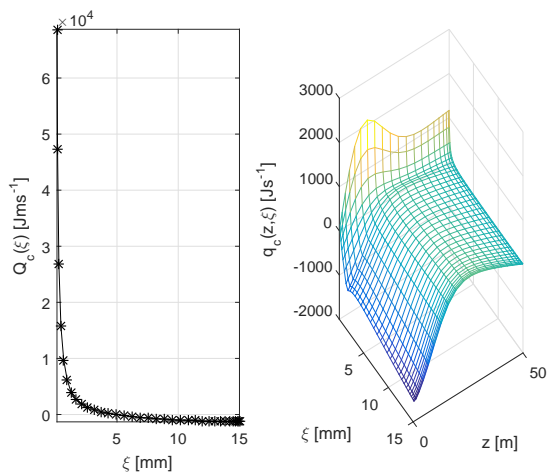


**Figure 6:** Heat flux for a single bubble as function of bubble size for bubble sizes 0.1 mm to 15 mm. Left: Heat flux for a single bubble integrated over the entire height of the reactor. Right: Heat flux as function of bubble size and axial direction for a single bubble.

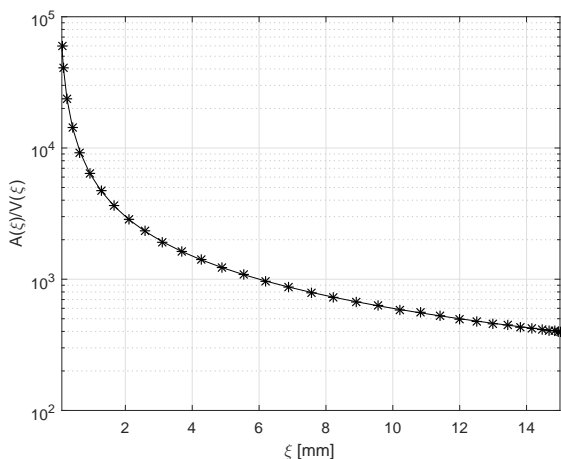


**Figure 7:** Surface area per volume for bubbles with diameter 0.1 to 15 mm.

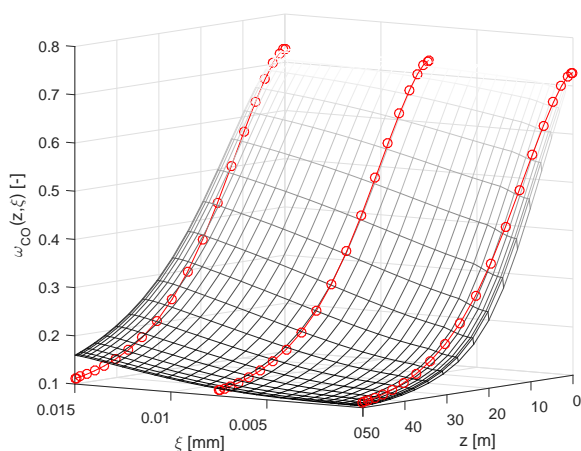


**Figure 8:** Weight fraction of CO (reactant) as function of bubble size and axial direction. Large bubbles have more reactant left in the bubble than the average. Small bubbles have less reactant left than the average.

cient by one order of magnitude. The nominal conversion at the outlet is 89%. Increasing the mass transfer coefficient by an order of magnitude gives 93%. Decreasing it gives a conversion of 48%. These numbers indicate that the mass transfer coefficient plays a significant role in the Fischer-Tropsch synthesis at the given operating conditions. The process is mass transfer limited at the given catalyst concentration (Table 1).

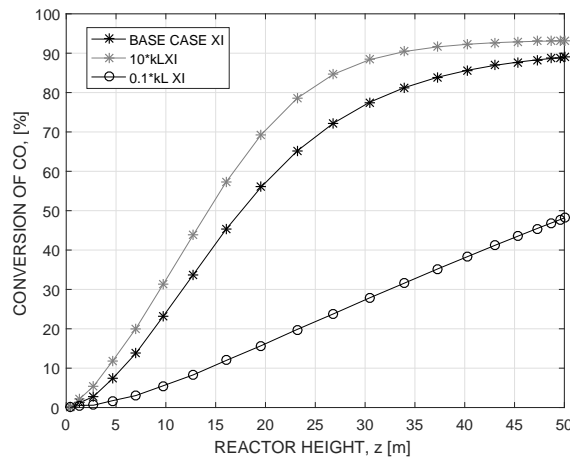


**Figure 9:** Conversion of CO in wt% as function of axial direction for increase and decrease in the liquid side mass transfer coefficient from the nominal value calculated from the small bubble correlation by Calderbank and Moo-Young (1961). Small  $k_L$  value is large mass transfer resistance, high  $k_L$  value is low mass transfer resistance. 45 wt% catalyst per volume of slurry.

It is noted that the base case simulation (Table 1) has a high catalyst loading of 45 wt% per volume of slurry. As a sensitivity a set of simulations with a 20 wt% catalyst concentration is given in Figure 10.

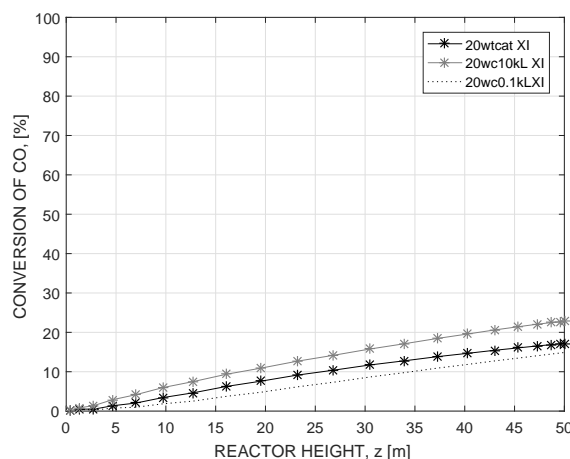


**Figure 10:** Conversion of CO in wt% as function of axial direction for increase and decrease in the liquid side mass transfer coefficient from the nominal value calculated by the formula from Calderbank and Moo-Young (1961). 20 wt% catalyst per volume of slurry.

The conversion of CO decreases from 89% to 17% for the nominal  $k_L$  value. For the tenfold increase, the conversion increases to 23%. For the low  $k_L$  value the result is a decrease from to 15%. The difference in conversion between the smallest and largest  $k_L$  values is smaller for lower catalyst

concentrations, as is expected. With a lower catalyst concentration it is less likely for the mass transfer to be the limiting resistance in the overall efficiency of the reactor. However, there is a potential to increase reactor efficiency by increasing mass transfer also at lower catalyst concentrations.

A detailed modelling of the mass transfer flux as function of the bubble size requires a good model for  $k_L$ , also its dependency on bubble size. Calderbank and Moo-Young (1961) claimed the bubble size of less importance and claimed  $k_L$  rather being a function of the liquid properties such as diffusivity than being a function of bubble size. However, the number of experimental studies of mass transfer at high pressures and with high gas flow rates is low (Rollbusch *et al.*, 2015), in particular if also requiring measurements in Fischer-Tropsch-like fluids.

### Size dependent velocity

Figure 11 shows the bubble size dependent velocity compared to the mass averaged velocity. For the smallest bubbles the difference is very large; the average is 0.4 to 0.6 m/s and the smallest bubble size in the field value has the same velocity as the liquid (set as boundary condition) of 0.02 m/s. The large variation in velocity as a function of bubble size is dictated by the drag coefficient for a single bubble by Tomiyama (1998). The coefficient is corrected by a factor  $p$ ;  $C_D = C'_D(1 - \alpha_G)^p$  to account for bubble interaction. In this work we use the value of 2 Ishii and Zuber (1979). The value of  $p$  is further discussed by Rampure *et al.* (2007). It is noted that the value of  $p$  is uncertain and has influence on the velocity.

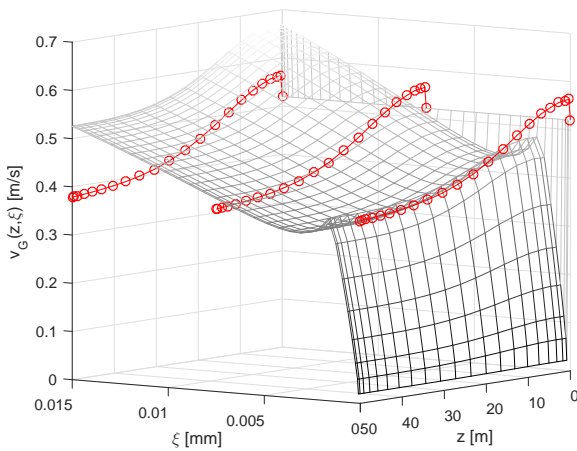


**Figure 11:** Velocity as function of bubble size  $\xi$  and axial direction  $z$ . The average value is shown as connected red circles. The difference in the velocity for the smallest and largest bubbles is 0.6 m/s.

### Size dependent temperature

Figure 12 shows the temperature as a function of bubble size and axial direction, with average values in red connected circles. The field deviates from the average value by less than 0.02K at all points. The maximal variation in the temperature profile along the axis is 10 K. The size dependency of the temperature is so small that it may be considered negligible for this system. It is noted that the gas and liquid phases are fed at the same temperature in this simulation. In case of difference between gas and liquid inlet temperatures or with lower values for the interfacial heat transfer coefficient the

bubble size dependency of the temperature may be important.

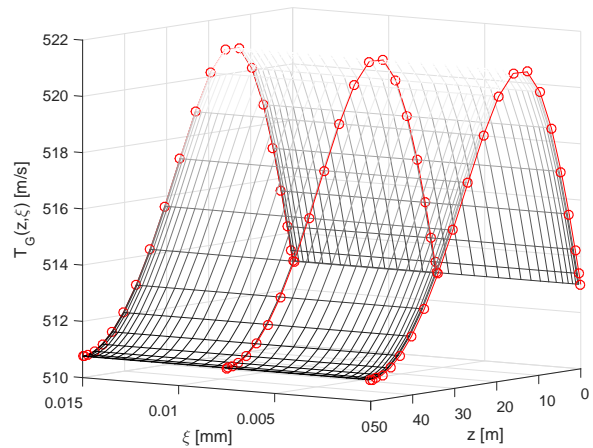


**Figure 12:** Temperature as function of bubble size  $\xi$  and axial direction  $z$ . The average value is shown with connected red circles. No variation in temperature as function of bubble size is visible.

### Effect of bubble size

A simulation was performed with a mean inlet bubble size of 15 mm instead of 10 mm. The results are shown in Figure 13. With an interfacial area reduced to about 50% of the nominal value, the conversion of CO decreases by 10 wt% points. The gas velocity increases as bigger bubbles are less slowed down by drag than smaller bubbles. The difference in outlet bubble size is shown in the lower left plot in Figure 13 and shows a difference of 8 mm for the peak bubble size. It is noted that the total bubble (gas) mass in the reactor was 9 % less in the sensitivity with a mean bubble size of 15 mm compared to the base case of 10 mm. The total bubble volume was 6 % less.

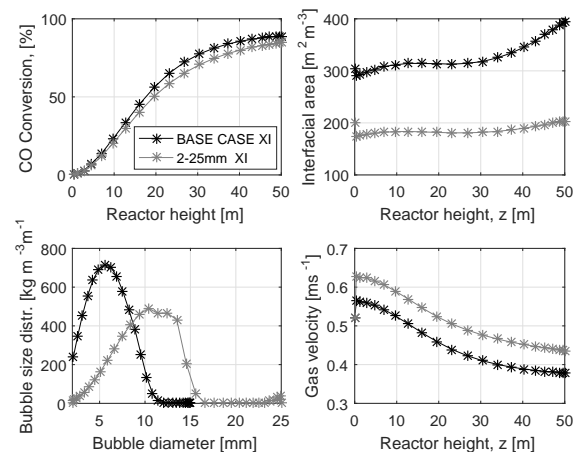


**Figure 13:** Conversion of CO, interfacial area, bubble size distribution at outlet and gas velocity for a mean inlet bubble size of 10 mm (base case) in black and 15 mm in gray.

### CONCLUSION

A bubble size dependent model for weight fractions, velocity and temperature has been developed and applied to the

Fischer-Tropsch synthesis in a slurry bubble column operating at industrial conditions.

The interfacial fluxes are inversely proportional to the bubble diameter and thus decrease with increasing diameter. The consequence is a higher mass, momentum (drag force) and heat transfer rate for the smaller bubbles than for the larger. Bubble size dependent velocity is known from the literature to give a valuable additional information compared to all bubbles having the same average velocity. This is also true here, as the drag force exerted on small bubbles is very different than for large bubbles resulting in a velocity profile highly dependent on bubble size. The difference in velocity for the smallest and largest bubbles is 0.6 m/s at its maximum which is significant as the average velocity is about 0.45 m/s. Bubble size dependent weight fractions show a concentration difference between the smallest and largest bubble sizes of maximum 0.2 at the conditions modelled here. With a weight fraction of reactant ranging from 0.1 to 0.7 this is a significant difference. Bubble size dependent weight fractions give more accurate description of the mass transfer in a reactor, given a proper  $k_L$  value for the system, preferably as a function of bubble size. This poses a challenge as  $k_L$  as a function of bubble size is difficult to measure at industrial conditions such high pressure, high temperature and multi-component viscous hydrocarbon fluids.

Bubble size dependent temperature does not add significant information new in the process studied here. The temperature as function of bubble size is relatively flat and the maximal deviation for any bubble size from the average temperature is 0.02 K. It is noted that the gas and liquid phases are fed at the same temperature in this simulation. In case of difference between gas and liquid inlet temperatures or with lower values for the interfacial heat transfer coefficient the bubble size dependency of the temperature may be important.

Given that mass transfer influences the overall conversion in the reactor, it is important to model this interfacial flux with the necessary level of detail. A bubble size dependent transfer flux combined with the information in the explicit density function  $f_d(z, \xi)$  provides a good starting point to increase the level of detail in modelling mass transfer in mass transfer limiting chemical and biochemical processes. It is noted that firm conclusions on the mass and heat transfer limitations can only be drawn when reliable estimates of the transfer coefficients are available.

## REFERENCES

ANDRESEN, E. (1990). *Statistical Approach to Continuum Models for Turbulent Gas-Particle Flows*. Ph.D. thesis, Technical University of Denmark.

CALDERBANK, P.H. and MOO-YOUNG, M.B. (1961). "The continuous phase heat and mass-transfer properties of dispersions". *Chemical Engineering Science*, **16**, 39–54.

CHAO, Z. (2012). *Modeling and Simulation of Reactive Three-phase Flows in Fluidized Bed Reactors Application to the SE-SMR Process*. Ph.D. thesis, Norwegian University of Science and Technology (NTNU).

COULALOGLOU, C. and TAVLARIDES, L. (1977). "Description of interaction processes in agitated liquid-liquid dispersions". *Chem. Eng. Sci.*, (**30**), 1289–1297.

DORAO, C.A. (2006). *High Order Methods for the Solution of the Population Balance Equation with Applications to Bubbly Flows*. Ph.D. thesis, Norwegian University of Science and Technology (NTNU).

FRANK, T., ZWART, P.J., SHI, J.M., KREPPER, E., LUCAS, D. and ROHDE, U. (2005). "Inhomogeneous musig

model - a population balance approach for polydispersed bubbly flows". *International Conference, Nuclear Energy for New Europe 2005*.

ISHII, M. and ZUBER, N. (1979). "Drag coefficient and relative velocity in bubbly, droplet or particulate flows". *AIChE Journal*, **25**, 843–855.

JAKOBSEN, H.A. (2008). *Chemical Reactor Modeling Multiphase Reactive Flows*. Springer.

KOHLER, M.A. (1986). "Comparison of mechanically agitated and bubble column slurry reactors". *Applied Catalysis*, **22**, 21–53.

LATHOUWERS, D. and BELLAN, J. (2000). "Modeling of dense gas-solid reactive mixtures applied to biomass pyrolysis in a fluidized bed". *Proceedings of the 2000 U.S. DOE Hydrogen Program Review NREL/CP-570-28890*.

MOREL, C. (2015). *Mathematical Modeling of Disperse Two-Phase Flows*. Springer International Publishing Switzerland.

NAYAK, A., BORKA, Z., PATRUNO, L., SPORLEDER, F., DORAO, C. and JAKOBSEN, H. (2011). "A combined multifluid-population balance model for vertical gas-liquid bubble-driven flows considering bubble column operating conditions". *Ind. Eng. Chem. Res.*, **50**(3), 1786–1798.

PATRUNO, L.E., DORAO, C.A., DUPUY, P.M., SVENDSEN, H.F. and JAKOBSEN, H.A. (2009). "Identification of droplet breakage kernel for population balance modelling". *Chemical Engineering Science*, **64**, 638–645.

RAMPURE, M.R., KULKARNI, A.A. and RANADE, V.V. (2007). "Hydrodynamics of bubble column reactors at high gas velocity Experiments and computational fluid dynamics (cfD) simulations". *Industrial & Engineering Chemical Research*, 8431–8447.

ROLLBUSCH, P., BOTHE, M., BECKER, M., LUDWIG, M., GRÜNEWALD, M., SCHLÜTER, M. and FRANKE, R. (2015). "Bubble columns operated under industrial relevant conditions - current understanding of design parameters". *Chemical Engineering Science*.

SIMONIN, O. (1996). "Continuum modelling of dispersed two-phase flows". *Combustion and turbulence in two-phase flows*, vol. 2, 1–47. van Karman Institute for fluid dynamics.

SOLSVIK, J. and JAKOBSEN, H.A. (2014). "A combined multifluid-population balance model applied to dispersed gas-liquid flows". *Journal for Dispersion Science and Technology*.

SPORLEDER, F. (2011). *Simulation of Chemical Reactors using the Least-Squares Spectral Element Method*. Ph.D. thesis, Norwegian University of Science and Technology (NTNU).

SPORLEDER, F., DORAO, C.A. and JAKOBSEN, H.A. (2011). "Model based on population balance for the simulation of bubble columns using methods of the least-square type". *Chemical Engineering Science*, **66**, 3133–3144.

TOMIYAMA, A. (1998). "Struggle with computational bubble dynamics". *Multiphase Science and Technology*, **10**(4), 369–405.

VANDU, C., KOOP, K. and KRISHNA, R. (2004). "Volumetric mass transfer coefficient in a slurry bubble column operating in the heterogeneous flow regime". *Chemical Engineering Science*, 4516–5423.

VIK, C.B., SOLSVIK, J., HILLESTAD, M. and JAKOBSEN, H.A. (2015). "Modeling of a slurry bubble column reactor for the production of biofuels via the fischer-tropsch synthesis". *Chemical Engineering & Technology*, **38**(4), 690–700. URL <http://dx.doi.org/10.1002/ce.22889>.

1002/ceat.201400647.

YATES, I.C. and SATTERFIELD, C.N. (1991). "Intrinsic kinetics of the fischer-tropsch synthesis on a cobalt catalyst". *Energy & Fuels*, **5(1)**, 168–173.

ZHU, Z. (2009). *The Least-Squares Spectral Element Method Solution of the Gas-Liquid Multi-fluid Model Coupled with the Population Balance Equation*. Ph.D. thesis, Norwegian University of Science and Technology (NTNU).

# CFD SIMULATION OF THE DROPLET SIZE DISTRIBUTION OF LIQUID-LIQUID EMULSIONS IN STIRRED TANK REACTORS

**Reza FARZAD<sup>1</sup>, Simon SCHNEIDERBAUER<sup>1,2</sup>**

<sup>1</sup> Christian Doppler Laboratory for Multi-Scale Modelling of Multiphase Processes, Johannes Kepler University, 4040 Linz, AUSTRIA

<sup>2</sup> Department of Particulate Flow Modelling, Johannes Kepler University, 4040 Linz, AUSTRIA

\* E-mail: reza.farzad@jku.at

## ABSTRACT

Predicting the drop size distribution (DSD) is essential in particulate flows such as emulsions as it affects mass transfer and heat transfer. In the current work we developed a novel numerical method to account for droplet breakup. The droplet breakup relies on an in-house developed correlation which depends on the local shear rate and some fluid properties. Commonly, a population balance equation (PBE) is employed to describe the breakup and coalescence of the droplets; however, such an approach does commonly not distinguish between different slip velocities of the smaller and larger droplets. Therefore, we propose a hybrid modelling strategy, which combines an Eulerian-Eulerian two-fluid model (TFM) and a Lagrangian discrete particle model (DPM), which is referred to as the Hybrid TFM-DPM model. This method enables the efficient evaluation of the poly-disperse liquid-liquid drag force from the local distribution of the different droplet diameters. The latter can be obtained by tracking statistically representative droplet trajectories for each droplet diameter class. Finally, we applied this novel approach to a liquid-liquid emulsion in a stirred tank presented. The results clearly show that the present method is able to predict the droplet size distribution for different rotational speeds of the stirrer.

**Keywords:** Emulsion, Droplet breakup, Coalescence, Hybrid TFM-DPM

## NOMENCLATURE

### Notation

$We$  Weber number, [-].

$Re$  Reynolds number, [-].

$A$  Dimensionless constant, [-].

$a$  Shear rate, [-].

$D_{32}$  Sauter mean diameter, [m].

$D_{90}$  90% of the droplets are smaller than this value, [m].

$F_k^{poly}$  Drag force acting on a parcel with  $d_k$ , [kg·m/s<sup>2</sup>].

$g$  Gravity acceleration, [m/s<sup>2</sup>].

$h$  Characteristic length, [m].

$K$  Interphase momentum exchange coefficient

$L$  Impeller diameter of stirred tank (Characteristic length), [m].

$\vec{u}$  Velocity field, [m/s].

$\tilde{u}$  Average velocity, [m/s].

### Greek Symbols

$\rho$  Mass density, [kg/m<sup>3</sup>].

$\mu$  Dynamic viscosity, [kg/m·s].

$\gamma$  Interfacial tension, [kg/s<sup>2</sup>].

$\varepsilon$  Turbulence dissipation rate. [m<sup>2</sup>/s<sup>3</sup>].

$\zeta$  Collision frequency, [#s].

$\lambda$  Coalescence efficiency, [-].

$\Gamma$  Coalescence frequency, [#s].

$\tau$  Shear stress, [kg/m·s<sup>2</sup>].

$\tau_{col,d}$  Collisional time scale.

$\phi$  Dispersed phase volume fraction. [-]

### Sub/superscripts

$c$  Continuous phase.

$d$  Dispersed phase.

$k$  Index of parcel.

$p$  Parcel.

## INTRODUCTION

Emulsions are widely used in the several industries such as food, pharmaceutical, cosmetic, chemical and petroleum. Drop size distribution (DSD) plays the key role as it controls mass transfer and heat transfer of the liquid-liquid system inside the reactor (Leng and Calabrese, 2004). Wide range of studies are done both numerically and experimentally to cover the DSD issues in the stirred tank reactor. There are several experimental studies focus on the single drop breakup experiment in order to define the breakup kernel for the Population balance equation (PBE) (Maaß et al., 2012; Solsvik et al., 2014; Solsvik and Jakobsen, 2015) and some others



investigated DSD regardless of the events happening to each droplet (Boxall et al., 2010; Calabrese et al., 1986; Coualaloglou and Tavlarides, 1977, 1976; Narsimhan et al., 1980; Ohtake et al., 1987; Wang and Calabrese, 1986). In addition, there are some additional studies, where computational fluid dynamic (CFD) in combination with PBE modelling is performed to predict the PSD of liquid-liquid emulsions (Agterof et al., 2003; Roudsari et al., 2012).

PBE is commonly used to take account for the break up and coalescence of the droplets, although it is computationally not affordable to consider the different slip velocities of the different droplet sizes. Furthermore, the PBE requires kernels for breakup and coalescence, which are difficult to obtain due to finding the parameters such as the breakage frequency (Ramkrishna, 2000). In the current work, a hybrid approach is proposed, which combines the Eulerian-Eulerian two fluid model (TFM) and the Lagrangian discrete particle model (DPM) (Schneiderbauer et al., 2016a, 2016b). Here, the breakup of the droplets can be evaluated based on individual representative droplets. Moreover, hybrid TFM-DPM strategy has the advantage to acquire the Sauter mean diameter from DPM side (Lagrangian) and deliver it to TFM in order to calculate the accurate interphase momentum exchange term (Schneiderbauer et al., 2015). However, this hybrid approach requires the local equilibrium droplet size distribution. In the literature there are correlations, which evaluate the global Sauter mean diameter in a stirred tank reactors. The early stage correlation was developed based on the Kolmogorov length scale (Kolmogorov, 1941) by the work of Shinnar and Church (Shinnar and Church, 1960) and Chen and Middleman (Chen and Middleman, 1967) which reads,

$$\frac{D_{32}}{L} = AWe^{-0.6} \quad (1)$$

There are similar works available, which give different correlations for the global Sauter mean diameter (Calabrese et al., 1986; Coualaloglou and Tavlarides, 1976; Wang and Calabrese, 1986). However, there is no available local correlation for Sauter mean diameter based on the local fluid dynamic parameters (such as turbulence dissipation rate,  $\epsilon$ ) as it is difficult to obtain. Therefore, we investigated the droplet breakup in a Taylor-couette flow, in which the measurement of fluid dynamic parameters such as shear rate is well defined (Farzad et al., 2016). The resulting correlation depends on the shear rate and the fluid physical properties like density, viscosity and interfacial tension which is written as below (Farzad et al., 2016),

$$\frac{D_{32}}{h} = We^{-\frac{1}{6}} Re^{-\frac{1}{4}} \left( \frac{\mu_d}{\mu_c} \right)^{0.33} \left( \frac{\rho_d}{\rho_c} \right)^{-6.6} \quad (2)$$

$$We = \frac{\rho_c a^2 h^3}{\gamma} \quad Re = \frac{\rho_c a h^2}{\mu_c}$$

Note that, the power of h becomes zero due to combination of the h, Weber number and Reynolds

number. Therefore, the normalized Sauter mean diameter is independent of the characteristic length (h). Finally, while the modelling of breakup can be efficiently realized on a droplet level, the coalescence of the droplets would require resolving the collisions between individual droplets. In the following, we present novel models for breakup and coalescence. On the one hand, the breakup model is connected to equation (2) and on the other hand, the coalescence model represents a different discretization strategy of the population balance equations.

## DROPLET BREAKUP MODEL

The present breakup model depends on the local Sauter mean diameter (equation 2), which can be obtained by using the local shear rate and the system's physical properties. Furthermore, our in-house experimental data (Farzad et al., 2016) reveals that the standard deviation scales linearly with the Sauter mean diameter, i.e.  $\sigma = 0.33D_{32}$ , and that the DSD follows a log-normal distribution; this observation is also consistent with literature (Boxall et al., 2010). Therefore, the full local equilibrium DSD can be determined by using the Sauter mean diameter from the correlation (equation 2) and  $\sigma = 0.33D_{32}$ . Thus, if a droplet is much larger than the the mean droplet size given from the DSD it might be prone to breakup. In this work, we employ the  $D_{90}$  for this threshold, which can be computed in each computational cell from the corresponding local DSD (Figure 1). If a droplet is larger  $D_{90}$  we sample a random number following the log-normal distribution. Only if this random number is larger than  $D_{90}$  as well, the droplet will break into two daughter droplets, where the diameter of the first daughter droplet is given by a second random number following the log-normal distribution. Note that, based on our assumption the local droplets (parcels) which are smaller than  $D_{90}$  remain stable as they are inside the local size distribution. Therefore, the local size distribution is constant and global size distribution changes till it reaches a steady state. Consequently, the diameter of the second daughter droplet can be easily computed from the volumes of the mother droplet and the first daughter droplet. This model was implemented as a user-defined function (UDF) to be used in the ANSYS FLUENT. The numerical implementation scheme will be discussed later. Note that breakup is not resolved for each droplet as it computationally costly and in most of the cases impossible; therefore, DPM uses parcels instead of particles which represent a group of particles with the identical diameter to reduce the computational costs.

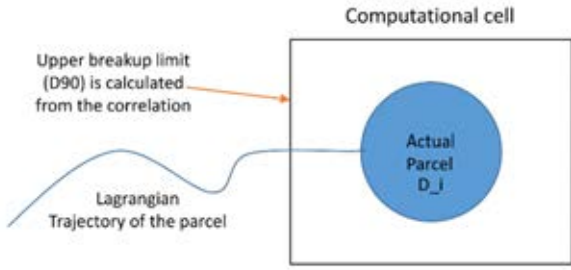


**Figure 1:** Schematic view of Lagrangian parcel which enters a specific computational cell with an upper breakup limit. If the parcel is larger than the limit then it breaks; otherwise, it remains unchanged.

## DROPLET COALESCENCE MODEL

Modelling coalescence is more demanding compared to the breakup. Coalescence can be thought as the combination of collision frequency  $\zeta(d, d')$  and coalescence efficiency  $\lambda(d, d')$ . Thus, a general form of the coalescence frequency reads (Coulaloglou and Tavlarides, 1977; Leng and Calabrese, 2004),

$$\Gamma(d, d') = \zeta(d, d')\lambda(d, d') \quad (3)$$

Computing the collision frequency directly from droplet interactions is computationally very demanding and would decline the benefits of the hybrid approach. Therefore, we follow Coulaloglou and Tavlarides (Coulaloglou and Tavlarides, 1977), who defined the collision frequency and coalescence efficiency as below:

$$\zeta(d, d') = c_1 \frac{\varepsilon^{1/3}}{1 + \phi} (d + d')^2 (d^{2/3} + d'^{2/3})^{1/2} \quad (4)$$

$$\lambda(d, d') = \exp(-c_2 \frac{\mu_c \rho_c \varepsilon}{\sigma^2 (1 + \phi)^3} (\frac{d \cdot d'}{d + d'})^4) \quad (5)$$

Coalescence may occur when at least two droplets collide with each other; however, as noted above computing  $\Gamma$  from the interactions of the Lagrangian parcels would considerably decrease the computational efficiency of the present model. Thus, a different strategy is required to compute the rate of coalescence for the actual Lagrangian parcel. This strategy is outlined in the following: First, similar to PBE modelling we introduce a specific number of diameter classes. For each of this diameter classes, we are able to compute the corresponding volume fraction from mapping the data coming from the Lagrangian parcels to the Eulerian grid used for the TFM solution. Second, based on these “imaginary coalescence partners” given from this binning, we are able to compute the individual rates of coalescence (equation (3)). Note that the representative diameter of each bin is given by its mid diameter. Therefore, if we have  $N$  parcels and  $M$  bins in a cell, there are  $M \times N$  combinations (e.g.  $N \approx 2 \times 10^6$   $M = 13$ ). Third, the amount of volume created due to coalescence is locally stored regarding to its new diameter class in the appropriate diameter bins. Note that all the coalescence which can produce droplets larger than local  $D_{90}$  were neglected in order to reduce the computational cost as they are prone to breakup again in the next time step.

After storing the volume of the created droplets, they should be off loaded correctly into the available parcels with appropriate diameter. The volume remains stored until an appropriate parcel enters the computational cell; this procedure is known as “Bus stop model” (Schellander et al., 2012). Bus stop model helps to reduce the computational cost since always injecting the coalescence volume as a new parcel increases the computation time. However, there might be no suitable parcel available (regarding to its diameter class) in the surrounding; then, a new parcel should be injected in the next time step (flow time).

## Two-fluid Model (TFM)

Resolving the motion of all droplets are computationally costly; therefore, it is more realistic to consider the averaged equation of motion and treat them as an Eulerian phase (Crowe et al., 2011). Continuity and momentum equations for the dispersed phase read (Ranade, 2001),

*Continuity equation*

$$\frac{\partial}{\partial t} (\alpha_d \rho_d) + \nabla \cdot (\alpha_d \rho_d \bar{u}_d) = 0 \quad (6)$$

*Momentum equation*

$$\frac{\partial}{\partial t} (\alpha_d \rho_d \bar{u}_d) + \nabla \cdot (\alpha_d \rho_d \bar{u}_d \bar{u}_d) = -\alpha_d \nabla p + \nabla \cdot (\alpha_d \tau_d) + F_d + \alpha_d \rho_d g \quad (7)$$

$F_d$  which denotes the interphase momentum exchange between the dispersed phase and the continuous phase reads,

$$F_d = K_{cd} (\bar{u}_c - \bar{u}_d) \quad (8)$$

In reality most of the dispersed multiphase flows such as droplets and particles are poly-disperse; therefore, Sauter mean diameter is required to calculate the interphase momentum exchange properly (Schneiderbauer et al., 2015).

Continuity and momentum equations for the continuous phase in a similar manner. This Eulerian-Eulerian approach is also known as TFM.

## Discrete phase model (DPM)

This model provides the movement of a single or a cluster of particles (parcel) and tracks them in the flow field. Tracking the parcel trajectories gives the Lagrangian information. The momentum equation for the parcel trajectory is,

$$\frac{\partial}{\partial t} (u_{p,k}) = F_k^{poly} + g \quad (7)$$

## Hybrid model

Combining Lagrangian and Eulerian models yields the hybrid model. The TFM model predicts the flow field by

solving the Navier-Stokes equation and the DPM model passes the extra information (e.g. Sauter mean diameter) to the TFM part in order to improve the accuracy of the Eulerian part (Schneiderbauer et al., 2015). Furthermore, sensitivity analysis on several numerical settings reveals that the hybrid model is reliable (Schneiderbauer et al., 2016b).

This model is able to calculate the local Sauter mean diameter which changes the poly-disperse drag force (Figure 2). The modified Lagrangian trajectory can be written as below (Schneiderbauer et al., 2016a),

$$\frac{\partial}{\partial t}(u_{p,k}) = -\frac{1}{\tau_{col,d}}(u_{p,k} - \tilde{u}_d) + F_k^{poly} + g \quad (7)$$



**Figure 2:** Single Lagrangian parcel trajectory (left side), the continuous droplets travels with local average velocity (middle), hybrid model in which consider the impact of the other existing droplets on the Lagrangian trajectory (right side)

## RESULTS AND DISCUSSION

The numerical work by Roudsari et al. (Roudsari et al., 2012) and the experimental data by Boxall et al. (Boxall et al., 2010) were used to validate the proposed models. These works are similar; however, the first one (Roudsari et al., 2012) explains the CFD simulation of the water-in-oil emulsion in stirred tank by applying PBE and validating their results by the second paper (Boxall et al., 2010) which contains the experimental data. The so called Conroe oil was used as the continuous phase and distilled water as the dispersed phase (Boxall et al., 2010). The Conroe oil density, viscosity and interfacial tensions are 842 kg/m<sup>3</sup>, 3.1 cP and 20 mN/m, respectively. The same geometry was used as Roudsari et al. (Roudsari et al., 2012). However, they used multiple reference frame (MRF) to simulate the impeller's rotation and ran the simulation in steady state but in the current work, dynamic simulation in combination with sliding mesh (SM) was carried out. Hexahedral mesh (Figure 3) of stirred tank reactor (Rushton turbine 6 blades and 4 baffles) was generated by using ANSYS ICEM (260,000 cells).

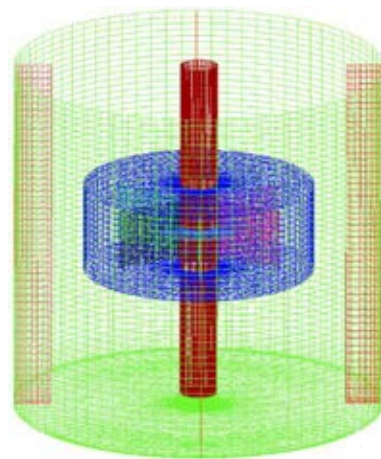


**Figure 3:** Stirred tank reactor mesh

As noted above, the Sauter mean diameter correlation, the breakup and the coalescence models were implemented as a UDF. The simulation of liquid-liquid system in stirred tank reactor including the hybrid TFM-DPM in combination with k-ε turbulence model was carried out by ANSYS FLUENT 16.2. The time step size was 0.01s.

## Breakup

The correlation of Sauter mean diameter (equation 2) was determined based on the dilute oil-water system (dispersed phase volume fraction was 1%) (Farzad et al., 2016); however, the volume fraction of dispersed phase in the experimental work of Boxall et al. (Boxall et al., 2010) is 15% and it can increase the Sauter mean diameter of the droplets due to coalescence (Coulaloglou and Tavlarides, 1976). Therefore, a linear correction factor was defined in the UDF based on the local volume fraction of the secondary phase in order to modify the correlation (equation 2) (Coulaloglou and Tavlarides, 1976).

$$D'_{32} = (1 + n\phi) D_{32}, \quad (8)$$

where n is set to 6.5. Simulation was ran for two rotational speeds, 300 RPM and 600 RPM. The initial droplets with diameter of 0.6 mm and 0.3 mm were injected at t=0 for the 300 RPM (Figure 4) and the 600 RPM (Figure 5) cases, respectively.

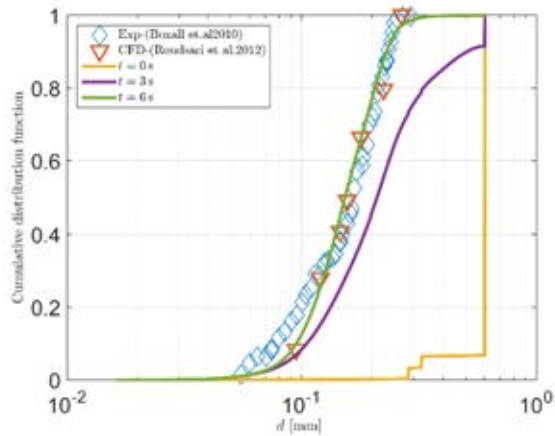


**Figure 4:** Cumulative drop size distribution at 300 RPM -Water in Conroe oil - Curves show the DSD (simulated) at  $t=0, 3$  and  $6$  second- shaped scattered experimental data are taken from Boxall et al. (Boxall et al., 2010)- Nabla shaped points are CFD simulation results taken from Roudsari et al. (Roudsari et al., 2012)

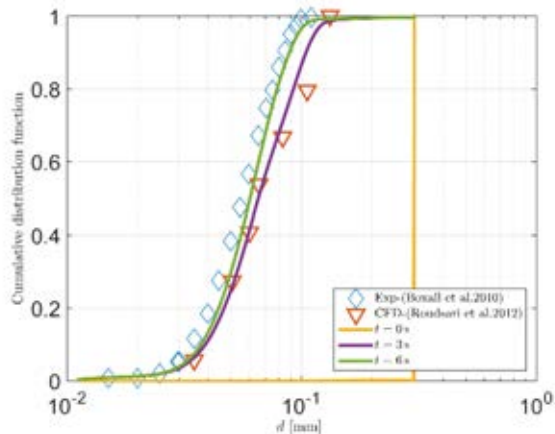


**Figure 5:** Cumulative drop size distribution at 600 RPM -Water in Conroe oil - Curves show the DSD (simulated) at  $t=0, 3$  and  $6$  second-Diamond shaped scattered experimental data are taken from Boxall et al. (Boxall et al., 2010)- Nabla shaped points are CFD simulation results taken from Roudsari et al. (Roudsari et al., 2012)

As it can be seen from figure 4 and 5, the final status of the simulated results are in a good agreement with the experimental data (Boxall et al., 2010). Comparing the figures at  $t=3s$  (real flow time) reveals that the simulation at 600 RPM reached faster to its final state is compared to the 300 RPM. Therefore, mixing process is happening faster at 600 RPM in comparison with 300 RPM. However, studying the mixing time is not in the scope of this work. In addition, simulated DSD at 600 RPM follows the experimental data (Boxall et al., 2010) more accurately than compared to the simulated data provided by Roudsari et al. (Roudsari et al., 2012). Furthermore, using Lagrangian tracer trajectories provides the possibility to distribute the final simulated results into a large number of bins (400) in order to get smooth DSD. Roudsari et al. (Roudsari et al., 2012) used 7 bins as a part of PBE model available on the ANSYS FLUENT; therefore, their results are not as smooth as the results in the current work.

## Coalescence

In order to validate the coalescence model, we study a process dominated by droplet coalescence. For example, when reducing the rotational speed was reduced from 600 RPM to 300 RPM breakup becomes negligible compared to coalescence. Nevertheless, both the breakup and the coalescence models were involved in this part of the simulation. The constant values of collision frequency,  $c_1 = 1.29e^{-5}$  and coalescence efficiency,  $c_2 = 7.32e^{12}$  were selected from (Maaß et al., 2007). However, the constant for the collision frequency was increased to  $c_1 = 1$ , in order to speed up the simulation to obtain the preliminary results. Figure 6 illustrates initial results of the coalescence model, where the curve at  $t=0$  is the DSD at 600 RPM and after 0.5s (real flow time) DSD is almost close the experimental data at 300 RPM (Boxall et al., 2010).

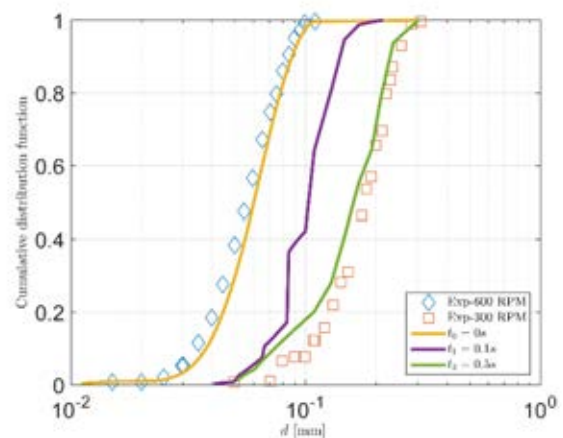


**Figure 6:** Cumulative drop size distribution evolves by time from 600 RPM to 300 RPM due to coalescence -Water in Crone oil - Curves show the DSD (simulated) at  $t=0, 0.1$  and  $0.5$  second-Diamond shaped and square shaped scattered experimental data are taken from Boxall et al. (Boxall et al., 2010)

## CONCLUSION

In this work, we presented novel breakup and coalescence models for liquid-liquid emulsions in combination with and Euerlian-Lagrangian Hybrid model. The main advantage compared to state of the art PBE modelling approaches is the Lagrangian nature of our approach, which allows the simple evaluation of, for example, residence time distribution.

The breakup model is based on an in-house correlation for Sauter mean diameter (Farzad et al., 2016), while the coalescence model is based on literature correlations. These models were combined with a hybrid TFM-DPM strategy, which allows the efficient analysis of poly-disperse systems. Final results for breakup show that the breakup model works fairly well for the validation case (Boxall et al., 2010; Roudsari et al., 2012). The initial results for the coalescence model are in a good agreement with the experiment (Boxall et al., 2010). However, these models, especially the model for coalescence require further investigation and more validation cases. Especially, larger systems will be subject to future investigations.

## REFERENCES

- Agterof, W.G.M., Vaessen, G.E.J., Haagh, G.A.A. V, Klahn, J.K., Janssen, J.J.M., 2003. Prediction of emulsion particle sizes using a computational fluid dynamics approach. *Colloids Surfaces B Biointerfaces* 31, 141–148. doi:10.1016/S0927-7765(03)00051-1
- Boxall, J.A., Koh, C.A., Sloan, E.D., Sum, A.K., Wu, D.T., 2010. Measurement and Calibration of Droplet Size Distributions in Water-in-Oil Emulsions by Particle Video Microscope and a Focused Beam Reflectance Method. *Ind. Eng. Chem. Res.* 49, 1412–1418. doi:10.1021/ie901228e
- Calabrese, R. V., Chang, T.P.K., Dang, P.T., 1986. Drop breakup in turbulent stirred tank contactors. Part I: Effect of dispersed phase viscosity. *AIChE J.* 32, 657–666. doi:10.1002/aic.690320416
- Chen, H.T., Middleman, S., 1967. Drop size distribution in agitated liquid-liquid systems. *AIChE J.* 13, 989–995. doi:10.1002/aic.690130529
- Coulaloglou, C.A., Tavlarides, L.L., 1977. Description of interaction processes in agitated liquid-liquid dispersions. *Chem. Eng. Sci.* 32, 1289–1297. doi:10.1016/0009-2509(77)85023-9
- Coulaloglou, C. a., Tavlarides, L.L., 1976. Drop Size Distributions and Coalescence Frequencies of Liquid-Liquid Dispersions in Flow Vessels. *AIChE J.* 22, 289–297. doi:10.1002/aic.690220211
- Crowe, C.T., Schwarzkopf, J.D., Sommerfeld, M., Tsuji, Y., 2011. *Multiphase Flows with Droplets and Particles*, Second Edition.
- Farzad, R., Puttering, S., Pirker, S., Schneiderbauer, S., 2016. Experimental investigation of liquid-liquid system drop size distribution in Taylor-Couette flow and its application in the CFD simulation. *Proc. Exp. Fluid Mech.* 2016 Conf. Lázně, Czech Repub.
- Kolmogorov, a N., 1941. The local structure of turbulence in incompressible viscous fluid for very large Reynolds numbers. *Dokl. Akad. Nauk Sssr* 30, 301–305. doi:10.1098/rspa.1991.0075
- Leng, D.E., Calabrese, R. V., 2004. Immiscible Liquid-Liquid Systems, in: Paul, E.L., Atiemo-Obeng, V.A., Kresta, S.M. (Eds.), *Handbook of Industrial Mixing*. John Wiley & Sons, Inc., pp. 639–753. doi:10.1002/0471451452.ch12
- Maaß, S., Gäbler, A., Zacccone, A., Paschedag, A.R., Kraume, M., 2007. Experimental Investigations and Modelling of Breakage Phenomena in Stirred Liquid/Liquid Systems. *Chem. Eng. Res. Des.* 85, 703–709. doi:10.1205/cherd06187
- Maaß, S., Paul, N., Kraume, M., 2012. Influence of the dispersed phase fraction on experimental and predicted drop size distributions in breakage dominated stirred systems. *Chem. Eng. Sci.* 76, 140–153. doi:10.1016/j.ces.2012.03.050
- Narsimhan, G., Ramkrishna, D., Gupta, J.P., 1980. Analysis of drop size distributions in lean liquid-liquid dispersions. *AIChE J.* 26, 991–1000. doi:10.1002/aic.690260614
- Ohtake, T., Hano, T., Takagi, K., Nakashio, F., 1987. Effects of Viscosity on Drop Diameter of W/O Emulsion Dispersed in a Stirred Tank. *J. Chem. Eng. Japan* 20, 443–447. doi:10.1252/jcej.20.443
- Ramkrishna, D., 2000. *Population Balances*, Chemical Engineering.
- Ranade, V. V., 2001. *Computational Flow Modeling for Chemical Reactor Engineering*.
- Roudsari, S.F., Turcotte, G., Dhib, R., Ein-Mozaffari, F., 2012. CFD modeling of the mixing of water in oil emulsions. *Comput. Chem. Eng.* 45, 124–136. doi:10.1016/j.compchemeng.2012.06.013
- Schellander, D., Schneiderbauer, S., Pirker, S., 2012. Numerical study of agglomeration modeling in polydispersed gas-solid flows with respect to particle separation. *Ninth Int. Conf. CFD Miner. Process Ind.* CSIRO, Melbourne, Aust.
- Schneiderbauer, S., Haider, M.F., Hauzenberger, F., Pirker, S., 2016a. A Lagrangian-Eulerian hybrid model for the simulation of industrial-scale gas-solid cyclones. *Powder Technol.* 304, 229–240. doi:10.1016/j.powtec.2016.07.064
- Schneiderbauer, S., Pirker, S., Puttering, S., Aguayo, P., Touloupidis, V., Joaristi, A.M., 2016b. A Lagrangian-Eulerian hybrid model for the simulation of poly-disperse fluidized beds: Application to industrial-scale olefin polymerization. *Powder Technol.* In Press. doi:10.1016/j.powtec.2016.12.063
- Schneiderbauer, S., Puttering, S., Pirker, S., Aguayo, P., Kanellopoulos, V., 2015. CFD modeling and simulation of industrial scale olefin polymerization fluidized bed reactors. *Chem. Eng. J.* 264, 99–112.
- Shinnar, R., Church, J.M., 1960. Statistical Theories of Turbulence in Predicting Particle Size in Agitated Dispersions. *Ind. Eng. Chem.* 52, 253–256. doi:10.1021/ie50603a036
- Solsvik, J., Becker, P.J., Sheibat-Othman, N., Mohallick, I., Farzad, R., Jakobsen, H.A., 2014. Viscous Drop Breakage in Liquid-Liquid Stirred Dispersions: Population Balance Modeling. *J. Dispers. Sci. Technol.* 36, 577–594.
- Solsvik, J., Jakobsen, H.A., 2015. Single drop breakup experiments in stirred liquid-liquid tank. *Chem. Eng. Sci.* 131, 219–234. doi:10.1016/j.ces.2015.03.059
- Wang, C.Y., Calabrese, R. V., 1986. Drop breakup in turbulent stirred-tank contactors. Part II: Relative influence of viscosity and interfacial tension. *AIChE J.* 32, 667–676. doi:10.1002/aic.690320417

## TOWARDS A CFD MODEL FOR BOILING FLOWS: VALIDATION OF QMOM PREDICTIONS WITH TOPFLOW EXPERIMENTS

Antonio BUFFO<sup>1</sup>, Marco VANNI<sup>1</sup>, Daniele L. MARCHISIO<sup>1</sup>, Gustavo MONTOYA<sup>2</sup>, Emilio BAGLIETTO<sup>2</sup>

<sup>1</sup>Department of Applied Science and Technology, Politecnico di Torino, ITALY

<sup>2</sup>Nuclear Science & Engineering, Massachusetts Institute of Technology, USA

### ABSTRACT

Boiling flows are very complex systems, usually confined in vertical pipes, where the liquid water moving upwards and the steam gas bubbles generated at the walls. The fluid dynamics of such systems is determined by the interplay of many different phenomena, including bubble nucleation, growth, condensation, coalescence, and breakage. For this reason, the development of a fully predictive computational fluid dynamics (CFD) model is very challenging, therefore we focus here only on some of the phenomena mentioned above (i.e. coalescence and breakage) by using population balance models (PBM). In this work, a coupled CFD-PBM model based on the two-fluid model and the quadrature method of moments (QMOM) was implemented in the open-source CFD code openFOAM. Simulation predictions obtained with this methodology are compared against the so-called TOPFLOW experiments for the first time, where simpler air-water cold systems that mimic the complexity of real boiling flows were investigated. Comparison between the available experimental data and the results show that great care must be paid on some modeling details, such as the inlet bubble size distribution (BSD) at the sparger and the coalescence and breakage rates modeling.

**Keywords:** Computational Fluid Dynamics, Population Balance Model, gas-liquid flows, top-flow experiments, boiling flow, coalescence, breakage, lift force. .

### NOMENCLATURE

#### Greek Symbols

$\alpha$	Volume fraction, [-].
$\beta$	Daughter distribution function, [1/m].
$\dot{\gamma}$	Shear strain rate, [1/s <sup>2</sup> ].
$\delta$	Dirac delta function, [-].
$\varepsilon$	Turbulent dissipation rate, [m <sup>2</sup> /s <sup>3</sup> ].
$\kappa$	Turbulent kinetic energy, [m <sup>2</sup> /s <sup>2</sup> ].
$\lambda$	Collision efficiency, [-].
$\mu$	Dynamic viscosity, [kg/ms].
$\rho$	Mass density, [kg/m <sup>3</sup> ].
$\sigma$	Surface tension, [kg/s <sup>2</sup> ].
$\sigma_{\kappa}$	$\kappa - \varepsilon$ model constant, [-].
$\sigma_{\varepsilon}$	$\kappa - \varepsilon$ model constant, [-].
$\sigma_{TD}$	Turbulent dispersion force parameter, [-].
$\tau$	Stress tensor, [kg/ms <sup>2</sup> ].

#### Latin Symbols

$a$	Coalescence kernel, [m <sup>3</sup> /s].
-----	--

$\bar{b}_k$	Generic order moment of the daughter distribution function, [m <sup>k</sup> ].
$C$	Model constant or coefficient, [-].
$C_{\mu}$	$\kappa - \varepsilon$ model constant, [-].
$C_{\varepsilon,1}$	$\kappa - \varepsilon$ model constant, [-].
$C_{\varepsilon,2}$	$\kappa - \varepsilon$ model constant, [-].
$d$	Diameter, [m].
$Eo$	Eötvös number, [-].
$\mathbf{F}$	Interfacial force per unit volume, [N/m <sup>3</sup> ].
$G$	Turbulence production rate, [m <sup>2</sup> /s <sup>3</sup> ].
$g$	Breakage frequency, [1/s].
$\mathbf{g}$	Gravity, [m/s <sup>2</sup> ].
$h$	Collision frequency, [m <sup>3</sup> /s].
$\mathbf{I}$	Identity matrix, [-].
$L$	Quadrature node (bubble size), [m].
$M_k$	k-th order moment, [m <sup>k-3</sup> ].
$n$	Number density function, [1/m <sup>4</sup> ].
$p$	Pressure, [Pa].
$Re$	Reynolds number, [-].
$\mathbf{S}$	Strain rate tensor, [1/s].
$\bar{S}_k$	Generic order moment transport equation source term, [m <sup>k-3</sup> /s].
$t$	Time, [s].
$\mathbf{U}$	Velocity, [m/s].
$w$	Quadrature weight, [1/m <sup>3</sup> ].
$We$	Weber number, [-].

#### Sub/superscripts

$\alpha$	Index $\alpha$ .
$b$	Bubbly gas phase.
$buoy$	Buoyancy.
$D$	Drag.
$eddy$	Eddy.
$eff$	Effective.
$i$	Index $i$ .
$j$	Index $j$ .
$k$	Index $k$ .
$l$	Liquid phase.
$L$	Lift or bubble size.
$shear$	Macroscopic shear.
$t$	Turbulent.
$T$	Terminal.
$TD$	Turbulent dispersion.
$tf$	Turbulent fluctuations.
$VM$	Virtual Mass.
$wake$	Wake.

### Abbreviations

BSD Bubble Size Distribution.  
 CFD Computational Fluid Dynamics.  
 CFL Courant-Friedrichs-Lewy.  
 MOC Methods of Classes.  
 NDF Number Density Function.  
 PBE Population Balance Equation.  
 PBM Population Balance Model.  
 QBMM Quadrature-Based Moment Method.  
 QMOM Quadrature Method Of Moments.

## INTRODUCTION

Boiling flows are omnipresent in the chemical, process and nuclear industries. Generally, the flow is confined in vertical pipes, with liquid water moving upwards and steam gas bubbles formed (via nucleation) at the wall and undergoing subsequent coalescence, breakage, growth and condensation. The movement of the steam gas bubbles is dictated by the interfacial forces, notably drag, lift and turbulent dispersion. In this particular flow configuration, the lift force plays a crucial role, as it is the main force pushing the bubbles away from the wall and into the core of the flow. The simulation of such flows is a challenge because of the variety and complexity of the phenomena involved, particularly the nucleation of gas bubbles at the wall and the interplay between interfacial forces, coalescence and breakage. In order to simplify the problem focusing only on fluid dynamics, very often steam bubble's nucleation, growth and condensation are not considered and the process investigated consists mainly on the injection of air bubbles at the wall, into a flow of cold water, mimicking the actual boiling flow (Schaffrath *et al.*, 2001; Prasser *et al.*, 2005; Lucas *et al.*, 2007). Computational fluid dynamics (CFD) coupled with population balance models (PBM) is commonly used to simulate such flows, by means of the Eulerian-Eulerian two-fluid model for the description of the air-water flow and the method of classes (MOC) for the solution of the PBM for the gas bubbles. However, this method is quite expensive and alternatives have been recently explored. In this work we want to replace the MOC with quadrature-based moments methods (QBMM) for the solution of the PBM. Among the different possible choices, QMOM is considered and different couplings with the CFD model are studied. In particular, the effect of the inlet bubble diameter on the final results is investigated. Moreover, different correlations for the interfacial forces (i.e. drag, lift, virtual mass and turbulent dispersion force), as well as different kernels for coalescence and breakage are here reviewed and analyzed, with the aim to be investigated in future communications. Simulations are performed with the open-source CFD code openFOAM by using the solver `compressibleTwoPhaseEulerFoam`, implementing the two-fluid model. The solver has been extensively modified to include QMOM, as illustrated in our previous work (Buffo *et al.*, 2016b). Simulation predictions are validated against the so-called TOPFLOW experiments (Prasser *et al.*, 2005; Lucas *et al.*, 2010), by comparing the bubble size distribution (BSD), the radial profiles of gas and liquid velocities, as well as gas volume fraction, at different heights of the test rig and under different operating conditions.

## MODEL DESCRIPTION

As previously mentioned, the Eulerian-Eulerian two-fluid model is here adopted to predict the behavior of the boiling

flow. The governing equations are briefly presented in the following (Buffo and Marchisio, 2014):

$$\frac{\partial \rho_k \alpha_k}{\partial t} + \nabla \cdot (\rho_k \alpha_k \mathbf{U}_k) = 0, \quad (1)$$

$$\begin{aligned} \frac{\partial \rho_k \alpha_k \mathbf{U}_k}{\partial t} + \nabla \cdot (\rho_k \alpha_k \mathbf{U}_k \mathbf{U}_k) = \\ - \nabla \cdot (\alpha_k \boldsymbol{\tau}_k) - \alpha_k \nabla p + \alpha_k \rho_k \mathbf{g} + \mathbf{F}_k, \end{aligned} \quad (2)$$

where the subscript  $k$  is equal to  $l$  for the continuous liquid phase and  $b$  for the bubbly gaseous phase, and where  $\alpha_k$  is the volume fraction,  $\rho_k$  is the density and  $\mathbf{U}_k$  is the Reynolds-averaged velocity for phase  $k$ . For instance, the stress tensor of the liquid phase  $\boldsymbol{\tau}_l$  is modeled considering a Newtonian fluid and the Boussinesq approach:

$$\boldsymbol{\tau}_l = \mu_{\text{eff},l} \left( (\nabla \mathbf{U}_l) + (\nabla \mathbf{U}_l)^T - \frac{2}{3} \mathbf{I} (\nabla \cdot \mathbf{U}_l) \right) \quad (3)$$

where  $\mu_{\text{eff},l}$  is the effective viscosity of the liquid phase:  $\mu_{\text{eff},l} = \mu_l + \mu_{t,l}$ , and where in turn  $\mu_l$  is the molecular viscosity of the liquid and  $\mu_{t,l} = \rho_l C_\mu \frac{\kappa^2}{\varepsilon}$ ,  $\kappa$  is the turbulent kinetic energy of the liquid phase and  $\varepsilon$  is the energy dissipation rate of the liquid phase. These two quantities are here calculated by using the multiphase extension of the  $\kappa - \varepsilon$  model (Kataoka and Serizawa, 1989), since it represents a good compromise between accuracy and computational time:

$$\frac{\partial \alpha_l \kappa}{\partial t} + \nabla \cdot (\alpha_l \kappa \mathbf{U}_l) - \nabla \cdot \left( \alpha_l \frac{\mu_{t,l}}{\rho_l \sigma_\kappa} \nabla \kappa \right) = \alpha_l (G - \varepsilon), \quad (4)$$

$$\begin{aligned} \frac{\partial \alpha_l \varepsilon}{\partial t} + \nabla \cdot (\alpha_l \varepsilon \mathbf{U}_l) - \nabla \cdot \left( \alpha_l \frac{\mu_{t,l}}{\rho_l \sigma_\varepsilon} \nabla \varepsilon \right) = \\ \alpha_l \left( C_{\varepsilon,1} \frac{\varepsilon}{\kappa} G - C_{\varepsilon,2} \frac{\varepsilon^2}{\kappa} \right). \end{aligned} \quad (5)$$

The model constants are those of the standard  $\kappa - \varepsilon$  model:  $C_\mu = 0.09$ ,  $\sigma_\kappa = 1.0$ ,  $\sigma_\varepsilon = 1.3$ ,  $C_{\varepsilon,1} = 1.44$ , and  $C_{\varepsilon,2} = 1.92$ . The term  $G$  is the turbulence production rate defined as:  $G = 2 \frac{\mu_{t,l}}{\rho_l} (\mathbf{S} : \nabla \mathbf{U}_l)$ , where the strain rate tensor is in turn defined as  $\mathbf{S} = \frac{1}{2} (\nabla \mathbf{U}_l + (\nabla \mathbf{U}_l)^T)$ .

It is important to remark that the term  $\mathbf{F}_k$  in Eq. (2) is crucial for a proper description of the fluid dynamics, since it is responsible for the momentum coupling between the phases by considering the different interfacial forces. Such term is usually described as a summation of different contributions, such as drag, lift, virtual mass, turbulent dispersion and wall lubrication forces (Lucas *et al.*, 2007; Buffo and Marchisio, 2014; Sugrue *et al.*, 2017). Although for standard equipment configurations as stirred tanks and bubble columns most of them can be neglected apart from the drag force (Buffo *et al.*, 2016a), in small diameter vertical pipes typical of boiling flows, where also the liquid phase raises through the column, and the gas is injected or formed laterally and then migrating towards the center of the column, all the forces may play a role (Lucas *et al.*, 2007; Lucas and Tomiyama, 2011). Therefore the term  $\mathbf{F}_b$  can be written as:

$$\mathbf{F}_b = -\mathbf{F}_l = \mathbf{F}_D + \mathbf{F}_L + \mathbf{F}_{VM} + \mathbf{F}_{TD}. \quad (6)$$

The drag force per unit volume  $F_D$  can be expressed as:

$$\mathbf{F}_D = -\frac{3}{4} \frac{\alpha_b \rho_l C_D}{d_b} |\mathbf{U}_b - \mathbf{U}_l| (\mathbf{U}_b - \mathbf{U}_l), \quad (7)$$

where  $d_b$  is the bubble diameter and  $C_D$  is the drag coefficient, which is here evaluated using the Tomiyama drag law (for slightly contaminated liquid) (Tomiyama *et al.*, 1998):

$$C_D = \max \left( \min \left( \frac{24}{\text{Re}_b} \left( 1 + 0.15 \text{Re}_b^{0.687} \right), \frac{72}{\text{Re}_b} \right), \frac{8}{3} \frac{\text{Eo}}{\text{Eo} + 4} \right) \quad (8)$$

where the bubble Reynolds number  $\text{Re}_b$  and the Eötvös number  $\text{Eo}$  can be written as:

$$\text{Re}_b = \frac{\rho_l |\mathbf{U}_b - \mathbf{U}_l| d_b}{\mu_l}, \quad (9)$$

$$\text{Eo} = \frac{g(\rho_l - \rho_b) d_b^2}{\sigma} \quad (10)$$

where  $\sigma$  is the surface tension and  $g$  is the gravity acceleration. The lift force per unit volume  $F_L$  can be written as (Lucas *et al.*, 2007):

$$\mathbf{F}_L = -C_L \alpha_b \rho_l (\mathbf{U}_b - \mathbf{U}_l) \times (\nabla \times \mathbf{U}_l), \quad (11)$$

where  $C_L$  is the lift coefficient. As can be observed in Eq. (6), in this work we do not model the wall lubrication as a separate force. We used the model of Shaver and Podowski (2015), where the wall lubrication phenomena is described by adjusting the lift coefficient according to the distance from the wall:

$$\begin{cases} 0 & \text{if } \frac{y}{d_b} < \frac{1}{2} \\ C_{L,0} \left( 3 \left( 2 \frac{y}{d_b} - 1 \right)^2 - 2 \left( 2 \frac{y}{d_b} - 1 \right)^3 \right) & \text{if } \frac{1}{2} \leq \frac{y}{d_b} \leq 1 \\ C_{L,0} & \text{if } 1 < \frac{y}{d_b} \end{cases} \quad (12)$$

The virtual mass force force can be expressed as (Lucas *et al.*, 2007):

$$\mathbf{F}_{VM} = -\alpha_b \rho_l C_{VM} \left( \frac{D\mathbf{U}_b}{Dt} - \frac{D\mathbf{U}_l}{Dt} \right), \quad (13)$$

where  $C_{VM}$  is the virtual mass coefficient and  $\frac{D}{Dt}$  is the substantial derivative. The turbulent dispersion force per unit volume  $F_{TD}$  can be written as (Burns *et al.*, 2004):

$$\mathbf{F}_{TD} = -\frac{3}{4} \frac{C_D \alpha_b \mu_{l,l}}{d_b \sigma_{TD}} |\mathbf{U}_b - \mathbf{U}_l| \left( \frac{1}{\alpha_l} + \frac{1}{\alpha_b} \right) \nabla \alpha_b, \quad (14)$$

where  $\sigma_{TD}$  is a constant equal to unity.

This short overview about the different interfacial forces is here reported for the sake of completeness. It is worth remarking here that, in this work, we focused on the population balance modeling (PBM). As far as the interfacial forces are concerned, we started including into the model gravity, buoyancy and drag, leaving the analysis of the effect of the different interfacial forces for future communications.

It is worth also remarking that in this investigation bubble nucleation and condensation are neglected, even though both are essential features of the boiling flows. In fact, the test cases simulated is a air-water system, where air bubbles are injected laterally to mimics the fluid dynamics of boiling flows. Bubble nucleation and condensation do not occur in this case and therefore they are neglected.

It is also useful to mention that the bubble diameter  $d_b$  appearing in Eq. (7) refers to the idealized monodisperse bubble distribution introduced with the two-fluid model. When a polydisperse bubble distribution is considered as in this case,  $d_b$  refers to the so-called mean Sauter diameter ( $d_{32}$ ) which is the ratio between the moment of order three and the moment of order two with respect to the bubble size. We will see in the following how to calculate this last term through the PBM.

## Population balance modeling

The PBM is based on the solution of the Population Balance Equation (PBE). For a thorough discussion on this equation, the reader may refer to the specialized literature (Ramkrishna, 2000; Marchisio and Fox, 2013). Among many methods to solve such complex integro-differential equation, the method here used is the Quadrature Method of Moments (QMOM) (Marchisio and Fox, 2013), which is based on the idea to approximate the bubble size distribution (BSD),  $n(L)$ , as a summation of Dirac delta functions :

$$n(L) \approx \sum_{\alpha=1}^N w_\alpha \delta(L - L_\alpha), \quad (15)$$

where  $w_\alpha$  and  $L_\alpha$  are the  $N$  weights and nodes of the quadrature approximation of order  $N$  and  $L$  is the bubble size. The nodes and weights can be calculated from the first  $2N$  moments of the BSD, with the generic order moment  $M_k$  being defined as:

$$M_k = \int_0^\infty n(L) L^k dL \approx \sum_{\alpha=1}^N w_\alpha L_\alpha^k, \quad (16)$$

where  $k \in 0, \dots, 2N - 1$  is the moment order. The way in which the weights and nodes of quadrature can be calculated from the moments is by means of the so-called moment inversion algorithms, such as for example the Product-Difference and Wheeler algorithms (Marchisio and Fox, 2013). The evolution of the generic order moment in space and time can be evaluated through the solution of the following transport equation:

$$\frac{\partial M_k}{\partial t} + \nabla \cdot (\mathbf{U}_b M_k) = \bar{S}_k, \quad (17)$$

which is derived from the PBE by applying the moment transform to such equation. In this way, the closure problem is solved, since the source term of Eq. (17) can be written as a function of the quadrature weights and nodes:

$$\begin{aligned} \bar{S}_k \approx & \frac{1}{2} \sum_{\alpha=1}^N \sum_{\beta=1}^N w_\alpha w_\beta a_{\alpha,\beta} \left[ \left( L_\alpha^3 + L_\beta^3 \right)^{k/3} - L_\alpha^k - L_\beta^k \right] \\ & + \sum_{\alpha=1}^N w_\alpha g_\alpha \left( \bar{b}_\alpha^k - L_\alpha^k \right), \end{aligned} \quad (18)$$

where  $a_{\alpha,\beta} = a(L_\alpha, L_\beta)$  is the coalescence kernel,  $g_\alpha = g(L_\alpha)$  is the breakage kernel and:

$$\bar{b}_\alpha^k = \int_0^\infty L^k \beta(L|L_\alpha) dL. \quad (19)$$

is the generic order moment of the daughter distribution function  $\beta(L|L_\alpha)$ . The value of the diameter  $d_b$  to be used in the expressions of the previous section can be calculated from the moments of the BSD. For instance the mean Sauter diameter is defined as follows:

$$d_b = d_{32} = \frac{M_3}{M_2}. \quad (20)$$

These models are essential for the proper solution of the PBM, since they represent the link between the mathematical method and the investigated physical phenomena. In this



work, we expressed the coalescence kernel in the following way:

$$a(L', L) = h(L', L)\lambda(L', L), \quad (21)$$

where  $h(L', L)$  is the collision frequency and  $\lambda(L', L)$  is the coalescence efficiency. The first term can be estimated by considering all the physical mechanisms that bring two bubbles close to each other and collide, while the second term relates the contact time during the collision and the time needed for the liquid film drainage between the colliding bubbles. The collision frequency is expressed as follows (Liao and Lucas, 2010; Liao *et al.*, 2015):

$$h(L', L) = h_{tf} + h_{shear} + h_{eddy} + h_{buoy} + h_{wake}, \quad (22)$$

where the first term accounts for the collisions induced by the turbulent fluctuations, the second for those by the macroscopic shear, the third for those due to bubbles trapped into large eddies, the fourth due to different terminal velocities given by the act of body forces (such as buoyancy) and the last term due to the small bubbles entrainment into the wake of large bubbles. It is important to remark that with Eq. (22) it is assumed that there are no interactions between these different mechanisms, in such a way that the frequencies can be summed up to give the overall coalescence frequency. This approximation is totally arbitrary from a physical point of view, although it is very complex to quantify the interactions between the different coalescence mechanisms.

For  $h_{tf}$  we used the well known model of Coulaloglou and Tavlarides (1977):

$$h(L', L)_{tf} = C_{tf} \frac{\pi}{4} (L' + L)^2 (L'^{2/3} + L^{2/3})^{1/2} \epsilon^{1/3}. \quad (23)$$

where  $C_{tf}$  is a model constant, equal to 0.88 from the theory but can be adjusted to fit different systems. For  $h_{shear}$  the model reported in the work of Liao *et al.* (2015) is used:

$$h(L', L)_{shear} = C_{shear} \frac{1}{8} (L' + L)^3 \dot{\gamma}_c, \quad (24)$$

where  $C_{shear}$  is parameter of the model and  $\dot{\gamma}_c$  is the shear strain rate of the continuous phase flow. A similar expression has also the term  $h_{eddy}$  (Liao *et al.*, 2015):

$$h(L', L)_{eddy} = C_{eddy} \frac{1}{8} (L' + L)^3 \dot{\gamma}_{eddy}, \quad (25)$$

where  $C_{eddy}$  is parameter of the model and the eddy shear strain rate  $\dot{\gamma}_{eddy}$  can be written as follows:

$$\dot{\gamma}_{eddy} = \sqrt{\frac{\rho_l \epsilon}{\mu_l}}. \quad (26)$$

The coalescence frequency due to body forces interactions,  $h(L', L)_{buoy}$ , can be estimated by considering the terminal velocities of the interacting bubbles as follows (Liao *et al.*, 2015):

$$h(L', L)_{buoy} = C_{buoy} \frac{\pi}{4} (L' + L)^2 |U_{T,L'} - U_{T,L}|, \quad (27)$$

where  $C_{buoy}$  is a constant parameter and  $U_{T,L}$  is the terminal velocity of the bubble with size  $L$  and can be assessed by means of well known correlations. The last term of Eq. (22) accounting for the bubble wake-entrainment is here calculated by using the model of Wang *et al.* (2005):

$$h(L', L)_{wake} = C_{wake} \frac{\pi}{4} [L'^2 U_{T,L'} C_{D,L'}^{1/3} \Theta_{L'} + L^2 U_{T,L} C_{D,L}^{1/3} \Theta_L], \quad (28)$$

where  $C_{wake}$  is a model constant,  $C_{D,L}$  is the drag coefficient for the bubble with size  $L$ , while  $\Theta_L$  is a function with the following expression (Wang *et al.*, 2005):

$$\Theta = \begin{cases} \frac{(L' - \frac{1}{2}L_{crit})^6}{(L' - \frac{1}{2}L_{crit})^6 + (\frac{1}{2}L_{crit})^6} & \text{se } L' \geq \frac{1}{2}L_{crit}; \\ 0 & \text{otherwise.} \end{cases} \quad (29)$$

The critical diameter  $L_{crit}$  can be assumed equal to 10 mm in air-water systems, or can be estimated through the following equation:

$$L_{crit} = 4.0 \sqrt{\frac{\sigma}{g(\rho_c - \rho_d)}}. \quad (30)$$

In this work, we restricted our analysis only on coalescence caused by turbulent fluctuations. Other coalescing mechanisms will be taken into account in future works.

The last missing portion of physics to estimate the coalescence kernel written in Eq. (21) is the coalescence efficiency  $\lambda(L', L)$ . With this simplified approach, a unique coalescence efficiency multiplies the overall coalescence frequency, although in principle each coalescence mechanism has its own efficiency. In the work of Liao *et al.* (2015), indeed the overall coalescence efficiency is calculated in such a way to consider all the coalescing mechanisms of Eq. (22), but it is assumed that the less efficient collision is the limiting efficiency, which might be a too strong approximation of the physical phenomena. For this reason, in this work we started by considering only the efficiency due to turbulent fluctuations  $\lambda_{tf}$ , and then all the other mechanisms will be progressively taken into account in the future. Different models were here considered, as the standard model of Coulaloglou and Tavlarides (1977), which is based on ratio between drainage and contact time:

$$h_{ft}(L', L) = \exp \left\{ -C_{tf} \frac{\mu_l \rho_l \epsilon}{\sigma^2} \left( \frac{L'L}{L'+L} \right)^4 \right\} \quad (31)$$

with the dimensioned parameter  $C_{tf}$  ( $m^{-2}$ ) being fitted with experimental data. In this work, the standard value of  $6 \cdot 10^9 m^{-2}$  is used. Another possible approach is the one given by Chesters (1991), which depends on bubbles Weber number, namely on the ratio between kinetic energy of the collision and the resisting surface energy to coalescence:

$$h_{ft}(L', L) = \exp \left\{ -C_{We} \sqrt{We_{i,j}} \right\} \quad (32)$$

where  $We_{i,j}$  is the Weber number defined as follows:

$$We_{i,j} = \frac{\rho_l \epsilon^{2/3}}{\sigma} \frac{L_i L_j}{L_i + L_j} (L_i^{2/3} + L_j^{2/3}). \quad (33)$$

Regarding the breakage kernel, the model of Laakkonen *et al.* (2007) based on the homogeneous isotropic turbulence theory and considering the size of the mother bubble compatible with the eddy length scale of the inertial subrange is here adopted:

$$g(L) = C_1 \epsilon^{1/3} \operatorname{erfc} \left( \sqrt{C_2 \frac{\sigma}{\rho_l \epsilon^{2/3} L^{5/3}} + C_3 \frac{\mu_l}{\sqrt{\rho_l \rho_b} \epsilon^{1/3} L^{4/3}}} \right) \quad (34)$$

where  $C_1 = 6.0$ ,  $C_2 = 0.04$  and  $C_3 = 0.01$  as in our previous works on gas-liquid systems (Buffo and Marchisio, 2014; Buffo *et al.*, 2016a). Although this is not the only breakage mechanism occurring in a real system, it is indeed the most

important and therefore the first to be considered here as a first approximation (Laakkonen *et al.*, 2006, 2007). Indeed, this aspect will be further investigated in future communications.

As far as the daughter distribution function is concerned, the following  $\beta$ -distribution function is used (Laakkonen *et al.*, 2006):

$$\beta(L, L') = 180 \left( \frac{L^2}{L'^3} \right) \left( \frac{L^3}{L'^3} \right)^2 \left( 1 - \frac{L^3}{L'^3} \right)^2 \quad (35)$$

where  $L$  is the size of the daughter bubble, created by the breakage of the mother bubble of size  $L'$ . This distribution is a bell-shaped distribution, where the symmetric breakage is the most probable event, due to the “activated” state in which the mother bubble is equilibrated by surface tension into two equally-sized fragments just before breaking. This choice was supported by comparison with experiments in previous works (Laakkonen *et al.*, 2006, 2007; Buffo *et al.*, 2016a). However other opposite approaches are debated in the literature, such as U-shaped and M-shaped distributions. The reader may refer to Liao and Lucas (2009) for further discussion.

## TEST CASE AND NUMERICAL DETAILS

As previously mentioned, the experimental setup here investigated for validation purposes is the TOPFLOW rig built at Helmholtz-Zentrum Dresden-Rossendorf (HZDR) (Schaf-frath *et al.*, 2001; Prasser *et al.*, 2005; Lucas *et al.*, 2010). This system consist of a vertical pipe of 195.3 mm diameter and 8000 mm tall, where liquid water raises from the bottom to the top of the column and air is injected laterally from holes placed at fixed distance along the circumference and at different heights of the column. The measurement apparatus is instead located at a fixed height of the vertical pipe, and it is composed by a mesh-wire sensor able to locally measure some of the most important property of the gas-liquid flow, such as the radial profiles of void fraction, gas velocity and bubble size distribution. Over the years a significant number of operating conditions were investigated by varying both liquid and gas flow rates, as exemplified in Table 1, where a small subset of the experiments carried out is reported.

**Table 1:** Some of the operating conditions investigated. Each number corresponds to a particular operating condition.

	Superf. gas vel. (m/s)					
	<b>0.0025</b>	<b>0.004</b>	<b>0.0062</b>	<b>0.0096</b>	<b>0.0235</b>	
Superf. liq. vel. (m/s)	<b>2.554</b>	010	021	032	043	065
	<b>1.611</b>	009	020	031	042	064
	<b>1.017</b>	008	019	030	041	063
	<b>0.405</b>	006	017	028	039	061
	<b>0.102</b>	003	014	025	036	058

Our own implementation of QMOM into the OpenFOAM (version 2.2.x) solver `compressibleTwoPhaseEulerFoam` was used to perform the three-dimensional transient numerical simulations. This implementation includes the transport equation for the moments of the BSD, and the Wheeler inversion algorithm to calculate the quadrature approximation from the transported moments (Buffo *et al.*, 2016b) and the calculation of the different submodels for the interfacial forces and the coalescence and breakage rates. In this work, only the first six moments of the BSD were calculated ( $M_0, M_1, M_2,$

$M_3, M_4, M_5$ ), corresponding to a quadrature approximation with three nodes:  $N = 3$ . Particular attention was paid to the problem of moment boundedness and realizability by means of a proper implementation of the moment transport equations (Buffo *et al.*, 2016b). As far as the inlet boundary conditions for the BSD is concerned, we adopted the same condition as our previous works (Buffo *et al.*, 2013, 2016a,b, 2017): a lognormal bubble size distribution with a standard deviation equal to 15% of the mean value, as suggested by Laakkonen *et al.* (2006) for holed sparger, and a mean value estimated through correlations or experimental evidences.

Different modeling aspects were taken into account in this work. First, a sensitivity analysis has been performed on the value of the inlet mean bubble diameter in order to assess the influence of this parameter on the predictions obtained with the PBM. The obtained results were also compared to the ones given by using the relationship of Changjun *et al.* (2013) to estimate the mean inlet bubble diameter, which takes into account the effect of the hole orientation in the physical space on the inlet mean bubble size. This procedure of Changjun *et al.* (2013) is based on the solution of ordinary differential equations for the position of the center of mass of the formed bubble and it is based on the balance of forces acting on the bubble before detaching from the sparger, namely buoyancy, gravity, drag, lift and virtual mass. Further details on its implementation can be found in the original work (Changjun *et al.*, 2013). Among all the operating conditions available, we picked the 008 and 042 points from Table 1, with the first operating condition corresponding to a gas superficial velocity of  $0.0025 \text{ m s}^{-1}$  and a liquid superficial velocity of  $1.017 \text{ m s}^{-1}$  and the second  $0.096 \text{ m s}^{-1}$  and  $1.611 \text{ m s}^{-1}$  respectively. It is worth mentioning that in all the performed simulations only the gravity, buoyancy and drag forces were considered as a first approximation. An in-depth analysis on the importance of different interfacial forces, especially to simulate operating conditions with higher gas superficial velocities is left to future communications.

## RESULTS

Let us start the discussion of the results with the sensitivity analysis on the inlet bubble size. This aspect is particularly important when a CFD-PBM approach is used, since different boundary conditions may lead to different solutions and there is always a certain degree of uncertainties about the estimations of the inlet bubble size through experiments or correlations. Fig. 1 shows the comparison between experimental data and numerical predictions for the axial profiles of the surface-averaged mean Sauter diameter for different values of the mean inlet bubble diameter. As it is possible to observe from the figure, all the simulations with the different inlet bubble diameter values shows a different initial part of the axial profile (i.e., close to the bubble injection section), while all reach approximately the same asymptotic value at the highest section of the vertical profile. This result is of great importance, since it proves that the steady-state reached by the system is not sensitive to this modeling parameter. Moreover, the profile obtained with the inlet value calculated with the correlation of Changjun *et al.* (2013) (i.e., 4.15 mm) is very close to the experimental points close to inlet section, while differs far from the inlet.

This mismatch can be caused by the approximations performed in the evaluation of the coalescence rates: at the moment in the model only the turbulent fluctuations are considered and most likely in the higher sections of the vertical pipe other mechanisms may become important, such as the body

forces (buoyancy) or macroscopic shear rate mechanisms. It is also interesting have a look at the radial profiles of volume fraction and axial gas velocity at different heights of the column. Figs. 2 and 3 report these two properties of the gas-liquid systems for the operating condition 008 (gas superficial velocity of  $0.0025 \text{ m s}^{-1}$  and liquid superficial velocity of  $1.017 \text{ m s}^{-1}$ ), while Figs. 4 and 5 for the operating condition 042 (gas superficial velocity of  $0.096 \text{ m s}^{-1}$  and liquid superficial velocity of  $1.611 \text{ m s}^{-1}$ ).

At it can be seen from the figures, the agreement with the experimental data is decent for both the analyzed properties and for both the operating conditions.

The largest deviation from the experimental data is observed for the closest and farthest sections from the inlet for both operating conditions for the local volume fraction profiles. It is worth reminding here that model at the moment does not consider any other additional interfacial forces apart from gravity, buoyancy and drag, as a first approximation. Therefore, the deviation observable is most likely due to this aspect: in fact, it is clear that close to the gas inlet the bubbles are

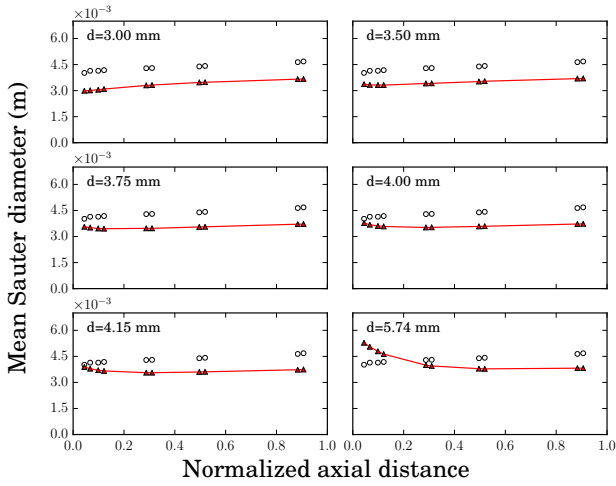


**Figure 1:** Axial profiles of the surface-averaged mean Sauter diameter for different values of the mean inlet bubble diameter. Operating condition 008. White circles: experimental data. Red triangles: simulation results

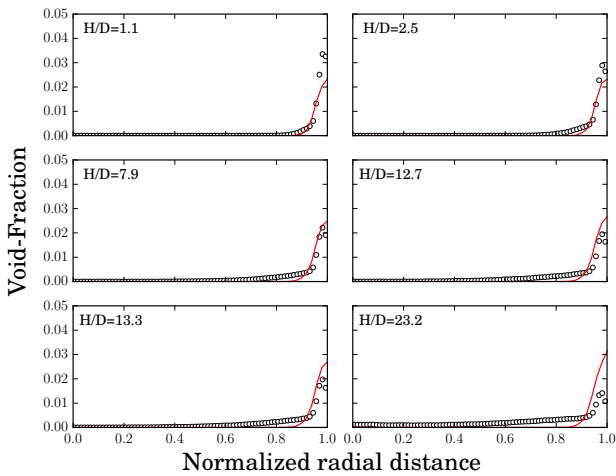


**Figure 2:** Void fraction radial profiles at different heights of the vertical pipe. Operating condition 008. White circles: experimental data. Red line: numerical results.

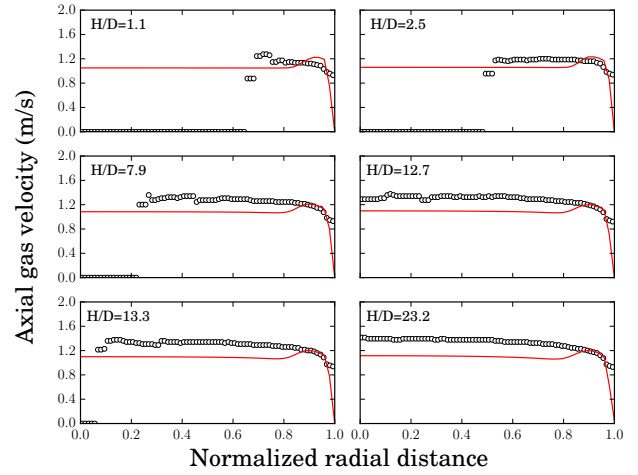


**Figure 3:** Axial velocity radial profiles at different heights of the vertical pipe. Operating condition 008. White circles: experimental data. Red line: numerical results.

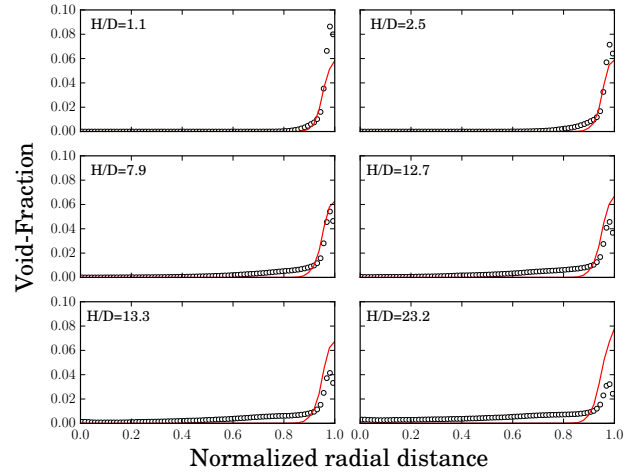


**Figure 4:** Void fraction radial profiles at different heights of the vertical pipe. Operating condition 042. White circles: experimental data. Red line: numerical results.

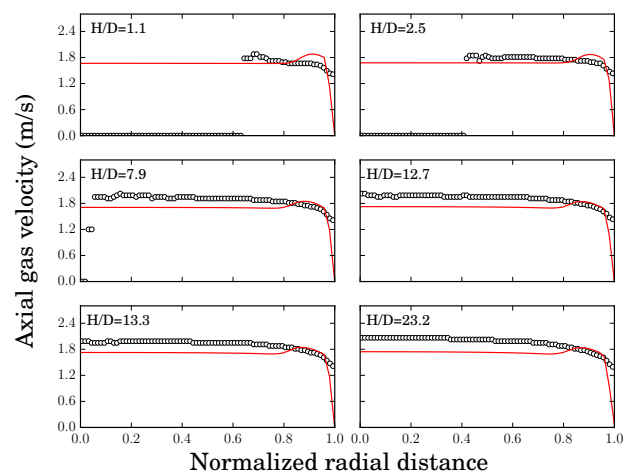


**Figure 5:** Axial velocity radial profiles at different heights of the vertical pipe. Operating condition 042. White circles: experimental data. Red line: numerical results.

small and the lift force tends to push them towards the wall, while for the highest values of the vertical pipe (where the bubbles are bigger due to coalescence) the turbulence dispersion force becomes important and moves the bubbles from the walls to the core of the vertical pipe.

From the comparison between the experimental data and the numerical predictions in terms of the axial gas velocity profiles reported in Figs. 3 and 5 it is instead possible to note that the agreement is good in the region close to the wall, where most of the bubbles can be found. When the normalized radial distance is lower than 0.9, the values of axial gas velocity do not have any physical meaning, since only few bubbles can be experimentally detected.

## CONCLUSION

In this work, a CFD-PBM methodology was applied to the simulation of an air-water system that mimics the conditions of a boiling flow, notably the TOPFLOW experiments. Simulations were performed with the open-source CFD code OpenFOAM (version 2.2.x) by using a modified version of the solver `compressibleTwoPhaseEulerFoam` which contains our own implementation of QMOM.

A sensitivity analysis on the boundary conditions for the PBM shows that the steady-state solution is not influenced by the inlet bubble diameter; moreover, the value of such parameter given by the model of Changjun *et al.* (2013) is able to reproduce well the behavior of the BSD in the regions close to the inlet sections. The comparison between experiments and predictions in terms of the void fraction and axial gas velocity profiles for two operating conditions available shows a good agreement, however an in-depth analysis on the effect of the different interfacial forces and the different coalescence mechanisms is need for the development of a general modeling tool that can be used for a larger number of operating conditions experimentally investigated.

## ACKNOWLEDGEMENTS

The authors wish to thank Prof. Dirk Lucas at Helmholtz-Zentrum Dresden-Rossendorf (HZDR). Access to the TOPFLOW data was kindly provided by HZDR in the framework of the HZDR-MIT collaboration. Moreover, the authors gratefully thank Salvatore Falzone, Mohsen Shia and Umberto Viscomi for their valuable contributions to this work. The financial support of the MITOR Project (Compagnia di San Paolo) is gratefully acknowledged.

## REFERENCES

BUFFO, A., VANNI, M., RENZE, P. and MARCHISIO, D. (2016a). "Empirical drag closure for polydisperse gas-liquid systems in bubbly flow regime: Bubble swarm and micro-scale turbulence". *Chemical Engineering Research and Design*, **113**, 284–303.

BUFFO, A., VANNI, M. and MARCHISIO, D. (2016b). "On the implementation of moment transport equations in OpenFOAM: Boundedness and realizability". *International Journal of Multiphase Flow*, **85**, 223–235.

BUFFO, A., VANNI, M. and MARCHISIO, D. (2017). "Simulation of a reacting gas-liquid bubbly flow with CFD and PBM: Validation with experiments". *Applied Mathematical Modelling*, **44**, 43–60.

BUFFO, A. and MARCHISIO, D.L. (2014). "Modeling and simulation of turbulent polydisperse gas-liquid systems via the generalized population balance equation". *Reviews in Chemical Engineering*, **30**(1), 73–126.

BUFFO, A., MARCHISIO, D.L., VANNI, M. and RENZE, P. (2013). "Simulation of polydisperse multiphase systems using population balances and example application to bubbly flows". *Chemical engineering research and design*, **91**(10), 1859–1875.

BURNS, A.D., FRANK, T., HAMILL, I. and SHI, J.M. (2004). "The Favre averaged drag model for turbulent dispersion in eulerian multi-phase flows". *5th international conference on multiphase flow, ICMF*, vol. 4, 1–17.

CHANGJUN, L., LIANG, B., SHENGWEI, T. and ENZE, M. (2013). "Effects of orifice orientation and gas-liquid flow pattern on initial bubble size". *Chinese Journal of Chemical Engineering*, **21**(11), 1206–1215.

CHESTERS, A.K. (1991). "The modelling of coalescence processes in fluid-liquid dispersions: a review of current understanding". *Chemical engineering research and design*, **69**(A4), 259–270.

COULALOGLOU, C.A. and TAVLARIDES, L.L. (1977). "Description of interaction processes in agitated liquid-liquid dispersions". *Chemical Engineering Science*, **32**, 1289–1297.

KATAOKA, I. and SERIZAWA, A. (1989). "Basic equations of turbulence in gas-liquid two-phase flow". *International Journal of Multiphase Flow*, **15**, 843–855.

LAAKKONEN, M., ALOPAEUS, V. and AITTAMAA, J. (2006). "Validation of bubble breakage, coalescence and mass transfer models for gas-liquid dispersion in agitated vessel". *Chemical Engineering Science*, **61**, 218–228.

LAAKKONEN, M., MOILANEN, P., ALOPAEUS, V. and AITTAMAA, J. (2007). "Modelling local bubble size distributions in agitated vessels". *Chemical Engineering Science*, **62**, 721–740.

LIAO, Y. and LUCAS, D. (2009). "A literature review of theoretical models for drop and bubble breakup in turbulent dispersions". *Chemical Engineering Science*, **64**, 3389–3406.

LIAO, Y. and LUCAS, D. (2010). "A literature review on mechanisms and models for the coalescence process of fluid particles". *Chemical Engineering Science*, **65**, 2851–2864.

LIAO, Y., RZEHA, R., LUCAS, D. and KREPPER, E. (2015). "Baseline closure model for dispersed bubbly flow: Bubble coalescence and breakup". *Chemical Engineering Science*, **122**, 336–349.

LUCAS, D. and TOMIYAMA, A. (2011). "On the role of the lateral lift force in poly-dispersed bubbly flows". *International Journal of Multiphase Flow*, **37**(9), 1178–1190.

LUCAS, D., KREPPER, E. and PRASSER, H.M. (2007). "Use of models for lift, wall and turbulent dispersion forces acting on bubbles for poly-disperse flows". *Chemical Engineering Science*, **62**, 4146–4157.

LUCAS, D., BEYER, M., SZALINSKI, P. and SCHUTZ, P. (2010). "A new database on the evolution of air-water flows along a large vertical pipe". *International journal of Thermal Sciences*, **49**, 664–674.

MARCHISIO, D.L. and FOX, R.O. (2013). *Computational Models for Polydisperse Particulate and Multiphase Systems*. Cambridge University Press, Cambridge, UK.

PRASSER, H.M., BEYER, M., BOTTGER, A., CARL, H., LUCAS, D., SCHAFFRATH, A., SCHUTZ, P., WEISS, F.P. and ZSCHAU, J. (2005). "Influence of the pipe diameter on the structure of the gas-liquid interface in a vertical two-phase pipe flow". *Nuclear Technology*, **152**, 3–22.

RAMKRISHNA, D. (2000). *Population balances: Theory and applications to particulate systems in engineering*. Academic press, San Diego, USA.

SCHAFFRATH, A., KRUSSENBERG, A., WEISS, F.P., HICKEN, E.F., BEYER, M., CARL, H., PRASSER, H., SCHUSTER, J., SCHUTZ, P., TAMME, M. *et al.* (2001). “Topflow-a new multipurpose thermalhydraulic test facility for the investigation of steady state and transient two phase flow phenomena”. *Kerntechnik-Bilingual Edition*-, **66(4)**, 209–213.

SHAVER, D. and PODOWSKI, M. (2015). “Modeling and validation of forced convection subcooled boiling”. *Proc. 16th Int. Topical Meeting on Nuclear Reactor Thermalhydraulics (NURETH-16)*, Chicago, IL.

SUGRUE, R., MAGOLAN, B., LUBCHENKO, N. and BAGLIETTO, E. (2017). “Assessment of a simplified set of momentum closure relations for low volume fraction regimes in star-ccm+ and openfoam”. *submitted to Annals of Nuclear Energy*.

TOMIYAMA, A., KATAOKA, I., ZUN, I. and SAKAGUCHI, T. (1998). “Drag coefficients of single bubbles under normal and micro gravity conditions”. *JSME International Journal, Series B: Fluids and Thermal Engineering*, **41**, 472–479.

WANG, T., WANG, J. and JIN, Y. (2005). “Theoretical prediction of flow regime transition in bubble columns by the population balance model”. *Chemical Engineering Science*, **60(22)**, 6199–6209.

## NUMERICAL SIMULATIONS OF TURBULENT LIQUID-LIQUID DISPERSIONS WITH QUADRATURE-BASED MOMENT METHODS

Antonio BUFFO<sup>1\*</sup>, Dongyue LI<sup>2</sup>, Wioletta PODGÓRSKA<sup>3</sup>, Marco VANNI<sup>1</sup>, Daniele L. MARCHISIO<sup>1</sup>

<sup>1</sup>Department of Applied Science and Technology, Politecnico di Torino, ITALY

<sup>2</sup>Department of Energy Process Engineering and Chemical Engineering, TU Bergakademie Freiberg, Freiberg, GERMANY

<sup>3</sup>Faculty of Chemical and Process Engineering, Warsaw University of Technology, Warsaw, POLAND

\* E-mail: antonio.buffo@polito.it

### ABSTRACT

The accurate description of droplet dynamics in turbulent liquid-liquid dispersions is of great importance in many industrial applications, especially when the economy of the process is determined by the involved mass transfer and chemical reaction rates. In this respect, the proper estimation of the spatial and time evolution of the droplet polydispersity can offer a useful tool to the modeler to design and scale-up relevant processes. In the latest years, computational fluid dynamics (CFD) and population balance modeling (PBM) have been coupled into a single computational tool, paving the way to full-predictive macro-scale models that incorporate sub-models for describing the rate of the relevant phenomena occurring at droplet-scale, such as coalescence, breakage, momentum and mass exchange with the continuous phase. In this work our recent advances on this topic are presented, with a particular attention to two distinct elements: 1) the choice of appropriate coalescence and breakage closures, pointing out the need to account for high-order turbulent phenomena, such as turbulent intermittency through the use of the so-called multifractal formalism; 2) the possibility to carry out simplified spatially homogeneous simulations when there is a clear separation of scales between coalescence/breakage and mixing. CFD simulations were carried out with our own implementation of the Quadrature Method of Moments (QMOM), combined with the two-fluid model, present in a solver of the open-source code OpenFOAM.

**Keywords:** Population Balance Methods, droplet dynamics, Multiphase heat and mass transfer, stirred tanks .

### INTRODUCTION

Turbulent polydisperse liquid-liquid systems, where droplets are immersed in a continuous liquid phase, are very common in several industrial applications, such as: cosmetic, pharmaceutical, oil and gas, polymer and food industries. Such dispersions are often generated in stirred tanks, where the power input is given to enhance mass, momentum and energy transfer rates between the phases in the desired processes (e.g., polymerization, extraction, separation and emulsification). The most important properties of the system to characterize is the droplet size distribution (DSD), as the dispersion stability, rheological properties and mass transfer rate strongly depend on it. The disperse droplets undergo coalescence and breakage causing changes in the DSD, which are known to depend on the geometry of the tank, the operating conditions

and locally within the tank (Alopaeus *et al.*, 2009). In fact, droplets break-up mostly occurs in the region close to the impeller, shifting the DSD towards smaller diameters, while coalescence likely takes place in the stagnant zones far from the impeller, skewing the DSD towards larger diameters.

In this context, the use of a computational tool capable of predicting the complex interaction between the phases can help the design and scale-up of liquid-liquid stirred tanks. The evolution of the DSD in space and time is often related with the flow field, and computational fluid dynamics (CFD) is nowadays commonly used to obtain such information. Moreover, CFD is often coupled with population balance models (PBM) to predict the evolution of the DSD and other properties of the dispersion. In the latter works, CFD-PBM models are used to simultaneously consider the flow inhomogeneities and the DSD evolution. However, there are still two main challenges related to this approach that still need to be addressed: the improvement of the computational efficiency of these calculations, through problem simplification, and the accuracy of the sub-models accounting for breakage and coalescence.

Regarding the first aspect, simplified approaches where the PBM is decoupled from the fluid dynamics description are often used, by prescribing for an entire vessel single volume-averaged values of the relevant properties, used to model the phenomena involved (e.g., coalescence, breakage and mass transfer). These “lumped” models usually stem on the volume-average turbulent dissipation rate, calculated from the stirring power input per unit mass, or estimated through correlations (Attarakih *et al.*, 2008, 2015; Bhole *et al.*, 2008). Although the solution methods in these cases is very fast from the computational point of view, these simplified approaches can be used only under certain conditions. In fact, simulation results obtained with detailed models, accounting for the detailed hydrodynamics under turbulent conditions, may significantly differ from the ones obtained with simplified models, where fluid dynamics homogeneity (and thus homogeneous distribution of all the properties of interest) is imposed (Marchisio *et al.*, 2003, 2006; Vanni and Sommerfeld, 1996).

As far as the second aspect is concerned, the modelling of droplet coalescence and breakage is the subject of many studies. One of the pioneering works on this topic, and still nowadays very popular for its simplicity, is the application of the Kolmogorov turbulence theory by Coualoglou and Tavlarides (1977). They used the statistical theory of tur-

bulence to derive the coalescence and breakage kernels; the same methodology was also applied by many others (Luo and Svendsen, 1996; Alopaeus *et al.*, 2002; Laakkonen *et al.*, 2007) to derive new and improved kernels. In this context, the developed kernels were also tested using multi-block (compartment) models, not only for liquid-liquid dispersions but also for gas-liquid (bubbly) systems. However, some important factors influencing the droplet coalescence and breakage rates, such as the disperse phase viscosity and turbulence intermittency, are neglected in the CT kernels. Based on the multifractal theory of turbulence, Baldyga and Podgórska (1998) and Podgórska and Baldyga (2001) derived new breakage and coalescence kernels, the so-called “multifractal” (MF) kernels, which include the effect of both disperse phase viscosity and turbulence intermittency.

In this work, we investigated both aspects. First, we formulated a consistent framework to derive and solve the governing equations for zero-dimensional (0D) “lumped” models (where the volume-averaged turbulent dissipation rate is used), 0D “homogeneous” models (where the volume-distribution of the turbulent dissipation rate is considered instead) and three-dimensional (3D) spatially inhomogeneous models (where CFD-PBM model is used). The comparison between these three different approaches is here performed through the investigation of the very same system, in order to point out the conditions (if any) where the 3D inhomogeneous model does not give any additional insight in the characterization of the system, offering the modeler the possibility to use simple 0D models and save computational time and resources. Then, we focused on the CFD-PBM model, by implementing and validating the MF coalescence and breakage kernels through comparison with experimental data. Our implementation of QMOM was employed to solve a PBM in the CFD code OpenFOAM-2.2.x to simulate turbulent liquid-liquid dispersions. The kernels developed by Coualaloglou and Tavlarides (1977) and by Baldyga and Podgórska (1998) and Podgórska and Baldyga (2001) were both employed and compared with the experimental data available.

## MODEL DESCRIPTION

### Three dimensional (3D) CFD-PBM model

The two-fluid model (TFM) is the CFD framework where PBM is implemented. In this model, both continuous and disperse phases are described by means of the definition of their volume fraction and other average field variables (such as momenta and enthalpies). The governing equations are here not reported for the sake of brevity, however the reader may refer to our previous works for a detailed discussion (Buffo and Marchisio, 2014; Buffo *et al.*, 2016a).

An important element of the CFD-PBM is the modeling of the momentum exchange between the phases, as this term takes into account the coupling between the DSD evolution and the fluid dynamics behavior of the system. In the present work, the only forces considered are gravity, buoyancy and drag. This simplification is possible for turbulent liquid-liquid stirred tanks, since the flow field is mainly determined by the motion of the stirrer. The drag force per unit volume can be estimated by means of the following equation:

$$\mathbf{F}_{\text{drag}} = \alpha_d \alpha_c \left( \frac{3}{4} C_D \frac{\rho_d}{d_{32}} |\mathbf{U}_r| \right) \mathbf{U}_r, \quad (1)$$

where  $\mathbf{U}_r = \mathbf{U}_c - \mathbf{U}_d$ ,  $\mathbf{U}_c$  and  $\mathbf{U}_d$  are respectively the average velocity of the continuous and disperse phases,  $d_{32}$  is the mean Sauter diameter of the droplets calculated through the

PBM,  $\alpha_d$  is the volume fraction of the disperse phase and  $\alpha_c$  is that of the continuous phase and  $C_D$  is the drag coefficient, calculated here through the Schiller and Naumann (1935) correlation.

The turbulence is here described through a RANS model, namely a multiphase extension of the  $k - \epsilon$  model is adopted: only two equations written in terms of the turbulent kinetic energy  $k$  and turbulent dissipation rate  $\epsilon$  of the continuous phase are solved. Although a certain turbulent anisotropy can be observed in stirred tank reactors operating at high Reynolds numbers, the RANS model based on homogeneous isotropic turbulence theory, represents the only feasible option for the simulation of large scale liquid-liquid systems, since it is a good compromise between computational costs and accuracy.

The CFD-PBM involves also the solution of the so-called Population Balance Equation (PBE). As previously mentioned, the method used to solve the equation is the Quadrature Method of Moments (QMOM). The general idea behind QMOM is to approximate the unknown DSD,  $n(\xi)$ , by a summation of Dirac delta functions (Marchisio and Fox, 2013):

$$n(\xi) \approx \sum_{\alpha=1}^N w_{\alpha} \delta(\xi - \xi_{\alpha}), \quad (2)$$

where  $w_{\alpha}$  and  $\xi_{\alpha}$  are the  $N$  weights and nodes of the quadrature approximation of order  $N$  and of course  $\xi$  is the droplet size. As well known the  $N$  nodes and weights are calculated in QMOM from the first  $2N$  moments of the DSD:

$$M_k = \int_0^{\infty} n(\xi) \xi^k d\xi \approx \sum_{\alpha=1}^N w_{\alpha} \xi_{\alpha}^k, \quad (3)$$

with  $k \in 0, \dots, 2N - 1$ , by using the so-called moment inversion algorithms, such as for example the Product-Difference and Wheeler algorithms (Marchisio and Fox, 2013). The moments of the DSD are, in turn, calculated by solving the following transport equations:

$$\frac{\partial M_k}{\partial t} + \nabla \cdot (\mathbf{U}_d M_k) = \bar{S}_k, \quad (4)$$

again with  $k \in 0, \dots, 2N - 1$ , derived by applying the moment transform to the PBE. By using the quadrature approximation, the source term of Eq. (4) can be written as:

$$\begin{aligned} \bar{S}_k \approx \frac{1}{2} \sum_{\alpha=1}^N \sum_{\beta=1}^N w_{\alpha} w_{\beta} a_{\alpha, \beta} \left[ \left( \xi_{\alpha}^3 + \xi_{\beta}^3 \right)^{k/3} - \xi_{\alpha}^k - \xi_{\beta}^k \right] \\ + \sum_{\alpha=1}^N w_{\alpha} g_{\alpha} \left( \bar{b}_{\alpha}^k - \xi_{\alpha}^k \right), \quad (5) \end{aligned}$$

where  $a_{\alpha, \beta} = a(\xi_{\alpha}, \xi_{\beta})$  is the coalescence kernel,  $g_{\alpha} = g(\xi_{\alpha})$  is the breakage kernel and:

$$\bar{b}_{\alpha}^k = \int_0^{\infty} \xi^k \beta(\xi | \xi_{\alpha}) d\xi. \quad (6)$$

is the generic order moment of the daughter distribution function  $\beta(\xi | \xi_{\alpha})$ . For further details on the corresponding mathematical theory, the reader is referred to the work of Marchisio and Fox (2013).

### Zero dimensional (0D) models

As previously mentioned, the DSD and all the other relevant properties in a stirred tank depend of the spatial coordinates and time. However, under certain limited operating conditions, the system can be considered as homogeneous and the evolution of the system can be described in terms of a volume-averaged DSD:

$$\bar{n}(t; \xi) = \frac{1}{V} \int_V n(t, \mathbf{x}; \xi) d\mathbf{x}, \quad (7)$$

where the volume averaging procedure is performed over the entire vessel with volume  $V$ . The volume-averaged PBE can be derived by applying the same averaging procedure and the mathematical details are here omitted for the sake of brevity (for a thorough discussion the reader may refer to Buffo *et al.*, 2016b). Here it is important to point out that the source term of the PBE depends not only on the DSD, but also on the turbulent dissipation rate, which presents a strong spatial inhomogeneity in stirred vessel. Therefore we can leave out the spatial dependency of the turbulent dissipation rate,  $\varepsilon = \varepsilon(\mathbf{x})$ , resulting in the following expression for the volume-averaged source term of the PBE:

$$\frac{\partial \bar{n}(t, \xi)}{\partial t} = \frac{1}{V} \int_V S(t, \mathbf{x}, \xi) d\mathbf{x} = \int_0^{+\infty} S(t, \varepsilon, \xi) f(\varepsilon) d\varepsilon = \bar{S}(t, \xi), \quad (8)$$

where  $f(\varepsilon)$  is the turbulent dissipation rate distribution in the stirred tank so that:  $f(\varepsilon)d\varepsilon$ , represents the volume fraction of fluid in the tank which experiences a turbulent dissipation rate between  $\varepsilon$  and  $\varepsilon + d\varepsilon$ . Then, by definition:

$$\int_0^{+\infty} f(\varepsilon) d\varepsilon = 1, \quad \int_0^{+\infty} f(\varepsilon) \varepsilon d\varepsilon = \bar{\varepsilon}, \quad (9)$$

where  $\bar{\varepsilon}$  is the volume-average turbulent dissipation rate in the tank. In fact, even if very intense mixing smooths out all the gradients of the DSD, allowing for the approximation of the DSD with its corresponding volume-averaged  $\bar{n}(t, \xi)$ , the source term may still depend on the spatial coordinate because of the turbulent dissipation rate,  $\varepsilon = \varepsilon(\mathbf{x})$ , through the term representing the turbulent dissipation rate distribution in the stirred tank  $f(\varepsilon)$ . This modeling approach is referred as 0D ‘‘homogeneous’’ model and it can be used to replace the 3D CFD-PBM model when the DSD is spatially uniform.

Due to the non-linear dependency on the turbulent dissipation rate of the coalescence and breakage kernels, as we will see in the following paragraph, the 0D ‘‘homogeneous’’ model differs from the 0D ‘‘lumped’’ model, where the kernels are simply evaluated with the volume-averaged value of the turbulent dissipation rate,  $\bar{\varepsilon}$ . In this latter case, the averaging procedure leads to the following volume-averaged PBE:

$$\frac{\partial \bar{n}(t, \xi)}{\partial t} = \frac{1}{V} \int_V S(t, \mathbf{x}, \xi) d\mathbf{x} = \bar{S}(t, \bar{\varepsilon}, \xi). \quad (10)$$

For a detailed derivation of the governing equations, the reader may refer to Buffo *et al.* (2016b) for further details.

### Coalescence and breakage kernels

Two different sets of kernels are used in this study to describe droplet breakage and coalescence: the Coualaloglou and Tavlarides (1977) (CT) kernels and the Baldyga and Podgórska (1998); Podgórska and Baldyga (2001) or multifractal (MF) kernels.

### CT kernels

Coualaloglou and Tavlarides (1977) proposed a breakage frequency model that takes into account the oscillations of the droplet surface caused by turbulent eddies. The breakage kernel reads as follows:

$$g_{CT}(\xi) = G_1 \frac{\varepsilon^{1/3}}{\xi^{2/3}} \exp\left(-G_2 \frac{\sigma}{\rho_c \varepsilon^{2/3} \xi^{5/3}}\right), \quad (11)$$

where  $\varepsilon$  is the turbulent energy dissipation rate,  $\xi$  is the droplet diameter,  $\rho_c$  is the density of the continuous phase and  $\sigma$  is the interfacial tension.  $G_1$  and  $G_2$  are dimensionless constants, typically derived by fitting with experiments and of limited validity. In this work,  $G_1 = 0.00481$  and  $G_2 = 0.08$ , as suggested in the literature (Liao and Lucas, 2009) and as done in our previous work (Gao *et al.*, 2016). Coalescence is instead determined by turbulent-induced collisions, that can be quantified through the homogeneous turbulence theory. Then a coalescence efficiency should be considered as not all the collisions will result in coalescence: this term is usually calculated as the exponential of the ratio of two characteristic time scales (i.e. film drainage and interaction time scales), resulting in the following coalescence kernel:

$$a_{CT}(\xi, \xi') = D_1 \varepsilon^{1/3} (\xi + \xi')^2 \left(\xi^{2/3} + \xi'^{2/3}\right)^{1/2} \exp\left(-D_2 \frac{\mu_c \rho_c \varepsilon}{\sigma^2} \left(\frac{\xi \xi'}{\xi + \xi'}\right)^4\right), \quad (12)$$

where  $\xi$  and  $\xi'$  are the diameters of the colliding droplets and  $\mu_c$  is the viscosity of the continuous phase.  $D_1$  is a dimensionless constant of order of magnitude of unity (Liao and Lucas, 2009) and generally taken equal to 0.88.  $D_2$  is another constant and generally fitted with experimental data. In this work, the value of  $9 \times 10^{15} \text{ m}^{-2}$  was used.

### MF kernels

As pointed out by Baldyga and Podgórska (1998), turbulence intermittency, namely the generation of transient and short-lived velocity gradients that result in an intermittent time evolution of the turbulent quantities, may have a great influence on the breakage rate and a non-negligible one on coalescence. Intermittency is usually described through the so-called multi-fractal theory of turbulence, resulting in the following breakage kernel:

$$g_{MF}(\xi) = C_g \sqrt{\ln\left(\frac{L}{\xi}\right)} \frac{\varepsilon^{1/3}}{\xi^{2/3}} \int_{\alpha_{\min}}^{\alpha_x} \left(\frac{\xi}{L}\right)^{\frac{\alpha+2-3f(\alpha)}{3}} d\alpha, \quad (13)$$

where  $C_g = 0.0035$  is derived from the theory. The integral turbulent length scale is calculated as follows:  $L = \frac{(2k/3)^{3/2}}{\varepsilon}$ ,  $\alpha_{\min} = 0.12$ , whereas the upper bound of multi-fractal exponent  $\alpha$  for vigorous eddies,  $\alpha_x$ , is given by the following expression:

$$\alpha_x = \frac{2.5 \ln\left(\frac{L \varepsilon^{0.4} \rho_c^{0.6}}{C_x \sigma^{0.6}}\right)}{\ln(L/\xi)} - 1.5, \quad (14)$$

where  $C_x = 0.23$ . Equation (14) is valid only for low viscosity of the disperse phase. The expression for  $\alpha_x$  that takes into account viscous effects can be found in Baldyga and Podgórska (1998).



The multi-fractal spectrum has a universal form derived from the experimental data of Meneveau and Sreenivasan (1991):

$$f(\alpha) = a + b\alpha + c\alpha^2 + d\alpha^3 + e\alpha^4 + f\alpha^5 + g\alpha^6 + h\alpha^7 + i\alpha^8, \quad (15)$$

with  $a = -3.51, b = 18.721, c = -55.918, d = 120.9, e = -162.54, f = 131.51, g = -62.572, h = 16.1, i = -1.7264$  for  $\alpha \geq 0.12$ .

Also the MF coalescence kernel is expressed as a product of the coalescence frequency and the coalescence efficiency, this latter expressed as an exponential of drainage time to interaction time ratio resulting in the following relationship (Podgórska and Baldyga, 2001):

$$a_{MF}(\xi, \xi') = \sqrt{\frac{8\pi}{3}} \varepsilon^{1/3} \left( \frac{\xi + \xi'}{2} \right)^{7/3} \left( \frac{\xi + \xi'}{2L} \right)^{0.027} \times \exp\left(-A_1 \frac{t_d}{t_i}\right), \quad (16)$$

where  $\xi$  and  $\xi'$  are the diameters of the colliding droplets and  $A_1$  is a dimensionless coefficient of the order of magnitude unity. In this model, the droplet interfaces are assumed partially mobile, in such a way that the film drainage is controlled by the motion of film surface, in turn controlled by shear stresses exerted on the film by fluid in the drop. Therefore, the drainage time is given as:

$$t_d = \frac{\mu_d \tilde{a} R_{eq}^{3/2}}{4\sigma R_L^{1/2}} \left( \frac{1}{h_c} \left( \frac{\xi^*}{L} \right)^{0.016} - \frac{1}{h_0} \left( \frac{\xi^*}{L} \right)^{-0.01} \right), \quad (17)$$

whereas the interaction time as:

$$t_i = \frac{1}{2} \left( \frac{8(\rho_d/\rho_c + \gamma)\rho_c R_S^3}{3\sigma(1 + \zeta^3)} \right)^{1/2}. \quad (18)$$

In these two latter equations,  $\gamma$  is the coefficient of virtual mass and  $L$  is the integral turbulent length scale.  $\xi^* = \frac{\xi + \xi'}{2}$ ,  $\zeta = \frac{R_S}{R_L}$ ,  $R_L = \max(\xi, \xi')/2$  and  $R_S = \min(\xi, \xi')/2$ ,  $R_{eq}$  is the equivalent radius expressed as:  $R_{eq} = \frac{\xi\xi'}{\xi + \xi'}$ ,  $\mu_d$  is the viscosity of the dispersed phase,  $\tilde{a}$  is the film radius derived under the assumption that the whole kinetic energy is transformed into excess surface energy (Podgórska, 2005):

$$\tilde{a} = \left( \frac{8(\rho_d/\rho_c + \gamma)\rho_c \varepsilon^{2/3} \xi^{*2/3} R_S}{3\sigma(1 + \zeta^3)} \right)^{1/4} (R_S R_L)^{1/2}. \quad (19)$$

The critical film thickness,  $h_c$ , is given by the following expression (Chesters, 1991):

$$h_c = \left( \frac{A R_{eq}}{8\pi\sigma} \right)^{1/3}, \quad (20)$$

where  $A$  is the Hamaker constant of the order of magnitude of:  $A \approx 10^{-20}$  J, for pure liquid-liquid systems. The initial film thickness,  $h_0$ , can be expressed as follows (Podgórska, 2005):

$$h_0 = \frac{\varepsilon^{1/6} \xi^{*1/6} \mu_d^{1/2} R_{eq}^{3/4} \tilde{a}^{1/2}}{2\sigma^{1/2} R_L^{1/4}}. \quad (21)$$

It is important to remark that  $A_1$  is the model constant that can be fine tuned and, with the fact that appears inside an exponential, model predictions are very sensitive to its value. In fact this constant, although of the order of magnitude of unity from the theory, includes all the modeling uncertainties which might be not of universal character, e.g. the uncertainty related to the Hamaker constant for different liquid-liquid systems.

### Daughter size distribution function

The daughter size distribution function  $\beta(\xi|\xi')$  is required to describe the droplet breakage event. A detailed discussion on the different daughter distribution functions can be found in the work of Liao and Lucas (2009). In this work, we assumed a binary breakage which is a reasonable assumption for coalescing systems here investigated. In fact, more than two daughter droplets can be detected only when very large droplets break-up (Podgórska, 2006). Therefore, the distribution proposed by Laakkonen *et al.* (2006) is here used:

$$\beta(\xi|\xi') = 180 \left( \frac{\xi^2}{\xi'^3} \right) \left( \frac{\xi^3}{\xi'^3} \right)^2 \left( 1 - \frac{\xi^3}{\xi'^3} \right)^2, \quad (22)$$

where  $\xi$  and  $\xi'$  are the daughter and mother droplets.

### Test cases and numerical details

Different simulations were performed in order to investigate the two aspects mentioned earlier. First, a realistic stirred tank reactor with water as the continuous phase and octanol as the disperse phase was considered, for investigating the differences in the results between the 0D ‘‘lumped’’ model, the 0D ‘‘homogeneous’’ model and the 3D CFD-PBM model. Different operating conditions were taken into account, combining different stirring rates of:  $N = 300, 500$  and  $600$  RPM, and different global concentrations of the disperse phase, corresponding to  $\phi_d : 0.1\%, 1\%$  and  $10\%$ .

Then two different sets of coalescence and breakage kernels, namely CT and MF, were used to simulate droplet breakage and coalescence in stirred tanks. Also in this case, different systems and operating conditions were investigated. Test cases correspond to the experimental data from Podgórska (2006, 2007). The time evolution of the volume-averaged mean Sauter diameter of the droplets is available for three different geometries (indicated as T1, T2 and T3), working under different stirring rates and viscosities of the disperse phase. In fact, different silicone oils with viscosity ranging from approximately  $1$  mPa s to  $500$  mPa s, and approximately the same interfacial tension were considered. The specific fluid properties, global disperse phase volume fraction,  $\phi_d$ , and stirring rate,  $N$ , are reported in Table 1. The geometrical details of the stirred tanks equipped with Rushton turbines for the different geometries investigated are reported in Fig. 1, 2 and 3.

**Table 1:** Fluid properties and operating conditions investigated in this work:  $\mu_c$  is the viscosity of the continuity phase (mPas),  $\mu_d$  is the viscosity of the dispersed phase (mPas),  $\rho_c$  is the density of continuity phase ( $\text{kg m}^{-3}$ ),  $\rho_d$  is the density of dispersed phase ( $\text{kg m}^{-3}$ ),  $\sigma$  is the surface tension between the two phases ( $\text{N m}^{-1}$ ),  $\phi_d$  is the global disperse phase volume fraction (-) and  $N$  is the impeller rotational speed (rpm).

Geom.	$\mu_c$	$\mu_d$	$\rho_c$	$\rho_d$	$\sigma$	$\phi_d$	$N$
T1	1.00	0.72	998	1022	0.0250	0.0020	300
T2	1.00	0.72	998	1022	0.0250	0.0020	392
T3	0.89	10.00	997	946	0.0458	0.0038	240
T3	0.89	10.00	997	946	0.0458	0.0038	350
T3	0.89	100.0	997	985	0.0464	0.0038	300
T3	0.89	100.0	997	985	0.0464	0.0038	350
T3	0.89	500.0	997	973	0.0505	0.0038	300
T3	0.89	500.0	997	973	0.0505	0.0038	350

The 0D simulations (‘‘lumped’’ and ‘‘homogeneous’’ models) of the first part of the work were carried out by means of a

short program written in Matlab. The set of ODEs was integrated by using the standard solver `ode15s`. The initial droplet population is assumed to follow a log-normal distribution with a mean estimated by correlation and standard deviation proportional to that mean.

The 3D simulations were instead performed using our own implementation of QMOM in OpenFOAM (version 2.2.x), that makes use of a modified version of the standard solver `compressibleTwoPhaseEulerFoam` including the transport equation for the moments of the DSD, and the Wheeler inversion algorithm to calculate the quadrature approximation from the transported moments (Buffo *et al.*,

2016a). In this work, only the first six moments of the DSD were calculated ( $M_0, M_1, M_2, M_3, M_4, M_5$ ), corresponding to a quadrature approximation with three nodes:  $N = 3$ . Particular attention was paid to the problem of moment boundedness and realizability by means of a proper implementation of the moment transport equations (Buffo *et al.*, 2016a). The rotation of the turbine was modelled using the multiple reference frame approach (MRF), which gives reasonable results and is significantly cheaper than the sliding mesh approach.

## RESULTS

Let us start the discussion of the results with the comparison of the approximate 0D models with the inhomogeneous 3D models. In Fig. 4 the turbulent dissipation rate distribution in the tank,  $f(\epsilon)$ , is shown for the three different stirring rates investigated as estimated from the 3D CFD-PBM model. As can be seen from the figure, at higher stirring rates very high values of  $\epsilon$  (up to  $135 \text{ m}^2 \text{ s}^{-3}$ ) are observed in the region close to the stirrer blade, while in the bulk zone, which represents the major part of the tank volume, much smaller values are observed. At lower impeller rotational speed instead the distribution of  $\epsilon$  shows that the turbulence is in general mild, with the values of turbulent dissipation rates concentrated on the left of the plot. It is therefore clear that the volume-averaged kernels for breakage and coalescence, as calculated with the 0D “homogeneous” model, may be significantly different from the kernels evaluated at the volume-average turbulent dissipation rate  $\bar{\epsilon}$ , as calculated with the 0D “lumped” model, and this difference will be much more significant with the increase of the rotational speed of the impeller.

It is important to remark that the 0D “homogeneous” model, together with the 3D CFD-PBM model, considers the turbulent dissipation rate distribution in the tank: while, the 3D model has a general validity (as long as all the sub-models for turbulence, drag forces, coalescence and breakage are accurate), the 0D “homogeneous” model is valid only in the case of uniform distribution of the disperse phase throughout the vessel, in such a way that the gradients of all other properties apart from  $\epsilon$  can be assumed null. The 0D lumped model, instead, makes use only of the volume-averaged turbulent dissipation rate  $\bar{\epsilon}$ , always neglecting the effect of the

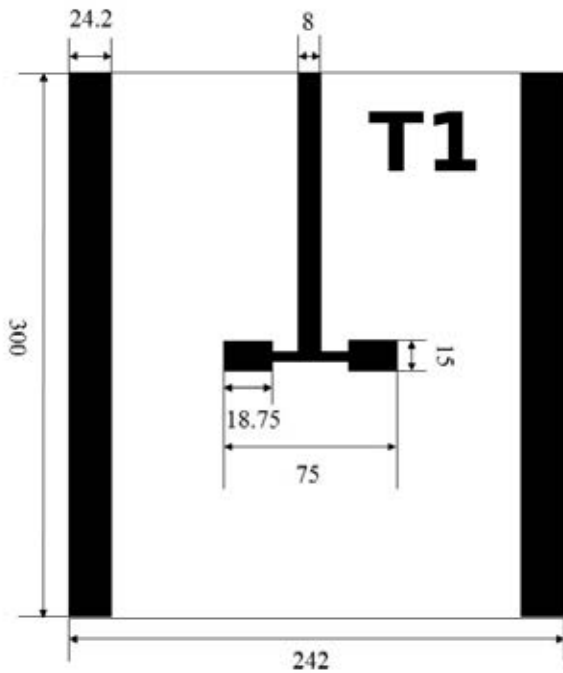


Figure 1: Geometry of the stirred tank T1. The units are in mm.

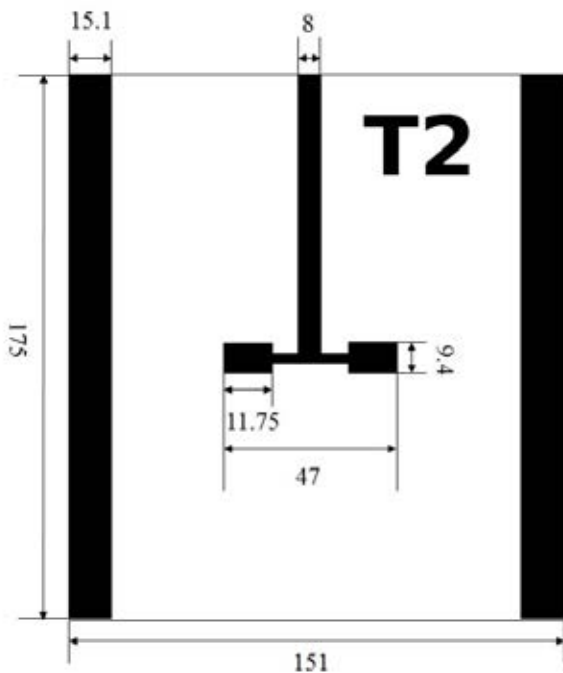


Figure 2: Geometry of the stirred tank T2. The units are in mm.

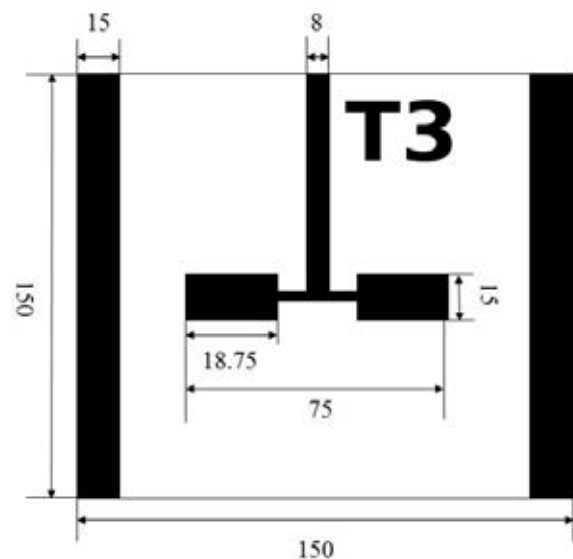


Figure 3: Geometry of the stirred tank T3. The units are in mm.

distribution of turbulent dissipation rate in the tank.

The values of the mean Sauter diameter ( $d_{32}$ ) at the steady state calculated with the three different methods are reported in Table 2 for two different operating conditions, while Table 3 shows the errors at the steady-state for the mean Sauter diameter as calculated with the 0D “homogeneous” model and the 0D “lumped” model, by using as a reference the predictions of the 3D model for all the different operating conditions investigated. Closer observation of Table 3 shows that 0D “homogeneous” model is able to give predictions that are very close to those given by the 3D CFD-PBM model. It is important to consider the fact that within the range of initial and operating conditions investigated, it was found that breakage always prevailed over coalescence, with the droplet size rapidly decreasing with time, until steady-state

**Table 2:** Values of the mean Sauter diameter at the steady state for two different operating conditions for all the approaches considered. The units are mm

Approach	300 rpm $\phi_d = 0.1\%$	600 rpm $\phi_d = 10\%$
0D “lumped”	0.239	0.085
0D “homogeneous”	0.046	0.038
3D CFD-PBM	0.047	0.058

**Table 3:** Difference between mean Sauter diameter calculated with 3D CFD-PBM model and 0D “homogeneous” (normal font) and 0D “lumped” simulations (bold font). Numbers are in percentage.

$\phi_d, \%$	RPM					
	300		500		600	
0.1	1.7	<b>249.6</b>	5.3	<b>236.3</b>	8.0	<b>227.5</b>
1.0	10.6	<b>164.7</b>	12.7	<b>163.0</b>	15.0	<b>159.3</b>
10.0	20.5	<b>85.1</b>	30.0	<b>65.0</b>	33.6	<b>60.0</b>

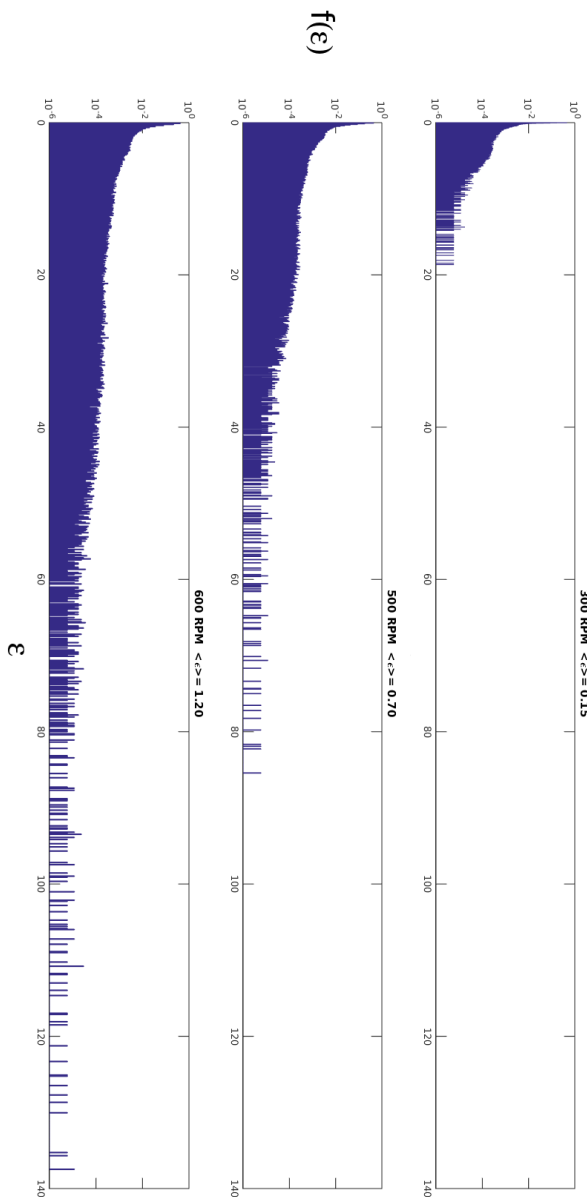


**Figure 4:** Distribution of the turbulent dissipation rate in the vessel for different operating conditions.

was reached. By using the 0D “lumped” model, in some cases of low stirring rate and high disperse phase volume fraction, coalescence prevailed over breakage, since the initial mean droplet diameter is of 1 mm. Moreover, the 0D “lumped” model underestimates the breakage rate in all the investigated cases, independently from the operating conditions, suggesting that this model should not be used even as a simple test case to study in detail the kinetics of coalescence and breakage (or in other words coalescence and breakage kernels) for such systems.

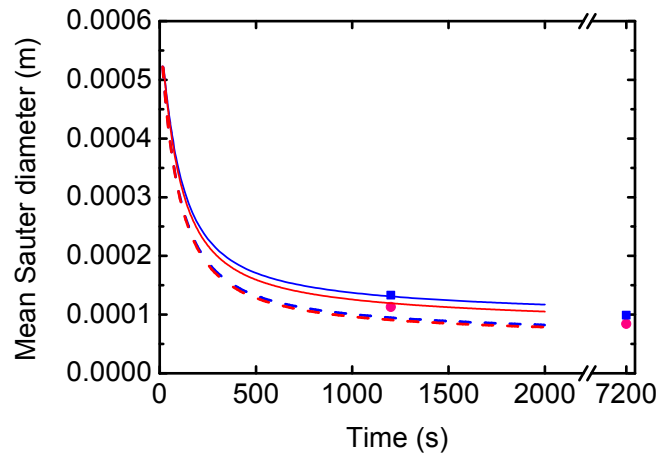


**Figure 5:** Time evolution of the volume-averaged mean Sauter diameter for T2,  $N = 392$  rpm (blue lines) and for T1,  $N = 300$  rpm (red lines). Viscosity of the disperse phase equal to  $0.72$  mPa s

It can be seen also that the 0D “lumped” model produces a very large error, whereas the error associated with the 0D “homogeneous” model is acceptable for some operating conditions. Moreover, it is possible to observe that the error increases both with the stirring rate and the global hold-up of the disperse phase. In particular for  $\phi_d = 0.1\%$ , the agreement with the reference solution is considerably good. As  $\phi_d$  increases to  $1.0\%$  the agreement for the mean Sauter diameter gets worse. A further increase of the disperse phase hold-up to  $\phi_d = 10.0\%$  significantly compromise the agreement between the predictions of the 3D CFD-PBM and 0D “homogeneous” models, regardless of the stirring rate. However, this behavior was expected: the 0D “homogeneous” model is in fact applicable only in dilute cases, when the DSD can be

considered uniform throughout the vessel. The error associated with the 0D “lumped” model, instead, is always significant for all the operating conditions investigated, showing

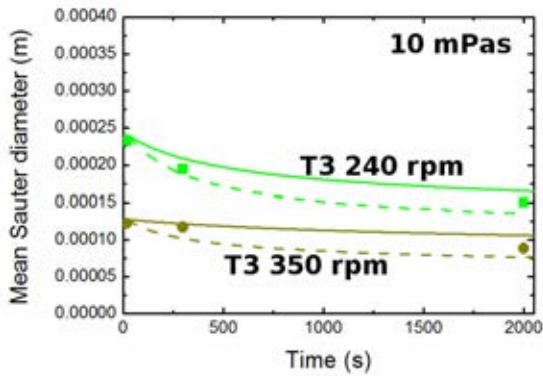


**Figure 6:** Time evolution of the volume-averaged mean Sauter diameter for T3,  $N = 240$  rpm (light green lines) and for T3,  $N = 350$  rpm (dark green lines). Viscosity of the disperse phase equal to 10 mPa s.

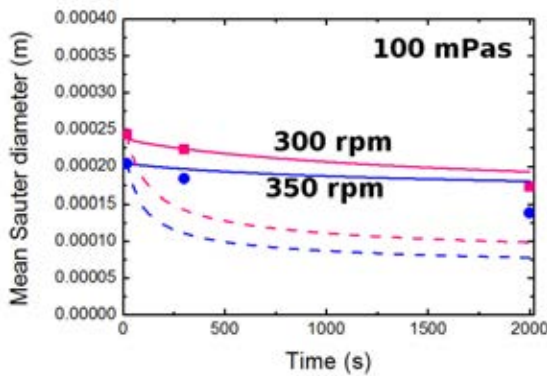


**Figure 7:** Time evolution of the volume-averaged mean Sauter diameter for T3,  $N = 300$  rpm (pink lines) and for T3,  $N = 350$  rpm (blue lines). Viscosity of the disperse phase equal to 100 mPa s.

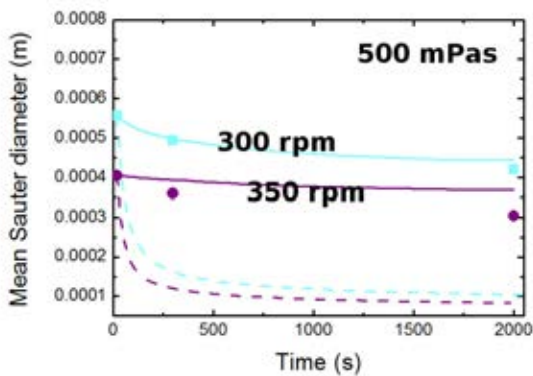


**Figure 8:** Time evolution of the volume-averaged mean Sauter diameter for T3,  $N = 300$  rpm (light blue lines) and for T3,  $N = 350$  rpm (purple lines). Viscosity of the disperse phase equal to 500 mPa s.

that the effect of the distribution of turbulent dissipation rate must be properly considered.

As far as the investigation on different sub-models for droplet coalescence and breakage is concerned, it is useful to compare the experimental data available and the numerical predictions in terms of the time evolution of the mean Sauter diameter. As it can be observed different test cases are reported, having different geometries, operating conditions and viscosity of the dispersed phase. It is useful to remind here that experimental data are in general affected by an uncertainty of about 5 %. The sensitivity of model predictions with respect to the key parameters was instead investigated in the cited literature where the kernels were first proposed. Figure 5 reports the comparison between predictions obtained with the CT kernels (dashed lines) and the MF kernels (continuous lines) for the two stirred tanks, T1 and T2, reported in Fig 1 and 2. T1 is the geometric scale up of T2 and the stirring rates are chosen in order to result with the same power dissipation per unit volume. As seen the CT kernels results in the very same predictions for the mean Sauter diameter, whereas only using the MF kernels a significant difference between the two tanks is observed, in perfect agreement with the experiments. This is due to the effect of intermittency, that is more important in the large tank (T1). The higher accuracy of the MF kernels is even more evident when the viscosity of the disperse phase is increased up to 10 mPa s, 100 mPa s and 500 mPa s as evident from 6, 7 and 8. In fact, predictions obtained with the MF kernels are close to experiments, whereas those obtained with the CT kernels are not able to reproduce the experimental trend. This is due to the fact that the CT kernels does not take into account the viscous forces that prevent the droplet to break, while the MF kernels properly include this important piece of physics into the model. Moreover, it is worth remarking that the MF kernels are capable of predicting with good accuracy also the dynamics of the investigated systems, which is another significant improvement with respect to the more common CT kernels.

## CONCLUSIONS

In this work two different aspects related to the simulation of liquid-liquid systems were considered. First, the predictions of a 3D CFD-PBM model, our own implementation of QMOM in OpenFOAM, were compared with those of two simpler (computationally cheaper and often used in the industrial practice) 0D models, derived from the 3D model with a simple volume-average procedure applied on the entire vessel. The results show that the model which assumes that the turbulence dissipation rate in the tank is uniform and equal to the volume-average value, namely the 0D “lumped” model, is not suitable in all the operating conditions here studied. This is due to the fact that the rates of coalescence and breakage are not homogeneous in the tank, regardless the spatial distribution of the droplet population. Whereas, the 0D “homogeneous” model, which is able to take into account the effect of the spatial distribution of the turbulent dissipation rate in the tank, can be used under certain operating conditions in replacement of the 3D model, when the spatial gradients of the DSD are negligible. This means that the knowledge of the spatial distribution of the turbulent dissipation rate in the tank is crucial for a proper calculation of the breakage and coalescence rates.

Moreover in this work, two different breakage kernels (the CT and the MF kernels) were considered in our simulations. Different test cases were simulated in three geometrically

different tanks working under different operating conditions and with different continuous and disperse phases. Eventually the mean Sauter diameters calculated from the CT kernel and MF kernel were compared with experimental data. The results show that, for dilute systems, the CT and MF kernels both are capable of capturing the evolution of the mean Sauter diameter, however the CT kernel under-predicts the mean Sauter diameter, especially in the case of high disperse phase viscosity, whereas the MF kernels results in satisfactory agreement.

## REFERENCES

- ALOPAEUS, V., KOSKINEN, J., KESKINEN, K. and MAJANDER, J. (2002). "Simulation of the population balances for liquid-liquid systems in a nonideal stirred tank. Part II: Parameter fitting and the use of the multiblock model for dense dispersions". *Chemical Engineering Science*, **57**(10), 1815–1825.
- ALOPAEUS, V., MOILANEN, P. and LAAKKONEN, M. (2009). "Analysis of stirred tanks with two-zone models". *AIChE Journal*, **55**(10), 2545–2552.
- ATTARAKIH, M., BART, H.J., STEINMETZ, T., DIETZEN, M. and FAQIR, N. (2008). "LLECMOD: A bivariate population balance simulation tool for liquid-liquid extraction columns". *Open Chem. Eng. J.*, **2**, 10–34.
- ATTARAKIH, M., HLAWITSCHKA, M., ABUKHADER, M., AL-ZYOD, S. and BART, H.J. (2015). "CFD-population balance modelling and simulation of coupled hydrodynamics and mass transfer in liquid extraction columns". *Applied Mathematical Modelling*, **39**, 5105–5120.
- BALDYGA, J. and PODGÓRSKA, W. (1998). "Drop break-up in intermittent turbulence: Maximum stable and transient sizes of drops". *The Canadian Journal of Chemical Engineering*, **76**, 456–470.
- BHOLE, M., JOSHI, J. and RAMKRISHNA, D. (2008). "CFD simulation of bubble columns incorporating population balance modeling". *Chemical Engineering Science*, **63**(8), 2267–2282.
- BUFFO, A. and MARCHISIO, D. (2014). "Modeling and simulation of turbulent polydisperse gas-liquid systems via the generalized population balance equation". *Reviews in Chemical Engineering*, **30**, 73–126.
- BUFFO, A., VANNI, M. and MARCHISIO, D. (2016a). "On the implementation of moment transport equations in OpenFOAM: Boundedness and realizability". *International Journal of Multiphase Flow*, **85**, 223–235.
- BUFFO, A., DE BONA, J., VANNI, M. and MARCHISIO, D. (2016b). "Simplified volume-averaged models for liquid-liquid dispersions: Correct derivation and comparison with other approaches". *Chemical Engineering Science*, **153**, 382–393.
- CHESTERS, A. (1991). "The modelling of coalescence processes in fluid-liquid dispersions: a review of current understanding". *Chemical Engineering Research and Design*, **69**, 259–270.
- COULALOGLOU, C. and TAVLARIDES, L. (1977). "Description of interaction processes in agitated liquid-liquid dispersions". *Chemical Engineering Science*, **32**(11), 1289–1297.
- GAO, Z., LI, D., BUFFO, A., PODGÓRSKA, W. and MARCHISIO, D. (2016). "Simulation of droplet breakage in turbulent liquid-liquid dispersions with CFD-PBM: Comparison of breakage kernels". *Chemical Engineering Science*, **142**, 277–288.
- LAAKKONEN, M., ALOPAEUS, V. and AITTAMAA, J. (2006). "Validation of bubble breakage, coalescence and mass transfer models for gas-liquid dispersion in agitated vessel". *Chemical Engineering Science*, **61**, 218–228.
- LAAKKONEN, M., MOILANEN, P., ALOPAEUS, V. and AITTAMAA, J. (2007). "Modelling local bubble size distributions in agitated vessels". *Chemical Engineering Science*, **62**(3), 721–740.
- LIAO, Y. and LUCAS, D. (2009). "A literature review of theoretical models for drop and bubble breakup in turbulent dispersions". *Chemical Engineering Science*, **64**, 3389–3406.
- LUO, H. and SVENDSEN, H. (1996). "Theoretical model for drop and bubble breakup in turbulent dispersions". *AIChE Journal*, **42**(5), 1225–1233.
- MARCHISIO, D. and FOX, R. (2013). *Computational models for polydisperse particulate and multiphase systems*. Cambridge University Press.
- MARCHISIO, D., VIGIL, R. and FOX, R. (2003). "Implementation of the quadrature method of moments in CFD codes for aggregation-breakage problems". *Chemical Engineering Science*, **58**(15), 3337–3351.
- MARCHISIO, D., SOOS, M., SEFCIK, J. and MORBIDELLI, M. (2006). "Role of turbulent shear rate distribution in aggregation and breakage processes". *AIChE journal*, **52**(1), 158–173.
- MENEVEAU, C. and SREENIVASAN, K. (1991). "The multifractal nature of turbulent energy dissipation". *Journal of Fluid Mechanics*, **224**, 429–484.
- PODGÓRSKA, W. (2005). "Scale-up effects in coalescing dispersions—Comparison of liquid-liquid systems differing in interface mobility". *Chemical Engineering Science*, **60**, 2115–2125.
- PODGÓRSKA, W. (2007). "Influence of dispersed phase viscosity on drop coalescence in turbulent flow". *Chemical Engineering Research and Design*, **85**, 721–729.
- PODGÓRSKA, W. and BALDYGA, J. (2001). "Scale-up effects on the drop size distribution of liquid-liquid dispersions in agitated vessels". *Chemical Engineering Science*, **56**, 741–746.
- PODGÓRSKA, W. (2006). "Modelling of high viscosity oil drop breakage process in intermittent turbulence". *Chemical Engineering Science*, **61**, 2986–2993.
- SCHILLER, L. and NAUMANN, A. (1935). "A drag coefficient correlation". *Vdi Zeitung*, **77**(318), 51–86.
- VANNI, M. and SOMMERFELD, M. (1996). "Aggregation of small particles in turbulent liquid flows". *Engineering Turbulence Modelling and Experiments*, **3**, 891–900.

# SIMULATION OF DISPERSION OF IMMISCIBLE FLUIDS IN A TURBULENT COUETTE FLOW

Alexander VIKHANSKY<sup>1</sup> , Dmitry ESKIN<sup>2\*</sup>

<sup>1</sup>Siemens PLM Software, Didcot, UK

<sup>2</sup> Schlumberger-Doll Research, Cambridge, MA, USA

\* E-mail: deskin@slb.com

## ABSTRACT

Dispersion of immiscible fluids in a Couette device, in which the inner cylinder rotates whereas the outer one is immobile, is modelled. Two different modelling approaches are employed. The 1st approach is based on solving a one-dimensional Advection-Diffusion-Population Balance equation. An influence of upper and bottom Couette device covers (the so-called end effect) is ignored in this case. The Prandtl mixing length model of turbulence, employed for modelling of a Couette flow field, allows obtaining an analytical expression for calculation of the energy dissipation rate distribution across Couette device gap. Fixed Pivot method is employed for numerical solution of the population balance equation.

The 2nd approach is based on the CFD-population balance A-MuSiG method, recently implemented into the STAR-CCM+ code of Siemens PLM Software. The Reynolds stress turbulence model along with the Daly & Harlow transport model are employed for modelling two-dimensional axisymmetric flow field in a Couette device.

In the present work, modelling is limited to only droplet breakup; i.e., only non-coalescing droplets are considered. A modified droplet breakup model of Coulaloglou and Tavlarides (1977) is employed for all the computations.

Computed droplet size distributions are compared with those obtained in a laboratory Couette device of a relatively small height that is a cause of the significant end effect. Dispersion of water droplets in silicone oil is studied. Coalescence is suppressed by a surfactant. The experimental droplet size distributions are reasonably well fitted by both the models employed.

The most significant advantage of the 3-D computations over the 1-D modelling is accounting for the end effect, that in its turn affects both velocity and energy dissipation rate distributions over the Couette device gap. Also, to better fit the experimental data, a weak coalescence was formally introduced into the 3-D computational code.

**Keywords:** Breakup, Dispersion, Droplets, Modelling, Population Balance, Turbulence

## NOMENCLATURE

### Greek Symbols

$\alpha$  Dispersed phase volume fraction  
 $\beta$  Droplet breakup density function

$\delta_{in}$  Thickness of the viscous layer at the inner Couette device wall, [m]  
 $\delta_o$  Thicknesses of the viscous layers at the outer Couette device wall, [m]  
 $\varepsilon$  Energy dissipation rate per unit mass, [W/kg]  
 $\rho$  Density, [kg/m<sup>3</sup>].  
 $\mu$  Dynamic viscosity, [kg/m s]  
 $\tau_R$  Reynolds stress, [Pa]  
 $\tau_{win}$  Shear stress at the outer cylinder wall, [Pa]  
 $\Omega$  Inner cylinder rotation speed, [Hz]  
 $\nu$  Droplet volume, [m<sup>3</sup>]

### Latin Symbols

$D$  Turbulent diffusivity of a droplet, [m<sup>2</sup>/s]  
 $d$  Droplet diameter, [Pa]  
 $f_{bv}$  Breakup volume fraction  
 $G$  Droplet breakup rate, [1/s]  
 $H$  Width of the Couette device gap, [m]  
 $L$  Couette device height, [m]  
 $M$  Maximum number of size fractions  
 $\dot{m}$  Mass transfer rate between size fractions, [kg/m<sup>3</sup>/s]  
 $N$  Number concentration of droplets per unit volume, [1/m<sup>3</sup>]  
 $P$  Pressure, [Pa]  
 $q$  Number flux of droplets, [1/m<sup>2</sup>/s]  
 $R$  Radius of the outer cylinder of a Couette device, [m]  
 $R_m$  Radius of the gap centreline, [m]  
 $r_{in}$  Radius of the inner cylinder of a Couette device, [m]  
 $Re$  Couette device Reynolds number  
 $u$  Velocity of a droplet averaged over a size fraction, [m/s]  
 $u_{o*}$  Friction velocity at the outer cylinder wall, [m/s]  
 $v$  Radial velocity component of a droplet, [m/s]  
 $We$  Weber number  
 $w$  Droplet fluctuation velocity, [m/s]

*Sub/superscripts.*

*cr* critical

*d* droplet

*f* fluid

*i, j* size fraction number

## INTRODUCTION

Emulsification (emulsion formation) is a process of dispersion of one immiscible fluid in another one, and also an important stage of many technologies. In some cases, emulsions are produced intentionally when high viscosity fluids are required for some purposes. For example, emulsions are widely used as different components in food industry, or in petroleum industry as displacing fluids for enhanced oil recovery as well as fracturing fluids for hydraulic fracturing. However, frequently, emulsion formation is a highly undesired phenomenon. An example is emulsion formation during oil production. Water almost always accompanies production of oil. A high viscosity water in oil emulsion, formed in a reservoir or a flowline, causes a significant increase in friction losses resulting in a production decrease. Moreover, natural surfactants, present in oil, may cause suppression of droplet coalescence and, as a result, formation of a stable emulsion that is characterized by a higher viscosity and smaller droplets. In this case, water-oil separation as well as some measurements, regularly conducted in a production tubing, are impaired. Injection of demulsifying chemicals is required to break a stable emulsion. To evaluate consequences of stable emulsion formation and make decision on necessity of demulsifier injection, a reliable model of the emulsification process is needed.

Droplet dispersion can be considered as a sequence of multiple droplet breakup and coalescence events. On large scale, the dispersion process can be most efficiently modelled by a well-known Population Balance (PB) method. There are many droplet breakup and coalescence models available in open literature (Liao and Lucas, 2009, 2010). However, superiority of certain models over others has never been proven.

In the current work, we consider droplet dispersion in a Couette device that consists of two coaxial cylinders (see Fig.1); the inner cylinder rotates whereas the outer is immobile. A flow pattern in such a device is somewhat similar to that in a pipe flow (Eskin et al., 2017); therefore, in some cases low-cost Couette device experiments can successfully substitute costly flow loop tests for laboratory studies of the droplet dispersion process. We will limit our analysis to Couette flows characterized by relatively high Reynolds numbers ( $Re > 13000$ ). In this case, scales of Taylor vorticities become comparable to scales of turbulent fluctuations and the boundary layer theory becomes applicable to a Couette flow (Lewis and Swinney, 1999). The Reynolds number, in this case, is calculated on the basis of the circumferential velocity of the inner cylinder and the Couette device gap.

Eskin et al. (2017) developed a one-dimensional model of droplet dispersion in a Couette device. Modelling was reduced to solution of an Advection-Diffusion-Population Balance equation. The model developed was assumed to

be valid for a device, the height of which significantly exceeds the outer radius. The latter condition makes an effect of bottom and upper walls on a flow field to be negligibly small. An applied flow model (Eskin, 2014) was based on the boundary layer theory.

The authors showed that the turbulence energy dissipation rate, which to a great extent determines the rate of droplet breakup and coalescence, is strongly non-uniform across the Couette device gap. The dissipation rate is highest at the inner wall and rapidly reduced to the gap centerline. The processes of droplet breakup and coalescence were modelled by a PB technique. As a breakup kernel, the authors employed the modified model of Coualaloglou and Tavlarides (1977), developed for an inertial regime of turbulence that takes place when sizes of breaking droplets significantly exceed the Kolmogoroff turbulence scale. The improved breakup model assumes the experimentally proven (Kuboi, 1972) three-dimensional Maxwellian distribution of turbulence eddy fluctuation velocity, whereas the original model is based on the unjustified assumption about the 2-D Maxwellian distribution.

The breakup model parameters were identified from the experimental data obtained using a laboratory Couette device. The experimental apparatus was of a relatively small height: the ratio of the outer radius to the gap width was  $\sim 1.42$ . The tests of different durations (2 and 10 min) were conducted for an oil/water mixture, characterized by a small volume fraction of water (2%), in presence of a surfactant suppressing droplet coalescence. The droplet size distributions were determined by analysis of the microscopic images of stabilized emulsion samples using image recognition software ImageJ (NIH). The computations showed that droplets, being dispersed in the laboratory Couette device, reach rather small sizes and are uniformly dispersed over the Couette device radius. The computed cumulative droplet size distributions were relatively close to the measured ones. However, the experimental distributions were wider; i.e., the smallest droplets measured were smaller, whereas the largest were larger than those computed. The authors (Eskin et al., 2017) suggested that this disagreement can be caused by the end effect associated with a small Couette device height, possible droplet coalescence as well partial occurrence of breakup in a viscous regime of turbulence, characterized by droplet sizes to be significantly smaller than the Kolmogoroff scale.

Dispersion of droplets, able to coalesce (no surfactant case), was analysed only numerically. The coalescence kernel of Coualaloglou and Tavlarides (1977) was employed for this purpose. The computations (Eskin et al., 2017) showed that in this case droplets are relatively large and, therefore, strongly stratified across the Couette device gap. An abrupt increase in droplet concentration at the outer wall indicates formation of a water layer. The conclusion was that a Couette device is hardly suitable for studies of turbulent flows of unstable emulsions in a turbulent flow. Therefore, in the present work, we will limit our studies only to modelling the dispersion process in absence of coalescence. We will compare the results, obtained by the engineering model based on the Advection-Diffusion Population Balance equation, with the data produced by the STAR-CCM+ CFD code of Siemens PLM Software in axisymmetric 3D formulation. The adaptive multiple size-groups (A-MuSiG) method,

recently implemented into the code, is employed for population balance modelling. The Reynolds stress turbulence model along with the Daly & Harlow transport model are used for computation of a Couette flow field.

## ENGINEERING MODELING APPROACH

Let us formulate and discuss the key modeling assumptions. The critical assumption employed in the current work is that droplets do not coalesce; i.e., an emulsion is stable. Emulsion can be stabilized by an

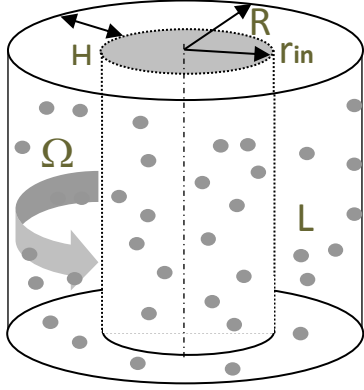


Figure 1: Couette device diagram

addition of chemicals (e.g., asphaltenes or other natural surfactants), molecules of which absorb on droplet surfaces making them rigid and as a result prevent coalescence. For the sake of simplicity, we assume that the emulsion stabilization process is short enough to be neglected. Eskin et al. (2017) showed also that a steady-state droplet size distribution, obtained in a laboratory Couette device in absence of coalescence, was practically independent on an initial droplet size. Also, the dispersion computations conducted for initially monodispersed droplets, uniformly distributed over the Couette device gap, showed that the volume averaged droplet size very rapidly decreases during a short period of stirring. During this initial stirring stage, the droplet size reduction rate greatly decreases and then droplet size distribution slowly approaches the steady-state. Based on these results, we neglect complex effects, associated with initial location of fluids to be stirred, and occurring on the initial dispersion stage. We will also assume that droplets maintain a spherical shape.

### Advection – Diffusion – Population Balance approach

Let us formulate the Advection-Diffusion-Population Balance equation for droplets, whose continuous size distribution is substituted with a discrete distribution represented by a finite number of size fractions. Note that in accordance with the analysis of Eskin et al. (2017) we neglect the droplet stratification due to gravity. Then, employment of one-dimensional governing equation is justified and it is written in polar coordinates as follows (Eskin et al., 2017):

$$\frac{\partial N_i}{\partial t} = \frac{1}{r} \frac{\partial}{\partial r} \left( D_i \frac{\partial N_i}{\partial r} - N_i v_i \right) + \left( \frac{\partial N_i}{\partial t} \right)_{PB}, \quad (1)$$

$i=1, \dots, M$

where  $D_i$  is the turbulent diffusivity of droplets of the  $i$ -th size fraction,  $M$  is the number of size fractions,  $N_i$  is the number concentration of droplets of the  $i$ -th size fraction per unit volume,  $v_i$  is the radial velocity component of a droplet of the  $i$ -th size fraction, and  $(\partial N_i / \partial t)_{PB}$  is the concentration change of the  $i$ -th size fraction droplets due to both breakup and coalescence (population balance term). All the terms of Eq. (1) are defined by local flow parameters, which can be determined using a simple engineering model of a Couette flow (e.g., Eskin 2010, 2014).

The boundary conditions for this equation are zero droplet fluxes through the inner and outer walls respectively. The corresponding equations for the number droplet fluxes are written as follows:

$$q_i(r_{in}) = \left( D_i \frac{\partial N_i}{\partial r} - N_i v_i \right) \Big|_{r_{in}} = 0 \quad (2)$$

$$q_i(R) = \left( D_i \frac{\partial N_i}{\partial r} - N_i v_i \right) \Big|_R = 0 \quad (3)$$

where  $r_{in}$  and  $R$  are radii of the inner and outer Couette device walls respectively.

Distributions of the radial velocity components of droplets and the droplet diffusivities are calculated using the Couette flow model (Eskin et al., 2017). Because droplets are small and the density difference between dispersed and continuous phases is moderate, it is possible to assume that droplets closely follow fluid. Then, the following assumptions are valid: 1) the circumferential velocities of a droplet and a fluid are equal; 2) the turbulent diffusivity of a droplet is equal to the eddy diffusivity. The droplet radial velocity is calculated from the balance between the centrifugal and the radial forces acting on a droplet. To calculate the eddy diffusivity we used the correlation of Notter and Sleicher (1971) for the near-wall region, and the relations, based on the Prandtl mixing length model of turbulence for a core flow (Eskin et al., 2011).

Let us now formulate the population balance term of Eq. (1). Neglecting coalescence we can formulate the corresponding equation for a continuous droplet size distribution as follows:

$$\frac{dN(\nu, t)}{dt} = \int_{\nu}^{\infty} \beta(\nu', \nu) G(\nu') N(\nu', t) d\nu' - G(\nu) N(\nu, t), \quad (4)$$

where  $G(\nu')$  is the breakup rate representing the breakup frequency of droplets of volume  $\nu'$ ;  $N(\nu, t)$  is the number concentration of droplets of volume  $\nu$ ;  $\beta(\nu', \nu)$  is the droplet breakup density function, expressing the number of daughter droplets of size  $\nu$  formed at breakup of a droplet, whose volume is in the range  $\nu' + d\nu'$ .

There are a significant number of different models of droplet breakup (Liao and Lucas, 2009). For all the computations in this work we will employ the modification



(Eskin et al., 2017) of the well-known breakup model of Coualoglou and Tavlarides (1977). This model is based on the assumption that a droplet can be broken only by an eddy of a scale equal to droplet diameter, whereas distribution of the fluctuation velocity of such an eddy is Maxwellian. The breakup event occurs when the dynamic pressure associated with the eddy fluctuation velocity exceeds the droplet capillary pressure. The Maxwellian distribution assumption is confirmed by the experimental data of Kuboi et al. (1972), who showed that droplet fluctuation velocity distribution in a turbulent flow is nearly Maxwellian and the droplet mean-square velocity is determined as:

$$\langle w^2(d) \rangle = 2(\varepsilon d)^{2/3} \quad (5)$$

where  $d$  is the particle size,  $\varepsilon$  is the energy dissipation rate per unit mass.

Those experimental results mean that mainly eddies of scales equal to diameters of droplets contribute into dynamics of droplet fluctuations; therefore, such eddies should be major contributors into droplet breakup. Thus, the breakup model of Coualoglou and Tavlarides (1977) has a reasonably strong physical background.

However, Coualoglou and Tavlarides (1977) wrongly assumed that the Maxwellian distribution is two-dimensional. Eskin et al. (2017) corrected this flaw by deriving an equation for the breakup rate that accounts for the three-dimensional Maxwellian velocity distribution. Thus, the breakup rate in the present work will be calculated as follows (Eskin et al., 2017):

$$G(v) = G(d) = K \frac{(\varepsilon d)^{1/3}}{d} \left[ \operatorname{erfc}(\Phi) + \frac{2}{\pi^{1/2}} \Phi^{1/2} \exp(-\Phi) \right] \quad (6)$$

where  $\operatorname{erfc}$  is the complementary error function,  $K$  is the model parameter,  $\Phi = 1.5We_{cr}/We$ ,  $We = 2\rho_f \varepsilon^{2/3} d^{5/3} / \gamma$  is the droplet Weber number,  $We_{cr}$  is the critical Weber number,  $\gamma$  is the interfacial tension,  $\rho_f$  is the continuous fluid density.

The model parameters  $K$  and  $We_{cr}$  need to be determined from experimental data.

Let us now formulate assumptions enabling to determine a number and sizes of daughter droplets formed at breakup of a mother droplet. We will employ a regular assumption of binary breakup; i.e., a droplet is always fragmented forming two daughter droplets. There are a number of known breakup density functions  $\beta$  (Liao and Lucas, 2009) determining probability of generation of daughter droplets of a certain volume ratio at a binary breakup event. Most frequently,  $\Pi$ -shaped functions are used for engineering computations. Such functions are characterized by maximum probability of formation of daughter droplets of equal sizes, whereas probability of generation of a droplet of infinitely small size is zero. According to calculations of Eskin et al. (2017), even large variations in shape of a function  $\beta$  do not cause significant changes in a steady-state droplet size distribution computed by the population balance equation. Therefore, following Eskin et al. (2017) in the present work we employed the droplet breakup density function

proposed by Lee et al. (1987) that in terms of the breakup volume fraction  $f_{bv}$  is formulated as:

$$\beta(f_{bv}) = 12f_{bv}(1 - f_{bv}), \quad (7)$$

where  $f_{bv} = v/v'$  characterizes the ratio of the daughter/mother droplet volumes.

In a turbulent flow the droplet breakup rate is mainly determined by the energy dissipation rate. Using the engineering flow model Eskin et al. (2017) calculated the energy dissipation rate as a specific power spent on friction between rotating fluid layers. In a core flow, the energy dissipation rate per unit mass is:

$$\varepsilon = \frac{\tau_{win} u_{o*}}{\rho_f \kappa} \frac{r_{in}^2 R}{r^3 (r - r_{in})} = \frac{u_{o*}^3}{\kappa} \left( \frac{R}{r} \right)^3 \frac{1}{r - r_{in}} \quad (8)$$

$$\text{at } r_{in} + \delta_{in} \leq r \leq R_m,$$

$$\varepsilon = \frac{\tau_{win} u_{o*}}{\rho_f \kappa} \frac{r_{in}^2 R}{r^3 (R - r)} = \frac{u_{o*}^3}{\kappa} \left( \frac{R}{r} \right)^3 \frac{1}{R - r} \quad (9)$$

$$\text{at } R_m < r \leq R - \delta_o$$

where  $u_{o*}$  is the friction velocity at the outer cylinder wall,

$\delta_{in}$  and  $\delta_o$  are the thicknesses of the viscous layers at the inner and the outer walls respectively,  $\kappa$  is the von-Karman constant,  $\tau_{win}$  is the shear stress at the outer cylinder wall.

The shear-stress distributions across the viscous layers are nearly constant and, therefore, assumed to be equal to the values calculated on the layer boundaries by Eqs. (8, 9).

The population-balance term in Eq. (1) was computed using the Fixed Pivot method (Kumar and Ramakrishna, 1996). In the computational code developed, the droplet volumes were discretised using a geometrical progression. The smallest droplet size was assumed to be 10% of the lowest value of the Kolmogoroff scale corresponding to the maximum energy dissipation rate that occurs at the inner wall. The radial coordinate along the gap was meshed as follows. The cells adjacent to both the walls were assumed to be equal to the thicknesses of the corresponding viscous layers  $\delta_{in} = \delta_o = 11.6 \delta_w$ , where  $\delta_w = \mu_f / \rho_f / u_*$  is the wall layer thickness. A geometric progression was used to distribute mesh sizes from the wall to the gap centreline. An explicit finite difference method was employed for numerical solution of Eq. (1). Independence of numerical solution on the chosen discretization of droplet volumes and the gap width, as well on the time step was verified by a number of trial computations.

## EXPERIMENT

The breakup model parameters were identified from the laboratory experiments, details of which are given in Eskin et al. (2017). An available Couette device, regularly used as a laboratory mixer, was employed for this purpose. The inner and the outer cylinder radii of this device are  $r_{in} = 14.35$  and  $R = 28.7$  mm; i.e.,  $r_{in}/R = 0.5$ . The

relatively small Couette device height,  $L = 20$  mm, leads to a significant effect of the boundary layers at the top and the bottom covers on the flow field (the end effect).

A water-in-oil emulsion, with the water volume fraction

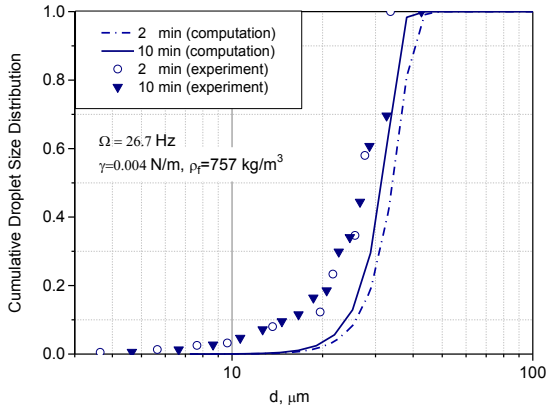


**Figure 2:** Computed and experimental droplet size distributions for the lower rotation speed

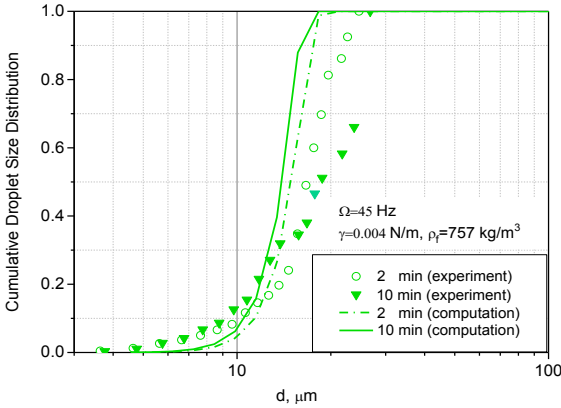


**Figure 3:** Computed and experimental droplet size distributions for the higher rotation speed

$\alpha = 0.02$  was prepared using mineral oil with the dynamic viscosity  $\mu_f = 0.002$  Pa s and the density  $\rho_f = 757$  kg/m<sup>3</sup> at the temperature 25 °C. Non-ionic surfactant was used for stabilization of dispersed droplets. The surfactant addition led to a significant reduction of the interfacial tension (from  $\gamma = 0.04$  to 0.004 N/m) causing generation of fine droplets. First, the Couette device was filled with the oil, and after that water was added on the top. The experiments were conducted at the defined rotation speeds and mixing durations. After the Couette device was stopped, samples were withdrawn by a pipette from three different locations across the gap. Then, these samples were analysed by a transmitted light microscope and after that the image recognition software was used to determine the droplet size distributions. We would like to emphasize the surfactant caused generation of small droplets, which are uniformly distributed across the gap due to turbulent dispersion; therefore, the droplet size distributions measured at the different locations were almost identical.

Based on the experimental data obtained for the two different rotation speeds,  $\Omega = 26.6$  and 45 Hz, and the two different stirring durations, 2 and 10 min, we identified the breakup model parameters in Eq. (6) as follows:  $K = 1$  and  $We_{cr} = 0.5$ . The identification accuracy was to some

extent impaired due to the limited experimental data for different durations, the end effect, partial shift of the breakup regime from the inertial subrange of turbulence to the viscous subrange, and not entirely suppressed droplet coalescence.

## COMPUTATIONAL FLUID DYNAMICS – POPULATION BALANCE MODELLING

The A-MuSiG method employed is adaptive; i.e., size discretization of a dispersed phase varies during computations as a result of breakup and coalescence. For each size fraction (size-group), its own mass and (if necessary) momentum balance equations can be formulated. The instantaneous mass balance equation for the  $i$ -th size fraction in a turbulent flow is:

$$\frac{\partial \alpha_i \rho_d}{\partial t} + \nabla \cdot (\alpha_i \rho_d \mathbf{u}_i) = \sum_j (\dot{m}_{ij} - \dot{m}_{ji}) \quad (10)$$

where  $\dot{m}_{ij}$  is the mass transfer rate from the  $j$ -th to the  $i$ -th size fraction,  $\mathbf{u}_i$  is the average velocity of the  $i$ -th size fraction,  $\alpha_i$  is the Reynolds averaged (RA) volume concentration of the size fraction  $i$ ,  $\rho_d$  is the droplet density.

The fraction-to-fraction mass transfer occurs due to breakup and coalescence, e.g., if a droplet is broken by turbulence, its mass and momentum are redistributed among smaller size fractions.

The RA Navier-Stokes (RANS) equations for the  $i$ -th size fraction of the dispersed phase are:

$$\frac{\partial \alpha_i \rho_d \mathbf{u}_i}{\partial t} + \nabla \cdot (\alpha_i \rho_d \mathbf{u}_i \mathbf{u}_i) = -\nabla P - \nabla \cdot \boldsymbol{\tau}_R + \sum_j (\dot{m}_{ij} \mathbf{u}_j - \dot{m}_{ji} \mathbf{u}_i), \quad (11)$$

where  $\boldsymbol{\tau}_R$  is the Reynolds stress.

It was assumed that the flow field is axisymmetric. Our experience shows that not every RANS model is capable to reproduce the swirl flow field: both  $k - \varepsilon$  and  $k - \omega$  models underestimate the torque at the Couette device spindle approximately by a factor of two. In the present study, we use the Reynolds-stress, linear pressure-strain turbulence model with the Daly-Harlow tensor diffusivity. The model predictions are in a very good agreement with the experimental data (Lewis and Swinney, 1999).

In the A-MuSiG method the number density equation is solved for each size fraction:

$$\frac{\partial N_i}{\partial t} + \nabla \cdot \{N_i (\mathbf{u}_i + D_i \nabla \ln v_i)\} = S_i, \quad (12)$$

where  $S_i$  is source term due to breakup and coalescence. As one can see, the volume of a single droplet  $v_i = \alpha_i / N_i$  is not prescribed a priori but varies in both time and space; it makes the method adaptive and our experience shows that from 3 to 7 size-fractions are sufficient for reliable engineering estimates.

One can see that there is an extra transport (diffusive) term in Eq. (12) that appears as a result of Reynolds-averaging of the instantaneous equation for  $N_i$ . The derivation details are given in Vikhansky and Splawski (2015).

As one can see, Eqs. (10)-(12) are presented in the standard form of multiphase fluid dynamics. A population balance

algorithm enters into these equations only through their source terms  $S_i$ ,  $\dot{m}_{ij}$ . In the present study, the source terms are calculated by the direct quadrature spanning tree method (Vikhansky, 2013).

### Computational examples

Examples are given for the laboratory Couette device employed in the present work for dispersion of water in mineral oil in presence of an emulsifying surfactant. The volume water fraction was fixed,  $\alpha=0.02$ . Other details of the experiments are given in the section ‘‘Experiment’’.

Let us start with a brief illustration of one-dimensional model performance that was in detail analysed by Eskin et al. (2017).

In Figs. 2, 3 we showed the experimental and computed cumulative droplet size distributions obtained in the Couette device at the spindle rotation speeds  $\Omega=26.7$  and 45 Hz respectively. The data are presented for the 2 and 10 min operation durations. Only droplet breakup was taken into account in the computations.

One can see that an increase in the spindle rotation speed leads to a significant droplet size reduction. Also, it is worth to note that the size distributions obtained during 2 and 10 min of operation are close to each other. Thus, the most intense dispersion occurs during a relatively short initial time period. The computed size distributions are noticeably narrower than the experimental ones. This disagreement is mainly caused by neglecting a coalescence, not fully suppressed by the surfactant, a limited accuracy of the 1-D model and the end effect associated with the relatively small Couette device height (see the brief discussion in ‘‘Introduction’’).

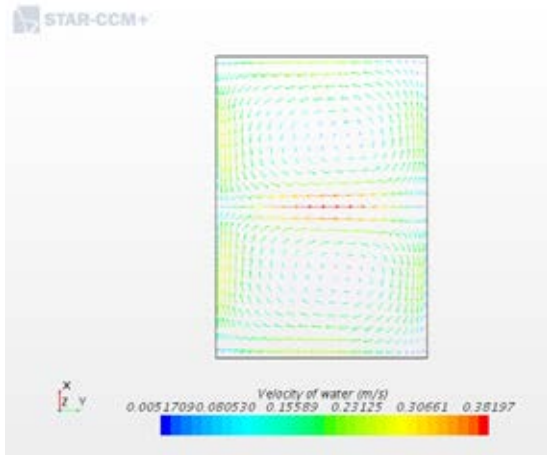


**Figure 4:** Distribution of the axial (x) and radial (y) velocity components over the radial Couette device gap cross-section.

Computations of droplet dispersion by the CFD code allowed us to better understand underlying process physics. The circumferential flow velocities in the investigated Couette flow regimes reach several meters per second. However, because the Couette device employed has relatively small height, secondary flows caused mainly by the end effect can be of relatively high intensities. The calculated velocity field of the secondary flows at the rotation speed  $\Omega=26.7$  Hz is shown in Fig.4. One can see the two nearly symmetric recirculation cells, characterized by velocities, which are relatively small but significant

enough to strongly influence droplet transport across the Couette device gap. Thus, accounting for the secondary flows is one of important advantages of the 3-D simulations over the 1-D model calculations.

Also, the end effect significantly reduces accuracy of computations of the shear stresses at the inner and the outer cylinders of the Couette device by the 1-D model. Stress distributions at both the cylinders are shown in Fig.5. The distributions are strongly non-uniform. Moreover, the mean stress at the inner cylinder wall is equal to 21.9 Pa, whereas at the outer cylinder - 3.38 Pa. For the given radii ratio of the cylinders, the 1-D model predicts the shear stress at the outer cylinder wall to be 5.48 Pa that by factor 1.6 exceeds the stress calculated by the 3-D code. This difference is caused by the end effect that is expected to decrease with an increase in the Couette device height.

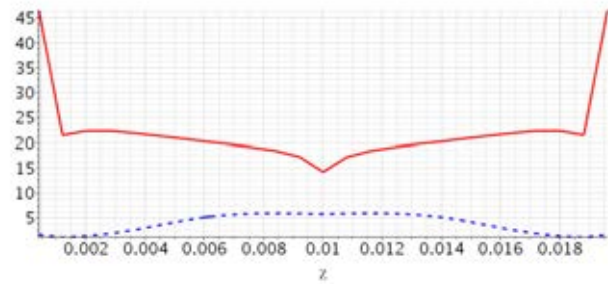


**Figure 5:** Shear stress ( Pa ) at the internal (solid line) and the external (dashed line) cylinder walls.

Let us now discuss the droplet dispersion results. The 3-D code, employing the same breakup kernel, Eq. (6), provides droplet size distributions, which are similar to those obtained using the 1-D model (Figs. 2, 3). I.e., the computed size distributions are still significantly narrower than the experimental ones. A highly possible reason of this discrepancy is that droplet coalescence was not entirely suppressed (Eskin et al., 2017) by surfactant. The discussion of this phenomenon is given in Eskin et al. (2017). Therefore, in further calculations by the 3-D code, besides breakup, we will also artificially introduce coalescence to more accurately fit the experimental data.

For coalescence modelling, we formally employ the model of Coulaloglou and Tavlarides (1977). Whereas the droplet collision rate, used in the present work, is exactly equal to that in Coulaloglou and Tavlarides (1977), the equation for the coalescence efficiency of the droplets of sizes  $d_i$  and  $d_j$  is different from the original one and written as:

$$\lambda_{ij} = \exp\left(-C \frac{\rho_f \mu_f \varepsilon d_{ij}^2}{\gamma^2}\right), \quad (13)$$

where  $d_{ij} = d_i d_j / (d_i + d_j)$ ,  $C$  is the empirical coefficient,  $\mu_f$  is the continuous fluid dynamic viscosity. Note, in Coulaloglou and Tavlarides (1977) one can find  $d_{ij}^4$  (not  $d_{ij}^2$ ) under the exponent. The authors of the model made a trivial typo in the derivations. Unfortunately, the erroneous equation has been widely used by numerous authors (e.g., Liao and Lucas, 2010).

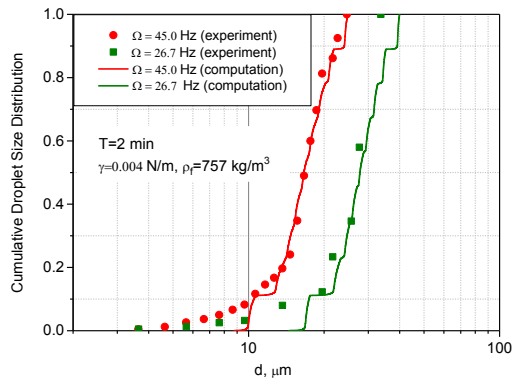


**Figure 6:** Cumulative size distribution for the 26.6 (right) and 45 Hz (left) rotation speeds: the experimental data (markers) and the CFD code (solid lines).

In the 3-D computations we use the same value of  $We_{cr}$  as in the 1-D case ( $We_{cr} = 0.5$ ). The coalescence related empirical coefficient, identified from the experimental droplet size distributions, is  $C = 3 \cdot 10^6$ . The calculated droplet size distributions for the 2-min duration experiments are shown in Fig.6. One can see a rather good agreement between the computed and the experimental curves. Note that the computations do not predict the left size distribution tails, caused by presence of small particles, because of the relatively small number of size fractions (9) employed for the 3-D computations.

We would like to also emphasize that Eq. (13) was derived assuming mobile droplet interfaces. In this work, we use this equation for modelling coalescence in presence of a surfactant that greatly reduces interface mobility. Thus, employment of Eq. (13) here does not have a solid physical justification and serves only for fitting the experimental data; therefore, the empirical coefficient identified is not suitable for modelling dispersion of fluids different from those used in the present work.

To illustrate the dispersion process mechanisms, in Fig.7 we plotted the distributions of both the breakup and coalescence rates over the Couette device gap under steady-state conditions at the rotation speed  $\Omega=26.7$  Hz. Note that the breakup plot is shown using logarithmic scale, whereas the coalescence plot - linear scale. As one can see, the breakup zone is located in the vicinity of the inner wall, where the turbulent dissipation rate is highest. In contrast to breakup, the coalescence rate is highest in the centres of the recirculation zones. We would like to also emphasize that the maximum breakup rate is much higher than the maximum coalescence rate. However, the total coalescence zone is much larger than the breakup one; therefore the total number of coalescence events is matched by the total number of breakup events.

To evaluate mixing quality in the considered Couette device, in Fig.8 we showed the steady-state distribution of the droplet Sauter diameter over the gap. Relatively small variations of this parameter over the gap, except the inner wall vicinity, show that the dispersed system is well-mixed. This observation means that the turbulent diffusion of droplets significantly contributes into droplet dispersion.

Thus, we performed a detailed studies of dispersion of chemically stabilized water droplets in a turbulent Couette flow using both the engineering 1-D model and the 3-D CFD code. Formal accounting for coalescence in 3-D modelling allowed to accurately fit the experimental data.

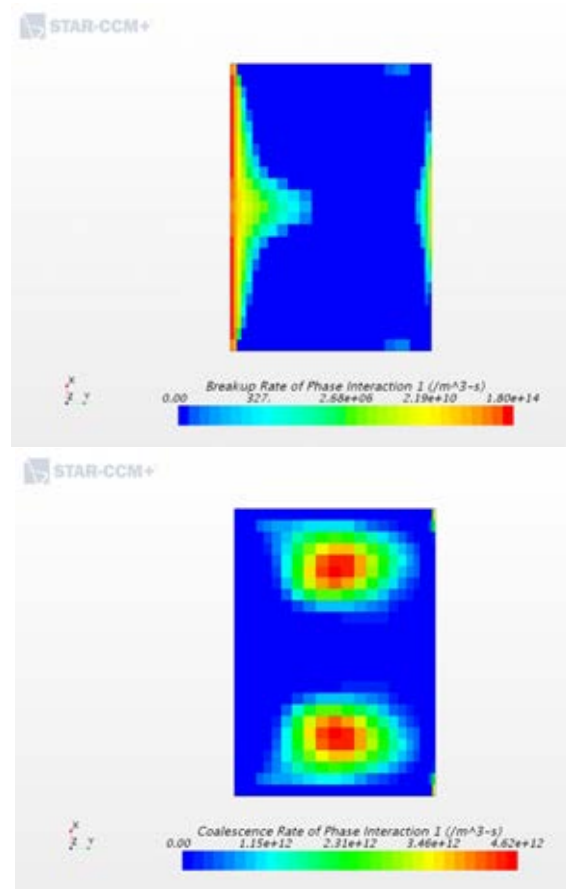


**Figure 7:** Distributions of the steady-state breakup (upper) and the coalescence (bottom) rates over the Couette device gap,  $\Omega=26.7$  Hz.

A number of the 3-D computations allowed us to reveal some peculiarities of the dispersion process. However, employment of the artificial approach to accounting for coalescence of partially stabilized droplets limits application of the identified model parameters to only the dispersion system that was studied in the current work.

## CONCLUSIONS

Dispersion of chemically stabilized water droplets in a turbulent Couette flow has been studied by both the 1-D and 3-D models. The 1-D model is based on solution of the Advection-Diffusion Population Balance equation. Three-dimensional modelling has been conducted using the CFD-population balance A-MuSiG method recently implemented into the STAR-CCM+ code of Siemens PLM Software. The same droplet breakup model has been employed for both the models. The 3-D computations revealed relatively intense circulation motion caused by the Couette device cover walls. Nevertheless, the droplet size distributions predicted by both the models were close to each other. An analysis of the experimental data showed that droplet coalescence is not fully suppressed by the surfactant; therefore, a coalescence was formally

introduced into the 3-D dispersion model to accurately fit the experimental data. The 3-D computations showed also that the dispersed phase is rather uniformly distributed over the Couette device gap that indicates a significant contribution of turbulent diffusion into the dispersion process.

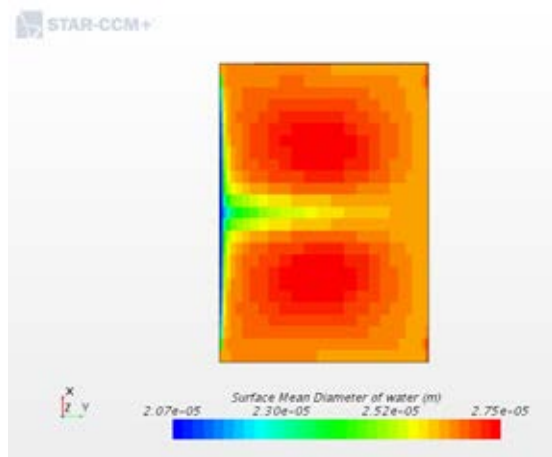


**Figure 8:** Distribution of the droplet Sauter diameter over the Couette device gap,  $\Omega=26.7$  Hz.

## REFERENCES

- COULALOGLOU C.A., TAVLARIDES L.L., (1977), "Description of interaction processes in agitated liquid-liquid dispersions", *Chem. Eng. Sci.*, **32**, 1289-1297.
- ESKIN D., RATULOWSKI J., AKBARZADEH K., PAN S., (2011), "Modelling asphaltene deposition in turbulent pipeline flows", *The Can. J. Chem. Eng.*, **89**, 421-441.
- ESKIN D., (2014), "Applicability of a Taylor-Couette device to characterization of turbulent drag reduction in a pipeline", *Chem. Eng. Sci.*, **116**, 275-283.
- ESKIN D., TAYLOR S., YANG D., (2017), "Modeling of droplet dispersion in a turbulent Taylor-Couette flow", *Chem. Eng. Sci.*, **161**, 36-47.
- KUBOI R., KOMASAWA I., and OTAKE T., (1972), "Behavior of dispersed particles in turbulent liquid flow", *J. Chem. Eng. Japan*, **5**, 349-355.
- KUMAR S., RAMAKRISNA, D., 1996. On the solution of population balance equations by discretization-I. A fixed pivot technique. *Chem. Eng. Sci.* 51, 1311-1332.
- LEE C.H., GLASGOW L.A., ERICKSON L.E., (1987), "Bubble breakup and coalescence in turbulent gas-liquid dispersions", *Chem. Eng. Commun.*, **59**, 65-84.
- LEWIS G.S., SWINNEY H.L., 1999, "Velocity structure functions scaling and transitions in high-Reynolds-number Couette-Taylor flow", *Phys. Rev. E*, **59**, 5457-5467.
- LIAO Y., LUCAS D., (2009), "A literature review of theoretical models for drop and bubble breakup in turbulent dispersions", *Chem. Eng. Sci.*, **64**, 3389-3406.
- LIAO Y., LUCAS D., (2010), "A literature review on mechanisms and models for the coalescence process of fluid particles", *Chem. Eng. Sci.*, **65**, 2851-2864.
- NOTTER R.H., SLEICHER C.A., (1971), "The eddy diffusivity in the turbulent boundary layer near a wall", *Chem. Eng. Sci.*, **26**, 161-171.
- VIKHANSKY A., (2013), "Direct quadrature spanning tree method for solution of the population balance equations", *Journal of Aerosol Science*, **55**, 78-88.
- VIKHANSKY A., SPLAWSKI A., (2015), "Adaptive multiple size group method for CFD-population balance modelling of polydisperse flows", *The Can. J. Chem. Eng.*, **93**, 1327-1334.

## SIMULATION OF GAS-LIQUID FLOWS IN SEPARATORS. A LAGRANGIAN APPROACH

John C. MORUD<sup>1\*</sup>, Sigrid K. DAHL<sup>1†</sup>

<sup>1</sup>SINTEF Materials and Chemistry, 7465 Trondheim, NORWAY

\* E-mail: john.morud@sintef.no

† E-mail: sigrid.k.dahl@sintef.no

### ABSTRACT

In order to simulate the separation efficiency of gas scrubbers, we have formulated and implemented a version of the Single-Particle Method. The method is suitable for CFD simulations of gas-droplet flows, and is based on using Lagrangian tracking of droplets. An implementation of the method has been made in a commercial CFD tool. The methodology and the CFD implementation have been validated against analytical results in the literature.

**Keywords:** CFD; fluid mechanics; two-phase; multi-phase; droplets; population balance .

$N$	Number of field particles in cell, [-]
$S$	Source term in population balance, [ $kg/m^3 \cdot m^3 \cdot s$ ]
$t$	Time, [s]
$\Delta t$	Time step, [s]
$T_L$	Lagrangian time scale of turbulence, [s]
$\mathbf{u}$	Velocity in pop. balance, [ $m/s$ ]
$\mathbf{u}_{fluid}$	Velocity of continuous fluid, [ $m/s$ ]
$v$	Droplet volume (size), [ $m^3$ ]
$V_{cell}$	Volume of Finite Volume cell, [ $m^3$ ]
$\mathbf{x}$	Position in space, [ $m$ ]
$y_i$	Volume (size) of field particle 'i', [ $m^3$ ]

### NOMENCLATURE

#### Greek Symbols

$\beta$	Under-relaxation factor for mass field, [-]
$\beta(v v')$	Mass distribution, daughter droplets in breakup, [ $m^{-3}$ ]
$\Gamma$	Breakup rate, [ $s^{-1}$ ]
$\delta$	Typical cell dimension, [ $m$ ]
$\varepsilon$	Turbulent dissipation rate, [ $W/kg$ ]
$\lambda$	Replacement rate constant for field particles, [ $1/s$ ]
$\xi$	Random number or process [-]
$\rho_{liq}$	Liquid density, [ $kg/m^3$ ]
$\tau$	Residence time for droplet, [s]
$\varphi_i$	Concentration of field particles, [ $kg/m^3$ ]
$\phi$	Particle field, [ $kg/m^3 \cdot m^3$ ]
$\chi$	Coalescence rate, [ $s^{-1}$ ]

#### Latin Symbols

$d$	Droplet diameter, [ $m$ ]
$F$	Cumulative size distribution, [-]
$K$	Coalescence kernel, [ $m^3/s$ ]
$k$	Turbulent kinetic energy, [ $m^2/s^2$ ]
$k_b$	Parameter in Case 1 and 3, [ $s^{-1}$ ]
$L_E$	Turbulent correlation length, [ $m$ ]
$m(v)$	Size distribution on mass basis, [ $kg/m^3 \cdot m^3$ ]
$\dot{m}$	Mass flow rate of droplets, [ $kg/s$ ]
$\tilde{M}$	Temporary field, [ $kg/cell$ ]
$M$	Mass of droplets in cell, [ $kg/cell$ ]

### INTRODUCTION

In many gas-liquid separation applications the separation efficiency is critically dependent on the particle size of the dispersed phase. Frequently, the use of an average particle size is sufficient for fluid flow simulations. However, there are a number of applications where one should consider the complete particle size distribution. The motivation for the work in this paper stems from high pressure gas-liquid separation (scrubbers) where there is a small amount of low surface tension liquid in a gas flow. However, most of the methodology is directly applicable to general multiphase flows as well as population balances occurring in Chemical Engineering applications, such as crystallizers.

The most important phenomena in scrubber applications are *droplet coalescence*, *droplet breakup*, *droplet deposition on walls* and *entrainment of droplets from walls*. The methodology in this paper is applicable to these, allowing a user to predict the performance of coalescence and breakup kernels and compare the predictions to experimental data. Actual physical models and validation against high pressure data will be a topic for a subsequent paper. Thus, in this paper we consider a droplet population balance with coalescence and breakup and show how it can be solved for arbitrary kernels.

There are a number of possible strategies for population balance simulations. One approach is to apply a quadrature rule to the integrals occurring in the population balance and track information in an Eulerian fashion. Among such methods are the Method of Classes (Ramkrishna, 2000); Galerkin methods; the method of Least Squares (Jiang, 1998; Dorao and Jakobsen, 2005); Orthogonal Collocation techniques and moment methods (McGraw, 1997). See also Morud (2011), Attarakih *et al.* (2004) and Attarakih *et al.* (2009).

Another way is by treating the dispersed phase as Lagrangian particles and track them throughout the flow field. The Lagrangian approach is particularly simple to implement for breakup dominated flows, as long as breakup events involve only the breaking particle and not the interaction between particles. Also aggregation events can be handled by counting and computing particle statistics in the numerical mesh (Haviland and Lavin, 1962).

In this paper we present a Lagrangian method based on the Single-Particle method of Vikhansky and Kraft (2005) together with the steady state Discrete-Particle-Method (DPM) in ANSYS FLUENT v13.0.0.

The paper is organized as follows: First the concept for handling coalescence by means of field particles is explained in an Eulerian framework. Then the Lagrangian formulation is described, explaining how to handle coalescence and breakup in the steady state DPM model. The methodology is validated against analytical solutions in the literature. Finally, we demonstrate our CFD implementation using a simple test example.

## MODEL DEVELOPMENT

We use a simple Eulerian population balance as a point of departure for the formulation of our Lagrangian model. In this manner the relation between source terms in the two formulations become apparent, allowing us to translate coalescence and breakup kernels from an Eulerian model into the Lagrangian model.

For laminar flow and at steady state the two stated models are equivalent, and can be directly compared. However, our Lagrangian formulation differs from the stated Eulerian model in that it is essentially a steady state model. Moreover, Lagrangian particles have individual velocities allowing for turbulent dispersion of equal particles. The stated Eulerian formulation is simpler in this respect as particles of equal size and position have the same velocity.

### Eulerian formulation

The droplet size distribution on mass basis at a given point in time and space,  $m(v)$ , is illustrated in Figure 1. Here  $v [m^3]$  is the droplet size (volume). Thus, within an infinitesimal size range between droplet size  $v [m^3]$  and  $v + dv [m^3]$ , the mass of droplets is  $m(v) dv [kg/m^3]$ .

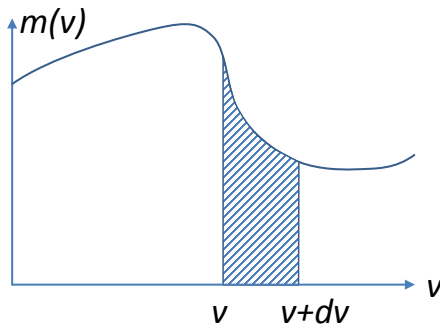


Figure 1: Droplet size distribution.

In an Eulerian framework the development of the droplet size distribution can be described by a population balance equa-

tion

$$\frac{\partial m(v, \mathbf{x}, t)}{\partial t} + \nabla \cdot (\mathbf{u}(v, \mathbf{x}, t) m(v, \mathbf{x}, t)) = S(v, \mathbf{x}, t) \quad (1)$$

where  $v$ ,  $\mathbf{x}$  and  $t$  are the droplet volume, position and time;  $\mathbf{u}(v, \mathbf{x}, t) [m/s]$  is the velocity field of the droplets and  $S(v, \mathbf{x}, t)$  is the source term consisting of birth and death of droplets due to coalescence and breakup. In the following we will omit  $\mathbf{x}$  and  $t$  for convenience as they are always present.

In particular, the birth by coalescence on mass basis is

$$S_{coal}^B(v) = \int_0^v \frac{K(v-v', v')}{\rho_{liq} v'} m(v') m(v-v') dv' \quad (2)$$

where  $K [m^3/s]$  is the coalescence kernel and  $\rho_{liq} [kg/m^3]$  is the liquid density. The integral combines all pairs of droplet sizes,  $v'$  and  $v-v'$ , that sums to droplet size  $v$ . Following Vikhansky and Kraft (2005) this can be written formally as

$$S_{coal}^B(v) = \int_0^v \frac{K(v-v', v')}{\rho_{liq} v'} \phi(v') m(v-v') dv' \quad (3)$$

where  $\phi(v)$  is equal to the mass distribution  $m(v)$  at a converged solution. We follow Vikhansky and Kraft (2005) and denote  $\phi(v)$  as the field (or target) particles. The basic principle is to keep an approximation to  $\phi(v)$  within each Finite Volume cell, whereas  $m(v)$  is represented by the Lagrangian simulation particles. An updating scheme is then introduced, which will make  $m(v)$  and  $\phi(v)$  equal at steady state.

The corresponding death term by coalescence becomes

$$S_{coal}^D(v) = - \int_0^\infty \frac{K(v, v')}{\rho_{liq} v'} \phi(v') m(v) dv' \quad (4)$$

Finally, we have the birth and death terms by breakup

$$S_{break}^B(v) = \int_v^\infty \Gamma(v') \beta_m(v|v') m(v') dv' \quad (5)$$

$$S_{break}^D(v) = -\Gamma(v) m(v) \quad (6)$$

where  $\Gamma(v) [1/s]$  is the breakage frequency and  $\beta_m(v|v')$  is the mass distribution of the daughter droplets resulting from the breakage of a droplet of size  $v'$ .

### Lagrangian formulation

The population balance, equation (1), can be written in a Lagrangian reference frame following a droplet:

$$\frac{d\mathbf{x}}{dt} = \mathbf{u} \quad (7)$$

$$\frac{d\mathbf{u}}{dt} = \mathbf{f}(v, \mathbf{u}, \mathbf{u}_{fluid}, \dots) \quad (8)$$

$$\frac{dv}{dt} = G(v) \quad (9)$$

$$\frac{dm}{dt} = S(v) - m \cdot \text{div}(\mathbf{u}) \quad (10)$$

where  $\mathbf{u}_{fluid}$  is the velocity of the continuous fluid,  $\mathbf{f}$  is the force per droplet mass and  $G$  is the growth rate of a droplet (normally zero in our models). As before,  $\mathbf{x}$  and  $t$  are omitted from the argument lists for convenience. Note that the continuous fluid is still represented in an Eulerian reference frame.

The two first equations are Newton's second law of motion for a droplet. In our case, we use the Discrete Particle Model (DPM) of FLUENT. Thus, we use the CFD code to track particles for us.

The third equation describes the growth of a droplet, which is normally zero in our models as we are considering breakup and coalescence only<sup>1</sup>.

The last equation shows that the mass density distribution along a droplet path varies due to (a) the source term,  $S$ , and (b) whether droplets approach each other or move apart. The equation is derived by applying the chain rule to  $m$  along a droplet track, i.e.

$$\frac{dm}{dt} = \frac{\partial m}{\partial t} + (\mathbf{u} \cdot \nabla) m = \underbrace{\frac{\partial m}{\partial t} + \nabla \cdot (\mathbf{u}m)}_{S(v)} - m (\nabla \cdot \mathbf{u}) \quad (11)$$

The source term for a Lagrangian **material volume**,  $\Omega(v)$ , of droplets of size  $v$  is the **same** as for the Eulerian formulation, namely  $S(v)$ . To see this, consider a material volume of droplets of size  $v$ , i.e. a material control volume with a boundary that follows the droplet velocity field for this size,  $\mathbf{u}(v)$ . There is no droplet flux of size- $v$  droplets across its boundary. The rate of change of the size distribution within this volume can then be found by using the Reynolds transport theorem followed by the Gauss theorem:

$$\begin{aligned} \frac{d}{dt} \left[ \int_{\Omega(v)} m dV \right] &= \int_{\Omega(v)} \frac{\partial m}{\partial t} dV + \int_{\partial\Omega(v)} m \mathbf{u} \cdot d\mathbf{A} \\ &= \int_{\Omega(v)} \frac{\partial m}{\partial t} dV + \int_{\Omega(v)} \nabla \cdot (\mathbf{u}m) dV \\ &= \int_{\Omega(v)} \left[ \frac{\partial m}{\partial t} + \nabla \cdot (\mathbf{u}m) \right] dV \\ &= \int_{\Omega(v)} S(v) dV \end{aligned} \quad (12)$$

Thus, in this interpretation the source term is the same for both the Eulerian and the Lagrangian frames.

### Lagrangian simulation particles

In our method we use the concept of *simulation particles*, which differs slightly from that of individual droplets. The use of simulation particles is abundant in the literature.

One extreme would be to represent every droplet by a simulation particle. We denote this as an *analog simulation*. This is not commonly used due to the computational cost, as the number of droplets in realistic cases is quite high. The other extreme is to consider Lagrangian tracking as a form of discretization of a continuous transport equation. Thus, the simulation particles are considered to be *virtual*. In this sense we can make simulation particles for any transport equation, say the equation for turbulent kinetic energy or for the dissipation rate.

In the present work, a simulation particle represents a group of droplets of similar size and follows the laws of motion of a representative droplet in the group. In the steady state model the path of the simulation particle represents a mass flow rate

<sup>1</sup> For the coalescence and breakage source terms, Equations (3), (4), (6), the growth term  $G$  becomes zero. This can be seen by subtracting  $\rho_{liq}v$  times the number density population balance from the mass density population balance, and thus obtain an equation for the evolution of droplet mass,  $d(\rho_{liq}v)/dt$ , in the Lagrangian frame. The breakup source term cancels. Due to the symmetry of the coalescence kernel,  $K(x,y) = K(y,x)$ , the coalescence term also cancels. Thus, droplets appear and disappear but do not grow or shrink by coalescence and breakup.

of droplets of similar size. Thus, we associate a mass flow rate,  $\dot{m}$  [kg/s], and a droplet size,  $v$  [ $m^3$ ], with the simulation particle.

### Monte Carlo methods

We are usually only interested in the average behavior of a large number of simulation particles, which means that techniques from Monte Carlo particle methods can be used (see Lux and Koblinger (1991)). Basically, we can choose how many realizations of a stochastic process we use provided that the number of realizations is large enough.

A basic Monte Carlo method is the one provided by the standard FLUENT DPM model with turbulent dispersion. We select particles randomly at the inlet based on the inlet size distribution and track them throughout the domain. Each of these particle tracks is associated with a liquid mass flow,  $\dot{m}$ .

There are a few observations to be made that greatly simplify our Lagrangian scheme. This is discussed in the following.

### Statistical weights

The key observation is that the mass flow,  $\dot{m}$ , of a particle track can be thought of as a statistical weight in the sense of Lux and Koblinger (1991). That is, given that a track is only one of a very large number of tracks, it results in only a small perturbation of the solution and the expected impact on the computed results becomes proportional to  $\dot{m}$ . Formally, and as a theoretical device for the subsequent discussion only, let us write this as

$$\Delta R = \dot{m} \cdot r(\mathbf{z}_0, \xi) \quad (13)$$

where  $\Delta R$  is the change in the results (i.e. some value, say the calculated separation efficiency),  $r$  is the impact on  $R$  per unit mass flow,  $\mathbf{z}_0$  is a state vector describing the initial state of the particle and  $\xi$  is a stochastic process (a vector of random numbers that decides what happens to the particle during tracking).

### Monte Carlo splitting

Assume that we choose to realize a given simulation particle by *two* particle tracks instead of one. We split the mass flow,  $\dot{m}$ , of the particle between the two realizations as  $\dot{m} = \dot{m}_1 + \dot{m}_2$  and simulate them independently. We then get an impact which is the sum of the two.

$$\Delta R_* = \dot{m}_1 \cdot r(\mathbf{z}_0, \xi_1) + \dot{m}_2 \cdot r(\mathbf{z}_0, \xi_2) \quad (14)$$

Note that the stochastic processes  $\xi_1$  and  $\xi_2$  are now different as there are two different realizations. Also note that two realizations use the same droplet size as the original particle; only the associated mass flow rates differ.

The expected value of  $r$  is independent of any actual realization  $\xi$  since it is the average of all possible realizations starting at state  $\mathbf{z}_0$ .

$$E[r(\mathbf{z}_0, \xi)] = E[r(\mathbf{z}_0, \xi_1)] = E[r(\mathbf{z}_0, \xi_2)] \quad (15)$$

Thus, the expected value stays the same as before:

$$\begin{aligned} E[\Delta R_*] &= \dot{m}_1 \cdot E[r(\mathbf{z}_0, \xi_1)] + \dot{m}_2 \cdot E[r(\mathbf{z}_0, \xi_2)] \\ &= (\dot{m}_1 + \dot{m}_2) \cdot E[r(\mathbf{z}_0, \xi)] \\ &= E[\Delta R] \end{aligned} \quad (16)$$



In summary, expected values do not change if we split a simulation particle into two and use different realizations for the two.

### Monte Carlo selection

Another modification is selection between two different particle tracks with mass flows  $\dot{m}_1$  and  $\dot{m}_2$ . We consider two different simulation particles with initial states,  $\mathbf{z}_1$  and  $\mathbf{z}_2$ . The impact of the two becomes

$$\Delta R_s = \dot{m}_1 \cdot r(\mathbf{z}_1, \xi_1) + \dot{m}_2 \cdot r(\mathbf{z}_2, \xi_2) \quad (17)$$

Now, consider realizing only one of the particles. With probability  $p_1 = \frac{\dot{m}_1}{\dot{m}_1 + \dot{m}_2}$  we simulate only particle 1. Otherwise, we simulate particle 2. We use the total mass flow for the selected particle. Thus with probability  $p_1$  we get

$$\Delta R_{s1} = (\dot{m}_1 + \dot{m}_2) \cdot r(\mathbf{z}_1, \xi_1) \quad (18)$$

otherwise, with probability  $p_2 = 1 - p_1$  we get

$$\Delta R_{s2} = (\dot{m}_1 + \dot{m}_2) \cdot r(\mathbf{z}_2, \xi_2) \quad (19)$$

The overall expected value of this operation becomes

$$\begin{aligned} & E[\Delta R_{s*}] \\ &= p_1 E[\Delta R_{s1}] + p_2 E[\Delta R_{s2}] \\ &= p_1 E[(\dot{m}_1 + \dot{m}_2) \cdot r(\mathbf{z}_1, \xi_1)] + p_2 E[(\dot{m}_1 + \dot{m}_2) \cdot r(\mathbf{z}_2, \xi_2)] \\ &= p_1 (\dot{m}_1 + \dot{m}_2) E[r(\mathbf{z}_1, \xi_1)] + p_2 (\dot{m}_1 + \dot{m}_2) E[r(\mathbf{z}_2, \xi_2)] \\ &= \dot{m}_1 E[r(\mathbf{z}_1, \xi_1)] + \dot{m}_2 E[r(\mathbf{z}_2, \xi_2)] \\ &= E[\Delta R_s] \end{aligned} \quad (20)$$

Thus, the expected value stays the same as if both particles were simulated. In summary, we are at liberty to pick two simulation particles (with mass flows  $\dot{m}_1$  and  $\dot{m}_2$ ), select one of these with probabilities  $p_1 = \dot{m}_1 / (\dot{m}_1 + \dot{m}_2)$  and  $p_2 = 1 - p_1$  respectively and simulating only the selected particle using a mass flow  $\dot{m} = \dot{m}_1 + \dot{m}_2$ .

### Application of splitting to coalescence events

Using Monte Carlo splitting, a simulation particle can be split into several simulation particles at any point of the particle track as long as the total mass flow rate of droplets stays the same. In particular, this means that the resulting droplet from a binary coalescence event can be represented by *two* simulation particles, with mass flows corresponding to the droplets entering the coalescence event. This simplifies book-keeping, since a binary coalescence can then be modeled as an interaction between two particle tracks where the simulation particles preserve their mass flows but change diameters in the interaction. In the actual implementation of the single-particle method, each of these simulation particles interacts only with the field particles, simplifying the book-keeping even further.

The model development proceeds in four stages, as illustrated in Figure 2.

- (a) We start with the coalescence event. Two particles with mass flows  $\dot{m}_1$  and  $\dot{m}_2$  collides, and a daughter particle with mass flow  $\dot{m}_1 + \dot{m}_2$  is produced. The droplet size becomes  $v_1 + v_2$

- (b) We could use two realizations to simulate the daughter particle. The realizations would have mass flows  $\dot{m}_1$  and  $\dot{m}_2$ . As explained in section this modification does not change expected values of the Monte Carlo simulation. That is, we obtain the same result on average as if we use scheme (a). Note that both daughter realizations have droplet size  $v_1 + v_2$ .
- (c) This is the same as (b), but illustrates that we could reuse the simulation particles entering the collision to simulate the two realizations of the daughter particle. Thus, the book-keeping becomes simpler as we consider a coalescence as an interaction between two simulation particles. The simulation particles change droplet size to  $v_1 + v_2$  during the interaction, whereas the mass flow,  $\dot{m}$ , stays the same.
- (d) Finally, we replace one of the simulation particles with the mean field,  $\phi$ , which is a statistical representation of the particles. In the present scheme, we sample simulation particles that pass through the Finite Volume cells and pick collision events randomly from this sample.

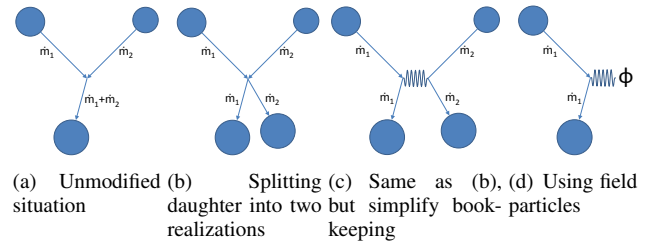


Figure 2: Development of coalescence scheme

### Application of selection to breakup events

In the same manner, we can simplify breakup events. When a droplet breaks into daughters we select one of the daughters by sampling a random droplet size,  $v$ , from the daughter distribution,  $\beta_m(v|v')$ . The mass flow of the simulation particle is thus kept during breakup events, whereas the diameter becomes that of the selected daughter. Expected values are preserved in this operation, meaning that the average behavior of a large number of tracks is the same as if every daughter were tracked. As before, we re-use the simulation particle entering the breakup event to simulate the selected daughter particle.

The situation is illustrated in Figure 3.

- (a) We start with a breakup event, illustrated by a binary breakup into droplets of size  $v_1$  and  $v_2$ .
- (b) Using Monte Carlo selection we realize only one of the daughters. We select a random droplet size by sampling the daughter distribution,  $\beta_m(v|v')$ , and using the total mass flow  $\dot{m}$ . This method is a continuous extension of the selection procedure explained in the section "Monte Carlo selection" above; thus this modification does not change expected values in the simulation.

### The FLUENT DPM model

To simulate particle tracks following Newton's second law of motion we use the Discrete Particle Model (DPM) of Ansys FLUENT. For turbulent flow, we use their standard

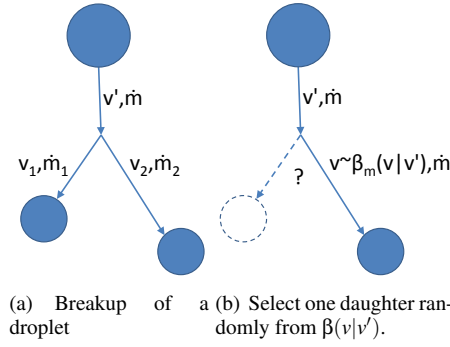


**Figure 3:** Development of breakup scheme

$k - \epsilon$  model together with the Discrete Random Walk (DRW) model. The DRW model simulates the interaction of a particle with a succession of discrete stylized turbulent eddies (Ansys Inc., Nov. 2010). Fluid velocity fluctuations are sampled from a Gaussian probability distribution assuming isotropic turbulence and a turbulent kinetic energy  $k$  provided by the  $k - \epsilon$  model. The interaction lasts for a duration that is the minimum of the Lagrangian time scale,  $T_L = C_L k / \epsilon$ , of the fluid and an eddy crossing time explained in the cited reference.

Thus, we write our population balance model on top of the existing DPM model in FLUENT by handling the population balances at the end of each time step of the DPM model. In this manner, our formulation inherits all the functionality of the DPM model. All we do is to add population balance functionality to the existing model.

### Lagrangian formulation for simulation particles

Thus, to simulate particle tracks we perform the following:

1. At the fluid inlet, pick simulation particles randomly from the inlet size distribution. The inverse distribution method is suitable, i.e. generate droplet volumes according to  $v = F^{-1}(\xi)$  where  $\xi$  is a uniform on  $[0,1]$  random number and  $F(v)$  is the cumulative size distribution, i.e. the fraction of the droplet mass below size  $v$ .
2. Simulate particle tracks according to Newton's second law of motion, and handle coalescence, breakup and deposition events at each time step. The actual tracking of the particle is handled by FLUENT's DPM model. All we do is to handle breakup and coalescence.

The details of the particle tracking are given in the following sections.

### Tracking particles

At each time step, perform the following tasks:

1. Update the overall mass holdup of droplets in the current FV-cell.
2. Update the field particles in the current cell.
3. Handle coalescence.
4. Handle breakup.

Each of these is described subsequently.

### Updating the overall mass holdup of droplets

As each particle track represents a mass flow rate,  $\dot{m}$ , of droplets, the mass holdup represented by one time step,  $\Delta t$ , of a simulation particle becomes  $\dot{m}\Delta t$ . Define a mass field of droplets,  $M$  [kg/cell], and a temporary field  $\tilde{M}$  [kg/cell].

Before each particle track: Set  $\tilde{M} = 0$ .

At each particle time step during a track: Add the holdup contribution  $\dot{m}\Delta t$  to the temporary field  $\tilde{M}$  of the current Finite Volume cell. If the cell differs from the previous cell, split the holdup contribution equally between the new and the previous cell (Nothing is gained by interpolating individual tracks linearly as the expected value of the split ratio is 50-50, which means that an equal split is correct on average for a large number of tracks).

At the end of a particle track: Update the mass field of droplets as  $M := \beta\tilde{M} + (1 - \beta)M$  where  $\beta$  is an under-relaxation factor. A typical value of  $\beta$  in our simulations is of the order of  $\beta \approx 0.01$ , which means that the mass field  $M$  is an exponential average of roughly the previous 100 particle tracks.

### Updating the field particles of the current cell

Updating the field particles in a Finite Volume (FV) cell is based on keeping statistics of the simulation particles that have visited the cell so far. This can be done in several ways, e.g. by means of histograms (Haviland and Lavin, 1962). Here, we follow Vikhansky and Kraft (2005) and represent the field particle ensemble in a FV cell by  $N$  particle groups with sizes  $y = [y_1, y_2, \dots, y_i, \dots, y_N]$ . A simple updating scheme is to pick a random number  $n$  using a Poisson distribution with parameter  $\lambda\Delta t$  where  $\Delta t$  is the time step and  $\lambda$  is a constant parameter. Replace  $n$  of the field particles in the current cell by the simulation particle. Store the size and the velocity of field particles.

Note that the number  $N$  of field particles in a FV cell is fixed. Moreover, this number can be small if the FV cells are small as long as the number of field particles per fluid volume is sufficient.

We choose the number of field particles per cell,  $N$ , to have a sufficient density of field particles. I.e.  $N/\delta^3$  should be sufficiently large, where  $\delta$  [m] is a typical cell dimension. The appropriate value of  $N$  should be selected from a sensitivity test.

We choose the parameter  $\lambda$  in the field particle replacement by setting the ratio  $\lambda\tau/N$  to a small value, say 0.01, where  $\tau$  is a typical residence time for a simulation particle in a cell. The ratio represents the fraction of the field particles in a cell that is replaced by a simulation particle on average.

### Handling coalescence

In the current scheme, simulation particles collide with field particles. There are  $N$  field particles in a FV cell with a total mass  $M$ , i.e. the mass of each field particle in a cell is  $M/N$ .

The field particles can be thought of as a discrete particle density distribution

$$\phi(v) = \sum_i \varphi_i \delta(v - y_i) = \sum_i \left( \frac{M}{NV_{cell}} \right) \delta(v - y_i) \quad (21)$$

where  $\phi_i = \frac{M}{NV_{cell}}$  is the mass concentration of field particle  $i$  in the cell,  $\delta(v - y_i)$  is a Dirac delta function at droplet volumes  $y_i$  and  $V_{cell}$  [ $m^3$ ] is the cell volume.

The death term for coalescence can then be written as:

$$\begin{aligned} S_{coal}^D(v) &= - \int \frac{K(v,v')}{\rho_{liq}v'} \phi(v') m(v) dv' \\ &= - \int \frac{K(v,v')}{\rho_{liq}v'} [\sum_i \phi_i \delta(v' - y_i)] m(v) dv' \\ &= -m(v) \sum_i \phi_i \underbrace{\frac{K(v,y_i)}{\rho_{liq}y_i}}_{\chi_i(v)} \end{aligned} \quad (22)$$

It follows that coalescence of a simulation particle against field particles is a Poisson process and that the rate of coalescence events,  $\chi_i(v)$  [1/s], for a simulation particle,  $v$ , against a particular field particle,  $y_i$ , is:

$$\chi_i(v) = \left( \frac{M}{NV_{cell}} \right) \frac{K(v,y_i)}{\rho_{liq}y_i} \quad (23)$$

The total coalescence rate against all field particles becomes:

$$\chi(v) = \sum_i \chi_i(v) = \left( \frac{M}{\rho_{liq}NV_{cell}} \right) \sum_i \frac{K(v,y_i)}{y_i} \quad (24)$$

This leads to the following scheme for coalescence events:

1. In a time step,  $\Delta t$ , select the number of coalescence events,  $n$ , randomly from a Poisson distribution with parameter  $\chi(v) \Delta t$ .
2. Pick  $n$  values,  $y_j$ ,  $j=1,2..n$ , randomly with probability  $P_i = \chi_i(v) / \chi(v)$  from the field particles (with replacement). Then update the simulation particle size as  $v := v + \sum_{j=1}^n y_j$

Note that more than one coalescence event during a time step should be a rare event. If not, the time step is too large and should be decreased.

## Handling breakup

There are a number of published breakup kernels in the literature (Liao and Lucas (2009)). Thus, select a breakup frequency model,  $\Gamma(v)$ . Select the number of breakages,  $n_{break}$  during a time step from a Poisson distribution with parameter  $\Gamma(v) \Delta t$ . Again, the time step should be sufficiently small that 0 and 1 events during the time step dominate.

For each breakup event we use Monte Carlo selection, and sample one daughter from the daughter distribution,  $\beta_m(v|v')$ , as explained in the section "Application of selection to breakup events" above. The cumulative daughter distribution is given by

$$F(v) = \int_0^v \beta_m(v|v') dv \quad (25)$$

The distribution can then be sampled by the inverse distribution method as  $v/v' = F^{-1}(\xi)$  where  $\xi$  is a uniform on [0 – 1] random number.

## VALIDATION OF THE METHODOLOGY

The methodology has been validated against analytical results for breakup and coalescence in Continuous Stirred Tank

Reactors (CSTR). A CSTR is similar to a single Finite Volume cell in the CFD code, and the methodology can be directly applied. For the validation we have used simple Matlab scripts.

### Case 1. CSTR with pure breakup

First, we demonstrate that the Monte Carlo selection procedure results in a correct daughter distribution. As a test case, we use 'Case 1' of Attarakih *et al.* (2004), for which there is an analytical solution.

Consider a Continuous Stirred Tank Reactor (CSTR). Assuming no spacial gradients, the population balance (1) can be integrated over the CSTR volume. Assuming no coalescence the population balance becomes

$$\begin{aligned} \frac{\partial m(v)}{\partial t} &= \frac{m_{feed}(v) - m(v)}{\tau} - \Gamma(v) m(v) \\ &+ \int_v^\infty \Gamma(v') \beta_m(v|v') m(v') dv' \end{aligned} \quad (26)$$

where  $m_{feed}$  is the feed distribution and  $\tau$  is the CSTR residence time.

The test case is:

$$\frac{m_{feed}(v)}{\rho_{liq}} = \frac{1}{v_0} \exp\left(-\frac{v}{v_0}\right) \quad (27)$$

$$\Gamma(v) = k_b \frac{v}{v_0} \quad (28)$$

$$\beta_m(v|v') = \frac{2v}{v'^2} \quad (29)$$

where  $v_0$  [ $m^3$ ] and  $k_b$  [1/s] are parameters.

Applying the described methodology, we arrive at the following algorithm. We select a fixed time step  $\Delta t$  that is sufficiently small compared to  $1/\Gamma$ .

1. **New simulation particle.** Select the size,  $v$ , of the simulation particle randomly from the feed distribution,  $m_{feed}$  (here: the exponential distribution with parameter  $v_0$ ).
2. **Outlet flow.** Particle can leave the CSTR during the time step  $\Delta t$ . This is a Poisson process. Thus, select a random number,  $n$ , from the Poisson distribution with parameter  $\Delta t/\tau$ . If  $n > 0$  the particle left the tank. Pick a new particle by restarting at step 1. Otherwise,  $n = 0$  and we continue with the next step.
3. **Particle breakage.** Select the number of breakages during the time step  $\Delta t$  from a Poisson distribution with parameter  $\Gamma \Delta t$ . The time step should be so small that two or more breakages during  $\Delta t$  happens rarely<sup>2</sup>. Zero and one events should dominate.
4. **Splitting into daughters.** By Monte Carlo splitting, select one daughter randomly from the  $\beta_m$ -distribution. In the present case we can select  $v = \sqrt{\xi} v'$  where  $\xi$  is a uniform on [0 – 1] random number<sup>3</sup>. Continue from step 2.

<sup>2</sup>In the present example we could select the time between events from an exponential distribution with parameter  $1/\Gamma$ , resulting in a variable time step  $\Delta t$ . However, in the CFD application this becomes impractical.

<sup>3</sup>The cumulative distribution of  $\beta_m$  is  $F(v) = \int_0^v \beta_m(v|v') dv = (v/v')^2$ . The inverse distribution method yields  $v/v' = F^{-1}(\xi)$ , or  $v = \sqrt{\xi} v'$ .

The analytical solution of Attarakih *et al.* (2004) at steady state can be written as

$$\frac{m(v)}{\rho_{liq}} = C v \left( \frac{1}{a} + \frac{2k_b \tau}{a^2} + \frac{2(k_b \tau)^3}{a^3} \right) \quad (30)$$

$$a = 1 + k_b \tau \frac{v}{v_0} \quad (31)$$

where  $C$  is a normalization constant.

Figure 4 shows a comparison between the cumulative mass distribution in our approach<sup>4</sup> and the analytical solution using  $N = 10\,000$  simulation particles,  $\tau = 100$  s,  $k_b = 1$  s<sup>-1</sup>,  $\Delta t = 1$  s and  $v_0 = 1$  mm<sup>3</sup>. As can be seen, the correspondence is excellent.

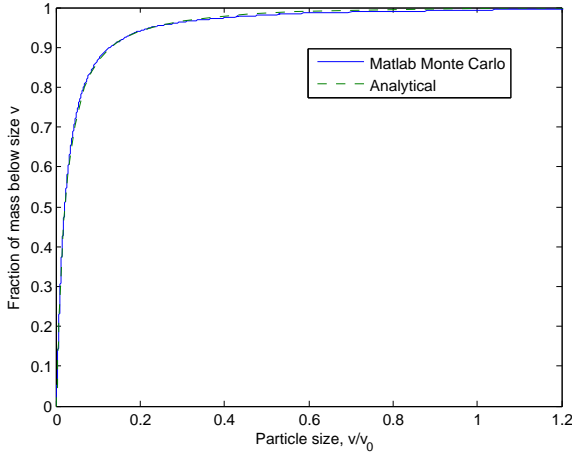


**Figure 4:** Case 1. Validation of daughter distribution from breakup.  $N = 10\,000$  simulation particles,  $\tau = 100$  s,  $k_b = 1$  s<sup>-1</sup>,  $\Delta t = 1$  s and  $v_0 = 1$  mm<sup>3</sup>.

## Case 2. CSTR with coalescence

We consider coalescence in a CSTR. Assuming no breakup and a constant breakup kernel,  $K(v, v') = K_0$ , the population balance becomes

$$\begin{aligned} \frac{\partial m(v)}{\partial t} = & \frac{m_{feed}(v) - m(v)}{\tau} \\ & + \int_0^v \frac{K_0}{\rho_{liq} v'} m(v') m(v-v') dv' \\ & - \int_0^\infty \frac{K_0}{\rho_{liq} v'} m(v') m(v) dv' \end{aligned} \quad (32)$$

where  $m_{feed}$  is the feed distribution and  $\tau$  is the CSTR residence time. The inlet mass distribution of the test case is

$$\frac{m_{feed}(v)}{\rho_{liq} N_0 v_0} = \frac{v}{v_0^2} \exp\left(-\frac{v}{v_0}\right) \quad (33)$$

where  $N_0$  and  $v_0$  are parameters.

An analytical solution to this problem is given in Nicmanis and Hounslow (1998) as

$$m(v) = \rho_{liq} N_0 \frac{v}{v_0} \frac{I_0\left(\frac{-tv}{v_0(1+2t)}\right) + I_1\left(\frac{-tv}{v_0(1+2t)}\right)}{\sqrt{1+2t} \exp\left[\frac{(1+t)v}{(1+2t)v_0}\right]} \quad (34)$$

<sup>4</sup>As all simulation particles represent the same amount of mass in our formulation, the plot is simply the accumulated mass fraction  $F = [1/N, 2/N, \dots, N/N]$  against a sorted vector of the simulation particles leaving the reactor,  $[v_1, v_2, \dots, v_N]$ .

where  $t = K_0 N_0 \tau$  and  $I_0, I_1$  are modified Bessel functions. Nicmanis and Hounslow (1998) also explain how to avoid overflow/underflow when evaluating this expression by using the asymptotic expression

$$m(v) = \rho_{liq} v \frac{\exp\left(\frac{-v}{2v_0 t}\right)}{\sqrt{\pi}(2t)^2 \left[\frac{v}{2v_0 t}\right]^{3/2}} \quad (35)$$

which is used when

$$\frac{-tv}{v_0(1+2t)} > 700 \quad (36)$$

We apply the algorithm given in sections through using  $N = 50\,000$  simulation particles,  $\tau = 200$  s,  $K_0 = 1$  mm<sup>3</sup>/s,  $N_0 = 1$  mm<sup>-3</sup>,  $v_0 = 1$  mm<sup>3</sup>,  $\Delta t = 2$  s,  $\beta = 0.01$ ,  $N_{field} = 100$  field particles,  $\lambda = 0.01 N_{field} / \tau = 0.005$ .

The resulting cumulative mass distribution is shown in Figure 5. The match between our scheme and the analytical result is excellent.

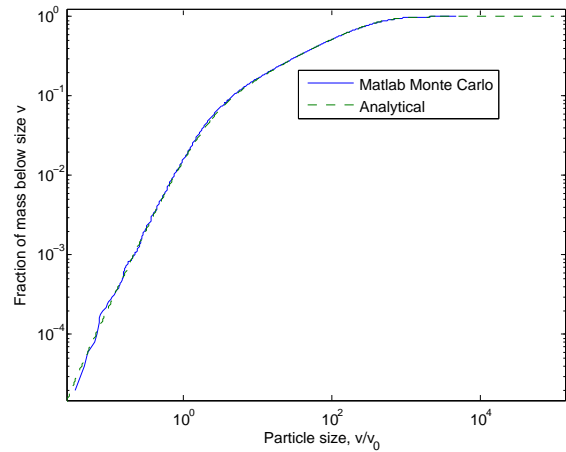


**Figure 5:** Case 2. Validation of coalescence using  $N = 50\,000$  simulation particles,  $\tau = 200$  s,  $K_0 = 1$  mm<sup>3</sup>/s,  $N_0 = 1$  mm<sup>-3</sup>,  $v_0 = 1$  mm<sup>3</sup>,  $\Delta t = 2$  s,  $\beta = 0.01$ ,  $N_{field} = 100$  field particles,  $\lambda = 0.01 N_{field} / \tau = 0.005$ .

## VALIDATION OF THE FLUENT IMPLEMENTATION

In order to validate the FLUENT implementation, we have simulated a simple plug flow reactor, as shown in Figure 6. Since this is a very simple problem it can be compared against the Matlab scripts that was validated in Case 1 and 2.

We emphasize that our implementation inherits all the functionality of the FLUENT DPM model. I.e. it works for unstructured 3D meshes, with momentum coupling between the particles and the continuous fluid, various boundary conditions etc. See the FLUENT theory guide (Ansys Inc., Nov. 2010) for details about functionality.

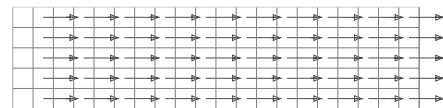


**Figure 6:** Case 3. Simple FLUENT mesh for plug flow test

## Validation of breakup implementation

The plug flow parameters used to validate the breakup implementation in FLUENT are identical to Case 1 above except for the plug flow aspect. The residence time in the reactor is 100 s as before.

As a comparison, we use the algorithm in section except that we replace the residence time in step 2 with the fixed value  $\tau$ . We reuse the Matlab script that was used for the Case 1 validation.

Figure 7 shows a comparison between the outlet size distribution by the FLUENT model and the corresponding Matlab result. The correspondence is excellent.

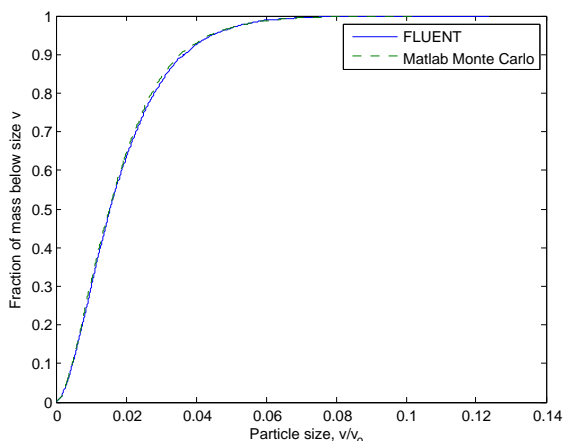


**Figure 7:** Case 3. Validation of daughter distribution from breakup using FLUENT.  $N = 10\,000$  simulation particles,  $\tau = 100$  s,  $k_b = 1\text{ s}^{-1}$  and  $v_0 = 1\text{ mm}^3$ .

## Validation of coalescence implementation

The plug flow parameters used to validate the coalescence implementation in FLUENT are identical to Case 2 above except for the plug flow aspect. The residence time in the reactor is 200 s as before. We use 10 field particles per cell; parameters  $\beta = 0.001$  and  $\lambda = 0.01$  in FLUENT.

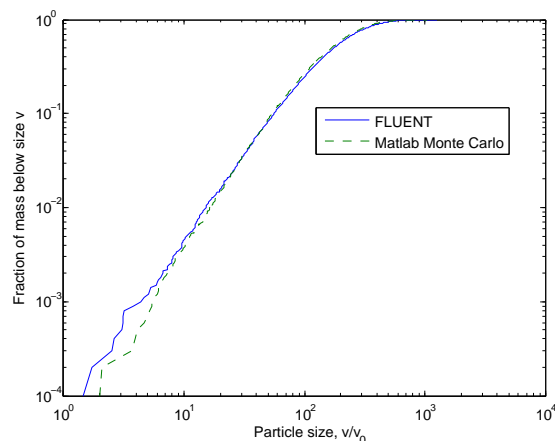
As a comparison we couple 20 CSTR's in series. We reuse the Matlab script for coalescence in a CSTR that was validated in Case 2.

Figure 8 shows a comparison between the outlet size distribution by the FLUENT model and the corresponding Matlab result. The correspondence is quite good. Note that there is inevitably a discrepancy at the tails of the distribution. Since we use 10000 particles, there are only 100 particles below an accumulated mass fraction of  $10^{-2}$ , and only 10 particles below  $10^{-3}$ .

## DISCUSSION AND CONCLUSION

One of the nice properties of the scheme presented in this paper is that there is global conservation of mass and momentum. A simulation particle has the same mass flow along the particle track even when there is breakup and coalescence. Thus, droplet mass will never appear or disappear.

The present paper focus on the general methodology, and not on actual kernels for coalescence and breakup. This is a subject of a subsequent paper. In turbulent flows one inevitably



**Figure 8:** Case 4. Validation of FLUENT daughter distribution from coalescence.  $N = 10\,000$  simulation particles,  $\tau = 200$  s,  $K_0 = 1\text{ mm}^3/\text{s}$ ,  $\beta = 0.001$ ,  $N_{field} = 10$  field particles per cell,  $\lambda = 0.01$  and  $v_0 = 1\text{ mm}^3$ .

has to make closure models when modelling coalescence and breakup. One of the purposes of our FLUENT model is to enable us to compare the predictions of coalescence and breakup kernels against experimental data.

In conclusion, the Monte Carlo, Single Particle method developed in this article can predict the solution of population balance equations. It is applicable to population balances in general, and in particular to droplet breakup and coalescence in gas-liquid flow. It has been shown how methods developed for Neutron transport, such as Monte Carlo splitting and selection, is directly applicable to population balances in Chemical Engineering applications.

The method has been implemented on top of the existing Discrete Particle Model (DPM) in FLUENT. Thus we have added population balance functionality to the DPM model without limiting the functionality of the DPM model.

The method has been validated against analytical solutions for breakup and coalescence.

## REFERENCES

- Anslys Inc. (Nov. 2010). *ANSYS FLUENT Theory Guide, Release 13.0*.
- ATTARAKIH, M., BART, H. and FAQIR, N. (2004). "Numerical solution of the spatially distributed population balance equation describing the hydrodynamics of interacting liquid-liquid dispersions". *Chemical Engineering Science*, **59**, 2567–2592.
- ATTARAKIH, M., DRUMM, C. and BART, H. (2009). "Solution of the population balance equation using the sectional quadrature method of moments (sqmom)". *Chemical Engineering Science*, **64**, 742–752.
- DORAO, C. and JAKOBSEN, H. (2005). "Application of the least square method to population balance problems". *Computers and Chemical Engineering*, **30**, 535–547.
- HAVILAND, J. and LAVIN, M. (1962). "Application of the monte carlo method to heat transfer in a rarified gas". *Physics of Fluids*, **11**, 1399–1405.
- JIANG, B. (1998). *The Least-Square Finite Element Method: Theory and Applications in Computational Fluid Dynamics and Electromagnetics*. Springer, Berlin.

LUX, I. and KOBLINGER, L. (1991). *Monte Carlo particle transport methods : Neutron and photon calculations*. Boca Raton : CRC Press, Cambridge.

MCGRAW, R. (1997). "Description of aerosol dynamics by the quadrature method of moments". *Aerosol Science and Technology*, **27**, 255–265.

MORUD, J. (2011). "Implementation of the sectional quadrature method of moments in fluent". *8th International Conference on CFD in Oil and Gas, Metallurgical and Process Industries SINTEF/NTNU, Trondheim Norway*.

NICMANIS, M. and HOUNSLOW, M.J. (1998). "Finite-element methods for steady-state population balance equations". *AIChE Journal*, **44(10)**, 2258–2272. URL <http://dx.doi.org/10.1002/aic.690441015>.

RAMKRISHNA, D. (2000). *Population balance-Theory and Applications to Particulate Processes in Engineering*. Academic Press, San Diego.

VIKHANSKY, A. and KRAFT, M. (2005). "Single-particle method for stochastic simulation of coagulation processes". *Chemical Engineering Science*, **60**, 963–967.



# CFD MODELLING TO PREDICT MASS TRANSFER IN PULSED SIEVE PLATE EXTRACTION COLUMNS

Nirvik SEN<sup>1\*</sup>, K.K. SINGH<sup>1,2</sup>, A.W. PATWARDHAN<sup>3</sup>, S. MUKHOPADHYAY<sup>1,2</sup>, K.T SHENOY<sup>2</sup>, S. MOHAN<sup>4</sup>

<sup>1</sup>Homi Bhabha National Institute, Mumbai, INDIA

<sup>2</sup>Chemical Engineering Division, Bhabha Atomic Research Centre, Mumbai, INDIA

<sup>3</sup>Institute of Chemical Technology, Mumbai, INDIA

<sup>4</sup>Chemical Engineering Group, Bhabha Atomic Research Centre, Mumbai, INDIA

Corresponding author's e-mail: nirvik@barc.gov.in

## ABSTRACT

A 2D CFD-PBM based numerical model to predict interphase mass transfer in a Pulsed Sieve Plate Column (PSPC) is reported. The model is based on Euler-Euler interpenetrating continuum approach. Drag law due to Schiller and Naumann is used to model the interphase momentum exchange term. Spatial and temporal variations of drop population are obtained by coupling Population Balance (PB) equations with flow equations. Suitable drop coalescence and breakage kernels are used in the PB equations. Species transport equation is solved in both phases to predict interphase mass. The developed model is validated against reported mass transfer experimental data in a 2 inch PSPC. Absolute average error in prediction is less than 5%. The validated model is used to understand the complex time periodic flow patterns inside the column.

**Keywords:** CFD, population balance equations, two phase flow, species transport equations, mass transfer. snap-shot approach.

## NOMENCLATURE

### Greek Symbols

- $\beta$  Coalescence kernel  
 $\phi$  Phase fraction, [-].  
 $\lambda$  Collision efficiency, [-].

### Latin Symbols

- $A$  Pulse amplitude, [m].  
 $a$  Breakage kernel,  
 $B^a$  Droplet birth due to aggregation, [ $1/m^3\cdot s$ ].  
 $B^b$  Droplet birth due to breakage, [ $1/m^3\cdot s$ ].  
 $b$  Daughter droplet distribution  
 $D^a$  Droplet death due to aggregation, [ $1/m^3\cdot s$ ].  
 $D^b$  Droplet death due to aggregation, [ $1/m^3\cdot s$ ].  
 $D$  Effective diffusion coefficient, [ $m^2/s$ ].  
 $f$  Pulse frequency, [ $1/s$ ].  
 $h$  Collision frequency [ $1/m^3\cdot s$ ]  
 $K_d$  Distribution coefficient, [-].  
 $K_{La}$  Overall volumetric mass transfer coefficient, [ $1/s$ ].  
 $L$  Characteristic drop size, [m].  
 $n$  Droplet number density, [ $m/s$ ].  
 $U$  Velocity vector, [ $m/s$ ].  
 $U_p$  Pulsing velocity, [ $m/s$ ]  
 $x$  Concentration of solute in aqueous phase, [-].  
 $y$  Concentration of solute in organic phase, [-].

### Subscripts

- $p$   $p^{\text{th}}$  phase.  
 $q$   $q^{\text{th}}$  phase.  
 $j$   $j^{\text{th}}$  species.

## INTRODUCTION

Pulsed sieve plate columns (PSPCs) are extensively used for solvent extraction in hydrometallurgical processes for extraction of important metal values (Grodfrey and Slator, 1994; Ferreira et al., 2010; Gameiro et al., 2010).

Typically pulsed column involves a cylindrical section comprising of plates with sieve holes. The construction is similar to that of a sieve plate. However, the percentage opening and hole size in the sieve plates are not sufficient to allow a counter-current flow (heavier aqueous phase moving downward while lighter organic phase moving upwards) solely due to gravity. Thus in a pulsed sieve plate the column contents are pneumatically pulsed from the bottom which forces the phases through the sieve plates ensuring counter-current flow in the column. During the positive peak of the pulse the lighter phase is forced up through the sieve holes. In doing so the lighter phase breaks up into small drops which increase the specific interfacial area for mass transfer. Pulsing also increases the turbulence in the column which increases the mass transfer coefficients. Thus a PSPC becomes more efficient than a typical sieve plate column.

PSPCs are characterised by high mass transfer efficiency and higher throughput. Another feature of PSPC is absence of any moving part which makes these columns highly reliable and maintenance-free. Even though there has been a large volume of work on PSPCs, most of it is experimental. There have been experimental studies on pressure drop and axial dispersion in two-phase flow (Miyachi and Oya, 1965; Novotny et al., 1970; Rao et al., 1978; Srinikethan et al., 1987). Experimental studies on mass transfer, dispersed phase hold up and drop size distribution have also been reported (Kumar and Hartland, 1988; Lorenz et al., 1990; Srinivasulu et al., 1997; Kumar and Hartland, 1999; Usman et al., 2009). Several experimental studies shed light on different regimes of operation and transitions from one regime to another (Sato et al., 1963; Boyadzhiev and Spassov, 1982; Kumar and



Hartland, 1983). Experiments to understand flooding characteristics have also been reported (Kagan et al., 1965, Tronton, 1957). The end results of most of the experimental studies on PSPCs are empirical correlations. Due to the large volume of experimental work that has been carried out, there exist many empirical correlations for PSPCs. Each of these correlations is valid for the range of the experimental data over which it has been regressed. However, there is no correlation that has been shown to be universal enough to be valid over a wide range of operational and design parameters. The existence of so many correlations has in fact caused a “problem of plenty” making it difficult to choose the best correlations to be used for designing a PSPC for a given duty (Yadav and Patwardhan, 2008).

As a result, design of industrial scale PSPCs still is based on the data generated using pilot-scale units and insights into the local hydrodynamics in the column are still rare. It becomes very difficult to experimentally investigate local hydrodynamics and drop dynamics in a column, especially large diameter columns. This makes use of CFD-based models very attractive. Such models can provide valuable insights into the functioning of the columns, help reduce experimentation and design of industrial-scale columns.

CFD and CFD coupled with population balance modeling (PBM) have been used to model dispersed liquid-liquid two-phase flow in different types of equipments (Wang and Mao, 2005; Gimbut et al., 2009; Kerdouss et al., 2008). Recently, several studies on CFD modelling of air pulsed columns have also been reported. But majority of these studies are on pulsed disc and doughnut columns (Retieb et al., 2007; Nabli et al., 1997; Saini and Bose, 2014). A CFD-PBM based approach to model pulsed disc and doughnut column was reported by Amokrane and coworker (Amokrane et al., 2014). Only drop breakage was considered in PBM. Single-phase CFD model was validated using experimental PIV data. The PBM was validated separately using the experimental data generated in a stirred tank. There after coupled CFD-PBM was used to predict the hydrodynamics in the column. However, the results of the CFD-PBM based model were not validated. In a recent study by the same group (Amokrane et al., 2016) a CFD-PBM approach considering both drop breakage and coalescence was reported. Drop size distribution in a 1 inch column was measured and used for optimization of the breakage and coalescence kernels. Only limited validation of the CFD-PBM approach was reported. Though there are several single-phase CFD studies on PSPCs (Kolhe et al., 2011; Xiaojin and Guangsheng, 2011; Sen et al., 2015) two-phase CFD studies on PSPCs are scarce. Yadav and Patwardhan, 2009 reported two-phase CFD modeling of a PSPC to study the effects of pulsing on column hydrodynamics, operating regimes and dispersed phase hold-up. However, the plates used in their work had downcomer (separate path/passage provided for the heavier phase to move down the column – similar to those provided in sieve/bubble cap plates in distillation columns for the downward movement of the heavier liquid phase). Plates typically used in PSPCs do not have downcomers. The

hydrodynamics in a column having plates with downcomers may be significantly different from those without downcomer. Din et al., 2010 reported a 2D two-phase CFD model of PSPC but the sieve plate section was modelled as a porous medium which is a significant simplification of the actual geometry. Recently we reported a 2D two-phase CFD model to predict hydrodynamics and dispersed phase holdup in PSPC (Sen et al., 2016). A comparison of different drag models, was carried out and validation against reported experimental data was done. To the best of our knowledge CFD-PBM simulation of PSPCs has not been reported so far. This study, therefore, represents the first implementation of CFD-PBM approach for PSPCs.

1D mathematical models to predict mass transfer in PSPCs have also been reported (Gonda and Matsuda, 1986; Torab-Mostaedi and Safdari, 2009). In fact, in nuclear fuel cycle several codes based on 1 D modelling are available (SOLVEX, SEPHIS-MOD4, Revised MIXSET, PULCO). However, each of these mathematical models embed several empirical correlations. With each correlation having its own uncertainty, using several of them in a mathematical model may result in significant overall uncertainty in the predictions of the model.

In the present work, we report, for the first time, 2D two-phase CFD-PBM simulations to directly predict mass transfer of a species/solute from organic to aqueous phase in a PSPC. The model is developed and validated against reported experimental data of a 2 inch diameter PSPC. The model provides insights into spatial and temporal variations of hydrodynamic variables inside the column under pulsing conditions and resultant effect on mass transfer in a 2D computational domain.

## MODEL DESCRIPTION

### Computational approach

Two fluid Euler–Euler approach was used to model two phase liquid-liquid flow in PSPC using a commercial finite volume based code. This approach has been widely used to simulate dispersed two-phase flows (Yadav and Patwardhan, 2009; Din et al., 2010; Ranade, 2002; Wang et al., 2014). The model solves the conservation equations for momentum and mass for both phases and assumes that both the phases can co-exist in every computational cell in the domain. The phase fraction (or hold up) of the dispersed phase in each cell is computed by solving a convection-diffusion transport equation for the phase fraction itself. The momentum exchange between the two phases is modelled through the interphase exchange coefficients which in turn is defined in terms of a drag coefficient.

Turbulence has been modelled using the mixture k- $\epsilon$  model in which the turbulence equations are solved for the mixture as a whole. This approach reduces the number of equations to be solved thus reducing computational time. The relevant equations can be found elsewhere (Sen et al., 2016) and are omitted here for brevity.

The exchange of momentum between the phases is only through the drag force which is quantified using the drag model of Schiller and Naumann.

One major simplification in two-phase CFD simulations of PSPCs reported till now has been the assumption of monodispersed drops. In such models the information on temporal and spatial variations of drop size is lost. In the present work a predictive CFD-PBM numerical approach is used to circumvent the monodispersed approximation in computational models of PSPCs. The method of classes is used to solve the population balance model (PBM).

Local drop size distribution inside PSPC depends on the initial drop size distribution in the feed, convective transport of the drops, breakage and coalescence rates of drops. In absence of mass transfer, the population balance equation for characteristic length of drop ( $L$ ) can be written as (Singh et al., 2009; Marchisio et al., 2003)

$$\frac{\partial}{\partial t}\{n(L, t)\} + \nabla \cdot (\mathbf{U} \cdot n(L, t)) = B^a(L; t) - D^a(L; t) + B^b(L; t) - D^b(L; t) \quad (1)$$

Here  $B^a$  and  $B^b$  are birth rates of droplet of size  $L$  at any time  $t$  due to coalescence and breakage respectively.  $D^a$  and  $D^b$  are the death rates of droplet of size  $L$  at any time  $t$  due to coalescence and breakage, respectively.  $n(L; t)$  is number density (per unit volume) of droplet having characteristic length  $L$  at any time  $t$ .

The expressions for the birth and death rates are given by Eq. (2) to (5).

$$B^a(L; t) = \frac{L^2}{2} \int_0^L \frac{\beta\{(L^3-\lambda^3)^{1/3}, \lambda\}}{(L^3-\lambda^3)^{2/3}} n\{(L^3 - \lambda^3)^{1/3}; t\} n(\lambda; t) d\lambda \quad (2)$$

$$D^a(L; t) = n(L; t) \int_0^\infty \beta(L, \lambda) n(\lambda; t) d\lambda \quad (3)$$

$$B^b(L; t) = \int_L^\infty a(\lambda) b(L|\lambda) n(\lambda; t) d\lambda \quad (4)$$

$$D^b(L; t) = a(L) n(L; t) \quad (5)$$

Where,  $\beta$  is the coalescence kernel,  $a$  is the breakage kernel,  $b$  is the daughter droplet distribution,  $h(L, \lambda)$  and  $\eta(L, \lambda)$  are collision frequency and collision efficiency, respectively. In literature, several kernels have been reported.

Breakage, daughter droplet distribution and coalescence kernels (and constants there in) proposed by Hsia and Tavlarides (Hsia and Tavlarides, 1980) have been used in the present work. Expression for these kernels are available elsewhere (Hsia and Tavlarides, 1980; Singh et al., 2009) and are omitted here for brevity.

The entire range of possible droplet size is divided into a fixed number of classes and a conservation equation is solved for each class. The rate of death and birth of drops in a specific class due to breakage and coalescence are accounted using respective kernels. In the present work, the range of drop sizes is considered to be from 0.5 mm to 4 mm. This choice of drop size is based on the values of drop sizes typically observed in a pulsed column (Lorentz et al., 1990, Usman et al., 2006).

Mass transfer of  $j^{\text{th}}$  solute (concentration  $x_j$ ) from one phase (phase  $p$ ) to the other phase (phase  $q$ ) is modelled

by solving species transport equation in both phases with mass exchange (source) terms as shown in Eqn. (6-7). Concentration of solute in the second phase (phase  $q$ ) is denoted by  $y_j$ .

$$\frac{\partial x_j}{\partial t} \phi_p + \phi_p \mathbf{U} \cdot \nabla x_j = \phi_p D_p \nabla^2 x_j - K_L a \left( x_j - \frac{y_j}{K_d} \right) \quad (6)$$

$$\frac{\partial y_j}{\partial t} \phi_q + \phi_q \mathbf{U} \cdot \nabla y_j = \phi_q D_q \nabla^2 y_j + K_L a \left( x_j - \frac{y_j}{K_d} \right) \quad (7)$$

where  $\phi_p$  is hold up of the  $p^{\text{th}}$  phase,  $D$  is the effective diffusivity (comprising of both eddy and molecular diffusion),  $K_L a$  is overall volumetric mass transfer coefficient,  $K_d$  is the distribution coefficient. Value of  $K_L a$  and  $K_d$  are estimated from the correlations reported in literature (Gonda and Matsuda, 1986). The mass transfer term (source term) is calculated based on the difference in concentration of the solute in the two phases and overall volumetric mass transfer coefficient. The two species transport equations are coupled with each other through the source terms. As the problem involves partitioning of one solute in two different phases, solute concentrations in the organic and the aqueous phases are related through the following equation.

$$y_j = K_d x_j \quad (8)$$

The pulsing action is introduced into the computational model using a pulsatile velocity at the pulse inlet, as given by Eq. (9).

$$U_p = \pi A f \text{Sin}(2\pi f t) \quad (9)$$

where  $U_p$  is the pulsing velocity,  $A$  is the amplitude and  $f$  is frequency (Hz) of pulsation.

As the solute concentration varies across the computational domain the density of both phases also varies. In other words as the solute is partitioned from organic phase into aqueous phase, the density of the organic phase reduces while that of the continuous phase increases. This effect has been incorporated in the model.

## Computational domain

For validation of the developed model, reported experimental data on solute end concentrations in a 2 inch PSPC are used (Gonda and Matsuda, 1986). Hence, the computational domain is based on the reported geometry. A standard sieve plate cartridge (23% opening area, 3 mm hole diameter, 5 cm inter-plate spacing) was used. The column was 2 m in height and had 36 plates. A pulse leg was connected the bottom disengagement section to provide pulsation to the column contents. The phase system used was 30% TBP in dodecane and 0.1 N Nitric acid.

In the present 2D computational model a reduced number of plates (5 plates) has been considered so as to limit the size of the computational domain and the resulting computational time. Suitability of using a 2D model and reduced number of plates for CFD modelling of PSPCs has been reported earlier (Kolhe et al., 2011; Yadav and Patwardhan, 2009; Sen et al., 2015; Sen et al., 2016). Transient simulations are carried out with a

time step of 0.01 sec which corresponds to Courant numbers less than 0.5 in all cases. A grid density of  $1.027 \times 10^6$  cells/m<sup>2</sup> has been used in the present work. This grid density is chosen based on the results of grid independence test carried out in our previous study on single-phase flow in pulsed sieve plate column (Sen et al., 2015). Similar grid density has been used in our recent work on two-phase flow in PSPC (Sen et al., 2016). In the model the hole diameter is kept at the original value (i.e. 3 mm) while the pitch is chosen such that percent free area is the same as in experimental setup. Fig. 1 shows the meshed computational domain and the quality of mesh in two inter-plate zones.

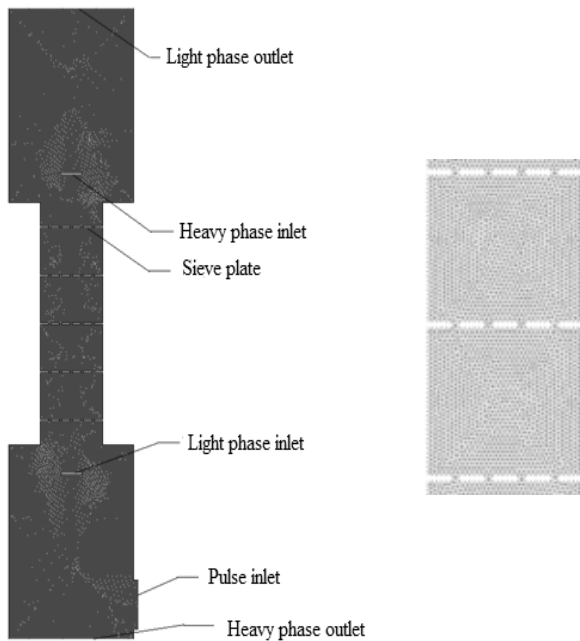


**Figure 1:** Meshed computational domain used to model 2 inch PSPC and zoomed view of the mesh in two inter-plate zones

## RESULTS AND DISCUSSION

### Validation

The mass transfer prediction of the developed CFD-PBM model is first validated against reported experimental results. Gonda and co-workers (Gonda and Matsuda, 1986) reported back extraction (stripping) of heavy metal solute from organic (dispersed phase) to aqueous (continuous phase) in a 2 inch diameter PSPC. Solute concentration in the organic phase fed to the column bottom was 97 gpl while the aqueous phase did not contain any solute. Solute concentration in each phase was reported at various locations along the column height leading to a solute concentration profile of each phase.

The computational model used in this work comprises of only 5 plates to ensure that computational time remains within reasonable limits. Solute concentration in organic phase entering the column and solute concentration in aqueous phase at the location of 5<sup>th</sup> plate from bottom goes into the model as inputs while the model predicts solute concentration in the aqueous phase exiting 1<sup>st</sup> plate from column bottom and in the organic phase exiting 5<sup>th</sup> plate from column bottom. Table 1 below shows the comparison of the predicted and reported values of solute concentration in the

organic phase at the 5<sup>th</sup> plate from bottom and in the aqueous phase at the location of 1<sup>st</sup> plate from column bottom. It is seen that the absolute average error in prediction of our model is 2.8 %. Hence the 2D CFD-PBM approach can directly predict mass transfer from one phase to another with good accuracy.

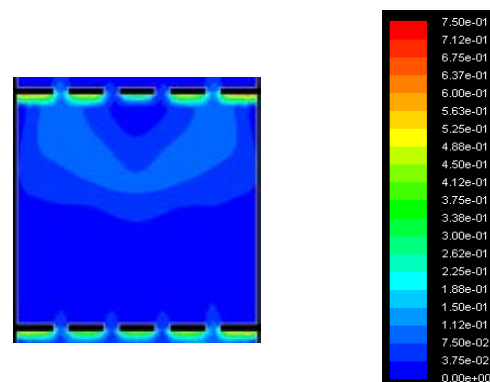
**Table 1:** Comparison of CFD\_PBM predicted values against experimental data

	CFD (gpl)	Experim ental (gpl)	Average Error (%)
Solute concentration at 5 <sup>th</sup> plate (from bottom) in organic phase	87.21	91.38	
Solute concentration at 1 <sup>st</sup> plate (from bottom) in aqueous phase	48.504	49	2.78

### Local hydrodynamic and mass transfer aspects

In this section we use the validated numerical model to understand the complex hydrodynamics in PSPC and its resultant effect on transport of species from one phase to another. Fig. 2 shows the spatial variations of dispersed phase hold up and Sauter mean drop diameter in a typical inter-plate zone. As the flow field is time varying due to pulsation the spatial variations are shown at positive peak of the pulse.

Accumulation of the dispersed phase is clearly seen below the sieve plates. The spatial variation of Sauter mean drop diameter reveals that drop of smaller size are formed at the location of the sieve holes and drop diameter increases as the dispersion moves above. This is due to the fact that turbulence dissipation rates are higher at the location of the holes (as evident from Fig. 3) which leads to increased breakage rates causing smaller drops at sieve holes. As the dispersion moves up and reaches the next plate drops tend to coalesce and increase in size. Fig. 3 shows the spatial variations of the turbulence dissipation rates, axial velocity of the continuous phase and axial velocity of the dispersed phase at the positive peak of the pulsing cycle.



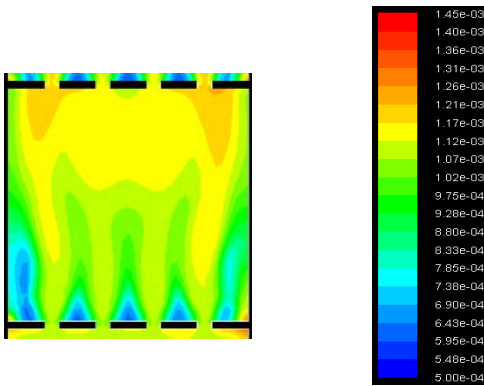


**Figure 2:** Spatial variation of dispersed phase hold up (-) (top) and Sauter mean drop diameter (m) (bottom)

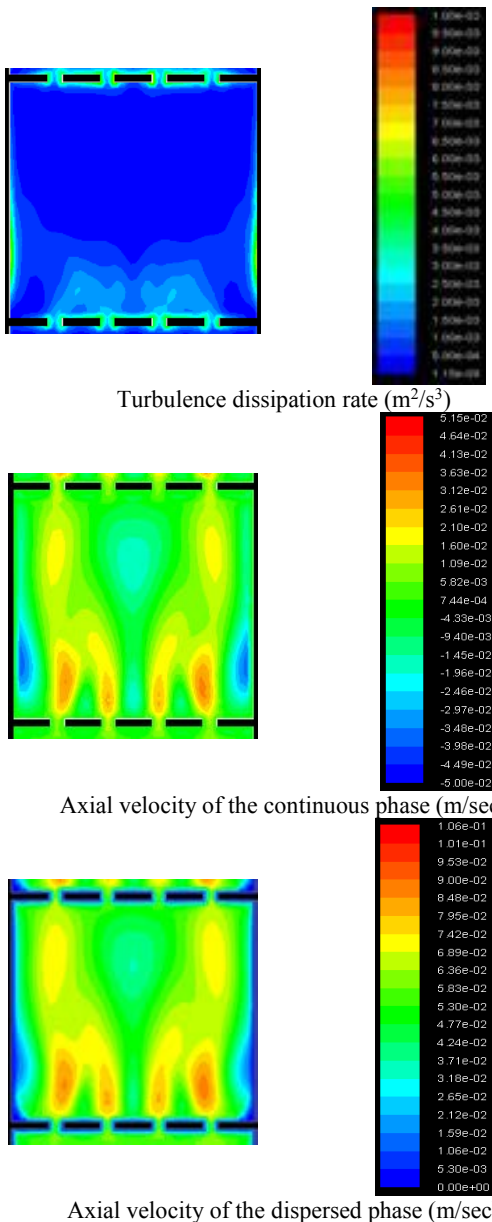


**Figure 3:** Spatial variations of turbulence dissipation rate, axial velocity of continuous phase, and axial velocity of the dispersed phase

It is seen that during the up stroke (i.e. positive peak of the pulse) both phases are being pushed up through the holes (indicated by positive axial velocities at the holes even though the general direction of flow of the continuous phase is downwards. Presence of small re-

circulations in the continuous phase visible near the wall (as evidenced by negative values of axial velocity of the continuous phase the wall). However, no circulations are observed for the dispersed phase as axial velocities are positive everywhere.

Fig. 4 shows the solute concentration (in terms of solute mass fraction) in the organic (dispersed) phase and the aqueous (continuous) phase.

A gradual decrease in concentration of the solute as the dispersed phase moves up is clearly observed. At the same time whatever solute leaves the dispersed (organic) phase is transferred to the continuous (aqueous) phase and is reflected as an increase in the solute concentration in the continuous phase as it flows downward.

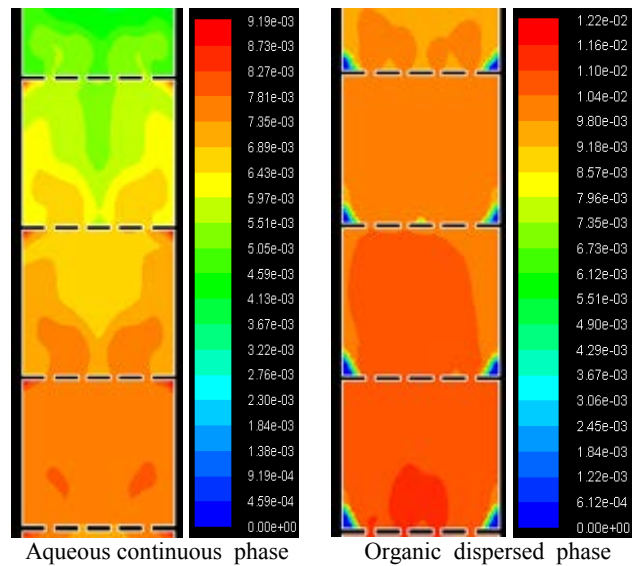


**Figure 4:** Spatial variations of solute mass fraction in continuous and dispersed phase.

Fig. 5 shows the spatial variation of the density of the organic phase in the entire computational domain. It is seen that density of the dispersed phase decreases as it flows upward along the column. In the model densities of both phases are composition dependent. Thus the density of the dispersed phase (organic) is seen to reduce as solute is transferred from the organic phase to the aqueous phase.

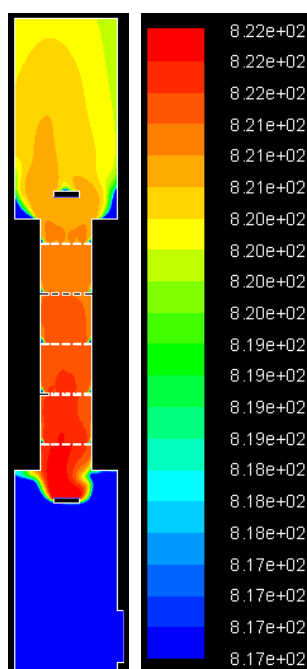


**Figure 5:** Spatial variation of the density of the dispersed phase ( $\text{kg/m}^3$ )

## CONCLUSION

The following conclusions could be drawn from this work

- 1) A 2D CFD-PBM numerical model is developed which could predict spatial and temporal variations of two-phase hydrodynamics and resultant inter-phase mass transfer in a pulsed sieve plate extraction column (PSPC).
- 2) The model is validated against reported experimental data on solute concentration in organic and aqueous phases in a 2 inch PSPC. The model predictions are very close to reported values, the absolute average error being 2.78%.
- 3) The validated model is then used to understand the spatial variations of different hydrodynamics parameters like dispersed phase hold up, Sauter mean drop diameter, turbulence dissipation rate and continuous and dispersed phase axial velocities. Transfer of mass from organic phase to aqueous was also clearly captured along the computational domain.
- 4) The model provides a way to directly estimate mass transfer performance of a PSPC from first principles with minimum empirical inputs.

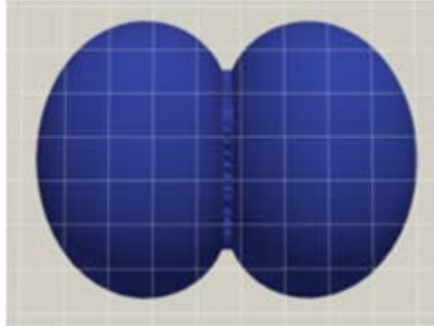
## REFERENCES

- AMOKRANE, A., CHARTON, S., LAMADIE, F., PAISANT, J. F. and PUEL, F., (2014), "Single-phase flow in a pulsed column: Particle Image Velocimetry Validation of a CFD based model", *Chemical Engineering Science*, **114**, 40-50.
- AMOKRANE, A., MAAß, S., LAMADIE, F., PUEL, F. and CHARTON, S., (2016), "On droplets size distribution in a pulsed column. Part I: In-situ measurements and corresponding CFD-PBE simulations", *Chemical Engineering Journal*, **296**, 366-376.
- BOYADZHIEV, L. and SPASSOV, M., (1982), "On the size of drops in pulsed and vibrating plate extraction columns", *Chem. Eng. Sci.*, **37**: 337-340.
- DIN, G.U., CHUGHTAI, I.R., INAYAT, M.H. and KHAN, I.H., (2010), "Modeling of a two-phase countercurrent pulsed sieve plate extraction column - A hybrid CFD and radiotracer RTD analysis approach", *Separation and Purification Technology*, **73** (2), 302-309.
- FERREIRA, A.E., AGARWAL, S., MACHADO, R., GAMEIRO, M.L.F., SANTOS, M., REIS, T.A., ISMAEL, M.R.C., CORREIA, J.N., CARVATHO, J.M.R., (2010), "Extraction of copper from acidic leach solution with Acorga M5640 using a pulsed sieve plate column". *Hydrometallurgy*, **104**(1), 66-75.
- GAMEIRO, M.L.F., MACHADO, R.M., ISMAEL, M.R.C., REIS, T.A., CARVATHO, J.M.R., (2010), "Copper extraction from ammoniacal medium in a pulsed sieve-plate column with LIX 84-I", *J. Hazardous Materials*, **183** (1-3), 165-175.
- GIMBUN, J., CHRIS D.R. and ZOLTAN K. N., (2009), "Modelling of mass transfer in gas-liquid stirred tanks agitated by Rushton turbine and CD-6 impeller: a scale-up study", *Chemical Engineering Research and Design*, **87**(4), 437-451.
- GODFREY, J.C. and SLATER, M.J. (1994) "Liquid-Liquid Extraction Equipment", Wiley, Chichester, U.K.
- GONDA, K. and MATSUDA, T., (1986), "Solvent extraction calculation model for PUREX process in pulsed sieve plate column", *J. Nuc. Sci. Tech.*, **23**(10), 883-895.
- HSIA, M. A. and TAVLARIDES, L. L., (1980), "A simulation model for homogeneous dispersion in stirred tank", *Chem. Eng. J.*, **20**, 225-236.
- KAGAN, S., AEROV, M., LONIK, V. and VOLKOVA, T., (1965), "Some hydrodynamic and mass transfer problems in pulsed sieve-plate extractors", *Int. Chem. Eng.*, **5** (4), 656-661.
- KERDOUSS, F., BANNARI, A., PROULX, P., BANNARI, R., SKRGA, M. and LABRECQUE, Y., (2008), "Two-phase mass transfer coefficient prediction in stirred vessel with a CFD model", *Computers & Chemical Engineering*, **32**(8), 1943-1955.
- KOLHE, N.S., MIRAGE, Y.H., PATWARDHAN, A.V., RATHOD, V.K., PANDEY, N.K., MUDALI, U.K. and NATARAJAN, R., (2011), "CFD and experimental studies of single phase axial dispersion coefficient in pulsed sieve plate", *Chemical Engineering Research and Design*, **89**(10), 1909-1918.
- KUMAR, A. and HARTLAND, S., (1983), "Correlations for dispersed phase hold-up in pulsed sieve-plate liquid-liquid extraction columns", *Chem. Eng. Res. Des.*, **61**, 248-252.
- KUMAR, A., and HARTLAND, S., (1988), "Prediction of dispersed phase hold-up in pulsed perforated-plate extraction columns", *Chem. Eng. Process. Proc. Int.*, **23**(1), 41-59.
- KUMAR, A. and HARTLAND, S., (1999), "Correlations for prediction of mass transfer coefficients in single

- drop systems and liquid–liquid extraction columns”, *Chem. Eng. Res. Des.*, **77** (5), 372–384.
- LORENZ, M., HAVERLAND, H., and VOGELPOHL, A., (1990), “Fluid dynamics of pulsed sieve plate extraction columns”, *Chem. Eng. Technol.*, **13**(1), 411–422.
- MARCHISIO, D. L., VIGIL, R. D. and FOX, R. O., (2003), “Implementation of the quadrature method of moments in CFD codes for aggregation–breakage problems”, *Chemical Engineering Science*, **58**(15), 3337–3351.
- MIYAUCHI, T. and OYA, H., (1965), “Longitudinal dispersion in pulsed perforated-plate columns”, *AIChEJ*, **11**(3), 395–402.
- NABLI, M.S.A., GUIRAUD, P. and GOURDON, C., (1997), “Numerical experiment: a tool to calculate axial dispersion coefficient in disc and doughnut pulsed extraction column”, *Chem. Eng. Sci.*, **52** (14), 2353–2368.
- NOVOTNY, P., PROCHAZKA, J., and LANDAU, J., (1970), “Axial dispersion study of single phase”, *Can. J. Chem. Eng.*, **48** (8), 405–410.
- RAO, K.V.K., JEELANI, S.A.K., and BALSUBRAMANIAN, G.R., (1978), “Backmixing in pulsed perforated plate columns”, *Can. J. Chem. Eng.*, **56**(1), 120–123.
- RETIEB, S., GUIRAUD, P., ANGELOV, G. and GOURDON, C., (2007), “Hold-up within two-phase counter current pulsed columns via Eulerian simulations”, *Chem. Eng. Sci.*, **62**(17), 4558–72.
- SAINI, R.K. and BOSE, M., (2014), “Stage holdup of dispersed phase in disc & doughnut pulsed column”, *Energy Procedia*, **54**, 796–803.
- SATO, T., SUGIHARA, K., and TANIYAMA, I., (1963), “Performance characteristics of pulsed perforated plate columns”, *Kogaku Kogaku*, **27**, 583–586.
- SEN, N., SINGH, K.K., PATWARDHAN, A.W., MUKHOPADHYAY, S. and SHENOY, K.T., (2015), “CFD Simulations of Pulsed Sieve Plate Column: Axial Dispersion in Single-Phase Flow”, *Separation Science and Technology*, **50**(16), 2485–2495.
- SEN, N., SINGH, K.K., PATWARDHAN, A.W., MUKHOPADHYAY, S. and SHENOY, K.T., (2016), “CFD Simulations of two phase flow in pulsed columns: Identification of drag law”, *Separation Science and Technology*, **51**(17), 2790–2803.
- SINGH, K. K., MAHAJANI, S. M., SHENOY, K. T. and GHOSH, S. K., (2009), “Population balance modelling of liquid–liquid dispersions in homogeneous continuous-flow stirred tank. *Industrial & Engineering Chemistry Research*, **48**(17), 8121–8133.
- SRINIKETHAN, G., PRABHAKAR, A., and VARMA, Y.G.B., (1987), “Axial dispersion in plate-pulsed columns”, *Bioprocess Eng.*, **2**(4), 161–168.
- SRINIVASULU, K., VENKATNARSAIAH, D. and VARMA, Y.B.G., (1997), “Drop size distribution in liquid pulsed columns”, *Bioprocess Eng.*, **17** (3), 189–195.
- TORAB-MOSTAEDI, M. and SAFDARI, J., (2009), “Prediction of mass transfer coefficients in a pulsed packed extraction column using effective diffusivity”, *Braz. J. Chem. Eng.*, **26**(4), 685–694.
- USMAN, M.R., SATTAR, H., HUSSAIN, S.N., MUHAMMAD, H., ASGHAR, A. and AFZAL, W., (2009), “Drop size in a liquid pulsed sieve plate extraction column”. *Braz. J. Chem. Engg.*, **26**(4), 677–683.
- WANG, F. and MAO, Z. S., (2005), “Numerical and experimental investigation of liquid-liquid two-phase flow in stirred tanks”, *Industrial & engineering chemistry research*, **44**(15), 5776–5787.
- XIAOJIN, T. and GUANGSHENG, L., (2011), “CFD simulations to flow characteristics in pulsed sieve plate extraction columns”, *Ind. Eng. Chem. Res.*, **50** (2): 1110–1114.
- YADAV, R.L. and PATWARDHAN, A.W., (2008), “Design aspects of pulsed sieve plate columns”, *Chem. Eng. J.*, **138**(1–3), 389–415.
- YADAV, R.L. and PATWARDHAN, A.W., (2009), “CFD modeling of sieve and pulsed- sieve plate extraction columns”, *Chem. Eng. Res. Des.*, **87** (1), 25–35.



# BREAKUP & COALESCENCE







# EXPERIMENTAL AND NUMERICAL STUDY ON SINGLE DROPLET BREAKAGE IN TURBULENT FLOW

Jing SHI\*, Eirik Helno HERØ, Jannike SOLSVIK, Hugo Atle JAKOBSEN\*

NTNU Department of Chemical Engineering, 7491 Trondheim, NORWAY

\* Correspondence concerning this article should be addressed to J. Shi at jingshi1988@gmail.com or H. A. Jakobsen at hugo.a.jakobsen@ntnu.no

## ABSTRACT

Droplet size distributions in liquid-liquid turbulent flow are determined by droplet breakage and coalescence. The current understanding of these processes are not sufficient. An experimental study on single droplet breakage in turbulent flow, where coalescence can be neglected, is presented in this paper to study the droplet breakage mechanism. A rectangular channel consisting of a pair of opposite steel walls having a series of stationary protuberances to enhance turbulence level, and a pair of opposite glass walls that are smooth to facilitate image capture of the droplet breakage process is used as the droplet breakage channel. The commercial CFD code FLUENT is utilised to simulate the continuous single-phase flow in the droplet breakage channel with interest particularly in the turbulent characteristics such as the turbulent kinetic energy and turbulent energy dissipation rate, as these parameters are closely related to the droplet breakage process. The large eddy simulation (LES) method was used to provide detailed features of the flow. Results from LES were also compared with those from a RANS model (SST k- $\omega$ ). The simulation results demonstrated that the turbulence level is enhanced across the pair of walls with protuberances. There are more coherent strong vortices in the region close to the wall with protuberances. Some preliminary experimental results on droplet breakage are also presented.

**Keywords:** Breakage, large eddy simulation (LES), turbulent energy dissipation rate, turbulent vortical structures.

## NOMENCLATURE

### Greek Symbols

- $\epsilon$  Turbulent energy dissipation rate, [ $\text{m}^2/\text{s}^3$ ].  
 $\langle \epsilon \rangle$  Time averaged turbulent energy dissipation rate, [ $\text{m}^2/\text{s}^3$ ].  
 $\kappa$  von Kármán constant, 0.4187, [-].  
 $\nu$  Molecular kinematic viscosity, [ $\text{m}^2/\text{s}$ ].  
 $\nu_{SGS}$  Subgrid eddy viscosity, [ $\text{m}^2/\text{s}$ ].  
 $\xi$  Length scale, [m].  
 $\tau_{ij}^{SGS}$  Subgrid stress tensor, [ $\text{m}^2/\text{s}^2$ ].  
 $\bar{\omega}_{ij}$  Vorticity tensor,  $\bar{\omega}_{ij} = \frac{1}{2} \left( \frac{\partial \bar{u}_i}{\partial x_j} - \frac{\partial \bar{u}_j}{\partial x_i} \right)$ , [1/s].  
 $\Delta$  Filter width, [m].  
 $\Omega$  Absolute value of vorticity,  $\Omega = \sqrt{2\bar{\omega}_{ij}\bar{\omega}_{ij}}$ , [1/s].

### Latin Symbols

- $C_s$  Smagorinsky constant, 0.1, [-].  
 $d$  Distance to the closest wall, [m].

- $G$  Filter function, [1/m].  
 $\langle \bar{k} \rangle$  Time averaged turbulent kinetic energy, [ $\text{m}^2/\text{s}^2$ ].  
 $L_s$  Mixing length for the subgrid scale, [m].  
 $\bar{p}$  Pressure, [Pa].  
 $Q$  Criterion for illustrating coherent vortices, [ $1/\text{s}^2$ ].  
 $\bar{S}_{ij}$  Rate of strain tensor,  $\bar{S}_{ij} = \frac{1}{2} \left( \frac{\partial \bar{u}_i}{\partial x_j} + \frac{\partial \bar{u}_j}{\partial x_i} \right)$ , [1/s].  
 $S$  Absolute value of the strain rate,  $S = \sqrt{2\bar{S}_{ij}\bar{S}_{ij}}$ , [1/s].  
 $t$  Time scale, [s].  
 $u_i$  Velocity, [m/s].  
 $\bar{u}$  Filtered/resolved velocity in LES, [m/s].  
 $u'_i$  Filtered residual velocity in LES, [m/s].  
 $\langle \bar{u}_i \rangle$  Time averaged velocity, [m/s].  
 $\bar{V}$  Mean velocity (experiments), [m/s].  
 $V_k$  Volume of a computational cell, [ $\text{m}^3$ ].  
 $x$  Length scale, [m].

### Sub/superscripts

- $i$  Index  $i$ .  
 $j$  Index  $j$ .  
 $k$  Index  $k$ .

## INTRODUCTION

Dispersed liquid-liquid systems are quite common in different industries, for example, the chemical, pharmaceutical, food, and petroleum industries. The fluid particle size is determined by equilibrium between various mechanisms of fluid particle breakage and coalescence. Most of the engineering flow problems are turbulent in nature. Many of the existing models that describe particle breakup in turbulent flow are based on the work of Coualaloglou and Tavlarides (1977). It is assumed that the droplets are in a turbulent flow field which is locally isotropic and the droplet size is within the inertial subrange. The authors proposed a premise that a drop would break if the turbulent kinetic energy transmitted to the drop from the turbulent eddies exceeds the drop surface energy and only eddies smaller than the particle diameter may transmit the energy. Reviews on the different models of particle breakage can be found in Lasheras et al. (2002), Liao and Lucas (2009) and Solsvik et al. (2013). The aforementioned reviews show that the predictions from different breakage models can be contradictory. Many of the models are derived from

assumptions that have not been validated experimentally. There is little reliable experimental data in the literature that can be used to validate different models. Therefore, it is of importance to experimentally investigate the breakage process and further obtain reliable data for model evaluation.

Many experimental studies on droplet breakage investigated the properties of final particle population, such as the maximum stable particle size, mean particle size and the particle size distribution as a function of the mean particle size (e.g., Sleicher, 1962; Sprow, 1967; Middleman, 1974; Calabrese et al., 1986; Wang and Calabrese, 1986; Angeli and Hewitt, 2000a; Azizi and Al Taweel, 2011). Experiments on single droplet breakage in turbulent flow, where coalescence can be neglected, have been undertaken by researchers more recently. Andersson and Andersson (2006) studied both bubble and droplet breakup in flow of immiscible fluids through a static mixer or channel reactor. The turbulence generated in this channel reactor in general is more homogeneous compared to a stirred tank reactor as turbulence is continuously produced and dissipated along the reactor. The experimental results from the above authors demonstrated differences in the bubble breakup and droplet breakup. The bubble breakup mainly resulted in two fragments while multiple breakup was more frequently observed in droplet breakup. Also, the bubble breakup often resulted in unequal size fragments while fragments upon droplet breakup had a higher probability of being approximately equal size than unequal size. Maaß et al. (2007) and Maaß and Kraume (2012) investigated single droplet breakage in turbulent flow in a breakage cell which was designed to reflect the flow field in the impeller region of a stirred tank. The breakage cell was a rectangular channel with a single blade representative of a section of a Rushton turbine inserted into the channel from one side. The results showed that the highest probability with regard to the number of fragments formed upon breakup was for the binary breakup. The average breakage time appeared to have a minimum for a certain mother drop diameter. The relative numbers of distributions of the breakage time were best fit with a  $\beta$ -distribution instead of normal distribution. Solsvik and Jakobsen (2015) experimentally investigated single droplet breakup in a stirred tank. It was reported that multiple breakup events (specifically, more than 2 daughter drops, and up to more than 9 fragments) were more frequently observed than binary breakup. Also, unequal-sized rather than equal-sized breakup was more frequently observed. For all of the aforementioned experimental studies on single droplet breakage, the high-speed imaging technique was applied to capture the breakage process. The statistical information on breakage process is obtained by further image processing. Detailed information which is of great value for evaluating the breakage models, e.g., the statistical distributions of breakage time, breakage probability, daughter numbers and sizes, can be obtained by experiments on single droplet breakage.

In addition to statistical information on droplet breakage, information of the underlying turbulent parameters, particularly the local turbulent energy dissipation rate,  $\varepsilon$ ,

is desirable. The local turbulent energy dissipation rate is one of the variables in most of the breakage models. As the local turbulent energy dissipation rate is usually not known, the average energy dissipation rate is used instead in many studies. Experimental measurement of the turbulent energy dissipation rate can be achieved by the particle image velocimetry (PIV) technique. However, the estimation of the turbulent energy dissipation rate from the PIV measurements is not straightforward and require careful evaluation (Jong et al., 2009). Since CFD has become a standard tool for flow prediction, the single-phase simulation could provide some useful information on the turbulent parameters. Bouaifi et al. (2004) conducted both PIV measurements and CFD simulation of the flow in a channel reactor which is the experimental system used in the particle breakage study reported in Andersson and Andersson (2006). Several different  $k$ - $\varepsilon$  models implemented in FLUENT were used in their CFD simulation. The turbulent parameters from the CFD simulations were comparable to those estimated from PIV measurements. Maaß et al. (2007) also used the  $k$ - $\varepsilon$  models to simulate the flow field of a breakage cell. The  $k$ - $\varepsilon$  models are practical turbulent models based on solving Reynolds Averaged Navier-Stokes Equations (RANS) together with the turbulence closures. The two-equation turbulent models (e.g.,  $k$ - $\varepsilon$  models,  $k$ - $\omega$  models) inherently apply an assumption of isotropic turbulent viscosity thus there could be large uncertainties in the CFD predictions of the flow where highly anisotropic turbulence exists. Another attractive method is Large Eddy Simulation (LES). In LES the Navier-Stokes equations are spatially filtered, which eliminates eddies whose scales are smaller than a filter width. Large eddies are directly resolved, while small eddies are modelled using subgrid scale models that describe the interactions between the large eddies and the unresolved smaller scales. LES results are theoretically more comparable to PIV measurements as the experimental data obtained by PIV are similar to the filtering method used in LES (Sheng et al., 2000). Ni et al. (2003) applied both LES and PIV to quantify turbulent properties in an oscillatory baffled column. The authors reported good agreement between these two techniques. Delafosse et al. (2008) performed simulations of flow in a stirred tank using both the standard  $k$ - $\varepsilon$  model and the LES model and compared the simulation results with PIV measurements. It was demonstrated that the LES gave better predictions in the turbulent parameters.

The aim of this study is to carry out an experimental campaign on single droplet breakage in turbulent flow to obtain the statistical information of the breakage process, and to perform CFD simulation of the single-phase flow using the LES method to have a picture of the underlying turbulent parameters related to droplet breakage. Results from the LES simulation were also compared with those from a steady RANS model (SST  $k$ - $\omega$ ). In this paper, the experimental setup is first introduced followed by introduction of the CFD models and simulation setup. In the following section on results, some preliminary experimental results are presented first, followed by the CFD results. Finally, the conclusions and some future work are presented.

## EXPERIMENTAL SETUP

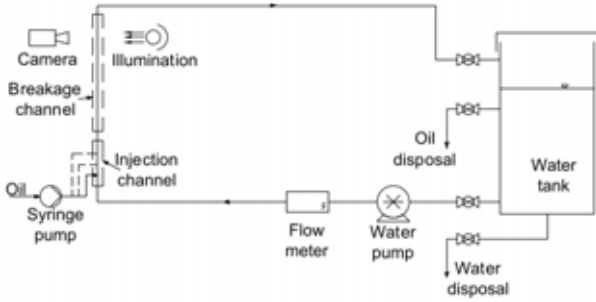


Figure 1: Schematic diagram of the experimental setup.

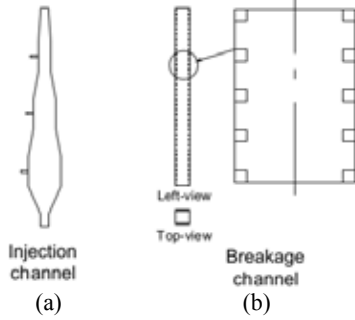


Figure 2: Schematic diagram of the injection channel (a) and the breakage channel (b).

The experimental setup used in this study is depicted in Figure 1. The de-ionized water is stored in a tank (capacity: 1 m<sup>3</sup>) and pumped by a positive displacement pump (PDP). The water flow is metered using an electromagnetic meter (SIEMENS SITRANS F M MAG 5100 W, DN 25). The water flows through a vertical pipeline which is the major part of the flow loop. The vertical line consists of two sections – the injection channel and the breakage channel. Dyed-oil pumped by a syringe pump is injected into the pipeline at the injection channel upstream of the vertical pipeline. This section is made from transparent glass and composed of three rectangular channels of different cross-sectional areas and the channels with varying cross-sections which smoothly connect the rectangular channels (see Figure 2 (a)). At a constant water flow rate in the flow loop, the size of the injected oil drop varies when injected via the different injection ports. Downstream of the injection channel is the breakage channel where the droplet breakage in turbulent water is investigated. This section is a rectangular channel (30×30×1000 mm<sup>3</sup>) consisting of a pair of opposite steel walls which have a series of stationary protuberances/tabs to enhance turbulence level, and a pair of opposite glass walls that are smooth to facilitate image capture of the droplet breakage process (see Figure 2 (b)). High-speed cameras (Photron FASTCAM Mini AX100) are used to record the breakage process of an oil droplet in turbulent flow with a frame rate of at least 4000 fps.

After the vertical pipeline, the fluids flow back to the water tank. Here the water tank also serves as a separator as the tank capacity is quite large and contains a large volume of water while the amount of oil used in experiments is very small compared to that of the water. The water in the lower part of the tank can be kept uncontaminated from oil thus cyclic operation can be

realised. The tank has a viewing window to allow for liquid level monitoring. Disposal of oil should be carried out when the purity of the water in the lower part of the tank would be affected with increased heights of the oil layer and the emulsion layer after some time of experiments with accumulation of oil droplets.

## NUMERICAL SIMULATION

### Governing Equations

The governing equations for LES are obtained by spatially filtering over small scales. A generalized filter can be defined by

$$\bar{u}_i(x, t) = \iiint G(x - \xi; \Delta) u_i(\xi, t) d^3 \xi \quad (1)$$

where the filter function is interpreted as acting to keep values of  $u_i$  occurring on scales larger than the filter width  $\Delta$ .  $G$  is some function that is effectively zero for values of  $u_i$  occurring at the small scales. By filtering the Navier–Stokes equations, the velocity field has the decomposition

$$u_i(x, t) = \bar{u}_i(x, t) + u'_i(x, t) \quad (2)$$

By filtering the Navier–Stokes equations, the governing equations employed for LES are obtained as

$$\frac{\partial \bar{u}_i}{\partial x_i} = 0 \quad (3)$$

$$\frac{\partial \bar{u}_i}{\partial t} + \frac{\partial \bar{u}_i \bar{u}_j}{\partial x_j} = -\frac{1}{\rho} \frac{\partial \bar{p}}{\partial x_i} + \frac{\partial}{\partial x_j} \left( \nu \frac{\partial \bar{u}_i}{\partial x_j} \right) - \frac{\partial \tau_{ij}^{SGS}}{\partial x_j} \quad (4)$$

where  $\tau_{ij}^{SGS} = \bar{u}_i \bar{u}_j - \bar{u}_i \bar{u}_j$ . The subgrid stress tensor  $\tau_{ij}^{SGS}$  describes the transfer of momentum by turbulence at scales that are smaller than the filter. The subgrid-scale stresses are unknown and require modelling. In this study, one frequently used subgrid model in the literature, namely, Smagorinski-Lily model, is used. The unresolved stresses follows

$$\tau_{ij}^{SGS} - \frac{1}{3} \tau_{kk}^{SGS} \delta_{ij} = -2\nu_{SGS} \bar{S}_{ij} \quad (5)$$

$$\nu_{SGS} = L_s^2 |\bar{S}| = L_s^2 \sqrt{2\bar{S}_{ij} \bar{S}_{ij}} \quad (6)$$

where  $\bar{S}_{ij}$  is the rate of strain tensor for the resolved scale,  $\bar{S}_{ij} = \frac{1}{2} \left( \frac{\partial \bar{u}_i}{\partial x_j} + \frac{\partial \bar{u}_j}{\partial x_i} \right)$ ;  $\nu_{SGS}$  is the subgrid eddy viscosity; and  $L_s$  the mixing length for the subgrid scale,  $L_s = \min(\kappa d, C_s V_k^{1/3})$ , in which  $\kappa$  denotes the von Kármán constant, 0.4187,  $d$  the distance to the closest wall,  $V_k$  the volume of a computational cell, and  $C_s$  the Smagorinsky constant. The default value in FLUENT,  $C_s = 0.1$ , was used in this study.

### Simulation Setup

The commercial CFD package FLUENT was used for the simulation. The simulation geometry is depicted in Figure 3 (a). The geometry resembles a short section of the experimental breakage channel along the flow direction, which is 60mm along Y-axis. Figure 3 (b) illustrates the mesh of the cross-section marked in Figure 3 (a). To satisfy the mesh requirement for LES simulation and to capture sufficiently detailed flow structures, the mesh (hexahedral cells) is very fine in general and is progressively finer near the walls (the lengths of cells ranged between 0.02-0.6 mm). The total number of cells

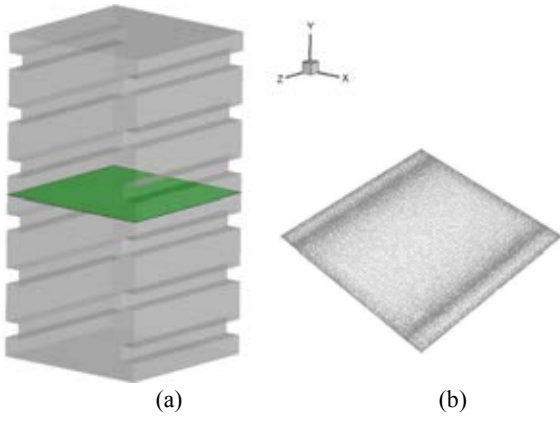


**Figure 3:** The simulation geometry (a) and mesh of a cross-section (b).

is about 7.4 million. The wall  $y^+$  for a flow rate of 2 m/s ranged between 0.01 and 5.9 with the majority of the cells having  $y^+$  between 0.01 and 3.

The fluid in this study was water (density: 998.2 kg/m<sup>3</sup>, viscosity: 1.003 mPa.s). The periodic flow boundary was applied to model the developed flow in the channel. The mass flow rate was specified (0.9 and 1.8 kg/s, corresponding average velocities of 1 and 2 m/s, respectively). A steady RANS simulation with the  $k-\omega$  SST model was first run before the LES simulation. The solutions from the RANS simulation were used as the initial conditions of the LES simulation.

The pressure-velocity coupling algorithm was used to solve the transport equations. The PRESTO! (pressure staggering option) scheme was used for the pressure interpolation. The SIMPLE (semi-implicit method for pressure linked equations) scheme was used for the pressure-velocity coupling. The bounded central differencing discretization scheme for momentum equations was applied. The bounded second order implicit scheme was used for the transient formulation. The time step used was  $2 \times 10^{-5}$  s. The pressure gradient was monitored as well as the residuals of the transport equations for the judgement of convergence. Convergence was regarded to be achieved when the monitored values are statically stable (that is after at least 3 flow-through time). The converged pressure gradients were close to theoretical predictions of developed channel flow for corresponding mass flow rates, thus the calculations were regarded as reasonable.

As the LES solves an approximately instantaneous velocity field, post-processing is needed to obtain the turbulent parameters of interest. This can be achieved by defining custom field functions and sampling the data in Fluent. The following definitions were applied to estimate ensemble/time averaged turbulent kinetic energy and dissipation rate (Ni et al., 2003; Delafosse et al., 2008).

*Turbulent kinetic energy:*

$$\langle \bar{k} \rangle = \frac{1}{2} \left( \frac{\sum_{n=1}^N \bar{u}_i \bar{u}_i}{N} - \langle \bar{u}_i \rangle^2 \right) \quad (7)$$

$$\langle \bar{u}_i \rangle = \frac{1}{N} \sum_{n=1}^N \bar{u}_i \quad (8)$$

*Turbulent energy dissipation rate:*

$$\langle \epsilon \rangle = \frac{1}{N} \sum_{n=1}^N \epsilon \quad (9)$$

$$\epsilon = 2(\nu_{SGS} + \nu) \bar{S}_{ij} \bar{S}_{ij} \quad (10)$$

where  $\langle \bar{k} \rangle$  denotes ensemble/time averaged turbulent kinetic energy over N samples,  $\bar{u}_i$  resolved velocity, and  $\langle \bar{u}_i \rangle$  ensemble/time averaged velocity over N samples.  $\langle \epsilon \rangle$  denotes ensemble/time averaged turbulent energy dissipation rate over N samples,  $\nu_{SGS}$  the subgrid kinematic eddy viscosity,  $\nu$  molecular kinematic viscosity, and  $\bar{S}_{ij}$  rate-of-strain tensor for the resolved scale.

With definitions of parameters of interest via custom field functions, data sampling was performed at a time interval of  $4 \times 10^{-5}$  s for at least 2 flow-through time, obtaining samples of a number of over 1000. With 64 parallel processors of 4 nodes from a cluster, the CPU time used was around 96h for a typical run.

## RESULTS

### Preliminary Experimental Results

Some preliminary tests were conducted using the food oil (olive oil). The approximate viscosity of the oil is 80 mPa.s. The interfacial tension between the un-dyed oil and water is around 16.4 mN/m. It is noted that the interfacial tension can be affected by the addition of the dye (Sudan Black B). The interfacial tensions between the dyed oils and water would be measured in the future.

Figure 4 illustrates the deformation process of a single droplet. The flow rate of the continuous flow is 1 m/s for this case. In this case, the droplet was slightly deformed in the central region of the channel, and it endured further deformation when it migrated into the region closer to the wall with protuberances. The highly deformed drop appeared dumbbell-shaped before it went out of the view area. To realize tracking the breakage process as complete as possible and at the same time obtaining high-speed photographs with sufficient spatial resolution, synchronized multiple high-speed cameras positioned along the flow direction will be applied in the future.

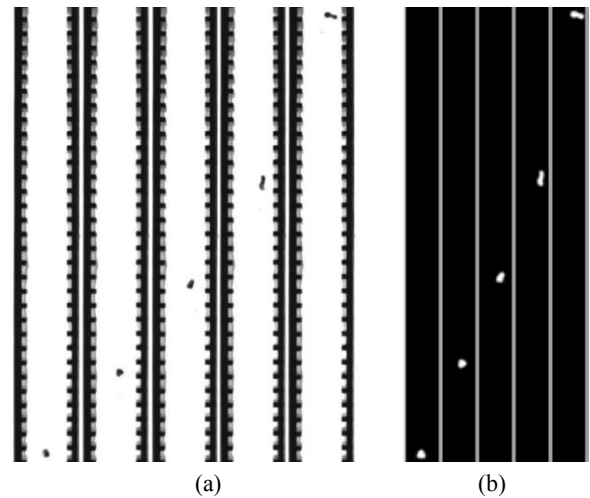


**Figure 4:** Illustration of the deformation process of a droplet. (a) High-speed images (b) Images after processing.

## CFD Results

### Velocity Field

The resolved velocity field from LES at one instant, which is approximately the instantaneous velocity field, is illustrated in Figure 5. It is demonstrated that there are backflow vortices below each protuberance/tab. The influence of the tabs on the pair of opposite walls is mainly 2-dimensional, with the flow field across the z-axis similar to that of a channel with smooth walls.

The profiles of the Y velocity (velocity component in the flow direction) along the lines of symmetry of a cross-section of the channel are described in Figure 6. In addition to the results from LES, the resolved velocities from the steady RANS simulation (SST k- $\omega$ ), which were in fact the initial conditions of the LES, are also depicted in Figure 6. The size of the protuberances is indicated by the dash lines in Figure 6 (b) as well as following relevant figures. In general, a good agreement is shown between the mean velocities from the LES and RANS simulation. However, it was shown from Figure 6 (b) that the highest backflow magnitude from the RANS simulation is slightly lower than that from LES. Also, the velocity profile from RANS is flatter across the central region of the channel.

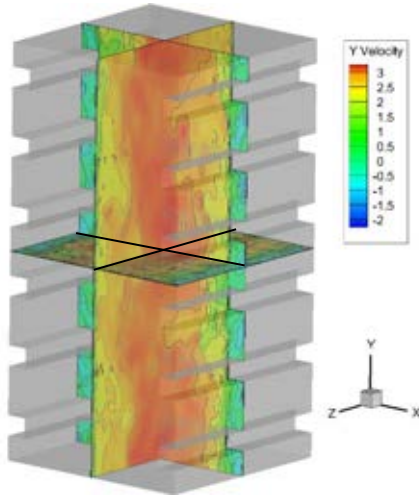
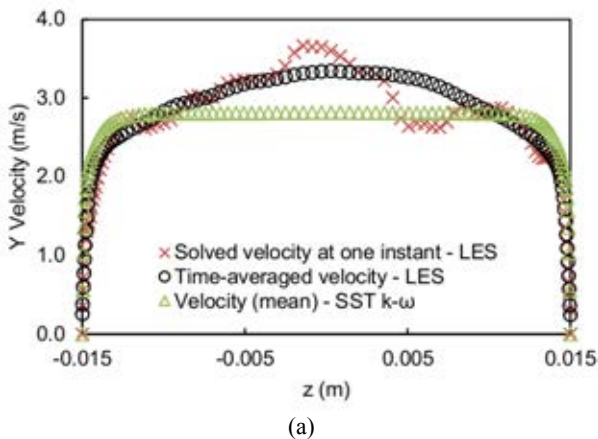


**Figure 5:** Contours of the resolved velocity (approximately the instantaneous velocity) at one instant from LES ( $\bar{V} = 2\text{m/s}$ ).



(a)

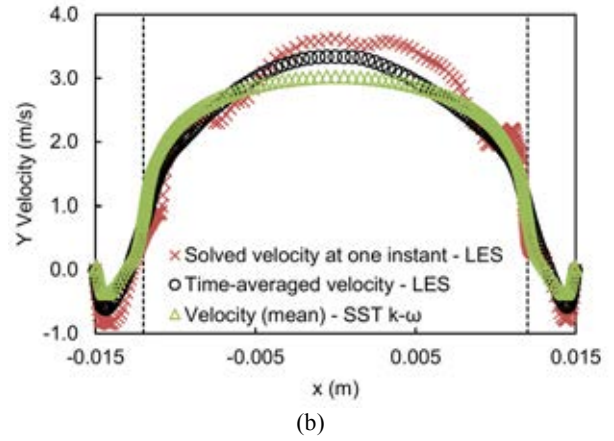
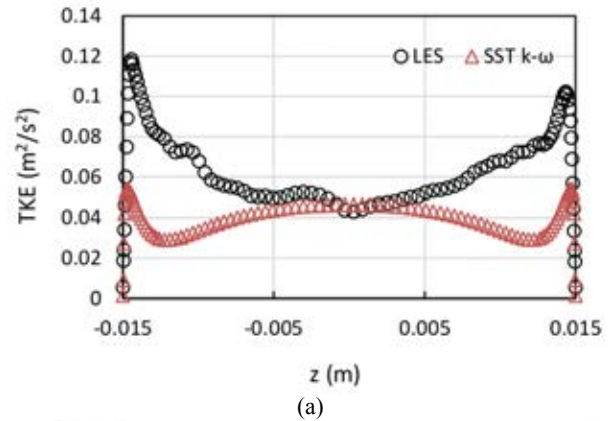


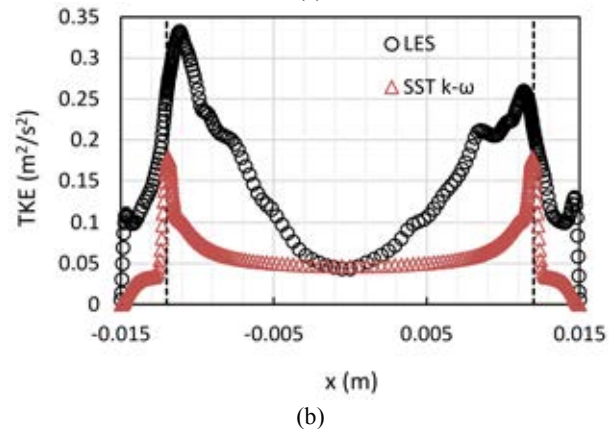
**Figure 6:** Y velocity along the lines of symmetry of a cross-section of the channel from LES and SST k- $\omega$  turbulence model ( $\bar{V} = 2\text{m/s}$ ). (a) Across the pair of smooth walls; (b) Across the pair of walls with tabs.

### Turbulent Kinetic Energy

The profiles of turbulent kinetic energy (TKE) along lines of symmetry of a cross-section of the channel are described in Figure 7. The TKE from LES illustrated are the ensemble/time averaged values calculated following Equations (7-8). The general trends of TKE from the LES and RANS simulation are consistent. However, the TKE from the LES is in general higher than that from the SST k- $\omega$  model. Similar magnitudes of TKE are shown in the central region of the channel, while the highest TKE locating close to walls/tabs from the LES is about one time higher than that from the SST k- $\omega$  turbulence model.

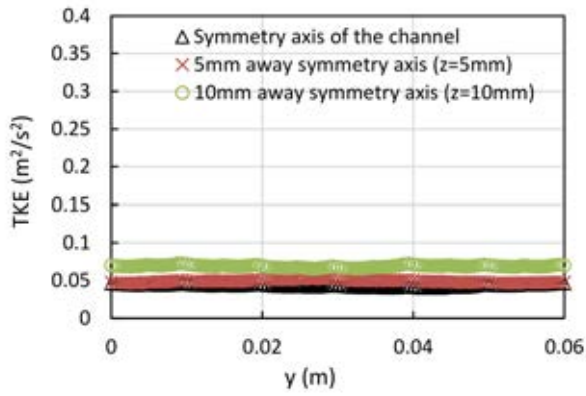


(a)

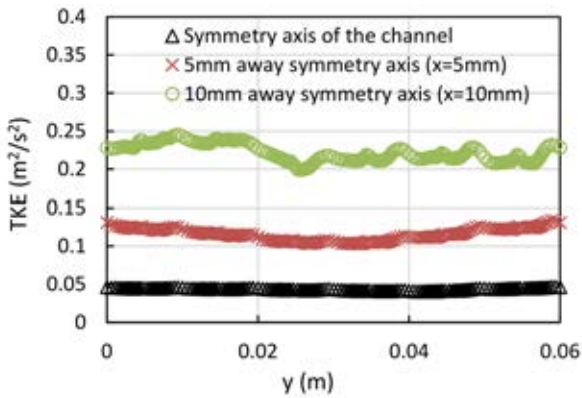


(b)

**Figure 7:** Turbulent kinetic energy along the lines of symmetry of a cross-section of the channel from LES and SST k- $\omega$  turbulence model ( $\bar{V} = 2\text{m/s}$ ). (a) Across the pair of smooth walls; (b) Across the pair of walls with tabs.



(a)



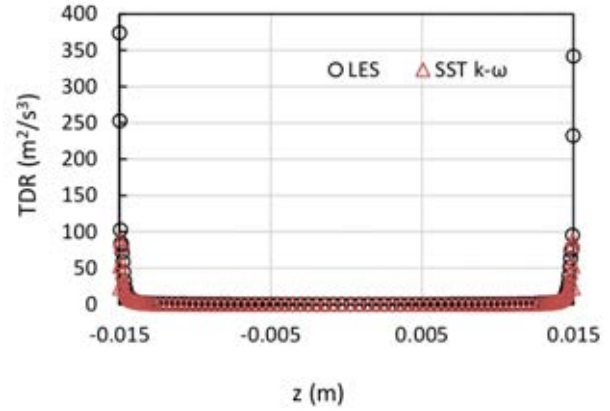
(b)

**Figure 8:** Turbulent kinetic energy from LES ( $\bar{V} = 2\text{m/s}$ ) along different lines parallel to the symmetry axis of the channel in symmetry planes of the channel. (a) In the symmetry plane across the pair of smooth walls; (b) In the symmetry plane across the pair of walls with tabs.

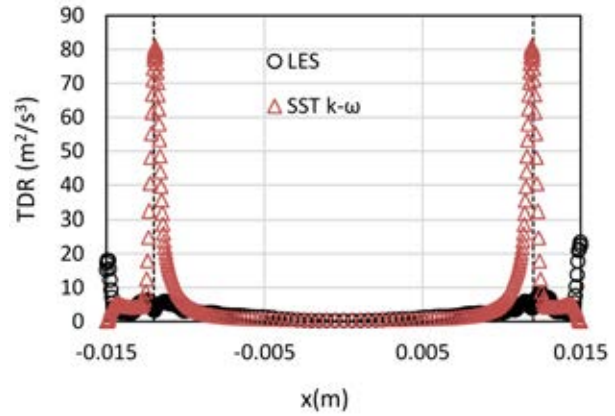
The SST  $k-\omega$  model inherently applies an assumption of isotropic turbulent viscosity thus there could be large uncertainties in the CFD predictions of the flow close to walls where highly anisotropic turbulence exists. The TKE from the LES shows less homogeneity in the central region of the channel than that from the SST  $k-\omega$  model in Figure 7 (b). Comparing Figure 7 (b) to Figure 7 (a), it is shown that the turbulence kinetic energy is increased across the pair of walls with tabs, which fits the purpose of increasing the turbulence level hence enhancing the occurrence of droplet breakage by using a pair of walls with increased roughness. The profiles of the turbulent kinetic energy along different lines parallel to the symmetry axis of the channel in symmetry planes of the channel are depicted in Figure 8. As have been demonstrated by Figure 7, Figure 8 in another way shows that the turbulence kinetic energy is increased across the pair of walls with tabs.

#### Turbulent Energy Dissipation Rate

The profiles of turbulent energy dissipation rate (TDR) along lines of symmetry of a cross-section of the channel are described in Figure 9. The general trends of TDR from the LES and the SST  $k-\omega$  model are consistent along the  $z$  direction, i.e., across the pair of smooth walls, as shown in Figure 9 (a). The magnitudes of TDR in the central region of the channel along the  $z$  direction from the LES and the SST  $k-\omega$  model are close. The LES



(a)



(b)

**Figure 9:** Turbulent energy dissipation rate along the lines of symmetry of a cross-section of the channel from LES and SST  $k-\omega$  turbulence model ( $\bar{V} = 2\text{m/s}$ ). (a) Across the pair of smooth walls; (b) Across the pair of walls with tabs.

predicts higher TDR in the near-wall region than the SST  $k-\omega$  model. Some inconsistency is demonstrated in the general trends of TDR from the LES and the SST  $k-\omega$  model along the  $x$  direction, i.e., across the pair of walls with tabs, as shown in Figure 9 (b). The predicted TDR across the pair of walls with tabs from LES has its highest value in the near-wall region, endures a decrease before it increases as approaching the region behind the tap wall (the tab wall is in alignment with  $x = \pm 0.012\text{ m}$ ); it gradually decreases again as approaching to the central region of the channel. The predicted TDR across the pair of walls with tabs from the SST  $k-\omega$  turbulence model is very low in the near-wall region, endures a gradual increase first then a sharp increase to its peak as approaching the region behind the tap wall. It decreases sharply as passing the region behind the tap wall. It is difficult to explain the different trends as the methods from which the turbulent energy dissipation rate are calculated. TDR from LES are calculated following Equations (9-10). The accuracy of the TDR from LES can be affected by the mesh scales and the subgrid-scale model. The  $k$ -equation and  $\omega$ -equation of the SST  $k-\omega$  turbulence model serve as empirical closures to solve the Reynolds Averaged Navier-Stokes Equations. The  $k$ -equation is directly deduced from Reynolds Averaged Navier-Stokes equations, denoting an exact equation for the turbulent kinetic energy. The greatest amount of uncertainty and controversy usually lies in the  $\omega$ -equation which is not directly derived from an exact equation (Wilcox, 1988). Also, as an assumption of

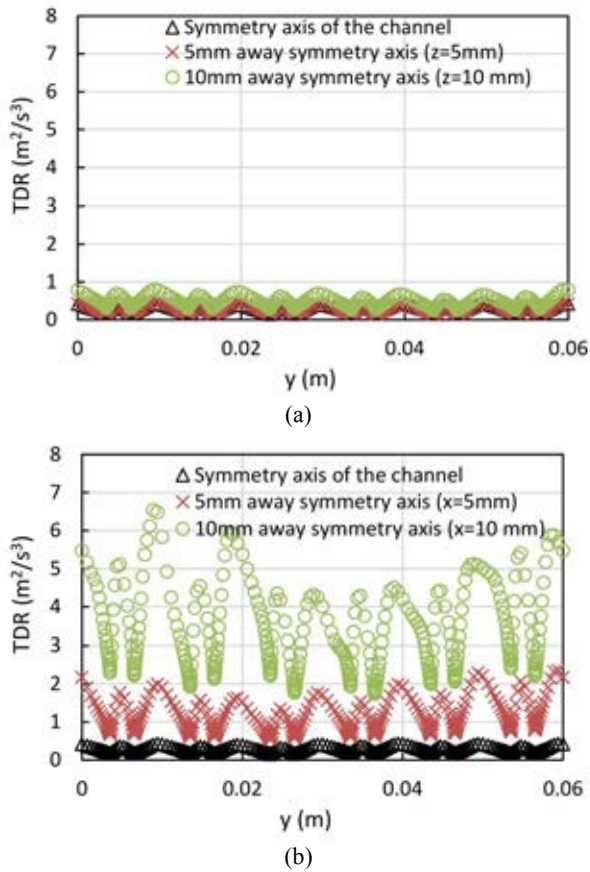


**Figure 10:** Turbulent energy dissipation rate from LES ( $\bar{V} = 2m/s$ ) along different lines parallel to the symmetry axis of the channel in symmetry planes of the channel. (a) In the symmetry plane across the pair of smooth walls; (b) In the symmetry plane across the pair of walls with tabs.

isotropic turbulent viscosity is used in RANS simulation, there could be large uncertainties in the CFD predictions of the flow behind the taps where highly anisotropic turbulence exists.

It is difficult to see whether the turbulent energy dissipation rate in the central region of the channel is increased or not across the wall with tabs from Figure 9 as the scale range is quite large. The profiles of the turbulent energy dissipation rate along different lines parallel to the symmetry axis of the channel in symmetry planes of the channel are depicted in Figure 10. Comparing Figure 10 (a) and (b), it is demonstrated that the turbulent energy dissipation rate in the central region of the channel is increased across the wall with tabs. Also, it shows that the turbulence in the central region of the channel is less homogenous across the pair of walls with tabs than across the pair of smooth walls.

#### Turbulent Vortical Structures

The iso-surfaces of the  $Q$ -criterion are depicted in Figure 11 to illustrate the coherent vortical structures. The definition of  $Q$  follows  $Q = \frac{1}{2}(\Omega^2 - S^2)$ , where  $\Omega$  and  $S$  are the absolute value of vorticity and strain rate, respectively ( $\Omega = \sqrt{2\bar{\omega}_{ij}\bar{\omega}_{ij}}$ ,  $S = \sqrt{2\bar{S}_{ij}\bar{S}_{ij}}$ ). Positive  $Q$  iso-surfaces isolate areas where the strength of rotation overcomes the strain, thus making those surfaces eligible

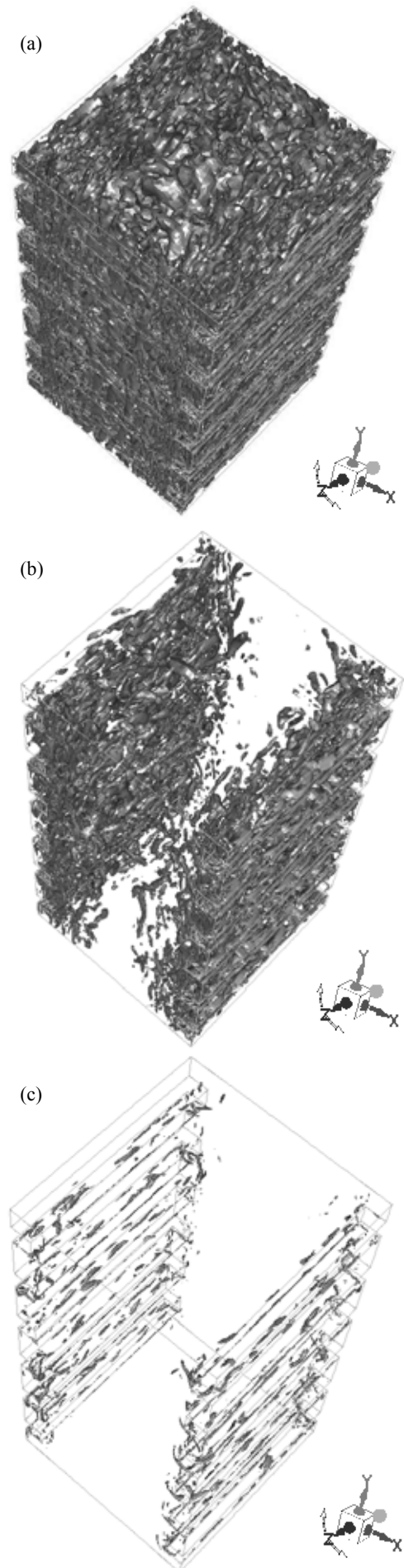


**Figure 11:** Iso-surfaces of the  $Q$ -criterion ( $\bar{V} = 2m/s$ ). (a)  $Q=10^4$ ; (b)  $Q=10^6$ ; (c)  $Q=10^7$ .



as vortex envelopes (Dubief and Delcayre, 2000; Jeong and Hussain, 1995). The dimensional  $Q$ -values can be very large and can vary greatly in the domain. For the case under consideration, the  $Q$ -values between  $10^{-9}$  and  $10^9$ . Iso-surfaces in the range of  $10^4$ – $10^7$  are sensible to illustrate the turbulent vortical structures for this case. Figures 11 (a) to (c) illustrate the iso-surfaces of  $Q$  values of  $10^4$ ,  $10^6$ , and  $10^7$ , respectively. It is demonstrated that there are more coherent strong vortices in the region close to the wall with tabs. Tip vortices are produced around the corners behind the tabs (see Figure 11 (c)). One basic question on droplet breakage is whether vortices smaller or larger than the droplets control the breakup rate. Earlier studies assumed that only eddies smaller than the particle diameter may transmit the energy to particles. More recent studies concluded that all scales of turbulent vortices affect the breakup (see for example, Andersson and Helmi, 2014; Ghasempour et al. 2014; Solsvik and Jakobsen, 2016a and 2016b; Solsvik, 2017). When experimental results on the probability of droplet breakage positions are obtained in the future, this information would be further used to provide some insight into the breakage mechanism.

## CONCLUSIONS

In this study, an experimental apparatus for investigating single droplet breakage in turbulent flow has been presented as well as some preliminary experimental results. CFD simulation of the single-phase flow in the experimental breakage channel was performed. The LES method was used for the simulation to provide detailed features of the flow. Results from LES were also compared with those from a RANS model (SST  $k-\omega$ ); different degrees of variance were shown in the profiles of velocity, turbulent kinetic energy, and the turbulent energy dissipation rate. The simulation results demonstrated that the turbulence level is enhanced across the pair of walls with protuberances/tabs. There are more coherent strong vortices in the region close to the wall with tabs. Systematic experimental tests will be carried out in the future to obtain statistical information on droplet breakage. The breakage mechanism will be investigated by analysing the experimental results together with the underlying turbulent information obtained from the present numerical study.

## ACKNOWLEDGEMENT

This work was carried out as a part of SUBPRO, a Research-based Innovation Centre within Subsea Production and Processing. The authors gratefully acknowledge the financial support from SUBPRO, which is financed by the Research Council of Norway, major industry partners and NTNU. Also, the authors would like to acknowledge the computational resources at NTNU provided by NOTUR, with which the CFD simulations were conducted.

## REFERENCES

Andersson, R. and Andersson, B. (2006) On the breakup of fluid particles in turbulent flows. *AIChE journal*, 52(6), pp. 2020-2030.  
 Andersson, R. and Helmi, A. (2014) Computational fluid dynamics simulation of fluid particle fragmentation

in turbulent flows. *Applied Mathematical Modelling*, 38(17), pp. 4186-4196.

Angeli, P. and Hewitt, G. F. (2000) Drop size distributions in horizontal oil-water dispersed flows. *Chemical Engineering Science*, 55(16), pp. 3133-3143.

Azizi, F. and Al Taweel, A. (2011) Turbulently flowing liquid-liquid dispersions. Part I: drop breakage and coalescence. *Chemical Engineering Journal*, 166(2), pp. 715-725.

Bouaifi, M., Mortensen, M., Andersson, R., Orciuch, W., Andersson, B., Chopard, F. and Noren, T. (2004) Experimental and numerical investigations of a jet mixing in a multifunctional channel reactor: Passive and reactive systems. *Chemical Engineering Research and Design*, 82(2), pp. 274-283.

Calabrese, R., Wang, C. and Bryner, N. (1986) Drop breakup in turbulent stirred-tank contactors. Part III: Correlations for mean size and drop size distribution. *AIChE journal*, 32(4), pp. 677-681.

Coulaloglou, C. and Tavlarides, L. (1976) Drop size distributions and coalescence frequencies of liquid-liquid dispersions in flow vessels. *AIChE journal*, 22(2), pp. 289-297.

de Jong, J., Cao, L., Woodward, S., Salazar, J., Collins, L. and Meng, H. (2009) Dissipation rate estimation from PIV in zero-mean isotropic turbulence. *Experiments in fluids*, 46(3), pp. 499-515.

Delafosse, A., Collignon, M.-L., Crine, M. and Toye, D. (2011) Estimation of the turbulent kinetic energy dissipation rate from 2D-PIV measurements in a vessel stirred by an axial Mixel TTP impeller. *Chemical Engineering Science*, 66(8), pp. 1728-1737.

Dubief, Y. and Delcayre, F. (2000) On coherent-vortex identification in turbulence. *Journal of turbulence*, 1(1), pp. 011-011.

Ghasempour, F., Andersson, R., Andersson, B. and Bergstrom, D. J. (2014) Number density of turbulent vortices in the entire energy spectrum. *AIChE journal*, 60(11), pp. 3989-3995.

Jeong, J. and Hussain, F. (1995) On the identification of a vortex. *Journal of Fluid Mechanics*, 285, pp. 69-94.

Lasheras, J. C., Eastwood, C., Martínez-Bazán, C. and Montañés, J. (2002) A review of statistical models for the break-up of an immiscible fluid immersed into a fully developed turbulent flow. *International Journal of Multiphase Flow*, 28(2), pp. 247-278.

Liao, Y. and Lucas, D. (2009) A literature review of theoretical models for drop and bubble breakup in turbulent dispersions. *Chemical Engineering Science*, 64(15), pp. 3389-3406.

Maaß, S., Gäbler, A., Zaccone, A., Paschedag, A. and Kraume, M. (2007) Experimental investigations and modelling of breakage phenomena in stirred liquid/liquid systems. *Chemical Engineering Research and Design*, 85(5), pp. 703-709.

Maaß, S. and Kraume, M. (2012) Determination of breakage rates using single drop experiments. *Chemical Engineering Science*, 70, pp. 146-164.

Middleman, S. (1974) Drop size distributions produced by turbulent pipe flow of immiscible fluids through a static mixer. *Industrial & Engineering Chemistry Process Design and Development*, 13(1), pp. 78-83.

Ni, X., Jian, H. and Fitch, A. (2003) Evaluation of turbulent integral length scale in an oscillatory baffled

column using large eddy simulation and digital particle image velocimetry. *Chemical Engineering Research and Design*, 81(8), pp. 842-853.

Sheng, J., Meng, H. and Fox, R. (2000) A large eddy PIV method for turbulence dissipation rate estimation. *Chemical Engineering Science*, 55(20), pp. 4423-4434.

Sleicher, C. (1962) Maximum stable drop size in turbulent flow. *AIChE journal*, 8(4), pp. 471-477.

Solsvik, J. and Jakobsen, H. A. (2015) Single drop breakup experiments in stirred liquid-liquid tank. *Chemical Engineering Science*, 131, pp. 219-234.

Solsvik, J., Tangen, S. and Jakobsen, H. A. (2013) On the constitutive equations for fluid particle breakage. *Reviews in Chemical Engineering*, 29(5), pp. 241-356.

Sprow, F. (1967) Distribution of drop sizes produced in turbulent liquid-liquid dispersion. *Chemical Engineering Science*, 22(3), pp. 435-442.

Wang, C. and Calabrese, R. V. (1986) Drop breakup in turbulent stirred-tank contactors. Part II: Relative influence of viscosity and interfacial tension. *AIChE journal*, 32(4), pp. 667-676.

Wilcox, D. C. (1998) *Turbulence modeling for CFD*, California: DCW industries



## IMPROVED COLLISION MODELLING FOR LIQUID METAL DROPLETS IN A COPPER SLAG CLEANING PROCESS

H. Yang<sup>1\*</sup>, J. Wolters<sup>1</sup>, P. Pischke<sup>2</sup>, H. Soltner<sup>1</sup>, S. Eckert<sup>3</sup>, J. Fröhlich<sup>4</sup>

<sup>1</sup> Forschungszentrum Jülich, Central Institute for Engineering, Electronics and Analytics, 52428 Jülich, Germany

<sup>2</sup> RWTH Aachen University, Institute of Heat- and Mass Transfer, 52062 Aachen, Germany

<sup>3</sup> HZDR, Department of Magneto-Hydrodynamics, 01067 Dresden, Germany

<sup>4</sup> TU Dresden, Institute of Fluid Mechanics, 01067 Dresden, Germany

\* E-mail: h.yang@fz-juelich.de

### ABSTRACT

Collision and coalescence among liquid metal droplets in a slag cleaning process enhanced by electromagnetic stirring were numerically studied. A hybrid collision algorithm was implemented to calculate the collision probability, which overcomes the mesh-dependency problem in a pure stochastic algorithm and is adaptive to both homogeneous and inhomogeneous cases. Theoretical analyses and numerical simulations based on the Volume-of-Fluid method were carried out in order to predict the result of droplet collisions, which are important for the copper slag cleaning process. Based on the numerical results, a new regime map, which is specific to the liquid metal droplet collisions driven by shear slag flow at low capillary numbers, is provided.

**Keywords:** copper slag cleaning, coalescence, volume-of-fluid method, liquid metal droplet

### NOMENCLATURE

#### Greek Symbols

- $\rho$  Mass density, [kg/m<sup>3</sup>].  
 $\mu$  Dynamic viscosity, [kg/m.s].  
 $\nu$  Kinematic viscosity, [m<sup>2</sup>/s].  
 $\sigma$  Surface tension, [N/m].  
 $\dot{\gamma}$  Shear rate, [1/s].  
 $\lambda$  Viscosity ratio, [-].  
 $\lambda_r$  Size ratio, [-].  
 $\psi$  Offset ratio, [-].  
 $\chi$  Mesh size, [m].  
 $\alpha$  Volume fraction, [-].  
 $\kappa$  Curvature, [-].  
 $\Theta$  Angular velocity, [rad/s].  
 $\Gamma$  Strain tensor, [-].  
 $\xi$  Dimensionless distance, [-].  
 $\varphi$  Angle, [rad].

#### Latin Symbols

- $p$  Pressure, [Pa].  
 $\mathbf{U}$  Velocity, [m/s].  
 $t$  Time, [s].  
 $g$  Gravitational acceleration, [m/s<sup>2</sup>].  
 $\mathbf{J}$  Current density, [A/m<sup>2</sup>].  
 $\mathbf{B}$  Magnetic flux density, [T].

- $\mathbf{F}$  Force, [N].  
 $h$  Distance, [m].  
 $R$  Radius, [m].  
 $V$  Volume, [m<sup>3</sup>].  
 $\mathbf{n}$  Surface normal vector, [-].  
 $\mathbf{r}$  Distance vector, [-].  
 $A_0$  Hamaker constant, [J].  
 $S_r$  Shape ratio [-].

#### Sub/superscripts

- ' Dimensionless  
 $d$  Droplet.  
 $f$  Fluid.  
 $0$  Initial value or external field.  
 $c$  Critical value.  
 $i$  Index  $i$ .

### INTRODUCTION

The recovery of valuable metallic material from industrial waste attracted increasing attention in past decades. In the copper production industry, slags from submerged arc furnaces (SAF) still contain up to 0.8 % of copper concentrate (Schlesinger and King, 2011). Single SAF furnaces generally produce 700,000 tons of slag per year, which represents a great economic recovery potential of the valuable copper material. As a result, a recovery furnace is conventionally arranged to recycle the remaining copper material from the SAF slag (cf. Figure 1), which allows gravitational settling of copper material onto the matte layer due to the density difference. In the slag, two thirds of the total copper is present in the form of entrained matte droplets with radii between 1 and 1000  $\mu\text{m}$  (Warczok and Riveros, 2003) whereas the rest is dissolved in the slag or matte as  $\text{Cu}^+$  ions bonded to  $\text{O}^{2-}$  or  $\text{S}^{2-}$ . A strong direct current (DC) is applied between the slag at the top and the matte layer at the bottom. The electric current generates Joule heat to keep the slag molten and to reduce the level of dissolved copper in the form of  $\text{Cu}_2\text{O}$  through electrode reactions, which segregate the dissolved copper near the anode. The segregated copper aggregates into fine dispersed droplets of 3 to 50  $\mu\text{m}$  diameter (Degel, et al., 2008). Considering the droplets with small size, the gravitational settling is too slow for an efficient cleaning

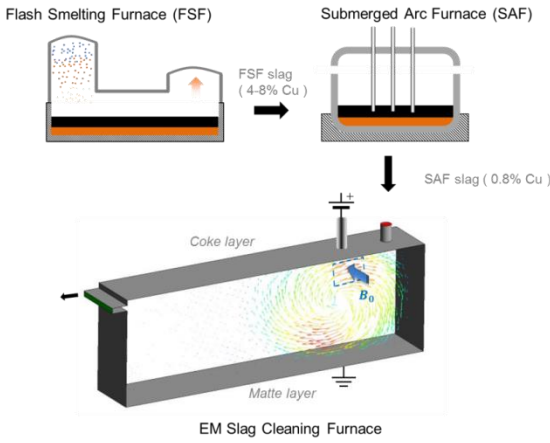


Figure 1: Flow diagram of an industrial copper production and slag cleaning process.

process. To increase the separation rate a magnetic field orthogonal to the electric field is introduced, which generates an intense stirring of the slag. Due to the stirring the probability of inter-droplet collisions is increased, which accelerates the droplet growth and results in a higher settling velocity.

In the recent years the feasibility and efficiency of the electromagnetic (EM) copper slag cleaning process has been tested experimentally at both laboratory and pilot scale (Kempken, et al., 2006). A few numerical investigations have also been published (Warczok and Riveros, 2007), which focused on predicting the dynamic and thermal behaviour of the slag phase. The inter-droplet collision and coalescence of the liquid metal droplets in molten slags, however, have not been numerically analysed despite of their dominating importance in the recovery process. Our project aims at advancing the understanding of the complex physical-chemical mechanisms in the copper slag cleaning process and optimizing the industrial process based on CFD calculations. Current numerical work is carried out using the commercial code ANSYS FLUENT.

The main focus of this paper is on analysing and modelling the outcome of binary collisions of liquid metal droplets in slags. Other numerical methods necessary to model the whole slag cleaning process, such as MHD (magneto-hydrodynamics) to simulate the forced stirring motion of the conducting slag and methods to determine the collision probability of droplets, will be mentioned but not discussed in detail.

## NUMERICAL MODELS

### Numerical scheme and governing equations

Our numerical investigations include multiphase modelling on the EM copper slag cleaning process, where the conducting slag is defined as the primary phase and entrained liquid metal droplets are defined as the dispersed secondary phase. The secondary phase features a small volume fraction but a massive number of droplets. Thus the current simulations are performed under an Euler–Lagrangian scheme, where the primary phase is treated as continuous phase and the secondary phase is treated as discrete phase.

For the continuous phase, the laminar flow of the conducting slag is driven and stirred by the Lorentz force. The Navier-Stokes equation for an incompressible conducting fluid under the influence of an external electromagnetic field can be expressed as:

$$\rho_f \left[ \frac{\partial \mathbf{U}}{\partial t} + (\mathbf{U} \cdot \nabla) \mathbf{U} \right] = -\nabla P + \rho_f \mathbf{g} + \mu_f \nabla^2 \mathbf{U} + \mathbf{J}_0 \times \mathbf{B}_0. \quad (1)$$

The term  $\mathbf{J}_0 \times \mathbf{B}_0$  is the Lorentz force density, which neglects the induction fields as the superposed field  $\mathbf{J}_0$  and  $\mathbf{B}_0$  are much stronger in comparison.

For the dispersed phase, the trajectory of the discrete droplet is predicted by solving the force balance equation:

$$m_d \frac{d\mathbf{U}_d}{dt} = \mathbf{F}_B + \mathbf{F}_D + \mathbf{F}_{VM} + \mathbf{F}_L + \mathbf{F}_{EC}. \quad (2)$$

Where  $\mathbf{F}_B$  is the buoyancy force,  $\mathbf{F}_D$  is the drag force,  $\mathbf{F}_{VM}$  is the virtual mass force,  $\mathbf{F}_L$  is the Lorentz force due to the higher conductivity of droplet and  $\mathbf{F}_{EC}$  is the electro-capillary force. More details on expressions of those forces can be found in (Warczok and Riveros, 2007) and (Choo and Toguri, 1992).

### Algorithm of collision probability calculation

In the present application, the direct modelling of collisions for all single droplets is prohibitive, since their large number would lead to unacceptable computational costs. This is avoided by a stochastic modelling, where the concept of parcels, representing a certain number of droplets with the same properties, is introduced. The most commonly used algorithm for collision modelling is a pure stochastic Monte Carlo algorithm, which is based on concepts of the kinetic gas theory (O'Rourke, 1981). It assumes that the droplets are homogeneously distributed in the collision volume. The collision probability depends on the mesh resolution, because the collision between droplets of two parcels is only possible when the centres of both parcels are located in the same cell of the continuous phase. The result of the pure stochastic algorithm highly depends on the spatial resolution and the error can become significant for cases with relatively coarse grids. The accuracy of this algorithm could be increased to second order through refining the control volume mesh. However, it may be computationally very costly to introduce such a refinement in geometrically complex simulations and it is difficult to estimate the appropriate mesh-resolution for different cases in advance. To overcome mesh dependency problems in the pure stochastic collision algorithm, a new hybrid Lagrangian collision algorithm was proposed by Pischke (2012). Here, the deterministic algorithm is transferred into a stochastic algorithm by redefining the number of collisions assuming a normal probability of presence of droplets around the centres of the parcels. The hybrid algorithm is absolutely mesh-independent and third-order accuracy can be achieved for inhomogeneous cases. Due to this advantage, the hybrid algorithm was chosen and implemented for the present simulations. In our former work (Yang, et al., 2016) we have investigated the differences between the two algorithms in detail.

### Prediction on collision outcome

To predict the collision outcome in a stochastic collision modelling, a regime map, which normally uses two or more parameters to identify the boundary among different possible collision outcomes, is required. Ready-to-use regime maps, such as suggested by Qian and Law (1997), are typically based on inertia-driven collisions in a gas-liquid-system with the Weber number ( $We$ ) as the main criterion. Those regime maps, however, are physically not suitable for our liquid metal droplet-slag system as stated in the following.

First of all the collision process of droplets in our system features very small Weber numbers, which would lead to droplet coalescence under the inertia-driven scheme. Instead of using criterion of an inertia-driven collision, it is physically more suitable to use the capillary number as the main criterion, which includes the influencing factors of shear-driven collisions like in our case.

Moreover, if the surfactant effect is neglected, collisions can be classified by the viscosity ratio between the droplet and fluid phase (Abid and Chesters, 1994). The outcome of a binary collision is determined by the drainage process of the thin film of the surrounding fluid trapped between confronting surfaces of the colliding droplets. The flow in the film can be described by the profile shown in Figure 2, depending on the viscosity ratio  $\lambda$ . When  $\lambda \gg 1$ , the interfaces are immobile and a Poiseuille flow type can be used to describe the drainage process. This is also the case for most of the Weber number based regime maps, where liquid droplets in gaseous environment are studied. When  $\lambda \sim 0$ , the film interfaces are fully mobile and the film drainage can be described as a plug flow. When  $\lambda$  has a moderate value, such as in our case for the liquid metal droplets-slag system, a partially mobile film interface is considered, where the drainage flow is a superposition of the Poiseuille and the plug flow. The regime maps which exclude such an influence brought by the viscosity ratio will cause an inaccurate prediction on the collision results.

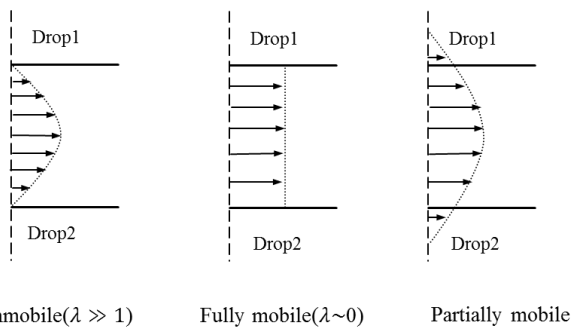


Figure 2: Classification of film drainage flow profile based on the viscosity ratio

Based on the above mentioned reasons, it is necessary to develop an appropriate outcome regime map for the liquid metal droplets-slag system. However, experimental results are difficult to achieve in such an opaque, high-temperature environment and no available experimental data have been found. Thus, in current investigations the collision process is studied theoretically and numerically to provide a suitable outcome regime map.

### ANALYSIS AND MODELLING OF THE BINARY COLLISION PROCESS

For numerically solving multiphase problems on two immiscible fluids with distinct interfaces, the volume of fluid (VoF) method is appropriate and is therefore chosen to model the binary collision process of liquid metal droplets entrained in a molten slag.

#### Fundamental principles of a shear driven binary collision

Similar to the analysis by Mousa (2001), a binary collision process in a simple shear flow can be illustrated according to Figure 3. The droplets are assumed to have equal size ( $R_1 = R_2 = R$ ) and droplet 2 is driven towards droplet 1 by the shear flow ( $\mathbf{U} = \sim(\dot{\gamma}\Delta y, 0, 0)$ ) in a straight line until they are close enough to interact with each other. At this point the confronting interfaces of the two droplets are flattened and the thin film of surrounding fluid starts to drain under the influence of hydrodynamic forces exerted by the shear flow and inter-molecular forces. If the drainage of the film is accomplished before droplets are separated by the external flow, the collision will end up in coalescence, at least temporarily. Otherwise, the droplets will slide along each other's surfaces and the collision ends up in bouncing.

The important dimensionless parameters to characterize the process are:

$$Ca = \mu_f \frac{\dot{\gamma}R}{\sigma}, \quad Re = \frac{\dot{\gamma}R^2}{\nu}, \quad \psi = \frac{\Delta y}{2R}, \quad \lambda = \frac{\mu_d}{\mu_f}$$

$$h'(t) = \frac{h(t)}{R}, \quad t' = \dot{\gamma}t.$$

Where,  $\dot{\gamma}$  is the shear rate,  $\sigma$  is surface tension,  $\nu$  is the kinetic viscosity,  $\mu_d$  and  $\mu_f$  are dynamic viscosity for droplet and bulk phase.

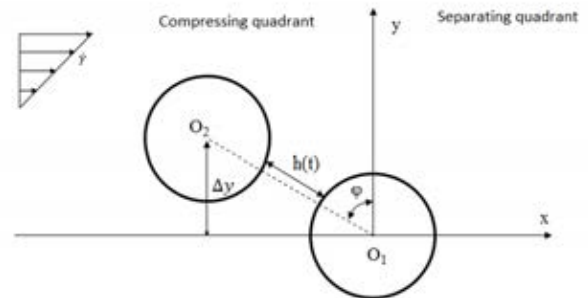


Figure 3: Sketch of a binary collision process

## Basics of the VoF method and governing equations

When the VoF method is used, additional transport equations for the volume fraction of phase  $i$  have to be solved. Under the prerequisites that no mass transfer between different phases is allowed and no mass source exists, the transport equation for the volume fraction  $\alpha_i$  for incompressible fluids is given by

$$\frac{D\alpha_i}{Dt} = \frac{\partial \alpha_i}{\partial t} + (\mathbf{U} \cdot \nabla)\alpha_i = 0. \quad (3)$$

In order to resolve the shape of the interface between different phases, a geometric reconstruction interpolation method (Young, 1982) is applied. This highly accurate, piecewise-linear approach recalculates a linear interface in each boundary cell filled with more than one phase based on the volume fraction and the corresponding derivative. To use the interface tracking method, an explicit scheme must be applied:

$$\frac{\alpha_i^{n+1} - \alpha_i^n}{\Delta t} + \frac{\sum_f (U_f^n \alpha_{i,f}^n)}{V} = 0. \quad (4)$$

Where  $V$  is the cell volume and  $f$  is the subscript that indicates a face value.

Compared with the implicit scheme, where the volume fraction value from the previous time step is not needed, the explicit scheme does not iteratively solve the transport equation of the volume fraction in each time step. The numerical diffusion of the interface is as a result less significant than in the implicit scheme and the prediction on the interface curvature is more accurate.

In the VoF method the intermolecular surface tension is normally modelled by solving the continuum surface force. At interface cells the gradient of the rise in pressure due to interfacial tension between different phases can be represented as volumetric body force  $F_{sf}$  (Brackbill, et al., 1992). The force is added as a source term in the momentum equation and can be expressed as:

$$\mathbf{F}_{sf} = 2 \cdot \alpha_1(t) \cdot \kappa(t) \cdot \mathbf{n}(t) \cdot \sigma. \quad (5)$$

$\mathbf{n}(t)$  is the surface normal vector, which is defined as the gradient of the second phase volume fraction:

$$\mathbf{n}(t) = \nabla \alpha_1(t). \quad (6)$$

$\kappa(t)$  is the local surface curvature and can be calculated by:

$$\kappa = \frac{1}{|\mathbf{n}|} \left[ \left( \frac{\mathbf{n}}{|\mathbf{n}|} \cdot \nabla \right) |\mathbf{n}| - (\nabla \cdot \mathbf{n}) \right]. \quad (7)$$

## Coalescence criterion

As mentioned before, the film drainage process is controlled by both hydrodynamic forces and inter-molecular forces, such as the Van der Waals force  $F_{vdw}$ . However, in the finite-volume modelling it is very difficult to precisely model the end of the drainage process in the case of coalescence ( $h(t) = 0$ ). Moreover, according to detailed calculations by Jiang and James (2007),  $F_{vdw}$  is only considerably large when  $h(t)$  is very small. Therefore, in our calculations coalescence is detected when

the critical thickness of the film  $h_c$  according to equation (8) is reached:

$$h_c = \left( \frac{AR}{8\pi\sigma} \right)^{\frac{1}{3}}. \quad (8)$$

According to the research by Chesters (1991), this approximate relationship is valid for flow-driven collisions between fluid-liquid dispersions at low capillary number. Once the critical film thickness is reached,  $F_{vdw}$  becomes significant and increases rapidly. The destabilization due to  $F_{vdw}$  dominates the film drainage, which leads to a film rupture and coalescence. This coalescence criterion was applied in several former researches, like for example in (Mousa, 2001). Mousa theoretically investigated collisions with partially and fully mobile interfaces at arbitrary approaching angles. In our calculations, we exclude the contribution of  $F_{vdw}$ , thus the collision is purely driven by the hydrodynamic forces and coalescence is reached if  $h(t)$  becomes less than  $h_c$ . The value of  $h(t)$  is determined by the minimum distance between the iso-surfaces of two droplets defined by the volume fraction.

The critical film thickness for metallic material in comparison to polymeric material is shown in Figure 4 as a function of the droplet size. The latter is extensively studied in experiments. A typical value for the Hamaker constant  $A$  of metallic material is  $40 \times 10^{-20} J$ , while for polymeric material it is  $1 \times 10^{-20} J$  (Chen, et al., 2009). The surface tension of copper droplets in slag is  $\sim 0.05 \frac{N}{m}$ , while for polymeric systems it is  $\sim 0.005 \frac{N}{m}$ . Thus the coalescence efficiency of copper droplets in a slag can be expected to be larger than that of polymeric material reported by Bruyn (2013).

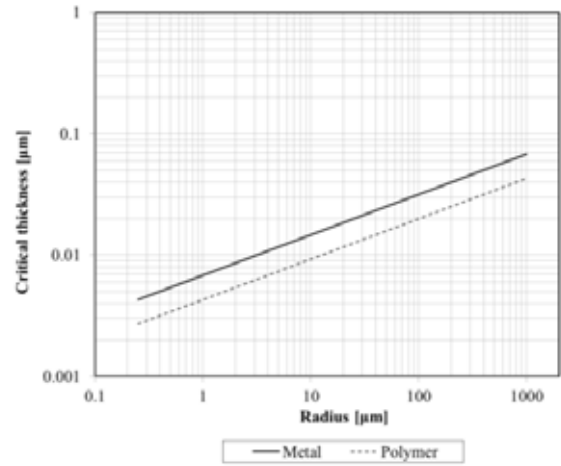


Figure 4: Critical film thickness for coalescence of metallic and polymeric material

## Numerical setups

### Geometry

A sketch of the 3D model to numerically simulate the binary collision process is shown in Figure 5. A simple shear flow at the desired shear rate is generated by two non-slip walls at the top and bottom of the domain, moving in opposite direction, and a periodic boundary condition. The centers of the two droplets are initially located in the middle of one symmetry plane at different y-positions, according to the demanded offset ratio. The initial distance in x-direction is fixed at  $\Delta x = 2.52R$  so

that the simulations start with non-interacting droplets until their shapes adapt to the flow field. The value of  $\Delta x$  is chosen according to the film drainage analysis (Chesters, 1991), where the film is established at the distance  $h(t) \leq 0.5 R$ . Similar to an experimental setup described by Bruyn (2013), the distance between the moving walls is  $36 R$  to avoid confinement effects. Periodic boundary conditions are used to ensure a fully developed shear flow. The distance between the two periodic planes is  $20 R$ , which is large enough to eliminate the influence due to the mirrored droplet pairs.

### Mesh

The modelling of the film drainage process requires meshes near the droplets surface with high resolution. However, it is computationally too expensive to generate meshes with identical sizes for the whole domain. Therefore a centre zone of size  $6R \times 6R \times 2R$  with sufficiently fine resolutions around the droplets is defined and the mesh resolution outside this zone is 10 times coarser. The boundary faces between the zone with fine and coarse mesh are defined as interfaces to allow mass and momentum transfer of the fluid. Furthermore, in the area near the droplets interface with the bulk phase, a 1-level dynamic adaptation of the mesh based on the gradient of the phase volume fraction is defined.

When choosing a proper mesh resolution, several aspects have to be considered:

First of all the mesh size  $\chi$  must be small enough to prevent the merging between interfaces of two droplets in the same cell before  $h(t)$  reaches the critical value  $h_c$  ( $\chi \leq \frac{h_c}{2}$ ).

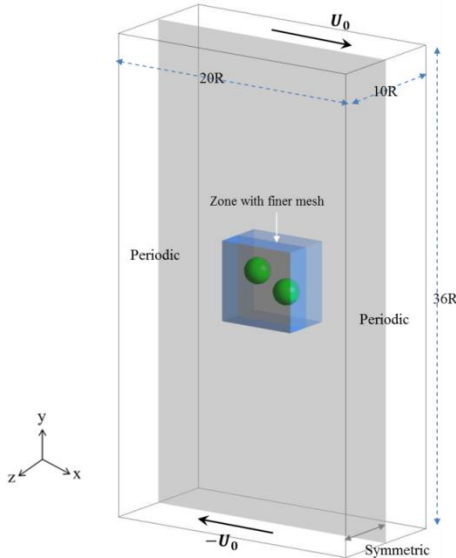


Figure 5: Geometry of the domain for modelling the binary collision

Moreover, the value of  $R/\chi$  must be sufficiently large to obtain a reasonable pressure distribution inside and outside of the droplet due to the Laplace pressure between the immiscible droplet and bulk phase (Sman and Graaf, 2008):

$$\Delta p = \frac{2\sigma}{R}. \quad (9)$$

In the VoF method, material is defined as a mixture of bulk and droplet phase in cells containing both phases, which physically do not exist. A finer mesh can reduce the error of the pressure distribution near the interface calculated with the VoF method in comparison to the theoretical value. This is important for modelling the film drainage process when interfaces of two droplets are close to each other.

On the other hand the value of  $R/\chi$  cannot be increased in the VoF method without limitation. One limitation is the error due to parasitic currents (unphysical flow near the interface) (Havie, et al., 2005), which is due to the local variations of the body force calculated by the surface tension algorithm. The magnitude of parasitic current becomes stronger with a finer mesh. The influence of the parasitic current is less significant in shear driven flows. But it will still cause diverging solutions on interface tracking when the magnitude of the parasitic current is too strong in comparison with the local external flow field.

Considering the above mentioned aspects and limitations due to the available computer cluster, the mesh resolution of studied cases is chosen as:

$$h_c = 2\chi, R = 126\chi.$$

According to the relationship between  $h_c$  and  $R$  in Figure 4, the physical size of the modelled droplets is  $R = 0.284 \mu\text{m}$ .

### Time step

The time step in an explicit VoF calculation must be small enough to ensure a stable iteration. In practice, the global Courant number should be smaller than 2. But in cases where a more accurate interface calculation is needed, it is preferred to choose a global Courant number smaller than 1. In the current calculations, the time steps are on the order of  $10 \text{ ns}$  leading to a maximum Courant number in the order of  $O(10^{-1})$ .

### Comparison of the time evolution of the film thickness from VoF calculations and far-field trajectory analyses

The binary collision between Newtonian droplets has been widely studied theoretically. At the present stage a trajectory analysis suggested in (Wang, et al., 1994) is used to verify the accuracy of the results from VoF calculations. This method assumes that two viscous droplets are approaching each other in a simple shear flow at a small capillary number and the shapes of droplets remain nearly spherical. Meanwhile the droplets are rotating at a constant angular velocity. The relative velocity of droplet 1 moving towards droplet 2 can be determined by:

$$\mathbf{V}_{12}(\mathbf{r}) = \boldsymbol{\Theta} \times \mathbf{r} + \boldsymbol{\Gamma} \cdot \mathbf{r} - \left[ \frac{A(\xi)\mathbf{r}\mathbf{r}}{r^2} + B(\xi) \left( \mathbf{I} - \frac{\mathbf{r}\mathbf{r}}{r^2} \right) \right] \cdot \boldsymbol{\Gamma} \cdot \mathbf{r}. \quad (10)$$



Where  $\mathbf{r}$  is the direction vector between the two droplet centers  $O_1$  and  $O_2$ ,  $\mathbf{I}$  is the unit second tensor,  $\boldsymbol{\Theta}$  is the angular velocity of the rotating droplet and  $\boldsymbol{\Gamma}$  is the strain tensor of the linear shear flow.  $\xi = h'(t) + 2$ ,  $A(\xi)$  and  $B(\xi)$  are relative mobility functions with respect of the viscosity ratio.

Due to the complexity of the flow situation when droplets are close to each other, the far-field expressions suggested in (Wang, et al., 1994) for the mobility functions are firstly considered:

$$A(\xi) = 4 \frac{(2 + 5\lambda)}{(1 + \lambda)} \frac{1}{\xi^3} - 48 \frac{\lambda(2 + \lambda) + \lambda(2 + 5\lambda)}{(1 + \lambda)(2 + 3\lambda)} \frac{1}{\xi^5} + o\left(\frac{1}{\xi^8}\right), \quad (11)$$

$$B(\xi) = 32 \frac{\lambda(2 + 3\lambda) + \lambda(2 + 5\lambda)}{(1 + \lambda)(2 + 3\lambda)} \frac{1}{\xi^5} + o\left(\frac{1}{\xi^6}\right). \quad (12)$$

The dimensionless trajectory equations are thereby given as:

$$\frac{d\xi}{dt'} = -(1 - A(\xi)) \xi \sin(2\alpha), \quad (13)$$

$$\frac{d\alpha}{dt'} = -\cos^2 \alpha - 0.5 B(\xi)(\sin^2 \alpha - \cos^2 \alpha). \quad (14)$$

The set of differential equations (13) and (14) is numerically solved by a fifth-order Runge-Kutta method. However, the expressions for the mobility functions given in (11) and (12) are only accurate when the dimensionless distance  $h(t)'$  is larger than  $\sim 0.1$ . To characterize the shape deformation of the droplets in a shear flow, a shape ratio  $S_r$  is defined as the ratio between the short axis length and the long axis length.

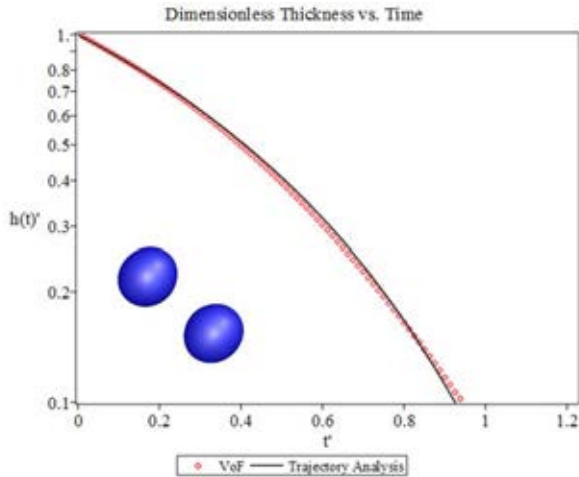


Figure 6: Time evolution of dimensionless distance between droplets' surfaces with VoF calculation and trajectory analysis ( $Ca = 0.05, \psi = 0.95, S_r = 0.9$ )

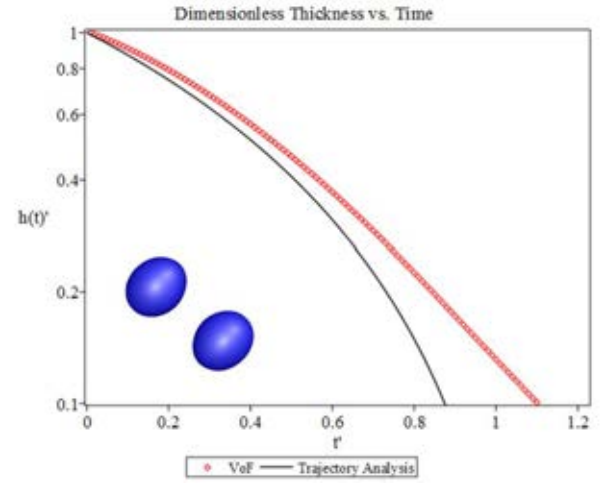


Figure 7: Time evolution of dimensionless distance between droplets' surfaces with VoF calculation and trajectory analysis ( $Ca = 0.1, \psi = 0.9, S_r = 0.8$ )

Binary collision test cases with  $Ca = 0.05, \psi = 0.95, S_r = 0.9$  and  $Ca = 0.1, \psi = 0.9, S_r = 0.8$  are used to compare the time evolutions of  $h(t)'$  solved by the trajectory analysis and VoF calculations up to a dimensionless distance  $h(t)' = 0.1$ . The tracking of film thickness starts at  $h(t)' = 1$ , which is shown in Figure 6 and Figure 7. Shapes of droplets at  $t' = 0$  are also shown in these figures. The given shape ratio  $S_r$  is due to the shear flow while the two droplets approach each other but do not yet interact. At low capillary numbers the deformation of the droplets does not affect the approaching process significantly and at large distances the results of the trajectory analysis and the VoF calculation agree well with each other (Figure 6). At larger capillary numbers the deformation of the droplets is more significant and the trajectory analysis for spherical droplets will overestimate the approaching speed (Figure 7).

### Collision outcome regime map of liquid metal droplets in a slag based on VoF calculations

As it was discussed before, in a simple shear flow at low capillary numbers the possible outcome after a binary collision is coalescence or bouncing (cf. Figure 8). To determine the critical offset ratio that separates the areas of coalescence and bouncing in an outcome regime map, for different capillary numbers a series of simulations were carried out approach the critical offset ratio  $\psi$  up to an accuracy of 2 decimal places by a bisection method. Coalescence is always considered permanent when the critical film thickness is reached, because according to (Shardt, 2013) a temporary bridge (temporary coalescence with subsequent separation) between droplets is only possible when  $R/h_c < 22$ . In our case this would mean that the corresponding droplets must have a very small physical size of  $R < 50$  nm, while the smallest droplets existing in the copper slag cleaning process have a size in the order of  $1 \mu\text{m}$ .

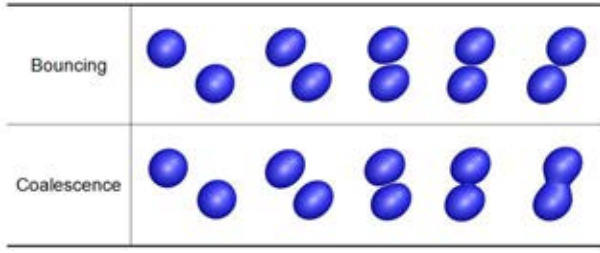


Figure 8: Possible collision outcomes in the VoF calculations

In Figure 9 the drainage process of the thin film and its possible outcome depending on the offset ratio is exemplarily shown for two different capillary numbers. In the VoF calculations, where the deformation of the droplets is balanced by the ambient pressure and surface tension, the droplets will gradually restore their shape after they pass the compressing quadrant ( $\varphi > 0$ , cf. Figure 3). The confronting faces of the droplets will still be pushed towards each other by the surface tension, although the hydrodynamic force tends to separate them. Therefore coalescence between droplets is still possible even if they are located in the separating quadrant of Figure 3 (cf. point  $\varphi = 0$  for curve 1 in Figure 9.). It should be noted that for the assessment of the collision process and the final regime map the previously defined capillary number is multiplied by an empirical factor  $\left(\frac{R}{\mu\text{m}}\right)^{0.84}$ , which reflects the influence due to the physical size of the droplets to the coalescence efficiency and will be discussed in the following section.

In a regime map where  $Ca \cdot \left(\frac{R}{\mu\text{m}}\right)^{0.84}$  is defined as x-axis and  $\psi$  is defined as y-axis, the curve of critical offset ratio that separates the zones of bouncing and coalescence is drawn by a polynomial interpolation (cf. Figure 10).

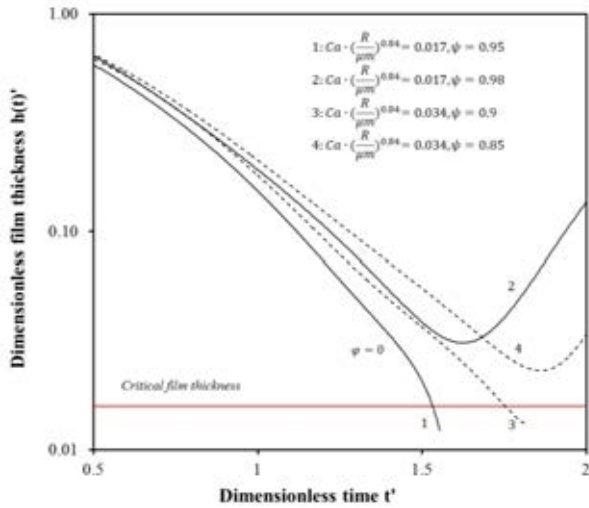
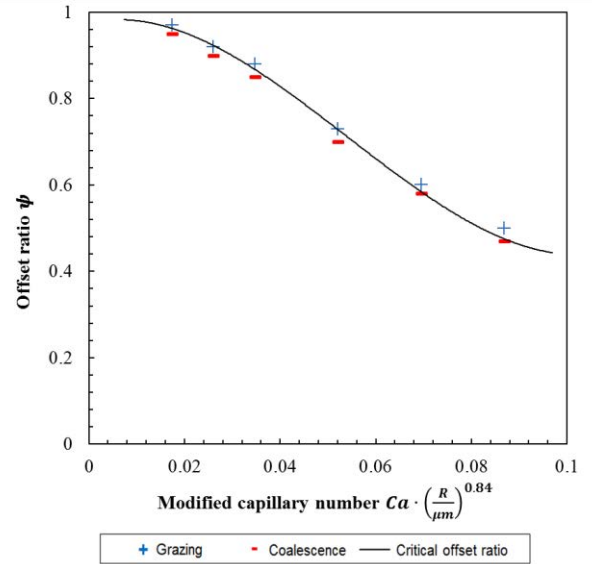

 Figure 9:  $h(t')$  versus  $t'$  for cases with different modified capillary number and offset ratio.


Figure 10: A capillary-number-based collision outcome regime map

## DISCUSSION

When the dielectric properties of the studied collision system are constant, the regime map suggested in Figure 10 depends on the following chosen physical parameters: the physical size of the droplets, the size ratio and the viscosity ratio. Their influence will be shortly discussed in the following.

### Physical size of the droplets

Instead of the pure capillary number  $Ca$ , a scaled number  $Ca \cdot \left(\frac{R}{\mu\text{m}}\right)^{0.84}$  is used in the regime map. The scaling factor is an empirical factor resulting from experiments described in (Hu, et al., 1989) and has been used to fit experimental data (Bruyn, et al., 2013). It indicates that for larger droplets the film drainage is slower than for smaller droplets if the same capillary number is considered. The numerical approach to examine the decrease in coalescence with a larger droplet size, however, is found to be difficult (Yoon, et al., 2007). In the corresponding simulations the decrease in coalescence efficiency is mainly due to the difference in the critical thickness calculated by equation ( 8) and the dependency of the dimensionless film drainage time on the droplet size is much weaker than that observed in the experiment. The possible reasons for this disagreement have been briefly discussed in the same literature. To avoid extra simulations with different droplet sizes, which will probably fail to provide a reliable correction factor, the modified capillary number  $Ca \cdot R^{0.84}$  is used currently to eliminate the effect of droplet size.

### Size ratio

The size ratio of two colliding droplets is defined as  $\lambda_r = R_{\text{smaller}}/R_{\text{larger}}$  and current investigations were under the assumption that two colliding droplets have an equal size ( $\lambda_r = 1$ ). Theoretical analyses (Wang, et al., 1994) and experimental observations (Mousa, et al., 2001) show that for a constant average radius the coalescence efficiency decreases if the difference in size increases ( $\lambda_r < 1$ ). This decrease in coalescence efficiency is due to the fact that smaller droplets tend to

follow the flow streamline bent around the larger droplet in the Stokes regime. The decreasing factor suggested by Mousa (1991) can be expressed as  $\left(\frac{4\lambda_r}{(1+\lambda_r)^2}\right)^\kappa$ , where  $\kappa$  is an empirical parameter, normally in the range from 1 to 6.

### Viscosity ratio

Based on the analyses in the former section it is clear that the viscosity ratio  $\lambda$ , which determines the mobility of the interfaces, has a great influence on the collision result. A simple power-law dependence of coalescence on  $\lambda$  was expected in some early investigations, for example, in the research by Hu (1989), a relationship of  $Ca_c \sim \lambda^{-2/3}$  using simple scaling theory is suggested, where  $Ca_c$  is the critical capillary number of coalescence for collision at fixed offset ratio. However, more recent researches (Yoon, et al., 2005) suggest that the influence on coalescence efficiency due to  $\lambda$  is more complex and it is not suitable to define a simple power-law dependency between those two parameters. To numerically investigate the influence due to the viscosity ratio simulations using the above mentioned setups with different  $\lambda$  were performed. The change of the critical offset ratios in the regime map based on the VoF simulations is shown in Figure 11. It can be seen that the influence of the viscosity ratio  $\lambda$  is more significant at higher capillary numbers. More investigations on this issue may be necessary. For the simulations on the copper slag cleaning process the influence of the viscosity ratio is important, since the temperature distribution in the slag is inhomogeneous and the viscosity ratio depends on the temperature.

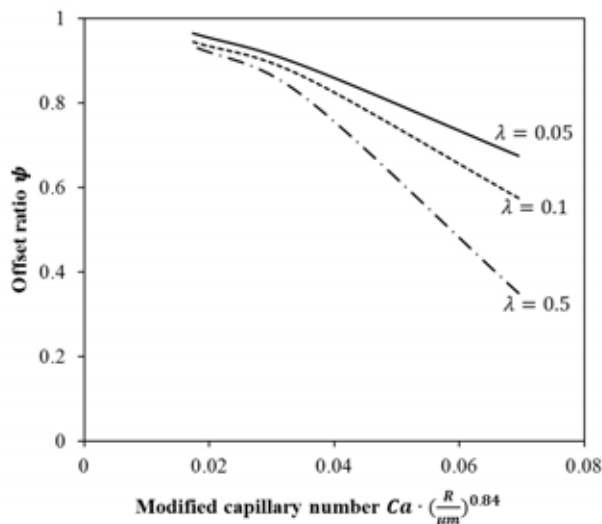


Figure 11: Critical offset ratio with respect of different viscosity ratios in the VoF calculations.

### CONCLUSIONS

Numerical approaches on modelling an enhanced copper slag cleaning process through electromagnetic stirring have been presented in this publication. An Euler-Lagrangian scheme of solving the multiphase problem is implemented, where slags are defined as continuous phase and liquid metal droplets are defined as dispersed phase. For the continuous phase, MHD (magneto-hydrodynamic) calculations on the conducting slags under the influence of orthogonally oriented magnetic

and electric fields were performed. For the dispersed phase tracking of the liquid metal droplet is realized by solving the force balance with consideration of special electromagnetic forces.

With respect to the inter-droplet collisions, a mesh-independent hybrid Lagrange-stochastic collision algorithm was introduced to calculate the collision probability, which has an excellent adaptability in both homogeneous and in-homogeneous cases.

In order to correctly predict the collision outcome in the stochastic collision modelling, a new outcome regime map was developed, taking into account the peculiarities of the slag cleaning process and physical properties of liquid metal droplets in slags. Since the collision of droplets in the slag is not driven by inertia effects but by a shear flow, the new regime map is based on the capillary number. The criteria for coalescence were derived by detailed numerical simulations on the binary collision of droplets in a slag using the Volume of Fluid (VoF) method, considering theoretical aspects and empirical findings. Intermolecular forces are not directly considered in the numerical simulation, but they determine the critical thickness of the film between the colliding droplets, for which coalescence is expected. The accuracy of the VoF calculation is verified by comparison with results from the far-field trajectory analysis. The influences due to some parameters, like droplet size, size ratio and viscosity ratio, are discussed and will also be considered in the application of the regime map.

The new regime map predicting the collision outcome in the stochastic collision model will be used in the overall copper slag cleaning process simulations. Based on these simulations an optimization of the process resulting in an improved recovery rate is envisaged in the near future.

### REFERENCES

- ABID, S. and CHESTERS, A.K., (1994), The drainage and rupture of partially mobile films between colliding drops at constant approach velocity, *Int. J. Multiphase. Flow*, Vol.20, No.3: 613-629.
- BRACKBILL, J. U., KOTHE, D. B., ZEMACH, C., (1992), A continuum method for modeling surface tension". *J.Comput. Phys.* 100. 335-354.
- BRUYN, P. D., CARDINAELS, R., MOLDENAERS, P., (2013), The effect of geometrical confinement on coalescence efficiency of droplet pairs in shear flow, *J. Colloid Interface Sci.* 409,183-192.
- CHESTERS, A., (1991), The modelling of coalescence processes in fluid-liquid dispersions, *Trans. IChemE*, 69, pp. 259-270.
- CHEN, D., CARDINAELS, R., MOLDENAERS, P., (2009), Effect of confinement on droplet coalescence in shear flow, *Langmuir*, 25(22): 12885-12893.
- CHOO, R.T.C. and TOGURI, J.M., (1992), The electrodynamic behavior of metal and metal sulphide droplets in slags, *Canadian Metallurgical Quarterly*, Vol.31, No.2: 113-126.
- DAVIS, R.H., SCHONBERG, J.A., RALLISON, J.M., (1989), The lubrication force between two viscous drops, *Phy. Fluids*, 1(1): 77-81.

DEGEL, R., OTERDOOM, H., KUNZE, J., WARCZOK, A., RIVEROS, G., (2008), Latest results of the slag cleaning reactor for copper recovery and its potential for the PGM industry, *Third International Platinum Conference 'Platinum in Transformation'*: 197-202.

HARVIE, D.J.E., DAVIDSON, M.R., RUDMAN, M., (2005), An analysis of parasitic current generation in volume of fluid simulations, *ANZIAM J.46*: ppC133-C146.

HU, Y.T., PINE, D.J., LEAL, L.G., (1989), Drop deformation, breakup, and coalescence with compatibilizer. *Phys. Fluids*, 12: 484-489.

JIANG, X. and JAMES, J., (2007), Numerical simulation of the head-on collision of two equal-sized drops with van der Waals force, *J. Eng. Math.* 59: 99-121.

KEMPKEN, J., DEGEL, R., SCHREITER, T., SCHMIEDEN, H., Rectangular furnace design and revolutionary DC-Slag cleaning technology for the PGM industry. (2006), *Metal world*, issue 12: 10-13.

MOUSA, H., AGTEROF, W., MELLEMA, J., (2001), Experimental investigation of the orthokinetic coalescence efficiency of droplets in simple shear flow, *J. Colloid Interface Sci.* 240: 340-348.

MOUSA, H. and VAN DE VEN, T.G.M., (1991), Stability of water-in-oil emulsions in simple shear flow 1. Determination of the orthokinetic coalescence efficiency, *Colloide surface*, 60: 19-38.

MOUSA, H., AGTEROF, W., MELLEMA, J., (2001), Theoretical and experimental investigation of the coalescence efficiency of droplets in simple shear flow, *Progr Colloid Polym Sci.*, 118, pp. 208-215.

O'ROURKE, P.J., (1981), Collective drop effects on vaporizing liquid sprays, Ph.D thesis, Department of Mechanical and Aerospace Engineering, Princeton University.

PISCHKE, P., CORDES, D., KNEER, R., (2012), A collision algorithm for anisotropic disperse flows based on ellipsoidal parcel representations, *Int. J. Multiphase Flow*, 38, pp. 1-16.

QIAN, J. and LAW, C.K., (1991), Regimes of coalescence and separation in droplet collision, *J. Fluid Mech.*, 331, pp. 59-80.

SHARDT, O., MITRA, S.K., DERKSEN, J.J., (2013), Simulations of Droplet Coalescence in Simple Shear Flow, *Langmuir*, 29, pp. 6201-6212.

WANG, H., ZINCHENKO, A., DAVIS, R., (1994), The collision rate of small drops in linear flow fields, *J. Fluid Mech.*, Vol.265: 161-188.

SCHLESINGER, M. and KING, M., (2011), *Extractive metallurgy of copper*, 5<sup>th</sup>ed., Elsevier, UK.

VAN DER SMAN, R.G.M. and VAN DER GRAAF, S., (2008), Emulsion droplet deformation and breakup with Lattice Boltzmann model, *Computer Physics Communications*, 178: 492-504.

WARCZOK, A. and RIVEROS, G., (2003), Effect of electric and magnetic fields on the metallic inclusions in a liquid slag, *Yazawa International Symposium-Metallurgical and materials processing and technology Volume 2*: 417-429.

WARCZOK, A. and RIVEROS, G., (2007), Slag cleaning in crossed electric and magnetic fields, *Miner.Eng.*, 20: 34-43.

YANG, H., WOLTERS, J., PISCHKE, P., Soltner, H., ECKERT, S., FRÖHLICH, J., (2016), Numerical

simulations on copper droplet collisions in the slag cleaning process, *9th International Conference on Multiphase Flow*, Firenze, Italy.

YOUNGS, D. L., (1982), Time-dependent multi-material flow with large fluid distortion. *Numerical Methods for Fluid Dynamics*, 24(2): 273-285.

YOON, Y., BORRELL, M., PARK, C.C., LEAL, L.G., (2007), Coalescence of two equal-sized deformable drops in an axisymmetric flow, *Phy. Fluids*, 19(10).

YOON, Y., BORRELL, M., PARK, C.C., LEAL, L.G., (2005), Viscosity ratio effects on the coalescence of two equal-sized drops in a two-dimensional linear flow, *J. Fluid Mech.*, vol.525: 355-379.



# MODELLING OF BUBBLE DYNAMICS IN SLAG DURING ITS HOT STAGE ENGINEERING

Y. WANG<sup>1\*</sup>, L. CAO<sup>1,2</sup>, B. BLANPAIN<sup>1</sup>, M. VANIERSCHOT<sup>3</sup>, M. GUO<sup>1</sup>

<sup>1</sup> KU LEUVEN Department of Materials Engineering, 3001 Leuven, BELGIUM

<sup>2</sup> UNIVERSITY OF SCIENCE AND TECHNOLOGY BEIJING State Key Laboratory of Advanced Metallurgy, 100083 Beijing, CHINA

<sup>3</sup> KU LEUVEN Mechanical Engineering Technology TC, Campus Group T, 3001 Leuven, BELGIUM

\* E-mail: yannan.wang@kuleuven.be

## ABSTRACT

Silica-rich additives are injected into the slag with N<sub>2</sub>/O<sub>2</sub> as carrier gas to stabilize free lime in BOF (Basic Oxygen Furnace) steelmaking slag. In order to understand the mixing behaviour of the additives, bubble dynamics and momentum transfer are to be clarified at first. The objective of this work is to investigate the bubble breakup and the injected momentum transfer. To this purpose, a Volume of Fluid (VOF) two phase model was developed using ANSYS FLUENT software to study the dynamic breakup process of the gas phase and the velocity attenuation along the injected axis. Particle Image Velocimetry (PIV) measurements were used to validate the corresponding computational modelling. The validation between experimental measurements and computational modelling is reasonable in the turbulence model. Bubble breakup begins very quickly in the region near the inlet. The momentum contained in the gas phase is dissipated within a short distance from the inlet.

**Keywords:** bubble breakup; momentum transfer; computational modelling; particle image velocimetry

## NOMENCLATURE

### Greek Symbols

$\alpha$  Volume fraction.

$\alpha_k, \alpha_\varepsilon$  Inverse effective Prandtl numbers.

$\mathcal{E}$  Turbulent dissipation rate, [m<sup>2</sup>/s<sup>3</sup>].

$\mu$  Dynamic viscosity, [kg/m.s].

$\mu_e$  Effective viscosity, [kg/m.s].

$\rho$  Mass density, [kg/m<sup>3</sup>].

=

$\tau$  Stress tensor.

### Latin Symbols

$A$  Inlet area, [m<sup>2</sup>].

$C_\mu, C_{1\varepsilon}, C_{2\varepsilon}$  Constant, 0.0845, 1.42, 1.68, respectively.

$F$  Momentum source term, [N/m<sup>3</sup>].

$g$  Gravitational acceleration, [m/s<sup>2</sup>].

$G_b$  Turbulence generation due to buoyancy.

$G_k$  Turbulence generation due to mean velocity gradient.

$\mathcal{K}$  Turbulence kinetic energy, [m<sup>2</sup>/s<sup>2</sup>].

$p$  Pressure, [Pa].

$Q$  gas flow rate, [Nm<sup>3</sup>/min].

$R_\varepsilon$  Additional term.

$S_\varepsilon$  Turbulence dissipation rate source term.

$S_k$  Turbulence kinetic energy source term.

$t$  Time, [s].

$T$  Temperature, [K].

$u_{in}$  Inlet velocity, [m/s].

$\mathbf{u}$  Velocity, [m/s].

$Y_M$  Contribution of the fluctuating dilatation.

### Sub/superscripts

o Operating condition.

s Standard condition.

## INTRODUCTION

Currently, about 10 million tonnes of BOF (Basic Oxygen Furnace) slag is annually produced as a main by-product during steelmaking in Europe (Euroslag, 2017). Therefore, the use of BOF slag becomes a very urgent issue since it causes land occupation, environmental problems and resource waste. However, BOF slag valorization is restricted by its volume swelling during natural aging due to the presence of free lime (Liu *et.al*, 2016). In order to solve this problem, silica-rich additives, which are used to stabilize the free lime at high temperature, are injected into the liquid slag with nitrogen or oxygen gas as carrier gas through a top submerged lance. As a result, a buoyancy-driven flow in the slag pot is generated by gas injection, and the additives can move with the flow and react with free lime and other compounds.

In this whole process, the mixing efficiency is usually considered as one of the most important performance parameters, therefore, one of the main objectives is to attain a good mixing effect in the slag pot. To this end, it

is beneficial to clearly understand the way that the injected gas affects the mixing characteristics. Regarding this topic, bubble dynamics and momentum transport phenomena are closely involved. A large body of research has been directed at a similar topic in ladle metallurgy that is the interaction between gas bubble and liquid metal (e.g. Cloete *et.al*, 2009; Li *et.al*, 2008; Olsen and Cloete, 2009). Based on the references, it can be predicted that the stirring and mixing of slag in a treatment is also mainly attributed to buoyant potential energy in the form of gas bubbles with different sizes formed by gas jet breakup. In other words, the gas breakup in the slag pot is very important to the flow pattern and mixing characteristics.

The purpose of the present study is to build a computational model to study the gas jet breakup and the momentum transfer in the slag pot. This can lay the foundation for the further investigation of mixing characteristics in the slag pot. In order to validate the turbulence modelling, Particle Image Velocimetry (PIV) measurements in a scaled cubic vessel was performed, and a detailed comparison between experimental and numerical results is made.

## MODEL DESCRIPTION

For the sake of reducing the computational cost, only a transient two-dimensional and two-phase (*g-l*) model is developed in the present study. The Volume of Fluid (VOF) multiphase flow model is adopted to investigate the gas jet breakup due to the immiscible property and the sharp interface between gas bubble and liquid slag. The RNG *k-ε* turbulence model is applied to study the turbulence characteristics in the slag pot.

### Volume of Fluid Model

The VOF model is designed for two or more immiscible fluids which, in our case, are liquid slag and gas, respectively. In the VOF model, a single set of momentum equations is shared by the fluids, and the volume fraction of each of the fluids in each computational cell is tracked throughout the domain. The continuity and momentum equations are listed as follows:

Continuity equation

$$\frac{\partial \rho}{\partial t} + \nabla \cdot (\rho \mathbf{u}) = 0 \quad (1)$$

Momentum equation

$$\frac{\partial \rho \mathbf{u}}{\partial t} + \nabla \cdot (\rho \mathbf{u} \mathbf{u}) = -\nabla p + \nabla \cdot \left( \frac{\tau}{\rho} \right) + \rho \mathbf{g} + \mathbf{F} \quad (2)$$

In the VOF model, all variables and properties are shared by the phases and represent volume-averaged values. Therefore, the variables and properties in any given control volume are either purely representative of one of the phases, or representative of a mixture of the phases, which depends on the volume fraction values. In our two-phase system, the volume fractions of slag and gas sum up to unity. The volume-averaged density and viscosity can be represented by the following mathematical equations.

$$\alpha_{\text{slag}} + \alpha_{\text{gas}} = 1 \quad (3)$$

$$\rho = \alpha_{\text{slag}} \rho_{\text{slag}} + \alpha_{\text{gas}} \rho_{\text{gas}} \quad (4)$$

$$\mu = \alpha_{\text{slag}} \mu_{\text{slag}} + \alpha_{\text{gas}} \mu_{\text{gas}} \quad (5)$$

### RNG *k-ε* Model

RNG *k-ε* turbulence model is derived from the instantaneous Navier-Stokes equations, using a statistical technique called “renormalization group” (RNG) method. It has a similar form to the standard *k-ε* turbulence model, but includes several refinements. It is more appropriate for rapidly strained and swirling flows than the standard *k-ε* turbulence model, and it also provides an analytically derived differential formula for effective viscosity that accounts for low-Reynolds number effects (ANSYS, Inc., 2015).

The turbulence kinetics energy, *k*, and its dissipation rate, *ε*, in the RNG *k-ε* model are obtained from the following transport equations:

$$\frac{\partial}{\partial t} (\rho k) + \frac{\partial}{\partial x_i} (\rho k u_i) \quad (6)$$

$$= \frac{\partial}{\partial x_j} \left( \alpha_k \mu_e \frac{\partial k}{\partial x_j} \right) + G_k + G_b - \rho \varepsilon - Y_M + S_k$$

$$\frac{\partial}{\partial t} (\rho \varepsilon) + \frac{\partial}{\partial x_i} (\rho \varepsilon u_i) \quad (7)$$

$$= \frac{\partial}{\partial x_j} \left( \alpha_\varepsilon \mu_e \frac{\partial \varepsilon}{\partial x_j} \right) + C_{1\varepsilon} \frac{\varepsilon}{k} (G_k + C_{3\varepsilon} G_b) - C_{2\varepsilon} \rho \frac{\varepsilon^2}{k} - R_\varepsilon + S_\varepsilon$$

The effective turbulent viscosity is solved by

$$\mu_e = \rho C_\mu \frac{k^2}{\varepsilon} + \mu \quad (8)$$

### Geometry and Operational Conditions

The geometry in the model consists of a slag pot and a lance. The slag pot is in the shape of a tapered cylinder and the lance is a simple cylinder. Liquid slag is contained in the slag pot with a certain height. The lance is submerged into the liquid slag from the slag level to a specific depth in the centre position. The dimensions and physical properties and operational conditions are listed in Table 1, 2 and 3, respectively. Since it is a symmetrical geometry, only half of it was built. The total node number is around 36000, which is large enough to obtain a sharp interface between gas bubble and liquid slag. The geometry with the grid is depicted in Figure 1.

**Table 1:** Geometrical dimensions of the pot.

Top diameter, mm	3360
Bottom diameter, mm	2390
Height, mm	3558
Lance diameter, mm	40

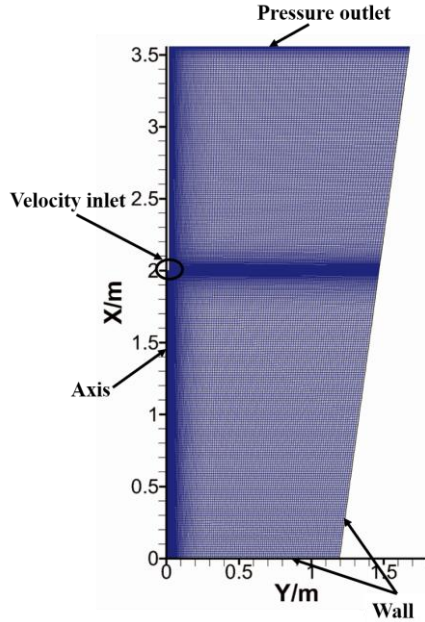
**Table 2:** Physical properties.

Density of slag, kg/m <sup>3</sup>	3000
Density of air, kg/m <sup>3</sup>	0.567*
Viscosity of slag, kg·m <sup>-1</sup> ·s <sup>-1</sup>	0.100
Viscosity of air, kg·m <sup>-1</sup> ·s <sup>-1</sup>	8.9e-5
Surface tension of slag/gas, N/m	0.55

“\*” indicates a lower air density due to the high temperature in real case.

**Table 3:** Operating conditions.

Air flow rate, Nm <sup>3</sup> /min	3
Inlet velocity, m/s	50.0 to 84.5
Operating temperature, K	1873
Operating pressure, Pa	3e5 to 5e5
Lance depth, mm	1000
Height of slag level, mm	3000

**Figure 1:** Geometry with grid.

The heat transfer is not in the scope of this study, therefore, the temperature gradient is neglected, which means that a uniform temperature field is assumed in this simulation. The inlet velocity of air is calculated based on the following equation.

$$u_{in} = \frac{Q_o}{A} = \left( \frac{p_s T_o}{p_o T_s} \right) \frac{Q_s}{A} \quad (9)$$

### Numerical Method

This model is implemented in FLUENT 16.2. Velocity inlet and pressure outlet boundary conditions are adopted for this simulation. For the solution methods, the Pressure-Implicit with Splitting Operators (PISO) pressure-velocity coupling scheme is used, which is recommended for a transient problem. PISO scheme has its own advantages that allows higher under-relaxation values for both momentum and pressure, leading to less iterations and faster convergence. In the spatial discretization part, the PREssure Stagging Option (PRESTO!) scheme and second order upwind scheme are performed for pressure and momentum, respectively. Convergence is monitored by means of the unscaled residual of the continuity equation. The reason is that the continuity equation is the most difficult one to converge. In this study, it is considered that the residual of the continuity equation must drop at least 3 orders of magnitude to obtain a sufficient accuracy. Therefore, the convergence criterion less than  $10^{-7}$  is chosen when the time step size is  $1 \times 10^{-4}$ .

The simulations were uploaded to a High Performance Computing (HPC) cluster. 2-5 nodes with 40-100 processors were required for the simulations.

### TURBULENCE MODEL VALIDATION

In order to validate the RNG  $k$ - $\epsilon$  turbulence model, PIV measurements and the corresponding simulations were conducted beforehand.

### Experimental setup

In the measurements, paraffin oil and compressed air are used to form a two-phase system. The vessel made of transparent glass is cubic shape with dimensions of  $135 \times 135 \times 195$  mm. A glass pipe with inner diameter of 5 mm taken as the top lance is also placed in the centre of the vessel. The operating conditions and physical properties are listed in Table 4.

The flow field in the vessel is measured by Time-Resolved PIV (TR-PIV). Since the vessel is axisymmetric, only the left zone is of interest. It can also be easily predicted that the liquid mainly flows in the upper part based on two considerations, one of which is that the upper part liquid is driven by the rising air, and the other one is that the injected air cannot penetrate very deeply, so the liquid in the lower part is almost still. Therefore, the selected area to be measured is located in the upper left part of the median plane, which is shown in Figure 2. A PIV laser (wavelength 527 nm, pulse energy 10 mJ @ 1000 Hz) from NewWave is employed to generate a laser sheet with a thickness of 0.5 mm which exactly overlaps the median plane of the vessel. The flow is seeded with hollow PMMA particles of diameters between 20 and 50  $\mu$ m. The particles are coated by Rhodamine B to exhibit fluorescence, which can help increase the signal to noise ratio when the back light of the laser sheet is filtered out by an optical filter. In order to correct for light refraction, the PIV system was calibrated by means of placing a calibration plate in the measured flow field, and the plate exactly overlaps the laser sheet. The images are recorded by a CMOS camera (HighSpeedStar 5) with a resolution of  $1024 \times 1024$  pixels. The calculation of velocity vector is processed by the Davis 8.1 software (LaVision GmbH). Further data processing is executed by Matlab software (R2016a) using specific code.

The corresponding numerical simulation is established with the same multiphase flow model (VOF) and the turbulence model (RNG  $k$ - $\epsilon$ ). The half meshing with around 5800 nodes is shown in Figure 4. The solution methods are also kept the same. These can ensure consistent approaches to the following simulation of flow field in the slag pot.

**Table 4:** Operating parameters and physical properties.

Air flow rate, NL/h	300
Inlet velocity, m/s	4.25
Submerged depth, m	0.044
Height of oil level, m	0.164
Density of oil, kg/m <sup>3</sup>	880
Density of air, kg/m <sup>3</sup>	1.225
Viscosity of oil, kg·m <sup>-1</sup> ·s <sup>-1</sup>	0.065
Viscosity of air, kg·m <sup>-1</sup> ·s <sup>-1</sup>	1.789e-5
Surface tension of oil/air, N/m	0.026



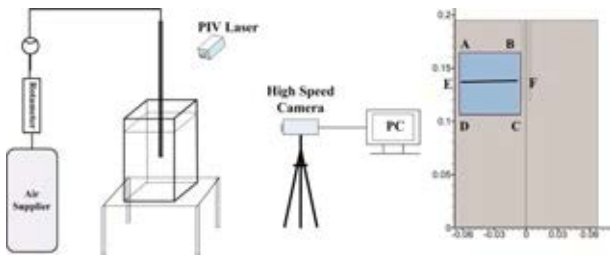


**Figure 2:** Schematic of the experimental setup and the measured area: A (-0.063, 0.164); B (-0.005, 0.164); C (-0.005, 0.106); D (-0.063, 0.106); E (-0.063, 0.135); F (-0.005, 0.135).

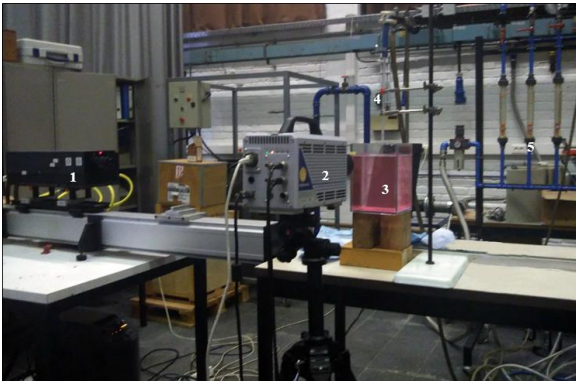


**Figure 3:** Photograph of the experimental setup. (1: laser generator; 2: highspeed camera; 3: paraffin oil with PMMA particles; 4: glass pipe; 5: rotameter)

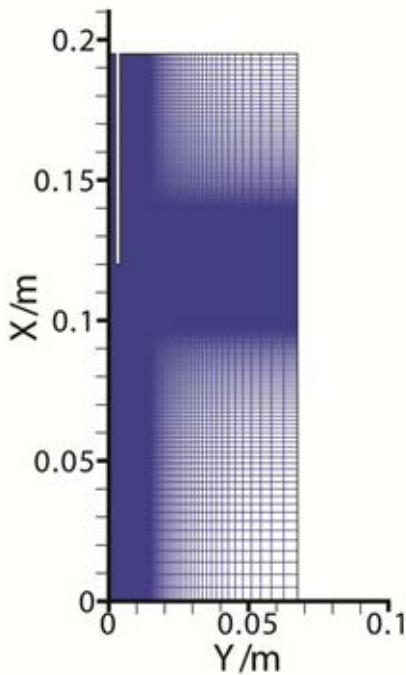


**Figure 4:** Meshing of the computing domain.

## RESULTS

### Model Validation

The turbulence model in numerical simulation is verified with experimental data by comparing the time-averaged velocity fields in the domain. The representative case with air flow rate of 300 NL/h is employed here, and the results are presented in Figure 5 and 6, respectively.

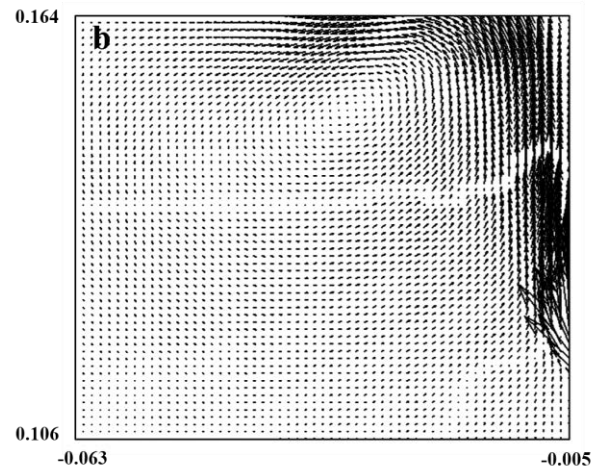
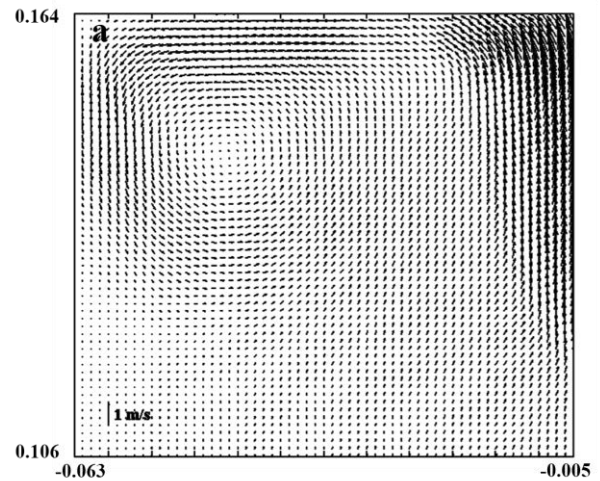


**Figure 5:** Comparison of the experimentally and numerically obtained time-averaged velocity fields (air flow rate: 300 NL/h). (a) velocity field of the PIV measurements and (b) velocity field of the numerical simulations.

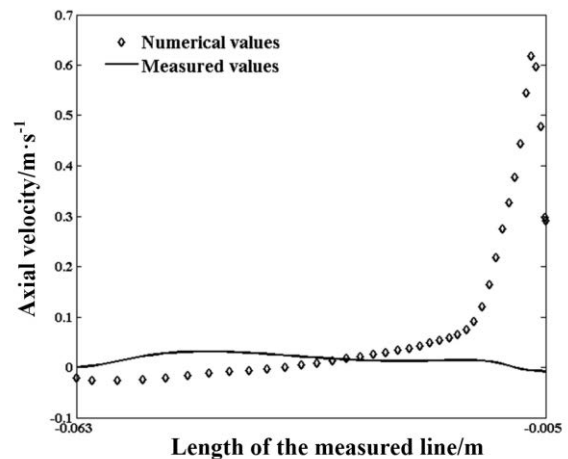


**Figure 6:** Axial velocity profile of the measured line EF shown in figure 2.

It can be seen from Figure 5 that a circulation zone consisting of a counter-clockwise rotating vortex is formed in the middle of the measured zone in the measurement, and a similar one can be observed in the corresponding numerical simulation, despite of a deviation of the location of the vortex centre. There may be a reason to explain it. Because a 2D axisymmetric model is used in this study, the domain will sweep 360 degree along  $x$ -axis by default, which makes the

computing domain more like a cylinder. However, the model in this study is a cubic one. This may be the reason for the deviation of the vortex centre. A further work of the corresponding 3D modelling will be established to determine the reason. It also can be observed that a large discrepancy appears in the very right region. This is because this measured region is very close to the gas pipe, and the gas bubbles rising along with this pipe posed serious influence on the measurement due to the refractive issues. In other words, the obtained data in the region close to the gas pipe is hardly reliable.

The axial velocity profile of the measured line shown in Figure 2 is depicted in Figure 6. Clearly, this is a big deviation in the right part, and the reason of it has been explained in the last paragraph. Apart from this, the rest seems acceptable since only minor errors appear. This may be attributed to the coarse meshing.

In conclusion, the results are still convincing since a similar circulation in the middle of the measured region and an acceptable quantitative validation can be observed, which means the flow patterns in the experiment and modelling resemble each other. However, there is, for sure, some space to improve the model. Based on the above description, the influence of the gas injection on the flow field is reasonably validated.

### Bubble Formation

In the slag valorization process, gas stirring is a key step. When the gas is injected into the slag through a submerged top lance, the continuous gas phase splits into discrete gas bubbles that move upward with high velocity. Soon a conical plume consisting of gas bubbles and liquid is shaped in the upward path. It is the moving bubbles that transfer momentum to the surrounding liquid and make the system stirred. Hence, gas breakage into bubbles is very important for transport phenomena in multiphase flow. For our study, gas breakage is the precondition for a better mixing, and it is well worth being investigated.

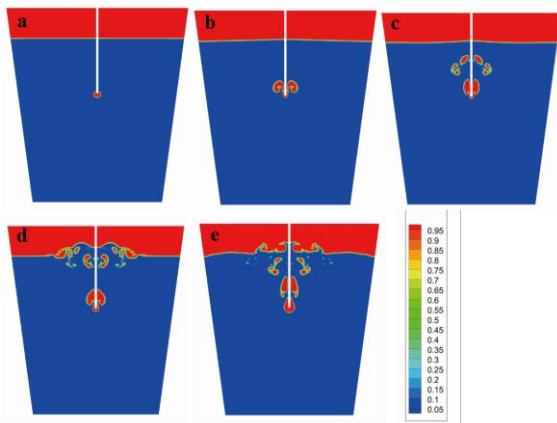


**Figure 7:** Gas bubble formation represented by the gas volume fraction (a: 0.02 s; b: 0.3 s; c: 0.75 s; d: 1.58 s; e: 2.70 s).

Figure 7 shows the dynamic breakage process of the gas phase in the slag pot. As can be seen in Figure 7(a), the gas phase comes out of the inlet and forms an

approximate circle. The upper part of the circle is a little deformed due to the pressure difference along the bubble surface. Later a dumbbell shape with a narrow neck forms near the inlet as the pressure difference continues increasing. Finally the gas phase splits into several gas bubbles. The gas bubbles keep moving up and can break up into even smaller bubbles.

It can be concluded that the gas phase begins breakup very soon near the inlet region, where large velocity gradient and turbulence kinetics energy exist. This will be further described in the following section. The formed bubbles can have secondary or several times breakup caused by turbulent eddies during rising up. Many studies in regard to bubble breakup can be found in chemical engineering, most of which, however, were performed in low temperature systems (e.g. Xing *et.al*, 2015; Luo and Svendsen, 1996; Hengel *et.al*, 2005). Nonetheless, these existing studies can supply important references for further investigation.

### Momentum Characteristics

In ladle metallurgy, the gas phase is injected from the bottom through plugs, and the gas flow rate is smaller compared to that in slag valorization. It has been proved that the injected momentum in ladle metallurgy is dissipated within a very short distance (Krishnapisharody and Irons, 2013). In Ausmelt TSL application, the gas phase is injected from the top via a top submerged lance. (Hoang *et.al*, 2009; Wood *et.al*, 2011). A violent stir can be obtained in the bath. Therefore, it is necessary to make clear if the injected momentum in the slag valorization can make an important contribution to system stirring. Three cases with initial inlet velocity of 84.5, 62.5 and 50.0 m/s, respectively, are discussed here. The time-averaged velocity and instantaneous results of turbulent kinetic energy and dissipation rate along the axis at 10.0 s are presented in Figure 8, 9 and 10, respectively.

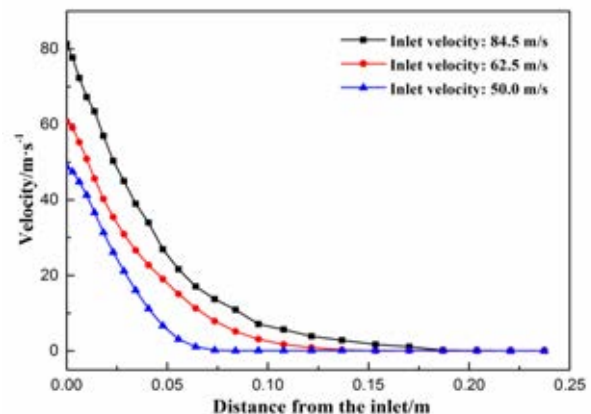


**Figure 8:** Velocity attenuation along the injected axis

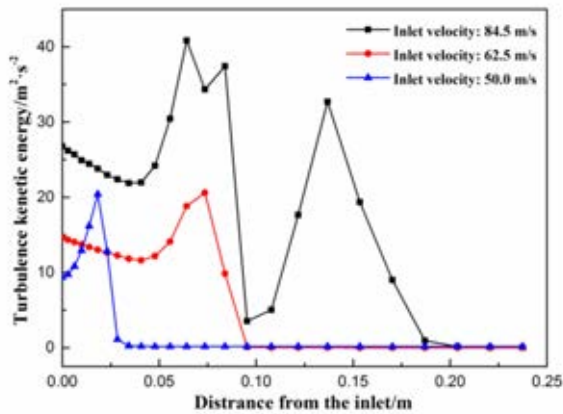


**Figure 9:** Attenuation of turbulence kinetic energy along the injected axis

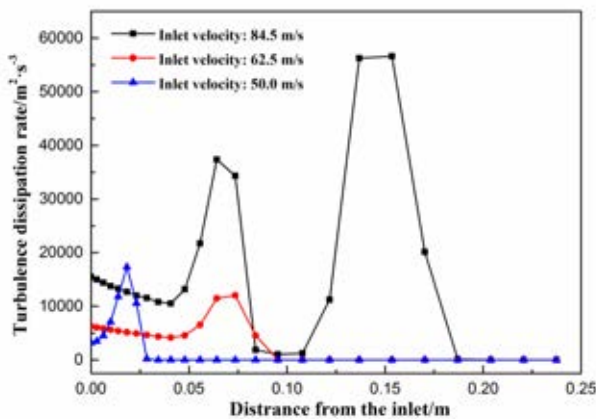


**Figure 10:** Attenuation of turbulence dissipation rate along the injected axis

The penetration depth is increased with increasing inlet velocity, which is clearly shown in Figure 8. However, the penetration depth is still quite small compared to the distance between the inlet and the bottom wall which is 2 m. This is because the density difference between the gas phase and slag is huge. Even with a very large inlet velocity, *e.g.* 84.5 m/s, the penetration depth is small compared to the slag bath height.

In Figure 9 and 10, the turbulence kinetic energy and its dissipation rate are depicted along the injected axis. The attenuations are consistent with the velocity attenuation, so the turbulence kinetic energy is dissipated in a short distance, which corresponds to other researchers' work mentioned previously. It can also be concluded that the turbulence kinetics energy and its dissipation rate are very unstable in this short distance according to the sharp peaks. Therefore, it can be imaged that turbulence in the adjacent area of the inlet is very violent. This can explain why the gas phase can split easily into bubbles in this region.

Now that it has been proved the injected momentum is limited in stirring the slag, it can be inferred that the flow is mainly driven by buoyancy of gas bubbles. This can be easily understood since the pressure difference between the top and bottom surfaces of bubbles is so large, which makes the bubble move upward with high velocity, and this high velocity can be transferred to the surrounding slag through interphase interactions. This is how gas bubbles drive liquid slag flow in the slag pot.

## CONCLUSIONS

The turbulence model used in our numerical simulation is quantitatively validated by comparing the velocity fields obtained from experiment and simulation, and the result is reasonable.

VOF model can successfully capture the dynamic breakup process of the gas phase. In our study, the gas phase breaks up into gas bubbles very quickly in the region adjacent to the inlet and the formed bubbles can undergo secondary or several times breakage while rising up.

The injected momentum is found to be dissipated in a short distance, very close to the inlet as indicated with measurements of the velocity attenuation and turbulence kinetic energy attenuation. This is consistent with the findings in the ladle metallurgy.

## ACKNOWLEDGEMENT

The financial support from IWT Grant 140514 (Belgium) and computer support from HPC (KU Leuven) are highly acknowledged. Yannan Wang and Lingling Cao want to thank the support of the China Scholarship Council (CSC).

## REFERENCES

- ANSYS, Inc., (2015), "Ansys fluent theory guide".
- CLOETE, S.W.P., EKSTEEN, J.J. and BRADSHAW, S.M., (2009), "A mathematical modelling study of fluid flow and mixing in full-scale gas-stirred ladles", *Progress in Computational Fluid Dynamics*, 9, 345-356.
- Euroslag: [www.euroslag.com](http://www.euroslag.com). Accessed on 20 February, 2017.
- HOANG, J., REUTER, M. A., MATUSEWICZ, R., HUGHES, S. and PIRET, N., (2009), "Top submerged lance direct zinc smelting", *Minerals Engineering*, 22, 742-751.
- HENGEL, E.I.V., DEEN, N.G. and KUIPERS, J.A.M., (2005), "Application of coalescence and breakup models in a discrete bubble model for bubble columns", *Industrial Engineering Chemistry Research*, 44, 5233-5245.
- KRISHNAPISHARODY, K and IRONS, G.A., (2013), "A critical review of the modified Froude number in ladle metallurgy", *Metallurgical and Materials Transaction B*, 44B, 1486-1498.
- LI, B., YIN, H., ZHOU, C. and TSUKIHASHI, F., (2008), "Modelling of three-phase flows and behaviour of slag/steel interface in an argon gas stirred ladle", *ISIJ International*, 48, 1704-1711.
- LIU C., GUO, M., PANDELAERS, L., BLANPAIN, B. and HUANG, S., (2016), "Stabilization of free lime in BOF slag by melting and solidification in air", *Metallurgical and Materials Transactions B*, 47B, 3237-3240.
- LUO, H. and SVENDSEN, F., (1996), "Theoretical model for drop and bubble breakup in turbulent dispersions", *AIChE Journal*, 42, 1225-1233.
- OLSEN, J.E. and CLOETE, S., (2009), "Coupled DPM and VOF model for analyses of gas stirred ladles at higher gas rates", 7<sup>th</sup> International Conference on CFD in the Minerals and Process Industries, CSIRO, Melbourne, Australia, December 9-11.

WOOD, J., CREEDY, S., MATUSEWICZ, R. and REUTER, M, (2011), “Secondary copper processing using Outotec Ausmelt TSL technology”, Proceedings of MetPlant, 460-467.

XING, C., WANG, T. and WANG, J., (2015), “A unified theoretical model for breakup of bubbles and droplets in turbulent flows”, AIChE Journal, 61, 1391-1403.



## CONTROLLED COALESCENCE WITH LOCAL FRONT RECONSTRUCTION METHOD

A. H. RAJKOTWALA<sup>1\*</sup>, H. MIRSANI<sup>1</sup>, E. A. J. F. PETERS<sup>1</sup>, M. W. BALTUSSEN<sup>1</sup>, C. W. M. VAN DER GELD<sup>2</sup>, J. G. M. KUERTEN<sup>3</sup>, J. A. M. KUIPERS<sup>1</sup>

<sup>1</sup>Multiphase Reactors Group, Department of Chemical Engineering and Chemistry, Eindhoven University of Technology, P.O. Box 513, 5600 MB Eindhoven, The Netherlands

<sup>2</sup>Process and Product Design Group, Department of Chemical Engineering and Chemistry, Eindhoven University of Technology, P.O. Box 513, 5600 MB Eindhoven, The Netherlands

<sup>3</sup>Multiphase and Reactive Flows Group, Department of Mechanical Engineering, Eindhoven University of Technology, P.O. Box 513, 5600 MB Eindhoven, The Netherlands

\* E-mail: a.rajkotwala@tue.nl

### ABSTRACT

The physics of droplet collisions involves a wide range of length scales. This poses a difficulty to accurately simulate such flows with traditional fixed grid methods due to their inability to resolve all scales with affordable number of computational grid cells. A solution is to couple a fixed grid method with simplified sub grid models that account for microscale effects. In this paper, we incorporate such framework in the Local Front Reconstruction Method (Shin *et al.*, 2011). To validate the new method, simulations of (near) head on collision of two equal tetradecane droplets are carried out at different Weber numbers corresponding to different collision regimes. The results show a better agreement with experimental data compared to other fixed grid methods like Front Tracking (Pan *et al.*, 2008) and Coupled Level Set and Volume of Fluid (CLSVOF) (Kwakkel *et al.*, 2013), especially at high impact velocities.

**Keywords:** Numerical Simulation, Multiphase flows, Front Tracking, LFRM, coalescence, break-up, droplet collision.

### NOMENCLATURE

#### Greek Symbols

$\rho$  Mass density, [kg/m<sup>3</sup>].  
 $\mu$  Dynamic viscosity, [kg/ms].  
 $\sigma$  Surface tension coefficient, [N/m].

#### Latin Symbols

$p$  Pressure, [Pa].  
 $\mathbf{u}$  Fluid Velocity, [m/s].  
 $\mathbf{g}$  Gravitational acceleration, [m/s<sup>2</sup>].  
 $\mathbf{F}_\sigma$  Surface tension force, [N/m<sup>3</sup>].  
 $t$  time, [s].  
 $\mathbf{n}$  Surface normal.  
 $t_c$  Contact time between droplets, [s].  
 $t_d$  Film drainage time, [s].  
 $R_0$  Initial droplet radius, [m].  
 $V_0$  Initial droplet speed, [m/s].  
 $b$  Offset distance between droplets, [m].

#### Sub/superscripts

$\Gamma$  Interface.  
 $l$  Liquid.

### INTRODUCTION

Droplet-laden flows play an important role in many industrial applications and natural processes (Crowe *et al.*, 1998). Some examples are spraying of fuel in combustion engines, spray drying of food products, liquid-liquid extraction, growth of rain droplets in clouds and pollution tracking. The interaction between droplets has a major influence on the dynamics of such flows, because of the coalescence and break-up that may occur upon collision. However, it is very difficult to accurately capture coalescence and break-up numerically because of the wide range of length scales involved. For example, the collision dynamics of droplets is influenced by the drainage of the thin gas film separating two colliding droplets (Mason *et al.*, 2012), causing bouncing of the droplets when the film is not drained during the collision event. Coalescence occurs when the gas film ruptures. The rupture is attributed to the van der Waals surface forces which become dominant at nanometer scale. It is not possible to capture all scales ranging from millimeter (droplet diameter) to nanometer (critical film thickness) using an affordable number of computational grid cells.

In our fixed grid method, the under resolved final stage of the film drainage process is accounted for by a sub-grid model. Few studies have been done previously using different fixed grid methods and sub-grid models (Kwakkel *et al.*, 2013, Mason *et al.*, 2012). The fixed grid methods for modeling multiphase flows can be divided into two types: front capturing and front tracking techniques (Tryggvason *et al.*, 2011). In front capturing methods, the interface is implicitly represented by a colour function. Common front capturing methods are Volume of Fluid (VOF) (van Sint Annaland *et al.*, 2005), Level Set (LS) (Sethian and Smereka, 2003) and Coupled Level Set and Volume of Fluid (CLSVOF) (van der Pijl *et al.*, 2005) methods. Generally, the droplets in these methods coalesce automatically when they share a common grid cell. However, this numerical coalescence can be avoided for the simulation of symmetric binary droplet collision using Volume of Fluid method. The coalescence can be controlled by prescribing a volume-fraction boundary condition on the collision plane using ghost cells (Mason *et al.*, 2012). When the boundary condition is set to zero volume fraction, the droplets will bounce; whereas a symmetry boundary condition will result in coalescence. A more general approach to avoid numerical coalescence is to use unique colour function for each droplet (Nikolopoulos *et al.*, 2009).

A big disadvantage of front capturing methods is the very fine grid resolution which is required for accurate surface

tension calculation especially when the droplets undergo complex topological changes (Kwakkel *et al.*, 2013). Front tracking methods (Dijkhuizen *et al.*, 2010, Shin *et al.*, 2011) are inherently better at surface tension calculation at coarse grid resolution. This is because a front tracking method directly tracks the interfaces using triangular marker elements, enabling accurate curvature calculation. However, in the traditional front tracking method, droplet coalescence is not possible. To incorporate coalescence, additional routines to merge the individual unstructured meshes belonging to different droplets are required (Nobari *et al.*, 1996). In the traditional front tracking method, the merging of the droplet meshes is complicated because the logical information about the marker connectivity should be updated. In addition, the merging of droplets with complex topology is very challenging. Therefore, we choose a front tracking method without connectivity, the Local Front Reconstruction Method (LFRM) by Shin *et al.*, 2011.

As logical connectivity between marker elements is not required, LFRM can handle complex topological changes like droplet coalescence and pinch off. It uses information from the original marker elements directly to reconstruct the interface in a mass conservative manner and thus, also ensures good local mass conservation. Because the interface is reconstructed independently in each individual reconstruction cell, the method can be highly parallelized. However, this cell-oriented reconstruction leads to numerical coalescence (similar to front capturing methods) in LFRM (Shin *et al.*, 2011). This is prevented in our implementation by storing the information about marker elements and marker points for each droplet separately. The coalescence is accomplished by merging data-structures of two droplets. Similarly, the break-up of a droplet is done by splitting the data-structure of the droplet. The details of these procedures are given in next section. We have improved the original LFRM method in certain areas which are also summarized in next section. Lastly, the results of simulations of (near) head on collision of two equal tetradecane droplets in different collision regimes are discussed. The discussion includes validation of simulations with experimental data and comparison with other fixed grid methods (Kwakkel *et al.*, 2013, Pan *et al.*, 2008).

## METHODOLOGY

### Local Front Reconstruction Method

Both fluids in the two phase flow are assumed to be incompressible, immiscible and Newtonian fluids. A one-fluid formulation is used and the governing equations are given by the continuity equations and the Navier-Stokes equations, where the physical properties depend on local phase fractions.

$$\nabla \cdot \mathbf{u} = 0 \quad (1)$$

$$\rho \frac{\partial \mathbf{u}}{\partial t} + \rho \nabla \cdot (\mathbf{u}\mathbf{u}) = -\nabla p + \rho \mathbf{g} + \nabla \cdot \mu \left[ \nabla \mathbf{u} + (\nabla \mathbf{u})^T \right] + \mathbf{F}_\sigma \quad (2)$$

where  $\mathbf{F}_\sigma$  is a singular source-term to represent the surface tension at the interface.

The following conditions are applied at the interface  $\Gamma$  to close the governing equations:

$$[\mathbf{u}]_\Gamma = 0 \quad (3)$$

$$\left[ -p\mathbf{n} + \mu \left( \nabla \mathbf{u} + (\nabla \mathbf{u})^T \right) \cdot \mathbf{n} \right]_\Gamma = \mathbf{S}_\sigma \cdot \mathbf{n} \quad (4)$$

where  $[\cdot]_\Gamma$  represents jump in a quantity across the interface from one phase to another and  $\mathbf{S}_\sigma$  is the surface force acting on interface due to surface tension.

The equations are discretized using a finite volume approach and are solved on a staggered computational grid by a fractional step method (Das *et al.*, 2017). The surface tension force  $\mathbf{F}_\sigma$  is calculated using hybrid surface tension model (Shin *et al.*, 2005) which has combined advantage of accurate curvature calculation (similar to the pull force model which is commonly used in front tracking methods) and proper balance of pressure and surface tension force at discrete level (similar to the continuum surface model which is commonly used in front capturing methods).

The fluid velocity is interpolated from Eulerian grid to Lagrangian grid using cubic spline interpolation and marker points are moved with the interpolated velocity using a 4<sup>th</sup> order Runge-Kutta scheme (Dijkhuizen *et al.*, 2010).

As mentioned before, the local phase fraction is required to calculate the averaged physical properties. This can be calculated by the geometric analysis using the positions of the marker points (Dijkhuizen *et al.*, 2010). This method of phase fraction calculation is exact and computationally more efficient than the traditional method of solving Poisson equation used in original LFRM method. From the calculated phase fractions, the average density and viscosity is calculated by algebraic and harmonic averaging, respectively.

Due to the advection of the marker points, the marker elements can become too large or too small. This poor grid quality decreases the accuracy of the surface tension force calculation. To maintain the mesh quality, a mesh reconstruction procedure of (Shin *et al.*, 2011) is implemented. The reconstruction procedure also allows to reconstruct the mesh when the multiple droplets coalesce or a droplet breaks-up. The implementation is improved by the use of linked-list data-structures for storing location of the three vertices of each marker. This ensures that each marker point has a unique identity, thus reducing the memory requirements and preventing precision problems.

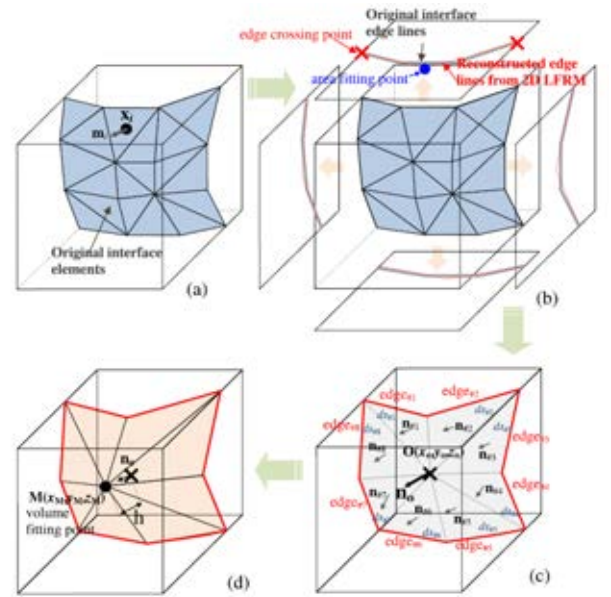


**Figure 1:** Schematic of the reconstruction procedure for LFRM (Shin *et al.*, 2011).

The overall reconstruction procedure consists of four simple steps as shown in Figure 1:

- (a) Localization - Interface of the discrete phase is cut by a reconstruction grid (similar to the Eulerian grid) such that each part of the interface lies completely inside one cell.
- (b) Edge line reconstruction - The edge line corresponding to the cut interface is traced out on relevant faces of the cell, and new edge line (containing only two edge points and a fitting point) is reconstructed in an area conservative manner.
- (c) Centroid calculation - Using edge points and fitting points of all the faces, a centroid is calculated. An intermediate interface is formed by connecting the centroid with intermediate edge lines.
- (d) Volume fitting - Finally, the centroid is moved in the normal direction of intermediate interface such that original volume of the dispersed phase is conserved in the given cell.

Flows involving coalescence and break-up of the dispersed phase are easily handled by LFRM. This is enabled by the marker reduction and the tetra-marching procedures, which allow merging and breaking of unstructured meshes of the dispersed phase. Details of these procedures can be found in (Shin *et al.*, 2011). In our implementation, the data-structure of each droplet is stored with a unique identity. However, this prevents coalescence completely. To enable coalescence between two droplets at a desired time, their data-structures have to be merged and the merged droplet has to be given a unique identifier, which is handled by the coalescence module. Similarly, each daughter droplet is given a unique identifier when formed after break-up of a droplet, which is handled by the break-up module.

### Coalescence Module

The coalescence module checks if there are multiple interfaces within the same reconstruction cell and combines the data-structures of two droplets depending on the calculated film drainage and contact time. The different steps in the coalescence module are given below:

- (a) Bounding box for droplets in terms of grid cell units is calculated (Figure 2(a)).
- (b) At each time step, it is checked if the bounding boxes of any two droplets are overlapping.
- (c) If the overlap exists, the cells containing interfaces from both droplets are flagged to check if any cell contains interface from both droplets (Figure 2(b)).
- (d) If one or more cells contain interface from both droplets, then these droplets are identified to be in 'contact' and added to a collision list (Figure 2(c)). The contact timer is initiated to keep track of contact time  $t_c$ .
- (e) At each time step, it is checked if the droplets pair is still in contact. If a pair is in contact, the contact time is compared to the film drainage time  $t_d$ . In this study, the film drainage time  $t_d$  is obtained from experiments. If the contact exists and  $t_c > t_d$ , the data-structures of two droplets are merged and reconstruction is performed to execute droplet coalescence (Figure 2(e)). If the contact ceases, the droplets are removed from the collision list and this leads to bouncing of droplets.

### Break-up Module

The numerical break-up of the droplet will take place based on the size of the reconstruction grid. As stated before, it is important to separate the data-structure of the droplets after break-up to avoid numerical coalescence. This separation is achieved by using a recursive flagging algorithm. The algorithm is used to find the disjoint droplets that are subsequently assigned a new 'droplet-number', see Figure 3.

### RESULTS

In case of (near) head-on collisions between equal sized hydrocarbon droplets, four regimes of collision outcome are observed with increasing Weber number (measure of droplet inertia compared to surface tension). As seen in Figure 4, these regimes are (I) Coalescence with minor deformation, (II) Bouncing, (III) Coalescence with major deformation and (IV) Coalescence with separation resulting in production of daughter droplets. To validate the modified LFRM method, a

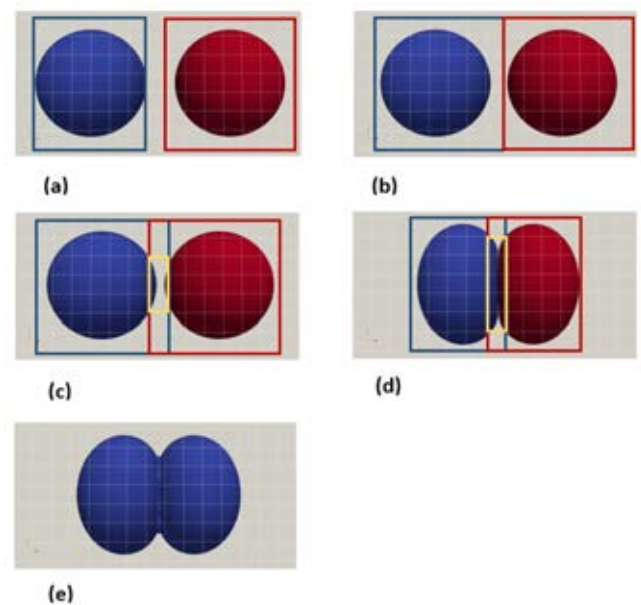


**Figure 2:** Schematic of the coalescence module. Blue and red boxes represent bounding boxes of blue and red droplets respectively. Yellow box represents cells containing interface from both droplets.

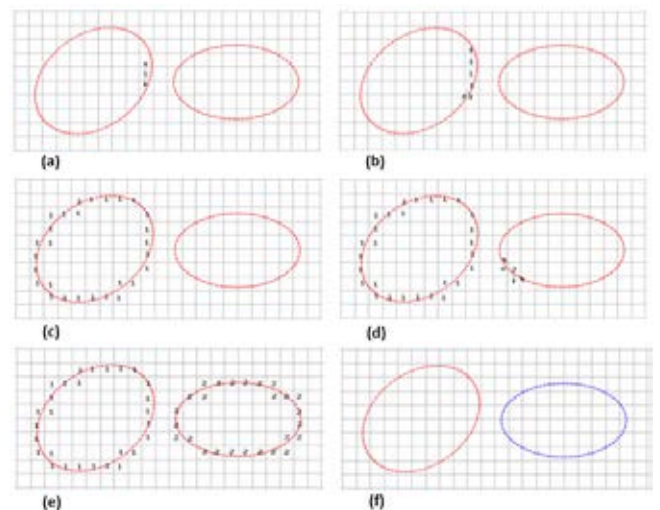


**Figure 3:** Steps of flagging algorithm in the break-up module.



case of binary droplet collision from each of these regimes is simulated and compared with experiments (Pan *et al.*, 2008 and Qian and Law, 1997) and other simulation methods (Pan *et al.*, 2008 and Kwakkel *et al.*, 2013).

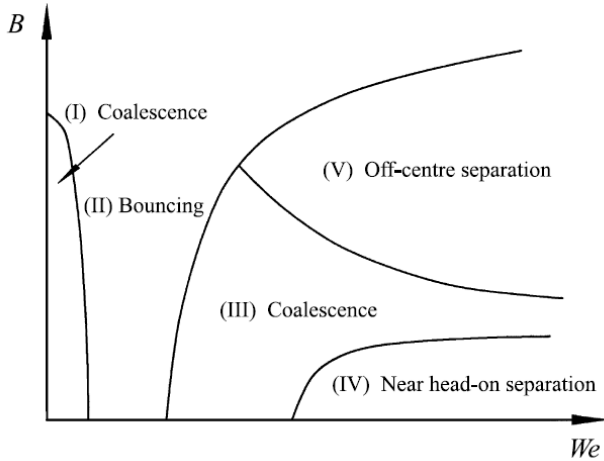


**Figure 4:** Schematic of collision regimes of two equal sized hydrocarbon droplets in atmospheric pressure. The parameter  $B$  represents the obliqueness of the collision and  $We$  represents the Weber number (Qian and Law, 1997).

The grid cell size is selected such that 12 grid cells are taken across the droplet radius ( $R_0$ ) (similar to grid size used in (Kwakkel *et al.*, 2013) for CLSVOF and (Pan *et al.*, 2008) for FT). The computational domain has dimensions  $8R_0 \times 10R_0 \times 8R_0$  with the largest dimension in the direction of the collision. Free slip boundary condition is used on all domain boundaries. The initial distance between the droplet centers is taken as  $2.8R_0$ . Each droplet is initialised with a uniform velocity field,  $V_0$ , but in the opposite direction. For each case, Weber number and impact parameter (Figure 5) are provided as an input. The film drainage time is provided by experimental observations (Pan *et al.*, 2008).

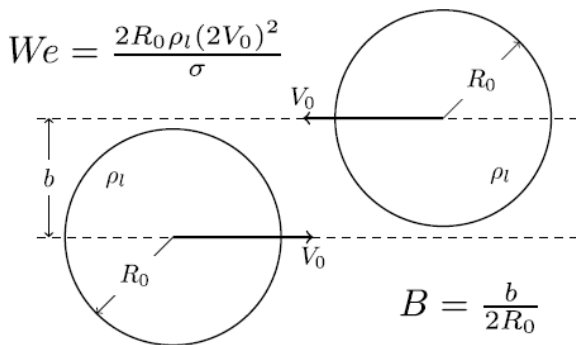


**Figure 5:** Nomenclature of general binary droplet collision (Kwakkel *et al.*, 2013).

### Regime I

This regime always results in coalescence, while the collisions are gentle (low Weber numbers). A collision of tetradecane droplets in 1 atm. air,  $R_0 = 107.2 \mu\text{m}$ ,  $V_0 = 0.305 \text{ m/s}$ ,  $We = 2.3$ , and  $B = 0$  is shown in Figure 6. The obtained result from LFRM matches well with results from the Coupled Level Set Volume of Fluid method (Kwakkel *et al.*, 2013),

the Front Tracking method (Pan *et al.*, 2008) and experimental data (Pan *et al.*, 2008). In such regime, the coalescence happens around maximum deformation. After the coalescence, the cusp at the merged interface is quickly flattened. This phenomenon is nicely captured by all the numerical simulations.

### Regime II

This regime always results in bouncing. A collision of tetradecane droplets in 1 atm. air,  $R_0 = 167.6 \mu\text{m}$ ,  $V_0 = 0.492 \text{ m/s}$ ,  $We = 9.33$ , and  $B = 0$  is shown in Figure 7. Again, the results obtained using LFRM agree well with experimental data (Pan *et al.*, 2008) and other simulation results with FT (Pan *et al.*, 2008) and CLSVOF (Kwakkel *et al.*, 2013).

### Regime III

This regime always results in coalescence, however the collisions are hard collision (high weber numbers) resulting in substantial deformation before merging. A collision of tetradecane droplets in 1 atm. air,  $R_0 = 169.7 \mu\text{m}$ ,  $V_0 = 0.591 \text{ m/s}$ ,  $We = 13.63$ , and  $B = 0$  is shown in Figure 8. The merging in this case occurs as the deformed droplet is flattened to a disk shape while the incoming mass at the center of the rear face is still heading forward resulting in dimpled shape between 370 and 500 ms. Although this is not very clear in the experimental results (Pan *et al.*, 2008) but it was captured properly by all the numerical simulations.

### Regime IV

This regime of near head on collision results in separation of droplets after merging as the kinetic energy is sufficient to overcome the surface energy. A collision of tetradecane droplets in 1 atm. nitrogen,  $R_0 = 168 \mu\text{m}$ ,  $V_0 = 1.260 \text{ m/s}$ ,  $We = 62.2$ , and  $B = 0.06$  is shown in Figure 9. A zero film drainage time (which is justified by high weber number) is used in the simulation. The different colour of droplets indicate that each droplet has different droplet number and separate data-structure.

The results obtained using LFRM match better with the experimental results (Qian and Law, 1997) compared to the CLSVOF (Kwakkel *et al.*, 2013). In Figure 9, a premature separation is seen for CLSVOF. As explained in (Kwakkel *et al.*, 2013), the origin of this premature separation is the less accurate curvature estimation in strongly deformed regions. These errors in curvature estimation have a direct consequence for the acting surface tension force, and over time the droplet shape. This indicates that LFRM has more accurate surface tension calculation for the same grid size. Also, the size of the satellite droplet resembles the experimental data better compared to the CLSVOF results.

## CONCLUSION

The local front reconstruction method has been improved and extended to allow for controlled coalescence. The new method has been successfully validated by carrying out simulations of binary (near) head on droplet collisions. By using experimentally observed film drainage times, a good match with experimental data is observed. This shows that if an accurate predictions of the film drainage time can be obtained from a sub-grid model, LFRM can capture collision dynamics in multiphase flows with physical realism. Finally, the results obtained using LFRM are compared with those of other methods and a better agreement with experimental data is seen, especially at high impact velocities.

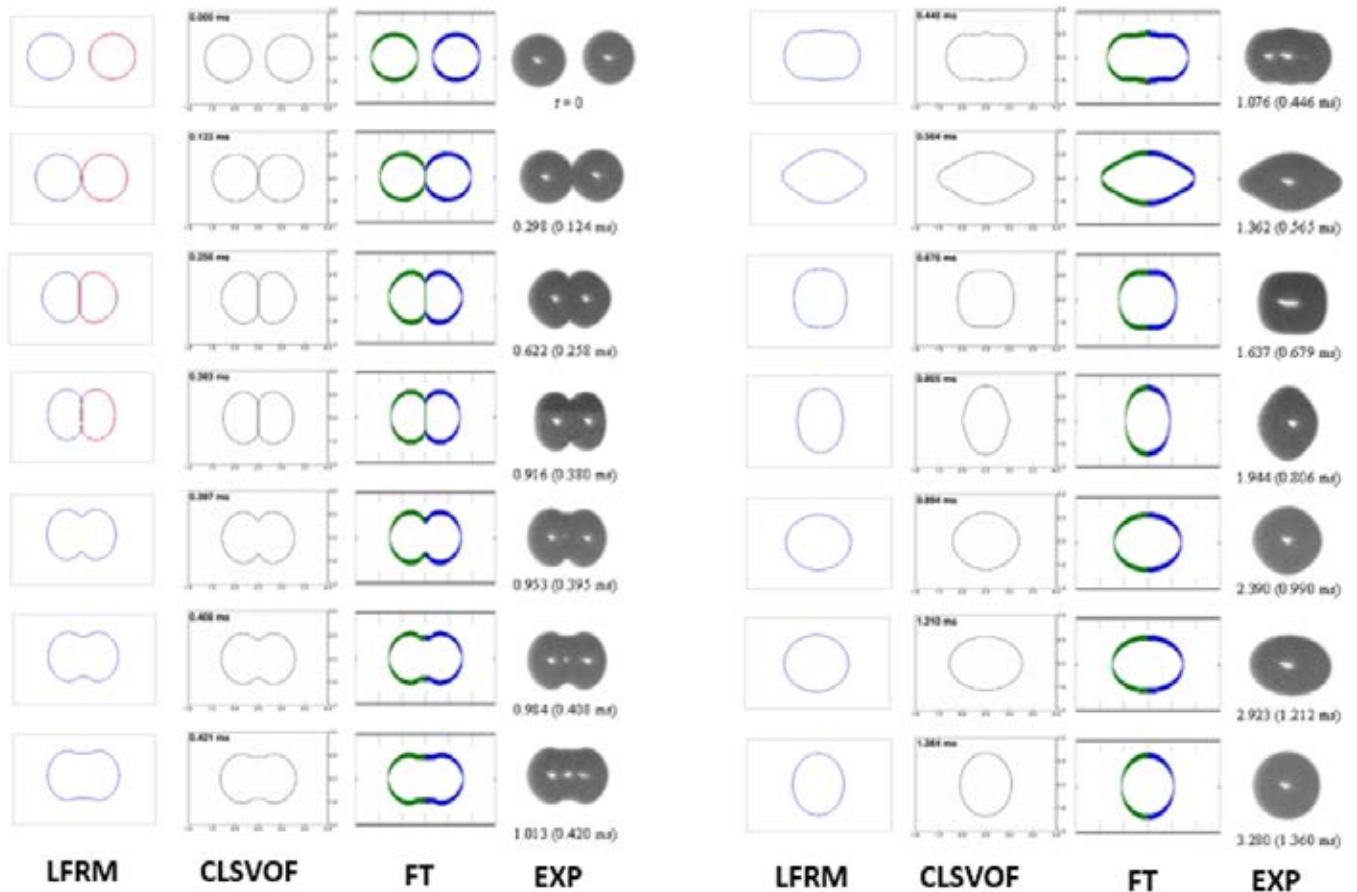


**Figure 6:** Merging collision sequence in regime I. LFRM results from present study, CLSVOF from (Kwakkel *et al.*, 2013), FT and experimental results from (Pan *et al.*, 2008). Conditions: tetradecane in 1 atm. air,  $R_0 = 107.2 \mu\text{m}$ ,  $V_0 = 0.305 \text{ m/s}$ ,  $We = 2.3$ , and  $B = 0$ . The film drainage time observed in experiments is  $t_d = 0.270 \text{ ms}$ .

## ACKNOWLEDGEMENT

This work is part of the research programme Open Technologieprogramma with project number 13781, which is (partly) financed by the Netherlands Organisation for Scientific Research (NWO) Domain Applied and Engineering Sciences (TTW, previously Technology Foundation STW).

## REFERENCES

- CROWE, C., SOMMERFELD, M. and TSUJI, Y. (1998). *Multiphase flows with droplets and particles*. CRC Press, Boca Raton.
- DAS, S., DEEN, N.G. and KUIPERS, J.A.M. (2017). “Immersed boundary method (ibm) based direct numerical simulation of open-cell solid foams: Hydrodynamics”. *AIChE Journal*, **63**(3), 1152–1173.
- DIJKHUIZEN, W., ROGHAI, I., ANNALAND, M.V.S. and KUIPERS, J. (2010). “DNS of gas bubbles behaviour using an improved 3d front tracking model - model development”. *Chemical Engineering Science*, **65**(4), 1427 – 1437.
- KWAKKEL, M., BREUGEM, W.P. and BOERSMA, B.J. (2013). “Extension of a CLSVOF method for droplet-laden flows with a coalescence/breakup model”. *Journal of Computational Physics*, **253**, 166 – 188.
- MASON, L., STEVENS, G. and HARVIE, D. (2012). “Multi-scale volume of fluid modelling of droplet coalescence”. *Ninth International Conference on CFD in the Minerals and Process Industries*. CSIRO, Melbourne, Australia.
- NIKOLOPOULOS, N., NIKAS, K.S. and BERGELES, G.

(2009). “A numerical investigation of central binary collision of droplets”. *Computers & Fluids*, **38**(6), 1191 – 1202.

NOBARI, M.R., JAN, Y.J. and TRYGGVASON, G. (1996). “Head-on collision of drops - a numerical investigation”. *Physics of Fluids*, **8**(1), 29–42.

PAN, K.L., LAW, C.K. and ZHOU, B. (2008). “Experimental and mechanistic description of merging and bouncing in head-on binary droplet collision”. *Journal of Applied Physics*, **103**(6), 064901.

QIAN, J. and LAW, C. (1997). “Regimes of coalescence and separation in droplet collision”. *Journal of Fluid Mechanics*, **331**, 59–80.

SETHIAN, J.A. and SMEREKA, P. (2003). “Level set methods for fluid interfaces”. *Annual Review of Fluid Mechanics*, **35**(1), 341–372.

SHIN, S., ABDEL-KHALIK, S.I., DARU, V. and JURIC, D. (2005). “Accurate representation of surface tension using the level contour reconstruction method”. *J. Comput. Phys.*, **203**(2), 493–516.

SHIN, S., YOON, I. and JURIC, D. (2011). “The local front reconstruction method for direct simulation of two- and three-dimensional multiphase flows”. *Journal of Computational Physics*, **230**(17), 6605 – 6646.

TRYGGVASON, G., SCARDOVELLI, R. and ZALESKI, S. (2011). *Direct Numerical Simulations of Gas-Liquid Multiphase Flows*. Cambridge University Press, Cambridge.

VAN DER PIJL, S., SEGAL, A., VUIK, C. and WESSELI, P. (2005). “A mass-conserving Level-Set method for modelling of multi-phase flows”. *International Journal for*

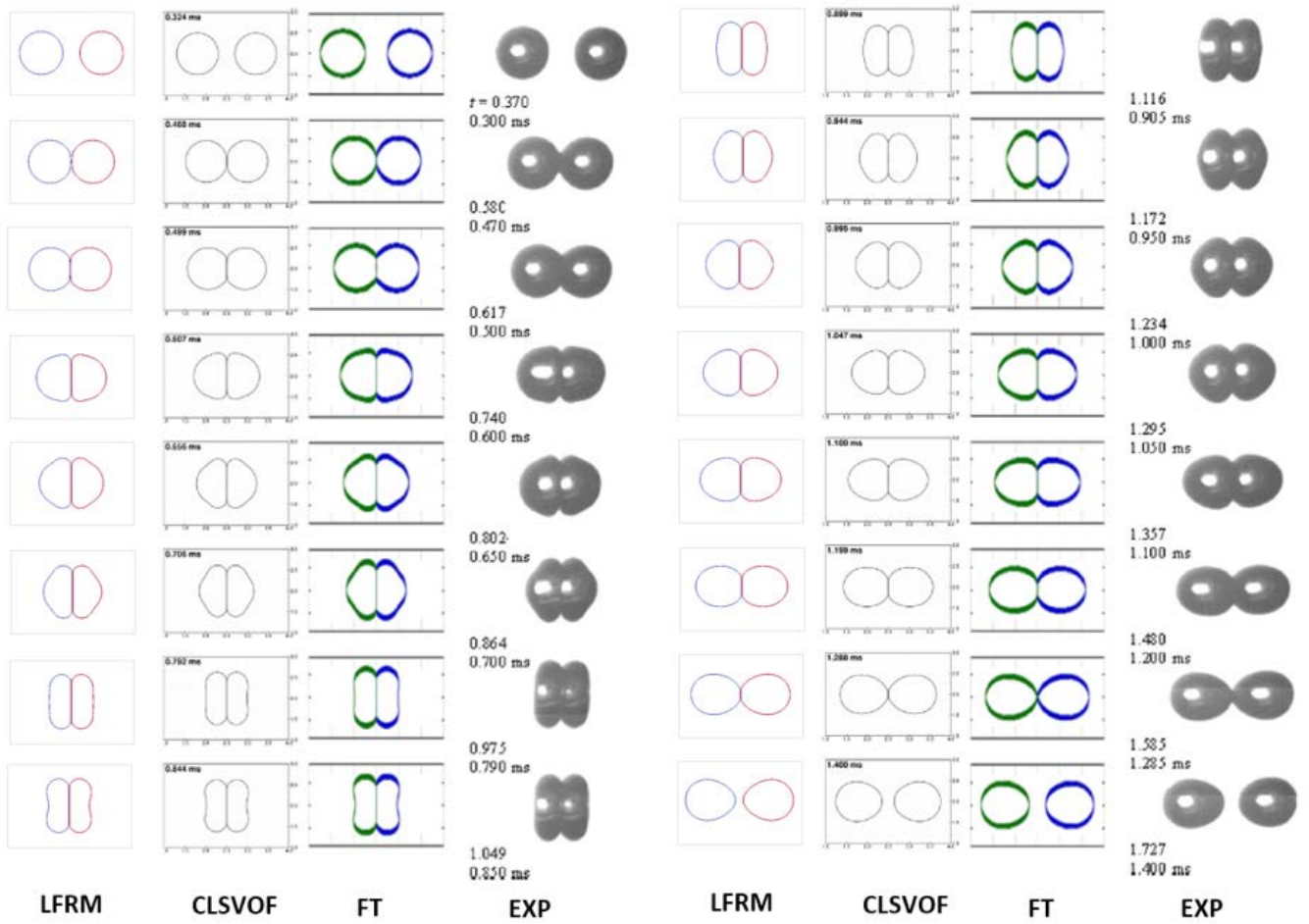


**Figure 7:** Bouncing collision sequence in regime II. LFRM results from present study, CLSVOF from (Kwakkel *et al.*, 2013), FT and experimental results from (Pan *et al.*, 2008). Conditions: tetradecane in 1 atm. air,  $R_0 = 167.6 \mu\text{m}$ ,  $V_0 = 0.492 \text{ m/s}$ ,  $We = 9.33$ , and  $B = 0$ .

*Numerical Methods in Fluids*, **47**, 339–361.

VAN SINT ANNALAND, M., DEEN, N. and KUIPERS, J. (2005). “Numerical simulation of gas bubbles behaviour using a three-dimensional volume of fluid method”. *Chemical Engineering Science*, **60(11)**, 2999–3011.

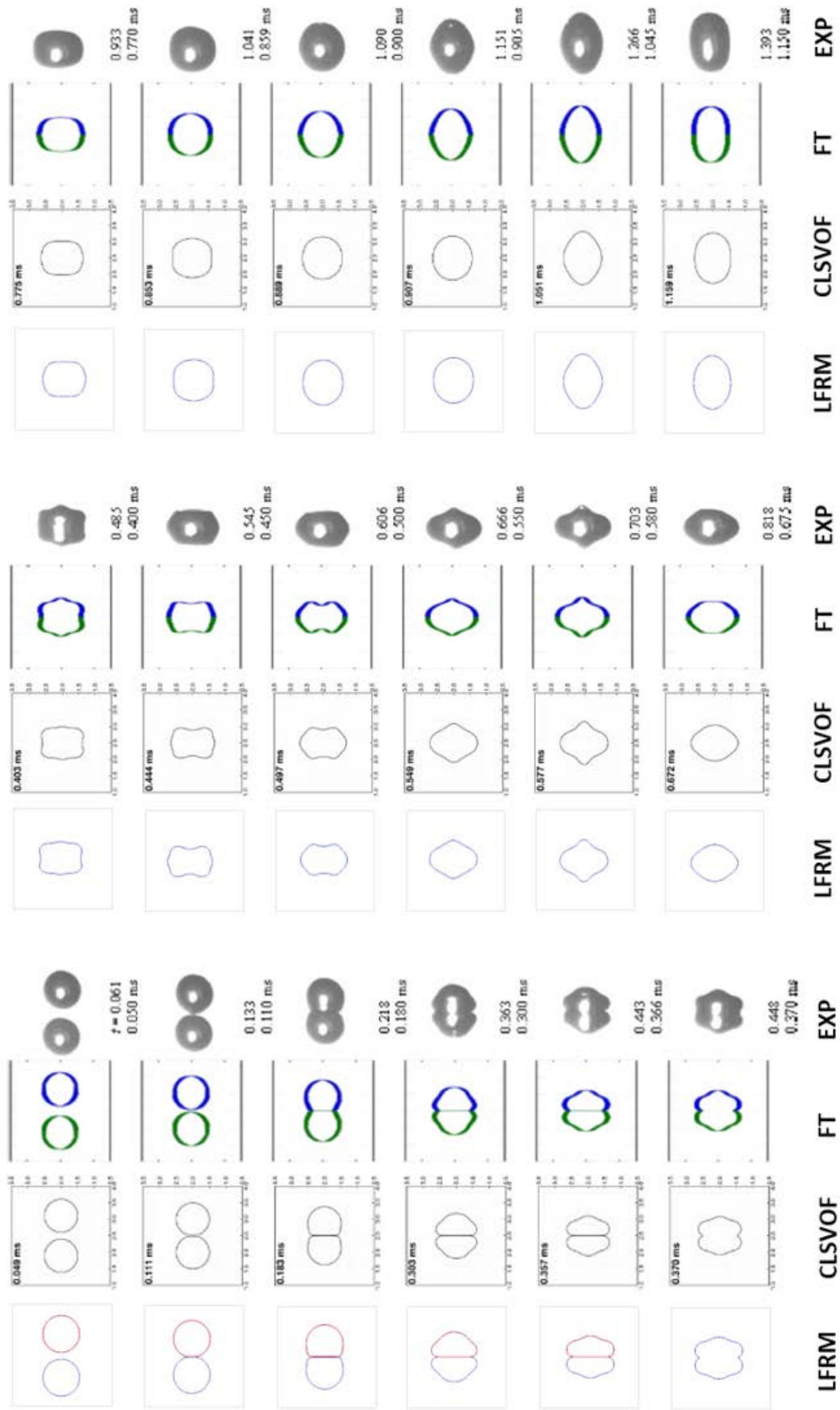


**Figure 8:** Merging collision sequence in regime III. LFRM results from present study, CLSVOF from (Kwakkel *et al.*, 2013), FT and experimental results from (Pan *et al.*, 2008). Conditions: tetradecane in 1 atm. air,  $R_0 = 169.7 \mu\text{m}$ ,  $V_0 = 0.591 \text{ m/s}$ ,  $We = 13.63$ , and  $B = 0$ . The film drainage time observed in experiments is  $t_d = 0.246 \text{ ms}$ .

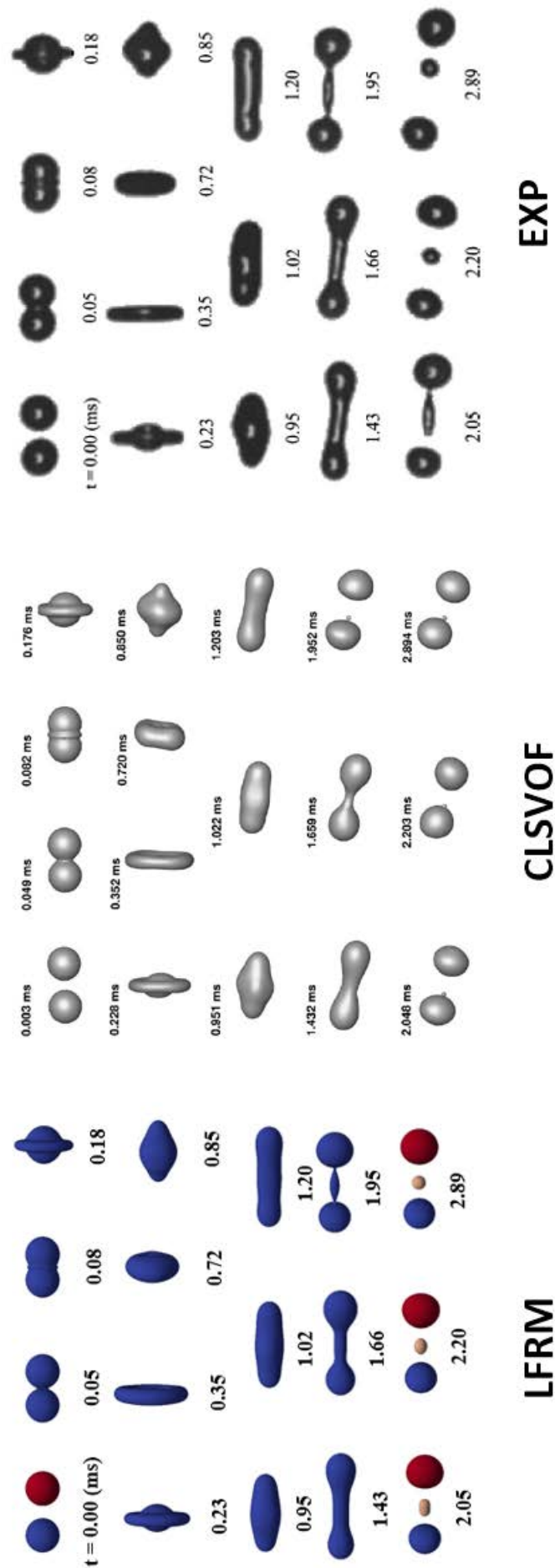
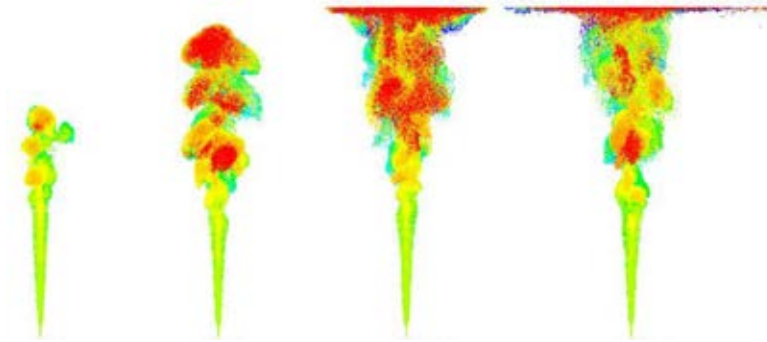


**Figure 9:** Near head on separating collision sequence in regime IV. LFRM results from present study, CLSVOF from (Kwakkel *et al.*, 2013) and experimental results from (Qian and Law, 1997). Conditions: tetradecane in 1 atm. nitrogen,  $R_0 = 168 \mu\text{m}$ ,  $V_0 = 1.260 \text{ m/s}$ ,  $We = 62.2$ , and  $B = 0.06$ . The film drainage time is assumed to be zero.

# BUBBLY FLOWS





## MODELING OF FLUID DYNAMICS, MASS TRANSFER, AND CHEMICAL REACTION IN BUBBLY FLOWS

**Roland Rzehak<sup>\*</sup>** and Manuel Krauß

Helmholtz-Zentrum Dresden - Rossendorf, Bautzner Landstrasse 400, 01328 Dresden, Germany

\* E-mail: r.rzehak@hzdr.de

### ABSTRACT

Mass transfer from gas bubbles to the surrounding liquid or vice versa is an important consideration in chemical engineering. Frequently such absorption or desorption processes are accompanied by a chemical reaction in the liquid phase. Compared with the fluid dynamics of bubbly flows, modeling and simulation of these processes is much less developed. The present work shows some recent advances made in validating closures for the Eulerian two-fluid framework of interpenetrating continua.

**Keywords:** dispersed gas liquid multiphase flow, Euler-Euler two-fluid model, CFD simulation, fluid dynamics, mass transfer, chemical reaction, absorption.

### NOMENCLATURE

#### Greek Symbols

$\alpha$	volume fraction [-]
$\mu$	viscosity [Pa s]
$\rho$	density [kg m <sup>-3</sup> ]
$\sigma$	surface tension [N m <sup>-1</sup> ]

#### Latin Symbols

$C^X$	Molar concentration of species X [kmol m <sup>-3</sup> ]
$d$	bubble diameter [m]
$D$	column diameter [m]
$D^X$	diffusion coefficient of species X [m <sup>2</sup> s <sup>-1</sup> ]
$E$	enhancement factor [-]
$Ha$	Hatta number [-]
$k$	specific turbulent kinetic energy [m <sup>2</sup> s <sup>-2</sup> ]
$k$	mass transfer coefficient [m s <sup>-1</sup> ]
$k^{\pm}$	for- (+) and backward (-) rate constant of reaction $\mathcal{E}$ with total reaction order $\xi$ [(m <sup>3</sup> kmol <sup>-1</sup> ) <sup><math>\xi-1</math></sup> s <sup>-1</sup> ]
$H$	column height [m]
$R$	pipe / column radius or halfwidth [m]
$Re$	Reynolds number [-]
$Sc$	Schmidt number [-]
$\mathbf{x}$	position [m]
$\mathbf{u}$	mean velocity [m s <sup>-1</sup> ]
$\mathbf{u}'$	fluctuating velocity [m s <sup>-1</sup> ]

#### Sub/superscripts

$a$	asymptotic limit of an instantaneous reaction
-----	---

$B$	bubble
$eff$	effective
$G$	gas
$L$	liquid
$mol$	molecular
$turb$	turbulent
$I$	first reaction
$II$	second reaction
$III$	third reaction
$+$	forward reaction
$-$	backward reaction

### INTRODUCTION

CFD simulations of dispersed bubbly flow on the scale of technical equipment are feasible within the Eulerian two-fluid framework of interpenetrating continua. However, accurate numerical predictions rely on suitable closure models. To achieve predictive capability, all details of the closures have to be fixed in advance without reference to any measurement data for the problem under investigation.

Concerning the fluid dynamics of bubbly flows a baseline model has recently been proposed to this end and shown to work for a range of different applications in a unified manner. This provides a reliable background which is well suited to add more complex physics.

Concerning mass transfer in bubbly flows both with and without an accompanying chemical reaction only few studies have been performed to date. Hence, a generally accepted closure model for the mass transfer coefficient has not emerged yet. This is partly due to a lack of experimental data suitable for model validation. Such data should provide spatially resolved measurements of concentration together with the bubble size distribution and cover a certain range of parameters known to be relevant, i.e. bubble size and turbulent fluctuations.

The effect of a chemical reaction on the mass transfer is commonly described by an enhancement factor which depends on the type of the reaction. For a meaningful validation of closure models a reliable characterization of the reaction kinetics is required in this case as well.

In the present contribution we consider a recent experiment on the absorption of CO<sub>2</sub> in aqueous NaOH in a bubble column (Hlawitschka et al., 2017), which



will be referred to as reactive case in the following. Fluid dynamical measurements have been conducted as well for CO<sub>2</sub> bubbles in water in the same column (Kovats et al., 2015, Rzehak et al., 2017), where effects of chemical reactions are vanishingly small, which is why this case will be referred to as non-reactive case. For both the non-reactive and the reactive case a comparison is made with Euler-Euler simulations using previously established closure models. Results for the non-reactive case have already been published (Rzehak et al., 2017) and a selection is shown for completeness here. Results for the reactive case are new.

## DATA

An experiment for which both fluid dynamics and reactive mass transfer were investigated has been presented recently by (Kovats et al., 2015, Rzehak et al., 2017, Hlawitschka et al., 2017). The geometry considered (Fig.1) was that of a round bubble column with an inner diameter of 142 mm. Initially, the column was filled up to a height of 730 mm either with de-ionized water or with aqueous NaOH at a pH of 9.5. CO<sub>2</sub> gas was supplied through four needles arranged in a line, spaced by 22 mm, and extending by 13 mm into the column. The gas flow rate was set to 6.4 l/h and an average size of the generated bubbles of  $d_b = 2.72$  mm resulted with a standard deviation of 0.33 mm. Even for the reactive case, this value did not vary appreciably throughout the column which means that the gas absorption rate is very low. The rise of the liquid surface due to the additional gas in the column was found negligible. The experiment was performed under ambient conditions.

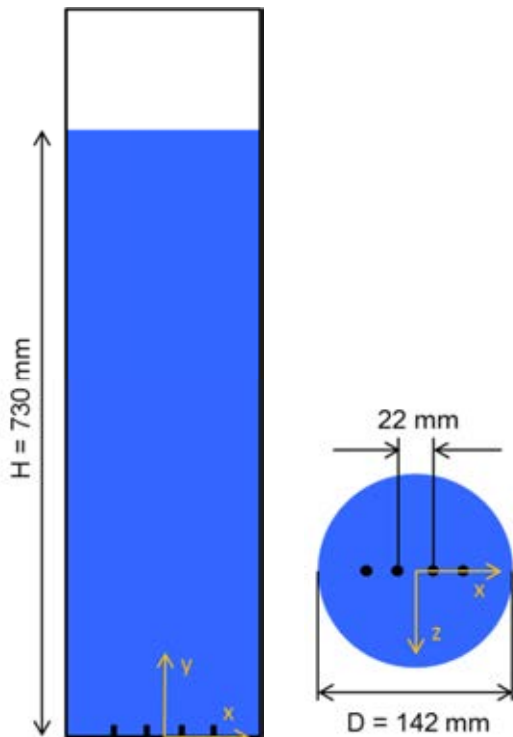


Figure 1: Schematic diagram of geometry.

Bubble location, velocity, and diameter were determined by shadowgraphy in a field of view extending up to a height of 300 mm with a depth of focus of  $\pm 20$  mm about the  $xy$ -plane in which the needles are located. From the bubble location data gas fractions were obtained by counting the number of bubbles falling into each cell of a grid covering the measurement plane. For comparison with the Euler-Euler simulations it has to be kept in mind that these gas fractions pertain to a slab with the thickness of the depth of focus and a corresponding average has to be taken in the simulation results.

Liquid velocity and its fluctuations were measured by PIV in five separate fields of view covering the entire column height with some overlap. Two-dimensional fields are obtained again in the  $xy$ -plane and for the two velocity components  $u$  and  $v$  lying in this plane.

Information about the pH-value can be discerned from LIF measurements by a calibration of the detected fluorescence intensity. The  $xy$ -plane was resolved in four separate fields of view over the column height.

For further details on the measurements we refer to the original papers (Kovats et al., 2015, Rzehak et al., 2017, Hlawitschka et al., 2017).

## MODELING

The entire model comprising multi-physics and chemistry is quite complex and space limitations preclude a full presentation. Detailed descriptions of modeling are available in previous works, i.e. Rzehak and Krepper (2013, 2015), Rzehak et al. (2014, 2015, 2017, 2017a), Rzehak and Kriebitzsch (2015), Ziegenhein et al. (2015, 2017), and Liao et al. (2016) for the fluid dynamics, Rzehak and Krepper (2016) for physical mass transfer and Krauß and Rzehak (2017, 2017a) for the chemical reactions and their effects on the mass transfer. In the following a brief summary is given, which emphasizes a few key issues concerning the reactive mass transfer.

The fluid dynamical part of the model comprises momentum exchange between the phases and liquid phase turbulence. The momentum exchange is governed by drag, (shear-) lift, wall (-lift), turbulent dispersion and virtual mass forces. The original works from which these correlations have been taken are summarized in Table 1. Turbulence is described by an SST-model common in single phase turbulence, which has been augmented by source terms describing the bubble-induced contribution (Rzehak and Krepper, 2013a).

For the mass transfer part, models are required for the mass transfer coefficient  $k_L$  and the turbulent diffusivity. Considering the resistance to mass transfer to be only on the liquid side, a correlation due to Brauer (1981) is applied, i.e.

$$k_L = \frac{D_{L,mol}^{CO_2}}{d_B} \left( 2 + 0.015 Re_B^{0.89} Sc_{L,mol}^{0.7} \right), \quad (1)$$

with Reynolds and Schmidt numbers defined as  $Re_B = |\mathbf{u}_L - \mathbf{u}_G| d_B \rho_L \mu_L^{-1}$  and  $Sc_{L,mol} = \mu_L (\rho_L D_{L,mol}^{CO_2})^{-1}$ .

This correlation was derived based on an analysis of mass transfer measurements on single bubbles in the

**Table 1:** Summary of bubble force correlations.

force	reference
drag	Ishii and Zuber (1979)
shear lift	Tomiya et al. (2002)
wall lift	Hosokawa et al. (2002)
turbulent dispersion	Burns et al. (2004)
virtual mass	constant coefficient $C^{VM} = 1/2$

wobbling regime which applies to gas bubbles of millimeter size in water.

The effective diffusivity in the liquid phase is the sum of a molecular contribution  $D_{L,mol}^{CO_2}$  and a turbulent contribution  $D_{L,turb}^{CO_2}$ . The latter is calculated from the turbulent kinematic viscosity by means of a turbulent Schmidt number for which the simple but frequently used assumption is made to take it as unity, i.e.

$$Sc_{L,turb} = \frac{\mu_{L,turb}}{\rho_L D_{L,turb}^{CO_2}} = 1. \quad (2)$$

The network of chemical reactions occurring during the absorption of  $CO_2$  in aqueous NaOH is shown in Fig. 2. The relative importance of the two reaction pathways, hydroxylation (superscript I in Fig. 2) and hydration (superscript III in Fig. 2), depends on the pH-value. Hydroxylation dominates for  $pH > 10$  and hydration dominates for  $pH < 8$ , while in between both reactions pathways are relevant (Kern, 1960). The need to include the hydration reaction to correctly capture the approach to the neutral point has been shown in Krauß and Rzehak (2017).

The effect of the chemical reactions on the mass transfer is modeled by an enhancement factor that depends on the type of reaction that occurs. Treating hydroxylation and hydration as independent parallel reactions (cf. van Swaaij and Versteeg, 1992) it can be seen that only the former is capable to cause a notable effect. Moreover, unless the temperature is increased or extra carbonate is added to the liquid, the equilibrium of reaction II lies far on the carbonate side so that the enhancement effect can be deduced from the effective overall reaction  $CO_2 + 2 OH^- \rightarrow CO_3^{2-} + H_2O$ , which is an irreversible bimolecular reaction (Krauß and Rzehak, 2017). An expression for the enhancement factor for this case has been derived by DeCoursey (1974) based on the renewal model as

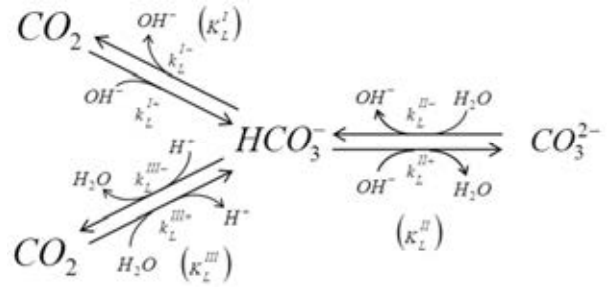
$$E = -\frac{Ha^2}{2(E_a - 1)} + \sqrt{\frac{Ha^4}{4(E_a - 1)^2} + E_a \frac{Ha^2}{(E_a - 1)} + 1}, \quad (3)$$

where the Hatta number is defined as

$$Ha = \frac{\sqrt{k_L^{I+} D_{L,mol}^{CO_2} C_L^{OH^-}}}{k_L} \quad (4)$$

and  $E_a$  gives the asymptotic limiting value for the enhancement factor of an instantaneous reaction.

Care has to be taken that a common approximation for the instantaneous enhancement factor  $E_a$  is not used outside its regime of validity which is restricted to large values. A fit formula that is applicable over a wide range of conditions has been proposed in Krauß and


**Figure 2:** Reaction scheme of  $CO_2$  in aqueous solution.

Rzehak (2017) and is used herein. With this fit formula, the enhancement factor converges to one for  $pH < 11.5$  which is why for the conditions of the present experiment no significant enhancement effect occurs. Correlations for reaction rates and physicochemical properties have been assembled in Rzehak and Krepper (2016) and Krauß and Rzehak (2017, 2017a).

## SIMULATIONS

Simulations have been performed for both the non-reactive and the reactive cases using a custom version of ANSYS CFX 14.5. The simulations were run in transient (URANS) mode on the full 3D domain. For both cases the domain was discretized using a grid with 86720 cells, which was found sufficient by a previously performed mesh study (Rzehak et al., 2017a). For the non-reactive case the time-step was set to  $1 \cdot 10^{-2}$  s, which guaranteed that the Courant-Friedrichs-Lewy number was always far below 1. For the reactive case smaller time-steps had to be used depending on the current pH-value, being lowered by hand from  $5 \cdot 10^{-4}$  s to  $1 \cdot 10^{-4}$  s as the simulation progressed. Time-averaged results have been averaged over a simulated physical time of 10 min discarding the initial transient until a statistically stationary state was attained. This time interval is sufficiently long that the resulting average does not change significantly anymore.

On the walls a no-slip condition holds for the continuous phase and a free-slip condition for the dispersed phase, assuming that direct contacts between the bubbles and the walls are negligible. To avoid the need to resolve the viscous sublayer, a single phase turbulent wall function assuming a smooth wall was used. For the mass fractions, the normal derivative vanishes on the walls as well as at the outlet at the top of the domain. In addition, a degassing condition was applied there, meaning an outlet condition for the dispersed phase and a free-slip and no-penetration condition for the continuous phase. The four needles were represented by point sources.

For the reactive case the continuous phase is considered as a mixture of sodium, hydroxide, bicarbonate and carbonate ions and carbon dioxide dissolved in water. While the initial concentrations of sodium and hydroxide ions were calculated with the initial pH-value of 9.5, all other concentrations were initially set to zero. The gas phase only consists of carbon dioxide. Bubble size distributions were narrow (Rzehak et al., 2017) and neither bubble coalescence and breakup nor shrinkage due to gas absorption was observed because the gas absorption rate was very small. Therefore a

monodisperse approximation with a constant bubble diameter of 2.72 mm was applied. Physicochemical properties were evaluated at atmospheric pressure and a temperature of 20°C.

## RESULTS

### Non-reactive case

For the non-reactive case, a statistically stationary state is attained after an initial transient when the gas flow is turned on. Thus, a time average of the experimental data is suitable for comparison with the Euler-Euler simulations. Since the simulations are run in URANS mode which allows to capture also time-dependent mean flows, such as e.g. bubble plume oscillations, a time average denoted as  $\langle \rangle$  is also performed on the simulation results.

A comparison between measured and calculated gas fractions is shown in Fig. 3. As already noted, an additional spatial average corresponding to the depth of focus of the shadowgraphy system has been applied to the simulations. The agreement between experiment and simulation is quite good. Special emphasis should be placed on the four peaks of gas fraction which are of the same width and get lower but broader with increasing height. This proves the suitability of the non-drag force models summarized in Table 1. However, the total amount of gas is a bit too high in the simulation.

This is confirmed by the comparison of the simulated and experimentally determined gas velocities shown in Fig. 4. The simulated velocities are close to the experimental ones. Both the experiment and the simulation show slightly lower velocities at the lowest height of 50 mm than at the other two positions. For all three heights the velocity is almost constant over the central portion of the column and decreases near the walls, but overall the simulated values are slightly too low. The consequence of this difference is a higher mean residence time of the gas bubbles and thus a slightly higher gas fraction as demonstrated in Fig. 3.

A comparison for the axial component of the mean liquid velocity is shown in Fig. 5. Close to the inlet region four peaks of velocity are visible matching the four peaks of gas fraction in Fig. 3 which is because most momentum is exchanged in regions of high buoyancy and consequently high drag forces. The simulated velocity is somewhat lower than in the experiment which is in accordance with the slightly lower gas velocities of the simulation in Fig. 4. It may be noted that in the experiment the second needle from the right apparently produced a faster liquid stream than the others. Since no difference is seen for this needle in the gas fraction, the reason for this is unclear, but the effect may be taken as an estimate of the magnitude of factors which are hard to control in laboratory experiments and which will inevitably be present in technical applications. A slight reminiscence of the resulting peak in the liquid velocity persists up to the higher level of 600 mm. Nevertheless, in consideration of the asymmetry of the experimental velocity profile the agreement between the experiment and the simulation is quite good.

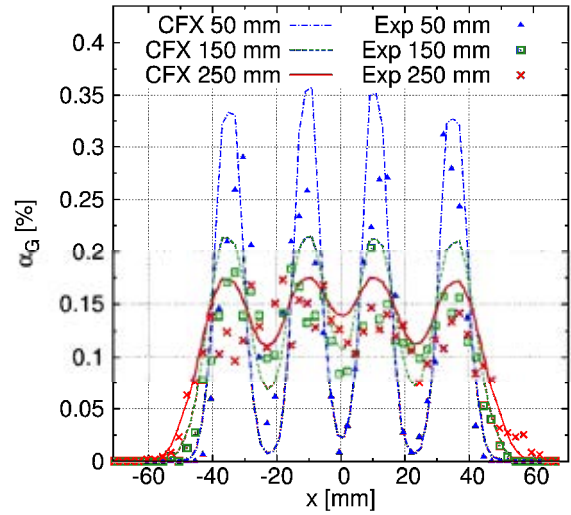


**Figure 3:** Comparison of gas fraction. Profiles at different heights as indicated in the legend.

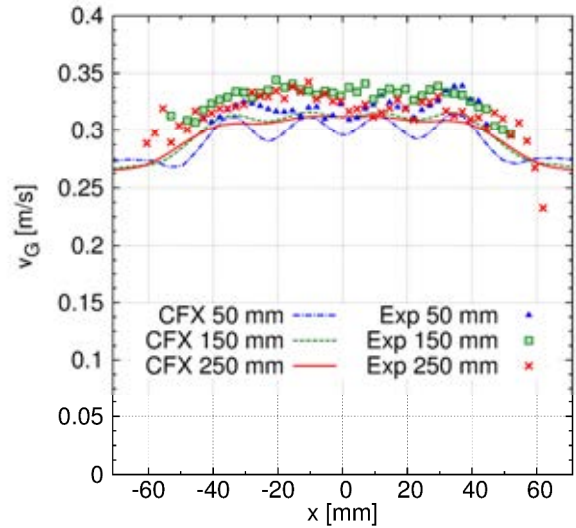


**Figure 4:** Comparison of gas velocity. Profiles at different heights as indicated in the legend.

Finally, the liquid velocity fluctuations are considered. For the simulations in URANS mode one has to take into account that there are two contributions to the covariance tensor of liquid velocity fluctuations  $\mathbf{u}'_L \mathbf{u}'_L$ : resolved and unresolved ones (Ziegenhein et al., 2015). The unresolved contribution is obtained from the averaged modeled turbulent kinetic energy  $k_L$  and is isotropic, while the resolved contribution is calculated from the time-dependent liquid velocity field and is anisotropic. The resulting expression is

$$\mathbf{u}'_L \mathbf{u}'_L = \langle (\mathbf{u}_L(t) - \mathbf{u}_L)(\mathbf{u}_L(t) - \mathbf{u}_L) \rangle + \frac{2}{3} \langle k_L(t) \rangle \mathbf{1} \quad (5)$$

where  $\mathbf{1}$  denotes the identity tensor. Fig. 6 shows the square root of the liquid velocity fluctuations in the axial direction. For the simulations in addition to the total fluctuations, which are compared with the experimental data, the resolved and unresolved contributions are also given separately. Agreement

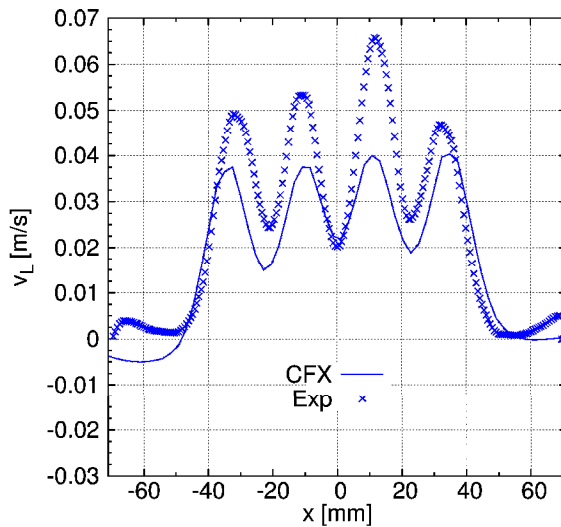
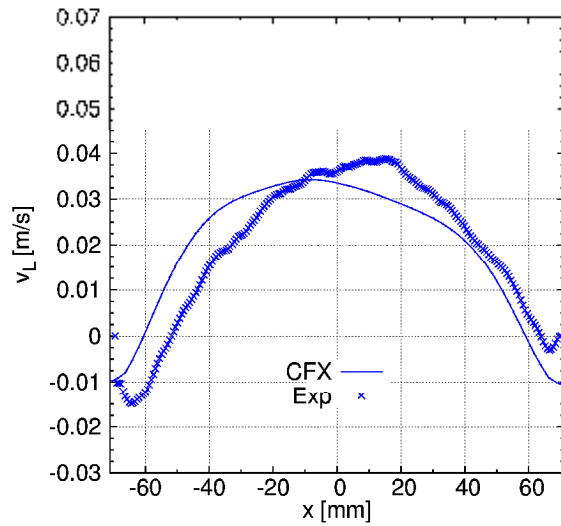


**Figure 5:** Comparison of axial liquid velocity. Profiles at different heights: bottom:  $H = 50$  mm; top:  $H = 600$  mm.

between simulation and experiment is good for both levels. In addition, it is observed that near the inlet needles the unresolved contribution dominates over the resolved one, while at larger heights, both contributions are of similar magnitude. Once again, four peaks are observed near the inlet needles matching the peaks in gas volume fraction and liquid velocity. In those regions of high gas volume fractions and their consequently high drag forces high contributions of bubble-induced turbulence are obtained. Furthermore, high liquid velocity gradients exist, which lead to high shear-induced turbulence contributions. For the upper level, where gradients of gas fraction and liquid velocity are clearly reduced, both contributions to the unresolved turbulence are much smaller.

### Reactive case

For the reactive case, the system behavior is time-dependent due to the accumulation of reaction products and dissolved carbon dioxide in the column. As an

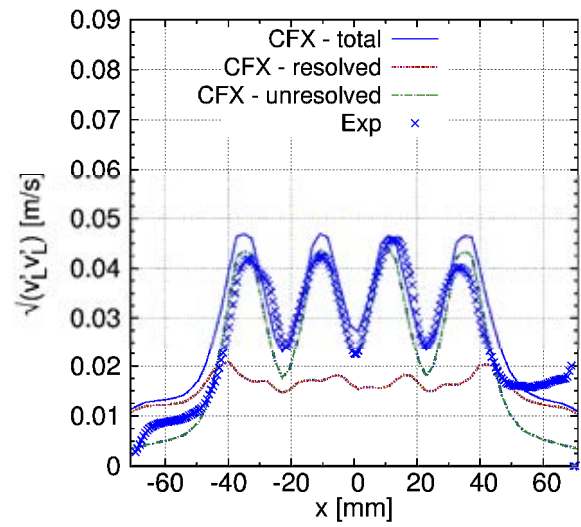
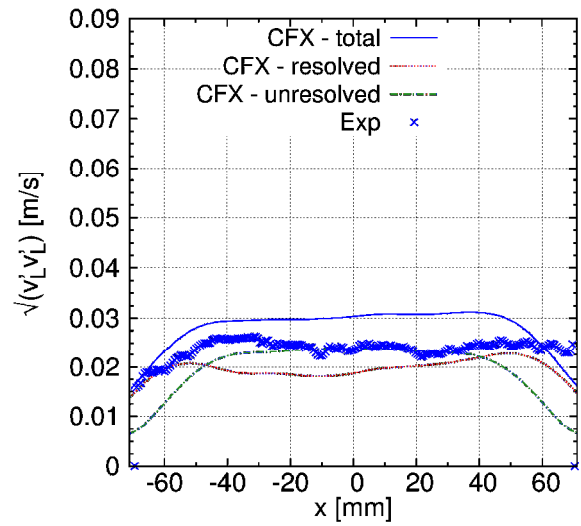


**Figure 6:** Comparison of axial liquid velocity fluctuations. Profiles at different heights: bottom:  $H = 50$  mm; top:  $H = 600$  mm.

illustration of this time dependency 2D fields of the simulated pH-value are shown in Fig. 7 at different physical times. Near the inlet liquid is carried upwards by the rising bubbles. Due to the high pH-values in the lower part of the column the absorbed gas is transformed to carbonate ions by the hydroxylation reaction pathway. During the decrease in pH-value with increasing height the carbonate ions are converted to bicarbonate ions by the second backward reaction. Furthermore, the hydration of carbon dioxide starts, whereby the pH-value continues to decrease. At a height of  $\sim 250$  mm accumulation of carbon dioxide by the liquid phase begins and the decrease in pH-value slows down. Near the outlet the slightly acidic liquid changes its direction of flow and moves downwards close to the column walls. This provides a continuous transport of fresh liquid downwards to the inlet needles until all of the liquid above  $\sim 250$  mm has been converted to an acidic environment. Only then does the reaction spread out to the lower part of the column.

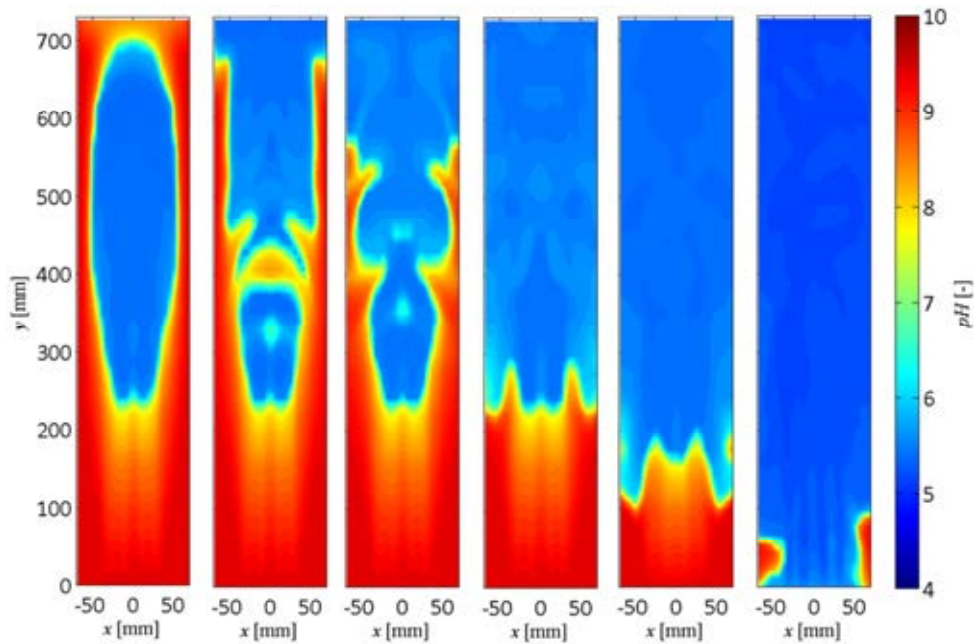


**Figure 7:** 2D fields of simulated pH-value. From left to right: simulation result after 11, 14, 18, 24, 34 and 60 s of gas supply.

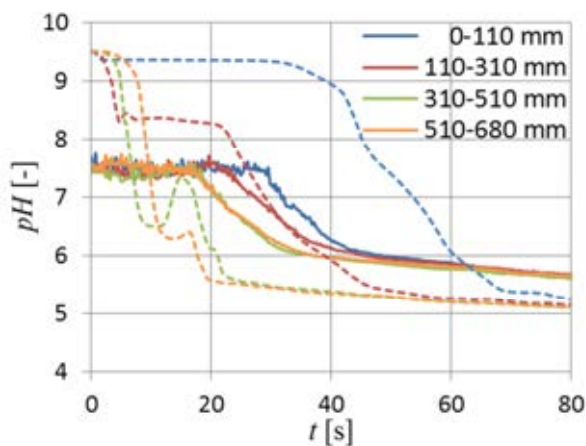


**Figure 8:** Comparison of the time-dependent pH-value, spatially averaged for the column height segments as indicated in the legend, between the simulation (dashed lines) and the experiment (solid lines). Note that the LIF method is limited to  $\text{pH} < \sim 7.6$ .

For a quantitative analysis, averages have been performed over the four column height segments corresponding to the separate fields of view in the experiment. The results are shown as the dashed lines in Fig. 8. It is seen that the drop in pH, which indicates the progress of the reactions, occurs first and almost simultaneously for the upper two segments from 310 mm to 680 mm. The segments from 110 mm to 310 mm and from 0 mm to 110 mm follow with a delay of  $\sim 20$  s each.

Quantitatively big differences are seen between the simulation and the experimental results, which were processed analogously and are shown by the solid lines in Fig. 8. Note that only values of  $\text{pH} < \sim 7.6$  are quantifiable by the LIF method applied here, because the fluorescence intensity is the same for all higher pH-values. The order in which the drop in pH occurs is the same in the experiment as in the simulation, but the starting times differ significantly. For the upper two

sections it starts later in the experiment than in the simulations, for the second section from below at about the same time and in the lowest section it starts earlier in the experiment than in the simulation. In addition the pH curves level off at  $\text{pH} \approx 6.0$  in the experiment but only at  $\text{pH} \approx 5.5$  in the simulations which could be a result of differences in chemical equilibrium evoked by differing conditions, such as temperature or initial pH-value. In the experiment the four separate segments were investigated sequentially in separate runs which requires a multiple preparation of the initial solution. In fact, the initial pH-values were not exactly identical, but there were differences up to 0.3. Also the precise value of temperature was not recorded in the experiment. The small peaks in the simulated pH-values of the upper two sections at  $\sim 15$  s are not observed in the experiment. They are caused by liquid of higher pH-values entering the measurement plane from other regions.

It must be noted that the deviations between the simulation and the experiment are substantially caused by experimental difficulties, in particular concerning the start-up process. The four needles do not start to supply gas simultaneously, but with considerable delays, which in addition are subject to large statistical variations. Therefore, the gas flow rate in the experiment does not change from zero to the nominal value instantaneously, but is ramped up over a time interval which is of the order of 7 to 20 s. In addition there are local variations of gas supply during this period which may have an impact on the bubble column hydrodynamics. Finally this ramp-up process is different for the different experimental runs from which the LIF data for the four segments were obtained. All of these effects could not be captured by the simulation where the gas supply starts instantaneously and for all needles simultaneously. To make a comparison, starting time for the experimental curves was chosen halfway in between the release of the first bubble by the first and the last needle.

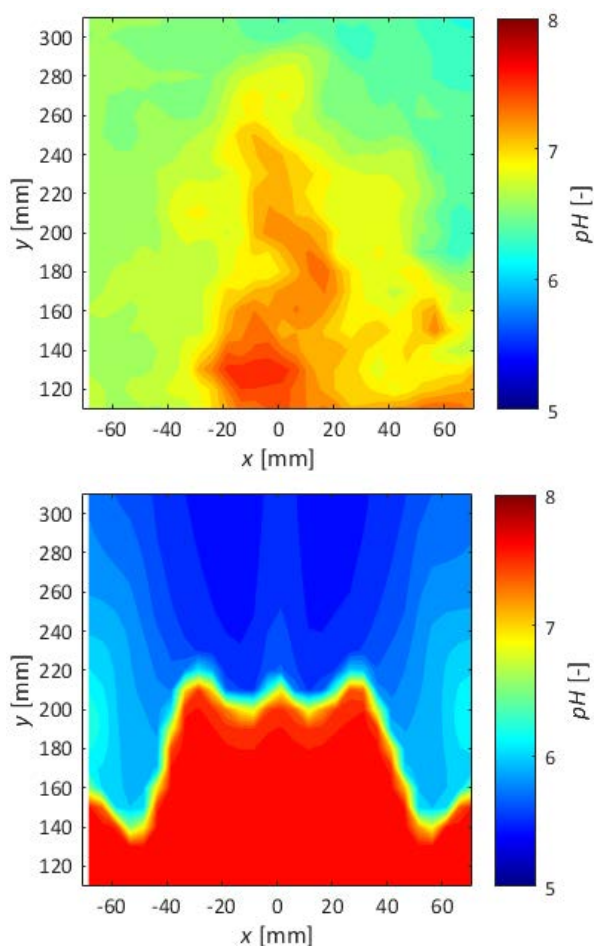


**Figure 9:** Comparison of 2D fields of the instantaneous pH-value between the simulation (bottom) and the experiment (top) at  $t = 30$  s in the segment from 110 mm to 310 mm.

In Fig. 9, the instantaneous 2D fields of pH-value at  $t = 30$  s of the experiment and the simulation are compared in the height segment from 110 mm to 310 mm. The highest pH-values of both fields are observed in the lower middle of the segment and decrease with increasing height. Slightly acidic liquid flows downwards next to the walls. The major difference between the simulation and the experiment is the significantly lower level of mixing in the simulation, which results in much stronger gradients of pH-value and therefore in substantial quantitative deviations.

In Fig. 10 the radially averaged pH-values at  $t = 30$  s are plotted over the column height for both experiment and simulation. Note that the simulated pH-values have been limited to  $\text{pH} < \sim 7.6$  in accordance with the sensitivity of the fluorescence to improve comparability. Both curves show a decrease in pH-value with increasing height which predominates at a height between 100 mm and 300 mm. However, according to the lower level of mixing in the simulation the decrease of the simulation is rather steep, whereas the decrease in the experiment is much more gradual. Moreover, the approximately constant pH-value for  $y > 300$  mm is  $\sim 0.5$  lower in the simulation than in the experiment. In addition to the aforementioned experimental difficulties this deviation could be again a result of differences in chemical equilibrium as already discussed above.

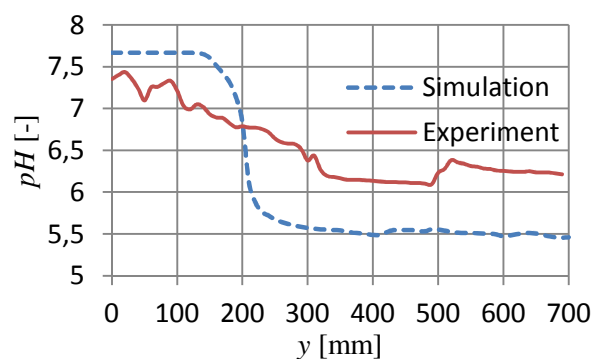


**Figure 10:** Comparison of radial averaged pH-value over height at  $t = 30$  s.

In view of the good agreement of the time-averaged results for the non-reactive case, the shortcoming of the reactive modeling is thus likely to be produced by errors in the reproduction of the dynamical flow behavior and the resulting poor mixing of the liquid phase in the simulation. It is likely that the high level of mixing in the experiment is evoked by small scale turbulence which cannot be resolved by the URANS approach used here.

## CONCLUSION

Simulations have been performed corresponding to a new experiment that comprises optical measurements of both fluid dynamics and reactive mass transfer. The Euler-Euler approach has been applied with closures that were previously established in independent investigations.

For the fluid dynamics, time-averaged results in the stationary state were investigated. Quite good agreement was found for the gas fraction, mean liquid velocity and turbulent fluctuations.

For the reactive mass transfer the ramp-up process of the chemisorption of carbon dioxide in sodium hydroxide solution was investigated. This ramp-up process provides stronger spatial differences in the concentration fields than the gas supply into a developed flow as studied in previous works, e.g. Darmana et al. (2007). Thus the configuration presently studied bears the possibility of a more conclusive model validation. While the potential of this approach can be confirmed from the qualitative similarities between simulation and experiment, the significant quantitative differences point to the need for its refinement.

In the course of the work it became apparent that the experiments were in some respects less well controlled than desirable for their use to validate CFD simulations. These issues are not completely obvious, hence the discussion may be useful to design future experiments with an increased reliability. In particular, for each experimental attempt crucial parameters like the initial pH-value and the ramp-up process of gas supply have to be identical for each repetition, especially when results from different runs are stitched together. Furthermore, the experimental error of the different measurement methods should be quantified in order to also access the quantitative model error.

Concerning the simulations, one may already draw the conclusion that the predicted mixing of chemical

species is significantly too weak. This is most likely due to a lack of resolving smaller scale turbulent structures, which are expected to be mainly responsible for mixing. Improvement could be achieved by applying a large eddy simulation, which is more able to resolve these kinds of turbulent structures, but requires much higher computational effort than the URANS model used here. Using the identical model for the setup of Darmana et al. (2007), a rectangular bubble column with higher superficial gas velocities, such severe problems were not observed. Presumably this is because the flow structures responsible for mixing in that case were fairly big and reasonably resolved by the URANS method, although some relatively minor deviations remained (Krauß and Rzehak, 2017a).

## ACKNOWLEDGEMENT

This work has been carried out in the frame of a research project (GZ: RZ 11/1-1) within the DFG Priority Programme 1740: “Reactive Bubbly Flows” funded by the DFG.

## REFERENCES

- BRAUER, H., (1981), “Particle/fluid transport processes”, *Prog. Chem. Eng.*, **19**, 81–111.
- BURNS, A.D., FRANK, T., HAMILL, I. and SHI, J.-M., (2004), “The Favre averaged drag model for turbulence dispersion in Eulerian multi-phase flows”, *5th Int. Conf. on Multiphase Flow (ICMF2004)*, Yokohama, Japan.
- DARMANA, D., HENKET, R., DEEN, N. and KUIPERS, J., (2007), “Detailed modelling of hydrodynamics, mass transfer and chemical reactions in a bubble column using a discrete bubble model: Chemisorption of CO<sub>2</sub> into NaOH solution, numerical and experimental study”, *Chem. Eng. Sci.*, **62**, 2556–2575.
- DeCOURSEY, W. J., (1974), “Absorption With Chemical Reaction: Development Of A New Relation For The Danckwerts Model”, *Chem. Eng. Sci.*, **29**, 1867–1872.
- HLAWITSCHKA, M., KOVÁTS, P., ZÄHRINGER, K. and BART, H.-J., (2017), “Simulation and experimental validation of reactive bubble column reactors”, *Chem. Eng. Sci.*, in press.
- HOSOKAWA, S., TOMIYAMA, A., MISAKI, S. and HAMADA, T., (2002), “Lateral Migration of Single Bubbles Due to the Presence of Wall”, *ASME Joint U.S.-European Fluids Engineering Division Conference (FEDSM 2002)*, Montreal, Canada.
- ISHII, M. and ZUBER, N., (1979), “Drag coefficient and relative velocity in bubbly, droplet or particulate flows”, *AIChE J.*, **25**, 843–855.
- KERN, D. M., (1960), “The hydration of carbon dioxide”, *J. Chem. Educ.*, **37**, 14–23.
- KOVÁTS, P., THÉVENIN, D. and ZÄHRINGER, K., (2015), “Fluid-dynamical Characterization of a Bubble Column for Investigation of Mass-transfer”, *Conference on Modelling Fluid Flow (CMFF’15)*, Budapest, Hungary.
- KRAUSS, M. and RZEHAK, R., (2017), “Reactive absorption of CO<sub>2</sub> in NaOH: Detailed study of enhancement factor models”, *Chem. Eng. Sci.*, **166**, 193–209.
- KRAUSS, M. and RZEHAK, R., (2017a), “Reactive absorption of CO<sub>2</sub> in NaOH: An Euler-Euler simulation study”, *Chem. Eng. Tech.*, submitted.
- LIAO, J., ZIEGENHEIN, T. and RZEHAK, R., (2016), “Bubbly flow in an airlift column: a CFD study”, *J. Chem. Tech. Biotech.*, **91**, 2904–2915.
- RZEHAK, R. and KREPPER, E., (2013), “Closure Models for turbulent bubbly flows: A CFD study”, *Nucl. Eng. Des.*, **265**, 701–711.
- RZEHAK, R. and KREPPER, E., (2013a), “CFD modeling of bubble-induced turbulence”, *Int. J. Multiphase Flow*, **55**, 138–155.
- RZEHAK, R., KREPPER, E., ZIEGENHEIN, T. and LUCAS, D., (2014), “A baseline model for monodisperse bubbly flows”, *10th International Conference on CFD in Oil & Gas, Metallurgical and Process Industries (CFD2014)*, Trondheim, Norway.
- RZEHAK, R. and KREPPER, E., (2015), “Bubbly flows with fixed polydispersity: validation of a baseline closure model”, *Nucl. Eng. Des.*, **287**, 108–118.
- RZEHAK, R. and KRIEBITZSCH, S., (2015), “Multiphase CFD-simulation of bubbly pipe flow: A code comparison”, *Int. J. Multiphase Flow*, **68**, 135–152.
- RZEHAK, R., KREPPER, E., LIAO, Y., ZIEGENHEIN, T., KRIEBITZSCH, S. and LUCAS, D., (2015), “Baseline model for the simulation of bubbly flows”, *Chem. Eng. Tech.*, **38**, 1972–1978.
- RZEHAK, R., (2016), “Modeling of mass-transfer in bubbly flows encompassing different mechanisms”, *Chem. Eng. Sci.*, **151**, 139–143.
- RZEHAK, R. and KREPPER, E., (2016), “Euler-Euler simulation of mass-transfer in bubbly flows”, *Chem. Eng. Sci.*, **155**, 459–468.
- RZEHAK, R., ZIEGENHEIN, T., KRIEBITZSCH, S., KREPPER, E. and LUCAS, D., (2017), “Unified modeling of bubbly flows in pipes, bubble columns, and airlift columns”, *Chem. Eng. Sci.*, **157**, 147–158.
- RZEHAK, R., KRAUSS, M., KOVÁTS, P. and ZÄHRINGER, K., (2017a), “Fluid dynamics in a bubble column: New experiments and simulations”, *Int. J. Multiphase Flow*, **89**, 299–312.
- TOMIYAMA, A., TAMAI, H., ZUN, I. and HOSOKAWA, S., (2002), “Transverse migration of single bubbles in simple shear flows”, *Chem. Eng. Sci.*, **57**, 1849–1858.
- ZIEGENHEIN, T., RZEHAK, R. and LUCAS, D., (2015), “Transient simulation for large scale flow in bubble columns”, *Chem. Eng. Sci.*, **122**, 1–13.
- ZIEGENHEIN, T., RZEHAK, R., MA, T. and LUCAS, D., (2017), “Towards a unified approach for modeling uniform and non-uniform bubbly flows”, *Can. J. Chem. Eng.*, **95**, 170–179.

## STOCHASTIC DSMC MODEL FOR LARGE SCALE DENSE BUBBLY FLOWS

Satish KAMATH<sup>1\*</sup>, Johan T. PADDING<sup>2</sup>, Kay A. BUIST<sup>1</sup>, J. A. M. KUIPERS<sup>1</sup>

<sup>1</sup>Multiphase Reactors Group, Department of Chemical Engineering & Chemistry, Eindhoven University of Technology, P.O. Box 513, 5600 MB Eindhoven, The Netherlands

<sup>2</sup>Process and Energy Department, Delft University of Technology, Building 34K Leeghwaterstraat 39  
2628 CB Delft, The Netherlands

\* E-mail: s.s.kamath@tue.nl

### ABSTRACT

Bubble columns are widely used in the chemical industry because of their simple design and high efficiency. The scale-up of these kinds of columns is challenging and time-consuming. Since high throughput is targeted, they are operated in the heterogeneous bubbling regime where the flow is complex and turbulent. Large-scale bubble columns can in principle be simulated using continuum models (TFM/MFM) with closures from more detailed models such as Front Tracking (FT) or Volume of Fluid (VOF). Multi-fluid models are capable of predicting the flow field, but to accurately describe mass transfer rates, an accurate interfacial area of the bubbles is required as well as mass transfer coefficients for dense bubble swarms. This requires the MFM to be coupled with models that can predict bubble size distributions. The Discrete Bubble Model (DBM) can be scaled up but the bubble-bubble interactions make it computationally very intensive.

Stochastic Direct Simulation Monte Carlo (DSMC) methods treat the bubbles in a discrete manner while more efficiently handling the collisions compared to the DBM. The DSMC model has earlier been used for very small particles in the size range of Angstroms to microns where the particles are purely inertial at high Stokes numbers. In the work of Pawar *et al.* (2014) this was used for micrometer sized particles/droplets where this method proved to be 60 to 70 times faster than more classical methods like the Discrete Particle Model (DPM).

In this work the DSMC method has been extended to finite sized bubbles/particles in the order of millimeters. A 4-way coupling (liquid-bubble-bubble) is achieved using the volume-averaged Navier Stokes equations. The model is verified first for mono-disperse impinging particle streams without gas. Then the model is verified with the DBM of a 3D periodic bubble driven system. The collision frequencies are all within 10 percent accuracy and the speed up achieved per DEM time step is nearly 10 times compared to the DBM, which facilitates simulation of large systems.

**Keywords:** Euler-Lagrange methods, bubble dynamics, optimization, stochastic methods, DSMC.

### NOMENCLATURE

#### Greek Symbols

$\rho$	Mass density, [ $kg/m^3$ ]
$\mu$	Dynamic viscosity, [ $kg/ms$ ]
$\varepsilon$	Porosity, [-]
$\tau$	Shear stress, [ $N/m^2$ ]
$\phi$	Volumetric momentum source term, [ $N/m^3$ ]

#### Latin Symbols

$\mathbf{F}$	Force (vector), [ $N$ ]
$P$	Pressure, [ $Pa$ ]
$\mathbf{u}$	Continuous phase velocity vector, [ $m/s$ ]
$\mathbf{v}$	Discrete phase velocity vector, [ $m/s$ ]
$\mathbf{g}$	Gravitational acceleration vector, [ $m/s^2$ ]
$V$	Discrete phase volume, [ $m^3$ ]
$R$	Bubble radius, [ $m$ ]

#### Sub/superscripts

$b$	discrete phase
$l$	continuous phase
$L$	Laminar
$T$	Turbulent
$bub$	bubble
$flow$	flow

### INTRODUCTION

#### Bubble columns

Bubble column reactors are widely used as gas-liquid contactors in the chemical and energy industries. A wide variety of processes like absorption, fermentation, Fischer-Tropsch synthesis, waste water treatment, bio-reactors etc. are operated in bubble columns. The design of such columns is based on parameters such as throughput, conversion, type of reactions etc. The industrial grade columns with large throughputs have volumes in the range of 100-300  $m^3$ . Larger columns are also employed for bio-processes like fermentation (3000  $m^3$ ) and waste water treatment (20000  $m^3$ ) (Deen *et al.*, 2012).

Figure 1 shows a schematic representation of a bubble column. Often, bubble columns are equipped with internal parts, depending on the application. If the reaction is highly exothermic, cooling tubes will be present inside the column. Catalyst particles may also be suspended in the liquid phase to facilitate faster conversion of the reactants.

The bubble dynamics and bubble size distribution inside the column dictate the liquid phase flow. This in turn controls the rate of mass transfer from the bubble to the liquid phase and also the heat transfer with submerged heat exchange tubes. Modeling of such bubble columns is very challenging and typically empirical correlations (Chaudhari and Ramachandran, 1980) are used even today. Recent advances in computational power and techniques have made



it possible to simulate the flow structures in such columns which occur at multiple time and length scales.

### Multi-scale approach

A multi-scale approach can be employed to simulate the complex fluid flow in a bubble column (see figure 2). At the lowest level methods such as Front-Tracking (Unverdi and Tryggvason, 1992) and Volume of Fluid (van Sint Annaland *et al.*, 2005) methods are used to simulate the behaviour of a single bubble or a group of interacting bubbles rising through the liquid phase. An Euler-Lagrange approach, such as the Discrete Bubble Model (DBM), is used to simulate larger length and time scales. This method uses closures from the above methods because the flow field around a bubble is not completely resolved. The DBM is a suitable method to understand the influence of bubble-bubble interactions and bubble wall encounters on large scale flow structures. The method becomes computationally expensive when simulating dense bubbly flows because every bubble is tracked explicitly and the bubble-bubble encounters have to be resolved in time. Therefore, at the industrial scale, Euler-Euler approaches are used with closures from the intermediate scale (Deen *et al.*, 2004a).

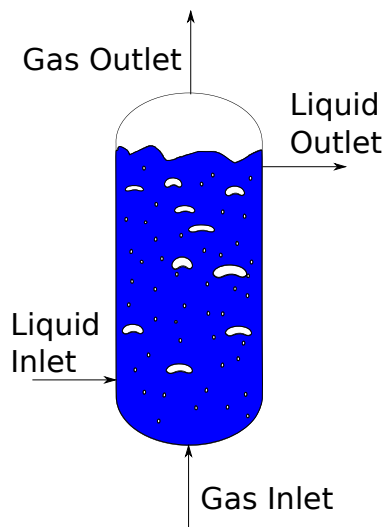


Figure 1: Schematic diagram of a bubble column.

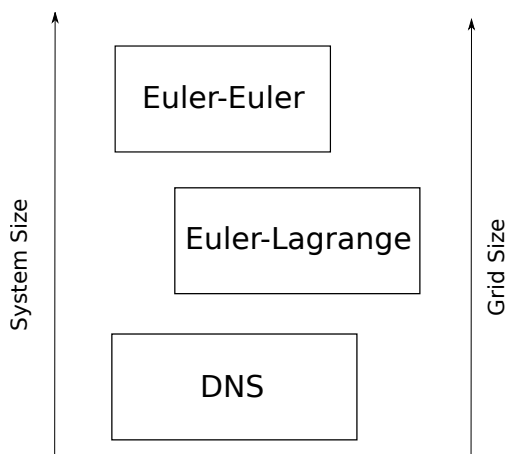


Figure 2: Multiscale approaches at different time and length scales.

### Problems with Euler-Euler approach

Euler-Euler approaches such as the Multi Fluid Model represent the bubble phase with different size classes. Coupled conservation equations are solved for each size class with suitable closures. The interactions among the different considered phases need to be explicitly defined. Bubble-bubble interactions are not accounted for nor the naturally occurring phenomena of coalescence and break-up. Dedicated external models, such as the population balance models, have to be integrated with the Multi-Fluid Model to account for coalescence and break-up (Zhang, 2007). In the work of (Zhang, 2007) the range of bubble sizes is assumed to be 2-4 mm while the other parameters such as drag, lift etc. are assumed to not vary much. Therefore a two-fluid approach is employed. This limits the range of bubble size, which influences the dynamics of the column.

### Objective

The main objective of this work is to develop an Euler-Lagrange model that can be used for large scale simulation of bubble columns (10-100  $m^3$ ). Bubble-bubble and bubble-wall interactions are one of the bottlenecks in the computational speed of the simulation. Therefore to resolve this issue, a stochastic Direct Simulation Monte-Carlo (DSMC) approach is used to execute the collisions. Pawar *et al.* (2014) and Du *et al.* (2011) have shown that the method is nearly two orders of magnitude faster than the DBM, but there are limitations to the approach with respect to the length scale of the simulation and the volume fraction of the discrete phase (Pawar *et al.*, 2014). This work aims to extend the DSMC approach to larger object sizes (in the order of millimeters) and to resolve the volume fraction limitation. Furthermore, this work aims to extend the method so that it can handle bubble-bubble collisions efficiently. Addition of a fluid phase where the fluid phase forces also contribute considerably to the bubble dynamics, adds an extra level of complexity because these have to be considered in the calculation of the collision frequency.

In the next sections, the method is briefly described and the model verification results are presented.

### MODEL DESCRIPTION

#### Discrete phase

DSMC methods are normally associated with a parcel approach where a group of discrete objects are represented by one simulated object. The systems for which this method was developed are molecular systems that have finite/large Knudsen number (Bird, 1994). In this work the DSMC method has been extended to larger discrete phase sizes (in the order of millimeters) with low Knudsen number. For simplicity a parcel size 1 is chosen, but in future work we will also explore larger parcel sizes. The bubbles are tracked individually where the momentum equations (see equations 1 and 2) need to be solved to obtain new velocities of the particles. Pawar *et al.* (2014) have reported a major speed boost with the DSMC model compared to the discrete particle approach with the same parcel size.

The bubble is assumed to be incompressible and the density of the bubble is also assumed to be constant. Forces considered here are gravitational ( $F_G$ ), pressure ( $F_P$ ), drag ( $F_D$ ),

lift ( $\mathbf{F}_L$ ), virtual mass ( $\mathbf{F}_{VM}$ ) and wall lubrication ( $\mathbf{F}_W$ ) (see equation 2).

$$\rho_b V_b \frac{d(\mathbf{v})}{dt} = \Sigma \mathbf{F} - (\rho_b \frac{d(V_b)}{dt}) \mathbf{v} \quad (1)$$

$$\Sigma \mathbf{F} = \mathbf{F}_G + \mathbf{F}_p + \mathbf{F}_D + \mathbf{F}_L + \mathbf{F}_{VM} + \mathbf{F}_W \quad (2)$$

The drag, lift and wall forces used here are from Tomiyama *et al.* (1995, 2002). The drag correction for bubble swarms is included from Roghair *et al.* (2011). A more detailed explanation about the forces and closures used can be found in works of Darmana *et al.* (2006); Jain *et al.* (2014).

### Liquid phase hydrodynamics

The liquid phase dynamics are described by the volume averaged Navier-Stokes equations coupled with the continuity equation (see equations 3 and 4).

$$\frac{\partial(\varepsilon_l \rho_l)}{\partial t} + \nabla \cdot \varepsilon_l \rho_l \mathbf{u} = 0 \quad (3)$$

$$\frac{\partial(\varepsilon_l \rho_l \mathbf{u})}{\partial t} + \nabla \cdot \varepsilon_l \rho_l \mathbf{u} \mathbf{u} = -\varepsilon_l \nabla P - \nabla \cdot \varepsilon_l \boldsymbol{\tau}_l + \varepsilon_l \rho_l \mathbf{g} + \phi \quad (4)$$

$\varepsilon_l$  represents the local liquid fraction and  $\phi$  represents the local momentum source term for the force exerted by the bubbles on the liquid. The shear stress term  $\boldsymbol{\tau}_l$  is given by:

$$\boldsymbol{\tau}_l = -\mu_{eff,l} ((\nabla \mathbf{u}) + (\nabla \mathbf{u})^T - \frac{2}{3} \mathbf{I}(\nabla \cdot \mathbf{u})) \quad (5)$$

where

$$\mu_{eff,l} = \mu_{L,l} + \mu_{T,l} \quad (6)$$

$\mu_{T,l}$  arises from the convection term when the Navier-Stokes equations are volume averaged and the Boussinesq eddy viscosity assumption. Deen *et al.* (2001) have compared different turbulence models with experimental data in the Euler-Euler framework for a square bubble column. They concluded that the large eddy simulation outperforms the  $k-\varepsilon$  model. Therefore, the same framework as Deen *et al.* (2001) was chosen for the liquid phase.  $\mu_{T,l}$  is closed with the sub-grid scale eddy viscosity expression given by Vreman (2004):

$$\mu_{T,l} = \rho_l c \sqrt{\frac{\beta_b}{\alpha_{ij} \alpha_{ij}}} \quad (7)$$

**Table 1:** Terms in the Vreman SGS model. Vreman (2004)

Term	Definition
$c$	$2.5 C_s^2$
$\alpha_{ij}$	$\frac{\partial \bar{u}_j}{\partial x_i}$
$\beta_{ij}$	$\Delta_m^2 \alpha_{mi} \alpha_{mj}$
$\beta_b$	$\beta_{11} \beta_{22} - \beta_{12}^2 + \beta_{11} \beta_{33} - \beta_{13}^2 + \beta_{22} \beta_{33} - \beta_{23}^2$

where  $C_s$  is the Smagorinsky constant, the rest of the parameters are given by table 1. A similar approach has been used by Darmana *et al.* (2006) and also by Jain *et al.* (2014).

## NUMERICAL SOLUTION METHOD

### Time marching

In most of the Euler-Lagrangian frameworks the discrete and the continuous phases are time-marched in an alternate fashion with intermediate coupling. Therefore there is a flow time-step  $\delta t_{flow}$  and a bubble time-step  $\delta t_{bub}$ .  $\delta t_{flow}$  is divided into a fixed number of sub-steps of duration  $\delta t_{bub}$ . During  $\delta t_{bub}$ , the forces acting on each bubble are recalculated based on the local Eulerian flow-field. The bubble time-step  $\delta t_{bub}$  can be divided into several more time steps based on the collision frequency calculated for every bubble. More details about this are given in the section "Discrete phase dynamics".

The major difference in time marching between the deterministic approach employed by Darmana *et al.* (2006) and the stochastic approach used in this work is the resolution of the lowest time scale. In the deterministic approach, the collision times are explicitly calculated and a list is maintained to sequentially perform the collisions in the ascending order of their collision times. In the stochastic approach, the collision times are not determined, but rather collisions take place based on a probabilistic approach. This is described with more details in section "Discrete phase dynamics".

### Coupling

The coupling between the phases dictates the flow field in the column. Therefore the mapping procedure between the grid cells has to be considered carefully. Kitagawa *et al.* (2001) have proposed to use a Lagrangian template function for the volume fraction of the dispersed phase. Similarly Deen *et al.* (2004b) proposed a fourth order polynomial function for mapping the forces and volume fraction. The width of the distribution is set based on the bubble size. This makes the mapping independent of the size of the Eulerian grid. Darmana *et al.* (2006) have also used it for their Discrete Bubble Model. This mapping is implemented in this work and is also suitable for comparison with the Discrete Bubble Model.

Lau *et al.* (2011) have performed an extensive parametric study for different mapping window sizes for the polynomial function in a bubble column. They found that the size of the mapping window does not have an effect on the predicted mean and fluctuating velocities when a drag correction is used that uses local gas fraction. Therefore a mapping window of  $2R_{bub}$  is used.

### Discrete phase dynamics

The discrete phase equations are solved using a first order explicit scheme for equation 1:

$$\mathbf{v}^{n+1} = \frac{\Sigma \mathbf{F}^n}{m_b} \delta t_{bub} + \mathbf{v}^n \quad (8)$$

The forces are mapped from the Eulerian grid cells based on the polynomial function method described in the previous section. Then the bubble dynamics is treated adapting the algorithm shown in Pawar *et al.* (2014) with a few important modifications described later in this section. Once the bubble marching along with the collisions are treated, the Lagrangian forces are collected in the volumetric momentum source term  $\phi$ . This is repeated until the discrete phase has moved for a full  $\delta t_{flow}$ . From the new bubble positions, the bubble volume fractions are computed and subsequently

mapped back to the Eulerian domain to determine  $\epsilon_l$ .

During every bubble time step, the bubbles are marched forward in time by  $\delta t_{bub}$ . The collisions that occur during this time interval can introduce a big computational overhead for a large scale system with bubbles/particles in the order of millions. The algorithm of a deterministic model like the Discrete Bubble Model (Darmana *et al.*, 2006) is inherently serial as the collisions need to occur in the order of their collision times. These collision-times are maintained in an encounter list and the minimum time needs to be searched every time a collision occurs due to changes in bubble positions and velocities. This implies a large overhead for dense systems, even with the implementation of efficient neighbour list concepts.

The speed-up in the DSMC algorithm is mainly due to choosing a collision partner using probabilistic rules. There are several methods used for choosing the right collision pairs in DSMC such as the time counter method, Nanbu method, modified Nanbu method (Lutišan, 1995). Pawar *et al.* (2014) and Du *et al.* (2011) have used the modified Nanbu method with their own modifications for the searching scope and collision conditions.

As the flow becomes more dense, the Knudsen number becomes smaller. In such situations the local relative velocities between bubbles are also comparatively small. Therefore they tend to continuously collide due to less availability of interstitial space, therefore a structural factor must be included in the algorithm. This factor is the radial distribution function at contact ( $g(r)_{contact}$ ).

The DSMC algorithm performs collisions in a stochastic manner with neighbouring particles located within a defined searching scope. The expression for the probability ( $P_{ij}$ ) that a particle  $i$  collides with another particle  $j$  defined within its searching scope is given by:

$$P_{ij} = \frac{|\mathbf{v}|_{ij} \sigma \Delta t_p}{V_{s,i}} g(r)_{contact} \quad (9)$$

where  $|\mathbf{v}|_{ij}$  is the relative velocity magnitude between the two particles,  $\sigma$  is the cross-sectional areas of the collision cylinder which is computed from the sum of the projected cross sectional area of the two particles,  $\Delta t_p$  is the time step and  $V_{s,i}$  is the volume of the searching scope of the particle with index  $i$ . It can be shown that for a given particle size, a minimum relative velocity is needed for the probability to be valid based on the Nanbu method. To account for relative velocities much lower than the limit, a nearest neighbour collision algorithm is included. The nearest neighbour is the most likely collision partner for an entity in a dynamic system (Bird, 2007). This was implemented without hampering the speed of the already existing algorithm.

The collisions are executed using the hard sphere model (Hoomans *et al.*, 1996) once the collision pairs are chosen. The normal component of the momentum is simply exchanged between the two bubbles/particles and the tangential component is retained.

### Liquid phase numerical scheme

The continuity equation and the momentum equations are solved in a coupled manner using SIMPLE (Patankar, 1980).

The unsteady part is discretized using the first order Euler scheme. The convective fluxes in the continuity equation are treated implicitly. The convective, diffusive and the source terms are treated explicitly in the momentum equations.

## VERIFICATION AND RESULTS

The Discrete Bubble Model from Darmana *et al.* (Darmana *et al.*, 2006) is taken as the verification model. The model is verified through two problems:

1. Impinging particle streams (P1)
2. 3D - periodic bubble rise from rest (P2)

System P1 consists of two nozzles facing each other at an angle (see figure 3). The solid particles flow through these nozzles, collide and spread across the domain based on the outcome of the collisions. There is no interstitial fluid phase for this test case, therefore the velocity field of the particles is purely set by the collisions. The mass flow-rate is set for each nozzle (see table 2). The parameters are the mean particle velocities and the standard deviation of the velocities. A Gaussian distribution is used to generate velocities in  $x$  and  $z$  direction with given mean velocity and standard deviation. The mean of the velocity in the  $y$  direction is 0.

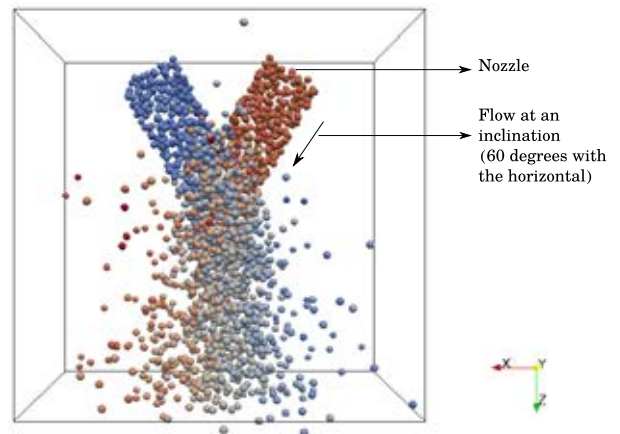


**Figure 3:** Schematic of the system for P1.

The 3D periodic system in P2 consists of an array of regularly spaced bubbles (see figure 4). The spacing between the bubbles is a little larger near the periodic planes than in the bulk of the domain. Therefore, there is a bias in bubble concentration towards the center. The bubbles start from rest and are coupled with an interstitial Newtonian liquid. Properties of air are used for the gas phase and water for the liquid phase.

### Impinging particle streams (P1)

The parameter space is defined in table 2. The DSMC collisions are velocity dependent. Therefore it is necessary to test the model at different velocity regimes. By changing the standard deviation of velocities we change the solid fraction at the impact region. Therefore two values for velocity standard deviations are chosen: one with the same order of magnitude as that of the mean velocity and one which is several orders of magnitude lower than the mean velocity. In

**Table 2:** Parameter space for particle size 2 mm.

Case	Mean velocity [m/s]	Std. deviation [m/s]	Mass flow rate [kg/s]
1	0.2	0.001	0.01
2	0.2	0.15	0.01
3	2.5	0.001	0.1
4	2.5	1.0	0.1

all cases, the total collisions and the collision frequency is measured for the entire domain.

The results are compared with the results obtained from the equivalent deterministic model. These are presented in figures 5 and 6. The initial condition is such that there are no particles in the domain. At  $t = 0$  the particles start flowing through the nozzles. They collide at the impact region and disperse, quickly achieving steady state.

The collision frequency increases exponentially initially and then reaches a steady state. The impact times of both streams match perfectly with the deterministic approach. The collision frequency in case 3 is over-predicted by about 5% compared to the equivalent DPM simulation. Since the DSMC smears out the collision window within its searching scope the size of the stochastic impact region in dense cases is slightly bigger than it actually is. Therefore, it takes into account some extra collisions.

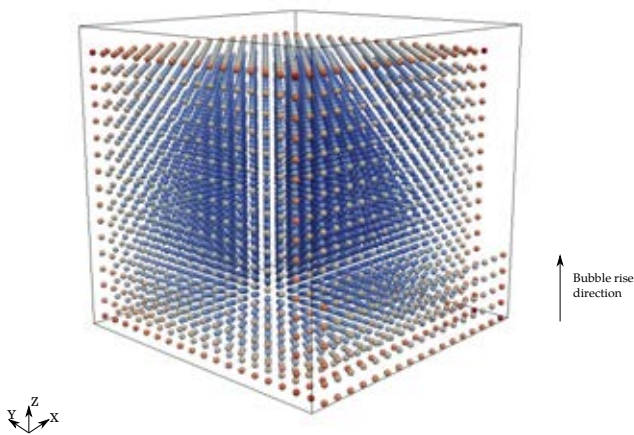


**Figure 4:** Schematic of the system for P2.

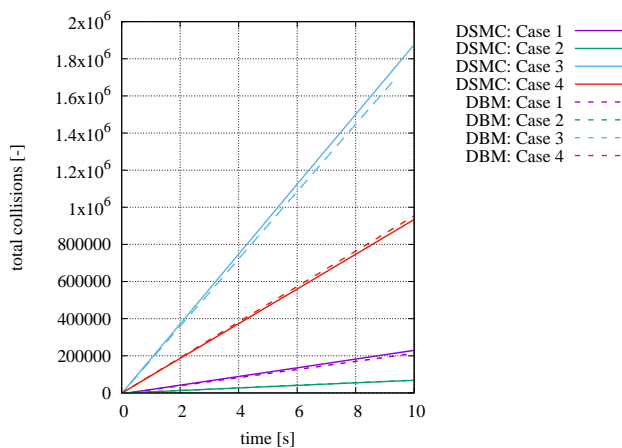


**Figure 5:** Total number of collisions occurring in the domain vs time for different cases, DBM vs DSMC.

### 3D-periodic bubble rise (P2)

The bubble rise starts from rest, with the initial condition as in figure 4. The bubbles rising in the wake of other bubbles experience less drag and tend to collide with the bubbles above them, pushing them forward. The bubbles act as small momentum sources at different locations in the domain and since the source terms are small the system needs some time before it reaches high velocities. This allows us to ob-

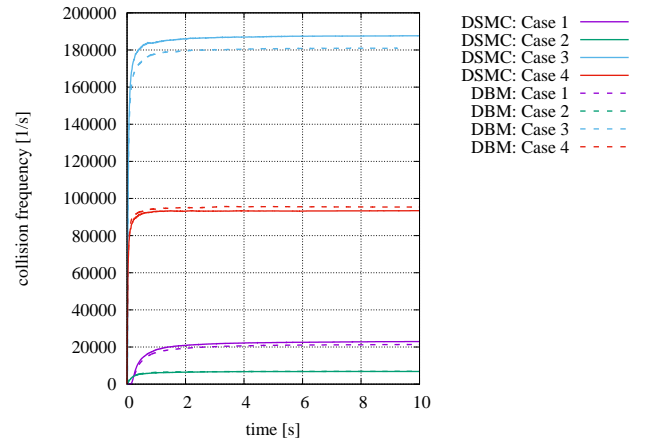


**Figure 6:** Collision frequency vs time for different cases, DBM vs DSMC.

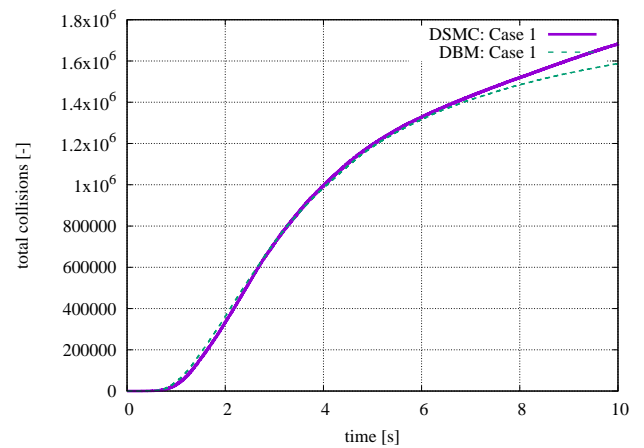


**Figure 7:** Total collisions occurring in domain vs time for different cases, DBM vs DSMC.

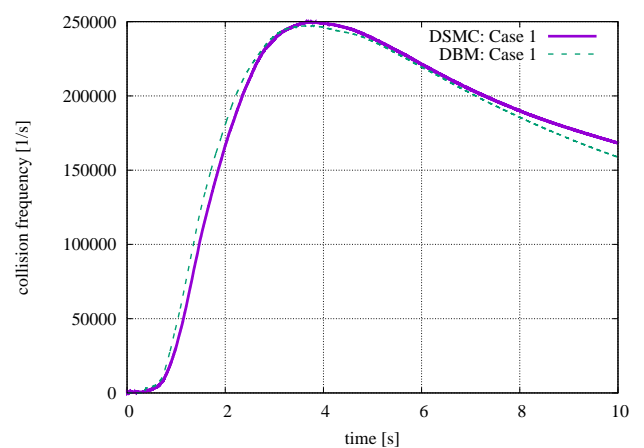


**Figure 8:** Collision frequency vs time for different cases, DBM vs DSMC.

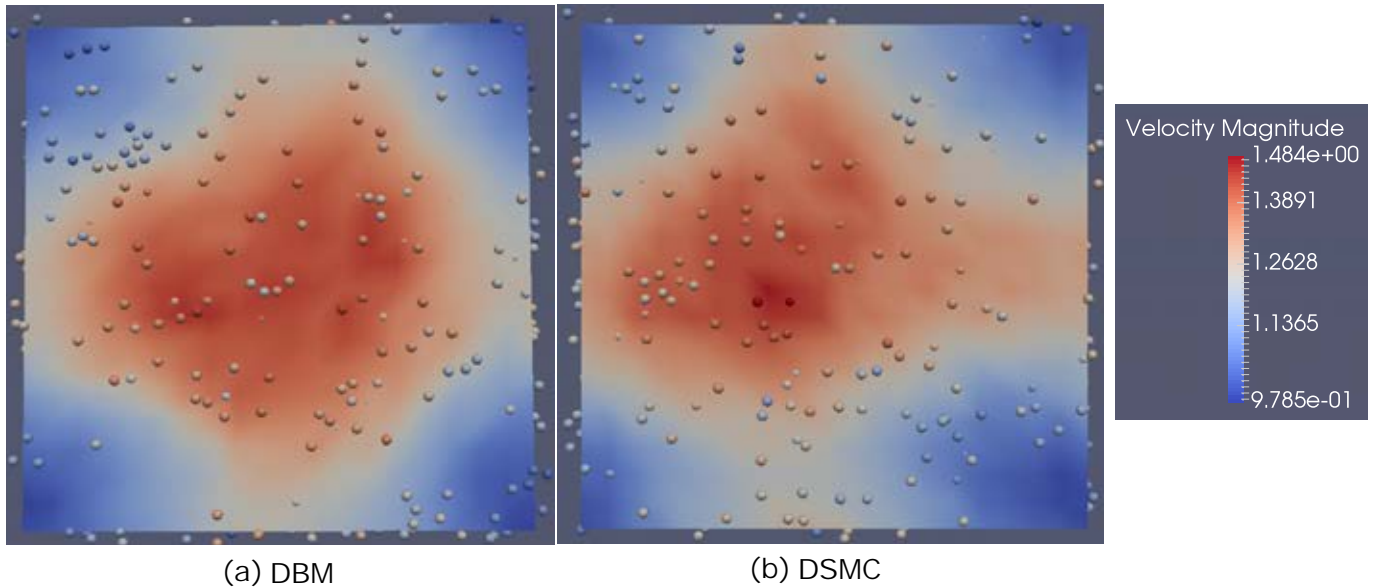


**Figure 9:** Instantaneous velocity profile after  $t = 10s$  in the x-y plane, DBM vs DSMC.

serve how bubbles behave in the bulk with different collision schemes and also the collision frequency at different transitioning velocity regimes which is important for a proper verification of the DSMC.

**Table 3:** Parameter space for 3D periodic bubble rise.

Case	Bubble size [mm]	Number of bubbles in domain [-]	Overall gas fraction ( $\epsilon_b$ ) [-]
1	2	5000	0.02

It can be observed from figures 7 and 8 that the DSMC model captures all the major phases of the bubble rise process. The different phases mainly refer to the changes in the structure of the system based on the bubble positions. The initial cubic arrangement in the system (see figure 4) breaks and homogenizes into a random arrangement as the simulation progresses. Since the bubble velocities change with time, it also has an effect on the collision frequency. The sudden rise in the collision frequency near time  $t = 1s$  is due to cluster formation of bubbles with memory of the initial configuration. Then the bubbles start layering and finally at higher velocities they homogenize, losing the memory of the initial configuration completely. The collision frequency starts decreasing after  $t = 4s$  because of the homogenization and constantly changing velocities due to accelerated liquid motion. The deviation in the collision frequency at higher velocities is due to slight over-compensation of the collisions in DSMC.

A high velocity core is observed in the velocity profile normal to the z-direction due to the biased initial configuration in the DBM (see figure 9). This effect is also well captured by the DSMC. When comparing DBM and DSMC results, the cores seem to be slightly shifted, but it should be emphasized that these are instantaneous snapshots, which are expected to be different for different sequences of bubble collisions (the so-called butterfly effect). When taking time averages the results are almost indistinguishable between the two methods.

The overall gas fraction is quite small. During the clustering the local gas volume fractions have reached up to 20 percent. A similar system with bubble size 4 mm is also simulated. The 4 mm system is much denser, therefore it reaches high velocities much faster than the 2 mm system. The collision frequency and total collisions match similar to the 2 mm case. The local gas fractions have reached values up to 39 percent in the 4 mm case.

## CONCLUSION

The DSMC model is extended to larger dispersed objects in the order of millimeters and also dense systems (up to 30-40 % gas fraction). The model has been verified for the mono-disperse systems and is currently being extended to poly-disperse systems. The next step is to further validate the model with experimental data of real bubble columns and parallelization of the method which is to be implemented for a large scale bubble column.

## ACKNOWLEDGEMENTS

This research has been funded by the NWO TOP grant "First principles based multi-scale modeling of transport in reactive three phase flows" (716.014.001).

## REFERENCES

- BIRD, G.A. (1994). *Molecular Gas Dynamics and Direct Simulation of Gas Flows*.
- BIRD, G. (2007). "Sophisticated DSMC". *DSMC07 meeting*, 1–49. URL <http://www.gab.com.au/dsmc07notes.pdf>.
- CHAUDHARI, R.V. and RAMACHANDRAN, P.A. (1980). "Three phase slurry reactors". *AIChE Journal*, **26(2)**, 177–201. URL <http://dx.doi.org/10.1002/aic.690260202>.
- DARMAHA, D., DEEN, N. and KUIPERS, J. (2006). "Parallelization of an Euler-Lagrange model using mixed domain decomposition and a mirror domain technique: Application to dispersed gas liquid two-phase flow". *Journal of Computational Physics*, **220(1)**, 216–248. URL <http://www.sciencedirect.com/science/article/pii/S0021999106002294>.

- DEEN, N.G., SOLBERG, T. and HJERTAGER, B.H. (2001). "Large eddy simulation of the Gas Liquid flow in a square cross sectioned bubble column". *Chemical Engineering Science*, **56**, 6341–6349.
- DEEN, N., VAN SINT ANNALAND, M. and KUIPERS, J. (2004a). "Multi scale modeling of dispersed gas liquid two-phase flow". *Chemical Engineering Science*, **59(8-9)**, 1853–1861. URL <http://www.sciencedirect.com/science/article/pii/S0009250904000971>.
- DEEN, N., MUDDE, R., KUIPERS, J., ZEHNER, P. and KRAUME, M. (2012). "Bubble Columns". *Ullman's Encyclopedia of Industrial Chemistry*, **6**, 359–379.
- DEEN, N.G., VAN SINT ANNALAND, M. and KUIPERS, J. (2004b). "Multi-scale modeling of dispersed gas–liquid two-phase flow". *Chemical Engineering Science*, **59(8)**, 1853–1861.
- DU, M., ZHAO, C., ZHOU, B., GUO, H. and HAO, Y. (2011). "A modified DSMC method for simulating gas–particle two-phase impinging streams". *Chemical Engineering Science*, **66(20)**, 4922–4931. URL <http://linkinghub.elsevier.com/retrieve/pii/S0009250911004477>.
- HOOMANS, B., KUIPERS, J., BRIELS, W. and VAN SWAAIJ, W. (1996). "Discrete particle simulation of bubble and slug formation in a two-dimensional gas-fluidised bed: a hard-sphere approach". *Chemical Engineering Science*, **51(1)**, 99–118.
- JAIN, D., KUIPERS, J. and DEEN, N.G. (2014). "Numerical study of coalescence and breakup in a bubble column using a hybrid volume of fluid and discrete bubble model approach". *Chemical Engineering Science*, **119**, 134–146. URL <http://www.sciencedirect.com/science/article/pii/S0009250914004448>.
- KITAGAWA, A., MURAI, Y. and YAMAMOTO, F. (2001). "Two-way coupling of Eulerian–Lagrangian model for dispersed multiphase flows using filtering functions". *International Journal of Multiphase Flow*, **27(12)**, 2129–2153.
- LAU, Y., ROGHAI, I., DEEN, N., VAN SINT ANNALAND, M. and KUIPERS, J. (2011). "Numerical investigation of the drag closure for bubbles in bubble swarms". *Chemical Engineering Science*, **66(14)**, 3309–3316.
- LUTIŠAN, J. (1995). "The treatment of molecular collisions in dsmc methods". *Molecular Simulation*, **14(3)**, 189–206.
- PATANKAR, S. (1980). *Numerical heat transfer and fluid flow*. CRC press.
- PAWAR, S., PADDING, J., DEEN, N., JONGSMA, A., INNINGS, F. and KUIPERS, J. (2014). "Lagrangian modelling of dilute granular flow modified stochastic DSMC versus deterministic DPM". *Chemical Engineering Science*, **105**, 132–142. URL <http://linkinghub.elsevier.com/retrieve/pii/S0009250913007331>.
- ROGHAI, I., LAU, Y., DEEN, N., SLAGTER, H., BALTUSSEN, M., ANNALAND, M.V.S. and KUIPERS, J. (2011). "On the drag force of bubbles in bubble swarms at intermediate and high reynolds numbers". *Chemical engineering science*, **66(14)**, 3204–3211.
- TOMIYAMA, A., MATSUOKA, T., FUKUDA, T. and SAKAGUCHI, T. (1995). "A simple numerical method for solving an incompressible two-fluid model in a general curvilinear coordinate system". *Multiphase Flow*, **95**.
- TOMIYAMA, A., TAMAI, H., ZUN, I. and HOSOKAWA, S. (2002). "Transverse migration of single bubbles in simple shear flows". *Chemical Engineering Science*, **57(11)**, 1849–1858.
- UNVERDI, S.O. and TRYGGVASON, G. (1992). "A front-tracking method for viscous, incompressible, multi-fluid flows". *Journal of computational physics*, **100(1)**, 25–37.
- VAN SINT ANNALAND, M., DEEN, N. and KUIPERS, J. (2005). "Numerical simulation of gas bubbles behaviour using a three-dimensional volume of fluid method". *Chemical Engineering Science*, **60(11)**, 2999–3011. URL <http://linkinghub.elsevier.com/retrieve/pii/S0009250905000564>.
- VREMAN, A. (2004). "An eddy-viscosity subgrid-scale model for turbulent shear flow: Algebraic theory and applications". *Physics of Fluids (1994-present)*, **16(10)**, 3670–3681.
- ZHANG, D. (2007). *Eulerian modeling of reactive gas-liquid flow in a bubble column*. phdthesis, University of Twente, Netherlands.



# ON THE SURFACING MECHANISM OF BUBBLE PLUMES FROM SUBSEA GAS RELEASE

Jan Erik OLSEN & Paal SKJETNE

SINTEF Materials and Chemistry, 7465 Trondheim, NORWAY

\* E-mail: jan.e.olsen@sintef.no

## ABSTRACT

A subsea release of gas poses a risk to humans and assets at the surface. Assessing this risk requires knowledge on how much gas reaches the surface and how it is distributed at the surface. This can be estimated by various modelling techniques, e.g. CFD. Reported surfacing flux can then be fed into a CFD model for atmospheric dispersion calculations. This paper briefly discusses how the surface flux can be calculated by CFD, but primarily focuses on the surfacing characteristics and discusses how the surface flux can be reported and issues related to this.

**Keywords:** CFD, bubbly flows, subsea gas release

## NOMENCLATURE

### Greek Symbols

- $\rho$  Mass density, [kg/m<sup>3</sup>].  
 $\sigma$  Standard deviation, [m].

### Latin Symbols

- $a$  Characteristic length, [m].  
 $\mathbf{F}$  Force, [N/m].  
 $\mathbf{g}$  Gravitational acceleration, [m/s<sup>2</sup>].  
 $J$  Gas flux, [kg/m<sup>2</sup>s].  
 $\dot{m}$  mass rate, [kg/s].  
 $r$  radius, [m].  
 $t$  Time, [s].  
 $\mathbf{u}$  Velocity, [m/s].

### Sub/superscripts

- $\theta$  Centre  
 $b$  Bubble.  
 $D$  Drag.  
 $VM$  Virtual mass.  
 $tot$  Total

## INTRODUCTION

A subsea gas release of hydrocarbons such as methane presents a risk of fire and explosions when the gas emerges into the atmosphere. Risk assessments are normally based on modelling of atmospheric dispersion of hazardous gases. Modelling of atmospheric dispersion

relies on a boundary condition which prescribes the flux of gas escaping from the ocean into the atmosphere. This flux will vary in time and position, although many assume it to be constant. In this work we try to characterize a surfacing profile and provide guidelines on how this can be represented as a boundary condition in atmospheric dispersion models.

The ocean surface boundary condition for atmospheric simulations can be provided by a subsea model of the bubble plume. Different modelling concepts are available for this. Traditionally, classical plume integral models, which are computationally fast, have been applied for this (Johansen, 2000; Morton *et al.*, 1956; Zheng & Yapa, 2002). These are based on a series of assumptions and calibration coefficients, but still have proven to reproduce experimental results at least at smaller scales. Transient 3-dimensional CFD modelling of these plumes are computationally expensive due to the large length scales involved, but they rely on fewer assumptions – especially in the surfacing region. The authors of this work have contributed to the development of a CFD model for bubble plumes from subsea gas releases (Cloete *et al.*, 2009; Olsen *et al.*, 2017).

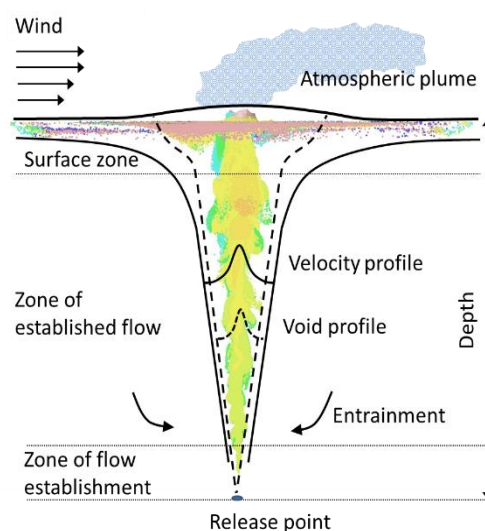
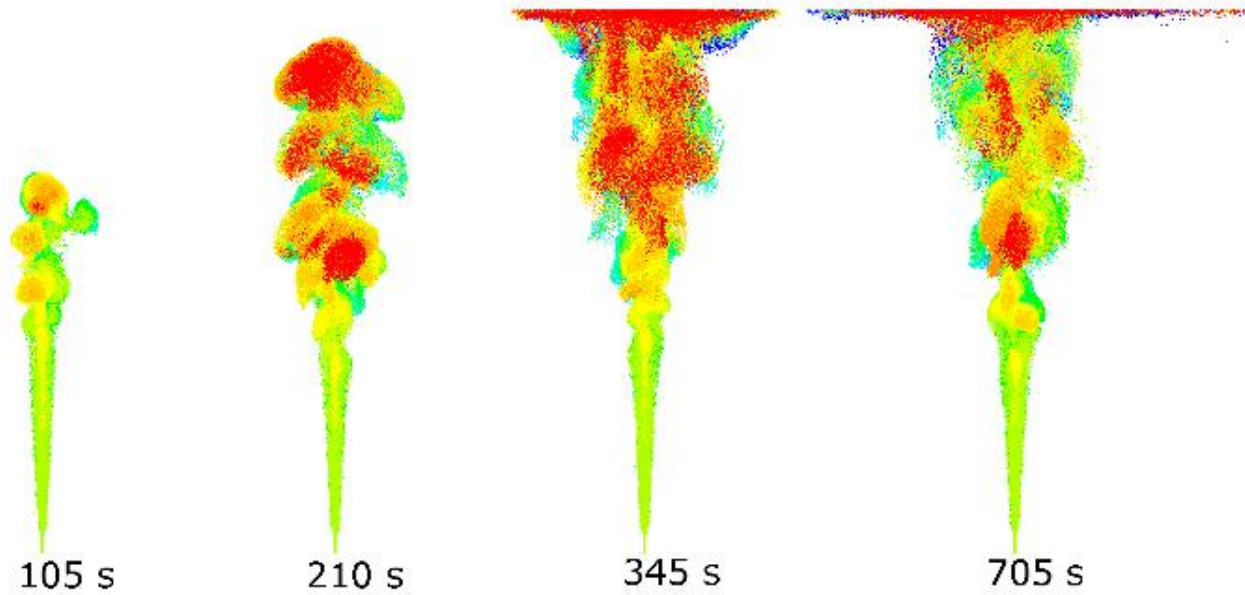


Figure 1: Illustration of subsea gas release.





**Figure 2:** Development of the starting plume from 300 m at a constant rate of 30 kg/s.

Gas released from the ocean floor rises as bubbles towards the surface. If the release rate is sufficient, the buoyancy of the bubbles will cause the water to accelerate and travel upwards with bubbles. At the surface the bubbles enter the atmosphere whereas the water is forced outwards in a radial flow. The CFD model quantifies where and when bubbles penetrate the surface and the strength of the radial outflow.

Here we apply the CFD model for a selected release scenario and analyse the surfacing characteristics. The resulting surfacing fluxes and radial outflow velocity are compared to mathematical profiles to verify if some of these are representative for the *true* surfacing profiles.

## MODEL DESCRIPTION

The CFD model developed to study large scale bubble plumes from subsea gas release is based on an Eulerian-Lagrangian modelling concept. The bubbles are treated as Lagrangian particles which move according to Newton's second law. The background fluid, i.e. the ocean, is governed by the Navier-Stokes equation in an Eulerian frame of reference. The interface between the ocean and the atmosphere is tracked by the *geo-reconstruct* algorithm. The details are provided in earlier publications (Olsen & Skjetne, 2016; Olsen *et al.*, 2017).

In a short summary it is worth mentioning that the model moves bubbles according to Newton's second law

$$\frac{d\mathbf{u}_b}{dt} = \frac{\mathbf{g}(\rho_b - \rho)}{\rho_b} + \mathbf{F}_D + \mathbf{F}_{VM} \quad (1)$$

where the forces on the right hand side are buoyancy, drag and virtual mass. The background fluids (ocean and atmosphere) are mathematically described by the principles of conservation of mass, momentum and energy through the continuity-, momentum- and heat-equation. The bubble motion and the flow of the background fluids are coupled through the drag term. Turbulence is modelled with a VLES model where

turbulent structures larger than the grid size are captured by the momentum equations and the subgrid turbulence is modelled by the k- $\epsilon$  model.

A model for the local mean bubble diameter is implemented accounting for break-up, coalescence, gas expansion and gas dissolution. Gas expansion is caused by the decrease in pressure and gas density as the bubbles rise upwards. Gas dissolution is driven by the difference in gas solubility and ocean saturation.

The model has been validated against meso scale experiments at 7, 30 and 50 meters depth and large scale data from 140 meters depth. The model is consistent with observations.

## RESULTS

The modelling concept mentioned above was applied to a release of 30 kg/s of methane from a depth of 300 meters with an ocean temperature at 10°C and ocean salinity of 35 psu. The simulation results have been analysed to shed light on the surfacing mechanism and to discuss how these results can be reported as a boundary condition to atmospheric dispersion modelling.

The resulting plume from the release is illustrated in Figure 2 as predicted by the CFD simulation. Turbulent eddies with gas bubbles surface after roughly 4 minutes. The eddies cause a fluctuating surface rate and flux which would not have been captured by a RANS turbulence model. Observations of ocean bubble plumes confirms the fluctuating behaviour qualitatively. The surfacing rate is plotted in Figure 3. The surfacing rate (kg/s) is the area integral of the surface flux (kg/m<sup>2</sup>s). It averages at 1.6 kg/s indicating that gas dissolution is significant since only 5% of the released gas reaches the surface. The fluctuations are also significant.

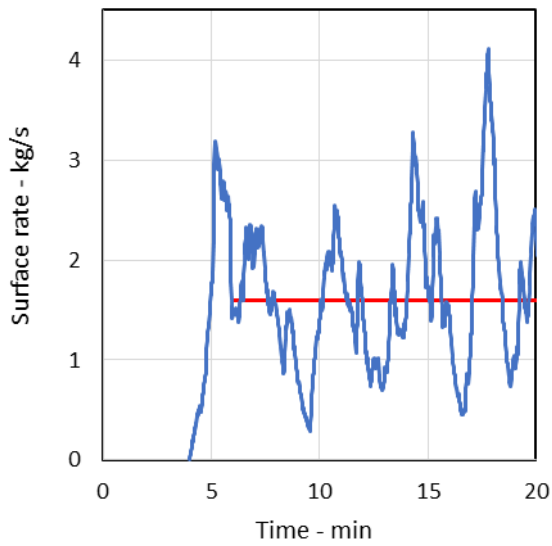


**Figure 3:** Surfacing rate as function of time, red line indicates average surfacing rate.

If we focus on the surfacing flux which varies in both time and space, we see that the fluctuations are even more significant. The resulting averaged surface flux using different averaging intervals are depicted in Figure 5 (next page). The two top plots are both with an averaging interval of 1 second, but from two different times (650 and 750 secs after release). There is a big difference in the peak flux and total surface rate between these two periods.

The flux is quite noisy. As the averaging interval increases, the flux distribution becomes more smooth and starts looking like a Gaussian distribution. Note that with an averaging period of 800 seconds the peak is less than ¼ of the maximum peaks in the fastest fluctuations. It is the long-averaged surface flux fitted to a Gaussian profile which is normally applied as a boundary condition in atmospheric dispersion modelling. This practice stems from modelling experiences with integral models and CFD models with RANS turbulence models. These models do not capture the fluctuations seen in Figures 3 and 5. Thus it can be questioned whether the conveniently long-averaged Gaussian profile is a proper boundary condition.

If we assume that a Gaussian profile is sufficiently representative of the surfacing flux, there are still some issues related on how to report the coefficients in the Gaussian expression. The Gaussian flux profile is given by

$$J = J_0 e^{-r^2/2\sigma^2} \quad (2)$$

where  $J_0$  is the centre flux (or peak flux) and  $\sigma$  is the standard deviation. If the long-averaged surface flux is truly Gaussian, a perfect fit between the surface flux from

the CFD simulation and a Gaussian profile exists. This is unfortunately not true.

All gas surfacing within the radius defined by the standard deviation amount to 39% of all gas surfacing in total (see Appendix). By analysing the surface flux from the CFD simulation, the radius within which 39% of the gas surfaces can be extracted and reported as a standard deviation. Applying the principle that the Gaussian profile shall fulfil mass conservation, the centre flux is obtained from

$$\dot{m}_{tot} = 2\pi J_0 \sigma^2 \quad (3)$$

From this procedure we get  $J_0=0.165 \text{ g/m}^2\text{s}$  and  $\sigma=28 \text{ m}$ . Alternatively we can quantify the coefficients by matching the Gaussian centre flux with the true peak flux and finding the standard deviation from mass conservation with Eq.(3). From this procedure we get  $J_0=0.39 \text{ g/m}^2\text{s}$  and  $\sigma=18 \text{ m}$ . The true long-averaged profile and the Gaussian curve fits are plotted below in Figure 4.

The two procedures for obtaining the Gaussian coefficients obviously produces two quite different sets of coefficients. From this we can conclude that the profile is not truly Gaussian. For a true Gaussian, both procedures would have resulted in the same set of coefficients. This gives rise to an important question; which procedure provides the most representative Gaussian profile for the long-averaged surface flux? Visually it is probably the procedure based on the centre flux which seems superior (see Figure 5). However, it is also fair to question whether a Gaussian profile is truly representative

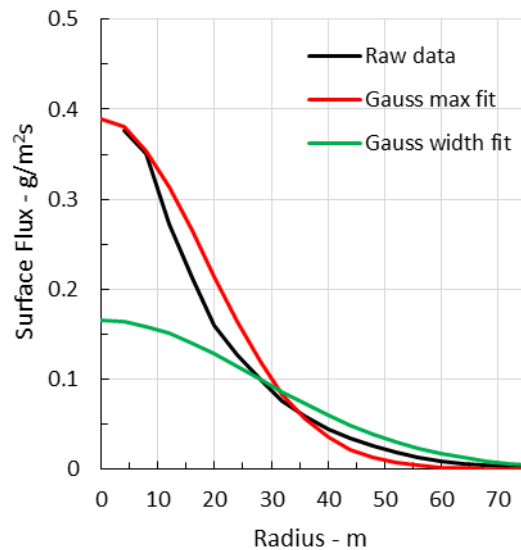
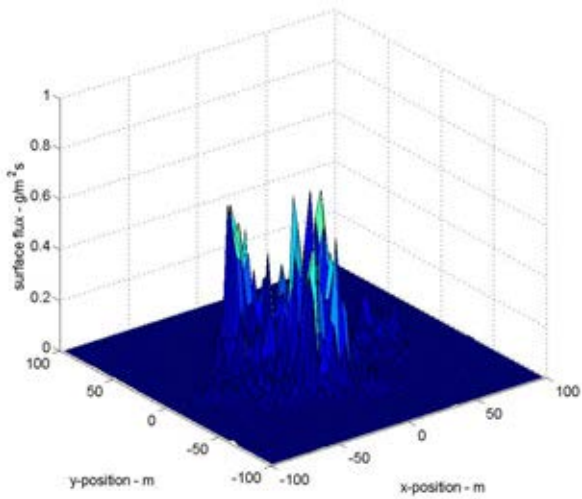
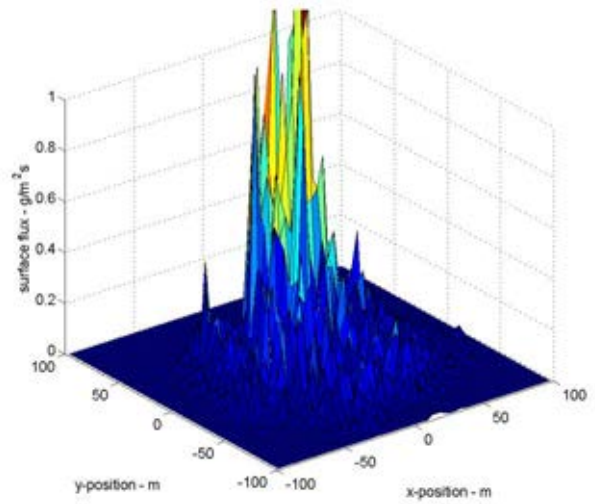


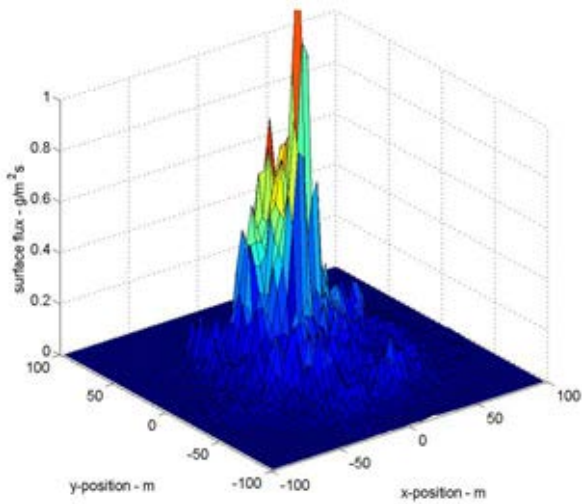
**Figure 4:** Surface flux



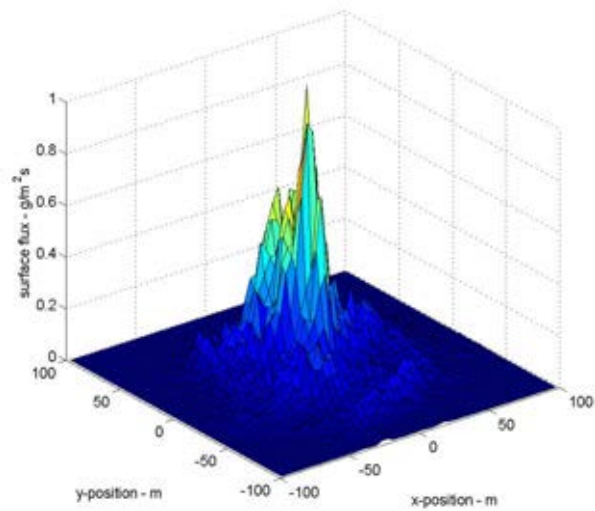
1 second averaging (at 750 secs)



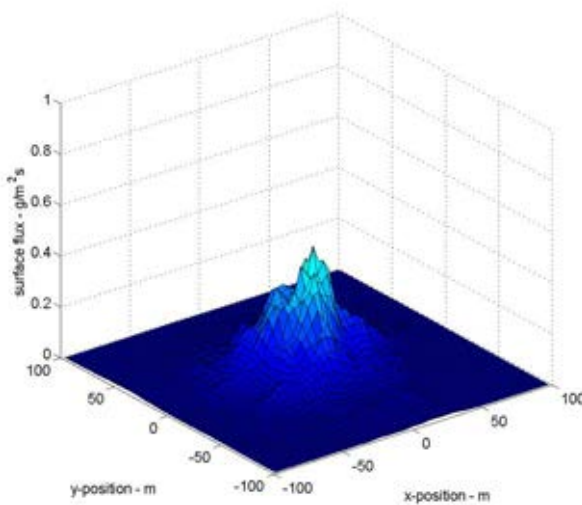
1 second averaging (at 650 secs)



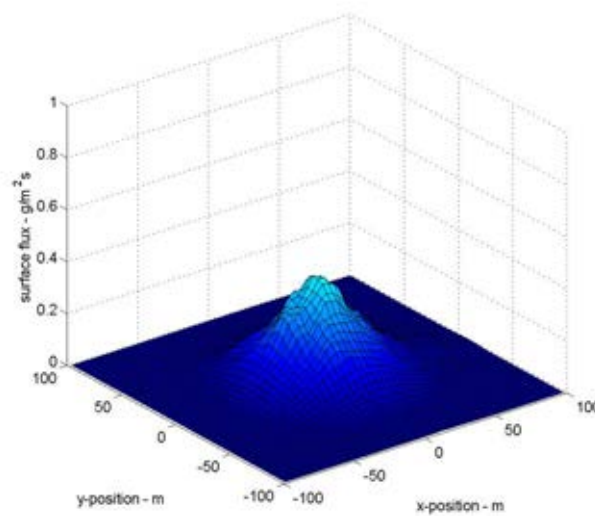
5 seconds averaging



10 seconds averaging



100 seconds averaging



800 seconds averaging

**Figure 5:** Surface flux for various averaging intervals. All averaging starts at 650 secs after start of release except top left example.

## CONCLUSIONS

A CFD model with a transient VLES model representing turbulence has been applied to study the surfacing mechanism of an ocean plume caused by a subsea gas release. The resulting surface rate and surface flux is clearly fluctuating. A surface flux profile based on time-averaging over 800 seconds has a smooth shape which can be fitted to a Gaussian profile, although a perfect fit cannot be achieved. This indicates that the surface flux is not truly Gaussian even if similarities exist. Two different procedures for quantifying the Gaussian profile yields two different sets of Gaussian coefficients.

A consequence of these findings is to further study which profile best matches the true surface flux with respect to a risk assessment (e.g. conservatism). Sensitivity studies with atmospheric dispersion modelling could reveal the significance on how to report the surfacing profile. This includes assessments on both the fluctuating nature of the surfacing mechanism and the influence of how the time averaged profile is represented.

## REFERENCES

- CLOETE, S., OLSEN, J.E., & SKJETNE, P. (2009). "CFD modeling of plume and free surface behavior resulting from a sub-sea gas release". *Applied Ocean Research*, **31**(3), 220-225.
- JOHANSEN, O. (2000). "DeepBlow - a Lagrangian plume model for deep water blowouts". *Spill Science & Technology Bulletin*, **6**(2), 103-111.
- MORTON, B.R., TAYLOR, G.I., & TURNER, J.S. (1956). "Turbulent gravitational convection from maintained and instantaneous sources". *Proc.Roy.Soc.A*, **234**, 171-178.
- OLSEN, J.E., & SKJETNE, P. (2016). "Modelling of underwater bubble plumes and gas dissolution with an Eulerian-Lagrangian CFD model". *Applied Ocean Research*, **59**, 193-200.
- OLSEN, J.E., SKJETNE, P., & JOHANSEN, S.T. (2017). "VLES turbulence model for an Eulerian-Lagrangian modeling concept for bubble plumes". *Applied Mathematical Modelling*, **000 Online**(1-11).
- ZHENG, L., & YAPA, P.D. (2002). "Modeling gas dissolution in deepwater oil/gas spills". *Journal of Marine Systems*, **31**, 299-309.

## APPENDIX A

A Gaussian flux profile is given by

$$J = J_0 e^{-r^2/2\sigma^2} \quad (4)$$

The total gas rate through the entire surface is given by

$$\begin{aligned} \dot{m}_{\text{tot}} &= 2\pi \int_0^{\infty} J_0 e^{-\frac{r^2}{2\sigma^2}} r \, dr \\ &= 2\pi J_0 \left[ -\sigma^2 e^{-\frac{r^2}{2\sigma^2}} \right]_0^{\infty} = 2\pi J_0 \sigma^2 \end{aligned} \quad (5)$$

The total gas rate through a surface limited by an outer radius  $R$ , is

$$\begin{aligned} \dot{m} &= 2\pi \int_0^R J_0 e^{-\frac{r^2}{2\sigma^2}} r \, dr \\ &= 2\pi J_0 \sigma^2 \left( 1 - e^{-\frac{R^2}{2\sigma^2}} \right) \end{aligned} \quad (6)$$

The ratio of mass surfacing inside a radius  $R$  and the total mass is thus

$$\frac{\dot{m}}{\dot{m}_{\text{tot}}} = 1 - e^{-\frac{R^2}{2\sigma^2}} \quad (7)$$

The relative amount of gas surfacing within the radius defined by the standard deviation,  $R = \sigma$ , is thus

$$\frac{\dot{m}_{\sigma}}{\dot{m}_{\text{tot}}} = 1 - e^{-\frac{1}{2}} = 0.39 \quad (8)$$

This means that 39% of all gas surfaces within a radius equal to the standard deviation, and subsequently 86% within 2 standard deviations and 99% within 3 standard deviations. Bear in mind that this is only true if the surfacing profile is perfectly described by a Gaussian profile.

This might come as a surprise since some might believe that the amount represented by the distribution within the extent of the standard deviation is 68%. This number comes from statistics where they perform a straight integration of the profile without multiplying with  $r$ .

$$\frac{\int_0^{\sigma} e^{-\frac{r^2}{2\sigma^2}} \, dr}{\int_0^{\infty} e^{-\frac{r^2}{2\sigma^2}} \, dr} = 0.68 \quad (9)$$

This is in principle a 1D version of the above derivation which holds for a 2D case.



# BUBBLE GENERATED TURBULENCE IN TWO FLUID SIMULATION OF BUBBLY FLOW

**M. Philip SCHWARZ<sup>1\*</sup>, Yuqing Feng<sup>1</sup>, Peter J. Witt<sup>1</sup>**

<sup>1</sup> CSIRO Minerals Resources, Clayton, AUSTRALIA

\* E-mail: phil.schwarz@csiro.au

## ABSTRACT

Bubbly flows are central to many processes in the minerals extraction and metal production industries, mainly because they enhance heat and mass transfer rates. These transfer rates depend on the turbulence level in the multiphase flow. Bubbles rising in a liquid give rise to an additional component of turbulence in the continuous phase, known as bubble-induced turbulence. Various models have been proposed in the literature to account for this mechanism in two-fluid Reynolds-averaged (RANS) simulations of bubbly flow, but there is considerable uncertainty about the form of terms that should be added to account for the effect, and even the flow physics underlying the phenomenon is poorly understood. Simulations are carried out of flow around a simplified bubble arrangement in order to clarify this flow physics, to allow a consistent definition of bubble-induced turbulence, and to point the way to a reliable determination of the source terms. It is argued that a component of the fluctuations due to flow around bubbles should not be considered to be turbulence since the energy of these fluctuations is actually recoverable. This fact seriously complicates efforts to obtain bubble-induced turbulence from experimental velocity measurements or direct numerical simulations. Simulations of flow around a bubble using the SST turbulence model allow the prediction of the source of actual bubble-induced turbulence for a single isolated rather than the pseudo-turbulence related to bubble motion. The source of actual turbulence for an isolated bubble of diameter 5 mm with a mobile interface is predicted to be very small, while for an immobile interface, a finite source is distributed in the wake of the bubble. The source of “bubble-induced” turbulence for a bubble swarm is a more complex issue, but the present simulations can give insights and point the way forward to a more complete formulation.

**Keywords:** Multiphase flow, bubble induced turbulence, two fluid simulation, turbulence kinetic energy, CFD.

## NOMENCLATURE

### *Greek Symbols*

- $\alpha$  Volume fraction, [-].
- $\varepsilon$  Dissipation rate of turbulence energy, [ $\text{m}^2/\text{s}^3$ ].
- $\kappa$  Empirical constant, [-].
- $\nu$  Kinematic viscosity, [ $\text{kg}/\text{m}\cdot\text{s}$ ].
- $\rho$  Mass density, [ $\text{kg}/\text{m}^3$ ].
- $\mu$  Dynamic viscosity, [ $\text{kg}/\text{m}\cdot\text{s}$ ].

$\tau$  Total shear stress, [ $\text{kg}/\text{m}\cdot\text{s}^2$ ].

### *Latin Symbols*

- $b_2$  Coefficient, [-].
- $c_2$  Coefficient, [-].
- $C_d$  Drag coefficient, [-].
- $C_{vm}$  Virtual mass coefficient, [-].
- $d_b$  Bubble diameter, [m].
- $k$  Kinetic energy of turbulence, [ $\text{m}^2/\text{s}^2$ ].
- $p$  Pressure, [Pa].
- $\mathbf{T}$  Tensor stress, [ $\text{kg}/\text{m}\cdot\text{s}^2$ ].
- $U_b$  Bubble slip velocity, [m/s].
- $U$  Velocity, [m/s].
- $y$  Coordinate perpendicular to velocity, [m].

### *Sub/superscripts*

- BI Bubble induced.
- BIT Bubble induced turbulence.
- $g$  Gas.
- $l$  Liquid.
- $t$  Turbulent.

## INTRODUCTION

Many processes in the chemicals and mineral processing industries involve injection of bubbles into a liquid, either as a direct reagent or to induce flow and mixing. Examples include bubble columns, three-phase fluidized beds, mineral flotation cells, some intensive smelting processes, as well as numerous specialized processes such as ladle refining, aluminium smelting, and so on. Computational Fluid Dynamics (CFD) modelling is a powerful tool to assist design and optimisation of such processes, but the complexity of the multi-scale flow involved means that approximations involving ‘modelling’ of micro- and meso-scale phenomena are required in order to simulate large-scale industrial systems (Schwarz and Feng, 2015).

In large-scale chemical and mineral reactors of the sort mentioned above, heat and mass transfer phenomena are usually central to the process operation. Bubbles can play a critical role here, both in participating directly through chemical reactions, and also by stirring the liquid. For example, in bubble columns and mineral flotation columns, the buoyancy of bubbles results in large-scale mixing within the reactor. At the same time, bubbles cause mixing at a wide range of length scales in such reactors, leading to local enhancement of heat and mass transfer rates, as well as overall mixing. So the ability to design and control the bubble flow and the associated transfer phenomena is crucial to the successful operation of such a process. This is the reason there has been an increasing trend of applying detailed multi-dimensional CFD modelling of the two-phase flow as a design tool.

The typical number of bubbles in large-scale reactors such as bubble columns and flotation cells is huge, so that direct simulation of the full detail of all bubble–liquid interactions is still not computationally feasible. For this reason, techniques have been developed in which the Navier-Stokes equations are averaged over fluctuations associated with individual bubbles. In this way, separate averaged equations are obtained for the liquid and gas phases, and for this reason, the approach is known as the multi-fluid model, (see, for example, Spalding, 1981). The gas and liquid velocity equations are coupled through interaction terms, that can in principle be determined as part of the averaging process. In practice, the flow interactions are usually so complex that theory and empiricism must be used to define and evaluate the interaction terms. The primary interaction term is of course drag, but there are several others such as the so-called lift force.

Bubbly flow in large-scale reactors is almost invariably turbulent. Because of the large scale and physico-chemical complexity, industrial simulations still treat turbulence in the flow using Reynolds averaging (the so-called RANS approach), and so in this case averaging is simultaneously carried out over fluctuations due to turbulence and over those due to individual bubble motion. Even in Large Eddy Simulations (LES), the very large scale of the reactor relative to bubble size means that sub-grid scale averaging occurs over both turbulence and bubble-related fluctuations. These fluctuations are coupled, in that bubble motion generates turbulence directly at a scale comparable to the bubble size, that is, so-called bubble-induced turbulence.

At this point it is important to distinguish between such bubble-induced turbulence and turbulence generated by decay of large-scale mean flows driven by bubbles. As an example of the latter, bubbles concentrated into a bubble plume can generate very strong upward flow, and the resulting shear generates turbulence through the conventional instability mechanism.

It is also important to distinguish bubble-generated turbulence from turbulence modulation caused by particles; this latter effect is generally understood to mean the damping of turbulence that arises from drag between particles by turbulence eddies. By contrast,

bubble-generated turbulence arises from the disturbance to liquid streamlines resulting from the movement of liquid around bubbles. Crowe (2000) presented data that indicates that turbulence enhancement occurs for large particles/bubbles, whereas damping occurs for small particles/bubbles. This paper deals with the enhancement effect, and focuses on bubbles, but most of the results would also be applicable to large particles.

Bubble-generated turbulence has been the subject of several theoretical studies, but no generally accepted formulation suitable for the multi-fluid model has yet been developed. Furthermore, experimental studies of the phenomena are few because of the difficulty of isolating the effect from the multitude of other related ones. The approach taken is usually a variant of that pioneered by Johansen and Boysen (1988), in which a theoretical expression for energy generation is modified by means of a multiplicative coefficient, which is determined by comparison of simulation results with experiment.

The theoretical approaches that have been used to account for bubble induced turbulence are reviewed briefly in the next section. The benefits and drawbacks of each approach will be discussed. Then, a simple CFD simulation for flow around a single bubble is discussed, in order to better understand the assumptions behind these theoretical approaches.

## THEORETICAL APPROACHES TO BUBBLE-INDUCED TURBULENCE

### Bubble-induced eddy viscosity

The first estimate of the shear stress associated with bubble motion was by Sato and Sekoguchi (1975), who assumed that the total shear stress,  $\tau$ , could be considered to be the sum of three components: that due to liquid viscosity, that due to momentum exchange resulting from conventional turbulence, and that due to momentum exchange resulting from bubble agitation:

$$\tau = \rho_l \alpha_g (\nu + \nu_t + \nu_{BIT}) \frac{d\bar{u}}{dy} \quad (1)$$

where  $\rho_l$  is the liquid density,  $\alpha_g$  is void fraction,  $\nu$  is kinematic viscosity, and  $\nu_t$  is turbulent eddy viscosity. A two-dimensional configuration was analyzed in which  $\bar{u}$  is the mean velocity perpendicular to the  $y$  direction. To evaluate the “bubble induced eddy viscosity”,  $\nu_{BIT}$ , they considered the liquid velocity fluctuations associated with flow past a bubble (assuming two-dimensional inviscid flow), as illustrated in Fig. 1. The fluctuations are the difference between velocities indicated in Fig. 1, and velocities in the flow without a bubble (or cylinder in 2D). They then averaged these fluctuations over a volume containing many such bubbles, to obtain:

$$\nu_{BIT} = \kappa \alpha d_b U_b, \quad (2)$$

where  $\kappa$  is an empirical constant,  $\alpha$  is gas void fraction, and  $d_b$  and  $U_b$  are average values of bubble diameter and relative velocity (or bubble slip velocity). Sato *et al.* (1981) recommend a value of 0.6 for  $\kappa$  based on

comparison with experimental data. They also point out that Eqn (1) is just a Prandtl mixing length expression for eddy viscosity in a wake behind a solid body based on a mixing length and velocity deficit.

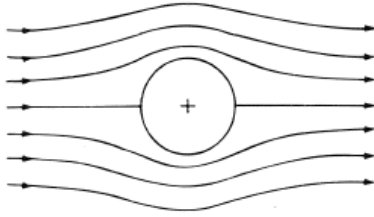


Figure 1: Streamlines for inviscid flow over a cylinder.

### Turbulent stress due to bubble disturbances

Arnold *et al* (1989) carried out a similar but more rigorous analysis for the turbulent stresses generated by bubble-induced velocity fluctuations. Their analysis was also based on inviscid flow, though in three dimensions (i.e. around spheres). Because they take a more rigorous approach to the averaging procedure, they obtain a much more complex expression for the tensor stress,  $\mathbf{T}$ , due to bubble-related fluctuations:

$$\mathbf{T} = a_2 \mathbf{I} + b_2 (\mathbf{U}_g - \mathbf{U}_l)(\mathbf{U}_g - \mathbf{U}_l) + \mathbf{T}^S \quad (3)$$

plus terms in the gradient of the slip velocity, which can be neglected if the bubble size is locally uniform, as is usually the case. Here  $\mathbf{I}$  is the identity tensor, and  $\mathbf{U}_g$  and  $\mathbf{U}_l$  are averaged gas and liquid phase velocities respectively. The coefficients were found to be:

$$a_2 = \frac{3}{20} \rho_l \alpha_g |\mathbf{U}_g - \mathbf{U}_l|^2 \quad (4)$$

$$b_2 = \frac{1}{20} \rho_l \alpha_g \quad (5)$$

The last term in Eqn. (3),  $\mathbf{T}^S$ , is a second order function of gradients of mean flow velocity, and is proportional to  $agdb^2$ . The authors argue that this implies that the effective eddy viscosity is also predicted to be proportional to  $agdb^2$ , and to mean velocity gradient. For Stokes flow,  $U_b \propto db$ , so it could be argued that the eddy viscosity should be of a similar form to the Sato and Sekoguchi [3] expression, eq.(1), except for the presence of the factor dependent on velocity gradient.

It is important to understand that Sato and Sekoguchi (1975) and Arnold *et al* (1989) (as well as various authors who have followed this approach such as Nigmatulin (1979)) consider the velocity deviations associated with the flow of liquid around the sphere to be turbulence. Now the assumption of irrotational flow around a sphere, as used by these authors implies no dissipation. For a single isolated bubble, the upstream and downstream flows are (mirror image) symmetrical in this model, so that while the liquid is associated with velocity deviations as it passes the sphere (or as a bubble moves upward through liquid), the energy associated with these deviations is completely recoverable. Consequently, these velocity deviations should not be considered to be turbulence in the true sense. A rising bubble “carries” these velocity deviations with it as it rises, so there is no

source of turbulence energy and no dissipation. If these deviations are indeed considered to be a form of pseudo “turbulence energy”, the value of this energy is constant: there is no net source or sink as bubbles rise.

If the flow is strictly inviscid, then there can be no “eddy viscosity” associated with the bubble-generated velocity deviations for a single isolated bubble. As a bubble rises, liquid elements will oscillate as a result of these deviations, but will then return to the original locations – there will be no diffusion of fluid concentrations or momentum, and hence zero effective eddy viscosity.

We argue here that even in less ideal flows where the inviscid assumption is relaxed, a component of the fluctuation energy associated with bubble rise will be recoverable in the sense of inviscid flow, and should not be counted as bubble-induced turbulence. We use the term “recoverable energy” to mean the pseudo-turbulence component of the fluctuation energy that is not dissipated.

Thus the fluctuations associated with bubble motion in a real liquid (with viscosity) can be considered to consist of two components. The first is the deformational motion of streamlines around the bubble that can be predicted for inviscid flow similar to that shown in Fig. 1. As mentioned above, the kinetic energy of this component is constant, and there is no source or sink. The second component is the motion within the wake. Unlike the first component these fluctuations are indeed dissipated, and so are likely to resemble turbulence.

Since the turbulence kinetic energy is  $k = \frac{1}{2} \overline{u'_i u'_i}$ , where  $u'_i$  is the  $i$ -th component of liquid phase fluctuation velocity and the summation convention applies, the Arnold *et al* (1989) expression, eqs.(4) and (5), implies that the kinetic energy of the disturbed motion around bubbles (the pseudo-turbulence) is:

$$k_{BI} = \frac{1}{4} \alpha_g |\mathbf{U}_g - \mathbf{U}_l|^2 \quad (6)$$

Lopez de Bertodano *et al* (1994) argued that since Eqn (6) was based on inviscid flow for which the virtual mass coefficient,  $C_{vm}$ , is  $\frac{1}{2}$ , and the turbulence energy relates to the volume in the wake, the equation can be written more generally as:

$$k_{BI} = \frac{1}{2} \alpha_g C_{vm} |\mathbf{U}_g - \mathbf{U}_l|^2 \quad (7)$$

They have used a CFD model incorporating the Sato *et al* (1981) bubble-induced eddy viscosity and Eqn (7) to simulate bubbly pipe flow, and have then compared the results with detailed measurements of velocity, turbulence and void fraction. Note that Eqn (7) was not used in determining eddy viscosity, but was needed to determine the total mean fluctuation in velocity (or equivalently the components of normal stress) for comparison with data. The best agreement is generally found for  $C_{vm} = 2$ . This value is consistent with theoretical calculations by Lance and Bataille (1991) for oblate bubbles moving in helical paths, which yield values between 1.2 and 3.4.



Extending the argument given by Lopez de Bertodano *et al* (1994), the turbulence energy in the wake component could be obtained by subtracting the pseudo-turbulence component from total energy as estimated from the virtual mass, in other words:

$$k_{\text{BI}} = \frac{1}{2} \alpha_g (C_{\text{vm}} - 0.5) |\mathbf{U}_g - \mathbf{U}_l|^2. \quad (8)$$

They also argue that their comparisons between CFD simulation and experiment suggests that  $C_{\text{vm}} = 2$  for bubbly flow in a pipe.

Lance and Bataille (1991) use a different argument. They roughly estimate the wake contribution to the kinetic energy from the dissipation rate, which is a fraction of the work performed by the drag force experienced by the bubbles,

$$\varepsilon_w \sim \alpha_g C_d |\mathbf{U}_g - \mathbf{U}_l|^3 / D. \quad (9)$$

where  $C_d$  is the drag coefficient and  $D$  is the bubble diameter, where the tilde here has the meaning approximately equal to within a factor of order unity. They then assume that the velocity fluctuations associated with this dissipation have a length scale  $\ell_w$ , then the r.m.s. value of the fluctuations satisfies

$$u'_w{}^3 / \ell_w \sim \alpha_g C_d |\mathbf{U}_g - \mathbf{U}_l|^3 / D. \quad (10)$$

Lance and Bataille (1991) argue that Eqn (10) implies that the energy associated with turbulence production in the wakes should vary as  $\alpha_g{}^{2/3}$ . This is different from the normal linear assumption.

Lance and Bataille (1991) appear to have understood the point we make that a fraction of the fluctuation energy associated with bubble rise is recoverable and does not contribute to real turbulence. They mention both “inviscid pseudo-turbulent contributions” and “the turbulent fluctuations produced by the wakes of the bubbles”, but the descriptions are not precise, and in later experimental work, the distinction is lost and the term “pseudo-turbulence” has become synonymous with bubble-induced turbulence (Wijngaarden, 1998; Hosokawa and Tomiyama, 2013).

The experimental LDA data collected by Lance and Bataille (1991) imply that the turbulent fluctuations produced by the wakes of the bubbles contribute only a small part of the overall fluctuating kinetic energy, with the vast majority contributed by the pseudo-turbulence. This of course means that it is extremely difficult (if not impossible) to determine an expression for bubble-induced turbulence from such experimental measurements. For the same reason, it would difficult to determine an expression for bubble-induced turbulence from direct numerical simulation of a bubbly flow. One possible alternative approach would be to numerically study the situation of flow around a single bubble, where it may be easier to separate the contributions of pseudo-turbulence and wake turbulence. This is the approach followed below.

## Generation rate of turbulence energy

Since a two-equation RANS model such as  $k$ - $\varepsilon$  is often used in industrial CFD modelling, it is natural to seek to incorporate bubble-induced turbulence into this formalism. The approach has been to determine source terms for the  $k$  and  $\varepsilon$  equations to characterize the bubble effect.

The expression usually used for the rate of generation of turbulence energy originates from analysis by Besnard and Harlow (1988) and Kataoka and Serizawa (1989) of the averaged two-phase Navier-Stokes equations. They identified the fluctuations generated by the dispersed phase as turbulence. The source term for this turbulence was shown to be, under certain assumptions, to the product difference between the mean velocities of the two phases and the drag force:

$$S_k = \mathbf{F}_D \bullet (\mathbf{U}_g - \mathbf{U}_l) \quad (11)$$

As argued above, the velocity fluctuations generated by bubbles include both pseudo-turbulence as well as true turbulence, so the suitability of this formula is suspect. Nonetheless, many researchers have used it as the source term describing bubble-induced turbulence in RANS simulations of bubbly flow, though generally with an empirically determined multiplying factor (e.g., Rzehak and Krepper, 2013; Feng *et al.*, 2015). Unfortunately, the value of the empirical factor is found to vary over a very wide range (two orders of magnitude) depending on the data used, and this limits the predictive value of the formula (Schwarz, 2015).

As discussed by Schwarz (2015) and Rzehak and Krepper (2013), the source term for  $\varepsilon$  is even more uncertain than that for  $k$ .

## CFD MODEL OF FLOW PAST A SINGLE BUBBLE

### CFD model formulation

A CFD model of liquid flow past a single bubble is developed and analysed to determine the strength of wake turbulence. The model is transformed to a frame of reference in which the bubble is stationary: this should be a reliable approach except in cases where a substantial spiralling motion occurs as the bubble rises.

The bubble is taken to be spherical, as would be the case for high surface tension. The simulations for spherical bubbles are useful as a base case, with which turbulence generation by deformed bubbles can later be compared.

Bubble diameter is taken to be 5 mm, and the rise velocity of the bubble is 0.2 m/s. The density and viscosity of the liquid are taken to be those of water. Simulations are run for both mobile and immobile bubble interface, by applying respectively free-slip and no-slip boundary conditions.

The CFD model is a transient Reynolds Averaged Navier-Stokes (RANS) model applying the SST turbulence model equations.

The inlet condition is taken to be constant velocity, and the outlet condition is set to a so-called “outlet”, in which pressure is uniform and the streamwise derivative of convected quantities is zero. The computational domain is taken to be a cylinder, with free-slip wall conditions sufficiently far from the sphere that they should not appreciably affect the flow (namely at 10 bubble diameters).

The flow equations are solved using ANSYS CFX.

### Model results (immobile interface)

The flowfield computed by the CFD model for immobile interface is illustrated in Figure 2 on a plane through the centre of the bubble. The entire domain is larger than that shown, but only the flowfield in the immediate vicinity of the bubble is of interest. There is clearly some asymmetry between upstream and downstream flows, which indicates the effect of viscosity. The computation is transient, but the computed Reynolds averaged flow is almost steady, with only a slight oscillation in the wake. Vortex shedding is expected to start for Reynolds number around 300 (Wu and Faeth, 1994) whereas the Re for the computed case is 1000. It is likely that the application of a turbulence model delays the onset of vortex shedding, and an LES or DNS simulation would undoubtedly give a more accurate prediction of the transition. However, the calculation and interpretation of a source of turbulence becomes more difficult for the results of such simulations. LES simulations will be analysed in the future.

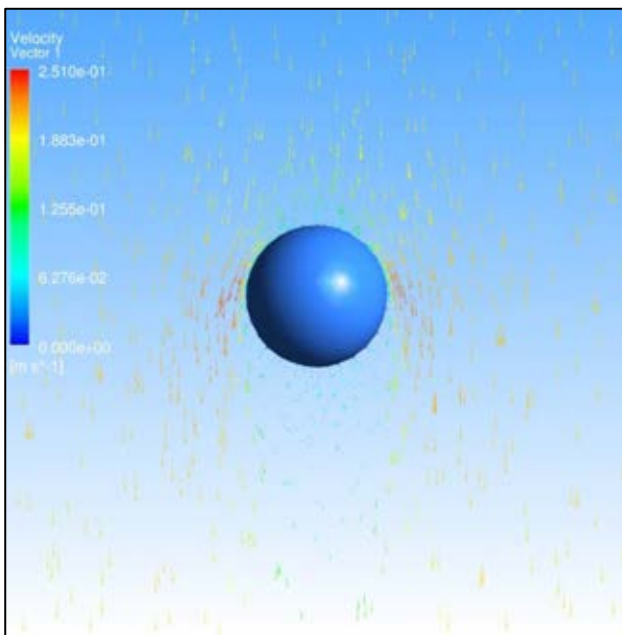


Figure 2: Computed flowfield past the spherical bubble (immobile interface). Colour indicates speed (m/s).

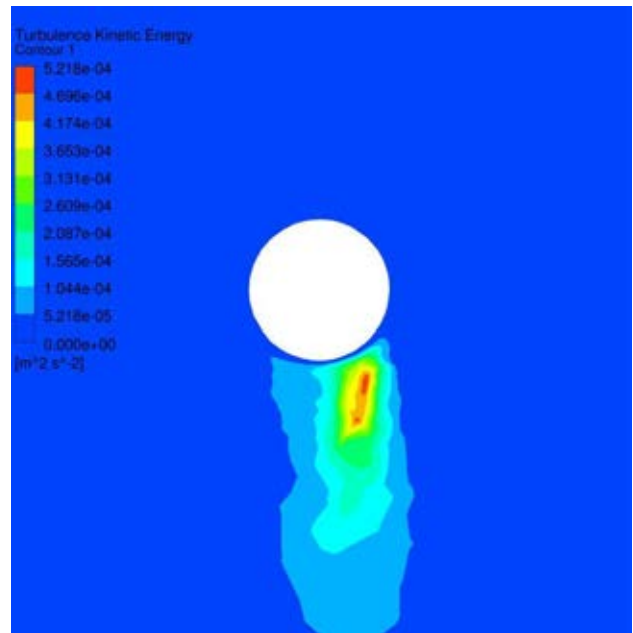


Figure 3: Contours of turbulence kinetic energy ( $\text{m}^2\text{s}^{-2}$ ) for the computed flow past spherical bubble (immobile interface).  
Maximum value:  $5.22 \times 10^{-4} \text{ m}^2\text{s}^{-2}$

Figure 3 plots contours of turbulence kinetic energy for the computed flow past the immobile interface spherical bubble, and Figure 4 plots contours of the turbulence frequency. The spatial distribution of the generation term for turbulence energy is plotted in Figure 5.

It should be mentioned that the standard  $k-\varepsilon$  turbulence model is not appropriate for this flow situation. Such a model predicts relatively high levels of turbulence generation in the boundary layer around the bubble, including the leading surface. The SST model is known to better capture flow in such boundary layers, and in fact, predicts a laminar boundary layer in this particular case. Turbulence generation only occurs in the wake.

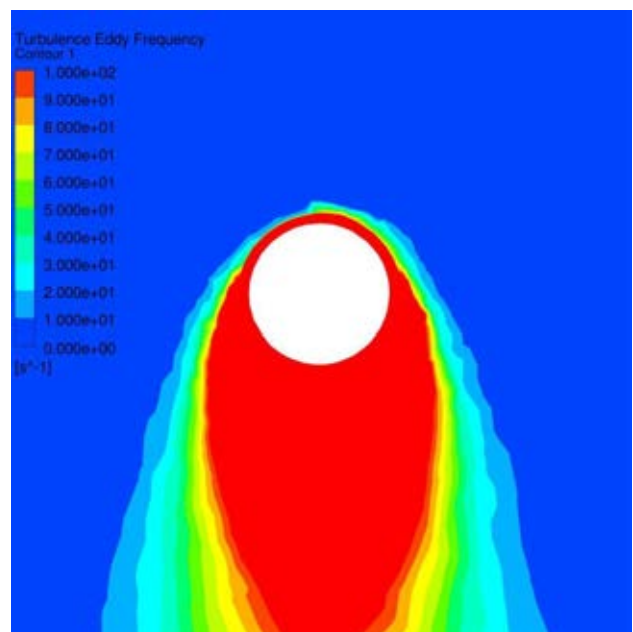
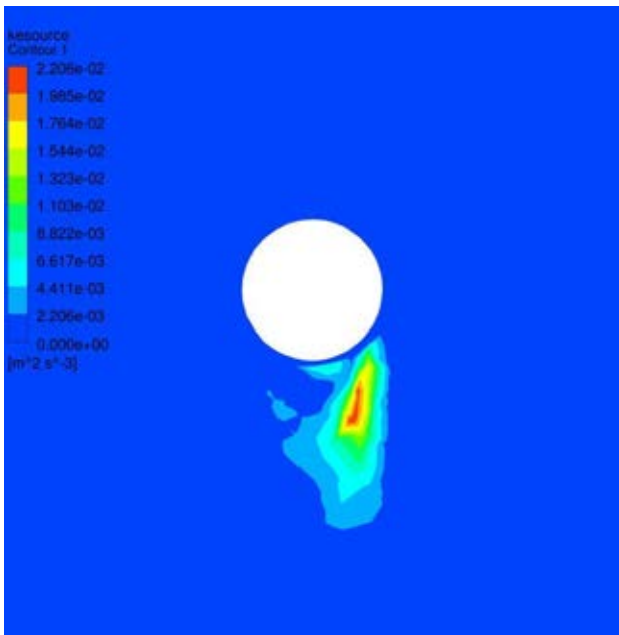
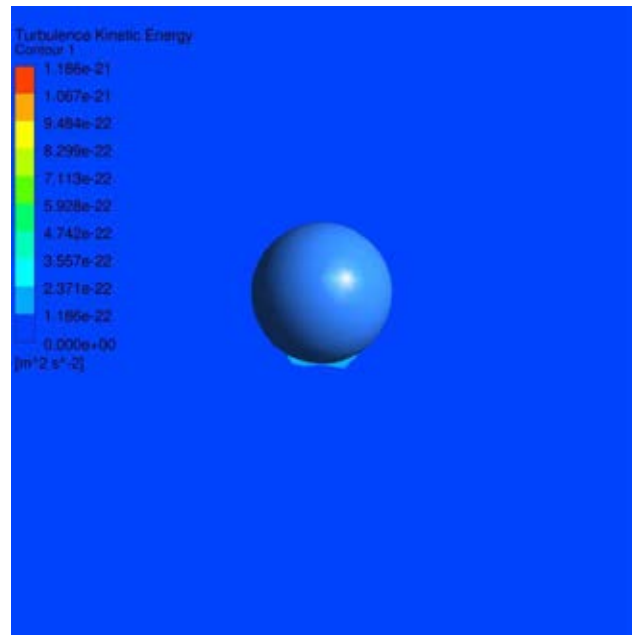


Figure 4: Contours of turbulence frequency ( $\text{s}^{-1}$ ) for the computed flow past spherical bubble (immobile interface).  
Maximum value:  $1.0 \times 10^2 \text{ s}^{-1}$



**Figure 5:** Contours of production rate of turbulence kinetic energy ( $\text{m}^2\text{s}^{-3}$ ) for the computed flow past spherical bubble (immobile interface). Maximum value:  $2.2 \times 10^{-2} \text{ m}^2\text{s}^{-3}$



**Figure 7:** Contours of turbulence kinetic energy ( $\text{m}^2\text{s}^{-2}$ ) for the computed flow past spherical bubble (mobile interface). Maximum value:  $1.19 \times 10^{-21} \text{ m}^2\text{s}^{-2}$

Figs 3 and 5 indicate that the turbulence energy and generation rate are distributed asymmetrically at this instant of time. While there is some movement in these zones as time progresses, they continue to be asymmetric. This is related to slight asymmetry in the computed flowfield which may be caused by an intrinsically unstable flow, perhaps aggravated by asymmetries in the computational mesh.

The total source of turbulence kinetic energy integrated over the entire domain is  $1.03 \times 10^{-6} \text{ kgm}^2\text{s}^{-3}$ .

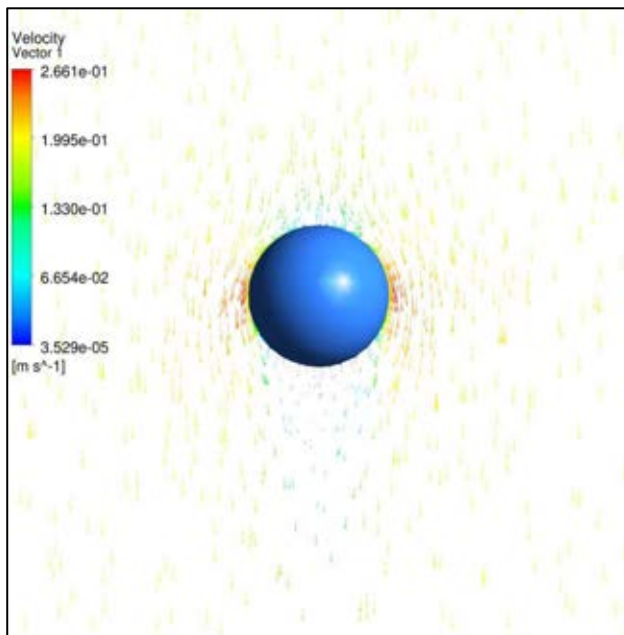


**Figure 6:** Computed flowfield past the spherical bubble (mobile interface). Colour indicates speed ( $\text{m/s}$ ).

### Model results (mobile interface)

The flowfield computed by the CFD model for a mobile interface is illustrated in Figure 6 on a plane through the centre of the bubble. The lateral and longitudinal extent of the wake region is reduced relative to that formed for an immobile interface (Figure 2).

Figure 7 plots contours of turbulence kinetic energy for the computed flow past the mobile interface spherical bubble, and Figure 8 plots contours of the turbulence frequency. The spatial distribution of the generation term for turbulence energy is plotted in Figure 9. These plots clearly indicate that the generation of turbulence energy in the wake is insignificant for a mobile interface when the bubble size is 5 mm.

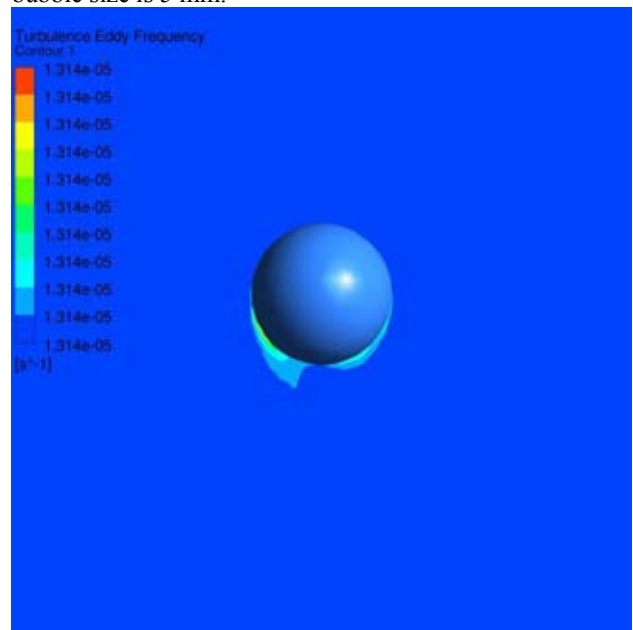


**Figure 8:** Contours of turbulence frequency ( $\text{s}^{-1}$ ) for the computed flow past spherical bubble (mobile interface). Maximum value:  $1.31 \times 10^{-5} \text{ s}^{-1}$

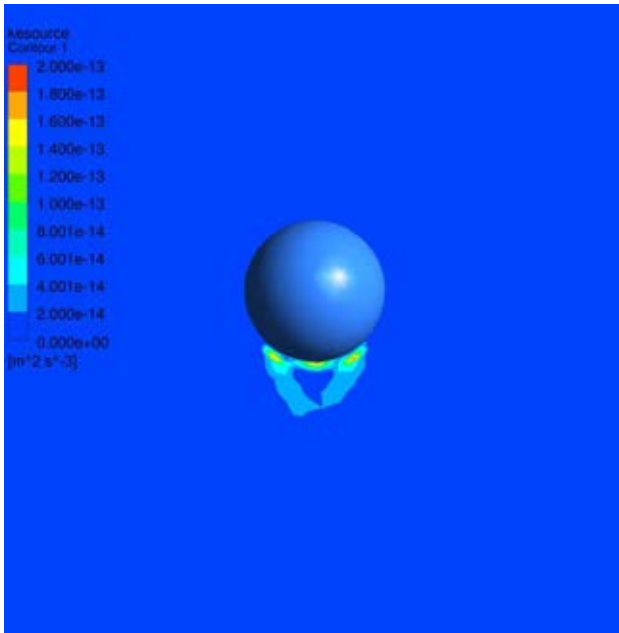


**Figure 9:** Contours of production rate of turbulence kinetic energy ( $\text{m}^2\text{s}^{-3}$ ) for the computed flow past spherical bubble (mobile interface). Maximum value:  $2.0 \times 10^{-13} \text{m}^2\text{s}^{-3}$

## DISCUSSION

As mentioned above, according to the turbulence model, the total source of turbulence kinetic energy integrated over the entire domain for the immobile interface bubble of size 5 mm is  $1.03 \times 10^{-6} \text{kgm}^2\text{s}^{-3}$ . One would expect that this source term would be one component of the source term for turbulence energy generated by the bubble.

The mean flow shown in Figure 2 consists of two components: the flow attached to the bubble whose energy is recoverable, and the energy in the wake which will contribute to the turbulence energy generated by the bubble. There is no well-defined procedure for separating these components, but we assume that the energy at two diameters downstream can be taken to be the wake energy. In this case (immobile interface bubble of size 5 mm) we find the energy source to be  $1.26 \times 10^{-6} \text{kgm}^2\text{s}^{-3}$ .

Now the theoretical argument encapsulated in Eqn (11) means that the turbulence energy generation should be given by the product of drag and slip velocity. If we assume that in steady state the drag force equals the buoyancy force on the bubble, then we can readily calculate the theoretical generation rate to be  $1.28 \times 10^{-4} \text{kgm}^2\text{s}^{-3}$ . This is substantially greater than the turbulence energy generation rate predicted by the CFD model. This difference can be explained by the fact that the product of drag and slip velocity is the total energy dissipation, but only part of that occurs through turbulence generation. The Reynolds number for the situation modelled is relatively low, so one would expect that a large fraction of the energy dissipation could occur directly through viscous forces, rather than indirectly via turbulence generation. After all, for laminar flow, the entire energy dissipation is directly through viscous forces. Thus, it appears that the theoretical formula often used as a basis for estimating bubble-induced turbulence

generation is not applicable for low Reynolds number (i.e. small bubbles).

Simulations are presently being carried out for larger bubbles, where it might be expected that higher rates of turbulence energy generation occurs, and the theoretical formula may better predict the generation rate. However, bubbles of size 1 cm and larger (at least in water) are subject to substantial distortion as they rise, so the simplified method used here would not be appropriate unless a greater surface tension was assumed.

The theoretical formula is even less applicable for the case of mobile interface. As seen in Figures 7-9, the generation rate of turbulence in this case is predicted to be negligible for the SST turbulence model. In effect, this flow is entirely viscous. Real bubbles will always have a certain degree of immobility, and in the case of water with surfactants, the interfaces can be substantially immobile. Larger bubbles with mobile interfaces will be subject to deformation, which will introduce additional sources of turbulence generation.

The equivalent values of turbulence dissipation rate can be computed for the SST model from turbulence energy and frequency. For the immobile case, the total dissipation rate is calculated from the CFD simulation results to be  $1.005 \times 10^{-6} \text{kgm}^2\text{s}^{-3}$ . It is noteworthy that this value is only slightly smaller than the total turbulence energy generation rate. That is to say, almost all the turbulence energy generated is dissipated locally, within the wake attached to the bubble. Very little energy is transported away from the bubble into the bulk flow.

## CONCLUSION

Models proposed to account for bubble-induced turbulence in two-fluid Reynolds-averaged (RANS) simulations of bubbly flow have been reviewed, and the assumptions underlying the models have been critically assessed.

1. There has been a neglect of the difference between so-called “false turbulence” (velocity fluctuations attached to the bubble whose energy is recoverable) and true turbulence (fluctuations not attached to the bubble, which can diffuse into the flow as modelled by the transport equation for  $k$ ).
2. The estimates of bubble-generated turbulence by Arnold *et al* (1989) and others are entirely of the false turbulence, since they assume inviscid flow, in which the “fluctuation energy” is entirely recovered.
3. Consideration of the false turbulence component of the fluctuations raises very real issues of definition of bubble induced turbulence, and also implies that direct measurement of real bubble induced turbulence (using LDA for example) will be very problematic.
4. Simulation of the rise of a 5 mm bubble underlines how most of the fluctuation energy is recoverable. Most of the energy dissipation is

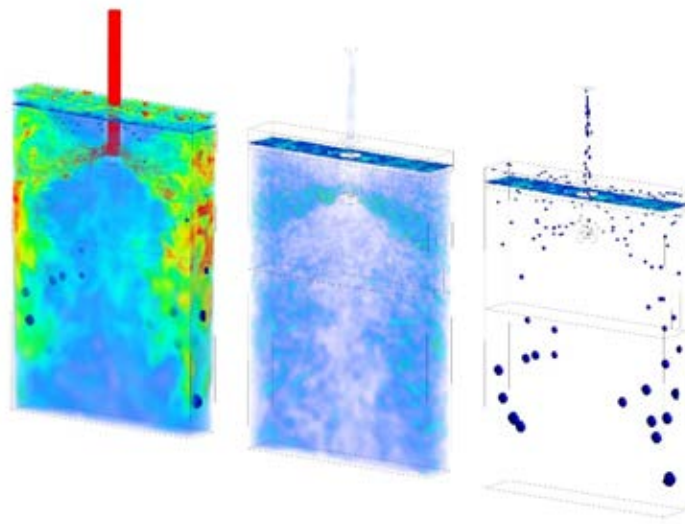
through direct viscous dissipation, rather than indirectly via generation of true turbulence.

5. Generation of true turbulence will undoubtedly be greater for larger bubbles and intrinsically unsteady bubble rise, but it is unclear whether the conventional theoretical formula for generation rate will be applicable, given that it does not appear to apply in the case of 5 mm bubbles.

## REFERENCES

- ARNOLD, G.S., DREW, D.A. and LAHEY, R.T., (1989), "Derivation of constitutive equations for interfacial force and Reynolds stress for a suspension of spheres using ensemble averaging", *Chem. Eng. Comm.*, **86**, 43–54.
- BESNARD, D.C. and HARLOW, F.H., (1988), "Turbulence in multiphase flow". *Int. J. Multiphase Flow*, **14**, 679–699.
- CROWE, C.T., (2000), "On models for turbulence modulation in fluid-particle flows", *Int. J. Multiphase Flow*, **26**, 719–727.
- FENG, Y.Q., SCHWARZ, M.P., YANG, W. and COOKSEY, M., (2015), "Two-phase CFD model of the bubble-driven flow in the molten electrolyte layer of a Hall-Héroult aluminum cell", *Metall. Mat. Trans. B*, **46**, 1959–1981.
- HOSOKAWA, S., and TOMIYAMA, A., (2013), "Bubble-induced pseudo turbulence in laminar pipe flows", *Inter. J. Heat and Fluid Flow*, **40**, 97–105.
- JOHANSEN, S.T. and BOYSAN, F., (1988), "Fluid Dynamics in Bubble Stirred Ladles; Part II: Mathematical Modelling", *Met. Trans. B*, **19**, 755–764.
- KATAOKA, I. and SERIZAWA, A., (1989), "Basic equations of turbulence in gas-liquid two-phase flow". *Int. J. Multiphase Flow*, **15**, 843–855.
- LANCE, M. and BATAILLE, J., (1991), "Turbulence in the liquid phase of a uniform bubbly air-water flow", *J. Fluid Mech.*, **222**, 95–118.
- LOPEZ DE BERTODANO, M., LAHEY, R.T. and JONES, O.C., (1994), "Development of a k- $\epsilon$  model for bubbly two-phase flow", *J. Fluids Eng. Trans ASME*, **116**, 128–134.
- NIGMATULIN, R.I., (1979), "Spatial averaging in the mechanics of heterogeneous and dispersed systems", *Int. J. Multiphase Flow*, **5**, 353–385.
- RZEHAK, R. and KREPPER, E., (2013), "CFD modeling of bubble-induced turbulence". *Int. J. Multiphase Flow*, **55**, 138–155.
- SATO, Y. and SEKOGUCHI, K., (1975), "Liquid velocity distribution in two-phase bubbly flow", *Int. J. Multiphase Flow*, **2**, 79–95.
- SATO, Y., SADATOMI, M and SEKOGUCHI, K., (1981), "Momentum and heat transfer in two-phase bubble flow", *Int. J. Multiphase Flow*, **7**, 167–177.
- SCHWARZ, M.P., (2015), "Bubble induced turbulence in two-fluid simulation of bubbly flow", *26th International Symposium on Transport Phenomena*, Leoben, Austria, 27 September–1 October 2015.
- SCHWARZ, M.P. and FENG, Y.Q., (2015), "Pragmatic CFD modelling approaches to complex multiphase processes", *Progress in Applied CFD*, J.E. Olsen and S.T. Johansen Eds, SINTEF, 25–38.
- SPALDING, D.B., (1981), "A general purpose computer program for multi-dimensional one- and two-phase flow", *Mathematics and Computers in Simulation*, **23**, 267–276.
- VAN WIJNGAARDEN, L., (1998), "On Pseudo Turbulence", *Theoret. Comput. Fluid Dynamics*, **10**, 449–458.
- WU, J.-S. and FAETH, G.M., (1994), "Sphere wakes at moderate Reynolds numbers in a turbulent environment", *AIAA J.*, **32**, 535–541.

# HEAT TRANSFER





## CFD-SIMULATION OF BOILING IN A HEATED PIPE INCLUDING FLOW PATTERN TRANSITIONS USING A MULTI-FIELD CONCEPT

Thomas HÖHNE\*, Eckhard KREPPER, Dirk LUCAS

Helmholtz-Zentrum Dresden-Rossendorf (HZDR) - Institute of Fluid Dynamics  
 P.O.Box 510119, D-01314 Dresden, GERMANY

\* E-mail: [t.hoehne@hzdr.de](mailto:t.hoehne@hzdr.de)

### ABSTRACT

The paper presents the extension of the GENTOP model for phase transfer and discusses the sub-models used. Boiling flow inside a wall heated vertical pipe is simulated by a multi-field CFD approach. Sub-cooled water enters the pipe from the lower end and heats up first in the near wall region leading to the generation of small bubbles. Further along the pipe larger and larger bubbles are generated by coalescence and evaporation. This leads to transitions of the two-phase flow patterns from bubbly to churn-turbulent and annular flow. The CFD simulation bases on the recently developed GGeneralized TwO Phase flow (GENTOP) concept. It is a multi-field model using the Euler-Euler approach. It allows the consideration of different local flow morphologies including transitions between them. Small steam bubbles are handled as dispersed phases while the interface of large gas structures is statistically resolved. The GENTOP sub-models and the Wall Boiling Model need a constant improvement and separate, intensive validation effort using CFD grade experiments.

**Keywords:** multi-phase, boiling, GENTOP, multi-scale, CFD

### NOMENCLATURE

$\alpha$	Void fraction
$\rho_k$	Density of the phase-k
$C_D$	Drag coefficient
$C_{clust}$	constant
$d_{lg}$	Interfacial length scale, i.e., the mean particle diameter for the particle model
$GasC$	potentially continuous gaseous phase
$GasD$	disperse gaseous phase
$\sigma$	Surface tension coefficient
$C_{cd}$	Interface drag force for the FAD turbulence dispersion model
$\Delta_\alpha$	Transition range width
$f_b$	blending function for bubble regime
$f_d$	blending function for droplet regime
$M_{kj}^i$	Interfacial momentum transfer per unit time between the fields k and j
$\mu$	Molecular (dynamic) viscosity

$\Psi_{surf}$	Blending Function
$\phi_{sf}$	Interface blending function
$\nu_t$	Kinematic eddy viscosity
$\dot{m}$	Evaporation mass transfer rate per unit wall area
Nu	Nusselt number
$h_{g,sat}$	Specific enthalpy of saturated vapor
$h_l$	Specific enthalpy of sub-cooled liquid
$c_{lg}^{(h)}$	Volumetric heat transfer coefficient
$\lambda$	Thermal conductivity
$T_s$	Interfacial temperature
$\tau_{dg \rightarrow cg}$	Time constant
$h_l$	Heat transfer coefficient for liquid
$h_g$	Heat transfer coefficient for gas

### 1. INTRODUCTION

Two-phase flows can be found in various industrial applications: nuclear power plants, processing industries, heat transfer systems, transport systems, and of course also in nature in general (ocean waves, river flooding).

Various classifications of two-phase flows exist and they are mainly based on flow morphologies. Such classifications are often difficult to make since the interface structure changes occur continuously. One of the two-phase flow classifications is divided in three major groups and several subgroups - flow regimes:

- Stratified flows (film flow, annular flow, horizontal stratified and jet flow),
- Mixed or transitional flows (cap, slug, churn-turbulent flow, bubbly annular flow, droplet annular flow and bubbly-droplet annular flow),



- Dispersed flows (bubbly flow, droplet flow and flow with solid particles).

Much progress has been achieved in establishing models to describe various multiphase flow phenomena using Computational Fluid Dynamics (CFD).

The GENTOP-concept (Hänsch et al., 2012) enables to consider such transitions in a consistent way as coalescence and breakup processes. The potential of this concept was demonstrated in Hänsch et al. (2012) and Hänsch et al. (2014) for adiabatic flows without heat and mass transfer. In this paper the GENTOP concept is applied to simulate boiling effects in a vertical pipe where transitions from bubbly flow to churn turbulent and then annular flow are involved.

Boiling is a process in which heat transfer causes liquid evaporation. Flow boiling refers to a boiling process when the fluid is imposed by a forced flow. It can be classified as saturated boiling and subcooled boiling. In the saturated boiling, the bulk temperature of the fluid is as equal as its saturation temperature, in the subcooled boiling regime the bulk temperature of the fluid is less than its saturation temperature. Due to latent heat transport, boiling heat transfer plays a very important role in wide number of applications in many technological and industrial areas including nuclear reactor cooling systems, car cooling and refrigeration systems.

Thus, in order to fully understand and predict the boiling phenomenon, the high gas volume fractions must be taken into account. Realizing this need, the GENTOP concept was utilized and further developed for flows with heat and mass transfer in this paper. It allows the modelling for bubbles smaller than the grid size and tracking the interface of large continuous bubbles (larger than the grid size). Thus, it is like a combination of Euler–Euler two fluid modeling and interface tracking techniques. It has been further advanced and validated for churn turbulent flow regimes (Montoya, 2014).

The concept has not yet applied to the situation involving transitions from bubbly flows to churn turbulent and then annular flows. This paper presents a simulation of a generic boiling phenomenon in a vertical pipe with the help of the GENTOP concept in ANSYS-CFX, where important new models have been discussed and applied.

## 2. CFD SIMULATION OF GAS-LIQUID TWO PHASE FLOWS

### 2.1 The generalized two phase flow (GENTOP) concept

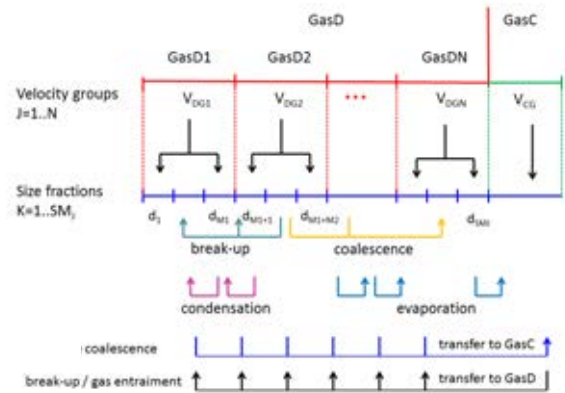


Figure 1 Scheme of the extended GENTOP model including phase transfer

The Generalized Two Phase flow (GENTOP) concept is based on a multi-field two-fluid approach. The flow is represented by a continuous liquid phase l, one or several poly-dispersed gas phases GasD and a continuous gas phase GasC.

The dispersed gas GasD is modelled in the framework of the inhomogeneous Multiple Size Group (iMUSIG) -approach to deal with different bubble size groups and associated velocity fields (Krepper et al. 2008). Within the poly-dispersed gas phases, transfers between different bubble size groups due to coalescence- and breakup as well as due to condensation and evaporation are taken into account by appropriate models.

The GENTOP concept has been developed as an extension of the inhomogeneous Multiple Size Group (iMUSIG) by adding a potentially continuous gas phase GasC which is included within the MUSIG framework. (Fig. 1). This last velocity group represents all gas structures which are larger than an equivalent spherical bubble diameter,  $d_{(dg,max)}$ . The interactions between GasC and the liquid phase are handled in a similar way like in the AIAD-concept (Höhne et al. 2011). This includes the blending for bubbly flow, interface and droplet regions allowing to apply e.g. for a low volume fraction of GasC closures for bubbly flow. For this reason it is called potentially continuous phase.

In the actual paper the GENTOP concept is extended by mass and heat transfer (Fig. 1).

## 2.2 Turbulence modeling

In terms of turbulence treatment, the dispersed phase zero equation is used for the dispersed gaseous phases, while the SST  $k-\omega$  approach is used for the liquid phase. One of the advantages of the  $k-\omega$  model over the  $k-\varepsilon$  is the treatment when in low Reynolds numbers for a position close to the wall. The effect of bubbles on the liquid turbulence is considered by additional source terms (Rzehak and Krepper, 2013).

## 2.3 Modeling of momentum transfer between the dispersed phases and liquid

Due to the averaging of the conservation equations all information on the interface is lost, but has to be reintroduced by the use of closure relations. The closure laws objective is to account for the mass and momentum transfer between the different fields and phases while providing the functional form expected from the interfacial forces. The present models are limited by the need of local condition dependent coefficients, derived from the fact that the closure laws have been developed for ideal bubbly flow and are now being applied to churn-turbulent flow and slug conditions.

Rzehak et al. (2015) have tested and successfully validated a number of poly-dispersed closure laws for Euler-Euler calculations and set up a so called Baseline Model for multiphase poly-dispersed bubbly flows (Table 1).

The total momentum exchange between dispersed gas and continuous liquid phase can be expressed as the superposition of several component forces (see Eq. 1).

$$\mathbf{M}_k^i = \mathbf{M}_k^D + \mathbf{M}_k^{VM} + \mathbf{M}_k^{TD} + \mathbf{M}_k^L + \mathbf{M}_k^W \quad (1)$$

In the baseline model (Rzehak et al., 2015) the drag force  $\mathbf{M}_k^D$  is calculated according to Ishii and Zuber (1979).

**Table 1:** Baseline model (Rzehak et al., 2015) for poly-dispersed flows used in GENTOP

Model	Name
Drag coefficient ( $C_{D,k}$ ),	Ishii and Zuber (1979)
Interfacial lift force	Tomiyama (2002)
Turbulent dispersion force	Burns (2004)
Wall lubrication force	Hosokawa (2002)

## 2.4 Handling of the potentially continuous phase GasC

### 2.4.1 Interface detection

To resolve the interface of continuous gas structures, the interface has to be localized. This is based on an appropriate blending function  $\Psi_{surf}$  (Gauß and Porombka, 2015). It bases on the volume fraction and its gradient and is designed in a generalized form capable for later applications describing not only bubble regions but also droplet regions. It replaces the blending taken from the AIAD model (Höhne, 2014) which was combined with a volume fraction based interface function in the original GENTOP concept of Hänsch et al. (2012).

The interface blending function is defined as

$$\psi_{FS} = \varphi_{sf}(f_b - f_d) \quad (2)$$

which is equal to zero for at a interphase boundary. Additionally, it provides information about the morphology:

$$\psi_{FS} = \begin{cases} 1 & \text{bubble region} \\ 0 & \text{interface} \\ -1 & \text{droplet region} \end{cases}$$

In the actual application only the bubble region and the interface region are of interest. The blending functions for the potentially continuous-phase bubble regime  $f_b$  and droplet regime  $f_d$  are given by:

$$f_b = \frac{1}{2} \left[ 1 + \cos \left( \pi \frac{\tilde{\alpha}^G - (\alpha_{b,crit} - \Delta_\alpha)}{2\Delta_\alpha} \right) \right] \quad (3)$$

$$f_d = \frac{1}{2} \left[ 1 + \cos \left( \pi \frac{\tilde{\alpha}^L - (\alpha_{d,crit} - \Delta_\alpha)}{2\Delta_\alpha} \right) \right] \quad (4)$$

The interface blending function is given by:

$$\varphi_{sf} = \frac{1}{2} \left[ 1 + \cos \left( \pi \frac{\nabla \tilde{\alpha}^c - (\nabla \alpha_{crit} - \Delta_{\nabla \alpha})}{2\Delta_{\nabla \alpha}} \right) \right] \quad (5)$$

### 2.4.2 Complete coalescence

During the calculation low fractions of dispersed gas in the region of mainly continuous gas might arise. To solve this unphysical situation a special coalescence method for complete gaseous mass transfer was established and is now included in the concept in order to replace the coalescence due to

the averaged coalescence models when the critical void fraction is reached. The coalescence rate is turning all the remained dispersed gas, within a specific grid cell, into continuous gas. The complete coalescence is turned off inside the interface in order to allow coalescence and breakup at those positions. The mass transfer is defined by:

$$S_{GasD \rightarrow GasC} = (1 - |\Psi|) \rho_{dg} \alpha_{dg} / \tau_{dg \rightarrow cg} \quad (6)$$

Where  $\tau_{dg \rightarrow cg} = \Delta t$  is a time constant that regulates how fast the mechanism occurs in consistency with the numerical scheme.

### 2.4.3 Clustering force

The clustering force (Figure 2) allows the transition from the dispersed towards the continuous gas phases using an aggregative effect within the volume fraction of the continuous gas. Modeling using an Eulerian approach will produce smearing of the volume fraction by numerical diffusion, thus this force produces interface stabilizing effects. This force is additional interfacial force acting exclusively between the continuous gas and the liquid phase and is included in the interfacial momentum transfer. This force acts proportionally to the gradient of the volume fraction of the liquid as given in the following eq. (7)

$$M_{cg}^{clust} = \max(\psi_{clust}, 0) c_{clust} \rho_l \nabla \alpha_l \quad (7)$$

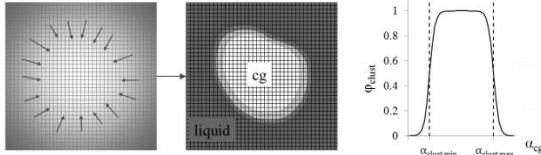


**Figure 2** Detail of a continuous gas liquid interface, and the blending function for a filtered interface (from Hänsch et al., 2012)

As soon as the specific critical void fraction of continuous gas is reached, this force will create regions of continuous gas volume fraction by inducing aggregation on the continuous gas phase volume fraction until a complete formation of gas structures is reached. The force acts outside the interface region, agglomerating the gas, and blends out as soon as the critical gradient of volume fraction appears, completely disappearing as soon as a fully formed interface occurs ( $\Psi_{surf} = 0$ ). The clustering force disappears within the continuous structure. A constant value of  $c_{clust} = 1$  is recommended for the GENTOP application.

### 2.4.4 Interfacial momentum transfer

The Algebraic Interfacial Area Density (AIAD) model, shown in Höhne et al. (2014), allows

detection of morphological form of two phase flow and is able to distinguish between bubbles, droplets and the interface through a corresponding switching via a blending function of each correlation from one object pair to another.

Based on  $\Psi_{surf}$  (blending function), formulations for interfacial area density and drag are defined as in eqs. (8) and (9),

$$A_{GasC} = (1 - |\Psi_{surf}|) A_{fs} + a_{sign} |\Psi_{surf}| A_b + (1 - a_{sign}) |\Psi_{surf}| A_d \quad (8)$$

$$C_{D, GasC} = (1 - |\Psi_{surf}|) C_{D, fs} + a_{sign} |\Psi_{surf}| C_{D, b} + (1 - a_{sign}) |\Psi_{surf}| C_{D, d} \quad (9)$$

## 2.5 Phase change model for GasD and GasC

For the simulation of boiling, the thermal phase change model has been used for the disperse gas phase (GasD) and liquid pair and the continuous gas phase (GasC) and liquid pair.

In our case of heat transfer between liquid and gas, the use of overall heat transfer coefficient is not sufficient to model the interphase heat transfer process. This model considers separate heat transfer process on each side of the phase interface. This is achieved by using two heat transfer coefficients defined on each side of the phase interface.

The sensible heat flux to liquid from the interface is given as:

$$q_l = h_l (T_s - T_l) \quad (10)$$

Similarly, the sensible heat flux to gas from the interface:

$$q_g = h_g (T_s - T_g) \quad (11)$$

The fluid specific Nusselt number is given by:

$$Nu_l = \frac{h_l d_{lg}}{\lambda_l} \quad (12)$$

For spherical bubbles the Ranz Marshall correlation can be applied to calculate the Nusselt number. In the present simulation the Ranz Marshall (1952) correlation was used for the the disperse gas phase (GasD) and liquid pair. The Hughes and Duffey (1991) model uses the surface renewal theory and is used for the potentially continuous gas phase (GasC) and liquid pair.

The wall boiling model is only activated for the disperse gas phase (GasD) and liquid pair. Initially, water is below its saturation temperature. Water becomes supersaturated locally, leading to the formation of bubbles. The bubbles will start

departing and before the formation of next bubble, some of heat will go in superheating the water. This process is known as quenching. In regions of the wall not affected by bubble growth, wall heat transfer to the water is described by single phase convective heat transfer.

In the actual paper the wall boiling heat flux partitioning model developed at RPI (Kurul, 1991) and implemented in CFX with its basic submodels and parameters is applied. In the present paper the basic framework of the GENTOP concept is in the focus of interest. A detailed discussion of the aspects of wall boiling can be found in Krepper et al. 2013.

### 3 DEMONSTRATION CASE OF A WALL HEATED TUBE

To illustrate the previous described concept a demonstration example of a vertical side wall heated tube is given. The tube has a length of 0.5 m and a diameter of 0.025 m. Water is considered at a pressure of 1 bar. At this pressure the saturation temperature amounts to 372 K. The initial temperature was set to a subcooling of 3 K. The temperature of the heated wall is set to a superheating of 13 K. The inlet velocity is 0.2 m/s.

#### 3.1 Geometry, mesh and general setup

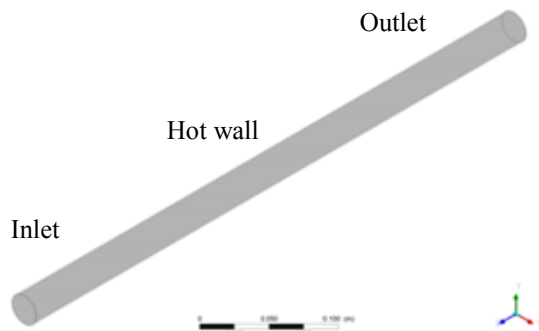


Figure 3 Pipe Geometry

The pipe is presented by a fully 3D geometry shown in Fig. 3 along with the name of the different zones (i.e., inlet, hot wall and outlet). The resulting mesh is made of approximately 127,300 hexahedral cells. A grid resolution study was conducted to ensure that convergence with respect to the spatial resolution has been achieved. A multiphase simulation was set up. Gas was described in the inhomogeneous poly-dispersed multiple size group (iMUSIG) framework by the dispersed gaseous phases GasD1 and GasD2 and the continuous gas phase GasC.

A total of four velocity fields, three gas and one for the continuous liquid were solved. Gas was assumed at saturation temperature. Properties of dry steam at saturation temperature have been taken from the steam tables. At the hot wall a wall boiling model generating GasD was applied. GasC then arise either by coalescence of GasD or by evaporation in the bulk. For the heat and mass transfer between gas and liquid in the bulk the implemented phase change models using the Ranz-Marshall correlation for the pair GasD/Liquid and the Hughes and Duffey (1991) model for the potentially continuous gas phase (GasC) and liquid pair were applied.

The following table 2 shows the numerical scheme used in the case:

Table 2 Solver setup

Advection scheme	Option	High Resolution
Transient scheme	Option $\Delta t$	Second Order Backward Euler 0.005 s
Convergence control	Timescale control Min./max. coeff. loops	Coefficient loops 4/50
Convergence criteria	Residual type Residual target	RMS 1e-04

#### 3.2 Overview of the settings and models used in the GENTOP framework

For the specified fluid water/steam at a pressure of 1 bar the critical bubble size, where the lift coefficient changes its sign, is found for  $d_B = 5.4$  mm. For GasD (dispersed gas) the iMUSIG model with 3 size fractions for GasD1 and 3 size fractions for GasD2 was applied. In this way the lift coefficient for GasD1 is clear different from the lift coefficient of GasD2. GasC was considered as last size fraction of the iMUSIG framework, to include it in the coalescence and fragmentation process. All gas structures equal or larger than 15 mm sphere equivalent diameter are assigned to GasC. The coalescence and breakup models according to Luo & Svendsen (1996) and Prince & Blanche (1990) with coefficients of  $F_B=0.01$  and  $F_C=2$  were applied. Momentum exchange between GasD and liquid was simulated considering all usually applied exchange terms for drag and non-drag forces were used. Concerning the drag between GasC and Liquid the formulation of AIAD was applied (Höhne 2014). The liquid phase was simulated as turbulent using the shear stress transport model. The influence of bubbles of GasD on the liquid

turbulence was considered. The exchange models were implemented using subdomains. Surface tension for the pair GasC and Liquid was implemented. Effects of numerical diffusion were compensated by an additional force, the Clustering force acting between GasC and Liquid to keep the interface between GasC and Liquid stable. The disappearance of unphysical fractions of dispersed gas in zones of prevailing GasC was enforced by complete coalescence. Concerning the turbulence of the liquid at the presence of an interface to GasC experiences with the AIAD model were used. Turbulence damping at the interface was considered and waves smaller as the grid resolution were treated as in the AIAD model.

### 1. RESULTS AND DISCUSSION

Figure 4 shows the time course of volume the averaged parameters in the whole flow domain. During the first 0.8 s only dispersed gas is generated by boiling (see Fig. 4b). After this time also continuous gas arises, mainly by coalescence of dispersed gas. After about 1 s the whole domain is heated up.

In Figure 5 the cross sectional averaged values of liquid temperature (a) and gas volume fractions (b to c) dependent on the height  $z$  are shown.

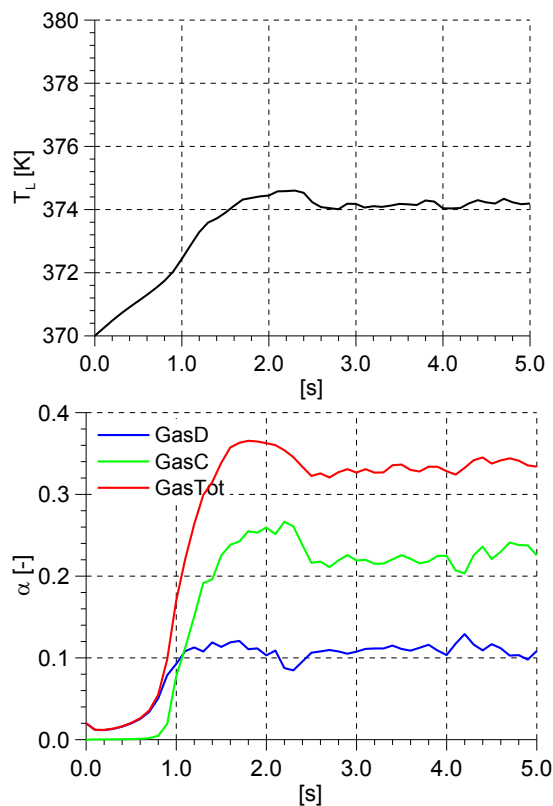


**Figure 4** Time course of the averaged liquid temperature (up) and the volume fractions for dispersed and continuous gas (down)

Figure 6 presents gas volume fractions for dispersed gas (GasD), continuous gas (GASC) and the sum of both (GasTot) after a heating time of 3.0 s. During this time a steady state oscillating period is reached (compare Fig. 4b).

At the beginning of the heating up process mainly small bubbles occur near the wall. The wall boiling model releases bubbles having a diameter of about 1 mm. By the agglomerative effect of the cluster-force and using the principles of the GENTOP-concept it is possible to create continuous gas structures out of a dispersed gas phase as demonstrated in Fig. 6. After the wall boiling of small bubble sizes the domain with the smallest bubble size group the dispersed gas phase is characterized by an increase of mean bubble diameter due to the coalescence processes in the MUSIG-framework.

When the mass transfer to the continuous gas begins and the volume fraction of GasC exceeds the threshold value  $\alpha_{cg} > \alpha_{clust,min}$ , here set to 0.5, the cluster-force agglomerates the continuous volume fraction until the complete coalescence replaces the dispersed gas fractions and large gas structures are resolved.

They further coalesce to larger gas structures forming distorted cap-bubbles and larger slugs represented in the picture (Fig. 6). In grid cells where the continuous gas volume fraction stays below the threshold value  $\alpha_{cg} < \alpha_{clust,min}$  the gas is treated as a dispersed phase following the particle model formulations.

Close observation of the GasD and GasC / Liquid interface show that the flow regimes discussed in chapter 1 except the annular mist flow regime can be found in the simulation.

The bubble flow regime occurs at relatively low gas flow rates, for which the gas phase appears in the form of small bubbles in the lower part of the pipe.

Later Bubbly-slug flow is characterized by the presence of relatively large cap-shaped bubbles, which occupy nearly the entire pipe cross-section and flow alongside smaller, deformable bubbles.

The tendency to annular flow can be seen clearly. The churn turbulent flow appears to be highly chaotic and frothy and may seem to move upwards at some instants and downwards at other instants.

Also in the annular flow regime at the end of the pipe, one may notice the existence of a gas core and a relatively uniform annular liquid film on the pipe wall as well as liquid slugs. The annular film mostly moves upwards but occasionally may seem to pause. This pause occurs when a liquid slug fills the

local cross-section of the pipe, thus blocking the flow of gas in the core.

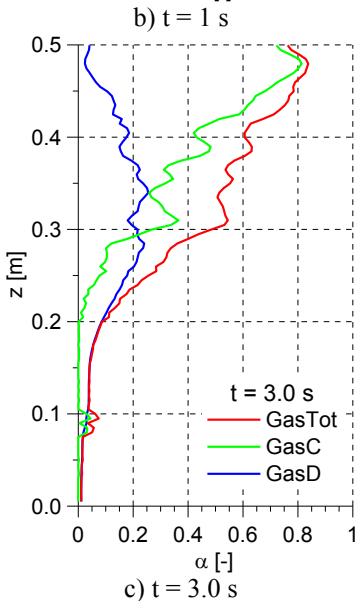
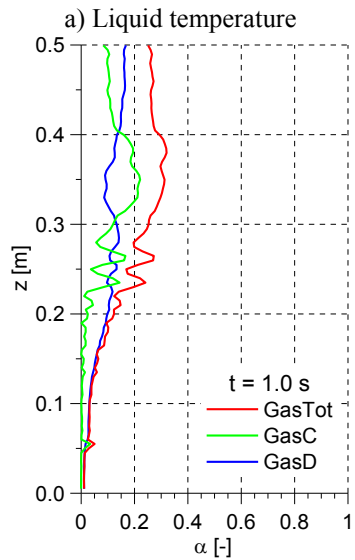
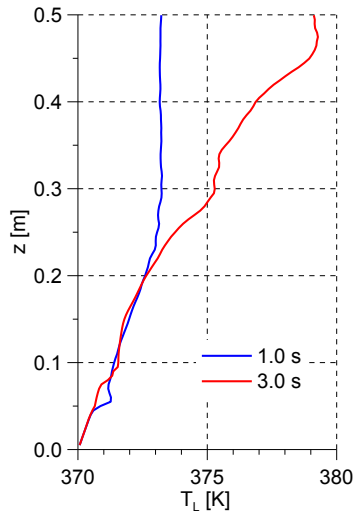


**Figure 5** Cross sectional averaged profiles for the liquid temperature (a) and the gas volume fractions for different times (b to c).

Shortly afterwards, however, the liquid slug gets penetrated by gas and the upward annular-type flow is resumed.

Fig. 7 represents essential GENTOP parameters at 2 s. The interface detection marks the identified interface. The cluster force is acting stabilizing the interface between GasC and Liquid. From the other side the surface tension force is acting in contradiction to the cluster force.

### SUMMARY AND FUTURE WORK

The GENTOP concept, which allows dealing with configurations involving dispersed and continuous interfacial structures, was coupled with a wall boiling model and extended to consider heat and mass transfer between gas and liquid in the bulk.

New model aspects of GENTOP were implemented and tested. Starting with a sub-cooled liquid in a hot pipe, bubbles (boiling) start to appear as soon as the liquid reaches its saturation temperature. Since the temperature of pipe wall is above the saturation temperature of the liquid, a series of flow regimes appear starting from bubbly flow, churn turbulent flow to annular flow. The simulation of the transitions between different flow regimes during boiling in a pipe is now feasible.

Next the demonstration case using the GENTOP-concept will follow experiments for a qualitative comparison of simulation results. The GENTOP sub-models and the Wall Boiling Model need a constant improvement and separate, intensive validation effort.

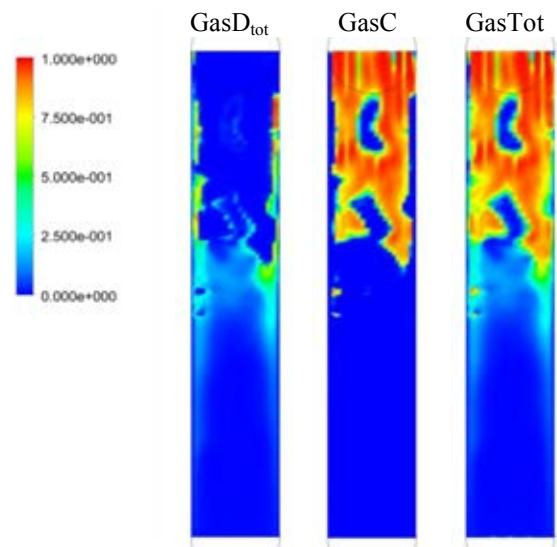


**Figure 6** Distribution of the gas volume fraction at 3.0 s (stretched height)

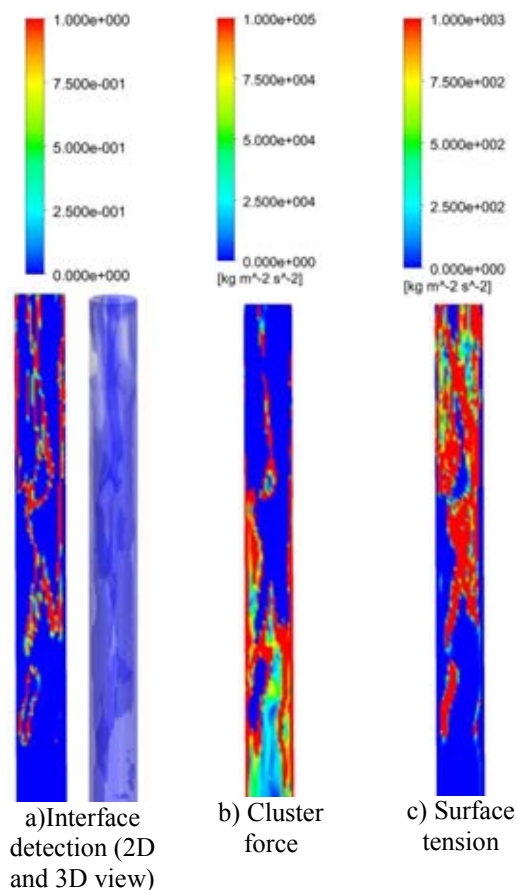


**Figure 7** Essential parameters of the GENTOP model framework at  $t=3$  s

## REFERENCES

- Burns, A.D., et al. The Favre averaged drag model for turbulent dispersion in Eulerian multi-phase flows. in 5th international conference on multiphase flow, ICMF. 2004.
- Gauß, F. and Porombka, P., Internal HZDR Communication, 2015
- Hänsch, S., et al., A multi-field two-fluid concept for transitions between different scales of interfacial structures. *International Journal of Multiphase Flow*, 2012. 47: p. 171-182.
- Hänsch, S.; Lucas, D.; Höhne, T.; Krepper, E., Application of a new concept for multi-scale interfacial structures to the dam-break case with an obstacle, *Nuclear Engineering and Design* 279(2014), 171-181
- Höhne, T. and J.-P. Mehlhoop, Validation of closure models for interfacial drag and turbulence in numerical simulations of horizontal stratified gas-liquid flows. *International Journal of Multiphase Flow*, 2014. 62(0): p. 1-16.
- Höhne, T.; Deendarlianto; Lucas, D., 2011. Numerical simulations of counter-current two-phase flow experiments in a PWR hot leg model using an area density model. *Int. J. Heat Fluid Flow* 32, Issue 5, 1047-1056.
- Hughes, E. D., Duffey, R. B. "Direct contact condensation and momentum-transfer in turbulent separated flows", *International Journal of Multiphase flow* 17, 599-619. (1991).
- Ishii, M.; Zuber, N. "Drag Coefficient and Relative Velocity in Bubbly, Droplet or Particle Flows". *AIChE J.*, 25: 843-855 (1979).
- Krepper, E., et al., The inhomogeneous MUSIG model for the simulation of poly-dispersed flows. *Nuclear Engineering and Design*, 2008. 238(7): p. 1690-1702.
- Krepper, E.; Rzehak, R.; Lifante, C.; Frank, T. 2013. CFD for subcooled flow boiling: Coupling wall boiling and population balance models, *Nuclear Engineering and Design* 255, 330-346
- Kurul, N. and M. Podowski. On the modeling of multidimensional effects in boiling channels. in *ANS Proceeding of the 27th National Heat Transfer Conference*. 1991.
- Luo, H. and H.F. Svendsen, Theoretical model for drop and bubble breakup in turbulent dispersions. *AIChE Journal-American Institute of Chemical Engineers*, 1996. 42(5): p. 1225-1233.
- Montoya, G., et al. Analysis and Applications of a Generalized Multi-Field Two-Fluid Approach for Treatment of Multi-Scale Interfacial Structures in High Void Fraction Regimes. in *Proc. Int. Congress on Adv. on Nucl. Power Plants. ICAPP2014-14230*, USA. 2014.
- Prince, M.J. and H.W. Blanch, Bubble coalescence and break-up in air-sparged bubble columns. *AIChE Journal*, 1990. 36(10): p. 1485-1499.
- Ranz, W. and W. Marshall, Evaporation from drops. *Chem. Eng. Prog.*, 1952. 48(3): p. 141-146
- Rzehak, R. & Krepper, E. CFD modeling of bubble-induced turbulence, *International Journal of Multiphase Flow*, 2013, 55, 138-155
- Rzehak, R.; Ziegenhein, T.; Liao, Y.; Kriebitzsch, S.; Krepper, E.; Lucas, D., Baseline model for simulation of bubbly flows, *Chemical Engineering & Technology* 38 (2015), 1972
- Tomiyama, A.; Sakoda, K.; Hayashi, K.; Sou, A.; Shimada, N.; Hosokawa, S., 2006. Modeling and Hybrid Simulation of Bubbly Flow. *Multiphase Sci. Tech.*, 18(1), 73-110.

## THE PEAR-SHAPED FATE OF AN ICE MELTING FRONT

James N. HEWETT<sup>1\*</sup>, Mathieu SELLIER<sup>1</sup>

<sup>1</sup>Department of Mechanical Engineering, University of Canterbury, Christchurch 8140, NEW ZEALAND

\* E-mail: james@hewett.nz

### ABSTRACT

A fluid-structure interaction problem with the melting of water around a heated horizontal circular cylinder is analysed with numerical simulations. Dynamic meshing was used for evolving the flow domain in time as the melting front extended radially outward from the cylinder; a node shuffle algorithm was used to retain mesh quality across the significant mesh deformation. We simulated one case above the density inversion point of water and one case below, yielding pear-shaped melting fronts due to thermal plumes either rising or falling from the cylinder, respectively. Results were compared with previous experimental studies and the melting front profiles matched reasonably well and melting rates were in agreement. We confirm that natural convection plays a significant role in the transport of energy as the melt zone increases, and needs to be considered for accurately modelling phase change under these conditions.

**Keywords:** Fluid-structure interaction, Stefan problem, melting, natural convection, density inversion.

### NOMENCLATURE

#### Greek Symbols

$\alpha$	Thermal diffusivity ( $k/\rho c_p$ ), [m <sup>2</sup> /s].
$\epsilon$	Strain tensor, [-].
$\theta$	Angle, [rad].
$\mu$	Dynamic viscosity, [kg/ms].
$\nu$	Kinematic viscosity ( $\mu/\rho$ ), [m <sup>2</sup> /s].
$\rho$	Mass density, [kg/m <sup>3</sup> ].
$\sigma$	Stress tensor, [Pa].
$\tau$	Dimensionless time ( $Fo \cdot Ste$ , Equation 5), [-].

#### Latin Symbols

$A$	Cross-sectional area, [m <sup>2</sup> ].
$c_p$	Specific heat, [J/kg K].
$C_T$	Temperature coefficient, [1/K].
$E$	Young's modulus, [Pa].
$Fo$	Fourier number ( $\alpha/R_w^2$ ), [-].
$g$	Acceleration due to gravity, [m/s <sup>2</sup> ].
$G$	Shear modulus, [Pa].
$\Delta h_f$	Latent heat of fusion, [J/kg].
$k$	Thermal conductivity, [W/m K].
$\mathbf{m}$	Mesh displacement vector, [m].
$\hat{\mathbf{n}}$	Unit normal vector to interface, [-].
$Nu$	Nusselt number (Equation 13), [-].
$Po$	Poisson's ratio (Equation 12), [-].

$q$	Temperature index, [-].
$r$	Radial coordinate, [m].
$R$	Radius, [m].
$Ra$	Rayleigh number (Equation 6), [-].
$Ste$	Stefan number (Equation 4), [-].
$t$	Time, [s].
$T$	Temperature, [°C].
$\mathbf{v}$	Velocity vector, [m/s].
$V$	Dimensionless volume ratio (Equation 1), [-].
$x$	Horizontal coordinate, [m].
$y$	Vertical coordinate, [m].

#### Sub/superscripts

0	Initial condition.
$f$	Fusion.
film	Evaluated at the film temperature ( $(T_i + T_f)/2$ ).
$i$	Interface.
$m$	Physical properties of water at 4.029325 °C.
$w$	Cylinder wall.

### INTRODUCTION

Thermal energy storage plays an important role in utilising energy resources effectively because often the timing of generation and consumption of energy can vary from hours to months. For example, solar energy is only available during the day and therefore effective energy storage is required for utilising solar energy during the night. Similarly, power stations must design for peak loads whereas adequate energy storage would allow more efficient use of generators as peak times can be offset by stored energy from off peak times. An efficient method of storing thermal energy is with latent heat which provides a high storage density and requires a smaller difference between storing and releasing temperatures compared with the sensible heat storage method (Farid *et al.*, 2004). There has also been recent studies on using phase change materials for passive cooling in buildings where latent heat is used to increase the thermal inertia of building envelopes, regularising the ambient temperature (Akeiber *et al.*, 2016).

The moving boundary problem where the solid and liquid phase change process occurs forms the classical Stefan problem (Stefan, 1891); named after the Slovene physicist Jožef Stefan (1835-1893). This moving boundary is a function of both time and space and is unknown a priori; creating a coupled fluid structure interaction problem to model. Heat transfer by conduction dominates as the mechanism responsible for melting in the initial stages, when a thin layer



of water is present. However, natural convection (due to the temperature dependent water density) plays an important role as the melting front advances outward from the heat source and the volume of the flow domain increases (White *et al.*, 1977; Sparrow *et al.*, 1978; Bathelt *et al.*, 1979). The flow induced from these buoyancy effects creates temperature fields which lead to a *pear-shaped* solid-liquid interface. Water has a density inversion near 4.0°C which influences the location of enhanced melting (either the warmer water rises or falls around the cylinder). An inverted pear-shaped interface was found for cylinder temperatures below 8.0°C (Herrmann *et al.*, 1984) and near concentric interface evolution at 8.0°C. We simulate one case below and another above this critical cylinder temperature to explore both scenarios due to the density inversion of water.

Experiments have previously been undertaken on the melting of phase change materials around horizontal cylindrical heat sources of: *n*-paraffins (*n*-heptadecane and *n*-octadecane) (Bathelt and Viskanta, 1980) where no density inversion exists; and water (White *et al.*, 1986) at temperatures around the density inversion point. We simulate water as the phase change material and quantitatively compare our results with the latter set of experiments.

Previous simulation approaches include numerical mapping techniques where the transformed domain morphs over time (Rieger *et al.*, 1982; Ho and Chen, 1986), and another by using the latent heat content which varies between zero (solid) and 1 (liquid) (Darzi *et al.*, 2012). The first approach involves tracking the melting interface via domain mapping and calculating the governing equations on a stationary grid. The second approach employs a single mesh where cells have a liquid fraction assigned and the interface is determined based on a fraction threshold criteria. Alternatively, we directly tracked the moving boundary by dynamically updating the mesh throughout the simulation based on the heat flux at the solid-liquid interface.

## METHODS

### Problem description

The physical problem studied in this paper is of ice melting radially outward from a horizontal isothermal heated cylinder. Initially, the ice has a uniform temperature of  $T_f$  and the cylinder is heated to  $T_w > T_f$ . We model the molten ice as a single phase with the interface boundary imitating the Stefan condition. The interface is tracked across discrete time steps where the mesh dynamically updates. Flow is solved in steady state at each time step, leading to a quasi-steady state simulation.

Considering the complexity of modelling phase change materials with dynamic boundaries, the following assumptions were made: (1) motion of water is laminar, 2-D and is incompressible; (2) thermophysical properties of water, except density, are constant across the temperature range modelled; (3) the Boussinesq approximation (density variations only feature in the buoyancy source term); (4) viscous dissipation and volume difference due to phase change are neglected; and (5) thermal equilibrium exists at the interface.

### Geometry and boundary conditions

The heated cylinder, bounded with a radius of  $R_w = 12.7$  mm, is located at the centre of the computational domain and remains stationary. We selected two cylinder wall temperature values:  $T_w = 2.3$ °C and  $T_w = 14.1$ °C, to directly compare our simulation results with existing experimental data (White

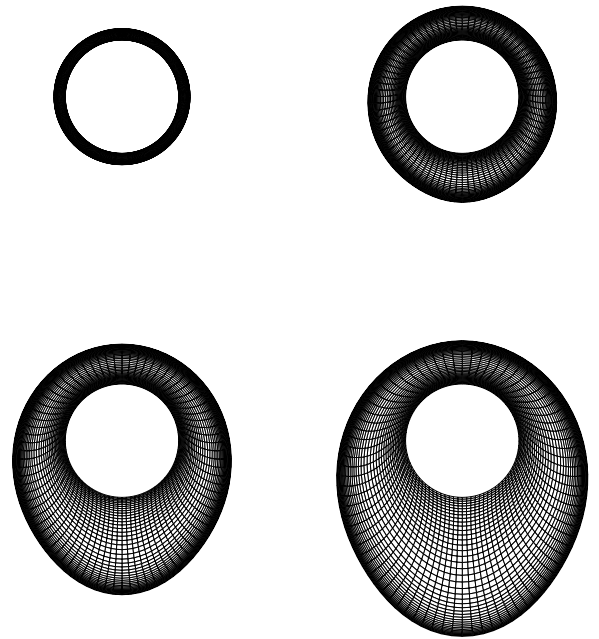


**Figure 1:** Computational mesh evolution from initial (top left) to final (bottom right) geometry for one of the simulations.

*et al.*, 1986); one below  $T_m$  (heat source sinks) and one above  $T_m$  (heat source rises).

Ice surrounds the cylinder outward to infinity and the interface between the ice and water is described with the radial distance  $R_i(\theta, \tau)$ . The computational domain resides between the heated cylinder wall boundary and the dynamic melting interface.

A dimensionless melted ice volume ratio was defined as the ratio of molten ice to the isothermal cylinder, calculated with

$$V = \frac{A_i - A_w}{A_w} \quad (1)$$

using cross-sectional areas because the depth is an arbitrary parameter for our 2-D model. The area enclosed by the interface  $A_i$  was calculated by treating the nodes outlining the boundary as a simple polygon, and the constant wall area was calculated with  $A_w = \pi R_w^2$ .

A structured O-grid mesh of  $40 \times 80$  (radial  $\times$  circumferential) was used in all of the simulations. Uniform cell lengths were specified around the perimeter and a bias was applied in the radial direction to cluster cells near both of the boundaries; in order to resolve the thermal boundary layers. The outer boundary (solid and molten ice interface) expands and the mesh dynamically updates accordingly throughout the simulation as shown in Figure 1. Computational cells within the mesh are deformed and translated without creating or destroying cells; a constant number of finite volume cells are retained throughout each simulation.

Dirichlet conditions were applied to the cylinder wall and interface boundaries with temperatures of  $T_w$  and  $T_i$  respectively, and no slip shear conditions were also imposed. The front and back boundaries of the O-grid domain were set as symmetry with one cell depth to enforce the 2-D assumption.

### Initial conditions

The experiments (White *et al.*, 1986) started with the solid ice in contact with the cylinder such that  $R_0 = R_w$  (no molten ice was present). However, our simulations require a fi-

nite volume to begin with and therefore we used  $R_0 = 1.2R_w$  and offset the time appropriately with  $t_0$  (as calculated based on the analytical solution of heat transfer by conduction described in the *Results* subsection on *Validation with uniform density*).

As the heat transport within the molten ice is dominated by conduction in the initial stages, we initialised the computational domain with the analytical solution to this conduction problem. Velocities were set to zero and the temperature field was initialised using

$$T = (T_i - T_w) \frac{\ln(r/R_w)}{\ln(R_i/R_w)} + T_w \quad (2)$$

with the substitution  $R_i = R_0$ .

#### Fluid properties

The nonlinear variation of water density was included in our simulations by using a  $\rho$  relation in the range of  $T = 0$  to  $20^\circ\text{C}$  (Gebhart and Mollendorf, 1977)

$$\rho = \rho_m(1 - C_T|T - T_m|^q) \quad (3)$$

where  $\rho_m = 999.9720\text{ kg/m}^3$ ,  $C_T = 9.297173 \times 10^{-6}/\text{K}$ ,  $T_m = 4.029325^\circ\text{C}$  and  $q = 1.894816$ .

Thermophysical properties of water were evaluated at an average temperature of  $T \approx 5^\circ\text{C}$ :  $c_p = 4.20\text{ kJ/kg K}$ ,  $\mu = 1.52\text{ g/ms}$  and  $k = 0.57\text{ W/m K}$ . These properties vary slightly across the temperature range simulated but have a negligible influence on the melting rate compared to the density variation.

The constant temperature of the heated cylinder  $T_w$  was non-dimensionalised with the Stefan number

$$\text{Ste} = \frac{c_p(T_w - T_f)}{\Delta h_f} \quad (4)$$

where  $\Delta h_f = 333.55\text{ kJ/kg}$ . The time was made dimensionless with the product of the Fourier and Stefan numbers with

$$\tau = \frac{\alpha}{R_w^2} \text{Ste} \quad (5)$$

The Rayleigh number is a measure of the intensity of natural convection within the molten ice. A density based definition (White *et al.*, 1986) was chosen to handle the non-linear density variation and density inversion feature, with

$$\text{Ra} = \frac{gR_w^3(\rho_m - \rho_{\text{film}})}{\nu\alpha\rho_m} \quad (6)$$

where  $g = 9.80665\text{ m/s}^2$ . Ra approaches zero at the density inversion point ( $T_w = 8.0^\circ\text{C}$  and therefore  $T_{\text{film}} = 4.0^\circ\text{C}$ ) where natural convection plays an insignificant role. Conversely, Ra increases further from this point and is positive for both upright and inverted pear-shaped melting fronts.

#### Numerical procedure

Our simulations were performed using ANSYS Fluent R17.0 as the computational fluid dynamics software. Data analysis and visualisation of results were coded in MATLAB 2016b.

#### Governing equations

Fluent is a cell centred finite volume solver and was employed to solve the momentum, continuity and energy equations. Second order spatial discretisation methods were set for the pressure, momentum and energy equations. Pressure

and velocity were coupled with the PISO scheme. Under-relaxation factors of 0.3 (pressure), 1 (density), 1 (body forces), 0.7 (momentum) and 0.7 (energy) were used.

The fluid time step specified in Fluent was  $1 \times 10^6\text{ s}$  (quasi-steady state assumption) whereas the dynamic mesh step used for deforming the interface was  $\Delta t = 250\text{ s}$  ( $\tau = 0.006$ ) resulting in 120 steps for the inverted pear-shape and  $\Delta t = 20\text{ s}$  ( $\tau = 0.003$ ) with 200 steps for the upright pear-shape case. A maximum number of 50 iterations per time step was used as this number gave iterative convergence of the solution.

#### Melting interface boundary

The velocity of the melting front at the solid-liquid water interface was given by the Stefan condition (Moore, 2017)

$$\mathbf{v}_i = -\frac{\alpha c_p}{\Delta h_f} \frac{dT}{dn} \Big|_i \hat{\mathbf{n}} \quad (7)$$

where  $\hat{\mathbf{n}}$  is directed toward the solid phase. The  $\mathbf{v}_i$  was positive for all cases because a negative temperature gradient existed at the interface boundary; yielding an outward melting front from the warm cylinder throughout the simulations.

#### Dynamic mesh

The dynamic mesh model in Fluent was employed for handling the changing mesh through time. Nodes on the interface boundary were displaced with

$$\Delta \mathbf{x}_i = \Delta t \mathbf{v}_i \quad (8)$$

using user-defined functions.

A node shuffle algorithm (Hewett and Sellier, 2017) was used to uniformly distribute the nodes around the interface at each mesh update. Without this algorithm, mesh quality degrades as the profile of the boundary morphs into its new shape and the simulation diverges.

The interior nodes were updated with a linearly elastic solid model (with the mesh smoothing based option in Fluent). Mesh motion was governed by

$$\nabla \cdot \underline{\boldsymbol{\sigma}}(\mathbf{m}) = \mathbf{0} \quad (9)$$

$$\underline{\boldsymbol{\sigma}}(\mathbf{m}) = E \text{tr}(\underline{\boldsymbol{\epsilon}}(\mathbf{m})) \mathbf{I} + 2G \underline{\boldsymbol{\epsilon}}(\mathbf{m}) \quad (10)$$

$$\underline{\boldsymbol{\epsilon}}(\mathbf{m}) = \frac{1}{2}(\nabla \mathbf{m} + (\nabla \mathbf{m})^T) \quad (11)$$

and was parameterised with Poisson's ratio

$$\text{Po} = \frac{1}{2(1 + G/E)} \quad (12)$$

where we used the default of  $\text{Po} = 0.45$  which gave robust mesh deformations and retained similar thermal boundary layer resolutions throughout the simulations.

## RESULTS

We first validated our model by using a phase change material with uniform density (no natural convection; conduction only) and compared the results with the analytical solution. Next, we simulated one case below the temperature threshold  $T_w = 8.0^\circ\text{C}$  where an inverted pear-shape interface developed, and one case above where an upright pear-shape melting front formed.

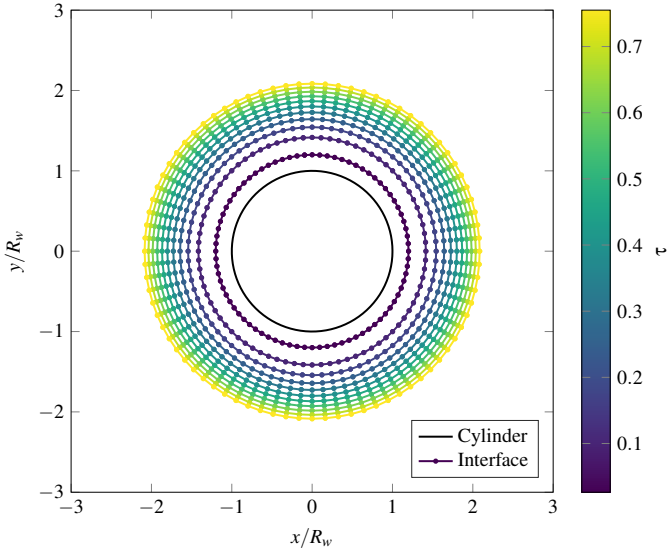


**Figure 2:** Melting interface evolution assuming uniform density with  $T_w = 2.3^\circ\text{C}$ . Profiles are equally spaced in time.

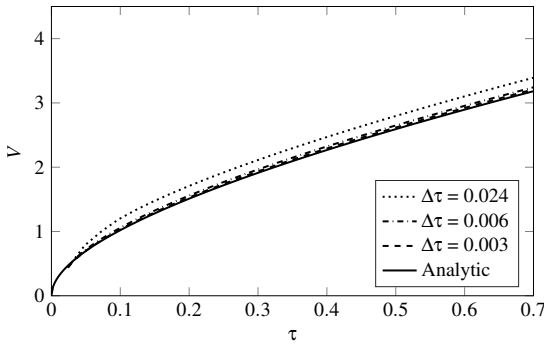


**Figure 3:** Time step convergence of melt volume over time for the uniform density case at  $T_w = 2.3^\circ\text{C}$ .

**Validation with uniform density**

The Stefan problem is simplified when a uniform fluid density is employed such that no natural convection exists and the heat is transferred exclusively by conduction. Equation 2 describes the temperature field throughout the melting evolution for this reduced one-dimensional case. The temperature gradient in Equation 7 was calculated by numerically differentiating the temperature at the interface boundary.

Evolution of the melting interface between the solid and liquid water phases are shown in Figure 2. All time interface profiles are concentric with the cylinder, caused by uniform temperature gradients at the boundary, because no flow was generated within the fluid. The melting front is quickest during the initial period where the ice is almost in contact with the heated cylinder and slows as the interface recedes outward.

The rate of melt volume (Figure 3) is greatest at the beginning and reduces over time; monotonically increasing. Simulations overestimate the melting rate because the temperature gradient was explicitly calculated at each step (essentially an Euler method). The coarse mesh time step of  $\Delta\tau = 0.024$  significantly overestimates the melt volume and time steps of  $\Delta\tau \leq 0.006$  agree well with the analytical solution.

Mesh independence was studied on a case by case basis as the flow features requiring varying mesh resolution levels differed across the cylinder temperatures and whether natural convection occurred or not. For example, the pure conduc-

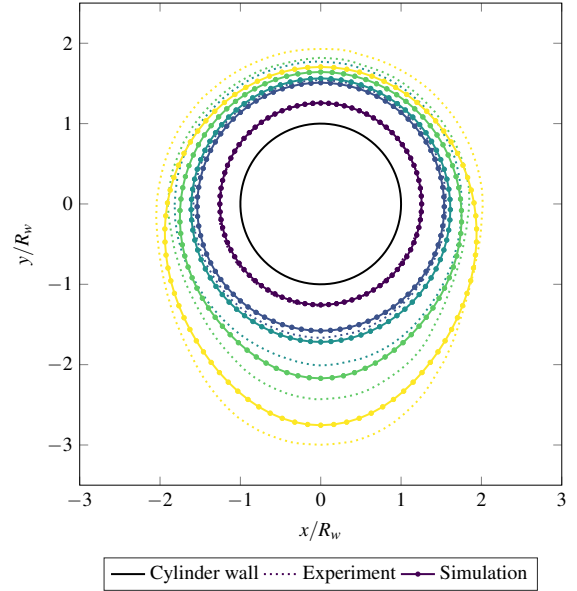


**Figure 4:** Melting interface profiles for  $T_w = 2.3^\circ\text{C}$ , comparing simulation with experiment using paired dimensionless times of  $\tau = 0.039, 0.172, 0.223, 0.350$  and  $0.524$  (extending outward from the cylinder respectively).

tion case achieved mesh independence with a coarser mesh than the cases where natural convection occurred; recirculation of the flow needed to be resolved. Similarly, the mesh time step was converged for each case.

**Inverted pear-shape ( $T < 8.0^\circ\text{C}$ )**

A low cylinder temperature of  $T_w = 2.3^\circ\text{C}$  ( $\text{Ste} = 0.029, \text{Ra} = 6700$ ) was chosen such that the coldest water had the lowest density (below the density inversion point). The melting interface, shown in Figure 4, initially advances concentrically from the cylinder at the same rate as the uniform density case (Figure 2).

Buoyancy driven flow develops as the melt volume increases causing recirculation as shown in Figure 5. The warm water sinks (due to the density variation specified via Equation 3), enhancing the melting rate at the base causing an inverted pear-shape form.

Molten ice volume over time is shown in Figure 6 where both our simulation and the experiment (White *et al.*, 1986) closely follows the uniform density during the early stages of melting. This uniform density approximation begins to deviate at  $\tau \approx 0.2$  where the fluid heat starts to be transported by natural convection in addition to conduction, causing the approximation to underestimate  $V$ .

A spike in  $V$  at  $\tau = 0.223$  was observed in the experiment (Figure 6) which was not featured in our results. However, the slope of  $V$  with  $\tau$  match closely between the final two experiment data points and the second half of our simulation. Furthermore, the shape  $R_i(\theta)$  closely resembles the experiment but lags slightly behind in time.

**Upright pear-shape ( $T > 8.0^\circ\text{C}$ )**

The final case included the density inversion effects of water by prescribing a cylinder boundary temperature of  $T_w = 14.1^\circ\text{C}$  ( $\text{Ste} = 0.178, \text{Ra} = 7400$ ). The melting interface for this case also begins with a concentrically evolving profile as shown in Figure 7.

A thermal plume develops as the molten ice volume increases and this plume generates two counter-rotating vortices as

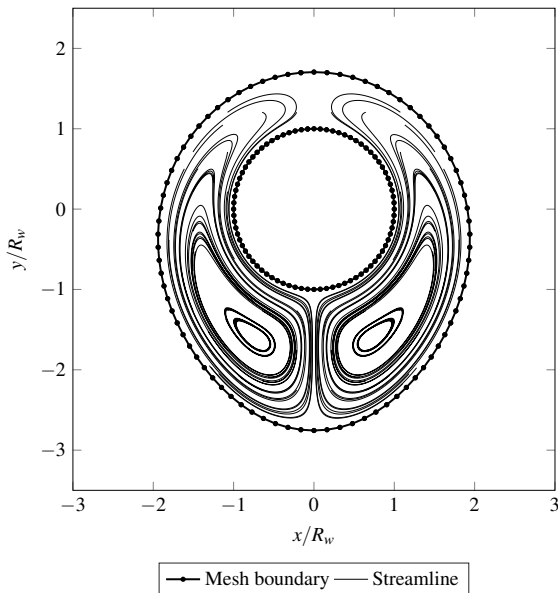


Figure 5: Streamlines for  $T_w = 2.3^\circ\text{C}$  at  $\tau = 0.524$ .

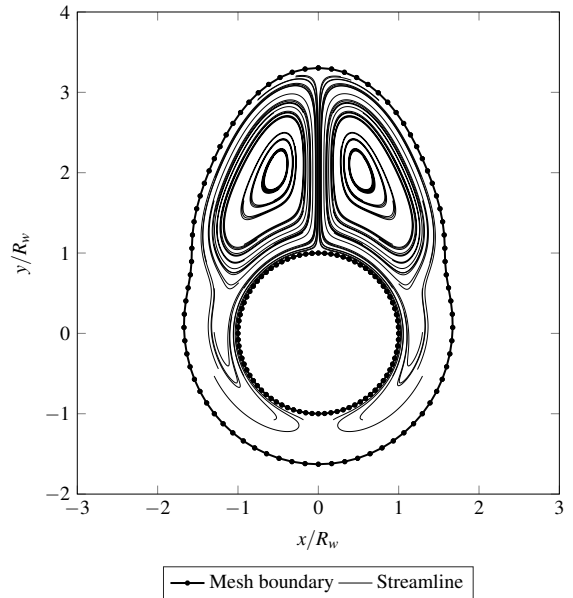


Figure 8: Streamlines for  $T_w = 14.1^\circ\text{C}$  at  $\tau = 0.370$ .

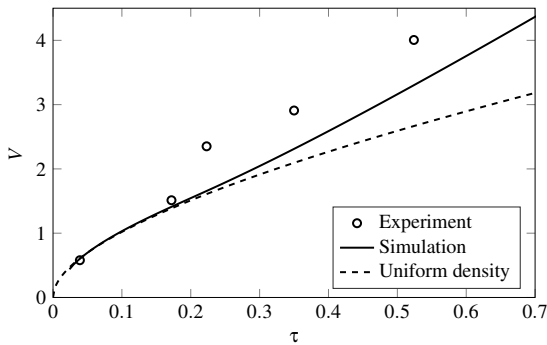


Figure 6: Molten ice volume over time with  $T_w = 2.3^\circ\text{C}$ .

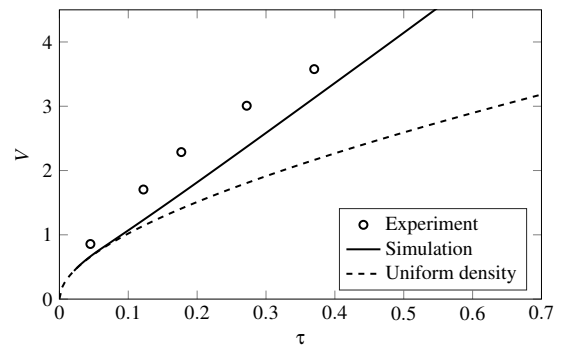


Figure 9: Molten ice volume over time with  $T_w = 14.1^\circ\text{C}$ .

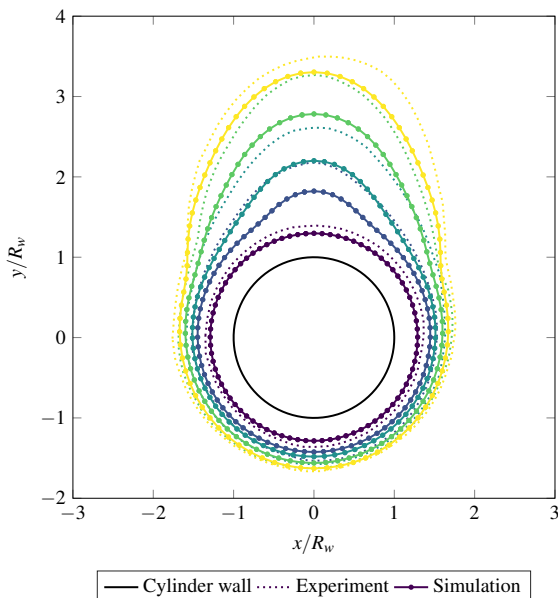


Figure 7: Melting interface profiles for  $T_w = 14.1^\circ\text{C}$ , comparing simulation with experiment using paired dimensionless times of  $\tau = 0.045, 0.122, 0.177, 0.272$  and  $0.370$  (extending outward from the cylinder respectively).

shown in Figure 8; these vortices were also observed in experiments (White *et al.*, 1986). This rising warm water and corresponding vortices causes an upright pear-shape profile to emerge.

The molten ice volume deviates from the uniform density approximation earlier for this warmer case as shown in Figure 9. The ice melting rate observed in the experiments appear to exceed that of by pure conduction even in the early stages of the process at  $\tau = 0.045$  whereas our simulations follow this rate until  $\tau \approx 0.1$ . Similar to the low temperature case, the slope of  $V$  with  $\tau$  match reasonably well between the experiment and our simulations during the natural convection dominated heat transfer regime.

Instantaneous interface profiles match closely with the experiment (Figure 7) but are out of sync; slightly lagging in time. Small asymmetric features were observed in the experiment during the final time snapshots whereas our simulations predicted symmetric profiles about the vertical plane.

## DISCUSSION

The solid-liquid interface advanced radially outward from the heated cylinder in all cases; causing a monotonically increasing melt volume. Resolidification of the molten ice was not allowed in our model as a positive temperature gradient was present at the interface boundary (since  $T > T_f$  throughout the domain); and resolidification was not observed in experiments (White *et al.*, 1986). The conduction only case exhibited uniform melting rates as a function of  $\theta$ , resulting in

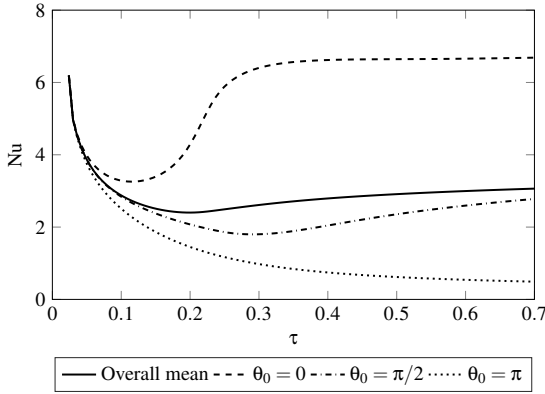


**Figure 10:** Variation of the local and total Nusselt numbers over time for the inverted pear-shape case ( $T_w = 2.3^\circ\text{C}$ ). Angle  $\theta$  is measured from the base of the cylinder and is positive in the anti-clockwise direction.

concentric interface profiles, whereas the other two cases involving natural convection featured eccentricity in their interface shapes beyond the initial conduction dominated period. The location of eccentricity was determined by the opposite direction of the thermal plume: either above or below the cylinder.

The local Nusselt number around the melting interface was defined as

$$\text{Nu}_i = \frac{R_i}{T_f - T_w} \left. \frac{dT}{dn} \right|_i \quad (13)$$

where an area averaged radius of  $R_i = \sqrt{A_i/\pi}$  was used to account for the time-dependent expansion of the domain. Figure 10 shows that the total heat transfer rapidly decreases in the early stages as the conduction heat transport mechanism accelerates the melting process. Heat transfer was uniform around the cylinder up until  $\tau \approx 0.05$  where the local angle dependent Nu numbers split and natural convection begins to develop. However, the melt volume rate deviates between the two cases at  $\tau \approx 0.2$  (Figure 6) indicating that the average melting rate is similar, regardless of the non-uniform melting rate, for  $0.05 < \tau < 0.2$ . Average Nu appears to plateau toward the end of the simulation ( $\tau > 0.6$ ), indicating that an equilibrium of the melting rate has been reached; also shown as the slope of  $V$  with  $\tau$  in Figure 6.

Heat transfer by conduction dominated the early stages of the process and natural convection became a significant factor as the molten ice volume expanded, allowing recirculation to occur (Figures 5 and 8). Experiments observed a spike in the rate of melting at the transition between the conduction and natural convection dominated heat transfer regimes. Our simulations did not capture this counter-intuitive local spike, possibly due to our simplified assumptions including 2-D steady flow. Local transient fluid motion induced from the transition from conduction to natural convection (unsteady flow) or 3-D effects may have been responsible for this enhanced melting rate. White *et al.* (1986) observed 3-D vortex motion in the later stages of the melting process causing ripples around the interface along the cylinder axis.

Standard uncertainties in measurements (either explicitly or implicitly via perturbing the rig) and values used for the thermophysical properties are other possible sources for the quantitative discrepancy between simulations and experiment. Melting rates and flow features are highly sensitive to the temperature of the heated cylinder. However, it is important to note that the interface shapes closely match throughout

the melting process; and only the time dependent interface evolution at the flow regime transition differs.

The Rayleigh numbers of the two pear-shape cases involving natural convection were similar: 6700 (inverted) and 7400 (upright). However, each case was either side of the density inversion point of water. The inverted pear-shape had a positive monotonic relationship of density to temperature yielding a relatively simple recirculation flow pattern on each side of the pear. In contrast, the upright pear-shape encompassed the density inversion point causing more complex flow features such as counter-rotating vortices above the cylinder separated by the thermal plume (Figure 8). An instability of the thermal plume was observed in the experiment (White *et al.*, 1986) at  $\tau \approx 0.3$  as the melt layer grew. These instabilities, and any unsteady flow features, are absent in our steady state model which could explain the discrepancy between the melt rates from  $\tau = 0.3$  for the  $T_w = 14.1^\circ\text{C}$  (Figure 9).

We assumed the flow field was in steady state for each discrete flow domain update (mesh step). The streamlines shown in images produced with an interferometer during the experiments (White *et al.*, 1986) indicate a mostly symmetric and steady flow field. However, slight perturbations and unsteady behaviour could cause greater heat mixing leading to faster melting, particularly for the  $T_w > 8.0^\circ\text{C}$  case. For example, assuming 2-D steady flow significantly overestimates the skin friction in the wake of an eroding cylinder evolving to a different shape than that of simulating with 3-D unsteady flow (Hewett and Sellier, 2017). Another step would be required for including these unsteady effects: the time-averaged wall temperature gradient must first be established before calculating  $\mathbf{v}_i$  or the mesh would be deformed based on instantaneous local transients.

## CONCLUSION

Numerical simulations were used to model the classical Stefan problem around a heated horizontal cylinder near the density inversion point of water by modelling both conduction and natural convection heat transfer. The melting front was explicitly tracked with a dynamic mesh and a node shuffle algorithm was employed to retain mesh quality through significant mesh deformation.

Heat transfer by conduction was dominant for the early stages of melting and natural convection played an important role as the melt zone increased. A stable steady flow field was found for the case below the density inversion point whereas a more complex and less stable flow was simulated when including the density inversion point. Pear-shaped melting interfaces developed as a thermal plume from the heated cylinder interacted with the solid-liquid boundary.

This paper provides a validation for modelling Stefan problems by tracking the melting front interface using only the local temperature gradient and fluid properties. The constitutive relation, along with the tools for handling the mesh deformation, form a useful approach for simulating this melting boundary problem found in latent heat thermal energy storage systems. This approach can also be applied to other scenarios of moving boundary problems.

## REFERENCES

AKEIBER, H., NEJAT, P., MAJID, M.Z.A., WAHID, M.A., JOMEHZADEH, F., ZEYNALI FAMILI, I., CALAUTIT, J.K., HUGHES, B.R. and ZAKI, S.A. (2016). "A review on phase change material (PCM) for sustainable passive cooling in building envelopes". *Renewable and Sustainable Energy Reviews*, **60**, 1470–1497.

BATHELT, A.G. and VISKANTA, R. (1980). "Heat transfer at the solid-liquid interface during melting from a horizontal cylinder". *International Journal of Heat and Mass Transfer*, **23(11)**, 1493–1503.

BATHELT, A.G., VISKANTA, R. and LEIDENFROST, W. (1979). "An experimental investigation of natural convection in the melted region around a heated horizontal cylinder". *Journal of Fluid Mechanics*, **90(2)**, 227–239.

DARZI, A.R., FARHADI, M. and SEDIGHI, K. (2012). "Numerical study of melting inside concentric and eccentric horizontal annulus". *Applied Mathematical Modelling*, **36(9)**, 4080–4086.

FARID, M.M., KHUDHAIR, A.M., RAZACK, S.A.K. and AL-HALLAJ, S. (2004). "A review on phase change energy storage: materials and applications". *Energy Conversion and Management*, **45(9-10)**, 1597–1615.

GEBHART, B. and MOLLENDORF, J.C. (1977). "A new density relation for pure and saline water". *Deep Sea Research*, **24(9)**, 831–848.

HERRMANN, J., LEIDENFROST, W. and VISKANTA, R. (1984). "Melting of ice around a horizontal isothermal cylindrical heat source". *Chemical Engineering Communications*, **25(1-6)**, 63–78.

HEWETT, J.N. and SELIER, M. (2017). "Evolution of an eroding cylinder in single and lattice arrangements". *Journal of Fluids and Structures*, **70**, 295–313.

HO, C.J. and CHEN, S. (1986). "Numerical simulation of melting of ice around a horizontal cylinder". *International Journal of Heat and Mass Transfer*, **29(9)**, 1359–1369.

MOORE, M.N.J. (2017). "Riemann-Hilbert problems for the shapes formed by bodies dissolving, melting, and eroding in fluid flows". *Communications on Pure and Applied Mathematics*.

RIEGER, H., PROJAHN, U. and BEER, H. (1982). "Analysis of the heat transport mechanisms during melting around a horizontal circular cylinder". *International Journal of Heat and Mass Transfer*, **25(1)**, 137–147.

SPARROW, E.M., SCHMIDT, R.R. and RAMSEY, J.W. (1978). "Experiments on the role of natural convection in the melting of solids". *Journal of Heat Transfer*, **100(1)**, 11–16.

STEFAN, J. (1891). "Über die theorie der eisbildung, insbesondere über die eisbildung im polarmeere". *Annalen der Physik*, **278(2)**, 269–286.

WHITE, D., VISKANTA, R. and LEIDENFROST, W. (1986). "Heat transfer during the melting of ice around a horizontal, isothermal cylinder". *Experiments in Fluids*, **4(3)**, 171–179.

WHITE, R.D., BATHELT, A.G., LEIDENFROST, W. and VISKANTA, R. (1977). "Study of heat transfer and melting front from a cylinder imbedded in a phase change material". *American Society of Mechanical Engineers (Paper)*, **77**.



## FLOW DYNAMICS STUDIES FOR FLEXIBLE OPERATION OF CONTINUOUS CASTERS (FLOW FLEX CC)

Tobias Forslund<sup>1,2</sup>, Henrik Barestrand<sup>2</sup>, Pavel E. Ramirez Lopez<sup>1</sup>, Pooria Jalali<sup>1</sup>, Christer Olofsson<sup>1</sup>  
Tobias Lindbäck<sup>1</sup> and Erik Roos<sup>3</sup>

<sup>1</sup>Process Metallurgy Department, Swerea MEFOS, Luleå, SWEDEN

<sup>2</sup>Luleå University of Technology (LTU), Luleå, SWEDEN

<sup>3</sup>SSAB Special Steels, Oxelösund, SWEDEN

\* E-mail: tobias.forslund@swerea.se

### ABSTRACT

Flow dynamics of liquid steel within the Continuous Casting (CC) mould are critical for process stability and the quality of final products. An “optimal” flow provides enough circulation of the metal to avoid freezing, but it is stable enough to avoid defects during solidification. This requires a trade-off between speed and stability that is difficult to achieve for the variety of conditions faced by the Scandinavian steel industry (e.g. small orders with high variability in size and steel grades). This is difficult to address with typical CFD models used by the industry and suppliers for design of flow control devices (nozzle, stoppers, etc.), since flow optimization requires a better understanding of the level instabilities inside the mould (i.e. free surface) and its highly turbulent behaviour. Consequently, CC requires advanced multiphase models as well as accurate turbulent and time scales resolution.

The investigation presented uses a multiphase approach (Volume of Fluid, VOF + Discrete Phase Modelling, DPM) to solve the molten steel and argon injection within the mould combined with Large Eddy Simulation (LES) to improve the resolution of turbulent scales compared to typical 2-equation models. CFD simulations were successfully validated with results from a Continuous Casting Simulator using a low melting point alloy. Then, these tools were used to design and test different SEN types for various mould sizes in order to optimize their flow pattern and performance in the mould. The project included a comprehensive set of plant trials at an industrial caster to validate/calibrate model predictions, test nozzle resistance and explore process improvement opportunities.

**Keywords:** Numerical modelling, Continuous Casting, SEN, LES, design, optimization.

### NOMENCLATURE

$g$ , Gravitational acceleration [ $m/s^2$ ]

$\phi$ , Velocity potential [ $m^2/s$ ]

$\{d, a, b\}$ , Spatial lengths [ $m$ ]

$\{x, y, z\}$ , Spatial coordinates [ $m$ ]

$\eta$ , Surface offset [ $m$ ]

$f$ , Frequency in Hz [ $1/s$ ]

$F_d(d)$ , Dimensionless scaling function

$\rho$ , Density [ $kg/m^3$ ]

$D$ , Nozzle port diameter (mm)

$\theta$ , Nozzle port angle (mm)

$V$ , Velocity [ $m/s$ ]

$\{m, n\}$ , integer numbers

### INTRODUCTION

The Swedish steel industry currently operates in a niche market where orders are small and products can differ significantly in composition and size. Thus, steelmakers seek a deeper process understanding to enhance quality for short production runs. Common quality problems in CC are related to flow instabilities in the mould, which may cause slag entrapment and cracking due to differences in shrinking and solidification for the variety of slab sizes ordered by the customers. The movement of liquid steel within the mould is critical to process stability and quality of final products where an “appropriate” behaviour of the metal level ensures a minimum of defects during solidification (Dauby, 2011). Therefore, there is a demand for a more flexible production where stable casting conditions are reached promptly to minimize defects. Consequently, the metal flow in the mould has been widely studied through simplified numerical models and physical models with water. Unfortunately, these approaches are not enough to capture the behaviour of the interface between metal and slag (e.g. single phase models) as well as the magnitude and frequency of level fluctuations at the interface due to different physical properties of liquid metal and water (e.g. water models). Advanced multiphase models are an efficient tool to address these shortcomings as well as testing different mould and nozzle geometries in a cost and time efficient manner. The advanced simulations carried out in this investigation use LES (Large Eddy Simulation) coupled to a DPM (Discrete Phase Model) model developed by Olsen *et al.* (Olsen *et al.*, 2009) for stirred ladles. This has been adapted to handle Argon gas injection in the nozzle and flow dynamics in the Continuous Casting mould (Ramirez Lopez *et al.*, 2014).



## The Continuous Casting (CC) process

Continuous Casting is a process by which molten metal is poured from a ladle into a copper mould through a Submerged Entry Nozzle (SEN). The metal fills the mould and forms a solidifying shell which contains the liquid steel as it is slowly pulled out at a specified casting speed ( $m/min$ ). Slag is added on top of the mould forming a slag-metal interface which prevents direct contact with air to avoid re-oxidation. As the strand is drawn out, it is bent by a series of cylindrical rolls. Once the strand has completely solidified it is cut into slabs by a gas torch. Figure 1 presents an overview of the CC process where red represents liquid metal, blue illustrates the solidified shell in the strand and grey represents the slag cover.

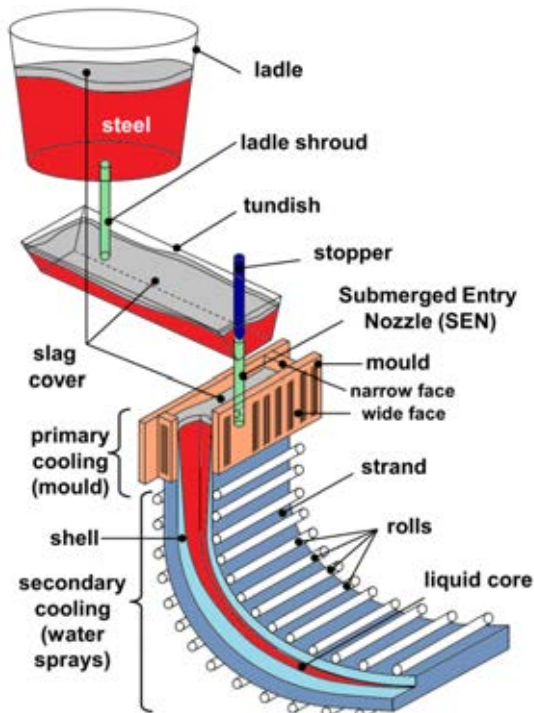


Figure 1: CC-Mould process.

## Numerical modelling

There are several complex physical processes acting simultaneously in the mould during casting. Firstly, there is a strong recirculating flow of liquid steel which is determined by the nozzle shape and mould size. Secondly, the injection of Argon (small bubbles, typically  $<5$  mm in  $\varnothing$ ) affects the main flow and disturbs the metal level as they leave the surface. Additionally, the slag acts as a semi-wall by dampening the fluctuations at the slag-metal interface (Pericleous *et al.*, 2010). This behaviour is highly dependent on the SEN design, mould and casting conditions. Furthermore, in some cases, external fields such as electro-magnetic breaking and/or stirring can be used to modify the flow. However, a model able to capture each of these phenomena to the smallest detail is not feasible for industrial application. Therefore, several simplifications have to be made in order to achieve predictions with enough accuracy at a reasonable computational cost. These include the following:

- Viscosity and density variations with temperature do not affect to a large extent the flow in the mould. Thus, the flow is assumed to be isothermal.
- The mushy zone close to the solidified shell in the mould walls can be approximated by a non-slip wall.
- The hydrostatic pressure and temperature variations in the liquid steel do not affect the Argon bubbles diameter significantly.
- The mesh is adapted for computational efficiency. Thus, boundary layers are not fully resolved at the walls (e.g. not ensuring  $y^+ \approx 1$ ) while time-step increments do not achieve Courant numbers below 1 in all of the geometry. However, it was concluded that an element count of  $\sim 2$  Million cells provides a good compromise between accuracy and computational time for the available resources. A mesh study has been carried out to verify the accuracy of the simulations (Barestrand *et al.*, 2016).

Figure 2 illustrates the geometry and different mesh zones for the model, (1) is a constant velocity inlet, (2) is a pressure outlet and (3) is a constant velocity outlet.

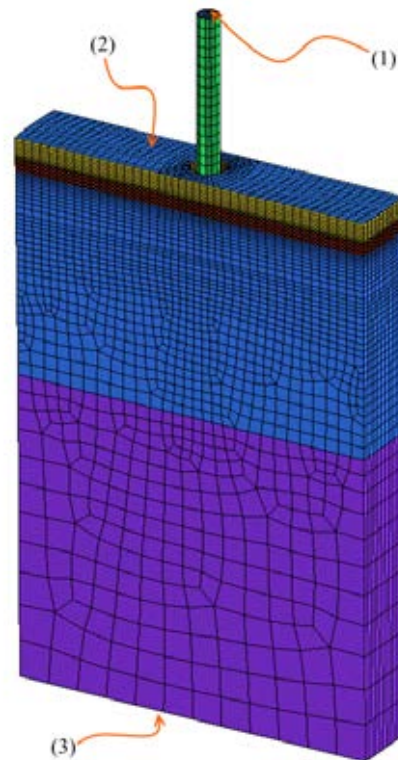


Figure 2: Mould model geometry & coarse mesh.

The mesh is completely conformal and joined by transition zones. It is highly refined at the metal level (red) and nozzle (green) to enable capturing of surface fluctuations and turbulence. The SIMPLE C-algorithm is used together with a Least Squares Cell Based gradient description for time-stepping. A body force weighted formulation was used for pressure, whereas a bounded central differencing is used for momentum. A second order upwind scheme is used for the volume fraction.

The following parameters were used for the LES (turbulence), VOF (Eulerian frame) and DPM (Lagrangian frame) sub-models for solving the Navier-Stokes equations:

- Large Eddy Simulation
  - WALE Subgrid model
  - WALE constant ( $C_w = 0.325$ )
- VOF: Eulerian frame type model
  - Implicit body force
  - Dispersed interface
  - Constant interfacial surface tension
- Discrete phase model:
  - Updated every third time-step
  - Coalescence
  - Custom User Defined Function (UDF) for drag-force
- Two-way coupling interaction between continuous phase (steel) and Disperse phase (Argon bubbles) including turbulent interactions.

Further details on the standard solver are not discussed here in detail since they can be found in the ANSYS-FLUENT theory manual (ANSYS-Inc., 2013) while specific changes to the solution procedure and User Defined Functions can be found in a detailed report (Barestrand *et al.*, 2016). ANSYS-FLUENT was executed on a 128 core cluster.

**Physical modelling**

A numerical model that aims to incorporate all the phenomena described previously needs substantial amounts of data for validation. This was partly done at a Continuous Casting simulator located at Swerea MEFOS. The simulator is based on a low-melting point alloy with similar properties to liquid steel. The properties used in the CFD simulations for steel and the low melting point alloy in the casting simulator is presented on Table 1.

**Table 1:** Casting Simulator Details and material properties

Continuous Casting Simulator specifications			
Mould size	1.2 x 0.22 x 0.9 m		
Tundish (metal holder)	h = 0.7-0.9 m		
Argon flow rate	Variable : up to 12 lit/min		
Immersion depth	Variable within 150 mm		
Bi-Sn alloy (MCP-137) & liquid steel properties			
	viscosity, $\mu$ (Pa-s x $10^{-3}$ )	density, $\rho$ (kg/m <sup>3</sup> )	kinematic viscosity, $\nu$ (m <sup>2</sup> /s x $10^{-6}$ )
Steel (1500 C°)	6.28	7193.7	0.9
MCP 137 (150 C°)	10.7	8580	1.25
MCP 137 (170 C°)	8.6	8580	1

Further details on the CC simulator were presented previously at CFD 2014 in Trondheim (Ramirez Lopez *et al.*, 2014) (Figure 3).



**Figure 3:** CCS-1.5 Continuous Casting SimulatorThe CC simulator was used to test two different SEN types; namely mountain and cup, based on the shape of the bottom of the nozzle and ports (Figure 4). The mountain and cup types are designated M and C, respectively.

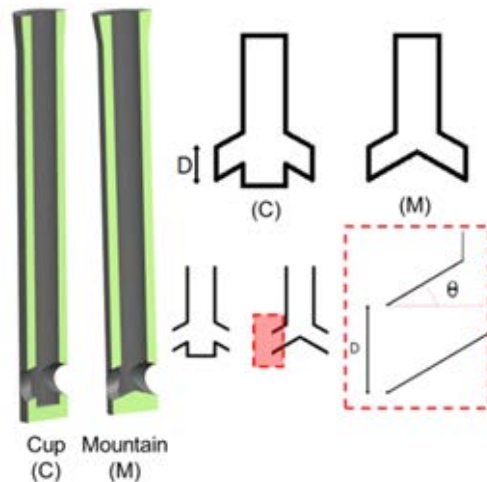


**Figure 4:** Mountain & Cup nozzle geometries and design parameters.

Experiments were carried out for all the casting conditions in the operational range of the industrial caster under investigation as well as testing the resistance and performance of the new nozzle designs. The industrial mould size varied between 1200 mm to 1680 mm in width and 220 mm to 290 mm in thickness, whereas validation in the CC simulator was carried out in a mould with 1200 mm width and 220 mm thickness for both nozzles. An optical probe was used for characterization of the surface fluctuations by means of a distance measurement with high acquisition rate, which resulted in reliable evaluation of the surface behaviour for the different nozzles and casting conditions (Figure 5a). The signal accuracy of the probe is up to 0.4  $\mu\text{m}$  with a sampling frequency of 1000 Hz. The probe was positioned at half the distance between the mould short face and nozzle as well as in the middle of the thickness for all measurements (Figure 5b-5c).

Large transient events were discarded in the processing of these signals, which leaves only the short period variations (e.g.  $T_s < 5s$ ) to characterize the fluctuations at the metal interface.



**Figure 5:** Measurement of fluctuations at the metal interface using an optical probe.

### Plant trials

A variety of velocity and surface profile measurements were carried out during actual production runs at an industrial CC machine. The velocity measurements were done using the nail board method where a rack of nails is dipped for a few seconds in the mould between the nozzle and narrow side. The steel forms a solidified tip whose profile can be related to the velocity and direction of the steel flow at that moment (Figure 6) (Liu *et al.*, 2011).

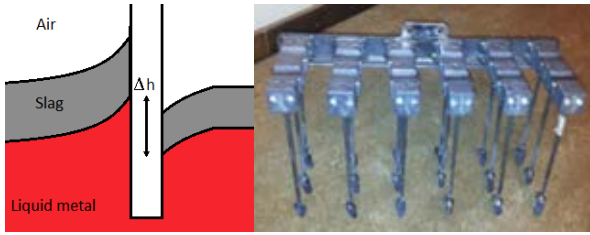


**Figure 6:** Schematics of nail dipped into the molten steel-slag interface (left) and nail board rack (right).

The velocity of the liquid metal at the nail position may be approximated by the formula.

$$\Delta h = \frac{V^2}{2g} \quad (1)$$

Where  $\Delta h$  is the difference in height between the two sides of the nail;  $V$  is the velocity at the interface and  $g$  is the gravitational acceleration. The nail board presented in Figure 6 (right) provides a 3x6 resolution map of the interface velocities. Furthermore, the main flow direction may be determined by measuring the positions of maximum and minimum height of solidified tip on the nail. These measurements were used as basis to validate the velocities and level fluctuations measured in the Casting Simulator and CFD models.

### Analytical model

The analytical behaviour of surface waves has been extensively studied for liquids with a free surface (Lighthill, 2001). Thus, the free surface frequencies of the metal in the mould can be derived by assuming two completely inviscid fluids with density ( $\rho$  and  $\rho_x$ )

separated by an interface ( $z = 0$ ) confined into a rectangular geometry of  $Size_i = \{a, b, d\}$ . The velocity potential in the fluids may be regarded as a general function dependent on spatial position and time. Further, it may be also assumed to be separable; so, the velocity potential can be written as:

$$\phi = \phi(x_j, t) = \phi_x(x)\phi_y(y)\phi_z(z)\phi_t(t) \quad (2)$$

Naturally, the velocity potential needs to satisfy the continuity equation since an incompressible fluid is assumed. Thus, this can be written as:

$$\frac{\partial^2 \phi}{\partial x_i \partial x_i} = 0 \quad (3)$$

If a new variable  $\eta$  is introduced to represent the offset of the surface from position  $z = 0$ , the boundary conditions for the domain can be written as:

$$\left. \frac{\partial \phi}{\partial z} \right|_{z=-d} = 0; \quad \left. \frac{\partial \phi}{\partial x} \right|_{x=0,a} = 0; \quad \left. \frac{\partial \phi}{\partial z} \right|_{z=0} = \frac{\partial \eta}{\partial t}; \quad \left. \frac{\partial \phi}{\partial y} \right|_{y=0,b} = 0 \quad (4)$$

Where  $a$  represents the width of the geometry containing the fluid,  $b$  is the length and  $d$  is the depth. The last condition for the interface comes from Bernoulli's equation for unsteady flows:

$$\frac{\partial \phi}{\partial t} + gz + \frac{p}{\rho} + \frac{1}{2}(\nabla \phi)^2 = 0 \quad (5)$$

Linearizing this equation (omitting  $(\nabla \phi)^2$ ) gives the final boundary condition for Equation 6:

$$\left. \frac{\partial \phi}{\partial t} \right|_{z=0} + g\eta(x, y, t) + \frac{p}{\rho} = 0 \quad (6)$$

The derivation is straightforward by inserting Equation 2 into Equation 3. An oscillatory solution with the frequency (Equation 7) is obtained after applying the boundary conditions (Equations 4 and 6):

$$\begin{cases} f_{mn}^2 = \frac{g}{4\pi} \sqrt{\left(\frac{m}{a}\right)^2 + \left(\frac{n}{b}\right)^2} F_d(d) \\ F_d(d) = \tanh\left(\pi d^2 \sqrt{\left(\frac{m}{a}\right)^2 + \left(\frac{n}{b}\right)^2}\right), (m, n) \in Z^+ \end{cases} \quad (7)$$

Where  $a$  and  $b$  are the side lengths (e.g. mould width and thickness) and  $g$  is the gravitational acceleration. Note that this expression only holds true when there is significant density differences between the fluids (e.g. water and air). The frequencies obtained through this equation are the *eigenfrequencies* at which the liquid steel within the mould resonates. These frequencies are independent of viscosity, density and all other properties of the fluid (i.e. these are only a result of the interaction between continuity and body forces). The general expression for the eigenfrequencies, ignoring the mould depth can be written as in Equation 8:

$$f_{mn}^2 = \frac{g}{4\pi} \sqrt{\left(\frac{m}{a}\right)^2 + \left(\frac{n}{b}\right)^2}, (m, n) \in Z^+ \quad (8)$$

Uneven whole numbers in this equation represent the so called “sloshing frequencies”, while even modes represent “symmetric frequencies” as observed in Figure 7. Generally even modes are induced by symmetric flow features and uneven modes by asymmetric structures (such as jet oscillation)(Gupta *et al.*, 1997).

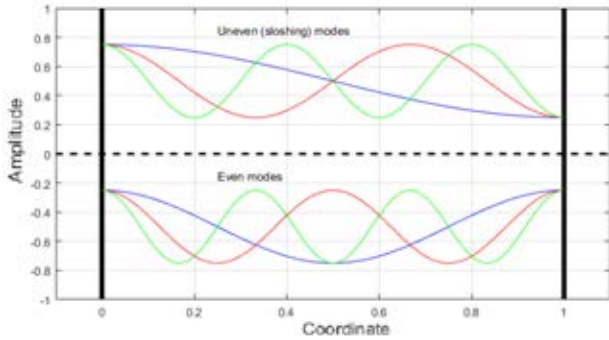


Figure 7: Sloshing and symmetric mould frequencies.

These frequencies naturally resonate with the mould and may lead to amplification of the surface waves (i.e. interface fluctuations in the mould); thereby, flow patterns in these frequency ranges must be avoided. Additionally, these frequencies affect the circulation time and roll frequencies. Ultimately the nozzle design affects all these flow structures and plays a major role on how these frequencies are induced.

## RESULTS & VALIDATION

### Overall flow patterns

Processing of CFD results is quite complex since it must portray the long-term behaviour of the flow pattern as well as its frequency fluctuations without simple averaging of the data. Figure 8 presents a volume render of velocities, eddy viscosity and Argon bubbles (i.e. DPM-distribution) for the 1200 x 220 mm mould.

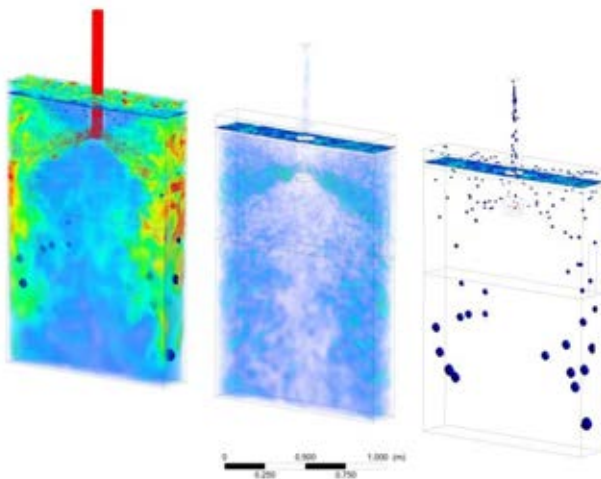


Figure 8: Volume render of velocity (left), eddy viscosity (centre) and Argon bubble distribution (right) for a 1200mm×220mm mould with M-type nozzle.

### Steel interface

The steel surface behaviour is of particular interest since the validation depends on the surface behaviour; thus, an iso-surface was used to define the steel-slag interface at VOF=0.5 steel fraction (Figures 9 and 10).

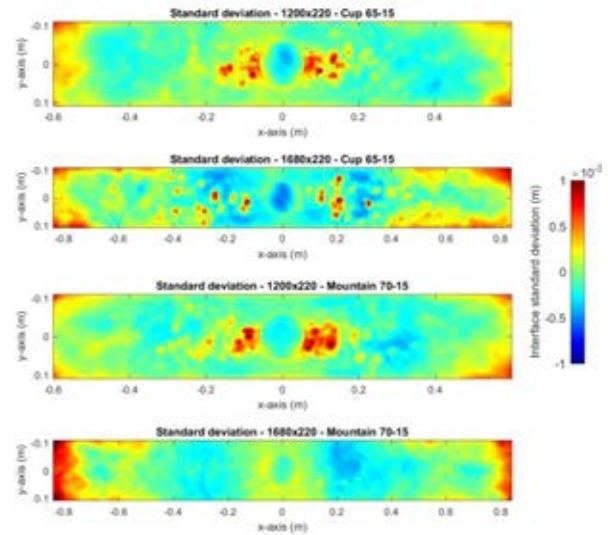


Figure 9: Standard Deviation of metal level fluctuations at the free surface.

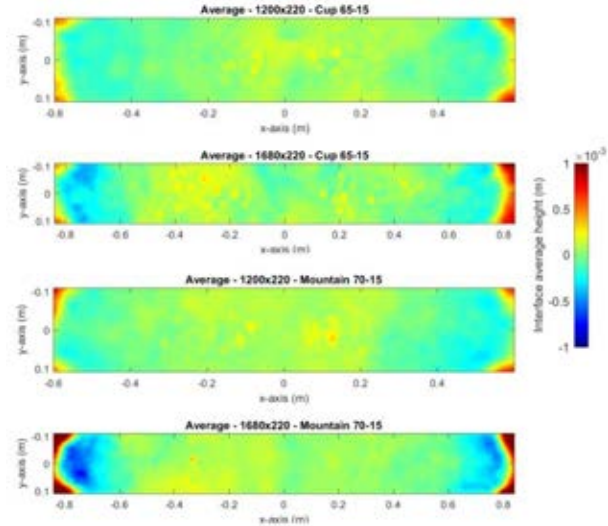


Figure 10: Averaging of metal level fluctuations at the free surface (red denotes an increase in level and blue denotes a decrease in level).

The surfaces in Figures 9 and 10 were extracted at a rate of 40 Hz and contain the height of the fluctuations measured from a steady reference level 0.0. (red denotes an increase in level and blue denotes a decrease in level). Figure 9 clearly indicates that the main source of surface fluctuations is the dissipation of momentum at the narrow sides as well as the bubble departure positions. Figure 10 indicates that the most prominent surface feature is the standing wave sending metal upwards due to momentum in the narrow walls and the neighbouring valley (i.e. level depression). This is an interface feature that was confirmed during the plant trials.

### Argon bubbles

The Discrete Phase Model (DPM) is able to predict the argon distribution and flow differences for the various mould sizes. However, there is no method available to map the bubble departure positions during industrial operation and/or liquid metal experiments. Therefore, the results are only indicative of the possible argon behaviour in the mould.

Nevertheless, the flow and velocity patterns observed during plant trials and experiments are similar to those predicted in the CFD simulations. This could well indicate that the argon model predictions are in line with the actual flow patterns in the mould. Bubble departure positions and termination points are presented in Figures 11 and 12, respectively. Figure 11 indicates that the bubble departure positions are spread more evenly for the larger geometry while bubbles tend to cluster around the nozzle for smaller moulds. This is mainly due to the different jet velocities for the widest (1680

mm) and narrowest (1200 mm) moulds. Bubble termination points in the x-y plane (parallel to the wide walls) are shown in Figure 12 where termination points indicate coalescence or escape. Results show that smaller geometries produce more coalescence in the upper part of the nozzle, while bubbles are more evenly distributed for larger geometries. This suggests that the residence times for smaller moulds are significantly larger, which allows more coalescence.

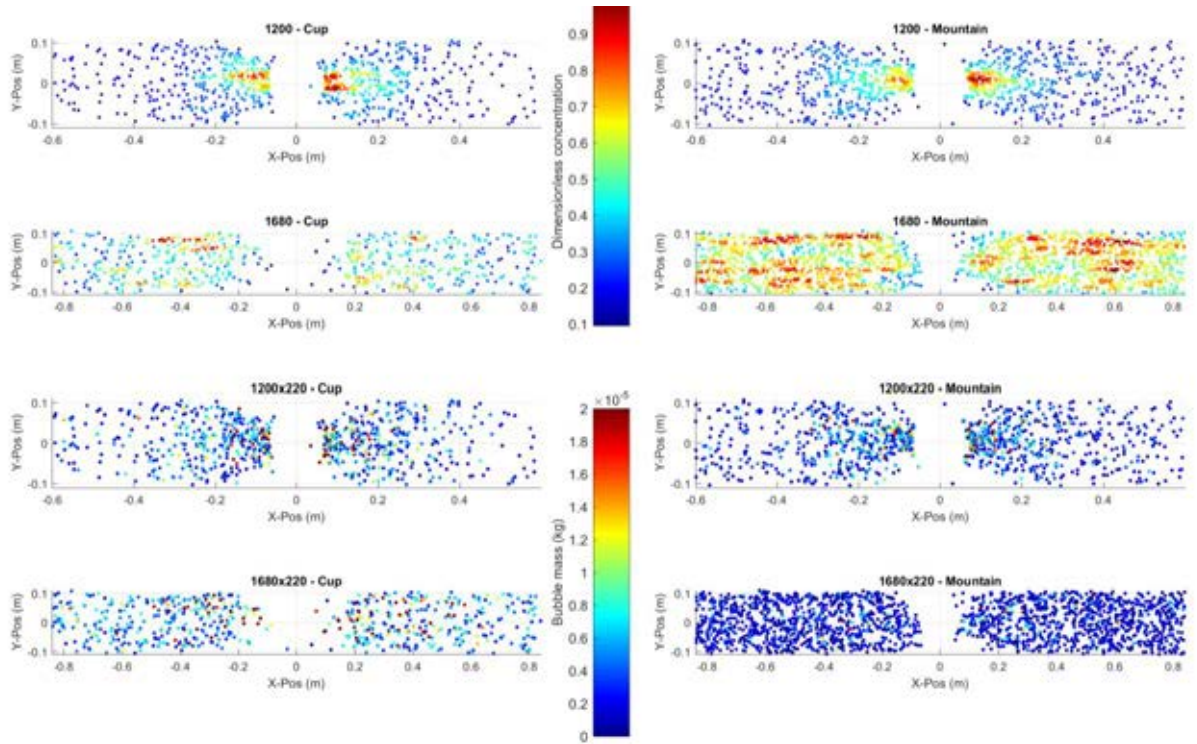


Figure 11: Scatter plot of bubble departure positions coloured by dimensionless concentration (upper) and particle mass (lower).

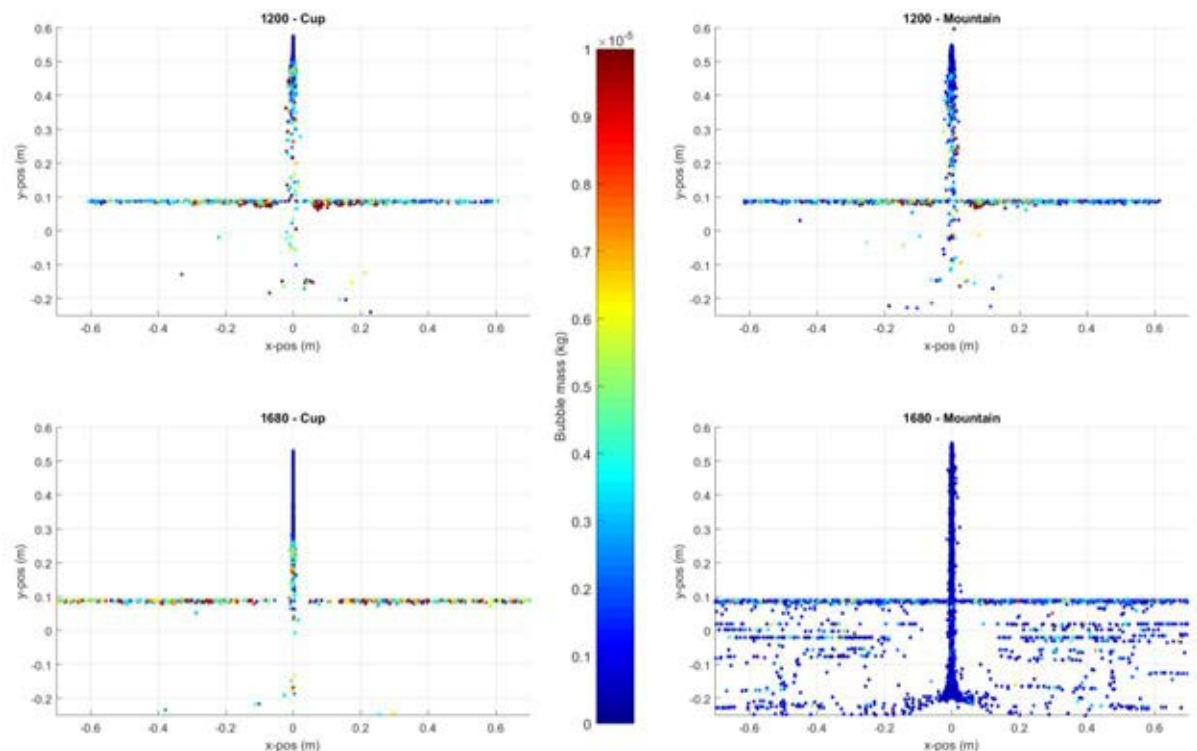


Figure 12: Bubbles termination points:  $y \approx 0.1$  indicates escape while  $y < 0$  or  $y > 0.1$  indicates coalescence (bubbles coloured by mass at termination).

### Nozzle frequency signature

Predictions show that nozzle performance is the main deciding factor for the length, distribution and periodicity of stable flows within the mould. Furthermore, each particular flow pattern gives rise to a *Nozzle Frequency Signature (NFS)* which varies with design, mould geometry and casting speed. Examples of these frequency signatures are presented in Figure 13.

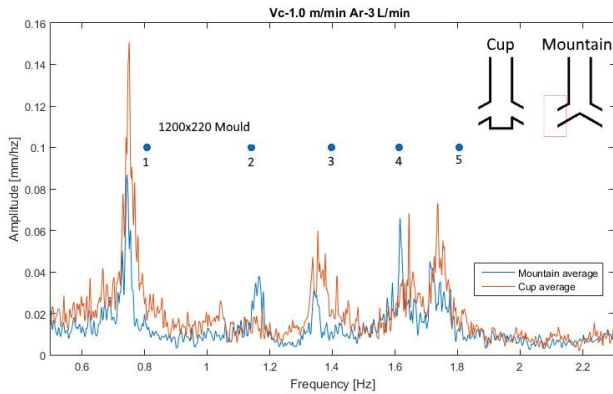


Figure 13: NFS for mountain and cup nozzles.

The main nozzle variables which affect NFS for a given mould and casting speed are:

- Inlet angle
- Inlet diameter
- Type (Mountain or Cup)

### Frequency comparison

Table 2 presents the predicted frequencies from analytical and numerical modelling compared to the actual frequencies measured in the physical caster.

Table 2: Frequency comparison in Hz

Peak #	1	2	3	4	5
Theoretical	0.8069	1.1412	1.3977	1.6140	1.8045
Numerical	0.7688	1.118	1.246	1.409	1.491
CCS-1.5	0.75	1.16	1.35	1.62	1.74

Results in Table 2 show a good agreement between Theoretical, Numerical and Experimental frequencies, which indicates the validity of the CFD and analytical models developed. Nevertheless, the offsetting of the modelling results towards lower frequencies reveals possible over relaxation as observed in Figure 14. The CFD predictions were further improved by disabling the sharp interface and interfacial anti-diffusion, which provides an excellent match for the Simulator frequencies in Table 3.

Table 3: Frequencies from numerical models in Hz (1/s). The number after C or M denotes the port diameter d in mm, while the inlet angle in  $\theta$  degrees is next. Frequencies in bold numbers have higher amplitudes.

Peak #	1	2	3	4	5
1200x220 - C 65-15	<b>0.778</b>	x	<b>1.328</b>	<b>1.612</b>	<b>1.745</b>
1200x220 - M 65-15	<b>0.709</b>	1.211	<b>1.471</b>	1.588	1.720
1200x220 - M 70-15	<b>0.782</b>	1.148	<b>1.339</b>	<b>1.61</b>	1.739

Substantially better agreement between models and experiments are evident by comparing these frequencies to the physical caster in Table 2. This means that anti-diffusion algorithms should be avoided when modelling mould frequencies and determining the NFS numerically

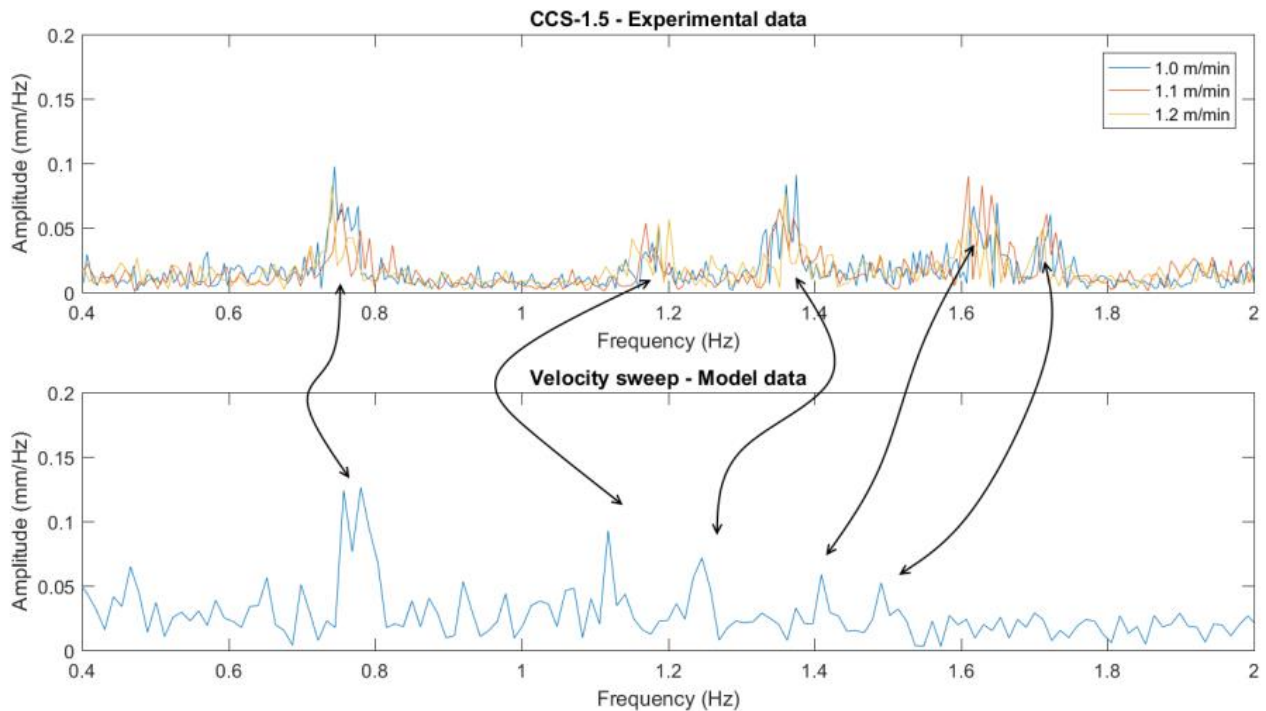
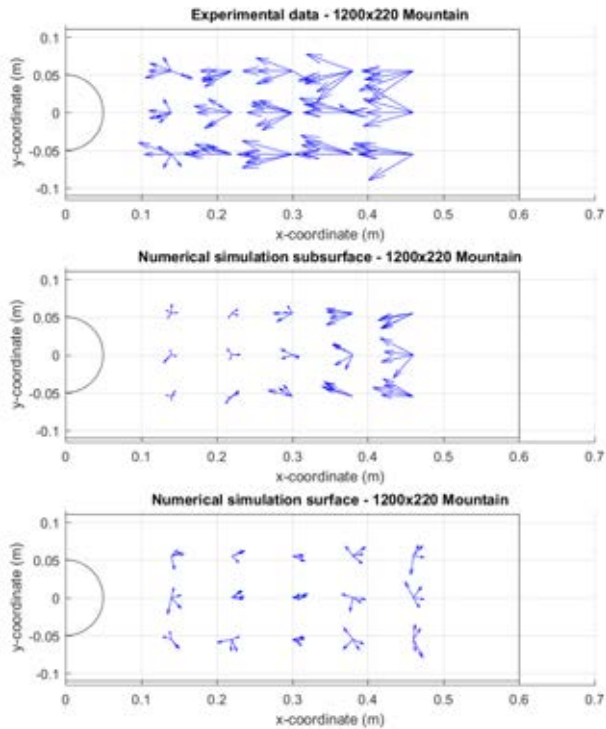


Figure 14: Sharp interface numerical model frequencies compared to physical.

### Surface velocity comparison

A comparison between surface velocities in the CFD models and plant measurements is presented in Figures 15 and 16. A dispersed phase formulation is used in Figure 15 for the velocity gradient resulting in poor agreement due to the dispersive layer. In contrast, a sharp anti-diffusive interface formulation is used in Figure 16 resulting in excellent agreement.



**Figure 15:** Interface velocities for the dispersed phase formulation compared to plant measurements.

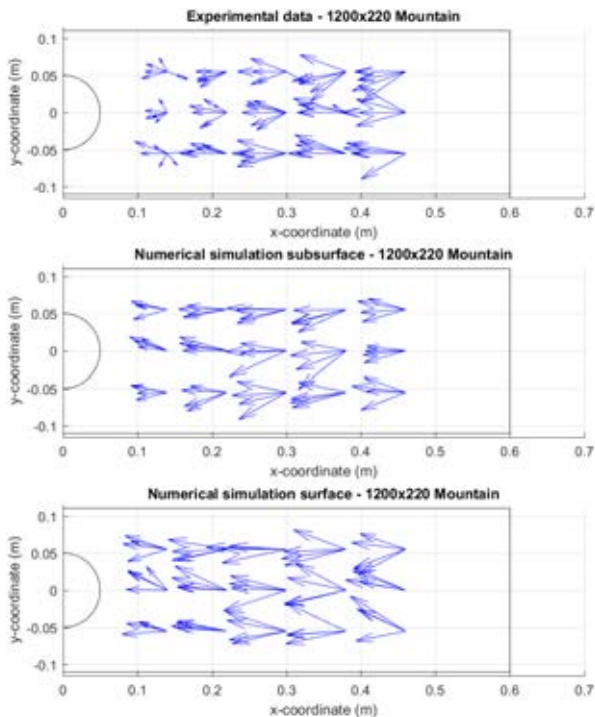


**Figure 16:** Interface velocities for sharp anti-diffusive interface formulation compared to plant measurements.

### DISCUSSION

The combination of LES+VOF+DPM seems suitable to predict the phenomena inside the mould and casting nozzle for different Argon loads and casting speeds. However; at this stage, the model does not account for bubble breakup which is expected to have a minor influence in the flow pattern (i.e. larger bubbles with more buoyancy would have a stronger effect on the flow). The surface velocity comparison shows that a non-dispersive model should be used in order to capture interface velocities with high accuracy. This is the opposite of the surface frequency results in the previous section. This requires further investigations and work is being carried out by the authors to explain and elaborate on these findings.

Ultimately, the aim of the present model is to find optimal conditions for caster operation which includes the ideal bubble size (to avoid entrapment of the bubbles in the solidifying shell). However, this requires coupling of LES with a more complex solidification model as those presented by the authors for a simpler turbulence model; k-epsilon (Ramirez Lopez *et al.*, 2014). This would also imply a non-isothermal solution with the subsequent thermal gradient effects on the continuous and dispersed phases (e.g. gas expansion, increased lift, convective effects, etc.). However, it is expected that these have a minimum impact on the flow since the argon temperature is already close to steel when reaching the injection point as observed by (Iguchi *et al.*, 1995) while the same minor influence can be expected for the convective effects since the inertial forces in the mould are considerably greater than any velocities induced by changes in density of the liquid steel. Even if those become more important towards the end of solidification further down the strand.

### CONCLUSIONS

The present investigation compared results from numerical and analytical models developed for Continuous Casting with Industrial trials and experiments on a Casting Simulator. The following conclusions can be drawn from these comparisons:

- *Eigenfrequencies* in the mould are almost exclusively dependent on the mould geometry, except for offsets in the frequency created by small differences in flow features. These are caused by minor changes in the nozzle design (e.g. port angle and diameter).
- The nozzle performance can be characterized by a Nozzle Frequency Signature (NFS) which varies between mould sizes and casting speed.
- The NFS can be evaluated using numerical methods validated on the Casting Simulator in liquid metal. This allows for a quick and efficient way to test the performance of a nozzle for a given geometry as well as finding optimal casting conditions.
- The analytical approach developed for prediction of frequencies in CC is in very good agreement with experiments and simulations, confirming the existence of the NFS.

- All measurements performed in the CC Simulator clearly show the presence of eigenfrequencies, although the uneven modes are offset compared to the theoretical ones by an average 0.06 Hz.
- It was confirmed that the amplitude of the eigenfrequencies is dependent on nozzle geometry, while the mode amplitudes are dependent on casting speed.
- The dispersed iso-surface VOF model for level monitoring and frequency analysis is proven to better capture the resonance frequencies. However, the sharp interface anti-diffusive interface formulation provides a better agreement with the interface velocities measured industrially.
- The major flow features can be captured using a relatively coarse mesh aiding computational efficiency.

A deeper study is undergoing to study the dependence of the flow patterns on different nozzle parameters such as how the interface, jets and argon-distribution are affected by changes in diameter and inlet angle of the nozzles.

## ACKNOWLEDGEMENTS

The research presented in this paper has been carried out within the project FLOWFLEX- Flow Dynamics studies for Flexible Operation of Continuous Casters (Diarienummer: 2014-01936) funded by the Swedish Innovation Agency, VINNOVA.

## REFERENCES

- ANSYS-INC.: "ANSYS Fluent v.12 - User's Guide", ANSYS Inc., (2013),
- BARESTRAND, H. and FORSLUND, T.: "Numerical & physical modelling of fluid flow in a continuous casting mould: Flow dynamics studies for flexible operation of continuous casters", (2016),
- BARESTRAND, H., FORSLUND, T., JALALI, P.N., RAMIREZ LOPEZ, P.E., OLOFSSON, C., ROOS, E. and JÖNSSON, P.: "Flow Dynamics Analysis of Continuous Casting Processes through numerical and Physical Modelling", 4th International Symposium on Cutting Edge of Computer Simulation of Solidification, Casting and Refining (CSSCR2016), (2016), Xi'an, CHINA.
- DAUBY, P.H.: "Real Flows in Continuous Casting Molds", *Iron and Steel Technology*, **8** (2011), 151-160.
- GUPTA, D., CHAKRABORTY, S. and LAHIRI, A.K.: "Asymmetry and oscillation of the fluid flow pattern in a continuous casting mould: a water model study", *ISIJ International*, **37** (1997), 654.
- IGUCHI, M., CHIHARA, T., TAKANASHI, N., OGAWA, Y., TOKUMITSU, N. and MORITA, Z.-I.: "X-ray fluoroscopic observation of bubble characteristics in a molten iron bath", *ISIJ International*, **35** (1995), 1354-1361.
- LIGHTHILL, J.: "Waves in fluids", Cambridge university press, (2001),
- LIU, R., SENGUPTA, J., CROSBIE, D., CHUNG, S., TRINH, M. and THOMAS, B.G.: "Measurement of molten steel surface velocity with SVC and nail dipping during continuous casting process", *TMS Annual Meeting*, (2011), 51-58.
- OLSEN, J.E. and CLOETE, S.W.P.: "COUPLED DPM AND VOF MODEL FOR ANALYSES OF GAS STIRRED LADLES AT HIGHER GAS RATES", *Seventh International Conference*

- on CFD in the Minerals and Process Industries*, (2009), Melbourne, Australia
- PERICLEOUS, K., KOUNTOURIOTIS, Z., DJAMBAZOV, G., DOMGIN, J.F. and GARDIN, P.: "Experimental and numerical simulation of the mould region of a steel continuous caster", *AIP Conf. Proc.*, **1281** (2010), 95-98.
- RAMIREZ LOPEZ, P.E., JALALI NAZEEM, P., SJÖSTRÖM, U. and NILSSON, C.: "Adding Argon Injection through the DPM+VOF Technique to an Advanced Multi-Physics and Multi-Scale Model for Continuous Casting of Steel", *10th International Conference on Computational Fluid Dynamics In the Oil & Gas, Metallurgical and Process Industries*, (2014), Trondheim, Norway.
- RAMIREZ LOPEZ, P.E., JALALI, P.N., BJÖRKVALL, J., SJÖSTRÖM, U. and NILSSON, C.: "Recent developments of a numerical model for continuous casting of steel: Model theory, setup and comparison to physical modelling with liquid metal", *ISIJ International*, **54** (2014), 342-350.





## AN EULER-EULER MODEL FOR GAS-LIQUID FLOWS IN A COIL WOUND HEAT EXCHANGER

Thomas ACHER<sup>1\*</sup>, Manuel KNAUP<sup>1</sup>, Konrad BRAUN<sup>1</sup>, Hans-Jörg ZANDER<sup>1</sup>

<sup>1</sup>The Linde Group - Engineering Division, Dr.-Carl-von-Linde-Straße 6-14, 82049 Pullach, GERMANY

\* E-mail: thomas.acher@linde.com

### ABSTRACT

Coil-wound heat exchangers (CWHE) are commonly adapted in process engineering for the efficient transfer of heat between fluids which feature wide temperature and pressure ranges. The field of application for this apparatus ranges from heating or cooling of single-phase flows, over the evaporation or condensation of fluids, to the utilization as isothermal reactor. Due to their large specific heat transfer area accompanied by a compact design, coil-wound heat exchangers are widely used in various process plants (e.g., LNG plants). Depending on the application, two-phase flows may occur at both, the tube- as well as the shell-side of the apparatus. For the design of a CWHE, the fluid and thermodynamic processes in the unit are commonly represented by a system of one-dimensional correlations. This approach implies uniform thermohydraulic conditions on horizontal cutting planes of the exchanger. Fluid and thermodynamic effects in the apparatus which result in radial parameter variations are inaccessible to these conventional design tools. To this end, a multidimensional CFD model has been established to enhance the representation of fluid and thermodynamic phenomena in CWHE design. The shell-side of the CWHE and all tube-side sections are each numerically represented by separate domains which are coupled by source terms to account for the thermodynamic interaction between tube- and shell-side. In each flow region, the hydraulic effect of the tube bundle is modeled as a porous medium with corresponding fluid dynamic characteristics. The gas-liquid dynamics in each flow region is modeled based on an Euler-Euler approach. Unlike classical Euler-Euler models, local phase fractions and fluid properties are calculated from species relations as well as pressure and temperature fields. This model framework is augmented by locally evaluated correlations for pressure drop and heat transfer to account for apparatus internals and thermal coupling. The models for gas-liquid interaction forces are derived from standard correlations and augmented by findings from detailed CFD studies. Remaining parameters are specified by a parameterization study based on experimental findings.

**Keywords:** process industry, heat exchanger, multiphase heat transfer, Euler-Euler approach.

### NOMENCLATURE

#### Greek Symbols

$\alpha$  Phase volume fraction, [-]  
 $\varepsilon$  Porosity, [-]

$\rho$  Mass density, [ $kg/m^3$ ]  
 $\tau$  Stress tensor, [ $N/m^3$ ]

#### Latin Symbols

$a$  Velocity profile coefficient, [-].  
 $A$  Area, [ $m^2$ ].  
 $C$  Model constant, [-].  
 $\vec{f}$  Volumetric force, [ $kg/ms^2$ ].  
 $g$  Gravitational acceleration, [ $m/s^2$ ].  
 $p$  Pressure, [ $Pa$ ].  
 $\vec{u}$  Velocity, [ $m/s$ ].

#### Sub/superscripts

$ax$  Axial.  
 $cent$  Centrifugal force.  
 $g$  Gas.  
 $h$  Homogeneous.  
 $i$  Phase indicator.  
 $j$  Phase indicator.  
 $l$  Liquid.  
 $lift$  Lift force.  
 $rad$  Radial  $i$ .

### INTRODUCTION

In various process engineering applications coil-wound heat exchangers (CWHE) are adopted for the efficient transfer of heat between fluids. The potential operating conditions of this type of apparatus feature a wide range of temperature and pressure levels and the transfer of heat between multiple fluid streams can be realized in one heat exchanger. CWHEs are specifically robust to transients of flow properties (Pacio and Dorao, 2011) and are characterized by a large specific heat transfer area per volume in combination with a comparably compact design. In a CWHE, multiple layers of tubes are wound helically around a central pipe (see Fig. 1) where several tubes are grouped into sections with varying fluid streams. Apparatuses with up to 10,000 tubes enable complex heat exchange processes with heating surfaces of 30,000  $m^2$  and more. Maximal bundle diameters of approx. 5,500 mm and unit heights up to 20 meters can be manufactured. (Walter *et al.*, 2014)

In many large scale plants for the production of liquified natural gas (LNG) CWHEs represent a key equipment. In these applications, the gaseous natural gas is fed to tube sections at the bottom of the apparatus and is cooled, liquified or subcooled while streaming upwards. In the

remaining tube sections the refrigerant is precooled by streaming concurrent to the natural gas. Subsequently, the refrigerant is applied to the top of the shell-side as a dispersed two-phase stream which evaporates while streaming towards the bottom of the CWHE. The natural gas liquification is driven by the complex thermodynamic interaction across the tube bundle with the multiphase flow at the shell-side of the CWHE. The gas-liquid flow characteristics determine local heat transfer and affect the efficiency and functionality of the entire apparatus.

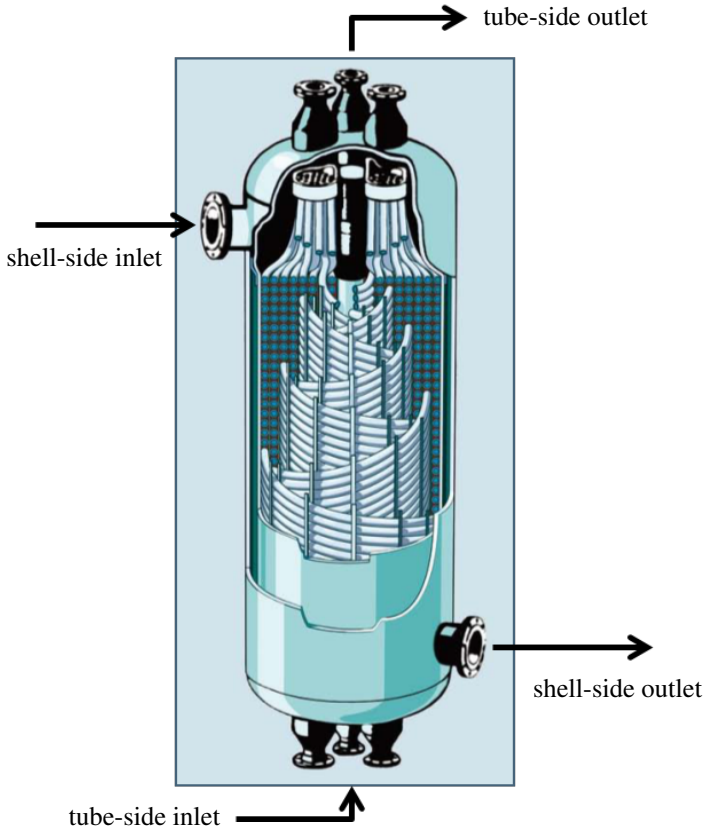


Figure 1: Exemplary sketch of a coil-wound heat exchanger.

In general, one-dimensional correlations are applied to represent fluid and thermodynamic processes in order to design CWHE apparatuses (Wang *et al.*, 2015). Merely axial variations of thermohydraulic parameters are captured by this approach while radial parameter variations, specifically fluiddynamic inhomogeneities, are neglected. In order to incorporate these potentially influential phenomena a two-dimensional CFD model has been developed. The following sections explicate this approach, specifically the gas-liquid flow representation as well as the effect of radial varying geometry parameters at the shell-side. Remaining model constants are specified by parameterization and CFD model results are presented.

## CFD MODEL DESCRIPTION

A numerically efficient representation of the CWHE is realized by the consideration of a two-dimensional cross-section of the cylindrical form (see Fig. 2). While assuming rotational symmetry of the apparatus, radial variations of thermohydraulic parameters are represented by this modeling setup. The individual fluid dynamic regions on the shell-side and the tube-side of the CWHE are reflected by separate simulation domains, where multiple tube sections are represented individually. To model the heat transfer between the shell- and the tube-side the independent flow regions are thermodynamically coupled by respective source terms and the hydraulic effect of the tube bundle is represented as a porous medium with corresponding fluid dynamic characteristics. This setup enables a coherent decomposition of the numerical meshes of the individual domains to allow for an efficient computation on multiple processors.

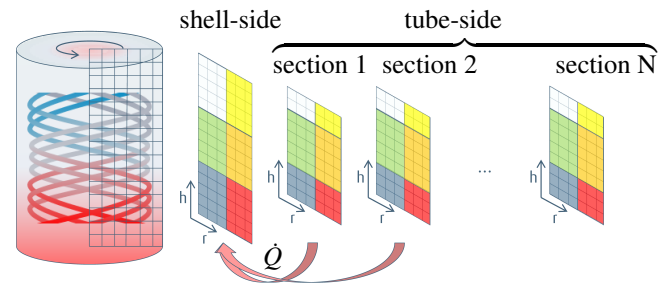


Figure 2: Two-dimensional representation of the CWHE with a shell-side domain and multiple tube sections (Göll *et al.*, 2013).

The fluid dynamics at both the tube- as well as the shell-side of the CWHE are modeled by an Euler-Euler approach (e.g., (Drew and Passman, 1999; Ishii and Hibiki, 2010)) since two-phase flows may occur at any flow region. The respective transport equations for momentum read

$$\frac{\partial}{\partial t} \alpha_i \rho_i \vec{u}_i + \nabla \cdot \alpha_i \rho_i \vec{u}_i \vec{u}_i = -\alpha_i \nabla p_i + \nabla \cdot \alpha_i \underline{\tau}_i + \alpha_i \rho_i \vec{g} + \vec{f}_{rad,i} + \vec{f}_{h,i} \quad (1)$$

where  $\alpha_i$ ,  $\rho_i$ ,  $\vec{u}_i$  and  $\tau_i$  denote the volume fraction, density, velocity and shear stress tensor of phase  $i$ . The fluid dynamic interaction between gas and liquid as well as the flow resistance in the porous media are modeled by the phase specific body forces in axial direction  $f_{h,i}$  and radial direction  $f_{rad,i}$ .

The Euler-Euler CFD solver *twoPhaseEulerFoam* of the program package OpenFOAM represents the basis for the model implementation which is interfaced to submodels for the evaluation of local void fractions and fluid parameters, pressure drop in the porous media and transferred heat between flow regions (see Fig. 3). In contrast to classical Euler-Euler models, local phase fractions are computed from the local composition of chemical species and thermodynamic conditions which requires the inclusion of transport equations of the comprised species instead of a respective formulation for local void fraction. Local thermodynamic equilibrium is assumed to determine relevant fluid properties (i.e. viscosity, density, thermal

conductivity and surface tension) and phase composition in each numerical cell based on local species concentrations and thermodynamic relations (Jakobsen, 2008). Local thermodynamic conditions are computed from the energy transport equation which includes source terms for the heat transfer across the simulation domains.

As depicted in Fig. 3 the evaluation of fluid parameters at vapor/liquid-equilibrium in each numerical cell is realized by coupling the CFD solver to Linde’s inhouse software. This program is used for cell-wise conduction of flash calculations (pH-flash) in order to evaluate local phase fractions and fluid properties. Energy transport equation source terms which represent heat transfer effects are based on one-dimensional correlations used for CWHE design at Linde which are determined by flow parameters and single- or two-phase flow conditions. At the shell-side as well as at the tube-side, the flow resistance due to the tube bundle is integrated in the CFD model by a porous zone. The corresponding pressure drop properties are evaluated from CWHE design correlations analogous to the heat transfer calculations. For additional information on the CFD model framework the reader is referred to previous publications (Acher *et al.*, 2016).

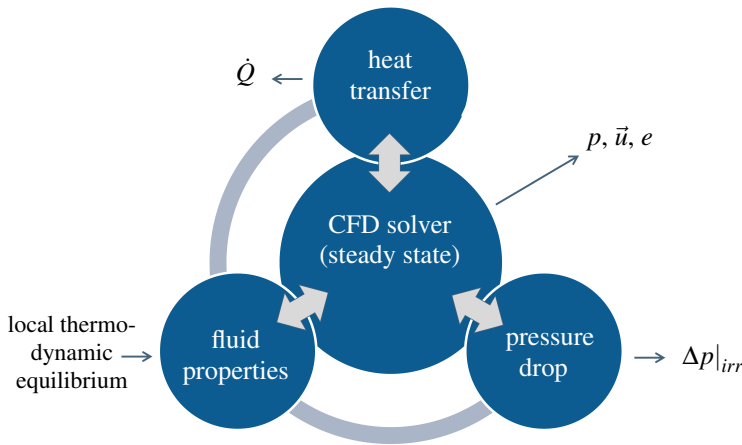


**Figure 3:** Depiction of numerical model components and their interaction.

As mentioned above, potential radial variations of fluid dynamic parameters might impact the heat transfer performance of the CWHE. These non-uniformities can originate from two-phase flow effects on the shell-side of the apparatus. The consideration of these phenomena necessitates the incorporation of submodels for an enhanced depiction of gas-liquid flow conditions.

**Two-phase flow model development**

The shell-side of the CWHE features a gas-liquid flow which is applied as a dispersed stream above the tube bundle and evaporates on its way to the bottom of the apparatus. The related thermohydraulic effects are commonly depicted by empirical correlations which resort to pseudo-homogenous parameters describing the multiphase flow. In contrast, in an Euler-Euler context the prevalent retaining and interfacial forces have to be modeled individually to yield phase-specific velocity fields (see Fig. 4).

In order to ensure consistency with the pseudo-homogeneous concept for a radially uniform flow field, the two-phase pressure drop characteristics along the bundle are

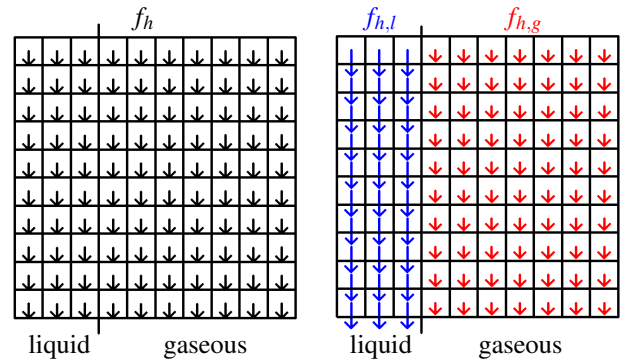


**Figure 4:** Schematic depiction of the volume force acting on fluid elements in a numerical cell (Knaup, 2015). Left: pseudo-homogenous flow resistance. Right: phase-specific flow resistance.

retained as specified by the one-dimensional model and the homogeneous force field  $f_h$  is divided into phase-specific contributions  $f_{h,i}$ :

$$f_{h,i} = C_i f_h = \frac{f_{ax,i}}{f_{ax,j} + f_{ax,i}} f_h \quad (2)$$

where the weighting coefficient  $C_i$  is a function of the axial forces acting on the gas phase  $f_{ax,g}$  and the liquid phase  $f_{ax,l}$  inside the tube bundle.

The axial retaining and interfacial forces for the individual phases  $f_{ax,g}$  and  $f_{ax,l}$  are further subdivided according to the bilateral interaction between gas, liquid and tube bundle. To do so, a basic perception of the gas-liquid flow pattern in the tube bundle is required. Figure 5 depicts the assumed liquid flow structures on the shell-side of the tube bundle which are comprised of vertical films enclosing the coiled tubes and dispersed droplets between tube layers.

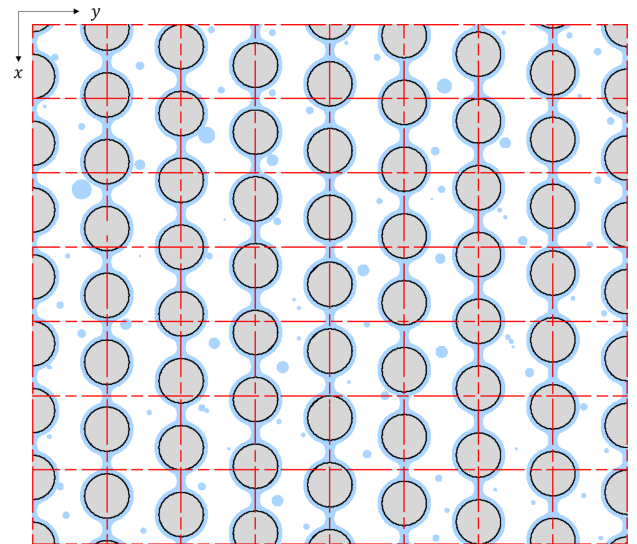


**Figure 5:** Sketch of the presumed gas-liquid flow conditions at the shell-side of the CWHE bundle

Due to their fundamentally different characteristics with regard to gas-liquid interaction the liquid film and droplets are modeled independently. Hence, the axial phase-specific forces at the shell-side are formulated as

$$f_{ax,g} = f_{gs} + f_{gl,d} + f_{gl,f}, \quad (3)$$

$$f_{ax,l} = f_{ls} - f_{gl,d} - f_{gl,f}. \quad (4)$$

Table 1 gives a description on each of the phase-specific interfacial forces and states the modeling approach selected for their evaluation. As the gas-liquid interaction  $f_{gl,d}$  is a function of the volume fraction of liquid droplets and drop sizes these parameters are derived from model correlations based on local fluid dynamic equilibrium considerations (Sirignano, 2010; Ishii and Mishima, 1989). Consistent to experimental observations, it is assumed that liquid velocities are dominated by the film around the tubes as the volumetric contribution of droplets is considered subordinate. This conception arguably justifies the adoption of simple approaches for the evaluation of droplet sizes and local volume ratios of droplet to film. Yet, this assumption is further validated by detailed 3D CFD simulations presented below.

Analogous to the representation of phase-specific axial forces the numerical model includes a formulation for radial volume forces  $f_{rad,i}$  in the Euler-Euler momentum equations Eqn. 1. Two prevalent mechanisms which induce radially acting volume forces were identified based on experimental findings, operational data analysis and detailed 3D CFD simulation of single- and multiphase flows. Table 2 gives a brief description of both the lift and centrifugal force. A more detailed explication with a focus on the origin of both effects with regard to the apparatus at hand is part of the following subsections.

The phase-specific cumulated effect of radial fluid dynamic processes is incorporated as

$$f_{rad,l} = f_{lift,l} + f_{cent,l}, \quad (5)$$

$$f_{rad,g} = -f_{lift,g} + f_{cent,g}. \quad (6)$$

The formulations for both radially acting forces  $f_{lift,i}$  and  $f_{cent,i}$  feature a model constant which has to be adjusted to experimental findings and is further explicated in the last section of this work.

The subdivision of retaining and interfacial forces  $f_{h,i}$ , explicated above, is a prerequisite to the evaluation of radial fluid dynamic processes as the respective models for  $f_{lift,i}$  and  $f_{cent,i}$  depend on individual phase velocities  $u_i$ . Locally determined phase-specific velocities which are inaccessible to common one-dimensional CWHE design correlations are required to investigate radial inhomogeneity of the two-phase flow on the shell-side of the apparatus. Radial parameter variations in the CWHE can be ascribed to radial inhomogeneity of the two-phase flow on the shell-side which impacts the efficiency of heat transfer processes.

#### Incorporation of the centrifugal force

The helical motion of gas in between the coiled tube rows as sketched in Fig. 6 effects a centrifugal force which is directed radially outward independent of the tube layer coiling direction. The gaseous flow pattern was confirmed by three-dimensional numerical simulations of single-phase flow through the resolved bundle geometry. It is assumed that liquid droplets follow this spiral motion (analogous to the flow in a cyclone used as a separator) and consequently are subject to the centrifugal force in radial direction.

#### Incorporation of the lift force

The lift force effect is initiated from radial variation of the axial gas flow velocity due to the geometrical inhomogeneity

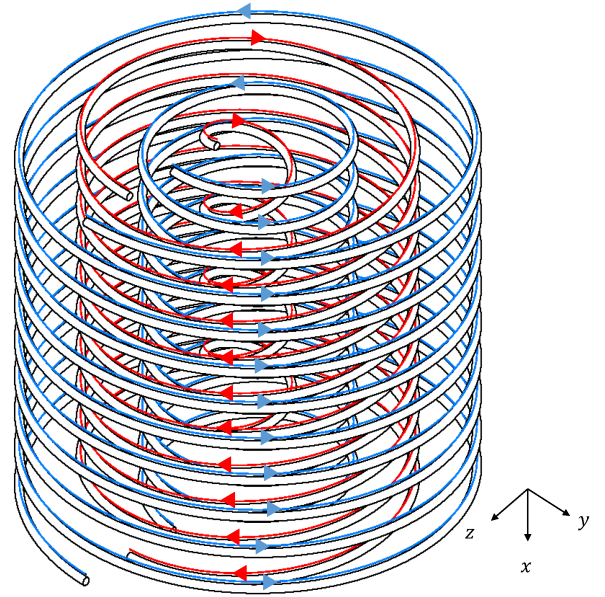


**Figure 6:** Delineation of the helical gas flow alternating in orientation for each tube layer. The arrows indicate the direction of the gas motion.

of the tube bundle. To illustrate this connection, a section of a CWHE tube bundle geometry for an experimental setup is depicted in Fig. 7. It shows several layers of coil-wound tubes in between the central pipe (i.e. the mandrel) and the outer shroud of the apparatus. A constant distance between tube rows and layers is maintained by tube spacers which are depicted in Fig. 7 in an abstracted manner by vertical beams. At different radii the spacers block varying portions of the free space between two layers of wound tubes. This results in a radial dependency of shell-side flow resistance which is to be adopted in the numerical modeling.

The non-uniform blocking of the free area between tube layers is represented in the CFD model via radially variant values of porosity defined as the ratio of actual void area to void area without any spacers:

$$\epsilon = \frac{A_{void} - A_{spacer}}{A_{void}} \quad (7)$$

Using this values of porosity a representative gas velocity for a heat exchanger without spacers can be derived from the local gas velocity:

$$u_{g,\infty} = \left(\frac{1}{\epsilon}\right)^a \cdot u_g \quad (8)$$

This velocity is the input for the calculation of the homogenous flow resistance  $f_h$  in equation 2 and leads to a radially varying flow resistance generating a velocity profile which can be adjusted by the coefficient  $a$  in equation 8. The parameter  $a$  is deduced from single phase 3D CFD simulations of the shell side flow through a representative section with detailed resolution of the tube bundle geometry as explained in the following section.

#### Submodel validation and parametrization

The aforementioned setup for the calculation of the gas-liquid flow through a coil wound heat exchanger requires many different sub-models, whose accuracy is crucial for

**Table 1:** Considered phase-specific axial forces on the two-phase flow at the shell-side of the CWHE bundle

	Description	Evaluation method
Gas-solid interaction $f_{gs}$	Retaining force on the gas flow by the partial blocking of the flow cross-section	Evaluation from single phase pressure drop correlation (Steinbauer and Hecht, 1996)
Liquid-solid interaction $f_{ls}$	Liquid film flow resistance due to tube wall friction	Adaption of the Nusselt water skin theory to flow across tubes (Rogers, 1981)
Gas-liquid droplet interaction $f_{gl,d}$	Drag force on droplets induced by the gaseous flow	Calculation from conventional drag force model (Schiller and Naumann, 1935)
Gas-liquid film interaction $f_{gl,f}$	Shear forces at the fluidic interface between gas and liquid film	Effect is considered as subordinate and therefore neglected

**Table 2:** Considered radial forces on the two-phase flow at the shell-side of the CWHE bundle

	Description	Evaluation method
Droplet lift force $f_{lift,i}$	Radial force on the droplet due to inhomogeneous gas flow through the porosity	Determination from common lift force approach with an adapted coefficient (Ishii and Hibiki, 2010)
Centrifugal force $f_{cent,i}$	Centrifugal effect on liquid droplets due to rotational motion of the gas	Definition of the centrifugal force on the droplet with a model factor

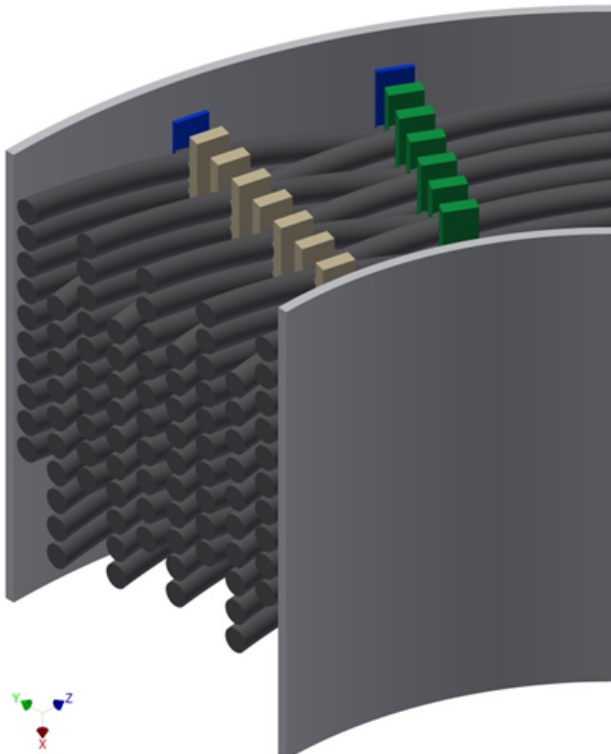


**Figure 7:** CAD model of a section of an experimental CWHE tube bundle with highlighted tube spacers. (Kiewat, 2015)

the correct prediction of the heat transfer inside the bundle. These models were derived under several assumptions and so have to be validated and parametrized with numerical and experimental data.

For the numerical investigation a CFD simulation resolving the gas-liquid and liquid-solid interface and most of the turbulence spectrum is required. In this case, the Volume-of-Fluid (VOF) method for the two-phase flow is coupled with an LES approach for the description of turbulence. With this approach the phase interaction and the effects of turbulence are derived directly from the Navier-Stokes-Equations instead of physical models.

The VOF approach is accompanied by a high computational effort to resolve most of the relevant length scales. In this case the smallest cell size was chosen to have a dimension of about 10 micrometers to resolve the vast majority of expected droplets. The total number of cells is decreased by limiting the simulation domain to a representative cutout of a coil wound heat exchanger using periodic boundary conditions as depicted in Figure 8 for one tube layer.

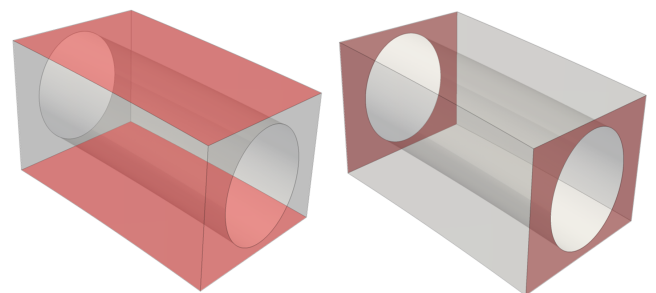


**Figure 8:** Schematic depiction of the periodicities in one layer of a coil wound heat exchanger (Bassfeld, 2017). Left: periodicity in axial direction; Right: periodicity in azimuthal direction.

To account for the interaction within the coil three layers were considered in the simulation setup. To this end, the non-overlapping boundaries resulting from the different orientated slope in the layers were associated with periodic boundary conditions as can be seen in Figure 9. As only fluidodynamical aspects were examined here, the flow was

regarded as incompressible without heat transfer from the tube-side or vaporization of the shell-side flow.

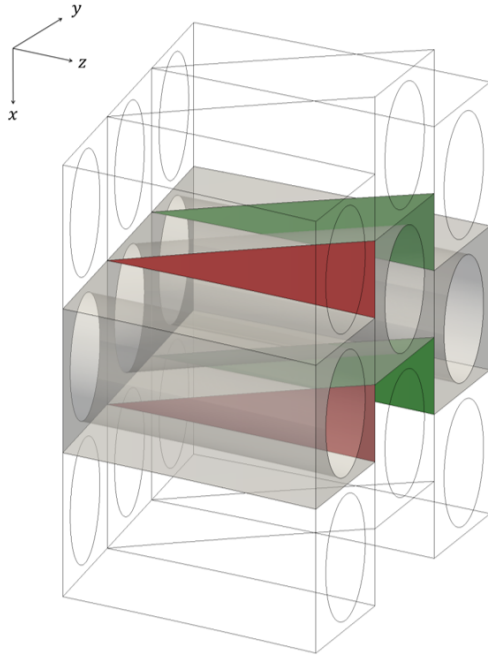


**Figure 9:** Schematic depiction of the periodicities in radial direction. (Bassfeld, 2017). Same colour indicates periodic connection. For better comprehension also one section above and below is depicted in transparent.

Figure 10 shows an instantaneous depiction of the liquid phase distribution which is color-coded by the local velocity. This confirms the current perception of gas-liquid pattern in the coil as shown in Figure 5. Especially the droplets' volume fraction of the whole liquid could be determined to about 0.05, justifying the rather simple approach for the droplet interaction in the previous section.

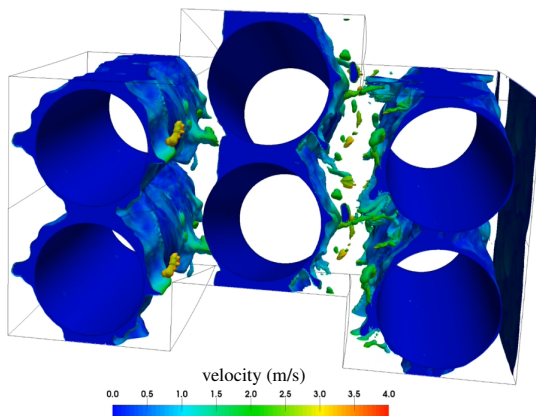


**Figure 10:** Isometric view of the liquid flow inside the tube bundle. (Bassfeld, 2017).

Most of the liquid is present as a falling film while the reminder forms droplets which are generated by liquid separation from film waves. These droplets are transported away from the tube layer and cause the radial migration of liquid. The accumulated effect is captured by the radial fluid interaction submodels in the Euler-Euler context in an abstracted manner.

The helical gas motion as sketched in Figure 6 is confirmed by the averaged velocity field resulting from the VOF

simulation. Figure 11 depicts the respective azimuthal component of the time-averaged gas flow indicating the swirl flow pattern.

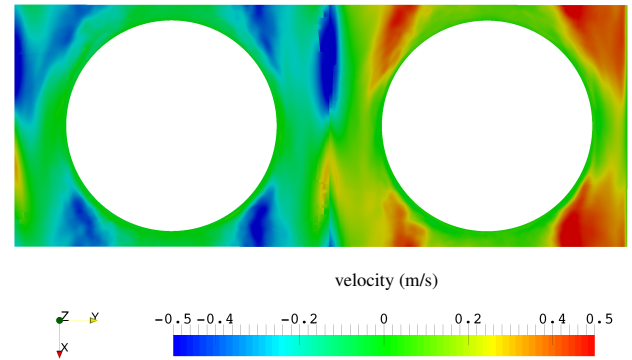


**Figure 11:** Plot of the azimuthal velocity component of the gas flow. (Bassfeld, 2017).

To determine the coefficients for the radial profile of the axial gas velocity a single phase RANS simulation was performed. The resulting profile is depicted in Figure 12. By adapting the coefficient  $a$  in equation 8 to a value of 2.5 this velocity profile could be reproduced in the Euler-Euler model.

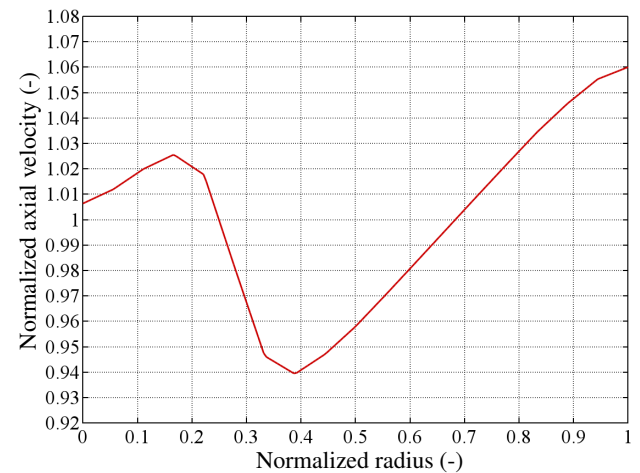


**Figure 12:** Plot of the axial velocity component of the gas flow over the radius. Local velocity values are normalized by average axial velocity.

To supplement the numerical data also an experimental campaign was launched using a pilot scale CWHE (see (Walter *et al.*, 2014) for details). It completes the validation data set for the measurement of the radial liquid distribution for many different flow conditions with and without heat transfer. These results were used for a parametrization study in order to specify model constants in the definition of the radial forces  $f_{lift,i}$  and  $f_{cent,i}$

## MODEL RESULTS

The final model setup was then used to simulate various experimental cases and the measured radial variation of the liquid distribution below the tube bundle was used to validate the CFD model setup.

The simulation results of the numerical model with a fixed parameter set show good accordance with the experimental findings for the entire spectrum of investigated fluid dynamic

parameters. As an example, a comparison of numerical and experimental results for two cases with strongly varying vapor quality is shown in Figures 13 and 14.

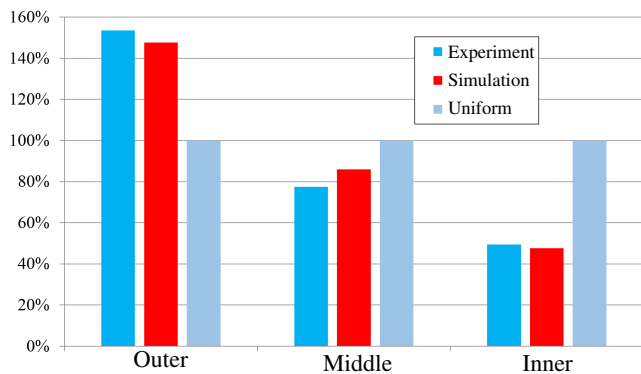


**Figure 13:** Liquid flow distribution at the bottom of the tube bundle for an experimental case with high gas throughput.

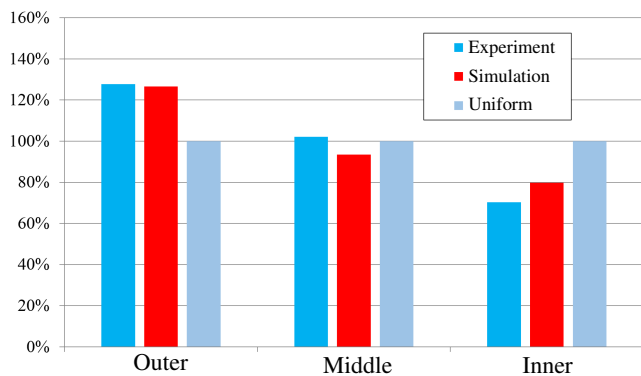


**Figure 14:** Liquid flow distribution at the bottom of the tube bundle for an experimental case with low gas throughput.

## CONCLUSION

A two-dimensional CFD model was introduced in the present work to represent the thermo- and fluid-dynamic processes in a coil-wound heat exchanger. Specifically the representation of the gas-liquid hydrodynamics is explicated with a focus on the incorporation of retaining and interfacial forces.

The model framework represents a modified Euler-Euler approach adopting the concept of local thermodynamic equilibrium to determine volume fractions and phase properties. The local heat transfer across the exchanger fluid regions is represented by one-dimensional model formulations which are commonly used for coil-wound heat exchanger design. These thermohydraulic correlations also determine the characteristics of the porous media model to consider the impact of the tube bundle on the fluid dynamics through and within the tube bundle.

The representation of individual retaining and interfacial forces at the shell-side of the tube bundle enables the computation of phase-specific velocities. In association with the consideration of radial geometry variations the differences in the phase velocities effect a radial motion of the liquid. This effect is superimposed by a centrifugal effect which is induced by the helical motion of the gaseous phase following the coiled tubes. Both fluid-dynamic processes are represented in the numerical model by the incorporation of corresponding source terms in the momentum equations.

Detailed 3D CFD simulation and experimental investigations have been conducted in order to validate specifics of phase interaction models. The Volume-of-fluid simulations indicated local liquid flow conditions, specifically with regard to droplet sizes, quality and behavior. Additionally these investigations confirmed observations regarding helical gas flow for a multiphase system. The experimental results were used to obtain the coefficients for the radial forces.

A comparison with experimental findings showed that the present two-dimensional CFD model was able to simulate the inhomogeneity of cross-sectional liquid distribution with agreement to measured values over a broad range of flow conditions.

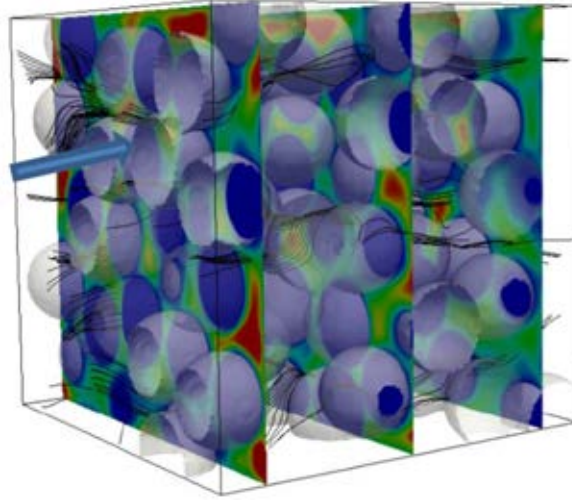
## REFERENCES

- ACHER, T., KNAUP, M., GÖLL, S., ZANDER, H.J., LENZ, S. and KERBER, C. (2016). "A two-dimensional CFD model for gas-liquid flows in a coil-wound heat exchanger". *Proceedings of the 9th International Conference on Multiphase Flow*.
- BASSFELD, J. (2017). *Untersuchung der Hydrodynamik in gewickelten Wärmetauschern*. Master's thesis, Technische Hochschule Nürnberg Georg Simon Ohm.
- DREW, D. and PASSMAN, S. (1999). *Theory of multicomponent fluids*. Springer.
- GÖLL, S., ZANDER, H.J., LENZ, S. and KERBER, C. (2013). "Entwicklung eines 2D-CFD-Modells zur Berechnung der Wärmeübertragung in spiralgewickelten Wärmeaustauschern". *Jahrestreffen der ProcessNet-Fachgruppen CFD, Mischvorgänge und Rheologie Würzburg*.
- ISHII, M. and HIBIKI, T. (2010). *Thermo-fluid dynamics of two-phase flow*. Springer.
- ISHII, M. and MISHIMA, K. (1989). "Droplet entrainment correlation in annular two-phase flow". *Int. J. Heat Mass Transf.*, **32**, 1835–1846.
- JAKOBSEN, H. (2008). *Chemical reactor modeling: multiphase reactive flows*. Springer.
- KIEWAT, M. (2015). *CFD SIMULATION OF COIL WOUND HEAT EXCHANGERS*. Master's thesis, Friedrich-Alexander-Universität Erlangen-Nürnberg.
- KNAUP, M. (2015). *Modellierung und numerische Simulation der Zweiphasenströmung in einem spiralgewickelten Wärmetauscher*. Master's thesis, Technische Universität München.
- PACIO, J.C. and DORAO, C.A. (2011). "A review on heat exchanger thermal hydraulic models for cryogenic applications". *Cryogenics*, **51**, 366–379.
- ROGERS, J.T. (1981). "Laminar Falling Film Flow and Heat Transfer Characteristics on Horizontal Tubes". *Can. J. Chem. Eng.*, **59**, 213–222.
- SCHILLER, L. and NAUMANN, K. (1935). "Über die grundlegenden Berechnungen bei der Schwerkraftaufbereitung". *Zeitschrift des Vereins der deutschen Ingenieure*, **77**, 316–320.
- SIRIGNANO, W. (2010). *Fluid Dynamics and Transport of Droplets and Sprays*. Cambridge University Press.
- STEINBAUER, M. and HECHT, T. (1996). "Optimised Calculation of Helical-Coiled Heat Exchangers in LNG Plants". *Eurogas 96 Conference*.
- WALTER, T., KERBER, C., BRAUN, K., RICHARDT, C. and STEINBAUER, M. (2014). "Coil wound heat exchangers for LNG - investigation of transport phenomena within the bundle". *Proceedings of the 3rd Trondheim Gas Technology Conference*.



WANG, T., DING, G., DUAN, Z., REN, T., CHEN, J. and PU, H. (2015). “A distributed-parameter model for LNG spiral wound heat exchanger based on graph theory”. *Applied Thermal Engineering*, **81**, 102 – 113.

# NON-NEWTONIAN FLOWS





# VISCOELASTIC FLOW SIMULATIONS IN DISORDERED POROUS MEDIA

**S. De, J.A.M. Kuipers, E.A.J.F. Peters**

Department of Chemical Engineering and Chemistry, Eindhoven University of Technology,  
The Netherlands

**J.T. Padding\***

\* Process & Energy department, Delft University of Technology, The Netherlands

E-mail: [s.de@tue.nl](mailto:s.de@tue.nl)  
[j.t.padding@tudelft.nl](mailto:j.t.padding@tudelft.nl)

## ABSTRACT

We investigate creeping flow of a viscoelastic fluid through a three dimensional random porous medium using computational fluid dynamics. The simulations are performed using a finite volume methodology with a staggered grid. The no slip boundary condition on the fluid-solid interface is implemented using a second order finite volume immersed boundary (FVM-IBM) methodology [1]. The viscoelastic fluid is modelled using a FENE-P type constitutive relation. The simulations reveal a transition of flow structure from a laminar Newtonian regime to a nonstationary non-Newtonian regime with increasing viscoelasticity. We find that the flow profiles are mainly governed by the porous microstructure. By choosing a proper length scale a universal curve for the flow transition can be obtained. A study of the flow topology shows how in such disordered porous media shear, extensional and rotational contributions to the flow evolve with increased viscoelasticity.

**Keywords:** CFD, IBM, Viscoelastic, Porous Media.

## NOMENCLATURE

### Greek Symbols

- $\rho$  Fluid density, [kg/m<sup>3</sup>].  
 $\eta_s$  Solvent viscosity, [kg/m.s].  
 $\eta_p$  Polymer zero shear viscosity, [kg/m.s].  
 $\eta$  Total viscosity, [kg/m.s].

### Latin Symbols

- $p$  Pressure, [Pa].  
 $\mathbf{u}$  Velocity, [m/s].  
 $\boldsymbol{\tau}$  Viscoelastic Stress tensor, [Pa].  
 $\lambda$  Relaxation time, [sec].  
 $L$  Maximum dumbbell extensibility.  
 $\beta$  Viscosity ratio ( $\eta_s / \eta$ ).  
 $\alpha$  Solid fraction.  
 $\phi$  Void fraction.  
 $d_p$  Particle diameter, [m].  
 $R_c$  Particle radius, [m].

- $N_p$  Particle Number  
 $k$  Permeability, [m<sup>2</sup>].  
 $\phi_i$  Fluid variable.

- De Deborah number.  
Re Reynolds number.

### Sub/superscripts

- $\nabla$  Second rank tensor.  
 $VE$  Viscoelastic fluids.  
 $N$  Newtonian fluids.

## INTRODUCTION

The flow of complex fluids through porous media is a field of considerable research due to its wide range of practical applications including enhanced oil recovery, blood flow, polymer processing, catalytic polymerization, bioprocessing, geology [2–4]. The flow of Newtonian fluids through porous media is relatively well understood in the framework of Darcy’s law [2]. Also, a significant effort has been made to understand flow through porous media of non-Newtonian fluids with a viscosity that depends on the instantaneous local shear-rate (inelastic non-Newtonian fluids, or quasi-Newtonian fluids), as reviewed by Chhabra et. al. [5] and Savins [6]. However, flow through disordered porous media of viscoelastic fluids, i.e. non-Newtonian fluids displaying elasticity, is far from being understood [5,7,8]. This is due to the complex interplay between the nonlinear fluid rheology and the porous geometry. Several types of numerical frameworks have been used to model flow of non-Newtonian fluids through porous media, including extensions of Darcy’s law [9], capillary based models [10], and direct numerical simulations based on computational fluid dynamics. Unfortunately, extensions of Darcy’s law and capillary based models are found to be inadequate to capture the complete physics of pore scale viscoelastic flow through porous media [11–13].

Many numerical studies focus on relatively simple geometries to learn about the essentials of non-Newtonian fluid flow through porous media [14–17]. Sometimes a full three-dimensional random porous medium is studied, which is already closer to a realistic pore geometry, but such studies are then usually limited to power-law fluids, which are the most commonly applied quasi-Newtonian fluids [11,18–20]. For example, Morais et al. [18] applied direct numerical simulations

to investigate the flow of power-law fluids through a disordered porous medium. Simulations of fully viscoelastic fluid flows are limited to two dimensional pore geometries [21–25]. It is now commonly agreed that including viscoelasticity is important: both numerically and experimentally, viscoelasticity is found to lead to profound effects such as enhanced pressure drop and elastic instabilities (sometimes referred to as elastic turbulence) [5,26–28]. So, although it is known that viscoelastic fluids behave more complex than inelastic non-Newtonian fluids, the current literatures shows a lack of detailed simulations of fully three dimensional flows of viscoelastic fluids through random porous media.

In this paper, we report on a numerical study of the flow of viscoelastic fluids through three dimensional random porous media consisting of packed arrangements of monodispersed spherical particles using a combined finite volume immersed boundary (FVM-IBM) methodology. Four different porosities are studied for a range of low to high Deborah numbers (defined later). We measure in detail the viscoelastic fluid flow structure and stress development in the porous medium. We will show a transition from a laminar Newtonian flow profile to an instable flow configuration, and will relate it to a strong increase in pressure drop. An analysis of the flow topology will show how shear, extensional and rotational dominated flow regimes change with increasing viscoelasticity for different porous structures. Finally, we will show how the distribution of energy dissipation in the porous medium changes with increasing viscoelasticity and correlate this with the flow topology. This analysis will help us to understand the interplay of pore structure and fluid rheology in three dimensional porous microstructures.

## MODEL DESCRIPTION

The fundamental equations for an isothermal incompressible viscoelastic flow are the equations of continuity and momentum, and a constitutive equation for the non-Newtonian stress components. The first two are as follows:

$$\nabla \cdot \mathbf{u} = 0 \quad (1)$$

$$\rho \left[ \frac{\partial \mathbf{u}}{\partial t} + \mathbf{u} \cdot \nabla \mathbf{u} \right] = -\nabla p + 2\eta_s \nabla \cdot \mathbf{D} + \nabla \cdot \boldsymbol{\tau} \quad (2)$$

The Newtonian solvent contribution is explicitly added to the stress and defined as  $2\eta_s \mathbf{D}$ , where the rate of strain is

$\mathbf{D} = (\nabla \mathbf{u} + (\nabla \mathbf{u})^T) / 2$ . The solvent viscosity  $\eta_s$  is assumed to be constant. In this work the viscoelastic polymer stress is modeled through the constitutive FENE-P model, which is based on the finitely extensible non-linear elastic dumbbell for polymeric materials, as explained in detail by Bird et al. [29]. The equation is derived from molecular theory, where a polymer chain is represented as a dumbbell consisting of two beads connected by an entropic spring. Other basic rheological models, such as the Maxwell model and Oldroyd-B model, take the elastic force between the beads to be proportional to the separation between the beads. The main disadvantage of such models is that the dumbbell can be stretched indefinitely, leading to divergent behavior and associated numerical instabilities in strong extensional flows. These problems are prevented by the use of a finitely extensible spring. The basic form of the FENE-P constitutive equation is:

$$f(\boldsymbol{\tau}) \boldsymbol{\tau} + \lambda \overset{\nabla}{\boldsymbol{\tau}} = 2a\eta_p \mathbf{D},$$

$$\text{with: } f(\boldsymbol{\tau}) = 1 + \frac{3a + (\lambda/\eta_p) \text{tr}(\boldsymbol{\tau})}{L^2}, \quad (3)$$

$$a = \frac{L^2}{L^2 - 3}$$

In equation (3) the operator  $\overset{\nabla}{\boldsymbol{\tau}}$  represents the upper-convected time derivative, defined as

$$\overset{\nabla}{\boldsymbol{\tau}} = \frac{\partial \boldsymbol{\tau}}{\partial t} + \mathbf{u} \cdot \nabla \boldsymbol{\tau} - \nabla \mathbf{u}^T \cdot \boldsymbol{\tau} - \boldsymbol{\tau} \cdot \nabla \mathbf{u} \quad (4)$$

In equation (3)  $\text{tr}(\boldsymbol{\tau})$  denotes the trace of the stress tensor. The parameter  $L$  equals the maximum length of a FENE dumbbell normalized by its equilibrium length. When  $L^2 \rightarrow \infty$  the Oldroyd-B model is recovered.

We simulate an unsteady viscoelastic flow through a static array of randomly arranged monodisperse spheres, constituting a model porous medium, using computational fluid dynamics (CFD). The primitive variables used in the formulation of the model are velocity, pressure and polymer stress. All the mass and momentum equations are considered and discretised in space and time. A coupled finite volume – immersed boundary methodology [1] (FVM - IBM) with a Cartesian staggered grid is applied. In the FVM, the computational domain is divided into small control volumes  $\Delta V$  and the primitive variables are solved in the control volumes in an integral form over a time interval  $\Delta t$ .

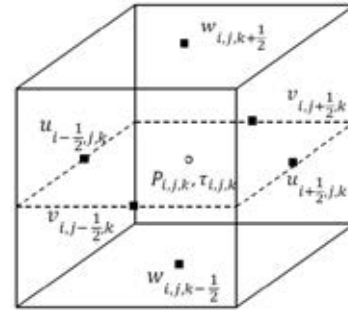


Figure 1. Location of primitive variables in a 3D control volume (fluid cell).

The location of all the primitive variables in a 3D cell are indicated in figure 1.

We apply the discrete elastic viscous stress splitting scheme (DEVSS), originally proposed by Guénette and Fortin [30], to introduce the viscoelastic stress terms in the Navier-Stokes equation because it stabilizes the momentum equation, which is especially important at larger polymer stresses. A uniform grid spacing is used in all directions. The temporal discretization for the momentum equation (2) is as follows,

$$\begin{aligned} \rho \mathbf{u}^{n+1} = & \rho \mathbf{u}^n + \Delta t \left\{ -\nabla p^{n+1} \right. \\ & - \left[ \mathbf{C}_f^{n+1} + (\mathbf{C}_m^n - \mathbf{C}_f^n) \right] \\ & \left. + \left[ (\eta_s + \eta_p) \nabla^2 \mathbf{u}^{n+1} + \nabla \cdot \boldsymbol{\tau}^n \right] - \mathbf{E}_p^n \right\} \end{aligned} \quad (5)$$

Here  $\eta_p \nabla^2 \mathbf{u}^{n+1}$  and  $\mathbf{E}_p^n = \eta_p \nabla^2 \mathbf{u}^n$  are the extra variables we introduce to obtain numerical stability, where  $n$  indicates the time index.  $\mathbf{C}$  represents the net convective momentum flux given by:

$$\mathbf{C} = \rho (\nabla \cdot \mathbf{u} \mathbf{u}) \quad (6)$$

Here the first order upwind scheme is used for the implicit evaluation of the convection term (called  $\mathbf{C}_f$ ). In the calculation of the convective term we have implemented a deferred correction method. The deferred correction contribution that is used to achieve second order spatial accuracy while maintaining stability is  $(\mathbf{C}_m^n - \mathbf{C}_f^n)$  and is treated explicitly. In this expression  $\mathbf{C}_m$  indicates the convective term evaluated by the total variation diminishing min-mod scheme. A second order central difference (CD) scheme is used for the discretization of diffusive terms.

In equation (5) the viscoelastic stress part  $\boldsymbol{\tau}$  is calculated by solving equation (3). The viscoelastic stress tensors are all located in the center of a fluid cell, and interpolated appropriately during the velocity updates. The convective part of equation (3) is solved by using the higher order upwind scheme.

Equation (5) is solved by a fractional step method, where the tentative velocity field in the first step is computed from:

$$\rho \mathbf{u}^{**} = \rho \mathbf{u}^n + \Delta t \left\{ \begin{aligned} & -\nabla p^{n+1} - \left[ \mathbf{C}_f^{**} + (\mathbf{C}_m^n - \mathbf{C}_f^n) \right] + \\ & \left[ (\eta_s + \eta_p) \nabla^2 \mathbf{u}^{**} + \nabla \cdot \boldsymbol{\tau}^n \right] + \rho \mathbf{g} - \mathbf{E}_p^n \end{aligned} \right\} \quad (7)$$

In equation (7) we need to solve a set of linear equations.

The velocity at the new time step  $n+1$  is related to the tentative velocity is as follows:

$$\mathbf{u}^{n+1} = \mathbf{u}^{**} - \frac{\Delta t}{\rho} \nabla (\delta p) \quad (8)$$

where  $\delta p = p^{n+1} - p^n$  is the pressure correction. As  $\mathbf{u}^{n+1}$  should satisfy the equation of continuity, the pressure Poisson equation is calculated as:

$$\nabla \cdot \left\{ \frac{\Delta t}{\rho} \nabla (\delta p) \right\} = \nabla \cdot \mathbf{u}^{**} \quad (9)$$

We use a robust and efficient block – incomplete Cholesky conjugate gradient (B-ICCG) algorithm to solve the resulting sparse matrix for each velocity component in a parallel computational environment. The solver iterations are performed until the norm of the residual matrix is less than the convergence criteria, which is set at  $10^{-14}$  for our simulations.

As the viscoelastic stress tensor components are coupled amongst themselves and with the momentum equation, the velocity at the new time level  $\mathbf{u}^{n+1}$  is used to calculate the stress value accordingly.

No-slip velocity boundary conditions at the interface between the viscoelastic fluid and solid objects are imposed through the immersed boundary method (IBM) at the level of the discretized momentum equations by extrapolating the velocity field along each Cartesian direction towards the body surface using a second order polynomial. To ensure a relatively high accuracy, we use a coupling method which works directly at the level of the discretized momentum equation (5). The discrete representation of the momentum equation is given by

$$a_c \phi_c + \sum_{nb} a_{nb} \phi_{nb} = b_c \quad (10)$$

Where  $\phi_i$  is a fluid phase variable (in this case a component of the fluid velocity). This equation indicates that the value of  $\phi_i$  for a fluid node “c” outside of the immersed object can be related to the values of its neighboring nodes “nb”, some of which may lie inside the immersed object. A schematic representation of this situation is shown in Figure 2.

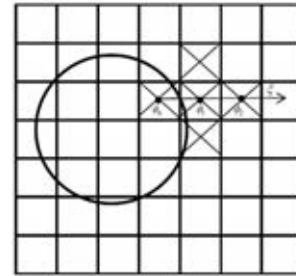


Figure 2. Immersed boundary method implementation strategy for a fluid variable  $\phi_i$

We use a second order interpolation to describe the value of  $\phi_i$  as a function of the local coordinate (see Figure 2).

This procedure is carried out for all solid nodes to ensure that the boundary condition is properly satisfied for all the solid nodes. The main advantage of using the immersed boundary method is that it requires no conformal meshing near the fluid-solid interface, and the method is computationally robust and cheap.

## RESULTS

We employ our method to investigate the flow of viscoelastic fluid through a static array of randomly arranged spherical particles in a 3D periodic domain (figure 3). The domain size is set by the solids volume fraction  $\alpha$ , the diameter of each particle  $d_p$  and number of particles  $N_p$ . To generate the random packing for  $\alpha \leq 0.45$ , a standard hard sphere Monte-Carlo (MC) method [31] is used. However, such a MC method does not provide sufficiently random configurations in highly dense packings [32]. Thus, to generate random configurations at  $\alpha > 0.45$ , an event driven method combined with a particle swelling procedure is applied [33]. This ensures the particles are randomly distributed. The same approach was followed by Tang et al. for Newtonian fluid simulations for a range of low to intermediate Reynolds numbers [34].

In all simulations the flow is driven by a constant body force exerted on the fluid in the  $x$ -direction, while maintaining periodic boundary conditions in all three directions. Simulations of random arrays are carried out with  $N_p = 108$  spheres arranged in different configurations. The particle diameter  $d_p$  is always kept constant. The solid fractions  $\alpha$  investigated are 0.3, 0.4, 0.5 and 0.6, respectively. Porosities therefore range from 0.7 to 0.4.

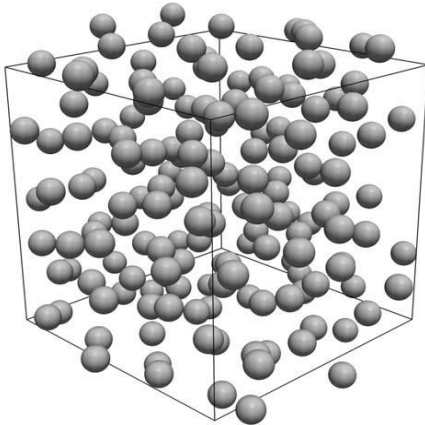


**Figure 3.** Particle configuration at solid fraction  $\alpha = 0.4$  of a random array of monodisperse spheres. Note that the particles are scaled by 50% for better visualization.

For the FENE-P viscoelastic fluid we use a constant extensional parameter ( $L^2$ ) of 100. The viscosity ratio is kept at 0.33. The  $\lambda$  is kept constant at 40 sec. As we want to study the interaction between the viscoelastic fluid and solid for different flow configurations we keep a constant value of  $L^2 = 100$ . For reference, we also simulate a Newtonian fluid with the same zero-shear viscosity as the polymer solution. In all our simulations we keep the Reynolds number low, below a value of 0.01, ensuring we are always in the creeping flow regime and any type of inertial effects will be insignificant. Deborah number is defined as  $De_R = \lambda U / R_c$ , based on the sphere radius and mean flow velocity  $U$ .

We have performed simulations for three different mesh sizes  $\Delta = R_c/30$ ,  $\Delta = R_c/40$  and  $\Delta = R_c/50$ . The results for  $\Delta = R_c/40$  and  $\Delta = R_c/50$  were virtually indistinguishable, even for  $De_R > 1$  (not shown). Thus all results in this paper are based on the mesh size  $\Delta = R_c/40$ . It should be noted that we need to keep the CFL number lower than 0.01 in all our simulations, leading to considerable computational costs. At  $De_R < 1$  a larger time step can be utilized but at  $De_R \geq 1$ , a small time step is required for smooth convergence.

Figure 4 shows viscoelastic flow streamlines through the random sphere packings at  $De_R=1$  for solid fractions 0.3 and 0.5. The flow direction is indicated by the arrow and selected planes are colored with the normalized averaged flow velocity.

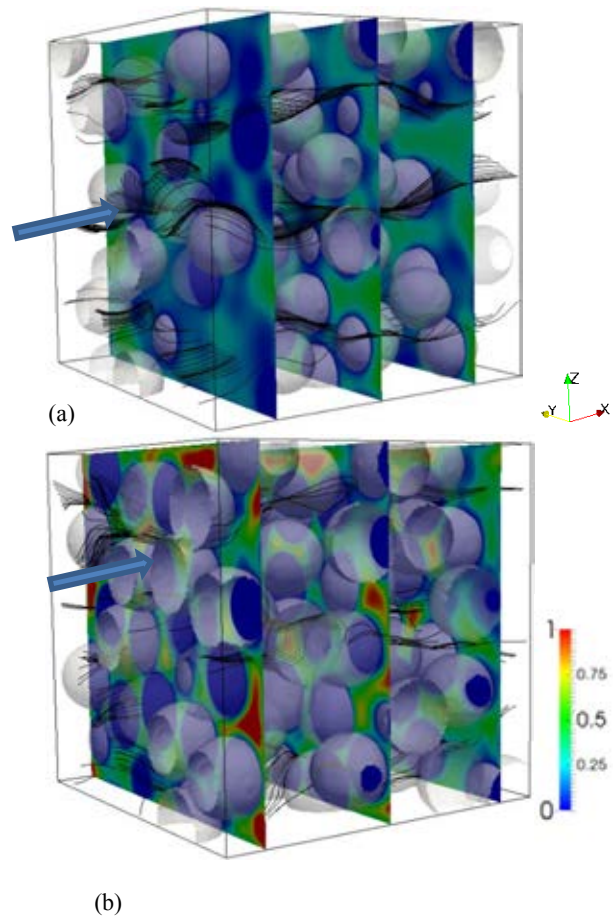


**Figure 4.** Viscoelastic flow streamlines through a random array of monodisperse spheres at  $De_R = 1.0$  for solid fractions (a)  $\alpha = 0.3$  and (b)  $\alpha = 0.5$ . The planes are colored with normalized averaged flow velocity (arrows showing the flow direction).

These streamlines provide an idea about the complex flow heterogeneity in the porous media. For solid fraction 0.3, the flow is rather homogeneous. However for solid fraction 0.5, the pore structure triggers more tortuous flow paths and more preferential pathways.

To quantify the viscoelastic effects we use the Darcy law for flow through porous media. The volume averaged fluid velocity  $\langle u \rangle$  in porous media is controlled by the pressure drop across the sample. According to Darcy's law, for a Newtonian fluid

the relation between the average pressure gradient  $-\partial p / \partial x$  and the average fluid velocity across the porous medium is:

$$\left( -\frac{dp}{dx} \right) = \frac{\eta \langle u \rangle}{k} \quad (12)$$

Here  $k$  is the permeability (units:  $m^2$ ), which is related to the porosity, pore size distribution and tortuosity of the porous medium. Eq. (12) presents an operational way of measuring the permeability  $k$  by flowing a Newtonian fluid of known viscosity through the porous medium. For a viscoelastic fluid, the viscosity is not a constant but generally depends on the flow conditions. However, if we assume  $k$  is constant for a specific porous medium, we can still define an *apparent* viscosity by using Darcy's law. Dividing the apparent viscosity by its corresponding flow rate limit gives us insight in the effective flow-induced thinning or thickening of the fluid in the porous medium. In detail, the apparent relative viscosity  $\eta_{app}$  of a viscoelastic fluid flowing with a volumetric flow rate  $q$  and pressure drop  $\Delta P$  through a porous medium is given by:

$$\eta_{app} = \frac{\left( \frac{\Delta P}{q} \right)_{VE}}{\left( \frac{\Delta P}{q} \right)_N} \quad (13)$$

Figure 5 depicts how the apparent relative viscosity changes with an increase in viscoelasticity for flow through configurations with different solid fractions. With increasing  $De_R$  we initially observe a (relatively weak) flow-induced thinning. Then beyond a certain flow rate we observe a strong flow-induced thickening, which means a sharp increase in flow resistance. With increasing solid fraction (decreasing porosity), the onset of this increased flow resistance shifts to a lower  $De$  number. This shows that the increased fluid-solid interaction facilitates the onset of such a flow resistance. Experimental evidence of this increase in apparent relative viscosity was previously reported in literature [5], especially for packed bed systems.

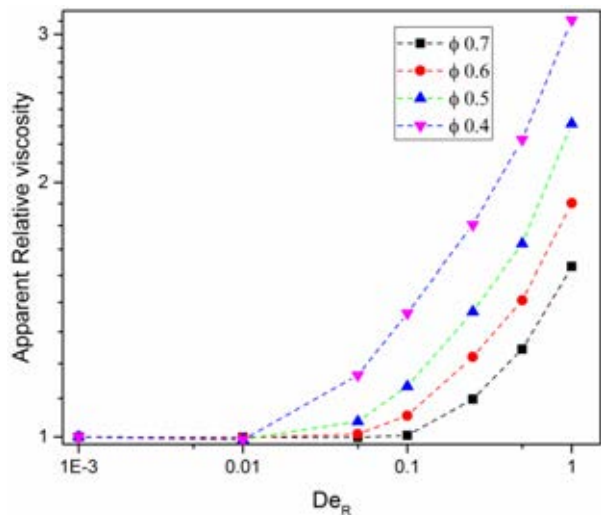


Figure 5. Apparent relative viscosity versus  $De_R$  number for different porosity  $\phi$ . Here  $De_R$  is based on the radius  $R_c$  of the sphere.

The pore porosity and pore geometry are very important for the increase in apparent relative viscosity, but this is not reflected in the  $De_R$  number based on the radius of the spheres. Therefore,

we next try to use the square root of the permeability,  $\sqrt{k}$  obtained from Newtonian flow simulations, as the characteristic length scale. This altered Deborah number is defined as

$$De_k = \frac{\lambda U}{\sqrt{k}} .$$

Figure 6 shows the apparent relative viscosity versus  $De_k$  for different solid fractions. We find a collapse of all data sets of figure 4 to a single curve for the entire range of  $De_k$  numbers. This is remarkable considering the fact that, despite the different arrangement of pore structures for the different porosities, the resulting increase in flow resistance follows the same universal thickening behaviour. However, we should keep in mind that these results are strictly only valid for a FENE-P type of fluid with  $L^2 = 100$  flowing through a random array of monodisperse spheres.

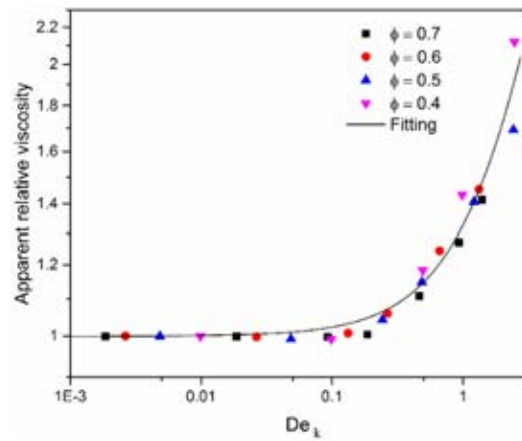


Figure 6. Apparent relative viscosity versus altered  $De_k$ , using

$\sqrt{k}$  as the characteristic length scale, for different solid fractions. Neglecting the slight flow-induced thinning around  $De_k = 0.1$ , most data can be fitted through the correlation

$$\eta_{app} = 1 + 0.32 De_k^{1.15} .$$

## CONCLUSION

We have employed a finite volume - immersed boundary methodology to study the flow of viscoelastic fluids through an array of randomly arranged equal-sized spheres representing a three dimensional disordered porous medium, for a range of solid fractions (or porosities). Irrespective of the solid fraction, we found a strong increase in flow resistance after a critical  $De$  number is reached. The increase in apparent relative viscosities measured for different solid fractions overlap with each other if the Deborah number is chosen with a length scale based on the

permeability of the pore space (more precisely,  $De_k = \frac{\lambda U}{\sqrt{k}}$ ,

with  $k$  the permeability of the medium for a Newtonian fluid. The flow profile suggest that with increasing viscoelasticity the flow become more asymmetric, and increasingly preferential flow paths are found.

A more detailed study of the flow topology (not given here) shows that for the porous media investigated in our study, shear



flow becomes more important than extensional or rotational flow at higher De number. So, even though the flow is shear dominated and the shear rheology is shear thinning, the apparent viscosity from a porous medium can be flow thickening. The likely cause of this thickening is the increased heterogeneity of the flow pattern, which is related to so-called elastic turbulence, and causes more energy dissipation.

More generally, simulations such as shown here help us to understand the complex interplay between the fluid rheology and pore structure in porous media. In our future work we will study flow through three dimensional realistic porous media which have a larger distribution in pore and throat sizes.

## 5. Acknowledgement

This work is part of the Industrial Partnership Programme (IPP) 'Computational sciences for energy research' of the Foundation for Fundamental Research on Matter (FOM), which is part of the Netherlands Organisation for Scientific Research (NWO). This research programme is co-financed by Shell Global Solutions International B.V. This work was carried out on the Dutch national e-infrastructure with the support of SURF Cooperative.

## References

- De, S., Das, S., Kuipers, J.A.M., et al. (2016) A coupled finite volume immersed boundary method for simulating 3D viscoelastic flows in complex geometries. *J. Nonnewton. Fluid Mech.*, **232**, 67–76.
- Dullien, F.A.L. (1979) *Porous Media-Fluid Transport and Pore Structure*, Academic, New York.
- Lake, L.W., Johns, R.T., Rossen, W.R. and Pope, G. (1986) *Fundamentals of enhanced oil recovery.*, Society of Petroleum Engineers.
- Soulis, J. V., Giannoglou, G.D., Chatzizisis, Y.S., et al. (2008) Non-Newtonian models for molecular viscosity and wall shear stress in a 3D reconstructed human left coronary artery. *Med. Eng. Phys.*, **30** (1), 9–19.
- Chhabra, R.P., Comiti, J., and Macha, I. (2001) Flow of non-Newtonian fluids in fixed and fluidised beds. *Chem. Eng. Sci.*, **56** (1), 1–27.
- Savins, J.G. (1969) Non-Newtonian Flow Through Porous Media. *Ind. Eng. Chem.*, **61** (10), 18–47.
- Tiu, C., Zhou, J.Z.Q., Nicolae, G., et al. (1997) Flow of viscoelastic polymer solutions in mixed beds of particles. *Can. J. Chem. Eng.*, **75** (1 993), 843–850.
- Zami-Pierre, F., De Loubens, R., Quintard, M., and Davit, Y. (2016) Transition in the Flow of Power-Law Fluids through Isotropic Porous Media. *Phys. Rev. Lett.*, **117** (7), 1–5.
- Pearson, J.R. a., and Tardy, P.M.J. (2002) Models for flow of non-Newtonian and complex fluids through porous media. *J. Nonnewton. Fluid Mech.*, **102**, 447–473.
- Sochi, T. (2007) Pore-Scale Modeling of Non-Newtonian Flow in Porous Media. *October*, **89** (October), 1–2.
- Singh, J.P., Padhy, S., Shaqfeh, E.S.G., and Koch, D.L. (2012) Flow of power-law fluids in fixed beds of cylinders or spheres. *J. Fluid Mech.*, **i** (2012), 1–37.
- Duda, J.L., Hong, S.A., and Klaus, E.E. (1983) Flow of polymer solutions in porous media: inadequacy of the capillary model. *Ind. Eng. Chem. Fundam.*, **22** (3), 299–305.
- Marshall, R.J., and Metzner, a. B. (1967) Flow of Viscoelastic Fluids through Porous Media. *Ind. Eng. Chem. Fundam.*, **6** (3), 393–400.
- Christopher, R.H., and Middleman, S. (1965) Power-law flow through a packed tube. *Ind. Eng. Chem. Fundam.*, **4**, 422–426.
- Bruschke, M. V., and Advani, S.G. (1993) Flow of generalized Newtonian fluids across a periodic array of cylinders. *J. Rheol.*, **37** (3), 479–498.
- Dazhi, G., and Tanner, R.I. (1985) The drag on a sphere in a power-law fluid. *J. Nonnewton. Fluid Mech.*, **17** (1), 1–12.
- Shahsavari, S., and McKinley, G.H. (2015) Mobility of power-law and Carreau fluids through fibrous media. *Phys. Rev. E - Stat. Nonlinear, Soft Matter Phys.*, **92** (6), 1–27.
- Morais, A.F., Seybold, H., Herrmann, H.J., and Andrade, J.S. (2009) Non-Newtonian Fluid Flow through Three-Dimensional Disordered Porous Media. *Phys. Rev. Lett.*, **103** (19), 1–5.
- Liu, H.L., Moon, J.S., and Hwang, W.R. (2012) Numerical simulation of a shear-thinning fluid through packed spheres. *Korea Aust. Rheol. J.*, **24** (4), 297–306.
- Sullivan, S.P., Gladden, L.F., and Johns, M.L. (2006) Simulation of power-law fluid flow through porous media using lattice Boltzmann techniques. *J. Nonnewton. Fluid Mech.*, **133** (2–3), 91–98.
- Liu, A.W., Bornside, D.E., Armstrong, R.C., and Brown, R.A. (1998) Viscoelastic flow of polymer solutions around a periodic, linear array of cylinders: comparisons of predictions for microstructure and flow fields. *J. Nonnewton. Fluid Mech.*, **77**, 153–190.
- Richter, D., Iaccarino, G., and Shaqfeh, E.S.G. (2010) Simulations of three-dimensional viscoelastic flows past a circular cylinder at moderate Reynolds numbers. *J. Fluid Mech.*, **651**, 415–442.
- Talwar, K.K. (1992) Application of higher order finite element methods to viscoelastic flow in porous media. *J. Rheol. (N. Y. N. Y.)*, **36** (7), 1377.
- Alcocer, F.J., and Singh, P. (2002) Permeability of periodic arrays of cylinders for viscoelastic flows. *Phys. Fluids*, **14** (7), 2578–2581.
- Souvaliotis, A., and Beris, A.N. (1996) Spectral collocation/domain decomposition method for viscoelastic flow simulations in model porous geometries. *Comput. Methods Appl. Mech. Eng.*, **129** (1–2), 9–28.
- Galindo-Rosales, F.J., Campo-Deafo, L., Pinho, F.T., et al. (2012) Microfluidic systems for the analysis of viscoelastic fluid flow phenomena in porous media. *Microfluid. Nanofluidics*, **12** (1–4), 485–498.
- Chmielewski, C., and Jayaraman, K. (1993) Elastic instability in crossflow of polymer solutions through periodic arrays of cylinders. *J. Nonnewton. Fluid Mech.*, **48** (3), 285–301.
- Gupta, R.K., and Sridhar, T. (1985) Viscoelastic effects in non-Newtonian flows through porous media. *Rheol. Acta*, **24** (2), 148–151.
- R. B. Bird, R. C. Armstrong, O.H. (1987) *Dynamics of Polymeric Liquids*.
- Guénette, R., and Fortin, M. (1995) A new mixed finite element method for computing viscoelastic flows. *J. Nonnewton. Fluid Mech.*, **60** (1), 27–52.
- Daan Frenkel and Berend Smit (2001) *Understanding Molecular Simulation From Algorithms to Applications*.
- Noya, E.G., Vega, C., and De Miguel, E. (2008) Determination of the melting point of hard spheres from direct coexistence simulation methods. *J. Chem. Phys.*, **128** (15), 1–7.
- N. Kumar, O. I. Imole, V. Magnanimo, S. Luding

- (2012) Deformation Modes for Assemblies of Frictionless Polydisperse Spheres. *Adv. Mater. Res.*, **508**, 160–165.
34. Tang, Y., Kriebitzsch, S.H.L., Peters, E.A.J.F., et al. (2014) A methodology for highly accurate results of direct numerical simulations: Drag force in dense gas-solid flows at intermediate Reynolds number. *Int. J. Multiph. Flow*, **62**, 73–86.



# TIRE RUBBER EXTRUDATE SWELL SIMULATION AND VERIFICATION WITH EXPERIMENTS

J Buist, DJ Van Dijk, TJ Mateboer\*

Windesheim University Professorship for Polymer Engineering, 8000 GB Zwolle, the Netherlands

\* E-mail: t.j.mateboer@windesheim.nl

## ABSTRACT

Extrudate swell simulations and experiments have been performed with a viscoelastic tire rubber compound at high flow rates through a circular die. A 3-mode PTT model was fitted onto rheological data of the rubber. The PTT model covers the range of shear rates present in the simulation. Convergence of the simulation was achieved with some wall slippage. The simulated and experimental extrudate swell is in good agreement at 20 mm from the die exit for a wide range of flow rates.

**Keywords:** CFD, extrudate swell, die swell, PTT, viscoelasticity, tire rubber compound

## NOMENCLATURE

### Greek Symbols

$\dot{\gamma}$	Shear rate, [ $s^{-1}$ ].
$\varepsilon$	Strain (elasticity) parameter of the PTT model, [-].
$\zeta$	Slip parameter of PTT model, [-] [1].
$\eta^*$	Dynamic viscosity, [ $Pa \cdot s$ ].
$\eta$	Viscosity, [ $Pa \cdot s$ ].
$\lambda$	relaxation time, [s].
$\rho$	Mass density, [ $kg \cdot m^{-3}$ ].
$\sigma_n$	Stress normal to plane direction, [Pa].
$\tau_{wall}$	The shear stress at the wall, [Pa].
$\omega$	Oscillation frequency, [ $rad \cdot s^{-1}$ ].

### Latin Symbols

$H$	Diameter of the extrudate, [m].
$H_0$	Diameter of the die, [m].
$\mathbf{D}$	Rate of deformation tensor, [ $s^{-1}$ ].
$\mathbf{g}$	Gravity field, [ $m \cdot s^{-2}$ ].
$G'$	Storage modulus, [Pa].
$G''$	Loss modulus, [Pa].
$k$	Slip coefficient, [ $kg \cdot m^{-2} \cdot s^{-1}$ ].
$m_{\eta^*}$	Power law coefficient, [ $Pa \cdot s^{n_{\eta^*}} \cdot Rad^{1-n_{\eta^*}}$ ].
$m_{G'}$	Power law coefficient, [ $Pa \cdot s^{n_{G'-1}} \cdot Rad^{1-n_{G'}}$ ].
$n_{\eta^*}$	power law index, [-].
$n_{G'}$	power law index, [-].
$p$	Pressure, [Pa].
$Q$	Flow rate, [ $m^3 \cdot s^{-1}$ ].

$r$	Viscosity ratio, [-].
rpm	Rotations per minute of the gear pump.
$S$	Swell ratio, [-].
$t$	Time, [s].
$T_g$	glass-liquid transition temperature, [ $^{\circ}C$ ].
$\mathbf{T}$	Stress tensor, [Pa].
$\Delta$	Upper-convected derivative of tensor $\mathbf{T}$ , [Pa].
$\nabla$	Lower-convected derivative of tensor $\mathbf{T}$ , [Pa].
$\mathbf{T}_1$	Lower-convected derivative of tensor $\mathbf{T}$ , [Pa].
$\mathbf{v}$	Velocity field, [m/s].
$v_s$	Velocity at the wall, the slip velocity, [ $m \cdot s^{-1}$ ].

## INTRODUCTION

Unvulcanized rubber extrusion is a key process in the tire industry. When rubber is extruded the extrudate will swell, a phenomenon called ‘extrudate swell’ or ‘die swell’. The degree of extrudate swell is dependent on many process parameters, among those parameters are the die shape, production rate, rubber composition and the elastic behavior of the rubber. Extrusion die design is a costly and time consuming process due to extrudate swell. Die design may be aided by numerical simulations of the extrusion process [2]. Flow patterns and pressure build up (flow resistance) within the die may be simulated with standard (fluid mechanics) numerical methods. However, extrudate swell poses specific problems because of the viscoelastic nature of the material, and because of the complex boundary conditions. There seems to be a growing interest in the tire making industry in simulating the extrusion of tire rubber [3-8]. This study proposes a procedure for aiding die design for industrial rubber extrusion by performing rheological measurements and numerical simulations. The simulated extrudate swell is verified with experimental extrudate swell.

## Theory

Extrudate swell is a complex phenomenon. There are several contributing factors identified [9]. Swelling due to rearrangement of the velocity field, which happens in Newtonian fluids and Non-Newtonian fluids alike. This is only a small contribution for viscoelastic fluids like

rubber. The main cause of extrudate swell in viscoelastic fluids is elastic recovery.

It is unlikely that an analytical solution can be found to calculate extrudate swell according to R. I. Tanner [9]. This is due to the stress singularity which occurs at the change of boundary conditions from zero velocity at the die wall into the free-surface.

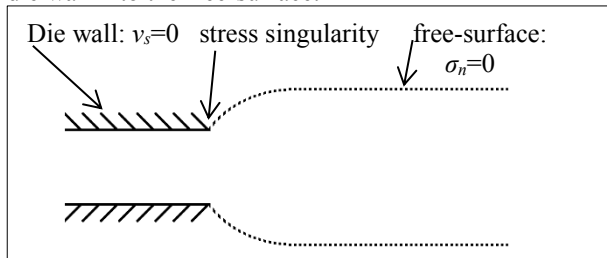


**Figure 1:** Schematic representation of extrudate swell. Velocities are zero at the die wall. At the free-surface the stresses normal to the free surface are zero [9].

Locating the free-surface is difficult. For this reason many attempts to calculate extrudate swell involve numerical methods. These methods need constitutive equations to describe the behavior of viscoelastic materials. Examples of viscoelastic models often applied in extrudate swell simulation studies are:

- Kaye-Bernstein-Kearsley-Zapas model [10-14]
- Pom-Pom model [14-17]
- Algebraic Extra-Stress Model [16, 18-20]
- Phan Thien & Tanner (PTT) model [8, 14-16, 20-30]

J.H. Kim and M.Y. Lyu have performed extrudate swell simulations with several viscoelastic models [16]. The PTT model shows good agreement with capillary rheometer experiments. Therefore the PTT model is applied in this study. Extrudate swell simulation studies are often conducted at relatively low flow rates and low shear rates [8, 14, 15, 31]. But in industrial rubber extrusion processes high flow rates and shear rates occur. This study is focused on extrudate swell at industrial flow rates.

## EXPERIMENTAL SETUP

### Extrusion experiments

Apollo tyres provided a rubber compound suitable for tire production. VMI Group performed several extrudate swell experiments. The rubber was extruded with a Shark 70 extruder, the shape and dimensions of the extrudate swell was captured on camera from above the extrudate.

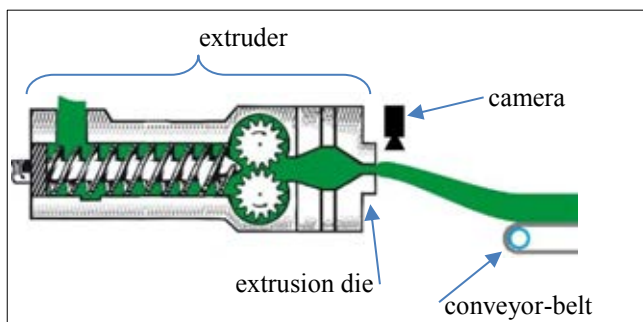


**Figure 2:** Schematic diagram of extrudate swell measurement setup.

The extrusion die is circular symmetrical and consist of a conical part and a capillary part.

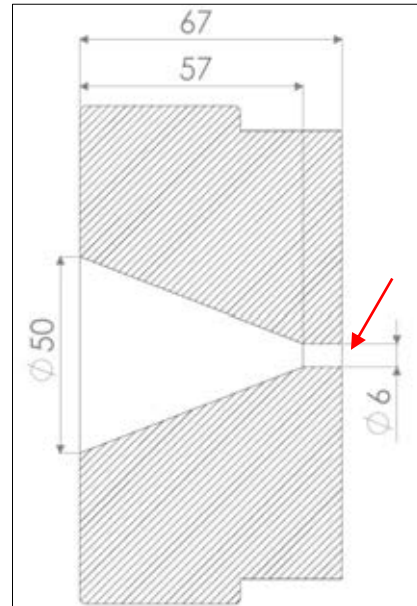


**Figure 3:** Cross-section of the circular symmetrical extrusion die, all dimensions are in mm. The rubber flow direction is from left to right. The red arrow points where the rubber exits the die.

A conveyor belt transported the rubber away from the extruder. The conveyor-belt speed was visually matched to the extrudate velocity to avoid pulling on the rubber extrudate. Pulling on the rubber decreases the extrudate swell. Camera imaging was used to measure the extrudate swell at several distances from the die exit. The rubber curves downward upon exiting the die since the conveyor-belt is positioned lower than the die exit, see Figure 4. This results in lower accuracy measurements of the extrudate swell at greater distances from the die exit.

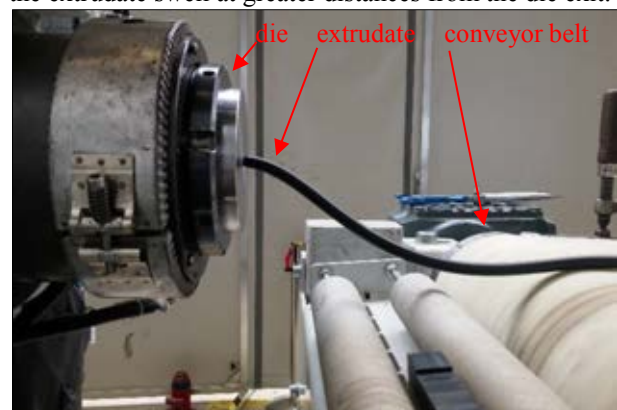


**Figure 4:** Photograph of the die, extruded rubber and conveyor belt, the camera is not included in this photograph.

The Shark 70 extruder consists of a conveying screw extruder and a gear-pump. The conveying screw extruder was set to produce a pressure of 30 Bar. Experiments have been performed at 4 different gear-pump speeds.

**Table 1:** Set gear-pump speeds and corresponding flow rates.

Gear pump speed	Flow rate
5 rpm	14.7 ml·s <sup>-1</sup>
10 rpm	29.3 ml·s <sup>-1</sup>
15 rpm	44.7 ml·s <sup>-1</sup>
20 rpm	58.7 ml·s <sup>-1</sup>

The flow rate was verified measuring the mass of extrudate collected during 36 s of extrusion. With each experiment, the temperature was measured at the inside of the extrudate. Extrudate swell ( $S$ ) is expressed as the ratio of the diameter of the die and the extrudate diameter:

$$S = \frac{H - H_0}{H_0} \quad 1$$

### Rheological measurement setup

The  $G'$ ,  $G''$  and  $\eta^*$  of the rubber compound were measured with an RPA2000 provided by the University of Twente. The RPA2000 is a cone-cone oscillatory rheometer. The cone geometry ensures that the shear rate is independent of the distance to the center of the cone.

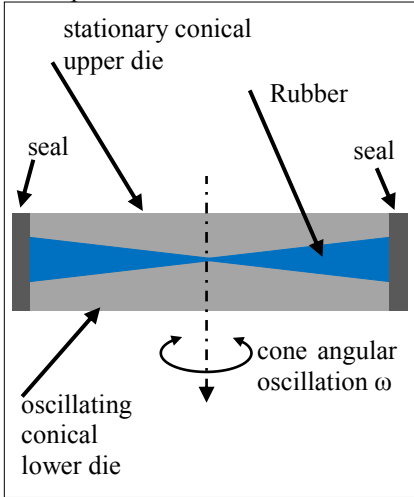


**Figure 5:** Schematic representation of the RPA2000, the conical dies are filled with a rubber specimen [32].

A rubber sample was subjected to a series of 9 measurements with a logarithmically increasing oscillation frequency of 0.07 rad·s<sup>-1</sup> up to 209 rad·s<sup>-1</sup>. Measurements with the RPA2000 were performed at 90 °C, 100 °C and 110 °C. The shear viscosity is calculated from the dynamic viscosity with the Cox-Merz rule [33].

$$\eta(\dot{\gamma}) = |\eta^*(\omega)|; \text{ with } \dot{\gamma} = \omega \quad 2$$

## SIMULATION SETUP

### Constitutive model

The numerical simulations have been performed with Polyflow of the Ansys 17.2 simulation suite. Polyflow is FEM software which is often used for viscoelastic extrusion simulations [8, 10, 13, 14, 16, 17, 20, 31, 34-36]. Polyflow calculates the extra stress tensor of the momentum conservation equation (3) with equation 4 [37].

$$\rho \left( \frac{\partial \mathbf{v}}{\partial t} + \nabla \cdot (\mathbf{v}\mathbf{v}) \right) = -\nabla p + \nabla \mathbf{T} + \rho \mathbf{g} \quad 3$$

$$\mathbf{T} = \mathbf{T}_1 + \mathbf{T}_2 \quad 4$$

$\mathbf{T}_2$  is a purely viscous component which improves the convergence of the numerical method [37].

$$\mathbf{T}_2 = 2\eta \frac{r}{1-r} \mathbf{D} \quad 5$$

$\mathbf{T}_1$  is calculated with the PTT viscoelastic model, equation 6 [37].

$$e^{\left[ \frac{\varepsilon \lambda}{\eta} \text{tr}(\mathbf{T}_1) \right]} \mathbf{T}_1 + \lambda \left[ \left( 1 - \frac{\xi}{2} \right) \nabla \cdot \mathbf{T}_1 + \frac{\xi}{2} \Delta \mathbf{T}_1 \right] = 2\eta \mathbf{D} \quad 6$$

When a multi-mode viscoelastic model is used, the total extra stress tensor is the sum of the individual viscoelastic components. In order to limit the computational costs only 3 modes have been used.

All the simulations are isothermal. The finite element method is used for solving the system of equations, which involves a combination of the discrete elastic viscous stress splitting (DEVSS) and the streamline upwind (SU) method [37].

### Curve fitting the PTT model parameters onto rheological data

The PTT model has several material specific parameters. The values of these parameters are found by fitting the PTT model onto the rheological data with Polymat. Polymat is an application for curve fitting and is available in Ansys 17.2.  $r$ ,  $\eta$ ,  $\varepsilon$  and  $\xi$  are fitted onto the measured  $G'$  and  $G''$ .  $\varepsilon$  and  $\xi$  are chosen to be identical for each PTT mode. The relaxation mechanism occurs near  $1/\dot{\gamma}$  [37]. The relaxation times are not curve fitted but set as the reciprocal of the typical shear rates of the simulation. These typical shear rates were determined with a trial simulation. The trial simulation is similar to the extrudate swell simulation. To limit computational costs, the extrudate and the free surface were not included in the trial simulation. A trial multimode PTT model with very high and a very short relaxation times was used, all the other parameters were curve fitted onto the measured data. The trial simulation shows that typical shear rates are between 1 s<sup>-1</sup> and 2000 s<sup>-1</sup>. In the final multimode PTT model the relaxation times were chosen as 0.667 ms, 0.02 s and 0.6 s, which correspond with the typical shear rates of the trial simulation. The simulations with the final multimode PTT model do not exceed shear rates of 2130 s<sup>-1</sup>.

### Extrapolation of the measured data

Measurements with the RPA2000 are limited to 208 Rad·s<sup>-1</sup> at a maximum. The typical shear rates of the simulation were much higher, therefore the measured  $\eta^*$ ,  $G'$  and  $G''$  were extrapolated in order to curve fit up to 1500 Rad·s<sup>-1</sup>. With many rubber compounds a shear thinning effect is measured up to very high shear rates [38-40]. It is assumed that a power law is applicable with shear rates up to 1500 s<sup>-1</sup>. Complex viscosity measurements are extrapolated using a power law which is fitted onto the rheological data. For  $G'$  an exponential relation was found. Finally  $G''$  is calculated with the extrapolated  $\eta^*$  and  $G'$ .

$$\eta^* = m_{\eta^*} \cdot \omega^{n_{\eta^*}-1} \quad 7$$

$$G' = m_{G'} \cdot \omega^{n_{G'}} \quad 8$$

$$G'' = \sqrt{\omega^2 \cdot \eta^{*2} - G'^2} \quad 9$$

### Boundary conditions

It was assumed that there is no wall slippage in the extrusion experiments, but the simulation would not converge without a certain amount of slippage at the die wall. This is most likely due to the high Weissenberg number problem. The high shear rates mostly occur near the die exit. Wall slippage was introduced in the extrudate swell simulations in order to temper the shear rates at the die exit. The wall slippage is enforced with equation 10 [37, 40].

$$v_s = -\frac{\tau_{wall}}{k} \quad 10$$

There is a full-slip condition when  $k=0 \text{ kg}\cdot\text{m}^{-2}\cdot\text{s}^{-1}$ , there is no slip if  $k=\infty \text{ kg}\cdot\text{m}^{-2}\cdot\text{s}^{-1}$ . Wall slippage decreases the pressure drop in the die. The pressure drop can be expressed as a function of slip coefficient  $k$ . It was decided that a simulation performs sufficiently if the pressure drop is not significantly influenced by the wall slippage.

A simplified simulation was performed in order to find the pressure drop within the die. The simplified simulation is without extrudate and free surface, the simulation does converge without wall slippage. The simplified simulation was subsequently subjected to an incrementally increasing wall slippage. At  $k=10^8 \text{ kg}\cdot\text{m}^{-2}\cdot\text{s}^{-1}$  the pressure drop became more than 95 % of that of the simulation without wall slippage. The extrudate swell simulations were performed with a wall slippage with a slip coefficient  $k=10^8 \text{ kg}\cdot\text{m}^{-2}\cdot\text{s}^{-1}$ .

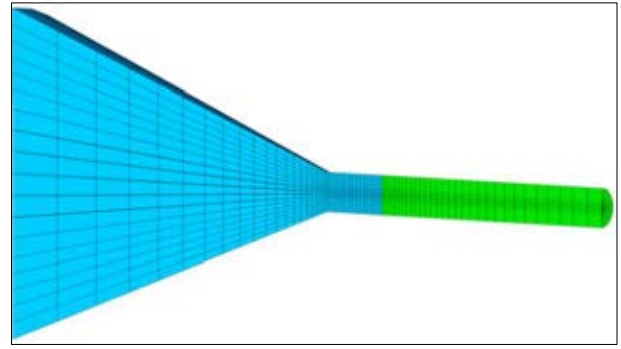
Finally, the surface of the extrudate is a free surface and the remeshing technique Optimesh-3D was applied [37]. At the outflow plane, a zero tangential and normal force condition was applied. This condition is applicable if the elastic tensions are completely dissipated.

### Mesh

Several 3D meshes of the die and 40 mm of extrudate were designed. Some design consideration are:

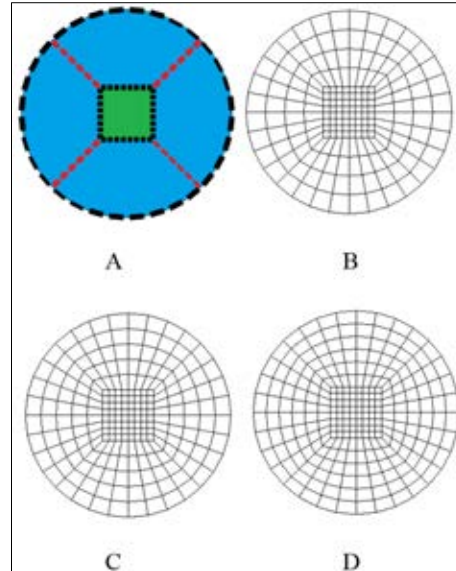
- High node density near the die exit is desirable since the greatest increase in extrudate diameter is expected to happen near the die exit.
- Practice shows that a structured mesh of hexagonal cells results in a more stable simulation than an unstructured mesh.
- The computational costs increases rapidly with an increase in the number of nodes.
- Sufficient node density near the die wall since the shear rates are greatest near the die wall.

Figure 6 shows the cross-section through the length of the die and extrudate, the node density is higher near the die exit.



**Figure 6:** A cross-section through the length of the die and extrudate. Blue is the rubber inside the die, green is extrudate with a free surface. Note the higher node density near the die exit and larger cells further away from the die exit.

Simulations with several meshes were performed in order to find a mesh with a sufficient node density near the die wall. The node density near the die wall was determined by one variable, all other design parameters are kept constant, see Figure 7.



**Figure 7:** Width cross-sections of the meshes. A: Schematic representation of the mesh designs, the mesh consists of a square mid-section (green) and a circular part (blue). The total number of nodes is determined by a constant number of nodes in the angular direction (black) and a variable number of nodes in the radial direction (red). B: Cross-section of a mesh with 4 nodes in the radial direction. C: Cross-section of a mesh with 5 nodes in the radial direction. D: Cross-section of a mesh with 6 nodes in the radial direction.

A mesh is sufficient if the extrudate does not increase much when the number of nodes increases. The diameter of the extrudate at 20 mm from the die exit as a function of the number of nodes is shown in Figure 8.

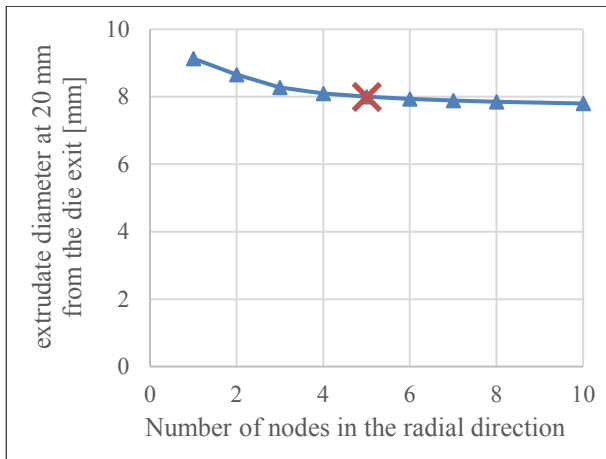


**Figure 8:** The extrudate diameter at 20 mm from the die exit as a function of the number of nodes in the radial direction with a flow rate of  $13.9 \text{ ml}\cdot\text{s}^{-1}$ . The red cross at 5 nodes in the radial direction, this is the mesh used for the extrudate swell simulations.

The mesh used in this study is with 5 nodes in the radial direction. The mesh is structured with hexagonal cells and contains 15906 cells.

## RESULTS AND DISCUSSION

### Rheological measurements and curve-fit

The  $G'$ ,  $G''$  and  $\eta$  were measured with the RPA2000, the rubber compound did not show a significant temperature dependence within the measured temperature range. This temperature independent behavior is expected since the rubber compound has a low  $T_g$  of less than  $0 \text{ }^\circ\text{C}$ . The measurements at  $100 \text{ }^\circ\text{C}$  have been used for extrapolation and curve-fitting. The measured  $G'$ ,  $G''$  and  $\eta$  and the extrapolated data is shown in Figure 9.

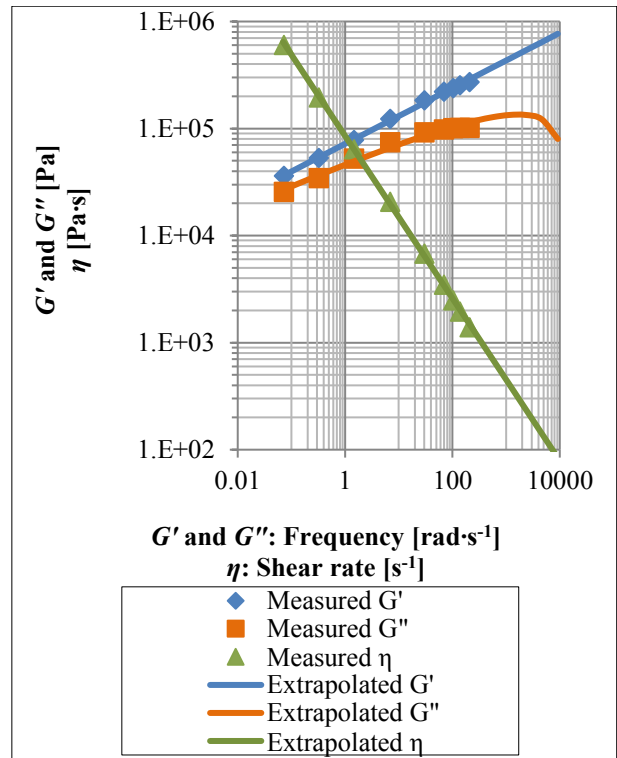


**Figure 9:** Measured and extrapolated  $G'$ ,  $G''$  and  $\eta$ . Note: the dimensions differ between  $G'$ ,  $G''$  and  $\eta$ . Note: all dimensions are presented on a logarithmic scale.

Equations 7, 8 and 9 are applied for the extrapolation of  $G'$ ,  $\eta$  and  $G''$ . The following values for the parameters of these equations were found:

- $m_{\eta^*} = 85422 \text{ Pa}\cdot\text{s}^{n_{\eta^*}}\cdot\text{Rad}^{1-n_{\eta^*}}$
- $n_{\eta^*} = 0.241$
- $m_{G'} = 72078 \text{ Pa}\cdot\text{s}^{n_{G'}}\cdot\text{Rad}^{-n_{G'}}$
- $n_{G'} = 0.259$

A curve fit was made onto the extrapolated data and is shown in Figure 10.



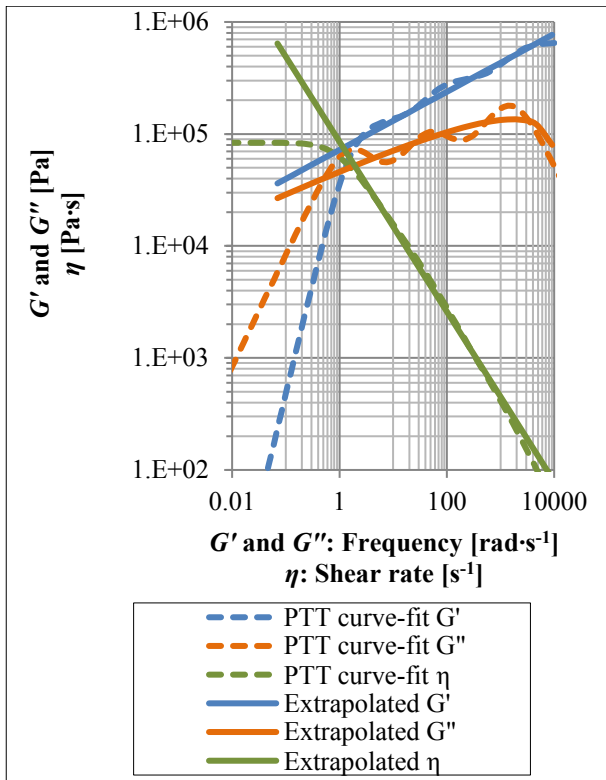


**Figure 10:** Extrapolated and curve fitted  $G'$ ,  $G''$  and  $\eta$ .  
 Note: the dimensions differ between  $G'$ ,  $G''$  and  $\eta$ .  
 Note: all dimensions are presented on a logarithmic scale.

The typical shear rates range between  $1 \text{ s}^{-1}$  and  $2000 \text{ s}^{-1}$  as was determined with the trial simulation. Note that the fit matches well in the range of typical shear rates, but poorly at the shear rates of less than  $1 \text{ s}^{-1}$ .

**Table 2:** Curve-fitted values of the 3 mode PTT model.  
 Note that there is only a single  $r$  for the multimode model, and that  $\varepsilon$  and  $\zeta$  are identical for each mode.

	First mode	Second mode	Third mode
$\lambda$	$0.667 \cdot 10^{-3} \text{ s}$	$2 \cdot 10^{-3} \text{ s}$	$0.6 \text{ s}$
$\eta$	$230.803 \text{ Pa}\cdot\text{s}$	$3539.3 \text{ Pa}\cdot\text{s}$	$79880.5 \text{ Pa}\cdot\text{s}$
$\varepsilon$	0.7508015	0.7508015	0.7508015
$\zeta$	0.1360633	0.1360633	0.1360633
$r$	$0.41343 \cdot 10^{-6}$	-	-

### Extrusion experiments

During the extrusion experiments the extrudate temperature and mass flow rate have been measured. Apollo tyres determined that the density of the rubber compound is  $1210 \text{ kg}\cdot\text{m}^{-3}$ .

**Table 3:** Measured flow rate and extrudate temperature for each experiment.

Gear pump speed	Flow rate	Extrudate temperature
5 rpm	$13.9 \text{ ml}\cdot\text{s}^{-1}$	$88 \text{ }^\circ\text{C}$
10 rpm	$27.4 \text{ ml}\cdot\text{s}^{-1}$	$95 \text{ }^\circ\text{C}$
15 rpm	$41.1 \text{ ml}\cdot\text{s}^{-1}$	$100 \text{ }^\circ\text{C}$
20 rpm	$54.2 \text{ ml}\cdot\text{s}^{-1}$	$105 \text{ }^\circ\text{C}$

The measured flow rates of Table 3 are used for the simulations.

### Shear rates in the simulations

The simulations show high shear rates within the capillary part of the die. At higher flow rates the shear rates increase, but do not surpass  $2130 \text{ s}^{-1}$ . Which is in agreement with the typical shear rates found with the trial simulations and the chosen relaxation times.

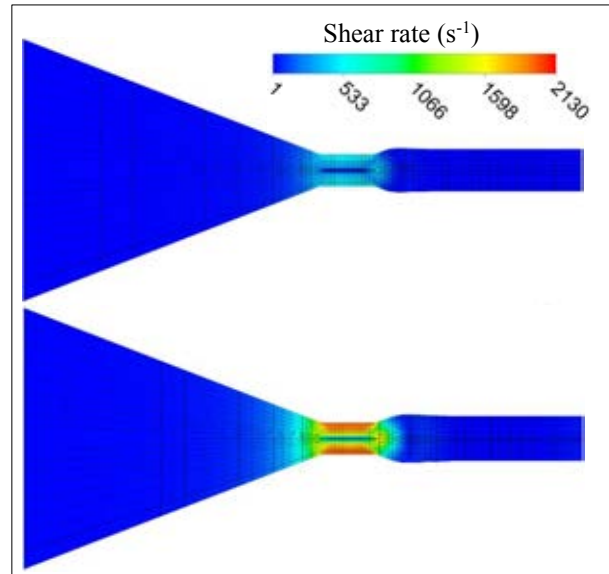


**Figure 11:** Shear rate in the extrudate swell simulations, upper diagram is 5 rpm, the lower diagram is 20 rpm.

### Extrudate swell

The measured extrudate swell and the simulated extrudate swell are shown as a function of distance from the die exit:

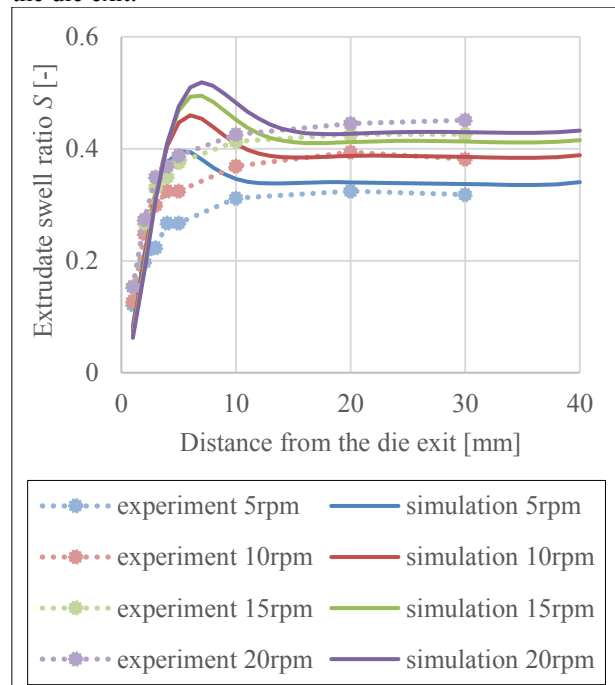


**Figure 12:** Experimental and simulated extrudate swell as a function of distance from the die exit, the legend shows the set gear pump speed of each experiment and simulation.

In these experiments the extrudate swell increases as a function of distance from the die exit up until 20 mm from the die exit. A small decrease in extrudate swell at

30 mm from the die exit can be observed. This is most likely a measurement error due to the downward curvature of the extrudate.

The simulations show a rapid increase in extrudate swell at a short distance from the die exit. The simulated extrudate swell seems to overshoot in comparison to the experiments. With more wall slippage, the overshoot disappeared.

The simulations show an increase of extrudate swell near the end of the 40 mm of simulated extrudate. This swell increases when the simulation is repeated with a shorter (20 mm) extrudate. A shorter extrudate has less time to relax. The extra swell near the end is most likely due to the boundary conditions at the outflow plane and the elastic tensions which have not completely been dissipated.

Figure 13 shows the simulated and experimental extrudate swell as a function of the flow rate at 20 mm from the die exit.

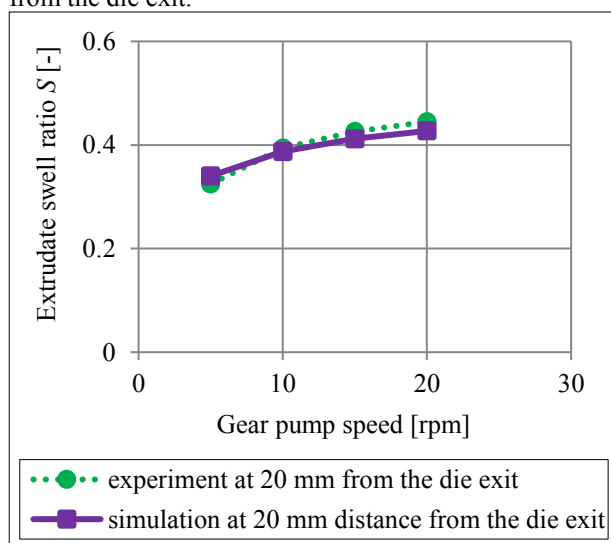


**Figure 13:** Experimental and simulated extrudate swell as a function of flow rate at 20 mm from the die exit.

There is strong agreement between the simulated and experimental extrudate swell. Both the simulated and experimental extrudate swell increase with higher flow rates, but the increase becomes less at higher flow rates.

## CONCLUSION

A procedure was proposed to simulate extrudate swell. A rubber compound was analyzed for its rheological behavior and a 3 mode PTT model was fitted onto the rheological data. Extrudate simulations at high flow rates and shear rates have been performed with the PTT model. Extrusion experiments at high flow rates and shear rates have been performed. The extrudate swell was measured, the accuracy of the extrudate swell measurement is decreases beyond 30 mm from the die exit. The simulated swell is overpredicted near the die exit, the simulated swell and the experimental swell is in good agreement at 20 mm from the die exit.

## Recommendations / Future work

The extrusion simulation was performed with a single circular die and a single tire rubber compound. Future work will focus on different die shapes and sizes,

different tire compounds and different viscoelastic models.

In this study, rheological data was extrapolated. Further study is needed to determine whether the behavior of rubber matches the extrapolation.

Further research is needed to determine whether wall slippage is present in the die and how this might be included in the simulations. Wall slippage is not present at low shear rates, but might be present at high shear rates. The presence of wall slippage might be determined by experiments and simulations at low and high flow rates and shear rates. This could also be a validation of the simulation procedure at low flow rates.

## ACKNOWLEDGEMENTS

This study was financially supported by Green Polymer Application Centre (Green PAC), Apollo tyres and VMI Group. The Windesheim University Professorship for Polymer Engineering conducted this study with project partners Apollo tyres, VMI Group and University of Twente. The project partners provided expert advice, essential equipment, materials and experimental data.

## REFERENCES

1. Coelho, P.M., F.T. Pinho, and P.J. Oliveira, *Fully developed forced convection of the Phan-Thien-Tanner fluid in ducts with a constant wall temperature*. International Journal of Heat and Mass Transfer, 2002. **45**(7): p. 1413-1423.
2. Pittman, J.F.T., *Computer-aided design and optimization of profile extrusion dies for thermoplastics and rubber: a review*. Proceedings of the Institution of Mechanical Engineers, Part E: Journal of Process Mechanical Engineering, 2011. **225**(4): p. 280-321.
3. Thais, L., L. Helin, and G. Mompean, *Numerical simulation of viscoelastic flows with Oldroyd-B constitutive equations and novel algebraic stress models*. Journal of Non-Newtonian Fluid Mechanics, 2006. **140**(1-3): p. 145-158.
4. Debbaut, B. *Eureka project ID 2799: Development and industrial applications of explicit algebraic fluid models*. Available from: <http://www.eurekanetwork.org/project/id/2799>.
5. Choi, S.H. and M.Y. Lyu, *Application of the PTT Model for Capillary Extrusion of Rubber Compounds*. International Polymer Processing, 2009. **24**(4): p. 326-333.
6. *29th Annual Meeting and Conference on Tire Science and Technology*. 2010.
7. Ashutosh A. Kudale, K.N., G. Karthick Raja, P. Sankarganesh 2, R. Rajesh Babu, *Extrusion Die Swell Simulation of Tire tread Compound using Phan Thien & Tanner (PTT) Model*.
8. Yang, C. and Z. Li, *Effects of wall slip on the rheological measurement and extrusion die design of a filled rubber compound*. Plastics, Rubber and Composites, 2016. **45**(7): p. 326-331.

9. Tanner, R.I., *Engineering rheology*. 1 ed. 1986: Oxford University Press.
10. Ahmed, R., R.F. Liang, and M.R. Mackley, *The experimental observation and numerical prediction of planar entry flow and die swell for molten polyethylenes*. *Journal of Non-Newtonian Fluid Mechanics*, 1995. **59**(2-3): p. 129-153.
11. Goublomme, A., B. Draily, and M.J. Crochet, *Numerical prediction of extrudate swell of a high-density polyethylene*. *Journal of Non-Newtonian Fluid Mechanics*, 1992. **44**: p. 171-195.
12. Goublomme, A. and M.J. Crochet, *Numerical prediction of extrudate swell of a high-density polyethylene: further results*. *Journal of Non-Newtonian Fluid Mechanics*, 1993. **47**: p. 281-287.
13. Konaganti, V.K., et al., *Extrudate Swell of High Density Polyethylenes in Slit (Flat) Dies*. *International Polymer Processing*, 2016. **31**(2): p. 262-272.
14. Konaganti, V.K., et al., *Extrudate swell of a high-density polyethylene melt: II. Modeling using integral and differential constitutive equations*. *Journal of Non-Newtonian Fluid Mechanics*, 2015. **225**: p. 94-105.
15. Ganvir, V., et al., *Extrudate swell of linear and branched polyethylenes: ALE simulations and comparison with experiments*. *Journal of Non-Newtonian Fluid Mechanics*, 2011. **166**(1-2): p. 12-24.
16. Kim, J.H. and M.Y. Lyu, *Predictions of flow behaviors and entrance pressure drop characteristics of a rubber compound in a capillary die using various rheological models*. *Polymer Engineering & Science*, 2014. **54**(10): p. 2441-2448.
17. Debbaut, B. and T. Marchal, *Numerical simulation of extrusion process and die design for industrial profile, using multimode pom-pom model*. *Plastics, Rubber and Composites*, 2008. **37**(2-4): p. 142-150.
18. Mompean, G., et al., *Numerical prediction of three-dimensional time-dependent viscoelastic extrudate swell using differential and algebraic models*. *Computers & Fluids*, 2011. **44**(1): p. 68-78.
19. Limtrakarn, W., et al., *Circular Die Swell Evaluation of LDPE Using Simplified Viscoelastic Model*. King Mongkut's University of Technology North Bangkok *International Journal of Applied Science and Technology*, 2013. **6**(3): p. 59-68.
20. Kim, J., et al., *Computer Simulation of Die Extrusion for Rubber Compound Using Simplified Viscoelastic Model*. *Elastomers and Composites*, 2011. **46**(1): p. 54-59.
21. Béraudo, C., et al., *A finite element method for computing the flow of multi-mode viscoelastic fluids: comparison with experiments*. *Journal of Non-Newtonian Fluid Mechanics*, 1998. **75**(1): p. 1-23.
22. Ganvir, V., et al. *Numerical and Experimental Studies on Extrudate Swell of Linear and Branched Polyethylenes*. in *The XV International Congress on Rheology, The Society of Rheology 80 Annual Meeting*. 2008. American Institute of Physics.
23. Ganvir, V., et al., *Prediction of extrudate swell in polymer melt extrusion using an Arbitrary Lagrangian Eulerian (ALE) based finite element method*. *Journal of Non-Newtonian Fluid Mechanics*, 2009. **156**(1-2): p. 21-28.
24. Mu, Y., et al., *Measurement and simulation of low-density polyethylene extrudate swell through a circular die*. *Polymer International*, 2009. **58**(5): p. 475-483.
25. Mu, Y., et al., *Finite-Element Simulation of Polymer Flow and Extrudate Swell Through Hollow Profile Extrusion Die with the Multimode Differential Viscoelastic Model*. *Advances in Polymer Technology*, 2013. **32**(S1): p. E1-E19.
26. Ganvir, V., et al., *Numerical and experimental studies on extrudate swell of branched polyethylene through axisymmetric and planar dies*. *Journal of Polymer Engineering*, 2011. **31**(2-3): p. 217-221.
27. Debbaut, B. and M.J. Crochet, *Further results on the flow of a viscoelastic fluid through an abrupt contraction*. *Journal of Non-Newtonian Fluid Mechanics*, 1986. **20**: p. 173-185.
28. Yang, C. and Z. Li, *An integrated numerical study of coextrusion flow inside and outside the die*. *Journal of Applied Polymer Science*, 2016. **133**(23).
29. Ren, Z., X.Y. Huang, and H.S. Liu, *3D Numerical study on the hollow profile polymer extrusion forming based on the gas-assisted technique*. *IOP Conference Series: Materials Science and Engineering*, 2016. **137**: p. 012007.
30. Pettas, D., et al., *On the origin of extrusion instabilities: Linear stability analysis of the viscoelastic die swell*. *Journal of Non-Newtonian Fluid Mechanics*, 2015. **224**: p. 61-77.
31. Konaganti, V.K., et al. *Study on extrudate swell of high-density polyethylenes in slit (flat) dies*. in *Annual Technical Conference - ANTEC, Conference Proceedings*. 2016. Alpha-Technologies, RPA2000.
32. Macosko, C.W., *Rheology: Principles, Measurements, and Applications*. 1994: WILEY-VCH.
33. Owens, R.G. and T.N. Phillips, *Computational rheology*. 2002: World Scientific.
34. Konaganti, V.K., et al., *The effect of damping function on extrudate swell*. *Journal of Non-Newtonian Fluid Mechanics*, 2016. **236**: p. 73-82.
35. Konaganti, V.K., et al., *Non-isothermal extrudate swell*. *Physics of Fluids*, 2016. **28**(12).
36. ANSYS, *Polyflow manual*.
37. Leblanc, J.L., *Rubber-filler interactions and rheological properties in filled compounds*.

- Progress in Polymer Science, 2002. **27**(4): p. 627-687.
39. Bhagawan, S.S., et al., *Effect of fillers on the rheological behavior of thermoplastic 1,2 polybutadiene rubber*. Polymer Engineering and Science, 1988. **28**(10): p. 648-654.
40. Yang, C. and Z. Li, *A study of wall slip in the capillary flow of a filled rubber compound*. Polymer Testing, 2014. **37**: p. 45-50.



## FRONT-TRACKING SIMULATIONS OF BUBBLES RISING IN NON-NEWTONIAN FLUIDS

**Alessandro BATTISTELLA<sup>1</sup>, Sebastian J.G. VAN SCHIJNDEL<sup>1</sup>, Maike W. BALTUSSEN<sup>2</sup>,  
 Ivo ROGHAIR<sup>1\*</sup>, Martin VAN SINT ANNALAND<sup>1</sup>**

<sup>1</sup>Chemical Process Intensification, Department of Chemical Engineering and Chemistry, Eindhoven University of Technology, Eindhoven, the Netherlands

<sup>2</sup>Multi-scale Modelling of Multiphase Flows, Department of Chemical Engineering and Chemistry, Eindhoven University of Technology, Eindhoven, the Netherlands

\* E-mail: i.roghair@tue.nl

### ABSTRACT

In the wide and complex field of multiphase flows, bubbly flows with non-Newtonian liquids are encountered in several important applications, such as in polymer solutions or fermentation broths. Despite the widespread application of non-Newtonian liquids, most of the models and closures used in industry are valid for Newtonian fluids only, if not even restricted to air-water systems. However, it is well known that the non-Newtonian rheology significantly influences the liquid and bubble behaviour. CFD represents a great tool to study such complex systems in more detail and gain useful insights on the dynamics of gas-liquid (and possibly solid) systems with the ultimate aim to help the development or the design of industrial reactors. In this study, a DNS Front Tracking (FT) method is applied to study the rise of bubbles in different power-law fluids. Detailed information is obtained regarding the flow of single or multiple bubbles, especially concerning the viscosity profile around single rising bubbles, their shapes and their rising velocity.

To describe the bubble rise velocity in less detailed model, a closure for the drag force is needed. With the use of Front Tracking, an existing drag correlation, which was derived for Newtonian fluids, is adapted and improved to non-Newtonian rheologies. When the effect of the viscosity changes are limited, such as for not extreme exponents ( $0.5 \leq n \leq 1.5$ ), the correlation can predict reasonably well the drag coefficient for power-law fluids.

**Keywords:** CFD, hydrodynamics, bubble and droplet dynamics, rheology, multiscale. .

### NOMENCLATURE

#### Greek Symbols

$\dot{\gamma}$	Shear rate, [ $s^{-1}$ ]
$\varepsilon$	Error, [-]
$\eta$	Apparent viscosity, [Pa s]
$\mu$	Dynamic viscosity, [Pa s]
$\rho$	Mass density, [ $kg\ m^{-3}$ ]
$\sigma$	Surface tension, [ $N\ m^{-1}$ ]
$\boldsymbol{\tau}$	Stress tensor, [ $N\ m^{-2}$ ]
$\phi$	Volume fraction, [-]

#### Latin Symbols

$A, S$	Surface, [m].
$C_D$	Drag coefficient, [-].
$d$	Diameter, [m].
Eö	Eötvös number $Eö = \frac{gd^2\rho}{\sigma}$ , [-].
$\mathbf{F}$	Force, [N].

$g$	Gravitational acceleration, [ $m\ s^{-2}$ ].
$K$	Power law consistency index, [ $Pa\ s^n$ ].
$L$	Half distance between plates, [m].
$n$	Power law index, [-].
$\mathbf{n}$	Normal, [-].
$p$	Pressure, [Pa].
Re	Reynolds number $Re = \frac{\rho u d}{\mu}$ , [-].
Re*	Generalized Reynolds number $Re^* = \frac{\rho u^{2-n} d^n}{K}$ , [-].
$t$	Time, [s].
$\mathbf{t}$	Tangent, [-].
$\mathbf{u}$	Velocity, [ $m\ s^{-1}$ ].
$V$	Volume, [ $m^3$ ].

#### Sub/superscripts

$a, b, c, i, m$	Marker indicators.
$G$	Gas.
$i$	Index $i$ .
$j$	Index $j$ .
$rel$	Relative.
$x, y$	Flow directions.

### INTRODUCTION

Non-Newtonian bubbly flows are widely present in nature as well as in many industrial applications, as for instance in a bioreactor (Al-Masry, 1999) where the design is crucial for the survival of microorganisms. Another well known application is polymer production, where many processes, for instance polycondensation or polymer devolatilization, involve multiphase flows with non-Newtonian fluids (Li, 1999).

An accurate description of the hydrodynamics as well as mass and heat transfer is decisive in rational the design of industrial reactors. For this reason, Computational Fluid Dynamics (CFD) represents a valuable tool to help gaining insights in the underlying physics as well as in the ultimate optimization and design. To this end, we adopted a multi-scale modelling technique (Deen *et al.*, 2004; van Sint Annaland *et al.*, 2003) where small-scale detailed models give insights for the higher, less computational expensive, scales. The latter can be summarized in two main categories: Euler-Lagrange models, where bubbles are represented by Lagrangian spheres moving in a continuum, and Euler-Euler methods where both phases are treated as a continuum. With the use of such tools, it is possible to describe small (lab) scale models up to an industrial scale reactor. However, they heavily rely on the accuracy of the used closure relations, needed to describe the interactions (drag, mass and

heat transfer) between the dispersed elements and the continuous phase.

The use of direct numerical simulations (DNS) to study the smallest scale and develop such closures has been demonstrated in the past for Newtonian fluids (Dijkhuizen *et al.*, 2010a; Roghair *et al.*, 2011). Out of the many forces involved, certainly the drag force, and hence the drag coefficient, represents one of the most relevant in determining the bubble's hydrodynamic. However, despite the widespread use of non-Newtonian fluids, a complete and comprehensive description of the drag on a sphere, bubble or droplet, in such fluids (Darby and Chhabra, 2016) is still missing. In most cases, the relatively scarce information comes from experimental results and it is usually limited as a consequence of the incredibly complex variety of fluids. In numerical studies, purely viscous cases, mainly power-law fluids represent the most common type of fluids studied (Chhabra, 2006).

Ohta *et al.* (2010, 2012) developed through the years a CLSVOF model which, together with experiments, was used to study bubble shapes and velocities in different non-Newtonian fluids (both shear-thinning and shear-thickening). Radl *et al.* (2007) examined the rising of bubbles in a range of purely viscous and viscoelastic media, including mass transfer. In their work they use a hybrid front tracking/front capturing model, restricted to 2D due to the high resolution needed by the species solver. Zhang *et al.* (2010) examined the velocity and viscosity distribution, motion and bubble shape of a single bubble rising in a purely viscous shear-thinning fluid, represented by the Carreau model. For the computation, a level-set numerical approach was adopted. Some attempts have been done in the past to adapt existing drag correlations to non-Newtonian power-law fluids, such as Rodrigue (2002), which considered shear-thinning polymers at low to moderate Reynolds numbers. The proposed correlation is not suitable for high Reynolds numbers, where it does not converge to a constant as it has been well established in the recent years.

The aim of this work is to give a description of the drag coefficient in non-Newtonian fluids (both shear-thickening and shear-thinning), starting from considering single bubbles rising in power-law fluids. In the following sections, the front-tracking model used in this work will be described and verified. Then, the bubble shapes and viscosity profiles will be investigated with the numerical setup. To conclude, an outline of the drag coefficient with different power-law fluids will be given.

## MODEL DESCRIPTION

The model used in this paper is a front tracking model which has been described in detail in Dijkhuizen *et al.* (2010b) and Roghair *et al.* (2015, 2016). In the following section a general description is provided, with focus on the implementation of the non-Newtonian viscosity model.

### Hydrodynamics modeling

The fluid flow is described by the incompressible Navier-Stokes equation and continuity equation:

$$\rho \frac{\partial \mathbf{u}}{\partial t} + \rho \nabla \cdot (\mathbf{u}\mathbf{u}) = -\nabla p + \rho \mathbf{g} + \nabla \cdot \boldsymbol{\tau} + \mathbf{F}_\sigma \quad (1a)$$

$$\nabla \cdot \mathbf{u} = 0 \quad (1b)$$

where  $\mathbf{u}$  is the fluid velocity and  $\mathbf{F}_\sigma$  represents a singular source-term for the surface tension at the interface. Here  $\boldsymbol{\tau}$  represents the stress tensor, which becomes the very well

known function of viscosity for Newtonian fluids. The velocity field is continuous even across interfaces, so a one-fluid formulation has been used. The equations are solved with a finite difference technique using a staggered discretisation (see Figure 1). The flow field is solved using a two-stage projection-correction method. After solving the momentum balance for each velocity component separately, a pressure-correction step is taken to satisfy the continuity equation. These steps use an incomplete Cholesky conjugate gradient (ICCG) method to solve the linearised equations. The boundary conditions can be adjusted between free-slip, no-slip and periodic, but only the first is used in this work. The formulation of  $\boldsymbol{\tau}$  will be discussed later.

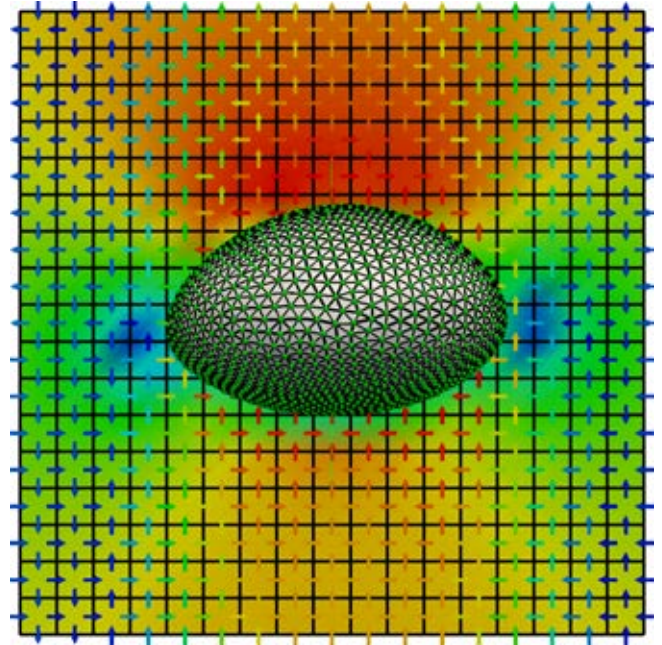


**Figure 1:** A zoomed snapshot of a rising FT bubble (at a very low resolution for illustration purposes), showing the tracking points and surface mesh, and the background grid with staggered velocity vectors. The colors of the background grid indicate the pressure profile, and the colors of the velocity vectors represent the magnitude.

### Surface mesh

The gas-liquid interface is tracked by Lagrangian control points, which connects to a mesh composed of triangular cells, called markers (Figure 2). At every time step, after the fluid flow has been calculated, the Lagrangian control points are moved with the interpolated velocity to their new locations. The velocity is interpolated with a cubic spline method. The actual movement is performed using a 4<sup>th</sup> order Runge-Kutta time stepping scheme.

#### Surface tension and pressure jump

$\mathbf{F}_\sigma$  is a force representing the surface tension, which can be directly calculated from the position of the interface markers. The individual pull-force of a general neighbouring marker  $i$  acting on marker  $m$  can be computed from their normal vectors and joint tangent as illustrated in Figure 2:

$$\mathbf{F}_{\sigma, i \rightarrow m} = \sigma (\mathbf{t}_{mi} \times \mathbf{n}_{mi}) \quad (2)$$

The sum of the surface forces of all markers yields the pres-

sure jump of the bubble as a whole.

$$\int_{\partial S} [p] dS = \int_{\partial S} \mathbf{F}_\sigma \cdot \mathbf{n} \quad (3)$$

$$[p] = \frac{\int_{\partial S} \mathbf{F}_\sigma \cdot \mathbf{n}}{\int_{\partial S} dS} = \frac{\sum_m \mathbf{F}_{\sigma,m} \cdot \mathbf{n}_m}{\sum_m S_m}$$

By distributing the total pressure jump equally back to the Eulerian mesh, the pressure jump is incorporated in the right-hand side of the momentum equations. For interfaces with a constant curvature (i.e. a sphere), the pressure jump and surface tension cancel each other out exactly, and if the curvature varies over the interface, only a relatively small net force will be transmitted to the Eulerian grid.

### Phase fraction and physical properties

Since the marker positions are exactly known, the phase fraction  $\phi$  in each Eulerian cell can be computed exactly using geometric analysis. With the phase fraction, the density of each Eulerian cell is calculated by weighted averaging. The viscosity (either Newtonian or the apparent non-Newtonian viscosity) is obtained by harmonic averaging of the kinematic viscosities (Prosperetti, 2002):

$$\rho(\mathbf{x}) = \sum_{p=0}^{n_{\text{phase}}-1} \phi_p(\mathbf{x}) \rho_p \quad (4a)$$

$$\frac{\rho(\mathbf{x})}{\eta(\mathbf{x})} = \sum_{p=0}^{n_{\text{phase}}-1} \phi_p(\mathbf{x}) \frac{\rho_p}{\eta_p} \quad (4b)$$

The bubble properties *i.e.* total surface area, volume and centroid position, can be efficiently obtained by summing over all triangular markers of an interface (Roghair *et al.*, 2015, 2016).

### Remeshing

Due to the advection of the interface control points, the markers' geometry changes at each time step, which may lead to too large or too small triangles. This distortion affects the grid quality and can decrease the accuracy in the surface tension forces computation. Moreover, due to the discrete nature of the interface, small changes in the enclosed volume appear

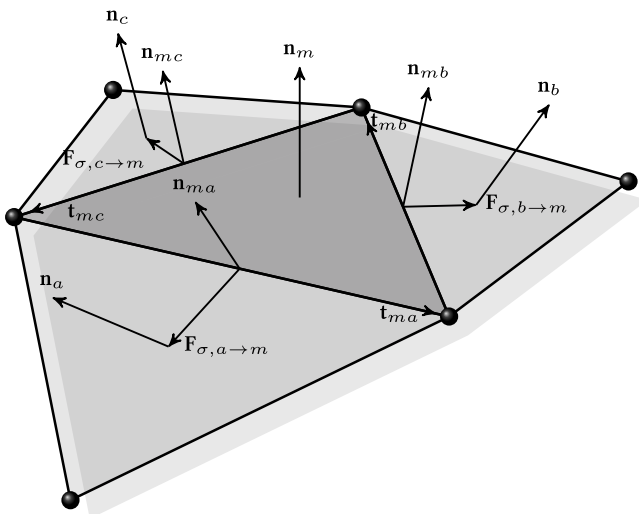


**Figure 2:** The surface tension calculation on marker involves the calculation of three pull-forces using the tangent and normal vectors shared with the neighbouring marker.

at every time step. Despite the small magnitude, the volume alterations can accumulate during the simulation time and must be prevented (Pivello *et al.*, 2013). The remeshing approach consists of three different parts: edge splitting and collapsing, edge swapping and smoothing. An edge is split (node addition) or collapsed (node removal) based on the edge length related to the Eulerian grid size. In some cases, it is preferable to swap an edge instead of changing the number of points: this procedure ensures that equilateral markers are preferred. Smoothing is used to enhance the quality of the grid and reduce the need for the other remeshing algorithms. The volume restoration/conservation is obtained using a method described by Kuprat *et al.* (2001). After each interface advection step and remeshing, a volume defect can be obtained by comparing the new volume with the original volume. This defect is then corrected by shifting the edges in order to restore the original volume, with particular attention on minimizing the impact on the actual geometry. A more detailed overview of the volume conservative remeshing has been presented in Roghair *et al.* (2015, 2016).

### Viscosity model

In (inelastic) non-Newtonian fluids, the viscosity is not a constant but is a function of the strain rate. When considering a Newtonian fluid, the stress tensor  $\boldsymbol{\tau}$  is given by:

$$\boldsymbol{\tau} = -\mu \left( \nabla \mathbf{u} + (\nabla \mathbf{u})^T \right) \equiv -\mu \dot{\boldsymbol{\gamma}} \quad (5)$$

in which  $\dot{\boldsymbol{\gamma}}$  represents the rate of strain tensor. A commonly used model to describe a non-Newtonian fluid is the so called *generalized Newtonian model*, consisting in simply replacing the viscosity  $\mu$  with an apparent viscosity  $\eta$ , which is a function of the shear rate (Bird *et al.*, 2007). The shear rate can be written as the magnitude of the rate of strain tensor:

$$\dot{\gamma} = \sqrt{\frac{1}{2}(\dot{\boldsymbol{\gamma}} : \dot{\boldsymbol{\gamma}})} \quad (6)$$

In this framework, the stress tensor is calculated as:

$$\boldsymbol{\tau} = -\eta \left( \nabla \mathbf{u} + (\nabla \mathbf{u})^T \right) \equiv -\eta \dot{\boldsymbol{\gamma}} \quad \text{with} \quad \eta = \eta(\dot{\gamma}) \quad (7)$$

Several empirical models are available to describe the relation between  $\eta$  and the shear rate, while the simplest and most widely used is the power-law model:

$$\eta = K \dot{\gamma}^{n-1} \quad (8)$$

Here  $K$  represents the consistency index while  $n$  is a constant characterizing the fluid: for  $n = 1$  the relation reduces to a Newtonian fluid, for  $n < 1$  the fluid is shear-thinning (viscosity reduces with the shear) and for  $n > 1$  is shear-thickening (viscosity increases with the shear). This model presents a very important physical and numerical limitation, as addressed by Gabbanelli *et al.* (2005). At zero shear, the viscosity becomes infinite for a shear-thinning and zero for a shear-thickening fluid. Furthermore, it is well known that most non-Newtonian fluids do not show this behaviour in the whole range of shear rates, but rather display Newtonian plateaus around a limited non-Newtonian region, depending on the fluid rheology. More complex models have been developed to overcome this problem, such as the Carreau model, but they usually hold for a limited type of fluid (e.g. shear-thinning). A simple solution is to use a *truncated power-law model* (Gabbanelli *et al.*, 2005):



$$\eta = \eta(\dot{\gamma}) = \begin{cases} \eta_0, & \dot{\gamma} < \dot{\gamma}_0 \\ K\dot{\gamma}^{n-1}, & \dot{\gamma}_0 \leq \dot{\gamma} \leq \dot{\gamma}_\infty \\ \eta_\infty, & \dot{\gamma} > \dot{\gamma}_\infty \end{cases} \quad (9)$$

Where  $\eta_0$  and  $\eta_\infty$  are the viscosities calculated with the respective shear rates. To keep consistency between the different cases, it has been selected to express the limits in terms of  $\eta$  as:

$$\begin{aligned} \eta_- &= 10^{-5} \text{ Pa s} \\ \eta_+ &= 10^{-1} \text{ Pa s} \end{aligned} \quad (10)$$

Note that in Equation 10 + or - represents 0 or  $\infty$  according to the type of fluid selected *i.e.* shear-thinning or shear-thickening. Those limits have been selected in order to guarantee numerical stability especially during the first time step, while at the same time obtaining power-law fluid rheology in the whole domain for the remaining of the simulations. Preliminary calculations showed that the limits are not reached in the domain when the bubble is at pseudo steady-state. On the other hand, this implicitly assumes that the viscosity at the walls is not the bulk viscosity ( $\eta_0$ ); this could have an influence because, due to the free slip boundary at the walls, the bulk viscosity is not  $\eta_0$ . Further investigation on this matter is needed, perhaps with a broader domain or different truncation limits (see Equation 9).

#### Verification

The front tracking model has been thoroughly validated in the past, both numerically (see Roghair *et al.* (2015)) and experimentally. For the latter, a drag correlation has been derived for single (Dijkhuizen *et al.*, 2010a) and multiple (Roghair *et al.*, 2013) bubbles rising in a initially quiescent liquid. Nonetheless, the addition of the non-Newtonian viscosity model must be verified as well. A simple test case to verify the correct implementation of the viscosity model is represented by a single phase unidirectional pressure-driven flow between two parallel plates, separated by a distance  $2L$  in the direction,  $y$ , orthogonal to the flow direction,  $x$ . Since the only non-zero component of the velocity is  $u_x(y)$ , the Navier-Stokes equations are simplified and it is possible to obtain the stationary solution as:

$$u_x = L \frac{n}{n+1} \left( \frac{L}{K} \frac{\partial p}{\partial x} \right)^{1/n} \left( 1 - \left| \frac{y}{L} \right|^{\frac{n+1}{n}} \right) \quad (11)$$

From this, it is possible to calculate the flux through the rectangular domain and thus, assuming it is a constant linear profile, the inlet velocity  $u_{in}$ . With some mathematical rearrangement, one can obtain the normalized velocity profile as:

$$\frac{u_x}{u_{in}} = \frac{2n+1}{n+1} \left( 1 - \left| \frac{y}{L} \right|^{\frac{n+1}{n}} \right) \quad (12)$$

where  $y$  represents the distance from the center of the channel in the positive or negative directions, as it is symmetric. It is very important to notice that the simulated flow is not entirely non-Newtonian, as in the regions close to the walls there is a high shear while in the center there is zero shear at  $y = 0$ . This will result in three separate regions:

- a Newtonian region close to the walls
- a power-law region in between
- a Newtonian region close to the center

Since the  $\dot{\gamma}$  limits are selected as broad as possible, it is possible to reduce the Newtonian regions to a very small fraction, thus assuming a power-law model in the whole domain. The simulations have been carried out with a rectangular domain where two dimensions are much larger (50 cm) than the distance between the two plates (12 mm). In the  $y$ -direction (perpendicular to the flow) a number of 100 grid nodes has been used. The two plates have a no slip boundary condition, while for the depth (the  $z$ -direction) a free slip boundary is applied. The remaining parameters are a time step of  $10^{-2}$  s, an inlet velocity of  $u_{in} = 0.01 \text{ m s}^{-1}$  and the fluid properties are those of water (with a consistency index  $K = 10^{-3} \text{ Pa s}^n$ ). A variety of different exponents has been tested, as well as a fully Newtonian case for completeness. The results of the validation are shown in Figure 3.

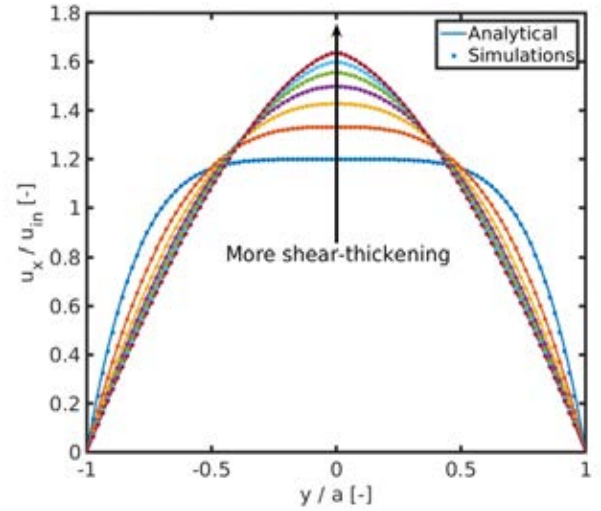


**Figure 3:** Comparison of simulations with the analytical solution for the steady-state velocity profiles of a 2D single phase non-Newtonian flow between parallel plates.

The simulation results match very well with the analytical solutions (see Table 1), thus confirming the validity of the power-law regime in the whole domain. The relative error has been calculated as in Equation 13 for all the cases.

$$\epsilon_{rel} = \frac{\left\| \mathbf{u}_x - \mathbf{u}_x^{analytical} \right\|_2}{\left\| \mathbf{u}_x^{analytical} \right\|_2} \quad (13)$$

Note that the relative error here is always a positive value, while the one in the next sections is calculated without the norm to show the sign of the deviations.

**Table 1:** Relative error between the numerical and analytical solutions of the velocity profile for a 2D single phase non-Newtonian flow between two parallel plates.

$n$	$\epsilon_{rel}$
0.2	0.36%
0.5	0.13%
0.8	0.11%
1	0.10%
1.2	0.10%
1.5	0.10%
1.8	0.10%

## RESULTS

### Numerical setup

The domain is a square box described by an Eulerian grid of  $100 \times 100 \times 100$  grid nodes. An initially spherical bubble is placed in an initially quiescent liquid with its center located at 60% of the height to gain additional information regarding its wake. While the bubble rises in a free slip domain, the window shifts so that the center of the bubble is in approximately the same position throughout the simulation (Deen *et al.*, 2004).

The typical simulation uses a time step of  $1 \times 10^{-5}$  s and it is performed for a total of 1 s. It is well known that, especially for larger bubbles, the velocity is oscillating. To determine the drag the terminal velocity is averaged starting from 0.2 s to discard initial start-up effects. In the case of viscous liquids, or in general when viscous effects are important, it is necessary to adequately describe the far field liquid motion. This was also investigated by Dijkhuizen *et al.* (2010a) for higher viscosity liquids. Since the objective of this work is to indeed study the influence of the change in viscosity, it has been decided to opt for a less resolved bubble (10 grid cells). Further investigations are ongoing to assess the validity of this assumption and eventually to resolve the bubble motion in more detail.

**Table 2:** Physical properties of the air-water system.

Property	Symbol	Value
Gas density	$\rho_g$	$1.25 \text{ kg m}^{-3}$
Gas viscosity	$\mu_g$	$1.8 \times 10^{-5} \text{ Pa s}$
Liquid density	$\rho_l$	$1000 \text{ kg m}^{-3}$
Surface tension	$\sigma$	$0.073 \text{ N m}^{-1}$

The physical properties of the system were chosen with the aim to resemble an air-water system for the Newtonian cases (see Table 2). The liquid viscosity is of course depending on the power-law behaviour of the fluid. Simulations have been performed for different exponents as well as bubble sizes (see Table 3). One case has been selected with a higher (100 times the one of the other cases)  $K$ , to investigate more viscous regimes. For this case, also the limits have been shifted by 2 orders of magnitude while keeping the same power-law window. For all these cases simulations with  $n = 0.2, 0.5, 0.8, 1, 1.2, 1.5, 1.8$  have been performed.

**Table 3:** Settings used in the different simulation cases.

Case	$d_b$ [mm]	$K \times 10^{-3}$ [Pa s <sup>n</sup> ]	Eö
1	0.5	1	$3.35 \times 10^{-2}$
2	2.0	1	0.54
3	4.0	1	2.15
4	4.0	100 <sup>1</sup>	2.15

<sup>1</sup> Different viscosity limits

### Viscosity profiles

As shown in the appendix, the non-Newtonian viscosity model has a large influence on bubble shape, as well as the bubble behaviour. In Figures 10, 11 and 12 in the appendix, some snapshots of the different cases are shown. As expected, in all the shear-thickening cases the bubble shape becomes more spherical as a consequence of the increased viscosity in the fluid immediately surrounding the bubble. Moreover, the bubble pattern is highly affected for the 4 mm

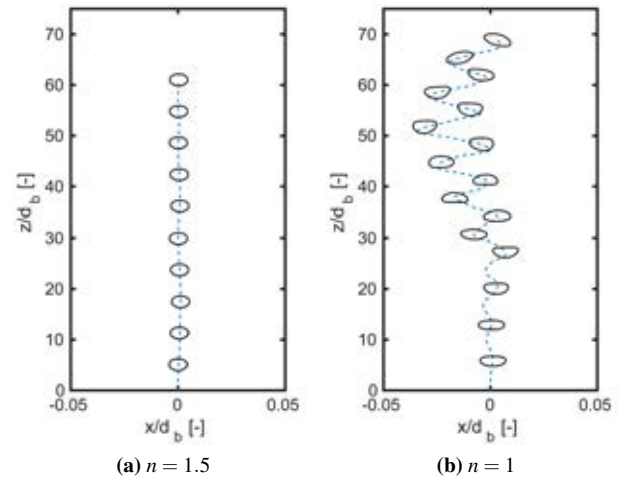
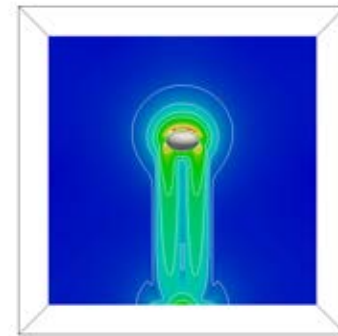
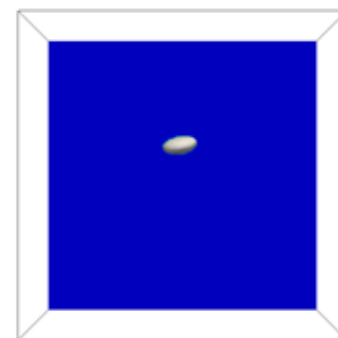


**Figure 4:** Comparison of the Newtonian and shear-thickening cases for a 4 mm bubble. It is possible to notice a remarkable change in shape and rising pattern, due to the viscosity alteration.



(a)  $n = 1.5$



(b)  $n = 1$

**Figure 5:** Snapshots of the viscosity profiles around a 4 mm bubble in a Newtonian and in a shear-thickening. The colors range from lower viscosity (blue) to higher viscosity (red).

case; the Newtonian case shows a meandering and wobbling bubble while it is rising in a straight line for the non-Newtonian cases, see also Figures 4 and 5. This is similar to a bubble rising in a more viscous fluid. The viscosity is mainly affected at the bubble front (where there is a highly shear-thickening region) and then the liquid passes the bub-

ble forming a higher viscosity tail in the wake. Since the larger bubble rises faster, the viscosity reaches a higher peak in front of the bubble, while the viscosity is affected in a larger part of the domain for the smaller 0.5 mm bubble. When inspecting the shear-thinning cases, one can observe that the shape is slightly less spherical. The meandering 4 mm bubble maintains the behaviour and this is also visible in the viscosity profile which follows the bubble pattern. In all three cases two higher viscosity regions can be observed at the walls (also observed in the past by Ohta *et al.* (2010)). Interestingly, unlike the shear-thickening case, the region with higher viscosity gradients is indeed at the walls, and mostly in the wake. In addition, again in this case the bubble rises faster for the 4 mm case, so the viscosity reaches higher (and lower) values due to higher velocity gradients. The quantification of the effects on the drag coefficient is discussed in the next sections.

### Drag coefficient

The front-tracking model has been used in the past to derive a drag correlation for both single bubble (Dijkhuizen *et al.*, 2010a) and bubbles rising in a swarm (Roghair *et al.*, 2011), to be used in higher scale model such as Euler-Lagrange models. The terminal velocity of a single bubble rising in a liquid is determined by the drag that the bubble experiences. The macroscopic force balance on a bubble is given by:

$$m \frac{d\mathbf{u}}{dt} = \mathbf{F}_G + \mathbf{F}_P + \mathbf{F}_D + \mathbf{F}_L + \mathbf{F}_{VM} + \mathbf{F}_W \quad (14)$$

Out of the many forces acting on the bubble, the drag force is the most important in determining its rise velocity. Assuming that the liquid is infinite (*i.e.* zero bulk velocity), this force can be expressed as:

$$\mathbf{F}_D = -\frac{1}{8} C_D \rho_l \pi d_b^2 |\mathbf{u}_\infty|^2 \quad (15)$$

When the bubble is rising in a pseudo steady-state, the drag force ( $\mathbf{F}_D$ ) balances the buoyancy force ( $\mathbf{F}_P + \mathbf{F}_G$ ); some mathematical rearrangement from Equation 14 neglecting the other forces leads to the well-known expression for the drag coefficient:

$$C_D = \frac{4}{3} \frac{d_b (\rho_l - \rho_g) \mathbf{g}}{\rho_l |\mathbf{u}_\infty|^2} \quad (16)$$

In many higher scale models, such as Euler-Euler or Euler-Lagrange models, the force balance on bubbles relies on the use of closure relations; for this reason it becomes unquestionably important to properly predict the drag coefficient. Many works exist in literature, starting from the drag on spherical particles (Stokes, 1851; Clift *et al.*, 1978) to arrive at the work of Tomiyama *et al.* (1998, 2002). This work is an extension to non-Newtonian fluids of the drag correlation obtained by Dijkhuizen *et al.* (2010a) and Roghair *et al.* (2011). In particular, Dijkhuizen *et al.* (2010a) described the drag coefficient as:

$$C_D = \sqrt{C_D(\text{Re})^2 + C_D(\text{Eö})^2} \quad (17)$$

where the Reynolds dependent part is described as (Mei *et al.*, 1994):

$$C_D(\text{Re}) = \frac{16}{\text{Re}} \left( 1 + \frac{2}{1 + \frac{16}{\text{Re}} + \frac{3.315}{\text{Re}}} \right) \quad (18)$$

and the Eötvös dependent part as:

$$C_D(\text{Eö}) = \frac{4\text{Eö}}{9.5 + \text{Eö}} \quad (19)$$

It is very important to notice that, while the Eötvös number can be easily calculated, for Equation 18 the Reynolds number includes the viscosity, which is not a constant for a power-law fluid. Therefore, a generalized Reynolds number for power-law fluids has been introduced (Chhabra, 2006):

$$\text{Re}^* = \frac{\rho u^{2-n} d_b^n}{K} \quad (20)$$

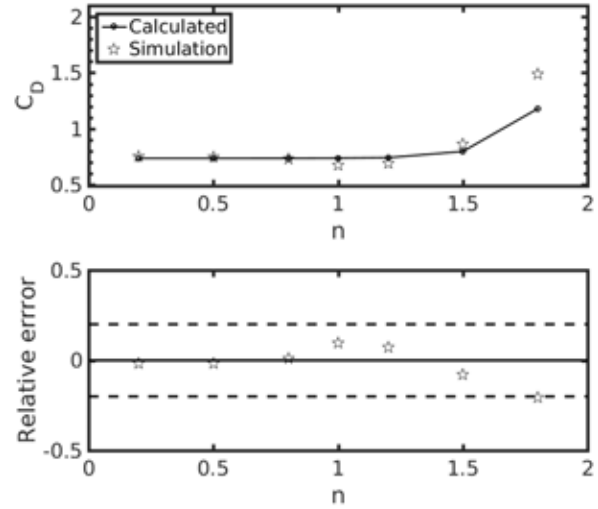


**Figure 6:** Drag coefficient ( $C_D$ ) of a 4 mm bubble rising in different power-law fluids, with consistency index  $K = 10^{-3} \text{ Pa s}^n$ . The relative error is shown with  $\pm 20\%$  error lines.

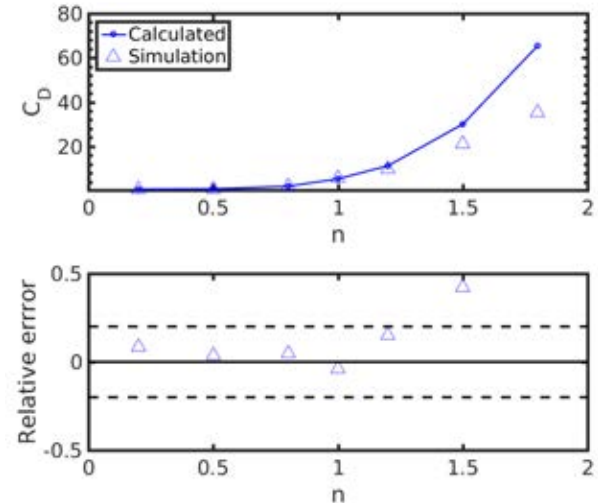


**Figure 7:** Drag coefficient ( $C_D$ ) of a 4 mm bubble rising in different power-law fluids, with consistency index  $K = 10^{-1} \text{ Pa s}^n$ . The relative error is shown with  $\pm 20\%$  error lines.

### Eötvös dominant regime

The drag coefficient is determined by two different contributions: the Eötvös and the Reynolds dependent parts. At high

Eötvös numbers, such as for bigger and deformed bubbles, the  $C_D(Eö)$  is dominant, while the  $C_D(Re)$  becomes negligible. This is visible in Figure 6, showing that the total drag is constant for most of the different exponents, as a result of the high  $C_D(Eö)$  contribution which is constant since the Eö number is not affected by the viscosity. When the exponent becomes higher, such as for  $n = 1.5$  or  $n = 1.8$ , the liquid is strongly shear-thickening. This affects the Re number, as the bubble is slowed down by the higher viscosity and becomes more spherical, and a considerable deviation occurs from the calculated drag coefficient. Despite this, for most of the cases the drag correlation is able to properly predict the total drag coefficient within a 20% deviation. When the consistency index  $K$  is increased by two orders of magnitude (see Figure 7), the effect of the highly shear thickening regime becomes much more pronounced with deviations up to 85%. In both cases, this deviation can be explained by considering the higher viscous contribution to the drag, which is more pronounced for the high viscosity case 4.

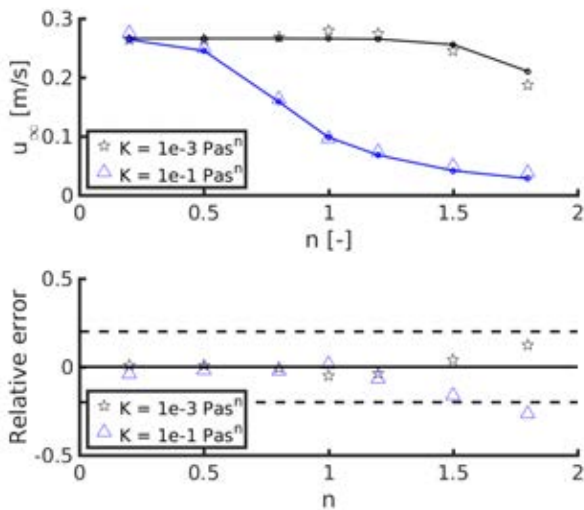


**Figure 8:** Terminal velocity of a 4mm bubble rising in different power-law fluids, with two different consistency indexes. The relative error is shown with  $\pm 20\%$  error lines.

The calculated drag coefficient has been used to determine the bubble terminal velocity (see Figure 8). The comparison with the simulation's data shows that the terminal velocity of case 3 can be reasonably well predicted for all the given exponents with a maximum relative error of 12% for the higher shear-thickening exponent, while for the other cases it is within 5%. Again, a more pronounced effect appears for case 4, where the error is within 6% for the other cases while it is 16% and 26% for the two higher exponents.

It is clear that the drag correlation of Dijkhuizen is able to predict within a reasonable accuracy the terminal velocity, until the fluid becomes very shear-thickening ( $n > 1.5$ ), where strong deviations occur.

#### Reynolds dominant regime

For smaller bubbles the Reynolds number decreases and the Reynolds dependent part of the drag starts to play a considerable role in the total drag coefficient.

A similar trend as in the previous section can be discerned from Figure 9. As soon as the exponent rises to  $n = 1.5$  or higher, the drag coefficient has a drastic increase and the velocity decreases. Despite the similar behaviour, it is possible

to notice how, for both bubbles, there is a clear trend in the error distribution, with many errors in the shear-thinning region outside the 50% area. This means that the correlation is not able to fully describe the drag force in this regime, which is where viscous effects are more important. Observing the bubble with  $d_b = 0.5$  mm, it is clearly visible that the error is large both in the shear-thickening and in the shear-thinning regions. Moreover, also the 2mm bubble (which is in the transition between the two regimes) shows a clear trend, with a large deviation for the most shear-thinning case.

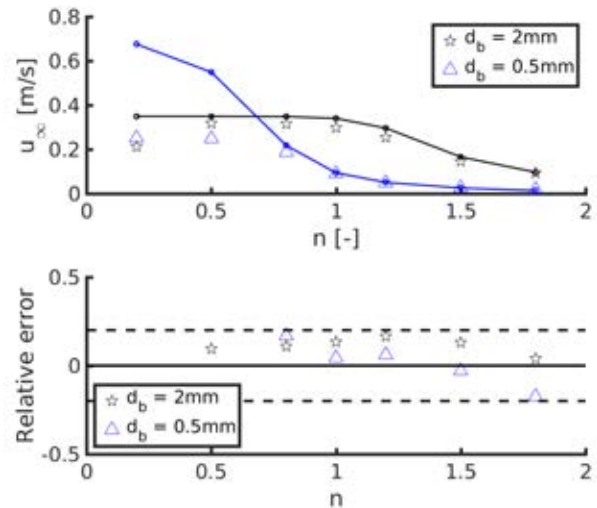


**Figure 9:** Terminal velocity of a 0.5mm and a 2mm bubble rising in different power-law fluids, with consistency index  $K = 10^{-3} \text{ Pas}^n$ . The relative error is shown with  $\pm 20\%$  error lines.

In Figure 9 the terminal velocities are calculated. It is immediately visible that there is a large deviation for the 0.5mm bubble, which reaches a plateau in the velocity for low exponents not described by the correlation. This might be due to the fact that, for extreme shear-thinning cases, the liquid viscosity approaches and even goes lower than the gas viscosity. Moreover, this could also be a consequence of an insufficient bubble or domain resolution, which needs to be further investigated.

Despite the somewhat expected deviations from the Newtonian correlation, it is noticeable how we can predict the drag coefficient with a reasonable agreement when the exponent does not reach extreme values (e.g. within  $\pm 0.5$  from 1).

## CONCLUDING REMARKS

This work has shown the possibility to verify and ultimately obtain drag information for single bubbles in non-Newtonian power-law fluids using Front-Tracking simulations. The drag relation proposed by Dijkhuizen is able to reasonably well predict the drag coefficient and hence the terminal velocity for moderately non-Newtonian fluids (e.g.  $0.5 \leq n \leq 1.5$ ) while more research has to be carried out for more extreme exponents. It is noticeable how the larger bubbles, where the Eö number is the most important in determining the drag, have in general a very good agreement with the correlation, due to the limited importance of viscous effects. On the other hand, for smaller bubbles large deviations occur from the correlation when the power-law exponent is higher (or lower). Moreover, special attention should be paid to the bubble resolution: more resolved simulations are being performed to

gain more insights. Eventually, the work will be extended to swarms of bubbles and the outcome will be used for the development of a Euler-Lagrange model in the multi-scale modelling approach.

## ACKNOWLEDGEMENTS

This work is part of the Industrial Partnership Programme i36 Dense Bubbly Flows that is carried out under an agreement between Akzo Nobel Chemicals International B.V., DSM Innovation Center B.V., Sabic Global Technologies B.V., Shell Global Solutions B.V., Tata Steel Nederland Technology B.V. and the Netherlands Organisation for Scientific Research (NWO).

## REFERENCES

- AL-MASRY, W.A. (1999). "Effect of scale-up on average shear rates for aerated non-Newtonian liquids in external loop airlift reactors." *Biotechnology and bioengineering*, **62(4)**, 494–498.
- BIRD, R.B., STEWART, W.E. and LIGHTFOOT, E.N. (2007). *Transport Phenomena*. Revised 2nd ed. John Wiley & Sons, New York.
- CHHABRA, R.P. (2006). *Bubbles, Drops, and Particles in Non-Newtonian Fluids, Second Edition*. Chemical Industries. CRC Press.
- CLIFT, R., GRACE, J.R. and WEBER, M.F. (1978). *Bubbles, Drops and Particles*. Academic Press, New York.
- DARBY, R. and CHHABRA, R.P. (2016). *Chemical Engineering Fluid Mechanics, Third Edition*. CRC Press.
- DEEN, N.G., VAN SINT ANNALAND, M. and KUIPERS, J.A.M. (2004). "Multi-scale modeling of dispersed gas-liquid two-phase flow". *Chem. Eng. Sci.*, **59(8-9)**, 1853–1861.
- DIJKHUIZEN, W., ROGHAIR, I., VAN SINT ANNALAND, M. and KUIPERS, J.A.M. (2010a). "DNS of gas bubbles behaviour using an improved 3D front tracking model—Drag force on isolated bubbles and comparison with experiments". *Chem. Eng. Sci.*, **65(4)**, 1415–1426.
- DIJKHUIZEN, W., ROGHAIR, I., VAN SINT ANNALAND, M. and KUIPERS, J.A.M. (2010b). "DNS of gas bubbles behaviour using an improved 3D front tracking model—Model development". *Chem. Eng. Sci.*, **65(4)**, 1427–1437.
- GABBANELLI, S., DRAZER, G. and KOPLIK, J. (2005). "Lattice Boltzmann method for non-Newtonian (power-law) fluids". *Physical Review E - Statistical, Nonlinear, and Soft Matter Physics*, **72(4)**, 046312.
- KUPRAT, A., KHAMAYSEH, A., GEORGE, D. and LARKEY, L. (2001). "Volume Conserving Smoothing for Piecewise Linear Curves, Surfaces, and Triple Lines". *J. Comp. Phys.*, **172(1)**, 99–118.
- LI, H.Z. (1999). "Bubbles in non-Newtonian fluids: Formation, interactions and coalescence". *Chemical Engineering Science*, **54(13-14)**, 2247–2254.
- MEI, R., KLAUSNER, J.F. and LAWRENCE, C.J. (1994). "A note on the history force on a spherical bubble at finite Reynolds number". *Phys. Fluids*, **6(1)**, 418–420.
- OHTA, M., YOSHIDA, Y. and SUSSMAN, M. (2010). "A computational study of the dynamic motion of a bubble rising in Carreau model fluids". *Fluid Dynamics Research*, **42(2)**, 025501.
- OHTA, M., KIMURA, S., FURUKAWA, T., YOSHIDA, Y. and SUSSMAN, M. (2012). "Numerical Simulations of a Bubble Rising through a Shear-Thickening Fluid". *Journal of Chemical Engineering of Japan*, **45(9)**, 713–720.
- PIVELLO, M., VILLAR, M., SERFATY, R., ROMA, A. and SILVEIRA-NETO, A. (2013). "A fully adaptive front tracking method for the simulation of two phase flows". *International Journal of Multiphase Flow*, **58**, 72–82.
- PROSPERETTI, A. (2002). "Navier-Stokes numerical algorithms for free-surface flow computations: an overview". *Drop-surface interaction*, **456**, 237–257.
- RADL, S., TRYGGVASON, G. and KHINAST, J.G. (2007). "Flow and mass transfer of fully resolved bubbles in non-Newtonian fluids". *AIChE Journal*, **53(7)**, 1861–1878.
- RODRIGUE, D. (2002). "A simple correlation for gas bubbles rising in power-law fluids". *The Canadian Journal of Chemical Engineering*, **80(2)**, 289–292.
- ROGHAIR, I., LAU, Y.M., DEEN, N.G., SLAGTER, H.M., BALTUSSEN, M.W., VAN SINT ANNALAND, M. and KUIPERS, J.A.M. (2011). "On the drag force of bubbles in bubble swarms at intermediate and high Reynolds numbers". *Chemical Engineering Science*, **66(14)**, 3204–3211.
- ROGHAIR, I., VAN SINT ANNALAND, M. and KUIPERS, J.A.M. (2016). "An improved Front-Tracking technique for the simulation of mass transfer in dense bubbly flows". *Chemical Engineering Science*, **152**, 351–369.
- ROGHAIR, I., VAN SINT ANNALAND, M. and KUIPERS, J.A.M. (2013). "Drag force and clustering in bubble swarms". *AIChE Journal*, **59(5)**, 1791–1800.
- ROGHAIR, I., VAN SINT ANNALAND, M. and KUIPERS, J.A.M. (2015). "An enhanced front tracking method featuring volume conservative remeshing and mass transfer". *Progress in Applied CFD*, 59–71.
- STOKES, G.G. (1851). "On the Effect of the Internal Friction of Fluids on the Motion of Pendulums". *Transactions of the Cambridge Philosophical Society*, **9(part II)**, 8–106.
- TOMIYAMA, A., KATAOKA, I., ZUN, I. and SAKAGUCHI, T. (1998). "Drag Coefficients of Single Bubbles under Normal and Micro Gravity Conditions." *JSME International Journal Series B*, **41(2)**, 472–479.
- TOMIYAMA, A., TAMAI, H., ZUN, I. and HOSOKAWA, S. (2002). "Transverse migration of single bubbles in simple shear flows". *Chemical Engineering Science*, **57(11)**, 1849–1858.
- VAN SINT ANNALAND, M., DEEN, N.G. and KUIPERS, J.A.M. (2003). *Multi-level modeling of dispersed gas-liquid two-phase flows*. Heat and mass transfer. Springer, Berlin.
- ZHANG, L., YANG, C. and MAO, Z.S. (2010). "Numerical simulation of a bubble rising in shear-thinning fluids". *Journal of Non-Newtonian Fluid Mechanics*, **165(11-12)**, 555–567.

APPENDIX

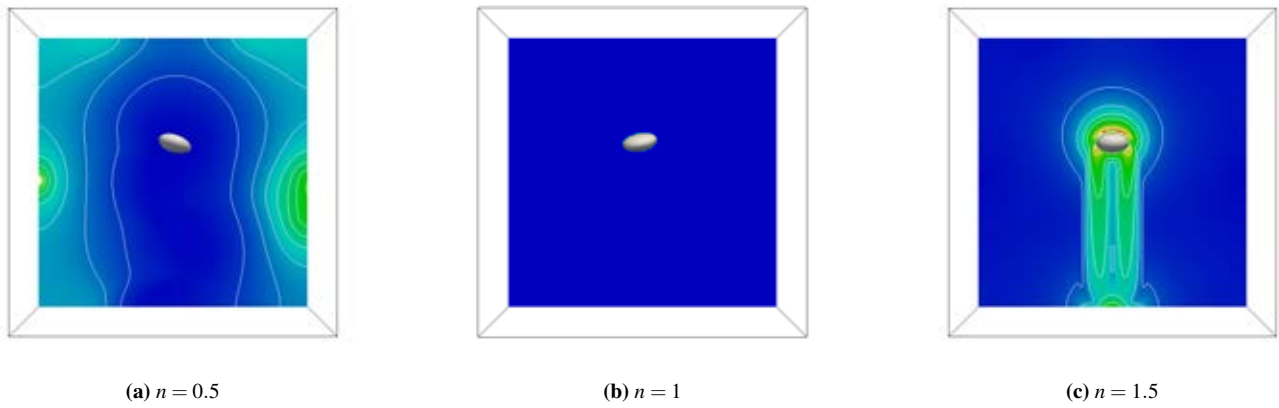


**Figure 10:** Snapshots of the viscosity profiles around a 4mm bubble in three different fluids: (a) shear-thinning, (b) Newtonian and (c) shear-thickening. The colors range from lower viscosity (blue) to higher viscosity (red).

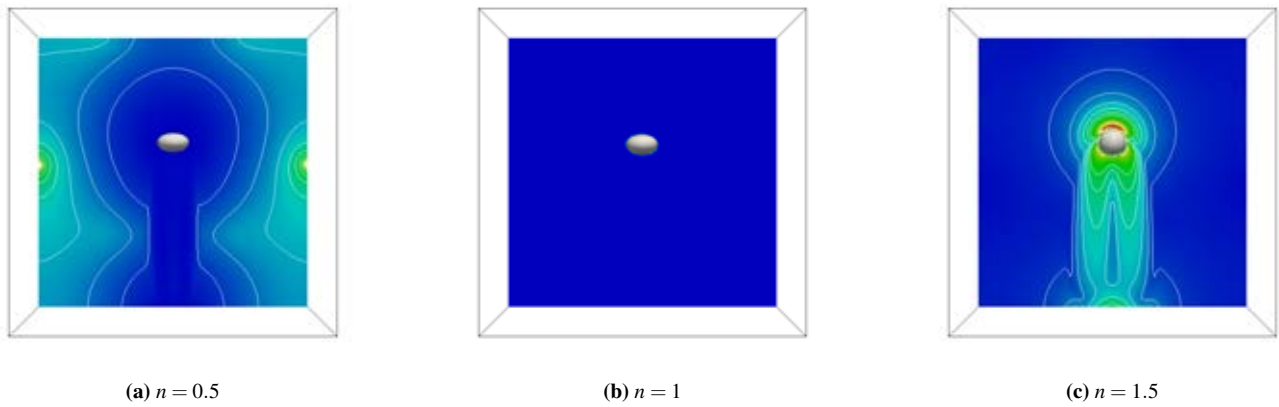


**Figure 11:** Snapshots of the viscosity profiles around a 2mm bubble in three different fluids: (a) shear-thinning, (b) Newtonian and (c) shear-thickening. The colors range from lower viscosity (blue) to higher viscosity (red).

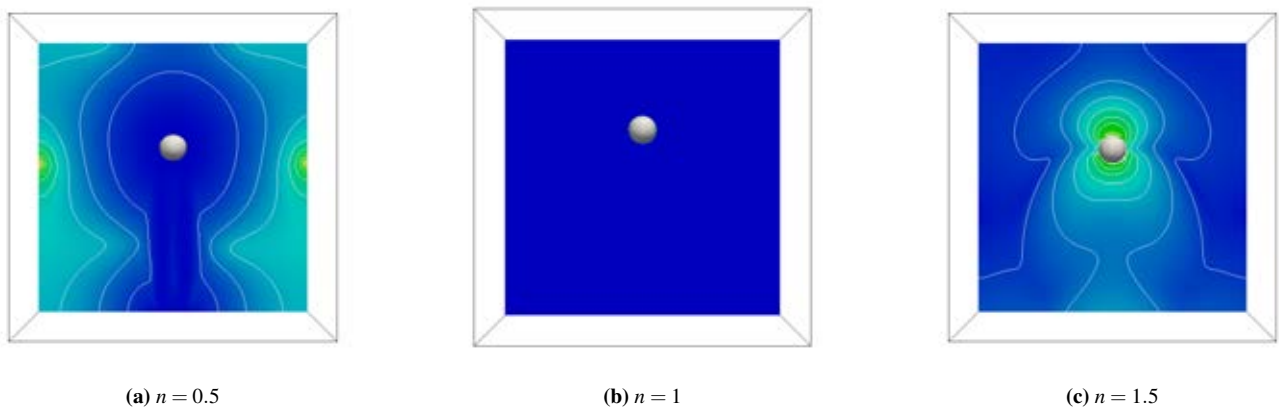


**Figure 12:** Snapshots of the viscosity profiles around a 0.5mm bubble in three different fluids: (a) shear-thinning, (b) Newtonian and (c) shear-thickening. The colors range from lower viscosity (blue) to higher viscosity (red).



# A 2D SEDIMENT BED MORPHODYNAMICS MODEL FOR TURBULENT, NON-NEWTONIAN, PARTICLE-LOADED FLOWS

Alexander BUSCH<sup>1\*</sup>, Milad KHATIBI<sup>2</sup>, Stein T. JOHANSEN<sup>1,3</sup>, Rune W. TIME<sup>2</sup>

<sup>1</sup> Norwegian University of Science and Technology (NTNU), Trondheim, NORWAY

<sup>2</sup> University of Stavanger (UiS), Stavanger, NORWAY

<sup>3</sup> SINTEF Materials and Chemistry, Trondheim, NORWAY

\* E-mail: [alexander.busch@ntnu.no](mailto:alexander.busch@ntnu.no)

## ABSTRACT

In petroleum drilling, cuttings transport problems, i.e. an accumulation of drilled solids in the wellbore, are a major contributor to well downtime and have therefore been extensively researched over the years, both experimentally and through simulation. In recent years, Computational Fluid Dynamics (CFD) has been used intensively due to increasing available computational power. Here, the problem of cuttings transport is typically investigated as a laminar/turbulent, potentially non-Newtonian (purely shear-thinning) multiphase problem. Typically, an Eulerian-Eulerian two-fluid model concept is utilized, where the particle phase is treated as a second continuous phase. Optionally, a granular flow model, based on the Kinetic Theory of Granular Flow (KTGF), may be used to account for the dense granular flow properties of cuttings forming a sediment bed. One issue of the state of the art CFD approach as described above is the proper resolution of the bed interface, as this may not be accurately resolved in an industrial-relevant CFD simulation.

In this paper, an alternative approach is taken based on modeling concepts used in environmental sediment transport research (rivers, deserts). Instead of including the sediment bed in the computational domain, the latter is limited to the part of the domain filled with the particle-loaded continuous fluid phase. Consequently, the bed interface becomes a deformable domain boundary, which is updated based on the solution of an additional scalar transport equation for the bed height, which is based on the so-called Exner equation (Exner, 1925), a mass conservation equation accounting for convection, and additionally deposition and erosion in the bed load layer. These convective fluxes are modeled with closures relating these fluxes to flow quantities.

As a first step, a 2D model was implemented in ANSYS Fluent R17.2 using Fluent's dynamic mesh capabilities and User-Defined Function (UDF) interfaces. The model accounts for local bed slope, hindered settling, and non-Newtonian, shear-thinning viscosity of the fluid phase as well as turbulence. Model results are benchmarked with experimental data for five different operating points. Most probably due to the utilized unsteady Reynolds-Averaging framework (URANS), the model is not capable of predicting flow-induced dunes; however, it does predict bed deformation as a consequence of for instance non-equilibrium boundary conditions. Other model issues such as e.g. non-Newtonian formulations of the closures are identified and discussed.

**Keywords:** Drilling, cuttings transport, particle transport, sediment transport, bed load, turbulence, non-Newtonian, multiphase, deforming mesh, CFD.

## NOMENCLATURE

### Greek Symbols

$\alpha$  Volume fraction, [-].  
 $\beta$  Local bed slope, [rad].

$\dot{\gamma}$  Shear rate, mag. of deformation rate tensor, [1/s].  
 $\rho$  Mass density, [kg/m<sup>3</sup>].  
 $\mu$  Dynamic viscosity, [kg/m.s].  
 $\nu$  Kinematic viscosity, [kg/m.s].  
 $\tau$  (Wall) Shear stress, [Pa].  
 $\phi$  Angle of repose, [rad].  
 $\theta$  Non-dimensional shear stress, Shields number, [-].  
 $\omega$  Specific dissipation rate [1/s].

### Latin Symbols

$c$  Coefficient of drag, [-].  
 $C$  Bed slope model constant,  $\approx 1.5$ , [-].  
 $d$  Diameter, [m].  
 $D$  Deposition, [m/s].  
 $\mathbf{D}$  Rate of deformation tensor, [m/s<sup>2</sup>].  
 $E$  Entrainment, [m/s].  
 $F$  Momentum exchange term, [kg/s<sup>2</sup>.m<sup>3</sup>].  
 $\mathbf{g}$  Gravitational acceleration, [m/s<sup>2</sup>].  
 $h$  Bed height, [m].  
 $k$  Turbulent kinetic energy, [m<sup>2</sup>/s<sup>2</sup>].  
 $n$  Exp. in rheo. models & hind. settling function, [-].  
 $q$  Vol. bed load transport rate per unit width, [m<sup>3</sup>/s.m].  
 $s$  Ratio of solid and fluid densities, [-].  
 $S$  Source term, [kg/s.m<sup>3</sup>].  
 $t$  Time, [s].  
 $\mathbf{T}$  Stress tensor, [kg.m/s<sup>2</sup>.m<sup>3</sup>].  
 $\mathbf{u}$  Velocity vector, [m/s].  
 $v$  Vertical velocity component, [m/s].  
 $V$  Volume, [m<sup>3</sup>].

### Sub/superscripts

$0$  Horizontal or initial or zero.  
 $*$  Non-dimensional.  
 $b$  Bed.  
 $cr$  Critical/Threshold.  
 $CR$  Cross.  
 $D$  Drag.  
 $f$  Fluid.  
 $i$  Phase index.  
 $PL$  Power-law.  
 $s$  Solid.  
 $t$  Turbulent.  
 $T$  Transposed.  
 $x$  x-direction in space.  
 $y$  y-direction in space.  
 $z$  z-direction in space.

### Abbreviations

2D Two-dimensional in space.  
3D Three-dimensional in space.  
CFD Computational Fluid Dynamics.



GNF	Generalized Newtonian Fluid.
H <sub>2</sub> O	Water.
KTGF	Kinetic theory of granular flow.
PAC	Polyanionic cellulose.
OBM	Oil-based muds.
UDF	User-Defined Function.
URANS	Unsteady Reynolds-Averaged-Navier-Stokes.
SST	Shear Stress Transport.
VLES	Very Large-Eddy Simulation.
WBM	Water-based muds.

## INTRODUCTION

### Existing research body and praxis

Cuttings transport in wellbores, herein termed wellbore flows, is a multiscale problem, both in space and time but also regarding the different levels of physical complexity. In general, wellbore flows incorporate non-Newtonian rheology, dispersed and potentially dense packed solids (cuttings forming a sediment bed) and the flow may be turbulent. The domain of interest is an annulus, formed by the drill pipe, which may also rotate, inside the wellbore.

Conceptually, the flow may be categorized into three layers: (1) A flowing mixture layer, where particles are transported in a heterogeneous suspension. (2) An intermediate layer, where particles roll and slide on top of each other, which is just a few particle diameters thick. (3) Depending on the various parameters involved, a densely packed, and in most cases stationary, cuttings bed may form at the lower part of the annulus.

Several scientists, e.g. Doron and Barnea (1993); Savage et al. (1996) or more recently Bello et al. (2011); Nossair et al. (2012); Goharzadeh et al. (2013); Corredor et al. (2016), have experimentally investigated wellbore flows in laboratory flow loops. Corredor et al. (2016) determined the critical velocities for the initiation of particle movement with rolling, saltation, and suspension. They found that the fluctuation of pressure gradient is due to the dune movement. Nossair et al. (2012) found a significant influence of pipe inclination on flow structure as a consequence of liquid-particle interaction at the bed interface and the suspension layer. Goharzadeh et al. (2013) found that an increased bed height in a horizontal pipe reduces the effective cross-sectional flow area and results in higher local liquid velocity, which is leading to higher shear forces at the solid-liquid interface. For solid particles, the dominant factors to induce the movement is the fluid shear force at the solid-liquid interface and the gravity force.

In recent years, CFD has been increasingly used to model wellbore flows. Different levels of complexity may be addressed by incorporating adequate models for multiphase flows, non-Newtonian fluid rheology, turbulence, and more physics. Mainly, the Eulerian-Eulerian two-fluid model has been used in recent research activities, for instance by Ofei et al. (2014); Sun et al. (2014); Manzar and Shah (2014); Han et al. (2010), where the fluid and solid phase are treated as two interpenetrating continua. In wellbore flows, a cuttings

bed may form under different conditions. Solids are not kept entirely in suspension, but settle out and agglomerate on the lower part of the annulus forming a stationary packed bed with maximum packing density ( $\alpha_s \approx 0.63$ ) and a moving dense layer ( $\alpha_s \approx 0.55$ ), where particles roll and slide on top of each other. This layer is usually only a few particle diameters thick. In terms of CFD modeling, the formation of a cuttings bed may be accounted for by incorporating the kinetic theory of granular flow (KTGF), as for instance used by Han et al. (2010). The KTGF describes the granular flow in the dense packed bed, where solid pressure and granular temperature become important flow variables.

### Position and Motivation

Utilizing the KTGF is computationally more expensive as additional transport equations have to be solved. Furthermore, the fine layer on top of the stationary cuttings bed, where particle roll and slide on top of each other, may not be resolved properly. Finally, the cuttings bed interface<sup>1</sup> may not be tracked properly, as interpolation of the various solids volume fraction values of different cells is required to yield the approximate position based on a threshold such as e.g.  $\alpha_s = 0.55$ .

In sediment transport research, CFD models usually utilize the so-called “Exner equation”, derived by Exner (1925), in order to track the development of the sediment bed height. The sediment bed height is usually taken as the distance from some reference level to the top or bottom of the so-called “bed load” layer. The “bed load” layer is located on top of the static bed and comprises a thin layer containing sediment flux, characterized by sliding and rolling particles. The dispersed solids are usually modelled by an additional species transport equation. Empirical formulas are used to model the bed load transport rate, where a variety of models exists to account for the deposition and entrainment fluxes. Examples of such a modeling approach are Solberg et al. (2006); Brørs (1999) or more recently Khosronejad et al. (2011); Khosronejad and Sotiropoulos (2014).

In order to simplify numerical cuttings transport studies, we will apply a combination of a multiphase treatment of the particle-loaded, potentially non-Newtonian flow and the Exner equation approach for tracking the bed interface. A two-dimensional (2D) model is implemented in ANSYS Fluent 17.2 and results are compared with respective experimental data for a set of different case parameters.

### Structure of this work

In the next section, we present a description of the modeling concept as well as the general flow and bed load models, along with different important model elements. Next, we provide an overview of the experimental setup and measurement techniques. In the following section, both numerical and experimental results will be presented, followed by a discussion of the results and comparison of CFD and experimental results. Finally, the last section provides a conclusion and outlook.

<sup>1</sup> This is an ambiguous term. In this study, it is considered to be the top of the sliding/rolling particle layer, where saltation processes just start to occur.

## NUMERICAL MODEL

This section provides a description of the general methodology used to model the evolution of the cuttings bed as well as a detailed description of the CFD model used in this study.

As a first step, the CFD model is built for a two-dimensional (2D) channel flow, where the domain is discretized with a structured quadrilateral grid as depicted in Figure 1.

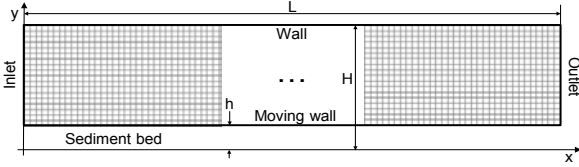


Figure 1: 2D channel domain.

Here, an initial cuttings or sediment bed is depicted. However, the cuttings bed is not part of the discretized domain. Instead, it is accounted for by setting the coordinate system appropriately, such that, in the given example, the y-coordinate is zero at the channel bottom, equal to the bed height at the lower end of the mesh and equal to the channel height at the top end of the mesh.

### General modeling concept

An overview of the general modeling concept is provided in Figure 2.

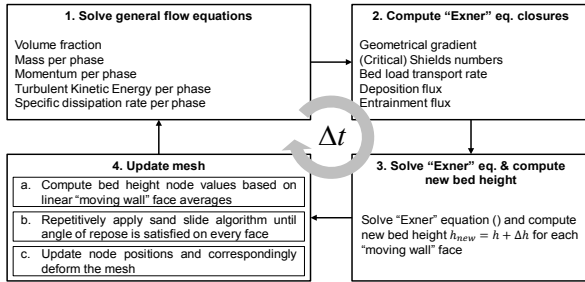


Figure 2: Overview of general modeling concept.

Four major steps per computational CFD time step are performed as follows:

1. Within the discretized domain of Figure 1, an Eulerian-Eulerian two fluid model is solved, where both the solvent and the dispersed phase are treated as interpenetrating continua.
2. Based on the solution, certain quantities required for modeling the evolution of the sediment bed are straightforwardly computed.
3. The evolution of the bed interface is described by the so-called "Exner equation", first introduced by Exner (1925). It is based on conservation of mass applied to a control volume, where the height of the volume may change with time due to the gain or loss of mass in the control volume. The evolution equation for the bed height  $h$  is:

$$\frac{\partial h}{\partial t} = -\frac{1}{(1-\alpha_b)} \left( \frac{\partial q_{bx}}{\partial x} + E - D \right) \quad (1)$$

Here,  $q_{bx}$  is the volumetric bed load transport rate per unit width, i.e. the amount of solids being transported in the bed load layer along the bed interface, and  $E$  and  $D$  are source terms representing volumetric entrainment and deposition fluxes of solids,

- respectively. The solution of equation (1) leads to a change in bed height for a given time step and grid cell.
4. Ensuring that the solids angle of repose is not violated and transferring face to node positions, the mesh is updated accordingly. Figure 3 shows a zoom of the near-bed region of Figure 1 at two subsequent time steps and illustrates that the computed change in bed height is used to accordingly deform the mesh on a per node and per time step basis.

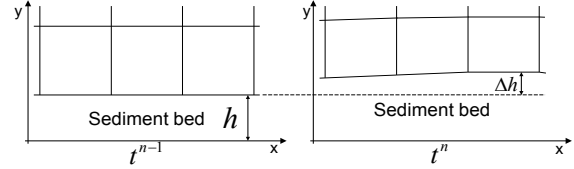


Figure 3: Mesh-deformation.

The CFD model, as further detailed in the next two subsections, is implemented in ANSYS Fluent R17.2 using its dynamic mesh capabilities and UDF functionalities.

### Flow field

The flow field, i.e. both the fluid and solid phase flowing through the discretized domain (Step 1. in Figure 2), is described in an Eulerian-Eulerian and unsteady Reynolds-Averaged (URANS) framework. Both the fluid and the solid phase are considered isothermal and incompressible. Hence, for an arbitrary volume element, the phase volume fractions have to sum to one.

$$V_i = \int_V \alpha_i dV \quad \wedge \quad \sum_i \alpha_i = 1 \quad \wedge \quad i \in \{f, s\} \quad (2)$$

### Transport of mass

The continuity equation for phase  $i \in \{f, s\}$  is expressed as

$$\frac{\partial}{\partial t} (\alpha_i \rho_i) + \nabla \cdot (\alpha_i \rho_i \mathbf{u}_i) = S_i \quad (3)$$

The source term  $S_i$  on the RHS is generally zero. However, in cells at the sediment bed interface, i.e. wall-adjacent cells of the bottom domain boundary "moving wall", mass may be added or removed as a consequence of solid deposition and entrainment processes taking place at the sediment bed interface.

### Transport of momentum

The momentum balance for the phase  $i \in \{f, s\}$  reads

$$\frac{\partial}{\partial t} (\alpha_i \rho_i \mathbf{u}_i) + \nabla \cdot (\alpha_i \rho_i \mathbf{u}_i \mathbf{u}_i) = \alpha_i \nabla \mathbf{T}_i + 2 \nabla \cdot (\alpha_i \mu_{t-i} \mathbf{D}_i) + \alpha_i \rho_i \mathbf{g} + K (\Delta \mathbf{u}_i) + \sum F_s \quad (4)$$

The stress tensor  $\mathbf{T}$  for a generalized Newtonian fluid (GNF) is

$$\mathbf{T}_i = -p \mathbf{1} + 2 \mu_i (\dot{\gamma}) \mathbf{D}_i \quad (5)$$

where  $\mathbf{D}_i$  is the rate of deformation tensor

$$\mathbf{D}_i = \frac{1}{2} (\nabla \mathbf{u}_i + \nabla \mathbf{u}_i^T) \quad (6)$$

and the shear rate  $\dot{\gamma}$  is a total shear measure defined as

$$\dot{\gamma} = \sqrt{2 \mathbf{D} : \mathbf{D}} \quad (7)$$

The turbulent Reynolds stresses are modelled using the gradient diffusion hypothesis (Boussinesq hypothesis), where turbulent Reynolds stresses are related to the mean velocity gradients and the turbulent viscosity  $\mu_{t-i}$ .

In the drag term,  $K$  is the interphase momentum exchange coefficient

$$K = \frac{A_s \rho_s}{6\tau_s} f(c_D) \quad (8)$$

with the particle relaxation time

$$\tau_s = \frac{\rho_s d_s^2}{18\mu_f} \quad (9)$$

and where the function  $f(c_D)$  represents the effect of a particular interphase momentum exchange model. Here, the model of Schiller and Naumann (1933) has been used. Other momentum exchange terms include lift, virtual mass, turbulent dispersion and turbulent interaction

$$\sum F = F_L + F_{VM} + F_{TD} + F_{TI} \quad (10)$$

where the standard Fluent formulation for the virtual mass force is used and lift is described by the model of Saffman (1965), turbulent dispersion by the model of Simonin and Viollet (1990b), and turbulent interaction as described by Simonin and Viollet (1990a).

Note, that, in accordance with the source term in the mass transport equation (3), the momentum equation (4) should feature a corresponding momentum source term to account for momentum exchange in the wall-adjacent grid cells. However, compared to the other terms in equation (4), the momentum source term due to mass exchange is expected to be of negligible order of magnitude.

#### Fluid rheology

Drilling fluids may be categorized as so-called water or oil based muds (WBM, OBM). These are generally engineered non-Newtonian (shear thinning, viscoelastic and thixotropic) fluid systems. However, usually, drilling fluids are modelled as GNF, i.e. purely viscous without elastic and time-dependent properties. Hence, the fluid apparent viscosity becomes a function of the second invariant of the rate of deformation tensor only, see equation (5), and may be expressed with different models depending on the fluids properties. In this study, experiments were performed for H<sub>2</sub>O and an aqueous solution of Poly-Anionic Cellulose with a concentration of 1 g/L (PAC1) as a WBM model system. PAC solutions are both shear-thinning and translucent which qualifies them for usage as WBM model systems in optical investigations. Preparation of the PAC1 solution and rheology measurements were described in previous studies, see Khatibi et al. (2016a), (2016b). Figure 4 shows the apparent dynamic viscosity  $\mu(\dot{\gamma})$  of H<sub>2</sub>O and PAC1 versus shear rate  $\dot{\gamma}$ .

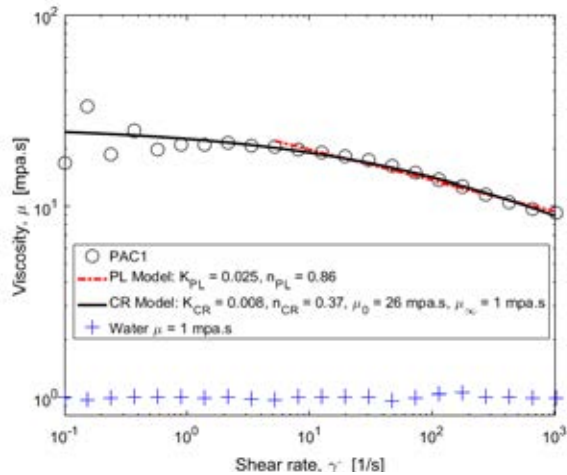


Figure 4: Rheology of water and PAC 1 g/l at 21 °C.

Power-law (PL) and Cross (CR) models, equations (11) and (12) respectively, were used for curve fitting of the PAC1 rheometric data. However, only the CR model was used in the CFD computations due to the better fit to the data.

$$\mu_{PL}(\dot{\gamma}) = K_{PL} \dot{\gamma}^{n_{PL}-1} \quad (11)$$

$$\mu_{CR}(\dot{\gamma}) = \frac{\mu_0 - \mu_\infty}{1 + (K_{CR} \dot{\gamma})^{n_{CR}}} + \mu_\infty \quad (12)$$

If required, the application of other models such as the Herschel-Bulkley model is straightforward. Density of H<sub>2</sub>O and PAC1 were approximately 1000 kg/m<sup>3</sup>. All liquids were measured at room temperature (21 °C) and atmospheric pressure ( $\approx 1.01$  bar).

#### Dispersed phase

In order to model drill cuttings, two different types of spherical glass beads with median diameters  $d_s = 0.3$  mm and  $d_s = 1.2$  mm were used in this study, with solids density  $\rho_s = 2500$  kg/m<sup>3</sup>.

#### Turbulence

As an URANS approach is taken to model the fluid flow, a turbulence model is required in order to compute the turbulent viscosity  $\mu_{t-i}$ . Here, the  $k-\omega$  SST model of Menter (1994) is used to model the two turbulent quantities, namely the turbulent kinetic energy  $k$  and the inverse turbulence time scale  $\omega$ . Roughness of a non-moving sand bed may be directly represented by the particle diameter. However, due to the moving sand particles, which may also slide, roll and saltate, bed roughness is taken to be equivalent to  $2d_s$ .

#### Bed load layer

As illustrated in Figure 3, the lower wall of the computational domain may deform based on the solution of the bed height transport equation (1). In order to solve equation (1), three closures are required, namely models for the volumetric bed load transport rate per unit width, the volumetric deposition flux and the volumetric entrainment flux (Step 2. in Figure 2).

#### Incipient motion

Bed load transport and entrainment only take place if the fluid has sufficient momentum to overcome a critical bed shear stress threshold, characterized by the Shields number. The Shields number is a non-dimensional shear stress acting on the bed and may also be seen as the ratio of shear force to gravitational force, acting on a particle at the top of the bed.

$$\theta = \frac{|\tau_b|}{gd_s(\rho_s - \rho_f)} \quad (13)$$

For a horizontal bed, the critical Shields number to overcome for bed load transport and entrainment to take place, may be estimated using an empirical expression of Soulsby (1997)

$$\theta_{cr,0} = \frac{0.24}{d_*} + 0.055(1 - e^{-0.02d_*}) \quad (14)$$

where  $d_*$  is a dimensionless particle diameter

$$d_* = \left( \frac{g(s-1)}{\nu_f^2} \right)^{\frac{1}{3}} d_s \quad (15)$$

Applying a force balance to a particle on a slope yields, for the 2D case, where shear stress always acts in the bed slope direction,

$$\theta_{cr} = \theta_{cr,0} \frac{\sin(\beta + \phi)}{\sin(\phi)} \quad (16)$$

where  $\phi$  is the solids angle of repose and  $\beta$  is the local bed slope.

#### Bed load transport rate

The bed load transport rate is mainly a function of the shear stress acting on the bed. Various empirical bed load formulas exist for different flow patterns and sediments. In this study, the expression of Nielsen (1992) is used,

$$q_{bx-0} = \begin{cases} 0 & \text{if } \theta \leq \theta_{cr} \\ 12\sqrt{g(s-1)d_s^3\theta(\theta-\theta_{cr})} & \text{if } \theta > \theta_{cr} \end{cases} \quad (17)$$

which is valid for a zero-slope bed. Following Struiksmas and Crosato (1989), a slope correction term is introduced as

$$q_{bx} = q_{bx-0} \left( \frac{u_f}{|u_f|} - C \frac{\partial h}{\partial x} \right) \quad (18)$$

where  $C$  is a constant and the direction of  $q_{bx}$  is assumed to be equivalent to the x-direction of the fluid velocity  $u_f$  in the wall-adjacent grid cell.

#### Deposition

The deposition flux  $D$ , i.e. particles leaving suspension and depositing on the bed, may be modeled as the product of the solid volume fraction and the suspension hindered settling velocity of Richardson and Zaki (1957)

$$D = \alpha_s (\alpha_f^n v_{set}) \quad (19)$$

where  $v_{set}$  is the settling velocity of an individual particle estimated with

$$v_{set} = -\sqrt{\frac{4(\rho_s - \rho_f)d_p g}{3\rho_f c_D}} \quad (20)$$

based on the drag coefficient  $c_D$  of Schiller and Naumann (1933). According to Garside and Al-Dibouni (1977), the exponent  $n$  in equation (19) is given by

$$n = \frac{0.27 \text{Re}_p^{0.9} + 5.1}{0.1 \text{Re}_p^{0.9} + 1} \quad (21)$$

#### Entrainment/Erosion

Following Celik and Rodi (1988), the entrainment flux  $E$ , i.e. particles leaving the bed and entering suspension due to near-bed turbulent eddies, may be expressed with the near-bed Reynolds flux of solids

$$E = \frac{\alpha_s' u_j'}{\rho_s} \approx -\frac{\mu_T}{\rho_s S c_T} \frac{\partial \alpha_s}{\partial y} \quad (22)$$

which may be modeled using the ratio of turbulent viscosity and the turbulent Schmidt number times the solid fraction gradient.

#### Sand slide

A pile of granular material will, under the pure influence of gravity, settle in such a way that the angle between its slope and the horizontal plane is equal to the materials angle of repose. The solution of equation (1) may lead to a violation of the angle of repose. Hence, a sand slide algorithm is required to avoid local violation of the angle of repose. The algorithm of Liang et al. (2005) is applied, where a face gradient is readjusted in a mass-conservative manner if the face slope is violating the angle of repose (Step 4. in Figure 2).

#### Boundary and initial conditions

Initially, the bed height is 5 mm in the entire domain and all the flow variables in the domain are zero.

At the inlet, a laminar velocity profile, which is adjusted to the potentially changing inlet size between step (4) and step (1) in Figure 2, is utilized for both the solid and the fluid phase. The velocity profile is defined in such a manner that the superficial velocities of the 2D channel flow CFD model and 3D pipe flow experiments match.

A zero bed load transport rate gradient is used as a BC for the volumetric bed load transport rate.

The solid volume fraction is assumed constant across the inlet. Reasonable values for the in-situ solid volume fraction were estimated based on the ratio of experimental superficial velocities

$$\alpha_s = \frac{U_{ss}}{U_{ss} + U_{sl}} \quad (23)$$

where the superficial particle velocity was calculated from the solids collection/injection rate and the superficial liquid velocity was calculated based on logged data from a Coriolis flow meter.

#### Implementation in ANSYS Fluent R17.2

With reference to Figure 2, the implementation in ANSYS Fluent R17.2 is as follows:

1. The flow field is solved in a standard manner using the Phase-Coupled SIMPLE scheme, spatial discretization is second order, with the exception of volume fraction where the QUICK scheme has been used. The time discretization is implicit second order.
2. After the flow field variables are available, the three closures (18), (19), and (22) are calculated using an EXECUTE\_AT\_END UDF.
3. In the same UDF, the bed height evolution equation (1) is solved with a first-order upwind scheme

$$h_x^{t+\Delta t} = h_x^t - \frac{\Delta t}{(1-\alpha_{\beta})\Delta x} (q_x^t - q_x^{t-\Delta t}) - \frac{\Delta t}{(1-\alpha_{\beta})} (E - D) \quad (24)$$

Note, that the volumetric transport rate  $q_x$  is a function of the transported property  $h$ . However, changes of the bed height  $h$  occur on a much larger time scale than changes of flow field variables such as velocity. Since the first-order upwind scheme, i.e. equation (24), is solved at the end of each CFD time step, no numerical instabilities are to be expected.

The net solid and fluid fluxes into/out of the wall-adjacent cell leads to a source term in these cells, as given in equation (3).

4. Finally, the computational domain is then updated by individual node movement using a DEFINE\_GRID\_MOTION UDF, where the new node positions are computed based on linear face position averages and the whole bed is repetitively swept with the sand slide algorithm until the angle of repose is satisfied at all bed faces. ANSYS Fluent's dynamic mesh capability is used to deform the mesh correspondingly. Here, the spring-based smoothing method is used, where the individual node displacements are obtained by treating the mesh as a network of connected springs. Displacements of the boundary nodes computed via equation (24) will be transmitted through the mesh by calculating adjacent node displacements based on Hooke's law.

## EXPERIMENTS

### Flow loop

The experiments were carried out in a medium-scale flow loop at the University of Stavanger. The flow loop, shown in Figure 5, is a closed loop, where the particles are separated and re-injected continuously to the test sections after collection in a hydrocyclone (10).

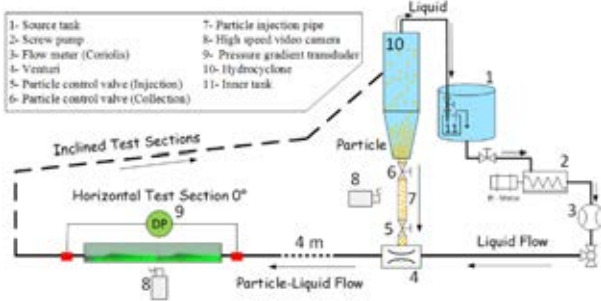


Figure 5: Medium-scale flow loop.

The flow loop features both a horizontal and an inclined test section, where the pipe is made of transparent plexiglas. The inner pipe diameter is 0.04 m, the total length of the horizontal test section is 6 m, with an upstream entrance length of 4 m. The test fluid was stored in a 350 L source tank (1). A PCM Moineau 2515 screw pump (2), regulated by a frequency inverter, provided the flow. Liquid flow rate and temperature were monitored by a Promass 80F DN50 Coriolis flow meter (3). The glass beads were mixed into the liquid through a Venturi shaped injector (4). The test section was located 4 m downstream of the injection point to minimize entrance flow effects and to let the particle-liquid patterns become fully developed. The pressure gradient data was measured over a length of 1.52 m by a Rosemount 3051 transducer (9). At the same position, flow pattern images were recorded using two high speed video cameras (8): A Basler camera with 500 fps at full resolution of 800x600 and a SpeedCam Mini e2 camera with 2500 fps at full resolution of 512x512 pixels. Particles and liquid were separated in the hydrocyclone (10), just after the inclined test section. The particles are then re-injected through the injection pipe (7) and the liquid is returned to the tank (1).

### Estimate of CFD boundary conditions

The solid superficial velocity required to specify the in-situ solid volume fraction used as a BC in the CFD model, i.e. equation (23), was estimated by measuring the injection and collection rate of particles. A time series of images of the injection pipe (7) was obtained, where one of the control valves (5, 6) was closed and the other one was open to collect or inject the particles. The changes of the packed particles height were calculated by analyzing the images in Matlab.

### Test matrix

Table 1 summarizes the relevant parameters used in the experiments (and corresponding simulations).

In all cases, glass beads with a density of 2500 kg/m<sup>3</sup> were used as solids.

The global  $\alpha_s$  represents the total volumetric loading of solids in the flow loop, whereas the in-situ  $\alpha_s$  represents the estimated solid volume fraction of moving solids

according to equation (23) used as a BC in the CFD simulations.

Table 1: Test matrix

Case	#1	#2	#3	#4	#5
Fluid	H <sub>2</sub> O	H <sub>2</sub> O	H <sub>2</sub> O	PAC1	PAC1
$U_{sl}$ [m/s]	0.26	0.43	0.44	0.45	0.81
$\mu_0$ [mPa.s]	-	-	-	26	26
$\mu_\infty$ [mPa.s]	1	1	1	1	1
$K_{CR}$ [Pa.s <sup>n<sub>CR</sub></sup> ]	-	-	-	0.008	0.008
$n_{CR}$ [-]	-	-	-	0.37	0.37
$d_s$ [mm]	0.3	0.3	1.2	1.2	1.2
$\alpha_s$ [-] global	0.08	0.08	0.12	0.12	0.12
$\alpha_s$ [-] in-situ	≈ 0.0015	≈ 0.0015	≈ 0.001	≈ 0.001	≈ 0.001

Pipe inclination was 0° in all cases, i.e. only the data from the horizontal test section was used in this study.

## RESULTS

### Numerical Modeling (CFD)

In the case of H<sub>2</sub>O, solids eventually accumulate into a pile at the inlet due to a developing recirculation zone, blocking more than half the inlet. For case #1, as depicted in Figure 6, and at approximately  $x \approx 1$  m, a static bed begins to form where the solids concentration profile as well as the bed height is constant with respect to  $x$ .

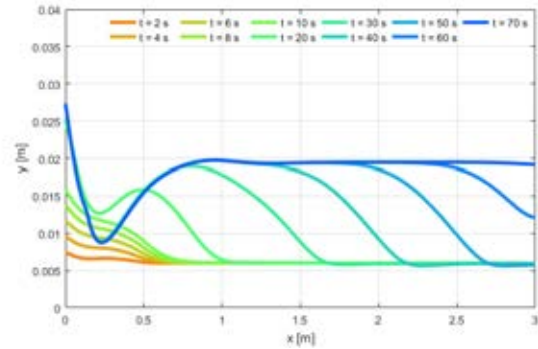


Figure 6: Bed height as a function of time, case #1.

For case #2, as illustrated in Figure 7, a large pile of solids develops in the domain (here depicted at  $t = 50$  s), which eventually is eroded.

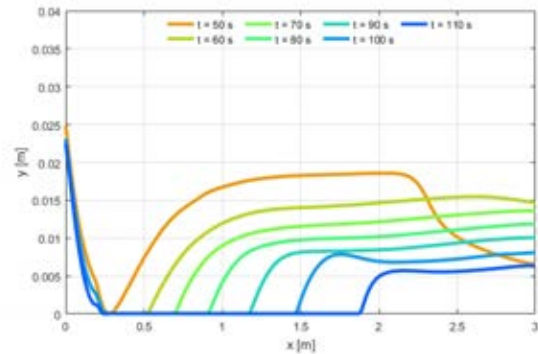


Figure 7: Bed height as a function of time, case #2.

For case #3, simulations were always diverging for a big variety of solver settings. Using time steps  $< 0.0005$  s lead to stable simulations; however, no results were obtained due to currently unavailable computational power required.

In case of PAC1, no pile build-up is observed at the inlet in either case. For case #4, as depicted in Figure 8, a dune starts to grow at  $x \approx 0.5$  m and eventually the bed approaches a steady-state with a bed height  $h = 0.0136$  m.

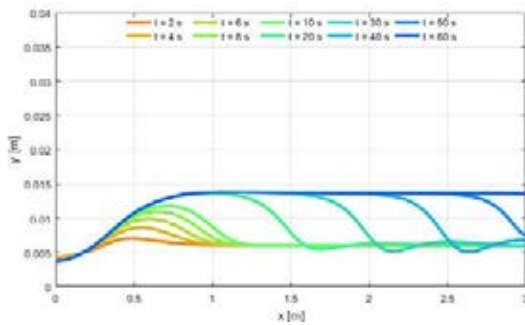


Figure 8: Bed height as a function of time, case #4.

For case #5, as illustrated in Figure 9, the bed is eroded from the start and yields a semi-steady-state bed height towards the outlet.

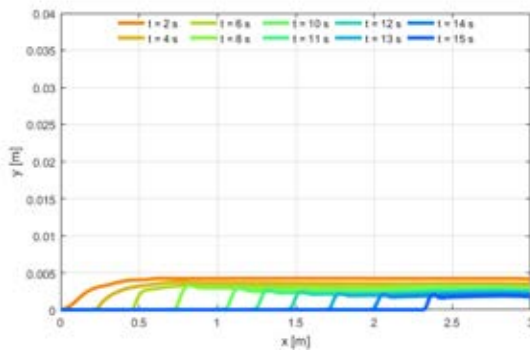


Figure 9: Bed height as a function of time, case #5.

However, the bed is eroded continuously, leading to zero bed height after the small dune traveling through the domain in the flow wise direction. No moving sand dunes were observed in the simulations.

### Experiments

In this study, only a subset of experimental results relevant for validation of CFD simulations are presented (horizontal test section, moving bed flow pattern). Figure 10 to Figure 14 show the corresponding experimental results for the cases #1 to #5.

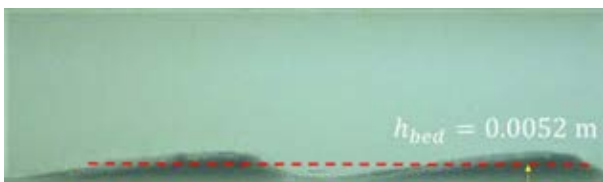


Figure 10: Exp. result case #1.



Figure 11: Exp. result case #2.

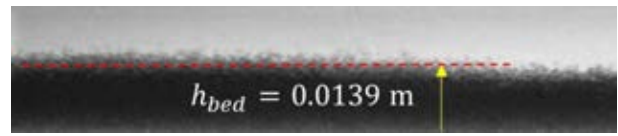


Figure 12: Exp. result case #3.



Figure 13: Exp. result case #4.



Figure 14: Exp. result case #5.

For case #1, #2 and #3, the fluid as well as particle properties are the same; with the only difference that the particle diameter  $d_s$  is 4 times larger in case #3 compared to case #1 and #2. Increasing the liquid superficial velocity  $U_{sl}$  leads to a higher bed height (case #2, Figure 11 vs. case #1, Figure 10), and changing the solids particle diameter  $d_s$  causes an even higher bed height (case #3, Figure 12).

For case #4 and #5, PAC1 was used as a fluid, having shear-thinning properties as shown in Figure 4. Changing the fluid properties from  $H_2O$  to the more viscous and shear-thinning PAC1 (case #4, Figure 8), changes the flow pattern and causes the bed to become much flatter but with a slightly higher bed height. By increasing the liquid superficial velocity  $U_{sl}$  (case #5, Figure 14), the bed height is reduced, and the flow pattern changes to stratified flow with more particles in suspension near the bed.

### DISCUSSION

First, the numerical results are discussed with a focus on model issues, followed by a brief discussion of the experimental results. Finally, numerical and experimental results are compared with each other.

#### Numerical Modeling (CFD)

##### *Dynamic bed forms and URANS concept*

Even though simulation results predict bed changes with respect to space and time, no dynamic bed forms such as dunes are observed. For case #1 and #4, a sediment bed with constant height in dynamic equilibrium with the interacting flow is obtained in the second half of the computational domain. For case #1 and #4, the bed seems to be eventually eroded; however, also no dunes are observed. The lack of dynamic morphodynamic bed shapes may be a direct consequence of the URANS concept employed. Here, only averaged turbulent quantities are considered. Hence, no flow-induced perturbations of the sand bed are observed away from the inlet. Similar results have also been obtained by other researchers in sediment transport research, e.g. Khosronejad et al. (2015). Hence, a URANS concept may only be used to predict an averaged bed height. A capability to resolve large scale turbulent structures seems required in order to obtain flow-induced bed

perturbations and dune dynamics. One computationally affordable concept may be the Very Large Eddy Scale (VLES) model introduced by Johansen et al. (2004), an approach that is currently investigated.

#### *Bed erosion & steady-state*

For case #2 and #5, the simulation results indicate a vanishing bed, i.e. the bed is eroding over time. Here, the solid transport capacity of the flow seems to be high enough to eventually transport all solids out of the domain, which is consistent with the comparatively high superficial velocity of the cases. However, as will be further discussed in section “Comparison of CFD and experimental results”, this is not in accordance with experiments, where a steady-state bed height is observed. Further simulation time is required to finally develop a full dynamic equilibrium, since, as Figure 7 and Figure 9 indicate, the eroding bed eventually leads to a fully flushed channel.

#### *Numerical instabilities*

For case #3, no converging solution could be obtained. In this case we have particles of  $d_s = 1.2$  mm in H<sub>2</sub>O. The settling velocity becomes large ( $v_{set} \approx 0.1$  m/s), imposing a considerable time step limitation. The problems observed here are expected to be related to the relative large hydrodynamic relaxation times of the larger particles leading to high deposition fluxes. These lead to short timescales for the Exner equation and consequently affect the numerical stability of our coupled equations.

#### *Bed load transport rate closure*

The used bed load transport rate is an empirical formula obtained for sand-water mixtures. Even though it is based on the non-dimensionalised wall shear stress in the form of the Shields number, it may not be adequate to quantify bed load transport for closed channel flows.

Furthermore, the applicability of bed load transport rate formulas for shear-thinning apparent viscosities is questionable.

The critical Shields number as the threshold for incipient motion was experimentally determined by Shields (1936) for a constant ratio of water-sand densities as well as  $a$ , with respect to the shear rate, constant water viscosity. Thus, for density ratios other than water-sand, as may be encountered in wellbore flows, and/or the varying apparent viscosity of drilling fluids, the standard Shields curve may not represent the correct threshold of motion.

#### *Node position update & mesh deformation*

The updated node positions are computed based on a simple face-averaging. In cases where the two neighboring faces of an arbitrary face do have a  $y$ -coordinate larger or smaller than the  $y$ -coordinate of the current face, the used averaging concept is not fully mass-conservative under all conditions. This may be easily deduced from Figure 3, where the third cell may be considered a local maximum. Since both the downstream and upstream face do have smaller  $y$ -coordinates, averaging node positions as described will lead to a new face value smaller than the actual computed face value. Ideally, the new node positions could be interpolated using e.g. splines with the constraint of mass conservation.

So far, mesh deformation was purely achieved without remeshing, since the local changes of the bed height occur on large time scales and, in relation to the channel height, comparatively small amplitudes. However, this may lead to cells with a very bad aspect ratio and/or improper  $y^+$ -values. A more sophisticated mesh deformation technique including boundary layer preservation and remeshing of inner cells is required.

An extension to 3D is planned to improve the applicability of the model for more complex flows, e.g. annular wellbore flows with drill pipe rotation. However, this will also require special treatment of the deforming boundary cells in case of contact with the drill pipe.

#### *BC & model parameters*

Appropriate BC as well as correct estimates of model parameters are major issues in all CFD simulations. Here, concerning BC, the transfer of a pipe cross-sectional geometry to a channel cross-sectional geometry is not fully consistent with regards to all parameters: Superficial velocities are matched; however, due to the different cross-sections, wall shear stress and Reynolds numbers are different.

For all cases, in the first half of the computational domain, the sand bed height changes with respect to space and time because of the various solid (bed load, deposition and entrainment) and corresponding fluid fluxes having different orders of magnitude and direction. This is mainly a consequence of the BC, i.e. the specified parabolic velocity profile and constant solid volume fraction across the inlet. These conditions do not represent a dynamic equilibrium. Since the velocity profile is updated based on the bed change at the inlet, a recirculation zone develops and the flow field and accordingly the sediment bed develop over an entrance length approximately equal to half the channel length. This may be circumvented by setting the first grid point constant, i.e. non-deforming. The two most prominent uncertain parameters are probably the estimated in-situ solid volume fraction given by equation (23) as well as the bed roughness required for the turbulence model. A sensitivity study may be required to identify the quantitative effect of these parameters on bed height.

Regarding solid fraction, a profile, for instance based on the Rouse concentration profile of suspended sediments, may be used. Together with a more realistic turbulent velocity profile, this may help to considerably reduce the required entrance length and thus speed up computations.

#### *Non-Newtonian rheology*

The apparent viscosity is based on the shear rate of the background fluid. For testing purposes, local, particle-induced shear rate and thus viscosity changes were taken into account for the settling velocity of solids in the wall-adjacent bed cells. However, this needs to be implemented into drag law formulations as well as shear-rate dependent force terms used in the two-fluid model. If not, solid velocities of the two fluid model and settling velocities of the bed load model would be inconsistent.

The utilized non-Newtonian rheology description as a GNF does not account for interdependencies of non-Newtonian fluid rheology and turbulence. Non-Newtonian rheology is only taken into account via the molecular viscosity, i.e. equation (5) and (12) whereas the effect of turbulence is only taken into account by the

corresponding models affecting the turbulent viscosity  $\mu_{t-i}$ . This is due to the conventional but simplified RANS treatment where the viscosity is first considered constant and later made variable by relating it to the shear rate, again see equation (5) and (12). Thus, terms representing the impact of fluctuations in strain rate on the fluids molecular viscosity as shown by Pinho (2003) as well as Gavrilov and Rudyak (2016) are ignored.

Adequate wall treatment for non-Newtonian fluids is not available so far, as the wall functions in ANSYS Fluent are based on the common Newtonian log-law concept. Hence, the boundary layer needs to be resolved down to  $y^+ < 1$  into the laminar sublayer or non-Newtonian wall laws have to be developed, e.g. based on Johansen (2015).

Drag, other momentum exchange terms and settling models utilized are based on Newtonian fluids. Here, further work is needed to account for non-constant viscosities, using available modeling concepts such as e.g. Childs et al. (2016); Ceylan et al. (1999); Li et al. (2012); Renaud et al. (2004); Shah et al. (2007); Shah (1986).

### Experiments

Recording of experimental data started after a flow stabilization sequence of 30 min, in order to yield dynamic equilibrium. An entrance length of 4 m upstream of the test section was sufficient to yield a well-developed particle-liquid flow in test section of the horizontal pipe, where the video images were recorded. The camera frame rate was sufficient to capture and track the movement of individual particles inside the test section.

Bed heights were measured from the video images and are in agreement with conventional theory.

Theoretically, the bed height should decrease with increasing liquid flowrate due to increased shear stress against the bed. Thus, both bed load and suspended load increase, which may be directly seen in Figure 13 and Figure 14 for the case of PAC1. However, in the case of H<sub>2</sub>O, an increase in bed height is observed, which may be explained by flow pattern transition from a rather stationary bed, where dunes are moving very slowly (case #1) to a moving bed, where dunes move much faster (case #2). In addition, beyond a threshold velocity, particle dunes disappear and the bed becomes flatter.

For constant particle mass density, the bed height increases with increasing particle diameter, due to increase in settling velocity, and decrease in entrainment rate.

Increased viscosity of shear-thinning fluid leads to decrease in bed height due to the increased solids transport capacity of the flow. This is mainly due to reduced settling velocity and consequently less deposition. It also leads to higher shear-stress acting on the bed and consequently more bed-load transport.

### Comparison of CFD and experimental results

As pointed out, the URANS-based numerical modeling approach does not yield any bed dynamics such as dunes. Therefore, comparison of CFD and experimental results may only be conducted based on a time/spatial average of the steady-state bed height.

Table 2 provides a quantitative comparison of the bed heights predicted by CFD simulations and the averaged bed heights obtained from experiments.

In case of the experiments, the averaged bed height was determined using Matlab Pixel-Viewer. By considering the grayscale color of each pixel (0 = black...255 = white), the interface of the sediment bed was determined and averaged over a sufficient length.

In case of the CFD results, the bed heights of case #2 and #5 are not representing the final steady state, as may be seen from the respective time series given in Figure 7 and Figure 9.

**Table 2: CFD vs. experimental averaged bed heights**

[#]	$h_{bed}$ (CFD) [m]	$h_{bed}$ (Exp) [m]	Ratio [-]
1	0.019	0.0052	3.65
2	0.0056	0.0093	0.60
3	n/a	0.0139	n/a
4	0.0136	0.0146	0.93
5	0.00157	0.0100	0.16

These time series actually indicate an eroding bed, which may eventually entirely vanish from the domain. This may be explained by (1) an overprediction of the solid transport capacity of the numerical model or (2) by an underestimation of the amount of solids entering the domain. In the case of (1), the bed load transport formula may need improvement with regards to the confined domain, non-Newtonian rheology or tuning of its model constants. The two latter aspects may also be valid for the entrainment model. Interestingly, the simulation result of case #1, does not support overprediction of solid transport capacity, as the bed height obtained from CFD simulations is 3.65 times the corresponding experimentally obtained bed height (see Table 2). In the case of (2), the amount of solids entering the domain could only be estimated based on equation (23) and corresponding experimental data. However, the estimated superficial velocities are global values, representing the respective superficial velocities on the entire flow loop system level. In order to improve on this BC estimate, measurements of the local superficial velocities at the test section inlet, or alternatively the solids concentration profile, would be required.

In general, comparison of the results is further complicated by the two different domains utilized in this study. In the experiments, a pipe geometry has been used, whereas in the CFD simulations, a 2D channel (with an infinitesimal long z-coordinate) has been used. As pointed out in subsection “BC & model parameters”, it is not straightforward to match these two different geometries with regards to BC. An extension of the model to 3D will mitigate this particular issue. Due to the uncertainties and shortcomings of the current status of the numerical model, as described in the subsection “Numerical Modeling”, a valid comparison of bed heights obtained from experiments and CFD simulations is not possible yet.

### CONCLUSION

1. The model developed so far does have major shortcomings when it comes to prediction of dunes and sediment bed dynamics as it may in principle only



predict the steady-state average bed height due to the utilized URANS approach. A simplified LES approach, e.g. the VLES concept currently investigated, may lead to a model capable of describing flow-induced dynamic bed shapes such as travelling dunes.

2. The current model status does not correctly predict the transport capacity of the flow, i.e. does not allow a quantitatively correct prediction of the steady-state bed height. An improved bed load transport model, together with a more realistic entrainment model, may yield more realistic transport capacities and consequently better predict the steady-state bed shape and bed height.
3. Improved inlet boundary conditions, in particular an inlet turbulent velocity profile together with a solid volume fraction profile, may considerably shorten entrance length effects and consequently speed up computations.
4. Further modeling work is required to adequately describe the effect of non-Newtonian rheology on various elements of the model: Non-Newtonian formulations for closures such as the bed load formula, the drag coefficient, the (critical) Shields number, and the hindered settling effect as well as non-Newtonian turbulence interdependencies may improve the model.
5. An investigation of the model's sensitivity with respect to bed roughness and in-situ solid volume fraction at the inlet is necessary in order to understand the effect of these two uncertain parameters.
6. An extension of the model to 3D will extend the applicability of the model for pipe flows, annular flows and potentially even more complex flows such as annular wellbore flows with drill pipe rotation, but at the same time require more sophisticated mesh deformation techniques.

## ACKNOWLEDGEMENTS

The project [Advanced Wellbore transport Modelling \(AdWell\)](#) with its sponsor, the Research Council of Norway and its partners Statoil, GDF SUEZ E&P Norge, IRIS, UiS, NTNU and SINTEF are gratefully acknowledged for funding and supporting part of this work.

## REFERENCES

BELLO, K. O. ET AL., (2011), "Minimum Transport Velocity Models for Suspended Particles in Multiphase Flow Revisited." *In* SPE Annual Technical Conference and Exhibition Society of Petroleum Engineers.

BRØRS, B., (1999), "Numerical Modeling of Flow and Scour at Pipelines." *Journal of Hydraulic Engineering* 125:511–523.

CELIK, I., AND RODI, W., (1988), "Modeling Suspended Sediment Transport in Nonequilibrium Situations." *Journal of Hydraulic Engineering* 114:1157–1191.

CEYLAN, K. ET AL., (1999), "A theoretical model for estimation of drag force in the flow of non-newtonian fluids around spherical solid particles." *Powder Technology* 103:286–291.

CHILDS, L. H. ET AL., (2016), "Dynamic settling of particles in shear flows of shear-thinning fluids." *Journal of Non-Newtonian Fluid Mechanics* 235:83–94.

CORREDOR, R. ET AL., (2016), "Experimental investigation of cuttings bed erosion in horizontal wells using water and drag reducing fluids." *Journal of Petroleum Science and Engineering* 147:129–142.

DORON, P., AND BARNEA, D., (1993), "A three-layer model for solid-liquid flow in horizontal pipes." *International Journal of Multiphase Flow* 19:1029–1043.

EXNER, F. M., (1925), "Über die Wechselwirkung zwischen Wasser und Geschiebe in Flüssen." *Akad. Wiss. Wien Math. Naturwiss. Klasse* 134:165–204.

GARSDIE, J., AND AL-DIBOUNI, M. R., (1977), "Velocity-Voidage Relationships for Fluidization and Sedimentation in Solid-Liquid Systems." *Industrial & Engineering Chemistry Process Design and Development* 16:206–214.

GAVRILOV, A. A., AND RUDYAK, V. Y., (2016), "Reynolds-averaged modeling of turbulent flows of power-law fluids." *Journal of Non-Newtonian Fluid Mechanics* 227:45–55.

GOHARZADEH, A. ET AL., (2013), "Experimental Characterization of Slug Flow on Solid Particle Transport in a 1 Deg Upward Inclined Pipeline." *Journal of Fluids Engineering* 135:081304.

HAN, S. M. ET AL., (2010), "Solid-liquid hydrodynamics in a slim hole drilling annulus." *Journal of Petroleum Science and Engineering* 70:308–319.

JOHANSEN, S. T., (2015), "Improved fluid control by proper non-Newtonian flow modeling." *In* Tekna – Flow Assurance Larvik.

JOHANSEN, S. T. ET AL., (2004), "Filter-based unsteady RANS computations." *International Journal of Heat and Fluid Flow* 25:10–21.

KHATIBI, M. ET AL., (2016a), "Experimental Investigation of Effect of Salts on Rheological Properties of Non-Newtonian Fluids." *In* Nordic Rheology Conference, University of Helsinki, Finland.

KHATIBI, M. ET AL., (2016b), "Particles Falling Through Viscoelastic Non-Newtonian Flows in a Horizontal Rectangular Channel Analyzed with PIV and PTV Techniques." *Journal of Non-Newtonian Fluid Mechanics* 235:143–153.

KHOSRONEJAD, A. ET AL., (2011), "Curvilinear immersed boundary method for simulating coupled flow and bed morphodynamic interactions due to sediment transport phenomena." *Advances in Water Resources* 34:829–843.

KHOSRONEJAD, A. ET AL., (2015), "Numerical simulation of large dunes in meandering streams and rivers with in-stream rock structures." *Fluvial Eco-Hydraulics And Morphodynamics* 81:45–61.

KHOSRONEJAD, A., AND SOTIROPOULOS, F., (2014), "Numerical simulation of sand waves in a turbulent open channel flow." *Journal of Fluid Mechanics* 753:150–216.

LI, S. ET AL., (2012), "The viscosity distribution around a rising bubble in shear-thinning non-newtonian fluids." *Brazilian Journal of Chemical Engineering* 29:265–274.

LIANG, D. ET AL., (2005), "Numerical modeling of flow and scour below a pipeline in currents - Part II. Scour simulation." *Coastal Engineering* 52:43–62.

MANZAR, M. A., AND SHAH, S. N., (2014), "Particle Distribution and Erosion During the Flow of Newtonian and Non-Newtonian Slurries in Straight and Coiled

Pipes.” *Engineering Applications of Computational Fluid Mechanics* 3:296–320.

MENTER, F. R., (1994), “Two-equation eddy-viscosity turbulence models for engineering applications.” *AIAA Journal* 32:1598–1605.

NIELSEN, P., (1992), “Coastal bottom boundary layers and sediment transport.” World Scientific Publishing Co Inc.

NOSSAIR, A. M. ET AL., (2012), “Influence of Pipeline Inclination on Hydraulic Conveying of Sand Particles.” In ASME 2012 International Mechanical Engineering Congress and Exposition pp. 2287–2293. American Society of Mechanical Engineers.

OFEL, T. N. ET AL., (2014), “CFD Method for Predicting Annular Pressure Losses and Cuttings Concentration in Eccentric Horizontal Wells.” *Journal of Petroleum Engineering* 2014:1–16.

PINHO, F. T., (2003), “A Model for the Effect of Turbulence on the Molecular Viscosity of Generalized Newtonian Fluids.” In 17th International Congress of Mechanical Engineering, Brazilian Society of Mechanical Sciences and Engineering (ABCM), Sao Paulo.

RENAUD, M. ET AL., (2004), “Power-Law Fluid Flow Over a Sphere: Average Shear Rate and Drag Coefficient.” *The Canadian Journal of Chemical Engineering* 82:1066–1070.

RICHARDSON, J. F., AND ZAKI, W. N., (1957), “Sedimentation and fluidisation: Part I.” *Chemical Engineering Research and Design* 75:S82–S100.

SAFFMAN, P. G., (1965), “The lift on a small sphere in a slow shear flow.” *Journal of Fluid Mechanics* 22:385.

SAVAGE, S. B. ET AL., (1996), “Solids transport, separation and classification.” *Powder technology* 88:323–333.

SCHILLER, L., AND NAUMANN, A., (1933), “Über die grundlegenden Berechnungen bei der

Schwerkraftaufbereitung.” *Z. Ver. Dtsch. Ing* 77:318–320.

SHAH, S. N., (1986), “Proppant-settling correlations for non-Newtonian Fluids.” *SPE Production Engineering* 1:446–448.

SHAH, S. N. ET AL., (2007), “New model for single spherical particle settling velocity in power law (visco-elastic) fluids.” *International Journal of Multiphase Flow* 33:51–66.

SHIELDS, A., (1936), “Anwendung der Ähnlichkeitsmechanik und der Turbulenzforschung auf die Geschiebebewegung.”

SIMONIN, C., AND VIOLLET, P., (1990a), “Predictions of an oxygen droplet pulverization in a compressible subsonic coflowing hydrogen flow.” *Numerical Methods for Multiphase Flows, FED91*:65–82.

SIMONIN, O., AND VIOLLET, P., (1990b), “Modelling of turbulent two-phase jets loaded with discrete particles.” *FG Hewitt, et al., Phenomena in multiphase flow*:259.

SOLBERG, T. ET AL., (2006), “CFD modelling of scour around offshore wind turbines in areas with strong currents.” In Offshore Wind Turbines situated in Areas with Strong Currents Offshore Center Danmark, Esbjerg.

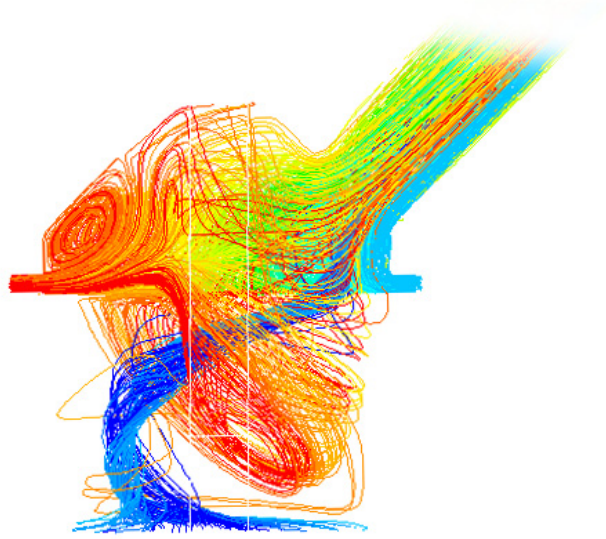
SOULSBY, R., (1997), “6. Threshold of motion.” In Dynamics of marine sands pp. 97–110. Thomas Telford Publishing.

STRUIKSMA, N., AND CROSATO, A., (1989), “Analysis of a 2-D bed topography model for rivers.” In Water Resources Monograph (S. Ikeda and G. Parker, eds.) pp. 153–180. American Geophysical Union, Washington, D. C.

SUN, X. ET AL., (2014), “Effect of drillpipe rotation on cuttings transport using computational fluid dynamics (CFD) in complex structure wells.” *Journal of Petroleum Exploration and Production Technology* 4:255–261.



# METALLURGICAL APPLICATIONS





## EXPERIMENTAL MODELLING OF METALLURGICAL PROCESSES

**Gunter Gerbeth\***, **Sven Eckert**

Helmholtz-Zentrum Dresden – Rossendorf (HZDR), Institute of Fluid Dynamics, 01328 Dresden, GERMANY

\* E-mail: g.gerbeth@hzdr.de

### ABSTRACT

Metallurgical processes often involve multi-phase flows of molten metals or molten slags. No doubt, CFD is a powerful tool to describe such flows, but for complex flow phenomena experimental data are needed for code validation. As for many melts such CFD grade data do not exist, liquid metal model experiments are more and more used in order to fill this gap. Several examples of it are described here.

**Keywords:** Liquid metal model experiments, measurement techniques.

### INTRODUCTION

Metallurgical processes involve a variety of molten metals or molten slags, which are opaque and typically at high temperatures. Measurements in such systems, e.g. of local velocities, temperatures, pressures, void fractions, impurity distributions, etc., are till today very scarce. CFD is a powerful tool in order to develop the necessary process understanding, but without relevant measurement data it is sometimes a bit lost, in particular in case of complex, often turbulent multi-phase processes. A powerful tool to validate related CFD codes consists in slightly simplified, low-temperature liquid metal model experiments. Water model experiments are, instead, often of limited value, particularly in the cases of strong temperature gradients, two-phase flows or flows exposed to electromagnetic fields.

Such liquid metal model experiments became a powerful tool over the past decade, mainly due to the development and availability of measurement techniques allowing to measure, e.g., the flow field in those melts almost completely up to melt temperatures of about 300°C. In the following we present, besides an overview on the measurement techniques, several examples for such kind of liquid metal model experiments. It involves mainly our experimental family LIMMCAST for modelling the continuous casting process of steel.

### MEASUREMENT TECHNIQUES FOR LIQUID METAL FLOWS

Commercial techniques for measuring the flow field in opaque liquids at higher temperatures are only barely available. Substantial research activities have been carried out at HZDR during the last 15 years on the

development and qualification of various methods to measure the velocity field in liquid metal flows. In this connection, we follow a twofold strategy. On one hand, we try to develop measuring techniques for applications under real industrial conditions. On the other hand, we use liquid metal models as an important tool to investigate the flow structure and related transport processes in melt flows being relevant for metallurgical applications. Besides the classical, invasive probes new ultrasonic or electromagnetic techniques came up and allow today a satisfying characterisation of flow quantities in the considered temperature range until 300°C. For reviews of those techniques we refer to Eckert et al. (2007, 2011) and Wondrak et al. (2014).

Today the Ultrasonic Doppler Velocimetry (UDV) and the newly developed Contactless Inductive Flow Tomography (CIFT) are most promising for the measurement of local velocity fields.

The Ultrasound Doppler method was developed in the early 1990's by Takeda (1991) and has been established in science and engineering for fluid flow measurements over the past two decades. UDV gives the one-dimensional velocity profile along the direction of the ultrasonic beam. The use and combination of multiple ultrasonic transducers expands the observation area or extends the number of velocity components which can be measured. The measurement can be done with a direct contact of the transducer to the fluid, but it can operate also through the wall of the liquid metal flow. Commercial transducers are available for temperatures up to about 230°C. For fluids at higher temperatures the concept of using an acoustic wave guide has been developed by Eckert et al. (2003) in order to achieve a thermal as well as a chemical decoupling between the active transducer and the hot fluid. The measurable velocity range extends from about 0.5 mm/s to 3...5 m/s with a spatial resolution of typically 1...5 mm and a temporal resolution of up to 30...50 Hz. The latter means that a full measurement of turbulent spectra is typically not possible with UDV, but the transient behaviour of practically relevant mean flow fields can certainly be monitored.

A new approach for a fully contactless and almost instantaneous detection of mean flow fields in metal melts is available today with CIFT. The melt volume is surrounded by one or two magnetic excitation fields. Magnetic field sensors mounted outside the melt detect

the induced magnetic field which arises from the interaction between the applied field and the flow. These flow-induced magnetic fields allow for a reconstruction of the three-dimensional mean velocity field in the melt as first demonstrated by Stefani et al. (2004). Successful applications of CIFT at single and two-phase flows typical for the continuous casting process have been reported by Wondrak et al. (2010, 2011). The main practical problem for CIFT typically consists in the low values of the flow-induced magnetic fields, which for an applied field of 1 mT are in the order of several ten's or hundred's of nT. This is often a challenging task due to disturbing electromagnetic fields (heaters, valves, pumps, etc.) which usually belong to the set-up at which CIFT shall be applied. Several solutions for an increased robustness of CIFT have recently been developed (AC field excitation, gradiometric pickup coils, improved reconstruction algorithms). Ratajczak et al. (2016) demonstrated that CIFT can operate reliably even in the presence of a strong external magnetic field such as an Electromagnetic Brake (EMBr) at a steel casting model. CIFT delivers mean three-dimensional flow fields with a temporal resolution of about 1 Hz. Measurements in the range of about 10 mm/s up to 5 m/s have been reported.

## LIMMCAST FACILITIES

For the modelling of flow problems in the continuous casting of metals meanwhile three different LIMMCAST facilities have been installed at HZDR. The LIMMCAST programme aims to model the essential features of the flow field in a continuous casting process, namely the flow field in the tundish, in the submerged entry nozzle (SEN) and in the mould as well as the solidification of the material in the strand. Figure 1 shows a photograph of the main, large LIMMCAST facility. All components are made from stainless steel. The low melting point alloy Sn60Bi40 is used as model liquid, whose temperature-dependent material data are well-known (Plevachuk et al., 2010). The liquidus temperature of 170°C allows for an operation of the facility in a temperature range between 200 and 400°C. The melt inventory is stored in two vessels with a capacity of 250 l each. An electromagnetic pump is used to transport the liquid metal into the tundish. The maximum flow rate, which is measured by an electromagnetic flow meter, is about 2.5 l/s.

Figure 2 shows a photograph of the test section containing the tundish, the SEN and the mould. From the tundish the melt pours through a pipe with an inner diameter of 54,5 mm into the mould with a rectangular cross section of 400 × 100 mm<sup>2</sup>. Argon gas bubbles can be injected with tuneable flow rates through the stopper rod into the SEN resulting in a two-phase flow inside the nozzle and the mould. Pipe connections with flanges are realized at various locations within the loop allowing a replacement of the particular components. This regards especially the nozzle, the mould, the tundish and parts of diverse test sections, which gives us a broad flexibility to modify the flow geometries for upcoming requirements.



Figure 1: Overall view of the LIMMCAST facility.

A main goal of the research at LIMMCAST consists in investigations on the impact of various types of magnetic fields on the flow in the mould and in the SEN. For instance, an EMBr with rectangular pole faces of 450 × 200 mm<sup>2</sup> has been used where a maximum electrical current of 2000 A provides a magnetic field strength up to 0.7 T within the pole gap of 200 mm. The flexible pole shoe design allows for the investigation of different magnetic field configurations, such as local brakes, ruler or even double ruler brakes.

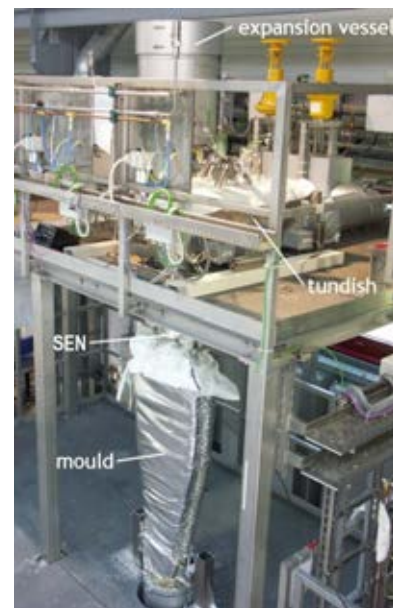


Figure 2: Photograph of the main test section with tundish, SEN and mould.

In addition to the main LIMMCAST facility the two smaller facilities Mini-LIMMCAST and X-LIMMCAST have been built up. Mini-LIMMCAST as shown in Fig. 3 uses the eutectic alloy Ga<sub>68</sub>In<sub>20</sub>Sn<sub>12</sub> as model fluid, which is liquid at room temperature. In contrast to the large LIMMCAST no heating is necessary and experiments can be performed either in a continuous or in a discontinuous way.

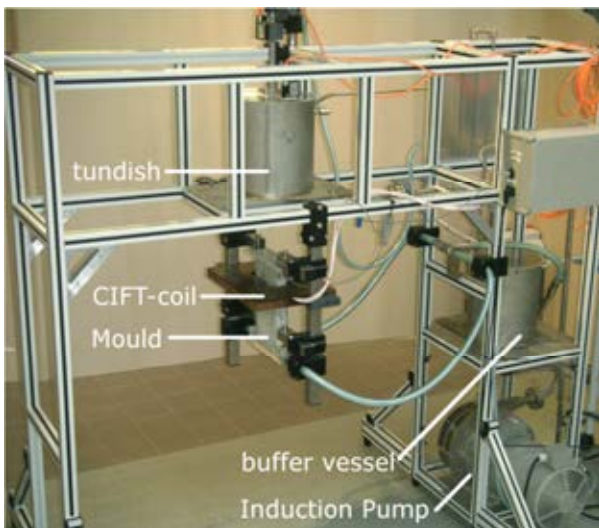


Figure 3: Photo of Mini-LIMMCAST.

The mould with a cross-section of  $140 \times 35 \text{ mm}^2$  and the nozzle with an inner diameter of 10 mm are made of acrylic glass. Stainless steel cylinders work as tundish and buffer vessel, respectively. In the discontinuous mode the tundish was filled with the alloy and then, after the lift of the stopper rod, the liquid metal pours through the nozzle into the mould. The total charge of about 6 litres of the alloy enables a measuring time of about 40 seconds with a mean flow rate of 100 ml/s. A detailed description of LIMMCAST and Mini-LIMMCAST is given by Timmel et al. (2010).

As model of an EMBr a DC magnet is utilized to supply a transverse magnetic field with a maximum field strength of  $B = 310 \text{ mT}$ . The pole faces of the magnet covered the wide side of the mould completely. We considered both situations of an electrically isolated and an electrically conducting mould, respectively. To simulate the case of the solidified shell in the real casting process, which actually exhibits a higher electrical conductivity as the liquid steel, the inner walls of the wide mould face were covered by brass plates with a thickness of 0.5 mm.

The **X-LIMMCAST** facility is a liquid metal loop constructed for use in the X-ray laboratory at HZDR. It is also operated with the model fluid GaInSn at room temperature. Visualisations of the liquid metal – argon two phase flows can be obtained by means of X-ray radioscopy. Figure 4 shows the experimental facility in the HZDR X-ray lab.

The melt is discharged through an acrylic glass tube with an inner square cross section of  $12 \times 12 \text{ mm}^2$  into the mould. The mould was also made from acrylic glass with a rectangular horizontal cross section of  $100 \times 15 \text{ mm}^2$  and a total length from the top lid to the bottom outlet of 426 mm. The liquid metal is circulated by an electromagnetic pump equipped with rotating permanent magnets. A maximum liquid metal flow rate of about 150 ml/s was achieved in the experiments if the stopper rod was brought into the highest position. During the two-phase flow experiments argon gas was injected at the tip of the stopper rod. Gas flow rates were adjusted in a wide range between 50 and 500  $\text{cm}^3/\text{min}$  by means of a mass flow controller. A more

detailed description of X-LIMMCAST and related results are given by Timmel et al. (2015).



Figure 4: Photo of X-LIMMCAST in the X-ray lab of HZDR.

## RESULTS OF THE LIMMCAST MODELS AND RELATED CFD RESULTS

There is meanwhile a vast of experimental and numerical results obtained with respect to the measurements at the LIMMCAST facilities. Here we point out a particular aspect which is interesting with respect to the relation between numerical and experimental modelling. The action of an EMBr was for many years considered as being almost fully understood in the sense that an external steady magnetic field always has a stabilizing influence on the flow of a liquid metal. The DC field was supposed to brake the mean flow and to reduce turbulent fluctuations in all configurations. Indeed, a vast of numerical simulations in the literature clearly showed this behaviour. Timmel et al. (2011) performed systematic studies of the mould flow at Mini-LIMMCAST with and without an external EMBr. Surprisingly it was found that the measured melt velocities showed the tendency of enhanced turbulent fluctuations for increasing magnetic field strength, in particular for the case of an electrically isolating mould wall. Figure 5 shows typical UDV velocity measurements at one fixed position in the core of the jet discharging from a port of the SEN. It clearly demonstrates that the velocity fluctuations in case of the electrically non-conducting mould are enhanced, whereas in case of a conducting mould wall the fluctuations are almost in the same range as without the EMBr. Figure 6 illustrates this behaviour with UDV velocity measurements of higher temporal resolution. Obviously, the steady magnetic field, i.e. the EMBr, triggers low-frequency velocity oscillations.



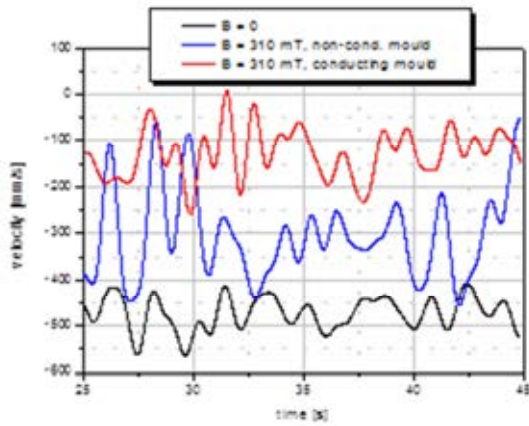


Figure 5: Measured velocities at a fixed position in the core of the jet.

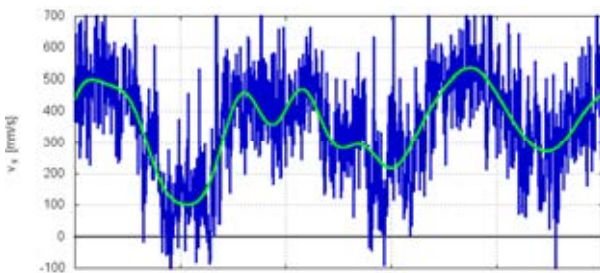


Figure 6: Measured velocity at a fixed position in the mould for electrically non-conducting mould walls.

Most interestingly, shortly after these experimental findings and the additional provision of detailed measurement data, refined numerical simulations by Chaudhary et al. (2012) and Miao et al. (2012) confirmed the results, in particular the tendency that the EMBr may enhance low-frequency oscillations in the velocity field.

There is no physical reason that the effect of a DC magnetic field on a liquid metal flow should only consist in a braking and turbulence damping action, in particular for fully three-dimensional flows. The magnetic field action is essentially determined by the closure of the electrical current, which geometrically results in local non-braking Lorentz forces, in particular for electrically non-conducting walls. Note that there is the case of the magnetorotational instability, which is a rotating flow which shows a laminar-turbulent transition solely due to an increasing external DC magnetic field (Stefani et al., 2006).

For a correct numerical simulation of the mould flow with EMBr two aspects turned out to be crucial:

- sufficient grid resolution of the typical electromagnetic Hartmann layers,
- anisotropic magnetic field effect in the turbulence modelling.

For more details we refer to Miao et al. (2012).

Regarding the two-phase flow in the nozzle and in the mould, the model experiments reported by Timmel et al. (2015) revealed that the gas bubble injection through the stopper rod results in the occurrence of rather large gas cavities in the upper, low-pressure region of the SEN as shown in Fig. 7.



Figure 7: Gas distribution in the upper part of the SEN. Experiments at X-LIMMCAST with a liquid flow rate of  $140 \text{ cm}^3/\text{s}$  and a gas flow rate of  $1.7 \text{ cm}^3/\text{s}$ .

To the best of the author's knowledge, there is not yet any CFD simulation of the two-phase flow in the SEN describing this phenomenon. Hence, a CFD modelling of the two-phase flow in the nozzle would be highly welcome for a critical assessment of the measurements published in Timmel et al. (2015). Further measurement data might be provided in case of interest.

Downstream in the mould the vast majority of bubbles leaving the nozzle are carried by the discharging jet into the lower circulation roll where they remain for many recirculation periods. The bubbles exhibit a long residence time in the lower circulation roll of the mould flow. Larger bubbles develop owing to coalescence and rise sporadically towards the free surface as visible in Fig. 8.

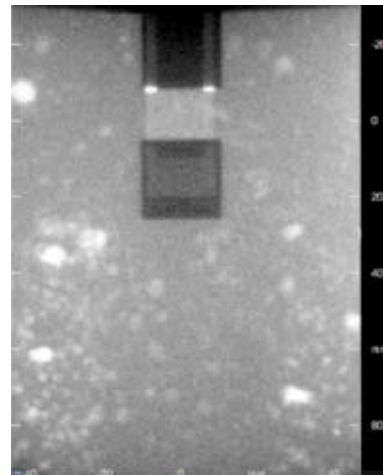


Figure 8: Snapshot showing the gas distribution in the mould at X-LIMMCAST with a liquid flow rate of  $140 \text{ cm}^3/\text{s}$  and a gas flow rate of  $0.7 \text{ cm}^3/\text{s}$ .

## FURTHER EXAMPLES OF LIQUID METAL MODEL EXPERIMENTS

Such model experiments are always useful as long as the real process under consideration is hardly accessible for experimental inspection. In the following we mention a few further examples.

The magnetic control of the down sprue flow in an industrial aluminum investment casting process was essentially based on GaInSn model experiments. They convincingly showed that the braking action of the external DC field can lead to a much more homogeneous distribution of the incoming melt over the cross-section of the duct, thus avoiding bubble or inclusion entrapment as they are typical for splashing melt fronts. For the particular casting part under consideration a significant reduction of the failure rate was obtained under industrial conditions. For more details we refer to Gerbeth et al. (2006).

Melt stirring by alternating magnetic fields is well-known for long. Standard stirring fields are the Rotating Magnetic Field (RMF), the Travelling Magnetic Field (TMF), or just the alternating magnetic field of a typical induction heater. Model experiments with the GaInSn melt allowed for verifying the calculated flow structures by direct velocity measurements. Interesting flow structures arise if the above stirring fields are superimposed. For instance, a certain combination of RMF and TMF gives rise to intense tornado-like flows as reported by Vogt et al. (2013). Note that these tornado-like flows by a suitable RMF-TMF combination have not yet been reproduced by CFD simulations in the turbulent parameter range.

Another focus of the experimental work is the investigation of the influence of electromagnetic fields on the process of solidification of metallic alloys. For that purpose an experimental setup has been made that enables for a simultaneous monitoring of the temporary position of the growth front, the temperature distribution and the flow pattern during solidification (see Fig. 9). This setup has been used for model experiments in Pb-Sn at temperatures of about 250°C and for investigations in Al-Si up to about 700°C.

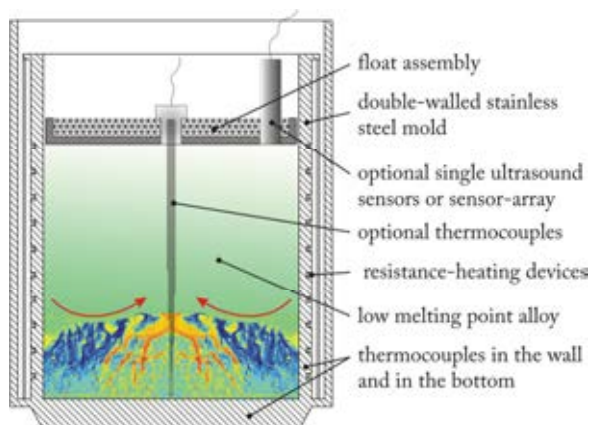


Figure 9: Schematic view of the setup for solidification experiments allowing for simultaneous observations of the front position, the temperature field and the velocity field.

The experiments provide an elaborate data base for the validation of numerical simulations. For that purpose, a network of cooperation exists with other numerical and experimental groups. A close collaboration with the University of Iowa focuses on fundamental aspects of the evolution of dendritic structures during the growth process and coarsening. The impact of fluid flow on the formation of segregation zones is investigated together with Oxford University (see Karagadde et al., 2014) and

Paris Mines Tech (see Saad et al., 2015). Furthermore, HZDR experimental data are also referred to on the webpage [www.solidification.org](http://www.solidification.org).

Electromagnetic stirring during solidification has been proved to be a striking method for achieving a purposeful alteration of the microstructure of casting ingots, such as grain refinement or the promotion of a transition from a columnar to an equiaxed dendritic growth (CET). However, the imposition of an RMF or a TMF also causes problems such as the occurrence of typical segregation pattern or a deflection of the upper free surface. A permanent radial inward (RMF and downward TMF) or outward (upward TMF) flow along the solidification front is responsible for the transport of solute to the axis or the wall of the ingot resulting in typical freckle segregation pattern filled with alloy of eutectic composition as shown for Al-Si experiments in Fig. 10a (freckles are highlighted by red framing). Our studies have been devoted to overcoming the handicaps of rotary stirring with the specific goal to generate a vigorous stirring in the bulk without considerable deformations of the free surface. So it was shown recently that the application of modulated AC magnetic fields offers considerable potential for optimizing the melt stirring. The secondary flow can be organized in such a way that periodic reversals of the flow direction occur adjacent to the solidification front, which has been proven as an important method to prevent flow-induced macrosegregation (see Eckert et al. (2007) and Willers et al. (2008)). Fig. 10b shows that the application of a pulsed RMF reduces the segregation effects significantly, which was demonstrated in Pb-Sn model experiments and afterwards also in Al-Si experiments.

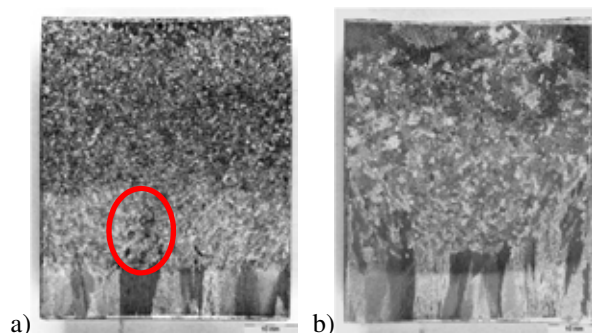


Figure 10: Comparison between a permanently applied RMF (left) and a modulated RMF (right) in Al-Si solidification: macrostructure of the longitudinal section.

## CONCLUSIONS

Liquid metal model experiments are a useful tool for various liquid metal processes, at least as long as the flow field and the related heat and mass transfer cannot be measured in the real, typically high-temperature processes. At much lower temperatures the model experiments allow today an almost complete measurement of the local flow field. This is of crucial importance for the validation of numerical simulations and for a better design or control of the corresponding liquid metal processes. The combination of numerical simulations with such model experiments often leads to a significantly improved insight into the processes.

## ACKNOWLEDGMENT

Financial support by the German Helmholtz Association in frame of the Helmholtz Alliance “Liquid Metal Technologies (LIMTECH)” is gratefully acknowledged.

## REFERENCES

- ECKERT, S. CRAMER, A. and GERBETH, G., (2007), “Velocity measurement techniques for liquid metal flows”, Molokov, S. et al. (Eds), *Magneto hydrodynamics – Historical Evolution and Trends*, 275-294, Springer.
- ECKERT, S. et al., (2011), “Some recent developments in the field of measuring techniques and instrumentation for liquid metal flows”, *J. Nucl. Sci. & Techn.*, **48**, 490-498.
- WONDRAK, T. et al., (2014), “Measurement techniques for the flow in a model of a continuous caster”, *Proc. 8<sup>th</sup> ECCO*, Graz, Austria, June 23-26, 2014, 247-256.
- TAKEDA, Y., (1991), “Development of an ultrasound velocity profile monitor”, *Nucl. Eng. Des.*, **126**, 277-284.
- ECKERT, S. GERBETH, G. and MELNIKOV, V.I., (2003), “Velocity measurements at high temperatures by ultrasound Doppler velocimetry using an acoustic wave guide”, *Exp. Fluids*, **35**, 381-388.
- STEFANI, F., GUNDRUM, T. and GERBETH, G., (2004), “Contactless inductive flow tomography”, *Phys. Rev. E*, **70**, 056306.
- WONDRAK, T. et al., (2010), “Contactless inductive flow tomography for a model of continuous steel casting”, *Meas. Sci. Technol.*, **21**, 045402.
- WONDRAK, T. et al., (2011), “Combined electromagnetic tomography for determining two-phase flow characteristics in the submerged entry nozzle and in the mould of a continuous casting model”, *Metall. Mater. Trans. B*, **42**, 1201-1210.
- RATAJCZAK, M., WONDRAK, T. and STEFANI, F., (2016), “A gradiometric version of contactless inductive flow tomography: theory and first applications”, *Phil. Trans. Royal Soc. A*, **374**, 20150330.
- PLEVACHUK, Y. et al., (2010), “Thermophysical properties of liquid tin-bismuth alloys”, *Int. J. Mater. Res.*, **101**, 839-844.
- TIMMEL, K. et al., (2010), “Experimental modeling of the continuous casting process of steel using low melting point metal alloys – the LIMMCAST program”, *ISIJ Int.*, **50**, 1134-1141.
- TIMMEL, K. et al., (2015), “Visualization of liquid metal two-phase flows in a physical model of the continuous casting process of steel”, *Metall. Mater. Trans. B*, **46**, 700-710.
- TIMMEL, K. et al., (2011), “Experimental investigation of the flow in a continuous-casting mold under the influence of a transverse, direct current magnetic field”, *Metall. Mater. Trans. B*, **42**, 68-80.
- CHAUDHARY, R., THOMAS, B.G. and VANKA, S.P., (2012), “Effect of electromagnetic ruler braking (EMBr) on transient turbulent flow in continuous slab casting using large eddy simulations”, *Metall. Mater. Trans. B*, **43**, 532-553.
- MIAO, X., et al., (2012), “Effect of an electromagnetic brake on the turbulent melt flow in a continuous-casting mold”, *Metall. Mater. Trans. B*, **43**, 954-972.
- STEFANI, F. et al., (2006), “Experimental evidence for magnetorotational instability in a Taylor-Couette flow under the influence of a helical magnetic field”, *Phys. Rev. Lett.*, **97**, 184502.
- GERBETH, G. et al., (2006), “Use of magnetic fields in aluminum investment casting”, *Proc. EPM 2006*, Sendai, Japan, Oct. 23-27, 323-328.
- VOGT, T. et al., (2013), “Spin-up of a magnetically driven tornado-like vortex”, *J. Fluid Mech.*, **736**, 641-662.
- KARAGADDE, S. et al., (2014), “3-D microstructural model of freckle formation validated using in-situ experiments”, *Acta Mater.*, **79**, 168-180.
- SAAD, A. et al., (2015), “Simulation of channel segregation during directional solidification of In-75wt%Ga alloy: Qualitative comparison with in-situ observations”, *Metall. Mater. Trans. A*, **46**, 4886-4897.
- ECKERT, S. et al., (2007), “Efficient Melt Stirring Using Pulse Sequences of a Rotating Magnetic Field-Part I – Flow Field in a Liquid Metal Column”, *Metall. Mater. Trans. B*, **38**, 977-988.
- WILLERS, B. et al., (2008), “Efficient Melt Stirring Using Pulse Sequences of a Rotating Magnetic Field-Part II – Application to Solidification of Al-Si Alloys”, *Metall. Mater. Trans. B*, **39**, 304-316.

# STATE OF THE ART: MACROSCOPIC MODELLING APPROACHES FOR THE DESCRIPTION OF MULTIPHYSICS PHENOMENA WITHIN THE ELECTROSLAG REMELTING PROCESS

**Christian SCHUBERT<sup>1\*</sup>, Antje RÜCKERT<sup>1†</sup>, Herbert PFEIFER<sup>1‡</sup>**

<sup>1</sup> RWTH Aachen University, Department for Industrial Furnaces and Heat Engineering, Kopernikusstr. 10, 52074 Aachen, GERMANY

\* E-mail: schubert@iob.rwth-aachen.de

† E-mail: arueckert@iob.rwth-aachen.de

‡ E-mail: pfeifer@iob.rwth-aachen.de

## ABSTRACT

The electroslag remelting (ESR) process, which is used to produce large ingots of high quality, bases on controlled solidification and chemical refinement mechanisms and is essential for the production of high quality steels and alloys designed for aeronautical, reactor chemical or nuclear applications. Due to this, it is indispensable to enable many high technological applications. Since the spreading of the industrial application of the ESR process in the 1960s, scientist and engineers worldwide are trying to deepen their understanding about this process to improve its flexibility, productivity and efficiency. Since the process conditions are very rough and measurements are quite costly, if possible at all, numerical simulation became the investigation tool of choice. Over the time, the models became more detailed and more phenomena could be taken into account. Today we are able to estimate electromagnetic fields, heat transfer, metallurgical flow and dendritic solidification in combination with each other within a macroscopic scale, based on actual physical models combined with the capabilities of numerical computing techniques. Out of this predictions about the influence of varied process control, or the occurring of macrosegregations and other defect types, became possible. In this paper state of the art, recent developments and critical aspects of the modelling of the ESR process will be shown. Common models, their strengths and weaknesses, as well as some possible approaches to presently less considered phenomena will be presented.

**Keywords:** Multiphase heat and mass transfer, Solidification modelling, Volume of Fluid, Electroslag remelting.

## NOMENCLATURE

### Greek Symbols

- $\alpha$  Phase fraction, [-].
- $\epsilon$  Electrical permittivity, [F/m].
- $\lambda$  Heat conductivity, [W/m].
- $\rho$  Mass density, [kg/m<sup>3</sup>].
- $\phi$  Electrical potential, [V].
- $\mu_D$  Dynamic viscosity, [kg/(m s)].
- $\mu$  Magnetic permeability, [N/A<sup>2</sup>].
- $\sigma$  Electrical conductivity, [S/m].
- $\tau$  Shear stress tensor, [Pa].

### Latin Symbols

- $A$  Magnetic vector potential, [V s m<sup>-1</sup>].
- $A_M$  Mushy zone constant, [kg/(m<sup>3</sup> s)].
- $B$  Magnetic field, [T].
- $D$  Displacement field, [C/m<sup>2</sup>].
- $E$  Electric field, [V/m].
- $E$  Internal energy, [J].
- $f_l$  Liquidus fraction, [-].
- $F_L$  Lorenz force, [N/m<sup>2</sup>].
- $F'_L$  Lorenz force, [N/m<sup>3</sup>].
- $F'_M$  Mushy zone damping force, [N/m<sup>3</sup>].
- $F'_V$  Volume specific force, [N/m<sup>3</sup>].
- $g$  Gravitational acceleration vector, [m/s<sup>2</sup>].
- $H$  Magnetic field intensity, [A/m].
- $I$  Identity tensor, [-].
- $J$  Electric current density, [A/m<sup>2</sup>].
- $K$  Intrinsic permeability of a medium, [m<sup>2</sup>].
- $p$  Pressure, [Pa].
- $Q_J$  Joule heat, [W/m<sup>3</sup>].
- $Q_{LH}$  Latent heat, [W/m<sup>3</sup>].
- $Q_S$  Heat source, [W/m<sup>3</sup>].
- $t$  Time, [s].
- $T$  Temperature, [K].
- $u$  Velocity vector, [m/s].
- $\phi$  Electrical potential, [V].

### Sub/superscripts

- $T$  Transpose
- eff* Effective quantities
- i* Index

## INTRODUCTION

The electroslag remelting respectively electroslag refining or electro-flux remelting (ESR) is a method to refine metals using a molten slag that is electrically heated up (Hoyle, 1983). It is applicable to a broad diversity of alloys and steels, for example titan- or nickel based alloys and tool steels. Hence, due to its outstanding chemical purification capabilities, it is vital for the production of certain kinds of highly stressed materials, especially those with aerospace, deep sea or reactor technology applications. Like the variety of materials and applications, several process variants based upon the ESR process exist (Nafziger, 1976, Hoyle, 1983).

In this paper, the ESR process and its common modelling methods will be described. Furthermore, we will discuss recent simulation approaches and their contribution to possible enhancements of general ESR simulations.

### Process description

Figure 1 shows a schematic diagram on the advanced stage of an exemplary ESR process.

The electrode is attached to a rod by a stub, through vertical movement of the rod the electrode is immersed into the slag. With the application of an electrical current (alternating or direct current) the slag, due to its high resistance, heats up and gets molten. The electrode influenced by the slag's temperature and its immersion depth begins to melt; at the bottom of the electrode a film of molten metal collects into droplets, finally falling through the slag layer, starting to form a liquid metal pool. Due to the water cooled copper mould the liquid metal starts to solidify from outside to inside, while the liquid metal pool sustains till the process is stopped. The zone in between the liquid metal and the already solidified metal is called mushy zone. Due to solidification and cooling of the metal an air gap is formed between electrode and mould, also a solidified slag layer is brought from the slag area to the solidified metal surface (more detailed shown in Figure 3), both effects have an critical impact on the heat transfer between solidified metal and mould (as well as on electrical conduction).

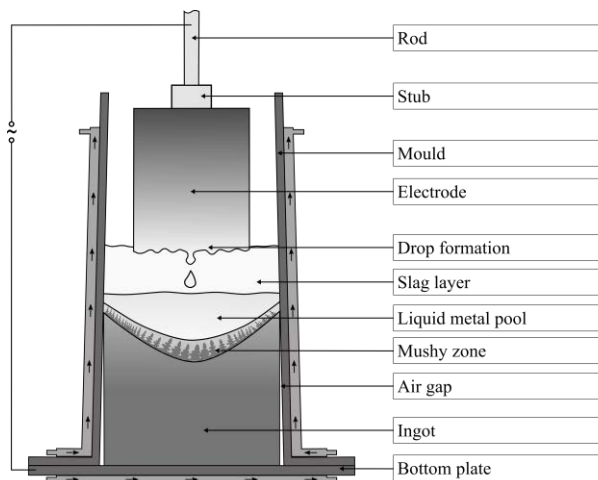


**Figure 1:** Schematic diagram showing an advanced stage during the ESR process.

Generally, the ESR process should reach some kind of stationary state, where the influence of the lower ingot can be neglected over the time. During these stationary phase many process parameter of the process are held constant, for example the electrode is generally controlled to hold a constant immersion depth into the slag. Due to the more or less stable conditions and its critical implication to the quality of the most of the ingot, this phase is the subject of the many ESR simulations.

### MODELLING

Numerical methods became a main tool to investigate the physical behavior of remelting processes, due to the rough process conditions, which hinder detailed experimental investigations.

However caused by the many mutual coupled physical, chemical and metallurgical phenomena it is not that trivial to build a viable model, making the right simplifications, choosing adequate boundary conditions and bringing it all together using an efficient computational method. While the first ESR computational modelling approaches were mostly based on handwritten finite difference codes, for example the model of Dilawari and Szekely (1977), today modern finite volume (FV) or finite element (FE) solvers are being used.

In the following, we will describe the present, most common modelling approaches regarding the ESR process and point out various modelling challenges.

The simulated area is typically reduced to the areas described by Figure 2. Where the one zone model is probably more physical, for example including the actual behavior of the slag / liquid metal pool interface (Rückert and Pfeifer, 2009, Kharicha et al., 2010), the two zone model can be way faster, especially regarding industrial size process geometries (Giesselmann et al., 2015).

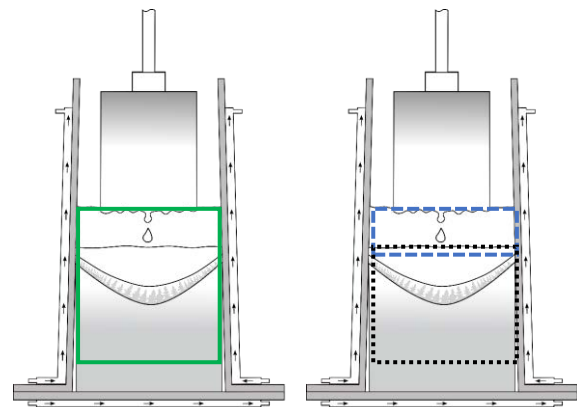


**Figure 2:** Common choices for computational domains within the ESR process, left side: one zone model approach and on the right side: two zone model approach

Usually a 2D axisymmetric simulation approach is used to model the ESR process, but especially in the region of the slag (see upper rectangle on the right side of Figure 2), according to Rückert (2012), Giesselmann (2014) or Karimi-Sibaki et al. (2016) this approach is only valid for the droplet behaviour in small lab scale size electrodes. It is not valid for industrial scale sized processes, as demonstrated by the non-axisymmetric dripping off behaviour, shown by the results from Kharicha et al. (2011) for full 3D models of industrial scale ESR plants. However according to Karimi-Sibaki et al. (2016) a 2D axisymmetric approach will be sufficient to model the solidification of larger ingot sizes. These findings are quite important since a 3D simulation of the whole process, speaking of real process times greater than a few seconds, will be quite unrealistic for the coming years, even utilizing the power of many core CPU clusters. So working out the right simplifications will still have a lot of impact on future simulations.

### Multiphase fluid flow

The most common modelling assumption for modeling the fluid flow inside the slag and liquid metal will be shown. Therefore, the Navier-Stokes equations consisting of continuity equation (1) and momentum equation (2) for incompressible fluid flow will be used.

$$\frac{\partial \rho}{\partial t} + \nabla \cdot (\rho \mathbf{u}) = 0 \quad (1)$$

$$\begin{aligned} \frac{\partial(\rho \mathbf{u})}{\partial t} + \nabla \cdot (\rho \mathbf{u} \mathbf{u}) \\ = -\nabla p + \nabla \cdot \boldsymbol{\tau} + \rho \mathbf{g} + \mathbf{F}'_L + \mathbf{F}'_M + \mathbf{F}'_V \end{aligned} \quad (2)$$

Different volume specific force vectors account for the induced Lorentz forces, Mushy zone damping forces and other possible volume specific forces. The shear stress tensor  $\boldsymbol{\tau}$  can be described according to equation (3) using the dynamic viscosity  $\mu_D$  and the velocity field  $\mathbf{u}$  (Giesselmann et al., 2015).

$$\boldsymbol{\tau} = \mu_D \left( (\nabla \mathbf{u} + \nabla \mathbf{u}^T) - \frac{2}{3} \nabla \cdot (\mathbf{u} \cdot \mathbf{I}) \right) \quad (3)$$

To describe the behavior of the liquid metal within the slag phase (see Figure 2) multiphase modelling approaches have to be used. Typically the volume of fluid (VOF) method is used for these kind of problems within FV methods (Kharicha et al., 2016, Wang et al., 2017). The VOF technique uses a single momentum equation, but solves these for each phase's volume fraction of the adapted continuity equation (4), while the sum of all volume fractions must be equal to unity as shown by equation (5).

$$\frac{1}{\rho_i} \left( \frac{\partial(\rho_i \alpha_i)}{\partial t} + \nabla \cdot (\rho_i \alpha_i \mathbf{u}) \right) = 0 \quad (4)$$

$$\sum_{i=1}^{n_{Phases}} \alpha_i = 1 \quad (5)$$

The interface between the different phases of the VOF cells can be tracked via interface reconstruction schemes (Hyman, 1984).

#### Short notice on turbulence modelling

A turbulence model should be used to account for the spatially nonuniform mixing in the molten pool (Kelkar et al., 2016) or the wake flow of liquid metal droplets inside the slag area. Often the standard k-epsilon model is used for describing the turbulent phenomena in ESR flows. However, with regard to Dong et al. (2016) using the RNG k-epsilon model may be more appropriate, due to the lower Reynolds number flow. While Giesselmann et al. (2015) is using the realizable k-epsilon model. As the realizable k-epsilon model, according to the ANSYS Theory Guide (ANSYS, 2017), has shown the best performance of all the model versions for several validations studies of separated flows and flows with complex secondary flow features.

Details about the above mentioned models can be found in the ANSYS Theory Guide (ANSYS, 2017). Depending on whichever turbulence model is chosen, equation (1) to (6) may vary.

#### Energy equation

With the use of a RANS turbulence model the energy conservation can be described via equation (6) additionally defining the Joule heating  $Q_J$  as well as the latent

heat  $Q_{LH}$ , taking care of solidification and melting heat, and possible other volumetric specific source terms  $Q_S$ .

$$\begin{aligned} \frac{\partial(\rho E)}{\partial t} + \nabla \cdot (\mathbf{u} \cdot (\rho E + p)) \\ = \nabla \cdot (\lambda_{eff} \cdot \nabla T + \boldsymbol{\tau}_{eff} \cdot \mathbf{u}) + Q_J + Q_{LH} \\ + Q_S \end{aligned} \quad (6)$$

#### MHD equations

The electromagnetic field occurring during the ESR process can be described using the macroscopic Maxwell's equations (7)-(10), neglecting the occurrence of displacement currents ( $\partial D / \partial t = 0$ ).

$$\nabla \times \mathbf{H} = \mathbf{J} + \frac{\partial \mathbf{D}}{\partial t} \quad (7)$$

$$\nabla \times \mathbf{E} = -\frac{\partial \mathbf{B}}{\partial t} \quad (8)$$

$$\nabla \cdot \mathbf{B} = 0 \quad (9)$$

$$\nabla \cdot \mathbf{D} = 0 \quad (10)$$

Furthermore, neglecting magnetization and polarization effects and assuming isotropic material behavior, the Maxwell equations can collectively be applied with the following material equations (11)-(13).

$$\mathbf{B} = \mu \mathbf{H} \quad (11)$$

$$\mathbf{D} = \epsilon \mathbf{E} \quad (12)$$

$$\mathbf{J} = \sigma (\mathbf{E} + \mathbf{u} \times \mathbf{B}) \quad (13)$$

Depending on the process geometry, the electrodynamic calculation should include the mold walls as well, to ensure a more accurate prediction of current flow and heat distribution in case's currents entering the mould (Kharicha et al., 2008). To describe the electrodynamic behavior various formulations can be used, for example the induction equation including various simplifications may be applied, but using the magnetic vector potential ( $A - \phi$ ) method seems to be the method of choice regarding more complex simulations. The  $A - \phi$  method states that due to equation (9) the magnetic field can be described with the rotation of an vector potential  $\mathbf{A}$  (equation (14)). Introducing this approach leads to another degree of freedom, which can be dealt with introducing the gradient of a scalar function  $\phi$ , which allows the electric field  $\mathbf{E}$  to be described by equation (15).

$$\mathbf{B} = \nabla \times \mathbf{A} \quad (14)$$

$$\mathbf{E} = -\frac{\partial \mathbf{A}}{\partial t} - \nabla \phi \quad (15)$$

By using these equations, the Maxwell and material equations are put to one equation (16). As described by Kost (1994), the Maxwell equations can then be solved numerically utilizing a suitable gauge condition for the divergence of  $\mathbf{A}$ .

$$\begin{aligned} \nabla \times \frac{1}{\mu} \nabla \times \mathbf{A} + \sigma \left( \frac{\partial \mathbf{A}}{\partial t} + \nabla \phi \right) \\ - \mathbf{u} \times \sigma \nabla \times \mathbf{A} = \mathbf{0} \end{aligned} \quad (16)$$

Since the time step size for the calculation of changing electromagnetic fields is usually significantly smaller than the time step size used for the solution of the multi-phase flow, the magnetic vector potential equation should further be simplified for stationary DC current or be solved in harmonic manner for the application of sinusoidal time varying currents.

The resulting quantities of the Lorentz force  $\mathbf{F}_L$  used in the momentum equation as well as the Joule heating  $Q_J$  term used in the energy conservation equation can be derived using the general equations (17) and (18).

$$\mathbf{F}_L = \mathbf{J} \times \mathbf{B} \quad (17)$$

$$Q_J = \frac{\mathbf{J} \cdot \mathbf{J}}{\sigma} \quad (18)$$

### Solidification

According to literature, a frequently used approach to model the macroscopic behavior of the solidifying metal during the ESR process is an enthalpy porosity technique introduced by Voller et al. (1990), assuming a dendritical solidification, where the interdendritic flow follows Darcy's law (equation (19)).

$$\nabla p = -\frac{\mu_D}{K} \mathbf{u} \quad (19)$$

Here the so called mushy zone constant  $A_M$  is used to describe the ratio between viscosity and permeability, as shown by equation (20). The function to calculate the liquids fraction  $f_l$  from the current temperature of the metal should be chosen in good agreement to the material behavior, for example the Scheil equation might be applied to various alloys.

$$\frac{\mu_D}{K} = \frac{1 - f_l}{f_l^3 + 0.001} \cdot A_M \quad (20)$$

As a result, velocity and turbulence quantities are lowered significantly in the mushy region. To determine the mushy zone constant the flow around the dendrites may be calculated, for example using the Lattice Boltzmann technique as shown by Böttger et al. (2016). However usually more simple approaches, for example the Kozeny–Carman equation, are used to approximate the permeability  $K$  over different liquidus fraction ranges (Singh et al., 2006).

### MODELLING CONSIDERATIONS

Even if the general modelling approaches are quite clear regarding the main fields and phenomena occurring inside the ESR process, there are still some difficulties to deal with. In this section, we will describe some of the recent problems which emerged out of past modelling approaches.

### Material data and electro chemical behavior

As often in CFD simulations appropriate material data is crucial for the calculation of plausible results. Since the thermal conditions inside the ESR process are very rough accurate measurements of density, viscosity, surface tensions and diverse electrical or thermal properties are not that easy, if possible at all. Therefore, often Computer Coupling of Phase Diagrams and Thermochemistry (CALPHAD) methods are being used to predict the high temperature material properties. Of course, using calculated material data brings another kind of uncertainty to every simulation, which generally requires some more effort in form of extensive sensitivity studies on these properties. Therefore, the research on high temperature material property measurement is an indispensable condition for the enhancement of ESR simulations.

Further problems are for example that in DC operating ESR processes the slag might undergo some electrolysis reactions, inhomogeneously influencing material properties and chemical purification reactions, but accounting for these kind of phenomena within a simulation will be quite costly speaking of modelling effort and computational expense.

### Electrode melting

The actual and changing shape of the electrode during the ESR process is of high interest, because of its influence to the film thickness and the actual dropping behavior of the liquid metal, which are a main indicator for the purification potential during the process.

Karimi-Sibaki et al. (2015) have shown a first dynamic mesh based approach to model the shape of the electrode during a ESR process, but it is still missing some essential aspects already implemented into the most other ESR models.

### Solidification phenomena

Due to solidification of the slag near the mold a thin slag skin layer is formed, which can be observed after the mould is removed from the ingot. This slag layer influences the heat- and electrical conductivity between mould and slag/ingot. Furthermore, with beginning of the solidification an air gap is formed between mould and ingot caused by thermal shrinkage and thermally induced stresses inside the ingot; also influencing the heat flux between ingot and mould.

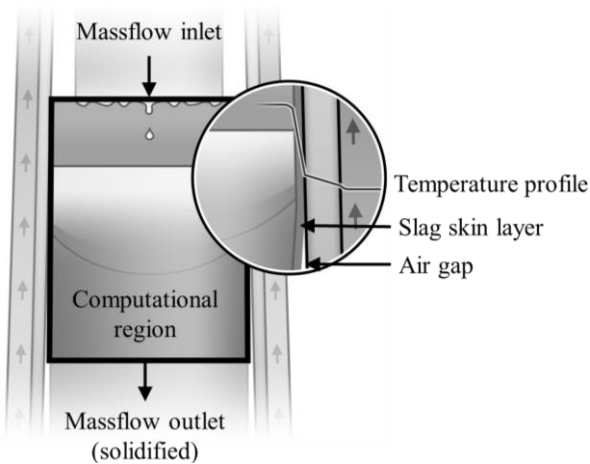


**Figure 3:** More detailed view of the computational region of the 1 zone model approach (Giesselmann et al., 2011) (modified)

Eickhoff et al. (2014) described an air gap developing model for the improved estimation of the air gap caused by thermally induced shrinkage, to improve the prediction of heat transfer between ingot and mould.

In many ESR simulations the slag skin is typically incorporated using a constant assumed slag skin thickness, in the best cases based on physical investigations of the represented process. Often these slag skin layer is assumed to electrically insulate the ingot area against the mould. However results of Kharicha et al. (2008), Kharicha et al. (2013) and Hugo et al. (2013) indicate that these assumption may not be right in many cases, which is essential for heat distribution and the simulated electromagnetic field and therefore probably should be context of further investigations.

Furthermore Yanke et al. (2015) incorporated the slag development of the slag skin into their ESR model, using the VOF technique, achieving quite accurate results.

#### *Mushy zone*

As mentioned in the previous section the solidification is modeled via the enthalpy-porosity approach, which can be applied assuming only dendritically solidification in the mushy zone area. Nevertheless it should be mentioned that according to Sinha et al. (1992) an anisotropic approach may be more appropriate than the isotropic approach described above in some cases.

Another problem is the that according to Giesselmann (2014) equiaxed crystal growth may occur in small sized laboratory ESR plants, in which case the aforementioned approaches are unsuitable. In the future other models available, see Wu et al. (2014), that also account for possible equiaxed crystal growth could be used.

#### *Solidification Defects*

The simulations of fluid flow, temperature and solidification are essential for understanding of the physical behavior during the ESR process. Nevertheless, the most relevant findings, at least for the industrial application of the numerical models, are the investigation or prediction of possible material defects, which might be introduced into the remolten ingot by using bad process parameters. As most solidification defects are introduced in the solidification area, for example the mushy zone, their simulative prediction strongly relies on the accurate mod-

elling of the solidifying area. Since the methods for prediction of certain defects, for example freckles or macrosegregations, are strongly related to the used metal or alloy, they will not be further covered within this paper. Nevertheless, it is important to notice that all the results of the possible defect prediction methods depend on the aforementioned problems settings.

## EXEMPLARY RESULTS

To facilitate some more insight into the process's simulation some results from the least year's research on ESR modelling at the Department for Industrial Furnaces and Heat Engineering (IOB) of the RWTH Aachen University will be shown. In Figure 4 some exemplary pictures for the slag area of a 2D axisymmetric ESR simulation are shown. The results are computed via coupling of simulations utilizing ANSYS Fluent and ANSYS EMAG. A regular sized rectangular mesh with a mesh size of around 0.5 mm is being used for the CFD and the electromagnetic simulation as well. The general simulation strategy is described in Giesselmann et al. (2011). It can be seen that the phase distribution has direct impact on the current distribution, which directly influences the joule heat generation shown in Figure 4, as you would aspect.

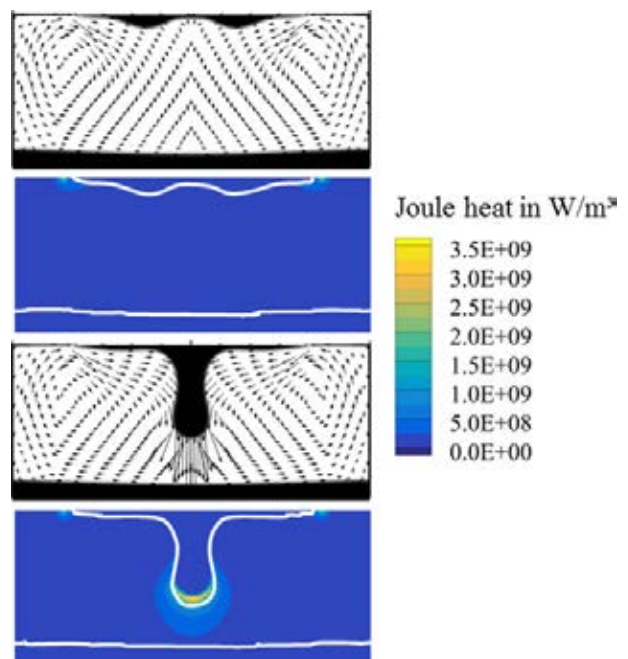


**Figure 4:** Exemplary view of 2D asymmetrical ESR simulation of small size ESR plant, diameter  $\sim 11$  cm, metal phase is drawn in black, black line in Joule heat contour plot represents the liquid metal isosurface line, vectors representing the velocity inside the slag phase

In Figure 5 the results in the metal zone/ingot of an ESR simulation with not appropriate parametrisation can be seen. The simulation strategy of these “second zone” within a two zone modelling approach is shown in Giesselmann (2014) or Giesselmann et al. (2015).

The illustrated results (Figure 5) were generated during a parameter study investigating the impact of different slag layer heat conductivities, mushy zone constants and air gap thicknesses. Obviously, the cooling effect of the mould is excessively low in this simulation, which leads to a deep liquid metal bath, and no solidification at the



mould walls in the recirculation area. This behaviour is not expected in a real ESR process.

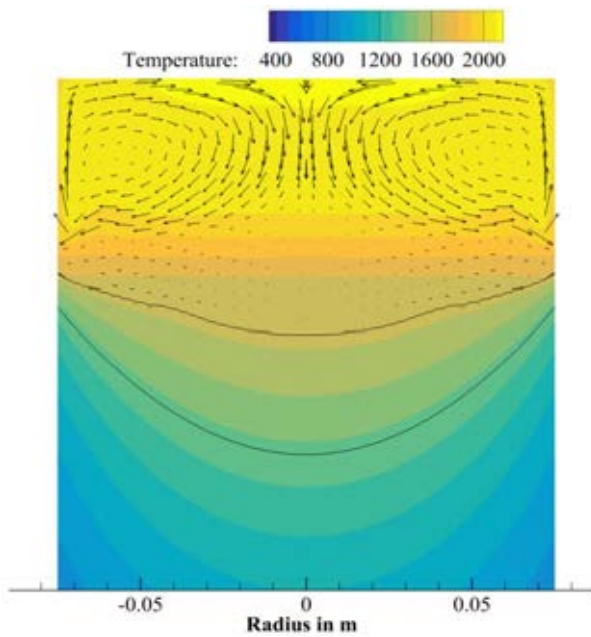


**Figure 5:** Contour of metal phase area of an inappropriately parametrized ESR simulation

At last, some notice should be given to the common validation method regarding ESR simulations. Since measurements at ESR plants are difficult to make during the stage of operation, typically the solidification line is determined out of the primary growth direction of the metallic grains/dendrites, extracted from prepared cross sections of a remolten ingot, as shown in Figure 6. This solidification line is taken as validation criteria by many authors.

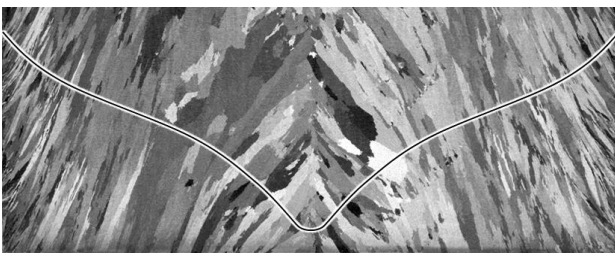


**Figure 6:** Cross section of etched ESR ingot with plotted solidification line (Giesselmann, 2014)

However, due to the many influencing factors to the solidification area combined with the many uncertainties in boundary conditions, material data etc., it cannot be guaranteed that a matching solidus line is sufficient to validate the whole process simulation.

## CONCLUSION AND OUTLOOK

In this paper, we gave a short comprehension of the ESR process and its current modelling approaches.

Even if the general modelling strategies and necessary field equations are sufficiently elaborated at the current time. There are several insufficient investigated phenomena, whose impact on the simulation accuracy are quite uncertain, for example the slag behavior in DC operation or the changing of the shape of the electrode during the process.

Further progress could be gained by improved understanding of the processed materials properties at high temperatures, since they are also a subject of uncertainty for many simulations.

Furthermore, new experiments investigating and validating boundary conditions would improve current models, for example, heat flow measurements through the mould wall may give further conclusions about the right treatment of boundary conditions and thereby strengthen the solidus line validation criteria/method.

To sum it up, it will still need quite some time to figure out a commonly efficient and consistent solution strategy for the ESR process simulation, also including important phenomena like the electrode shape simulation, slag layer- /air gap formation, defect occurrences and accounting for relevant 3D flow phenomena. As transient full 3D simulations of the whole process will not be a feasible option during the next years, due to the required computing power.

Furthermore, this will be difficult since it should be generally possible to simulate a decent range of real process time, to allow some phenomena to actually affect the solidification area and therefore the simulated solidus line, which is an import criterion for many investigations.

At last, it should be mentioned that due to the variety of problems and phenomena in the ESR process, simulative solutions or solution approaches might also influence the research on other more or less related (metallurgical) processes.

## ACKNOWLEDGMENT

The authors gratefully acknowledge the support of the German Research Foundation (Deutsche Forschungsgemeinschaft – DFG).

## REFERENCES

- ANSYS, INC., (2017), "ANSYS® Academic Research, Release 18.0, Help System, FLUENT Theory Guide".
- BÖTTGER, B., et al., (2016), "Cross-Permeability of the Semisolid Region in Directional Solidification: A Combined Phase-Field and Lattice-Boltzmann Simulation Approach", *JOM*, **68**, 27-36.
- DILAWARI, A.H. and SZEKELY, J., (1977), "A mathematical model of slag and metal flow in the ESR Process", *Metallurgical Transactions B*, **8**, 227-236.
- DONG, Y.-W., et al., (2016), "Comprehensive Mathematical Model for Simulating Electroslag Remelting", *Metallurgical and Materials Transactions B*, **47**, 1475-1488.
- EICKHOFF, M., et al., (2014), "Introducing an analytic approach on air gap formation during the ESR/VAR Process and numerical validation", *Ingot casting, rolling & forging : ICRF, ingot casting, rolling and forging 2014 ; 2nd International Conference ; Milan, Italy, 7 - 9 May 2014*.
- GIESSELMANN, N., (2014), "Numerische Untersuchungen des Elektroschlack-Umschmelzprozesses für Alloy 718", Dissertation, Aachen, RWTH Aachen University, Fakultät für Georesourcen und Materialtechnik, 140.

GIESSELMANN, N., et al., (2015), "Coupling of Multiple Numerical Models to Simulate Electroslag Remelting Process for Alloy 718", *ISIJ International*, **55**, 1408-1415.

GIESSELMANN, N., et al., (2011), "Mathematical modeling of the influence of process parameters on the solidification in the electroslag remelting process", "STEELSIM, International Conference Simulation and Modelling of Metallurgical Processes in Steelmaking, 4", Düsseldorf, TEMA Technologie Marketing AG, **4**.

HOYLE, G., (1983), "Electroslag processes: principles and practice", Applied Science Publishers.

HUGO, M., et al., (2013), "Impact of the Solidified Slag Skin on the Current Distribution during Electroslag Remelting", Proceedings of the 2013 International Symposium on Liquid Metal Processing and Casting, John Wiley & Sons, Inc. 79-85.

HYMAN, J.M., (1984), "Numerical methods for tracking interfaces", *Physica D: Nonlinear Phenomena*, **12**, 396-407.

KARIMI-SIBAKI, E., et al., (2015), "A Dynamic Mesh-Based Approach to Model Melting and Shape of an ESR Electrode", *Metallurgical and Materials Transactions B*, 1-13.

KARIMI-SIBAKI, E., et al., (2016), "On Validity of Axisymmetric Assumption for Modeling an Industrial Scale Electroslag Remelting Process", *Advanced engineering materials*, **18**, 224-230.

KELKAR, K.M., et al., (2016), "Computational Modeling of Electroslag Remelting (ESR) Process Used for the Production of High-Performance Alloys", Proceedings of the 2013 International Symposium on Liquid Metal Processing & Casting, M. J. M. Krane, A. Jardy, R. L. Williamson and J. J. Beaman, Cham, Springer International Publishing 3-12.

KHARICHA, A., et al., (2011), "3D Simulation of the melting during an industrial scale electro-slag remelting process", *International Symposium on Liquid Metal Processing and Casting*, Nancy, France, 41-48.

KHARICHA, A., et al., (2011), "Simulation of the melting of a flat electrode during an electro-slag remelting process", *STEELSIM, International Conference Simulation and Modelling of Metallurgical Processes in Steelmaking, 4, METEC InSteelCon, 2011*, Düsseldorf.

KHARICHA, A., et al., (2010), "Influence of the slag/pool interface on the solidification in an electroslag remelting process", *Materials science forum*, 229-236.

KHARICHA, A., et al., (2008), "On the Importance of Electric Currents Flowing directly into the Mould during an ESR Process", *steel research int.*, **Vol. 79**, 632-636.

KHARICHA, A., et al., (2013), "Contribution of the Mould Current to the Ingot Surface Quality in the Electroslag Remelting Process", Proceedings of the 2013 International Symposium on Liquid Metal Processing and Casting, John Wiley & Sons, Inc. 95-99.

KHARICHA, A., et al., (2016), "Simulation of the Electric Signal During the Formation and Departure of Droplets in the Electroslag Remelting Process", *Metallurgical and Materials Transactions B*, **47**, 1427-1434.

KOST, A., (1994), "Numerische Methoden in der Berechnung elektromagnetischer Felder", Springer-Verlag Berlin Heidelberg.

NAFZIGER, R.H., (1976), "The electroslag melting process", The electroslag melting process, U.S. Bureau of Mines.

RÜCKERT, A., (2012), "Mathematische Modellierung der Transportprozesse beim Elektroschlackeumschmelzen", Dissertation, Aachen, RWTH Aachen, Fakultät für Georessourcen und Materialtechnik, 135.

RÜCKERT, A. and PFEIFER, H., (2009), "Mathematical Modelling of the Flow Field, Temperature Distribution, Melting and Solidification in the Electroslag Remelting Process", *Magneto hydrodynamics*, **45**, 527-533.

SINGH, A.K., et al., (2006), "Role of appropriate permeability model on numerical prediction of macrosegregation", *Metallurgical and Materials Transactions B*, **37**, 799-809.

SINHA, S.K., et al., (1992), "A variable property analysis of alloy solidification using the anisotropic porous medium approach", *International Journal of Heat and Mass Transfer*, **35**, 2865-2877.

VOLLER, V.R., et al., (1990), "Modelling the mushy region in a binary alloy", *Applied Mathematical Modelling*, **14**, 320-326.

WANG, Q., et al., (2017), "A three-phase comprehensive mathematical model of desulfurization in electroslag remelting process", *Applied Thermal Engineering*, **114**, 874-886.

WU, M., et al., (2014), "Advanced Process Simulation of Solidification and Melting", *BHM Berg- und Hüttenmännische Monatshefte*, **159**, 30-40.

YANKE, J., et al., (2015), "Simulation of Slag-Skin Formation in Electroslag Remelting Using a Volume-of-Fluid Method", *Numerical Heat Transfer, Part A: Applications*, **67**, 268-292.



## LES-VOF SIMULATION OF TURBULENT INTERFACIAL FLOW IN THE CONTINUOUS CASTING MOLD

Mahdi SAEEDIPOUR<sup>1,2\*</sup>, Stefan PUTTINGER<sup>1†</sup>, Stefan PIRKER<sup>1‡</sup>

<sup>1</sup>Department of Particulate Flow Modelling, Johannes Kepler University, 4040 Linz, AUSTRIA

<sup>2</sup>Christian Doppler Laboratory for Multi-scale Modeling of Multiphase Processes, Johannes Kepler University, 4040 Linz, AUSTRIA

\* E-mail: mahdi.saeedipour@jku.at

† E-mail: stefan.puttinger@jku.at

‡ E-mail: stefan.pirker@jku.at

### ABSTRACT

Slag entrainment during continuous casting process is a multiscale problem strongly dependent on the molten metal flow in the mold. Large-scale flow structures in the mold interact with the slag layer at the top of the meniscus, and small-scale liquid structures in the form of slag droplets may be entrained into the solidifying metal. In this work a large eddy simulation - volume of fluid (LES-VOF) approach is applied to investigate the unsteady flow interaction with the metal-slag-air interface including the interface instability, deformation of the slag layer and its entrainment into the molten metal.

A benchmark experiment was designed to investigate the flow field in the proximity of a liquid-liquid interface for validation purposes. The experiment uses water and paraffinum liquidum to model the combination of liquid steel and the slag layer. While the entrainment of oil droplets can be visualized via shadowgraphy the flow field was measured via particle image velocimetry PIV. In combination, these two methods allow a qualitative and quantitative comparison of the unsteady flow characteristics with the CFD results.

The measurement data at different inflow conditions have been used to validate the simulation results. We compare the global flow characteristics and mean velocity of submerged entry nozzle jet upon injection to the mold. Furthermore, the statistics of turbulence including velocity fluctuations and turbulent kinetic energy are used to investigate the unsteady jet interaction with the slag layer as well as liquid-liquid interface dynamics. The comparison of CFD results and experimental data reveals fairly good agreement both quantitatively and qualitatively.

**Keywords:** Two-phase interfacial flow, large eddy simulation (LES), volume of fluid (VOF), particle image velocimetry (PIV), slag entrainment, continuous casting .

### NOMENCLATURE

#### Greek Symbols

$\rho$	Mass density, [ $kg/m^3$ ]
$\mu$	Dynamic viscosity, [ $kg/ms$ ]
$\sigma$	Surface tension coefficient, [ $N/m$ ]
$\alpha$	Volume of fluid, [-]
$\mu$	Dynamic viscosity, [ $kg/ms$ ]
$\delta$	Kronecker delta tensor, [-]
$\phi$	Arbitrary flow quantity, [-]
$\tau$	Sub-grid term, [-]
$\Delta$	Grid size, [ $m$ ]
$\kappa$	Curvature, [ $1/m$ ]
$\mathcal{G}$	Spatial filter operator, [-]
$\Theta$	Inlet angle, [ $deg$ ]

#### Latin Symbols

$p$	Pressure, [ $Pa$ ].
$\mathbf{U}$	Velocity, [ $m/s$ ].
$\mathbf{S}_\sigma$	Surface tension force, [ $N$ ].
$\mathbf{D}$	Rate of deformation, [ $1/s$ ].
$\mathbf{n}$	Interface normal vector, [-].
$C_s$	Smagorinsky constant, [-].

#### Sub/superscripts

$a$	air.
$o$	oil.
$w$	water.
$i$	Index $i$ .
$j$	Index $j$ .

### INTRODUCTION

Many industrial and environmental processes involve highly unsteady turbulent interfacial flows. Examples include liquid jet breakup, petroleum transportation, continuous casting process and many others. In continuous casting molds, the top surface of molten steel is covered by a slag layer in order to prevent steel from oxidation and heat loss as well as to use it as a lubricant between the solidifying steel and the mold (Iguchi *et al.*, 2000). Slag entrainment affects the quality of the final product strongly, if the entrained droplets become trapped in the solidifying metal. This draws much attention to the fundamental studying of slag entrainment in the casting industry over the recent decades, resulting in several proposed mechanisms (Hibbeler and Thomas, 2013).

According to several experimental investigations on mold flow, the shear-layer instability between the slag and molten metal, known as Kelvin-Helmholtz instability, has been identified as one of the mechanisms of slag entrainment. In addition, the formation of vortices behind the submerged entry nozzle (SEN), known as Karman vortex, can cause slag entrainment by pulling the slag layer down into the molten metal. It is also discussed by Iguchi *et al.* (2000) that the argon gas injection into the SEN to prevent clogging will result in bubble formation in the mold. The interaction between these bubbles and the slag interface is also introduced as another mechanism of slag entrainment.

All mentioned mechanisms are associated with the unsteady flow situation near the interface in particular due to the turbulence of the liquid steel pool (see Figure 1). Numerical simulation of such a multiphase turbulent flow remains a chal-

lenging topic, because a prospective approach must account for the turbulence modelling as well as capturing the interfacial topology between phases.

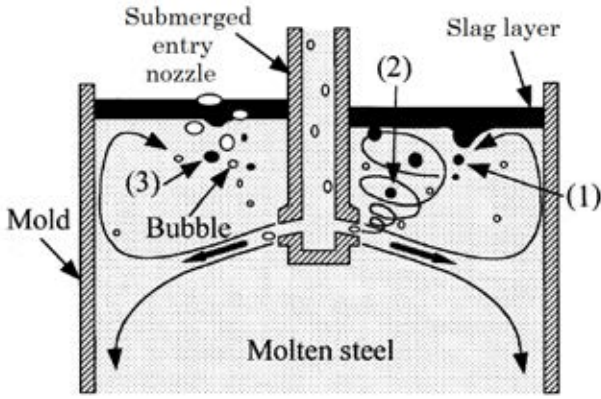


**Figure 1:** Schematic of slag entrainment mechanisms (reproduced from Iguchi *et al.* (2000)).

A variety of numerical studies on turbulent multiphase flows with different industrial application have been done within the last decade. In the case of modelling the continuous casting mold flow, Liu *et al.* (2013) carried out large eddy simulations to study the effect of argon gas injection through the SEN on the flow pattern in the mold. In this study they employed an Euler-Euler approach to model the molten metal flow and argon bubbles. In a similar work, they coupled a Lagrangian model with two-fluid model to study the influence of argon gas injection on the molten steel flow and particle transport behaviors (Liu *et al.*, 2014). Vakhrushev *et al.* (2014) studied the global behavior of mold flow around the SEN using a volume of fluid method. In this work a RANS-based turbulence model (i.e.  $k - \epsilon$ ) was coupled to three-phase VOF model to obtain the velocity field and the time-averaged oil-water interface position. They also validated the numerical results with a  $1/3$  scaled-down water model. Recently, the transient free surface behavior in a model mold is studied by Asad *et al.* (2015) using a RANS-VOF approach. In this work the impact of inlet velocity and nozzle depth on the free surface behavior and flow pattern was investigated and different flow regimes in the mold were observed.

Most of the aforementioned studies employed the RANS-based turbulence models which can only capture the global behavior of the unsteady flow in a large-scale domain; however, there are many small-scale phenomena involved in the slag entrainment that need to be captured by the numerical tool. Although RANS methods are computationally-efficient for industrial flow, they are not capable of capturing small-scale physics of multiphase flows. Even those studies that carried out LES do not report the conditions where several droplet-like slag structures are generated from the interface. Nevertheless, the entrainment of slag droplets into the water pool is observed in present benchmark experiments.

In the present work we aim at studying the mold flow three-phase using an LES-VOF approach which then provides us with an in-depth understanding of the physics of the flow in both large and small scales. Furthermore, the water-oil benchmark experiment is designed to visualize the global mold flow and measure the unsteady flow using PIV. The simulation results are then validated against the experiments at different conditions. The combination of experiments and modelling helps us to realize the shortcomings of LES approach in modelling of slag entrainment, especially at critical

conditions result in dispersed multiphase flow.

## MODEL DESCRIPTION

### Governing equations

From computational point of view, a feasible modelling strategy for interfacial turbulent flows including metal-slag-air flow in the continuous casting mold, must include proper treatment for (i) fluid flow governing equations (i.e. Navier-Stokes equations), (ii) capturing the interface between phases (i.e. VOF method (Hirt and Nichols, 1981) in the present study) and (iii) turbulence modelling. Therefore, the conservation equations governing the fully resolved motion of an unsteady, incompressible, immiscible, multiphase flow with single-fluid formulation are the continuity and Navier-Stokes equations together with the transport equation of volume of fluid as follows:

$$\frac{\partial \rho}{\partial t} + \nabla \cdot (\rho \mathbf{U}) = 0 \quad (1)$$

$$\frac{\partial (\rho \mathbf{U})}{\partial t} + \nabla \cdot (\rho \mathbf{U} \otimes \mathbf{U}) = -\nabla p + \nabla \cdot (2\mu \mathbf{D}) + \rho \mathbf{g} + \mathbf{S}_\sigma \quad (2)$$

$$\frac{\partial \alpha}{\partial t} + \nabla \cdot (\alpha \mathbf{U}) = 0 \quad (3)$$

For incompressible flows where  $\rho = \text{const}$ , the continuity equation reduces to  $\nabla \cdot \mathbf{U} = 0$ .

In this single-fluid formulation,  $\bar{\mathbf{U}}$  is the mixture velocity field shared with all phases.  $p$  is the pressure and  $\mathbf{D}$  is the rate of deformation tensor in the form of  $\mathbf{D} = \frac{1}{2}(\nabla \mathbf{U} + \nabla^T \mathbf{U})$ . The scalar function  $\alpha$  is the volume of fluid field which determines the physical properties of the flow in one-fluid formulation based on properties of each phase, as follows:

$$\rho = \alpha \rho_1 + (1 - \alpha) \rho_2 \quad (4a)$$

$$\mu = \alpha \mu_1 + (1 - \alpha) \mu_2 \quad (4b)$$

$\mathbf{S}_\sigma$  is the surface tension force which is treated by the Continuous Surface Force (CSF) method (Brackbill *et al.*, 1992). This method considers surface tension effects as a volumetric source term in the momentum equation acting only on the interfacial areas. Following the CSF method, the interface normal vector  $\hat{\mathbf{n}}$  and interface curvature  $\kappa$  (i.e. the first and second derivatives of the phase indicator function) are of significant importance in the determination of the surface tension force.

The most common method in estimation of the curvature and normal vector for each computational cell is based on interface orientation approach by Youngs (1982). In this approach a basic definition of interface normal vector is applied based on the gradient of VOF function, then the unit interface normal, and its curvature are determined as

$$\hat{\mathbf{n}} = \frac{\nabla \alpha}{|\nabla \alpha|} \quad (5)$$

$$\kappa = -\nabla \cdot \hat{\mathbf{n}} = -\nabla \cdot \left( \frac{\nabla \alpha}{|\nabla \alpha|} \right) \quad (6)$$

Finally, the surface tension force can be computed by the CSF method and reads

$$\mathbf{S}_\sigma = \sigma \kappa \hat{\mathbf{n}} \delta_s \quad (7)$$

where  $\sigma$  is the surface tension coefficient and  $\delta_s$  is the Dirac delta function that equals unity at the interface and zero elsewhere. The numerical procedure to solve this system of equations for two phases is implemented in the open source CFD framework of OpenFOAM (Greenshields, 2015) within the solver called *interFoam*. As an extension to this solver, for the multiphase flows with more than two different phases, the solver *multiphaseInterFoam* is adopted. The main difference between these two solvers is the way for computation of the curvature. *multiphaseInterFoam* uses a pair-averaged gradient of the volume fraction (Vakhrushev *et al.*, 2014) for computing the unit interface normal in equation (5). Thus  $\hat{\mathbf{n}}$  is reformulated for interface between each pair of phases and reads

$$\hat{\mathbf{n}}_{ij} = \frac{\alpha_j \nabla \alpha_i - \alpha_i \nabla \alpha_j}{|\alpha_j \nabla \alpha_i - \alpha_i \nabla \alpha_j|} \quad (8)$$

where  $\alpha_i$  and  $\alpha_j$  are the volume fractions of each pair of phases ( $i, j$ ). This solver is utilized in the present study to capture the interface between molten metal, slag and air. It should be noted that the equations (4a) and (4b) are also including the third phase properties to be consistent with the mixture assumption.

### Large eddy simulation

Large eddy simulation (LES) is typically considered as an intermediate approach for modelling turbulent flows. The principal idea behind LES is to reduce the computational efforts by spatial filtering the small-scale motions (i.e. by a low-pass filter operation) and only resolve the largest ones. By applying a spatial filter operator  $\mathcal{G}$  to a flow quantity  $\phi(\mathbf{x}, t)$ , the filtered quantity reads:

$$\bar{\phi}(\mathbf{x}, t) = \mathcal{G} * \phi(\mathbf{x}, t) = \int_D \mathcal{G}(\mathbf{x} - \mathbf{x}') \phi(\mathbf{x}', t) d\mathbf{x}' \quad (9)$$

where  $(\cdot)$  indicates the spatial filtering.

Introducing the filter operation into equations (1) to (3) and assuming that the filter commutes with both the time and spatial derivatives, the filtered governing equations can be derived as follows:

$$\nabla \cdot \bar{\mathbf{U}} = 0 \quad (10a)$$

$$\begin{aligned} \frac{\partial(\bar{\rho}\bar{\mathbf{U}})}{\partial t} + \nabla \cdot (\bar{\rho}\bar{\mathbf{U}} \otimes \bar{\mathbf{U}}) = & -\nabla \bar{p} + \nabla \cdot (2\bar{\mu}\bar{\mathbf{D}}) + \rho\bar{\mathbf{g}} + \sigma\bar{\kappa}\nabla\bar{\alpha} \\ & + \nabla \cdot (\tau_{\mu D} - \tau_{uu}) + \tau_\sigma - \tau_{tt} \end{aligned} \quad (10b)$$

$$\frac{\partial\bar{\alpha}}{\partial t} + \nabla \cdot (\bar{\alpha}\bar{\mathbf{U}}) = \nabla \cdot \tau_{\alpha u} \quad (10c)$$

This operation results in appearance of different sub-grid scale (SGS) terms in the equations.

$$\tau_{uu} = \overline{\rho\mathbf{U} \otimes \mathbf{U}} - \bar{\rho}\bar{\mathbf{U}} \otimes \bar{\mathbf{U}} \quad (11a)$$

$$\tau_{\mu D} = \overline{\mu(\nabla\mathbf{U} + \nabla^T\mathbf{U})} - \bar{\mu}(\nabla\bar{\mathbf{U}} + \nabla^T\bar{\mathbf{U}}) \quad (11b)$$

$$\tau_{tt} = \frac{\partial(\bar{\rho}\bar{\mathbf{U}})}{\partial t} - \frac{\partial(\bar{\rho}\bar{\mathbf{U}})}{\partial t} \quad (11c)$$

$$\tau_\sigma = \overline{\sigma\kappa\nabla\alpha} - \sigma\bar{\kappa}\nabla\bar{\alpha} \quad (11d)$$

$$\tau_{\alpha u} = \overline{\alpha\bar{\mathbf{U}}} - \bar{\alpha}\bar{\mathbf{U}} \quad (11e)$$

The sub-grid scale of convective, viscous and unsteady terms in equations (11a) to (11c) are present in classical single phase LES while the sub-grid surface tension effects as well as the sub-grid of interfacial transport in equations (11d) and (11e) appear specifically in two-phase flows.

It is reported by several DNS studies that in most of single phase turbulent flows, the contribution of the sub-grid scale convective term to the turbulent kinetic energy budget is predominant (Labourasse *et al.*, 2007). This provides the basis for the closure of the single phase LES formulation by the eddy-viscosity approach (Versteeg and Malalasekera, 2006). Nevertheless, in the context of turbulent interfacial flows, the contribution of sub-grid scale surface tension and volume of fluid transport is not negligible specially at small-scale interfacial topological changes. But due to the lack of general model for those sub-grid terms, only the sub-grid convective term is accounted for in the present study. Therefore, the anisotropic part of the sub-grid stress tensor is modelled by eddy-viscosity approximation as follows:

$$\tau_{uu} - \frac{1}{3} \text{Tr}(\tau_{uu})\mathbf{I} = -2\mu_t \bar{\mathbf{D}} \quad (12)$$

In this formulation, the turbulent eddy-viscosity reads

$$\mu_t = (C_s \Delta)^2 |\bar{\mathbf{D}}| \quad (13)$$

where  $C_s$  is the model constant and  $\Delta$  is the grid size. As the turbulence modelling is a generic feature of most of the OpenFOAM solvers, the classical Smagorinsky model (Smagorinsky, 1963) is chosen in *multiphaseInterFoam* to close the system of equations.

### EXPERIMENTS

To provide experimental data for comparison with our CFD model we built up a simplified mold flow experiment in the lab as shown in Figure 2. It represents a 1/3 model of a continuous casting mold. As a replacement for steel and slag we use water and colored paraffinum oil. In order to investigate the interaction of the jet with the water-oil interface for various inlet angles ( $\Theta$ ), we use a central symmetry plane with an adjustable inlet nozzle instead of a SEN. This gives more flexibility and allows to check worst case scenarios with strong interaction of the jet with the liquid-liquid interface for positive inlet angles. The water circuit is driven by an impeller pump and all shown results were obtained at a flow rate of 0.26 l/s. To avoid upstream disturbances in the mold flow caused by the water outlet, the main basin is decoupled from the outlet area by a porous plate. The dimensions of the experiment are shown in Table 1. The physical properties of water and paraffinum oil are found in Table 2. Data is recorded with an ordinary video camera to get a qualitative impression of the jet-interface interaction and slag entrainment as well as 2D particle image velocimetry (PIV). In the latter case the center plane of the basin is illuminated with

**Table 1: Dimensions of the lab experiment.**

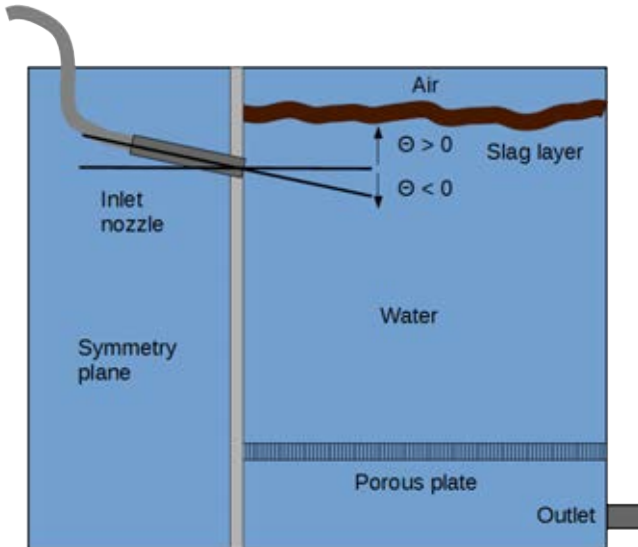
Dimensions	250 x 400 x 75 mm
Diameter of inlet nozzle	19 mm
Water level above inlet	8 cm
Thickness of oil layer	1.5 cm

**Table 2: Physical properties of water and paraffinum oil at 20°C.**

Water (w)			Paraffinum Liquidum (o)		
$\mu$	1	mPa · s	$\mu$	189	mPa · s
$\rho$	1000	kg/m <sup>3</sup>	$\rho$	863.3	kg/m <sup>3</sup>
$\sigma$	0.07275	N/m	$\sigma$	0.026	N/m

a Nd:YAG laser and plastic powder is used as tracer particles for PIV processing. A total number of 1000 double frames is recorded for each case to provide sufficient data for averaging the flow fields.

For comparison of CFD results with experimental data both data sources are interpolated to a common equidistant grid using MATLAB.


**Figure 2: The sketch of lab experiment.**

## RESULTS AND DISCUSSION

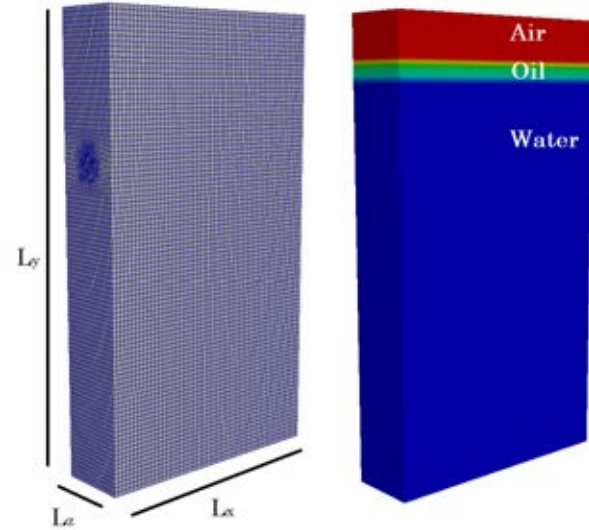
### Simulation setup

In order to perform numerical simulation, a three-dimensional geometry ( $L_x = 250$  mm,  $L_y = 400$  mm and  $L_z = 70$  mm) with a circular inlet was created as the computational domain. Then structured computational grid networks were generated with the lowest grid spacing of 1.5 mm as shown in Figure 3. The initial value of volume fraction for each phase is adjusted similar to the experimental case.

Pressure outlet and wall boundary conditions were imposed on the surrounding boundaries of computational domain. Since generating inflow boundary conditions for LES is not a straightforward task, a turbulent velocity boundary condition was used at the inlet to initiate the injection with a randomly-perturbed velocity profile with the intensity of 0.1. The PIMPLE algorithm is adopted for pressure-velocity coupling and pressure correction. The VOF transport equation is solved by a specific algorithm in OpenFOAM called MULES solver (Multidimensional Universal Limiter with Explicit Solution).

This method guarantees the robustness of the VOF method when using an artificial compression term to improve the interface resolution (Greenshields, 2015). The simulation time steps are determined based on CFL criterion to keep the maximum Courant number about 0.6.

All the fluid properties in the simulation were taken similar to the experiments. The interfacial tension between water and oil is  $\sigma_{w/o} = 0.048$  N/m. The air properties were used at standard room temperature  $\rho_a = 1.2$  kg/m<sup>3</sup> and  $\mu_a = 0.017$  mPa·s.


**Figure 3: The sketch of computational domain.**

### Global flow characteristics

Numerical simulations were performed for two cases at different inlet angles of  $\Theta = -10$  and 0 degree. In order to validate the CFD results with PIV measurements, the first quantity to look at is the average velocity field in the mold. For this purpose the simulations were run long enough to obtain sufficient instantaneous velocity fields at every 5 ms at the mid-plane in z-direction. The average velocity magnitude from the CFD results for  $\Theta = -10$  and 0 degree are shown in Figures 4 and 5, respectively. To reveal a comparison with the PIV results, the average velocity profiles from CFD and experiments are plotted along with the constant horizontal and vertical distances of  $x = 200$  mm and  $y = 70$  mm as shown in Figures 6 to 9. The overall comparison demonstrates fairly good agreement between the simulation and experiments.

Furthermore, the velocity fields obtained from the CFD simulation are used to compute the energy spectra. Therefore, a fast Fourier transform was carried out and the energy spectrum reveals that the present LES model yields good agreement with the Kolmogorov spectrum (Pope, 2000). However, for validating the dynamic behavior of the CFD simulation we need time-resolved experimental data, which we will obtain by high-speed PIV in the near future.

### Slag entrainment depth

To investigate the interaction of the mold flow with the slag layer we extracted the point of maximum slag entrainment depth. Figure 10 shows an example of the shadowgraphy experiments where the colored layer of oil can be clearly distinguished from the water phase. The position of the deepest oil entrainment can simply be extracted via digital image processing. The same procedure was applied to CFD data

by using the volume of fluid field of oil at iso-surfaces of  $\alpha_o = 0.5$ . The CFD and experimental results are compared in Figures 11 and 12 for the cases with  $\Theta = -10$  and 0 degree inclination, respectively. One can see that the positions of maximum slag entrainment correspond quite well between CFD and experimental results. Nevertheless the spreading of data in the experiment is larger which can also be noticed as

a higher dynamics of the interface movement in the recorded videos.

### CONCLUSION AND OUTLOOK

In this paper, the turbulent interfacial flow in the continuous casting mold was numerically and experimentally studied. An LES-VOF approach is applied to investigate the unsteady flow interaction with the metal-slag-air interface. A water-oil benchmark experiment was designed for validation purposes. While the entrainment of slag into the mold was

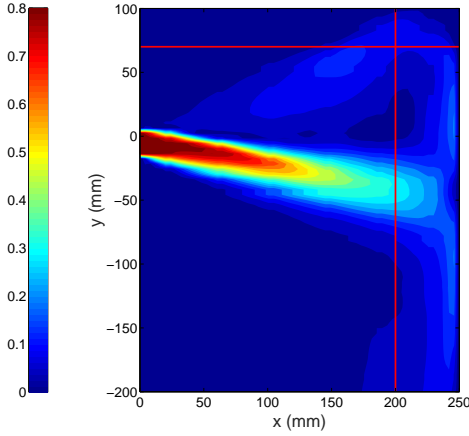


Figure 4: The average velocity magnitude at mid-plane for  $\Theta = -10$  deg. The contour is plotted in SI unit.

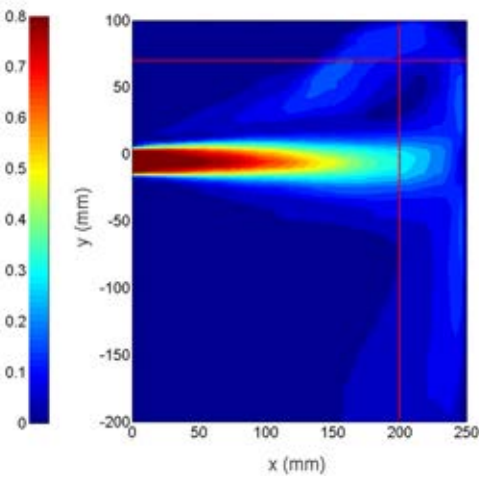


Figure 5: The average velocity magnitude at mid-plane for  $\Theta = 0$  deg. The contour is plotted in SI unit.

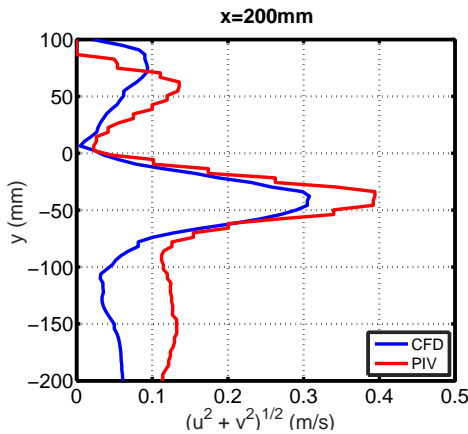


Figure 6: CFD-PIV comparison of the average velocity profile at  $x = 200$  mm for  $\Theta = -10$  deg.

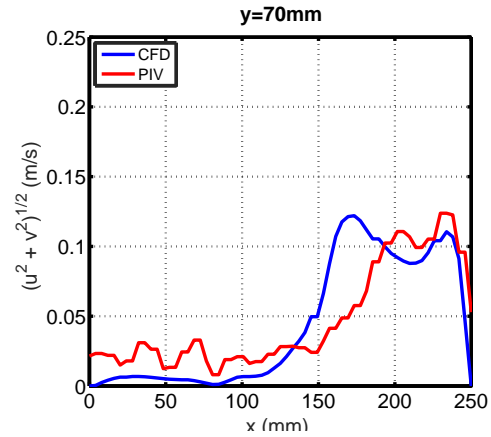


Figure 7: CFD-PIV comparison of the average velocity profile at  $y = 70$  mm for  $\Theta = -10$  deg.

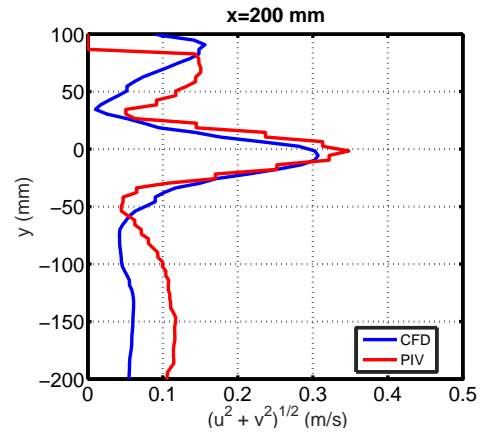


Figure 8: CFD-PIV comparison of the average velocity profile at  $x = 200$  mm for  $\Theta = 0$  deg.

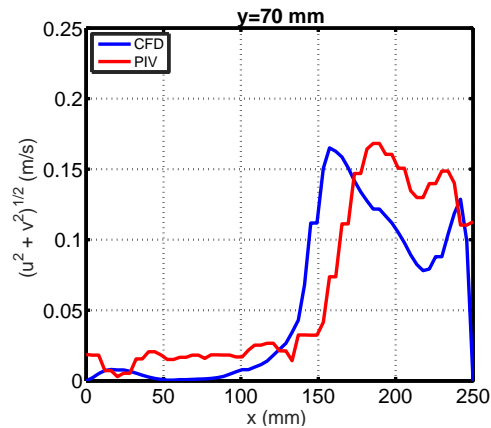
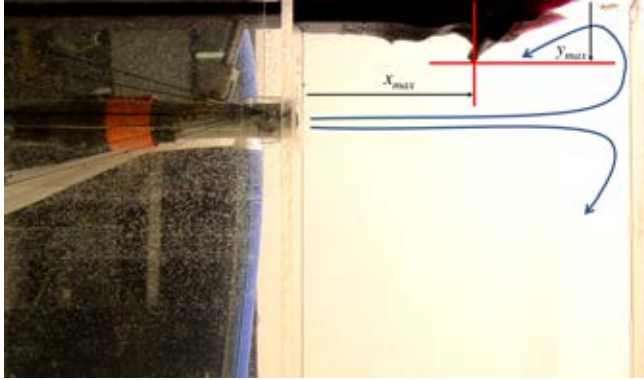


Figure 9: CFD-PIV comparison of the average velocity profile at  $y = 70$  mm for  $\Theta = 0$  deg.



visualized via shadowgraphy, the flow field was measured via particle image velocimetry. In combination these two methods allow a qualitative and quantitative comparison of the unsteady flow characteristics with the CFD results. First, we compared the global flow behavior for different inflow conditions by using the average velocity fields obtained from the CFD and PIV. The general agreement of CFD results and experimental data is very promising. Then, we investigated the



**Figure 10:** Example image from the mold flow experiment showing the position of maximum slag layer entrainment.

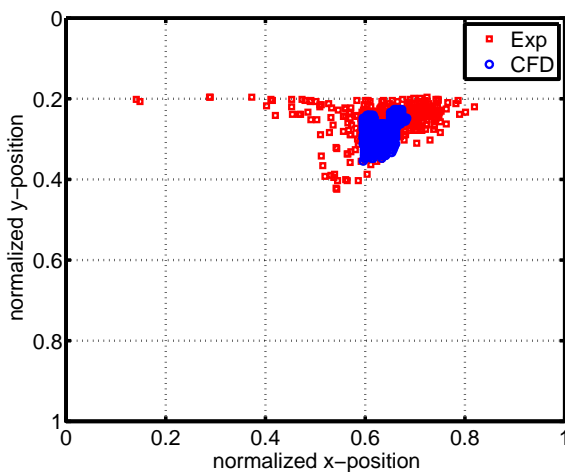


**Figure 11:** The positions of maximum slag entrainment for  $\Theta = -10$  degree from simulation and experiment.

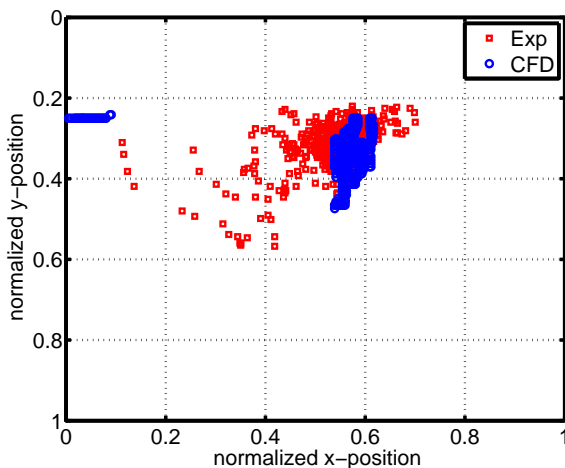


**Figure 12:** The positions of maximum slag entrainment for  $\Theta = 0$  degree from simulation and experiment.

interaction of the unsteady flow field with the liquid-liquid interface. The entrainment depth from the simulation match the experimental visualization quite well while the dynamics of the interface motion is much lower in the CFD simulation than in the experiments.

However, there are some shortcomings to be considered for future improvements of the model such as employing a more accurate inflow boundary condition for LES simulation. Although the entrainment of small-scale oil droplets cannot be captured with the current level of modelling, it can be deduced that LES-VOF approach is a feasible way to model the slag entrainment at critical conditions where the droplet-like slag structures become dispersed in the mold. To this end, improvement of the current LES-VOF by sub-grid modification seems inevitable. Future studies will also focus on numerical modelling and experimental investigation of other mechanisms for slag entrainment including the Karman vortex formation.

## ACKNOWLEDGMENTS

The authors gratefully acknowledge the funding support of K1-MET GmbH, metallurgical competence center. The research program of the competence center K1-MET is supported by COMET (Competence Center for Excellent Technologies), the Austrian program for competence centers. COMET is funded by the Federal Ministry for Transport, Innovation and Technology, the Federal Ministry for Science, Research and Economy, the province of Upper Austria, Tyrol, and Styria and the Styrian Business Promotion Agency.

## REFERENCES

- ASAD, A., KRATZSCH, C. and SCHWARZE, R. (2015). "Numerical Investigation of the Free Surface in a Model Mold". *Steel Research International*, **86**, 1–10.
- BRACKBILL, J., KOTHE, D. and ZEMACH, C. (1992). "A continuum method for modeling surface tension". *Journal of Computational Physics*, **100**, 335–354.
- GREENSHIELDS, C.J. (2015). "OpenFOAM The Open Source CFD Toolbox". Tech. rep. URL <http://www.openfoam.com>.
- HIBBELER, L.C. and THOMAS, B.G. (2013). "Mold slag entrainment mechanisms in continuous casting molds". *Iron and Steel Technology*, **10(10)**, 121–136.
- HIRT, C. and NICHOLS, B. (1981). "Volume of fluid (VOF) method for the dynamics of free boundaries". *Journal of Computational Physics*, **39**, 201–225.
- IGUCHI, M., YOSHIDA, J., SHIMIZU, T. and MIZUNO, Y. (2000). "Model Study on the Entrapment of Mold Powder into Molten Steel." *ISIJ International*, **40(7)**, 685–691.
- LABOURASSE, E., LACANETTE, D., TOUTANT, A., LUBIN, P., VINCENT, S., LEBAGUE, O., CALTAGIRONE, J.P. and SAGAUT, P. (2007). "Towards large eddy simulation of isothermal two-phase flows: Governing equations and a priori tests". *International Journal of Multiphase Flow*, **33(1)**, 1–39.
- LIU, Z.Q., LI, B.K., JIANG, M.F. and TSUKIHASHI, F. (2013). "Modeling of Transient Two-Phase Flow in a Continuous Casting Mold Using Euler-Euler Large Eddy Simulation Scheme". *ISIJ International*, **53(3)**, 484–492.
- LIU, Z.Q., LI, B.K., JIANG, M.F. and TSUKIHASHI, F. (2014). "Euler-Euler-Lagrangian Modeling for Two-Phase Flow and Particle Transport in Continuous Casting Mold". *ISIJ International*, **54(6)**, 1314–1323.
- POPE, S. (2000). *Turbulent Flows*. Cambridge University Press.

SMAGORINSKY, J. (1963). “General circulation experiments with the primitive equations, I. the basic experiment”. *Monthly Weather Review*, **91**, 99–164.

VAKHRUSHEV, A., WU, M., LUDWIG, A., NITZL, G., TANG, Y. and HACKL, G. (2014). “Experimental verification of a 3-phase Continuous casting simulation using a water model”. *8th European Continuous Casting Conference*. Graz, Austria.

VERSTEEG, H.K. and MALALASEKERA, W. (2006). *An Introduction to Computational Fluid Dynamics Second Edition*. Pearson Education Limited.

YOUNGS, D. (1982). “Time-Dependent Multi- material Flow with Large Fluid Distortion”. *Numerical methods for fluid dynamics*, 273–285. Academic Press, New York.



# CFD-DEM MODELLING OF BLAST FURNACE TAPPING

Mathias VÅNGÖ<sup>1\*</sup>, Stefan PIRKER<sup>1</sup>, Thomas LICHTENEGGER<sup>1,2</sup>

<sup>1</sup>Department of Particulate Flow Modelling, Johannes Kepler University, 4040 Linz, AUSTRIA

<sup>2</sup>Linz Institute of Technology (LIT), Johannes Kepler University, 4040 Linz, AUSTRIA

\* E-mail: mathias.vangoe@jku.at

## ABSTRACT

The campaign length of a blast furnace is limited by the hearth inner lining lifetime. In order to maximize the campaign length and ensure a good draining of hot metal and slag, a good understanding of the flow in the hearth is essential. Challenges in modelling the flow involve several continuous phases (hot metal, slag and hot blast) as well as the presence of the deadman, a dense bed of coke particles. The shape and position of the deadman depend on the weight of the burden column above and the buoyancy forces from the liquids in the hearth.

A numerical coupled CFD (Computational Fluid Dynamics) – DEM (Discrete Element Method) model was developed and implemented in *CFDEMcoupling* (Goniva *et al.*, 2012), intended for future flow pattern investigation of the hearth during tapping. A VOF (Volume of Fluid) method is used to model the multiple continuous phases and DEM to model the discrete particles. The VOF and DEM models are coupled together in a 2-way manner, resulting in a complete 4-way coupled CFD-DEM model. We report the experimental validation of the model, performed on a small-scale particle filled tank. The tank was drained of water through the dense particle bed and the mass flow rate was measured.

Difficulties in choosing a fine enough mesh for the VOF method to correctly resolve the interface and simultaneously ensure a stable and accurate void fraction calculation arose. Different methods was proposed to enable particle sizes in the same range of the CFD cells, involving alternative methods for mapping the void fraction field onto the CFD mesh, as well as smoothing of the void fraction. With the smoothing model of Radl *et al.* (2014), the simulation was stable and very good agreements were found with the experimental measurements.

**Keywords:** VOF-method, DEM, multiphase flow, particle bed, blast furnace hearth .

## NOMENCLATURE

### Greek Symbols

$\alpha$	volume fraction, [–]
$\varepsilon$	void fraction, [–]
$\rho$	density, [ $kg/m^3$ ]
$\mu$	dynamic viscosity / friction coefficient, [ $kg/ms/–$ ]
$\nu$	kinematic viscosity / Poisson’s ratio, [ $m^2/s/–$ ]
$\tau$	viscous stress tensor, [ $N/m^2$ ]
$\sigma$	surface tension, [ $N/m$ ]
$\kappa$	interface curvature, [ $1/m$ ]
$\omega$	angular velocity, [ $rad/s$ ]

$\Delta t$  time step, [ $s$ ]

### Latin Symbols

$\mathbf{u}$	velocity, [ $m/s$ ].
$p$	pressure, [ $Pa$ ].
$p^*$	non-hydrostatic pressure, [ $Pa$ ].
$\mathbf{g}$	gravity, [ $m/s^2$ ].
$\mathbf{x}$	coordinate, [ $m$ ].
$\mathbf{F}$	force, [ $N$ ].
$m$	mass, [ $kg$ ].
$I$	moment of inertia, [ $kg\ m^2$ ].
$M$	torque, [ $Nm$ ].
$d$	diameter, [ $m$ ].
$V$	volume, [ $m^3$ ].
$COR$	coefficient of restitution, [–].
$N$	number of particles, [–].

### Sub/superscripts

$f$	fluid.
$p$	particle.
$i$	phase $i$ / particle $i$ .
$c$	compression.
$\sigma$	surface tension.
$pf$	particle–fluid interaction.
$pp$	particle–particle interaction.
$T$	turbulent.
$a.m$	added mass.
$semi – sat.$	semi-saturated.

## INTRODUCTION

The blast furnace hearth condition has been proven to be critical to the campaign length as well as ensuring a stable operation. Increasing the blast furnace campaign length is of great importance because the re-lining is an expensive operation and causes a significant downtime in production (Shao, 2013; Zhang *et al.*, 2008). The hearth is an extremely harsh environment, temperatures exceeding 2000°C and high fluid velocities close to the tap holes cause great wear on the lining. Thus understanding the fluid flow pattern in the hearth is essential in order to optimize the campaign length (Ariyama *et al.*, 2014; Guo *et al.*, 2008).

The hearth is filled with liquid iron and slag, which settles in immiscible layers due to their different densities. Additionally, dense packed coke particles form a permeable structure often referred to as the deadman (Nnanna *et al.*, 2004; Tanzil *et al.*, 1984). The shape and position of the deadman depend on the operation, it is depending on the weight of the bur-

den column above and the buoyancy forces from the liquid metal and slag in the hearth. Due to the harsh environment, accurate measurements are difficult to perform, hence accurate models are essential in the understanding of the hearth (Huang *et al.*, 2005). In order to accurately model the tapping procedure it is important to consider the dynamics of the deadman.

Therefore, in this work a coupled CFD - DEM model was developed and implemented in the open-source software *CFDEMcoupling*, intended to be used in future work for flow pattern- and deadman dynamics investigation during tapping. In DEM, each individual particle is solved for, giving the model capabilities of accounting for the deadman dynamics at the expense of being extremely computationally demanding. The well known interface tracking method VOF (Hirt and Nichols, 1981; Gueyffier *et al.*, 1999), is used to model the multiple immiscible fluids.

## MODEL DESCRIPTION

The CFD-DEM model is based on the theory for unresolved particle-fluid interaction, in which the flow around each particle is not resolved. Typically the CFD grid cells are larger than the particles and volume-averaged quantities are used on cell-size scale level. Sacrificing the smallest scale phenomena to solve for larger systems.

### CFD governing equations

In order to model the multiple continuous phases, a VOF approach is used to track the interface. It is based on a mixture approach, where an indicator function ranging from 0 to 1 is used to distinguish between the fluids. The evolution of the interface is described by solving the advection equation,

$$\frac{\partial \alpha}{\partial t} + \nabla \cdot (\alpha \mathbf{u}_f) = 0, \quad (1)$$

where  $\alpha$  is the volume fraction and  $\mathbf{u}_f$  the fluid velocity (Hirt and Nichols, 1981; Li *et al.*, 1999). If the particle phase is considered as well as introducing a compression term to sharpen the interface, as done by Rusche (2002), a final set of transport equations for the volume fractions  $\alpha_i$  can be written as,

$$\frac{\partial \varepsilon \alpha_i}{\partial t} + \nabla \cdot (\varepsilon \alpha_i \mathbf{u}_f) - \nabla \cdot (\mathbf{u}_c \alpha_i (1 - \alpha_i)) = 0, \quad (2)$$

where  $\varepsilon$  is the local void fraction and  $\mathbf{u}_c$  is the artificial compression velocity. The local fluid properties are determined by taking the volume weighted average of all the phases physical values as shown in Equation (3) and (4) for  $k$  continuous phases.

$$\rho_f = \sum_{i=1}^k \alpha_i \rho_i \quad (3)$$

$$\mu_f = \sum_{i=1}^k \alpha_i \mu_i \quad (4)$$

The flow is described by the Navier-Stokes (NS) equations in the form from Anderson and Jackson (1967). In VOF methodology only one momentum equation is solved, using the mixture fluid properties. Due to the presence of discrete particles, the void fraction term has been incorporated into the governing equations. The continuity equation is given by Equation (5) and the momentum equation by Equation (6).

$$\frac{\partial \varepsilon}{\partial t} + \nabla \cdot (\varepsilon \mathbf{u}_f) = 0 \quad (5)$$

$$\frac{\partial \varepsilon \rho_f \mathbf{u}_f}{\partial t} + \nabla \cdot (\varepsilon \rho_f \mathbf{u}_f \mathbf{u}_f) = -\varepsilon \nabla p^* + \varepsilon \nabla \cdot \boldsymbol{\tau} - \varepsilon (\mathbf{g} \cdot \mathbf{x}) \nabla \rho_f + \mathbf{F}^\sigma + \mathbf{F}^{pf} \quad (6)$$

The formulation of pressure in Equation (6) is different from e.g. Anderson and Jackson (1967) and Sun and Sakai (2015). According to Rusche (2002), solving for a modified pressure  $p^*$ , defined as  $p^* = p - (\mathbf{g} \cdot \mathbf{x}) \rho_f$ , where  $\mathbf{g}$  is the gravity vector and  $\mathbf{x}$  the coordinate vector, simplifies the assignment of pressure boundary conditions as well as it offers a numerically better way of handling the strong density gradient at the interface. Physically,  $p^*$  can be interpreted as the pressure without the hydrostatic contribution. Furthermore,  $\boldsymbol{\tau}$  denotes the viscous stress tensor, which is usually written as  $\boldsymbol{\tau} = \mu_f (\nabla \mathbf{u}_f + \nabla \mathbf{u}_f^T)$ .  $F^\sigma$  is the surface tension force, defined as  $F^\sigma = \sigma \kappa \nabla \alpha$ , where  $\sigma$  denotes the surface tension and  $\kappa$  is the interface curvature.  $F^{pf}$  is a source term arising from the momentum exchange between the fluids and particles, which is further described in the following section.

### DEM governing equations

The discrete particles are described with DEM. It is a well known numerical method for solving granular flows and it is based on the theory of Cundall and Strack (1979). Each particle is solved individually by determining its trajectory with Newton's laws of motion as,

$$m_i \frac{d\mathbf{u}_{p,i}}{dt} = \mathbf{F}_i^{pp} + \mathbf{F}_i^{pf} + m_i \mathbf{g}, \quad (7)$$

$$I_i \frac{d\boldsymbol{\omega}_{p,i}}{dt} = \mathbf{M}_i^{pp} + \mathbf{M}_i^{pf}, \quad (8)$$

where  $\mathbf{u}_{p,i}$  is the particle velocity and  $\boldsymbol{\omega}_{p,i}$  the angular velocity.  $\mathbf{F}_i^{pp}$  denotes the inter-particle force and  $\mathbf{F}_i^{pf}$  the particle-fluid interaction force. In this work, relatively large particles are used ( $d_p \sim O(10^{-3}m)$ ), thus neglecting any cohesive forces which can be important for e.g. powders. The particle-particle interaction term is then described only by the collision forces.

The particle-fluid interaction term,  $\mathbf{F}_i^{pf}$ , is fully defined as:

$$\mathbf{F}_i^{pf} = \mathbf{F}_{drag,i} + \mathbf{F}_{\nabla p,i} + \mathbf{F}_{\tau,i} + \mathbf{F}_{Basset,i} + \mathbf{F}_{a.m,i} + \mathbf{F}_{Saffman,i} + \mathbf{F}_{Magnus,i}, \quad (9)$$

where the components on the right hand side are respectively the drag force, pressure gradient force, viscous force, Basset force, added-mass force, Saffman- and Magnus-lift force. In this work, the Basset-, added-mass-, Saffman- and Magnus-forces are neglected because it is expected that the drag-, pressure gradient- and viscous-forces are dominant (Zhou *et al.*, 2010). Equation (7) can then be rewritten as,

$$m_i \frac{d\mathbf{u}_{p,i}}{dt} = \sum_{i=1}^n \mathbf{F}_i^{contact} + \mathbf{F}_{drag,i} + \mathbf{F}_{\nabla p,i} + \mathbf{F}_{\tau,i} + m_i \mathbf{g}, \quad (10)$$

where  $\mathbf{F}_{\nabla p,i} = -V_{p,i} \nabla p$  and  $\mathbf{F}_i = V_{p,i} \nabla \cdot \boldsymbol{\tau}$ . In this work the Koch and Hill drag model (Hill *et al.*, 2001; van Buijtenen *et al.*, 2011) was used.

## Smoothing

One contradiction arises due to the nature of the model. In VOF methodology, a fine mesh is desired to resolve the interface, where as for unresolved CFD-DEM, the cell size should be larger than the particles in order to accurately map the void fraction field onto the mesh. A few alternative methods for calculating the void fraction have been suggested to enable for particle sizes in the range of the cell sizes. For example, Jing (2016) used an approach where the particles are artificially enlarged to influence more surrounding cells, while keeping the volume constant.

Additionally, Peng *et al.* (2014) reported that, small inaccuracies in mapping the void fraction onto the mesh eventually causes local pressure fluctuations due to the formulation of the governing equations. Reducing these fluctuations is of great importance in order to ensure stable simulations. Additional treatment of the exchange fields can be performed to improve stability, as done by e.g. Pirker *et al.* (2011), Radl *et al.* (2014) and Capecelatro and Desjardins (2013), where a diffusion equation,

$$\frac{\partial \phi}{\partial t} = D \nabla^2 \phi, \quad (11)$$

for the quantity in question  $\phi$  is solved.  $D$  is the diffusion coefficient, which can be defined as  $D = l^2 / \Delta t$ , where  $l$  is interpreted as the smoothing length. By performing this operation, the exchange fields are "smeared" over nearby cells.

## EXPERIMENTAL SETUP

The tank was a transparent box with the dimensions 330x150x400 mm. A cylindrical tap hole with the diameter  $d_{outlet} = 27.5$  mm was located at the bottom of the side. A schematical view of the setup is shown in Figure 1. A valve was used to control the tapping and the total bulk mass tapped was measured with a load cell. Because coke particles are buoyant in the blast furnace hearth, wood particles were chosen in order to be buoyant in water. The measured particle properties are listed in Table 1. As a result of choosing wooden particles, the particle properties varied between wet or dry because the wood soaked water. The particles were measured and weighed in between ten experimental runs. A semi-saturated state of the particles was reached after five instances where-after for the following five runs, the particle-diameter and density were determined to  $d_p = 6.5$  mm and  $\rho_p = 850$  kg/m<sup>3</sup> respectively.

**Table 1:** Particle properties

$N_p$	40000
$\rho_{p,dry}$	600 kg/m <sup>3</sup>
$\rho_{p,semi-sat.}$	850 kg/m <sup>3</sup>
$d_{p,dry}$	6.0 mm
$d_{p,semi-sat.}$	6.5 mm

For a first test run, a sitting particle bed was considered. The initial water level was set to 300 mm and the buoyant particles were held down by a grid as shown in Figure 1. Another grid was placed at the outlet to hinder the particles from leaving the tank.

## SIMULATION SETUP

The computational domain is shown in Figure 2. Its outer dimensions are 330x150x350 mm and it is divided in 1920 hexahedral cells, with the smallest cell size,  $\Delta x_{min} = 11$  mm

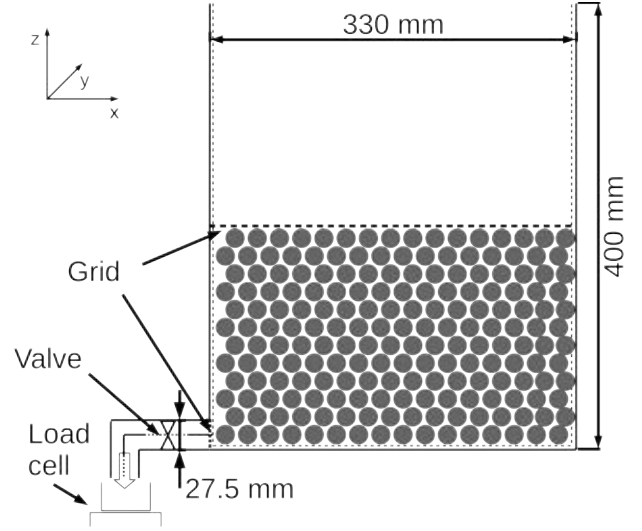


**Figure 1:** Schematic diagram of the experimental setup.

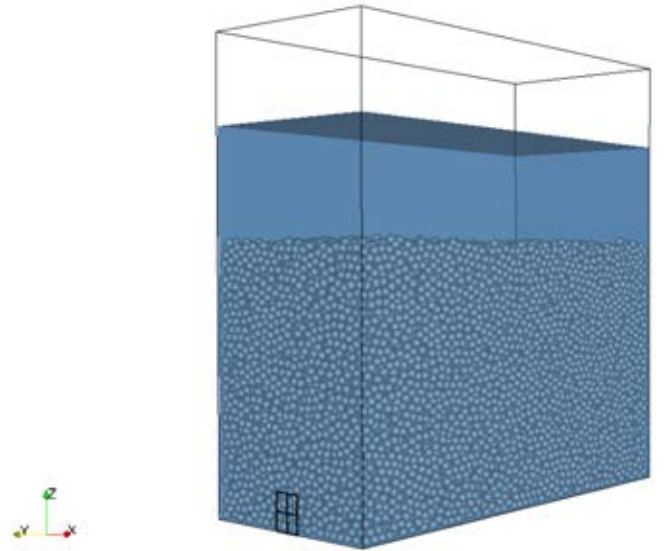


**Figure 2:** Computational domain and the initial state of the particle bed and water level.

and the biggest,  $\Delta x_{max} = 25$  mm. It should be noted that a few assumptions were made to the tap hole. In the simulation, the tap hole was modeled as a square instead of a circle with the side,  $a$ , calculated as:

$$a = \frac{1}{2} \sqrt{\pi d_{outlet}^2}, \quad (12)$$

Additionally, the pipe from the experimental setup was not modeled in the simulation. Thus it was assumed that the pipe pressure drop could be neglected. Figure 2 also shows the initial state the simulation. In order to ensure that the particles remain on the bottom, the particle density is set to 2500 kg/m<sup>3</sup>. The full list of simulation parameters are listed in Table 2 and 3, where  $\nu_p$  denotes the Poisson's ratio, COR the coefficient of restitution and  $\mu_p$  the friction coefficient. It should be noted that the particle time step size was 100 times smaller than the fluid time step, meaning that 100 sub-iterations of DEM calculations were performed for every CFD time step.

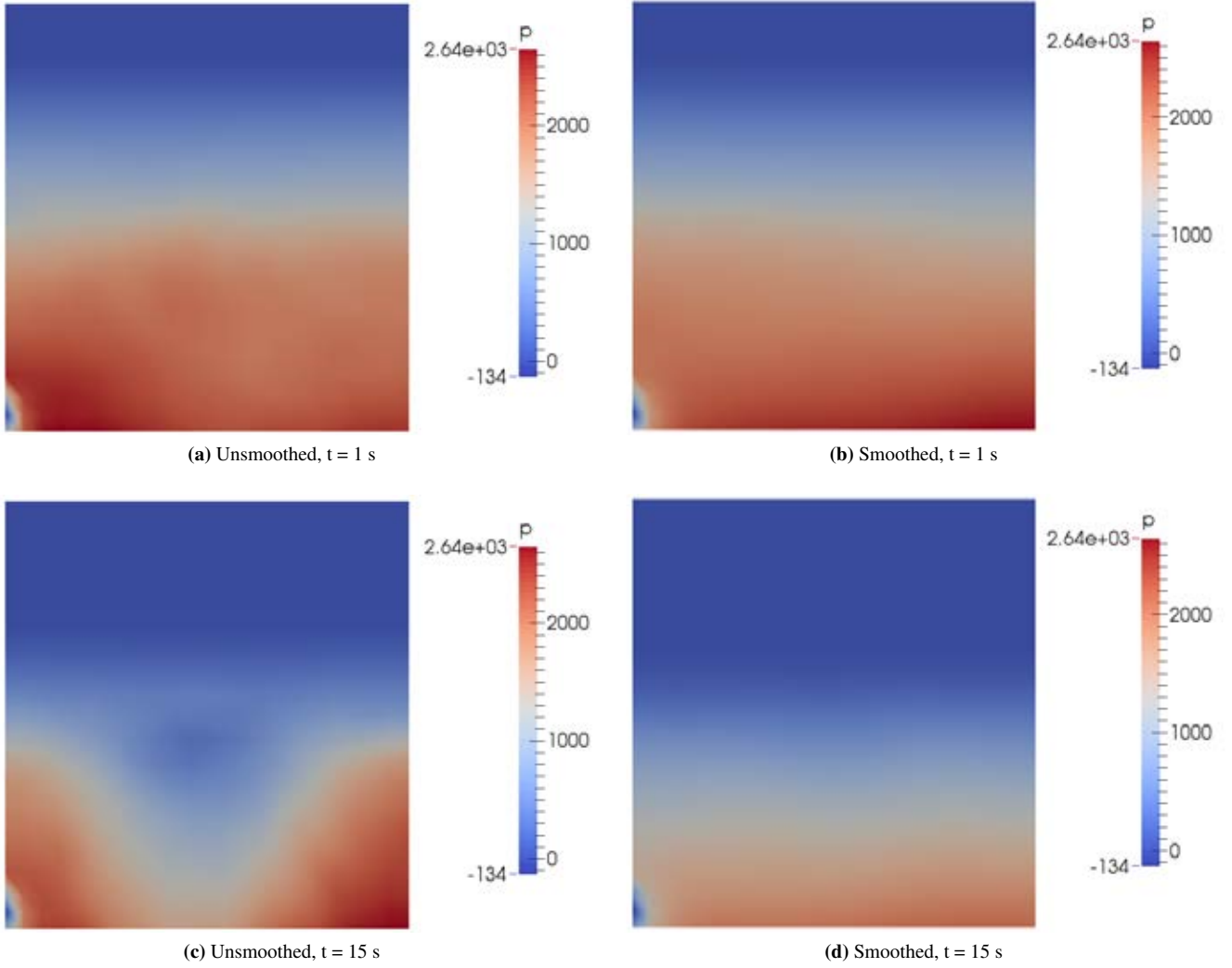


**Figure 3:** Pressure for the unsmoothed- (left) and smoothed (right) simulation at the central plane for various time steps.

**Table 2:** Simulation parameters: fluid

$\Delta t_f$	$5 \cdot 10^{-3}$ s
$\rho_{water}$	1000 kg/m <sup>3</sup>
$\rho_{air}$	1.0 kg/m <sup>3</sup>
$v_{water}$	$1.0 \cdot 10^{-6}$ m <sup>2</sup> /s
$v_{air}$	$1.0 \cdot 10^{-5}$ m <sup>2</sup> /s
$\sigma_{water-air}$	0.07 N/m

**Table 3:** Simulation parameters: particle

$\Delta t_p$	$5 \cdot 10^{-5}$ s
$\rho_p$	<b>2500</b> kg/m <sup>3</sup>
$d_p$	6.5 mm
$N_p$	40000
Young's modulus	$5 \cdot 10^{-6}$ Pa
$v_p$	0.45
COR	0.3
$\mu_p$	0.5

## RESULTS

The effect of smoothing on the pressure is depicted in Figure 3. Two different simulations were carried out, one unsmoothed and one with the smoothing model previously described active with the smoothing length  $l = 3d_p$ . The top row shows the resulting pressure at  $t = 1$  s and the bottom row at  $t = 15$  s. One would expect a linearly increasing pressure towards the bottom due to the hydrostatic pressure. Consequently, the maximum pressure at the bottom would decrease as the water level decreased. The expected behavior can be observed in the smoothed simulation, while the pressure in the unsmoothed shows an odd behavior. Thus, validation was performed with the smoothing model active. Figure 4 illustrates the instantaneous flow field at  $t = 8$  s. Due to atmospheric pressure at the outlet, the fluid is drained and high fluid velocities are observed at the outlet. The monitored mass flow rate is shown in Figure 5. As expected, the mass flow rate was high at the beginning and decreased over time as the water level decreased and the tank was fully drained after approximately 80 s. In order to compare the simulation with the experimental results, the mass flow rate was integrated over time. It is depicted in Figure 6 together with the measurements. The experimental data is presented by error bars, which represents the minimum-, mean- and maximum-value of five experimental runs (as motivated in the previous section). The dotted line represents the initial

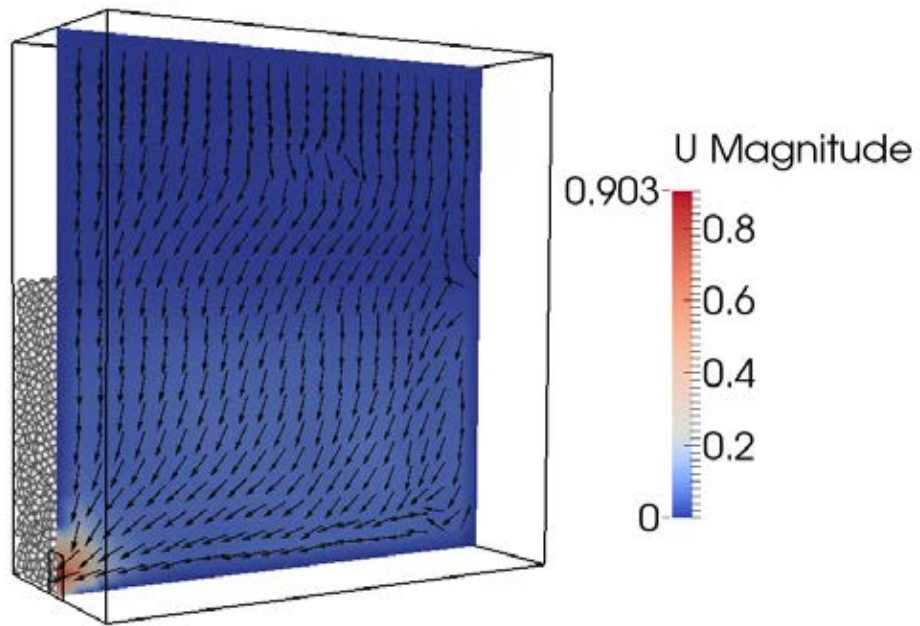


**Figure 4:** Illustration of the flow field at  $t = 8$  s.

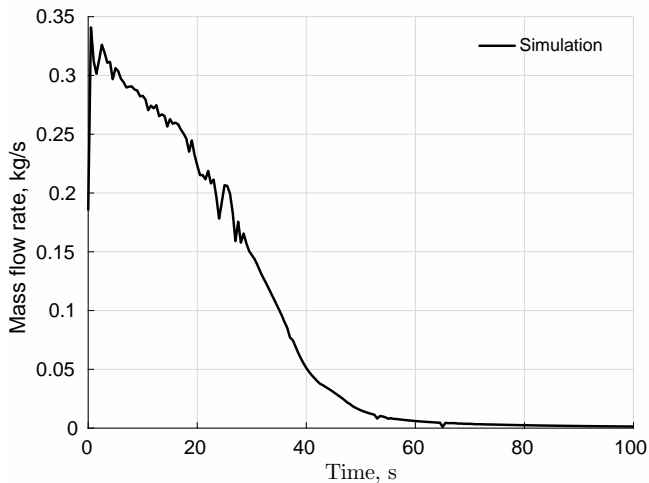


**Figure 5:** Tapping mass flow rate over time for a simulation of the experimental setup.

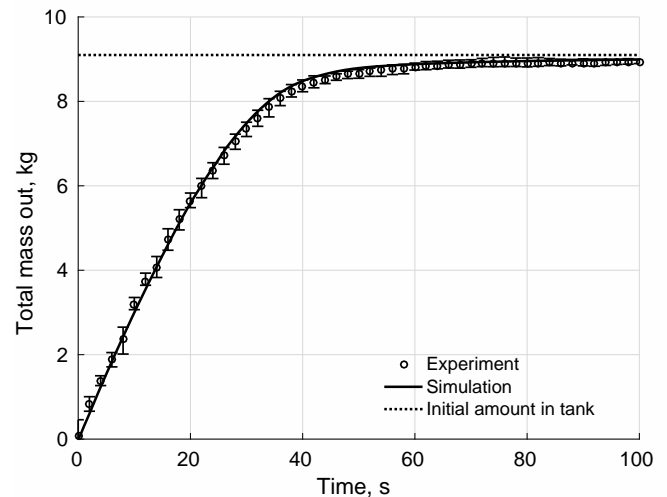


**Figure 6:** Integrated mass flow rate over time, compared with experimental measurements.

amount of water in the tank.

It can be seen that the simulation successfully reproduced the drainage pattern observed in the experiments. Both the simulation result and the measurements converged towards the expected amount drained and a small liquid hold up was noticeable in the experiments as well as in the simulations.

## CONCLUSION

A VOF-DEM coupled solver was successfully implemented in the open-source software *CFDEMcoupling*, with capabilities of handling  $n$  continuous phases in conjunction with discrete particles.

A tank-draining experiment was set up to provide experimental measurements to validate the model. Water was drained through a sitting particle bed, consisting of wooden particles and the flow rate was measured.

Numerical instabilities were encountered due to a relatively fine mesh. Alternative ways of calculating the void fraction, as well as smoothing of the exchange fields were performed with success. With the smoothing model of Radl *et al.*

(2014), very good agreement was found for the mass flow rate compared to the experimental measurements.

## REFERENCES

- ANDERSON, T.B. and JACKSON, R.O.Y. (1967). “A Fluid Mechanical Description of Fluidized Beds”. *Industrial & Engineering Chemistry Fundamentals*, **6(4)**, 527–539.
- ARIYAMA, T., NATSUI, S., KON, T., UEDA, S., KIKUCHI, S. and NOGAMI, H. (2014). “Recent Progress on Advanced Blast Furnace Mathematical Models Based on Discrete Method”. *ISIJ International*, **54(7)**, 1457–1471.
- CAPECELATRO, J. and DESJARDINS, O. (2013). “An Euler-Lagrange strategy for simulating particle-laden flows”. *Journal of Computational Physics*, **238**, 1–31.
- CUNDALL, P.A. and STRACK, O.D.L. (1979). “A discrete numerical model for granular assemblies”. *Géotechnique*, **29(1)**, 47–65.
- GONIVA, C., KLOSS, C., DEEN, N.G., KUIPERS,



- J.A.M. and PIRKER, S. (2012). "Influence of rolling friction on single spout fluidized bed simulation". *Particuology*, **10(5)**, 582–591.
- GUEYFFIER, D., LI, J., NADIM, A., SCARDOVELLI, S. and ZALESKI, S. (1999). "Volume of fluid interface tracking with smoothed surface stress methods for three-dimensional flows". *J. Comput. Phys.*, **152**, 423–456.
- GUO, B.Y., MALDONADO, D., ZULLI, P. and YU, A.B. (2008). "CFD Modelling of Liquid Metal Flow and Heat Transfer in Blast Furnace Hearth". *ISIJ International*, **48(12)**, 1676–1685.
- HILL, R.J., KOCH, D.L. and LADD, A.J.C. (2001). "The first effects of fluid inertia on flows in ordered and random arrays of spheres". *Journal of Fluid Mechanics*, **448(2001)**, 243–278.
- HIRT, C.W. and NICHOLS, B.D. (1981). "Volume of fluid (VOF) method for the dynamics of free boundaries". *Journal of Computational Physics*, **39(1)**, 201–225.
- HUANG, D.F., YAN, F., MILLOVACHI, P., CHAUBAL, P. and ZHOU, C.Q. (2005). "Numerical Investigation of Transient Hot Metal Flows in a Blast Furnace Hearth". *Ais-tech 2005*, **I(1)**, 199–207.
- JING, L. KWOK, C.L.Y.S.Y.D. (2016). "Extended CFD-DEM for free-surface flow with multi-size granules". *International Journal for Numerical and Analytical Methods in Geomechanics*, **40**, 62–79.
- LI, Y., ZHANG, J. and FAN, L.S. (1999). "Numerical simulation of gas–liquid–solid fluidization systems using a combined CFD-VOF-DPM method: bubble wake behavior". *Chemical Engineering Science*, **54(21)**, 5101–5107.
- NNANNA, A.G.A., ULUDOGAN, A., ROLDAN, D. and ZHOU, C.Q. (2004). "Water Model of a Blast Furnace Hearth for Flow Pattern Investigation". *AISTech 2004 Proceedings*, vol. I, 35–46.
- PENG, Z., DOROODCHI, E., LUO, C. and MOGH-TADERI, B. (2014). "Influence of Void Fraction Calculation on Fidelity of CFD-DEM Simulation of Gas-Solid Bubbling Fluidized Beds". *AIChE Journal*, **60(6)**, 2000–2018.
- PIRKER, S., KAHRIMANOVIC, D. and GONIVA, C. (2011). "Improving the applicability of discrete phase simulations by smoothening their exchange fields". *Applied Mathematical Modelling*, **35(5)**, 2479–2488.
- RADL, S., GONZALEZ, B., GONIVA, C. and PIRKER, S. (2014). "State of the Art in Mapping Schemes for Dilute and Dense Euler-Lagrange Simulations". *10th International Conference on CFD in Oil & Gas, Metallurgical and Process Industries*, **(June)**, 1–9.
- RUSCHE, H. (2002). *Computational Fluid Dynamics of Dispersed Two-Phase Flows at High Phase Fractions*. Ph.D. thesis, Imperial College of Science, Technology & Medicine.
- SHAO, L. (2013). *Model-Based Estimation of Liquid Flows in the Blast Furnace Hearth and Taphole*. Ph.D. thesis, Åbo Akademi University.
- SUN, X. and SAKAI, M. (2015). "Three-dimensional simulation of gas–solid–liquid flows using the DEM–VOF method". *Chemical Engineering Science*, **134**, 531–548.
- TANZIL, W., ZULLI, P., BURGESS, J.M. and V., P.W. (1984). "Experimental Model Study of the Physical Mechanisms Governing Blast Furnace Hearth Drainage". *Transactions of the Iron and Steel Institute of Japan*, **24(3)**, 197–205.
- VAN BUIJTENEN, M.S., VAN DIJK, W.J., DEEN, N.G., KUIPERS, J., LEADBEATER, T. and PARKER, D. (2011). "Numerical and experimental study on multiple-spout fluidized beds". *Chemical Engineering Science*, **66(11)**, 2368–2376.
- ZHANG, Y., DESHPANDE, R., HUANG, D.F., CHAUBAL, P. and ZHOU, C.Q. (2008). "Numerical analysis of blast furnace hearth inner profile by using CFD and heat transfer model for different time periods". *International Journal of Heat and Mass Transfer*, **51(1-2)**, 186–197.
- ZHOU, Z.Y., KUANG, S.B., CHU, K.W. and YU, A.B. (2010). "Discrete particle simulation of particle–fluid flow: model formulations and their applicability". *Journal of Fluid Mechanics*, **661**, 482–510.

# MULTIPHASE FLUID FLOW MODELLING OF FURNACE TAPHOLES

Quinn G. REYNOLDS<sup>1\*</sup>, Markus W. ERWEE<sup>1\*\*</sup>

<sup>1</sup> MINTEK Pyrometallurgy Division, Randburg, Johannesburg, 2125, SOUTH AFRICA

\* E-mail: [quinnr@mintek.co.za](mailto:quinnr@mintek.co.za)

\*\* E-mail: [markuse@mintek.co.za](mailto:markuse@mintek.co.za)

## ABSTRACT

Pyrometallurgical furnaces of many varieties make use of tapholes in order to facilitate the removal of molten process material from inside the vessel. Correct understanding and operation of the taphole is essential for optimal performance of such furnaces.

The present work makes use of computational fluid dynamics models generated using the OpenFOAM<sup>®</sup> framework in order to study flow behaviour in the taphole system. Single-phase large-eddy simulation models are used to quantify the discharge rate and laminar-turbulent transitions as a function of parameters such as height of material inside the furnace vessel, taphole geometry, and fluid properties. The results are used to inform boundary conditions in multiphase fluid flow models used for prediction of the qualitative behaviour of the free surface in the launder and tapping ladle for selected cases.

**Keywords:** CFD, Pyrometallurgy, Tapholes, Furnace.

## NOMENCLATURE

### Greek Symbols

$\rho$  Mass density, [kg/m<sup>3</sup>].

$\mu$  Dynamic viscosity, [kg/m.s].

### Latin Symbols

$D$  Diameter of taphole, [m].

$L$  Length of taphole [m].

$P$  Pressure, [Pa].

$\mathbf{u}$  Velocity, [m/s].

### Dimensionless

$N_{Re}$  Reynolds number.

$N_L$  Geometry ratio.

$N_T$   $N_{Eu} \cdot \sqrt{N_{Re}}$ .

$N_{Eu}$  Euler number.

$K_L$  Discharge coefficient.

## INTRODUCTION

Many important commodities such as iron and steel, aluminium, ferro-alloys, and precious metals are produced in part using pyrometallurgical furnaces (Jones et al., 2006). The majority of these units make use of tapholes, specially-designed openings in the furnace wall, in order to remove the molten process products from the furnace (Nelson et al., 2016). Depending on the commodity being produced, the furnace may use a single taphole for all material, or separate tapholes for different phases such as slag and metal. Tapholes are typically located in a taphole assembly, a section of the furnace sidewall designed for this purpose. The taphole assembly may consist of several cylindrical or rectangular inserts made of copper, graphite, or refractory material through which the taphole itself runs, mounted within a steel frame which provides structural support and a contact point for water cooling (McDougall, 2014).



**Figure 1:** Tapping in operation on a DC furnace pilot plant, (l) and (m) slag, (r) metal (images courtesy Mintek)

After the taphole is opened by lancing or drilling, molten material drains out of the vessel due to differences in hydrostatic pressure (see Figure 1). The rate of drainage is primarily determined by a combination of the inlet geometry and the length of the taphole channel, as well as the physical and thermochemical properties of the material passing through the taphole. Characterisation of the flow behaviour inside the taphole channel is challenging due to the wide variation in physical properties of the fluid phases encountered in furnaces; metals and sulphide mattes tend to be high-density and low-viscosity, while oxide slags are the opposite. Transitions between turbulent and laminar flow may occur during a tap or even within the taphole itself, especially for higher-viscosity materials; such transitions affect not only the discharge rate of material through the taphole but also the mechanical forces on the taphole

surfaces which contribute to erosion and wear, and may be exacerbated by gas entrainment during tapping (He et al., 2002).

Upon exiting the taphole, the molten material passes through an open channel (the tapping launder) and into a steel or refractory-lined container vessel (the tapping ladle). The launder and ladle system is a multiphase free surface flow problem, behaviour of the fluid flow is highly dependent on the physical properties of the material being tapped. In practice launders may be angled both vertically and horizontally in order to reach tapping ladles located below, ladles may be positioned incorrectly, and wear on the lining of the launder may change its shape from the original design. As a result, substantial splashing and intermixing of the molten phase with the surrounding air may occur. Although this is undesirable in the case of reduction smelting or high-purity product requirements, the degree of contact between the air and the molten product is generally small and can be further mitigated by careful launder and ladle design and operation (Leong et al., 2006).

To date, much research has been conducted in the field of computational modelling of taphole flow behaviour using advanced modelling techniques (e.g. (Kadkhodabeigi et al., 2011) and (Shao et al., 2013)). However, due to the high resource demands of accurate computational fluid dynamics modelling, there is generally a strong focus on specific design problems or process parameters, using computational fluid dynamics as a post hoc design analysis or failure forensics tool. In the present work, the intention is to use computational modelling as a virtual experimentation platform in order to gain insight into the behaviour of taphole systems at a more generalised and simplified level.

## FLOW THROUGH THE TAPHOLE – THEORY AND DIMENSIONAL CONSIDERATIONS

For the taphole region geometry as described in Figure 2, it is instructive to consider initially a simple theoretical expression for the fluid flow into and through the taphole. Similar work has been performed elsewhere (e.g. (Guthrie, 1992) using the Bernoulli equation to relate the imposed pressure differential across the taphole to the flowrate of material through it. This approach results in:

$$\Delta P = \frac{\rho u^2}{2} + P_P + P_E \quad (1)$$

Where  $\Delta P$  is the pressure difference between the furnace interior and exterior as a result of static head of molten material and any additional forces,  $\rho$  is the fluid density,  $u$  is the bulk average velocity of fluid in the taphole, and  $P_P$  and  $P_E$  are the irreversible pressure losses due to viscous flow inside the taphole channel and friction in the taphole entry geometry respectively. Bulk velocity of the fluid in the furnace interior is assumed to be close to zero.

If fully-developed laminar flow in the taphole channel is assumed, (1) may be written as:

$$\Delta P = \frac{32\mu Lu}{D^2} + (1 + K_L) \frac{\rho u^2}{2} \quad (2)$$

where  $\mu$  is the fluid viscosity,  $L$  and  $D$  are the taphole length and diameter respectively, and  $K_L$  is the discharge coefficient for a given entry geometry (0.5 for sharp-edged pipe entries, reducing to negligible values for well-rounded inlets resulting from advanced taphole wear). Rearranging (2) in terms of dimensionless quantities yields:

$$N_T^2 = \frac{1 + K_L}{2} N_{Re}^2 + 32N_L N_{Re} \quad (3)$$

Here,  $N_{Re}$  is the Reynolds number,  $N_L$  is a simple geometry ratio, and  $N_T$  is the product of the Reynolds number and the square root of the Euler number. By the principles of dimensional analysis only these three groups are needed to completely define the problem regardless of the flow regime; their definitions are shown in Table 1.

**Table 1:** Dimensionless groups used to characterise taphole flow

$N_{Re}$	$N_L$	$N_T$
$\frac{Du\rho}{\mu}$	$\frac{L}{D}$	$\frac{D\sqrt{\rho\Delta P}}{\mu}$

This particular set of dimensionless groups is preferred since only one ( $N_{Re}$ ) is dependent on the fluid velocity, which is often a poorly-known quantity in tapping operations. This allows tapping velocity to be represented explicitly as a function of the taphole design, the properties of the fluid being tapped, and the applied pressure.

## MODEL DEVELOPMENT

In order to model different aspects of the behaviour of taphole systems most effectively, several simplifications were made.

Although the effect of heat transfer and phase change on the molten material being tapped is an important aspect of the taphole's behaviour, this study focuses only on flow in order to isolate behaviour related to fluid dynamics. Coupled heat transfer models will be considered at a later stage but are not within the scope of the present work.

In addition, the taphole system was divided into two separate computational models – one covering the single-phase flow from the furnace interior to the exit point of the taphole, and another covering the multiphase flow from the taphole exit through the launder and into the ladle. The rationale for this approach as opposed to a single unified model is that different research questions are posed in the different regions – in flow through the taphole, it is desirable to perform high fidelity

simulations in order to resolve near-wall turbulence and accurately quantify the discharge rate as a function of taphole geometry and fluid properties, whereas with flow in the launder and ladle the primary aim is to identify broad qualitative differences in the patterns of free surface flow in response to variations in material properties and equipment design.

Both computational models were implemented using the finite volume method, in OpenFOAM® version 4.1 (OpenFOAM, 2017). For the taphole region model, a modified version of the “ *pisoFoam* ” solver was written to allow for adaptive time-stepping using a specified Courant number. For the launder and ladle region model, the standard “ *interFoam* ” solver was used without modification. Hexahedral-element-dominant computational meshes were generated using  *cfMesh*  version 1.1.1 ( *cfMesh* , 2017), with mesh sizes ranging from between 1 and 2 million elements for the taphole region models, up to ~4 million elements for the launder and ladle region models.

### Taphole region model

Flow in the taphole region is modelled using large eddy simulation (LES) methods to capture the turbulent flow behaviour. LES methods directly compute the unsteady, dynamic behaviour in turbulent flow at length scales above a certain level, and approximate the turbulent stresses using sub-grid scale (SGS) models at length scales below it. The critical length scale is commonly taken as the resolution of the numerical mesh. This approach results in a filtered version of the Navier Stokes equations for the resolved components of the pressure and fluid velocity, containing source terms which are closed using the chosen SGS model. LES models generally require higher-fidelity meshes than Reynolds-averaged (RANS) turbulence models, but are considerably less computationally demanding than direct numerical simulation. They are more adept than RANS models with regard to predicting laminar-turbulent transition behaviour as well as temporal structures in turbulent flows, both of which are relevant to the present study.

For the taphole region a dynamic *k*-equation model (Kim et al., 1995) is used as the SGS model together with standard box filtering at the mesh resolution. Near-wall mesh refinement was used to ensure that the dimensionless wall distance  $y^+$  remained below unity.

The entry region and taphole channel are modelled as a large plenum zone (representing the furnace interior) connected to a cylindrical pipe section (representing the taphole itself). The lip of the taphole is treated as a sharp edge, and assumes that little or no wear of the taphole materials of construction has occurred. The geometry of the model region is shown in Figure 2.

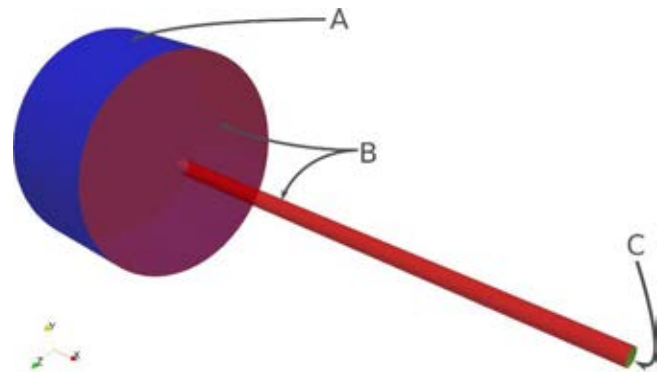


**Figure 2:** Taphole model geometry

Boundary conditions are applied as shown in Table 2.

**Table 2:** Boundary conditions for taphole region model

Boundary	$\mathbf{u}$	$p$	$k$
A (inlet)	$\frac{\partial u_n}{\partial \mathbf{n}} = 0$ $u_\tau = 0$	$p = \frac{\Delta P}{\rho} - \frac{1}{2}  \mathbf{u} ^2$	$k = 0$
B (walls)	$\mathbf{u} = 0$	$\frac{\partial p}{\partial \mathbf{n}} = 0$	$k = 0$
C (outlet)	$\frac{\partial \mathbf{u}}{\partial \mathbf{n}} = 0$	$p = 0$	$\frac{\partial k}{\partial \mathbf{n}} = 0$

In the case of the reduced pressure boundary condition on boundary A, the boundary pressure value of  $p$  is calculated using the total applied pressure difference across the domain (a specified parameter, as used in equations (1) to (3)) and the local velocity at the boundary, which is obtained after calculation of the velocity field boundary condition.

Here,  $\mathbf{u}$  is the fluid velocity vector field (with components  $u_n$  and  $u_\tau$  normal and tangential to the boundary respectively),  $p$  is the reduced pressure field,  $k$  is the turbulent kinetic energy field, and  $\mathbf{n}$  are unit vectors normal to the boundary surface.

### Launder and ladle region model

In the region after the molten material exits the taphole, the behaviour is modelled using the volume of fluid (VOF) method for multiphase fluid flow (Hirt et al., 1981). VOF tracks the fluid interface using a phase field  $\alpha$ , representing the volume fraction of the first phase (in a two-phase system, the volume fraction of the second phase is then  $1 - \alpha$ ). The evolution of  $\alpha$  is modelled with a convection equation using gradient compression schemes to maintain a sharp interface between phases. Source terms are added to the Navier Stokes equations in the interface regions to account for the additional forces arising from surface tension effects.

The launder and ladle are modelled as solid walls surrounded by open atmosphere as shown in Figure 3. The ladle is treated as a simple truncated conical vessel in all cases, but the launder is modelled with different designs (rectangular and v-shaped channel profiles) to examine the effect on the flow patterns while tapping. Slag and metal materials are modelled in each case to

examine the effect of the physical properties of the molten phase on the behaviour of the system. A range of taphole exit velocities is considered based on results obtained from the taphole region model. Static mesh refinement is performed in each case by running an initial simulation at low resolution, and using the resulting phase field to refine the mesh to higher resolution in areas where the gas-liquid interface is present. Boundary conditions used are shown in Table 3.

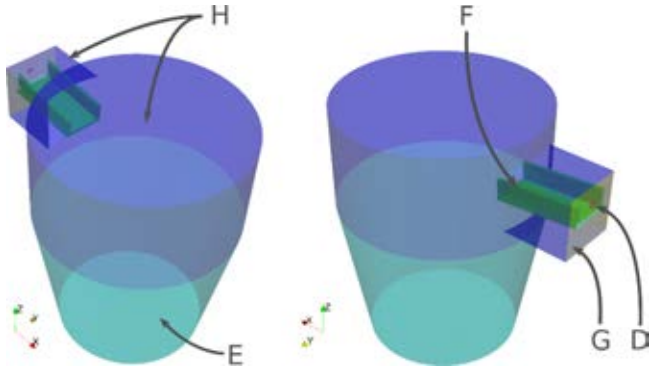


**Figure 3:** Geometry of launder and ladle models

**Table 3:** Boundary conditions for ladle and launder region model

Boundary	$\mathbf{u}$	P	$\alpha$
D (inlet)	$\mathbf{u} = \mathbf{u}_0$	$\frac{\partial P}{\partial \mathbf{n}} = 0$	$\alpha = 1$
E, F, G (walls)	$\mathbf{u} = 0$	$\frac{\partial P}{\partial \mathbf{n}} = 0$	$\frac{\partial \alpha}{\partial \mathbf{n}} = 0$
H (atmosphere)	$\begin{cases} \frac{\partial u_n}{\partial \mathbf{n}} = 0, u_\tau = 0 \\ \frac{\partial \mathbf{u}}{\partial \mathbf{n}} = 0 \end{cases}$	$\begin{cases} P = P_0 - \frac{1}{2} \rho  \mathbf{u} ^2 \\ P = P_0 \end{cases}$	$\begin{cases} \alpha = 0 \\ \frac{\partial \alpha}{\partial \mathbf{n}} = 0 \end{cases}$

In the case of the absolute pressure boundary condition on boundary H, the boundary value of P is calculated using the specified total atmospheric pressure and the local velocity at the boundary, which is obtained after calculation of the velocity field boundary condition.

Here, P is the absolute pressure field, and  $P_0$  is atmospheric pressure in the region around the launder and ladle.  $\alpha$  represents the volume fraction of molten material. At the atmosphere boundary F, it is possible for fluid to flow both into and out of the domain – for each field, the first expression is used in the case of inflow, the second in the case of outflow.

### Model parameters

The viscosities, densities and surface tension values of slags, mattes and metals vary with both composition and temperature. These properties are often difficult to measure, due to the extreme temperatures at which these

phases are molten. A detailed summary of the viscosity and density values for various commodity smelting operations is given in (Nelson et al., 2016). For iron and steel production, ferroalloys such as ferrochromium and ferromanganese, the viscosity of the metal phase at temperature varies between 0.004 and 0.007 Pa.s. For mattes (e.g. from copper and nickel smelting operations), the values can be higher – varying from 0.003 to 0.05 Pa.s. The viscosity of slags from these operations varies between 0.1 to 1.5 Pa.s across operations, except for copper smelting where the slag viscosity values are as low as 0.03 Pa.s. Notably, the viscosity of slags in any operation can increase dramatically when solids precipitate from the melt.

Density values vary from 5500 to 7500 kg/m<sup>3</sup> for ferrous-based processes, typically 4200-4500 kg/m<sup>3</sup> for mattes. Slag density values vary between 2600-3200 kg/m<sup>3</sup> for most slags, except for, for example copper and nickel process slags, which generally slightly higher densities, roughly 3500 – 4000 kg/m<sup>3</sup>.

The surface tension values for metals and slags in pyrometallurgical processes are quite high (when compared to common fluids). These values vary across commodities, but is roughly 0.5 N/m for most common slags, mattes and metals (Tanaka et al., 2014).

In terms of the physical design and operation parameters of the taphole region, typical lengths and diameters for slag, metal, and matte tapholes have been reported in several sources, for example (Nelson et al., 2016), (van Beek et al., 2014), and (Nolet, 2014). A summary of the industrial data is shown in Table 4. Although the internal furnace pressure in the case of certain processes such as blast furnaces can be extremely high (up to 5 bar (Nelson et al., 2016)), in open-bath smelting furnaces the primary source of the pressure is most often the head of molten material above the level of the taphole. Typical values across several different processes are reported in (Nelson et al., 2016) and summarised in Table 5.

**Table 4:** Geometry parameters for industrial furnace tapholes

Material	Taphole diameter	Taphole length
Slag	0.04 – 0.1 m	< 1.3 m
Matte	0.04 – 0.1 m	1 – 1.5 m
Metal	0.04 – 0.07 m	1 – 1.5 m

**Table 5:** Head of molten material above tapholes for slag and metal/matte systems

Material	Above slag taphole	Above metal/matte taphole
Slag	0.2 – 1 m	0.4 – 2 m
Metal/matte	-	0.15 – 0.6 m

In order to demonstrate the use of the multiphase flow model of the launder and ladle region, dimensions based on pilot-scale DC furnace equipment in use at Mintek were selected. Two different launder cross sections, a square channel profile and a v-shaped channel profile, were studied at different flowrates of slag and metal material to determine their impact on the flow pattern into the ladle. Dimensions of the model system are shown in Table 6.

**Table 6:** Geometry parameters for launder and ladle models

Parameter	Value	Parameter	Value
Taphole diameter	0.03 m	Ladle diameter	1 m
Launder length	0.4 m	Ladle height	0.75 m
Launder width	0.2 m	Launder height above ladle	0.2 m
Launder inclination	5°		

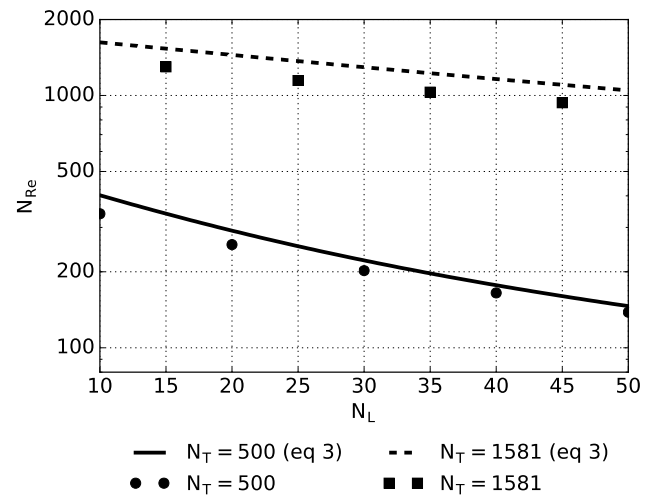
## RESULTS AND DISCUSSION

### Taphole region models

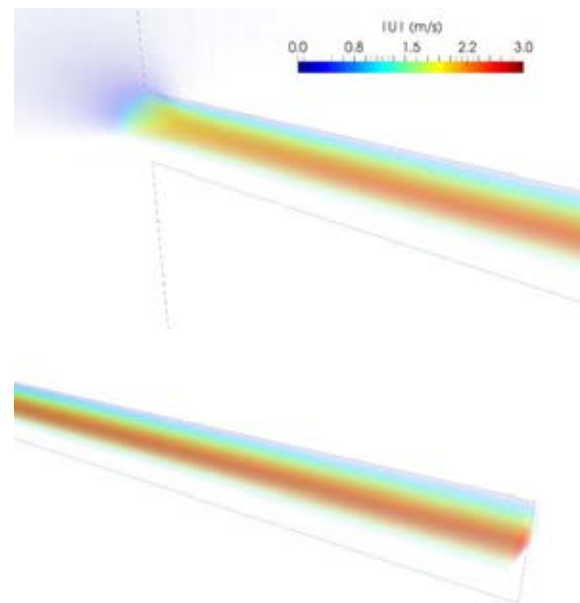
In order to study a broad range of typical taphole conditions and designs representative of most electric smelting processes, a set of simulations was executed to cover the ranges  $500 < N_T < 500000$ , and  $10 < N_L < 50$ . This was achieved in the computational model by fixing taphole diameter (0.02 m), fluid density ( $7000 \text{ kg/m}^3$ ), and applied pressure (89286 Pa), and calculating the required taphole length and fluid viscosity in each case based on the desired values of  $N_T$  and  $N_L$  using the expressions in Table 1.

Once the initial conditions had decayed sufficiently (typically after 1 s of simulation time), a time- and area-averaged velocity at the taphole outlet was computed and used to calculate  $N_{Re}$ . The laminar or turbulent nature of the flow was assessed using the relative variability in time of the velocity field at the outlet – this was calculated by finding the difference between the minimum and maximum velocity values at the taphole centreline over the final 0.2 s of simulation time divided by the average outlet velocity over the same time period. A total of 32 separate cases were simulated using the sharp-edged entry geometry shown in Figure 2, each taking between 10 and 20 hours of wall time on 16 Intel Xeon CPUs.

For model validation purposes, the simulation results were compared to the predictions of equation (3) in the laminar flow region. This is shown in Figure 4. The agreement in both qualitative trends and values is fairly good, with the computational model under-predicting slightly relative to (3). This is expected since (3) assumes that the flow in the taphole is fully developed along its entire length, whereas in reality there will be an entrance length over which the wall boundary layer expands before full Hagen-Poiseuille flow is reached. In this entry region, the wall shear forces are higher and will therefore restrict the flow to a greater degree, resulting in lower flowrates than those predicted by (3).

**Figure 4:** Model validation against equation (3)

Visualisations of the instantaneous flow patterns in and around the taphole are presented in Figures 5 to 7, for cases in which the value of  $N_L$  was fixed at 30 and the value of  $N_T$  was changed. All visualisations are shown at the end of the simulation, time = 1 s. The upper section of each image shows the velocity profile through the 3D volume, and the lower section shows a contour plot of turbulent viscosity  $\nu_t$ .

**Figure 5:** Velocity field (coloured) and contour of  $\nu_t = 7.5 \times 10^{-6} \text{ m}^2/\text{s}$  for case  $N_L = 30$  and  $N_T = 500$ , (top) taphole entry (bottom) taphole exit

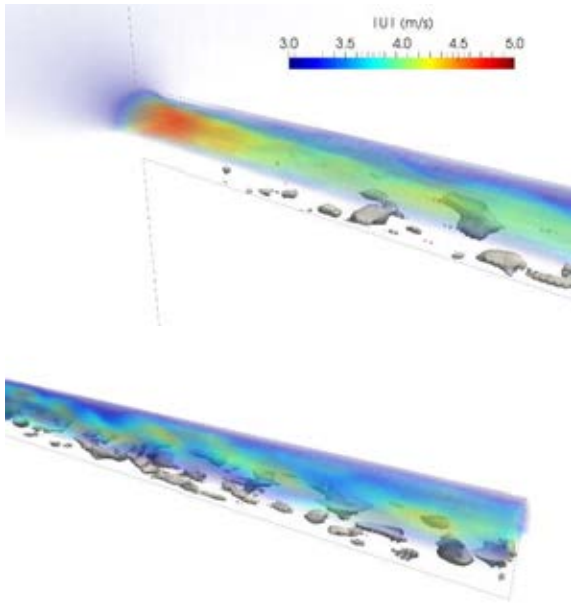


**Figure 6:** Velocity field (coloured) and contour of  $v_t = 7.5 \times 10^{-6} \text{ m}^2/\text{s}$  for case  $N_L = 30$  and  $N_T = 5000$ , (top) taphole entry (bottom) taphole exit

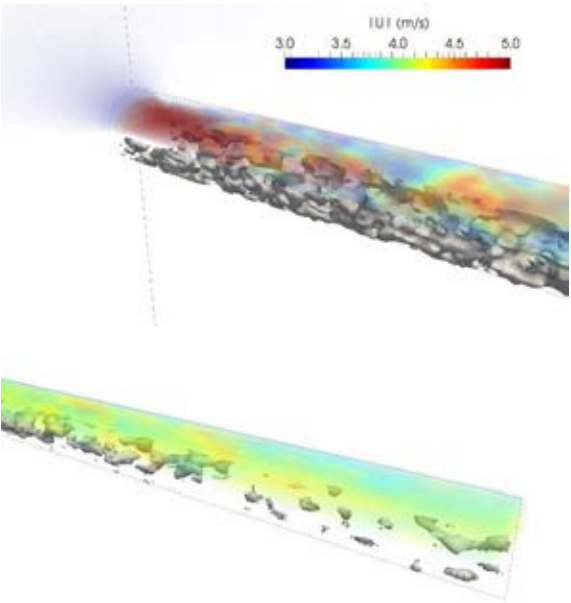


**Figure 7:** Velocity field (coloured) and contour of  $v_t = 7.5 \times 10^{-6} \text{ m}^2/\text{s}$  for case  $N_L = 30$  and  $N_T = 500000$ , (top) taphole entry (bottom) taphole exit

As  $N_T$  increases, a transition from laminar to unsteady, turbulent flow occurs. In particular, a vena contracta with flow separation forms in the entry region of the taphole due to the sharp-edged entry, and this acts as a strong trigger for turbulent flow to develop in this area at high  $N_T$ . Average flow velocity increases steadily from approximately 1.5 m/s at  $N_T = 500$  to 4 m/s at  $N_T = 500000$ . Detail of the evolution of the velocity field along the centreline of the taphole over time is shown in Figure 8 and 9 for cases of laminar and turbulent flow (in both cases,  $x/L = 0.2$  indicates the location of the taphole entry). It may be seen that the turbulent flow case exhibits erratic and unsteady flow starting within one or two diameters of the taphole inlet at approximately 0.1 s, and

propagating down the taphole channel at the bulk average flow velocity.

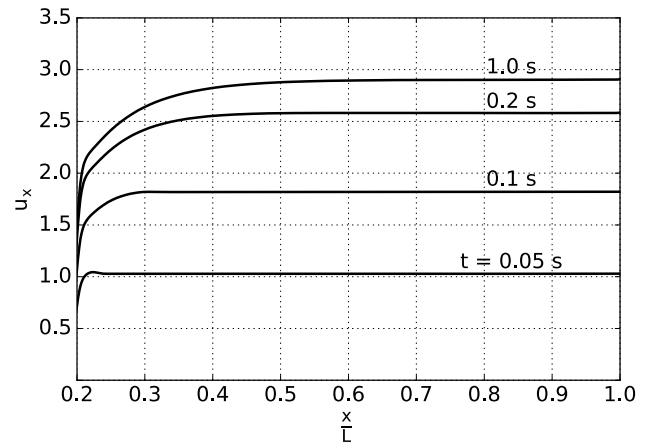


**Figure 8:** Evolution of instantaneous velocity profile along taphole centreline as a function of time, case  $N_L = 30$  and  $N_T = 500$  (laminar flow)

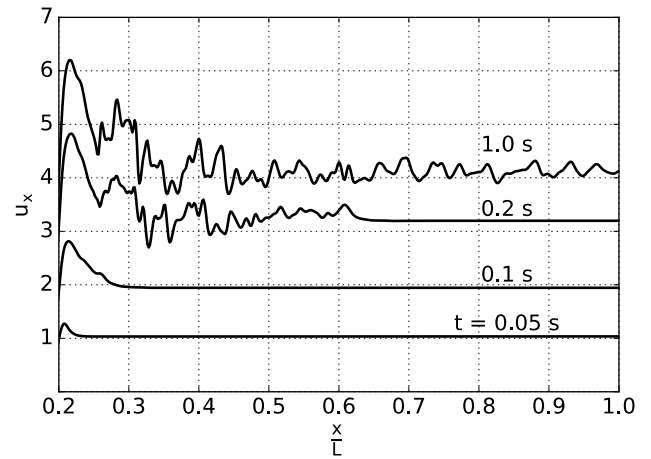


**Figure 9:** Evolution of instantaneous velocity profile along taphole centreline as a function of time, case  $N_L = 30$  and  $N_T = 500000$  (turbulent flow)

Changing the length of the taphole while holding  $N_T$  constant results in less extreme changes in the behaviour of the flow, however certain differences are visible. Visualisation of the flow patterns for short and long tapholes are presented in Figures 10 and 11. In the case of tapholes with early turbulent triggering as is the case with sharp-edged entry geometry, the level of turbulence at the taphole exit is generally seen to be higher for shorter tapholes (this is somewhat exacerbated by the fact that shorter tapholes result in higher discharge velocities, although this is a second-order effect). Turbulence levels settle within 10 to 15 taphole diameters and remain constant in longer tapholes. This suggests that mechanical wear patterns may be expected to be more uniform in longer tapholes away from the entry region.

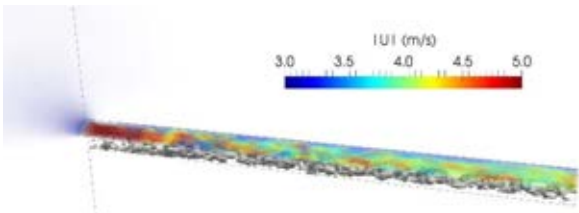


**Figure 10:** Velocity field (coloured) and contour of  $v_t = 7.5 \times 10^{-6} \text{ m}^2/\text{s}$  for case  $N_L = 15$  and  $N_T = 15811$

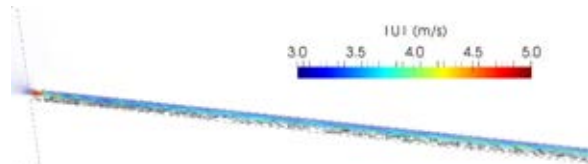


**Figure 11:** Velocity field (coloured) and contour of  $v_t = 7.5 \times 10^{-6} \text{ m}^2/\text{s}$  for case  $N_L = 45$  and  $N_T = 15811$

The full set of computational model results for the prediction of  $N_{Re}$  as a function of  $N_L$  and  $N_T$  was linearly interpolated and is presented in Figure 12. It can be seen that increasing the taphole length has a significant effect on the discharge velocity only at relatively low values of  $N_T$ , below about  $10^4$ . Dependence of  $N_{Re}$  on  $N_T$  is strong in all operating regions, increasing approximately linearly as  $N_T$  and  $N_L$  become large – this is expected since  $N_T$  is proportional to the square root of the applied pressure, which is the driving force for the flow. It is also interesting to note that since  $N_{Re}$  and  $N_T$  are both proportional to  $D/\mu$ , the viscosity and taphole diameter have a relatively small effect on the discharge velocity in this range; it is instead dominated by the density of the molten material and the applied pressure at the taphole entrance.

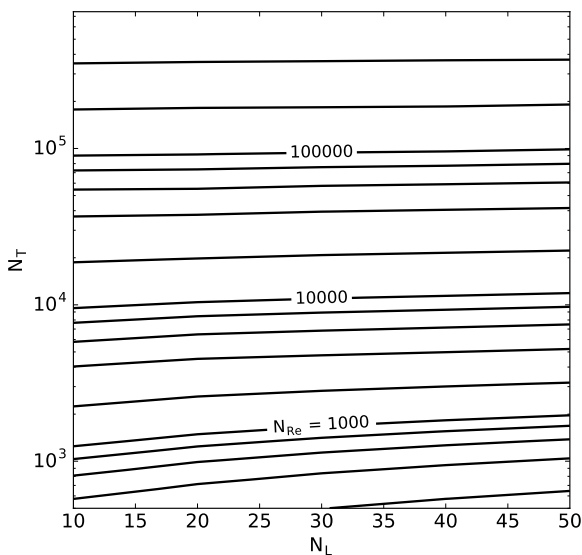


**Figure 12:**  $N_{Re}$  calculated by computational model as a function of  $N_L$  and  $N_T$

In Figure 13, the transition from laminar to turbulent flow as calculated from the model results using the variability of the velocity at the taphole outlet is presented. The transition region is assumed to be a function of  $N_{Re}$  for a

given taphole geometry – the bounds were estimated using the lowest value of calculated  $N_{Re}$  for which the model predicted unsteady flow, and the highest value of  $N_{Re}$  for which steady laminar flow was predicted. When indicative operating regions for slag, matte, and metal tapholes are imposed on the chart, it can be seen that metals and mattes are in general very likely to exhibit turbulent flow in at least part of the taphole, whereas slags may be laminar or turbulent (or even transition from one to the other during a single tap) depending on the conditions. This has implications for the wear mechanisms occurring at the taphole channel surface; in general, turbulent flow may be expected to exacerbate mechanical wear of the taphole.

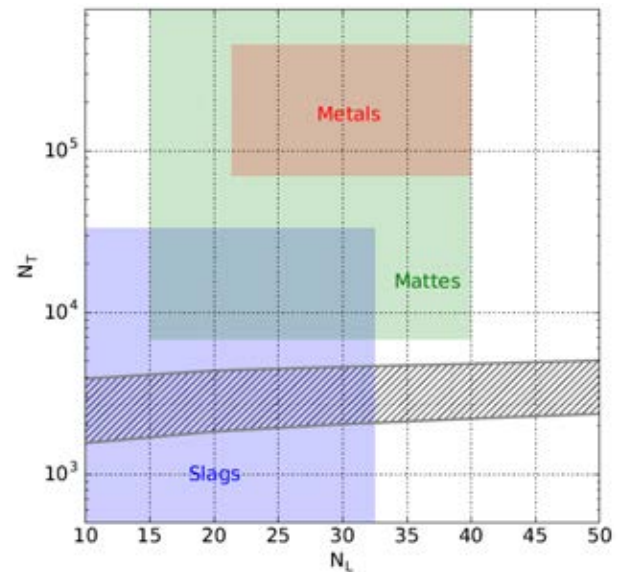


**Figure 13:** Laminar-turbulent transition region (grey hatching) showing typical operating windows for slag, metal, and matte tapholes

Although results for sharp-edged entries are useful for predicting flow through new tapholes, it is also of interest to consider how the flow patterns change once the taphole has worn after repeated use. Taphole wear patterns are typically concentrated in the entry region, resulting in conical (Thomson, 2014) or rounded (Steenkamp et al., 2014) inlets. Computational models of worn tapholes were constructed assuming an increase in the channel radius at the entry point of 0.05 m, and wear into the channel to a depth of 0.05 m. Visualisations of the flow patterns from models at  $N_L = 30$  and  $N_T = 50000$  are shown in Figures 14 and 15. When compared to results from the sharp-edged taphole models, it can be seen that the smoother the entrance geometry relative to the local direction of flow, the lower the level of turbulence generated in the taphole entrance region. This is particularly obvious in the case of the rounded entrance, in which the onset of turbulent flow is postponed an appreciable distance down the taphole channel even at high values of  $N_T$ . This observation suggests that the pattern of mechanical wear in furnace tapholes may change as the taphole ages – wear is initially concentrated in the entrance region, but reduces and moves into the main body of the taphole as time goes on.



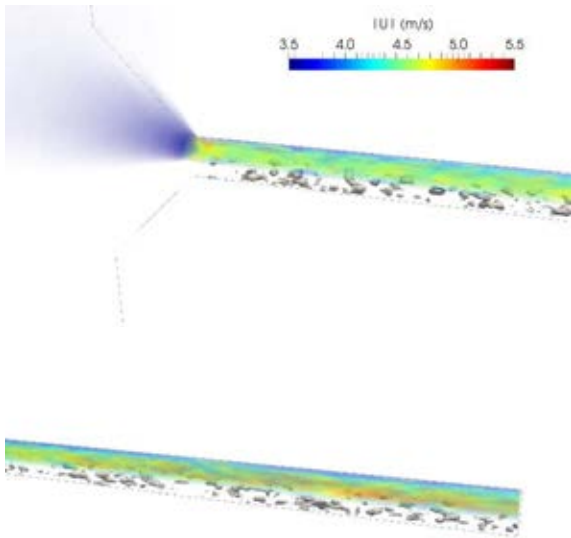


**Figure 14:** Velocity field (coloured) and contour of  $v_t = 7.5 \times 10^{-6} \text{ m}^2/\text{s}$  for case  $N_L = 30$  and  $N_T = 50000$  with conical entrance, (top) taphole entry (bottom) taphole exit

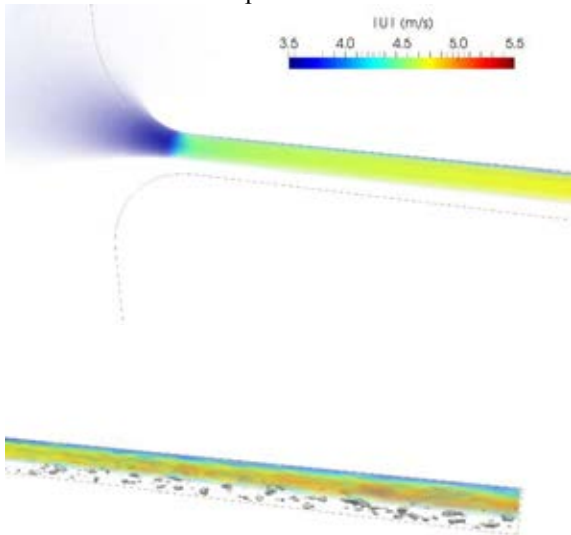


**Figure 15:** Velocity field (coloured) and contour of  $v_t = 7.5 \times 10^{-6} \text{ m}^2/\text{s}$  for case  $N_L = 30$  and  $N_T = 50000$  with rounded entrance, (bottom) taphole entry (top) taphole exit

Although there are considerable qualitative differences in the flow patterns and turbulence onset, the quantitative differences in flow velocity are relatively small for different entry configurations. Figure 16 shows a comparison of the sharp-edged entry results with those from conical and rounded entry models.

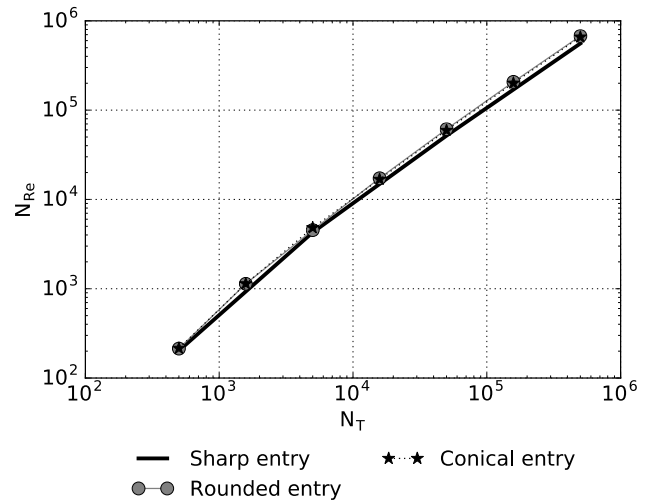


**Figure 16:**  $N_{Re}$  calculated by computational model as a function of  $N_T$  at  $N_L = 30$ , for different entry geometries

It can be seen that the tapping velocities match within 10-20 % across a wide range of  $N_T$  for all geometries tested, although more comprehensive study is recommended to verify this result.

### Ladle and launder region models

The results from the taphole region model determine appropriate ranges on the taphole exit velocity, which is required as an input boundary condition for the launder and ladle region model – in the case of a pilot-scale furnace as modelled here, exit velocities between 1 and 3 m/s were applied. For the liquid phase being tapped, both slag ( $\mu = 0.1 \text{ Pa}\cdot\text{s}$ ,  $\rho = 2500 \text{ kg}/\text{m}^3$ ) and metal ( $\mu = 0.005 \text{ Pa}\cdot\text{s}$ ,  $\rho = 7000 \text{ kg}/\text{m}^3$ ) materials were used. For the surrounding gas phase, the properties of air were used.

Results comparing different materials and flowrates for the rectangular launder design are shown in Figures 17 to 20, in all cases at time 4 s after taphole opening. The contour of  $\alpha = 0.1$  is used to show the liquid surface, and coloured according to the local velocity field.

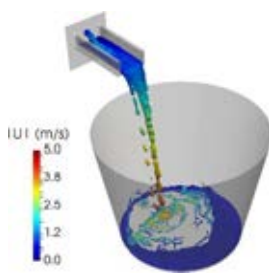


**Figure 17:** Rectangular profile launder, slag tapping at 1 m/s

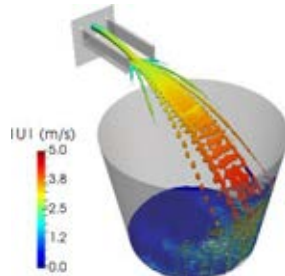


**Figure 18:** Rectangular profile launder, slag tapping at 3 m/s

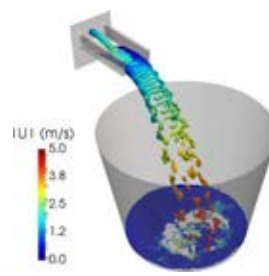


**Figure 21:** Rectangular launder profile, slag tapping at 2 m/s

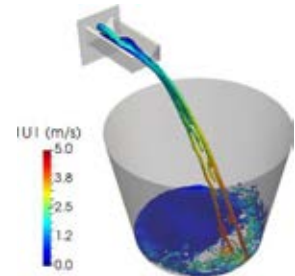


**Figure 22:** V-shaped launder profile, slag tapping at 2 m/s

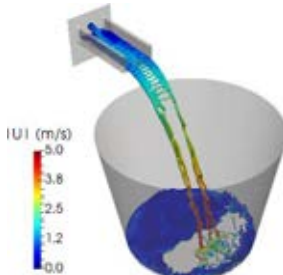


**Figure 19:** Rectangular launder profile, metal tapping at 1 m/s

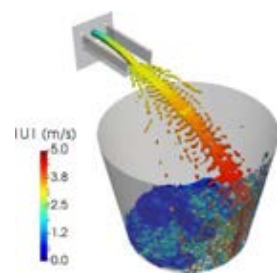


**Figure 20:** Rectangular launder profile, metal tapping at 3 m/s

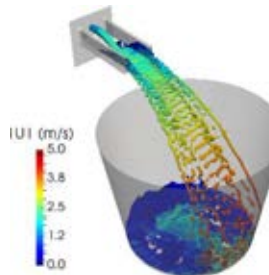


**Figure 23:** Rectangular launder profile, metal tapping at 2 m/s

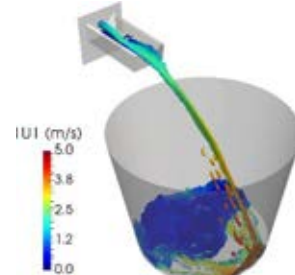


**Figure 24:** V-shaped launder profile, metal tapping at 2 m/s

At low flowrates, the tapping stream is generally well contained within the launder channel with minimal splashing before exiting into the ladle. At high flowrates (typical of when the taphole is newly opened) it is clear that this particular launder design is too short – the tapping stream catches the edge of the launder and spreads the tapped material out into a fan shape as it enters the ladle. This would not be an optimal configuration for tapping metal, as the increased surface area may result in undesirable re-oxidation of the material by the surrounding air as it enters the ladle.

Comparing different materials, it can be seen that in the case of metal the flow tends to separate out into smaller droplets and streams than in the case of slag; it is likely that this is related to the lower viscosity of molten metals. The flow patterns at low tapping velocities are particularly different, due to the development of open-channel flow patterns in the launder in addition to the free-surface flow as the material exits into the ladle.

Results comparing a simple variation on the launder design are shown in Figures 21 to 24. Flow behaviour at a fixed tapping velocity (2 m/s) is shown in all cases, with visualisations performed at 4 s after the taphole was opened. The contour of  $\alpha = 0.1$  is used to show the liquid surface, and coloured according to the local velocity field.

Changing the cross-sectional shape of the launder has a significant impact on the shape and structure of the flow regardless of the material being tapped. In the case of the v-shaped launder, the channel flow is kept contained in a narrower cross-section as it traverses the launder, resulting in a more contained stream flowing into the ladle. This results in less break-up of the stream into droplets, keeping the surface area exposed to air lower. The intense, directed flow of the stream into the ladle may however cause high localised heat transfer and mechanical wear of the ladle lining – this would have to be managed carefully to avoid premature ladle failure.

## CONCLUSIONS

Characterisation of the flow behaviour in furnace taphole systems is a complex subject. Due to the practical challenges associated with handling of molten materials at high temperatures, computational modelling can be used very effectively as a complement to experimental work in this area. Development of preliminary computational models of the fluid flow behaviour both inside the taphole and after the material exits it have been successful, and study of a range of operating parameters and designs was conducted.

The taphole region models demonstrated that for typical material properties and taphole geometries, the nature of the flow inside the taphole can be expected to be turbulent for metals and mattes, but may be laminar or turbulent for slags depending on conditions. Quantification of the taphole exit velocities in terms of dimensionless parameters was obtained, with dependence of  $N_{Re}$  on  $N_T$  being much stronger than on  $N_L$ . The effect of taphole entrance geometry on turbulence onset and flow patterns in the taphole channel was found to be appreciable, however, the exit velocities were not particularly sensitive to this change.

The results from the taphole region model were used as boundary conditions for multiphase flow models of the launder and ladle outside the furnace. The scope of this work was limited to comparing the flow behaviour in a simple design at pilot-plant furnace scale. It was found that differences in flow patterns between slag and metal were exaggerated at low tapping velocities, with metal flows tending to break up into smaller droplets and streams. Launder channel shape also had a large effect on the nature of the free surface flow between the launder and the ladle, suggesting that proper launder design and maintenance is critical for repeatable tapping flow behaviour.

This work is intended to be a preliminary starting point for computational modelling of taphole flow behaviour, and as such, there is considerable scope for further research in this area. In the taphole region, more detailed studies of fluid dynamics in the taphole channel using LES or direct numerical simulation models which include the effect of taphole wear on geometry and surface roughness would be of value. In the launder and ladle region, evolution of the model into a virtual prototype capable of comparative performance testing of various designs is anticipated. In all cases the impact of coupling additional phenomena (in particular heat transfer and phase change) to the flow model should be investigated further, and ultimately integrated into the thermal design of the taphole assembly.

## ACKNOWLEDGEMENTS

This paper is published by permission of Mintek. The CSIR Centre for High Performance Computing provided computational resources for execution of all modelling work. The authors gratefully acknowledge useful interactions with Lloyd Nelson and Rodney Hundermark (Anglo American plc), and Joalet Steenkamp (Mintek).

## REFERENCES

- JONES, R.T. and CURR, T.R. (2006). "Pyrometallurgy at Mintek", *Proc. SAIMM Southern African Pyrometallurgy 2006*, Johannesburg, South Africa, p 127.
- NELSON, L.R. and HUNDERMARK, R.J. (2016). "'The taphole' – key to furnace performance", *J. SAIMM*, 116(5), p 465.
- MCDUGALL, I. (2014). "Water cooled tap-hole blocks", *Proc. SAIMM Furnace Tapping Conference 2014*, Muldersdrift, South Africa, p 183.
- HE, Q., ZULLI, P., TANZIL, F., LEE, B., DUNNING, J., and EVANS, G. (2002). "Flow characteristics of a blast furnace taphole stream and its effects on trough refractory wear", *ISIJ*, 42(3), p 235.
- LEONG, B. and JOUBERT, H. (2006). "Innovative and safe copper launder design", *Proc. SAIMM Southern African Pyrometallurgy 2006*, Johannesburg, South Africa, p 385.

KADKHODABEIGI, M., TVEIT, H., and JOHANSEN, S.T. (2011). "Modelling the tapping process in submerged arc furnaces used in high silicon alloys production", *ISIJ*, 51(2), p 193.

SHAO, L. and SAXEN, H. (2013). "A simulation study of two-liquid flow in the taphole of the blast furnace", *ISIJ*, 53(6), p 988.

GUTHRIE, R.I.L. (1992). "Engineering in process metallurgy", Oxford University Press, Oxford, United Kingdom.

OpenFOAM (2017). <https://www.openfoam.org/>, accessed 10/02/2017.

cfMesh (2017). <http://cfmesh.com/>, accessed 10/02/2017.

KIM, W.-W. and MENON, S. (1995). "A new dynamic one-equation subgrid-scale model for large eddy simulations", *Proc. AIAA 33<sup>rd</sup> Aerospace Sciences Meeting and Exhibit*, Reno NV, USA, paper 1995-0356.

HIRT, C.W. and NICHOLS, B.D. (1981). "Volume of fluid (VOF) method for the dynamics of free boundaries", *J. Comput. Phys.*, 39(1), p 201.

TANAKA, T. and SCHELLER, P.R. "Interfacial Phenomena in High Temperature Metallurgy", *Chapter 1 in Treatise on Process Metallurgy Volume 2: Process Phenomena*, edited by Seetharaman, S., McLean, A., Guthrie, R. and Sridhar, S., Elsevier, 2014, pp.46-50.

VAN BEEK, W.S.B., GOFF, T.J., NEL, P.E., and REX, E. (2014). "An overview of the design, operation, and maintenance practices relating to tap-hole management of a PGM smelting furnace", *Proc. SAIMM Furnace Tapping Conference 2014*, Muldersdrift, South Africa, p 113.

NOLET, I. (2014). "Tapping of PGM-Ni mattes: an industry survey", *Proc. SAIMM Furnace Tapping Conference 2014*, Muldersdrift, South Africa, p 223.

THOMSON, L. (2014). "Monitoring, repair, and safety practices for electric furnace matte tapping", *Proc. SAIMM Furnace Tapping Conference 2014*, Muldersdrift, South Africa, p 87.

STEENKAMP, J.D, GOUS, J.P., PISTORIUS, P.C., TANGSTAD, M., and ZIETSMAN, J.H. (2014). "Wear analysis of a tap-hole from a SiMn production furnace", *Proc. SAIMM Furnace Tapping Conference 2014*, Muldersdrift, South Africa, p 51.

## NUMERICAL PREDICTIONS OF THE SHAPE AND SIZE OF THE RACEWAY ZONE IN A BLAST FURNACE

Dmitry SAFRONOV<sup>1\*</sup>, Andreas RICHTER<sup>1†</sup>, Bernd MEYER<sup>1‡</sup>

<sup>1</sup>TU Bergakademie Freiberg, IEC, 09599 Freiberg, Germany

\* E-mail: dmitry.safronov@vtc.tu-freiberg.de

† E-mail: a.richter@vtc.tu-freiberg.de

‡ E-mail: bernd.meyer@iec.tu-freiberg.de

### ABSTRACT

A 3D transient numerical model has been developed to predict the shape and size of the raceway zone created by the force of the blast air injected through the tuyeres in the coke bed of a blast furnace. The model is based on the solution of conservation equations of both gas and solid phases as interpenetrating continua on an Eulerian-Eulerian frame of reference. A modified  $k$ - $\epsilon$  model has been adopted for gas phase turbulence including gas-coke turbulent interaction. The solid phase is characterized by the solid pressure, bulk viscosity and shear viscosity, which are evaluated by applying kinetic theory to granular flows. The influences of the air blast velocity, granular properties of the coke phase, and tuyere diameter on the shape and size of the raceway zone have been predicted by numerical simulations and described using semi-empirical relations. The effect of the cohesive zone on the raceway geometry is also taken into account. The trends of the derived results are compared with experimental data reported by various researchers with reasonable agreement.

**Keywords:** Process metallurgy, Ironmaking, Blast furnace, Raceway, CFD, Fluidized/packed beds, Granular flows.

### NOMENCLATURE

#### Greek Symbols

$\alpha$	Volume fraction, —
$\beta$	Momentum exchange coefficient, $\text{kg m}^{-3} \text{s}^{-1}$
$\epsilon$	Turbulent energy dissipation, $\text{m}^2 \text{s}^{-3}$
$\Theta$	Granular temperature, K
$\mu$	Dynamic (shear) viscosity, Pa s
$\rho$	Density, $\text{kg m}^{-3}$
$\bar{\tau}$	Stress tensor, Pa
$\phi$	Angle of internal friction, degree
$\zeta$	Bulk viscosity, Pa s

#### Latin Symbols

$C_d$	Drag coefficient, —
$C_{td}$	Turbulent dispersion coefficient, —
$C_V$	Added mass coefficient, —
$D$	Depth, m
$d$	Diameter, m
$e$	Coefficient of restitution, —
$\vec{F}$	Volume-specific force, $\text{N m}^{-3}$
$g_0$	Radial distribution function, —
$H$	Height, m

$\vec{g}$	Standard acceleration due to gravity, $\text{m s}^{-2}$
$\vec{I}$	Unit tensor, —
$k$	Turbulent kinetic energy, $\text{J kg}^{-1}$
$L$	Length, m
$p$	Pressure, Pa
$Re$	Reynolds number, —
$\vec{R}$	Interphase momentum exchange, $\text{N m}^{-3}$
$R_u$	Universal gas constant, $\text{J mol}^{-1} \text{K}^{-1}$
$S$	Cross-sectional area, $\text{m}^2$
$t$	Time, s
$T$	Temperature, K
$\vec{U}$	Velocity, $\text{m s}^{-1}$
$\dot{V}$	Volumetric flow, $\text{m}^3 \text{s}^{-1}$
$W$	Width, m

#### Sub/superscripts

0	Standard state
eff	Effective value
g	Gas phase
in	Inlet
$i$	Phase $i$
$j$	Phase $j$
max	Maximal value
rw	Raceway
s	Solid phase
t	Turbulent
td	Turbulent dispersion
tuyere	Tuyere

### INTRODUCTION

The blast furnace (BF) that converts iron ore into molten iron is an important component in iron-steel making and a capital and energy intensive process. To maintain and improve the competitiveness of the blast furnace process, it is necessary to achieve a considerable decrease in the coke and total energy consumption for primary metal production along with minimization of environmental impacts. Injection of auxiliary fuels such as pulverized coal or oil has continuously made a considerable contribution toward reducing the requirement on expensive metallurgical coke in the last decades. The high coal injection rates and low coke rate is a common goal for reducing the cost of the hot metal production (Geerdes *et al.*, 2015). However, for an efficient and stable operation of the blast furnace towards increased injection rates, one has to understand the different physical processes and recognize the key parameters governing the processes.

In a blast furnace, iron-bearing materials and coke with flux are charged in alternate layers into the top of the furnace, as shown in Fig. 1. Preheated air and fuel (gas, oil or pulverized coal) are injected at high velocity into the lower part of the furnace through tuyeres, forming a cavity known as a raceway. In this raceway zone the injected fuel and some of the coke descending from the top of the furnace are combusted and gasified (see Fig. 2). The shape and size of the raceway greatly affect the conversion of the coke and the injected fuel. In the previous decades, tremendous work had been conducted to investigate the kinetics of raceway formation. The works related to the prediction of the raceway size and shape can be classified into experimental, analytical, semi-empirical, and numerical types. Analytical and semi-empirical studies have considered dimensional analysis (Szekely and Poveromo, 1975; VDE, 1976; Flint and Burgess, 1992; Ohno *et al.*, 1994; Rajneesh *et al.*, 2004; Singh *et al.*, 2006; Gupta and Rudolph, 2006) or macroscopic mass and momentum balance above the raceway (Nomura,

1986) to find a correlation for the size of the raceway, which often was considered to be spherical or having other predefined simple geometrical shape. These works are often accompanied with experimental investigations of the raceway formation using simplified two- or three-dimensional physical models for determination of the modeling parameters. Numerical works can in turn be classified into particle-resolved Discrete Element Modeling (DEM) and continuous Eulerian modeling. The literature shows that the DEM method has great potential but still has some significant challenges (Xu *et al.*, 2000; Nogami *et al.*, 2004; Yuu *et al.*, 2005; Hellberg *et al.*, 2005; Umekage *et al.*, 2007; Natsui *et al.*, 2011). All DEM models are significantly simplified, either by scaling up particles for industrial-scale furnaces, or scaled-down furnace size for real-size particles. This simplification lowers the computational load by reducing the number of particles. The geometry is further reduced in size by using a slot or thin pie-slice instead of the full cylindrical blast furnace shape, again reducing the number of particles in the simulation due to the high demand on computational resources.

In this work a comprehensive Eulerian approach is selected to describe the gas-coke particle flow. Aoki *et al.* (Aoki *et al.*, 1993) utilized the Eulerian approach to model the formation of raceway, but the authors neglected the effects of particles on gas phase turbulence in predicting the shape and size of the raceway zone. Mondal *et al.* (Mondal *et al.*, 2005) investigated the impact of coke bed and blast rates on the raceway shape and size applying Euler-Euler approach to a simplified two-dimensional BF geometry. More recently Selvarasu *et al.* (Selvarasu *et al.*, 2006, 2007) studied the raceway formation using geometry and operational parameters based on a real BF. However, no details on turbulent interaction between the gas and the solid phases can be found in the articles.

It has been recognized for many years that other blast furnace operation factors, such as the cohesive zone, arrangement of tuyeres and burden distribution also play an important role in the raceway formation and determine its size and shape. However, the effect of all those practical conditions on the raceway formation has not been studied very well. In order to improve our understanding of underlying physical processes, a three-dimensional Euler-Euler CFD model for simulation of the raceway formation process was developed. This work investigated the effect of tuyere geometry, air blast velocity, and coke particle size on the raceway formation. Possibilities to use the numerical predictions in real-time applications via reduced-order modeling approach are also discussed.

## MODEL DESCRIPTION

Fig. 3 shows the geometry used in the simulations, which is based on the geometry of ArcelorMittal Eisenhüttenstadt BF 5A blast furnace. The computational domain consists of three tuyeres and includes the coke bed below the cohesive zone. The approximate shape and location of the cohesive zone is known from an analysis of vertical probing. The detailed size and shape of the deadman is dependent on the furnace inner profile and the shape and location of the cohesive zone.

## Assumptions

The computational setup is based on the following basic assumptions:

- Coke particles are spheres of same size

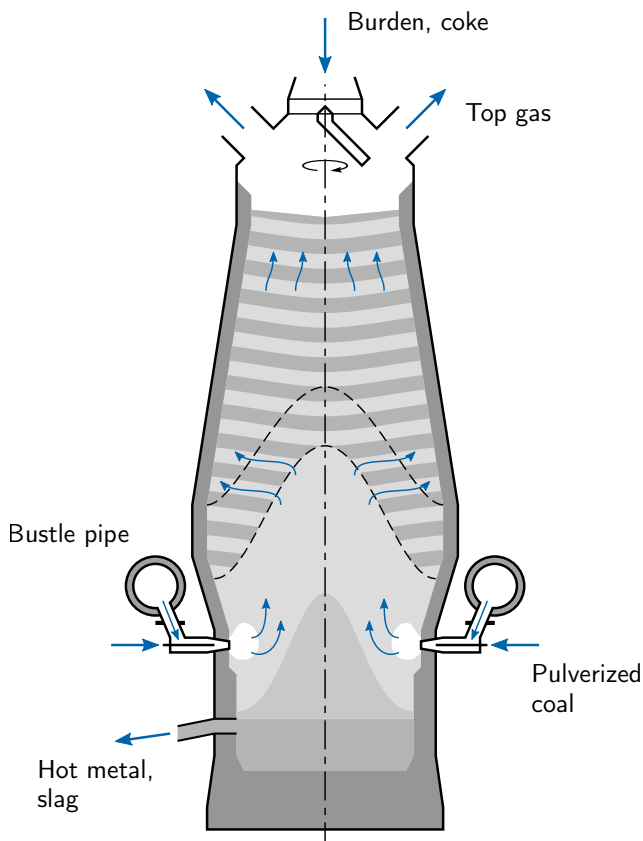


Figure 1: Ironmaking blast furnace (overview)

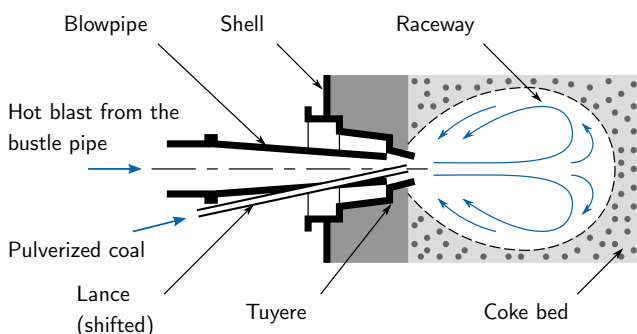


Figure 2: Coal injection in the raceway (tuyere level)

- Particle collisions are considered as binary and inelastic
- Effect of fuel injection is not considered

### Governing Equations

In the Eulerian approach, the different phases  $i$  are described mathematically as interpenetrating continua characterized by their volume fraction  $\alpha_i$ . The volume fractions are assumed to be continuous functions of space and time and their sum is equal to one:  $\sum_i \alpha_i = 1$ . In this work two different phases are considered. The coke particles are represented by the solid granular phase and the blast air is referred as the gas phase. Momentum and continuity equations are obtained for each phase in terms of its volume fraction. The continuity equation for phase  $i$  is

$$\frac{\partial(\alpha_i \rho_i)}{\partial t} + \nabla \cdot (\alpha_i \rho_i \vec{U}_i) = 0. \quad (1)$$

The momentum balance for phase  $i$  yields

$$\begin{aligned} \frac{\partial(\alpha_i \rho_i \vec{U}_i)}{\partial t} + \nabla \cdot (\alpha_i \rho_i \vec{U}_i \vec{U}_i) = \\ - \alpha_i \nabla p_i + \nabla \cdot \bar{\tau}_i + \alpha_i \rho_i \vec{g} + \vec{R}_{ij} + \vec{F}_{td,i}, \end{aligned} \quad (2)$$

where  $\bar{\tau}_i$  is the stress-strain tensor for phase  $i$

$$\bar{\tau}_i = \alpha_i \mu_i \left( \nabla \vec{U}_i + \nabla \vec{U}_i^T \right) + \alpha_i \left( \xi_i - \frac{2}{3} \mu_i \right) \nabla \cdot \vec{U}_i \vec{I}, \quad (3)$$

with  $\mu_i$  and  $\xi_i$  as the shear and bulk viscosities of phase  $i$ . The interphase momentum exchange term  $\vec{R}_{ij}$  describes the momentum transfer between the solid and the gas phase:

$$\vec{R}_{gs} = \beta (\vec{U}_g - \vec{U}_s), \quad \vec{R}_{sg} = \beta (\vec{U}_s - \vec{U}_g). \quad (4)$$

The interphase momentum exchange coefficient  $\beta$  was calculated according to the Gidaspow model (Gidaspow *et al.*,

1992), which is a combination of the Wen and Yu model (Wen and Yu, 1966) and the Ergun's equation (Ergun, 1952). For  $\alpha_g > 0.8$  the fluid–solid exchange coefficient  $\beta$  is based on the drag force of the fluid acting on a single particle:

$$\beta = \frac{3}{4} C_{d,s} \frac{\alpha_s \alpha_g \rho_g}{d_s} \left| \vec{U}_s - \vec{U}_g \right| \alpha_g^{-2.65} \quad (5)$$

and if  $\alpha_g \leq 0.8$ , the exchange coefficient is described by Ergun's equation for dense granular systems as

$$\beta = 150 \frac{\alpha_s^2 \mu_g}{\alpha_g^2 d_s^2} + 1.75 \frac{\rho_g \alpha_s}{\alpha_g d_s} \left| \vec{U}_s - \vec{U}_g \right|. \quad (6)$$

The interphase drag coefficient  $C_{d,s}$  in Eqn. (5) is given by

$$C_{d,s} = \frac{24}{Re_s} \left( 1 + 0.15 Re_s^{0.687} \right), \quad (7)$$

where the relative Reynolds number is defined as

$$Re_s = \frac{\rho_g d_s \left| \vec{U}_s - \vec{U}_g \right|}{\mu_g}. \quad (8)$$

The turbulent dispersion force  $\vec{F}_{td,i}$  in Eqn. (2) arises from averaging the interphase drag term  $\vec{R}_{ij}$ . For modeling of the turbulent dispersion force the formulation proposed by Lopez de Bertodano (de Bertodano, 1991) was used:

$$\vec{F}_{td,g} = -\vec{F}_{td,s} = C_{td} \rho_g k_g \nabla \alpha_s, \quad C_{td} = 1 \quad (9)$$

The bulk viscosity of the gas phase is considered to be zero

$$\xi_g = 0 \quad (10)$$

and the effective dynamic viscosity (shear viscosity) is calculated from the molecular and turbulent viscosities as follows:

$$\mu_{eff,g} = \mu_g + \mu_{t,g}. \quad (11)$$

The turbulent viscosity,  $\mu_{t,g}$ , is modeled by modified  $k$ - $\epsilon$  closure equations for turbulence

$$\mu_{t,g} = \rho_g C_\mu \frac{k_g^2}{\epsilon_g}, \quad (12)$$

where the turbulent kinetic energy,  $k_g$ , and turbulent kinetic energy dissipation rate,  $\epsilon_g$ , are determined from their respective conservation equations (13) and (14) considering the effect of solid particles.

$$\begin{aligned} \frac{\partial(\alpha_g \rho_g k_g)}{\partial t} + \nabla \cdot (\alpha_g \rho_g \vec{U}_g k_g) = \nabla \cdot \left( \alpha_g \frac{\mu_{t,g}}{\sigma_k} \nabla k_g \right) + \\ \alpha_g G_{k,g} - \alpha_g \rho_g \epsilon_g + \underbrace{\beta (k_{sg} - 2k_g)}_{\text{phase interaction}}, \end{aligned} \quad (13)$$

$$\begin{aligned} \frac{\partial(\alpha_g \rho_g \epsilon_g)}{\partial t} + \nabla \cdot (\alpha_g \rho_g \vec{U}_g \epsilon_g) = \\ \nabla \cdot \left( \alpha_g \frac{\mu_{t,g}}{\sigma_\epsilon} \nabla \epsilon_g \right) + \alpha_g \frac{\epsilon_g}{k_g} \left( C_{1\epsilon} G_{k,g} - C_{2\epsilon} \rho_g \epsilon_g \right) + \\ \underbrace{C_{3\epsilon} \frac{\epsilon_g}{k_g} \beta (k_{sg} - 2k_g)}_{\text{phase interaction}}. \end{aligned} \quad (14)$$

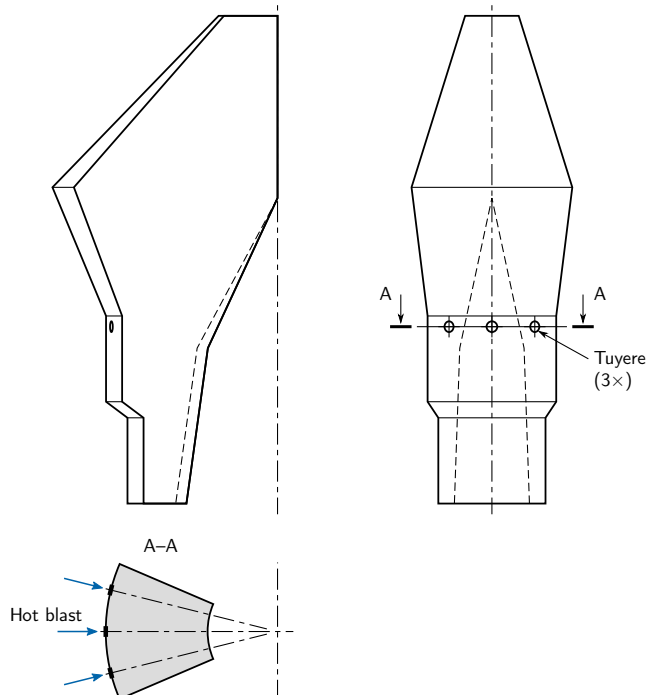


Figure 3: Computational domain for the raceway simulation

$G_{k,g}$  in Eqn. (13) is the production of turbulent kinetic energy in the gas phase. The last term in both the equations represents the influence of the dispersed phases (solid phase) on the continuous phase (Elgobashi and Abou, 1983). The constants for the  $k$ - $\epsilon$  model are (Launder and Spalding, 1972, 1974; Ferziger and Perić, 2002)

$$C_\mu = 0.09, \quad C_{1\epsilon} = 1.44, \quad C_{2\epsilon} = 1.92, \quad C_{3\epsilon} = 1.2, \\ \sigma_k = 1.0, \quad \sigma_\epsilon = 1.3. \quad (15)$$

The term  $k_{sg}$  in Eqn. (13) and (14) is the covariance of the velocities of the continuous phase and the solid phase (Simonin and Viollet, 1990) and is given by

$$k_{sg} = 2k_g \left( \frac{b + \eta_{sg}}{1 + \eta_{sg}} \right), \quad (16)$$

where the term  $b$  can be expressed as

$$b = (1 + C_V) \left( \frac{\rho_s}{\rho_g} + C_V \right)^{-1} \quad (17)$$

with  $C_V = 0.5$  as added-mass coefficient.

The term  $\eta_{sg}$  can be written as the ratio of the Lagrangian integral time scale and the characteristic particle relaxation time scale as

$$\eta_{sg} = \frac{\tau_{t,sg}}{\tau_{F,sg}}. \quad (18)$$

The characteristic particle relaxation time scale connected with inertial effects acting on a dispersed phase is defined as

$$\tau_{F,sg} = \alpha_s \rho_s \beta^{-1} \left( \frac{\rho_s}{\rho_g} + C_V \right). \quad (19)$$

The eddy particle interaction time is mainly affected by the crossing-trajectory effect (Csanady, 1963) and defined as

$$\tau_{t,sg} = \frac{\tau_{t,g}}{\sqrt{(1 + C_\beta \xi^2)}}, \quad (20)$$

where

$$\xi = \frac{|\vec{U}_{sg}| \tau_{t,g}}{L_{t,g}} \quad (21)$$

and

$$C_\beta = 1.8 - 1.35 \cos^2 \theta. \quad (22)$$

$\theta$  is the angle between the mean particle velocity  $\vec{U}_s$  and the mean relative velocity  $\vec{U}_{sg}$ .

The time scale of the energetic turbulent eddies appearing in Eqn. (20) is defined as

$$\tau_{t,g} = \frac{3}{2} C_\mu \frac{k_g}{\epsilon_g} \quad (23)$$

and the length scale of the turbulent eddies appearing in Eqn. (21) is given by

$$L_{t,g} = \sqrt{\frac{3}{2}} C_\mu \frac{k_g^{3/2}}{\epsilon_g}. \quad (24)$$

The solid phase is characterized by the solid pressure, bulk viscosity and shear viscosity, which are evaluated by applying kinetic theory to granular flows. All the three quantities, namely,  $p_s$ ,  $\xi_s$ , and  $\mu_s$ , arise from the momentum transport

due to the movement and interaction (translation, collision, and friction) of coke particles.

The solids pressure represents the particle normal forces (Gidaspow, 1994; Gidaspow *et al.*, 1992; Huilin *et al.*, 2003; Ding and Gidaspow, 1990) and is composed of a kinetic term and a second term due to particle collisions:

$$p_s = \alpha_s \rho_s \Theta_s + 2\rho_s (1 + e_{ss}) \alpha_s^2 g_{0,ss} \Theta_s, \quad (25)$$

where  $e_{ss}$  is the coefficient of restitution for particle collisions,  $\Theta_s$  is the granular temperature, and  $g_{0,ss}$  is the radial distribution function.

The distribution function  $g_{0,ss}$  describes the transition from the ‘‘compressible’’ condition ( $\alpha_s < \alpha_{s,max}$ ), where the spacing between the solid particles can continue to decrease, to the ‘‘incompressible’’ one, where no further decrease in the spacing is possible:

$$g_{0,ss} = \frac{3}{5} \left[ 1 - \left( \frac{\alpha_s}{\alpha_{s,max}} \right)^{1/3} \right]^{-1}, \quad (26)$$

where  $\alpha_{s,max}$  is the packing limit for the solid phase.

The granular temperature  $\Theta_s$  is proportional to the kinetic energy of the fluctuating particle motion. The energy transport equation for the solid granular phase in terms of granular temperature  $\Theta_s$  derived from kinetic theory takes the form (Gidaspow *et al.*, 1992; Ding and Gidaspow, 1990):

$$\frac{3}{2} \frac{\partial (\rho_s \alpha_s \Theta_s)}{\partial t} + \frac{3}{2} \nabla \cdot (\rho_s \alpha_s \vec{U}_s \Theta_s) = \bar{\tau}_s : \nabla \vec{U}_s + \\ \nabla \cdot (k_{\Theta_s} \nabla \Theta_s) - \gamma_{\Theta_s} - 3\beta \Theta_s, \quad (27)$$

where the first term on the right-hand side represents the generation of energy by the solid stress tensor, the second term represents the diffusion of energy, the third term represents the collisional dissipation of energy and the last term represents the exchange of kinetic energy from the solid phase to the gas phase.

The diffusion coefficient  $k_{\Theta_s}$  and collisional dissipation of granular energy  $\gamma_{\Theta_s}$  in Eqn. (27) can be expressed (Gidaspow *et al.*, 1992; Huilin *et al.*, 2003; Ding and Gidaspow, 1990) as

$$k_{\Theta_s} = \frac{150 \rho_s d_s \sqrt{\Theta_s \pi}}{384 (1 + e_{ss}) g_{0,ss}} \left[ 1 + \frac{6}{5} g_{0,ss} \alpha_s (1 + e_{ss}) \right]^2 + \\ 2 \alpha_s^2 \rho_s d_s g_{0,ss} (1 + e_{ss}) \left( \frac{\Theta_s}{\pi} \right)^{1/2}, \quad (28)$$

$$\gamma_{\Theta_s} = 3 (1 - e_{ss}^2) g_{0,ss} \rho_s \alpha_s^2 \Theta_s \times \\ \left[ \frac{4}{d_s} \left( \frac{\Theta_s}{\pi} \right)^{1/2} - \nabla \cdot \vec{U}_s \right]. \quad (29)$$

The shear viscosity and bulk viscosity appearing in Eqn. (3) for the solid granular phase can be written (Gidaspow, 1994; Gidaspow *et al.*, 1992; Huilin *et al.*, 2003; Ding and Gi-

daspow, 1990; Schaffer, 1987; Lun *et al.*, 1984) as

$$\mu_s = \underbrace{\frac{4}{5} \alpha_s^2 \rho_s d_s g_{0,ss} (1 + e_{ss}) \left( \frac{\Theta_s}{\pi} \right)^{1/2}}_{\text{collisional part}} + \underbrace{\frac{10 \rho_s d_s \sqrt{\Theta_s \pi}}{96 (1 + e_{ss}) g_{0,ss} \left[ 1 + \frac{4}{5} g_{0,ss} \alpha_s (1 + e_{ss}) \right]^2}}_{\text{kinetic part}} + \underbrace{\frac{p_s \sin \phi_s}{2 \sqrt{I_{2D}}}}_{\text{frictional part}}, \quad (30)$$

$$\xi_s = \frac{4}{3} \alpha_s^2 \rho_s d_s g_{0,ss} (1 + e_{ss}) \left( \frac{\Theta_s}{\pi} \right)^{1/2}, \quad (31)$$

where  $\phi_s$  is the angle of internal friction for the solid phase,  $p_s$  is the solid pressure, and  $I_{2D}$  is the second invariant of the deviatoric stress tensor.

### CFD SETUP AND VALIDATION

The conservation equations for the gas and the solid phase were solved using an implicit Finite Volume Method (FVM). A coupling between the pressure and velocity was accomplished using the Phase Coupled SIMPLE (PC-SIMPLE) algorithm for the pressure–velocity coupling. The velocities are solved coupled by phases, but in a segregated fashion. Pressure and velocities are then corrected by solving a pressure correction equation to satisfy the continuity constraint. The space derivatives of the diffusion terms were discretized by a central differencing scheme, while the advection terms were discretized by a power law scheme.

The computational domain consists of approximately  $10^6$  control volumes after a grid sensitivity study. At the hot blast inlet, the air velocity was considered to be uniform and the volume fraction of gas was unity ( $\alpha_{g,in} = 1$ ). The pressure was defined at the outlet and the axial gradients of all other variables were set to zero. In order to specify the pressure at the outlet of the computational domain, the effect of assumed burden distribution was modeled separately using the full BF inner profile and considering the pressure drop due to the cohesive zone measured by a vertical probing. Turbulent quantities  $k$  and  $\epsilon$  in the near-wall cells were prescribed from a logarithmic wall function. Symmetric boundary conditions (normal gradient is zero) were applied at the side walls. A no-slip condition was set at the wall for the gas phase calculations. The solid normal velocity was also set to zero at the wall. The burden properties used in the calculations are summarized in Table 1.

The validity of the computational model is examined using the data reported by Nomura for Newcastle No. 1 BF in Australia (Nomura, 1986). The conditions used for the validation are listed in Table 2. Fig. 4 shows the comparison in the raceway depth  $L_{rw}$  between CFD simulation results and the experimental results. It can be seen that the CFD model is in reasonable agreement with experimental work and is also able to predict actual physical trends accurately and within acceptable limits.

### SIMULATION CONDITIONS

The various conditions for the parametric studies are shown in Table 3. These parameters are collected from an actual operation case.

**Table 1:** Granulometric and mechanic properties of the granular phase (Adema, 2014; Natsui *et al.*, 2011; Yuu *et al.*, 2010)

Parameter	Coke	Ore
Particle size	38 mm	38 mm
Particle density	1100 kg m <sup>-3</sup>	4000 kg m <sup>-3</sup>
Volumetric fraction in the burden above cohesive zone	0.4	0.6
Volumetric fraction in the burden below cohesive zone	1.0	0.0
Shear modulus	10 <sup>7</sup> Pa	10 <sup>7</sup> Pa
Coefficient of restitution	0.8	0.8
Angle of internal friction	45°	45°
Packing limit $\alpha_{s,max}$	0.63	0.63

**Table 2:** Validation conditions

Tuyere diameter	152 mm
Coke particle size	41–49 mm
Blast velocity	90–120 m s <sup>-1</sup>
Blast temperature	973 K

### RESULTS

Figs. 5 and 6 show the distribution of the volume fraction of the solid phase  $\alpha_s$  in the region near tuyeres. A macroscopically stable raceway is formed in front of the tuyere under the combined effect of the gas flow and the motion of the solid particles. The boundary of the raceway zone separating it from the coke bed is characterized by the lines of constant volume fraction which is equal to the initial volume fraction of solid,  $\alpha_s$ . The raceway is characterized by a central high void region and circulating particle region near the raceway boundary. Although the boundary may show some fluctuation, the overall raceway size remains almost unchanged. The blast air incurs a relatively large momentum exchange with the solid phase in the radial direction and results in convecting the solid particles radially towards the furnace axis. Through the momentum exchange the air flow loses its kinetic energy and is predominantly moving upward as expected (see Fig. 7).

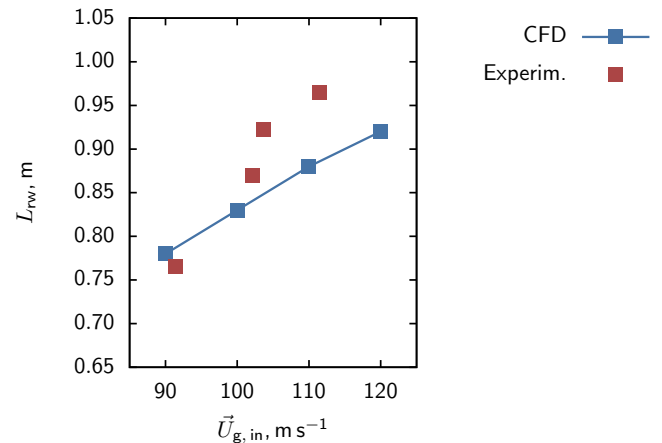


**Figure 4:** Comparison in the raceway depth  $L_{rw}$  between CFD simulation results and experimental data reported by Nomura (Nomura, 1986)



**Table 3:** Operating conditions

Tuyere diameter	123 mm
Tuyere angle	4°
Coke particle size	25–38 mm
Blast velocity	140–300 ms <sup>-1</sup>
Blast temperature	1413 K

The velocity distribution inside the raceway is an important factor that decides the conversion behavior of the coke and injected fuels. Fig. 8 shows the streamlines of the gas phase inside the raceway and in the surrounding coke bed. At the top and bottom of the raceway near the wall of the furnace stagnation zones can be observed. Their existence can also be verified by some particle-resolved simulations (Hilton and Cleary, 2012). In the middle of the raceway a recirculation

area is formed. This area defines the extent of the raceway and influences the residence time of the injected fuel particles.

The effect of the blast velocity is shown in Fig. 9, 10, and 11. The raceway size increases as the tuyere velocity rises. An increase in the gas velocity increases the momentum of the gas phase, which in turn causes a larger momentum exchange with the solid particles, moving them further away from the tuyere towards the center of the furnace. The raceway is larger for a higher tuyere velocity. It is also observed that the interaction between the different raceways increases with the increased tuyere velocity.

The effect of coke particle size is shown in Fig. 12. The results show that the raceway size increases as the coke size decreases, because smaller particles have larger specific surface area and gains stronger drag force from the gas flow with respect to their weight. This is in agreement with various experimental observations and correlations (Rajneesh *et al.*, 2004; Gupta, 2005; Gupta and Rudolph, 2006), where it is observed that the raceway shape is inversely proportional

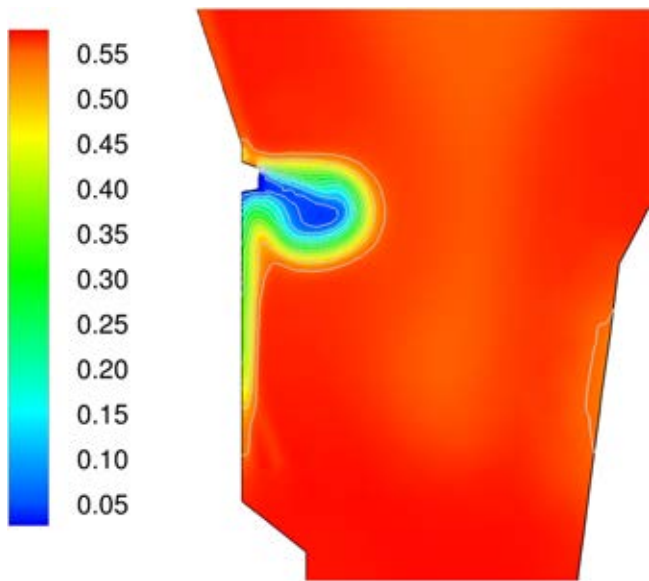


**Figure 5:** Spatial distribution of the granular phase volume fraction  $\alpha_s$  for the inlet velocity  $\vec{U}_{g,in} = 230 \text{ ms}^{-1}$  and the coke particle size  $d_s = 0.038 \text{ m}$  (axial cross-section)

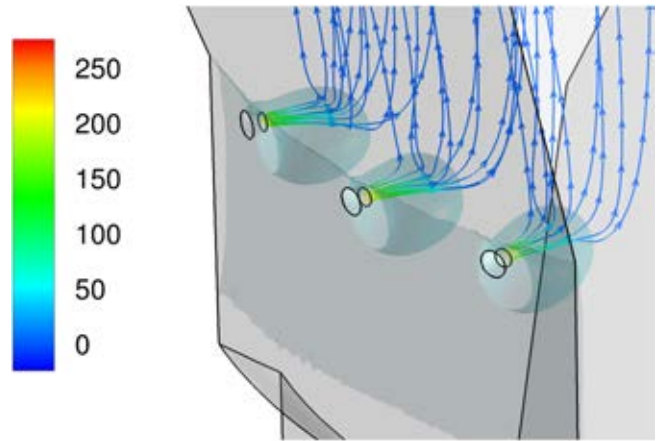


**Figure 7:** Streamlines of the gas phase colored by the gas velocity  $\vec{U}_g \text{ (ms}^{-1}\text{)}$  and iso-surfaces of the granular phase volume fraction  $\alpha_s$  (filled) for the inlet velocity  $\vec{U}_{g,in} = 230 \text{ ms}^{-1}$  and the coke particle size  $d_s = 0.038 \text{ m}$

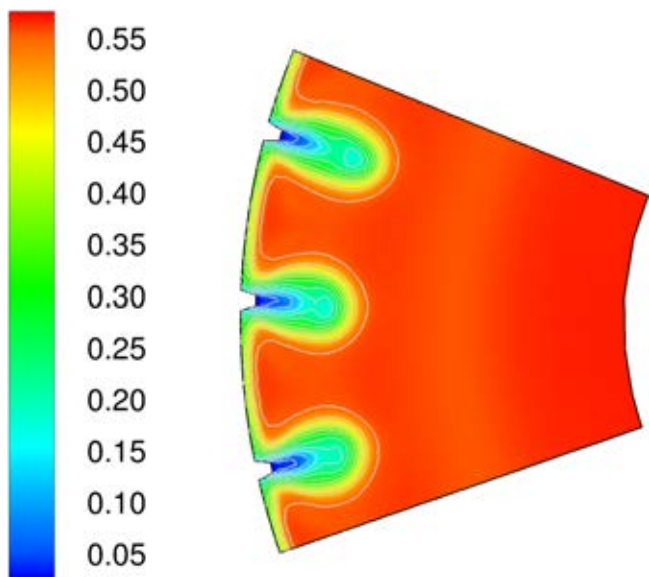


**Figure 6:** Spatial distribution of the granular phase volume fraction  $\alpha_s$  for the inlet velocity  $\vec{U}_{g,in} = 230 \text{ ms}^{-1}$  and the coke particle size  $d_s = 0.038 \text{ m}$  (tuyere level)

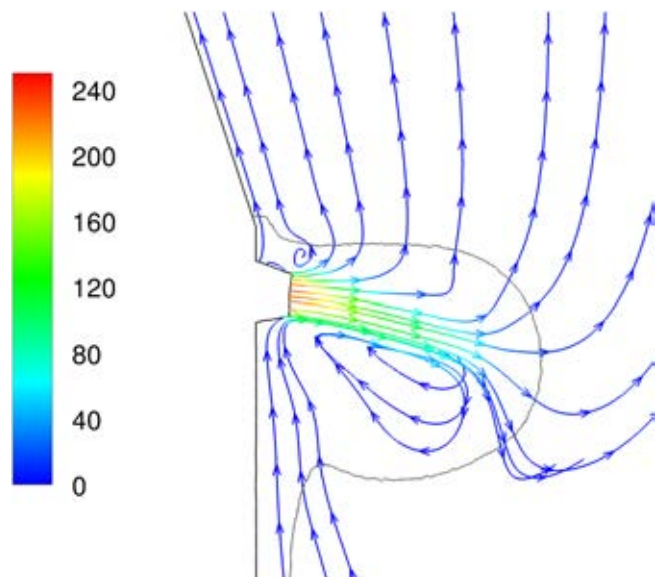


**Figure 8:** Streamlines of the gas phase colored by the gas velocity  $\vec{U}_g \text{ (ms}^{-1}\text{)}$  for the inlet velocity  $\vec{U}_{g,in} = 230 \text{ ms}^{-1}$  and the coke particle size  $d_s = 0.038 \text{ m}$  (axial cross-section)

to the coke particle diameter. Numerous numerical studies (Nogami *et al.*, 2004; Gupta and Rudolph, 2006; Selvarasu *et al.*, 2006; Rangarajan *et al.*, 2014) also confirm this observation.

Furthermore, an inspection of the coke velocities shown in Fig. 13 suggests that the formation of the raceway does not change the bed structure very much, i.e., the raceway is quite localized; particles in the bed can adjust themselves in response to the disturbance. Such a phenomenon has also been observed experimentally and was confirmed by numerical calculations using the DEM approach (Xu *et al.*, 2000; Goto *et al.*, 2002; Xu, 2003; Feng *et al.*, 2003; Nogami *et al.*, 2004; Yuu *et al.*, 2005; Umekage *et al.*, 2007; Zhu *et al.*, 2011; Hilton and Cleary, 2012; Adema, 2014).

Numerical models for raceway formation are complex and computationally demanding. Although, they capture various aspects of process behavior in a multidimensional frame-

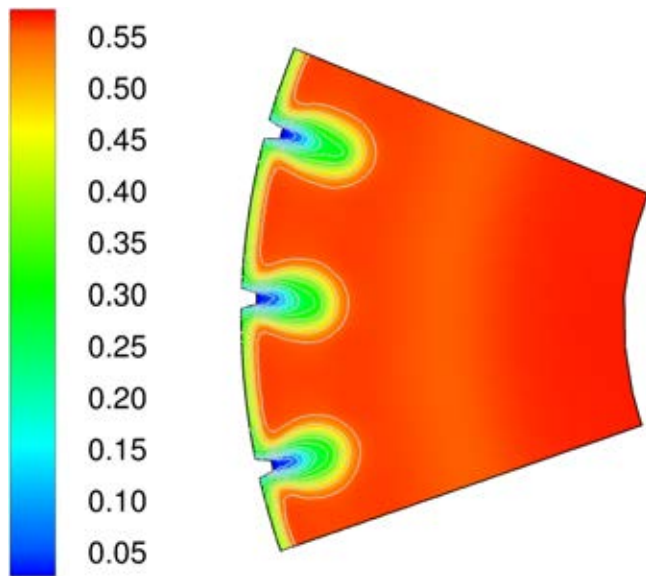


**Figure 9:** Spatial distribution of the granular phase volume fraction  $\alpha_s$  for the inlet velocity  $\bar{U}_{g,in} = 180 \text{ m s}^{-1}$  and the coke particle size  $d_s = 0.038 \text{ m}$  (tuyere level)

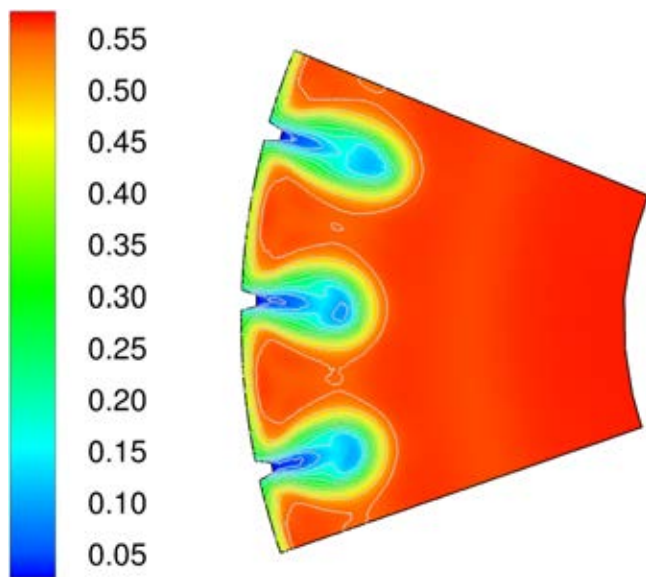


**Figure 10:** Spatial distribution of the granular phase volume fraction  $\alpha_s$  for the inlet velocity  $\bar{U}_{g,in} = 300 \text{ m s}^{-1}$  and the coke particle size  $d_s = 0.038 \text{ m}$  (tuyere level)

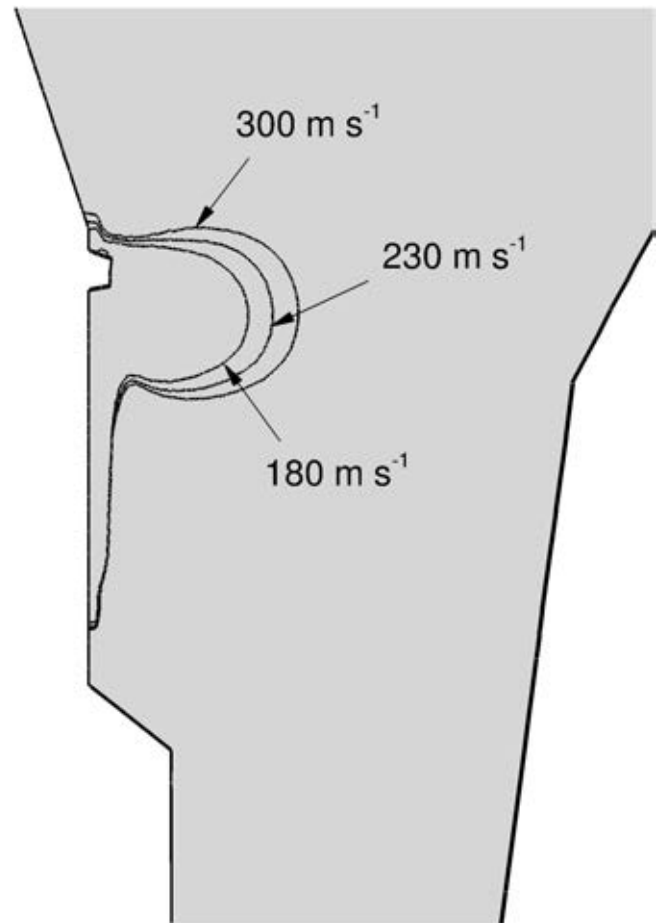


**Figure 11:** Shape and size of raceway zone for the coke particle size  $d_s = 0.038 \text{ m}$  and different inlet velocities  $\bar{U}_{g,in}$  (axial cross-section)

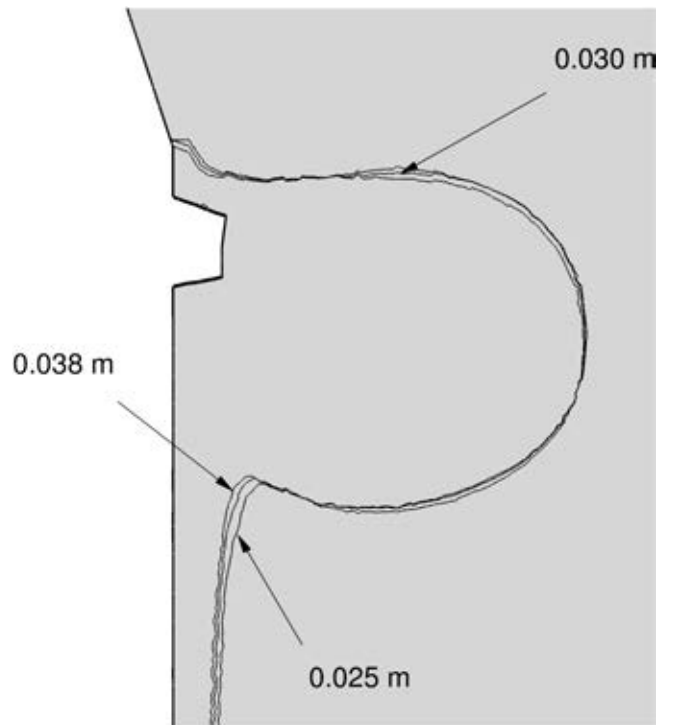


**Figure 12:** Shape and size of raceway zone for the inlet velocity  $\bar{U}_{g,in} = 230 \text{ m s}^{-1}$  and different coke particle size  $d_s$  (axial cross-section)

work, the approach is not suitable for real-time application due to its long computational time. In order to make process models amenable for real-time application, it becomes imperative to minimize the computational time significantly such that the real-time predictions can be made in synchronization with the plant operational data. For such applications, reduced-order models of the blast furnace processes need to be implemented in a real-time mode, which can be synchronized with the distributed control system (DCS) for an operating blast furnace. As discussed above, the reduced-order models for predicting raceway size and shape are primarily based on force and momentum balance and incorporate semi-empirical formalism to capture the process behavior without sacrificing the important phenomenology.

In this work the approach by Nomura (Nomura, 1986) was used. The predefined geometry of the raceway is described by using its depth,  $D_{rw}$ , width,  $W_{rw}$ , and height,  $H_{rw}$ , which are determined from a force balance formulated for two different points on the surface of the raceway boundary. The resulting correlation for the depth, width, and height of the

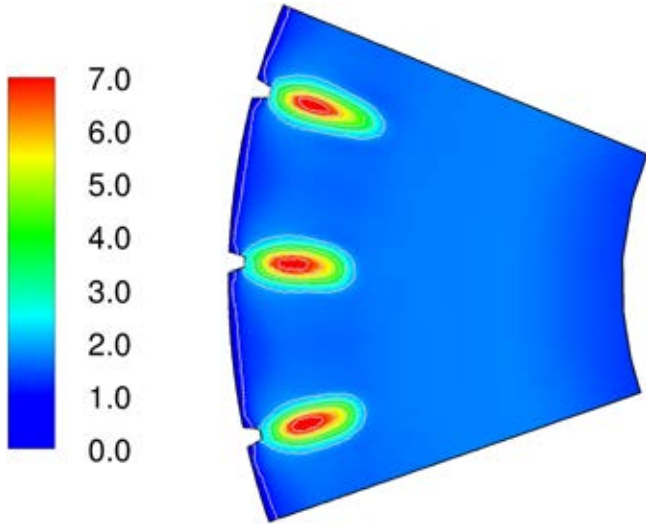


**Figure 13:** Spatial distribution of the granular phase velocity  $\vec{U}_s$  for the inlet velocity  $\vec{U}_{g,in} = 300 \text{ m s}^{-1}$  and the coke particle size  $d_s = 0.038 \text{ m}$  (tuyere level)

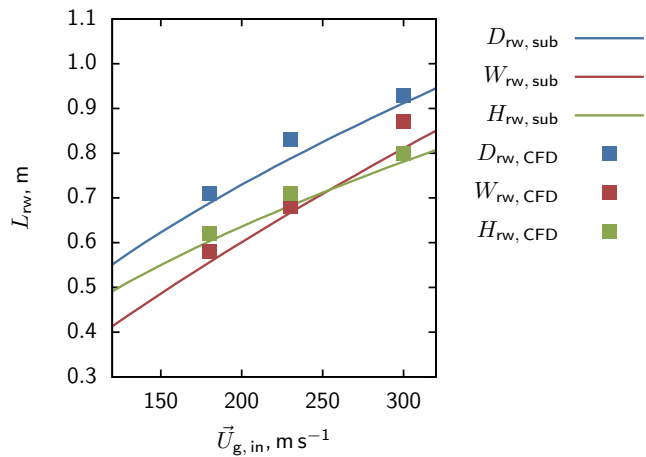


**Figure 14:** Dimensions of the raceway zone as a function of the gas inlet velocity for  $d_s = 0.038 \text{ m}$

**Table 4:** Model parameters for semi-empirical relations

$C_1$	$C_2$	$C_3$	$C_4$	$C_5$	$C_6$
1.8	0.275	0.45	1.34	1.4	2.18

raceway are

$$\frac{D_{rw}}{D_{tuyere}} = C_1 \left[ \rho_{g,0} \left( \frac{\dot{V}_{g,0}}{S_{tuyere}} \right)^2 \frac{p_0 T_g}{p T_0} \frac{1}{\bar{g} d_s \rho_s} \right]^{C_2}, \quad (32)$$

$$\frac{W_{rw}}{D_{tuyere}} = C_3 \left( \frac{D_{rw}}{D_{tuyere}} \right)^{C_4}, \quad (33)$$

$$\frac{(4H_{rw}^2 + D_{rw}^2) W_{rw}}{H_{rw} D_{tuyere}^2} = C_5 \left( \frac{D_{rw}}{D_{tuyere}} \right)^{C_6}. \quad (34)$$

In the work of Nomura (Nomura, 1986) the model parameters  $C_1, C_2, \dots, C_6$  are determined by using a comprehensive set of experimental data including data from other researchers as well as own data for different industrial-scale BFs. In order to achieve better approximation for the BF geometry under consideration the model parameters can be redefined using numerical data discussed above.

Figs. 14 and 15 show the resulting raceway dimensions as functions of the operational parameters for the newly defined set of model parameters. The new model parameters are summarized in Table 4.

## CONCLUSION

The shape and size of the raceway zone of an industrial-scale blast furnace have been numerically predicted in the Eulerian-Eulerian frame of reference for different blast velocities and coke particle sizes. The major observations are:

- An increase in the blast velocity increases the size of the raceway zone and the interaction with the neighbor ones.
- Increasing the size of the coke particles leads to decreasing of the raceway zone mainly due to the different mass-to-surface ratio of the coke particles.
- The real-time prediction of the shape and size of the raceway zone can be implemented using semi-empirical models based on force balance.

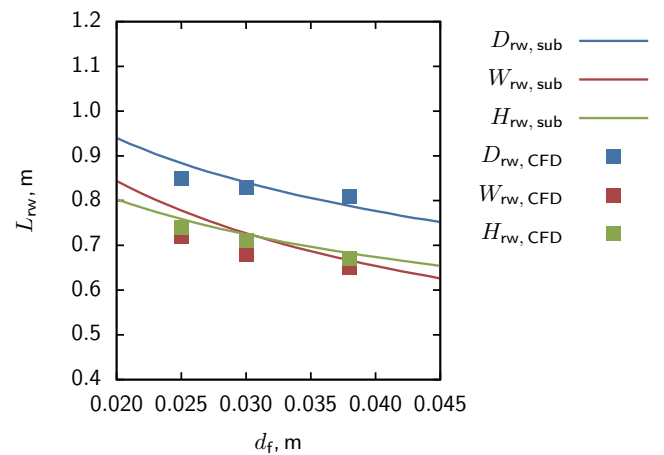


**Figure 15:** Dimensions of the raceway zone as a function of the coke particle size for  $\vec{U}_{g,in} = 230 \text{ m s}^{-1}$

## ACKNOWLEDGEMENT

This research has been funded by ArcelorMittal Eisenhüttenstadt GmbH and ArcelorMittal Bremen GmbH. The authors gratefully acknowledge the financial support.

## REFERENCES

- ADEMA, A. (2014). *DEM-CFD modelling of the iron-making blast furnace*. Ph.D. thesis, Delft University of Technology.
- AOKI, H., NOGAMI, H., TSUGE, H., MIURA, T. and FURUKAWA, T. (1993). "Simulation of transport phenomena around the raceway zone in the blast furnace with and without pulverized coal injection". *ISIJ International*, **33**(6), 646–654.
- CSANADY, G.T. (1963). "Turbulent diffusion of heavy particles in atmosphere". *Journal of the Atmospheric Sciences*, **20**, 201–208.
- DE BERTODANO, M.L. (1991). *Turbulent bubbly flow in a triangular duct*. Ph.D. thesis, Rensselaer Polytechnic Institute, Troy, New York.
- DING, J. and GIDASPOW, D. (1990). "A bubbling fluidization model using kinetic theory of granular flow". *AIChE Journal*, **36**, 523–538.
- ELGOBASHI, S.E. and ABOU, T.W. (1983). "A two equation turbulence model for two phase flows". *Physics of Fluids*, **26**, 931–938.
- ERGUN, S. (1952). "Fluid flow through packed columns". *Chemical Engineering Progress*, **48**(2), 89–94.
- FENG, Y.Q., PINSON, D., YU, A.B., CHEW, S.J. and ZULLI, P. (2003). "Numerical study of gas–solid flow in the raceway of a blast furnace". *Steel Research International*, **74**(9), 523–530.
- FERZIGER, J. and PERIĆ, M. (2002). *Computational Methods for Fluid Dynamics*. 3rd ed. Springer, Berlin.
- FLINT, P.J. and BURGESS, J.M. (1992). "A fundamental study of raceway size in two dimensions". *Metallurgical transactions B*, **23B**, 267–283.
- GEERDES, M., CHAIGNEAU, R., KURUNOV, I., LINGIARDI, O. and RICKETTS, J. (eds.) (2015). *Modern Blast Furnace Ironmaking: An Introduction*. 3rd ed. IOS Press, Netherlands.
- GIDASPOW, D. (1994). *Multiphase Flow and Fluidization: Continuum and Kinetic Theory Descriptions*. Academic Press, Boston.
- GIDASPOW, D., BEZBURUAH, R. and DING, J. (1992). "Hydrodynamics of circulating fluidized beds: Kinetic theory approach". *Proceedings of the 7th Engineering Foundation Conference on Fluidization*, 75–82. Brisbane, Australia.
- GOTO, K., MURAI, R., MURAO, A., SATO, M., ASANUMA, M. and ARIYAMA, T. (2002). "Massive combustion technology of solid fuel injected into blast furnace". *International Blast Furnace Lower Zone Symposium*, 1. Australasian Institute of Mining and Metallurgy (AusIMM), Wollongong, Australia.
- GUPTA, G.S. (2005). "Prediction of cavity size in the packed bed systems using new correlations and mathematical model". International Application Published under the Patent Cooperation Treaty (PCT). International Publication Number: WO 2005/010218 A1.
- GUPTA, G.S. and RUDOLPH, V. (2006). "Comparison of blast furnace raceway size with theory". *ISIJ International*, **46**(2), 196–201.
- HELLBERG, P., JONSSON, T.L.I., JÖNSSON, P.G. and SHENG, D.Y. (2005). "A model of gas injection into a blast furnace tuyere". *Fourth International Conference on CFD in the Oil and Gas, Metallurgical & Process Industries*, 1–5. SINTEF/NTNU.
- HILTON, J.E. and CLEARY, P.W. (2012). "Raceway formation in laterally gas-driven particle beds". *Chemical Engineering Science*, **80**, 306–316.
- HUILIN, L., GIDASPOW, D., BOUILLARD, J. and WENTIE, L. (2003). "Hydrodynamic simulation of gas–solid flow in a riser using kinetic theory of granular flow". *Chemical Engineering Journal*, **95**, 1–13.
- LAUNDER, B.E. and SPALDING, D.B. (1972). *Lectures in Mathematical Models of Turbulence*. Academic Press, London, England.
- LAUNDER, B.E. and SPALDING, D.B. (1974). "The numerical computation of turbulent flows". *Computer Methods in Applied Mechanics and Engineering*, **3**(2), 269–289.
- LUN, C.K.K., SAVAGE, S.B., JEFFREY, D.J. and CHEPURNIY, N. (1984). "Kinetic theory for granular flow, inelastic particles in Couette flow and slightly inelastic particles in a general flow field". *Journal of Fluid Mechanics*, **140**, 223–56.
- MONDAL, S.S., SOM, S.K. and DASH, S.K. (2005). "Numerical predictions on the influences of the air blast velocity, initial bed porosity and bed height on the shape and size of raceway zone in a blast furnace". *Journal of Physics D: Applied Physics*, **38**, 1301–1307.
- NATSUI, S., NOGAMI, H., UEDA, S., KANO, J., INOUE, R. and ARIYAMA, T. (2011). "Simultaneous three-dimensional analysis of gas–solid flow in blast furnace by combining discrete element method and computational fluid dynamics". *ISIJ International*, **51**(1), 41–50.
- NOGAMI, H., YAMAOKA, H. and TAKATANI, K. (2004). "Raceway design for the innovative blast furnace". *ISIJ International*, **44**, 2150–2158.
- NOMURA, S. (1986). "A simple treatment on the geometry of raceway zone". *Transactions ISIJ*, **26**, 107–113.
- OHNO, Y., FURUKAWA, T. and MATSU-URA, M. (1994). "Combustion behavior of pulverized coal in a raceway cavity of blast furnace and its application to a large amount injection". *ISIJ International*, **34**(8), 641–648.
- RAJNEESH, S., SARKAR, S. and GUPTA, G.S. (2004). "Prediction of raceway size in blast furnace from two dimensional experimental correlations". *ISIJ International*, **44**(8), 1298–1307.
- RANGARAJAN, D., SHIOZAWA, T., SHEN, Y., CURTIS, J.S. and YU, A. (2014). "Influence of operating parameters on raceway properties in a model blast furnace using a two-fluid model". *Industrial & Engineering Chemistry Research*, **53**, 4983–4990.
- SCHAFFER, D.G. (1987). "Instability in the evolution equations describing incompressible granular flow". *Journal of Differential Equations*, **66**(19–50).
- SELVARASU, N., GU, M., ZHOU, C. and ZHAO, Y. (2007). "Computer modeling of blast furnace raceway formation kinetics". *Proceedings of the Iron and Steel Technology Conference*, vol. 1, 425–433. Association for Iron & Steel Technology AISTech.
- SELVARASU, N.K., HUANG, D., CHEN, Z., GU, M., ZHAO, Y., CHAUBAL, P. and ZHOU, C.Q. (2006). "Prediction of raceway in a blast furnace". *Proceedings of IMECE2006*, 297–303. ASME, ASME. 2006 ASME International Mechanical Engineering Congress and Exposition.
- SIMONIN, C. and VIOLLET, P.L. (1990). "Predictions of an oxygen droplet pulverization in a compressible subsonic co-flowing hydrogen flow". *Numerical Methods for Multiphase Flows, FED'91*, 65–82.

SINGH, V., GUPTA, G.S. and RAJNEESH, S. (2006). "Modelling of void initiation and breaking phenomena in a packed bed". *Ironmaking and Steelmaking*, **33(2)**, 101–110.

SZEKELY, J. and POVEROMO, J.J. (1975). "A mathematical and physical representation of the raceway region in the iron blast furnace". *Metallurgical Transactions B*, **6B**, 119–130.

UMEKAGE, T., KADOWAKI, M. and YUU, S. (2007). "Numerical simulation of effect of tuyere angle and wall scaffolding on unsteady gas and particle flows including raceway in blast furnace". *ISIJ International*, **47(5)**, 659–668.

VDE (1976). "Automatisierung des Hochofenverfahrens, Teil 2: Modelluntersuchungen über die Ausbildung der Zirkulationszone vor den Blasformen von Hochöfen". Tech. rep., Kommission der Europäischen Gemeinschaften, Düsseldorf.

WEN, C.Y. and YU, Y.H. (1966). "Mechanics of fluidization". *Chemical Engineering Progress Symposium Series*, vol. 62, 100–111.

XU, B.H. (2003). "Modelling of the gas fluidization of a mixture of cohesive and cohesionless particles by a combined continuum and discrete model". *KONA Powder and Particle Journal*, **21**, 100–108.

XU, B.H., YU, A.B., CHEW, S.J. and ZULLI, P. (2000). "Numerical simulation of the gas–solid flow in a bed with lateral gas blasting". *Powder Technology*, **109**, 13–26.

YUU, S., UMEKAGE, T. and MIYAHARA, T. (2005). "Prediction of stable and unstable flows in blast furnace raceway using numerical simulation methods for gas and particles". *ISIJ International*, **45(10)**, 1406–1415.

YUU, S., UMEKAGE, T., MATSUZAKI, S., KADOWAKI, M. and KUNITOMO, K. (2010). "Large scale simulation of coke and iron ore particle motions and air flow in actual blast furnace". *ISIJ International*, **50(7)**, 962–971.

ZHU, H.P., ZHOU, Z.Y., HOU, Q.F. and YU, A.B. (2011). "Linking discrete particle simulation to continuum process modelling for granular matter: Theory and application". *Particuology*, **9**, 342–357.

# MODELLING AND MEASUREMENTS IN THE ALUMINIUM INDUSTRY

## WHERE ARE THE OBSTACLES?

Eirik MANGER<sup>1</sup>

<sup>1</sup> Hydro Aluminium, PMT, Hydrovegen 67, Porsgrunn, NORWAY

\* E-mail: eirik.manger@hydro.com

### ABSTRACT

In this paper the necessity of obtaining experimental data with good enough quality for model verification is addressed. Relevant examples from the aluminium industry are shown to illustrate some cases where measurements and model results work hand in hand on identifying bottlenecks and improving the situation. Moreover, measurements and their interpretation are briefly touched upon, trying to enlighten a few of the challenges on data collection in industrial environments and comparison with models.

Realising that measurements only uncovers parts of the real picture, an approach to estimate data interpretation errors is briefly outlined. A good model can and should rule out erroneous measurements – with the right use it can even give some guidelines on where to get good measurements.

**Keywords:** Measurements, CFD, Aluminium, Ducting.

### NOMENCLATURE

*Greek Symbols*

$\rho$  Mass density, [kg/m<sup>3</sup>].

*Latin Symbols*

$C$  Constant, [-].

$p$  Pressure, [Pa].

$u$  Velocity, [m/s].

### INTRODUCTION

The development in computer hardware combined with more sophisticated modelling tools have during the last decades opened up a wealth of new possibilities to understand and explain physical phenomena in complex systems. This is indeed true also for the aluminium industry, where the processes range from “simple” gas flow all the way to multiphase flow and phase changes coupled with electromagnetic forces.

Models are however still only approximations of the real processes, and comparison with measurements is crucial and necessary. A previous presentation Manger (2014) showed the importance of correct problem descriptions. Along the same line, and equally important, are the access to and the quality of experimental data.

In this paper modelling combined with measurements are used to identify bottlenecks and other challenges in gas flow duct systems. Two different case studies will be used as examples, focusing on the area between matches and differences.

### CASE STUDY I

The first case study is concentrated around a suction system for a quite old pot line, built in the mid 80's. Significant pressure drop increase in the ducting system during the last years has reduced the net pot suction rates and led to an unacceptable situation in terms of plant emissions. Measurements pointed towards deposits in the system, but there were questions on where and how much.

#### Original ducting system

Before moving on to the problem analysis, a brief overview of gas suction systems and their designs in aluminium plants is given.

#### *Design*

Gas suction systems for aluminium plants start at the individual pot by collecting fume gases from underneath the hooding. This is done via a gas channel with distributed openings along the pot's length, usually located behind the anode beams at the top of the superstructure – see Figure 1. To avoid emissions from the pot, the suction rates must be high enough to keep the fume gases inside the pot hooding. Necessary rates will depend on i.a. hooding efficiency, size and temperature, typically varying from 4500 to 6500 Nm<sup>3</sup>/h/pot. Insufficient suction rates on the pots will cause undesirable emissions to the pot room and to the environment.



**Figure 1:** Gas channels at the top of the super structure.

Designing pot gas channels is a relatively straightforward task, with a few guidelines:

- Pressure drop should be quite low
- Deposits in the channel should be avoided
- The suction should be even along the entire pot
- The construction must be simple and robust

Avoiding deposits in the pot gas channels can be (and often is) a challenge, particularly at the opposite end of the outlet where the channel dimensions lead to low velocities. This again changes the properties of the system and has undesirable effects.

The suction rate from each individual pot is controlled by dampers. The fume gas is led into one of several larger branches transporting the gas towards the Fume Treatment Plant, shortened FTP. Number of pots per branch varies, typically from 16 to 32, but there are systems with as many as 60 pots on one single line. Figure 2 shows the particular gas systems of interest, including which pot numbers that are connected to the different sections. The system might not look impressive at first glimpse, but the reader should note that the total length of the channels is 500 metres, with channel cross sections varying from 2.5 m<sup>2</sup> to approximately 8 m<sup>2</sup>. The main inlets to the FTP have a cross section of nearly 30 m<sup>2</sup>.

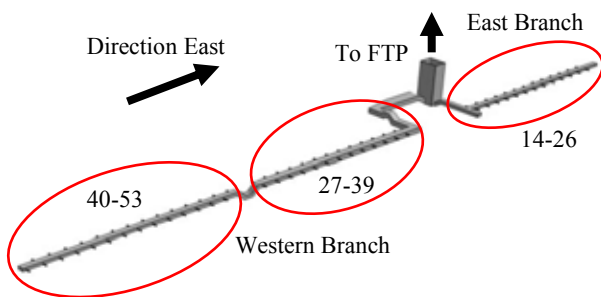


**Figure 2:** Gas ducting system.

### Modelling

To get an impression of the ducting system performance, several CFD models were established.

First the sizes of the opening slots in the pot gas channel were investigated. A simple model based the existing layout was established having ~24K hexahedral cells. Constant density for air at 120°C was assumed, and the Relizable k-ε model handled turbulence. The flow distribution could then be determined by using a pressure inlet with a fixed outlet flux. Slot sizes decrease towards the outlet to compensate for the increased suction pressure (lower static pressure), mainly caused by increased gas velocity towards this side. The geometric model is shown in Figure 3, whereas the predicted static pressure just outside and inside the pot gas channel is shown in Figure 4.



**Figure 3:** Geometric model, pot gas channel.

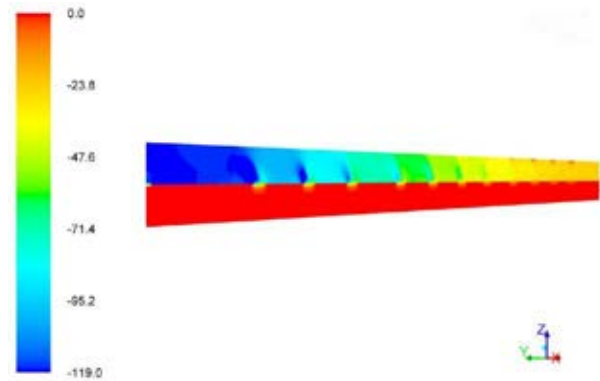


**Figure 4:** Static pressure outside and inside the pot gas channel.

Analysing the flux through each of the slots revealed that the openings towards the outlet actually were too small, as can be seen in Figure 5. By adjusting the size of these, a more even suction from the pot could be achieved. In addition, the net pressure drop through this part of the system was reduced with nearly 25%.

The CFD model for the entire duct system became a bit more complicated. A mesh with approximately 3.8M polyhedral cells was constructed. Similar models and boundary conditions as for the hooding simulations were used, except that the inlet pressure from each pot had to be handled separately.

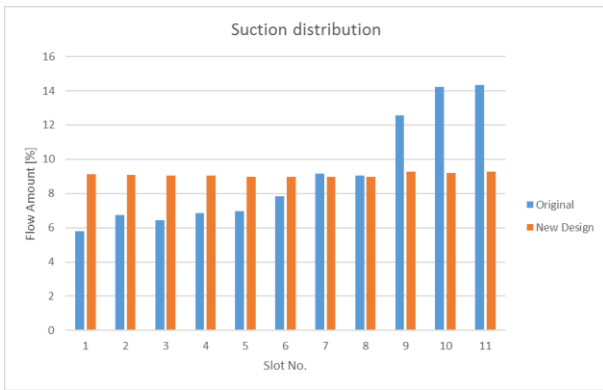


**Figure 5:** Original and new suction distribution.

Adding the measured pressure drop through the interface towards the ducting branches (will be touched upon later) gave a reasonable estimate for the total inlet pressure drop into the channel. This pressure drop is modelled as a turbulent dynamic resistance on the form

$$\Delta p \approx C \cdot \frac{1}{2} \rho u^2 \quad (1)$$

The calculated pot suction rates for the unbalanced system are depicted in Figure 6. The results show, as expected, that the pots closest to the FTP intake have significantly higher suction rates compared against the end pots. Furthermore, the branch east of the FTP inlet generally have more suction compared to the western branch. This is also as expected, since there are a number of restrictions along the western flow path.

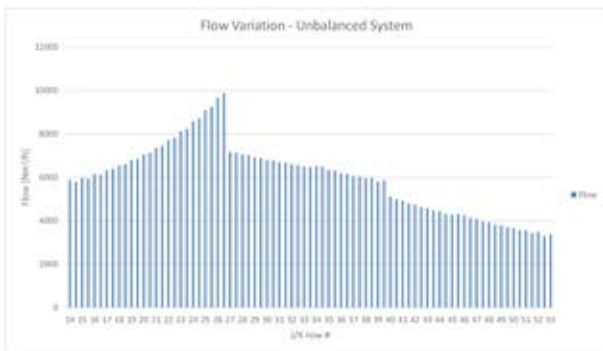


**Figure 6:** Calculated flow rates for an unbalanced system.

Before moving on to investigate if, and if so where, there are deposits in the system, the flow must be balanced theoretically. In real life this is done by measurements, so there might be some deviations to the actual damper settings, but this represents the closest match achievable between modelling and measurements.

The estimated resistance coefficients for balancing the system are shown in Figure 7. From correlations it can be shown that a resistance factor of around 4 represents blocking approximately half the available flow area. After balancing the systems, the average flow rate is predicted to some 6000 Nm<sup>3</sup>/h/pot at 130°C and a suction pressure around 1500 Pa at the FTP inlets.

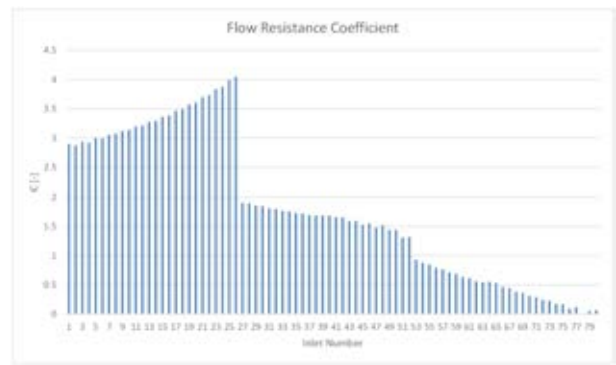


**Figure 7:** Estimated resistance coefficients for balancing the suction system.

### Deposit analysis

With a balanced system in place, the search for obstacles and deposits could commence. Measured static pressures are shown in Figure 8. These correspond to effective suction pressures on the pots and were obtained by M. Karlsen (2016). Pots 1 to 13 in the series are connected to another FTP and not subject to analysis here, so focus should be on the pots in the range from 14 to 55. A first inspection shows that there is a big jump in suction pressure between the pots 40 and 41.

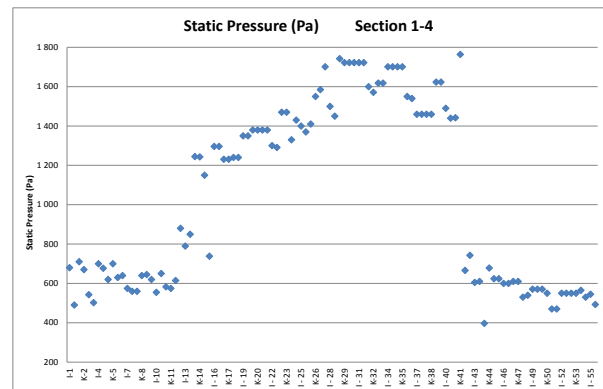


**Figure 8:** Measured suction pressure in the system.

Putting the simulation results on top of this shows that there is also a predicted jump in the pressure profile not seen in the measurements. In addition to the rather obvious restriction between pots 41 and 42, this indicates that something might be blocking the path from the eastern branch as well.

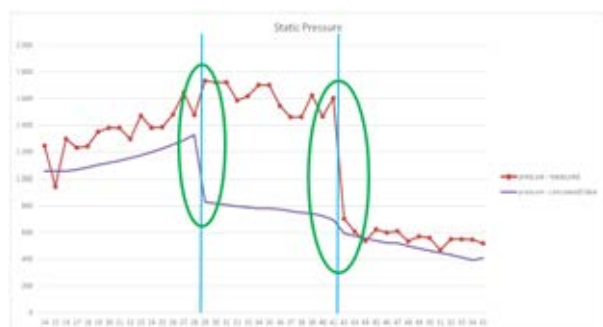


**Figure 9:** Comparison between simulated and measured pressure profile.



To investigate the effect of deposits and put numbers on the amount of material, the geometry was altered by blocking part of the lowest section in the channel dip, as can be seen in Figure 10. By trial error the deposit height in the channel dip was predicted to around one meter, leaving an open space only around 60 cm high from the originally 165 cm. Again, the pictures might not justify the dimensions – with one meter deposits as shown here, the blocked volume is some 12-13 m<sup>3</sup>.

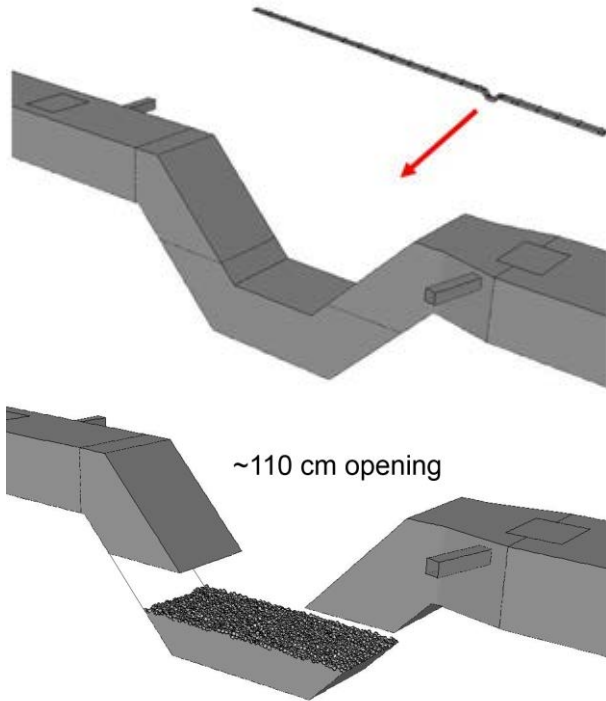


**Figure 10:** Top; the original channel dip layout. Bottom; channel dip partially filled with deposits.

The yellow line in Figure 11 shows the revised pressure profile with deposits in the channel dip. The match between measurements and simulations is now quite good for the eastern part of the system. By adding a restriction between the FTP inlets and the western branch, an even better agreement can be achieved, as shown with the green line. The amount of deposits and exact location for this have however not been followed further in the simulations.

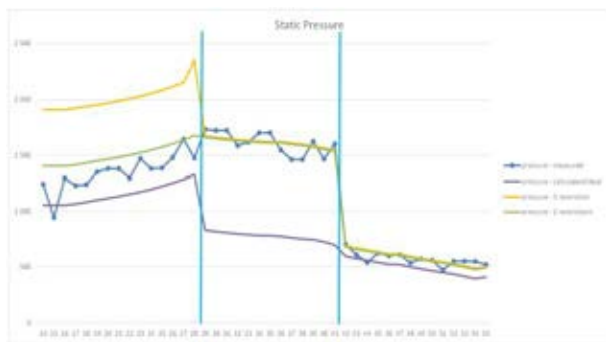


**Figure 11:** Estimated resistance coefficients for balancing the suction system.

### Optimising the pot gas channel

In a situation where every extra Pascal of suction pressure matters in trying to improve the emissions, especially for the end pots, also the construction of the pot channel interface towards the gas channel branch has been addressed. The original design had several obstructions and small openings, which can be seen in Figure 12. Streamlining, removing obstacles, and increasing the smallest openings with minor adjustments, as showed in Figure 13, reduce the pressure drop with approximately 25%, which also will contribute to larger net suction rates for the pots.

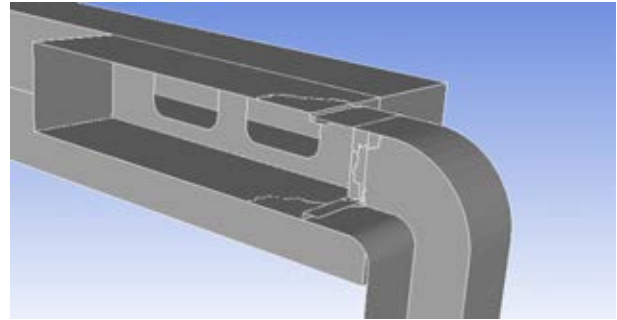


**Figure 12:** Original pot channel outlet.

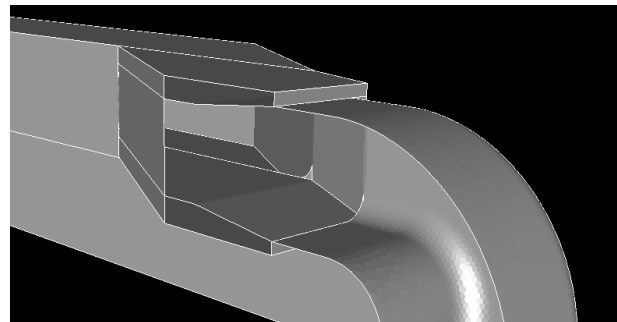


**Figure 13:** Optimised pot channel outlet.

### Current status

Comparing measurements and calculations strongly indicated that deposits reduced the pot suction rates significantly upstream the channel dip in the western branch. Opening some small hatches confirmed these conclusions, and actions could be planned.

#### Deposit removal

With evidence on significant amounts of deposits in the channel dip, it was decided to send in personnel to inspect the situation. Large amounts of rock solid material were found at the bottom, and the smallest opening height was measured to around 60 cm – in very good agreement with the simulations. It was further decided to try to remove some of the deposits.

Before starting the work, however, a there was a question asking how much of the material that should be removed to see an impact on the end pots. Thus, a series of simulations were run looking at the dependence between end pot suction rate and deposit height. Results from the simulations, plotted in Figure 14, show that there seems to be a minimum threshold value around

one meter. For opening heights larger than this, the net gain of removing deposits is relatively low per unit, whereas below this value the suction pressure on the end pots decrease rapidly.

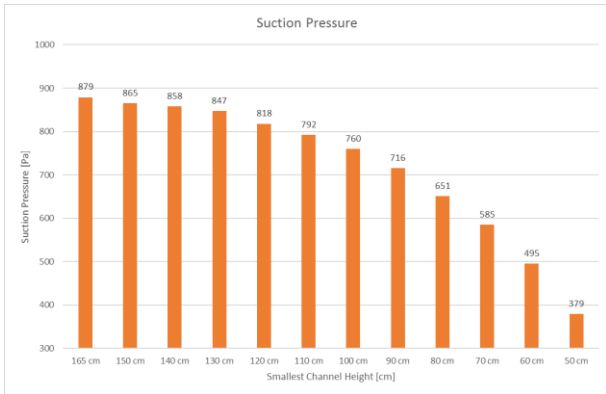


**Figure 14:** Effect of smallest opening height on end pot suction rate.

Personnel has done a magnificent job in digging and removing deposited material from the channel dip. Currently the smallest opening height has been increased to almost one meter, as recommended from the calculations. The duct system has responded well, again in quite good agreement with the model, and the suction pressure on the end pots is now close to 800 Pa.

*Superstructure modifications*

The proposed changes on the pot gas channel interface has also been accepted by the plant management. The changes are implemented when the pots are relined, and will slowly contribute to an even better emission picture.

*Final comments*

This work has shown how measurements combined with CFD models can be used to analyse and identify obstacles in a gas ducting system. The essence, perhaps not stated very directly, is that even quite simple models (no boundary layers, k-ε based turbulence model etc.) perform well enough when uncertainties on e.g. geometry, deposits and measurements are added to the picture. There is no point in striving for the last 1% accuracy in simulation models when other deviations easily can be a factor 10-20 above this. For us this is pragmatic modelling.

**CASE STUDY II**

The second case study is also concentrated around a suction system for a rather old pot line. Increasing the line current has altered the performance, and larger suction rates were needed to avoid substantial emissions.

Rather than looking at the entire system, the focus will be towards the suction rates from single pots. When analysing the system, there were large discrepancies between pitot tube measurements and the simulation results. To explain these differences a deep dive into measurement interpretation was needed, forming a basis of what could be referred to as model assisted measurements.

**Superstructure gas channel**

To get an understanding of the pots’ suction rates, the superstructure gas channels were simulated. Again a very simple model with some 54K polyhedral cells, constant density, Relizable k-ε, in combination with pressure inlet and fixed mass outflow, but it should still be able to capture the main features of the design. The geometric layout is shown in Figure 15, whereas the predicted velocities are plotted below in Figure 16. The velocities at the inlets are quite low, and the channel outlet velocity is around 16 m/s.

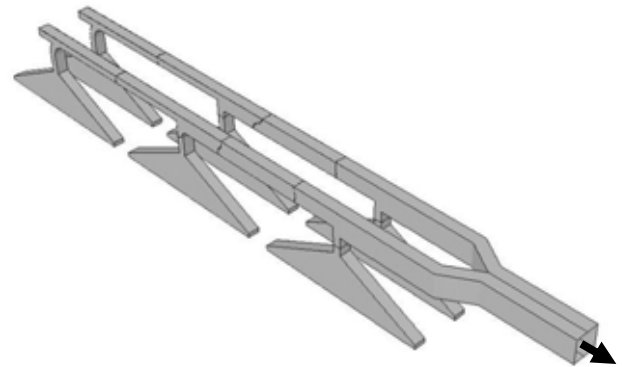


**Figure 15:** Gas channel design in the superstructure.

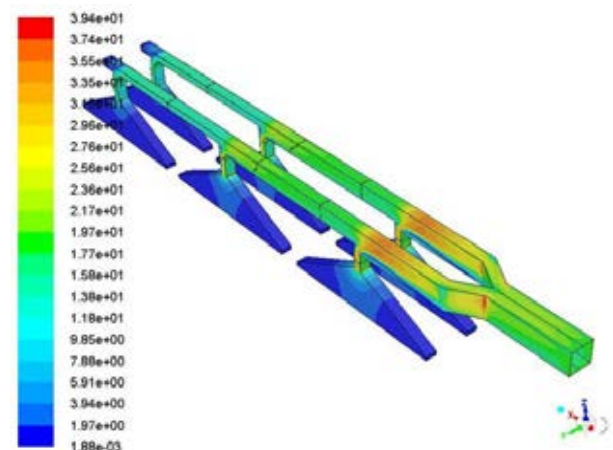


**Figure 16:** Predicted velocities in the superstructure gas channel.

In general, the pressure drop through the superstructure gas channel will depend on the flow rate as well the density – or implicitly, on temperature. Figure 17 shows the relationship between pressure drop and flow rate, given in units of Nm<sup>3</sup>/h (which actually is equivalent to a mass flow rate), for three different temperatures.

In addition, the pressure drop is given for two different states of the gas channel. The inlets from each hooding contain dampers to control and balance the flow. When fully open, the gas suction is not even along the pots. When balancing the flow, the pressure drop is increased with some 30%.

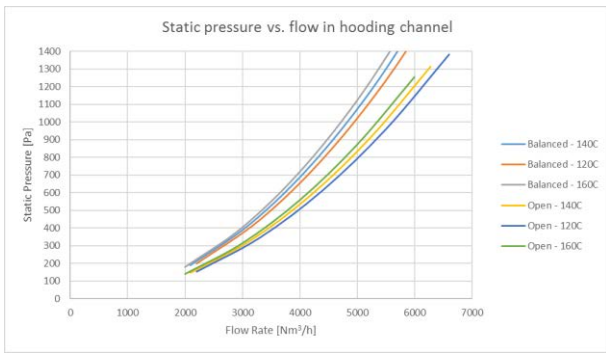


**Figure 17:** Gas channel design in the superstructure.

Ideally, calculated flow rates should of course match the measurements. However, when comparing these, there were large deviations, as can be seen in Figure 18. Here only the pressure drop curves for 140°C have been shown for simplicity. The estimated flow rates, from seven profile points across the pipe using a pitot tube, seem to indicate pressure drops of the order 800 Pa for flow rates around 6000 Nm<sup>3</sup>/h. The calculations predict 1100-1200 Pa at the same rates – or even higher if the superstructure gas channel was balanced.

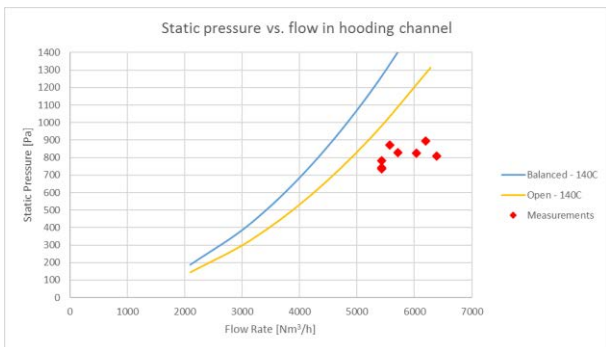


**Figure 18:** Comparing measurements with simulation results.

### Measurement interpretation

In search for explanations there were no reasons to disbelieve in the measurements – these were of excellent quality, with low variation and good repeatability. At the same time, adjusting and refining the CFD model had little impact on the calculated pressure drop.

After some discussions back and forth, the measurement interpretation came up as a point that might be questioned. Due to the channel outlet design, which has an expander from Ø200 to Ø460, and the location of the measurement point just downstream of this (access restrictions), the measured velocities showed a clear parabolic profile in the pipe, see Figure 19. Since the flow is highly turbulent, such a profile is not exactly expected, also indicating that the flow is not fully developed. In addition, for a circular pipe as measured here, the cross-sectional area covered by each point increases radially. Thus, utilizing our standard way of measurement interpretation, i.e. simple averaging, might not be good enough in this case.

The reader should note that the number of points in the velocity profile plot differs from the actual number of measurements points. Using an interpretation template, the user should specify both wall distance from first/last point, as well as the distances between the points. The values at the wall, constituting the first and the last points in the velocity profile, can either be set to zero or be found from extrapolation – representing a best possible reconstruction of the velocity profile.

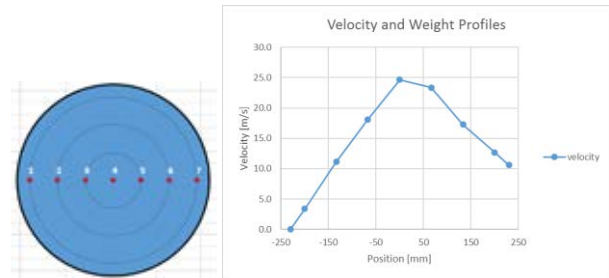


**Figure 19:** Measured velocity profile and corresponding measurement points.

To overcome the hurdles on measurements/model discrepancy, a revised method on measurement interpretation was outlined and used. The method will be discussed briefly in the next section, but for now concentrate on the numbers found. The new interpretation puts the pressure drops as function of flow rates right on top of the model predictions, see Figure 20, and it was concluded that this was the main cause for the deviations.

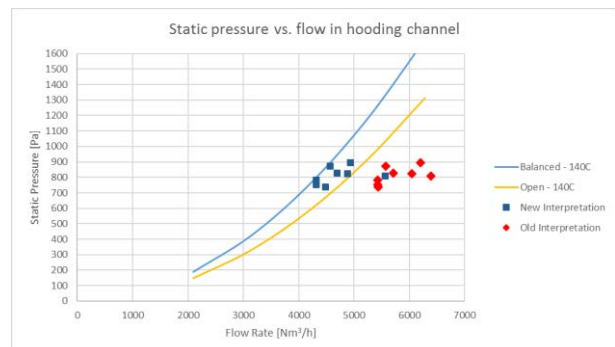


**Figure 20:** Changing the measurement interpretation.

### Model assisted measurements

It is no understatement to claim that out in the field, measurements must often be performed based on availability, which not necessarily corresponds to the optimal location. Based on the findings in this last project, there is now a recommendation on always combining measurements and models with the aim to say something about the conditions at the measurement location.

To give an example of how interpretation can influence the flow predictions from measurements, two rather simple geometries are considered – a straight pipe and an expander, the last one being showed in Figure 21.

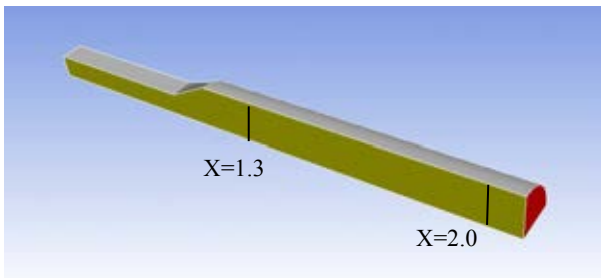


**Figure 21:** The expander, to be measured virtually.

The flow is simulated using a fixed velocity inlet, and monitoring points are added at two downstream locations to measure velocities virtually. These are then again used to calculate the flow rates (or rather the mean velocity). Three different approaches for calculating the mean velocity are considered:

- Simple arithmetic averaging
- Area weighted averaging
- Linear reconstruction of the velocity profile

The results from the virtual measurements are given in Table 1, whereas the calculated mean velocities and the deviations when using the different methods are shown in Table 2. Note that the real average velocity should be around 8.9 m/s.

As can be seen from the tables, there are only small discrepancies for the straight pipe section, independent of which calculation method used. For the expander, the story is however quite different. Close to the expander (at  $X=1.3$ ), the mean velocity based on arithmetic averaging is overestimated with 50%. Using area based averages improves the figure somewhat, but there is still a deviation of almost 35%. The calculation based on linear reconstruction of the velocity profile is however superior to the others, with only 10% deviation even at this position (which is quite close to the expansion and far from optimal). Further downstream the expansion the deviations decrease.

**Table 1:** Virtual measurements in a pipe and an expansion.

Point No.	Straight		Expansion	
	$X = 1.3$	$X = 2.0$	$X = 1.3$	$X = 2.0$
1	8.96	9.13	8.7	8.8
2	8.97	9.23	14.5	9.7
3	8.97	9.23	15.3	10.3
4	8.97	9.23	15.3	12.5
5	8.97	9.23	15.3	10.3
6	8.97	9.23	14.5	9.7
7	8.96	9.13	8.7	8.8

**Table 2:** Estimated mean velocities based on the virtual measurements, and the deviations from real values.

Method/Variable	Straight		Expansion	
	$X = 1.3$	$X = 2.0$	$X = 1.3$	$X = 2.0$
<i>Avg. Velocity</i>				
Simple Arithmetic	9.0 m/s	9.2 m/s	13.2 m/s	10.0 m/s
Area Weighted	9.0 m/s	9.2 m/s	11.8 m/s	9.4 m/s
Linear Flow Interp.	9.0 m/s	9.1 m/s	9.8 m/s	9.1 m/s
<i>Deviation</i>				
Simple Arithmetic	1.9 %	4.6 %	49.8 %	13.8 %
Area Weighted	1.9 %	4.3 %	34.2 %	7.0 %
Linear Flow Interp.	1.8 %	3.9 %	11.2 %	3.2 %

The latter represents an example on how to use simulations in “assisting” with interpretation and perform quality control of measurements. In the future more work will follow this line.

## CONCLUSION

The conclusions are:

1. With the powerful CFD tools available today, simulation errors due to e.g. model selection or settings are often smaller than the measurement errors in an industrial environment. This is of course true only if the models are utilized in a correct manner.
2. Measurements, even though not of the best quality, can hand in hand with simulations prove to be a valuable tool for finding faults and obstacles in existing systems. Keep focus on the discrepancies.
3. Always have a knowledge of what is measured and how to interpret and convert the results into other numbers. A wrong interpretation and understanding will evidently lead to inaccurate figures and deviations.

## ACKNOWLEDGEMENT

Interaction between measurements and modelling is a teamwork requiring expertise in both areas. The author wishes to acknowledge M. Karlsen and A. Dyrøy (2016) for excellent field work, discussions and contributions through the work.

## REFERENCES

- MANGER, E. (2014), “CFD in Problem Analysis and Optimisation – the Importance of Correct Boundary Conditions”, *Proc. CFD 2014 – 10<sup>th</sup> Int. Conf. on CFD in the Oil & Gas, Metallurgical and Process Industries*, Trondheim, Norway, June 17-19.
- KARLSEN, M. and DYRØY, A. (2016), *Private Communications*.



## MODELLING OF CHEMICAL REACTIONS IN METALLURGICAL PROCESSES

M. Efe KINACI<sup>1\*</sup>, Thomas LICHTENEGGER<sup>2,3†</sup>, Simon SCHNEIDERBAUER<sup>1‡</sup>

<sup>1</sup>Christian Doppler Laboratory for Multi-Scale Modelling of Multiphase Processes, 4040 Linz, AUSTRIA

<sup>2</sup>Linz Institute of Technology (LIT), Johannes Kepler University, 4040 Linz, AUSTRIA

<sup>3</sup>Department of Particulate Flow Modelling, Johannes Kepler University, 4040 Linz, Austria

\* E-mail: mustafa\_efe.kinaci@jku.at

† E-mail: thomas.lichtenegger@jku.at

‡ E-mail: simon.schneiderbauer@jku.at

### ABSTRACT

Iron-ore reduction has attracted much interest in the last three decades since it can be considered as a core process in steel industry. The iron-ore is reduced to iron with the use of blast furnace and fluidized bed technologies. To investigate the harsh conditions inside fluidized bed reactors, computational tools can be utilized. One such tool is the CFD-DEM method, in which the gas phase reactions and governing equations are calculated in the Eulerian (CFD) side, whereas the particle reactions and equation of motion are calculated in the Lagrangian (DEM) side. In this work, this method has been extended to cover the most common types of representation models for the reactions of solids submerged in fluids. These models are the Shrinking Particle Model (SPM) and the Unreacted Shrinking Core Model (USCM). With the use of the SPM, the implemented communication framework between the CFD and DEM sides have been verified by running some preliminary cases and comparing the species mass balances. In the modelling of iron-oxide reduction the SPM is insufficient to represent the different reaction steps, therefore a three-layered USCM is utilized. The implemented USCM is validated by running some preliminary cases.

**Keywords:** CFD-DEM, iron-ore reduction, chemical models, particle shrinkage, unreacted-core model .

### INTRODUCTION

The rising energy demands, the deterioration of the quality of ore and coal due to high costs and low availability related with the shortage of resources, as well as the increased usage of mini mills, which might replace the conventional route of steel-making with the use of scrap or scrap substitutes, has lead to the development of new ways for the direct reduction of iron ores (Habermann *et al.*, 2000; Yang *et al.*, 2010). The practical importance of being used as feedstock in iron- and steel-making processes has also played a role at encouraging researchers to give attention to the reduction of iron-oxides (Donskoi and McElwain, 2003; Turkdogan and Vinters, 1971). Currently, the three available iron-making technologies are the blast furnace, smelting reduction and direct reduction technologies.

The leading process used in iron-making is the blast furnace, which consists of a moving bed reactor with countercurrent flow of the solid reactants against a reducing gas. In the blast furnace process, the iron ore fines which built up around 80% of iron ores, need to go through a pelletizing or sintering process (Schenk, 2011). In some cases, fine ores can directly

be charged into the reduction process such as the fluidized bed technology, making it highly advantageous. Such fluidized bed reactors are used in the pre-reduction stage of the FINEX<sup>®</sup> process (Habermann *et al.*, 2000; Primetals, 2015). The FINEX<sup>®</sup> process produces hot metal in the same quality as traditional blast furnaces, however the coke making and sintering of the fine ores are avoided. The iron-ores that are charged into the process go through fluidized bed reactors where they are heated and reduced to DRI (Direct Reduced Iron), which is charged into the melter gasifier where final reduction and melting as well as the production of reducing gas by gasification of coal with oxygen takes place. Another advantage of the FINEX<sup>®</sup> process is the exhaust gas, which can be used for various other applications such as heating within a steel plant, power generation and so forth (Plaul *et al.*, 2009).

The main reactions for the reduction of metallic oxide with a gaseous reductant of carbon monoxide (CO) and hydrogen (H<sub>2</sub>) can be expressed with the following steps:

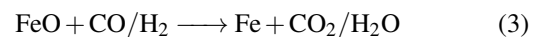
Hematite to Magnetite:



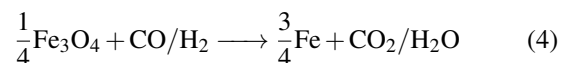
Magnetite to Wustite:



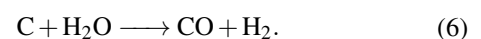
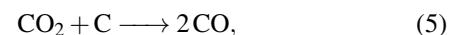
Wustite to Iron:



If the reaction temperature is below 570°C, then there is no wustite formation and magnetite reduces directly to metallic iron with the reaction



The carbon monoxide that is utilized in the indirect reduction of iron-oxide comes from the gasification of carbon with carbon-dioxide that is described with the homogeneous, endothermic Boudouard reaction (5) and from the water-gas reaction (6), which can be defined as



Since access to the reactor is limited due to harsh conditions inside, carrying out measurements to investigate the processes is complicated. Thus, in order to better understand the

reactors and to make improvements on the processes, simulation methods and computational tools are utilized. One such tool is the Two-Fluid Model (TFM), which is an Euler-Euler approach that treats the solid and the fluid phases as a continuum. However, this model lacks the proper representation of particle size description and the related physical phenomena. In order to represent micro-scale phenomena, the TFM would require a fine spatial grid and that would make the process unaffordable for industrial scale utilization. If a coarse-graining is carried out there would be a loss of unresolved (small) scales and lead to errors (van der Hoef *et al.*, 2006; Schneiderbauer and Pirker, 2014). Another tool uses the coupling of CFD (Computational Fluid Dynamics) for the continuous fluid phase (i.e. the reduction gas) and the DEM (Discrete Element Method) for the discrete particles such as iron-ore and coal. These methods are coupled in a CFD-DEM approach based on the open source software packages OpenFOAM (OpenCFD Ltd. 2009) and LIGGGHTS (LIGGGHTS, 2011). DEM provides an easier way to evaluate the per-particle chemistry such as the shrink/growth of particles due to reactions and it does not require to transfer these reactions to a continuum representation. However, to tackle industrial scale operations with the CFD-DEM a coarse-graining needs to be carried out in order to reduce the computational demands, which is an upcoming investigation of this research. Another method that can be thought of would be the hybrid Lagrangian-Eulerian model that combines the Lagrangian discrete phase model (DPM) and a coarse-grained two-fluid model (TFM) such as in the works of (Schneiderbauer *et al.*, 2016).

## MODELLING OF IRON-ORE REDUCTION

An effective investigation of iron-ore reduction needs to consider the thermodynamic aspects of the reduction reaction such as the conditions required for the reaction to take place or even if it is possible for the reaction to occur, as well as the kinetic aspects such as the reaction rates and concentration changes (Schmidt, 1998).

### Thermochemical Aspects

In chemical reactions, spontaneity defines if the reaction occurs without being driven by an outside force. If a reaction is spontaneous the entropy of the reaction increases, and it can be considered that the system is able to release its *free energy* and move to a more stable state. The free energy is the part of the total enthalpy that can be converted into useful work. The free energy, just like enthalpy, cannot be measured by itself. However, the change of free energy can be calculated with

$$\Delta G_T^\circ = \Delta H_T^\circ - T\Delta S_T^\circ. \quad (7)$$

The change of free energy of a system is at its minimum value, if the system is in an equilibrium. The values for the standard free energies can be found in the thermodynamic data tables available in literature's from (Von Bogdandy and Engell, 2013), (Turkdogan, 1980), and the JANAF-Thermochemical tables. An error, no matter how small, in the value of  $\Delta G$  leads to a great amount of change in the shape of the equilibrium curves in an equilibrium phase diagram (Von Bogdandy and Engell, 2013). The chemical equilibrium can be defined with the equilibrium constants of the reaction. The various correlations defining the equilibrium constants can help to define the stability areas for the different iron oxides depending on temperature and composition of the reducing gas. The equilibrium constants can be considered as the ratio of molar concentrations of products

to the reactants such as in the case of a general reaction  $aA + bB \longrightarrow cC + dD$ , the equilibrium constant can be defined as

$$K_c = \frac{[C]^c [D]^d}{[A]^a [B]^b} \quad (8)$$

or with the standard free energy change as (Levenspiel, 1999)

$$\ln K = \frac{-\Delta G^\circ}{RT}. \quad (9)$$

An equilibrium phase diagram for the thermodynamically stable phases that occur in the reduction of iron-oxide to metallic iron is one of the most useful phase diagrams in the reduction process. One such diagram demonstrates the reduction processes of the iron-oxygen-carbon system, which is also called the *Baur-Glaessner Diagram*. In this diagram, as it is demonstrated in Fig. 1, the stabilities for the iron-oxides and iron phases are depicted as a function of temperature and CO/CO<sub>2</sub> mixture with the available correlations for the equilibrium constant from literature and the ones calculated.

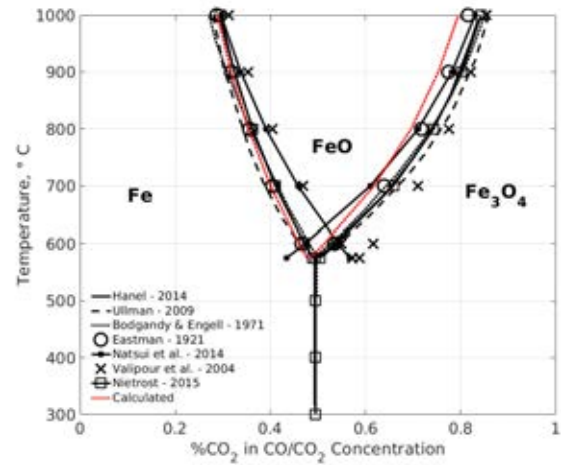


**Figure 1:** Equilibrium gas composition depending on the temperature for the iron-oxygen-carbon system at 1 atmospheric pressure.

The concentration molar fraction of the relative gas species can be determined with the use of the equilibrium constant as

$$\frac{x_{CO_2}^{eq}}{x_{CO}^{eq}} = Ke_{Fe_xO_y, CO}, \quad (10)$$

thus the molar fraction of the mixture can be defined with,

$$x_{CO_2}^{eq} = k_c \frac{Ke_{Fe_xO_y, CO}}{1 + Ke_{Fe_xO_y, CO}} \quad (11)$$

or

$$x_{CO}^{eq} = k_c \frac{1}{1 + Ke_{Fe_xO_y, CO}}, \quad (12)$$

in which  $k_c$  represents the total content of carbon in the system that can be expressed with

$$x_{CO}^{eq} + x_{CO_2}^{eq} = k_c. \quad (13)$$

As a more advanced method one might consider a four-component gas mixture of CO, H<sub>2</sub>, CO<sub>2</sub> and H<sub>2</sub>O to be represented in a single Baur-Glaessner Diagram with an abscissa of CO + H<sub>2</sub> or H<sub>2</sub> + CO<sub>2</sub> content.

## Reaction Kinetics

To depict the progress of the fluid-solid reactions a model is chosen that is similar to reality. The most common types of representation models for the non-catalytic reactions of solids submerged in fluids is the shrinking particle model (SPM) and the unreacted shrinking core model (USCM) (Levenspiel, 1999).

In the SPM, only the surface of the particle is reacting with the surrounding fluid. In, this type of model there are no layer formations due to reaction and the products diffuse directly into gas. As the reaction progresses, the particle size shrinks and eventually disappears completely. In Fig. 2, the SPM is depicted, in which the particle shrinks and disappears with time.

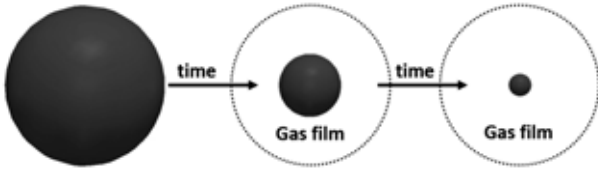


**Figure 2:** A schematic of the SPM, where the solid particle is reacting with the fluid without an ash layer formation.

The rate of change for the shrinkage/growth of a sphere can be expressed with (Levenspiel, 1999; Schmidt, 1998)

$$\frac{1}{4\pi R^2} \frac{dN_B}{dt} = \frac{b}{4\pi R^2} \frac{dN_A}{dt} = bkC_A \quad (14)$$

where  $k$  is the rate coefficient of surface reaction per unit area,  $C_A$  is the concentration of fluid species A at the surface of the particle,  $b$  is the stoichiometric coefficient for the reacting solid,  $N_B$  is the number of moles of solid B, which can be defined with

$$N_B = \frac{4\pi R^3 \rho_B}{3M_B} = \frac{m_B}{M_B} \quad (15)$$

$m_B$  is the mass of B,  $M_B$  is the molar mass of B,  $R$  is the radius of the particle,  $\rho_B$  is the density of solid particle. If we combine Eq. 14 and Eq. 15 than we can get for the rate of mass change for the gas species A as

$$\frac{dm_A}{dt} = k_g C_A M_A A_p \quad (16)$$

The unreacted shrinking core model is one of the most precise models to represent the real-life fluid-solid reaction (Levenspiel, 1999; Homma *et al.*, 2005; Schmidt, 1998). The main reactions for the direct reduction of iron with a gaseous reductant can be expressed in three reaction steps with CO/H<sub>2</sub> reducing gas as shown in Reactions 1 - 4. The three layer unreacted shrinking core model developed by Philbrook, Spitzer and Manning (Tsay *et al.*, 1976) is able to represent the three interfaces of hematite/magnetite, magnetite/wustite and wustite/iron. An illustration of the model layer structure with corresponding radiuses, and a snapshot of a polished section of sintered hematite pellet that has been reduced 30% by H<sub>2</sub> is given as comparison to the USCM in Fig. 3.

The removal of oxygen follows these steps (Tsay *et al.*, 1976);

- The reducing gas is transported through the gas film onto the particle surface.

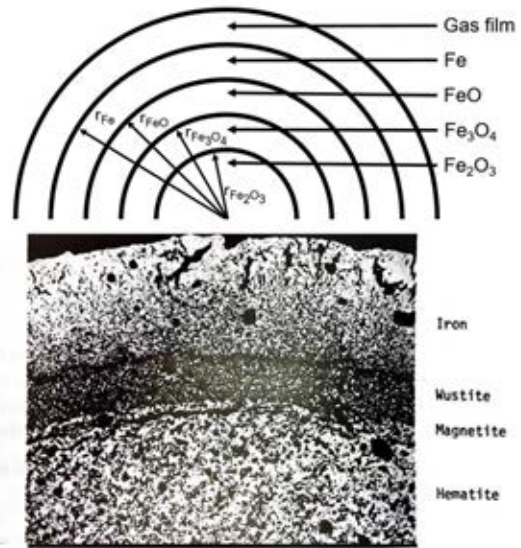


**Figure 3:** A schematic of the three layer unreacted shrinking core model (top) and a snapshot of a sintered pellet that has been reduced 30% (bottom) (Turkdogan, 1980).

- The reductant gas then diffuses through the porous iron layer.
- Part of the reductant reacts with wustite at the wustite/iron interface producing iron and gaseous product.
- Rest of the reducing gas diffuses through the wustite layer onto the wustite/magnetite interface.
- A portion of the gas reacts with magnetite at layer surface producing wustite and gaseous product.
- The balance gas diffuses through the magnetite layer onto the magnetite/hematite interface.
- Chemical reaction of the leftover gas occurs at the hematite core and produces magnetite and a gaseous product.
- The gaseous product diffuses outwards through the pores of the pellet.

Since each step is a resistance to the total reduction of the pellet, the reduction pattern of a single pellet can be considered to follow a resistance network such as an electrical resistance circuit network as illustrated in Fig. 4.

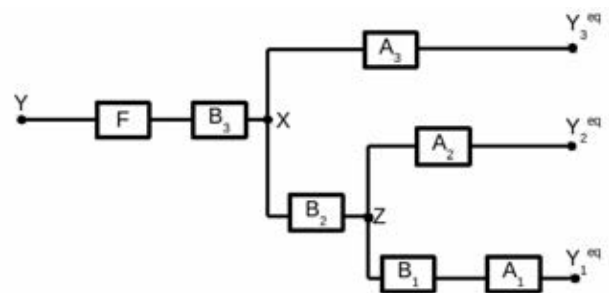


**Figure 4:** Resistance network diagram that illustrates the resistance of an iron-ore pellet that goes through in the reduction process.



The solution of this resistance network yields the reaction flow rate of  $\dot{Y}_{j,i}$  of the gas species for the relative layers yields as;

- from hematite to magnetite as

$$\begin{aligned} \dot{Y}_{h,i} = & ([A_3(A_2 + B_2 + B_3 + F) + (A_2 + B_2)(B_3 + F)](Y - Y_1^{eq}) \\ & - [A_3(B_2 + B_3 + F) + B_2(B_3 + F)](Y - Y_2^{eq}) \\ & - [A_2(B_3 + F)](Y - Y_3^{eq})) \frac{1}{W_{3,i}}, \end{aligned} \quad (17)$$

- from magnetite to wustite as

$$\begin{aligned} \dot{Y}_{m,i} = & ((A_1 + B_1 + B_2)(A_3 + B_3 + F) + A_3(B_3 + F)](Y - Y_2^{eq}) \\ & - [B_2(A_3 + B_3 + F) + A_3(B_3 + F)](Y - Y_1^{eq}) \\ & - [(A_1 + B_1)(B_3 + F)](Y - Y_3^{eq})) \frac{1}{W_{3,i}}, \end{aligned} \quad (18)$$

- from wustite to iron as

$$\begin{aligned} \dot{Y}_{w,i} = & ((A_1 + B_1)(A_2 + B_2 + B_3 + F) + A_2(B_2 + B_3 + F)] \\ & (Y - Y_3^{eq}) - [A_2(B_3 + F)](Y - Y_1^{eq}) \\ & - [(A_1 + B_1)(B_3 + F)](Y - Y_2^{eq})) \frac{1}{W_{3,i}} \end{aligned} \quad (19)$$

in which  $A_j$  represents the relative chemical reaction resistance term,  $B_j$  the relative diffusivity resistance term,  $j$  represents the layers hematite, magnetite and wustite and  $i$  the reducing gas species.  $F$  is the mass transfer resistance term, which is defined with  $1/k_f$ .  $Y$  is the bulk gas mole fraction and  $Y_j^{eq}$  the relative layer equilibrium mole fractions. The denominator  $W_{3,i}$  is expressed as

$$W = [(A_1 + B_1)(A_3(A_2 + B_2 + B_3 + F) + (A_2 + B_2)(B_3 + F)) + A_2(A_3(B_2 + B_3 + F) + B_2(B_3 + F))]. \quad (20)$$

The chemical reaction resistance term  $A_{j,i}$  can be expressed as

$$A_{j,i} = \left[ \frac{1}{(1 - f_j)^{\frac{2}{3}}} \frac{1}{k_j \left(1 - \frac{1}{Ke_j}\right)} \right]_i \quad (21)$$

in which  $j$  represents the reduction layer,  $i$  the reducing gas,  $k$  the reaction rate constant and  $f_j$  is the local fractional reduction of the relative layer that is calculated as

$$f_j = 1 - \left( \frac{r_j}{r_p} \right)^3. \quad (22)$$

The diffusivity resistance term  $B_{j,i}$  can be calculated for the relative iron oxide component as (Valipour *et al.*, 2006; Valipour, 2009)

$$B_{h,i} = \left[ \frac{(1 - f_m)^{\frac{1}{3}} - (1 - f_h)^{\frac{1}{3}}}{(1 - f_m)^{\frac{1}{3}}(1 - f_h)^{\frac{1}{3}}} \frac{r_g}{De_h} \right]_i, \quad (23)$$

$$B_{m,i} = \left[ \frac{(1 - f_w)^{\frac{1}{3}} - (1 - f_m)^{\frac{1}{3}}}{(1 - f_w)^{\frac{1}{3}}(1 - f_m)^{\frac{1}{3}}} \frac{r_g}{De_m} \right]_i, \quad (24)$$

$$B_{w,i} = \left[ \frac{1 - (1 - f_w)^{\frac{1}{3}}}{(1 - f_w)^{\frac{1}{3}}} \frac{r_g}{De_w} \right]_i, \quad (25)$$

in which  $De_j$  represents the diffusion coefficient of the relative layer.

With the use of the reaction flow rate  $\dot{Y}_{j,i}$  the relative mass flow rates of reactant gas between layers can be defined in a similar manner as in Eq. 16 with

$$\frac{dm_i}{dt} = C_i M_i A_p \dot{Y}_{j,i}. \quad (26)$$

#### Mass and Heat Transfer Coefficient

The mass transfer coefficient  $k_f$  which is used in the determination of the mass transfer term can be calculated through the Sherwood number or the Nusselt number as

$$\begin{aligned} Sh &= \frac{k_f d}{D_e}, \\ Nu &= \frac{k_f}{k}, \end{aligned} \quad (27)$$

where  $d$  is the diameter of pellet,  $D_e$  the diffusion coefficient and  $k$  the thermal conductivity. A number of correlations for determining the Sherwood number exist in literature. Lee and Barrow (Lee and Barrow, 1968) proposed a model through investigating the boundary layer and wake regions around the sphere leading to a Sherwood number of

$$Sh_t = (0.51Re^{0.5} + 0.02235Re^{0.78})Sc^{0.33}, \quad (28)$$

where  $Sc$  stands for the Schmidt number and defined as  $\frac{\nu}{D_e}$ . In more recent works from Valipour (Valipour, 2009) and Nouri *et al.* (Nouri *et al.*, 2011) the Sherwood and Nusselt numbers are expressed as

$$\begin{aligned} Sh &= 2 + 0.6Re^{0.5}Sc^{0.33}, \\ Nu &= 2 + 0.6Re^{0.5}Pr^{0.33}. \end{aligned} \quad (29)$$

$Pr$  represents the Prandtl number and is expressed as the specific heat times the viscosity over thermal conductivity  $c_p \mu / k$ .

#### Diffusivity Coefficient

Diffusivity of a gaseous species depends on properties such as the pore size distribution, void fraction and tortuosity. For example, according to (Tsay *et al.*, 1976) a pore size of  $2\mu$  to  $5\mu$  the Knudsen diffusion has been found to be 10 times faster than molecular diffusion, therefore in their work the Knudsen diffusion has been neglected and the effective binary gas diffusion was calculated with

$$[D_{j,i}]_{eff} = D_{j,i} \frac{\epsilon}{\tau} \quad (30)$$

where  $\epsilon$  represents the dimensionless void fraction,  $\tau$  the tortuosity. (Valipour, 2009; Valipour *et al.*, 2006) has used the Fuller-Schettler-Giddings equation to determine the effective diffusivity as

$$D_{j,i} = \frac{10^{-7} T^{1.75}}{(P_t (\dot{v}_j^{1/3} + \dot{v}_i^{1/3}))^2} \left( \frac{1}{M_j} + \frac{1}{M_i} \right)^{0.5} \quad (31)$$

in which the  $\dot{v}$  is the diffusion volume of the relative species,  $M$  is the molecular weight,  $P_t$  the total flow pressure and  $T$  the temperature in Kelvin.

### Reaction Rate Coefficient

For many reactions the rate expression can be expressed as a temperature-dependent term. It has been established that in these kinds of reactions, the reaction rate constant can be expressed with the Arrhenius' law (Levenspiel, 1999) as follows

$$k = k_0 \exp\left(\frac{-E_a}{RT}\right), \quad (32)$$

in which  $k_0$  represents the frequency factor or the pre-exponential factor,  $E_a$  the activation energy,  $R$  the universal gas constant and  $T$  the temperature. The values for the pre-exponential factor and the activation energy can be found through various works (Tsay *et al.*, 1976; Valipour, 2009).

### RESULTS

Firstly, the CFD-DEM coupling library is extended to cover the SPM, in which the particle reacts with the fluid without forming a layer. Afterwards with the use of the SPM, the communication framework between the Eulerian CFD side and the Lagrangian DEM side is verified.

A simple test case is developed, consisting of a single carbon particle that reacts with the reactant gas of  $O_2$  with a user defined reaction rate constant. The communication of DEM and CFD works by first initializing the particles in the DEM side and transferring their information such as the locations and velocities onto the CFD side. This information is then used to localize the particles and determine the voidfraction, fluid density, temperature, drag force and the species concentration (mass fractions) at particle locations, which is communicated back to the DEM side. The newly transferred data is then used to determine the particle movement, the change in particle size and change of gas concentrations due to the chemical reactions for the new time step and is transferred back to CFD side. This process continues until a specified amount of time steps have been reached.

The test case results are verified by comparing the species mass balances. The particle only reacts with the  $O_2$  present, and stops after the total amount of  $O_2$  has been depleted. The mass change of the reactant and product gas species is investigated in relation to particle shrinking. The simulation results are compared with theoretical data that is calculated with the same species concentration as the simulation, which proves to be in a good agreement within. The mass of change of the gas species is illustrated depending on the time in Fig. 5.

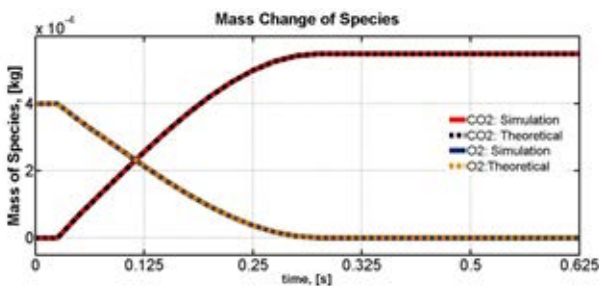


**Figure 5:** The change of mass of reacting gas species  $O_2$  and product gas  $CO_2$  depending on time.

After the communication framework is verified, the USCM is implemented into the DEM library. First, a correlation to determine the equilibrium constant  $Ke_{Fe_xO_y}$  for every layer is implemented, and the relative equilibrium mole fractions of reactant and product gases are calculated as in Eq. 11 and 12. Therewith, the implemented reaction flow rates  $\dot{Y}_{j,i}$ ,

defined in Eq. 17 -19, are calculated and the mass flow rate of reactant gas between layers is determined. The mass flow rate of the reactant gas is used to calculate the mass transfer of every layer with the expression

$$\frac{dm_{B,l}}{dt} = \frac{dm_{A,l}}{dt} \frac{\nu_{B,l} M_{B,l}}{\nu_{A,l} M_{A,l}}, \quad (33)$$

which is used to determine the radii of every iron-oxide layer. Since the model implemented at this time, only consider the chemical reaction resistance term  $A_{j,i}$ , only the reduction of layers for a single particle is investigated. Therefore, a preliminary test case is constructed that considers, just as in the SPM test case, a single particle, and the fractional reduction rate of every iron-oxide layer is investigated depending on time. An illustration of this reduction rate can be found in Fig. 6.

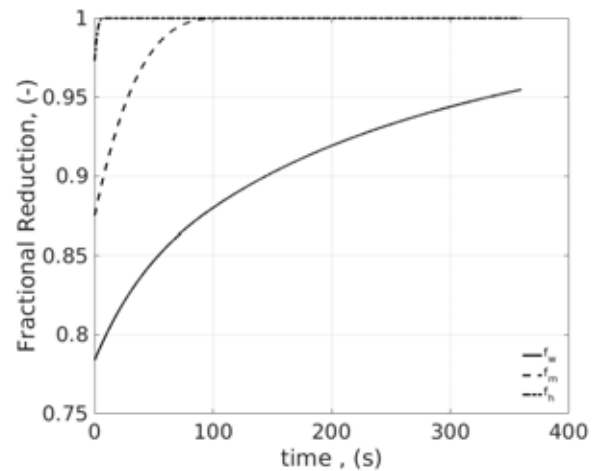


**Figure 6:** The fractional reduction of every iron oxide layer with time.

### CONCLUSION AND OUTLOOK

In order to use the CFD-DEM method to investigate the reduction of iron-ore inside the fluidized bed reactors, the mathematical models representing the fluid-solid chemical reactions have been implemented into the DEM library. First, the SPM has been verified and used to test the communication framework between CFD and DEM sides. As these results were highly satisfactory, the framework is expanded to cover the three-layered USCM for a realistic representation of the iron-ore reduction. Since the investigation of the implemented model is still under way, some preliminary results from the shrinking of the layers of a single particle depending only on the chemical reaction resistance have been presented. For further research, valid correlations for the diffusion resistance term and the mass transfer term will be added to the DEM model. After the successful verification of the USCM with all its resistance terms is concluded, a coarse-graining of the CFD-DEM approach will be carried out and maybe a combination of the TFM and DPM for industrial scale simulations.

### ACKNOWLEDGEMENTS

This work was funded by the Christian-Doppler Research Association, the Austrian Federal Ministry of Economy, Family and Youth, and the Austrian National Foundation

for Research, Technology and Development. The author also want to acknowledge the financial support from the KIMET center for metallurgical research in Austria ([www.k1-met.com](http://www.k1-met.com)).

## REFERENCES

- DONSKOI, E. and MCELWAIN, D.L.S. (2003). "Estimation and modeling of parameters for direct reduction in iron ore/coal composites: Part I. Physical parameters". *Metallurgical and Materials Transactions B*, **34(1)**, 93–102.
- HABERMANN, A., WINTER, F., HOFBAUER, H., ZIRNGAST, J. and SCHENK, J.L. (2000). "An Experimental Study on the Kinetics of Fluidized Bed Iron Ore Reduction". *ISIJ International*, **40(10)**, 935–942.
- HOMMA, S., OGATA, S., KOGA, J. and MATSUMOTO, S. (2005). "Gas-solid reaction model for a shrinking spherical particle with unreacted shrinking core". *Chemical Engineering Science*, **60(18)**, 4971–4980.
- LEE, K. and BARROW, H. (1968). "Transport processes in flow around a sphere with particular reference to the transfer of mass". *International Journal of Heat and Mass Transfer*, **11(6)**, 1013–1026.
- LEVENSPIEL, O. (1999). *Chemical Reaction Engineering*.
- NOURI, S.M.M., Ale Ebrahim, H. and JAMSHIDI, E. (2011). "Simulation of direct reduction reactor by the grain model". *Chemical Engineering Journal*, **166(2)**, 704–709.
- PLAUL, F.J., BÖHM, C. and SCHENK, J.L. (2009). "Fluidized-bed technology for the production of iron products for steelmaking". *Journal of the Southern African Institute of Mining and Metallurgy*, **109(2)**, 121–128.
- PRIMETALS (2015). "The finex process". Brochure. URL <http://primetals.com/en/technologies/ironmaking/finex%C2%AE/Lists/FurtherInformation/The%20Finex%20process.pdf>.
- SCHENK, J.L. (2011). "Recent status of fluidized bed technologies for producing iron input materials for steelmaking". *Particuology*, **9(1)**, 14–23.
- SCHMIDT, L.D. (1998). "The engineering of chemical reactions". 536.
- SCHNEIDERBAUER, S., PIRKER, S., PUTTINGER, S., AGUAYO, P., TOULOUPIDIS, V. and Martínez Joaristi, A. (2016). "A Lagrangian-Eulerian Hybrid Model for the Simulation of Poly-disperse Fluidized Beds: Application to Industrial-scale Olefin Polymerization". *submitted to Powder Technology*. URL <http://dx.doi.org/10.1016/j.powtec.2016.12.063>.
- SCHNEIDERBAUER, S. and PIRKER, S. (2014). "Filtered and Heterogeneity-Based Subgrid Modifications for Gas-Solid Drag and Solid Stresses in Bubbling Fluidized Beds". *American Institute of Chemical Engineers*, **60(3)**, 839–854.
- TSAY, Q.T., RAY, W.H. and SZEKLEY, J. (1976). "The modeling of hematite reduction with hydrogen plus carbon monoxide mixture". *AIChE J*, **22(6)**, 1064–1076.
- TURKDOGAN, E. and VINTERS, J. (1971). "Gaseous reduction of iron oxides: Part I. Reduction of hematite in hydrogen". *Metallurgical Transactions*, **2(11)**, 3175–3188.
- TURKDOGAN, E.T. (1980). "Physical chemistry of high temperature technology".
- VALIPOUR, M.S. (2009). "Mathematical Modeling of a Non-Catalytic Gas-Solid Reaction : Hematite Pellet Reduction with Syngas". *Chemical Engineering*, **16(2)**, 108–124.
- VALIPOUR, M.S., HASHEMI, M.Y.M. and SABOOHI, Y. (2006). "Mathematical modeling of the reaction in an iron ore pellet using a mixture of hydrogen, water vapor, carbon monoxide and carbon dioxide: an isothermal study". *Advanced Powder Technology*, **17(3)**, 277–295.
- VAN DER HOEF, M.A., YE, M., van Sint Annaland, M., ANDREWS, A.T., SUNDARESAN, S. and KUIPERS, J.A.M. (2006). "Multiscale Modeling of Gas-Fluidized Beds". *Advances in Chemical Engineering*, **31**, 65–149.
- VON BOGDANDY, L. and ENGELL, H.J. (2013). *The reduction of iron ores: scientific basis and technology*. Springer Science & Business Media.
- YANG, K., CHOI, S., CHUNG, J. and YAGI, J.I. (2010). "Numerical Modeling of Reaction and Flow Characteristics in a Blast Furnace with Consideration of Layered Burden". *ISIJ International*, **50(7)**, 972–980.

## USING CFD ANALYSIS TO OPTIMISE TOP SUBMERGED LANCE FURNACE GEOMETRIES

Stephen GWYNN-JONES<sup>1\*</sup>, Phil CONRADIE<sup>2</sup>, Stanko NIKOLIC<sup>1</sup>, Bennie HENNING<sup>2</sup>, Martin BAKKER<sup>1</sup>,  
Hugo JOUBERT<sup>1</sup>, Brett FRANCIS<sup>1</sup>

<sup>1</sup> Tenova PYROMET, Brisbane, QLD, AUSTRALIA

<sup>2</sup> Tenova PYROMET, Midrand, GAUTENG, SOUTH AFRICA

\*Corresponding author's e-mail: Stephen.Gwynn-Jones@tenova.com

### ABSTRACT

The gas offtake design is an important aspect of the Top Submerged Lance (TSL) furnace technology. CFD modelling has been used to investigate the gas offtake geometry to better understand and address common industrial issues. The objective of the study was to understand how the shape of the offtake affected emissions from the roof ports, and influenced both the location of the post combustion reactions and the flow profile of the gas within the vessel and waste heat boiler (WHB). The conditions and gas species included in the modelling are based on typical large industrial copper smelters. Commercial software (ANSYS-FLUENT) has been used to investigate design variants by incorporating the effects of momentum, multi-component mixing, radiative and convective heat transfer, combustion reactions, and buoyancy. The learnings from the CFD modelling were integrated into the design of the new Novasmelt™ TSL technology.

**Keywords:** CFD, TSL, copper smelting, offtake.

### NOMENCLATURE

Greek Symbols

$\rho$  Mass density, [kg/m<sup>3</sup>].

$\theta$  Roof angle, [°].

Latin Symbols

$P$  Pressure, [Pa].

$T$  Temperature, [°C].

$t$  Time, [s].

$v$  Velocity, [m/s].

$\dot{m}$  Mass flow, [kg/s].

Sub/superscripts

$b$  Bath inlet.

$whb$  WHB outlet.

$fp$  Feed port opening.

$lp$  Lance port post combustion inlet.

$dc$  WHB downcomer post combustion inlet.

### INTRODUCTION

The Top Submerged Lance (TSL) furnace technology was originally developed by the Commonwealth Scientific Industrial Research Organisation (CSIRO) in Australia in the 1970s under the name Sirosmelt (J.M.

Floyd & Conochie, 1984). Originally starting in the field of tin smelting, the technology has since been adopted for copper, lead, nickel and zinc production (J. M. Floyd, 2005), becoming a popular choice for many base metal smelters. The TSL technology involves a cylindrical furnace vessel with material continuously fed via a roof opening into a molten bath. The bath is vigorously stirred by submerged gas injection from the centrally inserted lance. In sulfide smelting TSL furnaces, the bath reactions and bubbling creates a continuous stream of high concentration sulfur dioxide (SO<sub>2</sub>) containing off-gas. The off-gas is typically cooled in a waste heat boiler (WHB), often consisting of two vertical radiation shafts and followed by either a spray quencher or a horizontal heat recovery convection section (Köster, 2010). The cooled off-gas is then delivered to an electrostatic precipitator for de-dusting before being sent to an acid plant for sulfur recovery.

The TSL furnace has been the focus of CFD studies in the past, although primarily in the bath region rather than the gas offtake. Morsi et al. (2001) used a CFX model, validated by an experimental setup, of gas injection into a liquid bath to study the impact of gas injection angular momentum (swirl) on the liquid recirculation patterns. Pan and Langberg (2010) used a CFX model and experimental test-work to study the free surface behaviour of large collapsing gas bubbles in a liquid bath (such as those created at the tip of the lance in TSL furnace). Huda et al. (2009) used CFD to study the bath mixing differences when the lance submergence, flow rate and swirl angle were varied. Huda then constructed a model to simulate the submerged zinc fuming reactions that occur in a pilot plant TSL (Huda, Naser, Brooks, Reuter, & Matuszewicz 2012).

Off-gas dynamics has been the subject of study in other copper smelting furnaces. (Pelton, 1995) created a CFD model of the radiation and convection sections of a flash furnace to study the effect of changing the geometry. (Li, Brink, & Hupa, 2009) simulated the particle deposition in a flash furnace WHB radiation section to study locations of accretion formation and resulting impact on heat transfer. However, there appears to be no public domain information specifically addressing the effect of the TSL off-take geometry on the furnace off-

gas flow patterns. This study aims to fill this gap in TSL furnace understanding and discusses how the offtake geometry design can address common industrial issues. The outcomes of this study have been incorporated into the next generation of TSL furnace, the Novasmelt™, with solutions being supplied both to existing operations and for new facilities.

## BACKGROUND

### TSL Furnace Offtakes

The volume above the bath of the TSL furnace is commonly referred to as the gas offtake. The offtake is shaped to connect the cylindrical barrel section to the roof openings and the gas treatment system. The offtake design must allow for post-combustion reaction management, splash containment, lance and feed entry, and emissions control. Operating TSLs have reported a variety of issues with their offtakes, including: accretion formation, corrosion and steam leakages, feed chute blockages, and roof panel or refractory failures (Bhappu, Larson, & Tunis, 1994; Binengar, 1995; Herrera & Mariscal, 2013; Viviers & Hines, 2005).

There are two main furnace offtake shapes for the TSL vessel in use by industry, a flat roof design and a sloped roof design as shown schematically in Figure 1. Originally the majority of TSL furnaces had sloped roofs, and the flat roof furnace design was introduced to offer cost saving advantages and improve the access for operators when compared to the sloped roof, supposedly without detracting from the off-gas flow dynamics (Arthur & Hunt, 2005). There is no indication in the literature that the latter claim was substantiated, and it is the intent of the present study to address this gap.

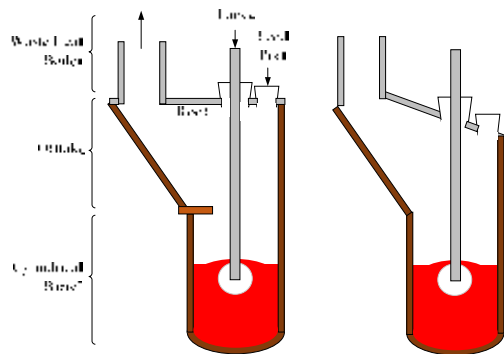


**Figure 1:** Typical TSL furnace shapes; flat roof design (left), sloped roof design (right)

The materials of construction of TSL furnace offtakes vary in existing designs, with the walls of the offtake typically being refractory lined, although more recently boiler tubes have also been employed (Peippo & Lankinen, 2010). The furnace roof is typically constructed of either copper panels or boiler tubes (Arthur & Hunt, 2005). Refractory bricked furnace offtakes must maintain a minimum shell curvature to ensure brick stability, whereas boiler tubes do not have this restriction and may be shaped to better accommodate fluid flow and remove dead zones. Recently, it has been proposed that additional cost savings could be realised if the entire furnace offtake,

including the walls are manufactured from flat panel boiler tubes, creating a polygonal shape (Peippo & Lankinen, 2010). The effect of the polygonal offtake on the gas flows was not discussed, and it is a further intent of the present work to make use of simplified cases to understand how such a design would impact fluid flow behaviour.

Some flat roof TSL furnace offtakes include a splash mitigation device (Voltura, 2004). The device reduces the amount of splash from the bath that enters the gas offtake and would otherwise form accretion. By providing a physical barrier the splash instead contacts the block, and forms an accretion inside the offtake or returns to the bath. The device is typically a large water cooled copper element. There is no indication that the impact of this geometry on the gas flows within the furnace has been investigated in the literature.

Early TSL furnaces used an angled (rather than vertical) first shaft for the WHB, which resulted in significant issues with accretions. Some of these installations opted to redesign their offtake hood to be vertical to help alleviate these issues (Binengar, 1995; Viviers & Hines, 2005).

### Heat Transfer in TSL Furnace Offtakes and WHBs

The WHB is required to cool the off-gas to enable subsequent volatile element precipitation, de-dusting and sulfur recovery from the gas stream. The boiler produces a low pressure steam which requires additional heating for recovery of the heat to power via a turbo-alternator. Alternatively the steam is simply re-condensed. The route chosen by the operation depends on local economics. The heat transfer in this application is complex as high temperature gas (1200 °C), with up to 60 wt. % SO<sub>2</sub> content and laden with reacting dusts, is cooled by a combination of radiative and convective heat exchange with the boiler tube walls. Inside the TSL furnace offtake the heat transfer and combustion reactions are further complicated by three dimensional flow patterns and recirculation. Air/oxygen, at lower temperature than the furnace gases (between 50 – 400 °C depending on whether preheating is used), is usually added to the furnace to provide sufficient oxygen for post combustion reactions. The SO<sub>2</sub> content in the off-gas is the primary species involved in the grey gas radiative heat transfer in the WHB radiation section (Pelton, 1995). Over cooling the gas is problematic, because temperatures below 220 °C can result in weak acid condensation inside the off-take or boiler, leading to corrosion and a loss of sidewall integrity. The boiler water/steam temperature is thus selected, through the boiler pressure setting, to operate above 240 °C to prevent such low temperatures from occurring.

### Ingress Air and Draught

Air/oxygen is not only injected into the furnace offtake and boiler, but is also added in a less controlled manner via ingress of additional air through the multiple openings in the furnace as it operates under slight negative pressure. The main source of ingress is air drawn into the open feed port. The negative gauge pressure measured at the port is often called the furnace

draught. Furnace draught is controlled by the downstream off-gas system using an Induced Draught (ID) fan. Engineers typically specify that a TSL furnace should have an ingress air flow rate to suit the process requirements for the off-gas treatment, which results in an off-gas containing 2-2.5 vol% free oxygen at the WHB outlet (Herrera & Mariscal, 2013).

In practice the internal pressure within the TSL vessel fluctuates significantly during operation. At times, the furnace pressure may become positive which results in emission of the furnace gas into the surrounding atmosphere. This is undesirable as these fugitive emissions are hazardous for both the workplace and general environment. Controlling furnace ingress air and preventing fugitive emissions is challenging. The primary causes of the pressure fluctuations within the TSL vessel are predicted to be bath bubble collapse from the submerged lance and the rapid vaporisation of the moisture in the feed as it falls through the furnace top-space. The frequency of the bubble collapse has previously been calculated to be between 1.2-3.4 Hz (Player, 1996), and the magnitude of the pulse will be dependent on the size of the bubble, which is inversely proportional to the bubble frequency. Deeper lance immersion depth has been suggested to increase the bubble size, and reduce the bubble frequency (De Antunes, 2009). The frequency and magnitude of pressure fluctuation from the vaporisation of the feed moisture will be dependent on the stability of the feed rate into the furnace, the moisture content and the homogeneity of the feed.

In addition to the internal causes of TSL furnace pressure fluctuation, there are also external causes. Sulfide smelting TSL furnaces typically interface with complex off-gas handling systems carrying sulfur dioxide laden gases from multiple furnaces to the site sulfuric acid plant(s). If these other furnaces are in batch operating mode, as is typical of converting furnaces (i.e. Peirce-Smith Converters), they can cause rapid changes in the pressure of the entire off-gas system when they roll in or out of the blowing position, requiring ID fan control adjustments to stabilise the TSL furnace pressure. Consequently, the TSL furnace control philosophy requires continual adjustment of the furnace draught in an effort to minimise both excessive accretion in the TSL furnace from too much cold ingress air, and potential release of hazardous fugitive emissions from the furnace ports arising from process pressure spikes.

In the present work, the relationship between furnace draught, bath off-gas flow and ingress air is studied for several different furnace offtake geometries to understand how changing the offtake design affects the gas flows. The different furnace offtake designs are then compared in terms of ability to help achieve process targets and minimise operational issues. Given the current modelling context (complex models exhibiting step change behaviour, qualitative and quantitative targets, limited validation data and lack of directly relevant literature) the analysis is executed using a simplistic approach: changing the design incrementally

and studying the impact. For the sake of brevity, this paper will focus on the findings of the work related to offtake shape. Optimisation for the post combustion air addition (size, quantity, locations, and flow enhancements) and boiler transition piece shapes have been excluded.

## MODEL DESCRIPTION

### Scope

The CFD model in the present work is intended to focus only on the furnace gas flows. Thus, the model does not consider splash, accretion formation on the walls, or the falling feed. The modelled domain includes the furnace gas space, port openings, WHB uptake, and downcomer. The outlet of the WHB radiation downcomer was set to be of equal height to the feed port.

The geometry used for this study is based on scaling publically available dimensions, drawings and site photos (Chitundu, 2009; Herrera & Mariscal, 2013), and can be considered a reasonable approximation of a typical large TSL copper smelter.

As the intended use of the modelling results was to understand the relative impact of changes, it was decided to limit the complexity to only include the physics that were likely to affect the offtake design.

### Main Assumptions

The main assumptions made during the modelling of the gas offtake are:

1. Particulate media are not included in the model to reduce computational time.
2. Heat associated with solid-gas reactions is excluded.
3. Combustion reactions are simplified to include only carbon monoxide (CO), with the remainder of the combustibles recalculated to an equivalent CO flow/concentration as outlined in the process conditions section below.
4. SO<sub>2</sub> reactions are completed in the bath and SO<sub>2</sub> does not participate in the gas-space reactions.

### Model Settings

The CFD model was built using the commercial code ANSYS FLUENT<sup>®</sup> 17.2, utilising the pressure-based Navier-Stokes equations. The simulations were set up using a steady state solver approach, with the pseudo-transient option enabled to aid in convergence. The simulation used the k-epsilon 2 equation realizable turbulence model. As the focus was on the macro flow field and small scale recirculation is not expected, the Realizable k-e model was considered adequate for this analysis. Near-wall turbulence was approximated by the accompanying Standard Wall Function and care was taken to maintain an appropriate y+ using three inflation layers for most of the domain. Radiation was implemented using the Discrete Ordinates Radiation Model. The emissivity was calculated depending on the gas composition using the weighted-sum-of-grey-gases model (WSGGM) approach. Due to the high

temperatures inside the furnace, the rate of reaction for the CO oxidation is expected to be primarily controlled by the turbulent mixing. Thus the turbulence/chemistry interactions were modelled using eddy-dissipation, which assumes an instantaneous burn upon mixing. The simulations were executed using double precision. The second order scheme was used for the scalars and energy equations. The PRESTO! Scheme was used for pressure.

**Process Conditions**

Typical industrial copper smelter process data from the Mt Isa Copper Smelter (Edwards, 1998) was combined with Tenova Pyromet’s in-house copper smelting process model to calculate the gas flows and temperatures. The inputs to this process model were the elemental compositions (Edwards, 1998), which were speciated to their mineralogical components for proper incorporation into the system enthalpy balance. The mineralogical inputs were then bulk reacted to their respective liquid metal oxide slag and liquid metal sulfide matte phases with the remaining sulfur and carbon species partially combusted to the gaseous phase (Yazawa, Nakazawa, & Takeda, 1983). The reaction extents were determined by the output compositional data for the matte grade, mass percent copper in matte, and slag magnetite concentration, as listed in (Edwards, 1998). Combustion of the feed was completed by added air/oxygen, which carries with it both the oxygen for reaction and nitrogen. From a chemical reaction perspective the nitrogen gas component is inert, but this gas is responsible for the generation of bubbles at the end of the submerged lance and therefore ensures the bath is turbulent and that the reactions are completed to their required extents.

The outputs of the process model were converted into the boundary conditions for the CFD model that are specified in **Figure 2**, **Table 1** and **Table 2**. These conditions were kept constant across all of the models to provide a comparison between the different geometries. The thermal boundary condition values were selected based on typical industry values. It should be noted that the gas flow rates and compositions can vary significantly between operations, thus although the findings will hold, the specific flow patterns and calculated outcomes may not apply to operations with significantly different process inputs.

The CO mass flow has been calculated such that it will provide the same total heat energy as all of the other combustible gases arising from the furnace bath (hydrogen, hydrogen sulfide, sulfur gas, methane, etc.). This simplification does not account for the heat energy released from the additional reactions of dust particles entrained in the gas stream. This assumption is not expected to significantly impact on the results.

The wall boundary conditions included heat transfer effects by specifying an effective thermal resistance to the temperatures listed in **Table 2**, and was calculated using a 1D approach based on typical refractory or boiler tube designs. The copper splash mitigation device was set to have the same thermal resistance as the

refractory bricks, based on the assumption that it would be coated in a thick slag layer during operation.

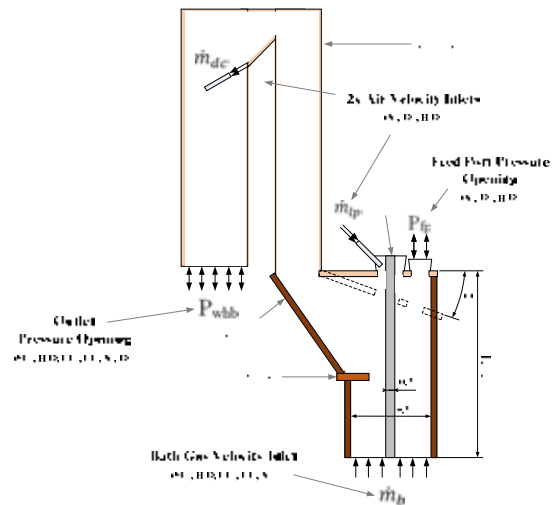


**Figure 2:** Boundary condition locations and key dimensions on CFD model

**Table 1:** Fluid boundaries

Boundary Condition	Value	Units	Temperature (°C)
$\dot{m}_b$	27.4	kg/s	1180
$P_{fp}$	0	Pa (g)	20
$P_{whb}$	-100 to -10	Pa (g)	580
$\dot{m}_{tp}$	1.68	kg/s	50
$\dot{m}_{dc}$	1.87	kg/s	50

**Table 2:** Thermal boundaries

Boundary	Heat Transfer Coefficient (W/m <sup>2</sup> -K)	Temperature (°C)	Internal Emissivity
Refractory Brick	2.64 <sup>(1)</sup>	20	0.38 <sup>(2)</sup>
Steel	0 (adiabatic)	NA	1
Boiler Tubes	30 <sup>(3)</sup>	280	0.8 <sup>(4)</sup>
Copper	2.64	20	0.38
Bath Inlet	NA	1180	1
Boiler Outlet	NA	580	1

<sup>(1)</sup> Calculated assuming brick, backing lining and steel layers with natural convection.

<sup>(2)</sup> Magnesite brick emissivity at 1000 °C

<sup>(3)</sup> Typical industrial value for overall heat transfer in TSL WHB

<sup>(4)</sup> Combination of frozen slag and oxidised steel surface values

**Mesh Strategy**

An unstructured tetrahedral mesh was created in ANSYS meshing consisting of approximately 2 million cells. An example of a typical mesh can be viewed in Figure 3. The mesh was refined in the region of the roof ports and post combustion air injection, and inflation layers were used at all walls to capture the boundary layer effects. The tetrahedral mesh was imported into ANSYS FLUENT® and converted to be a polyhedral mesh, reducing the total element count to approximately 0.8 million cells.

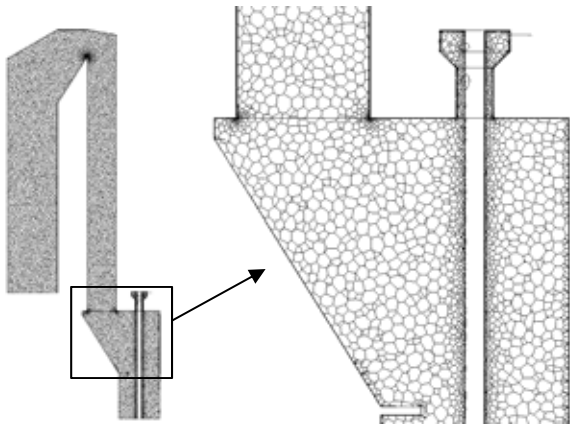


**Figure 3:** Typical polyhedral mesh on domain centreline. All walls have inflation layers.

**Cases**

The list of geometry cases is contained in Table 3. The angled roof geometries were created by removing a segment of the offtake volume and lowering the lance and feed ports to suit the angled shape. The flat panel geometries were constructed by matching the offtake width to the WHB. Examples of the geometries are included in Figure 4.

**Table 3:** CFD Geometry cases

Case	Roof Angle $\theta$ (°)	Offtake Wall Material	Splash Mitigation Device	Offtake Wall	Notes
1.	0	Bricks	Y	Curved Shell	
2.	0	Bricks	N	Curved Shell	
3.	30	Bricks	Y	Curved Shell	
4.	30	Bricks	N	Curved Shell	
5.	0	Boiler Tubes	N	Flat Panels	
6.	15	Boiler Tubes	N	Flat Panels	
7.	30	Boiler Tubes	N	Flat Panels	
8.	45	Boiler Tubes	N	Flat Panels	
9.	45	Boiler Tubes	N	Flat Panels	FP Length x2
10.	0	Bricks	Y	Curved Shell	FP Length x2

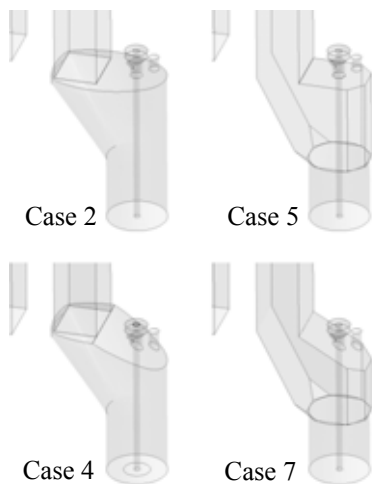


**Figure 4:** Example geometries for various cases

**RESULTS**

**Convergence**

The models typically required 2000 iterations to achieve acceptable convergence from initialisation. Subsequent runs of the same geometry at varying boundary

conditions were run for an additional 1000-1500 iterations depending upon the convergence of the boundary mass flows and temperatures.

**Heat Transfer Comparison to Process Assumptions**

The process model predicted the WHB radiation section outlet temperature to be approximately 581 °C based on typical operational experience, equating to a total heat loss of 22.1 MW from the boiler tubes and refractory bricks.

The CFD model for Case 1 predicts that the total heat loss through the walls is 15.6 MW by summing the total heat transfer across those surfaces, and is mostly from radiation as shown in Figure 5, which is expected since the model only includes the radiation section of the boiler. When compared to the process model heat loss of 22.1 MW the result indicates that the CFD model may be under-predicting the heat loss in the WHB. While it would have been possible to adjust the heat transfer coefficient for the boiler tubes to be a higher value, the boiler itself is not the focus of the present study. Further, altering the boiler heat transfer was only expected to have a minimal impact on the gas flows in the furnace offtake.

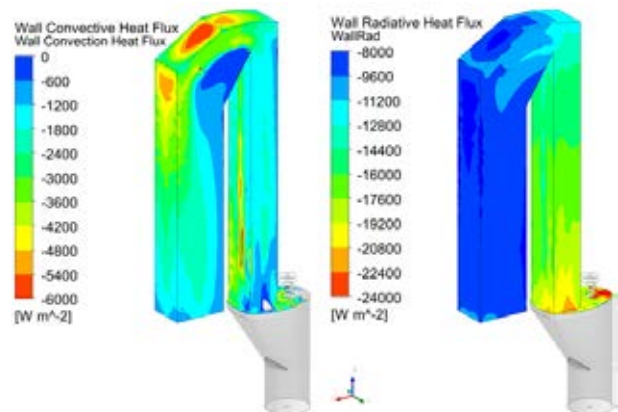


**Figure 5:** Convective (left) and radiative (right) heat on the boiler tube boundary condition for Case 1 with  $P_{whb} = -10$  Pa. Negative heat flux is heat leaving the domain.

**Comparison to Site Data**

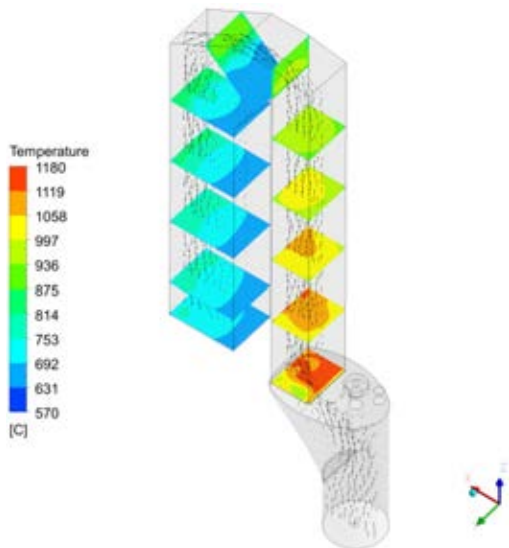
The complexity of the present model requires that it be validated against site data to provide some confidence in its ability to simulate actual furnace conditions. Unfortunately it is only possible to perform limited validation for two reasons: firstly, the geometry and boundary conditions of the CFD model were pieced together from public data sourced from multiple TSL furnaces (Mt Isa, Mopani and SPCC), and secondly, there is limited information in the literature that can be used to validate the CFD predictions. The available plant data for gas temperatures provided by Herrera and Mariscal (2013) are plant measurements from a large scale copper smelter (SPCC) of a similar design throughout to the modelled case.

Case 1 was selected for the model validation as it best matched the offtake design of the Southern Peru Copper Corporation furnace (Cuadros Rojas, 2010). The boiler outlet pressure was set to -10 Pa as this resulted in a



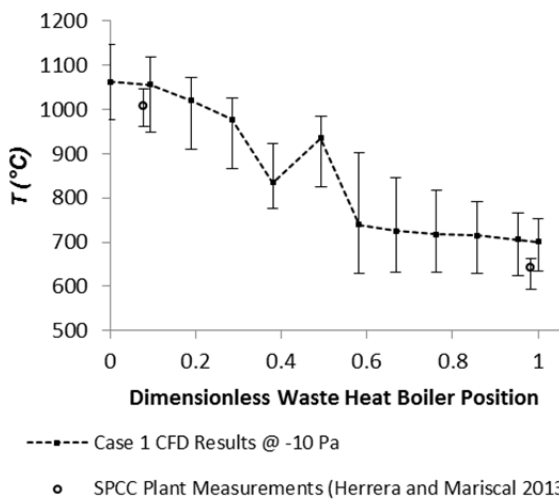
feed port ingress of 2.04 kg/s, where the target value from the process model was 2.05 kg/s.

Figure 6 illustrates the CFD results for temperature cross sections at 12 locations along the WHB. The results show that the CFD model predicts a range of temperatures at each location depending upon the localised flow field.



**Figure 6:** Temperature cross sections along WHB in Case 1 with  $P_{whb} = -10$  Pa.

In **Figure 7** the CFD results for temperature at each location are compared against the values from Herrera and Mariscal (2013). As no precise information was provided about the location used to collect the plant temperature measurements, the CFD data is presented as a range for comparison purposes. While the CFD prediction of temperature range overlaps the measured plant data at both measurement locations, the CFD average is higher; this is consistent with the comparison to the process model.



**Figure 7:** Comparing CFD prediction of off-gas temperature (Case 1 with  $P_{whb} = -10$  Pa) to 2 years of copper smelter plant data from Herrera and Mariscal (2013). Error bars on CFD result indicate the range of values of temperatures at each cross section.

There are several reasons that the CFD model might predict slightly different temperatures than the industrial data. The heat transfer coefficient of the boiler tubes used in the model is a typical value, and has not been the subject of rigorous analysis. In the industrial case the curved shape of the boiler tube panels increases the heat transfer area compared to the flat surfaces used in the CFD model. As the boiler is below atmospheric pressure it would be drawing in cold atmospheric air through any openings or gaps between panels, which is not permitted to occur in CFD. Overall the CFD model showed reasonable agreement with site data, indicating it could be used for comparing the relative impact of changes to the geometry.

### Impact of a Splash Mitigation Device

The impact of including a splash mitigation device in the design can be assessed by comparing Cases 1 and 2. Note that cases 3 and 4 showed the same change. **Figure 8** shows a velocity contour plot on the furnace centreline. The results indicate that the splash mitigation device creates a large recirculation zone as the rising gas flows around it. The ‘dead zone’ of flow created by the recirculation acts to reduce the effective cross sectional area for the furnace gases, increasing the gas velocity.

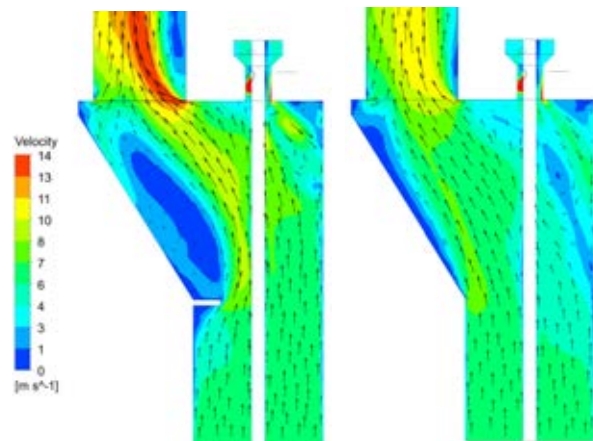


**Figure 8:** The impact of the splash mitigation device. Velocity contours for case 1 (left) and case 2 (right) at  $P_{whb} = -10$  Pa. Splash mitigation device creates large recirculation zone in furnace off-take.

TSL furnace off-takes are typically designed to keep the linear velocity of the gas at the boiler inlet below 10 m/s (Köster, 2010) to ensure homogenous heat transfer and temperature profiles. The presence of the splash mitigation device creates instantaneous velocities up to 14 m/s at the boiler inlet leading to recirculation in the boiler.

### Impact of Roof Angle

The air streamlines from the introduction of post combustion air into the furnace lance and feed ports for Cases 1, 2, 3, and 4 are compared in **Figure 9** to understand the impact of adding a slope to the furnace roof and the impact of a splash mitigation device. One of the main differences observable in these results is that the feed port ingress air and the injected lance port air behave differently depending on these geometrical factors. When the roof is flat (Cases 1 and 2), a

recirculation zone is created in the relatively cold stagnant zone below the feed port. The stagnation zone occupies a similar shape to the volume of fluid removed when converting to an angled roof, and is larger when there is no splash mitigation device. When the roof is sloped there is no stagnant zone, and the air is entrained into the furnace gas flow before entering the offtake, and better mixing is observed when there is no splash mitigation device.

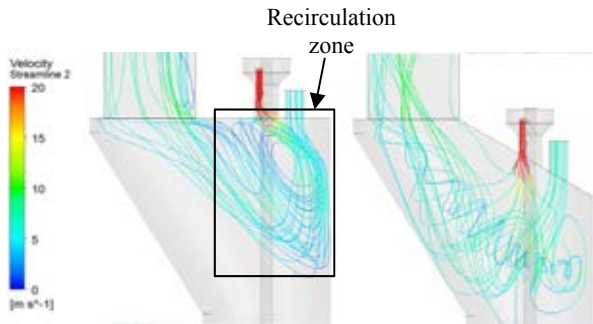


**Figure 9:** Air streamlines from feed port and lance port post combustion air for case 1 (left), and case 2 (right). Recirculation is evident in the flat roof case.

In order to compare the performance of multiple furnace offtake geometries it is convenient to map the system response for feed port ingress air to changing boiler suction as a series of steady state simulations. The slope of the curve relating ingress air to suction pressure indicates the rapidness with which the furnace will transition from ingress to emission, i.e. “puffing” furnace gas into the atmosphere, for a given pressure pulse.

The simulation results relating the feed port mass flow ( $\dot{m}_{fp}$ ) to the vessel roof angle ( $\theta$ ) is summarised in Figure 10. The following observations may be made:

- Increasing the slope angle of the roof at a constant -10 Pa at the WHB inlet increases the ingress air flow. This suggests that sloped roof furnaces could run less ID fan suction to meet the same ingress air requirements. The increased angle more effectively channels the gases into the boiler, causing the gas to flow parallel to the roof.
- The presence of a splash mitigation device does not significantly impact the feed port mass flow.

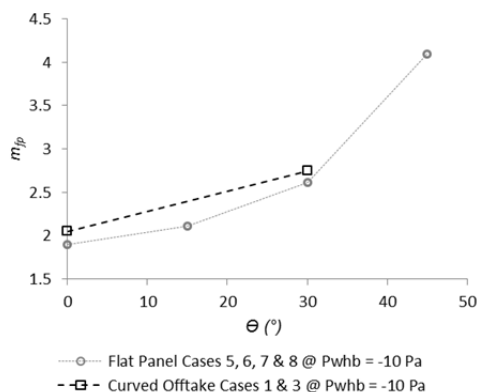


**Figure 10:** The relationship between feed port ingress air at  $P_{whb} = -10$  Pa and vessel roof angle. Increasing the

roof angle increases the ingress air, likely due to increased entrainment.

**Flat panel offtake performance**

The flat panel boiler tube offtake design is an opportunity to improve the offtake service life, and reduce the complexity and operating costs associated with curved refractory offtakes. Figure 11 and Figure 12 show the air streamlines from the introduction of post combustion air into the lance and feed ports for the curved offtake design (Case 2) and flat panel design (Case 5) for a flat roof TSL. The flat panel geometry reduces the recirculation of the ingress air, likely due to it not having the stagnant zones around the entrance to the boiler as in the curved offtake design. These same benefits were evident in the angled offtake cases that utilised flat panels.

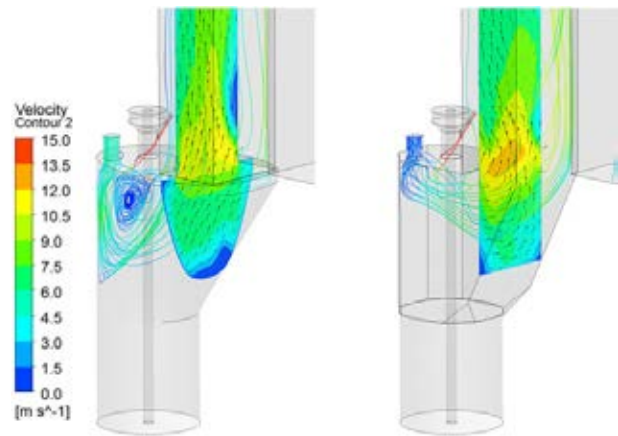


**Figure 11:** Streamlines and contours showing velocity for Case 2 (left) and 5 (right). The flat panel design has less dead zones around the offtake and fewer recirculation zones.

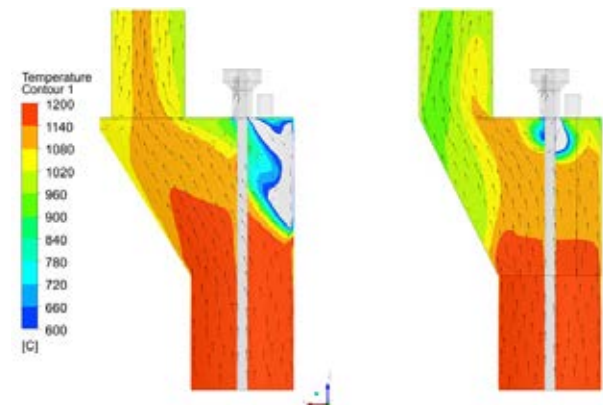


**Figure 12:** Temperature contours for Case 2 (left) and 5 (right). The inclusion of boiler tube flat panels reduces the gas temperatures in the offtake compared to the bricked design.

**Combustion near the splash mitigation device**

The results for Case 1, as highlighted previously in Figure 8, show a recirculation region around the splash mitigation device. In conditions representative of higher feed rates there was a deeper penetration of the feed port air combined with the higher volume flow of bath gas generated. The recirculating region is supplied with

oxygen by the feed port air ingress, which results in a combustion zone at the interface with the rising furnace gases. The resulting combustion zone extends the entire length of the splash mitigation device and is in contact with the offtake walls on either side as shown in Figure 13. For refractory furnaces it is suspected that this combustion zone will create local hot spots on the refractory resulting in accelerated wear. This can be mitigated by the application of cooled elements such as plate, SafeCool® or MAXICOOL® coolers (Joubert, Nikolic, Bakker, & McDougall, 2016), which can be retrofitted to existing furnaces. Alternatively boiler tube offtake walls can also perform this function, as investigated in the current work.

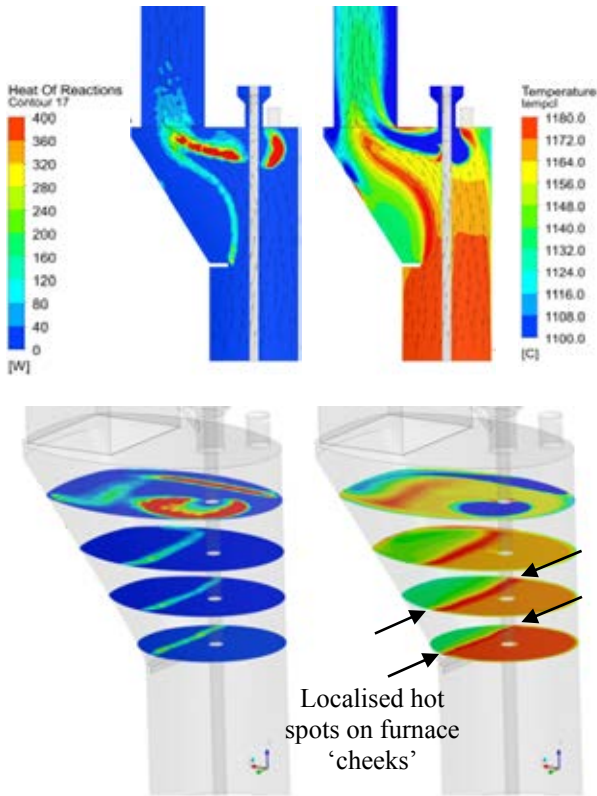


**Figure 13:** Combustion cross sections (top left and bottom left) and temperature cross sections (top right and bottom right) around the splash mitigation device for Case 1 at  $P_{whb} = -40$  Pa for boundary conditions representative of increased feed rates. High localised temperatures around sides of furnace caused by splash mitigation device recirculation region.

**Transient simulation of “puffing”**

In operating TSL furnaces, the intermittent emission or “puffing” of gases from open ports can occur rapidly and frequently. It is proposed that this puffing is strongly influenced by the bubble collapsing in the bath from the submerged lance gas injection. In order to study this assumption a transient simulation was created. As the bubble frequency has been demonstrated to be related to nitrogen flow, and not the total flow (Player, 1996), it is expected that the bubble expels mainly nitrogen. To simulate these conditions the nitrogen flow rate from the bath was set to fluctuate at +/- 100% from the nominal value in a sinusoidal nature, to provide a generalisation of flow variation due to

bubble collapse. The frequency of the pulsing flow was set at 2 Hz based on the findings of Player (1996).

The boundary conditions used for the transient simulation of bath gas over a one second period are summarised in Figure 14. The simulation was run using FLUENT’s default under-relaxation factors and a time step of 0.025 s. It can be seen that, at its peak, the fluctuating nitrogen component has a similar velocity contribution as all of the other gas species combined.

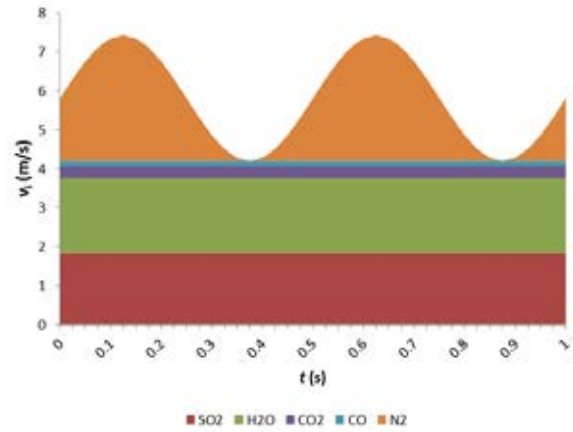


**Figure 14:** Volume contribution of individual gas species to bath inlet flow velocity for transient simulation case over a 1 second time period. Nitrogen flow is pulsing at 2 Hz.

The results for the total mass flow and mass flow of SO<sub>2</sub> over the feed port boundary with time for case 1 and Case 8 are summarised in Figure 15. SO<sub>2</sub> is selected for this comparison because it is hazardous and is one of the primary constituents of the bath gas. SO<sub>2</sub> is emitted only when the feed port mass flow is net outwards from the domain (negative values). The feed port mass flow can be seen to have a peak when the bath gas velocity has a trough, indicating an inverse relationship. The results also indicate that there is very little difference in performance between the flat roof geometry with splash mitigation device (Case 1) and the 45° angled roof (Case 8), despite the significant geometrical changes to the offtake.

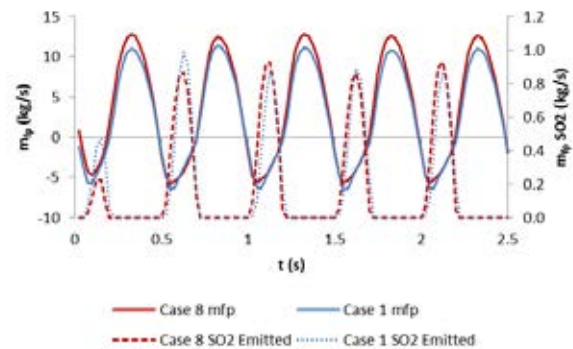


**Figure 15:** Feed port mass flow for Cases 1 and 8 at  $P_{whb} = -10$  Pa in response to pulsing nitrogen flow. Both cases exhibit similar feed port mass flow and SO<sub>2</sub> emissions.

### Longer feed port

Additional cases were created to examine the impact of changing the feed port geometry on SO<sub>2</sub> emissions using the transient models. The results of these analyses are summarised in **Figure 16** for Case 9 and 10, which are simply Case 8 and 1 with doubled feed port heights. The results indicate that doubling the feed port height reduces the SO<sub>2</sub> emissions by an order of magnitude. This is because there is insufficient time for the SO<sub>2</sub> to travel along the length of the feed port before the flow is reversed, as per **Figure 17**. This suggests a longer feed port will emit less SO<sub>2</sub> for a given set of pressure pulsing conditions by acting as an increased length buffer zone. In existing TSL furnaces with angled roofs, the layout of the floor levels has resulted in feed port lengths that are approximately twice as long as those found on flat roofed furnaces, perhaps unintentionally conveying these benefits to those operations. Ostensibly the effectiveness of using a longer feed port to reduce puffing will depend on the magnitude of the pulses in the bath gas flow, which will be specific to each operation.

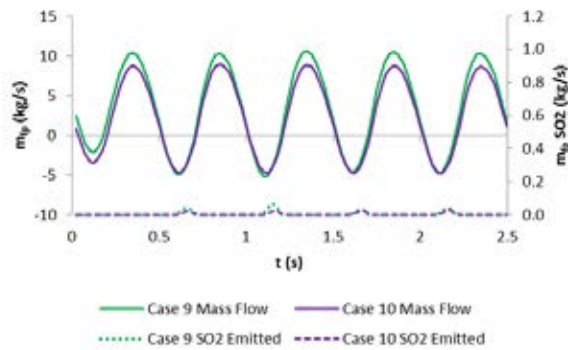


**Figure 16:** Feed port mass flow for Cases 9 and 10 at  $P_{\text{whb}} = -10$  Pa in response to pulsing nitrogen flow. Both cases have 2x feed port length and display a substantial reduction in SO<sub>2</sub> emissions.

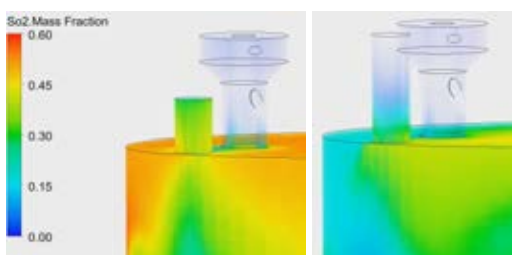


**Figure 17:** SO<sub>2</sub> mass fraction volume rendering for Case 1 (left) and 10 (right) at  $t = 1.625$  s displaying maximum outward mass flow. The longer feed chute exhibits lower SO<sub>2</sub> emissions by increasing the buffer zone.

### Dust sulfation and oxidation locations

The off-gas in a TSL furnace is typically laden with dust, which originates from entrainment of small particles or condensation of vapours (Swinbourne, Simak, & Yazawa, 2002). Managing the dust reactions is an important part of designing the off-gas system and post combustion addition. It is important to balance the flows between the furnace and WHB downcomer to prevent accretion formation in the WHB and furnace offtake (Herrera & Mariscal, 2013). While dust

oxidation/sulfation reactions are occurring, the dust is sticky and soft (Ranki-Kilpinen, 2004), which increases the likelihood of accretion formation. In order to predict the regions of accretion formation, temperature contours were added to the Case 8 steady state CFD results to examine the regions where various sulfation reactions are likely to occur (Figure 18). Note that as the CFD model does not incorporate these additional species these contours are only based on the specified temperatures ranges. The results indicate that the simulated WHB would have minimal sulfation reactions occurring in the top of the boiler, reducing the likelihood of accretion formation in this area.

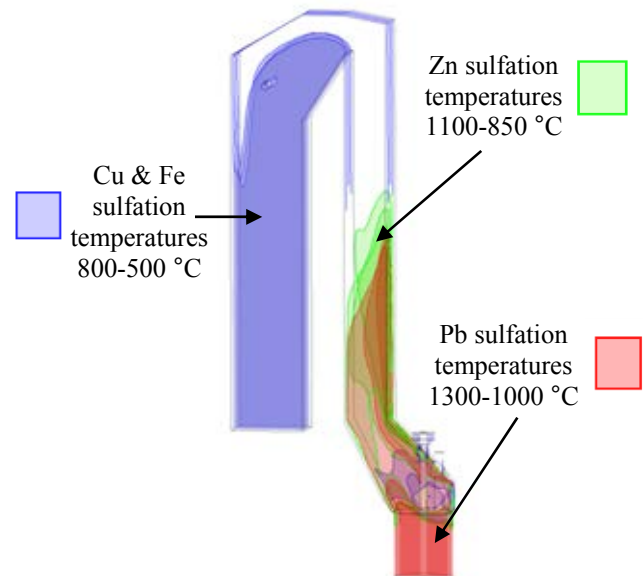


**Figure 18:** Approximate dust sulfation reaction locations based on temperatures in case 8 at  $P_{\text{whb}} = -10$  Pa.

### CONCLUSIONS

The TSL furnace gas offtake is an important part of the furnace design that performs a range of essential functions. There is scant evidence in the public domain that the offtake design has been subject to previous rigorous analysis, despite it being the source of numerous issues in operating plants, and the two different designs used throughout industry. The present work has focused on the development of a CFD model that captures key aspects of fluid flow and heat transfer in different TSL furnace offtake geometries. This CFD model was then used to assess the impact of a range of design changes. This CFD model may also be used to investigate off-gas dynamics in existing TSL operations, as long as the site specific boundary conditions and geometry are used.

The learnings from the present work regarding the optimisation of TSL furnace offtakes have been integrated into the new Novasmelt™ TSL design. An optimised TSL furnace offtake geometry would achieve the following:

- Reduction in SO<sub>2</sub> emissions and excessive ingress air from puffing.

- Reduction in damaging post-combustion reactions and ‘hot spots’ near the refractory sidewalls, or use of more robust materials such as boiler tubes.
- Increased homogeneity of flow at inlet to WHB to improve heat transfer and reduce accretion formation.
- Minimise velocities in offtake to reduce carryover of un-smelted feed.
- Sulfation reactions located in vertical sections of boiler to reduce risk of sticky accretion formation in stagnant flow areas.

The following may be concluded from the present work:

1. The inclusion of a splash mitigation device at the bottom of the offtake creates a large recirculation zone, resulting in increased combustion at the furnace sidewalls, higher gas velocities in the offtake, reduced mixing of post combustion air, and less homogenous gas flow in the WHB.
2. Flat roof offtake geometry tends to create a recirculation zone of air underneath the feed port. This can lead to increased carryover, localised accretion formation and thermal shock of the refractory in extreme cases.
3. Angled roof offtake geometry causes ingress air and injected post combustion air to be entrained into the furnace gas bulk flow without recirculation and results in improved mixing.
4. Flat panel offtake geometry using boiler tubes rather than bricks can be used to remove dead zones and reduce gas recirculation, and also results in lower overall temperatures in the offtake.
5. Longer feed ports should result in less furnace “puffing” and significant reductions in SO<sub>2</sub> emissions.

## REFERENCES

- ARTHUR, P. S., & HUNT, S. P. (2005). “Isasmelt - 25 Years of Continuous Evolution”, *Paper presented at the John Floyd International Symposium on Sustainable Developments in Metals Processing*, Melbourne, Australia.
- BEZUIDENHOUT, J. J., YANG, Y., & EKSTEEN, J. J. (2008). “Computational fluid dynamic modelling of a waste-heat boiler associated with flash smelting of base metal sulphides” *The Journal of The Southern African Institute of Mining and Metallurgy*, 108(MARCH), 179 - 188.
- BHAPPU, R. R., LARSON, K. H., & TUNIS, R. D. (1994). “Cyprus Miami Mining Corporation Smelter Modernization Project Summary and Status”, *Paper presented at the EPD Congress 1994*.
- BINEGAR, A. H. (1995). “Cyprus Isasmelt start-up and operating experience”. *Paper presented at the Copper 95*, Santiago, Chile.
- CHITUNDU, K. (2009). “Smelter Start-Up of new ISA Furnace and Progress to Date”. *Paper presented at the Presentations from the SAIMM Branch Event*, Chingola, Zambia.
- CUADROS ROJAS, A. (2010). “Reduccion de las Peridadas de Cobre en las Escorias del Proceso IsaSmelt de la Fundicion de Ilo de SPCC”. *Universidad Nacional de Ingenieria*.
- DE ANTUNES, H. M. A. (2009). “Experimental Study of Lance Bubbling Phenomena”. (Diploma of Engineering), Von Karman Institute, Rhode-Saint-Genève.
- EDWARDS, J. S. (1998). “Isasmelt-A 250 000 TPA Copper Smelting Furnace”. *Paper presented at the AUSIMM '98 - The Mining Cycle*, Mt Isa.
- FLOYD, J. M. (2005). “Converting an idea into a worldwide business commercializing smelting technology”. *Metall. Mater. Trans. B*, 36(5), 557-575. doi:10.1007/s11663-005-0047-7
- FLOYD, J. M., & CONOCHIE, D. S. (1984). “SiroSmelt - The First Ten Years”. *Paper presented at the Symposium on Extractive Metallurgy*, AusIMM, Melbourne, Australia.
- HERRERA, E., & MARISCAL, L. (2013). “Controlling SO<sub>3</sub> Formation in the Off-Gases Process From the IsaSmelt Furnace at Southern Peru Ilo Smelter”. *Paper presented at the Copper 2013*, Santiago, Chile.
- HUDA, N., NASER, J., BROOKS, G., REUTER, M. A., & MATUSEWICZ, R. W. (2009). “CFD Modeling of Swirl and Nonswirl Gas Injections into Liquid Baths Using Top Submerged Lances.” *Metallurgical and Materials Transactions B*, 41B(February 2010), 35-50.
- HUDA, N., NASER, J., BROOKS, G., REUTER, M. A., & MATUSEWICZ, R. W. (2012). “Computational Fluid Dynamic Modeling of Zinc Slag Fuming Process in Top-Submerged Lance Smelting Furnace”. *METALLURGICAL AND MATERIALS TRANSACTIONS B*, 43B, 39-55.
- JOUBERT, H., NIKOLIC, S., BAKKER, M. L., & MCDUGALL, I. (2016). “Tenova Pyromet - Cooled Copper Furnace Elements”. *Paper presented at the Copper 2016*, Kobe, Japan.
- KÖSTER, S. (2010). “Waste Heat Recovery Systems Downstream of Pyrometallurgical Processes for Lead and Zinc”. *Paper presented at the Lead-Zinc 2010*, Vancouver, Canada.
- LI, B., BRINK, A., & HUPA, M. (2009). “CFD Investigations of deposition in a heat recovery boiler: Part II - deposit growth modelling”. *Progress in Computational Fluid Dynamics*, 9(8), 453-459.
- MORSI, Y. S., YANG, W., ACHIM, D., & ACQUADRO, A. (2001). “Numerical and experimental investigation of top submerged gas injection system”. *Transactions on Modelling and Simulation*, 30, 95-104.
- PAN, Y., & LANGBERG, D. (2010). “Two-Dimensional Physical and CFD Modelling of Large Gas Bubble Behaviour in Bath Smelting Furnaces”. *The Journal of Computational Multiphase Flows*, 2(3), 151-164. doi:10.1260/1757-482X.2.3.151
- PEIPPO, R., & LANKINEN, H. (2010). “TSL-Furnace Wall Cooling by Boiler Tubes”. *Presented at Copper 2010*, Vancouver, Canada.
- PLAYER, R. (1996). “Copper Isasmelt - Process Investigation”. *Paper presented at the International symposium, Injection in pyrometallurgy*, Melbourne; Australia.
- RANKI-KILPINEN, T. (2004). “Sulphation of Cuprous and Cupric Oxide Dusts and Heterogeneous Copper Matte Particles in Simulated Flash Smelting Heat Recovery Boiler Conditions”. (Doctor of Science in Technology), Helsinki University of Technology. (TKK-ME-DT-1)
- SWINBOURNE, D. R., SIMAK, E., & YAZAWA, A. (2002). “Accretion and Dust Formation in Copper Smelting - Thermodynamic Considerations”. *Paper presented at the Sulfide Smelting 2002*, Warrendale, PA.
- VIVIERS, P., & HINES, K. (2005). “The New Anglo Platinum Converting Project”. *Paper presented at the First Extractive Metallurgy Operators’ Conference*, Brisbane.
- VOLTURA, S. A. (2004). “Continuous Improvements at the Phelps Dodge Miami Mining Smelter”. *Paper presented at the SME Annual Meeting, Denver, Colorado*.
- YAZAWA, A., NAKAZAWA, S., & TAKEDA, Y. (1983). “Distribution Behaviour of Various Elements in Copper Smelting Systems”. *Paper presented at the Advances in Sulfide Smelting Symposium*.

# NUMERICAL ANALYSIS OF THE TEMPERATURE DISTRIBUTION IN A MARTENSITIC STAINLESS STEEL STRIP DURING HARDENING

**Pouyan Pirouznia**<sup>1,2,3</sup>, **Nils Å. I. Andersson**<sup>1\*</sup>, **Anders Tilliander**<sup>1</sup>, **Pär G. Jönsson**<sup>1</sup>

<sup>1</sup> Division of Processes, Department of Material Science and Engineering, KTH Royal Institute of Technology, SE-100 44 Stockholm, Sweden

<sup>2</sup> Department of Material Science and Engineering, Dalarna University, SE-791 88 Falun, Sweden

<sup>3</sup> Research & Development Department, voestalpine Precision Strip AB, SE-684 28, Munkfors, Sweden

\* E-mail: nilsande@kth.se

## ABSTRACT

Due to the increasing demands on higher qualities of thin martensitic steel strips, a great attention needs to be paid to the dimension quality of the finished product within the hardening line. The temperature distribution within the strip during the process influences the flatness of the finished product. Therefore, a FEM model was developed based on physical theories. Specifically, the temperature for the section before martensitic transformation was predicted by using a steady state approach. In addition, the results of the numerical predictions were compared to measured temperature performed in industry by using infrared thermal imaging. The results showed that a significant temperature difference exists across the width of the strip. This difference was 41°C and 48°C at the position close to the bath interface according to the thermal imaging and modelling results, respectively. Furthermore, the temperature measurements showed that the temperature of the strip decreased by 245°C from the furnace temperature within the gas box beyond the hardening furnace. The measurements were performed at a position about 21mm away from the molten metal bath interface. Overall, the results of this study can be seen as initial fundamental knowledge of the modelling of the hardening process. Thereby, this knowledge can be used to modify the current hardening process as well as be used as input to study the stress in strip in future investigations.

**Keywords:** Process industries, Hardening process, Martempering, Heat transfer, Numerical modelling, Strip.

## NOMENCLATURE

### *Greek Symbols*

- $\rho$  Mass density, [kg/m<sup>3</sup>].  
 $\mu$  Dynamic viscosity, [Pa.s].  
 $\varepsilon$  Emissivity.  
 $\gamma$  Specific heat ratio.  
 $\sigma_b$  Stefan–Boltzmann constant, [W/ (m<sup>2</sup>.K<sup>4</sup>)].

### *Latin Symbols*

- $c_p$  Heat capacity at a constant pressure, [J/ (kg.K)].  
 $G$  Incoming radiative heat flux, [W/m<sup>2</sup>].  
 $h$  Heat transfer coefficient, [W/ (m<sup>2</sup>.K)].  
 $\mathbf{I}$  Identity matrix.

- $k$  Thermal conductivity, [W/ (m.K)].  
 $p$  Pressure, [Pa].  
 $T$  Temperature, [K] unless otherwise stated.  
 $\mathbf{u}$  Velocity, [m/s].

### *Sub/superscripts*

- $\tau$  Transpose matrix.

## INTRODUCTION

Advanced thin martensitic stainless steel strips, are commonly produced by using a hardening and tempering line or a by using a continuous martempering process. The hardening stage consists of a controlled atmosphere hardening furnace, a martempering media where the strip is cooled to the temperature just above the martensitic transformation, and a finishing step where the strip is quenched to the room temperature. The purpose of the hardening process is to form a desired martensitic structure.

For a conventional batch hardening of a component, hot oils up to 205°C and a molten salts in the range of 160 to 400°C are commonly used as the martempering media (Webster and Laird (1991)). Furthermore, Ebner (1983) indicated that if a molten lead-bismuth eutectic (LBE) alloy is used as a martempering media and afterwards cooled by an air jet, considerable advantages with regards to the flatness can be obtained compared to when using quenching in oil. Later, Lochner (1994) compared different cooling methods such as quenching in a molten metal bath, hydrogen jet and oil and their effects on the flatness of the strip. Later, Lochner (2006) demonstrated the advantages of using a LBE bath as the martempering media when comparing it to various methods of cooling the LBE bath to obtain a natural convection in the media. In addition, the important advantages of selecting LBE as martempering media were summarized, especially with respect to improvements in the flatness and dimensional qualities of the strip.

A LBE bath is used as a media in the continuous hardening process, where mainly: thin strips for springs,

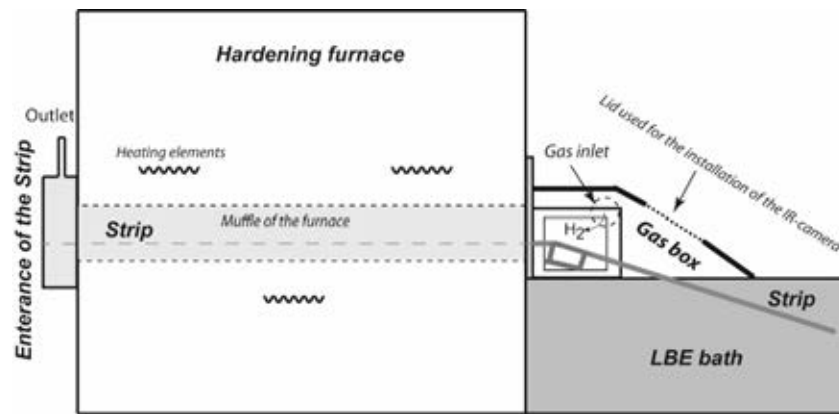


**Figure 1:** Schematic view of the part of the hardening process which takes place before a martensitic phase transformation at voestalpine Precision Strip AB, Munkfors, Sweden.

blades for the paper & printing industry- and valve steels are produced. A schematic view of the specific hardening process, before the martensitic transformation step, is illustrated in Figure 1. The so called gas box, is a sealing box in which the strip is transported from the muffle of the furnace into the LBE bath. The reducing hydrogen atmosphere of the furnace is provided from the gas inlet located inside the gas box.

Despite all advantages of using LBE as a media in the hardening process, geometrical and flatness defects are still found in the produced strip. In order to investigate how these may form, a better comprehension of the process is required with a focus on the temperature distribution in the strip.

Many researchers referred to the uneven temperature difference as one of the main reasons for the cause of flatness defects. Dimensional changes during case hardening were discussed by Thelning (1984) and he showed that thermal stresses; created during cooling, are the main causes of dimensional changes. In addition, Yoshida (1984) analysed the edge wave of a hot rolled strip after cooling. He established a numerical method to predict the temperature and thermal stresses in the strip. He showed that wavy edges can be removed by using a uniform transverse temperature difference. Wang et al. (1996) studied the deflection problems of the thermomechanical controlled process (TMCP) plates manufactured by the accelerated cooling process. Specifically, the correlation between the temperature variation resulted in thermal stresses and deflections were studied. Different types of flatness deflections, based on the non-uniform cooling in the different directions, were found. Also, Zhou et al. (2007) proved that cooling of a hot rolled strip on the run-out table caused an increased transverse temperature difference between the centre and edges of the strip. This led to an increased buckling tendency. In addition, Wang et al. (2008) showed that uneven transverse temperature distributions in strips are the main reason for flatness defects during a run-out table cooling during rolling of hot steel strips. Furthermore, they developed a numerical model to calculate the amount of thermal stresses that developed during the cooling period. Here, thermal image measurement data across the transverse direction at the exit of the rolling mill were used as the initial conditions in the finite element model (FEM) simulations. Furthermore, model including both thermal and mechanical investigations to predict the flatness of

steel strips during the quenching after the last mill stand during hot strip rolling was carried out by Wang et al. (2012). The results by Wang et al. (2013), showed that uneven transverse temperature difference and microstructure differences were the main causes for an edge wave formation of steel strips during the run-out cooling procedure. Moreover, personal communications with experts in the industry (2012), has indicated that the quenching in the molten metal bath has an essential influence on the dimensional attributes of the stainless steel strip.

In spite of all studies regarding the importance of the nature of the temperature on the steel strip quality, very little focus has been put on the temperature distribution of the strip after it leaves the hardening furnace. Therefore, a numerical model was developed which considers the heat transfer of the strip after it leaves the furnace and goes in to the molten metal quenching area. In addition, an infrared thermal imaging camera was used to obtain data to enable validations of the model predictions and to better understand the process. Thus, this study aims to give a better insight into the quenching step in the hardening process as well as to determine the temperature distribution pattern during the cooling of the strip. The results of this study will be used as a base for the investigation of flatness defects in real industrial processes.

## MODEL DESCRIPTION

The numerical model was based on the conditions of the hardening process at voestalpine in Munkfors, Sweden. The thermal analysis model was carried out by using Comsol Multiphysics, COMSOL (2015). The focus of the modelling was to study the temperature pattern within the strip as well as in the gas box and the LBE quenching bath.

## Mathematical Formulation

The computational model focused on predicting the cooling process of the stainless steel strip and with a specific aim to predict the temperature distribution in the strip. The following assumptions were used in the definition of the numerical model:

I. The laminar Navier-Stokes equation combined with the energy balance and continuity equations were solved numerically for the hydrogen filled gas box domain, where thermal interactions between the strip and the hydrogen gas flow take place.

II. A non-isothermal laminar flow was employed for the hydrogen flow, due to the low Reynolds number of around 485.

III. The Mach number was about 0.00093. Thus, a weak compressibility for the flow was also considered.

IV. Only heat transfer by conduction was considered for the thermal interaction between the strip and the LBE bath.

V. Transient effects (time dependency) were neglected and a steady state solution was chosen for the model simulations.

VI. The gravitational force was neglected. Based on these assumptions, the following governing equations were solved:

- Continuity equation:  

$$\nabla \cdot (\rho \mathbf{u}) = 0 \quad (1)$$

- Momentum equation:  

$$\rho \mathbf{u} \cdot \nabla \mathbf{u} = -\nabla p + \nabla \cdot (\mu(\nabla \mathbf{u} + (\nabla \mathbf{u})^T) - \frac{2}{3}\mu(\nabla \cdot \mathbf{u})\mathbf{I}) \quad (2)$$

- Energy balance equation:  

$$\rho c_p \mathbf{u} \cdot \nabla T = \nabla \cdot (k \nabla T) \quad (3)$$

### Mesh and the Geometry used in the Numerical Simulation

The geometry of the numerical model was designed based upon the real process conditions. A heated stainless steel strip with a thickness of 0.2mm and a width of 310mm enters the gas box after passing through the hardening furnace. The latter is filled with hydrogen to achieve a reducing atmosphere. Thereafter, a further quenching is provided by the Lead-Bismuth eutectic bath. A schematic view of the three-dimensional solution

domain, for which the governing equations were solved, is shown in Figure 2. Furthermore, a complete list of the dimensions used in the mathematical model is given in Table 1.

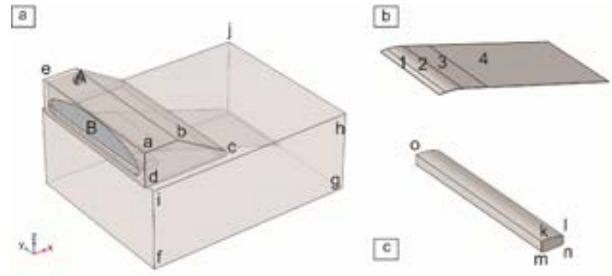


**Figure 2:** View of computational domains, Length are found in Table 1: (a) three-dimensional solution domains, (b) Stainless steel strip, (c) Gliding material

**Table 1:** Geometry specifications of the model [mm]. The distances are defined in Figure 2.

Strip (Figure 2b)	1	2	3	4			
	310.0×23.5	310.0×61.3	310.0×97.0	310.0 × 500.0			
LBE bath	$\bar{h}_i$	$\bar{f}_i$		$\bar{h}_j$			
	805.0	300.0		645.0			
Gas box	$\bar{a}\bar{b}$	$\bar{b}\bar{c}$	$\bar{c}\bar{d}$	* $R_{\bar{c}}$	$\bar{a}\bar{d}$	$\bar{a}\bar{e}$	
	129.8	222.6	317.6	10	130.0	585.0	
Gliding material (Figure 2c)	$\bar{l}\bar{m}$	$\bar{m}\bar{n}$	$\bar{k}\bar{n}$	$\bar{k}\bar{l}$	* $R_{\bar{k}\bar{l}}$	* $R_{\bar{m}}, R_{\bar{n}}$	$\bar{k}\bar{o}$
	15.8	49.0	25.0	59.9	195	5	450.0

\*R: radius

The gas box and LBE bath domain correspond to the extrusion of the surfaces of a – d and f – i by the length of  $\bar{a}\bar{e}$  and  $\bar{h}_j$  in the y-direction respectively. The thickness of the gas box walls is 10mm. The gliding material defines the extrusion of k – n by the dimension of  $\bar{k}\bar{o}$  in

**Table 2:** Boundary conditions used in the model

Surface(s)	Boundary conditions	Expressions
Inner side of the ceiling of the gas box	• No - slip	$\mathbf{u} = 0$
Segments 1-3 of the strip (Figure 2b)	• Moving wall	$\mathbf{u}_{u,d} = \mathbf{u}_{strip} (<0.17 \text{ m/s})$ $u, d : \text{up, down}$
Gas inlet, surface A (Figure 2a)	• Velocity inlet • A Quantified temperature was assumed due to the measured value of the walls of the gas inlet	$3.3 \text{ Nm}^3/h$ $(u = 1.18 \text{ m/s for flow at } 200^\circ\text{C})$ $T_A = 200^\circ\text{C}$
Surface B and its connected surfaces (Figure 2a)	• A furnace temperature	$T = 1000^\circ\text{C}$
Surface B (Figure 2a)	• Pressure outlet (backflow is allowed)	$P_0 = P_{Furnace}$
Outside of the ceiling of the gas box	• Convective heat flux to air (assumed $h$ )	$-k\nabla T = h \cdot (T_{external} - T)$ $T_{external} = 20^\circ\text{C}, h = 0.5 \text{ W/m}^2\text{K}$
Inner side of the ceiling of the gas box, Surface B (Figure 2a), top surface of segments 1, 2 (Figure 2b), both sides of segment 3 (Figure 2b) of the strip, the surface of the LBE bath in the gas box	• Surface to Surface radiation	$-k\nabla T = \varepsilon \cdot (G - \sigma T^4)$ COMSOL (2015)
Bottom surface of the bath	• Setpoint temperature	$T_{bath} = 300^\circ\text{C}$
Top surface of the bath, outside of the gas box	• Convective heat flux to air (Low value of $h$ was assumed due to the surface oxidation)	$-k\nabla T = h \cdot (T_{external} - T)$ $T_{external} = 20^\circ\text{C}, h = 0.1 \text{ W/m}^2\text{K}$



a mentioned direction as well. The stainless steel strip is shown by the four transverse segments 1 – 4 to simplify the adjustment of the boundary conditions, so that they are similar to the industrial process. In addition, the strip was assumed to be a shell due to its thickness. The required hydrogen flow for the hardening furnace is provided from surface A in the gas box ( $d_A = 40\text{mm}$ ) and where surface B (Area =  $31780\text{mm}^2$ ) is specified as an outlet.

According to the complexity of the model, various grid sizes were tested in the model simulations. Specifically the numerical modelling was carried out with three different numbers of elements, i.e. 82310, 289517 and 525884. This was done to improve the calculation time and to achieve mesh-independent results. These meshes contain various amount of grids in the shape of tetrahedral, pyramid, prism, triangular, edge and vertex elements.

### Method of solution and boundary conditions

The temperature calculation was based on the consideration of the following statements

- I. A heat conduction in the strip.
- II. A convective heat transfer within the gas box, i.e. a heat convection between the strip – fluid, fluid – walls of the gas box and the wall of the gas box – the surroundings.
- III. A heat radiation, (surface to surface radiation) in the gas box between the surface of the strip, the inner side of the ceiling, and the surface of the LBE bath.
- IV. A conduction of heat transfer between the strip and the liquid bath.

The boundary conditions and the initial values used for the numerical model are shown in Table 2, which contains some process-defined values as well as some assumed values. The labels from Figure 2 are used for a clarification of the given values.

### Physical parameters used in the model

A chromium stainless steel, uddeholmstrip SS716, was the main target of this study. Its physical parameters used in the model are based on the data sheets of the nearest equivalent steel grade, EN 1.4034 or AISI 420 (Spittel and Spittel (2009)). Also, the physical parameters of the LBE used in the model were based on data from the literature (OECD (2007)) as well as from data from the production of strips. The physical parameters which typically vary with the temperature have an essential influence on the results of the numerical model. Table 3 shows linear relationship of the physical parameters as well as a summary of the material physical parameters for each domain, which are being used in the model. Surface emissivity values of 0.5 and 0.4 were assumed for those parts of the strip that contain higher and lower temperatures, i.e. segments 1 and 2 in Figure 2b, respectively. These values were taken from the literature (Wen (2010)), where it was shown that the value of the surface emissivity increased with an increased temperature for an AISI 420 alloy. In addition, these high emissivities were chosen due to the bright surface of the strip resulting from the reducing atmosphere of the furnace. Also, accurate values of the physical properties for hydrogen were taken from NIST (National Institute of Standard and Technology), which extracted their data

from Kunz et al. (2007), Leachman et al. (2009) and McCarty et al. (1981). A regression of the data was made and it is shown for the physical parameters of the hydrogen and the thermal conductivity of gliding material and strip.

**Table 3:** Physical properties of materials used in the model

	<i>Symbol</i>	<i>Value(s)</i>
Strip	$k$	$10^{-7} \cdot T^2 + 0.0024 \cdot T + 24.817$
	$\varepsilon$	0.5, 0.4
Wall of the gas box	$k$	44.5
	$\rho$	7850
	$C_p$	475
	$\varepsilon$	0.4, 0.6
Hydrogen	$k$	$0.0014 \cdot T^{0.8501}$
	$\rho$	24.507/T
	$C_p$	$5.96 \cdot 10^{-11} \cdot T^5 - 2.05 \cdot 10^{-7} \cdot T^4 + 2.76 \cdot 10^{-4} \cdot T^3 - 0.18 \cdot T^2 + 56.8 \cdot T + 7500$
	$\mu$	$2 \cdot 10^{-7} \cdot T^{0.6801}$
	$\gamma$	1.40
LBE	$k$	$3.61 + 1.517 \cdot 10^{-2} \cdot T - 1.741 \cdot 10^{-6} \cdot T^2$
	$\rho$	$11096 - 1.3236 \cdot T$
	$C_p$	$159 - 2.72 \cdot 10^{-2} \cdot T + 7.12 \cdot 10^{-6} \cdot T^2$
	$\varepsilon$	0.35
Gliding material	$k$	$10^{-7} \cdot T^2 + 7 \cdot 10^{-6} \cdot T + 0.0253$
	$\rho$	350
	$C_p$	1050

In this study, the wall of the gas box and the gliding material were estimated to be equivalent to those of an AISI 4340 alloy and for a typical high temperature board used in this application, respectively. In addition, a surface emissivity of 0.35 was introduced for a bright surface of molten lead according Trinks et al. (2007). Therefore, this value was assumed for the surface emissivity of the molten metal bath. According to a study by Wen (2010), the surface emissivity of steel varies between 0.4 to 0.7, based on the type of steel and the temperature. In this study, a surface emissivity of 0.6 was assumed for the surface which was defined as an outlet or interface of the gas box and the furnace that, which implies an incoming radiated heat from the furnace. This assumed value is based on the fact that the steel muffle is located inside the furnace, where the strip is hardened. For the inner side of the ceiling with a lower temperature, a value of 0.4 was assumed for the surface emissivity.

### TEMPERATURE MEASUREMENT IN THE HARDENING PROCESS

Real process temperature measurements were performed by using a DIAS Infrared thermal imaging camera in order to investigate the accuracy of the finite element model and to achieve a better insight about the temperature distribution across the strip. Measurements were carried out in the temperature range of 300 to  $1200^\circ\text{C}$  and using  $320 \times 256$  pixels. The temperature measurements were performed when the process reached its steady state situation in order to gain consistent results. Also, the measurements were carried out on the segment of the strip, just before it entered the LBE bath. This was due to the limited accessibility at the gas box and the installation limitations of the camera such as its

working temperature. The schematic view of the temporary setup of the process for the measurement is shown by Figure 3. A surface emissivity of 0.4 was set for the camera, which is the same value as was used for the initial condition of the strip in the numerical model within this area.

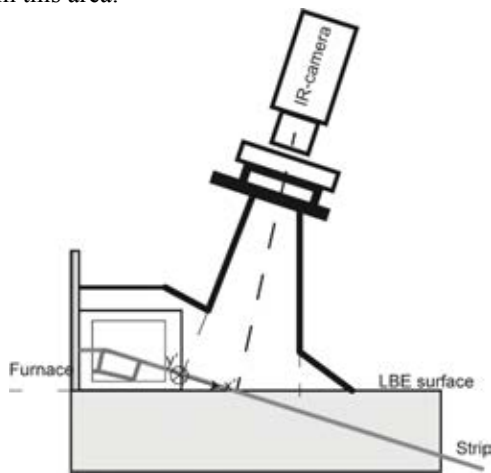


**Figure 3:** Schematic view of the temporary setup used in the temperature measurement in the industrial hardening process.

## RESULTS

### Model verification

Three numbers of mesh elements were applied into the FEM model in order to study if mesh-independent results as well as an improved convergence time could be obtained. Also, the temperature distribution across a line in a y-direction (strip's width) with different meshes was investigated and the results are illustrated in Figure 4.

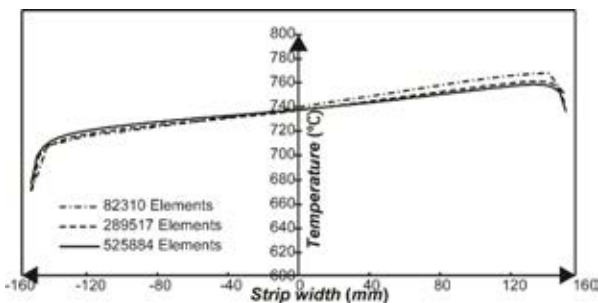


**Figure 4:** The influence of mesh size on the temperature predictions across the width of strip.

This comparison was done for a line located 63mm before the interface of strip and the bath. The results show that the maximum temperature deviation of the model, meshed with 82310 elements in comparison with the model meshed with 525884 elements is around 1.4%. Furthermore, that this difference decreased to 0.3% when a model with 289517 elements was compared to one with 525884 elements. In addition, the solution time is about 3 times larger when using 525884 elements in comparison to when using 289517 elements. Therefore, the numerical model containing 289517 elements was chosen as the optimum grid for the remaining investigations presented in the current study.

### Results of the Computational model

The quenching of a thin stainless steel strip within the hardening line was modelled. In addition, a thermal analysis was performed for the strip in the gas box.

Furthermore, the cooling process of the strip within the LBE bath was considered in the model. The hydrogen flow pattern resulting from the computational model of the laminar flow together with its temperature is illustrated in Figure 5.

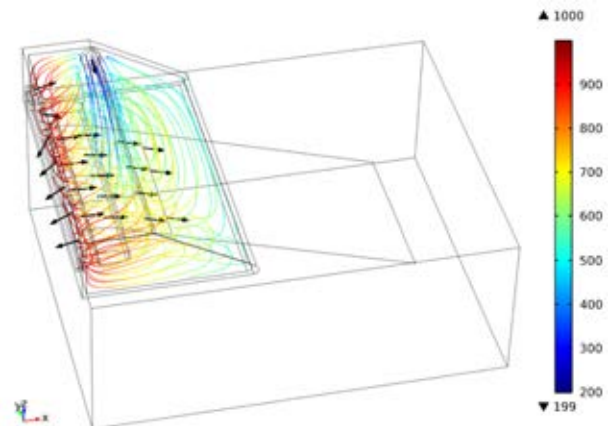


**Figure 5:** Hydrogen flow pattern and its temperature variation[°C].

As can be seen in this figure, the strip faces a colder flow at the area closest to the inlet. Furthermore, due to a mixture of the fluid and the heat from the strip, a warmer flow is available for the other segments of the strip before its entry to the quenching bath.

The prediction of the temperature pattern for the stainless steel strip was one of the main aims of this project. The temperature distribution within the strip after cooling, caused by the laminar flow and the quenching bath, is shown by Figure 6. The temperature at the exit of the hardening furnace is about 1000°C. However, as it can be seen, this value decreases to about 630°C after cooling by the cold hydrogen flow in the gas box. Also, the temperature drop is more significant on the strip side located nearest to the flow inlet compared to other parts of the strip. A non-uniform temperature distribution within the strip remains visible, especially across its transverse direction in the gas box. Therefore, a uniform temperature pattern is gradually becoming visible after a quenching of the strip by the liquid metal bath.

Figure 7 illustrates the temperature difference across the two edges and the centre of the strip. It can be seen that the strip temperature decreases dramatically from 1000°C to about 630°C before quenching by the molten metal, which occurs at a length of 175mm from the exit of the furnace.

At the position between 50-150mm, it can be seen that the strip at the opposite side of the gas inlet is subjected to less cooling than at the side close to the cold hydrogen gas inflow. Due to this result, the temperature of the strip decreases dramatically to a value of about 681°C. Also, significant transverse temperature difference between the two edges at the introductory part of cooling can be observed explicitly. Specifically, it can be up to about 73°C at the longitudinal position of 93mm. In addition, the centre part of the strip is exposed to the cold flow as well. Therefore, the far edges shows a maximum value of the temperature at the initial part of the cooling zone.

At the area between 150-175mm, the centre part shows a higher temperature value of in comparison to at the edges of the strip. This is caused by the mixture of the gas with the incoming heat from the furnace and the heat from the

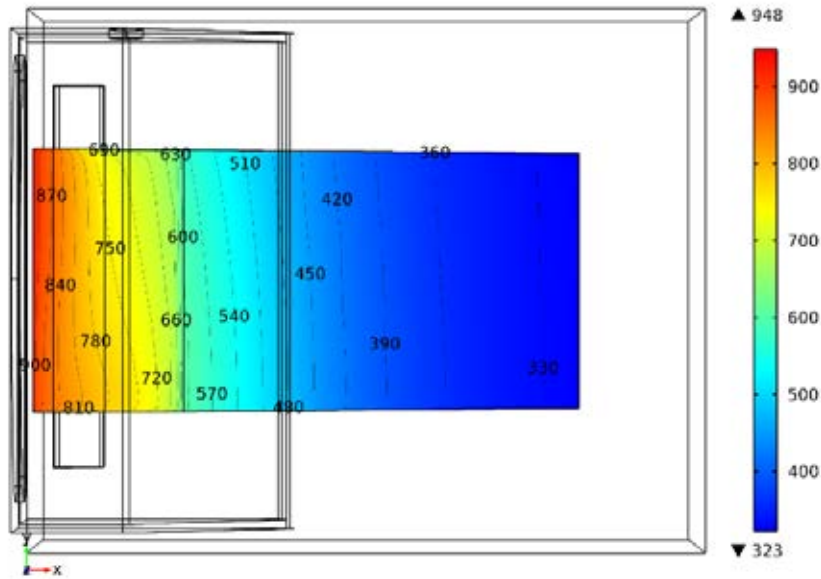


Figure 6: Temperature pattern within the strip [°C].

strip as well as by the three way heat convection at the edges. Therefore, a lower transverse temperature difference can be seen in the further cooling part of the strip. However, as shown in Figure 6, the strip at the area far from the inlet has its warmest area before the quenching by the bath. Also, a non-symmetrical temperature difference is present in the strip.

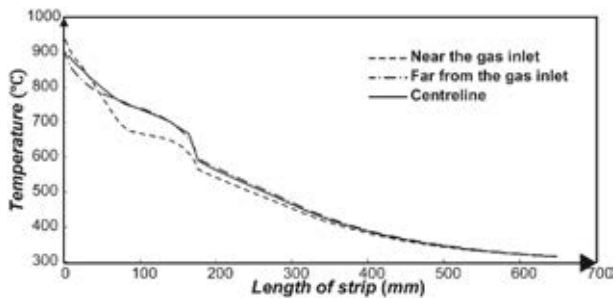


Figure 7: Temperature trajectories across the two edges and at the centre of the strip.

### Measured temperatures versus model predictions

A direct comparison of the real process temperature measurement and the predicted result is shown in Figure 8. Figure 8a shows the predicted temperature results from the model at the area where the real process temperature measurements had been carried out. Moreover, a result of the measured temperature done by the infrared thermal imaging camera is shown in Figure 8b. GS stands for the gas inlet side at which the inflow of gas is located in the gas box and OS defines the Operator side. Two straight lines named *I-I* and *II-II* were used for the validation of the numerical model across the transverse and along the longitudinal direction respectively. According to the thermal image analysis, the strip is slightly buckled at the entry of the quenching by the LBE bath. As shown in Figure 8, the same tendency of the transverse temperature distribution can be seen in both the measured and predicted results. It has been shown that the area located furthest from the gas inlet had the highest temperature in comparison to the other positions.

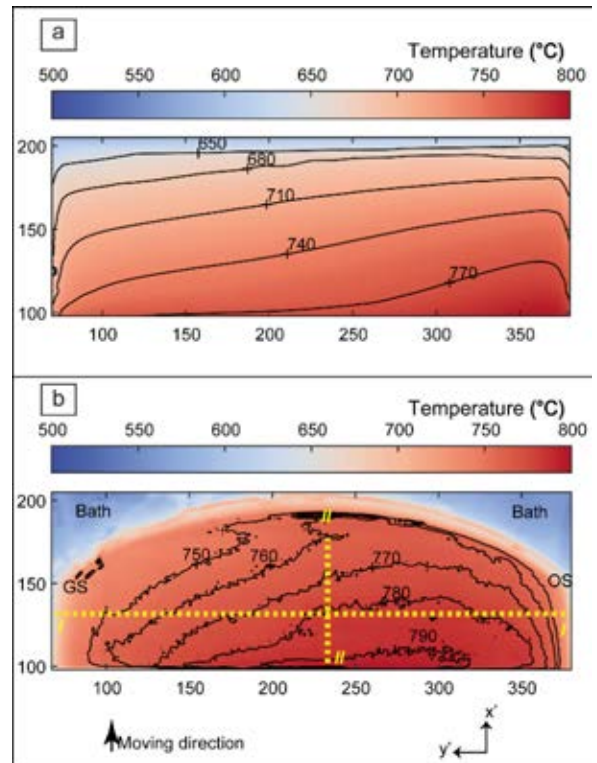


Figure 8: Temperature results (a) Predicted result from the numerical model, (b) A result from the measurements using the infrared thermal imaging camera to measure the temperature distribution on the strip

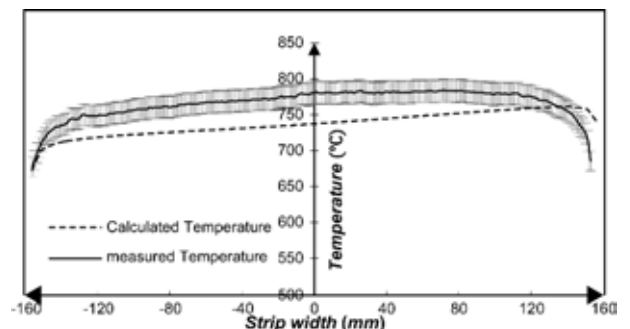
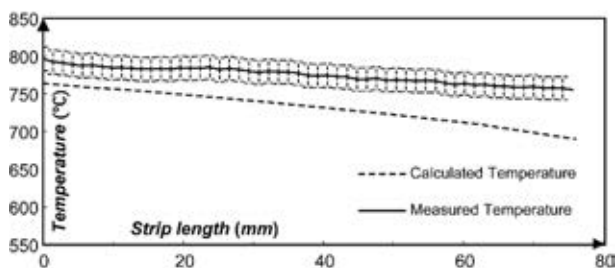


Figure 9: Comparison between the result of the predicted and measured temperatures across the width of strip, where line *I-I* is defined in Figure 8.

A Comparison of the numerical calculation results and measured temperature distribution across the strips' transverse direction, line *I-I* in Figure 8, is shown in Figure 9. This comparison was done at a position about 63mm from the bath interface. However, it was quite complicated to define the same line for the thermal image analysis and the model. In addition, a  $\pm 2\%$  of measured value was considered as the measurement uncertainty of the camera, based on the information given by the manufacturer (DIAS). This uncertainty is shown as an error bar in the diagram. The deviation between the calculated results and the real process data for the maximum temperature is 2.9%. However, the deviation for the minimum temperature is 0.6%. Also a significant transverse temperature difference is visible across the strips width. Specifically, this value was 107°C and 88°C for the measured temperatures and the model predictions, respectively. At the centre of the strip, the deviation between the predicted temperature and the measured value is 5.5%. Furthermore, a cooling at the edges can be seen from the predictions and measured results.

The temperature distribution along the strip's longitudinal direction, line *II-II* in Figure 8, is shown in Figure 10.



**Figure 10:** Temperature distribution along the strip's longitudinal direction, where line *II-II* is defined in Figure 8.

The length of the assumed line is about 76mm and it ends at a position about 21mm away from the bath interface. A definition of the exact line with the same position in the model and the thermal image can be identified as the limitation in this specific comparison. The same relationship for the temperature distribution is also found between the model predictions and the measured camera values. Also, the temperatures within the assumed line decrease by about 41°C and 73°C according to the temperature measurement and the model prediction, respectively. This result indicates that a cooling of the strips occur as it passes the gas box. By using a thermal image analysis and model predictions, it can be seen that the temperature of the strip dropped significantly within the gas box before a further quenching by the liquid metal bath took place. Specifically, the temperature of the strip decreased from 1000°C and the furnace temperature to about 755°C and 690°C, according to the thermal analysis and the model results, respectively.

## DISCUSSION

The object of this research was to study the quenching process of a thin stainless steel strip within the hardening line. Numerical simulations and empirical temperature measurements by using infrared thermal imaging were performed. The precision of the temperature distribution is an essential parameter to know in order to achieve an accurate comparison between the results of the model

predictions and the measured temperatures. In addition, accurate temperature measurements can assist in future investigations of thermal stresses analyses of strips. For instance, Wang et al. (2008) used measured data from the real process as its initial condition parameters for residual stress calculations in steel strips.

According to the results achieved by the numerical model in Figure 6 and Figure 7, the temperature of the strip drops significantly within the gas box. This is due to the existence of a hydrogen flow. The gas inflow in the box was preliminary designed to provide a reducing atmosphere in the hardening furnace. However, a high cooling effect on the stainless steel strip was also observed. Also, a stronger cooling effect has been seen at the area near to the cold gas flow inlet compared to the other parts of the furnace. This resulted in a distinguishable non-uniform temperature distribution within the strip, especially across its transverse direction. Regarding the various cooling conditions of the strip, a drop of the temperature at the edges is not avoidable. This phenomenon was also shown by Suebsomran and Butdee (2013) and Wang et al. (2008) in the cooling process modelling of strip steel on a run-out table in a hot rolling process, where the strip was quenched by an external fluid.

The trajectories of the temperature measured empirically and a comparison with the results of the numerical predictions are shown in Figure 9 and Figure 10. From this comparison, it can be seen that the warmest area of the strip is located at the area away from the gas inlet. Moreover, a significant transverse temperature difference (*y*-direction) can clearly be observed. The variation of the temperature values between the measured and the model data can be due to the limitations of each approach and due to an error in the comparison method.

A location of an assumed line for the investigation of temperature pattern within the prediction model and the thermal image analysis was performed as good as possible, but it was not perfect. Therefore, it may be difficult to consider precise values of the temperature, as a main target of a comparison. This limitation can also be called a potential error in the comparison of the results.

Various parameters can influence the results of the thermal image results. To obtain a precise value of the measured temperature in the closed gas box is an enormously hard task to achieve. As described in the literature by Minkina and Dudzik (2009), errors in an IR cameras' temperature measurement can be classified into the following reasons: errors of method, calibration errors, and electronic path errors. Many parameters cause errors in the method, which in turn cause a deviation from the actual value of the measured temperature. The following reasons can result in an error of the measuring method; i) an incorrect value of the emissivity of the object, ii) an influence of the ambient radiation which arrives to the detector of the camera directly or that is reflected by the surface of the object, and iii) the atmospheric temperature. Therefore, the definition of the surface emissivity value has an essential influence on the measurements. The object emissivity depends on the temperature of the material, the state of the surface, and the direction of observations (Minkina and Dudzik (2009)).

One of the main primary settings for the thermal imaging camera surface is the surface emissivity of the object. Furthermore, this parameter changes by the temperature of the strip (Wen (2010)). The real process temperature measurements showed that there is about a 4% temperature difference between the values resulting from surface emissivity values of 0.3 and 0.4. Therefore, the setting of a reliable surface emissivity for the whole object area is a quite hard task to perform, since colder areas are located near the edges. In addition, the curved shape of the strip in the LBE bath contact surface imply a buckling of the strip in the gas box. This incident influences the measured temperature of the strip on the top surface and the edges as well by means of changes in the state of the surface.

According to the lens variant of the IR-camera, the camera should be installed at the specific height to obtain accurate measurements. This height is defined based on the HFOV and VFOV, namely the Horizontal Field Of View and Vertical Field Of View, respectively. An implied buckled strip at the area before quenching by the bath, affects these two parameters by changing the height of the camera and the angle of the imaging to the strip. Consequently, this phenomenon causes errors in temperature measurements as well as reflections. This means that the mentioned uncertainty percentage of the measurements and errors caused by a variation of the surface emissivity can be increased.

The calibration error of the camera is  $\pm 2\%$  of the measured value according to the manufacturer (DIAS). This parameter is considered as the accuracy when operating the camera under specified laboratory conditions for a black body radiator and for an ambient temperature of 25°C (DIAS). In practical measurements, this uncertainty may be significantly higher (Minkina and Dudzik (2009)).

The errors in the electronic path of camera are below  $\pm 1\%$  for the ambient temperature. For non-contact temperature measurements by infrared cameras, errors in the method are generally the main source of uncertainty, which even can reach values of up to several percent (Minkina and Dudzik (2009)).

Therefore, these limitations can explain the differences between the measured data and calculated values in Figure 9. Therefore, by neglecting the temperature values at the edges (20mm from each side), the maximum value of the temperature for the measured data and the calculated result are 784°C and 761°C, respectively. However, there is about a 62mm difference between their locations. Moreover, the minimum values were 743°C and 713°C. The transverse temperature difference (y-direction), between the maximum and minimum values, at the assumed line in the thermal imaging process is about 41°C. However, this value is increased to 48°C in the numerical predictions. These values stand for a correct conformity between the measured temperatures and the numerical results.

Limitations in the model should always be considered in the comparison of the results with the measured temperatures. The current complex heat transfer model contains many boundary conditions based on the real process. Also, many material parameters also vary with the temperature. Physical parameters, used in the model, were chosen to be as accurate as possible. However, it is

still an enormous struggle to find a precise value and a temperature correlation for all the parameters of the different domains. In addition, fluid flow investigations were performed for a hydrogen flow in the gas box and the conduction was the only physics which was considered for the metal quenching bath. Therefore, due to the complexity of the model, the movement of the strip in the LBE bath were not considered. Moreover, to quantify the difference in the measured temperature and the model results in Figure 10, further investigations focusing on the heat convection in the bath are necessary.

## CONCLUSIONS

In this study, a thermal analysis numerical model was established and thereafter utilized to investigate the temperature distribution within the molten metal quenching step of a hardening process. Predicted temperatures of the strip were compared to real process thermal measurements using an infrared camera thermal imaging technique. The conclusions of this study may be summarized as follows:

1. The computational model results gave a better insight into the hardening process and a description of the temperature distribution within the quenching step in various domains. A hydrogen flow pattern within the gas box was revealed, which contributes to a better understanding of the temperature distribution on the strip.
2. An infrared thermal imaging used in this study exposed the temperature difference on the strip just before quenching. In addition, a buckled surface of the strip was revealed by these measurements.
3. The surface emissivity had the strongest influence on the results as the initial parameter for the temperature measurement analysis. There was a 4% temperature variation between the results from surface emissivity values of 0.3 and 0.4. Therefore, a calibration of the camera by using different surface emissivity values is suggested in future studies.
4. It has been proven that the strip faced a stronger cooling effect at the area close to the gas inlet, which resulted in a significant transverse temperature. Based on the literature data, extreme temperature difference across the transverse direction can be the source of flatness defects found within the strip.
5. By neglecting the temperature values at the edges (20mm from each side), the transverse temperature differences (y-direction) are about 41°C and 48°C in the real process measurements and the numerical predictions, respectively. Also, the mathematical model showed the same tendency for the temperature distribution within the strip in comparison to the thermal image analysis results. Therefore, the numerical model is deemed to be valid to be used for predictions of temperature distributions in strips.
6. The temperature of the strip, decreases dramatically within the gas box, between the exit of the hardening furnace and the entry of the quenching bath. The temperature of the strip, at 21mm from the bath interface, after the furnace decreased from 1000°C to about 755°C and 690°C according to the thermal analysis and the model results, respectively. It can be concluded that the hydrogen gas flow has a significant cooling effect on the strip, even though it

was preliminary designed to provide a reducing atmosphere in the hardening furnace. Therefore, a change of the gas inlet location might reduce temperature difference across the width of the strip.

7. This study can be used as a fundamental knowledge base for further investigations regarding the thermal stresses caused from non-uniform transverse temperature difference in the quenching step of the hardening process. This, in turn, will help to reduce the flatness problems in industrial hardening processes.

## ACKNOWLEDGMENTS

The authors would like to thank Mr. Chris Millward and Mr. Stellan Ericsson of voestalpine Precision Strip AB, for the fruitful discussion and great support with the temperature measurements as well as Mr. Nihat Palanci of Snesotest, Sweden to provide the possibility to use the Infrared camera for the industrial measurements. This study was carried out with a financial support from the Regional Development Council of Dalarna, Regional Development Council of Gävleborg, County Administrative Board of Gävleborg, the Swedish Steel Producers' Association, Dalarna University, Sandviken Municipality and voestalpine Precision Strip AB.

## REFERENCES

- (2012). Personal communication with Mr. Stellan Eriksson, R&D process technology, voestalpine precision strip AB, Munkfors, Sweden
- COMSOL, [www.comsol.com/release/5.1](http://www.comsol.com/release/5.1), date of access 2017-02-22, Heat Transfer Module User's Guide, Version 5.1, (2015).
- DIAS, PYROVIEW 320N, [www.dias-infrared.com/pdf/pyroview320n\\_eng\\_mail.pdf](http://www.dias-infrared.com/pdf/pyroview320n_eng_mail.pdf), date of access 2017-02-22.
- Ebner, J., (1983), "Bright Heat Treating of Carbon Steel Strip Using a Lead Quench", *Mach. Steel Austria*, 4.
- Kunz, O., Klimeck, R., Wagner, W., Jaeschke, M., (2007), "The GERG-2004 Wide-Range Equation of State for Natural Gases and Other Mixtures", GERG Technical Monograph 15 and Fortschr.-Ber., VDI-Verlag, Düsseldorf.
- Leachman, J.W., Jacobsen, R.T., Penoncello, S.G., Lemmon, E.W., (2009), "Fundamental Equations of State for Parahydrogen, Normal Hydrogen, and Orthohydrogen", *J. Phys. Chem. Ref. Data*, **38**, 721-748.
- Lochner, H., (1994), "Hardening of strip in a molten-metal bath or hydrogen jet cooler", *Steel Times*, **222**, 350.
- Lochner, H., (2006), "Steel strip hardening and tempering lines for medium and high carbon steels and alloyed grades part I: Production lines with liquid metal quenching", *Proc. IFHTSE - Int. Fed. Heat Treat. Surf. Eng. Cong. 2006*. ASMET, Vienna, 43.
- McCarty, R.D., Hord, J., Roder, H., (1981), "Selected properties of hydrogen (engineering design data)", National Engineering Lab (NBS), Boulder, CO (USA).
- Minkina, W., Dudzik, S., (2009), "Errors of Measurements in Infrared Thermography, Infrared Thermography", John Wiley & Sons, Ltd, New Jersey, 61.
- OECD NEA. Nuclear Science Committee, (2007), "Handbook on Lead-bismuth Eutectic Alloy and Lead Properties, Materials Compatibility, Thermal-hydraulics and Technologies", OECD Nuclear Energy Agency, France, 25.
- Spittel, M., Spittel, T., (2009), "Metal Forming Data of Ferrous Alloys - deformation behaviour", Springer Berlin Heidelberg, Berlin, 588.
- Suebsomran, A., Butdee, S., (2013), "Cooling process on a run-out table by the simulation method", *Case stud. therm. eng.* **1**, 51-56.
- Thelning, K.-E., (1984), "Steel and its Heat Treatment", Second Edition ed. Butterworth-Heinemann, Oxford, 581.
- Trinks, W., Mawhinney, M.H., Shannon, R.A., Reed, R.J., Garvey, J.R., (2007), "Industrial Furnaces", John Wiley & Sons, Inc., New Jersey, 190.
- Wang, S.-C., Chiu, F.-J., Ho, T.-Y., (1996), "Characteristics and prevention of thermomechanical controlled process plate deflection resulting from uneven cooling", *Mater. Sci. and Technol.* **12**, 64-71.
- Wang, X.-d., Li, F., Jiang, Z.-y., (2012), "Thermal, Microstructural and Mechanical Coupling Analysis Model for Flatness Change Prediction During Run-Out Table Cooling in Hot Strip Rolling", *J. Iron Steel Res. Int.*, **19**, 43-51.
- Wang, X., Li, F., Yang, Q., He, A., (2013), "FEM analysis for residual stress prediction in hot rolled steel strip during the run-out table cooling", *App. Math. Model.*, **37**, 586.
- Wang, X., Yang, Q., He, A., (2008), "Calculation of thermal stress affecting strip flatness change during run-out table cooling in hot steel strip rolling", *J. Mater. Proc. Technol.*, **207**, 130-146.
- Webster, H., Laird, W.J., (1991), "ASM Handbook", ASM International, 137-151.
- Wen, C.-D., (2010), "Investigation of steel emissivity behaviors: Examination of Multispectral Radiation Thermometry (MRT) emissivity models", *Int. J. Heat and Mass Transf.*, **53**, 2035-2043.
- Yoshida, H., (1984), "Analysis of Flatness of Hot Rolled Steel Strip after Cooling", *Trans. Iron Steel Inst. Jpn.*, **24**, 212-220.
- Zhou, Z., Lam, Y., Thomson, P.F., Yuen, D.D.W., (2007), "Numerical Analysis of the Flatness of Thin, Rolled Steel Strip on the Runout Table" *Proc. Inst. Mech. Eng., B J. Eng. Manuf.*, **221**, 241-254.



## VALIDATION OF A RAPID SLAG VISCOSITY MEASUREMENT BY CFD

B. Vandensande, E. Nagels\*, S. Arnout

InsPyro, Kapeldreef 60, 3001 Leuven, Belgium

\* E-mail: els.nagels@inspyro.be

### ABSTRACT

Slag viscosity is an important property in daily process practice, as well as for modelling flows in metallurgical processes accurately. Measuring slag viscosities is a challenging task, and usually requires a specific high-temperature furnace set-up, which needs to be gas tight and still allow for e.g. torque measurements on a well-aligned rotating viscometer spindle. The inclined plane technique is an alternative, requiring little time and no complex instruments. A slag sample, heated in a crucible or from an industrial furnace, is poured onto an inclined steel plate, and runs down while solidifying, to form a ribbon of a certain length. The ribbon length has been experimentally proven to be correlated rather accurately to the high temperature viscosity. However, as the viscosity increases sharply during cooling, the ribbon length should also depend on the temperature dependence of the viscosity. To study these effects, a CFD model has been built in this project. This model also allows to understand the effect of slag weight, steel plate thickness, temperature, and inclination, which could influence the results. The model is based on a VOF description for the slag surface and uses accurate heat capacity and viscosity functions based on thermodynamic calculations. This approach allows to increase the reliability of the fast slag viscosity measurement.

**Keywords:** CFD, metallurgy, viscosity, slag

### NOMENCLATURE.

#### Greek Symbols

- $\alpha$  Angle of inclined plane, [ $^{\circ}$ ] or Volume fraction, [-].  
 $\Gamma$  Diffusion coefficient, [ $\text{m}^2/\text{s}$ ].  
 $\eta$  Viscosity, [ $\text{Pa s}$ ] or [Poise].  
 $\rho$  Mass density, [ $\text{kg}/\text{m}^3$ ].  
 $\phi$  A conserved scalar

#### Latin Symbols

- A Parameter of Wayman-Frenkel relationship, [ $\text{Pa.s}/\text{K}$ ].  
B Parameter of Wayman-Frenkel relationship, [K].  
 $c_p$  Heat capacity, [ $\text{J}/\text{kg.K}$ ].  
L Ribbon length, [m].  
 $\dot{m}_{pq}$  Mass transfer from phase p to phase q, [ $\text{kg}/\text{m}^3$ ].  
 $n$  Number of phases, [-].  
 $S_{\phi}$  A source term of conserved scalar  $\phi$

- T Temperature, [K] or [ $^{\circ}\text{C}$ ].  
 $\mathbf{v}$  Velocity, [m/s].  
X Molecular fraction, [-].

#### Sub/superscripts

- p Phase p.  
q Phase q.

### INTRODUCTION

Within the metal producing industry, slag control is often instrumental for the efficiency of the production. Controlling the slag composition is key to have a good metal yield in any smelting or refining activity (Reis, 2014). Next to composition, which defines the chemical equilibria of reactions, also the physical property viscosity has a direct impact on the production process. To remove a slag from the furnace, it is commonly tapped as a liquid. This procedure requires a slag with a low viscosity, allowing it to flow. A low viscosity has the additional advantage that the metal-slag reactions will encounter less kinetic difficulties, e.g. due to better mixing. However, a low viscosity slag with a high reactivity towards the furnace lining could accelerate the refractory wear (Chen, 2016). Viscosity is thus a very important, although hard to measure, property of the slag. This research project explores the possibilities of an experimental measurement called the inclined plane technique. The measurement is tested in a lab environment and is modelled by CFD, which allows for a sensitivity analysis. It is clear that when this technique is installed in an industrial environment, some initial validation is needed. From this study with both CFD and experiments, a first indication of the most influential parameters is obtained.

### MODEL DESCRIPTION

#### Inclined plane technique

The inclined plane technique is a relatively simple and robust set-up. This gives the opportunity to use the measurement both in industrial as well as in lab environments. In this method, a certain amount of a slag is placed in a graphite or platinum crucible and heated to a temperature above the melting temperature. Industrially, it can be taken directly from the furnace or from the slag stream during tapping. The molten slag is then quickly poured onto a V-shaped stainless steel plate, set at a certain inclination (the inclined plane).



The slag flows down the inclined plane until it solidifies and forms a slag ribbon. The experimental set-up used by Dey and Riaz (2012) is shown in Figure 1. The length of the slag ribbon ( $L$ ) has been found to be exponentially related to the viscosity ( $\eta$ ) (Dey, 2012; Mills, 1997). To estimate the slag viscosity by the Inclined Plane Method, a ( $L$ ,  $\eta$ ) curve must be constructed first. The ( $L$ ,  $\eta$ ) curve can be constructed experimentally by measuring the ribbon length of slags with known viscosities. Subsequently, when the ( $L$ ,  $\eta$ ) curve is available, a slag sample with unknown viscosity is poured and then its ribbon length is measured. With the measured ribbon length and the available ( $L$ ,  $\eta$ ) curve, the viscosity of the studied slag can be estimated. This gives a quantitative technique to evaluate the flow properties of slag.

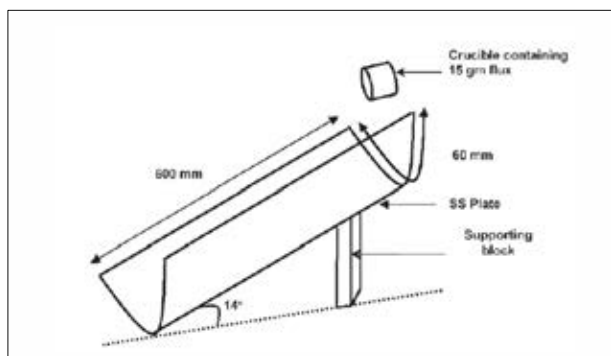


**Figure 1: Schematic representation of set-up for the inclined plane technique (After Dey, 2012)**

The experimental technique was evaluated and proven to be a fast technique with a good repeatability of the results. In this experimental phase, the angle of the set-up, the amount of material and initial temperature were considered as parameters, as shown in Table 1. Complementing this, the aim of the CFD calculations is to evaluate the robustness of the technique towards the experimental parameters, and towards parameters which are harder to vary experimentally, such as the thickness of the inclined plate, the temperature dependence of the viscosity and the initial temperature of this plate.

**Table 1: Experimental parameters**

Series	T(°C)	Inclination	Mass of slag	Composition
1	1300	12.5°	15g	1-6
2	1350	12.5°	15g	1-6
3	1400	12.5°	15g	1-6
4	1300	25°	15g	1-3
5	1300	12.5°	30g	1-3

#### Viscosity model

In literature, several models are described for the viscosity of a slag as a function of composition and temperature. In general, slags are formed by a solution of oxides and silicates. For the sake of viscosity, generally three types of oxides, namely acidic oxides, basic oxides and amphoteric oxides, are considered (Slag Atlas, 1995).



**Figure 2: Picture of the experimental set-up**

Acidic oxides such as  $\text{SiO}_2$ ,  $\text{P}_2\text{O}_5$ ,  $\text{B}_2\text{O}_3$  possess stiff, highly covalent metal-oxygen bonds.  $\text{SiO}_2$  forms tetrahedral anionic molecules of  $\text{SiO}_4^{4-}$  (silicate) which polymerize with each other to form more complicated polymer structures and even 3D networks, leading to high viscosities (Slag Atlas, 1995 and Kekkonen, 2012). With addition of basic oxides such as  $\text{CaO}$ ,  $\text{Na}_2\text{O}$ ,  $\text{MgO}$  with ionic metal-oxygen bonds, which do not require defined bond angles, the network breaks down, and consequently the viscosity of the slag decreases. The magnitude of the network-breaking effect depends strongly on the components and their proportions present in the slag. Amphoteric oxides, such as  $\text{Al}_2\text{O}_3$ ,  $\text{Fe}_2\text{O}_3$ , may act either as a network former or a breaker, depending on the composition of the slag (Kekkonen, 2012).

The temperature dependence of slag viscosity is mostly expressed in the form of the Wayman-Frenkel relationship (Equation 1) in which A and B are viscosity parameters and T is the temperature in K.

Wayman-Frenkel relationship

$$\eta = AT \exp\left(\frac{B}{T}\right) \quad (1)$$

#### CFD model specifications

##### Geometry and mesh of 2D model

The flow of the liquid slag in a V-shaped gutter is simplified to a 2D geometry to decrease the calculation time. The third dimension is modelled as a symmetry plane which corresponds with an infinite long plate over which a wave of liquid slag flows. Clearly, this has consequences for the cooling of the slag which will be discussed further when comparing the 2D to 3D situation. For now, the aim is to verify the influence of some parameters on the length of the formed ribbon which can qualitatively be understood from the 2D case. The mesh contains 30668 quad elements. A small cell size of  $2.5 \cdot 10^{-7} \text{ m}^2$  and 2<sup>nd</sup> order upwind schemes are used to capture the strong temperature and viscosity gradients present. The steel plate is meshed as well to capture the heat transfer in the solid domain. The mesh dependency of the ribbon length is illustrated in Table 2. A variation of -6% in the final ribbon length is significant and indicates that mesh effects are present. However, these deviations are within the experimental error margin.

**Table 2: Validation of mesh dependency**

Series	Mesh elements [-]	Final ribbon length [m]
1	13137	0,1577
2	30668	0,1547
3	54627	0,1449

#### Governing equations

Modelling the inclined plane technique is a multiphase problem with steep viscosity and temperature gradients. By using the volume of fluid (VOF) approach only one set of continuity equations must be solved for each iteration (Ansys, 2017). In its most general form the conservation of a scalar can be written as in Equation 2 (Ferziger, 2002 and Versteeg, 2007).

#### General transport equation

$$\frac{\partial \rho \phi}{\partial t} + \text{div}(\rho \phi \mathbf{v}) = \text{div}(\Gamma \text{grad} \phi) + S_{\phi} \quad (2)$$

with  $\mathbf{v}$  the velocity vector,  $S_{\phi}$  the source term of conserved parameter  $\phi$  and  $\Gamma$  the diffusion coefficient. The conserved variable  $\phi$  can be taken equal to 1, equal to the velocity in x, y, z direction or equal to the temperature. The conservation equations of mass, x-momentum, y-momentum, z-momentum or energy will be found respectively (Versteeg, 2007). Equation 3 gives as an example the continuity equation for mass conservation.

#### Continuity equation

$$\frac{\partial \rho}{\partial t} + \text{div}(\rho \mathbf{v}) = \text{div}(\Gamma \text{grad}(1)) + S_{\phi} = 0 \quad (3)$$

Additionally, in the Eulerian VOF description the interface is tracked by solving an additional continuity equation of the volume fraction for one or more phases (Ansys, 2017). The continuity equation for phase  $q$  in a simulation with  $n$  phases is given in Equation 4 (Ansys, 2017).

$$\frac{1}{\rho_q} \left[ \frac{\partial \rho_q \alpha_q}{\partial t} + \text{div}(\rho_q \alpha_q \mathbf{v}_q) \right] = \frac{1}{\rho_q} \left[ \sum_{p=1}^n (\dot{m}_{pq} - \dot{m}_{qp}) + S_{\alpha q} \right] \quad (4)$$

with  $\dot{m}_{pq}$  being the mass transfer from phase  $p$  to phase  $q$ . The interface is reconstructed from the volume fractions. For this model the Compressive Interface Capturing Scheme for Arbitrary Meshes (CISAM) is used due to its ability to cope with large differences in viscosity (Ansys, 2017).

#### Material properties and boundary conditions

The material properties used in the CFD model are given in Table 3 (Ansys, 2017 and Bale et al., 2016 and Slag Atlas, 1995). The slag properties correspond to the reference slag M1 of Dey and Riaz (2012).

**Table 3: Material properties used for modelling**

Property	Air	Slag	Steel
$c_p$ [J/kgK]	1006	1273	502
$\rho$ [kg/m <sup>3</sup> ]	1.225	2580	8030
$\alpha$ [W/mK]	0.024	0.8	16.3
$\sigma$ [N/m]	-	0.4 (with air)	-
$\eta$ [Pa.s]	$1.78 \cdot 10^{-5}$	UDF (see below)	-

The viscosity of the slag phase is implemented in Fluent 18.0 using a user defined function (UDF). The temperature dependence of the viscosity is calculated with the Riboud model. This model gives the coefficients of the Wayman-Frenkel relation based on the composition for the slag (Slag Atlas, 1995). These estimated coefficients are then used in the UDF to calculate the viscosity in each cell depending on the cell temperature. The viscosity calculated by the UDF is limited to 1000 Pa.s. This limitation is necessary to avoid the extreme gradients for lower temperatures. Without this limitation, the viscosities predicted by the Wayman-Frenkel equation cause the solver to diverge. This behaviour is observed for both the 2D and 3D situation. A limit of 1000 Pa.s is not expected to have an influence on the end result as the achieved solution displays no further movement of the slag.

The outer walls of the solid domain (steel plate) are modelled by a convection wall with a heat transfer coefficient of 15 W/(m<sup>2</sup>K) and a free stream temperature of 21 °C. The outer walls of the fluid domain are set to a fixed temperature of 21 °C. In the contact area between liquid and solid, the temperatures are coupled. ‘‘No slip’’ boundaries are used on all boundaries of the fluid domain.

The initial parameters of the base case are given in Table 4. The inclination is implemented by the orientation of the gravity. This allows the inclination to be changed more easily because the world reference and mesh can remain the same. The initial slag area corresponds to a cross section of the 3D case with 15g of slag.

**Table 4: Initial conditions of base case**

Inclination	12.5°
Initial temperature of steel plate	21°C
Initial temperature of air	21°C
Initial temperature of slag	1300°C
Initial area of slag	$48.1 \cdot 10^{-6}$ m <sup>2</sup>
Time step	0.0005s (except first 1000 iterations where it is 0.0001s)

In the experiments, the slag solidifies when it runs down the plate. In the simulations, the slag is said to be solidified when the slag ribbon length remains constant for at least one second.

## RESULTS

### Inclined plane technique test results

It is expected that the temperature of the liquid slag has a direct influence on the slag viscosity following the Wayman-Frenkel relation. In the experiments, it is indeed seen that a higher initial temperature results in a longer ribbon length (Figure 3). The compositions in Figure 3 correspond to earlier work by Dey and Riaz (2012). For all tested compositions, the influence of temperature seems to have an equal effect. From Figure 4, it is learned that the initial temperature has no influence on the relation between ribbon length and the viscosity, indicating that temperature information is not necessary to measure the viscosity with this technique. This means, the technique can be used to measure the viscosity at any experimental temperature, without knowing the temperature.

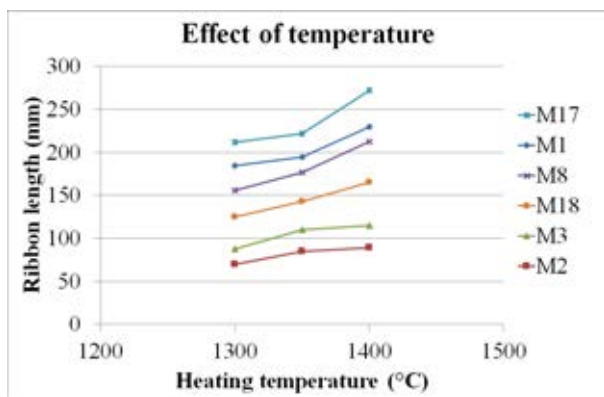


Figure 3: Increasing the initial temperature results in a larger ribbon length, corresponding to the viscosity dependence on temperature and composition

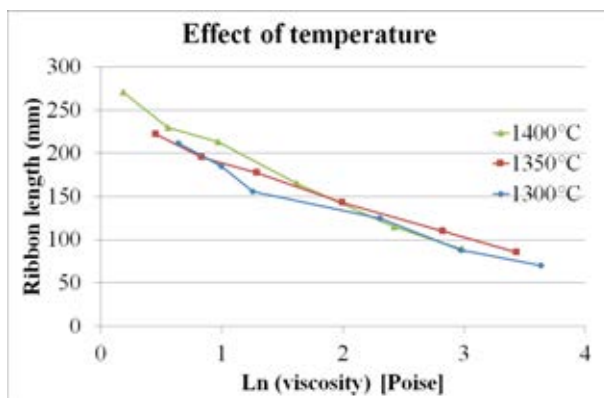


Figure 4: Ribbon length displays a linear relation with the logarithm of the viscosity over different initial temperatures

The second slag-related parameter for this test is the amount of material used for the inclined plane measurement. Obviously, when more material is present, a longer ribbon is expected. For three compositions, tests with both 15 g and 30 g are performed. An overview of the resulting ribbon lengths is given in Figure 5. These results indicate that a correction factor for the amount of slag will indeed be necessary. Roughly estimated from the limited number of experiments, doubling the weight of slag leads to a 50% longer ribbon. The amount of slag can be weighed

after cooling, so correcting the length after the measurement is feasible in an industrial set-up. A calibration is needed and expected to be possible, but from the limited amount of trials in this test series, it is not yet clear how many data points are needed for an accurate weight correction.

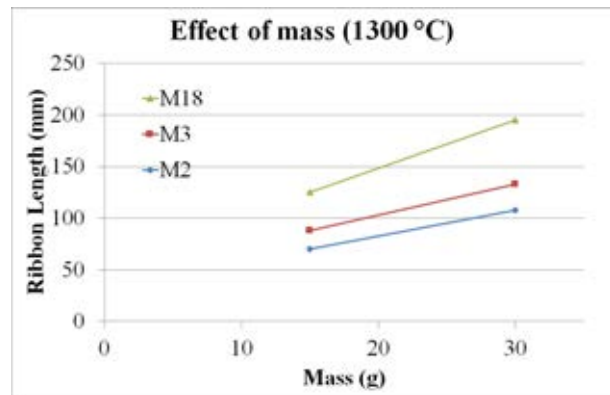


Figure 5: An increasing slag amount results in a longer ribbon

### CFD model results

All results are compared to the base case as described earlier in the model specifications (Table 4). The flow of the base case is illustrated in Figure 6. The first frame, the red rectangle, illustrates the initial position of the slag phase. During the simulations, the slag will stream down the plate and form the slag ribbon. The last frame illustrates how the final slag ribbon looks like. This shape agrees with the experimental observed solidified slag ribbons. During the simulation, the temperature decreases, due to the contact with the steel plate. Consequently, the viscosity increases. The velocity of slag slows down due to this increasing viscosity. This can also be observed in Figure 7. In this figure, the length evolution of three different calculations is compared, in which the temperature dependence of the viscosity is changed as shown in Figure 8. The steeper the dependency of the slag viscosity on the temperature, the faster the velocity of the slag decreases, resulting in a shorter ribbon.

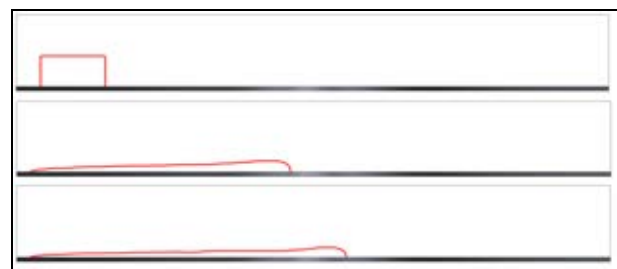
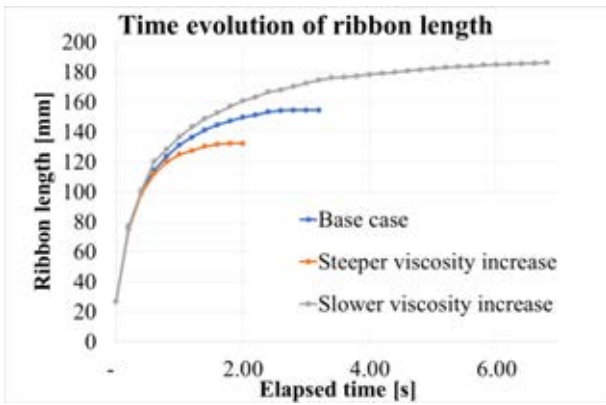


Figure 6: Contour evolution of the slag phase in the base case. From top to down: 0.0s, 0.5s and 1.0s



**Figure 7: Time evolution of different temperature dependent cases**

Figure 6 and Figure 7 prove that the maximum viscosity used in the UDF is sufficiently high to approximate the solidification. The ribbon length and shape of the slag phase all remain stable. For these length scales and forces, a liquid with a viscosity of 1000 Pa.s is practically solid.

Two types of parameters have been studied: set-up variations and material properties variations. The set-up variations include:

- increasing the inclination to 25°,
- increasing the initial temperature of the steel plate to 100 °C and 200 °C,
- increasing thickness of the steel plate to 5 mm,
- increasing the volume of slag by 59%, which corresponds to doubling a 3D cubic volume equally in all directions.

The material variations include:

- increasing/decreasing the slope of the Wayman-Frenkel relationship with a factor 2 while keeping the viscosity constant at 1300 °C (increased/decreased temperature dependency with the same start viscosity, dashed black lines in Figure 8),
- increasing the initial temperature of the slag to 1400 °C,
- doubling the initial viscosity with same temperature dependency (solid black line in Figure 8).

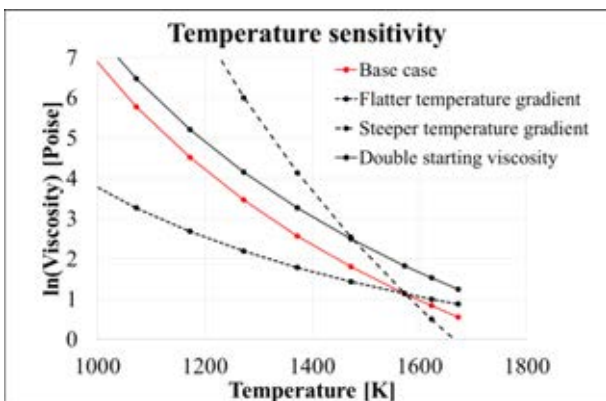


**Figure 8: Temperature dependency of different cases. Red line is the base case scenario, the black lines represent changes in temperature dependency**

The effect of the set-up parameters is summarized in Figure 9. By modelling the inclined plane, it can be concluded that the effect of both thickness and initial temperature of the plate are negligible for the final ribbon length. Consequently, doing sequential experiments, effectively increasing the initial temperature of the plate, will not largely influence the measured ribbon length. On the other hand, the angle of the plate and amount of material are to be calibrated for to obtain the actual viscosity from the ribbon length. In the model, the final length scales linearly with the amount of slag. This contradicts earlier experimental observations. This is due to neglecting the V-shape of the plate in the 2D model. In reality the system would react differently to an increasing amount of poured material. A 3D model seems prerequisite to correctly model the effect of a volume change.

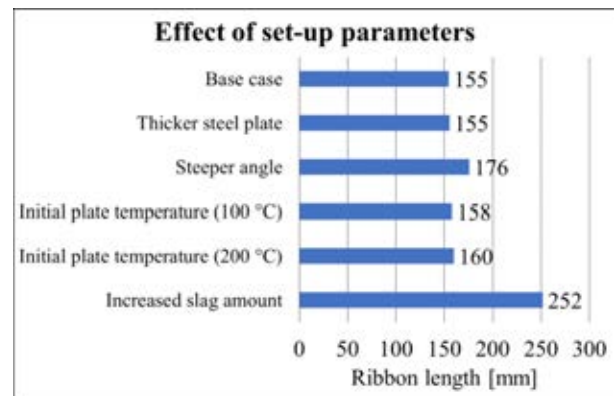


**Figure 9: Effect of set-up parameters on ribbon length**

The effect of the material property variations is summarized in Figure 10. The temperature dependency of the different cases is illustrated by Figure 8. Simulations with the same temperature dependency follow the experimentally observed linear relationship of Figure 4. However, Figure 10 indicates that the linear relationship between the final ribbon length and the viscosity is not depending on only the starting viscosity. In fact, the viscosity dependency on the temperature could cause serious deviations on the experimentally observed linear relationship.

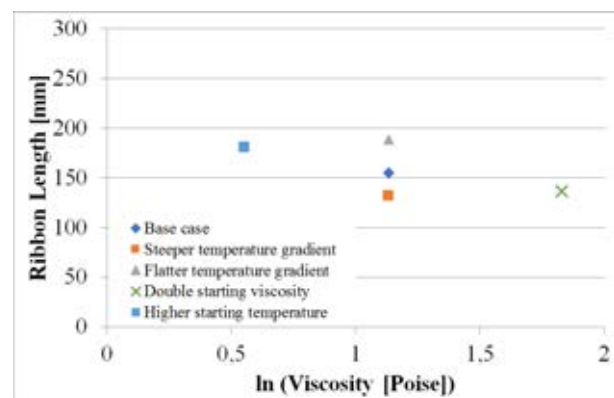


**Figure 10: Effect of viscosity parameters on ribbon length**

The inclined plane method therefore has the most comparative value if the temperature dependency for

different samples is similar. This will be the case in an industrial set-up where the same type of slag is always produced. This is also valid for the tested samples, for which the change in viscosity as a function of temperature is given in Figure 11. The Riboud model theoretically predicts the temperature dependency from the composition of the slag (Slag Atlas, 1995):

$$B = 31140 - 23896X_{CaO} - 46356X_{CaF_2} - 39159X_{Na_2O} + 68833X_{Al_2O_3} \quad (5)$$

with  $X$  being the molecular fraction of the different compounds. Consequently, the predicted values will change rather limited unless the molar fraction of aluminium is largely affected. For example, an increase of the molar fraction of alumina by 10% in the base case (with a decrease of calcium fluoride) will only lead to a change in temperature dependency of around 3%.

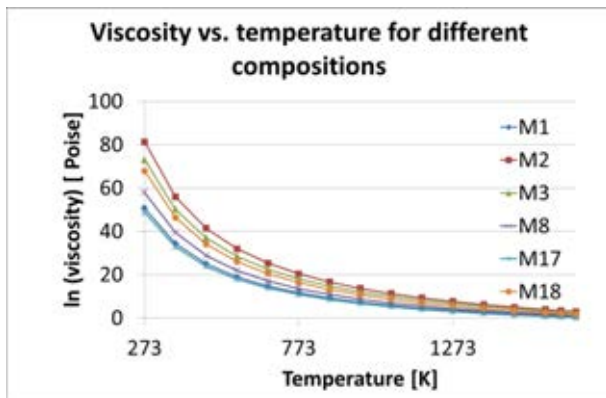


**Figure 11: Viscosity dependencies on temperature for the different composition of the test campaign**

### Future Research

To validate the current model to the experimental data and to predict absolute ribbon lengths, a 3D model is necessary. Certain effects were neglected in the 2D model such as the stream of the slag to the centre of the gutter, a larger contact area with the steel plate, and a larger heat sink in the steel plate next to the sample. These effects make any quantitative and predictive model impossible when working in 2D.

Unfortunately, artefacts exist when working with high viscosity liquids in Fluent 18.0 with the current approach. The slag phase does not fully make contact with the metal plate, but a certain volume fraction of air remains present at the interface. This distorts the heat transfer. Currently this problem can also be recreated in 2D by increasing the viscosity. The effect is not present in the simulations used in this paper.

In Figure 12 a first result of the 3D model is given. Although the shape and movement of the slag look realistic, some optimisation steps are necessary to increase the credibility of the result, especially concerning the heat transfer at the boundary conditions.

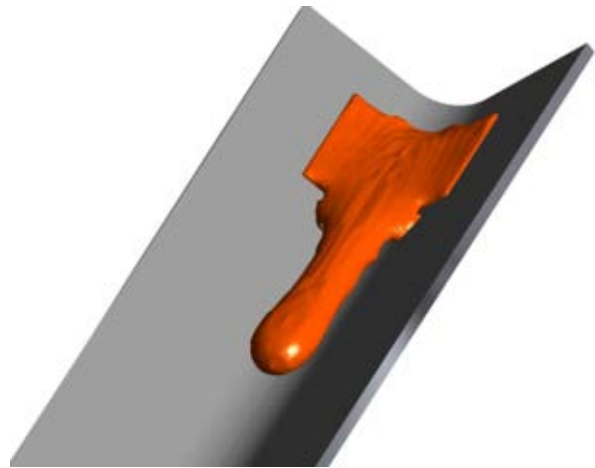


**Figure 12: Illustration of 3D model**

### CONCLUSION

In this work, CFD was used to complement the outcome of a testing campaign to validate the inclined plane set-up as a technique to measure slag viscosity. CFD allowed to verify the influence of several material and set-up parameters which are difficult to test in lab environment. It was concluded that the inclined plane technique is a reliable and robust technique, which looks promising to be used in an industrial environment for fast measurements of viscosity. CFD showed that sequential testing does not pose too large deviations due to heating of the equipment and it proved that if the composition changes are not too large, a quantitative comparison of ribbon lengths and related viscosities is possible. Given the positive outcome of this study, further effort will be done to calibrate the measurement to make it available for industry.

### ACKNOWLEDGEMENT

The authors would like to thank Kopila Gurung for performing the experiments.

### REFERENCES

- ANSYS, (2017), "Fluent 18.0 documentation", Ansys Help 18.0.
- BALE, C.W., BELISLE, E., CHARTRAND, P., DECTEROY, S.A., ERIKSSON, G., CHERIBI, A.E., HACK, K., JUNG, I.H., KANG, Y.B., MELANCON, J. and PELTON, A.D., PETERSEN, S., ROBELIN, C., STANGSTER, J. and VAN ENDE, M.A. (2010-2016), "FactSage Thermochemical Software and Databases", *Calphad*, vol. 54, pp 35-53, 2016.
- CHEN, L., LI, S., JONES, P.T., MUXING, G., BLANPAIN, B. and MALFLIET, A. (2016), "Identification of magnesia-chromite refractory degradation mechanisms of secondary copper smelter linings", *Journal of the European Ceramic Society*, vol. 36, nr. 8, pp. 2119-2132.
- DEY, A. and RIAZ, S. (2012), "Viscosity measurement of mould fluxes using inclined plane test and development of mathematical model," *Ironmaking & Steelmaking*, vol. 39, nr. 6, pp. 391-397.

FERZIGER, J.H. and PERIC, M. (2002), “*Computational methods for fluid dynamics*”. Springer.

KEKKONEN, M., OGHBASILASIE, H. and LOUHENKILPI, S. (2012) “Viscosity models for molten slags”, School of chemical technology, Helsinki.

MILLS, K.C., HALALI, M., LÖRZ, H.P., KINDER, A., POMFRET, R. and WALKER, B. (1997), “A Simple Test for the Measurement of Slag viscosities”, *Molten Slags, Fluxes and Salts*.

REIS, B.H., BIELEFELDT, W.V. and VILELA, A.C.F., (2014), “Absorption of non-metallic inclusions by steelmaking slags – a review”, *Journal of Materials Research and Technology*, vol. 3(2) pp179-185.

SLAG ATLAS. 2<sup>nd</sup> edition, (1995), *Verlag Stahleisen GmbH*, Düsseldorf.

VERSTEEG, H.K. and MALALASEKERA, W., (2007), “An introduction to computational fluid dynamics: the finite volume method”, *Pearson Education Ltd*, Harlow.



# SOLIDIFICATION MODELING WITH USER DEFINED FUNCTION IN ANSYS FLUENT

**Moritz EICKHOFF<sup>1\*</sup>, Antje RÜCKERT<sup>1</sup>, Herbert PFEIFER<sup>1</sup>**

<sup>1</sup> RWTH Aachen University, Department for Industrial Furnaces and Heat Engineering, Kopernikusstr. 10, 52074 Aachen, GERMANY

\* E-mail: eickhoff@iob.rwth-aachen.de

## ABSTRACT

The modelling of solidification processes in combination with fluid flow is one main application of ANSYS Fluent. The solidification is modelled with the enthalpy porosity technique. Therefore the fluid flow is damped like a flow through a porous media of dendrites. In case of materials with large solidification ranges, like the nickel based superalloy 718, the adjustment possibilities of ANSYS Fluent are often not adequate. The program postulates a linear dependency between liquid fraction and temperature. To improve the simulation, the solidification was implemented by a user defined function (UDF). The principal modelling of fluid flow is based on the theory of ANSYS Fluent, but it is now possible to adjust the liquid fraction in fine temperature steps.

**Keywords:** Rheology, Interphases, Casting and solidification, Process metallurgy, Alloy 718.

## NOMENCLATURE

### Greek Symbols

$\epsilon$	Turbulent dissipation rate, [-].
$\lambda$	Thermal conductivity, [W/(m K)].
$\mu_D$	Dynamic viscosity, [kg/(m s)].
$\nabla$	Divergence operator, [-].
$\rho$	Density, [kg/m <sup>3</sup> ].
$\tau$	Shear stress tensor, [N/m <sup>2</sup> ].

### Latin Symbols

$A_{mush}$	Mushy zone constant, [kg/(m <sup>3</sup> s)].
$e$	Internal energy, [J].
$f$	Fraction, [-].
$F$	Force against fluid flow per volume, [N/m <sup>3</sup> ].
$g$	Gravity, [m/s <sup>2</sup> ].
$k$	Turbulent kinetic energy, [-].
$K$	Permeability, [m <sup>2</sup> ].
$l$	Small number, [-].
$p$	Pressure, [Pa].
$Q_e$	volumetric energy source, [J/m <sup>3</sup> ].
$S$	Momentum sink for turbulence, [kg/(m <sup>3</sup> s)].
$v$	Velocity, [m/s].
$t$	Time, [s].
$T$	Temperature, [K].

### Sub/superscripts

eff	Effective (molecular + turbulent).
ESR	Electro slag remelting.
$\epsilon$	Turbulent dissipation rate.
k	Turbulent kinetic energy.
liq	Liquidus / liquid.
p	Pulling (movement of the solid).
sol	Solidus.
UDF	User-defined function.
UDM	User-defined memory.
VAR	Vacuum arc remelting.
x	X-direction.
y	Y-direction.
z	Z-direction.

## INTRODUCTION

Metallurgical processes are often modeled to obtain details of the inner fluid flow or temperature distribution, due to the difficult observation possibilities with classical measurement methods. The modelling of solidification processes is in focus of research since the 1970s (Erickson, 1975).

One of the common simulation programs ANSYS Fluent uses the enthalpy-porosity approach (ANSYS Inc., Release 14.5, 2012) which was introduced by Poirier (1987). ANSYS Fluent uses the assumption that the liquid fraction is proportional to the temperature in the solidification range. For many standard steels, this assumption will be an appropriate approach. In case of some nickel based superalloys, like alloy 718, the supposition is far-out the real material behavior.

Therefore, user-defined functions implement the solidification to reproduce the real material behavior.

## SOLIDIFICATION PHENOMENA

Important for the simulation of solidification processes are the damping of the fluid flow in the mushy region and the solidification enthalpy. The damping is adjustable with the material specific mushy zone constant (Voller et al., 1990) and considers the liquid fraction also.

Figure 1 shows the liquid fraction of an alloy 718 in respect to the temperature in the solidification range calculated by JMatPro. Obviously, the linear approximation made by ANSYS Fluent is not appropriate for this material. After a cooling of 25 % of the temperature range the liquid fraction is not 75 % but only 40 %. Therefore, the



damping of the fluid flow is underestimated by ANSYS Fluent.

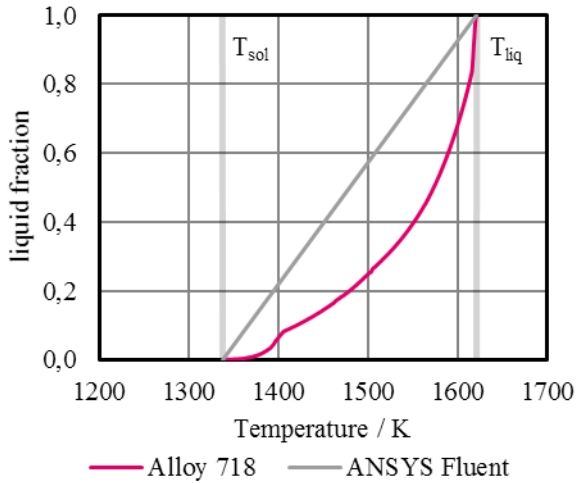


**Figure 1:** Liquid fraction of alloy 718 (Giesselmann et al., 2015) in comparison to ANSYS Fluent

The deviation of the liquid fraction from alloy 718 results in a nonlinear behavior of the enthalpy in the solidification range, because the solidification enthalpy is dependent on the liquid fraction.

Figure 2 shows the comparison of solidification enthalpies in respect to the temperature in the solidification range. The grey line shows the linear implementation of ANSYS Fluent. Obviously, the change in enthalpy of the mild steel (Koric and Thomas, 2008) is close to the approximation from ANSYS Fluent. Whereas, the red line, representing Alloy 718 (Overfelt et al., 1994), shows a considerably different behavior.

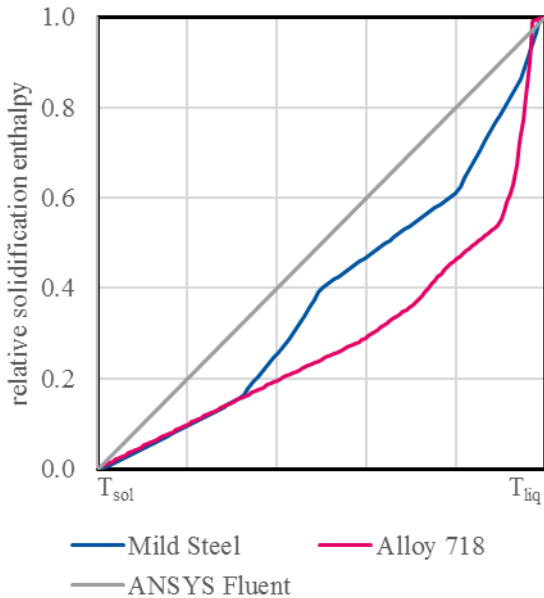


**Figure 2:** Comparison of solidification enthalpies (Overfelt et al., 1994, Koric and Thomas, 2008)

## BUILT-IN SOLIDIFICATION IN ANSYS FLUENT

The solidification module from ANSYS Inc. (Release 14.5, 2012) uses the enthalpy-porosity approach to implement the damping of the fluid flow in the mushy region. Poirier (1987) shows, that the inter dendritic flow follows Darcy's law (Darcy, 1856):

Darcy's law

$$\nabla p = -\frac{\mu_D}{K} \cdot \mathbf{v} \quad (1)$$

Voller and Prakash (1987) implemented the awareness of Poirier (1987) in the fluid flow modeling. Later, a mushy zone constant was introduced to replace the dynamic viscosity  $\mu_D$  and the unknown permeability  $K$  (Voller et al., 1990). The liquid fraction  $f_{liq}$  represents the change in permeability, whereas the mushy zone constant  $A_{mush}$  implements the different material behavior (2). The small number  $\epsilon$  is equal 0.001 to avoid a division by zero (ANSYS Inc., Release 14.5, 2012).

$$\frac{\mu_D}{K} = \frac{(1 - f_{liq})^2}{f_{liq}^3 - l} \cdot A_{mush} \quad (2)$$

The ratio between viscosity and permeability (see formula (2)) is then inserted in the equations (3) and (4) to formulate the force  $F$  against the fluid flow  $\mathbf{v}$  as well as the momentum  $S$  against the turbulence quantities  $\Phi$ .

$$\mathbf{F} = \frac{(1 - f_{liq})^2}{f_{liq}^3 - \epsilon} \cdot A_{mush} \cdot (\mathbf{v} - \mathbf{v}_p) \quad (3)$$

$$S = \frac{(1 - f_{liq})^2}{f_{liq}^3 - \epsilon} \cdot A_{mush} \cdot \Phi \quad (4)$$

The necessary turbulence quantities depend on the used turbulence model. Equation (4) is equal for all quantities like turbulent dissipation rate  $\epsilon$ , turbulent kinetic energy  $k$ , specific dissipation  $\omega$  and so on (ANSYS Inc., Release 14.5, 2012).

To show the implementation of the formula above, the momentum equation of the solver (5) is given below. The damping force  $F$  of the fluid flow (Equation (4)) is inserted in the last term.

$$\frac{\partial}{\partial t} (\rho \cdot \mathbf{v}) + \nabla \cdot (\rho \cdot \mathbf{v} \cdot \mathbf{v}) = -\nabla p + \nabla \cdot (\boldsymbol{\tau}) + \rho \cdot \mathbf{g} + \mathbf{F} \quad (5)$$

As mentioned in the previous chapter, the solidification enthalpy is distributed linear over the temperature range of solidification and implemented as source term  $S_m$  in the energy equation (6).

$$\frac{\partial}{\partial t} (\rho \cdot e) + \nabla \cdot (\mathbf{v} \cdot (\rho \cdot e + p)) = \nabla \cdot (\lambda_{eff} \cdot \nabla T + \boldsymbol{\tau}_{eff} \cdot \mathbf{v}) + Q_e \quad (6)$$

## USER-DEFINED SOLIDIFICATION MODEL

To reconstruct the real material behavior of alloy 718 an in-house developed solidification model based on UDFs is used for several process models, like electro slag remelting (ESR) and vacuum arc remelting (VAR).

### Approach

The aim of the modified solidification model is to implement the nonlinear behavior of the liquid fraction in respect to the temperature. The curve progression can be received for example from a Scheil-Gulliver approach like in Figure 1 or other calculation programs for thermo-physical data.

The idea was to reconstruct the solidification model of ANSYS Fluent by user-defined functions. Therefore, the main equations ((3) and (4)) for the damping are also used.

The solidification enthalpy is included in the heat capacity of the material.

### Implementation

The implementation of the modified solidification model is based on a DEFINE\_ADJUST function for the liquid fraction and several DEFINE\_SOURCE functions for the damping. A modified heat capacity includes the change in enthalpy.

The liquid fraction should be adjusted very detailed to represent the real fluid flow. Therefore, liquid fraction and solidification enthalpy out of the thermophysical database are divided in 1 K steps.

#### Damping of the fluid flow

A DEFINE\_ADJUST UDF loops over all the cells in the fluid regions to get the temperature of the cells. A look-up function searches the corresponding liquid fraction for these temperatures out of the tabulated liquid fractions. The liquid fraction is saved in a user-defined memory (UDM) for post processing.

Analog to the calculation procedure in ANSYS Fluent the ratio between viscosity and permeability is calculated with equation (2) and saved in another UDM. This ratio is the damping term of velocities and turbulence quantities (see equation (3) and (4)).

The damping force and momentum values are calculated in several DEFINE\_SOURCE UDFs. One UDF for each velocity direction and the turbulence quantities, typical turbulent dissipation rate  $\epsilon$  and turbulent kinetic energy  $k$ . The source value is the negative product of the damping term with the velocity or turbulence value (See equations (7) to (11)). If a pull velocity  $v_p$  moves the solid region, it has to be subtracted from the fluid velocity, here in the x direction:

$$F_x = -\frac{(1 - f_{liq})^2}{f_{liq}^3 - \epsilon} \cdot A_{mush} \cdot (v_x - v_p) \quad (7)$$

$$F_y = -\frac{(1 - f_{liq})^2}{f_{liq}^3 - \epsilon} \cdot A_{mush} \cdot v_y \quad (8)$$

$$F_z = -\frac{(1 - f_{liq})^2}{f_{liq}^3 - \epsilon} \cdot A_{mush} \cdot v_z \quad (9)$$

$$S_k = -\frac{(1 - f_{liq})^2}{f_{liq}^3 - \epsilon} \cdot A_{mush} \cdot k \quad (10)$$

$$S_\epsilon = -\frac{(1 - f_{liq})^2}{f_{liq}^3 - \epsilon} \cdot A_{mush} \cdot \epsilon \quad (11)$$

The five source terms have to be included for the corresponding values in the ANSYS Fluent interface. The program implements the source terms in the momentum equation (5) as well as the turbulence model.

#### Solidification enthalpy

To implement the nonlinear behavior of the solidification enthalpy (see Figure 2) the enthalpy is included in the heat capacity of the material (see Figure 3). Therefore, it is not necessary to modify the energy equation (6) of the solver.

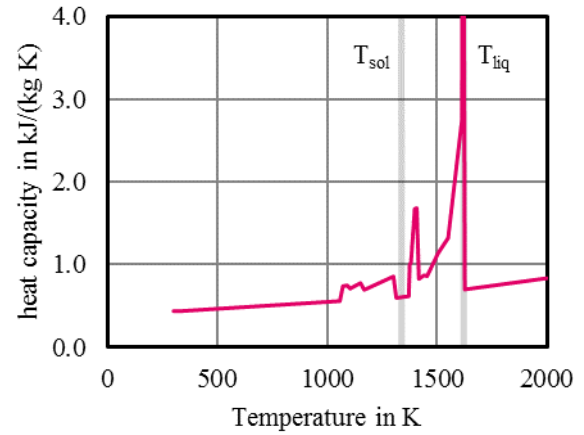


**Figure 3:** Heat capacity of alloy 718 including the solidification enthalpy (Giesselmann, 2014)

Obviously, most of the solidification enthalpy is needed or set free near to the liquidus temperature. This refers to the steep slope of the liquidus fraction in this area (compare Figure 1).

Another possibility to implement the enthalpy of solidification would be a DEFINE\_SOURCE UDF. The advantage of the presented solution is the reversible character of the heat capacity. Because some parts of the simulated region maybe melt on again, the solution with source term would be more elaborate. Whereas the heat capacity offers directly the possibility for change of sign in the temperature derivation.

## COMPARISON OF THE MODELS

To compare the built-in solidification of ANSYS Fluent with the UDF based solidification model a test case was set up. Figure 4 and Figure 5 show the flow of hot metal through a cooled pipe. The left face is a velocity inlet of hot liquid metal. The top wall is at constant temperature, which is lower than the solidus temperature. At the right side, the boundary is an outflow. The contour plot visualizes the liquid fraction from one (white) to zero (black). The black line symbolizes the position of 1 % solid fraction. The vectors and their lengths show the velocity. In Figure 4 the solidification model of ANSYS Fluent was used. Therefore, the liquid fraction increases uniformly over the whole solidification range.

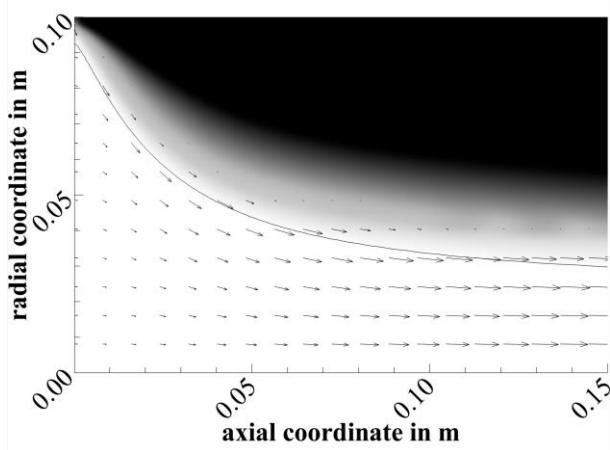


**Figure 4:** Test case: Built-in Fluent solidification model

Figure 5 shows the same test case simulation as Figure 4 with the UDF based solidification model. Obviously, the shape of the solidified area is slightly different, but more interesting is the case that there is sharp edge in the middle of the gray scale. Therefore, the fluid flow is damped at this position abruptly.

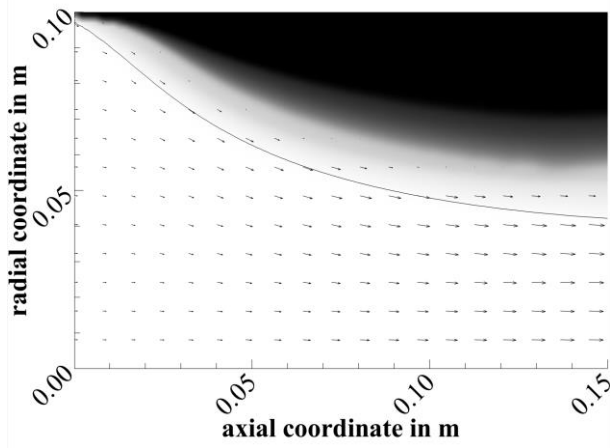


**Figure 5:** Test case: UDF solidification model

The comparison of the two test cases show the similarity of the models as well as the decisive differences. Whereas the flow in first case is damped smoothly, the damping with the UDF based model is more abrupt.

## CONCLUSION

A modified solidification model for ANSYS Fluent was introduced. It offers the possibility to reproduce the real material behavior in context of liquid fraction in respect to temperature. Which is important for the damping of the fluid flow in the mushy region as well as the distribution of the solidification enthalpy over temperature.

The solidification model of ANSYS Fluent was modified and calculated in a user-defined function to adjust the liquid fraction concerning the cell temperature properly. The damping of the motion values is then implemented by source terms for velocities and turbulence quantities. The solidification enthalpy is included in the heat capacity of the material. Therefore, the enthalpy can be fitted very detailed.

A test case shows the similarities and differences of the two models. The modified solidification implements a more abrupt damping of the fluid flow.

The modified solidification model is able to replicate the material behavior more detailed than the built-in solidification module of ANSYS Fluent.

## REFERENCES

ANSYS INC., (Release 14.5, 2012), "ANSYS® Academic Research Help System".

DARCY, H.P.G., (1856), "Dètermination des lois d'écoulement de l'eau à travers le sable".

ERICKSON, W.C., (1975), "Use of a general-purpose heat-transfer code for casting simulation", United States.

GIESSELMANN, N., (2014), "Numerische Untersuchungen des Elektroschlack-Umschmelzprozesses für Alloy 718", Dissertation, Aachen, RWTH Aachen University, Fakultät für Georesourcen und Materialtechnik, 140.

GIESSELMANN, N., et al., (2015), "Coupling of Multiple Numerical Models to Simulate Electroslag Remelting Process for Alloy 718", *ISIJ International*, **55**, 1408-1415.

KORIC, S. and THOMAS, B.G., (2008), "Thermo-mechanical models of steel solidification based on two elastic visco-plastic constitutive laws", *Journal of Materials Processing Technology*, **197**, 408-418.

OVERFELT, R.A., et al., (1994), "Porosity in cast equiaxed alloy 718", *International Symposium on Superalloys 718, 625, 706 and Various Derivatives*, Pittsburgh, 189-200.

POIRIER, D., (1987), "Permeability for flow of interdendritic liquid in columnar-dendritic alloys", *Metallurgical and Materials Transactions B*, **18**, 245-255.

VOLLER, V.R., et al., (1990), "Modelling the mushy region in a binary alloy", *Applied Mathematical Modelling*, **14**, 320-326.

VOLLER, V.R. and PRAKASH, C., (1987), "A fixed grid numerical modelling methodology for convection-diffusion mushy region phase-change problems", *International Journal of Heat and Mass Transfer*, **30**, 1709-1719.

# CLEANING OF POLYCYCLIC AROMATIC HYDROCARBONS (PAH) OBTAINED FROM FERROALLOYS PLANT

**Balram Panjwani, Stefan Andersson, Bernd Wittgens, and Jan Erik Olsen**

SINTEF Materials and Chemistry, 7465 Trondheim, NORWAY

\* E-mail: balram.panjwani@sintef.no

## ABSTRACT

Polycyclic Aromatic hydrocarbons (PAHs) are organic compounds consisting of only hydrogen and aromatic carbon rings. PAHs are neutral, non-polar molecules that are produced due to incomplete combustion of organic matter. These compounds are carcinogenic and interact with biological nucleophiles to inhibit the normal metabolic functions of the cells. In Norway, the most important sources of PAH pollution are considered to be metallurgical industries, offshore oil industries, transport and wood burning. Stricter governmental regulations regarding emissions to the outer and internal environment combined with increased awareness of the potential health effects have motivated Norwegian metal industries to increase their efforts to reduce emissions considerably. One of the objective of the ongoing industry and Norwegian research council supported "SCORE" project at SINTEF is to remove PAH from a hot gas stream through controlled combustion of the PAH inside a dedicated combustion chamber. The sizing and configuration of the combustion chamber depends on the properties of the bulk gas stream and the properties of the PAH itself. In order to achieve efficient and complete combustion of the PAH, the residence time and temperature need to be optimized. In the present study, the oxidation of pure PAH and PAH mixed with process gas is modelled using a Perfectly Stirred Reactor (PSR) concept. PSR concept was useful for understanding the influence of residence time and temperature on the oxidation of PAH to CO<sub>2</sub> and water. Furthermore, a computationally fast approach based on Chemical Reactor Network (CRN) is proposed for understanding the oxidation of PAH inside complex geometries. The Chemical Reactor Network (CRN) yields a detailed composition regarding species and temperature in the combustion chamber.

**Keywords:** PAH, PSR, Energy recovery, Ferro alloy furnace

## INTRODUCTION

Polycyclic Aromatic Hydrocarbons (PAHs) are one of the most stable classes of compounds and the largest organic chemical species known so far. It was in existence even before life started on Earth and it is considered to be one of the building blocks responsible for life on Earth. In the universe, PAH molecules are formed from carbon-rich, dying, giant red stars. These molecules grow in size and finally become larger dust particles. Formation of a nucleus takes place at around

2000 K and then the growth from nucleus to the larger PAH structure happen continuously. In Earth's atmosphere, PAHs are formed as a result of incomplete combustion of organic material or natural gas and also due to smoking and sometimes also natural processes such as carbonization. There are several hundred available PAHs and among them benzo[a]pyrene (BaP) is widely known and most frequently detected. The PAHs are found in air, water, food, and soil. In submerged arc furnaces, PAHs are major components formed during coal pyrolysis and combustion processes. Efficient pyrolysis of coal should result in the breakdown of large organic molecules to smaller hydrocarbons and in efficient combustion the only products should be CO<sub>2</sub>, H<sub>2</sub>O, CO etc. However, such complete degradation of coal rarely occurs and fairly large organic compounds, including PAHs, can be released from combustion sources. The formation of PAHs during coal combustion follows a complex pathway. Their formation depends on many variables such as temperature, oxygen concentration, and carbon-to-hydrogen ratio of the fuel. In principle it is difficult to control the PAH formation especially when the metal reduction processes take place inside the submerged arc furnace. Since controlling the formation of PAH is a challenge, a post-treatment of the PAH is therefore a viable option. There are many treatment methods for removal of PAH from liquids (e.g., liquid-liquid extraction, column liquid chromatography, and solid-phase extraction). However, few of these methods can be applied for efficient removal from gaseous streams (i.e., absorbent or adsorbent injection). Most of the available technologies are also expensive and some of them require dealing with complex chemicals. In these processes PAHs are not removed, but are merely transferred to another phase, up-concentrated and treated as a waste stream.

One of the byproducts during the metal reduction process is energy-rich off-gas and usually this energy is not harnessed. SINTEF Materials and Chemistry along with Ferroalloy industry is developing a novel concept for energy recovery from ferroalloy furnaces. The concept is based on the idea of introducing a combustion chamber in the off-gas section, in which controlled combustion of process gas will be carried out. A

combustion chamber will be designed in which the process gas consisting of PAH obtained from furnace will be oxidized with air. This oxidation process is performed inside a combustion chamber and the design of the combustion chamber has been presented elsewhere (Panjwani 2017). The oxidation rate of PAH depends on the local temperature and reaction kinetics of the PAH. There is a plethora of kinetic data available on the formation of PAH during pyrolysis or combustion, but the kinetic data on mechanisms dealing with oxidation of PAH are very limited. It has become apparent that PAH combustion at high temperature is not the most actively studied field, but rather closely related fields such as PAH and soot formation from smaller hydrocarbons as well as room temperature atmospheric oxidation of PAHs. Such related studies do contain highly relevant data for the study of PAH combustion as well, but care must be taken to find and extract relevant data on the complete combustion of PAHs. The paper by Mati et al. (Mati et al. 2007) stands out in this respect, reporting on a study of 1-methylnaphthalene combustion involving both experiments as well as including a kinetics model with 146 species and 1041 reactions. The kinetic data used in the model consists of a mixture of literature data and estimated data based on chemical considerations and similar reactions wherever literature data were unavailable. The oxidation of methylnaphthalene has been performed experimentally by Mati et al. in a Jet stirred Reactor (JSR) over a wide range of temperatures (800–1421 K) at 1 atm and 10 atm pressure, and residence times 0.5 to 1.5 s. The 1-methylnaphthalene kinetic mechanism consists of 146 species and 1041 elementary reactions. There is also a wealth of useful kinetics models from the CRECK Modelling group (<http://creckmodeling.chem.polimi.it/>) in Milan who deal with kinetics modelling of combustion and pyrolysis systems involving, e.g., conversion from coal and biomass to PAHs and small molecules as well as from small hydrocarbons to PAHs and soot.

An accurate prediction of PAH combustion inside a combustion chamber requires a coupling between complex chemical kinetics and CFD. Incorporating reaction kinetics of 1-methylnaphthalene within Computational Fluid Dynamics (CFD) requires solving around 150 transport equations which is indeed computationally demanding and the computational cost will increase further when including more complex PAH. Therefore a simplified approach is developed in which oxidation of 1-methylnaphthalene is studied independently at different pressures, temperatures and species concentration. It is assumed that the oxidation of PAH will not affect the overall flow pattern or temperature. The temperature, pressure and species concentration including PAH concentration will be obtained from the CFD simulation of a combustion chamber. The present study is divided into two parts. In part-1, the kinetic study using a perfectly stirred reactor is performed to estimate a minimum residence time and temperature required for oxidation of 1-methylnaphthalene in the presence of process gas

consisting of mainly CO and H<sub>2</sub>O. This information has been used for the sizing of the combustion chamber<sup>1</sup>. In part-2, the oxidation of 1-methylnaphthalene inside the combustion chamber will be assessed using the Chemical Reactor Network (CRN) approach (Falcitelli et al. 2002; Fichet et al. 2010; Skjøth-Rasmussen et al. 2004). An algorithm to construct CRN was proposed by Falcitelli et al. (Falcitelli et al. 2002) They showed that this methodology could be successfully applied to several industrial cases and in each case, the NO<sub>x</sub> prediction presents a great accuracy compared to measurements with less than a 5% error.

## EXPERIMENTAL AND THEORETICAL SOURCES OF KINETIC DATA

Even though there is a limited amount of literature data on kinetics, one can find data on PAH oxidation in for instance the atmospheric chemistry literature, which deals with reactions of a large number of different PAHs emitted to the atmosphere (Keyte, Harrison, and Lammel 2013; Saggese et al. 2014). The most well studied oxidizing species are OH, O<sub>3</sub>, and NO<sub>x</sub>. One must remember that contrary to combustion, such reactions, typically studied at room temperature, give only partially oxidized PAH derivatives rather than leading to complete destruction. These reaction products are of particular interest not only as intermediates in the degradation of PAHs, but also since they potentially are more toxic than the parent PAHs. The crucial rate-determining steps are in these cases found in the first few reaction steps of PAH oxidation, since the products generally are more reactive than the PAHs themselves.

Reactions with OH will be particularly relevant if there is a significant amount of water vapour is available in the gas. With some caution the room temperature kinetic data could be extrapolated to combustion conditions. A useful support in this case is to complement experimental data with atomic-scale quantum chemistry calculations, as has been performed on the oxidation of naphthalene (Qu, Zhang, and Wang 2006; Zhang, Lin, and Wang 2012). Such calculations can be used to directly calculate activation energies, allowing for safer extrapolation of kinetic data from one temperature to another. One should just be careful to validate the calculated data against reliable benchmark literature data as far as possible. Such comparisons have for instance been made for the chemically related initial steps of benzene oxidation (Taatjes et al. 2010).

## ALTERNATIVE PROCESSES FOR PAH OXIDATION AND DESTRUCTION

One alternative way of oxidizing PAHs is to use suitable catalysts. Recent work by Varela-Gandía et al. (Varela-Gandía et al. 2013) focused on achieving complete oxidation of naphthalene by using palladium nanoparticles protected by polymers sitting in porous support materials, such as zeolites and alumina. The results were very promising and 100% conversion was achieved between 165°C and 180°C. Best performance and stability were found using the BETA zeolite as support.

A number of research groups are also working on plasma-assisted conversion of PAHs (Chun, Kim, and Yoshikawa 2011; Odeyemi, Rabinovich, and Fridman 2012; Yu, Li, et al. 2010; Yu, Tu, et al. 2010). The studies by Yu et al. (Yu, Li, et al. 2010; Yu, Tu, et al. 2010) report on the destruction of naphthalene, acenaphthene, fluorene, anthracene and pyrene in a direct current gliding arc plasma reactor at a temperature of 130°C. The PAHs are found to be destroyed to within 93-98% in pure oxygen, with slightly lower values in air. The products are mainly CO, CO<sub>2</sub>, H<sub>2</sub>O and O<sub>3</sub>. In air a rather significant amount of NO<sub>x</sub> is also formed along with partially oxidized PAH molecules containing keto and NO<sub>2</sub> groups. These PAH derivatives will likely react further much more readily than the parent PAH molecules.

#### METHOD AND TOOLS:

The residence time and flame temperature are very important for designing the combustion system. These two parameters are estimated using a perfectly stirred reactor (PSR) (Ellen M. 1996). The PSR is an ideal reactor in which uniform mixing is assumed inside the control volume due to diffusion and forced turbulent mixing. This means the rate of reaction is mainly governed through chemical kinetics and not through mixing. In other words the mixing time scale is much shorter than the chemical time scale. The residence time ( $\tau$ ) inside the reactor is defined as  $\tau = \frac{V_r}{\dot{m}}$ , where  $V_r$  is volume of the reactor. Figure 1 illustrates the conceptual representation of the reaction, where the reactant is introduced at the inlet with specified temperature and species concentration. The reactants are ignited inside the reactor at constant pressure. The product will be formed depending on the kinetic of the reactants.

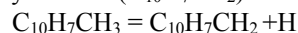


Figure 1 Schematic of PSR

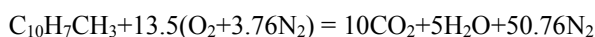
The product leaving the reactor has a certain composition and temperature. If the residence time is too short or the temperature is too low there will be an insignificant amount of reactions occurring and in that situation the outlet properties (temperature and species composition) will be same as those of the inlet. Before using the PSR concept for more realistic problems a verification test case is performed. A suitable test case for verification of the PSR approach would be oxidation of a hydrocarbon. Here, an oxidation study of methane with air at different equivalence ratio ( $\phi$ ) is performed using the PSR code. Figure 2 illustrates the comparison of the present study (symbol) with literature data (solid line) (W.-C. Chang and J.-Y. Chen). The results show that the reactor temperature is well predicted for both lean ( $\phi=0.7$ ) and rich ( $\phi=1.2$ ) fuel conditions for an initial temperature of 295K and atmospheric pressure.

#### OXIDATION CHARACTERISTIC OF PAH

The oxidation of a PAH is mainly governed by temperature and residence time and will only take place if temperature and residence time are above critical values. These critical values depend on the kinetic data of the PAH itself. In the mechanism (Mati et al. 2007), the initiation reactions for the oxidation of methylnaphthalene includes C-H bond cleavage yielding the methylnaphthyl radical (C<sub>10</sub>H<sub>7</sub>CH<sub>2</sub>).



A detailed description involving the different chains of reactions and intermediate products has been given by Mati et al. (Mati et al. 2007). It is worth mentioning that the oxidation of 1-methylnaphthalene also produces many complex intermediate such as Indene, A2R5C2H, A3R5AC, etc. The stoichiometric chemical reaction between 1-methylnaphthalene and air is given below. Oxidation of 1 mole of methylnaphthalene requires 13.5 mole of air.



While performing PSR simulations; 0.0153 moles of C<sub>10</sub>H<sub>7</sub>CH<sub>3</sub>, and 0.207 moles of O<sub>2</sub> and 0.77 moles of N<sub>2</sub> were fed at the inlet of PSR reactor. For a given inlet the temperature and pressure of the reactor were maintained constant but the residence time was increased from 0.2 to 2 s. The resulting output of the PSR was mole fractions of the reactant and product. Figure 3 illustrates 1-methylnaphthalene mole fraction (y-axis log scale) as a function of residence time at temperature from 800-1600°C. The results show that the oxidation of 1-methylnaphthalene will not take place below 800°C and a residence time shorter than 0.2 s. For a given inlet temperature, the increase in residence time accelerates the rate of oxidation of 1-methylnaphthalene. Figure 4 illustrates the CO<sub>2</sub> mole fraction (y-axis log scale) as a function of residence time at different temperature (800-1600 °C). The formation rate of CO<sub>2</sub> is also very small at temperatures below 800°C since there are no reactions occurring at this temperature.

The results obtained from this study have been utilized for sizing of the combustion chamber (Panjwani 2017). While designing the combustion chamber it was ensured that the temperature inside the combustion chamber is not lower than 800 °C and that the residence time of the PAH component should be more than 2 s. Current study was useful for finding intermediate during the oxidation of PAH. The detail of the full combustion chamber design is not presented here but a simplified 2D axisymmetric design is presented and discussed here. The simplified design is used for understanding the PAH oxidation. The results from the study will make a platform for designing the full scale 3D combustion chamber design.

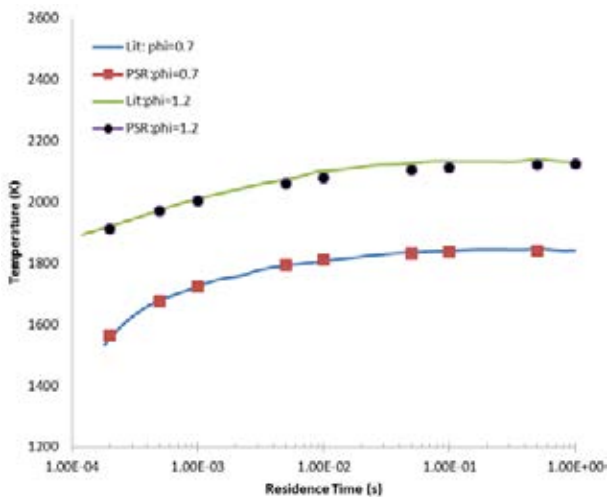


Figure 2 Effect of residence time on the reactor temperature

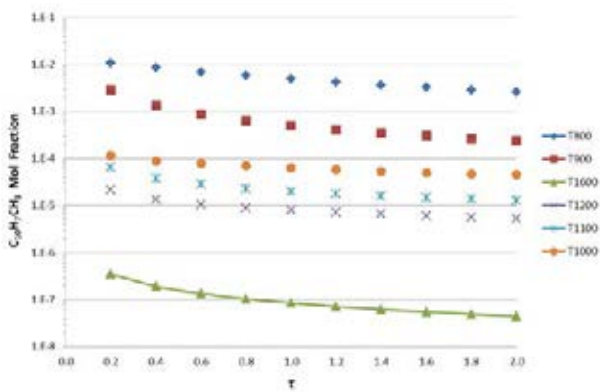


Figure 3 Mole fraction of 1-methylnaphthalene at different temperature as a function of residence time

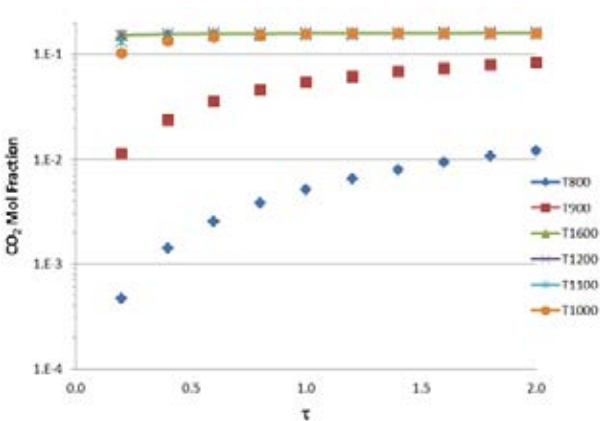


Figure 4 CO<sub>2</sub> mole fraction at different temperature as a function of residence time

## GEOMETRY AND MODELLING SETUP

The design and operation of the combustion chamber depend on many parameters, including the total power capacity of the combustion chamber, and the residence time for combusting the complex PAH, NO<sub>x</sub>. The process gas mainly consists of CO, H<sub>2</sub>O, CO<sub>2</sub> and Si components in a Ferro Silicon furnace and Mn components in a Ferro Manganese furnace. The process gases also consist of a certain amount of PAH and the treatment of these PAH is a challenge due to their stable

complex rings. Axisymmetric combustion chamber has been proposed for PAH oxidation.

A CFD-based approach has been used for designing the combustion chamber. CFD has become mature enough to be used for designing any industrial or laboratory scale system involving flow, heat and mass transfer. The commercial CFD software ANSYS FLUENT (ANSYS 2016) has been utilized for this purpose.

An axisymmetric combustion chamber with primary and secondary inlets for air has been proposed (see Figure 5). The geometry and mesh were generated using the ANSYS design modeler. The generated mesh was imported into the FLUENT (Finite Volume Solver). In the model setup, the convective and diffusive terms in the transport equation were discretized using second-order schemes. The turbulence-chemistry was modeled with the eddy dissipation concept model. Turbulence was handled with the k- $\epsilon$  model and for radiation a well-known Discrete Ordinance (DO) model was employed. The process gas mainly consists of 70-75% of CO and 20-25 % of H<sub>2</sub>O. The oxidation mechanism of CO with air was modeled using a detailed chemical kinetic mechanism involving 12 species and 28 elementary reactions (Drake and Blint 1988). Pressure-velocity coupling was achieved by the SIMPLE algorithm. The PAH modelling principle described in the earlier sections has only been validated for one set of conditions such as pressure, temperature and species concentration. However, in the actual combustion chamber all these parameters i.e. pressure, temperature, species concentration, residence time and PAH concentration vary with time and space. CFD modelling of complex hydrocarbons having hundreds of species and thousands of reaction mechanisms is a computationally demanding task.

Furthermore, performing CFD simulation for several flow conditions will be a daunting task. In the present study an approach called chemical reactor network (CRN) analysis is utilized in which flow parameters such as concentrations of major species (CO, CO<sub>2</sub>, H<sub>2</sub>O), temperature and pressure are extracted from the CFD simulation. These variables are subsequently supplied to a stand-alone reactor. In principle each numerical cell of the CFD is treated as a PSR. Here we assumed that the temperature and concentration changes due to oxidation of the PAH has insignificant effects on the global flow parameters i.e. velocity, temperature and pressure. The approach has previously been applied to different furnace geometries, such as pilot-scale and full scale boilers, low-NO<sub>x</sub> burner flames, incinerators and glass furnaces. A similar approach was introduced by Skjøth-Rasmussen et al. (Skjøth-Rasmussen et al. 2004) who solved larger geometrical problems considering each computational cell of the CFD grid as a perfectly stirred reactor. The results obtained from this approach were encouraging therefore this approach is utilized for current study.

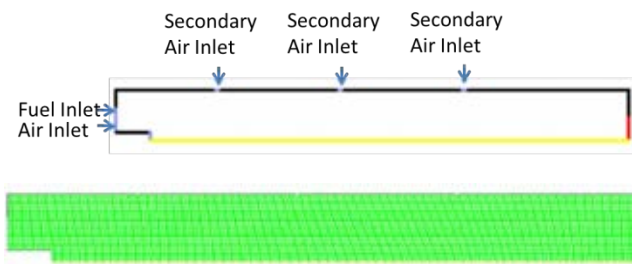


Figure 5 Geometry and Mesh of the combustion chamber

## RESULTS AND DISCUSSION

Results obtained from CFD simulations without PAH oxidation is presented. The temperature distribution on the middle plane of the combustion chamber is shown in Figure 6. There are mainly four hot pockets, one close to the primary air inlet and the remaining three hot pockets are close to the secondary air inlets. The maximum temperature is around 1700°C for a chosen fuel/air ratio. The peak temperature varies for different fuel/air compositions.

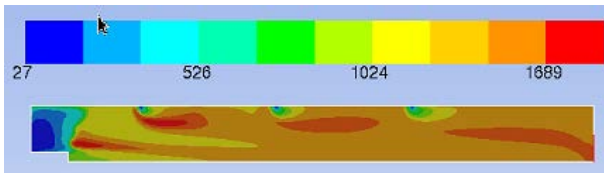


Figure 6 Contours of Static Temperature ( $^{\circ}$ C)

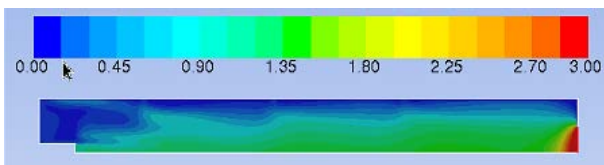


Figure 7 Contours of velocity magnitude (m/s)

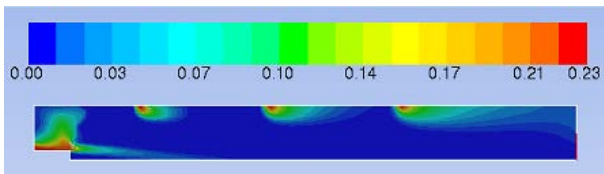


Figure 8 Contours of O<sub>2</sub> mass fraction (-)

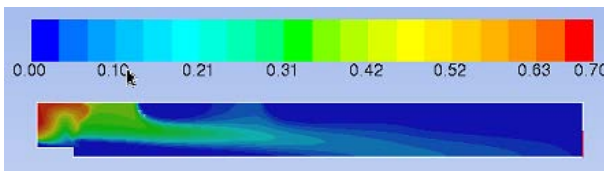


Figure 9 Contours of CO mass fraction (-)

Ignition of the process gas starts when it comes into contact of fresh air. The magnitude of velocity is shown in Figure 7. The average velocity is around 1.5 m/s and the maximum exit velocity is around 3 m/s. A distribution of O<sub>2</sub> mass fraction is shown in Figure 8. The maximum mass fraction is close to the inlet. It can be observed that air is not able to penetrate due to strong axial momentum force. As soon as air is injected from the secondary inlets

it is subjected to an axial force and it follows along the direction of the combustion chamber. The incoming CO mixes with the air and starts combusting close to the secondary air inlets. A contour plot of CO mass fraction is shown in Figure 9. It can be seen that the CO mass fraction is much higher ahead of the secondary air inlets. The CO will start combusting when it mixes with air coming from the secondary air inlets.

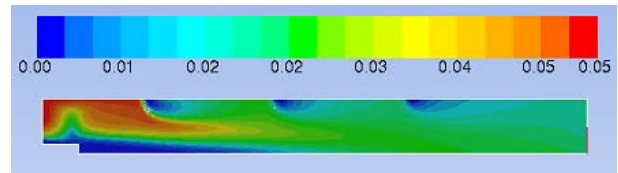


Figure 10 Contours of PAH mass fraction (Without any oxidation)

A contour of PAH distribution without any oxidation is shown in Figure 10. In the CFD study PAH is behaving as a non-reacting species because an oxidation process of PAH is not considered. This PAH concentration along with other species such O<sub>2</sub>, N<sub>2</sub>, CH<sub>4</sub>, CO<sub>2</sub>, CO will be input to the PSR reactor model. As mentioned earlier, each numerical cell of the CFD is treated as a PSR. The major output from the PSR reactor model will be change in PAH, O<sub>2</sub>, N<sub>2</sub>, CH<sub>4</sub>, CO<sub>2</sub>, CO concentration and intermediate species concentration. It is assumed that the flow is frozen and in steady state and effect of change in temperature and species concentration due to PAH oxidation is insignificant on the global flow field.

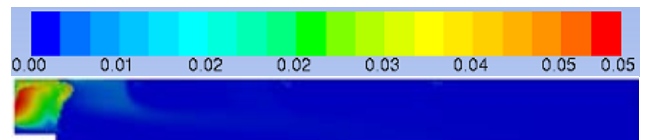


Figure 11 Contours of PAH mass fraction (after PSR simulations)

Results from CRN analyses is shown in Figure 11, which is illustrating the contours of PAH mass fraction after PSR simulation. Higher mass fraction can be observed at entrance of the combustion chamber due to unavailability of the oxidizer, lower temperature and lower residence time. As we move further downstream, the PAH concentration keeps on diminishing. It should be mentioned that during the PSR calculation a residence time of 2 s was assumed everywhere. In reality, however, this residence time will be a function of space. This varying residence time might have some impact on the PAH concentration but is not considered in the present study.

## CONCLUSIONS

Estimating the chemical kinetics data of PAH is a challenging task. An extensive literature survey was performed for finding the chemical kinetic data of PAH and based on this study we were only able to find kinetic data for 1-methylnaphthalene. A PSR simulation of 1-methylnaphthalene for a given set of chemical mechanisms clearly indicates that the combustion of 1-methylnaphthalene depends on the residence time and



initial temperature. The minimum temperature at which combustion of 1-methylnaphthalene starts is around 800°C. This study shows that the effect of residence time is weaker than the effect of temperature on the combustion of 1-methylnaphthalene. A residence time of 2s is essential for the oxidation of methylnaphthalene. A CRN analysis approach is utilized for understanding the oxidation of PAH inside the combustion chamber. The oxidation of PAH occurs at much longer time scales than the oxidation of process gas, which occurs on time scales on the order of micro- to milli-seconds. The study clearly showed that almost all the PAH is oxidized as far as 1-methylnaphthalene is concerned. However, we do not have any kinetic data on the complex PAHs and with the present results we cannot make definite conclusions about the oxidation behavior of these more complex species.

#### ACKNOWLEDGMENT

The research work carried out in this article is funded by SCORE (Staged Combustion for Energy Recovery in Ferroalloy industry) project funded by Norwegian research council and The Norwegian Ferroalloy Producers Research Association (Ferrolegeringsindustriens Forskningsforening (FFF)). Funding from the SCORE project is greatly acknowledged

#### REFERENCES

- ANSYS, INC. 2016. *ANSYS FLUENT Theory Guide*.
- Chun, Young Nam, Seong Cheon Kim, and Kunio Yoshikawa. 2011. 'Destruction of anthracene using a gliding arc plasma reformer', *Korean Journal of Chemical Engineering*, 28: 1713.
- Drake, Michael C., and Richard J. Blint. 1988. 'Structure of Laminar Opposed-flow Diffusion Flames With CO/H<sub>2</sub>/N<sub>2</sub> Fuel', *Combustion Science and Technology*, 61: 187-224.
- Ellen M., Harry K. M., Joseph F. G., and Robert J. K. 1996. "A FORTRAN Program for Modeling Well Stirred Plasma and Thermal Reactors with Gas and Surface Reactions " In.: Sandia.
- Falcitelli, M., S. Pasini, N. Rossi, and L. Tognotti. 2002. 'CFD+reactor network analysis: an integrated methodology for the modeling and optimisation of industrial systems for energy saving and pollution reduction', *Applied Thermal Engineering*, 22: 971-79.
- Fichet, Vincent, Mohamed Kanneche, Pierre Plion, and Olivier Gicquel. 2010. 'A reactor network model for predicting NO<sub>x</sub> emissions in gas turbines', *Fuel*, 89: 2202-10.
- Keyte, Ian J., Roy M. Harrison, and Gerhard Lammel. 2013. 'Chemical reactivity and long-range transport potential of polycyclic aromatic hydrocarbons - a review', *Chemical Society Reviews*, 42: 9333-91.
- Mati, Karim, Alain Ristori, Gaëlle Pengloan, and Philippe Dagaut. 2007. 'Oxidation of 1-Methylnaphthalene at 1–13 atm: Experimental Study in a JSR and Detailed Chemical Kinetic Modeling', *Combustion Science and Technology*, 179: 1261-85.
- Odeyemi, F., A. Rabinovich, and A. Fridman. 2012. 'Gliding Arc Plasma-Stimulated Conversion of Pyrogas into Synthesis Gas', *IEEE Transactions on Plasma Science*, 40: 1124-30.
- Panjwani, B., Wittgens, B., Olsen, J.E. 2017. "COMBUSTION CHAMBER SCALING FOR ENERGY RECOVERY FROM FURNACE PROCESS GAS: WASTE TO VALUE " In.
- Qu, Xiaohui, Qingzhu Zhang, and Wenxing Wang. 2006. 'Mechanism for OH-initiated photooxidation of naphthalene in the presence of O<sub>2</sub> and NO<sub>x</sub>: A DFT study', *Chemical Physics Letters*, 429: 77-85.
- Saggese, Chiara, Nazly E. Sánchez, Alessio Frassoldati, Alberto Cuoci, Tiziano Faravelli, María U. Alzueta, and Eliseo Ranzi. 2014. 'Kinetic Modeling Study of Polycyclic Aromatic Hydrocarbons and Soot Formation in Acetylene Pyrolysis', *Energy & Fuels*, 28: 1489-501.
- Skjøth-Rasmussen, M. S., O. Holm-Christensen, M. Østberg, T. S. Christensen, T. Johannessen, A. D. Jensen, P. Glarborg, and H. Livbjerg. 2004. 'Post-processing of detailed chemical kinetic mechanisms onto CFD simulations', *Computers & Chemical Engineering*, 28: 2351-61.
- Taatjes, Craig A., David L. Osborn, Talitha M. Selby, Giovanni Meloni, Adam J. Trevitt, Evgeny Epifanovsky, Anna I. Krylov, Baptiste Sirjean, Enoch Dames, and Hai Wang. 2010. 'Products of the Benzene + O(3P) Reaction', *The Journal of Physical Chemistry A*, 114: 3355-70.
- Varela-Gandía, Francisco J., Ángel Berenguer-Murcia, Dolores Lozano-Castelló, Diego Cazorla-Amorós, David R. Sellick, and Stuart H. Taylor. 2013. 'Total oxidation of naphthalene using palladium nanoparticles supported on BETA, ZSM-5, SAPO-5 and alumina powders', *Applied Catalysis B: Environmental*, 129: 98-105.
- W.-C. Chang and J.-Y. Chen. <http://firebrand.me.berkeley.edu/griredu.html>, Accessed 28/04/2017.
- Yu, Liang, Xiaodong Li, Xin Tu, Yu Wang, Shengyong Lu, and Jianhua Yan. 2010. 'Decomposition of Naphthalene by dc Gliding Arc Gas Discharge', *The Journal of Physical Chemistry A*, 114: 360-68.
- Yu, Liang, Xin Tu, Xiaodong Li, Yu Wang, Yong Chi, and Jianhua Yan. 2010. 'Destruction of acenaphthene, fluorene, anthracene and pyrene by a dc gliding arc plasma reactor', *Journal of Hazardous Materials*, 180: 449-55.
- Zhang, Zhijie, Ling Lin, and Liming Wang. 2012. 'Atmospheric oxidation mechanism of naphthalene initiated by OH radical. A theoretical study', *Physical Chemistry Chemical Physics*, 14: 2645-50.

# GRANULAR FLOW DESCRIBED BY FICTITIOUS FLUIDS: A SUITABLE METHODOLOGY FOR PROCESS SIMULATIONS

**Manuel SPARTA\***, Sverren Anton HALVORSEN

Teknova AS, 4612 Kristiansand, NORWAY

\* E-mail: manuel.sparta@teknova.no

## ABSTRACT

The flow of granular materials is often present in metallurgical reactors. Metallurgical simulations are typically multidisciplinary and the granular flow will often have a significant effect on the temperature distribution. The flow of bulk materials exhibits patterns that can be very different from fluid flows. Standard fluid flow methods are not applicable to describe such flows.

For simple bulk flows with plug flow sections and mass flow hoppers, a reasonable flow field can, however, be computed with a standard CFD tool. The trick is to apply appropriate, non-standard, moving wall boundary conditions.

This simple approach does not work for complex flow cases, including sections with one or more free boundaries. For such cases, we apply the Discrete Element Method (DEM), which has emerged to be the preferred choice for simulation of granular flow. A suitable method has been developed to compute the volume averaged flow field by DEM and then import it into a code for multiphysics simulations.

To reduce the high computational cost of DEM simulations a hybrid approach is recommended. DEM simulations are then used for the complex flow regions while the simple model is used wherever applicable. In the multiphysics program the flow field is forced to be equal, or very close to, the DEM results by applying a suitable volume force.

**Keywords:** Granular flow, Fictitious fluids, Standard CFD software, Process metallurgy.

## NOMENCLATURE

- $\Phi$  Total flow, [m<sup>3</sup>/s]
- $\Omega$  Cross section, [m<sup>2</sup>]
- $a$  Characteristic length, [m]
- $z$  Vertical coordinate, [m]
- $\mathbf{u}$  Velocity, [m/s]
- $\bar{w}(z)$  Average vertical velocity, [m/s]
- $u$  radial component of the velocity, [m/s]
- $w$  vertical component of the velocity, [m/s]
- $K$  Force factor, [Ns/m<sup>4</sup>]
- $s_\Phi$  Total flow scaling factor, [1]

## INTRODUCTION

The flow of granular material is ubiquitous in metal production with the transport of ores and carbonaceous materials in furnaces being a primary example. Granular flows exhibit patterns that can be very different from fluid flows (Jenike, 1964). For example, arc formation can clog outlets, small change in the hopper angle may result in the transition from funnel flow (with stagnant areas) to mass flow (with flow in the whole cross section). If obstacles are present, upstream stagnant zones and empty cavities downstream are easily formed. All these effects can sum up counterintuitively, to the extent that the placement of obstacles can increase the flow rate (obstacles are routinely inserted before outlet opening in silos). These unique features imply that standard fluid models do not provide good approximations to granular flow. Significant efforts have been spent to derive numerical models for granular materials (for a recent review we refer to the work of Tang et al. (2015)), but such methods may not be implemented in common multiphysics programs.

Metallurgical simulations are typically multidisciplinary and the granular flow will often have a significant effect on the temperature distribution. For many applications, the general flow patterns are essential, while details can be neglected. It is most convenient if these patterns can be available within the computational tool you normally apply for multidisciplinary simulations.

We follow the the spirit of application-driven pragmatic modeling, i.e. deriving simplest possible model which can give fast, and sufficiently accurate answers (c.f. Zoric et al. 2014). We started to test whether standard CFD tools might be suitably adapted, to describe granular flow.

This article is organized as follows, a fictitious model geometry showing some challenges of a metallurgic reactor is presented. In first approximation, we attempt to enforce a granular-like flow applying available boundary conditions. Secondly, we show how to derive a template flow using Discrete Element Methods simulations and import it into a Multiphysics environment. Finally, we discuss the capabilities of a hybrid approach. All our testing is done in COMSOL Multiphysics (COMSOL, 2016), which is the tool that we routinely use.

## Model Geometry

After some initial trials, we chose to test our ideas on an axially symmetric geometry shown in Figure 1. This geometry is not based on any real reactor, but was designed to test some common patterns for granular flow:

- A straight section at the top where plug flow is expected
- A mass flow hopper
- Another straight section with plug flow
- A sharp widening of the domain where there will be a free surface, given by the angle of repose for the bulk material.
- Stagnant (non-moving) particles on top of an obstacle (grey section)
- A cavity just beneath the obstacle

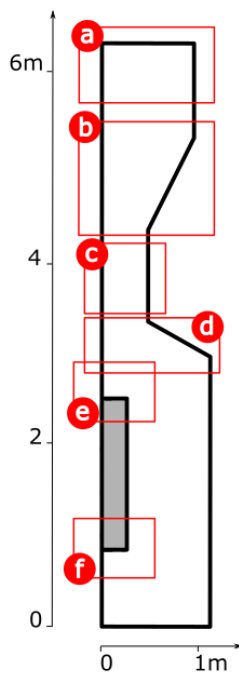


**Figure 1:** Geometry of the cylindrical model investigated. Areas of interest are highlighted: a) Plug flow zone b) Mass flow hopper c) Plug flow zone d) Abrupt widening with a free surface e) Stagnant particles on top of an obstacle f) Cavity right underneath the obstacle.

## SIMULATIONS

### Simple adaptation of viscous flow

First we considered the upper part of our test reactor, consisting of sections a), b), and c). The flow here is comparatively simple with plug flow in a) and c) and a velocity gradient in b).

For our case, we set the velocity in the hopper center to be roughly twice as big as at the wall. This seems realistic for particulate flow (Jenike, 1964). Further, a parabolic velocity profile seems reasonable here. Hence, the flow field in b) should be properly described by viscous laminar flow.

We then applied boundary conditions to achieve the desired flow patterns for the upper sections.

For the vertical walls, there are two options:

- 1) *Slip* condition – Wall without friction. The flow is only forced to move parallel to the wall.
- 2) *No slip* and a *moving wall* with a prescribed vertical velocity, given by the plug flow requirement. The viscous fluid will then match the velocity of the wall.

For a long straight section of fluid domain, the 2 approaches show the same result, plug flow. We favor, however, the second option as the boundary condition then plays an active role near geometrical transitions.

For the hopper section, we again rely on the moving wall condition. The first step is to compute the average vertical velocity as a function of the z-coordinate.

$$-\bar{w}(z) = \frac{\Phi}{\Omega(z)} \quad (1)$$

where  $\Phi$  is the total flow, and  $\Omega(z)$  is the horizontal cross section area.

Then, we let the vertical velocity at the wall be equal to the average velocity scaled by a suitable factor, in our case 2/3 worked well. An appropriate radial component is set to ensure that the flow is parallel to the wall, hence the wall velocity at the hopper wall is equal to:

$$\mathbf{u}_f = \left[ -2 \frac{\bar{w}(z)}{3}, -2 \frac{\bar{w}(z)}{3} \tan(\alpha) \right] \quad (2)$$

where  $\alpha$  is the hopper angle.

The flow field obtained with this setup is shown in Figure 2, where the total flow rate is set to  $1 \text{ m}^3/\text{h}$ . The first panel shows the radial component of the flow velocity and, as expected, this is zero except in the hopper. The vertical component has a flat profile in the zones a) and c) as described by the plug flow and the acceleration occurs in the hopper.

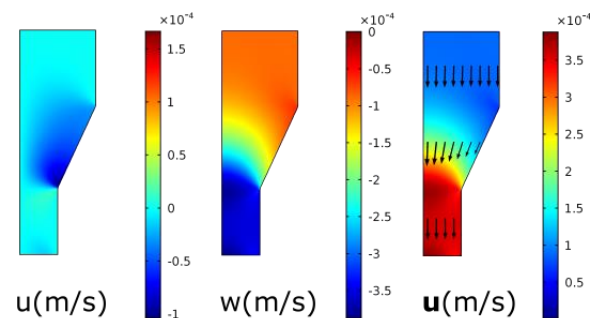


**Figure 2:** Top section of the model system, flow obtained imposing “No Slip condition” and prescribed wall velocities.

The simple approach gives a realistic particulate flow field. A fictitious fluid flow is computed as the boundary conditions are not realistic for viscous flow.

For a given geometry it is sufficient with one CFD computation. If the results for another value of the total flow is required, the computed velocities are simply multiplied with the appropriate factor, to get the correct total flow. Granular flow is gravity driven and does not change pattern significantly as long as the motion is sufficiently small, i.e. inertia effects can be neglected.

### Flow at a free boundary

While laminar viscous flow worked well with adapted boundary conditions, this approach failed to describe the conditions at the free boundary in region d). At the free surface, there will be a thin layer, a few particle diameters thick, where the particles will move at a comparatively high speed (Shinohara, 1987 and Williams, 1976). Below this layer, the bulk velocity will be much slower. Such sharp change in the fluid velocity cannot be described by simply adapting the boundary conditions for a viscous fluid.

We tried to add one or more inner walls to enforce a suitable boundary layer at the free surface, but were not able to adapt a reasonable bulk flow pattern. We cannot preclude that such a procedure may succeed, but based on our trials, it does not look promising.

### Application of Discrete Element Model (DEM)

To obtain an accurate description of the problematic areas d)-f) we turn to the use of a Discrete Element Method simulations.

The Discrete Element Method (DEM) was first introduced by Cundall and Strack (1979) and in recent years, thanks to increasing of computational power and the development of efficient programs, it has become widely used to investigate granular flow. In a nutshell, DEM predicts the bulk properties of a granular flow by analyzing the time propagation of position and momentum of each individual particle. Each particle is represented by a simple and well defined geometrical entity in most cases a sphere. The translational and angular accelerations are computed as the result of the corresponding momentum balances (Ariyama et al., 2014; Guo and Curtis, 2015). Realistic simulations involve, however, a huge number of particles and the computational time may be correspondingly high. Furthermore, the method can be appropriate to obtain the flow patterns, but it is unsuitable to include in multidisciplinary iterations. For the latter case, our special application of standard CFD software is clearly preferable.

For our case, the workflow is organized as follows:

- Set up and run a DEM simulation for a suitable 3D model of the system under investigation, c.f. Appendix A.
- By means of space and time averaging, turn the information of the DEM snapshots into a discretized flow field (Appendix B).
- Import the computed flow field into COMSOL Multiphysics.

The detailed description of the DEM simulation can be found in Appendix A. Briefly, the 3D model for the system of interest is constructed starting from the 2D axisymmetric model. Auxiliary structural elements functional to the keep the operation during the DEM simulation steady (see Figure 3) are added. In this case, a sufficiently large reservoir of particles was introduced above section a), to ensure particles flowing uniformly into our test reactor. A hopper section was applied, but a cylindrical region could alternatively have been chosen. The lower part was extended and a flat plate was introduced. This plate was lowered at a constant speed,

to control the gravity driven flow. The vertical velocity at the bottom was set to 0.01 m/s. This seems like an unreasonable high flow, but as already stated: the flow patterns do not depend on the speed, as long as inertia effect can be neglected.

A 200 s simulation time was applied and a snapshot of the system was taken every 0.04 s. Each snapshot contains for each particle its Cartesian coordinates, radius and velocity in Cartesian components.

The free surface is clearly visible in Figure 3. The model also showed a void beneath the obstacle, section f). This void is not visible as the figure is in 3D, i.e. just beneath the obstacles we see the particles behind the void.

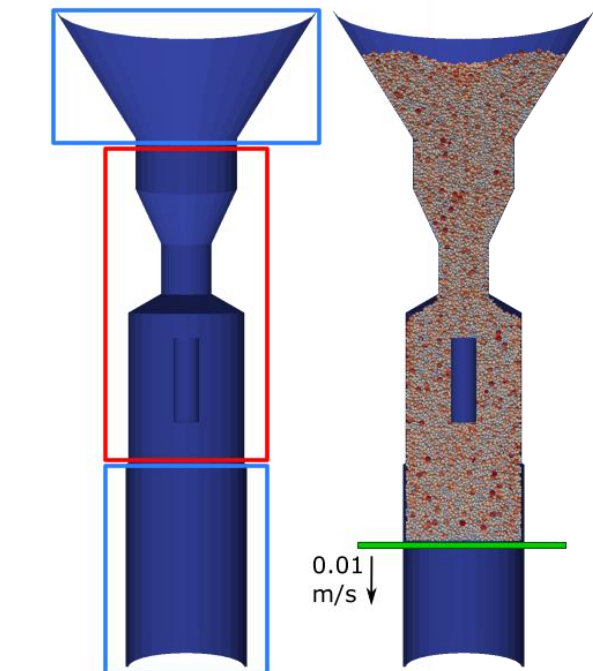


**Figure 3:** Left side: 3D model of the reactor walls. The original area of interest is highlighted with a red box. Auxiliary feeder and output sections are marked with light blue. Right: Snapshot of the DEM simulation.

After a sufficiently long simulation, the information collected in the snapshots are transformed into a suitable flow field. Details of these steps are given in Appendix B. Briefly, for one snapshot, particle velocities in 3D space are projected into a fine grid (grid elements smaller than the particles) in a 2D subdomain as shown in Figure 4 (space average). Subsequently, the information from several snapshots is combined (time average) and this greatly reduces the granularity of the field as seen in Figure 4.

The time average results are adjusted to ensure that the flow is correct at each level and smoothed using convolutions with a 5x5 Gaussian kernel (Davies, 1990) as shown in Figure 5.

The result of the procedure is shown in Figure 6 where the radial and vertical component of the flow velocity are depicted. Both components have the expected characteristics, the radial term vanishes in all the straight

sections and it assumes relatively large values only at the widening of the domain in the d) zone.

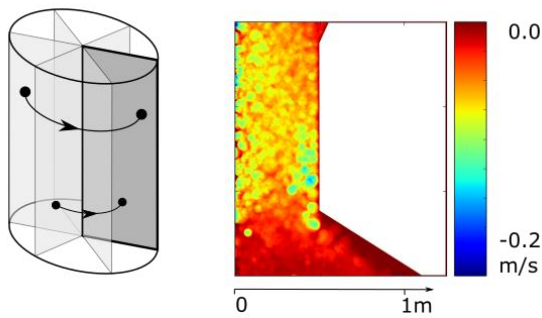


**Figure 4:** Left: The particles on the 3D DEM model are projected into a grid in the 2D subspace. Right: Details of the projection of one DEM snapshot.

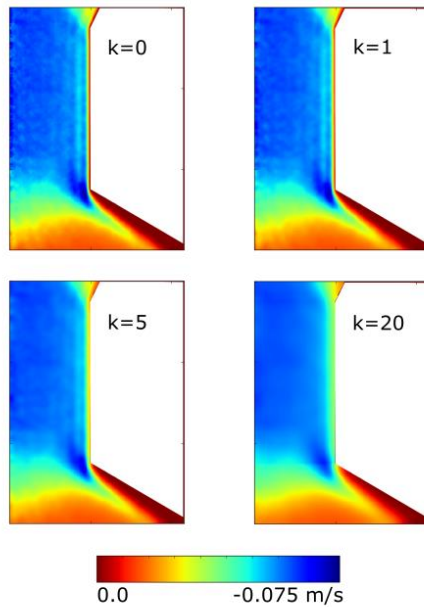


**Figure 5:** Detail of the vertical component of the flow field, smoothing with Gaussian convolution. Effect of subsequent applications ( $k$ ) of the filter.

The voids in sections d) and f) are shown as regions of zero velocities. Observe that the highest velocity is not shown at the free surface in zone d), but slightly below. At the free surface, the particles will flow at the highest velocity. We have, however, computed the average volume flow. Since there are fewer particles found *at* the free boundary than *slightly below*, the average volume flow is diminished very close to the boundary. Further, the center of the particles will always be at least one radius away from the void region. Hence, moving towards the free boundary, a smaller and smaller fraction of a particle can be present. The average volume velocity will then gradually be lowered and reaching zero at the boundary. This latter effect also causes the average velocity to approach zero at any boundary, c.f. Figure 5 for  $k = 0$ . A stagnant zone is visible in the vertical component of the velocity in the e) zone.

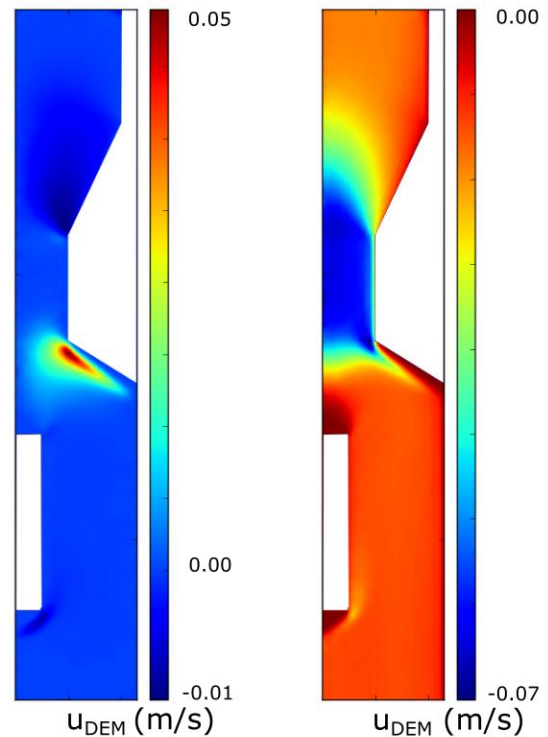


**Figure 6:** Components of the velocity field extracted from a DEM simulation. Left: radial component, Right: vertical component.

The data are saved in a text file that can be imported via the interpolated function feature of COMSOL. Here, after re-scaling with the appropriate total flow, the velocities can be natively used in multiphysics applications.

Having the fictitious fluid velocities obtained with DEM it is interesting to evaluate the performance of the approach based on wall speeds. The flows, apart from a scaling factor due to the higher DEM flow, are qualitatively similar (see Figure 2 and Figure 6). The only obvious difference is that with DEM one always obtains a boundary effect near walls whereas the simple approach gives a homogeneous velocity profile. Since the total flow is exact in both cases, the simple approach overestimates the fluid velocities near the boundaries (approximately 2-3 particle radiuses) and slightly underestimate elsewhere.

### Hybrid approach

In the previous section, we demonstrated how to construct and analyze a DEM simulation to obtain a bulk flow field that can be used within COMSOL. An obvious disadvantage is that the DEM simulation can be costly in terms of resources and computational time when applied to metallurgical systems. One possible solution is to use the DEM approach only for the zones that are foreseen to be problematic. In the example considered in this work, an experienced practitioner may realize that the section comprising the zones d) and e) and the region including zone f) require DEM treatment. An *ad hoc* sub-model can then be extracted and treated with the outlined DEM procedure (see Figure 7). We found that the smaller DEM model only required half the simulation time.

Once the DEM simulation is processed as described above, the resulting flow field is mapped back into the original geometry and it is used as a “flow template”. Within the two applicable regions we add a volume force that will force the flow to be equal, or very close to the DEM flow field. We applied stationary simulation and a proportional controller, that is we used the volume forces:

$$F_r(r, z) = K(s_\phi u_{DEM} - u) \quad (3)$$

$$F_z(r, z) = K(s_\phi w_{DEM} - w) \quad (4)$$

where  $u_{DEM}$ , and  $w_{DEM}$  are the velocity components from DEM,  $K$  is a suitable large number and  $s_\phi$  is the scaling factor to ensure that the DEM total flow matches the CFD simulation. Other methods can be applied.

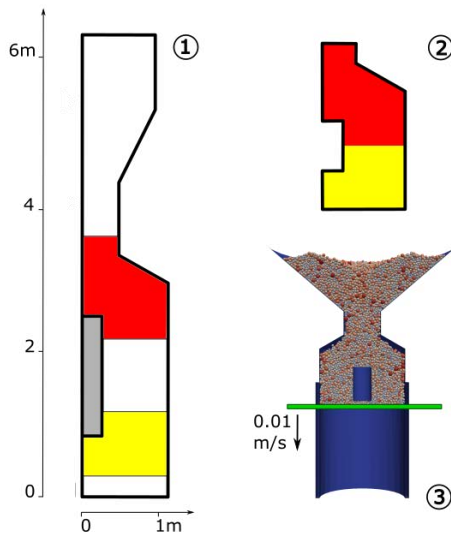


**Figure 7:** 1) Problematic sections of the system are identified. 2) A subsystem is constructed. 3) Snapshot of the DEM simulation.

To avoid discontinuities, we recommend the use of a smoothing function in the transition between forced (velocities from DEM) and free zones.

The results of the hybrid procedure are shown in Figure 8 where the velocity components of the fictitious fluid flow are shown. These are in excellent agreement with the DEM results of Figure 6 (apart from a scaling factor since the DEM simulation have applied a higher flow).

In this example, the complexity/cost of the DEM calculation is reduced by only a factor of 2. While this may not justify the use of a hybrid approach, it demonstrates that complex systems can be partitioned in subdomains to be solved individually. A model can then be incrementally improved by adding subsequent sections where flow velocities are DEM-derived.

There are small details that the approach cannot cover. For example, the simplified approach imposes a uniform velocity across any cross section of any straight domain. This is in contrast with the DEM results that predict a small boundary effect at the walls. As explained above, the velocity will approach zero at any (non-moving) boundary. For this reason, at the transition between the forced and free zones, small artefacts in the fluid flow can occur.

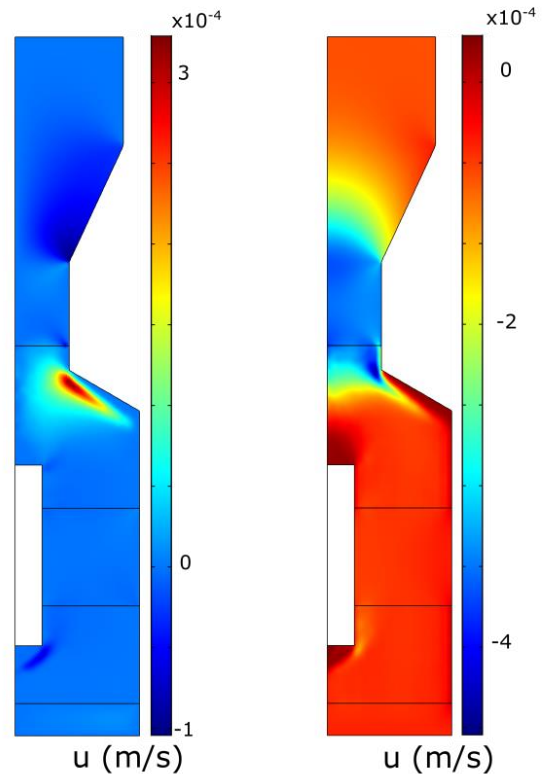


**Figure 8:** Components of the velocity field extracted from a DEM simulation.

## CONCLUSIONS

For comparatively simple bulk flow like plug flow sections and mass flow hoppers, a reasonable flow field can be computed applying viscous laminar flow with appropriate moving wall boundary conditions.

This simple approach does not work for more complex flows, e.g. regions with a free boundary. The flow field must then be found by other methods, for instance a DEM simulation.

A suitable method has been developed to average DEM results and import the flow field into a program for Multiphysics simulations.

To reduce the computational cost of DEM simulations a hybrid approach is recommended. DEM simulations are then used for the complex flow regions while the simple model is used wherever applicable.

## REFERENCES

- ARIYAMA, T., NATSUI, S., KON, T., UEDA, S., KIKUCHI, S., NOGAMI, H., (2014) “Recent Progress on Advanced Blast Furnace Mathematical Models Based on Discrete Method.” *ISIJ International*, **54**, 1457-1471.
- CUNDALL, P.A. and STRACK, O.D.L., (1979), “A discrete element model for granular assemblies”, *Geotechnique*, **29**, 47-65.
- COMSOL Multiphysics® v.5.2a. (2016) [www.comsol.com](http://www.comsol.com). COMSOL AB, Stockholm, Sweden.
- DAVIES, E., (1990), “Machine Vision: Theory, Algorithms and Practicalities”, Academic Press, 42-44.
- GUO, Y., CURTIS, J.S., (2015) “Discrete Element Method Simulations for Complex Granular Flows”, *Annu. Rev. Fluid Mech.*, **47**, 21-46.

KLOSS, C., GONIVA, C., HAGER, A., AMBERGER, S., PIRKER, S., (2012), "Models, algorithms and validation for opensource DEM and CFD-DEM", *Prog. Comput. Fluid Dy.*, **12**, 140-152.

JENIKE, A.W., (1964), "Storage and Flow of Solids", Bulletin 123, University of Utah Engineering Station, USA.

NATSUI, S., UEDA, S., FAN, Z., ANDERSSON, N., KANO, J., INOUE, R., ARIYAMA, T., (2009), "Characteristics of Solid Flow and Stress Distribution Including Asymmetric Phenomena in Blast Furnace Analyzed by Discrete Element Method", *ISIJ International*, **50**, 207-214.

SAKAI, M., ABE, M., SHIGETO, Y., MIZUTANI, S., TAKAHASHI, H., VIRE, A., PERCIVAL, J., XIANG, J., PAIN, C., (2016), "Verification and validation of a coarse grain model of the DEM in a bubbling fluidized bed", *Chem Eng J*, **244**, 33-43.

SHINOHARA, K., (1987), "General Mechanism of Particle Segregation during Filling Hoppers", Proceedings of 9th CHISA Congress, section H: Particulate Solids, H.3.5, Prague.

TANG, Y., ZHANG, L., GUO, Q., (2015), "A review on numerical models for granular flow inside hoppers and its applications in PBR", *J. Nucl. Sci. Technol.*, **52**, 759-768.

WILLIAMS, J.C., (1976), "The segregation of particulate materials", *Powder Technol.*, **15**, 245-256.

ZORIC, J., JOHANSEN, S.T., EINARSRUD, K.T. SOLHEIM, A., (2014) "On pragmatism in industrial modeling," in CFD 2014 - 10th International Conference on Computational Fluid Dynamics in the Oil & Gas, Metallurgical and Process Industries, Trondheim, 1-16.

## APPENDIX A – DEM CALCULATION

The descriptions of complex flow zones in the granular flow calls for the use of DEM simulations. The first step in this endeavor is the construction of a 3D mesh. Having the 2D axisymmetric projection of the fluid domain already implemented in COMSOL greatly simplifies this operation and the 3D model of the wall is obtained by revolving the trace of the fluid domain, obtaining a volume of approximately 19 m<sup>3</sup>. At this stage, the 3D model should be equipped with a feeder zone and output zone designed to keep the flow steady and control with precision the flux. These two features are shown in the left panel of Figure 3. The DEM simulation was carried out using LIGGGHTS® (Kloss et al., 2012). The particles have density equal to 1000 kg/m<sup>3</sup> and a radius normally distributed around the mean value 3 cm (standard deviation 1 cm). The granular model "Hertz" was used to compute the frictional force between two granular particles; the evolution of the tangential overlap during particles - particle contact is used to modify the spring part of the tangential. Finally, an additional torque contribution is added via the epsd2 rolling friction model. The following material properties and interactions were used for the simulation: Young's modulus 4.7\*10<sup>9</sup> Pa; Poisson's ratio 0.35; coefficient of restitution 0.43; coefficient of friction 0.73, coefficient of rolling friction 0.21. The time step was set to 10<sup>-5</sup> s. The right panel of Figure 3 depicts a snapshot of the DEM simulations with the system loaded with approximately 134000 spherical particles. While this number of particles is representative

of an industrial application using rather lumpy material, DEM simulations employing large particles are common in the field (see e.g. Natsui et al., 2009) and Coarse Grain approximations are emerging as a viable tool to reduce computational costs (Sakai, 2016). After equilibration of the loaded particles, 200 s simulation was performed and a snapshot was saved every 4000 time steps. During this time the wall at the bottom of the system was moving downward at a constant speed of 0.01 m/s, corresponding to a flow of 4.2\*10<sup>-2</sup> m<sup>3</sup>/s. These values exceed normal metallurgical operational conditions but ensures that each particle travels enough space to be able to collect a representative picture with a relative short simulation. For reference, the DEM calculations took approximately 4 days on a standard desktop PC.

## APPENDIX B – HOMOGENEIZATION

This appendix describes the transformation of the information collected in the DEM snapshots into the flow field of a fictitious fluid.

The first step to be accomplished is the space averaging as depicted in Figure 4. In practice, the Cartesian coordinates and velocity components for each particle are transformed in cylindrical coordinates and projected into the 2D subspace of the axisymmetric model. The projection occurs over a discretized grid whose elements are smaller than the particles. The space average takes into consideration both the volume of the particle and the total volume extruded over the projection itself.

A detail of the outcome of the space average is shown in the right panel of Figure 4 where the magnitude of the vertical component of the velocity is rendered. Although the space averaging successfully collects all the information of the 3D model and translated it into a bidimensional field component, the granular nature of the system is still evident and "shadows" of the individual particles are still visible.

The second step consists of combining data from several snapshots into a time average. In the specific case, we used 450 snapshots collected every 0.4 s in the range 20-200 s of the DEM simulation.

At this stage, it is important to realize that the approach so far does not include the movement of the "empty" fraction of the bulk. A possible solution is to scale all the velocities with a factor inversely proportional to the packing density of the system. Alternatively, the bulk flux (imposed in the DEM simulation), can be used to scale the flux for each row of the grid in the 2D subspace. An example of the results at this stage is shown in the top left section of Figure 5. Although the flux of the fictitious fluid is now exact by design, some noise is still present in the flow fields and small artefacts emerge near the walls (see vertical striations in Figure 5). This can be corrected using a smoothing function. Here we use repeated convolutions with a 5x5 Gaussian kernel (Davies, 1990).

The operations described in this section refer to a 2D axisymmetric COMSOL simulation. However, only small modifications of the projection function and smoothing procedure are needed to address Cartesian 2D and full 3D cases.

# A MULTISCALE NUMERICAL APPROACH OF THE DRIPPING SLAG IN THE COKE BED ZONE OF A PILOT SCALE SI-MN FURNACE

Sebastien LETOUT<sup>1\*</sup>, Arne-Peter RATVIK<sup>2</sup>, Merete TANGSTAD<sup>1</sup>, Stein-Tore JOHANSEN<sup>2</sup>,  
Jan-Erik OLSEN<sup>2</sup>

<sup>1</sup>NTNU Department of Materials Science and Engineering, 7491 Trondheim, NORWAY

<sup>2</sup>SINTEF Materials and Chemistry, 7465 Trondheim, NORWAY

\* E-mail: sebastien.letout@ntnu.no

## ABSTRACT

The Si-Mn alloy process production in submerged arc furnaces (SAF) is investigated. The aim of the studies currently in progress is an enhancement of the knowledge about the key reactions and the mass transport phenomenon related to the metal production. Some small scale experiments on raw materials and bigger pilot scale experiments are done to understand local kinetic and its extension to real condition production furnaces. As it is impossible to observe what is happening in the core of the furnace during operation, excavation of the pilot scale furnace are realised after operations. Based on bibliographical description of similar processes, observations and species analyses after excavation, a numerical simulation is currently in development to test the hypothesis formulated about the internal behaviour of the furnace. As it is difficult to model the complex entire furnace, the work presented here is focusing on what are the phenomenas inside the coke bed, in the dripping zone where the slags flow around the carbon particles before reaching the bottom of the furnace. The thrickling of the slags across the coke bed can be evaluated by a simulation of the droplets finding their path by gravity through the packing of carbon particles. This study has to be very local in space and time, but can give some useful informations such as velocities and drag force. At a larger scale (ie furnace scale), the coke bed particles are modelled by a granular phase in an eulerian-eulerian representation where the slag phase flow interact in the same way as in the local study. The slag is found to flow across the coke bed under the form of droplets of a maximum diameter of 10mm. The apparent velocity of the fluid is about 0,12 m/s. However the residence time of the droplets is longer due to the liquid trapped along the coke bed.

**Keywords:** Packed bed, Granular flow, Free surface flow, Multi-phase mass transfer, Multiscale .

## NOMENCLATURE

### Greek Symbols

$\rho$  Mass density, [ $kg/m^3$ ]  
 $\mu$  Dynamic viscosity, [ $kg/ms$ ]  
 $\alpha$  Surface tension, [ $kg/s^2$ ]

### Latin Symbols

**u** Averaged volume Velocity, [ $m/s$ ].  
**K** Momentum exchange Coefficient, [ $1/s$ ].  
**F** Volumic Force, [ $kg/m^2.s^{-2}$ ].  
**g** Gravitational Acceleration, [ $m/s^{-2}$ ].

$\Delta H$  Reaction enthalpie, [ $J/mol$ ].  
**q** Heat flux, [ $J/m^2.s$ ].  
**h** Convective heat transfer coefficient, [ $J/m^2.s.K$ ].  
**rr** Reaction rate, [ $mol/m^3.s$ ].  
**T** Temperature, [ $K$ ].  
**A<sub>dst</sub>** Area density, [ $m^2/m^3$ ].

### Sub/superscripts

*p* particle.  
*s* slag.  
*g* gas.  
*eq* equilibrium.

## INTRODUCTION

In the steel industry, manganese is an important element needed in order to produce specific grades of steel, ranging from materials having a great toughness, a high strength or containing low carbon. Manganese is added into the steel production furnace in the form of alloys and mainly ferroalloys. Silico-manganese, also called SiMn is another alloy which is privileged in the production of silicon and manganese containing steel.

The major part of SiMn is produced in submerged arc furnace (SAF) by carbothermic reduction of oxidic raw materials. An experimental effort has been conducted these last years at NTNU, operating a pilot scale SAF to investigate the parameters limiting the conversion of slag into metal alloy. Currently about 35 % of the mass is tapped from the production furnace as a metal, leaving the 65% remaining in a slag form.

To facilitate the understanding of the furnace, a modeling effort of the furnace is conducted in order to give different scenarios conducting to the conversion of slag into metal. Hypothesis has to be made to describe the furnace, and, to reduce the complexity of the problem, the whole problem has been split into more elementary part.

This paper is focusing on the modeling strategy used to depict one part, identified as the dripping part of the furnace.



## FURNACE DESCRIPTION

The pilot scale furnace (Ringdalen and Tangstad, 2013) is a cylindrical container of 450 mm of inner diameter and the charge height is around 700mm. The furnace is filled with ores and the charge is always maintained up to its maximum height level during operations. There are two electrodes; a top one situated in the furnace and a bottom one situated under the furnace. Their role is to bring thermal energy to the particles due to ohmic dissipation inside the conducting material which is mostly carbon particles.

The furnace is usually reported to be composed of two parts that is the pre-reduction zone and the reduction zone. The pre-reduction zone is the upper part of the furnace where the ores are reduced ( $\text{FeO}$ ) or pre-reduced ( $\text{Mn}_3\text{O}_4$ ,  $\text{Mn}_2\text{O}_3$ ,  $\text{MnO}_2$ ). This zone is heated by the exothermic pre-reduction reactions as well as by the hot flux of  $\text{CO}$  gas ascending from the reduction zone which is at the same time a reactant in the pre-reduction reactions (figure 1). The reduction zone is located on the bottom half of the furnace. In this zone, due to Joule dissipation in the carbon particles, the ores are melted and reduced into metal by carbo-reduction. The general layout of the reducing steps and the kinetic associated is not yet well known and are the object of the current investigations. Poor pre-reduction of the ores as well as limited ores reduction lead to partial conversion of the slag into metal.

As the core of the metal production process is happening in the reduction zone, it is interesting to investigate this zone more deeply.

## PHYSIC OF THE PROCESS

The process involves various different physical phenomena which are coupled together such as electricity, thermodynamics, turbulent hydrodynamics, heat radiation and chemical reactions. The complexity of the interdependency of these phenomena both in a mathematical way and due to the existence of different zones inside the furnace lead to challenging modeling where some choices have to be done.

**Phases** At least 4 phases have to be taken into account that is the gas phase, the solid phase and two liquid phases. The oxides form the liquid slag phase, whereas the reduced oxides are combined together into another liquid phase which is the metal phase. The pre-reduction zone is mainly constituted of solid and gas whereas in the reduction zone, the two liquids are flowing through a bed of solid particles.

**Species** The number of species present can be quite large due to the wide variety of ore materials used. In those materials some elements participate only in the slag phase ( $\text{CaO}$ ,  $\text{MgO}$ ,  $\text{BaO}$ ,  $\text{Al}_2\text{O}_3$ ), as they seem not to be involved into the reacting system of metal production. The solid material are mainly  $\text{Mn}_x\text{O}_y$ ,  $\text{SiO}_2$ , and the carbon represented as coke. The fluid species can be classified in two types that is the oxides and the metallic compounds. The slag components taking part of the reaction are mainly  $\text{SiO}_2$  and  $\text{MnO}$  whereas the metallic component are by order of importance Mn, Fe and Si. The gas phase is composed of  $\text{CO}$  and  $\text{CO}_2$ , but only  $\text{CO}$  is present into the whole furnace.

In this paper we focus on the way the melting ores are dripping on carbon particles.

## DATAS AVAILABLE TO PROCESS THE MODELING.

Due to the temperature, the size, and the opacity of the system, it is difficult to monitor internal parameters such as the

temperature, the flow rate, or the reduction rate in the furnace.

The data available during a run are mostly external parameters that is the power supplied to the installation and the variation of resistance measured in between the electrodes, the quantity of molten slag and metal collected every 30 min, the temperature of the tapped liquid and the analysis of this liquid components after operations.

At the end of the operations the furnace is cooled down and the void areas are filled with epoxy. A slice along the diameter of the furnace is realised. This slice, called the excavation plate, gives us a picture of the furnace at the instant when the electrical power is shutdown. The informations extracted from it can help us to understand the internal process during operations. The hypothesis made is that no reduction happens during the cooling process as not enough power is supplied to continue the reduction. From the excavation of the furnace some informations about the solid phase packing can be extracted, as well as the composition of some phases remaining. According to these excavations, it seems that 90% of the reduction happens on a thin layer situated at the top of the reduction zone, at the interface with the pre-reduction zone, where the reacting ores, already liquid are reduced. The 10% remaining reduction should happen in the coke bed by dripping down through it.

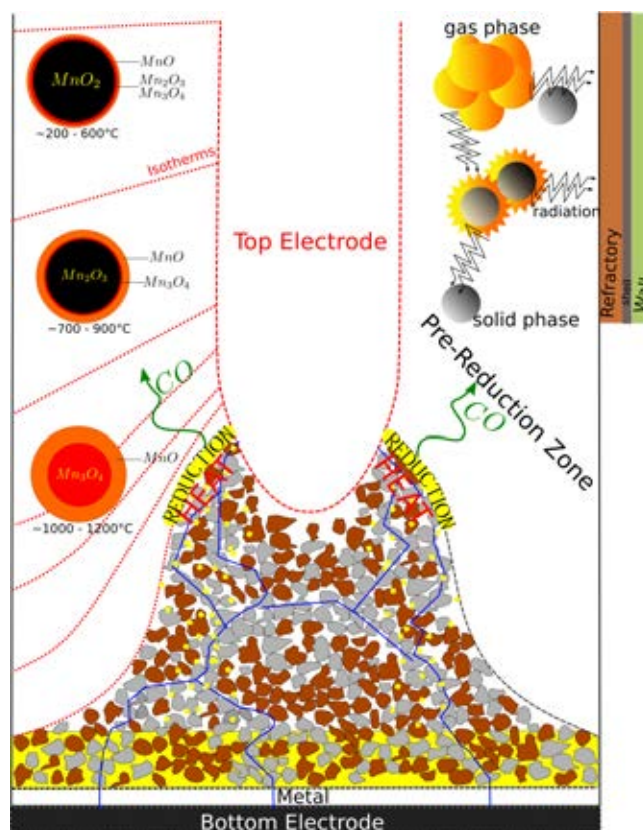


Figure 1: Scheme of the Si-Mn pilot-scale furnace

## COKE BED, THE DRIPPING ZONE

As the phenomena explaining that most of the reduction operations happen on the top of the coke bed are not yet well identified and just hypothesis, it is difficult to model the entire coke bed as a whole. Indeed the slag in liquid state has to stay long enough on the top of the coke bed to be reduced without flowing in the down part of the coke bed.

To decouple the problem, we focus on the way the liquid slag flow through the coke bed (see figure 1). This zone is referred to the dripping zone. It is the zone where the slag flow by gravity around the carbon particles. The description we depict now is similar to the one observed in the blast furnace where the dripping zone is described as a zone of great importance to the mass transfer of elements (Husslage *et al.*, 2005).

To study this zone we are using two different numerical models involving two different scales :

- one local model where the interstitial space between carbon particles is meshed, and where the interface of the flowing fluid slag is tracked with the help of the Volume of Fluid method
- one global model where the phases fractions are tracked in each cells with the Euler-Euler method. In this model, the cells are bigger than the inter-poral space and the whole dripping zone is modeled.

In the dripping zone the temperature is assumed to be maintained at a value of about 1873 K. It is the temperature measured of the tapped metal, and just above the temperature of reduction of the ores.

## THE TWO SCALES MODEL

### The local model

This part of the calculations referred to the local model are done in order to give a representation about the intensity and the configuration of the dripping slag into the coke bed.

We consider a 2D box representing some carbon particles digitized from the real geometry (figure 2). In this box only the poral space around the carbon particles is meshed, using the snappyHexMesh tool of OpenFoam 4.1 (OF4.1).

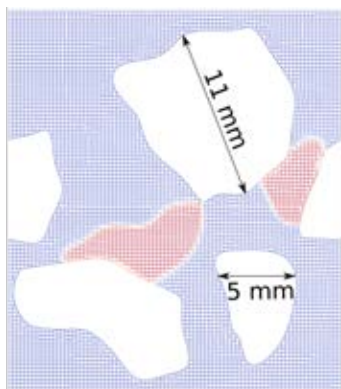


**Figure 2:** 2D box for slag droplet simulation

This box have to be small enough to permit a fine meshing of the poral space and large enough to contain at least some droplets free to move.

The solid fraction in the box is representative of the average solid fraction of the real packing in the pilot scale experiment. The slag phase is introduced by initializing its phase fraction to 1 into a geometrical zone representing the desired quantity of liquid, This liquid is initially at rest (zero velocity), and flows by gravity.

Periodic boundary conditions are used on top and bottom of the box, and non matching cyclic boundary conditions are used on the right and left side of the box.

The method used is the Volume Of Fluid method which solve all the phases with one set of conservation equations. The

solver is the interFlow solver based on interFoam version of OF 4.1.

In this solver, the interface reconstruction algorithm used is the recent isoAdvector algorithm (Roenby *et al.*, 2016), which oppositely to MULES, use geometrical interface reconstruction and advection instead of algebraic interface compression. This algorithm has been found to be more accurate in interface advection and reducing splashing of small parts of the volume fraction out of the main fluid flow. The performance of the algorithm is also very good in comparison to others geometrical reconstruction algorithm. Additionally the advection of the interface is almost not affected by the type and shape of cell used.

The solver is modified to introduce the gravity field into the momentum equation instead of the pressure equation, to avoid problems due to the non periodicity of the pressure field. The average slag velocity in the box is calculated with the velocity of the liquid phase along the dripping path of the slag. The volume of fluid reported divided by the height of the box and the final velocity, gives us the flow rate obtained when the slag reaches the bottom of the coke bed.

The goal of this calculation is to depict the behaviour of the slag when the flowrate calculated at the bottom of the coke bed is similar to the one deduced from the quantity of liquid obtained from each tapping of the pilot-scale experiment. This calculation is done iteratively by correcting the quantity of liquid introduced and the size of the simulation box until reaching some result in accordance with the experimental quantities obtained.

The hypothesis done during the calculation is that the slags are flowing homogeneously in the whole dripping zone and that the flow rate stay constant during all the process. The thickness of the droplets is estimated as being the average of the diameter of the flowing droplets considered. This study can be completed by taking into account the variation of the viscosity, surface tension, density and contact angle along the path, due to composition variation. As it is still a bit difficult to obtain the correct informations into both spatial variations of composition and properties evolutions related to these composition variation, the properties have been, in this attempt, kept constant.

This averaged velocity of the dripping slag has been reinterpreted in terms of drag coefficient of the coke bed :

$$F_{drag} = \alpha_s \rho_s (\mathbf{u}_p - \mathbf{u}_s) K_{p-s} + \alpha_s \rho_s (\mathbf{u}_g - \mathbf{u}_s) K_{g-s} = \alpha_s \rho_s \mathbf{g}$$

If we consider that there is no drag interaction between the gas and the slag phase and that the solid particles are not moving, we can then estimate the value of  $K_{p-s}$  with the expression  $K_{p-s} = \mathbf{g}/u_s$ . We can also deduce an order of size of the droplets by following the liquid phase in spaces without particles where the droplets are not combined together. Both datas can be used in a large scale modeling which will be presented in the next part.

The physical properties used to calculate the flow are based on the composition of the slag tapped after experiment. These properties are summarized in table 2 for an average slag composition obtained over several tapping given in 1.

**Table 1:** Slag composition (mass %) at the temperature T=1778K

Temperature	MnO	SiO <sub>2</sub>	CaO	MgO	Al <sub>2</sub> O <sub>3</sub>
1778	21	39	19	8	13

**Table 2:** Physical properties of the slag whose composition is given in table 1

$\rho(kg.m^{-3})$	$\mu(Pa.s)$	$\sigma(N.m^{-1})$	$\theta$	dynamic $\theta$
3280	0.1	0.49	125	$\pm 10$

### The global model

The Euler-Euler model of Fluent 17.2 is used to represent the dripping part of the whole furnace. This model offer the possibility to study a process on a large scale geometry. This model has been used to simulate several complex processes involving several phases and reactions. In metal production it has been used to simulate the trends of the silicon production process in an industrial configuration (Darmana *et al.*, 2012). In this model particle, liquids and gas phases are present in each cell. The phase fraction of the phases are tracked as well as their averaged velocity and temperature in each cell. Only one pressure field is calculated for all the phases, and the turbulent quantities  $k$  and  $\epsilon$  are calculated for the mixture. The evolution of these continuous fields are calculated with the help of correlations to describe the inter-phase interaction inside the cells. These terms are added as source terms in the fluid flow equations (momentum and/or energy) of each phase. The study is axi-symmetric.

**Solid phase** The granular model is used to model the coke particles. The coke bed is represented as a packed bed with no velocity. The solid phase fraction is taken as the same as the one used in the local model (0.39). The size of the particles is also taken as representative of the coke bed (0.01 m).

**Liquid phase** The main parameter of the liquid phase is the size of the droplets flowing through the solid phase. The droplet size is assumed to be homogeneous in the whole furnace and the value is estimated from the calculations of the local model. The phase fraction in the domain is calculated from the imposed boundary conditions.

**Gas phase** The gas phase is the main or continuous phase which means that its phase fraction is calculated with the space non occupied by the other phases following  $\alpha_{solid} + \alpha_{liquid} + \alpha_{gas} = 1$ .

**Geometry** The geometry boundary are sketched from :

1. The walls of the furnace for the down and side boundary
2. The shape of the reduction zone determined from the excavation plate of the furnace.

The shape of the reduction zone can be located as the fictive boundary separating the zones with different solid composition. On the upper part a mix of solid coke and ore particles can be observed whereas on the lower part there is just solid coke remaining. The mesh generated with the Delaunay algorithm for quad (Remacle *et al.*, 2010) of the GMSH utility, is represented on figure 3.

**Boundary conditions** The fluid is entering the top part of the coke bed near the electrode, and the fluid is free to leave the coke bed (pressure outlet conditions) on both the lower part and the upper part of the coke bed (figure 3). The velocity inlet conditions are set in a way to respect the global flowrate of the experiment. The velocity is set at a similar value as the main value wanted into the coke bed, and the inlet phase fraction is adapted to this value.

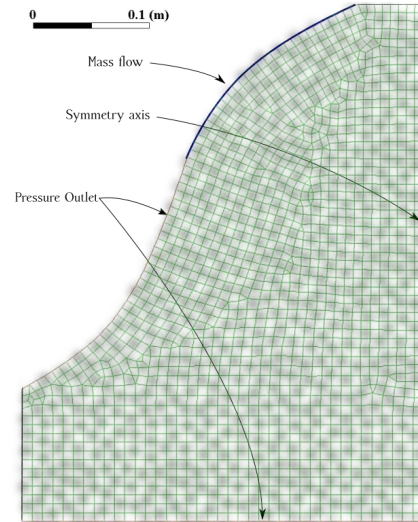


**Figure 3:** Geometry and mesh of the coke bed zone

**Drag coefficient** For the calculations of the drag coefficient between fluids the Schiller-Naumann correlation is used. For the drag interaction between the liquid and the solid, the  $K_{p-s}$  coefficient calculated previously and adapted to the dimensions required by the equation solved by Fluent ( $kg.m^{-3}.s^{-1}$ ) is used.

## RESULTS

### Local model

The VOF model gives us several informations about the distribution of the droplets into the coke bed.

First, small droplets (diameter  $< 9mm$ ) will flow quickly in places where the pore size is superior to their size. Depending on their velocity these droplets will go through smaller interpores. If the smaller interpore zone is smaller than the droplet diameter, and its inertia is not sufficient to cross the obstacle, then the droplet will get stuck. These droplets may fragment into smaller droplets when they impact a bigger particle with a high velocity (0.5 m/s), but usually due to the high surface tension and the friction along the coke bed, these droplets rarely split.

The high density (3 times higher than water), and the relatively low dynamic viscosity (comparable to olive oil) permit the slag phase to flow easily into the coke bed. Oppositely, the contact angle and the high surface tension oppose a resistance when it comes to zone with smaller pore dimensions.

Big droplets (diameter  $> 10mm$ ) split in smaller droplets during their trickling path through the coke bed. The dynamic of the obtained droplets depends on the size of these droplets. As long as the smallest pores between particles is not filled with slag, the droplets will partially attach to the carbon particles which leads to a non steady flow rate, and a residence time of a droplet which vary at the beginning of the simulation. As these poral spaces of the coke bed are filled

with slag, we have a continuous process which begin, one droplet pushing the precedent droplet out to feel the cavity or to extract the totality of the fluid, releasing each time new droplets. The size and the dynamic of the new droplet depend on the quantity of liquid extracted from the cavity.

In this pseudo stationary regime the movement of fluid is estimated to be around 0.12 m/s with velocities ranging from 0m/s for the droplets trapped into the coke bed up to about 0.5 m/s during (free fall of some small droplets). The velocity of the droplets vary depending on how many filled cavities are met along the droplet path inside the coke bed. If we consider that the liquid pushed out of the cavity is the continuity of the one pushing the liquid then the velocity of one bubble of a diameter of 9 mm is about 0.12 m/s. The final size of the droplet at the bottom of the furnace does not depend directly of the size of the initial droplet but also of the quantity of liquid trapped into the pores. If the size of droplets stemming from the top of the coke bed is stationary then the size of a droplet trapped is about the same size and the size of the bubble released is also approximatively the same.

The wetting of the particles is a key parameter to determine the contact area between the slag and the solid particles. It depends on the physical properties of the fluid, in particular the contact angle, but also on the geometry of the particles and the interstitial space where the droplets are trapped. The scarcity of the droplets flowing through the coke bed and the high value of the contact angle explain that only a few part of the coke surface is wet by the slag in the dripping zone.

### Global model

Introducing the correct order of magnitude of the particle size, coke bed void fraction and drag coefficient permit to simulate an averaged situation which is representative of our local simulation. The droplets of the predetermined size (4 mm in our simulations) flow in a coke bed at the approximate velocity of 0.1 m/s. This lead to a distribution of the phase fraction given by the calculation on figure 5. This model as such does not give more informations as it reproduces in a modeled way the results obtained with the local model.

The idea behind the use of this model is to add an energy balance calculation in the system by choosing the appropriate boundary conditions, energy sources and energy consumption inside the coke bed. This needs an accurate description of the thermo-physical properties of the system, electrical power released and of the kinetic of the reaction system. A first attempt has been made in this direction using the simplified system

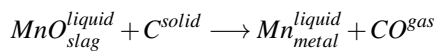


Figure 4: 3-6 mm droplets flowing along coke particles

involving just one component in each phase. The subscript specify the liquid phase whereas the superscript specify the physical state of the compound. The slag phase is composed of MnO, the metal phase of Mn, the solid phase is made of carbon and the gas phase is composed of CO. This means that in contact with carbon our slag phase transform into the metal phase. The reaction is endothermic, needing an external energy source to supply thermal power to the system.

The kinetics of the process is still in investigation, and, in this attempt we used a heat transfer correlation, the Gunn correlation to estimate the heat transfer coefficient  $h$  between the carbon phase and the slag phase. The reaction is temperature driven and the kinetics is based on the heat flux received by the material :  $rr = A_{dst} \cdot q / \Delta H$  with  $q = h(T_p - T_{eq})$ . The value of the area concentration  $A_{dst}$  can be use to model the surface of contact between slag droplets and coke particles available for chemical reactions.

In the figure 6 we can see the calculated reaction rate of our implementation. The results are homogeneous on most of the part of the furnace, and a bit higher on the top zone of the furnace where the fluid is slower.

It is not yet a goal in this paper to reproduce the real reduction behavior of the furnace, but to present the modeling strategy used to help understanding the furnace operations by adapting the input datas of the model to the observations.

### DISCUSSION

This modeling answers some questions :

1. The fluidity of the slag in a fully liquid state cannot explain that 90% of the reduction happen at the top of the

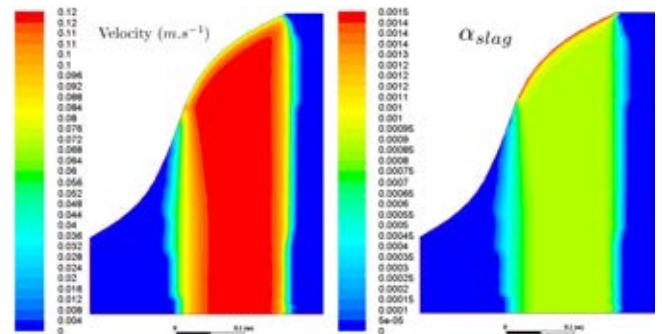


Figure 5: Velocity and phase fraction of the slag phase dripping into the coke bed

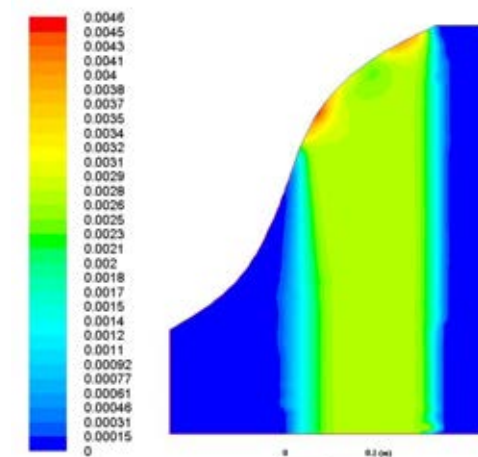


Figure 6: Reaction rate in the coke bed volume ( $kmol.m^{-3}.s^{-1}$ )

coke bed. Another explanation has to be found to explain the residence time of the slags on this part of the furnace.

2. The slag is not flowing down through the coke bed as a continuous flow but by succession of droplets coming from the reduction zone at the top of the coke bed.
3. The chemical composition of these droplets is not just evolving by reaction along the path imposed to them by the gravity, which would result in very few reduction as their residence time would be small.

Instead, some droplets stay at some places into the coke bed until another droplet push it down. There is certainly a permanent renewal of the chemical concentration of these droplets which are trapped. So it can be considered that a real droplet has an average residence time in the coke bed which is superior to the impression it gives when flowing from cavity to cavity. In addition the renewal of the droplet may depend on the position in the coke bed. On the peripheral part of the main dripping zone, some droplets are renewed less often than in the main flow leading probably to a less important reduction rate. In 3D also there are more accessible places for a droplet to stay before being pushed by another one. In addition, the modification of the chemical composition of the droplets modifies the physical properties. The trajectories of these droplets are very sensible to the physical properties due to the combination of variation of properties as the contact angle, the surface tension and the viscosity. The trajectories of the flow will probably defer from droplet to droplet leading to an exploration of the whole geometry and a lower renewal of droplets trapped in the coke bed, increasing their residence time. However in some conditions, the limited height of the coke bed allow for some droplets to flow without being trapped.

All these considerations can be taken into account in the global modeling by adapting the  $K_{p-s}$  drag coefficient to a value consistent with the evaluated residence time in the coke bed. This will be a parameter which will influence the way the reaction rate will be calculated and need to be taken into account.

Here the reduction rate calculated is not in accordance with the real transformation rate. Some thermal datas used are not totally accurate and the real kinetic need to be reformulated with the last datas obtained about the Si-Mn reduction process in order to be compared with a real production rate. In addition the gunn correlation is not well adapted when the liquid is not the continuous phase.

However, the modeling strategy presented here, can give some useful informations about the reality of some hypothesis formulated, and may assess if it is realistic to estimate that 10% of the slag reduction occur in the coke bed.

## CONCLUSIONS

A modeling strategy to simulate the behaviour of a Pilot-scale Si-Mn production furnace in relation with experiments analysis has been proposed. For this purpose, a 2D numerical model of the dripping slag across the coke bed zone is detailed.

The developed numerical model is based on two different scales using two different approach of the multiphase modeling.

1. The first one is a detailed model on a small scale aiming at using the fluid properties of the slag to describe how

it can flow into a dry coke bed when traveling from the reduction zone to the bottom of the furnace.

2. The second one use hydrodynamic results of the interaction between the solid phase and the slag phase calculated in the first one to describe the whole geometry with averaged quantities.

The first one use the VOF-isoAdvector method when the other one use the Euler-Euler model. The results show us that the liquid slag is flowing through the coke-bed by a succession of droplet and that the averaged flowing velocity is about 0.12 m/s. The diameter of the droplet cannot be higher than 9-10 mm to avoid their break-up. The residence time of the droplets should be greater than the apparent velocity of the fluid to take into account that the droplets stay often trapped into the coke-bed. These effects can be taken into account into the big scale model by introducing the appropriate drag coefficient. This model can be used to simulate the reductions reaction and validate a thermal balance of the coke bed zone.

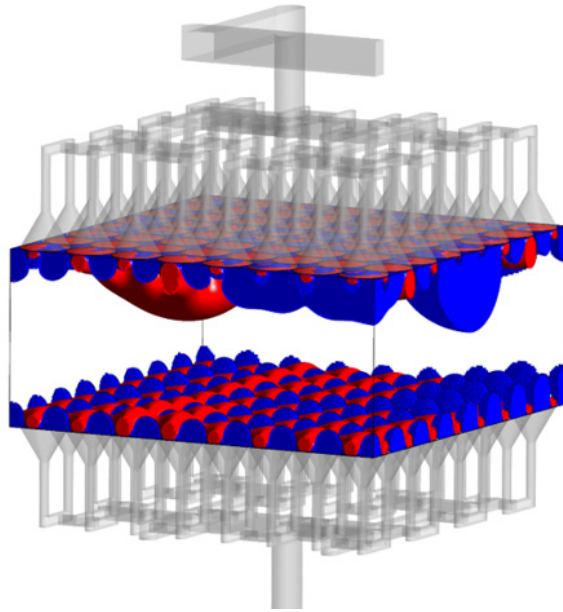
## ACKNOWLEDGEMENTS

The work reported herein was funded by the Norwegian Research Council through the Centre for Research-Based Innovation Metal Production.

## REFERENCES

- DARMANA, D., OLSEN, J., TANG, K. and RINGDALEN, E. (2012). "Modelling concept for submerged arc furnaces". *Ninth International Conference on CFD in the Minerals and Process Industries CSIRO, Melbourne, Australia 10-12 December 2012*. URL [http://www.cfd.com.au/cfd\\_conf12/PDFs/062DAR.pdf](http://www.cfd.com.au/cfd_conf12/PDFs/062DAR.pdf).
- HUSSLAG, W.M., BAKKER, T., STEEGHS, A.G.S., REUTER, M.A. and HEEREMA, R.H. (2005). "Flow of molten slag and iron at 1500 c to 1600 c through packed coke beds". *Metallurgical and Materials Transactions B*, **36(6)**, 765–776. URL <http://dx.doi.org/10.1007/s11663-005-0080-6>.
- REMACLE, J.F., HENROTTE, F., CARRIER-BAUDOIN, T., E, B. and MERCHANDISE, E. (2010). "A frontal delaunay quad mesh generator using the linf norm". *Int. J. Numer. Meth. Engng.* URL <http://onlinelibrary.wiley.com/doi/10.1002/nme.4458/abstract>.
- RINGDALEN, E. and TANGSTAD, M. (2013). "Study of simn production in pilot scale experiments". *INFACON*. URL <http://www.pyro.co.za/InfaconXIII/0195-Ringdalen.pdf>.
- ROENBY, J., BREDMOSE, H. and JASAK, H. (2016). "A computational method for sharp interface advection". *Royal Society Open Science*, **3(11)**. <http://rsos.royalsocietypublishing.org/content/3/11/160405.full.pdf>, URL <http://rsos.royalsocietypublishing.org/content/3/11/160405>.

# INDUSTRIAL APPLICATIONS





# USE OF CFD AS A DESIGN TOOL FOR A PHOSPHORIC ACID PLANT COOLING POND

**Aurélien DAVAILLES<sup>1\*</sup>**, Sylvain DEVYNCK<sup>1</sup>

TechnipFMC - Paris Operating Center, Paris la Défense, FRANCE

\* Corresponding author, E-mail: aurelien.davailles@technipfmc.com

## ABSTRACT

Phosphate fertilizer plants are installations constantly evolving which make their design a challenging task. Phosphogypsum, a by-product of the manufacture of phosphoric acid, is piled up, forming stacks which may eventually alter the process efficiency as they encroach on process cooling ponds and locally modify the airflow fields. The easier access to high performance computing and the improvement of software capabilities allow to fully consider today the use of CFD within tight-schedule industrial projects, even the ones involving large-size geometry. As an example we describe how CFD can be efficiently used as a design tool for the revamping of a phosphate fertilizer complex. The use of recently emerged multi-software optimization tool is also explored as a way to enhance the engineering time dedicated to this problem.

**Keywords:** CFD, Fluid-Fluid interaction, Heat exchange, Optimization, Pollutant dispersion.

## NOMENCLATURE

### *Greek Symbols*

$\alpha$  Water mass fraction.

### *Latin Symbols*

V Velocity, [m/s].

T Temperature [°C].

$z_0$  Roughness length, [m].

### *Sub/superscripts*

a Air.

p Pond

## INTRODUCTION

The enhanced accessibility to faster cores has led to an important evolution of high computing performance (HPC) for CFD. In addition, most of the current commercial softwares are now well optimized to take advantage of this available higher power resources, allowing large-size geometry parallelization. This has opened up new opportunities for CFD to be part of industrial projects as a design tool in domains where it was not a conceivable option just a few years ago, due to the incompatibility between the project schedules and the

time consuming calculations. Furthermore, CFD studies on the atmospheric boundary layer are now common [DUYNKERKE, 1988] [VENDEL et al, 2010] and allow to model a complete plant subjected to various weather conditions. Based on Pasquill classes [PASQUILL, 1971], different wind velocity, temperature and turbulence profiles can be applied to represent real atmospheric conditions. In Oil & Gas industry, two frequent examples are the Hot Air Recirculation studies performed on Liquefied Natural Gas (LNG) trains and the pollutant dispersion studies around onshore and/or offshore installations [DEVYNCK, 2016]. Another less familiar application involving the modeling of large geometry and for which CFD can be a helpful design option is the phosphate fertilizer plant.

This kind of plant may be associated with several problematics such as fluoride dispersion, steam fog formation or process thermal management. Fluoride is a major pollutant involved in the phosphoric acid production process which usually consists of the reaction between phosphate rock and sulphuric acid (wet process). Its release in the atmosphere from the evaporative cooling pond surface must be carefully monitored to ensure the respect of the regulations. Moreover, the cooling process taking place in the ponds leads to an important increase of the water content in the ambient air, which can cause steam fog formation under unfavourable weather conditions. Whether it is for the dispersion of fluoride or the steam fog formation prediction, not only CFD can allow to assess the situation but also to explore improvement solutions.

Another concern regarding the phosphate fertilizer plants comes from the formation over time of large phosphogypsum stacks which may eventually lead to the necessity to revamp the plant. The phosphogypsum, a by-product of the manufacture of the phosphoric acid during the so called wet process, is mixed with water to form a slurry, then continuously piled up in settling ponds which will turn into massive gypsum stacks after years of service. About 5 tons of phosphogypsum are produced for each ton of phosphoric acid [GOWARIKER et al, 2009]. To allow the gypsum stack expansion, new deposit areas must be defined. The conversion of a cooling pond into a settling pond is then a possible solution even though it leads to the reduction of the heat



exchange surface. As a result, new ways to exchange energy or to reduce the process total heat duty requirement must be found. The easiest way to achieve this may be by revamping the process in order to reduce the total dissipated energy and to optimize the remaining exchange surface. Revamping plants is a quite common task for Oil & Gas engineering companies nowadays and CFD can be used to support the optimization of the remaining pond surface.

## MODEL DESCRIPTION

### Overall geometry

To account for a phosphate site production, a typical area has been reproduced. It consists in two gypsum stacks whose only one is still active with a settling pond at the top. Three cooling ponds are used on that plant, including one at the top of the non-active gypstack. Surrounding elements such as process units and houses of the residential area have also been modeled (Figure 1). The atmospheric part of the domain is modeled by a box whose dimensions are 2km x 2.5km x 1km.

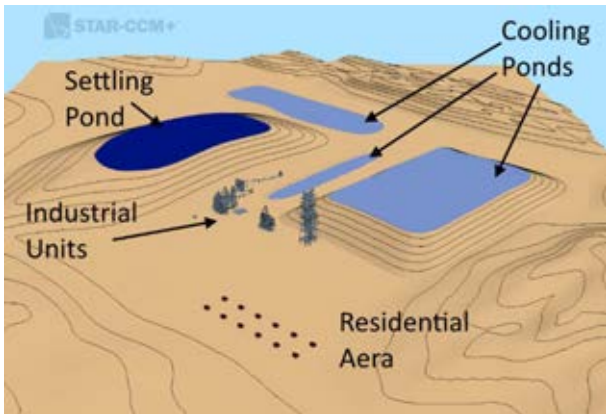


Figure 1: Overall domain

The presence of irregular terrain close to the site can be included into the simulation starting either from 2D elevation lines or directly from a 3D topography surface. Using STAR-CCM+ surface wrapper we reconstructed a CFD compatible ground surface.

In the following demonstration study, the irregular terrain elevation has been imported as STL files while stacks have been entirely built from the 3D-CAD modeler of STAR-CCM+. All parts of interest for the study must be included in the computational domain in order to take into account the congestion and the air flow disturbance. Moreover, this could also be of importance for controlling precisely the amount of pollutant in the installation area.

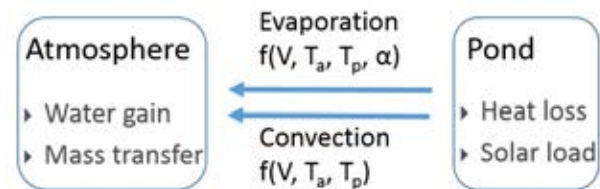
A residential area represented by 12 houses has been implemented at about 500 meters of the closest pond. Likewise, process industrial structures are positioned at about 100 m from the pond.

### Fluid-Fluid interaction

To account for the evaporation taking place from the pond surface without computing the real gas-liquid

interface, we modeled it as a fluid-structure interface. Two independent fluid regions are exchanging data through the interface in order to compute the calibrated heat and mass exchange. Several benefits come from the separation of the two regions: the physics is simplified as there is no more need for multiphase flow modeling. Instead, two single phase flow calculations are performed simultaneously and only an exchange of some specific values at the interface is required. Using data mapping technique with nearest neighbour interpolation, water temperature value is sent to the atmosphere region whereas the calculated evaporative and convective heat fluxes values are transmitted to the pond region to cool down the liquid.

Several field functions accounting for the evaporative and convective heat fluxes and the water mass flow rate at the air/pond interface have been defined. The main local parameters used by the solver to feed those functions are the air velocity, the air temperature, the relative humidity and the water temperature. The different exchanges taking place between the two fluid domains are summarized by the following diagram.



The evaporation correlation is based on daily experimental data measurements over several years and is detailed in § Heat management computations.

Another important advantage arising from the flat interface hypothesis is to allow the use of coarser meshes. Table 1 gives a comparison of the mesh size of two identical domains varying only by the modeling approach (1 fluid region versus 2 fluid regions).

Table 1: Number of cells

	Air	Water	TOTAL
2 regions	184,858	102,090	286,948
1 region	2,240,000	717,066	2,957,142

It is obvious that adopting the two separated fluid zone modeling will allow a significant computational time reduction which is preferable for the purpose of conducting optimization study which can require to perform numerous simulation runs.

### Mesh

Due to the large surface and the very small depth of the ponds, the thin mesher technique has been used in the water region. Ten cells have been generated over the water depth to discretise sufficiently the cooling pond. There is no need to use a conformal mesh at the interface due to the employed interpolation technique (§ Fluid-Fluid Interaction). Thus, with a cell size of the same magnitude at both interface sides, yet adopting two

different meshing method for the fluid zones, the final mesh can be coarser while remaining relevant to model the heat exchange and the flow in the two regions. In the air zone, a trimmed mesh has been used with one prism layer generated on the ground. The ground surface cell size has been set to 5m while a 2m size has been imposed on the pond surface. During the surface wrapping operation, different target sizes have been defined on the structure elements according to the desired level of precision. The minimum cell size allowable has been set to 10 % of the base size.

The Figure 2 shows the differences between the initial faceted surface (STL) and two generated surface meshes set with different base sizes, respectively 5 m and 10 m.

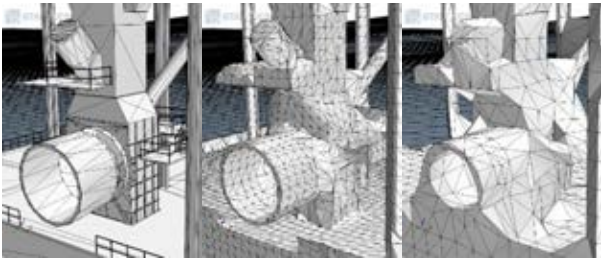


**Figure 2: STL file, Wrap 5m, Wrap 10m**

Given the potential for the rapid growth of the total cell number, only the areas of interest, such as the air intakes or the areas nearby the workers should be precisely discretised.

### Pond Optimization

Following the removal of one of the cooling pond to allow space for the active gypsum stack expansion, a significant surface which was dedicated to the dissipation of the energy is no longer available. Consequently, modifications must be made to the process to recover the lost heat duty, thus ensuring to maintain the process efficiency. In order to achieve this objective, the remaining cooling ponds must be optimized as well to make them the most efficient possible.

On this basis, the second pond which offers the highest potential due to its larger size, has been modeled separately with the purpose to optimize the surface heat exchange. As the overall geometry of the pond cannot be modified, only realistic on-site implementations have been explored such as modification of the water inlets/outlets position and the addition of elements to modify the water distribution, such as dikes.

Figure 3 highlights the CFD study domain which includes only the cooling pond and the non-active gypsum stack to keep the number of cells to a reasonable amount. Indeed, the optimization study can require a lot of calculation runs to determine the global optimum or to plot a Pareto front which helps to determine the feasible designs depending on the defined constraints and objectives.

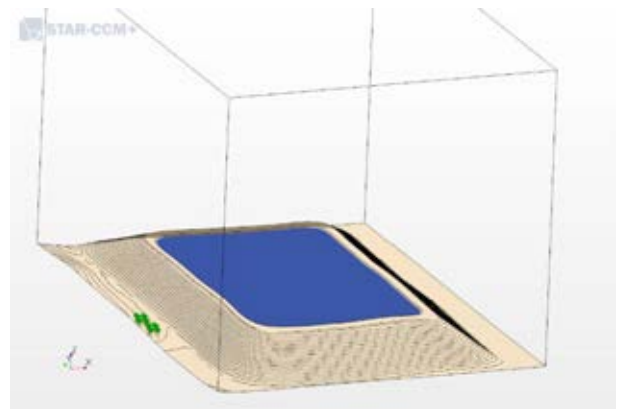


**Figure 3: Optimization domain**

The optimization tool used for this study is HEEDS which is a multidisciplinary design exploration software from Siemens PLM Software. After the definition of several parameters adjustable by the solver and several target objectives, the selected optimization algorithm will explore the whole space design in order to find local or global optimum. As this exploration process is automated within HEEDS, the final geometry and mesh model must be robust to ensure the good convergence of the different calculations. Consequently, all the standard manual manipulations such as “surface repair” or “diagnostics” are avoided and must be configured to be automatically performed.

In order to modify the water distribution inside the pond, dikes have been created via the 3D-CAD modeler to be added to the pond model. The parameters defined as being modifiable by the software to find the better designs are:

- Number of dikes (from 1 to 10).
- Depth of the pond (from 0.5m to 5m)
- Orientation of the dikes (North-South or East-West)
- Aperture between side of the pond and dikes (20 to 200m)

A JAVA macro is also executed before the start of the simulation in order to modify the position of the water inlet inside the pond. Indeed, depending on the number of dikes and their orientation, the inlet may be located at three different locations, while the outlet remains fixed.

As a finer mesh is required close to the dikes, the total number of cells in the domain will change significantly according to the parameter set configuration. The total number of cells can vary between 300,000 cells and 2,500,000 cells.

Two objectives have been defined: improve the surface heat transfer and reduce the investment costs (CAPEX). On a practical level, this involves the lowest outlet temperature possible while minimizing the dikes length.

## Boundary and Operating conditions

### Air domain

The atmospheric domain has been set to orient the cell faces perpendicularly to the wind direction. Wind is coming from the east direction with a neutral wind stability profile (Pasquill class D). Wind velocity is 3 m/s at 10 m elevation. The wind temperature is assumed to be constant and equal to 25°C.

The two side faces parallel to the wind direction are considered as symmetry planes, such as the top of the atmospheric box. The last bounding box face has been set as a pressure outlet.

The atmospheric boundary layer has been modeled through the best practices of STAR-CCM+ and the roughness of the ground has been set to represent an agricultural land with some large obstacles by a distance of 500 meters ( $z_0=0.035$ ).

On the water surface, a slip condition for air has been set. That leads to increase the wind velocity far from the side of the pond. A water mass flux source term has been defined. It depends on the wind velocity, the air temperature, the water content and the water temperature (see § Fluid-Fluid Interaction). Convective and evaporative heat transfer are computed via the correlations explained above. A realizable k-epsilon turbulence model has been used.

### Water domain

The pond's bottom and side faces are considered adiabatic with a no-slip condition. The interface is treated like a free surface, i.e with a slip condition and with a thermal heat sink corresponding to the evaporation and the convection heat flux. A realizable k-epsilon turbulence model has been used.

## RESULTS

### Pollutant dispersion

Fluoride emissions from the ponds may raise concerns if the concentration reaches the regulatory limits. Safety and environmental studies are a large part of all the industrial projects. They aim to ensure the protection of the site workers and the population living in the plant vicinity. It is for this reason that the fluoride released by the eastern stack surface has been studied using a multi-gas approach.

The Figure 4 represents an overhead view of the plant and highlights the fluoride plume expansion. The wind coming from the right face of the atmospheric box (south east direction) drives the pollutant towards the installations and the residential area.

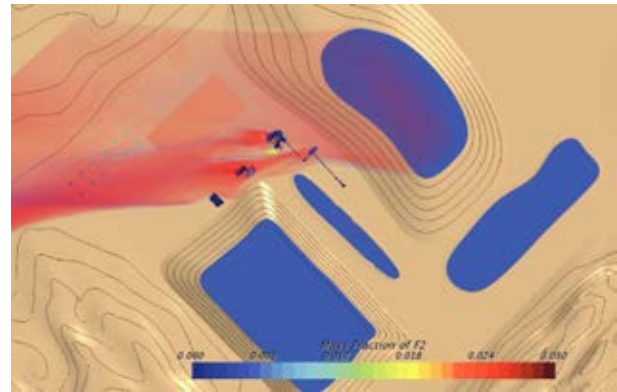


Figure 4: Fluorine plume expansion

The concentration of fluoride can also be displayed on the wall of the area of interest such as the residential area or the process equipment. Due to the discrepancy between the regulatory limits regarding the working area and the residential area (8 hour exposures vs yearly exposure) two scales of concentration must be plotted. On that example, an 8-hour mass fraction exposure limit of 0.027 (fictional value) of fluoride is drawn in Figure 5 on working area and a yearly mass fraction exposure limit of 0.015 (fictional value) of fluoride on the houses representing the residential area on Figure 6.

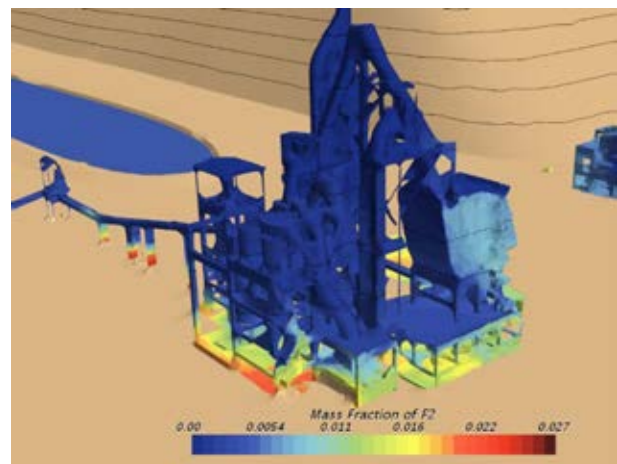


Figure 5: 8Hr exposure limit on working area

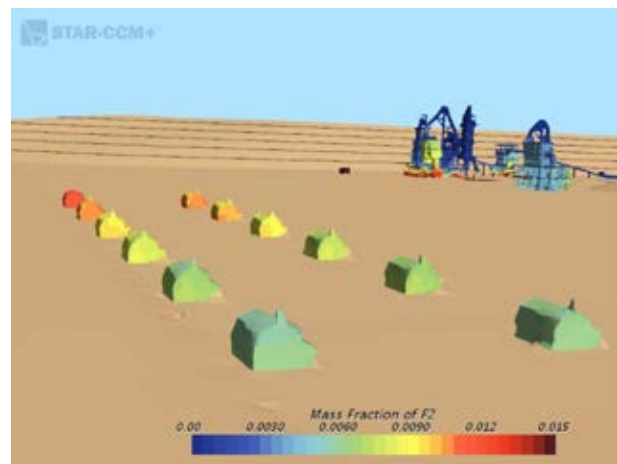


Figure 6: 1yr exposure limit on residential area

## Heat management computations

The main role of the cooling ponds is to exchange a large amount of heat with the atmosphere, thus reducing the process water temperature. Any modification of the upstream process (inlet water temperature, water flowrate, etc) or of the cooling pond surface will affect its performances.

### Base case

First of all, the active configuration has been modeled and compared to experimental on-site measurements. Three ponds are used to cool the process water, two on the ground level and one at the top of an old gypsum stack.

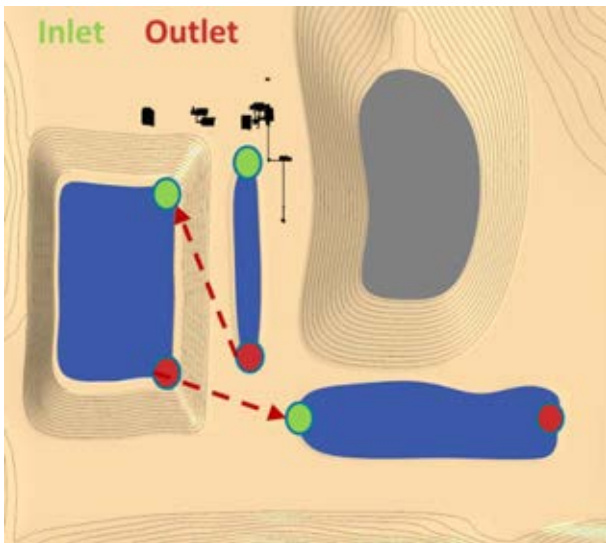


Figure 7: Base case modeling

According to on-site daily measurements, an evaporation correlation has been established depending on wind velocity, air temperature, water content in air (moisture) and water temperature. The way to exchange the values between the water and the air is described in § Fluid-Fluid Interaction. The convective heat transfer has also been taken into account depending on wind velocity, air temperature and water temperature.

Figure 7 represents the running order of the three ponds. The water is entering in the first and smaller pond at 48°C. Figure 8 shows the computed water surface temperature in the different ponds.

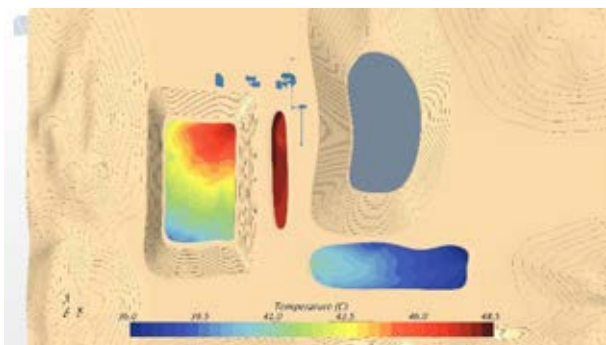


Figure 8: Base case surface temperature

The calculation allowed to highlight the contribution of the last – and soon to be remove - pond to the total heat exchange. Water temperature drops by 4°C in this pond which represents 52 MW (about 30% of total heat exchange).

### Pond optimization

All the results extracted from STARCCM+ by HEEDS have been compared to a base case without dikes and a pond depth of 2m (Figure 9). The outlet temperature is 44.43°C and the error margin has been estimated to be 0.2°C (5% of the heat exchange). More than 120 computations have been performed, including less than 15% that have failed due to divergence problems or results inconsistency.

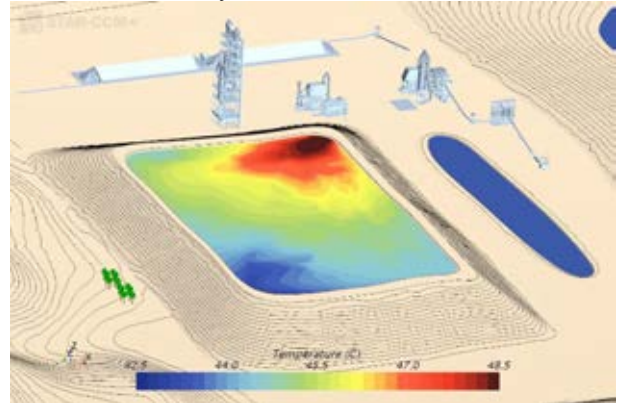


Figure 9: Optimization - No dikes, 2m depth

Some of the optimization results were very close to each other, within the error margin. That led to select not one, but several “best design” and to extract the trends regarding the effects of the different parameters.

As an example, we present two different solution designs leading to an equivalent outlet temperature (Figure 10 and Figure 11):

- 6 horizontal dikes, large opening, small depth  
Outlet temperature = 43.8°C  
Heat duty gain = 15.2%

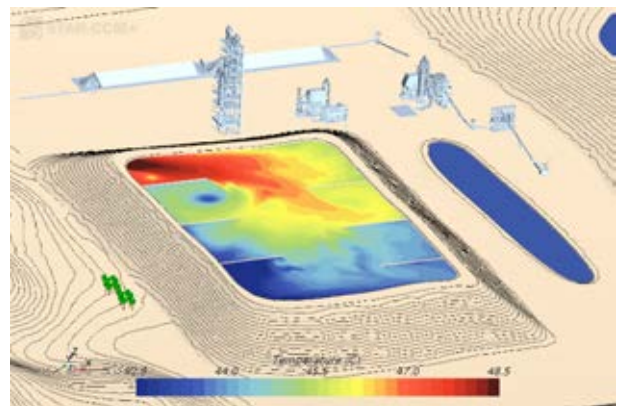


Figure 10: 6 horiz. dikes, large opening, small depth

- 1 horizontal dike, large opening, small depth  
Outlet temperature = 43.65°C  
Heat duty gain = 19%

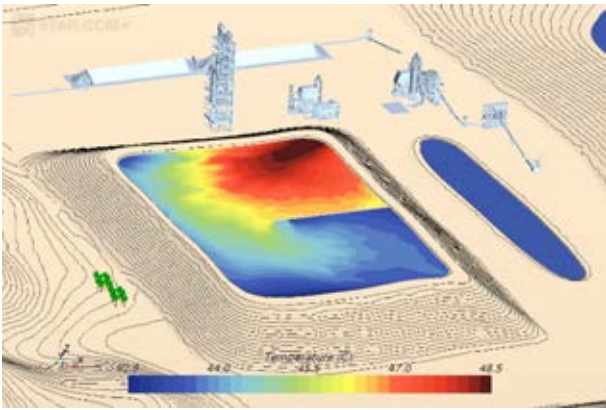


Figure 11: 1 horiz. dike, large opening, small depth

Figure 12 describes an analysis chart coming from HEEDS which allows to quickly identify trends by understanding the connections between the different design parameters. In our case it allowed to identify the following trends:

- Both horizontal and vertical dike positioning are possible
- The number of dikes may change from 1 to 7 in the best designs
- The aperture at the end of the dikes may be large or medium, depending on the number of dikes
- Depth seems to be the most influencing parameter and should be kept to a low value to improve the results.

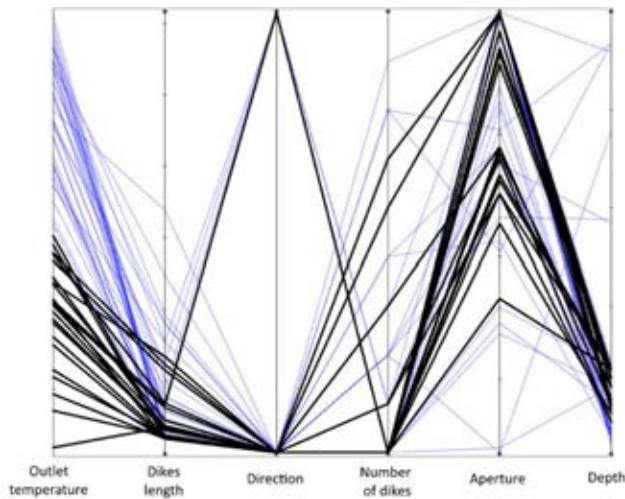


Figure 12: Connections between design parameters

## CONCLUSION

Through the example of the revamping of a phosphate fertilizer plant, we have demonstrated that using CFD as

a design exploration tool for large installations is no longer a pipe dream. Even without a proper 3D-CAD model to start from, different strategies to reconstruct the model into the CFD software are possible, such as using the surface wrapper tool. Although the use of this wrapping technique makes more difficult the calibration and automation of the exchanges between the CFD and Design exploration softwares, it is something achievable.

In the case we have studied, a first CFD model of the active plant configuration has been developed and the simulations that followed have allowed to quantify the heat duty provided by each of the plant cooling ponds. In order to find solutions to recover the lost duty, the multidisciplinary design exploration software HEEDS has been used to drive numerous CFD simulation runs. These calculations did not allow to establish a typical Pareto front as the defined two objectives weren't incompatible with each other. No parameters among the ones we allowed the software to explore turned out to be a real game changer by itself regarding the pond efficiency. However, a list of best designs has been determined quickly thanks to the software, allowing to increase the pond efficiency of about 20%.

While we are just starting to explore the use of design exploration software to drive our CFD simulations, this test case has shown us very promising results regarding the quantity of valuable information that can be extracted in a very short time using this approach.

## REFERENCES

- DEVYNCK, S., (2016) "Using Computational Fluid Dynamics to increase profitability", *In.Brief, GPA*, 09-2016
- DUYNKERKE, P. G. (1988). "Application of the E-ε turbulence closure model to the neutral and stable atmospheric boundary layer", *Journal of the atmospheric sciences*, 45(5), 865-880.
- GOWARIKER, V, et al. "The fertilizer encyclopedia." *John Wiley & Sons*, 2009.
- PASQUILL, F. "Wind structure in the atmospheric boundary layer." *Philosophical Transactions of the Royal Society of London A: Mathematical, Physical and Engineering Sciences*, 1971, vol. 269, no 1199, p. 439-456.
- VENDEL, F., et al. (2010). "Modelling diabatic atmospheric boundary layer using a RANS CFD code with k-epsilon turbulence closure". *13th Conference on Harmonisation within Atmospheric Dispersion Modelling for Regulatory Purposes*.

# NUMERICAL EVALUATION OF CO-FIRING SOLID RECOVERED FUEL WITH PETROLEUM COKE IN A CEMENT ROTARY KILN - EFFECT OF FUEL MOISTURE

David Jayanth ISAAC<sup>1\*</sup>, Morten Nedergaard PEDERSEN<sup>3</sup>, Damien GRÉVAIN<sup>2</sup>, Lars Skaarup JENSEN<sup>2</sup>, and Mads NIELSEN<sup>2</sup>

<sup>1</sup> FLSmidth Private Limited, 34, Egatoot, Kelambakkam, India

<sup>2</sup> FLSmidth A/S, Vigerslev Allé 77, DK-2500 Valby, Copenhagen, Denmark

<sup>3</sup> Technical University of Denmark, DK-2800 Lyngby, Denmark

\*E-mail: david.jayanth@flsmidth.com

## ABSTRACT

This paper presents a numerical simulation model for co-combustion of coarse Solid Recovered Fuel (SRF) with pulverised petroleum coke in a rotary kiln producing cement clinker. The objective is to derive a reliable modelling methodology for design and optimisation of a kiln burner and for the control of the co-combustion process. In this simulation model both the solid fuels are treated as dispersed phases using the Lagrangian method. Two separate shape factors are used to account for the thermodynamic and aerodynamic behaviour of the coarse irregular-shaped SRF particles. Both the fuels undergo similar combustion process - heating, drying, devolatilisation followed by volatile and char combustion. Using such a numerical model the influence of fuel moisture on ignition, flame intensity, fuel burnout and heat output is evaluated. Further insight into the behaviour of SRF particles and the flame characteristics are obtained from video images of the combustion process recorded at a cement plant.

**Keywords:** Multi-Fuel Burner, Rotary Cement Kiln, Co-firing, SRF, Fuel Moisture, Combustion Modelling.

## NOMENCLATURE

### Greek Symbols

- $\rho$  Density, [kg/m<sup>3</sup>].
- $\tau$  Stress tensor, [N/m<sup>2</sup>].
- $\lambda$  Thermal conductivity, [W/m.K].
- $\Gamma$  Diffusion coefficient, [m<sup>2</sup>/s].
- $\Phi$  Reaction rate, [kg/m<sup>3</sup>.s].

### Latin Symbols

- $A$  Pre-exponential factor.
- $CS$  Cross-section area, [m<sup>2</sup>].
- $D$  Kiln diameter, [m].
- $D_{eq}$  Equivalent diameter of spherical particle, [m].
- $E_a$  Activation energy, [kcal/mol].
- $g$  Acceleration due to gravity, [m/s<sup>2</sup>].
- $h_t$  Total enthalpy, [m<sup>2</sup>/s<sup>2</sup>].
- $k$  Reaction rate constant.
- $p$  Static pressure, [Pa].
- $R$  Universal gas constant, [J/mol K].
- $SA$  Cross-section area, [m<sup>2</sup>].

- $T$  Temperature, [K].
- $T_a$  Activation temperature, [K].
- $\mathbf{u}$  Velocity, [m/s].
- $V$  Volume of particles, [m<sup>3</sup>].
- $Y_i$  Mass fraction of species  $i$ .
- $z$  Axial distance inside the kiln, [m].

## INTRODUCTION

In the cement industry rotary kilns are widely used for the production of cement clinker. This process is energy intensive and requires large quantities of fuels. Coal and other fossil fuels have traditionally been used as fuels in cement kilns. Driven by incentives to lower energy costs and waste co-processing, many cement companies increasingly substitute conventional fossil fuels such as coal, oil and natural gas with alternate fuels derived from waste. Solid Recovered Fuel (SRF) is one such alternative and is a solid fuel prepared from non-hazardous waste materials intended for firing in industrial furnaces. SRF consists of large amount of combustible materials like biomass and plastic. While it is attractive to substitute conventional fuels with biomass based fuels in economic and environmental terms, there are some characteristics of these fuels that can impact the kiln process adversely, and may for example reduce clinker quality and production rate.

A modern kiln burner must often be able to perform with high degree of SRF substitution. Hence it is vital to recognize the impacts of burning such alternate fuels in order to design and optimize the kiln combustion system. Irregular particle shape, inhomogeneous nature, high moisture content and prevention of unburnt SRF particle from reaching the clinker bed, while still maintaining a stable combustion, are some of the challenges to be overcome by an optimal burner design. Numerical simulations, with appropriate models for SRF combustion incorporated, is a useful tool for the control and investigation of the combustion process. It is possible to simulate in advance different co-firing concepts and scenarios giving valuable inputs to burner designers and kiln operators.

A number of studies have dealt with CFD simulations of the combustion of pulverized coal in cement kilns [1–4], but only a few papers have studied the effect of alternative fuels. Ariyaratne et al. [5] used CFD to compare the co-combustion of coal, meat and bone meal in the cement kiln, and Liedmann et al. [6] simulated the co-firing of lignite and SRF. Both studies found that the use of alternative fuels resulted in a lower gas phase temperature, due to an increased conversion time of the relatively large alternative fuel particles with high moisture content. A number of studies have also described CFD modelling and impact of SRF co-firing in cement calciners [7] and in power plants [8, 9]. The current study focuses on CFD modelling of co-firing SRF with petroleum coke in a cement rotary kiln.

## CEMENT ROTARY KILN

A rotary kiln is a pyro processing device used to raise materials to a high temperature to enable clinker formation reactions in a cement plant. Figure 1 shows a rotary kiln positioned between the preheater tower and the clinker cooler.

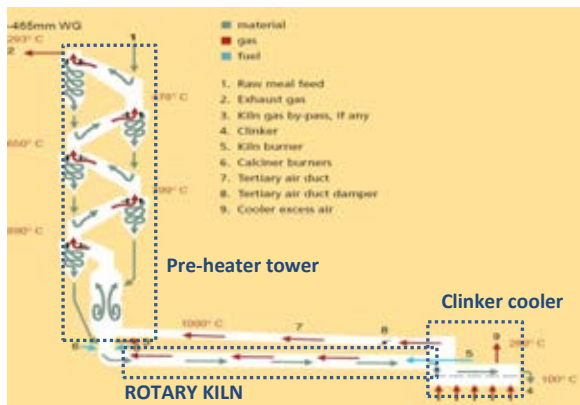


Figure 1: Schematic of a modern cement kiln system

The kiln is a long, cylindrical tube consisting of an outer steel shell and an inner refractory lining. In the material outlet end the kiln is equipped with a burner. The main function of the burner is to form a flame to provide energy for clinkerisation. The flame should be short, narrow and strongly radiant in order to achieve a good heat transfer from the flame to the materials in the bed.

The burner fires the kiln with pulverized coal or coke, oil, natural gas or even as in this case secondary fuels such as plastic chips, wood chips, paper, packing material, etc. Most of the air required for combustion is the hot secondary air from the cooler entrained into the fuel jet and the rest is cold primary air introduced through the burner. The primary air is further divided into multiple channels to impart axial and tangential momentum which helps in controlling the flame shape and also to assist in fuel conveying and cooling the burner tip.

## COMPUTATIONAL METHOD

The modelling method is based upon the solution of the equations governing compressible fluid flow on a finite volume mesh representing the inside of a kiln with a burner, as illustrated in Figure 2. The commercial CFD software ANSYS CFX, was used for modelling and simulation of the combustion process. The governing equations of conservation of mass, momentum, energy and species mass fraction in the continuous gas phase is described in equations 1 to 4.

$$\frac{\partial \rho}{\partial t} + \nabla \cdot (\rho \mathbf{u}) = S_m \quad (1)$$

$$\frac{\partial (\rho \mathbf{u})}{\partial t} + \nabla \cdot (\rho \mathbf{u} \mathbf{u}) = -\nabla p + \nabla \cdot (\tau) + \rho \mathbf{g} + F \quad (2)$$

$$\frac{\partial (\rho h_i)}{\partial t} - \frac{\partial (p)}{\partial t} + \nabla \cdot (\rho \mathbf{u} h_i) = \nabla \cdot (\lambda \nabla T) + \nabla \cdot (\mathbf{u} \cdot \tau) + S_e \quad (3)$$

$$\frac{\partial (\rho Y_i)}{\partial t} + \nabla \cdot (\rho \mathbf{u} Y_i) = \nabla \cdot (\rho \Gamma_i \nabla Y_i) + \Phi_i \quad (4)$$

Here,  $S_m$  is the mass source added to the continuous phase (due to evaporation, devolatilisation and char reaction);  $F$  is the external body force that arises due to interaction with the dispersed phase;  $S_e$  represents the heat source due to combustion;  $\Gamma$  is the diffusion coefficient of species  $i$  and  $\Phi$  is the reaction rate. In addition the two equation model of Shear Stress Transport (SST) is used to predict turbulence, as the flow has moderate swirl generated by the burner. Heat transfer by radiation is computed using the discrete transfer radiation model.

The finite volume mesh must be adequate to capture the presence of a large range of length scales that needs to be resolved, ranging from the dimensions of individual primary air nozzles (hydraulic diameter  $\approx 25$  mm) to the overall size of the kiln (diameter=5m; length=75 m).

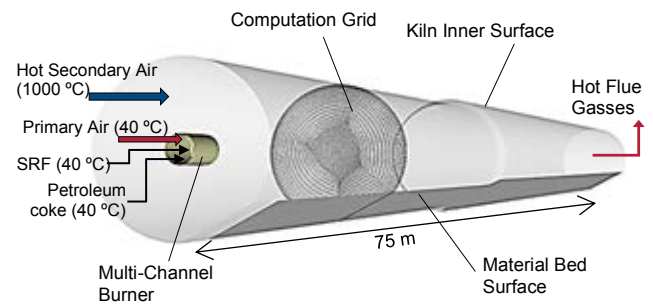
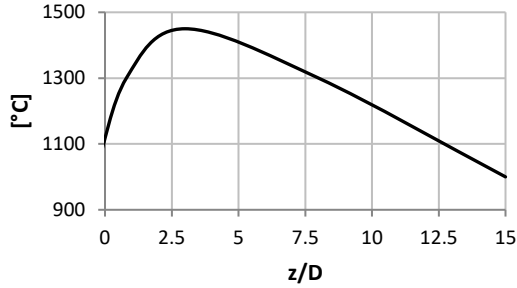


Figure 2: Computation domain and boundary conditions

All the gas and particle inflow boundaries are defined by specified mass flow rate and temperature, while the outlet has a defined pressure.

In this simulation model the actual process of clinkerisation is not modeled instead a predefined temperature profile (Figure 3) is applied to the inner walls of kiln and the material bed thereby representing the surfaces from which heat is transferred to and from the flame or process gasses.



**Figure 3:** Predefined material bed surface and kiln wall temperature<sup>[1]</sup> applied in the computational method

The two fuels, petroleum coke and SRF, are tracked using the Lagrangian particle transport model. Petroleum coke is a conventional fuel and is ground to a fine degree to be completely burnt in the kiln. The particle size distribution of petroleum coke is represented in figure 4. A Rosin-Rammler distribution is fitted to the PSD data and is used to model injection of petroleum coke particles.

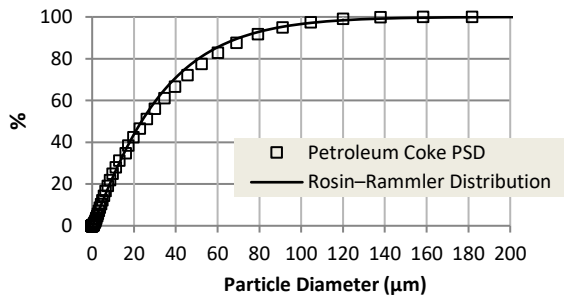


**Figure 4:** Cumulative particle size distribution of petroleum coke

SRF on the other hand, is coarse and has an irregular shape, mostly flat 2D foils of paper, cardboard, packing material and plastics [6 and 11]. For the purpose of modelling all SRF particles are considered to be flat particles of size 10mm wide, 20mm long and 0.1mm thick. Each flat particle is represented by a spherical particle with an equivalent diameter computed based on volume (Figure 5).

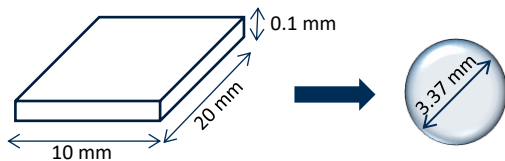


**Figure 5:** Representation of flat SRF particle as a sphere

*Equivalent diameter of spherical particle*

$$D_{eq} = \sqrt[3]{\frac{6 \times V}{\pi}} \quad (5)$$

The coarse irregular-shaped SRF particles are specially treated with shape factors to account for variations in thermodynamic behaviour and aerodynamic behaviour (Parameter values summarised in Table 1).

The Cross Sectional Area Factor (CSAF) is included to account for the influence of drag force of a non-spherical particle on the assumed spherical particle.

$$CSAF = \frac{CS}{\pi \left( \frac{D_{eq}}{2} \right)^2} \quad (6)$$

Similarly the Surface Area Factor (SAF) is applied to account for mass and heat transfer correlations of a non-spherical particle on a spherical particle. It is defined as the ratio of the actual surface area to the surface area of a spherical particle with the same equivalent diameter:

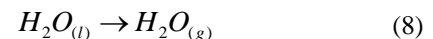
$$SAF = \frac{SA_{cuboidal}}{SA_{sphere}} \quad (7)$$

**Table 1:** SRF particle size and shape factors used in the simulations.

	Units	Value
<b>Flat Particle</b>		
Width	mm	10
Length	mm	20
Thickness	mm	0.1
Volume (V)	mm <sup>3</sup>	20
Cross Section Area (CS)	mm <sup>2</sup>	200
Surface Area (SA)	mm <sup>2</sup>	406
<b>Equivalent Spherical Particle</b>		
Diameter (D <sub>eq</sub> )	mm	3.37
Surface Area (SA)	mm <sup>2</sup>	35.63
Surface Area Factor (SAF)		11.39
Cross Sectional Area Factor (CSAF)		22.45

Combustion of both the solid fuels is divided into four stages: heating, drying, devolatilisation followed by volatile and char combustion. These stages are illustrated in figure 6.

After initial heating to approximately 100°C, moisture is evaporated and transported away from the particles:





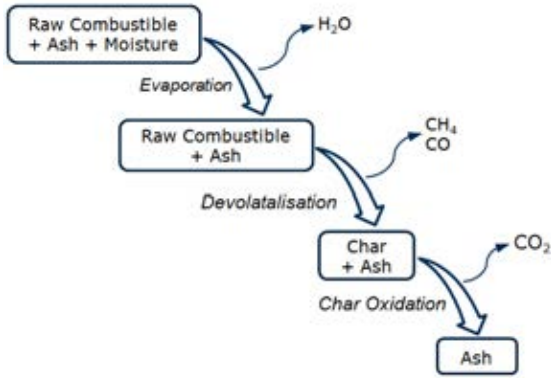
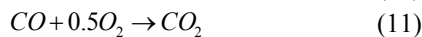
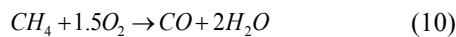


**Figure 6:** Stages of solid fuel combustion

The next step is devolatilisation, which is the release of volatiles into the gas stream. The process is initiated by external heating when the particle surface temperature reaches the lower devolatilisation temperature. This is an endothermic reaction absorbing heat from the surrounding environment. In the current study the volatile gas is assumed to consist of only CH<sub>4</sub> and CO. The distribution of CH<sub>4</sub> and CO in volatiles is adjusted such that the total energy in the fuel is balanced:

$$\left( \begin{array}{c} \text{Energy in Volatiles} \\ (CH_4 + CO) \end{array} \right) = \left( \begin{array}{c} \text{Energy in} \\ \text{Raw Combustible} \end{array} \right) - \left( \begin{array}{c} \text{Energy in} \\ \text{Char} \end{array} \right) \quad (9)$$

In an oxygen environment the devolatilised products ignite in a flame front, above the outer surface and undergo volatile oxidation, enhancing heat transfer to the surface. This accelerates the overall devolatilisation process. A two-step process defined by Westbrook Dryer WD2 [10] is considered to define homogenous volatile oxidation:



The final step is char combustion where the remaining fuel particle consisting almost entirely of carbon and ash is converted into ash. During the char conversion process, oxygen is transported from the surrounding gas to the solid fuel outer surface and eventually into the porous surfaces by diffusion, where it reacts with solid carbon to release carbon dioxide.



All the reactions including evaporation are modelled using a kinetic approach with an Arrhenius type equation. The dependence of the rate constant  $k$  of the chemical reactions on the temperature  $T$  and activation energy  $E_a$  is computed as shown in equation 13.

$$k = A \times e^{-\left(\frac{E_a}{T}\right)} \quad (\text{or}) \quad k = A \times e^{-\left(\frac{E_a}{RT}\right)} \quad (13)$$

**Table 2:** Adopted kinetics for multiphase reactions

	Units	Pet coke <sup>[12]</sup>	SRF <sup>[11]</sup>
<b>Evaporation</b>			
Pre-exp. factor (A)	s <sup>-1</sup>	1.00E+10	1.00E+10
Activation Temperature (T <sub>a</sub> )	K	9273	9273
<b>Devolatilisation</b>			
Pre-exp. factor (A)	s <sup>-1</sup>	1.05E+13	3.01E+16
Activation Temperature (T <sub>a</sub> )	K	25227	26110
<b>Char Oxidation</b>			
Pre-exp. factor (A)	g/cm <sup>2</sup> s	7	5.69E+08
Activation Energy (E <sub>a</sub> )	kcal/mol	19.7	35.80

Evaporation, devolatilisation and char oxidation are multiphase reactions involving solid and gaseous phases. Whereas the volatile oxidation is a homogenous reaction where all the reactants and products are in gaseous phase. Table 2 and 3 summarises the kinetic parameters used in the model.

**Table 3:** Adopted kinetics for volatile oxidation <sup>[10]</sup>

	Units	
<b>Methane oxidation</b>		
Pre-exp. factor (A)	s <sup>-1</sup>	1.5E+07
Activation Energy (E <sub>a</sub> )	kcal/mol	30
<b>CO oxidation</b>		
Pre-exp. factor (A)	m <sup>2.25</sup> s <sup>-1</sup> mol <sup>-0.750</sup>	1.26e+10
Activation Energy (E <sub>a</sub> )	kcal/mol	40

## SIMULATED CONDITIONS AND RESULTS

This CFD modelling study examines the effect of moisture in SRF, when co-firing with pulverized petroleum coke, on flame intensity, fuel burnout and heat output. Moisture content in the fuel is an important issue to consider when burning SRF in kilns. During operation the burner can receive SRFs with varying degree of moisture. The heating value of the fuel decreases with increased moisture content. High moisture content will reduce the combustion temperature, hindering the amount of heat transferred to the material bed resulting in poor quality of clinker. In such an event the operator will increase the rate of fuel flow or reduce the substitution rate to maintain the combustion temperature in the kiln.

Conditions for simulation represent co-firing at a substitution rate of 70% with SRF. Substitution rate here refers to the amount of conventional fuel substituted by secondary fuels like SRF, calculated based on the burner's thermal output. Three grades of SRF are considered for this study with varying amounts of moisture in the fuel. The ultimate and proximate analysis of these three SRFs and petroleum coke is summarised in table 4.

**Table 4:** Proximate and Ultimate analysis

	Pet coke	SRF10	SRF20	SRF40
<i>Proximate (% wt as received)</i>				
Moisture	0.52	10.00	20.00	40.00
Volatiles	12.94	64.35	57.20	42.90
Fixed Carbon	77.48	6.89	6.12	4.69
Ash	9.07	18.77	16.68	12.51
<i>Ultimate (% wt as received)</i>				
C	82.46	47.05	41.82	31.37
H	3.84	6.68	5.94	4.46
N	2.15	0.38	0.34	0.26
O	0.43	16.52	14.68	11.01
S	1.54	0.08	0.07	0.05
Cl	0.00	0.53	0.47	0.35
Net Calorific Value (MJ/kg)	32.7	20.14	17.62	12.69
Mass Flow Rate (kg/s)	0.56	2.13	2.43	3.40

With the increase in fuel moisture, the quantity of SRF fuel is increased to keep the burner's total thermal power output unchanged. The mass of primary air remains same in the three cases, thereby keeping the axial and swirl momentums from the burner constant. The amount of secondary air though is varied such that the equivalence ratio of the combustion system is maintained at 1.2 for all cases.

Petroleum coke enters the kiln through an annular channel in the burner, devolatilises and undergoes volatile combustion setting the ignition point of the flame. The high temperatures generated by combustion of petroleum coke, accelerates heating and drying of the coarse SRF particles which are injected through a separate circular central channel. The devolatilized gasses from SRF burn to complete the flame. Only 30% of the total burner power is derived from petroleum coke. Hence it attains almost complete combustion with very little unburnt char left, which are normally carried away with the flue gasses. On the contrary, the larger SRF particles fall to the material bed (Figure 7). These particles undergo partial char combustion while they are in suspension and the rest burns on the material bed when enough oxygen is available.

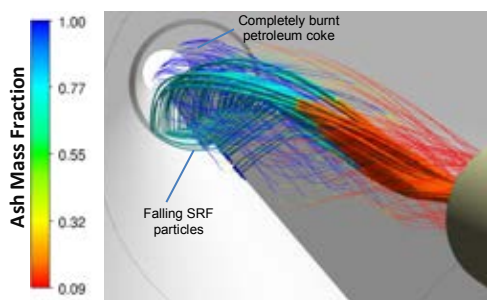


**Figure 7:** Particle tracks of SRF and petroleum coke

In this simulation the Lagrangian particles are no longer tracked after 200s. This time interval is sufficient for the particles to reach the material bed, but is not enough to ensure complete combustion of the char particles on the bed. Limiting the particle tracking time, leads to a fraction of the total heat energy to be unaccounted in the model. Fortunately this unaccounted heat, that is lost as unburnt char particles along with their sensible heat, is a good indication of the degree of fuel not burning while in suspension.

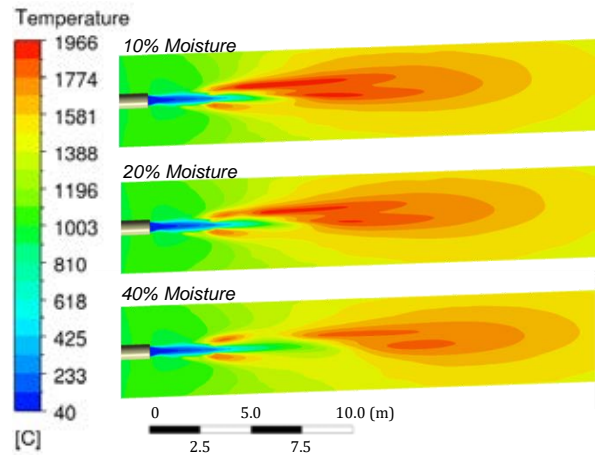


**Figure 8:** Temperature contours determined for the three SRF moisture contents

Temperature plots of flames produced in the three scenarios (shown in figure 8), reveal that when operating at 70% substitution, the influence of moisture is more felt when the fraction of moisture is very high. SRF with 10% and 20% moisture show little difference in flame shape, ignition and useful heat output. Ignition in all cases is controlled by the flame produced by burning of petroleum coke.

The SRF particles are heated to evaporation temperature, by the hot secondary air and by radiations from the walls. In the low moisture cases, rapid release of moisture happens in the vicinity of high temperatures generated by the petroleum coke flame (Figure 9). This initial flame provides enough heat to overcome the latent heat required for vaporisation and promote further heating of SRF particles to devolatilization temperature. In this scenario the petroleum coke flame and the SRF flame appear attached to each other.

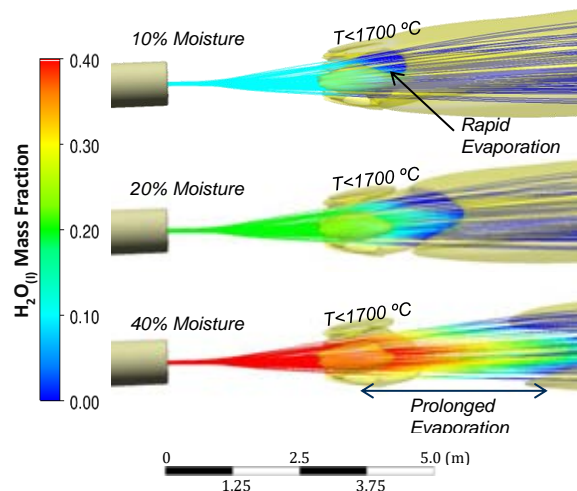


**Figure 9:** Particle tracks coloured with mass fraction of water

In the high moisture case, the particle heating and evaporation phase is prolonged. Moisture release happens outside the high temperature zone created by the combustion of petroleum coke. Under this condition, reduction in gas temperatures are observed in the near burner zone ( $z/D < 2$ ) (Figure 9 and 10) owing to a stretched evaporation phase, further delaying devolatilisation and volatile combustion. A gap develops between the flames from the two fuels.

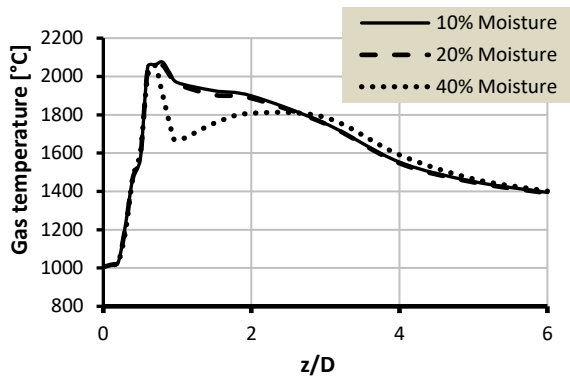


**Figure 10:** Peak gas temperatures in the burning zone plotted as a function of distance/diameter (z/D)

The comparison of the total distribution of heat among the three moisture cases is shown in figure 11. A big fraction of input heat (in the form of fuel firing) is available for clinkerisation. A portion is lost as unburnt carbon in char and the rest are the heat lost through the kiln shells and the heat carried away by the flue gasses.

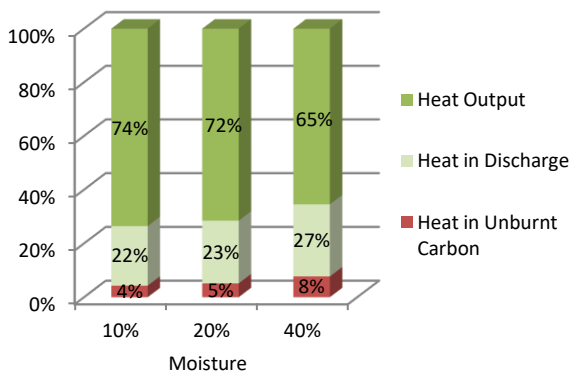


**Figure 11:** Heat distribution between: Bed and walls (Heat output); Gas stream leaving kiln (heat in discharge); and Unburnt fuel.

Heat available for clinkerisation is measured in each simulation as a heat flux on the material bed and the kiln walls. This is used as a parameter to evaluate the performance at different operating conditions. Figure 12 compares the cumulative heat transferred to the material surface and kiln walls for the three scenarios. The rate of heat transferred is rapid in the near burner flow field where most of the combustion occurs and is gradual in the regions away from the burner.

The amount of heat transferred in the burning zone (z/D<5) influences the process of clinkerisation. With 40% moisture in the fuel the cumulative heat flux in the burning zone reduces by 6MW.

Quite clearly the higher moisture content reduces the amount of heat available for clinkerisation even when the total burner power is maintained by firing additional quantities of fuel. The influence of moisture can be expected to become more significant when the substitution rate is further increased beyond 70%.

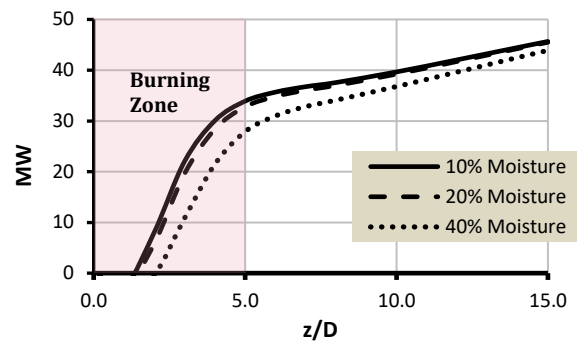


**Figure 12:** Cumulative heat flux on the walls and bed surface

## INDUSTRIAL TESTS

It was also desirable to use industrial measurements to investigate the effect of different fuels and burner settings on the flame and also to derive input conditions for CFD simulations and to validate models. A number of measurements have been performed at a full-scale cement plant firing a mix of petroleum coke and SRF. A water-cooled camera probe was developed to obtain detailed video images of the combustion process in the cement kiln. This made it possible to insert a camera in the hot environment next to the kiln burner (Figure 13).

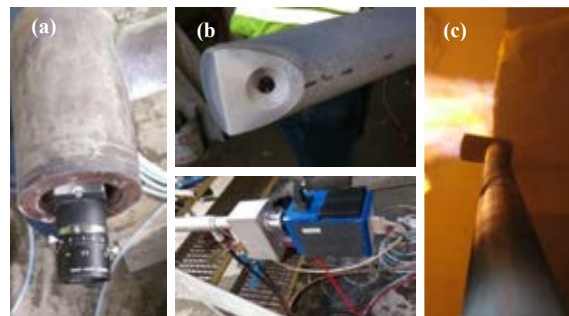


**Figure 13:** (a) Visual camera (b) infra-red camera and (c) video probe inserted into the kiln hood

The images are used to compare the differences in ignition point, flame shape, and fuel flow of a petroleum coke flame and a co-fired flame.

An example comparison is shown in figure 14. The petroleum coke flame (figure 14a) ignites earlier than the co-fired flame (figure 14b), which is due to a larger particle size of SRF and higher moisture content, that cools the flame. It is estimated that the ignition point is approx. 2-3 m from the burner tip when using petroleum coke, and that the ignition point is delayed 1 to 2 meter further when SRF is co-fired.

The petroleum coke flame plume is also wider due to the petroleum coke being added through an annular channel, where it can more readily expand than the SRF, which is added through a central pipe.

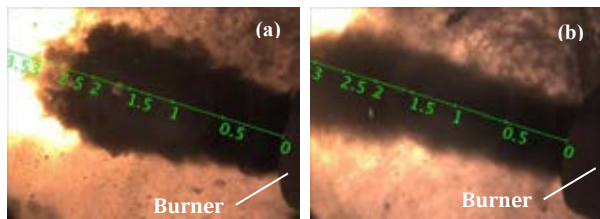


**Figure 14:** Images of a) Petroleum coke flame, b) co-fired flame (scale is in 'm')



**Figure 15:** Images of co-fired flame with infrared camera.

The image in Figure 15 is recorded with the use of an infrared camera. This is well suited to track the flight behaviour of SRF particles inside the kiln. The SRF is shown as large dark particles in the IR image, which indicate a low particle temperature. The cold particles can be tracked relatively far inside the kiln, indicating a low conversion. This will likely result in some of the SRF particles landing in the kiln bed unconverted, as also indicated in the CFD simulations.

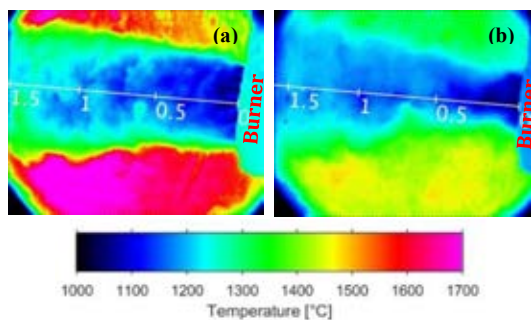


**Figure 16:** Temperature estimation (a) petroleum coke firing and (b) co-firing with SRF, (scale is in 'm')

The infrared camera was calibrated using a black body inserted in an oven, to get a relationship between the temperature of the unit and the camera image intensity. This allows for an estimate of the temperature in the near burner zone constituting approximately the first 5 meters of the kiln. An example is shown in Figure 16 with the temperature of a petroleum coke flame (figure 16a) and the co-fired flame (figure 16b). The temperatures for the petroleum coke flame are significantly higher, with the highest temperature exceeding 1700 °C. For the co-fired flame the maximum temperature in the near burner zone is around 1500 °C.

## CONCLUSIONS AND OUTLOOK

The presented work studies the influence of moisture in the fuel on combustion characteristics and useful heat output while co-firing a cement kiln with petroleum coke and SRF at 70% thermal substitution. The results give an overview of the capabilities of CFD in the field of combustion modelling of large sized secondary fuels typically burnt in the cement industry. An overview of the models that have to be considered is presented. Trends of the simulated results compare qualitatively with video recordings.

Focused analysis of the results provides a deeper insight into the physical and thermal behaviour of such fuels. Model predictions from CFD simulations can be further sharpened by proper assumptions of reaction rate of the char burnout reaction of SRF along with better definitions of the composition of the volatile gases, their formation during devolatilisation and combustion modelled with more complex reaction schemes. Such a model can be used further to understand the influence of different operating parameters and investigate different injection concepts to optimise burner designs.

## REFERENCES

- [1] WANG, S., LU, J., LI, W., LI, J., and HU, Z., (2006), "Modeling of Pulverized Coal Combustion in Cement Rotary Kiln", *Energy & Fuels* 2006, 20, 2350-2356.
- [2] LOCKWOOD, F. C, and SHEN, B., (1994), "Performance predictions of pulverised-coal flames of power station furnace and cement kiln types", *Twenty-Fifth Symposium (International) on Combustion*, 1994, pp. 503–509.
- [3] MASTORAKOS, E., MASSIAS, A., TSAKIROGLOU, C.D., GOUSSIS, D.A., BURGANOS, V.N., and PAYATAKES, A.C., (1999), "CFD predictions for cement kilns including flame modelling, heat transfer and clinker chemistry", *Applied Mathematical Modelling*, 1999, 23, 55–76.
- [4] MUJUMDAR, K.S., and RANADE, V.V., (2008), "CFD modeling of rotary cement kilns", *Asia-Pacific Journal of Chemical Engineering*, 2008, 3, 106–118.
- [5] ARIYARATNE, W.K.H., MALAGALAGE, A., MELAAEN, M.C., and TOKHEIM, L.-A., (2014), "CFD Modeling of Meat and Bone Meal Combustion in a Rotary Cement Kiln", *International Journal of Modeling and Optimization*, 2014, 4, 263–272.
- [6] LIEDMANN, B., ARNOLD, W., WIRTZ, S., SCHERER, V., KRÜGER, B., MROTZEK, A., HÜNDGEN, W., and TOPP, O., (2015), "Refuse Derived Fuel Co-Firing in Cement Rotary Kilns – A methodology to specify a customized fuel by numerical simulation and fuel characterisation", *10th European Conference on Industrial Furnaces and Boilers*, 2015, pp. 1–11.

[7] NAKHAEI, M., WU, H., GLARBORG, P., DAM-JOHANSEN, K., GRÉVAIN, D., and JENSEN, L.S., (2016), "CFD simulation of a full-scale RDF-fired calciner", *Proceedings of the 2nd International Workshop on CFD and Biomass Thermochemical Conversion*, Leipzig, 9 September 2016.

[8] LIEDMANN, B., ARNOLD, W., KRÜGER, B., BECKER, A., KRUSCH, S., WIRTZ, S., and SCHERER, V., (2017), "An approach to model the thermal conversion and flight behaviour of Refuse Derived Fuel", *Fuel*, 2017, 200, 252–271.

[9] AGRANIOTIS, M., NIKOLOPOULOS, N., NIKOLOPOULOS, A., GRAMMELIS, P., and KAKARAS, E., (2010), "Numerical investigation of Solid Recovered Fuels' co-firing with brown coal in large scale boilers - Evaluation of different co-combustion modes", *Fuel*, 2010, 89, 3693–3709.

[10] WESTBROOK, C.K., DRYER, F.L., (1981), "Simplified Reaction Mechanisms for the Oxidation of Hydrocarbon Fuels in Flames", *Combustion Science and Technology*, 1981 Vol. 27, pp. 31-43.

[11] PEDERSEN, P.N., (2015), "Single particle combustion of refuse derived fuel", *Technical report, Technical University of Denmark, Department of Chemical and Biochemical Engineering*.

[12] SMITH, I. W., (1982), "The Combustion Rates Of Coal Chars: A Review", *Nineteenth Symposium (International) on Combustion/The Combustion Institute*, 1982/pp. 1045-1065.

## EXPERIMENTAL AND CFD INVESTIGATIONS OF FRACTAL DISTRIBUTOR ON A NOVEL PLATE AND FRAME ION-EXCHANGER

Gongqiang He<sup>1</sup>, Vadim Kochergin<sup>2</sup>, Yuehao Li<sup>1</sup>, Krishnaswamy Nandakumar<sup>1\*</sup>

<sup>1</sup> Louisiana State University, Baton Rouge, LA, USA

<sup>2</sup> Amalgamated Research LLC (ARi), ID, USA

\* E-mail: nandakumar@lsu.edu

### ABSTRACT

Conventional pressure based flow distributors face challenges in the form of operational limits as their low outlet density and non-uniform flow distribution path, often act as bottleneck in the overall chemical equipment efficiency. Recently, a new distributor design inspired by the concept of fractal shows promising performance over a wide range of applications and operating conditions. The inherent scaling symmetry from such fractal distributors allows identical hydraulic flow path length to all outlets as well as much higher outlet density. In this study, we have designed a novel 12" by 12" plate and frame type ion-exchanger called "Fractal Pack" and tested it in pilot scale adopting fractal distributors with 256 outlets under operating flow rates ranging from  $6.31 \times 10^{-5}$  m<sup>3</sup>/s to  $2.52 \times 10^{-4}$  m<sup>3</sup>/s. For comparison, ion-exchanger with 16 distributor outlets has also been assembled to mimic the performance of conventional pressure-based design. Both residence time distribution test and CFD investigations have been conducted. From CFD results, at highest flow rate, we found the overall pressure drop for ion-exchanger with 16 outlets is about 6 times larger than with fractal distributor and 78% of its pressure drop is caused by sudden expansion and contraction at 16 outlets. In addition, a key index, degree of heterogeneity which measures the percentage of mal-distribution zones inside resin, has been defined to quantify flow distribution inside resin. The distributor equipped with 16 outlets shows 4 times more mal-distribution zones than 256 outlets at highest flow rate. This work demonstrates that fractal distributors can reliably provide superior performance over conventional distributors in a compact design framework; by introduction of symmetry, fractal distributors can aid process intensifications for many chemical processes that are plagued by heterogeneities and poor process efficiencies. The work also demonstrates how CFD can assist in avoiding ad-hoc design decision on dimensions and systematically explore the design space for optimum design decisions, using optimization criteria like coefficient of variation, degree of dispersion or heterogeneity.

**Keywords:** CFD, flow distribution, fractal geometry, fluid distributor, RTD

### NOMENCLATURE

#### Greek Symbols

$\alpha$  Permeability, [m<sup>2</sup>].

$\delta_{ij}$  Kronecker delta function.

$\epsilon$  Turbulence energy dissipation rate, [m<sup>2</sup>/s<sup>2</sup>].

$\mu$  Dynamic viscosity, [kg/m.s].

$\mu_t$  Turbulent viscosity, [kg/m.s].

$\rho$  Mass density, [kg/m<sup>3</sup>].

$\sigma$  Turbulent Prandtl number.

#### Latin Symbols

$C$  Tracer concentration, [mol/m<sup>3</sup>].

$d$  Channel depth, [m].

$D_d$  Diffusivity of the tracer, [m<sup>2</sup>/s].

$D_p$  Diameter of resin bead, [m].

$g$  Gravity, [m/s<sup>2</sup>].

$G_k$  Generation of turbulent kinetic energy due to the mean velocity gradients, [m<sup>2</sup>/s<sup>2</sup>].

$G_b$  Generation of turbulent kinetic energy due to buoyance, [m<sup>2</sup>/s<sup>2</sup>].

$h$  Channel width, [m].

$k$  Turbulent kinetic energy, [m<sup>2</sup>/s<sup>2</sup>].

$p$  Pressure, [Pa].

$R$  Resistance in the resin section, [Pa/m].

$u_i$  Velocity component in  $i^{\text{th}}$  spatial component, [m/s].

$x_i$   $i^{\text{th}}$  spatial component, [m].

#### Sub/superscripts

$i$  Index  $i$ .

$j$  Index  $j$ .

$\rightarrow$  Vector form.

### INTRODUCTION

Since its emergence in 1970s, process intensification, as one promising innovation paths in chemical process industry, has been attracting extensive research interests from both academic and industrial sectors. Process intensification consists of the development of novel apparatuses and techniques that can lead to drastic improvement in chemical processes by reduction of equipment size, energy consumption or water utilization. Such characteristics are highly desired as they make the chemical industry more sustainable and environment-friendly (H. Liu et al., 2010). One good topic of process intensification is the innovation of flow distributors (V. Kochergin and M. Kearney, 2006). Flow distributors are extensively integrated by chemical equipment to distribute incoming feed streams uniformly

prior to the subsequent operations, whether it is reaction, mixing or separation. The efficiency of the flow distributor plays a key role in determining the overall performance of the chemical equipment. When the distributors have low efficiencies, the chemical equipment has to be oversized as a compensation, resulting in increased material and energy consumption and reduced efficiency. In order to achieve process intensification, innovative flow distributors that offer uniform flow distribution and close residence time distribution of the feed streams are in urgent need by the chemical industry.

Conventional flow distributors utilize the pressure-based and trough-type designs, of which the typical diagrams are shown in Figure 1(a) and (b), respectively. The pressure-based designs, i.e., spray nozzle distributors as seen in Figure 1(a), position their outlets on the branches with certain interval. The flow paths from the distributor to each outlet are varying between each other. In order to achieve uniform flow distribution, each outlet has to be sized accordingly based on its flow paths. Such design concept is associated with several inherent disadvantages. As the outlet are designed based on particular operating flow rates, the performance of such distributors are undermined when the operating flow rates deviate from the designed value significantly. For example, the process fluid may drip only from those center outlets when the operating flow rate is much lower than the designed one. In addition, the varying flow path results in different residence time of each stream. Furthermore, the scale-up of such distributors requires significant efforts as the design lacks symmetry. The outlet density, which is defined as the number of outlets per unit cross-sectional area, is usually limited below 250 openings per square meters (V.J. Inglezakis and S.G. Pouloupoulos, 2006).

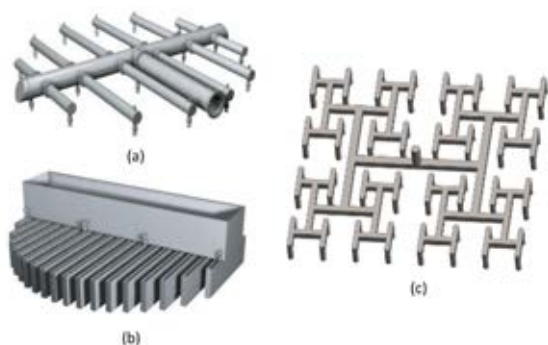


**Figure 1** (a) a conventional spray nozzle distributor (Sulzer Chemtech Ltd). (b) A trough-type liquid distributor (Sulzer Chemtech Ltd). (c) A fractal distributor

First proposed in 1994 (M.M. Kearney et al., 1994), fractal distributors are now attracting extensive research interests. Such distributors are inspired by the fractal patterns existing in nature, i.e., human's lung systems, leaf veins and river basins. The key feature shared by fractal patterns is the self-similarity (B. Mandelbrot, 1982). In other words, these patterns contain pieces that are duplications of the same pattern on successively increasing finer scales. By adopting such a feature in engineering, fractal distributors utilize symmetric pipe systems to distribute fluid flow as seen in Figure 1(c). Since such designs rely on the symmetry rather than

pressure drop or hydraulic head, they show superior performances over conventional distributors in various aspects. First, the fractal distributor allows easy scale up due to the self-similarity feature; as a result, the distributors can achieve much higher outlet density than conventional distributors. Second, the feed streams have close residence time distribution, as their flow paths are almost identical. In addition, fractal patterns regulate turbulent eddies by subdividing large eddies into smaller ones. The flow lamination helps to improve the homogeneity in the downstream chemical equipment.

In this study, we present our experimental and CFD investigations of a novel fractal distributor integrated into a "fractal pack" based ion exchanger. Such an ion exchanger consists of multiple plates fabricated by polymethyl-methacrylate (PMMA). The internal channels of the fractal are machined inside PMMA plates. The distributor was assembled with either 16 or 256 outlets. The 16-outlet distributor mimics the outlet density of a conventional pressure-based design. However, it is noted that the 16-outlet design used in this study is still a fractal configuration and includes the benefits of hydraulic symmetry to all outlets. Therefore, for this paper, the 16-outlet distributor can be considered a "best case" pressure-based design. Conventional pressure-based designs, such as spray nozzle distributors, would be expected to perform in a less favourable manner than presented here for the 16 outlet fractal device. There are three aims of this work: (1) to develop and validate a CFD model that captures the fluid flow inside the fractal distributor and other components of the ion exchanger; (2) to compare the performance of a fractal distributor with a "best case" hydraulically symmetric pressure-based distributor; (3) to explore design space for optimizing fractal distributor performance, using optimization criteria like coefficient of variation in flow rate.

## EXPERIMENTAL SETUP

In collaboration with Amalgamated Research LLC, a novel ion exchanger at pilot scale was fabricated using PMMA. As shown in Figure 2, such exchanger is composed by three components: a fractal distributor, a resin exchanging bed and a fractal collector. The detailed illustrations of each component are shown in Figure 2. The fractal distributor is assembled by three plates. The 1st plate consists of an H-shape channel which distributes the incoming fluid stream from the fractal inlet to 4 outlets. Leaving those outlets, the distributed fluid streams then enter the 2nd plate where they are distributed again to 16 outlets. Similarly, the incoming fluid streams are again further distributed to 256 outlets on the 3rd plate. Each outlet in the 3rd plate has a cone-shape expansion which maximizes the contact area between the distributed stream and the resin bed downstream. These plates were assembled carefully to ensure that the outlets of the previous plate were aligned to the inlets of the next plate precisely.

After the fluid streams leave the fractal distributor, they enter the resin bed as shown as plate 4 in Figure 2. The resin bed is comprised by 310-micron ion-exchange resin beads which are confined inside the resin frame. The porosity of the resin bed is about 0.44. The particular

ion exchange resin used in these tests does not adsorb food dye (FD&C Blue No.1) and only acts as a simple porous media for RTD and visualization testing. Post to the resin section, the fluid streams are collected by a fractal collector. Such a collector is identical to the fractal distributor, but the three plates (5th, 6th, and 7th) are assembled in a reverse order. The process streams merge from these inlets into one. The thickness of each plate in the distributor and the collector is about 25.3 mm.

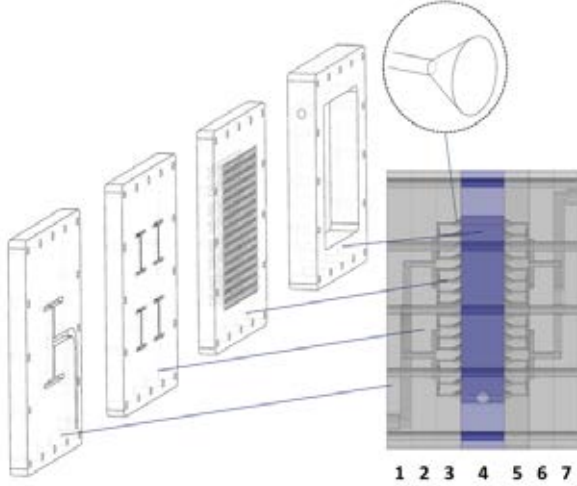


**Figure 2** Schematic view of the ion-exchange system: (1) the 1<sup>st</sup> plate consisting of one inlet and H-shape channel with four outlets; (2) the 2<sup>nd</sup> plate consisting of 16 outlets; (3) the 3<sup>rd</sup> plate consisting of 256 outlets with cone shape expansion; (4) resin frame where resin is stuffed inside; (5), (6) & (7) collector plates with identical structure as those in the distributor but in a reverse direction.

The flow visualization experiment and the residence time distribution (RTD) analyses were carried out during the experiments to visualize the fluid flow inside the fractal distributor.

## MODEL DESCRIPTION

As the process fluid satisfies the incompressible and Newtonian conditions, the fluid flow can be described by the incompressible Navier-Stokes equations. The Reynolds number in the fractal inlet, corresponding to flow rate as  $2.52 \times 10^{-4} \text{ m}^3/\text{s}$ , is 14400 ( $\text{Re} = \rho U D_h / \mu$ , in which  $\rho$  is fluid density;  $U$  is the superficial velocity in the inlet;  $D_h$  is the hydraulic diameter of the inlet;  $\mu$  is fluid viscosity), indicating that the flow is in the fully-developed turbulent regime. Therefore, the Reynolds-averaged Navier-Stokes (RANS) equations were adopted to describe the turbulent flow:

$$\frac{\partial}{\partial x_i} u_i = 0 \quad (1)$$

$$\rho \frac{\partial}{\partial x_j} (u_i u_j) = -\frac{\partial}{\partial x_i} p + \frac{\partial}{\partial x_j} \left[ \mu \left( \frac{\partial}{\partial x_j} u_i + \frac{\partial}{\partial x_i} u_j \right) \right] - \rho \frac{\partial}{\partial x_j} (\overline{u'_i u'_j}) + \rho \vec{g} + \vec{R} \quad (2)$$

in which  $u$  is the mean velocity vector, and the subscripts  $i, j$  and  $k$  stand for the components on  $x, y$  and  $z$  directions;  $x$  is the spatial vector;  $\rho$  is fluid density;  $p$  is pressure;  $\mu$  is fluid viscosity;  $u'_i$  and  $u'_j$  are the fluctuating velocity components;  $\vec{g}$  is the gravitational vector; and  $\vec{R}$  is the resistance in the resin section which is estimated by the Ergun equation.

In order to close the RANS equations, the Reynolds stresses term,  $-\rho(\overline{u'_i u'_j})$ , are modeled by employing the Boussinesq hypothesis:

$$-\rho \overline{u'_i u'_j} = \mu_t \left( \frac{\partial}{\partial x_j} u_i + \frac{\partial}{\partial x_i} u_j \right) - \frac{2}{3} \left( \rho k + \mu_t \frac{\partial}{\partial x_k} u_k \right) \delta_{ij} \quad (3)$$

in which  $\mu_t$  is the turbulent viscosity;  $k$  is the turbulent kinetic energy;  $\delta_{ij}$  is the unit component in the stress tensor.

In this study,  $\mu_t$  and  $k$  are estimated by the realizable  $k$ - $\epsilon$  model. Compared to the standard  $k$ - $\epsilon$  model, the realizable  $k$ - $\epsilon$  model modifies the  $\epsilon$  equation to improve the accuracy of predicting turbulent kinetic energy dissipation rate. Therefore, it shows superior abilities to capture complex flow structures in fractal channels. The model remains valid at low Reynolds number flow regions where  $k, \epsilon$  and hence  $\mu_t$  tend to zero with fluid flow determined solely by NSE model.

The realizable  $k$ - $\epsilon$  model solves two transport equations for the turbulence kinetic energy  $k$  and its dissipation rate  $\epsilon$ :

$$\begin{aligned} \rho \frac{\partial}{\partial x_j} k u_j &= \frac{\partial}{\partial x_j} \left[ \left( \mu + \frac{\mu_t}{\sigma_k} \right) \frac{\partial}{\partial x_j} k \right] + G_k + G_b - \rho \epsilon \quad (4) \\ \rho \frac{\partial}{\partial x_j} \epsilon u_j &= \frac{\partial}{\partial x_j} \left[ \left( \mu + \frac{\mu_t}{\sigma_\epsilon} \right) \frac{\partial}{\partial x_j} \epsilon \right] + \rho C_1 S \epsilon - \rho C_2 \frac{\epsilon^2}{k + \sqrt{v \epsilon}} + C_{1\epsilon} \frac{\epsilon}{k} C_{3\epsilon} G_b \quad (5) \end{aligned}$$

and the turbulent viscosity  $\mu_t$  is computed by

$$\mu_t = \rho C_\mu k^2 / \epsilon \quad (6)$$

In the above equations,  $G_k$  and  $G_b$  are the generation of turbulent kinetic energy due to the mean velocity gradients and buoyancy, respectively;  $\sigma_k = 1.0$  and  $\sigma_\epsilon = 1.2$  are the turbulent Prandtl number for  $k$  and  $\epsilon$ , respectively;  $C_{1\epsilon} = 1.44$  and  $C_2 = 1.9$  are the model constants. The detailed expression of  $G_k, G_b, C_1, S$  and other variables can be found in the reference (T.-H. Shih et al., 1995).

In the resin section, the porous media exerts strong resistance to the fluid flow. Such resistance is accounted into the RANS equations as a source term,  $\vec{R}$ . The component of  $\vec{R}$  is estimated by the classic Ergun equation as:

$$R_i = - \left( \frac{\mu}{\alpha} u_i + C_{R2} \rho |u_i| |u_i| \right) \quad (7)$$

in which  $\alpha$  is the permeability, and  $C_{R2}$  is the inertial resistant coefficient. They are expressed as:

$$\alpha = \frac{D_p^2}{150} \frac{\epsilon^3}{(1-\epsilon)^2} \quad (8)$$

$$C_{R2} = \frac{3.5(1-\epsilon)}{D_p \epsilon^3} \quad (9)$$

Where,  $D_p$  is the diameter of resin bead, which is 310  $\mu\text{m}$ ;  $\epsilon$  is the porosity of the resin section, which is 0.44.

The RTD analyses in the model were conducted by solving the species transport equation:

$$\frac{\partial}{\partial t} C + \frac{\partial}{\partial x_i} (u_i C) = D_d \frac{\partial}{\partial x_i} \left( \frac{\partial}{\partial x_i} C \right) \quad (10)$$

in which  $C$  is concentration of tracer;  $u_i$  is the velocity vector predicted by the N-S equations, and  $D_d$  is the diffusivity of the tracer which is specified as  $4 \times 10^{-5} \text{ m}^2/\text{s}$ .



## CFD SIMULATION SETUP

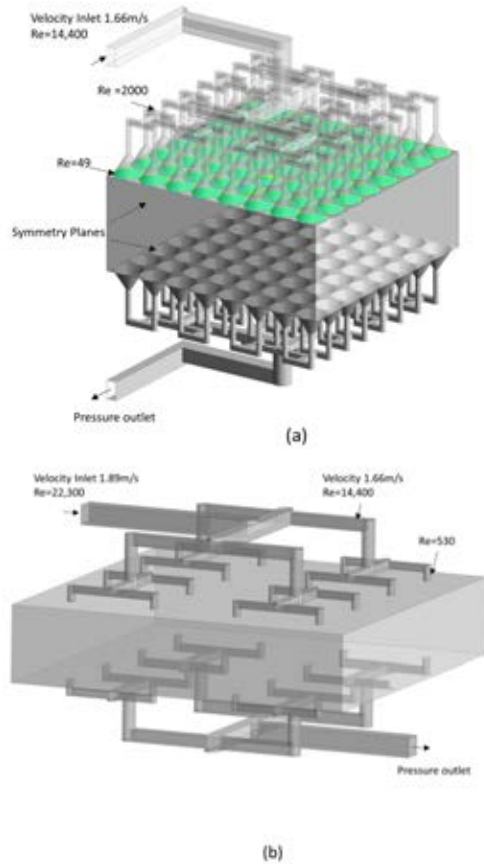


**Figure 3** Illustration about the computational domains of the two ion exchangers: (a) The 1st ion exchanger with the fractal distributor of 256 outlets in total and only  $\frac{1}{4}$  part (64 outlets) has been shown as computation domain. (b) The 2nd ion exchanger with the fractal distributor of 16 outlets. The typical Re in certain locations of the distributors are denoted in the figures.

The computational domain of the two ion exchangers is shown in Figure 3. The corresponding fractal distributors used by these two exchangers consist of 256 and 16 outlets, respectively. For the one of 256 outlets, only a quarter of the ion exchanger was simulated utilizing the symmetry condition. The location of symmetry planes have been shown in Figure 3(a). The inlet velocity was 1.660 m/s, corresponding to the volumetric flow rate of  $2.52 \times 10^{-4} \text{ m}^3/\text{s}$ . For one of 16 outlets, the entire ion exchanger was simulated. The inlet velocity was specified as 1.89 m/s with same flow rate. The geometry of distributor with 16 outlets was created in a way that it followed the same dimension with the main branches from the distributor with 256 outlets, but without further splitting of outlets from 16 to 256 at the last horizontal plane.

The outlets of the collectors were specified as the pressure outlet with 0 Pa. No-slip conditions incorporating with the scalable wall function were specified to all wall boundaries. Dimensionless wall distance ( $y^+$ ) vary around 20-10 based on local flow field and Re.

The SIMPLE (Semi-Implicit Method for Pressure-Linked Equations) scheme was used to couple the momentum and continuity equations. For spatial discretization, least-squares cell-based method was adopted for gradient; standard method, which

interpolates the pressure on the faces using the cell center values, was used for pressure interpolation; second-order upwind was used for momentum, turbulent kinetic energy and turbulent dissipation rate.

All simulations have been performed with ANSYS FLUENT 16 with 40 processors on Supermike HPC located at Louisiana State University. The steady-state solutions of the N-S equations were obtained usually within 5000 iterations with convergence criteria at  $1\text{E-}4$ . Then the corresponding velocity field from steady state solution was supplied to the species transport equation, which adopted transient simulations. A typical time step used by the simulations was 0.005s. The entire simulation took about 10 hours.

## MODEL VALIDATION

The CFD model is validated by comparing the predicted RTD curves and pressure drops of the ion exchanger with the ones from the experiments. The simulations and the experiments were carried out with the two ion exchangers shown in Figure 4. Figure 4(a) plots the RTD curves predicted by simulations and the corresponding ones measured from experiments. The good agreement between the model and experiments suggests that the model successfully captured the flow inside the ion exchangers.

In this study, a mesh dependence test was performed prior to the parametric study in order to eliminate the potential numerical error resulted from the insufficient grid resolutions. Three types of grids with different resolutions were generated by the CutCell algorithm in Ansys Meshing. Figure 4(b) shows Velocity profiles along the sampling lines in the 1 ion exchanger with three mesh densities. The test results suggested that the flow profile in resin became independent from grid solutions when the total mesh elements exceeded 2.7 million. Therefore, such a mesh was selected for the following parametric studies.

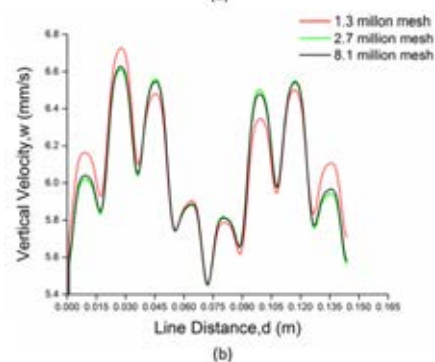
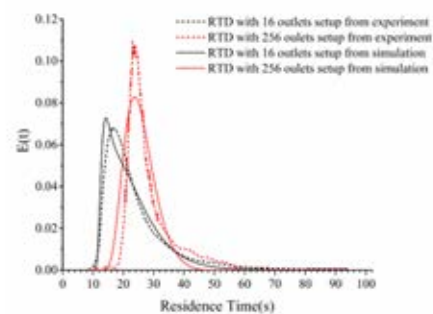


**Figure 4** (a) Comparison of the RTD curves of the 1st and 2nd ion exchangers measured from experiments and predicted by the CFD simulations. The mesh with 2.7 million elements has been adopted for 1st ion exchanger. The exchangers were operated with a flow rate of  $6.31E-5 \text{ m}^3/\text{s}$ . (b) Vertical velocity profiles along the sampling lines (cross line at 5mm depth inside resin) in the 1st ion exchanger with three mesh densities.

### VELOCITY PROFILE COMPARISON OF TWO DISTRIBUTORS

In this section, we will compare the performance of a fractal distributor with a “best case” hydraulically symmetric pressure-based distributor.

In order to understand how the flow distribution influences the performance of ion exchangers, the detail flow profiles inside the resin bed were analysed with the aid of simulation results. For both 1st and 2nd distributor, the simulations were performed with same flow rate ( $2.52 \times 10^{-4} \text{ m}^3/\text{s}$ ). Taking the 1st ion exchanger as an example, Figure 5 shows the overview of velocity profiles on three representative planes of the resin bed. The locations of these three planes are denoted in Figure 5(a). They are Plane 1 which is the top surface of the resin bed (0 mm), Plane 2 which is 5 mm below the top surface and Plane 3 which is 15 mm below.

In order to observe the velocity evolution quantitatively, three lines were sampled along the diagonal of planes of different depths as illustrated in Figure 6(a). The locations of these lines are denoted in Figure 5(a). They locate on the planes that are 5, 10 and 15 mm below the top surface of the resin bed, respectively. The corresponding velocity profiles plot in Figure 5(b) clearly demonstrates the homogenizing process of the velocity profiles along the transversal flow direction. When the process streams enter the resin bed,

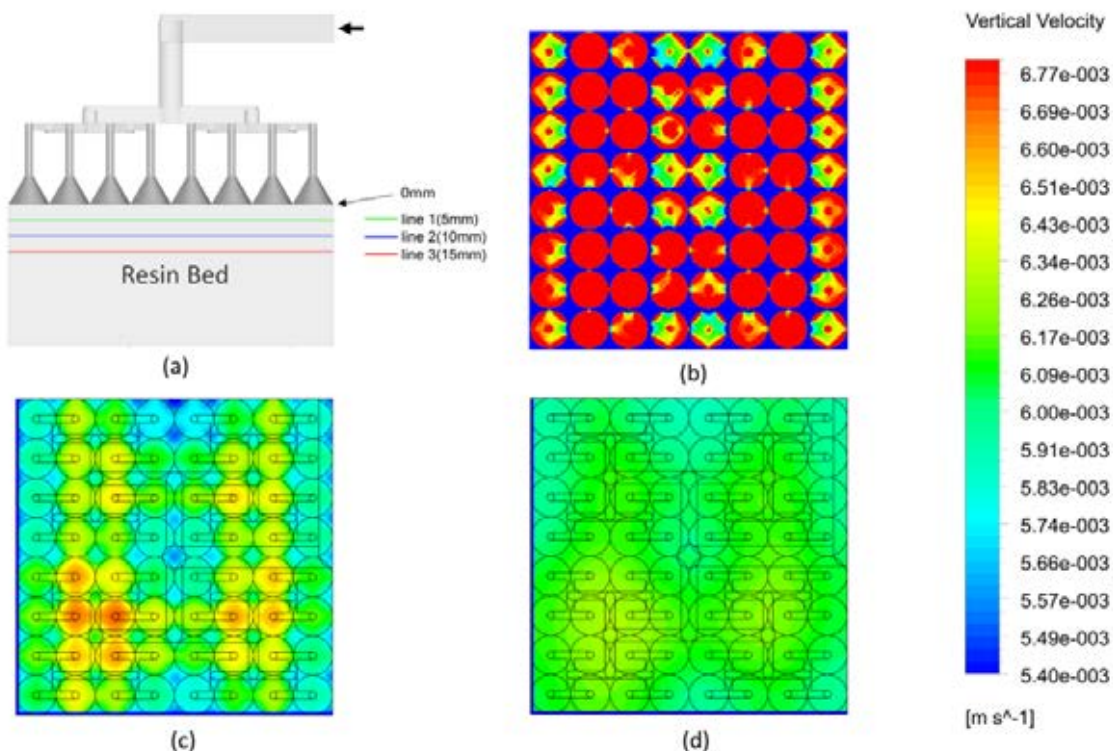
the fluid elements tend to take the shortcut to travel through the resin bed. Those regions on the flow track have large velocity magnitudes while the other regions off the track have lower ones. As a result, the velocity profiles shows fluctuations in magnitude, of which the maximum variation is about 1.20 mm/s. On the other hand, the resistant force exerted by the resin bed tends to homogenize the velocity profile. As indicated in Figure 6(b), the peak values is reduced along the transversal direction due to the resistance force. When the process stream reaches 15 mm plane, the maximum velocity variation is reduced to 0.25 mm, indicating that the flow profile approaches the plug pattern.

Figure 6 (c) compares the velocity profiles of the 1st and 2nd ion exchanger sampled at 5 mm plane with  $\frac{1}{4}$  part of the whole domain. Clearly, the velocity profile of the 2nd ion exchanger shows a much larger variation than that of the 1st ion exchanger. The significant velocity variation is due to the inefficient initial distribution. As a result, the 2nd ion exchanger requires a much deeper resin bed than that of the 1st ion exchanger so as to attain a uniform velocity profile. On the other hand, the large velocity variation results in malfunctioning operations in the resin bed.

### MALFUNCTIONING OPERATIONS OF THE RESIN BED

As illustrated in Figure 6, the inefficient distribution of the process stream causes significant variations in velocity profiles. Consequently, it leads to the malfunctioning operations of the resin bed such as “dead space” and “channelling”.

The term “dead space” is commonly used in industry to name those regions where the fluid elements have



**Figure 5** (a) Locations of the three representative planes: Plane 1 which is the top surface of the resin bed (0 mm), Plane 2 which 5 mm below the top surface and Plane 3 which is 15 mm below the top surface. (b), (c) and (d): Contours of vertical velocity in the flow direction on Plane 1, Plane 2 and Plane 3, respectively.

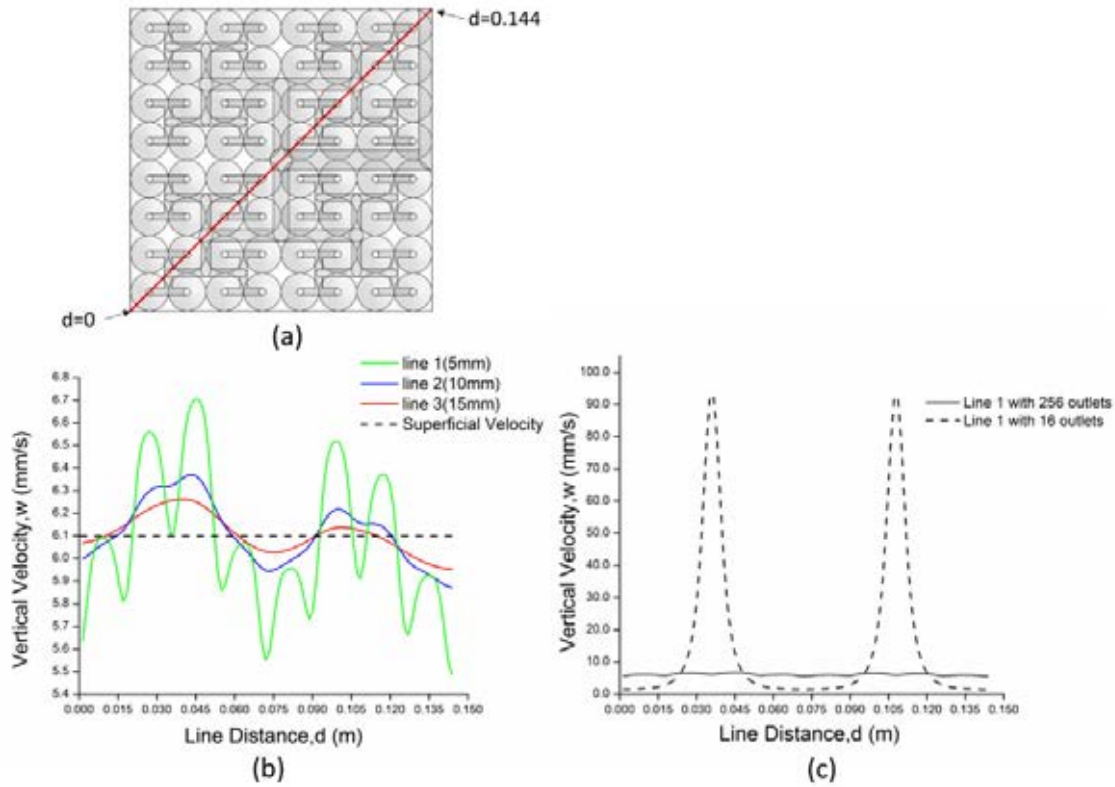


**Figure 6** (a) Illustration about the location of the sampling lines. (b) Velocity profiles along the sampling lines in the 1st ion exchanger. (c) Comparison of velocity profiles along Line 3 between the 1st and 2nd ion exchangers.

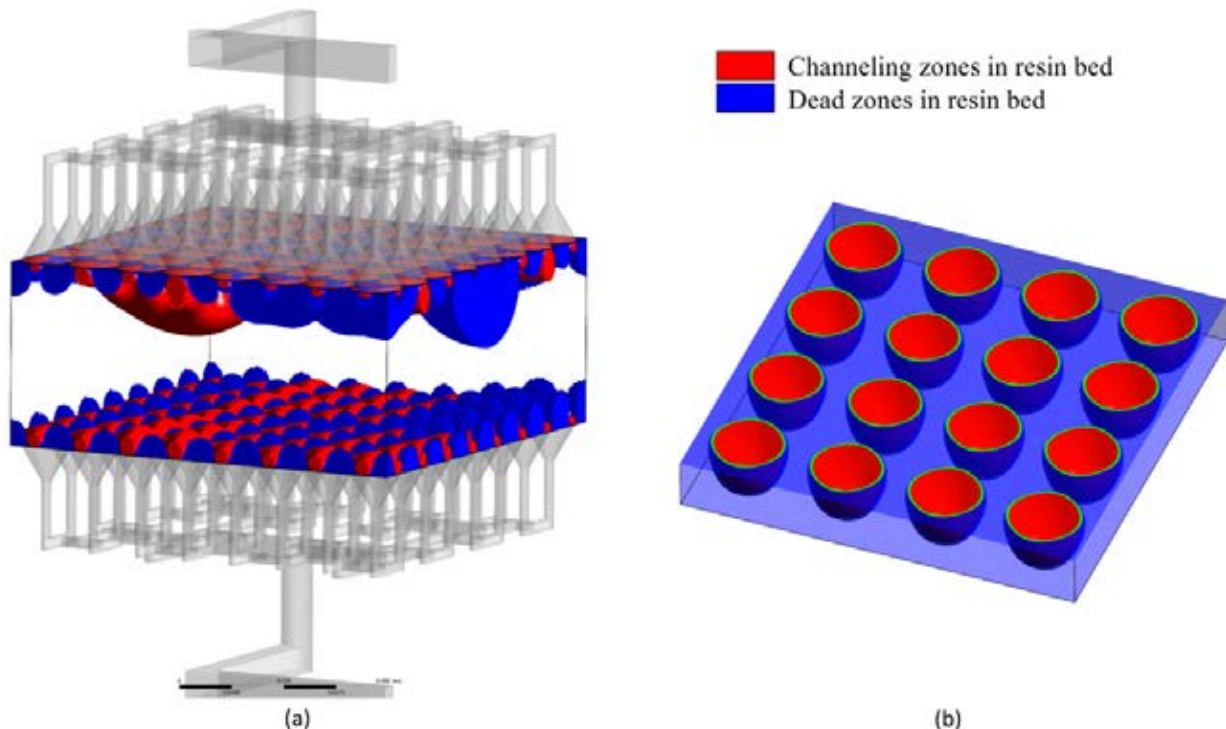


**Figure 7** Locations of the malfunctioning zones in (a) the 1st and (b) the 2nd ion exchangers.

much lower velocities than the superficial velocity. In the dead space, the fluid elements have prolonged residence time due to their low velocities. Herein, the dead space is defined as the region where the velocity magnitude of the process stream is 2.5% below the superficial velocity. In contrast, “channelling” refers to the phenomenon that fluid passes through bed prematurely with a much shorter residence time. A zone with the fluid velocity that is 2.5% over the superficial one is defined as “channelling”

zones. In order to quantify the malfunctioning operations, the volumetric percentages of the dead space and channelling zones were estimated based on the modelling results. For example, the percentage of the dead space is defined as:

$$\text{Dead space percent} = \frac{\text{volume of the dead space}}{\text{total volume of the resin bed}}$$

A universal index, “degree of heterogeneity”, was used to evaluate the operation of the resin bed. The degree of heterogeneity is defined as the sum of dead space percentage and channelling zone percentage.

Figure 7 plots the corresponding locations of the dead space and channelling zones in the resin beds of the 1st and 2nd ion exchanger, respectively. The dead space is marked in blue while the channelling zone is in red. As discussed previously, the fractal distributor of the 1st ion exchanger provides efficient initial distribution. The velocity profile reaches plug flow within 15 mm of bed depth. Because of efficient initial distribution, the majority of the resin bed in the 1st ion exchanger shows normal operation as indicated in Figure 7(a). The malfunctioning zones appear only in the vicinity of the top and bottom surface of the resin bed where the flow has expansions and contractions due to the existence of the fractal distributor and collector. As shown in Table 1, the dead space takes 6.28% of the resin bed, and the channelling zones is 16.14%. The total degree of heterogeneity of the resin bed is 22.42%, indicating that the majority of the resin bed has uniform velocity distribution thus good operation.

In contrast, the resin bed in the 2nd ion exchanger has malfunctioning operations. As shown in Figure 7(b), the process streams leave the fractal distributor and travel through the resin bed with a high velocity. As a result, those regions in their flow track forms the channelling zone. According to Figure 7(b) and Table 1, the channelling zones spread from the fractal distributor to the fractal collector, taking up 22.97% of the resin bed. In contrast, a majority of the resin bed is dead space, taking up about 68.14% of the resin bed. The total degree of heterogeneity is 91.11%, suggesting that the entire bed is in malfunctioning.

Table 1 Summary of the malfunctioning zones

	Dead Space percentage	Channeling zone percentage	Degree of heterogeneity
1st Ion exchanger	6.28%	16.14%	22.42%
2nd Ion exchanger	68.14%	22.97%	91.11%

**PRESSURE DROPS OF THE TWO ION EXCHANGERS**

The pressure drop across the ion exchanger is an important parameter as it determines the required pressure head and subsequently operating cost. The

Pressure drop	Across the resin bed (Pa)	Across the entire ion exchanger (Pa)	Percentage of resin bed
1st Ion exchanger	$8.1 \times 10^3$	$1.6 \times 10^4$	51%
2nd Ion exchanger	$9.9 \times 10^3$	$9.7 \times 10^4$	10%

modelling results indicate that the design of the fractal distributor impacts not only the velocity profiles in the resin bed but also the pressure drop across the ion exchanger. When the ion exchangers are operated with a

flow rate of  $2.52 \times 10^{-4}$  m/s, the corresponding pressure drops across the fractal distributor and the resin bed are summarized in Table 2.

Table 2 Summary of the pressure drops across the ion exchangers

When these two ion exchangers were operated with same flow rate, the total pressure drop of the 1st one is only about 16% of the 2nd one. The pressure drops across the resin beds of these two ion exchangers are close to each other, and that of the 2nd ion exchanger is slightly higher due to the channelling zones and dead space. The modelling results suggest that the significant pressure drop in the 2nd ion exchanger is resulted from the sudden expansion and contraction of the process streams.

Figure 8 plots the pressure distributions inside the outlets of the fractal distributors in the 1st and 2nd ion exchangers. The fractal distributor equipped by the 1st ion-exchanger has a cone-shape expansion in its outlet. Such design provides a smooth expansion to the fluid; as a result, the corresponding pressure drop in the outlet is only about 270 Pa. In contrast, the outlets of the fractal distributor in the 2nd ion exchanger is designed with straight channels. Leaving the outlet, the process stream has a steep expansion. Such a steep expansion results in a significant pressure loss. The pressure drop of the outlet is about  $3.7 \times 10^4$  Pa, which is almost two orders of magnitude higher than that of the 1st fractal distributor. The resin beads closed to outlets may be washed away in the real world. Although this phenomena cannot be captured in our lumped model, the steep expansion may still have significant impact on system pressure drop.

Based on the modelling results, one may conclude that the steep expansion of the streams leads to excessive pressure drop. As illustrated in Figure 1, the outlet designs in most of conventional distributors are similar to that of the 2nd fractal distributor. These conventional distributors inevitably result in large pressure drops. The modification of outlet design can reduce the pressure drop and subsequently saves the operating cost.

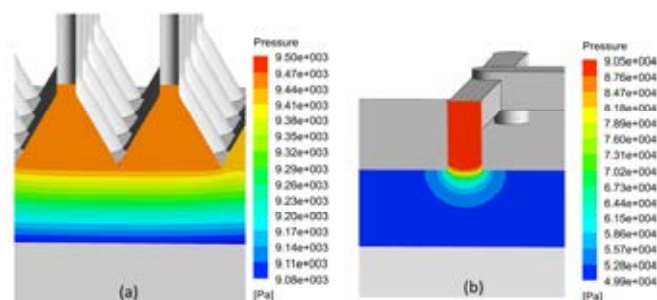


Figure 8 Pressure distributions in the outlets of (a) the fractal distributor of the 1st ion exchanger and (b) the fractal distributor of the 2nd ion exchanger.

**COMPARISON OF THE RTDS OF THE TWO ION EXCHANGERS**

According to the previous sections, the design of a fractal distributor determines the velocity profiles inside the resin bed. Due to the low outlet density of the 2nd fractal distributor, the velocity profile inside the resin bed of the 2nd ion exchanger is not uniform. A majority of the resin bed has dead space and channeling zones. In

order to understand the effect of outlet density on the residence time distribution (RTD) of process streams, RTD analyses were carried out with the two ion exchangers. The flow rate of the process stream was set as  $6.31 \times 10^{-5} \text{ m}^3/\text{s}$ , and the resultant RTD curves are shown in Figure 9.

As discussed earlier, the fractal distributor in the 2nd ion exchanger cannot distribute the incoming process stream uniformly due to its low outlet density. The corresponding RTD curve confirms the existence of the channelling zone and the dead space. The mean residence time,  $t_m$ , of the 2nd ion exchanger, which is 24.1 s, is smaller than that of the 1st ion exchanger. The smaller  $t_m$  suggesting that a significant amount of tracer leaves the resin bed through the shortcut of channelling zones, which is generally known as “channelling” phenomenon. On the other hand, the curve has a long tail, suggesting that the corresponding the rest tracer elements have prolonged residence time due to the dead space. The dimensionless second moment,  $\tau$ , which is defined as

$$\tau = \frac{\text{second moment } (\sigma^2)}{t_m^2}$$

evaluates the overall dispersion in RTD response. From the table in Figure 9, the 2nd ion exchanger has a larger  $\tau$  than the 1st ion exchanger, indicating that the tracer is widely spread when it passes through the 2nd ion exchanger.

In comparison, the RTD curve corresponding to the 1st ion exchanger is close to that of a plug flow. The shape is close to symmetric response and has less dispersion. Such shape is consistent with the velocity profiles shown in Figures 5 and 6. As the velocity profiles become plug shape within a short distance, the tracer travels through the resin bed with fairly uniform residence time.

Based on Figure 9, one may conclude that the outlet density of a fractal distributor plays a key role in determining the performance of the downstream resin bed. Conventional pressure-based distributors are similar to the fractal distributor of the 2nd ion exchanger, which generally have low outlet densities. The low outlet density undermines the overall performance of the resin bed. In comparison, fractal distributors can achieve large outlet density easily because of the inherent scaling symmetry. Since they provide uniform distributions, the fractal distributors can ensure high efficiencies of resin beds with reduced dead space and narrower residence time distribution.

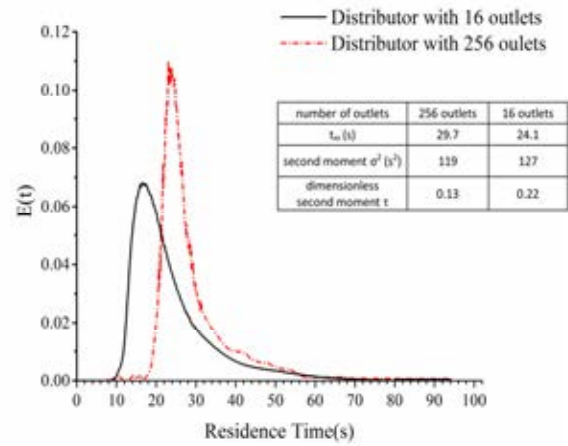


**Figure 9** RTD curves of the 1st and 2nd ion exchangers operated with an incoming flow rate of  $6.31 \times 10^{-5} \text{ m}^3/\text{s}$ . The embedded table lists the mean residence time and second moments.

### FRACTAL DISTRIBUTOR GEOMETRY FLOW UNIFORMITY OPTIMIZATION

CFD can assist in avoiding ad-hoc design decision on dimensions and systematically explore the design space for optimum design decisions.

In this section, the hydrodynamics of fractal distributor has been discussed. For simplification purpose, CFD fluid domain contains only main branches of previous fractal distributor geometry where the degree of preferential flow is higher. The modelling setup is very similar to the previous setup but zero pressure outlet boundary condition. Figure 10(a) show case the velocity vector distribution inside the original configuration at 3 GPM.

Parametric study has been performed with different scaling of width and depth based on previous configuration. For example,  $0.625 \cdot d$  means all channel depth is 0.625 of previous design. With a total of 25 different configurations automatic generated from ANSYS WORKBENCH, we collected the coefficient of variation of flow rate at all outlets for each case. The response surface was plotted in Figure 10(b). From the result, we can conclude that 1) with channel depth fixed, decreasing channel width may improve flow uniformity. 2) with channel width fixed, increasing channel depth generally can increase the performance but there may be some optimized depth to width ratio. 3) Since there is no back pressure at outlet, the Coefficient of Variation (CV) may overestimated in this setup. With addition of resin bed, CV values may drop significantly. However, the relative relationship of width and depth ratio to CV may still hold and the response surface offers a useful guide line for design of fractal distributor. 4) 1.265 as channel depth to width ratio (aspect ratio) is recommended for high flow distribution performance.

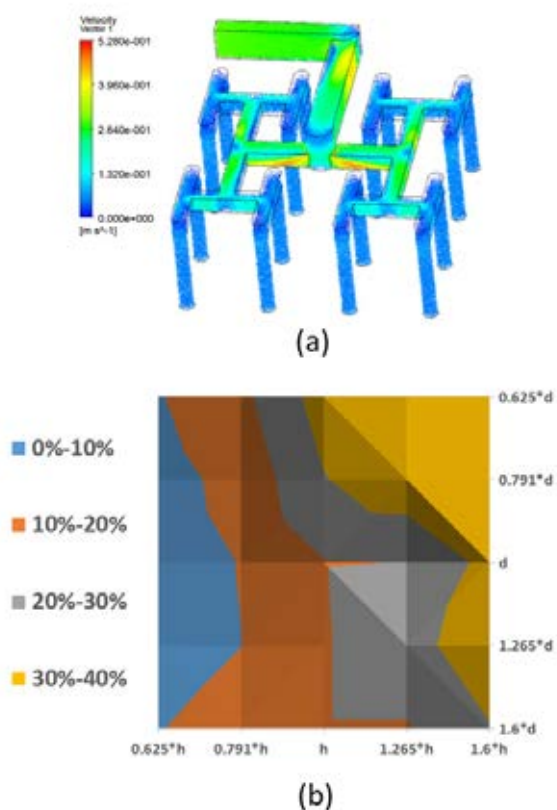


**Figure 10** (a) velocity vector plot for flow rate at 3 GPM. (b) Response surface of coefficient of variation based on the flow rate at each outlet at 3 GPM.

## Conclusion

In this work, a novel filter press-based ion exchanger equipped with a fractal distributor and a fractal collector was fabricated using PMMA. Two ion exchanger configurations, of which the 1st one includes a fractal distributor of 256 outlets and the 2nd one with a fractal distributor of 16 outlets, respectively, were investigated by CFD simulations and experiments including residence time distribution (RTD) analysis and dye visualization experiments.

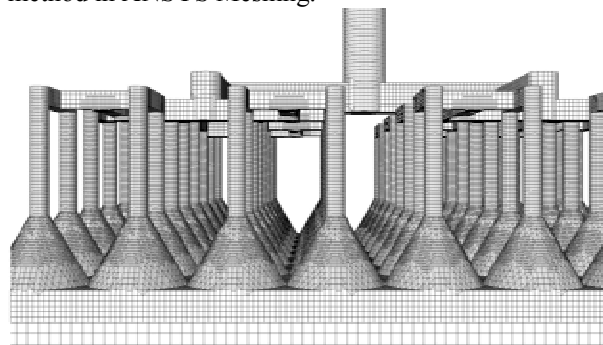
The results indicate that the outlet density of a fractal distributor plays a key role in determining the overall performance of an ion exchanger. When the fractal distributor has a high outlet density, the process stream reaches a uniform velocity profile similar to a plug flow with a short depth inside the resin bed. As a result, the process stream has a uniform residence time distribution in the ion exchanger. In contrast, the insufficient outlet density leads to large velocity variations in the process stream. Consequently, from CFD investigations, a majority of the resin bed shows malfunctioning operations including dead space and channelling. Due to the non-uniform distribution, the process stream passes through the resin bed with a broad RTD which

undermines the overall performance of the ion exchanger. From the response surface with channel width and depth scale as input parameter, we found out that 1.265 as channel aspect ratio may result in high quality of flow distribution. CFD can assist in avoiding ad-hoc design decision on dimensions and systematically explore the design space for optimum design decisions.

This study may enhance the understanding of fractal distributors and may benefit the process intensification using fractal distributors.

## APPENDIX A

A snapshot of the mesh with 2.7 million elements for 1st ion exchanger. The mesh was generated with Cutcell method in ANSYS Meshing.

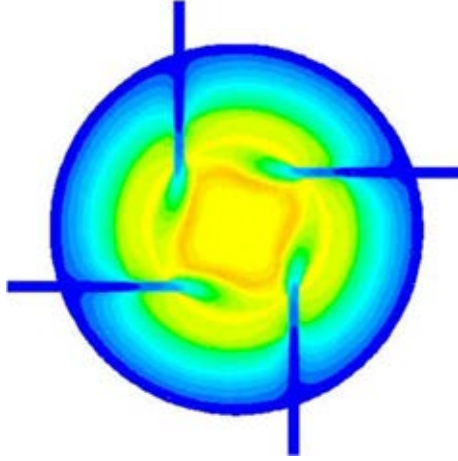


## REFERENCES

- INGLEZAKIS, V.J., POULOPOULOS, S.G., 2006. 3 - Heterogeneous Processes and Reactor Analysis, in: Inglezakis, V.J., Pouloupoulos, S.G. (Eds.), Adsorption, Ion Exchange and Catalysis. Elsevier, Amsterdam, pp. 57-242.
- KEARNEY, M.M., MUMM, M.W., PETERSEN, K.R., VERVLOET, T., (1994), "Fluid transfer system with uniform fluid distributor", US Patent. The Amalgamated Sugar Company, Ogden, Utah, U.S.
- KOCHERGIN, V., KEARNEY, M., (2006), "Existing biorefinery operations that benefit from fractal-based process intensification", *Applied Biochemistry and Biotechnology*, **130**, 349-360.
- LIU, H., LIANG, X., YANG, L., CHEN, J., (2010), "Challenges and innovations in green process intensification", *Science China Chemistry*, **53**, 1470-1475.
- MANDELBROT, B., 1982. The fractal geometry of nature. W.H. Freeman.
- T.-H. SHIH, W. W. LIOU, A. SHABBIR, Z. YANG, ZHU, J., (1995), "A New Eddy-Viscosity Model for High Reynolds Number Turbulent Flows - Model Development and Validation", *Computers Fluids*, **24**, 227-238.



# COMBUSTION







# CFD MODELING OF A COMMERCIAL-SIZE CIRCLE-DRAFT BIOMASS GASIFIER

Hui LIU<sup>1</sup>, Robert J. CATTOLICA<sup>1\*</sup>, Reinhard SEISER<sup>1</sup>  
Chang-hsien LIAO<sup>2</sup> and Matthew SUMMERS<sup>2</sup>

<sup>1</sup>University of California, San Diego, 9500 Gilman Drive, La Jolla, CA 92093, USA

<sup>2</sup>West Biofuels, 14958 County Road 100B, Woodland, CA 95776, USA

\*Corresponding Author, E-mail: rjcat@ucsd.edu

## ABSTRACT

This work was focused on a commercial-size (2MWth.) circle-draft biomass gasifier. In this work a three-dimensional transient CFD (computational fluid dynamics) model was established to simulate the circle-draft biomass gasifier. The MP-PIC (multiphase particle-in-cell) method was applied to simulate multiphase reactive flows in the gasifier. In the MP-PIC method, the Navier-Stokes equation coupled with the large-eddy simulation (LES) was applied to describe the gas phase. The particulate phase was described in a Lagrangian way by computing the trajectories of parcels of particles solving Newtonian equations of motion for each parcel. The mass and energy transport equations were coupled with the momentum equation to simulate mass and energy transfer in the circle-draft gasifier. The heterogeneous solid-gas and homogeneous gas-phase reaction kinetics were integrated with the transport equations to simulate biomass drying, gasification, combustion, and other gas-phase reactions. The simulation results were compared with experimental data to validate the CFD model. The CFD model predicted gas species distribution, reaction zone temperatures, and producer gas composition in the circle-draft biomass gasifier.

## NOMENCLATURE

### Greek Symbols

$\alpha$	volume fraction
$\rho$	density
$\tau$	stress tensor

### Latin Symbols

$A_p$	particle surface area
$C_d$	drag model coefficient
$C_v$	specific heat capacity
$C_{p,n}$	solid species $n$ concentration
$D$	drag function
$f$	particle size distribution function
$F$	drag force
$g$	standard gravity
$k_d$	solid thermal conductivity
$m_p$	particle mass

$M_{w,p,n}$	molecular weight of solid species $n$
$Nu$	Nusselt number
$u$	velocity
$p$	pressure
$P_s$	model constant
$T$	temperature
$V$	computational cell volume

### Subscripts

$cp$	close pack condition
$g$	gas phase
$n$	solid species
$lam$	laminar flows
$t$	turbulence

## INTRODUCTION

Fossil fuels are still the primary energy sources in the world. Since natural resources are limited, finding alternative energy sources becomes necessary. Biomass is abundantly available in the nature and can be an alternative to fossil fuels. Additionally, biomass is a renewable energy source. Utilizing bio-energy from biomass doesn't increase CO<sub>2</sub> emission, which is beneficial to environmental protection (Huang, Wu, Wu and Gao 2017). Bio-energy can be released through thermal chemical processes such as biomass pyrolysis, gasification, and combustion. Among them, biomass gasification is a promising technology. During the process, biomass is utilized to generate syngas, which can be further applied to generate chemicals and electricity (Ismail and El-Salam 2017).

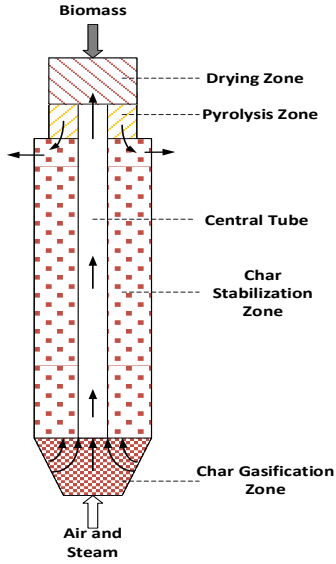


Figure 1: A circle-draft (2MWth.) biomass gasifier  
 In this work a circle-draft biomass gasifier was studied. As shown in Figure 1, biomass is fed at the top while air and steam are fed at the bottom of the gasifier. After biomass is fed to the gasifier, it is dried in the drying zone and then falls down to the pyrolysis zone where biomass is decomposed into char and volatile gases. Char particles continue to fall down and go through the stabilization zone to reach the char gasification zone where char reacts with air and steam to generate syngas. The generated syngas penetrates through the solid bed and flows upwards through a central tube to reach the upper pyrolysis zone. Biomass is heated in the pyrolysis zone while the hot syngas is flowing through the zone. Finally, the syngas is extracted through 4 outlets at the side of the gasifier.

In this work a three-dimensional CFD (computational fluid dynamics) model was developed to simulate the circle-draft biomass gasifier. In this model the MP-PIC (Multiphase Particle-In-Cell) method was applied to simulate gas-solid flows in the circle-draft biomass gasifier. The heterogeneous and homogeneous reaction kinetics were integrated with the momentum, mass, and energy transport equations to predict producer gas distribution and reactor temperature profile in the circle-draft biomass gasifier.

## MODEL DESCRIPTION

The MP-PIC method is an Eulerian-Lagrangian method. This model was built in Barracuda VR (virtual reactor). In the software, the Navier-Stokes equation was coupled with LES to simulate the gas phase. The particulate phase is calculated with the particle acceleration equation (O'Rourke and Snider 2014), based on Newton's motion law for each particle parcel. The momentum transport equation was coupled with the mass and energy transport equations to simulate mass and energy transfer in the circle-draft biomass gasifier. The calculation of thermal radiation in the MP-PIC method was based on Stefan-

Boltzmann law. The finite volume method was applied to solve the discretized governing equations.

## Governing Equations

The continuity and momentum equations for the gas phase are shown as follows:

$$\frac{\partial(\alpha_g \rho_g)}{\partial t} + \nabla \cdot (\alpha_g \rho_g u_g) = \delta m_p \quad (1)$$

$$\frac{\partial(\alpha_g \rho_g u_g)}{\partial t} + \nabla \cdot (\alpha_g \rho_g u_g u_g) = -\nabla p - F + \alpha_g \rho_g g + \nabla \cdot \tau \quad (2)$$

$$\tau = \mu \left( \frac{\partial u_{g,i}}{\partial x_j} + \frac{\partial u_{g,j}}{\partial x_i} \right) - \frac{2}{3} \mu \delta_{ij} \frac{\partial u_k}{\partial x_k} \quad (3)$$

$$\mu = \mu_{lam} + \mu_{eddy} \quad (4)$$

$\mu_{eddy}$  is calculated by the sub-grid scale (SGS) model (Smagorinsky 1963) as shown below:

$$\mu_t = \frac{1}{2} C \rho_g \Delta^2 \sqrt{\left( \frac{\partial u_{g,i}}{\partial x_j} + \frac{\partial u_{g,j}}{\partial x_i} \right)^2} \quad (5)$$

$$\Delta = \sqrt[3]{V} \quad (6)$$

$C$  is a model constant of 0.01. The particle acceleration equation is applied to calculate the particle velocity as follows (O'Rourke and Snider 2010):

$$\frac{du_p}{dt} = D_p (u_g - u_p) - \frac{\nabla p}{\rho_p} - \frac{\nabla \tau_p}{\rho_p \alpha_p} + g + \frac{\bar{u}_p - u_p}{2\tau_D} \quad (7)$$

The solid stress tensor,  $\tau_D$ , is modeled by the following equation:

$$\tau_p = \frac{10 P_s \alpha_p^\beta}{\max\{(\alpha_{cp} - \alpha_p), \varepsilon(1 - \alpha_p)\}} \quad (8)$$

$\alpha_{cp}$  is the close-pack volume fraction of the particulate phase. In this work it was set as 0.42, based on experimental data. The solid volume fraction,  $\alpha_p$ , is calculated as follows:

$$\alpha_p = \iiint f \frac{m_p}{\rho_p} dm_p du_p dT_p \quad (9)$$

The interphase momentum exchange between the gas and particle phase is given by:

$$F = \iiint f \left\{ m_p \left[ D(u_g - u_p) - \frac{\nabla p}{\rho_p} \right] + u_p \frac{dm_p}{dt} \right\} dm_p du_p dT_p \quad (10)$$

The drag function of  $D$  is described as follows (Gidaspow 1994):

$$D_{p1} = \frac{6}{8} C_d \frac{\rho_g |u_g - u_p|}{\rho_p d_p} \quad (11)$$

$$C_d = \begin{cases} \frac{24\alpha_g^{-2.65}}{Re}, Re < 0.5 \\ \frac{24\alpha_g^{-2.65}}{Re} (1 + 0.15Re^{0.687}), 0.5 \leq Re \leq 1000 \\ 0.44\alpha_g^{-2.65}, Re > 1000 \end{cases} \quad (12)$$

$$D_{p2} = 0.5 \left( \frac{180\alpha_p}{\alpha_g Re} + 2 \right) \frac{2\rho_g |u_g - u_p|}{d_p \rho_p} \quad (13)$$

$$D_p = \begin{cases} D_{p1} & \alpha_p < 0.75\alpha_{cp} \\ (D_{p2} - D_{p1}) \left( \frac{\alpha_p - 0.75\alpha_{cp}}{0.1\alpha_{cp}} \right) + D_{p1} & 0.85\alpha_{cp} \geq \alpha_p \geq 0.75\alpha_{cp} \\ D_{p2} & \alpha_p > 0.85\alpha_{cp} \end{cases} \quad (14)$$

The mass and energy transport equations for the particulate phase are (Snider, Clark and O'Rourke 2011):

$$\delta m_p = - \iiint f \frac{dm_p}{dt} dm_p du_p dT_p \quad (15)$$

$$\frac{dm_p}{dt} = \sum_{i=1}^N \frac{dm_{p,n}}{dt} \quad (16)$$

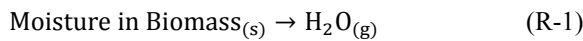
$$\frac{dm_{p,n}}{dt} = \frac{\alpha_g M_{w_{p,n}}}{\rho_p \alpha_p} m_p \frac{dc_{p,n}}{dt} \quad (17)$$

$$C_V \frac{dT_p}{dt} = \frac{1}{m_p} \frac{k_d Nu}{d_p} A_p (T_g - T_p) \quad (18)$$

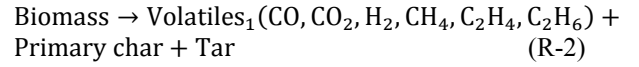
## Reaction Kinetics

In the circle-draft gasifier, biomass is fed at the top and then drops into the drying zone where moisture is released from biomass. Dry biomass continues to fall into the pyrolysis zone. Volatiles are released and char is generated from biomass pyrolysis. Char particles pass through the stabilization zone and reach gasification zone. Char particles react with air and steam injected from the bottom to generate syngas. The residual char and ash fall down into the bottom region where are removed from the gasifier with an ash auger. In this model heterogeneous reactions including biomass drying, pyrolysis, partial combustion of primary char, char and CO<sub>2</sub> reaction, char and steam reaction, and methane formation are included. The homogeneous reactions such as water gas shift reaction and gas oxidation reactions are also considered in this model.

Heterogeneous reactions (Walker Jr, Rusinko Jr and Austin 1959, Yu, et al. 2011, Xu and Qiao 2012):

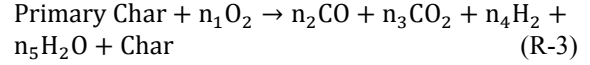


$$r_1 = 5.13 \times 10^{10} \exp\left(\frac{-10585}{T_p}\right) m_{\text{biomass}}$$



$$r_2 = 1.49 \times 10^5 \exp\left(\frac{-1340}{T_p}\right) m_{\text{biomass}}$$

The reaction rate of primary pyrolysis was calculated with a single-step global reaction mechanism (Yu, et al. 2011) and the pre-exponential factor of  $1.49 \times 10^5$  was selected to fit experimental data in this work.



$$r_3 = 8.68 \times 10^6 m_{\text{prim.char}} T_p \exp\left(\frac{-29160}{T_p}\right) [\text{O}_2]$$

The primary char generated in biomass pyrolysis was defined as CH<sub>1.286</sub>O<sub>0.4585</sub> according to experimental data. To simplify the model, char generated in the partial combustion of primary char is assumed to be pure carbon. Tar generated in biomass pyrolysis is defined as CH<sub>1.331</sub>O<sub>0.6979</sub> (Ingram, et al. 2008). The



$$r_{4f} = 1.272 m_c T_p \exp\left(\frac{-22645}{T_p}\right) [\text{CO}_2]$$

$$r_{4r} = 1.044 \times 10^{-4} m_c T_p^2 \exp\left(\frac{-2363}{T_p} - 20.92\right) [\text{CO}]^2$$



$$r_{5f} = 1.088 m_c T_p \exp\left(\frac{-22645}{T_p}\right) [\text{H}_2\text{O}]$$

$$r_{5r} = 1.044 \times 10^{-4} m_c T_p^2 \exp\left(\frac{-6319}{T_p} - 17.29\right) [\text{H}_2][\text{CO}]$$



$$r_6 = 1.18 \times 10^{-5} m_c T \exp\left(\frac{-17921}{T_p}\right) [\text{H}_2]$$

Homogeneous reactions (Padban and Becher 2005, Gómez-Barea and Leckner 2010, Lu and Wang 2013):



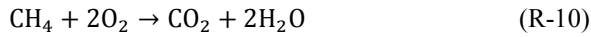
$$r_7 = 2.75 \exp\left(\frac{-10079}{T_g}\right) [\text{CO}][\text{H}_2\text{O}]$$



$$r_8 = 1.00 \times 10^{10} \exp\left(\frac{-15155}{T_g}\right) [\text{CO}][\text{O}_2]^2$$



$$r_9 = 2.2 \times 10^9 \exp\left(\frac{-13110}{T_g}\right) [\text{H}_2][\text{O}_2]^2$$



$$r_{10} = 2.8 \times 10^9 \exp\left(\frac{-24417}{T_g}\right) [\text{CH}_4][\text{O}_2]^2$$

### Simulation Setup

The CFD model was built in Barracuda Virtual Reactor<sup>®</sup> using the MP-PIC method to simulate a 2MWth circle-draft biomass gasifier at Woodland Biomass Research Center, Woodland, California, as shown in Figure 2. The height of the gasifier is 10.4 meters and the diameter of the gasifier is 1.7 meters.

The boundary settings of the circle-draft biomass gasifier are shown in Figure 3. Biomass feeding points are defined at the top, 4 gas outlets are set at the side, and steam & air injections are defined at the bottom of the gasifier.

A central tube is built in the center of the gasifier. Note that the structure of the central tube is in the shape of a rectangular box for simplicity, instead of the original cylindrical-tube shape. The total volume of the structure is still the same as that of the original central tube, which ensures that the predicted flow pattern in the gasifier is not dramatically affected by the shape change of the central tube. In the software of Barracuda VR<sup>®</sup>, geometries are meshed by orthogonal grids. For round-shaped geometries, more gridlines and cells are needed to capture necessary geometry details. In comparison, geometries with straight edges require less gridlines and computational cells. Therefore, in this work a rectangular-box channel is built to simplify the geometry to achieve better computation efficiency.

The ultimate analysis data of biomass used in experiments are shown in Table 1 and the model settings of base case are listed in Table 2. A normal distribution with a standard deviation of  $0.2d_p$  was applied to describe the size distribution of biomass particles. The thermal conductivity was set as 0.12 W/(mK) and the heat capacity of biomass was set as 1760 kJ/kgK.



Figure 2: A 2MWth circle-draft biomass gasifier

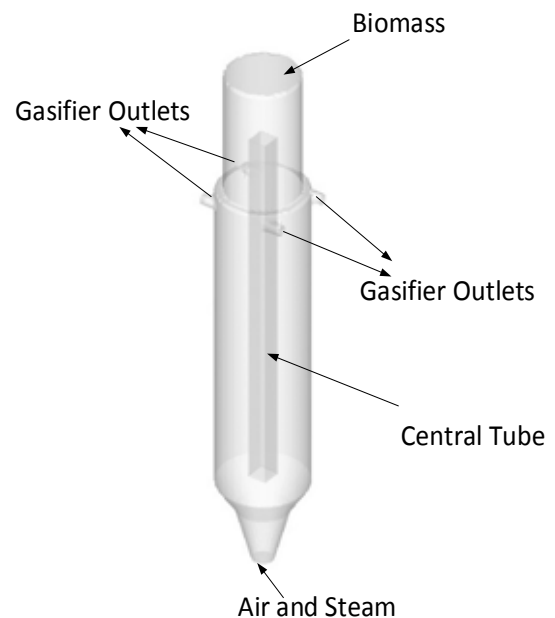


Figure 3: Boundary settings of the circle-draft gasifier

Table 1: Ultimate analysis of biomass feedstock

Elements	wt %
Moisture	17.23
C	43.16
H	5.06
O	33.26
N	0.10
Ash	1.19

Table 2: Base case settings

Description	Value
Biomass particle diameter (mm)	5.64
Biomass density (kg/m <sup>3</sup> )	662.85
Initial solid packing	0.42
Outlet pressure (atm, abs.)	1
Biomass feeding rate (kg/h)	101.42
Air feeding rate (kg/h)	77.44

The model was solved with the control volume method. A computational grid with 111,537 grid was applied for the CFD model. A grid resolution study was implemented by using three computational grids with 88,750, 111,537, and 168,175 cells. The difference of the simulation results between the three cases are less than 5%. Considering relative low computational cost and acceptable model accuracy, the grid with 111,537 cells was selected for the base case. The simulation time was set as 1000 seconds to reach the steady-state. The convergence criterions for volume, pressure, velocity, and energy were set as  $10^{-6}$ ,  $10^{-7}$ ,  $10^{-6}$ , and  $10^{-7}$ . The iteration numbers were set as 10, 2000, 50, and 100 for each transport equations, respectively. The size of time step is in the range of  $10^{-3}$  to  $10^{-5}$  seconds and is automatically controlled by the Courant-Friedrichs-Lewy (CFL) scheme (Courant, Friedrichs and Lewy 1967) to achieve a converged solution. The model was computed using the GPU-accelerated computing technology on a computer with an Intel® i7 CPU @3.50 GHz and a GeForce GTX TITAN graphics card. The 1000-s simulation took about 5 days to be completed.

## RESULTS

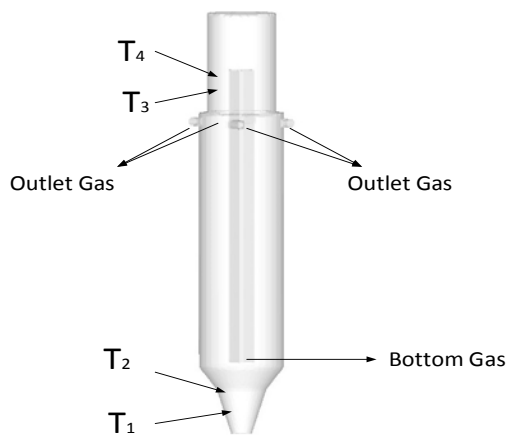


Figure 4: Temperature sensor and gas sampling locations

Figure 4 shows the locations of temperature sensors and producer gas sampling points. Considering the air and steam inlet as the bottom surface, the temperatures of T<sub>1</sub>, T<sub>2</sub>, T<sub>3</sub>, and T<sub>4</sub> were measured for char gasification and pyrolysis zones at the heights of 0.95, 1.44, 8.68, and 9.17 meters. Producer gas was sampled from the bottom entry point of the central tube and 4 gas outlets as the bottom

producer gas and the final producer gas output, respectively.

In Figure 5, the predicted producer gas composition in the bottom region is compared with experimental data. It is observed that the gas composition prediction in the bottom region is consistent with experiment measurement. The bottom producer gas in experiments was sampled at the bottom surface of the central tube in the circle-draft gasifier.

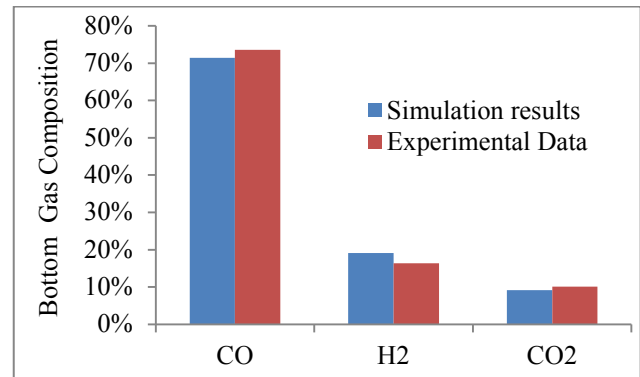


Figure 5: Comparison of bottom producer gas

The predicted outlet gas composition is also compared with experimental data. As seen in Figure 6, the difference between the simulation results and experimental data is averagely less than 3%.

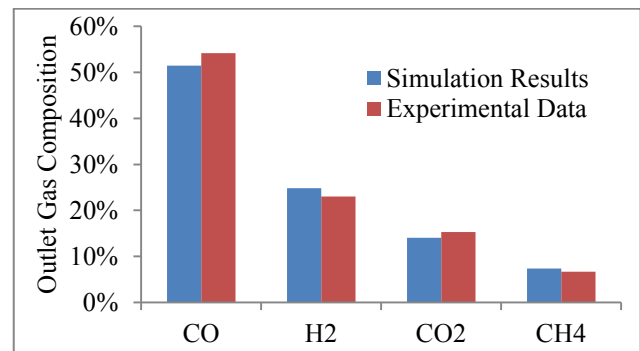


Figure 6: Comparison of outlet producer gas

Figure 7 demonstrates the comparison of the gasifier temperatures in biomass pyrolysis and char gasification zones. As seen in the figure, the temperature predictions agree well with temperature measurements.

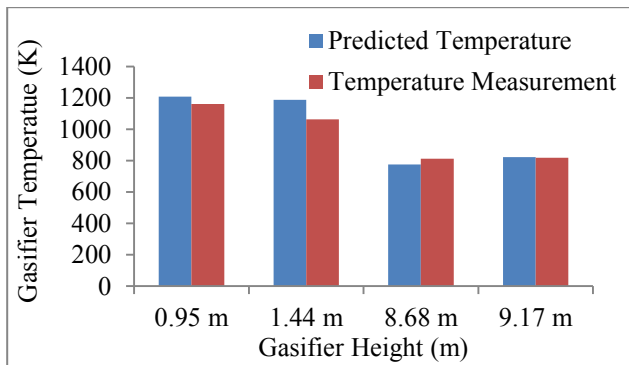


Figure 7: Comparison of gasifier temperature

Figure 8 demonstrates the transient distribution of CO molar fraction in the circle-draft gasifier. As shown in the figure, CO is generated in the bottom region due to gasification and then flows through the solid bed to reach the central tube. The gas rises through the central tube to the pyrolysis zone in the upper region of the gasifier, where more CO is generated from biomass pyrolysis. Two streams of CO from the bottom and upper regions merges and accumulates in the upper region of the gasifier. Meanwhile, the rest of CO generated in the bottom region gradually penetrates through the annular region surrounding the central tube and reaches the upper region. All of CO from the bottom and upper regions is eventually extracted from 4 gas outlets at the side of the gasifier.

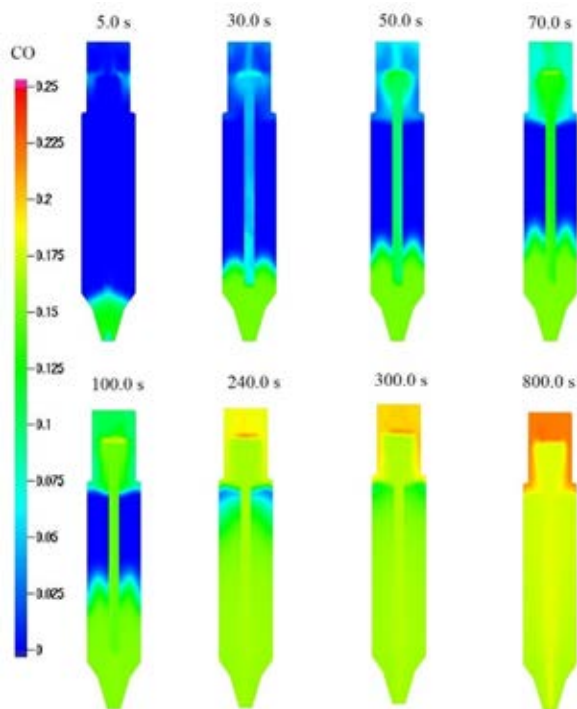


Figure 8: Transient CO distribution

Figure 9 shows transient tar distribution in the circle-draft gasifier. It is observed that tar is only generated in the pyrolysis zone which is in the upper region of the gasifier. Tar gradually accumulates in the region and finally leaves

the gasifier through the gas outlets. As predicted in the model, since tar is generated in the upper region and is extracted together with other gases from the gas outlets, tar concentration in the final gas output is expectedly high, which matches our observations in the experiment.

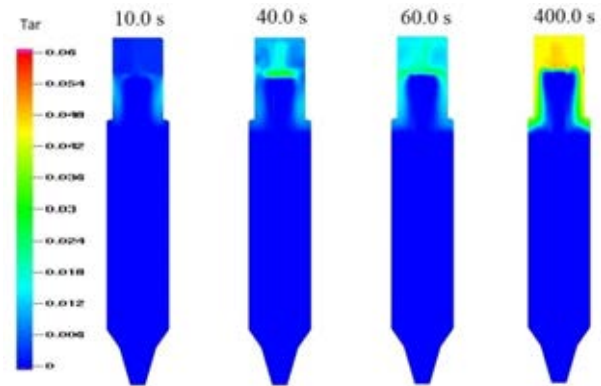


Figure 9: Transient tar distribution

The molar fractions of CO, H<sub>2</sub>, CO<sub>2</sub>, and Tar in the steady-state are shown in Figure 10. As seen in the figure, CO, H<sub>2</sub>, and CO<sub>2</sub> are generated in both of char gasification and biomass pyrolysis zones. CO and H<sub>2</sub> are concentrated in the central region, which is mainly due to producer gas production from water gas shift reaction. On the other hand, tar is only generated from the top region and is eventually extracted together with other gases through the gas outlets.

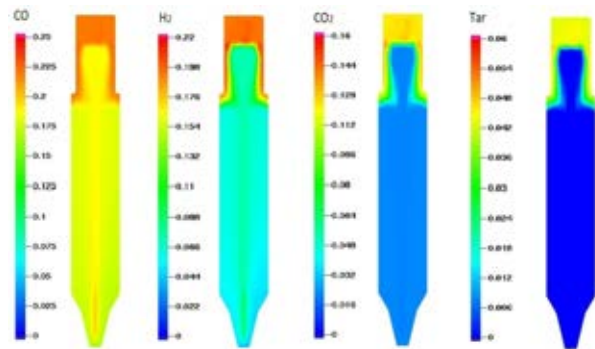


Figure 10: Steady-state producer gas composition

The temperature distribution in the circle-draft gasifier is shown in Figure 11. As indicated in the figure, the central region in the bottom region is hot due to partial combustion of char and the temperature in the upper region is lower due to biomass gasification.

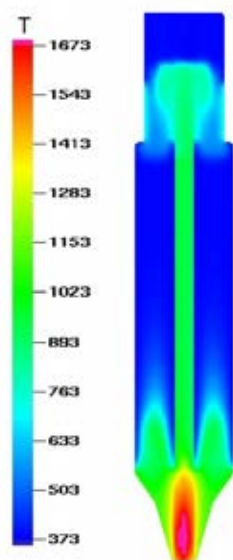


Figure 11: Temperature distribution of circle-draft biomass gasifier

## CONCLUSION

In this paper a transient three-dimensional CFD model was built to simulate a circle-draft biomass gasifier. The MP-PIC method was used to simulate gas-particle flows in the gasifier. The CFD model was applied to predict flow pattern, producer gas distribution, and reactor temperature profiles in the circle-draft biomass gasifier. The predicted gas composition and reactor temperatures were compared with experimental data and good agreement between the simulation results and experimental data was achieved.

## ACKNOWLEDGEMENT

The authors gratefully acknowledge the financial support from the California Energy Commission Grant (PIR-11-008) through West Biofuels. Additional support was provided by the University of California Discovery Pilot Research and Training Program (Award 211974).

## REFERENCES

Courant, R., Friedrichs, K., and Lewy, H. (1967), "On the Partial Difference Equations of Mathematical Physics," IBM Journal.

Gidaspow, D. (1994), "Multiphase Flow and Fluidization. Continuum and Kinetics Theory Description," Academic Press, Boston.

Gómez-Barea, A., and Leckner, B. (2010), "Modeling of Biomass Gasification in Fluidized Bed," *Progress in Energy and Combustion Science*, 36, 444-509.

Huang, S., Wu, S., Wu, Y., and Gao, J. (2017), "Structure Characteristics and Gasification Activity of Residual Carbon from Updraft Fixed-Bed Biomass Gasification

Ash," *Energy Conversion and Management*, 136, 108-118.

Ingram, L., et al. (2008), "Pyrolysis of Wood and Bark in an Auger Reactor: Physical Properties and Chemical Analysis of the Produced Bio-Oils," *Energy & Fuels*, 22, 614-625.

Ismail, T. M., and El-Salam, M. A. (2017), "Parametric Studies on Biomass Gasification Process on Updraft Gasifier High Temperature Air Gasification," *Applied Thermal Engineering*, 112, 1460-1473.

Lu, X., and Wang, T. (2013), "Water-Gas Shift Modeling in Coal Gasification in an Entrained-Flow Gasifier – Part 2: Gasification Application," *Fuel*, 108, 620-628.

O'Rourke, P. J., and Snider, D. M. (2014), "A New Blended Acceleration Model for the Particle Contact Forces Induced by an Interstitial Fluid in Dense Particle/Fluid Flows," *Powder Technology*, 256, 39-51.

O'Rourke, P. J., and Snider, D. M. (2010), "An Improved Collision Damping Time for Mp-Pic Calculations of Dense Particle Flows with Applications to Polydisperse Sedimenting Beds and Colliding Particle Jets," *Chemical Engineering Science*, 65, 6014-6028.

Padban, N., and Becher, V. (2005), "Clean Hydrogen-Rich Synthesis Gas," *CHRISGAS*, fuel from biomass.

Smagorinsky, J. (1963), "General Circulation Experiments with the Primitive Equations," *Monthly Weather Review*, 91, 99-164.

Snider, D. M., Clark, S. M., and O'Rourke, P. J. (2011), "Eulerian-Lagrangian Method for Three-Dimensional Thermal Reacting Flow with Application to Coal Gasifiers," *Chemical Engineering Science*, 66, 1285-1295.

Walker Jr, P. L., Rusinko Jr, F., and Austin, L. G. (1959), "Gas Reactions of Carbon," in *Advances in Catalysis* (Vol. Volume 11), eds. P. W. S. D.D. Eley and B. W. Paul, Academic Press, pp. 133-221.

Xu, J., and Qiao, L. (2012), "Mathematical Modeling of Coal Gasification Processes in a Well-Stirred Reactor: Effects of Devolatilization and Moisture Content," *Energy & Fuels*, 26, 5759-5768.

Yu, J., et al. (2011), "Biomass Pyrolysis in a Micro-Fluidized Bed Reactor: Characterization and Kinetics," *Chemical Engineering Journal*, 168, 839-847.





## NUMERICAL STUDY OF COAL PARTICLE GASIFICATION UP TO REYNOLDS NUMBERS OF 1000

Sebastian KRIEBITZSCH<sup>1\*</sup>, Andreas RICHTER<sup>1†</sup>

<sup>1</sup>CIC Virtuhcon, Institute of Energy Process Engineering and Chemical Engineering,  
 TU Bergakademie Freiberg, 09599 Freiberg, GERMANY

\* E-mail: sebastian.kriebitzsch@vtc.tu-freiberg.de

† E-mail: a.richter@vtc.tu-freiberg.de

### ABSTRACT

The influence of turbulent structures on the gasification of coal particles, in particular on the char consumption and surface temperature, is studied. Existing submodels for char gasification are mainly based on results for laminar flow only, therefore the capability of these models to predict gasification at higher particle Reynolds numbers is evaluated using the simulation results. Two representative scenarios were studied: the gasification of a 2 mm particle at atmospheric pressure in a O<sub>2</sub>/CO<sub>2</sub>/H<sub>2</sub>O atmosphere at 2006 K and the gasification of a 263 μm particle at 30 bar in a different O<sub>2</sub>/CO<sub>2</sub>/H<sub>2</sub>O atmosphere at 1480 K. The simulation conditions were based on data obtained from the simulations of two different entrained-flow gasifiers. ANSYS Fluent<sup>TM</sup> was used to solve the Navier-Stokes equations for the flow field coupled with energy and species conservation equations. The model for the reaction system incorporates six gaseous chemical species H<sub>2</sub>, O<sub>2</sub>, CO, CO<sub>2</sub>, H<sub>2</sub>O, N<sub>2</sub> and solid carbon. A semi-global reaction mechanism was applied for the homogeneous gas-phase reactions and the water gas reaction, the Boudouard reaction and the oxidation of carbon to carbon monoxide were considered as heterogeneous gas-solid reactions. In the present work it is shown how the reaction zone is modified due to the change in wake structure, the impact of the turbulent effects on the overall carbon conversion rate are discussed, and hints how to adjust existing submodels to correctly predict char conversion at high particle Reynolds numbers are given.

**Keywords:** CFD, gasification, turbulence, heterogeneous reactions.

### NOMENCLATURE

#### Greek Symbols

$\lambda_{ij}$  stoichiometric coefficient of species  $i$  in reaction  $j$ ,  $[-]$   
 $\theta$  empirical factor,  $[-]$   
 $\nu$  kinematic viscosity,  $[m^2/s]$

#### Latin Symbols

$c_i$  molar concentration of species  $i$ ,  $[kmol/m^3]$ .  
 $d_p$  particle diameter,  $[m]$ .  
 $k$  reaction rate constant, in SI units.  
 $k^\infty$  pre-exponential factor, in SI units.  
 $n$  exponent of power law kinetic rate equations,  $[-]$ .  
 $p_i$  partial pressure of species  $i$ ,  $[Pa]$ .  
 $p_{op}$  operating pressure,  $[Pa]$ .  
 $r$  molar reaction rate,  $[kmol/m^3s]$ .

$u$  magnitude of velocity,  $[m/s]$ .  
 $D_{eff}$  effective diffusion coefficient in a porous medium,  $[m^2/s]$ .  
 $E_a$  activation energy,  $[J/kmol]$ .  
 $K$  inhibition constant,  $[1/Pa]$ .  
 $R$  universal gas constant,  $[J/kmol\cdot K]$ .  
 $Re$  particle Reynolds number:  $Re = u_{in} \cdot d_p / \nu$ ,  $[-]$ .  
 $S_V$  Specific surface area per volume,  $[m^2/m^3]$ .  
 $X$  char conversion,  $[-]$ .  
 $Y$  mass fraction,  $[-]$ .

#### Sub/superscripts

$in$  at the inlet boundary

### INTRODUCTION

Due to the multiscale character of coal combustion and gasification processes, the use of sub-models describing particle-gas interaction is unavoidable, and the correct prediction of the burning rate and the particle temperature based on this sub-models is an essential part of successfully modeling of such reactors (Edge *et al.*, 2011; Schulze *et al.*, 2013; Richter *et al.*, 2016). An analysis of existing computational burnout sub-models reveals that e. g. the influence of particle velocity on carbon consumption and particle temperature is not well understood. Thus, particle-resolved numerical simulations of single burning particles can highlight different physical phenomena and correlations and therefore they can help to better understand the complex combustion physics. Examples for this approach are given in Refs. (Lee *et al.*, 1996; Higuera, 2008; Kestel *et al.*, 2012; Richter *et al.*, 2013, 2015; Wittig *et al.*, 2016).

To the authors best knowledge almost all single-particle studies published in literature considered laminar flow regimes only and most consider only one heterogeneous reaction i.e. Boudouard, watergas or carbon oxidation. In different technological applications much larger particle Reynolds numbers are possible and all three above mentioned reactions proceed in parallel. For that reason the char-particle burnout corresponding to turbulent flow up to particle Reynolds number equals 1000 in two different O<sub>2</sub>/CO<sub>2</sub>/H<sub>2</sub>O atmospheres is investigated. At these Reynolds numbers time periodicity and the planar symmetry of the vortex shedding are lost and the wake becomes turbulent (Jones and Clarke, 2008; Campregher *et al.*, 2009). The operating conditions, that means pressure, temperature and gas phase composition, are based

on data obtained from simulations of two different entrained-flow gasifiers.

## MODEL DESCRIPTION

The gasification is studied for a single spherical particle in embedded in a large domain as schematically shown in Figure 1. As the heterogeneous reaction time scales are much

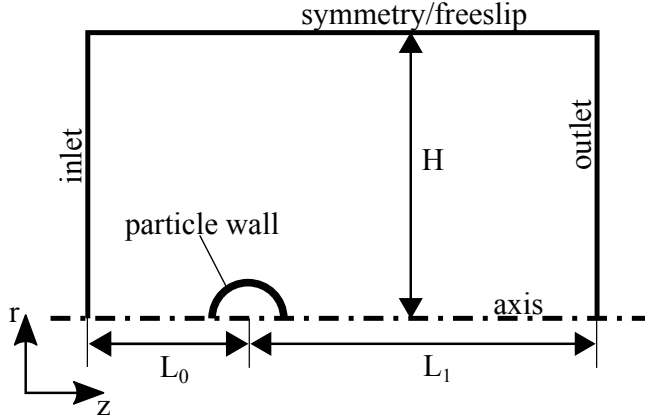
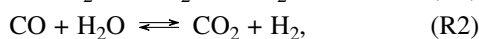
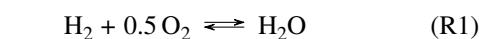


**Figure 1:** Schematic drawing of the 2D domain used in the simulations.

larger than the flow time scales (Sundaresan and Amundson, 1980; Richter *et al.*, 2013), the pseudo-steady state approach was assumed valid, hence no particle-shrinking was taken into account and the steady-state form of the governing equations are solved. Indeed this assumption is confirmed from the simulations results. The lowest value of the ratio of carbon consumption time scale and fluid time scale is found to be of the order  $O(10)$ , but in most of the cases it is higher. Fluid flow is modelled coupled with species and energy transport as well as coupled with heat conduction inside the solid particle. Buoyancy effects are neglected, hence gravity is set to zero but the density still varies due to e.g. changes in temperature. Turbulence is taken into account using the  $k$ - $\omega$ -SST model in the steady RANS simulations for particle Reynolds numbers larger than  $Re = 200$ . The Maxwell-Stefan equations are used to describe diffusional mass flux in the multi-component gas mixture and gas-gas radiation is included via the P1 radiation model. The heterogeneous reactions are assumed to take place on the outer particle surface only, however the internal structure of the char particle is considered through an effectiveness factor, which is defined in the next section. The gas phase is modelled as an incompressible ideal gas and all physical properties of the components are modelled using polynomial expressions or kinetic theory. The chemical system incorporates pure carbon as solid and  $H_2$ ,  $O_2$ ,  $H_2O$ ,  $CO$ , and  $CO_2$  as gaseous species. Details of the finite-rate chemical mechanism are discussed in the next section. The process and inlet condition for the two different cases studied in this work are shown in Table 1. Uniform profiles are prescribed for velocity, temperature and species concentrations at the inlet.

## Chemical reactions

The semi-global mechanism to describe the homogeneous gas phase reactions are modelled using a mechanism proposed by Jones and Lindstedt (1988):



	case	
	1	2
$d_P/m$	$2 \cdot 10^{-3}$	$0.263 \cdot 10^{-3}$
$P_{op}/bar$	1.013	30
$T_{in}/K$	2006	1480
$Re_{in}$	1 – 500	1 – 1000
$u_{in}/m/s$	0.1932 – 95.58	0.03192 – 31.92
$Y_{CO_2,in}$	0.223	0.223
$Y_{H_2O,in}$	0.123	0.221
$Y_{O_2,in}$	0.366	0.187

**Table 1:** Process and inlet conditions for both cases considered.

however with modified reaction rate kinetics for the hydrogen oxidation R1 as used by Kim *et al.* (2008). A simple power law is used to compute the reaction rates for R1

$$r_{R1} = k_{\infty} \cdot \exp\left\{-\frac{E_a}{R \cdot T}\right\} \cdot c_{O_2}^{0.5} \cdot c_{H_2} \quad (1)$$

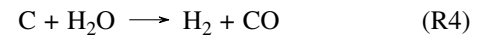
and for R2:

$$r_{R2} = k_{\infty} \cdot \exp\left\{-\frac{E_a}{R \cdot T}\right\} \cdot c_{CO} \cdot c_{H_2O}, \quad (2)$$

	$k_{\infty}$	$E_a/(J/kmol)$
R1	$5.69 \cdot 10^{11}$	$1.465 \cdot 10^8$
R2	$2.75 \cdot 10^9$	$8.368 \cdot 10^7$

**Table 2:** Kinetic constants for the gas phase reactions.

The Boudouard and water-gas reaction as well as the oxidation of the carbon are considered as heterogeneous reactions of the particles with the gas phase:



Different sets of kinetic rate equations are used for atmospheric conditions (case 1) and pressurized case (case 2). For the atmospheric conditions of case 1 the model for the effective reaction rates proposed by Vascellari *et al.* (2014) is used:

$$r_{R3,1} = \theta(X) \cdot k_{\infty} \cdot \exp\left\{-\frac{E_a}{R \cdot T}\right\} \cdot \frac{p_{CO_2}^n}{1 + K_{CO} \cdot p_{CO}}, \quad (3)$$

$$r_{R4,1} = \theta(X) \cdot k_{\infty} \cdot \exp\left\{-\frac{E_a}{R \cdot T}\right\} \cdot \frac{p_{H_2O}^n}{1 + K_{H_2} \cdot p_{H_2}}, \quad (4)$$

$$r_{R5,1} = \theta(X) \cdot k_{\infty} \cdot \exp\left\{-\frac{E_a}{R \cdot T}\right\} \cdot p_{O_2}^n, \quad (5)$$

The rate constants are taken from Richter *et al.* (2016) and are given in Table 3.

$\theta(X)$  is an empirical factor to account for the inner structure of the particle, which is calculated as described in Vascellari *et al.* (2014).

	$k_{\infty}/(kmol/(m^3sPa^n))$	$E_a/(J/kmol)$	n	$K/(1/Pa)$
R3	$9.04 \cdot 10^3$	$1.3063 \cdot 10^8$	0.76	$5,47 \cdot 10^{-6}$
R4	7.30	$1.0676 \cdot 10^8$	0.97	$3.19 \cdot 10^{-7}$
R5	$1.77 \cdot 10^4$	$1.771 \cdot 10^8$	1	

**Table 3:** Kinetic constants for the effective reaction rates of the boudouard, water gas and oxidation reactions from Richter *et al.* (2016).

At 30bar operating pressure (case 2), the intrinsic reaction rate data of Hla *et al.* (2007) is taken and modified with an effectiveness factor  $\eta_p$  to account for the transport resistances inside the particle. Hence the effective reaction rates are:

$$r_{R3,2} = \eta_{p,CO_2} \cdot S_V \cdot k_{\infty} \cdot \exp\left\{-\frac{E_a}{R \cdot T}\right\} \cdot p_{CO_2}^n, \quad (6)$$

$$r_{R4,2} = \eta_{p,H_2O} \cdot S_V \cdot k_{\infty} \cdot \exp\left\{-\frac{E_a}{R \cdot T}\right\} \cdot p_{H_2O}^n, \quad (7)$$

$$r_{R5,2} = \eta_{p,O_2} \cdot S_V \cdot k_{\infty} \cdot \exp\left\{-\frac{E_a}{R \cdot T}\right\} \cdot p_{O_2}^n, \quad (8)$$

The rate constants are given in Table 4.

	$k_{\infty}/(kmol/(m^2sPa^n))$	$E_a/(J/kmol)$	n
R3	$3.331 \cdot 10^{-2}$	$2.11 \cdot 10^8$	0.4
R4	2.485	$2.31 \cdot 10^8$	0.4
R5	$1.236 \cdot 10^{-3}$	$1.36 \cdot 10^8$	0.8

**Table 4:** Kinetic constants for the intrinsic reaction rates of the boudouard, water gas and oxidation reactions from Hla *et al.* (2007) for coal CRC272.

The effectivity for the species  $i$  and reaction  $j$  is estimated as

$$\eta_j(\Phi_{ij}) = \frac{1}{\Phi_{ij}} \left( \frac{1}{\tanh(3\Phi_{ij})} - \frac{1}{3\Phi_{ij}} \right), \quad (9)$$

using a generalized Thiele modules  $\Phi_{ij}$  which is (almost) independent of the particle shape. For a power-law kinetic reaction rate defined it is defined as:

$$\Phi_{ij} = \frac{V_P}{S_P} \sqrt{\frac{n+1}{2} \frac{\lambda_{ij} \cdot k_{\infty,j} \cdot \exp\left\{-\frac{E_{a,j}}{R \cdot T}\right\} \cdot S_V \cdot p_i^{n-1}}{D_{eff,i}}} \quad (10)$$

### Simulation settings

ANSYS Fluent™ V 17.2 was used to solve the Navier-Stokes equations coupled with species and energy transport. The pressure based solver was used and the differential equations were discretized using second order schemes in space and time. Only the convective fluxes were discretized with a third-order MUSCL scheme in the steady RANS simulations. For the 2D-axisymmetric simulations the domain extends  $L_0 = 30d_p$  in upstream,  $L_1 = 100d_p$  in downstream and  $H = 40d_p$  in radial direction. Based on the 2D results, the 3D-domain has been chosen slightly smaller. The cuboid extends  $L_0 = 8d_p$  in upstream,  $L_1 = 24d_p$  in downstream and  $H = 8d_p$  in the lateral directions. The number of grid cells used is 27,750 for the 2D simulations and 4,085,112 for the 3D simulations. Grid-independence has been confirmed in previous investigations by Richter *et al.* (2015, 2016). A comprehensive validation of the model setup against different experimental data is given in Richter *et al.* (2013).

## RESULTS

In order to reduce the computational effort, as the final aim of this research is to study gasification in high detail with three-dimensional transient LES simulations, a semi-global mechanism is used in this work. Hence for comparison simulations have been done with the detailed drmm22-mechanism proposed by Kazakov and Frenklach (1994). Results for the atmospheric case at  $Re = 500$  are shown in Figure 2 and for the pressurized case at  $Re = 1000$  in Figure 3. The general features of the flame structure are repro-

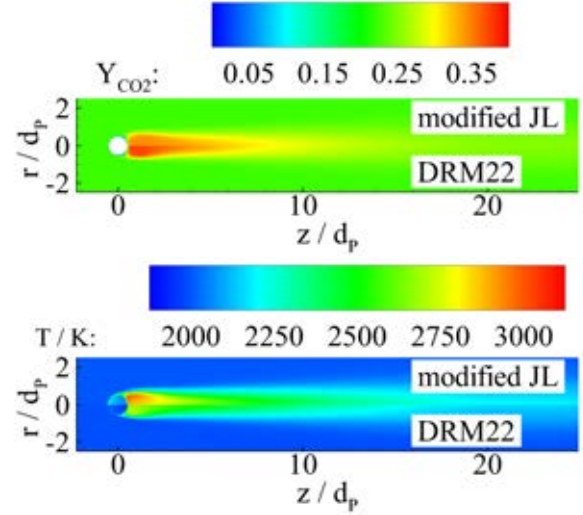


**Figure 2:** Contours of the mass fraction  $Y_{CO_2}$  and Temperature  $T$  at  $Re = 500$  for case 1. The upper half shows results obtained with the semi-global mechanism proposed by Kim *et al.* (2008), which is used in this work, and the lower half results obtained with the detailed chemical mechanism drmm22 by Kazakov and Frenklach (1994).

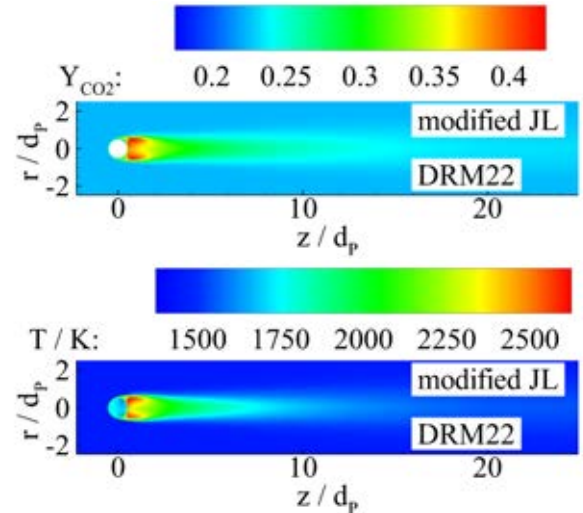


**Figure 3:** As in Figure 2, however for case 2 at  $Re = 1000$ .

duced with the semi-global mechanism, however some differences can be observed in particular in the contours shown for the atmospheric case 1. The maximum temperature is higher and the high temperature zone is more pronounced for the semi-global mechanism. The maximum  $CO_2$  mass fraction is larger when using the detailed mechanism, however the shape of the  $CO_2$ -rich zone is similar. The higher  $CO_2$  mass fraction can be explained by the simplified semi-global mechanism, which only considers the hydrogen oxi-

dition R1 and the water-gas shift reaction R2, whereas the detailed DRM22 mechanism also includes the oxidation of CO to CO<sub>2</sub>. Under the pressurized conditions of case 2 the differences in the results using the different mechanisms are less pronounced. Please note that the same gas phase mechanisms have been used in both cases, only the heterogeneous gas-surface reactions and the operating conditions are changed. The flame zone is slightly larger for the semi-global mechanism and the maximum temperature is slightly higher. Secondly the influence of turbulence on the gasifica-

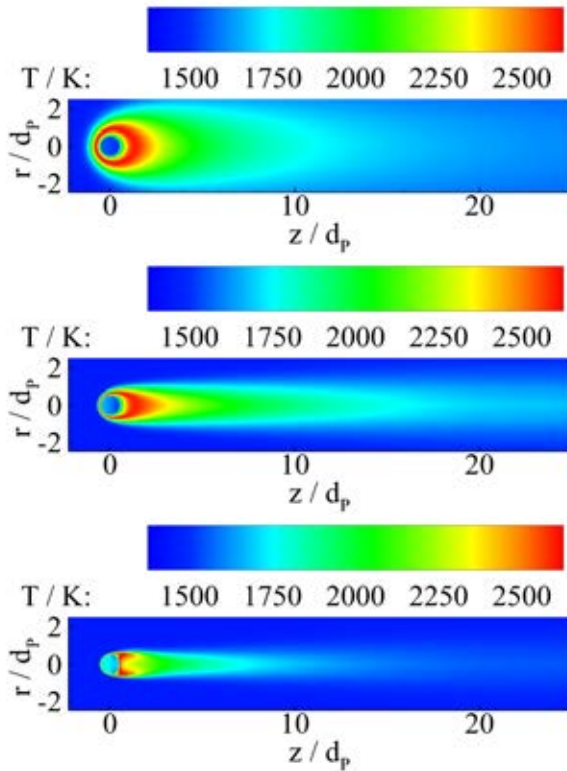


**Figure 4:** Contours of the temperature  $T$  for different particle Reynolds numbers. From top to bottom:  $Re = 10, 100, 1000$  for case 2.

tion is studied. A qualitative comparison is presented in Figure 4, which shows the contours of the temperature for case 2 at different particle Reynolds-numbers. A similar picture is obtained for the atmospheric pressure case 1. The maximum temperature remains almost constant, however the shape and size of the flame zone significantly change with increasing particle Reynolds number. Fully engulfing the particle at low particle Reynolds numbers, the flame zone is gradually thinning with particle Reynolds number accompanied by an increasing fore-aft asymmetry such that a separated reaction zone persists at higher particle Reynolds numbers.

Quantitative data are given in Figures 5 and 6, which show the average temperature on the particle surface and the average carbon mass flux for case 1 and for case 2, respectively. Results are presented for 2D-axisymmetric RANS simulations and for 3D RANS simulations at the highest particle Reynolds number. The differences between the 2D and the 3D results are small, which shows that the 2D axisymmetric assumption is justified. Initially the eddy dissipation concept (EDC) model for turbulence-chemistry interaction has been used for all simulations with  $Re > 200$ . However in the graphs of the average surface temperature and also the species mass fractions a sudden jump has been found in the results rather than a smooth transition, which is considered

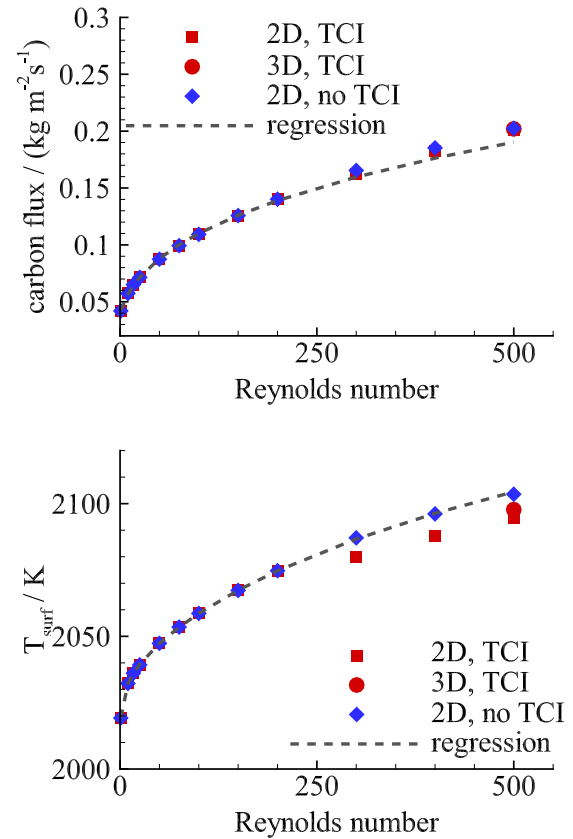


**Figure 5:** Carbon mass flux and temperature as a function of the particle Reynolds number for case 1. TCI denotes simulations using the eddy dissipation concept (EDC) to account for turbulence-chemistry interaction.

non-physical. The red squares in the graphs for the surface temperature of Figures 5 and 6 show these findings. As the EDC model has originally been developed for highly turbulent flows, this model is considered the main suspect for the observed non-physical behaviour. Hence simulations with exactly the same simulations have been done, only with the turbulence-chemistry model turned off. The results are shown by the blue symbols in Figures 5 and 6. The jump has disappeared and a continuous change of surface temperature with particle Reynolds number can be seen. The contours of CO<sub>2</sub> mass fraction and temperature shown in Figure 7 for case 2 at  $Re = 1000$  shed some lights on this question. Note that similar results are found for case 1 and for different particle Reynolds numbers. Qualitatively similar results are obtained for the simulations with and without turbulence-chemistry interaction turned on, only a higher temperatures and a higher CO<sub>2</sub> mass fraction are observed in the very thin flame zone close to the particle surface. However in this region the flow conditions are laminar and the grid is fine enough such that all scales are resolved. Hence the EDC model, which is based on the assumption of fully turbulent conditions, too strongly dampens the reactions which leads to the non-physical jump in the results. The carbon flux on the other hand is almost unaffected by the use of the EDC model and no clear jump is visible.

Finally, the dashed-lines in Figures 5 and 6 are a regression based on the laminar results, i.e. for  $Re \leq 200$ . One sees that the extrapolation of the laminar results to higher particle Reynolds number still give a reasonable prediction of the carbon consumption, the maximum difference is about 10%.

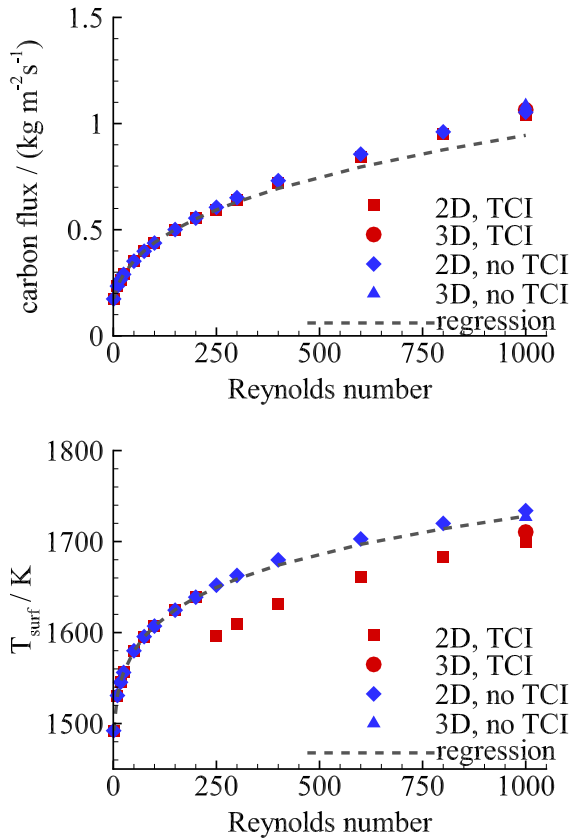


**Figure 6:** Carbon mass flux and temperature as a function of the particle Reynolds number for case 2. TCI denotes simulations using the eddy dissipation concept (EDC) to account for turbulence-chemistry interaction.

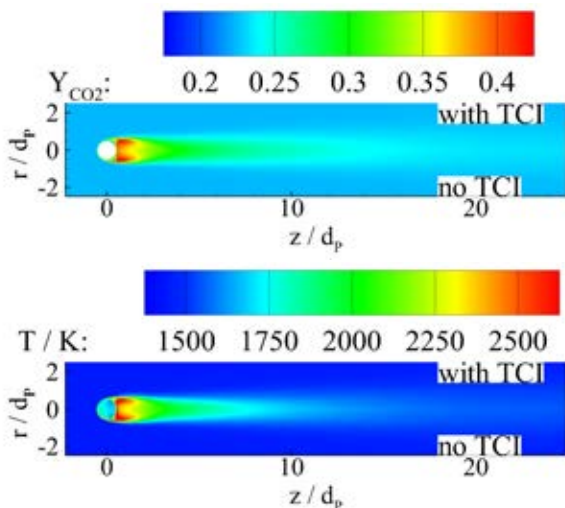


**Figure 7:** Influence of turbulence-chemistry interaction for case 2 at  $Re = 1000$ . The upper half shows results obtained using the EDC model for turbulent-chemistry interaction, which is turned off in the lower half

## CONCLUSIONS AND OUTLOOK

In this work the interplay between a turbulent chemically-reacting flow and heterogeneous gasification and combustion on a particle surface has been studied. It has been shown that the main features of the flame-zone are well captured using a simple semi-global gas phase mechanism and that the use of axisymmetric 2D simulations is justified. The use

of the EDC turbulence-chemistry interaction leads to a too strong damping of the gas phase reactions near the particles, which strongly affects the surface temperature and species distribution, however the total carbon consumption rate is only mildly influenced. The reaction zone is strongly modified due to the change in wake structure. From engulfing the whole particle at low particle Reynolds numbers, a increasing fore-aft asymmetry has been found which lead to a separated flame zone at high particle Reynolds numbers. Despite the strong changes in the shape of the reaction zone, extrapolation of the laminar results into the turbulent regime gives a reasonable prediction of the carbon consumption rate and the surface temperature. This shows that models, based on laminar flow conditions, which are capable of capturing the fore-aft symmetry, can at least as a first estimate be used to also model gasification at larger particle Reynolds numbers. Finally as a completion of this work, currently 3D LES simulations are under way to study the effect of turbulent fluctuations on the overall carbon consumptions rate.

## REFERENCES

- CAMPREGHER, R., MILITZER, J., MANSUR, S.S. and DA SILVEIRA NETO, A. (2009). "Computations of the flow past a still sphere at moderate reynolds numbers using and immersed boundary method". *J. Braz. Soc. Mech. Sci. & Eng.*, **31**, 344–352.
- EDGE, P., GHAREBAGHI, M., IRONS, R., PORTER, R., PORTER, R.T.J., POURKASHANIAN, M., SMITH, D., STEPHENSON, P. and WILLIAMS, A. (2011). "Combustion modelling opportunities and challenges for oxy-coal carbon capture technology". *Chem. Eng. Res. Des.*, **89**, 1470–1493.
- HIGUERA, F.J. (2008). "Combustion of a coal char particle in a stream of dry gas". *Combust. & Flame*, **152**, 230–244.
- HLA, S.S., HARRIS, D. and ROBERTS, D. (2007). "Gasification conversion model – PEFR". Research report 80. Cooperative research centre for coal in sustainable development.
- JONES, D.A. and CLARKE, D.B. (2008). "Simulations of flow past a sphere using the fluent code". Technical report. Austral. Gov., Dep. of Def., Def. Sc. and Techn. Org.
- JONES, W.P. and LINDSTEDT, R.P. (1988). "Global reaction schemes for hydrocarbon combustion". *Combust. & Flame*, **73**, 233–249.
- KAZAKOV, A. and FRENKLACH, M. (1994). "Reduced reaction sets based on gri-mech 1.2". <http://www.me.berkeley.edu/drm/>.
- KESTEL, M., NIKRITYUK, P.A., HENNIG, O. and HASSE, C. (2012). "Numerical study of the partial oxidation of a coal particle in steam and dry air atmospheres". *IMA J. Appl. Math.*, **77**, 32–46.
- KIM, J.P., SCHNELL, U. and SCHEFFKNECHT, G. (2008). "Comparison of different global reaction mechanisms for MILD combustion of natural gas". *Comb. Sci. Technol.*, **180**, 565–592.
- LEE, J., TOMBOULIDES, A.G., ORSZAG, S.A., YETTER, R.A. and DRYER, F.L. (1996). "A transient two-dimensional chemically reactive flow model: Fuel particle combustion in a nonquiescent environment". *Proc. Combust. Inst.*, **26**, 3059–3065.
- RICHTER, A., NIKRITYUK, P.A. and KESTEL, M. (2013). "Numerical investigation of a chemically reacting carbon particle moving in a hot O<sub>2</sub>/CO<sub>2</sub> atmosphere". *Ind. Eng. Chem.*, **52**, 5815–5824.

RICHTER, A., NIKRITYUK, P.A. and MEYER, B. (2015). “Three-dimensional calculation of a chemically reacting porous particle moving in a hot O<sub>2</sub>/CO<sub>2</sub> atmosphere”. *Int. J. Heat Mass Transfer*, **83**, 244–258.

RICHTER, A., VASCELLARI, M., NIKRITYUK, P.A. and HASSE, C. (2016). “Detailed analysis of reacting particles in an entrained-flow gasifier”. *Fuel Process. Technol.*, **144**, 95–108.

SCHULZE, S., KESTEL, M., NIKRITYUK, P.A. and SAFRONOV, D. (2013). “From detailed description of chemical reacting carbon particles to subgrid models for CFD”. *Oil Gas Sci. Technol.*, **68**, 1007–1026.

SUNDARESAN, S. and AMUNDSON, N.R. (1980). “Diffusion and reaction in a stagnant boundary layer about a carbon particle. 5. pseudo-steady-state structure and parameter sensitivity”. *Ind. Eng. Chem. Fundam.*, **19**, 344–351.

VASCELLARI, M., ARORA, R. and HASSE, C. (2014). “Simulation of entrained flow gasification with advanced coal conversion submodels. part 2: Char conversion”. *Fuel*, **118**, 369 – 384.

WITTIG, K., NIKRITYUK, P.A., SCHULZE, S. and RICHTER, A. (2016). “Three-dimensional modeling of porosity development during the gasification of a char particle”. *AICJE J.*, available online.

## MODELLING COMBUSTION OF PULVERIZED COAL AND ALTERNATIVE CARBON MATERIALS IN THE BLAST FURNACE RACEWAY

**Martin ÖLUND<sup>1\*</sup>, Lena S. ÖKVIST<sup>1,2</sup>, Lars-Erik FROM<sup>1</sup>, Dan SANDSTRÖM<sup>1</sup>, Johanna ALATALO<sup>3</sup>**

<sup>1</sup> Swerea MEFOS, Process Metallurgy Department, Luleå, Sweden

<sup>2</sup> Luleå University of Technology, Division of Minerals and Metallurgical Research, Luleå, Sweden

<sup>3</sup> LKAB, R&D, Luleå, Sweden

\* E-mail: martin.olund@swerea.se

### ABSTRACT

The impact of injection lance design and injection materials on the combustion conditions inside the raceway of the blast furnace has been investigated. Operational injection tests in LKAB's Experimental blast furnace have been conducted and data describing particle dispersion and temperatures at the tuyere was gathered. A three-dimensional, multiphase numerical model of pulverized material injection (pulverized coal and alternative carbon materials) was developed in order to increase the understanding of raceway conditions in terms of combustion efficiency and reaction rates. In total two different injection lances and two alternative carbon materials in varying blend ratios with pulverized coal were investigated in the numerical study. Simulation results agreed quite well to the experimental data. Furthermore, simulation results agree with published findings regarding the general effect of material properties of pulverized coal on combustion efficiency.

**Keywords:** Process metallurgy, Blast furnace, Coal injection, Numerical modelling, Combustion, Gasification

### NOMENCLATURE

#### Latin Symbols

$A, A_2$	Pre-exponential factors for devolatilization and homogeneous reactions, [1/s]
$A_c$	Pre-exponential factor for heterogeneous reactions, [kg/m <sup>2</sup> .s.Pa]
$A_p$	Particle surface area, [m <sup>2</sup> ]
$A_{EDM}$	Empirical constant for Eddy-dissipation model
$a, b$	Rate exponents
$B_{EDM}$	Empirical constant for Eddy-dissipation model
$C_1$	Diffusion rate constant, [kg/m <sup>2</sup> .s.Pa.K <sup>0.75</sup> ].
$C_{j,n}$	Molar concentration of species $j$ in the reaction $n$ , [kmol/m <sup>3</sup> ]
$d_p$	Particle diameter, [m]
$E, E_2, E_c$	Activation energy, [J/kmol]
$f_s$	Mass fraction of reacting solid species
$f_{VM,0}$	Initial volatile matter mass fraction
$k, k_2$	Kinetic rate, [1/s]
$m_a$	Mass of ash, [kg]
$m_p$	Particle mass, [kg]
$m_{p,0}$	Initial particle mass, [kg]
$m_{VM}$	Mass of volatile matter, [kg]
$M_i$	Molecule weight of species $i$ , [kg/kmol]

$p_g$	Bulk partial pressure of the reacting gas species, [Pa]
$R$	Universal gas constant, [J/kmol.K]
$R_c$	Heterogeneous reaction rate, [kg/s]
$R_D$	Diffusion rate, [kg/m <sup>2</sup> .s.Pa]
$R_K$	Kinetic rate, [kg/m <sup>2</sup> .s.Pa]
$R_{i,n}$	Finite reaction rate of species $i$ and reaction $n$ , [kg/s]
$R_{VM}$	Devolatilization rate, [kg/s]
$T$	Temperature, [K]

#### Greek Symbols

$\alpha, \alpha_2$	Yield factors
--------------------	---------------

#### Sub/superscripts

$g$	Gas
$p$	Particle
$s$	Solid
$i$	Index $i$
$j$	Index $j$
$n$	Index $n$

### INTRODUCTION

Tuyere injection of auxiliary reducing agents, mainly pulverised coal (PC), has been used in the past few decades to replace some of the coke used in the blast furnace (BF). The main concept of the BF processes is illustrated in Figure 1. Injection of auxiliary reducing agents aims to decrease the use of coke, lowering the total use of carbon and fossil coals in the process. At the same time, this contributes to lower CO<sub>2</sub> emissions and increases the short term heat level control.

When un-burnt PC (char) passes through the raceway boundary entering the packed coke bed, it is consumed together with coke fines in high temperature regions by reduction with CO<sub>2</sub> in reduction gas and FeO in slag. As char is more reactive than coke, accumulation of coke fines may occur (Ishii, 2000) causing permeability problems, channelling and low gas efficiency. Therefore, a high char burnout in the raceway is needed to overcome those issues (Mathieson et al., 2005, Hutny et al., 1991). High injection rates are requested by industry as well as increased flexibility of the process, making the use of alternative carbon material (ACM) injection a relevant topic. The decrease in CO<sub>2</sub> emissions from the BF process would be



significant by both enabling increased injection rates and replacing fossil auxiliary reducing agents.

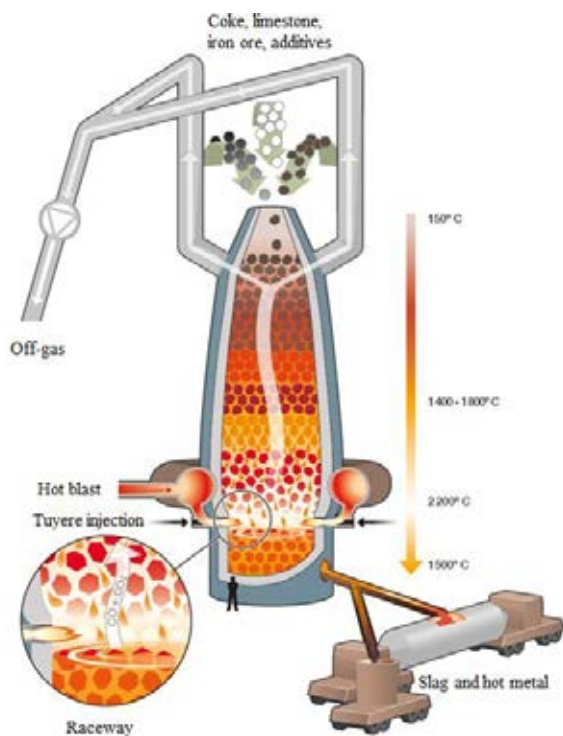


**Figure 1: Schematic illustration of the BF process.**

The effect of material properties of PC and operational conditions on combustion efficiency has been investigated; combustion efficiency is in general enhanced with increased volatile matter (VM) in PC, decreased particle size, increased blast temperature and enhanced oxygen supply to the PC plume (Pichard, 2001, Ishii, 2000, Mathieson et al., 2005, Shen et al., 2009a). However, PC with lower VM has usually higher replacement ratio to coke (Sundqvist-Ökvist et al., 2016, Ishii, 2000), i.e. more carbon will be converted for the same injection rate even if the combustion efficiency decreases.

The injection system for auxiliary reducing agents varies from BF to BF; hence optimization to enhance the oxygen supply to the PC plume has to be customized (Gudenau et al., 1994). By enhancing particle dispersion the contacting chance for particles and oxygen in the blast will increase. Using a swirl-tip lance instead of an ordinary coaxial air-cooled lance is one method to increase particle dispersion and oxygen utilization. Installation of a swirl-tip lance under oxy-coal conditions made it possible to increase the PC injection rate at LKAB Experimental BF (EBF) (Hallin and Wikström, 2003) and the concept was found to improve combustion conditions in an industrial BF (Wikström et al., 1996). However, using a swirled annular cooling flow doesn't necessarily enhance particle dispersion. In a numerical study the dispersion was found to increase in the tuyere when turning of the swirled cooling flow (Majeski et al., 2012). It must be noted that the thermal effect on the lance by such implementation was not investigated in the study. The purpose of implementing the cooling flow is to prevent excessive heating of the injection lance and thereby prolong lifetime, hence this

action might be unrealistic to implement by practical reasons.

Combustion within the tuyere and the raceway cavity is a complex process where multiphase flow in high velocity conditions interacts with intricate chemistry. The requirement of stable operation makes comprehensive research difficult to implement on industrial BFs. Therefore, experiments in laboratory scale (e.g. Vamvuka et al., 1996) and pilot scale are widely used. A compilation of pilot scale test rigs used for evaluation of coal combustion are described by Mathieson et al. (2005). Lack of similarities to the complex industrial process, e.g. the present raceway condition where coke interaction affect the dynamics, might obstruct a direct transfer of findings made at a test rigs handling PC coal combustion only. The LKAB EBF provides a quite rare possibility to overcome those obstacles since pilot scale trials can be conducted in an industrial environment. Since the plant was taken into operation in 1997, a total of 32 campaigns have been conducted. General information about EBF construction and operational conditions has been described elsewhere (Sundqvist-Ökvist et al., 2016, Hallin and Wikström, 2003). The similarities to industrial scale BF conditions retain the harsh environment inside the process and limiting process monitoring opportunities. Hence, insight information to fully explain and understand process improvements caused by different actions is difficult to gather. Therefore, the use of computational fluid dynamics (CFD) in combination with available process data provides a comprehensive tool to increase the understanding of the in-furnace phenomena, provided that the process characteristics are fully captured by the applied mathematical formulation.

In practice, by looking into tuyere and injection lance setup, three-dimensional (3D) models are needed to fully resolve the fluid dynamics in the process. A number of 3D models describing combustion of auxiliary reducing agents in BF like conditions have been carried out by different approaches, such as tuyere combustion models (Du et al., 2007, Majeski et al., 2012), tuyere-raceway combustion models (Guo et al., 2005, Shen et al., 2009, Shen et al., 2016) and tuyere-raceway-coke bed combustion models (Shen et al., 2011, Shen et al., 2012, Maier et al., 2014). Tuyere combustion models have a great potential to resolve the particle dispersion in detail due to the relatively small computational domain. However, the geometrical representation of the raceway region has been stated to have a major impact on the particle dispersion (Mathieson et al., 2005), meaning that results from tuyere combustion models cannot be transferred directly to make conclusions about the overall combustion efficiency in the combustion zone of the BF. In the tuyere-raceway models, the raceway was simplified by a cylindrical combustion chamber where its diameter was enlarged compared to the tuyere diameter. This model approach gives the opportunity to resolve the free shear flow (jet) in the raceway region and capture the effect on particle dispersion and combustion efficiency. Interaction with coke was neglected for those three tuyere-raceway combustion models, chemical reactions and gas composition were direct results of PC combustion and gasification only. The tuyere-raceway-

coke bed combustion models include combustion of coke in the packed coke bed. Raceway shape was not calculated explicitly, but defined as a boundary condition to limit computational efforts. The raceway was represented by a balloon shaped cavity (total void) by Shen et al., (2011, 2012a, 2012b), while Maier et al. (2014) used a more circular shape with gradients in void fraction in the raceway boundary. Even though both definitions were based on literature sources, there was a significant difference in gas flow field in the raceway cavity between both models. Shen found that low speed recirculation of small auxiliary reduction agent particles occurred due to gas recirculation and strongly affected the combustion conditions while Maier et al. (2014) did not stated any gas recirculation. However, the model presented by Maier included coke bed movement and showed that inter-phase momentum transfer made coke particles recirculating in the upper part of the raceway falling into the jet and being partly combusted in the blast. This behaviour has been reported earlier from experimental observations (Kase et al., 1982) and has also been observed within the experiments conducted in connection to this study. Hence, the model presented by Maier et al. (2014) is the only one of the reviewed models that has captured this behaviour.

The CFD model presented in this paper follows the tuyere-raceway modelling approach in order to ensure detailed particle trajectories in the blast. In extension to similar models, coke interaction and subsequent chemical reactions are included to properly evaluate the combustion in BF raceway like conditions.

## MODEL DESCRIPTION

### Gas-solid flow

The CFD simulations were carried out using the software platform ANSYS FLUENT, release 16.2. The continuous phase was modelled by a set of 3D, steady state Reynolds average Navier-Stokes (RANS) equations with a realizable k- $\epsilon$  turbulence model using enhanced wall treatment. Also the energy equation and the species transport equation were solved in addition to the RANS-equations. The Discrete Ordinates (DO) radiation model was enabled to solve the radiative heat transfer equation. The Euler-Lagrange approach was used to model the dynamics of the multiphase flow, where the solid phase was solved for steady state by tracking a certain number of spherical particles throughout the computational domain. The particles could exchange mass, momentum and energy with the continuous phase. A stochastic tracing model was used to predict the dispersion of the discrete phase due to turbulence. The particle radiation interaction model was enabled to involve the particles in the radiation model. A Rosin-Rammler particle diameter distribution (RRD) was used to simulate the particle size distribution (PSD) data obtained from material screening.

### Chemical reactions

The conversion of pulverized auxiliary reduction agents is defined by four steps considering pre-heating, devolatilization, homogenous reactions (gas-gas reactions) and heterogeneous reactions (gas-particle surface reactions). An outline of the considered

chemical reactions is presented in Table 1, where (R5) and (R6) is the reversible water-gas shift reaction.

**Table 1: Chemical reactions considered.**

Devolatilization	
$Raw\ coal \xrightarrow{Volatile\ Matter\ (VM)}$	<b>(R1)</b>
$\xrightarrow{Char\ (C_{<S>)} + Residue\ (Ash)}$	
Homogenous reactions	
$VM + O_2 \rightarrow Products$	<b>(R2)</b>
$CO + 0.5 O_2 \rightarrow CO_2$	<b>(R3)</b>
$H_2 + 0.5 O_2 \rightarrow H_2O$	<b>(R4)</b>
$CO + H_2O \rightarrow CO_2 + H_2$	<b>(R5)</b>
$CO_2 + H_2 \rightarrow CO + H_2O$	<b>(R6)</b>
Heterogeneous reactions	
$C_{<S>} + 0.75 O_2 \rightarrow 0.5CO + 0.5CO_2$	<b>(R7)</b>
$C_{<S>} + CO_2 \rightarrow 2 CO$	<b>(R8)</b>
$C_{<S>} + H_2O \rightarrow CO + H_2$	<b>(R9)</b>

Kinetic parameters for reaction (R1), (R7) and (R8) were deduced from thermogravimetric analysis (TGA), where the sample mass was logged over time in different atmospheres. The same TG program was used for all evaluated materials, i.e. the heating rate was equal. The measured kinetic rate was then adjusted to BF-like conditions by normalizing the pre-exponential factors to a higher ambient temperature. Details of the experimental setup can be found elsewhere (Sundqvist-Ökvist et al., 2016).

### Devolatilization

Devolatilization starts when the combusting particle reaches the vaporization temperature and remains while the mass of the particle,  $m_p$ , exceeds the mass of non-volatiles in the particles:

$$m_p > (1 - f_{VM,0})m_{p,0} \quad (1)$$

where  $f_{VM,0}$  is the mass fraction of VM from the proximate analyse and  $m_{p,0}$  is the initial particle mass. Depending of the behaviour of the material analysed in the TGA, either a single kinetic rate model or a two-competing rate model has been considered to simulate the devolatilization rate of the evaluated injection agent. The single kinetic rate model (Badzioch and Hawksley, 1970) assumes the devolatilization rate,  $R_{VM}$ , has a first-order dependency of remaining mass of VM,  $m_{VM}$ , in the particle:

$$R_{VM} = \frac{dm_{VM}}{dt} = km_{VM} \quad (2)$$

where  $dm_{VM}$  is the mass change of VM,  $dt$  is change in time and  $k$  is the kinetic rate constant, defined by the Arrhenius equation:

$$k = Ae^{-\frac{E}{RT}} \quad (3)$$

where  $A$  is the pre-exponential factor,  $E$  is the activation energy,  $R$  is the universal gas constant and  $T$  is the temperature. The competing rate model (Kobayashi et al., 1976) assume that two competing kinetic rates,  $k$  and  $k_2$ , controls the devolatilization rate over different temperatures. The two kinetic rates are weighted to yield an expression for the devolatilization:

$$R_{VM} = (\alpha k + \alpha_2 k_2)(m_p - m_a) \quad (4)$$

where  $\alpha$  and  $\alpha_2$  are yield factors and  $m_a$  is mass of ash.

#### Homogenous reactions

The rates of homogeneous reactions are determined by either the kinetics or turbulent mixing. The finite reaction rate model calculates the reaction rate,  $R_{i,n}$ , for species  $i$  and reaction  $n$  as:

$$R_{i,n} = M_i k [C_{j,n}]^{a+b} \quad (5)$$

where  $M_i$  is the molecule weight of species  $i$ ,  $k$  is the kinetic rate following the Arrhenius approach as described in equation (3),  $C_{j,n}$  is the molar concentration of species  $j$  in reaction  $n$ ,  $a$  and  $b$  are rate exponents. Reaction rate due to turbulent mixing is determined by the Eddy-dissipation model (EDM) (Magnussen and Hjertager, 1976), which requires input of two empirical constants; notated as  $A_{EDM}$  and  $B_{EDM}$  in this paper. The net reaction rate is taken as the minimum of these two rates. In practice, the finite rate acts as a kinetic switch, preventing reaction before the flame holder. Once the flame is ignited, the Eddy-dissipation rate is generally smaller than the Arrhenius rate, and the reactions are mixing limited.

#### Heterogeneous reactions

Heterogeneous reactions of PC/ACM and coke with gas species are considering oxidation and gasification with  $\text{CO}_2$  and  $\text{H}_2\text{O}$ . Therefore, a multiple surface reactions model was applied. The model assumes that the particle surface reaction rate,  $R_C$ , is determined either by the kinetic rate,  $R_K$ , or by the diffusion rate,  $R_D$ , such as:

$$R_C = A_p f_s p_g \frac{R_K R_D}{R_K + R_D} \quad (6)$$

where  $A_p$  is the particle surface area,  $f_s$  is the mass fraction of reacting solid species in the particle and  $p_g$  is the bulk partial pressure of the reacting gas species. The kinetic rate follows the Arrhenius approach as described in equation (3). The diffusion rate is defined as:

$$R_D = C_1 \frac{T_m^{0.75}}{d_p} \quad (7)$$

where  $C_1$  is the diffusion rate constant,  $d_p$  is the particle diameter and  $T_m$  is the mean value of particle surface temperature and bulk gas temperature. This model is based on oxidation studies of char particles, but it is also applicable to gas-solid reactions in general, not only to char oxidation reactions.

## SIMULATION CONDITIONS

### Computational domain

The computational domain, shown in Figure 2, corresponded to the lance and tuyere geometry of the EBF. The main focus when creating the computational domain was to minimize the control volume, without changing the nature of the flow. Initial temperature and velocity of injected material (gas and particles) are important for the combustion conditions. Therefore, the flow in the lance is modelled completely inside the blowpipe-tuyere region, allowing fully developed

velocity profiles and temperature increase by convective and radiant heat transfer from the blast respectively the downstream combustion. Mass flow inlets were applied for the blast, cooling gas, carrying gas and auxiliary reducing agents. The raceway cavity was simplified as a cylinder with a length specified in proportion to the furnace diameter. A pressure outlet with a backflow temperature of  $1600^\circ\text{C}$  was applied as boundary condition on the outer surface, the upper part also served as a mass flow inlet for discrete particles (coke). A consequence by applying a pressure outlet with constant gauge pressure all over the cylinder surface was that no recirculation of reaction products and/or unburned particles could occur. However, findings in literature are inconsistent regarding gas and particle (auxiliary reducing agents) recirculation and its effects on combustion conditions in the raceway cavity. Recirculation was either non-existing (Maier et al., 2014), rather small (Zhang et al., 2010) or significant for evaluation of combustion efficiency (Shen et al., 2012). Hence, no definitely recommendations on model setup in this area could be deduced from the reviewed literature.

The computational domain and the boundary conditions applied were assumed to capture enough of the main process conditions without compromising on the details of particle trajectories to be able to evaluate alternative lance designs and injection of ACMs. The computational domain was discretized by an unstructured grid with prism layers in the near-wall region and locally refinements in the lance and close to the lance tip, see Figure 3.

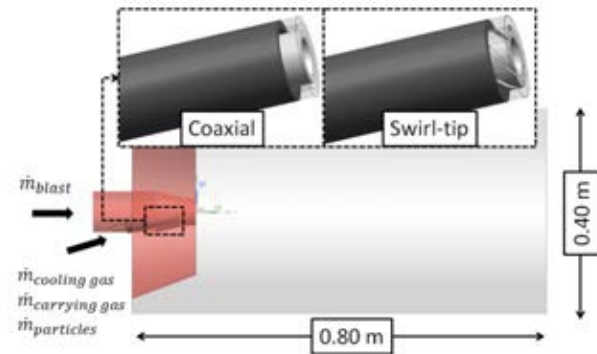


**Figure 2: Computational domain and evaluated lance designs seen from the right. The tip (5 mm) of the outer lance pipe is illustrated as transparent to demonstrate the difference in design.**

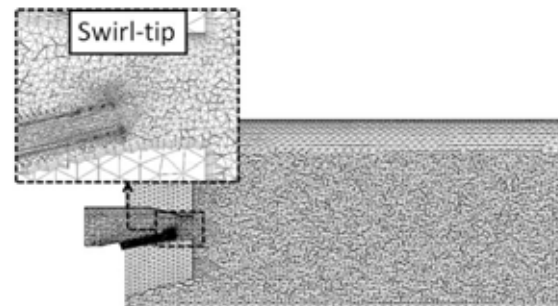


**Figure 3: Lance parallel cross-section of the discretized computational domain seen from the right.**

## Material properties and boundary conditions

In experimental trials (EBF campaign no. 31) three different auxiliary reducing agents were injected: one type of PC, activated lignite coke (ALC) and torrefied biomass (BIO). Material analysis, heating values and vaporization temperature (from TGA) are presented in Table 2. Evaporation of moisture was not considered in the model formulation of chemical reactions, instead the lower heating value was applied to calculate the heat of combustion.

Oxidation of VM, reaction (R2) in Table 1, is dependent of the material properties. Considered oxidation reaction, deduced from the material analysis, for each material is presented in Table 3.

**Table 2: Material analysis.**

	PC	ALC	BIO
Proximate analysis [wt%]			
VM	18.4	3.1	50.3
Char	69.6	87.0	47.2
Ash	10.8	8.7	0.9
Moisture	1.2	1.15	1.62
Ultimate analysis [wt%]			
S	0.3	0.4	0.0
C	88.6	98.9	71.1
H	4.4	0.2	5.1
O	4.5	0.1	23.7
N	2.2	0.4	0.1
Lower heating value [kJ/kg]	30.5	30.3	27.1
Vaporization temp. [°C]	384	616	276

**Table 3: Considered oxidation of VM.**

Devolatilization	
$1 VM_{PC} + 3.37 O_2$	(R2a)
$\rightarrow 1.62 CO + 0.47 CO_2$	
$+ 4.74 H_2O + 0.17 N_2$	
$+ 0.02 SO_2$	
$1 VM_{ALC} + 2.58 O_2$	(R2b)
$\rightarrow 2.29 CO + 0.66 CO_2$	
$+ 1.31 H_2O + 0.19 N_2$	
$+ 0.17 SO_2$	
$1 VM_{BIO} + 1.71 O_2$	(R2c)
$\rightarrow 1.58 CO + 0.46 CO_2$	
$+ 2.23 H_2O + 0.003 N_2$	
$+ 0.00 SO_2$	

**Table 4: Boundary conditions for the CFD model, based on the operational conditions of the EBF.**

Injected auxiliary reducing agent	
Total flow rate [kg/s]	0.021
Temperature [°C]	47
Carrier gas (N <sub>2</sub> )	
Flow rate [kg/s]	0.0035
Temperature [°C]	47
Cooling gas (air)	
Flow rate [kg/s]	0.0097
Temperature [°C]	27
O <sub>2</sub> and H <sub>2</sub> O <sub>(g)</sub> mole fractions [-]	0.21/0.0
Blast (oxygen enriched air)	
Flow rate [kg/s]	0.183
Temperature [°C]	1097
O <sub>2</sub> and H <sub>2</sub> O <sub>(g)</sub> mole fractions [-]	0.285/0.019
Top gas pressure [Bar]	2.01

The particle size distribution from material screening is presented in Figure 4 together with the mathematical representation used in the CFD model. The applied boundary conditions are presented in Table 4. During the EBF trials the operational conditions were kept constant, except in terms of lance type and blend ratio of PC/ALC/BIO.

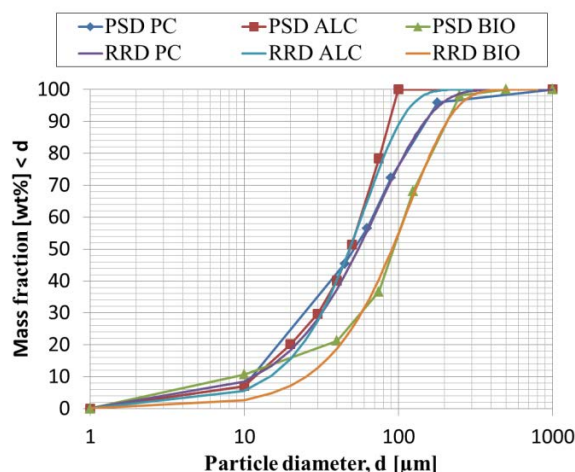
CFD model setup should be close to process conditions to evaluate PC and ACM in terms of combustion efficiency inside the BF raceway. Interaction of coke in the EBF raceway is illustrated in Figure 5, hence coke particles need to be included in the model formulation. However, coke flow rate in the raceway is difficult to measure, instead the assumption that the oxygen content should reach zero when reaching the raceway boundary is used to specify coke boundary conditions. The properties of coke are chosen similar to the coke used in the EBF. The content is considered to be carbon and ash, VM is neglected due to the initial low VM content from the material analysis (<1wt%). Spherical coke particles with a uniform diameter of 15.0 mm and a temperature of 1600°C is injected through the top half of the raceway, in the normal direction, with a flow rate of 1.00 kg/s and an initial velocity of 0.50 m/s. Activation energy for combustion and gasification with CO<sub>2</sub> is taken from related literature (Shen et al., 2010).

Table 5 presents the six different conditions evaluated in the parametric CFD study, where five cases correspond to operational conditions from experimental trials. Case 6 was decided to be evaluated additionally in the CFD model due to its potential to decrease the net CO<sub>2</sub> emissions from the BF process. Considered parameters to describe chemical reactions in the CFD model are presented in Table 6.

**Table 5: Boundary conditions for parametric study.**

Case	Lance type	Blend PC/ALC/BIO
1. Coaxial PC	Coaxial	100/0/0
2. Swirl PC	Swirl-tip	100/0/0
3. ALC20	Swirl-tip	80/20/0
4. ALC40	Swirl-tip	60/40/0
5. BIO20	Swirl-tip	80/0/20
6. BIO100*	Swirl-tip	0/0/100

\* not evaluated in the experimental trials



**Figure 4: Particle size distribution and mathematical representation by a Rosin-Rammler distribution.**

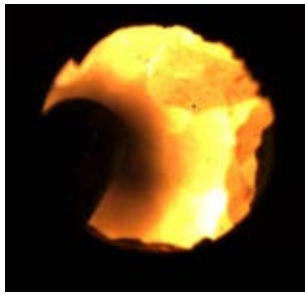


**Figure 5: Single frame from high-speed monitoring of tuyere injection in the EBF.**

**Table 6: Parameters as input in chemical reaction models.**

Devolatilization				
	PC	ALC	BIO	
$A_{(R1)}$	1.05E+09	2.30E+13	1.42E+11	
$E_{(R1)}$	9.93E+07	1.85E+08	9.40E+07	
$\alpha_{(R1)}$	0.184	-	-	
$A_{2(R1)}$	1.29E+12	-	-	
$E_{2(R1)}$	1.74E+08	-	-	
$\alpha_{2(R1)}$	1.00	-	-	
Homogenous reactions				
$A_{(R2)}$		2.12E+11		
$E_{(R2)}$		2.03E+08		
$A_{(R3)-(R6)}$		1.00E+15		
$E_{(R3)-(R6)}$		1.00E+08		
$A_{EDM}$		4.00		
$B_{EDM}$		0.500		
Heterogeneous reactions				
	PC	ALC	BIO	Coke
$A_{c(R7)}$	2.20	4.40E+05	3.57E+04	2.20
$E_{c(R7)}$	9.79E+07	1.38E+08	1.20E+08	9.00E+07
$A_{c(R8)}$	1.33	22.9	1.88E+6	1.33
$E_{c(R8)}$	1.86E+08	1.69E+08	2.46E+08	2.40E+08
$A_{c(R9)}$	1.5	1.5	1.5	-
$E_{c(R9)}$	1.50E+08	1.50E+08	1.50E+08	-
$C_1$	5.00E-12	5.00E-12	5.00E-12	2.50E-08

## RESULTS

### Validation

High-speed video recordings and temperature measurements from EBF campaign no. 31 have been used to validate model results. A visual validation was carried out by comparing high-speed videos with post-processed model images. A contour plot of the particle mass concentration at tuyere outlet is compared to a single frame from the high-speed videos in Figure 6 (presented cases are Coaxial PC and Swirl PC). As can be seen, there is some difference in lance location between the process images and the model images. However, the trends in dispersion are similar for the high-speed images and the model image since the main coal plume area is located perpendicular to the lance outlet for Coaxial PC, while the swirling flow from the swirl-tip makes the main coal plume area located to the right of the lance.

Even though the way of particles dispersion is stated to differ between coaxial and the swirl-tip lance, the image analysis of the high-speed images did not detect any major differences in terms of area of particle dispersion. The area seems to be at equal size by just

visually comparing the model images in Figure 6. A more accurate picture is given when removing the injection lances in Figure 7. The difference in particle dispersion becomes hereby obvious.

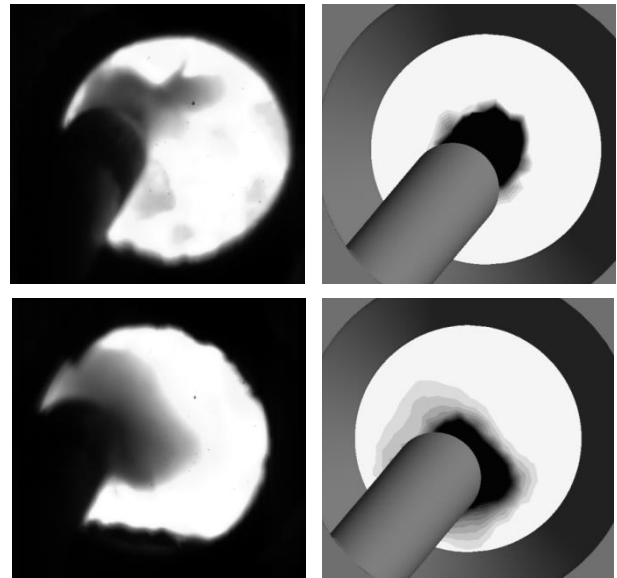


**Figure 6: Visual comparison between high-speed image of the EBF process (left) and the CFD model (right), for Coaxial PC (upper) and Swirl PC (lower).**

In Figure 8 the average gas temperature for the cross-sectional plane generating the highest value (varies depending on start of combustion, particle dispersion etc.) are compared to spectrometer measurements and theoretical calculations of the raceway adiabatic flame temperature (RAFT). Optical fibres were used to guide light from the tuyere to the spectrometer for the spectrometer measurement.

As expected, RAFT generates the highest temperatures overall. Spectrometer measurements retain the same trend as RAFT, even though the temperature is decreased. The same trend is obtained when comparing CFD model results to RAFT and spectrometer measurements, Coaxial PC has the lowest flame temperature and ALC40 has the highest. The maximum divergence in temperature between spectrometer and CFD model are found for ALC40 where the divergence amounts to 0.9%. Overall, the changes in injected material generate reasonable results. The temperature increase for ALC40 in the model cannot be seen in the same extent as for RAFT and spectrometer measurements. Further, the model seems to underestimate the temperature for Coaxial PC to a minor extent. A possible explanation might be that the coke particles in the raceway region affect the dispersion of PC particles by collisions; increasing the PC dispersion. This effect should be greater for Coaxial PC compared to the Swirl PC due to a less dispersed plume when reaching the raceway region. The effect of particle collision is not included in the model formulation.

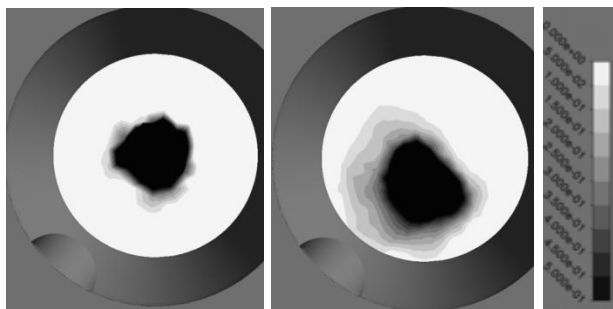


**Figure 7: Contour plot of particle mass concentration ( $\text{kg/m}^3$ ) at tuyere outlet, no lance displayed (Coaxial PC left, Swirl PC right)**

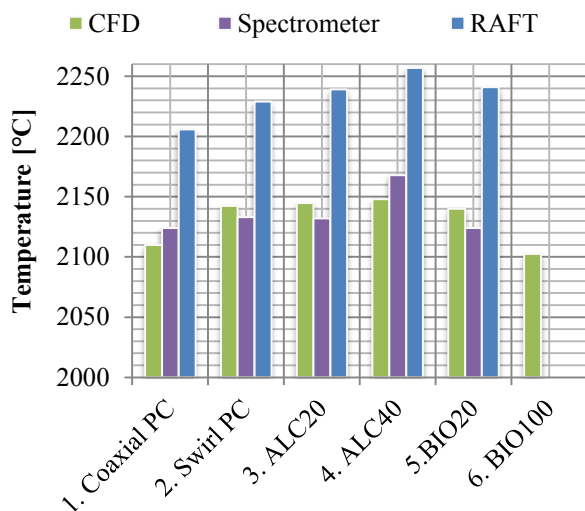


**Figure 8: CFD model temperatures compared to spectrometer measurements and RAFT.**

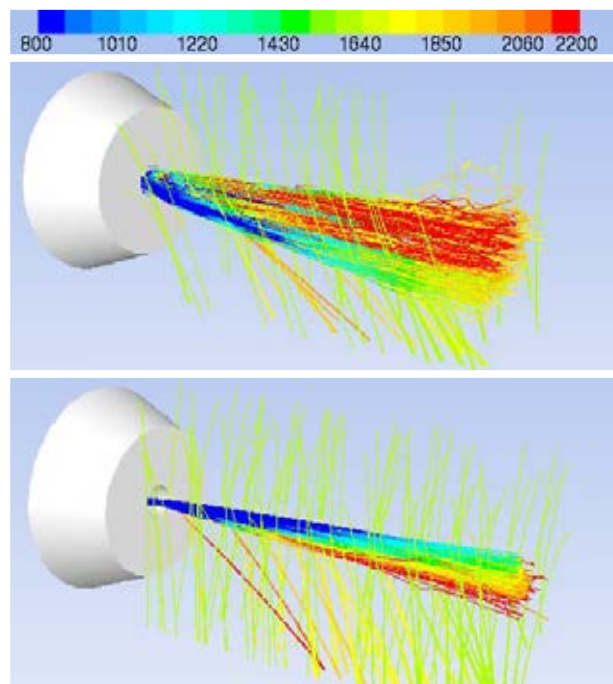


**Figure 9: Particle trajectories for Swirl PC (upper) and Coaxial PC (lower) coloured by particle temperature ( $^{\circ}\text{C}$ ). PC particles enter the raceway through the injection lance inside the tuyere, while coke particles are injected from the top of raceway.**

### Alternative lance design

Particle trajectories, coloured by particle temperature, of PC and coke for Coaxial PC and Swirl PC are presented in Figure 9. Unlike the image analysis of particle dispersion, the difference in dispersion is clear. The swirl-tip lance increases particle dispersion significantly resulting in earlier ignition (Figure 11) and increased carbon conversion of PC (Table 7). Especially carbon converted via combustion is increased by Swirl PC, illustrated in Figure 10. For Swirl PC the heterogeneous reaction rate of combustion is the fastest, followed by carbon solution loss and last gasification with water vapour, while for Coaxial PC the behaviour is vice versa. This might be explained by the differences in particle dispersion, where worse PC dispersion makes larger regions of the blast stream unoccupied and limits the conversion by oxidation. With the current model formulation this oxygen will react with coke, making the total carbon conversion the highest for Coaxial PC (Table 7). This explains why the highest average temperature does not diverge that much. By looking into the reaction rates and comparing the net enthalpy change the difference should be larger if only comparing PC conversion. However, total carbon conversion is not a proper measurement to evaluate the combustion efficiency. One main purpose of injecting auxiliary reducing agents in the raceway is to decrease the total use of carbon, by replacing some of the coke. This should be done by converting as much carbon as possible of the injected material in the raceway region to avoid unstable BF operation.

### Alternative carbon materials

For case 2-6 the swirl lance has been used. Differences in combustion efficiency and characteristics are all connected to differences in the properties of the injected materials; such as PSD, analysis and reaction parameters. BIO100 has the earliest start of combustion followed by BIO20, see Figure 11 and Table 7. Start of combustion depends on injected material and lance type used. For the swirl-tip lance, the deciding factor seems to be the VM content in the injected material/blend. As a consequence, the highest carbon burnout of the injected material is reached for the BIO-cases. In general, increased VM leads to increased combustion efficiency in terms of carbon burnout. BIO has larger particle size compared to ALC and PC, which might counter the efficiency enhancement from the increase in VM. The extent of this factor has not been investigated in this work. Further, ALC40 converts the most carbon from the injected materials. The observed behaviour corresponds to earlier findings presented in reviewed literature. However, BIO20 has a higher amount of VM compared to Swirl PC but increases not only the combustion efficiency, but also the carbon conversion. This might be motivated by the synergetic effect; where BIO releases more VM, helping form a higher gas temperature field in an earlier stage promoting PC devolatilization and combustion. This theory is supported by Shen et al. (2009b).

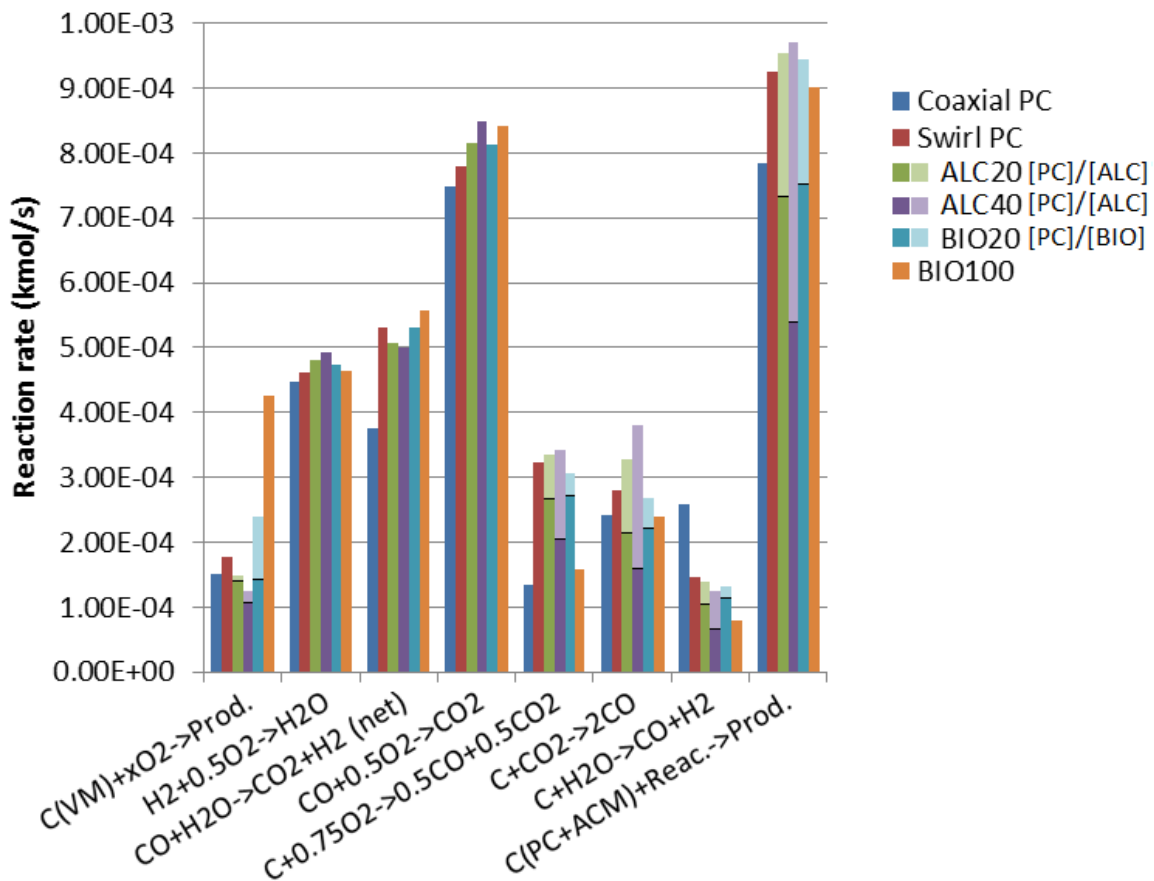


Figure 10: Reaction rates in kmol/s. Cases with blends (ALC20, ALC40 and BIO20) are presented in total rate, where darker shade corresponds to carbon originates from PC and lighter shade to carbon originates from ACM.

Table 7: Combustion characteristics for all evaluated cases.

	Coaxial PC	Swirl PC	ALC20		ALC40		BIO20		BIO100
PC and ACMs only									
Auxiliary reducing agent	PC	PC	ALC	PC	ALC	PC	BIO	PC	BIO
C in VM converted [g/s]	1.81	2.13	0.10	1.72	0.21	1.29	1.15	1.73	5.15
VM burnout [%]	84.4	99.4	100.0	99.7	100.0	99.8	100.0	99.9	89.6
C <sub>∞</sub> converted [g/s]	7.61	9.00	2.57	7.09	4.99	5.22	1.14	7.34	5.73
C <sub>∞</sub> burnout [%]	53.3	63.1	69.7	61.9	68.5	60.9	63.5	64.1	64.3
C converted [g/s]	<b>9.42</b>	<b>11.13</b>	<b>11.48</b>		<b>11.71</b>		<b>11.36</b>		<b>10.88</b>
C burnout [burnout]	<b>57.4</b>	<b>67.8</b>	<b>67.7</b>		<b>67.5</b>		<b>70.4</b>		<b>74.2</b>
Including coke									
C <sub>∞</sub> in coke converted [g/s]	15.82	11.63	11.98		12.36		11.41		11.84
Total C converted [g/s]	<b>25.24</b>	<b>22.76</b>	<b>23.46</b>		<b>24.07</b>		<b>22.77</b>		<b>22.72</b>
Total C burnout [%]	<b>3.13</b>	<b>2.82</b>	<b>2.90</b>		<b>2.98</b>		<b>2.82</b>		<b>2.82</b>
Other comb. characteristics									
Start of combustion [mm]	146	29	32		35		22		12
Plane position for highest avg. temp. [mm]	490	340	340		390		340		390
Highest avg. temp., T <sub>avg.</sub> [°C]	<b>2110</b>	<b>2142</b>	<b>2145</b>		<b>2148</b>		<b>2140</b>		<b>2102</b>

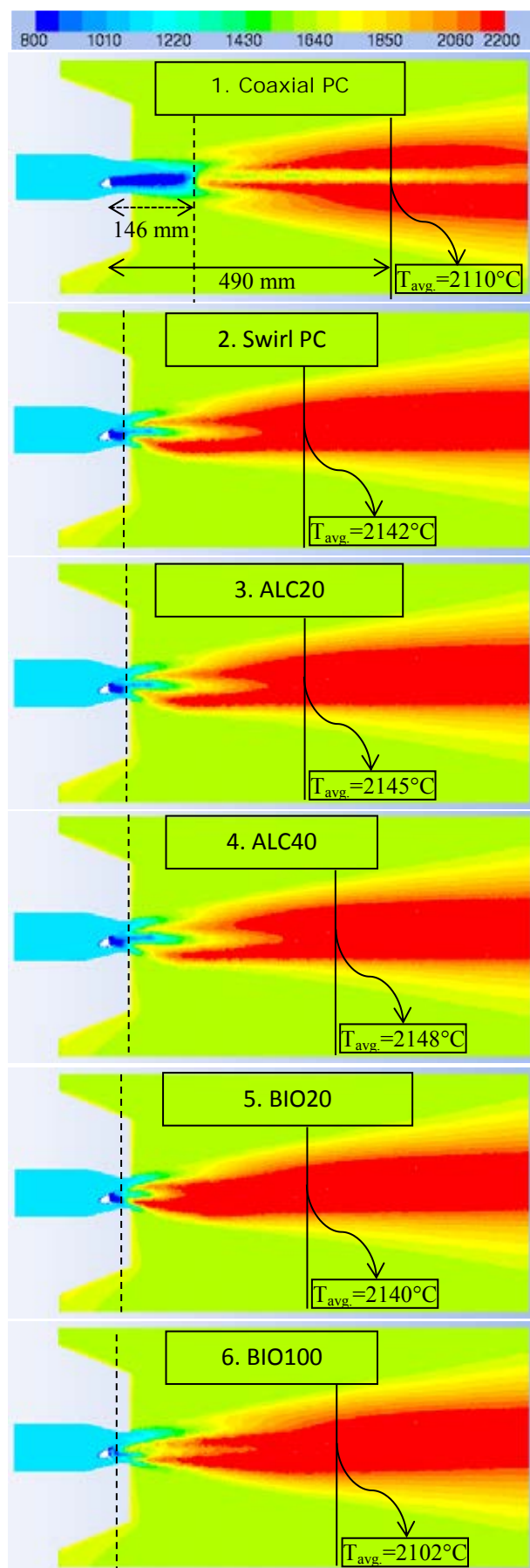


Figure 11: Contour plot of temperature (°C) at cross-sectional plane (tuyere seen from the right). Solid line indicates position of plane for highest average temperature and dashed line indicates start of combustion.

By comparing the flame distribution for the swirl-tip cases in Figure 11 there are some minor differences, most likely explained by differences in PSD between the materials. BIO is deviant in PSD compared to PC and ALC, which might explain the decreased flame distribution close to the tuyere outlet. It will take longer time for the particles to change direction due to the increased momentum. Making the PSD for BIO closer to the other two materials will most likely enhance the combustion efficiency even further.

In Table 7 and Figure 11 it can be seen that the highest average temperature is found in different positions downstream the lance tip. Highest average temperatures are found further downstream for Coaxial PC, ALC40 and BIO100 compared to Swirl PC, ALC20 and BIO20 that all have the highest temperature at approximately 340 mm downstream the lance tip. For Coaxial PC, later ignition leads to postponed combustion of solid carbon in PC. The ignition for ALC40 is postponed as well, but to a minor extent. The increased activation energy needed to combust solid carbon in ALC compared to PC is assumed to be the explanation. The same explanation partly applies to BIO100, together with the increased PSD.

The highest average temperature is found for ALC40, while BIO100 generates the lowest. By only comparing the heating value for full combustion the temperature difference appears to be too small. However, the complexity of the process is high and full combustion is not the case. By looking into the reaction behaviour and comparing reaction rates and net enthalpy change this is reasonable.

## CONCLUSION

A three-dimensional, steady-state CFD model has been developed to investigate the impact of injection lance design and injection materials on the combustion conditions inside the raceway of the blast furnace. In total, two injection lances and three injection materials were evaluated under uniform operation conditions. A detailed geometric representation of the injection lance and tuyere was included in the model. The model was found suitable for evaluating alternative lance designs and alternative carbon materials for injection in the BF by validation against measurements from experimental trials. The developed modelling technique can advantageously be transferred to any industrial BF.

Compared to the ordinary coaxial lance, the swirl-tip lance was found to significantly enhance the combustion efficiency of PC, increasing carbon conversion and raceway temperature. Model results indicate that the swirl-tip lance enables increased injection rates of auxiliary reducing agents without making any major impact on the tuyere installation. BIO (torrefied biomass) showed overall good results in the CFD model, making it a suitable candidate to reduce the total amount of fossil coal used in the BF process. With a blend of 20 wt% BIO in PC the temperature remained stable and both carbon conversion and combustion efficiency were increased. Further, the low sulphur content in BIO compared to PC reduces the production of sulphur dioxide in the process.



The CFD model presented is a useful tool for BF tuyere injection evaluation by complementing available measurements and providing further insights in the harsh BF process.

## ACKNOWLEDGMENTS

The research presented in this paper has been carried out within the project IMPCO RFSR-CT-2012-00002, co-founded by the Research fund for coal and steel, RFCS. The Swedish Energy Agency is greatly acknowledged for additional financial contribution to the project. The paper is a contribution from CAMM, Centre of Advanced Mining and Metallurgy, at Luleå University of Technology supporting the presented research scientifically and economically.

## REFERENCES

BADZIOCH, S. and HAWKSLEY, P. G.W., (1970) "Kinetics of thermal decomposition of pulverized coal particles", *Ind. eng. chem. process design and development*, **9**, 521–530.

DU, S-W., CHEN, W-H. and LUCAS, J., (2007) "Performances of pulverized coal injection in blowpipe and tuyere at various operational conditions", *Energy conversion and management*, **48**, 2069-2076.

GUDENAU, H.W., PETERS, M., JOKSCH, M., (1994) "Steigerung der Kohleeinblasrate am Hochofen durch Optimierung der Einblasanlagen", *Stahl und Eisen*, **114**, 69-73.

GUO, B., ZULLI, P., ROGERS, H., MATHIESON, J.G., and YU, A., (2005) "Three-dimensional simulation of flow and combustion for pulverized coal injection", *ISIJ Int.*, **45**, 1272-1281.

HALLIN, M. and WIKSTRÖM, J-O., (2003) "Ways to improve the blast furnace operation – The Use of an Experimental Blast Furnace", *Sci. and tech. of innovative ironmaking for aiming at energy half consumption*, Tokyo, Japan, November 27-28.

HUTNY, W.P., LEE, G.K. and PRICE, J.T., (1991) "Fundamentals of coal combustion during injection into blast furnace", *Prog. Energy Comb. Sci.*, **17**, 373-395.

ISHII, K., (2000) "Advanced pulverized coal injection technology and blast furnace operation", *research group of pulverized coal combustion in blast furnace ironmaking in JSPS 54<sup>th</sup> Committee*.

KASE, M., SUGATA, M., YAMAGUCHI, K. and NAKAGOME, M., (1982) "Analysis of coke behavior in raceway using endoscope and high-speed camera", *Transactions of the iron and steel inst. of Japan*, **22**, 811-819.

KOBAYASHI, H., HOWARD, J. B. and SAROFIM, A. F., (1976) "Coal devolatilization at high temperatures", *In 16<sup>th</sup> symp. (Int'l.) on combustion. The combustion institute*.

MAGNUSSEN, B.F. and HJERTAGER, B. H., (1976) "On mathematical models of turbulent combustion with special emphasis on soot formation and combustion", *In 16<sup>th</sup> symp. (Int'l.) on combustion. The combustion institute*.

MAIER, C., JORDAN, C., FEILMAYR, C., and HARASEK, M., (2014) "Multi-scale modelling of hydrocarbon injection into the blast furnace raceway", *10<sup>th</sup> int. conf. on CFD in oil & gas, metallurgical and*

*process industries*, SINTEF, Trondheim, Norway, June 17-19.

MAJESKI, A., RUNSTEDTLER, A., D’ALESSIO, J., MACFADYEN, N. and FERRON, K., (2012) "The effects of lance positioning and design on the co-injection of pulverized coal and natural gas into blast furnace", *Ninth int. conf. on CFD in Minerals and process ind.*, CSIRO, Melbourne, Australia, December 10-12.

MATHIESON, J.G., TRUELOVE, J.S. and ROGERS, H., (2005) "Towards an understanding of coal combustion in blast furnace tuyere injection", *Fuel*, **84**, 1229-1237.

Picard, M., (2001) "Pulverized coal combustion in the blast furnace raceway, using a 3D numerical simulation", *Ironmaking Conf. Proc.*, Baltimore.

SHEN, Y., GUO, B. and ZULLI, P., (2009a) "Model study of the effects of coal properties on pulverized coal combustion", *ISIJ int.*, **49**, 819-826.

SHEN, Y.S., GUO, B.Y., YU, A.B., and ZULLI, P., (2009b) "A three-dimensional numerical study of the combustion of coal blends in blast furnace", *Fuel*, **88**, 255-263.

SHEN, Y.S., GUO, B.Y., YU, A.B., AUSTIN, P.R. and ZULLI, P., (2011) "Three-dimensional modelling of in-furnace coal/coke combustion in a blast furnace", *Fuel*, **90**, 728-738.

SHEN, Y.S., YU, A.B., AUSTIN, P.R. and ZULLI, P., (2012a) "CFD study of in-furnace phenomena of pulverized coal injection in blast furnace: Effects of operating conditions", *Powder technology*, **223**, 27-38.

SHEN, Y., YU, A., AUSTIN, P. and ZULLI, P., (2012b) "Modelling in-furnace phenomena of pulverized coal injection in ironmaking blast furnace: Effects of bed porosities", *Minerals engineering*, **33**, 54-65.

SHEN, Y.S. and YU, A.B., (2016) "Modelling of injecting a ternary coal blend into a model ironmaking blast furnace", *Minerals engineering*, **90**, 98-95.

SUNDQVIST-ÖKVIST, L., ÖLUND, M., SANDSTRÖM, D., FROM, L-E. and ALATALO, J., (2016) "Impact on combustion conditions from tuyere injection settings", *7<sup>th</sup> European coke and ironmaking congress*, Linz.

VAMVUKA, D., SCHWANEKAMP, G. and GUDENAU, H.W., (1996) "Combustion of pulverized coal with additives under conditions simulating blast furnace injection", *Fuel*, **75**, 1145-1150.

WIKSTRÖM, J-O., SKÖLD, B-E. and KÄRSRUD, K., (1996) "SSAB/MEFOS oxy-coal system - 3 years of industrial experience", *55th Ironmaking Conf. Proc.*, Pittsburgh, USA.

ZHANG, S., BAI, C., WEN, L., QIU, G. and LÜ, X., (2010) "Gas-particle flow and combustion characteristics of pulverized coal injection in blast furnace raceway", *Journal of iron and steel research, int.*, **17**, 8-12.

# COMBUSTION CHAMBER SCALING FOR ENERGY RECOVERY FROM FURNACE PROCESS GAS: WASTE TO VALUE

**Balram Panjwani, Bernd Wittgens, and Jan Erik Olsen**

SINTEF Materials and Chemistry, 7465 Trondheim, NORWAY

\* E-mail: balram.panjwani@sintef.no

## ABSTRACT

One of the byproducts during the metal reduction process is energy rich off-gas of which the energy is normally not used. In the present paper, a novel concept for energy recovery from process gas is discussed. The concept is founded on the idea of introducing a combustion chamber in the off-gas section, which will provide an additional degree of freedom for optimizing energy recovery and minimizing Polycyclic Aromatic Hydrocarbon (PAH) and NO<sub>x</sub> concentrations. Design and operation of the combustion chamber depend on many parameters, including the total power capacity of the combustion chamber, residence time for combusting the complex PAH. The design criteria for the combustion chamber have been identified and discussed. The scaling of the combustion chamber based on proposed design criteria is presented. Engineering methods and Computational Fluid Dynamics (CFD) has been utilized extensively for scaling the combustion chamber. The results from our CFD simulations of the flow in the combustion chamber, exploring different off-gas fuel compositions, are presented. In brief, the paper covers all aspects which influences the scaling of the combustion chamber, including insulation thickness, choice of insulating material, heat transfer through extended surfaces, multi-staging and secondary air injection.

**Keywords:** CFD, Combustion chamber, Ferro Alloys, Furnace.

## NOMENCLATURE

A complete list of symbols used, with dimensions, is required.

### Greek Symbols

$\rho$  Mass density, [kg/m<sup>3</sup>].

$\lambda$  Thermal Conductivity,  $\lambda$ , [W/m.s].

### Latin Symbols

$h$  Heat transfer coefficient, [m].

$p$  Pressure, [Pa].

$r_e$  outer radius of the chamber, [m].

$r_i$  inner radius of the chamber, [m].

$r_n$  Radius of nth insulating radius, [m].

### Sub/superscripts

$i$  Index  $i$ .

$j$  Index  $j$ .

## INTRODUCTION

Ferrous alloys is produced in submerged arc furnaces (SAF) where ore and carbon (coke, coal, etc.) are mixed into a charge and allowed to react when electric energy is supplied through electrodes. The reactions produce alloys and an energy rich process gas. The alloys sink to the bottom where it is collected in ladles through a tapping hole. Hot process gas rises upwards through the charge surface into a furnace hood. Simultaneously, in case of open furnace hood, air is sucked into the hood through various open areas due to the pressure drop. The air and process gas reacts inside the hood through a combustion process and produces an off-gas potentially containing CO<sub>2</sub>, H<sub>2</sub>O and other components. This is illustrated in Figure 1. Most of the energy of the process gas is lost due to uncontrolled combustion of CO inside the hood. This is a kind of intriguing system where first energy is supplied to produce a desirable metal and then the energy rich by products are not used. A viable solution to the problem is to recover the energy from the process gas. There are two main potential sources for energy recovery; 1) an off-gas with a high temperature and 2) the cooling water used for cooling the system. An energy analysis carried out by Kamfjord et al. (Kamfjord et al. 2010) has shown utilization of hot water obtained from the furnace for other industries including agriculture, sports etc.

Currently, most of the Si furnaces are open, where use of the energy available in the process gas for electricity production is a challenge. However, in closed furnace the process gas CO does not go through the uncontrolled combustion inside the hood and therefore it is possible to utilize the energy for electricity generation. Heimir Hjartarson et al. (Heimir Hjartarson, Halldor Palsson, and Saevarsdottir 2010) performed an energy and exergy analysis on a 47 MW SAF producing FeSi75 based on measurements. It was concluded that the production of ferrosilicon involves large exergy destruction, estimated to be 46.5 MW, and the exergetic efficiency of the

furnace is about 30%. The energy analysis shows that much of the energy used in the production of ferrosilicon goes into the environment as a waste heat. Only 35.6 MW of the 98 MW of the energy supplied to the process are retrieved as chemical energy in the product.

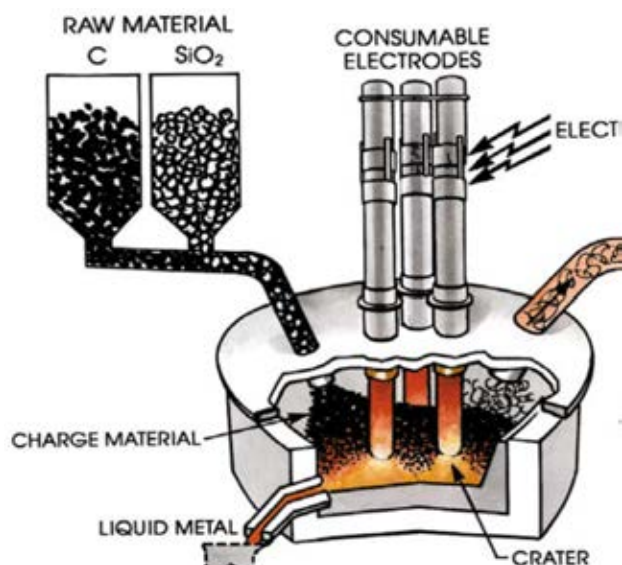


Figure 1: Principle sketch of the metal reduction process. Schei et al (Schei, Tuset, and Tveit 1997)

To obtain energy from the submerged arc furnace, a heat recovery system needs to be designed. One of the principle requirement of heat recovery system is that it should not affect the quantity and quality of the product and it should not increase primary energy (coal, oil or natural gas) consumption. The heat recovery system should extract energy available in sensible heat of waste hot water and from chemical energy available in flue gas. The recovery system needs to be safe, reliable, sustainable, and stable with reduced amount of smoke/dust and other pollutant production. Proposed waste heat recovery system is based on the utilization of the chemical energy available in process gas. The system includes a combustion chamber and the primary objective of the proposed combustion chamber is to combust the process gases obtained either from Ferro manganese or from Ferro silicon furnace. The process gas mainly consists of CO, H<sub>2</sub>O, CO<sub>2</sub> and Si component (dust/gas) in Ferro Silicon furnace and Mn components (dust/gas) in Ferromanganese furnace. The process gas also consist of some amount of PAH and oxidation of the PAH is a challenge due to their stable complex rings. One of the objectives of the proposed combustion chamber is to oxidize the PAH. The minimum residence time and temperature to oxidize these PAH rings is around 2s and 800°C respectively (Mati et al. 2007). The other requirement for this combustion chamber is to have better control of the NO<sub>x</sub> formation, which again depends on the temperature and residence time. The peak temperature and simultaneous higher residence time leads to higher NO<sub>x</sub> formation. Thus the two requirements of complete PAH combustion and minimized NO<sub>x</sub> formation are contradictory to each other. However, it is possible to meet both requirements

by having more uniform temperature. Temperature should not exceed the critical temperature responsible for the higher NO<sub>x</sub> formation. The critical temperature for thermal NO<sub>x</sub> formation is above 1500°C. It is possible to optimize the chamber with respect to temperature and residence time. The residence time of the combustion chamber can be calculated either with Langrangian approach or with species transport. Langrangian approach is computationally demanding and therefore approach based on the species transport is employed. In this approach an inert specie/tracer is released from the process gas inlet. It is assumed that effect of tracer on the global flow field is insignificant. Residence time is calculated by solving an unsteady transport equation for inert specie. The concentration of inert specie over a time is monitored at the outlet.

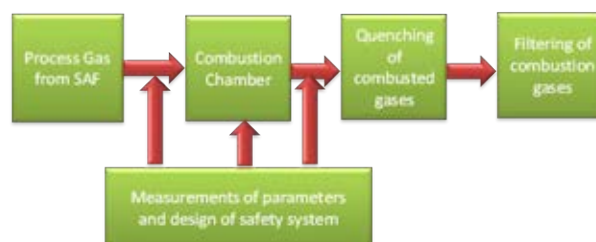


Figure 2: Flow diagram of heat recovery system from flue gas.

An overall concept of the entire system is shown in Figure 2. The objective of the lab scale plant is only to demonstrate the functioning of the combustion chamber and therefore the current lab scale plant is not equipped with a power generation system. Process gas from the SAF is transported to the combustion chamber via a suitable connection. Measurements of temperature, species concentration, and other emissions is performed not only downstream and upstream of the combustion chamber, but also inside the combustion chamber. A robust safety system integrated with measurement system is developed to avoid any accidents. The hot exhaust gases from the combustion chamber is quenched to a suitable temperature before entering into the filter unit.

#### DESIGN CRITERION OF COMBUSTION CHAMBER

The combustion chamber is normally designed considering two different types of flames, either diffusion or premix. In the diffusion or non-premixed flame, fuel and oxidizer come from a separate stream prior to entering the combustion chamber. However, in the premixed flame both fuel and oxidizer are mixed prior to entering the combustion chamber. Apart from type of flames, the combustor performance is also governed by the size and shape of the combustion chamber. Historically, most of the research has been done for the jet engine combustion chamber scaling and therefore most of the design criteria have been laid down for the jet engines combustion chamber. In addition, the existing gas fired boiler/furnaces design criteria do not meet our requirements and therefore the new design criteria are needed to design a combustion chamber to meet our requirements. These are some of the proposed design criteria for scaling the combustion chamber.

1) The combustion chamber has to be based on the pure diffusion flame concept. Operating the combustion chamber with a premixed flame is a challenge due to uncontrolled flame that can affect the furnace safety.

2) Transport of the process gas from the furnace to the combustion chamber requires special attention to avoid any clogging of the pipes due to dust and tar available in the process gas. There are also possibilities of condensation of SiO gas inside the transport pipes and this has to be considered while scaling the transport pipes.

3) The residence time and temperature of the gases inside the combustion chamber should be sufficiently high to achieve a proper mixing and subsequent combustion of PAH.

4) The inner wall temperature of the combustion chamber should not exceed the critical temperature at which the insulating materials have been designed.

5) The maximum temperature on the outer wall of the combustion chamber should not be very high. The outer wall temperature of the combustion chamber shall not exceed 60-100 °C.

7) The temperature of the combusted gases out of the combustion chamber should not be more than 800°C otherwise cooling of the exhaust hot gases will be a challenge.

8) The capacity of the combustion chamber should be around 30 kW. Aim of the combustion chamber was not to produce power but to show an oxidation of PAH and NOx formation. Therefore combustion chamber with small capacity was designed.

9) Last but not least is the price and weight of the whole assembly should not exceed the limit. It is difficult to come with price now and this information is sensitive and could not be shared. It was made sure that pipe size, chamber internal and outer dimension, insulations are of standard dimensions to avoid unnecessary costs.

**COMPUTATIONAL FLUID DYNAMICS (CFD) MODEL OF COMBUSTION CHAMBER**

CFD has been matured enough to be used for designing any industrial or laboratory scale system involving flow, heat and mass transfer. In the present study CFD is utilized for designing and scaling the combustion chamber. All the design parameters discussed earlier have been independently evaluated with CFD. Commercial CFD software ANSYS FLUENT (ANSYS 2016) has been utilized for studies. The geometry and mesh was generated using ANSYS design modeler. The generated mesh was imported into the FLUENT flow solver.

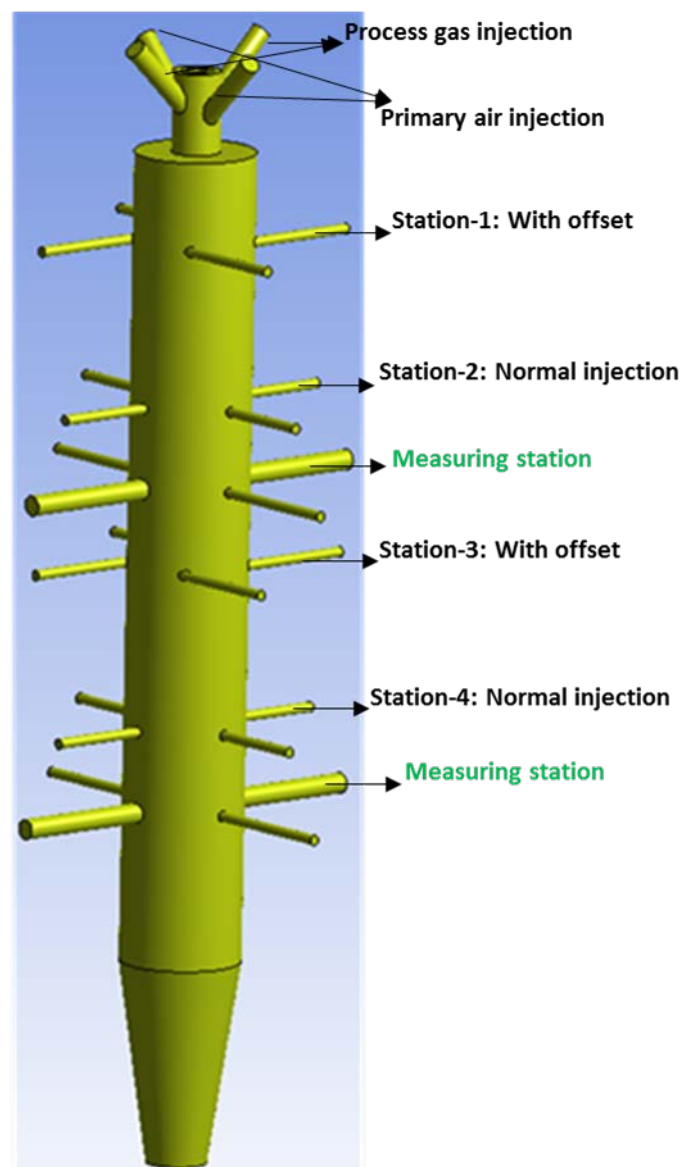


Figure 3: Combustion chamber

In current steady state CFD model setup, the convective and diffusive terms in all the transport equations (mass, momentum, energy, turbulence and species) were discretized using first order accurate scheme during the initial phase of chamber scaling, however, for final scaling, second order scheme was employed. The turbulence-chemistry was modeled with the eddy dissipation concept model. Turbulence was handled with k-e model and for radiation, Discrete Ordinance (DO) model was employed. The process gas mainly consists of 70-75% of CO and 20-25 % of H2O. Oxidation of CO with air was modeled using a detailed chemical kinetic mechanism involving 12 species and 28 elementary reactions (Drake and Blint 1988) as shown in Table-1. The pressure-velocity coupling was achieved by SIMPLE algorithm. Meshing of the geometry was carried out using ANSYS MESH.

Table-1: CO/air mechanism used for present study

```
ELEMENTS
H O C N
END
```

SPECIES

H O2 O OH H2 H2O HO2 CO CO2 HCO H2O2 N2

END

REACTIONS CAL/MOLE

Units are moles, cubic centimeters, and calories per mole. Temperature in Kelvin.

H+O2=O+OH	5.10E+16	-0.816	16507
OH+H2=H2O+H	1.20E+09	1.3	3630
H2+O=H+OH	1.80E+10	1	8920
OH+OH=H2O+O	1.50E+09	1.14	0
H+HO2=OH+OH	1.50E+14	0	1000
H+HO2=H2+O2	2.50E+13	0	690
H+HO2=H2O+O	1.00E+13	0	1073
HO2+OH=H2O+O2	1.50E+13	0	0
HO2+O=O2+OH	2.00E+13	0	0
H2O2+OH=H2O+HO2	1.00E+13	0	1800
HO2+HO2=H2O2+O2	2.00E+12	0	0
H2O2+H=HO2+H2	1.70E+12	0	3750
H+O2+M=HO2+M	2.30E+18	-0.8	0
H2O2+M=OH+OH+M	1.20E+17	0	45500
CO+OH=CO2+H	1.50E+07	1.3	-770
CO+HO2=CO2+OH	1.50E+14	0	23650
CO2+O=CO+O2	2.80E+12	0	43830
HCO+M=H+CO+M	7.10E+14	0	16800
HCO+H=CO+H2	2.00E+14	0	0
HCO+OH=CO+H2O	5.00E+13	0	0
HCO+O2=CO+HO2	5.00E+11	0.5	835
H+H+M=H2+M	9.00E+16	-0.6	0
H+OH+M=H2O+M	2.20E+22	-2	0
O+H+M=OH+M	6.20E+16	-0.6	0
CO+O+M=CO2+M	5.80E+13	0	0
HCO+O=CO+OH	3.00E+13	0	0
HCO+O=CO2+H	3.00E+13	0	0

The model initial mesh was 6.5 million tetrahedral cells, which was converted into polyhedral mesh of 1.8 million cells. The grid was refined close to all walls. In addition, a boundary layer mesh was generated. While converting from tetrahedral mesh to polyhedral mesh, the boundary layer mesh does not change. Global stoichiometric ratio of combustion system is maintain closer to one. Amount of process gas was calculated considering the combustion chamber of 30 kW. The air need for complete combustion is calculated based on the amount of process gas. 20% of air was supplied at the primary air inlet located at the top and remaining 80% of the air was equally distributed into the secondary air inlet. Optimization of stoichiometric ratio through secondary air injection is not performed in the present study.

#### DESIGN CRITERIA FOR COMBUSTION CHAMBER SIZING

The length and diameter of the combustion chamber were based on two parameters initially 1) desired power

capacity of combustor which is around 30 kW and 2) desired residence time require for oxidation of PAH. However, controlling the temperature and residence time only through chamber diameter and length was a challenge; therefore some other parameters/functions on the combustion chamber need to be introduced. The other parameter that can control the residence time inside the combustion chamber could be the arrangement of the air supply. In the combustion chamber, the fuel and oxidizer can be supplied either coaxially or circumferentially. In a coaxial arrangement of fuel and air inlet, the dominating flow direction is along the axis of the combustion chamber and some of the air might travels in a lateral direction due to diffusion. However, in this configuration the residence time is mainly governed by the fuel and air inlet velocities at the coaxial inlet and length of the chamber. Based on our initial finding it was found that the coaxial configuration does not give residence time of 2s necessary for the PAH oxidation. Furthermore, coaxial injection does not provide uniform mixing. The other possibility to improve the residence time is to supply air circumferentially. The air supplied circumferentially is referred here as a secondary air injection. These secondary injections are provided at the offset (see Figure 4) to improve a mixing between fuel and oxidizer.

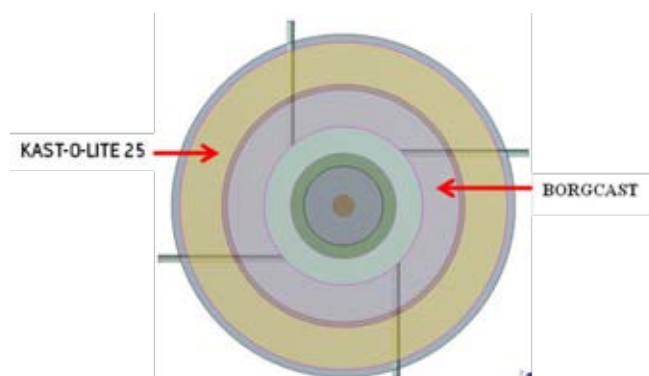


Figure 4: Cross section of the combustion chamber with secondary air injection in offset plane

Figure 4 shows cross section of the combustion chamber with secondary air injection in offset plane. The secondary air was injected at four different locations along the length of the combustion chamber (see Figure 3). At each longitudinal locations four air inlet pipes were provided. In the initial design phase of combustion chamber, all the four pipes were provided circumferentially at offset from the center to obtain the circulation pattern inside the combustion chamber which helps to improve the mixing and subsequent combustion. This arrangement of inlet pipes also increases the residence time of the gases and maintain the gas temperature at lower level, which helps in reduced NOx formation.

However, a challenging problem with this arrangement is a lesser penetration of air deep inside the chamber where most of the process gas is available. This problem was solved by removing offset for the secondary air inlet at second and fourth stations. The offset was only provided at first and second station for secondary air

inlet. The perpendicular locations of air inlet at second and fourth gave deeper penetration of the air. This configuration also gave sufficiently enough residence time required for the oxidation of PAH.

One of the major requirements of the combustion chamber is the outer casing temperature of the combustion chamber should be order of 100-150°C. This can be achieved via two ways, first by providing insulating layers on the combustion chamber and second by passing a coolant fluid on the walls of the combustion chamber. The second alternative is quite complicated at this stage and therefore first alternative was chosen for further study. Parameters such as thermal shocks, thermal gradients, structural properties, thermal conductivity of insulating material were considered while selecting the insulating material. The combustion chamber was designed using three different insulating layers. Thickness of each layer of insulating material was estimated based on temperature gradient requirements. For estimating the insulating thickness initially an engineering approach was used (see Equation 1).

$$R = \frac{1}{2\pi h_i r_1} + \sum_{k=1}^{n-1} \frac{\ln\left(\frac{r^{(k+1)}}{r_k}\right)}{2\pi \lambda_k} + \frac{1}{2\pi h_e r_n} \quad (1)$$

A final check on the effect of insulating materials on the heat distribution was carried out using CFD. Any discrepancy between the estimated insulating layer thickness using engineering model and CFD was adjusted in the final design of the combustion chamber.

Controlling the outer layer temperature only with insulating material is a challenge due to non-linear behavior of insulation thickness on the temperature drop through insulating layers. The study indicated that the effect of insulation thickness and insulating material properties on the temperature drop is non-linear and beyond certain insulation thickness the temperature of the outer shell does not reduce significantly. On the other hand, the outer diameter and weight of the combustion chamber should not exceed the critical values. The outer diameter of the combustion chamber was fixed at 650 mm. Controlling the outer temperature with insulating material alone was not sufficient and therefore extended surfaces (Fins) were provided to achieve the higher heat transfer rates. The fin was very useful in controlling the outer wall temperature.

After going through many iterations the final design and size of the combustion chamber was proposed and shown in Figure 3. CFD simulations of the final configuration was performed and presented in following sections. The CFD results of intermediate design is not presented here and it is beyond the scope of the paper.

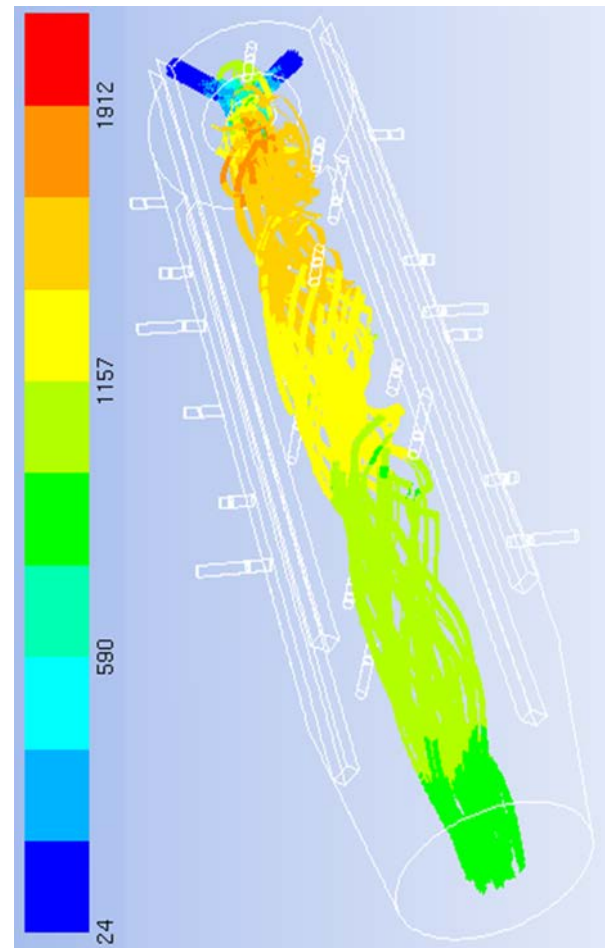


Figure 5: Pathlines coloured with gas temperature (°C)

## RESULTS AND DISCUSSIONS

A maximum velocity at the outlet of the chamber is around 4 m/s. The first and third stations had offset for secondary air injection (see Figure 3 and Figure 8/9), but second and fourth air injections were perpendicular to the chamber (see Figure 10/11). The second and fourth station of secondary air injection is supplying air normal to the combustion chamber to achieve a deeper penetration of the air. The penetrated air interacts strongly with process gas and thus helps in better combustion of the process gases. The converging section of the combustion chamber close to the outlet makes flow streamline along the wall of the combustion chamber. The flow inside the combustion chamber is somewhat complicated due to offset supply of air (see Figure 5). The pathlines from the fuel inlet is shown in Figure 5. The pathlines are colored with gas temperature. Highest temperature is nearly 1900 °C. A circulating pattern of the gas stream can be seen in the Figure 5. The gas released from the co-axial fuel/air inlet is along the direction of the combustion chamber, the gas undergoes to a circulation flow pattern when it meets the secondary air released from the offset injection (first stations of secondary air inlet). This circulating pattern helps in increasing the residence time of the PAH gas components. It can also be observed that the temperature of the gas stream is never less than 850°C, which ensure a possibility of having the complete combustion of PAH.

The maximum temperature is also not more than 1950 °C which is very helpful for not allowing the substantial NOx. Formation. There are mainly three routes for NOx formation; 1) thermal NOx, 2) fuel NOx, and 3) prompt Nox, among them the rate of thermal NOx formation exponentially varies with the gas temperature and for every increase in 90 degree the rate of NOx formation doubles at temperature above 1927 °C .

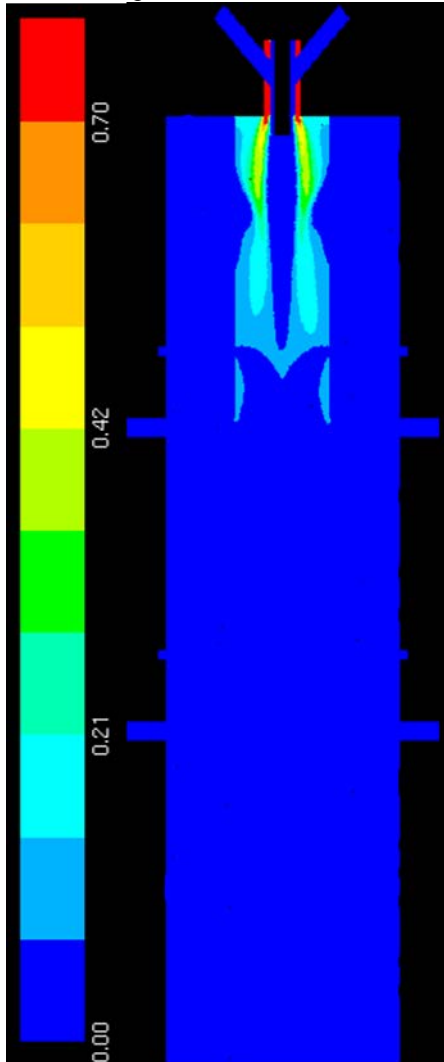


Figure 6: CO mass fraction in the central plane

CO in the middle plane of the combustion chamber is illustrated in Figure 6. It can be seen that the most of the CO is consumed before the second station for secondary air injection. However, increasing the secondary air injection velocity beyond optimum at injection perpendicular to the combustion chamber might lead to the some challenges.

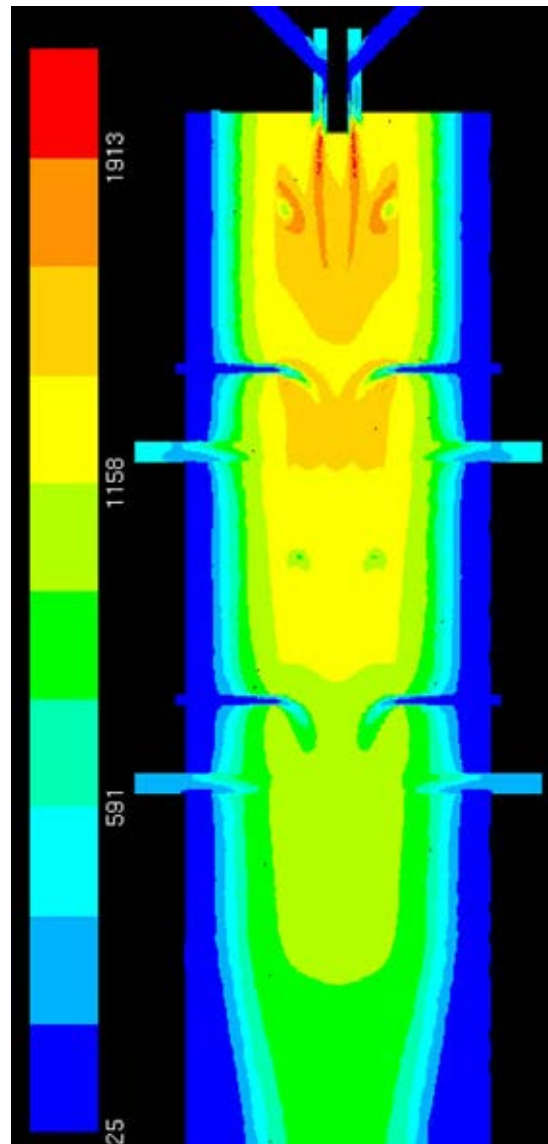


Figure 7: Temperature distribution in the central plane (°C)

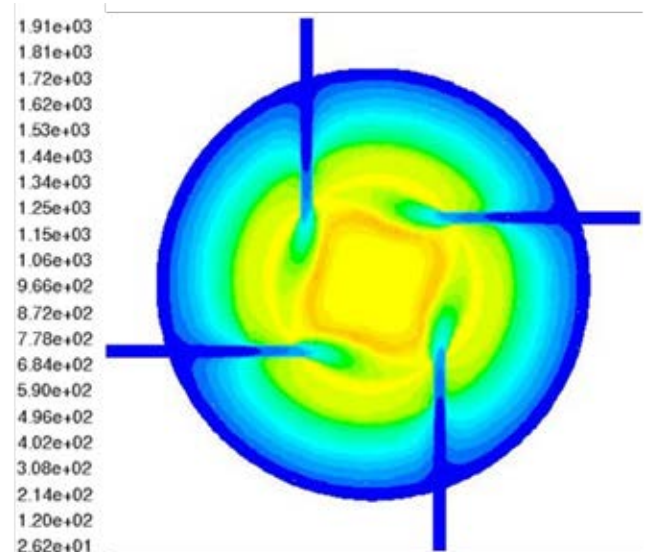


Figure 8: Temperature distribution at first station of secondary air injection

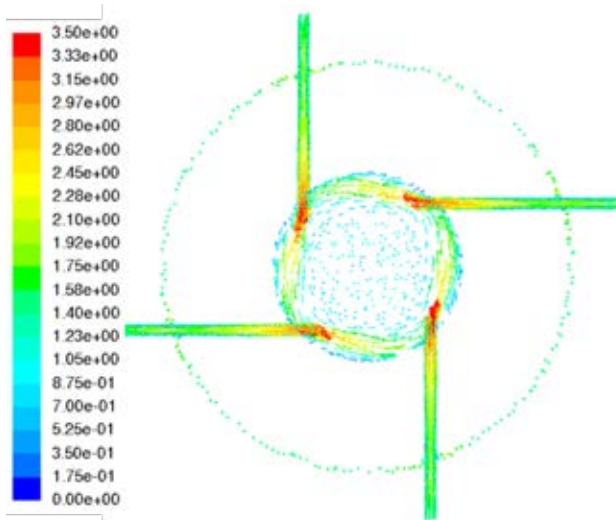


Figure 9: Velocity vector colored by velocity magnitude (m/s) at the first station

Temperature distribution in the central plane is shown in Figure 7. The highest temperature of gas is around 1950 °C and the outlet temperature of the gas is around 850 °C. The peak temperature occurs close to the lab burner region, in this region fuel and oxidizer reacts and develops a stabilized flame. The temperature distribution of the combustion chamber section at first secondary air inlet is shown in Figure 8. A flame (squared shape high temperature zone) is visible at a location where fresh air from the secondary air inlet interacts with gas coming from co-axial fuel and air inlets. In the same location, velocity distribution is shown in Figure 9. The velocity distribution shows two distinct pattern first one is recirculating pattern due to secondary air injection and the second zone is due to co-axial flow. The temperature and velocity distributions are completely different at the second station for secondary air injection (see Figure 10 and Figure 11). The circulation pattern around the secondary air injection is not visible anymore and air is penetrating deeper inside the combustion chamber.

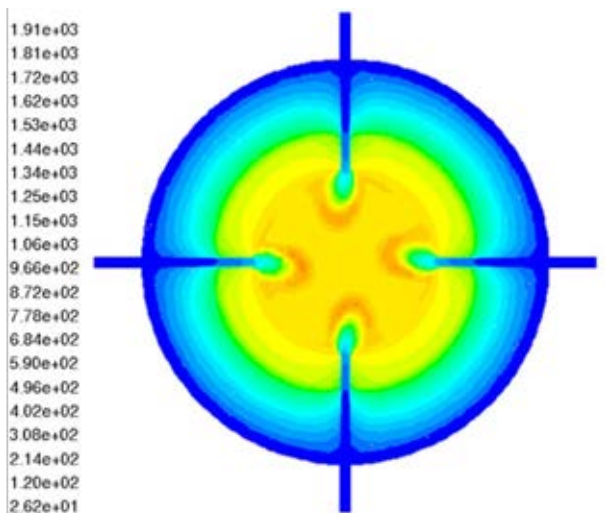


Figure 10: Temperature distribution at second station of secondary air injection

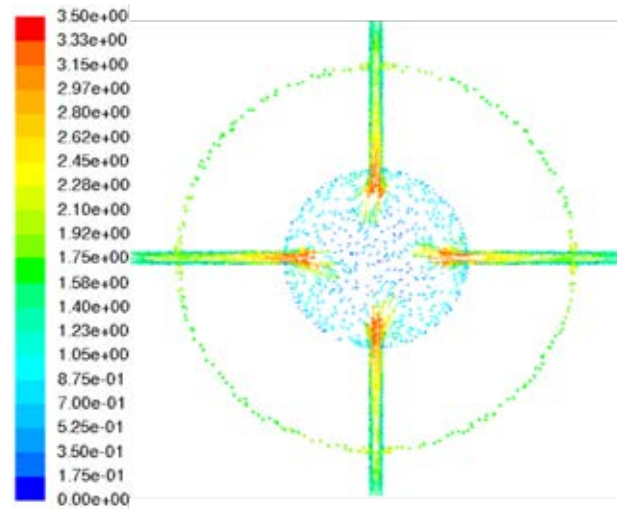


Figure 11: Velocity vector colored by velocity magnitude at the second station

## CONCLUSION

The design concept of combustion chamber for combusting the process gas obtained during the SAF reduction process has been presented. Design principle of the proposed combustion chamber is different from the traditional jet engine combustion chamber and boiler/furnace combustion chamber. New design principle of combustion chamber has been presented for scaling the combustion chamber design. The major parameter such as residence time and maximum/average temperature of the process gas, outer diameter and outer shell temperature of chamber and power of the combustion chamber are considered while designing the combustion chamber. CFD studies have shown that the secondary air injection is necessary for minimization of NO<sub>x</sub> formation. The secondary air injection also increases the residence time of the process gas while maintaining a uniform temperature inside the chamber, which is required for an efficient combustion of the PAH. The proposed combustion chamber gave an average residence time of 2s and an average temperature of around 800 °C suitable for PAH oxidation.

## ACKNOWLEDGMENT

The research work carried out in this article is funded by SCORE (Staged Combustion for Energy Recovery in Ferroalloy industry) project funded by Norwegian research council and The Norwegian Ferroalloy Producers Research Association (Ferrolegeringsindustriens Forskningsforening (FFF)). Funding from the SCORE project is greatly acknowledged

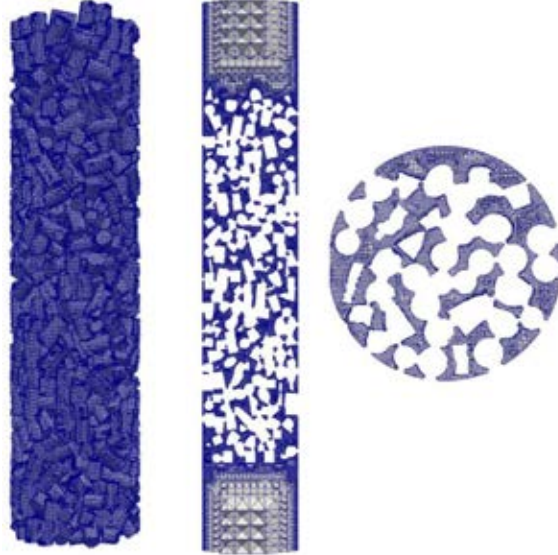
## REFERENCES

- ANSYS, INC. 2016. *ANSYS FLUENT Theory Guide*.
- Drake, Michael C., and Richard J. Blint. 1988. 'Structure of Laminar Opposed-flow Diffusion Flames With CO/H<sub>2</sub>/N<sub>2</sub> Fuel', *Combustion Science and Technology*, 61: 187-224.
- Heimir Hjartarson, Halldor Palsson, and Gudrun Saevarsdottir. 2010. "Waste Heat Utilization From A Submerged



- Arc Furnace Producing Ferrosilicon." In *The Twelfth International Ferroalloys Congress Sustainable Future*. Helsinki, Finland: INFACON.
- Kamfjord, N.E., E. H. Myrhaug, H Tveit, and Wittgens B. 2010. "Energy Balance Of A 45 Mw (Ferro-) Silicon Submerged Arc Furnace." In *The Twelfth International Ferroalloys Congress Sustainable Future*. Helsinki, Finland: INFACON.
- Mati, Karim, Alain Ristori, GaËlle Pengloan, and Philippe Dagaut. 2007. 'Oxidation of 1-Methylnaphthalene at 1–13 atm: Experimental Study in a JSR and Detailed Chemical Kinetic Modeling', *Combustion Science and Technology*, 179: 1261-85.
- Schei, A., J. K. Tuset, and H. Tveit. 1997. *Production of High Silicon Alloys* (Tapir).

# PACKED BED





# COMPARISON OF PARTICLE-RESOLVED DIRECT NUMERICAL SIMULATION AND 1D MODELLING OF CATALYTIC REACTIONS IN A PACKED BED

Arpit Singhal <sup>a, b\*</sup>, Schalk Cloete <sup>c</sup>, Stefan Radl <sup>d</sup>, Rosa Quinta-Ferreira <sup>b</sup> and Shahriar Amini <sup>a, c</sup>

<sup>a</sup> NTNU (Norwegian University of Science and Technology), Department of Energy and Process Engineering, Kolbjørn hejes v 1B, NO-7491, Trondheim, Norway

<sup>b</sup> University of Coimbra, Department of Chemical Engineering, Rua Sílvio Lima, Polo II, 3030-790 Coimbra, Portugal

<sup>c</sup> SINTEF Materials and Chemistry, Flow Technology Department, S. P. Andersens veg 15 B, NO-7031, Trondheim, Norway

<sup>d</sup> TU Graz, Institute of Process and Particle Engineering, 8010 Graz, Inffeldgasse 13/III, Austria

Corresponding author's e-mail: arpit.singhal@ntnu.no

## ABSTRACT

The work presents a comparison of catalytic gas-solid reactions in a packed bed as simulated on two widely different scales: direct numerical simulation (capable of accurately predicting transfer phenomena in and around a few particles) and 1D modelling (capable of engineering simulations of industrial scale reactors).

Particle-resolved direct numerical simulation (PR-DNS) is performed on a small geometry containing ~100 realistically packed monodisperse spherical particles generated via the discrete element method (DEM). These results are compared to a 1D packed bed reactor model using the effectiveness factor approach to account for intra-particle mass transfer and a suitable closure for gas-particle heat transfer.

The differences between the results from the two modelling approaches are quantified over a range of Thiele moduli, Prandtl numbers and reaction enthalpies. Results showed that existing 1D-model closures perform well for a simple first order catalytic reaction. Heat transfer completely dominates the overall reaction system when large reaction enthalpies are simulated, while mass transfer limitations dominate at low reaction enthalpies. Future work will extend this comparative approach to packings with more complex particle shapes and complex reactions.

**Keywords:** Direct numerical simulation (DNS), CFD-DEM, packed bed, catalytic gas-solid reaction, reaction rate, heat transfer, multiscale.

## NOMENCLATURE

### Greek Symbols

$\alpha$	Volume fraction
$\varepsilon$	Void fraction
$\phi$	Thiele modulus (Th)
$\eta$	Effectiveness factor

### Latin Symbols

$C_p$	Specific heat capacity of fluid [J/kg.K]
$C_A$	Concentration of species A [mol/m <sup>3</sup> ]
$D$	Molecular diffusivity [m <sup>2</sup> /s]
$d_p$	Diameter of the cylindrical particle [m]
$E$	Activation energy [J/mol]
$h$	Heat transfer coefficient [W/m <sup>2</sup> K]
$k_0$	Arrhenius constant [1/s]

$K_f$	Thermal Conductivity of fluid [W/m.K]
$Nu$	Nusselt number ( $hd_p/K_f$ )
$Pr$	Prandtl number ( $\mu C_p/K_f$ )
$R$	Gas constant [8.314 J/mol/K]
$R_{cat}$	Catalytic reaction rate [mol/m <sup>3</sup> s]
$r$	Radius [m]
$Re$	Reynolds number ( $\rho u_s d_p/\mu$ )
$T$	Temperature [K]
$u_s$	Superficial velocity of the fluid [m/s].

### Sub/superscripts

f	Fluid
s	Solid.
p	Particle.

## INTRODUCTION

Gas-solid reaction systems in packed beds are of great industrial influence, with the application widespread from process to metallurgical industries. The catalytic or non-catalytic role of the solid defines the complexity involved in the gas-solid reactions.

There are several advanced models available in literature for gas-solid reaction systems. The non-catalytic reaction systems are considered more complicated as they are transient in nature. The detailed review of such systems is described by (Ramachandran and Doraiswamy, 1982) and more recently by (Nashtae and Khoshandam, 2014). Meanwhile, (Ishida and Wen, 1968) have described the effectiveness factor ( $\eta$ ) in catalytic reactions for gas-solid systems. The effectiveness factor in heterogeneous catalyst reaction to obtain the intra particle diffusion in porous particles is suggested in (Levenspiel, 1999).

The recent work from (Yang et al., 2016) described an effectiveness factor for general reaction forms. They presented an analytical expression, which is applicable to wide range of reaction rate forms and provides a direct and computationally efficient approach of obtaining effectiveness factor in packed bed reactors. The validity of such a simplified model when added with heat transfer limitations motivates the current work. Hence, the objective of the work is to obtain a comparison in prediction of effectiveness factor for a catalytic gas-solid reaction on two distinct scales. Firstly, a PR-DNS study of a packed bed of ~100 spherical particles now involving a catalytic reaction based on our previously published work (Singhal et al., 2017) gives insight into a phenomenon of intra particle diffusion along with heat transfer limitations. Secondly, a 1D packed bed reactor model coupled with the effectiveness

factor model from (Yang et al., 2016) describes the intra-particle heat and mass transfer. The results obtained from both the approaches are compared and documented.

## METHODOLOGY

### Thiele Modulus and Effectiveness Factor

The effectiveness factor concept in heterogenous catalytic gas-solid reactions can be explained as the effect of intra particle diffusion on the reaction rate (Ishida and Wen, 1968; Levenspiel, 1999).

$$\eta = \frac{\text{actual reaction rate}}{\text{reaction rate without diffusion limitations}}$$

Thus, the effectiveness factor in catalytic reactions is directly linked with the Thiele modulus (Thiele, 1939). Thiele modulus is explained as:

$$\phi \approx \frac{\text{reaction rate}}{\text{diffusion rate}}$$

### PR-DNS Simulation Setup

The spherical particle bed is generated using DEM (Discrete Element Method) integrated in ANSYS FLUENT following the procedure described in the paper (Singhal et al., 2017). The geometry is meshed with fine body-fitted polyhedral elements both inside and outside the particles with resolution of  $dp/30$  on the particle surfaces and the growth rate of 20% (Figure 1).

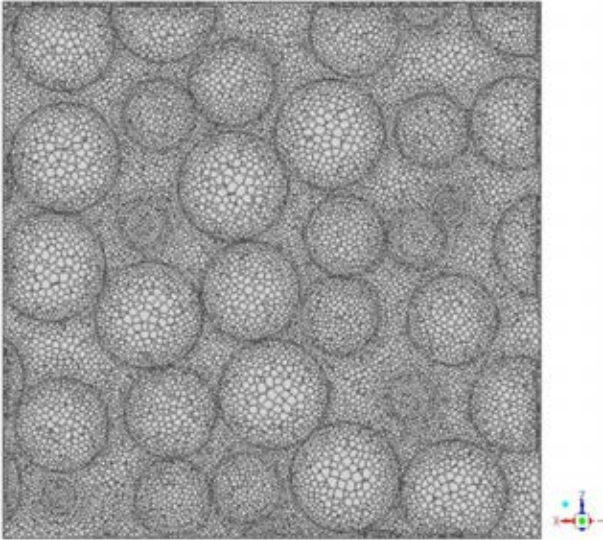
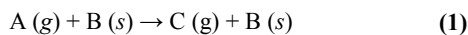


**Figure 1: A section ( $y = 0$ ) through the geometry meshed with polyhedral elements.**

ANSYS FLUENT is used to complete steady state DNS using the SIMPLE algorithm for pressure-velocity coupling with 2<sup>nd</sup> order spatial discretization of other equations. Steady state DNS was found to be sufficient for this case since no transient fluctuations occurred in the small spaces between particles (Singhal et al., 2017). The geometry incorporates a velocity inlet, a pressure outlet and a no-slip condition on the wall. The reaction takes place in the porous solid particles (grain model (Szekely, 1976)) modelled by the Eq. (1). The simulation parameters used in the DNS simulations are describe in the Table 1.



The reaction rate is described in the conventional way:

$$R_{cat} = \alpha_s k C_A \quad (2)$$

$$k = k_0 \exp\left(\frac{-E}{RT}\right) \quad (3)$$

Simulations were completed at three different levels of mass transfer resistance (Thiele modulus), heat transfer resistance (Prandtl number) and reaction enthalpy as outlined in Table 1. Mass and heat transfer was adjusted by setting the molecular diffusivity and gas-phase thermal conductivity according to the Th and Pr numbers specified in Table 1. No solids phase thermal conductivity was included in order to accentuate heat transfer resistances in the particle. For the reaction rate, the pre-exponential factor in Eq. (3) was chosen to result in a reaction rate constant of 10000 1/s at a temperature of 1000 K. A large activation energy is selected to accentuate coupling between heat and mass transfer.

**Table 1: Simulation parameters for PR-DNS**

Parameters	Value
Particle diameter ( $d_p$ ) (m)	0.001
Packed bed voidage	0.355
Particle void fraction (internal)	0.3
Density ( $\text{kg/m}^3$ )	Fluid :1    Particles :2500
Fluid velocity (m/s)	1
Inlet mole fraction (A)	0.1
Specific heat capacity ( $C_p$ ) ( $\text{J/kg/k}$ )	1000
Thiele moduli (Th)	5, 10, 20
Prandtl numbers (Pr)	0.4, 1.6, 6.4
Heat of reaction ( $\text{kJ/mol}$ )	100, 10, 0

### 1D Packed Bed Model

A detailed outline of the setup of the 1D model used in this work can be viewed in a recent work by the authors (Cloete et al., 2016). The model is solved in the commercial CFD code, ANSYS FLUENT 16.2, on a domain with 100 cells arranged in only one direction. In order to simulate a packed bed, the Eulerian Two Fluid Model approach is followed and the velocity of the solids phase is fixed to zero in all cells. Conservation equations for mass, momentum, species and energy are then solved in the conventional manner.

In the present study, the most important closures are the effectiveness factor for modelling intra-particle mass transfer limitations (Levenspiel, 1999) and the gas-particle heat transfer coefficient for modelling external heat transfer limitations (Gunn, 1978). The effectiveness factor for the simple first order catalytic reaction considered in this study is written as follows:

$$\eta = \frac{3}{\phi^2} (\phi \coth(\phi) - 1) \quad (4)$$

$$\phi = r_p \sqrt{\frac{k}{D_e}} \quad (5)$$

$$D_e = \frac{D\varepsilon}{\tau} \quad (6)$$

The Thiele modulus ( $\phi$ ) represents the ratio of kinetic rate to diffusion rate, so higher values represent greater mass transfer limitation. The effective diffusivity ( $D_e$ ) is composed of the molecular diffusivity ( $D$ ), the void fraction of porous particles ( $\varepsilon = 0.3$ ) and the tortuosity ( $\tau = 1$ ).

The classical Gunn correlation for gas-particle heat transfer is written as follows:

$$Nu = (7 - 10\varepsilon + 5\varepsilon^2) \left( 1 + 0.7Re^{0.2}Pr^{\frac{1}{3}} \right) + (1.33 - 2.44\varepsilon) + 1.2\varepsilon^2 Re^{0.7} Pr^{\frac{1}{3}} \quad (7)$$

Inlet and outlet boundary conditions as well as the domain length are set to identical values as the PR-DNS simulations. The solids volume fraction in the bed is taken as the product of

the mean solids volume fraction in the PR-DNS domain (0.645) and the solids volume fraction in the particles (0.7).

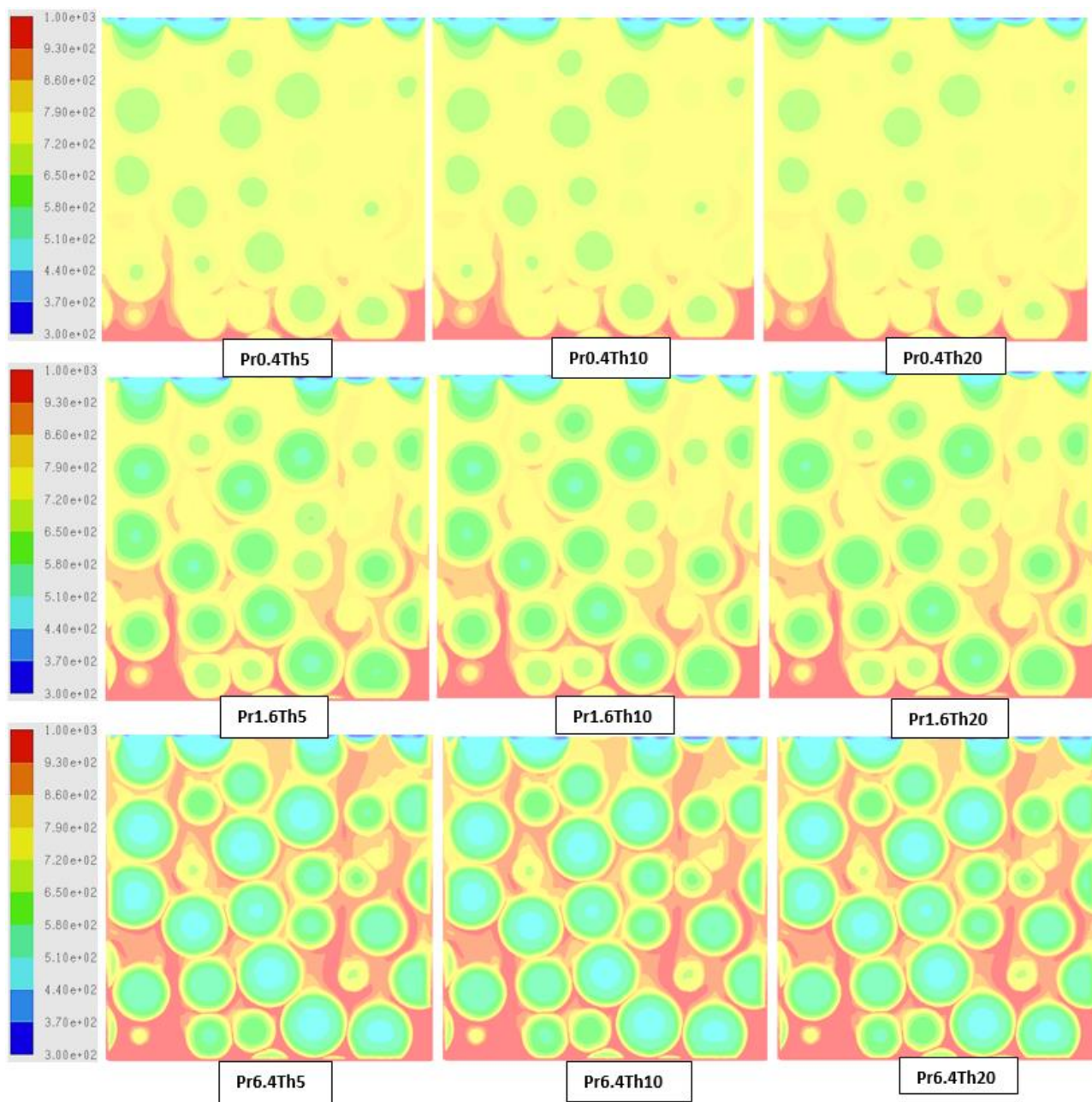


Figure 2: The PR-DNS results for the temperature variation in the packed bed of spherical particles for different Prandtl numbers (Pr) and Thiele moduli (Th)

## RESULTS AND DISCUSSIONS

### Heat and Mass Transfer in Densely Packed Bed

PR-DNS results for simulations completed with different Thiele moduli and Prandtl numbers for the highly endothermic reaction ( $dH_{rxn} = 100 \text{ kJ/mol}$ ) are shown in Figure 2 and Figure 3. The temperature variation in Figure 2 illustrates the increasing effect of the heat transfer resistance as Pr is increased by decreasing the gas-phase thermal conductivity. Even though the thermal conductivity is also very low inside the particle, it is clear that external gas-particle heat transfer still dominates.

This is most clearly visible in the Pr6.4 cases in Figure 2 where the temperature gradient inside the particles is small relative to the temperature gradient in the fluid film around the particles. Figure 3 illustrates the mass transfer resistances. It is immediately evident that mass transfer resistances are much less influential in this case than heat transfer resistances because the species concentration gradients are small relative to the temperature gradients in Figure 2. The Pr0.4Th20 case shows some intra-particle mass transfer resistance as a clear species gradient within the particles. The importance of heat transfer resistance relative to mass transfer resistance for this particular case will be further discussed in the next sections.

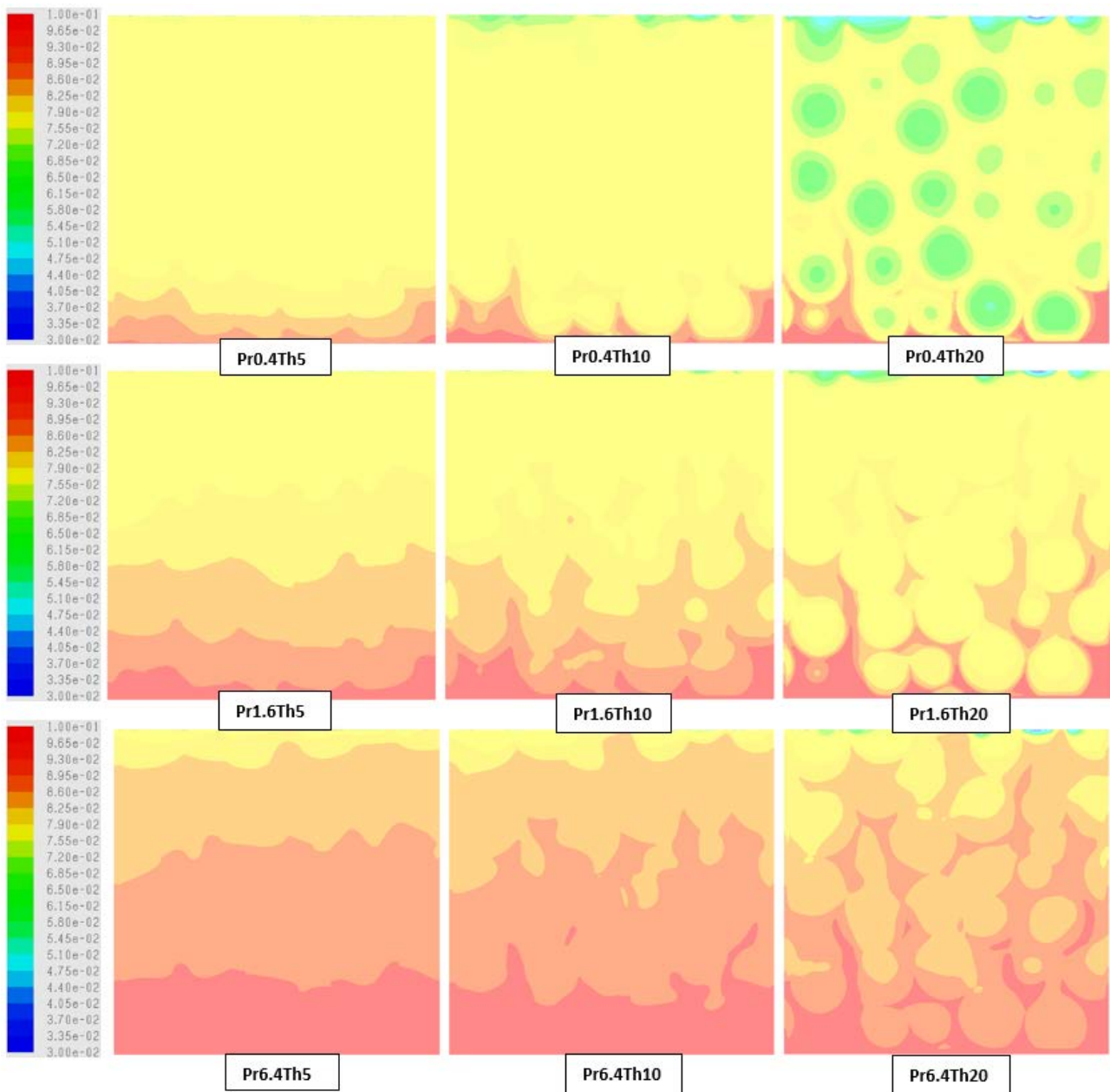


Figure 3: The PR-DNS results for the reactant (A) mole fraction in the packed bed of spherical particles for different Prandtl numbers (Pr) and Thiele moduli (Th).

### Individual Particle Data

The PR-DNS approach allows for extraction of detailed data from individual particles within the domain. In this way, the effectiveness factor for individual particles can be extracted and compared. This will be done for the case with the largest heat and mass transfer limitations (Th20-Pr6.4). The definition of the effectiveness factor becomes very important in this case. Three different approaches will be followed (Figure 4):

- **Species:** Comparing the species concentration on the particle surface to the average concentration in the particle (the effectiveness factor for an isothermal first order reaction)
- **Surface:** Comparing the average reaction rate in the particle to the reaction rate that would occur using species concentration and temperature on the particle surface.
- **Volume:** The same as the previous point, only using data averaged over the volume of the particle.

The fact that the “species” effectiveness factor is close to unity implies that mass transfer plays essentially no role in this particular case (the reactant concentration on the particle surface is essentially the same as the reactant concentration in the particle volume). This case is therefore almost exclusively controlled by heat transfer (as seen in the Th20-Pr6.4 case of Figure 2 and Figure 3).

The heat transfer limitation becomes clear when looking at the “surface” effectiveness factor. The temperature on the particle surface is a lot higher than inside the particle volume where the reaction takes place. Calculating the reaction based on the particle surface temperature would therefore result in large errors.

Interestingly, the “volume” effectiveness factor is larger than unity. This implies that there is a significant amount of temperature variation inside the particle, brought about by the assumption of zero thermal conductivity by the solid material. Naturally, this will not be the case in most catalyst particles, but it presents an interesting phenomenon. Given the exponential increase in reaction kinetics with temperature, any variation in temperature around the mean will strongly increase the average

kinetic rate inside the particle. This is what happened in this case: the actual reaction rate inside the particle was higher than the reaction rate calculated based on the average particle temperature.

### 1D Model Predictions

Comparisons between PR-DNS and 1D model results are discussed in this section. Firstly, the 1D model will be compared to PR-DNS results over a range of Prandtl numbers and Thiele moduli. Secondly, the reaction enthalpy will be changed and the models will be compared again. Finally, an important observation regarding the implementation of the 1D model will be presented.

#### Variation of Prandtl number and Thiele modulus

A comparison of axial reactant concentration is given in Figure 5 for nine combinations Prandtl number and Thiele modulus. It is clear that the 1D model successfully predicts the PR-DNS results.

In addition, the dominance of heat transfer limitations is clear in all cases because results for different Thiele moduli are essentially identical, whereas results for different Prandtl numbers differ substantially. As may be expected, the amount of reaction in this endothermic system decreases as Pr is increased by decreasing the gas phase thermal conductivity. A lower thermal conductivity implies greater gas-particle heat transfer resistance, thereby allowing less heat to enter and sustain the highly endothermic reaction.

The continued dominance of heat transfer resistance at  $Pr = 0.4$  is interesting given the clear intra-particle species gradients that can be observed in the Th20-Pr0.4 case in Figure 2. This is because the outer shell of the particles is slightly hotter than the centre, implying that reduced species concentrations in the centre of the particle (where the temperature is lower and the kinetics is slower) does not have such a large impact on the overall reaction rate.

Figure 6 shows the axial evolution of the difference between the average gas temperature and the average particle temperature. Again, it is clear that mass transfer limitations are essentially negligible, while gas-particle heat transfer dominates the system.

In this case, there is a clear deviation between the PR-DNS and 1D-simulation results: PR-DNS consistently predicts a larger difference between the average gas and particle temperatures. This implies that the PR-DNS predicts a lower particle temperature than the 1D simulations (gas temperature reduces with gas species concentration and is almost identical between the PR-DNS and 1D simulations). As mentioned in the previous section, the temperature variation inside the particle in the PR-DNS allows the reaction rate to be higher than that implied by the average particle temperature. On the other hand, the 1D simulation inherently assumes constant temperature in all particles. For this reason, the two models predict the same overall reaction rate at different average particle temperatures.

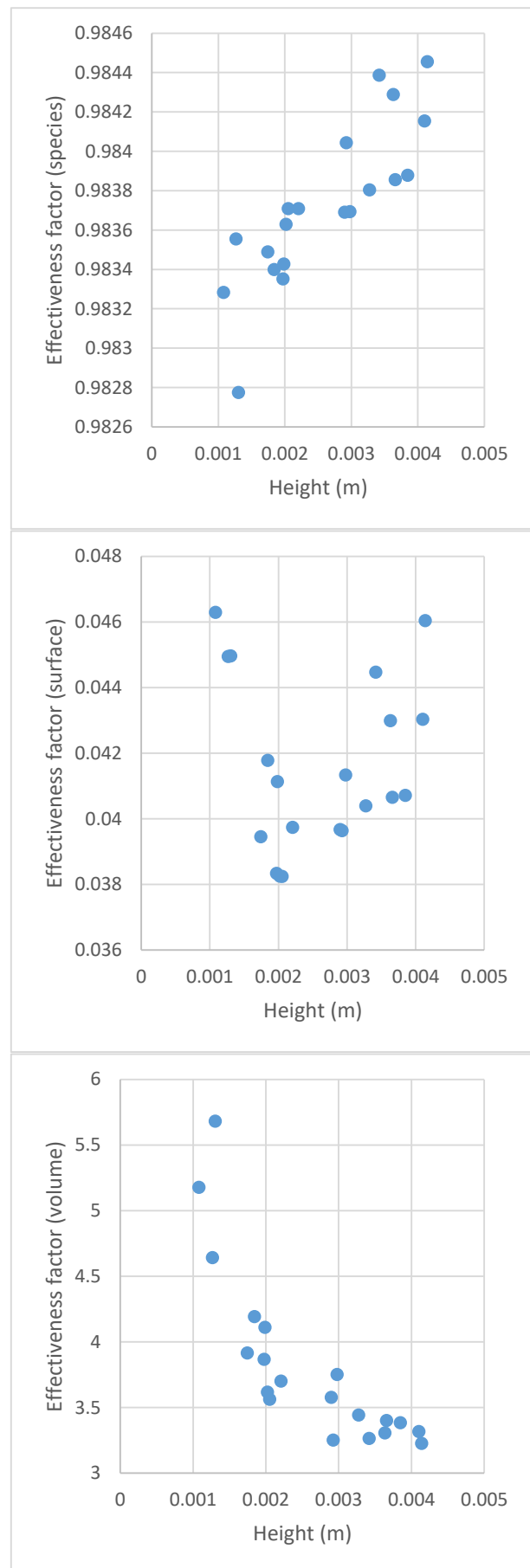
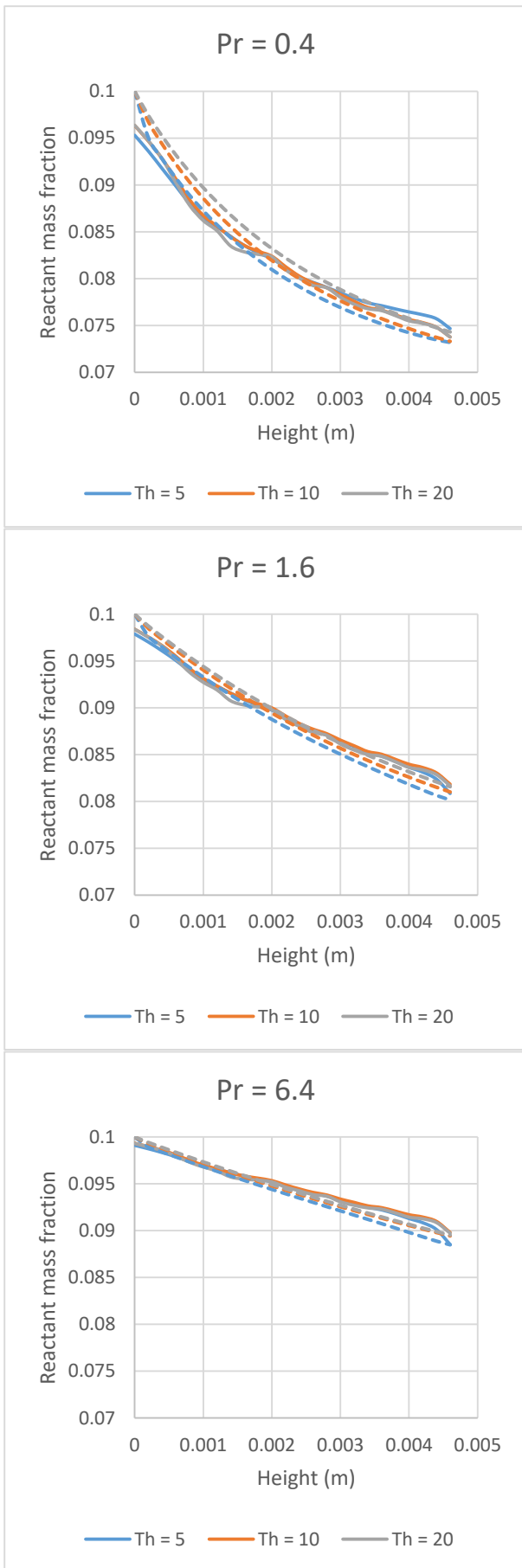
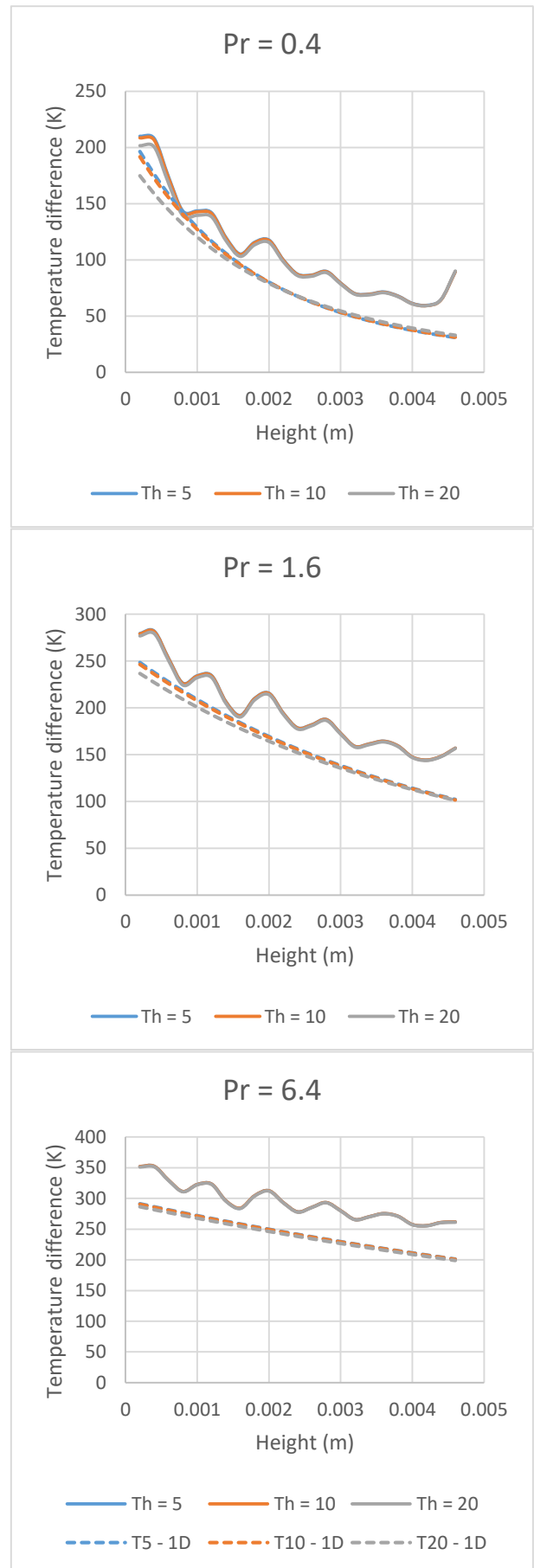


Figure 4: Three different representations of effectiveness factors for 20 particles from the Th20-P6.4 case.





**Figure 5: Comparison of axial species profiles between PR-DNS (solid lines) and 1D simulations (dashed lines) for different Prandtl numbers (Pr) and Thiele moduli (Th).**



**Figure 6: Comparison of axial gas-particle temperature difference between PR-DNS (solid lines) and 1D simulations (dashed lines) for different Prandtl numbers (Pr) and Thiele moduli (Th).**

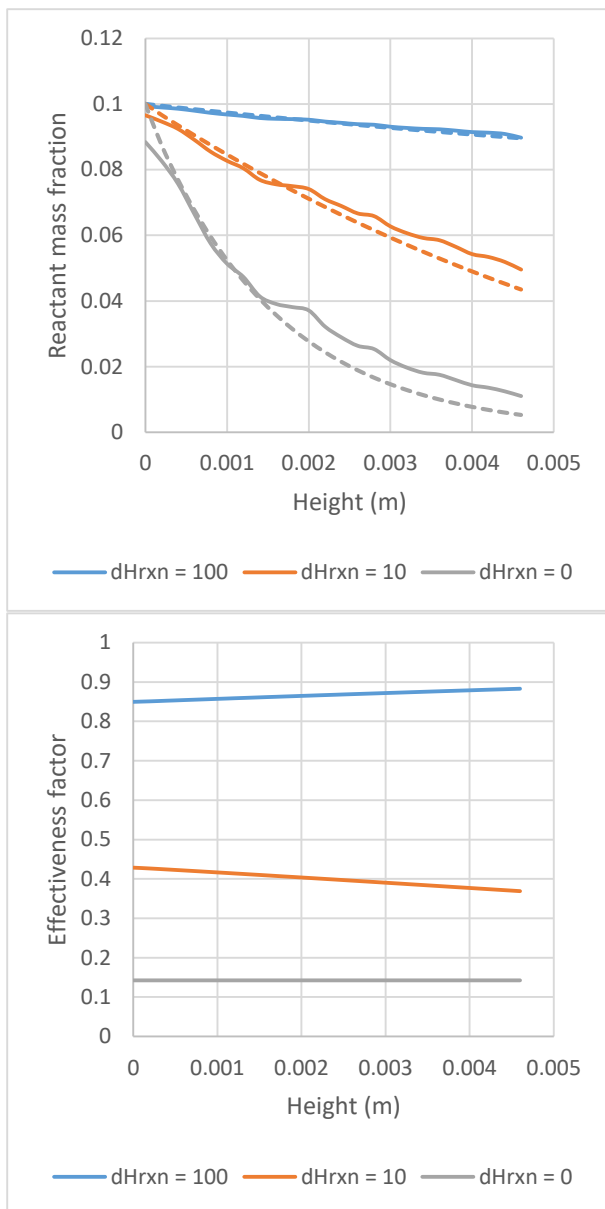


**Figure 7: Comparison of axial species profiles between PR-DNS (solid lines) and 1D simulations (dashed lines) for different reaction enthalpies ( $dH_{rxn}$  in kJ/mol). The effectiveness factor predicted by the 1D model is also shown for the different cases.**

#### Variation of reaction enthalpy

Results in the previous section were generated with a strongly endothermic reaction ( $dH_{rxn} = 100$  kJ/mol). This section will investigate three additional reaction enthalpies on the case with the greatest mass and heat transfer resistances (Th20-Pr6.4). Figure 7 shows the effect of reaction enthalpy on the reactant conversion. It is clear that a decrease in the reaction enthalpy greatly increased reactant conversion and that the 1D model accurately predicts the results from PR-DNS.

The increase in conversion with a decrease in the endothermicity of the reaction is simply due to the large heat transfer resistances included in this case. As the reaction becomes less endothermic, the requirement for heat flow into the particle reduces, thereby lessening the impact of this limitation. As a result, mass transfer becomes the controlling phenomenon, as can be seen from the reduction in the effectiveness factor in Figure 7.

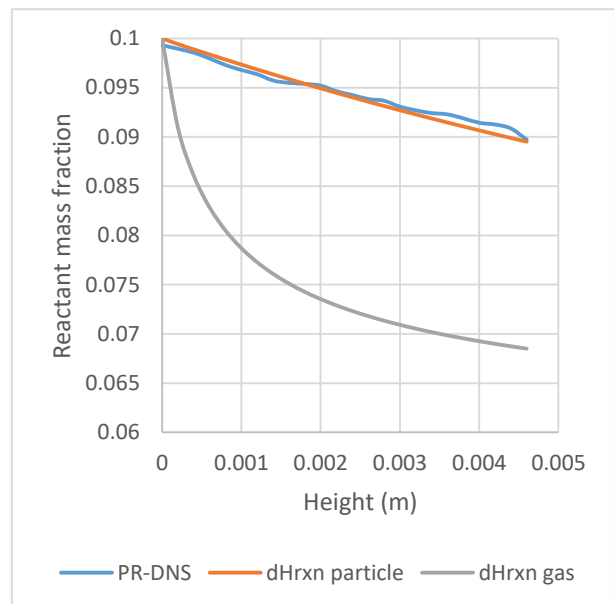


**Figure 8: Comparison of the 1D simulations to the PR-DNS results illustrating the importance of assigning the reaction heat to the particle phase.**

#### Importance of the reaction enthalpy source term

Finally, an important observation regarding the 1D-modelling of gas-solid reaction systems with significant reaction enthalpies can be shared. It is intuitive to add the energy source term related to a reaction involving gas species to the gas phase, but this results in large errors if significant gas-particle heat transfer limitations exist. To get accurate predictions, all reaction enthalpy must be assigned to the particle phase in the 1D simulation. This practice mimics the real case where all reaction heat is released or consumed within the particle, even if only gas species is involved in the reaction.

As an illustration of the importance of this observation, the axial species profiles from the Th20-Pr6.4 case with  $dH_{rxn} = 100$  kJ/mol are presented in Figure 8. It is clear that assigning the reaction heat to the gas phase completely over-predicts the reaction. This is because the large gas-particle heat transfer limitation observed in earlier sections is essentially eliminated if the heat is not extracted in the particle phase.

## CONCLUSION

This work presented a comparison of particle-resolved direct numerical simulations (PR-DNS) results with 1D modelling of a reactive gas-particle system with large heat and mass transfer limitations. Existing 1D model closures for intra-particle mass transfer and gas-particle heat transfer compared well to the PR-DNS results. However, it was shown that it is vitally important that all reaction heat must be assigned as a source term in the particle phase, even if only gas species are reacting.

When a highly endothermic reaction ( $dH_{rxn} = 100$  kJ/mol) is simulated, gas-particle heat transfer completely dominates the reaction phenomena in the particle assembly. Large heat consumption in the particle requires large quantities of heat to enter the particle from the gas phase. Mass transfer resistances become increasingly important as the reaction enthalpy becomes smaller until the system becomes exclusively mass transfer controlled when no reaction heat is simulated.

It was also interesting to observe that the 1D model still produced good results even though significant intra-particle heat transfer limitations were included to generate some temperature gradients inside the particles. This finding, combined with the knowledge that a constant particle temperature is normally a safe assumption, suggests that good models for external gas-particle heat transfer and internal mass

transfer are sufficient for accurate 1D model predictions of packed bed reactors.

## ACKNOWLEDGEMENT

This work is a part of a European Union project under Seventh research framework program (FP7/2007-2013) under grant agreement n° 604656 - A multi-scale Simulation based design platform for Cost effective CO<sub>2</sub> capture Processes using Nano-structured materials (NanoSim). The authors are grateful to European Research Council for its support. Additionally, the computational resources at NTNU provided by NOTUR, <http://www.notur.no>, were used during this project.

## REFERENCES

- Cloete, S., Gallucci, F., van Sint Annaland, M., Amini, S., (2016). "Gas Switching as a Practical Alternative for Scaleup of Chemical Looping Combustion". *Energy Technology* **4**, 1286-1298.
- Gunn, D.J., (1978). "Transfer of heat or mass to particles in fixed and fluidised beds". *International Journal of Heat and Mass Transfer* **21**, 467-476.
- Ishida, M., Wen, C.Y., (1968). "Comparison of kinetic and diffusional models for solid-gas reactions". *AIChE Journal* **14**, 311-317.
- Levenspiel, O., (1999). "Chemical Reaction Engineering, 3rd ed". John Wiley & Sons, New York.
- Nashtae, P.S.b., Khoshandam, B., (2014). "Noncatalytic gas-solid reactions in packed bed reactors: a comparison between numerical and approximate solution techniques". *Chemical Engineering Communications* **201**, 120-152.
- Ramachandran, P.A., Doraiswamy, L.K., (1982). "Modeling of noncatalytic gas-solid reactions". *AIChE Journal* **28**, 881-900.
- Singhal, A., Cloete, S., Radl, S., Quinta-Ferreira, R., Amini, S., (2017). "Heat transfer to a gas from densely packed beds of monodisperse spherical particles". *Chemical Engineering Journal* **314**, 27-37.
- Szekely, J., Evans, J.W., Sohn, H.Y., (1976). "Gas-solid reactions". Academic Press, New York.
- Thiele, E.W., (1939). "Relation between Catalytic Activity and Size of Particle". *Industrial & Engineering Chemistry* **31**, 916-920.
- Yang, W., Cloete, S., Morud, J., Amini, S., (2016). "An Effective Reaction Rate Model for Gas-Solid Reactions with High Intra-Particle Diffusion Resistance", *International Journal of Chemical Reactor Engineering*, p. 331.

## NUMERICAL INVESTIGATION OF PARTICLE TYPES INFLUENCE ON PACKED BED ADSORBER BEHAVIOUR

**Bahram HADDADI<sup>1\*</sup>, Christian JORDAN<sup>1</sup>, Hamid R. NOROUZI<sup>2</sup>, Michael HARASEK<sup>1</sup>**

<sup>1</sup> Technische Universität Wien, Institute of Chemical Engineering, Getreidemarkt 9/166, A-1060 Vienna, AUSTRIA

<sup>2</sup> Shahid Beheshti University, Department of Pharmaceutical Engineering, Medical Plants and Drug Research Institute, Tehran, IRAN

\* E-mail: bahram.haddadi.sisakht@tuwien.ac.at

### ABSTRACT

Packings are an inseparable part of Chemical Engineering processes like adsorption. Computational Fluid Dynamics (CFD) simulations on fully resolved packed beds can provide local flow information (e.g. wall effects and flow bypasses) which cannot be identified using “black box” and/or one-dimensional modelling, which can have severe influence on the adsorption characteristics.

Creation of random packed beds is one of the main challenges in studying fully resolved packings; this can be covered using Discrete Element Methods (DEM). In this study the effect of using different types of particles on the fluid flow pattern in the packings was investigated. Three different types of particles (mono-disperse spheres, mono-disperse cylinders and poly-disperse cylinders) were packed into beds with identical dimensions (same height, same diameter) using custom DEM code and meshed using open source tools.

CFD simulations were performed using adsorpFoam, a newly developed solver for modelling adsorption, based on open source CFD code OpenFOAM<sup>®</sup>. In this stage of study particles were considered as non-reactive to investigate fluid flow only.

From simulated packings porosities as well as particle arrangements and positions have been analysed. Frequency and positions of high velocity spots were extracted. The residence time distributions were also analysed.

Furthermore, experiments with the identical types of particles were performed to verify the validity of the packing structure and global simulation results. The pressure drops derived from simulations were compared to the measured values from the beds in the lab and also available correlations and a good agreement was observed.

**Keywords:** Computational Fluid Dynamics, Packed bed, Particle, Discrete Element Method, Bypass, Pressure drop, OpenFOAM<sup>®</sup>.

### NOMENCLATURE

#### Latin Symbols

D	Bed diameter [m]
d	Particle diameter [m]
m	Mass [kg]
p	Pressure [Pa]
q	Energy [J]
S	Source term [ $\text{kg}/\text{m}^3/\text{s}$ , $\text{J}/\text{m}^3/\text{s}$ ]
T	Temperature [K]

<b>u</b>	Velocity [m/s]
<b>Y</b>	Mass fraction

#### Sub/superscripts

fluid	Fluid phase
solid	Solid phase
M	Mass
E	Energy
i	Specie i

### INTRODUCTION

In chemical engineering operations usually large contact surface areas are required for improving mass and heat transfer between phases. Packed beds are devices used for providing large surface area between fluids and solids. They are used in different processes like adsorption and chromatography. Packed beds are typically a column filled with solid particles. The shape of column, particles and D/d can have a critical effect on the performance and efficiency of the packed beds. A not optimally packed bed can have bypasses which causes small contact time and area between fluid and solid or it can have dead zones where there is no flow and that can cause very low mass and heat transfer (which are mainly driven by diffusion) and creation of hot spots inside the bed (Wakao and Kagei, 1982). There are different approaches to study design and packing of packed beds, e.g. zero or one dimensional process simulation approaches. Among available approaches computational fluid dynamics (CFD) can provide three dimensional spatial resolution besides time resolution which makes this tool very promising for studying local effects (e.g. bypasses and hot spots) in the packed beds (Calis et al., 2001).

Eppinger et al. (2010) introduced a new meshing method of beds filled with mono sized spherical particles by flattening the particle-particle and particle-wall contact points. They studied the pressure drop and the porosity of the beds with D/d between 3 and 10 using CFD. Behnam et al. (2013) suggested a new approach for modelling radial thermal convection based on averaged radial and axial velocity components from detailed CFD simulation of spherical packed beds. Dixon and Nijemeisland (2001) showed how CFD can

be used as a tool for studying packed beds in detail. They suggested development of reduced models which are detailed enough to be used for design purposes based on the detailed CFD simulations. They studied low  $D/d$  (2-4) bed behaviour for spherical particles. Taskin et al. (2010) used CFD for refining cylindrical particles for investigation of the flow, transport and reaction interactions in this beds and they observed non-uniform and non-symmetric surface and intra-particle variations and also steep temperature gradients at tube wall. Bey and Eigenberger (1996) performed experiments on different sphere, ring and cylinder sizes ( $3.3 < D/d < 11$ ) and measured the radial velocity profiles below the beds and used the data for derivation of a model for predicting the porosity inside the beds. Beavers et al. (1973) performing experiments studied the effect of bed size on the porosity and flow characteristics of spherical random packed beds and they found out the porosity of the beds is not influenced by the bed size for  $D/d > 15$ . Experimental measurements performed by Ribeiro and Pinho (2010) on random packed beds of mono sized spheres were used for developing of a correlation for average bed porosity. Haughey and Beveridge (1969) analysed regular and random packed beds of spheres as a basis for examination of more general random packed beds. Dixon et al. (2011) studied the meshing of a single spherical particle and its effect on the quality of the simulations for heat transfer and fluid flow, they (Dixon et al., 2013) used this pre-study to investigated the effect of meshing and mesh quality at particle-particle and particle-wall contact points of spherical packings on the fluid dynamics and heat transfer inside the beds. They suggested using bridges between particles and also between particles and wall to reduce the error in calculated drag force and heat transfer.

Usually previous studies on packed beds limited to low  $D/d$  ratio or just one type of particles. The presented approach in this study is has been used with packings with  $D/d > 25$  and including functionalized particles (e.g. adsorption) with internal heat and mass transfer and different particle types and particle size distribution. With this analysis it would be possible to investigate local overheating effects during e.g. adsorption process etc. However due to experimental limitations the columns with  $D/d \sim 6$  was used for this validation study. Spherical and cylindrical particle types are commonly used in packed beds (Mueller, 1992 – Giese et al., 1998). In this study three different types of particles (spheres, mono disperse cylinders and particle size distribution) were packed in the identical bed geometries using an in-house discrete element method (DEM) code. Similar packings were also built in the lab to verify the packing creation, meshing and CFD simulation of the beds. Different packing parameters from CFD/DEM (e.g. porosity, velocity distribution...) were investigated and compared for these three packings.

## SIMULATION WORKFLOW

### Packing creation

The first step in preparation for CFD simulations was creation of packings. For this purpose an in-house

discrete element method (DEM) code was used. DEM is a numerical approach for modelling large number of particles interacting with each other and the surrounding geometry (Munjiza, 2004). Granular mediums of random shapes can be modelled with different methods. Multi-sphere approach is a powerful method for modelling random shapes. In this approach each particle is represented by a set of overlapping spheres which are treated as a unit and move together. However the diameter of spheres representing a particle is smaller, a more accurate representation of the particle shape is created. On the other hand by increasing the number of sub-spheres computational efforts also increases, therefore it is important to select a reasonable sub-sphere number to get the best possible simulation of the particles in reasonable time (Kruggel-Emden, 2008).

**Table 1:** Particle types and sizes.

Packing	Distribution type	Characteristic diameter [m]	Characteristic Length [m]
Sphere	Mono sized	0.006	-
Cylinder type 1	Mono sized	0.00506	0.00513
Cylinder type 2	Particle size distribution	0.0039 (0.0025 – 0.0044)	0.0054 (0.0029 – 0.0094)

Particle types and their sizes can be seen in table 1. Mono-disperse sphere particle and two types of cylindrical particles were packed into the beds. The cylinder type 2 particles have a varying aspect ratio ( $l/d$ ) from 0.8 to 2.3. Particles were released into a cylindrical bed with inner diameter of 0.032 m from the height of 0.2 m from bottom of the bed. Particles were falling freely into the bed by gravity ( $9.8 \text{ m/s}^2$ ) in the direction of main bed axis.



**Figure 1:** Packing creation for mono-disperse cylinders: a – filling the beds with DEM code, b – correcting the bed heights to 0.013 m and exporting the STL, c – merging the main bed and particles STLs.

The filling was continued till a filling height more than 0.13 m was achieved (figure 1-a). Then the heights of beds were corrected to 0.13 m by keeping only the particles which were complete below this height. Particles were exported as STereoLithography (STL)

file format (Jacobs, 1992) from the DEM code (figure 1-b). Bed geometry were also drawn in Catia® (3DS, 2017) and exported as STL. Particles and bed STLs were merged to create the final STL for meshing (figure 1-c).

### Meshing

Prepared geometries in STL format were meshed using an open-source tool snappyHexMesh® which is an automatic mesher supplied with OpenFOAM® (OpenFOAM, 2017).



**Figure 2:** Mesh created for mono-disperse cylinders: a – mesh on the particles surfaces, b – mesh on the vertical centre cut plane, c – mesh on the horizontal centre cut plane.

In this mesher the main geometry is mapped into a base hexahedral mesh by refining the mesh close to STL surfaces and removing of the parts of the mesh which are not needed and snapping the mesh to STL surface (figure 2). The background mesh had a cell size [cubes] of 0.005 m and was refined on the STL surface up to four levels. In each level, the mesh is cut into half in each direction. The final meshes had around 1.5 million cells. In this study a new method for treating the contact points between particles and particles and walls was introduced. Creating the meshes using this method a bridge connection between the particles was created similar to Dixon et al. (2013) and Ookawara et al. (2007). Unlike their approach in this study the bridge is introduced by mesh and its size can be controlled by the minimum mesh size. The meshes had good quality and for improving the quality the very few skewed cells (< 10 cells in total) were removed from the meshes.

### Solution

For simulating the flow through the packed bed a solver based on the open-source CFD code OpenFOAM® was developed. The new solver (adsorpFoam) is capable of modelling adsorption in the packed beds. In adsorption process target molecules are removed selectively from fluid by the solid (De Boer, 1956).

In the figure 3 the algorithm for adsorpFoam is shown. At the beginning of the time step the coupled Navier-Stokes and continuity equations are solved using the pressure implicit with splitting of operator algorithm

(PISO) based on the pressure and velocity values from previous time step or initial conditions. Using the calculated pressure and velocity fields and based on the adsorption model applied, sink and source terms for heat and mass transfer are calculated. In the next step mass and heat transfer equations are solved and boundary conditions and also fluid and solid properties are updated.

Since the focus in this study is on the flow structure in the packed beds, the adsorption was deactivated to just simulate the flow through the beds.

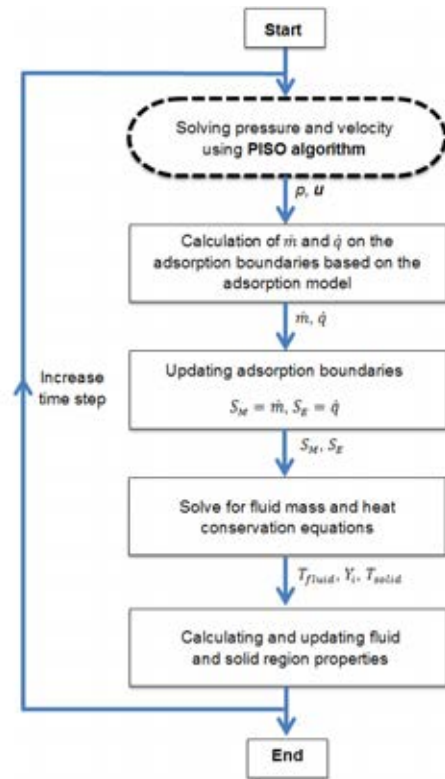


**Figure 3:** adsorpFoam algorithm.

### Data extraction and evaluation

For analysing the simulation results data were extracted using open-source tool ParaView® (ParaView, 2017). An automation script was written for ParaView® to extract the radial and axial data from simulated beds. Two types of data were extracted and compared from beds:

- Geometrical information: number of particles, average porosities, particle centre positions, particles angles and axial porosities.
- Flow properties: bypasses, velocities, velocity distribution along radius and height, high velocity points, pressure drops and residence time distributions (RTD).

As it can be seen from figure 4 two sets of angles were extracted and analysed for cylindrical particles. The first angle (in this text it is referenced as “Horizontal angle”) is the angle between the axial particle centre line and the horizontal plane (figure 4-a) and the second angle (in this text it is referenced as “Radial angle”) is the angle between the particle centre line and the line which passes from centre of bed to the centre of mass of the particle (figure 4-b).

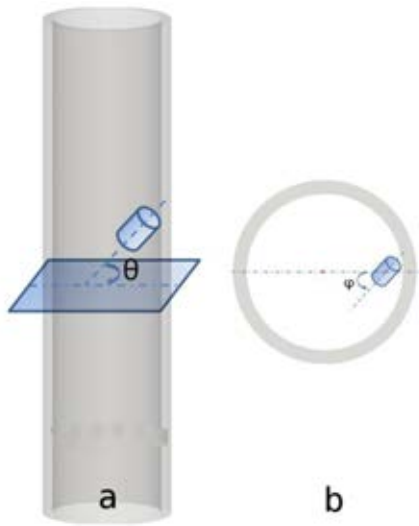


**Figure 4:** Particles angles: a – Horizontal angle: angle with horizontal plane, b – Radial angle: angle with line passing centres of particle and bed central axis.

**EXPERIMENTAL**

To verify the work flow for creation and simulation of the packings a similar bed with the same dimensions was built and packed with similar particle types.

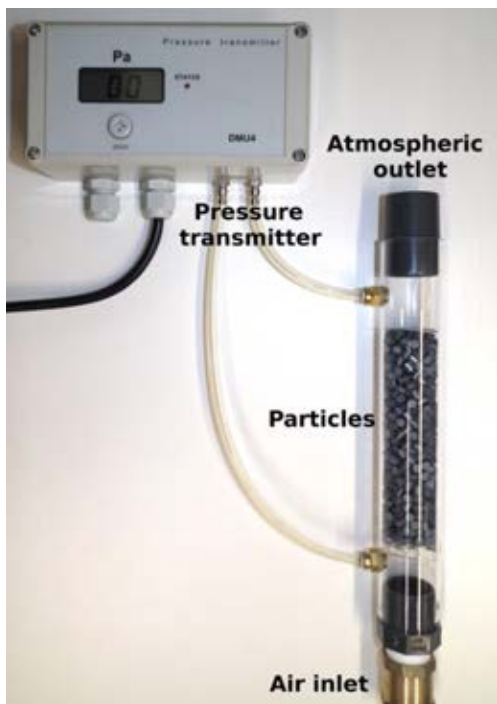


**Figure 5:** Experimental setup for mono-disperse cylinder packed bed.

As it can be seen in figure 5 air at ambient conditions (298 K and  $10^5$  Pa) enters the bed at the bottom and exits after passing the particles from atmospheric outlet. Average porosity and number of particles for all three types of particles were measured and compared to the results from DEM simulation. Also the pressure drop at different inlet velocities was measured and compared to the simulations.

**SIMULATION SETTINGS**

Identical to the experiments the fluid used for simulations was air at ambient conditions (298 K and  $10^5$  Pa). Walls and particles surfaces were treated with no-slip and isothermal boundary conditions. The outlet was set to pressure-outlet with absolute constant pressure of  $10^5$  Pa and zero-gradient velocity. For comparison between simulation and experiments the simulation inlet was set to velocity inlet and it was varied from 0.1 m/s to 1.6 m/s. The comparisons between simulations of three different types of packings were done at an inlet velocity of 0.829 m/s. No turbulence model was used since the Reynolds number in the packings are less than 2500 based on both Reynolds definitions: superficial velocity and bed diameter and also local velocities and particle diameters.

**RESULTS AND DISCUSSIONS**

**Simulations verification**

Similar packings using DEM code and in lab were created. The beds were packed (for both experiments and DEM) by releasing the particles from the plane positioned at distance two times the final beds height (26 cm) from bottom of the beds to create consistent packed beds in both methods. Different values from simulations were compared to the lab experiments. In table 2 in the second column (Number of particles) needed particles to fill the bed up to 0.13 m for both simulations and experiments were counted and compared. As it can be seen there is less than 2 % difference between number of particles packed into the beds using the DEM code and particles which were packed into the beds in the lab. In the third column the calculated and measured porosity from both methods are compared. In this case the deviation between simulations and lab experiments is bigger compared to the number of counts; it is mainly because the meshing in the areas where two particles collide, these regions were not fully resolved to keep the mesh computationally affordable. Also the particles used in reality were not perfect (especially cylinders) and that also caused larger deviation between the simulation and lab results.

**Table 2:** Comparison between DEM simulations and experimental measurements (the deviation between two methods is shown as percentage).

Packing	Number of particles (DEM/Reality)	Overall porosity (DEM/Reality)
Sphere	533/525 ( $\Delta = 1.5\%$ )	0.429/0.432 ( $\Delta = 0.7\%$ )
Cylinder type 1	599/605 ( $\Delta = 1.0\%$ )	0.406/0.38 ( $\Delta = 6.4\%$ )
Cylinder type 2	1007/1000 ( $\Delta = 0.7\%$ )	0.418/0.393 ( $\Delta = 6.0\%$ )

Figure 6 shows the measured and simulated pressure drop for spheres at different inlet (superficial) velocities. The results are also compared to very well-known Ergun equation (Ergun, 1949). As it can be seen good agreement between simulation, correlation and experiment can be observed.

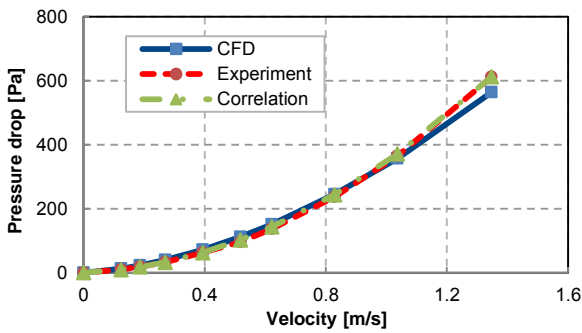


**Figure 6:** Pressure drop for spheres packed bed, simulation, correlation (Ergun) and experiments.

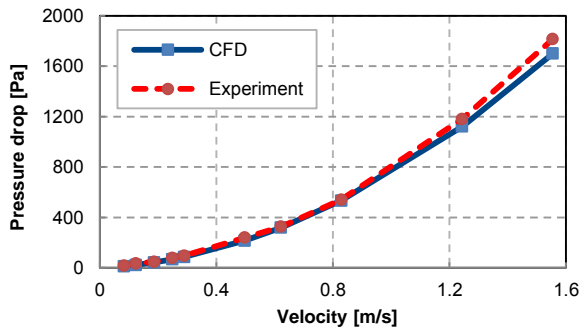


**Figure 7:** Pressure drop for cylinders type 1 packed bed, simulation and experiments.

The same comparison was also performed for the packed bed with cylindrical particles. The measured values from lab setup were compared to the simulations and good agreement was observed (figure 7 and figure 8). The slight deviation between measurements and experiments can be justified by the small difference in the created and simulated packed beds porosities.

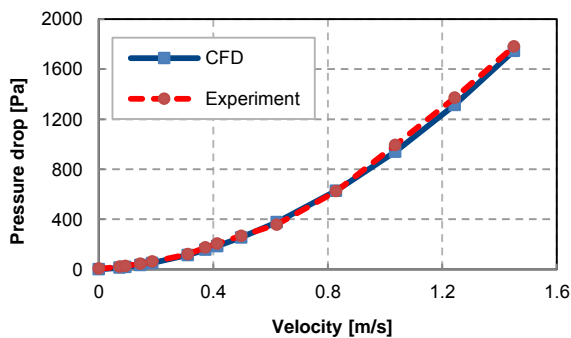


**Figure 8:** Pressure drop for cylinders type 2 packed bed, simulation and experiments.

### Radial and axial porosities

Besides overall porosities calculated and reported for all three types of particles (table 2), local porosities in the bed radial direction and also bed axial direction were extracted and analysed.

As it can be seen from figure 9 by moving from centre of bed towards the walls the porosity fluctuates and reaches its maximum at bed walls (the data was extracted from 64 co-centric cylindrical cuts). The porosity for spherical particles was also compared to available correlations from literature (De Klerk, 2003) and a good agreement can be observed in the predicted frequency and amplitude of porosities fluctuations.

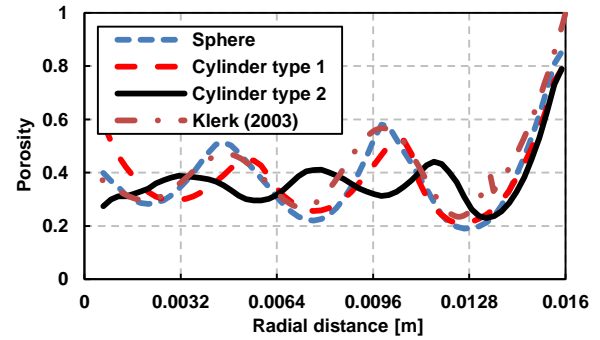


**Figure 9:** Average porosity on cylindrical co-centric cuts for all three types of particles vs. distance from centre of beds and also comparison to available correlation for spheres.

Higher porosity at walls creates possible fluid bypasses at walls. As it can be seen spheres have the biggest fluctuations in the porosity along the radius compared to the cylindrical packings. By changing the particle shape from spheres to cylinders these fluctuations reduces and in the case of cylinder type 2 particles (cylindrical particles with particle size distribution) packed into the bed the fluctuations in the porosity are smallest. The frequency of repetition of these fluctuations correlate with particles equivalent diameters which can be seen more clearly in figure 10, where the centres of mass of all of the particles are mapped to the top view. With spheres a clearer pattern in the centres of particles can be seen and this fades with going to particle size distribution cylinders.

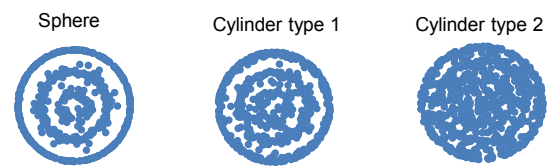


**Figure 10:** Centres of mass of particles mapped on the top view.

Figure 11 shows how the porosity changes over bed height for the different types of particles (data extracted over 520 planes along the bed height and the moving average of porosity with 20 points).

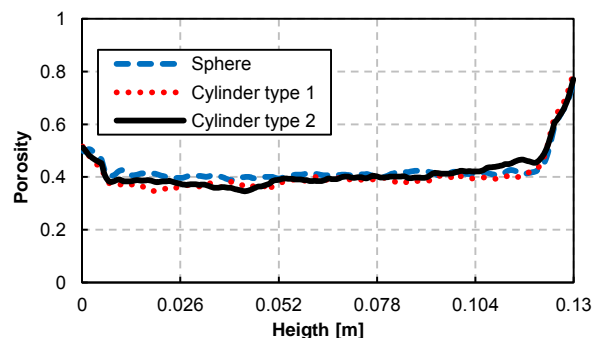


**Figure 11:** Moving average porosity along bed height for all three types of particles.

The porosity is almost constant and close to average porosity for spheres but it increases slightly along the bed height for cylinders because of the shaking effect of particles during the filling and repositioning of already filled particles. At the beginning and end of the bed the porosity increases, because of the end effects of particle

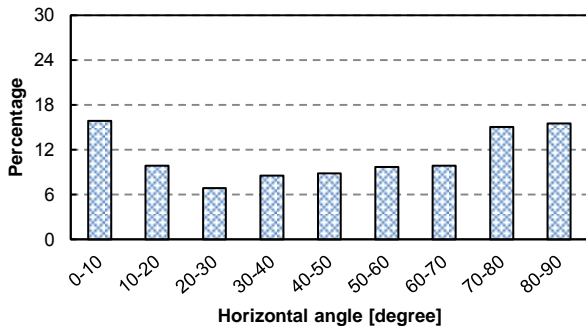


contact with inlet section and also not smooth end of the bed.

**Particles alignment**

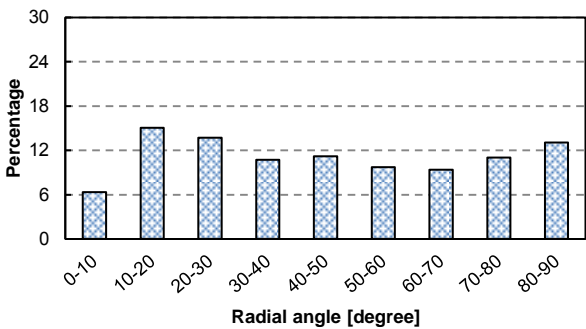
Another interesting parameter to be investigated for cylindrical particles is how particles align during their packing in the beds and effects of size distribution on their arrangement. If the particles tend to align along a specific direction (e.g. bed main axis) it is more probable channelling happens and that causes low fluid residence time and (short contact between fluid and solid) and decrease in adsorption performance.

Figure 12 shows how horizontal angle varies for cylinder type 1. As it can be seen for the full packing particles tend to be positioned more horizontally/vertically compared to incline in the bed.



**Figure 12:** Horizontal angle distribution for mono-disperse cylinders.

In comparison particles distribution at all radial angles (figure 13) is similar and particles are frequently positioned more randomly compared to their horizontal angle.



**Figure 13:** Radial angle distribution for mono-disperse cylinders.

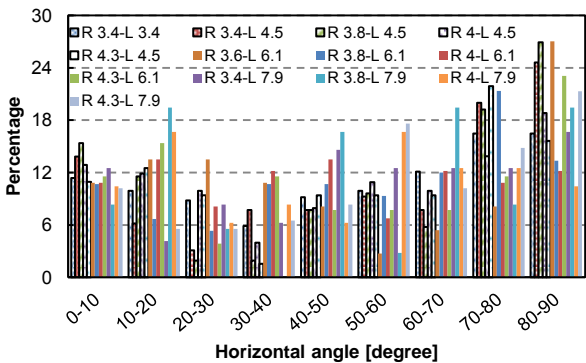


**Figure 14:** Horizontal angle distribution for particle size distribution cylinders.

In the bed with cylinder type 2 (particle size distribution) particles tend to be more vertical than horizontal or inclined. As particles become shorter in length they are more positioned vertically compared to longer particles (figure 14).

As it can be seen in figure 15 like mono-disperse cylinders, cylinder packing with particle size distribution has also more random spread of particles radial angles.

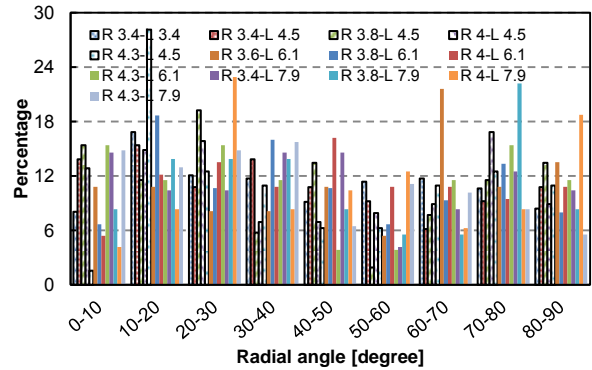


**Figure 15:** Radial angle distribution for particle size distribution cylinders.

**Pressure drop**

One of the parameters in operating cost of packed beds is the bed pressure drop. However this pressure drop is higher more energy is needed to pass the fluid through the bed. In figure 16 pressure drop for the beds is shown and compared. Pressures are average pressure extracted over 11 equally spaced planes along bed height. As it can be seen cylinders with particle size distribution have the highest pressure drop compared to the other two types of packings (as they have lowest void fraction). The pressure drop for sphere packing is more linear compared to the other beds, since the spheres are positioned more arranged and do not reposition and become denser by adding layers of particles. In the beds with cylinders adding more layers cause the lower layers to rearrange and become denser. This caused denser packing at the lower parts of the bed and contributed to the higher slope of the pressure drop curve in the lower zone. This effect can be seen more in the bed with particle size distribution.

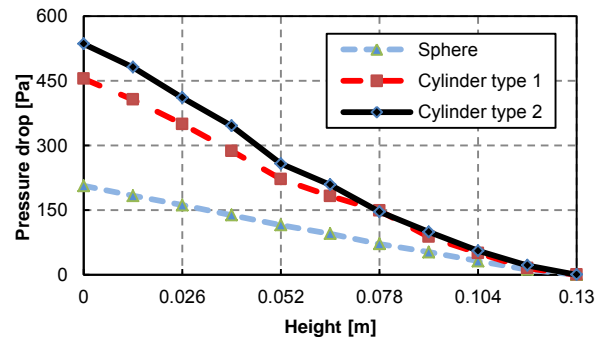


**Figure 16:** Pressure drop along bed height for different types of packing.

**Velocity**

Table 3 shows the average physical velocity magnitude (axial velocity difference less than 1 %) and also the peak velocities occurring in the beds (inlet and outlet

sections are excluded). The average velocity is very similar the same in all of the beds since the average porosity was also similar. But maximum velocity in the beds is much higher in the bed with particle size distribution particles (more than two times more than spheres bed).

**Table 3:** Average and maximum physical velocity for the beds.

Packing	Average velocity magnitude [m/s]	Maximum velocity magnitude [m/s]
Sphere	1.93	7.5
Cylinder type 1	2.04	13.2
Cylinder type 2	1.98	15.6

Figure 17 shows how this high velocity points are distributed along the height and radius of the bed geometry. All the regions with velocity eight times bigger than inlet velocity are extracted and shown in this figure. In the upper part of the figure the beds are shown from front view and high velocity points are coloured with their distance from centre of the bed. In the lower part of the figure the same high velocity points are shown on the top view but coloured with their height from beginning of the packings.

As it can be seen and high velocity points happen more often in the cylindrical packed beds compared to sphere bed. In the sphere bed there are just a few high velocity points which shows the homogeneous distribution of the flow in the beds compare to the other beds. High velocity points are located mostly close to walls which can be justified by wall effects and higher porosities at the walls and they are randomly distributed along the bed height.

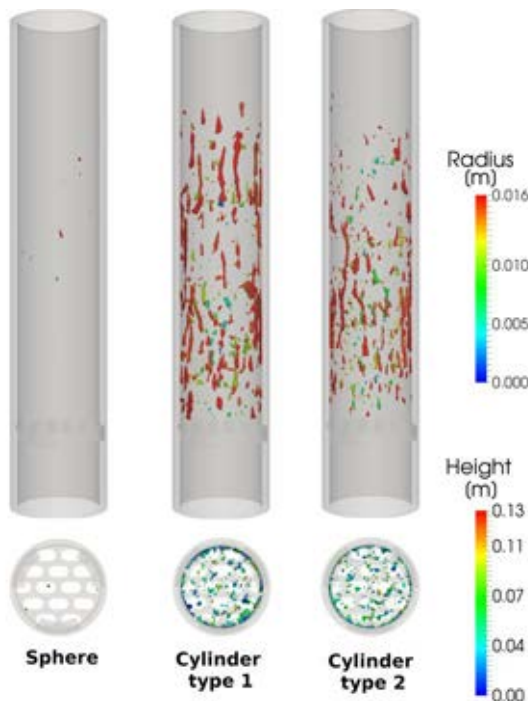


**Figure 17:** High velocity points (higher than eight times inlet velocity) in the beds: upper picture coloured with their distance from centre of the bed, lower pictures coloured with their distance form bottom of the packings.

The radial and axial velocity distributions in the beds follow similar pattern as the radial and axial porosity in

the beds. Overall the velocities are higher close to walls compared to centre of the beds (figure 9).

**Residence time distribution**

Using residence time distribution (RTD) the amount of time a fluid element spends inside the beds can be evaluated and compared to the behaviour of a plug flow reactor. For simulating RTD a tracer was inserted uniformly at the beds inlet and its concentration at the outlet was recorded and compared for all three beds over the time.

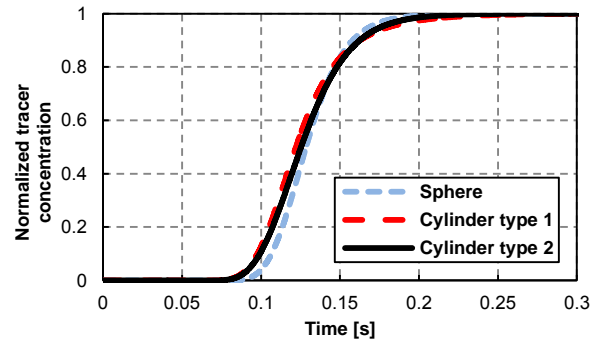


**Figure 18:** Residence time distribution for all three beds.

Figure 18 shows the RTD for three different types of bed. RTD curves look very similar since the porosities are comparable. Just in the sphere bed the breakthrough curve is steeper which shows it has a closer behaviour to plug flow and less channelling inside the bed. Tracer iso volumes (normalized concentration higher than 0.5) at  $t = 135$  ms can be seen in figure 19.

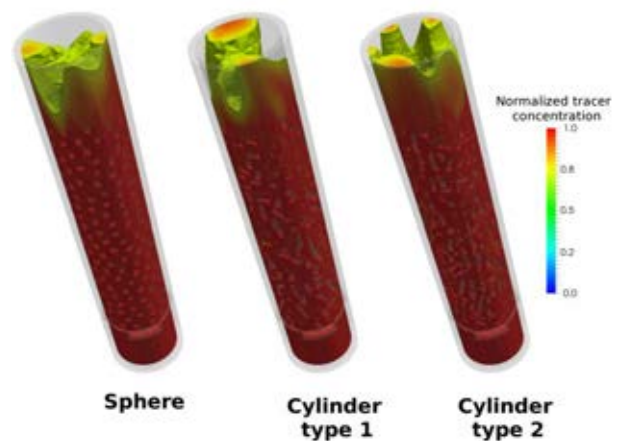


**Figure 19:** Tracer iso volumes (normalized concentration higher than 0.5) coloured with Normalized tracer concentration at  $t = 135$  ms.

**CONCLUSION**

In this study the effects of particle type on the packing and packing properties were investigated. For this purpose three different types of particles (spheres, mono-disperse cylinders and particle size distribution particles) were packed into the same bed geometry up to the same height using a custom DEM code and simulated with a new solver developed based on the OpenFOAM® platform for simulation of adsorption phenomena. Experiments with similar types of particles in a bed with the same dimensions as simulated were performed to confirm the validity of the creation and

analysis of the packings. Overall porosity of the beds, particle counts and also pressure drop of the beds at different inlet velocities were compared between experiments and simulations and good agreement was observed. In the next step the simulated packings were investigated in more detail to get a better and deeper understanding of their behaviour. Various parameters were investigated, pressure drop, particles angles, velocities and residence time distributions in the beds. Among investigated beds, the bed filled with spherical particles had the best flow distribution (less axial dispersion) and also the least pressure drop and the mono-disperse cylinders packed bed was the second for flow distribution and pressure drop. Residence time distributions were very similar for all three beds except a little sharper breakthrough for the spheres packed bed which also shows less axial dispersion for this packed bed.

## ACKNOWLEDGEMENT

Financial support was provided by the Austrian research funding association (FFG) under the scope of the COMET programme within the research project –Industrial Methods for Process Analytical Chemistry - From Measurement Technologies to Information Systems (imPACts, [www.k-pac.at](http://www.k-pac.at))” (contract # 843546).

## REFERENCES

- Beavers, G. S., Sparrow, E. M., Rodenz, D. E. (1973). Influence of bed size on the flow characteristics and porosity of randomly packed beds of spheres. *ASME. J. Appl. Mech.* 1973;40(3):655-660. doi:10.1115/1.3423067.
- Behnam, M., Dixon, A. G., Nijemeisland, M., & Stitt, E. H. (2013). A new approach to fixed bed radial heat transfer modeling using velocity fields from computational fluid dynamics simulations. *Industrial & Engineering Chemistry Research*, 52(44), 15244-15261.
- Bey, O., & Eigenberger, G. (1996). Fluid flow through catalyst filled tubes. *Chemical Engineering Science*, 52(8), 1365-1376.
- Calis, H. P. A., Nijenhuis, J., Paikert, B. C., Dautzenberg, F. M., & Van Den Bleek, C. M. (2001). CFD modelling and experimental validation of pressure drop and flow profile in a novel structured catalytic reactor packing. *Chemical Engineering Science*, 56(4), 1713-1720.
- De Boer, J. H. (1956). Adsorption phenomena. *Advances in Catalysis*, 8, 17-161.
- De Klerk, A. (2003). Voidage variation in packed beds at small column to particle diameter ratio. *AICHE journal*, 49(8), 2022-2029.
- Dixon, A. G., & Nijemeisland, M. (2001). CFD as a design tool for fixed-bed reactors. *Industrial & Engineering Chemistry Research*, 40(23), 5246-5254.
- Dixon, A. G., Taskin, M. E., Nijemeisland, M., & Stitt, E. H. (2011). Systematic mesh development for 3D CFD simulation of fixed beds: Single sphere study. *Computers & Chemical Engineering*, 35(7), 1171-1185.
- Dixon, A. G., Nijemeisland, M., & Stitt, E. H. (2013). Systematic mesh development for 3D CFD simulation of fixed beds: Contact points study. *Computers & Chemical Engineering*, 48, 135-153.
- Eppinger, T., Seidler, K., & Kraume, M. (2010). DEM-CFD simulations of fixed bed reactors with small tube to particle diameter ratios. *Chemical Engineering Journal*, 166(1), 324-331.
- Ergun, S., & Orning, A. A. (1949). Fluid flow through randomly packed columns and fluidized beds. *Industrial & Engineering Chemistry*, 41(6), 1179-1184.
- Giese, M., Rottschäfer, K., & Vortmeyer, D. (1998). Measured and modeled superficial flow profiles in packed beds with liquid flow. *AICHE Journal*, 44(2), 484-490.
- Haughey, D. P., & Beveridge, G. S. G. (1969). Structural properties of packed beds—a review. *The Canadian Journal of Chemical Engineering*, 47(2), 130-140.
- Jacobs, P. F. (1992). Rapid prototyping & manufacturing: fundamentals of stereolithography. Society of Manufacturing Engineers.
- Kruggel-Emden, H., Rickelt, S., Wirtz, S., & Scherer, V. (2008). A study on the validity of the multi-sphere Discrete Element Method. *Powder Technology*, 188(2), 153-165.
- Mueller, G. E. (1992). Radial void fraction distributions in randomly packed fixed beds of uniformly sized spheres in cylindrical containers. *Powder technology*, 72(3), 269-275.
- Munjiza, A. A. (2004). The combined finite-discrete element method. John Wiley & Sons.
- Ookawara, S., Kuroki, M., Street, D., & Ogawa, K. (2007, September). High-fidelity DEM-CFD modeling of packed bed reactors for process intensification. In *Proceedings of European Congress of Chemical Engineering (ECCE-6)*, Copenhagen (pp. 16-20).
- Ribeiro, A. M., Neto, P., & Pinho, C. (2010). Mean porosity and pressure drop measurements in packed beds of monosized spheres: side wall effects. *International Review of Chemical Engineering*, 2(1), 40-46.
- Taskin, M. E., Troupel, A., Dixon, A. G., Nijemeisland, M., & Stitt, E. H. (2010). Flow, transport, and reaction interactions for cylindrical particles with strongly endothermic reactions. *Industrial & Engineering Chemistry Research*, 49(19), 9026-9037.
- Wakao, N., & Kagei, S. (1982). Heat and mass transfer in packed beds (Vol. 1). Taylor & Francis.
- [www.3ds.com/products-services/catia/](http://www.3ds.com/products-services/catia/), Last visit: February 2017
- [www.openfoam.com](http://www.openfoam.com), Last visit: February 2017
- [www.paraview.org](http://www.paraview.org), Last visit: February 2017

## CFD BASED STUDY OF DENSE MEDIUM DRUM SEPARATION PROCESSES

Arne EGGERS<sup>1\*</sup>, Wim DEWULF<sup>1†</sup>, Martine BAELMANS<sup>1‡</sup>, Maarten VANIERSCHOT<sup>1§</sup>

<sup>1</sup>KU Leuven Mechanical Engineering Department, 3000 Leuven, BELGIUM

\* E-mail: arne.eggerts@kuleuven.be

† E-mail: wim.dewulf@kuleuven.be

‡ E-mail: martine.baelmans@kuleuven.be

§ E-mail: maarten.vanierschot@kuleuven.be

### ABSTRACT

Dense Medium Drum (DMD) separation is applied particularly in the coal and recycling industries. Characteristic of the process is a separation based on density, driven by the buoyancy and gravitational forces acting on an object moving in a free surface flow. The fundamental phenomena occurring in a DMD have been widely investigated by (Napier-Munn, 1991). However, in contrary to other separation methods, such as the Dense Medium Cyclone which was investigated extensively by (Kuang *et al.*, 2014) and others, no Computational Fluid Dynamics (CFD) studies have been conducted for the DMD separation. Even recent studies, like (Meyer and Craig, 2015), use first order models which need to be calibrated with performance data of the investigated drum. Hence, important parameters like the flow-velocity and the detailed design of the drum are only taken into account indirectly.

This paper reports a detailed CFD analysis of the flow in a generic DMD separation process. The study comprises, a general understanding of the flow field and an analysis of the impact of different process parameters. Furthermore, the model predicts the actual separation performance of the DMD at different working points. To the authors' knowledge, this is the first study which conducts a CFD analysis of a DMD separation process. Therefore, findings concerning the flow field and its influence on the separation efficiency will be reported on. Moreover, the separation model can be used to derive the coefficients for highly used first order models without the need of experimental data. Like this, the early design phase of DMD separation processes can improve immensely.

**Keywords:** CFD, Process industries, separation, free surface flow

### NOMENCLATURE

#### Greek Symbols

$\varepsilon$	Relative error, [-]
$\eta$	Separation efficiency, [-]
$\mu$	Kinematic viscosity, [ $m^2/s$ ]
$\rho$	Mass density, [ $kg/m^3$ ]
$\phi$	Medium volume fraction, [-]
$\omega$	Turbulent Frequency, [ $1/s$ ]

#### Latin Symbols

$C_D$	Drag Coefficient, [-]
$d$	Diameter, [ $m$ ]
$dir$	Direction, [-]
$F$	Force, [ $N$ ]
$F_s$	Safety coefficient for the GCI, [-]

$g$	Gravitational acceleration, [ $m/s^2$ ].
$GCI$	Grid convergence index, [-].
$k$	Turbulent Kinetic Energy, [ $m^2/s^2$ ].
$m$	Mass, [ $kg$ ].
$n$	Number of objects, [-].
$p$	Pressure, [ $Pa$ ].
$po$	Order of grid convergence, [-].
$r$	Grid refinement factor, [-].
$Re$	Reynolds number, [-].
$t$	Time, [ $s$ ].
$T$	Viscous stress tensor, [ $N/m^2$ ].
$u$	Velocity, [ $m/s$ ].
$V$	Volume, [ $m^3$ ].
$x$	Location, [ $m$ ].

#### Sub/superscripts

$B$	Buoyancy,
$c$	Carrier fluid,
$cg$	Coarse grid,
$D$	Drag,
$eff$	Effective.
$i$	Index i.
$j$	Index j.
$p$	Particle or Object.
$turb$	Turbulent.
$r$	Relative.

### INTRODUCTION

In the environmental action plan for the circular economy, the European Union sets ambitious targets for recycling rates. This makes the development and optimization of current recycling processes mandatory. Dense Medium Drums (DMDs) are density separation machines frequently used in the coal and the recycling industry. In general the medium is a suspension of a high density powder with water. As illustrated in figure 1, objects with a density lower than the medium density float and leave the drum on the surface through the light fraction outlet. Other objects sink and are extracted from the drum by collectors or spirals which are driven by the rotation of the drum. Medium is supplied through inlet tubes and a small angle of inclination assures a constant stream towards the light fraction outlet of the drum. Although the coal industry applies DMD separation already for several decades, the approaches of modeling the process are restricted to first order models which get tuned by measurement data (Napier-Munn, 1991). These models predict for instance the behavior of the Wemco Drum, taking

different diameters of the separation objects into account (P.J. Baguley and T.J. Napier-Munn, 1996). The modeling of sub-processes like the DMD is accompanied by macroscopic analyses of the complete process in a plant (King, 1999). Furthermore, a recent study improves the modeling approaches by proposing a method, based on solving a system of differential equations, designed to be applied in the control of DMDs (Meyer and Craig, 2015). None of these studies directly investigates the flow in the drum and its influence on the separation process. This can only be achieved by utilizing experimental techniques or Computational Fluid Dynamics (CFD). DMDs for the application of plastic separation have been investigated experimentally (Dodbiba *et al.*, 2002). However, none of these studies applies CFD. CFD enables the possibility to base models for the design of DMDs on the flow simulation. This makes an optimization of the actual process during the design phase possible.

The modeling of a DMD based on CFD can be divided into two different major problems: The simulation of the free surface flow and the modeling of separation objects. Free surface flow simulation make currently mainly use of two models. The level-set method tracks the surface, directly storing its position in a distance field (Stanley Osher and James A. Sethian, 1988). Hence, a sharp interface is conserved. The second method makes use of the volume of fluid (VOF) method (C. W. Hirt and B.D. Nichols, 1981). One of the phases is marked using a coloring function which is advected passively with the local flow field. The interface is not necessarily sharp. To estimate its exact position an interface reconstruction, based on the distribution of the color function, is needed.

The modeling of the objects in flows can be characterized by its description of the object domain. Objects which are considered to be large compared to the grid cell size have to be resolved and simulated. These methods are physically accurate, on the one hand, but computationally expensive, on the other (G. Houzeaux *et al.*, 2010). Smaller objects, often referred to as particles, can be described as point mass (Dehbi, 2008). This makes the modeling of huge amounts of objects with reasonable computational costs possible.

In the present research a generic DMD will be simulated. The free surface is modeled using the VOF method (Omno Ubbink, 1997). Although the separation objects are considered to be large, the model describes them as point masses. To prevent nonphysical flow behavior due to the large point masses a one-way coupling, which neglects the influence of the objects onto the flow, is applied. Thus, the separation performance of the generic drum in dependency of different flow parameters can be estimated.

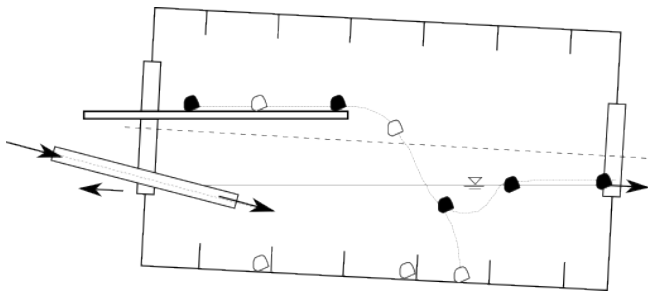


Figure 1: Sketch of a generic DMD.

## MODEL DESCRIPTION

The model has been implemented into the existing framework of the OpenFOAM toolbox. Hence, all equations and models described below are solved using this toolbox. The incompressible Reynolds averaged Navier-Stokes (RANS) equations are solved,

$$\frac{\partial \bar{u}_i}{\partial x_j} = 0, \quad (1)$$

$$\frac{\partial \bar{u}_i}{\partial t} + \bar{u}_j \frac{\partial \bar{u}_i}{\partial x_j} = -\frac{1}{\rho} \frac{\partial \bar{p}}{\partial x_i} + \frac{\partial}{\partial x_j} \left( \frac{1}{\rho} T_{ij} - \overline{u'_i u'_j} \right) + g_i. \quad (2)$$

As these equations on their own are not closed, a  $k-\omega$  SST model is applied to model the Reynolds stress tensor and the turbulent viscosity. This model solves an extra set of equations for the turbulent kinetic energy and the turbulent frequency. A detailed description of it can be found in the literature (Menter, 1994). A finite volume scheme with a first order upwind interpolation was used for the spatial discretization. For the time derivation an Euler forward scheme has been applied.

In the investigated generic drum geometry the medium is a suspension out of Ferro Silicon powder and water. The model assumes that the powder and the water is in perfect suspension at any place and time and hence behaves as one continuum with constant fluid dynamical properties. The VOF method models the free surface between the air phase and the medium phase in the drum (Omno Ubbink, 1997). A color function  $\phi$  is utilized which indicates the volume proportion of the medium phase at a certain location of the drum.  $\phi = 1$  in the medium phase,  $\phi = 0$  in the air phase and  $0 < \phi < 1$  in the interface area. The color function advects passively with local flow field,

$$\frac{\partial \phi}{\partial t} + \bar{u}_j \frac{\partial \phi}{\partial x_j} = 0. \quad (3)$$

## Object Tracking

The Lagrangian equations of motion describe the movement of the objects in the flow,

$$\frac{dx_{p,i}}{dt} = u_{p,i}, \quad (4)$$

$$\frac{du_{p,i}}{dt} = \frac{1}{m_p} (F_{D,i} + F_{B,i}). \quad (5)$$

The summed forces in equation 5 consist out of two contributions: the drag force and the buoyancy force. Equation 5 is integrated using a first order explicit Euler scheme. The forces are modeled as described in the following.

### Buoyancy Force

The difference in density between the objects and carrier fluids introduces a buoyancy force which drives the separation of the objects. The buoyancy force can be calculated,

$$F_{B,i} = \rho_p \cdot V_p \cdot g_i \cdot \left( 1 - \frac{\rho_c}{\rho_p} \right). \quad (6)$$

### Drag Force

The drag force is modeled based on a drag coefficient,

$$F_{D,i} = \frac{1}{2} \cdot C_D(Re_p) \cdot |u_{r,i}| \cdot u_{r,i} \cdot A_p. \quad (7)$$

Here  $u_{r,i}$  is the relative velocity between the local flow field and the object.  $Re_p$  is defined as the particle Reynolds number,

$$Re_p = \frac{|u_{r,i}| \cdot d_p}{\mu} \quad (8)$$

The drag coefficient of a sphere can be estimated,

$$C_D(Re) = \begin{cases} 0.424, & \text{if } Re \geq 1000 \\ 24(1 + 0.15 \cdot Re^{0.678}), & \text{otherwise} \end{cases} \quad (9)$$

Equation 7 computes the forces acting on an object based on the averaged flow field from the solution of the RANS equations. As stated in previous studies one of the major influences on the separation process are the turbulent fluctuations of the flow which effects the objects in a stochastic way (P.J. Baguley and T.J. Napier-Munn, 1996). The computed averaged flow does not include any information about these fluctuations. However, the  $k-\omega$  SST turbulence model conserves turbulent quantities, namely the turbulent kinetic energy and the turbulent frequency, which can be used to model the influence of the fluctuation statistically. Here, this is done using a popular Eddy Interaction Model (EIM) (Gosman and Ioannides, 1983). Without taking the turbulent fluctuations into account, objects with a density higher than the medium will get sorted as heavy fraction and all others as light fraction, if the drum is sufficiently large and the velocities small.

If an object enters the domain the forces are summed up and equation 5 is integrated. However, before the drag force is computed the turbulent fluctuations are added to the local velocity to calculate the effective local velocity,

$$u_{eff,i} = u_i + u_{turb,i} \quad (10)$$

The magnitude of the turbulent fluctuations is sampled from a Gaussian normal distribution, with an expectation value of 0 and a standard deviation of 1, and scaled with the expected magnitude,

$$|u_{turb,i}| = \sqrt{\frac{2k}{3}} \cdot Gauss(0, 1) \quad (11)$$

Turbulence models, as the applied  $k-\omega$  SST model, utilizes an eddy viscosity hypothesis. As such, it assumes homogeneous turbulence. Hence, the same assumption is applied for the turbulent dispersion modeling leading to randomly sampled turbulent fluctuation,

$$dir_{turb,i} = \begin{bmatrix} rnd() \\ rnd() \\ rnd() \end{bmatrix} \text{ with } |dir_{turb,i}| = 1. \quad (12)$$

The turbulent fluctuation velocity can now be estimated,

$$u_{turb,i} = |u_{turb,i}| \cdot dir_{turb,i} \quad (13)$$

This process samples a new turbulent velocity when equation 5 has been integrated for the duration of one turbulent time scale,

$$t_{turb} = \frac{1}{\omega} \quad (14)$$

### Coupling

Although the objects in this model are considered to be large, they are still modeled as spherical point masses. As such a drag coefficient can model the influence from the flow onto the object and the simulation of large amounts of objects

is enabled. Several models exist to account for the influence from the objects onto the flow. However none of them can cope with large objects experiencing directional forces. Hence, this model utilizes, in a first pragmatic approach, a one-way coupling.

This might be a too strong assumption for a accurate simulation of the flow in the drum. However, the model is designed to deliver a reliable prediction of the separation efficiency of a DMD. In this context the assumption might be accurate enough. The algorithm updates the positions of the objects at first and then solves the flow and turbulence equations.

### Separation Performance

In classical separation modeling first order models generate separation curves. These curves describe the separation number, the probability that an object gets separated as heavy or light in dependency of the object density or its theoretical terminal velocity.

To achieve these curves based on a CFD calculation the paths of a huge amount of objects have to be tracked. The number of objects leaving the drum through the light and the heavy fraction outlet can be used to calculate the separation efficiency,

$$\eta_{heavy} = \frac{n_{heavy\ outlet}}{n_{heavy\ outlet} + n_{light\ outlet}}, \quad (15)$$

$$\eta_{light} = \frac{n_{light\ outlet}}{n_{heavy\ outlet} + n_{light\ outlet}} \quad (16)$$

For these equations it is assumed that all objects are supposed to be heavy fraction, in case of equation 15, or light fraction, in case of equation 16, independently from their density and the medium density. The efficiency is assumed to be converged if the statistical error is below 0.1%.

### RESULTS

In this study a generic drum geometry is simulated and its performance is predicted for different densities and object diameters. For the calculation of the separation efficiency it is assumed that all objects are supposed to be sorted as heavy fraction. Hence, equation 15 is utilized. Based on these results separation curves for different object diameters are computed. Furthermore, a grid study is conducted and the medium flow field is investigated.

### Geometry

Major dimensions and a general overview on the geometry are given in figure 2. It is a simplified, generic version of a real applied drum. No collectors for the heavy fraction objects are taken into account and the drum is not rotating. The separation zone of the drum is long enough to ensure a sufficient residence time. The whole lower part of the inlet side, in figure 2 marked as a and b, is defined as medium inlet. Here medium enters the drum with a low velocity generating a slow and steady inflow. Separation objects are released through the middle part of the inflow section, in figure 2 marked as b. The complete curved wall of the drum, in figure 2 marked as d, is defined as heavy fraction outlet. Through this outlet only separation objects but no medium can leave the drum. On the outlet side of the drum the higher light fraction outlet is located, in figure 2 marked as c. This outlet allows medium and objects to leave the drum.

### Computational Grid

The computational grid, which is shown in figure 3, consists of 344640 cells. This structured grid is used for performance predictions. For the grid study a second grid with 849216 grid cells has been used.

### Grid Study

For the grid study two grids are used. At first the two flow fields of the medium phase are compared and then their influence onto the separation efficiency is assessed.

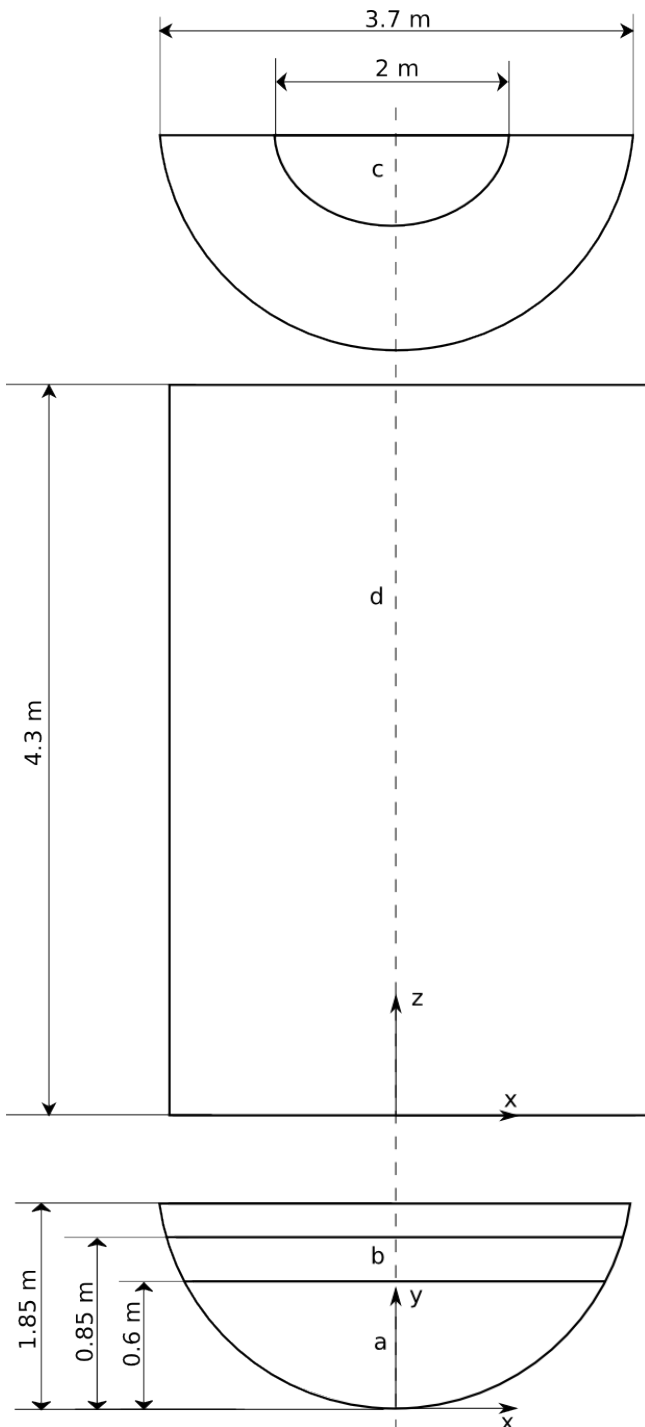


**Figure 2:** Sketch of the computational domain. With views on the light fraction outlet (c) (top), on the heavy fraction outlet (d) (middle), on the water inlet (a) and on the water objects mixture inlet (b) (bottom).

### Medium Flow Field

In figure 4 the medium velocity profiles in the symmetry plane of the drum ( $x=0$ ) are compared. After the medium enters the drum a steady flow field with a maximum velocity of approximately  $u_z = 0.25 \frac{m}{s}$  develops. In this area the solutions of both grids align very well and can be considered grid independent.

However, this changes as the medium passes through the drum and gets influenced by the outlet of the drum. Compared to the fine grid, the coarse grid underpredicts the outlet vortex and hence the back flow area in the lower part of the drum is smaller. Furthermore, the fine grid predicts a slightly higher peak velocity at the outlet.

### Separation Efficiency

The grid convergence of the separation efficiency is assessed using the grid convergence index (GCI) (P. J. Roache, 1994),

$$GCI_{cg} = \frac{F_s \cdot |\epsilon| \cdot r^{po}}{r^{po} - 1} \quad (17)$$

The grid refinement factor is  $r = 3$ , the safety coefficient is  $F_s = 3$  and the order of grid convergence is assumed to be  $p = 2$ . The results are summarized in table 1. Although the medium flow field differs between the two grids, the GCI for the separation efficiency remains low. Hence, the separation efficiency can be examined using the coarsest grid. The GCI drops with increasing object density as the buoyancy forces increase while the drag force remains constant. The grid study has been conducted only for objects with a diameter of  $d = 0.005$ . It is expected that the grid influence is bigger for smaller objects as in these cases the grid independent buoyancy force is less important compared to the drag force.

### Medium Flow Field

The medium is entering the drum through the lower part of the inlet side, which is visible in figure 2 (a and b). The inlet velocity is defined to be  $u_{in} = 0.1 \frac{m}{s}$ . The combination of a large inlet area and a low velocity generates a slow and steady flow in the drum.

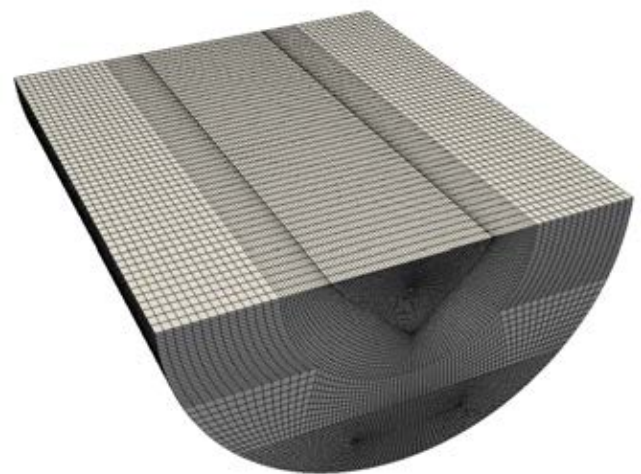


**Figure 3:** The computational grid used for the performance prediction.

**Table 1:** GCI and error in mean for objects of diameter  $d = 0.005$  and different densities.

Density ( $kg/m^3$ )	GCI (%)	error in mean
900	0.0	1.348e-05
990	2.531	5.07e-05
1000	1.635	0.0002
1020	0.329	0.0003
1030	0.075	0.0002

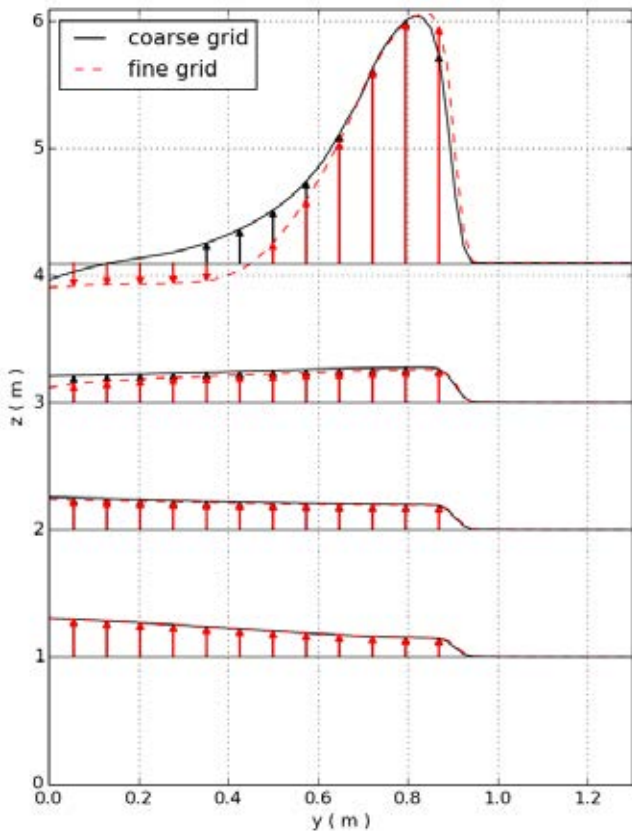
The smaller outlet drives an acceleration of the medium. As shown in figure 5, a vortex is created under the outlet. Separation objects which do not leave the drum through the light fraction outlet get dragged towards the heavy fraction outlet by this vortex. The acceleration is strongest in the symmetry plane ( $x=0$ ) and gets less in the side planes of the drum. The same trend is observed for the outlet vortex.

**Performance Prediction**

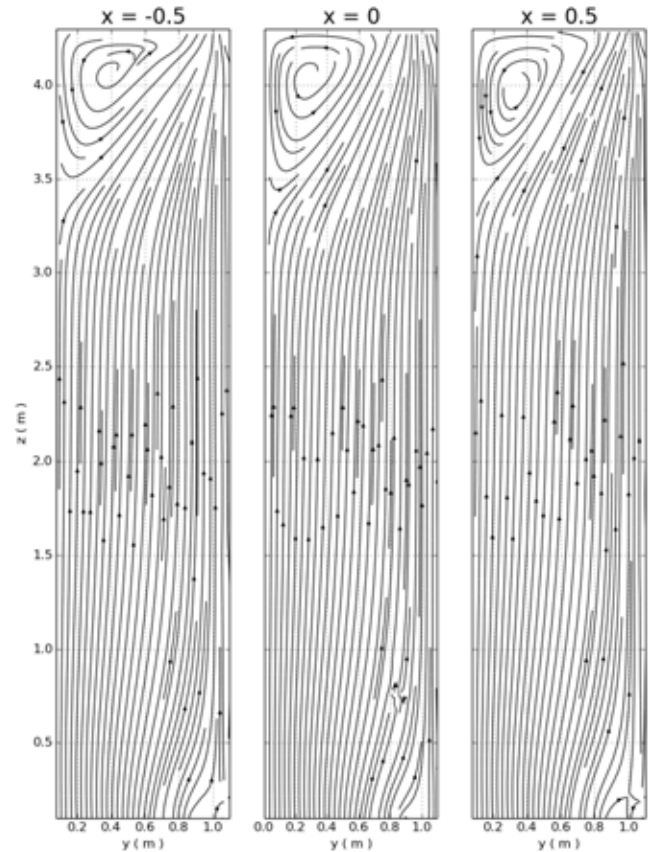
For the prediction of the separation performance of the generic geometry, depending on the flow and object properties, multiple hundred thousand of objects have to be traced on their path through the drum.

Figure 6 shows a typical convergence curve of the separation efficiency. The efficiency, which is calculated based on equation 15, starts with a value of one, as separation objects enter the drum over its full width. Hence, a small number of objects enter the computational domain close to the heavy fraction outlet and an even smaller amount gets dragged through it. As objects need approximately 15 seconds to pass the drum, no objects leave through the light fraction outlet at this point and an efficiency of one is computed. However, it drops

as soon as objects reach the light fraction outlet. Once the outflow of objects through the heavy and light fraction outlet stabilizes at a constant value, the computed separation efficiency will converge to a statistically constant value as well. As no object-object interactions and no back-coupling from the objects onto the flow have been taken into account, the mass flow of separation objects does not influence the predicted efficiency. The case shown in figure 6 reaches convergence approximately after 80 seconds and more than 500000 tracked objects. A simulation like this predicts a separation efficiency for a specified object density and diameter. Hence,



**Figure 4:** Medium velocity profiles in the symmetry plane ( $x=0$ ) of the drum on the fine and the coarse mesh.



**Figure 5:** Streamlines in three different planes in the medium zone of the drum. The outlet is in the top ( $z=4.3$ ) and the inlet in the bottom ( $z=0$ ) of the figure.

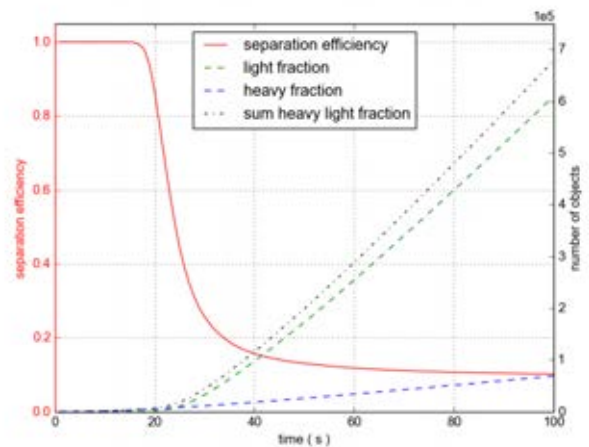


**Figure 6:** Computed separation efficiency and number of objects, which left the drum, over simulated time.



it delivers one point in a separation curve. If simulations are conducted for different densities and diameters the whole separation curve can be predicted.

Figure 7 shows the predicted partitioning curves for the generic geometry of different object diameters. The typical S-shape and the influence of the object diameter size is recognizable in the same way as in figure 8. Furthermore, the generic drum slightly tends to separate objects as light fraction, although their density is higher than the medium density. This is due to the high medium mass flow which accelerates towards the outlet. However, particularly for the larger object diameters the generic drum has a high separation efficiency, which leads to a very sharp S-shape of the partitioning curve. For smaller objects the influence of the buoyancy force, which drives the separation, becomes less dominant compared to the drag force. Hence, the separation efficiency for these cases are much lower and the S-shape is more blurry.

## CONCLUSION

A CFD based model, which predicts the separation efficiency of a DMD has been proposed. It has been applied to a generic

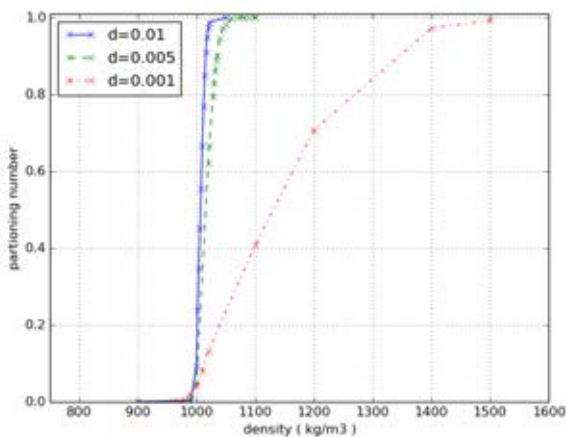


**Figure 7:** Partitioning curves of the generic DMD for different object diameters.

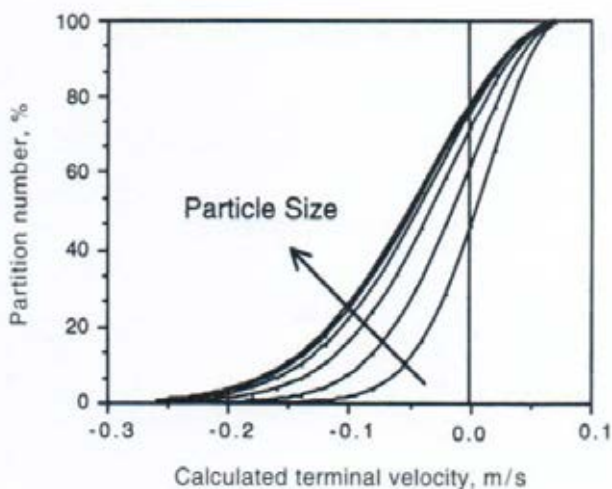


**Figure 8:** Typical S-shape of a drum separation curve and the influence of different object diameters on it (P.J. Baguley and T.J. Napier-Munn, 1996).

and simplified drum geometry. As the CFD simulations deliver information on the general flow field in the drum, this has been investigated as well and key structures like the outlet vortex have been discussed.

The model reproduces the characteristic S-shape of separation curves for DMDs including its trend for objects with different size. Hence, in a next step a real DMD, for which geometrical data and partitioning curves are available, will be investigated. Thus, the performance of the model can be assessed. Furthermore, in real drums a suspension is used as medium. This enables sedimentation effects, which might influence the separation process.

## REFERENCES

- C. W. Hirt and B.D. Nichols (1981). "Volume of Fluid (VOF) Method for the Dynamics of Free Boundaries". *Journal of Computational Physics*, **39**, 201–225.
- DEHBI, A. (2008). "A CFD model for particle dispersion in turbulent boundary layer flows". *Nuclear Engineering and Design*, **238(3)**, 707–715.
- DODDIBA, G., HARUKI, N., SHIBAYAMA, A., MIYAZAKI, T. and FUJITA, T. (2002). "Combination of sink&float separation and flotation technique for purification of shredded PET-bottle from PE or PP flakes". *International Journal of Mineral Processing*, **65(1)**, 11–29.
- G. Houzeaux, C. Samaniego, H. Calmet, R. Aubry, M. Vazquez and P. Rem (2010). "Simulation of Magnetic Fluid Applied to Plastic Sorting". *The open Waste Management Journal*, **3**, 127–138.
- GOSMAN, A.D. and LOANNIDES, E. (1983). "Aspects of Computer Simulation of Liquid-Fueled Combustors". *Journal of Energy*, **7(6)**, 482–490.
- KING, R.P. (1999). "Practical Optimization Strategies for Coal-washing Plants". *Coal Preparation*, **20(1-2)**, 13–34.
- KUANG, S., QI, Z., YU, A., VINCE, A., BARNETT, G. and BARNETT, P. (2014). "CFD modeling and analysis of the multiphase flow and performance of dense medium cyclones". *Minerals Engineering*, **62**, 43–54.
- MENTER, F.R. (1994). "Two-equation eddy-viscosity turbulence models for engineering applications". *AIAA Journal*, **32(8)**, 1598–1605.
- MEYER, E. and CRAIG, I. (2015). "Dynamic model for a dense medium drum separator in coal beneficiation". *Minerals Engineering*, **77**, 78–85.
- Napier-Munn (1991). "Modelling and Simulating Dense Medium Separation Processes - A Progress Report". **4**, 329–346.
- Omno Ubbink (1997). *Numerical prediction of two fluid system with sharp interfaces*. Ph.D. thesis, Imperial College of Science, Technology & Science.
- P. J. Roache (1994). "Perspective: A Method for Uniform Reporting of Grid Refinement Studies". *Journal of Fluids Engineering*, **116**, 405–413.
- P.J. Baguley and T.J. Napier-Munn (1996). "Mathematical model of the dense-medium drum". **105(Jan-April)**, C1–C8.
- Stanley Osher and James A. Sethian (1988). "Fronts Propagating with Curvature-Dependent Speed: Algorithms Based on Hamilton-Jacobi Formulations". *Journal of Computational Physics*, **79**, 12–49.

# A MULTI-DOMAIN 1D PARTICLE-REACTOR MODEL FOR PACKED BED REACTOR APPLICATIONS

Mandar TABIB, Schalk CLOETE, John MORUD, Magne LYSBERG, Shahriar AMINI

SINTEF, Trondheim, NORWAY

\* E-mail: mandar.tabib@sintef.no,shahriar.amini@sintef.no,john.morud.sintef.no

## ABSTRACT

A validated multi-domain 1D particle-reactor model has been developed to simulate packed bed reactor operation. Two main components of the model are: (1) a particle model for simulating the radial distribution of chemical species and temperature within the catalyst particles and (2) a 1D reactor model for solving mass and energy transport along the length of the reactor. The model captures the effect of intra-particle heat and mass transfer phenomena on the reactor performance. Its efficacy and usability is evaluated using a thorough verification and validation campaign. Validation has been carried out through comparisons to analytical solutions for: (a) the transient thermal response of the fixed bed to a step-change in inlet feed temperature and for (b) the maximum temperature rise during an exothermic oxidation process in a chemical looping combustion (CLC) operation. Further, its performance has been verified with two well-established solvers (a 1D Euler-Euler packed bed model developed in ANSYS FLUENT and a previously published 1D model) for simulating a realistic 500kW cyclic packed bed chemical looping combustion system involving dynamic fuel-air cycling. This successful verification demonstrates the ability of the model to simulate complex cyclic packed bed reactor processes involving stiff kinetics in an efficient manner. Further, significance of particle model is evaluated for mass transfer limiting condition and this reinforces the advantage of using the proposed 1D particle-reactor model in such cases.

**Keywords:** 1D model, packed bed reactor, chemical looping combustion.

## NOMENCLATURE

Ck	Concentration species "k"	[kmol/m <sup>3</sup> ]
Cp	Heat capacity	[J/kg.K]
Ctot	Total gas concentration	[kmol/m <sup>3</sup> ]
$D_{eff,kg}$	Effective diffusivity of gas species 'k'	[m <sup>2</sup> /s]
$D_{eff,ks}$	Effective diffusivity of gas species 'k' in the pores of the particle.	[m <sup>2</sup> /s]
dp	Particle diameter	[m]
Fh	Flux of enthalpy	[J/m <sup>2</sup> .s]
Fk	Flux of species "k"	[kmol/m <sup>2</sup> .s]
Ftot	Total gas flow rate	[kmol/m <sup>2</sup> .s]
G	Mass flux of gas	[kg/m <sup>2</sup> .s]
H	Enthalpy	[J]
hc	Heat transfer coefficient	[W/m <sup>2</sup> .K]
$\bar{j}$	Diffusive flux	[kg/m <sup>2</sup> .s]
$K_{sg}$	Interphase momentum exchange coefficient	[kg/m <sup>3</sup> .s]
kg	Mass transfer coefficient	[m/s]
M	Molecular Weight	[Kg/kmol]
Nu	Nusselt number	
p,P	Pressure	[bar]
R	Particle radius	[m]
Rg	Gas constant	[J/kmol.K]

$R^H$	Het. reaction rate	(kmol/m <sup>3</sup> .s)
S	Source term	
T	Temperature	[K]
T0	Initial temperature	[K]
U	Internal energy	[J/m <sup>3</sup> ]
Xj	Conversion of species j during reaction	[-]
vg	Superficial gas velocity	[m/s]
wf	Fluid mass flow rate	[Kg/s]
wact,j	weight fraction of active solid species j in pellet.	[-]
wg,i	Weight fraction of gas species i	[-]
Z	Axial position	[m]
$c_\infty$	Concentration at infinity	[any consistent]

## Greek Symbols

$\alpha$	Volume fraction	
$\gamma$	Stoichiometric coefficient	[-]
$H_{sg}$	Interphase energy exchange coefficient	[-]
$\bar{\tau}$	Stress tensor	
$\vec{v}$	Velocity vector	[m/s]
$-\Delta H_{rx}$	Heat of reaction	[J/kmol]
$\epsilon$	Void fraction	[-]
$\epsilon_s$	Pore fraction is Oxygen carrier	[-]
$\eta$	Reaction efficiency factor	[-]
$\xi$	Ratio of moles of gas to solid needed for the oxidation reaction	
$\Gamma_k$	Source term for species "k"	[kmol/m <sup>3</sup> .s]
$\Gamma_u$	Source term for enthalpy	[J/m <sup>3</sup> .s]
$\lambda$	Thermal conductivity in particles	[W/m.K]
$\lambda_{ax}$	Effective axial thermal conductivity in bed	[W/m.K]
$\mu$	Gas viscosity	[kg/m.s]
$\rho$	Gas density	[kg/m <sup>3</sup> ]
$\rho_s$	Oxygen carrier density	[kg/m <sup>3</sup> ]
$\tau$	Oxygen carrier tortuosity	[-]
$\beta$	Ratio of thermal capacity of solid and gas.	[-]

## Latin Symbols

a	Characteristic length, [m].
p	Pressure, [Pa].
u	Velocity, [m/s].

## Sub/superscripts

p or s	Particle/Solid
g or gas	Gas phase
k	Species "k"
l	Reaction "l"

## INTRODUCTION

Packed bed reactors are commonly utilized in processes involving solid-catalysed reactions and/or heterogeneous gas-solid reactions [1, 2]. These reactors are used ubiquitously in the petroleum and petrochemical industry for processes involving reforming, hydro-cracking, polymerization, etc. Recently, gas-solid processes have been developed for reducing greenhouse gas emissions. For example, the Packed Bed Chemical Looping Combustion (PBCLC) process has enjoyed significant research attention as a potential solution for cost effective power production with integrated CO<sub>2</sub> capture [3, 4].

A validated stand-alone packed bed reactor simulator will help to ensure a safe and efficient packed bed reactor operation. Hence, a computationally efficient 1D particle-reactor model has been developed to accurately capture the physics. The concept of multi-domain 1D particle-reactor models have been used effectively by different researchers [5-9]. Different researchers have used different set of equations and solution techniques in their models. However, in most cases, the models have been applied on a single stage operation rather than on cyclic operations. In present work, the equations and solvers/solution techniques used are different than those proposed in earlier models. The usability and efficiency of the proposed model is evaluated by verifying it with other popular well-established solvers, like ANSYS FLUENT and a published 1D model from the Eindhoven University of Technology [3, 7, 8]. The verification is done for a realistic cyclic packed bed chemical looping combustion (PBCLC) process operation. The cyclic reduction-oxidation process involves very stiff kinetics and is useful to test the robustness and accuracy of our software. Further, validation of the proposed model has also been presented by comparing it with analytical solutions for: (a) the transient thermal response of the fixed bed to a step-change in inlet feed temperature and for (b) the maximum temperature rise during an exothermic oxidation process in a chemical looping combustion (CLC) operation.

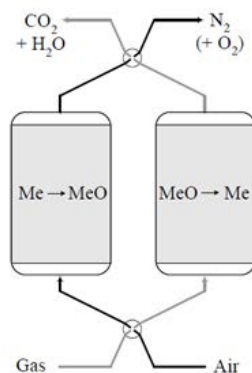


Figure 1: Chemical Looping Combustion process in a packed bed reactor.

The PBCLC process involves cyclic gas-solid non-catalytic reaction operations, wherein the bed material (typically a metal oxide oxygen carrier) is alternatively exposed to a fuel stream (reduction cycle) and an air stream (oxidation cycle). Figure 1 shows a schematic representation of a PBCLC reactor system. During the fuel stage, the oxygen carrier supplies oxygen to the fuel,

resulting in a hot stream of carbon dioxide and super-heated steam which can subsequently be processed into a high-purity CO<sub>2</sub> stream following heat recovery and purification. The reduced metal oxide bed is then exposed to the air stream, which re-oxidizes it. This highly exothermic oxidation stage produces a high-volume stream of hot gas that can also be used for efficient electricity generation in a combined cycle. The reduction-oxidation cycle is then repeated continuously, leading to power generation with integrated CO<sub>2</sub> capture. The 1D particle-reactor model can help to determine the operating conditions (flow rates, flow composition and feed inlet temperatures) and reactor size for efficient PBCLC operation.

## MODEL DESCRIPTION

A 1D model assuming plug flow conditions can be safely applied to industrial scale packed bed reactors because the effect of near wall phenomena in packed beds (oscillations in radial volume fraction profile) is confined to a very small zone (typically about 5 particle diameters from the wall). Radial variations in volume fraction and velocity are negligible beyond this small near-wall zone. In addition to the plug-flow assumption, the present 1D model also considers the process to be adiabatic and the ideal gas law is considered to be valid. The model accounts for (a) external heat and mass transfer resistances, which influence the transport of reactants and energy from bulk fluid up to a catalyst pellet, (b) intra-particle transport (diffusion limited) resistances, which influence the transport of mass and energy from the external surface of the particle to grains inside the porous pellet, and (c) the kinetic rate, which accounts for the reactions occurring on internal grains as the fluid phase reactant reaches it. These physical phenomena are captured by solving species mass balance and energy balance equations for the fluid phase and the reaction-diffusion equations within the particle. The particle model provides the source-term for the mass and energy balances of the fluid phase by computing the component and energy fluxes at the particle surface. Thus, the particle model and reactor model are coupled together by the source terms. The equation system is described in more detail below.

### Gas phase Equations

#### Ideal gas equation of state

$$P = C_{tot} R_g T_g \quad (1)$$

#### Ergun pressure drop equation

$$\frac{\partial P}{\partial z} = -\frac{G}{\rho d_p} \left( \frac{1-\varepsilon}{\varepsilon^3} \right) \left( \frac{150(1-\varepsilon)\mu}{d_p} + 1.75 G \right) \quad (2)$$

#### Material balance for species "k" in gas phase

$$\varepsilon \frac{\partial C_k}{\partial t} + \frac{\partial F_k}{\partial z} = \Gamma_k$$

$$\text{where, } F_k = F_{tot} X_k - C_{tot} D_{eff,kg} \frac{\partial X_k}{\partial z} \quad (3)$$

#### Energy balance for gas phase

$$\varepsilon \frac{\partial U}{\partial t} + \frac{\partial F_h}{\partial z} = \Gamma_U$$

$$\text{where, } F_h = F_{tot}h - \lambda_{ax} \frac{\partial T}{\partial z} \quad (4)$$

Boundary conditions for gas phase

$z=0$ : Inlet flux

$z=L$ :

$$\frac{\partial C_k}{\partial z} = 0, \quad \frac{\partial T}{\partial z} = 0 \quad (5)$$

Source terms for gas phase mass- and energy balance arising due to mass and heat transfer at the gas-particle interface.

$$\Gamma_k = k_g a (C_{k,r=R}^s - C_k) \quad (6)$$

$$\Gamma_U = h_c a (T_{r=R}^s - T) \quad (7)$$

Where,  $h_c$  is the heat transfer coefficient and  $k_g$  is the mass transfer coefficient.

Solid particle model (particle could be oxygen carrier or catalyst)

Mass balance for species "k" inside catalyst particles

$$\varepsilon_s \frac{\partial C_k^s}{\partial t} = \frac{\varepsilon_s D_{eff,ks}}{\tau} \nabla^2 C_k^s + \rho_s r_k \quad (8)$$

Energy balance for catalyst particles

$$\rho_s C_{ps} \frac{\partial T^s}{\partial t} = \lambda \nabla^2 T^s + \rho_s \sum_l r_l (-\Delta H_{rx,l}) \quad (9)$$

Boundary conditions for catalyst particles

Symmetry at  $r=0$ :

$$\frac{\partial C_k^s}{\partial r} = 0, \quad \frac{\partial T^s}{\partial r} = 0 \quad (10)$$

Catalyst surface,  $r=R$ :

$$-\frac{\varepsilon_s D_{eff,ks}}{\tau} \frac{\partial C_k^s}{\partial r} = k_g (C_{k,r=R}^s - C_k) \quad (11)$$

$$-\lambda \frac{\partial T^s}{\partial r} = h(T^s - T) \quad (12)$$

Numerical solution of this equation system results in temperature and composition profiles along the length of the bed for both the gas and solid particle. The velocity of the solid particle is set to zero. The pressure at any given cell is obtained by ideal gas law (Equation 1) and pressure drop between this cell and the outlet is obtained. This pressure drop is used to compute the gas phase velocity using a pressure drop correlation (Equation 2). The pressure drop correlation accounts for the resistance offered by the particles to the gas flowing through the interstitial region. The closures used by the 1D model are dependent on particle shape and size. A spherical particle of size 3 mm is used in this work. For spherical particles, the following well-established correlations have been used : (a) the pressure drop correlation by Ergun [10] as in Equation 2, (b) the heat transfer correlation using the multi-particle Ranz-

Marshal correlation [11] for computing external heat transfer coefficient and (c) the mass transfer correlation for computing mass transfer coefficient. Further, information on (a) the volume fraction of the gas phase and (b) the particle surface area per unit volume of the reactor, are also needed as closures by the model. For packed beds comprising of spherical particles, the solid volume fraction in the bed (around 0.6) and surface area of particle per unit volume of reactor,  $a$ , are known. Thus, well-known closures and correlations for the spherical particle are used in this study. For many non-spherical particle shapes, however, these critical closure values are not known. One way of obtaining them is using a 3D CFD-DEM modelling approach such as developed by Tabib [12].

## NUMERICAL IMPLEMENTATION AND SOLVER DETAILS

The set of partial differential equations (Equations 3-12) are solved using Finite Volume discretization for the gas phase in the reactor (where the bed is spatially divided into small volumes in the axial direction) and an orthogonal collocation technique for the particle. The orthogonal collocation technique resolves the radial variations of temperature and chemical composition within the particle at each axial location of the bed. Figure 2 shows the schematic representation of this implementation. The mass and energy balances are formulated for gas and particle phases and solved for each cell volume.

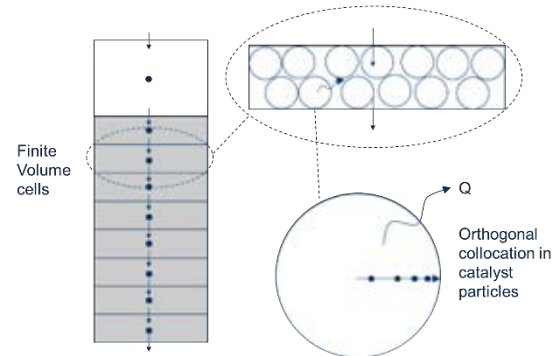


Figure 2: Implementation of 1D Particle-Reactor Model.

The partial differential equations are converted into a set of ordinary differential equations (ODE) by discretizing the spatial terms of the gas phase equation. An upwind scheme is used to obtain the flux at cell faces for computing the convective term in the discretized equation. The resulting ODE equation set can be solved by using any available standard ode-solver that can solve for stiff equations. An ODE solver proposed by Hindmarsh's group [13-15] has been used in this work. The temporal discretization is done using an implicit multi-step backward differentiation formula and the Adam-Moulton scheme. This implicit temporal discretization forms a non-linear algebraic equation system that needs to be solved at each time-step. A Newton scheme is used to solve these non-linear equations iteratively.

The Newton scheme uses a Jacobian matrix of the system of equations. This Jacobian matrix can be a banded matrix or a full matrix depending upon the way

equations are arranged and solved. A banded Jacobian matrix implementation ensures faster and more efficient solution. The equations to be solved (Equations 3-12) are arranged in a manner so as to produce a banded Jacobian matrix. Here, the equations (variables) to be solved are arranged cell-wise, i.e., equations in the first cell volume are arranged first (all gas species mass balance equations in the first cell, all solids species mass balance equations in the first cell, one gas energy equation in the first cell, one solid energy equation at first cell), followed by the same variables in the second cell volume, then the third cell volume and so on. This produces a banded Jacobian pattern. If we arrange the equations in a different way and not cell-wise (such that equations of a particular variable for all N cells are solved first), then it leads to an inefficient solution involving the full Jacobian matrix. Hence, a banded Jacobian solver implementation is executed.

## MODEL VALIDATION

Packed beds are characterized by the presence of either or both a thermal front and the reaction front. The thermal dynamics of the bed and movement of the thermal front influences many processes, like catalytic chemical reactors, adsorption columns, ion exchange columns, and the chromatographic process. In heterogeneous gas-solid reactions (e.g., chemical looping combustion), the reaction front is also present along with the thermal front. Both these fronts are identifiable via the temperature and concentration profiles along the bed.

The reaction front velocity is determined by the reactant species concentration in gas and solid phase, the molecular weights of reacting species, and the stoichiometry of the reaction rate. An identifiable feature of this reaction front is the presence of a fully converted solid bed upstream of the front (i.e., no solid reactant species exist and no reaction takes place upstream of the reaction front), while the solid bed region that is downstream of the reaction front will be fully unconverted and will react on being exposed to a gaseous reactant. Depending upon the rate of the reaction, the reaction front can be diffused or sharp. A rise in temperature of gas and solid bed occurs owing to the heat generated at the reaction front. The reaction front can also be identified by temperature profiles as there will be a drop in bed-temperature just downstream of the reaction front (if the reaction is exothermic). On upstream regions of the reaction front, hot temperatures will prevail till certain distance until the bed is cooled down by incoming gas. This temperature difference between the incoming cold gas and the hot converted solid bed leads to heat transfer and establishment of a thermal front. Velocity of this thermal front is determined by relative thermal heat capacity of the fluid and the bed (depends upon material properties like heat capacity and density). The above description assumes that reaction front velocity is faster than thermal front velocity. A 1D model should be able to accurately capture the movement of these two fronts (thermal and reaction fronts). Hence, validation of the 1D model is done by comparing it with analytical results for the movement of the fronts and the maximum temperature rise experienced in the reaction front. The validation for the two cases is discussed below.

## VALIDATION

### Case - Transient thermal response of the bed involving a step change in feed temperature

The 1D model is used to simulate the transient temperature response in the bed for a step increase in the inlet feed stream temperature and no reactions are considered. There exists an analytical solution [16] for this case if the following idealizations are considered: (a) negligible thermal capacity of the reactor walls, (b) negligible radial or azimuthal temperature gradients in the fluid and solid phases, (c) plug flow is assumed, (d) negligible axial mixing of fluid due to dispersion, (e) negligible axial conduction of heat in either fluid or solid media and (f) negligible temperature gradients within the solid particles. The equations (equation 13-14) to be solved analytically can then be represented by the following heat balances on both the fluid and solid.

Heat balance in fluid medium

$$\rho_g C_{p,g} \varepsilon A \frac{\partial T_g}{\partial t} + w C_f \frac{\partial T_g}{\partial x} = h a A (T_s - T_g) \quad (13)$$

Heat balance in solid medium

$$\rho_s C_s (1 - \varepsilon) A \frac{\partial T_s}{\partial t} = h a A (T_g - T_s) \quad (14)$$

Initial condition: Both solid and fluid at same uniform temperature,  $T_0$ .

Boundary condition: A step change in fluid temperature at the bed inlet.

$$T(0, t) = T_0 + \alpha T \quad (15)$$

The dependent variables above (temperature) can be normalized using a step change in temperature, and independent variables (time and spatial location) can be normalized by dividing it with fluid residence time and reactor length respectively. The new equations in terms of normalized variables can be written as:

$$\frac{\partial \theta}{\partial \tau} + \frac{\partial \theta}{\partial z} = H(\phi - \theta) \quad 16$$

$$\frac{\partial \phi}{\partial \tau} = H\beta(\theta - \phi) \quad 17$$

$$\text{IC} \quad \theta(z, 0) = \phi(z, 0) = 0$$

$$\text{BC} \quad \theta(0, \tau) = U(\tau)$$

$$\text{where,} \quad \tau = \frac{tv}{L}, \quad z = \frac{x}{L}, \quad \phi = \frac{T_s - T_0}{\alpha}, \quad \theta = \frac{T - T_0}{\alpha}, \quad H = \frac{h a L}{\rho_f C_f \varepsilon v}, \quad \beta = \frac{\rho_f C_f \varepsilon}{(1 - \varepsilon) \rho_s C_s}$$

The "average response time" is dependent on the number of fluid transits, H (fluid residence time) needed to supply the thermal capacity of the bed, which is determined by  $\beta$  (ratio of heat capacitance).

Equations 16-17 are solved analytically by subjecting them to Laplace transform and substituting for the particle temperature in the fluid energy balance, which leads to the equation 18 below.

$$\theta(s, z) = \frac{1}{s} \exp \left[ -sz - \frac{Hsz}{s + H\beta} \right] \quad 18$$

Inverse Laplace transform of above equation can provide us with the solution for fluid temperature at any location (z) at any time (t) as shown in Figure 3 for the case below.

Case Studied

Consider a packed bed reactor with an inlet gas fed at a temperature equal to the initial temperature of the bed (say, at 571 K). A step change in feed

temperature is provided and inlet gas temperature is increased to 623 K (a step change of 52 K). The transient response of bed is studied for fixed material properties of the gas and solids phases (fixed heat capacity ratio,  $\beta$  of  $2 \times 10^{-4}$ ) for three different cases. The three cases have been studied by varying the external heat transfer coefficient between gas and solid (at  $h = 6 \text{ W/m}^2\text{K}$ ,  $60 \text{ W/m}^2\text{K}$  and  $600 \text{ W/m}^2\text{K}$ ).

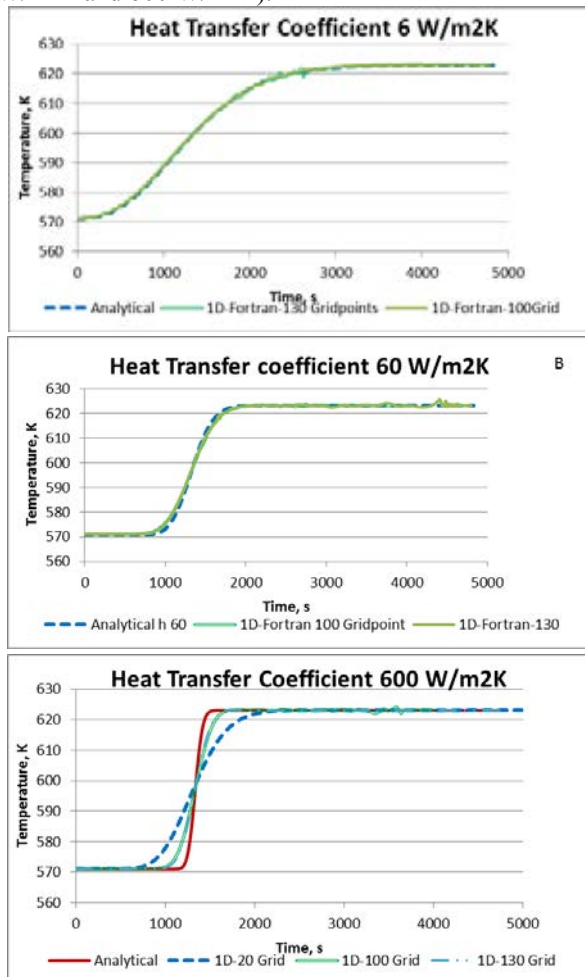


Figure 3: Validation of transient thermal bed response.

The 1D model has been compared to the analytical solution for these three different cases (Figure 3A-C) using three different grid sizes (20, 100 and 130 grid points). Grid-independence has been achieved with 100 grid points. The velocity of the thermal front and the average response time for the effect of inlet step change to be felt at any particular location is dependent on the ratio of thermal capacities of gas and solid ( $\beta$ ). The three figures show that for the chosen value of  $\beta = 2 \times 10^{-4}$ , the average response time for the effect of inlet step change to be felt at reactor bed outlet is 1334 s.

The rate of fluid-particle heat transfer (or heat transfer coefficient) has no influence on the average response time, but determines the sharpness of the temperature profile. A very high heat transfer coefficient value results in faster gas-solid heat transfer and low (or negligible) dispersion in the temperature profile around the average response time (i.e. the outlet temperature profile will then resemble the inlet step change profile), while a lower heat transfer coefficient will result in highly diffused response

to the step change. This effect can be seen in Figure 3(A-C).

The 1D model correctly captures the more diffused heat front at heat transfer coefficient of  $6 \text{ W/m}^2\text{K}$  and  $60 \text{ W/m}^2\text{K}$ , but the solution for the high heat transfer coefficient ( $600 \text{ W/m}^2\text{K}$ ) could not be fully replicated. This sharp step change response can be captured by using very high number of grid points and significant numerical diffusion is still observed for the finest grid investigated (130 grid points). A higher order scheme (like, central difference) may perhaps show lower dispersion than an upwind scheme, but it may also introduce spurious oscillations and is known to be unstable for flows with Peclet number greater than 2 [17]. However, typically the gas-solid heat transfer coefficient in a packed bed will not be as high as  $600 \text{ W/m}^2\text{K}$  and the cyclic CLC process studied here has a heat transfer coefficient of  $100 \text{ W/m}^2\text{K}$ . Thus, it can be concluded that the present 1D model is able to capture the thermal front movement for moderate heat transfer coefficients which are typical of packed beds.

### Case - Validation of Temperature Rise During An Exothermic Reaction

In order to validate reactive behaviour, the 1D model is used to simulate the movement of the reaction and thermal fronts during the oxidation stage of a PBCLC process. The movement of fronts and the maximum temperature rise predicted by the 1D model is compared to that predicted by an analytical model [3]. There exists an analytical solution if the following conditions are assumed: (a) the rate of non-catalytic gas-solid reaction is infinite, (b) axial conduction and dispersion effects are negligible, (c) heat and mass transfer limitations between the gas and solid phase are negligible and (d) intra-particle diffusion limitations are negligible. The case considered initially has the solid bed (the oxygen carrier) made of ilmenite ( $\text{FeO-Fe}_2\text{O}_3\text{-TiO}_2$ ) in a fully reduced state (i.e. no  $\text{Fe}_2\text{O}_3$ , but only  $\text{FeO-TiO}_2$ ). The solid particle has a density of  $2591 \text{ kg/m}^3$ , a heat capacity of  $922 \text{ J/KgK}$  and an active  $\text{FeO}$  weight fraction of 0.21. The initial gas present in the bed (nitrogen) is non-reactive. Both phases are initialized at a uniform temperature of  $923 \text{ K}$ . The system is fed with air at inlet temperature of  $923 \text{ K}$  and air pressure (density varies as per ideal gas law). As the oxygen is exposed to the solid limonite particle, the exothermic oxidation reaction ( $4\text{FeO} + \text{O}_2 \rightarrow 2\text{Fe}_2\text{O}_3$ ) takes place and proceeds to completion. The resulting reaction front propagates through the bed at a velocity shown by Equation 24. The expression for computing reaction front velocity assumes that all the gaseous reactant reacts with a known stoichiometric amount of the solid material.

$$W_r = \frac{\rho_g w_{g,i}^{in} v_g M_{act,i}}{\epsilon_s \rho_s w_{act,j} X_j M_i \xi} \quad 24$$

The reaction front velocity obtained for the present case (as per equation 24) is  $7.67 \times 10^{-2} \text{ m/s}$ , allowing the distance travelled in 15 s of oxidation to be calculated as 1.15 m. Figure 4 shows the results obtained by the 1D model simulation for five different grid sizes (20, 40, 60, 80 and 100 grid points) and one result is shown by making transport resistances negligible (i.e., employing very high values for mass diffusivity). The grid-independent results show a dispersed (diffused) reaction

front and the mid-point of this dispersed reaction front is at 1.15 m from the inlet of reaction bed. The reaction front dispersal is along the expected lines as the overall reaction rate is not infinite as is assumed in equation 24. Figure 4 also shows that particle-scale mass transfer resistances (captured by the particle model) cause the fronts to become more diffused. Thus, it can be concluded that the 1D model correctly captures the movement of the reaction front.

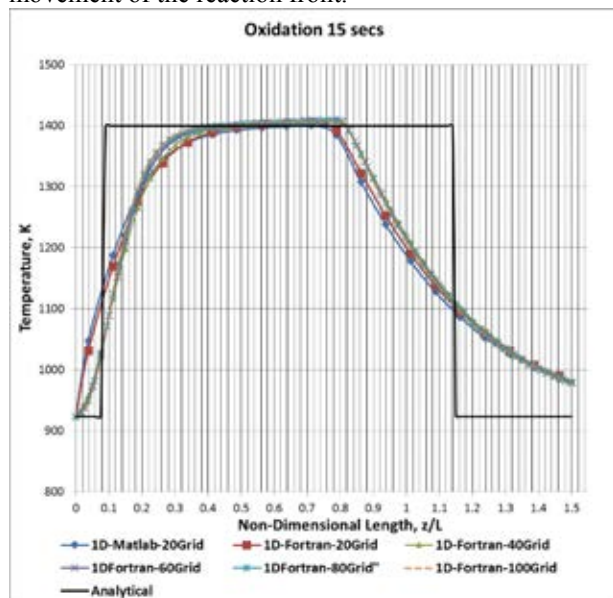


Figure 4: Validation of 1D model for front movement and temperature rise for an exothermic reaction : Analytical model (solid black line) compared with results from 1D-model at five different grid points (20,40,60,80,100) and from 1D model with no diffusional limitation (at 100 grid points).

The heat released during the exothermic reaction leads to the establishment of a higher maximum temperature upstream of the reaction front (which is discussed in a later section). Bed material upstream of the reaction front will remain hot for some distance until it is cooled down by incoming gas. The incoming gas (at 923 K) on getting exposed to a hot and fully converted bed, will therefore establish a thermal front as described in the previous section.

The thermal front moves at a velocity  $w_h$  as expressed by equation 25. This expression assumes that at the heat front, the heat present in the solid material is instantaneously transferred to the gas phase.

$$W_h = \frac{\rho_g V_g C_{p,g}}{\epsilon_s \rho_s C_{p,s}} \quad 25$$

The thermal front velocity predicted by the above equation for the current case is  $5.76 \times 10^{-3}$  m/s (around one order of magnitude slower than the reaction front). In 15 s of oxidation, the thermal front would travel 0.086 m inside the reactor bed. Figure 4 obtained by the 1D model shows the thermal front to be dispersed around 0.086 m from inlet of the bed due to the finite heat transfer coefficient. The model thus predicts the movement of the thermal-front reasonably well.

The maximum temperature that can be reached in the bed due to the heat of reaction can be obtained using an energy balance. The energy balance

formulation assumes that the volumetric heat capacity of the gas phase can be neglected and that the reaction front propagates more rapidly than the heat front. The energy balance equation can be written as:

$$\frac{\rho_g V_g w_{g,i}^{in}}{M_{g,i}} (-\Delta H_{R,i}) = \epsilon_s \rho_s C_{p,s} (w_r - w_h) (T - T_0) \quad 26$$

Equations (24)–(26) can then be combined to obtain the expected temperature change (as shown in equation 27).

$$\Delta T = \frac{(-\Delta H_{R,i})}{\frac{C_{p,s} M_{a,i}}{w_{act,j} X_j \tau} - \frac{C_{p,g} M_i}{w_{g,i}^{in}}} \quad 27$$

Equation 27 shows that the maximum temperature in the reactor is independent of the process inlet gas flow rate and is dependent upon the heat of reaction, material properties, stoichiometry and reactant species composition in gas inlet and initial solid bed. The maximum temperature change predicted by equation 27 is about 477 K which is correctly reproduced by the model as shown in Figure 4. Thus, the 1D model is able to capture the movement of the thermal and reaction fronts as well as the maximum temperature rise. This validates the use of 1D model for heterogeneous gas-solid reactions such as those taking place in the PBCLC process.

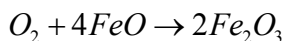
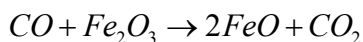
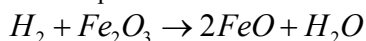
## VERIFICATION

The 1D particle-reactor model has been verified by comparing its performance with a 1D Euler-Euler model developed in ANSYS FLUENT and with a well-established 1D model developed at the Eindhoven University of Technology (TU/e). The ANSYS FLUENT solver is recognized for being robust, computationally efficient (high convergence speed) and numerically stable (use of large time-steps). It is widely used and has been extensively validated for reactive multi-phase applications. The TU/e model has been used in a number of publications [7, 8, 18] implying that its validity is broadly accepted within the scientific community. These two simulation tools therefore present an excellent verification benchmark.

The verification has been done for realistic cyclic operating conditions suggested for the 500 kW demonstration scale CLC reactor [18]. The simulation with these operating process conditions (see B1 strategy from Table 4 of [18]) will help to evaluate the model for real behaviour of an industrial packed bed reactor. This operating cycle strategy includes four distinct phases of operation: a reduction phase (with synthesis gas as fuel) for 300 s, a heat removal phase with an inert gas stream for 300 s, an oxidation phase with air (until the oxidation reaction front reaches the end of the reactor) for 300 s, and a purge phase for 10s. This 910 s cycle of reduction-heat removal-oxidation-purge is repeated continuously. The advantage of this approach is that the reduction phase is carried out when almost the entire bed is at the maximum temperature (owing to a prior oxidation phase). At lower temperatures, the reduction reaction rates are quite low. Hence, a bed at maximum temperature enables a higher reduction reaction rate and avoids early fuel-slip of H<sub>2</sub> and CO.

The proposed model must be able to capture the effect of a typical cyclic operation, wherein the initial bed conditions (bed temperature and species) for a newly starting phase is a result of a previous phase in the cycle. These process conditions therefore serve as a very stringent test of the model's ability to accurately capture the thermal and chemical dynamics of packed bed reactors.

The reduction and oxidation reactions taking place for the ilmenite particle can be described as :



All three models use the same reaction kinetics provided by Abad et. al. (2011). However, the set of equations and modelling approach used by all the three models are different. The FLUENT model does not have a particle model, while the TU/e model has both a particle model and reactor model [7, 8]. However, the TU/e cyclic simulations presented by Spallina et. al. [18] were conducted without the use of a particle model (using an effectiveness factor approach with near unity value of effectiveness factor) for efficient computation. The next section describes the 1D Fluent model in brief.

#### 1D Fluent Model

The 1D FLUENT model uses an Eulerian-Eulerian multiphase flow modelling approach, where the two participating phases (gas and solids) are treated as interpenetrating continua or fluids. The mass, momentum, energy and species are conserved for each phase individually. Table 1 lists the conservation equations being solved by the FLUENT solver and the closure laws (Ergun drag model and multi-particle Ranz-Marshall heat transfer coefficient) used. For maintaining the packed bed, the solid phase velocity is fixed to zero and the volume fraction of both solid and gas phase are also fixed.

The reactor geometry comprises of a plane (0.3 m x 2.8 m), which is spatially discretized only in axial direction (100 grid cells in axial direction) and has no radial space discretization. This enables for only the 1D effect to be solved. Grid independence was achieved for the 100 axial grid point employed. The solutions have been obtained using a phase-coupled SIMPLE algorithm [17] for pressure-velocity coupling. The QUICK scheme [19] has been employed for convective terms discretization in all the equations and a 1st order implicit scheme temporal discretization has been used. The comparison of the three models is as below :

The three models (1D Fluent, 1D TU/e and 1D particle-reactor) have been compared for predicting the axial temperature profile (Figure 5) at the end of oxidation phase, at the end of reduction phase and at the end of heat removal phase in a cyclic operation. In addition, the reduction reaction front movement (Figure 6) and the exit gas temperature in a cycle (Figure 7) are also compared.

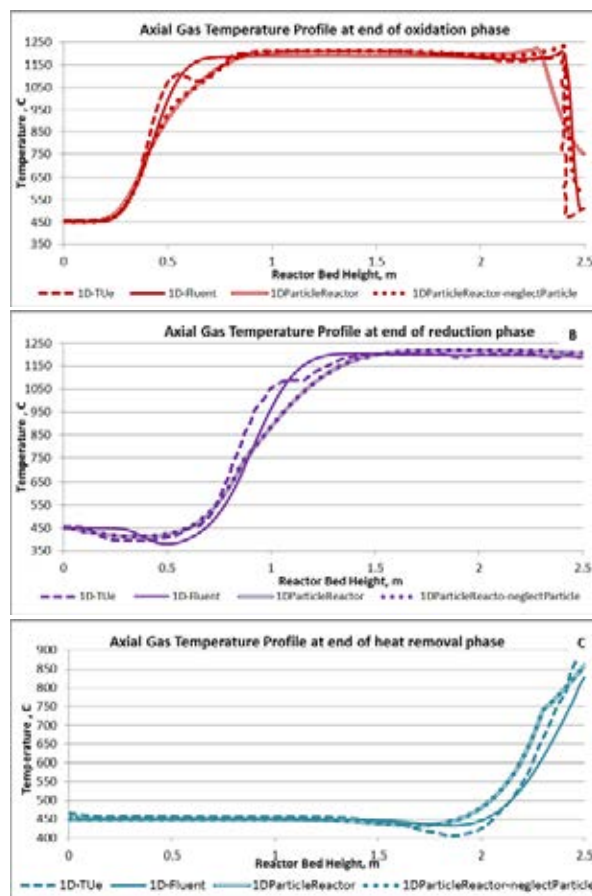


Figure 5 Verification - comparison of different 1D model in predicting the axial temperature profile at: (A) the end of oxidation phase, (B) at the end of reduction phase and (C) at the end of heat removal phase.

Simulations have also been conducted to check the effect of diffusive resistances within the particle on the whole cyclic process. To make the particle effect of negligible, the 1D particle-reactor model has been simulated with high intra-particle gas species diffusivity and high external heat/mass transfer coefficients (see the results with legend 1DParticleReactor-neglectParticle in Figures 8-11). The inclusion of the particle model has a significant impact. The oxidation reaction front (towards reactor end in Figure 5A) and reduction reaction front (in Figure 5B) are more diffused with the particle effect on (legend named 1DParticleReactor) than without the particle effect (legend named 1DParticleReactor-neglectParticle). This diffused front is caused by a reduction in the effective reaction rate due to inclusion of intra-pellet mass-transfer limitations with the particle. For this particular case, the diffusional resistance offered by the 3 mm spherical particles is high enough to have an impact on the cyclic reactor performance. For example, Figure 8 shows much earlier fuel slip in the model with intra-particle diffusive resistances activated than in the model without these resistances. Such fuel slip would require a significantly shorter fuel stage, thereby changing the overall cycle dynamic.

This significant effect of intra-particle diffusion is expected because diffusivity of species lowers owing to the reduction in mean free path with increasing pressure, implying that diffusivity is low at the 20 bar operating pressure. The effective diffusivity in the particle after



accounting for the particle void fraction and tortuosity leads to a lower diffusion rate constant (around  $1.3 \text{ s}^{-1}$ ) for the 1.5mm radius particle. The Thiele modulus (diffusion time over reaction time) for the present condition is in the order of 100 due to the higher effective reaction rate constant. This implies that the process is mass transfer dominated and provides the theoretical basis for the observed results (as predicted by the inclusion of the particle model).

Hence, the results with inclusion of the particle model give more dispersed profiles as compared to the 1D Fluent and 1D TU/e model results. The inclusion of the particle model in the 1D model helps to correctly identify the significant amount of fuel slip taking place during the reduction phase as seen in Figure 8, which will lead to more accurate reactor design and cycle-time predictions. However, the 1D particle-reactor model with neglected particle effect (legend named 1DParticleReactor-neglectParticle) gives similar results as the 1D TU/e model and the 1D Fluent model.

The oxidation phase temperature rise and the oxidation thermal front velocity predicted by these three models (in Figure 5A) are also quite similar but for some minor deviations. These minor deviations are acceptable and are caused by some minor differences in the material properties data (heat capacity as a function of temperature) and differences in the means of computation of heat of reaction. The TU/e model computes the heat of reaction using an input correlation of heat of reaction as a function of temperature, while the other two 1D models compute the heat of reaction from the input heat capacity data and standard enthalpy of formation.

These three models also show good agreement on the location of the oxidation reaction front (Figure 5A) and the reduction reaction front (Figure 6). The oxidation reaction front is located towards the reactor end (seen in Figure 5A) as the results are compared at the end of the oxidation phase. In Figure 6, the reduction reaction front is located mid-way of the reactor (as the results are compared after 150 s from start of the 300 s reduction phase). The reaction front movement is independent of the reaction rate, but the slope of the front (sharp or diffused) is dependent upon reaction rate. As mentioned earlier, the results of 1D particle-reactor model with particle effect neglected (legend named 1DParticleReactor-neglectParticle) is closer to the 1D Fluent and 1D TU/e model (sharper reaction front) for both the oxidation and reduction reaction front. This is expected as both the 1D Fluent and 1D TU/e model do not include the effect of intra-particle diffusion. The comparison of thermal fronts predicted by the three models at the end of reduction (Figure 5B) and at the end of heat-removal (Figure 5C) shows some minor deviations within acceptable limit. As suggested earlier, these deviations are a result of uncertainty in exact closure data (heat capacity material properties) used by the TU/e model. The heat capacity data and heat of reaction data for a given material system predicted by different thermodynamic software packages and suggested in different material database handbooks may slightly differ from each other, resulting in this acceptable deviation.

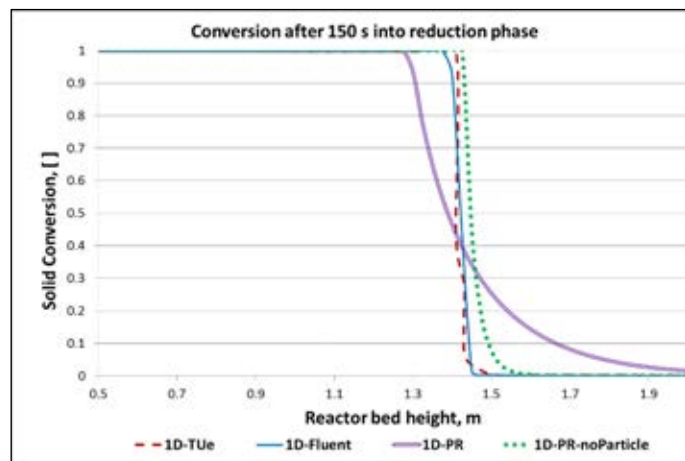


Figure 6 Verification - Comparison of different 1D models in predicting the reaction front velocity during the reduction phase (PR in the legend stands for our particle-reactor model).

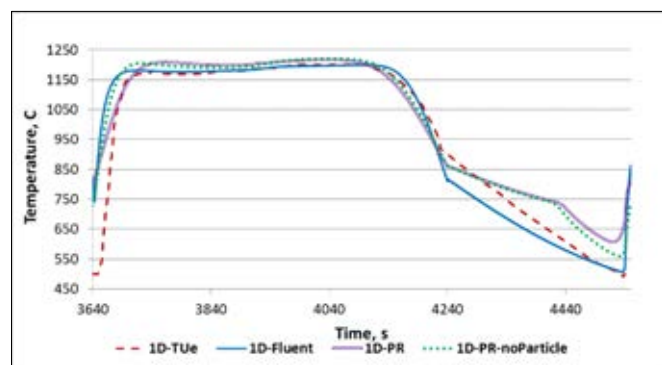


Figure 7 Comparison of different 1D models in predicting the exit gas temperature dynamics in a cycle. (PR in the legend stands for our particle-reactor model).

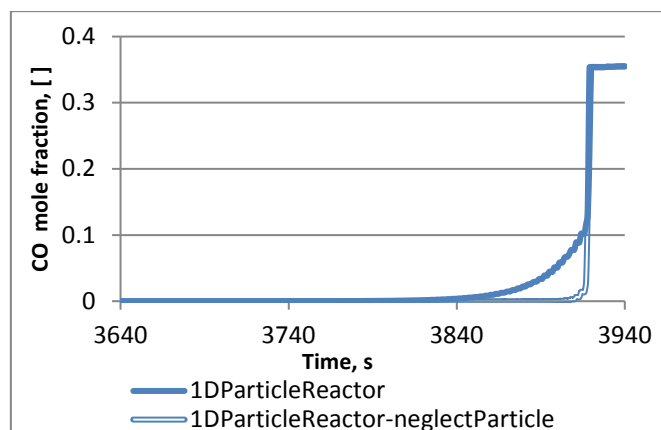


Figure 8. Effect of particle model on Fuel-slip: Outlet concentration of CO mole fraction at reactor exit during the reduction stage.

This uncertainty in material property data also explains the deviation in the last segment of the exit gas temperature profile (Figure 7). However, all three models predict the same maximum outlet temperature (nearly  $1200 \text{ }^\circ\text{C}$ ) for a similar duration of time. Despite the minor deviations caused by uncertainties regarding material property data, the present comparative results on axial temperature profile and solid conversion profile provide

a credible verification of the accuracy of the 1D-particle-reactor model solver developed in this work. The next section covers in brief the performance and advantages of the proposed solver.

Regarding solver efficiency of 1D model, using 100 grid points (for ensuring comparison with grid independent FLUENT results) and using very high tolerances (absolute tolerance of  $1 \times 10^{-6}$  and relative tolerance of  $1 \times 10^{-9}$ ), the 1D particle-reactor model takes 4960 s (about 1.37 hrs) of computational time to simulate 4550 s of cyclic reactor operation. The 4550 s of cyclic reactor operation corresponds to 5 cycles ( $5 \times 910 \text{ s} = 4550 \text{ s}$ ). The results after 4 cycles are already compared and discussed in Figure 5-8. Figure 9 shows results from 1D Fluent model. The 1D simulation was run on a desktop personal computer with 2.7GHz Intel® core™ i7-2620M CPU. With 70 grid points, this 1D model gives as accurate results as 100 grid points (nearly grid-independent result), in computational time faster than real-time (i.e. the 4550 s of reactor operation is simulated in 3018 s of computational time). While with 20 grid points, the 4550 s cyclic reactor operation is simulated in just 520 s of computational time, but there is loss of accuracy owing to numerical diffusion (the fronts are more diffused). Comparatively, when the FLUENT solver is run without any convergence criteria, then it is 7 times faster than the 1D model with 100 grid points and ensures real-time operation (simulates 4500 s cycle in just 700 s of computational time). However, the 1D Fluent model does not account for the particle effect. This ANSYS Fluent simulation is carried out on a server machine on a single processor (2.4GHz Intel® Xeon® E-5645 CPU). With convergence criteria on (convergence criteria of  $1 \times 10^{-3}$  for all equations), the ANSYS FLUENT 13 solver (with 100 grid points) takes 19 hrs of to simulate the 4550 s cycle. However, the FLUENT solver has been able to capture the front movements in the cycle accurately with little loss of accuracy when run without any convergence control criteria. The segregated solver in conjunction with Algebraic Multigrid method in ANSYS Fluent ensures efficient solution. However, the cost of ANSYS FLUENT licenses along with need for a server infrastructure makes it costly, while the present 1D model provides results as numerically accurate as FLUENT in a very cost-effective way. In addition, the proposed 1D model also simulates for the effect of intra-particle diffusion and makes it physically more complete. Further, the implicit solver utilized makes the model computationally efficient for stiff kinetics. It is not practically feasible to solve the stiff kinetics using explicit schemes as it requires very low time-steps (a fact tested using the explicit ode45 solvers in MATLAB®). The current implicit solver runs with an average time step of  $1 \times 10^{-3}$  s for the stiff kinetics as compared to  $1 \times 10^{-8}$  s required by the explicit solver. Further, with increasing grid density, an explicit solver performance becomes much slower than the implicit solver. An explicit solver needs to lower the time-step to meet the Courant number criteria for stability, while an implicit solver is not limited by stability but will lower the time-step to meet accuracy (for increasing grid density). The present implicit solver thus ensures faster convergence.

The choice of programming language also ensures faster solutions. The present Fortran-90 implementation makes

the code much faster as Fortran-90 is a compiled scripting language. This 1D model implemented in Fortran-90 is two orders of magnitude faster than a similar implicit Matlab® solver (Matlab® being an interpreted scripting language takes longer time).

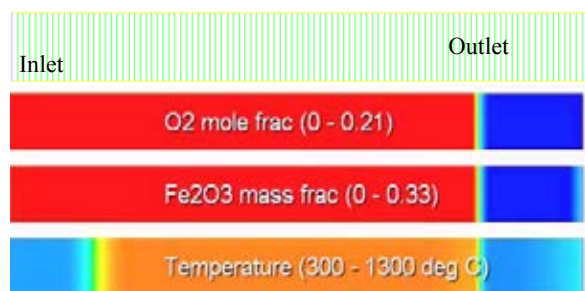


Figure 9 shows the grid and geometry used for 1D Fluent and the location of reaction front and thermal front captured by it during the oxidation phase of the cycle.

Thus, both the validation and verification of the proposed multi-domain 1D particle-reactor model shows that it offers good numerical accuracy, is computationally efficient in solving systems with stiff kinetics, is physically complete as it simulates the particle effect, and is cost-effective for practical operations.

## CONCLUSIONS

The 1D multi-domain packed bed model is a combination of (1) a particle model for the radial distribution of chemical species and temperature within a catalyst particle and (2) a 1D reactor model for mass and energy transport along the reactor. The 1D particle-reactor model has been successfully validated against analytical solutions for (a) transient thermal behaviour of a fixed bed to a step-change in inlet feed temperature and for (b) maximum temperature rise and front movement during an exothermic oxidation stage in a packed bed chemical looping combustion process. The 1D model predicts similar results as the analytical models, thus giving confidence in its accuracy and usage. Further, the proposed 1D model is also successfully verified by comparing it with the popular commercial ANSYS FLUENT solver and a well-established 1D packed bed reactor model from the Eindhoven University of Technology. The models are compared for simulating a realistic 500kW cyclic chemical looping combustion process involving stiff redox kinetics over multiple cycles, wherein each cycle comprises of reduction phase, heat-removal phase, oxidation phase and purging phase. These process conditions serve as a very stringent test of the model's ability to accurately capture the thermal and chemical dynamics of packed bed reactors. The comparison reveals that the proposed model is able to accurately capture the thermal front and reaction front dynamics arising in the realistic 500kW cyclic PBCLC process. The proposed 1D model predicts similar results as the 1D FLUENT and 1D TU/E model when the particle effects are made negligible by using high transport coefficients. The comparison also highlights the need and significance of a particle model when the mass transfer limitation dominates, and thus successfully showcases the advantages with using the proposed 1D particle-reactor model. The validated and verified 1D

model is also compared for the solver performance. The choice of an implicit multi-step backward differentiation formula makes the model computationally efficient while solving stiff reaction kinetics. Overall, the proposed 1D model is efficient and also physically more complete owing to the inclusion of a particle model. Hence, the proposed 1D particle-reactor model can help to design and operationalize all kinds of gas-solid packed bed reactions.

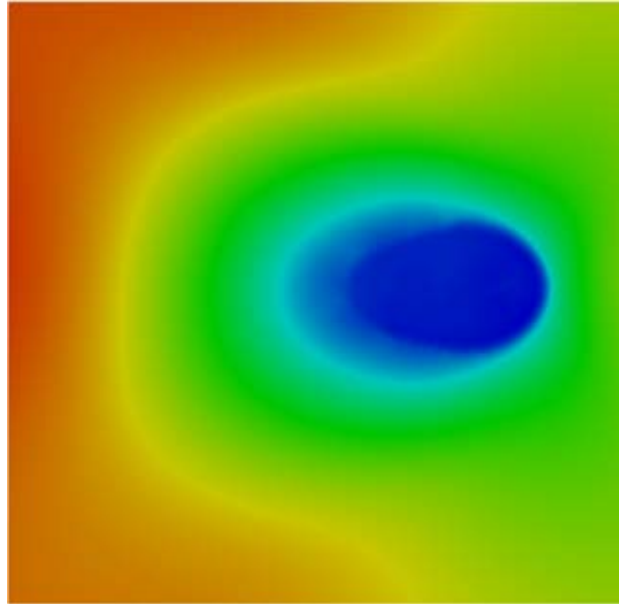
## ACKNOWLEDGMENT

The work has been carried out as a part of a POP-SEP funding from SINTEF Materials and Chemistry and funding from the European Union Seventh Framework Programme (FP7/2007–2013) under grant agreement n° 268112 (Project acronym DEMOCLOCK).

## REFERENCES

- [1] G. Eigenberger, Catalytic Fixed-Bed Reactors. Handbook of Heterogeneous Catalysis. , 2008, p. 2075.
- [2] J.B. Joshi, L.K. Doraiswamy, Chemical Reaction Engineering, in Albright's Chemical Engineering Handbook, CRC Press. Albright, Boca , Raton, FL, 2009, p.
- [3] S. Noorman, Packed bed reactor technology for chemical-looping combustion, Univ. **2009**, p.
- [4] S. Noorman, F. Gallucci, M. Van Sint Annaland, J.A.M. Kuipers, *Industrial and Engineering Chemistry Research* **2011**, *50*, 1968.
- [5] K.R. Rout, H.A. Jakobsen, *Fuel Processing Technology* **2013**, *106*, 231.
- [6] K.R. Rout, J. Solsvik, A.K. Nayak, H.A. Jakobsen, *Chem Eng Sci* **2011**, *66*, 4111.
- [7] S. Noorman, F. Gallucci, M. Van Sint Annaland, J.A.M. Kuipers, *Chemical Engineering Journal* **2011**, *167*, 297.
- [8] S. Noorman, F. Gallucci, M.M. van Sint Annaland, J.A.M. Kuipers, *Chemical Engineering Journal* **2011**, *167*, 369.
- [9] G.D. Ingram, I.T. Cameron, K.M. Hangos, *Chem Eng Sci* **2004**, *59*, 2171.
- [10] S. Ergun, *Chem. Eng. Prog* **1952**, *48*, 89.
- [11] W.E. Ranz, W.R. Marshall, *Chem. Eng. Prog.* **1952**, *48*, 173.
- [12] M.V. Tabib , S.T. Johansen , A. Shahriar, *Industrial and Engineering Chemistry Research* **2013**, *52 (34)* 12041.
- [13] A.C. Hindmarsh, R.S. Stepleman, "ODEPACK, a Systematized Collection of ODE Solvers" Scientific Computing, RR. S. Stepleman et al., eds., North-Holland, Amsterdam, 1983, p. 55.
- [14] G.D. Byrne, A.C. Hindmarsh, *ACM Trans. Math. Software* **1975**, *1*, 71.
- [15] P.N. Brown, G.D. Byrne, A.C. Hindmarsh, *SIAM J. Sci. Stat. Comput.* **1989**, *10*, 1038.
- [16] J.E. Crider, A.S. Foss, *AIChE J.* **1968**, *14*, 77.
- [17] S.V. Patankar, Numerical heat transfer and fluid flow / Suhas V. Patankar, Hemisphere Pub. Corp. ; McGraw-Hill, Washington : New York, **1980**, p.
- [18] V. Spallina, F. Gallucci, M.C. Romano, P. Chiesa, G. Lozza, M. van Sint Annaland, *Chemical Engineering Journal* **2013**, *225*, 174.
- [19] B.P. Leonard, S. Mokhtari, ULTRA-SHARP Nonoscillatory Convection Schemes for High-Speed Steady Multidimensional Flow, NASA TM 1-2568 (ICOMP-90-12) NASA Lewis Research Center, 1990, p.

# SPECIES TRANSPORT & INTERFACES





## MODELLING AND NUMERICAL SIMULATION OF SURFACE ACTIVE SPECIES TRANSPORT - REACTION IN WELDING PROCESSES

**Kateryna DOROGAN**

Industrial Risk Management Department, EDF R&D, 78401 Chatou Cedex, FRANCE

E-mail: kateryna.dorogan@edf.fr

### ABSTRACT

This paper deals with the modelling of steel melting process during TIG welding operations on the nuclear power plants. The issue of the quality assurance of welding operations on some components is of great importance for the nuclear safety management. However, there are many parameters involved in the process which makes the uncertainty of the whole operation important. Moreover, some repair operations make impossible the quality control of the final weld bead. This is the case of one such a weld this study focus on. A way to ensure the quality of such weld beads could be based on the weld pool shape prediction by the numerical simulation. Thus, giving the operating parameters such as arc energy distribution, the flow simulation inside the weld pool could provide the information on the final weld pool dimensions.

The model describing the metal flow during the welding process developed in this work is based on the classical MHD and the enthalpy equations. Yet, the flow in the weld pool is mainly governed by variable surface tension force, the phenomenon known as Marangoni effect. The surface tension variation is in this case highly dependent on the thermal and the surfactant concentration gradients. In order to better evaluate this force, in this work, we present a new formulation of transport-reaction equations for surfactant and relative species in the molten steel. Moreover, this model takes into account species chemical reaction and evaporation. This allows mass fractions and gradients computation at the weld pool surface, and by this mean a better prediction of the surface tension force in case of variable chemical composition. The results of the simulations are compared to experimental data on the weld pool dimensions.

**Keywords:** Surfactants and interface, CFD, Free surface flow, MHD, Casting and solidification .

### NOMENCLATURE

#### Greek Symbols

$\beta$	Thermal expansion coefficient, $[1/K]$
$\Gamma_s$	Excess of S concentration in solute, $[kg\cdot mol/m^2]$
$\gamma$	Surface tension force, $[N/m]$
$\gamma_m^0$	Surface tension of a pure metal at $T_f$ , $[N/m]$
$\varepsilon$	Emissivity of the weld pool surface, $[1]$
$\eta$	Yield of the TIG process, $[1]$
$\lambda$	Thermal conductivity, $[W/m\cdot K]$
$\mu$	Dynamic viscosity, $[kg/ms]$
$\mu_0$	Vacuum permeability, $[V\cdot s/A\cdot m]$
$\rho$	Mass density, $[kg/m^3]$

$\rho_{ref}$	Density of the steel at the liquidus temperature, $[kg/m^3]$
$\sigma$	Electrical conductivity, $[Ohm\cdot m]$
$\sigma_{SB}$	Stefan-Boltzmann constant, $[W/m^2\cdot K^4]$

#### Latin Symbols

<b>A</b>	Magnetic potential, $[V\cdot s/m]$
$\bar{A}$	Thermal surface tension gradient for a pure material, $[N/(m\cdot K)]$
$a_s$	Sulfur activity, $[1]$
<b>B</b>	Magnetic field, $[T]$
$C_p$	Specific heat, $[J/K]$
<b>c</b>	Vector of mass concentrations, $[kg/m^3]$
$c_s$	Sulfur mass concentration, $[kg/m^3]$
$D_j^i$	Diffusion coefficient of species $i$ in solute $j$ , $[m^2/s]$
$D_0^i$	Frequency factor for species $i$ , $[m^2/s]$
<b>E</b>	Electric field, $[V]$
$F_b$	Buoyancy, $[Pa/m]$
$f_l$	Liquid fraction, $[1]$
<b>g</b>	Gravity, $[m/s^2]$
<b>H</b>	Total enthalpy, $[J]$
$\Delta H$	Heat of adsorption, $[J/(kg\cdot mol)]$
$\Delta H_s^{Cr}$	Partial molar enthalpy of Cr-S interaction, $[J]$
$h$	Specific enthalpy, $[J/kg]$
$\tilde{h}$	Convective exchange coefficient, $[W/m^2\cdot K]$
<b>I</b>	Current intensity, $[A]$
<b>j</b>	Current density, $[A/m^2]$
<b>k</b>	Segregation entropy factor, $[1]$
<b>n</b>	Outward normal vector, $[m]$
$P_R$	Electric potential, $[V]$
$p$	Pressure, $[Pa]$
$Q^i$	Activation energy for $i$ -species, $[J/mol]$
<b>R</b>	Gas constant, $[J/mol\cdot K]$
$r$	Distance from heat source, $[m]$
$r_H$	Heat source dispersion, $[m]$
$r_J$	Current source dispersion, $[m]$
$S_R^u$	Carman-Kozeny term, $[Pa/m]$
<b>T</b>	Temperature, $[K]$
$T_f$	Melting point, $[K]$
$T_l$	Liquidus temperature, $[K]$
$T_{ref}$	Reference temperature, $[K]$
$T_s$	Solidus temperature, $[K]$
$T_0$	Ambient temperature, $[K]$
$t$	time, $[s]$
<b>U</b>	Current tension, $[V]$
<b>u</b>	Fluid velocity, $[m/s]$
<b>v</b>	Welding torch speed, $[m/s]$

$\mathbf{x}$  Space coordinates vector, [m]  
 $Y_i$  i-species mass fraction, [1]

#### Sub/superscripts

$Cr$  Chromium  
 $Fe$  Iron  
 $Mn$  Manganese  
 $S$  Sulfur

## INTRODUCTION

This paper is aimed at proposing a new modelling of reacting metal flow formed in the weld pool during Tungsten Inert Gas (TIG) welding operations. Welding being one of the most used repair processes in nuclear engineering, the quality assessment of weld beads appears to be one of the important issues both from nuclear safety and industrial costs points of view. For instance, we are interested in reproducing numerically one such a weld found on French nuclear power plants. This weld appears to be difficult to control and reproduce experimentally due to local variations in chemical composition of welded materials. Moreover, the process make impossible the weld quality control upside down the pieces so that some internal defects could remain unrevealed. Till today, several experimental studies were made in order to understand and reproduce the most critical of those, but these attempts have been mostly unsuccessful.

An alternative approach to tackle this problem could be based on the weld pool shape predictions using numerical simulation tools. The model the most widely used to predict the flow pattern in the weld pool is based on the unsteady MHD equations taking into account the Marangoni effect which consists in modelling the surface tension force as a function of temperature and of surfactant concentration on the weld pool surface (Belton, 1976; Heiple and Roper, 1982; Sahoo *et al.*, 1988; McNallan and DebRoy, 1991; Mills *et al.*, 1998; Sampath and Zabaras, 2001).

However, these simulations were only successful in the case of constant chemical composition. In fact, in most practical situations, when two or more different materials are welded, the local variation of the surfactant content causes the modification of the flow characteristics, and an important difference on the weld pool shape may appear. This is for instance the case for sulfur which is known to modify the surface tension of the molten steel. It was found that the surface tension variation with the temperature is non monotonous and highly dependent on the sulfur concentration and its gradient. Moreover, the sulfur concentration in the liquid steel varies with the time and with the temperature since sulfur may create solid inclusions with manganese. Therefore, an accurate evaluation of species mass fractions in the unsteady metal flow is essential for the correct prediction of the surface tension force in these situations.

Thus, this paper presents the new transport-reaction equations of surfactant and relative species in the molten steel together with the MHD and the enthalpy equations describing the flow in the weld pool. It takes into account sulfur and manganese reversible chemical reaction and manganese evaporation.

## WELD POOL MODEL DESCRIPTION

### Geometry and Mesh

We deal with two fitted steel plates each of size  $80 \times 40 \text{ mm}^2$  and of thickness  $2 \text{ mm}$  put together, thus forming the whole domain of dimensions  $80 \text{ mm} \times 80 \text{ mm} \times 2 \text{ mm}$ , Fig. 1. In the figure, the red line shows the separation between pieces by the plane  $y = 0$ .

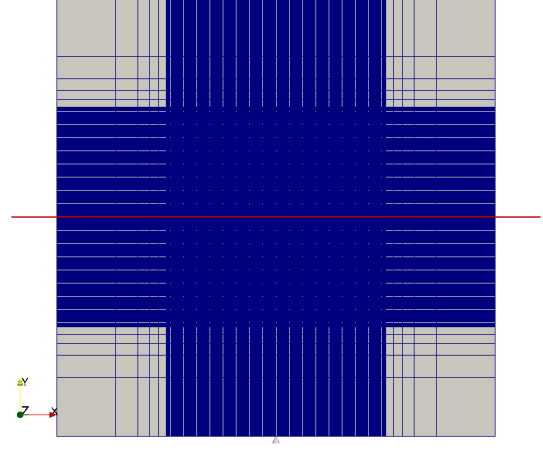


Figure 1: Geometry and mesh of the domain, 2d-cut.

The mesh shown in Fig. 1 is orthogonal and composed of  $1.4 \times 10^6$  cells with the size of  $1.25 \times 10^{-4} \text{ m}$  in the finest central square region of size  $40 \times 40 \text{ mm}^2$ .

### Magnetohydrodynamics equations

The model is a system of incompressible Navier-Stokes and Maxwell equations. For  $\mathbf{x} \in R^3$ ,  $t > 0$  and the state vector  $(\mathbf{u}, p, h, P_R, \mathbf{A})^t(\mathbf{x}, t)$  we solve numerically :

*Mass continuity equation :*

$$\nabla(\rho \mathbf{u}) = 0, \quad (1)$$

*Momentum conservation :*

$$\frac{\partial(\rho \mathbf{u})}{\partial t} + \nabla(\rho \mathbf{u} \otimes \mathbf{u}) = -\nabla p + \mu \Delta \mathbf{u} + \mathbf{j} \times \mathbf{B} + \mathbf{F}_b + \mathbf{S}_R''', \quad (2)$$

*Specific enthalpy conservation :*

$$\frac{\partial(\rho h)}{\partial t} + \nabla(\rho \mathbf{u} h) = \nabla \left( \frac{\lambda}{C_p} \nabla h \right) + \mathbf{j} \cdot \mathbf{E}, \quad (3)$$

*Charge continuity equation :*

$$\nabla(\sigma \nabla P_R) = 0, \quad (4)$$

*Ampere's circuital law :*

$$\Delta \mathbf{A} = -\mu_0 \mathbf{j}, \quad (5)$$

with initial and boundary conditions detailed below. In (1)-(5),  $\mathbf{u}$  denotes the fluid velocity,  $p$  the total pressure,  $h$  the specific enthalpy,  $P_R$  the real part of the scalar electric potential and  $\mathbf{A}$  the vector magnetic potential. The thermodynamical properties of material are the density  $\rho$ , the dynamic viscosity  $\mu$ , the specific heat  $C_p$ , the thermal conductivity  $\lambda$  and the electric conductivity  $\sigma$ , all varying as functions of the temperature (Kim, 1975).

The source terms in the momentum equation (2) correspond to the Laplace forces (expressed via the current density  $\mathbf{j}$

and the magnetic field  $\mathbf{B}$ ), the buoyancy  $\mathbf{F}_b$  and the Carman-Kozeny term describing the velocity relaxation in the porous media during the liquid-solid transition  $\mathbf{S}_R^u$  (Kozeny, 1927; Carman, 1956). The buoyancy is expressed using Boussinesq approximation:

$$\mathbf{F}_b = \rho_{ref} [1 - \beta(T)(T - T_{ref})] \mathbf{g}, \quad (6)$$

with  $\beta$  the thermal expansion coefficient,  $T_{ref}$  the liquidus temperature of the steel,  $\rho_{ref}$  the density of the steel at  $T_{ref}$  and  $\mathbf{g}$  the gravity. In the enthalpy conservation equation (3), the rhs term  $\mathbf{j} \cdot \mathbf{E}$  represents the Joule effect,  $\mathbf{E}$  denoting the electric field.

The form of equations (4), (5) is based on two assumptions: the fluid is supposed electrically neutral; the electric and magnetic fields are quasi stationary. Using the simplified Ohm's law:  $\mathbf{j} = \sigma \mathbf{E}$ , the system (1)-(5) is completed by the following relations:

$$\begin{aligned} \mathbf{E} &= -\nabla P_R, \\ \mathbf{B} &= \text{rot } \mathbf{A}. \end{aligned} \quad (7)$$

#### Initial conditions

We fix the initial difference of the electric potential between the electrodes  $U = 11 \text{ V}$  as well as the current intensity  $I = 135 \text{ A}$ , thus giving the initial values to  $P_R$  and  $\mathbf{A}$ . At  $t = 0$ , we consider the workpiece in a solid state at ambient temperature  $T_0 = 300 \text{ K}$ , and atmospheric pressure,  $p_0 = 101325 \text{ Pa}$ . Then, the corresponding values of other properties for these values of pressure and temperature are:  $\rho_0 = 7500 \text{ kg/m}^3$ ,  $C_{p,0} = 602 \text{ J K}^{-1} \text{ kg}^{-1}$  et  $\mathbf{u}_0 = \mathbf{0}$ .

#### Boundary conditions

The boundary conditions will be only detailed for the top (heated) surface of the plates. On the other boundary faces the default wall boundary conditions are fixed. Moreover, in practice there is no mass or momentum flux on these sides since they remain always in solid state.

- *Pressure:*  $\partial P / \partial n = 0$ .
- *Velocity:* We fix  $\mathbf{u} \cdot \mathbf{n} = 0$  and add a flux related to the weld pool surface tension variation, the surface tension  $\gamma(\mathbf{c}, T)$  being a function of the temperature  $T$  and of the chemical concentration of species composing the steel  $\mathbf{c}$  (Belton, 1976):

$$\mu \frac{\partial \mathbf{u}}{\partial n} = f_l \cdot \sum_i \frac{\partial \gamma(\mathbf{c}, T)}{\partial c_i} \cdot \nabla c_i + f_l \cdot \frac{\partial \gamma(\mathbf{c}, T)}{\partial T} \cdot \nabla T. \quad (8)$$

with the liquid fraction  $f_l$ , defined as follows:

$$f_l = \begin{cases} 1, & T > T_l, \\ (T - T_s) / (T_l - T_s), & T_s \leq T \leq T_l, \\ 0, & T < T_s. \end{cases} \quad (9)$$

Among several surface active species which may be found in the steel during melting, sulfur is one that may be beforehand quantified since it is introduced in the steel during steel making process. It is also known to modify to a great extent the surface tension of binary Fe-S alloys (Heiple and Roper, 1982).

The most general expression of the surface tension force of the liquid metal containing surface active inclusions

(for instance, sulfur) and varying with temperature is given by (Belton, 1976; Heiple and Roper, 1982; Sahoo *et al.*, 1988):

$$\gamma(c_s, T) = \gamma_m^0 - \tilde{A}(T - T_m) - RT \Gamma_s \ln[1 + Ka_s], \quad [N/m] \quad (10)$$

with

$$K = ke^{-\Delta H/RT}, \quad (11)$$

and with  $\gamma_m^0$  the surface tension of a pure metal at  $T_f$  (with no inclusions),  $\tilde{A}$  the opposite of  $\partial \gamma(c_s, T) / \partial T$  for a pure material (without surface active inclusions),  $\Gamma_s$  the excess of sulfur concentration in solute,  $R$  the gas constant,  $k$  the segregation entropy,  $\Delta H$  the heat of adsorption and  $a_s$  the sulfur activity.

Then, considering a more recent work (McNallan and DebRoy, 1991) which takes into account S-Cr interaction in liquid steel, the expression of the surface tension gradients induced by temperature and by sulfur concentration are written in the following form:

$$\begin{aligned} \frac{\partial \gamma(c_s, T)}{\partial T} &= -A - RT \Gamma_s \left[ \ln(1 + Ka_s) + \frac{Ka_s}{1 + Ka_s} \frac{\Delta H - \Delta H_s^{\text{Cr}}}{RT} \right], \\ \frac{\partial \gamma(c_s, T)}{\partial c_s} &= -\frac{RTK\Gamma_s}{1 + Ka_s} \end{aligned} \quad (12)$$

with

$$a_s = 10^{e_s^{\text{Cr}} [\text{pct Cr}]} \cdot [\text{pct S}], \quad (13)$$

$$e_s^{\text{Cr}} = -94.2/T + 0.0396 \quad (14)$$

and with  $\Delta H_s^{\text{Cr}}$  the partial molar enthalpy of Cr-S interaction in solute:

$$\Delta H_s^{\text{Cr}} = -94.2R[\text{pct Cr}] \ln 10. \quad (15)$$

Expression (8) describes the phenomenon known as the *Marangoni effect* which consists in the mass transfer along an interface between two fluids due to surface tension gradient. The latter is one of the most important forces acting in the weld pool.

- *Enthalpy:* The enthalpy flux fixed on the top surface is composed of the Gaussian-distributed heat source, radiative and convective heat exchange contributions moving with the torch speed in the  $x$ -direction:

$$\frac{\lambda}{C_p} \frac{\partial h}{\partial n} = \frac{\eta UI}{2\pi r_H^2} \exp\left(-\frac{r^2}{2r_H^2}\right) + \varepsilon \sigma_{SB}(T^4 - T_0^4) + h(T - T_0), \quad (16)$$

with  $r_H$  the heat source dispersion,  $I$  the current intensity,  $U$  the current tension,  $\eta$  the yield of the process,  $\sigma_{SB} = 5.67 \times 10^{-8} \text{ W m}^{-2} \text{ K}^{-4}$  the Stefan-Boltzmann constant,  $\varepsilon = 0.5$  the emissivity of the weld pool surface,  $T_0 = 300 \text{ K}$  the ambient temperature and  $h = 15 \text{ W m}^{-2} \text{ K}^{-1}$  the convective exchange coefficient.

- *Scalar electric potential and vector magnetic potential:*

$$\begin{aligned} \sigma \frac{\partial P_R}{\partial n} &= \frac{I}{2\pi r_j^2} \exp\left(-\frac{r^2}{2r_j^2}\right), \\ \frac{1}{\mu_0} \frac{\partial \mathbf{A}}{\partial n} &= 0. \end{aligned} \quad (17)$$

For the sake of simplicity, we assume the current source dispersion  $r_j = r_H$ .



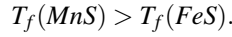
## Species transport-reaction equations

Since the surface tension gradients (12) are highly dependent on the sulfur concentration in the weld pool, it is essential to know the sulfur concentration at each time and position in the weld pool. Thus, in this section we detail the transport-reaction equations of the surface-active and related species. For instance, it is well known that Manganese addition is used in steel making processes to capture sulfur particles in order to prevent the steel from hot cracking during manufacturing. In fact, free-state sulfur atoms induce steel liquefaction by forming liquid inclusions with  $Fe$ :



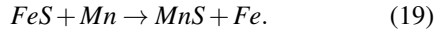
which are characterized by an extremely low melting point:  $T_f(FeS) = 1261 K$ , thus reducing the melting point of the steel alloy. This may result in hot cracking defects.

To overcome this problem, desulfurization agents such as Manganese ( $Mn$ ) are added in the steel during melting which allows the liquid inclusions  $FeS$  to be replaced by solid inclusions  $MnS$  with a higher melting point,  $T_f(MnS) = 1893 K$ :



Therefore, in the present work, we are interested in modelling the following species-related phenomena:

- The sulfur content in the steel is limited to 0.03% weighted percent, and the Manganese content to 2%.
- **The chemical reaction** between sulfur in solute and Manganese to form  $MnS$  takes place during cooling at  $T_{reac} = 1853 K$ :



Since this reaction takes place at the temperature below the  $MnS$  melting point, it results in solid inclusions in liquid steel. These inclusions are created in the region with the appropriate temperature level and especially during the solidification.

- **Manganese evaporation** which takes place at temperatures  $T > 2000K$  depending on the saturation pressure and boiling temperature (Pischke, 1994).
- **Diffusion coefficients of species** dependent on the chemical composition of the steel are rather difficult to determine at high temperatures. They are generally expressed as:

$$D_{304L}^i(T) = D_0^i e^{(-Q^i/RT)} \quad [m^2/s], \quad (20)$$

with  $D_0^i$  the frequency factor and  $Q^i$  activation energy. Following some references (Potard, 1972; Chybanova, 2000), we found the following expressions of these coefficients for sulfur and Manganese:

$$\begin{aligned} D_0^S &= 2.33 \times 10^{-7} m^2/s \quad \text{et} \quad Q^S = 52200 J/mol, \\ D_0^{Mn} &= 3.85 \times 10^{-7} m^2/s \quad \text{et} \quad Q^{Mn} = 69500 J/mol. \end{aligned} \quad (21)$$

- **Thermophoresis (Soret effect)**. Considering Lewis number which gives the rate of the thermal diffusion to the mass diffusion is high enough,  $Le(T) \approx 10^2$  as well

as Prandtl number which gives the rate of the momentum diffusivity to the thermal diffusivity,  $Pr(T) \approx 0.05$ , it seems that the thermophoresis is an important phenomenon to be taken into account. It mainly depends on the thermal gradient referred to the domain size. However, the definition of the thermo diffusion coefficient in the liquid metal seems quite complicated, since most of ten found expressions are based on gas theory and never for high temperature liquid (Talbot *et al.*, 1980; Alam *et al.*, 2009).

In generalized form, the transport-reaction equation of  $Y_i$  species ( $S, Mn$ ) is written :

$$\begin{aligned} \partial_t(\rho Y_i) + \nabla(\rho \mathbf{u} Y_i) - \nabla \cdot \left( \rho \mathbf{D}_{304L}^{Y_i} \nabla Y_i \right) &= \nabla \cdot \left[ \left( \mathbf{D}_{th}^{Y_i} \frac{\nabla T}{T} \right) \rho Y_i \right] \\ &- K(T) \rho Y_i Y_j + S_{evap}^{Y_i}, \quad \text{with} \quad K = K_0 e^{(-\frac{E_a}{RT})} \end{aligned} \quad (22)$$

with  $Y_i$  the  $i$ -species mass fraction,  $Y_i \in [0, 1]$ ,  $\mathbf{D}_{304L}^{Y_i}$  the mass diffusion coefficient of the  $i$ -species in the alloy (20),  $\mathbf{D}_{th}^{Y_i}$  the thermophoretic diffusion coefficient of the  $i$ -species,  $K(T)$  the rate constant for a bimolecular phase reaction,  $S_{evap}^{Y_i}$  evaporation source term involved in  $Mn$  equation only. Moreover, we note that the  $MnS$  chemical reaction takes place at  $T = 1853 K$ . Then, the enthalpy equation in (1)-(5) is modified to take into account these contributions: the concentration gradients, the latent heat of evaporation and chemical reaction contribution (though, in this case  $MnS$  reaction is isothermal).

Equations (22) together with system (1)-(5), (7) with initial and boundary conditions described in the previous section allow a more physical modelling of the surface tension variations (8) in the case of important thermal and concentration gradients.

## RESULTS

The simulations were performed with *Code\_Saturne* open source CFD software developed by EDF (Archambeau *et al.*, 2004). It is devoted to unsteady single phase simulations with complex reactive physics, turbulence and scalar transport. It is mainly based on the pressure correction algorithm and uses the finite volume numerical schemes. For more detailed presentation, the reader is referred to the technical documentation available online, <http://code-saturne.org>.

Given the welding parameters :

- the initial difference of the electric potential  $U = 11 V$ ,
- the current intensity  $I = 135 A$ ,
- the welding torch speed  $v = 16.3 cm/min$ ,

as well as the geometry and the mesh described in ‘‘Geometry and Mesh’’ section (Fig. 1) with the cell size of  $1.25 \times 10^{-4} m$  and the time step  $\Delta t = 10^{-3} s$ , we present here some results coming from weld pool simulations of a practical welding operation used as a validation test case. The pieces to be welded include a discontinuity of the chemical composition which corresponds for instance to an initial discontinuity in sulfur content as shown in Fig. 2, 3 with Low sulfur content of 0.0008 wt% (blue) and

High sulfur content of 0.005 wt% (red). In this example, High sulfur material represents the filler metal often used in welding operations to improve the weld pool penetration.

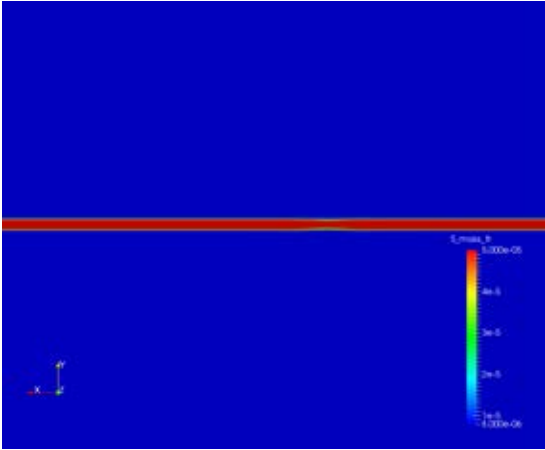


**Figure 2:** The sulfur mass fraction presenting a discontinuity (the filler metal) at  $t = 0$  s, top surface view,  $z = 0.002$ .



**Figure 3:** The sulfur mass fraction presenting a discontinuity (the filler metal) at  $t = 0$  s,  $x = 0$  cut.

The results presented in Fig.4 - Fig.9 show the velocity, pressure, temperature and surface tension gradient wrt the temperature approximations as well as the spatial distribution of the sulfur mass fraction in the weld pool at the stationary state. We can see that the negative values of the surface tension gradient wrt the temperature imply the outward fluid velocities on the top surface which result in more spreading weld pool.

We've also performed a sensitivity analysis of the results on the mean sulfur content in the weld pool. It appeared that the external weld pool width is decreasing with a growing sulfur concentration and that at the same time, the internal width is increasing for the sulfur content above 0.006 wt%. This is a quite relevant conclusion which reflects the correct treatment of the surface tension variation with sulfur content. In fact, the surface tension force on the weld pool surface is known to decrease with an increasing sulfur concentration. Moreover, the surface tension gradient wrt the temperature changes the sign when the sulfur concentration exceeds 0.005 wt%. Thus, the flow direction in the weld pool turns opposite : we expect to have a more penetrating weld pool for high sulfur concentration versus a more spreading one for low sulfur content (Heiple and Roper, 1982; McNallan and DebRoy, 1991).

Then, Figures 10 and 11 show the final weld pool shape in a stationary state whose dimensions (external and internal widths) are highly dependent on the initial sulfur content. We compare these dimensions with the experimental data provided by operating company for a welding operation performed in the same operating conditions. We note that

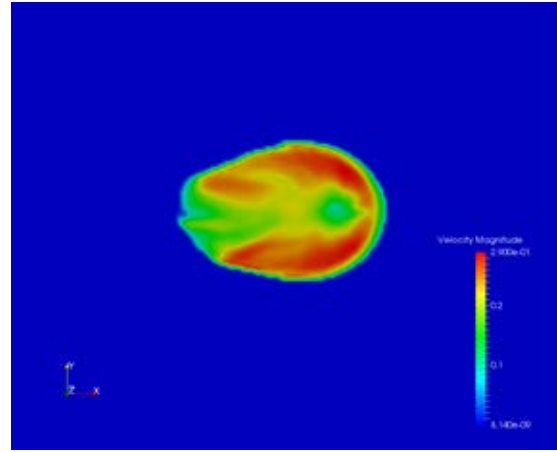


**Figure 4:** The fluid velocity in the stationary regime, top surface view with  $z = 0.002$ .

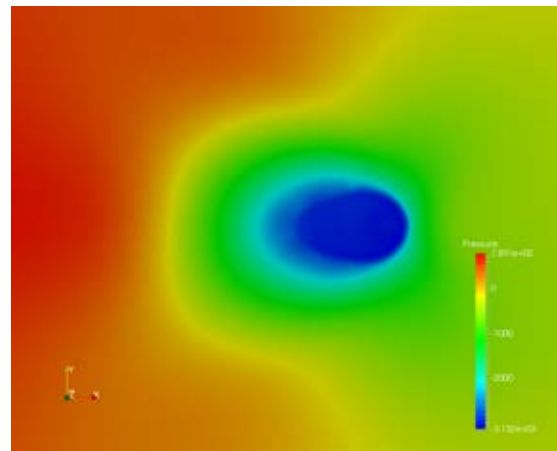


**Figure 5:** The pressure approximation in the stationary regime, top surface view with  $z = 0.002$ .

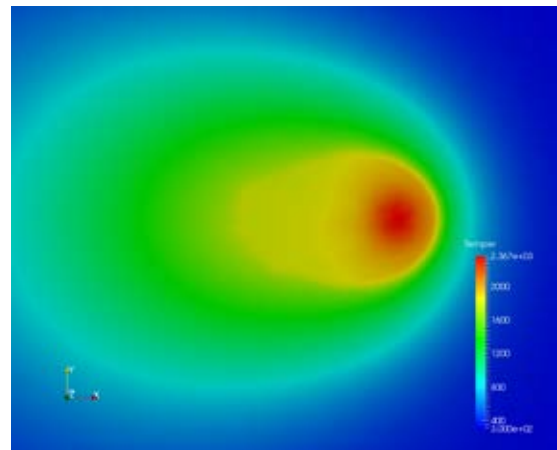


**Figure 6:** The temperature approximation in the stationary regime, top surface view with  $z = 0.002$ .

the data on the weld pool dimensions obtained in this case are in quite good agreement (Table1).

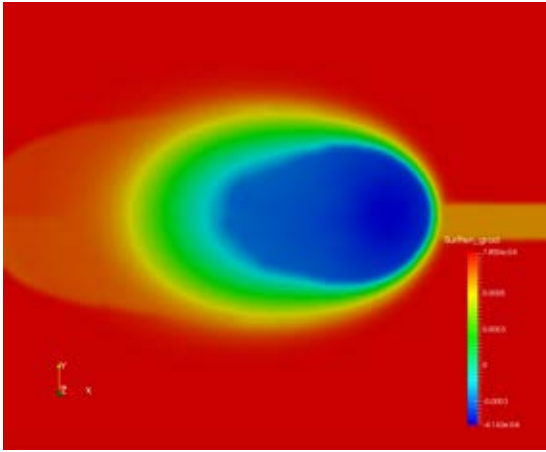


**Figure 7:** The surface tension gradient induced by temperature in the stationary regime, top surface view with  $z = 0.002$ .

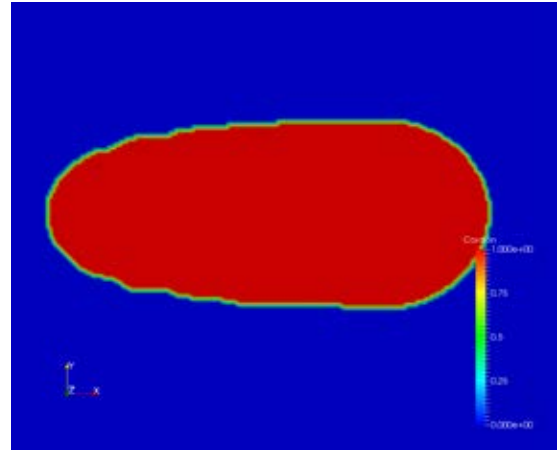


**Figure 10:** Final weld bead shape, top surface view with  $z = 0.002$ .

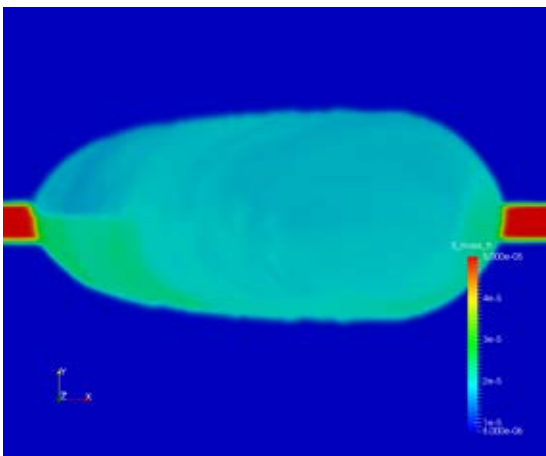


**Figure 8:** The sulfur mass fraction in the stationary regime, top surface view with  $z = 0.002$ .



**Figure 11:** Final weld bead shape,  $x = 0.005$  cut.

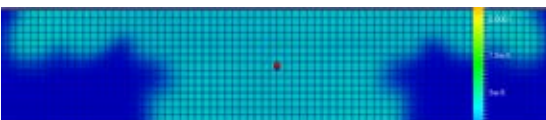


**Figure 9:** The sulfur mass fraction in the stationary regime,  $x = 0.005$  cut.

**Table 1:** Comparison of weld pool dimensions

	Simulation	Measurement
External width (mm)	8.4	8.2
Internal width (mm)	4.26	4.5

## CONCLUSION

Based on a practical case of a welding operation, we have introduced in this paper a new transport - reaction equations for surface active and related species which are involved in the surface tension modelling when studying welding and metal melting processes. This modelling is new and offers a tool for the unsteady quantification of the sulfur content in the molten steel all along the welding operation and the solidification. It takes into account sulfur and manganese chemical reaction, temperature dependent mass diffusion, manganese evaporation and thermophoresis. Moreover, the surface ten-

sion law accounts for sulfur and chromium interaction, which influences the sulfur surface activity. Some sensitivity analysis has also been made to study the global effect of the sulfur content on the weld pool dimensions. The numerical results obtained with these simulations are in good agreement with the experimental data, the conclusion which allows to validate both the modelling and the numerical approach for the present case.

## REFERENCES

- ALAM, M., RAHMAN, M. and SATTAR, M. (2009). "Transient magnetohydrodynamic free convective heat and mass transfer flow with thermophoresis past a radiate inclined permeable plate in the presence of variable chemical reaction and temperature dependent viscosity". *Nonlinear Analysis: Modelling and Control*, **14(1)**, 3–20.
- ARCHAMBEAU, F., MECHITOUA, N. and SAKIZ, M. (2004). "Code\_saturne: a finite volume code for the computation of turbulent incompressible flows". *Int. J. Finite Volumes*, **1**, 1–62.
- BELTON, G. (1976). *Metall.Trans. B*, **7B**, 35–42.
- CARMAN, P. (1956). *Flow of gases through porous media*. Butterworths, London ed.
- CHYBANOVA, L. (2000). *Proprietes physico-chimiques des metaux liquides contenant des sulfures et des oxydes et la cinetique des echanges a la limite avec les materiaux de construction*. Ph.D. thesis, Oural Technical University.
- HEIPLE, C. and ROPER, R. (1982). "Mechanism for minor element effect on gta fusion zone geometry". *Weld. J.*, **61(4)**.
- KIM, C.S. (1975). "Thermophysical properties of stainless steels". *Argonne National Laboratory*.
- KOZENY, J. (1927). "Ueber kapillare leitung des wassers im boden". *Sitzungsber Akad. Wiss., Wien*, **136(2a)**, 271–306.
- MCNALLAN, M. and DEBROY, T. (1991). "Effect of temperature and composition on surface tension in fe-ni-cr

alloys containing sulfur". *Metallurgical Transactions*, **22B**, 551–560.

MILLS, K., KEENE, B., BROOKS, R. and SHIRALI, A. (1998). "Marangoni effects in welding". *Phil. Trans. R. Soc. Lond.*, **356**, 911–925.

POTARD, C. (1972). *Contribution a l'etude de la diffusion dans les alliages liquides ternaires. Application a la solidification*. Ph.D. thesis, Grenoble.

SAHOO, P., DEBROY, T. and MCNALLAN, M.J. (1988). "Surface tension of binary metals - surface active solute systems under conditions relevant to welding metallurgy". *Metallurgical Transactions*, **19B(483)**.

SAMPATH, R. and ZABARAS, N. (2001). "Numerical study of convection in the directional solidification of a binary alloy driven by the combined action of buoyancy, surface tension, and electromagnetic forces". *Journal of Computational Physics*, **168**, 384–411.

TALBOT, L., CHENG, R., SCHEFER, A. and WILLS, D. (1980). "Thermophoresis of particles in a heated boundary layer". *J. Fluid Mech.*, **101**, 737–758.



## MULTISCALE APPROACH TO FULLY RESOLVED BOUNDARY LAYERS USING ADAPTIVE GRIDS

A. PANDA<sup>1\*</sup>, E.A.J.F. PETERS<sup>1</sup>, M.W. BALTUSSEN<sup>1</sup>, J.A.M. KUIPERS<sup>1</sup>

<sup>1</sup>Multiphase Reactors Group, Department of Chemical Engineering and Chemistry,  
Eindhoven University of Technology, 5600 MB Eindhoven, THE NETHERLANDS

\* E-mail: a.panda@tue.nl

### ABSTRACT

Bubbly flows are omnipresent in most industrial processes. Often the intended use of such processes is to facilitate efficient mass and heat transfer for reactive flows. Mass and heat transfer coupled with fluid flow in gas-liquid systems gives rise to multiscale transport phenomena. Because of large Schmidt and (possibly) Prandtl numbers in the liquid phase the concentration and temperature boundary layers are much thinner than the momentum boundary layers. When using fully resolved CFD modeling on an uniform grid, these small scales would demand an overall refinement which requires an immense computational effort. Here, however, a hybrid mesh approach is used which couples a fixed Cartesian grid for the hydrodynamics and a tree structure based mesh, which can be adaptively refined for heat and mass transfer. Tree based adaptive refinements commonly suffer from low order accurate numerical schemes. A higher order finite volume scheme on a parallel tree data structure for solving the convection-diffusion equation has been implemented using an implicit formulation. The resulting set of linear algebraic equations are then solved with AMG class of matrix solvers. This approach presents a solution to resolve the fine boundary layers of scalar transport for realistic range of Schmidt and Prandtl numbers. The present study will demonstrate the robustness of this framework to capture sharp boundary layers in fairly simple analytical flow fields. A detailed comparison is performed with overall refined simulations on multi core parallel architectures.

**Keywords:** adaptive grids, fully resolved simulation, boundary layer, multiscale transport, heat and mass transfer .

### NOMENCLATURE

#### Greek Symbols

$\rho$  Mass density, [ $kg/m^3$ ]  
 $\mu$  Dynamic viscosity, [ $kg/ms$ ]  
 $\phi$  General scalar, [-]

#### Latin Symbols

$Sc$  Schmidt Number, [-]  
 $Pr$  Prandtl Number, [-]  
 $h$  Cell size, [-]  
 $L$  Cell level, [-]  
 $L_i$  Error norms, [-]  
 $p$  Pressure, [ $Pa$ ].  
 $\mathbf{u}$  Velocity, [ $m/s$ ].  
 $V$  Volume of cell, [ $m^3$ ].  
 $a$  Area of cell face, [ $m^2$ ].  
 $c$  Concentration, [ $mol/L$ ]

$T$  Temperature, [ $^{\circ}C, ^{\circ}K$ ]  
 $C$  Cell, [-]

#### Sub/superscripts

$d$  Direction.  
 $f$  Face centre.  
 $n$  Time step.  
 $i$  Index  $i$ .  
 $j$  Index  $j$ .  
 $1, 2, \infty$  Type of error norm.

### INTRODUCTION

Bubble columns are one of the widely used and very interesting processing units for contacting gas-liquid flows in the chemical industry. In these bubble columns the gas phase is dispersed in the continuous liquid phase. The rising bubbles increase the mixing of the liquid phase thus providing improved mass and heat transfer properties. In spite of the simple structure of bubble columns, the physical phenomena occurring at the gas liquid interface is still not completely understood. Therefore, the design of the columns is mainly based on experimental data and empirical or semi-empirical correlations. To improve the design of bubble columns, a deeper understanding of the physics is necessary.

Due to the increase of computational power, it is possible to simulate many flow situations using direct numerical simulation (DNS), which simulates the flow based solely on first principles. Although, the methods to determine the hydrodynamics of multiphase flows are well known, adding new physics i.e. mass transfer, heat effects or chemical reaction still are faced with a lot of challenges. The challenges occur due to the multitude of length scales and time scales these phenomena possess. From the dimensionless numbers which describe these phenomena, such as Schmidt ( $Sc$ ) number in case of mass transfer and Prandtl ( $Pr$ ) number in case of heat transfer, it can be determined that the boundary layers in many industrial cases can vary by several orders of magnitude. For example, in case of mass transfer from a bubble to liquid, the mass diffusivity is generally at least two to three orders of magnitude smaller than momentum diffusivity. This condition enforces a constraint on the mesh resolution and the time step required for sufficiently resolving mass transfer boundary layer at the bubble interface thus increasing the computational cost.

Several different methods can be used to enable the computation of all of these different length and time scales. First of

all the overall mesh can be refined (Darmana *et al.*, 2006; Roghair *et al.*, 2016). However, the overall mesh refinement leads to billions of cells to solve boundary layer problems corresponding to realistic  $Sc$  ( $Sc \sim 10^3$ ). This requires a lot of computational effort therefore, leading to limitation of simulating systems which have very modest  $Sc$  numbers ( $1 \lesssim Sc \lesssim 10$ ). Secondly the boundary layer can be approximated by using subgrid scale models (Aboulhasanzadeh *et al.*, 2012; Gründing *et al.*, 2016), which are based on self similar solutions corresponding to the mass boundary layer. However, in industrial reactors, the flow patterns are complex due to frequent bubble-bubble interactions, which significantly affect the bubble hydrodynamics and thereby influencing the interfacial mass transfer. In such dense bubbly flow regimes validity of overly simplistic boundary layer assumptions is not well established. Finally, the mesh could be adapted according to the local gradients in scalar field (Deising *et al.*, 2016). Adaptive mesh refinement (AMR) has its own set of computational challenges specific to different methods of mesh refinement. It's one of the advanced research areas in CFD as many well formulated methods which work on simple Cartesian grids cannot be simply extended to adaptive meshes.

Among many different AMR strategies, notable are block structured AMR, overset or Chimera grids, tree based AMR etc. For non deformable interfaces, a Chimera or overset grid presents a plausible solution to resolve the boundary layer. For interfaces which are deformable such as those occurring in bubbly flows and for an optimal mesh count, a tree based grid adaption is well suited. Tree based AMR also suffers from some limitations such as efficient data structures, parallelization, load balancing using graph partitioning methods and efficient matrix solvers. It is important to note the third limitation pertaining to matrix solvers is more stringent, as the linear system of equations on such adaptive grids leads to unsymmetric matrices which are computationally expensive to solve. Algebraic multigrid class of matrix solvers are suited for such systems which, if combined with parallelization can give a performance improvement. In any CFD calculations, most of the time is spent on solving the Poisson problem arising from the incompressibility constraint on the momentum equation. Solving it becomes even more difficult for multiphase flows with high density ratios such as air-water system. AMR grids based on a dynamic data structure such as quadtree or octree are considerably slower for the same grid count because of issues related to dynamic memory layout and reduced vectorization in comparison to array based data structures which are used for Cartesian grids.

To circumvent this problem, a novel hybrid grid based method is proposed for fully resolved multiscale transport on adaptive grids. The essence of the idea is to only solve the scalar transport equations on the AMR grid while solving the hydrodynamics on the Cartesian grid. The methodology and implementation of a general scalar convection diffusion equation on parallel adaptive mesh refined grids is described in later sections. The resulting convection diffusion solver is verified and validated with model test cases. Also, a methodology is presented to encode a staggered velocity field onto an AMR grid, which can then be used to fetch velocity values from a staggered Cartesian hydrodynamics grid. A divergence free interpolation is also presented, for interpolating velocity values during mesh refinement on to the finer grid.

## MODEL DESCRIPTION

## Spatial Discretization

Generally, a flow domain can be represented in the form of control volumes which are square in 2D (or a cube in 3D). These square (or cubic) meshes are adapted using a quadtree (or octtree) data structure which also finds its use in image processing & computer graphics (Popinet, 2003). Figure 1 depicts a representation of such discretization in case of a 2D tree. Each control volume is called as a *cell* and can have 4 descendants (8 in case of 3D) called *children*, in which case, the cell is called as *parent* of these children. A cell which has no parent cell is called as the *root* cell while cells which do not have any children are called as *leaf* cells. The length of any cell edge is denoted by  $h$ . The *level* of a cell is defined with the root cell as reference 0 and children being one level higher than the parents. The spatial discretization in the form of quadtree needs to satisfy 2:1 balance constraint, which states that adjacent cells' levels must not differ by more than one i.e. a maximum one hanging node is possible at any cell face. This constraint restricts the number of possible cases which in a way helps in devising efficient numerical schemes on such spatial discretization.

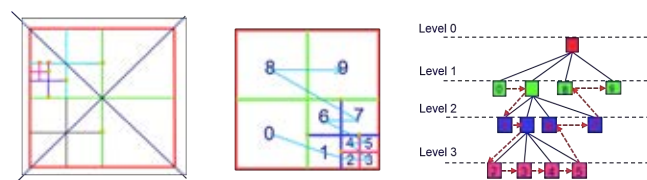


Figure 1: Schematic diagram of quadtree spatial discretization.

## Governing Equations

The generalised scalar convection-diffusion equation along with the Navier Stokes equation can be written as :

*Scalar Convection Diffusion Equation*

$$\frac{\partial \phi}{\partial t} + \mathbf{u} \cdot \nabla \phi = D \nabla^2 \phi + F_s \quad (1)$$

*Navier-Stokes Equation*

$$\rho \frac{\partial \mathbf{u}}{\partial t} + \rho \nabla \cdot (\mathbf{u}\mathbf{u}) = -\nabla p + \rho \mathbf{g} + \nabla \cdot \mu (\nabla \mathbf{u} + (\nabla \mathbf{u})^T) + \mathbf{F}_\sigma \quad (2)$$

*Continuity Equation*

$$\nabla \cdot \mathbf{u} = 0 \quad (3)$$

Although, the Navier-Stokes equations are solved on a regular Cartesian grid, the scalar transport equations are solved on a grid that can be adaptively refined as the solution proceeds in time. Here  $\phi$  can be any generalized scalar such as the concentration or the temperature. For the accurate representation of the velocity field on this grid, a Cartesian grid which is sufficiently fine to resolve the hydrodynamics of multiphase flows is used. Generally the hydrodynamic boundary layer, can be resolved accurately with a coarser grid in comparison to mass transfer boundary layer. Also, solving a Poisson problem to meet the incompressibility criterion especially in case of multiphase flows with high density ratios is the most time consuming task amongst the whole solution time. Hence, solving only the scalar transport equations on an AMR grid leads to a decrease in computational effort compared to a situation where the hydrodynamics and scalar transport are both solved on the same grid. Finally, a Cartesian grid results in symmetric matrices forming the system

of linear algebraic equations which can then be solved with robust matrix solvers with efficient vectorization and parallelization.

### Convection

The unsteady convection part of the problem can be written as follows:

$$\frac{\partial \phi}{\partial t} + \nabla \cdot (\mathbf{u}\phi) = 0 \quad (4)$$

The above equation can be discretized using finite volume technique, resulting into

$$\phi^{n+1} = \phi^n + \frac{\Delta t}{\Delta V} \left( \sum_{faces} u_f^{n+1} \phi_f^n h^2 \right) \quad (5)$$

The convection of a scalar can be numerically resolved using upwind class of methods which have good transport properties. For an adaptive grid based on a 2:1 balanced tree data structure, in combination with a first order method, two cases on a cell face can occur either both of the sides are at the same level or else there is a hanging node at the face resulting from level difference on either side (see figure 2). For a conventional Cartesian grid the convective flux at face center can be obtained for an upwind scheme, by the upwinded value of scalar at the face given as  $\phi_f = \phi$  whereas, in case of face with a hanging node, the upwinded scalar in each subface,  $\phi_{f1}$  and  $\phi_{f2}$  is calculated first and is then averaged to obtain the upwinded scalar viz.  $\phi_f = (\phi_{f1} + \phi_{f2})/2$ . The flux can then be estimated assuming that the value of velocity at the face is known a priori.

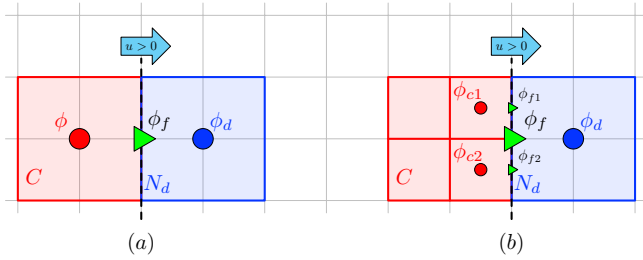


**Figure 2:** Upwind method on quadtree (a) both cells are at same level (b) neighbor is not a leaf cell.

### Diffusion

The unsteady state diffusion part of the problem can be written as:

$$\frac{\partial \phi}{\partial t} = \nabla \cdot (D\nabla\phi) + S_\phi \quad (6)$$

When equation 6 is discretized using a semi-implicit scheme, equation 7 will be obtained.

$$\frac{\phi^{n+1} - \phi^n}{\Delta t} \Delta V = (1 - \beta) \nabla \cdot (D^n \nabla \phi^n) + \beta \nabla \cdot (D^{n+1} \nabla \phi^{n+1}) + S_\phi^n \quad (7)$$

To calculate the diffusive flux at each face, a numerical estimation of the gradient of the scalar has to be determined at the cell face. For conventional Cartesian grid, this is normally done by central differencing, which is second order accurate for cells of same size. However, when this scheme is applied for cell face with a hanging node, the scheme is first

order accurate instead of second order accurate. This type of differencing would result in schemes with inconsistent order of convergence, across the whole domain. To circumvent this problem, one needs to specifically look for schemes which are overall second order accurate. In this paper, a scheme is implemented which is overall second order accurate for the Laplacian operator in space. To verify the implementation of the Laplacian operator, the order of convergence is studied and compared with Gerris flow solver (Popinet, 2003), which uses the same discretization scheme for the pressure Poisson equation.

To enable the calculation of the transport via diffusion, the gradient at the face centers should be discretized. While this is trivial on a regular Cartesian grid, this is more difficult within the adaptive framework. In practice, only three cases are possible for the construction of face centered gradients for a cell  $C$  with a neighbor  $N_d$  in the direction  $d$  (see figure 3).

- (I)  $N_d$  is at the same level and is a leaf cell
- (II)  $N_d$  is at a lower level than the cell  $C$ , or double the size of cell  $C$
- (III)  $N_d$  is at a higher level than the cell  $C$ , or half the size of cell  $C$

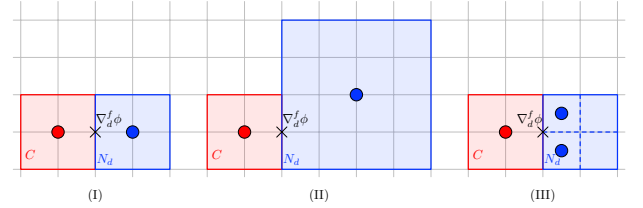


**Figure 3:** Different cases while calculating gradient at faces.

In case of (I) the stencil reduces down to a conventional Cartesian grid and thus one can write the simple centered difference discretization. In case of (II) a second order polynomial is fitted passing through the cell,  $C$ , the neighbor  $N_d$  and the opposite cell  $\hat{\phi}_d$ . Using the slope of the polynomial at the examined interface, the gradient at the face center can be calculated. Based on the configuration of the opposite cell, two subcases can arise due to 2:1 balanced tree: an undivided leaf cell at the same level of cell  $C$  or a parent cell with 4 leaf cells (8 in 3D). With the definition of  $\phi_6$  and  $\phi_7$  from figure 4, the expression for, respectively, an undivided and divided left neighbor are:

$$h\nabla_d^f \phi = -\frac{\phi}{3} - \frac{\hat{\phi}_d}{5} + \frac{8}{15}\phi_6 \quad (8)$$

$$h\nabla_d^f \phi = -\frac{2}{9}\phi - \frac{8}{27}\phi_7 + \frac{14}{27}\phi_6 \quad (9)$$

However as shown in figure 4,  $\phi_6$  should also be interpolated from the values of scalar in the cells neighboring the neighbor  $N_d$ , in the perpendicular direction to  $d$  ( $\hat{N}_{\perp d}$  and  $N_{\perp d}$ ) leading to more cases which needs to be included in an efficient fashion (Popinet, 2003). A sample case is shown in figure 4. Additional issues arise when extending to 3D because the two perpendicular that needs to be traversed to obtain the value of  $\phi_6$  are non-intersecting unlike the case in 2D. The details of this have been left out of the scope of this paper. In case (III),  $N_d$  is at the same level but not a leaf cell. In this case the gradient at the face is constructed as the average of



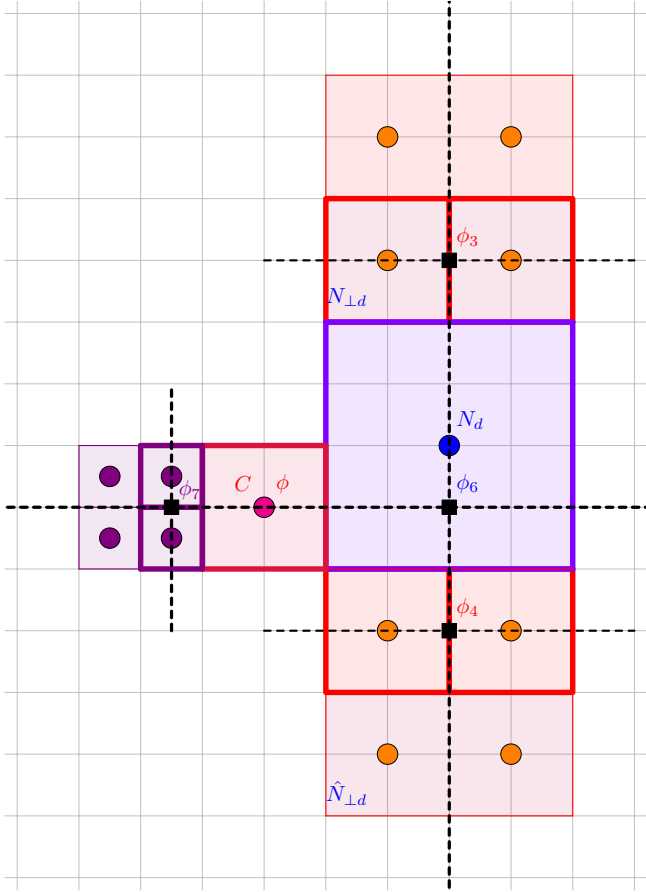


**Figure 4:** Sample stencil for face centered gradient calculation in case where  $\hat{\phi}_d$ ,  $\hat{N}_{\perp d}$  and  $N_{\perp d}$  is not a leaf cell.

the gradients constructed from the children cells of  $N_d$  which share the face with the cell  $C$ . These gradients can then be computed by following the same scheme as case (II).

The resulting set of simultaneous linear equations resulting from this discretization of the Laplace operator is solved using robust matrix solver based on algebraic multigrid (AMG) method. Specifically, an open source library called HYPRE (Falgout and Yang, 2002) is used to solve the resultant equations using the boomerAMG module. The solver scales to  $10^3$  number of processors based on the MPI model and uses parallel graph partitioning methods for load balancing. The base framework used for implementation of the code is an open source library which provides efficient parallel tree data structure, called p4est (Burstedde *et al.*, 2011).

### Boundary Conditions

At the domain boundary, both Dirichlet and Neumann boundary conditions can be applied with second order accuracy. For case (I) a ghost cell based approach is used to enforce Dirichlet boundary condition for the cell face at the boundary. For cases (II) and (III) where the value is interpolated in case  $N_d$  is a boundary cell, a ghost cell across the boundary face is created. This cell is of the same size of the neighbor cell  $N_d$  leaving only two possibilities in each case and thus resulting 4 additional stencils in 2D.

### Staggered Velocity Field

The velocity needed to calculate the convective fluxes of the scalar is only known on the hydrodynamics mesh. The velocities are, however, needed on the smaller adaptive grid for the scalar transport. Hence, to obtain the values of veloc-

ity on the adaptive grid, the velocity should be transferred to the adaptive grid. Generally in an unstructured grid data structures, it is a common practice to encode all the possible state variables at a collocated grid, but the in house hydrodynamics code for gas-liquid interfaces has been developed on a staggered grid framework. The used staggered arrangement is beneficial for the upwind advection scheme used for the convection. To ensure a divergence free field a piecewise linear interpolation method is used to interpolate the velocity field (Roghair *et al.*, 2016). The interpolation can be visualized in figure 5. For example, the velocity field in the  $x$ -direction is calculated using the following set of equations:

$$u_{x,i,j-\frac{1}{4}} = u_{x,i,j+\frac{1}{4}} = \frac{u_{x,i-\frac{1}{2},j} + u_{x,i+\frac{1}{2},j}}{2} \quad (10)$$

$$u_{x,i-\frac{1}{2},j-\frac{1}{4}} = u_{x,i-\frac{1}{2},j+\frac{1}{4}} = u_{x,i-\frac{1}{2},j} \quad (11)$$

$$u_{x,i+\frac{1}{2},j-\frac{1}{4}} = u_{x,i+\frac{1}{2},j+\frac{1}{4}} = u_{x,i+\frac{1}{2},j} \quad (12)$$

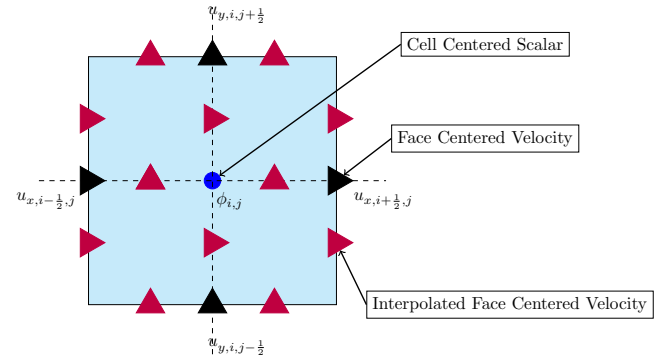


**Figure 5:** Staggered velocity interpolation.

## Results

### Convection

To test the implementation of the convection of scalar, a blob of a material is advected through a steady shear-free velocity field. To ensure the problem is a pure convection problem, diffusivity is set to zero. Typically the blob is given a conical distribution. The 2D transport equation for a scalar  $\phi$  is solved over a unit square centered at the origin, domain boundaries being  $x = \pm 0.5$  and  $y = \pm 0.5$ . The initial scalar distribution is prescribed to be zero except within a region of conical blob located with center at  $(0,0)$  and radius  $r = 0.1$ , where the distribution of  $\phi$  is given as  $\sin^2((\pi/2)(1 - \frac{r}{0.1}))$ . The test was carried out for two values of velocities viz.  $u = 1, v = 0$  and  $u = 1, v = 1$ . Figure 6 shows two snapshots for an inclined flow profile (a), and a parallel flow field (b). As with any other first order upwind method, this method suffers in principle from artificial diffusion, however here, the numerical diffusion is very small because of adaptive grids. In the test case with inclined flow field, a 94% reduction in grid requirements in adaptive framework (limited to maximum refinement of 10) was observed in comparison to a Cartesian grid at 10 levels of refinement ( $2^{2 \times 10} = 1048576$  grid cells) for the same numerical diffusion. The time step for advection is chosen in such a way that the CFL Number ( $u_{max}\Delta t / \Delta x_{min}$ ) is always less than 0.5, where  $\Delta x_{min}$  is the cell size of the smallest quadrant in the domain and  $u_{max}$  is the maximum velocity in the domain.

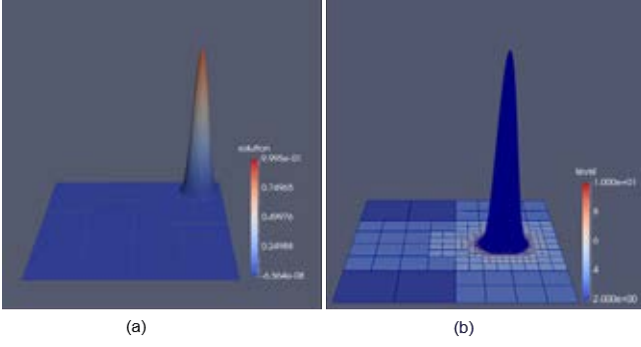


**Figure 6:** Convection of Scalar in (a) inclined flow field (solution), (b) parallel flow field (grid)

### Diffusion

To test the implementation of the transport of scalar diffusion, the heat conduction equation on a rectangular slab of length,  $L$  and width,  $W$  is simulated. The slab is exposed to Dirichlet boundary conditions on all boundaries. In this test case, the top surface is maintained at  $100\text{ }^\circ\text{C}$  while the rest of the boundaries are maintained at  $0\text{ }^\circ\text{C}$ . The analytical solution of this steady state problem in terms of non dimensionalised temperature,  $\theta$  is given by Equation 13.

$$\theta(x,y) = \frac{2}{\pi} \sum_{n=1}^{\infty} \frac{(-1)^{n+1} + 1}{n} \sin \frac{n\pi x}{L} \frac{\sinh(n\pi y/L)}{\sinh(n\pi W/L)} \quad (13)$$

Figure 7 shows the contour lines of the non-dimensionalised temperature and a comparison with this analytical solution. The  $L_1$ ,  $L_2$  and  $L_\infty$  error norms for the test problem were obtained to be  $1.60\text{e-}05$ ,  $2.60\text{e-}4$  and  $0.022$  respectively.

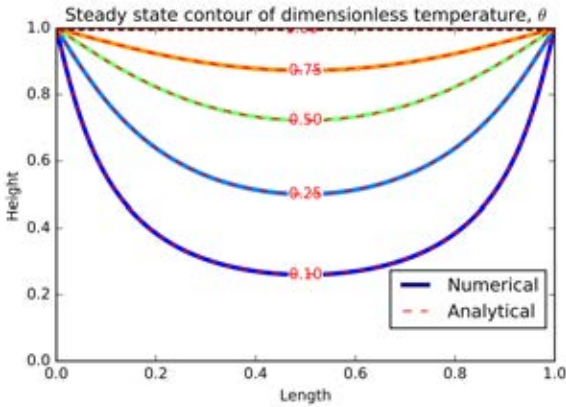


**Figure 7:** Heat Conduction in a Slab : Contour lines of dimensionless temperature in adaptive grid with analytical solution.

To ascertain the second order convergence of the Laplace operator, a convergence test is performed on Cartesian and adaptive grids. In this test a pressure Poisson equation is solved on a unit square domain centered around origin. The divergence of the intermediate velocity field is given by equation 14. When  $k = l = 3$ , the analytical solution is given by the pressure field of equation 15 using Neumann boundary conditions on all sides.  $\kappa$  in equation 15, is an arbitrary constant which in this case is the average value of the computed pressure over the entire domain.

$$\nabla \cdot U^{**}(x,y) = -\pi^2(k^2 + l^2) \sin(\pi kx) \sin(\pi ly) \quad (14)$$

$$\phi(x,y) = \sin(\pi kx) \sin(\pi ly) + \kappa \quad (15)$$

The initial guess for the pressure field is a constant field. The problem is solved for two different domains: a domain at the  $L^{\text{th}}$  level of refinement (figure 8(a)) and the same domain with a circular patch of radius,  $R = 0.25$  which is at  $(L+2)^{\text{th}}$  level of refinement (figure 8(b)). To estimate the order of convergence, the problem is solved for different levels of refinement,  $L$  ranging from 3 to 10. For each simulation case, the volume (area in 2D) weighted norm of the error,  $\|ae\|$  is shown in figure 9. The figure shows that the order of convergence is indeed two.

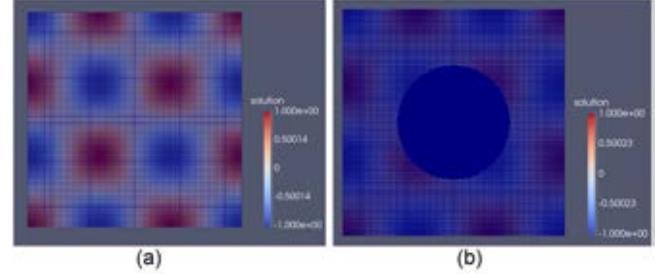


**Figure 8:** Domain for test case of Poisson equation (a) Cartesian grid ( $L = 7$ ) (b) Grid used for evaluation of coarse/fine gradient operator ( $L = 7$ ).

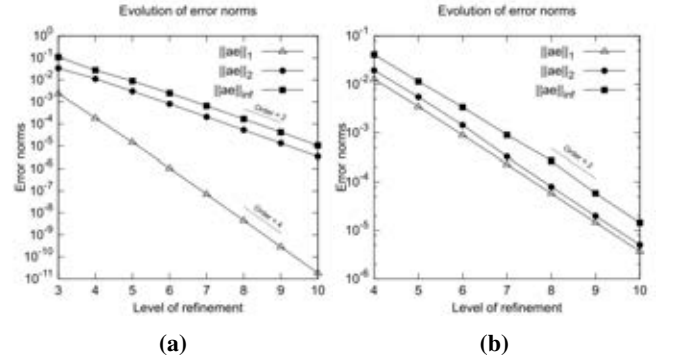


**Figure 9:** Order of convergence test showing error norms for (a) Cartesian grid (b) Adaptive grid

### Staggered Velocity Interpolation

For testing of staggered grid velocity interpolation, the grid was initiated with a divergence free analytical flow field at each face center. The velocity profile considered is given by Equation 16.

$$\mathbf{u}(x,y,z) = (0, -2\sin^2(\pi y)\sin(\pi z)\cos(\pi z), 2\sin^2(\pi z)\sin(\pi y)\cos(\pi y)) \quad (16)$$

The simulation is started at different level of refinements ( $3^{\text{rd}} - 11^{\text{th}}$  level). Figure 10 shows the error with respect to the analytical solution after the interpolation of the velocity field. Because the initial level of refinement influences the error in the interpolated solution, the figure shows the error with respect to the level at which the original solution was created. Figure 11 shows a velocity vector plot for the refined grid at level 10 obtained from the initiated grid at level 8. The divergence has also been quantified in each of these refinement operations and was indeed found to be accurate to machine precision, i.e.  $10^{-15}$  and  $10^{-16}$ .

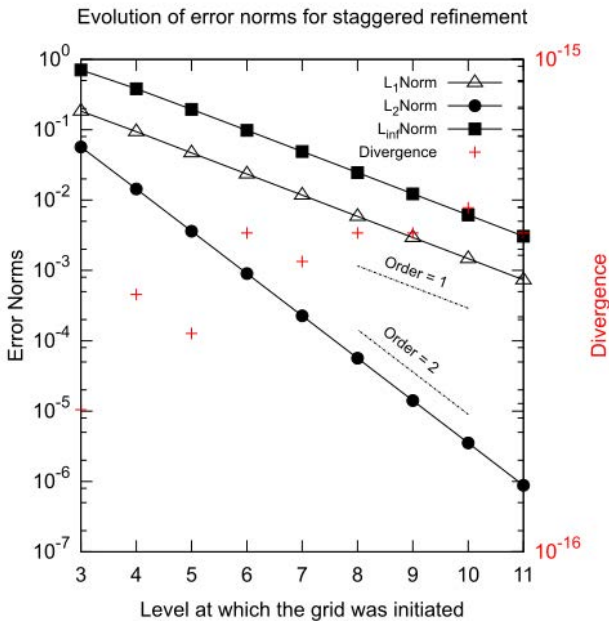


Figure 10: Error norms and divergence for staggered grid interpolation corresponding to different levels of refinement.

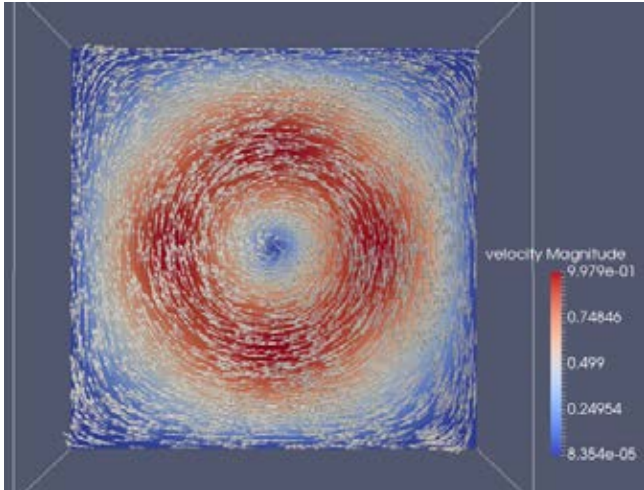


Figure 11: Velocity vector plot at 10<sup>th</sup> level of refinement obtained from staggered grid interpolation of analytical flow field at 8<sup>th</sup> level of refinement.

### Concentration boundary layers

This test considers a stationary spherical bubble with radius  $R$  in a quiescent, zero gravity pool of liquid. The concentration within the sphere is initialized with a dimensionless concentration of 1. As, mass diffuses through the interface, a concentration boundary layer profile will evolve over time. The domain is refined at the 7<sup>th</sup> level, while a zone near the bubble interface is refined upto the 12<sup>th</sup> level (see figure 12). The bubble is simulated to be an infinite source by fixing the concentration inside the bubble to be 1. The concentration profiles are shown in figure 13.

For a diffusion equation written in spherical coordinates for a stationary bubble, an analytical solution can be obtained by imposing the boundary conditions:  $c = c_0$  for  $r = R$ ,  $c = 0$  for  $r = \infty$  and initial condition  $c = 0$  for  $r > R$ . Because the simulation domain is finite, Neumann conditions are applied at the domain boundaries with a zero gradient. A diffusion coefficient  $D = 10^{-6}$  m<sup>2</sup>/s. was used. Figure 14 shows the

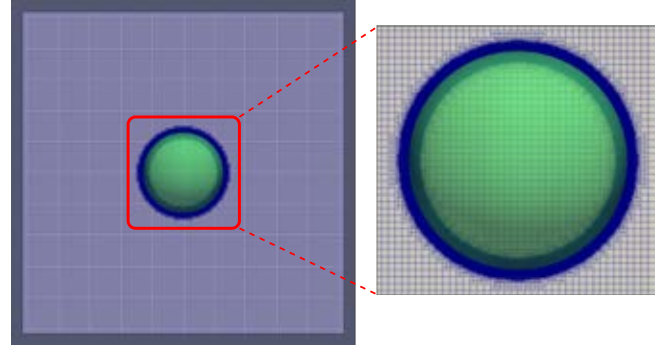


Figure 12: Initial grid for the species diffusion test.

concentration profile around a 4 mm sphere along the x-axis from the interface of the bubble and is compared with the exact solution. The interface is resolved with 8<sup>th</sup> level of refinement with total cell count during 500<sup>th</sup> time step to be 440784 which is 2.62 % that of a respective Cartesian mesh ( 16777216 cells ).

$$\frac{c(r)}{H \cdot c_0} = \frac{R}{r} \left( 1 - \operatorname{erf} \left( \frac{r-R}{\sqrt{4Dt}} \right) \right) \quad (17)$$

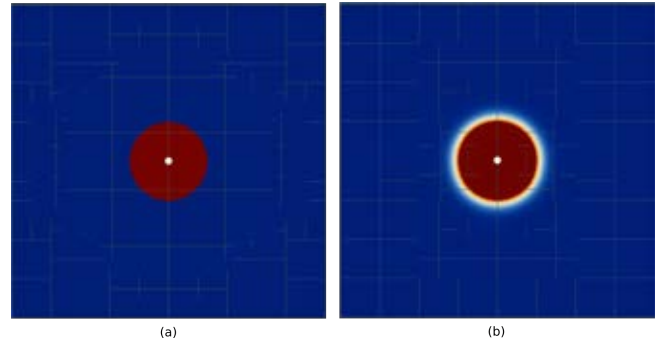


Figure 13: (a) Initial concentration profile inside stationary sphere. (b) Concentration profile around the sphere after 500 time steps.

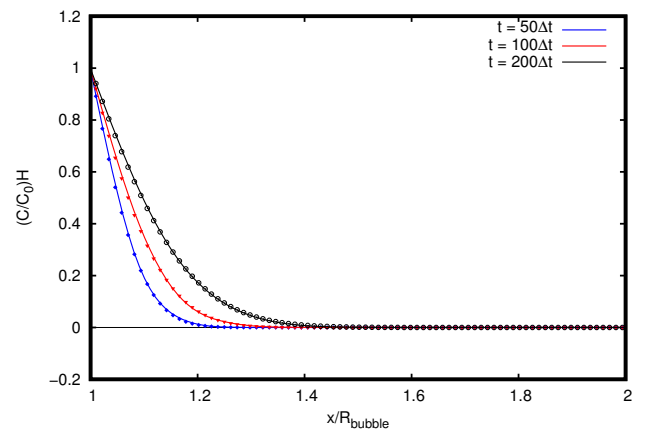


Figure 14: Dimensionless concentration profile in the vicinity of a stationary sphere, along the x-axis (lines) compared to the exact solution (markers).

### CONCLUSION

In this paper, a methodology is proposed to solve heat and mass transfer equations on a different adaptive grid than the

fixed Cartesian hydrodynamics grid. The details of the velocity access will be addressed in future work. The current work presents a robust way to set up a higher order accurate convection diffusion solver. The combined framework is tested for accuracy and order of convergence and furthermore, the method is found to be suitable for resolving boundary layers in bubbly flows. A methodology is also presented to encode staggered velocities on adaptive grids and to handle the grid adaptation without violating the divergence free criteria. In future research this methodology will be applied for the 3D simulation of bubbly flows with coupled heat and mass transfer.

## ACKNOWLEDGMENT

This work is part of the Industrial Partnership Programme i36 Dense Bubbly Flows that is carried out under an agreement between Akzo Nobel Chemicals International B.V., DSM Innovation Center B.V., Sabic Global Technologies B.V., Shell Global Solutions B.V., Tata Steel Nederland Technology B.V. and the Netherlands Organisation for Scientific Research (NWO).

## REFERENCES

- ABOULHASANZADEH, B., THOMAS, S., TAEIBI-RAHNI, M. and TRYGGVASON, G. (2012). “Multi-scale computations of mass transfer from buoyant bubbles”. *Chemical Engineering Science*, **75**, 456 – 467.
- BURSTEDDE, C., WILCOX, L.C. and GHATTAS, O. (2011). “p4est: Scalable algorithms for parallel adaptive mesh refinement on forests of octrees”. *SIAM Journal on Scientific Computing*, **33**(3), 1103–1133.
- DARMANA, D., DEEN, N.G. and KUIPERS, J.A.M. (2006). “Detailed 3d modeling of mass transfer processes in two-phase flows with dynamic interfaces”. *Chemical Engineering & Technology*, **29**(9), 1027–1033.
- DEISING, D., MARSCHALL, H. and BOTHE, D. (2016). “A unified single-field model framework for volume-of-fluid simulations of interfacial species transfer applied to bubbly flows”. *Chemical Engineering Science*, **139**, 173 – 195.
- FALGOUT, R.D. and YANG, U.M. (2002). *hypre: A Library of High Performance Preconditioners*, 632–641. Springer Berlin Heidelberg, Berlin, Heidelberg.
- GRÜNDING, D., FLECKENSTEIN, S. and BOTHE, D. (2016). “A subgrid-scale model for reactive concentration boundary layers for 3d mass transfer simulations with deformable fluid interfaces”. *International Journal of Heat and Mass Transfer*, **101**, 476 – 487.
- POPINET, S. (2003). “Gerris: a tree-based adaptive solver for the incompressible euler equations in complex geometries”. *Journal of Computational Physics*, **190**(2), 572 – 600.
- ROGHAIR, I., VAN SINT ANNALAND, M. and KUIPERS, J.A.M. (2016). “An improved front-tracking technique for the simulation of mass transfer in dense bubbly flows”. *Chemical Engineering Science*, **152**, 351 – 369.



## IMPLEMENTATION, DEMONSTRATION AND VALIDATION OF A USER-DEFINED WALL FUNCTION FOR DIRECT PRECIPITATION FOULING IN ANSYS FLUENT

Sverre G. JOHNSEN<sup>1\*</sup>, Tiina M. PÄÄKKÖNEN<sup>2</sup>, Stein T. JOHANSEN<sup>1,3</sup>, Riitta L. KEISKI<sup>2</sup>, Bernd WITTGENS<sup>1</sup>

<sup>1</sup>SINTEF Materials and Chemistry, NO-7465 Trondheim, NORWAY

<sup>2</sup>University of Oulu, Environmental and Chemical Engineering, FI-90014 Oulu, FINLAND

<sup>3</sup>NTNU, Dept. of Energy and Process Engineering, NO-7491 Trondheim, NORWAY

\* E-mail: sverre.g.johnsen@sintef.no

### ABSTRACT

In a previous paper (Johnsen *et al.*, 2015) and presentation (Johnsen *et al.*, 2016), we developed and demonstrated a generic modelling framework for the modelling of direct precipitation fouling from multi-component fluid mixtures that become super-saturated at the wall. The modelling concept involves the 1-dimensional transport of the fluid species through the turbulent boundary layer close to the wall. The governing equations include the Reynolds-averaged (RANS) advection-diffusion equations for each fluid species, and the axial momentum and energy equations for the fluid mixture. The driving force for the diffusive transport is the local gradient in the species' chemical potential. Adsorption mechanisms are not modelled per se, but the time-scale of adsorption is reflected in the choice of Dirichlet boundary conditions for the depositing species, at the fluid-solid interface.

In this paper, the modelling framework is implemented as a user-defined function (UDF) for the CFD software ANSYS Fluent, to act as a wall boundary condition for mass-transfer to the wall. The subgrid, 1-dimensional formulation of the model reduces the computational cost associated with resolving the fine length-scales at which the boundary-layer mass transfer is determined, and allows for efficient modelling of industry-scale heat exchangers suffering from fouling.

The current paper describes the modelling framework, and demonstrates and validates its applicability in a simplified 2D heat exchanger geometry (experimental and detailed CFD modelling data by Pääkkönen *et al.* (2012, 2016)). By tuning the diffusivity, only, good agreement with the experimental data and the detailed CFD model was obtained, in terms of area-averaged deposition rates.

**Keywords:** CFD, Heat Exchangers, Mass transfer, Multiscale, UDF, Wall function, Fouling .

### NOMENCLATURE

#### Greek Symbols

$\partial_{y^+} \equiv \partial/\partial y^+$  Dimensionless derivative in the wall-normal direction, [–].

$\kappa = 0.42$  von Kármán constant, [–].

$\mu$  Dynamic viscosity, [Pa·s].

$\rho_f$  Fluid mixture mass density, [kg/m<sup>3</sup>].

$\tau_w$  Wall shear stress, [Pa].

#### Latin Symbols

$c_p$  Specific heat capacity, [J/kgK].

$C$  Concentration, [kg/m<sup>3</sup>].

$E_a$  Activation energy, [J/mol].

$\mathbf{g}$  Gravity vector, [m/s<sup>2</sup>].

$h_{sens}$	Specific sensible enthalpy, [J/kg].
$J_{dep}$	Deposition rate, [kg/m <sup>2</sup> s].
$\mathbf{j}$	Mass flux vector, [kg/m <sup>2</sup> s].
$k_0$	Pre-exponential factor, [m <sup>4</sup> /kgs <sup>2</sup> ].
$k'_r$	Surface integration rate constant, [m <sup>4</sup> /kgs <sup>2</sup> ].
$k$	Thermal conductivity, [W/mK].
$N$	Number of species, [–].
$P$	Pressure, [Pa].
$Pr$	Prandtl number, [–].
$q_w$	Wall heat flux, [W/m <sup>2</sup> ].
$\mathcal{R}$	Universal gas constant, [8.3144598J/Kmol].
$Sc$	Schmidt number, [–].
$T$	Absolute temperature, [K].
$u_\tau \equiv \sqrt{\tau_w/\rho_{f,w}}$	Shear velocity, [m/s].
$u_{f,x}$	Fluid velocity parallel to the wall, [m/s].
$\mathbf{u}_f$	Mass-averaged advective fluid velocity vector, [m/s].
$x$	Cartesian coordinate, parallel to the wall, [m].
$X$	Mass fraction, [kg/kg].
$y$	Cartesian coordinate, normal to the wall, [m].
$z$	Mole fraction, [mol/mol].

#### Sub/superscripts

+	Dimensionless variable.
$a, b, c$	Curve-fit parameters.
$bulk$	Value in the bulk.
$d$	Diffusive.
$f$	Property of the fluid mixture.
$i$	Species index.
$I$	Solid-fluid interface.
$in$	Value at inlet.
$reg$	Regression value.
$Sat$	Saturation value.
$t$	Turbulent.
$w$	Value at the wall.

### INTRODUCTION

Fouling of solid surfaces and heat exchanger surfaces in particular, is a common and much studied problem in most process industries, as reflected in the review paper by Müller-Steinhagen (2011). Fouling is defined as the unwanted accumulation of solid (or semi-solid) material on solid surfaces. A similar phenomenon is the desired accumulation of solids e.g. in chemical vapor deposition (Krishnan *et al.*, 1994; Kleijn *et al.*, 1989). A common and costly problem in many industrial applications is the direct precipitation of super saturated fluids on heat exchanger surfaces. Typical examples

are found in e.g. the high-temperature off-gas from waste incineration, metal production, or in power plants, where efficient heat recovery is key to sustainable production, and where a combination of direct precipitation and deposition of e.g. solid metal oxides is a major showstopper. Similar issues can be found in almost all process industries, and in the current work we study the deposition of a low-solubility salt (calcium carbonate,  $\text{CaCO}_3$ ) from liquid water. By precipitation, we understand all types of phase transitions from a fluid to a relatively denser phase, e.g. gas  $\rightarrow$  liquid (condensation), gas  $\rightarrow$  solid (sublimation), liquid  $\rightarrow$  solid (solidification). For some materials, the precipitate may have a crystalline structure (crystallization) (e.g.  $\text{CaCO}_3$ ).

In our modelling work, fouling due to mass deposition from a fluid phase is grouped into two different classes; 1) particulate fouling, where particles carried by the fluid phase penetrate through the laminar boundary layer and stick to the wall (e.g. precipitates, dust, or soot particles) (Johansen, 1991; Johnsen and Johansen, 2009); and 2) direct precipitation where the fluid is super-saturated close to the wall and a phase-transition occurs at the wall (current paper). The direct precipitation on solid surfaces is due to the molecular diffusion through the stagnant boundary layer close to the wall. This is a complex physical process where the diffusion flux of each species is coupled to the diffusion fluxes and thermodynamic/chemical properties of all the species present. Commonly, a combination of 1 and 2 takes place. Fouling can only occur if the adhesive forces between the foulant and the wall are strong enough to overcome the flow-induced shear forces at the wall.

In previous papers, we developed frameworks for the mathematical modelling of particle deposition and re-entrainment (Johansen, 1991; Johnsen and Johansen, 2009) and direct precipitation (Johnsen *et al.*, 2015). In presentations (Johnsen *et al.*, 2010, 2016), it was demonstrated how these models could be employed as wall boundary conditions (mass sinks) for CFD models. Pääkkönen *et al.* (2016) compared CFD simulations with experimental results with respect to  $\text{CaCO}_3$  deposition in a lab-scale heat exchanger setup. In the current paper we apply the wall function approach published in (Johnsen *et al.*, 2015), in a coarse grid CFD model, and test it against the detailed CFD modelling results and experimental data obtained by Pääkkönen *et al.* (2012, 2016).

## EXPERIMENTAL SETUP

The modelling results are validated against experimental data from crystallization fouling on a heated surface. The experimental setup includes a flow-loop with a test-section (a rectangular flow channel), with ohmically heated test surfaces. In the present work, we investigate the case where the wall heat flux was a constant  $q_w = 52.5 \text{ kW/m}^2$ . A water-based test liquid, supersaturated with respect to  $\text{CaCO}_3$ , is circulated from a mixing tank and is filtered before entering the test section (average inlet velocities ranging from  $u_{f,x,in} = 0.2 - 0.4 \text{ m/s}$  and temperature of  $T_{in} = 303 \text{ K}$ ), where  $\text{CaCO}_3$  precipitates and deposits on the heated test surface. The growth of the fouling layer is monitored by measuring the temperature at the test surface. The decreased overall heat transfer coefficient due to the fouling layer (fouling resistance) will cause the test-section surface temperature to increase. Details of the experimental setup, procedure and results were described by Pääkkönen *et al.* (2012).

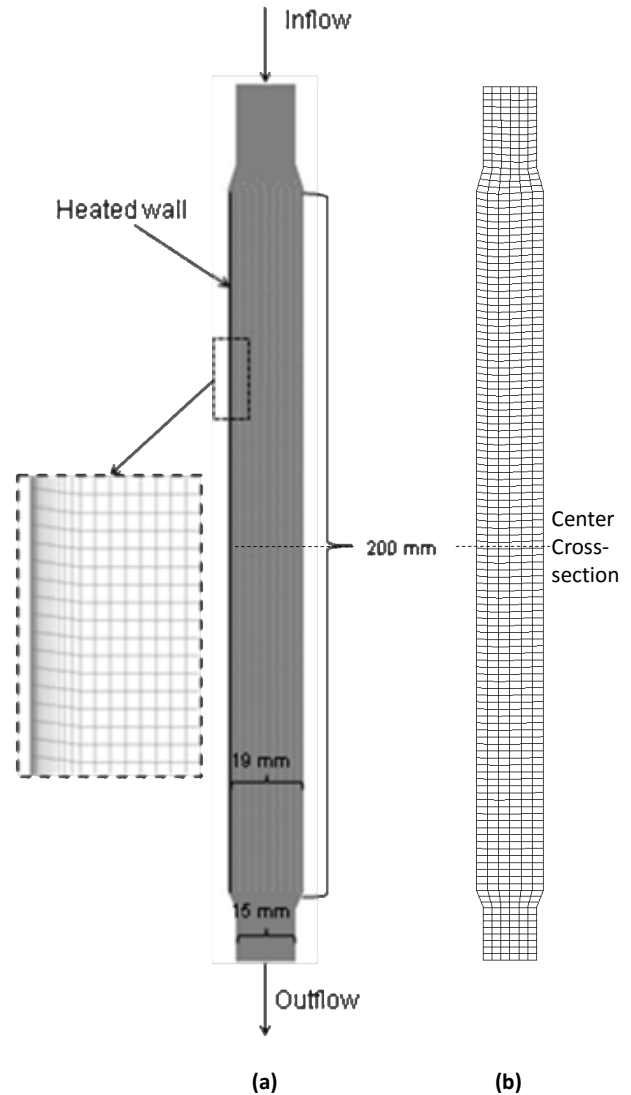


**Figure 1:** Computational geometry and fine-mesh (a), for two-step fouling model (Pääkkönen *et al.*, 2016), and coarse mesh (b), for fouling wall function model.

## MODEL DESCRIPTION

In the present paper, CFD is used to model experiments performed in the aforementioned experimental setup. Two different modelling approaches are employed; 1) *Two-step fouling model* (Pääkkönen *et al.*, 2016); and 2) *Fouling wall function* for direct precipitation fouling (Johnsen *et al.*, 2015, 2016). These two differ fundamentally in the way they approach the problem. Model 1 relies on a detailed CFD mesh close to the wall in order to be able to model the boundary layer phenomena correctly, and employs the traditional two-step approach (see e.g. (Mullin, 2001)) to model the deposition rate. Model 2, on the other hand, relies on a relatively coarse mesh, where the cell centers of the cells residing at the wall are in the log-layer. This approach employs a subgrid model to calculate the deposition rates from a set of simplified governing equations. For more details, see descriptions below as well as mentioned references. The main objective of the current paper is to shed light on the applicability of the wall function approach, since the successful application of such a method would be an essential step towards the cost-efficient modelling of many industry scale applications.

## Geometry and Computational Mesh

Figure 1 presents the 2D geometry used in the CFD simulations. The figure shows a 2D-representation of the liquid-filled gap between two parallel, vertical heat transfer surfaces. The liquid enters from the top and exits through the bottom. For more details about the experimental set-up, refer to Pääkkönen *et al.* (2012).

Two different meshes were applied for the two different modelling approaches described below; namely a fine mesh, as shown in Figure 1a (Pääkkönen *et al.*, 2016), and a coarse mesh as shown in Figure 1b. The coarse mesh was used with the wall function model (Johnsen *et al.*, 2015) whereas the fine mesh was used with the two-step model (Pääkkönen *et al.*, 2016). With the fine mesh, the  $y^+$  value at the surface is about 0.08, and the total number of cells is 76000. In the coarse mesh, the  $y^+$  value at the wall is between 20 (for the  $u_{f,x,in} = 0.2\text{m/s}$  case) and 36 (for the  $u_{f,x,in} = 0.4\text{m/s}$  case), and the total number of cells is 276. In addition, the wall function utilizes a 1-dimensional, logarithmic subgrid consisting of 300 computational nodes, the first node at a wall-distance equal to  $1/10000$ th of the distance to the cell center in the coarse CFD mesh ( $\sim 2.34 \cdot 10^{-7}\text{m}$ ).

## Model Fluid

The test liquid in the experiments was a mixture of various salts dissolved in water. Refer to (Pääkkönen *et al.*, 2015) for details. In the current modelling work it was assumed that the test fluid was a pure calcium carbonate,  $\text{CaCO}_3$ , solution in water. Thus, the mixture was considered as a dilute, electrically quasi-neutral ideal mixture with no chemical reactions. In the present paper, the  $\text{CaCO}_3$  mass-fraction of  $4.197 \cdot 10^{-4}\text{kg/kg}$  was used for the test fluid entering the model geometry. Temperature-dependent fluid properties (mass density, viscosity, diffusivity) were modelled in accordance with Table 2 in (Pääkkönen *et al.*, 2015).

## Fouling Models

Traditionally mass deposition at the wall surface, in crystallization fouling, is modelled based on a two-step approach. In the two-step modelling approach, the fouling process consists of 1) transport from the bulk to the vicinity of the wall, and 2) surface integration (i.e. adsorption onto the fouling layer). The species transport to the vicinity of the crystal-fluid interface, is based on the difference between the bulk and interface concentrations. The mass transfer coefficient is typically estimated from empirical correlations. At the surface, the integration of the species into the crystal body is modelled as a pseudo chemical reaction driven by the difference between the interface and saturation concentrations. When the two steps are combined, the interfacial concentration, which is often unknown, cancels out of the model. The two-step approach has been used as a stand-alone model (Bansal *et al.*, 2008; Helalizadeha *et al.*, 2005; Augustin and Bohnet, 1995) as well as part of a CFD model (Mwaba *et al.*, 2006; Brahim *et al.*, 2003).

### Two-step fouling model

Pääkkönen *et al.* (2016) implemented the two-step model into CFD by utilizing the ability of CFD to model the transport of species to the vicinity of the surface, and thus provide the interfacial concentration difference between the surface and the fluid. To account for the wall shear-stress dependency of the adhesion probability seen in experiments (Pääkkönen *et al.*, 2015), a time scaling factor was included in the model to scale the fluid residence time at the wall.

The mass deposition rate to the surface, based on the two-step approach, including the effect of the residence time (Pääkkönen *et al.*, 2015) can be expressed as

$$j_{dep} = \beta \left[ \frac{1}{2} \left( \frac{\beta \rho_f u_\tau^2}{k'_r \mu_f} \right) + (C_b - C_{Sat}) - \sqrt{\frac{1}{4} \left( \frac{\beta \rho_f u_\tau^2}{k'_r \mu_f} \right)^2 + \frac{\beta \rho_f u_\tau^2}{k'_r \mu_f} (C_b - C_{Sat})} \right]. \quad (1)$$

From the experiments, it was determined that the fouling process was controlled by surface integration (Pääkkönen *et al.*, 2012). Thus, Eq. (1) reduces to

$$j_{dep} = k'_r (C_b - C_{Sat})^2 \frac{\mu_f}{\rho_f u_\tau^2}, \quad (2)$$

where the rate constant for the surface integration can be determined from

$$k'_r = k_0 \exp(-E_a/\mathcal{R}T). \quad (3)$$

The pre-exponential factor  $k_0 = 1.62 \cdot 10^{22}\text{m}^4/\text{kg}\text{s}^2$ , and the activation energy  $E_a = 148\text{kJ/mol}$  were determined from the experiments, for the surface integration controlled fouling process (Pääkkönen *et al.*, 2015). The two-step fouling model was implemented into CFD as mass and momentum sink terms.

### Fouling wall function

The core idea of the fouling wall function approach is to formulate the species transport equations on one-dimensional form by applying appropriate approximations and simplifications in the turbulent boundary layer. Next, the simplified governing equations are solved on a local subgrid for each grid cell residing at the wall, to obtain the cell-specific deposition mass flux. Thus, the calculated species mass fluxes, at the wall, can be used as mass sinks in the CFD grid cells next to the wall.

The set of steady-state governing equations consists of the Advection-Diffusion equation (ADE) for each species,

$$\nabla \cdot (\rho_f X_i \mathbf{u}_f) + \nabla \cdot \mathbf{j}_{d,i} = 0, \quad (4)$$

the fluid mixture momentum and energy equations,

$$\nabla \cdot (\rho_f \mathbf{u}_f \mathbf{u}_f) = -\nabla P + \nabla \tau + \rho_f \mathbf{g}, \quad (5)$$

$$\nabla \cdot (\rho_f h_{sens,f} \mathbf{u}_f) = \nabla \cdot (k_f \nabla T) - \nabla \cdot \left( \sum_i \mathbf{j}_{i,d} h_{sens,i} \right), \quad (6)$$

and the restriction that the mass- and mole-fractions must sum to unity,

$$\sum_i X_i = \sum_i z_i = 1. \quad (7)$$

Introducing turbulence, dimensionless variables and appropriate simplifications, the simplified governing equations are obtained:

$$\partial_{y^+} \left[ \frac{v_i^+}{Sc_i} \rho_f^+ \partial_{y^+} X_i \right] + \partial_{y^+} j_{d,i,y}^+ = 0 \quad (8)$$

gives the mass-fraction profiles;

$$\partial_{y^+} u_{f,x}^+ = 1/(\mu^+ + \mu_i^+) \quad (9)$$



**Table 1:** Wall  $y^+$  values at the centre cross-section, for selected coarse grids with uniform node spacing, for inlet velocities 0.2 and 0.4 m/s .

No. of cells across channel	4	6	8	10
Inlet velocity				
0.2 m/s	30	20	15	11
0.4 m/s	49	36	25	20

gives the dimensionless axial fluid mixture velocity profile; and

$$\partial_{y^+} \left[ K_{(0)}^+ T^+ + K_{(1)}^+ \partial_{y^+} T^+ \right] = 0 \quad (10)$$

gives the dimensionless temperature profile.

$$K_{(0)}^+ \equiv \left( k_{f,c}^+ + k_{f,t}^+ \right) \left( \partial_{y^+} \ln c_P^+ \right) - Pr_w \sum_{i=1}^N c_{P,i}^+, \quad (11)$$

and

$$K_{(1)}^+ \equiv k_f^+ + k_{f,t}^+ + k_{f,c}^+ \quad (12)$$

express the dimensionless groups in Eq. (10). For more details, refer to (Johnsen *et al.*, 2015).

Due to the assumed weak effect of thermophoresis (due to small temperature gradients) and the lack of good estimates of the thermophoretic diffusivity, only diffusiophoresis (concentration gradient diffusion) was considered in the current work. Furthermore, it was assumed that the model fluid could be treated as a dilute, ideal mixture. This reduces the Maxwell-Stefan diffusion model to the Fickian diffusion model. The mixture mass density and viscosity was modelled in accordance with (Pääkkönen *et al.*, 2015), while constant mixture thermal conductivity and specific heat capacity 0.6637 W/m<sup>2</sup> of and 4182 J/kgK, respectively, were used. The turbulent Schmidt number was set to 1. The Maxwell-Stefan binary diffusivity was tuned so that the area averaged deposition rate matched that of the experiments, for the  $u_{f,x,in} = 0.2 \text{ m/s}$  data-point, and was kept constant for the other inlet velocities. This resulted in a Fickian diffusivity of  $3.64 \cdot 10^{-5} \text{ m}^2/\text{s}$ .

### CFD Models

CFD modelling was performed using the ANSYS FLUENT 16.2 CFD software. Turbulence is modelled with the standard  $k - \epsilon$  turbulence model. In the fine-mesh CFD model, the Enhanced Wall Treatment is employed to resolve the near wall region in the fine mesh model.

Temperature dependent fluid properties were implemented via user-defined functions (UDFs) in accordance with (Pääkkönen *et al.*, 2015). The fouling models were also implemented via UDFs and hooked into ANSYS Fluent via the adjust function hook. Due to the low deposition rates observed, it was expected that the mass transfer to the wall would have a very small effect on the bulk conditions in the coarse mesh. Thus, the fouling wall function was not utilized as a mass source, but was run on a frozen flow field.

### Coarse-Mesh Velocity Wall Function

The fouling wall function was designed to work on grids where the grid cells residing on the wall are in the log-layer. The main reason for this is that its bulk boundary conditions were chosen to be valid for fully developed turbulent flow. In the current experimental set-up, however, due to the low Reynolds numbers, such a stringent requirement of the wall

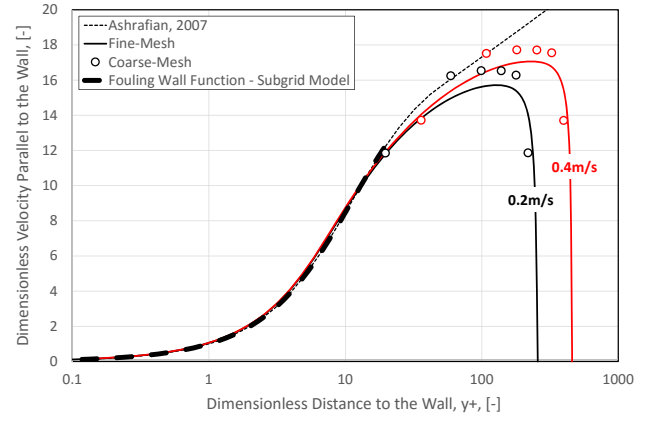


**Figure 2:** Comparison of dimensionless velocities as functions of dimensionless wall distance at the center cross-section (isothermal conditions), for the coarse- (circles) and fine-mesh (solid lines) CFD models, the fouling wall function subgrid model (dashed, black line), and theoretical velocity profile (Ashrafian and Johansen, 2007) (dotted, black line).

$y^+$  left us with very coarse meshes. In Table 1, the approximate wall  $y^+$  value at the center cross-section (see Figure 1) is shown for various coarse meshes where the node spacing is constant across the channel.

In order to predict the wall shear stress and general velocity profile accurately, on the coarse mesh, the wall function proposed by Ashrafian and Johansen (2007), was employed;

$$u_{f,x}^+(y^+) = \begin{cases} 11.4 \arctan \left( \frac{y^+}{11.4} \right), & y^+ \leq y_*^+ \\ \frac{1}{\kappa} \ln \left( \frac{1 + \kappa y^+}{1 + \kappa y_*^+} \right) + u_{f,x}^+(y_*^+), & y^+ > y_*^+ \end{cases}, \quad (13)$$

with the dimensionless turbulent kinematic viscosity

$$v_t^+ = \begin{cases} \left( \frac{y^+}{11.4} \right)^2 & y^+ \leq y_*^+ \\ \kappa y^+ & y^+ > y_*^+ \end{cases}, \quad (14)$$

where dimensionless velocity is defined as  $u_{f,x}^+ = u_{f,x}/u_\tau$ , dimensionless wall distance is defined as  $y^+ = u_\tau y/\nu$ ,  $y_*^+ = 51.98$ , and  $\kappa = 0.42$  is the von Kármán constant.

A sensitivity study was done to investigate how the coarse meshes performed against the fine-mesh CFD model and the Ashrafian-Johansen wall function. It was determined that the mesh with 6 cells across the channel reproduced the fine-mesh velocity and temperature profiles quite well and at the same time gave an acceptable wall  $y^+$  value. In Figure 2, it is shown how the fine-mesh and coarse-mesh CFD models perform against the profile published by Ashrafian and Johansen (2007) under isothermal conditions (no heating), in terms of dimensionless variables. The deviations at high  $y^+$  values are due to the effect of the opposing channel wall and the relatively low Reynolds numbers investigated. For the coarse-mesh CFD model, the fouling wall function subgrid model is included for validation of the subgrid velocity profile. In Figure 3a, the coarse and fine-mesh axial velocity profiles at the center cross-section are compared, and in Figure 3b, the temperature profiles are compared. It can be seen that generally, the axial velocity was underpredicted, in the coarse-mesh CFD model, whereas the temperature was overpredicted.

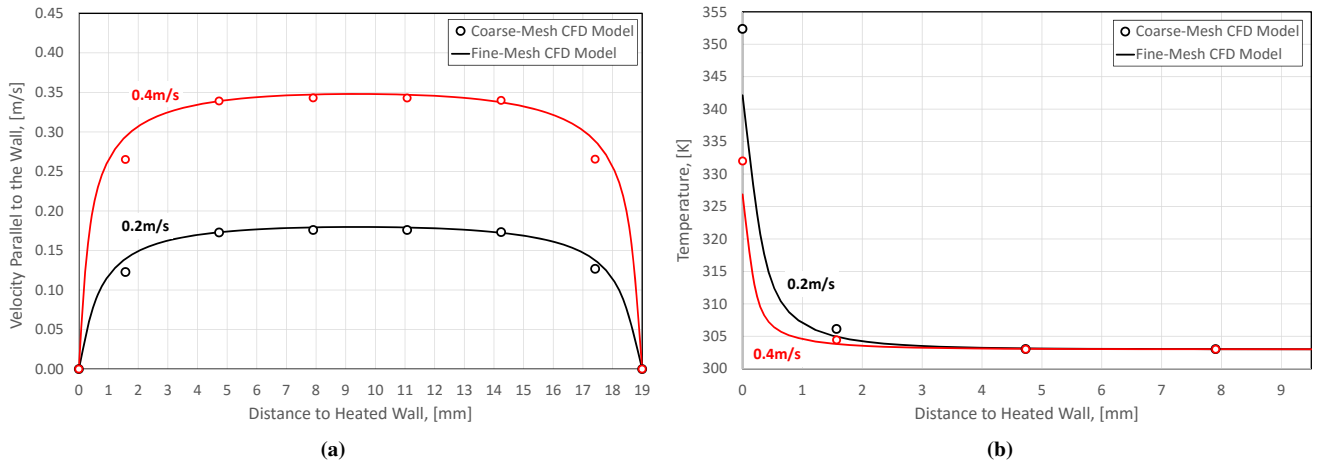


**Figure 3:** Comparison of parallel-to-wall flow velocity profiles (a) and temperature profiles (b) at the center duct cross-section ( $x = 100\text{mm}$ ), for coarse and fine-mesh CFD models, for wall heat flux of  $52.5\text{kW}/\text{m}^2$  and inlet velocities  $0.2\text{m}/\text{s}$  and  $0.4\text{m}/\text{s}$ .

### Boundary Conditions for the Fouling Wall Function

The fouling wall function requires boundary conditions for temperature and species mass-fractions at the wall as well as axial velocity, temperature and species mass-fractions in the bulk. The bulk values as well as the wall temperature are taken directly from the CFD model via the inbuilt macro library in ANSYS Fluent, and utilized as Dirichlet boundary conditions in the subgrid model. The species-specific mass-fraction boundary conditions at the wall, however, require special attention. First, the type of boundary condition depends on whether the species is depositing or not; second, they depend on which diffusive transport mechanisms are dominating close to the wall (Johnsen *et al.*, 2017).

E.g., consider the case where diffusion due to mass-fraction gradients (diffusiophoresis) is the sole transport mechanism close to the wall. For the non-depositing species, the mass-fraction gradient at the wall must be zero to ensure zero deposition flux, and we employ the Neuman BC for the ADE, at the wall. For the depositing species, however, we do not have a priori knowledge of the deposition flux, so we cannot use the mass-fraction gradient as a BC. We have to use the Dirichlet BC. That is, we need to specify the mass-fractions of the depositing species, at the wall.

The mass-fractions at the wall (interface mass-fractions) are consequences of the balance between transport through the turbulent boundary layer and the species integration into the crystal lattice. Therefore, it is a function of e.g. temperature, temperature gradient, composition, composition gradients, wall shear stress, crystal properties, etc. Thus, the interface mass-fraction is not just a fixed boundary condition, but is in fact part of the solution itself. If the kinetics of the surface reaction are known, it is possible to estimate the interface mass-fractions. Then, an iterative procedure can be employed to find the interface mass-fraction that ensures that the transport rate through the boundary layer and the integration rate into the crystal are identical (Johnsen *et al.*, 2017). Lacking accurate predictions of the surface reaction rates, the current wall function model employed interface concentrations obtained from the fine-mesh CFD model (see Figure 4). These concentrations are dependent on both wall temperature and inlet velocity (wall shear stress). By curve fitting the Logistic function,

$$X_{l,reg} = \frac{a}{1 + (T_w/b)^c}, \quad (15)$$

**Table 2:** Curve fit polynomial coefficients for velocity dependence of interface mass-fractions (Eqs. 16-18).

	$a$	$b$	$c$
<b>0</b>	0.251654	342.436	409.600
<b>1</b>	1.28476	26.6133	-2179.69
<b>2</b>	-3.57731	-112.872	4968.05
<b>3</b>	3.41471		

to the fine-mesh CFD data, we obtained good representations of the interface mass-fractions for each inlet velocity case. The inlet velocity-dependent fitting parameters,  $a$ ,  $b$ , and  $c$ , are shown in Figure 5, and could be accurately described in terms of 3rd and 2nd order polynomials;

$$a = a_0 + a_1 u_{f,x,in} + a_2 u_{f,x,in}^2 + a_3 u_{f,x,in}^3, \quad (16)$$

$$b = b_0 + b_1 u_{f,x,in} + b_2 u_{f,x,in}^2, \quad (17)$$

$$c = c_0 + c_1 u_{f,x,in} + c_2 u_{f,x,in}^2. \quad (18)$$

The coefficients are given in Table 2. Employing Eq. (15) with coefficients given by Eqs. 16-18, we got a good, general representation of the CFD-data (see black circles in Figure 5).

Figure 6 shows the temperature dependence of the calculated interface mass-fraction (Eq. (15)), for selected inlet velocity cases. It is seen that the interface mass-fraction drops from close to the bulk value to zero, at a certain threshold temperature, which appears to be dependent on the inlet velocity. In reality, this is a consequence of the complex interplay between mass deposition rate, interface mass-fraction, wall temperature, and wall shear stress. We will be content, however, to consider this as an inlet velocity dependent feature. At temperatures below the threshold, the deposition regime is interface controlled, whereas at higher temperatures it is diffusion controlled. Pääkkönen *et al.* (2012) concluded that the fouling regime was interface controlled, in these experiments, since the over-all deposition rate is not increasing for increasing flow-velocities, as would be expected for a mass transfer controlled fouling regime. However, various segments of the heated wall may be in different fouling regimes depending on the local flow conditions and wall temperature, as indicated in Figure 7. In general, the higher the difference between the bulk and interface mass-fractions, the higher

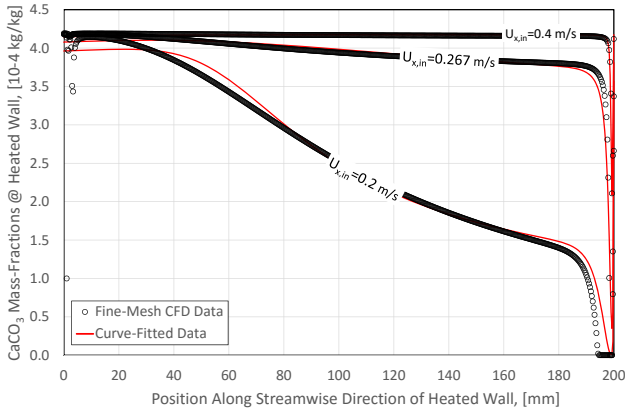


**Figure 4:** Comparison of fine-mesh CFD (black circles) and best-fit (red lines)  $CaCO_3$  mass-fractions at the wall plotted against the axial position along the heated wall, for selected inlet velocities.

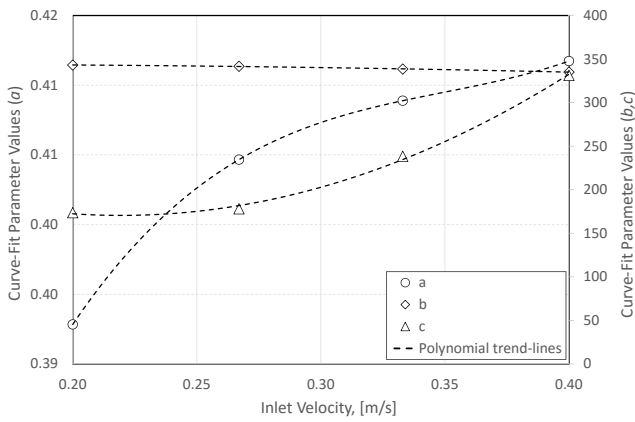


**Figure 5:** Curve-fit parameters  $a$ ,  $b$ , and  $c$  (see Eq. (15)) plotted as functions of inlet velocity, along with best-fit polynomial trend-lines (see Eqs. 16-18 and Table 2).

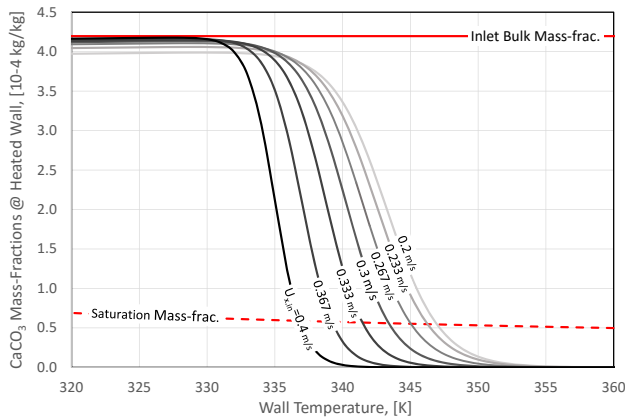


**Figure 6:** Comparison of temperature dependency of  $CaCO_3$  bulk (red line), saturation (dashed red line), and interface (calculated for various inlet velocities, from Eq. (15): black=  $0.4m/s$ , light gray=  $0.2m/s$ ) mass-fractions, at the wall.

the deposition rate (mind that at interface mass-fractions below the metastable equilibrium mass-fraction, fouling might not take place at all). Thus, the deposition rate at locations with wall temperatures above the threshold can be expected to dominate. Since the coarse-mesh CFD model is

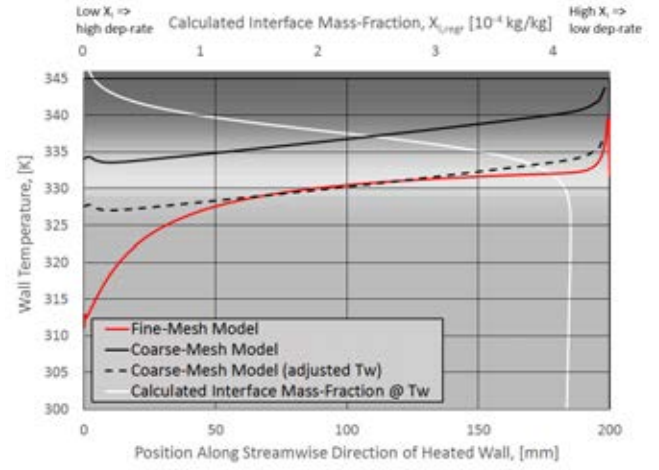


**Figure 7:** Wall temperature vs. position along the heated wall, for the  $u_{f,x,in} = 0.333m/s$  case, for the fine-mesh model (red), coarse-mesh model (solid black), and adjusted coarse-mesh wall-temperature ( $-6.5K$ ) (dashed black). The relationship between the wall temperature and the interface mass-fraction is shown by the white curve. The contour plot in the background corresponds to the interface mass-fraction values at given wall temperatures (dark gray corresponds to low  $X_I$ , and light gray corresponds to high  $X_I$ ) and links the modelled, local wall temperatures with an expected local interface mass-fraction.

prone to overpredict the wall temperature, as was discussed above (see Figure 3b), there is a risk that the interface mass-fraction is severely underpredicted if the true wall temperature is lower than, but close to the threshold temperature. To reduce the risk of overprediction of deposition rates, a fixed  $6.5K$  was subtracted from the wall temperature when calculating the interface mass-fraction from Eq. (15). Figure 7 shows that a greater part of the overpredicted wall temperature curve (solid black) is in the low interface mass-fraction region (dark gray area) than the fine-mesh model wall temperature curve (red). Hence, a greater part of the wall will have low interface mass-fraction in the coarse-mesh model than in the fine-mesh model. The corrected wall temperature curve (dashed black), however, is more similar to the fine-mesh model temperature curve. Furthermore, interface mass-fractions below the saturation mass-fraction indicate that the fluid is undersaturated at the crystal surface. Physically this means that deposition is unfavorable with respect to minimizing the Gibbs free energy, thus no deposition will take place (Johnsen *et al.*, 2017). Therefore, the Dirichlet boundary condition for the  $CaCO_3$  was set to

$$X_{I, CaCO_3} = \max(X_{I,reg}, X_{Sat}) \quad (19)$$

## RESULTS AND DISCUSSION

The ambition in the current work was to demonstrate the applicability of a previously developed fouling wall function framework (Johnsen *et al.*, 2015), in practice. To approach this objective, its implementation, as a user-defined function in ANSYS Fluent 16.2, was employed to demonstrate how it performs against a more traditional two-step fouling modelling approach (Pääkkönen *et al.*, 2016), in the context of a well-controlled laboratory experiment (Pääkkönen *et al.*, 2012).

The main motivation for developing the fouling wall function was to eliminate the need to resolve the turbulent boundary layer and enable efficient fouling modelling in industry scale

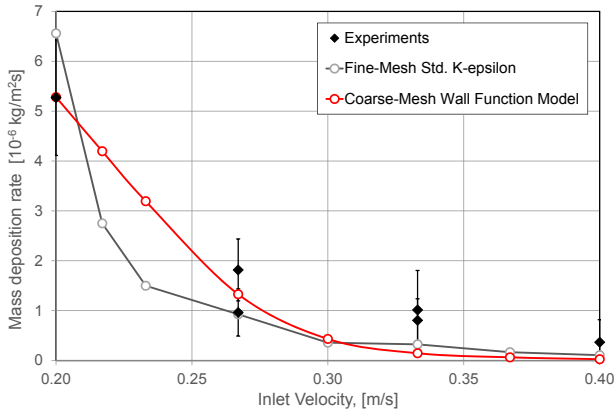


**Figure 8:** Comparison of the area averaged mass deposition rates from the fine-mesh two-step model and the coarse-mesh fouling wall function model with the experimental data.

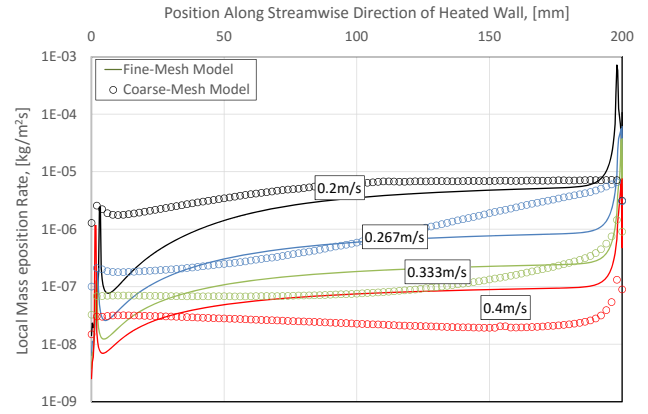


**Figure 9:** Comparison of the local mass deposition rates calculated by the fine-mesh two-step model (lines) and the coarse-mesh fouling wall function model (circles), at selected inlet velocities.

CFD simulations. Hence, the modelling framework relies on relatively high wall  $y^+$  values in the CFD cells residing at the wall. This proved to be challenging in the employment of the above cited experimental and simulation data, for comparison. Due to the low Reynolds numbers encountered in the data from Pääkkönen et al., it was necessary to confide in a very coarse CFD mesh as basis for the fouling wall function modelling (see Figure 1).

The mass deposition rates predicted by the fouling wall function are depending directly on the wall function boundary conditions;

- wall mass-fractions for the depositing species,
- bulk and wall temperatures,
- bulk velocity parallel to the wall,

where *bulk* refers to the center of the CFD grid cells residing at the wall. Thus, accurate prediction of the deposition rates rely heavily on the accurate CFD modelling of these quantities.

By utilizing the wall function published by Ashrafiyan and Johansen (2007), we managed to reproduce the fine-mesh CFD model velocity and temperature profiles fairly well, qualitatively. However, the quantitative discrepancy turned out to be the major source of error in the fouling wall function modelling results. In Figure 2, it can be seen how the dimensionless velocity profiles are comparable in the absence of heating, and in Figure 3 it can be seen how dimensional velocity and temperature profiles are comparable under constant heating of  $52.5kW/m^2$ . The effect on the velocity profiles, by turning on/off heating was minimal.

Since thermophoresis was neglected in the current work, the role of the temperature was to provide the temperature dependent fluid properties (mass density, viscosity, and saturation mass-fraction), and interface mass-fraction for the depositing species. Although the inaccurate prediction of any of these will affect the predicted mass deposition rate to some extent, it seemed that the effect of the inaccurate prediction of the interface mass-fraction was the most severe. As was indicated in figures 6 and 7, even modest errors in the local wall temperature could result in a severely miss-represented interface mass-fraction. Since the mass deposition rate is expected to scale approximately linearly with the difference between the bulk and interface mass-fractions, the mass deposition rate can be off by an order of magnitude by just a slight overprediction of the wall temperature, as seen in Figure 6. To avoid underpredicting the interface mass-fraction due to overprediction of the wall temperature, the temperature was

subtracted a fixed  $6.5K$  when calculating the interface mass-fractions (see Figure 7).

Figure 8 presents a comparison between the experimental data, the fine-mesh two-step fouling model data, and the data obtained from the coarse-mesh fouling wall function model. In the absence of reliable measurements/calculations of the diffusivity, it was treated as a calibration parameter, for the fouling wall function. The fouling wall function data were thus obtained with a tuned diffusivity of  $3.64 \cdot 10^{-5}m^2/s$ , reproducing the  $u_{f,x,in} = 0.2m/s$  experimental data point. The same, constant diffusivity was used in all grid cells along the wall, for all the inlet velocity cases. Despite the issues with predicting the required boundary conditions for the fouling wall function model accurately, the modelling results compared very well with the results from the fine-mesh two-step fouling modelling and the experimental data, in terms of the area averaged mass deposition rate.

In Figure 9, the local deposition rates are compared for the fine-mesh two-step model and the coarse-mesh fouling wall function model. It can be seen that even if the area-averaged values compared well, the local values differs significantly. The mismatch seems primarily to be due to

- inaccurate prediction of interface mass-fraction;
- inaccurate prediction of wall temperature in the coarse mesh;
- inaccurate prediction of bulk velocity in the coarse mesh.

The most crucial improvement to the fouling wall function model would be to get accurate interface mass-fractions. An in-depth study of these effects are left to future investigations. In the meantime, we are content to summarize that the fouling wall function approach performed very well in a scenario, slightly outside the design specifications of the modelling framework, with respect to the Reynolds number. The model fluid used in the current paper is a coarse simplification of the actual fluid employed in the cited experiments. The real fluid was a salt-water solution involving a multitude of chemically reacting ions and molecules. This is reflected by the fact that the content of dissolved  $CaCO_3$  in the model fluid, is much higher than the saturation concentration. Thus, the modelled  $CaCO_3$  may be seen as a pseudo-component representing e.g. the true  $CaCO_3$  fraction in addition to  $Ca^{2+}$ ,  $CO_3^{2-}$  and possibly other species. In the present case, at relatively low concentrations, this simplification seems to be justified in both modelling approaches

employed. However, this may be part of the explanation of the local difference between deposition rates resulting from the two modelling methods.

The present demonstration case indicates that in industry-scale applications, where very fine meshes are infeasible, the wall function approach may provide a means to do physically detailed simulations of complex fluids, in complex geometries, at reasonable computational cost. In particular, if it can be assumed that the deposition rates are so small that they do not affect the flow field significantly, the savings in computational cost will be great. Then, the fouling wall function can be run on a frozen flow-field, and sensitivity studies or optimization studies on e.g. diffusivities, wall surface properties, etc., that does not affect the macro scale flow-fields can be performed without the need to update the frozen flow-field. Establishing the frozen flow-field on the coarse mesh, without the fouling wall function activated is very efficient due to the low number of computational cells needed. Then, running multiple fouling scenarios can be done on that flow-field just by changing input parameters to the fouling wall function and running one single CFD iteration, for each fouling scenario, with the fouling wall function activated.

## CONCLUSION

Two different CFD modelling approaches were compared with experimental data on mass deposition rates in an experimental heat exchanger set-up. The two CFD strategies resolved the fine length-scales determining the mass transfer through the turbulent boundary layer, in two different ways: 1) the refinement was done in the 2D CFD mesh, resulting in a relatively high number of grid cells and a wall  $y^+$  of ca. 0.08; and 2) the refinement was taken into account in a wall function utilizing a 1-dimensional subgrid, allowing for a coarse CFD mesh with wall  $y^+$  of about 30. The fine-mesh CFD model utilized a traditional two-step modelling approach for the mass deposition modelling, complemented with the fluid residence-time at the wall, whereas the coarse-mesh CFD model wall function solved the coupled Advection-Diffusion, momentum and energy equations on a local subgrid to estimate the mass deposition rates.

The coarse-mesh model performed very well compared to the fine-mesh model and experimental data, with respect to area average deposition rates. Significant mismatch was observed, however, in the local deposition rates. The lacking accuracy in the coarse-mesh model was mainly due to the challenges in predicting interface mass-fractions, wall temperatures and bulk velocities, on the very coarse mesh.

The over-all good performance of the coarse-mesh model gives strong support to the idea that the wall function approach may provide a means to do physically detailed simulations of complex fluids, in complex, industry-scale geometries, at a reasonable computational cost.

## ACKNOWLEDGEMENTS

This work was funded by the Research Council of Norway and The Norwegian Ferroalloy Producers Research Association, through the SCORE project (Wittgens, 2013). Sverre expresses his gratitude towards the University of Oulu, Environmental and Chemical Engineering, FINLAND, for hosting him and his family during August 2016.

## REFERENCES

ASHRAFIAN, A. and JOHANSEN, S.T. (2007). "Wall boundary conditions for rough walls". *Progress in Computational Fluid Dynamics*, **7(2-4)**, 230–236.

AUGUSTIN, W. and BOHNET, M. (1995). "Influence of the ratio of free hydrogen ions on crystallization fouling". *Chemical Engineering and Processing: Process Intensification*, **34(2)**, 79–85.

BANSAL, B., CHEN, X.D. and MÜLLER-STEINHAGEN, H. (2008). "Analysis of 'classical' deposition rate law for crystallisation fouling". *Chem. Eng. Process.: Process Intensification*, **47**, 1201–1210.

BRAHIM, F., AUGUSTIN, W. and BOHNET, M. (2003). "Numerical simulation of the fouling process". *International Journal of Thermal Sciences*, **42(3)**, 323 – 334.

HELALIZADEHA, A., MÜLLER-STEINHAGEN, H. and JAMIALAHMADIA, M. (2005). "Mathematical modelling of mixed salt precipitation during convective heat transfer and sub-cooled flowboiling". *Chemical Engineering Science*.

JOHANSEN, S.T. (1991). "The deposition of particles on vertical walls". *International Journal of Multiphase Flow*, **17(3)**, 355–376.

JOHANSEN, S.G. and JOHANSEN, S.T. (2009). "Deposition modelling from multi-phase dispersed flow - a boundary layer wall function approach". *Heat Exchanger Fouling and Cleaning VIII - 2009*.

JOHANSEN, S.G., ÅBERG, M. and JOHANSEN, S.T. (2010). "Implementation and demonstration of a boundary condition wall function for industrial scale particulate fouling cfd modeling". *ICMF 2010 7th International Conference on Multiphase Flow, Tampa, Florida, USA*.

JOHANSEN, S.G., JOHANSEN, S.T. and WITTGENS, B. (2015). "A wall-function approach for direct precipitation/crystallization fouling in cfd modelling". *Heat Exchanger Fouling and Cleaning XI - 2015*.

JOHANSEN, S.G., JOHANSEN, S.T. and WITTGENS, B. (2016). "Implementation and demonstration of a boundary condition wall function for direct precipitation fouling cfd modelling". *ICMF 2016 9th International Conference on Multiphase Flow, Firenze, Italy*.

JOHANSEN, S.G., PÄÄKKÖNEN, T.M., ANDERSSON, S., JOHANSEN, S.T. and WITTGENS, B. (2017). "On the wall boundary conditions for species-specific mass conservation equations in mathematical modelling of direct precipitation fouling from supersaturated, multi-component fluid mixtures". *arXiv:1703.01448 [physics.flu-dyn]*.

KLEIJN, C.R., VAN DER MEER, T.H. and HOOGENDOORN, C.J. (1989). "A mathematical model for lpcvd in a single wafer reactor". *Journal of The Electrochemical Society*, **136(11)**, 3423–3433.

KRISHNAN, A., NING, Z. and PRZEKWAS, A. (1994). "A computational model for chemical vapor deposition processes in industrial reactors". *4th InterSociety Conference on Thermal Phenomena in Electronic Systems (I-THERM)*, 222–236.

MÜLLER-STEINHAGEN, H. (2011). "Heat transfer fouling: 50 years after the kern and seaton model". *Heat Transfer Engineering*, **32(1)**, 1–13.

MULLIN, J.W. (2001). *Crystallization*. Butterworth-Heinemann.

MWABA, M.G., GOLRIZ, M.R. and GU, J. (2006). "A semi-empirical correlation for crystallization fouling on heat exchange surfaces". *Applied Thermal Engineering*, **26(4)**, 440–447.

PÄÄKKÖNEN, T.M., RIIHIMÄKI, M., SIMONSON, C.J., MUURINEN, E. and KEISKI, R.L. (2012). "Crystallization fouling of  $CaCO_3$  - analysis of experimental thermal

resistance and its uncertainty”. *International Journal of Heat and Mass Transfer*, **55(23-24)**, 6927 – 6937.

PÄÄKKÖNEN, T.M., RIIHIMÄKI, M., SIMONSON, C.J., MUURINEN, E. and KEISKI, R.L. (2015). “Modeling  $CaCO_3$  crystallization fouling on a heat exchanger surface - definition of fouling layer properties and model parameters”. *International Journal of Heat and Mass Transfer*, **83**, 84–98.

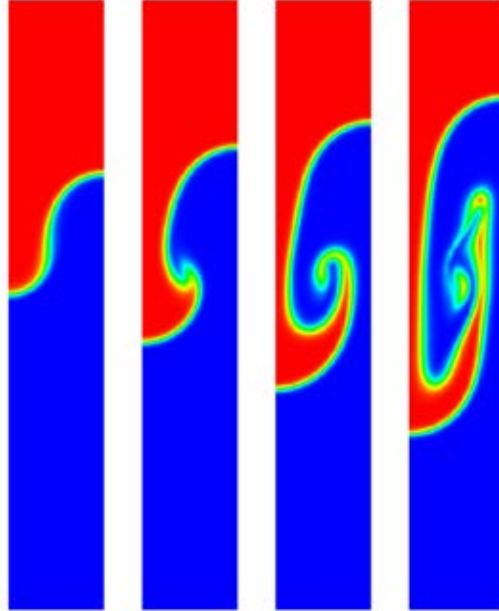
PÄÄKKÖNEN, T.M., OJANIEMI, U., PÄTTIKANGAS,

T., MANNINEN, M., MUURINEN, E., KEISKI, R.L. and SIMONSON, C.J. (2016). “CFD modelling of  $CaCO_3$  crystallization fouling on heat transfer surfaces”. *International Journal of Heat and Mass Transfer*, **97**, 618 – 630.

WITTGENS, B. (2013). “Score - staged combustion for energy recovery in ferroalloy industry”. <http://www.sintef.no/en/projects/score-staged-combustion-for-energy-recovery-in-fer/>.



# FREE SURFACE FLOW & WAVES







# UNRESOLVED CFD-DEM IN ENVIRONMENTAL ENGINEERING: SUBMARINE SLOPE STABILITY AND OTHER APPLICATIONS

Alice HAGER<sup>1\*</sup>, Manuela KANITZ<sup>2</sup>, Jürgen GRABE<sup>2</sup>, Christoph KLOSS<sup>1</sup>, Christoph GONIVA<sup>1</sup>

<sup>1</sup> DCS Computing GmbH, 4020 Linz, AUSTRIA

<sup>2</sup> TUHH, Institute of Geotechnical Engineering and Construction Management, 21079 Hamburg, GERMANY

\* E-mail: alice.hager@dcs-computing.com

## ABSTRACT

When installing gravity foundations for offshore structures such as wind power stations or oil platforms, the seabed needs to be excavated for providing enough stability. To minimize the impact on the surrounding fauna and the installation costs, steep but stable slopes are desired. The work presented is done in a research project on the numerical investigation of the stability of submarine slopes, particularly under the impact of influences like material removal or wave-induced disturbances.

The method used in the current project is coupled CFD-DEM: while the dynamics of the fluid phase (water and in some cases water and air) are handled with computational fluid dynamics (CFD), the soil is modelled by spheres, whose motion is calculated with a discrete element method (DEM). Force models are used for considering the particles' effect on the fluid and vice versa, a void fraction field accounts for the volume of the particles on the CFD side. Due to the high number of particles in the domain only unresolved CFD-DEM (cf., e.g. Zhou (2010)) is suitable: in this case the particles are smaller than the cells of the CFD mesh.

In the presented work the investigations concentrated on the validation of the CFD-DEM models against small-scale experiments that were conducted by the authors. In a first step, the used materials were characterized and a lubrication force model was implemented. Furthermore, some basic investigations on the topic of dilatancy were carried out. Then an experimental setup and an according simulation were compared. In addition to that a three phase (air, water, particles) solver was used to depict the effect of surface waves onto the particle bed.

For the calculations CFDEM@coupling was used. CFDEM@coupling is an Open Source software for coupled CFD-DEM simulations. It uses the CFD framework of the Open Source CFD code OpenFOAM® and the DEM framework of the Open Source code LIGGGHTS®. Both CFDEM@coupling and LIGGGHTS® have been presented before (cf., e.g. Goniva et al. (2012), Kloss et al. (2012)), the used model equations were validated against analytical solutions and literature.

**Keywords:** Lagrangian methods, granular flows, unresolved CFD-DEM.

## NOMENCLATURE

### *Greek Symbols*

- $\alpha$  Volume fraction.
- $\rho$  Mass density, [kg/m<sup>3</sup>].
- $\mu$  Dynamic viscosity, [kg/m.s].
- $\omega$  Angular velocity, [rad/s].

### *Latin Symbols*

- $F$  Force, [N].
- $g$  Gravitational acceleration, [m/s<sup>2</sup>].
- $h$  Minimal surface distance of two particles, [m].
- $m$  Mass, [kg].
- $p$  Pressure, [Pa].
- $r$  Particle radius, [m].
- $U$  Velocity, [m/s].
- $v$  Velocity [m/s].
- $R_{sl}$  Solid-liquid interaction force, [kg/(m.s)<sup>2</sup>].
- $T$  Torque, [N.m].

### *Sub/superscripts*

- $f$  Fluid
- $i$  Index  $i$
- $j$  Index  $j$
- $p$  Particle
- $w$  Wall

## INTRODUCTION

The reasons for producing under water slopes are manifold: they occur when sand or gravel is harvested as well as when foundations for off-shore wind power plants or oil platforms are required. For both economic and ecological reasons it is desirable to build steep and yet stable slopes. The stability of the slopes and their formation can either be influenced by the production process itself (e.g. grab or suction dredging) or environmental phenomena such as surface waves. A joint research project between TUHH and DCS Computing GmbH aims on modelling different phenomena at the soil-water interface. The presented contents were developed within the course of this project.

First, the implementation and validation of a lubrication force model is discussed and the capability of depicting

dilatancy is demonstrated. Modelling the effect of dilatancy is crucial for simulating saturated sand beds. Due to shear loading, dilatancy leads to a local hardening of the soil bed as the pore volume increases. This effect causes a negative excess pore water pressure and hence suction occurs until the inflowing pore water fills the volume between the soil grains. In a second part two application cases are considered:

- (i) the effect of suction dredging on an underwater slope is investigated numerically and compared to experimental data
- (ii) a three-phase solver is used to proof the feasibility of simulating wave induced disturbances on particle beds

The presented work is realized with the Open Source software packages LIGGGHTS® (Kloss et al. (2012)) and CFDEM®coupling (Goniva et al. (2012)).

## MODEL DESCRIPTION

A coupled CFD-DEM model was used to compute the dynamics of the fluid and particle phases and their interaction. On the CFD side the computational domain was discretised and a finite volume solver was applied. For the granular phase a Lagrangian method was used, in which each particle was considered individually.

## Governing equations

The governing equations for the presented CFD-DEM method are the volume averaged Navier-Stokes equations:

*Continuity equation*

$$\frac{\partial \alpha_f \rho_f}{\partial t} + \nabla \cdot (\alpha_f \rho_f U) = 0 \quad (1)$$

*Momentum equation*

$$\frac{\partial \alpha_f \rho_f U}{\partial t} + \nabla \cdot (\alpha_f \rho_f U U) = -\alpha_f \nabla p + R_{sl} + \alpha_f \rho_f g \quad (2)$$

The term  $R_{sl}$  denotes the fluid-structure interaction force density, which is computed with the aid of particle-data. In the DEM method used for the calculation of the particle phase, the trajectory of each particle is calculated separately, using Newton's second law:

$$m_p \frac{dU_p}{dt} = \sum F_{p,p} + \sum F_{p,w} + m_p g + F_p + F_f \quad (3)$$

$$I_p \frac{d\omega_p}{dt} = T_p \quad (4)$$

The right-hand side of equation (3) consists of the particle-particle and particle-wall interaction forces, for their calculation a soft-sphere approach was used. The term  $m_p g$  represents the mass-force due to gravity and  $F_p$  stands for the pressure forces. The term  $F_f$  represents the forces exerted by the fluid. In the current case the drag force, the pressure gradient force and the viscous force were identified as dominating forces. The drag force model by Koch and Hill (2001) was used. As the particle-particle contacts take place under water also a lubrication force model was implemented and validated.

## Lubrication force model

If two particles collide within a fluid the displacement of the fluid in the gap between them causes a force – the lubrication force. While for many processes where fluids with relatively low viscosities are present the effect of the force is negligible, it might be worth considering in the presented applications. The classical formulation of the lubrication force is given as

$$F_{\text{lub}} = -6 \cdot \pi \cdot \mu \cdot r_{ij}^2 \cdot \left( \frac{1}{h} \right) \cdot v_n, \quad (5)$$

where  $r_{ij}$  is the effective radius defined as

$$\frac{1}{r_{ij}} = \frac{1}{r_i} + \frac{1}{r_j}, \quad (6)$$

with  $i$  and  $j$  denoting arbitrary different particles.  $h$  is the minimal surface distance between two particles and one has to make sure that the lubrication force does not become infinitely large when the particles are in contact with each other. Therefore, the radius of action of the lubrication force was limited to a certain minimal distance between two particles. This approach was also used by Sun and Xiao (2016) in their implementation.

## Validation of the lubrication force model

In the considered cases particle-particle interactions have by far more impact than particle-wall interactions. Therefore, also the validation test-case focused on particle-particle interaction: a sphere was fixed at a specific position while another sphere was released “directly” above it, with different initial velocities and for different fluid viscosities.

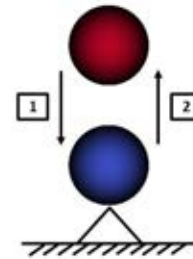


**Figure 1:** Basic test case for the validation of the lubrication force model.

During the simulation, the velocity of the moving particle was measured right before and after the collision. The velocity before the impact,  $v_1$ , was used to calculate the Stokes number as following (cf., e.g. Tomac (2013)):

$$St = \frac{m v_1}{6 \pi \mu r^2}. \quad (7)$$

The coefficient of restitution was determined as

$$c_{\text{rest}} = \frac{v_2}{v_1}. \quad (8)$$

In the diagram in Fig. 2 the coefficients of restitution for different fluid viscosities are displayed over the according Stokes numbers. The results of the implemented model are compared to values presented by Zhang et al. (2005) and by Tomac and Gutierrez (2013), a good accordance could be obtained.

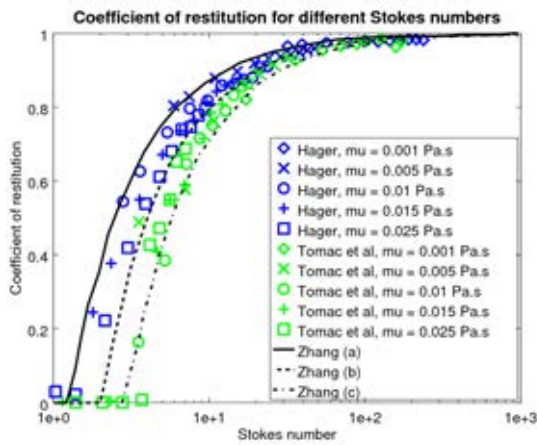


Figure 2: Validation of the lubrication force model.

### Depiction of dilatancy

The qualitative test for demonstrating the capability of depicting dilatancy was the following: three packings with the same volume but of different volume fractions were generated (0.75, 0.80, 0.85), the packings consisted of about 3000 particles. For keeping the particle packing in place, fixed side walls were chosen, while the upper and the lower wall were moving: for the top wall a so-called servo wall was used that exerted a constant pressure force on the bed, while the lower wall was moved horizontally. The force of the servo wall was chosen such that the particle bed was at an equilibrium at the beginning of the test.

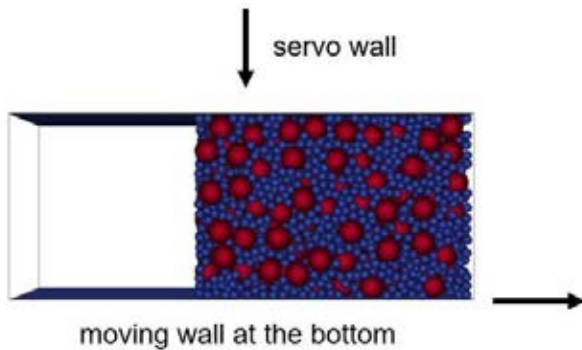


Figure 3: Setup of the dilatancy test case.

As soon as the motion of the lower wall started, the particles started to re-arrange and thus expand. The expansion showed in a lifting of the top plate, increasing with increasing initial volume fraction (cf. Fig. 4).

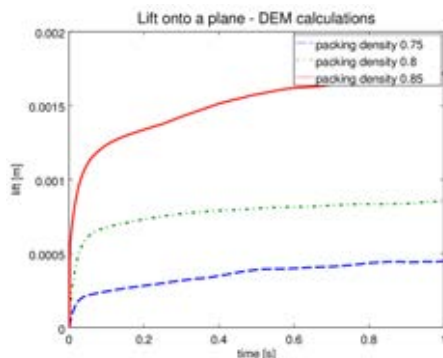


Figure 4: Displacement of the upper wall for different packing densities.

With this simple test the ability to depict dilatancy could be shown.

## FORMATION OF UNDER WATER SLOPES

When extracting sand and gravel from under-water regions one often uses suction dredgers. In this process pumps deliver sand/gravel and water mixtures. Grabe (2005) presented a detailed small-scale experimental study of the effect of grab dredging onto the formation of an under-water slope. The material used in the experiments was described as sand with a critical angle of friction of  $34^\circ$ .

### Material calibration

Accurate simulations require detailed knowledge of the used material. The material parameters can be divided in two groups: Some quantities can be measured directly, like for example density, grain size distribution or the volume fraction, while the set of model parameters needs to be determined otherwise. These describe the physical behaviour of the bulk material. Examples are the coefficient of friction and the coefficient of rolling friction. For obtaining these coefficients, a set of three well-established calibration experiments and simulations was conducted:

#### 1. The shear cell test

The coefficient of friction between the particles can be determined with a shear cell. For the experiments Jenike shear testers with cylinder diameters of about 10 cm were used. These devices consist of an upper and a lower hollow cylinder which are filled with the granular material. One of these cylinders is fixed, the other one can be displaced linearly in horizontal direction. For the tests a weight is placed on top of the granular material (exerting a normal force) and the non-fixed cylinder is moved slowly in horizontal direction. The resulting shear stress is measured and compared to the shear stresses obtained by the ring shear cell test in the simulation.



Figure 5: Calibrating the particle-particle coefficient of friction with shear cell experiments and simulations.

#### 2. Inclined plate

This experiment serves the purpose of determining the coefficient of rolling/sliding friction between particles and a wall. A small sample of grains is placed on a plate which is then inclined gradually. From a certain inclination (target angle) particles start to roll or slide down the plate, depending on whether the sliding or rolling friction is stronger.



Figure 6: Inclined plate test.

In the simulation particles are placed on a horizontal plate and the gravity vector is chosen such that the target angle is obtained. One then looks for the smallest coefficient of rolling friction, for which the particles are at rest (cf., Fig. 7).

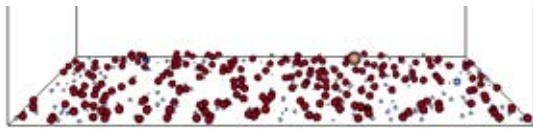


Figure 7: Simulation of the inclined plate test.

### 3. Angle of repose

The angle of repose experiment is used to determine the particle-particle coefficient of rolling friction. The setup used for the test is the following: a hollow cylinder is placed on an elevated circular plate with the same diameter as the cylinder. The cylinder is filled with granular material and the lifted slowly and uniformly, which leads to the formation of a conical heap. In the simulation the coefficient of rolling friction is varied until the angle of the cone matches the result of the experiment (cf., Fig. 8).

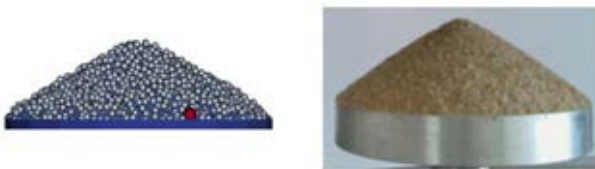


Figure 8: The particle-particle coefficient of rolling friction dominates the formation of the angle of repose.

The grain size distribution was identified by sieving, the average coefficient of restitution was determined with drop tests.

### Simulation setup

As the experiment was carried out in a small scale it was possible to simulate the process at original scale. A slope with an inclination angle of  $30^\circ$  (smaller than the critical angle) was generated (cf., Fig. 9). The simulation domain had a length of 40 cm and a height of 25 cm. The maximal height of the particle bed was 20 cm. For reducing the number of particles in the simulation domain periodic boundary conditions were used for the front and back wall both on the CFD and the DEM side. The complete set of velocity and pressure boundary conditions is summed up in Table 1. The bed was initialized with a pure DEM calculation.

	velocity (U, m/s)	pressure (p, Pa)
top	zeroGradient	fixedValue (0)
bottom	fixedValue (0,0,0)	zeroGradient
front/back	cyclic	cyclic
left wall	fixedValue, (0,0,0)	zeroGradient
right wall	zeroGradient	fixedValue (0)

Table 1: Velocity and pressure boundary conditions for the CFD calculation.

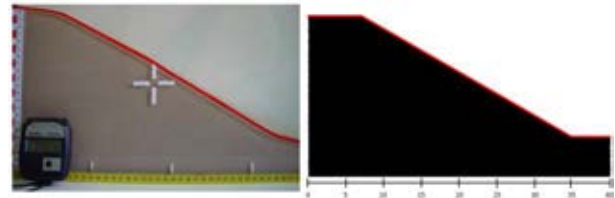


Figure 9: Initial slope (experiment vs. simulation)

In the current investigation, the focus lay on the formation of the slope after the extraction of the particles, thus the particles were removed at once in the simulation (cf., Fig. 10).

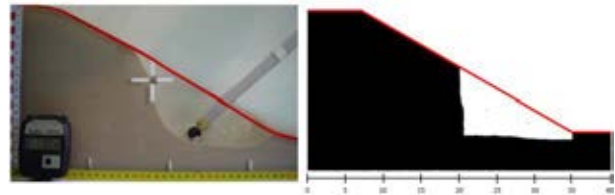


Figure 10: Slope after suction dredging is completed.

### Results

After the removal of the particles in the dredging region the coupled CFD-DEM calculation was launched and the settling process started. In Fig. 11 two images of unstable slopes during the settling process in experiment and simulation are compared.

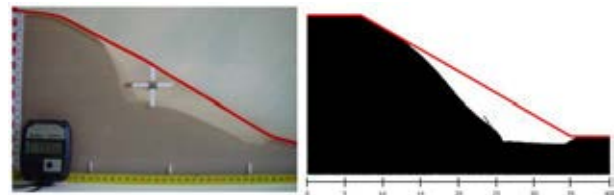


Figure 11: Slope during settling process (unstable).

It can be observed that while the reformation of the slope is ongoing, it develops slightly different in simulation and experiment. Furthermore, the time scale is smaller in the simulation, i.e. the changes of the slope occur faster. This difference could stem from an under-representation of the pore pressure in the simulation, but will be subject to future investigations as well. However, as can be seen in Fig. 12, in both cases the resulting final slope has an inclination of about  $34^\circ$ , which is the critical angle of the sand used.

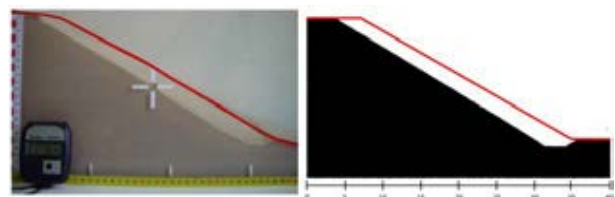
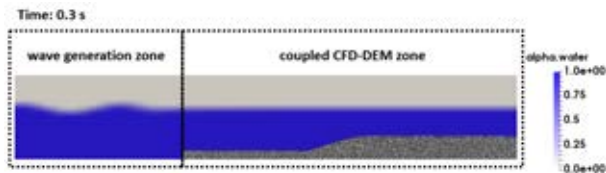


Figure 12: Final slope.

### WAVE INDUCED DISTURBANCES

The purpose of this application example was to show the feasibility of combining a three-phase solver (two-phase fluid and particles) with the wave generation toolbox

waves2foam (cf., Jacobsen et al. (2011)). waves2foam uses a zone in which the waves are generated. For making sure that the manipulations of the equations due to wave generation and those due to the presence of a granular phase do not interfere, a separate wave generation zone without particles was used (cf., Fig. 13). The granular material used for these calculations were 3mm glass beads, their properties were determined as described in the previous section. The total length of the CFD domain was 1.2 m, whereas the first 0.4 m were used as wave generation zone. The height of the domain was 0.2 m and due to the application of periodic boundary conditions a domain depth of 0.05 m could be used.



**Figure 13:** The waves were generated in a zone without particles.

As can be seen in Fig. 14 the waves propagate through the whole domain, their shape is influenced by the ascending sea bed.

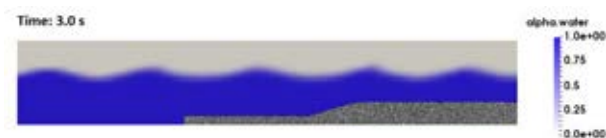


**Figure 14:** The waves propagate through the whole domain; the particle bed influences their shape.

When considering the force which the fluid exerts on the particle bed (here termed as drag force), the influence of the waves onto the soil becomes visible (cf. Fig. 15). The higher/lower force values onto the particles are in direct relation with the fluid pressure field  $\rho_{rgh}$  (total pressure minus hydrostatic pressure): it is lower underneath wave troughs and higher in wave crest areas and acts similar as a lift force.

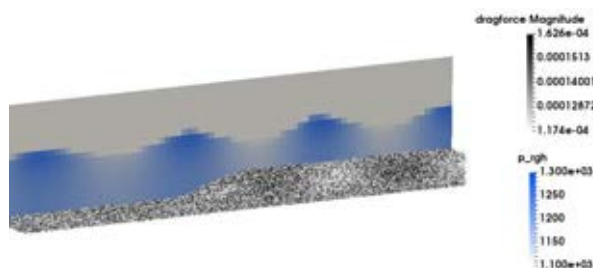


**Figure 15:** underneath the wave troughs the drag force onto the particles is increased while it is decreased underneath the wave crests.

These calculations showed that it is possible to apply wave boundary conditions to three phase problems within CFDEM@coupling. The observed behaviour matches the expectations and future experiments will be used for validation.

## CONCLUSION AND OUTLOOK

A lubrication force model was implemented and validated and it was demonstrated that dilatancy can be depicted. The simulation of a suction dredging case was in good accordance with the experiments. Furthermore, the feasibility and plausibility of the combination of a three-phase solver and the toolbox waves2foam was shown by a small-scale test case, experiments for validating the new solver are planned.

## ACKNOWLEDGEMENTS

The authors are grateful to the Austrian Science Fund (FWF) for supporting this research under project I 2257 (DACH project).

## REFERENCES

- GONIVA, C., KLOSS, C., KUIPERS, J.A.M. and PIRKER, S., (2012), "Influence of rolling friction modelling on single spout fluidized bed simulations", *Particuology*, **10** (5), 582-591.
- GRABE, J., (2005), "Phänomene an der Grenzschicht zwischen Wasser und Boden", *Grenzschicht Wasser und Boden – Phänomene und Ansätze, Veröffentlichungen des Instituts für Geotechnik und Baubetrieb der TU Hamburg-Harburg*, **9**, 3-30.
- JACOBSEN, N.G., FUHRMAN, D.R. and FREDSSØE, J., (2011), "A wave generation toolbox for the open-source CFD library: OpenFOAM®", *Int. J. Numer. Meth. Fluids*, **70** (9), 1073-1088.
- KLOSS, C., GONIVA, C., HAGER, A., AMBERGER, S. and PIRKER, S., (2012), "Models, algorithms and validation for opensource DEM and CFD-DEM", *Prog. Comput. Fluid. Dy., An. Int. J.* 2012, **12** (2/3), 140-152.
- KOCH, I. and HILL, R.J., (2001), "Inertial effects in suspension and porous-media flows", *Ann. Rev. of Fluid Mechanics*, **33**, 619-647.
- OpenCFD Ltd., (2004-2017), "OpenFOAM – The Open Source CFD-toolbox", URL: [www.openfoam.com](http://www.openfoam.com).
- SUN, R. and XIAO, H., (2016), "SediFOAM: A general-purpose, open-source CFD-DEM solver for particle-laden flow with emphasis on sediment transport", *Comput. Geosci.*, **89**, 207-219.
- TAESERI, D., LAUE, J., OTSUBO, M. and TOWHATA, I., (2016), "New mitigation method for pipeline uplift during seismic event", *Geotechnical Research*, **3** (2), 54-64.
- TOMAC, I. and GUTIERREZ, M., (2013), "Discrete element modelling of non-linear submerged particle collisions", *Granul. Matter*, **15**, 759-769.
- ZHANG, W., NODA, R. and HORIO, M., (2005), "Evaluation of lubrication force on colliding particles for DEM simulation of fluidized beds", *Powder Technol.*, **158**, 92-101.
- ZHOU, Z.Y., KUANG, S.B., CHU, K.W. and YU, A.B., (2010), "Discrete particle simulation of particle-fluid flow: model formulations and their applicability", *J. Fluid Mech.*, **661**, 482-510.



## INFLUENCE OF THE UPSTREAM CYLINDER AND WAVE BREAKING POINT ON THE BREAKING WAVE FORCES ON THE DOWNSTREAM CYLINDER

Arun KAMATH<sup>1\*</sup>, Mayilvahanan ALAGAN CHELLA<sup>1†</sup>, Hans BIHS<sup>1‡</sup>, Øivind A. ARNTSEN<sup>1§</sup>

<sup>1</sup>NTNU Department of Civil and Transport Engineering, 7491 Trondheim, NORWAY

\* E-mail: arun.kamath@ntnu.no

† E-mail: acm@ntnu.no

‡ E-mail: hans.bihs@ntnu.no

§ E-mail: oivind.arntsen@ntnu.no

### ABSTRACT

The interaction of breaking waves with marine structures involves complex free surface deformation and instantaneous loading on the structural members. A typical offshore platform or a coastal structure consists of several vertical and horizontal members exposed to breaking wave action. The breaking wave hydrodynamics and the effect of neighbouring cylinders on multiple cylinders placed in near vicinity is important due to force amplification or reduction resulting from interaction between the cylinders. The kinematics of breaking waves and the hydrodynamics of breaking wave interaction with a single vertical cylinder have been studied in detail in current literature. Studies have established that the location of a cylinder with respect to the wave breaking point has a major influence on the breaking wave forces on the cylinder. These studies have to be extended to investigate the hydrodynamics of cylinders placed close to each other to understand the modifications in the force regime due to the presence of neighbouring cylinders under a breaking wave regime.

In this paper, the open-source Computational Fluid Dynamics (CFD) model REEF3D is used to simulate breaking wave interaction with a pair of tandem cylinders. The focus of the study is on the location of the wave breaking point with respect to the upstream cylinder and the consequences for the downstream cylinder. The free surface features associated with the incident breaking wave and the evolution of the free surface after interaction with the upstream cylinder are investigated. The overturning wave crest and the associated free surface deformation have a major influence on the wave that is then incident on the downstream cylinder. The development of a downstream jet behind the upstream cylinder leads to the negation of the shadowing effect on the downstream cylinder. This can lead to an unexpected higher force on the downstream cylinder. The evolution of this downstream jet and the extent of this phenomenon changes the character of the otherwise shadow region behind the upstream cylinder. A detailed understanding of this phenomenon can provide new insights into the wave hydrodynamics related to multiple cylinders placed in close vicinity under a breaking wave regime. The knowledge regarding force amplification or reduction on downstream cylinders will aid in designing a safer and reliable substructure for marine installations.

**Keywords:** CFD, hydrodynamics, breaking wave, wave force, tandem cylinders .

### NOMENCLATURE

#### Greek Symbols

$\Gamma$  Relaxation function,  $\Gamma$

$\rho$  Fluid density,  $[kg/m^3]$   
 $\nu$  Kinematic viscosity,  $[m^2/s]$   
 $\nu_t$  Eddy viscosity,  $[m^2/s]$   
 $\omega$  Specific turbulent dissipation rate,  $[1/s]$   
 $\Omega$  Surface of object,  $[m^2]$   
 $\phi(\vec{x}, t)$  Level set function,  $[m]$   
 $\eta$  Free surface elevation,  $[m]$   
 $\tau$  viscous shear stress tensor,  $[N/m^2]$

#### Latin Symbols

$d$  still water level,  $[m]$ .  
 $p$  Pressure,  $[Pa]$ .  
 $g$  Acceleration due to gravity,  $[m/s^2]$ .  
 $D$  Cylinder diameter,  $[m]$ .  
 $F$  Total force,  $[N]$ .  
 $H$  Wave height,  $[m]$ .  
 $S$  centre to centre separation distance between the cylinders,  $[m]$ .  
 $T$  Wave period,  $[s]$ .  
 $U$  time-averaged velocity,  $[m/s]$ .

#### Sub/superscripts

$i$  Index  $i$ .  
 $j$  Index  $j$ .

### INTRODUCTION

Simulating the propagation and interaction of breaking waves produced by reducing water depth presents challenges due to the complex physical processes involved, with highly non-linear interactions and rapid variations in the free surface. Several numerical investigations have attempted to model wave breaking over plane slopes such as Lin and Liu (1998); Zhao *et al.* (2004); ALAGAN CHELLA *et al.* (2015a). With the help of these studies, detailed information about breaking wave characteristics and the geometric properties of breaking waves under different incident conditions and bottom slope have been obtained. The empirical coefficients used for the evaluation of breaking wave forces in other structural models and design considerations are determined using the breaking wave parameters quantified by these studies. With the advances in computational modelling and with the establishment of CFD models that can represent the breaking process in a satisfactory manner, breaking wave forces on structures can be calculated. In current literature, Bredmose and Jacobsen (2010) present breaking



wave impact forces due to focussed waves with the JoN-SWAP wave spectrum for input and carried out computations for half the domain assuming lateral symmetry of the problem using OpenFOAM. Mo *et al.* (2013) measured and modelled solitary wave breaking and its interaction with a slender cylinder over a plane slope for a single case using the filtered Navier-Stokes equations with large eddy simulation (LES) turbulence modelling. Choi *et al.* (2015) investigated breaking wave impact forces on a vertical cylinder and two cases of inclined cylinders for one incident wave using the modified Navier-Stokes equations with the volume of fluid (VOF) method for interface capturing to study the dynamic amplification factor due to structural response. These investigations present results for breaking wave interaction with a single cylinder, while breaking wave forces on tandem cylinders, the effect of neighbouring cylinders on the breaking wave forces on the cylinders along with the complex free surface deformations associated with the interaction are not presented in detail.

In the current study, the open source CFD model REEF3D (Bihs *et al.*, 2016) is used to simulate periodic breaking wave forces on tandem cylinders in a three-dimensional wave tank without assuming lateral symmetry. The model has been previously used to simulate the wave breaking process under different conditions (ALAGAN CHELLA *et al.*, 2015b,c) and the wave breaking kinematics were fully represented including the motion of the jet, air pocket formation and the reconnection of the jet with the preceding wave trough. Following the work presented in (Kamath *et al.*, 2016), the effect of breaker location and the upstream cylinder on the wave forces on a second cylinder placed downstream in tandem is investigated.

## MODEL DESCRIPTION

### Governing Equations

In the numerical wave tank REEF3D, the incompressible three-dimensional Reynolds-Averaged Navier-Stokes (RANS) equations are solved in conjunction with the continuity equation:

$$\frac{\partial U_i}{\partial x_i} = 0 \quad (1)$$

$$\frac{\partial U_i}{\partial t} + U_j \frac{\partial U_i}{\partial x_j} = -\frac{1}{\rho} \frac{\partial p}{\partial x_i} + \frac{\partial}{\partial x_j} \left[ (\nu + \nu_t) \left( \frac{\partial U_i}{\partial x_j} + \frac{\partial U_j}{\partial x_i} \right) \right] + g_i \quad (2)$$

where  $U$  is the velocity,  $\rho$  is the density of the fluid,  $p$  is the pressure,  $\nu$  is the kinematic viscosity,  $\nu_t$  is the eddy viscosity and  $g$  the acceleration due to gravity.

### Discretisation Schemes

The convective terms of the RANS equations are discretised using the fifth-order conservative finite difference Weighted Essentially Non-Oscillatory (WENO) scheme (Jiang and Shu, 1996) and time advancement is carried out using a Total Variation Diminishing (TVD) third-order Runge-Kutta explicit time scheme (Shu and Osher, 1988). The CFL criterion is used in an adaptive time stepping algorithm to determine the optimal time step for each step in the simulation. An implicit time scheme is used for diffusion to remove it from the CFL criterion. The projection method (Chorin, 1968) is applied for pressure treatment and the Poisson pressure equation is solved with a PFMG preconditioned (Ashby and Flagout, 1996) BiCGStab solver (van der Vorst, 1992) from

the high performance solver library HYPRE (hyp, 2015). The code is parallelised using the MPI (Message Passing Interface) framework. A staggered Cartesian grid is employed in the model and complex geometries are accounted for using the ghost cell immersed boundary method

### Free surface and Turbulence modelling

The two equation  $k$ - $\omega$  model is employed for turbulence closure (Wilcox, 1994) along with eddy viscosity limiters (Durbin, 2009) and a free surface turbulence damping scheme (Naot and Rodi, 1982). The hydrodynamics are modelled in a two-phase flow approach, calculating the flow for both water and air. The level set method (Osher and Sethian, 1988) captures the interface between the two fluids. (Berthelsen and Faltinsen, 2008). Further details regarding the numerical model REEF3D can be obtained in Bihs *et al.* (2016).

### Numerical Wave Tank

The numerical model is used as a numerical wave tank to model and calculate wave hydrodynamics. Waves are generated on one end of the tank using the relaxation method (Larsen and Dancy, 1983) with the relaxation functions presented by Jacobsen *et al.* (2012). The velocity and the free surface in the relaxation generation zone is modulated as follows:

$$\begin{aligned} U_{relaxed} &= \Gamma(x)u_{analytical} + (1 - \Gamma(x))u_{computational} \\ \phi_{relaxed} &= \Gamma(x)\phi_{analytical} + (1 - \Gamma(x))\phi_{computational} \end{aligned} \quad (3)$$

where  $\Gamma(x)$  is a relaxation function and  $x \in [0, 1]$  is the  $x$ -coordinate scaled to the length of the relaxation zone. The relaxation function shown in Eq. (4) is used in the current numerical model (Jacobsen *et al.*, 2012):

$$\Gamma(x) = 1 - \frac{e^{(1-x)^{3.5}} - 1}{e - 1} \quad (4)$$

The generation zone is generally one wavelength long and is not considered an active part of the numerical wave tank. A similar relaxation zone can be defined to absorb all the wave energy at the other end of the tank, the numerical beach. In the current model, in order to reduce the size of the computational domain, an active wave absorption method is employed. At the downstream boundary, waves opposite to the reflected waves are generated, achieving a net cancellation of the wave energy at the end of the domain. A horizontal velocity following the shallow water theory is prescribed (Schäffer and Klopman, 2000) on the downstream boundary.

$$U(t) = -\sqrt{\frac{g}{d}} \xi(t) \quad (5)$$

$$\xi(t) = \eta(t) - d \quad (6)$$

Here,  $\eta(t)$  is the actual free surface location along the downstream boundary and  $d$  the water depth.

### Numerical evaluation of wave forces

The total breaking wave forces on a cylinder are calculated by integrating the pressure  $p$  and the surface normal component of the viscous shear stress tensor  $\tau$  on the surface of the solid objects as follows:

$$F = \int_{\Omega} (-n p + n \cdot \tau) d\Omega \quad (7)$$

where  $\mathbf{n}$  is the unit normal vector pointing into the fluid and  $\Omega$  is the surface of the object.

## RESULTS

### Validation: Breaking wave force on a single cylinder

The breaking wave forces on a single vertical cylinder are calculated and compared to experimental data from the experiments were carried out at the Large Wave Flume (GWK), Hannover, Germany (Irschik *et al.*, 2002). The cylinder has a diameter  $D = 0.7$  m, placed in a water depth of  $d = 3.80$  m. Regular waves of period  $T = 4.0$  s and height  $H = 1.30$  m are incident on the cylinder that is placed at the crest of a 23 m long 1 : 10 slope. The still water depth at the cylinder is  $d = 1.50$  m in the experimental setup.

In the numerical setup the wave tank is 56 m long, 5 m wide and 7 m high. A grid size of  $dx = 0.05$  m is used, resulting in a total of 15.68 million cells. A cylinder with  $D = 0.7$  m is placed at the crest of a 23 m long 1 : 10 slope, with its centre at 44.0 m with the incident waves of period  $T = 4.0$  s breaking exactly on the front surface of the cylinder. The numerical setup is illustrated in Fig. (1), where except for the total length of the tank, the other conditions are similar to the experimental setup. Further details regarding the numerical setup can be obtained in Kamath *et al.* (2016).

The numerically calculated wave force is compared to the EMD (Empirical Mode Decomposition) treated experimental data from Choi *et al.* (2015) to filter out the dynamic amplification of the wave forces due to the vibration of the cylinder in Fig. (2). A good agreement is seen between the numerical and experimental breaking wave forces on a single vertical cylinder.

### Breaking wave force on tandem cylinders

The breaking wave interaction with a single vertical cylinder results in several distinct free surface features such as the separation of the breaking wavefront around the cylinder, the subsequent meeting of the separated wave front and the formation of a water jet downstream of the cylinder. These features have been presented and discussed by Kamath *et al.* (2016). Here, the effect of the free surfaces features from breaking wave interaction with the upstream cylinder on the hydrodynamics of a cylinder placed downstream is studied in different scenarios: when the wave breaking point is on the surface of the upstream cylinder and when the wave breaking point is just behind the upstream cylinder. For each of the breaking scenarios, the distance between the two cylinders is varied and the effect on the breaking wave forces on the downstream cylinder is investigated.

#### *Breaking point on the front surface of the upstream cylinder*

In this scenario, the wave breaking point is on the surface of the upstream cylinder and the downstream cylinder is placed at distances of  $S = 1D, 2D, 3D, 4D$  and  $5D$  from the upstream cylinder. The breaking wave force on a single cylinder in this scenario is 13900 N. The variation of the total breaking wave force on the downstream cylinder with the distance of the downstream cylinder from the upstream cylinder is presented in Fig. (3).

The wave force on the downstream cylinder is seen to increase as the distance between the cylinders is increased from  $S = 1D$  to  $3D$ . At a centre-to-centre distance of  $S = 3D$ , the force on the downstream cylinder is seen to be the maximum under this scenario of wave impact. A further increase in

the distance between the cylinders results in a decrease in the total breaking wave force. At a centre-to-centre distance of  $S = 5D$ , the total breaking wave force on the downstream cylinder is similar to that at  $S = 1D$ .

The variation of the total breaking wave forces on the downstream cylinder is a consequence of the free surface features associated with the breaking wave interaction with the upstream cylinder and the resulting wave incident on the downstream cylinder. The downstream cylinder is within the shadow region of the upstream cylinder at a separation distance of  $S = 1D$ . Here, the overturning wave crest incident on the upstream cylinder with a vertical wavefront gets separated around the upstream cylinder. The downstream cylinder is then in the shadow zone and impacted by a smaller mass of water compared to the upstream cylinder. This leads to smaller breaking wave forces on the downstream cylinder. As the separation distance is increased, the downstream cylinder moves out side the shadow region. The cylinder is then impacted by a larger mass of water formed by the rejoining of the separated wavefront, downstream of the first cylinder. This results in increasing total breaking wave forces on the downstream cylinder, with a maximum seen for  $S = 3D$ .

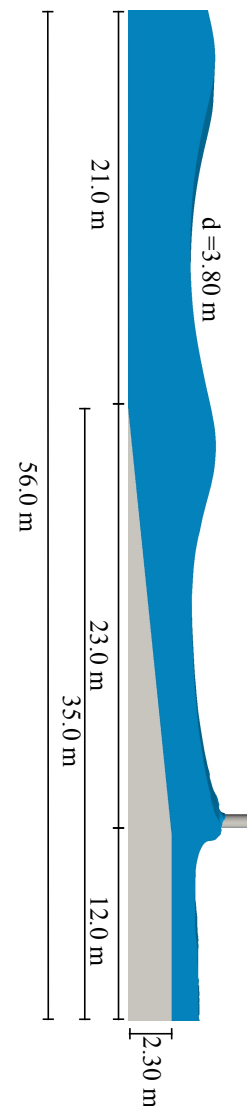


**Figure 1:** Numerical setup used for investigate breaking wave forces on a cylinder

As the separation distance is further increased beyond  $S = 3D$ , the downstream cylinder is outside the shadow region, but now impacted by the splash up from the overturned wave crest. With increasing distance from this point onwards, the total breaking wave force on the downstream cylinder is reduced.

The free surface features associated with breaking wave interaction with a pair of tandem cylinders placed with a separation distance  $S = 2D$  is presented in Fig. (4). The incident wave on the upstream cylinder, impacting the cylinder with a vertical wave front crest is seen in Fig. (4a). The separation of the wavefront around the upstream cylinder as the incident wave crest begins to overturn is shown in Fig. (4b). The downstream cylinder is in the shadow zone in Fig. (4c), where the overturning wave crest impacts the cylinder with significantly smaller mass of water due to the separation of the wavefront around the upstream cylinder. Fig. (4d) shows the overturned wave crest after it passes the downstream cylinder and the runup on the downstream cylinder due to the water jet formed behind the upstream cylinder.

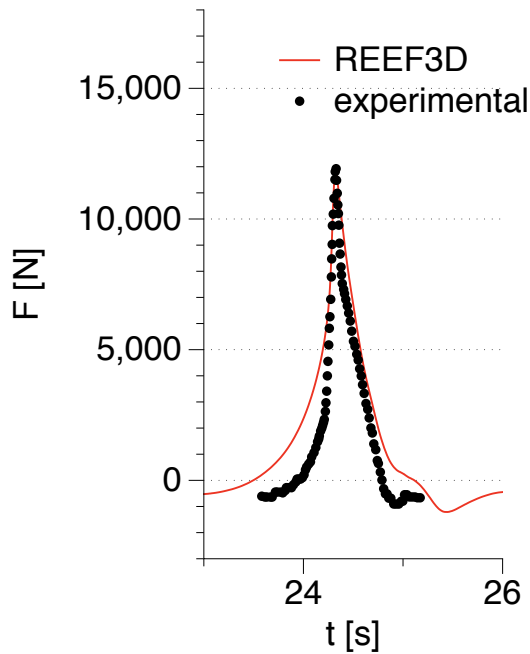


**Figure 2:** Comparison on numerical and experimental breaking wave forces on the single cylinder

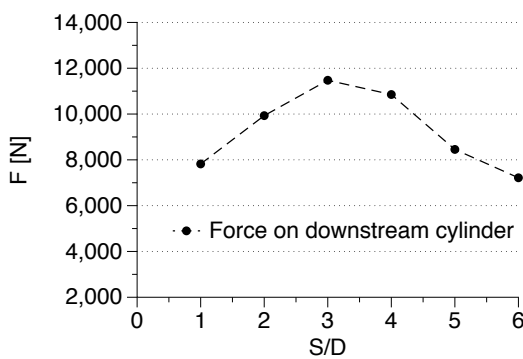


**Figure 3:** Variation of the breaking wave forces on the downstream cylinder with increasing distance from the upstream cylinder when the wave breaks on the surface of the upstream cylinder

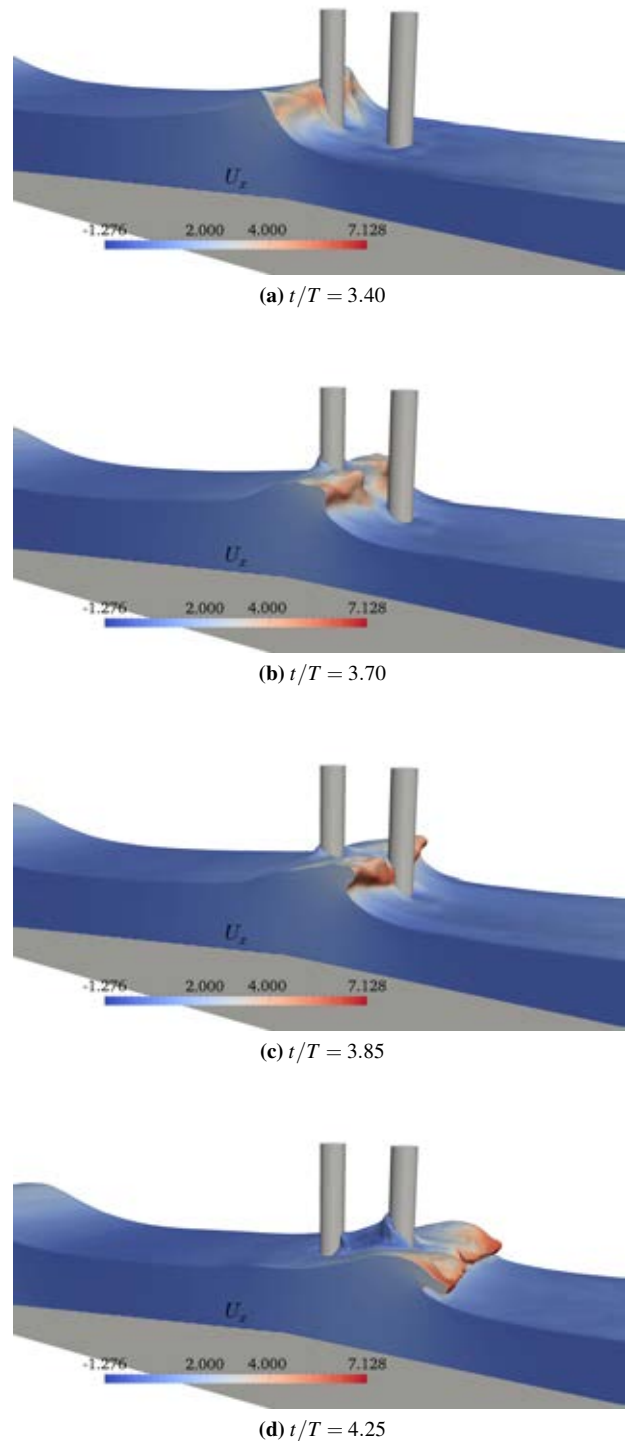


**Figure 4:** Breaking wave interaction with tandem cylinders placed with a distance of  $2D$  between their centers, with the wave breaking point on the surface of the upstream cylinder

At a separation distance of  $S = 4D$ , the downstream cylinder is outside the shadow region of the upstream cylinder. The vertical incident wave crest front on the upstream cylinder in this case is presented in Fig. (5a). The separation of the overturning wave crest around the upstream cylinder and the development of the plunger are seen in Figs. (5b) and (5c) respectively. Fig. (5d) shows the impact of the overturned wave crest on the downstream cylinder. The downstream cylinder is outside the shadow region behind the upstream cylinder, but is impacted by the plunger before it reconnects with the

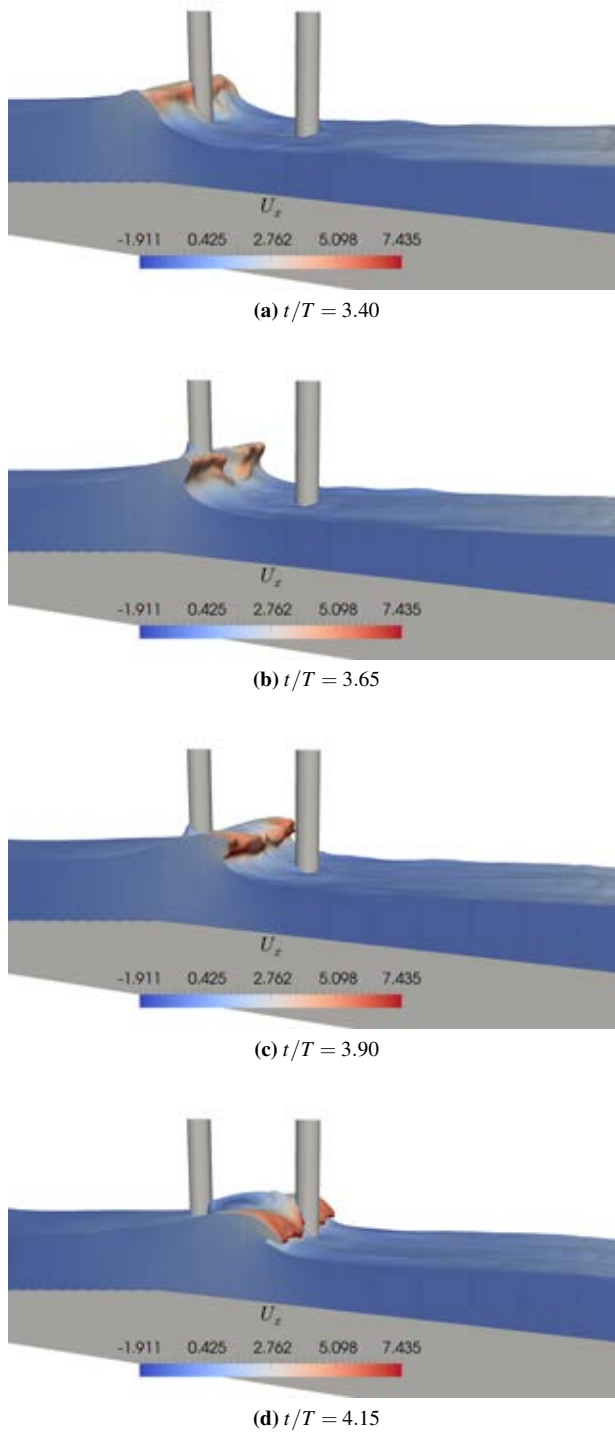


**Figure 5:** Breaking wave interaction with tandem cylinders placed with a distance of  $4D$  between their centres, with the wave breaking point on the surface of the upstream cylinder

preceding wave crest. While the breaking wave forces on the downstream cylinder in this case are lower than than for  $S = 3D$ , they are higher than for  $S = 1D$  and  $2D$ . In the case of  $S = 3D$ , the plunger would impact the cylinder just under the wave crest level and thus result in the highest wave force on the cylinder in this scenario of wave impact, following Irschik *et al.* (2002), Irschik *et al.* (2004) and Kamath *et al.* (2016).

*Breaking point behind the upstream cylinder*

In this scenario, the wave breaking point is just behind the upstream cylinder and the downstream cylinder is placed at distances of  $1D$ ,  $2D$ ,  $3D$ ,  $4D$  and  $5D$  from the upstream cylinder. The breaking wave force on a single cylinder in this scenario is  $9800$  N. Fig. (6) shows the variation of the total breaking wave forces on the downstream cylinder with the distance between the two cylinders in this scenario. In this scenario of wave impact, the total breaking wave forces on the downstream cylinder are seen to increase with increasing separation distance  $S$ , until  $S = 5D$ . Further increase in  $S$  results in a reduction in the breaking wave force.

The variation of the total breaking wave force on the downstream cylinder seen in Fig. (6) is justified as follows. As the wave breaking point is behind the upstream cylinder, the downstream cylinder is effectively in direct exposure to the breaking wave impact. With increasing  $S$ , the downstream cylinder is placed in positions which result in higher total breaking wave forces. According to the results presented by Irschik *et al.* (2004) and Kamath *et al.* (2016), the total breaking wave forces on a single vertical cylinder are the highest when the overturning wave crest impact the cylinder just below the wave crest level followed by wave impact around crest level and vertical impact. From the results for breaking wave interaction with cylinders placed in tandem, similar conclusions can be drawn.

The breaking wave interaction with the tandem cylinders placed with a separation distance of  $S = 1D$  is presented in Fig. (7). The wave incident on the upstream cylinder is yet to obtain a vertical wave crest front in Fig. (7a). The incident wavefront is separated around the upstream cylinder and attains a vertical wave crest front profile just passing the cylinder in Fig. (7b). The impact of the overturning wave crest on the downstream cylinder is seen in Fig. (7c). Here, the impacting overturning wave crest is still separated and thus the wave impact on the downstream cylinder is by a lower mass of water, resulting in the lowest breaking wave forces in this scenario. The runoff on the downstream cylinder as the overturning wave crest passes the downstream cylinder is seen in Fig. (7d).

In the case of separation distance  $S = 5D$ , the total breaking wave forces on the downstream cylinder are the maximum in this scenario of breaking wave impact. Fig. (8a) shows the wave incident on the upstream cylinder which has not yet attained a vertical wave crest front. The incident wave is separated and attains a vertical wave crest front in

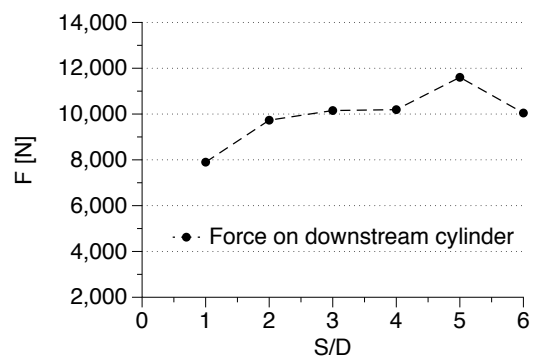


**Figure 6:** Variation of the breaking wave forces on the downstream cylinder with increasing distance from the upstream cylinder when the wave breaks just behind the upstream cylinder

Fig. (8b) as it passes the upstream cylinder. The overturning wave crest propagating between the two cylinders is seen in Fig. (8c). Finally, the impact of the overturning wave crest on the downstream cylinder, just below the wave crest level is seen in Fig. (8d). Thus, in this impact scenario where the wave breaking point is just behind the upstream cylinder, the wave forces on the downstream cylinder increase with increase in  $S$ , due to the cylinder moving away from the shadow zone and being exposed to the overturning wave crest under conditions of impact that result in higher total breaking wave forces.

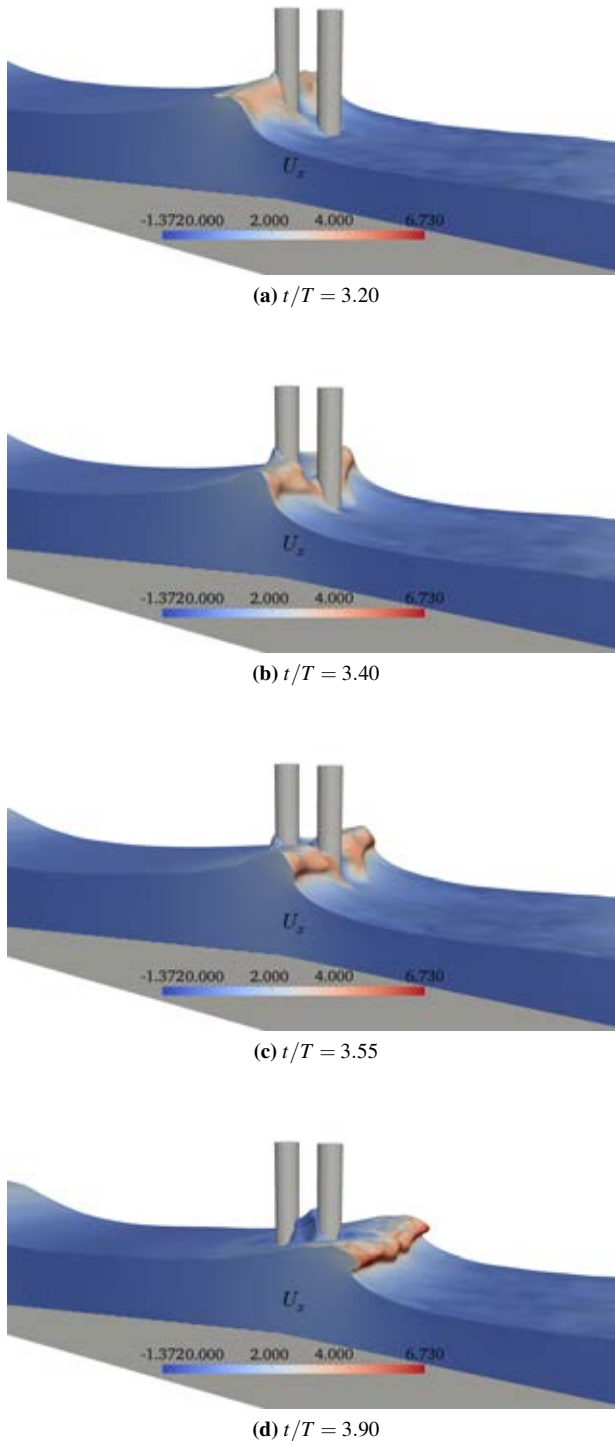


**Figure 7:** Breaking wave interaction with tandem cylinders placed with a distance of  $1D$  between their centers, with the wave breaking point just behind the upstream cylinder

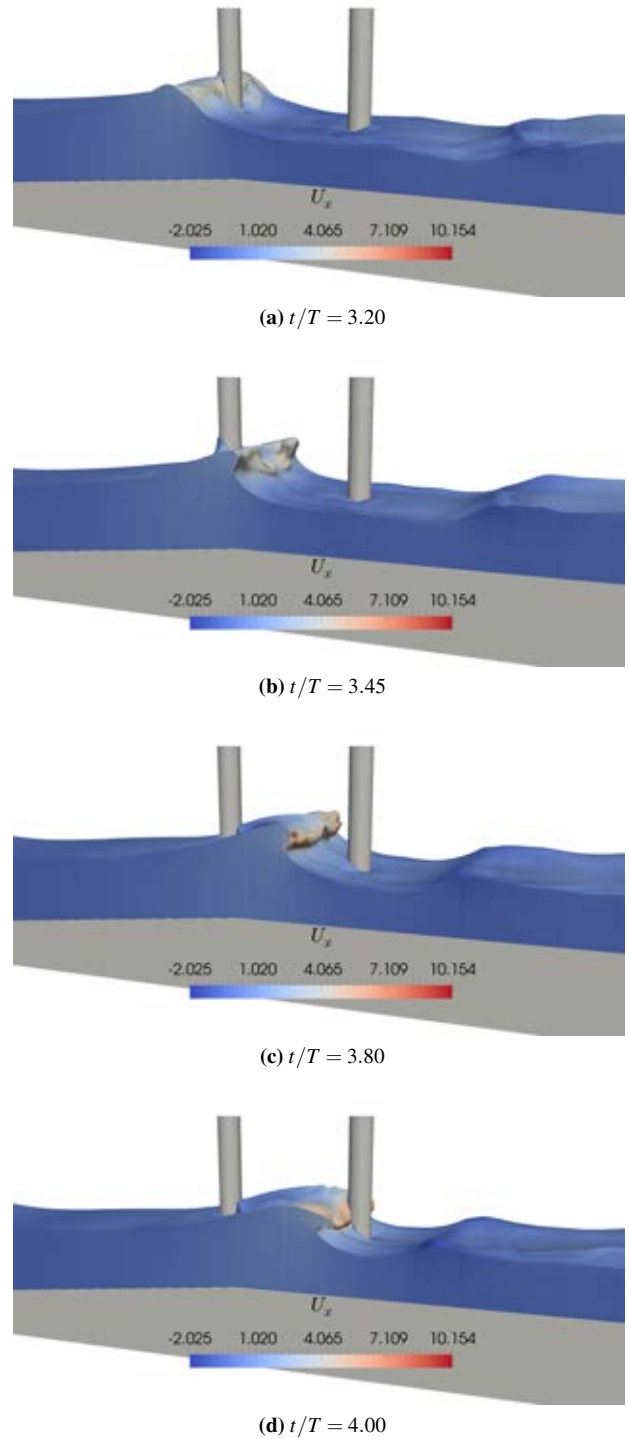


**Figure 8:** Breaking wave interaction with tandem cylinders placed with a distance of  $5D$  between their centres, with the wave breaking point just behind the upstream cylinder

**CONCLUSION**

The conclusions are:

1. Breaking wave forces on the downstream cylinder in a tandem arrangement follow a similar trend as that observed for a single cylinder, with maximum breaking wave forces calculated for the case where the overturning wave crest impacts the cylinder just below the wave crest level.
2. The free surface features due to breaking wave interaction with the upstream cylinder such as the separation of

the wavefront, rejoining of the separated wavefront and the formation of the water jet influence the wave forces on the downstream cylinder.

3. The shadow zone behind the upstream cylinder is less than  $3D$  for vertical wave crest impact on the upstream cylinder, while it is about  $1D$  for wave breaking just behind the upstream cylinder.
4. The breaking wave force on the downstream cylinder can be equal to or higher than the breaking wave force on a single cylinder under certain arrangements.

## REFERENCES

- (2015). *HYPRE high performance preconditioners - User's Manual*. Center for Applied Scientific Computing, Lawrence Livermore National Laboratory.
- ALAGAN CHELLA, M., BIHS, H., MYRHAUG, D. and MUSKULUS, M. (2015a). "Breaking characteristics and geometric properties of spilling breakers over slopes". *Coastal Engineering*, **95**, 4–19.
- ALAGAN CHELLA, M., BIHS, H. and MYRHAUG, D. (2015b). "Characteristics and profile asymmetry properties of waves breaking over an impermeable submerged reef". *Coastal Engineering*, **100**, 26–36.
- ALAGAN CHELLA, M., BIHS, H., MYRHAUG, D. and MUSKULUS, M. (2015c). "Hydrodynamic characteristics and geometric properties of plunging and spilling breakers over impermeable slopes". *Ocean Modelling, Virtual Special Issue: Ocean Surface Waves*, 1–20.
- ASHBY, S.F. and FLAGOUT, R.D. (1996). "A parallel multigrid preconditioned conjugate gradient algorithm for groundwater flow simulations". *Nuclear Science and Engineering*, **124**(1), 145–159.
- BERTHELSEN, P.A. and FALTINSEN, O.M. (2008). "A local directional ghost cell approach for incompressible viscous flow problems with irregular boundaries". *Journal of Computational Physics*, **227**, 4354–4397.
- BIHS, H., KAMATH, A., ALAGAN CHELLA, M., AGGARWAL, A. and ARNTSEN, Ø.A. (2016). "A new level set numerical wave tank with improved density interpolation for complex wave hydrodynamics". *Computers & Fluids*, **140**, 191–208.
- BREDMOSE, H. and JACOBSEN, N.G. (2010). "Breaking wave impacts on offshore wind turbine foundations: focused wave groups and CFD". *Proc., 29th International Conference on Ocean, Offshore and Arctic Engineering, Shanghai, China*.
- CHOI, S.J., LEE, K.H. and GUDMESTAD, O.T. (2015). "The effect of dynamic amplification due to a structure's vibration on breaking wave impact". *Ocean Engineering*, **96**, 8–20.
- CHORIN, A. (1968). "Numerical solution of the Navier-Stokes equations". *Mathematics of Computation*, **22**, 745–762.
- DURBIN, P.A. (2009). "Limiters and wall treatments in applied turbulence modeling". *Fluid Dynamics Research*, **41**, 1–18.
- IRSCHIK, K., SPARBOOM, U. and OUMERACI, H. (2002). "Breaking wave characteristics for the loading of a slender pile". *Proc. 28th International Conference on Coastal Engineering, Cardiff, Wales*.
- IRSCHIK, K., SPARBOOM, U. and OUMERACI, H. (2004). "Breaking wave loads on a slender pile in shallow water". *Proc. 29th International Conference on Coastal Engineering, Lisbon, Portugal*.
- JACOBSEN, N.G., FUHRMAN, D.R. and FREDSSØE, J. (2012). "A wave generation toolbox for the open-source CFD library: OpenFOAM". *International Journal for Numerical Methods in Fluids*, **70**(9), 1073–1088.
- JIANG, G.S. and SHU, C.W. (1996). "Efficient implementation of weighted ENO schemes". *Journal of Computational Physics*, **126**, 202–228.
- KAMATH, A., ALAGAN CHELLA, M., BIHS, H. and ARNTSEN, Ø.A. (2016). "Breaking wave interaction with a vertical cylinder and the effect of breaker location". *Ocean Engineering*, **128**, 105–115.
- LARSEN, J. and DANCY, H. (1983). "Open boundaries in short wave simulations - a new approach". *Coastal Engineering*, **7**, 285–297.
- LIN, P. and LIU, P.L.F. (1998). "A numerical study of breaking waves in the surf zone". *Journal of Fluid Mechanics*, **359**, 239–264.
- MO, W., JENSEN, A. and LIU, P.L.F. (2013). "Plunging solitary wave and its interaction with a slender cylinder on a sloping beach". *Ocean Engineering*, **74**, 48–60.
- NAOT, D. and RODI, W. (1982). "Calculation of secondary currents in channel flow". *Journal of the Hydraulic Division, ASCE*, **108**(8), 948–968.
- OSHER, S. and SETHIAN, J.A. (1988). "Fronts propagating with curvature-dependent speed: algorithms based on Hamilton-Jacobi formulations". *Journal of Computational Physics*, **79**, 12–49.
- SCHÄFFER, H.A. and KLOPMAN, G. (2000). "Review of multidirectional active wave absorption methods". *Journal of Waterway, Port, Coastal, and Ocean Engineering*, **126**(2), 88–97.
- SHU, C.W. and OSHER, S. (1988). "Efficient implementation of essentially non-oscillatory shock capturing schemes". *Journal of Computational Physics*, **77**, 439–471.
- VAN DER VORST, H. (1992). "BiCGStab: A fast and smoothly converging variant of Bi-CG for the solution of nonsymmetric linear systems". *SIAM Journal on Scientific and Statistical Computing*, **13**, 631–644.
- WILCOX, D.C. (1994). *Turbulence modeling for CFD*. DCW Industries Inc., La Canada, California.
- ZHAO, Q., ARMFIELD, S. and TANIMOTO, K. (2004). "Numerical simulation of breaking waves by a multi-scale turbulence model". *Coastal Engineering*, **51**(1), 53–80.



## RECENT DEVELOPMENTS FOR THE COMPUTATION OF THE NECESSARY SUBMERGENCE OF PUMP INTAKES WITH FREE SURFACES

Frank BLOEMELING\*, Ralf LAWALL

TUEV NORD EnSys GmbH & Co. KG, 22525 Hamburg, GERMANY

\* E-mail: fbloemeling@tuev-nord.de

### ABSTRACT

Swirling flow and gas entrainment induced by vortex formation at pump intakes are possible causes for pump failures and damages. Thus, the avoidance of hollow surface vortices is a safety-related issue for all plants which require a reliable pump operation.

The most efficient measure to avoid these problems is a sufficient submergence of the intake. An acceptable submergence can be determined by means of costly experiments, complex CFD calculations or special correlations. When using correlations their applicability for the specific case has to be taken into account carefully, because a universally applicable correlation is not available yet. Hence, there is a present need for improved correlations or numerical methods which are capable to compute the necessary submergence.

Within the research alliance SAVE experiments and numerical simulations were performed to investigate the occurrence of surface vortices at industrial scales. Amongst others, the lengths of the gas cores of the surface vortices were measured with varying boundary conditions and the velocity fields were determined by means of PIV (Particle Image Velocimetry) measurements. These experiments were accompanied by CFD simulations, the results were compared with the experimental data. A methodology was developed based on single phase CFD simulations with ANSYS CFX in combination with the Burgers-Rott vortex model which can be used to compute the gas core length with very good accuracy. Additionally, two phase CFD simulations were performed which use a free surface model based on recent developments.

In order to develop an improved correlation for the computation of the necessary submergence, which considers in particular the circulation in the approaching flow, several parameter studies were performed. As a result of these studies two new theoretical approaches for the limiting cases of very small and very large circulation were developed which yield new correlations for the computation of the necessary submergence of pump intakes.

**Keywords:** pump intake design, submergence, free surface flow, surface vortices.

### NOMENCLATURE

#### Greek Symbols

$\alpha$	Volume fraction, [m <sup>3</sup> /m <sup>3</sup> ].
$\gamma$	Interfacial area density, [1/m].
$\Gamma$	Circulation, [m <sup>2</sup> /s].
$\rho$	Mass density, [kg/m <sup>3</sup> ].
$\mu_{eff}$	Effective dynamic viscosity, [Pa s].
$\nu$	Kinematic viscosity, [m <sup>2</sup> /s].
$\Theta$	Interfacial mass transfer, [kg/(m <sup>3</sup> s)].
$\Psi$	Interfacial momentum transfer, [N/m <sup>3</sup> ].

#### Latin Symbols

$a$	Suction parameter, [1/s].
$C_D$	Drag coefficient, [-].
$d$	Suction pipe diameter, [m].
$d_V$	Vessel diameter, [Pa].
$F_D$	Drag force, [N/m <sup>3</sup> ].
$g, \mathbf{g}$	Gravity acceleration, [m/s <sup>2</sup> ].
$\mathbf{I}$	Identity matrix, [-].
$h$	Submergence, [m].
$l$	Gas core length, [m].
$M$	Mass flow rate, [kg/s].
$\mathbf{n}$	Surface normal vector, [-].
$p$	Pressure, [Pa].
$Q$	Volume flow rate, [m <sup>3</sup> /s].
$r$	Radial coordinate, [m].
$r_{max}$	Characteristic radius, [m].
$\mathbf{S}$	Mean strain-rate tensor, [1/s].
$t$	Time, [s].
$\mathbf{u}$	Velocity, [m/s].
$u$	Velocity in the suction pipe, [m/s].
$W$	Kinetic energy per unit time, [J/s].
$z$	Axial coordinate, [m].

#### Dimensionless numbers

$A$	Dimensionless suction parameter, [-].
$Fr$	Froude number, [-].
$H$	Dimensionless submergence, [-].
$L$	Dimensionless gas core length, [-].
$N$	Circulation number, [-].



$Re$  Reynolds number, [-].

#### Sub/superscripts

$g, l$  Gaseous and liquid phase, respectively.

$r$  Radial component.

$\theta$  Azimuthal component.

$crit$  Critical.

$ref$  Reference.

## INTRODUCTION

In many industrial applications a reliable operation of pumps is required. The applications range from the simple emptying of fluid tanks or tank ships over dewatering or wastewater applications to cooling in the nuclear industry. Depending on their intended use disturbances of the pumps may lead to consequences like production downtimes or even safety-relevant problems, if for instance cooling, fire-extinguishing or dewatering systems are affected.

Since gas entrainment and swirl caused by surface vortices at free surfaces are two main sources of possible pump problems, the occurrence of surface vortices should be prevented. The consequences of swirl and gas entrainment include for instance a decreased flow rate up to a complete blockage of the pump, vibrations, noise and mechanical damage. The most effective measure to avoid surface vortices is a sufficient submergence of the pump intake.

But the necessary submergence depends on several site specific parameters like the intake geometry, the flow rate or the circulation of the inflow. Therefore, a lot of work has been done and is still going on to provide methods to determine the necessary submergence of pump intakes. This includes the design of model experiments and the development of numerical methods as well as easy-to-use correlations.

Although several correlations are available, they are all linked with certain ranges of applicability or boundary conditions, respectively. For instance the American National Standard for pump intake design represented by the Hydraulic Institute recommends the so-called ANSI correlation (Hydraulic Institute, 2012). According to this standard this correlation is only applicable for cases with moderate circulation. A universally applicable and reliable correlation does not exist.

Therefore, the research alliance SAVE investigated the conditions for the occurrence and the shape of surface vortices. Amongst others, the aim was to improve existing design recommendations with particular consideration of the influence of circulation on the surface vortices.

For this purpose an industrial scale experimental facility was built at the Hamburg University of Technology (TUHH) (Szeliga, 2016). The experiments at this facility were used to develop and to validate numerical methods which are able to compute the onset and the shape of surface vortices. Furthermore, the results of the experiments and simulations were used to develop new correlations which can be applied for the determination of the necessary pump submergence.

In the following the experimental setup at the TUHH is presented first. The corresponding single and multi-phase CFD models are explained next. In the subse-

quent section a short overview of selected analytical vortex models is given. These vortex models are used in the following sections which start with the validation of the CFD models. In the next section a theoretical model is proposed which yields new correlations for the determination of the necessary submergence in the presence of strong circulation. Moreover, the new model is validated with available experimental data. Finally also a second model is proposed for the opposite case of very small circulation. This model is confirmed by different parameter studies. The paper closes with a summary and some conclusions.

## EXPERIMENTAL SETUP

Many experiments dealing with surface vortices were performed at small scale test facilities. In order to exclude scaling effects from the outset, a test facility was built at the TUHH that on one hand has typical industrial dimensions and on the other hand is flexible enough to allow the examination of all relevant parameters which affect the surface vortices. The test facility consists mainly of a large cylindrical vessel with 4 m diameter and 4 m height (see figure 1).

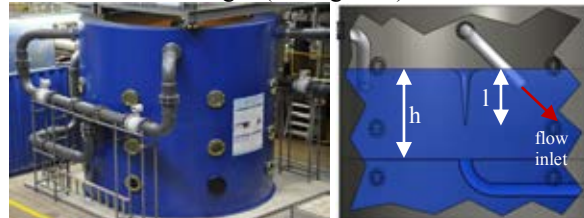


**Figure 1:** Test facility at the TUHH (left: exterior view; right: sketch of the interior) (Szeliga, 2016)

The water enters the test vessel via four adjustable DN200 inlet pipes. The water jets from these pipes generate an angular momentum, which causes a circulation that depends on the pipes' inclination. The pump suction intake is located at the centre of an intermediate floor. Its shape can be altered in order to examine the influence of the intake geometry. The basic configuration is a flush mounted suction pipe with 0.2 m inner diameter. Optical measurements are possible through small windows in the vessel. Due to the symmetrical setup different types of stable, hollow vortices can be generated in the centre of the vessel. The types range from swirl without any surface deformation to fully developed gas cores which reach into the suction line. Gas cores whose lengths equal exactly the submergence are of particular importance. They characterise the so-called critical submergence. Submergences lower than the critical one usually lead to continuous gas entrainment into the pump.

Among others, the gas core lengths as well as the tangential fluid velocities were measured during the experiments under varying boundary conditions.

## CFD MODELS

To numerically analyse the experiments different CFD models were set up with ANSYS CFX. First a single-phase model was built that simulates only the liquid phase. Compared to two-phase simulations this approach is much less computationally expensive. But a direct computation of a surface deformation is not pos-

sible by applying this kind of simulations. Therefore, additionally a two-phase model was developed that considers also the gaseous phase and is capable to track the water surface.

### Single-phase model

The single-phase model consists only of the liquid phase (water at 20° C). The geometry and the boundary conditions are shown in figure 2. Because of symmetry only a model of a quarter of the test vessel geometry is required. At the vertical cut planes a rotational periodicity is used. A mass flow rate and a pressure boundary condition define the inlet and the outlet, respectively. The water surface at 1.467 m is replaced by a non-deformable free slip wall at which the water can move freely in azimuthal and radial direction.

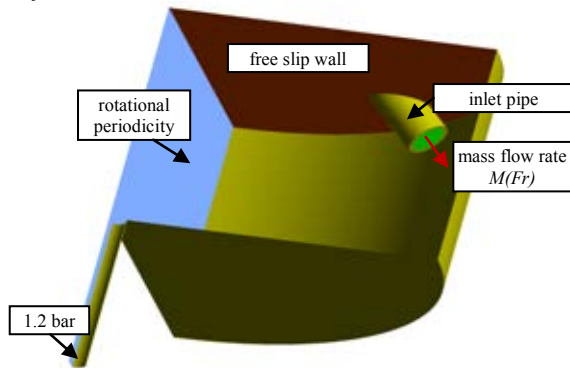


Figure 2: Single-phase CFD model

The underlying equations are the incompressible Reynolds averaged Navier-Stokes equations (RANS) (Wilcox, 1993). Thus, the influence of turbulence is modelled by the Reynolds stress tensor in the momentum equations. To close the system of equations the Shear Stress Transport model (SST) is used with automatic wall functions. The SST model is a two equation turbulence model based on the turbulent kinetic energy and the turbulent dissipation frequency (Menter, 1994). It is crucial to turn on the built-in curvature correction (Spalart and Shur, 1997), because otherwise the SST model is not an appropriate choice for strongly swirling flow. The curvature correction considers the swirling flow and enhances or damps the turbulence production appropriately.

ANSYS CFX applies a co-located, vertex-centered Finite Volume Method (ANSYS, 2016). In the present case a high resolution scheme is used to discretise the advection terms of the conservation equations and the transient parts are discretised by an implicit second order Euler method.

In figure 3 the grid is shown that is mainly structured and consists of hexahedral cells. Only the vicinity of the inclined inlet pipe is meshed with tetrahedral cells in order to achieve a better grid quality. The grid is locally refined at walls and the vessel centre. The maximum edge length is 40 mm. In the centre the grid resolution is much finer. The horizontal edge length in this region is between 3 and 4 mm. Altogether the grid contains ca. 0.5 million cells.

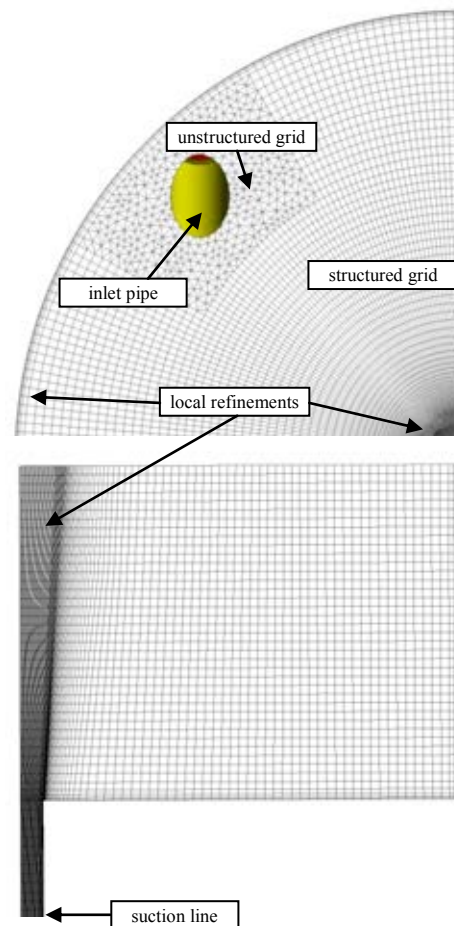


Figure 3: Computational grid (top and side view)

### Two-phase model

In the two-phase case both the liquid phase and the gaseous phase above the free surface are modelled (water and air). Therefore, it is necessary to extend the model by an air domain above the water surface (see figure 4). The air is treated as an ideal gas. In contrast to the single-phase model the top is now modelled by a no-slip wall. The other boundary conditions remain unchanged. The air domain is obtained by extruding the grid shown in figure 3. Thus, the principle grid structure and the grid quality do not change.

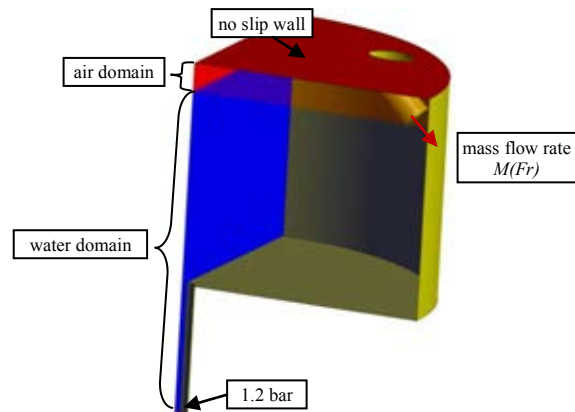


Figure 4: Two-phase CFD model

In the two-phase model each phase has its own continuity and momentum equation which now contain the volume fractions  $\alpha_g$  and  $\alpha_l$  of the gaseous and liquid phase, respectively. Furthermore, the terms  $\Theta_k$  and  $\Psi_k$

for interfacial mass and momentum transfer are included.

Continuity equation:

$$\frac{\partial(\alpha_k \rho_k)}{\partial t} + \nabla \cdot (\alpha_k \rho_k \mathbf{u}) = \Theta_k \quad (1)$$

Momentum equation:

$$\frac{\partial(\alpha_k \rho_k \mathbf{u}_k)}{\partial t} + \nabla \cdot (\alpha_k \rho_k \mathbf{u}_k \otimes \mathbf{u}_k) = -\alpha_k \nabla p + \nabla \cdot (\alpha_k \mu_{eff,k} \mathbf{S}_k) + \alpha_k \rho_k \mathbf{g} + \Psi_k \quad (2)$$

with  $k \in \{g, l\}$  and

$$\mathbf{S}_k = \nabla \mathbf{u}_k + \nabla \mathbf{u}_k^T - \frac{2}{3} (\nabla \cdot \mathbf{u}_k) \mathbf{I}$$

is the main strain-rate tensor. Since no mass transfer occurs between the two phases, the transfer term  $\Theta_k$  vanishes.

Although there were several successful attempts in the past to use the Volume-of-Fluid Method in order to simulate hollow surface vortices (Ito, 2010a, or Merzari, 2008), the above Two-Fluid Model was chosen in this case. The main reason is that recent developments show that this model can be applied successfully in order to cover different flow regimes simultaneously (Haensch, 2012). Thus, it is a promising candidate for future simulations that aim to quantify the gas entrainment, since this involves free surface and dispersed flow regimes. The use of the Volume-of-Fluid Method for this purpose is probably too costly, since also small bubbles have to be resolved.

For the computation of the remaining momentum transfer term the concept of the Algebraic Interfacial Area Density Model (AIAD) (Hoehne, 2011) was adopted. In the case of free surface flows ANSYS CFX computes the interfacial area density from the volume fraction gradient

$$\gamma = \|\nabla \alpha\| \quad (3)$$

and the momentum transfer is

$$\Psi_f = C_D (\alpha_g \rho_g + \alpha_l \rho_l) \gamma \|\mathbf{u}_g - \mathbf{u}_l\| (\mathbf{u}_g - \mathbf{u}_l). \quad (4)$$

Equation (4) describes an interfacial drag force that is dependent on the drag coefficient  $C_D$ . This drag coefficient is computed in the AIAD model, as if the water surface acted like a wall. Then the phase specific drag force  $\mathbf{F}_{D,k}$  can be computed via

$$\mathbf{F}_{D,k} = \gamma \mu_k (\mathbf{I} - \mathbf{n}_k \otimes \mathbf{n}_k) \mathbf{S}_k \cdot \mathbf{n}_k \quad (5)$$

with the surface normal vector

$$\mathbf{n}_k = -\frac{\nabla \alpha_k}{\gamma}. \quad (6)$$

So finally the drag coefficient can be calculated from

$$C_D (\alpha_g \rho_g + \alpha_l \rho_l) \gamma \|\mathbf{u}_g - \mathbf{u}_l\|^2 = \alpha_g \|\mathbf{F}_{D,g}\| + \alpha_l \|\mathbf{F}_{D,l}\|. \quad (7)$$

The other settings are very similar to the single-phase case. For instance the SST turbulence model with curvature correction is used again. However, the time step has to be chosen much smaller than in the single-phase simulations in order to keep the Courant number smaller than one. This makes the two-phase simulations very time consuming. However, some time can be saved, when a single-phase simulation is used as initial conditions.

## ANALYTICAL VORTEX MODELS

As already mentioned it is not possible to determine any surface deformation with the single-phase model. But by means of an analytical vortex model this situation can be remedied.

The probably simplest vortex model is the Rankine model (Wu et. al, 2006) that divides the vortex into two regions, an outer free vortex region and a core region. The core region behaves like a rotating solid. Therefore, the tangential velocity of the vortex can be expressed by

$$u_\theta = \frac{\Gamma}{2\pi r} \begin{cases} 1, & \text{for } r \geq r_{max} \\ \left(\frac{r}{r_{max}}\right)^2, & \text{for } r < r_{max}. \end{cases} \quad (8)$$

The model depends on the parameter  $r_{max}$  that characterises the location, where the velocity attains its maximum. Furthermore, the model depends on the circulation  $\Gamma$ .

A more evolved model is the model of Burgers and Rott (Rott, 1958). It describes a rotationally symmetrical stagnation-point flow. Inserting this assumption into the Navier-Stokes equations leads to the following tangential velocity.

$$u_\theta = \frac{\Gamma}{2\pi r} \left[ 1 - \exp\left(-a \frac{r^2}{4\nu}\right) \right]. \quad (9)$$

Again, two parameters have to be provided by the user of equation (9). Beside the circulation  $\Gamma$  the so-called suction parameter (or downward velocity gradient)  $a$  has to be specified. The suction parameter is related to  $r_{max}$  via the equation

$$\frac{r_{max}}{1.1209} = 2 \sqrt{\frac{\nu}{a}}. \quad (10)$$

Note that the shape of the water surface is characterised by a constant pressure condition. By applying this condition one obtains the ordinary differential equation

$$\frac{dz}{dr} = -\frac{u_\theta^2}{g r} \quad (11)$$

that describes the deflection of the water surface. Substituting equation (9) in equation (11) and integration yields the formula

$$l = \frac{a \ln(2)}{\nu g} \left( \frac{\Gamma}{4\pi} \right)^2 \quad (12)$$

for the gas core length of surface vortices (Ito, 2010). The difficulty with the application of the analytical vortex model of Burgers and Rott is the determination of the parameters circulation  $\Gamma$  and suction parameter  $a$  for arbitrary or even for simple intake geometries. For this task CFD is an excellent tool. By determining the circulation and the suction parameter from the CFD results and by applying equation (9) or (12), respectively, it is possible to compute the shape and the length of gas cores of hollow vortices. This is even possible, if only single-phase CFD simulations are performed, which require much less effort compared to two-phase models.

There exist several other analytical vortex models of comparable complexity. But there are also attempts to obtain a more general description of vortex flow. One is given by Granger who developed a sequence of systems of partial differential equations resulting from a power series expansion based on the radial Reynolds number (Granger, 1966). The 0<sup>th</sup> order model of Granger, i.e. the

first term of the power series, consists of two partial differential equations for the dimensionless stream function and the dimensionless circulation. The solution of these partial differential equations requires the knowledge of the centre line distribution of vorticity and axial velocity or alternatively the application of numerical methods. In the present case the 0<sup>th</sup> order Granger model was used in parameter studies and the equations were solved with a second order finite difference method.

**VALIDATION OF THE CFD MODELS**

The single-phase CFD model in combination with the Burgers-Rott vortex model as well as the two-phase CFD model were validated by the comparison of gas core lengths and tangential velocities with corresponding experimental measurements.

Figure 5 shows the tangential velocities determined with the single-phase CFD model for Froude number

$$Fr = \frac{u}{\sqrt{g d}} = 1.2. \tag{13}$$

This Froude number corresponds to a total mass flow of 53 kg/s. At this mass flow the submergence became critical in the experiments. The computed tangential velocities are evaluated along three lines at different elevations. There are only slight differences in the core region of the vortex between these positions. Additionally, the tangential velocities according to the Burgers-Rott model with adjusted parameters are included in the figure. The Burgers-Rott model agrees well with the CFD results.

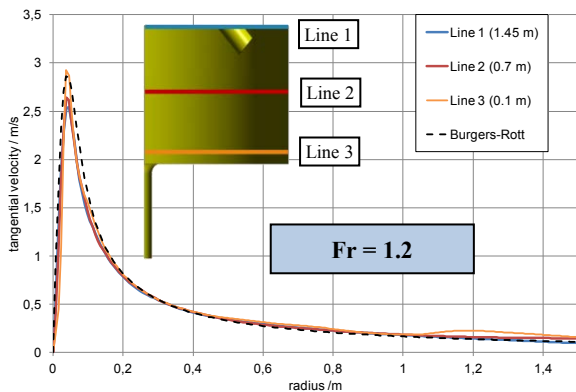


**Figure 5:** Tangential velocities according to CFX and the Burgers-Rott vortex model; Fr = 1.2

Once the parameters of the Burgers-Rott model are determined equations (11) and (12) can be used to compute the gas core shape. Figure 6 shows the gas core shapes, which are determined by the vortex model of Burgers and Rott, for two different mass flows and the maximal deflection of the water surface observed in the corresponding experiments. In both cases the length of the gas cores matches the experimental data with very good accuracy. Even the critical conditions at Fr = 1.2, for which the gas cores lengths equal exactly the submergence, are well predicted.

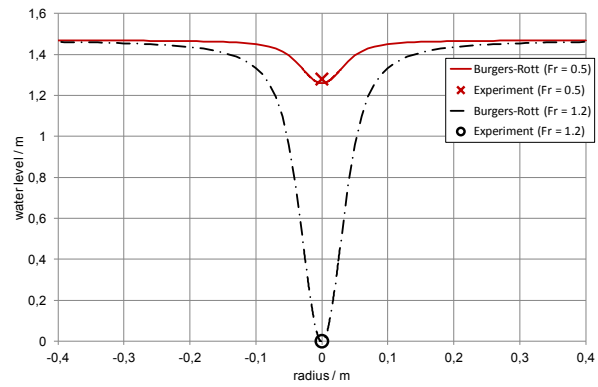


**Figure 6:** Gas core shapes for different mass flows

For the case with lower Froude number (Fr = 0.5) measurements of the tangential velocities are available (Szeliga, 2016). They were obtained by Particle Image Velocimetry (PIV). A comparison of the measurements and the CFD simulation results is presented in figure 7. Obviously also the measured and computed tangential velocities coincide well.

So far it was demonstrated that the combination of single-phase CFD simulations with the Burgers-Rott model is an accurate approach for the determination of the gas core length. Therefore, the attention is now turned on the two-phase model that allows the computation of the water surface directly without applying an analytical vortex model.

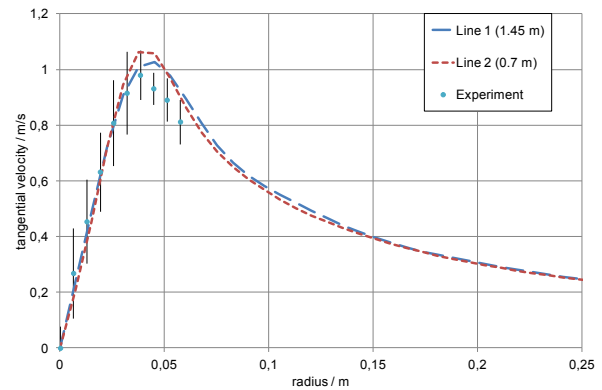


**Figure 7:** Comparison between measured and computed tangential velocities, Fr = 0.5

For the two-phase simulations a Froude number Fr = 1 was used, corresponding to 45 kg/s mass flow. Thus, critical conditions are not reached yet, but the experimentally observed gas core length of the surface vortex is about 70 % of the submergence. To simplify the simulations they were started with the single-phase results as initial conditions. After a simulation time of approximately 1 s an elongated gas core was formed during the simulations which corresponds very well with the experimental observations and the Burgers-Rott model (see figure 8). By continuing the simulation it turned out that the gas core became thinner and tore off at some point. As a consequence the surface vortex vanishes and has to develop again. However, the two-phase model has proved its suitability and ability to reproduce the shape of the surface vortex.

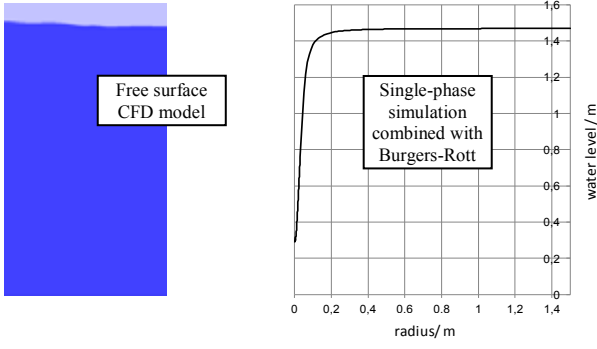


**Figure 8:** Comparison between CFD simulation (left) and Burgers-Rott model (right)

### COMPUTATION OF THE GAS CORE LENGTH AND THE NECESSARY SUBMERGENCE IN THE PRESENCE OF LARGE CIRCULATION

According to equation (12) the computation of the gas core length of a surface vortex requires the knowledge of the circulation  $\Gamma$  and the suction parameter  $a$ . The circulation is a parameter that depends strongly on the specific geometry. For the TUHH experiment the CFD simulations reveal an affine linear relationship between the angular momentum induced by the inlet pipes and the circulation in the vessel. This relation can be expressed for a given submergence and inclination of the inlet pipes by a simple equation. For instance the formula

$$\frac{\Gamma}{m^2/s} = (0.258 + 0.542 Fr^2) \quad (14)$$

can be derived for a submergence of 1.467 m and inlet pipes that are inclined at an angle of  $45^\circ$ .

While the circulation is highly system-dependent the suction parameter can be obtained by a theoretical approach that is described in the following.

A rotating fluid without any suction behaves like a rotating solid, because in this case the kinetic energy attains a minimum for a given circulation. This can be easily demonstrated with the Rankine model in equation (8). Enlarging  $r_{max}$  reduces the tangential velocities. Therefore, the kinetic energy in the cylindrical vessel reaches a minimum, if  $r_{max}$  attains a maximum, e.g.  $r_{max} = d_v / 2$ . In this case the entire fluid can be interpreted as solid body. But pumping changes the character of the flow. The typical tangential velocity profile (cmp. figure 5) consisting of a free vortex and a solid body rotation appears. This happens because a certain portion of kinetic energy is detracted from the vessel through the suction line. However, to sustain the rotation with the same circulation it is necessary that the rotating fluid also contains this additional portion of kinetic energy. This can be controlled by the parameter  $r_{max}$ .

The kinetic energy per unit time which is detracted through the suction line can be expressed by

$$\Delta W = \frac{\rho}{2} \frac{Q^3}{(\pi/4 d^2)^2}. \quad (15)$$

Because in strongly rotating flow the tangential velocity dominates the axial and radial velocities, the radial and axial components can be neglected in the cylindrical vessel. Therefore, the kinetic energy that passes a certain radius per unit time becomes

$$W = \frac{\rho}{2} Q u_0^2. \quad (16)$$

As explained this expression becomes minimal, if the characteristic radius is chosen as half of the cylinder diameter which yields the reference kinetic energy per unit time

$$W_{ref} = \frac{\rho}{2} Q \left( \frac{\Gamma}{\pi d_v} \right)^2 \left( \frac{2r}{d_v} \right)^2. \quad (17)$$

By subtracting equation (17) from equation (16) and evaluation at  $r = r_{max}$  one obtains

$$(W - W_{ref})_{r=r_{max}} = \frac{\rho}{2} Q \left( \frac{\Gamma}{\pi d_v} \right)^2 \left( \left( \frac{d_v}{2r_{max}} \right)^2 - \left( \frac{2r_{max}}{d_v} \right)^2 \right) \quad (18)$$

for the additional energy flux resulting from a certain choice of the parameter  $r_{max}$ . This additional flux must equal the expression in equation (15) to compensate the loss of energy through the suction line. This condition finally leads to the equation

$$\left( 4 \frac{Q}{d^2} \frac{d_v}{\Gamma} \right)^2 = \frac{1 - \xi^4}{\xi^2}, \quad \text{with } \xi := \frac{2r_{max}}{d_v} \quad (19)$$

which is a quadratic equation in  $\xi^2$  with the solution

$$\xi = \sqrt{\sqrt{1 + \frac{\varepsilon^2}{4}} - \frac{\varepsilon}{2}}, \quad \text{with } \varepsilon := \left( 0.25 \frac{d}{d_v} N \right)^{-2}. \quad (20)$$

In the above equation (20) the circulation  $\Gamma$  has been replaced by the dimensionless circulation number

$$N = \frac{\Gamma d}{Q}. \quad (21)$$

The Rankine model is a model with simplifications and it doesn't yield the correct kinetic energy distribution. For this reason a correction factor  $\kappa = 0.41$  is introduced, when the parameter  $r_{max}$  is determined from the definition of  $\xi$ , i.e.

$$r_{max} = \kappa \frac{d_v}{2} \xi. \quad (22)$$

The correction factor is derived from the experimental data. Now the suction parameter  $a$  can be computed with equation (10).

Usually it is preferable to use dimensionless quantities. The dimensionless suction parameter  $A$  can be defined by

$$A = \frac{a d^3}{Q}. \quad (23)$$

Substituting equation (10) and rewriting equation (22) by using equation (23) leads to the dimensionless equation

$$A = \frac{150}{Re} \frac{1}{\xi^2} \left( \frac{d}{d_v} \right)^2, \quad (24)$$

where  $Re$  denotes the Reynolds number

$$Re = \frac{u d}{\nu}. \quad (25)$$

Note that equation (20) is already written in dimensionless form.

The dimensionless version of equation (12) is given by

$$L = \frac{\pi \ln(2)}{4^5} A Re Fr^2 N^2. \quad (26)$$

Equation (26) contains two more dimensionless quantities, i.e. the dimensionless gas core length

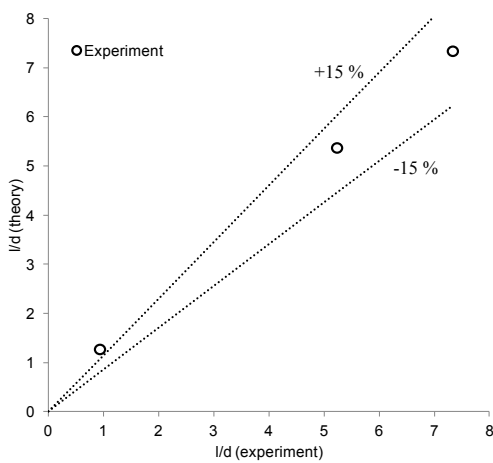
$$L = \frac{l}{d} \quad (27)$$

and the Froude number.

The equations (26), (24) and (20) form a new mathematical model for the computation of the gas core length which uses the Reynolds, Froude and circulation number as input parameters. This new model is applicable for surface vortices with strong circulation. Note that the circulation number depends on the circulation which therefore has to be given for instance by a relation like equation (14).

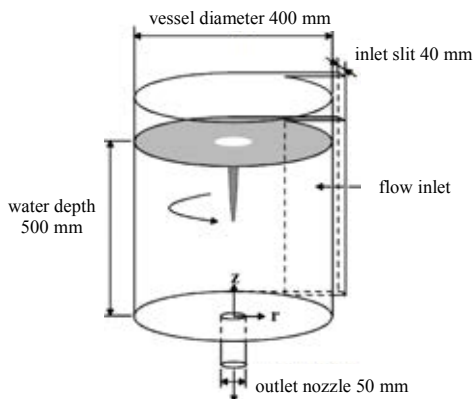
In the following the model is validated with the experimental data gained from the TUHH experiments and with data from the independent experiment of Moriya (Ito, 2010).

Figure 9 shows a comparison of the theoretical gas core lengths obtained from equation (26) with experimentally observed gas core lengths from the TUHH. The accuracy of the theory is very good in particular for larger gas cores.



**Figure 9:** Theoretical vs. experimental gas core lengths; TUHH experiments for Froude numbers  $Fr = 0.5, 1, 1.2$

In order to compare the theory also with independent measurements the experiment of Moriya was additionally considered. The setup of this experiment is similar to the TUHH experiments. The test facility consists also of a cylindrical vessel with a vertical pump suction intake (see figure 10). The main differences are the dimensions and the flow inlet. In Moriya’s experiment the water enters the test vessel tangentially through an inlet slit that causes the circulation in the vessel. The circulation is known (equation (41) in the paper of Ito, 2010) and it depends solely on the volume flow rate for fixed submergence.



**Figure 10:** Moriya’s experiment (Ito, 2010)

So, the circulation number  $N$  is already given via equation (21). The second parameter, the suction parameter  $A$ , can be computed with the above theory (equation (24)). Afterwards the gas core length follows from equation (26). The results are plotted in figure 11.

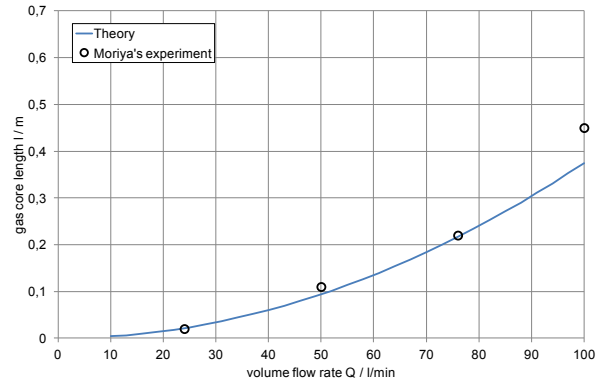


**Figure 11:** Validation against Moriya’s experiment

Again the theory matches the experimental data with very good accuracy. Only at a high flow rate of 100 l/min the theory deviates slightly from the corresponding measurement.

Since the developed theory allows the determination of the gas core length, only a small modification of equation (26) yields a new correlation for the computation of the critical submergence. By definition the critical submergence is reached, if the gas core length equals the submergence, i.e.  $l = h$ . Therefore, the dimensionless critical submergence  $H_{crit} = h_{crit}/d$  results from equation (26) by simply setting

$$H_{crit} = \frac{\pi \ln(2)}{4^5} A Re Fr^2 N^2. \quad (28)$$

The suction parameter  $A$  and the circulation number  $N$  are in general functions of the submergence, i.e.

$$A = A(H_{crit}), N = N(H_{crit}). \quad (29)$$

This is a nonlinear implicit equation that has to be solved for  $H_{crit}$ .

### EXTENSION OF THE THEORY TO SMALL AND MODERATE CIRCULATION

The theoretical approach that leads to the suction parameter in equation (24) is valid for strongly circulating flow. Therefore, it is applicable to the TUHH experiments and Moriya’s experiment. To examine if it is also suitable for moderate circulation further parameter studies were performed.

So firstly, cases without any circulation were investigated. For this purpose the 0<sup>th</sup> order Granger model was solved with a second order finite difference method. This procedure was chosen, because it allows the variation of the suction line diameter and the submergence without the necessity of complex remeshing steps.

The variations of the submergence and the suction line diameter in the Granger model reveal a relationship between the dimensionless suction parameter  $A$  and the dimensionless submergence  $H$  that fits very well to the equation

$$A = 1.1 H^{-2.88}. \quad (30)$$

Both the results from the Granger model and the graph of the derived correlation are shown in figure 12.

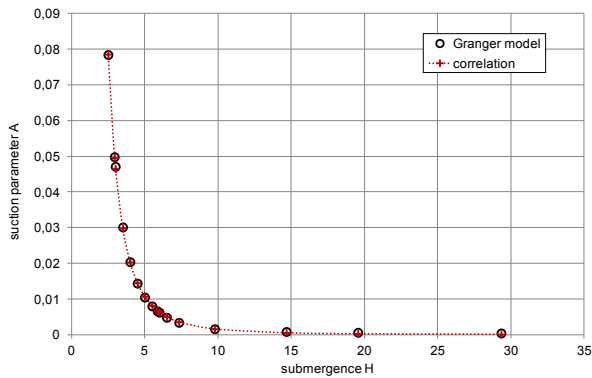


**Figure 12:** Suction parameter in dependency of the submergence (cases without circulation)

Since the applied finite difference solver of the Granger model considers no circulation, more parameter studies were performed with another generic ANSYS CFX model. This generic model consists of a simple cylindrical domain, but it is possible to generate a specified moderate circulation by imposing an inflow angle at the circumference. All parameter studies as a whole yield a correlation for cases with small circulation which is given by the following equation

$$A = 1.1 H^{-2.88} \left( 1 - \frac{2 \arctan(NH)}{\pi} \right). \quad (31)$$

Equation (24) and equation (31) represent two different correlations developed for the limiting cases of large and small circulation. The corresponding graphs for a pump intake diameter of 0.2 m, 45 kg/s mass flow and a submergence of 1.467 m as well as varying circulation numbers are plotted in figure 13.

Obviously the theory for small circulation fits well to the simulations with the Granger model and the generic CFX model, while the theory for large circulation fits well to the simulation of the TUHH experiment with an inlet pipe inclination of 45°. Hence, both theories are confirmed by CFD simulations and in particular the theory for large circulation is also validated with experimental results. Moreover, the experimental data of Jain (1978) indicates that the desired suction parameter for moderate circulation lies indeed between both theories. Therefore, an appropriate interpolation between both theories is required to capture the correct suction parameter in cases with moderate circulation. This will be the topic of future investigations.

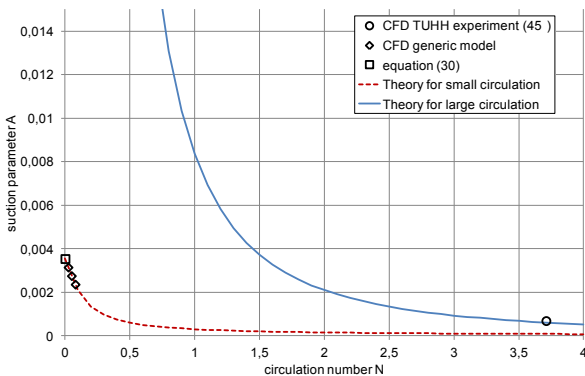


**Figure 13:** Dimensionless suction parameter over circulation number according to the theories of large and small circulation

## SUMMARY AND CONCLUSIONS

The avoidance of gas entrainment and a homogenous flow without swirl are basic requirements for an undisturbed pump operation. As a consequence surface vortices, which might occur at free surfaces, have to be prevented. The most effective measure in this regard is a sufficient submergence of the intake. But the determination of the critical submergence requires either elaborate model experiments or estimations by means of some correlation. Due to the lack of an universally applicable and reliable correlation, there is an ongoing need for improved correlations.

Therefore, an industrial scale test facility has been built at the TUHH in order to examine the conditions for the occurrence and the shape of surface vortices. In particular the length of gas cores of those hollow vortices was analysed with varying boundary conditions. The so gained experimental data was used to develop appropriate strategies for the computation of the gas core lengths, the vortex shapes and therefore also the critical submergence. Numerical methods were applied based on single- and multi-phase CFD models. The multiphase CFD approach has shown its ability to calculate the shape of the gas cores directly, but the computational effort of the multiphase simulations is very high. In fact, it turned out that it is possible to accurately compute the shape of the surface vortices with single-phase CFD simulations in combination with the Burgers-Rott vortex model that is a much more efficient approach. Both methods were applied to simulate the TUHH experiments and they were validated with the corresponding measurements.

Furthermore, two new theories have been developed which yield new correlations for the computation of the gas core length of surface vortices and the critical submergence, respectively. The first theory results from an energy balance and is applicable for flows with strong circulation. In addition it was validated with the TUHH experiments and the independent experiment of Moriya. The second approach is based on parameter studies with CFD and yields a correlation for flows with very low circulation. These theories represent the two limiting cases for swirling flows. Cases with moderate circulation like Jain’s experiment lie in between and require an adequate interpolation between both theories.

## ACKNOWLEDGMENTS

This work is sponsored by the German Federal Ministry of Education and Research (BMBF) under the contract number 02NUK023C. The responsibility for the content of this publication lies with the author.

## REFERENCES

- ANSYS Germany GmbH, (2016), ANSYS CFX 17, <http://www.ansys.com/products/fluids/ansys-cfx>
- GRANGER, R., (1966), “Steady three-dimensional vortex flow”, *J. Fluid Mech.*, **25** (3), 557-576
- HAENSCH, S., (2012), “A multi-field two-fluid concept for transition between different scales of interfacial structures”, *International Journal of Multiphase Flow*, **47**, 171-182
- HOEHNE, T., et al., (2011), “Numerical simulations of counter-current two-phase flow experiments in a PWR hot leg

- model using an interfacial area density model”, *International Journal of Heat and Fluid Flow*, **32**, 1047-1056
- HYDRAULIC INSTITUTE, (2012), “Rotodynamic Pumps”, ISBN 978-880952-70-2
- ITO, K. et al., (2010), “Improvement of Gas Entrainment Prediction Method –Introduction of Surface Tension Effect–”, *Journal of Nuclear Science and Technology*, **47 (9)**, 771-778
- ITO, K. et al., (2010a), “CFD-based Evaluation of Interfacial Flows”, *INTECH*, Croatia
- JAIN, A.K. et al., (1978), “Vortex Formation at Vertical Pipe Intakes”, *Journal of the Hydraulics Division*, **HY10**, 1429-1445
- MENTER, F.R., (1994), “Two-Equation Eddy-Viscosity Turbulence Models for Engineering Applications”, *AIAA Journal*, **32 (8)**, 1598-1605, August 1994
- MERZARI, E. et al., (2008), “Numerical Simulation of Free-Surface Vortices”, *Nuclear Technology*, **165**, 313-320
- ROTT, N., (1958), “On the Viscous Core of a Line Vortex”, *Journal of Applied Mathematics and Physics (ZAMP)*, **9**, 543-553
- SPALART, P.R. and SHUR, M., (1997), “On the Sensitization of Turbulence Models to Rotation and Curvature”, *Aerospace Science and Technology*, **4**, 297-302
- SZELIGA, N. et al., (2016), “Determination of the Influence of Tangential Momentum on Air-Core Vortex Formation at Pump Intakes by Means of Particle Image Velocimetry”, *GALA 2016*, 30-1 – 30-9, ISBN: 978-3-9816764-2-6.12
- WILCOX, D.C., (1993), “Turbulence Modelling for CFD”, DCW Industries, Inc., ISBN 0-9636051-0-0
- WU, J.-Z. and MA, H.-Y. and ZHOU, M.-D., (2006), “Vorticity and Vortex Dynamics”, Springer



# PARALLEL MULTIPHASE FLOW SOFTWARE FOR SOLVING THE NAVIER-STOKES EQUATIONS

Fahad S. AL-RASHED<sup>1\*</sup>, Maher M. SHARIFF<sup>1†</sup>

<sup>1</sup>Saudi Aramco, Dhahran, SAUDI ARABIA

\* E-mail: fahad.rashed@aramco.com

† E-mail: maher.shariff@aramco.com

## ABSTRACT

A code based on finite element method was built and applied on the variable density incompressible Navier-Stokes equations for accurately simulating immiscible two phase flows. The algorithm simulates the interface between the two liquid phases with high accuracy; it utilizes both the level-set method with a third order strong stability property Runge-Kutta (SSPRK) time integrator and a second-order projection method for the momentum equation. The solver developed is based on deal.II, an open source framework code. Numerical assessments on the transport and momentum equations are presented to verify the code accuracy. Nonconforming manufactured solutions are shown to produce the expected convergence rate of the used numerical schemes. Simulation of classical Rayleigh-Taylor instability was carried out and shown to match those in the published work.

**Keywords:** CFD, projection methods, level set, LES .

## NOMENCLATURE

### Greek Symbols

$\rho$	Density
$\mu$	Dynamic viscosity
$\nu$	Kinematic viscosity
$\phi$	Level set

### Latin Symbols

$\mathbf{u}$	Velocity
$p$	Pressure
$t$	Time
$V$	An appropriate space with proper boundary conditions

All symbols are non-dimensional.

## METHOD

The *variable density incompressible Navier-Stokes equations* are defined as follows:

$$\begin{aligned} \partial_t \rho + \operatorname{div}(\rho \mathbf{u}) &= 0, & \text{in } \Omega \times (0, T], & (1) \\ \rho[\partial_t \mathbf{u} + (\mathbf{u} \cdot \nabla) \mathbf{u}] - 2\mu \operatorname{div}(\nabla^s \mathbf{u}) \\ &+ \nabla p = \rho \mathbf{f}, & \text{in } \Omega \times (0, T], & (2) \\ \operatorname{div}(\mathbf{u}) &= 0, & \text{in } \Omega \times (0, T], & (3) \end{aligned}$$

where  $\Omega \subset \mathbb{R}^{2,3}$  and  $\partial\Omega$  is the boundary,  $\rho(\mathbf{x}, t)$  is the density at  $(\mathbf{x}, t) \in \Omega \times [0, T]$ ,  $\mathbf{u}(\mathbf{x}, t)$  is the velocity vector field,  $\mu$

is the dynamic viscosity, and  $p(\mathbf{x}, t)$  is the pressure. **Bold** variables are vector valued. Equation (1) is referred to as the transport equation, (2) is the momentum equation and (3) is the incompressibility constraint.

## Transport equation weak formulation

The weak formulation for the transport equation is: Find  $\rho(\mathbf{x}, t) \in V(\Omega)$  such that:

$$\int_{\Omega} v \left( \frac{\partial}{\partial t} \rho + \mathbf{u} \cdot \nabla \rho \right) dx = 0, \quad \forall v \in V(\Omega), \quad (4)$$

$$\rho(\mathbf{x}, t) = \rho_{\partial\Omega}, \quad \text{in } \partial\Omega_-, \quad (5)$$

$$\rho(\mathbf{x}, 0) = \rho_0, \quad \rho_0 > 0, \quad (6)$$

where  $V$  is an appropriate space for the transport equation with appropriate boundary conditions.

To accurately capture the density field  $\rho$ , we choose the 3<sup>rd</sup> order time integration method "Strong Stability Preserving Runge-Kutta" with three steps (abbreviated as SSPRK(3,3)) as described by (Gottlieb, 2005). The SSPRK(3,3) steps are:

$$y^{(1)} = y^k + \Delta t f(t^k, y^k), \quad (7)$$

$$y^{(2)} = \frac{1}{4} \left( 3y^k + y^{(1)} + \Delta t f(t^{k+1}, y^{(1)}) \right), \quad (8)$$

$$y^{k+1} = \frac{1}{3} \left( y^k + 2y^{(2)} + 2\Delta t f(t^{k+\frac{1}{2}}, y^{(2)}) \right). \quad (9)$$

The strong stability preserving property is  $\|y^{k+1}\| \leq \|y^k\|$ . This makes it attractive in the transport equation case. The SSP property comes from the maximum principle preserving property of the Forward Euler method.

## The Level Set Model

The fluid mixture we are interested in modeling with the transport equations has two phases: oil, and water. Each has a different density value  $\rho$ . Since they do not mix, it is important that each phase must be distinct when modeled and the volume of each phase in  $\Omega$  be conserved. Otherwise, the incompressibility condition  $\operatorname{div}(\mathbf{u}) = 0$  will be violated. As a consequence, when solving the approximation of the transport equation, one needs to make sure the interface between two phases is tracked with enough accuracy. There are many methods to achieve such accuracy, which can be divided into two classes. In the first one, the interface is implicitly tracked by a function defined on the whole domain. Such methods include the level set method, and volume of fluid method. In

the second class, the interface is explicitly tracked with front-tracking methods. We will use the level set method between two phases.

The level set method was first introduced by (Osher and Sethian, 1988) to evolve the interface with speeds depending on the curvature of a given velocity field. The interface is tracked with a function  $\Phi(\mathbf{x})$  to represent the  $n - 1$  dimensional interface  $\Gamma \subset \Omega$  separating  $\Omega$  into two phases  $\Omega_1$  and  $\Omega_2$ . There are many ways to define  $\Gamma$  but we are going to use the tanh function with the interface at  $\Phi(\mathbf{x}) = 0.5$ . The tanh function is defined as:

$$\Phi(\mathbf{x}) := \frac{1}{2} \left( 1 + \tanh \left( \frac{d(\mathbf{x})}{\gamma} \right) \right), \quad (10)$$

where  $d$  is a distance from the interface function and  $\gamma$  controls how steep the interface is. To describe the evolution of an interface that is transported along with a fluid, we can use  $\Phi$  instead of  $\rho$  in (4):

$$\int_{\Omega} v \left( \frac{\partial}{\partial t} \Phi + \mathbf{u} \cdot \nabla \Phi \right) dx = 0, \quad \forall v \in V(\Omega), \quad (11)$$

$$\Phi(\mathbf{x}, t) = \Phi_{\partial\Omega}, \quad \text{in } \partial\Omega, \quad (12)$$

$$\Phi(\mathbf{x}, 0) = \Phi_0, \quad \Phi_0 > 0. \quad (13)$$

This essentially transports the  $\Phi$  function instead of the density  $\rho$ . To reconstruct  $\rho$  from  $\Phi$ , we use the function  $H(\Phi)$ :

$$H(\Phi(\mathbf{x})) = \begin{cases} \rho_1, & \Phi(\mathbf{x}) < 0.5, \\ \rho_2, & \Phi(\mathbf{x}) \geq 0.5, \end{cases} \quad (14)$$

where  $\rho_1, \rho_2$  are the densities of the fluids in  $\Omega_1$  and  $\Omega_2$  respectively ( $\rho_1 < \rho_2$ ).  $H(\Phi)$  will produce density fields that have discontinuous transitions between phases, which are undesirable when dealing with PDEs that expect smooth enough functions. There are many functions that create smoother transitions such as:

$$H(\Phi(\mathbf{x})) = \frac{\rho_2 - \rho_1}{2} + \frac{\rho_2 + \rho_1}{2} \tanh \left( \frac{\Phi(\mathbf{x})}{\gamma} \right), \quad (15)$$

where  $\alpha$  controls how steep the transition between the two densities is. The advantage of this reconstruction is that it produces the closest density field close to (14) with some retained smoothness. Another candidate  $H$  function is:

$$H(\Phi(\mathbf{x})) = (\rho_2 - \rho_1)\Phi(\mathbf{x}) + \rho_1, \quad (16)$$

which is a linear scaling of the level set to the densities in  $\Omega$ . It is robust but translates the undesirable oscillations that extends beyond  $\Phi(\mathbf{x}) > 1$  or  $\Phi(\mathbf{x}) < 0$ . This issue may be solved by clipping the reconstruction at a certain radius  $\alpha$  around 0.5 ( $0 \leq \alpha \leq 0.5$ ):

$$H(\Phi(\mathbf{x})) = \begin{cases} \rho_1, & \Phi(\mathbf{x}) \leq 0.5 - \alpha, \\ \rho_2, & \Phi(\mathbf{x}) \geq 0.5 + \alpha, \\ (\Phi(\mathbf{x}) - (0.5 - \alpha)) \frac{\rho_2 - \rho_1}{2\alpha} + \rho_1, & \text{otherwise.} \end{cases} \quad (17)$$

This reconstruction introduces relatively sharp changes in the density gradient and affects the stability of simulation runs. Finally, the last reconstruction we are going to introduce has the property of having slope zero at the  $0.5 \pm \alpha$  points and

being a transition polynomial of third degree ( $0 \leq \alpha \leq 0.5$ ):

$$H(\Phi(\mathbf{x})) = \begin{cases} \rho_1, & \text{if } \Phi(\mathbf{x}) \leq 0.5 - \alpha, \\ \rho_2, & \text{if } \Phi(\mathbf{x}) \geq 0.5 + \alpha, \\ \frac{(4\alpha - 2\Phi(\mathbf{x}) + 1)(2\alpha + 2\Phi(\mathbf{x}) - 1)^2}{32\alpha^3} & (18) \\ (\rho_2 - \rho_1) + \rho_1, & \text{otherwise.} \end{cases}$$

Compared to the clipped reconstruction (17), the above has smooth gradient transitions and was found to have a stabilizing effect when used in the simulations below. This transition is comparable to the Heaviside function (14) in (Sussman and Fatemi, 1999) but has the advantage of being polynomial in nature.

### Entropy-Viscosity

The Entropy-Viscosity is (at least) a second-order stabilization term introduced by (Guermont *et al.*, 2011a) and (Guermont and Pasquetti, 2011). It has the advantage of having a less diffusive effect on the solution and thus allowing the construction of stabilized second order numerical schemes. Using the transport equation weak form:

$$\int_{\Omega} v_h \left( \frac{\partial \rho_h}{\partial t} + \mathbf{u}_h \cdot \nabla \rho_h - \text{div} (v \nabla \rho) \right) dx = 0, \quad \forall v_h \in V_h(\Omega), \quad (19)$$

and  $v$  is calculated for each cell separately as follows. Define  $E(\phi)$  as convex functions that satisfies the differential inequality:

$$\partial_t E(\phi) + \mathbf{u} \cdot \nabla E(\phi) < 0, \quad (20)$$

where  $\phi$  is the level set function mentioned in section and  $E(\phi)$  is the entropy function. For examples, one can use:

$$E(\phi) = \begin{cases} \frac{1}{p} (\phi - \frac{1}{2})^p & \text{where } p = 1, 2, \dots, \\ -\log(|\phi(1 - \phi)| + 10^{-14}). \end{cases} \quad (21)$$

In the fully discretized setting, use  $\phi^n, \phi^{n-1}$  and compute the following values for each quadrature points  $q_k, q_f$  in cell  $k$  and face  $f$ :

$$R^{n+1/2}(q_k) = \frac{\Pi_{\mathcal{T}_h} E(\phi^n) - \Pi_{\mathcal{T}_h} E(\phi^{n-1})}{\Delta t} + \quad (22)$$

$$\frac{1}{2} (\mathbf{u}^n \cdot \nabla \Pi_{\mathcal{T}_h} E(\phi^n) + \mathbf{u}^{n-1} \cdot \nabla \Pi_{\mathcal{T}_h} E(\phi^{n-1}))$$

$$J^n(q_f) = \mathbf{u}^n \cdot \mathbf{n} [\partial_n \Pi_{\mathcal{T}_h} E(\phi^n)]|_f. \quad (23)$$

Then get the maximum  $R_k^{n+1/2} = \max_{q_k \in k} |R^{n+1/2}(q_k)|$  and  $J_k^n = \max_{f \in k} \max_{q_f \in f} |J^n(q_f)|$ . Note that we are using the Crank-Nicolson scheme to calculate  $R$  giving us a second order accurate value for  $R$ . The viscosity  $\nu_k$  will then be:

$$\nu_k = \min \left( C_m h |\mathbf{u}|_{L^\infty}, C_e h^2 \frac{R^{n+1/2} + J_k^n}{\|E(\phi^n) - \overline{E(\phi^n)}\|_{L^\infty(\Omega)}} \right), \quad (24)$$

where  $\overline{E(\phi)} = \frac{1}{|\Omega|} \int_{\Omega} E(\phi)$  and  $\|E(\phi^n) - \overline{E(\phi^n)}\|_{L^\infty(\Omega)}$  is a normalization factor. The amount of artificial viscosity is proportional to the entropy production but bounded from above by the linear artificial viscosity. If the solution is smooth and entropy production is very small, little or no artificial viscosity is added. Some disadvantages remain such as coefficients  $C_e, C_m$  to tune and the ambiguity of  $h$ .

### Compression for the Level Set

For the level set method to work, the curved shape of the level set function over the boundary must be maintained to prevent adding non-physical effects to the model. The stabilization viscosity diffuses the level set interface as the simulation marches in time. Consequently, with the presence of the diffusion term, we add the compression (or anti-diffusion) term  $\text{div}\left(C_K \frac{v}{h} (1 - \phi_h) \phi_h \frac{\nabla \phi_h}{|\nabla \phi_h|}\right)$  to the transport equation (4):

$$\int_{\Omega \times [0, T]} \frac{\partial}{\partial t} \phi_h + \mathbf{u} \cdot \nabla \phi_h - \text{div}\left(v \nabla \phi_h - C_K \frac{v}{h} \phi_h (1 - \phi_h) \frac{\nabla \phi_h}{|\nabla \phi_h|}\right) dxdt = 0, \quad (25)$$

where the level set  $\phi \in [0, 1]$  and defined at  $\phi = 0.5$ . This compression term eliminates the need for a separate reinitialization step. In practice, it has been observed that the compression term in (25) induces ‘‘fingering’’ effect in simulations. It is the result of perturbations in the initial level set that the compression term gradually propagates resulting in the level set extending like fingers. To mitigate that, a smoothed out  $\phi_h^*$  is used in the normal of the compression front  $\frac{\nabla \phi_h}{|\nabla \phi_h|}$  where  $\phi_h^*$  is the solution to  $\phi_h^* - h^2 \Delta \phi_h^* = \phi$ ,  $\nabla \phi_h^* \cdot \mathbf{n} = 0$  on  $\partial\Omega$ . We will denote  $S$  as the operator that maps  $\phi$  to the corresponding  $\phi^*$  (i.e.  $S\phi_h = \phi_h^*$ ).

Let us detail the algorithm for solving (25):

1. Initialize the level set by normalizing the initial density scalar field.

$$\phi_h^0 = \frac{\rho_h^0 - \rho_{\min}}{\rho_{\max} - \rho_{\min}},$$

2. For each of the SSPRK(3,3) steps below, we need to solve the following:

$$L^n(\mathbf{u}_h, \phi_h, \phi_h^*) = -\mathbf{u}_h \cdot \nabla \phi_h - \text{div}\left(v \nabla \phi_h - C_K \frac{v}{h} \phi_h (1 - \phi_h) \frac{\nabla \phi_h^*}{|\nabla \phi_h^*|}\right), \quad (26)$$

when solved for each of the three steps below, the values are

$$\phi_h^{(1)} = \phi_h^n + \Delta t L^n(\mathbf{u}_h^n, \phi_h^n, S\phi_h^n), \quad (27)$$

$$\phi_h^{(2)} = \frac{1}{4} \left( 3\phi_h^n + \phi_h^{(1)} + \Delta t L^{n+1}(2\mathbf{u}_h^n - \mathbf{u}_h^{n-1}, \phi_h^{(1)}, S\phi_h^{(1)}) \right), \quad (28)$$

$$\phi_h^{n+1} = \frac{1}{3} \left( \phi_h^n + 2\phi_h^{(2)} + 2\Delta t L^{n+\frac{1}{2}} \left( \frac{1}{2} [3\mathbf{u}_h^n - \mathbf{u}_h^{n-1}], \phi_h^{(2)}, S\phi_h^{(2)} \right) \right). \quad (29)$$

3. Lastly, we ‘‘denormalize’’ the level set with a reconstruction function such as:

$$\rho_h^{n+1} = H(\phi_h)(\rho_{\max} - \rho_{\min}) + \rho_{\min}. \quad (30)$$

It is worth mentioning that when the entropy-viscosity vanishes in well resolved regions of the solution, the compression stops working and the sharpness of the level set interface is lost. This may be remedied by using some ‘‘antivanish’’ viscosity  $\mathbf{v}_{\text{antivanish}} = \mathbf{v} + \mathbf{v}_\epsilon$  where  $\mathbf{v}_\epsilon$  is a small positive amount of viscosity that maintains the balance between diffusion and compression and, thus, maintains the slope of the level set.

### Projection method for the momentum equation

Initialize the algorithm with  $\rho^0 = \rho_0$ ,  $\mathbf{u}^0 = \mathbf{u}_0$ ,  $p^0 = p_0$ ,  $\phi^0 = q^0 = 0$  then proceed as follows:

1. Setup intermediate variables:

$$\begin{aligned} \rho^* &= \rho^{n+1} + \frac{1}{6} \text{BDF}_2(\rho^{n+1}), \\ &\quad \text{where } \text{BDF}_2(\phi^{n+1}) = 3\phi^{n+1} - 4\phi^n + \phi^{n-1}, \\ p^* &= p^n + \frac{1}{3} \left( 4\delta\psi^n - \delta\psi^{n-1} \right), \\ \mathbf{u}^* &= 2\mathbf{u}^n - \mathbf{u}^{n-1}. \end{aligned}$$

2. Prediction:

$$\begin{aligned} &\frac{3\rho^* \mathbf{u}^{n+1} - 4\rho^{n+1} \mathbf{u}^n + \rho^{n+1} \mathbf{u}^{n-1}}{2\Delta t} - \rho^{n+1} \mathbf{u}^* \cdot \nabla \mathbf{u}^{n+1} \\ &+ \frac{1}{2} \text{div}(\rho^{k+1} \mathbf{u}^*) \mathbf{u}^{n+1} - \mu \Delta \mathbf{u}^{n+1} + \nabla p^* = \rho^{n+1} \mathbf{f}^{n+1}, \\ &\quad \mathbf{u}^{n+1}|_{\partial\Omega} = 0, \end{aligned}$$

3. Projection:

$$\begin{aligned} \Delta \delta\psi^{n+1} &= \frac{3\rho_{\min}}{2\Delta t} \text{div}(\mathbf{u}^{k+1}), \quad \partial_n \delta\psi^{n+1} = 0, \\ \delta q^{n+1} &= -\text{div}(\mathbf{u}^{n+1}), \end{aligned}$$

4. Pressure correction:  $p^{n+1} = \psi^{n+1} - \mu q^{n+1}$ .

where BDF stands for Backwards Difference Formula.

This variable density projection method is shown to have an error of  $O(\Delta t^2)$  in the  $L^2$  norm. The stability proof can be found in (Guermont and Salgado, 2011, §5.4)

### Large Eddy Simulation

The Large Eddy Simulation (LES) is based on the – at least – 2<sup>nd</sup> order entropy-viscosity method (Guermont *et al.*, 2011b). The concept behind LES is separating the flow into large – or resolved – and small – or subgrid – scales. For a good overview of LES, see (John, 2004).

When dealing with the Navier-Stokes equations, LES is added as a cell-wise viscosity  $\nu_K \geq 0$  to the term  $-2\nu \text{div}(\nabla^s \mathbf{u})$ . The result is a viscosity  $\mathbf{v} + \nu_K$ . The classical Smagorinsky model ((Smagorinsky, 1963)) uses:

$$\nu_K := C_s \delta_K^2 \|\nabla^s \mathbf{u}\|,$$

where  $C_s$  is the Smagorinsky constant and  $\delta_K$  is the width of the filter (which is proportional to  $h_K$ ). (Guermont *et al.*, 2011c) proposed the following Entropy-Viscosity approach:

$$\nu_K := \min \left( C_m h_K |\mathbf{u}|, C_e h_K^2 \frac{|D_h(\mathbf{x}, t)|}{\|\mathbf{u}_h^2\|_{L^\infty(\Omega)}} \right),$$

where

$$\begin{aligned} D_h(\mathbf{x}, t) &:= \\ \partial_t \left( \frac{1}{2} \mathbf{u}_h^2 \right) + \text{div} \left( \left( \frac{1}{2} \mathbf{u}_h^2 + p_h \right) \mathbf{u}_h \right) - Re^{-1} \Delta \left( \frac{1}{2} \mathbf{u}_h^2 \right) \\ &\quad + Re^{-1} (\nabla \mathbf{u}_h)^2 - \mathbf{f} \cdot \mathbf{u}_h \end{aligned} \quad (31)$$

where  $h_K$  is the mesh size locally,  $\|\mathbf{u}_h^2\|_{L^\infty(\Omega)}$  is a normalizing term, and  $C_m, C_e$  are appropriate constants. The first term  $C_m h_K |\mathbf{u}|$  is the first order artificial viscosity. When the mesh is fine enough to simulate all the scales,  $h_K^2 |D_h(\mathbf{x}, t)|$  is much smaller than the first-order artificial viscosity. This makes  $\nu_K$  a consistent viscosity that vanishes when scales of all levels are resolved.

## NUMERICAL RESULTS

We test the schemes discussed in the previous sections numerically and present them here.

### Validation

Here, we will present the validation of the projection method with density  $\rho(\mathbf{x}, t) = 1$ . This is a constant density test performed on a variable density equation for validation purposes. Using  $\Omega = (0, 1)^d$  domain with a uniform mesh and cell-wise  $[\mathbb{Q}_2]^d$  continuous finite elements, we introduce the following simple linear polynomial manufactured solution for the momentum equation:

$$\mathbf{u}(\mathbf{x}, t) = (1+t) \begin{pmatrix} x+y \\ x-y \end{pmatrix}, \quad p(\mathbf{x}, t) = (1+t)xy, \quad (32)$$

$$\mathbf{u}(\mathbf{x}, t) = (1+t) \begin{pmatrix} 1+z \\ 1+x \\ 1+y \end{pmatrix}, \quad p(\mathbf{x}, t) = (1+t)xyz. \quad (33)$$

for  $d = 2, 3$  respectively. We solve the equation (2) with  $\mu = 1$  running until final time  $T = 1$ . The projection step is disabled, which means that the exact pressure is interpolated every time step. The boundary condition  $\mathbf{u}|_{\partial\Omega} = \mathbf{u}(\mathbf{x}, t)|_{\partial\Omega}$  is enforced. The time step is changed to roughly achieve a Courant-Friedrichs-Lewy condition (CFL) of 0.25. As expected, table 1 shows that the error is machine epsilon which means that the algorithm reproduces the conforming manufactured solutions exactly.

	cells	$\mathbf{u}_{\text{dofs}}$	$\Delta t$	$\ e_{\mathbf{u}}\ _{L2}$	$\ e_{\mathbf{u}}\ _{H1}$	$\text{CFL}_{\text{max}}$
2D	16	162	8E-03	3E-13	1E-12	0.2621
	64	578	4E-03	1E-15	2E-14	0.2606
	256	2178	2E-03	1E-14	8E-14	0.2607
3D	8	375	3E-02	9E-16	1E-14	0.2601
	64	2187	1E-02	5E-15	3E-14	0.2614
	512	14739	7E-03	7E-15	7E-14	0.2613

**Table 1:** Error values for running conforming manufactured solutions in a unit cube. We get the expected value of machine epsilon.

### Projection Scheme

Using  $\Omega = (0, 1)^d$  domain with a uniform mesh and cell-wise  $[\mathbb{Q}_2]^d/\mathbb{Q}_1$  Taylor-Hood continuous finite elements, we introduce the following simple linear polynomial manufactured solution for the momentum equation:

$$\mathbf{u}(\mathbf{x}, t) = (1+t) \begin{pmatrix} x+y \\ x-y \end{pmatrix}, \quad p(\mathbf{x}, t) = (1+t)xy, \quad (34)$$

$$\mathbf{u}(\mathbf{x}, t) = (1+t) \begin{pmatrix} 1+z \\ 1+x \\ 1+y \end{pmatrix}, \quad p(\mathbf{x}, t) = (1+t)xyz. \quad (35)$$

with  $d = 2, 3$  respectively. We solve the equation (2) with  $\mu = 1$  running until final time  $T = 1$ . The projection step is disabled, which means that the exact pressure is interpolated from the exact solution to the discrete space every time step. We enforce the following boundary condition  $\mathbf{u}|_{\partial\Omega} = \mathbf{u}(\mathbf{x}, t)|_{\partial\Omega}$ . The source term is modified to reflect the exact solutions. As expected, table 2 shows that the error is machine epsilon ( $\sim 0$ ), which means that the algorithm reproduces the conforming manufactured solutions exactly.

	cells	$\mathbf{u}_{\text{dofs}}$	$\Delta t$	$\ e_{\mathbf{u}}\ _{L2}$	$\ e_{\mathbf{u}}\ _{H1}$
2D	16	162	1E-02	8E-16	1E-14
	64	578	5E-03	6E-15	4E-14
	256	2178	3E-03	2E-14	1E-13
3D	8	375	2E-02	1E-15	1E-14
	64	2187	1E-02	3E-15	3E-14
	512	14739	5E-03	9E-15	8E-14

**Table 2:** Error values for running conforming manufactured solutions in a unit cube. We get a machine epsilon as expected.

Now, we validate the scheme by running a convergence rate test. We use the same 2D setup as before with the following nonconforming manufactured solutions:

$$\mathbf{u}(\mathbf{x}, t) = \begin{pmatrix} \cos(x) + \cos(y+t) \\ \sin(x) + \sin(y+t) \end{pmatrix}, \quad (36)$$

$$p(\mathbf{x}, t) = \cos(x+y+t).$$

We see in table 3 that we get the  $O(\Delta t^2)$  in the  $L^2$  norm as expected. The  $H^1$  norms are a bit higher than the expected  $O(\Delta t^{\frac{3}{2}})$ .

$\mathbf{u}_{\text{dofs}}$	$\Delta t$	$\ e_{\mathbf{u}}\ _{L2}$	rate	$\ e_{\mathbf{u}}\ _{H1}$	rate
4802	2E-02	1.54E-04	-	1.04E-03	-
18818	1E-02	4.28E-05	1.85	3.11E-04	1.75
74498	5E-03	1.14E-05	1.9	9.01E-05	1.79
296450	2.5E-03	2.98E-06	1.94	2.57E-05	1.81

$\mathbf{u}_{\text{dofs}}$	$\Delta t$	$\ e_p\ _{L2}$	rate	$\ e_p\ _{H1}$	rate
4802	2E-02	1.37E-03	-	2.22E-02	-
18818	1E-02	4.10E-04	1.74	8.63E-03	1.36
74498	5E-03	1.18E-04	1.8	3.27E-03	1.4
296450	2.5E-03	3.31E-05	1.83	1.22E-03	1.42

**Table 3:** Convergence rate for the constant density projection method. The  $\text{CFL}_{\text{max}}$  is at 0.64.

### Realistic Models

In this section, we will study the applications of variable density projection scheme on a more realistic model; the Rayleigh-Taylor instability test. We compare our results with the work of (Guermont *et al.*, 2011a). Specifically in the early times before turbulent behavior.

### Rayleigh-Taylor Instability

We now apply the method to a more realistic problem. We use the Rayleigh-Taylor instability test that (Tryggvason, 1988) used. Two fluids are initially at rest in the 2D domain  $(-d/2, d/2) \times (-2d, 2d)$  and the heavier fluid is on top. The transition of the phase-field variable  $\rho$  is as follows:

$$\rho(x, y, t = 0) = \frac{\rho_{\text{max}} + \rho_{\text{min}}}{2} + \frac{\rho_{\text{max}} - \rho_{\text{min}}}{2} \tanh\left(\frac{y + \mu(x)}{\alpha d}\right), \quad (37)$$

where  $\alpha \approx 0.04$  and the initial interface is slightly perturbed as follows:

$$\mu(x) = 0.1 \cos(2\pi x/d). \quad (38)$$

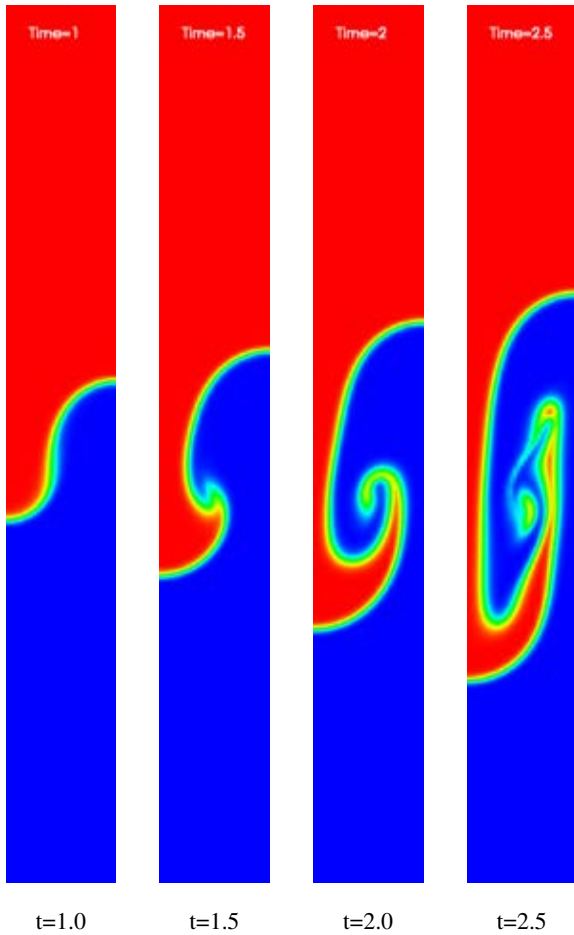


**Figure 1:** The Rayleigh-Taylor instability with density ratio of 3.

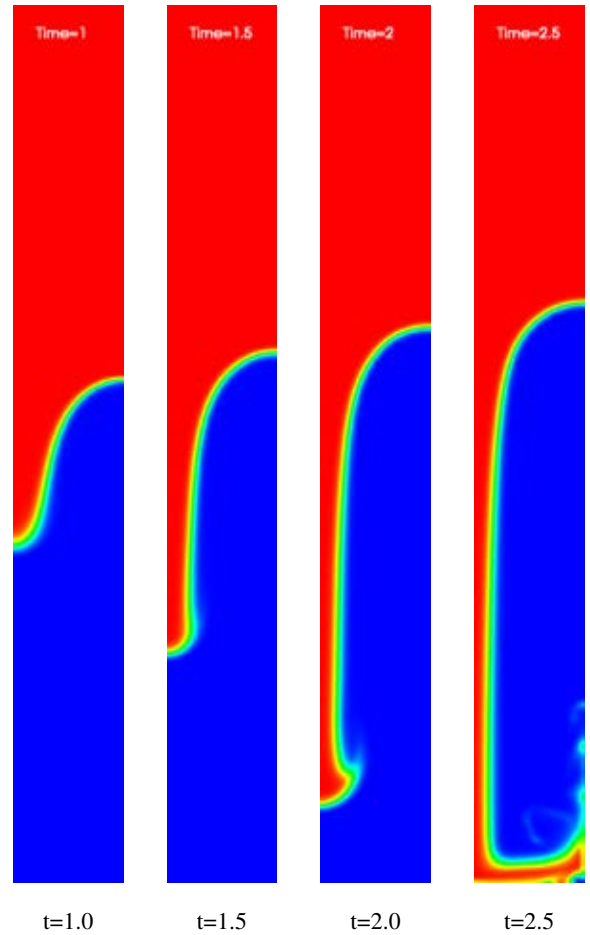


**Figure 2:** The Rayleigh-Taylor instability with density ratio of 100.

The time is also scaled using the Atwood number in Tryggvason as  $t_{\text{Tryg}} = t\sqrt{A_t}$

$$A_t = \frac{\rho_0^{\max} - \rho_0^{\min}}{\rho_0^{\max} + \rho_0^{\min}}, \quad (39)$$

where  $\rho_0^{\max} := \max_{\mathbf{x} \in \Omega} \rho_0(\mathbf{x})$  and  $\rho_0^{\min} := \min_{\mathbf{x} \in \Omega} \rho_0(\mathbf{x})$ . As the system progresses at  $t > 0$ , the heavy fluid will fall into the lighter fluid as a result of having the momentum equation gravity source term is  $\rho \mathbf{g}$

We non-dimensionalize the equations as follows. We divide by:  $\rho_0^{\min}$  for the density  $\rho$ ,  $d$  for length, and  $d^{1/2}/|\mathbf{g}|^{1/2}$  for time. Consequently,  $d^{1/2}|\mathbf{g}|^{1/2}$  is the velocity reference and the Reynolds number is  $Re = \rho_0^{\min} d^{1/2} |\mathbf{g}|^{1/2} d / \mu$ . We will restrict ourselves to the domain  $(0, d/2) \times (-2d, 2d)$  because we assume that the symmetry of the initial setup continues as time progresses. The top and bottom parts have no-slip boundary conditions and the left and right sides have  $\mathbf{u} \cdot \mathbf{n} = 0$ ,  $(\mathbf{I} - \mathbf{n} \otimes \mathbf{n}) \mathbf{v} \nabla \mathbf{u} = 0$  boundary conditions (known as symmetry or free boundary conditions).

*Remark.* Note that we must integrate the pressure term by parts in the weak form for  $p$  to be in  $L^2$ . In this experiment, we tested both integrating by parts and leaving the pressure term as is. This leads to different boundary conditions for each case:  $(\mathbf{I} - \mathbf{n} \otimes \mathbf{n})(\mathbf{v} \nabla \mathbf{u} - \mathbf{I}p) = 0$ , and  $(\mathbf{I} - \mathbf{n} \otimes \mathbf{n}) \mathbf{v} \nabla \mathbf{u} = 0$  respectively. In this experiment, both were numerically stable and gave almost exactly the same results when compared to previous papers. By not integrating by parts,  $p$  will be in  $H^1$  and we have to answer the question: Is the discrete Ladyzhenskaya-Babuska-Brezzi (LBB) condition sat-

isfied for the space pair  $H^1, H^1$ ? In this experiment specifically, the numerical scheme seems to be stable but we cannot generalize to all possible cases without a rigorous proof.

As hyperbolic equations need stabilization, we do so with the nonlinear entropy viscosity (Guermond *et al.*, 2011a) using the entropy function  $E(x) = -\log |\rho(1-\rho) + 10^{-14}|$ . In figure 1, the evolution of the density field of ratio 3 at times 1, 1.5, 2, and 2.5 in Tryggvason time scale  $t_{\text{Tryg}} = t\sqrt{A_t}$  with  $Re = 1000$ . The same times are shown in figure 2 with density ratio of 100. There are 8484  $Q_2$  degrees of freedom for  $\rho$  with uniform mesh size of 2048 cells. The time stepping is variable and maintains a maximum CFL of 0.4.

Now, we want to conduct a more challenging test. Specifically, we will test with density ratio 100 to check the robustness of the scheme – see, for example, (Sussman *et al.*, 1994). As figure 2 shows, the simulation holds nicely. Also, when figure 1 is visually compared with the results in (Guermond *et al.*, 2015), they are visually almost identical.

## CONCLUSION

The Navier-Stokes equations were solved using a code developed based on finite element method to accurately simulate immiscible two phase flows. A proprietary massively parallel Navier-Stokes solver code based on the open source software deal.II was successfully implemented to simulate the interface between the two liquid phases with good accuracy. The utilization of both the level set method with a third order strong stability property Runge-Kutta (SSPRK) time integrator and a second-order projection method for the momentum equation was deemed successful. Numerical val-

idations of the transport and momentum equations were presented; they confirmed the code accuracy. The convergence rate of the numerical schemes selected for modeling the non-conforming manufactured solutions were shown to be within expected convergence rate values. Classical Rayleigh-Taylor instability results were shown to be in good agreement with previously published work.

## ACKNOWLEDGEMENT

The authors would like to thank Saudi Aramco for technical and financial support which made this study possible.

## REFERENCES

GOTTLIEB, S. (2005). “On high order strong stability preserving runge–kutta and multi step time discretizations”. *Journal of Scientific Computing*, **25**(1), 105–128.

GUERMOND, J.L. and PASQUETTI, R. (2011). “Entropy viscosity method for high-order approximations of conservation laws”. J.S. Hesthaven and E.M. Rønquist (eds.), *Spectral and High Order Methods for Partial Differential Equations*, vol. 76 of *Lecture Notes in Computational Science and Engineering*, 411–418. Springer Berlin Heidelberg. URL [http://dx.doi.org/10.1007/978-3-642-15337-2\\_39](http://dx.doi.org/10.1007/978-3-642-15337-2_39).

GUERMOND, J.L. and SALGADO, A.J. (2011). “Error analysis of a fractional time-stepping technique for incompressible flows with variable density”. *SIAM J. Numer. Anal.*, **49**(3), 917–944. URL <http://dx.doi.org/10.1137/090768758>.

GUERMOND, J.L., PASQUETTI, R. and POPOV, B. (2011a). “Entropy viscosity method for nonlinear conservation laws”. *Journal of Computational Physics*, **230**(11), 4248–4267.

GUERMOND, J.L., PASQUETTI, R. and POPOV, B. (2011b). “Entropy viscosity method for nonlinear conservation laws”. *Journal of Computational Physics*, **230**(11), 4248 – 4267. Special issue High Order Methods for CFD Problems, URL <http://www.sciencedirect.com/science/article/pii/S0021999110006583>.

GUERMOND, J.L., PASQUETTI, R. and POPOV, B. (2011c). “From suitable weak solutions to entropy viscosity”. *Journal of Scientific Computing*, **49**(1), 35–50. URL <http://dx.doi.org/10.1007/s10915-010-9445-3>.

GUERMOND, J.L., SALGADO, A.J. and SHEN, J. (2015). “Splitting for variable density flows”. *in preparation*.

JOHN, V. (2004). *Large Eddy Simulation of Turbulent Incompressible Flows: Analytical and Numerical Results for a Class of Les Models*. Lecture Notes in Computational Science and Engineering. Springer Berlin Heidelberg. URL <http://books.google.com/books?id=Y-Z0qMEiwdUC>.

OSHER, S. and SETHIAN, J.A. (1988). “Fronts propagating with curvature-dependent speed: Algorithms based on hamilton-jacobi formulations”. *Journal of Computational Physics*, **79**(1), 12 – 49. URL <http://www.sciencedirect.com/science/article/pii/0021999188900022>.

SMAGORINSKY, J. (1963). “General circulation experiments with the primitive equations”. *Monthly Weather Review*, **91**(3), 99–164. URL [http://dx.doi.org/10.1175/1520-0493\(1963\)091<0099:GCEWTP>2.3.CO;2](http://dx.doi.org/10.1175/1520-0493(1963)091<0099:GCEWTP>2.3.CO;2).

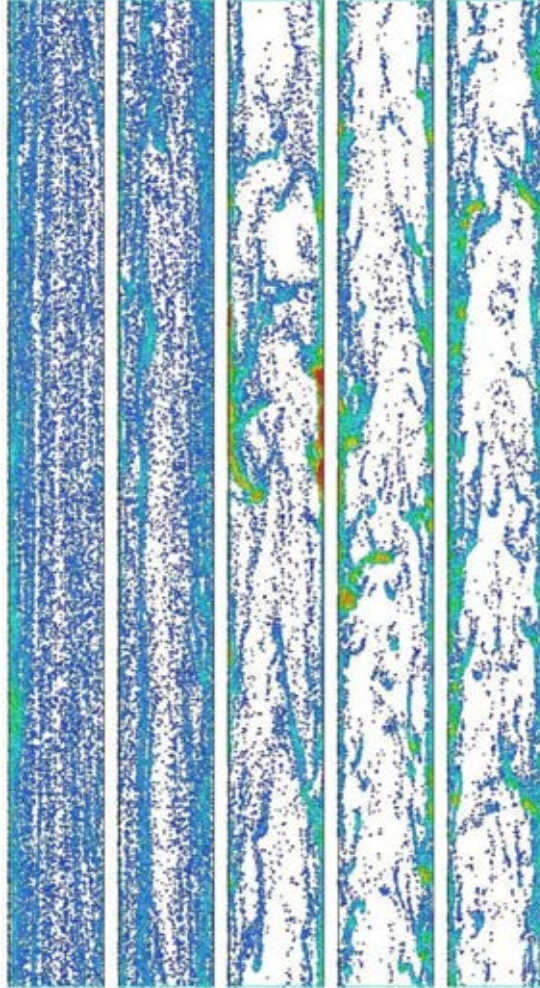
SUSSMAN, M. and FATEMI, E. (1999). “An efficient, interface-preserving level set redistancing algorithm and its application to interfacial incompressible fluid flow”. *SIAM Journal on scientific computing*, **20**(4), 1165–1191.

SUSSMAN, M., SMEREKA, P. and OSHER, S. (1994). “A level set approach for computing solutions to incompressible two-phase flow”. *Journal of Computational Physics*, **114**(1), 146 – 159. URL <http://www.sciencedirect.com/science/article/pii/S0021999184711557>.

TRYGGVASON, G. (1988). “Numerical simulations of the rayleigh-taylor instability”. *J. Comput. Phys.*, **75**(2), 253–282. URL [http://dx.doi.org/10.1016/0021-9991\(88\)90112-X](http://dx.doi.org/10.1016/0021-9991(88)90112-X).



# PARTICLE METHODS







## A NUMERICAL APPROACH TO MODEL AGGREGATE RESTRUCTURING IN SHEAR FLOW USING DEM IN LATTICE-BOLTZMANN SIMULATIONS

Akash SAXENA<sup>1\*</sup>, Jean-Sébastien KROLL-RABOTIN<sup>2†</sup>, R. Sean SANDERS<sup>1‡</sup>

<sup>1</sup>Department of Chemical Engineering, University of Alberta, CANADA

<sup>2</sup>Institut Jean-Lamour, UMR 9871, CNRS, Université de Lorraine-CNRS, Nancy, FRANCE

Laboratory of Excellence for Design of Alloy Metals for Low-mass Structures, FRANCE

\* E-mail: asaxena@ualberta.ca

† E-mail: jean-sebastien.kroll-rabotin@univ-lorraine.fr

‡ E-mail: ssanders@ualberta.ca

### ABSTRACT

Aggregate shape and structure significantly impact rheological properties of fluids in many fields such as extractive metallurgy, oil field drilling and mineral processing. The morphology of the aggregates determines the porosity of solid structures and their dimensions, which in turn affects the solid-liquid and solid-solid interactions in the mixture, and hence the rheology of the system. Aggregates can undergo morphological changes induced by shear flow. The response of aggregate mixtures in terms of rheology as a function of their shear history has thus been studied in many fields (Coufort *et al.*, 2005) with experimental approaches. Numerical investigations of aggregation dynamics and aggregate restructuring have also been conducted in low Reynolds conditions (Fringieri and Vanni, 2016), or using free draining approximation, in which the fluid particle interactions are exclusively through Stokesian drag (Eggersdorfer *et al.*, 2010). In this study, a fully coupled Eulerian-Lagrangian approach is developed to evaluate the restructuring of aggregates in shear flows for low Reynolds numbers. In particular, a Discrete Element Method (DEM) is used for particle tracking, coupled with Lattice Boltzmann Method (LBM) for solving the liquid flow. An Immersed Boundary Method (IBM) is incorporated so that primary particle shapes and hydrodynamic interactions between particles are fully resolved (Niu *et al.*, 2006). Selected particle-particle interaction models have been implemented in the DEM to represent the mechanical behaviour of aggregates. General attractive and repulsive force models, and the bending moment as described by Pantina and Furst (2005) have been included.

Artificial aggregates were created and characterized using fractal dimension and radius of gyration. The evolution of these shape indicators over time has been studied while aggregates are subjected to a shear flow. Preliminary results obtained with fully coupled liquid-solid simulations were also compared with results based on the free draining approximation. In fully coupled simulations, significant perturbations in the flow field were observed due to the presence of particles, which leads to a significant difference in aggregate's restructuring. Different solid interaction contributions and their underlying impact on aggregate restructuring have been compared, at a given shear rate. While increasing shear or maximum cohesion forces lead to denser aggregates, effect of tangential forces on the aggregate's morphology appears to be more complex. Also, tangential forces were found to have a tendency to favor aggregate breakage.

**Keywords:** Aggregates, shear flow, restructuring, CFD-DEM, free draining, lattice-Boltzmann method, immersed boundary method. .

### NOMENCLATURE

#### Greek Symbols

$\alpha$	Acceleration force coefficient, [ $kg$ ].
$\beta$	Velocity force coefficient, [ $kg \cdot s$ ].
$\gamma$	Force contribution, [ $N$ ].
$\dot{\gamma}$	Shear rate, [ $s^{-1}$ ].
$\rho$	Mass density, [ $kg \cdot m^{-3}$ ].
$\mu$	Dynamic viscosity, [ $Pa \cdot s$ ].
$\xi$	Spring elongation, [ $m$ ].
$\omega$	angular velocity, [ $rad \cdot s^{-1}$ ].
$\Omega$	LBM collision operator, [ $]$ ].
$\delta$	Regularized Dirac function, [ $]$ ].
$\Delta$	Step, [ $]$ ].

#### Latin Symbols

$A_H$	Hamaker constant, [ $J$ ].
$\mathcal{A}$	Surface area, [ $m^2$ ].
$D_f$	Fractal dimension, [ $]$ ].
$f$	LBM quantities, [ $]$ ].
$f$	Volume force, [ $N \cdot m^{-3}$ ].
$F$	Force, [ $N$ ].
$J$	Tensor of inertia, [ $kg \cdot m$ ].
$m$	Mass, [ $kg$ ].
$N$	Number of particles, [ $]$ ].
$N_{Born}$	Born constant, [ $]$ ].
$P$	Projection matrix, [ $]$ ].
$q$	LBM solution vector, [ $]$ ].
$R_g$	Radius of gyration, [ $m$ ].
$R_p$	Particle radius, [ $m$ ].
$S$	Structure factor, [ $]$ ].
$T$	Torque, [ $N \cdot m$ ].
$t$	Time, [ $s$ ].
$v$	Velocity, [ $m \cdot s^{-1}$ ].
$V$	Force potential, [ $J$ ].

#### Sub/superscripts

$f$	Fluid.
$i$	Index $i$ .
$j$	Index $j$ .
$M$	Marker point.
$n$	Normal component.
$t$	Tangential component.
$p$	Particle.

## INTRODUCTION

The efficiency of most industrial processes involving fluid-solid systems strongly depends on aggregate behaviours, either directly or through their impact on rheological parameters of the fluid-solid mixture. In mineral processing (Laskowski and Ralston, 2015) or liquid metal treatments (Zhang and Thomas, 2003), shear induced aggregation is often used to form bigger aggregates which are easier to recover. In extractive metallurgy as well as in the oil sand industry, aggregation of colloidal clay particles in the tailings is necessary to separate them out (Plumpton, 2013). Whatever the material they are made of, floc and aggregate properties are conditioned by the flow conditions (Vaezi G. *et al.*, 2011; Khashayar Rastegari *et al.*, 2004; Coufort *et al.*, 2005; Daoud *et al.*, 2011).

Aggregates are formed by primary particles that come sufficiently close to each other, so that they undergo cohesive forces. When they are transported in a fluid phase, they experience hydrodynamic forces that compete with the cohesive forces holding them together. Consequently, in such conditions, their morphology evolves, which impacts both the distributions of the hydrodynamic stresses and the contact/cohesive forces within the aggregate.

Early attempts to predict the aggregation kinetics are a century old, when Smoluchowski (1917) first gave the equation to predict the net rate of aggregation of particles based on collision frequency. However, his work did not explain the underlying mechanics. Earlier, due to the complexity of the physics, the aggregates were assumed to be of simple shapes such as spheres, and stresses across the sphere were calculated in shear flow to predict its rupture (Bagster and Tomi, 1974). Later, porosity of aggregates was taken into account by Adler and Mills (1979). However, it was concluded by Sonntag and Russel (1987) that this approach was not supported by experimental data as it did not take into account the complex shapes of aggregates.

With the advancements in computational resources, attempts were made to model evolution of aggregates composed of discrete particles. Using the Discrete Element Method (DEM) (Cundall and Strack, 1979), it became possible to model the forces between every primary particle. For hydrodynamic forces, free-draining approximation has been extensively used (Chen and Doi, 1989; Potanin, 1993; Becker *et al.*, 2009; Eggersdorfer *et al.*, 2010). It assumes that each particle experiences Stokesian drag as if no other particle were present in its vicinity. Brady and Bossis (1988) developed Stokesian Dynamics (SD) which accurately accounts for the impacts of hydrodynamic interactions on aggregates (Harshe *et al.*, 2011; Vanni and Gastaldi, 2011; Seto *et al.*, 2012; Harshe and Lattuada, 2012; Conchuir *et al.*, 2014; Ren *et al.*, 2015). However, SD is only valid for spheres and is accurate only for low Reynolds conditions. Schlauch *et al.* (2013) have developed a Finite Element Method (FEM) in which Stokes equation is discretized and solved over the surface. Again, this approach is limited to low Reynolds conditions, but allows complex shape primary particles. Immersed Boundary Method (IBM) (Peskin, 1972) is now being widely used for full coupling between complex shape objects and full Navier-Stokes flow solver. Different variants of IBM have proven able to handle even high Reynolds conditions (Yang and Stern, 2013; Taira and Colonius, 2007; Lācis *et al.*, 2016). Schlauch *et al.* (2013) have done a comparative study of these coupling methods (namely, FEM, SD and LBM), however, their particles were fixed in a fluid flow. Till

now, fully coupled liquid-solid simulations are still very rare due to their high computation cost, thus there remains a lack of understanding about the impact of hydrodynamic interactions on the aggregate structures.

Lattice Boltzmann methods (LBM) have proved efficient to solve the flow field around complex shapes. Binder *et al.* (2006) used LBM to compare results with accelerated SD and Schlauch *et al.* (2013) used LBM to resolve the flow around their fixed aggregates.

In various studies, different force models have been used depending on the physical system. Commonly used models include spring-dashpot model (Kadau *et al.*, 2002; Iwashita and Oda, 1998; Seto *et al.*, 2012). Other studies have used DLVO model to describe the normal forces in colloidal systems (Becker and Briesen, 2008; Becker *et al.*, 2009; Ren *et al.*, 2015; Conchuir *et al.*, 2014; Harshe *et al.*, 2011). Even magnetic models have been used in specific studies (Dominik and Nübold, 2002). Normal forces have thus been extensively studied, however, in many systems such as colloidal suspensions, tangential forces have also been observed (Pantina and Furst, 2005) and modelled (Becker and Briesen, 2008). Still, no study has been done so far to quantify the relative effect of the involved forces in restructuring of an aggregate.

From all these works that have been conducted so far, it appears that in many systems, cohesive forces between primary particles have both tangential and normal components. The way the hydrodynamic forces are balanced by the contact forces is what drives the restructuring of aggregates. It is thus expected that the relative weight of the two contributions of the cohesive force may significantly impact the morphological changes of the aggregates. Using fractal dimension to characterize aggregate morphology, we have compared the relative effect of selected forces in a shear flow. The forces that we have considered are maximum attractive force, drag force and maximum bending moment.

Due to the major role of the drag force in the problem, preliminary studies using IBM in Lattice-Boltzmann simulations have also been conducted and compared to the free-draining approximation.

## SIMULATION SETUP AND NUMERICAL METHODS

### Generation and characterization of initial aggregates

Aggregate size and density are the most natural quantities to characterize aggregates (Gregory, 1997). Several studies have worked on relating these two properties through the concept of fractal dimension (Gregory, 1997; Woodfield and Bickert, 2001; LI and Ganczarzyk, 1989; Bushell *et al.*, 2002). It is defined on the basis that the mass of an aggregate scales as a power of its size, this power being the fractal dimension. This allows to characterize morphology using a unique quantity. To ensure that fractal dimension is a valid way to characterize aggregate morphological evolutions, simulations have been run for 10 different aggregates with the same fractal dimension ( $D_f$ ) and the same number of particles ( $N$ ), namely  $D_f = 2.30 \pm 0.01$ , radius of gyration ( $R_g$ ) =  $22.76 \pm .01 \mu\text{m}$  and  $N = 50$ , as represented in figure 1. To estimate the fractal dimension, it has been derived from the number of particles and the radius of gyration, which are straightforward to calculate.

$$N = S \left( \frac{R_g}{R_p} \right)^{D_f} \quad (1)$$

In equation (1),  $S$  is the static structure factor, for which there

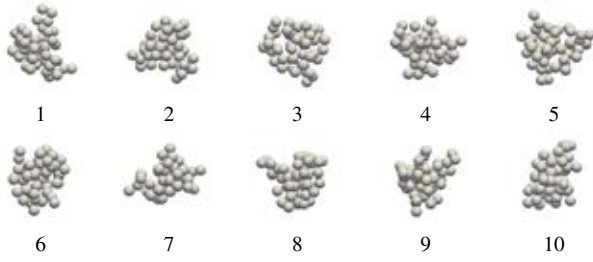


**Figure 1:** The 10 artificially created initial aggregates that have been used in the simulations ( $N = 50$ ,  $D_f = 2.30 \pm 0.01$ ),  $R_g = 22.76 \pm .01 \mu\text{m}$

exists an empirical expression as a function of the fractal dimension (Gmachowski, 2002).

$$S = \left( \sqrt{1.56 - \left(1.728 - \frac{D_f}{2}\right)^2} - 0.228 \right)^{D_f} \left( \frac{2 + D_f}{D_p} \right)^{\frac{D_f}{2}} \quad (2)$$

Some studies (Harshe *et al.*, 2011) also include radius of gyration ( $R_g$ ) to characterize an aggregate. However, since equation (1) includes  $R_g$ , there is no need to track it along with  $D_f$ .

The initial structures of the simulated aggregates (see figure 1) were produced algorithmically. An initial sphere is placed, then all the other spheres are added one after the other to the aggregate. Each new sphere is placed at random position relative to another existing sphere. Sixteen (16) random positions are tested for every new sphere, and the chosen position is the one that yields the fractal dimension that is closest to the target fractal dimension. This process is repeated until the aggregate contains the desired number of primary spheres.

### Discrete Element Method

To study the restructuring of an aggregate, each particle has to be tracked independently. In the Discrete Element Method (DEM) (Cundall and Strack, 1979), all forces acting on every individual particle are calculated, and the equations of motion for all particles are solved.

Forces are evaluated at each time step by iterating over every individual particle and all particle pairs that are closer than a given maximum interaction distance. Then particle velocities and positions are updated. After that, the next time step starts again by calculating the forces applied to each particle, as well as computing interphase coupling forces when the liquid flow is resolved, and so on. The forces applied to each individual particles (driving forces) and to particle pairs (interaction forces) are described in the next section. Particle velocities are calculated by solving Newton's equations of motion for every particle.

$$m \frac{d\vec{v}_i}{dt} = \sum \vec{F}_i \quad (3)$$

$$J \frac{d\vec{\omega}_i}{dt} = \sum \vec{T}_i \quad (4)$$

To solve these equations, we use a semi-explicit approach where all forces that depend on particle acceleration and velocity are accounted for as linear functions, represented by coefficients  $\alpha$  and  $\beta$  in equation (5).

$$m_p \frac{d\vec{v}}{dt} = \alpha \frac{d\vec{v}}{dt} + \beta \vec{v} + \vec{\gamma} \quad (5)$$

The term  $\vec{\gamma}$  contains the forces that do not depend on particle motion. The velocity calculation at each time step comes directly from equation (5) following a semi-implicit approach, which yields a simple linear equation.

$$m_p \frac{\vec{v}(t + \Delta t) - \vec{v}(t)}{\Delta t} = \alpha \frac{\vec{v}(t + \Delta t) - \vec{v}(t)}{\Delta t} + \beta \vec{v}(t + \Delta t) + \vec{\gamma} \quad (6)$$

Equation (6) is solved for  $\vec{v}(t + \Delta t)$ .

$$\vec{v}(t + \Delta t) = \frac{\left( \frac{m_p - \alpha}{\Delta t} \right) \vec{v}(t) + \vec{\gamma}}{\frac{m_p - \alpha}{\Delta t} - \beta} \quad (7)$$

The equation for the angular moment is expressed in the same way, and it is solved similarly.

In this specific study,  $\alpha = 0$  and particle inertia is negligible, so equation (7) practically boils down to  $\vec{v} = -\vec{\gamma}/\beta$ . However, inertia has been kept in the solver since it helps stabilize the particle motion when interaction forces see very steep variations, and it is physically there anyway. Finally, particle position is updated with the new velocity.

$$\vec{x}(t + \Delta t) = \vec{x}(t) + \Delta t \vec{v}(t + \Delta t) + \frac{\Delta t}{2} (\vec{v}(t + \Delta t) - \vec{v}(t)) \quad (8)$$

This integration scheme, while not being of high order accuracy, helps stabilizing the interactions between primary particles since it dissipates energy from the otherwise purely elastic interactions, but it preserves the maximum values of the different forces. Due to the low inertia of the particles, the acceleration term is negligible, except for the few time steps when new bonds are created between primary particles.

The DEM is only a tracking method for the primary particles that the aggregate is made of. All the interesting physics must be captured by the force models that are included. The forces here are of two nature, driving forces and pair particle interactions.

### Forces involved

In a solid-liquid system, the dynamics of every primary particle is governed by primarily two types of interactions: inter-particle forces and hydrodynamic forces.

DLVO theory has been used to represent particle interactions, which includes Van der Waals forces as cohesive forces. Normal forces then derive from a potential ( $V$ ). Since the considered primary particles are spherical, a simplified form for the potential has been used (Hamaker, 1937).

$$V_{VDW}(s) = -\frac{A_H}{12(s-2)} \quad (9)$$

Here,  $A_H$  is the Hamaker constant, and  $s$  is the non-dimensional distance between two particles. Attractive Van der Waals forces must be balanced by a steeper very short range force that prevents particle from overlapping. Born repulsion (Feke *et al.*, 1984) plays this role.

$$V_{Born}(s) = \frac{A_H N_{Born}}{s} \left[ \frac{s^2 - 14s + 54}{(s-2)^7} + \frac{60 - 2s^2}{s^7} + \frac{s^2 + 14s + 54}{(s+2)^7} \right] \quad (10)$$

Here,  $N_{born}$  is the Born constant. When combined, these two attractive and repulsive contributions form an energy barrier that must be overcome for particles to separate. This energy barrier corresponds to a maximum attractive force.

Moreover, a tangential force has been included. This tangential force is responsible for providing a bending moment to the aggregates similar to that seen in an elastic rod (Becker and Briesen, 2008). In this model, when two particles come close and stick to each other due to cohesive forces, they interact in an elastic manner modelled by springs ( $k_t$ ) whose elongation ( $\xi$ ) corresponds to the relative tangential displacement of the interacting particles.

$$\frac{d\vec{\xi}_{ij}}{dt} = (1 - \vec{n}_{ij} \otimes \vec{n}_{ij})(\vec{v}_j - \vec{v}_i) - 2R_p(\vec{\omega}_j \times \vec{n}_{ij}) \quad (11)$$

where  $i$  and  $j$  are particle indices,  $\vec{v}$  is their velocity,  $\vec{\omega}$  is their angular velocity and  $n_{ij}$  is the unit vector pointing from the center of particle  $i$  to the center of particle  $j$ . Force and moment depend on spring elongation ( $\xi$ ).

$$\vec{F}_j = k_t(\vec{\xi}_{ij} - \vec{\xi}_{ji}) \quad (12)$$

$$\vec{T}_j = 2R_p k_t \vec{n}_{ji} \times \vec{\xi}_{ji} \quad (13)$$

The maximum bending moment that particles can exert on each other is fixed through a critical elongation ( $d_{max}$ ) after which springs can no longer elongate. Thus, the maximum tangential force between a pair of particles is  $k_t \cdot d_{max}$ .

All the values for the constants ( $A_H$ ,  $N_{Born}$ ,  $k_t$  and  $d_{max}$ ) were chosen so that the forces cover a range that is expected for 2  $\mu\text{m}$  clay particles in water. The overall set of conditions that have been tested is summarized in tables 1 and 2. ( $d_{max}$ ) has been chosen as 2% of particle's diameter.

The driving forces for aggregate restructuring are hydrodynamic forces. In this study, two approaches have been considered: Free Draining Approximation and Immersed Boundary Method.

### Free Draining Approximation

In the free draining approximation, it is assumed that the hydrodynamic forces acting on a particle are not affected by the presence of other particles. They do not account for the perturbation of particles on the fluid flow. Thus, it is only a one-way coupling. It tends to overestimate the forces as it does not compensate the surface area of primary particles shielded by other particles. It is calculated using Stokes' law, since the particle Reynolds number remains small in the considered cases. A pure shear flow is imposed for the liquid phase.

$$\vec{F}_{f/p} = 6\pi\mu R_p(\vec{v}_p - \dot{\gamma}z\vec{e}_x) \quad (14)$$

$$\vec{T}_{f/p} = 8\pi\mu R_p^3(\vec{\omega}_p - \frac{1}{2}\dot{\gamma}\vec{e}_y) \quad (15)$$

where  $\mu$  is the dynamic viscosity of the fluid, index  $p$  is for particle properties and  $\dot{\gamma}$  is the shear rate in liquid flow.

To resolve the hydrodynamic interactions between particle, such as shielding, two-way coupling is required and a flow solver is needed. A lattice Boltzmann method has been used for that.

### Lattice Boltzmann Method

Aggregate restructuring is driven by particle contacts. Interaction forces have very steep variations according to inter-particle distance and collision are instantaneous events, thus

the time and the length scales induced by the particle interactions are much shorter than the ones of the liquid flow. Thus, an explicit method is well suited to solve for the fluid flow, since flow evolutions will be slow compared to other physical mechanisms that put stronger constraints on the time steps.

Lattice Boltzmann methods have become the most common explicit flow solvers. Moreover, the inherent difficulty to use complex meshes in such methods has also led to the development of several ways to represent solid boundaries inside the fluid phase, which is also a significant asset for the study of aggregate restructuring, since changes in the contacts between particle make it particularly difficult to represent particles using mesh boundaries.

For these reasons, a lattice Boltzmann method has been used for simulations in which the liquid flow was resolved. Lattice Boltzmann methods are based on the resolution of the Boltzmann equation (16) in which the flow field variables are only solved as moments of the probabilities ( $f$ ) associated to a given mass at a given position in space, moving at a given velocity.

$$\frac{\partial f}{\partial t} + \vec{c} \cdot \vec{\nabla}_x f = \Omega(f) - \vec{f} \cdot \vec{\nabla}_c f \quad (16)$$

$$\rho = \int_{\mathbb{R}^3} f(\vec{c}) d\vec{c} \quad \rho \vec{u} = \int_{\mathbb{R}^3} \vec{c} f(\vec{c}) d\vec{c}$$

Once discretized over a lattice, that is a finite set of positions in space and a finite set of velocities ( $\vec{c}_i$ ) at which mass probabilities can travel from one node to its neighbours during a time step, the Boltzmann equation can be solved explicitly using a time-splitting approach, where the dynamics are solved in two steps: collision and streaming. Hereafter, external volume forces ( $\vec{f}$ ) are accounted for during the collision step, that is, included into the so-called collision operator ( $\Omega$ ).

$$\overbrace{f_i(\vec{x} + \vec{c}_i \Delta t, t + \Delta t)}^{\text{streaming}} = \overbrace{f_i(\vec{x}, t) + \Omega_i(f(\vec{x}, t), \vec{f}(\vec{x}, t))}_{\text{collision}} \Delta t \quad (17)$$

Bhatnagar *et al.* (1954) have expressed the collision operator as a relaxation towards an equilibrium state (which for kinetic theory of gases corresponds to the lattice-discretized Maxwell distribution) and through which the flow dynamics can satisfy the Navier-Stokes equations, under the condition that some unphysical high order terms that appear due to the discretization remain low. More recently developed lattice-Boltzmann methods operate the relaxation in a projection of the probabilities ( $f$ ) on another basis than lattice velocities ( $\vec{c}_i$ ), which allows to relax different combinations of their moments with different relaxation coefficients. Such Multiple-Relaxation-Time (MRT) approaches (D'Humières *et al.*, 2002) offer a way to segregate between physical and unphysical terms in the equation and to damp the unphysical high order terms, widening the set of conditions under which Navier-Stokes equations are satisfied with a good accuracy.

There is then a matrix  $[P]$  to operate the projection between the probabilities and the set of moments that are relaxed. In this study, the collision operator described by Eggels and Somers (1995) is used. The relaxed moments are chosen so that flow field quantities directly appear in a so-called solu-

tion vector ( $q$ ).

$$f(\vec{x} + \vec{c}, t + 1) = [\mathbf{P}]^{-1} \underbrace{([1] + [\Omega])}_{q^+} \overbrace{[\mathbf{P}] f(\vec{x}, t)}^{q^-} \quad (18)$$

$$q^\pm = \begin{cases} \rho \\ \rho \vec{u} \pm \frac{1}{2} \vec{f} \\ \rho([\vec{u} \otimes \vec{u}]) + \rho \frac{\pm 1 - 6\nu}{6\nu} ([\nabla \vec{u}] + [\nabla \vec{u}]^\top) \end{cases}$$

One of the nice properties of such a collision operator is that the external forces are applied during the collision step, and the projection matrix ( $[\mathbf{P}]$ ) gives a direct relation between the probabilities ( $f$ ) and the corresponding momentum change at each time step (that is the relaxation of the first order moments of the probabilities). It has been leveraged for the solid-liquid coupling method, as well as for boundary conditions, where shear stress was imposed as an external force to get a shear flow.

### Immersed boundary method

Due to the ease to exchange momentum with the liquid phase through the chosen collision operator, the coupling with the solids is achieved using the momentum exchange based boundary developed by Niu *et al.* (2006). The surface of the particles is described by marker points, distributed as regularly as can be on the particle surface, each weighted to the area of the surface element it corresponds to, as shown on figure 2.

The coupling between the marker points ( $M$ ) of the solids and the lattice nodes for the liquid is achieved by interpolating the quantities using regularized Dirac functions ( $\delta$ ) as described by Roma *et al.* (1999). The values of the probabilities are thus interpolated at the marker point position ( $\vec{x}_M$ ), and the force contribution of each marker point to the coupling between the two phases is calculated using bounce-back (stopping the flow) and adding the momentum that corresponds to the solid phase at this position, weighted by surface element area. The resulting force ( $\vec{f}_{p/f}$ ) is then distributed on the fluid

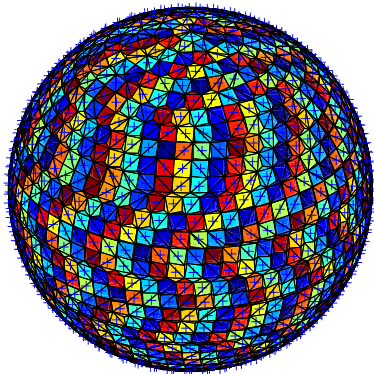


**Figure 2:** Representation of a sphere using a surface distribution of marker points (+) and their corresponding surface elements (each represented with a different color)

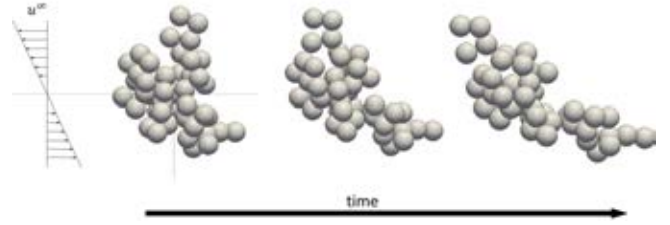


**Figure 3:** Aggregate 1 (see figure 1) placed in a pure shear flow so that its center of mass lies in the zero velocity plane

nodes using the same regularized Dirac function.

$$f_M = \sum_{\vec{x}} f(\vec{x}) \delta(\vec{x}_M - \vec{x}) \quad (19)$$

$$\vec{f}_M = \underbrace{\mathcal{A}_M}_{\text{marker weight}} \sum_i \left( \underbrace{f_M(-\vec{c}_i) - f_M(\vec{c}_i)}_{\text{full way bounce back}} + \underbrace{[\mathbf{P}]_{(\vec{c}_i)}^{-1} \rho \vec{u}_M}_{\text{solid velocity}} \right) \vec{c}_i \quad (20)$$

$$\vec{f}_{p/f}(\vec{x}) = \sum_M \vec{f}_M \delta(\vec{x}_M - \vec{x}) \quad (21)$$

Due to the way of computing the coupling force ( $\vec{f}_{p/f}$ ), it ensures that the fluid velocity, after the collision operator is applied, is the velocity of the solid. On the other hand, the force and the torque acting on the solids are the sum of the reciprocal actions.

$$\vec{F}_{f/p} = - \sum_M \vec{f}_M \quad (22)$$

$$\vec{T}_{f/p}^O = - \sum_M (\vec{x}_M - \vec{x}_O) \times \vec{f}_M \quad (23)$$

Since this coupling method forces the fluid surface corresponding to the solid boundary to behave like a solid, the action of the fluid inside the solid must be cancelled. To do that, in the equation of motion that is solved in the DEM, another external force is applied to every resolved particle that opposes inner fluid inertia. To make sure that this force can be easily estimated, another surface boundary is forced inside the particle, so that viscous effects between the forced layers make the motion of the inner fluid follow a solid body motion.

Then, the inertia of the inner fluid should be removed by introducing a virtual force in the DEM as a coefficient for the acceleration term, see  $\alpha$  in equation (5), but here, since the particle density and the fluid density are the same it would have made the equation degenerate. Inner fluid inertia has been kept for numerical reasons, but it has no impact on the physical results since particle Stokes number is very low anyway.

### Simulation cases

Initial aggregates as presented in figure 1 were introduced in laminar pure shear flows, as shown is figure 3. Aggregates restructure due to the forces it experiences from the flow and the fractal dimensions ( $D_f$ ) are recorded over time.

To study the relative effect of the different forces on the evolution of fractal dimension, several variations of the forces were considered. Equations 9 and 10 show that for a given particle diameter, the maximum cohesive force depends on the Hamaker constant  $A_H$ . For clay colloidal systems,  $A_H$  is generally of the order  $10^{-20}$  J and Born ( $N_{\text{Born}}$ ) constant can have values between  $10^{-18}$  to  $10^{-23}$ , which gives maximum cohesive force in the order  $10^{-9}$  N. Pantina and Furst (2005)

$A_H$ (J)	$(F_n)_{\max}$ (N)	$k_t$ (N/m)	$(F_t)_{\max}$ (N)	$\dot{\gamma}$ (s <sup>-1</sup> )	$(F_{f/p})_{\max}$ (N)
$5.92 \times 10^{-21}$	$10^{-9}$	$2.5 \times 10^{-2}$	$10^{-9}$	2652.59	$10^{-9}$
$5.92 \times 10^{-22}$	$10^{-10}$	$2.5 \times 10^{-3}$	$10^{-10}$	265.259	$10^{-10}$
$5.92 \times 10^{-23}$	$10^{-11}$	$2.5 \times 10^{-4}$	$10^{-11}$	26.5259	$10^{-11}$

**Table 1:** Simulation parameters: values of the physical constants and corresponding maximum forces

suggest that the maximum tangential force is of the order  $10^{-11}$  N. Also, it is common to see shear rates of  $100 \text{ s}^{-1}$  in experiments involving colloidal aggregates. The maximum shear-induced force between two particles can be estimated based on the drag force and the variation of velocity across a particle diameter.

$$F_{f/p} \sim 12\pi\mu\dot{\gamma}R_p^2 \quad (24)$$

The cohesive interactions within the whole aggregate will need to balance the driving force. However, these cohesive interactions are summed over chains of particles that all see different flow velocities. In the 50 particle aggregates, particle chains are about a dozen of primary particles long. This is why the estimation of  $(F_{f/p})_{\max}$  was increased by an order of magnitude than the calculated value from equation (24). For a clay colloidal system with primary particles that would be  $2 \mu\text{m}$  in diameter, this gives a value of the order of  $10^{-10}$  N.

The reference case was then chosen with a maximum attraction force  $((F_n)_{\max} = \max(\|\vec{F}_{VDW} + \vec{F}_{Born}\|))$  of  $10^{-9}$  N, a maximum tangential force  $((F_{tang.})_{\max})$  of  $10^{-11}$  N and a shear induced force  $((F_{f/p})_{\max})$  of  $10^{-10}$  N. To reflect the relative variations of these parameters, forces have been expressed as their ratio to the shear induced force, which were then varied from 0.01 to 100. Table 1 lists all the physical values  $A_H$ ,  $k_t$  and  $\dot{\gamma}$  that have been varied for the simulations, and their corresponding force magnitudes. Table 2 lists all the simulation cases and the corresponding force ratios. In such conditions, the Reynolds number, calculated based on the shear rate, varies from  $10^{-4}$  to  $10^{-2}$ .

The LBM and DEM schemes used for this research follow the same approach as described in Kroll-Rabotin *et al.* (2012). In this study, the simulations were performed in a domain of  $200^3$  nodes, with each node of size  $0.2\mu\text{m}$ . Time step for each iteration was of the order  $10^{-9}$  s.

## RESULTS AND DISCUSSION

### Fractal Dimension as a morphology indicator

To address the question of the relevance of fractal dimensions ( $D_f$ ) as the single morphology indicator, all tested conditions have been repeated for 10 aggregates with the same fractal dimension. The number of particles and the primary particle diameter were always kept constant.

Figure 4 shows the evolution over time of the fractal dimension of the 10 aggregates (see figure 1) for various force ratios. Although it is hard to make any quantitative observation from such different curves, all these plots show that in all cases, all 10 aggregates follow the same trend and undergo the overall same transformation after some time, be it breakage or reaching about the same fractal dimension. The behaviour of aggregates number 8 (in the second line) and number 7 (right hand side of the third line) give confidence in the fact that observations extracted from the whole set of aggregates can be interpreted as general rules. Indeed, its apparent initial imbalance makes it behave quite differently from all other aggregates during most simulation's early stages.

However, after some morphological evolution, it ends up following the same trends and reach the same fractal dimension as all the others. The final states that are observed thus seem not to be too dependent on the initial structure of the aggregates.

Due to the negligible inertia in different cases, the evolution trends of the aggregate morphologies did not depend on the force magnitudes, only the time scale of the problem would change. As a consequence, cases with the same force ratios were not repeated to see effectiveness of  $D_f$  as the single morphological parameter. Table 2 lists all the cases that have been considered along with the resulting morphological evolution of the aggregates. When aggregates did not break, their morphology has been characterized by their time averaged fractal dimension over a rotation. Indeed, the antisymmetric part of the deformation rate in the flow corresponds to a rotation with a revolution period of  $4\pi/\dot{\gamma}$ . Since aggregates never stop rotating in such a flow, and their fractal dimension may keep changing with their orientation relative to the shear direction, only time averaged fractal dimensions  $(\langle D_f \rangle)$  displayed in table 2.

$$\langle D_f \rangle = \lim_{\tau \rightarrow \infty} \frac{1}{4\pi/\dot{\gamma}} \int_{\tau-4\pi/\dot{\gamma}}^{\tau} D_f dt \quad (25)$$

Several force ratios yield aggregate breakage, in which case it is meaningless to compare the fractal dimension of the parts to the one of the initial aggregate, since the limited number of particles in aggregates has a strong influence on the fractal dimension. In such cases, the time before breakage of the aggregate in such conditions is reported in table 2, since this is the most significant parameter to capture the breakage rate in population balance studies that could make use of the results presented here.

### Relative effect of the different force components

In table 2, highlighted cells in light red are those which broke during the simulation run, while those in grey broke in the very beginning of the simulation.

When shear prevails compared to attractive forces  $((F_n^*) < 1)$ , aggregates break immediately. This can obviously be explained since normal forces are the ones that oppose the tearing apart of primary particles, and prevent the aggregate from breaking. Aggregate cohesion in the end boils down to cohesive interactions between primary particles. However, as soon as there is enough cohesion between primary particles, the way forces are distributed within the aggregate will vary depending on the relative contributions of the tangential and normal interactions.

When  $(F_n^*)$  is kept constant, tangential forces appear to have a significant impact on aggregate breakage or structure. Increasing  $(F_t^*)$  tends to favor aggregate breakage. Indeed, as general rule of thumb tangential forces within the aggregate reduce the normal forces between particles. If forces acting on an aggregate are transmitted between primary particle through tangential interactions, there is less attractive contribution opposing the total tearing force, which means that

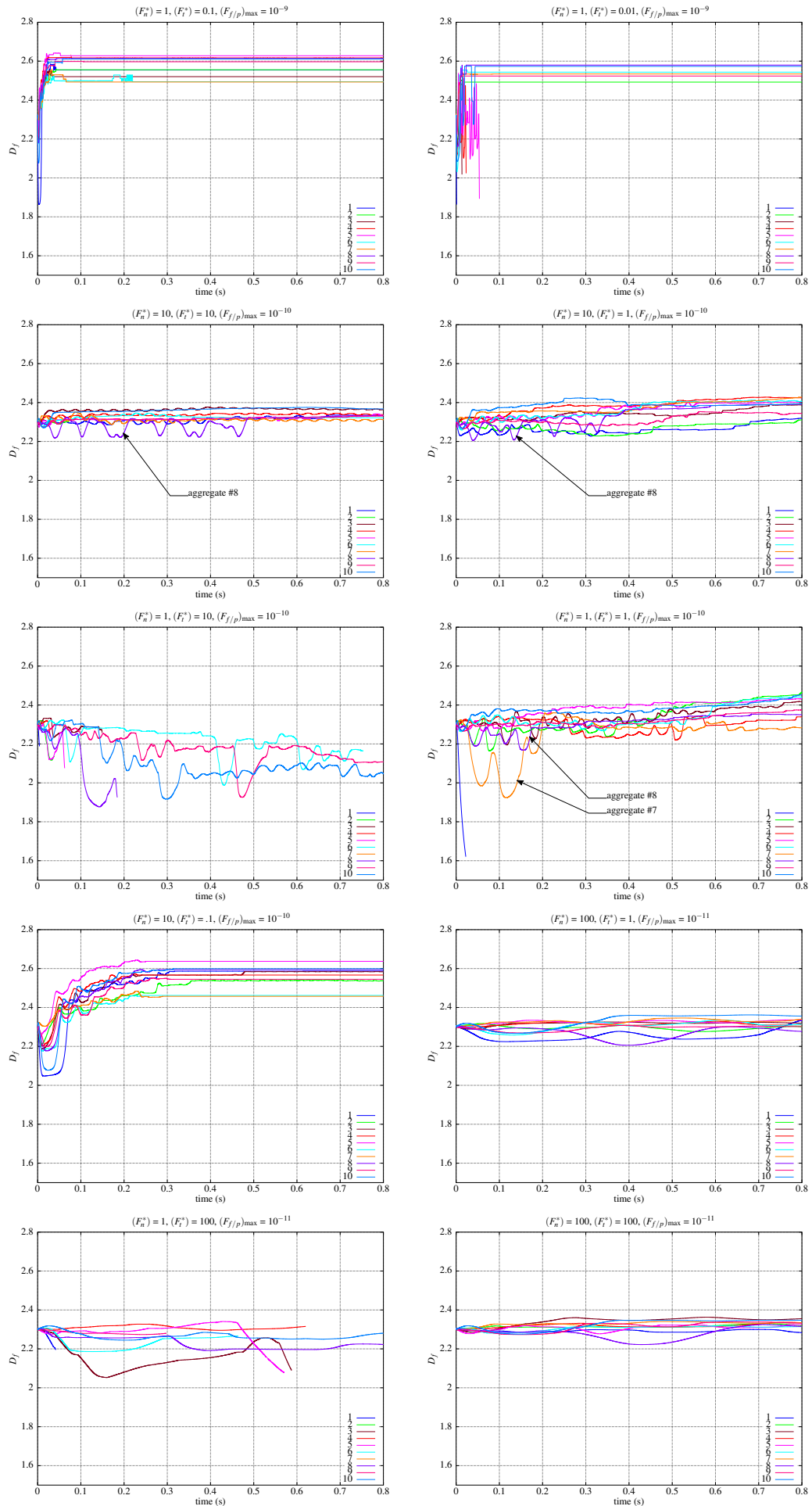


**Figure 4:** Evolution of fractal dimension ( $D_f$ ) over time for several force ratios. Lines stopping before the end of the time axis mean that the corresponding aggregate broke in such conditions.



$(F_f/p)_{\max}$	$(F_n^*)$	$(F_t^*)$	Aggregate label (see figure 1)									
			1	2	3	4	5	6	7	8	9	10
$10^{-11}$	1	1	44.0	2.2579	2.3057	2.3183	2.2806	2.3188	2.0364	2.2106	2.2954	2.3524
$10^{-11}$	1	10	44.0	248.0	2.3218	752.0	644.0	2.2626	67.0	2.2085	2.2878	2.2971
$10^{-11}$	1	100	42.0	14.0	587.56	620.0	570.6	464.0	16.0	2.2043	298.0	2.2628
$10^{-11}$	10	1	2.2483	2.2793	2.3218	2.3171	2.3120	2.3093	2.3398	2.2592	2.2982	2.3608
$10^{-11}$	10	10	2.2979	2.2961	2.3574	2.3271	2.3113	2.3098	2.3136	2.2759	2.3043	2.3485
$10^{-11}$	10	100	2.2995	2.2818	2.2944	2.3074	2.2991	2.3168	68.04	2.2769	2.3055	2.3481
$10^{-11}$	100	1	2.2611	2.2924	2.3219	2.3155	2.3275	2.3173	2.3331	2.2607	2.3021	2.3575
$10^{-11}$	100	10	2.3155	2.295	2.3131	2.3269	2.3351	2.3135	2.3219	2.2754	2.3073	2.3437
$10^{-11}$	100	100	2.2928	2.3181	2.3531	2.3195	2.3114	2.3137	2.3342	2.2736	2.3295	2.3454
$10^{-10}$	0.1	0.1	0.2	0.12	0.2	1.12	0.16	0.24	0.2	0.2	0.2	0.16
$10^{-10}$	0.1	1	0.12	0.08	0.08	0.08	0.08	0.08	0.08	0.04	0.08	0.04
$10^{-10}$	0.1	10	0.08	0.12	0.04	0.2	0.04	0.16	0.04	0.04	0.08	0.04
$10^{-10}$	1	0.1	2.6101	2.5396	2.6218	2.6094	2.6200	2.5492	2.4305	2.6330	2.6223	2.5729
$10^{-10}$	1	1	5.2	2.4513	2.4131	2.327	2.4308	2.3605	2.2812	2.3508	2.371	2.4401
$10^{-10}$	1	10	4.32	38.16	149.2	28.8	62.52	753.2	6.68	184.2	2.1066	2.0403
$10^{-10}$	10	0.1	2.5875	2.5370	2.5839	2.5666	2.6371	2.4621	2.4574	2.5947	2.5449	2.5992
$10^{-10}$	10	1	2.3161	2.2998	2.3875	2.4255	2.4025	2.4078	2.4232	2.3905	2.3423	2.3926
$10^{-10}$	10	10	2.3342	72	2.3646	2.3379	2.3346	2.3220	2.3103	2.3325	2.3304	2.3676
$10^{-09}$	0.01	0.01	0.04	0.04	0.04	0.04	0.04	0.04	0.04	0.04	0.04	0.04
$10^{-09}$	0.01	0.1	0.04	0.08	0.04	0.04	0.04	0.04	0.04	0.04	0.04	0.04
$10^{-09}$	0.01	1	0.04	0.08	0.04	0.04	0.04	0.04	0.04	0.04	0.04	0.04
$10^{-09}$	0.1	0.01	0.24	0.28	0.56	0.2	0.24	0.16	0.04	0.48	0.04	0.16
$10^{-09}$	0.1	0.1	0.16	0.16	0.04	0.12	0.04	0.32	0.04	0.04	0.04	0.04
$10^{-09}$	0.1	1	0.24	0.04	0.04	0.04	0.04	0.04	0.04	0.04	0.04	0.04
$10^{-09}$	1	0.01	1.12	2.4923	13.48	23.08	53.8	2.5436	2.5342	2.5799	2.5237	2.5734
$10^{-09}$	1	0.1	2.5546	2.5559	2.5205	2.6169	2.6278	2.4944	2.4929	2.6138	2.5969	2.6111
$10^{-09}$	1	1	0.56	2.6076	2.5966	2.5247	2.6154	2.5426	2.5405	2.5636	2.5354	2.5772

**Table 2:** Overview of the simulation results in terms of fractal dimension ( $\langle D_f \rangle$ ) or time undergoing shear (in milliseconds) until breakage (in highlighted cells) for all 10 aggregates. Cells in grey indicate that the aggregates broke at the very beginning of the simulation. In cases highlighted in red, aggregates broke after significant morphological evolution.

$(F_f/p)_{\max}$	$(F_n^*)$	$(F_t^*)$	Aggregate label (see figure 1)									
			1	2	3	4	5	6	7	8	9	10
$10^{-11}$	1	1	2.1897									
$10^{-11}$	1	10	2.1839	2.1254		2.2886	2.0721		2.3174			
$10^{-11}$	1	100	2.1949	2.3079	2.0888	2.3153	2.077	2.2667	2.3019		2.28	
$10^{-11}$	10	100							2.3183			
$10^{-10}$	0.1	0.1	2.2966	2.3016	2.298	2.2979	2.302	2.3049	2.3	2.3053	2.2967	2.2999
$10^{-10}$	0.1	1	2.2979	2.3012	2.2989	2.303	2.3014	2.3047	2.2998	2.3049	2.2963	2.2995
$10^{-10}$	0.1	10	2.2986	2.2998	2.2992	2.2991	2.3019	2.3042	2.2993	2.3043	2.2958	2.2991
$10^{-10}$	1	1	2.1487									
$10^{-10}$	1	10	2.188	2.138	2.2568	2.2377	2.0754	2.1651	2.3176	1.9251		
$10^{-10}$	10	10		2.3007								
$10^{-09}$	0.01	0.01	2.2887	2.2961	2.2921	2.2974	2.3002	2.3052	2.3027	2.3001	2.2988	2.3061
$10^{-09}$	0.01	0.1	2.2872	2.2937	2.2895	2.2953	2.2953	2.3022	2.2998	2.2952	2.2949	2.3017
$10^{-09}$	0.01	1	2.2851	2.2744	2.2873	2.2938	2.2904	2.2979	2.2969	2.2924	2.289	2.2982
$10^{-09}$	0.1	0.01	2.1961	2.2205	2.0394	2.2584	2.2624	2.2927	2.3048	2.3031	2.3017	2.3091
$10^{-09}$	0.1	0.1	2.238	2.2515	2.2938	2.2781	2.2975	2.2133	2.302	2.2979	2.298	2.3054
$10^{-09}$	0.1	1	2.1839	2.2911	2.2898	2.2958	2.2925	2.3014	2.2989	2.2924	2.2924	2.3007
$10^{-09}$	1	0.01	1.8635		2.0177	2.0238	1.8928					
$10^{-09}$	1	1	2.1292									

**Table 3:** Instantaneous fractal dimension ( $D_f$ ) just before breakage (see table 2)

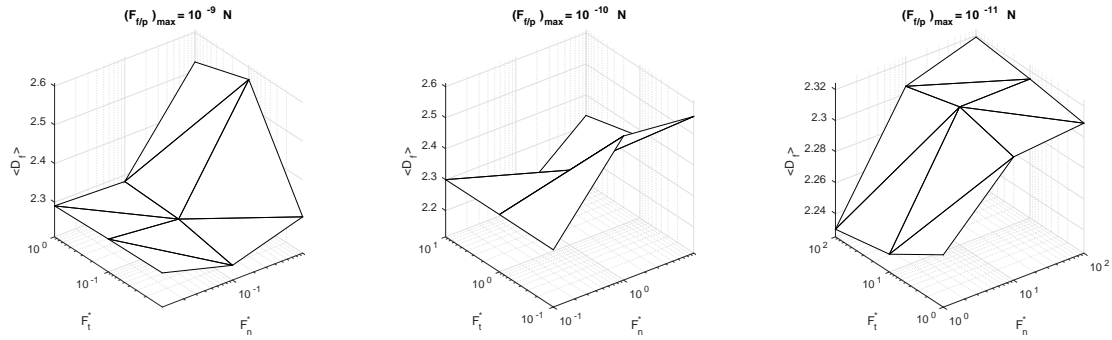


**Figure 5:** Mean fractal dimension as a function of the two interaction force contributions

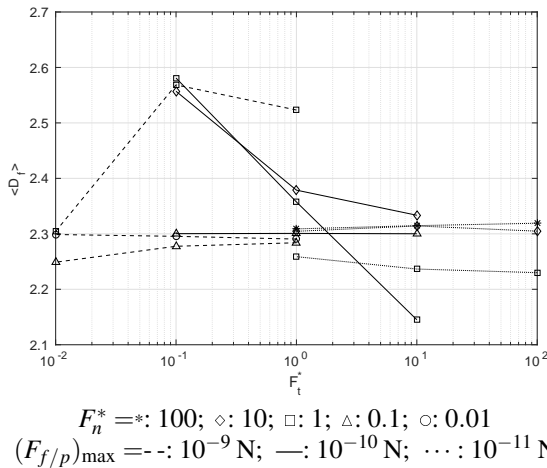


**Figure 6:** Evolution of the mean fractal dimension as a function of tangential interactions

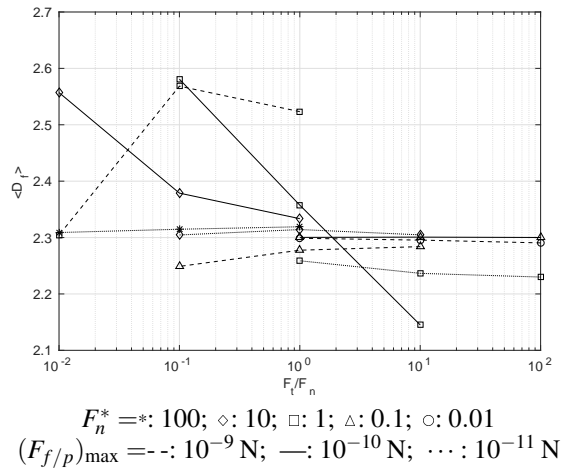


**Figure 7:** Evolution of the mean fractal dimension as a function of the ratio of the two components of particle interactions

the tearing force must oppose a weaker net attractive force in order to break the aggregate.

Comparing the final fractal dimension ( $\langle D_f \rangle$ ) of aggregates in conditions where they do not break, shows the impact of the different force contributions on the final shape of the aggregate. As expected, when  $(F_n^*)$  varies while  $(F_t^*)$  remains constant, aggregates tend to be denser: they show a higher fractal dimension. Conversely, the higher  $(F_{f/p})_{max}$  (in the non-breaking range), the higher  $\langle D_f \rangle$ .

However, the dependence of fractal dimension on the tangential force ratio ( $F_t^*$ ), when other forces are kept constant, shows that the rule of thumb derived from breakage observation only captures very approximately the role of such forces. Indeed, figure 5 shows that their actual impact differs depending on other parameters, such as the value of  $(F_n^*)$ , but there is no clear trend. Some cases show a steep decrease of the fractal dimension when  $F_t^*$  increases, but others, corresponding to relatively high values of  $F_n^*$ , show an inverse relation, though in a much less sensitive manner.

Another way to look at the relative effects of the different forces is presented in figure 6. In this figure, a single value for the fractal dimension is reported for every simulated condition, it is calculated by averaging all the fractal dimensions of the 10 aggregates, with the aim to observe general trends. In order to try to capture as much morphological evolutions as possible in this single characteristic value, in cases where aggregates broke, their instantaneous fractal dimension at the instant they broke was used for the averaging step. These instantaneous fractal dimensions  $D_f$  are shown in table 3.

All curves in figures 6 and 7 relate evolutions of the fractal dimension to the tangential force ratio, for various combinations of the other forces. Tangential force ratios have been scaled relatively to the drag (figure 6) and to the normal force component figure 7) but none of these comparisons show any definite trend. There is an expected overall tendency of the fractal dimension to increase when tangential interactions are low, however, the most striking feature of figures 6 and 7 is the particularly high number of data points that fall outside of the main trend.

### Results from IBM

Since free draining approximation does not account for the flow perturbation induced by particles on the force acting on every particles, results from such an assumption are expected to be inaccurate in cases where fractal dimension ( $D_f$ ) increases to high values over time. A few simulations were run with fully resolved flows using an LBM+IBM approach, to account for the impact of multiphase coupling on the aggregate behaviour.

Figure 8 shows how aggregate number 1 evolved under high shear and with interaction forces of the same order of magnitude as the shear induced force. First, in such conditions, this aggregate broke quickly when using the free draining approximation, while the LBM+IBM simulation did not give such result. This difference, in itself, shows an obvious impact of the coupling on the aggregate behaviour. Now, when looking at the flow perturbation induced by the presence of the aggregate in the pure shear, this tells a little more about

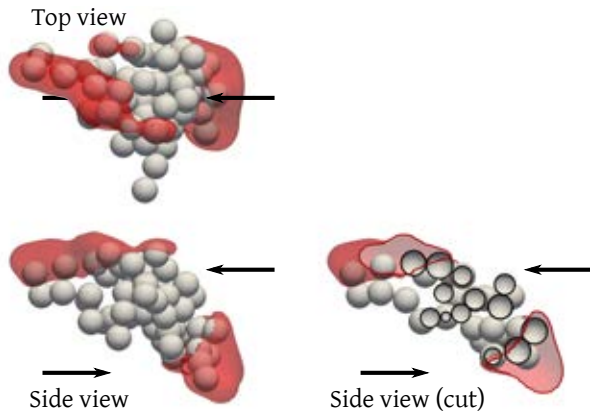


**Figure 8:** Aggregate 1 (see figure 1) after 1.2 ms under similar conditions as the last line of table 2 but resolved with LBM+IBM. The red surface is an iso-surface of the velocity perturbation for the characteristic velocity difference due to the shear at the scale of primary particles, see (26)

the difference in behaviour.

The flow perturbation is represented with an iso-surface of the velocity difference between the pure shear and the resolved flow with the aggregate. The value corresponding of the iso-surface is the velocity scale given by the shear rate and the diameter of primary particles.

$$\|\vec{v} - \dot{\gamma}z\vec{e}_x\| = 2\dot{\gamma}R_p \quad (26)$$

The arrows on figure 8 show the liquid velocity direction, and consequently the shear experienced by the aggregate. From this, it clearly appears that particle chains aligned with the flow are shielded by the aggregate region that faces the flow. Many particles, inside the red bubbles, are much more protected from the shear forces than what is considered in the free draining approximation.

Simulations with resolved flows take much longer to run, but also, the complex nature of the hydrodynamic interactions between particles make them hard to study in a similar way as what has been done with fractal dimension. To capture their impact and shed light on some trends, many more simulations must be run, but more importantly pre- and post processing tools and methods must be developed so that the simulation results can be properly interpreted.

## CONCLUSION

In this work, a preliminary attempt at understanding the relative roles of the multiple forces acting within an aggregate undergoing shear has been presented. While the effect of cohesive forces and shear forces was well established, the relative study of tangential forces showed that their combined effect with other forces is complex. Although no quantitative observations nor clear tendencies depending with respect to other forces could be derived from the results, it was confirmed that tangential forces tend to decrease the cohesive forces within the aggregate. Although the force ratios that characterize the flow conditions and aggregate properties in this study seem similar to Shields numbers, as commonly defined to characterize granular flows (Ouriemi *et al.*, 2009) the systems that it was applied to are too different from ours to directly correlate our study with them. The elastic nature of the interactions within colloidal systems, and the importance of discrete interactions in relatively small aggregates yield

very different behaviours so that no critical Shields number seem to characterize aggregate restructuring.

This work is a pioneer in using IBM to couple solids with fluid in aggregate restructuring studies. The behaviour of an aggregate as simulated using LBM+IBM was compared to its free draining approximation counterpart. It showed that there is a significant difference in aggregate behavior when hydrodynamic interactions are taken into account. Thus, numerical simulations with LBM+IBM will give more accurate results than free draining approximation, as the flow perturbations due to every particles will be fully resolved.

Finally, all these preliminary numerical investigations already confirmed a few expected restructuring behaviours, and illustrated the complexity of studying aggregate restructuring even under very controlled conditions, with simplified interactions. But more importantly, they have demonstrated the feasibility and the suitability of the LBM+DEM+IBM approach for such a problem, and confirmed the need for such numerical investigations. Now that the method has been developed and applied to this problem, more extensive studies covering various interactions and flow conditions involving higher Reynolds and Stokes numbers promise to yield valuable knowledge on aggregate restructuring.

## REFERENCES

- ADLER, P.M. and MILLS, P.M. (1979). "Motion and rupture of a porous sphere in a linear flow field". *Journal of Rheology*, **23**(1), 25–37.
- BAGSTER, D.F. and TOMI, D. (1974). "The stresses within a sphere in simple flow fields". *Chemical Engineering Science*, **29**(8), 1773–1783.
- BECKER, V. and BRIESEN, H. (2008). "Tangential-force model for interactions between bonded colloidal particles". *Physical Review E*, **78**(6), 061404.
- BECKER, V., SCHLAUCH, E., BEHR, M. and BRIESEN, H. (2009). "Restructuring of colloidal aggregates in shear flows and limitations of the free-draining approximation". *Journal of Colloid and Interface Science*, **339**(2), 362–372.
- BHATNAGAR, P.L., GROSS, E.P. and KROOK, M. (1954). "A model for collision processes in gases. I. small amplitude processes in charged and neutral one-component systems". *Physical Review*, **94**, 511–525.
- BINDER, C., FEICHTINGER, C., SCHMID, H.J., THÜREY, N., PEUKERT, W. and RÜDE, U. (2006). "Simulation of the hydrodynamic drag of aggregated particles". *Journal of Colloid and Interface Science*, **301**(1), 155–167.
- BRADY, J.F. and BOSSIS, G. (1988). "Stokesian dynamics". *Annual Review of Fluid Mechanics*, **20**(1), 111–157.
- BUSHHELL, G.C., YAN, Y.D., WOODFIELD, D., RAPER, J. and AMAL, R. (2002). "On techniques for the measurement of the mass fractal dimension of aggregates". *Advances in Colloid and Interface Science*, **95**(1), 1–50.
- CHEN, D. and DOI, M. (1989). "Simulation of aggregating colloids in shear flow. II". *The Journal of Chemical Physics*, **91**(4), 2656–2663.
- CONCHUIR, B.O., HARSHE, Y.M., LATTUADA, M. and ZACCONE, A. (2014). "Analytical model of fractal aggregate stability and restructuring in shear flows". *Industrial & Engineering Chemistry Research*, **53**(22), 9109–9119.
- COUFORT, C., BOUYER, D. and LINÉ, A. (2005). "Flocculation related to local hydrodynamics in a Taylor-Couette reactor and in a jar". *Chemical Engineering Science*, **60**(8), 2179–2192.
- CUNDALL, P.A. and STRACK, O.D. (1979). "A discrete

numerical model for granular assemblies". *Geotechnique*, **29(1)**, 47–65.

DAOUD, I.L.A., RIMBERT, N., JARDY, A., OESTERLÉ, B., HANS, S. and BELLOT, J.P. (2011). "3d modeling of the aggregation of oxide inclusions in a liquid steel ladle: two numerical approaches". *Advanced Engineering Materials*, **13**, 543–549.

D'HUMIÈRES, D., GINZBURG, I., KRAFczyk, M., LALLEMAND, P. and LUO, L.S. (2002). "Multiple-relaxation-time lattice Boltzmann models in three dimensions". *Philosophical Transactions of the Royal Society of London A: Mathematical, Physical and Engineering Sciences*, **360**, 437–451.

DOMINIK, C. and NÜBOLD, H. (2002). "Magnetic aggregation: dynamics and numerical modeling". *Icarus*, **157(1)**, 173–186.

EGGELS, J.G.M. and SOMERS, J.A. (1995). "Numerical simulation of free convective flow using the lattice-Boltzmann scheme". *International Journal of Heat and Fluid Flow*, **16(5)**, 357–364.

EGGERSDORFER, M.L., KADAU, D., HERRMANN, H.J. and PRATSINIS, S.E. (2010). "Fragmentation and restructuring of soft-agglomerates under shear". *Journal of Colloid and Interface Science*, **342(2)**, 261–268.

FEKE, D.L., PRABHU, N.D., MANN, J.A.J. and MANN, J.A.L. (1984). "A formulation of the short-range repulsion between spherical colloidal particles". *The Journal of Physical Chemistry*, **88(23)**, 5735–5739.

FRUNGIERI, G. and VANNI, M. (2016). "Dynamics of a shear-induced aggregation process by a combined Monte Carlo-Stokesian dynamics approach". *International Conference on Multiphase Flow*. Firenze.

GMACHOWSKI, L. (2002). "Calculation of the fractal dimension of aggregates". *Colloids and Surfaces A: Physicochemical and Engineering Aspects*, **211(2)**, 197–203.

GREGORY, J. (1997). "The density of particle aggregates". *Water Science and Technology*, **36(4)**, 1–13.

HAMAKER, H.C. (1937). "The London-van der Waals attraction between spherical particles". *Physica*, **4(10)**, 1058–1072.

HARSHE, Y.M. and LATTUADA, M. (2012). "Breakage rate of colloidal aggregates in shear flow through Stokesian dynamics". *Langmuir*, **28(1)**, 283–292.

HARSHE, Y.M., LATTUADA, M. and SOOS, M. (2011). "Experimental and modeling study of breakage and restructuring of open and dense colloidal aggregates". *Langmuir*, **27(10)**, 5739–5752.

IWASHITA, K. and ODA, M. (1998). "Rolling resistance at contacts in simulation of shear band development by DEM". *Journal of Engineering Mechanics*, **124(3)**, 285–292.

KADAU, D., BARTELS, G., BRENDDEL, L. and WOLF, D.E. (2002). "Contact dynamics simulations of compacting cohesive granular systems". *Computer Physics Communications*, **147(1-2)**, 190–193.

Khashayar Rastegari, William Y. Svrcek and YARRANTON\*, H.W. (2004). "Kinetics of asphaltene flocculation". *Industrial & Engineering Chemistry Research*, **43(21)**, 6861–6870.

KROLL-RABOTIN, J.S., SUNGKORN, R., HASHEMI, S.A., DERKSEN, J.J. and SANDERS, R.S. (2012). "Large eddy simulation of a solid-liquid fluidized bed using the lattice-boltzmann method and a soft-sphere collision model". *Proc. Ninth Int. Conference on CFD in Minerals and Process Industries*. Melbourne, Australia.

LĀCIS, U., TAIRA, K. and BAGHERI, S. (2016). "A stable fluid-structure interaction solver for low-density rigid bodies using the immersed boundary projection method". *Journal of Computational Physics*, **305**, 300–318.

LASKOWSKI, J.J. and RALSTON, J. (2015). *Colloid chemistry in mineral processing*. Elsevier.

LI, D.H. and GANCZARCZYK, J. (1989). "Fractal geometry of particle aggregates generated in water and wastewater treatment processes". *Environmental science & technology*, **23(11)**, 1385–1389.

NIU, X.D., SHU, C., CHEW, Y.T. and PENG, Y. (2006). "A momentum exchange-based immersed boundary-lattice Boltzmann method for simulating incompressible viscous flows". *Physics Letters A*, **354**, 173–182.

OURIEMI, M., AUSSILLOUS, P. and GUAZZELLI, E. (2009). "Sediment dynamics. part 1. bed-load transport by laminar shearing flows". *Journal of Fluid Mechanics*, **636**, 295–319.

PANTINA, J.P. and FURST, E.M. (2005). "Elasticity and critical bending moment of model colloidal aggregates". *Physical Review Letters*, **94(13)**, 138301.

PESKIN, C.S. (1972). "Flow patterns around heart valves: a numerical method". *Journal of Computational Physics*, **10(2)**, 252–271.

PLUMPTON, A.J. (2013). *Production and Processing of Fine Particles: Proceedings of the International Symposium on the Production and Processing of Fine Particles, Montreal, August 28-31, 1988*. Elsevier.

POTANIN, A.A. (1993). "On the computer simulation of the deformation and breakup of colloidal aggregates in shear flow". *Journal of Colloid and Interface Science*, **157(2)**, 399–410.

REN, Z., HARSHE, Y.M. and LATTUADA, M. (2015). "Influence of the potential well on the breakage rate of colloidal aggregates in simple shear and uniaxial extensional flows". *Langmuir*, **31(21)**, 5712–5721.

ROMA, A.M., PESKIN, C.S. and BERGER, M.J. (1999). "An adaptive version of the immersed boundary method". *Journal of Computational Physics*, **153**, 509–534.

SCHLAUCH, E., ERNST, M., SETO, R., BRIESEN, H., SOMMERFELD, M. and BEHR, M. (2013). "Comparison of three simulation methods for colloidal aggregates in Stokes flow: finite elements, lattice Boltzmann and Stokesian dynamics". *Computers & Fluids*, **86**, 199–209.

SETO, R., BOTET, R., AUERNHAMMER, G.K. and BRIESEN, H. (2012). "Restructuring of colloidal aggregates in shear flow". *The European Physical Journal E*, **35(12)**, 128.

SMOLUCHOWSKI, M.V. (1917). "Grundriß der Koagulationskinetik kolloider Lösungen". *Kolloid-Zeitschrift*, **21(3)**, 98–104.

SONNTAG, R.C. and RUSSEL, W.B. (1987). "Structure and breakup of flocs subjected to fluid stresses". *Journal of Colloid and Interface Science*, **115(2)**, 390–395.

TAIRA, K. and COLONIUS, T. (2007). "The immersed boundary method: a projection approach". *Journal of Computational Physics*, **225(2)**, 2118–2137.

VAEZI G., F., SANDERS, R.S. and MASLIYAH, J.H. (2011). "Flocculation kinetics and aggregate structure of kaolin mixtures in laminar tube flow". *Journal of Colloid and Interface Science*, **355**, 96–105.

VANNI, M. and GASTALDI, A. (2011). "Hydrodynamic forces and critical stresses in low-density aggregates under shear flow". *Langmuir*, **27(21)**, 12822–12833.

WOODFIELD, D. and BICKERT, G. (2001). "An im-

proved permeability model for fractal aggregates settling in creeping flow”. *Water Research*, **35(16)**, 3801–3806.

YANG, J. and STERN, F. (2013). “Fully resolved simulation of particulate flow using a sharp interface direct forcing immersed boundary method”. *ASME 2013 Fluids Engineering Division Summer Meeting*, V01AT08A006. ASME, Nevada.

ZHANG, L. and THOMAS, B.G. (2003). “State of the art in evaluation and control of steel cleanliness.” *ISIJ International*, **43(3)**, 271–291.

## ADAPTIVE COARSE-GRAINING FOR LARGE-SCALE DEM SIMULATIONS

**Daniel QUETESCHINER<sup>1\*</sup>, Thomas LICHTENEGGER<sup>2,3†</sup>, Simon SCHNEIDERBAUER<sup>1‡</sup>, Stefan PIRKER<sup>2§</sup>**

<sup>1</sup>CD Laboratory for Multi-Scale Modelling of Multiphase Processes, 4040 Linz, AUSTRIA

<sup>2</sup>Department of Particulate Flow Modelling, Johannes Kepler University Linz, 4040 Linz, AUSTRIA

<sup>3</sup>Linz Institute of Technology (LIT), Johannes Kepler University Linz, 4040 Linz, AUSTRIA

\* E-mail: daniel.queteschiner@jku.at

† E-mail: thomas.lichtenegger@jku.at

‡ E-mail: simon.schneiderbauer@jku.at

§ E-mail: stefan.pirker@jku.at

### ABSTRACT

The large time and length scales and, not least, the vast number of particles involved in industrial-scale simulations inflate the computational costs of the Discrete Element Method (DEM) excessively. Coarse grain models can help to lower the computational demands significantly. However, for effects that intrinsically depend on particle size, coarse grain models fail to correctly predict the behaviour of the granular system.

To solve this problem we have developed a new technique based on the efficient combination of fine-scale and coarse grain DEM models. The method is designed to capture the details of the granular system in spatially confined sub-regions while keeping the computational benefits of the coarse grain model where a lower resolution is sufficient. To this end, our method establishes two-way coupling between resolved and coarse grain parts of the system by volumetric passing of boundary conditions. Even more, multiple levels of coarse-graining may be combined to achieve an optimal balance between accuracy and speedup. This approach enables us to reach large time and length scales while retaining specifics of crucial regions. Furthermore, the presented model can be extended to coupled CFD-DEM simulations, where the resolution of the CFD mesh may be changed adaptively as well.

**Keywords:** DEM, Multilevel/Multiscale .

### NOMENCLATURE

#### Greek Symbols

$\alpha$	Coarse grain ratio.
$\gamma$	Damping coefficient, $[kg/s]$ .
$\delta$	Overlap, $[m]$ .
$\kappa$	Constant in the Beverloo Eq.
$\mu$	Friction coefficient.
$\rho$	Mass density, $[kg/m^3]$
$\sigma$	Granular stress, $[N/m^2]$
$\dot{\omega}$	Angular acceleration, $[rad/s^2]$ .

#### Latin Symbols

$C$	Constant in the Beverloo Eq.
$d$	Particle diameter, $[m]$ .
$D$	Diameter, $[m]$ .
$e$	Coefficient of restitution.
$E$	Young's modulus, $[N/m^2]$ .
$\mathbf{f}$	Force, $[N]$ .
$g$	Gravitational acceleration, $[m/s^2]$ .
$G$	Shear modulus, $[N/m^2]$ .
$I$	Moment of inertia, $[N]$ .
$k$	Stiffness coefficient, $[N/m]$ .

$m$	Mass, $[kg]$ .
$\dot{m}$	Discharge rate, $[kg/s]$ .
$P$	Granular pressure, $[N/m^2]$ .
$\mathbf{r}$	Contact vector, $[m]$ .
$R$	Particle radius, $[m]$ .
$\mathbf{t}$	Torque, $[Nm]$ .
$\mathbf{v}$	Particle velocity, $[m/s]$ .
$\mathbf{v}'$	Particle velocity relative to mean streaming velocity, $[m/s]$ .
$V$	Box volume, $[m^3]$ .
$\ddot{\mathbf{x}}$	Acceleration, $[m/s^2]$ .

#### Sub/superscripts

$eff$	Effective.
$i$	Index $i$ .
$j$	Index $j$ .
$n$	Normal direction.
$o$	Orifice.
$t$	Tangential direction.
$z$	Z-direction.

### INTRODUCTION

Since its introduction (Cundall and Strack, 1979), the Discrete Element Method (DEM) has proven to be a viable tool for the analysis of granular flows. Supported by the ever growing computational power, the DEM has found its way into numerous branches of industry such as the minerals and mining industries (Cleary, 2001), the transport of consumer goods (Raji and Favier, 2004), the pharmaceutical industry (Ketterhagen *et al.*, 2009), as well as the iron and steel making industry (Mio *et al.*, 2012).

The major shortcoming of the DEM, however, is its computational cost that increases with the amount of particles involved in the simulation. This hinders the application of the DEM to large-scale systems of industrial size. A coarse grain (CG) model of the DEM has been described (Bierwisch *et al.*, 2009; Sakai and Koshizuka, 2009; Radl *et al.*, 2011) to improve this situation. Using straightforward scaling rules, a group of particles gets replaced by a representative coarse particle. This effectively reduces the number of particles that need to be processed. The weak point of this approach is that the scaling rules break down when effects depending on the particle size determine the behaviour of the system. Unfortunately, more often than not, industrial facilities operate at multiple scales. Hence, for such large-scale simulations, a method is needed, that combines the speedup of the coarse grain model and the resolution of a fine-scale simulation in

critical regions. To this end, we propose a concurrent coupling for DEM simulations of different resolution, where one or more fine-scale domains can be embedded in the coarse grain simulation of the overall system.

Indeed, coupling simulations of different resolution or applying models to correct a coarse simulation is not an unusual approach to bridge the scale-gap (Praprotnik *et al.*, 2005; Rojek and Oñate, 2007; Wellmann and Wriggers, 2012; Schneiderbauer *et al.*, 2012, 2013, 2015).

## MODEL DESCRIPTION

### Discrete Element Method

In the DEM each particle  $i = 1, \dots, N$  is advanced in time according to Newton's equations of motion

$$m_i \ddot{\mathbf{x}}_i = \mathbf{f}_i \quad (1)$$

$$I_i \dot{\boldsymbol{\omega}}_i = \mathbf{t}_i \quad (2)$$

The total force  $\mathbf{f}_i$  acting on a particle includes external forces such as gravity, as well as the normal and tangential contact forces due to binary collisions:

$$\mathbf{f}_{n,ij} = k_n \delta_{n,ij} - \gamma_n \dot{\delta}_{n,ij} \quad (3)$$

$$\mathbf{f}_{t,ij} = k_t \delta_{t,ij} - \gamma_t \dot{\delta}_{t,ij} \quad (4)$$

The tangential overlap is truncated such that

$$f_{t,ij} \leq \mu f_{n,ij} \quad (5)$$

where  $\mu$  is a Coulomb-like friction coefficient. The expressions for  $k_{n,t}$  and  $\gamma_{n,t}$  depend on the applied contact model. In this study we used a non-linear damped Hertzian spring-dashpot model (Tsuiji *et al.*, 1992; Antypov and Elliott, 2011). Thereby, the stiffness and damping coefficients read

$$\begin{aligned} k_n &= \frac{4}{3} E_{\text{eff}} \sqrt{R_{\text{eff}} \delta_{n,ij}} \\ \gamma_n &= -\beta \sqrt{5 m_{\text{eff}} k_n} \\ k_t &= 8 G_{\text{eff}} \sqrt{R_{\text{eff}} \delta_{n,ij}} \\ \gamma_t &= -\beta \sqrt{\frac{10}{3} m_{\text{eff}} k_t} \\ \beta &= \frac{\ln(e)}{\sqrt{\ln^2(e) + \pi^2}} \end{aligned} \quad (6)$$

### Coarse Grain Model

The coarse grain model of the DEM replaces several particles of original size by a single coarse particle and establishes scaling rules based on the assumption of consistent energy densities (Bierwisch *et al.*, 2009; Radl *et al.*, 2011). The scaling rules follow from a dimensional analysis of Eqs. (3) and (4) and are applicable to the contact model used in this work (Nasato *et al.*, 2015). In detail, the particle density, the coefficient of restitution, the Young's modulus and the coefficient of friction need to be kept constant. The particle radius is scaled with the constant coarse grain ratio  $\alpha$ . The stiffness coefficients  $k_{n,t}$  scale with  $\alpha$  and the damping coefficients  $\gamma_{n,t}$  scale with  $\alpha^2$ .

### Multi-Level Coarse Grain Model

To combine the advantages of the fine-scale and coarse grain DEM models, we embed one or multiple fine-scale subdomains in the coarse grain simulation using equivalent external forces and the same geometries in any part of the system.

This can be done recursively to nest multiple coarse grain levels.

At the boundary surface of the fine-scale region we measure the mass flow rate, the particle velocity and size distribution of the coarse grain particles. To this end, we divide the surface into tetragonal cells that are about three to ten coarse grain diameters in size.

We consider ensembles of particles instead of tracking each individual grain to retain the local size distribution while avoiding the introduction of artificial clusters of equal particles due to a one-to-one replacement of particles.

Over the course of a coupling interval the particle velocity per cell is Favre averaged. We use the data thus obtained to insert the corresponding fine-scale particles cell by cell by means of a simple sequential inhibition (SSI) algorithm (Diggle *et al.*, 1976).

Furthermore, we introduce a boundary layer inside the fine-scale subdomain to establish proper boundary conditions and ensure a smooth transition between the differently resolved representations. Analogous to the boundary surface, this region is subdivided into a single layer of hexahedral cells, which are used to obtain Eulerian properties of the material such as the macroscopic stress (Chialvo *et al.*, 2012),

$$\boldsymbol{\sigma} = \frac{1}{V} \sum_i \left[ \sum_{j \neq i} \frac{1}{2} \mathbf{r}_{ij} \mathbf{f}_{ij} + m_i (\mathbf{v}'_i) (\mathbf{v}'_i) \right] \quad (7)$$

the volume fraction and the average as well as the maximum particle velocities per cell.

To transfer the granular stress from the coarse grain simulation to the fine-scale simulation, a discrete proportional-integral (PI) controller is used with the fine-scale normal stress components as process variable and the corresponding coarse grain properties as setpoint. This results in a correcting force that is applied to the fine-scale particles in the transition layer. We limit the force such that the resulting particle velocity will not exceed the maximum velocity in the master coarse grain simulation. Furthermore, we let the force induced by the mismatch of the normal stress components fade out after  $3/2$  of a fine-scale particle diameter, which is sufficient to account for the missing particles at the boundaries.

We could now handle the transition from the fine-scale subdomain to the master coarse-grain simulation in a similar way, thus establishing a symmetric coupling scheme. However, this introduces additional particle insertion events, which are typically a costly operation in DEM simulations as they invalidate the current neighbour list. Furthermore, the determination of appropriate insertion locations for coarse grain particles may become a non-trivial task. To ensure the strict conservation of mass, this may involve a complicated gathering step to accumulate fine-scale particles crossing the boundary surface. In addition, another transition layer and controller forces may decrease the stability of the system.

To avoid these potential problems, we instead preserve the coarse grain particles and apply correcting forces, if necessary, to ensure an accurate overall behaviour of the coarse grain system.

These corrections are realized analogous to the establishing of boundary conditions in the transition layer. We introduce a hexahedral grid inside the fine-scale region and thus obtain volume-averaged particle properties. These are fed into a controller to be transferred to the coarse grain particles. Typically, the property that needs to be corrected is either velocity or mass flow rate, where it may be necessary to sacrifice one over the other to achieve a correct overall behaviour of the

coarse grain system outside the fine-scale domain. In case of correcting the mass flow rate, we typically need to increase the velocity of the coarse grain particles due to a reduced volume fraction. Hence, we simply multiply the fine-scale velocity by the volume-fraction mismatch. A simple proportional controller is sufficient for velocity and mass flow adjustments. The advantage over directly setting the velocity is a smoother transition across cells.

Despite the corrections applied to the coarse grain system, at any given location the evaluation of data should be performed using the highest resolution available.

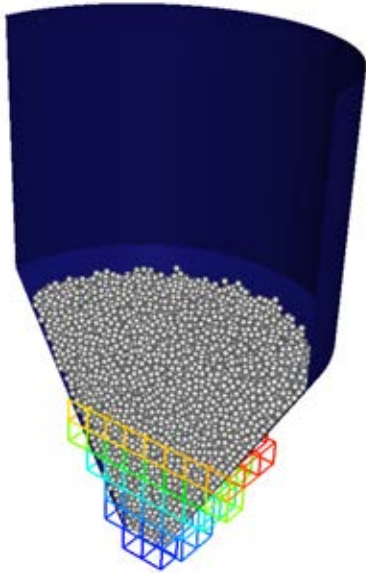


**Figure 1:** Particles filled into the silo (only coarse grain particles shown). The grid indicated at the bottom is used to establish the coupling between the different coarse grain levels.

## RESULTS

To test the behavior and performance of our multi-level coarse grain implementation, the filling and discharge of a silo was studied. This test case has previously been used to illustrate the performance of an MPI/OpenMP hybrid parallelization of the LIGGGHTS open source DEM code (Berger *et al.*, 2015). Considering the Beverloo equation (Beverloo *et al.*, 1961)

$$\dot{m} = C\rho\sqrt{g}(D_o - \kappa d)^{5/2} \quad (8)$$

which predicts the discharge rate of monodisperse granular material through a circular orifice, a dependence on the particle size is clearly evident. Thus, we can expect a different behaviour of the coarse grain and the fine-scale simulation. To testify this prediction, we compare a reference simulation with particles of original size to a conventional coarse grain simulation and a simulation using our model with two levels of resolution. The reference simulation consists of 187 504 particles with a diameter of 2.8 mm. The coarse grain simulation uses a coarse grain ratio of  $\alpha = 2$ , i.e., 23 438 particles with a diameter of 5.6 mm. Finally, the multi-level coarse grain simulation is constituted of 23 438 particles scaled with  $\alpha = 2$ , and about 44 000 particles of original size in the lower quarter of the silo. The simulation parameters are given in Table 1.

The particles are poured into a silo of 40 cm height. The top half of the silo is a cylinder with a diameter of 27 cm, while the lower conical half narrows to a 4 cm diameter. After an

incipient filling and settling phase of 0.7 s, the orifice at the bottom is opened, letting the particles flow out for 1.0 s. Figure 1 shows a cross-section of the silo after the initial phase. The grid illustrated at the bottom of the silo in Fig. 1 indicates the fine-scale subdomain of the multi-level setup and is used to obtain volume-averaged quantities for the coupling procedure. The grid is made up of 172 cubic cells with an edge length of 2 cm. The top layer consisting of 60 cells is used for the transition from the coarse-scale to the fine-scale representation of the particles. The cells below are used for mass flow corrections of the coarse-scale simulation. The discharge rate is measured 1 cm below the orifice with a sampling rate of 100 Hz.

All simulations were performed on an Intel Core i5-4570 CPU using a  $2 \times 2 \times 1$  partitioning of the simulation domain.

**Table 1:** Simulation parameters of silo example.

Young's modulus	$2.5 \times 10^7$ N/m <sup>2</sup>
Poisson's ratio	0.25
Coefficient of restitution	0.5
Coefficient of friction (particle-particle)	0.2
Coefficient of friction (particle-wall)	0.175
Particle density	1000 kg/m <sup>3</sup>
Particle diameter	2.8 mm
Time step	$10^{-6}$ s
Duration	$1.7 \times 10^6$ steps

## Silo Filling

Concentrating on the filling part of the simulation allows us to focus on the transition from the coarse-scale representation to the fine-scale description of the system. In the multi-level coarse grain variant of this test case, the original size particles at the top of their subdomain are lacking the pressure exerted from the particles further above. The stress-based PI controller of our model is to correct this deficiency.

Figure 2 shows the average granular pressure in the four central cells of the transition region as a function of time for the reference simulation and the fine-scale region of the two-level coarse grain simulation with and without corrections. To fill up the silo, particles are inserted from  $t = 0$  s to  $t = 0.47$  s at the top of the silo with an initial velocity of

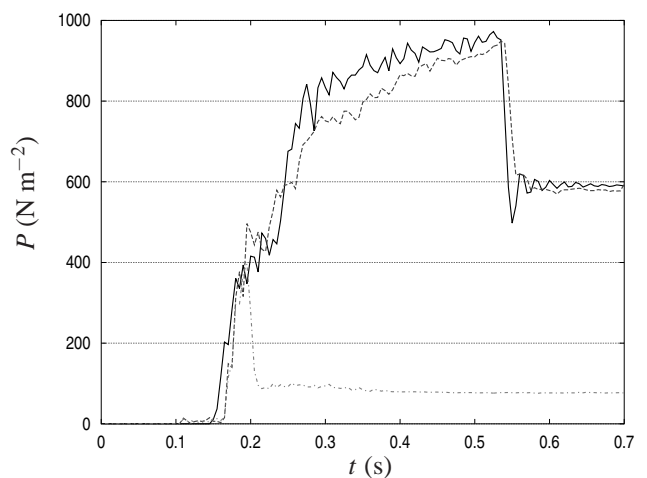


**Figure 2:** Average granular pressure in  $\text{N m}^{-2}$  in the four central cells of the transition layer as a function of time. — reference simulation, -- fine-scale subdomain with pressure correction and - · - without pressure correction.



$v_z = -3$  m/s. From the diagram in Fig. 2 we find a change in pressure around  $t = 0.15$  s. At this point, the heap of particles reaches the lower boundary of the transition region. Between  $t = 0.15$  s and  $t = 0.2$  s the transition region is filled up. For the uncorrected fine-scale subdomain, the pressure drops at this point and levels off at about  $77$  N/m<sup>2</sup>. The reference simulation, however, shows a further increase of the pressure due to additional particles falling on top of the fill. The pressure drop at  $t = 0.55$  s marks the start of the settling phase where all particles come to rest. This is accompanied by a pressure relaxation.

By applying the granular stress from the master coarse-scale simulation via the PI controller with an update every 15 time steps, this behaviour can be reproduced in good agreement in the embedded fine-scale simulation.

### Silo Discharge

The discharge phase of the simulation lends itself to study the correction of the coarse grain simulation using properties of the particles in the fine-scale subregion. Based on Eq. (8), we can assume that the conventional coarse grain model will fail to correctly predict the discharge rate from the silo.

Indeed, the computed mass flow rates of the reference and

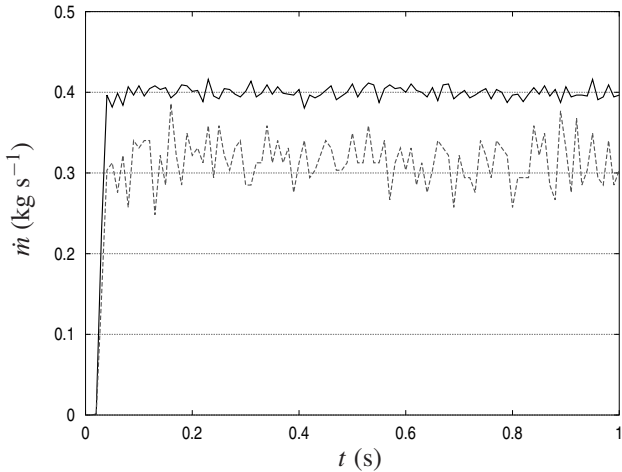


**Figure 3:** The rate of discharge in  $\text{kg s}^{-1}$  of 2.8 mm particles as a function of time. — reference simulation and -- coarse grain simulation ( $\alpha = 2$ )

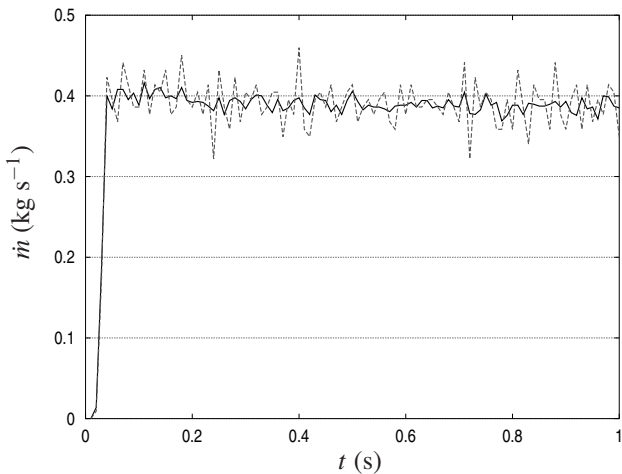


**Figure 4:** The rate of discharge in  $\text{kg s}^{-1}$  of 2.8 mm particles as a function of time. Two size levels: — original size particles and -- coarse grain particles ( $\alpha = 2$ )

coarse grain simulations depicted in Fig. 3 confirm that the setup containing the coarse particles exhibits a substantially lower discharge rate. While the reference simulation yields an average of  $0.4$  kg/s, the coarse grain equivalent underpredicts the mass flow rate with  $0.315$  kg/s by more than 20% (cf. Table 2). In addition, we observe larger fluctuations in the discharge rate of the coarse grain simulation. These are mainly due to the discrete nature of mass in the granular material. The detection of a single particle in the coarse grain simulation corresponds to  $\alpha^3$  particles in the fine-scale description. On the other hand, the time span between detection events of coarse grains is larger due to their increased size and thus an increased distance between individual particles in flow direction.

Also, due to kinematic constraints, the volume fraction in the coarse grain simulation is lower near the outlet. Thus, for the coupling method in our model it is insufficient to solely correct the particle velocity. It is essential to take the volume fraction mismatch into account as an additional parameter. In fact, reaching the same velocity and mass flow rate in the coarse grain simulation and the fine-scale simulation at the same time is mutually exclusive in this region. In this regard, it should be noted that once the coarse-scale particles have passed the orifice, a pure velocity coupling is to be applied to ensure a correct flow velocity in any adjacent coarse-scale regions.

Applying this procedure, an average discharge rate of  $0.39$  kg/s was computed in our two-level simulation (cf. Table 2). This means no more than 2.5% deviation from the reference value. Figure 4 depicts the discharge rate as a function of time and shows that the coarse grain part of the coupled simulation follows the fine-scale part closely. Also, the fluctuations of the discharge rate in the coupled simulation are comparable to those in the corresponding reference and coarse grain simulations. Hence, we can conclude that our controlling scheme does not add any significant noise to the flow characteristics.

**Table 2:** Computed averaged discharge rates  $\langle \dot{m} \rangle$  with corresponding standard deviation  $\sigma(\dot{m}) = \sqrt{\langle (\dot{m} - \langle \dot{m} \rangle)^2 \rangle}$  in  $\text{kg s}^{-1}$ . The speedup of the simulation runtime is given relative to the reference simulation.

	$\langle \dot{m} \rangle$	$\sigma(\dot{m})$	speedup
Reference Simulation	0.400	0.007	1.0×
CG Model ( $\alpha = 2$ )	0.315	0.028	10.1×
MLCG Model ( $\alpha = 1$ )	0.390	0.009	
MLCG Model ( $\alpha = 2$ )	0.391	0.026	2.4×

### Simulation Runtimes

A list of the relative runtimes of the reference, conventional coarse grain and multi-level coarse grain simulations is given in Table 2. We note that the  $10.1\times$  speedup of the conventional coarse grain simulation is slightly higher than one may expect from the ratio of the number of coarse grain particles to the number of fine-scale particles. Although it is difficult to determine the exact source for this additional speedup, a somewhat reduced number of average neighbour particles and fewer neighbour list rebuilds in the coarse grain simulation are assumed to contribute to the effect.

In the multi-level coarse grain simulation, the total number of particles after filling is  $2.78\times$  lower than in the reference simulation. However, this ratio gets worse during discharge, as the net amount of particles in the lower quarter of

the silo does not change significantly. Furthermore, the insertion of particles into the fine-scale subdomain, which occurs at regular intervals, triggers additional neighbour list rebuilds adding to the runtime. Also, the calculation of the cell-averaged particle properties adds a minor overhead. Hence, the measured speedup of  $2.4\times$  comes up to expectations, especially when we consider the low coarse grain ratio  $\alpha$  and the - for demonstration purpose - exaggerated fine-scale region in the presented test case.

A more realistic scenario may be imagined by reducing the particle size by a factor of 32 and conversely increasing the amount of particles by  $32^3$ , resulting in about 6.14 billion particles in the full system. Assume we establish a recursive coupling of five coarse grain levels  $l = 1, \dots, 5$  with  $\alpha_l = 2^{l-1}$ . Furthermore, let the subdomains be defined such that the volume filled with particles is quartered compared to the next coarser level. This means that in each level  $l$  we end up with about  $6.14 \times 10^9 \times \alpha_l^{-3} \times 4^{l-5}$  particles. This amounts to approximately 46.5 million particles in total and we may estimate a speedup of more than  $100\times$ .

The runtime of the simulation can be further improved when taking into account the dependency of the time step on the particle size. In the DEM, the time step needs to be chosen such that the overlap of particles during contact can be resolved. This implies that, in accordance with the particle size, the time step may be scaled with  $\alpha$ . Ultimately, the speedup depends on the size of the region required to resolve the critical area in the system, as well as the desired level of accuracy.

## CONCLUSION

We described a new technique to concurrently simulate granular flows at different coarse grain levels, where spatially confined subdomains of finer scale are embedded into coarser representations of the system. We presented data to confirm the proper establishing of boundary conditions for the fine-scale region. This was achieved by applying stress-based controller forces within a predefined transition region. Furthermore, we demonstrated that the more precise data of the fine-scale subdomain can be used to amend the overall behaviour of the coarse-scale simulation. We have validated the method by comparing the computed Eulerian properties of the multi-level coarse grain model with the corresponding properties of the fully resolved reference system.

The computational speedup in the presented test case was nearly proportional to the number of particles saved. This means that our method introduces only a minor overhead compared to the overall computational costs per particle. As the amount of particles is generally the major limiting factor, our method performs best for systems that require full resolution only in small regions of the simulation domain and allow for large coarse grain ratios in the rest of the system.

The presented method can be easily extended to improve the performance of coupled CFD-DEM simulations, where the DEM component typically takes up the major part of the computational resources. The different coarse grain representations of the granular material can be treated separately on the CFD side using appropriately scaled drag laws. The DEM part can then merge the different levels as demonstrated in this study. Furthermore, the resolution of the CFD mesh can be chosen according to the DEM coarse grain level in the corresponding region.

## ACKNOWLEDGEMENTS

This work was funded by the Christian-Doppler Research Association, the Austrian Federal Ministry of Economy, Family and Youth, and the Austrian National Foundation for Research, Technology and Development. Furthermore, the authors want to thank the K1-MET center for metallurgical research in Austria, which is partly funded by the Austrian government (www.ffg.at), for its financial contribution.

## REFERENCES

- ANTYPOV, D. and ELLIOTT, J.A. (2011). "On an analytical solution for the damped Hertzian spring". *EPL*, **94**(5), 50004.
- BERGER, R., KLOSS, C., KOHLMAYER, A. and PIRKER, S. (2015). "Hybrid parallelization of the LIGGGHTS open-source DEM code". *Powder Technol.*, **278**, 234–247.
- BEVERLOO, W., LENIGER, H. and VAN DE VELDE, J. (1961). "The flow of granular solids through orifices". *Chem. Eng. Sci.*, **15**(3-4), 260–269.
- BIERWISCH, C., KRAFT, T., RIEDEL, H. and MOSELER, M. (2009). "Three-dimensional discrete element models for the granular statics and dynamics of powders in cavity filling". *J. Mech. Phys. Solids*, **57**(1), 10–31.
- CHIALVO, S., SUN, J. and SUNDARESAN, S. (2012). "Bridging the rheology of granular flows in three regimes". *Phys. Rev. E*, **85**, 021305.
- CLEARY, P. (2001). "Modelling comminution devices using DEM". *Int. J. Numer. Anal. Meth. Geomech.*, **25**(1), 83–105.
- CUNDALL, P.A. and STRACK, O.D.L. (1979). "A discrete numerical model for granular assemblies". *Géotechnique*, **29**(1), 47–65.
- DIGGLE, P.J., BESAG, J. and GLEAVES, J.T. (1976). "Statistical Analysis of Spatial Point Patterns by Means of Distance Methods". *Biometrics*, **32**(3), 659–667.
- KETTERHAGEN, W.R., AM ENDE, M.T. and HANCOCK, B.C. (2009). "Process Modeling in the Pharmaceutical Industry using the Discrete Element Method". *J. Pharm. Sci.*, **98**(2), 442–470.
- MIO, H., KADOWAKI, M., MATSUZAKI, S. and KUNITOMO, K. (2012). "Development of particle flow simulator in charging process of blast furnace by discrete element method". *Miner. Eng.*, **33**, 27–33.
- NASATO, D.S., GONIVA, C., PIRKER, S. and KLOSS, C. (2015). "Coarse Graining for Large-scale DEM Simulations of Particle Flow - An Investigation on Contact and Cohesion Models". *Procedia Eng.*, **102**, 1484–1490.
- PRAPROTNIK, M., DELLE SITE, L. and KREMER, K. (2005). "Adaptive resolution molecular-dynamics simulation: Changing the degrees of freedom on the fly". *J. Chem. Phys.*, **123**(22), 224106.
- RADL, S., RADEKE, C., KHINAST, J. and SUNDARESAN, S. (2011). "Parcel-Based Approach for the Simulation of Gas-Particle Flows". J.E.Ø. Olsen and S.T. Johansen (eds.), *Proceedings of the 8th International Conference on CFD in Oil & Gas, Metallurgical and Process Industries*, 124/1–124/10. Flow Technology.
- RAJI, A. and FAVIER, J. (2004). "Model for the deformation in agricultural and food particulate materials under bulk compressive loading using discrete element method. I: Theory, model development and validation". *J. Food Eng.*, **64**(3), 359–371.
- ROJEK, J. and OÑATE, E. (2007). "Multiscale analy-

sis using a coupled discrete/finite element model”. *Interact. Multiscale Mech.*, **1(1)**, 1–31.

SAKAI, M. and KOSHIZUKA, S. (2009). “Large-scale discrete element modeling in pneumatic conveying”. *Chem. Eng. Sci.*, **64(3)**, 533–539.

SCHNEIDERBAUER, S., AIGNER, A. and PIRKER, S. (2012). “A comprehensive frictional-kinetic model for gas-particle flows: Analysis of fluidized and moving bed regimes”. *Chem. Eng. Sci.*, **80**, 279–292.

SCHNEIDERBAUER, S., PUTTINGER, S. and PIRKER, S. (2013). “Comparative analysis of subgrid drag modifications for dense gas-particle flows in bubbling fluidized beds”. *AIChE J.*, **59(11)**, 4077–4099.

SCHNEIDERBAUER, S., PUTTINGER, S., PIRKER, S., AGUAYO, P. and KANELLOPOULOS, V. (2015). “CFD modeling and simulation of industrial scale olefin polymerization fluidized bed reactors”. *Chem. Eng. J.*, **264**, 99–112.

TSUJI, Y., TANAKA, T. and ISHIDA, T. (1992). “Lagrangian numerical simulation of plug flow of cohesionless particles in a horizontal pipe”. *Powder Technol.*, **71(3)**, 239–250.

WELLMANN, C. and WRIGGERS, P. (2012). “A two-scale model of granular materials”. *Comput. Meth. Appl. M.*, **205-208**, 46–58.

## NOVEL EFFICIENT HYBRID-DEM COLLISION INTEGRATION SCHEME

**Kay A. BUIST<sup>1\*</sup>, Luuk J.H. SEELEN<sup>1</sup>, Niels G. DEEN<sup>2</sup>, Johan T. PADDING<sup>3</sup>, Hans J.A.M. KUIPERS<sup>1</sup>**

<sup>1</sup>Multiphase Reactors group, Department of Chemical Engineering & Chemistry, Eindhoven University of Technology, P.O. box 513, 5600 MB Eindhoven, The Netherlands

<sup>2</sup>Multiphase & Reactive Flows Group, Department of Mechanical Engineering, Eindhoven University of Technology, P.O. Box 513, 5600 MB Eindhoven, The Netherlands

<sup>3</sup>Intensified Reaction and Separation Systems Group, Process & Energy department, Delft University of Technology, Leeghwaterstraat 39, 2628 CA Delft, The Netherlands

\* E-mail: k.a.buist@tue.nl

### ABSTRACT

A hybrid collision integration scheme is introduced, benefiting from the efficient handling of binary collisions in the hard sphere scheme and the robust time scaling of the soft sphere scheme. In typical dynamic dense granular flow, simulated with the soft sphere scheme, the amount of collisions involving more than two particles are limited, and necessarily so because of loss of energy decay otherwise. Because most collisions are binary, these collisions can be handled within one time step without the necessary numerical integration as needed in a soft sphere method. The remainder of the collisions can still be handled with the classical soft sphere scheme. In this work the hybrid collisions integration scheme is shortly described and tested with a bounding box problem. The hybrid scheme is capable of solving the same problem as a classic soft sphere scheme but is roughly one order of magnitude faster.

**Keywords:** Discrete Element Method, Collision integration scheme, optimization .

$p$  position, [m].  
 $d$  diameter, [m].  
 $c$  integration constant, [-].

### Sub/superscripts

0 old time step  
 $n$  normal  
 $d$  dampened  
 $t$  tangential  
 $coll$  collision  
 $a, b$  particles a, b  
 $last$  duration of lasting collision  
 $i$  index i  
 $max$  maximum  
 $s$  solids  
 $eff$  effective

### NOMENCLATURE

#### Greek Symbols

$\delta$  overlap, [m]  
 $\omega$  frequency, [1/s]  
 $\zeta$  damping ratio, [-]  
 $\eta$  damping coefficient, [Ns/m]  
 $\mu$  friction coefficient, [-]  
 $\beta$  tangential restitution coefficient, [kg/m<sup>3</sup>]  
 $\rho$  density, [kg/m<sup>3</sup>]  
 $\phi$  solids volume fraction, [-]

#### Latin Symbols

$\vec{F}$  force, [kgm/s<sup>2</sup>].  
 $\vec{J}$  impuls, [kgm/s].  
 $B$  collision constant, [kg<sup>-1</sup>].  
 $R$  norm of distance, [m].  
 $N$  number of particles, [-].  
 $\vec{v}$  velocity, [m/s].  
 $t$  time, [s].  
 $m$  mass, [kg].  
 $k$  spring stiffness, [N/m].  
 $\vec{n}$  normal unit vector, [-].  
 $e$  restitution coefficient, [-].  
 $f$  frequency, [1/s].  
 $\vec{x}$  position vector, [m].  
 $\vec{r}$  distance vector, [m].

### INTRODUCTION

Since the introduction of the Distinct Element Model (DEM) by Cundall and Strack (1979) for perfect spheres the field of granular flow modelling has expanded dramatically. The model by Cundall and Strack (1979) has since then been extended for various external forces (Xu and Yu, 1997; Pournin *et al.*, 2005; Lu *et al.*, 2015; Marshall, 2009; Mikami *et al.*, 1998; Korevaar *et al.*, 2014; Zastawny *et al.*, 2012). For an overview of the relevant inter-particle and particle-fluid forces see Zhu *et al.* (2007). DEM has been used to model various granular flows as found in industrial applications, ranging from; fluidized beds (Van Buijtenen *et al.*, 2011), rotating drums (Gonzalez Briones *et al.*, 2015; Yang *et al.*, 2008) and tumbling mills, chute flow (Shirsath *et al.*, 2014) to sedimentation and hoppers (Cleary and Sawley, 2002). A more comprehensive overview of these applications can be found in the work of Zhu *et al.* (2008).

The foundation of these models is however the contact model, of which the hard sphere model as discussed by Hoomans *et al.* (1996) and a soft sphere model by Tsuji *et al.* (1993) are the most well known. The hard-sphere approach works on the assumption that all collisions are binary and instantaneous. As such the model only handles particle-pair interactions that follow each other in chronological order. Therefore the hard-sphere model is an event-driven scheme and the simulation time scales with the collision frequency, which scales with the solids fraction and the granular temperature of the system. The hard-sphere scheme is most suited for rather dilute systems, as with increasing solids fraction

and granular temperature the number of collisions increases drastically.

For more dense and highly dynamic systems a soft-sphere method is more often used. The soft-sphere method allows for particle-particle overlap and represents the forces associated with the indentation of the solids with a spring-dashpot system. The spring handles the repulsion and the dashpot handles energy dissipation. The duration of the collision is no longer instantaneous and scales with the ratio of the spring stiffness and the mass of the particle. Because of the finite duration of the collision multiple particles can be in contact at the same time, in this work denoted as Multi-Body Collisions (MBC). Numerical integration of the forces over time allows for proper treatment of the collisions. The soft-sphere method is thus a time-driven scheme.

Both methodologies have their strengths and limitations. The hard-sphere model benefits from the immediate handling of a collision, while the soft-sphere method benefits from the relaxation of the spring-stiffness and thus larger time step. The most time-consuming step in the simulations however is the collision detection, which for the hard-sphere has to be updated with a frequency related to the number of events and for the soft-sphere has to be performed every particle time step; roughly ten times per duration of the collision. Reducing the number of collision detection evaluations thus massively increases the simulation efficiency.

In the soft-sphere method, for dynamical systems, most of the collisions will still be binary. And they have to be mostly binary, because else the energy dissipation rate is no longer maintained, as we will show later. In one of our simulations from earlier work (Buist *et al.* (2015)) we indeed found that most collisions involved only two particles, as can be seen in figure 1.

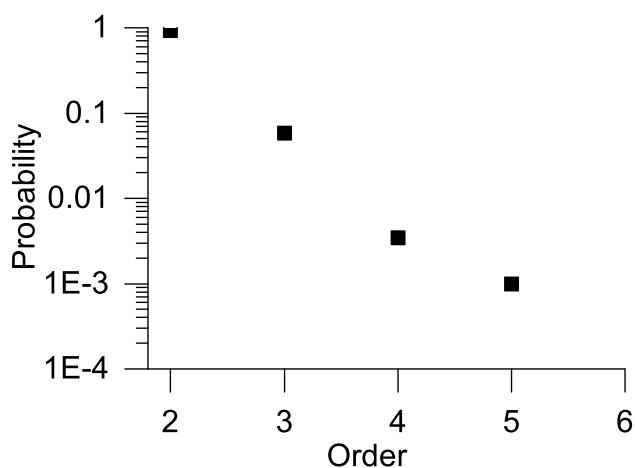


**Figure 1:** Collision order probability from a simulation of a pseudo 2D fluidized bed, with  $\varepsilon = 0 - 0.6$ ,  $u_{mf} = 3.5$  m/s,  $e = 1$ ,  $\beta = 0.33$ ,  $\mu = 0.1$ .

All of these binary collisions can of course be handled instantaneously, following the analytical solution of the damped harmonic oscillator. The binary collision maintains a finite duration and the task that remains is to be able to distinguish between binary collisions and Multi-Body contacts. These MBC's have to be solved with a classical soft-sphere method. The collisions have to be determined only once, and only for the particles colliding in two subsequent time steps additional checks have to be made. The time-step of the simulation is now exactly the duration of a collision, and collision-detection has to be performed only once for most

of the particles. This work is a short version of a publication in Chemical Engineering Science, containing the main idea of the hybrid collision integration scheme and the main results. For more details the interested reader is referred to Buist *et al.* (2016).

## MODEL DESCRIPTION

The hybrid model is in spirit somewhere in between a hard sphere and a soft sphere methodology. In this work however we will not go into the details of these two methods, for an extensive explanation of both schemes the interested reader is referred to Deen *et al.* (2007).

### Hybrid DEM

The new integration scheme can either be viewed as a time-driven hard sphere model with a finite collision duration or as a semi one-step soft sphere model. A time-driven hard sphere approach was first developed by Helland *et al.* (2002). In their work however, each collision is still quasi-instantaneous. The first to couple a hard sphere and a soft sphere approach was Gui *et al.* (2016). In their work however the time step used is still considerably smaller than the duration of a collision. The use of a hard sphere methodology however allows for an accurate description of collisions, while maintaining a  $\sim 10$  times larger time step with respect to a classical visco-elastic methodology for non-spherical particles.

In the hybrid collision integration scheme that is presented here, the chosen time step is exactly the same as the duration of a collision, following the linear spring dashpot model. Because most collisions are assumed to be binary these collisions can be handled at once, following a modified hard sphere approach. And because the time step is the same as the collision duration, only one collision per particle per time step can happen. The only exceptions are the multi-body collisions, that are handled with the classical soft sphere methodology. For the particles involved in a multi-body collision, the time step is divided in ten sub steps. A short schematic overview is given in table 1.

The gain in speed-up is in the use of the collision detection algorithm, which generally has to take place only once every time step, instead of ten times in the classical soft-sphere scheme. Of course the actual choice of the type of collision detection algorithm will have a major impact on the final performance of the codes. In this work the same collision detection algorithm is used for both the classical soft-sphere method and the hybrid method; a kd-tree algorithm from Matlab.

In the next few sections we will discuss in a bit more detail binary collisions and multi-body collisions. Finally an overview of the model is given that shows the main extra steps that need to be taken into account.

### Binary collisions

We assume particles are of equal size and mass possessing no tangential component ( $\mu = 0$  and  $v_{t,0} = 0$ ). For a binary collision it follows that:

$$\bar{v}_n = \bar{v}_{n,0} - \frac{1+e}{2} \bar{v}_{ab,n} \quad (1)$$

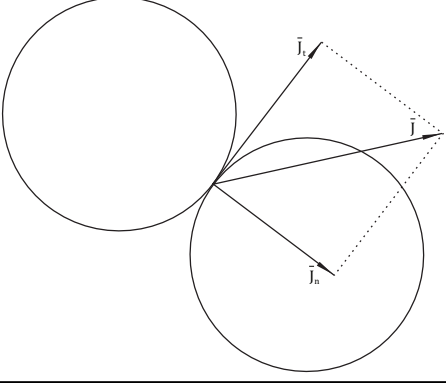
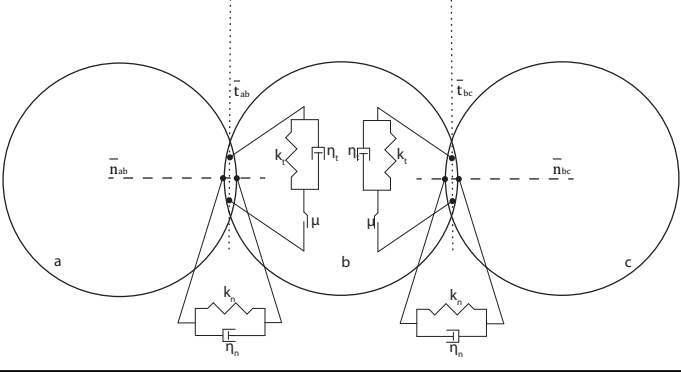
with  $\bar{v}_{ab}$  defined as the relative velocity at the point of contact:

$$\bar{v}_{ab} = \bar{v}_a - \bar{v}_b + (\bar{\omega}_a R_a + \bar{\omega}_b R_b) \times \bar{n}_{ab} \quad (2)$$

which consists of a normal and a tangential component:

$$\bar{v}_{ab,n} = (\bar{v}_{ab} \cdot \bar{n}_{ab}) \bar{n}_{ab} \quad (3)$$

**Table 1:** Short overview of the hybrid collisions schemes.

Hybrid model	
	
<p><b>Binary</b></p> $\bar{v}_{n,a} = \bar{v}_{n,a,0} - \frac{1+e}{2} \bar{v}_{ab,n}$ $\bar{x}_a = \bar{x}_{a,0} + \frac{\bar{v}_a + \bar{v}_b}{2} \Delta t + (\bar{v}_a - \bar{v}_{n,a,0}) t_{last}$ $t_{last} = \frac{(\bar{r}_{ab} \cdot \bar{v}_{ab} + \sqrt{(\bar{r}_{ab} \cdot \bar{v}_{ab})^2 - ( \bar{r}_{ab}  - (R_a + R_b))^2  \bar{v}_{ab} })}{ \bar{v}_{ab} }$	<p><b>Multibody</b></p> $\bar{F}_n = -k_n \delta_n \bar{n}_{ab} - \eta_n \bar{v}_{ab,n}$ $\bar{F}_t = -k_t \delta_t \bar{t}_{ab} - \eta_t \bar{v}_{ab,t}$ <p>or in case of sliding (<math>\bar{F}_t &gt; \mu  \bar{F}_n </math>):</p> $\bar{F}_t = -\mu  \bar{F}_n  \bar{t}_{ab}$
<p><b>Time scale collision</b></p> $t_{coll} = \frac{\pi}{\omega_d}$	<p><b>Time scale collision</b></p> $t_{coll} \leq \frac{\pi}{\omega_d}$
<p><b>Time step</b></p> $\Delta t = t_{coll}$	<p><b>Time step dilation in case of multibody</b></p> $\Delta t = \frac{t_{coll}}{10}$

$$\bar{v}_{ab,t} = \bar{v}_{ab} - \bar{v}_{ab,n} \quad (4)$$

$$\bar{n}_{ab} = \frac{\bar{x}_b - \bar{x}_a}{|\bar{x}_b - \bar{x}_a|} \quad (5)$$

$$\bar{t}_{ab} = \frac{\bar{v}_{ab,t}}{|\bar{v}_{ab,t}|} \quad (6)$$

Finally the position is defined as:

$$\bar{x} = \bar{x}_0 - \bar{v}_0 t_{last} + \frac{\bar{v}_a + \bar{v}_b}{2} \Delta t + \bar{v} t_{last} \quad (7)$$

That is, the new position is the sum of respectively the old position, the displacement until collision based on the old velocity, a shared mean displacement of the two particles during collision and a displacement after the collision till the end of the time step.

Here,  $\bar{x}_0$  and  $\bar{v}_0$  are the position and velocity at the time step before collision, and  $\bar{x}$  and  $\bar{v}$  the position and velocity at the time step after the collision.  $t_{last}$  is the time between the moment of first contact until the end of the time step. These are given by:

$$\bar{r}_{ab} = \bar{x}_{a,0} - \bar{x}_{b,0}$$

$$\bar{v}_{ab} = \bar{v}_{a,0} - \bar{v}_{b,0}$$

$$t_{last} = \frac{(\bar{r}_{ab} \cdot \bar{v}_{ab} + \sqrt{(\bar{r}_{ab} \cdot \bar{v}_{ab})^2 - (|\bar{r}_{ab}| - (R_a + R_b))^2 |\bar{v}_{ab}|})}{|\bar{v}_{ab}|} \quad (8)$$

### Multi-body collisions

The analytical solution to multi-body contacts follows a very similar equation as those for binary collisions:

$$x_i(t) = \sum_{i=1}^n e^{-\zeta \omega_n t} (d_{1,i} \cos(\omega_{d,i} t) + d_{2,i} \sin(\omega_{d,i} t)) \quad (9)$$

where n is the number of contacts. Even though it is possible to determine trajectory and the change of velocity of the MBC, it is not possible to determine the duration of the collision analytically, as the sum of sinusoids with differing frequencies and amplitudes cannot be easily simplified. As such it is not possible to determine the outcome of a MBC in this particular way. On top of this because of the added amplitudes and frequencies the collision can take both longer and shorter than the original binary collision duration.

Keeping the above in mind it is simpler to use the classical soft sphere treatment, and divide the contact time into a number of steps only for the particles in an MBC, see also table 1.

### Overview of DEM code

Here we will give a brief description of the code. The code is build using MATLAB for simple training purposes. To allow each binary collision to be uniquely described the time step is taken as exactly the duration of a collision following the soft-sphere approach, given by:

$$\Delta t = t_{coll} = \frac{\pi}{\omega_d} = \frac{\pi}{\sqrt{\frac{k_n}{m_{eff}} (\sqrt{1 - \zeta^2})}} \quad (10)$$

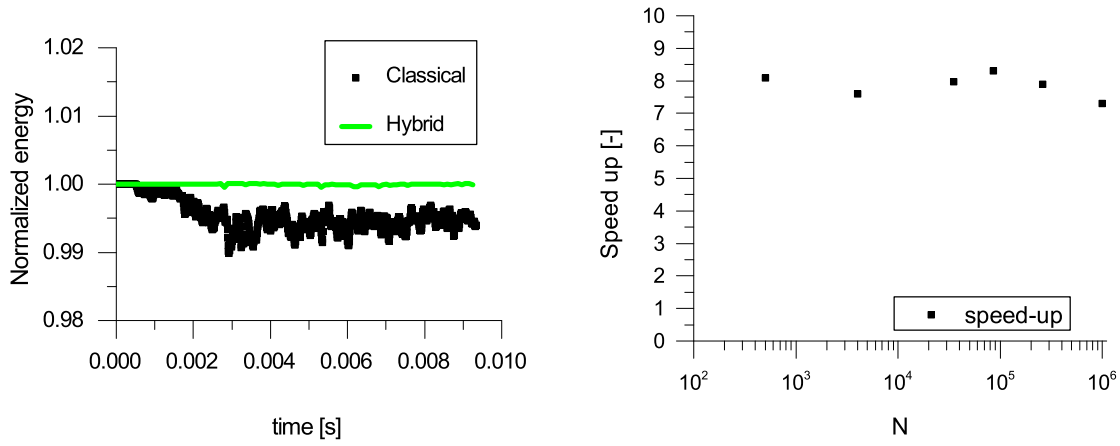


**Figure 2:** Normalized energy levels per time step for a bounding box problem with  $e=1$ . In black the classical soft-sphere method is given, in green the new hybrid model (left). Speed up as a function of the number of particles  $N$  (right).

where  $\omega_d$  is the dampened frequency defined as:

$$\omega_d = \sqrt{\frac{k_n}{m_{eff}}} \left( \sqrt{1 - \zeta^2} \right)$$

where  $\zeta$  is the damping ratio defined as:

$$\frac{-\ln(e)}{\sqrt{\pi^2 + \ln(e)^2}}$$

A collision detection algorithm; a kd-tree searcher, from MATLAB is used to detect all particles that have overlap. For these particles the duration of the contact is determined using equation 8 and subsequently the collision is processed with the method described earlier. For multi-body collisions the duration of a collision can be slightly longer or shorter as described before. In case the collision takes longer the information has to be appropriately transferred across time steps.

Additionally, checks have to be made for particles that are colliding in two subsequent time steps, because the two collisions might be overlapping, in essence being a multi-body collision. this has extensively been discussed in Buist *et al.* (2016).

## RESULTS

**Table 2:** Parameter values used for the simulations.

parameter	value	
$\phi_s$	0.4-0.5	
$N_p$	$10^3 - 10^6$	
$d_p$	0.003	$m$
$\rho$	2500	$kg/m^3$
$k_n$	20000	$N/m$
$e$	0.7-1.0	
$\beta$	1	
$\mu$	0	
$\langle v_n \rangle$	0	$m/s$
$v_t$	0	$m/s$
$v_{max}$	$\pm 0.15$	$m/s$

In this section the first results of the new integration scheme will be shown. First tests are done for a bounding box problem. This problem consists of a cubic box randomly filled

with particles, with sizes ranging from 8 to 100 times the particle diameter. The particles have zero mean velocity and are given a velocity drawn from a Gaussian distribution. The maximum velocity, solids fraction and the box size can be varied to scale the problem. The simulation data is given in table 2 and are inspired by simulations of a fluidized bed (see figure 1), to match the solids holdup and granular temperature. For the particle-wall contacts we assume the same restitution coefficient as for particle-particle contacts.

### Speed up & Scalability

The first test involves a bounding box containing 4000 particles with a solids volume fraction of 40%. The particles are allowed to freely bounce in the box for 0.1 s of real time. Simulations were conducted using both the new collision integration scheme as well as the classical soft sphere scheme. This resulted in on average 50 collisions per particle and 0.4 multibody collisions per particle. In this test the particles have ideal collision properties. This implies that the total energy in the system should remain constant. The normalized total kinetic energy of the particles is shown in figure 2. The total energy is normalized to the energy given at  $t=0$ .

The classical soft sphere method shows regular dips in the energy-level, associated with energy being stored in the springs as a consequence of the collisions. The hybrid model has a largely static energy profile as most collisions are binary. Both models are capable of maintaining proper energy conservation, as expected. The difference is however that the hybrid model is about eight times faster.

To test for the scalability of the hybrid model and the robustness of the gained speed up, the size of the bounding box is gradually increased to include  $10^6$  particles. The relative speed up for these systems is shown in figure 2. It can be seen that an average speed up of a factor 7 to 8 is possible with the new hybrid collision integration scheme. This speed up can be attributed to the lower number of collision detection evaluations that are necessary. The maximum possible speed-up factor 10 is not reached because of the overhead associated with the check for overlapping collisions, as discussed in the previous section.

### Number of contact partners

For the new hybrid model to be competitive with the classical soft sphere model, it has to be capable of dealing with sys-

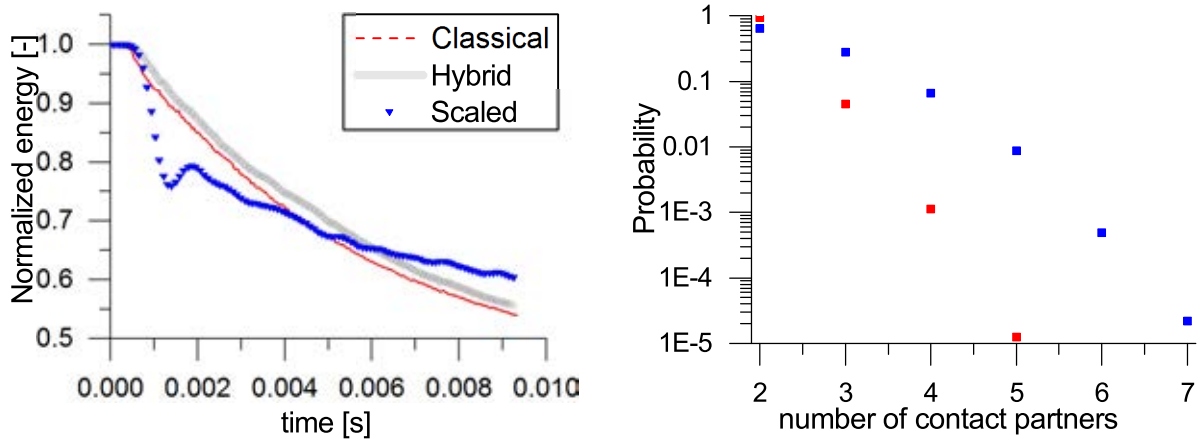


**Figure 3:** Normalized energy loss over time for the two schemes (left), collision order probability (right), for a bounding box problem with  $\varepsilon = 0.5$ ,  $e = 0.9$ ,  $\mu = 0$ .

tems with similar solids fractions and granular temperatures. It is the combination of these two parameters that determines the amount of multibody collisions. For this reason a simulation was run with a solids fraction of 50% and a maximum velocity of 0.15 m/s. The results are shown in figure 3. The left figure shows the normalized energy of the system for the two schemes, the figure on the right shows the probability of the number of contact partners, with 2 being binary and every higher number signifying extra particles participating in the collision. It can be seen that the two models show the same trend, now with more energy stored in the springs for the classic model. The amount of multibody collisions add up to about 5% of all collisions which matches the result of figure 3. The hybrid model is thus able to match the density and energy of systems in which typically a soft sphere model is used.

### Relaxing the classical scheme

In the classical scheme it is also possible to scale the duration of a collision by scaling the spring stiffness. By reducing the spring stiffness by a factor 100, the duration of a collision is multiplied by a factor ten, i.e. the same as for our hybrid model. This will reduce computation time but will also increase the overlap between colliding particles.

To see if this affects the energy balance of the system, the results of such scaling of the spring stiffness is quantified for the same simulation as before, figure 3 in comparison to the classical and the hybrid schemes. The number of contact partners is also shown for the scaled model. The first thing that can be seen is that the scaled scheme has a very sudden and large drop in energy, associated with a lot of particles entering collision mode at the same time, often with multiple collision partners. Binary collisions only make up for 65 % of all collisions. The rate of energy loss is also much smaller than for the classical and the hybrid schemes.

This underestimation of the dissipation rate is entirely attributable to the number of multibody contacts and was also found for pure multibody contacts in Pournin *et al.* (2001). The relative speed up of the scaled model is only in the order of 2.5. The poor performance of this scaled classic model, in terms of both the energy conservation and the speed up of the model, shows the power and need of a hybrid model all the more. Second, the lower rate of energy dissipation means that the choice of a proper spring stiffness is critical in obtaining meaningful results, especially for dense dynamical

systems.

### CONCLUSIONS

Most collisions in a soft-sphere granular flow problem are necessarily binary that can be accurately described within one time step. Because of the possible distinction between binary and multi-body contacts a hybrid collision integration scheme was proposed. The binary collisions are solved with a modified hard-sphere approach with a collision duration equal to the classic linear spring dashpot and all multi-body contacts are handled with the classic soft-sphere approach.

The larger time-step of this hybrid integration scheme and the lower amount of collision detection evaluations allows for a factor 7 to 8 computational speed-up. Meanwhile retaining energy and momentum conservation. Because a lower amount of energy is stored in the springs of the spring-dashpot model the energy state of the hybrid scheme more accurately describes the granular behaviour of the system.

The results of this scheme were shown to be scalable with the number of particles up to at least  $O(10^6)$  and is capable of handling systems with a solids hold-up and granular temperature resembling the collision dynamics in an actual granular flow system.

Further relaxation of the spring-stiffness in the classical scheme to allow for a similar increase in time-step has proven to be inadequate to quantitatively capture the energy decay of a dense dynamic granular system and was proven to be less computationally efficient as the presented hybrid scheme.

### ACKNOWLEDGEMENTS

This research was funded by the European Research Council, under the Advanced Investigator Grant Scheme, contract no. 247298 (Multiscale Flows).

### REFERENCES

- BUIST, K.A., VAN ERDEWIJK, T.W., DEEN, N.G. and KUIPERS, J.A.M. (2015). "Determination and comparison of rotational velocity in a pseudo 2-d fluidized bed using magnetic particle tracking and discrete particle modeling". *AIChE Journal*, **61**(10), 3198–3207.
- BUIST, K.A., SEELEN, L., DEEN, N., PADDING, J. and KUIPERS, J. (2016). "On an efficient hybrid soft and hard sphere collision integration scheme for dem". *Chemical Engineering Science*, **153**, 363–373.
- CLEARY, P.W. and SAWLEY, M.L. (2002). "Dem modelling of industrial granular flows: 3d case studies and the



effect of particle shape on hopper discharge”. *Applied Mathematical Modelling*, **26(2)**, 89–111.

CUNDALL, P.A. and STRACK, O.D. (1979). “A discrete numerical model for granular assemblies”. *Geotechnique*, **29(1)**, 47–65.

DEEN, N.G., VAN SINT ANNALAND, M., VAN DER HOEF, M.A. and KUIPERS, J.A.M. (2007). “Review of discrete particle modeling of fluidized beds”. *Chemical Engineering Science*, **62(1)**, 28–44.

GONZALEZ BRIONES, J.S.L., WINDOWS-YULE, C.R., LUDING, S., PARKER, D.J. and THORNTON, A.R. (2015). “Shaping segregation: Convexity vs. concavity”. *Physical review B: Condensed matter*, 1–5.

GUI, N., YANG, X., JIANG, S., TU, J. and FAN, J. (2016). “Extended hpm–dem coupled simulation of drainage of square particles in a 2d hopper flow”. *AIChE Journal*.

HELLAND, E., OCCELLI, R. and TADRIST, L. (2002). “Computational study of fluctuating motions and cluster structures in gas–particle flows”. *International Journal of Multiphase Flow*, **28(2)**, 199–223.

HOOMANS, B.P.B., KUIPERS, J.A.M., BRIELS, W.J. and VAN SWAAIJ, W.P.M. (1996). “Discrete particle simulation of bubble and slug formation in a two-dimensional gas-fluidised bed: a hard-sphere approach”. *Chemical Engineering Science*, **51(1)**, 99–118.

KOREVAAR, M.W., PADDING, J.T., VAN DER HOEF, M.A. and KUIPERS, J.A.M. (2014). “Integrated dem–cfD modeling of the contact charging of pneumatically conveyed powders”. *Powder technology*, **258**, 144–156.

LU, G., THIRD, J.R. and MÜLLER, C.R. (2015). “Discrete element models for non-spherical particle systems: From theoretical developments to applications”. *Chemical Engineering Science*, **127**, 425–465.

MARSHALL, J.S. (2009). “Discrete-element modeling of particulate aerosol flows”. *Journal of Computational Physics*, **228(5)**, 1541–1561.

MIKAMI, T., KAMIYA, H. and HORIO, M. (1998). “Numerical simulation of cohesive powder behavior in a fluidized bed”. *Chemical Engineering Science*, **53(10)**, 1927–1940.

POURNIN, L., LIEBLING, T.M. and MOCELLIN, A. (2001). “Molecular-dynamics force models for better control of energy dissipation in numerical simulations of dense granular media”. *Physical Review E*, **65(1)**, 011302.

POURNIN, L., WEBER, M., TSUKAHARA, M., FERREZ, J.A., RAMAIOLI, M. and LIEBLING, T.M. (2005). “Three-dimensional distinct element simulation of spherocylinder crystallization”. *Granular Matter*, **7(2-3)**, 119–126.

SHIRSATH, S.S., PADDING, J.T., KUIPERS, J.A.M., PEETERS, T.W.J. and CLERCX, H.J.H. (2014). “Numerical investigation of monodisperse granular flow through an inclined rotating chute”. *AIChE journal*, **60(10)**, 3424–3441.

TSUJI, Y., KAWAGUCHI, T. and TANAKA, T. (1993). “Discrete particle simulation of two-dimensional fluidized bed”. *Powder technology*, **77(1)**, 79–87.

VAN BUIJTENEN, M.S., BÖRNER, M., DEEN, N.G., HEINRICH, S., ANTONYUK, S. and KUIPERS, J.A.M. (2011). “An experimental study of the effect of collision properties on spout fluidized bed dynamics”. *Powder Technology*, **206(1)**, 139–148.

XU, B.H. and YU, A.B. (1997). “Numerical simulation of the gas-solid flow in a fluidized bed by combining discrete particle method with computational fluid dynamics”. *Chemical Engineering Science*, **52(16)**, 2785–2809.

YANG, R.Y., YU, A.B., MCELROY, L. and BAO, J.

(2008). “Numerical simulation of particle dynamics in different flow regimes in a rotating drum”. *Powder Technology*, **188(2)**, 170–177.

ZASTAWNY, M., MALLOUPPAS, G., ZHAO, F. and VAN WACHEM, B. (2012). “Derivation of drag and lift force and torque coefficients for non-spherical particles in flows”. *International Journal of Multiphase Flow*, **39**, 227–239.

ZHU, H.P., ZHOU, Z.Y., YANG, R.Y. and YU, A.B. (2007). “Discrete particle simulation of particulate systems: theoretical developments”. *Chemical Engineering Science*, **62(13)**, 3378–3396.

ZHU, H.P., ZHOU, Z.Y., YANG, R.Y. and YU, A.B. (2008). “Discrete particle simulation of particulate systems: a review of major applications and findings”. *Chemical Engineering Science*, **63(23)**, 5728–5770.

# IMPLEMENTING THE KINETIC THEORY OF GRANULAR FLOWS INTO THE LAGRANGIAN DENSE DISCRETE PHASE MODEL

Schalk Cloete, Shahriar Amini\*

SINTEF Materials and Chemistry, 7465 Trondheim, NORWAY

\* E-mail: Shahriar.amini@sintef.no

## ABSTRACT

The dense discrete phase model (DDPM) is a promising method for detailed simulation of fluidized bed reactors. It can resolve particle clusters on much coarser grids than the conventional two fluid model (TFM) and allows for a more natural inclusion of particle size distributions. However, the discrete nature of the DDPM presents challenges when implementing the kinetic theory of granular flows (KTGF), which is required for adequate predictions of fluidized bed behaviour. This paper outlines several methods for accomplishing this task. A good match with experimental and TFM data was achieved with different methods for implementing the KTGF, thus building confidence in the DDPM as a method for fluidized bed reactor modelling. It was also shown that the model completely fails in dilute riser flows when the KTGF is only partially implemented or neglected completely.

**Keywords:** Kinetic theory of granular flows, dense discrete phase model, granular temperature, fluidized bed.

## NOMENCLATURE

### Greek Symbols

- $\alpha$  Volume fraction  
 $\Delta t$  Time step size [s]  
 $\phi_{gs}$  Interphase energy exchange rate [W/m<sup>3</sup>]  
 $\gamma_{\Theta}$  Energy dissipation rate [W/m<sup>3</sup>]  
 $\Theta$  Granular temperature [m<sup>2</sup>/s<sup>2</sup>]  
 $\rho$  Density [kg/m<sup>3</sup>]  
 $\bar{\tau}$  Stress tensor [kg/m.s<sup>2</sup>]  
 $\tau_c$  Collisional relaxation time [s]  
 $\vec{v}$  Velocity vector [m/s]  
 $\vec{v}'$  Uncorrelated velocity vector [m/s]  
 $\omega_{\Theta}$  Granular temperature generation [m<sup>2</sup>/s<sup>3</sup>]

### Latin Symbols

- $d$  Diameter [m]  
 $e_{ss}$  Particle-particle restitution coefficient

- $\vec{F}$  Specific force vector [N/kg]  
 $F_d$  Drag force coefficient [1/s]  
 $\vec{g}$  Gravitational acceleration [m/s<sup>2</sup>]  
 $g_0$  Radial distribution function  
 $k_{\Theta}$  Granular temperature diffusion coefficient [kg/m.s]  
 $K_{sg}$  Interphase momentum exchange coefficient [kg/m<sup>3</sup>s]  
 $n_p$  Number of particle parcels in a cell  
 $p$  Pressure [Pa]  
 $t$  Time [s]

### Sub/superscripts

- $g$  Gas  
 $p$  Particle  
 $pc$  Particle parcel  
 $s$  Solids

### Acronyms

- CFD Computational fluid dynamics  
DDPM Dense discrete phase model  
fTFM Filtered two fluid model  
GT Granular temperature  
KTGF Kinetic theory of granular flows  
ODE Ordinary differential equation  
PDE Partial differential equation  
RHS Right hand side  
TFM Two fluid model  
ToGT Transport of granular temperature

## INTRODUCTION

Fluidized bed reactors are used across a wide range of process industries. The complex flow patterns, tightly coupled with mass and heat transfer phenomena, present challenges related to the design and operation of these reactors. These challenges have motivated several decades of research into accurate modelling of fluidized beds, both in terms of 1D phenomenological models and more fundamental CFD approaches.

The most established CFD approach is the two fluid model (TFM) closed by the kinetic theory of granular flows (KTGF) (Jenkins and Savage 1983, Gidaspow,

Bezburuah et al. 1992). In this method, particles in the fluidized bed are modelled as a fluid and closure laws are derived to model the dispersive effects of particle collisions and random translations as stresses experienced by this granular fluid. Closure laws derived from the KTGF are based on the likeness of granular motions to the motions of gas molecules, leading to a modelled pressure and viscosity.

The TFM-KTGF approach has been developed to a good level of maturity over the past three decades. It gives good representations of small scale fluidized beds (Cloete, Zaabout et al. 2013, Cloete, Johansen et al. 2015), but cannot be used for 3D simulations of fluidized beds larger than laboratory scale (Cloete, Johansen et al. 2015). The reason for this restriction is the tendency of particles to cluster together during fluidization. This clustering behaviour strongly impacts all transfer phenomena inside the reactor and must be resolved to achieve accurate results. Due to the dynamic nature of these clusters, TFM-KTGF simulations generally require very fine spatial and temporal resolution, leading to great computational expense.

To overcome this challenge, a promising approach called the filtered TFM (fTFM) (Igci, Andrews et al. 2008) is currently under development. This approach utilizes multiscale modelling principles to derive models capable of modelling the presence of particle clusters on grid sizes larger than the cell size used in the CFD simulation, thereby reducing computational costs by several orders of magnitude. However, this approach is still under development.

The dense discrete phase model (DDPM) approach (Popoff and Braun 2007), which is the subject of this paper, is another promising method for reducing computational costs relative to the TFM. This approach tracks parcels of particles through the domain in the Lagrangian sense, but also interpolates information such as volume fraction and velocity onto an Eulerian computation grid. In this way, the DDPM eliminates numerical diffusion, thereby allowing clusters to be resolved on much fewer cells than the TFM, thus resulting in 1-2 orders of magnitude speed-up. Since particle clusters still need to be resolved, the DDPM approach remains limited for large reactors fluidizing fine powders (Cloete, Cloete et al. 2016), but it can simulate much larger reactors than the TFM. In addition, the method allows a more natural inclusion of the wide particle size distribution typical of many fluidized bed applications.

An important challenge related to the DDPM approach is the implementation of the KTGF for correctly modelling the effects of unresolved particle collisions on the motion of particle parcels. Due to the discrete nature of the DDPM, the flow fields interpolated onto the Eulerian grid from the Lagrangian particle data are not continuous, thus creating problems when implementing the KTGF where many gradient operations are required. It is also challenging to convect the granular temperature (kinetic energy in the random particle motions) – a key variable in the KTGF. This paper will investigate ways to incorporate the KTGF into the DDPM framework and evaluate the performance of the resulting DDPM-KTGF model in 2D riser flows.

## SIMULATIONS

### Model description

The DDPM is a hybrid Lagrangian-Eulerian approach, tracking the particle phase using Newton's second law (Eq. (1)), while gas-phase motion is solved by the Navier-Stokes equations (momentum conservation as in Eq. (2)). Solids phase volume fraction and velocity are interpolated from the particle data in each computational cell. A more complete presentation of the equation system is given in (Cloete, Johansen et al. 2012).

$$\frac{d\vec{v}_p}{dt} = F_D (\vec{v} - \vec{v}_p) + \frac{\vec{g}(\rho_p - \rho)}{\rho_p} + \vec{F}_{KTGF} \quad (1)$$

$$\frac{\partial}{\partial t} (\alpha_g \rho_g \vec{v}_g) + \nabla \cdot (\alpha_g \rho_g \vec{v}_g \vec{v}_g) = -\alpha_g \nabla p + \nabla \cdot \vec{\tau}_g + \alpha_g \rho_g \vec{g} + K_{sg} (\vec{v}_s - \vec{v}_g) \quad (2)$$

Five different possibilities for modelling particle collisions and random translations are investigated in this work:

1. **No KTGF:** No additional modelling
2. **No ToGT:** Algebraic granular temperature conservation and modelling of the solids pressure
3. **Full KTGF:** Transport of granular temperature on the particle parcels and modelling of the full solids phase stress tensor
4. **Parcel relax:** The full KTGF implementation including a relaxation of parcel velocity to the mean in each cell
5. **Parcel GT:** Modelling granular temperature generation through the particle parcel velocity distribution in each cell and modelling the solids pressure

In the “**No KTGF**” approach, the final term in Eq. (1) is simply ignored to illustrate the effect of completely excluding the KTGF.

The “**No ToGT**” approach calculates the local generation and dissipation of granular temperature in each cell, but ignores convection and diffusion of granular temperature. This simplifying assumption reduces the granular temperature equation from a PDE to an ODE, simplifying implementation. However, this assumption is generally not valid in dilute systems as was selected for this study. The resulting granular temperature is then used to calculate the solids pressure, which is used to model the effect of particle collisions and random translations on the motion of particle parcels via the final term in Eq. (1):

$$\vec{F}_{KTGF} = \frac{-1}{\alpha_p \rho_p} \nabla \bar{\tau}_s \approx \frac{-1}{\alpha_p \rho_p} \nabla p_s \quad (3)$$

As indicated in Eq. (3), this is also a simplifying assumption, ignoring the shear stress components of the solids stress tensor.

The “**Full KTGF**” approach completes the modelling described above by including the transport of granular temperature and the full stress tensor. Granular temperature is naturally convected on the particle parcels as described in (Cloete, Johansen et al. 2012) through the ODE shown in Eq. (4).

$$\frac{3}{2} \alpha_s \rho_s \frac{d\Theta}{dt} = \bar{\tau}_s : \nabla \bar{\mathbf{v}}_s + \nabla \cdot (k_\Theta \nabla \Theta) - \gamma_\Theta + \phi_{gs} \quad (4)$$

The second order derivatives present in the full stress tensor (Eq. (3)) require some smoothing of the solids velocity field interpolated from the particle data as described in (Cloete, Johansen et al. 2012).

An additional modification is made in the “**Particle relax**” approach by removing the parcel-scale granular temperature (caused by the difference between the velocities of the tracked particle parcels) in each cell. This is done through the relaxation term in Eq (5):

$$\tau_c = \left( \frac{24 \alpha_s}{\sqrt{\pi} d_p} g_0 \sqrt{\Theta_{pc}} \right)^{-1} \quad (5)$$

Each particle parcel is then accelerated according to a modified Eq. (3) where an additional particle acceleration is implemented which is proportional to the deviation of the particle velocity from the mean velocity in the cell:

$$\bar{\mathbf{F}}_{KTGF} = \frac{-1}{\alpha_p \rho_p} \nabla \bar{\tau}_s - \frac{\bar{\mathbf{v}}'}{\tau_c} \quad (6)$$

The reasoning behind this action is to remove the additional dispersion of momentum and granular temperature by uncorrelated motions of the particle parcels in each cell. If the full kinetic theory is implemented as in the “Full KTGF” approach, the modelled granular temperature should account for all the effects of uncorrelated particle motions, implying that additional dispersive effects are superfluous.

Finally, the “**Parcel GT**” approach models the generation of granular temperature from the uncorrelated motions of particle parcels in each cell. This is done by implementing Eqs. (5) and (6) to relax particle parcels towards the mean velocity in each cell, but conserving energy by adding a generation of granular temperature. In fact, Eqs. (5) and (6) conserve momentum, but assume completely inelastic collisions, thereby dissipating all the kinetic energy associated with the uncorrelated particle motions. Granular temperature generation in each cell was therefore approximated from the projected difference in kinetic energy in the particle parcels before and after the relaxation in each timestep:

$$\omega_\Theta = \left( \sum_1^{n_p} \bar{\mathbf{v}}_p^2 - \sum_1^{n_p} \left( \bar{\mathbf{v}}_p - \frac{\bar{\mathbf{v}}'}{\tau_c} \Delta t \right)^2 \right) e_{ss}^2 / n_p \Delta t \quad (7)$$

The product of Eq. (7) and the particle mass then replaced the first term on the RHS of Eq. (4) to increase the granular temperature stored on each particle parcel. In addition, the second term on the RHS of Eq. (4) was neglected on the assumption that the uncorrelated motions of the particle parcels, each carrying a certain amount of granular temperature, adequately describe the diffusion of granular temperature.

To keep consistency with this parcel-scale approach to the KTGF implementation, the effect of granular temperature was implemented by simply displacing each parcel by the distance that would be covered by the uncorrelated motion in each timestep in a random direction:

$$\Delta \mathbf{x} = \sqrt{\Theta} \Delta t \quad (8)$$

This simplified approach captures the essence of the KTGF by dispersing particles away from regions of high uncorrelated motions where many particle collisions and random translations would take place. This dispersion of particles carrying momentum and granular temperature then naturally leads to a dispersion of momentum and granular temperature without requiring additional modelling. Dispersion of a particle parcel into a cell with a very different mean velocity then leads to the generation of additional granular temperature since particle velocities in this parcel would be very different from that of the other particles in the cell.

#### Geometry, boundary conditions and material properties

A simple 2D planar geometry with periodic boundaries in the axial direction is utilized in this work (see Figure 1 and Figure 2 for visualization). This geometry has been used in detailed validation studies of the TFM approach in riser flows (Cloete, Amini et al. 2011). It will therefore be informative to observe whether the DDPM can achieve a similarly good match to experimental data as the TFM.

Similar to (Cloete, Amini et al. 2011), the geometry is 0.8 m in height and 0.076 m in width. The geometry was meshed with 8288 square cells – about 8 times fewer than was needed for the TFM study in (Cloete, Amini et al. 2011). The coarser mesh is due to the superior cluster resolution capability of the DDPM.

The side boundaries of the geometry were designated as walls with a no-slip boundary condition for the gas. For the solids, normal and tangential restitution coefficients of 0.9 and 0.2 were specified (FLUENT defaults). A more advanced formulation accounting for the granular temperature on each particle may be implemented in future works, but this simple implementation was deemed sufficient for this comparative study.

The top and bottom boundaries of the geometry were specified as periodic. A variable pressure gradient was specified across the geometry via a negative feedback mechanism to keep the average gas superficial velocity through the geometry close to 4.48 m/s (Cloete, Amini et al. 2011).

A total of 80000 particle parcels were included in the simulation so that the average solids volume fraction in the domain amounts to 0.0372. The particle size, density

and restitution coefficient were specified as  $67 \mu\text{m}$ ,  $1500 \text{ kg/m}^3$  and  $0.9$  respectively. The gas was standard air at room temperature.

#### Solver settings

The commercial flow solver ANSYS Fluent 16 was used to complete the calculations. The phase coupled SIMPLE algorithm was used for pressure-velocity coupling, while all other variables were discretized using the QUICK scheme. First order temporal discretization was used since this was found to be adequate in (Cloete, Johansen et al. 2012).

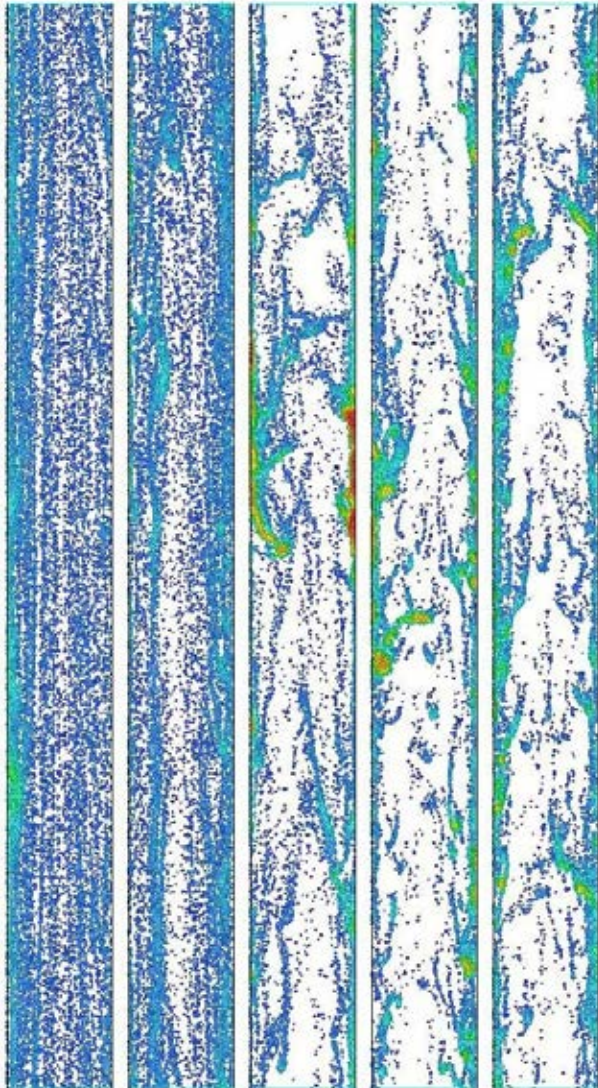


**Figure 1: Instantaneous particle parcel positions for the five modelling approaches investigated in this study. Parcels are coloured according to local solids volume fraction where blue is zero and red is 0.6. From left to right: no KTGF implementation (No KTGF), no transport of granular temperature (No ToGT), complete KTGF implementation (Full KTGF), complete KTGF implementation with particle relaxation towards the mean velocity in each cell (Particle relax), and granular temperature generation from the uncorrelated motions between particle parcels (Parcel GT).**

## RESULTS

#### Qualitative analysis

Figure 1 shows instantaneous distributions of particle parcels in the geometry for the five different modelling approaches investigated in this study. It is clear that the first two approaches did not capture the expected clustering at the walls of the geometry, while the latter three approaches captured this phenomenon due to the more complete implementation of the kinetic theory of granular flows.

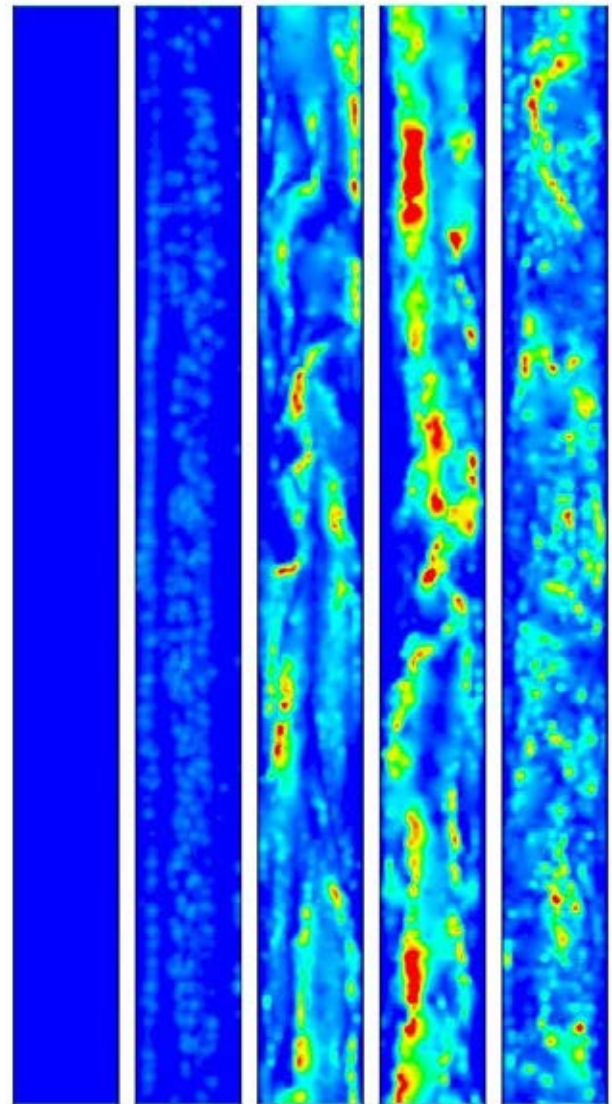


**Figure 2: Instantaneous contours of granular temperature at the same instance as Figure 1. Blue represents zero and red  $0.3 \text{ m}^2/\text{s}^2$ .**

Adequate representation of cluster formation at the walls of the geometry is primarily due to the formation of regions of high granular temperature in the dilute central regions of the geometry (Figure 2). These regions of high uncorrelated particle motion cause particles to migrate away from these regions towards the denser clusters at the walls. In these denser regions, granular temperature is rapidly dissipated due to inelastic collisions, thereby preserving the formed clusters until they are broken up by the rising gas flow (drag).

### Quantitative analysis

Results presented in the previous section clearly showed that the inclusion of a proper KTGF implementation is essential for reasonable predictions in riser flows. The three complete KTGF implementations investigated in this work all performed well in a qualitative sense by predicting reasonable cluster formation and breakup behaviour at the walls (Figure 1). Quantitative results presented in this section will aim to better distinguish the differences between these three approaches.

Time averaged lateral profiles of solids volume fraction and axial velocity are shown in Figure 3 and Figure 4 for all five cases investigated in the study. It is clear that the incomplete KTGF implementations (“No KTGF” and “No ToGT”) completely fail to predict the flow in the simulated riser section. This is especially evident in Figure 4 where very large upward velocities in the centre and downward velocities at the walls are shown. The reason for this great error is simply that the proper dispersion of momentum caused by the KTGF is not accounted for, thereby allowing very large velocity gradients to form. In addition, limited cross-stream particle parcel motion (due to the final term in Eq. (1) being very small or neglected) cause very few impacts with the wall to slow down falling particles. The result is a lateral velocity profile that is far too pronounced.

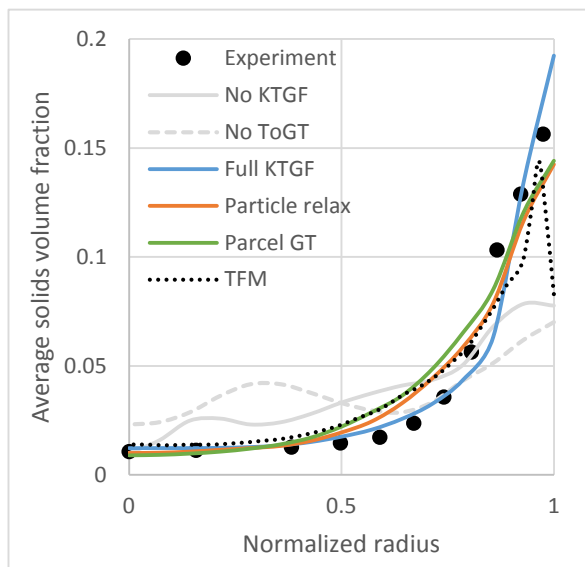


**Figure 3: Time averaged lateral volume fraction profiles of the five cases compared to experiments (Yan and Zhu 2004) and TFM predictions (Cloete, Amini et al. 2011). Legend: No KTGF = no KTGF implementation, No ToGT = no transport of granular temperature, Full KTGF = Complete KTGF implementation, Particle relax = Complete KTGF implementation with particle relaxation towards the mean velocity in each cell, and Parcel GT = Granular temperature generation from the uncorrelated motions between particle parcels.**

The three cases with more complete implementations of the KTGF perform much better. Figure 3 shows very similar profiles for the “Particle relax” and “Parcel GT” case, and a somewhat more pronounced lateral solids volume fraction profile for the “Full KTGF” case.

The similarity between the “Particle relax” and “Parcel GT” cases is the relaxation of particle parcels towards the mean cell velocity through Eqs. (5) and (6). This implementation has a large impact on particle parcel motion, but is strongly dependent on the granular temperature. Remarkably, the completely different methods used to represent the granular temperature in the “Particle relax” and “Parcel GT” cases returned similar granular temperature predictions (Figure 5). This is a positive result for the “Parcel GT” implementation, given its relative simplicity relative to the “Particle relax” and “Full KTGF” cases.

An important effect of the particle relaxation implementation in Eqs. (5) and (6) is that it slowed down falling particle clusters at the wall. This resulted from the effect of particle parcels hitting the wall and losing axial momentum (tangential restitution coefficient of 0.2) being transmitted to all parcels in the first cell next to the wall. Given that the cell size in this case was equivalent to 40 particle diameters, it is likely to be incorrect that parcels being slowed down on one side of the cell will exchange momentum with parcels on the opposite side of the cell. This implementation may therefore be grid dependent in regions of high solids velocity gradients (e.g. walls). Further work is needed on this topic.

It is clear from Figure 4 that the “Full KTGF” implementation resulted in more cluster slip at the walls because all particle parcels in the first cell next to the wall were not directly affected by momentum exchange with the wall as described in the previous paragraph.

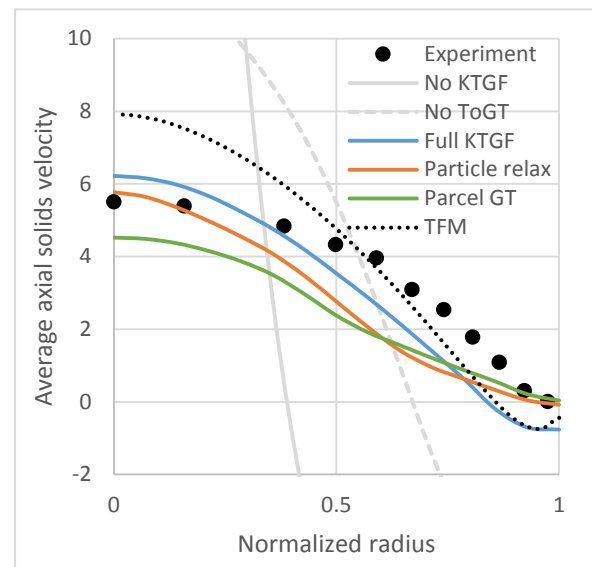


**Figure 4: Time averaged lateral profiles of axial velocity compared to experiments (Yan and Zhu 2004) and TFM predictions (Cloete, Amini et al. 2011). Values were weighted by the solids volume fraction in the averaging process. See the caption of Figure 3 to interpret the legend.**

The granular temperature profiles in Figure 5 show similar results for the three different cases with adequate KTGF implementations. The “Full KTGF” profile is shifted more towards the wall due to the formation of smaller, but more concentrated clusters at the wall (a higher solids concentration at the wall in Figure 3). As

mentioned earlier, the profile of the “Parcel GT” case is remarkably similar to the others even though a very different implementation of the KTGF was done in this case.

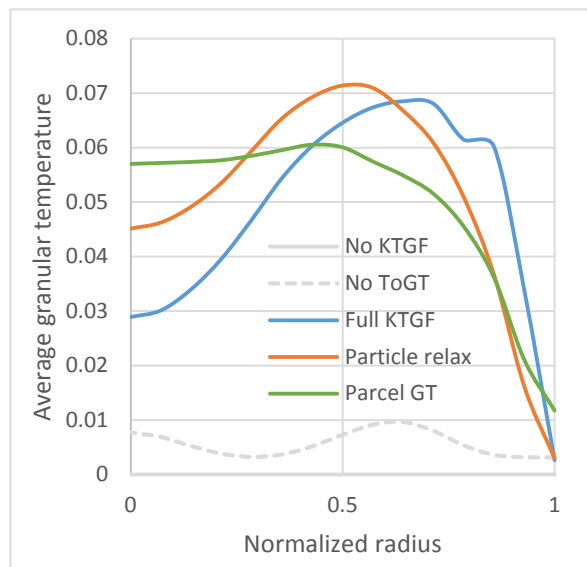


**Figure 5: Time averaged lateral profiles of granular temperature. Values were weighted by the solids volume fraction in the averaging process. See the caption of Figure 3 to interpret the legend. Note that the “No KTGF” case has no granular temperature.**

## CONCLUSION

This paper presented five different methods for modelling dilute granular flows using the hybrid Lagrangian-Eulerian dense discrete phase model (DDPM). It was firmly established that proper implementation of the KTGF is essential for capturing the flow dynamics in riser flows. If this is not done, momentum dispersion is under-predicted and excessive velocity gradients can form.

Three different approaches to a more complete KTGF implementation all performed well when compared to experiments and predictions by the conventional Eulerian two fluid model (TFM). In all the approaches, transport of granular temperature is naturally completed by convecting a granular temperature property on each tracked particle parcel.

Results also showed that generation of granular temperature and the resulting momentum dispersion can be well approximated via data regarding the uncorrelated motions in the tracked particle parcels. This is a simpler approach relative to the conventional KTGF implementation where gradient operations are required, creating challenges due to the discrete nature of the DDPM.

In general, positive results from this study showed that different pathways exist towards a complete implementation of granular physics into the promising DDPM framework. Further evaluation of these methods in a broader range of cases is strongly recommended.

## ACKNOWLEDGEMENT

The authors gratefully acknowledge financial support from the Research Council of Norway under the FRINATEK programme (Acronym: CSR, project number: 221902)

## REFERENCES

- Cloete, S., S. Amini and S. T. Johansen (2011). "A fine resolution parametric study on the numerical simulation of gas-solid flows in a periodic riser section." *Powder Technology* **205**(1-3): 103-111.
- Cloete, S., S. Amini and S. T. Johansen (2011). "On the effect of cluster resolution in riser flows on momentum and reaction kinetic interaction." *Powder Technology* **210**(1): 6-17.
- Cloete, S., J. H. Cloete and S. Amini (2016). *Comparison of the Filtered Two Fluid Model and Dense Discrete Phase Model for Large-Scale Fluidized Bed Reactor Simulations*. AIChE Annual Meeting, San Francisco, USA.
- Cloete, S., S. T. Johansen and S. Amini (2012). "Performance evaluation of a complete Lagrangian KTGF approach for dilute granular flow modelling." *Powder Technology* **226**: 43-52.
- Cloete, S., S. T. Johansen and S. Amini (2015). "Grid independence behaviour of fluidized bed reactor simulations using the Two Fluid Model: Effect of particle size." *Powder Technology* **269**(0): 153-165.
- Cloete, S., S. T. Johansen, A. Zaabout, M. van Sint Annaland, F. Gallucci and S. Amini (2015). "The effect of frictional pressure, geometry and wall friction on the modelling of a pseudo-2D bubbling fluidised bed reactor." *Powder Technology* **283**: 85-102.
- Cloete, S., A. Zaabout, S. T. Johansen, M. van Sint Annaland, F. Gallucci and S. Amini (2013). "The generality of the standard 2D TFM approach in predicting bubbling fluidized bed hydrodynamics." *Powder Technology* **235**(0): 735-746.
- Gidaspow, D., R. Bezburuah and J. Ding (1992). *Hydrodynamics of Circulating Fluidized Beds, Kinetic Theory Approach*. *7th Engineering Foundation Conference on Fluidization* 75-82.
- Igci, Y., A. T. Andrews, S. Sundaresan, S. Pannala and T. O'Brien (2008). "Filtered two-fluid models for fluidized gas-particle suspensions." *AIChE Journal* **54**(6): 1431-1448.
- Jenkins, J. T. and S. B. Savage (1983). "Theory for the rapid flow of identical, smooth, nearly elastic, spherical particles." *Journal of Fluid Mechanics* **130**: 187-202.
- Popoff, B. and M. Braun (2007). *A Lagrangian Approach to Dense Particulate Flows*. *6th International Conference on Multiphase Flow*. Leipzig, Germany.
- Yan, A. and J. Zhu (2004). "Scale-Up Effect of Riser Reactors (1) Axial and Radial Solids Concentration Distribution and Flow Development." *Industrial & Engineering Chemistry Research* **43**(18): 5810-5819.

## IMPORTANCE OF THE DIFFERENT FLUID FORCES ON PARTICLE DISPERSION IN FLUID PHASE RESONANCE MIXERS

Silvio SCHMALFUSS<sup>1\*</sup>, Martin SOMMERFELD<sup>1</sup>

<sup>1</sup> Otto-von-Guericke-University Magdeburg, 06130 Halle (Saale), GERMANY

\* E-mail: silvio.schmalfuss@ovgu.de

### ABSTRACT

In Fluid Phase Resonance (FPR) mixers, a central pipe reaches into the liquid phase inside a mixing vessel. Thus two closed gas cushions are formed above the liquid – one inside the pipe and one above the liquid inside the vessel. A drive attached at the top of the pipe creates low frequency (typically in a range from  $1 \text{ s}^{-1}$  to  $5 \text{ s}^{-1}$ ) harmonical pressure oscillations in the gas cushion inside the pipe, which in turn induce a motion inside all the liquid in the vessel. This motion of the liquid is utilised for the purpose of mixing and dispersion of particles.

Simulations are performed for four different geometries of the central pipe's lower exit and for different particle Stokes numbers. Particle Stokes numbers are varied from  $9.7 \cdot 10^{-4}$  to 2.7 by changing the particle diameter and density. The flow field inside the vessel was simulated with a Volume-of-Fluid solver to capture the free surface and the influence of the gas cushions, which act like springs, until a quasi-steady state was reached. One of these simulations was verified with Laser Doppler Anemometry measurements. For each simulation, the flow fields of the last full oscillation period are stored. The particles are then repeatedly tracked through these flow fields for 15 oscillations with an Euler-Lagrange approach with one-way-coupling, so that there is no need to recalculate the flow fields. The particles are considered as point masses, which are exposed to added mass, buoyancy, drag, gravity, history, pressure gradient, rotational lift, and shear lift force. Hydrodynamic torque is also considered, as well as a Langevin model for turbulent dispersion and a wall collision model accounting for rotation.

Mixing quality and time are determined by means of correlation dimension and the 90% lifting criterion whereby one of the four pipe exit configurations was identified as the best one. For this configuration two more oscillation frequencies are also investigated. Increasing the frequency to the resonance frequency leads to a more intense mixing process. Increasing it further drastically reduces the fluid velocity and deteriorates the mixing properties.

Furthermore, the influence of the different forces on the particles is investigated. The often neglected added mass and history forces are quite relevant for all particles investigated, having always more than 10% of the drag force's magnitude, with maximum values of up to 142% for added mass and up to 66% for history force. Pressure gradient force is highly relevant for larger particles. The rotational lift force is important for large particles only. Finally, the shear lift force is highly important, especially for larger and denser particle, but negligible for small, light particles.

**Keywords:** CFD, Euler-Lagrange, particle forces, LDA, mixing, Fluid Phase Resonance mixer.

### NOMENCLATURE

#### Greek Symbols

$\varepsilon$	Turbulent dissipation rate, [ $\text{m}^2/\text{s}^3$ ]
$\mu_F$	Fluid dynamic viscosity, [ $\text{kg}/(\text{m} \cdot \text{s})$ ]
$\rho_F$	Fluid density, [ $\text{kg}/\text{m}^3$ ]
$\rho_P$	Particle density, [ $\text{kg}/\text{m}^3$ ]
$\tau_F$	Fluid time scale, [s]
$\tau_P$	Particle time scale, [s]
$\omega$	Turbulent frequency, [ $\text{s}^{-1}$ ]

#### Latin Symbols

$d_2$	Correlation dimension, [-]
$d_p$	Particle diameter, [m]
$f$	Frequency, [ $\text{s}^{-1}$ ]
$F_{drag}$	Drag force, [N]
$\vec{F}_i$	Force i, [N]
$i$	Index i, [-]
$k$	Turbulent kinetic energy, [ $\text{m}^2/\text{s}^2$ ]
$m_p$	Particle mass, [kg]
$P_2$	Number of pairs, [-]
$r$	Distance, [m]
$St$	Stokes number, [-]
$T$	Oscillation period, [s]
$t$	Time, [s]
$U$	Velocity, [m/s]
$u'$	Turbulent velocity fluctuation, [m/s]
$U_{i,max/min}$	Max/min velocity in direction i, [m/s]
$U_{i,max/min,turb}$	Max/min velocity in direction i including turbulent fluctuation, [m/s]
$\vec{u}_p$	Particle velocity, [m/s]
$\bar{U}_Z$	Average velocity in axial direction, [m/s]
$U_{Z,max}$	Maximum velocity in axial direction, [m/s]
$U_{Z,min}$	Minimum velocity in axial direction, [m/s]
$V$	Volume, [ $\text{m}^3$ ]
$\vec{x}_p$	Particle position, [m]



## INTRODUCTION

FPR mixers are a comparatively new kind of mixing technology. Instead of a stirrer, here a central pipe reaches into a liquid contained in a mixing vessel. Two closed gas cushions are formed, one outside and one inside the central pipe. The latter is exposed to a harmonically oscillating pressure created by a drive attached to the central pipe, causing an oscillating movement of the liquid inside the pipe, which in turn induces a non-zero mean flow inside all the liquid as shown in Schmalfuß et al (2012). This flow is in this case utilised for the dispersion of solid particles. Usually, the oscillation frequencies are in a range between  $1 \text{ s}^{-1}$  and  $5 \text{ s}^{-1}$ . According to Schmalfuß and Sommerfeld (2017) the flow properties and therefore also the mixing properties (e.g. velocity magnitude, turbulence, structure) are mainly defined by the central pipe's geometry and the oscillating frequency. On the one hand, this work investigates these influences to improve the mixing quality of FPR mixers. On the other hand, also the influence of different forces acting on the particles is analysed. Considered forces are drag force, added mass force, Basset force (or history force), pressure gradient force, gravity force including buoyancy, and the transverse lift forces due to shear and rotational lift. Some of these forces are usually neglected when it comes to the simulation of industrial scale processes, especially added mass and Basset force. The present work shall reveal if this practice is justified.

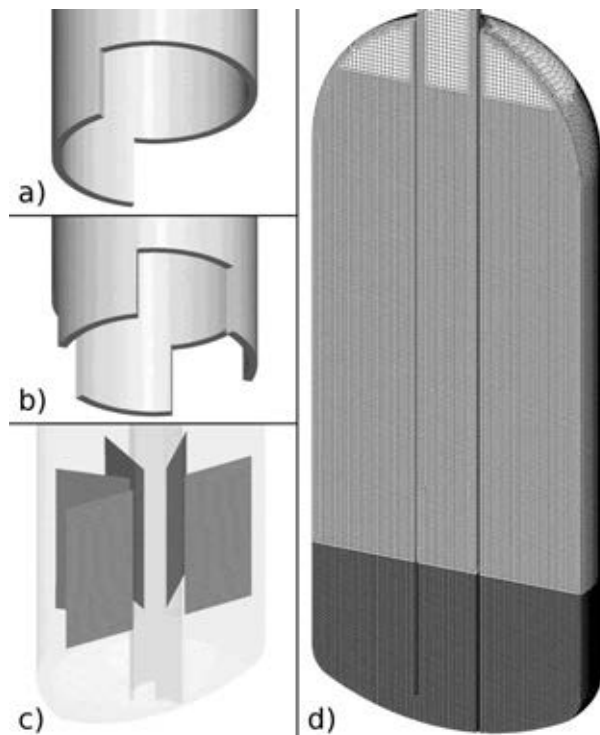


**Figure 1:** Geometry and computational domain; a) one-sided cutout pipe end; b) tripod pipe end; c) measurement planes (left:  $0^\circ$ , right:  $180^\circ$ ); d) computational grid.

## GEOMETRY AND PROCESS PARAMETERS

A vessel with a torispherical bottom is used as mixing vessel. Its geometrical properties are summarised in Table 1 and the different central pipe ends are shown in Figure 1 a) and b). Having a diameter of 0.45 m and a

filling height of 0.7 m results in a filling-height to diameter ratio of  $\sim 1.6$ . The first pipe end is a  $225^\circ$ -cutout, leaving a kind of nose at the end of the pipe and it will be referred to as “one-sided cutout”. The second pipe end consists of three  $60^\circ$ -cutouts, resulting in a tripod-like shape with three  $60^\circ$ -noses, henceforth referred to as “tripod”. Both central pipes have an inner diameter of 0.1 m. For each pipe two different mounting heights are considered. One time the pipe ends directly at the vessel bottom, leaving only small gaps at the cutouts, the other time the pipe is lifted by 20 mm. These two pipe heights will be referred to as “at bottom” or “lifted”, respectively. The drive frequency is  $1.2 \text{ s}^{-1}$  for all configurations. For the configuration “tripod at bottom” two higher frequencies, namely  $1.5 \text{ s}^{-1}$  and  $2.0 \text{ s}^{-1}$ , are used to investigate the frequency's influence. Water and air at room temperature and ambient pressure are used as the two phases. Their properties are listed in Table 2. The particles have densities of  $1050 \text{ kg/m}^3$ ,  $1500 \text{ kg/m}^3$ , and  $2500 \text{ kg/m}^3$ . Their diameters are  $80 \mu\text{m}$ ,  $500 \mu\text{m}$ ,  $1500 \mu\text{m}$ , and  $2500 \mu\text{m}$ .

**Table 1:** Geometry parameters.

Pipe		At bottom	Lifted
Vessel diameter	[m]	0.45	
Vessel height	[m]	1.1	
Filling height	[m]	0.70	
Pipe diameter	[m]	0.1	
Pipe height	[m]	-	0.020
Cutout height	[m]	0.04	

**Table 2:** Fluid phase material parameters.

		Water	Air
Density	$[\text{kg/m}^3]$	1000	1.3
Kinematic viscosity	$[\text{m}^2/\text{s}]$	$1 \cdot 10^{-6}$	$13 \cdot 10^{-6}$
Compressibility	$[\text{s}^2/\text{m}^2]$	$4.7 \cdot 10^{-10}$	$9.9 \cdot 10^{-6}$
Surface tension	$[\text{kg/s}^2]$	0.073	

## NUMERICAL AND EXPERIMENTAL METHODS

### Fluid flow

The fluid flow is simulated as an unsteady, compressible flow of two separate phases, namely water and air. OpenFOAM's solver compressibleInterFoam, employing a Volume-of-Fluid approach with interface compression, is used for this task. The geometries are discretised into approximately 4 million cells, whereby a symmetry plane is used as shown in Figure 1d) to lower the requirements on computational resources. At the top of the central pipe, a harmonically oscillating velocity normal to the surface is used as boundary condition, according to the parameters given by the drive attached to the pipe. At the symmetry plane a symmetry boundary condition is used and at the walls a no-slip condition is applied. Previous simulations by Schmalfuß et al (2012) have shown that the  $k-\omega$ -SST turbulence model gives the best results compared to

others. Thus, it is also used here. To ensure a quasi-steady flow, where after one oscillation the same flow field is found again, the flow is simulated for 20 periods. The averaged velocity components for the simulations are the arithmetic means of the three velocity components or the velocity magnitude, respectively, over the time of one period at the end of the simulation. Maximum and minimum velocities  $U_{i,max/min,turb}$  in directions  $i$  are calculated with the corresponding velocities during the analysed time period and the turbulent velocity fluctuations  $u'$ , which are estimated from turbulent kinetic energy  $k$ , assuming isotropic turbulence:

$$U_{i,max/min,turb} = U_{i,max/min} \pm u' = U_{i,max/min} \pm \sqrt{\frac{2}{3}k} \quad (1)$$

As another means of comparison between the configurations, the temporally and spatially averaged values of the turbulent kinetic energy and dissipation rate  $\varepsilon$  inside the liquid phase have been calculated.

The results of the flow field simulations are also used to calculate the turbulence characteristic time scale  $\tau_F$  of the fluid as a temporally and spatially averaged value of the ratio of turbulent kinetic energy and turbulent dissipation rate:

$$\tau_F = \frac{1}{T} \int_t^{t+T} \frac{1}{V} \int_V \frac{k}{\varepsilon} dV dt \quad (2)$$

The temporal averaging is done over one oscillation period with duration  $T$  starting at time  $t$ , and the spatial averaging is done over the total liquid volume  $V$ .

Measurements with a one component Laser Doppler Anemometer (LDA) have been conducted in five planes for the configuration “one-sided cutout at bottom” to verify the simulations. The measurement planes can be seen in Figure 1c). There are two planes in the symmetry plane (one on each side of the pipe) and three planes between those two, each shifted by 45°. In each plane there are 156 measurement points, where axial and radial velocity components have been measured. Unfortunately, the tangential velocity component could not be measured in this geometry. Tracer particles with a diameter of 40  $\mu\text{m}$  and a density of 1050  $\text{kg/m}^3$  are used. For LDA measurements it is important that these tracer particles follow the flow largely without slip, which means the particle Stokes number should be considerably below unity. Schmalfuß et al. (2012) have shown that the highest particle Stokes number occurs only in a very small region at the lower end of the immersed pipe with a value of about 0.14. Hence, the tracer particles should follow the flow to a large extent. In each measurement location 3000 Doppler signals are collected and statistically analysed. For the comparison of measurements and calculations, three different values are used: average, maximum and minimum velocities. The maximum and minimum velocities are determined for each point by the 0.05- or 0.95-quantile, respectively, of the 3000 values collected per point. The average is determined by an arrival time weighted average.

### Particle motion and mixing properties

An Euler-Lagrange approach, where particles are treated as point masses, is used to calculate the particle behaviour. The flow field for these calculations is taken

from the flow simulations described above. For the last oscillation, the transient flow field is stored with a time step of 0.01 s. The particles are repeatedly tracked through these stored flow fields. After one oscillation the flow field states are used again. Of course, with this approach only one-way-coupling is possible, meaning that the particles do not have any influence on the flow field, implying that for the moment only low particle concentrations are considered. Consequently inter-particle collisions are also neglected. As a Lagrangian approach is used, the particle motion is calculated by:

$$\frac{d\vec{x}_p}{dt} = \vec{u}_p \quad (3)$$

$$\frac{d\vec{x}_p}{dt} m_p = \sum_i \vec{F}_i \quad (4)$$

Here,  $u_p$  and  $m_p$  are the particle velocity and mass,  $t$  is the time and  $F_i$  are the forces acting on the particle. The forces considered are added mass force, Basset force (also called history force), drag force, gravity and buoyancy force, pressure gradient force, and the transverse lift forces due to rotational and shear slip, see e.g. Sommerfeld et al (2008) or Crowe et al (2012). Shear lift is modelled according to the findings of Mei (1992) and rotational lift according to Oesterlé and Bui Dinh (1998). Added mass and Basset force are implemented according to Michaelides and Roig (2011). For the Basset force, the approximation of Hinsberg et al (2011) is used for solving the integro-differential equation. Otherwise, either the tail in Basset force calculation would have to be truncated or its calculation would lead to all but impossibly high needs in computational resources.

Additionally, the hydrodynamic torque is considered. It is calculated with correlations taken from Sommerfeld et al. (2008), which are based on experiments by Dennis et al. (1980) and Sawatzki (1970).

Wall collisions account for kinetic energy loss and friction and can alter the angular velocity of the particles, as described by Decker (2005).

The fluctuating velocities due to turbulence are not resolved when a RANS-model, like  $k-\omega$ -SST in this case, is used to describe the turbulence. To model the turbulent velocity fluctuations seen by the particles, a single-step Langevin dispersion model is employed, as suggested by Sommerfeld et al. (1993).

At the beginning of the particle simulations, approximately 100,000 particles are randomly distributed near the bottom of the vessel with a velocity magnitude of zero. These particles are then, as described above, repeatedly tracked through the oscillating flow fields for 15 periods, which corresponds to a time of 12.5 s for the cases with  $f = 1.2 \text{ s}^{-1}$ .

The mixing properties are investigated using two parameters, namely mixing time and mixing quality. To judge about the mixing speed, the mixing time is defined as the 90% lifting criterion. This criterion is fulfilled as soon as the first particle reaches a height corresponding to 90% of the filling level. The mixing quality is investigated by means of the correlation dimension, which indicates how well the particle positions represent a random three dimensional distribution. Its values can vary between unity, representing a one-dimensional distribution, e.g. along a

line, and three, representing a random three dimensional distribution, e.g. in a spherical arrangement. The correlation dimension  $d_2$  is temporally averaged over the last oscillation period and is calculated as:

$$d_2(r) = \lim_{r \rightarrow 0} \frac{d \ln P_2(r)}{d \ln r} \quad (5)$$

with  $P_2(r)$  being the number of particle pairs closer than distance  $r$  to each other.

### Influence of the different particle forces

The magnitude of all the forces acting on the particles is stored every 0.001 s for the last two oscillation periods. To analyse their influence, the values are averaged over the above mentioned last two periods and then normalised with the magnitude of the drag force. An averaged particle Stokes number is used as parameter for judging on the influence of the forces. This number describes the ability of the particles to follow the flow field and is defined as:

$$St = \frac{\tau_P}{\tau_F} \quad (6)$$

The fluid time scale  $\tau_F$  has already been described above and is an average turbulence time scale in the entire liquid region. The Stokesian particle response time is

$$\tau_P = \frac{(\rho_P + 0.5\rho_F)d_P^2}{18\mu_F} \quad (7)$$

with  $\mu_F$  and  $\rho_F$  being the dynamic viscosity and density of the fluid and  $\rho_P$  the particle density.

## RESULTS

### Fluid flow

The configuration “one-sided cutout at bottom” is also investigated by means of LDA. In Figure 2 the average, maximum, and minimum values of the vertical velocities in the five planes depicted in Figure 1c) are compared. In general, the comparison between measurement and simulation shows good agreement. Discrepancies can be seen especially at the 180° plane. This might be because this is the symmetry plane in the simulation, so there is a zero velocity imposed perpendicular to that plane, which in turn might cause higher flow rates in the directions parallel to the symmetry plane. In reality, of course, this is not the case. Furthermore, the extremal values are not always met in the measured observations compared to the numerical computations. This could be caused by the comparatively coarse measurement grid.

In Figure 3 the temporal averaged velocity magnitude, turbulent kinetic energy, and turbulent dissipation rate in the symmetry plane of the four configurations are compared. Regarding the velocities it can be seen that the highest values occur inside the pipe. A lifted central pipe results in higher velocities inside, but lower velocities outside the pipe. With a pipe at the bottom, there is a large region with high velocities at the vessel wall opposite the opening of the pipe for both, one-sided cutout and tripod. For a lifted pipe with the one-sided cutout, this region is considerably smaller and for the lifted tripod it is even at the opposite side. The pipe exit geometry seems to have only low influence on the velocity magnitude.

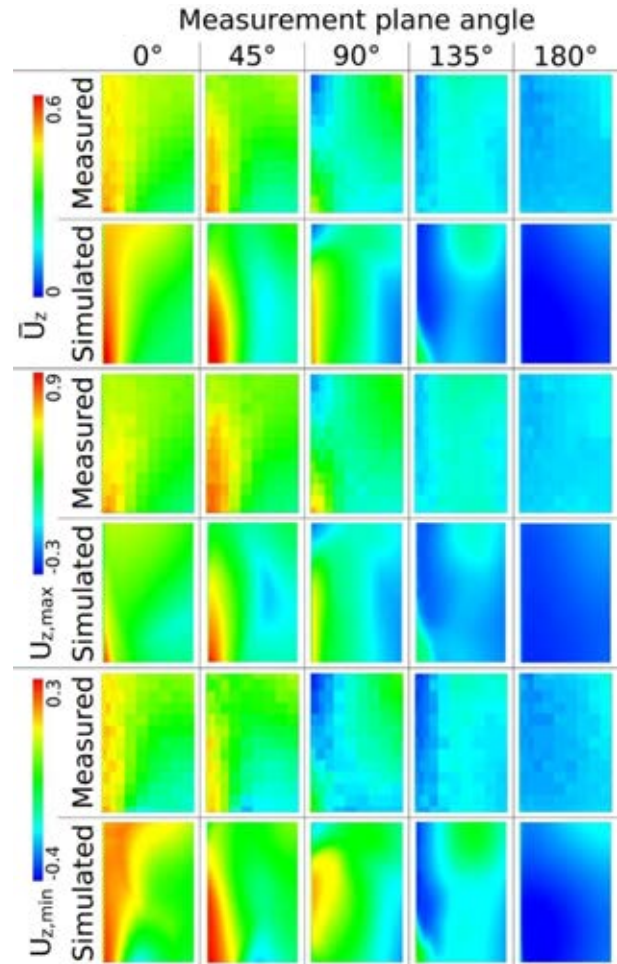


**Figure 2:** Comparison of temporal average, maximum, and minimum values of measured and calculated velocities (m/s) in axial direction in the measurement planes shown in Fig. 1c), for “one-sided cutout at bottom”.

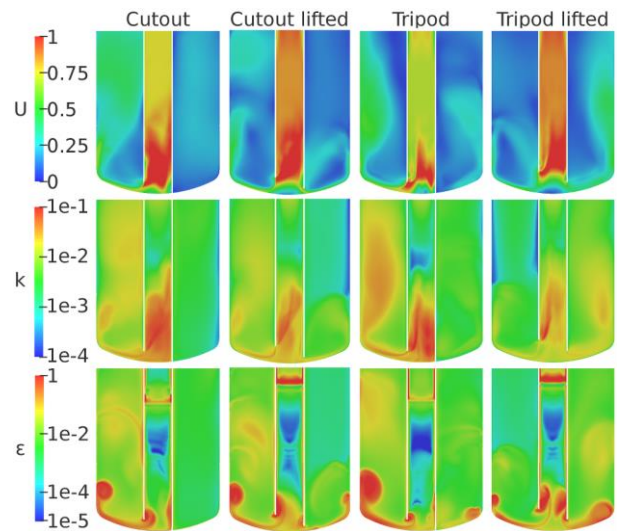


**Figure 3:** Comparison of temporal averaged values of velocity magnitude  $U$  in m/s, turbulent kinetic energy  $k$  in  $\text{m}^2/\text{s}^2$ , and dissipation rate  $\varepsilon$  in  $\text{m}^2/\text{s}^3$  for the different configurations in the symmetry plane

Turbulent kinetic energy  $k$  has its highest values inside the pipe near the pipe exit. With a pipe at the bottom, it has the same pattern for one-sided cutout and tripod, but it is higher for the tripod in most regions. Similar to the velocities, the lifted pipe versions show lower values

outside the pipe and for the lifted tripod a reversed left-to-right image with high values at the right vessel wall. Contrary to the findings for the velocities, the turbulent kinetic energy inside the pipe is higher for the pipe-at-bottom configurations. Overall it seems that  $k$  is higher for the versions with a pipe at the bottom.

Comparing the dissipation rate between the two one-sided cutout versions reveals that lifting the pipe leads to higher dissipation at the right side of the bottom. In the upper parts of the symmetry plane the dissipation rate seems to be almost the same for these two versions. The tripod at bottom has much larger regions with high dissipation rates than a one-sided cutout opposite to the pipe opening. Additionally there is also a region with high dissipation rates at the right side of the bottom. This region even increases for the version with the lifted tripod. But here the dissipation rate at the left side is significantly lower.

Figure 4 shows the influence of the drive's frequency on velocity, turbulent kinetic energy and dissipation rate. Increasing the frequency from  $1.2 \text{ s}^{-1}$  to  $1.5 \text{ s}^{-1}$  significantly increases all three quantities. This is because  $1.5 \text{ s}^{-1}$  is the resonance frequency of the system and so the movement of the liquid is the most intense. The higher velocities lead in turn to higher turbulence and thus to higher turbulent kinetic energy and dissipation rates. Increasing the frequency further to  $2.0 \text{ s}^{-1}$ , which means to a value clearly above the resonance frequency, leads to a heavy drop in all of the three quantities. This is because the oscillating system now cannot follow the excitation from the drive because it is too inertial.

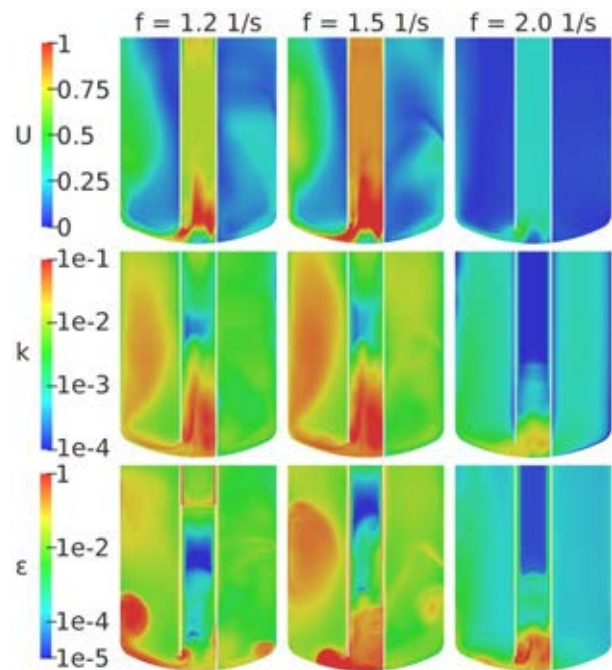
### Particle motion and mixing properties

Figure 5 shows exemplary results for the frozen particle positions after 15 oscillations in the "lifted tripod" configuration for particles with a density of  $1500 \text{ kg/m}^3$  and with diameters from  $80 \mu\text{m}$  to  $2500 \mu\text{m}$ , leading to Stokes numbers of 0.0013 to 1.2. The particles are colour coded by particle velocity magnitude. Unsurprisingly, the particles with low Stokes numbers seem to be distributed quite uniformly, whereas the more inertial particles tend to remain in the lower parts of the vessel, hence dispersion is not sufficient.

The relative mixing times, i.e. the times to fulfil the 90% lifting criterion normalised with the period duration, are shown in Table 3. Where no value is given, the criterion was not fulfilled. Considering only the configurations with an oscillation of  $f = 1.2 \text{ s}^{-1}$ , the "tripod at bottom" configuration reveals the best mixing speed for most of the investigated particle properties, which is why this configuration was also analysed at other frequencies. Only for particles having a diameter of  $2500 \mu\text{m}$  and a density of  $2500 \text{ kg/m}^3$  another configuration, namely the "one-sided cutout at bottom", has a shorter mixing time than the "tripod at bottom".

Raising the frequency to  $1.5 \text{ s}^{-1}$  gives even faster mixing speeds. This is due to the higher fluid velocities in the vessel. Due to resonance, the decrease in mixing time seems to be not linear, otherwise the relative mixing time should have been the same as for the lower frequency. Apparently, this is also the case when increasing the frequency above the resonance frequency, but here the relative mixing time rapidly

increases. This fits the observation of low velocities in the fluid flow simulations.



**Figure 4:** Influence of frequency on temporal averaged values of velocity magnitude  $U$  in m/s, turbulent kinetic energy  $k$  in  $\text{m}^2/\text{s}^2$ , and dissipation rate  $\epsilon$  in  $\text{m}^2/\text{s}^3$  in the symmetry plane for "tripod at bottom".

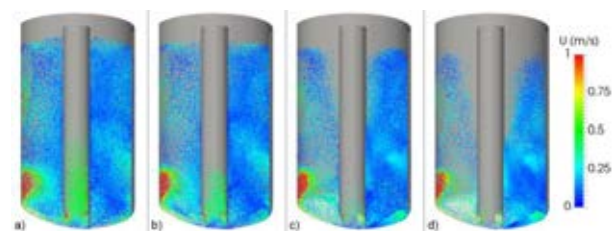


**Figure 5:** 3-dimensional view of particle positions and velocities at the end of 15 oscillations in the "tripod at bottom" with  $\rho_p = 1500 \text{ kg/m}^3$ ; a)  $d_p = 80 \mu\text{m}$ ,  $St = 0.0013$ ,  $d_2 = 2.84$ ; b)  $d_p = 500 \mu\text{m}$ ,  $St = 0.049$ ,  $d_2 = 2.20$ ; c)  $d_p = 1500 \mu\text{m}$ ,  $St = 0.44$ ,  $d_2 = 2.07$ ; d)  $d_p = 2500 \mu\text{m}$ ,  $St = 1.2$ ,  $d_2 = 2.05$ .

Table 4 lists the correlation dimensions at the end of the simulations for all considered particles. As might be expected, the correlation dimensions tend to lower values for higher particle diameters and densities. But there are some discrepancies to this overall trend. For example  $d_2$  rises in the "one-sided cutout at bottom" and the "lifted tripod" when increasing the particle diameter from  $1500 \mu\text{m}$  to  $2500 \mu\text{m}$  for a particle density of  $2500 \text{ kg/m}^3$ . This might be due to the fact that the correlation dimension does not account for the distribution of particles in the liquid volume, but only gives an estimate of how the particles are distributed at their locations. So for the large, heavy particles this means that they are quite randomly distributed, but only in a small region at the lower part of the vessel. The standard deviation of the particle concentration would prevent this drawback, but the particle concentrations considered are too small to provide sufficient information in every computational cell. Despite this, the  $d_2$ -values indicate two configurations for best mixing, namely "tripod at bottom" for small and light particles and "lifted one-

sided cutout” for larger and heavier particles. Overall, the “tripod at bottom”-configuration seems to offer the best combination of mixing speed and quality.

**Table 3:** Relative mixing times for all simulations; bold letters denote the fastest mixing time for  $f = 1.2 \text{ s}^{-1}$ .

$\rho_p$ [kg/m <sup>3</sup> ]	$d_p$ [ $\mu\text{m}$ ]	One-sided cutout at bottom	One-sided cutout lifted	Tripod at bottom	Tripod lifted	Tripod at bottom $f = 1.5 \text{ s}^{-1}$	Tripod at bottom $f = 2.0 \text{ s}^{-1}$
1050	80	<b>1.2</b>	1.3	<b>1.2</b>	<b>1.2</b>	0.90	5.6
	500	1.3	1.7	<b>1.1</b>	1.6	0.86	5.7
	1500	1.3	1.7	<b>1.1</b>	1.3	0.81	6.7
	2500	1.3	1.7	<b>1.0</b>	1.3	0.81	8.3
1500	80	1.2	1.3	<b>1.1</b>	1.2	0.84	5.6
	500	1.3	1.7	<b>1.2</b>	1.7	0.83	7.2
	1500	1.3	2.0	<b>1.1</b>	2.3	0.90	-
	2500	<b>1.3</b>	3.8	<b>1.3</b>	<b>1.3</b>	0.95	-
2500	80	1.3	1.3	<b>1.1</b>	1.2	0.86	5.6
	500	1.3	1.8	<b>1.2</b>	1.9	0.83	-
	1500	1.8	-	<b>1.5</b>	-	1.1	-
	2500	<b>2.3</b>	-	3.7	-	1.3	-

**Table 4:** Correlation dimensions for all simulations; bold letters denote the best (i.e. highest) values for  $f = 1.2 \text{ s}^{-1}$ .

$\rho_p$ [kg/m <sup>3</sup> ]	$d_p$ [ $\mu\text{m}$ ]	One-sided cutout at bottom	One-sided cutout lifted	Tripod at bottom	Tripod lifted	Tripod at bottom $f = 1.5 \text{ s}^{-1}$	Tripod at bottom $f = 2.0 \text{ s}^{-1}$
1050	80	2.79	2.80	<b>2.84</b>	2.77	2.81	2.70
	500	2.63	2.74	<b>2.79</b>	2.74	2.78	2.44
	1500	2.24	<b>2.75</b>	<b>2.75</b>	2.73	2.77	1.91
	2500	2.18	<b>2.76</b>	2.75	2.72	2.77	1.64
1500	80	2.78	2.81	<b>2.84</b>	2.78	2.81	2.67
	500	1.52	<b>2.76</b>	2.20	2.73	2.37	1.70
	1500	1.30	<b>2.65</b>	2.07	2.10	1.78	1.46
	2500	1.48	<b>2.47</b>	2.05	1.74	1.61	2.24
2500	80	2.70	2.80	<b>2.85</b>	2.80	2.80	2.42
	500	1.82	<b>2.37</b>	1.66	1.97	1.77	1.56
	1500	1.42	<b>2.36</b>	1.91	1.94	1.74	2.13
	2500	1.58	1.76	1.72	<b>2.19</b>	1.82	1.80

### Influence of the different particle forces

The influence of the different forces acting on particles with different Stokes numbers is shown in the graphs in Figure 6 for fixed particle densities. These values are averaged over all particles during the last two oscillation periods over all configurations with oscillation frequency  $f = 1.2 \text{ s}^{-1}$ , and afterwards the averages are normalised with regard to the average drag force magnitude. At small Stokes numbers the Basset force is the most important force after the drag force. It can be seen that the Basset force decreases with increasing diameter or Stokes number, respectively, whereas all other forces increase. This might be due to the circumstance that the Basset force tail is “deleted” when a particle hits a wall. Usually, more inertial particles are more likely to collide with walls than particles that

mainly follow the fluid flow. For higher Stokes numbers, all forces seem to have an influence on the particles with magnitudes of more than 10% of the drag force. For small Stokes numbers, some forces are relatively unimportant, namely pressure gradient and the two lift forces. For density ratios near unity, even the gravity and buoyancy force becomes negligible, leaving added mass and Basset force as the only two forces beneath drag force with a considerable contribution to the particle motion.

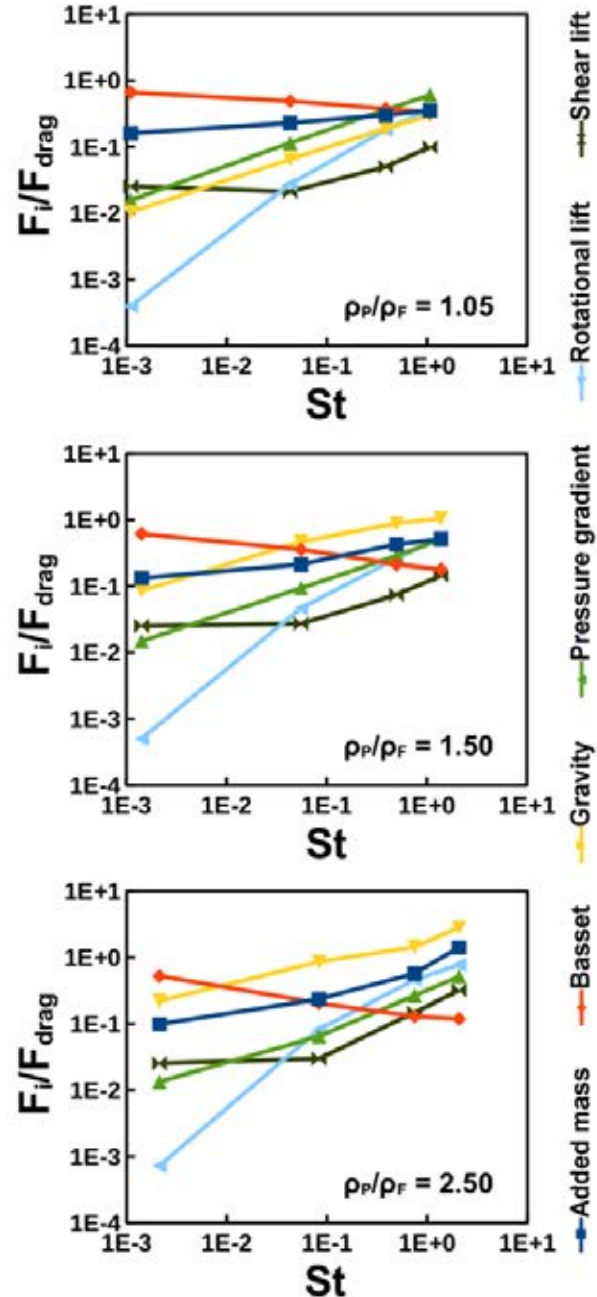


**Figure 6:** Averaged magnitude of considered forces  $F_i$  normalised by drag force  $F_{drag}$  for fixed density ratios  $\rho_p/\rho_F$  in dependence of particle Stokes number  $St$ .

Especially the fact that the magnitudes of added mass and Basset force are always higher than 10% of the drag force's magnitude should be emphasised. Due to their comparatively high demands for computational resources, these two forces are mostly neglected in particle simulations for industrial liquid-solid

multiphase flows like in mixing vessels. This is in this case clearly not justified. The same holds true for the two lift forces at higher Stokes number, meaning particles with large diameters or high density ratios. But it should be noted that this statement should be verified for other processes, as the flow in the FPR mixers is not necessarily comparable to flows in standard stirred vessels. On the other hand, in a stirred vessel the flow is much more inhomogeneous so that unsteady forces and the lift forces should be even more important.

## CONCLUSIONS AND OUTLOOK

The fluid-flow simulation of FPR mixing vessels has been done and was verified with LDA measurements.

Regarding the influence of pipe geometry the conclusions are that lifting the pipe has a much larger influence on the flow than changing its exit geometry.

Furthermore, the oscillation frequency seems to have even more influence. Increasing it from a low frequency to the system's resonance frequency leads to a much more intense flow with higher velocities and higher turbulent kinetic energy and dissipation rates.

However, increasing the frequency further, above the resonance frequency, drastically decreases the velocities and the turbulence properties.

Several particle simulations have been done with the calculated flow fields, covering Stokes numbers from  $9.7 \cdot 10^{-4}$  to 2.7. Mixing speed and mixing quality have been determined by means of the 90% lifting criterion and the correlation dimension. Overall the configuration "tripod at bottom" seems to have the best combination of mixing time and quality, even though the mixing quality of the "lifted one-sided cutout" is better for more inertial particles.

Eventually, the influence of the different particle forces considered has been investigated. The magnitudes of the often neglected added mass force and Basset force are always higher than 10% of the drag force's magnitude and reach values of 142% regarding added mass force, and 66% regarding Basset force. The lift forces are quite low for small Stokes numbers, but are not negligible for higher Stokes numbers. Summing up, it should not be taken for granted that neglecting all these forces is always justified.

The particle simulations are not verified yet, so measurements, e.g. with particle image velocimetry should be done. Additionally, the simulations could be improved, for example by including particle collisions, as suggested by Sommerfeld and Decker (2004), at least for high Stokes numbers, which lead to high particle concentrations at the bottom, or by extending the simulations to a fully 3-dimensional domain without a symmetry plane.

The different forces naturally strongly depend on the fluid flow and the flow inside FPR mixing vessels surely differs from flows obtained with standard stirrers. This holds true even more for flows in other processes. Thus, the statements about the influence of the forces should also be investigated for other stirrers and industry scale processes.

## REFERENCES

- CROWE, C., SCHWARZKOPF, J.D., SOMMERFELD, M. and TSUJI, Y., (2012), "Multiphase Flow with Droplets and Particles", 2<sup>nd</sup> Edition, *CRC Press*, Boca Raton, ISBN: 978-1-4398-4050-4.
- DECKER, S., (2005), "Zur Berechnung von gerührten Suspensionen mit dem Euler-Lagrange-Verfahren", PhD-Thesis, Martin-Luther-University Halle (Saale) (Germany).
- DENNIS, S.C.R., SINGH, S.N., INGHAM, D.B., (1980), "The steady flow due to a rotating sphere at low and moderate Reynolds numbers", *J. Fluid Mech.*, **101**, 257-279.
- VAN HINSBERG, M.A.T., TEN THIJE BOONKAMP, J.H.M. and CLERCX, H.J.H., (2011), "An efficient, second order method for the approximation of the Basset history force", *J. Comp. Phys.*, **230**, 1465-1478.
- MEI, R., (1992), "An approximate expression for the shear lift force on a spherical particle at finite Reynolds number", *Int. J. Multiph. Flow*, **18**, 145-147.
- MICHAELIDES, E.E. and ROIG, A., (2011), "A reinterpretation of the Odar and Hamilton data on the unsteady equation of motion of particles", *AIChE J.*, **57**, 2997-3002.
- OESTERLÉ, B. and BUI DINH, T., (1998), "Experiments on the lift of a spinning sphere in a range of intermediate Reynolds numbers", *Exp. Fluids*, **25**, 16-22.
- SAWATZKI, O., (1980), „Über den Einfluß der Rotation und der Wandstöße auf die Flugbahn kugelig Teilchen im Luftstrom“, PhD-Thesis, University Karlsruhe (Germany).
- SCHMALFUSS, S., SÄUBERLICH, R. and SOMMERFELD, M., (2012), "CFD-Simulation und LDA-Messung der Strömungsvorgänge beim Fluidphasenresonanzmischen", *Chem. Ing. Tech.*, **84**, 547-552.
- SCHMALFUSS, S. and SOMMERFELD, M., (2017), "Numerical and experimental analysis of Fluid Phase Resonance mixers", *submitted to Chem. Eng. Sci.*
- SOMMERFELD, M. and DECKER, S., (2004), "State of the Art and Future Trends in CFD Simulation of Stirred Vessel Hydrodynamics", *Chem. Eng. Technol.*, **27**, 215-224.
- SOMMERFELD, M., KOHNEN, G. and RÜGER, M., (1993), „Some open questions and inconsistencies of Lagrangian particle dispersion models“, *Proceedings Ninth Symposium on Turbulent Shear Flows*, Kyoto (Japan), Paper No. 15-1.
- SOMMERFELD, M., VAN WACHEM, B., OLIEMANS, R., (2008), "Best Practice Guidelines for Computational Fluid Dynamics of Dispersed Multiphase Flows", ERCOFTAC (European Research Community on Flow, Turbulence and Combustion), ISBN 978-91-633-3564-8.

## LARGE SCALE MODELLING OF BUBBLE FORMATION AND GROWTH IN A SUPERSATURATED LIQUID

**Alessandro BATTISTELLA<sup>1</sup>, Sander S.C. AELEN<sup>1</sup>, Ivo ROGHAIR<sup>1\*</sup>,  
 Martin VAN SINT ANNALAND<sup>1</sup>**

<sup>1</sup>Chemical Process Intensification, Department of Chemical Engineering and Chemistry, Eindhoven University of Technology, Eindhoven, the Netherlands

\* E-mail: i.roghair@tue.nl

### ABSTRACT

Bubble formation due to supersaturation or superheating plays an important role in many different areas from boiling flows to reactions producing gases, such as in electrolytic processes or fermentation. The predominant mechanism for bubble formation is heterogeneous nucleation and, while it has been studied on the micro-scale, the effect of bubble nucleation on the large-scale performance of bubble column reactors is still scarcely investigated.

This work presents a modelling and simulation study on phase transition in bubble column reactors on the meso-scale using a discrete bubble model (DBM). The Discrete Bubble Model is an Euler-Lagrange model which tracks each bubble individually. The model has been extended to include the formation of bubbles due to the presence of supersaturation.

With this model, phase transition from liquid to gas in a supersaturated liquid has been studied for two cases: bubble formation on a solid surface and in a liquid bulk. The second case shows a larger number of bubbles formed, with a bigger size. The concentration front presents differences, as in the first case it shifts from a lower concentration at the bottom to the opposite.

To conclude, a starting point for simulations of phase transition due to supersaturation has been given in this work, showing that the choice of the mechanisms of bubble formation highly influence bubble densities, sizes and movements in the considered liquid.

**Keywords:** CFD, Bubble and droplet dynamics, Lagrangian methods, Multiphase heat and mass transfer. .

### NOMENCLATURE

#### Greek Symbols

$\alpha$	Volume fraction, [-]
$\Gamma$	Transport coefficient, [ms <sup>-1</sup> ]
$\zeta$	Supersaturation ratio, [-]
$\theta$	Film thickness, [m]
$\mu$	Dynamic viscosity, [Pas]
$\rho$	Mass density, [kilog/m <sup>3</sup> ]
$\sigma$	Surface tension, [Nm <sup>-1</sup> ]
$\tau$	Stress tensor, [N <sup>2</sup> m <sup>-1</sup> ]
$\Phi$	Interphase momentum transfer, [Nm <sup>-1</sup> ]

#### Latin Symbols

$A$	Surface area, [m].
$C$	Model coefficients, [-].
$c$	Concentration, [kmol m <sup>-1</sup> ].
$d_{eq}$	Equivalent diameter $d_{eq} = \left(\frac{1}{d_i} + \frac{1}{d_j}\right)^{-1}$ , [m].

$D_b$	Bubble diameter, [m].
$\mathcal{D}$	Diffusion coefficient, [ms <sup>-1</sup> ].
$E\ddot{o}$	Eötvös number $E\ddot{o} = \frac{gD_b^2\rho}{\sigma}$ , [-].
$E_b$	Bubble aspect ratio, [-].
$\mathbf{F}$	Force, [N].
$g$	Gravitational acceleration, [m <sup>2</sup> s <sup>-1</sup> ].
$k_l$	Mass transfer coefficient, [ms <sup>-1</sup> ].
$H$	Henry constant, [-].
$\dot{M}$	Volume averaged interfacial mass transfer, [kg s <sup>-1</sup> m <sup>-1</sup> ].
$m$	Individual bubble mass transfer, [kg s <sup>-1</sup> ].
$p$	Pressure, [Pa].
$Re$	Reynolds number $Re = \frac{\rho u D_b}{\mu}$ , [-].
$R_b$	Radius, [m].
$S$	Source term (reaction), [kg s <sup>-1</sup> m <sup>-1</sup> ].
$Sc$	Schmidt number $Sc = \frac{\mu}{\rho \mathcal{D}}$ , [-].
$Sh$	Sherwood number $Sh = \frac{k_l D_b}{\mathcal{D}}$ , [-].
$t$	Time, [s].
$\mathbf{u}$	Liquid velocity, [ms <sup>-1</sup> ].
$\mathbf{v}$	Gas velocity, [ms <sup>-1</sup> ].
$V$	Volume, [m].
$We$	Weber number $We = \frac{\rho_l (v_{n,i} - v_{n,j})^2 D_b}{\sigma}$ , [-].
$Y_j$	Mass fraction of component $j$ , [-].

#### Sub/superscripts

$b$	Bubble.
$c$	Critical.
$d$	Distorted.
$i, j$	Indexes.
$eff$	Effective.
$l$	Liquid.
$n$	Normal.
$rel$	Relative.
$s$	Saturation.
$T$	Turbulent.

### INTRODUCTION

Bubble columns, and in general bubbly flows, are widely used in industrial applications due to contact a gas and liquid in processes where reaction or heat/mass transport takes place between the phases. Despite the widespread applications of these systems, detailed knowledge on the complex interactions between hydrodynamics and mass/heat transport is still lacking, especially in the region of dense flows and

their effect on the large-scale performance of bubble column reactors. The use of Computational Fluid Dynamics (CFD) to model and study these systems is becoming more and more widespread resulting from large improvements in computational power. Different levels of detail (length scales) can be identified ranging from large Euler-Euler simulations to detailed DNS. At an intermediate level, Euler-Lagrange models, where each bubble is tracked individually in a Lagrangian manner, play an important role in gaining details on swarms with a large number of bubbles (van Sint Annaland *et al.*, 2003).

Phase transition as a consequence of supersaturation occurs in a variety of natural and industrial processes. For instance, a well known example is opening a bottle of soda: the sudden change in pressure creates a local supersaturation and bubbles form on the surface of the bottle. Another mechanism to obtain local supersaturation is when a reaction produces gas in excess. Relevant industrial applications are in the field of bio-reactors, such as fermenters for the production of bio-ethanol, where gaseous CO<sub>2</sub> is produced, or in electrolytic processes where gas (such as H<sub>2</sub> in the electrolysis of brine) bubbles are formed on the electrodes (Volanschi *et al.*, 1996). Models describing phase transition are very relevant for industry, but still lacking in practice.

The aim of this work is to give a starting point for Eulerian-Lagrangian simulations of large scale bubbly flows where phase transition occurs. In the following sections, the used model and the numerical setup will be described and verified. Then, an outline of bubble formation due to supersaturation by heterogeneous nucleation will be given.

## MODEL DESCRIPTION

The Discrete Bubble Model (DBM) is an Euler-Lagrange CFD model which is based on the work of Delnoij *et al.* (1999) subsequently expanded and improved by Darmana *et al.* (2005) and Lau *et al.* (2014). The model tracks each bubble separately using Newton's laws of motion and accounts for bubble-bubble interactions (collisions, coalescences and breakups), mass transport and it has been expanded in this work to account for phase transition. A detailed description of the model will be given in the following sections. For more details the reader can refer to the aforementioned works.

### Hydrodynamics modeling

The fluid flow is described by the volume-averaged Navier-Stokes equations:

$$\frac{\partial}{\partial t} (\rho_l \alpha_l \mathbf{u}) + \nabla \cdot (\rho_l \alpha_l \mathbf{u} \mathbf{u}) = -\alpha_l \nabla p + \alpha_l \rho \mathbf{g} + \nabla \cdot \alpha_l \boldsymbol{\tau}_l + \Phi \quad (1a)$$

$$\frac{\partial}{\partial t} (\rho_l \alpha_l) + \nabla \cdot \rho_l \alpha_l \mathbf{u} = \dot{M} \quad (1b)$$

where  $\mathbf{u}$  is the fluid velocity,  $\alpha_l$  denotes the liquid fraction and  $\Phi$  represents the momentum coupling between the liquid and the discrete gas phase. In this equation  $\boldsymbol{\tau}$  represents the stress tensor, which is described with the very well known Equation 2 for Newtonian fluids.

$$\boldsymbol{\tau}_l = -\mu_{eff} \left[ \nabla \mathbf{u} + (\nabla \mathbf{u})^T - \frac{2}{3} \mathbf{I} (\nabla \cdot \mathbf{u}) \right] \quad (2)$$

The effective viscosity considers the contribution of the LES sub-grid scale turbulent viscosity, which is calculated using the model developed by Vreman (2004).

## Bubble dynamics

Each individual bubble is tracked using Newton's law of motion accounting for the forces that the bubble experiences. For a spherical incompressible bubble, its motion is described as:

$$\rho_b V_b \frac{d\mathbf{v}}{dt} = \sum \mathbf{F} - \left( \rho_b \frac{dV_b}{dt} \right) \mathbf{v} \quad (3)$$

where  $\mathbf{v}$  represents the bubble velocity. The sum of the forces on bubbles is composed of drag (Roghair *et al.*, 2011), lift (Tomiyama *et al.*, 2002), buoyancy, virtual mass (Auton, 1987) and wall-interactions (Tomiyama *et al.*, 1995), as given by Equation 4:

$$\sum \mathbf{F} = \mathbf{F}_G + \mathbf{F}_P + \mathbf{F}_D + \mathbf{F}_L + \mathbf{F}_{VM} + \mathbf{F}_W \quad (4)$$

The description of the forces considered is given in Table 1. The interphase coupling is performed through polynomial mapping, to transfer information from the discrete phase to the Eulerian grid and vice versa. The chosen technique is a clipped fourth-order polynomial following the work of Deen *et al.* (2004).

An important aspect is the volume change due to the inter-phase mass transfer. This is accounted for as:

$$\rho_b \frac{dV_b}{dt} = \dot{m} \quad (5)$$

More details on the mass transfer will be given in the following sections.

### Bubble interactions

Bubble collisions, coalescence and breakup have been taken into account in the model. Since each bubble position, velocity and size are readily available as part of the solution, bubble encounters (with other bubbles or with a wall) are relatively easy to track. The collision model used in this work is based on the hard-sphere approach of Hoomans *et al.* (1996). The (binary) encounters are event-based and are treated as perfectly elastic collisions, unless coalescence takes place. To speed up the collision routines, a neighbour list concept as described by Darmana *et al.* (2005) is used. Since collisions are perfectly elastic, the tangential velocity component is not altered by the encounter while the normal component (assuming bubbles  $i$  and  $j$  collide) is calculated as:

$$v_{n,i}^{new} = 2 \frac{m_i v_{n,i} + m_j v_{n,j}}{m_i + m_j} - v_{n,i} \quad (6)$$

In performing the collision, the shrinkage or growth of bubbles as a consequence of mass transfer needs to be considered; in some specific cases the two elements are slowly diverging from each other but a collision can still take place if the radius is growing. In this case, the velocity sign should not be changed as the two bubbles are already diverging.

In addition to elastic collisions, bubbles can coalesce when sufficiently long in contact. Many theories and models exist on bubble coalescence (see Lau *et al.* (2014)). In this work the film drainage model as implemented by Darmana *et al.* (2005) is used. When two bubbles are colliding, they will coalesce if the contact time is larger than the time that it takes for the thin film of liquid trapped between them to drain (see Equation 7 and 8).

$$t_{contact} \geq t_{drainage} \quad (7)$$



**Table 1:** Forces acting on a bubble

Force	Closure relation
$\mathbf{F}_G = \rho_b V_b \mathbf{g}$	-
$\mathbf{F}_P = -V_b \nabla P$	-
$\mathbf{F}_D = -\frac{1}{2} C_D \rho_l \pi R_b^2  \mathbf{v} - \mathbf{u}  (\mathbf{v} - \mathbf{u})$	$\frac{C_D}{C_{D,\infty}} = \left(1 + \frac{18}{E\ddot{o}} \alpha_b\right) \alpha_l$ $C_{D,\infty} = \sqrt{C_{D,\infty}(\text{Re})^2 + C_{D,\infty}(E\ddot{o})^2}$ $C_{D,\infty}(\text{Re}) = \frac{16}{\text{Re}} \left(1 + \frac{1}{1 + \frac{16}{\text{Re}} + \frac{3.315}{\sqrt{\text{Re}}}}\right)$ $C_{D,\infty}(E\ddot{o}) = \frac{4E\ddot{o}}{E\ddot{o} + 9.5}$
$\mathbf{F}_L = -C_L \rho_l V_b (\mathbf{v} - \mathbf{u}) \times (\nabla \times \mathbf{u})$	$C_L = \begin{cases} \min[0.288 \tanh(0.121 \text{Re}), f(E\ddot{o}_d)] & E\ddot{o} < 4 \\ f(E\ddot{o}_d) & 4 \leq E\ddot{o} \leq 10 \\ -0.29 & E\ddot{o} > 10 \end{cases}$ $f(E\ddot{o}_d) = 0.00105 E\ddot{o}_d^3 - 0.0159 E\ddot{o}_d^2 - 0.0204 E\ddot{o}_d + 0.474$ $E\ddot{o}_d = \frac{E\ddot{o}}{E_b}, \quad E_b = \frac{1}{1 + 0.163 E\ddot{o}^{0.757}}$
$\mathbf{F}_{VM} = -C_{VM} \rho_l V_b \left(\frac{D\mathbf{v}}{Dt} - \frac{D\mathbf{u}}{Dt}\right)$	$C_{VM} = 0.5$
$\mathbf{F}_W = -C_W R_b \left(\frac{1}{y^2} - \frac{1}{(L-y)^2}\right) \rho_l  (\mathbf{v} - \mathbf{u}) \cdot \mathbf{n}_z ^2 \mathbf{n}_v$	$C_W = \begin{cases} e^{(-0.933 E\ddot{o} + 0.179)} & 1 \leq E\ddot{o} \leq 5 \\ 0.007 E\ddot{o} + 0.04 & 5 \leq E\ddot{o} \leq 33 \end{cases}$

Prince and Blanch (1990) calculated the drainage time as:

$$t_{\text{drainage}} = \sqrt{\frac{d_{eq}^3 \rho_l}{128 \sigma}} \ln \frac{\theta_0}{\theta_f} \quad (8)$$

where  $\theta_0$  and  $\theta_f$  represents respectively the initial and final film thickness during the drainage process, which are equal to  $1 \times 10^{-4}$  m and  $1 \times 10^{-8}$  m respectively (Darmana *et al.*, 2005). Since the velocities and the sizes of each colliding couple are available, it is possible to calculate the contact time as proposed by Sommerfeld *et al.* (2003), assuming that it is proportional to a deformation distance divided by the normal component of the two bubbles' velocities:

$$t_{\text{contact}} = \frac{C_{co} d_{eq}}{2 |v_{n,i} - v_{n,j}|} \quad (9)$$

The coalescence constant ( $C_{co}$ ) represents the deformation distance normalized by the effective bubble diameter. To conclude, for each pair of colliding bubbles it is possible to calculate both of the times and check whether a collision or a coalescence takes place. In the latter event, the resulting bubble will have a volume equal to the sum of the two parents.

Together with binary interactions between bubbles, a break-up model (described by Lau *et al.* (2014)) is implemented in the DBM. This model assumes that break-up occurs when the inertial forces acting on the bubble (which deform the bubble) are higher than the surface tension force. The break-up criterion is described in the form of a critical Weber number as (for spherical bubbles):

$$\text{We} = \frac{\rho_l (v_{n,i} - v_{n,j})^2 d_{eq}}{\sigma} \geq 12 \quad (10)$$

The daughter bubbles sizes are described by a U shaped daughter size distribution; since the location of the bubble is necessary for the DBM, it is assumed that it coincides with the parent for the largest bubble while the smaller is located randomly in the proximity of the other, avoiding immediate subsequent coalescence (see Lau *et al.* (2014)).

### Species transport and mass transfer

The DBM includes species transport, mass transfer and reaction (Darmana *et al.*, 2005). A transport equation for each species is implemented as:

$$\frac{\partial}{\partial t} (\alpha_l \rho_l Y_l^j) + \nabla \cdot (\alpha_l (\rho_l \mathbf{u} Y_l^j - \Gamma_{eff}^j \nabla Y_l^j)) = \dot{M} + \alpha_l S^j \quad (11)$$

where  $S^j$  represents the source/sink term accounting for chemical reactions and  $\Gamma_{eff}$  is calculated as:

$$\Gamma_{eff}^j = \rho_l \mathcal{D}_l^j + \frac{\mu T}{Sc_T^j} \quad (12)$$

where the turbulent Schmidt number is approximated to  $Sc_T^j = 1$  (Jain *et al.*, 2015). The transport equations are solved for N-1 components, while the last component is solved enforcing the summation equation:

$$\sum_{j=1}^{N_S} Y_l^j = 1 \quad (13)$$

The physical properties of the mixture are calculated as the weighted average of each specie. The interphase mass transfer is a function of the concentration difference between the bubble (assumed to be composed entirely of one gas, namely CO<sub>2</sub>) and the liquid. This has been expressed by (Darmana *et al.*, 2005) as:

$$\dot{m}_b^j = k_l^j A_b \rho_l (Y_l^{j*} - Y_l^j) \quad (14)$$

The mass transfer coefficient is determined by a Sherwood relation (Bird *et al.*, 2007):

$$\text{Sh} = 2 + 0.6415 (\text{Re} \text{Sc}^j)^{1/2} \quad (15)$$

The gas side mass fraction is calculated from the Henry constant:

$$Y_l^{j*} = H^j Y_b^j \frac{\rho_b}{\rho_l} \quad (16)$$

The transport equation is discretized implicitly (with a semi-implicit source term for the reaction) on the Eulerian grid and the resulting linear system is solved using a biconjugate gradient method implemented in the scientific library PETSc (Balay *et al.*, 2016, 1997).

## Verification

The hydrodynamics of the DBM has been verified in the past by Lau *et al.* (2014), with the use of experimental data from a square bubble column, performed by Deen *et al.* (2001). On the other hand, the species solver has been modified since Darmana *et al.* (2005) and a verification is required to assess the numerical validity of the results. A few unidirectional validation cases have been performed, as will be detailed in the following sections.

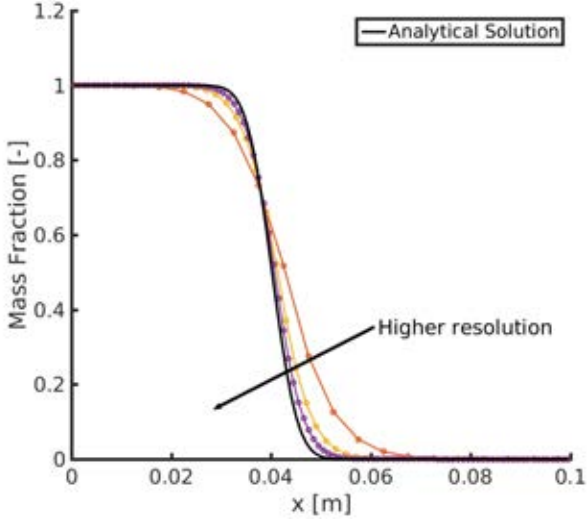


**Figure 1:** Comparison of the DBM species solver with the analytical solution for a unidirectional convection-diffusion flow, for different grid resolutions. The analytical solution is represented by the black line.

### 1D convection-diffusion

In this case, a unidirectional flow in the domain is considered where the concentration of the component of interest is initially zero. The density is assumed constant. A flow from one side (where the mass fraction is  $Y_l = 1$ ) is started and diffusion takes place. Equation 11 simplifies to:

$$\frac{\partial c}{\partial t} + u \frac{\partial c}{\partial x} = \mathcal{D} \frac{\partial^2 c}{\partial x^2} \quad (17)$$

The analytical solution for this system has been derived by Ogata and Banks (1961) as:

$$\frac{c}{c_0} = \frac{1}{2} \left[ \operatorname{erfc} \left( \frac{x-ut}{2\sqrt{\mathcal{D}t}} \right) + \exp \left( \frac{ux}{\mathcal{D}} \right) \operatorname{erfc} \left( \frac{x+ut}{2\sqrt{\mathcal{D}t}} \right) \right] \quad (18)$$

It is visible that the grid resolution plays an important role (due to the well known numerical diffusion) but the solver approaches very well the analytical solution at high enough (100 in this case) number of grid elements.

### Batch reaction

It is very important to verify the correct implementation of the semi-implicit discretization for the source/sink term and mass transfer. A simple reaction  $A \rightarrow B$  is implemented with a first and a second order kinetics, assuming an ideally mixed batch reactor. In this case, Equation 11 simplifies to:

$$\frac{dc}{dt} = R = \begin{cases} -k_R c & 1^{st} \text{ order reaction} \\ -k_R c^2 & 2^{nd} \text{ order reaction} \end{cases} \quad (19)$$

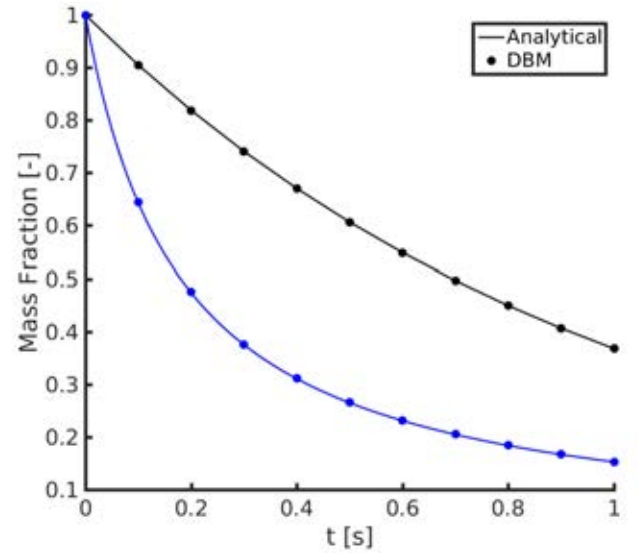


**Figure 2:** First (top line) and second (bottom line) order reactions in a batch reactor: comparison with the analytical solutions.

where  $k_R$  represents the reaction rate. Integration of Equation 19 yields to the analytical solutions:

$$c = \begin{cases} c_0 \exp(-k_R t) & 1^{st} \text{ order reaction} \\ \frac{1}{1/c_0 + k_R t} & 2^{nd} \text{ order reaction} \end{cases} \quad (20)$$

As shown in Figure 2, the DBM results match very well with the analytical solutions.

## Phase transition

### Theoretical overview

An important concept is supersaturation: a liquid is (locally) supersaturated when the concentration is higher than the equilibrium concentration, which can be expressed, for instance, by Henry's law as done in Equation 16. A relevant parameter, called the *supersaturation ratio*, is introduced as (Enrriquez *et al.*, 2013):

$$\zeta = \frac{c}{c_s} - 1 \quad (21)$$

It is visible that, for phase transition to occur,  $\zeta > 0$ . The equilibrium condition is when this ratio is equal to 0.

The mechanism of a gas bubble formation is not new in literature (Jones *et al.*, 1999). Several possible ways are accounted for, where two different classes are distinguished: homogeneous and heterogeneous nucleation. The first occurs when a bubble is formed, together with a completely new interface, anywhere in the liquid bulk where supersaturation exists. However, the energy barrier required for this mechanism to occur is high, so that homogeneous nucleation happens only when the supersaturation ratio is extremely large, as for  $\zeta > 1000$  (Wilt, 1986). On the other hand, the supersaturation of common drinks like soda and champagne reaches much lower levels of  $\zeta$ , which is in the order of  $\sim 2$  to 5 (Enrriquez *et al.*, 2013; Liger-Belair *et al.*, 2002). For this case, bubbles are forming in large numbers via heterogeneous nucleation. This mechanism describes the formation of gas bubbles on so-called *nucleation sites*, such as impurities in the liquid bulk, small cavities on the container or other gas bubbles. In those sites, a gas-pocket can be easily

formed and grow. The size of the nucleation site is crucial in describing the formation and growth of a bubble, as it determines whether a bubble will grow or be dissolved back into the liquid. Only nucleation sites with a radius larger than a critical value (related to the Laplace pressure) can host a growing bubble:

$$R_c = \frac{2\sigma}{p_s \zeta} \quad (22)$$

#### Implementation in the DBM

The DBM has been extended to account for local supersaturation. For every Eulerian grid cell, the local supersaturation ratio is calculated, as described by Equation 21. It is then possible to calculate the local critical radius (see Equation 22), which represents the minimal size a bubble should have in order to grow and not dissolve again. Since the volume of the Eulerian cell is known as well as  $\zeta$ , it is possible to calculate the excess mass (or volume) of gas which is present in each cell. From this, the volume of a possible nucleated bubble it is easily derived and compared to the critical radius. If the candidate bubble is large enough, it is generated (and the transferred mass is accounted for as described in the previous sections) with the critical radius and randomly placed in the cell, avoiding possible overlaps with neighbouring bubbles. An important limitation to this is that a single bubble is created for every cell (since the preferred way to reduce the supersaturation is mass transfer to neighbouring bubbles) which makes it depending on the grid size. Research is currently ongoing to study, with the help of experiments, bubble formation rates and how to link them to the DBM in a Lagrangian manner (such as discrete nucleation sites with their own properties as size or contact angle).

## RESULTS

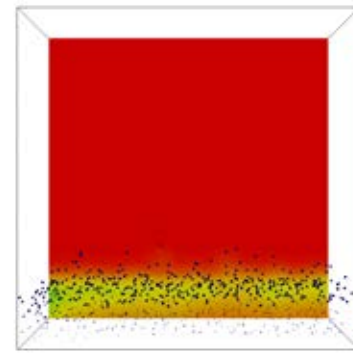
### Numerical setup

The considered domain is a square box of 15 cm described by an Eulerian grid of  $30 \times 30 \times 30$  grid nodes. The liquid is water and its properties are at standard conditions ( $\rho_l = 1000 \text{ kg m}^{-3}$ ,  $\sigma = 0.073 \text{ N m}^{-1}$  and  $\mu_l = 10^{-3} \text{ Pa s}$ ). The dissolved gas is  $\text{CO}_2$ , which is perfectly mixed in the liquid bulk with a mass fraction of  $Y_{\text{CO}_2} = 0.003$ , corresponding to an initial supersaturation ratio  $\zeta = 0.783$ . This has been arbitrarily chosen to avoid forming very small or very large bubbles. The typical time step is 1 ms for both the species and the flow solvers while bubbles moves at a pace 20 times smaller. Two different mechanisms have been implemented, heterogeneous nucleation on the bottom surface and nucleation in the liquid bulk. Even though it has been already explained that the predominant mechanism for bubble nucleation is the first, it is still worth to do a comparison between the two as, in principle, a bubble can use a nucleation site which is suspended in the liquid such as solid impurities.

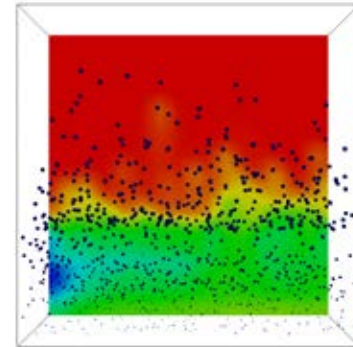
### Bubble formation

#### Heterogeneous nucleation on a surface

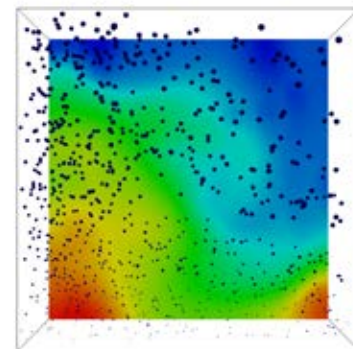
In this implementation, bubbles are forced to form only in the lower plane of the box, which represents a solid surface. In the bottom plane (represented in this case by all the grid cells in the  $x$  and  $y$  directions with  $z$  between 0 and  $\Delta z$ ), each bubble is generated with a random position in all directions in order to avoid overlap with walls and/or other neighbouring bubbles. As shown in Figure 3, small bubbles are formed at the bottom plane, which immediately start rising and increase their size due to mass transfer and coalescence. A



(a)  $t = 0.65 \text{ s}$



(b)  $t = 1.15 \text{ s}$



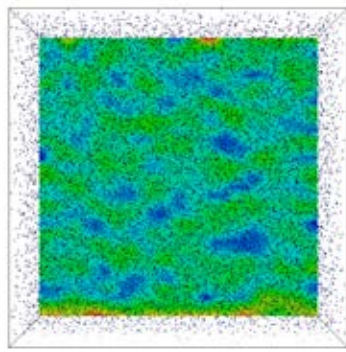
(c)  $t = 7.5 \text{ s}$

**Figure 3:** Snapshots of the concentration profiles around bubbles for the surface nucleation case. The color range from higher dissolved gas concentration (red) to lower (blue).

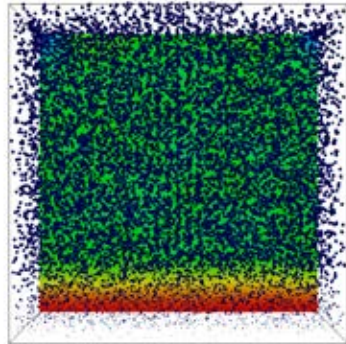
bubble front is formed in the first time steps, due to the initialization technique. After the startup of the phase transition, bubbles induce mixing with strong circulation patterns (see Figure 3c) and the lower concentration area shifts to the top, as expected since bubbles are rising upwards and the dissolved gas is transferred to them. In Figure 3c a large vortex is visible, induced by the bubble movement.

#### Heterogeneous nucleation in the liquid bulk

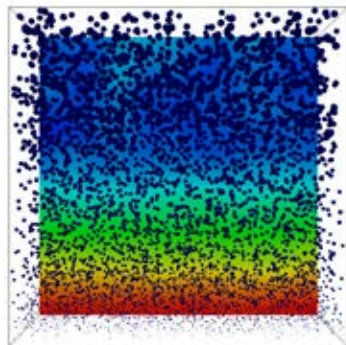
In this case bubbles are free to nucleate in the whole domain, mimicking a liquid which contains enough solid impurities that act as nucleation sites. As a consequence, at the first time step a large (equal to the number of grid elements) number of bubbles are formed (see Figure 4). It is noticeable how, at first, smaller bubbles are formed all over the bulk but later, as a consequence of mass transfer, the average size is consider-



(a)  $t = 0.25$  s



(b)  $t = 1$  s



(c)  $t = 2$  s

**Figure 4:** Snapshots of the concentration profiles around bubbles for the bulk nucleation case. The color range from higher dissolved gas concentration (red) to lower (blue).

ably higher at the top of the domain, similarly to the previous case. Also in this case, a concentration front which goes from the bottom to the top can be clearly discerned, following the direction of the rising bubbles. In this situation, it appears that the bubbles create less vortices, probably because they are distributed more uniformly throughout the domain.

#### Comparison

A comparison of the bubble diameter is shown in Figure 5. It is immediately clear that the average diameter is at first the same, because the supersaturation ratio  $\zeta$  is the same and thus bubbles are formed with an equal size. Despite the bubble numbers are clearly not the same (see Figure 6 for a comparison) and a large number of small bubbles is formed for the nucleation in the liquid bulk, the two profiles for the average bubble diameter follow the same trends. At the startup, the

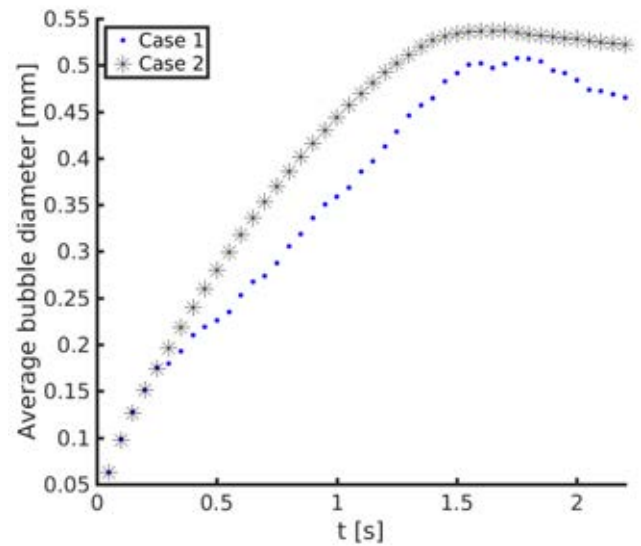


**Figure 5:** Comparison of the average bubble diameter in the column for the two cases: Case 1 nucleation on a surface and Case 2 in the liquid bulk.

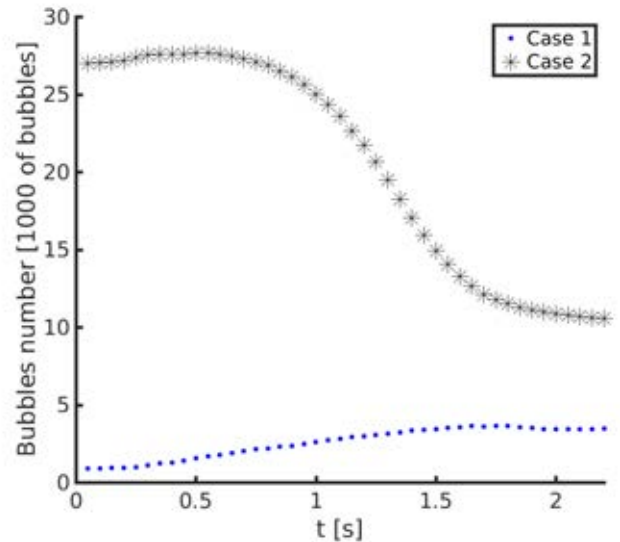


**Figure 6:** Comparison of the bubble density in the column for the two cases: Case 1 nucleation on a surface and Case 2 in the liquid bulk.

bubble size is small and immediately starts to increase as a consequence of mass transfer but even more importantly of coalescence. Since more bubbles are present in the second case, they have a higher probability to coalesce, leading to a slightly larger average bubble size.

A comparison of the bubble numbers is provided in Figure 6. It is particularly interesting to notice the opposite behaviour of the two cases. While for the second case the, at first large, number of bubbles is reduced, the other case sees an increase. This can be explained by the effect of coalescence for the second case, which also explains the larger average bubble diameter. In addition, a second effect contributes to the difference: in the second case bubbles are not free anymore to nucleate, because most of the cells already contain a bubble. In the second case, on the other hand, the domain is almost empty and, as soon as the first bubbles leave the bottom plane, new bubbles will form while the others are still in

the domain.

## CONCLUDING REMARKS

This work represents a starting point to model bubble formation in a liquid. A first algorithm has been set up to study the formation of bubbles both on a solid surface and in the liquid bulk. The choice of the bubble formation mechanism has a large influence in determining the bubble numbers, which are consistently larger for the bulk nucleation case. Moreover, the concentration front shows a different behaviour for the first case, where it shifts from a lower concentration at the bottom to the opposite situation. In addition, bubble sizes are also changed, as a consequence of coalescence.

However, this model is not yet complete. Currently, we are working on expanding the model to account for Lagrangian nucleation sites, where with mass transfer a bubble can grow and detach, avoiding the influence of the grid size. Moreover, an experimental setup is under construction to first study nucleation rates, bubble numbers and sizes at an intermediate scale and eventually validate the results of the DBM. To conclude, the inclusion of phase transition as a consequence of superheating (boiling case) will also be considered.

## ACKNOWLEDGEMENTS

This work is part of the Industrial Partnership Programme i36 Dense Bubbly Flows that is carried out under an agreement between Akzo Nobel Chemicals International B.V., DSM Innovation Center B.V., Sabic Global Technologies B.V., Shell Global Solutions B.V., Tata Steel Nederland Technology B.V. and the Netherlands Organisation for Scientific Research (NWO). The authors thank Stan Thewissen for his contribution to the simulation results.

## REFERENCES

AUTON, T.R. (1987). "The lift force on a spherical rotational flow". *J. Fluid Mech.*, **183**, 199–218.

BALAY, S., GROPP, W.D., MCINNES, L.C. and SMITH, B.F. (1997). "Efficient Management of Parallelism in Object Oriented Numerical Software Libraries". E. Arge, A.M. Bruaset and H.P. Langtangen (eds.), *Modern Software Tools in Scientific Computing*, 163–202. Birkhäuser Press.

BALAY, S., ABHYANKAR, S., ADAMS, M.F., BROWN, J., BRUNE, P., BUSCHELMAN, K., DALCIN, L., EIJKHOUT, V., GROPP, W.D., KAUSHIK, D., KNEPLEY, M.G., MCINNES, L.C., RUPP, K., SMITH, B.F., ZAMPINI, S., ZHANG, H. and ZHANG, H. (2016). "PETSc Users Manual". Tech. Rep. ANL-95/11 - Revision 3.7, Argonne National Laboratory.

BIRD, R.B., STEWART, W.E. and LIGHTFOOT, E.N. (2007). *Transport Phenomena*. Revised 2nd ed. John Wiley & Sons, New York.

DARMANA, D., DEEN, N.G. and KUIPERS, J.A.M. (2005). "Detailed modeling of hydrodynamics, mass transfer and chemical reactions in a bubble column using a discrete bubble model". *Chemical Engineering Science*, **60(12)**, 3383–3404.

DEEN, N.G., SOLBERG, T. and HJERTAGER, B.H. (2001). "Large eddy simulation of the Gas-Liquid flow in a square cross-sectioned bubble column". *Chemical Engineering Science*, **56(21)**, 6341–6349.

DEEN, N.G., VAN SINT ANNALAND, M. and KUIPERS, J.A.M. (2004). "Multi-scale modeling of dispersed gas-liquid two-phase flow". *Chem. Eng. Sci.*, **59(8-9)**, 1853–1861.

DELNOIJ, E., KUIPERS, J.A.M. and VAN SWAAIJ, W.P.M. (1999). "A three-dimensional CFD model for gas-liquid bubble columns". *Chemical Engineering Science*, **54(13-14)**, 2217–2226.

ENRÍQUEZ, O.R., HUMMELINK, C., BRUGGERT, G.W., LOHSE, D., PROSPERETTI, A., VAN DER MEER, D. and SUN, C. (2013). "Growing bubbles in a slightly supersaturated liquid solution". *Review of Scientific Instruments*, **84**, 065111.

HOOMANS, B.P.B., KUIPERS, J.A.M., BRIELS, W.J. and VAN SWAAIJ, W.P.M. (1996). "Discrete particle simulation of bubble and slug formation in a two-dimensional gas-fluidised bed: A hard-sphere approach". *Chemical Engineering Science*, **51(1)**, 99–118.

JAIN, D., DEEN, N.G. and KUIPERS, J.A.M. (2015). "Numerical modeling of carbon dioxide chemisorption in sodium hydroxide solution in a micro-structured bubble column". *Chem. Eng. Sci.*, **137**, 685–696.

JONES, S.F., EVANS, G.M. and GALVIN, K.P. (1999). "Bubble nucleation from gas cavities - a review". *Advances in Colloid and Interface Science*, **80(1)**, 27–50.

LAU, Y.M., BAI, W., DEEN, N.G. and KUIPERS, J.A.M. (2014). "Numerical study of bubble break-up in bubbly flows using a deterministic Euler-Lagrange framework". *Chemical Engineering Science*, **108**, 9–22.

LIGER-BELAIR, G., VIGNES-ADLER, M., VOISIN, C., Bertrand Robillard and JEANDET, P. (2002). "Kinetics of Gas Discharging in a Glass of Champagne: The Role of Nucleation Sites". *Langmuir*, **18(4)**, 1294–1301.

OGATA, A. and BANKS, R.B. (1961). "A solution of the differential equation of longitudinal dispersion in porous media". Tech. rep.

PRINCE, M.J. and BLANCH, H.W. (1990). "Bubble coalescence and break-up in air-sparged bubble columns". *AIChE Journal*, **36(10)**, 1485–1499.

ROGHAIR, I., LAU, Y.M., DEEN, N.G., SLAGTER, H.M., BALTUSSEN, M.W., VAN SINT ANNALAND, M. and KUIPERS, J.A.M. (2011). "On the drag force of bubbles in bubble swarms at intermediate and high Reynolds numbers". *Chemical Engineering Science*, **66(14)**, 3204–3211.

SOMMERFELD, M., BOURLOUTSKI, E. and BRÖDER, D. (2003). "Euler/Lagrange Calculations of Bubbly Flows with Consideration of Bubble Coalescence". *The Canadian Journal of Chemical Engineering*, **81(3-4)**, 508–518.

TOMIYAMA, A., MATSUOKA, T., FUKUDA, T. and SAKAGUCHI, T. (1995). "A Simple Numerical Method for Solving an Incompressible Two-Fluid Model in a General Curvilinear Coordinate System". *Multiphase Flow 1995*, 241–252.

TOMIYAMA, A., TAMAI, H., ZUN, I. and HOSOKAWA, S. (2002). "Transverse migration of single bubbles in simple shear flows". *Chemical Engineering Science*, **57(11)**, 1849–1858.

VAN SINT ANNALAND, M., DEEN, N.G. and KUIPERS, J.A.M. (2003). *Multi-level modeling of dispersed gas-liquid two-phase flows*. Heat and mass transfer. Springer, Berlin.

VOLANSCHI, A., OUDEJANS, D., OLTHUIS, W. and BERGVELD, P. (1996). "Gas phase nucleation core electrodes for the electrolytical method of measuring the dynamic surface tension in aqueous solutions". *Sensors and Actuators B*, **35-36**, 73–79.

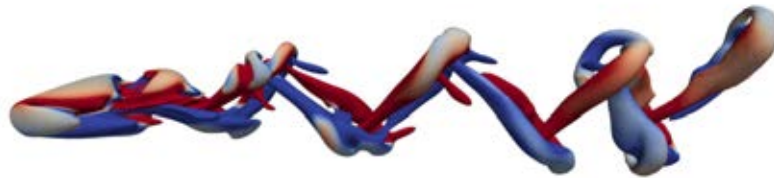
VREMAN, A.W. (2004). "An eddy-viscosity subgrid-scale model for turbulent shear flow: Algebraic theory and

applications". *Physics of Fluids*, **16(10)**, 3670–3681.

WILT, P.M. (1986). "Nucleation rates and bubble stability in water-carbon dioxide solutions". *Journal of Colloid and Interface Science*, **112(2)**, 530–538.



# FUNDAMENTAL FLUID DYNAMICS







## FLOW PAST A YAWED CYLINDER OF FINITE LENGTH USING A FICTITIOUS DOMAIN METHOD

Jean-Lou PIERSON<sup>1\*</sup>, Abdelkader HAMMOUTI<sup>1</sup>, Franck AUGUSTE<sup>2</sup>, Anthony WACHS<sup>3</sup>

<sup>1</sup>IFP Energies nouvelles, 69360 Solaize, France

<sup>2</sup>UMR5318-CECI, CERFACS/CNRS, Toulouse, France & IMFT, Allée du Professeur Camille Soula,  
31400 Toulouse

<sup>3</sup>Department of Mathematics, University of British Columbia, 1984 Mathematics Road, Vancouver, BC,  
Canada V6T 1Z2, Department of Chemical & Biological Engineering, University of British Columbia,  
2360 East Mall, Vancouver, BC, Canada V6T 1Z3

\* E-mail: jean-lou.pierson@ifpen.fr

### ABSTRACT

In this work, the flow past a finite-end yawed cylinder is studied. This constitutes a first step to understand the motion of freely moving particles. To this aim the Finite Volume / Fictitious Domain (FV/FD) method developed in the PeliGRIFF code (Wachs *et al.*, 2015) is intensively used. This method is validated using numerical results of the literature for a cylinder of finite length whose direction is parallel to the flow (Auguste, 2010). Efforts and vortex shedding frequencies are carefully analysed giving strong confidence in the numerical methodology. A detail study of the flow past a cylinder of aspect ratio  $L/D = 3$  (where  $D$  is the diameter and  $L$  the length) at moderate Reynolds numbers ( $Re = \rho U D / \mu = 200$ ) is also carried out. The influence of the yaw angle (ranging from  $0^\circ$  to  $90^\circ$ ) is identified both on the wake and on the hydrodynamic efforts. Three different regimes are successively encountered including standing-eddy pattern as unsteady vortex shedding. Otherwise the independence principle which states that the normal force on the cylinder only depends on the normal component of the velocity (Sears, 1948), is compared to the numerical simulations. Results indicate that the independence principle is inaccurate in this flow regime. A linear law obtained in the Stokes regime should be preferred.

**Keywords:** Fictitious domain method, finite-end cylinder, hydrodynamic forces, wake instability .

### INTRODUCTION

Fixed and fluidized beds are frequently encountered in various industrial processes such as catalyse and biomass gasification. Despite the large numbers of studies describing the flow past spherical particles, much less is known concerning cylindrical particles which are frequently used in fixed and bubbling fluidised bed. In order to fill that gap direct numerical simulation have been used to study the flow through a packed bed of cylinders. For instance (Dorai *et al.*, 2015) highlight the impact of the particle shape on the pressure drop through the bed. For computational reasons, Euler-Lagrange methods are usually preferred to direct numerical simulation to deal with a large number of fluidized particles. Those methods have been applied with success for spouted bed configurations and bubbling fluidized bed of spherical particles (Capecelatro and Desjardins, 2013; Bernard *et al.*, 2016). However the averaging procedure used to derive the Euler-Lagrange equations brings out more unknown than equations (Jackson, 2000). Closure law and especially hydrodynamic force exerted on the body are thus needed to

solve the problem. To this aim the flow past a finite-length yawed cylinder is studied numerically as a first step to understand the efforts acting on many of them.

One of the earliest study of the flow past a cylinder oriented perpendicularly to the streamwise direction is the one of Wieselsberger (1922). Both infinite and two free ends cylinder were considered. For the former the aspect ratio  $L/D$  was 5, where  $L$  is the length of the cylinder and  $D$  its diameter. He covered a large range of Reynolds numbers  $Re = \rho D U / \mu$  from 400 to  $8 \times 10^5$  where  $\mu$ ,  $\rho$  and  $U$  are respectively the dynamic viscosity, density and inlet velocity. The drag coefficient was found to decrease when decreasing  $L/D$ . Zdravkovich *et al.* (1989) studied the flow past a perpendicular cylinder of finite aspect ratio ( $1 \leq L/D \leq 10$ ) at high Reynolds numbers ( $6 \times 10^4 \leq Re \leq 2.6 \times 10^5$ ). The drag coefficient was also observed to decrease when decreasing  $L/D$ . He observed a kind of vortex shedding in the range  $2 \leq L/D \leq 8$  and an asymmetric flow pattern for  $1 \leq L/D \leq 3$ . Inoue and Sakuragi (2008) performed a detailed numerical study of the flow past finite length cylinder. The prescribed  $L/D$  and Reynolds number were respectively  $0.5 \leq L/D \leq 100$  and  $40 \leq Re \leq 300$ . They identify five different vortex shedding patterns depending on both aspect ratio and Reynolds number. They also showed that the critical Reynolds number, for the onset of the unsteady regime, decreased with  $L/D$ .

Studies of the flow past yawed or aligned cylinders (whose symmetry axis is parallel to the incoming flow) are more sparse comparatively to the large amount of works on perpendicular cylinder. Auguste (2010) and Auguste *et al.* (2010) numerically studied the wakes of disks ( $0 \leq L/D \leq 1$ ) parallel to the flow direction. The Reynolds number prescribed was  $0 \leq Re \leq 400$ . Auguste (2010) observed that the critical Reynolds for appearance of unsteady regime as the wake patterns are strongly varying function of the aspect ratio. To the author knowledge the bifurcation scenario for  $L/D > 1$  have not been studied so far. Recently Chrust *et al.* (2010) evidenced the effect of  $L/D$  over the wake of spheroids parallel to the flow direction. Ramberg (1983) studied experimentally the flow past free-ended yawed cylinders and yawed cylinders fitted with end-plates in the Reynolds number range  $160 \leq Re \leq 1100$ . Cylinders were oriented to the flow direction at an angle  $\theta$ . He showed that the results were very sensitive to the cylinder end conditions. Sears (1948) has theoretically demonstrated, using boundary layer theory, that the flow past a

yawed cylinder is determined by the normal component of the velocity. In other words the force on cylinder with a yawed angle  $\theta$  was identical to the force on a cylinder in cross-flow with velocity  $U \sin \theta$ . This law called independence principle has been widely used to predict the force on a yawed cylinder. However this principle suffers from some limitation summarized in Zdravkovich (2003, p 955). Recently Vakil and Green (2009) performed a complete numerical analysis of the flow past a yawed cylinder ( $2 \leq L/D \leq 20$ ) for moderate Reynolds number ( $1 \leq Re \leq 40$ ). They proposed an empirical relation for the drag and lift force on the cylinder. They also checked the validity of the independence principle. Even if the range of Reynolds number studied was lower than the one for strict application of boundary layer theory they obtain relatively good agreement for large  $\theta > 45^\circ$ .

Thus there is a large amount of works especially on the flow past perpendicular cylinder. An exhaustive review can be found in the two monographs of Zdravkovich (1997, 2003). A large part of the numerical study dealing with that subject make use of boundary-fitted method to describe the flow around the particle (Auguste, 2010; Inoue and Sakuragi, 2008; Vakil and Green, 2009). Those methods are very accurate but not designed to deal with a large number of mobile particles since they need re-meshing at each time steps (Hu *et al.*, 1992). For this kind of applications fictitious domain method are usually preferred. Indeed the boundary conditions on the particle are defined on the Eulerian grid using forcing terms added to the governing equations (Mittal and Iaccarino, 2005). Those methods have been used and validated for the settling of spheroidal particles (Uhlmann and Dušek, 2014; Ardekani *et al.*, 2016). To the authors knowledge, analysis of the flow past a yawed cylinder using a fictitious domain method have not been done so far. Therefore before studying the flow past a yawed cylinder in inertial regimes, we will carefully validate our numerical method with existing results of the literature.

The outline of the paper is the following. In the first section the numerical method, flow geometry and boundary conditions are described. In the second section the flow past a yawed cylinder is studied. The first part of the second section is devoted to the comparison of our numerical results to those of the literature. The second part describes the flow past a  $L/D = 3$  cylinder at  $Re = 200$  for various yawed angles. Main conclusions and future work are presented in the last section.

## NUMERICAL PROCEDURES

Computations are carried out using the fictitious domain method of the PeliGRIFF code. A set of Lagrange points are distributed throughout the body in order to enforce the boundary conditions. In the rest of the section we summarize the principal features of the fictitious domain method developed by Wachs *et al.* (2015).

### Time discretization scheme

The three dimensional unsteady incompressible Navier-Stokes equations are solved using a second-order time accurate Adams-Bashforth / Crank-Nicolson scheme. However due to a first-order Marchuk-Yanenko time splitting strategy the overall time algorithm is first-order accurate. Incompressibility is enforced at the end of the fluid time step through a projection method. The linear systems obtained from both Crank-Nicolson and projection step are solved using PETSC library.

The overall time advancement procedure is described in the following.

- At the beginning of the time step the velocity of the fluid  $\mathbf{u}^n$  and the pressure  $p^n$  are known. The  $n$  index refers to the time step.
- A mixed Adams-Bashforth / Crank-Nicolson scheme is employed to compute  $\tilde{\mathbf{u}}^{n+1}$ . Then a Poisson equation is solved to find a divergence free velocity  $\hat{\mathbf{u}}^{n+1}$  and  $p^{n+1}$  :

$$\frac{\tilde{\mathbf{u}}^{n+1} - \mathbf{u}^n}{\Delta t} - \frac{1}{2} \frac{\mu}{\rho} \nabla^2 \tilde{\mathbf{u}}^{n+1} = -\frac{1}{\rho} \nabla p^n + \frac{1}{2} \frac{\mu}{\rho} \nabla^2 \mathbf{u}^n - \frac{1}{2} (3\mathbf{u}^n \cdot \nabla \mathbf{u}^n - \mathbf{u}^{n-1} \cdot \nabla \mathbf{u}^{n-1}) - \mathbf{f}^n, \quad (1a)$$

$$\nabla^2 \psi^{n+1} = \frac{1}{\Delta t} \nabla \cdot \tilde{\mathbf{u}}^{n+1}, \quad (1b)$$

$$\hat{\mathbf{u}}^{n+1} = \tilde{\mathbf{u}}^{n+1} - \Delta t \nabla \psi^{n+1}, \quad (1c)$$

$$p^{n+1} = p^n + \psi^{n+1} - \frac{1}{2} \frac{\Delta t \mu}{\rho} \nabla^2 \psi^{n+1} \quad (1d)$$

where  $\rho$  is the fluid density,  $\mu$  the viscosity,  $\psi^n$  the auxiliary potential and  $\mathbf{f}^n$  is the explicit forcing term used to take into account the presence of the rigid body.

- A fictitious domain problem which is solved using an Uzawa algorithm Wachs (2009). For a fixed body configuration the problem can be written such that  $\mathbf{u}^{n+1}$  and  $\mathbf{f}^{n+1}$  satisfy in the body region :

$$\frac{\mathbf{u}^{n+1} - \hat{\mathbf{u}}^{n+1}}{\Delta t} + \mathbf{f}^{n+1} = \mathbf{f}^n, \quad (2a)$$

$$\mathbf{u}^{n+1} = \mathbf{0} \quad (2b)$$

Unlike Uhlmann (2005); Bigot *et al.* (2014), the incompressibility condition is enforced before the imposition of boundary conditions on the particle. The main consequence is that the mass conservation is not exactly satisfied while the boundary conditions are exactly satisfied.

The hydrodynamic force and torque on the body can be written respectively  $\mathbf{F} = \int_S \boldsymbol{\sigma} \cdot \mathbf{n} dS$  and  $\mathbf{T} = \int_S \mathbf{r} \times \boldsymbol{\sigma} \cdot \mathbf{n} dS$  where  $\boldsymbol{\sigma}$  is the stress tensor,  $\mathbf{r}$  the local position relative to the solid centroid and  $\mathbf{n}$  the unit normal to the body surface  $S$ . The direct evaluation of these terms are complicated due to the many interpolations required. An approach similar to the one

proposed by Uhlmann (2005) was preferred. The surface integral of the hydrodynamic force and torque are replaced by  $\rho \int_V \mathbf{f}^{n+1} dV$  and  $\rho \int_V \mathbf{r} \times \mathbf{f}^{n+1} dV$  where  $V$  is the particle volume.

### Space discretization scheme

Equations (1a)-(1d) are solved on a staggered cartesian grid with a finite volume approach. A second order central discretization scheme is employed for the diffusion term while the convective term is treated with a total variation diminishing (TVD) scheme and Superbee flux limiter. However due to the presence of the immersed boundary, the method is not fully second order in space (Wachs *et al.*, 2015).

In order to enforce the boundary conditions on the body, a set of lagrangian points are distributed along the surface and inside the particle. Interior points are distributed on the staggered grid at the same location that the velocity points. Distribute points uniformly along the particle surface is much more challenging. The detailed method developed in the PeliGRIFF code is described in a companion paper (Pierson *et al.*, 2017). The basic idea is to divide the cylinder in two main areas : its length and the two ending disks. The area defined along the length of the body can be mapped using a diamond-shaped mesh while the disks can be mapped with a specific spiral distribution. This methodology ensures that the points are uniformly and isotropically distributed. This property have been proved to be important for computation of the flow past a sphere (Wachs *et al.*, 2015).

The explicit forcing term in equation 1 is smoothed using a simple hat function of 3 cells length support. This simple procedure have proven to be efficient in all cases studied by the past (Wachs *et al.*, 2015; Rahmani and Wachs, 2014) and contain some similarities with the delta function used by Uhlmann (2005) and Kempe and Fröhlich (2012). While it would be possible to use the same type of delta function to interpolate the forcing term on the Lagrangian points, a quadratic interpolation operator was preferred (Wachs *et al.*, 2015). Indeed, since the construction of the 3D stencil of this operator relies on the orientation of the outward normal vector to the particle boundary, a good spatial accuracy can be achieved (Wachs *et al.*, 2015).

### Computational domain

The building of a relevant numerical domain valid in all configurations studied (various aspect ratios and yawed angles) while keeping its size reasonable is a challenging task. To our knowledge there is no consensus in the literature on the size of the domain to used. In the following we briefly review several computational domains used by the past in the literature. The length and radius of the cylindrical domain used by Auguste (2010) are respectively  $25D$  and  $10D$  where  $D$  is the diameter of the disk. He focused on the flow past various disks of aspect ratio varying from zero to one. Special attention is paid to the distance between the disk and the outlet boundary condition which have to be at least of  $15D$  to avoid errors on the computation of the hydrodynamic force. Inoue and Sakuragi (2008) studied the flow past cylinders directed perpendicular to the flow. In their study, the aspect ratio varied from 0.5 to 100. They defined five computational domain depending on the range of aspect ratio studied. In particular the length of the domains range from  $115D$  to  $190D$ . The height of the domains, whose normal is parallel to the axis of the cylinder, vary linearly with  $L$  (as  $L + 60D$ ) while its depth is equal to  $= 60D$  and is thus fixed for all aspect ratio studied. Vakil and Green (2009) studied the flow

past a yawed cylinder of variable aspect ratio ranging from 2 to 20. Their computational domain shares some similarities with the one of Inoue and Sakuragi (2008). Indeed the length and the height depend on  $L$  and equal respectively  $25L$  and  $12$ , while the depth is fixed and equals to  $50D$ .

After numerous calculations the size of the domain was defined using a length proportional to the equivalent spherical diameter (the diameter of a sphere with equivalent volume) :  $D_e = (LD^2)^{1/3}$ . This choice ensures that the domain evolves with the size of the particle while remaining relatively small. Several test cases have shown that this convention remains valid up to  $L/D = 10$ .

The simulations are performed in a cuboid domain on an irregular cartesian grid. Its dimension evolves with the size and angle of the particle with the inflow. Indeed the length  $L_x$ , height  $L_y$  and depth  $L_z$  of the domain are respectively  $30D_e + L \cos \theta$ ,  $20D_e + L/2 \cos \theta$  and  $20D_e$  (figure 1), where  $\theta$  is the angle between the symmetry axis of the cylinder and the incoming flow.  $L_y$  and  $L_z$  are chosen sufficiently large to avoid wall effect in low Reynolds number flow. On the other hand  $L_z$  is defined in such a way that the wake can grow without being perturbed by the outer boundary. The domain can be divided in two main regions. An inner region around the cylinder which is made of regular cell. The dimension of this subdomain ( $L_{xb}, L_{yb}, L_{zb}$ ) are specified in figure 1.  $L_{xb}$  is larger downstream of the cylinder to ensure that the near wake is well captured. The outer region is made of stretched cell which smoothly match the size of cells of the inner region.

Boundary conditions are prescribed as follow. Symmetry boundary conditions are imposed on the lateral walls :  $\partial u / \partial n = 0, v = 0, w = 0$  where  $u, v, w$  are respectively the  $x, y$  and  $z$  components of the velocity vector. At the inlet a uniform velocity profile is imposed  $(U, 0, 0)$ . The imposition of the outlet boundary condition is not straightforward and different choices can be found in the literature (Prosperetti and Tryggvason, 2009, p. 36). The choice made in the PeliGRIFF code is a zero gradient condition  $\partial \mathbf{u} / \partial n = 0$  which have been used with success by the past to study the unsteady force on a sphere (Kim and Elghobashi, 1998). In all computations the time step was fixed to  $\Delta t = 2.5 \times 10^{-3}$  and specified in order to satisfy the CFL condition.

## RESULTS

In the following subsections, the numerical method described above is applied to the study of the flow past a yawed cylinder of finite-length. Before analysing our results a mesh sensitivity analysis is performed by comparing our solutions to those of Auguste (2010). His results for a cylinder aligned with the flow direction  $\theta = 0$  obtained with boundary fitted method are considered as references. The range  $Re \in [25; 200]$  and  $Re = 360$  are analysed in detail. Then the flow past a yawed cylinder  $0 \leq \theta \leq 90$  of aspect ratio 3 is studied. The Reynolds number  $Re = \rho U D / \mu$  is set to 200. The choice of the lengthscale for the Reynolds numbers is far from straightforward. Indeed several conventions are used in the literature : Sears (1948) used the length of the cylinder, Vakil and Green (2009) used the diameter and Hölzer and Sommerfeld (2009) the equivalent diameter. Our choice is guided by its simplicity. The Reynolds number, the yawed angle  $\theta$  and the aspect ratio  $L/D$ , fully characterized the system. The analysis to come involves other dimensionless parameters. The Strouhal  $St = fD/U$  number is commonly defined when the wake and the force experienced by the body become unsteady and periodic. It compares the frequency of vortex shedding  $f$  to

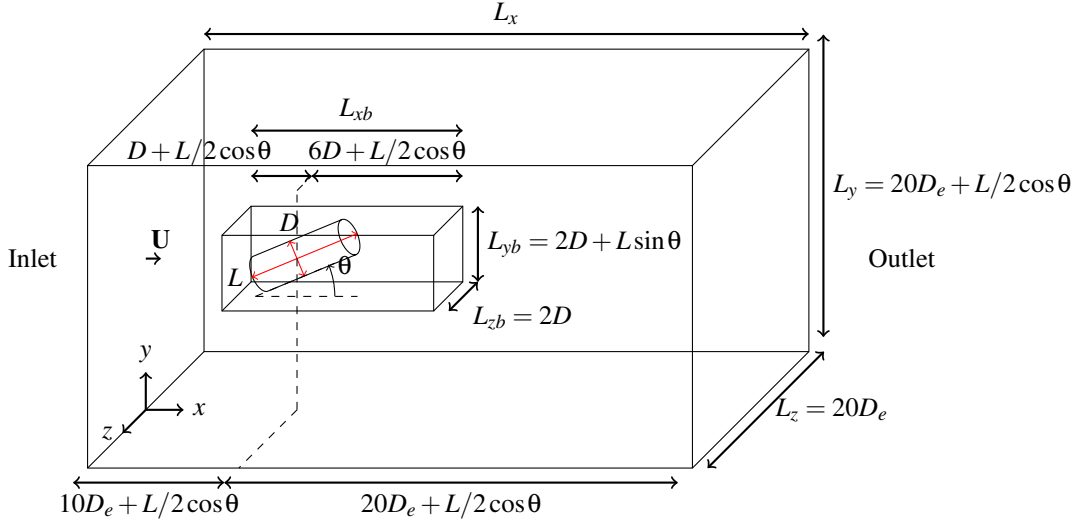


Figure 1: Scheme of the computational domain.

the characteristic frequency of the flow  $U/D$ . To describe the efforts exerted on the body the drag coefficient is defined as follow  $C_D = F_x/(1/2\rho U^2 LD)$ . This is the ratio between the hydrodynamic force in the streamwise direction  $F_x$  and a characteristic pressure force in inertial regime  $1/2\rho U^2 LD$  where  $LD$  is proportional to the lateral area of the cylinder. It is common in practise to define the drag coefficient of a bluff body using the area of the projection of the body on a plane normal to the streamwise direction (Batchelor, 1967, p 339). Our choice to used  $LD$  as the reference area for the drag coefficient was guided by two main reasons. When  $L \gg D$  and  $\theta > 0$  the projected area of the disk becomes negligible compared to the lateral area of the cylinder. Moreover, since the reference area does not depend on  $\theta$ , comparison between hydrodynamic efforts at different yaw angles are made simpler.

### Flow past a $L/D = 1$ cylinder with $\theta = 0$

In this subsection our results are compared with those of Auguste (2010) obtained with the IMFT/JADIM code. A cylinder of aspect ratio 1 aligned in the streamwise direction is considered. Auguste (2010) identify 6 regimes depending on the Reynolds number. For  $Re \lesssim 278$  the wake is stationary and axisymmetric : a toroidal vortex remains downstream of the cylinder. This vortex is usually called standing eddy (Batchelor, 1967, p 330). In the range  $278 \lesssim Re \lesssim 355$  the axial symmetry is lost. However the wake still maintain a plan of symmetry with two counter rotating vortices downstream of the cylinder. This regime called bifid wake is also observed for the flow past a sphere for  $212 \lesssim Re \lesssim 273$  (Ern *et al.*, 2012; Ghidersa and Dusek, 2000). For higher Reynolds number ( $355 \lesssim Re \lesssim 395$ ) the wake becomes unsteady while keeping its planar symmetry. This regime is characterized by one vortex shedding frequency. The two first bifurcations encountered with  $L/D = 1$  ( $\theta = 0$ ) are consistent with those observed for the sphere (Ern *et al.*, 2012) and for  $L/D = 1/3$  ( $\theta = 0$ ) (Auguste *et al.*, 2010). An intermediate regime arises for ( $395 \lesssim Re \lesssim 420$ ) where a second frequency close to the third of the primary one appears. The bifurcation scenario is distinct from the one observed with  $L/D = 1/3$  where the planar symmetry is lost (regime called Knit-Knot mode in Auguste *et al.* (2010)). For higher Reynolds number the planar symmetry is partially broken. The planar symmetry is fully broken for  $Re = 450$

and the wake becomes fully three dimensional and chaotic. To demonstrate the ability of our approach to describe the flow past a yawed cylinder, we selected two regimes described above : the stationary regime with axial symmetry and the first unsteady regime.

		$C_D$	$E(C_D)\%$	$l_R$	$E(l_R)\%$
$Re = 25$	Auguste (2010)	9.2868	-	0.430	-
	16 cells/D	9.4441	1.6933	0.453	5.35
	32 cells/D	9.3591	0.77811	0.447	3.84
$Re = 50$	Auguste (2010)	6.1591	-	0.720	-
	16 cells/D	6.2668	1.7486	0.741	2.99
	32 cells/D	6.2034	0.72013	0.732	1.67
$Re = 100$	Auguste (2010)	4.2210	-	1.12	-
	16 cells/D	4.3533	3.1338	1.17	4.02
	32 cells/D	4.2532	0.76104	1.14	1.43
$Re = 200$	Auguste (2010)	2.9468	-	1.630	-
	16 cells/D	3.2466	10.173	1.86	14.1
	32 cells/D	3.0324	2.9033	1.68	2.79

Table 1: Comparison of drag coefficient and length of standing eddy given by our numerical method and the one of (Auguste, 2010). The number of cells distributed along the cylinder diameter varies from 16 to 32.  $E(C_D)$  and  $E(l_R)$  represent respectively the relative error made on the drag and on the length of the standing eddy.

Table 1 shows the drag force and recirculation length for different Reynolds numbers and increasingly refined meshes. The length  $l_R$  is taken from the downstream extremity of the cylinder to the end of the eddy. This former point is fitted with a fourth-order polynomial. The error made on the drag coefficient using the coarsest grid (16 points per diameter) is less than 3.5% except for the highest Reynolds number. Since the thickness of the boundary layer scales as  $O(D/Re^{1/2})$ , there is approximately one point to describe the viscous layer at  $Re = 200$ . This is far from being sufficient, since even for boundary fitted mesh 5 five points are necessary to accurately describe the viscous boundary layer (Auguste, 2010). The error made on  $l_R$  using the coarsest grid is large for all Reynolds number. This error decreases significantly using a grid twice more refined. However we can still note that the error made on  $l_R$  is higher than 3% for the smaller Reynolds number. The increase of numerical errors for low Reynolds number flows was pointed out by

Wachs *et al.* (2015). <sup>1</sup>Indeed the error made with the time splitting strategy scales as  $\Delta t/Re$  (Perot, 1993).



**Figure 2:** Wake patterns of a  $L/D = 1$  cylinder aligned with the streamwise direction at  $Re = 360$ . 96 cells are distributed along the cylinder diameter. The wake is visualized using the  $Q$  criterion. Isosurface of  $Q = 10^{-3}$  are shown. Those isosurfaces are coloured by the horizontal vorticity ranging from  $-0.2$  to  $0.2$ .

Figure 2 shows the vortex shedding behind a cylinder at  $Re = 360$  (the wake is visualized using the  $Q$  criterion (Hunt *et al.*, 1988)). The wake keep a planar symmetry in the  $(x, y)$ . Hairpin vortices are shed periodically behind the cylinder. This type of wake is a distinctive feature of wake instability since it has been observed by the past for the flow past a sphere (Sakamoto and Haniu, 1990), cylinder (Inoue and Sakuragi, 2008) and even when a sphere cross a fluid-fluid interface (Pierson and Magnaudet, 2017a). The vortex structure are double-sided that is opposite oriented hairpin vortices are shed alternatively (Inoue and Sakuragi, 2008). Moreover the hairpin vortices are not symmetric. Indeed the top vortices extend longitudinally after the hairpin loop while the bottom one not. This asymmetry of the hairpin cortices induces an averaged non-zero lift force on the body (the direction of the lift force is defined unambiguously in that case owing of the wake symmetry plane).

		$C_D$	$E(C_D)\%$	$St$	$E(St)\%$
$Re = 360$	Auguste (2010)	0.578	-	0.118	-
	16 cells/ $D$	0.808	39.8	-	-
	32 cells/ $D$	0.678	17.3	0.124	4.67
	64 cells/ $D$	0.609	5.44	0.118	0.113
	96 cells/ $D$	0.597	3.36	0.117	0.762

**Table 2:** Comparison of mean drag coefficient and Strouhal number given by our numerical method and the one of (Auguste, 2010). The number of cells distributed along the cylinder diameter vary from 16 to 96.  $E(C_D)$  and  $E(St)$  represent respectively the relative error made on the drag an on the Strouhal number.

Table 2 shows the drag coefficient and Strouhal number for increasingly refined mesh. The value of the drag coefficient given is averaged on at least 10 periods. For the coarsest grid (16 cells per diameter) the error made on the drag coefficient is closed to 40%. Moreover the wake is chaotic which prevent from defining a characteristic frequency of vortex shedding and thus the Strouhal number. The error made on the drag is less than 20% when 32 cells are distributed along the cylinder diameter. The wake (not shown here) consist of hairpin vortices which are not shed periodically. Indeed a second frequency appears in the wake (close to the fourth of the expected one) which is a pure numerical artefact. It remains possible to define the Strouhal number based on the highest frequency: the resulting error is less than 5%. The

<sup>1</sup>The increase of numerical errors for low Reynolds number flow past immersed boundaries were also observed by Kempe and Fröhlich (2012) and Pierson and Magnaudet (2017b). In their cases this was a direct consequences of the imposition of the Immersed boundary forcing before the implicit step of the Cranck-Nicholson method. This create an error on the forcing term which scales as  $O(\Delta t \mu/\rho)$ .

spurious frequency disappear when using the 64 cells per diameter mesh. For that case, table 2 illustrates that the error made on  $C_D$  is more than 5% while the error made on  $St$  is less than 1%. For the more refined mesh the error on  $C_D$  is less than 3.5%.

Tables 1 and 2 point out an interesting behaviour of our fictitious domain approach. For all configuration studied the drag is always overestimated in comparison to the reference results. Numerical diffusion is a possible candidate for this overestimation. The source of this numerical error is investigated by our team. In light of those results it appears necessary to used at least 64 points per diameter to accurately describe the unsteady regime.

### Flow past a yawed cylinder $L/D = 3$ cylinder

So far the present numerical method was used for comparison with existing results of the literature. We now focus on the other main motivation of this paper which is the investigation of the impact of the yawed angle on the flow structures and the efforts acting on the cylinder. The flow past a cylinder of aspect ratio three is considered. This setup is particularly relevant for chemical engineering applications since cylindrical pellets of this kind of aspect ratio are frequently used in fixed bed reactors. The Reynolds number is fixed and equals 200 which seems to be sufficiently high to see the appearance of wake instabilities (Inoue and Sakuragi, 2008). 64 cells are distributed along the diameter of the cylinder. Seven angles of inclination are studied ranging from  $0^\circ$  to  $90^\circ$  by step of  $15^\circ$ . The size of the resulting mesh vary from  $61 \times 10^6$  cells to  $91 \times 10^6$  cells. For the sake of brevity we will only focus on the wake of a few configurations which show contrasted behaviour. Then we will study the force and torque experienced by the particle.

#### Wake patterns



**Figure 3:** Standing eddy behind a  $L/D = 3$  cylinder at  $Re = 200$ . Instantaneous streamlines on the  $y-z$  plane are coloured by the axial velocity.

Figure 3 shows the streamline patterns for  $L/D = 3$ ,  $\theta = 0$  and  $Re = 200$ . The wake is steady and a toroidal vortex appeared behind the cylinder. The length of the recirculation zone is  $1.31D$  smaller than the one observed for  $L/D = 1$  at the same Reynolds number (table 1).



**Figure 4:** Vortical structure for a cylinder tilted with an angle  $\theta = 15^\circ$  at  $Re = 200$ . Isosurface of  $Q = 10^{-2}$  coloured by the longitudinal vorticity ranging from  $-0.2$  to  $0.2$ .

Figure 4 shows two streamwise vortices, which look like the arms of a squid, in the wake of  $\theta = 15^\circ$  cylinder. The two vortices are steady and form a counter rotating vortex pair. This regime called bifid wake for a sphere was described

in the previous section. The bottom region of the cylinder presents a bulge made of contra-rotative vortices. The entire wake keeps a reflectional symmetry with respect to the  $(x, y)$  plane.

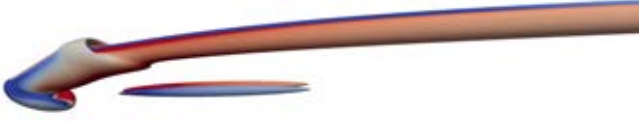


**Figure 5:** Vortical structure for a cylinder tilted with an angle  $\theta = 30^\circ$  at  $Re = 200$ . Isosurface of  $Q = 10^{-3}$  coloured by the longitudinal vorticity ranging from  $-0.2$  to  $0.2$ .

The flow past a  $\theta = 30^\circ$  cylinder is closed to the flow past a  $\theta = 15^\circ$  cylinder even if we note the apparition of another vortex pair below the first one (figure 5). The sense of rotation of the four vortices is alternate as shown by the sense of the streamwise vorticity. This regime bears similarities with the "octopus" regime first observed by Inoue and Sakuragi (2008) for the flow past a  $L/D = 1$ ,  $\theta = 90^\circ$  cylinder at Reynolds 150. The main difference between both regimes (ours and the one of Inoue and Sakuragi (2008)) is the asymmetry between the magnitude of the two vortex pairs.



**Figure 6:** Vortical structure for a cylinder tilted with an angle  $\theta = 75^\circ$  at  $Re = 200$ . Isosurface of  $Q = 10^{-2}$  coloured by the longitudinal vorticity ranging from  $-0.2$  to  $0.2$ .

For yawed angles larger than  $60^\circ$ , the wake becomes unsteady. Figure 6 shows the wake behind a  $\theta = 75^\circ$  cylinder. Hairpin vortices are shed periodically. Those vortices are double sided in the sense that vortices of opposite sense of rotation are shed. The wake seems to be symmetric with respect to the  $(x, z)$  plane but the hairpin vortices are tilted and not mutually parallel.

$C_D$	$C_{Ly}$	$C_{Lz}$	$St_y$	$St$
0.83	-0.16	$8.6 \times 10^{-4}$	0.056	0.126

**Table 3:** Drag, lift coefficients and Strouhal number for a  $L/D = 3$ ,  $\theta = 75^\circ$  cylinder at  $Re = 200$ .  $C_D$ ,  $C_{Ly}$  and  $C_{Lz}$  are respectively the mean drag, mean lift on  $y$  and  $z$  direction. The Strouhal numbers  $St_y$  and  $St$  are given respectively by the frequency of oscillation of  $C_{Ly}$  and the vortex shedding frequency.

Table 3 shows the drag and side force exerted on the body in the case of figure 6. The side coefficients  $C_{Ly}$  and  $C_{Lz}$  are calculated using the same convention as for  $C_D$ . The mean of  $C_{Ly}$  is non-zero which tends to confirm the absence of a reflectional symmetry plane with respect to  $(x, z)$ . On the other hand  $C_{Lz}$  is really close to zero since the force oscillations along  $z$  are almost periodic. The Strouhal number  $St$  is approximatively 15% smaller than the one observed when  $\theta = 90^\circ$  (not shown here) for the same Reynolds number. Decrease of the Strouhal number when decreasing  $\theta$  has been

observed by the past by Ramberg (1983) for long cylinders ( $L/D \geq 20$ ). The impact of the yaw angle on the vortex shedding frequency of short cylinder is let for future research. The Strouhal number  $St_y$  obtained using the frequency of force oscillations in the  $y$  direction is approximatively two times smaller than  $St$ . Two vortex are shed during one oscillation period of  $C_{Ly}$ .

For  $\theta = 90^\circ$  double-sided hairpin vortices are still observed (not shown here). Since this regime was observed by Inoue and Sakuragi (2008) until  $Re = 100$  this extend the range of Reynolds number for the appearance of this regime.

#### Drag, lift and torque coefficients

In this section the efforts on the  $L/D = 3$  yawed cylinder at  $Re = 200$  are investigated. A summary of current approaches to describe the force and momentum on a yawed cylinder can be found in appendix.

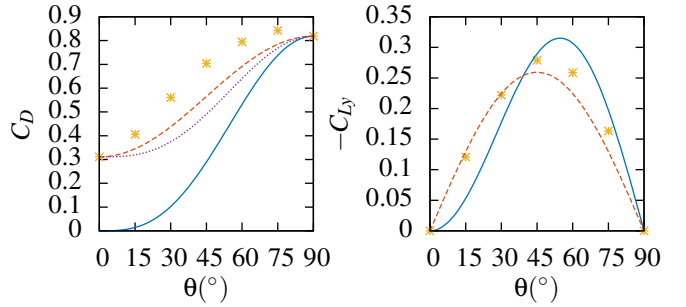


**Figure 7:** Drag and lift coefficient at various yaw angle. \*: numerical results, — : principle of independence (equation 5 and 6), - - : linear law (equation 3 and 4), . . : empirical relation of Rosendahl (2000) (equation 7).

The independence principle in its original form (equation 5) does not fit well with numerical results (figure 7 left) since the drag of the cylinder when  $\theta = 0$  is not taken into account. When this drag is taken into account (equation 7) the agreement is better but there are still important difference in the range  $30^\circ \leq \theta \leq 60^\circ$ . For all the angles of incidence studied the linear law gives better results than the independence principle and its modification due to Rosendahl (2000).

The agreement between the independence principle and the numerical results is better for the lift force (figure 7 right). However the linear law (equation 4) is still more accurate especially for  $\theta \leq 30^\circ$ . This lack of accuracy of the independence principle may be due to the fact that all computations were made with a fixed Reynolds number. The Reynolds number could be adapted in function of the yawed angle as in the numerical experiments of Vakil and Green (2009).

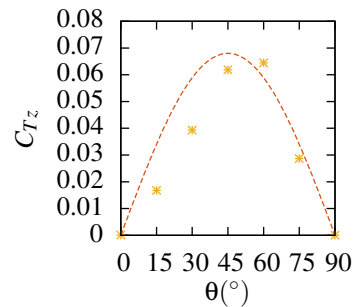


**Figure 8:** Torque coefficient at various yaw angle. \*: numerical results, - - :  $C_{Tz} = 0.068 \sin(2\theta)$  (appendix).

Figure 8 shows the torque coefficient  $C_{Tz} =$

$T_z/(1/2\rho U^2 L^2 D)$  where  $T_z$  is the hydrodynamic torque along the  $z$  direction, for various angles of inclination. The numerical results are compared to an analytical law obtained in the Oseen regime (Khayat and Cox) :  $C_{T_z} = C_{T_z\theta=45^\circ} \sin(2\theta)$  where  $C_{T_z\theta=45^\circ}$  is a coefficient fitted to the numerical results. The torque are zero for  $\theta = 0^\circ$  and  $\theta = 90^\circ$ , but Khayat and Cox explained that the only stable configuration is  $\theta = 90^\circ$ . The agreement between the numerical results and the law of Khayat and Cox is pretty good even if the numerical results curve is staggered in the high  $\theta$  direction. Therefore the maximal torque is obtained for  $\theta \geq 45^\circ$ .

## CONCLUSION

The aim of this work was to demonstrate the ability of a fictitious domain method to accurately simulate the flow past a finite-end cylinder tilted to the flow. The flow past a  $L/D = 1$  cylinder aligned with the flow direction was computed and compared with the results of Auguste (2010) who used a boundary-fitted method. The obtained results compares favourably with the one of Auguste (2010) when 32 points per diameter are distributed along the cylinder diameter in steady flow and 64 points in unsteady flow.

The present approach was then applied to the flow past a  $L/D = 3$  yawed cylinder at  $Re = 200$ . Three different regimes were observed depending on the yaw angle  $\theta$ . For  $\theta = 0^\circ$  the wake pattern behind the body is a steady axisymmetric toroidal vortex. A first bifurcation is observed in the range  $0^\circ \leq \theta \leq 15^\circ$  : the wake breaks the axisymmetry but retains a reflectional symmetry with respect to the  $(x,y)$  plane. This regime is characterized by two steady counter-rotating vortices. Two other counter-rotating vortices appears below the first one for  $\theta = 30^\circ$ . The wake becomes unsteady for  $\theta \leq 60^\circ$ . The plane of symmetry is partially broken and double-sided hairpin vortices are shed alternatively. The independence principle was shown to be poorly accurate to describe the drag force on a yawed cylinder. For the aspect ratio and Reynolds number studied the linear law given by the Stokes regime seems to be better suited. Thus the range of validity of the independence principle (in terms of Reynolds number and aspect ratio) must be investigated deeper. Indeed it gives very accurate results for yawed cylinder of infinite length at high Reynolds number (Zhao *et al.*, 2009).

Despite the good agreement between our results and the one of Auguste (2010) several points need to be clarified. First the effect of the numerical scheme used to discretize the convective term of the momentum equation have to be investigated. This may give some hints for the source of numerical diffusion observed in the second section. Secondly several tests have to be performed for the case  $L/D = 3$ ,  $Re = 200$   $\theta = 75^\circ$  in order to investigate if the oscillations of the side force along  $y$  are numerical errors or not.

Finally it would be interesting to study the flow past cylinder aligned with the flow, in order to obtain a lower bound for the drag on the same cylinder tilted with the flow. Several points may be investigated. Batchelor (1967, p. 337) pointed out that the boundary layer detachment occurs when the body is not sufficiently slender. It would be interesting to quantify the impact of  $L/D$  over the apparition of the standing eddy. On the other hand Ern *et al.* (2012) gave a threshold value for the Reynolds number associated with the first bifurcation of a disk ( $L/D \leq 1$ ). It is estimated as  $Re_c = 116.5(1 + L/D)$ . The investigation of the validity of this law for  $L/D \geq 1$  constitute a promising task.

## ACKNOWLEDGEMENTS

This work was granted access to the HPC resources of CINES under the allocation c20162a7728.

## REFERENCES

- ARDEKANI, M.N., COSTA, P., BREUGEM, W.P. and BRANDT, L. (2016). "Numerical study of the sedimentation of spheroidal particles". *International Journal of Multiphase Flow*, **87**, 16–34.
- AUGUSTE, F. (2010). "Instabilités de sillage générées derrière un corps solide cylindrique, fixe ou mobile dans un fluide visqueux". *These de doctorat*.



- AUGUSTE, F., FABRE, D. and MAGNAUDET, J. (2010). "Bifurcations in the wake of a thick circular disk". *Theoretical and Computational Fluid Dynamics*, **24**(1), 305–313.
- BATCHELOR, G.K. (1967). *An introduction to fluid dynamics*. Cambridge university press.
- BERNARD, M., CLIMENT, E. and WACHS, A. (2016). "Controlling the quality of two-way euler/lagrange numerical modeling of bubbling and spouted fluidized beds dynamics". *Industrial & Engineering Chemistry Research*.
- BIGOT, B., BONOMETTI, T., LACAIZE, L. and THUAL, O. (2014). "A simple immersed-boundary method for solid-fluid interaction in constant-and stratified-density flows". *Computers & Fluids*, **97**, 126–142.
- CAPECELATRO, J. and DESJARDINS, O. (2013). "An euler-lagrange strategy for simulating particle-laden flows". *Journal of Computational Physics*, **238**, 1–31.
- CHRUST, M., BOUCHET, G. and DUŠEK, J. (2010). "Parametric study of the transition in the wake of oblate spheroids and flat cylinders". *Journal of Fluid Mechanics*, **665**, 199–208.
- DORAI, F., TEIXEIRA, C.M., ROLLAND, M., CLIMENT, E., MARCOUX, M. and WACHS, A. (2015). "Fully resolved simulations of the flow through a packed bed of cylinders: Effect of size distribution". *Chemical Engineering Science*, **129**, 180–192.
- ERN, P., RISSO, F., FABRE, D. and MAGNAUDET, J. (2012). "Wake-induced oscillatory paths of bodies freely rising or falling in fluids". *Annual Review of Fluid Mechanics*, **44**, 97–121.
- GHIDERSA, B. and DUSEK, J. (2000). "Breaking of axisymmetry and onset of unsteadiness in the wake of a sphere". *Journal of Fluid Mechanics*, **423**, 33–69.
- HOERNER, S.F. (1965). *Fluid-dynamic drag: practical information on aerodynamic drag and hydrodynamic resistance*. Hoerner Fluid Dynamics Midland Park, NJ.
- HÖLZER, A. and SOMMERFELD, M. (2008). "New simple correlation formula for the drag coefficient of non-spherical particles". *Powder Technology*, **184**(3), 361–365.
- HÖLZER, A. and SOMMERFELD, M. (2009). "Lattice boltzmann simulations to determine drag, lift and torque acting on non-spherical particles". *Computers & Fluids*, **38**(3), 572–589.
- HU, H.H., JOSEPH, D.D. and CROCHET, M.J. (1992). "Direct simulation of fluid particle motions". *Theoretical and Computational Fluid Dynamics*, **3**, 285–306.
- HUNT, J.C., WRAY, A.A. and MOIN, P. (1988). "Eddies, streams, and convergence zones in turbulent flows".
- INOUE, O. and SAKURAGI, A. (2008). "Vortex shedding from a circular cylinder of finite length at low reynolds numbers". *Physics of Fluids*, **20**(3), 033601.
- JACKSON, R. (2000). *The dynamics of fluidized particles*. Cambridge University Press.
- KEMPE, T. and FRÖHLICH, J. (2012). "An improved immersed boundary method with direct forcing for the simulation of particle laden flows". *Journal of Computational Physics*, **231**(9), 3663–3684.
- KHAYAT, R. and COX, R. (). "Inertia effects on the motion of long slender bodies". *Journal of Fluid Mechanics*, **209**.
- KIM, I. and ELGHOBASHI, S. (1998). "On the equation for spherical-particle motion: effect of reynolds and acceleration numbers". *Journal of Fluid Mechanics*, **367**(1), 221–253.
- MITTAL, R. and IACCARINO, G. (2005). "Immersed boundary methods". *Annu. Rev. Fluid Mech.*, **37**, 239–261.
- PEROT, J.B. (1993). "An analysis of the fractional step method". *Journal of Computational Physics*, **108**(1), 51–58.
- PIERSON, J.L. and MAGNAUDET, J. (2017a). "Inertial settling of a sphere through an interface. part 1: From sphere flotation to wake fragmentation". *J. Fluid Mech (submitted)*.
- PIERSON, J.L. and MAGNAUDET, J. (2017b). "Inertial settling of a sphere through an interface. part 2: Sphere and tail dynamics". *J. Fluid Mech (submitted)*.
- PIERSON, J.L., HAMMOUTI, A., AUGUSTE, F. and WACHS, A. (2017). "Direct numerical simulation of the flow past a finite-end yawed cylinder : a fictitious domain approach". (*in preparation*).
- PROSPERETTI, A. and TRYGGVASON, G. (2009). *Computational methods for multiphase flow*. Cambridge university press.
- RAHMANI, M. and WACHS, A. (2014). "Free falling and rising of spherical and angular particles". *Physics of Fluids*, **26**(8), 083301.
- RAMBERG, S. (1983). "The effects of yaw and finite length upon the vortex wakes of stationary and vibrating circular cylinders". *Journal of Fluid Mechanics*, **128**, 81–107.
- ROSENDAHL, L. (2000). "Using a multi-parameter particle shape description to predict the motion of non-spherical particle shapes in swirling flow". *Applied Mathematical Modelling*, **24**(1), 11–25.
- SAKAMOTO, H. and HANIU, H. (1990). "A study on vortex shedding from spheres in a uniform flow". *ASME, Transactions, Journal of Fluids Engineering*, **112**, 386–392.
- SEARS, W.R. (1948). "The boundary layer of yawed cylinders". *Journal of the aeronautical sciences*.
- UHLMANN, M. (2005). "An immersed boundary method with direct forcing for the simulation of particulate flows". *Journal of Computational Physics*, **209**, 448 – 476.
- UHLMANN, M. and DUŠEK, J. (2014). "The motion of a single heavy sphere in ambient fluid: a benchmark for interface-resolved particulate flow simulations with significant relative velocities". *International Journal of Multiphase Flow*, **59**, 221–243.
- VAKIL, A. and GREEN, S.I. (2009). "Drag and lift coefficients of inclined finite circular cylinders at moderate reynolds numbers". *Computers & Fluids*, **38**(9), 1771–1781.
- WACHS, A. (2009). "A dem-dlm/fd method for direct numerical simulation of particulate flows: Sedimentation of polygonal isometric particles in a newtonian fluid with collisions". *Computers & Fluids*, **38**(8), 1608–1628.
- WACHS, A., HAMMOUTI, A., VINAY, G. and RAHMANI, M. (2015). "Accuracy of finite volume/staggered grid distributed lagrange multiplier/fictitious domain simulations of particulate flows". *Computers & Fluids*, **115**, 154–172.
- WIESELSBERGER, C. (1922). "Further data on the law of liquid and air drag". *Phys. Z*, **23**, 219–224.
- ZDRAVKOVICH, M., BRAND, V., MATHEW, G. and WESTON, A. (1989). "Flow past short circular cylinders with two free ends". *Journal of fluid mechanics*, **203**, 557–575.
- ZDRAVKOVICH, M.M. (1997). *Flow around Circular Cylinders: Volume 1: Fundamentals*, vol. 1. Oxford university press.
- ZDRAVKOVICH, M.M. (2003). *Flow around Circular Cylinders: Volume 2: Applications*, vol. 2. Oxford university press.
- ZHAO, M., CHENG, L. and ZHOU, T. (2009). "Direct numerical simulation of three-dimensional flow past a yawed circular cylinder of infinite length". *Journal of Fluids and Structures*, **25**(5), 831–847.

## APPENDIX : EFFORTS ON A YAWED CYLINDER

The force and torque experienced by a finite cylinder in a stationary flow are not known exactly even in the Stokes flow regime. However in this regime owing to the linearity of the equations, the force on a cylinder tilted with an angle  $\theta$  (figure 1) can be related to the force on the same object tilted with angles  $\theta = 0$  and  $\theta = 90$  as :

$$C_D = C_{D\theta=0^\circ} \cos^2(\theta) + C_{D\theta=90^\circ} \sin^2(\theta) \quad (3)$$

$$C_{Ly} = C_{Dy\theta=0^\circ} \cos(\theta) \sin(\theta) - C_{Dy\theta=90^\circ} \sin(\theta) \cos(\theta) \quad (4)$$

In the Stokes flow regime, the torque on a cylinder is  $\mathbf{0}$ . A cylinder will keep its initial orientation while falling under gravity. This specific property is lost when including weak effect of inertia (Khayat and Cox). When  $Re \ll 1$  the torque along  $z$  evolves as  $T_z \propto \sin(2\theta)$ .

For high Reynolds numbers there is another interesting theory which relates the force on a yawed cylinder to the force on the same cylinder perpendicular to the flow. Indeed the independence principle states that the normal force on an infinitely long yawed cylinder in a flow of velocity  $U$  is the same that the one exerted upon the same cylinder placed in a cross flow of velocity  $U \sin(\theta)$  (Sears, 1948). The drag and lift coefficients can be written as (Hoerner, 1965) :

$$C_D = C_{D\theta=90^\circ} \sin^3(\theta) \quad (5)$$

$$C_{Ly} = C_{Dy\theta=90^\circ} \sin^2(\theta) \cos(\theta) \quad (6)$$

In order to take into account into the drag the force experienced by a cylinder aligned with the flow direction Rosendahl (2000) proposed the empirical relation :

$$C_D = C_{D\theta=0^\circ} + (C_{D\theta=90^\circ} - C_{D\theta=0^\circ}) \sin^3(\theta) \quad (7)$$

There are several other empirical and semi-empirical laws derived for the drag on non spherical-particles including the one of (Hölzer and Sommerfeld, 2008). Instead of using explicitly the orientation of the particle, they proposed to use the lengthwise and crosswise sphericity (whose definition can be found in their article). Their correlation give excellent agreement with existing results in the literature.



## A NUMERICAL EVALUATION OF THE EFFECT OF ELECTRO-MAGNETIC FORCE ON BUBBLE FLOW IN ALUMINIUM SMELTING PROCESS

**Yuqing FENG<sup>1,\*</sup>, Peter J. WITT<sup>1</sup>, Zhibin ZHAO<sup>1,2</sup>, Kaiyu ZHANG<sup>3</sup>, M. Philip SCHWARZ<sup>1</sup>, Zhaowen WANG<sup>2</sup>**

<sup>1</sup> CSIRO Mineral Resources, Victoria 3169, AUSTRALIA

<sup>2</sup> NORTHEASTERN UNIVERSITY School of Metallurgy, Shenyang, CHINA

<sup>3</sup> Hefei University of Technology, CHINA

\*E-mail: Yuqing.Feng@csiro.au

### ABSTRACT

This paper aims to investigate the effect of electro-magnetic forces on bubble flow under an anode using a computational fluid dynamics (CFD) model with the volume-of-fluid (VOF) method to capture the gas-liquid interface. Current flow was solved simultaneously to determine the Lorentz forces. As an initial phase of investigation, the investigation was conducted using part of a single anode geometry as a test bed. The CFD model was run with a fixed bubble volume and two anode inclination angles. The effect of Lorentz forces was assessed in terms of bubble sliding velocities, bubble shapes and trajectories.

**Keywords:** CFD, Aluminium Electrolytic Cell, Bubble Flow, Electro-Magnetic Force.

### NOMENCLATURE

#### Greek Symbols

- $\alpha$  Volume fraction.
- $\rho$  Mass density, [ $\text{kg m}^{-3}$ ].
- $\phi$  Electric potential [V].
- $\sigma$  Electrical conductivity, [ $\text{S m}^{-1}$ ].
- $\mu$  Dynamic viscosity, [ $\text{kg m}^{-1} \text{s}^{-1}$ ].

#### Latin Symbols

- B** Magnetic flux density, [T].
- E** Electric field, [ $\text{V m}^{-1}$ ].
- F<sub>L</sub>** Volumetric Lorentz force, [ $\text{N m}^{-3}$ ].
- F<sub>S</sub>** Surface tension force, [ $\text{N m}^{-3}$ ].
- g** Gravity vector [ $\text{m s}^{-2}$ ].
- J** Electric current density, [ $\text{A m}^{-2}$ ].
- p** Pressure, [Pa].
- t** Time [s].
- u** Velocity, [ $\text{m s}^{-1}$ ].

#### Sub/superscripts

- g* Gas.
- l* Liquid.

### INTRODUCTION

Bubble flow is an inherent phenomena in Hall- Héroult reduction cells for aluminium smelting, and plays an import role in determining cell performance. A better understanding of the bubble dynamics and the resulting liquid flow is key to improving cell performance. Due to the corrosive and high temperature environment, bubble dynamics are traditionally studied using substitute physical models, including water models, low temperature electrolytic models, small-scale high-temperature electrolytic cells. A detailed summary of these models was made in a recent publication (Zhao et al., 2016a). Due to the limitation of measurement technology, the detailed bubble dynamics cannot be studied quantitatively in physical models at or near industrial scale. In the last decade, numerical modelling has been used increasingly to study bubble dynamics in the aluminium smelting system. These studies have focused on different areas, such as bubble detachment on the effect of aluminium-cryolite interfaces (Einarsrud, 2010), bubble detachment and sliding mechanism (Das et al., 2011), anode edge shape on bubble release (Wang and Zhang, 2010) and the effect of MHD forces on global bubble behaviour and voltage fluctuation (Einarsrud et al., 2012).

The CSIRO CFD team, in collaboration with a number of aluminium smelting companies, has developed a multi-scale CFD modelling approach to study bubble induced bath flow in aluminium smelting cells. This bath flow model (Feng et al., 2010, 2015) was developed using a local averaged approach accompanied with PIV measurement for model validation (Cooksey and Yang, 2006). To understand detailed bubble dynamics a micro-approach based on the Volume of Fluid (VOF) model was developed in parallel. Using the latter approach, for the first time, the difference in bubble dynamics between air-water and CO<sub>2</sub>-cryolite systems were quantified for motion of a single bubble in the ACD (anode-cathode distance) and for continuous bubbles motion in side

channels (Zhang et al., 2013; Zhao et al., 2015). In the detailed bubble model the electro-magnetic force, or Lorentz force, was not included.

Bojarevics and Roy (2012) performed an analytical evaluation of the electro-magnetic force on a hemispherical stationary bubble under an anode, and suggested that the presence of the electro-magnetic force could significantly affect the bubble transport, concentration and detachment. In a recent physical model study using aqueous CuSO<sub>4</sub> electrolysis (Das et al., 2015), the superposition of a magnetic field significantly affected the bubble density, coalescence, velocity and the overall sliding characteristics. Using a multiscale modelling approach, Einarsrud et al (2012) found that the inclusion of Lorentz force did not appear to influence global bubble behaviour and voltage fluctuations significantly. However, the Lorentz force appeared to enhance bubble departure by 7 and 12% in the two cases they investigated. To quantitatively evaluate the effect of electric-magnetic force on bubble behaviour, it is necessary to simulate the motion of individual bubbles in three dimensions.

This paper aims to further investigate the effect of electro-magnetic forces on bubble flow under an anode using a computational fluid dynamics (CFD) model with the volume-of-fluid (VOF) method used to capture the gas-liquid interface. Current flow was solved simultaneously to determine the Lorentz force. The investigation was conducted using part of a single anode geometry as a test bed. The CFD model was run for a single bubble with fixed bubble volume and two anode inclination angles with different directions of the electro-magnetic field. The effect of Lorentz force was assessed in terms of bubble sliding velocities, bubble shape and trajectories.

## MODEL DESCRIPTION

### Gas-Liquid Flow Model

Transient fluid dynamics of the gas and liquid bath are simulated by solving transport equations for the conservation of mass and momentum. The governing equations for the two-phase mixture are:

*Global continuity equation*

$$\nabla \cdot \mathbf{u} = 0 \quad (1)$$

*Momentum equation*

$$\frac{\partial(\rho \mathbf{u})}{\partial t} + \nabla \cdot (\rho \mathbf{u} \mathbf{u}) = -\nabla p + \nabla \cdot [\mu(\nabla \mathbf{u} + \nabla \mathbf{u}^T)] + \rho \mathbf{g} + \mathbf{F}_s + \mathbf{F}_L \quad (2)$$

Mixture density and viscosity are weighted based on volume fraction in the following manner:

$$\rho = \alpha_g \rho_g + \alpha_l \rho_l \quad (3)$$

$$\mu = \alpha_g \mu_g + \alpha_l \mu_l \quad (4)$$

The interface location between the two phases is calculated using the volume of fluid (VOF) approach in which a transport equation for the gas volume fraction is solved.

*Gas phase continuity equation*

$$\frac{\partial(\rho_g \alpha_g)}{\partial t} + \nabla \cdot (\rho_g \alpha_g \mathbf{u}) = 0 \quad (5)$$

### Electro-Magnetic Model

The Lorentz force in equation (2) is given by:

$$\mathbf{F}_L = \mathbf{J} \times \mathbf{B} \quad (6)$$

where the current density,  $\mathbf{J}$ , is;

$$\mathbf{J} = \sigma(\mathbf{E} + \mathbf{u} \times \mathbf{B}) \quad (7)$$

noting that the electrical conductivity,  $\sigma$ , is phase weighted as the other fluid properties (e.g. density). Since the velocities are small the induced current term on the right hand side is small and ignored in this work. The electric field can be defined in terms of a scalar potential ( $\mathbf{E} = -\nabla\phi$ ) then from equation (7) and current conservation the potential equation to be solved is:

$$\nabla \cdot (\sigma \nabla \phi) = 0 \quad (8)$$

### Geometry and Boundary Conditions

The model geometry is a 0.15[m] wide three dimensional slice of a section of the anode and bath from a reduction cell. The model domain and boundary condition locations for the model are shown in Figure 1, consisting of a solid domain for the anode and fluid domain for the cryolite-CO<sub>2</sub> mixture. The brown slice is through the centre of the anode, which has a height of 0.4 [m] and a length of 0.65 [m] in Z and Y directions respectively. A uniform current density of 9 [kA m<sup>-2</sup>] is applied to the top pink coloured surface.

A plane through the centre of the bath coloured, by volume fraction, shows the initial conditions for the blue CO<sub>2</sub> and red cryolite fluids. The fluid domain consists of the volume under the anode in the ACD, which has a depth of 40 [mm], and the volume in the centre channel beside the anode. Centre channel half width is 0.12 [m] with the top light blue face set as an outlet boundary at zero gauge pressure. Initial liquid height in the centre channel is 0.15 [m] above the base of the bath. The grey base of the bath is a non-slip wall set at a fixed voltage of 0 [V] and represents the top surface of the metal pad in an operating cell. Two surfaces couple the anode and bath domains via conducting walls that allow current to pass between the domains. For the fluid side the flow boundary condition is a non-slip wall. The high and low x-direction surfaces are set as symmetry planes or effectively free-slip insulating walls. Other surfaces and insulated non-slip walls.

A small surface, 5 [mm] by 5 [mm] square and 0.07 [m] from the low y end of the anode, is located on the base of the anode. As detailed nucleation of the gas is not considered here, it is assumed that CO<sub>2</sub> gas enters the domain at this surface to form a bubble. Inclination of the anode is accounted for by altering the direction of the gravity vector.

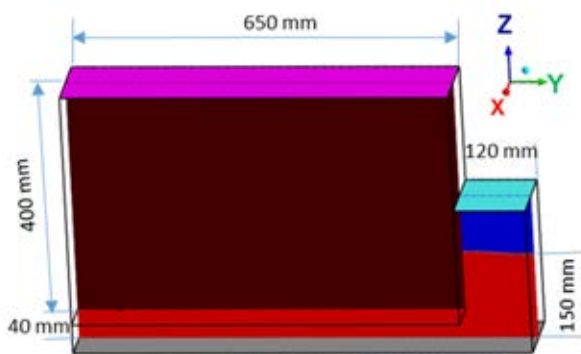


Figure 1: Schematic diagram of geometry.

Initially the domain is meshed using 620,000 hexahedral cells with 485,000 in the anode domain and 135,000 in the fluid domain. This cell size is consistent with our previous work in Zhao et al., (2015). To resolve details of the bubble interface three levels of adaptive meshing was used based on the gradient of volume fraction. Figure 2 shows the cut-cell mesh refinement around the bubble at 0.22 [s] with the green line indicating the gas-liquid interface. The grey surface in Figure 2 is in the X-Y (horizontal) plane and the colored surface is a Y-Z (vertical) plane. With mesh refinement the cell count increases to approximately 1.2 million cells with most of the increase being in the fluid domain.

Gas is added to cells adjacent to the 5 [mm] x 5 [mm] square “nucleation site” at a rate of  $2.5 \times 10^{-6}$  [kg s<sup>-1</sup>] for a period of 0.16 seconds. Thus, a single bubble with an equivalent bubble size of 25.2 [mm] is formed, with an approximate thickness of 2 [mm]. For cases with a magnetic field, it was applied at a uniform strength of 0.02 [T] in either the x or y direction as defined in Figure 1.

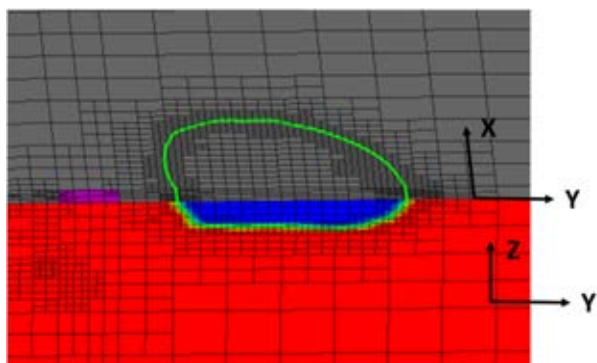


Figure 2: Mesh refinement around bubble at 0.22 [s], grey surface - anode base, blue - CO<sub>2</sub>, red - cryolite, pink – gas “nucleation site”.

### Material Properties

Properties were based on typical values for operating industrial cells as are summarised in Table 1.

Table 1: Physical Properties.

Cryolite Density	2100 [kg m <sup>-3</sup> ]
CO <sub>2</sub> Density	0.4 [kg m <sup>-3</sup> ]
Cryolite Dynamic Viscosity	0.003 [Pa s]
CO <sub>2</sub> Dynamic Viscosity	$1.37 \times 10^{-5}$ [Pa s]
Cryolite-CO <sub>2</sub> Surface Tension	0.132 [N m <sup>-1</sup> ]
Contact angle Cryolite-CO <sub>2</sub>	120°
Cryolite Electrical Conductivity	222 [S m <sup>-1</sup> ]
CO <sub>2</sub> Electrical Conductivity	1 [S m <sup>-1</sup> ]
Carbon Anode Electrical Conductivity	21,430 [S m <sup>-1</sup> ]

### Solution Scheme

Model results were obtained using ANSYS-Fluent 17.1 to solve equations (1,2,5 and 8) in the fluid domain and equation (8) in the solid domain by a finite volume scheme. PISO is used for pressure velocity coupling and a second order upwind scheme used for momentum. A first order implicit transient scheme with adaptive time stepping is used for time advancement. The time step is determined by targeting a Courant number of 0.5, typically this results in a time step of 0.0002 seconds and approximately 8-12 iterations are required to converge each time step.

The location of the gas-liquid interface is predicted using the explicit VOF formulation and geometric reconstruction of the interface shape. Surface tension effects in equation (2) are calculated using the continuum surface force model with wall adhesion.

Equation (8) is solved as a user defined scalar equation with no transient or convective terms, using a second order central difference scheme. User defined functions are used to calculate the current density and Lorentz force. UDFs are also used to add mass source terms for gas nucleation at the base of the anode.

## RESULTS

### No Lorentz Force

To obtain a baseline for the bubble behaviour the model was run with no magnetic field and thus no Lorentz force. The gravity vector was orientated such that the base of the anode was sloping upward toward the centre channel at 1.5° to the horizontal. This being representative of an anode that has worn to the shape of a metal pad with significant heave.

Iso-surfaces showing the gas-liquid interface are plotted at a number of time instants in Figure 3. Results are plotted looking upward from the metal pad to the anode and from the side of the cell. The first image is at 0.16 seconds at the time that CO<sub>2</sub> gas stops entering the model.

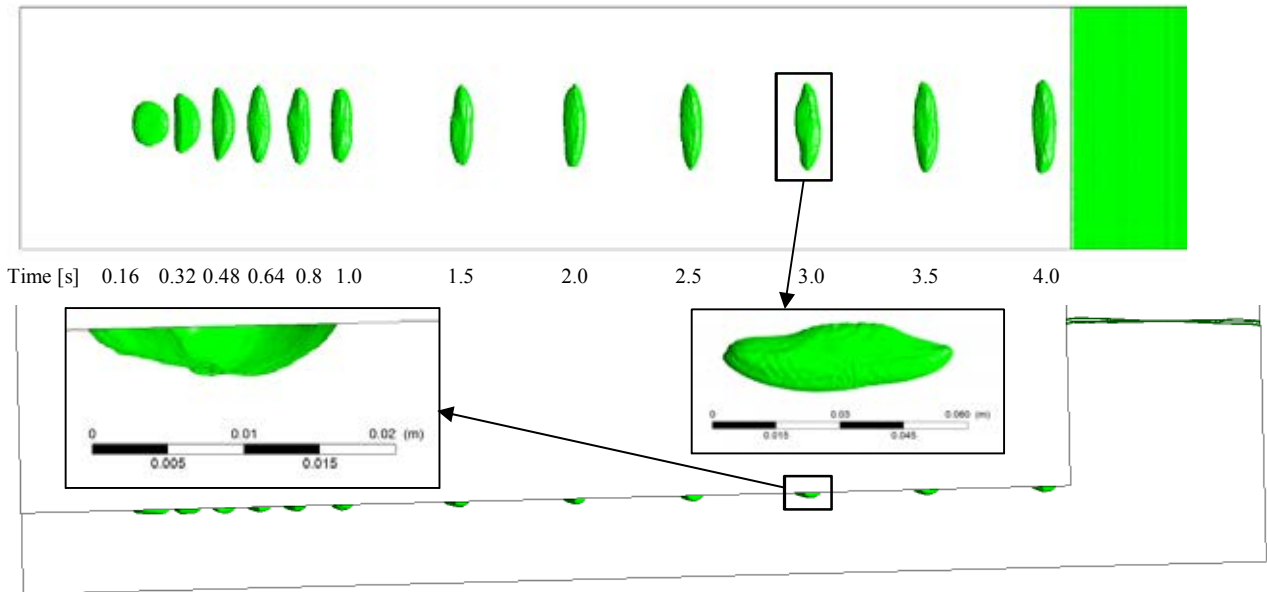


**Figure 3:** Bubble interface locations at various time instants with no Lorentz force a  $1.5^\circ$  anode slope, View from underneath (top) View from side (bottom). Insets shows details of the bubble shape and size at 3.0 seconds.

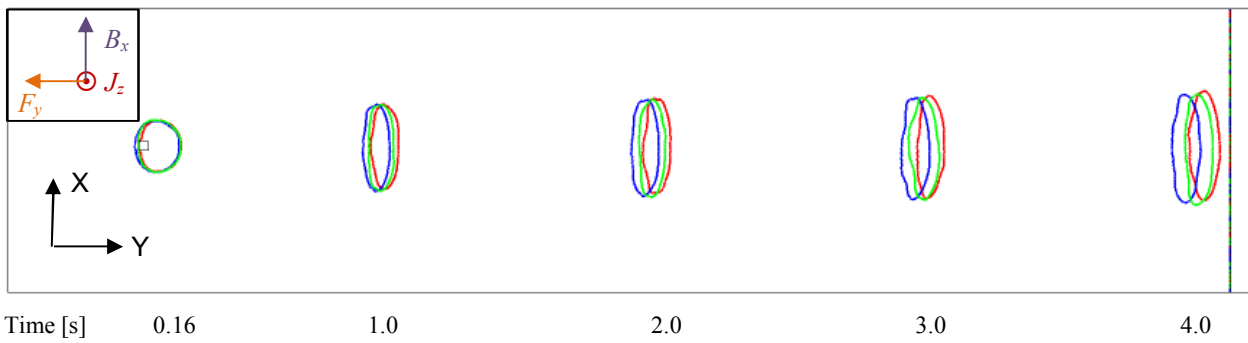


**Figure 4:** View from underneath of bubble outline at various time instants with a  $1.5^\circ$  anode slope and with — no Lorentz force, —  $B_x=-0.02$  [T], —  $B_x=0.02$  [T]. Inset shows direction of the fields and force for  $B_x=0.02$  [T].

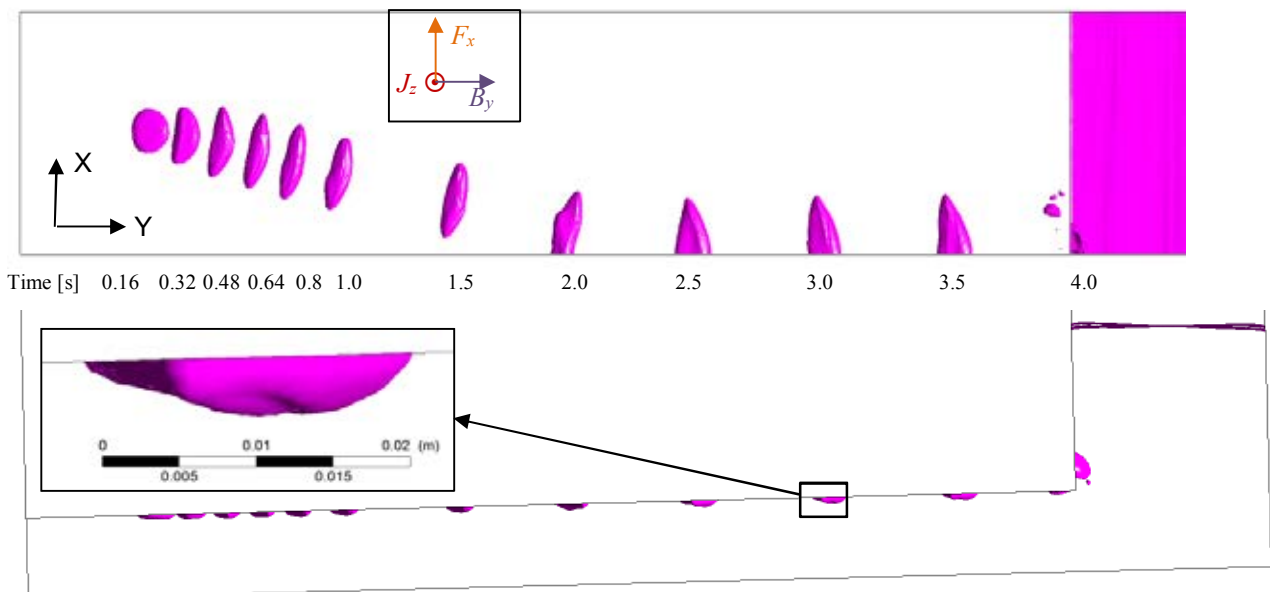


**Figure 5:** Bubble interface locations at various time instants with a  $1.5^\circ$  anode slope and a magnetic field of  $B_y=0.02$  [T], View from underneath (top) View from side (bottom). Inset shows details of the bubble shape and size at 3.0 seconds.

**Table 2:** Predicted average bubble dimensions.

Magnetic Field	Anode base angle 1.5°				Anode base angle 0.5°	
	0	$B_x=0.02$ [T]	$B_x=-0.02$ [T]	$B_y=0.02$ [T]	$B_x=0.02$ [T]	$B_x=-0.02$ [T]
Width [m] (Y direction)	0.0149	0.0147	0.0146	0.0212	0.0196	0.0260
Length [m] (X direction)	0.0529	0.0528	0.0517	0.0372	0.0391	0.0297
Aspect Ratio	3.6	3.6	3.5	1.8	2.0	1.1
Velocity [ $m\ s^{-1}$ ]	0.145	0.146	0.144	0.156	0.121	0.056
Thickness [mm]	1.99	2.00	2.00	2.24	1.88	1.75

At this time the bubble has moved under buoyancy to the right with the left edge of the bubble just exposing the edge of the nucleation site. As shown in previous work (Zhao *et al.*, 2015) the bubble is initially circular and deforms to a sausage bubble as it moves towards the centre channel under buoyancy.

Bubble dimensions obtained by averaging the bubble position at half second intervals between 1.5 and 3.5 seconds are given in Table 2. The predicted behaviour, thickness, aspect ratio and velocity are in agreement with those reported and validated by Zhao *et al.* (2015) for a similar system using a similar modelling methodology.

**Effect of Transverse Magnetic Field**

To identify if the Lorentz force has an effect on bubble motion, a magnetic field of 0.02 [T], typical of that found in industrial potlines, was applied in the x-direction and in the negative x-direction. From equation (6) for a downward current,  $J_z$ , and transverse magnetic field,  $B_x$ , the Lorentz force acts in the negative y-direction, away from the centre channel, as shown schematically in the top left of Figure 4. When the magnetic field is applied in the negative x-direction the force acts in the positive y-direction, towards the centre channel. Figure 4 shows the bubble position at four time instants for the case with no magnetic field and two cases with the magnetic field in the x-direction.

As evident by the results in Figure 4 and Table 2 the Lorentz force arising from  $B_x$  causes a small change in the bubble velocity and thus motion of the bubble with time.

**Effect of Longitudinal Magnetic Field**

Results from a simulation with the magnetic field acting in the y-direction are presented in Figure 5. Reorienting the magnetic field also changes the force direction with it now acting in positive x-direction. The bubble trajectory is plotted in Figure 5 and shows that the bubble is moved across the base of the anode and at approximately 2.0 seconds contacts the model boundary. In the model the boundary is effectively a free slip wall thus the bubble travels along the wall before rising along the anodes in the centre channel. From Table 2 the bubble length reduces and its thickness increases changing its profile and thus drag, resulting in an increased velocity. In a reduction cell this change would not occur and the bubble would continue traversing across the anode base until it reached a slot or edge of the anode.

**Effect of Anode Base Angle**

The two cases with the magnetic field in the positive and negative x-direction were run with the anode inclination angle reduced from 1.5° to 0.5°. Figure 6 shows plots of the bubble locations for the reduced inclination cases.

With the buoyancy force reduced, the Lorentz force has a stronger effect on the bubble. As shown in Table 2 and Figure 6, when the Lorentz force acts in the same direction as the buoyancy force on the bubble, the bubble velocity is reduced to half of that when compared to the case with the Lorentz force opposing to the buoyancy force.

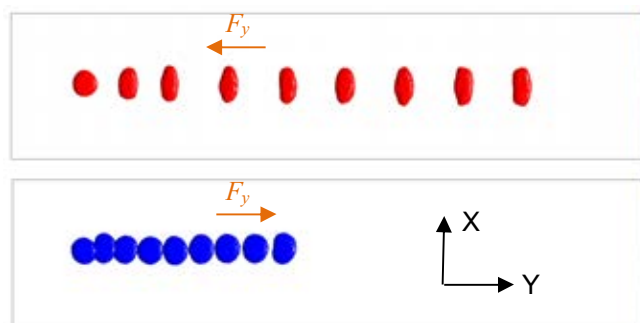


**Figure 6:** View from underneath of bubble interface locations at various time instants for a 0.5° anode slope and with Lorentz force of  $B_x=-0.02$  [T] (bottom) and  $B_x=0.02$  [T] (top). Time [s] from left to right are: 0.16 0.64 1.0 1.5 2.0 2.5 3.0 3.5 4.0.

**CONCLUSION**

Numerical simulations of CO<sub>2</sub> bubbles moving in cryolite bath under an anode in the presence of a magnetic and electric field were performed using a three dimensional VOF model. Results show that the Lorentz force produced by the electro-magnetic fields alters the behaviour of the CO<sub>2</sub> bubbles.

Bubbles are predicted to move in the direction opposing the MHD force acting on the liquid. For a case with the anode at an angle of 1.5° and a transverse magnetic field the effect on bubble motion was small. For the same geometry but when the magnetic field is aligned in the longitudinal direction of the anode the MHD force cause the bubbles to move transverse to their trajectory when only buoyancy is acting.

With a reduced anode inclination angle of 0.5° the MHD force had a strong influence on the bubble velocity with



the velocity varying between 0.056 and 0.121 [m s<sup>-1</sup>] depending on the direction of the magnetic field.

This work demonstrates that the electro-magnetic force in aluminium reduction cells has the potential to alter the behaviour of gas bubbles.

## ACKNOWLEDGEMENT

Zhibin Zhao and Kaiyu Zhang would like to thank the China Scholarship Council (CSC) and the National Natural Science Foundation of China (Grant No. 51529401) for their visiting Ph.D. scholarships to study at CSIRO.

## REFERENCES

BOJAREVICS, V. and ROY, A., (2012), "Effect of magnetic forces on bubble transport and MHD stability of aluminium electrolysis cells", *Magnetohydrodynamics*, 48, 125-136.

COOKSEY, M.A. and YANG, W., (2006), "PIV measurements on physical models of aluminium reduction cells", *Light Metals*, 359-365.

DAS, S., MORSI, Y., BROOKS, G., YANG, W. and CHEN, J. J. J., "The principal characteristics of the detachment and sliding mechanism of gas bubble under an inclined anode", 10th Australasian Aluminium Smelting Technology Conference. Launceston, Tasmania, 2011.

DAS, S., WEERASIRI, L.D. and JEGATHEESAN, V., (2015), "Bubble flow in a static magnetic field", *Light Metals* 2015, 789-793.

EINARSRUD, K. E., (2010), "The effect of detaching bubbles on aluminum-cryolite interfaces: An experimental and numerical investigation", *Metall. Mater. Trans. B.*, 41, 560.

EINARSRUD, K. E., JOHANSEN, S. T. and ERIC, I., (2012), "Anodic bubble behaviour in Hall-Heroult cells", *Light Metals*, 875-880.

FENG, Y.Q., YANG, W., COOKSEY, M. and SCHWARZ, M.P., (2010), "Development of Bubble Driven Flow CFD Model Applied for Aluminium Smelting Cells", *J. Comp. Multiphase Flows*, 2(3), 179-188.

FENG, Y.Q., SCHWARZ, M.P., YANG, W. and COOKSEY, M.A., (2015), "Two-phase CFD model of the bubble-driven flow in the molten electrolyte layer of a Hall-Heroult aluminum cell", *Metall and Materi Trans B.*, 46, 1959-1981.

WANG, Y. F. and ZHANG, L. F., "Numerical modelling on the fluid flow-related phenomena in an aluminium electrolysis cell", *Light Metal* 2010, 14.

ZHANG, K., FENG, Y.Q., SCHWARZ, P., WANG, Z. and COOKSEY, M., (2013), "Computational fluid dynamics (CFD) modeling of bubble dynamics in the aluminum smelting process", *Ind. Eng. Chem. Res.*, 52 (33), 11378-11390.

ZHAO, Z.B., GAO, B.L., WANG, Z.W., HU, X.W., FENG, Y.Q., (2016a), "Anodic Bubble Behaviour and Voltage Drop in a Laboratory Transparent Aluminium Electrolytic Cell", *METALLURGICAL AND MATERIALS TRANSACTIONS B*, 47B, 1962-1975

ZHAO, Z.B., FENG, Y.Q., SCHWARZ, M.P., WITT, P.J., WANG, Z.W. and COOKSEY, M., (2016b), "Numerical modeling of flow dynamics in the aluminum smelting process: Comparison between Air-Water and CO<sub>2</sub>-Cryolite systems", *Metall and Materi Trans B*, 2016.

## A DNS STUDY OF DROPLET SPREADING AND PENETRATION ON A POROUS MEDIUM

S DAS<sup>1\*</sup>, E MILACIC<sup>1</sup>, H.V. PATEL<sup>1</sup>, N.G. DEEN<sup>2</sup>, J.A.M. KUIPERS<sup>1</sup>

<sup>1</sup>Multiphase Reactors Group, Dept. of Chemical Engineering and Chemistry, Eindhoven University of Technology, P.O. Box 513, 5600 MB Eindhoven, The Netherlands

<sup>2</sup>Multiphase and Reactive Flows Group, Department of Mechanical Engineering, Eindhoven University of Technology, P.O. Box 513, 5600 MB Eindhoven, The Netherlands

\* E-mail: s.das@tue.nl

### ABSTRACT

We have investigated the dynamics of droplet spreading and liquid penetration at the surface of a porous medium at zero-gravity condition. A coupled IBM-VOF finite volume code has been used to perform pore-scale level fully resolved numerical simulations. The geometrical details of the solid porous matrix are resolved by a sharp interface immersed boundary method (IBM) on a Cartesian grid, whereas the motion of the gas-liquid interface is tracked by a mass conservative volume of fluid (VOF) method. At small scales, the contact line dynamics mainly govern the spreading and capillary penetration. In the present case, the motion of the gas-liquid interface at the immersed boundary is modeled by imposing the contact angle as a boundary condition at the three-phase contact line. All the simulations are performed using a model porous structure that is approximated by a 3D cubic scaffold with cylindrical struts. The porosity ( $\epsilon$ ) of the porous structure is varied from  $\epsilon = 0$  (flat plate) to  $\epsilon = 0.65$  and the equilibrium contact angle  $\Theta$  is varied from  $\Theta = 30^\circ$  (hydrophilic) to  $\Theta = 135^\circ$  (hydrophobic). The effect of porosity and contact angle on the transient evolution of penetration and spreading have been presented and compared with classical models.

**Keywords:** Three phase flow, immersed boundary method (IBM), volume of fluid (VOF), contact line dynamics, capillary penetration

### NOMENCLATURE

#### Notations

$p$	Pressure, [Pa]
$t$	Time, [s]
$D$	Droplet diameter, [m]
$F$	Fluid phase fraction, [-]
$H$	Droplet height, [m]
$La$	Laplace number, [-]
$S$	Spreading diameter, [m]
$V$	Penetration volume, [m <sup>3</sup> ]

#### Greek Symbols

$\rho$	Mass density, [kg/m <sup>3</sup> ]
$\mu$	Dynamic viscosity, [Pa·s]
$\sigma$	Surface tension, [N/m]
$\Theta$	(Static) contact angle, [degree]
$\epsilon$	Porosity, [-]
$\tau$	Non-dimensional time, [-]
$\bar{\tau}$	Stress tensor, [N/m <sup>2</sup> ]

#### Vectors

$\mathbf{u}$	Velocity, [m/s]
$\mathbf{F}_\sigma$	Surface tension force, [N]
$\mathbf{g}$	Gravitational acceleration, [m/s <sup>2</sup> ]

#### Sub/superscripts

$V_0$	Total droplet volume, [m <sup>3</sup> ]
-------	---

### INTRODUCTION

When a droplet of liquid is placed on the surface of a solid substrate, the liquid interface will evolve until it reaches an equilibrium condition. Depending on liquid-gas, solid-liquid and liquid-gas surface tensions, the liquid droplet attains a finite angle with the solid surface and this can be described by Young's equation. While Young's equation assumes that the surface is smooth, the equilibrium contact angle  $\Theta$  depends on, (i) surface roughness or surface topography ( $\mu\text{m}$  scale) and (ii) material properties that involve intermolecular forces acting at the very thin meniscus of liquid film at the gas-liquid-solid contact line acts at  $\text{nm}$  scale. On engineering scales, for very slow flow for a given gas-liquid-solid system it can be assumed that  $\Theta$  is fixed (i.e. a static contact angle) throughout the evolution of droplet from initial to equilibrium condition. In absence of gravity, at the equilibrium condition, the droplet will always remain a spherical cap and the intermediate motion of the gas-liquid interface is governed by the relative contribution of the surface tension, liquid inertia and viscous forces. A series of experimental and numerical studies (Yang and Xu, 2017; Frank and Perre, 2012; Legendre and Maglio, 2013) are available in the literature which deals with the transient evolution of the droplet shape in presence of a flat solid surface. The present work deals with understanding the wetting, spreading and capillary imbibition of a liquid droplet in contact with a *porous surface* or *porous structure*. This phenomenon is important for many engineering applications and scientific research, such as ink-jet printing, enhanced oil recovery (EOR), several micro-fluidics devices, biological systems, surface coating of porous material etc. The typical length scale of the porous medium is in the order of  $\sim 10^{-3}\text{m}$  and it can be assumed that the evolving droplet maintains a constant equilibrium contact angle ( $\Theta$ ) with each parts of the porous structure. Numerical prediction of the dynamics of a droplet in contact with a porous structure demands a state-of-the-art direct numerical model/ technique for coupling the contact line

motion at the solid surface and capillary penetration. As a result very few fully resolved pore-scale level numerical simulations are available attacking this complex flow behavior. Frank *et al.* (Frank and Perre, 2012; Frank *et al.*, 2015) performed a direct numerical simulation for droplet spreading on a porous medium using a lattice Boltzmann method (LBM) under zero gravity conditions. In their study, a porous structure made of longitudinal cavities is considered, that only allows the capillary penetration unidirectionally. The motion of the fluid in the transverse direction, inside the porous structure is restricted, which is not a true representation of a realistic porous medium. They have chosen a system of low Laplace number (ratio of surface tension to momentum transport) for smooth motion of the liquid. Meng *et al.* (2014) performed a similar pore-scale level study using smoothed particle hydrodynamics (SPH) in a model porous medium with and without gravity condition. Hyväluoma *et al.* (2006) performed pore-resolved LBM simulations for droplet penetration in paper board. 3D micro-tomographic images of paper board were used in their numerical study.

In the present work, the porous structure is approximated by a 3D cubic scaffold with cylindrical struts, where motion of the liquid in both the longitudinal and transverse directions are studied. The geometrical details of the solid porous matrix are resolved by a sharp interface immersed boundary method (IBM) (Deen *et al.*, 2012; Das *et al.*, 2016) on a Cartesian grid, whereas the motion of the gas-liquid interface is tracked by a mass conservative volume of fluid (VOF) method (Van Sint Annaland *et al.*, 2005). The motion of the gas-liquid interface at the immersed boundary is modeled by imposing the contact angle as a boundary condition at the three-phase contact line (Patel *et al.*, 2017).

## GOVERNING EQUATIONS AND SOLUTION METHODOLOGY

In the present single-field/ single-equation formulation for two-fluid flows, the mass and momentum conservation equations for both the fluids are given as follows:

$$\nabla \cdot \mathbf{u} = 0 \quad (1)$$

$$\rho \frac{\partial \mathbf{u}}{\partial t} + \rho \nabla \cdot (\mathbf{u}\mathbf{u}) = -\nabla p + \nabla \cdot \bar{\boldsymbol{\tau}} + \rho \mathbf{g} + \mathbf{F}_\sigma \quad (2)$$

where  $\bar{\boldsymbol{\tau}} = \mu[\nabla \mathbf{u} + (\nabla \mathbf{u})^T]$  is the fluid stress tensor;  $\rho$  and  $\mu$  are local averaged density and viscosity. The volumetric source term  $\mathbf{F}_\sigma$  appearing in the momentum equation is due to surface tension ( $\sigma$ ) between the two fluids and acts only in the vicinity of the interface (Brackbill *et al.*, 1992). The dynamics of the interface is captured by a Volume of Fluid (VOF) method (Van Sint Annaland *et al.*, 2005) where the two different fluids are identified by a color function  $F$ . It indicates the fractional amount of fluid present at a certain computational cell. The motion of the interface is evolved by advecting the color function ( $F$ ) with the local fluid velocity as,

$$\frac{\partial F}{\partial t} + \mathbf{u} \cdot \nabla F = 0 \quad (3)$$

In Eq. 2, the local density ( $\rho$ ) is calculated by linear averaging of the densities of the fluid 1 and fluid 2. However, the local viscosity ( $\mu$ ) is calculated by harmonic averaging of the kinematic viscosities of the individual fluid phases. A

geometrical advection scheme is used to solve Eq. 3 which allows to achieve a very high degree of mass conservation.

In the Cartesian domain, the no-slip condition at the solid non-conforming boundary is imposed by an implicit (direct) second-order accurate Immersed Boundary Method (IBM) (Deen *et al.*, 2012; Das *et al.*, 2016). In the presence of fluid-fluid interfaces with immersed solids, contact line dynamics plays a major role in wetting phenomena. It is incorporated by applying the apparent contact angle ( $\Theta$ ) as a boundary condition for interface at the contact lines (Patel *et al.*, 2017). The effect of the contact angle is taken into account by modifying the fluid-fluid interface normals at the solid boundaries. The detailed implementation and thorough validation of the present IBM-VOF coupling strategy has been reported in Patel *et al.* (2017).

## RESULTS AND DISCUSSIONS

### Droplet spreading on a flat plate

As a base case, we start with analyzing the droplet spreading on a flat surface. When a spherical droplet is placed gently on a flat surface, at the very first instance the air layer between the droplet and the surface is drained; and a small liquid bridge is formed between the drop and the surface. To maintain the wettability condition, an initial perturbation travels upward in the form of a capillary wave. If the fluid has a large inertia for a very small  $\Theta$ , the larger size of the capillary waves may raise up to the drop surface and 'pinch-off' may occur. The Laplace number ( $La = \frac{\rho \sigma^{0.5} D}{\mu^2}$ ), compares the inertia and surface tension to viscosity effect, and can be used as a dimensionless quantity to predict droplet pinch-off. At a very high  $La$ , the capillary wave and eventual pinch-off of the droplet may create satellite droplets.

If we study the transient development of wetted area, characterised by the equivalent spreading diameter  $S(t)$ , for a completely wetting case ( $\Theta \approx 0$ ), the droplet spreading phenomena can be divided into an early stage inertia dominant wetting, following a power-law  $S(t) \sim t^n$  with  $n = \frac{1}{2}$  and a second stage consisting of a viscous regime, where  $n = \frac{1}{10}$ , according to Tanner's law (Tanner, 1979). Varying the relative contributions between the inertia, viscous force, surface tension and gravity different evolutions have been reported in the literature:  $n = 1/8, 1/7, 1/5, 1/4$ . To check the accuracy of our numerical model, at first we have studied droplet spreading on a flat surface using the same settings of experimental work by Winkels *et al.* (2012). The flat surface is represented by an immersed surface at the [111] plane, which does not conform the Cartesian grid. Across the diameter of the droplet 40 grid cells are used. In Fig. 1 the transient evolution of spreading diameter is shown. Similar to the experiments, a water droplet in air has been considered which corresponds to  $La = 36 \times 10^3$ . As a results the initial spreading is purely governed by the inertial force and we expect  $S(t) \sim t^{0.5}$  as temporal evolution. The spreading diameter ( $S$ ) is non-dimensionalized by the initial diameter of the droplet ( $D$ ) and time ( $t$ ) is normalized by the inertial scale, i.e.  $\tau = t/(\rho(D/2)^3/\sigma)^{0.5}$ . In sub-fig (a) to (d) the simulations snapshots are presented: (a) initial spherical droplet, (b) capillary wave propagating in the upward direction, (c) pinch-off at the upper portion of the droplet and (d) at the end of inertial spreading leaving a spherical cap shape of the droplet. After inertial spreading the bubble interface oscillates a few times before it finally reaches the equilibrium condition. Fig. 1 shows a very good match with experiments and indeed we observe a  $\sim t^{0.5}$

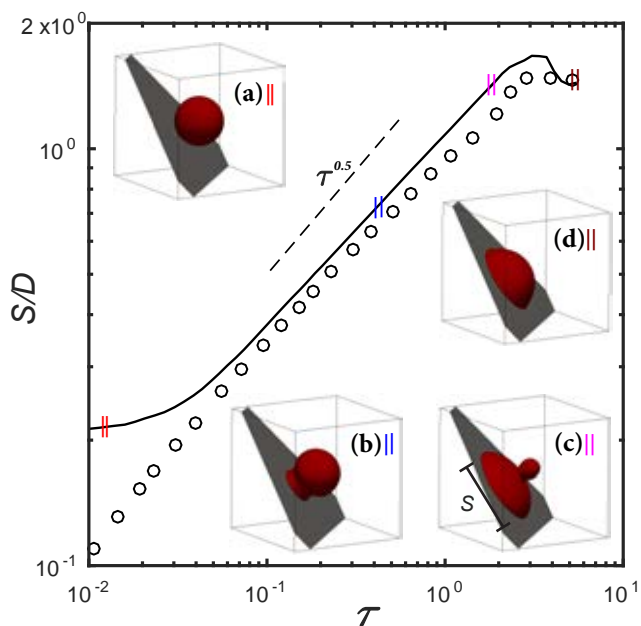


**Figure 1:** Transient evolution of spreading diameter ( $S/D$ ) with non-dimensionalised time ( $\tau$ ) for droplet spreading on a flat surface with  $\Theta = 65^\circ$ . In a Cartesian grid the flat surface is represented as an immersed surface. The line indicates the simulation results and the markers are for the experimental results. The simulation snapshots at four different time intervals are also shown.

evolution of spreading diameter. Please note, unlike the experimental results, in our simulation the initial spreading radius is not zero due to finite grid resolution. In reality, at the very beginning, there exists a point contact (zero surface area) between the droplet and the solid surface. However, due to the finite grid resolution in our numerical simulation there will always be some overlap between the droplet and surface to initiate the spreading. At very high grid resolution  $S(0) \rightarrow 0$ , nevertheless with the current grid resolution we are able to capture the  $S(t) \sim t^n$  trend very accurately.

### Droplet spreading and capillary penetration on a porous block

The computational setup of the main system studied in this work is shown in Fig. 2, where a liquid droplet is put in contact with a porous block. Each ligament and each pore size of the porous structure is resolved by at least 12 grid cells. The simulations are performed in a single quarter of the domain using a symmetry boundary condition. The total number of computational cells are reported as  $\sim 9 \times 10^6$ . The time-step size ( $\sim 10^{-6} s$ ) has been restricted by both the CFL and capillary wave constraint (Patel *et al.*, 2017). The diameter ( $D$ ) of the droplet is 4 mm and the fluid properties are:  $\mu = 0.034 Pa-s$ ,  $\rho = 809 kg/m^3$  and  $\sigma = 0.032 N/m$ . The surrounding medium is air. It corresponds to an air-squalane oil system with  $La = 45$ . The porous block is made of equidistant cylindrical ligaments and the size of the representative elementary volume (REV) is 0.67 mm. Due to the capillarity and the wetting condition, the droplet spreads as well as penetrates inside the porous slab. Porous structures of three different porosities,  $\epsilon = 0.35, 0.5$  and  $0.65$  have been considered. The equilibrium contact angle ( $\Theta$ ) between the air-oil interface with the solid ligaments is varied from  $30^\circ$  to  $135^\circ$ . As  $La = 45$ , spreading is dominated by inertia. However, the magnitude of the capillary wave is not very

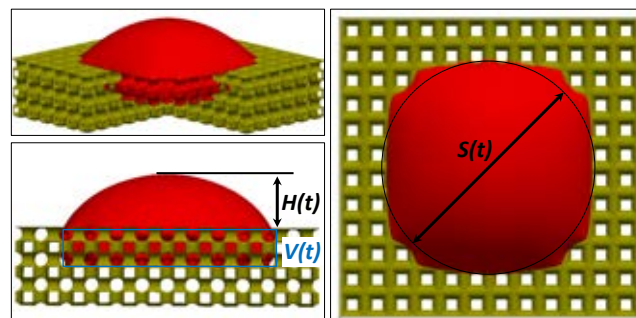


**Figure 2:** Droplet spreading and capillary penetration on a porous block: physical description of the problem.  $H(t)$  represents the transient evolution of the height of the droplet,  $S(t)$  represents the equivalent spreading radius and the penetration volume is represented by  $V(t)$ .

vigorous to pinch-off the droplet from its top surface. At each time-step we capture the droplet height ( $H$ ), the equivalent spreading diameter ( $S$ ) at the porous surface and the volume of the penetrated liquid ( $V$ ).

The transient development of droplet shape, spreading and capillary imbibition are shown in Fig. 3 for a typical case ( $\epsilon = 0.5$  and  $\Theta = 30^\circ$ ). Please notice that the simulation snapshots are not taken at equal intervals. From the initial position ( $\tau = 0$ ) to  $\tau = 1.03$ , the upper portion of the droplet does not move, liquid slightly penetrates inside the porous structure and finally forms a cylindrical shape. In reality, when the droplet touches the solid, to satisfy the wetting condition, a perturbation is generated at the contact point. It travels upward as a capillary wave and reaches the top of the droplet. Until this time the upper portion of the droplet does not move. In Fig. 3,  $\tau = 1.53$  to  $\tau = 2.18$  corresponds to the fast inertial spreading where the height of the droplet rapidly decreases. Also, it spreads rapidly over the porous surface. The simultaneous capillary penetration and viscous spreading is clearly visible at  $\tau = 2.36$  to  $\tau = 6.04$ , where the rate of change of droplet height is low. Both the phenomena are comparatively very slow where capillary force is balanced by the viscous shear stress at the solid surfaces. In the next section, all these phenomena are quantitatively analyzed.

### Droplet height ( $H$ )

The normalized droplet height ( $H/D$ ) from the surface of the porous block with time ( $\tau$ ) is shown in Fig. 4 for varying contact angle ( $\Theta$ ) when  $\epsilon = 0.5$ . For  $\Theta = 30^\circ$  and  $\Theta = 45^\circ$ , three different zones, capillary wave propagation, fast inertial spreading; and then simultaneous viscous spreading and capillary penetration, can easily be observed. When  $\Theta = 90^\circ$ , inertial spreading is rather small and the droplet interface oscillates at the end of the inertial spreading before it reaches the equilibrium condition. When the solid surfaces are made hydrophobic ( $\Theta = 135^\circ$ ), the height does not change much with time. At a first glance, it seems that there is no spreading. However, from the plot of spreading diameter ( $S$ ) with time, the spreading can still be identified. This will be discussed in the next section. Fig. 5 shows the effect of porosity on transient variation of the droplet height when  $\Theta = 45^\circ$ . Simulation results for the flat plate ( $\epsilon = 0$ ) are also shown. The effect of porosity on the transient variation of the droplet height is comparatively small. It is interesting to observe that with an increase in porosity, the rate of change of height ( $\delta H/\delta \tau$ ) decreases. This phenomenon is also observed

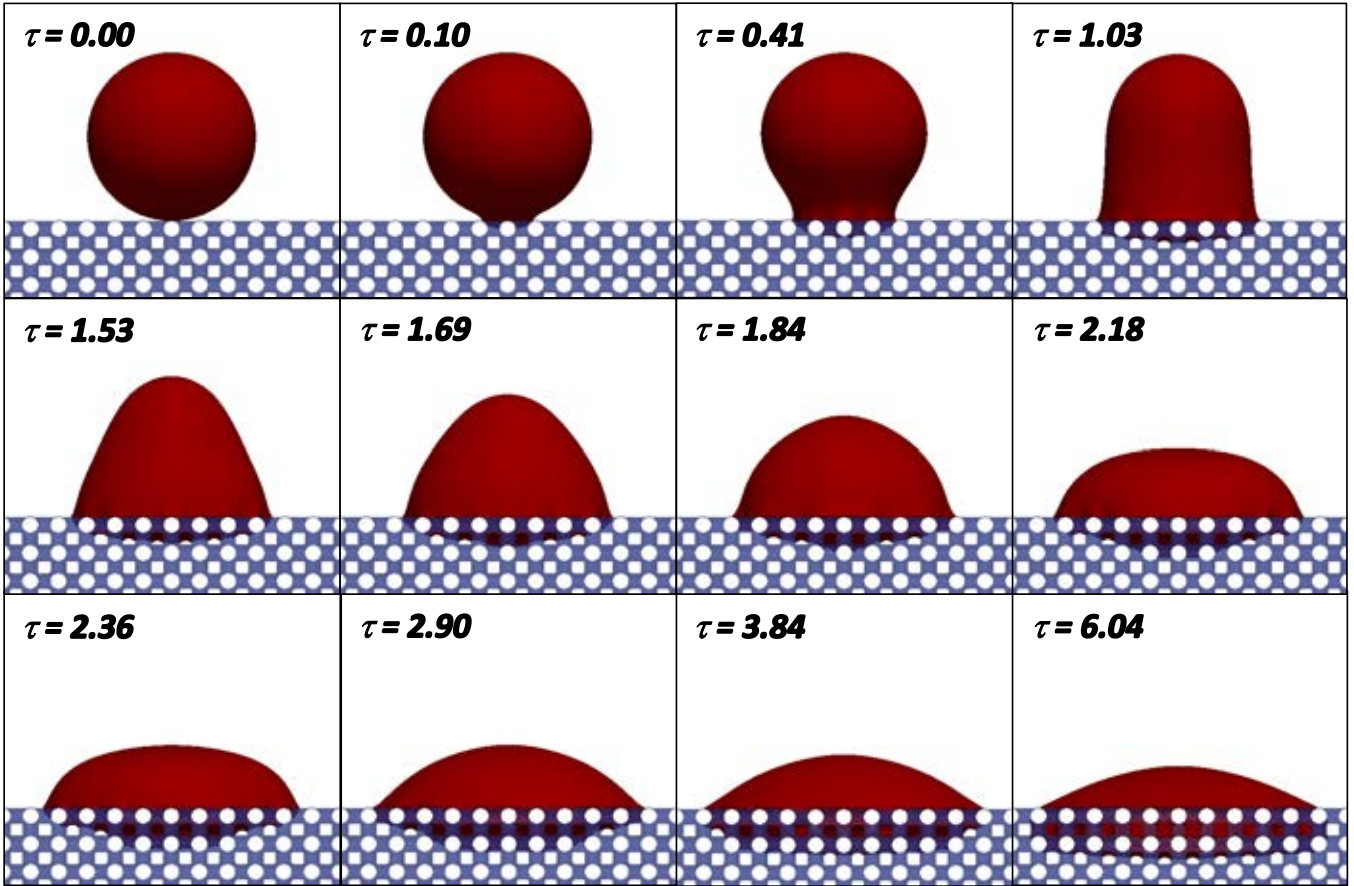


**Figure 3:** Droplet shape evolution during spreading and capillary penetration on a porous block of porosity  $\epsilon = 0.5$  and equilibrium contact angle  $\Theta = 30^\circ$ .  $\tau$  is the non-dimensional time.

by Frank and Perre (2012) through LBM simulation. At a particular time, the total height of the droplet depends on both the inertial spreading and capillary penetration. When the porosity increases, the inertial spreading slows down while the capillary penetration increases. The time-scale for inertial spreading is high compared to the capillary penetration. Hence, the relative contribution of the inertial spreading is higher and mainly governs the height of the droplet. With decrease in the porosity, the inertial spreading increases and as a result the total height decreases faster.

*Equivalent spreading diameter (S)*

Unlike the droplet spreading over a flat plate, the imprint of the contact line on the surface of the porous block is not always circular. Based on the spread area, just above the porous block, we have calculated an equivalent spreading diameter ( $S$ ) at each time-step. The variation of the normalized spreading diameter ( $S/D$ ) with non-dimensional time ( $\tau$ ) is shown in Fig. 6 for varying  $\Theta$  and in Fig. 7 for varying  $\epsilon$ . Here too, it is very clearly visible that, for all the cases the inertial fast spreading lasts up to approximately  $\tau \approx 2$ . Similar to spreading over a flat surface, power-law variation of spreading, i.e.  $S \sim C\tau^n$  is still valid for all the cases. From Fig. 6, we can observe that the spreading is faster when the contact angle is low and it is slower for the hydrophobic case. Fig. 7 clearly shows that spreading is fastest for the flat plate, slowed down with increasing

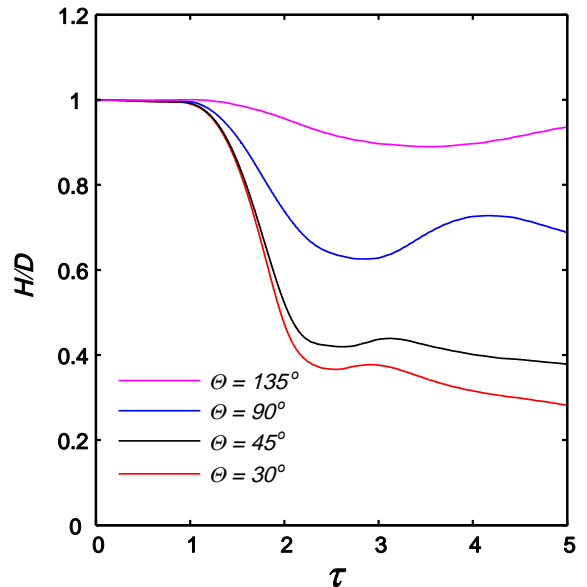


**Figure 4:** Droplet height ( $H/D$ ) evolution for  $\epsilon = 0.5$ : effect of  $\Theta$ .

porosity. After the inertial spreading,  $S$  decreases slowly with time for higher porosity cases, due to capillary penetration of the liquid.

To study quantitatively, the effect of  $\epsilon$  and  $\Theta$  on spreading dynamics ( $S$ ), both the exponent ( $n$ ) and pre-factor ( $S$ ) of the

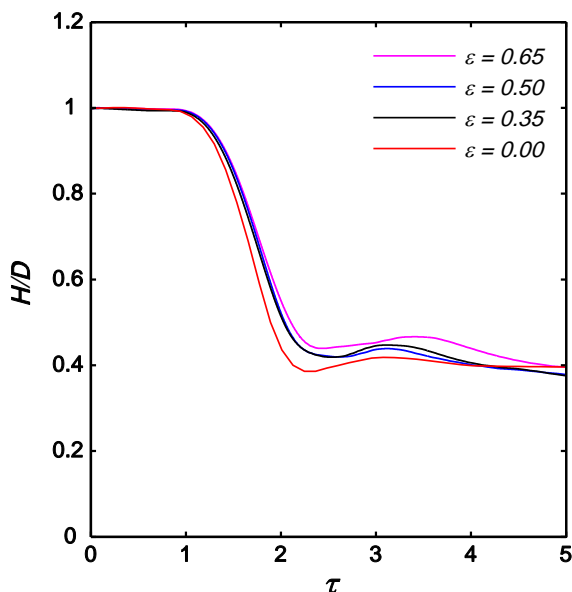


Figure 5: Droplet height ( $H/D$ ) evolution for  $\Theta = 45^\circ$ : effect of  $\epsilon$ .

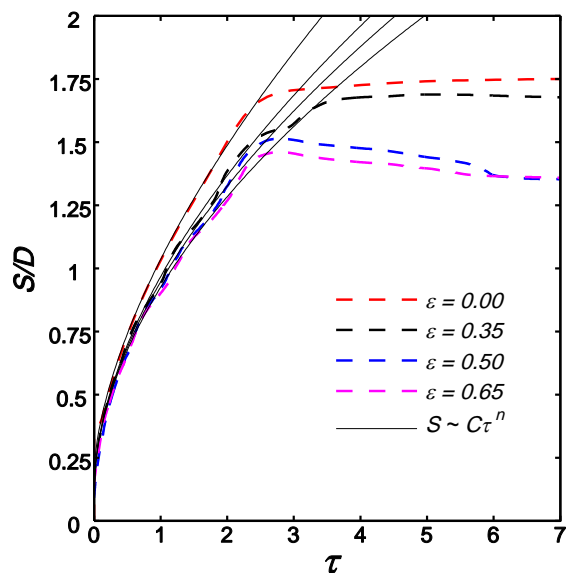


Figure 7: Evolution of equivalent spreading diameter ( $S/D$ ) for  $\Theta = 45^\circ$ : effect of  $\epsilon$ .

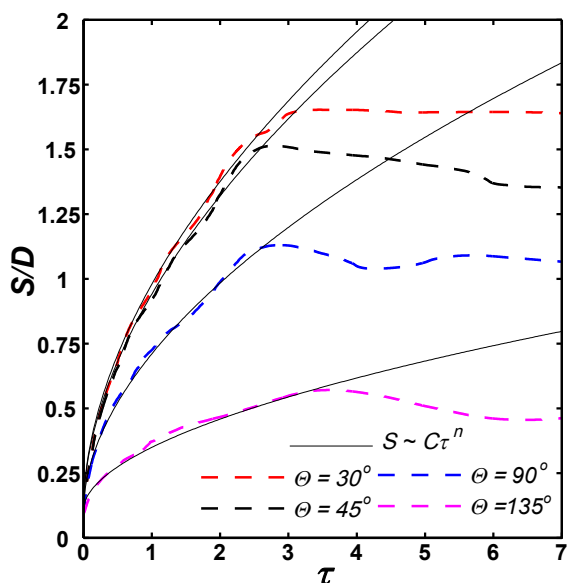


Figure 6: Evolution of equivalent spreading diameter ( $S/D$ ) for  $\epsilon = 0.5$ : effect of  $\Theta$ .

$S/D = C\tau^n$  fit have been evaluated for all the cases. Fig. 8 shows the variation of  $n$  and  $S$  with  $\epsilon$  and  $\Theta$ . For spreading over a flat plate, for all the contact angle, Legendre (Legendre and Maglio, 2013) observed that  $n$  varies from 0.5 to 0.66 for  $La = 72000$  to  $La = 7$ . In the present case, for  $La = 45$ , we found  $n = 0.62$  for the case of flat plate. In our simulation it is observed that  $n$  is almost constant with  $\Theta$ , however, decreases linearly with porosity. On the other hand, the pre-factor  $C$  decreases drastically with  $\Theta$ , which indicated slower spreading for hydrophobic surfaces. The pre-factor  $C$  also decreases with increase in porosity, however, the variation is comparatively less.

#### Liquid penetration ( $V$ )

Finally, we have studied the amount of liquid penetration inside the porous block with time. The volume of penetrated liquid ( $V$ ) normalized by the total volume of the droplet

( $V_0$ ) is plotted against time in Fig. 9 for different  $\Theta$ . For  $\Theta = 30^\circ$  and  $\Theta = 60^\circ$  the penetration is faster, the equilibrium condition is only reached when the full droplet drained into the porous block. For the rest of the cases, only a single layer of the porous block get wet by the liquid. An equilibrium condition is achieved when the contact force at the triple lines of the upper surface of the porous medium is balanced by the contact force inside the porous block.

Fig. 10 shows the effect of porosity on capillary penetration. For  $\Theta = 60^\circ$ , the equilibrium condition is achieved after only a small amount of liquid penetration. However, for  $\Theta = 30^\circ$ , the liquid penetration is faster and a strong function of  $\epsilon$ . In this stage, the capillary force is balanced by the viscous forces. The magnitude of viscous resistance can be estimated by the Kozeny–Carman equation, which shows a non-linear increase in viscous resistance with an increase in solid fraction ( $1 - \epsilon$ ). For higher porosity, the lower viscous resistance increases the capillary imbibition.

## CONCLUSIONS

For the first time, the very complex interaction between a droplet and a porous media has been studied by an accurate IBM-VOF method based finite volume code. The complex physical phenomena, like contact line motion, inertial spreading, and capillary imbibition have been successfully studied, analysed and qualitatively compared with literature results for a range of porosities and contact angles. It is found that the transient behaviour of spreading follows a power law with time, similar to the droplet interaction with a flat plate. For smaller contact angles and lower porosities, the spreading is fast, which forces a quick reduction in droplet height in a short time. Irrespective of porosity, the capillary imbibition stalls for contact angle  $60^\circ$  and above. However, this limiting value depends on the geometrical details of the porous structures. Viscous penetration is comparatively slow, and the rate of volumetric imbibition is a strong function of the porosity. For the present moderate or low Laplace number simulations, the motion of the droplet is smooth,

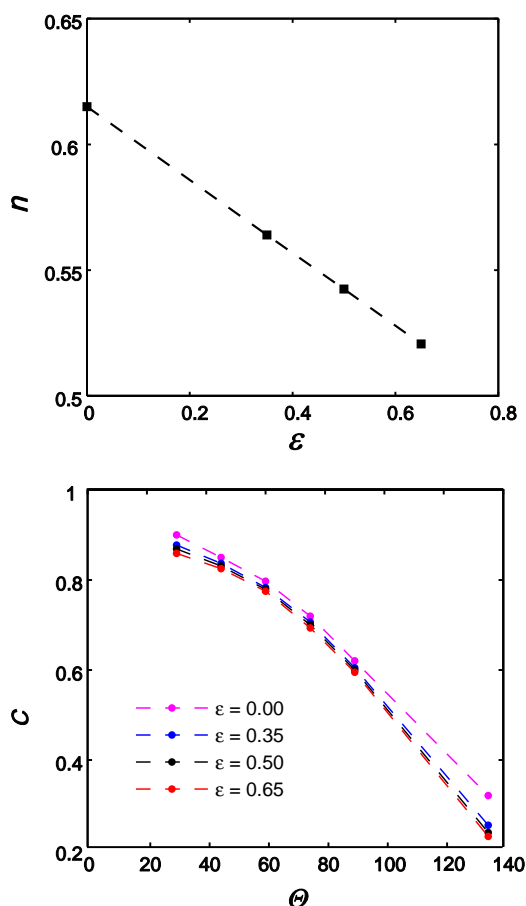


**Figure 8:** Exponent ( $n$ ) and pre-factor ( $C$ ) of power-law ( $S/D = C\tau^n$ ) evolution of spreading diameter for different cases.

however, our code is also capable of simulating systems of very large Laplace number. In the next stage of our research, we intend to study the effect of Laplace number on droplet pinch-off and satellite droplet formation.

## REFERENCES

- BRACKBILL, J.U., KOTHE, D.B. and ZEMACH, C. (1992). "A continuum method for modeling surface tension". *Journal of computational physics*, **100**(2), 335–354.
- DAS, S., DEEN, N.G. and KUIPERS, J.A.M. (2016). "Immersed boundary method (ibm) based direct numerical simulation of open-cell solid foams: Hydrodynamics". *AIChE Journal*.
- DEEN, N.G., KRIEBITZSCH, S.H., VAN DER HOEF, M.A. and KUIPERS, J.A.M. (2012). "Direct numerical simulation of flow and heat transfer in dense fluid-particle systems". *Chemical Engineering Science*, **81**, 329–344.
- FRANK, X. and PERRE, P. (2012). "Droplet spreading on a porous surface: A lattice boltzmann study". *Physics of Fluids*, **24**(4), 042101.
- FRANK, X., PERRÉ, P. and LI, H.Z. (2015). "Lattice boltzmann investigation of droplet inertial spreading on various porous surfaces". *Physical Review E*, **91**(5), 052405.
- HYVÄLUOMA, J., RAISKINMÄKI, P., JÄSBERG, A., KOPONEN, A., KATAJA, M. and TIMONEN, J. (2006). "Simulation of liquid penetration in paper". *Physical Review E*, **73**(3), 036705.
- LEGENDRE, D. and MAGLIO, M. (2013). "Numerical simulation of spreading drops". *Colloids and Surfaces A: Physicochemical and Engineering Aspects*, **432**, 29–37.

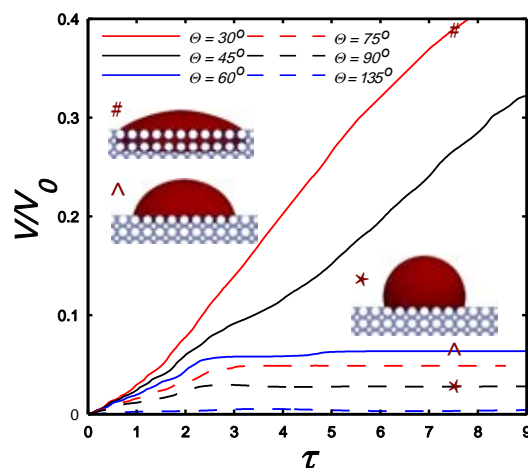


**Figure 9:** Volume of penetrated liquid ( $V/V_0$ ) with time ( $\tau$ ) for  $\varepsilon = 0.35$ : effect of  $\theta$ .

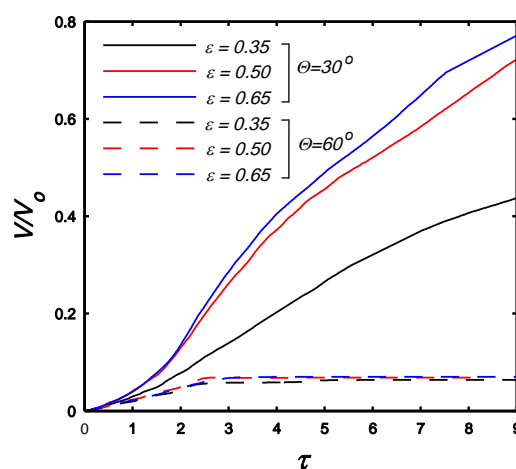


**Figure 10:** Volume of penetrated liquid ( $V/V_0$ ) with time ( $\tau$ ) for  $\theta = 30^\circ$  and  $60^\circ$ : effect of  $\varepsilon$ .

- MENG, S., YANG, R., WU, J.S. and ZHANG, H. (2014). "Simulation of droplet spreading on porous substrates using smoothed particle hydrodynamics". *International Journal of Heat and Mass Transfer*, **77**, 828–833.
- PATEL, H., DAS, S., KUIPERS, J.A.M., PADDING, J.T. and PETERS, E.A.J.F. (2017). "A coupled volume of fluid and immersed boundary method for simulating 3d multiphase flows with contact line dynamics in complex geometries". *Chemical Engineering Science*.
- TANNER, L. (1979). "The spreading of silicone oil drops on horizontal surfaces". *Journal of Physics D: Applied Physics*, **12**(9), 1473.
- VAN SINT ANNALAND, M., DEEN, N.G. and KUIPERS, J.A.M. (2005). "Numerical simulation of gas bubbles behaviour using a three-dimensional volume of fluid method". *Chemical Engineering Science*, **60**(11), 2999–3011.
- WINKELS, K.G., WEIJS, J.H., EDDI, A. and SNOEIJER, J.H. (2012). "Initial spreading of low-viscosity drops on partially wetting surfaces". *Physical Review E*, **85**(5), 055301.
- YANG, W. and XU, J. (2017). "Drop spreading and penetrating on micro/nano particle sintering porous with multiscale structure". *Colloids and Surfaces A: Physicochemical and Engineering Aspects*, **516**, 9–22.

## FROM LINEAR TO NONLINEAR: TRANSIENT GROWTH IN CONFINED MAGNETOHYDRODYNAMIC FLOWS

Oliver G. W. CASSELLS<sup>1\*</sup>, Tony VO<sup>1†</sup>, Alban POTHÉRAT<sup>2‡</sup>, Gregory J. SHEARD<sup>1§</sup>

<sup>1</sup>Department of Mechanical and Aerospace Engineering, Monash University, Victoria 3800, Australia

<sup>2</sup>Applied Mathematics Research Centre, Coventry University, Coventry, CV15FB, United Kingdom

\* E-mail: oliver.cassells@monash.edu

† E-mail: tony.vo@monash.edu

‡ E-mail: aa4111@coventry.ac.uk

§ E-mail: greg.sheard@monash.edu

### ABSTRACT

The underlying flow mechanisms for the destabilisation of an electrically conducting fluid under the influence of a transverse magnetic field in a square duct are investigated. Such flows are applicable to metallurgical processes where magnetic fields are used to dampen disturbances to increase homogeneity in material production, in addition to cooling blankets of nuclear fusion reactors, where flow disturbances can aid in improving convective heat transfer. A preliminary investigation into optimal linear growths at Hartmann numbers  $10 \leq Ha \leq 1000$  and Reynolds number  $Re = 5000$  identifies two regimes for the scaling of optimal linear growths; when perturbation structures are dominated by three-dimensional variation in the vertical side-wall boundary layers, and for when quasi-two-dimensional (Q2D) disturbances are prevalent. Through comparison with existing literature, the Q2D model of Sommeria & Moreau (1982) is shown to be an excellent predictor of fundamental growth mechanisms for  $Ha > 150$ . A two-step method incorporating the seeding of an unperturbed base flow with optimal linear perturbations in a high magnetic field strength regime shows that no increase in energy amplification can be achieved via initial seeding energies in the range  $10^{-6} \leq E_p \leq 10^{-2}$ . The dominant dissipative mechanisms for these different seeding energies are also analysed, where it is shown that strong magnetic damping does not always necessitate the smoothing of the velocity field towards pure anisotropy, which has potentially useful applications for aiding convective heat transfer in magnetically damped flows.

**Keywords:** CFD, transient linear growth, magnetohydrodynamics, liquid metal, fusion reactor, metallurgy.

### NOMENCLATURE

#### Greek Symbols

$\delta$	Boundary layer thickness
$\epsilon$	Viscous dissipation
$\mu$	Magnetic dissipation
$\nu$	Kinematic viscosity
$\Omega$	Spatial domain
$\phi$	Electric scalar potential
$\rho$	Mass density
$\sigma$	Electrical conductivity
$\tau$	Time period
$\xi$	Shape function $L_i$ spatial coordinate

#### Latin Symbols

$\mathcal{A}$	State-transition operator
$a$	Duct width
$\mathbf{B}_0$	Magnetic field vector
$B_0$	Magnetic field magnitude
$C_d$	Viscous drag coefficient
$E$	Kinetic energy
$G$	Perturbation energy amplification
$\mathcal{G}$	Anisotropy coefficient
$Ha$	Hartmann number
$\mathbf{j}$	Electric current density vector
$\mathbf{k}$	Wavenumber vector
$k$	Streamwise wavenumber.
$L$	Linear time evolution operator.
$L_i$	Lagrangian polynomial shape function.
$L_z$	Periodicity duct length
$\mathcal{L}^2$	Vector space
$m$	Fourier mode
$N_p$	Shape function polynomial order
$p$	Pressure
$Re$	Reynolds number
$Re_m$	Magnetic Reynolds number
$t$	Time
$U_0$	Peak base flow streamwise velocity
$u$	$x$ -velocity component of $\mathbf{V}$
$\mathbf{V}$	Velocity vector
$v$	$y$ -velocity component of $\mathbf{V}$
$w$	$z$ -velocity component of $\mathbf{V}$
$x$	Cartesian coordinate (spanwise direction)
$y$	Cartesian coordinate (spanwise direction)
$z$	Cartesian coordinate (streamwise direction)

#### Sub/superscripts

$g$	Nodal index
$Ha$	Hartmann layer
$i$	Nodal index
$m$	Fourier coefficient
max	Global maximum
$n$	Non-linear solution
opt	Optimal value at global maximum
$p$	Perturbation field
$Sh$	Shercliff layer
$0$	Base flow
$\hat{\phantom{x}}$	Fourier transform
$l$	Linear perturbation
$*$	Adjoint



## INTRODUCTION

Electrically conducting fluids under the influence of strong magnetic fields come under the class of magnetohydrodynamic (MHD) flows. Understanding the stability mechanisms of such flows has potentially significant implications to metallurgical processes, and more pertinently the viability of clean energy sources, such as magnetic confinement fusion reactors. For the latter, the strong transverse magnetic fields that exist to contain the plasma have a strong damping effect on the flow differentials in the adjacent liquid metal cooling blankets. In these flows, motion-derived electric currents interact with an externally applied magnetic field to induce electro-magnetic forces known as Lorentz forces (Hunt and Stewartson, 1965). The Lorentz force acts to suppress velocity differentials in perpendicular planes, while flow structures also become elongated and aligned with the external magnetic field vector (Sommeria and Moreau, 1982; Sommeria, 1988). Furthermore, boundary layers develop along walls aligned with the magnetic field (called Shercliff layers) and orthogonal to it (Hartmann layers). Both become thinner at higher magnetic fields, as their thicknesses respectively scale as  $\delta_{Sh} = O(Ha^{-1/2})$  and  $\delta_{Ha} = O(Ha^{-1})$ . Here,  $Ha$  is the Hartmann number describing the ratio of electromagnetic to viscous forces in the flow and is a function of the geometry and material properties of the fluid.

A resulting effect of these flow modulations is inefficient convective heat transport; a detriment to the thermal performance in maintaining safe operating temperatures of the reactor, and in the heat exchange process used in the production of electrical energy. To overcome these issues, several works have been conducted with the aim of mechanically enhancing the convective heat transfer performance (Cassells *et al.*, 2016; Hamid *et al.*, 2016). While these methods certainly hold an important place in furthering our current understanding, as well as our ability to meet the viability constraints of fusion reactors, they are not always practicable. Thus, a further understanding of the underlying instability mechanisms which can aid in convection across a broader range of operational parameters is needed.

An issue with respect to studying the stability of MHD flows in the limit of strong magnetic fields is the discrepancy between the critical regime parameters predicted through the growth of exponentially growing perturbations and that observed in experiments. For example, it has been shown that the Hartmann boundary layers become linearly unstable for  $Re/Ha \geq 48311$ , whereas experimental observations show transition occurring for  $Re/Ha \geq 380$  (Takashima, 1996; Moresco and Alboussiere, 2004; Krasnov *et al.*, 2004, 2010). One explanation is that the non-normality of the Orr–Sommerfeld modes can create transient amplifications leading to a subcritical instability. In other words, the linearisation around a base state may predict asymptotically decaying eigenvalues, yet, interactions between suboptimal modes could result in sufficient non-linear transient amplifications to render the base flow unstable (N araigh, 2015). The initial conditions that undergo the maximum growth in kinetic energy are commonly referred to as the optimal perturbations or modes.

The three-dimensional nature of MHD flows and the reduction in boundary layer thickness (relative to hydrodynamic flows) means that numerically such analysis comes at a large computational cost. Quasi-two-dimensional (Q2D) numerical models for approximating these flows at high mag-

netic field strengths are often utilised by assuming the flow outside of laminar Hartmann boundary layers are predominantly two dimensional. First developed by Sommeria and Moreau (1982) (hereafter SM82), this model has proved promising from a kinematic standpoint for when both the Hartmann number and the interaction parameter, defined as  $N = Ha^2/Re$ , are much greater than unity, where  $Re$  is the Reynolds number representing the ratio of inertial to viscous forces in the flow (Sommeria and Moreau, 1982; Poth erat *et al.*, 2000; Hamid *et al.*, 2015; Cassells *et al.*, 2016).

Poth erat (2007) studied the effects of the Shercliff layers on the stability of confined MHD flows using the SM82 model. In this framework, the three-dimensional component of the wavenumber and MHD equivalent Orr–Sommerfeld modes was assumed zero, an assumption expected to become valid when  $Ha > 200$ . It was further assumed that only the MHD equivalent of the Orr–Sommerfeld modes were available to contribute to non-modal growths. However, the validity of these Q2D approximations on resolving the all-important stability characteristics in three-dimensional MHD flows has been the focus of little to no empirical research. To the best of the authors knowledge, the only methodologically comparable research to that presented in the present work is by Krasnov *et al.* (2010), who employed 3D transient growth analysis to show a scaling of global dominant modes following a  $Ha^{-3/2}$  relation in the limited range of  $10 \leq Ha \leq 50$  for  $Re = 5000$  in square ducts.

The presence and structure of these optimal modes have been shown to form a fundamental part in the processes leading to flow destabilisation and subsequently the transition of fully turbulent flows (Boeck *et al.*, 2008). From an industrial standpoint, effective flow control strategies, such as periodic suppression and/or excitation of electro-magnetic fields, can be implemented to promote or discourage flow destabilisation by utilising the knowledge of the modal and spatial characteristics of these linear growth mechanisms. Potential end uses being the destabilisation of liquid metal cooling blankets to aid convective heat transfer coefficients in nuclear fusion reactors, or the promotion of flow stability to aid in homogeneity of material production in metallurgical applications (Smolentsev *et al.*, 2012).

Motivated by an investigation into the stability of Hartmann layers by Krasnov *et al.* (2004), a two-step method incorporating the seeding of a basic flow in a three-dimensional MHD duct with the optimal disturbance modes will also be investigated in the present work. For Hartmann flows, this method has shown a strong correlation in relation to the types of flow structures which appear during transition and onset of turbulence in full-3D-DNS seeded with small-amplitude random noise and experimental works with varying surface roughness (Krasnov *et al.*, 2004; Moresco and Alboussiere, 2004).

To date, it is not properly understood if Q2D models are accurate predictors of the dominant disturbance mechanisms towards high magnetic field strengths, nor is there an extensive body of work on the physical structures which develop through their transition to a Q2D-dominated state. Therefore, the present work aims to address this gap in knowledge by elucidating the processes for when and how specific linear transient amplifications present over a wide range of  $Ha$ , and the processes through which the 3D states at low magnetic field strengths give way to anisotropic 2D structures at higher field strengths. Furthermore, as the energetic response of seeding fully confined 3D MHD flows with opti-

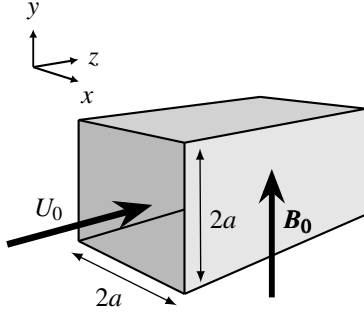


**Figure 1:** Schematic depicting the flow configuration and parameters pertaining to this investigation.

mal perturbation modes has not been investigated, and poses promising potential applications, it is therefore an additional aim of the present work to extend this to the confined MHD case incorporating the sidewall Shercliff layers. The energetic response for high  $Ha$ , in addition to a quantification of the dominant dissipation mechanisms affecting the evolution of kinetic energy and the formation of flow structures will be also investigated.

## MODEL DESCRIPTION

### Problem Definition and Mathematical Formulation

A fluid with electrical conductivity  $\sigma$ , kinematic viscosity  $\nu$  and density  $\rho$ , flows through a square duct with cross-sectional width  $2a$ . The electrically insulated vertical and horizontal duct walls are respectively located at  $x = \pm a$  and  $y = \pm a$ . A constant external homogeneous magnetic field  $\mathbf{B}_0 = B_0 \mathbf{e}$  is imposed on the flow tangential to the vertical sidewalls such that the unit vector  $\mathbf{e} \equiv \langle e_x, e_y, e_z \rangle = \langle 0, 1, 0 \rangle$  (see figure 1). The flow is driven by a constant pressure gradient  $\nabla p$  with no-slip conditions applied on all solid boundaries. The MHD equations are written in the quasi-static, low-magnetic number approximation. In this approximation, the magnetic field generated by the motion-induced currents of the conducting fluid in comparison to the externally applied field  $B_0$  are small. Hence, the agglomerated magnetic field remains of nearly equal magnitude to  $B_0$ . This approximation is valid for target applications and in laboratory experiments of moderate intensity and size (typically liquid metals flowing under  $1m/s$  in a domain smaller than  $1m$ ) (Krasnov *et al.*, 2010; Smolentsev *et al.*, 2010). Non-dimensionalisation of the governing equations is achieved by taking the proper scales for length  $a$ , pressure  $\rho U_0^2$ , where  $U_0$  is the peak inlet velocity, time  $a/U_0$ , magnetic field  $B_0$  and lastly, for the electric potential  $aU_0 B_0$ . It follows that the dimensionless quasi-static momentum and continuity equations can be written as

$$\frac{\partial \mathbf{V}}{\partial t} + (\mathbf{V} \cdot \nabla) \mathbf{V} = -\nabla p + \frac{1}{Re} \nabla^2 \mathbf{V} + \frac{Ha^2}{Re} (\mathbf{j} \times \mathbf{B}_0), \quad (1)$$

$$\nabla \cdot \mathbf{V} = 0, \quad (2)$$

where  $\mathbf{V}(x, y, z, t) = \langle u, v, w \rangle$  and  $\mathbf{j} = -\nabla \phi + \mathbf{V} \times \mathbf{B}_0$  are the velocity and electric current density vectors, respectively. Here  $\phi$  is the electric scalar potential. The dimensionless groups  $Re$  and  $Ha$  are respectively the Reynolds number,  $Re \equiv U_0 a / \nu$ , representing the ratio of inertial to viscous forces in the flow, and the Hartmann number,  $Ha \equiv a B_0 \sqrt{\sigma / \rho \nu}$ , representing the ratio of electromagnetic to the viscous forces in the flow. In the present work, Hartmann numbers between  $10 \leq Ha \leq 1000$  are investigated which

significantly extends the range covered by Krasnov *et al.* (2010). The aim being to bridge the gap between 3D and Q2D models for transient growth analysis of optimal linear amplifications. Here a fixed Reynolds number of  $Re = 5000$  is used both for comparison reasons with existing literature, but also as it is below the exponential instability limit found for hydrodynamic Poiseuille flows.

### Transient growth analysis

The transient growth of linear three-dimensional infinitesimal perturbations of the form

$$[\mathbf{V}_p, \phi_p, p_p](x, y, z, t) = (u', v', w', \phi', p'), \quad (3)$$

to a streamwise independent two-dimensional steady-state base flow

$$[\mathbf{V}_0, \phi_0, p_0] = (u(x, y), v(x, y), w(x, y), \phi(x, y), p(z)), \quad (4)$$

is conducted by tracking their energy amplification over a finite time interval  $\tau$ . The flow solution then takes the general form

$$[\mathbf{V}, \phi, p] = (\mathbf{V}_0, \phi_0, p_0) + (\mathbf{V}_p, \phi_p, p_p), \quad (5)$$

with the perturbations being considered through the form of decoupled normal Fourier modes

$$[\mathbf{V}_p, \phi_p, p_p] = (\hat{u}, \hat{v}, \hat{w}, \hat{\phi}, \hat{p})(x, y, t) \cdot e^{ikz}, \quad (6)$$

where  $k$  is a streamwise wavenumber. For brevity, the full system of linearised equations describing the evolution of these perturbed flows is not given. The reader may refer to Krasnov *et al.* (2010) for a form consistent with this work.

The growth in perturbation kinetic energy over a given time interval  $t = \tau$  can be written as a ratio of volume integrals over domain  $\Omega$  of the standard  $L^2$  space inner products of  $\mathbf{V}_p(t)$  at  $t = \tau$  over the initial state at  $t = 0$

$$G(\tau) = \frac{\int_{\Omega} \mathbf{V}_p(\tau) \cdot \mathbf{V}_p(\tau) d\Omega}{\int_{\Omega} \mathbf{V}_p(0) \cdot \mathbf{V}_p(0) d\Omega}. \quad (7)$$

Here the adjoint evolution method outlined in Barkley *et al.* (2007) is employed, where the introduction of a state-transition operator  $\mathcal{A} = e^{L\tau}$ , where  $L$  is a linear operator, allows for the time evolution of an arbitrary initial perturbation  $\mathbf{V}_p$  to  $t = \tau$  to be described by

$$\mathbf{V}_p(\tau) = \mathcal{A}(\tau) \mathbf{V}_p(0). \quad (8)$$

By further introducing an adjoint evolution operator  $\mathcal{A}^*(\tau)$  of  $\mathcal{A}$ , that evolves an equivalent adjoint variable  $\mathbf{V}_p^*$  backwards in time from  $t = \tau$  to  $t = 0$ , (7) can be rewritten as

$$G(\tau) = \frac{\int_{\Omega} \mathbf{V}_p(0) \cdot \mathcal{A}^*(\tau) \mathcal{A}(\tau) \mathbf{V}_p(0) d\Omega}{\int_{\Omega} \mathbf{V}_p(0) \cdot \mathbf{V}_p(0) d\Omega}. \quad (9)$$

In this form, the optimal disturbance mode leading to  $G(\tau)_{\max}$  is found through the determination of the leading eigenvalue and corresponding eigenvector of the operator  $\mathcal{A}^* \mathcal{A}$ . This optimal perturbation mode presents as the real and orthonormal right singular vector determined through the singular value decomposition of  $\mathcal{A}^* \mathcal{A}$ ; which is solved using an implicitly restarted Arnoldi iterative method. The aim of the optimal linear growth portion of the present work can be formally written as

$$G(\tau)_{\max} = \max_{\mathbf{V}_p(0)} \frac{\int_{\Omega} \mathbf{V}_p(0) \cdot \mathcal{A}^*(\tau) \mathcal{A}(\tau) \mathbf{V}_p(0) dV}{\int_{\Omega} \mathbf{V}_p(0) \cdot \mathbf{V}_p(0) dV}. \quad (10)$$

The global maximum amplification  $G_{\max}$  occurs at the optimal time interval  $\tau_{\text{opt}}$  having streamwise wavenumber  $k_{\text{opt}}$ . From a physical perspective,  $G_{\max}$  defines the global maximum growth in kinetic energy due to initial optimal linear conditions  $\mathbf{V}_{p,\text{opt}}(0)$  evolved to time  $\tau_{\text{opt}}$ . This is referred to as the optimal growth as it is the largest achievable gain in energy for all spatial wavenumbers  $k$  for a given  $Re$  and  $Ha$  dependent flow regime.

### Numerical Methodology

A spatial high order nodal spectral element method incorporating a third-order time integration scheme based on backward-differencing is employed to discretise the governing equations and implement the transient growth analysis methodology. The domain is meshed using an average of 425 quadrilateral macro-elements with internally applied Lagrangian polynomial shape functions defined as

$$L_i(\xi) = \prod_{g=1, g \neq i}^{N_p+1} \frac{\xi - \xi_g}{\xi_i - \xi_g}, \quad (11)$$

where  $\xi$  is the spatial coordinate,  $i$  and  $g$  the nodal indices, and  $N_p$  the polynomial order, which is varied to control spatial resolution in the spanwise  $x$ - $y$  cross-plane. The nodal points within each element are spaced and weighted to correspond to Gauss-Legendre-Lobatto quadrature integration points, which reduce computational costs by forming diagonal mass matrices and leading to exponential spatial convergence. A graded element distribution was employed towards all solid surfaces to resolve regions that experience large flow gradients. The spacing of macro elements are scaled with respect to the  $Ha$  dependent boundary layer thickness; ensuring that a minimum of 8 macro elements span their height. Boundary conditions consist of zero velocities on all solid surfaces, a fully developed inlet velocity profile, along with high order pressure field Neumann boundary conditions on all domain perimeters to maintain third-order time accuracy (Karniadakis *et al.*, 1991).

A spectral-element-Fourier method analogous to the cylindrical formulation constructed in Blackburn and Sherwin (2004) is employed to capture three-dimensional flow variation in the streamwise  $z$ -direction. This method is well suited to simulation of flows where the geometry can be arbitrarily complex in a cross-plane but is infinite or periodic in an orthogonal direction (Karniadakis, 1990; Blackburn and Sherwin, 2004; Sheard *et al.*, 2009; Vo *et al.*, 2015). The velocity, pressure and electric potential fields are decomposed using this Fourier expansion in  $z$  with  $m$  streamwise modes such that

$$\begin{bmatrix} u(x, y, z, t) \\ v(x, y, z, t) \\ w(x, y, z, t) \\ p(x, y, z, t) \\ \phi(x, y, z, t) \end{bmatrix} = \sum_{j=0}^{m-1} \begin{bmatrix} u_m(x, y, t) \\ v_m(x, y, t) \\ w_m(x, y, t) \\ p_m(x, y, t) \\ \phi_m(x, y, t) \end{bmatrix} e^{ikmz} \quad (12)$$

where  $k = 2\pi/L_z$  is the associated wavenumber in the  $z$  direction, and  $L_z$  is the periodicity length of the domain also in the  $z$  direction. The number of Fourier modes determines the spatial resolution in the orthogonal streamwise direction. The basic flow solution described by the fundamental Fourier mode was validated against the analytical solution for fully developed MHD flow as developed by Hunt and Stewartson (1965). For the transient growth analysis, the linearised equations require the construction of a single non-zero Fourier mode in the  $z$ -direction to completely define the

eigenmodes as per (6). Streamwise wavenumbers are investigated between  $0 \leq k \leq 80$ , with the local maxima resolved to an accuracy of at least 0.1. To ensure that the optimal growths were captured sufficiently, and a monotonic decay in amplifications were achieved at higher  $\tau$ , the analysis was conducted over time intervals extending to  $\tau = 5\tau_{\text{opt}}$ . Eigenvalue convergence of better than 0.01% was ensured for all the values presented in this paper. The linearised component of this solver has also been previously verified and implemented in works such as Hussam *et al.* (2012) and Tsai *et al.* (2016).

Local mesh refinement ( $h$ -refinement), shape function polynomial degree refinement ( $p$ -refinement) and Fourier mode refinement (where applicable) are used in ensuring grid independence and the convergence of the viscous drag coefficient  $C_d$  and the  $L^2$  norm. A polynomial order of  $N_p = 8$  was deemed sufficient with a convergence of better than 0.3% achieved for all reference parameters. The minimum wavenumber (and in turn the maximum duct length  $L_z$  discretisation) required for the 3D simulations incorporating the non-linear MHD governing equations is given by the respective  $k$  of the optimal mode used to seed the base flow. For all but the highest initial perturbation energies ( $10^{-6} \leq E_p \leq 10^{-3}$ ), 8 Fourier modes were found to be satisfactory for resolving the flow dynamics. For the highest perturbation case ( $E_p = 10^{-2}$ ), 32 Fourier modes were required in congruence with an additional anti-aliasing method coming in the form of the two-thirds low-pass filtering technique outlined in Orszag (1971).

## RESULTS AND DISCUSSION

### Optimal Linear Transient Growth

The optimal modal gain in perturbation kinetic energy as a function of Hartmann number are presented and discussed in this section. The global maximum amplification  $G_{\max}$  for  $10 \leq Ha \leq 1000$  are provided in figure 2. Here, the results from Krasnov *et al.* (2010) and Pothérat (2007) are also shown for comparison. Transient growth was found to occur for all  $Ha$  present in this study, however, the magnitude of these amplifications is progressively suppressed with increasing Hartmann number. The monotonic reduction in energy growth is most likely due to the increased Joule dissipation found with higher magnetic field strengths. For  $10 \leq Ha \leq 100$  the global maximum amplification is found in the present work to follow the trend  $G_{\max} \approx 11.45 \times 10^3 Ha^{-1.6}$ . This is in close agreement with the  $G_{\max} \approx 8.8 \times 10^3 Ha^{-1.5}$  relationship obtained by the optimal growth analysis in Krasnov *et al.* (2010) over the limited range of  $10 \leq Ha \leq 50$  as shown in figure 2. This also serves as further validation for the numerical framework used in this study.

For  $150 \leq Ha \leq 1000$ , the rate of change of  $G_{\max}$  lessens with increasing Hartmann number. The scaling and growth rate predictions in this regime demonstrate a remarkable consistency with the SM82 model results from Pothérat (2007). For this higher  $Ha$  regime, the global maximum amplification recovers an approximate  $-1/3$  power scaling of  $G_{\max} \approx 25 \times 10^3 Ha^{-0.37}$ . This is in stark contrast to the behaviour observed at lower field strengths  $Ha \leq 150$ , where there is a significant deviation between the scaling and energy gains predicted by both 3D and Q2D models. The mechanism producing maximum transient amplifications in low- $Ha$  MHD flows and 3D Poiseuille flows result from the coupling of modes both invariant and variant in the vertical direction. These modes are the respective MHD equivalent of the well

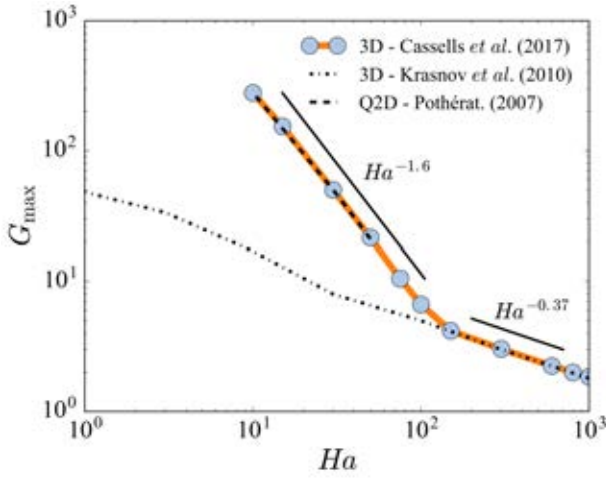


**Figure 2:** Global maximum amplifications as a function of Hartmann number. Here, pre-existing transient growth analysis data using a SM82 model (Pothérat, 2007) (dash-dotted line) and quasi-static MHD analysis (Krasnov *et al.*, 2010) (dashed line) are plotted for comparison against current results (orange line, grey markers).

known Orr–Sommerfeld and Squire modes found in hydrodynamic flows. Being of Q2D nature, the SM82 model can only combine the two-dimensional Orr–Sommerfeld equivalent modes for energy amplification. As the present findings show such strong alignment of the 3D duct optimal growths predictions for  $150 \leq Ha \leq 1000$  with the SM82 model, this suggests that for adequately large field strengths (here  $Ha \geq 150$ ), suppression of the streamwise invariant modes has occurred to allow the SM82 model to be an excellent predictor of optimal linear growth. Conversely, the coupling between streamwise variant and invariant modes plays a fundamental part in the enhancement of transient amplifications for  $Ha \leq 150$ ; leading to the deviation between predicted growth rates at smaller  $Ha$ .

This explanation for the development of two well defined scaling regimes are further illustrated through a qualitative analysis of the perturbation field structures. The evolution of the eigenvector fields to time of maximum energy gain  $\tau_{\text{opt}}$  for  $Ha = 10, 100, 150$  and  $600$  are visualised via iso-surfaces of the spanwise component ( $x$ - $z$  plane) of vorticity in figure 3. The perturbation fields for low to moderate  $Ha$  (figures 3 (a) and (b)) form complex overlapping homothetic structures within the sidewall layers. These streamwise aligned cigar-shaped modes are consistent with those producing maximum transient amplification in pure hydrodynamic flows (Pothérat, 2007). As  $Ha$  is increased in the first scaling regime  $10 \leq Ha \leq 100$ , the number of rolls in the vertical  $y$  direction also increase but maintain well defined periodicity. These disturbance modes also become increasingly flattened and localised within the thinning Shercliff layers in combination with a significant decrease in the optimal streamwise wavenumber.

In the second regime between  $150 \leq Ha \leq 1000$ , periodicity in  $y$  is lost, with a breakdown of the streamwise vortices occurring, as highlighted in figures 3(c,d). The flow becomes increasingly invariant in the magnetic field direction, such that by  $Ha = 600$  only remnants of streamwise variation of vorticity remain, which are predominantly confined to the corner regions of the duct. The two-dimensionalisation of the optimal modes, and the relative invariance of the vortic-

ity disturbance field in figures 3(c,d) 3(c,d), helps to illustrate the suspected diminishing influence of the Squire equivalent modes on the overall transient amplification of energy for  $Ha \geq 150$ . From a numerical methodology perspective this can have quite significant and meaningful implications. As Hartmann numbers in fusion reactor applications are typically quite large ( $O(10^3)$ ), the ability of the SM82 model to accurately predict the dominant transient amplifications mechanisms at these larger field strengths allows for modelling to be conducted at significantly reduced computational costs. The reason being that the thin Hartmann layers do not require resolving when employing this Q2D model.

### Nonlinear Temporal Evolution of Optimal Perturbations at High Hartmann Numbers

A three-dimensional basic flow seeded with optimal linear perturbations at varying initial energies for  $Ha = 600$  and  $Re = 5000$  will be analysed in this section. These flow regime parameters were chosen with a view towards representative magnetic field strengths seen in industrial applications (Smolentsev *et al.*, 2010). The energy of the perturbation field is given as a relative fraction of the unperturbed base flow energy, and defined using the ratio of volume integrals

$$E(t) = \frac{\int_{\Omega} \mathbf{V}_p \cdot \mathbf{V}_p \, d\Omega}{\int_{\Omega} \mathbf{V}_0 \cdot \mathbf{V}_0 \, d\Omega}. \quad (13)$$

The initial seeding energy of the optimal perturbation modes is defined as  $E_p \equiv E(0)$ , where  $10^{-6} \leq E_p \leq 10^{-2}$  is presented here. The energy amplification of the perturbed flow can thus be measured using the temporal relation

$$G_n(t) = \frac{E(t)}{E_p}. \quad (14)$$

The energetic response due to the seeding of the base flow as a function of time is illustrated in figure 4. For the smallest initial seeding energy  $E_p = 10^{-6}$ , a very strong alignment with the temporal energy evolution modelled using the linearised governing equations is seen. As the seeding energy is increased, the magnitude of amplification is successively diminished in conjunction with a shortening of the time period at which the maximum occurs. For the maximum seeding energy  $E_p = 10^{-2}$ , no energy gain is observed for any time periods measured. For  $E_p \leq 10^{-3}$ , only single peaks in energy amplification are detected before a monotonic decay presents as  $t \rightarrow \infty$ . For a better understanding of the flow dynamics during these stages of transient growth, we introduce quantitative measures for viscous and magnetic dissipation, which are respectively defined as

$$\epsilon = 2\nu \sum_{\mathbf{k}} k^2 [\mathbf{V}(\mathbf{k}) \cdot \mathbf{V}(-\mathbf{k})], \quad (15)$$

$$\mu = \frac{\sigma}{\rho} \sum_{\mathbf{k}} \frac{(\mathbf{B}_0 \cdot \mathbf{k})}{k^2} [\mathbf{V}(\mathbf{k}) \cdot \mathbf{V}(-\mathbf{k})]. \quad (16)$$

Here  $\mathbf{k}$  is the wavenumber vector associated with a 3D Fourier decomposition. This is achieved through implementing a fast Fourier transform technique on discretely sampled data in the  $x$ - $y$  plane in conjunction with a modal expansion using (12). The total viscous and magnetic dissipation normalised by their respective initial seeding energies are plotted as a function of time in figures 5 and 6, respectively. For  $10^{-6} \leq E_p \leq 10^{-3}$ , a significant increase in viscous dissipation is observed immediately after the base flow is seeded

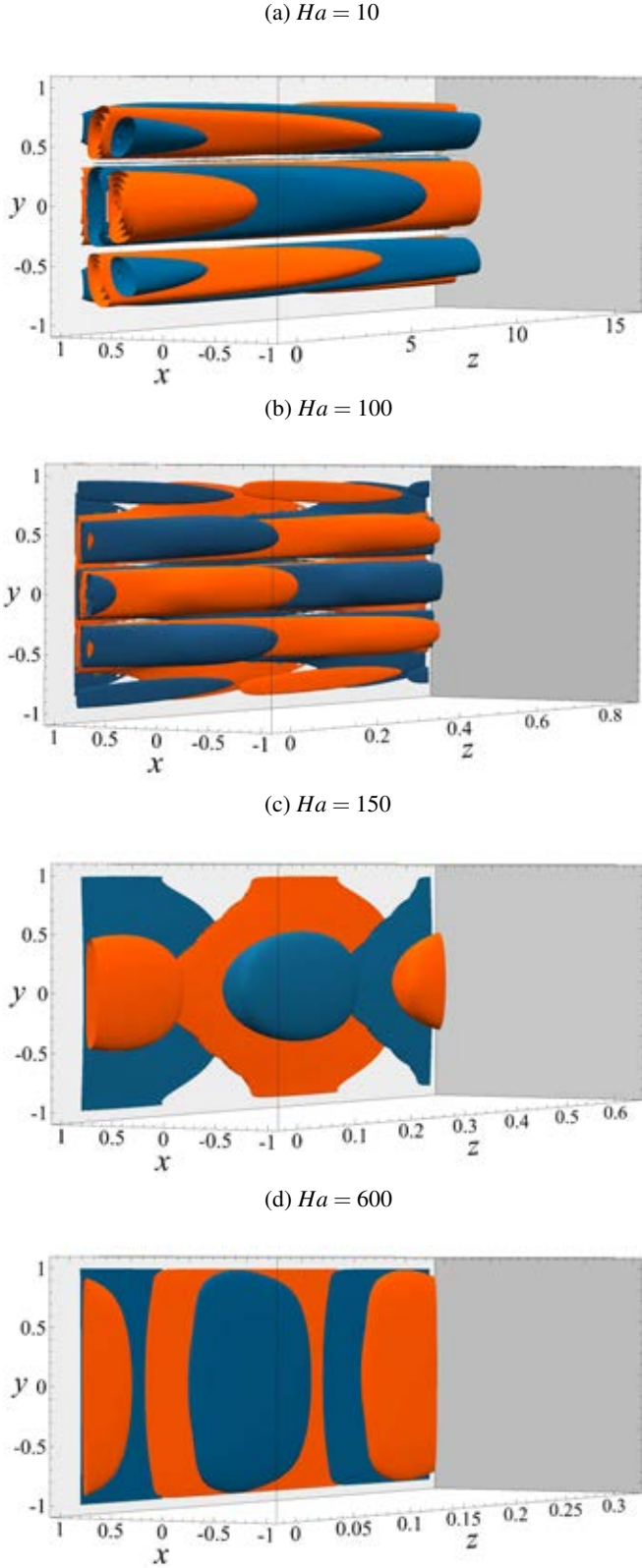


**Figure 3:** Vorticity iso-surfaces of the eigenvector fields producing the maximum transient amplification  $G_{\max}$  evolved to  $\tau_{\text{opt}}$  for  $Ha = 10, 100, 150$  and  $600$  at  $Re = 5000$ . Blue and orange contours represent positive and negative spanwise vorticity, respectively. Contour levels are adjusted to approximately 90% of the maximum magnitude of vorticity. The flow is from left to right in the positive  $z$ -direction, with the magnetic field orientated vertically in the positive  $y$ -direction. For clarity, the vorticity is only plotted for  $0 \leq x \leq 1$ .

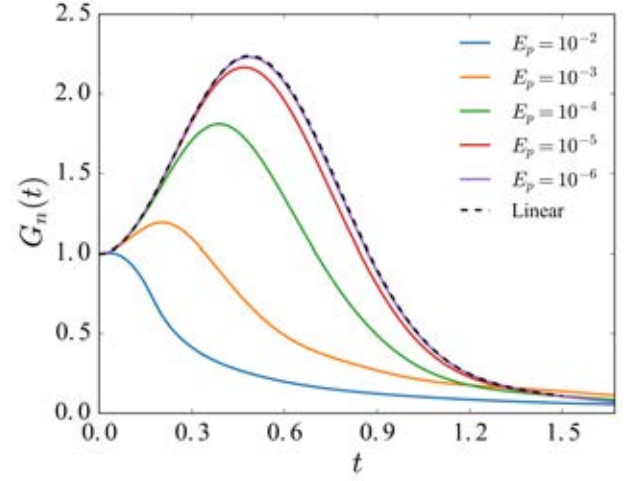


**Figure 4:** Temporal evolution of energy amplification due to seeding of the unperturbed base flow with the optimal disturbance mode corresponding to  $Ha = 600$  at  $Re = 5000$  for initial perturbation energies  $10^{-6} \leq E_p \leq 10^{-2}$ . Here the predicted growth rate using the linearised governing equations is also plotted (dashed line).

with the optimal mode. For  $10^{-6} \leq E_p \leq 10^{-4}$ , the peak in both magnetic dissipation and viscous dissipation appears to be strongly correlated with the corresponding time of maximum amplification seen in figure 4. For  $E_p = 10^{-3}$  only the latter is strongly correlated, with no relationship seen for  $E_p = 10^{-2}$ . At  $t \approx 0.2$ , a sharp increase in  $\epsilon$  and a corresponding decrease in  $\mu$  is observed for the highest energy  $E_p = 10^{-2}$  case. At this point in time, the ratio  $\mu/\epsilon \approx 1.1$  indicates that viscous dissipation is contributing in almost equal measure to the total dissipation rates in the flow. However, magnetic dissipation remains the dominant energy loss mechanism for all  $E_p$  and  $t$  investigated here. After reaching their respective peaks in dissipation rates, both  $\epsilon$  and  $\mu$  are observed to decay (not necessarily monotonically) as  $t \rightarrow \infty$ .

It is interesting to note here that as the initial seeding energy approaches the infinitesimal limit described by the linearised equations, the time rate of change of both dissipation mechanisms converge. In other words,  $\partial\epsilon/\partial t \approx \partial\mu/\partial t$  as  $E_p \rightarrow 10^{-\infty}$ . It also appears that as the initial seeding energy is increased, and the relative importance of nonlinear terms in the solution in turn grows, a weakening of magnetic dissipation and conversely strengthening of viscous dissipation is produced. A partial explanation for the difference is through the larger cascade of energy transfer to higher Fourier mode wavenumbers seen for greater seeding energies (not published here). Magnetic dissipation acts equally on all scales, whereas the dissipating effects of viscosity are more pronounced for higher  $k$ . Hence, nonlinearity is seen to promote transfer of energy to high wavenumbers, where viscous damping is dominant, rather than dissipating energy through Joule damping at larger scales.

For further quantification of the dominant flow structures leading to observed energy growth and dissipative trends, we introduce a flow anisotropy measure

$$\mathcal{G} = \frac{\mathcal{G}_1 + \mathcal{G}_2}{2}, \quad (17)$$

where  $\mathcal{G}_1$  and  $\mathcal{G}_2$  are calculated using the normalised mean-

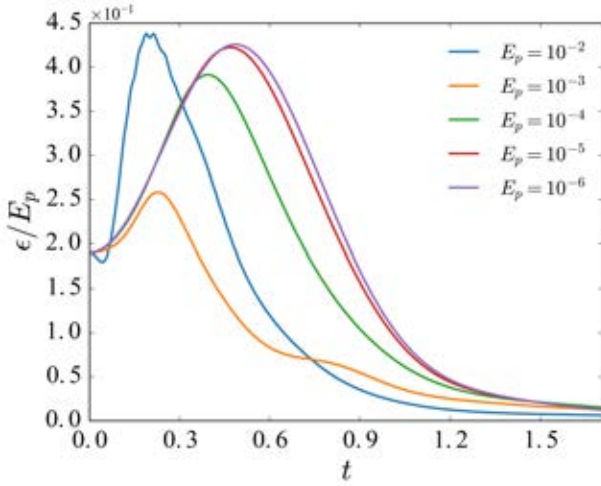


**Figure 5:** Temporal evolution of normalised viscous dissipation due to seeding of the unperturbed base flow with the optimal disturbance mode corresponding to  $Ha = 600$  at  $Re = 5000$  for initial perturbation energies  $10^{-6} \leq E_p \leq 10^{-2}$ .

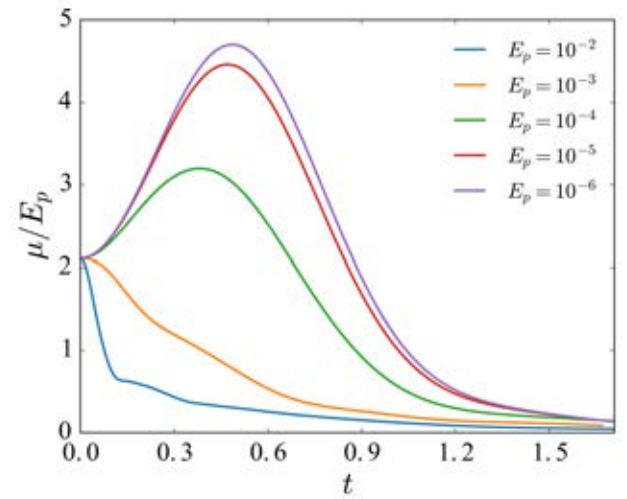


**Figure 6:** Temporal evolution of normalised magnetic dissipation due to seeding of the unperturbed base flow with the optimal disturbance mode corresponding to  $Ha = 600$  at  $Re = 5000$  for initial perturbation energies  $10^{-6} \leq E_p \leq 10^{-2}$ .

square velocity gradients

$$\mathcal{G}_1 = \frac{\langle (\partial u / \partial y)^2 \rangle}{2 \langle (\partial u / \partial x)^2 \rangle} \quad \text{and} \quad \mathcal{G}_2 = \frac{2 \langle (\partial v / \partial y)^2 \rangle}{\langle (\partial v / \partial x)^2 \rangle}. \quad (18)$$

These anisotropy coefficients characterises the difference between the magnitudes of flow velocity derivatives taken along  $(\partial/\partial y)$  and across  $(\partial/\partial x)$  the magnetic field direction. They tend towards unity as a flow reaches a purely isotropic state, and towards zero in magnetic field direction independent anisotropic flow (Schumann, 1976). The primary cause for the changes in these derivatives are known to be due to the Joule dissipative effects found in MHD flows (Vorobev *et al.*, 2005). For 3D anisotropic flows, both coefficients in (18) tend towards one another. Hence, the average of the two, which are considered in (17), provide a good measure for the overall level of anisotropy in the flow.

The time history of (17) is plotted for varying optimal mode seeding energies in figure 7. Immediately onwards from  $t = 0$ , a rapid increase in  $\mathcal{G}$  is observed for all  $E_p$  cases. Multiple peaks in flow isotropy are detected for all cases, where the initial peak occurs at a slightly delayed time interval in comparison to the time of maximum energy gain seen in figure 4. It is important to note that the measured decrease in flow anisotropy is small for all cases ( $O(10^{-2}) - O(10^{-1})$ ). The flow remains dominated by anisotropic structures, yet has small but finite intermittent bursts of relative isotropy. For  $10^{-4} \leq E_p \leq 10^{-2}$  the secondary peaks in  $\mathcal{G}$  are equal to or greater than the initial peak magnitude. In contrast, for lower seeding energies  $E_p \leq 10^{-5}$ , the degree of anisotropy increases after reaching a minimum at the first initial maxima seen in figure 7. It is interesting to note here that although Joule dissipation remains strong for all  $E_p$ , as seen in figure 6, this does not necessitate the temporal smoothing of the velocity field so that a monotonic trend towards a purely anisotropic state occurs. Exploiting this behaviour could pose as useful for future investigations into eliciting further transient growth and, potentially, instabilities.

## CONCLUSION

The global maximum transient amplifications of an electrically conducting fluid under the influence of a transverse

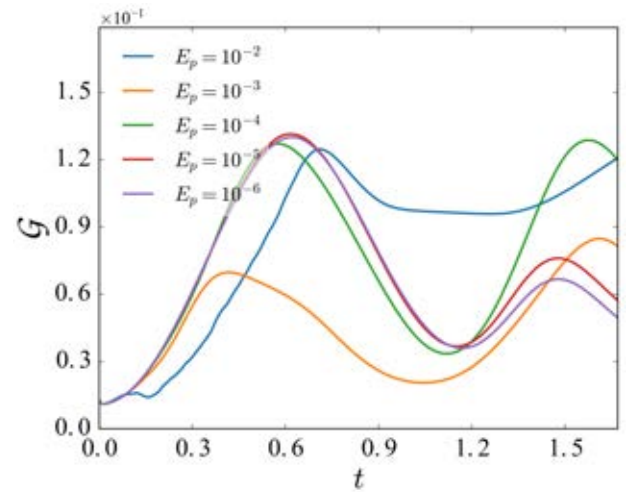


**Figure 7:** Temporal evolution of the degree of anisotropy due to seeding of the unperturbed base flow with the optimal disturbance mode corresponding to  $Ha = 600$  at  $Re = 5000$  for initial perturbation energies  $10^{-6} \leq E_p \leq 10^{-2}$ .

magnetic field were investigated. A range of Hartmann numbers for  $10 \leq Ha \leq 1000$  were studied at a fixed  $Re = 5000$ . It was shown that two regimes exists for scaling of maximum transient growth amplification; when perturbation structures are dominated by 3D modes a scaling of  $G_{\max} \propto Ha^{-1.6}$  for  $10 \leq Ha \leq 100$  was found, and  $G_{\max} \propto Ha^{-0.37}$  in the range of  $150 \leq Ha \leq 1000$  for when optimal disturbances become predominantly Q2D. Through comparison with existing literature, the SM82 model for Q2D MHD flow was found to be a valid predictor of optimal linear growths in this regime.

A subsequent investigation into seeding of an optimal mode corresponding to a high  $Ha$  regime into an unperturbed base flow to study the dynamic response was also conducted. At  $Ha = 600$  and  $Re = 5000$ , it was determined that the initial energy of the perturbation modes plays a fundamental role in not only in the transient growth of energy, but also in the dominant dissipation and anisotropy forming mechanisms. No energy amplification above the linear prediction was ob-

served for any nonlinear case. As the seeding energy amplitude reduces in magnitude, it more closely recovers the linear growth predictions. Additionally, the time at which their respective maxima in energy occurs is closely correlated with the time of maximum dissipation. However, this time interval is increasingly shortened as the perturbation seeding energy magnitude grows. It was found that no growth occurs for  $E_p = 10^{-2}$ , which is in congruence with a sharp increase in viscous dissipation and combined decrease in magnetic dissipation. The likely reason being that as the initial energy is increased, and nonlinear terms in the solution become more significant, a greater transfer of energy to larger wavenumbers  $k$  tends to occur. Lastly, it was shown that the flow is dominated by anisotropy for all  $t$  and  $E_p$ , but experiences intermittent bursts of increased isotropy.

## ACKNOWLEDGEMENTS

O. G. W. C. was supported by an Engineering Research Living Allowance (ERLA) scholarship from the Faculty of Engineering, Monash University. This research was supported by Discovery Grant DP150102920 from the Australian Research Council, and was undertaken with the assistance of resources from the National Computational Infrastructure (NCI), which is supported by the Australian Government.

## REFERENCES

- BARKLEY, D., BLACKBURN, H. and SHERWIN, S. (2007). “Direct optimal growth analysis for timesteppers”. *Int. J. Numer. Methods Fluids*, **231**, 1–20.
- BLACKBURN, H.M. and SHERWIN, S. (2004). “Formulation of a Galerkin spectral element–Fourier method for three-dimensional incompressible flows in cylindrical geometries”. *Journal of Computational Physics*, **197(2)**, 759–778.
- BOECK, T., KRASNOV, D., THESS, A. and ZIKANOV, O. (2008). “Large-scale intermittency of liquid-metal channel flow in a magnetic field”. *Phys. Rev. Lett.*, **101(24)**, 244501.
- CASSELLS, O.G.W., HUSSAM, W.K. and SHEARD, G.J. (2016). “Heat transfer enhancement using rectangular vortex promoters in confined quasi-two-dimensional magnetohydrodynamic flows”. *Int. J. Heat Mass Transfer*, **93**, 186–199.
- HAMID, A.H.A., HUSSAM, W.K. and SHEARD, G.J. (2016). “Combining an obstacle and electrically driven vortices to enhance heat transfer in a quasi-two-dimensional MHD duct flow”. *J. Fluid Mech.*, **792**, 364–396.
- HAMID, A.H., HUSSAM, W.K., POTHÉRAT, A. and SHEARD, G.J. (2015). “Spatial evolution of a quasi-two-dimensional Kármán vortex street subjected to a strong uniform magnetic field”. *Phys. Fluids*, **27(5)**, 053602.
- HUNT, J.C.R. and STEWARTSON, K. (1965). “Magnetohydrodynamic flow in rectangular ducts. ii”. *J. Fluid Mech.*, **23(3)**, 563–581.
- HUSSAM, W.K., THOMPSON, M.C. and SHEARD, G.J. (2012). “Optimal transient disturbances behind a circular cylinder in a quasi-two-dimensional magnetohydrodynamic duct flow”. *Phys. Fluids*, **24**, 024105.
- KARNIADAKIS, G. (1990). “Spectral element-fourier methods for incompressible turbulent flows”. *Computer Methods in Applied Mechanics and Engineering*, **80(1)**, 367–380.
- KARNIADAKIS, G.E., ISRAELI, M. and ORSZAG, S.A. (1991). “High-order splitting methods for the incompressible Navier-Stokes equations”. *Journal of computational physics*, **97(2)**, 414–443.
- KRASNOV, D., ZIKANOV, O., ROSSI, M. and BOECK, T. (2010). “Optimal linear growth in magnetohydrodynamic duct flow”. *J. Fluid Mech.*, **653(1)**, 273–299.
- KRASNOV, D., ZIENICKE, E., ZIKANOV, O., BOECK, T. and THESS, A. (2004). “Numerical study of the instability of the Hartmann layer”. *J. Fluid Mech.*, **504**, 183–211.
- MORESCO, P. and ALBOUSSIÈRE, T. (2004). “Experimental study of the instability of the hartmann layer”. *J. Fluid Mech.*, **504**, 167–181.
- NÁRAIGH, LENNON, O. (2015). “Global modes in nonlinear non-normal evolutionary models: Exact solutions, perturbation theory, direct numerical simulation, and chaos”. *Physica D*, **309**, 20–36.
- ORSZAG, S.A. (1971). “On the elimination of aliasing in finite-difference schemes by filtering high-wavenumber components”. *Journal of the Atmospheric sciences*, **28(6)**, 1074–1074.
- POTHÉRAT, A. (2007). “Quasi-two-dimensional perturbations in duct flows under transverse magnetic field”. *Phys. Fluids*, **19**, 074104.
- POTHÉRAT, A., SOMMERIA, J. and MOREAU, R. (2000). “An effective two-dimensional model for MHD flows with transverse magnetic field”. *J. Fluid Mech.*, **424**, 75–100.
- SCHUMANN, U. (1976). “Numerical simulation of the transition from three- to two-dimensional turbulence under a uniform magnetic field”. *J. Fluid Mech.*, **74(01)**, 31–58.
- SHEARD, G.J., FITZGERALD, M.J. and RYAN, K. (2009). “Cylinders with square cross-section: wake instabilities with incidence angle variation”. *J. Fluid Mech.*, **630**, 43–69.
- SMOLENTSEV, S., VETCHA, N. and MOREAU, R. (2012). “Study of instabilities and transitions for a family of quasi-two-dimensional magnetohydrodynamic flows based on a parametrical model”. *Phys. Fluids*, **24**, 024101.
- SMOLENTSEV, S., WONG, C., MALANG, S., DAGHER, M. and ABDOU, M. (2010). “MHD considerations for the DCLL inboard blanket and access ducts”. *Fus. Eng. Des.*, **85(7)**, 1007–1011.
- SOMMERIA, J. (1988). “Electrically driven vortices in a strong magnetic field”. *J. Fluid Mech.*, **189**, 553–569.
- SOMMERIA, J. and MOREAU, R. (1982). “Why, how, and when, MHD turbulence becomes two-dimensional”. *J. Fluid Mech.*, **118**, 507–518.
- TAKASHIMA, M. (1996). “The stability of the modified plane poiseuille flow in the presence of a transverse magnetic field”. *Fluid dynamics research*, **17(6)**, 293–310.
- TSAI, T., HUSSAM, W.K., FOURAS, A. and SHEARD, G.J. (2016). “The origin of instability in enclosed horizontally driven convection”. *Int. J. Heat Mass Transfer*, **94**, 509–515.
- VO, T., MONTABONE, L., READ, P.L. and SHEARD, G.J. (2015). “Non-axisymmetric flows in a differential-disk rotating system”. *J. Fluid Mech.*, **775**, 349–386.
- VOROBÉV, A., ZIKANOV, O., DAVIDSON, P.A. and KNAEPEN, B. (2005). “Anisotropy of magnetohydrodynamic turbulence at low magnetic reynolds number”. *Phys. Fluids*, **17(12)**, 125105.

